



AD-A280 385



The American Physical Society



# Proceedings of the 1993 Particle Accelerator Conference

Volume 4 of 5  
Pages 2546-3218

DTIC ELECTE JUN 13 1994  
S F D

This document has been approved for public release and sale; its distribution is unlimited.

87608 94-17986

Papers from the fifteenth biennial Particle Accelerator Conference, an international forum on accelerator science and technology held May 17-20, 1993, in Washington, D.C., organized by the Continuous Electron Beam Accelerator Facility (CEBAF), jointly sponsored by the Institute of Electrical and Electronics Engineers Nuclear and Plasma Sciences Society and the American Physical Society Division of Physics of Beams, and conducted with support from the U.S. Department of Energy, the National Science Foundation, and the Office of Naval Research.

94 6 10 094

DTIC QUALITY INSPECTED

**Best  
Available  
Copy**

**1993 IEEE Particle Accelerator Conference**

Abstracting is permitted with credit to the source. Libraries are permitted to photocopy beyond the limits of U.S. Copyright law for private use of patrons those articles in this volume that carry a code at the bottom of the first page, provided the per-copy fee indicated in the code is paid through the Copyright Clearance Center, 27 Congress Street, Salem, MA 01970. For other copying, reprint, or republications permission, write to the IEEE Copyright Manager, IEEE Service Center, 445 Hoes Lane, P.O. Box 1331, Piscataway, NJ 08855-1331. All rights reserved. Printed in the USA. Copyright © 1993 by The Institute of Electrical and Electronics Engineers, Inc.

IEEE Catalog Number: 93CH3279-7

Library of Congress Number: 88-647453

Additional copies of this publication are available from

ISBN Softbound: 0-7803-1203-1

Casebound: 0-7803-1204-x

Microfiche: 0-7803-1205-8

IEEE Service Center

445 Hoes Lane

Piscataway, NJ 08854-4150



The  
American  
Physical  
Society

1993 Particle Accelerator Conference, Washington, D.C., 17-20 May

Conference Chairman  
Christoph Leemann, *CEBAF*  
Annie Soltys, Executive Assistant  
Telephone: (804) 249-7575  
E-mail: [soltys@cebaf.gov](mailto:soltys@cebaf.gov)  
Fax: (804) 249-5024

18-May-94  
Box 2 of 2

Organizing Committee

M. Allen, *SLAC*  
W. Barletta, *LLNL*  
K. Beckner, *LBL*  
D. Beasley, *NFS*  
J. Bisognano, *CEBAF*  
R. Briggs, *SSCL*  
Y. Cho, *ANL*  
L. Costrell, *NBS*  
M. Craddock, *U. of BC*  
W. K. Dawson, *TRIUMF*  
H. Edwards, *FNAL*  
S. Holmes, *FNAL*  
S. Krinsky, *BNL*  
H. Lustig, *APS*  
C. Roberson, *ONR*  
S. Schriber, *LANL*  
D. Sutter, *DOE*  
S. Tazzari, *U. of Rome II & INFN*  
M. Tigner, *Cornell*  
W. T. Weng, *BNL*

Program Committee

J. Bisognano, Chair, *CEBAF*  
Telephone: (804) 249-7521  
E-mail: [bisognano@cebaf.gov](mailto:bisognano@cebaf.gov)  
H. Edwards, Deputy Chair, *FNAL*

Program Treasurer

Julie Leverenz  
Telephone: (804) 249-7642  
E-mail: [leverenz@cebaf.gov](mailto:leverenz@cebaf.gov)

Conference Editor

Steven T. Corneliussen, *CEBAF*  
Telephone: (804) 249-7582  
E-mail: [corneliussen@cebaf.gov](mailto:corneliussen@cebaf.gov)

Editorial Assistant

Linda Carlton  
Telephone: (804) 249-7690  
E-mail: [carlton@cebaf.gov](mailto:carlton@cebaf.gov)  
Fax: (804) 249-5024

DEFENSE TECHNICAL INFORMATION CENTER  
BUILDING 5, CAMERON STATION  
ALEXANDRIA, VA 22304-6145

REF.: GRANT NO. N00014-93-1-0623

Dear Sir or Madam:

Enclosed please find two (2) copies of the Proceedings of the 1993 Particle Accelerator Conference (PAC93). The above-referenced \$15,000 grant from the Office of Naval Research helped fund the cost of publishing the Proceedings, enabling us to keep the registration fee to a minimum.

On behalf of the conference organizers and the more than 1300 participants, thank you for supporting PAC93.

Sincerely,

Christoph W. Leemann  
Conference Chairman

cc: D. Galicki, IEEE

DTIC QUALITY INSPECTED 1

# Five-Volume Contents

Each volume begins with this five-volume table of contents and ends with the five-volume author index. The chairmen's foreword and a list of conference organizers and staff appear as front matter in Volume 1. A list of conference participants precedes the author index in Volume 5.

## Volume 1

### Opening Plenary

Chair: *J. Bisognano*

HERA Operations and Physics — *B. H. Wiik, U. Hamburg and DESY*..... 1

### Single-Particle Beam Dynamics

Chair: *W. Weng*

Nonlinear Beam Dynamics Experiments at the IUCF Cooler Ring ( <i>Invited Paper</i> ) — <i>S. Y. Lee, Indiana University</i> .....	6
The Preservation of Low Emittance Flat Beams ( <i>Invited Paper</i> ) — <i>T. O. Raubenheimer, SLAC</i> .....	11
Long-Term Stability Studies for CERN-LHC ( <i>Invited Paper</i> ) — <i>W. Scandale, CERN</i> .....	16
Emittance Growth in a Low Energy Proton Beam ( <i>Invited Paper</i> ) — <i>J. A. Palkovic, SSCL</i> .....	21
Proton Extraction from the CERN-SPS by a Bent Crystal — <i>S. Weisz and the RD22 Collaboration; CERN</i> .....	26
Longitudinal Tracking with Phase and Amplitude Modulated RF — <i>D. D. Caussyn, M. Ball, B. Brabson, J. Budnick, J. Collins, V. Derenchuk, G. East, M. Ellison, T. Ellison, D. Friesel, B. Hamilton, H. Huang, W. P. Jones, S. Y. Lee, D. Li, S. Nagaitsev, X. Pei, T. Sloan, Y. Wang, IUCF; A. W. Chao, S. Dutt, M. Syphers, Y. T. Yan, P. L. Zhang, SSCL; M. G. Minty, SLAC; K. Y. Ng, FNAL</i> .....	29
Measurement of Spin Motions in a Storage Ring Outside the Stable Polarization Direction — <i>N. Akchurin, A. Bravar, J. McPherson, F. Olchowski, Y. Onel, U. Iowa; L. Badano, M. Conte, INFN Genova; A. Penzo, INFN Trieste; J. Hall, U. New Mexico; A. Pisent, INFN Legnaro; M. Pusterla, INFN Padova; T. Rinckel, Indiana U.; R. Rossmanith, CERN; H. Kreiser, U. Hamburg</i> .....	32
A Clean Way to Measure Nonlinear Momentum Compaction Factor $a_1$ — <i>J. P. Shan, I. Kourbanis, D. McGinnis, K. Y. Ng, S. Peggs, FNAL</i> .....	35
Long-Term Tracking with Symplectic Implicit One-Turn Maps — <i>Y. T. Yan, M. Li, M. J. Syphers, SSCL; P. J. Channell, LANL</i> .....	38
Injection Method Using the Third Order Resonance at TARN II — <i>M. Tomizawa, Y. Arakaki, K. Chida, S. Watanabe, T. Watanabe, T. Katayama, M. Yoshizawa, INS Tokyo; A. Noda, Kyoto U.</i> .....	41
Effects of Tidal Forces on the Beam Energy in LEP — <i>L. Arnaudon, F. Bordry, W. Coosemans, B. Dehning, K. Henrichsen, A. Hofmann, R. Jacobsen, J. P. Koutchouk, L. Lawson-Chroco, M. Mayoud, J. Miles, R. Olsen, M. Placidi, G. Ramseier, R. Schmidt, J. Wenninger, CERN; A. Blondel, Ec. Polytech. Paris; R. Assmann, MPI Munich; G. E. Fischer, C. Pan, SLAC; R. Olivier, Lausanne U.</i> .....	44

### Poster presentations:

The Appearance of Beam Lines — <i>D. C. Carey, FNAL</i> .....	47
Multipole Channel Parameters for Equalization of Beam Intensity Distribution — <i>Y. K. Batygin, MEPI</i> .....	50
Single Beam Effects Due to Errors in Crab Compensation — <i>D. Sagan, Cornell</i> .....	53
Lattice Design of the LANL Spallation-Source Compressor Ring — <i>B. Blind, A. J. Jason, F. Neri, LANL</i> .....	56
Optics Simulations of the 5 MeV NPBSE FOX Telescope — <i>M. F. Reusch, D. L. Bruhwiler, Grumman Corp.</i> .....	59
Longitudinal Kinetic Energy Spread from Focusing in Charged Particle Beams — <i>N. Brown, M. Reiser, D. Kehne, D. X. Wang, J. G. Wang, U. Maryland</i> .....	62
Numerical and Experimental Studies of Halo Formation Due to Mismatch in a Space-Charge-Dominated Electron Beam — <i>D. Kehne, M. Reiser, U. Maryland; H. Rudd</i> .....	65
Suppression of the Main LEP Coupling Source — <i>J. Billan, J.-P. Gourber, J.-P. Koutchouk, V. Remondino, CERN</i> .....	68
Applications of Matrix Optics to Acceptance Studies in Low-Beta Ion Linacs — <i>K. Joh, J. A. Nolen, ANL</i> .....	71
Analytical Evaluation of the Second Order Momentum Compaction Factor and Comparison with MAD Results — <i>J. P. Shan, S. G. Peggs, S. A. Bogacz, FNAL</i> .....	74
Chromaticity Compensation Scheme for the Main Injector — <i>S. A. Bogacz, FNAL</i> .....	77

Dist	even and/or Special
A-1	

*Proceedings of the 1993 Particle Accelerator Conference*

Accelerator Physics Analysis with Interactive Tools — J. A. Holt, L. Michelotti, FNAL .....	80
The 50 MeV Beam Test Facility at LBL — W. Leemans, G. Behrsing, K.-J. Kim, J. Krupnick, C. Matuk, F. Selph, S. Chattopadhyay, LBL .....	83
Knowledge Rule Base for the Beam Optics Program TRACE 3-D — G. H. Gillespie, P. K. Van Straagen, B. W. Hill, G. H. Gillespie Assoc. ....	86
Beam Dynamics Studies of Four-Gap Low-Beta Superconducting Resonators — J. A. Nolen, K. Joh, ANL .....	89
Third-Order Corrections to the SLC Final Focus — N. J. Walker, R. Helm, J. Irwin, M. Woodley, SLAC .....	92
Global Tuning Knobs for the SLC Final Focus — N. J. Walker, J. Irwin, M. Woodley, SLAC .....	95
Sigma Matrix Reconstruction in the SLC Final Focus — P. Raimondi, P. J. Emma, N. Toge, N. J. Walker, V. Ziemann, SLAC .....	98
Beam Based Alignment of the SLC Final Focus Superconducting Final Triplets — P. Raimondi, P. J. Emma, N. Toge, N. J. Walker, V. Ziemann, SLAC .....	100
A Design of a Quasi-Isochronous Storage Ring — S. Y. Lee, Indiana U.; K. Y. Ng, FNAL; D. Trbojevic, BNL .....	102
Optimization Method for Orbit Correction in Accelerators — E. Bozoki, A. Friedman, BNL .....	105
A Fast Model-Calibration Procedure for Storage Rings — W. J. Corbett, M. J. Lee, V. Ziemann, SLAC .....	108
Dynamic Accelerator Modeling — H. Nishimura, LBL .....	111
Procedure for Determining Quadrupole and BPM Offset Values in Storage Rings — W. J. Corbett, V. Ziemann, SLAC .....	114
Beam Based Alignment of the SLC Final Focus Sextupoles — P. Emma, J. Irwin, N. Phinney, P. Raimondi, N. Toge, N. J. Walker, V. Ziemann, SLAC .....	116
Analysis of Higher Order Optical Aberrations in the SLC Final Focus Using Lie Algebra Techniques — N. J. Walker, J. Irwin, M. Woodley, SLAC .....	119
Simulation Support for Commissioning and Operating the SSC Linac — F. W. Guy, J. W. Hurd, C. R. Chang, D. Raparia, C. Y. Yao, SSCL .....	122
The Provision of IP Crossing Angles for the SSC — Y. Nosochkov, SSCL; D. M. Ritson, SLAC .....	125
Interactive Simulation of LEB Commissioning Procedure on a Hypercube Parallel Computer — G. Bourianoff, M. Botlo, B. Cole, S. Hunt, N. Malitsky, A. Romero, SSCL .....	128
Localized Chromaticity Correction of Low-Beta Insertions in Storage Rings — M. Donald, R. Helm, J. Irwin, H. Moshhammer, SLAC; E. Forest, D. Robin, A. Zholents, LBL; M. Sullivan, U. Ca., SLAC .....	131
Amplitude Function Mismatch — M. J. Syphers, T. Sen, SSCL; D. A. Edwards, DESY/Fermilab .....	134
SSC Collider Arc Lattice — M. J. Syphers, E. D. Courant, A. A. Garren, S. K. Kauffmann, T. Sen, SSCL .....	137
Second Order Chromaticity of the Interaction Regions in the Collider — T. Sen, M. J. Syphers, SSCL .....	140
Chromaticity Correction for the SSC Collider Rings — T. Sen, Y. Nosochkov, F. Pilat, R. Stiening, SSCL; D. M. Ritson, SLAC .....	143
Effect of Power Supply Ripple on Emittance Growth in the Collider — T. Sen, M. J. Syphers, SSCL .....	146
The QBA Optics for the 3.2 GeV Synchrotron Light Source ROSY II — D. Einfeld, Res. Ctr. Rossendorf; M. Plesko, Sincrotrone Trieste .....	149
Dynamic Aperture of the 2.5 GeV Synchrotron Radiation Source LISA — D. Einfeld, Fachhochschule Ostfriesland; D. Husmann, U. Bonn; M. Plesko, Sincrotrone Trieste .....	152
Four-Cell Third-Order Achromats and Their Application to Multi-Pass Time-of-Flight Spectrometers — W. Wan, M. Berz, MSU-NSCL .....	155
An Automatic Finder of Field Defects in a Large A.G. Machine — A. Verdier, J. Chappelier, CERN .....	158
Automatic and Expert Systems for Orbit Analysis — A. Verdier, J. Chappelier, CERN .....	161
Symplectic Scaling, a DA Based Tool — G. H. Hoffstätter, M. Berz, NSCL-MSU .....	164
New Features in DIMAD — R. V. Servranckx, TRIUMF .....	167
A First Order Matched Transition Jump at RHIC — S. Peggs, S. Tepikian, D. Trbojevic, BNL .....	168
Comparison of Aperture Determinations on RHIC for Single Particles Tracked 10 <sup>6</sup> Turns and 100 Particles, Having Randomly Generated Initial Coordinates, Tracked for 1000 Turns — G. F. Dell, BNL .....	171
Status of the Variable Momentum Compaction Storage Ring Experiment in SPEAR — P. Tran, A. Amiry, C. Pellegrini, UCLA; J. Corbett, M. Cornacchia, M. Lee, H.-D. Nuhn, H. Winick, D. Wu, SLAC; A. Hofmann, CERN; D. Robin, LBL .....	173
SSC High Energy Booster Resonance Corrector and Dynamic Tune Scanning Simulation — P. Zhang, S. Machida, SSCL .....	176
Transport Properties of the CEBAF Cavity — Z. Li, Coll. of William & Mary/CEBAF; J. J. Bisognano, B. C. Yunn, CEBAF .....	179

*Each volume begins with this five-volume table of contents and ends with the five-volume author index. The chairman's foreword and a list of conference organizers and staff appear as front matter in Volume 1. A list of conference participants precedes the author index in Volume 5.*

Five-Volume Contents

Global Coupling and Decoupling of the APS Storage Ring — <i>Y. C. Chae, J. Liu, L. C. Teng, ANL</i> .....	182
Conventional Collimation and Linac Protection — <i>J. Irwin, R. Helm, W. R. Nelson, D. Walz, SLAC</i> .....	185
Measurement of Beta-Function and Phase Using the Response Matrix — <i>Y. Chung, G. Decker, K. Evans, Jr., ANL</i> ..	188
MATCH 1.0: The Program for Analytical Matching of Insertion — <i>I. P. Yudin, JINR Moscow</i> .....	191
The Application Package DeCA for Calculating Cyclic Accelerators — <i>P. I. Gladkikh, A. Yu. Zelinsky,</i> <i>M. A. Strelkov, Kharkov Inst.</i> .....	194
Echo Effect in Accelerators — <i>G. V. Stupakov, S. K. Kauffmann, SSCL</i> .....	197
Tune Shift Effect Due to the Sextupole Longitudinal Periodic Structure in the Superconducting Dipole Magnets — <i>G. López, S. Chen, SSCL</i> .....	200
Decoupling Schemes for the SSC Collider — <i>Y. Cai, G. Bourianoff, B. Cole, R. Meinke, J. Peterson, F. Pilat,</i> <i>S. Stampke, M. Syphers, R. Talman, SSCL</i> .....	203
Matrix Nonlinear Beam Dynamics in Curvilinear Space-Time — <i>A. Dymnikov, U. St. Petersburg; R. Hellborg,</i> <i>U. Lund</i> .....	206
A Numerical Check of the Thermal Wave-Model for Particle-Beam Dynamics — <i>R. Fedele, G. Miele,</i> <i>U. Napoli; F. Galluccio, INFN Napoli</i> .....	209
Longitudinal Dynamics for Electrons in the Thermal Wave Model for Charged Particle Beams — <i>R. Fedele, G. Miele,</i> <i>U. Napoli/INFN Napoli; L. Palumbo, U. Roma/INFN-LNF</i> .....	212
Experimental Measurement of Dynamic Aperture at the Photon Factory Storage Ring — <i>Y. Kobayashi, T. Mitsuhashi,</i> <i>A. Ueda, KEK; T. Yamakawa, Tohoku U.</i> .....	215
Lattice and Dynamic Aperture of the Duke FEL Storage Ring — <i>Y. Wu, V. N. Litvinenko, J. M. J. Madey, Duke</i> ...	218
Synchrotron Coupling Effects in Alternating Phase Focusing — <i>W. Cheng, R. L. Gluckstern, H. Okamoto,</i> <i>U. Maryland</i> .....	221
Experimental Determination of a Betatron Difference Resonance — <i>M. Ellison, M. Ball, B. Brabson, J. Budnick,</i> <i>D. D. Caussyn, J. Collins, V. Derenchuk, G. East, T. Ellison, D. Friesel, B. Hamilton, H. Huang,</i> <i>W. P. Jones, S. Y. Lee, D. Li, S. Nagaitsev, T. Sloan, Y. Wang, IUCF; A. W. Chao, S. Dutt, M. Syphers,</i> <i>Y. T. Yan, P. L. Zhang, SSCL; M. Minty, SLAC; K. Y. Ng, FNAL; L. Teng, ANL; X. Pei, BNL</i> .....	224
Experimental Results of the Betatron Sum Resonance — <i>Y. Wang, M. Ball, B. Brabson, J. Budnick, D. D. Caussyn,</i> <i>J. Collins, V. Derenchuk, G. East, M. Ellison, D. Friesel, B. Hamilton, H. Huang, S. Y. Lee,</i> <i>W. P. Jones, D. Li, S. Nagaitsev, T. Sloan, IUCF; A. W. Chao, S. Dutt, M. Syphers, Y. T. Yan,</i> <i>P. L. Zhang, SSCL; K. Y. Ng, FNAL; M. Minty, SLAC; X. Pei, BNL</i> .....	227
Chromaticity Compensation and Dynamic Aperture Limitation of SIBERIA-2 — <i>V. Korchuganov, E. Levichev,</i> <i>V. Sajaev, BINP</i> .....	230
RF Voltage Modulation at Discrete Frequencies, for Application to Proton Extraction Using Crystal Channeling — <i>W. E. Gabella, J. Rosenzweig, UCLA; R. Kick, IMSA; S. Peggs, BNL</i> .....	233
Modification of the Short Straight Sections of the High Energy Booster of the SSC — <i>M. Li, D. Johnson, P. Kocur,</i> <i>R. Schailey, R. Servranckx, R. Talman, Y. Yan, R. York, V. Yarba, SSCL</i> .....	236
Dynamic Aperture of the Chromatically Corrected Collider Lattice — <i>F. Pilat, Y. Nosochkov, T. Sen, R. Stiening,</i> <i>SSCL</i> .....	239
An Optimized Formulation for Deprit-Type Lie Transformations of Taylor Maps for Symplectic Systems — <i>J. Shi,</i> <i>U. Houston; Y. T. Yan, SSCL</i> .....	242
Symmetric Integrable-Polynomial Factorization for Symplectic One-Turn-Map Tracking — <i>J. Shi, U. Houston;</i> <i>Y. T. Yan, SSCL</i> .....	243
Recent Results from the Dynamic Aperture Experiment at the SPS — <i>W. Fischer, J. Gareyte, M. Giovannozzi,</i> <i>T. Risselada, W. Scandale, F. Schmidt, CERN</i> .....	246
Higher Order Tune Derivatives Due to Low- $\beta$ Insertions — <i>A. Verdier, CERN</i> .....	249
A Quasi-Isochronous Operation Mode for the LNLS UVX Storage Ring — <i>L. Lin, C. E. T. Gonçalves da Silva,</i> <i>Unicamp/LNLS Brazil</i> .....	252
Tracking Studies and Machine Performance Simulation of the SSC Low Energy Booster — <i>X. Wu, R. York,</i> <i>R. Servranckx, S. Machida, J. F. Knox-Seith, U. Wienands, SSCL</i> .....	255
Magnetic Correction of RHIC Triplets — <i>J. Wei, R. Gupta, S. Peggs, BNL</i> .....	258
Beam-Beam Modulational Diffusion in 2 1/2 Dimensions — <i>T. Satogata, S. Peggs, BNL</i> .....	261
Preparation of an Experiment to Investigate Nonlinear Beam Dynamics at the Storage Ring DELTA — <i>M. Schürmann,</i> <i>U. Dortmund</i> .....	264
Statistics of the Half-Integer Stopband — <i>S. Dutt, F. Chautard, R. Gerig, S. Kauffman, SSCL</i> .....	267
Stochastic Dynamics for Accelerators — <i>A. Pauluhn, DESY</i> .....	270

**Proceedings of the 1993 Particle Accelerator Conference**

Diffusion Phenomena in Simple Hamiltonian Systems: Some Analytical and Numerical Results — A. Bazzani, S. Rambaldi, G. Turchetti, U. Bologna; M. Giovannozzi, CERN .....	273
Particle Acceleration in Extremely Strong Electromagnetic Wave Fields — K. O. Thielheim, U. Kiel .....	276
Laser Powered Beam Conditioner for Free Electron Lasers and Synchrotrons — H. Liu, G. Neil, CEBAF .....	279
Tracking Studies of Insertion Device Effects on Dynamic Aperture in the APS Storage Ring — Y. Chae, U. Houston; E. A. Crosbie, ANL .....	282
Particle Diffusion from Resonance Islands in Aladdin at SRC — J. Liu, E. Crosbie, L. Teng, J. Bridges, D. Ciarlette, R. Kustom, D. Voss, F. Mills, M. Borland, ANL; K. Symon, U. Wisc. Madison; W. Trzeciak, SRC Stoughton .....	285
Alternating-Phase Focusing with Amplitude Modulation — L. Sagalovsky, J. R. Delayen, ANL .....	288
Full-Turn Symplectic Map from a Generator in a Fourier-Spline Basis — J. S. Berg, R. L. Warnock, R. D. Ruth, SLAC; É. Forest, LBL .....	291
Synchrotron Resonances Due to Crab Cavities — S. Kurokawa, KEK; D. Pestrikov, KEK/BINP Novosibirsk .....	294
Third-Order Bending Magnet Optics for Cartesian Coordinates — V. V. Andreev, I. P. Yudin, JINR Moscow .....	297
Effects of Plane Undulator (Wiggler) Fields on Beam Dynamics at Large Orbit Distortion — S. Efimov, E. Bulyak, Kharkov Inst. ....	300
Bunching Property of High Current Injector with Subharmonic Prebuncher in Linac — Z. Zhang, Y. Chen, CIAE China .....	303
Beam Transport Line of CIAE Medical Cyclotron and Its Magnetic Elements Design Studies — T. Zhang, C. Chu, M. Fan, CIAE China .....	306
Resonant Beam Extraction with Constant Separatrix — K. Hiramoto, M. Tadokoro, J. Hirota, M. Nishi, Hitachi Ltd. ....	309
The On-Line Control Software for BEPC Beam Transport Lines — X. Zhang, K. Wei, C. Zhang, IHEP China.....	312
About Extraction of 70-GeV Protons by a Bent Crystal from the IHEP Accelerator to the Proza Setup — A. A. Asseev, A. N. Vasil'ev, E. A. Ludmirsky, V. A. Maishev, S. B. Nurushev, Yu. S. Fedotov, IHEP Russia .....	315
Increase a Bent Crystal Extraction Efficiency by Means of Thin Internal Target — A. A. Asseev, E. A. Myae, S. V. Sokolov, Yu. S. Fedotov, IHEP Russia.....	318
Influence of Thin Internal Target on the Bent Crystal Extraction Efficiency — A. A. Asseev, S. V. Sokolov, IHEP Russia .....	320
Extraction of 50 GeV Protons from IHEP Accelerator by Bent Crystal — A. A. Asseev, V. A. Maishev, E. A. Myae, IHEP Russia.....	322
On Using the Thin Target at Extraction of Protons from the Accelerators by Bent Crystal — A. A. Asseev, IHEP Russia .....	324
A Digital Computer Program for the Simulation of Positive or Negative Particle Beams on a PC — J. E. Boers, Thunderbird Simulations .....	327
Antiproton Extraction in the Fermilab Antiproton Accumulator — M. Church, S. O'Day, FNAL .....	330
Beam Optics of LEB-MEB Transfer Line for Superconducting Super Collider — N. Mao, J. A. McGill, K. L. Brown, R. E. Gerig, SSCL .....	333
Acceleration and Bunching by a Gap — S. Kulinski, INFN-LNF .....	336
The New Slow Extraction System of the CERN PS — Ch. Steinbach, H. Stucki, M. Thivent, CERN .....	339
Simulation of Slow Extraction in the Main Injector — C. S. Mishra, F. A. Harfoush, J. Johnstone, FNAL .....	342
Stability of Beam in the Fermilab Main Injector — C. S. Mishra, F. A. Harfoush, FNAL .....	345
Correction Schemes to Improve the Dynamical Aperture of the Main Injector — C. S. Mishra, F. A. Harfoush, FNAL .....	348
Defining the Systematic and Random Multipole Errors for Main Injector Tracking — F. A. Harfoush, B. C. Brown, H. D. Glass, C. S. Mishra, S. Peggs, FNAL.....	351
Experience with the New Reverse Injection Scheme in the Tevatron — S. Saritepe, G. Goderre, J. Annala, B. Hanna, A. Braun, FNAL .....	354
Injection and Extraction Performance at the SIS/ESR Facility — H. Eickhoff, K. Blasche, U. Blell, B. Franzke, J. Pinkow, GSI Darmstadt .....	357
The AGS-Booster Complex for the g-2 Experiment and RHIC Injection — M. Tanaka, Y. Y. Lee, BNL .....	360
First-Turn Losses in the LAMPF Proton Storage Ring (PSR) — R. Hutson, R. Macek, LANL .....	363

*Each volume begins with this five-volume table of contents and ends with the five-volume author index. The chairmen's foreword and a list of conference organizers and staff appear as front matter in Volume 1. A list of conference participants precedes the author index in Volume 5.*

Five-Volume Contents

Stripper-Foil Scan Studies of the First-Turn Beam Loss Mechanism in the LAMPF Proton Storage Ring (PSR) — <i>R. Hutson, D. Fitzgerald, S. Frankle, R. Macek, M. Plum, C. Wilkinson, LANL</i> .....	366
Measurement of H <sup>0</sup> Excited States Produced by Foil Stripping of 800-MeV H <sup>-</sup> Ions — <i>J. Donahue, D. Clark, S. Cohen, D. Fitzgerald, S. Frankle, R. Hutson, R. Macek, E. Mackerrow, O. van Dyck, C. Wilkinson, LANL; H. Bryant, M. Gulley, M. Halka, P. Keating, W. Miller, U. New Mexico</i> .....	369
Reducing Phase-Dependent Emittance Growth with Local Flattopping — <i>R. E. Laxdal, T. Kuo, G. H. Mackenzie, L. Root, TRIUMF; A. Papash, INR Kiev</i> .....	372
An Ion-Source Model for First-Order Beam Dynamic Codes — <i>C. L. Fink, B. P. Curry, ANL</i> .....	375
Lattice Design and Injection Issues for the 2 TeV SSCL High Energy Booster to Collider Injection Lines — <i>F. Wang, R. Schailey, J. McGill, D. Johnson, SSCL; K. L. Brown, SLAC</i> .....	378
Detailed Studies on the Beam Transfer Line from Linac to Low Energy Booster Synchrotron for the SSC — <i>R. Bhandari, J. McGill, F. Wang, S. Penner, SSCL</i> .....	381
200 GeV Beam Transfer Lines at the SSC — <i>F. G. Mariam, J. McGill, SSCL; K. Brown, SLAC</i> .....	384
Effect of Betatron Motion on the Septum Flux in Superslow Extraction at the SSC — <i>B. S. Newberger, U. Texas, Austin; H.-J. Shih, SSCL; J. A. Ellison, U. NM</i> .....	387
Study of Energy Ramping Process Applied to the LNLS Synchrotron Light Source (Brazil) — <i>L. Jahnel, C. E. T. Gonçalves da Silva, Unicamp/LNLS Brazil</i> .....	390
Extraction System Design for the SSC Low Energy Booster — <i>X. Wu, R. York, U. Wienands, T. Hunter, S. Sheynin, SSCL</i> .....	393
Tests and Analysis for SLC Damping Ring Data — <i>J. E. Spencer, SLAC</i> .....	396
RF Capture Studies for Injection into a Synchrotron — <i>E. S. Lessner, Y. Cho, ANL</i> .....	399
Results from Beam Diffusion and Collimation Measurements in Preparation for Fermilab Tevatron Crystal Extraction — <i>G. Jackson, FNAL</i> .....	402
Operational Experience with Third Harmonic RF Cavity for Improved Beam Acceleration Through Transition in the Fermilab Main Ring — <i>C. M. Bhat, J. Dey, J. Griffin, I. Kourbanis, J. MacLachlan, M. Martens, K. Meisner, K. Y. Ng, J. Shan, D. Wildman, FNAL</i> .....	405
New Method for Control of Longitudinal Emittance During Transition in Proton Synchrotrons — <i>J. E. Griffin, FNAL (Ret.)</i> .....	408
Remarks on the Differential Luminosity in the Weak Disruption and the Transition Region — <i>H. Heydari, TUB Germany</i> .....	411
Flat Beam Studies in the SLC Linac — <i>C. Adolphsen, F.-J. Decker, J. T. Seeman, SLAC</i> .....	414
Method to Evaluate Steering and Alignment Algorithms for Controlling Emittance Growth — <i>C. Adolphsen, T. Raubenheimer, SLAC</i> .....	417
Experimental Simulation of Ground Motion Effects — <i>M. J. Syphers, A. W. Chao, S. Dutt, Y. T. Yan, P. L. Zhang, SSCL; M. Ball, B. Brabson, J. Budnick, D. D. Caussyn, J. Collins, V. Derenchuk, G. East, M. Ellison, T. Ellison, D. Friesel, B. Hamilton, H. Huang, W. P. Jones, S. Y. Lee, D. Li, S. Nagaitsev, X. Pei, G. Rondeau, T. Sloan, Y. Wang, IUCF; M. G. Minty, SLAC; W. Gabella, K. Y. Ng, FNAL; L. Teng, ANL; S. Tepikian, BNL</i> .....	420
Bunch Coalescing Studies for the SSC — <i>N. Mahale, Y. T. Yan, J. Ellison, SSCL</i> .....	423
Compensation of RF-Induced Energy Spread in the CEBAF Injector Chopping System — <i>M. G. Tiefenback, G. A. Krafft, CEBAF</i> .....	426
The North Arc of the SLC as a Spin Rotator — <i>T. Limberg, P. Emma, SLAC; R. Rossmannith, CEBAF</i> .....	429
The Evolution of Tensor Polarization — <i>H. Huang, S. Y. Lee, IUCF, L. Ratner, BNL</i> .....	432
Even Order Snake Resonances — <i>S. Y. Lee, Indiana U.</i> .....	435
Wiggler as Spin Rotators for RHIC — <i>A. Luccio, BNL; M. Conte, U. Genova</i> .....	438
Taylor Map and Calculation of Equilibrium Polarization for Proton Storage Rings — <i>V. Balandin, N. Golubeva, INR Moscow</i> .....	441
Investigation of Spin Resonance Crossing in Proton Circular Accelerators — <i>V. Balandin, N. Golubeva, INR Moscow</i> .....	444
Electron Beam Depolarization in a Damping Ring — <i>M. Minty, SLAC</i> .....	447
SPINLIB: New Computer Code for Polarization Calculation — <i>Yu. Eidelman, V. Yakimenko, BINP</i> .....	450
IHEP Polarized Proton Beam — <i>V. N. Zapol'sky, Yu. A. Chesnokov, A. Dyshkant, N. A. Galyaev, V. I. Kotov, V. I. Kryshkin, R. A. Rzaev, R. M. Sulyaev, S. V. Tsarik, V. G. Zaruchevsky, IHEP Moscow</i> .....	454
Measurement of Longitudinal Beam Polarization by Synchrotron Radiation — <i>I. P. Karabekov, Yerevan/CEBAF, R. Rossmannith, CEBAF</i> .....	457

Volume 1: 1-747  
 Volume 2: 748-1640  
 Volume 3: 1641-2545  
 Volume 4: 2546-3218  
 Volume 5: 3219-3933

**Proceedings of the 1993 Particle Accelerator Conference**

The Status of Polarization Studies at HERA — <i>M. Böge, DESY</i> .....	460
Computer Assisted Accelerator Tuning — <i>J. K. Boyd, LLNL</i> .....	463
Pulse-to-Pulse Simulation of Orbit Feedback for JLC Final Focus System — <i>N. Yamamoto, K. Hirata, K. Oide, KEK</i> .....	466
Multi-Dimensional Beam Emittance and $\beta$ -Functions — <i>J. Buon, LAL Orsay</i> .....	469
Observation of the Coalescing of Beam into an Asymmetric RF Bucket by Stochastic Cooling — <i>A. M. Halling, X. P. Lu, FNAL</i> .....	472
Effects of Transverse Coupling on Transverse Beam Size, Simulation and Measurements — <i>A. M. Halling, FNAL</i> ...	474
One of Methods to Extract Truncated Taylor Map for Orbital and Spin Motion in Proton Storage Rings — <i>V. Balandin, INR Moscow</i> .....	477
Skew Quadrupole Effects in the IBM Compact Synchrotron — <i>C. N. Archie, IBM Semiconductor R&amp;D Ctr.</i> .....	480
A Simulation Study of Linear Coupling Effects and Their Correction in RHIC — <i>G. Parzen, BNL</i> .....	483
Eigenfunctions of the Transfer Matrix in the Presence of Linear Coupling — <i>G. Parzen, BNL</i> .....	486
Emittance and Beam Size Distortion Due to Linear Coupling — <i>G. Parzen, BNL</i> .....	489
Use of Regularization Method in the Determination of Ring Parameters and Orbit Correction — <i>Y. N. Tang, S. Krinsky, NSLS-BNL</i> .....	492
Automatic Differentiation of Limit Functions — <i>L. Michelotti, FNAL</i> .....	495
Corrector Ironing in the SLC Final Focus — <i>V. Ziemann, SLAC</i> .....	498
General Normal Form Procedure to Correct Tune-Shift and Non-Linear Chromaticity for Large Accelerators like the LHC — <i>M. Giovannozzi, F. Schmidt, CERN</i> .....	500
Review of Recent Optical Issues in LEP — <i>F. Ruggiero, CERN</i> .....	503
Emittance and Damping of Electrons in the Neighborhood of Resonance Fixed Points — <i>E. A. Crosbie, ANL</i> .....	506
Effects of the Third Order Transfer Maps and Solenoid on a High Brightness Beam — <i>Z. Parsa, BNL</i> .....	509
Simultaneous Cancellation of Beam Emittance and Energy Spread in the CEBAF Nuclear Physics Injector Chopping System — <i>H. Liu, J. Bisognano, CEBAF</i> .....	512
The Linkage of Zlib to TEAPOT for Auto-Differentiation Map Extraction and Nonlinear Analysis — <i>N. Sun, Y. T. Yan, F. Pilat, G. Bourianoff, SSCL</i> .....	515
Influence of the Ionization Loss in the Diagnostic Foil on the Phase Motion in the Phasotron — <i>O. N. Borisov, L. M. Onischenko, JINR, Dubna</i> .....	518
<b>Lepton RF Linacs and Linear Colliders</b> <span style="float: right;"><i>Chair: Y. Kimura</i></span>	
Recent SLC Developments ( <i>Invited Paper</i> ) — <i>M. Ross, SLAC</i> .....	522
CEBAF Commissioning Status ( <i>Invited Paper</i> ) — <i>A. Hutton, CEBAF</i> .....	527
Overview of Linear Collider Designs ( <i>Invited Paper</i> ) — <i>R. H. Siemann, SLAC</i> .....	532
Progress Report on the TESLA Test Facility — <i>H. T. Edwards and the TESLA Collaboration, DESY/FNAL</i> .....	537
The CERN Linear Collider — <i>The CLIC Study Group, CERN</i> .....	540
The Next Linear Collider Test Accelerator — <i>R. D. Ruth, C. Adolphsen, K. Bane, R. F. Boyce, D. L. Burke, R. Callin, G. Caryotakis, R. Cassel, S. L. Clark, H. Deruyter, K. Fant, R. Fuller, S. Heifets, H. Hoag, R. Humphrey, S. Kheifets, R. Koontz, T. Lavine, G. A. Loew, A. Menegat, R. H. Miller, J. M. Paterson, C. Pearson, R. Phillips, J. Rifkin, J. Spencer, S. Tantawi, K. A. Thompson, A. Vlieks, V. Vylet, J. W. Wang, P. B. Wilson, A. Yeremian, B. Youngman, SLAC; N. M. Kroll, UC San Diego; C. Nantista, UCLA</i> .....	543
High Power CW Linac in PNC — <i>S. Toyama, Y. L. Wang, T. Emoto, M. Nomura, N. Takahashi, H. Oshita, K. Hirano, Y. Himeno, PNC Japan; I. Sato, A. Enomoto, M. Ono, KEK</i> .....	546
<b>Poster presentations:</b>	
A mm-Wave Planar Microcavity Structure for Electron Linear Accelerator System — <i>Y. W. Kang, R. Kustom, F. Mills, G. Mavrogenes, ANL; H. Henke, TU Berlin</i> .....	549
SCANUR: A Subcritical Reactor with Electron Linacs for Transmutation of Nuclear Wastes — <i>A. Krasnykh, Yu. Popov, V. Rudenko, L. Somov, JINR Dubna; L. Men'schikov, V. Prusakov, S. Subbotin, Kurchatov Inst., Moscow</i> .....	552
New Irradiation Field Shaping Systems of High Voltage Electron Accelerators for Industry — <i>A. S. Ivanov, V. P. Ovchinnikov, M. P. Svinin, N. G. Tolstun, Efremov Inst.</i> .....	555
A Versatile 2 MeV, 200 mA Compact X-Band Linac — <i>C. E. Clayton, K. A. Marsh, UCLA</i> .....	558

*Each volume begins with this five-volume table of contents and ends with the five-volume author index. The chairmen's foreword and a list of conference organizers and staff appear as front matter in Volume 1. A list of conference participants precedes the author index in Volume 5.*

Five-Volume Contents

Emittance Measurements of the 4.5 MeV UCLA RF Photo-Injector — S. C. Hartman, N. Barov, S. Park, C. Pellegrini, J. Rosenzweig, G. Travish, R. Zhang, P. Davis, C. Joshi, G. Hairapetian, UCLA .....	561
Commissioning of the SIBERIA-2 Preinjector and First Beam Results — V. Korchuganov, G. Kulipanov, E. Levichev, O. Nezhevenko, G. Ostreiko, A. Philipchenko, G. Serdobintsev, E. Shaimerdenov, V. Ushakov, INP Novosibirsk; A. Kadnikov, Yu. Krylov, S. Kuznetsov, V. Ushkov, Yu. Yupinov, Kurchatov Inst.....	564
Emittance Measurement and Modeling of the ALS 50 MeV Linac to Booster Line — J. Bengtsson, W. Leemans, T. Byrne, LBL .....	567
Extended Version of an S-Band RF Gun — S. Park, C. Pellegrini, UCLA .....	570
Progress Report on the Commissioning of the Lisa 25 MeV SC Linac — F. Tazzioli, M. Castellano, M. Ferrario, S. Kulinski, M. Minestrini, P. Patteri, INFN-LNF; L. Catani, S. Tazzari, INFN Roma .....	573
The Plane Wave Transformer Linac Development at UCLA — R. Zhang, S. Hartman, C. Pellegrini, UCLA .....	575
Nanosecond MOSFET Gun Pulser for the CESR High Intensity Linac Injector — C. R. Dunnam, R. E. Meller, Cornell .....	578
Progress of PLS 2-GeV Linac — W. Namkung, I. Ko, M. Cho, C. Ryu, J. Bak, S. Nam, H. Lee, POSTECH .....	581
Lattice Design Principles for a Recirculated, High Energy, SRF Electron Accelerator — D. R. Douglas, CEBAF .....	584
Commissioning and Operation Experience with the CEBAF Recirculation Arc Beam Transport System — Y. Chao, M. Crofford, N. Dobeck, D. Douglas, A. Hofler, C. Hovater, G. A. Krafft, R. Legg, J. Perry, E. Price, S. Suhring, M. Tiefenback, J. van Zeijts, CEBAF .....	587
Linac Upgrade Plan for the KEK B-Factory — A. Enomoto, S. Anami, T. Kamitani, H. Hanaki, T. Shidara, I. Sato, KEK .....	590
Performance Characteristics of the Pulsed High Power Klystron Tube for PLS 2-GeV Linac — M. H. Cho, S. H. Nam, J. S. Oh, S. S. Park, H. S. Lee, J. S. Bak, I. S. Ko, W. Namkung, POSTECH .....	593
Electron Transport of a Linac Coherent Light Source (LCLS) Using the SLAC Linac — K. L. Bane, T. O. Raubenheimer, J. T. Seeman, SLAC .....	596
Phasing Schemes for the CEBAF Cavities — S. N. Simrock, R. Kazimi, G. A. Krafft, L. Merminga, L. Ninan, S. Witherspoon, CEBAF .....	599
Initial Data of Linac Preinjector for SPring-8 — S. Suzuki, H. Yoshikawa, T. Hori, K. Yanagida, A. Mizuno, K. Tamezane, K. Mashiko, H. Yokomizo, JAERI .....	602
Status of the Advanced Photon Source (APS) Linear Accelerator — M. White, W. Berg, R. Fuja, A. Grelick, G. Mavrogenes, A. Nassiri, T. Russell, W. Wesolowski, ANL .....	605
200 MeV RF Linac for Brookhaven National Laboratory — K. Whitham, H. Anamkath, S. Lyons, J. Manca, R. Miller, P. Treas, T. Zante, Titan Beta; R. Miller, SLAC; R. Heese, J. Keane, BNL .....	608
Design of the e <sup>+</sup> /e <sup>-</sup> Frascati Linear Accelerator for DaFne — K. Whitham, H. Anamkath, S. Lyons, J. Manca, R. Miller, T. Zante, P. Treas, D. Nett, Titan Beta; R. Miller, SLAC; R. Boni, H. Hsieh, S. Kulinski, F. Sannibale, B. Spataro, M. Vescovi, G. Vignola, INFN-Frascati .....	611
The Possibility of Introducing Additional Focusing Caused by the Circular Irises in Iris Loaded Accelerator Sections — M. Kurz, P. Hülsmann, H.-W. Glock, H. Klein, Inst. f. Ang. Physik .....	614
Disruption Effects from the Collision of Quasi-Flat Beams — P. Chen, SLAC .....	617
Accelerator and RF System Development for NLC — A. E. Vlieks, R. Callin, H. Deruyter, R. Early, K. S. Fant, Z. D. Farkas, W. R. Fowkes, C. Galloway, H. A. Hoag, R. Koontz, G. A. Loew, T. L. Lavine, A. Menegat, R. H. Miller, D. Palmer, C. C. Pearson, R. D. Ruth, S. G. Tantawi, P. B. Wilson, J. W. Wang, C. Yoneda, SLAC; N. Kroll, UCSD; C. Nantista, UCLA .....	620
Rise Time of the Amplitudes of Time Harmonic Fields in Multicell Cavities — H.-W. Glock, M. Kurz, P. Hülsmann, H. Klein, Inst. f. Ang. Physik .....	623
CLIC Drive Beam Generation by Induction Linac and FEL Experimental Studies for the CERN Linear Collider — R. Corsini, C. D. Johnson, CERN; J. Gardelle, J. Grenier, CESTA .....	626
Beam Instabilities Related to Different Focusing Schemes in TESLA — A. Mosnier, CE Saclay .....	629
A Large Aperture Final Focus System for TESLA — O. Napoly, CE Saclay .....	632
Chicane and Wiggler Based Bunch Compressors for Future Linear Colliders — T. O. Raubenheimer, P. Emma, S. Kheifets, SLAC .....	635
An "NLC-Style" Short Bunch Length Compressor in the SLAC Linac — J. T. Seeman, R. Holtzapple, SLAC .....	638
Multibunching Studies for CLIC — I. Wilson, W. Wuensch, CERN .....	641
Linear Collider Systems and Costs — G. A. Loew, SLAC .....	644
Application of the Monte Carlo Method to Estimate the Tenth-Value Thickness for X-Rays in Medical Electron Accelerators — J. Ródenas, G. Verdú, U. Politécnica, Valencia .....	647

Volume 1: 1-747  
 Volume 2: 748-1640  
 Volume 3: 1641-2545  
 Volume 4: 2546-3218  
 Volume 5: 3219-3933

**Proceedings of the 1993 Particle Accelerator Conference**

Burst-Mode Electron Gun Pulser for FEL with the ISIR Linac — <i>K. Tsumori, Sumitomo Elect. Ind.; S. Okuda, T. Yamamoto, S. Suemine, S. Takamuku, Osaka U.</i> .....	650
Positron Accumulation Ring for the SPring-8 Project — <i>Y. Miyahara, JAERI-RIKEN</i> .....	653

**High-Current Accelerators**

*Chair: T. Fessenden*

Induction Accelerator Development for Heavy Ion Fusion ( <i>Invited Paper</i> ) — <i>L. L. Reginato, LBL</i> .....	656
Generation and Focusing of High Energy, 35-kA Electron Beams for Pulsed-Diode Radiographic Machines: Theory and Experiment — <i>R. L. Carlson, M. J. George, LANL; T. P. Hughes, D. R. Welch, MRC</i> .....	661
Numerical Investigation of High-Current Ion Beam Acceleration and Charge Compensation in Two Accelerating Gaps of Induction Linac — <i>N. G. Belova, Russian Acad.; V. I. Karas', Kharkov Inst.</i> .....	664
The Light-Ion Pulsed Power Induction Accelerator for the Laboratory Microfusion Facility (LMF) — <i>M. G. Mazarakis, D. L. Smith, L. F. Bennett, T. R. Lockner, R. E. Olson, J. W. Poukey, J. Boyes, Sandia Nat. Lab.</i> .....	667

*Poster presentations:*

First Operation of the LELIA Induction Accelerator at CESTA — <i>Ph. Eyharts, Ph. Anthouard, J. Bardy, C. Bonnafond, Ph. Delsart, A. Devin, P. Eyl, P. Grua, J. Labrousche, J. Launspach, P. Le Taillandier, J. de Mascureau, E. Merle, A. Roques, M. Thevenot, D. Villate, CEA-CESTA</i> .....	670
An Induction Linac and Pulsed Power System at KEK — <i>J. Kishiro, K. Ebihara, S. Hiramatsu, Y. Kimura, T. Ozaki, K. Takayama, D. H. Whittum, K. Saito, KEK</i> .....	673
Design and Operation of Inductive Acceleration Modules for FEL with Controlled Voltage Ramp — <i>S. Kawasaki, Saitama U.; H. Ishizuka, Fukuoka Inst.; A. Tokuchi, Nichicon Corp.; Y. Yamashita, S. Nakajima, Hitachi; S. Sakamoto, H. Maeda, M. Shiho, JAERI</i> .....	676
Study on Induction Accelerator for Industrial Applications — <i>Y. S. Cho, K. H. Baik, K. H. Chung, Seoul Nat. U.; B. H. Choi, Korea Atomic Energy Res. Inst.</i> .....	679
Linear Induction Accelerators for Industrial Applications — <i>M. I. Demsky, Yu. P. Vakhrushin, A. E. Baranovsky, A. A. Volzhev, A. P. Kuprianov, D. E. Trifonov, Efremov Inst.</i> .....	682
High Power, High Brightness Electron Beam Generation in a Pulse-Line Driven Pseudospark Discharge — <i>W. W. Destler, Z. Segalov, J. Rodgers, K. Ramaswamy, M. Reiser, U. Maryland</i> .....	685
Experimental Study of Post-Acceleration and Transport of a Pseudospark-Produced Electron Beam — <i>C. J. Liu, M. J. Rhee, U. Maryland</i> .....	688
Compound-Lens Injector for a 19-MeV, 700-kA Electron Beam — <i>T. W. L. Sanford, J. W. Poukey, J. A. Halbleib, Sandia Nat. Lab.; R. C. Mock, Ktech Corp.</i> .....	691
Electron Flow in the SABRE Linear Induction Adder in Positive Polarity — <i>J. R. Smith, Titan/Spectra; J. W. Poukey, M. E. Cuneo, D. L. Hanson, S. E. Rosenthal, M. Bernard, Sandia Nat. Lab.</i> .....	694
Design and Progress of the AIRIX Induction Accelerator — <i>J. de Mascureau, Ph. Anthouard, J. Bardy, C. Bonnafond, Ph. Delsart, A. Devin, Ph. Eyharts, P. Eyl, P. Grua, J. Labrousche, J. Launspach, P. Le Taillandier, E. Merle, A. Roques, B. Sacepe, M. Thevenot, D. Villate, CEA-CESTA</i> .....	697
Nuclear Fusion of Protons with Ions of Boron — <i>A. G. Ruggiero, BNL</i> .....	700
Heavy Ion Fusion Injector Program — <i>S. Yu, S. Eylon, W. W. Chupp, A. Faltens, T. Fessenden, E. Henestroza, R. Hipple, D. Judd, C. Peters, L. Reginato, H. Rutkowski, J. Stoker, D. Vanecek, LBL; J. Barnard, G. Caporaso, Y. J. Chen, F. Deadrick, A. Friedman, D. Grote, D. Hewett, LLNL</i> .....	703
Ion Pulse Propagation Through a Previously Unfilled Electrostatic Aperture Lens Accelerating Column — <i>H. L. Rutkowski, S. Eylon, D. S. Keeney, LBL; Y. J. Chen, D. W. Hewett, J. Barnard, LLNL</i> .....	706
ILSE-ESQ Injector Scaled Experiment — <i>E. Henestroza, S. Eylon, S. Yu, LBL; D. Grote, LLNL</i> .....	709
One Dimensional Simulations of Transients in Heavy Ion Injectors — <i>J. J. Barnard, G. J. Caporaso, LLNL; S. S. Yu, S. Eylon, LBL</i> .....	712
Analysis of Beam Loading in Electrostatic Columns — <i>G. J. Caporaso, J. J. Barnard, LLNL</i> .....	715
Simulation of Transient Effects in the Heavy Ion Fusion Injectors — <i>Y. Chen, D. W. Hewett, LLNL</i> .....	718
Electrostatic Quadrupoles for Heavy-Ion Fusion — <i>P. Seidl, A. Faltens, LBL</i> .....	721
Simulation Studies of Space-Charge-Dominated Beam Transport in Large Aperture Ratio Quadrupoles — <i>W. M. Fawley, L. J. Laslett, C. M. Celata, A. Faltens, LBL; I. Haber, NRL</i> .....	724

*Each volume begins with this five-volume table of contents and ends with the five-volume author index. The chairmen's foreword and a list of conference organizers and staff appear as front matter in Volume 1. A list of conference participants precedes the author index in Volume 5.*

Three Dimensional PIC Simulation of Heavy Ion Fusion Beams: Recent Improvements to and Applications of WARP — <i>D. P. Grote, A. Friedman, LLNL; I. Haber, NRL</i> .....	727
Longitudinal Beam Dynamics for Heavy Ion Fusion — <i>D. A. Callahan, A. B. Langdon, A. Friedman, LLNL; I. Haber, NRL</i> .....	730
Correction of Longitudinal Errors in Accelerators for Heavy-Ion Fusion — <i>W. M. Sharp, D. A. Callahan, J. J. Barnard, A. B. Langdon, LLNL; T. J. Fessenden, LBL</i> .....	733
System Modeling for the Longitudinal Beam Dynamics Control Problem in Heavy Ion Induction Accelerators — <i>A. N. Payne, LLNL</i> .....	736
Development of FET-Switched Induction Accelerator Cells for Heavy-Ion Fusion Recirculators — <i>M. A. Newton, W. R. Cravey, S. A. Hawkins, H. C. Kirbie, C. W. Ollis, LLNL</i> .....	739
Parametric Studies for Recirculating Induction Accelerators as Drivers for Heavy-Ion Fusion — <i>R. L. Bieri, Schafer Assoc.</i> .....	742
A Fusion Device of the Continuous Electron Beam Confinement Used by the Accumulating Ring with the Continuous Injection — <i>S. Gao, G. Qian, CIAE China</i> .....	745

## Volume 2

### RF Structures

Chair: *D. Reid*

Operating Experience with High Beta Superconducting RF Cavities ( <i>Invited Paper</i> ) — <i>H. F. Dylla, L. R. Doolittle, J. F. Benesch, CEBAF</i> .....	748
Perpendicular Biased Ferrite-Tuned Cavities ( <i>Invited Paper</i> ) — <i>R. L. Poirier, TRIUMF</i> .....	753
SRF Cavities for Future Applications ( <i>Invited Paper</i> ) — <i>D. Proch, DESY</i> .....	758
Preparation and Testing of a Superconducting Cavity for CESR-B — <i>D. Moffat, P. Barnes, J. Kirchgessner, H. Padamsee, J. Sears, Cornell</i> .....	763
High Power Operation of Single-Cell 352-MHz Cavity for the Advanced Photon Source (APS) — <i>J. F. Bridges, Y. W. Kang, R. L. Kustom, K. Primdahl, ANL</i> .....	766

### Poster presentations:

Development of Crab Cavity for CESR-B — <i>K. Akai, J. Kirchgessner, D. Moffat, H. Padamsee, J. Sears, M. Tigner, Cornell</i> .....	769
A New 3-D Electromagnetic Solver for the Design of Arbitrarily Shaped Accelerating Cavities — <i>P. Arcioni, M. Bressan, L. Perregrini, U. Pavia</i> .....	772
Design Study for the ELFA Linac — <i>W. A. Barletta, LBL; G. Bellomo, INFN/ U. Milan; G. Gemme, R. Parodi, INFN Genova; V. Stagno, V. Variale, INFN Bari</i> .....	775
The RF Cavity for DAFNE — <i>S. Bartalucci, R. Boni, A. Gallo, L. Palumbo, R. Parodi, M. Serio, B. Spataro, INFN-LNF</i> .....	778
Mechanical Results of the CEBAF Cavity Series Production — <i>J. Mammoser, J. F. Benesch, CEBAF</i> .....	781
Fabrication of Complex Mechanical Components — <i>Y. Beroud, SICN</i> .....	784
Measurements of Higher Order Modes in 3rd Harmonic RF Cavity at Fermilab — <i>C. M. Bhat, FNAL</i> .....	787
POISSON/SUPERFISH on PC Compatibles — <i>J. H. Billen, L. M. Young, LANL</i> .....	790
Radio Frequency Measurement and Analysis Codes — <i>J. H. Billen, LANL</i> .....	793
Progress on RF Superconductivity at Saclay — <i>Groupe d'Etudes des Cavités Supraconductrices, CE Saclay and Institut de Physique Nucléaire, Orsay</i> .....	796
A New Surface Treatment for Niobium Superconducting Cavities — <i>B. Bonin, C. Henriot, C. Antoine, B. Coadou, F. Koechlin, J. P. Rodriguez, E. Lemaitre, P. Greiner, CE Saclay</i> .....	798
Using the Panofsky-Wenzel Theorem in the Analysis of Radio-Frequency Deflectors — <i>M. J. Browman, LANL</i> .....	800
The Effects of Temperature and RF Power Level on the Tuning of the Water-Cooled SSC Low-Energy Booster Cavity — <i>C. Friedrichs, LANL; G. Hulsey, SSSL</i> .....	803
Superconducting Cavities for the LEP Energy Upgrade — <i>G. Cavallari, C. Benvenuti, P. Bernard, D. Bloess, E. Chiaveri, F. Genesis, E. Haebel, N. Hilleret, J. Tuckmantel, W. Weingarten, CERN</i> .....	806
TESLA Input Coupler Development — <i>M. Champion, D. Peterson, T. Peterson, C. Reid, M. Ruschman, FNAL</i> ....	809

*Proceedings of the 1993 Particle Accelerator Conference*

Computer Simulation and Cold Model Testing of CCL Cavities — C. R. Chang, C. G. Yao, D. A. Swenson, L. W. Funk, SSCL .....	812
Drive Linac for the Argonne Wakefield Accelerator — E. Chojnacki, R. Konecny, M. Rosing, J. Simpson, ANL .....	815
Choice of the RF Cavity for the SSC Collider — W. Chou, SSCL .....	818
High Field Conditioning of Cryogenic RF Cavities — M. Cole, T. Debiak, C. Lom, W. Shephard, J. Sredniawski, Grumman .....	821
Status of the SSC LEB RF Cavity — P. Coleman, F. Brandeberry, C. Friedrichs, Y. Goren, T. Grimm, G. Hulsey, S. Kwiatkowski, A. Propp, L. Taylor, L. Walling, SSCL; J. Averbukh, M. Karliner, V. Petrov, S. Yakovlev, BINP .....	824
RF Commissioning of the Superconducting Super Collider Radio Frequency Quadrupole Accelerator — R. I. Cutler, G. Arbique, J. Grippe, S. Marsden, O. Marrufo, R. Rodriguez, SSCL .....	827
Design of a Tuner and Adjustable RF Coupler for a CW 2856 MHz RF Cavity — M. S. de Jong, F. P. Adams, R. J. Burton, R. M. Hutcheon, T. Tran-Ngoc, AECL, Chalk River; A. Zolfaghari, P. T. Demos, MIT-Bates .....	829
A 2856 MHz RF Cavity for the MIT-Bates South Hall Ring — M. S. de Jong, F. P. Adams, R. J. Burton, R. M. Hutcheon, T. Tran-Ngoc, AECL, Chalk River; A. Zolfaghari, P. T. Demos, MIT-Bates .....	832
Cavity RF Mode Analysis Using a Boundary-Integral Method — M. S. de Jong, F. P. Adams, AECL, Chalk River ..	835
Design Considerations for High-Current Superconducting RFQ's — J. R. Delayen, C. L. Bohn, W. L. Kennedy, L. Sagalovsky, ANL .....	838
Commissioning of the CEBAF Cryomodules — M. Drury, T. Lee, J. Marshall, J. Preble, Q. Saulter, W. Schneider, M. Spata, M. Wiseman, CEBAF .....	841
Design and Fabrication of High Gradient Accelerating Structure Prototype at 36.5 GHz — V. A. Dvornikov, I. A. Kuzmin, MEPI Russia.....	844
The SSC RFQ-DTL Matching Section Buncher Cavities — T. Enegren, C. M. Combs, Y. Goren, M. D. Hayworth, A. D. Ringwall, D. A. Swenson, SSCL.....	846
Bulk Niobium Low-, Medium- and High- $\beta$ Superconducting Quarter Wave Resonators for the ALPI Postaccelerator — A. Facco, J. S. Sokolowski, INFN Legnaro; I. Ben-Zvi, BNL; E. Chiaveri, CERN; B. V. Elkonin, Weizmann Inst. ....	849
A Numerical Method for Determining the Coupling Strengths and Resonant Frequencies of a Nonperiodic Coupled Cavity Chain — M. Foley, T. Jurgens, FNAL .....	852
Thermal Study of HOM Couplers for Superconducting RF Cavities — M. Fouaidy, T. Junquera, IPN Orsay; S. Chel, A. Mosnier, Saclay .....	855
Very Wide Range and Short Accelerating Cavity for MIMAS — C. Fougeron, P. Ausset, D. de Menezes, J. Peyromaure, G. Charruau, LNS-CE Saclay .....	858
Fundamental Mode Detuned Travelling Wave Accelerating Structure — J. Gao, LAL Orsay .....	862
Demi-Disc Travelling Wave Accelerating Structure — J. Gao, LAL Orsay .....	865
Analytical Formulae for the Coupling Coefficient $\beta$ Between a Waveguide and a Travelling Wave Structure — J. Gao, LAL Orsay .....	868
Automated Bead-Positioning System for Measuring Impedances of RF Cavity Modes — D. A. Goldberg, R. A. Rimmer, LBL .....	871
Measurements of Higher-Order Mode Damping in the PEP-II Low-Power Test Cavity — R. A. Rimmer, D. A. Goldberg, LBL .....	874
Nonlinear Effects in Ferrite Tuned Cavities — Y. Goren, N. K. Mahale, L. Walling, T. Enegren, G. Hulsey, SSCL; V. P. Yakovlev, V. M. Petrov, BINP .....	877
Eddy Current Analysis for the SSC Low Energy Booster Cavity — Y. Goren, L. Walling, F. Brandeberry, N. Spayd, SSCL .....	880
Voltage Counter-Phasing in the SSC Low Energy Booster — Y. Goren, SSCL; T. F. Wang, LANL .....	883
An Update on High Peak Power (HPP) RF Processing of 3 GHz Nine-Cell Niobium Accelerator Cavities — P. Barnes, J. Kirchgessner, D. Moffat, H. Padamsee, J. Sears, Cornell; C. Crawford, FNAL; J. Graber, P. Schmäuser, DESY .....	886
Microscopic Investigation of RF Surfaces of 3 GHz Niobium Accelerator Cavities Following RF Processing — P. Barnes, T. Flynn, J. Kirchgessner, J. Knobloch, D. Moffat, H. Muller, H. Padamsee, J. Sears, Cornell; J. Graber, DESY .....	889
A World Record Accelerating Gradient in a Niobium Superconducting Accelerator Cavity — P. Barnes, J. Kirchgessner, D. Moffat, H. Padamsee, J. Sears, Cornell; J. Graber, DESY .....	892

*Each volume begins with this five-volume table of contents and ends with the five-volume author index. The chairmen's foreword and a list of conference organizers and staff appear as front matter in Volume 1. A list of conference participants precedes the author index in Volume 5.*

Five-Volume Contents

Characterization of NSLS Accelerating Cavities Using Impedance Measurement Techniques — <i>S. M. Hanna, P. M. Stefan, NSLS-BNL</i> .....	895
In Search of Trapped Modes in the Single-Cell Cavity Prototype for CESR-B — <i>W. Hartung, Cornell; E. Haebel, CERN</i> .....	898
Envelope Equations for Transients in Linear Chains of Resonators — <i>H. Henke, M. Filtz, TU Berlin</i> .....	901
A Broad-Band Side Coupled mm-Wave Accelerating Structure for Electrons — <i>H. Henke, W. Bruns, TU Berlin</i> .....	904
Accelerator Structure Development for NLC — <i>H. A. Hoag, H. Deruyter, C. Pearson, R. D. Ruth, J. W. Wang, SLAC; J. Schaefer, Texas Inst.</i> .....	907
HOM Damping with Coaxial Dampers in a Pillbox Cavity Without the Fundamental Mode Frequency Rejection Filter — <i>Y. W. Kang, R. L. Kustom, J. F. Bridges, ANL</i> .....	910
Reduced Length Design of 9.8 MHz RF Accelerating Cavity for the Positron Accumulator Ring (PAR) of the Advanced Photon Source (APS) — <i>Y. W. Kang, J. F. Bridges, R. L. Kustom, ANL</i> .....	913
Higher Order Mode Damping System in the UNK RF Cavity — <i>V. Katalev, V. Kudryavtsev, I. Sulygin, IHEP</i> .....	916
Status and Outlook for High Power Processing of 1.3 GHz TESLA Multicell Cavities — <i>J. Kirchgessner, P. Barnes, J. Graber, D. Metzger, D. Moffat, H. Muller, H. Padamsee, J. Sears, M. Tigner, Cornell; L. Bartelson, M. Champion, C. Crawford, H. Edwards, K. Koepke, M. Kuchnir, H. Pfeffer, FNAL; A. Matheisen, M. Pekeler, P. Schmüser, DESY</i> .....	918
20 MV/m Accelerating Gradient with Heat Treatment of a Six Cell, 1.5 GHz Cavity for TESLA — <i>J. Kirchgessner, P. Barnes, W. Hartung, D. Moffat, H. Padamsee, D. Rubin, J. Sears, M. Tigner, Cornell; M. Hiller, Babcock &amp; Wilcox; D. Saraniti, SLAC; Q. S. Shu, SSCL</i> .....	921
A New 50 MHz RF Cavity for Aladdin — <i>K. J. Kleman, SRC Madison</i> .....	924
Performance of a CEBAF Production Cavity After High-Temperature Heat Treatment — <i>P. Kneisel, M. G. Rao, CEBAF</i> .....	927
Suppression of Higher-Order Modes in an RF Cavity by Resistive Material — <i>T. Koseki, Y. Kamiya, ISSP Tokyo; M. Izawa, KEK</i> .....	930
A Coaxial-Type Accelerating System with Amorphous Material — <i>V. A. Krasnopolsky, MRTI Russia</i> .....	933
Applications and Comparisons of Methods of Computing the S Matrix of 2-Ports — <i>R. M. Jones, K. Ko, S. Tantawi, SLAC; N. Kroll, UCSD/SLAC; D. U. L. Yu, DULY Res.</i> .....	936
Construction of the CEBAF RF Separator — <i>A. Krycuk, J. Fugitt, A. Johnson, R. Kazimi, L. Turlington, CEBAF</i> .....	939
RF Cavity for the Medium Energy Booster for SSCL — <i>S. Kwiatkowski, J. Curbow, T. Enegren, A. Propp, SSCL; V. P. Yakovlev, V. M. Petrov, Budker Inst.</i> .....	941
New Achievements in RF Cavity Manufacturing — <i>G. Lippmann, K. Pimiskern, H. Kaiser, Dornier GmbH</i> .....	944
Analysis of Mechanical Fabrication Experience with CEBAF's Production SRF Cavities — <i>J. Mammosser, P. Kneisel, J. F. Benesch, CEBAF</i> .....	947
Microphonic Analysis of Cryo-Module Design — <i>A. Marziali, H. A. Schwettman, Stanford U.</i> .....	950
The Design of a Pill-Box Cavity with Waveguide HOM Suppressors — <i>A. Massarotti, G. D'Auria, A. Fabris, C. Pasotti, C. Rossi, M. Svandrlík, Sinc. Trieste</i> .....	953
Power Conditioning of the RF Cavities for ELETTRA — <i>A. Massarotti, G. D'Auria, A. Fabris, C. Pasotti, C. Rossi, M. Svandrlík, Sinc. Trieste</i> .....	956
High Power Test of a SLED System with Dual Side-Wall Coupling Irises for Linear Colliders — <i>H. Matsumoto, H. Baba, A. Miura, S. Yamaguchi, KEK</i> .....	959
Performance Tests of a Ferrite-Loaded Cavity Under Operation Conditions — <i>S. Papureanu, Ch. Hamm, A. Schnase, H. Meuth, Jülich</i> .....	962
CLIC Transfer Structure (CTS) Simulations Using "MAFIA" — <i>A. Millich, CERN</i> .....	965
Magnetron Sputtering Configuration for Coating 1.3 GHz Cavities with a Nb Film — <i>M. Minestrini, M. Ferrario, S. Kulinski, INFN-LNF; S. Tazzari, INFN Roma</i> .....	968
Accelerator Structure for Low-Energy Electron Beam — <i>A. V. Mishin, MEPI Moscow</i> .....	971
Higher Order Mode Dampers for the KAON Booster Cavity — <i>A. K. Mitra, TRIUMF</i> .....	974
Design and Fabrication of a Ferrite-Lined HOM Load for CESR-B — <i>D. Moffat, P. Barnes, J. Kirchgessner, H. Padamsee, J. Sears, M. Tigner, A. Tribendis, V. Veshcherevich, Cornell</i> .....	977
High-Beta Linac Accelerating Structure — <i>V. G. Andreev, G. I. Batskikh, B. I. Bondarev, B. P. Murin, MRTI</i> .....	980
Design of a 90° Overmoded Waveguide Bend — <i>C. Nantista, UCLA; N. M. Kroll, UCSD/SLAC; E. M. Nelson, SLAC</i> .....	983
Numerical Simulation of Coupler Cavities for Linacs — <i>C.-K. Ng, H. Deruyter, K. Ko, SLAC</i> .....	986

Volume 1: 1-747  
 Volume 2: 748-1640  
 Volume 3: 1641-2545  
 Volume 4: 2546-3218  
 Volume 5: 3219-3933

*Proceedings of the 1993 Particle Accelerator Conference*

TESLA Vertical Test Dewar Cryogenic and Mechanical Design — <i>T. H. Nicol, D. E. Arnold, M.S. Champion, FNAL</i> .....	989
Update of the TRISTAN Superconducting RF System — <i>S. Noguchi, K. Akai, E. Kako, K. Kubo, T. Shishido, KEK</i> .....	992
Cryostat for a Beam Test with the CESR-B Cavity — <i>E. Nordberg, P. Barnes, R. Ehrlich, J. Kirchgessner, D. Metzger, D. Moffat, H. Muller, H. Padamsee, J. Sears, K. She, M. Tigner, Cornell; W. Fox, LANL; H. Heinrichs, U. Wuppertal</i> .....	995
A Statistical Model for Field Emission in Superconducting Cavities — <i>H. Padamsee, K. Green, W. Jost, B. Wright, Cornell</i> .....	998
Design and Test of Prototype Cavities for the ELFA Linac — <i>G. Bellomo, R. Parodi, G. Gemme, P. Fabbriatore, R. Musenich, B. Zhang, INFN</i> .....	1001
Frequency Domain Determination of the Waveguide Loaded <i>Q</i> for the SSCL Drift Tube Linac — <i>J. Petillo, W. Krueger, A. Mondelli, SAIC; J. Potter, AccSys Technology</i> .....	1004
Some Operational Characteristics of CEBAF RF Windows at 2 K — <i>H. L. Phillips, C. Reece, T. Powers, V. Nguyen-Tuong, CEBAF</i> .....	1007
Photoemission Phenomena on CEBAF RF Windows at Cryogenic Temperatures — <i>T. Powers, P. Kneisel, M. Vaidya, CEBAF</i> .....	1010
Fabrication of the APS Storage Ring Radio Frequency Accelerating Cavities — <i>K. Primdahl, J. Bridges, F. Depaola, R. Kustom, ANL; D. Snee, FNAL</i> .....	1013
Performance of Production SRF Cavities for CEBAF — <i>C. Reece, J. Benesch, P. Kneisel, P. Kushnick, J. Mammoser, T. Powers, CEBAF</i> .....	1016
A New 15 MHz, 4 MV/m RF-Deflector for the Munich Heavy Ion Recoil Spectrometer (MRS)— <i>K. Rudolph, P. Jaenker, U. Munich</i> .....	1019
Superconducting Multicell Cavity Development Program at Los Alamos — <i>B. Rusnak, G. Spalek, E. Gray, J. N. DiMarco, R. DeHaven, J. Novak, P. Walstrom, J. Zumbro, H. A. Thiessen, J. Langenbrunner, LANL</i> ..	1021
L-Band Superconducting Cavities at KEK for TESLA — <i>K. Saito, S. Noguchi, E. Kako, M. Ono, T. Shishido, T. Tajima, M. Matsuoka, H. Miwa, T. Suzuki, H. Umezawa, KEK</i> .....	1024
Design of a HOM Damped Cavity for the ATF Damping Ring — <i>S. Sakanaka, K. Kubo, T. Higo, KEK</i> .....	1027
Measurement of Microwave Properties of X-Band Accelerating Structure Under Pulsed High-Power Operation at Liquid Nitrogen Temperature — <i>A. J. Saversky, I. S. Shchedrin, MEPI Moscow</i> .....	1030
RF Systems Engineering for the SSC Collider Rings — <i>G. Schaffer, P. D. Coleman, R. E. Mustaine, J. D. Wallace, X. Q. Wang, Y. Zhao, J. D. Rogers, SSCL</i> .....	1033
Impedance Calculations for a Coaxial Liner — <i>M. Filtz, T. Scholz, TU Berlin</i> .....	1036
Design of a High-Power Test Model of the PEP-II RF Cavity — <i>H. D. Schwarz, R. A. Bell, J. A. Hodgson, J. G. Judkins, K. Ko, N. Kroll, C. K. Ng, R. P. Pendleton, K. Skarpaas, SLAC; G. Lambertson, R. Rimmer, LBL; M. S. deJong, T. Tran-Ngoc, F. P. Adams, M. G. Lipsett, W. Mellors, AECL</i> .....	1039
Construction of a Superconducting RFQ Structure — <i>K. W. Shepard, W. L. Kennedy, ANL; K. R. Crandall, AccSys Technology</i> .....	1042
Niobium Coaxial Quarter-Wave Cavities for the New Delhi Booster Linac — <i>K. W. Shepard, ANL; A. Roy, P. N. Potukuchi, Nuc. Science Ctr., New Delhi</i> .....	1045
Design of High Power Model of Damped Linear Accelerating Structure Using Choke Mode Cavity — <i>T. Shintake, KEK</i> .....	1048
Suppression of Longitudinal Coupled-Bunch Instability Using Energy Storage Cavity in B-Factory RF System — <i>T. Shintake, KEK</i> .....	1051
A Two-Gap Booster Synchrotron RF Cavity — <i>W. R. Smythe, D. C. Van Westrum, U. Colorado</i> .....	1054
HOM (Higher-Order Mode) Test of the Storage Ring Single-Cell Cavity with a 20-MeV <i>e</i> <sup>-</sup> Beam for the Advanced Photon Source (APS) — <i>J. Song, Y. W. Kang, R. Kustom, ANL</i> .....	1057
Performance of a 1500 MHz Niobium Cavity with 2K-LHe Channel Cooling — <i>J. Susta, P. Kneisel, M. Wiseman, CEBAF</i> .....	1060
Large Scale Production at Ansaldo of 352 MHz Niobium Coated LEP-CERN Cavities: Development Activities and First Results — <i>A. Bixio, P. Gagliardi, M. Marin, S. Moz, W. Scitutto, F. Terzi, G. Zoni, Ansaldo</i> .....	1063
RF Hardware Development Work for the CLIC Drive Beam — <i>G. Carron, L. Thorndahl, CERN</i> .....	1066
Accelerating Frequency Shift Minimization — <i>A. V. Tiunov, V. I. Shvedunov, INP Moscow</i> .....	1069

*Each volume begins with this five-volume table of contents and ends with the five-volume author index. The chairman's foreword and a list of conference organizers and staff appear as front matter in Volume 1. A list of conference participants precedes the author index in Volume 5.*



*Proceedings of the 1993 Particle Accelerator Conference*

Test Results of the AGS Booster Low Frequency RF System — R. T. Sanders, P. Cameron, R. Damm, A. Dunbar, M. Goldman, D. Kasha, A. Mc Nerney, M. Meth, A. Ratti, R. Spitz, BNL .....	1166
Design and Test Results of a 600-kW Tetrode Amplifier for the Superconducting Super Collider — D. E. Rees, D. L. Brittain, LANL ; J. M. Grippe, O. Maruffo, SSCL .....	1169
Conceptual Design of the 26.7. MHz RF System for RHIC — J. Rose, D. P. Deng, R. McKenzie-Wilson, W. Pirkl, A. Ratti, BNL .....	1172
Operation of a High-Power CW Klystron with the RFQ1 Facility — J. Y. Sheikh, A. D. Davidson, G. E. McMichael, L. W. Shankland, B. H. Smith, AECL, Chalk River .....	1175
Design and Results of a 1.3 MW CW Klystron for LEP — E.-G. Schweppe, R. Bachmor, E. Demmel, Philips RHW .....	1178
Interleaved Wide and Narrow Pulses for the KAON Factory 1 MHz Chopper — G. D. Wait, M. J. Barnes, D. Bishop, G. Waters, TRIUMF .....	1181
Considerations Regarding the Efficiency of High Power RF Sources for Particle Accelerators — G. Clerc, C. Bearz M. Bres, G. Faillon, Ph. Guidee, Thomson Tubes Elect. ....	1184
Initial Commissioning of High Power, Long Pulse Klystrons for SSC Injector Linacs — P. Collet, J. C. Terrien, Ph. Guidee, Thomson Tubes Elect. ....	1187
Simulation of Traveling-Wave Output Structures for High Power rf Tubes — K. R. Eppley, SLAC .....	1190
Upgrade of an RF Source of the Linac for the B-Factory Project — S. Fukuda, S. Anami, Y. Saito, S. Michizono, K. Nakao, I. Sato, KEK .....	1193
High-Power RF Pulse Compression with SLED-II at SLAC — C. Nantista, UCLA; Z. D. Farkas, T. L. Lavine, A. Menegat, R. D. Ruth, S. G. Tantawi, A. E. Vlieks, SLAC; N. M. Kroll, UCSD .....	1196
Rigid-Beam Model of a High-Efficiency Magnicon — D. E. Rees, P. J. Tallerico, LANL; S. J. Humphries, Jr., UNM .....	1199
High Power Operation Results of the X-Band SLED System — S. Tokumoto, H. Mizuno, KEK; O. Azuma, IHI Japan .....	1202
Automated Testing of a High-Power RF Microwave Tube — A. Young, D. E. Rees, A. Vergamini, LANL .....	1205
Two-Klystron Binary Pulse Compression at SLAC — Z. D. Farkas, T. L. Lavine, A. Menegat, A. E. Vlieks, J. W. Wang, P. B. Wilson, SLAC .....	1208
New Compact Mode Converters for SLAC RF Pulse Power Compression System — G. Luo, SRRRC Taiwan .....	1211
Performance of Litton 805 MHz, 12 MW Klystrons — Q. Kerns, M. B. Popovic, C. Kerns, A. Moretti, FNAL .....	1214
Higher-Order Modes in the APS Storage Ring Waveguides — S.O. Brauer, R. L. Kustom, ANL .....	1217
The Design and Production of the Higher-Order-Mode Loads for CEBAF — I. E. Campisi, L. K. Summers, B. H. Branson, A. M. Johnson, A. Betto, CEBAF .....	1220
The High Level RF System for Transition Crossing Without RF Focusing in the Main Ring at Fermilab — J. Dey, C. M. Bhat, A. Crawford, D. Wildman, FNAL .....	1223
RF System of the CW Race-Track Microtron-Recuperator for FELs — V. Arbuzov, S. Belomestnykh, A. Bushuyev, M. Fomin, N. Gavrilov, E. Gorniker, A. Kondakov, I. Kuptsov, G. Kurkin, V. Petrov, I. Sedlyarov, V. Veshcherevich, BINR, Russia.....	1226
Three Years of Operational Experience with the LEP RF System — S. Hansen, CERN .....	1229
Measured Performance of the GTA RF Systems — P. M. Denney, S. P. Jachim, LANL .....	1232
Improved RF System for Aladdin — K. J. Kleman, SRC Madison .....	1235
The ALS Storage Ring RF System — B. Taylor, C. C. Lo, K. Baptiste, J. Guigli, J. Julian, LBL .....	1238
The Upgrade Project for the RF System for the Brookhaven AGS — J. M. Brennan, D. J. Ciardullo, T. Hayes, M. Meth, A. J. Mc Nerney, A. Otis, W. Pirkl, R. Sanders, R. Spitz, F. Toldo, A. Zaltsman, BNL .....	1241
Acceptance Test Performance of the Rocketdyne Radio Frequency Power System — M. Curtin, J. Hall, P. Metty, Rocketdyne; E. Gower, J. Manca, K. Whitham, Titan-Beta Corp.....	1244
The LEP II RF Power Generation System — H. Frischholz, CERN .....	1247
Overview and Status of RF Systems for the SSC Linac — J. Mynk, J. Grippe, R. I. Cutler, R. Rodriguez, SSCL .....	1250
Possibilities and Limitations for a Fully Digital RF Signal Synthesis and Control — H. Meuth, A. Schnase, H. Halling, Jülich .....	1253
RF System Analyses for the SSC Collider Rings — J. D. Rogers, P. D. Coleman, G. Schaffer, J. D. Wallace, X. Q. Wang, Y. Zhao, SSCL .....	1256
PEP-II Prototype Klystron — W. R. Fowkes, G. Caryotakis, T. G. Lee, C. Pearson, E. L. Wright, SLAC .....	1259

*Each volume begins with this five-volume table of contents and ends with the five-volume author index. The chairmen's foreword and a list of conference organizers and staff appear as front matter in Volume 1. A list of conference participants precedes the author index in Volume 5.*

Five-Volume Contents

Low Cost Concepts to Reduce the Voltage Ripple of the DC Power Supply — <i>Y. Cheng, K. Liu, SRRC Taiwan</i> .....	1262
Magnet Power Supply System for the ALS Storage Ring and Booster — <i>L. T. Jackson, K. Luchini, I. Lutz, LBL</i> ....	1265
Design and Development of Bipolar Power Supply for APS Storage Ring Correctors — <i>Y. G. Kang, ANL</i> .....	1268
Circuit Description of Unipolar DC-to-DC Converters for APS Storage Ring Quadrupoles and Sextupoles — <i>D. G. McGhee, ANL</i> .....	1271
PLL Subsystem for NSLS Booster Ring Power Supplies — <i>J. Murray, Stony Brook; R. Olsen, J. Dabrowski, BNL</i> .....	1274
Control and Performance of the AGS and AGS Booster Main Magnet Power Supplies — <i>R. K. Reece, R. Casella, B. Culwick, J. Geller, I. Marneris, J. Sandberg, A. Soukas, S. Y. Zhang, BNL</i> .....	1277
Hierarchical Modelling of Line Commutated Power Systems Used in Particle Accelerators Using Saber — <i>J. A. Reimund, SSCL</i> .....	1280
Independent Resonant System Tracking Considerations — <i>K. W. Reiniger, TRIUMF</i> .....	1283
Electrical Characteristics of the SSC Low-Energy Booster Magnet System — <i>A. Young, B. E. Shafer, LANL</i> .....	1285
Analysis and Design of a High-Current, High-Voltage Accurate Power Supply for the APS Storage Ring — <i>M. Fathizadeh, ANL</i> .....	1288
Design of the HIMAC Synchrotron Power Supply — <i>M. Kumada, K. Sato, A. Itano, M. Kanazawa, E. Takada, K. Noda, M. Sudou, T. Kohno, H. Ogawa, S. Yamada, Y. Sato, T. Yamada, A. Kitagawa, J. Yoshizawa, T. Murakami, Y. Hirao, NIRS; S. Matsumoto, Dokkyo U.; H. Sato, T. Sueno, T. Kato, K. Endo, KEK; K. Utino, Tsukuba Tech.; Y. Takada, U. Tsukuba; A. Noda, Kyoto U.; T. Tanabe, S. Watanabe, INS; S. Koseki, H. Kubo, Hitachi</i> .....	1291
A 2-Megawatt Load for Testing High Voltage DC Power Supplies — <i>D. Horan, R. Kustom, M. Ferguson, K. Primdahl, ANL</i> .....	1294
Energy Storage Inductor for the Low Energy Booster Resonant Power Supply System — <i>C. Jach, SSCL; A. Medvedko, S. Petrov, INP Moscow; V. Vinnik, Y. Fishler, UETM Russia</i> .....	1297
A High Power Water Cooled Resistor for the High Voltage Power Supply in the TRIUMF RF System — <i>K. Jensen, G. Blaker, R. Kuramoto, TRIUMF</i> .....	1300
Filament Power Supply Improvement of the TRIUMF RF System — <i>A. K. Mitra, J. J. Lu, TRIUMF</i> .....	1303
Advances in the Development of the Nested High Voltage Generator — <i>R. J. Adler, R. J. Richter-Sand, North Star Res. Corp.</i> .....	1306
High-Power Klystron Modulator Using a Pulse-Forming Line and Magnetic Switch — <i>M. Akemoto, S. Takeda, KEK</i> .....	1309
A Compact Modulator for RF Source Development — <i>J. D. Ivers, G. S. Kerslick, J. A. Nation, L. Schachter, Cornell</i> .....	1312
High Power Pulse Modulator for PLS Linac — <i>S. H. Nam, M. H. Cho, J. S. Oh, S. S. Park, W. Namkung, POSTECH</i> .....	1315
Pulse Modulator Developments in Support of Klystron Testing at SLAC — <i>R. F. Koontz, R. Cassel, J. de Lamare, D. Ficklin, S. Gold, K. Harris, SLAC</i> .....	1318
A Blumlein Type Modulator for 100-MW Class X-Band Klystron — <i>H. Mizuno, KEK; T. Majima, S. Sakamoto, Y. Kobayashi, IHI Japan</i> .....	1321
Noise Reduction Techniques Used on the High Power Klystron Modulators at Argonne National Laboratory — <i>T. J. Russell, ANL</i> .....	1324
Novel Gigawatt Power Modulator for RF Sources — <i>I. Yampolsky, G. Kirkman, N. Reinhardt, J. Hur, B. Jiang, Integrated App. Physics Inc.</i> .....	1327
Optimization of Speed-Up Network Component Values for the 30 $\Omega$ Resistively Terminated Prototype Kicker Magnet — <i>M. J. Barnes, G. D. Wait, TRIUMF</i> .....	1330
Test Results of the 8.35 kA, 15 kV, 10 pps Pulser for the Elettra Kickers — <i>R. Fabris, P. Tosolini, Sinc. Trieste</i> ....	1333
Preliminary Testing of the LEB to MEB Transfer Kicker Modulator Prototype — <i>G. C. Pappas, D. R. Askew, SSCL</i> .....	1336
A Novel Technique for Pulsing Magnet Strings with a Single Switch — <i>R. J. Sachtschale, C. Dickey, P. Morcombe, Duke</i> .....	1339
Linac Pulsed Quad Power Supply — <i>L. Bartelson, FNAL</i> .....	1342
The AGS New Fast Extracted Beam System Orbit Bump Pulser — <i>J. S. Chang, A. V. Soukas, BNL</i> .....	1345
Experimental Investigation of High Voltage Nanosecond Generators of Injection System for SIBERIA-2 Storage Ring — <i>A. Kadnikov, Y. Matveev, BINP</i> .....	1348

Volume 1: 1-747  
 Volume 2: 748-1640  
 Volume 3: 1641-2545  
 Volume 4: 2546-3218  
 Volume 5: 3219-3933

*Proceedings of the 1993 Particle Accelerator Conference*

Design and Preliminary Results for a Fast Bipolar Resonant Discharge Pulser Using SCR Switches for Driving the Injection Bump Magnets at the ALS — <i>G. Stover, L. Reginato, LBL</i> .....	1351
Design and Preliminary Testing of the LEB Extraction Kicker Magnet at the SSC — <i>D. E. Anderson, L. X. Schneider, SSCL</i> .....	1354
Development of a High Quality Kicker Magnet System — <i>J. Dinkel, B. Hanna, C. Jensen, D. Qunell, R. Reilly, FNAL</i> .....	1357
Consequences of Kicker Failure During HEB to Collider Injection and Possible Mitigation — <i>R. Soundranayagam, A. I. Drozhdin, N. V. Mokhov, B. Parker, R. Schailey, F. Wang, SSCL</i> .....	1360
High Efficiency Beam Deflection by Planar Channeling in Bent Silicon Crystals — <i>K. Elsener, M. Clément, N. Doble, L. Gatignon, P. Grafström, CERN; S. P. Møller, E. Uggerhøj, T. Worm, ISA-Aarhus; M. Hage-Ali, P. Siffert, Strasbourg</i> .....	1363
Extraction from the Fermilab Tevatron Using Channeling with a Bent Crystal — <i>G. Jackson, FNAL</i> .....	1366
2 TeV HEB Beam Abort at the SSCL — <i>R. Schailey, J. Bull, T. Clayton, P. Kocur, N. V. Mokhov, SSCL</i> .....	1369
Electrostatic Septa Design and Performance for Injection and Extraction to and from the MIT-Bates South Hall Ring (SHR) — <i>S. Sobczynski, R. Averill, M. Farkhondeh, W. Sapp, C. Sibley, MIT-Bates</i> .....	1372
Injection into the Elettra Storage Ring — <i>D. Tommasini, Sinc. Trieste</i> .....	1375
The Septum Magnets System of Elettra — <i>R. Fabris, F. Daclon, M. Giannini, D. Tommasini, P. Tosolini, Sinc. Trieste</i> .....	1378
High Voltage Vacuum Insulation in Crossed Magnetic and Electric Fields — <i>W. T. Diamond, AECL</i> .....	1381
Injection System for the SIBERIA-2 Storage Ring — <i>G. Erg, A. Evstigneev, V. Korchuganov, G. Kulipanov, E. Levichev, Yu. Matveev, A. Philipchenko, L. Schegolev, V. Ushakov, BINP</i> .....	1384
Fixed Target to Collider Changeover at A0 — <i>K. J. Weber, FNAL</i> .....	1387
Surface Resistivity Tailoring of Ceramic Accelerator Components — <i>S. Anders, A. Anders, I. Brown, LBL</i> .....	1390
Compensation of Field Shaking Due to the Magnetic Vibration — <i>Y. Cheng, C. Hwang, SRRC Taiwan</i> .....	1393
Superconducting Cavity Tuner Performance at CEBAF — <i>J. Marshall, J. Preble, W. Schneider, CEBAF</i> .....	1396
Test Results and Design Considerations for a 500 MHz, 500 kW Vacuum Window for CESR-B — <i>D. Metzger, P. Barnes, A. Helser, J. Kirchgessner, H. Padamsee, Cornell</i> .....	1399
An Experimental and Analytical Study of a Buoyancy Driven Cooling System for a Particle Accelerator — <i>B. Campbell, R. Ranganathan, SSCL</i> .....	1402
Collider Bypass Diode Thermal Simulations and Measurements for the SSCL — <i>C. Rostamzadeh, G. Tool, SSCL</i> ..	1405
Frequency-Feedback Tuning for Single-Cell Cavity Under RF Heating — <i>J. D. Stepp, J. F. Bridges, ANL</i> .....	1408
A Device of Amplitude and Phase Stabilization for the FEL Injector in the L-Band — <i>Q. Zhang, X. Wang, Y. Sun, S. Bu, M. Zhang, G. Su, CIAE China</i> .....	1411
A Jet Neutralizer Concept — <i>T. E. Horton, U. Mississippi</i> .....	1413
Modulator Upgrade of the KEK 2.5-GeV Linac — <i>T. Shidara, H. Honma, S. Anami, I. Sato, KEK</i> .....	1416
NSLS X-Ray Ring RF System Upgrade — <i>M. G. Thomas, R. Biscardi, W. Broome, S. Buda, R. D'Alsace, S. Hanna, J. Keane, P. Mortazavi, G. Ramirez, J. M. Wang, NSLS-BNL</i> .....	1419
A Wide Tuning Range Rf Cavity with External Ferrite Biasing — <i>X. Pei, BNL; S. Anderson, D. Jenner, D. McCammon, T. Sloan, IUCF</i> .....	1421
Longitudinal Rf Matching During AGS-RHIC Beam Transfer — <i>X. Pei, BNL</i> .....	1424
<b>Photon Sources</b> <i>Chair: J. Galayda</i>	
Commissioning and Performance of the ESRF ( <i>Invited Paper</i> ) — <i>J. L. Laclare and the Project Team, ESRF</i> .....	1427
Commissioning and Performance of the Advanced Light Source ( <i>Invited Paper</i> ) — <i>A. Jackson, LBL</i> .....	1432
Status of BESSY II, a High-Brilliance Synchrotron Radiation Source in the VUV to XUV Range ( <i>Invited Paper</i> ) — <i>D. Krämer, BESSY</i> .....	1436
A Superconducting Short Period Undulator for a Harmonic Generation FEL Experiment — <i>G. Ingold, L. Solomon, I. Ben-Zvi, S. Krinsky, D. Li, D. Lynch, J. Sheehan, M. Woodle, X. Z. Qiu, L. H. Yu, X. Zhang, NSLS-BNL; W. Sampson, M. Gardner, K. Robins, BNL; I. Lehrman, R. Heuer, J. Sheehan, D. Weissenburger, Grumman Corp.</i> .....	1439
UV-VUV FEL Program at Duke Storage Ring with OK-4 Optical Klystron — <i>V. N. Litvinenko, J. M. J. Madey, Duke; N. A. Vinokurov, BINP-Novosibirsk</i> .....	1442

*Each volume begins with this five-volume table of contents and ends with the five-volume author index. The chairmen's foreword and a list of conference organizers and staff appear as front matter in Volume 1. A list of conference participants precedes the author index in Volume 5.*

## Five-Volume Contents

A 2-4 nm Linac Coherent Light Source (LCLS) Using the SLAC Linac — <i>H. Winick, K. Bane, R. Boyce, G. Loew, P. Morton, H.-D. Nuhn, J. Paterson, P. Pianetta, T. Raubenheimer, J. Seeman, R. Tatchyn, V. Vylet, SLAC; C. Pellegrini, J. Rosenzweig, G. Travish, UCLA; D. Prosnitz, T. Scharlemann, LLNL; K. Halbach, K.-J. Kim, M. Xie, LBL</i>	1445
The Vanderbilt University Compton Scattering X-Ray Experiment — <i>P. A. Tompkins, C. A. Brau, W. W. Dong, J. W. Waters, Vanderbilt U.; F. E. Carroll, D. R. Pickens, R. R. Price, VUMC</i>	1448
Observations of Effects of Ion Accumulation in the Maxwell Model 1.2-400 Synchrotron Light Source — <i>R. P. Johnson (now at CEBAF), D. Y. Wang, Maxwell Labs; H. Bluem, LSU</i>	1451
A Progress Report on the Laboratório Nacional de Luz Síncrotron (Brazil) — <i>A. R. D. Rodrigues, C. E. T. Gonçalves da Silva, D. Wisnivesky, LNLS Brazil</i>	1454
An Overview of the PLS Project — <i>T. Lee, POSTECH</i>	1457
Present Status of SRRC — <i>E. Yen, SRRC</i>	1460
<i>Poster presentations:</i>	
SOLEIL, a New Synchrotron Radiation Source for LURE — <i>M. P. Level, P. Brunelle, P. Marin, A. Nadji, M. Sommer, H. Zyngier, LURE; J. Faure, J. Payet, A. Tkatchenko, LNS</i>	1465
Conceptual Design of a Compact Electron Storage Ring System Dedicated to Coronary Angiography — <i>Y. Oku, K. Aizawa, S. Nakagawa, Kawasaki Heavy Ind.; M. Ando, K. Hyodo, S. Kamada, PF, KEK; H. Shiwaku, JAERI</i>	1468
Report on DELTA, One Year Before Routine Operation — <i>N. Marquardt, U. Dortmund</i>	1471
Lattice Design for the 1.7-GeV Light Source BESSY II — <i>E. Jaeschke, D. Krämer, B. Kuske, P. Kuske, M. Scheer, E. Wehreter, G. Wüstefeld, BESSY</i>	1474
The Synchrotron Light Source ROSY — <i>D. Einfeld, H. Büttig, S. Dienel, W. Gläser, H. Guratzsch, B. Hartmann, D. Janssen, H. Krug, J. Linnemann, W. Matz, W. Neumann, W. Oehme, D. Pröhl, R. Schlenk, H. Tyrroff, Res. Ctr. Rossendorf; Th. Goetz, M. Picard, U. Bonn; J. B. Murphy, BNL; M. Plesko, D. Tomassini, Sincrotrone Trieste; R. Rossmannith, CEBAF</i>	1477
A Source of Synchrotron Radiation for Research and Technology Applications — <i>E. Bulyak, V. Chechetenko, A. Dovbnya, S. Efimov, A. Gevchuk, P. Gladkikh, I. Karnaukhov, V. Kozin, S. Kononenko, V. Likhachev, V. Lyashchenko, V. Markov, N. Mocheshnikov, V. Moskalenko, A. Mytsykov, Yu. Popkov, A. Shcherbakov, M. Strelkov, A. Tarasenko, Yu. Telegin, V. Trotsenko, A. Zelinsky, Kharkov Inst.; V. Bar'yakhtar, V. Molodkin, V. Nemoshkalenko, A. Shpak, Metallophysics Inst.</i>	1480
Optimum Steering of Photon Beam Lines in SPEAR — <i>W. J. Corbett, B. Fong, M. Lee, V. Ziemann, SLAC</i>	1483
Establishment of a Tolerance Budget for the Advanced Photon Source Storage Ring — <i>H. Bizek, E. Crosbie, E. Lessner, L. Teng, ANL</i>	1485
Study of Transverse Coupled Bunch Instabilities by Using Non-Linear Taylor Maps for the Advanced Light Source (ALS) — <i>M. Meddahi, J. Bengtsson, LBL</i>	1488
Plans to Increase Source Brightness of NSLS X-Ray Ring — <i>J. Safranek, S. Krinsky, NSLS-BNL</i>	1491
A Design Concept for the Inclusion of Superconducting Dipoles Within a Synchrotron Light Source Lattice — <i>M. W. Poole, J. A. Clarke, S. L. Smith, V. P. Suller, L. A. Welbourne, SERC Daresbury; N. A. Mezentsev, BINP Russia</i>	1494
A Conceptual Design and Thermal Analysis of High Heat Load Crotch Absorber — <i>I. C. Sheng, S. Sharma, E. Rotela, J. Howell, ANL</i>	1497
Thermal Analysis of the Beam Missteering in APS Storage Ring — <i>I. C. Sheng, J. Howell, S. Sharma, ANL</i>	1500
Dynamic Response Analysis of the LBL Advanced Light Source Synchrotron Radiation Storage Ring — <i>K. K. Leung, SSCL</i>	1503
The Study of Seismic Vibration of SR Source "Zelenograd" — <i>S. Kuznetsov, Kurchatov Inst.; E. Levichev, BINP</i>	1506
Measurement of the Orbit Parameters at SOR-RING — <i>H. Kudo, K. Shinoe, H. Takaki, T. Koseki, H. Ohkuma, Y. Kamiya, ISSP Tokyo</i>	1509
Challenging Issues During ESRF Storage Ring Commissioning — <i>A. Roper, ESRF</i>	1512
Upgrading to 500 mA of the Stored Beam Current at SORTEC 1-GeV Source Facility — <i>M. Kodaira, N. Awaji, T. Kishimoto, K. Mukugi, M. Watanabe, SORTEC; T. Iida, H. Tsuchidate, Mitsubishi Corp.</i>	1515
Performance of Upgraded SORTEC 1-GeV 500-mA SR Source Facility — <i>T. Kishimoto, M. Kodaira, N. Awaji, K. Mukugi, M. Araki, SORTEC; Y. Kijima, M. Haraguchi, Mitsubishi Corp.</i>	1518

Volume 1: 1-747  
 Volume 2: 748-1640  
 Volume 3: 1641-2545  
 Volume 4: 2546-3218  
 Volume 5: 3219-3933

**Proceedings of the 1993 Particle Accelerator Conference**

Design of Test Linac for Free Electron Laser — <i>H. Kang, I. Ko, M. Cho, W. Namkung, POSTECH</i> .....	1521
The Revised ELFA Project — <i>E. Acerbi, F. Alessandria, G. Baccaglioni, G. Bellomo, C. Birattari, R. Bonifacio, I. Boscolo, A. Bosotti, F. Broggi, R. Corsini, L. De Salvo, D. Giove, C. Maroli, P. Pierini, N. Piovela, M. Pullia, G. Rivoltella, L. Rossi, G. Varisco, INFN/ U. Milan; P. Arcioni, M. Bressan, G. Conciauro, INFN Pavia; W. A. Barletta, LBL; G. Gemme, R. Parodi, INFN Genova; V. Stagno, V. Variale, INFN Bari</i> .....	1524
Design and Construction of a Compact Infra Red Free Electron Laser CIRFEL — <i>J. Krishnaswamy, I. S. Lehrman, J. Sheehan, R. L. Heuer, M. F. Reusch, R. Hartley, Grumman Aerospace Corp.</i> .....	1527
Coherence and Linewidth Studies of a 4-nm High Power FEL — <i>W. M. Fawley, A. M. Sessler, LBL; E. T. Scharlemann, LLNL</i> .....	1530
Performance Characteristics, Optimization, and Error Tolerances of a 4 nm FEL Based on the SLAC Linac — <i>K.-J. Kim, M. Xie, LBL; E. T. Scharlemann, LLNL; C. Pellegrini, G. Travish, UCLA</i> .....	1533
X-Ray Beam Lines and Beam Line Components for the SLAC Linac Coherent Light Source (LCLS) — <i>R. Tatchyn, P. Pianetta, SLAC</i> .....	1536
Photon Pulse Filtering and Modulation Based on the Extreme Temporal Compression and Correlated Energy Spread of the Electron Bunches in the SLAC Linac Coherent Light Source (LCLS) — <i>R. Tatchyn, SLAC</i> .....	1539
Infrared (IR) vs. X-Ray Power Generation in the SLAC Linac Coherent Light Source (LCLS) — <i>R. Tatchyn, SLAC</i> .....	1542
Saturation of a High Gain FEL — <i>R. L. Gluckstern, Maryland; S. Krinsky, BNL; H. Okamoto, Kyoto U.</i> .....	1545
Numerical Studies of Strong Focusing in Planar Undulators — <i>G. Travish, J. Rosenzweig, UCLA</i> .....	1548
Generation of High Power 140 GHz Microwaves with an FEL for the MTX Experiment — <i>S. L. Allen, C. J. Lasnier, B. Felker, M. Fenstermacher, S. W. Ferguson, S. Fields, E. B. Hooper, S. Hulsey, M. Makowski, J. Moller, W. Meyer, D. Petersen, E. T. Scharlemann, B. Stallard, R. Wood, LLNL</i> .....	1551
Burst Mode FEL with the ETA-III Induction Linac — <i>C. J. Lasnier, S. L. Allen, B. Felker, M. E. Fenstermacher, S. W. Ferguson, S. D. Hulsey, E. B. Hooper, M. C. Jackson, M. A. Makowski, W. H. Meyer, J. M. Moller, D. E. Petersen, S. E. Sampayan, B. W. Stallard, W. F. Fields, LLNL; K. Oasa, JAERI</i> .....	1554
Design and Experiment of SG-1 FEL — <i>Z. Hui, IEE China</i> .....	1557
Electron Beam Quality Limitations and Beam Conditioning in Free Electron Lasers — <i>P. Sprangle, G. Joyce, NRL; B. Hafizi, Icarus Res.; P. Serafim, Northeastern U.</i> .....	1560
An Optical Approach to Emittance Compensation in FELs — <i>G. R. Neil, H. Liu, CEBAF</i> .....	1563
Ultrahigh-Brightness Microbeams: Considerations for Their Generation and Relevance to FEL — <i>H. Ishizuka, Y. Nakahara, Fukuoka Inst. Tech.; S. Kawasaki, Saitama U.; K. Sakamoto, A. Watanabe, N. Ogiwara, M. Shiho, JAERI</i> .....	1566
The Groove Guide: A Non-Conventional Interaction Structure for Microwave FEL Experiments — <i>P. Arcioni, M. Bressan, G. Conciauro, U. of Pavia; F. Broggi, P. Pierini, INFN Milano</i> .....	1569
First Undulators for the Advanced Light Source — <i>E. Hoyer, J. Akre, J. Chin, B. Gath, D. Humphries, B. Kincaid, S. Marks, P. Pipersky, D. Plate, G. Portmann, R. Schlueter, LBL; W. Hassenzahl, LLNL</i> .....	1572
Insertion Device Magnet Measurements for the Advanced Light Source — <i>S. Marks, C. Cork, E. Hoyer, D. Humphries, B. Kincaid, D. Plate, A. Robb, R. Schlueter, C. Wang, LBL; W. V. Hassenzahl, LLNL</i> .....	1575
Spectral Quality of ALS U5.0 Undulator and Field Error Effects — <i>C. Wang, S. Marks, B. Kincaid, LBL</i> .....	1578
Modeling and Measurement of the ALS U5 Undulator End Magnetic Structures — <i>D. Humphries, K. Halbach, E. Hoyer, B. Kincaid, S. Marks, R. Schlueter, LBL</i> .....	1581
Flux Shunts for Undulators — <i>E. Hoyer, J. Chin, LBL; W. V. Hassenzahl, LLNL</i> .....	1584
Design, Construction and Testing of Insertion Devices for ELETTRA — <i>R. P. Walker, R. Bracco, A. Codutti, B. Diviacco, D. Millo, D. Zangrando, Sinc. Trieste; C. Poloni, U. Trieste</i> .....	1587
Performance Optimization of Pure Permanent Magnet Undulators — <i>B. Diviacco, Sin. Trieste</i> .....	1590
Magnetic Interaction Effects in ELETTRA Segmented Pure Permanent Magnet Undulators — <i>B. Diviacco, R. P. Walker, Sinc. Trieste</i> .....	1593
Planar Helical Undulator Sources of Circularly Polarized X-Rays — <i>R. Carr, SSRL</i> .....	1596
Polarized Wiggler for NSLS X-Ray Ring — <i>A. Friedman, X. Zhang, S. Krinsky, E. B. Blum, NSLS-BNL; K. Halbach, LBL</i> .....	1599
Magnetic Field Measurements of a Superconducting Undulator for a Harmonic Generation FEL Experiment at the NSLS — <i>L. Solomon, G. Ingold, I. Ben-Zvi, S. Krinsky, L. H. Yu, NSLS-BNL; W. Sampson, K. Robins, BNL</i> .....	1602

*Each volume begins with this five-volume table of contents and ends with the five-volume author index. The chairmen's foreword and a list of conference organizers and staff appear as front matter in Volume 1. A list of conference participants precedes the author index in Volume 5.*

Magnetic Performance of the NSLS Prototype Small-Gap Undulator — G. Rakowsky, R. Cover, Rockwell; L. Solomon, NSLS-BNL .....	1605
Design Considerations for a 60 Meter Pure Permanent Magnet Undulator for the SLAC Linac Coherent Light Source (LCLS) — R. Tatchyn, R. Boyce, K. Halbach, H.-D. Nuhn, J. Seeman, H. Winick, SLAC; C. Pellegrini, UCLA .....	1608
Adjustment and Measurement of a Hybrid Undulator — B. Wu, Y. Ma, B. Liu, Z. Zhang, CIAE China .....	1611
Coherent Radiation at Submillimeter and Millimeter Wavelengths — M. Oyamada, R. Kato, T. Nakazato, S. Urasawa, T. Yamakawa, M. Yoshioka, M. Ikezawa, K. Ishi, T. Kanai, Y. Shibata, T. Takahashi, Tohoku U. ....	1614
Suppression of Coherent Synchrotron Radiation in Conducting Boundaries — R. Kato, T. Nakazato, M. Oyamada, S. Urasawa, T. Yamakawa, M. Yoshioka, M. Ikezawa, K. Ishi, T. Kanai, Y. Shibata, T. Takahashi, Tohoku U. ....	1617
A Compact Tunable X-Ray Source Based on Parametric X-Ray Generation by Moderate Energy Linacs — X. K. Maruyama, K. Dinova, D. Snyder, Naval Postgraduate School; M. A. Piestrup, Q. Li, Adelphi Tech.; R. B. Fiorito, D. W. Rule, NSWC .....	1620
Fundamental and Harmonics of Thomson Backscattered X-Rays from an Intense Laser Beam — C. Tang, NRL; B. Hafizi, Icarus Res.; S. K. Ride, UCSD .....	1623
Generation of Intensive Long-Wavelength Edge Radiation in High-Energy Electron Storage Rings — O. V. Chubar, N. V. Smolyakov, Kurchatov Inst. ....	1626
The Radiation Emission by a High Energy Electron-Positron Pair and Ultrarelativistic Hydrogen-Like Atom Moving Through Thick Target — A. V. Koshelkin, MEPI .....	1629
Bremsstrahlung by the Bunch of Ultrarelativistic Charged Particles into a Thick Target — A. V. Koshelkin, MEPI ..	1632
Construction and Commissioning of the SRRC Storage Ring — Y. C. Liu, J. R. Chen, C. C. Kuo, SRRC .....	1635
Commissioning a Second Superconducting Wiggler in the Daresbury SRS — M. W. Poole, J. A. Clarke, P. D. Quinn, S. L. Smith, V. P. Suller, L. A. Welbourn, Daresbury .....	1638

## Volume 3

### Hadron RF Linacs, Cyclotrons, Radioactive Beams

Chair: R. Pollock

An Overview of Radioactive Beam Concepts ( <i>Invited Paper</i> ) — J. M. D'Auria, TRIUMF .....	1641
Heavy Ion Beam Accumulation, Cooling, and Experiments at the ESR ( <i>Invited Paper</i> ) — B. Franzke, K. Beckert, F. Bosch, H. Eickhoff, B. Franczak, A. Gruber, O. Klepper, F. Nolden, P. Raabe, H. Reich, P. Spädtke, M. Steck, J. Struckmeier, GSI Darmstadt .....	1645
The Research Center for Nuclear Physics Ring Cyclotron ( <i>Invited Paper</i> ) — I. Miura, Osaka U. ....	1650
The Fermilab 400-MeV Linac Upgrade ( <i>Invited Paper</i> ) — C. W. Schmidt, FNAL .....	1655
Use of the Holifield Facility 25-MV Tandem Accelerator in the Oak Ridge Radioactive Ion Beam Project — C. M. Jones, R. C. Juras, M. J. Meigs, D. K. Olsen, ORNL .....	1660
Realistic Modeling of Radiation Transmission Inspection Systems — K. E. Sale, LLNL .....	1663
Overview of Accelerators in Medicine — A. J. Lennox, FNAL/Rush U. ....	1666
Commissioning of the First Drift Tube Linac Module in the Ground Test Accelerator — K. F. Johnson, O. R. Sander, W. H. Atkins, G. O. Bolme, S. Bowling, R. Cole, R. Connolly, P. Denney, J. Erickson, J. D. Gilpatrick, W. B. Ingalls, D. Kersteins, R. Kraus, W. P. Lysenko, D. McMurry, C. T. Mottershead, J. Power, C. Rose, D. P. Rusthoi, D. P. Sandoval, J. D. Schneider, M. Smith, G. Vaughn, E. A. Wadlinger, R. Weiss, V. Yuan, LANL .....	1669
Acceleration and Isobaric Separation of Radioactive Ion Beams With the Louvain-la-Neuve Isochronous Cyclotrons — M. Loiselet, N. Postiau, G. Ryckewaert, U. Catholique de Louvain; A. Morduev, R. Oganessian, JINR .....	1672
Linear Accelerator for Plutonium Conversion and Transmutation of NPP Wastes — I. M. Kapchinskiy, I. V. Chuvilo, A. A. Kolomiets, N. V. Lazarev, I. M. Lipkin, V. K. Plotnikov, I. A. Vorobjov, ITEP Moscow .....	1675

### Poster presentations:

Acceleration and Transverse Focusing of Ion Beams in Lineondutron — E. S. Masunov, MEPI .....	1681
Linac Design Study for an Intense Neutron-Source Driver — M. T. Lynch, A. Browman, R. DeHaven, R. Jameson, A. Jason, G. Neuschaefer, P. Tallerico, A. Regan, LANL .....	1683

*Proceedings of the 1993 Particle Accelerator Conference*

Design and Operation of the HIMAC Injector — T. Murakami, H. Ogawa, S. Yamada, Y. Sato, T. Yamada, A. Kitagawa, J. Yoshizawa, S. Fu, T. Kohno, K. Sato, A. Itano, M. Kumada, E. Takada, M. Kanazawa, K. Noda, M. Sudou, Y. Hirao, Nat. Inst. of Radiological Sciences; O. Morishita, K. Sawada, Sumitomo Heavy Ind. ....	1686
Time-of-Flight Measurements of Absolute Beam Energy in the Fermilab Linac — M. B. Popovic, T. L. Owens, T. K. Kroc, L. J. Allen, C. W. Schmidt, FNAL .....	1689
Phase Scan Signature Matching for Linac Tuning — T. L. Owens, M. B. Popovic, E. S. McCrory, C. W. Schmidt, L. J. Allen, FNAL .....	1691
Operational Status of the Uranium Beam Upgrade of the ATLAS Accelerator — R. C. Pardo, L. M. Bollinger, J. A. Nolen, K. W. Shepard, P. Billquist, J. M. Bogaty, B. E. Clift, R. Harkewicz, F. H. Munson, J. E. Specht, G. P. Zinkann, ANL .....	1694
One Year Operation of the 7 MeV Proton Linac — T. Shirai, H. Dewa, H. Fujita, M. Ikegami, Y. Iwashita, S. Kakigi, H. Okamoto, A. Noda, M. Inoue, Kyoto U. ....	1697
The SSC Linear Accelerator — L. W. Funk, SSCL .....	1700
Finalized Design of the SSC RFQ-DTL Matching Section — M. Haworth, C. Combs, P. Datte, T. Enegren, W. Funk, Y. Goren, F. Guy, J. Hurd, G. Jamieson, D. Martin, A. Ringwall, R. Sethi, D. Swenson, SSCL; D. Barlow, R. Kraus, R. Meyer, LANL .....	1703
Accelerator Readiness Review Process for the SSC Linac — J. F. Tooker, T. Benke, L. W. Funk, V. Oliphant, SSCL .....	1706
Commissioning Status of the Continuous Wave Deuterium Demonstrator — P. Den Hartog, J. Dooling, M. Lorello, J. Rathke, Grumman Aerospace; J. Carwardine, D. Godden, G. Pile, Culham Lab.; T. Yule, T. Zinneman, ANL .....	1709
Design Study for a Superconducting Proton Linac From 20 to 100 MeV — T. P. Wangler, R. Garnett, F. Krawczyk, J. Billen, N. Bultman, K. Christensen, W. Fox, R. Wood, LANL .....	1712
Design Considerations for High-Current Superconducting Ion Linacs — J. R. Delayen, C. L. Bohn, B. J. Micklich, C. T. Roche, L. Sagalovsky, ANL .....	1715
Special Design Problems and Solutions for High Powered Continuous Duty Linacs — D. Liska, L. Carlisle, G. McCauley, LANL; S. Ellis, P. Smith, Grumman Aerospace .....	1718
Status of CIAE Medical Cyclotron — X. Zhang, Z. Li, M. Fan, CIAE China .....	1721
A 600 MeV Cyclotron for Radioactive Beam Production — D. J. Clark, LBL .....	1724
Development of a Compact Permanent Magnet Cyclotron for Accelerator Mass Spectrometry — A. T. Young, D. J. Clark, K. Halbach, W. B. Kunkel, K. N. Leung, C. Y. Li, A. Rawlins, R. D. Schlueter, M. E. Stuart, R. P. Wells, LBL; J. X. Yu, Beijing U.; K. J. Bertsche, SSCL .....	1727
Performance of H <sup>+</sup> /D <sup>-</sup> Cyclotron Using Internal Source — T. T. Y. Kuo, TRIUMF; G. O. Hendry, Cyclotron Inc. ....	1730
Operation of the TR30 "Industrial" Cyclotron — K. Erdman, R. Dawson, Ebco Tech./TRIUMF; B. Milton, N. Stevenson, TRIUMF .....	1733
The First Year with Electron Cooling at CRYRING — K. Abrahamsson, G. Andler, L. Bagge, E. Beebe, P. Carlé, H. Danared, K. Ehrnstén, M. Engström, Å. Engström, C. J. Herrlander, J. Hilke, J. Jeansson, A. Källberg, S. Leontein, L. Liljeby, A. Nilsson, A. Paál, A. Pikin, K.-G. Rensfelt, U. Rosengård, J. Starker, M. af Ugglas, Manne Siegbahn Inst. Stockholm .....	1735
Electron Cooling of Heavy Ions at GSI — M. Steck, K. Beckert, H. Eickhoff, B. Franzke, F. Nolden, P. Spädtké, GSI Darmstadt .....	1738
The Aarhus Storage Ring for Ions and Electrons ASTRID — S. P. Møller, Aarhus U. ....	1741
Recent Developments at the Gustaf Werner Cyclotron and CELSIUS — D. Reistad, Svedberg Lab. ....	1744
Ion Beam Acceleration and New Operation Modes at the TSR Heidelberg — M. Grieser, D. Habs, R.v. Hahn, B. Hochadel, C. M. Kleffner, J. Liebmann, R. Repnow, D. Schwalm, MPI Heidelberg; G. Bisoffi, INFN Legnaro; E. Jaeschke, BESSY; S. Papureanu, IFIN Bucarest.....	1747
A New Design for an EMIS-CYCLOTRON System, for Direct Production of Gaseous PET Radioisotopes — H. Ayvazian, Ion Beam App. Lab. ....	1750
The Chandigarh Variable Energy Cyclotron and Its Application for Trace Element Analysis Using PIXE Techniques — I. M. Govil, Panjab U. ....	1753
Proton Linacs for Boron Neutron Capture Therapy — A. J. Lennox, FNAL /Rush U. ....	1756
Modeling and System Specifications for an Integrated 3-D Proton Treatment Delivery System — J. W. Staples, B. A. Ludewigt, LBL .....	1759

*Each volume begins with this five-volume table of contents and ends with the five-volume author index. The chairmen's foreword and a list of conference organizers and staff appear as front matter in Volume 1. A list of conference participants precedes the author index in Volume 5.*

## Five-Volume Contents

Shielding and Activation Study for Proton Medical Accelerators — <i>H. B. Knowles, J. L. Orthel, B. W. Hill, G. H. Gillespie Assoc.</i> .....	1762
Beam Dynamics Studies for Proposed Proton Therapy Facility — <i>D. Raparia, W. Funk, SSCL</i> .....	1765
Compact Protontherapy Unit Pre-design — <i>D. Tronc, G.E.</i> .....	1768
High Energy Accelerator Technology in Radiology — <i>J. F. Crawford, B. Larsson, H. Reist, U. Zurich/PSI; L. Goldin, ITEP Moscow; H. Condé, K. Elmgren, E. Grusell, B. Nilsson, O. Pettersson, T. Rönqvist, U. Uppsala</i> .....	1771
The Neutral Particle Beam Space Experiment (NPBSE) Accelerator Designs — <i>C. C. Paulson, A. M. M. Todd, S. L. Mendelsohn, Grumman</i> .....	1774
The Continuous Wave Deuterium Demonstrator (CWDD) Design and Status — <i>A. M. M. Todd, Grumman; M. P. S. Nightingale, Culham Lab.; T. J. Yule, ANL</i> .....	1777
Beam Matching Section in the INS Heavy Ion Linac Complex — <i>K. Niki, S. Arai, Y. Hashimoto, H. Masuda, M. Tomizawa, K. Yoshida, INS Tokyo</i> .....	1780
A Heavy Ion Linac Complex for Unstable Nuclei — <i>S. Arai, M. Doi, Y. Hashimoto, A. Imanishi, T. Katayama, H. Masuda, K. Niki, Y. Takeda, N. Tokuda, M. Tomizawa, E. Tojyo, K. Yoshida, M. Yoshizawa, INS Tokyo; T. Hattori, Tokyo Inst. of Tech.</i> .....	1783
Interdigital-H Linac for Unstable Nuclei at INS — <i>M. Tomizawa, S. Arai, M. Doi, T. Katayama, K. Niki, M. Yoshizawa, INS Tokyo; T. Hattori, Tokyo Inst. of Tech.</i> .....	1786
SPIRAL: A Radioactive Ion Beam Facility at GANIL — <i>A. Joubert, R. Anne, P. Bertrand, MP. Bourgarel, C. Bieth, B. Bru, A. Chabert, M. Duval, R. Leroy, Ch. Ricaud, P. Sortais, GANIL</i> .....	1789
On Line Isotopic Separator Test Benches at GANIL — <i>R. Anne, B. Bru, A. Joubert, R. Leroy, M. Lewitowicz, P. Sortais, M. G. Saint Laurent, C. Tribouillard, GANIL; J. Obert, J. C. Putaux, IPN Orsay; C. F. Liang, P. Paris, CSNSM Orsay; N. Orr, J. C. Steckmeyer, LPC-ISMRA</i> .....	1792
The Outlook of MPC-10 Cyclotron Use for the Solution of Applied Problems — <i>S. T. Latushkin, V. V. Leonov, A. A. Ogloblin, L. I. Yudin, V. E. Yarosh, D. I. Yartsev, Kurchatov Inst.</i> .....	1795
ITEP Heavy Ion Alternating Phase Focusing Linac — <i>V. V. Kushin, N. A. Nesterov, I. O. Parshin, S. V. Plotnikov, ITEP Moscow</i> .....	1798
<b>Accelerator Control Systems</b> <i>Chair: D. Gurd</i>	
Sharing Control System Software ( <i>Invited Paper</i> ) — <i>P. Clout, Vista Systems</i> .....	1801
Control System Architecture: The Standard and Non-Standard Models ( <i>Invited Paper</i> ) — <i>M. E. Thuot, L. R. Dalesio, LANL</i> .....	1806
Anatomy of a Control System: A System Designer's View — <i>S. Magyary, LBL</i> .....	1811
Beam Position Monitor Data Acquisition for the Advanced Photon Source — <i>F. R. Lenkszus, E. Kahana, A. J. Votaw, G. A. Decker, Y. Chung, D. J. Ciarlette, R. J. Laird, ANL</i> .....	1814
New Tevatron Cryogenic Control System — <i>B. Lublinsky, J. Firebaugh, J. Smolucha, FNAL</i> .....	1817
Control Software for EUTERPE — <i>P. D. V. van der Stok, F. van den Berk, R. Deckers, Y. van de Vijver, J. I. M. Botman, J. L. Delhez, C. J. Timmermans, Tech. U., Eindhoven</i> .....	1820
<i>Poster presentations:</i>	
Network Management of Real-Time Embedded Processors — <i>C. Kalbfleisch, S. Hunt, K. Low, D. Mathieson, SSCL</i> .....	1823
High Speed Serial Communications for Control Systems — <i>D. Mathieson, C. Kalbfleisch, S. Hunt, K. Low, SSCL</i> .....	1826
"BUBBANET": A High Performance Network for the SSC Accelerator Control System — <i>S. Hunt, C. Kalbfleisch, K. Low, D. Mathieson, SSCL</i> .....	1829
Gateway for Inter-Network Connection in the Pohang Light Source Control System — <i>S. C. Won, S. Kwon, POSTECH</i> .....	1832
The Star, a Dynamically Configured Dataflow Director for Realtime Control — <i>M. Bickley, J. Kewisch, CEBAF</i> .....	1835
The SSCL Linac Control System — <i>J. Heefner, C. Cuevas, S. Hunt, D. Murray, J. Sage, SSCL</i> .....	1838
Proposal to Use Failure Prediction as a Means of Meeting Availability Requirements at the SSC — <i>S. Sarkar, W. Merz, F. Meyer, SSCL</i> .....	1841
Control, Timing, and Data Acquisition for the Argonne Wakefield Accelerator (AWA) — <i>P. Schoessow, C. Ho, J. Power, E. Chojnacki, ANL</i> .....	1844

Volume 1: 1-747  
 Volume 2: 748-1640  
 Volume 3: 1641-2545  
 Volume 4: 2546-3218  
 Volume 5: 3219-3933

*Proceedings of the 1993 Particle Accelerator Conference*

The High Level Programmer and User Interface of the NSLS Control System — Y. N. Tang, J. D. Smith, NSLS-BNL; S. Sathe, AGS-BNL .....	1846
NSLS Control Monitor and Its Upgrade — S. Ramamoorthy, J. D. Smith, NSLS-BNL .....	1849
NSLS Control System Upgrade Status — J. Smith, S. Ramamoorthy, Y. Tang, J. Flannigan, S. Sathe, J. Keane, S. Krinsky, NSLS-BNL .....	1852
Digital Signal Array Processor for NSLS Booster Power Supply Upgrade — R. Olsen, J. Dabrowski, BNL; J. Murray, Stony Brook .....	1855
Control System for NSLS Booster Power Supply Upgrade II — R. Olsen, J. Dabrowski, BNL; J. Murray, Stony Brook .....	1858
Software Environment and Configuration for the DSP Controlled NSLS Booster Power Supplies — R. Olsen, J. Dabrowski, NSLS-BNL; J. Murray, Stony Brook .....	1861
Control Units for APS Power Supplies — O. D. Despe, C. Saunders, D. McGhee, ANL .....	1864
High Resolution ADC Interface to Main Magnet Power Supply at the NSLS — M. Bordoley, NSLS-BNL .....	1867
Design of the Advanced Light Source Timing System — M. Fahmie, LBL .....	1869
Ring Diagnostics and Consistency Test of the Model for the AGS Booster — A. Luccio, E. H. Auerbach, BNL .....	1872
Use of Design Codes for On-Line Beam Diagnostics at the MIT-Bates Accelerator — K. D. Jacobs, B. G. McAllister, J. B. Flanz, MIT Bates .....	1875
A Graphical User-Interface Control System at SRRC — J. S. Chen, C. J. Wang, S. J. Chen, G. J. Jan, SRRC Taiwan .....	1878
Machine Protection System Algorithm Compiler and Simulator — G. R. White, G. Sherwin, SLAC .....	1881
MPS VAX Monitor and Control Software Architecture — S. Allison, N. Spencer, K. Underwood, D. VanOlst, M. Zelanzy, SLAC .....	1884
The Continuous and Seamless Replacement of a Running Control System Succeeded — G.v. Egan-Krieger, R. Müller, J. Rahn, BESSY .....	1887
Control and Data Acquisition System of Electron Accelerator for Radiation Processing — W. Maciszewski, J. Lukasiewicz, W. Migdal, A. G. Chmielewski, Inst. of Nuc. Tech., Warsaw .....	1890
Expert System for Magnetic Systems Investigations — S. Lima, R. V. Poliakova, F. F. Nodarse, I. P. Yudin, JINR Moscow .....	1892
Orbit Correction Implementation at CEBAF — M. Bickley, B. A. Bowling, D. Douglas, A. Hofler, J. Kewisch, G. A. Krafft, CEBAF .....	1895
Controls Interface Protocols for the SSC Correction and 'DC' Magnet Power Supplies — S. Sarkar, J. Gannon, W. Merz, F. Meyer, SSCL .....	1898
Parametrization of the AmPS Magnets for the Control System — Y. Wu, G. van Garderen, R. Hart, J. van der Laan, R. Maas, F. Schimmel, NIKHEF-K .....	1901
Global Voltage Control for the LEP RF System — E. Ciapala, A. Butterworth, E. Peschardt, CERN .....	1903
Designing RF Control Subsystems Using the VXibus Standard — J. D. Stepp, F. C. Vong, J. F. Bridges, ANL .....	1906
Automated Measurement of Cavity Frequency and Cavity Tuning at CEBAF — R. Li, S. N. Simrock, B. C. Yunn, CEBAF .....	1909
A Beam Position Monitor Data Acquisition System for the New Fermilab 400 MeV Line — S. Lackey, J. Firebaugh, C. Johnstone, W. Marsh, J. Smolucha, K. Woodbury, FNAL .....	1912
A VME Based Quench Protection Monitor for the Tevatron Low Beta Quadrupoles — S. Lackey, C. Briegel, L. Chapman, R. Flora, K. Martin, FNAL; T. Savord, SSCL .....	1914
Experience with the TRIUMF Main Tank Vacuum Control System — S. Sarkar, D. P. Gurd, SSCL; J. C. Yandon W. Sievers, P. Bennett, P. Harmer, J. Nelson, TRIUMF .....	1916
Laser Power Stabilization in the TRIUMF Optically Pumped Polarized H <sup>-</sup> Ion Source — S. Sarkar, SSCL .....	1919
MPS Beam Control Software Architecture — K. Krauter, M. Crane, SLAC .....	1922
The CEBAF Analog Monitor System — K. Crawford, M. O'Sullivan, J. Perry, S. Simrock, CEBAF .....	1925
Techniques for Increasing the Reliability of Accelerator Control System Electronics — J. Utterback, FNAL .....	1928
WindoWorks: A Flexible Program for Computerized Testing of Accelerator Control System Electronic Circuit Boards — J. Utterback, FNAL .....	1931
Switching the Fermilab Accelerator Control System to a Relational Database — S. Shtirbu, FNAL .....	1934
The Impact of New Accelerator Control Software on LEP Performance — R. Bailey, A. Belk, P. Collier, M. Lamons, G. de Rijk, M. Tarrant, CERN .....	1937

*Each volume begins with this five-volume table of contents and ends with the five-volume author index. The chairmen's foreword and a list of conference organizers and staff appear as front matter in Volume 1. A list of conference participants precedes the author index in Volume 5.*

## Five-Volume Contents

A Software System for Modeling and Controlling Accelerator Physics Parameters at the Advanced Light Source — <i>L. Schachinger, V. Paxson, LBL</i> .....	1940
Machine Physics Application Program for Control, Commissioning and Error Findings for Storage Rings — <i>H. P. Chang, C. H. Chng, C. C. Kuo, M. H. Wang, J. C. Lee, J. Y. Fan, H. J. Tsai, SRRC Taiwan;</i> <i>C. S. Hsue, SRRC/Nat. Tsing Hua U.</i> .....	1943
CATER: An Online Problem Tracking Facility for SLC — <i>R. C. Sass, H. Shoaee, SLAC</i> .....	1946
Ramping Control Using a Spreadsheet — <i>D. Y. Wang, R. P. Johnson (now at CEBAF), L. S. B. Ng, W. J. Pearce,</i> <i>Maxwell Labs</i> .....	1949
Easy and Effective Applications Programs Using DataViews — <i>E. S. McCrory, FNAL</i> .....	1952
The Graphic Environment for Transport Line Control and Beam Diagnostics — <i>S. Kuznetsov,</i> <i>Kurchatov Inst.</i> .....	1955
An I/O Subnet for the APS Control System: The BITBUS Universal Gateway — <i>G. J. Nawrocki, N. D. Arnold,</i> <i>M. G. Hoffberg, J. R. Winans, S. J. Benes, ANL</i> .....	1957
Status and Design of the Advanced Photon Source Control System — <i>W. McDowell, M. Knott, F. Lenkszus,</i> <i>M. Kraimer, N. Arnold, R. Daly, ANL</i> .....	1960
Controlling the Third Harmonic Cavity During Focus Free Transition Crossing in the Fermilab Main Ring — <i>M. A. Martens, FNAL</i> .....	1963
AMS: Area Message Service for SLC — <i>M. Crane, R. Mackenzie, D. Millsom, M. Zelazny, SLAC</i> .....	1966
Adding PCs to SLC Control System — <i>T. Lahey, S. Levitt, R. MacKenzie, N. Spencer, K. Underwood, SLAC</i> .....	1969
Precise System Stabilization at SLC Using Dither Techniques — <i>M. C. Ross, L. Hendrickson, T. Himel, E. Miller,</i> <i>SLAC</i> .....	1972
Thermal Stabilization of Low Level RF Distribution Systems at SLAC — <i>D. McCormick, M. Ross, T. Himel,</i> <i>N. Spencer, SLAC</i> .....	1975
 <b>Lepton Circular Colliders, Synchrotrons, and Microtrons</b> <span style="float: right;"><i>Chair: A. Sessler</i></span>	
CESR Luminosity Upgrades and Experiments ( <i>Invited Paper</i> ) — <i>D. Rice, Cornell</i> .....	1978
LEP Status and Future Plans ( <i>Invited Paper</i> ) — <i>L. R. Evans, CERN</i> .....	1983
Challenges on the High Luminosity Frontier of $e^+e^-$ Factories ( <i>Invited Paper</i> ) — <i>W. A. Barletta, LBL/UCLA</i> .....	1988
DAFNE, The Frascati F-Factory ( <i>Invited Paper</i> ) — <i>G. Vignola, INFN-LNF</i> .....	1993
Commissioning Results of the Amsterdam Pulse Stretcher/Storage Ring AmPS — <i>R. Maas, F. Kroes,</i> <i>J. van der Laan, G. Luijckx, J. Noomen, Y. Wu, NIKHEF</i> .....	1998
 <i>Poster presentations:</i>	
LEP Operation in 1992 with a 90° Optics — <i>R. Bailey, T. Bohl, F. Bordry, H. Burkhardt, K. Cornelis, P. Collier,</i> <i>B. Desforges, A. Faugier, V. Hatton, M. Jonker, M. Lamont, J. Miles, G. de Rijk, H. Schmickler, CERN</i> .....	2001
Status of TRISTAN-II Project — <i>S. Kurokawa, KEK</i> .....	2004
The Long Range Beam-Beam Interaction at CESR: Experiments, Simulations and Phenomenology — <i>A. B. Temnykh, INP Novosibirsk; J. J. Welch, D. H. Rice, Cornell</i> .....	2007
PEP-II Design Update and R&D Results — <i>W. Barletta, M. S. Zisman, LBL; R. A. Bell, J. M. Dorfan, SLAC</i> .....	2010
Commissioning and Operation of the LEP Pretzel Scheme — <i>R. Bailey, J. M. Jowett, W. Kalbreier, D. Wang,</i> <i>CERN</i> .....	2013
Progress of the LEP Energy Upgrade Project — <i>C. Wyss, CERN</i> .....	2016
Flat Beams in the SLC — <i>C. Adolphsen, T. Barklow, D. Burke, F.-J. Decker, P. Emma, M. Hildreth, T. Himel,</i> <i>P. Krejcik, T. Limberg, M. Minty, N. Phinney, P. Raimondi, T. Raubenheimer, M. Ross, J. Seeman,</i> <i>R. Siemann, W. Spence, N. Walker, M. Woodley, SLAC</i> .....	2019
The Damping Ring For Novosibirsk F- and B-Factories — <i>V. V. Anashin, S. E. Belomestnykh, A. A. Didenko,</i> <i>N. S. Dikansky, B. I. Grishanov, P. M. Ivanov, V. A. Kiselev, V. I. Kudelainen, N. A. Kuznetsov,</i> <i>V. A. Lebedev, B. L. Militsin, S. I. Mishnev, V. V. Parkhomchuk, A. N. Voroshilov,</i> <i>M. N. Zakhvatkin, BINP, Russia</i> .....	2022
A Possible Redesign of the SLAC SLC Damping Rings — <i>T. O. Raubenheimer, R. Early, T. Limberg,</i> <i>H. Moshammer, J. Spencer, SLAC</i> .....	2025
Update on the Argonne Positron Accumulator Ring — <i>M. Borland, ANL</i> .....	2028
Measurement on the SRRC 1.3 GeV Electron Booster Synchrotron Operation Parameters and the Ramping Behavior — <i>K. K. Lin, K. T. Hsu, T. S. Ueng, SRRC Taiwan</i> .....	2031

Volume 1: 1-747  
 Volume 2: 748-1640  
 Volume 3: 1641-2545  
 Volume 4: 2546-3218  
 Volume 5: 3219-3933

*Proceedings of the 1993 Particle Accelerator Conference*

1.3 GeV Electron Synchrotron — <i>J. Mod�er, Scanditronix</i> .....	2034
Performance of the ALS Injection System — <i>C. H. Kim, LBL</i> .....	2036
Synchrotron of SPring-8 — <i>H. Yonehara, H. Suzuki, T. Aoki, S. Yoneyama, Y. Ueyama, Y. Sasaki, T. Nagafuchi, S. Hayashi, H. Yokomizo, JAERI</i> .....	2039
Further Study of JINR Tau-Charm Factory Design — <i>E. Perelstein, V. Alexandrov, V. Antropov, O. Arkhipov, P. Beloshitsky, L. Bobyleva, V. Kazacha, N. Kazarinov, A. Krasnykh, V. Mironov, D. Kaltchev, L. Onischenko, A. Sissakian, Yu. Smirnov, Ts. Vylov, JINR Dubna; V. Belov, B. Mudiugin, A. Popov, D. Serebrennikov, SRI St. Petersburg; I. Kvashonkin, E. Petrov, I. Umansky, Russian Inst., St. Petersburg ...</i>	2042
A Versatile Lattice for a Tau-Charm Factory That Includes a Monochromatization Scheme (Low Emittance) and a Standard Scheme (High Emittance) — <i>A. Faus-Golfe, U. Valencia; J. Le Duff, LAL Orsay</i> .....	2045
DAFNE Interaction Region Design — <i>M. Bassetti, M. E. Biagini, C. Biscari, M. A. Preger, G. Raffone, G. Vignola, INFN-LNF</i> .....	2048
On an Asymmetric Correlated Flavor Factory — <i>D. Cline, A. Boden, W. Gabella, A. Garren, X. Wang, UCLA</i> .....	2051
Status of the MIT-Bates South Hall Ring Commissioning — <i>J. B. Flanz, K. D. Jacobs, B. McAllister, R. Averill, S. Bradley, A. Carter, K. Dow, M. Farkondeh, E. Ihloff, S. Kowalski, W. Sapp, C. Sibley, D. Tieger, C. Tschalaer, A. Zolfaghari, MIT-Bates</i> .....	2054
Current Status of the Design of the Kharkov Pulse Stretcher Ring PSR-2000 — <i>S. Efimov, P. Gladkikh, Y. Grigor'ev, I. Guk, I. Karnaukhov, V. Kozin, S. Kononenko, V. Likhachev, V. Markov, N. Mocheshnikov, V. Moskalenko, A. Mytsykov, Yu. Popkov, A. Shcherbakov, M. Strelkov, A. Tarasenko, Yu. Telegin, A. Zelynsky, Kharkov Inst.; M. Nagaenko, Yu. Severgin, ESRI</i> .....	2057
Moscow State University CW Race-Track Microtron Status — <i>V. I. Shvedunov, A. S. Alimov, A. S. Chepurinov, O. V. Chubarov, I. V. Gribov, B. S. Ishkhanov, I. V. Surma, A. V. Tiunov, INP Moscow</i> .....	2059
Optical Design of the 75-MeV Eindhoven Racetrack Microtron — <i>G. A. Webers, J. L. Delhez, J. I. M. Botman, H. L. Hagedoorn, Eindhoven U. of Tech.</i> .....	2062
Example Application for the Hamiltonian Description of an Azimuthally Varying Field Racetrack Microtron — <i>J. L. Delhez, W. J. G. M. Kleeven, H. L. Hagedoorn, J. I. M. Botman, G. A. Webers, Eindhoven U. of Tech.</i> .....	2065
A 100-MeV Racetrack Microtron — <i>P. Lidbj�rk, J. �str�m, Scanditronix</i> .....	2068
Electrostatic Quadrupole Focusing in the AGS g-2 Storage Ring — <i>G. Bennett, R. Larsen, W. Morse, Y. Semertzidis, J. Yelk, BNL; Z. Liu, Boston U.</i> .....	2070
Design of 8-GeV Rapid-Cycle Booster Synchrotron for the KEK B-Factory — <i>S. Kurokawa, KEK; P. Zenkevich, ITEP Moscow</i> .....	2073

**Instrumentation and Beam Feedback**

*Chair: R. Shafer*

Feedback Control of Coupled-Bunch Instabilities ( <i>Invited Paper</i> ) — <i>J. D. Fox, N. Eisen, H. Hindi, I. Linscott, G. Oxoby, L. Sapozhnikov, SLAC; M. Serio, INFN Frascati</i> .....	2076
Electro-Optical Technology Applied to Accelerator Beam Measurement and Control ( <i>Invited Paper</i> ) — <i>R. J. Pasquinelli, FNAL</i> .....	2081
RF-Synchronized Imaging for Particle and Photon Beam Characterizations ( <i>Invited Paper</i> ) — <i>A. H. Lumpkin, ANL</i> .....	2086
Diagnostic Instrumentation System for the SRRC 1.3 GeV Synchrotron Radiation Light Source — <i>K. T. Hsu, G. J. Jan, C. H. Kuo, K. H. Hu, SRRC Taiwan</i> .....	2091
Overview and Status of Beam Instrumentation at the SSC — <i>R. C. Webber, SSCL</i> .....	2094
Performance of Advanced Light Source Particle Beam Diagnostics — <i>J. Hinkson, LBL</i> .....	2097
Damping in the Fermilab Booster — <i>J. M. Steimel, Jr., D. McGinnis, FNAL</i> .....	2100
Betatron Function Measurement at LEP Using the BOM 1000 Turns Facility — <i>P. Castro, IFIC, Spain; J. Borer, A. Burns, G. Morpurgo, R. Schmidt, CERN</i> .....	2103
Adaptive Cascaded Beam-Based Feedback at the SLC — <i>T. Himel, S. Allison, P. Grossberg, L. Hendrickson, R. Sass, H. Shoaee, SLAC</i> .....	2106
Design of the ALS Transverse Coupled-Bunch Feedback System — <i>W. Barry, J. M. Byrd, J. N. Corlett, J. Hinkson, J. Johnson, G. R. Lambertson, LBL; J. D. Fox, SLAC</i> .....	2109

*Each volume begins with this five-volume table of contents and ends with the five-volume author index. The chairmen's foreword and a list of conference organizers and staff appear as front matter in Volume 1. A list of conference participants precedes the author index in Volume 5.*

## Five-Volume Contents

### Poster presentations:

Results of Prototype Particle-Beam Diagnostics Tests for the Advanced Photon Source (APS) — A. H. Lumpkin, Y. Chung, E. Kahana, D. Patterson, W. Sellyey, A. Votaw, X. Wang, ANL .....	2112
Diagnostics Development for High Current Electron Accelerators at CESTA — J. de Mascureau, C. Bonnafond, A. Devin, E. Merle, G. Ployard, D. Villate, CESTA .....	2115
Beam Instrumentation for the SSC RFQ — P. Datte, G. Jamieson, R. Aiello, D. Beechy, A. Jones, D. Martin, J. Riordon, R. Webber, F. Wood, SSCL .....	2118
High Density Data Recording for SSCL Linac — A. L. VanDeusen, Allied Signal; C. Crist, SSCL .....	2121
Physic Requirements of Commissioning Diagnostics for SSCL Linac — J. W. Hurd, G. M. Arbique, C. E. Crist, F. W. Guy, M. Haworth, G. T. Leifeste, K. Saadatmand, SSCL; M. Krogh, K. McGinnis, D. Stittsworth, A. Vandeusen, S. Wright, Allied Signal .....	2124
Beam Diagnostic Layout Requirements for SSCL Linac — J. W. Hurd, F. W. Guy, G. Jamieson, D. Raparia, K. Saadatmand, SSCL .....	2127
SSCL Linac Commissioning Diagnostic Cart — C. E. Crist, L. W. Funk, J. W. Hurd, G. T. Leifeste, SSCL; M. Krogh, K. McGinnis, D. Stittsworth, A. Vandeusen, S. Wright, Allied Signal .....	2130
A Method for LEBT Automation — J. Sredniawski, L. Solensten, R. Schmidt, J. Porter, Y. Ng, C. Lom, Grumman; W. Newman, AMTEX .....	2133
Beam Energy Measurement Using the Hall C Beam Line — C. Yan, R. Carlini, D. Neuffer, CEBAF .....	2136
A Wide Range and High Speed Automatic Gain Control — E. J. Tacconi, C. F. Christiansen, SSCL/ UNLP Argentina.....	2139
A Beamline Design and Data Acquisition with the 20-MeV, 20-ps Electron Beam for the Higher-Order-Mode Studies of the APS SR-RF Cavities — J. Song, A. Nassiri, R. Daly, ANL .....	2142
A Bunch Killer for the NSLS X-Ray Electron Storage Ring — R. J. Nawrocky, U. Bergmann, D. P. Siddons, NSLS BNL .....	2145
The Mechanical Design of a Bunched Beam Stochastic Cooling Tank for the FNAL Tevatron — P. Hurh, G. Jackson, FNAL .....	2148
Design Study of Laser Compton Scattering with Relativistic Electron to Measure the Electron Beam Energy — I. Hsu, H. Chen, C. Cho, Y. Liu, Nat. Tsing Hua U. ....	2151
Transverse Beam Impedance Measurement: A New Coaxial Method — M. Cardito, F. Galluccio, R. Losito, M. R. Masullo, V. Vaccaro, INFN Napoli ; G. Di Massa, U. Calabria .....	2154
A Novel Method of Noise Suppression in Beam Transfer Function Measurements — F. Caspers, M. Chanel, U. Oeftiger, CERN .....	2157
Beam Dispersion Measurements with Wire Scanners in the SLC Final Focus Systems — P. Emma, D. McCormick, M. C. Ross, SLAC .....	2160
Comprehensive Beam Jitter Study for the Commissioning of the Intermediate Matching Section and Drift Tube Linac at Ground Test Accelerator — D. S. Barr, J. D. Gilpatrick, LANL .....	2163
A New Method of Ion Beam Diagnostics — A. S. Artiomov, JINR Dubna .....	2166
Correlation Method of Measurements of Ion Beam Parameters — A. S. Artiomov, JINR Dubna .....	2169
The Compton Polarimeter at the SLC — G. Shapiro, S. Bethke, O. Chamberlain, R. Fuzesy, M. Kowitz, D. Pripstein, B. Schumm, H. Steiner, M. Zolotorev, LBL; P. Rowson, Columbia; D. Blockus, H. Ogren, M. Settles, Indiana; M. Fero, A. Lath, MIT; D. Calloway, R. Elia, E. Hughes, T. Junk, R. King, T. Maruyama, K. Moffeit, M. Petradza, M. Swartz, M. Woods, SLAC; G. Zapalac, Wisconsin .....	2172
Measurement of the Spin of a Particle Using Undulator Radiation — A. Luccio, BNL .....	2175
Quantum Geometrical Phase Signal of NLC Bunch Cross Section Carried by Virtual Photons — J. Shen, IHEP Beijing .....	2178
Response of Air-Filled Ion Chambers to High-Intensity Radiation Pulses — M. Plum, D. Brown, LANL .....	2181
The CEBAF Beam Loss Sensors — J. Perry, E. Woodworth, L. Meringa, S. Simrock, R. May, CEBAF; G. Stapleton, SSCL .....	2184
A Scintillating Fiber Beam Halo Detector for Heavy Ion Beam Diagnostics — M. A. McMahan, A. Assang, S. Herr, F. McCormack, G. Krebs, B. Feinberg, LBL .....	2187

*Proceedings of the 1993 Particle Accelerator Conference*

Development and Investigation of the $2\pi$ Beam Loss Monitors for Super-High-Energy Accelerators, Part 1: Quad-BLM for "Warm" Machines — S. N. Lapitsky, I. A. Kurochkin, V. S. Seleznev, IHEP Russia .....	2190
The Design and Performance of a High Sensitivity Loss Monitor System for Use in the Fermilab Antiproton Rings — A. M. Halling, J. R. Zagel, A. Hahn, FNAL .....	2193
Abort Interlock Diagnostic for Protection of APS Vacuum Chamber — G. Decker, ANL .....	2196
Experience with Radiation Protection for a Silicon Vertex Detector at a Hadronic Collider — P. F. Derwent, D. Amidei, A. Dunn, T. Song, S. Vejcek, U. Michigan; R. Crouch, R. Ducar, D. Herrup, FNAL; C. Haber, LBL .....	2199
Design of a New Generation of Collimators for LEP 200 — R. Jung, R. Perret, R. Valbuena, CERN .....	2202
Synchrotron Radiation Damage Test of Insulating Materials in the TRISTAN MR — H. Mitsui, R. Kumazawa, T. Tanii, T. Chugun, Toshiba Corp.; Y. Ohsawa, T. Ozaki, K. Takayama, KEK .....	2205
Insulating and Metal-Ceramic Materials for Particle Accelerators — Yu. P. Severgin, M. Z. Filimonov, Efremov Inst. ....	2208
The Advanced Light Source (ALS) Radiation Safety System — A. L. Ritchie, D. E. Oldfather, A. F. Lindner, LBL ..	2210
Radiation Measurements During Cavities Conditioning on APS RF Test Stand — D. M. Grudzien, R. L. Kustom, H. J. Moe, J. J. Song, ANL .....	2213
Application of a Simple Analytical Model to Estimate Effectiveness of Radiation Shielding for Neutrons — S. Frankle, D. Fitzgerald, R. Hutson, R. Macek, C. Wilkinson, LANL .....	2216
Monte Carlo Based Formula for Radiation Shielding Assessment in the Forward Direction — C. Wilkinson, D. Fitzgerald, S. Frankle, R. Hutson, R. Macek, LANL .....	2219
A High Reliability Oxygen Deficiency Monitoring System — R. Parry, G. Claborn, A. Haas, R. Landis, W. Page, J. Smith, SSCL .....	2222
Programmable Electronic Safety Systems — R. R. Parry, SSCL .....	2225
A Pseudo Real Time Tune Meter for the Fermilab Booster — G. Wu, V. Bharadwaj, J. Lackey, D. McGinnis, R. Tomlin, FNAL .....	2228
Measurement Techniques Using the Tektronix® 3052 DSP System — J. M. Steimel, Jr., D. McGinnis, FNAL .....	2231
Using Transient Waveform Recorders to Measure and Store Beam Parameters — R. E. Stege, Jr., R. K. Jobe, M. Ross, SLAC .....	2234
Tune Measurement in the APS Rings — W. Selvyey, E. Kahana, X. Wang, ANL .....	2237
Integrating Log-Ratio Position Processing for the Los Alamos Proton Storage Ring Extraction Line — T. W. Hardek, A. Band, LANL .....	2240
Betatron "Ping" Tune Measurement System for the IUCF Cooler Synchrotron/Storage Ring — B. J. Hamilton, M. S. Ball, T. J. P. Ellison, IUCF .....	2243
Tune Measurement in the NSLS Booster Synchrotron — E. B. Blum, R. Nawrocky, BNL .....	2246
A Realtime Feedback Microprocessor for the Tevatron — D. A. Herrup, L. Chapman, A. Franck, T. Groves, B. Lublinsky, FNAL .....	2249
A New Study of the Main Ring Physical Aperture — G. Wu, S. Pruss, D. Capista, FNAL .....	2252
Electron Beam Stability and Beam Peak to Peak Motion Data for NSLS X-Ray Storage Ring — O. Singh, BNL .....	2254
Test of Fast-Digital Beamline Feedback Control at the Photon Factory — N. Nakamura, T. Katsura, KEK .....	2257
Horizontal Movement of the Storage Ring Floor at the Photon Factory — T. Katsura, H. Nakamura, Y. Kamiya, KEK; Y. Fujita, Shimizu Corp. ....	2260
Closed Orbit Correction Using Singular Value Decomposition of the Response Matrix — Y. Chung, G. Decker, K. Evans, Jr., ANL .....	2263
Compensation for the Effect of Vacuum Chamber Eddy Current by Digital Signal Processing for Closed Orbit Feedback — Y. Chung, L. Emery, J. Kirchman, ANL .....	2266
Dynamic Closed Orbit Correction — Y. Cheng, SRRC Taiwan .....	2269
A Closed-Loop Photon Beam Control Study for the Advanced Light Source — G. Portmann, J. Bengtsson, LBL .....	2272
Global DC Closed Orbit Correction Experiments on the NSLS X-Ray Ring and SPEAR — Y. Chung, G. Decker, K. Evans, Jr., ANL; J. Safranek, I. So, Y. Tang, BNL; W. J. Corbett, R. Hettel, SSRI .....	2275
FFT-Oriented Feedback — F.-J. Decker, SLAC .....	2278
Issues of the Transverse Feedback Systems Design at the SSC — W. Chou, J. Peterson, SSCL .....	2281
A Digital Feedback System for Orbit Stabilization — A. Friedman, E. Bozoki, O. Singh, J. Smith, BNL .....	2284
Results from the AGS Booster Transverse Damper — D. Russo, M. Brennan, M. Meth, T. Roser, BNL .....	2286
Single Board Op-Amp Beam Position Monitors Electronics — M. Ball, T. J. P. Ellison, B. J. Hamilton, IUCF .....	2289

*Each volume begins with this five-volume table of contents and ends with the five-volume author index. The chairmen's foreword and a list of conference organizers and staff appear as front matter in Volume 1. A list of conference participants precedes the author index in Volume 5.*

## Five-Volume Contents

A Single-Passage Beam-Position Monitor in the TRISTAN AR-to-MR Transport Lines — <i>T. Ieiri, M. Arinaga, KEK</i> .....	2292
Beam Position Monitoring System Using PIN Diode Switches — <i>K. Shinoe, T. Koseki, Y. Kamiya, ISSP Tokyo; N. Nakamura, T. Katsura, T. Ieiri, KEK</i> .....	2295
Performance of the CEBAF Arc Beam Position Monitors — <i>A. S. Hofler, B. A. Bowling, C. S. Higgins, P. K. Kloeppel, G. A. Krafft, K. L. Mahoney, CEBAF</i> .....	2298
The Million Turn Data Acquisition System BOSC — <i>A. Burns, W. Fischer, H. Jakob, I. Milstead, F. Schmidt, L. Vos, CERN</i> .....	2301
Beam Position Monitor Calibration for the Advanced Photon Source — <i>Y. Chung, G. Decker, E. Kahana, F. Lenkszus, A. Lumpkin, W. Sellyey, ANL</i> .....	2304
Self Triggered Single Pulse Beam Position Monitor — <i>J. L. Rothman, E. B. Blum, NSLS-BNL</i> .....	2307
A Prototype BPM Electronics Module for RHIC — <i>W. A. Ryan, T. J. Shea, P. Cerniglia, C. M. Degen, BNL</i> .....	2310
Dynamic Range Extension of BPM at the NSLS — <i>M. Bordoley, NSLS-BNL</i> .....	2313
Beam Position Monitoring in the 100-MHz to 500-MHz Frequency Range Using the Log-Ratio Technique — <i>F. D. Wells, R. E. Shafer, J. D. Gilpatrick, LANL</i> .....	2316
Beam Pinging, Sweeping, Shaking, and Electron/Ion Collecting, at the Proton Storage Ring — <i>T. Hardek, R. Macek, M. Plum, T.-S. Wang, LANL</i> .....	2319
Test Results of the SSC Log-Ratio Beam Position Monitor Electronics — <i>G. R. Aiello, M. R. Mills, R. E. Gonzalez, SSCL</i> .....	2322
RF Beam Position Monitors for the TESLA Test Facility — <i>R. Lorenz, TU Berlin</i> .....	2325
RHIC Beam Position Monitor Assemblies — <i>P. R. Cameron, M. C. Grau, W. A. Ryan, T. J. Shea, R. E. Sikora, BNL</i> .....	2328
Stripline Beam Position Monitor for the MIT-Bates South Hall Ring — <i>J. B. Flanz, R. Averill, E. Ihloff, K. D. Jacobs, D. Wang, A. Zolfaghari, MIT-Bates</i> .....	2331
Design and Operation of Button-Probe, Beam-Position Measurements — <i>J. D. Gilpatrick, J. F. Power, R. E. Meyer, C. R. Rose, LANL</i> .....	2334
Design and Calibration of Pickup-Electrodes for Beam Position Monitoring at SOR-RING — <i>K. Shinoe, Y. Kamiya, ISSP Tokyo; N. Nakamura, T. Katsura, KEK</i> .....	2337
The Position Monitor Using Stretched Wire Technique — <i>T. Mimashi, S. Kuroda, H. Nakayama, K. Oide, R. Sugahara, N. Yamamoto, KEK</i> .....	2340
An Over-Moded Stripline Beam Position Monitor — <i>J. G. Noomen, J. Bijleveld, F. Kroes, T. Sluijk, NIKHEF-K</i> ...	2343
Loss of Precision in Resonant Beam Position Monitors Due to Finite $Q$ — <i>J. P. H. Sladen, W. Wuensch, CERN</i> ....	2346
Simulation of the ALS Longitudinal Multibunch Feedback System — <i>J. Byrd, LBL</i> .....	2349
Analysis of DSP-Based Longitudinal Feedback System: Trials at SPEAR and ALS — <i>H. Hindi, N. Eisen, J. Fox, I. Linscott, G. Oxoby, L. Sapozhnikov, SLAC; M. Serio, INFN</i> .....	2352
VXI Based Low Level RF System for Fermilab Linac Upgrade — <i>B. E. Chase, R. J. Pasquinelli, FNAL</i> .....	2355
Longitudinal Feedback in LEP — <i>J. P. Boiteux, P. Brown, E. Ciapala, H. Frischholz, G. Geschonke, J. C. Juillard, E. Peschardt, CERN</i> .....	2358
Performance of the Upgraded Stacktail Momentum Cooling System in the Fermilab Antiproton Source — <i>R. J. Pasquinelli, D. McGinnis, FNAL</i> .....	2361
Energy Vernier System for CEBAF — <i>G. A. Krafft, J. J. Bisognano, M. T. Crofford, J. C. Hovater, L. Merminga, S. N. Simrock, S. D. Witherspoon, CEBAF; K. Kubo, KEK</i> .....	2364
A Digital Approach for Phase Measurement Applied to Delta- $t$ Tuneup Procedure — <i>G. R. Aiello, SSCL</i> .....	2367
RF Feedback for Beam Loading Compensation in the SLC Damping Rings — <i>P. Krejcik, P. Corredoura, M. Minty, R. Siemann, R. Tighe, SLAC; F. Pedersen, CERN</i> .....	2370
Simulation and Analysis of RF Feedback Systems on the SLC Damping Rings — <i>M. Minty, T. Himel, P. Krejcik, R. H. Siemann, R. Tighe, SLAC</i> .....	2373
Improved Impedance Reduction in the CERN SPS Superconducting Cavities for High Intensity Proton Operation — <i>D. Boussard, G. Lambert, T. P. R. Linnecar, CERN</i> .....	2376
Damping of Phase Errors at Injection in the LHC — <i>D. Boussard, E. Onillon, CERN</i> .....	2379
A Digital Beam Phase Loop for the Low Energy Booster — <i>L. K. Mestha, V. Brouk, R. C. Webber, J. Mangino, T. Uher, SSCL</i> .....	2382
General Time-Varying State-Space Control Model and Its Application for Transient Beam Loading Compensation — <i>L. K. Mestha, C. M. Kwan, SSCL; K. S. Yeung, UTA</i> .....	2385
A Digital Phase and Amplitude Feedforward Correction System — <i>D. Yu, P. Conway, DULY Res. Inc.</i> .....	2388

*Proceedings of the 1993 Particle Accelerator Conference*

Results of Adaptive Feedforward on GTA — C. D. Ziomek, P. M. Denney, A. H. Regan, M. T. Lynch, S. P. Jachim, L. E. Eaton, E. F. Natter, LANL .....	2391
Fast Bunch-to-Bunch Current Sampling in the Cornell Electron-Positron Collider — C. R. Dunnam, Cornell; K. B. Unser, CERN .....	2394
A Method for Measuring Dark Current Electron Beams in an RF Linac — X. K. Maruyama, T. Fasanello, H. Rietydyk, Naval Postgraduate School; M. A. Piestrup, Adelphi Tech.; D. W. Rule, R. B. Fiorito, NSWC .....	2397
High Bandwidth Beam Current Monitor — R. M. Baltrusaitis, C. A. Ekdahl, LANL; R. G. Cooper, E. Peterson, C. E. Warn, EG&G .....	2400
Rapid Measurements of Two-Dimensional Ion Beam Current Distribution for Pulsed Neutron Source — A. M. Tron, MEPI .....	2403
Short Bunch Length Detector for Ion Beam with High Bunch Density — A. M. Tron, V. V. Shako, MEPI .....	2406
Measurement of Bunch Time-Structure in KEK-PF — M. Tobiyama, T. Kasuga, T. Takeo, T. Obina, K. Tamura, Hiroshima U.; T. Katsura, KEK .....	2409
A Fifth Harmonic RF Bunch Monitor for the ANL-APS Electron Linac — A. Nassiri, A. Grelick, ANL .....	2412
Characterization of Subnanosecond Heavy-Ion Bunches at the TASSC Superconducting Cyclotron — G. R. Mitchel, N. A. Towne, AECL .....	2415
Design, Implementation, and Results from a Longitudinal Phase Space Tomography (PST) Monitor in the Fermilab Main Ring — G. Jackson, FNAL .....	2418
An Electrostatic Sweep Plate Device for Emittance Measurement of Ion Beams to 2 MeV — T. W. Debiak, J. Porter, R. Heuer, I. Birnbaum, Grumman .....	2420
Length Monitor for 1 mm SLC Bunches — E. Babenko, BINP Novosibirsk; R. K. Jobe, D. McCormick, J. T. Seeman, SLAC .....	2423
Bunch Shape Monitor for SSCL Linac — J. W. Hurd, G. M. Arbiqye, C. E. Crist, F. W. Guy, G. T. Leifeste, D. Raparia, K. Saadatmand, D. A. Swenson, SSCL; S. Esin, A. Feschenko, A. Stepanov, A. Mirzajan, INR Moscow .....	2426
A Field-Based Technique for the Longitudinal Profiling of Ultrarelativistic Electron or Positron Bunches Down to Lengths of $\leq 10$ Microns — R. Tatchyn, SLAC .....	2429
Performance Limits of a Streak Camera in Real Time Three-Dimensional Measurement of Bunch Oscillation in LEP — E. Rossa, CERN; F. Tecker, RWTH Aachen; J.C. Mathae, ARP Strasbourg .....	2432
Bunch Length Measurements in the SLC Damping Ring — F.-J. Decker, T. Limberg, M. Minty, M. Ross, SLAC ..	2435
Virtual Photon Impulse of Bunch, Beampipe Response, Coherent RF Beamstrahlung; and BEPC Bunch Length, BES Jam, Virtual Acceleration — J. Shen, IHEP Beijing .....	2438
Development on Multistrip Monitor for Nonintercepting Measurement of Beam Geometric Moments — Y. Yin, TRIUMF .....	2441
Wire Scanner Data Analysis for the SSC Linac Emittance Measurement — C. Y. Yao, J. W. Hurd, J. Sage, SSCL .....	2444
Real-Time Spot Size Measurement for Pulsed High-Energy Radiographic Machines — S. A. Watson, LANL .....	2447
High Resolution Beam Monitoring with Optical Transition Radiation at 3 MeV Electron Energy — A. Specka, D. Bernard, R. Guirlet, F. Jacquet, P. Miné, B. Montès, R. Morano, P. Poilleux, LPNHE; F. Amiranoff, LULI; J. Morillo, LSI .....	2450
Beam Profiling with Optical Transition Radiation — D. W. Rule, R. B. Fiorito, NSWCDD .....	2453
Beam Emittance from Coherent Cherenkov Radiation in a Solid Dielectric — R. D. Richardson, R. C. Platt, SAIC; C. E. Crist, SNL .....	2456
A 10 $\mu$ m Resolution Secondary Emission Monitor for Fermilab's Targeting Station — P. Hurh, S. O'Day, R. Dombrowski, T. Page, FNAL .....	2459
Construction of a High Resolution Electron Beam Profile Monitor — J. Norem, J. Dawson, W. Haberichter, W. Novak, L. Reed, X-F. Yang, ANL .....	2462
Design Study of Beam Profile Monitor of Storage Ring by Using Synchrotron Radiation — I. C. Hs, T. H. Huang, Nat. Tsing Hua U./SRRC .....	2465
Limitations of a Residual Gas Ionization Beam Profile Monitor for the SSC Collider — R. Meinke, W. Nexsen, E. Tsyganov, A. Zinchenko, SSCL .....	2468
Full Cycle Beam Diagnostics with an Ionization Profile Monitor — A. Stillman, R. E. Thern, BNL .....	2471
Electron Beam Diagnostics by Means of Edge Radiation — O. V. Chubar, Kurchatov Inst.; E. S. Masunov, MEPI .....	2474
CEBAF Beam Viewer Imaging Software — B. A. Bowling, C. McDowell, CEBAF .....	2477

*Each volume begins with this five-volume table of contents and ends with the five-volume author index. The chairmen's foreword and a list of conference organizers and staff appear as front matter in Volume 1. A list of conference participants precedes the author index in Volume 5.*

## Five-Volume Contents

Prototype Flying-Wire Beam-Profile Monitor — <i>D. B. Barlow, C. M. Fortgang, J. D. Gilpatrick, R. E. Meyer, A. M. Rendon, D. S. Warren, M. D. Wilke, LANL</i> .....	2480
Emittance Measurement and Data Analysis for the SSC Linac Injector Lab — <i>J. E. Hébert, P. Datte, F. W. Guy, N. C. Okay, K. Saadatmand, J. Sage, D. M. Wetherholt, W. A. Whittenberg, SSCL</i> .....	2483
Automatic Emittance Measurement at the ATF — <i>X. J. Wang, R. Malone, K. Batchelor, I. Ben-Zvi, BNL</i> .....	2486
Electron Beam Emittance Monitor for the SSC — <i>E. Tsyganov, R. Meinke, W. Nexsen, S. Kauffmann, A. Zinchenko, A. Taratin, SSCL</i> .....	2489
Measurement of Vertical Emittance at LEP from Hard X-Rays — <i>H. Akbari, J. Borer, C. Bovet, Ch. Delmere, A. Manarin, E. Rossa, M. Sillanoli, J. Spanggaard, CERN</i> .....	2492
Performance and Operational Experience of the LEP Synchrotron Light Telescopes — <i>G. Burtin, R. J. Colchester, J. J. Gras, R. Jung, J. M. Vouillot, CERN</i> .....	2495
High Sensitivity Beam Intensity and Profile Monitors for the SPS Extracted Beams — <i>J. Camas, G. Ferioli, R. Jung, J. Mann, CERN</i> .....	2498
High Density Harp for SSCL Linac — <i>C. T. Fritsche, M. L. Krogh, AlliedSignal; C. E. Crist, SSCL</i> .....	2501
High Resolution Measurements of Lepton Beam Transverse Distributions With the LEP Wire Scanners — <i>J. Camas, G. Crockford, G. Ferioli, C. Fischer, J. J. Gras, R. Jung, J. Koopman, J. Mann, CERN</i> .....	2504
Beam Size Measurements with Noninterceptive Off-Axis Screens — <i>F.-J. Decker, R. Brown, J. T. Seeman, SLAC</i> ...	2507
Resolution Improvement in Beam Profile Measurements with Synchrotron Light — <i>O. V. Chubar, MEPI</i> .....	2510
The Orsay Spot Size Monitor for the Final Focus Test Beam — <i>J. Buon, B. Delcourt, J. Jeanjean, F. Le Diberder, V. Lepeltier, P. Puzo, LAL Orsay</i> .....	2513
Beam Monitor Utilizing Transition Radiation — <i>Y. Ogawa, J. Choi, T. Suwada, T. Kamitani, T. Urano, K. Furukawa, S. Ohsawa, A. Enomoto, I. Sato, KEK</i> .....	2516
Fermilab Main Ring Low Level RF System Modifications for Focus Free Transition Beam Tests — <i>R. G. Scala, K. Meisner, FNAL</i> .....	2519
RF Synchronous Transfer into Specific Buckets Between Fermilab Main Ring and Tevatron Accelerators — <i>K. Meisner, FNAL</i> .....	2522
Main Ring Bunch Length Monitor — <i>K. Meisner, G. Jackson, FNAL</i> .....	2525
A VX1/LabVIEW-based Beamline Tuner — <i>W. Blokland, FNAL</i> .....	2528
A Frequency-Domain Directivity Enhancement of Beam Position Stripline Detectors — <i>E. L. Barsotti, FNAL</i> .....	2531
The Control System of ROSY I — <i>T. Goetz, M. Picard, U. Bonn; M. Plesko, Sinc. Trieste</i> .....	2534
Measuring Emittance Using Beam Position Monitors — <i>S. J. Russell, B. E. Carlsten, LANL</i> .....	2537
On the Reliability of Measured Results by Non-Destructive Beam Profile Monitor — <i>T. Kawakubo, E. Kadokura, KEK; T. Ishida, Mitsubishi Elect.</i> .....	2540
Transverse Feedback System with Digital Filter — <i>V. M. Zhabitsky, JINR; I. L. Korenev, L. A. Yudin, MRTI</i> .....	2543

## Volume 4

<b>Advanced Accelerator Concepts</b> <i>Chair: C. Joshi</i>	
R. R. Wilson Prize Lecture: Adventures with Accelerators ( <i>Invited Paper</i> ) — <i>J. P. Blewett, BNL (ret.)</i> .....	2546
Demonstration of Plasma Beat Wave Acceleration of Electrons from 2 MeV to 20 MeV ( <i>Invited Paper</i> ) — <i>C. E. Clayton, K. A. Marsh, M. Everett, A. Lal, C. Joshi, UCLA</i> .....	2551
Laser Wakefield Accelerator Experiments Using 1 ps 30 TW Nd:glass Laser — <i>K. Nakajima, H. Nakanishi, T. Kawakubo, A. Ogata, KEK; Y. Kitagawa, H. Shiraga, R. Kodama, T. Zhang, K. Suzuki, Y. Kato, Osaka U.; Y. Sakawa, T. Shoji, Nagoya U.; Y. Nishida, N. Yugami, Utsunomiya U.; T. Tajima, U. Texas, Austin</i> .....	2556
Photonic Band Gap Resonators for High Energy Accelerators ( <i>Invited Paper</i> ) — <i>S. Schultz, D. R. Smith, UCSD; N. Kroll, UCSD/SLAC</i> .....	2559
Update on the ATF Inverse Cherenkov Laser Acceleration Experiment — <i>W. D. Kimura, L. C. Steinhauer, G. H. Kim, S. C. Tidwell, STI Optronics; I. Pogorelsky, K. P. Kusche, BNL/STI Optronics</i> .....	2564
New Directions in RF Sources ( <i>Invited Paper</i> ) — <i>L. Schüchter, Cornell</i> .....	2567
Criteria for Comparing the Suitability of Microwave Amplifiers for Driving TeV Linear Colliders — <i>V. I. Granatstein, G. S. Nusinovich, U. Maryland</i> .....	2572

Volume 1: 1-747  
 Volume 2: 748-1640  
 Volume 3: 1641-2545  
 Volume 4: 2546-3218  
 Volume 5: 3219-3933

**Proceedings of the 1993 Particle Accelerator Conference**

High Gradient Acceleration in a 17 GHz Photocathode RF Gun — S. C. Chen, J. Gonichon, L. C-L. Lin, R. J. Temkin, S. Trotz, B. G. Danly, J. S. Wurtele, MIT .....	2575
An Inverse Free-Electron-Laser Accelerator — A. S. Fisher, J. C. Gallardo, A. van Steenberg, S. Ulc, M. Woodle, BNL; J. Sandweiss, Yale; J. Fang, Columbia U. ....	2578
Phase Control in High-Gradient Laser Particle Accelerators — L. C. Steinhauer, W. D. Kimura, STI Optronics .....	2581
<b>Poster presentations:</b>	
Beam Quality in a Cyclotron Autoreonance Accelerator — B. Hafizi, Icarus Res.; P. Sprangle, NRL; J. L. Hirshfield, Omega-P Inc. ....	2584
Superlattice Crystal Accelerator: Acceleration Beyond GeV/m — S. A. Bogacz, FNAL .....	2587
Design Study of a Microwave Driver for a Relativistic Klystron Two-Beam Accelerator — T. L. Houck, LLNL .....	2590
The Standing Wave FEL/TBA: Realistic Cavity Geometry and Energy Extraction — J. Kim, A. M. Sessler, LBL; H. Henke, TU Berlin; W. M. Sharp, LLNL .....	2593
The Argonne Wakefield Accelerator: Overview and Status — P. Schoessow, E. Chojnacki, W. Gai, C. Ho, R. Konecny, J. Power, M. Rosing, J. Simpson, ANL .....	2596
A Self-Consistent Theory of Ferromagnetic Waveguide Accelerators Driven by Electron Beams — H. S. Uhm, NSWC .....	2599
Wakefield Accelerator Driven by a Relativistic Electron Beam in a Ferromagnetic Waveguide — H. S. Uhm, NSWC .....	2602
Magnetic Field-Decay Accelerator Driven by a Relativistic Electron Beam in a Ferromagnetic Waveguide — H. S. Uhm, NSWC .....	2605
Three-Dimensional Simulation Analysis of the First Sections of a Standing-Wave Free-Electron Laser Two-Beam Accelerator — C. Wang, A. M. Sessler, LBL .....	2608
Reacceleration Experiment to Demonstrate the Concept of Efficiency Enhancement in a Relativistic Klystron Two- Beam Accelerator — G. A. Westenskow, T. L. Houck, LLNL .....	2611
Design Analysis for a 100-MeV Inverse Cherenkov Laser Accelerator — J. R. Fontana, UCSB; W. D. Kimura, L. C. Steinhauer, STI Optronics; I. Pogorelsky, BNL/STI Optronics .....	2614
An Inverse Free Electron Laser Driven Linear Collider Electron-Positron B-Factor — N. Barov, C. Pellegrini, UCLA; J. Sandweiss, Yale .....	2617
2.5D Numerical Simulation of Relativistic Electron Bunches (REB) Interaction with Underdense and Overdense Plasmas — O. V. Batishchev, Y. S. Sigov, Keldysh Inst.; V. I. Karas', Y. B. Fainberg, Kharkov Inst. ....	2620
Propagation of Short Electron Pulses in Underdense Plasmas — N. Barov, J. Rosenzweig, UCLA .....	2623
Numerical Simulations of Driving Beam Dynamics in the Plasma Wakefield Accelerator — G. Joyce, J. Krall, E. Esarey, NRL .....	2626
Self-Modulated-Laser Wakefield Accelerator — J. Krall, A. Ting, E. Esarey, P. Sprangle, NRL .....	2629
A 100 MeV Proof-of-Principle Laser Wakefield Accelerator Experiment — A. Ting, A. Fisher, R. Fischer, J. Grun, J. Krall, E. Esarey, P. Sprangle, NRL; D. Umstadter, G. Mourou, U. Michigan .....	2632
Recent Work on Short Pulse Laser-Plasma Accelerators — T. Katsouleas, T. C. Chiou, USC; W. B. Mori, C. Decker, UCLA; J. S. Wurtele, G. Shvets, MIT .....	2635
Plasma Lens Experiments at the Final Focus Test Beam — J. Norem, ANL; D. Cline, W. Gabella, P. Kwok, S. Rajagopalan, J. Rosenzweig, UCLA; B. Barletta, UCLA/LBL; R. Williams, Florida A&M; S. Chattopadhyay, W. Leemans, A. Sessler, LBL; G. Westenskow, LLNL; J. Wurtele, MIT; J. J. Su, NCU Taiwan; K. Nakajima, H. Nakanishi, A. Ogata, D. Whittum, KEK; I. Hsu, NTU Taiwan; D. D. Meyerhofer, U. Rochester; T. Katsouleas, P. Lai, R. Liou, USC; P. Chen, W. Craddock, C. K. Ng, J. Spencer, SLAC; Y. Nishida, Utsunomiya U. ....	2638
A Plasma Lens and Accelerator Based Upon Magnetically Driven Charge Separation — S. Robertson, U. Colorado .....	2641
The NRL X-Band Magnicon Amplifier Experiment — S. H. Gold, C. A. Sullivan, W. M. Manheimer, NRL; B. Hafizi, Icarus Res. ....	2644
Theoretical Investigation of Magnicon Efficiency — B. Hafizi, Icarus Res.; S. H. Gold, W. M. Manheimer, P. Sprangle, NRL .....	2647
First Test of the X-Band Pulsed Magnicon — O. Nezhevenko, I. Kazarezov, E. Kozyrev, G. Kuznetsov, I. Makarov, A. Nikiforov, B. Persov, G. Serdobintsev, M. Tiunov, V. Yakovlev, I. Zapryagaev, BINP Russia .....	2650

Each volume begins with this five-volume table of contents and ends with the five-volume author index. The chairmen's foreword and a list of conference organizers and staff appear as front matter in Volume 1. A list of conference participants precedes the author index in Volume 5.

Five-Volume Contents

TM-FEL With a Longitudinal Wiggler and an Annular Beam — L. Schächter, T. J. Davis, J. A. Nation, Cornell	2653
CARM and Harmonic Gyro-Amplifier Experiments at 17 GHz — W. L. Menninger, B. G. Danly, S. Alberti, C. Chen, E. Gignot, J. L. Rullier, R. J. Temkin, MIT	2656
Stability of Gyrotwistrons — P. E. Latham, G. S. Nusinovich, J. Cheng, U. Maryland	2659
Optimum Operation of Gyrotwistrons — P. E. Latham, G. S. Nusinovich, U. Maryland	2661
Large Orbit Gyroklystron Development at Los Alamos — R. M. Stringfield, R. M. Wheat, D. J. Brown, M.V. Fazio, J. Kinross-Wright, B. E. Carlsten, G. Rodenz, R. J. Faehl, R. F. Hoeberling, LANL	2664
Initial Operation of a High Power, K-Band, Harmonic Gyroklystron for Accelerator Applications — J. P. Calame, H. W. Matthews, W. Lawson, B. Hogan, M. K. E. Lee, J. Cheng, V. L. Granatstein, M. Reiser, C. D. Striffler, U. Maryland	2667
Design of a 100 MW, 17 GHz Second Harmonic Gyroklystron Experiment — W. Lawson, P. E. Latham, V. Specht, M. K. E. Lee, Q. Qian, J. P. Calame, B. Hogan, V. L. Granatstein, M. Reiser, C. D. Striffler, U. Maryland	2670
Some Concepts of Relativistic Gyroamplifiers for Particle Acceleration — G. S. Nusinovich, P. E. Latham, V. L. Granatstein, U. Maryland	2673
Experimental Progress Toward a 1 GW, 1 ns Pulse Length, High Current Relativistic Klystron — M. Fazio, B. Carlsten, R. Faehl, W. Haynes, T. Kwan, R. Stringfield, LANL	2675
Relativistic Plasma Klystron Amplifier in Connection with Application to High Gradient Accelerators — H. S. Uhm, NSWC	2678
Sheet-Beam Klystron RF Cavities — D. Yu, DULY Res. Inc.; P. Wilson, SLAC	2681
Beam-Wave Interaction in a Quasi-Periodic Structure — L. Schächter, J. A. Nation, Cornell	2684
Two-Stage, High Power X-Band Amplifier Experiment — E. Kuang, T. J. Davis, J. D. Ivers, G. S. Kerslick, J. A. Nation, L. Schächter, Cornell	2687
Long-Pulse, High-Power, X-Band Relativistic Traveling-Wave Tube Amplifier — T. Kimura, S. Alberti, B. G. Danly, R. J. Temkin, MIT	2690
Tapered Tube, Microsecond Electron Beam Gyrotron Backward-Wave Oscillators — R. M. Gilgenbach, M. T. Walter, P. R. Menge, T. A. Spencer, U. Michigan	2693
Quiet Start and Autotasking for PARMELA — J. Gonichon, S. C. Chen, L. C.-L. Lin, R. J. Temkin, MIT	2696
Waveguide Side-Wall Coupling in RF Guns — L. C.-L. Lin, S. C. Chen, J. Gonichon, S. Trotz, J. S. Wurtele, MIT	2699
A High-Current Micro-Pulse Electron Gun — F. M. Mako, W. Peter, FM Tech. Inc.	2702
Knife-Edge Thin Film Field Emission Cathodes — B. Lee, H. P. Demroff, M. M. Drew, T. S. Elliot, T. K. Mazumdar, P. M. McIntyre, Y. Pang, D. D. Smith, H.-J. Trost, Texas A&M	2705
The Oxidized Porous Silicon Field Emission Array — D. D. Smith, H. P. Demroff, T. S. Elliott, T. B. Kasproicz, B. Lee, T. K. Mazumdar, P. M. McIntyre, Y. Pang, H.-J. Trost, Texas A&M	2708
Study of Porous Silicon Morphologies for Electron Transport — Y. Pang, H. Demroff, T. S. Elliott, B. Lee, J. Lu, V. B. Madduri, T. K. Mazumdar, P. M. McIntyre, D. D. Smith, H.-J. Trost, Texas A&M	2711
Cold Test Measurements of a BWO Slow-Wave Structure — W. Main, Y. Carmel, K. Ogura, J. Weaver, S. Watanabe, U. Maryland	2714
Collective Accelerator with Variable Energy and Wide Spectrum of Accelerated Ions — R. Meshcherov, G. Batskikh, V. Krasnopolsky, V. Rybalko, V. Sazhin, MRTI Moscow; A. Vasiliev, MAE Russia	2717
High Gradient Experiments with Nanosecond Pulses — V. Baglin, H. Haseroth, J. Knott, CERN; F. Chautard, SSCL	2720
Development of the Alternate Entry Port for the ATF — Z. Parsa, BNL	2723

**Magnets, Cryogenics, and Alignment**

Chair: J. Strait

Status of Superconducting Magnet Development (SSC, RHIC, LHC) (Invited Paper) — P. Wanderer, BNL	2726
Electrical Performance Characteristics of the SSC Accelerator System String Test (Invited Paper) — W. Robinson, W. Burgett, T. Dombek, J. Gannon, P. Kraushaar, A. McInturff, T. Savord, G. Tool, SSCL	2731
Overview of the Final Focus Test Beam Alignment System — V. E. Bressler, R. E. Ruland, D. Plouffe, SLAC	2736
Long Term Experience with Cryoplant Operation for Superconducting Magnets and RF Cavities at CERN — D. Delikaris, J.-P. Dauvergne, P. K. Frandsen, F. Haug, G. Passardi, J.-M. Rieubland, J. Schmid, CERN	2739
Axial Variations in the Magnetic Field of Superconducting Dipoles and Quadrupoles — A. K. Ghosh, K. E. Robins, W. B. Sampson, BNL	2742

Volume 1: 1-747  
 Volume 2: 748-1640  
 Volume 3: 1641-2545  
 Volume 4: 2546-3218  
 Volume 5: 3219-3933

**Proceedings of the 1993 Particle Accelerator Conference**

<b>Large Aperture Quadrupoles for RHIC Interaction Regions — R. Gupta, M. Anerella, G. Ganetis, M. Garber, A. Ghosh, A. Greene, A. Jain, S. Kahn, E. Kelly, E. Killian, G. Morgan, A. Morgillo, J. Muratore, A. Prodell, M. Rehak, W. Sampson, R. Shutt, P. Thomson, P. Wanderer, E. Willen, BNL .....</b>	<b>2745</b>
<b>Poster presentations:</b>	
<b>Design of Superconducting Quadrupole Magnets for CEBAF's Hall A Spectrometer — R. Kreuz, E. Brüttsch, K. Dreher, H. Grüneberg, H. Lütkehaus, W. Nick, H. Peschel, B. Rzezonka, F. Sommer, P. Schäfer, Siemens AG .....</b>	<b>2748</b>
<b>Design of a Superconducting Wiggler for the PLS — B. K. Kang, Y. M. Koo, D. E. Kim, H. S. Seo, Y. U. Sohn, Pohang; P. D. Vobly, N. A. Mezentsev, G. N. Kulipanov, BINP .....</b>	<b>2751</b>
<b>Calculations of Magnetic Field for the End Design of the RHIC Arc Dipole — S. A. Kahn, R. C. Gupta, A. K. Jain, G. H. Morgan, P. A. Thompson, BNL .....</b>	<b>2754</b>
<b>Collider Scenario Implications of ASST Operation — A. D. McInturff, W. Burgett, M. Christianson, T. Dombeck, J. Gannon, D. Haenni, P. Kraushaar, M. Levin, M. McAshan, G. Mulholland, D. Murray, W. Robinson, T. Savord, R. Smellie, F. Spinós, G. Tool, J. Weisend II, J. Zatopek, SSCL .....</b>	<b>2757</b>
<b>Preliminary Analysis of Coil Wedge Dimensional Variation in SSC Prototype Dipole Magnets — D. Pollock, G. Brown, S. Dwyer, R. Gattu, D. Warner, SSCL .....</b>	<b>2760</b>
<b>SSC String Test Facility for Superconducting Magnets: Testing Capabilities and Program for Collider Magnets — P. Kraushaar, W. Burgett, T. Dombeck, A. McInturff, W. Robinson, V. Saladin, SSCL .....</b>	<b>2763</b>
<b>"B" Series RHIC Arc Quadrupoles — P. Thompson, M. Anerella, G. Ganetis, M. Garber, A. Ghosh, A. Greene, R. Gupta, A. Jain, S. A. Kahn, G. Morgan, A. Morgillo, J. Muratore, A. Prodell, M. Rehak, W. Sampson, P. Wanderer, E. Willen, BNL .....</b>	<b>2766</b>
<b>Fermilab-Built SSC Collider Dipoles Using Low Temperature Curing Insulation Systems With and Without Glass Tape — T. S. Jaffery, R. Coombes, A. Devred, J. DiMarco, T. Ogitsu, R. E. Sims, J. C. Tompkins, M. Wake, SSCL; R. Bossert, J. Carson, S. W. Delchamps, I. Gonczy, S. Gourlay, R. Hanft, M. J. Lamm, P. Mazur, D. Orris, J. Strait, FNAL .....</b>	<b>2769</b>
<b>Design and Tests of UNK Superconducting Correction Magnet Models — E. Rybakov, N. Bogatov, I. Dmitrieva, M. Kosyakin, Yu. Severgin, V. Fedorov, V. Shan'gin, Efremov Inst.; P. Chirkov, S. Kozub, K. Myznikov, V. Sychev, IHEP Moscow; A. Rychagov, V. Sytnikov, A. Taran, All-Union R&amp;D Inst. ....</b>	<b>2772</b>
<b>Quench and Quench Protection for the SSC Collider Correctors — A. He, SSCL.....</b>	<b>2775</b>
<b>Variation in <math>a_1</math> Saturation in SSC Collider Dipoles — R. C. Gupta, A. K. Jain, BNL .....</b>	<b>2778</b>
<b>Spool Pieces at the SSCL — T. Clayton, Y. Cai, R. Smellie, S. Stampke, SSCL .....</b>	<b>2781</b>
<b>Quench Simulations of the 40 mm Aperture SSC-Quadrupole Magnet Connected in Series with 50 mm Aperture SSC-Dipole Magnets — G. López, SSCL .....</b>	<b>2784</b>
<b>Effective Stress of the SSC 80 K Synchrotron Radiation Liner in a Quenching Dipole Magnet — K. K. Leung, Q. S. Shu, K. Yu, J. Zbasnik, SSCL .....</b>	<b>2787</b>
<b>Improved Cable Insulation for Superconducting Magnets — M. Anerella, A. K. Ghosh, E. Kelley, J. Schmalzle, E. Willen, BNL; J. Fraivillig, J. Ochsner, D. J. Parish, DuPont .....</b>	<b>2790</b>
<b>Treatment of the Results of Magnetic Mapping of the SIBERIA-2 Magnets — V. Korchuganov, E. Levichev, A. Philipchenko, BINP .....</b>	<b>2793</b>
<b>Prototype Quadrupole Magnets for the PLS Storage Ring — Y. M. Koo, D. E. Kim, Y. G. Nah, H. S. Han, B. K. Kang, K. H. Park, J. R. Yoon, H. K. Lee, J. E. Milburn, Pohang .....</b>	<b>2796</b>
<b>Magnetic Measurement Data of the Injector Synchrotron Dipole Magnets for the 7-GeV Advanced Photon Source — K. Kim, S. H. Kim, L. R. Turner, C. L. Doose, R. Hogrefe, R. Merl, ANL .....</b>	<b>2799</b>
<b>Magnet Measurement Facility for the 7-GeV Advanced Photon Source — S. H. Kim, K. Kim, C. Doose, R. Hogrefe, R. Merl, ANL .....</b>	<b>2802</b>
<b>Magnetic Measurements of the Storage Ring Quadrupole Magnets for the 7-GeV Advanced Photon Source — S. H. Kim, K. Kim, C. Doose, R. Hogrefe, R. Merl, ANL .....</b>	<b>2805</b>
<b>Design and Tests of the Injector Synchrotron Magnets for the 7-GeV Advanced Photon Source (APS) — K. Kim, S. H. Kim, K. M. Thompson, L. R. Turner, ANL .....</b>	<b>2808</b>
<b>Final Analysis of the ALS Lattice Magnet Data — R. Keller, LBL .....</b>	<b>2811</b>
<b>Design and Measurement of the Sextupole Magnet for the APS Storage Ring — L. R. Turner, K. M. Thompson, S. H. Kim, K. Kim, ANL .....</b>	<b>2814</b>
<b>A Pulsed Septum Magnet for the APS — L. R. Turner, D. G. McGhee, F. E. Mills, S. Reeves, ANL .....</b>	<b>2817</b>

*Each volume begins with this five-volume table of contents and ends with the five-volume author index. The chairmen's foreword and a list of conference organizers and staff appear as front matter in Volume 1. A list of conference participants precedes the author index in Volume 5.*

## Five-Volume Contents

The ELETTRA Storage Ring Magnets — <i>G. Petrucci, D. Tommasini, Sinc. Trieste/CERN</i> .....	2820
Experience with the Source Evaluation Board Method of Procuring Technical Components for the Fermilab Main Injector — <i>D. J. Harding, J. P. Collins, G. R. Kobliska, N. S. Chester, E. G. Pewitt, W. B. Fowler, FNAL</i> ..	2823
Sextupole Magnets for the Fermilab Main Injector — <i>D. J. Harding, N. Chester, R. Baiod, FNAL</i> .....	2826
Design and Measurements of Prototype Fermilab Main Injector Dipole Endpacks — <i>D. J. Harding, H. D. Glass, J.-F. Ostiguy, B. C. Brown, F. A. Harfoush, C. S. Mishra, FNAL</i> .....	2829
Magnetic Measurement of Quadrupole and Sextupole Magnets for the MIT-Bates South Hall Ring (SHR) — <i>D. R. Tieger, J. D. Zumbro, W. W. Sapp, MIT Bates</i> .....	2832
A Permanent Magnet Dipole Correction Element for the Tevatron — <i>J. E. Goodwin, T. Anderson, A. Franck, N. Gelfand, H. Jostlein, FNAL</i> .....	2835
Precision Measurement of Transport Components — <i>P. Tenenbaum, J. K. Cobb, D. R. Jensen, D. Sawyer, W. Wagner, H. V. Walz, S. H. Williams, SLAC</i> .....	2838
Measurement and Adjustment of CIAE Medical Cyclotron Magnet — <i>M. Fan, X. Zhang, T. Zhang, C. Liang, Q. Tao, Z. Zhao, C. Chu, T. Li, Y. Hu, Y. Chen, H. Zhang, H. Jia, C. Jiao, J. Liu, W. Zhang, C. Zhou, J. Jiao, Y. Hou, CIAE China</i> .....	2841
Magnetic Measurement and Alignment of the ELETTRA Storage Ring Quadrupole, Sextupole and Steerer Magnets — <i>D. Zangrando, R. P. Walker, Sinc. Trieste</i> .....	2844
Measurement and Correction of the ELETTRA Storage Ring Dipole Magnets — <i>R. P. Walker, D. Zangrando, Sinc. Trieste</i> .....	2847
Magnet Costs for the Advanced Light Source — <i>J. Tanabe, J. Krupnick, E. Hoyer, A. Paterson, LBL</i> .....	2850
Automatic Bench for Precise Magnetic Measurements of Linac Multipole Focusing Elements — <i>V. S. Skachkov, M. A. Kozchekin, R. P. Koujbida, V. I. Lulevich, A. V. Selin, O. S. Sergeeva, ITEP Moscow</i> .....	2853
Measurements of Loma Linda Proton Therapy Gantry Dipoles — <i>H. D. Glass, P. O. Mazur, J. W. Sim, FNAL</i> .....	2856
Techniques for Measurement of Dipole Endfields with a Rigid Integrating Coil — <i>H. D. Glass, FNAL</i> .....	2859
Lamination and End Plate Design Studies of SSC Low Energy Booster Magnet Prototypes — <i>N. Li, SSCL</i> .....	2862
Design and Fabrication of a Multi-Purpose Panofsky Magnet — <i>J. Budnick, T. Hall, D. Li, S. Y. Lee, IUCF</i> .....	2865
Magnetic Septa Design and Performance for Injection and Extraction to and from the MIT-Bates South Hall Ring (SHR) — <i>R. Averill, K. Dow, H. Enge, J. Flanz, E. Ihloff, M. Farkhondeh, C. Sibley, MIT-Bates</i> .....	2868
Octupole Magnet Design for the 1/2 Integer Resonant Extraction of Electrons from the MIT-Bates South Hall Ring (SHR) — <i>R. Averill, J. Flanz, E. Ihloff, D. Tieger, MIT-Bates</i> .....	2871
Ramped Quadrupole Design and Performance for the MIT-Bates South Hall Ring (SHR) — <i>R. Averill, J. Flanz, E. Ihloff, D. Tieger, MIT-Bates</i> .....	2874
Lambertson Upgrade Program — <i>K. J. Weber, FNAL</i> .....	2877
Computer Studies of a Combined-Function Bend Magnet for a Proposed Redesign of the SLAC SLC Damping Rings — <i>R. A. Early, T. O. Raubenheimer, SLAC</i> .....	2880
Comparison of Computer Predictions and Magnetic Field Measurements for an Iron Spectrometer Magnet — <i>G. T. Danby, J. W. Jackson, W. Meng, C. Spataro, BNL</i> .....	2883
Design and Performance of the Dipole Magnet for the SRRC Storage Ring — <i>C. H. Chang, H. C. Liu, G. J. Hwang, SRRC Taiwan</i> .....	2886
Specific Features of Magnet Design for the Duke FEL Storage Ring — <i>B. Burnham, N. Hower, V. N. Litvinenko, J. M. J. Madey, Y. Wu, Duke</i> .....	2889
Dipole Design for the EUTL RPE Storage Ring — <i>J. I. M. Botman, C. J. Timmermans, B. Xi, H. Heller, H. L. Hagedoorn, P. Brinkgreve, E. Dekkers, J. Moerel, Eindhoven,</i> .....	2892
Design of a Lambertson Injection Magnet for the RHIC Machine — <i>E. Rodger, N. Tsoupas, J. Claus, H. W. Foelsche, BNL</i> .....	2895
Combined AC Corrector Magnets — <i>A. J. Otter, P. A. Reeve, TRIUMF; N. Marks, Daresbury</i> .....	2898
Longitudinal Profile and Effective Length of a Conventional Dipole Magnet — <i>J. Ostiguy, FNAL</i> .....	2901
Magnetic Flux Shielding for the Muon g-2 Storage Ring Superconducting Inflectors — <i>W. Meng, W. B. Sampson, M. Suenaga, BNL</i> .....	2904
Three Dimensional Field Analysis for the AGS Combined Function Magnets — <i>W. Meng, M. Tanaka, BNL</i> .....	2907
Survey and Alignment Data Analysis for the ALS Storage Ring — <i>R. Keller, LBL</i> .....	2910
A Mechanical System for the Positioning of Accelerator Magnets — <i>R. Viola, R. Martin, SSCL</i> .....	2913
Preliminary Studies on a Magneto-Optical Procedure for Aligning RHIC Magnets — <i>M. A. Goldman, R. E. Sikora, T. J. Shea, BNL</i> .....	2916

Volume 1: 1-747  
 Volume 2: 748-1640  
 Volume 3: 1641-2545  
 Volume 4: 2546-3218  
 Volume 5: 3219-3933



## Poster presentations:

Design and Construction of a Full Copper Photocathode RF Gun — X. J. Wang, K. Batchelor, I. Ben-Zvi, D. Lynch, J. Sheehan, M. Woodle, BNL .....	3000
Streak Camera Measurements of Electron Bunch Length from a Copper Photocathode in an RF Gun — G. Hairapetian, P. Davis, M. Everett, C. Clayton, C. Joshi, S. Hartman, S. Park, C. Pellegrini, UCLA .....	3003
Possible Efficiency-Enhancement of Metal Photocathode for DISKTRON Electrostatic Accelerator — T. Tanabe, Y. Kawamura, K. Toyoda, RIKEN; D. Li, Changchun Inst., China .....	3006
Cold Test of Rocketdyne RF Gun — M. Lampel, Rockwell; R. Zhang, UCLA .....	3009
Design and Construction of a High-Duty-Factor Photocathode Electron Gun — I. S. Lehrman, I. A. Birnbaum, M. Cole, R. L. Heuer, E. Sheedy, Grumman; I. Ben-Zvi, K. Batchelor, J. C. Gallardo, H. G. Kirk, T. Srinivasan-Rao, BNL .....	3012
An Improved Thermionic Microwave Gun and Emittance-Preserving Transport Line — M. Borland, ANL .....	3015
Experience with a Radio Frequency Gun on the SSRL Injector Linac — J. N. Weaver, R. D. Genin, P. Golceff, H. Morales, J. Sebek, SLAC .....	3018
Design of a High Duty Cycle, Asymmetric Emittance RF Photocathode Injector for Linear Collider Applications — J. B. Rosenzweig, E. Colby, UCLA; G. Jackson, T. Nicol, FNAL .....	3021
Design of a High Brightness RF Photoinjector for the SLAC Linear Coherent Light Source — J. Rosenzweig, UCLA; L. Serafini, INFN Milan .....	3024
Performance of the SLC Polarized Electron Source and Injector with the SLAC 3 km Linac Configured for Fixed Target Experiments — A. D. Yeremian, R. K. Alley, J. E. Clendenin, J. C. Frisch, C. L. Garden, L. A. Klaisner, A. V. Kulikov, R. H. Miller, C. Y. Prescott, P. J. Saez, D. C. Schultz, H. Tang, J. L. Turner, M. B. Woods, M. Zolotarev, SLAC .....	3027
An In-Situ Photocathode Loading System for the SLC Polarized Electron Gun — R. E. Kirby, G. J. Collet, K. Skarpaas, SLAC .....	3030
High Voltage Processing of the SLC Polarized Electron Gun — P. Sáez, J. Clendenin, C. Garden, E. Hoyt, L. Klaisner, C. Prescott, D. Schultz, H. Tang, SLAC .....	3033
Study of Non-Linear Photoemission Effects in III-V Semiconductors — H. Tang, R. K. Alley, J. E. Clendenin, J. C. Frisch, C. L. Garden, E. W. Hoyt, R. E. Kirby, L. A. Klaisner, A. V. Kulikov, C. Y. Prescott, P. J. Sáez, D. C. Schultz, J. L. Turner, M. Woods, M. S. Zolotarev, SLAC; H. Aoyagi, Nagoya U. ....	3036
Photocathode Performance Measurements for the SLC Polarized Electron Gun — C. L. Garden, E. W. Hoyt, D. C. Schultz, H. Tang, SLAC .....	3039
Electron Quantum Yields from a Barium Photocathode Illuminated with Polarized Light — M. E. Conde, S. Chattopadhyay, K.-J. Kim, K.-N. Leung, A. T. Young, LBL; S.-I. Kwon, Kyonggi U. ....	3042
The 1992 Polarized Light Source — R. Alley, M. Woods, M. Browne, J. Frisch, M. Zolotarev, SLAC .....	3045
Operation of a Ti:Sapphire Laser for the SLAC Polarized Electron Source — J. Frisch, R. Alley, M. Browne, M. Woods, SLAC .....	3047
The Argonne Wakefield Accelerator (AWA) Laser System and Its Laser Pulse Shaper — W. Gai, N. Hill, C. Ho, P. Schoessow, J. Simpson, ANL .....	3050
CANDELA Photo-injector: The Drive Laser — P. Georges, P. Thomas, Inst. d'Opt. Theor. Appl., Orsay; B. Leblond, C. Travier, LAL Orsay .....	3053
A Flat-Cathode Thermionic Injector for the PHERMEX Radiographic Facility — T. Kauppila, L. Builta, M. Burns, W. Gregory, D. Honaberger, S. Watson, LANL; T. Hughes, Mission Res. Corp. ....	3055
The ALS Gun Electronics System — C. C. Lo, LBL .....	3058
Witness Gun for the Argonne Wakefield Accelerator — J. Power, J. Simpson, E. Chojnacki, ANL .....	3061
Parametric Studies with PARMELA to Improve SLC Performance — T. A. Jones, A. D. Yeremian, R. H. Miller, SLAC .....	3063
High Current, Low Energy Electron Beams Produced During the High Current Phase of a Pseudospark — T. Hsu, R. Liou, M. A. Gundersen, USC; G. Kirkman, Integrated App. Phys. ....	3066
Theoretical and Experimental Study of Pseudospark Electron Beam Generation — L. Pitchford, J. P. Boeuf, U. Paul Sabatier; V. Puech, U. de Paris-Sud; R. Liou, M. Gundersen, USC .....	3069
A Variable Pulse-Length Electron Beam From the Back-Lighted Thyatron — R. Liou, T. Hsu, G. Roth, M. Gundersen, USC; G. Kirkman, Integrated App. Phys. ....	3072

*Proceedings of the 1993 Particle Accelerator Conference*

One-Dimensional Simulation Studies of Breakdown and Electron Beam Generation Processes for a Hollow Cathode Pseudospark Discharge — S. Y. Cai, C. D. Striffler, U. Maryland .....	3075
A High Brightness Electron Beam Produced by a Ferroelectric Cathode — B. Jiang, G. Kirkman, N. Reinhardt, Integrated App. Physics .....	3078
The UV-FEL at the NSLS: Straight Injection Configuration — X. Zhang, J. C. Gallardo, BNL .....	3081
Progress on PEP-II Injection R&D — E. Bloom, F. Bulos, T. Fieguth, G. Godfrey, G. Loew, R. Miller, SLAC .....	3084
New Pre-Injector of the KEK 2.5-GeV Linac and Its Performance — S. Ohsawa, I. Abe, S. Anami, J.-Y. Choi, A. Enomoto, K. Furukawa, H. Hanaki, K. Kakihara, N. Kamikubota, T. Kamitani, H. Kobayashi, Y. Ogawa, T. Oogoe, I. Sato, T. Suwada, Y. Yamazaki, M. Yokota, KEK; A. Asami, Naruto U. ....	3087
Hydrodynamic Calculations of 20-TeV Beam Interactions with the SSC Beam Dump — D. C. Wilson, C. A. Wingate, J. C. Goldstein, R. P. Godwin, LANL; N. V. Mokhov, SSCL .....	3090
First Results Concerning a Crystal Radiator Dedicated to Positron Production by Photons from Channeled Multi-GeV Electrons — R. Chehab, T. Baier, P. Jean, LAL Orsay; X. Artru, M. Chevallier, R. Kirsch, J. C. Poizat, J. Remillieux, IPNL Lyon; A. Jejcic, J. Maillard, J. Silva, LPC Paris; E. Hourany, G. Renou, J. P. Didelez, A. Elayi, L. Rosier, IPN Orsay; V. N. Baier, V. M. Katkov, V. M. Strakhovenko, BINP Novosibirsk; K. Maier, MPI Stuttgart .....	3093
New Target Results from the FNAL Antiproton Source — S. O'Day, F. Bieniosek, K. Anderson, FNAL .....	3096
High Current Radioisotope Production with Solid Target System — W. Z. Gelbart, N. R. Stevenson, R. R. Johnson, J. Orzechowski, F. Cifarelli, TRIUMF; F. Nortier, NAC Faure .....	3099
Isospin Target-Ion Source Shielding — M. M. Barbier, Marcel Barbier Inc. ....	3102
Beam Raster System at CEBAF — C. Yan, J. Beaufait, P. Brindza, R. Carlini, W. Vulcan, R. Wines, CEBAF.....	3103
Monitoring Production Target Thickness — M. A. Othoudt, LANL.....	3106
Beam Loss Handling at the SSC — I. S. Baishev, A. I. Drozhdin, N. V. Mokhov, SSCL .....	3109
Analytical Study of RFQ Channel by Means of the Equivalent Charges Model — V. M. Pirozhenko, O. V. Plink, MRTI .....	3112
Design of an 80-MHz RFQ Linac for Heavy Ions — O. Takeda, Y. Tanabe, K. Satoh, S. Kawazu, Toshiba; Y. Oguri, M. Okamura, T. Hattori, Tokyo Inst. of Tech. ....	3115
Operational Characteristics of a 100-mA, 2-MeV Radio-Frequency Quadrupole — K. F. Johnson, W. B. Cottingham, G. O. Bolme, C. M. Fortgang, W. Ingalls, J. Marquardt, D. P. Rusthoi, O. R. Sander, M. Smith, G. T. Worth, LANL .....	3118
Analysis of the End Regions of the CERN Lead-Ion 4-Rod RFQ — V. A. Andreev, ITEP Moscow; A. Lombardi, G. Parisi, INFN Legnaro; M. Vretenar, CERN .....	3121
90°-Apart-Stem RFQ Structure for Wide Range of Frequencies — V. A. Andreev, ITEP Moscow; G. Parisi, INFN Legnaro .....	3124
The SSCL RFQ System Integration — G. Arbique, A. Calo, C. Cuevas, P. Datte, D. Evans, J. Hurd, E. Marsden, K. Saadatmand, J. Sage, SSCL .....	3127
SSC Radio-Frequency-Quadrupole Beam: Comparison of Experimental and Simulated Results — F. W. Guy, J. W. Hurd, D. Raparia, K. Saadatmand, W. A. Whittenberg, SSCL .....	3130
Mechanical Integration of an RF Volume Source and Einzel Lens LEBT to the SSC RFQ — R. A. Valicenti, J. Lenz, N. C. Okay, L. Plesea, K. Saadatmand, SSCL .....	3133
Segmented Resonantly Coupled Radio-Frequency Quadrupole (RFQ) — L. M. Young, LANL .....	3136
Experiments with the High Current RFQ Prototype for GSI — A. Kipper, A. Schempp, H. Deitinghoff, J. Madlung, T. Ludwig, K. Volk, O. Engels, A. Firjahn-Andersch, H. Vormann, Inst. f. Angew. Physik .....	3139
Transport of Ions in RFQ-Accelerators — J. Dehen, W. Barth, A. Schempp, H. Deitinghoff, Inst. f. Angew. Physik .....	3142
An ESQ Lens System for Low Energy Beam Transport Experiments on the SSC Test Stand — S. K. Guharay, C. K. Allen, M. Reiser, U. Maryland; K. Saadatmand, SSCL .....	3145
Test of the Transport Properties of a Helical Electrostatic Quadrupole and Quasi-Octupole — L. Xiu, S. Ohnuma, K. Wang, U. Houston; C. R. Meitzler, Y. Xu, Sam Houston State U. ....	3148
Comparison of Experimental and Simulated Results for the SSC LEBT — J. W. Lenz, J. Hebert, N. Okay, D. Raparia, K. Saadatmand, SSCL .....	3151
Axial Magnetic Field Lens with Permanent Magnet — Y. Iwashita, Kyoto U. ....	3154
Design of a Merging Beamlet Pre-Accelerator for an Electrostatic Quadrupole Accelerator (ESQ) — C. F. Chan, M. C. Vella, LBL .....	3157
Low Energy H <sup>-</sup> Injector Design for SSC RFQ — C. F. Chan, K.-N. Leung, LBL .....	3160

Each volume begins with this five-volume table of contents and ends with the five-volume author index. The chairmen's foreword and a list of conference organizers and staff appear as front matter in Volume 1. A list of conference participants precedes the author index in Volume 5.

## Five-Volume Contents

Lithium Lens for Focusing Protons on Target in the Fermilab Antiproton Source — <i>F. M. Bieniosek, K. Anderson, FNAL</i> .....	3163
Injector Design for High-Current CW Proton Linacs — <i>R. R. Stevens, Jr., J. D. Sherman, J. D. Schneider, LANL</i> ...	3166
A High Power Long Pulse RF-Driven H <sup>-</sup> Source — <i>J. W. Kwan, G. D. Ackerman, W. S. Cooper, G. J. deVries, K. N. Leung, R. P. Wells, LBL</i> .....	3169
Initial Operation of the CW 8X H <sup>-</sup> Ion Source Discharge — <i>H. V. Smith, Jr., P. Allison, C. Geisik, D. R. Schmitt, J. D. Schneider, J. E. Stelzer, LANL</i> .....	3172
Volume H <sup>-</sup> Ion Source Development at LAMPF — <i>R. L. York, D. Tupa, D. R. Swenson, R. Damjanovich, LANL</i> .....	3175
Further Development with Heavy Ion Sources at Brookhaven National Laboratory's Tandem Van de Graaff Facility — <i>M. J. Zarcone, D. B. Steski, K. S. Smith, P. Thieberger, BNL</i> .....	3178
A Dual-Optically-Pumped Polarized Negative Deuterium Ion Source — <i>Y. Mori, M. Kinsho, KEK</i> .....	3181
The IUCF High Intensity Polarized Ion Source Project — <i>M. Wedekind, R. Brown, V. Derenchuk, D. Friesel, J. Hicks, P. Schwandt, IUCF</i> .....	3184
The High Current Ion Source System HOLCROSS — <i>N. R. Lobanov, MEPI Moscow</i> .....	3187
Positive Hydrogen Ion Beam Production by an RF-Driven Multicusp Source — <i>K. N. Leung, D. A. Bachman, P. R. Herz, D. S. McDonald, L. T. Perkins, LBL; M. Olivo, PSI</i> .....	3190
Measurements of Emittance and Species Fractions of a Positive Hydrogen Ion Beam Extracted from an RF-Driven Multicusp Source — <i>G. Gammel, T. W. Debiak, S. Melnychuk, J. Sredniawski, Grunman</i> .....	3193
A New Design of the Sputter Type Metal Ion Source and Its Characteristics of Ion Beam Extraction — <i>W. Kim, B. H. Choi, J. T. Jin, K.-S. Jung, Korea Atomic Energy Res. Inst.; S. H. Do, Pusan Nat. Fishers U.; K. H. Chung, Seoul Nat. U.</i> .....	3196
K <sup>+</sup> Ion Source for the Heavy Ion Induction Linac System Experiment ILSE — <i>S. Eylon, E. Henestroza, W. W. Chupp, S. Yu, LBL</i> .....	3199
On the Magnetic Compression and Guiding of Electron Beams in E.B.I. S. or E.B.I.T — <i>J. L. Bobin, E. Mercier, UPMC Paris; G. Giardino, LPAN</i> .....	3202
Choice of Hexapole Parameters for ECR Ion Source — <i>V. P. Kukhtin, E. A. Lamzin, Yu. P. Severgin, S. E. Sytchevsky, Efremov Inst.</i> .....	3205
Stripping Efficiencies for 277 MeV/amu Gold Beam on Copper Foils — <i>T. Roser, BNL</i> .....	3207
Management of High Current Transients in the CWDD Injector 200 kV Power System — <i>J. A. Carwardine, G. Pile, AEA Tech. Culham Lab; T. E. Zinneman, ANL</i> .....	3210
Design and Results of the Radio Frequency Quadrupole RF System at the Superconducting Super Collider Laboratory — <i>J. Grippe, E. Marsden, O. Marrufo, SSCL; A. Regan, D. Rees, C. Ziomek, LANL</i> .....	3213
Initial Operation and Beam Characteristics of the UCLA S-Band Photo-Injector — <i>C. Pellegrini, N. Barov, P. Davis, G. Hairapetian, S. C. Hartman, C. Joshi, S. Park, J. Rosenzweig, G. Travish, R. Zhang, UCLA</i> .....	3216

## Volume 5

### Multiparticle Beam Dynamics

Chair: *M. Reiser*

Methods of Impedance Calculation ( <i>Invited Paper</i> ) — <i>R. L. Gluckstern, Maryland</i> .....	3219
Space-Charge Calculations in Synchrotrons ( <i>Invited Paper</i> ) — <i>S. Machida, SSCL</i> .....	3224
Advanced Computers and Simulation ( <i>Invited Paper</i> ) — <i>R. D. Ryne, LANL</i> .....	3229
Measured Optimum BNS Damping Configuration of the SLC Linac — <i>J. T. Seeman, F.-J. Decker, R. L. Holtzapple, W. L. Spence, SLAC</i> .....	3234
Single Beam Phenomena in BEPC — <i>Z. Y. Guo, X. Bai, G. X. Li, J. Qin, Q. Qin, G. Xu, C. Zhang, X. L. Zhang, Z. T. Zhao, IHEP, Academia Sinica</i> .....	3237
High Intensity Bunch Length Instabilities in the SLC Damping Rings — <i>P. Krejcik, K. Bane, P. Corredoura, F.-J. Decker, J. Judkins, T. Limberg, M. Minty, R. H. Siemann, SLAC; F. Pedersen, CERN</i> .....	3240
Investigation on Relaxations in Electron Beams — <i>A. Aleksandrov, N. Dikansky, N. Ch. Kot, V. Kudelainen, V. A. Lebedev, P. Logachov, BINP; R. Calabrese, G. Ciullo, V. Guidi, G. Lamanna, P. Lenisa, B. Maciga, L. Tecchio, B. Yang, INFN</i> .....	3243
Studies of Multipass Beam Breakup and Energy Recovery Using the CEBAF Injector Linac — <i>N. S. Sereno, L. S. Cardman, U. Illinois; G. A. Krafft, C. K. Sinclair, J. J. Bisognano, CEBAF</i> .....	3246

Volume 1: 1-747  
 Volume 2: 748-1640  
 Volume 3: 1641-2545  
 Volume 4: 2546-3218  
 Volume 5: 3219-3933

## Proceedings of the 1993 Particle Accelerator Conference

### Poster presentations:

The Longitudinal and Transverse Beam Dynamics Simulation in the MMF Storage Ring — V. A. Moiseev, INR Moscow .....	3249
Control of Longitudinal Instabilities in the LEB — T. L. Grimm, P. D. Coleman, SSCL .....	3252
Simulation of the Transverse Dipole Mode Multibunch Instability for the SSC Collider — S. Chen, G. López, SSCL .....	3255
HOM RF Cavity Dampers for Suppressing Coupled Bunch Instabilities in the Fermilab Booster — D. Wildman, FNAL; K. Harkay, Purdue .....	3258
Longitudinal Instabilities in the MEB — J. A. Palkovic, SSCL .....	3261
A New Formulation of Longitudinal Coherent Instabilities — S. Y. Zhang, W. T. Weng, BNL .....	3264
Three-Dimensional Simulations for Accelerator Physics Using ARGUS — A. Mondelli, A. Manakofsky, J. Petillo, W. Krueger, C. Kostas, A. Drobot, SAIC; R. Ryne, R. K. Cooper, G. Rodenz, M. J. Brownman, LANL .....	3267
A Higher-Order Moment Simulation Model — K. T. Tsang, C. Kostas, A. Mondelli, SAIC .....	3270
Collective Effects of the PLS 2 GeV Storage Ring — M. Yoon, J. Choi, T. Lee, Pohang .....	3273
Nonlinear Evolution of Longitudinal Bunched-Beam Instabilities — A. Gerasimov, FNAL .....	3276
Multi-Bunch Dynamics in Accelerating Structures Including Interaction with Higher Order Modes — M. Ferrario, F. Tazzioli, INFN-LNF; L. Serafini, INFN Milano .....	3279
Generation of Space-Charge Waves due to Localized Perturbations — J. G. Wang, D. X. Wang, D. Kehne, M. Reiser, U. Maryland .....	3282
Three Dimensional Multipole Decomposition of Fields — K. Hahn, LBL .....	3285
Multi-Bunch Beam Break-Up Studies for a SWFEL/TBA — J. S. Kim, A. M. Sessler, LBL; D. H. Whittum, KEK; H. Henke, TU Berlin .....	3288
RF Noise Revisited: The Effect of Coherence — A. Gerasimov, FNAL; S. Y. Lee, Indiana U. ....	3291
TSD Versus TRL Calibration and Applications to Beam Impedance Measurements — M. Foley, P. Colestock, E. Barsotti, Jr., FNAL .....	3294
Recent Study of Beam Stability in the PSR — T. Wang, R. Cooper, D. Fitzgerald, S. Frankle, T. Hardek, R. Hutson, R. Macek, C. Ohmori, M. Plum, H. Thiessen, C. Wilkinson, LANL; E. Colton, DOE; D. Neuffer, CEBAF; G. Rees, RAL .....	3297
Impedance Budget and Beam Stability Analysis of the Fermilab Main Injector — M. A. Martens, K. Y. Ng, FNAL ..	3300
Trapped Ions and Beam Coherent Instability — P. Zhou, P. L. Colestock, S. J. Werkema, FNAL .....	3303
Comparison of the Coupled-Bunch Mode Theory to Experimental Observations in the Fermilab Booster — K. C. Harkay, Purdue; P. L. Colestock, FNAL .....	3306
Measurement of Trapped Ion Pockets and Control of Ion Instabilities in the Fermilab Antiproton Accumulator — S. J. Werkema, K. D. Fullett, P. Zhou, FNAL .....	3309
Study of Possible Energy Upgrade for the ALS and Modeling of the "Real Lattice" for the Diagnosis of Lattice Problems — M. Meddahi, J. Bengtsson, LBL .....	3312
Study of Coupled-Bunch Collective Effects in the PEP-II B-Factory — J. Byrd, LBL .....	3315
Study of Coupled-Bunch Collective Effects in the ALS — J. M. Byrd, J. N. Corlett, LBL .....	3318
Time Domain Solutions for a Coasting Beam with Impedance Feedback — M. Blaskiewicz, BNL .....	3321
Longitudinal Impedance and Stability Thresholds of the AGS Booster — M. Blaskiewicz, BNL .....	3324
Calculation of the Bunch Lengthening Threshold — X. T. Yu, J. S. Wurtele, MIT .....	3327
Computation of Longitudinal Bunched Beam Instability Thresholds — R. Baartman, TRIUMF; M. D'Yachkov, U. British Columbia .....	3330
Bunch Lengthening Observed Using Real-Time Bunch-Length Monitor in the TRISTAN AR — T. Ieiri, KEK .....	3333
Transverse Stability in Multibunch Mode for CLIC — G. Guignard, CERN .....	3336
Simulations of the Longitudinal Instability in the SLC Damping Rings — K. L. F. Bane, SLAC; K. Oide, KEK .....	3339
Multibunch Beam Break-Up in Detuned Structures — K. A. Thompson, C. Adolphsen, K. L. F. Bane, SLAC .....	3342
Longitudinal Head-Tail Instability in a Non-Harmonic Potential Well — B. Chen, A. W. Chao, SSCL .....	3345
Bunch Lengthening Effect and Localized Impedance — B. Chen, A. W. Chao, SSCL .....	3348
Experimental Reduction of Electron Beam Breakup Instability Using External Coupled Cavities — P. R. Menge, R. M. Gilgenbach, Y. Y. Lau, M. Walter, C. H. Ching, U. Michigan .....	3351
Beam Breakup in an Annular Beam — Y. Y. Lau, J. W. Luginsland, P. M. Gilgenbach, U. Michigan .....	3354

Each volume begins with this five-volume table of contents and ends with the five-volume author index. The chairmen's foreword and a list of conference organizers and staff appear as front matter in Volume 1. A list of conference participants precedes the author index in Volume 5.

Five-Volume Contents

RF Focusing Effects and Multi-Bunch Beam Breakup in Superconducting Linear Colliders — <i>J. Rosenzweig, S. Hartman, J. Stevens, UCLA</i> .....	3357
Required Cavity HOM deQing Calculated from Probability Estimates of Coupled Bunch Instabilities in the APS Ring — <i>L. Emery, ANL</i> .....	3360
Measurement and Analysis of Transverse Beam Transfer Functions in the Fermilab Main Ring — <i>P. J. Chou, G. Jackson, FNAL</i> .....	3363
Observation of a Short Bunch Train Longitudinal Instability in the Fermilab Main Ring — <i>X. Lu, G. Jackson, FNAL</i> .....	3366
Suppression of Longitudinal Coupled-Bunch Instabilities by a Passive Higher Harmonic Cavity — <i>R. A. Bosch, C. S. Hsue, SRRC Taiwan</i> .....	3369
The Longitudinal Coupling Impedance of a Slot on the SSC Collider Liner — <i>V. Thiagarajan, SSCL</i> .....	3372
Impedance of a Small-Gap Undulator Vacuum Chamber — <i>K. Bane, SLAC; S. Krinsky, NSLS-BNL</i> .....	3375
A Formula for the High Frequency Longitudinal Impedance of a Tube With Smoothly Varying Radius — <i>R. L. Warnock, SLAC</i> .....	3378
A Bench Set-Up for Low-Beta Beam-Current Test Measurements with COSY — <i>Ch. Günther, A. Schnase, H. Meuth, IKP Jülich; F. Caspers, CERN</i> .....	3381
A Generalized Model for Parametric Coupling of Longitudinal Modes in Synchrotrons — <i>P. L. Colestock, L. Klamp, FNAL</i> .....	3384
Longitudinal Coupling Impedance of a Cavity — <i>I. Gjaja, R. L. Gluckstern, U. Maryland</i> .....	3387
Transverse Impedance of an Iris in a Beam Pipe — <i>S. Jiang, R. L. Gluckstern, U. Maryland; H. Okamoto, Kyoto U.</i> .....	3390
RF Characteristics of the APS Storage Ring Isolation Valve — <i>J. J. Song, R. L. Kustom, ANL</i> .....	3393
Coupling Impedance of Vacuum Pumping Holes for the APS Storage Ring — <i>J. Zhou, J. J. Song, R. L. Kustom, ANL</i> .....	3396
Impedance Formalism for an Arbitrary Cumulative Instability — <i>X. T. Yu, J. S. Wurtele, MIT; D. H. Whitum, KEK</i> .....	3399
Longitudinal Impedance of a Prototype Kicker Magnet System — <i>H. J. Tran, M. J. Barnes, G. D. Wait, Y. Yan, TRIUMF</i> .....	3402
Beam Coupling Impedance Measurements and Simulations of a Beam Pipe Liner with Pumping Holes or Slots — <i>E. Ruiz, L. Walling, Y. Goren, N. Spayd, SSCL</i> .....	3405
Measurement and Computation of the Higher Order Modes of the ALS 500 MHz Accelerating Cavities — <i>J. N. Corlett, J. M. Byrd, LBL</i> .....	3408
Impedance Measurements of Components for the ALS — <i>J. N. Corlett, R. A. Rimmer, LBL</i> .....	3411
Advances and Applications of ABCI — <i>Y. H. Chin, LBL</i> .....	3414
On Coupling Impedances of Pumping Holes — <i>S. S. Kurennoy, SSCL</i> .....	3417
Using a Ceramic Chamber in Kicker Magnets — <i>S. S. Kurennoy, SSCL</i> .....	3420
An Analytical Treatment of Self Fields in a Relativistic Bunch of Charged Particles in a Circular Orbit — <i>J. L. Delhez, J. M. A. Hofman, J. I. M. Botman, H. L. Hagedoorn, W. J. G. M. Kleeven, G. A. Webers, Eindhoven U. of Tech.</i> .....	3423
Transverse Wake Fields in the CLIC Transfer Structure — <i>G. Guignard, G. Carron, A. Millich, L. Thorndahl, CERN</i> .....	3426
The LEP Impedance Model — <i>D. Brandt, K. Cornelis, V. Danilov, A. Hofmann, C. Juillard, E. Perevedentsev, E. Peschardt, E. Rossa, F. Tecker, D. Wang, B. Zotter, CERN; L. Rivkin, PSI</i> .....	3429
Impedance Calculations for the Improved SLC Damping Rings — <i>K. L. F. Bane, C.-K. Ng, SLAC</i> .....	3432
Broadband Impedance of Azimuthally Symmetric Devices in RHIC — <i>V. Mane, BNL</i> .....	3435
Software Development with Two Port Calibration Techniques for RHIC Impedance Measurements — <i>V. Mane, T. Shea, BNL</i> .....	3438
Resistive Wall Wake Function for Arbitrary Pipe Cross Section — <i>K. Yokoya, KEK</i> .....	3441
Impedance of a Perforated Liner and Its Impact on the SSC Collider — <i>W. Chou, T. Barts, SSCL</i> .....	3444
A Generalized Method for Calculating Wake Potentials — <i>O. Napoly, Saclay; Y. H. Chin, LBL; B. Zotter, CERN</i> ...	3447
The Interaction of a Beam With a Beam Line Higher-Order-Mode Absorber — <i>W. Hartung, K. Akai, J. DeFord, T. Hays, J. Kirchgessner, D. Metzger, D. Moffat, H. Padamsee, D. Rubin, M. Tigner, A. Tribendis, V. Veshcherevich, Cornell</i> .....	3450
Persistent Wakefields Associated with Waveguide Damping of Higher Order Modes — <i>N. M. Kroll, X. Lin, UCSD/SLAC</i> .....	3453

Volume 1: 1-747  
 Volume 2: 748-1640  
 Volume 3: 1641-2545  
 Volume 4: 2546-3218  
 Volume 5: 3219-3933

*Proceedings of the 1993 Particle Accelerator Conference*

Perturbation Theory of Broadband Impedances — <i>S. Heifets, SLAC</i> .....	3456
Broadband Impedance of the B Factory — <i>S. Heifets, SLAC</i> .....	3459
Study of a Detuned Accelerating Section With the Computer Program PROGON — <i>S. A. Heifets, S. A. Kheifets, SLAC</i> .....	3462
Estimation of Broad Band Impedance of the SPring-8 Storage Ring — <i>T. Nakamura, JAERI</i> .....	3464
Head-On and Long Range Beam-Beam Tune Shift Spread in the SSC — <i>G. López, SSCL</i> .....	3467
Beam-Beam Effects with Errors in the Crab Compensation — <i>D. Sagan, Cornell</i> .....	3470
A Strong-Strong Simulation on the Beam-Beam Effect in a Linac/Ring B-Factory — <i>R. Li, J. J. Bisognano, CEBAF</i> .....	3473
Some Aspects of the Long Range Beam-Beam Interaction in Storage Rings — <i>A. B. Temnykh, INP; J. J. Welch, Cornell</i> .....	3476
Experimental Study of Crossing Angle Collision — <i>T. Chen, SLAC; D. Rice, D. Rubin, D. Sagan, M. Tigner, Cornell</i> .....	3479
Beam-Beam Experiments in the Tevatron — <i>D. Siergie, G. Goderre, FNAL</i> .....	3482
Beam-Beam Effects for the PEP-II B Factory — <i>M. A. Furman, LBL; J. R. Eden, U. Washington</i> .....	3485
Equivalent Equations and Incoherent Lifetime Calculated from $e^+e^-$ Beam-Beam Simulation — <i>Y. Orlov, Cornell</i> .....	3488
Simulation of Beam-Beam Effects in Electron-Positron Rings — <i>K. Hirata, S. Matsumoto, KEK</i> .....	3491
Longitudinal Beam-Beam Effects in Circular Colliders — <i>M. Hogan, J. Rosenzweig, UCLA</i> .....	3494
Strong-Weak Beam-Beam Simulation with a Six Dimension Symplectic Code — <i>Y. Funakoshi, H. Koiso, KEK</i> .....	3497
Synchrotron Beam-Loading Stability with a Higher RF Harmonic — <i>T. F. Wang, LANL</i> .....	3500
Compensation of Bunch Position Shift Using Sub-RF Cavity in a Damping Ring — <i>K. Kubo, T. Higo, S. Sakanaka, KEK</i> .....	3503
Analytic Criteria for Stability of Beam-Loaded RF Systems — <i>S. R. Koscielniak, TRIUMF</i> .....	3506
Beam Loading Effect in SSCL Coupled Cavity Linac — <i>Yu. Senichev, R. Cutler, J. Hurd, D. Raparia, SSCL</i> .....	3509
The Ion Core Density in Electron Storage Rings with Clearing Electrodes — <i>E. V. Bulyak, Kharkov Inst.</i> .....	3512
Operation of the CEBAF Linac with High Beam Loading — <i>L. Merminga, J. J. Bisognano, C. Hovater, G. A. Krafft, S. N. Simrock, CEBAF; K. Kubo, KEK</i> .....	3515
An Idea of Dynamical Cooling of Electron Beam in SR Ring — <i>S. Kato, Osaka U.</i> .....	3518
The Principle of Ultra-Fast Automatic Cooling for Beams — <i>S. Gao, G. Qian, CIAE</i> .....	3521
On the Longitudinal Stability of Cooled Coasting Ion Beams — <i>S. Nagaitsev, IUCF</i> .....	3524
Crystalline Beam Ground State — <i>J. Wei, BNL; X. Li, Rutgers; A. M. Sessler, LBL</i> .....	3527
Confinement and Stability of a Crystal Beam — <i>A. G. Ruggiero, BNL</i> .....	3530
Bunched Beam Stochastic Cooling in the Fermilab Tevatron Collider — <i>G. Jackson, E. Buchanan, J. Budlong, E. Harms, P. Hurh, D. McGinnis, R. Pasquinelli, D. Peterson, D. Poll, P. Seifrid, FNAL</i> .....	3533
Longitudinally Space Charge Dominated Beams in a Synchrotron — <i>T. J. P. Ellison, S. S. Nagaitsev, M. S. Ball, D. D. Caussyn, M. J. Ellison, B. J. Hamilton, IUCF</i> .....	3536
High Density Plasma Source for Plasma Lens Experiments — <i>K. Nakamura, R. Liou, M. Gundersen, USC</i> .....	3537
Measurement of Escaping Ions in the Fermilab Antiproton Accumulator — <i>P. Zhou, P. L. Colestock, K. Junck, C. A. Crawford, FNAL</i> .....	3540
Experimental Demonstration of Plasma Lens Focusing — <i>G. Hairapetian, P. Davis, C. E. Clayton, C. Joshi, S. Hartman, C. Pelligrini, UCLA; T. Katsouleas, USC</i> .....	3543
Numerical Modelling of Time-Space Behavior of High-Current Relativistic Electron Beam in Plasma Waveguide — <i>V. I. Karas', Kharkov Inst.; N. G. Belova, Russian Acad.</i> .....	3546
IPROP Simulations of the GAMBLE II Proton Transport Experiment — <i>D. R. Welch, Mission Res. Corp.</i> .....	3549
Plasma Lens and Plasma Wakefield Acceleration Experiments Using Twin Linacs— <i>A. Ogata, H. Nakanishi, K. Nakajima, T. Kawakubo, D. Whittum, M. Arinaga, KEK; Y. Yoshida, T. Ueda, T. Kobayashi, Nucl. Eng. Res. Lab, Tokyo U.; H. Shibata, S. Tagawa, Res. Ctr. Nucl. Sci. Tech., Tokyo U.; N. Yugami, Y. Nishida, Utsunomiya U.</i> .....	3552
Plasma Focusing of the Final Test Beam — <i>S. Rajagopalan, UCLA</i> .....	3555
Emittance Growth in MEB and Its Control — <i>Y. Huang, S. Machida, R. Gerig, SSCL</i> .....	3558
Longitudinal Diffusion as Inflicted by Arbitrary Band-Width Random-Modulated Currents in Feeders of Detuned Cavities — <i>S. Ivanov, IHEP Moscow</i> .....	3561
Induced Beam Oscillations from Quadrupole Vibrations in the SLC Linac — <i>J. T. Seeman, R. L. Holtzapple, M. C. Ross, SLAC</i> .....	3564

*Each volume begins with this five-volume table of contents and ends with the five-volume author index. The chairmen's foreword and a list of conference organizers and staff appear as front matter in Volume 1. A list of conference participants precedes the author index in Volume 5.*

Five-Volume Contents

Effects of Magnetic Focusing on Longitudinal Emittance and Energy Dispersion of an Intense Short Accelerating Electron Pulse — <i>J.-M. Dolique, J. C. Coacolo, U. Joseph Fourier/CEA</i> .....	3567
Measurement and Reduction of Transverse Emittance Blow-Up Induced by Space Charge Effects — <i>R. Cappi, R. Garoby, S. Hancock, M. Martini, J. P. Riinaud, CERN</i> .....	3570
Transverse Emittance Growth in the Fermilab Antiproton Accumulator with High-Current Antiproton Stacks — <i>S. J. Werkema, D. W. Peterson, P. Zhou, FNAL</i> .....	3573
Transverse Tails and Higher Order Moments — <i>W. L. Spence, F.-J. Decker, M. D. Woodley, SLAC</i> .....	3576
Simulation of Emittance Dilution in Electron Storage Ring from Compton Backscattering — <i>L. N. Blumberg, E. Blum, BNL</i> .....	3579
Transverse Effects of Longitudinal Wakefields at High Dispersion — <i>F. Decker, SLAC</i> .....	3582
Error and Tolerance Studies for the SSC Linac — <i>D. Raparia, C. R. Chang, F. Guy, J. W. Hurd, W. Funk, SSCL; K. R. Crandall, AccSys</i> .....	3585
Emittance Growth Due to Dipole Ripple and Sextupole — <i>H.-J. Shih, J. A. Ellison, M. J. Syphers, B. S. Newberger, SSCL</i> .....	3588
Proton-Proton Scattering Contribution to Emittance Growth — <i>T. Garavaglia, SSCL</i> .....	3591
Source Size Variation and Ion Effects in the SRS at Daresbury — <i>J. A. Clarke, D. M. Dykes, S. F. Hill, E. A. Hughes, M. W. Poole, P. D. Quinn, S. L. Smith, V. P. Suller, L. A. Welbourne, SERC Daresbury</i> .....	3594
Global Trajectory Correction Algorithms in CLIC and Main Linac Alignment Tolerances — <i>C. Fischer, CERN</i> .....	3597
Lattice Scaling and Emittance Control in the CLIC Main Linac — <i>G. Guignard, CERN</i> .....	3600
Decoherence and Recoherence of Beam in Phase Space — <i>J. Shi, S. Ohnuma, U. Houston</i> .....	3603
Space-Charge-Induced Emittance Growth in an Elliptical Charged Particle Beam with a Parabolic Density Distribution — <i>T. P. Wangler, LANL; P. Lapostolle, A. Lombardi, CERN</i> .....	3606
Emittance and Luminosity Evolution During Collisions in the SSC Collider — <i>W. Chow, S. Dutt, T. Garavaglia, K. Kauffmann, SSCL</i> .....	3609
Emittance Growth in Displaced, Space-Charge-Dominated Beams with Energy Spread — <i>J. J. Barnard, J. Miller, LLNL; I. Haber, NRL</i> .....	3612
An Injection Scheme for the Brookhaven ATF Utilizing Space-Charge Emittance Growth Compensation — <i>J. C. Gallardo, H. G. Kirk, BNL</i> .....	3615
A Matrix Theory of the Motion of an Ellipsoidal Bunch in a Beam Control System with a Rectilinear Optical Axis and with Space Charge — <i>A. Dymnikov, U. St. Petersburg; R. Hellborg, U. Lund</i> .....	3618
Space-Charge Dominated Beam Envelope Transport with Rotatable Axes — <i>E. Y. Tsiang</i> .....	3621
Effect of Space Charge Forces on Particle Tracking and Generation of High-Order Maps — <i>D. L. Bruhwiler, M. F. Reusch, Grumman</i> .....	3624
Experimental Study of Longitudinal Dynamics of Space-Charge Dominated Parabolic Bunches — <i>D. X. Wang, J. G. Wang, D. Kehne, M. Reiser, U. Maryland; I. Haber, Naval Res. Lab.</i> .....	3627
Transition Crossing in the Fermilab Main Ring, Past and Present — <i>I. Kourbanis, K. Y. Ng, FNAL</i> .....	3630
Observation and Correction of Resonance Stopbands in the AGS Booster — <i>C. Gardner, L. Ahrens, J. W. Glenn, Y. Y. Lee, T. Roser, A. Soukas, W. van Asselt, W. T. Weng, BNL; Y. Shoji, KEK</i> .....	3633
The Stability of Ions in a Storage Ring in the Presence of Small Gap Insertion Devices — <i>E. Bozoki, BNL</i> .....	3636
Simulation of Space-Charge Dominated Beam Dynamics in an Isochronous AVF Cyclotron — <i>S. R. Koscielniak, TRIUMF; S. R. Adam, PSI Switzerland</i> .....	3639
Passage Through a Half-Integer Resonance Due to Space Charge for Different Initial Distributions — <i>A. Budzko, INR; Yu. Senichev, SSCL</i> .....	3642
Estimation of Collective Effects for the EUTERPE Ring — <i>B. Xi, J. I. M. Botman, J. van Laar, C. J. Timmermans, H. L. Hagedoorn, Eindhoven U. of Tech.</i> .....	3645
A Moment Method Laplace Solver for Low Energy Beam Transport Codes — <i>C. K. Allen, S. K. Guharay, M. Reiser, U. Maryland</i> .....	3648
Evolution of Hadron Beams Under Intrabeam Scattering — <i>J. Wei, BNL</i> .....	3651
Simulation Study of Ion Trapping in PLS Storage Ring — <i>J. Jung, I. Ko, POSTECH</i> .....	3654
Beam Halo Formation From Space-Charge Dominated Beams in Uniform Focusing Channels — <i>J. S. O'Connell, Booz, Allen &amp; Hamilton; T. P. Wangler, R. S. Mills, LANL; K. R. Crandall, AccSys Tech.</i> .....	3657
Computer Simulation of the Maryland Transport Experiment — <i>I. Haber, Naval Res. Lab.; D. A. Callahan, A. B. Langdon, LLNL; M. Reiser, D. X. Wang, J. G. Wang, U. Maryland</i> .....	3660
Integrated Numerical Modeling of a Laser Gun Injector — <i>H. Liu, S. Benson, J. Bisognano, P. Liger, G. Neil, D. Neuffer, C. Sinclair, B. Yunn, CEBAF</i> .....	3663

## Proceedings of the 1993 Particle Accelerator Conference

Halo Formation in Mismatched, Space-Charge-Dominated Beams — C. L. Bohn, J. R. Delayen, ANL .....	3666
Collective Effects in the VEPP-3 Storage Ring — S. A. Belomestnykh, A. N. Voroshilov, BINP .....	3669
Single Bunch Effects in the Daresbury SRS — L. A. Welbourne, J. A. Clarke, D. M. Dykes, S. F. Hill, E. A. Hughes, M. W. Poole, P. D. Quinn, S. L. Smith, V. P. Suller, SERC Daresbury .....	3672
The Effects of Coulomb Beam Interaction in Multiaperture Linac — A. I. Balabin, G. N. Kropachev, I. O. Parshin, D. G. Skachkov, ITEP Moscow .....	3675
Longitudinal Instability of an Induction Linac with Acceleration — L. Smith, E. P. Lee, LBL .....	3678
On Solvable Model with Synchrotron Mode-Coupling — D. V. Pestrikov, BINP/KEK .....	3681
On Limitations on Low- $\alpha$ Rings Performance Due to —Z-Instabilities — N. S. Dikansky, BINP Russia; D. V. Pestrikov, KEK .....	3684
On Landau Damping of Collective Beam-Beam Modes — D. V. Pestrikov, BINP/KEK .....	3687
Synchronous Phase Changes Due to the Gap in the Bunch Train — Z. Greenwald, M. Tigner, Cornell .....	3690
Simulation and Compensation of Multibunch Energy Variation in NLC — K. A. Thompson, R. D. Ruth, SLAC ....	3693
The Physical Mechanism of Ultra-Fast Automatic Cooling for Beams in the Six-Dimensional Emittance Space — S. Gao, G. Qian, D. Liang, H. Sun, CIAE China .....	3696
An Exact Expression for the Momentum Dependence of the Space Charge Tune Shift in a Gaussian Bunch — M. Martini, CERN .....	3699
Stored Beam Lifetime Evaluation Formulae for Electron Storage Rings — A.V. Makulkin, All-Russ. Res. Inst. ....	3702
A Simulation Study on Beam Bunching in the KEK 2.5-GeV Linac New Pre-Injector — T. Kamitani, J.-Y. Choi, A. Enomoto, S. Ohsawa, Y. Ogawa, T. Urano, T. Suwada, K. Furukawa, I. Sato, KEK .....	3705
New Outlooks on Bunched Beam Instabilities in Particle Accelerators: A Proposal for a Simple Method to Release a Potential Self-Consistent High Quality Beam — M. Bergher, LURE .....	3708
Experimental Study of Collective Effects in BEP Storage Ring with High Stored Current — V. Danilov, I. Koop, A. Lysenko, B. Militsyn, I. Nesterenko, E. Perevedentsev, E. Pozdeev, V. Ptitsin, Yu. Shatunov, I. Vasserman, BINP .....	3711
Beam Coupling Impedances of Axial Symmetric Structures — W. Bruns, Technische Universität Berlin .....	3714

### Hadron and e-p Colliders and Hadron Synchrotrons

Chair: D. Edwards

Accelerator Physics Issues at the SSC (Invited Paper) — G. F. Dugan, SSCL .....	3717
Fermilab Collider Upgrade: Recent Results and Plans (Invited Paper) — D. A. Finley, FNAL .....	3721
Operation of the Brookhaven AGS with the Booster (Invited Paper) — W. T. Weng, BNL .....	3726
Overview of Future Spallation Neutron Sources (Invited Paper) — G. H. Rees, Rutherford Appleton .....	3731
The Heavy Ion Synchrotron SIS: A Progress Report — K. Blasche, B. Franczak, B. Langenbeck, G. Moritz, C. Riedel, GSI .....	3736
Status of the PSR Improvement Program — R. J. Macek, D. H. Fitzgerald, M. Hoehn, R. Ryder, R. York, LANL .....	3739

### Poster presentations:

First Experience with Colliding Electron-Proton Beams in HERA — R. Brinkmann, F. Willeke, DESY .....	3742
The Development of a Prototype Multi-MeV Electron Cooling System — D. Anderson, M. Ball, D. Caussyn, T. Ellison, B. Hamilton, S. Nagaitsev, P. Schwandt, UCF; J. Adney, J. Ferry, M. Sundquist, Nat. Electr. Corp.; D. Reistad, Svedberg Lab.; M. Sedlacek, Alfvén Lab. ....	3745
The Bevalac Long Spill — C. M. Celata, S. Abbott, M. Bennett, M. Bordua, J. Calvert, R. Dwinell, D. Howard, D. Hunt, B. Feinberg, R. Force, R. Frias, J. Halliwell, J. Kalnins, S. Lewis, M. Nyman, L. Shalz, M. Tekawa, LBL; R. Solomons, RAFAEL, Israel .....	3748
Capture from Pair Production as a Beam Loss Mechanism for Heavy Ions at RHIC — B. Feinberg, A. Belkacem, R. Bossingham, H. Gould, LBL; W. E. Meyerhof, Stanford U. ....	3751
Acceleration of Deuteron Beam in the KEK Proton Synchrotron — Y. Mori, KEK .....	3754
Conceptual Design for a One Megawatt Spallation Neutron Source at Argonne — Y. Cho, J. Bailey, B. Brown, F. Brumwell, J. Carpenter, K. Crawford, D. Horan, D. Jerng, R. Kleb, A. Knox, R. Kustom, E. Lessner, D. McGhee, F. Mills, H. Moe, R. Nielsen, C. Potts, A. Rauchas, K. Thompson, ANL .....	3757
A Los Alamos Design Study for a High-Power Spallation-Neutron-Source Driver — A. J. Jason, R. A. Hardekopf, R. W. Macek, S. O. Schriber, H. A. Thiessen, R. Woods, LANL .....	3760

Each volume begins with this five-volume table of contents and ends with the five-volume author index. The chairmen's foreword and a list of conference organizers and staff appear as front matter in Volume 1. A list of conference participants precedes the author index in Volume 5.

## Five-Volume Contents

On the High Intensity Aspects of AGS Booster Proton Operation — R. K. Reece, L. A. Ahrens, E. J. Bleser, J. M. Brennan, C. Gardner, J. W. Glenn, T. Roser, Y. Shoji, W. vanAsselt, W. T. Weng, BNL .....	3763
Results from Commissioning the AGS Booster Orbit System — E. Bleser, BNL .....	3766
The Effect of Global Survey Misalignment on the SSC — T. Garavaglia, N. Mahale, J. Peterson, SSCL .....	3769
Dealing with Abort Kicker Prefire in the Superconducting Super Collider — A. I. Drozhdin, I. S. Baishev, N. V. Mokhov, B. Parker, R. D. Richardson, J. Zhou, SSCL .....	3772
Design Status Report on the Collider Utility Straight Insertions — B. Parker, SSCL .....	3775
Current Design of the SSC Interaction Regions — Y. Nosochkov, A. Garren, T. Sen, R. Stiening, SSCL; E. Courant, BNL; D. M. Ritson, SLAC .....	3778
The Parameter Spreadsheets and Their Applications — R. Schwitters, A. Chao, W. Chou, J. Peterson, SSCL .....	3781
Lattice Studies for KAON Factory Accumulator and Booster Rings — A. Iliev, A. V. Budzko, INR-Troitsk; R. V. Servranckx, TRIUMF .....	3784
Reducing the Coupled-Bunch Oscillation in the Fermilab Booster by Optimizing RF Voltage — J. P. Shan, D. McGinnis, R. Tomlin, FNAL .....	3787
Beta Measurements and Modeling the Tevatron — N. M. Gelfand, FNAL .....	3790
The Status of the Fermilab Main Injector Project — D. Bogert, W. Fowler, S. Holmes, P. Martin, T. Pawlak, FNAL .....	3793
Constructing High Energy Accelerators Under DOE's "New Culture" for Environment and Safety: An Example, the Fermilab 150 GeV Main Injector Proton Synchrotron — W. Fowler, FNAL .....	3796
Performance and Comparison of the Different Coalescing Schemes Used in the Fermilab Main Ring — I. Kourbanis, G. P. Jackson, X. Lu, FNAL .....	3799
Operational Experience with Collimators in the Tevatron Collider — S. M. Pruss, FNAL .....	3802
Reliability of the Fermilab Antiproton Source — E. Harms, Jr., FNAL .....	3803
Multibunch Operation in the Tevatron Collider — J. A. Holt, D. A. Finley, V. Bharadwaj, FNAL .....	3806
Operational Experience with the Tevatron Collider Using Separated Orbits — G. Annala, FNAL .....	3808
Fermilab Antiproton Accumulator in the Main Injector Era — V. Visnjic, FNAL .....	3811
Study of Betatron Stochastic Cooling in Fermilab Antiproton Debuncher — V. Visnjic, M. Halling, FNAL .....	3814
Energy and Luminosity Limits of Hadron Supercolliders — W. A. Barletta, LBL/UCLA .....	3817
Ions Acceleration in the Synchrotrons with Constant RF of Electrical Field — V. P. Belov, Yu. P. Severgin, Efremov Inst. ....	3820
Ion Storage Ring of the INR Storage-Accelerating Complex — A. V. Dolinsky, A. I. Papash, S. N. Pavlov, A. T. Rudchik, A. E. Val'kov, I. N. Vishnevsky, A. V. Zhmendak, INR Kiev; V. P. Belov, A. A. Kapustin, V. S. Kashihin, A. M. Kokorin, A. A. Makarov, B. G. Mud'jugin, B. V. Rogdestvensky, Yu. P. Severgin, L. A. Schukeilo, M. N. Tarovik, Efremov Inst. ....	3822
A Compensated Dispersion-Free Long Insertion for an FFAG Synchrotron — P. F. Meads, Jr. ....	3825
 <b>Vacuum Technology</b> <i>Chair: D. Edwards</i>	
Vacuum Technology for Superconducting Colliders ( <i>Invited Paper</i> ) — A. G. Mathewson, CERN .....	3828
Dynamic Vacuum in the Beam Tube of the SSCL Collider: Cold Beam Tube and Liner Options — W. C. Turner, SSCL .....	3833
Distributed Ion Pump Testing for PEP-II, Asymmetric B-Factory Collider — M. Calderon, F. Holdener, W. Barletta, D. Petersen, LLNL; C. Foerster, BNL .....	3836
High Capacity Getter Pump for UHV Operation — P. Manini, M. Marino, F. Belloni, M. Porro, SAES Getters .....	3839
 <i>Poster presentations:</i>	
ELETTRA Vacuum System — M. Bernardini, F. Daclon, F. Giacuzzo, R. Kersevan, J. Miertusova, F. Pradal, Sinc. Trieste .....	3842
Vacuum Chamber and Crotch Absorber for the SPring-8 Storage Ring Vacuum System — K. Watanabe, S. H. Be, Y. Oikawa, H. A. Sakaue, C. Y. Xu, S. Yokouchi, Y. Wang, JAERI-RIKEN; S. Takahashi, Kobe Steel; M. Tsuchiya, IHI; Y. Yanagi, Hitachi .....	3845
SYNRAD, a Montecarlo Synchrotron Radiation Ray-Tracing Program — R. Kersevan, SSCL .....	3848
Vacuum System Design of the MIT-Bates South Hall Ring — E. Ihloff, R. Averill, J. Flanz, K. Jacobs, S. Sobczynski, D. Wang, A. Zolfaghari, MIT-Bates .....	3851
Design of Vacuum Chambers for Experimental Regions of Colliding Beam Machines — C. Hauviller, CERN .....	3854

**Proceedings of the 1993 Particle Accelerator Conference**

Distributed Non-Evaporable Getter Pumps for the Storage Ring of the APS — <i>R. Dortwegt, R. Benaroya, ANL</i> .....	3857
Test Fabrication of a Copper Beam Duct for the KEK B-Factory — <i>Y. Suetsugu, K. Kanazawa, KEK</i> .....	3860
FNAL Main Injector Quadrupole Vacuum Chamber — <i>L. Sauer, FNAL</i> .....	3863
FNAL Main Injector Dipole Installation Equipment — <i>K. Moravec, F. Lange, J. Leibfritz, L. Sauer, FNAL</i> .....	3864
Solvents and Pumpdown Characteristics of SRF Nb Cavities — <i>M. G. Rao, P. Kneisel, H. F. Dylla, CEBAF</i> .....	3867
Leak Checker Data Acquisition System — <i>J. Payne, J. Gannon, SSCL</i> .....	3870
Theoretical and Experimental Study of Sorption Processes on Non-Evaporable Getters St 707 — <i>J. Miertusova, F. Daclon, Sinc. Trieste</i> .....	3873
Photodesorption Experiments on SSC Collider Beam Tube Configurations — <i>I. Maslennikov, W. Turner, SSCL; V. Anashin, O. Malyshev, V. Osipov, V. Nazmov, V. Pindyurin, A. Salimov, BINP; C. Foerster, C. Lanni, BNL</i> .....	3876
The Heat Load of an 80 K Liner for the SSC — <i>J. Maddocks, A. Yücel, SSCL</i> .....	3879
Design of Large Aperture, Low Mass Vacuum Windows — <i>W. J. Leonhardt, M. Mapes, BNL</i> .....	3882
Observation and Analysis for Motions of Trapped Microparticles in the TRISTAN Accumulation Ring — <i>H. Saeki, Japan SRRI; T. Momose, Miyagi; H. Ishimaru, KEK</i> .....	3885
Overview of an 80 K Liner Design for Synchrotron Light Interception in SSCL Collider — <i>Q.-S. Shu, W. Chou, D. Clark, W. Clay, Y. Goren, R. Kersevan, V. Kovachev, P. Kraushaar, K. Leung, J. Maddocks, D. Martin, D. Meyer, R. Mihelic, G. Morales, J. Simmons, G. Snitchler, M. Tuli, W. Turner, L. Walling, K. Yu, J. Zbasnik, SSCL</i> .....	3888
Thermal Model and Associated Novel Approach for Synchrotron Radiation Liner with End Cooling — <i>Q.-S. Shu, K. Yu, W. Clay, J. Maddocks, G. Morales, J. Zbasnik, SSCL</i> .....	3891
Design of ECR Ion Source Vacuum Systems — <i>J. Pivarc, JINR Dubna</i> .....	3894
Development of Distributed Ion Pumps for g-2 Beam Vacuum System — <i>H. C. Hseuh, M. Mapes, L. Snyderstrup, BNL</i> .....	3897
What Joining Method for the New Generation of Accelerators (SSC and LHC) — <i>R. Gillier, Helicoflex; J. Montuclard, M. Lefrancois, Ch. Rouaud, LeCarbone-Lorraine, France</i> .....	3900
Surface Treatments and Photodesorption of Oxygen Free Copper Used in an Accelerator — <i>T. Kobari, M. Matumoto, S. Ueda, MERL Hitachi; M. Kobayashi, Y. Hori, KEK</i> .....	3903
The DAFNE Main Ring Vacuum System — <i>V. Chimenti, A. Clozza, H. Hsieh, G. Raffone, C. Vaccarezza, INFN-LNF</i> .....	3906
Vacuum Tracking — <i>V. Ziemann, SLAC</i> .....	3909
<b>Closing Plenary</b> <i>Chair: W. Hess</i>	
Future Accelerators in Japan — <i>N. Toge, KEK</i> .....	3912
LHC Progress and Status — <i>G. Brianti and the LHC Machine Group, CERN</i> .....	3917
Status of the SSC — <i>R. J. Briggs, SSCL</i> .....	3922
Design for Low Beam Loss in Accelerators for Intense Neutron Source Applications — <i>R. A. Jameson, LANL</i> .....	3926
Is There a Future for High Energy Accelerators? — <i>M. Tigner, Cornell</i> .....	3931

*Each volume begins with this five-volume table of contents and ends with the five-volume author index. The chairmen's foreword and a list of conference organizers and staff appear as front matter in Volume 1. A list of conference participants precedes the author index in Volume 5.*

## R.R. Wilson Prize Lecture: Adventures with Accelerators

John P. Blewett

Brookhaven National Laboratory (Retired), 310 West 106th Street, New York, NY 10025

In this paper I plan to cover 60 years of accelerator history in half a hour. In 60 years there are a little over a million half hours, so this will be a compression by a factor of  $10^6$ . I can't be very complete—just a few glances at that history as seen from wherever I was at the time.

My first contacts with big accelerators were in the mid-thirties when I was a graduate student at Princeton. Every year we students made our way to Washington for the spring meeting of the American Physical Society, held at the Bureau of Standards which then was a cozy affair out Connecticut Avenue about a mile past the Shoreham Hotel. First we found a cheap rooming house, then we made our way out to the meeting; about five hundred physicists attended in those days and everybody knew everybody else. We looked forward to the annual debate between Millikan, Compton, and Swann about what were the cosmic rays and where did they come from. Then we would troop to the Department of Terrestrial Magnetism to see Merle Tuve, Larry Hafstad, and Odd Dahl and their 1.3 million volt Van de Graaff machine—one of the most spectacular physics operations to be seen anywhere in those days.

The next contact was back at Princeton where Milton White and Malcolm Henderson had just arrived, bringing us the cyclotron gospel from California. They were to build a machine with a 40-inch pole; its magnet yoke proved to be so huge that it would not go through the laboratory door. A big hole had to be knocked out of the outside wall. The rest of us, doing tabletop experiments for our theses, were stupefied by the grandeur of this operation.

From Princeton I went to England—to the Cavendish Laboratory—for a year of work under the direction of Lord Rutherford and Mark Oliphant. Cockcroft and Walton's voltage multiplier was still standing, but was superseded by a new multiplier built by Philips in Holland. An intriguing feature was an electric typewriter built by Wynn-Williams to record data from the Cockcroft-Walton set. But Wynn-Williams had left and nobody else could make the typewriter work.

My work was on the range-energy relation for slow alpha particles—relatively unimportant, but every day "the Lord," as Rutherford was affectionately called by his students, came around about noon to ask how the work was going.

I returned to the U.S.A. to a job, paying \$3,000 a year, in the Research Laboratory of the General Electric Company in Schenectady.

Coolidge, the Lab's Director, was famous for his development of X-ray apparatus. He considered the betatron to be an important X-ray source and, in 1941, he welcomed Don Kerst who had built the first betatron at the University of Illinois. With the help of GE's engineers, Kerst built a 20 MeV machine and then returned to Urbana. But GE's interest continued and it was decided to build a 100 MeV machine at the GE Research Lab. This was done, primarily under the direction of one of GE's best engineers, Willi Westendorp. This was quite a spectacular machine operating at 60 Hz, making a deafening noise and producing a truly lethal X-ray beam.

During the war we were distracted from accelerators by the need for equipment to jam the German and Japanese radar systems. This, with the cooperation of the Radio Research Laboratory at Harvard, we accomplished quite easily.

In 1944 a letter to the editor of the *Physical Review* came to my attention. The Russians, Iwanenko and Pomeranchuk, presented a formula for energy losses by electrons in circular paths and suggested that this might set a limit to the energy to which electrons could be accelerated. Since the formula indicated energy losses proportional to the fourth power of the energy, this evidently deserved attention.

All innocent of the fact that the same formula had been worked out by Lienard in 1899, I worked through the electromagnetic theory and concluded that the Russians were right. Moreover, it appeared that the effects on a 100 MeV beam should be easily detectable. The theory indicated also that the radiation should be in a very narrow beam directed straight ahead of the radiating electron, and so should exist in a spectrum with a great many harmonics of the revolution frequency. But the vacuum chamber of the 100-MeV machine at GE was opaque, so nothing could be seen. However, it was easy to show that energy losses should make the radius of the electron orbit shrink appreciably at the end of the acceleration period. Westendorp had already observed an unexplained orbit shrinkage; I calculated its predicted amount and found complete agreement with the observations.

I published my calculations and our observations on the 100-MeV machine in 1946. Only later did I become aware of Lienard's work (remember, he was the one who invented retarded potentials) and of another monumental opus, the 327-page Adams Prize Essay of 1908 by G.A. Schott,

scholar of Trinity College, Cambridge on "Electromagnetic Radiation." That essay contained the complete theory of radiation from accelerated charged particles. Its only weakness was that the formula describing the spectrum of the radiation was expressed in Bessel functions of very high order not to be found in available tables. This was rectified in 1949 when Julian Schwinger published his elegant paper, "On the Classical Radiation of Accelerated Electrons," in which he converted Schott's spectrum formula to one using tabulated functions.

It should be noted that, at that time and for some time thereafter, this radiation was regarded as nothing but a nuisance, setting an upper limit to achievable energies. No one appreciated the possibility that the radiation might be a useful experimental tool.

It was then that the synchrotron appeared on the scene. We read Ed McMillan's paper with fascination. Did his phase oscillation equation indicate a stable oscillation? To the mathematically sophisticate it was evidently OK, but I thought it would be nice to solve it with a new calculating engine that GE's engineers had created. It performed integration with a system of discs revolving in contact with the surfaces of other rotating discs and took up a room 85 feet long. It had been quite useful in solving some problems of electron orbits in vacuum tubes, so I fed it the phase oscillation differential equation. To my distress, it supplied a solution that continually increased in amplitude. After some thought, I decided to feed it the equation for an undamped sine wave. To my relief, the machine again yielded an increasing amplitude. The conclusion was that backlash in the integrating mechanisms made the machine unsuitable for equations with periodic solutions.

About this time Ed McMillan himself appeared in Schenectady to ask for advice on how to construct the laminated magnet for his proposed 300-MeV synchrotron. Westendorp and I, with several others, spent a good deal of time with him, showing him our solutions to problems with the betatron magnet. Then he went home and we began to think about our skill in building machines and about all the parts we had lying around. Herb Pollock, Bob Langmuir and I, with several of our associates, said to ourselves, "Suppose we put together a machine for, say 70 MeV? We could be the first in the world to produce an operating synchrotron." And, indeed, that is what we did. Our machine operated in 1947; it had a transparent vacuum chamber and almost immediately the electron radiation was observed, a small bluish white spot at the side of the chamber where the beam was approaching the observer. At lower energies the spot changed color; at 40 MeV it was yellow and at 30 MeV it became red and very

faint. So now it is called "synchrotron radiation" although it was first detected in a betatron.

We were not the first to produce an operating synchrotron. The British team of Goward and Barnes had very quickly thrown together a tiny 8-MeV machine which worked long before ours was finished.

In 1946 I heard about the founding of the Brookhaven National Laboratory; it was to be a center for all sciences involving the nucleus and it was to build equipment so big that single universities could not afford it. Stan Livingston who, with Ernest Lawrence had built the first cyclotron, was to head the accelerator group. He wanted to build the largest cyclotron ever seen for 750 MeV but he was overruled by I.I. Rabi who decreed that Brookhaven's first accelerator should surpass a billion volts. This meant that it had to be a proton synchrotron—a machine that presented many unsolved problems. All of this was very exciting for me and I decided to leave GE and get in on the founding of the new Laboratory. So I departed Schenectady and moved to Long Island. Unfortunately the 70 MeV synchrotron at GE wasn't finished yet, so I missed the first eyeballing of synchrotron radiation.

The Cosmotron, as we named our prospective proton synchrotron, presented rather terrifying problems associated with size and shape. Electron synchrotrons like McMillan's 300 MeV machine involved relatively small magnets arranged around a circular orbit about six feet across. His vacuum chamber was a toroid with an aperture of a couple of inches in the radial direction and about one inch high. But our energy was ten times higher—we chose to aim for three billion volts—and protons are not bent into circular orbits as easily as are electrons; our orbit would be at least sixty feet in diameter. How much space needed to be provided in the vacuum chamber for proton excursions from the equilibrium orbit restrained only by weak focusing? Remember, strong focusing had yet to be invented.

The problem of aperture also was faced at Berkeley at Ernest Lawrence's Radiation Laboratory, which had been approved at the same time as we were for a machine twice as big as ours to be called the "Bevatron." Estimates of necessary aperture at Berkeley ran from one by four feet to four by fourteen feet. The Bevatron finally was built so that the aperture could be four by fourteen feet, but pole pieces could be inserted if it turned out that all that space wasn't needed. As a check on these guesses, they built a quarter-scale model of their machine with shutters that could be closed down to see at what aperture the beam disappeared.

Our approach was quite different. Our little group included two very bright young theorists,

Ernest Courant and Nelson Blachman. They worked out the details of the proton orbits, taking into account the achievable vacuum and all effects of component misalignments, and concluded that a gap nine inches high and thirty-six inches wide would be quite adequate. With considerable daring, we decided to disregard the Berkeley guesses and build as we were told by Courant and Blachman. After deep thought, I proposed the magnet structure shown

in Fig. 1. The final shape of the gap was the result of magnet model measurements and many hours of tedious calculation. We tried to get help from a "computing bureau" in New York that consisted of twenty people with mechanical adding machines, but they were virtually useless and the complex relaxation calculations of field patterns in the end were done by Hildred Blewett.

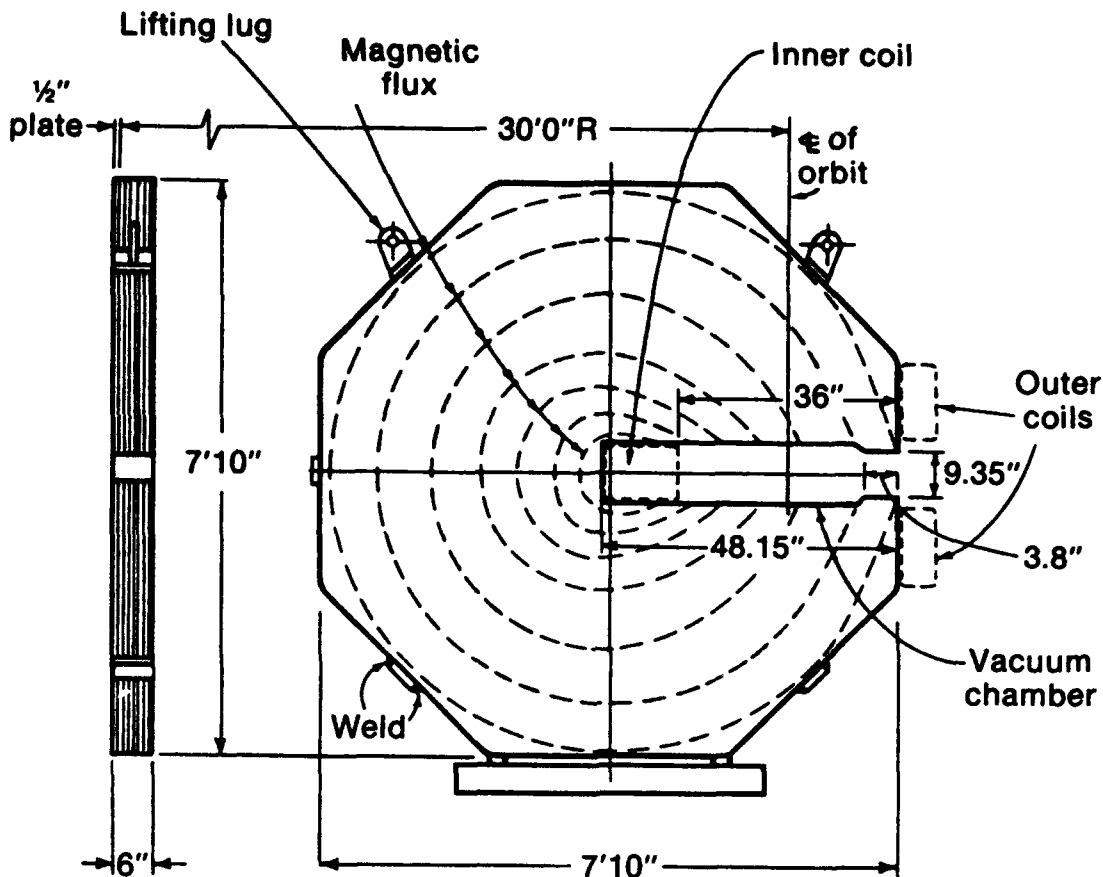


Figure 1. Cross section of the Cosmotron magnet

There were a host of other problems to be solved in the first proton synchrotrons. With injection at 4 million volts from High Voltage Engineering's first Van de Graaff machine, the proton velocity is less than one tenth of the final velocity—which is quite close to the velocity of light. So the radio frequency accelerating field must change in frequency by more than a factor of ten and the accelerating cavity had to be tuned over that range. For this purpose, we introduced to the United States the ferromagnetic ferrites that had just been discovered at the Philips Laboratories in the Netherlands.

We wanted very badly to be first in the world to a billion volts, but we were terrified that the mighty Berkeley powerhouse of talent and experience would beat us to it. Then, in 1949, the

Berkeley quarter-scale model was completed and tests on it showed that the beam was lost at an aperture larger than we were building into our 2000-ton magnet. Today it is evident that the model did not meet the mechanical tolerances that we built into the Cosmotron, but at the time we were very scared.

Then Fortune befriended us. At Berkeley and Livermore a huge, very secret project was started aimed at production of fissionable material for the national defense program. The whole Bevatron staff was transferred to this project for two years and we were given the chance to be first to a billion volts. We made it in May of 1952. It was a glorious victory; it was indeed a critical victory. If the Cosmotron had failed, Brookhaven's splendid program in high energy physics might never have been started.

Consequently, I feel that the Cosmotron was about the most important project in my career.

That summer of 1952 we heard about the organization of the CERN Laboratory, to be a new European center for high-energy physics. They were well impressed by the design of the Cosmotron and planned to build a scaled-up version of our machine to reach 10 billion volts. We learned that they would visit us during the summer of 1952 to ask our advice about a variety of problems. Livingston was anxious to be of all assistance possible and he suggested a design change to reach higher fields in our magnet. The Cosmotron magnetic field pattern above about 13 kilogauss was affected by saturation effects so that the field gradient increased to levels where weak focusing was no longer possible. Livingston suggested placing some magnet returns outside the orbit so that the high gradients would average out to the low gradient required. He asked Ernest Courant to analyze the effects of alternating gradients on the orbits and to Ernest's surprise, he found that the focusing was much improved when the gradients were such as alternately to focus and defocus the beam. The higher the gradients, the better was the focusing strength. Hartland Snyder came by and reminded us of the optical analog: the combination of a focusing lens and a defocusing lens of equal strength is focusing, no matter which comes first. Thus was strong focusing born. Immediately it was evident to me that this was the solution to the fundamentally defocusing accelerating fields in linear accelerators. All that is necessary is to include alternating focusing and defocusing quadrupoles—either electrostatic or magnetic—and proton or ion linear accelerators of high intensity become possible. Our papers on the strong focusing synchrotron and focusing in linear accelerators appeared in *The Physical Review* in December of 1952.

The visitors from CERN—Odd Dahl, Frank Goward and Rolf Widerøe—appeared shortly after this discovery. We told them our story; they lost no time in abandoning their 10-GeV Cosmotron and raised their sights to a new strong focusing machine in the energy range of 30 GeV—almost exactly the machine which we now had in mind. Also, they invited Ernest Courant, Hildred Blewett and me to come to Europe and help organize CERN's proton synchrotron effort. Hildred and I accepted, and early in 1953 we found ourselves located in Bergen, Norway where Odd Dahl, the head of CERN's PS group, lived as head of the Mikelsens Institute. We soon made friends with a promising young Norwegian protege of Dahl's—Kjell Johnsen—and found ourselves established in the Physics Department of Bergen University. They had just built a betatron and had some magnet laminations

left over, so we very quickly built a small model of a strong focusing, high-gradient magnet that provided the basis for the first CERN magnet design. But the most important project we undertook for CERN was to persuade them that PS design projects scattered all over Europe would make no real progress until all were assembled in Geneva, the final site of CERN. In September of 1953 at last we all moved to Geneva. A month later the CERN group was subjected to a public examination by accelerator experts from all over the world. Though suffering from beginners' terrors, they passed the examination with flying colors. In 1954 we came home, confident that CERN was headed for a brilliant future. We indeed were justified.

I note in passing that confidence in strong focusing was not universal. We, CERN and Bob Wilson at Cornell proceeded with strong focusing machines. But, even after our announcement of the new method, old fashioned weak focusing machines were built at Argonne (the ZGS), at Princeton (the Princeton-Penn accelerator), and at the Rutherford Laboratory (Nimrod).

We returned to find Brookhaven's AGS well underway. While we were at CERN, BNL had decided to build an "Electron Analog" to test our ability to pass through the "phase transition"—a sudden phase shift that hadn't existed in the Cosmotron, but would be necessary in the AGS. I took a dim view of this project. Kjell Johnsen had analyzed the problem and concluded that it would be easily solved. Anyway, the analog worked as Johnsen had predicted and people no longer feared the phase transition.

The AGS and the CERN PS worked as expected and, indeed, are still working after over 30 years. Meantime a group of us turned our attention to the next big accelerator. Official Washington decided that this was to be for 200 GeV, that it was to be designed at the University of California, that the Atomic Energy Commission would conduct a site search and that Brookhaven should study future machines for up to 1000 GeV. After a fair amount of administrative foolishness and disagreement within the high energy physics community, the Fermilab emerged to become the distinguished center that it now is.

Meantime at Brookhaven, Luke Yuan and I organized a number of studies of "super energy" machines and raised questions with the high energy physics community about what they wanted in the future. In 1963 at a Brookhaven summer study, we could find only three experts who favored colliding beams. Under pressure from the Columbia group headed by Leon Lederman, it was decided that colliding beams should be left to CERN. Brookhaven should concentrate on souping up the

intensity of the AGS for improved studies on neutrinos.

Eventually, we came to a design for a new colliding beam machine, known as ISABELLE—ISA for "intersecting storage accelerators" and BELLE for good measure. ISABELLE lived long enough for us to construct a two-mile tunnel, now about to house RHIC, a heavy ion colliding beam ring. I think it fair to suggest that ISABELLE was an important stepping stone on the way to the SSC.

During President Carter's regime, I organized a program at Brookhaven for development of energy sources, but eventually I found my way back to accelerators and formed an alliance with Ken Green, Rena Chasman and Jules Godel to start a project for a synchrotron light source for Brookhaven. By now it had become evident that synchrotron radiation could be useful in a great number of fields. The pioneers in this area were at Cornell and at the University of Wisconsin, where the remains of MURA (Midwestern Universities Research Association) had refused to die and had begun to exploit the radiation from one of MURA's electron models. Now it seemed appropriate for Brookhaven to provide a "National Synchrotron Light Source." I edited the proposal and Ken and Rena provided the basic design. We were quickly approved and, as I am

sure you know, the project has been a great success with, by now, over two thousand users from universities, industry and other institutions.

Now, light sources are springing up world wide. I am particularly attached to a 1.3 GeV ring in Taiwan having been a member of its Technical Review Committee since 1984. It is a beautiful machine and is just now coming into operation. Its staff reminds me of Cosmotron days when a collection of beginners gradually turned into professional accelerator builders.

I conclude with a mention of a graph which I evolved around 1960 of logarithm of achieved accelerator energy against date. This proved to be a reasonably straight line indicating an increase of energy by a factor of ten every six years. Stan Livingston and I wrote a book about accelerators in 1962 in which we published this graph. It is interesting to see how this plot looks at present. In adding points for colliding beams I use the equivalent energy required for a static target. The linearity of the graph persists quite nicely—still a factor of ten every six years. Drawing the line as carefully as I can, it seems to predict that the LHC will be completed around the year 1998, while the SSC is not due until the year 2003.

# Demonstration of Plasma Beat Wave Acceleration of Electrons from 2 MeV to 20 MeV

C. E. Clayton, K. A. Marsh, M. Everett, A. Lal, and C. Joshi  
Department of Electrical Engineering  
University of California at Los Angeles  
56-125B Engineering IV  
Los Angeles, CA 90024

## Abstract

We describe the results from recent experiments<sup>1</sup> on the plasma beat wave accelerator (PBWA) scheme at UCLA. A relativistic electron plasma wave (which is the accelerating structure) is resonantly excited in a plasma by the beating of two co-propagating electromagnetic waves (obtained from a CO<sub>2</sub> laser operating simultaneously on two wavelengths). A 2 MeV, 200 mA (peak-current) electron beam, roughly 1 nsec (FWHM) in duration is used as a source of test particles for measuring the longitudinal fields of the plasma wave which itself is moving with a relativistic Lorentz factor of about 34. Accelerated electrons are energy-selected with an imaging sector magnet and detected simultaneously with a cloud chamber and surface barrier detectors. Initial experiments show that electrons are accelerated up to 20 MeV over roughly 1 cm (the uniform length of plasma) indicating an gradient of acceleration of more than 1.8 GeV/m.

## INTRODUCTION

In the last 5 or 10 years, there has been a great deal of interest in advanced accelerator concepts.<sup>2</sup> The primary motivation behind this research is to increase acceleration gradients to levels beyond the  $\sim 100$  MeV/m limit of conventional rf technology. Much of this effort has been in the area of collective acceleration using plasmas.<sup>3</sup> Plasma technology has the potential for 10–100 $\times$  higher gradients than state-of-the-art rf technology. For example, for a working

(eV/cm) for  $n_e$  expressed in electrons/cm<sup>3</sup>. This gives  $1 < E_{accel} < 10$  GeV/m for  $10^{15} < n_e < 10^{17}$  cm<sup>-3</sup> and a modest wave amplitude of 30%. Potential applications of this technology are in compact GeV-scale linacs and perhaps more affordable TeV-scale linear colliders. This paper presents some recent experimental results on one such plasma accelerator concept, namely the plasma beat wave accelerator.

## PHYSICAL MECHANISM

The accelerator structure in the plasma beat wave scheme is an electron plasma wave which is a normal mode of the plasma. The means by which this wave is excited is illustrated in Fig. 1. When two laser beams of slightly different frequency are propagating together, there is constructive and destructive interference of their transverse electric fields forming a beat envelope as shown in Fig. 1(a). In this case, there is a longitudinal modulation to the total field intensity. The plasma electrons experience a force, called the ponderomotive force, which is proportional to the gradient of the field intensity and is thus directed towards the local minima of the beat-envelope pattern. This tends to bunch the electrons into the minima of the beat envelope (as shown in Fig. 1(b)) with a period given by the difference wavenumber  $\Delta k$ . As the beat envelope propagates (to the right in Fig. 1), the electrons oscillate longitudinally at the difference frequency  $\Delta\omega$ . Now, because the plasma ions are too massive to respond to the beating force, they do not move and so the electrons will also feel a restoring force due to the space-charge field between the bunched electrons and the still uniform ions. The plasma frequency  $\omega_{pe}$  is the natural frequency of this mode of oscillation (where plasma electrons are displaced from their equilibrium position). If the plasma density and thus the plasma frequency is chosen such that  $\omega_{pe} = \Delta\omega$ , then the plasma wave will grow rapidly with time until a nonlinear relativistic saturation<sup>4</sup> limits the amplitude to  $\epsilon \approx 40\%$  (typically) for our experimental parameters.

## OVERVIEW OF EXPERIMENT

A cartoon of the top-view of the experiment is shown in Fig. 2. The two-frequency laser beam<sup>5</sup> is focused into a vacuum chamber filled with about 140 mT of hydrogen gas. The plasma is formed by laser-ionization of the gas through tunneling ionization.<sup>6</sup> Upon full ionization, the plasma wave grows up and, since the bunched electrons resemble a grating, the wave can scatter optical beams, thus allowing optical diagnostics of the wave. The parameters for the laser and

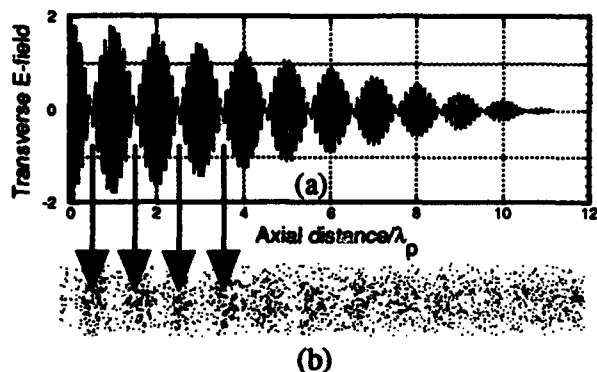


Figure 1: (a) Interference or beat pattern formed by two laser beams of slightly different frequencies. (b) Density bunching caused by the longitudinal ponderomotive force from the intensity gradients in (a).

plasma density of  $n_e$  and a plasma wave amplitude of  $\epsilon$ , the accelerating electric field  $E_{accel}$  is given by  $E_{accel} \approx \epsilon(n_e)^{1/2}$

plasma/plasma wave are given in Table 1. An important point to note is that the Rayleigh range is about 1 cm and this will be one of the limiting factors in the experiment. The electric fields of the wave are probed directly by injecting electrons from an electron linac.<sup>7</sup> The linac parameters are also summarized in Table 1. The electrons are focused through a

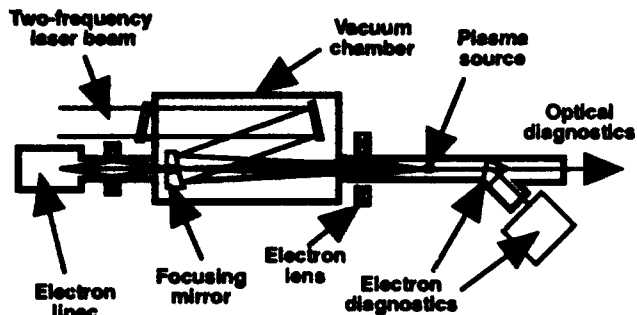


Figure 2: Cartoon overview of the main experimental apparatus.

small hole drilled in the large CO<sub>2</sub> laser focusing mirror, allowing the electrons and laser to propagate collinearly as is necessary for the experiment. The electrons are focused to a spot of about 260 μm diam which is smaller than the laser spot allowing good coupling of the electrons to the plasma wave. A double-focusing sector magnet selects the energy of the accelerated electrons which are detected by the electron diagnostics. These will be discussed in more detail in a later section.

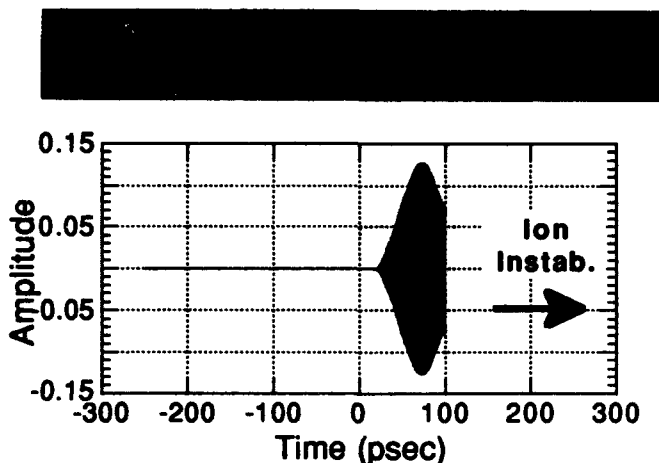


Figure 3: Bottom graph shows a calculation of the plasma wave amplitude vs. time for our laser parameters and the laser rising at  $t=0$  psec. The model cannot predict what happens later in time due to ion instabilities. The top image is an actual streak of Cherenkov light from the linac electrons with the same time scale as the graph.

## MODELING OF THE EXPERIMENT

With the laser parameters listed in Table 1, one can model the experiment<sup>8</sup> to find out what sort of dynamics to expect in the experiment. For example, the plasma formation can be modeled using the proven tunneling ionization theory<sup>9</sup> and the

Table 1: Experimental parameters for the laser, plasma, plasma wave, and electron injector.

Laser	
Source	CO <sub>2</sub> laser
Wavelengths	10.591, 10.289 μm
Energy per line (typ.)	60 J, 15 J
Spot radius $w_0$	150 μm
Rayleigh range $2z_0$	1.3 cm
Electron quiver vel.	0.17, 0.07
Pulse risetime	150 psec
Pulse FWHM	300 psec
Plasma	
Source	Tunnel ionization
Density	$8.6 \times 10^{15} \text{ cm}^{-3}$
Gas	Hydrogen
Plasma period $v_p^{-1}$	1.2 psec
Plasma wave wavelength	360 μm
Lorentz factor $\gamma_{ph}$	34
Accel. gradient for 11% wave	1 GeV/m
Electrons	
Source	RF LINAC
Energy	2 MeV
Peak current	200 mA
Emittance	$6\pi \text{ mm-mrad}$
Focused spot radius	130 μm
RF frequency	9.3 GHz
Micropulse separation	107 psec
Electrons per micropulse	$1.7 \times 10^7$
Micropulse length	10 psec

time-dependent density one thereby calculates can be inserted into a computation of the plasma wave growth. The result of such a modeling is shown in Fig. 3. The plasma reaches full ionization at best focus after about 25 psec into the 150 psec rise of the laser pulse. At this point, the plasma wave begins to grow until relativistic saturation occurs after about 70 psec. This particular calculation was for  $\omega_{pe} = \Delta\omega$ . If one sets  $\omega_{pe}$  slightly above  $\Delta\omega$ , the relativistic saturation is delayed and a peak wave amplitude of 40% can be expected.<sup>10</sup>

The timing of the CO<sub>2</sub> laser and the 1 nsec FWHM linac macropulse is set to within  $\pm 100$  psec. However, due to the technique by which the CO<sub>2</sub> pulse is generated, it is not possible to phase the exact micropulse timing to the timing of the peak fields in the plasma wave. A typical streak of the electrons (from Cherenkov light) is shown in the image above the graph in Fig. 3. One can see that there will be roughly a 50% probability that a micropulse will interact with a field of at least half the maximum fields of the plasma wave. The probability of interacting with higher and higher fields continues to drop until there is an approximately 10% chance of a micropulse interacting with the peak plasma wave fields.

## DETAILED EXPERIMENTAL SETUP

A more detailed view of the experimental setup is shown in Fig. 4. The CO<sub>2</sub> laser and the electrons are both focused into

the plasma which is located at the center of a cross piece in the vacuum chamber. The back- and forward-scattered CO<sub>2</sub> light as well as the Thomson scattered probe beam are indicated by arrows. These three scattering diagnostics comprise the optical diagnostics of the wave amplitude mentioned earlier.

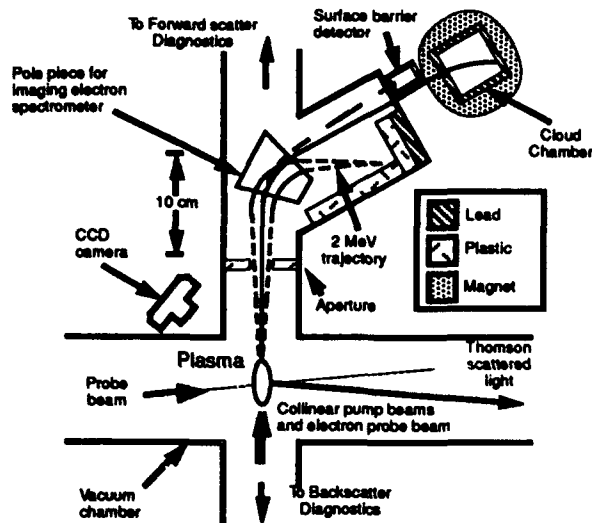


Figure 4: Detailed view of the experimental setup.

Injected electrons which do not interact with the plasma wave follow a small-radius trajectory and are dumped in a plastic beam dump as shown in Fig. 4. Electrons which are accelerated follow a larger radius trajectory and are detected in one of the electron diagnostics: a silicon surface barrier detector (SBD) or a diffusion cloud chamber.

The SBD, along with a preamplifier, produces a signal of about 20 mV per electron and can thus easily detect single electrons. It also has the advantage of providing a quantitative measurement of the number of electrons over a large dynamic range (by changing the preamplifier gain). But it has one major disadvantage and that is its sensitivity to x-rays. In fact, one cannot discern the difference between an electron signal and an x-ray signal except through the statistics of many data shots and null tests. For the experimental setup shown in Fig. 4, the contribution from x-ray noise varies from about 30 electrons worth of signal when the electron spectrometer is set to 3.5 MeV down to < 1 electron worth of signal when the spectrometer is set to 20 MeV.

The other electron detector is a simple, home-made diffusion cloud chamber<sup>11</sup> which uses a methanol bath at dry ice temperature in a chamber of 1 ATM of dry air. A piece of felt wicks the methanol up to the top of the chamber and the methanol vapor falls back into the bath, going through a region of supersaturation. The electrons ionize the air and the methanol condenses on the ions along the electrons' path. The chamber is shielded in lead and surrounded by a coil which can be energized to provide a  $\approx 260$  G vertical magnetic field throughout the active region of the cloud chamber. The tracks are recorded by frame-grabbing CCD camera. The big advantage of the cloud chamber over the SBD is that it is essentially immune to x-ray noise. Although x-rays do

produce some ionization of the gas and thus visible tracks, the tracks are typically short and kinked as they are due to low energy (<50 keV) electrons which are kicked out by the x-ray absorption in the dry air. The actual signal due to accelerated electrons should appear quite distinct from these tracks. They should be straight tracks, traversing the entire field of view of the camera and they should appear to originate from the aperture in the chamber.

## EXPERIMENTAL RESULTS

### Null tests

Ideally, the presence of signals on the two electron detectors should only occur if the three main components of the experiment are present. These are; (1) the plasma, (2) the injected electrons, and (3) the beat wave. If any of these are turned off, we would expect that there would be no signal on the electron detectors unless some other physics is occurring besides beat wave acceleration. The result of these null tests are summarized in Table 2. As indicated in the third column, we see no evidence of acceleration by the laser beam itself, of acceleration of non-injected electrons (from for example, instability-heated electrons), or of spontaneous generation of an accelerating structure through some mechanism other than beat wave (as in, for example, Raman forward scattering).

### Cloud chamber data

When the plasma, external electron source, and two-frequency laser are fired up simultaneously in about 140 mT of hydrogen gas, tracks are observed in the cloud chamber as seen in Fig. 5. For the image in Fig. 5(a), the electron spectrometer was set to direct 5.2 MeV electrons into the aperture of the cloud chamber and the magnetic field surrounding the cloud chamber was off. The tracks have the characteristics of high-energy electrons discussed earlier; that is, straight lines, long range, and directionality. The scatter in the angles is probably dominated by scatter in the 25  $\mu$ m Mylar vacuum-exit window and the  $\approx 6$  cm of 1 ATM air between the vacuum window and the beginning of the field of view. Subsequent calibrations indicate that Fig. 5(a) is

Table 2: Summary of the key null tests performed.

Condition	Result	Conclusion
Linac & 2-frequency laser but no plasma (chamber evacuated).	Only usual* x-ray noise.	No acceleration by laser only.
2-frequency laser & plasma but no linac (linac beam blocked).	No signal at all $\ddagger$ .	No trapping of background plasma electrons or SRS-generated tail.
Single-line laser & linac & plasma (no second frequency).	Only usual* x-ray noise.	No substantial level of stimulated Raman forward scattering.

\* Usual x-ray noise  $\approx 10$  electrons worth of signal.

$\ddagger$  No signal  $\Rightarrow$  less than 1 electrons worth of signal.

composed of about  $10^3$  tracks.<sup>12</sup> For Fig. 5(b), the external magnetic field was energized causing the electron trajectories and therefore the tracks to bend. For this shot, the electron spectrometer was again set to 5.2 MeV as in Fig. 5(a). An image with a small number of tracks was chosen in order to see individual tracks. Three theoretical trajectories calculated for 5.2 MeV electrons are overlaid onto this image. The good agreement indicates that the electrons were within 10% of 5 MeV; i.e., 2.5 times higher energy than the injection energy of 2 MeV.

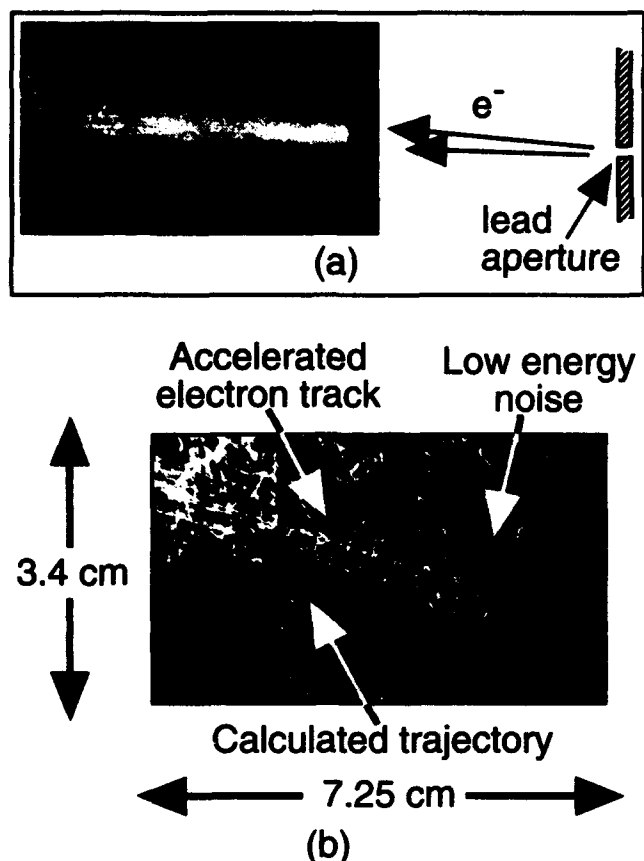


Figure 5: Images of tracks in cloud chamber with the electron spectrometer set to send 5.2 MeV electrons into the aperture of the cloud chamber. (a) No external magnetic field. Relative location of the aperture is shown. (b) With 260 G external field. Calculated trajectories are overlaid as the thin white curves.

#### Surface barrier detector data

While the cloud chamber dramatically confirms the existence of accelerated electrons, it is not a very quantitative diagnostic. The SBD, however, is quantitative since the signal level is directly proportional to the number of electrons striking the silicon detector. Figure 6 shows the SBD signal vs. fill pressure of  $H_2$  gas in the vacuum chamber for a variety of electron spectrometer settings. Since we expect that the gas is fully ionized and since the beatwave is a resonant phenomena, we can predict the range of pressures over which a substantial level of plasma wave will exist. This is shown by the hatched bar along the pressure axis near 135 mT. Experimentally, we find that we must overfill the chamber by

about 8% or so. This is probably due to hydrodynamic expansion of the plasma column during the  $\sim 100$  psec time scale of the interaction. The individual points on Fig. 6 are single laser shots. All the shots which show electrons signals above the x-ray noise (which is around 200–300 mV) also show evidence for a large-amplitude plasma wave on the three optical diagnostics.<sup>8</sup> Shots with small electron signals

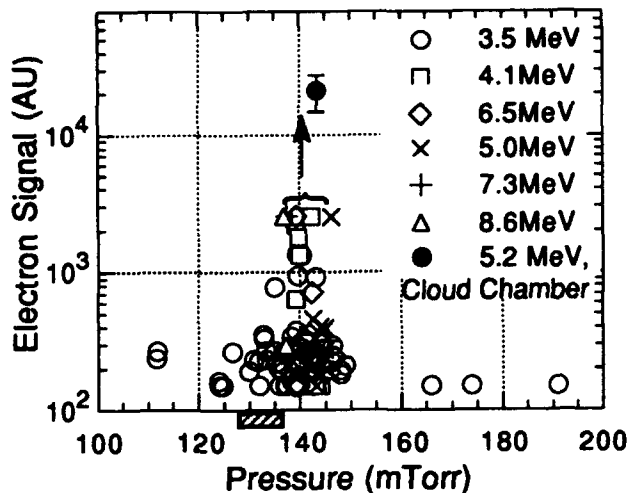


Figure 6: SBD signal vs. vacuum-chamber fill pressure for various settings of the electron spectrometer. The open points are from Detector A and the solid point is from a calibration of the intensity of the tracks in Fig. 5(a). The hatched bar is the range of the expected resonance.

near 140 mT either did not have a plasma wave (according to the optical diagnostics) due to lack of two frequencies in the laser or they did have a plasma wave but the electrons were unsynchronized due to the micropulse structure of the linac beam. The data in Fig. 6 were taken with the experimental arrangement of Fig. 4 and for this arrangement, the SBD detector is referred to Detector A.

Detector A is limited to viewing energies below 9 MeV due to the maximum field obtainable in the electrons spectrometer. To extend the electron energy measurements to energies beyond 9 MeV, a new port was added to the electron spectrometer at about  $5\times$  the radius of curvature shown by the long-dashed curve in Fig. 4. In this case, two SBD's were collecting data for each shot: Detector B at the low energy position and Detector C at the high energy position. A summary of the number of detected electrons (SBD signal in mV times electrons/mV sensitivity of the detector/preamp combination, corrected for any limiting lead apertures placed over the detectors) vs. the energy location of the detectors. Although this data was accumulated over many laser shots, we can see that the numbers are falling off rapidly with energy, going out to 20 MeV. This rapid fall-off with energy can be expected for two reasons. First, the electrons are not pre-bunched and therefore occupy all phases in the acceleration buckets. Secondly, energy-bunching is expected to occur only for longer acceleration lengths where transient or start-up phase

slippage is not important. In this experiment, however, the electrons execute a large swing in phase as they accelerate from  $\gamma = 5$  (well below the Lorentz factor for the wave,  $\gamma_{ph}$ ) to  $\gamma = 20$  (slightly above  $\gamma_{ph}$ ).

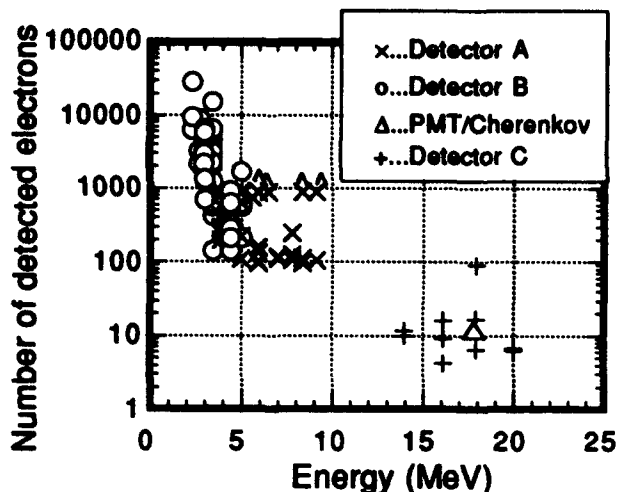


Figure 7: Number of detected electrons vs. energy location of the detectors. Data is from many shots. Detectors B and C were on-line together. Triangle point is from a gaseous Cherenkov tube coupled to a photomultiplier.

The maximum energy seen in these shots was 20 MeV. This is an energy gain of 18 MeV over the nominal 1 cm of interaction length which corresponds to an average accelerating gradient of 1.8 GeV/m. From the engineering formula given in the introduction, this corresponds to a wave amplitude of  $\epsilon = 20\%$ . This is within a factor of two of the best one would expect for our experimental parameters. The maximum energy gain may be limited by the dynamics discussed in connection with Fig. 6.

## CONCLUSION

To summarize, the acceleration of an externally injected beam of electrons in a relativistic electron plasma wave has been demonstrated. Acceleration is only observed when the linac injector, the two-frequency laser, and the plasma are all on simultaneously. The numbers of accelerated electrons is correlated with independent optical diagnostics. Energies out to 20 MeV have been observed implying an average gradient (over  $\approx 1$  cm) of about 1.8 GeV/m, only about 2 times lower than the optimum expected for our experimental parameters.

To conclude, it appears that the plasma beat wave accelerator concept can be relied upon to provide energy gains nearly in accordance with theory. If one chooses a different parameter space—for example, replacing the CO<sub>2</sub> laser with a two-frequency laser operating at a wavelengths around 1  $\mu\text{m}$ —one can find theoretical energy gains of several hundred MeV from gradients approximately 10 $\times$  higher than demonstrated in this experiment.<sup>8</sup> Such an experiment would essentially be an extension of the current CO<sub>2</sub> laser experiment in that it requires no new physics. Thus, with today's glass laser

technology, one could envision building a small plasma accelerator based on the beat wave concept which would approach the GeV energy range.

## ACKNOWLEDGMENTS

The authors would like to acknowledge useful discussions with Drs. W. B. Mori and P. Mora, and Professors J. M. Dawson, T. Katsouleas, and R. Williams and thank D. Gordon for his technical assistance. This work is supported by the U. S. Department of Energy under grant no. DE-FG03-92ER40727.

## REFERENCES

1. C. E. Clayton, K. A. Marsh, A. Dyson, M. Everett, A. Lal, W. P. Leemans, R. Williams, and C. Joshi, "Ultrahigh-gradient acceleration of injected electrons by laser-excited relativistic electron plasma waves", *Phys. Rev. Lett.* **70**, 37 (1993).
2. See, for example, *Advanced Accelerator Concepts*, ed. by C. Joshi, AIP Conf. Proc. No. 193 (Amer. Inst. Phys., New York, 1989).
3. See, for example, the Special Issue on Plasma-Based High Energy Accelerators, *IEEE Trans. Plasma Sc.*, **PS-15**, (1987) and C. Joshi, W. B. Mori, T. Katsouleas, J. M. Dawson, J. M. Kindel, and D. W. Forslund, "Ultrahigh gradient particle acceleration by intense laser-driven plasma density waves", *Nature* **311**, 525 (1984).
4. M. Rosenbluth and C. S. Liu, "Excitation of plasma waves by two laser beams", *Phys. Rev. Lett.* **29**, 701, (1972).
5. C. E. Clayton, K. A. Marsh, W. P. Leemans, M. Everett, and C. Joshi, "A terawatt, short-pulse, multiline CO<sub>2</sub> laser facility based on optical free-induction decay" (to be published).
6. W. P. Leemans, C. E. Clayton, W. B. Mori, K. A. Marsh, A. Dyson, and C. Joshi, "Plasma physics aspects of tunnel-ionized gases", *Phys. Rev. Lett.* **68**, 321 (1992) and W. P. Leemans, C. E. Clayton, W. B. Mori, K. A. Marsh, P. K. Kaw, A. Dyson and C. Joshi, "Experiments and simulations of tunnel-ionized plasmas", *Phys. Rev. A* **46**, 1091 (1992).
7. C. E. Clayton and K. A. Marsh, "A 2 MeV, 100 mA electron accelerator for a small laboratory environment", *Rev. Sci. Instr.*, **64**, 728 (1993) and C. E. Clayton and K. A. Marsh, "A versatile 2 MeV, 200 mA compact x-band linac", (this proceedings).
8. C. Joshi, C. E. Clayton, K. A. Marsh, A. Dyson, M. Everett, A. Lal, W. P. Leemans, R. Williams, T. Katsouleas, and W. B. Mori, "Acceleration of injected electrons by the plasma beat wave accelerator", in AIP Proceedings of Workshop on Advanced Accelerator Concepts, Port Jefferson, Ed. J. Wurtele, to be published (1992).
9. P. B. Corkum, N. H. Burnett and F. Brunel, "Above-threshold ionization in the long-wavelength limit," *Phys. Rev. Lett.*, vol. 62, pp. 1259-62, March 1989.
10. C. M. Tang, P. Sprangle, and R. N. Sudan, "Dynamics of space-charge waves in the laser beat wave accelerator", *Phys. Fluids* **28**, 1974 (1985).
11. A. Langsdorf, Jr., "A continuously sensitive diffusion cloud chamber", *Rev. Sci. Instr.* **10**, 91 (1939).
12. C. E. Clayton, K. A. Marsh, A. Dyson, M. Everett, A. Lal, W. P. Leemans, R. Williams, and C. Joshi, "Experimental Demonstration of Laser Acceleration of Electrons via Relativistic Plasma Waves", *Proc. of the SPIE OE-LASE '93 Conf.*, Jan. 16-23, 1993, Los Angeles, CA.

# Laser Wakefield Accelerator Experiments Using 1ps 30TW Nd:glass Laser

K. Nakajima, H. Nakanishi, T. Kawakubo, A. Ogata  
KEK, National Laboratory for High Energy Physics, Tsukuba, Ibaraki, Japan

Y. Kitagawa, H. Shiraga, R. Kodama, T. Zhang, K. Suzuki, Y. Kato  
Institute of Laser Engineering, Osaka University, Osaka, Japan

Y. Sakawa, T. Shoji  
Plasma Science Center, Nagoya University, Nagoya, Japan

Y. Nishida, N. Yugami  
Department of Electric and Electronic Engineering, Utsunomiya University, Utsunomiya, Japan

T. Tajima  
Institute for Fusion Studies, The University of Texas at Austin, Austin, Texas, USA

## Abstract

The peak power of 30TW and the pulse width of 1ps produced by the Nd:glass laser system is capable of creating a highly-ionized plasma of a moderate density gas on an ultrafast time scale and generating a large amplitude plasma wave with an accelerating gradient of the order of GeV/m. We are going to demonstrate particle acceleration injecting electrons of a few MeV emitted from a solid target by intense laser irradiation.

## 1 INTRODUCTION

Recent progress in ultrashort super-intense lasers allows us to test the principle of the Laser Wakefield Accelerator (LWFA) [1]. An intense, short laser pulse with peak power of 30TW and pulse width of 1ps is delivered by the Nd:glass laser system GMII in Osaka University. This laser achieves  $10^{17} - 10^{18} \text{W/cm}^2$  intensity, strong enough to create a fully-ionized plasma on an ultrafast time scale by the tunneling ionization process. In a plasma with appropriate density, a large amplitude of wakefield is generated behind the laser pulse propagating through the plasma due to the ponderomotive force. The phase velocity of the plasma wave is highly relativistic so that the wakefield can accelerate charged particles trapped by the plasma oscillation.

In these experiments, a chamber is filled with  $\text{H}_2$  or He gas beforehand, whose pressure mates with the optimum plasma density for acceleration if it is completely ionized. Two  $1.052\mu\text{m}$  Nd:glass laser beams are injected into the chamber. One with 200ps duration and 200GW peak power bombarded a solid target to produce test electrons whose energy ranges to the order of MeV. The other, with 1ps duration and 30TW peak power, ionizes the gas

and excites wakefields in the resultant plasma in synchronism with the first laser. Energy change of the test electrons caused by the wakefield is measured by an energy analyzer.

We have not yet conditioned the 1ps laser to attain the full power. Consequently, no conclusive demonstration of the acceleration has not yet observed.

## 2 THEORETICAL PREDICTIONS

We assume the Gaussian beam optics, in which the laser beam has the wavelength  $\lambda_0$ , the peak power  $P$ , the radius  $w_0(z)$  at the waist and the vacuum Rayleigh length  $z_R$ . The linear model with an unmagnetized, cold plasma of classical electrons and immobile ions gives the longitudinal wakefield excited by the Gaussian laser pulse as [2]

$$eE_z = \frac{m_e c^2 \epsilon_0 \cos(k_p z - \omega_p t)}{z_R [1 + (z/z_R)^2]} \exp\left(-\frac{r^2}{w_0^2 [1 + (z/z_R)^2]}\right), \quad (1)$$

with the vacuum resistivity  $\Omega_0 = 377\Omega$ , the plasma frequency  $\omega_p$ ,  $k_p = \omega_p/v_p$  with a phase velocity of the plasma wave  $v_p$ , and

$$\epsilon_0 = \frac{\Omega_0 P}{\sqrt{\pi} m_e^2 c^4} \left(\frac{\lambda_0}{\lambda_p}\right) k_p \sigma_z \exp\left(-\frac{k_p^2 \sigma_z^2}{4}\right), \quad (2)$$

where  $\sigma_z$  is the rms pulse length. The wakefield is maximum when the plasma density gives the relation  $\lambda_p = \pi \sigma_z$ .

The maximum energy gained by an electron with velocity equal to the phase velocity of the plasma wave is obtained by integrating the axial wakefield along the laser beam axis,

$$(\Delta E)_{\max} = \int_{-\infty}^{\infty} E_z(z) dz = \pi m_e c^2 \epsilon_0. \quad (3)$$

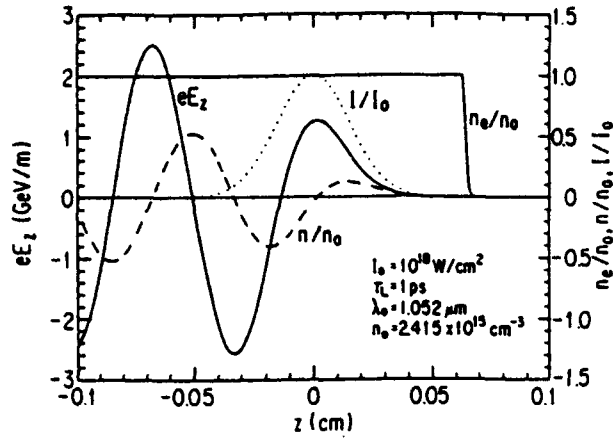


Figure 1: Evolution of the electron density  $n_e$ , the density perturbation  $n$  and the axial electric field  $E_z$  excited by a 1 ps Nd:glass laser pulse of the peak intensity  $10^{18}$  W/cm<sup>2</sup>.

The 1ps, 30TW laser pulse at wavelength  $\lambda_0 = 1.052\mu\text{m}$  should be able to produce the maximum energy gain of 45MeV.

The trapping condition for an electron with energy  $\gamma$  and velocity  $\beta = v/c$  is given by

$$eE_z/(m_e c \omega_p) \geq \gamma(1 - \beta_\phi \beta) - 1/\gamma_\phi. \quad (4)$$

where  $\beta_\phi$  is the phase velocity of the plasma wave and  $\gamma_\phi$  is the relativistic factor of its phase velocity defined as

$$\beta_\phi = \frac{v_p}{c} = \sqrt{1 - \frac{\omega_p^2}{\omega_0^2}}, \quad \gamma_\phi = \frac{1}{\sqrt{1 - \beta_\phi^2}} = \frac{\omega_0}{\omega_p}. \quad (5)$$

The trapping and the acceleration occur at the waist in the Rayleigh length. The minimum threshold kinetic energy to be trapped by the plasma wake is about 40keV for excitation of a  $10^{18}$ W/cm<sup>2</sup> intensity.

The present experiments utilizes the ability of tunneling ionization of a short pulse laser. The phenomenon on an ultrafast time scale ( $\leq 10$ fs) is distinct when the intensity is greater than  $10^{15}$ W/cm<sup>2</sup>. The onset of tunneling ionization is predicted by a simple Coulomb-barrier model. The threshold intensity [4] for the production of charge state  $Z$  of the atom or ion with the ionization potential  $U_i$  is given by

$$I_{th} = 2.2 \times 10^{15} Z^{-2} (U_i/27.21)^4 \text{ W/cm}^2. \quad (6)$$

The ionization rate [5] for a hydrogen atom is given by ,

$$W_H = 1.61 \omega_{a.u.} \left[ \frac{10.87 E_{a.u.}}{E_0} \right]^{1/2} \exp \left[ -\frac{2E_{a.u.}}{3E_0} \right], \quad (7)$$

where  $\omega_{a.u.}$  is the atomic unit of frequency ( $4.1 \times 10^{16} \text{ s}^{-1}$ ) and  $E_{a.u.}$  is the atomic field strength ( $5.1 \times 10^9 \text{ V/cm}$ ).

Fig. 1 depicts the evolution of electron density in hydrogen plasma with initial atomic density  $n_0 = 2.415 \times 10^{15}$

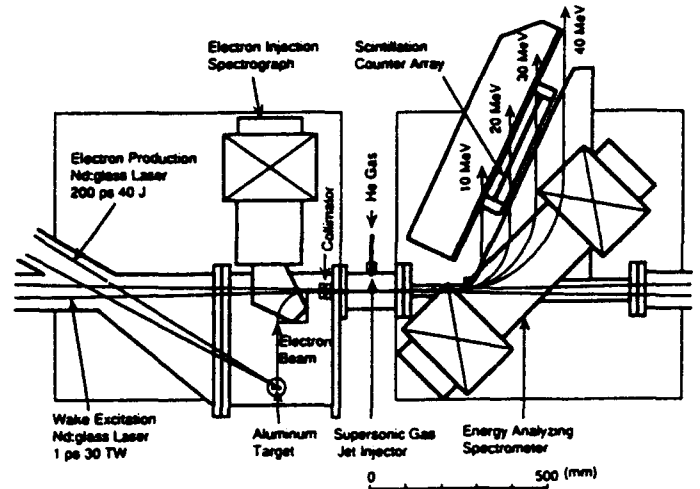


Figure 2: Experimental layout for electron acceleration.

cm<sup>-3</sup>, the density perturbation and the axial electric field excited by a 1 ps laser pulse with the peak intensity  $I_0 = 10^{18}$ W/cm<sup>2</sup>.

### 3 EXPERIMENTAL APPARATUS

The chamber is filled with H<sub>2</sub> or He gas beforehand with static pressure to mate with the optimum plasma density for acceleration when completely ionized. It is also possible to feed the gas pulsively in synchronous with the laser pulse. Two 1.052 $\mu\text{m}$  Nd:glass laser beams are injected into the chamber. One bombards a solid target to produce test electrons whose energy ranges to the order of MeV. The other with 1ps duration and 30TW peak power ionizes the gas and excites wakefield in the resultant plasma in synchronism with the first laser. The energy change of the test electrons caused by the wakefield is measured by an energy analyzer.

The lasers are almost linear polarized. They are processed as follows[3]. A primary Nd:YAG laser pulse of 130ps duration is coupled to a single mode fiber of 1.85km in length. The beam is split into two at the exit of the fiber, each has 200ps duration and 1.8nm bandwidth. One is amplified and used for the electron production. The other is also amplified to an energy of 41J with a beam diameter of 14cm, and it is finally compressed to a pulse width of 1ps by a pair of gratings. The output from the compression stage is focused into a vacuum chamber containing H<sub>2</sub> or He gas with a focal spot size of  $\sim 100\mu\text{m}$ . Because the wavelength for maximum gain in the amplifiers (1053nm) is different from the central wavelength of the chirped pulse(1052.3nm), the spectrum of each of the two amplified pulses is shifted downwards.

The repetition rate of the laser system is less than once per hour. The pair of gratings, a focusing lens and the setups of Fig. 2 are contained in the chamber and evacuated to  $\sim 10^{-5}$  torr. The laser power and the time structure

can be measured at the exit of the plasma chamber by a calorimeter and a streak camera with 0.6ps time resolution, respectively. In the course of optical alignment and timing adjustment, the source Nd:YAG laser is used at the pulse rate of 5Hz. The alignment used a metal sphere with a radius of  $100\mu\text{m}$ , which was placed at the point to be focused and whose image was observed by a CCD camera from the end windows. The direction and the position of a final mirror were adjusted so that the sphere hides the laser beam completely.

The test electrons with energy satisfying the trapping condition are produced by irradiating a solid target by the 40J, 200ps laser. The electron production may be explained by the Raman instability or resonance absorption of the laser radiation[6]. In order to inject electrons emitted from the target into the laser wakefield at the waist of the laser beam, a dipole magnet is used to select the electron energy in the range of 0.2 – 3MeV. This spectrograph is placed between the target and the image point of electrons, as shown in Fig. 2. The electrons are injected along the axis of the main laser beam. The time delay between two laser beams are adjusted by the optical path lengths of two laser pulses. It takes account of the time-of-flight of the electrons, which amounts to 1.8ns for electrons of 1.5MeV/c. The test electrons are thus selected both by the spectrograph and the time-of-flight.

The acceleration occurs at the waist of the laser beam characterized by a Rayleigh length of 25mm in the plasma chamber. The test electrons are bent by an angle of  $90^\circ$  in the dipole field of the spectrometer placed in the exit of the plasma chamber. This spectrometer covers the energy range of 10 – 45 MeV at the dipole field of 4.3kG. The electron detector is an array of 32 scintillation counters each of which is assembled with a 1cm wide scintillator and a 1/2-in. H3165 photomultiplier. Shields of lead blocks and plates were necessary to reject background noise. The pulse heights of the detector array are measured by the fast multichannel CAMAC ADCs gated in coincidence with the laser pulse. The energy resolution of the spectrometer is 1.3MeV per channel.

#### 4 EXPERIMENTAL RESULTS

No conclusive demonstration of the acceleration has not yet observed. We have not yet transmitted the full power of the 1ps laser to the plasma chamber.

As the target to produce test electrons, an aluminum rod and a gold plate were tried, but no substantial difference was found. The maximum electron energy was around 1MeV. The increase of the laser energy increased not the energy but the number of electrons. The energy spectrum of test electrons from the aluminum target produced by the 200ps, 25.9J laser beam is shown in Fig. 3.

We had prepared optical plasma diagnostics to measure the plasma density, the Stark broadening[7], the blueshifting of the incident laser spectrum[8], etc.. However, sufficient light intensity for such diagnostics has not obtained

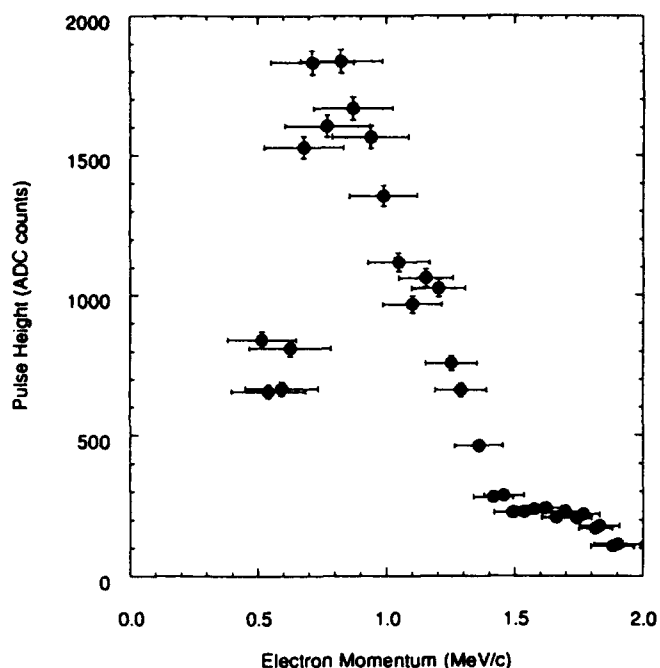


Figure 3: Energy spectrum of test electrons.

from the plasma. We have to calculate the plasma density from the gas pressure at the present.

We have tried acceleration experiments using the 1ps laser beam with power less than 5TW. It is found that the energy spectra of electrons are certainly different with and without the existence of the test electrons; i.e., with and without the operation of the 200ps laser. However, because of the poor signal-to-noise ratio of the energy spectra, we refrain from publishing the results. The ratio has been predicted by the simulation which numerically integrates the two-dimensional equation of motion. It gives the probability of the electron trapping in this range of laser power to be  $< 10^{-4}$ . We expect that the 1ps laser with the designed power will give clear results.

#### 5 REFERENCES

- [1] T. Tajima and J.M. Dawson, *Phy. Rev. Lett.* **43**(1979) 267; P. Sprangle *et al.*, *Appl. Phys. Lett.* **53**(1988)2146.
- [2] K. Nakajima *et al.*, 1992 Linac Conf. Proc., Ottawa (Chalk River Lab., AECL-10728) p332.
- [3] K. Yamakawa *et al.*, *Opt. Lett.* **16** (1991)1593 .
- [4] B.M. Penetrante and J.N. Bardsley, *Phys. Rev. A* **43** (1991)3100 .
- [5] M.V. Ammosov, N.B. Delone and V.P. Krainov, *Zh. Eksp. Teor. Fiz.* **91**(1986)2008.
- [6] S. Aithal *et al.*, *Phys. Fluids* **30** (1987)3825 .
- [7] H. R. Griem, "*Spectral Line Broadening by Plasma*" (Academic Press, New York, 1974.)
- [8] Wm. M. Wood *et al.*, *Phys. Rev. Lett.* **67**(1991)3532.

# Photonic Band Gap Resonators for High Energy Accelerators\*

S. Schultz<sup>1</sup>, D. R. Smith<sup>1</sup>, and N. Kroll<sup>1,2</sup>

(1) Department of Physics, University of California, San Diego  
9500 Gilman Drive, La Jolla, CA 92093-0319

(2) Stanford Linear Accelerator Center, Stanford University  
Stanford, CA 94309

## Abstract

We have proposed that a new type of microwave resonator, based on Photonic Band Gap (PBG) structures, may be particularly useful for high energy accelerators. We provide an explanation of the PBG concept and present data which illustrate some of the special properties associated with such structures. Further evaluation of the utility of PBG resonators requires laboratory testing of model structures at cryogenic temperatures, and at high fields. We provide a brief discussion of our test program, which is currently in progress.

## I. INTRODUCTION

The use of high Q cavity resonators has become an integral part of the accelerator technology applicable to present and future experiments in high energy particle physics. Currently, the resonators in use or under construction, are based on geometric structures where the normal modes are readily understood as a consequence of the electric field satisfying the boundary conditions imposed by the metal walls of the cavity. The nature of both the fundamental and higher order modes can often be qualitatively visualized, even though accurate evaluation of the mode frequencies may be numerically demanding. In contrast, the resonant cavities that we have proposed for potential use in a future generation of accelerators are based on what has been termed Photonic Band Gap (PBG) structures, and they are sufficiently different from both the traditional metal walled cavities or the diverse types of dielectric resonators, that they have to be analyzed and evaluated in their own right. Because the criteria for establishing the resonant modes in a PBG structure are so different, they (presently) cannot be designed or evaluated with the level of intuition normally applicable to the traditional cavity designs. Indeed, the difference in mode densities may be one of the principal advantages of PBG structures, with the possibility, for example, of designs that have negligible or even no higher order modes.

In this paper, for the convenience of the reader, we present a physical explanation of the PBG structure and its

key properties, followed by illustrative data and numerical simulations. We conclude with a brief discussion of a typical configuration for a PBG cavity suitable for an accelerator, and an outline of our test program. We have presented a more detailed introduction to the idea of utilizing PBG structures as accelerator cavities [1]. We refer the reader to several prior articles that may also be specifically useful [2,3].

## II. A PHYSICAL EXPLANATION OF THE PBG RESONATOR

The principal component of a PBG resonator is a photonic lattice; that is, a configuration which has a periodically varying dielectric constant in at least one direction, and is uniform in all other potential directions. We define the dimension of the PBG element as the number of directions in which the dielectric function varies periodically. A 1-D PBG structure, for example, could be a waveguide filled with a set of dielectric slabs periodically spaced along its length. A 2-D PBG system could be a lattice of very long parallel dielectric rods. A 3-D PBG structure could be composed of dielectric scatterers placed, for example, on a diamond lattice.<sup>4</sup> The dimension of the photonic lattice plays an important role in determining the electromagnetic mode characteristics of the PBG resonator.

Any actual PBG resonator will contain a dielectric lattice terminated in some way (e.g., conducting walls or absorber). While it is difficult to solve the general boundary value problem, Maxwell's equations for an infinite periodic dielectric lattice can be solved numerically with relative ease, and the solutions obtained reflect the dominant properties of any significantly large, but finite, section of such material. The essential characteristic of a periodically varying dielectric medium, common to any dimension, is that regions of frequency exist for which no propagating modes are present for waves traveling in a particular set of directions in the lattice. These frequency regions are called band gaps. In general, one finds band gaps for every direction of propagation for which there is periodic modulation of the dielectric constant. However, if there is a frequency region where these band gaps overlap for all the possible propagation directions, then the system is said to possess a complete photonic (i.e., electromagnetic wave) band gap. In 1-D some complete band gaps are guaranteed for any periodicity in the dielectric constant, since there is only one

\*This work supported by the National Science Foundation DMR-93-02913, and the Department of Energy, contracts DE-FG-03-93ER40793 and DE-AC-03-76SF00515.

direction of propagation. In higher dimensions, whether or not a complete PBG exists depends on the type of lattice, filling factor, dielectric mismatch, and scatterer structure.

Once we have identified an infinite dielectric lattice with a complete PBG, we may then ask how a finite section of such a lattice will behave. Rather than having absolute forbidden frequency regions, a finite lattice will now have modes in the band gap region which grow or decay in some direction with exponential dependence. As a practical example, if we imagine varying the frequency of a wave incident on a lattice and measuring the power which is transmitted, we would find regions of nearly perfect transmittance, usually designated as pass bands, separated by regions of strong attenuation corresponding to the band gaps. If we are to apply the solutions obtained from the infinite lattice to a finite lattice, we require that the length scale of that lattice be at least several times larger than the largest attenuation length in the lattice.

Having defined a PBG structure, how can it be useful for devices requiring a cavity-like resonance? Let us now restrict our discussion to a specific 2-D geometry. Our PBG structure simply consists of a periodic array of dielectric cylinders, with the axes of the cylinders perpendicular to a pair of bounding conducting plates on top and bottom. This configuration may be tested (either in the laboratory or via numerical simulation) and it is found that indeed there are regions of frequencies for which the transmission through a finite length of the structure is exponentially attenuated for waves incident from any direction. We will see later that it is quite practical to find such configurations for 2-D systems at microwave frequencies, and that the characteristic attenuation lengths can be comparable to the lattice constant.

We now consider a sample of the structure that is made with any circumferential geometry, as long as the distance from boundary to center is many times the value of the longest attenuation length for the frequency range of interest. One can make a perturbation to the dielectric region near the center of this lattice, and arrange to couple energy into that region via a small probe placed in a hole drilled through one of the metal plates above the perturbed site. We know that no energy radiating from the probe will propagate radially outward, because waves in all directions are exponentially attenuated for frequencies within a complete PBG. Thus, in general, the energy incident via the probe will be fully reflected. However, if the perturbation to the dielectric is strong enough, it may be possible that for some frequency, occurring within the PBG region, the electromagnetic fields may just match onto the exponentially decaying waves perfectly, for all directions, and constitute a resonant mode of that system. Indeed, we find that we can make configurations with the properties just described. The perturbation is termed a "defect", and the resonant mode is a defect mode. In this special circumstance we would find that energy can be coupled into the "cavity" where the electromagnetic fields corresponding to that mode will build up until the losses equal the incident power flow. As it turns out, completely removing a cylinder from an otherwise

periodic lattice often produces a defect mode with the desired properties.

To utilize the preceding type of resonance to accelerate an electron beam we consider modes where the electric rf field is everywhere normal to the metal plates with a maximum at the center (i.e. a monopole character). The bunched electron beam, suitably phased, would enter via a hole in one plate, and emerge with increased energy through a similar hole in the other plate. As with other types of resonant cavities, there would have to be provisions for coupling drive power into a cavity, which in turn could feed many other resonant cavities all at the same frequency, and suitably coupled by adjustments to the intercavity apertures. An illustration of a possible 3 section,  $2\pi$  accelerator modular unit based on a triangular periodic lattice is presented in Figure 1. As we shall discuss, the triangular lattice appears to be particularly advantageous as a PBG-defect resonant cavity for accelerator applications.

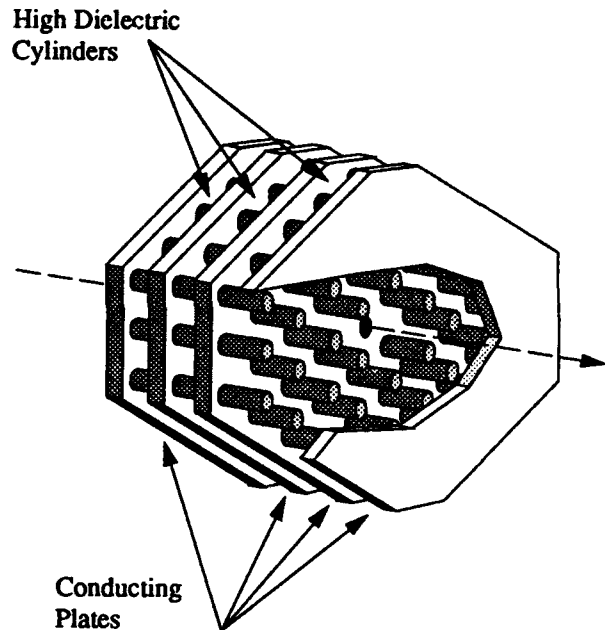


Figure 1. A schematic view of the proposed  $2\pi$  accelerator unit. In this example the unit consists of three triangular photonic lattices, separated by superconducting sheets. Each of the lattices has a cylinder removed to allow the formation of a defect mode with an electric field maximum in the center. Holes drilled through the conducting plates would allow a particle beam to be accelerated through the unit.

### III. NUMERICAL SIMULATIONS AND ILLUSTRATIVE EXPERIMENTS

As a first approach to designing a potential PBG accelerator cavity, we need to determine whether the structure has complete photonic band gaps. This information can be found by computing what has come to be termed the photonic band structure. Since we are concerned with 2-D configurations, and we wish to accelerate particles from one

plate to the next, we restrict our attention to modes in which the electric fields are polarized along the cylinder axes (TM modes). Thus, the wave equation we solve reduces to:

$$\nabla^2 E(\vec{x}) = -\frac{\omega^2}{c^2} \epsilon(\vec{x}) E(\vec{x}) \quad (1)$$

where the dielectric function satisfies

$$\epsilon(\vec{x} + \vec{d}) = \epsilon(\vec{x}) \quad (2)$$

The vector  $\vec{d}$  is any primitive lattice vector. The methods for solving Eq. (1) are well-known [1-5]; the solutions are Bloch waves, which have the form

$$E(\vec{x}) = u_{\vec{k}}(\vec{x}) e^{i\vec{k}\cdot\vec{x}} \quad (3)$$

where  $u_{\vec{k}}(\vec{x} + \vec{d}) = u_{\vec{k}}(\vec{x})$ . The vector  $\vec{k}$  indexes solutions, and is referred to as the wave vector. For each value of  $\vec{k}$  there is a discrete set of solutions with a discrete set of frequencies  $\{\omega_n(\vec{k})\}$ . The solutions for a given  $n$  are continuous as a function of the wave vector, forming sheets in reciprocal space. These sheets are known as bands, and  $n$ , the band index, refers to a given sheet. The bands, due to the periodicity of the lattice in coordinate space, are also periodic in reciprocal space; it is thus sufficient to view the solutions in a restricted region of reciprocal space called the Brillouin Zone (BZ). Because the real lattice has fourfold rotational and reflection symmetries, only the solutions for a single octant of the square BZ are unique. A plot of the mode frequencies  $\{\omega_n(\vec{k})\}$  corresponding to lattice vectors along the boundary of the BZ comprises the photonic band structure. The Brillouin Zones and band structures for lattices with other symmetries can be similarly defined.

When we calculate the band structure for a given lattice configuration, we expect to learn at what frequencies complete band gaps occur, and how large the band gaps are. An example of a photonic band structure calculation is shown in Figure 2, where we find three band gaps in the spectrum within the lowest fourteen bands. We and others [5,6] have systematically studied the behavior of band gaps for 2-D lattices over a large variation of dielectric constants and filling factors, and for a variety of lattice types. The lattice configurations include the square and triangular lattices with dielectric cylinders at the lattice sites, as well as the inverse cases of dielectric hosts with holes ( $\epsilon=1$ ) at the lattice sites.

Experimental confirmation of photonic band gaps can be readily obtained through transmission experiments. As discussed above, waves incident on a photonic lattice with frequencies corresponding to the band gap region of the lattice, decay into the lattice with exponential dependence. Thus, band gaps in the band structure will be manifest as regions of attenuation in a transmission measurement. A schematic diagram of our test apparatus is found in reference [3]. We are able to make simple transmission measurements with the equipment, as well as make measurements of the electric energy density of standing wave modes. In Figure 3 we present the transmission spectrum through a square lattice

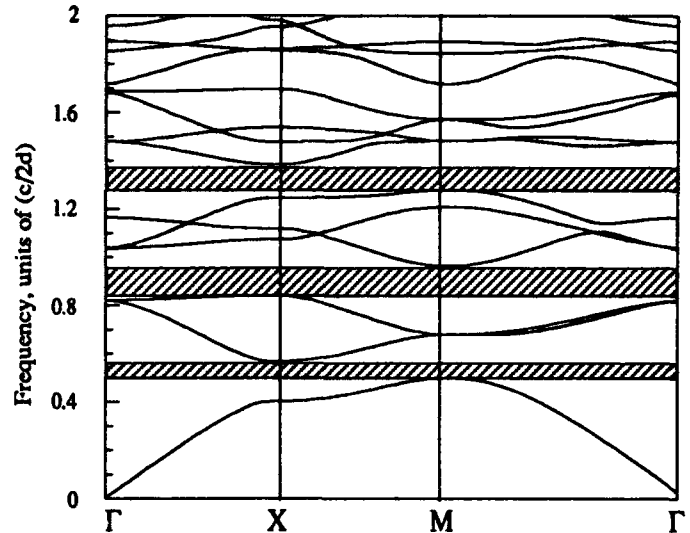


Figure 2. The photonic bandstructure for the square lattice of cylinders with dielectric constant  $\epsilon=9$ . The lattice cylinder diameter is 1 cm, and the lattice spacing is 1.27 cm. The three band gaps are indicated by the shaded area.

along the (10) direction. The sample was a 7 X 19 array of cylinders, with dielectric constant  $\epsilon=9$ , set in a precision drilled Styrofoam template. Microwave absorber was placed surrounding the scattering region, which minimized reflection back into the lattice. Note the sharp attenuation at frequencies corresponding to the gap region in the calculated bandstructure of Figure 2. The transmittance is reduced by over 40 dB, and has reached the noise floor of the microwave sweeper (a Hewlett-Packard 8756A scalar network analyzer). The configuration used for Figure 3 also had one central cylinder removed. Note the appearance of the sharp resonance in the gap, corresponding to the resonant defect mode.

In Figure 4 we present a detailed mapping of the electric energy density ( $\epsilon E^2$ ) as a function of the distance around a removed cylinder from a square lattice. The mode corresponds to a resonance similar to the one shown in Figure 3, except the lattice spacing is 1.33 cm. The defect mode shown is a monopole mode (antinode in the center), has the four fold symmetry of the lattice, and is well localized. The fields decay most gradually along the (10) and related symmetry directions. A plot along a cut in these directions logarithmically revealed the  $1/e$  decay length to be approximately 0.6 lattice constants. We will compare this value with numerical simulations in Section IV.

#### IV COMPLEX BANDSTRUCTURE

In addition to the Bloch type of solutions with real wave vector  $\vec{k}$ , the wave equation also has solutions with real frequency corresponding to complex values of  $\vec{k}$ . These solutions will exist only when the periodicity of the lattice is broken, for example at a surface or defect. The analytic

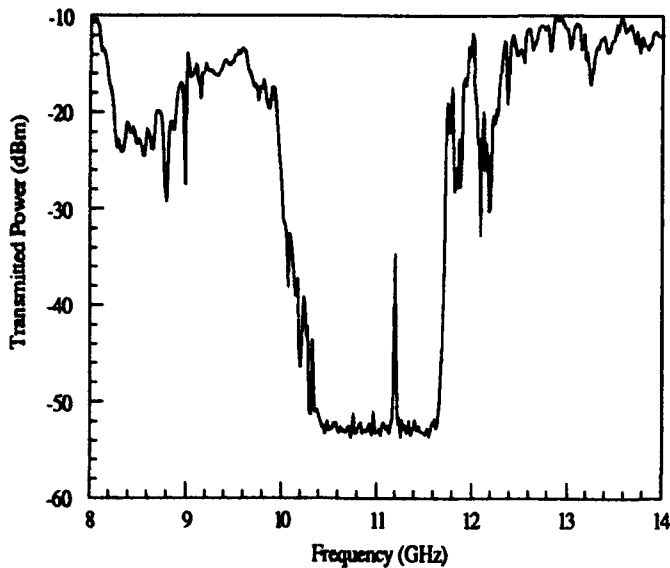


Figure 3. Transmittance vs. frequency of microwaves through a square lattice of  $7 \times 19$  cylinders. The cylinders have radius  $a=1$  cm, and lattice constant  $d=1.27$  cm (0.5"). The dielectric constant of the cylinders is  $\epsilon=9$ . The gap which is shown corresponds to the second photonic band gap in Figure 2. The sharp spike in the band gap occurs only after a single central cylinder is removed and is the resonance of interest.

properties of the solutions to the Scrodinger equation with a periodic potential have been rather thoroughly analyzed [7]. For illustration we restrict the propagation vector to lie along the (10) direction of the lattice. In Figure 5 we present the calculated complex bandstructure for the (10) direction of a square lattice. The dimensions of the lattice are the same as the lattice used to make the defect mode in Figure 4. Real frequency lines with complex  $k$  must either form loops

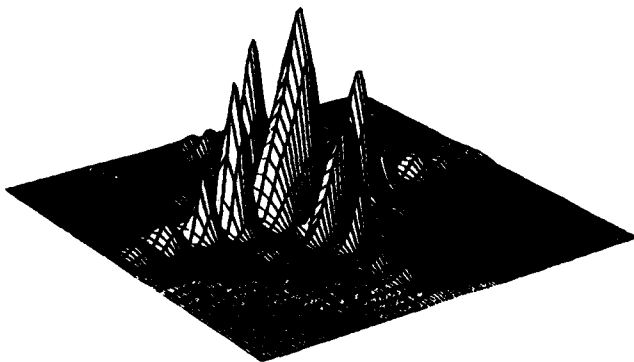


Figure 4. A spatial map of the electric energy density of a defect mode corresponding to the resonance shown in the band gap in Figure 3. All parameters of the lattice are the same as those for Figure 3, except for the lattice constant which in this case was  $d = 1.33$  cm.

connecting one band to another, or must come up from minus infinity and connect to a band. The trajectory of any given real frequency line must increase monotonically with

frequency; the collection of these real frequency lines form paths which wind their way through the bandstructure. If we select any given frequency, we find each path gives us no more than one solution at that frequency.

The complex bandstructure provides us with relatively quick insight which can be useful in many instances. As an example, when we consider a lattice geometry for possible use as a PBG structure, we can find from the complex bandstructure not only the size of the gaps, but also the attenuation length of the given gap. The longest attenuation length available to the system will dictate the minimum lateral dimension of the structure; parameters can thus be roughly optimized to find a smallest structure. Note that in the second gap there are three real frequency paths shown with imaginary  $k$  (there are, of course, infinitely many solutions with imaginary  $k$  at any frequency); however, the smallest imaginary  $k$  has a mid-gap value of 0.83, corresponding to a field decay length of  $\lambda=1.21$  lattice constants. This is in good agreement with the power decay length of 0.6 lattice constant along the (10) direction of the defect mode, measured from the experimental data above. While the complex bandstructure is important for insight and for certain calculations such as surface modes and transmission spectrums, it is necessary to perform a complete calculation to verify the existence of a desired defect mode, and then to evaluate near field shape, symmetry, etc., of the

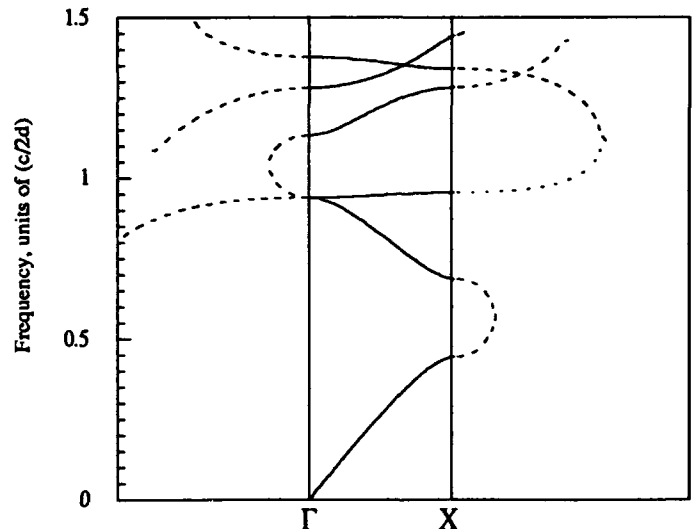


Figure 5. Complex band structure for the (10) direction. The parameters for this calculation match those used for the lattice used in Figure 4. The solid lines between  $\Gamma$  and  $X$  correspond to pure traveling waves. The dotted lines on either side of that region correspond to the imaginary (i.e., attenuative) part of the complex wave vector.

mode. Calculations such as these have been successfully carried out with very good accuracy for both two- and three-dimensional structures [8].

## V. DISCUSSION AND FUTURE EXPERIMENTS

Extensive numerical simulation studies are required to design an optimum PBG resonant structure. An important criterion will be to find a structure that has no resonant higher order modes. As another example, we find that the exponential decay of the fields for a triangular lattice can be ~30% faster than that of the square lattice with similar parameters. This in turn means that one can have a smaller physical structure for a given design value of unloaded Q (The periphery of a PBG resonator has absorber so as to reduce the Q of all other frequencies, and this in turn means that the unloaded Q will be set by the net Poynting energy flow to the periphery of the finite PBG lattice). Using superconducting niobium plates and high purity sapphire for the dielectric cylinders, we can expect to achieve intrinsic unloaded Q values of  $>10^9$ . While such high unloaded Q values are required for the regions cooled to liquid helium temperature, we note that the loaded Q for other superconducting designs is typically only  $\sim 10^6$ . For the structures discussed, we can expect to reach such Q values with a radius of  $<10$  lattice constants.

Our immediate experimental program is to determine several key properties via measurements in a cryogenic apparatus. These include the demonstration of unloaded Q  $>10^9$ , operation at high gradients ( $>10$  MV/m), and an investigation of the frequency stability, tunability, intercavity coupling, and external power coupling. One may expect particular difficulties due to dielectric breakdown at high field strengths. Once the cryogenic tests are successful, we plan to place a modest multi-cavity unit on a beam line and determine for the presently available superconducting cavities. However, we feel this effort is particularly worthwhile because the properties of PBG structures are so very different the limitations set by multipaction, charging, etc. Clearly

there are formidable problems to be investigated and solved in order to make PBG resonant structures a practical replacement than those of the usual resonant cavities. We suggest that other interesting applications may arise, particularly as the special features of PBG structures and resonators become fully appreciated.

## VII. REFERENCES

- [1] N. Kroll, D. Smith, S. Schultz, "Photonic band-gap structures: a new approach to accelerator cavities," to appear in the Proceedings of the Advanced Accelerator Concepts Workshop, Port Jefferson, New York., June 1992.
- [2] S. L. McCall, P. M. Platzman, R. Dalichaouch, D. Smith, S. Schultz, *Phys. Rev. Lett.*, **67**, 2017 (1991)
- [3] D. R. Smith, R. Dalichaouch, N. Kroll, S. Schultz, S. L. McCall, P. M. Platzman, *J. Opt. Soc. Am. B*, **10**, 314 (1993)
- [4] E. Yablonovitch, *Phys. Rev. Lett.*, **58**, 2059 (1987)
- [5] R. D. Meade, K. D. Brommer, A. M. Rappe, and J. D. Joannopoulos, "Existence of a photonic band gap in two dimensions," *Appl. Phys. Lett.*, **61**, 495 (1992)
- [6] M. Plihal, A. Shambrook, A. A. Maradudin, "Photonic bandstructure of two-dimensional photonic band structures," *Opt. Commun.*, **80**, 199 (1991)
- [7] V. Heine, *Proc. Phys. Soc.*, **81**, 300 (1963)
- [8] R. D. Meade, A. M. Rappe, K. D. Brommer, and J. D. Joannopoulos, "Accurate theoretical analysis of photonic band-gap materials", preprint, submitted to *Phys. Rev. Lett.* (1992)

# Update on the ATF Inverse Čerenkov Laser Acceleration Experiment\*

W. D. Kimura, L. C. Steinhauer, G. H. Kim, and S. C. Tidwell  
STI Optronics, Inc.  
2755 Northup Way, Bellevue, WA 98004

I. Pogorelsky and K. P. Kusche  
Brookhaven National Laboratory/STI Optronics, Inc.  
ATF/Bldg. 820, Brookhaven National Laboratory, Upton, NY 11973

## Abstract

The inverse Čerenkov acceleration (ICA) experiment is being performed on the Accelerator Test Facility (ATF) located at Brookhaven National Laboratory. This facility presently features a 50 MeV  $e$ -beam and a  $\sim 10$  GW peak power  $\text{CO}_2$  laser. In the experiment 1.7 atm of  $\text{H}_2$  gas is used to slow the phase velocity of the light wave to match the electron velocity. The Čerenkov angle is 20 mrad and the interaction length is 20 cm. A peak energy gain of  $\sim 12$  MeV is predicted assuming 5-GW of laser peak power delivered to the interaction region. An update of the experiment's progress is presented.

## I. INTRODUCTION

The Accelerator Test Facility (ATF) has been constructed at Brookhaven National Laboratory and is available for laser acceleration experiments. This new facility features a 50-MeV linac and a high peak power ( $\sim 10$  GW)  $\text{CO}_2$  laser. The inverse Čerenkov acceleration (ICA) experiment will be the first laser acceleration experiment to use the new facility.

ICA was first demonstrated at Stanford University in 1981 [1]. The ATF ICA experiment will be investigating an improved configuration developed by Fontana and Pantell [2]. This is illustrated in Figure 1. A radially polarized laser beam [3] is focused by an axicon onto the  $e$ -beam inside a gas cell at the Čerenkov angle  $\theta_c$  given by  $\cos \theta_c = (1/n\beta)$ , where  $n$  is the index of refraction of the gas and  $\beta$  is the ratio of electron velocity to

the velocity of light. This arrangement has several advantages over the earlier Stanford experiment [2]. The ATF  $\text{CO}_2$  laser has  $>150$  times higher peak power than the Stanford laser. This will result in over 10 times more energy gain than the Stanford experiment.

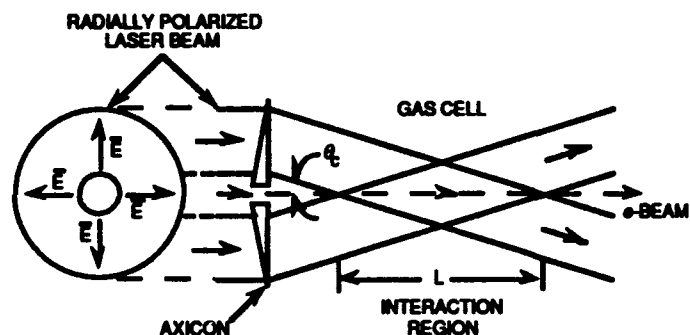


Figure 1. Basic arrangement for inverse Čerenkov acceleration.

## II. REVIEW OF MODEL PREDICTIONS

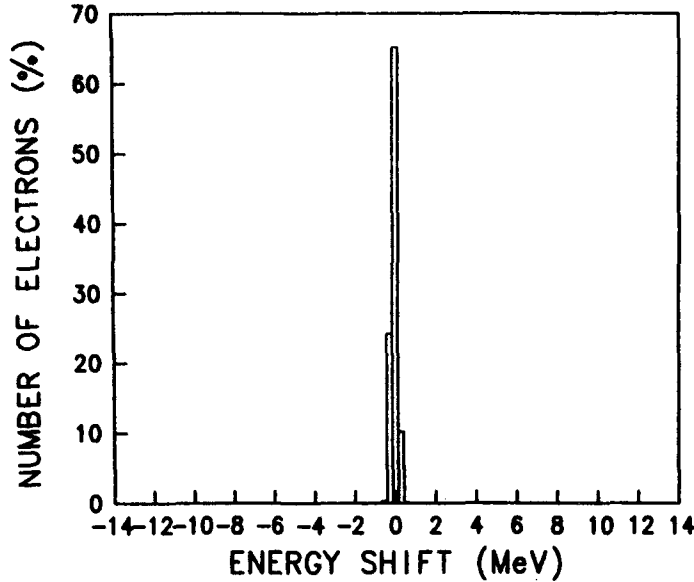
A Monte Carlo computer model of the ICA process has been developed [4] and used to predict the performance of the experiment. These predictions are shown in Figure 2. (Note, we assume a 50% efficient optical system resulting in 5 GW of peak power delivered to the interaction region.)

A peak energy gain of  $>12$  MeV is predicted corresponding to 24% energy gain and an acceleration gradient of  $>60$  MeV/m. Since the gain scales as the square root of the laser peak power [2], a 50-GW delivered laser beam would produce  $\sim 38$  MeV energy gain and an acceleration gradient of 190 MeV/m.

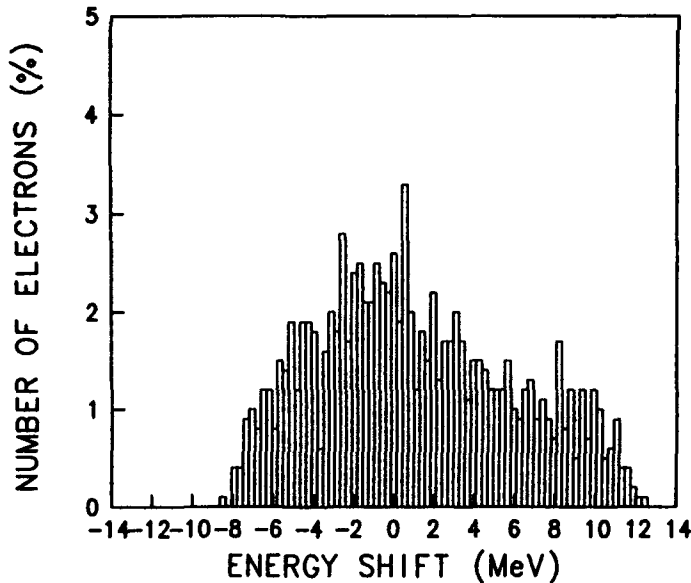
\* Supported by US DOE Contract No. DE-AC06-83ER40128.

### III. DESCRIPTION OF EXPERIMENTAL APPARATUS

The experimental hardware has been fabricated and installed at the ATF. It consists of



(a) No Laser Present



(b) Laser Present

Figure 2. Model predictions for the ATF ICA experiment for  $\theta_c = 20$  mrad,  $L = 20$  cm, laser beam OD = 1 cm,  $P = 1.7$  atm  $H_2$ ,  $e$ -beam focused to  $r = 0.18 \mu\text{m}$ , and  $2.1\text{-}\mu\text{m}$  thick diamond  $e$ -beam windows are used. (a) No laser present; (b) laser present at a delivered peak power of 5 GW.

a gas cell where the ICA interaction occurs, an electron beamline system, and an optical system for converting the linearly polarized ATF  $CO_2$  laser beam into one with radial polarization. Figure 3 is a schematic of the beamline system.

A schematic plan view of the internal gas cell components is given in Figure 4. An axicon mirror is used rather than a transmissive axicon (see Figure 1). The incoming laser beam enters the gas cell and reflects off a  $45^\circ$  mirror towards the axicon. Both the  $45^\circ$  mirror and axicon have a central hole for the  $e$ -beam to pass through. The axicon focuses the laser beam onto the  $e$ -beam, which enters and exits through  $2.1\text{-}\mu\text{m}$  thick diamond windows sealed on the ends of the gas cell. Phosphor screens inside the cell are used to monitor the position of the  $e$ -beam.

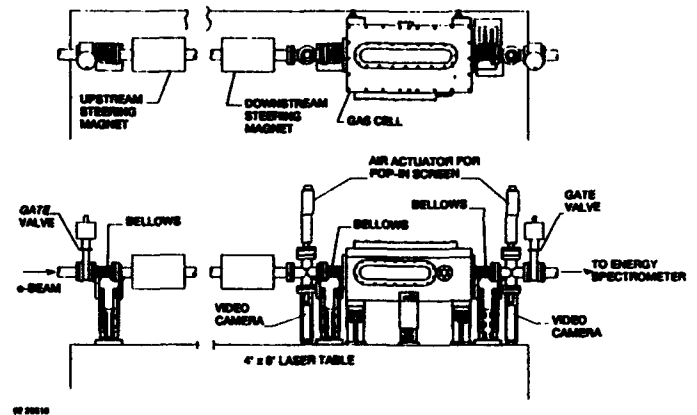


Figure 3. Schematic of ATF ICA beamline system.

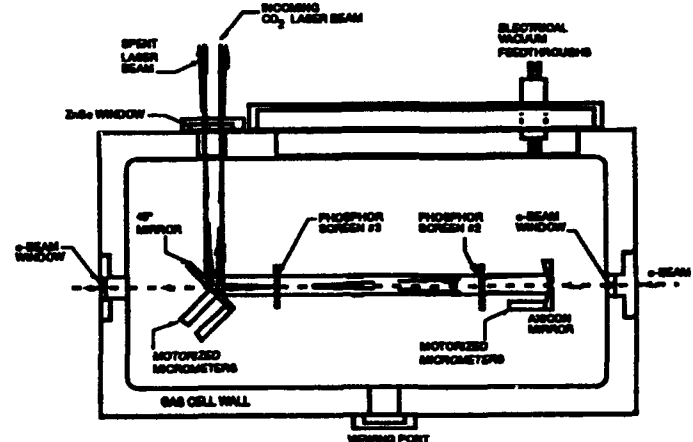


Figure 4. Schematic plan view of gas cell.

#### IV. EXPERIMENT UPDATE

The experiment is divided into two phases. Phase I consisted of laser only experiments without the ATF  $e$ -beam, and were completed last year. During Phase I the radial polarization converter system was successfully tested with the ATF CO<sub>2</sub> laser beam. Alignment and focusing of the laser beam into the gas cell was also demonstrated. Initial investigations of any possible nonlinear effects (e.g. gas breakdown) occurring in the gas due to the presence of the high peak power laser beam proved negative. Critical optical components also passed optical damage tests, and the  $e$ -beam windows survived exposure to an  $e$ -beam provided by the National Synchrotron Light Source (NSLS).

Phase II is the actual electron acceleration experiment in which the Phase I ICA hardware is fully integrated with the ATF linac. This integration has been completed and the first Phase II experiments have begun.

At the time of this writing (May 1993), the first run with the laser and  $e$ -beam has been completed. The  $e$ -beam was successfully sent through the gas cell, including the 1-mm diameter entrance and exit diamond windows, and the 1-mm diameter holes in the axicon and 45° mirrors (see Figure 4). Approximately 4 GW of laser peak power was delivered to the interaction region.

This first run revealed several modifications to the experimental system that need to be implemented. First, the system devised to view the positions of the  $e$ -beam and laser beam within the gas cell needs to be improved. This is important to ensure the physical overlap of the beams within the gas cell. Second, the high power laser beam tends to damage the 45° mirror and axicon around the holes in their centers. This is because the radially polarized beam is not purely annular in shape and a significant amount of laser energy strikes the edges of the holes.

#### V. FUTURE WORK

Modifications to the experimental system will be made before the second run to rectify the problems encountered during the first run. We expect to observe acceleration of electrons within the next several months.

#### VI. REFERENCES

- [1] J. A. Edgiffer, W. D. Kimura, R. H. Pantell, M. A. Piestrup, and D. Y. Wang, *Phys. Rev. A* 23, No. 4, 1848 (1981).
- [2] J. R. Fontana and R. H. Pantell, *J. Appl. Phys.* 54, No. 8, 4285 (1983).
- [3] S.C. Tidwell, D.H. Ford, and W.D. Kimura, *Appl. Optics* 29, No. 15, 2234 (1990).
- [4] R. D. Romea and W. D. Kimura, *Phys. Rev. D* 42, No. 5, 1807 (1990).

# New Directions in RF Sources \*

Levi Schächter

Laboratory of Plasma Studies and School of Electrical Engineering  
Cornell University, Ithaca, NY 14853 USA

## Abstract

We examine the various high power RF sources on the basis of the next linear collider requirements. The discussion is based on classification of the sources according to what we consider the most informative criteria. In the conventional acceleration scheme (e.g. SLAC) multiple sources generate the RF power. A variety of sources are considered and they cover the spectrum from 9 to 19GHz. In the two beam accelerator scheme all the modules are driven by the same beam which has multi MeV (LBL/LLNL) up to a few GeV (CERN) electrons; the current carried by the beam is of order of kA. Two types of RF sources have been suggested: traveling wave (TW) structures and free electron laser (FEL). The operating frequency varies from device to device in the range of 9 to 35GHz.

## I. INTRODUCTION

The typical requirements from an RF source for the next linear collider (NLC) are: 200MW/m at 10–30GHz with an efficiency above 40%. The pulse duration varies from one scheme to another, but the net pulse for acceleration is expected to be above 100nsec and to generate a gradient on the order of 100MV/m. The luminosity requirements determine the repetition rate and according to the system it can vary from 50–1400Hz<sup>(1)</sup>. The detailed specifications of any RF source are established as part of the design of an entire system. According to the acceleration system one can divide these sources into two groups: sources which drive (i) a Two Beam Accelerator (TBA) e.g. at LBL/LLNL/MIT, KEK, JINR(Dubna) and CERN in which a single beam generates the whole required power and (ii) a conventional multiple sources system e.g. SLAC, KEK, DESY, VLEPP, Cornell and Univ. of Maryland; see Fig. 1. This is our first classification criterion.

If in the past the klystron was practically the only RF source used for acceleration purposes, the beam-wave interaction in today's systems tends to expand beyond the limits of a fraction of the (vacuum) wavelength. The main reason for this trend is the breakdown problem associated with the high power, frequency and efficiency imposed by the NLC requirements. The approach followed to overcome the breakdown problem provides our second classification criterion. There are several such approaches. (i) It is possible to increase the frequency (to 30GHz and above as is the case for the TBA); doing so the power level required is much smaller since for the same gradient the power scales like  $f^{-2}$ . Thus an increase by a factor of 3 in the frequency lowers the power requirement by almost an order of magnitude. However a problem

with this approach is that the geometrical (alignment and manufacturing) tolerances at small dimensions, associated with the increased frequency, become very tight (0.5 $\mu$ m). (ii) Another approach is that of pulse compression adopted by SLAC and KEK in which an X-band (11.4GHz) klystron generates 50MW for 1.5 $\mu$ sec. This pulse is then compressed 4 times in power and 6 times in time such that the nominal pulse is 200MW for 250nsec. A similar approach was adopted at VLEPP which operates at 14GHz and the compression method is different; we shall discuss this system later in more detail. (iii) The last approach to overcome the breakdown problem is to use a distributed interaction in a TW structure. This approach has proven to be successful at SLAC<sup>(2)</sup>, Cornell<sup>(3)</sup> and with the Choppertron<sup>(4)</sup> (Haimson/LLNL). The idea here is to generate a high power pulse (100–400MW) for the duration required for acceleration (> 100nsec). TW structures are also part of the CLIC extraction section.

The issue of distributed interaction leads us to the third classification criterion namely, we would like to distinguish here between (i) slow wave devices (Cerenkov) and (ii) fast wave devices (FEL, CARM<sup>(5)</sup>, Gyrotron<sup>(6-7)</sup> and Magnicon<sup>(8-9)</sup>). This is schematically presented in Fig. 2. Each of these categories has its own advantages and disadvantages. If we limit for a moment the discussion to traveling wave amplifiers (TWA) and gyrotrons then the former operates in a single TM mode whereas in the latter a massive higher mode suppression is necessary for "single mode operation". On the other hand in the TWA the breakdown at the corrugated walls remains a problem (though not as severe as in the klystron) whereas in the gyrotron the smooth walls minimize this problem. As for now it is difficult to assess what weight to attribute to the cost of the applied magnetic field and its required accuracy<sup>(7)</sup> since the power levels reported so far are almost one order of magnitude lower than the TWA<sup>(10)</sup>. For 27MW at 9.85GHz a field less than 6kG was required with an accuracy of 50G. This magnitude is similar to that of the guiding field in either TWA or relativistic klystron but these two are practically insensitive to variations in the magnetic field - on the scale mentioned above. We shall now examine some of the RF sources which have been investigated recently in the view of the classification mentioned above.

## II. TWO BEAM ACCELERATOR

The TBA concept first suggested in 1982 by A. Sessler<sup>(11)</sup> relies on the interaction of a single high power beam with a radiation field in the presence of a wiggler. The radiation power is extracted from discrete (extended) cavities, thus

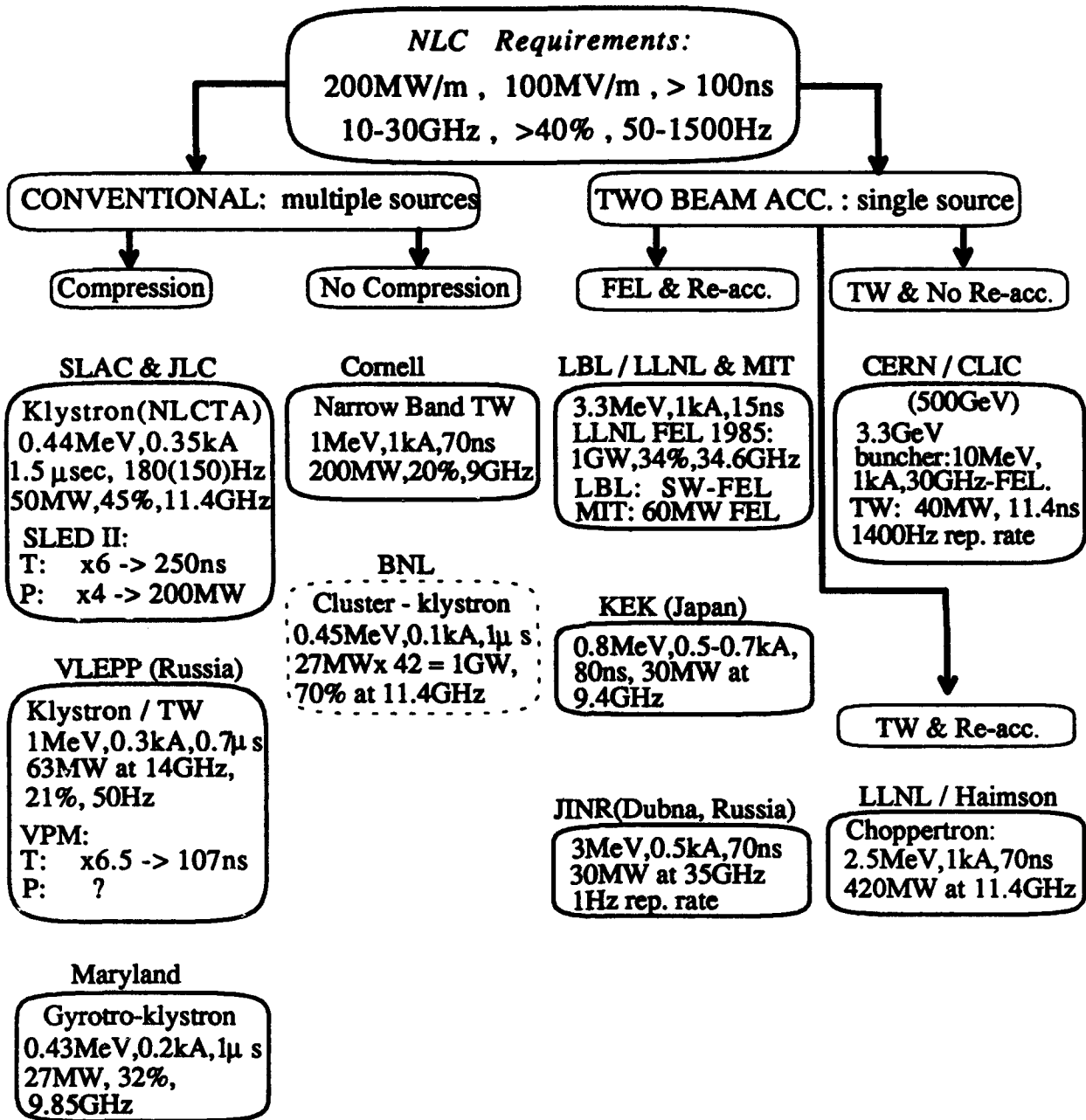


Fig.1: Classification of RF sources according to acceleration scheme.

the notion of standing wave FEL. The proof of principle dates back to 1985 when a  $3.3\text{MeV}$ ,  $1\text{kA}$  beam generated  $1\text{GW}$  of power for  $15\text{nsec}$  at  $34.6\text{GHz}$  corresponding to 34% efficiency<sup>(12)</sup>. Recently  $30\text{MW}$  at  $9.4\text{GHz}$  were generated at KEK<sup>(13)</sup> for  $80\text{nsec}$  with  $0.8\text{MeV}$ ,  $0.5 - 0.7\text{kA}$  in an FEL. At JINR(Dubna)<sup>(14)</sup>, a similar amount of power was generated for  $70\text{nsec}$  but at  $35\text{GHz}$  with a  $3\text{MeV}$ ,  $0.5\text{kA}$  beam. All three have the FEL interaction in common. The beam is planned to be re-accelerated by induction linac cells which are crucial for the adequate operation of the following RF extraction units. According to our third classification the standing wave FEL is a fast wave device. There is no reason why the fast-wave interacting cells can not be replaced with slow-wave type cells. This is the case in the LLNL/Haimson<sup>(4)</sup> experiment (Choppertron) in which a  $2.5\text{MeV}$ ,  $1\text{kA}$ ,  $70\text{nsec}$  beam is injected in two consecutive traveling wave structures; power in excess of  $400\text{MW}$  at  $11.4\text{GHz}$  was measured in this case. Similar structures are used at CLIC following a very unique design. The electrons are bunched by an FEL when injected with an initial energy of  $10\text{MeV}$  ( $1\text{kA}$  of current). They are bunched at  $30\text{GHz}$  in this stage and then accelerated to  $3.9\text{GeV}$ . This beam feeds short traveling wave sections which generate about  $40\text{MW}$  of power, each for  $11.4\text{nsec}$ . Note that the  $40\text{MW}$  in this design can generate a similar gradient as the  $400\text{MW}$  of the Choppertron at  $11.4\text{GHz}$ .

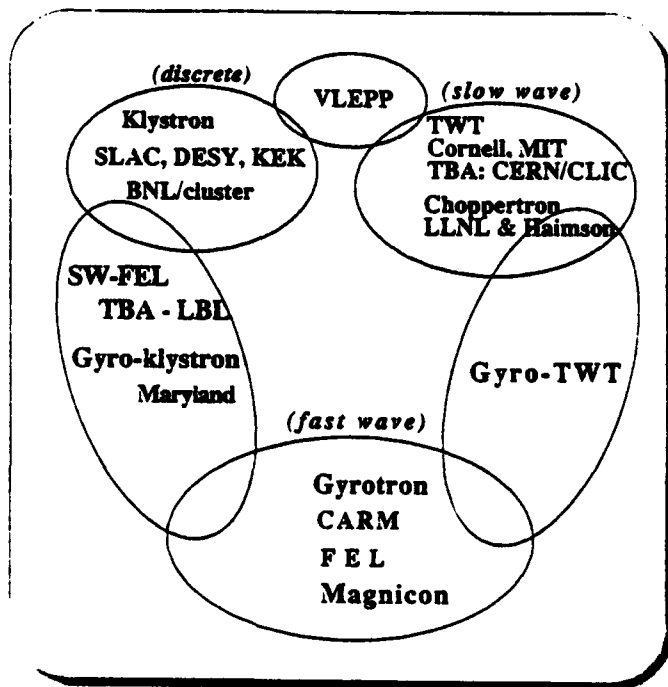


Fig. 2: Classification of RF sources according to interaction type.

### III. CONVENTIONAL SOURCES

When examining conventional sources it is convenient to divide them according to the interaction type. We shall discuss first the fast wave devices. In this presentation we

shall limit the discussion to a single representative from this family namely, the gyrotron. The gyrotron<sup>(6-7)</sup> or its combination with TW and klystron version called gyro-twystron has a significant appeal since the TW structure helps to keep the magnetic field at relatively low levels when the RF power levels (and thus the current) are significantly higher. The operation of the extraction section designed to fit the second frequency harmonic is also in progress.

In the category of the bare klystron we would like to mention the Cluster Klystron. As presently envisaged it is to be driven by a  $0.45\text{MeV}$ ,  $0.1\text{kA}$ ,  $1\mu\text{sec}$  beam. There will be 42 such beams generated on the same cathode by magnetron injector guns which will generate beams with a local current density as high as  $40\text{A/cm}^2$ . At about 70% efficiency each klystron will generate  $26\text{MW}$  with an overall  $1.1\text{GW}$  RF power at  $11.4\text{GHz}$ ; this is the first system discussed so far that has not been tested experimentally. Basically there are two major obstacles this system has to overcome: the generation of controllable multiple beams from a single cathode and, assuming that this was accomplished, the combination of all outputs in a single waveguide at a well defined phase.

As illustrated in Fig.2 the VLEPP klystron lies somewhere between the slow wave devices and the klystron family. It consists of a series of cavities but its extraction section is unique: the electrons are generated and guided by a  $25\text{kV}$  electrostatic optic system and afterwards accelerated by a  $1\text{MV}$  dc voltage source. Since the driving voltage is high, the required power can be supplied by injecting a modest amount of current ( $300\text{A}$ ). This fact has two implications: (i) the beam can be guided by a permanent periodic magnetic field and (ii) according to V. Balakin<sup>(15)</sup> it has the potential of a very efficient device due to its low (0.3) micro-perveance. The dc guiding of the beam makes the device very attractive from the financial point of view since a significant portion of the cost of an RF generator is the cost of the magnets. The design of this system is very ambitious and it is planned to reach almost 80% efficiency. At the present time the output is  $63\text{MW}$  which corresponds to 21% efficiency. This is the typical efficiency one can expect from an uniform TW section without any optimization.

The last subject to be considered in the category of conventional sources is the traveling wave amplifier (TWA). We have investigated this device at Cornell both experimentally and theoretically in the past several years. In a two stage TWA we have reported generation of more than  $400\text{MW}$  in the X-band for a pulse duration of  $70\text{nsec}$  using a  $1\text{MV}$ ,  $1\text{kA}$  beam. However the spectrum of the signal was unacceptably broad ( $300\text{MHz}$ ) due to the presence of asymmetric sidebands. Theoretical studies indicated that these effects are a result of amplified noise at frequencies which are selected by the interference of the two waves which bounce between the two ends of the TW

structure. In order to eliminate the problem of the reflections (the increased noise is unavoidably part of the modulation process) we suggested<sup>(16)</sup> building an amplifier in which the time it takes the EM energy to reach the input end after being reflected from the output end, is of the same order of magnitude as the electron pulse duration. In order to satisfy the above condition the group velocity has to be very small (in our case less than  $0.01c$ ). This subject is presented in Ref.10. The output in the most recent experiments indicate power levels of about  $200MW$  at  $9GHz$  in a frequency range which is less than  $50MHz$ . This has been achieved in a uniform structure in which the only optimization was making the last disk  $1mm$  thick instead of  $6mm$ . This allows the EM mode to leave the system since for the disk radius this wave is well below cutoff<sup>(18)</sup>. This result can be probably improved significantly by a better design of the output TW section.

#### IV. DISCUSSION

Although the variety of concepts and devices is not particularly helpful in the attempt to identify a global trend, we believe that there are clear indications of local trends. The clearer among these trends is that of the TBA source: neither of the devices under consideration use the klystron as a basis for their RF generator. In fact it is fairly clear that the *distributed* interaction either in a fast or slow wave device replaces the *local* beam-wave interaction of a klystron. However the cavity effects, say in a standing wave FEL, are still there, and as was indicated in Ref.(17) the analogy to klystrons can be quite helpful.

With respect to conventional schemes, the scaling of the klystron to the X-band and to long pulse operation in conjunction with the compression scheme indicates that the klystron is still a potentially viable competitor for the next linear collider RF source. As an intermediary stage the compression schemes proposed by SLAC and VLEPP will probably meet the requirements but they will not solve the long term problem. Over the long term we have to remember the limitations of both the klystron and the compression schemes - especially with respect to breakdown. One of the alternatives we mentioned in our second classification criterion was a medium length ( $100-200nsec$ ) high power ( $100-400MW$ ) pulse. This kind of system eliminates the necessity for compression and still provides the required power levels. But to withstand high electric field associated with these power levels it will require a TW output section<sup>(2-4)</sup>. Since this scheme has the potential to solve the problem it seems probable that TW output sections will become an integral part of future RF extraction systems. It is this trend which we wish to further discuss next.

The starting point is the constraint imposed by the NLC requirements on the RF structure. The output frequency requirement limits the input section of any source to a very good frequency selective device. From this perspective the klystron cavity or a combination of a cavity with a magnetic field as in the case of the Choppertron or an

FEL, are the natural candidates for the *input section* of any RF system. The *main section* can be a set of isolated cavities as in a klystron, a TW section or a combination of the two. However the breakdown problem will force us to use a TW structure as an *output section* with one or more extraction ports. This brings us to the last subject which is discussed in more detail in another work<sup>(18)</sup> regarding the beam-wave interaction in quasi-periodic structures.

A high power traveling wave structure is conceived as a section of a periodic disk loaded structure and its electromagnetic characteristics are determined as if the system was infinitely long. Practically these are a set of cavities which are *coupled* through the disk aperture. At the other extreme, the klystron is a set of a few *isolated* cavities. In the former case the beam interacts with a wave continuously, whereas in the klystron the beam interacts with the field in the close vicinity of the cavity. The interaction in a uniform periodic structure (TWA) or in a few uncoupled cavities (klystron) is relatively well understood. But we lack analytical or even quasi-analytical tools to accurately investigate the interaction in transition region of a high power microwave device - which is exactly what is required for construction of an adequate output section. For this purpose we have developed an analytical method to investigate the beam-wave interaction in a quasi-periodic structure. The method relies on an arbitrary number of pill-box like cavities of any dimension and an arbitrary number of radial arms. The only constraint is that the radius of the coupling pipe has to be fixed. So far we have successfully employed this method for cold design - in particular for the extraction region of the two stage amplifier reported in Ref.(10).

#### V. SUMMARY

Let us now summarize the main conclusions regarding high power radiation sources for acceleration applications: (i) There is a clear advantage to operate at the highest frequency the alignment constraints permit. (ii) At very high power local beam-wave interaction (as in a klystron) is disadvantageous comparing to distributed interaction in traveling wave structures due to the breakdown problem. (iii) Radiation sources need to expand further beyond the limits of the bare klystron. (iv) The expansion so far is "equally" divided towards fast and slow wave devices. (v) In two beam accelerators the klystron, in its present configuration, will play little, if any, role. (vi) In conventional sources the traveling wave structure with one or multiple output ports will have an increasing role at least in the output section of a high power RF source. Accordingly the interaction in transition regions will require more and more attention.

#### VI. ACKNOWLEDGEMENT

I would like to thank J.A. Nation for his help in gathering the information and for the clarifying discussions at various stages of this work.

## VII. REFERENCES

- [\*] This work was supported by the United States Department of Energy.
- [1] There is no world wide consensus regarding the exact specification of the source for the next linear collider therefore we shall consider the figures above as figures of merit.
- [2] "High-gradient electron accelerator powered by a relativistic klystron", M.A. Allen *et. al.* Phys. Rev. Lett. 63 p.2472 (1989).
- [3] "Two Stage High Power Traveling Wave Amplifier" D. Shiffler, J. D. Ivers, G. S. Kerslick, J. A. Nation and L. Schächter, *Appl. Phys. Lett.*, 58, 899, (1991).
- [4] Suppression of beam induced pulse shortening modes in high power RF generator TW output structures", J. Haimson *et. al.* SPIE Proc. Vol.1629 p.209 (1992).
- [5] "CARM Amplifier experiment at 17GHz" W. Menninger, B. Danley, S. Allberti, C.Chen, E.Giguet, J.Rullier, J.Wurtele and R. Temkin MIT in the Proceedings of this Meeting.
- [6] "Initial Operation of a High Power K-Band, Harmonic Gyro-Klystron" J. Calame, H. Matthews, B. Hogan, M. Lee, J. Cheng, C. Striffler, V. Granatstein and M. Reiser U. Maryland in the Proceedings of this Meeting.
- [7] "Gyroklystron Research for Application to TeV Linear Colliders" M. Reiser *et. al.* in XV<sup>th</sup> International Conference on High Energy Accelerators, HEACC'92 Hamburg 1992,p. 924.
- [8] "The NRL X-band Magnicon Amplifier" S.Gold, C. Sullivan and W. Manheimer and B. Hafizi in the Proceedings of this Meeting.
- [9] "First Test of the X-band Pulsed Magnicon", O. Nezhevenko *et. al.* in the Proceedings of this Meeting.
- [10] "Two Stage, High Power X-band Amplifier Experiment", E. Kuang, G.S. Kerslick, J.D. Ivers, J.A. Nation and L. Schächter; in the Proceedings of this Meeting.
- [11] "The FEL as a power source for a high gradient accelerating structure" A.M. Sessler, AIP Conf. Proc. 91 p.154 (1982).
- [12] "High Efficiency extraction microwave radiation from a tapered wiggler FEL" T.J. Orzechowsky *et. al.* Phys. Rev. Lett. 57, 2172(1986).
- [13] "Two-beam linear colliders" by K. Hubner in XV<sup>th</sup> International Conference on High Energy Accelerators, HEACC'92 Hamburg 1992,p. 791.
- [14] "FEL as an RF source for the Linear Collider" A.A. Kaminsky, in XV<sup>th</sup> International Conference on High Energy Accelerators, HEACC'92 Hamburg 1992,p. 900.
- [15] "14GHz VLEPP Klystron", V. Balakin, in Proc. of the 3<sup>rd</sup> EPAC, Berlin, Germany 1992.
- [16] "Narrow Band High Power Traveling Wave Amplifier", L.Schächter and J.A. Nation; The third Workshop on Advanced Acceleration Concepts, Port Jefferson, Long Island, NY 14-20 June 1992.
- [17] "Common Analysis of the Relativistic Klystron and the Standing Wave FEL" J.S. Wurtele, D.H. Whittum and A.M. Sessler in XV<sup>th</sup> International Conference on High Energy Accelerators, HEACC'92 Hamburg 1992,p. 508.
- [18] "Beam-wave interaction in quasi-periodic structures" L. Schächter and J.A. Nation see the Proceedings of this Meeting.

# Criteria for Comparing the Suitability of Microwave Amplifiers for Driving TeV Linear Colliders

V.L. Granatstein and G.S. Nusinovich

Laboratory for Plasma Research, University of Maryland, College Park, MD 20742, USA

## I. INTRODUCTION

Many types of microwave amplifiers are being considered at various institutions as candidate sources for driving future linear colliders. The choice of operating frequency ranges from 2.85 GHz to 35 GHz. Peak microwave output power and pulse duration also vary widely. In this paper, we propose three criteria for evaluating and comparing amplifier options. These are as follows: 1)  $N_t$ , the number of amplifiers required to drive an accelerator with a given final energy and a given accelerating gradient; 2)  $V$ , the voltage required to operate the microwave amplifier; and 3)  $\eta_T$ , the overall efficiency including the output efficiency of the amplifier, the efficiency of the pulse compression circuit if any is used, and the high voltage modulator pulse-shape efficiency. All of these criteria will affect the cost of a linear collider system. The cost of the microwave amplifiers will, of course, equal the cost of each amplifier (with its associated power supplies, magnets, and pulse compression circuit) multiplied by the number of amplifiers,  $N_t$ . The cost of each amplifier and its power supply/modulator will increase with the voltage,  $V$ . In fact, we have chosen to restrict our consideration of specific amplifiers to those in which  $V < 1$  MV; at voltages above 1 MV very large insulators and more exotic pulsed power supplies such as induction linacs would be required and these might be excessively costly. Overall efficiency will, of course, influence average power consumption as well as the size and cost of power supplies.

## II. THE NUMBER OF AMPLIFIERS REQUIRED TO DRIVE A COLLIDER

First, consider the relationship between peak microwave power required per unit accelerator length,  $p$ , the accelerator gradient,  $E_a$ , and the microwave wavelength,  $\lambda$ . Perry Wilson has recently presented<sup>1</sup> the result that for an accelerator structure consisting of a chain of pillbox TM<sub>010</sub> resonators, the microwave power per unit length is given by

$$p \approx 1.2 \times 10^{-7} E_a^2 \lambda^{1/2} \quad (1)$$

(throughout this paper mks units are used unless otherwise noted), while the structure fill-time is given by

$$t_f \approx 2.3 \times 10^{-5} \lambda^{3/2}. \quad (2)$$

Thus, the required microwave pulse energy per unit length is

$$u = p t_f \approx 2.8 \times 10^{-12} E_a^2 \lambda^2. \quad (3)$$

Then, a single microwave amplifier with peak output power,  $P_p$ , and pulse duration  $\tau_p \geq t_f$  would be able to drive a length of accelerator structure

$$\ell_1 = \frac{P_p \tau_p \eta_c}{u} \approx 3.6 \times 10^{11} \frac{P_p \tau_p \eta_c}{E_a^2 \lambda^2}, \quad (4)$$

where we have used Eq. (3), and  $\eta_c$  is the efficiency of any pulse compression circuit that is used. If we estimate that each factor of 2 in pulse compression can be achieved with 90% efficiency,<sup>2</sup> then

$$\eta_c = 0.9 \exp [\log_2(\tau_p/t_f)]. \quad (5)$$

The required overall length of an accelerator with final energy,  $U_f$ , is

$$L = U_f / e E_a \quad (6)$$

while the total number of microwave tubes required is obtained from Eqs. (4) and (6) as

$$N_t = \frac{L}{\ell_1} \approx 1.7 \times 10^7 \frac{U_f E_a \lambda^2}{P_p \tau_p \eta_c}. \quad (7)$$

Accelerator cost will increase both with the length of the required tunnel,  $L$ , and with the number of microwave tubes,  $N_t$ . However, since  $L \sim E_a^{-1}$  and  $N_t \sim E_a$ , the choice of an optimum  $E_a$  is not obvious, and involves a complicated analysis of such factors as tunnel cost versus microwave tube cost.

Once  $U_f$  and  $\lambda$  are chosen for a collider, Eq. (6) together with (7) and (2) may be used to evaluate  $N_t$ . It may be seen from Eq. (6) that  $N_t$  could be decreased by choosing a higher microwave frequency if  $P_p \tau_p$  decreased less rapidly than  $\lambda^2$ . In addition,

high frequency has the advantages of increased limiting values of  $E_a$  as determined by rf breakdown<sup>3</sup> and increased pulse repetition frequency<sup>4</sup> which diminishes problems caused by ground jitter. However, there is a practical upper limit on frequency that is currently estimated to be in the neighborhood of 35 GHz. At higher frequency, fabricating and aligning the smaller accelerator structures becomes increasingly difficult; this might be alleviated however by using higher order transverse modes in the accelerator cavities which would not substantially affect the values of  $\ell_1$  or  $N_t$ .

### III. OVERALL MICROWAVE AMPLIFIER SYSTEM EFFICIENCY

A typical microwave amplifier system consists of the microwave tube, the pulse compression circuit, and the high voltage modulator (plus other elements which will not be considered in this first-cut analysis). Accordingly, the total system efficiency may be defined as

$$\eta_T = \eta_a \eta_c \eta_v \quad (8)$$

where  $\eta_a$  is the output efficiency of the microwave amplifier (i.e. microwave output power divided by the power of the electron beam in the amplifier),  $\eta_c$  is defined in Eq. (5), and  $\eta_v$  is the pulse-shape efficiency of the high voltage modulator.

In contrast to the behavior of pulse compression efficiency, the high voltage modulator pulse-shape efficiency,  $\eta_v$ , decreases as pulse duration  $\tau_p$  becomes shorter due to the increasing fraction of pulse energy in the rise and fall of regions of the modulator pulse. The efficiency  $\eta_v$  is thought<sup>1</sup> to have the form

$$\eta_v = \frac{\tau_p}{\tau_p + \sqrt{\alpha \tau_p}} \quad (9)$$

where we estimate empirically that the constant  $\alpha = 0.25 \times 10^{-6}$  sec.

### IV. COMPARISON OF EXPERIMENTAL MICROWAVE AMPLIFIERS

The performance parameters of a number of leading microwave amplifier experiments are displayed in Table 1 together with the calculated values of  $\eta_T$  and  $N_t$ . The various experimental studies are in different stages of maturity and so the tabulated data indicates only what has been demonstrated by the beginning of 1993 and not ultimate potential. For

purposes of comparison the performance characteristics of the S-band SLC klystron is tabulated on the first line.

It will be noted that both the X-band klystron and the two gyroklystron experiments show significant progress in reducing the value of  $N_t$  from the SLC klystron value. The free electron laser, extended interaction klystron and traveling wave tube would have lower values of  $N_t$  if they could be made to operate with longer pulses. An acceptable value of  $N_t$  might be 1000-2000 and thus new higher power experiments are of interest. For example, a 17.4 GHz amplifier operating with an output pulse of  $P_p = 100$  MW and  $\tau_p = 1 \mu\text{s}$  would have  $N_t \approx 1300$ .

It will also be noted that none of the higher frequency amplifier experiments have yet equalled the SLC klystron in efficiency and improvement in  $\eta_T$  is emphatically called for. Perhaps energy recovery schemes such as depressed collectors should be seriously studied.

This work was supported by the U.S. Department of Energy.

### V. REFERENCES

1. P. B. Wilson, "Pulsed RF Technology for Future Linear Colliders," invited talk presented at the Washington, DC meeting of the American Physical Society, April 21, 1992 (*Bull. Am. Phys. Soc.* **37**, 941 (1992)).
2. Z. D. Farkas, G. Spalek and P. B. Wilson, "RF Pulse Compression Experiments at SLAC," SLAC-PUB-4911, March 1989.
3. W. D. Kilpatrick, *Rev. Sci. Instru.* **28**, 824 (1957).
4. V. L. Granatstein and A. Mondelli, "Microwave Sources and Parameter Scaling for High Frequency Linacs," in *Phys. Particle Accelerators*, ed. M. Month and M. Dienes, AIP Conference Proceedings 153 (New York: 1987) pp. 1506-1571.
5. G. Caryotakis, private discussions.
6. W. Lawson, et al., *Phys. Rev. Lett.* **67**, 520 (1991).
7. S.G. Tantawi, et al., *IEEE Trans. Plasma Sci.* **20**, 205 (1992).
8. J. Calame, et al., these proceedings.
9. M.E. Conde and G. Bekefi, *Phys. Rev. Lett.* **67**, 3082 (1991).
10. D.L. Goodman, et al., *Proc. SPIE* **1407**, 217 (1991).

11. D. Shiffler, et al., *J. Appl. Phys.* **70**, 106 (1991).

Table 1. Demonstrated amplifier performance ( $V \leq 800$  kV);  $N_t$  is the total number of amplifiers required to drive a 1 TeV accelerator with  $E_a = 100$  MV/m.

Type of Amplifier	Research Institution	$f$ (GHz)	$P_p$ (MW)	$\tau_p$ ( $\mu$ s)	$\eta_a$ (%)	$V$ (kV)	$N_t$	$\eta_T$ (%)
SLC klystron	SLAC	2.856	65	3.5	45	350	17 k	28
X-band klystron <sup>5</sup>	SLAC	11.4	50	1.0	22	447	5.6 k	10
X-band gyrokystron <sup>6,7</sup>	U. Md.	9.85	27	1.4	32	425	10 k	15
K-band gyrokystron <sup>8,**</sup>	U. Md.	19.7	30	0.8	27	440	4.2 k	11
Free electron laser <sup>9</sup>	MIT	33	61	0.02	27	750	19 k	6
Extended interaction klystron <sup>10</sup>	SRL*	11.4	100	0.05	43	440	42 k	13
Traveling wave tube <sup>11</sup>	Cornell	8.76	200	0.1	24	800	16 k	9

\*Science Research Laboratory in collaboration with Haimson Research Corp. and MIT.

\*\*In the K-band gyrokystron the output cavity operates at twice the input frequency.

## High Gradient Acceleration in a 17 GHz Photocathode RF Gun\*

S. C. Chen, J. Gonichon, L. C-L. Lin, R. J. Temkin, S. Trotz, B. G. Danly, and J. S. Wurtele  
Plasma Fusion Center, Massachusetts Institute of Technology

### Abstract

The physics and technological issues involved in high gradient particle acceleration at high microwave (RF) frequencies are under study at MIT. The 17 GHz photocathode RF gun has a  $1\frac{1}{2}$  cell room temperature copper cavity with a peak accelerating gradient of about 250 MV/m. The anticipated beam parameters, when operating with a photoemission cathode, are: energy 2 MeV, normalized emittance  $0.43\pi$  mm-mrad, energy spread 0.18%, bunch charge 0.1 nC, and bunch length 0.39 ps. The goal is to study particle acceleration at high field gradients and to generate high quality electron beams for potential applications in next generation linear colliders and free electron lasers. The experimental setup and status are described.

### I. INTRODUCTION

To meet the stringent requirements set by future applications such as high-energy linear colliders and next generation free electron lasers, efforts have been made recently to create novel electron beam sources.[1] While existing RF guns operate 144 MHz to 3 GHz, a 17.136 GHz photocathode RF gun has been constructed and is currently under cold test at MIT.[2] The 17.136 GHz operation is very attractive despite potential technical difficulties and physics issues associated with high frequencies. It allows us to achieve a high accelerating gradient, to make the system compact, and to generate high brightness beams. In this paper, the status of the 17 GHz photocathode RF gun experiment is presented in detail. A general layout of the experiment is shown in Fig.1. It consists of three parts: (1) the RF gun cavity and the transport line (including the power source and the vacuum system), (2) the laser and timing system, and (3) the beam transport and diagnostic line. Each of these subjects is described successively in Sections 2, 3, and 4. Section 5 summarizes the status of the experiment.

### II. RF CAVITY AND TRANSPORT LINE

#### A. RF Cavity and Waveguide Coupling

Figure 2 shows the vacuum assembly that houses the RF gun structure and the coupling waveguide. A vacuum of  $10^{-9}$  Torr has been achieved inside the RF gun chamber. The peak accelerating gradient is chosen to be 250 MV/m, corresponding to a peak surface field around 300 MV/m.

— \* This research is supported by DOE under Grant DE-FG02-91-ER40648

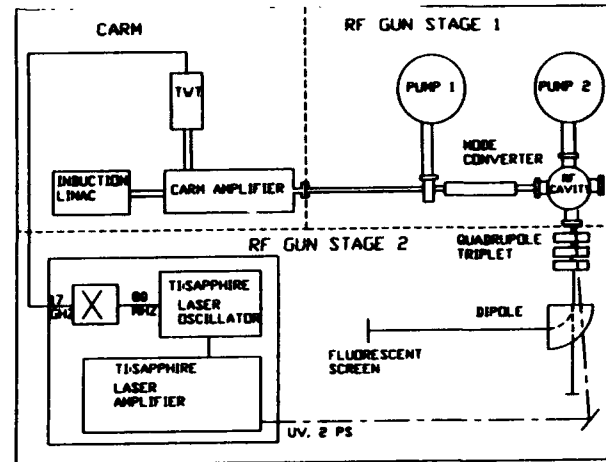


Fig. 1: Schematic of the 17 GHz photocathode RF gun experiment

The beam dynamics and the interplay between time-dependent RF forces, space-charge forces, and nonlinear RF forces have been studied using the simulation code MAGIC [3]. The main operating parameters at 17 GHz are summarized in Table 1.

Table 1: 17 GHz RFG Designed Beam Parameters

Peak accelerating gradient	250MV/m
Laser pulse length	1.4ps
Final bunch length	0.39ps
RF phase for laser pulse	$12^\circ$
Current density	$6.7kA/cm^2$
Cathode radius	0.525mm
Bunch charge	0.1 nC
Emittance	$0.43\pi$ mm-mrad
Energy spread	0.18%
Current	258A
Brightness	$1.43 \times 10^{14} \frac{A}{(mrad)^2}$

The  $TE_{10}$  waveguide mode is coupled to the cavity through two rectangular apertures, one on each cell of

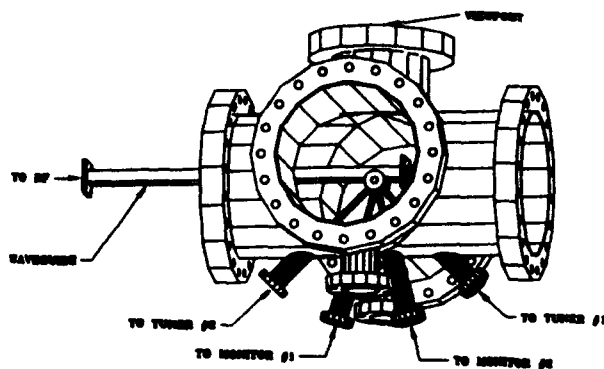


Fig. 2: RF Gun Vacuum chamber. The gun structure is located at the center of the chamber.

the cavity, to excite the  $\pi$  mode resonance. An intensive study of this waveguide sidewall coupling scheme has been conducted both theoretically and experimentally.[4] We have cold tested both electroformed and machined/brazed OFHC copper cavities with similar results. The reflected power from the waveguide-fed RF gun cavities was measured using a network analyzer. Fig.3 shows the reflected power as a function of frequency of an untuned gun cavity. The two resonances are about 100 MHz apart and each cavity has a Q value of about 1000. Each cavity absorbs over 80% of the incident power.

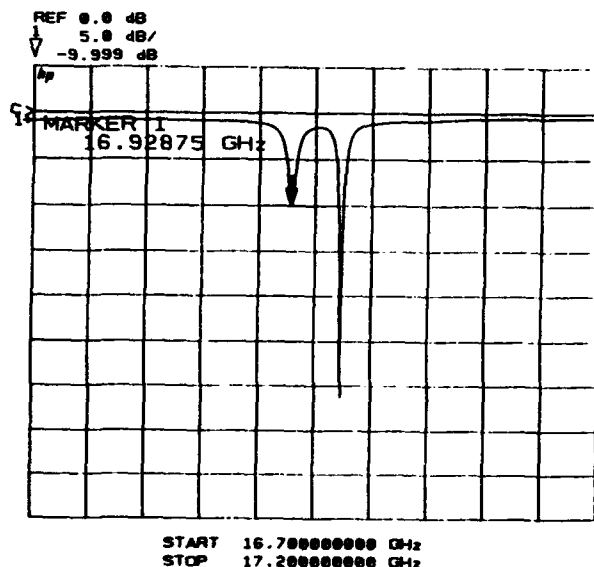


Fig. 3: Reflection as a function of frequency of an untuned gun structure

Figure 4 shows the reflection as a function of frequency after the gun cavities are tuned. The single resonance absorbs more than 90% of the input

power. The theoretical modelling of the waveguide-cavity coupling is presented in a companion paper in this volume[4].

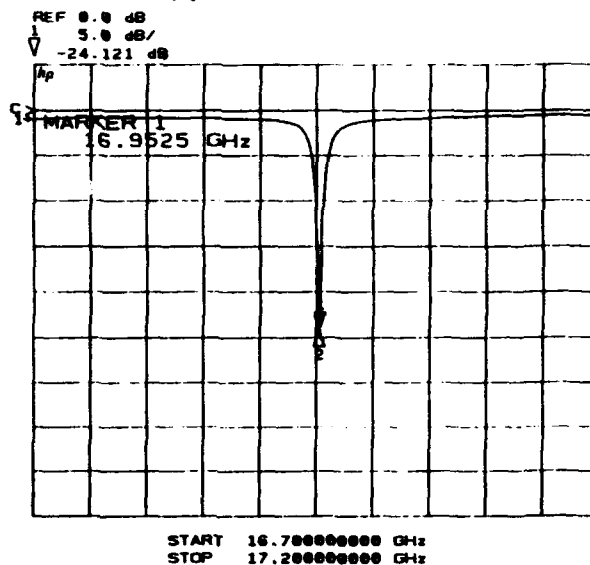


Fig. 4: Reflected Power as a function of frequency of a tuned gun structure

### B. RF Source and Transport

The power source used to feed the RF cavity is a gyro-amplifier under development at MIT [5]. The RF source will deliver 5-10 MW peak power in a pulse of 30 ns at a repetition rate of 10 Hz. The output RF is in a circularly polarized  $TE_{31}$  mode and must be converted to the  $TE_{10}$  mode in the rectangular waveguide that couples to the RF cavity. The RF transport line consists of a long overmoded 2" guide, a 2" to 1" taper, a  $TE_{31}$  to  $TE_{11}$  converter, a  $TE_{11}$  (rotating) to  $TE_{11}$  (linear) polarization converter, and a circular to rectangular transition. The line is followed by a dual directional coupler, a high-vacuum RF window, a flexible waveguide, and (optionally) an arc sensor. The  $TE_{31}$  to  $TE_{11}$  converter is under fabrication. The RF source is transit time isolated from the gun cavity by the 10 ft transport line.

The complete RF line, less the  $TE_{31}$  to  $TE_{11}$  converter, has been assembled and vacuum leak checked at  $10^{-5}$  Torr. The VSWR for the flexible waveguide is 1.23. The VSWR for the high power window does not exceed 1.2 between 16.9 and 17.1 GHz. The efficiency of the mode converter is at least 98 %.

## III. LASER AND TIMING SYSTEM

### A. Laser

The parameters of the laser system are summarized in Table 2.

**Table 2. Parameters of the Laser System**

Wavelength	220-280 nm
Repetition rate	0-10 Hz (adjustable)
Energy	200 $\mu$ J
Energy fluctuation	$\leq \pm 10$ %
Pulse Length	<2 ps
Phase Jitter	<1 ps
Timing Jitter	<3 ns
Polarization	> 99 %
Beam Divergence	0.5 to 1 mrad
Beam Pointing Error	< 10 $\mu$ rad
Mode-Lock Frequency	82 MHz

An Argon Ion pumped Ti:Sapphire laser oscillator produces a regeneratiely modelocked CW train of microjoule pulses which enter a pulsed Ti:Sapphire laser amplifier. The amplifier is pumped by a 1J Nd:YAG laser. The amplified IR pulse is then frequency tripled into the ultraviolet by an KDP/BBO combination and is directed into the RF cavity.

#### B. Timing

As shown in our simulation studies [3], the electron beam quality is strongly dependent on the RF phase of photoemission. The phase jitter is required to be less than 1 ps in our experiment. The highly stable Ti:Sapphire laser system serves as the system clock in the timing chain. The modelock frequency of 82 MHz is defined by the round-trip time of the laser cavity. The laser oscillator cavity mirrors are mounted on Invar tubes to minimize length variations. The 82 MHz signal is multiplied up by a solid state frequency multiplier (x 204) into 17 GHz to drive the RF amplifier chain.

#### IV. BEAM LINE AND DIAGNOSTICS

The beam line consists of a quadrupole triplet and a bending magnet. The 90° bend forms a point-to-point imaging system to be used for energy spread measurement. The position and the horizontal thickness of the fluorescent spot give the energy and the energy spread, respectively. The quadrupole triplet can also be used to measure the emittance: the bending magnet is switched off and the spot produced by the electrons on another screen positioned along the RF gun axis is observed. The gradient of one of the quadrupoles is varied in order to vary the spot size on the screen. A least-square analysis of the beam transverse dimension vs. the gradient in the quad gives the transverse emittance.

The program TRACE3d was used to obtain a preliminary design. Simulations of the same line with the program PARMELA show that the resolution of the spectrometer should be better than

0.1%. The charge will be measured with a Faraday cup. Several methods for measuring the bunch length are under investigation.

#### V. SUMMARY

A 17 GHz photocathode RF gun experiment is under developments. The designed peak accelerating gradient on axis is 250 MV/m. The accelerating structure and the RF transport line have been fully cold tested. The first stage experiment involves powering the structure with high power 17 GHz microwaves. The goal of the initial experiment is to condition the cavity, and to study field emission and RF breakdown at 17 GHz.

The second stage of the experiment will integrate the laser system with the RF source and the gun system. Detail characterization of the beam property are planned. The following systems will be integrated with the 17 GHz RF gun system in the second stage of the experiment. A UV laser system and the related timing system are being tested to generate picosecond electron bunches through photoemission from the cavity wall. Successful acceleration of these bunches under high field gradient will provide high brightness electron beams suitable for applications in next generation linear colliders and in short wavelength free electron lasers.

#### VI. REFERENCES

- [1] For a review, see C. Travier, "RF guns, bright injectors for FEL", Nuclear Instruments and Methods in Physics Research, A304, p 285, (1991) and the references therein.
- [2] S.C. Chen, J. Gonichon, C.L. Lin, R.J. Temkin, S. Trotz, B.G. Danly, and J.S. Wurtele, "High Gradient Acceleration in a 17 GHz Photocathode RF Gun", in *Advanced Accelerator Concepts*, AIP, New York (1993).
- [3] C.L. Lin, S.C. Chen, J.S. Wurtele, R.J. Temkin, and B.G. Danly, "Design and Modelling of a 17 GHz Photocathode RF Gun", Proc. 1991 IEEE Particle Accelerator Conf., p. 2026 (May, 1991)
- [4] C.L. Lin, S.C. Chen, J. Gonichon, and J.S. Wurtele, "A Study on the Waveguide Sidewall Coupling Problem for Photocathode RF Guns", in this Proceedings.
- [5] W.L. Menninger, B.G. Danly, C. Chen, K.D. Pendergast, and R.J. Temkin, "CARM Amplifiers for RF Accelerator Drivers", Proc. 1991 IEEE Particle Accelerator Conf., p. 754 (May, 1991). See also the paper in this Conference Proceedings.

# An Inverse Free-Electron-Laser Accelerator\*

A.S. Fisher, J.C. Gallardo, A. van Steenbergen, S. Ulc, M. Woodle  
National Synchrotron Light Source and Physics Department  
Brookhaven National Laboratory, Upton, NY 11973

J. Sandweiss  
Department of Physics, Yale University, New Haven, CT 06511

Jyan-Min Fang  
Department of Applied Physics, Columbia University, New York, NY 10027

## Abstract

Recent work at BNL on electron acceleration using the Inverse Free-Electron Laser (IFEL) has considered a low-energy, high-gradient, multi-stage linear accelerator. Experiments are planned at BNL's Accelerator Test Facility using its 50-MeV linac and 100-GW CO<sub>2</sub> laser. We have built and tested a fast-excitation wiggler magnet with constant field, tapered period, and overall length of 47 cm. Vanadium-Permendur ferromagnetic laminations are stacked in alternation with copper, eddy-current-induced, field reflectors to achieve a 1.4-T peak field with a 4-mm gap and a typical period of 3 cm. The laser beam will pass through the wiggler in a low-loss, dielectric-coated stainless-steel, rectangular waveguide. The attenuation and transverse mode has been measured in waveguide sections of various lengths, with and without the dielectric. Results of 1-D and 3-D IFEL simulations, including wiggler errors, will be presented for several cases: the initial, single-module experiment with  $\Delta E = 39$  MeV, a four-module design giving  $\Delta E = 100$  MeV in a total length of 2 m, and an eight-module IFEL with  $\Delta E = 210$  MeV.

## I. IFEL ACCELERATOR DESIGNS

An inverse free-electron laser (IFEL) accelerates an electron beam through its interaction with high-power laser radiation and a periodic wiggler field. This concept has been pursued at Brookhaven National Laboratory for several years [1-4], most recently in the form of low-energy ( $\leq 1$  GeV), high-gradient, multistage, linear accelerators [5].

Three sets of IFEL parameters are presented in Table 1. All use constant-field wigglers (described in the following section), assembled in 60-cm-long modules. In an initial demonstration of IFEL acceleration [6], a single-stage IFEL will be tested with the 50-MeV electron beam at Brookhaven's Accelerator Test Facility (ATF), which offers a high-brightness 50-MeV electron beam and a high-power picosecond CO<sub>2</sub> laser. Assuming that a 200-GW peak power in a 6-ps pulse will then be available (20 GW in 30 ps has been demonstrated to date, but shorter pulses with higher powers are under development), an acceleration gradient of 83 MV/m should result. Extending this design to eight modules and higher laser power gives an exit energy of 257 MeV. A third set of parameters [7] responds to the challenge presented at the Port Jefferson Workshop on Advanced Accelerator Concepts (June 1992), for an energy increase of 100 MeV in a total length of 2 m, by using four modules and a relatively modest laser power of 100 GW.

## II. FAST-EXCITATION WIGGLER

To maintain synchronism as an electron accelerates in a laser field with a constant wavelength  $\lambda_l$ , the wiggler must be tapered. The taper can be accomplished while holding

the wiggler parameter  $K_w$ , the period  $\lambda_w$ , or the field  $B_w$  fixed. The choice is restricted by the maximum practical wiggler field and the minimum wiggler period. The maximum rate of acceleration, averaged over the full accelerator length, is obtained for a constant- $B_w$  accelerator [5], and this choice is made for the IFELs in Table 1. Although such a structure could be constructed using permanent magnets, the variable period would be costly and difficult to adjust. Instead, we have developed a fast-excitation electromagnet [8-10] with stackable, geometrically alternating substacks of identical ferromagnetic (Vanadium Permendur, VaP) laminations, assembled in  $(\lambda_w/4)$ -thickness substacks separated by nonmagnetic laminations (Fig. 1). Four straight conductive rods, parallel to the axis and interconnected only at the ends of the assembly, constitute the single loop that drives the wiggler. The stacks are easily assembled, are compressed by simple tie rods, and allow any combination of wiggler periods. A dramatic improvement results from using copper for the nonmagnetic laminations, so that the induced fields from the eddy currents uncouple the wiggler's "up" fields from the "down" fields. These "field reflectors" significantly enhance the maximum achievable field on axis.

Both two-dimensional mesh computations (POISSON) and measurements of short wigglers were used to develop the lamination design. Reference [11] presents measurements of a full-length prototype with a tapered period. The wiggler is able to satisfy the requirements of Table 1. Measurements with a constant period of 3.75 cm [12] found an rms field error of under 0.15% and low harmonic content (3% in the 3<sup>rd</sup> harmonic).

## III. CO<sub>2</sub> LASER WAVEGUIDES

Since the wiggler gap is 4 mm, the maximum practical inside diameter for a beam pipe through the wiggler is 3 mm. If a Gaussian laser beam is focused to a 1-mm radius  $\omega_0$  (where the power drops by  $e^{-2}$ ), then the corresponding Rayleigh length  $z_R$  is 30 cm. Waveguiding can occur even in the 47-cm length of the wiggler for the single-stage IFEL, since the free-space beam radius  $\omega(z)$  will exceed the aperture of the waveguide. In a multistage IFEL, waveguiding will be unavoidable—and helpful in confining the beam. Consequently, we are investigating the mode structure and attenuation in CO<sub>2</sub>-laser waveguides.

Our present design uses rectangular stainless-steel guides, with an inside cross section of 2.8 mm  $\times$  2.8 mm. Stainless has good vacuum properties and a conductivity low enough to allow penetration of the pulsed wiggler field. To reduce the expected attenuation, some of the test waveguides were prepared (following Zakowics [13]) with a 1/4-wavelength dielectric coating (germanium) deposited on two opposite inner walls, in order to reduce surface currents. Subsequently,

it was realized that this model strictly applies at lower frequencies, where the metal walls can be treated as nearly perfect conductors. At infrared wavelengths and glancing angles, the metal behaves mostly as a dielectric, and the wall losses are greatly reduced, even without the germanium.

To investigate coupling into the waveguides, transmission loss, and transverse mode structure, eight test guides were built, half with the germanium coating. Six guide sections were 10-inches (254-mm) long; two were 5-inches (127-mm) long. All had precision alignment pins and sockets to permit accurate assembly of lengths of up to 35 inches (889 mm) of either coated or uncoated guide. The beam was focused to a Gaussian waist with an adjustable radius at the entrance to the first guide. The beam profile was measured using a pyroelectric vidicon TV camera and a digital frame grabber.

The coupling tests demonstrated optimum coupling near a waist radius of 1.0 mm. The transmission (including both coupling and attenuation losses) ranged between 80 and 95%, measured with lengths from 10 to 35 in, for entering waists of 1.0 and 1.3 mm, and for both coated and uncoated guides. In all cases, the transmission of the coated guide was  $\approx 2\%$  greater than the uncoated guide. For the longest length tested (35 in), the best result was 88% for the coated guide with a 1-mm entering beam radius.

To measure the transverse beam profile versus distance, the camera was placed within a few millimeters of the exit for guides of various lengths. Fig. 2 shows that when no guide was present, the beam diverged according to  $z_R$ , but within a guide, the beam radius decreased and oscillated about a smaller value, suggesting that some of the energy was in higher-order modes. The beam sizes were not the same for the coated and uncoated guides. Any misalignment of the beam entering the guides or of the junctions between guide sections produced a mode that was not symmetric. The transmission was much less sensitive to alignment.

The laser power must be efficiently coupled into the desired mode. Approximating with an overlap integral, Zakowics [13] predicted a coupling efficiency of 95% for a beam focused at the guide entrance to a diameter equal to 71% of the guide aperture. To determine the transition region over which the mode becomes established, we performed a series of 2-D ( $zz$ ) scalar diffraction calculations to find the fields propagating from the coupling aperture. The mode pattern transforms from the input Gaussian to a stable field distribution over a distance which is comparable to  $z_R$ . For our waist sizes, after the mode has stabilized (in about 50 cm), the amplitude typically fluctuates by  $\pm 5\%$  and the phase by  $\pm 0.05$  radian, due to a coupling into high-order modes. These calculations suggest a 90% coupling efficiency into the desired mode, but because of the 2-D scalar approximation, the coupling into the real waveguides may not be as pure.

#### IV. IFEL SIMULATIONS

To model the acceleration process in a waveguide IFEL, we have developed a 1-D particle simulation code incorporating self-consistently the longitudinal electron dynamics and the laser field. The code also takes into account the properties of a realistic electron beam, i.e., finite radius, emittance and energy spread. Subsequently, the multiparticle-simulation linac code PARMELA [14] was modified to simulate the full 3-D aspects of the IFEL interaction. The electron beam dynamics include: (a) an arbitrary initial electron distribution in "trace"

Table 1: Simulation parameters for the single-module IFEL experiment, an 8-stage IFEL, and an IFEL with  $\Delta E = 100$  MeV.

	Single	8-Stage	100 MeV	
<b>Electron Beam</b>				
Injection energy	48.9	48.9	49	MeV
Exit energy	88.0	256.9	150	MeV
Mean gradient	83	53	50	MV/m
Charge	1	1	1	nC
Peak current	100	100	100	A
Emittance $\epsilon_n$ ( $\sigma$ )	$7\pi$	$7\pi$	$7\pi$	$\mu\text{m}$
Radius ( $\sigma$ )	0.3	0.3	0.3	mm
<b>Wiggler</b>				
Number of modules	1	8	4	
Module length	60	60	60	cm
Total wiggler length	47	395	200	cm
First period	2.86	2.86	2.86	cm
Last period	4.32	9.08	6.29	cm
Gap	4	4	4	mm
Peak field	1.25	1.25	1.25	T
<b>Laser</b>				
Power	200	620	100	GW
Peak electric field	13.6	24	9.6	GV/m
Wavelength	10.2	10.2	10.2	$\mu\text{m}$
Pulse length	6	6	6	ps

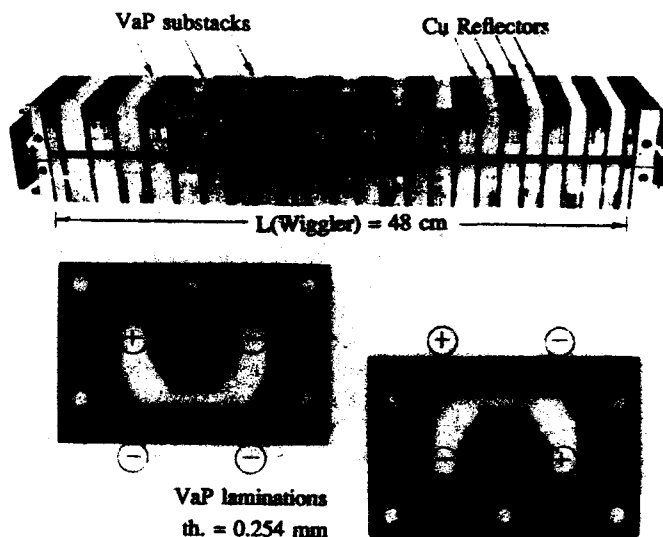


Figure 1: The fast-excitation, variable-period wiggler. The lower portion shows the VaP laminations configured for the two field polarities.

space ( $x, dx/dz, y, dy/dz$ ), determined by the Twiss parameters  $\alpha_x, \beta_x, \alpha_y, \beta_y$  and the transverse emittances  $\epsilon_x$  and  $\epsilon_y$ ; (b) an arbitrary longitudinal initial electron distribution in phase  $\phi$  and energy  $W$ ; (c) a realistic piecewise-constant tapered wiggler, allowing for both horizontal and vertical focusing.

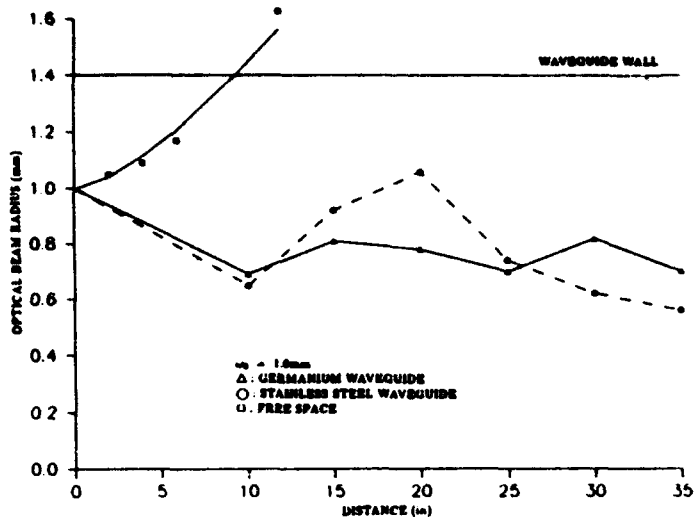


Figure 2: Beam radius  $\omega$  at the exit of stainless-steel waveguides of various lengths, with and without a germanium coating, for beam waist radius  $\omega_0$  of 1.0 mm at the guide entrance. The radius without a waveguide is also shown.

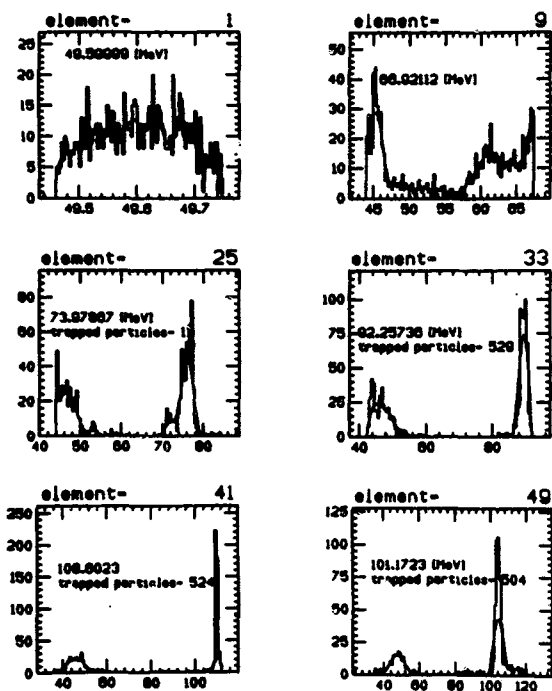


Figure 3: A 3-D simulation of the evolution of the energy spectrum in the early portion of the multistage accelerator.

The results of these calculations are given more fully in Reference [7]. The transverse phase space at the end of the wiggler shows some emittance growth in the horizontal plane and two well defined groups of electrons (accelerated

and non-accelerated) in the vertical plane; the emittances are comparable to the initial value. The evolution of the energy spectrum along the wiggler, in Fig. 3, clearly illustrates the fraction of accelerated electrons ( $\approx 50\%$ ).

For the eight-stage IFEL of Table 1, the 1-D simulation code was used to optimize the sequence of tapered wigglers for a given laser power, resonance phase angle and peak wiggler field. The vertical transverse focusing action of the planar wiggler was taken into account. Instead of shaping the wiggler poles for horizontal focusing, external focusing was added.

## V. CONCLUSION

The study of the IFEL accelerator is continuing with near-term emphasis on low-loss guide development, transverse and longitudinal phase space transport and the further optimization of a multimodule 1-GeV accelerator. For a single demonstration stage, aimed at approximately doubling the beam energy, a  $\text{CO}_2$  laser power of  $10^{11}$  W is satisfactory. A cascaded IFEL accelerating to 1 GeV would require a laser power of  $10^{12}$  W to make the overall device technically competitive.

We wish to acknowledge the assistance of T. Romano and J. Armendaris (wiggler measurements), and of S. Coe and M. Weng (waveguide measurements).

## VI. REFERENCES

\*U.S. Department of Energy contract DE-AC02-76-CH00016.

1. R.B. Palmer, *J. Appl. Phys.* **43**, 3014 (1972).
2. C. Pellegrini, P. Sprangle, W. Zakowics, *Int. Conf. on High-Energy Accelerators* (1983).
3. E.D. Courant, C. Pellegrini, W. Zakowics, *Phys. Rev.* **A32**, 2813 (1985).
4. E. Courant, J. Sandweiss, BNL-38915.
5. A. van Steenbergen, *Experimental Program, ATF*, BNL-41664 (1988); "IFEL Accelerator Demonstration Stage," BNL-43702 (1989).
6. E. Courant et al., "Inverse Free Electron Laser (IFEL) Accelerator Development," *ATF Users Meeting*, Oct. 1991, BNL-47000, CAP 81-ATF-91P, ed. H.G. Kirk, p. 235.
7. A. Fisher, J. Gallardo, J. Sandweiss, A. van Steenbergen, "Inverse Free Electron Laser Accelerator," BNL-47974, to be published in *Third Workshop on Advanced Accelerator Concepts*, Port Jefferson, NY, June 1992.
8. A. van Steenbergen, J. Gallardo, T. Romano, M. Woodle, "Fast Excitation Wiggler Development," *Workshop on Prospects for a 1-Å FEL*, Sag Harbor, NY, April 1990, BNL-52273, ed. J. Gallardo, p. 79.
9. A. van Steenbergen, U.S. Patent Application 368618, June 1989, issued Aug. 1990.
10. A. van Steenbergen, J. Gallardo, T. Romano, M. Woodle, "Fast Excitation Variable Period Wiggler," *1991 IEEE Particle Accelerator Conf.*, San Francisco, CA (IEEE, Piscataway, NJ, 1991), p. 2724.
11. J. Armendaris, J. Gallardo, T. Romano, A. van Steenbergen, "Fast Excitation Wiggler Field Measurement Results," BNL-47928, August 1992.
12. J.C. Gallardo, T. Romano, A. van Steenbergen, "Magnetic Performance of a Fast Excitation Wiggler," BNL-48675, March 1993.
13. W. Zakowics, *J. Appl. Phys.* **55**, 3421 (1984); BNL-34347.
14. L. Young, "PARMELA," 1991 version, private communication.

# Phase Control in High-Gradient Laser Particle Accelerators\*

L.C. Steinhauer and W.D. Kimura  
STI Optronics, Inc.  
2755 Northup Way, Bellevue, WA 98004

## Abstract

High gradient acceleration can be achieved in a free-space laser particle accelerator by generating an interference pattern in the laser wave in which electrons move in phase with the laser in regions of constructive interference and out of phase in regions of destructive interference. The desired interference pattern is created by proper design of a holographic grating on the surface of the entrance optic. The approach for designing such a system is described and examples are presented.

## I. INTRODUCTION

Laser particle acceleration (LPA) is a promising method for high-gradient acceleration. The most difficult aspect of LPA is phase matching between the laser wave and the electron beam. Proposed solutions have either introduced gaseous or plasma media into the interaction region, or else have conditioned the electron beam (using a magnetic wiggler) or the light wave (using evanescent waves from a nearby grating). A recently proposed alternative is to operate in vacuum and limit the length of the laser-*e*-beam interaction region [1]. Such *free-space acceleration* does not require exact phase matching between electrons and the light wave. A novel approach is examined here that creates an interference pattern which achieves both high acceleration gradient and reduced laser intensity on optical surfaces.

## II. PHYSICAL ARRANGEMENT

The arrangement of one section of a free space accelerator is shown in Figure 1. This geometry is axisymmetric and the laser beam axis coincides with the electron beam path. The incoming laser beam is annular and radially-polarized and has been prefocused by an axicon

mirror. The *entrance optic*, nominally a flat mirror with a central hole for passage of electrons, reflects the incoming laser wave through the interaction zone (shown as a shaded area in the figure). This zone is terminated downstream by the *exit optic*, another flat mirror with a central hole. As described later, the surface of the entrance optic will be suitably engraved with a holographic grating surface to achieve the desired interference pattern in the *e*-beam path.

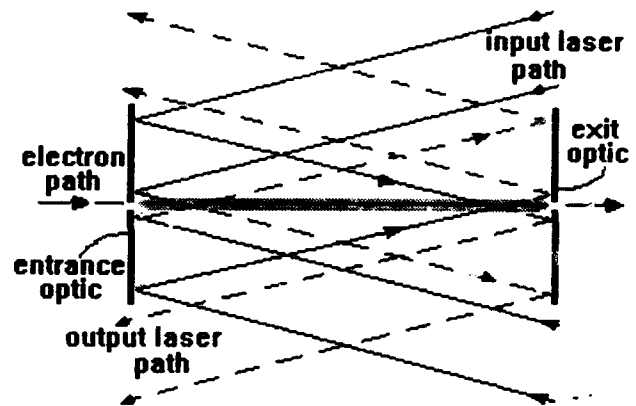


Figure 1. Basic laser-*e*-beam interaction zone design.

In some ways this arrangement resembles a cavity. Note, however, that the surfaces at each end cannot be perfectly flat mirrors else no net acceleration can occur. The actual surface shape will be discussed briefly in Section V.

## III. ELECTRIC FIELD "DESIGN"

By limiting the length of the interaction zone, net acceleration can occur even though the electrons slip relative to the laser wavefronts. This was shown in Reference [1]; although, no attempt was made there to improve performance by tailoring the intensity and phase structure of the incoming laser wave. The objective here is to *design* the electric field structure with two purposes in mind: (1) maximize the energy gain

\* Supported by US DOE Contract No. DE-AC06-83ER40128.

for a given laser power; and (2) minimize the peak laser intensity on optical surfaces.

The approach here is to assume a desired longitudinal electric field structure on the geometric axis

$$E_z(r=0, z) = F(z) \sin(k_M z) e^{i\omega t}, \quad (1)$$

where  $F(z)$  is the *envelope*, the sine function gives the phase structure, and  $\omega$  is the laser frequency. The envelope function is assumed symmetric about  $z = L/2$ , where the interaction zone in Figure 1 is between the range  $0 < z < L$ . In order to realize propagating waves that cross the geometric axis, the propagation constant  $k_M$  must be less than  $k \equiv \omega/c$ . The phase factor is assumed to have the same symmetry about  $z = L/2$  and to vanish at the boundaries (consistent with low laser intensity at the optical surfaces). Thus,  $k_M = (2N-1)\pi/L$ , where  $N$  is an integer. The given field structure can be Fourier analyzed using a sine series on the interval  $0 < z < L$ . Then the electric field on axis can be expressed in terms of Fourier modes:

$$E_z = \sum_{j=1}^{\infty} A_j \sin(\kappa_j z) e^{i\omega t}, \quad (2)$$

where  $A_j$  is the amplitude and  $\kappa_j$  is the propagation constant for each mode,  $\kappa_j = (2j-1)\pi/L$ . Only *odd* harmonics are used because the function is symmetric about  $z = L/2$ . Indeed only input functions with this symmetry property are of interest since only the odd harmonics produce net acceleration.

Given the  $E_z$  structure on axis (Eq. 2), the corresponding electromagnetic field structure elsewhere can be found using familiar Bessel function solutions. Assuming only that the fields are axisymmetric and radially polarized:

$$E_z(r, z, t) = \sum_{j=1}^{\infty} A_j J_0(\alpha_j r) \sin(\kappa_j z) e^{i\omega t}, \quad (3)$$

$$E_r(r, z, t) = \sum_{j=1}^{\infty} A_j \frac{\kappa_j}{\alpha_j} J_1(\alpha_j r) \cos(\kappa_j z) e^{i\omega t}. \quad (4)$$

The factors  $\alpha_j$  and  $\kappa_j$  are the radial and longitudinal components of the wave vector for

each mode and are related as follows:

$$\alpha_j^2 + \kappa_j^2 = k^2, \quad (5)$$

where  $k = 2\pi/\lambda$ , and  $\lambda$  is the laser wavelength.

Using these electric fields and making the Born approximation, the energy gain by an on-axis electron traversing the interaction region is

$$\Delta W = eL \sum_{j=1}^{\infty} A_j (\tilde{W}_{Cj} \cos \psi_0 + \tilde{W}_{Sj} \sin \psi_0), \quad (6)$$

where  $\psi_0$  is the electron entrance phase ( $z = 0$ );  $e$  is the electron charge; and

$$\tilde{W}_{Cj} \equiv \frac{\cos \sigma_j - 1}{2\sigma_j}; \quad \tilde{W}_{Sj} \equiv \frac{\sin \sigma_j}{2\sigma_j}; \quad (7)$$

$$\sigma_j \equiv \frac{k}{\beta} \pm (2j-1)\pi. \quad (8)$$

Here  $\beta$  is the relativistic parameter. The  $\pm$  in Eq. 8 indicate left and right moving waves, respectively. [The  $\sin(k_M z)$  phase structure includes both.] Only right moving waves ( $+z$  direction) need be considered since only they cause significant acceleration of right moving electrons.

#### IV. PERFORMANCE IN EXAMPLE CASES

The acceleration and other properties are found for the following example envelope function,

$$F(z) = \sin(\pi z/L) \sin^2(N_L \pi z/L), \quad (9)$$

where  $N_L$  is the number of lobes desired in the interference pattern. Figure 2 shows the electric field on the axis for a particular example. This example has a relatively short interaction zone ( $L/\lambda = 108$ ) and a steep principal crossing angle ( $\theta_m = 397$  mrad, where  $k_m/k = \cos \theta_m$ ). Given  $L/\lambda$ , an optimal combination of  $N$  and  $N_L$  was chosen so that the electron with the proper initial phase will be in phase with the wave in the regions of high field amplitude (constructive interference) and out of phase in the regions of low amplitude (destructive interference).

The electric fields at the entrance optic for the same case are shown in Figure 3. The fields

shown are actually those on a viewing cone at an angle which minimizes the apparent phase

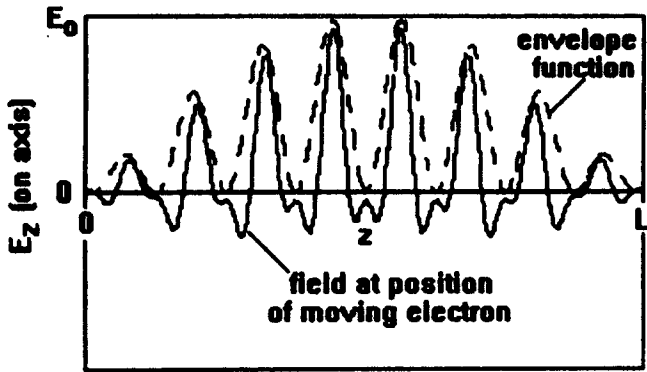


Figure 2.  $E_z$  on axis for the case  $L/\lambda = 108$ ,  $N = 100$ ,  $N_L = 8$ .

variation (modulation) of the wave. The electric field scale,  $E_0$ , is the same as in the beam path shown in Figure 2. Here the radial scale is  $a = L/\cos\theta_m$ ; a ray of light at the principal crossing angle  $\theta_m$  passing through  $r = a$  at  $z = 0$  will cross the axis at  $z = L$ .

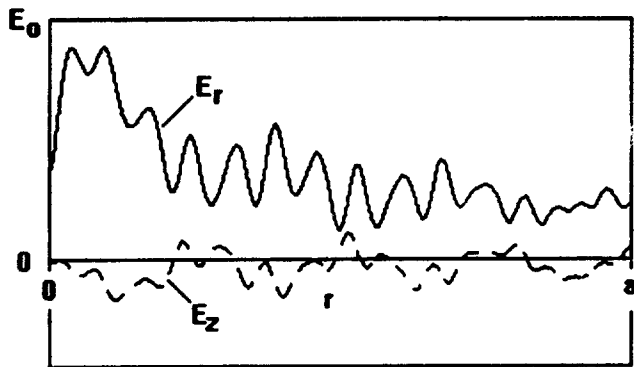


Figure 3. Fields at entrance optic (on viewing cone:  $r = s \cos\theta_p$ ,  $z = s \sin\theta_p$  ( $0 < s < a$ ) where  $\theta_p = 85.2$  mrad is the crossing angle of the last propagating mode ( $j = 108$ ).

In this example the maximum electric field on the entrance optic is  $E_{max} = 0.89E_0$ , i.e. it is slightly less than the nominal peak acceleration field experienced by the electron (Fig. 2).

Examples of this concept are summarized in Table I based upon a  $\text{CO}_2$  laser. Evidently, high acceleration gradients of hundreds of GeV/m over single section lengths of order 1 cm are possible. These examples also have reduced laser intensity at optical surfaces; the maximum electric field at the entrance optic is less than the accelerating field in the electron path.

Table I. Examples for 10.2  $\mu\text{m}$  Laser Wavelength.

$L$ (cm)	$a$ (cm)	$P_L$	$\langle \frac{dW}{dz} \rangle$ (MeV/m)	$\frac{E_{max}}{E_0}$
0.42	0.11	50 GW	470	0.55
1.04	0.18	50 GW	190	0.95
1.04	0.18	1 TW	850	0.95
1.04	0.18	10 TW	2700	0.95

## V. DISCUSSION

The examples here show that properly designed interference patterns allow electrons to effectively remain in phase with a laser wave over significant distances. The question then is how to produce input waves with electric field patterns like that shown in Figure 3. This is possible by (1) optically modifying the incoming laser beam intensity pattern and (2) engraving the proper holographic grating structure on the entrance optic. Since the required electric field distribution can be analytically calculated, the necessary holographic structure can also be numerically computed. Computer controlled diamond machining can then be used to cut the holographic structure on the entrance optic. Similarly, a holographic grating on the exit optic can be used to convert the laser beam back into one that can be recycled for another interaction with the  $e$ -beam.

Future work on this concept will address several topics: (1) optimization of the design for a single interaction cell and (2) recycling the laser beam, i.e., collecting and reinjecting the exit laser wave into the adjacent interaction cell. (See Figure 1).

## VI. REFERENCES

- [1] L.C. Steinhauer and W.D. Kimura, J. Appl. Phys. 72, 3237 (1992).

# Beam Quality in a Cyclotron Autoresonance Accelerator<sup>1</sup>

B. Hafizi<sup>†</sup>, P. Sprangle<sup>‡</sup> and J. L. Hirshfield<sup>§</sup>

<sup>†</sup>Icarus Research, 7113 Exfair Road, Bethesda, MD 20814

<sup>‡</sup>Beam Physics Branch, Plasma Physics Division

Naval Research Laboratory, Washington, DC 20375

<sup>§</sup>Omega-P, Inc., 2008 Yale Station, New Haven, CT 06520

and Yale University, PO Box 6666, New Haven, CT 06511

**Abstract** – The axial velocity spread for a gyrating electron beam produced by cyclotron autoresonant acceleration is determined. The parameter range chosen for analysis is that of interest in harmonic generation of cm-wavelength radiation to drive a next-generation electron-positron collider.

## I. Introduction

The cyclotron autoresonant accelerator (CARA) may have application as a compact, low-energy injector for a high-gradient accelerator or for use in a source of radiation that requires low-energy electrons. Recent calculations of the efficiency for production of rf power at a harmonic of the rotation frequency for an electron beam prepared using a CARA show that good beam quality is important for achieving high efficiency.<sup>1</sup> For example, when a nonlinear (resonant) taper in magnetic field is employed in the harmonic converter, 5-th harmonic conversion efficiency at 14.25 GHz was predicted to fall from 70% to 30% when the axial velocity spread was increased from zero to 2% in a 7 A, 150 kV electron beam. It is thus crucial to understand the origins of finite velocity spread during cyclotron autoresonant acceleration, in order to design accelerators capable of producing beams with spreads below 1%. This paper presents preliminary results of a numerical study of the evolution of axial velocity spread during acceleration by a CARA operating in the TE<sub>11</sub> mode at S-band.

Prior theoretical studies of the acceleration process<sup>2</sup> have shown that rapid trapping of particles occurs at the resonant phase<sup>3</sup>, that substantial energy gain can be obtained<sup>4</sup>, but that a practical upper limit to beam energy will exist when a fast wave rf accelerating field is employed<sup>5</sup>. If an accelerating field with a phase velocity equal exactly to the light velocity is employed then—in principle—unlimited accel-

eration can occur. Means for arranging this in practice include the use of dielectrically-lined waveguides or coaxial waveguides operating in the TEM mode. For the former, acceleration gradients determined in our analysis to date have been smaller than those for fast wave unlined waveguides. For the latter, elementary considerations show that axicentric orbits experience acceleration to an energy no greater than the potential drop between the inner and outer conductors. For properly phased electrons with fixed, small off-axis displacement of guiding centers, the energy increases with time like  $t^{2/5}$  in the asymptotic limit. This is to be compared with the  $t^{2/3}$  scaling for the conventional autoresonance acceleration. As a result, consideration here will be limited to fast-wave accelerators for producing 20-100 MW beams in the energy range up to 1 MeV for use in the harmonic generation of cm-wavelength radiation to drive a next-generation electron-positron collider. In this paper we present results from time-dependent simulation of the CARA to illustrate the quality of the electron beam generated, as measured by the axial velocity spread.

## II. Numerical Results

The simulation results presented here are obtained by following the motion of a group of 100 electrons in the field of a TE<sub>11</sub> mode in a circular waveguide which is immersed in a guide magnetic field. The amplitude of the rf field is assumed to vary slowly due to beam loading of the circuit. The guide field is tapered along the  $z$  axis in order to maintain resonance, i.e.,  $\Omega_0/\gamma = \omega(1 - n\beta_z)$ , where  $\Omega_0 = |e|B_0/mc$  is the gyrofrequency in the axial component of the guide field  $B_0(z)$ ,  $e$  is the charge and  $m$  is the mass of an electron,  $c$  is the vacuum speed of light,  $\gamma$  is the relativistic mass factor,  $\beta_z = v_z/c$  is the ratio of the axial velocity to  $c$ ,  $\omega$  is the rf frequency and  $n = c/(\omega/k_z)$  is the refractive index for the waveguide mode with axial wavenumber  $k_z$ . Tapering of the axial component

<sup>1</sup>Supported by ONR & DoE

of the guide field implies the presence of transverse components since the magnetic field is solenoidal and approximately irrotational. The Lorentz equations of motion for the electrons are simplified by retaining only the resonant terms and integrated by a 4-th order Runge-Kutta method, using  $10^4$  mesh points. The slow-scale spatial variation of the rf is expressed as  $\exp\{i \int_0^z dz' [\Delta k(z') + i\Gamma(z')]\}$ , where  $\Delta k(z)$  is the wavenumber shift and  $\Gamma(z)$  is the damping rate. The slow-scale Maxwell equations then lead to explicit expressions for  $\Delta k(z)$  and  $\Gamma(z)$ . The electrons enter the waveguide as a pencil beam consisting of axicentric orbits, but with finite emittance. The parameters for the simulation results presented here are shown in Table 1. The initial emittance value of 14.14 mm-mrad is twice the ideal emittance for a 50 A beam drawn from a  $5 \text{ cm}^2$  thermionic cathode at a temperature of 0.16 eV.

Table 1

Frequency $\omega/2\pi$	2.85	GHz
Input Power	50	MW
Waveguide Radius	8.824	cm
Refractive Index	0.937	
Waveguide Length	168	cm
Initial Energy	100	keV
Final Energy	1	MeV
Current	50	A
Initial Normalised Emittance	14.14	mm-mrad
Initial Beam Radius	0.638	mm
Final Beam Radius	2.7	cm
Initial Axial Velocity Spread	0.015	%
Final Axial Velocity Spread	0.11	%
Initial Magnetic Field	0.592	kG
Final Magnetic Field	1.45	kG

Table 1: Parameters for simulation of CARA at S-band.

The waveguide radius is chosen to be large enough so that the refractive index is close to unity and, therefore, the interaction is close to autoresonance. As a consequence the waveguide is somewhat overmoded and supports all TE and TM modes through  $TM_{21}$ . However, other simulations show that CARA operation below cutoff for the  $TM_{11}$  mode is also possible.

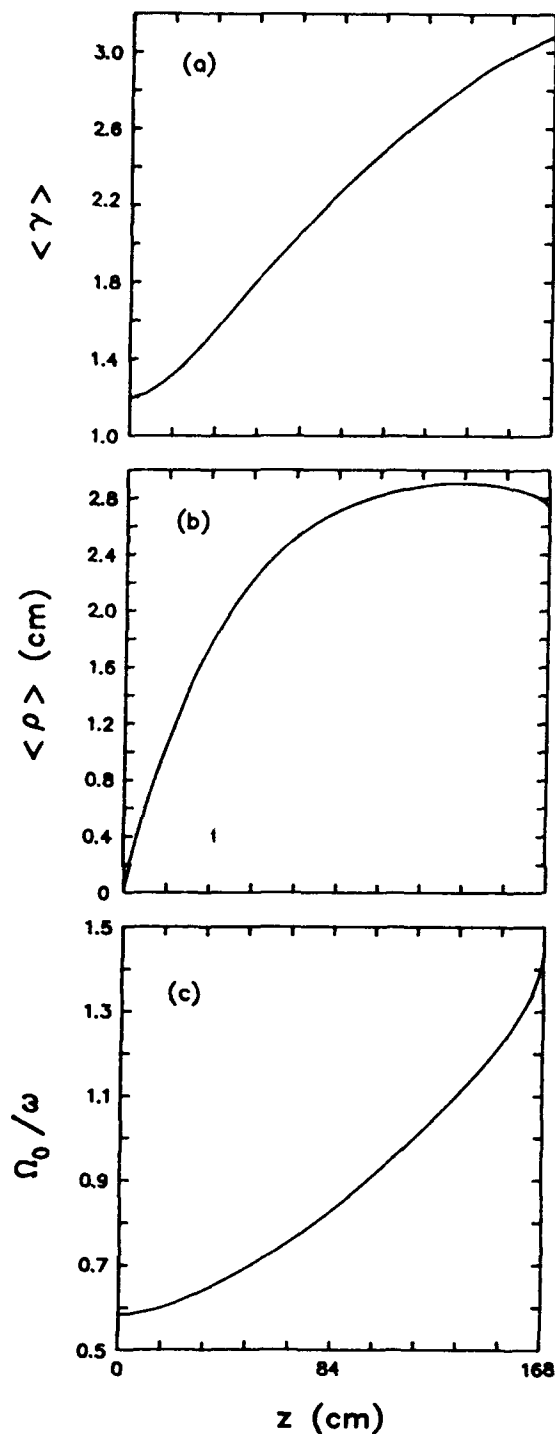


Fig. 1: Results from numerical simulation of CARA operating at S-band with 100 keV initial electron energy. (a) Mean beam relativistic factor;  $\langle \rangle$  indicates an average over the electron distribution. (b) Mean beam gyroradius. (c) Ratio of gyrofrequency to rf frequency.

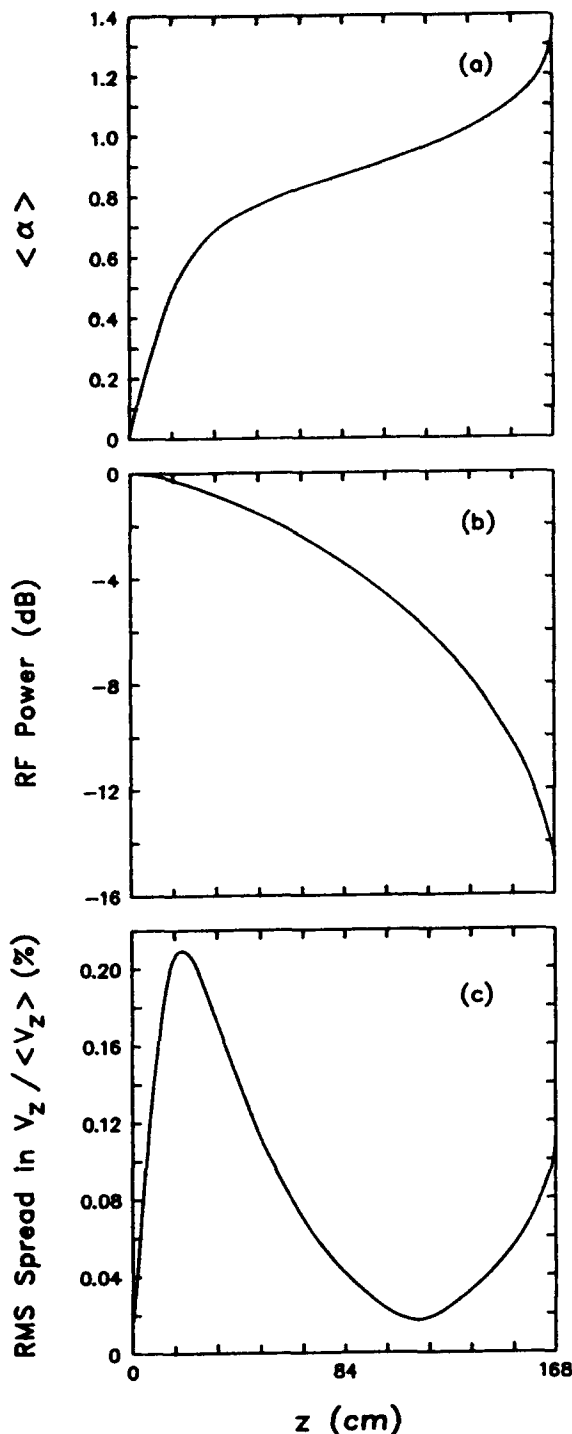


Fig. 2: Results from numerical simulation of CARA operating at S-band with 100 keV initial electron energy. (a) Mean beam  $\alpha$ . (b) Depletion of rf power. (c) Ratio of root-mean-square spread in axial velocity to mean axial velocity.

Figures 1(a), (b) and (c) show the mean  $\gamma$  (averaged over the ensemble of electrons), the mean gyroradius,  $\rho = \gamma v_{\perp} / \Omega_0$  where  $v_{\perp}$  is the transverse component of the electron velocity, and the ratio of the gyrofrequency to the rf frequency,  $\Omega_0 / \omega$ , all as functions of axial distance  $z$ . (In the figures,  $\langle \rangle$  indicates the average over the electron distribution.) Figure 1(a) shows that the beam energy increases to about 1 MeV in a distance of 168 cm. Beyond  $\sim 100$  cm, the rise in energy is principally directed into the transverse component of the electron velocity. To maintain resonance this is accompanied by a rise in the magnetic field which tends to reduce the axial electron velocity due to the transverse components of the magnetic field. This, in turn, leads to a further rise in the field to preserve the resonance. The net effect is the rapid rise observed in Fig. 1 (c) and is responsible for restraining the beam radius from approaching the waveguide radius, as indicated in Fig. 1(b).

Figure 2(a) shows the increase in the mean beam  $\alpha \equiv v_{\perp} / v_z$  as the electrons are accelerated. The acceleration process, of course, leads to depletion of the rf power down the waveguide, as shown in Fig. 2(c). Finally, the root-mean-square (rms) spread in the axial velocity of the electrons, normalized to the mean axial velocity, is shown in Fig. 2(c). It is observed that the spread in the axial velocity, which is the key figure-of-merit in evaluating the quality of the beam for radiation generation purposes, is much smaller than 1%.

### III. Conclusion

We have presented some preliminary numerical results for a  $> 95\%$  efficient CARA operating at S-band. In particular, we have shown that the quality of the electron beam generated by this accelerator, as measured by the axial velocity spread on the beam, is consistent with the requirement for efficient generation of cm-wavelength radiation in a 5-th harmonic converter.

### References

- [1] J. L. Hirshfield, Phys. Rev. A **46**, 5161 (1992); A. K. Ganguly and J. L. Hirshfield, Phys. Rev. Lett. **70**, 291 (1993).
- [2] C. S. Roberts and S. J. Buchsbaum, Phys. Rev. **135**, 381 (1964).
- [3] P. Sprangle, L. Vlahos and C. M. Tang, IEEE Trans Nucl. Sci. NS-**30**, 3177 (1983).
- [4] R. Shpitalnik, J. Appl. Phys. **71**, 1583 (1992).
- [5] C. Chen, Phys. Rev. A **46**, 6654 (1992).

# Superlattice Crystal Accelerator: Acceleration Beyond GeV/m

S.A. Bogacz

Accelerator Physics Department, Fermi National Accelerator Laboratory  
P.O. Box 500, Batavia, IL 60510 USA

## Abstract

Here, an idea of using a visible light wave to accelerate relativistic particles via the inverse FEL mechanism is explored. A strain modulated crystal structure – the superlattice, plays the role of a microscopic undulator providing very strong ponderomotive coupling between the beam and the light wave. Purely classical treatment of relativistic protons channeling through a superlattice is performed in a self consistent fashion involving the Maxwell wave equation for the accelerating electromagnetic field and the relativistic Boltzmann equation for the protons. It yields the accelerating efficiency in terms of the negative gain coefficient for the amplitude of the electromagnetic wave – the rate the energy is extracted from the light by the beam. Presented analytic formalism allows one to find the acceleration rate in a simple closed form, which is further evaluated for a model beam – optical cavity system to verify feasibility of this scheme.

## I. INTRODUCTION

The main idea of using a modulated crystal structure as an undulator is illustrated schematically in Figure 1. A beam of relativistic particles while channeling through the crystal follows well defined trajectories. The particles are periodically accelerated perpendicular to their flight path as they traverse the channel. The undulator wavelengths typically fall in the range 50–500 Å, far shorter than those of any macroscopic undulator.

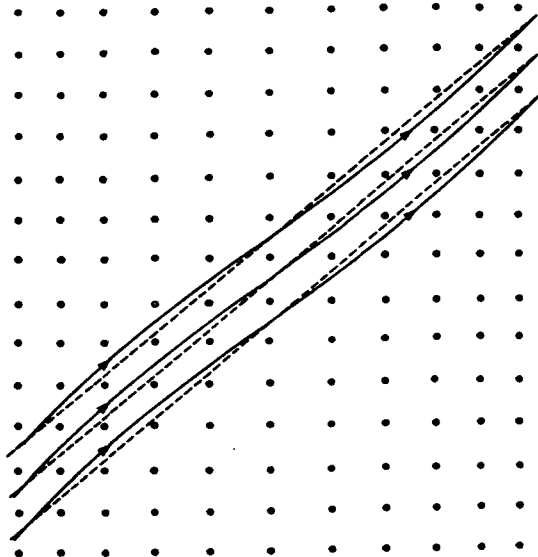


Figure 1 Center of the channeling trajectory in [110] direction in a strain-modulated superlattice.

Furthermore, the electrostatic crystal fields involve the line averaged nuclear field and can be two or more orders of magnitude larger than the equivalent fields of macroscopic magnetic undulators. Both of these factors hold the promise of greatly enhanced coupling between the beam and the accelerating electromagnetic wave.

## II. SUPERLATTICE CHANNELING

One can describe a high intensity proton beam in terms of a classical distribution function,  $f(p, x, t)$ , governed by the relativistic Boltzmann equation. The transverse dynamics of relativistic protons propagating in a strain modulated superlattice is modeled by a harmonic crystal field potential<sup>1</sup> and leads to generation of a transverse current. This couples the Vlasov equation to the Maxwell wave equation. Therefore, presented problem reduces to a self consistent solution of the Vlasov and the wave equations.

Collective behavior of a particle beam channeling along the  $z$  axis can be described in terms of the relativistic Vlasov equation

$$\frac{\partial f}{\partial t} + \frac{1}{m\gamma} \left( p^\alpha - \frac{e}{c} A^\alpha \right) \frac{\partial f}{\partial x^\alpha} + \left[ \frac{e}{mc\gamma} \left( p^\beta - \frac{e}{c} A^\beta \right) \frac{\partial A^\beta}{\partial x^\alpha} - e \frac{\partial \phi}{\partial x^\alpha} \right] \frac{\partial f}{\partial p^\alpha} = 0. \quad (1)$$

Here  $A$  is a vector potential of an electromagnetic field and  $\phi$  is a phenomenological harmonic crystal-field potential<sup>2</sup>, which describes both transverse focusing of the beam and longitudinal modulation of the minimum of the harmonic potential well.

$$\phi = \phi_0 + \frac{1}{2} \phi_1 (x - x_1 \cos gz)^2, \quad (2)$$

where  $g = 2\pi/l$ ,  $l$  is the strain modulation periodicity and  $x_1, \phi_1, \phi_0$  are parameters of the potential.

Eq. (1) will be treated iteratively and only linear terms in the  $A$ -field will be retained. In the 0-th order solution  $A = 0$ , and the corresponding distribution function  $f = f^{(0)}$  is obtained from the solution of

$$\frac{\partial f^{(0)}}{\partial t} + \frac{p^\alpha}{m\gamma} \frac{\partial f^{(0)}}{\partial x^\alpha} - e \frac{\partial \phi}{\partial x^\alpha} \frac{\partial f^{(0)}}{\partial p^\alpha} = 0. \quad (3)$$

A class of solutions,  $f^{(0)}$ , describing a beam with a sharply peaked initial momentum distribution,  $\Lambda$  can be constructed as follows

$$f^{(0)} = n_0 \delta(x - x^{(0)}) \delta(p_x - p_x^{(0)}) \Lambda(p_z - p_0). \quad (4)$$

where  $n_0$  is a concentration of particles per unit area of the channeling plane and the steady state trajectory is described as follows

$$x^{(0)} = \frac{x_1}{1 - U^2} \cos(gz) \quad (5)$$

$$p_x^{(0)} = p_z \frac{\partial x^{(0)}}{\partial z}$$

Here  $U = g/k_\beta$ , where,  $k_\beta$  is a focusing strength of the crystal channel given explicitly below

$$k_\beta^2 = \frac{e\phi_1}{p_z v_z} \quad (6)$$

We have assumed that only the transverse component of the A-field is present and  $A_x \equiv A(z, t)$ . We seek a perturbed solution,  $f^{(1)}$ , in the following form

$$f^{(1)} = n_0 \delta(x - x^{(0)}) \delta(p_x - p_x^{(0)}) h(z, p_z, t), \quad (7)$$

where  $h$  describes bunching of particles due to the presence of the A-field. Substituting Eqs.(4)–(7) and (2) into Eq.(1) leads to the following kinetic equation for  $h$

$$\frac{\partial h}{\partial t} + \frac{p_z}{m\gamma} \frac{\partial h}{\partial z} + \frac{e}{c} \frac{p_x}{m\gamma} \frac{g x_1}{1 - U^2} \frac{\partial A}{\partial z} \frac{\partial \Lambda}{\partial p_z} \sin gz = 0. \quad (8)$$

The inhomogeneous term in the above equation plays the role of a driving force representing acceleration of the particles by the ponderomotive force due to the transverse motion (induced by the crystal field) in the presence of the A-field. The resulting transverse current couples Eq.(8) to the following wave equation

$$\left( \frac{\partial^2}{\partial z^2} - \frac{1}{c^2} \frac{\partial^2}{\partial t^2} \right) A = \frac{4\pi n e}{c} \int_{-\infty}^{\infty} dp_z h \frac{p_z}{m\gamma} \frac{g x_1}{1 - U^2} \sin gz, \quad (9)$$

resulting in a closed system of equations for  $h$  and  $A$ . Here the A-field can be identified as a sum of the macroscopic driving field and a self consistent electromagnetic field propagating in the crystal structure. We start with a single plane wave solution of arbitrary  $\omega$  and  $k$  propagating in free space along the  $z$  axis in both directions and use it as a 0-th order iteration step

$$A_{\pm}^{(0)} = A_0 e^{-i\omega t \pm ikz} \quad (10)$$

Putting  $A = A_{\pm}^{(0)}$  (left and right propagating waves) in Eq.(9), one can solve it analytically for  $h = h_{\pm}^{(1)}$  by constructing a Green's function with the appropriate boundary conditions built in it. The solutions for  $A_{\pm}^{(1)}(z)$  can be written explicitly in terms of the Green's function for the Helmholtz equation. On the other hand,

one can model the effect of coupling by adding a small complex part  $ik^{\pm} = \alpha^{\pm} + i\beta^{\pm}$  to the  $k$ -vector; here  $\alpha$  is a gain/loss coefficient and  $\beta$  describes a small shift in the phase velocity of the optical mode. Deamplification of the back traveling wave can be summarized by the following expression

$$\alpha^- = -\frac{\pi}{4} n \int_{-\infty}^{\infty} dp_z Q^2 \frac{p_z}{m\gamma} \frac{\partial \Lambda}{\partial p_z} L\Gamma(v^-), \quad (11)$$

where

$$v^- = m\gamma kc/p_z + k - g, \quad (12)$$

and

$$Q = \frac{e}{c} \frac{g x_1}{1 - U^2} \quad (13)$$

Here,

$$\Gamma(x) \equiv \left( \frac{\sin(xL/2)}{xL/2} \right)^2 \quad (14)$$

is the characteristic form occurring in diffraction theory, with the principal maximum at  $x = 0$ .

### III. ACCELERATION RATE

Imposing resonant condition,  $v^- = 0$ , in Eq.(11) fixes the wave vector of the optical mode as follows

$$g = m\gamma kc/p_z + k \quad (15)$$

One can notice that, apart from a slowly varying function  $Q$ , the remaining functions occurring in the integrand in Eq.(11), namely,  $\Lambda$  and  $\Gamma$  are sharply peaked functions of momentum characterized by the respective widths:

$$\left( \frac{\Delta p}{p} \right)_{\Lambda} \text{ and } \left( \frac{\Delta p}{p} \right)_{\Gamma} = \frac{l}{L} \quad (16)$$

Now one can compare relative sharpness of both functions;  $\Lambda$  and  $\Gamma$ . Typical value of the relative momentum spread is of the order of  $10^{-4}$ . Assuming superlattice modulation of 500Å and crystal length of 5 cm allows one to evaluate the width of  $\Gamma$ . Both characteristic widths can be summarized as follows

$$\left( \frac{\Delta p}{p} \right)_{\Lambda} = 10^{-4}, \quad \left( \frac{\Delta p}{p} \right)_{\Gamma} = 10^{-6}. \quad (17)$$

The integration in Eq.(11) is carried out assuming that the sharper function, namely  $\Gamma$ , is approximated by the  $\delta$ -function. This reduces the gain/loss coefficient to the following simple expression

$$\alpha = -\frac{\pi}{2} n \frac{Q^2}{m} \gamma l \left( \frac{\Delta p}{p} \right)_{\Lambda}^{-2}. \quad (18)$$

The above final result will serve as a starting point for further feasibility discussion.

#### IV. THREE WAVE MIXING

Spontaneous bunching of the proton beam channeling through a superlattice and interacting with the electromagnetic wave results in energy flow from the wave to the beam. This particular kind of particle density fluctuation,  $h$ , has the form of a propagating plane wave of the same frequency,  $\omega$ , as the emitted electromagnetic wave. The phase velocity of the moving bunch matches the velocity of protons in the beam. Therefore, the quantity  $\gamma m \omega / p_z = k_b$  represents the wave vector of the propagating particle density bunch. Keeping in mind that the periodicity of the undulator represents a static wave with a wave vector  $g$ , and that  $k$  is the wave vector of the electromagnetic wave, we can analyze our results in the language of three wave mixing<sup>3</sup>.

Furthermore "momentum" conservation of all three modes yields the,  $v^- = 0$  conditions. The last condition,  $k_b = g - k$ , is equivalent to a momentum "recoil" between the particle density "bunch" and the electromagnetic wave (deamplification of the backward propagating wave), where a four momentum  $(0, g)$  is transferred from the backward propagating wave to the forward moving proton bunch.

#### V. FEASIBILITY ASSESSMENT

We will discuss the feasibility of the proposed scheme by considering (110) planar channeling in a strain modulated Si crystal<sup>4</sup>. We write the undulator period as  $l = Nd$ , where  $d = 1.92 \text{ \AA}$  is the spacing between successive lattice planes and  $N$  is the number of such planes. The strain modulation, of course, requires a second component, such as Ge; however, we will use the parameters of Si for convenience.

Relativistic particles while channeling along the path undergo transverse harmonic oscillations from the crystal field potential, an analog of the betatron oscillations, with the characteristic frequency  $\omega_b = \sqrt{e\phi_1/m}$ . One can see from Eq.(13) that if the angular velocity of a particle traversing the strain modulated path,  $\omega = 2\pi v/l$ , approaches  $\omega_b/\sqrt{\gamma}$  (Doppler shifted betatron frequency), the undulator parameter,  $Q$ , has a resonance ( $U \rightarrow 1$ ), which would enormously enhance the gain/loss coefficient. However, the excessive growth of the undulator parameter would soon result in a rapid dechanneling of the particles. One can see this easily if  $Q$  is rewritten in the following form

$$Q = \frac{e}{c} \frac{v_{\perp}^{\max}}{v_{\parallel}} \quad (19)$$

where  $v_{\perp}, v_{\parallel}$  are transverse and longitudinal components of the particle velocity, respectively.

For small values of  $\gamma$  ( $U \approx 1$ ), the following simple physical criterion allows one to estimate the maximum value of  $Q$ . Dechanneling will occur if the transverse kinetic energy of the particle exceeds the binding energy of the harmonic potential (a particle leaves the channel). If the maximum transverse velocity of a channeling particle is  $v_{\perp}$  and  $a$  is the distance between adjacent channels (for (110) channeling in Si  $a = 5 \text{ \AA}$ ), the above condition can be written as follows:

$$v_{\perp}^2 \geq \frac{e\phi_1}{m\gamma} \left(\frac{a}{2}\right)^2 \quad (20)$$

The equality sign in Eq.(20) along with Eq.(19) fix the maximum allowed value of the undulator parameter as

$$Q^{\max} = \frac{e}{c} \frac{a}{2} \sqrt{\frac{e\phi_1}{m\gamma c^2} \frac{\gamma}{\gamma^2 - 1}} \quad (21)$$

The above expression can be evaluated for relativistic protons channeling through our model superlattice as

$$Q^{\max} = 7.5 \times \sqrt{\frac{\gamma}{\gamma^2 - 1}} \times 10^{-24} \text{ cm}^{1/2} \text{ g}^{1/2} \quad (22)$$

Now, one can evaluate Eq.(11) assuming only one proton - by assigning  $n$  to be an inverse area of the channeling plane per one particle for typical values of the beam concentration<sup>5</sup>,  $n = 10^{16} \text{ cm}^{-2}$ . This way  $\alpha$  describes the rate of optical amplitude depletion per one particle - the acceleration rate. Assuming  $\gamma$  of 2,  $l = 500 \text{ \AA}$  and

$$\left(\frac{\Delta p}{p}\right)_{\Lambda} = 10^{-4} \quad (23)$$

yields the following value of the acceleration rate

$$\alpha = 3.53 \times 10^{-4} \text{ cm}^{-1} \quad (24)$$

The nominal acceleration efficiency in units of eV/cm will, obviously, depend on the energy density of the actual optical cavity, which is left out for further discussion elsewhere.

#### REFERENCES

1. B. L. Berman, et al, Nuclear Instruments and Methods in Physics Research B, 2, 90 (1984).
2. J. A. Ellison, S. T. Picraux, W. R. Allen and W. K. Chu, Phys. Rev. B, 37, 7290 (1988).
3. J. A. Ellison, Phys. Rev. B, 18, 5948 (1978).
4. S. Datz, et al, Nuclear Instruments and Methods in Physics Research B, 2, 74 (1984).
5. M. A. Kumakhov, Sov. Phys. JEPT, 4, 781 (1977).

# Design Study of a Microwave Driver for a Relativistic Klystron Two-Beam Accelerator\*

T.L. Houck

Lawrence Livermore National Laboratory  
University of California, Livermore, California 94550 USA

## Abstract

In two-beam accelerators, the reacceleration of a modulated drive beam can enable high conversion efficiency of electron beam energy to rf energy. However, the stability issues involved with the transport of high current electron beams through rf extraction structures and induction accelerator cells are critical. We report on theoretical studies and computer simulations of a two-beam accelerator design using traveling-wave extraction structures. Specific issues addressed include regenerative and cumulative transverse instabilities.

## I. Introduction

A collaboration between the Lawrence Livermore National Laboratory's (LLNL) Microwave Source Facility and the Lawrence Berkeley Laboratory's Collider Physics Group has been studying the feasibility of a Relativistic Klystron-Two Beam Accelerator (RK-TBA) as a possible linear collider. In a RK-TBA, one beam line is a high-gradient rf linac which accelerates electrons or positrons to very high energies. The second beam line, the subject of this paper, is an induction linac which includes microwave generating structures located at regular intervals along the beam line. These structures extract energy in the form of microwaves which are then used to drive the rf linac. In a RK-TBA design, the microwave generating structures are rf structures, e.g. standing-wave cavities or traveling-wave structures (TWS). Experiments at LLNL have shown that traveling-wave structures are capable of producing the desired high-power microwave pulses (100's MW per output).<sup>1</sup> However, these experiments also indicated that the major difficulty in designing a feasible RK-TBA is the transverse instabilities resulting from the propagation of kiloamperes of average current through the narrow apertures of x-band microwave structures.<sup>2</sup> This paper addresses both analytical and numerical modeling performed to study damping of the transverse instability in such systems.

## II. Analytical Modeling

To model the RK-TBA, I have used Caporaso's technique<sup>3</sup> for studying the growth of transverse insta-

\*The work was performed under the auspices of the U.S. Department of Energy by Lawrence Livermore National Laboratory under contract W-7405-ENG-48.

bilities in induction accelerators. The microwave extraction cavities are treated as a continuous distribution along the drive beam of the RK-TBA. The transverse instability is assumed to be due to the excitation of a single dipole resonant mode with frequency  $\omega_0$ . Within this frame work the asymptotic behavior of the transverse instability can be studied using the well-known multicavity model equations:<sup>4,5</sup>

$$\left(\frac{\partial^2}{\partial t^2} + \frac{\omega_0}{Q} \frac{\partial}{\partial t} + \omega_0^2\right) \Delta = \omega_0^2 G \xi / \gamma \quad (1)$$

$$\frac{\partial}{\partial z} \left[ \gamma \frac{\partial \xi}{\partial z} \right] + \gamma k_\beta^2 \xi = \gamma \Delta, \quad (2)$$

where  $\xi$  is the transverse displacement of the beam centroid from the axis.  $\Delta \equiv \Delta p_\perp / (L_g p_z)$  is the normalized z-averaged transverse angular change of the beam centroid per unit length,  $L_g$  is the cavity spacing,  $\Delta p_\perp$  is the change in transverse momentum, and  $p_z$  is the longitudinal momentum. The strength of the coupling between the beam and the dipole field is represented by the term  $G = c \omega_0 (Z_1/Q) I / (L_g I_0)$ , where  $I_0 = mc^3/e = 17$  kA. For solenoidal focusing  $k_\beta$  should be interpreted as one half of the cyclotron wave number and  $\xi$  is equal to the phasor  $x + iy$ . In the RK-TBA concept the average energy of the induction beam remains constant over an extraction-reacceleration cycle. In the continuous distribution approximation I will treat  $\gamma$  as a constant.

Equations (1) and (2) can be solved by Fourier transforming from  $t$  to  $\omega$  and using the WKB method. The transform inversion to recover  $\xi$  can only be done analytically in a few special cases of initial/boundary conditions. However, general information on the growth of the transverse instability can be obtained if two simplifying assumptions are made;

$$k_\beta^2 \gg \frac{\omega_0^2 G}{\gamma (\omega_0^2 - \omega^2 - i \omega_0 \omega / Q)}$$

and the instability growth is sharply peaked near the resonance,  $\omega = \omega_0$ . The solution can then be approximated as:

$$\xi \approx \frac{A(\omega_0) \omega_0}{2\pi Q} \exp\left(-i\omega_0 t + i \int_0^z k_\beta - \frac{i G Q}{2\gamma k_\beta} dz\right) \sim \exp\left[\frac{G Q z}{2\gamma k_\beta}\right], \quad (3)$$

where  $A(\omega_0)$  is determine by boundary conditions. Equation (3) exhibits the exponential growth with distance that is characteristic of this instability.

Phase mixed damping due to a spread in energy across the beam can be included in the analysis by using

the techniques of hose instability theory.<sup>6</sup> The beam is divided into "beamlets" with different energies, oscillation amplitudes, and betatron wavelengths such that  $k_\eta^2 = \eta k_\beta^2$ , where  $k_\beta$  is the maximum wave number,  $0 \leq \eta \leq 1$ , and  $\xi_\eta$  are the associated oscillation amplitudes. The model equations are

$$\left(\frac{\partial^2}{\partial t^2} + \frac{\omega_0}{Q} \frac{\partial}{\partial t} + \omega_0^2\right) \Delta = \omega_0^2 G(\xi)/\gamma, \text{ and} \quad (4)$$

$$\frac{\partial^2 \xi_\eta}{\partial z^2} + k_\eta^2 \xi_\eta = \Delta, \text{ where} \quad (5)$$

$$G(\xi) = \int_0^1 g(\eta) \xi_\eta d\eta, \gamma = \int_0^1 g(\eta) \gamma_\eta d\eta, \text{ and} \int_0^1 g(\eta) d\eta = 1.$$

For this analysis, let the distribution function be:

$$g(\eta) = \begin{cases} 0 & \text{for } 0 \leq \eta < 1 - \epsilon \\ 1/\epsilon & \text{for } 1 - \epsilon < \eta \leq 1 \end{cases} \quad (6)$$

A dispersion relationship can be obtained from equations (4) and (5) by Fourier transforming  $\omega$  to  $t$  and  $z$  to  $k$  and using the distribution in equation (6):

$$1 = \frac{\omega_0^2 G}{\gamma (\omega_0^2 - \omega^2 - i \omega_0 \omega / Q) \epsilon k_\beta^2} \ln \left[ \frac{k_\beta^2 - k^2}{k_\beta^2 (1 - \epsilon) - k^2} \right] \quad (7)$$

I will again assume that the greatest growth in the instability occurs when  $\omega = \omega_0$ , and then solve for  $k$ :

$$k^2 = k_\beta^2 \left( 1 + \frac{\epsilon e^{i\phi}}{1 - e^{i\phi}} \right) = k_\beta^2 \left( 1 - \frac{\epsilon}{2} + i \frac{\epsilon}{2} \cot \left( \frac{\phi}{2} \right) \right) \quad (8)$$

where  $\phi = \epsilon \gamma k_\beta^2 / (GQ)$ . If  $\phi = \pi$ ,  $k$  will be a purely real number and  $\xi$  will not exhibit exponential growth.

### III. Numerical Modeling

The Beam Breakup (BBU) Code<sup>7</sup> developed at LLNL was used to numerically study the transverse instability in a microwave generator comprised of many equally spaced traveling-wave structures (TWS). The BBU Code assumes a single dipole cavity mode is dominant and the x-polarization of the electric field in the  $n^{\text{th}}$  cavity can be expressed as

$$\vec{E}_n(\vec{r}, t) = f_n(t) \vec{\xi}_n(\vec{r}) e^{i\omega t}, \quad (9)$$

where  $\vec{\xi}_n$  denotes an eigenmode with eigenfrequency  $\omega_n$ . Here  $\omega$  denotes a characteristic frequency of the generator assumed near the transverse instability resonance. It is possible to show that the excitation amplitudes  $f_n$  are governed by the following circuit equations:

$$\frac{\partial^2 f_n}{\partial t^2} + \left( \frac{\omega_n}{Q_n} - 2i\omega \right) \frac{\partial f_n}{\partial t} + \left( \omega_n^2 - \omega^2 - \frac{i\omega\omega_n}{Q_n} \right) f_n =$$

$$K_n^{n-1} f_{n-1} + K_n^{n+1} f_{n+1} + \frac{\omega_n^3}{\epsilon c^2} \left( \frac{Z_\perp}{Q} \right)_n \frac{\partial I_x}{\partial t} e^{-i(\omega t + \phi_n)}, \quad (10)$$

where  $Q_n$  is the quality factor of the  $n^{\text{th}}$  cavity,  $K_n^{n\pm 1}$  denotes the coupling of the  $n$  and  $n\pm 1$  cavities,  $I$  is the current,  $x$  is the transverse displacement of the beam centroid in the  $x$  direction from the center line,  $\phi$  is a phase advance, and  $Z_\perp$  is the transverse impedance. A

second equation is used for the y-polarization as well as single particle equations of motion in the  $x$  and  $y$  directions. While equation (10) is similar to equation (4), there are several features in the BBU Code necessary for modeling a realistic structure:

- RF structures are treated as separate entities with specific rf properties,
- RF structures have a finite longitudinal length,
- Electromagnetic coupling can exist between adjacent rf cavities (needed for TWS cells),
- Variable current profiles can be used, and
- Actual solenoidal fields included for focusing.

The electromagnetic coupling of cells allows the effect of regenerative BBU to be modeled. A limitation is that the beam is treated as a series of rigid disks. Thus, beam parameters such as current and energy can only be varied longitudinally.

Modeling parameters used in the simulations presented below are given in Table 1. For some simulations five different configurations of TWS's were used. Two configurations were modeled after TWS's tested during the Choppertron experiments,<sup>1</sup> and a third after a structure to be tested in the near future. The final two configurations have rf characteristics bracketed by the others. De-Q-ing circuits<sup>8</sup> mentioned below refer to a technique for damping the dipole modes in TWS's used at LLNL. TWS's that are de-Q-ed are simulated by reducing the  $Q$  of the first two cells to about 20. In all the simulations the current is modulated at 11.4 GHz, the  $2\pi/3$  longitudinal mode of the TWS's, with each microbunch covering  $120^\circ$  of phase. Beam energy is kept constant, although it is possible to simulate energy extraction and reacceleration with the BBU Code.

TABLE 1.  
TWS Modeling Parameters in Simulations

dipole mode	lower "HEM <sub>11</sub> branch"
frequency (GHz)	13.75, 13.675, 13.6, 13.525, 13.45
phase advance	142.5° per cell
# cells per TWS	7
TWS electrical length	6.1278 cm
cell aperture (mm)	13, 13.5, 14, 15, 16
group velocity	0.12 c, 0.13c, 0.14c, 0.15c, 0.16c
$Q_{\text{wall}}$ (cells)	3000 (2), 7000 (5)
$Q_{\text{ext}}$ (damped cells)	20
$Z_\perp / Q_{\text{wall}}$	18.33 $\Omega$ /cell
TWS spacing	50 cm (center to center)
dc/rf currents	650/600 amps
pulse length	110 ns (includes 5 ns ramp time)
beam energy	10 MeV
initial offset	0.1 mm
solenoidal field ( $B_z$ )	8 KG

Figure 1 illustrates the effect of adding de-Q-ing circuits to the first two cells of the TWS's. The displacement of the beam centroid is measured midway between TWS's. Points are plotted whenever the centroid displacement has doubled after passing

through a TWS. The abrupt growth in the case of no de-Q-ing indicates the current was above the threshold for regenerative BBU in an individual TWS. With sufficient damping, as in the de-Q-ed case, cumulative BBU is the principle mechanism for instability growth. Figure 2 shows the effect of varying structures along the beam line (staggered tuning). For example the curve "5 TWS" represents a beam line comprised of repeating sets of five different TWS's. Structures are de-Q-ed in all cases. This effect is similar to lowering the Q for a single configuration. Figure 3 shows the effect of phase

mixed damping due to a longitudinal variation in energy along the beam (modulated at 11.4 GHz). Five different de-Q-ed TWS's are used in all cases. Larger spreads in gamma,  $\Delta\gamma$ , would require greater resolution (thinner current disks) for accuracy.

#### IV. Conclusions

It is essential to sufficiently damp the BBU resonances within individual TWS's to prevent the onset of regenerative BBU. It is also necessary to limit electromagnetic coupling between adjacent TWS's to avoid regenerative BBU between TWS's. This condition was assumed in the simulations. Phase mixing is the best means of defeating the cumulative instability, although large energy spreads will make beam transport more difficult. To further increase the practical number of rf output structures in an RK-TBA, I will examine more aggressive de-Q-ing, different TWS geometry's, and the use of standing-wave cavities. Also, additional work needs to be accomplished to determine a more realistic current density distribution and to model two-dimensional phase mixing.

#### V. Acknowledgments

I would like to thank G. Caporaso, J. Haimson, V.K. Neil, D. Whittum, and S. Yu for their advice and insights on beam instabilities. I thank G. Westenskow for guidance and encouragement.

#### VI. References

- [1] T.L. Houck and G.A. Westenskow, "Status of the Choppertron Experiments," Proc. 16<sup>th</sup> Int'l LINAC Conf., Aug, 1992, pp. 498-500.
- [2] G.A. Westenskow, et. al., "Transverse Instabilities in a Relativistic Klystron Two-Beam Accelerator," Proc. 16<sup>th</sup> Int'l LINAC Conf., Aug, 1992, pp.263-267.
- [3] G.J. Caporaso, "The Control of Beam Dynamics in High Energy Induction LINACS," Proc. 13<sup>th</sup> Int'l LINAC Conf., June, 1986, pp. 17-21.
- [4] W.K.H. Panofsky and M. Bander, "Asymptotic Theory of Beam Break-Up in Linear Accelerators," Rev. Sci. Instrum. **39**, 206 (1968).
- [5] V.K. Neil and R.K. Cooper, "Coherent Instabilities in High Current Linear Induction Accelerators," Part. Accel. **1**, 111 (1970).
- [6] E.P. Lee, "Resistive Hose Instability of a Beam with the Bennett Profile," Physics Fluids **21**, Aug 1978, pp. 1327-1343.
- [7] T.L. Houck, et. al., "BBU Code Development for High-Power Microwave Generators," Proc. 16<sup>th</sup> Int'l LINAC Conference, Aug, 1992, pp. 495-497.
- [8] J.Haimson and B.Meckenburg, "Suppression of beam induced pulse shortening ...," SPIE Vol. 1629 Intense Microwave and Part. Beams III (1992), pp. 209-219.

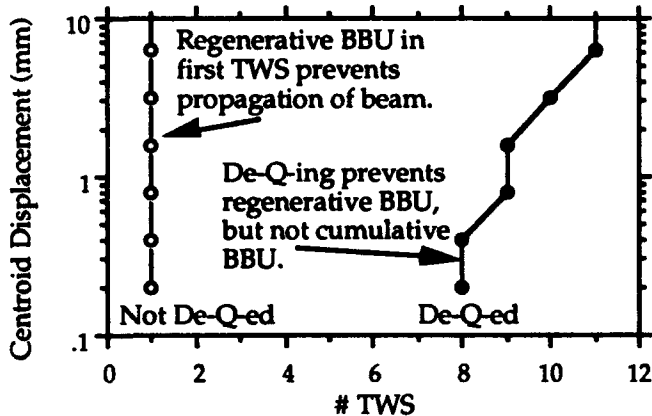


Figure 1. Effect of the de-Q-ing circuit.

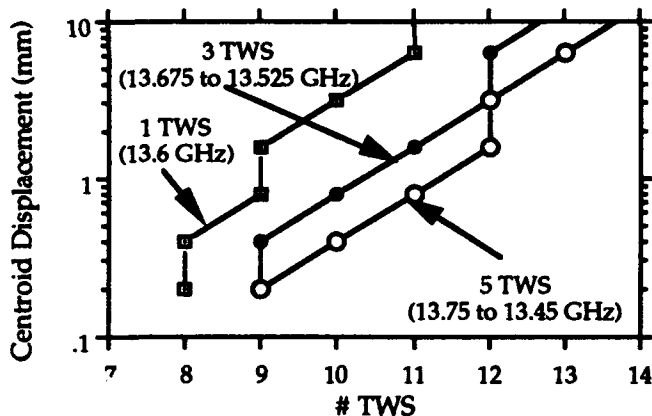


Figure 2. Effect of staggered tuning.

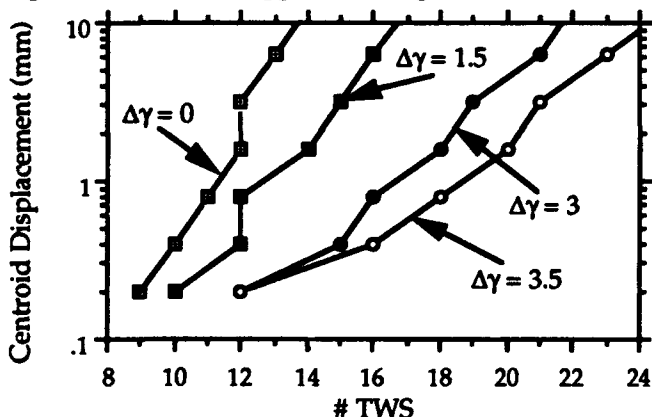


Figure 3. Effect of phase mixing due to energy spread.

# The Standing Wave FEL/TBA: Realistic Cavity Geometry and Energy Extraction\*

Jin-Soo Kim, Heino Henke<sup>(a)</sup>, Andrew M. Sessler, and William M. Sharp<sup>(b)</sup>  
Lawrence Berkeley Laboratory  
University of California, Berkeley, California 94720

## Abstract

A set of parameters for standing wave free electron laser two beam accelerators (SWFEL/TBA) is evaluated for realistic cavity geometry taking into account beam-break-up and the sensitivity of output power to imperfections. Also given is a power extraction system using cavity coupled wave guides.

## I. INTRODUCTION

For the next generation linear colliders, a high gradient acceleration structure is necessary. As a possible source of energy for such colliders, a SWFEL/TBA has been proposed[1,2]. A schematic diagram of a FEL/TBA is shown in Figure 1.

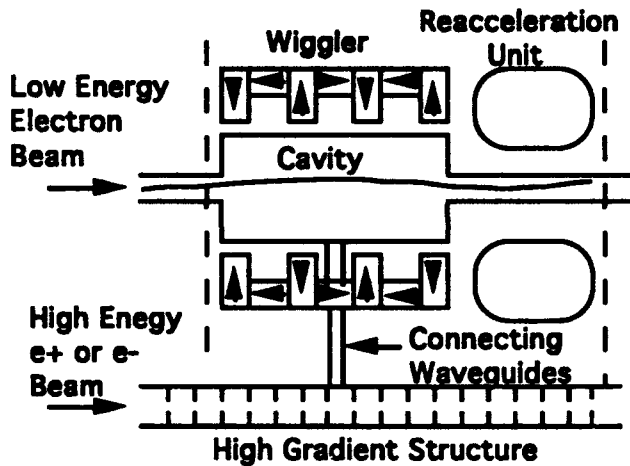


Figure 1. Schematic diagram of SWFEL/TBA

There have been some parameter studies of SWFEL/TBA parameters. Preliminary optimizations were made for the constancy of output energy and phase with respect to de-tuned energy for short pulse bunches[3]. The sensitivity has been reduced further by utilizing drift tubes between the cavities[4].

In this paper, we optimize the parameters with

\* The work was supported by the Director, Office of Energy Research, Office of High Energy and Nuclear Physics, Division of High Energy Physics, of the U. S. Department of Energy under Contract No. DE-AC03-76SF00098.

- (a) Permanent address: Technische Universitat Berlin, Institute fur Theoretische Elektrotechnik, Einsteinufer 17, D-1000 Berlin 10, Germany.  
(b) Permanent address: Lawrence Livermore National Laboratory, University of California, Livermore, California 94550, USA.

longer pulses (for better efficiency), with longer cavities (for BBU considerations[5]) than previously considered, and with realistic engineering constraints. Induction linacs have leakage current the order of 100 A and need much higher current than this level to be efficient. Switching time for such a high current takes about 10 nsec and thus beam pulse lengths significantly longer than this are needed for a good efficiency. An output energy of about 10 J/m is desired. Reacceleration can also not be too large, since about 30 cm long ferrite material is needed for 0.25 MeV reacceleration. With these constraints transverse and longitudinal beam dynamics are considered and lead to a set of parameters for SWFEL/TBA.

## II. BASIC MODEL

Within a cavity the particles and fields of a SWFEL can be examined by the conventional wiggler-averaged FEL equations[6]. Using the subscripts *s* for signal waves and *w* for wiggler quantities, and representing the vector potential by the usual normalized quantity  $a = A/(mc^2/e)$ , the equations for particle phase,  $\theta_j$ , the *j*-th particle energy,  $\gamma_j$ , and the field amplitude,  $a_s$ , with phase,  $\phi$ , are given by the following.

$$\frac{d\theta_j}{dz} = k_s + k_w - \frac{\omega_s}{c} - \frac{\omega_s}{2c\gamma_j^2} \left[ 1 + \frac{a_w^2}{2} - 2D_x a_w a_s \cos(\vartheta_j + \phi) \right],$$

$$\frac{d\gamma_j}{dz} = -D_x \frac{\omega_s}{c} \frac{a_w}{\gamma_j} a_s \sin(\vartheta_j + \phi), \quad (1)$$

$$\frac{d(a_s e^{i\phi})}{ds} = ic \left( \frac{2\gamma_r^2}{a_w} \right) \left( \frac{R}{Q} \right) \left( \frac{I}{I_a} \right) \left( \frac{e^{-i\vartheta_j}}{\gamma_j} \right)$$

Here,  $\gamma_r$  is the resonant beam energy, *I* is the average beam current, *z* is the axial coordinate, *s* is the distance from the leading bunch, and the jitter term  $D_x \approx 1/2$ . The angle brackets are averages over particles of a bunch. The brackets are redundant since in our analysis we make the approximation that only one macro particle per bunch. The shunt impedance is then given by

$$\frac{R}{Q} = \frac{4\pi}{VL\omega} \left| \int_{-L/2}^{+L/2} dz \frac{\bar{v}(z)}{v_z} \cdot \bar{a}(z) \exp\left(-\frac{i\omega z}{v_z}\right) \right|^2, \quad (2)$$

where  $\bar{v}$  is the particle velocity,  $v_z$  is the *z* component of the velocity,  $\omega$  is the FEL mode angular frequency, *V* is the volume of the cavity, and *L* is the length of the cavity.

Once a particle leaves a cavity, the FEL field bounces back to the other end of the cavity as a standing wave. Thus, the field should be updated accordingly.

The bunches in a pulse are then considered as blocks of  $2N$ . Since the particles do not interact much with the reflected waves, the first  $2N$  bunches behave identically where  $N = L/c$ . The next  $2N$  bunches see the reflected field of the previous  $2N$  bunches. Thus we need to examine only one bunch per every  $2N$  bunches. Utilizing the drift tubes between cavities, and by adjusting the beam energy for each  $2N$  particles, it is possible to make each  $2N$  particles behave identically through each cavity, thus yielding a stable high power energy for a long device as described in Reference [4].

The output energy is then proportional to the square of  $R/Q$  and the total charge of the pulse  $IL_p$ .

$$W_{out} \propto (IL_p)^2 \left(\frac{R}{Q}\right)^2 \quad (3)$$

The proportionality constant not shown in the above equation, depends on the geometry of the cavity.

### III. GEOMETRY EFFECT

The geometry of cavities and irises affect the field equation, the third equation of Eq.(1), through  $R/Q$ . Although the quantity  $R/Q$  depends on the beam energy and wiggler fields, the geometry dependence affects the FEL performance through this quantity only. Thus, we can evaluate FEL performance for various geometry by simply evaluating this quantity and using the usual FEL equations.

Now it is easy to understand the geometry effect since the geometry term affects only the field equation, and at the same time the averaged beam current affects only the field equation. Therefore, the geometry effect can be easily compensated by adjusting current, keeping  $IR/Q$  constant. Thus sensitivity of output power to various errors is as in an ideal cavity. The output energy may be different. This, however, is not a problem since it is necessary to have constant output energy but the magnitude of the energy is not so important.

### IV. NUMERICAL RESULTS

Eq.(1) is advanced by the fourth order Runge-Katta method. Assuming no slippage between particles and fields, the field equations are evolved in  $z$  (replacing  $s$  by  $z$ ). The initial field phase was set to zero and the initial particle phase is given as  $\pi/3$ .

A typical evolution of FEL variables, in the absence of errors, are illustrated in Figure 2. In the absence of any errors, the dynamics of each  $2N$  block is the same for the cavities. Thus only the first 3 cavities are shown. The particle lose energy (a) as it traverses a cavity while the field amplitude increases (b). The lost energy of the particle is replenished before entering the next cavity, thus repeating the same motion again. In (c) particle phase, field phase, and the ponderomotive phase are shown.

For stable FEL performance, it is important to keep the ponderomotive phase  $\psi = \theta_j + \phi$  invariant. In principle we do not have to consider phase change of  $\theta$  and  $\phi$  independently. However, best results are obtained by minimizing the variation of the particle phase within a cavity,

by making the nonsinusoidal component of the particle phase equation in Eq.(1) small. For 17.1 GHz,  $k_w=0.16$  is good.

A set of parameters is summarized in Table 1, taking into account BBU, beam sensitivity and engineering

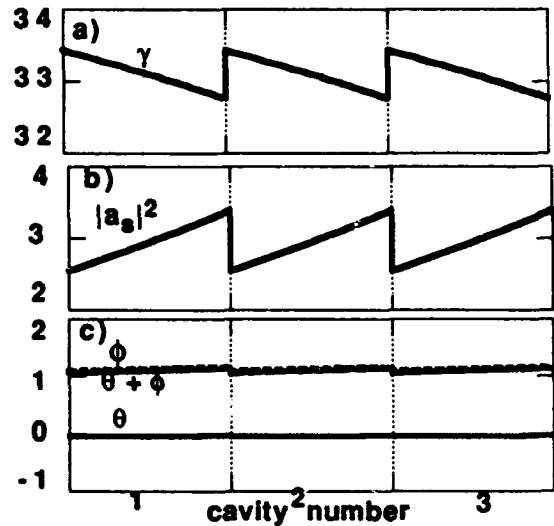


Figure 2. Particle energy (a), field energy (b), particle phase, field phase, and the ponderomotive phase (c) of  $j$ -th particle for the first three cavities. Drift tube regions are not shown, and simply indicated as a vertical dotted line.

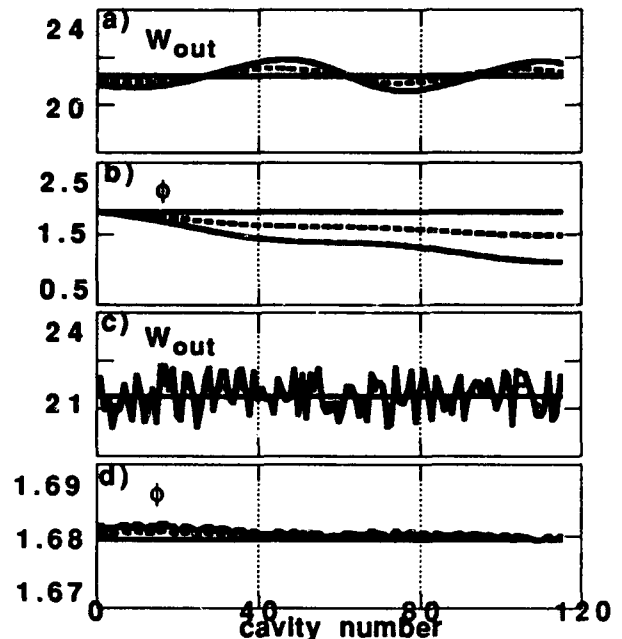


Figure 3. Output energy (a) and field phase (b) versus device length for 0% (straight line), 0.5% (dotted curve), and 1% (solid curve) de-tune in beam energy for the parameters in Table 1. The same quantities are shown in (c) and (d) for 0% (straight line), 2% (dotted curve), and 4% (solid curve) for random cavity errors in  $R/Q$ .

The bunches in a pulse are then considered as blocks of  $2N$ . Since the particles do not interact much with the reflected waves, the first  $2N$  bunches behave identically where  $N = L/c$ . The next  $2N$  bunches see the reflected field of the previous  $2N$  bunches. Thus we need to examine only one bunch per every  $2N$  bunches. Utilizing the drift tubes between cavities, and by adjusting the beam energy for each  $2N$  particles, it is possible to make each  $2N$  particles behave identically through each cavity, thus yielding a stable high power energy for a long device as described in Reference [4].

The output energy is then proportional to the square of  $R/Q$  and the total charge of the pulse  $IL_p$ .

$$W_{out} \propto (IL_p)^2 \left(\frac{R}{Q}\right)^2. \quad (3)$$

The proportionality constant not shown in the above equation, depends on the geometry of the cavity.

### III. GEOMETRY EFFECT

The geometry of cavities and irises affect the field equation, the third equation of Eq.(1), through  $R/Q$ . Although the quantity  $R/Q$  depends on the beam energy and wiggler fields, the geometry dependence affects the FEL performance through this quantity only. Thus, we can evaluate FEL performance for various geometry by simply evaluating this quantity and using the usual FEL equations.

Now it is easy to understand the geometry effect since the geometry term affects only the field equation, and at the same time the averaged beam current affects only the field equation. Therefore, the geometry effect can be easily compensated by adjusting current, keeping  $IR/Q$  constant. Thus sensitivity of output power to various errors is as in an ideal cavity. The output energy may be different. This, however, is not a problem since it is necessary to have constant output energy but the magnitude of the energy is not so important.

### IV. NUMERICAL RESULTS

Eq.(1) is advanced by the fourth order Runge-Katta method. Assuming no slippage between particles and fields, the field equations are evolved in  $z$  (replacing  $s$  by  $z$ ). The initial field phase was set to zero and the initial particle phase is given as  $\pi/3$ .

A typical evolution of FEL variables, in the absence of errors, are illustrated in Figure 2. In the absence of any errors, the dynamics of each  $2N$  block is the same for the cavities. Thus only the first 3 cavities are shown. The particle lose energy (a) as it traverses a cavity while the field amplitude increases (b). The lost energy of the particle is replenished before entering the next cavity, thus repeating the same motion again. In (c) particle phase, field phase, and the ponderomotive phase are shown.

For stable FEL performance, it is important to keep the ponderomotive phase  $\psi = \theta_j + \phi$  invariant. In principle we do not have to consider phase change of  $\theta$  and  $\phi$  independently. However, best results are obtained by minimizing the variation of the particle phase within a cavity,

by making the nonsinusoidal component of the particle phase equation in Eq.(1) small. For 17.1 GHz,  $k_w=0.16$  is good.

A set of parameters is summarized in Table 1, taking into account BBU, beam sensitivity and engineering

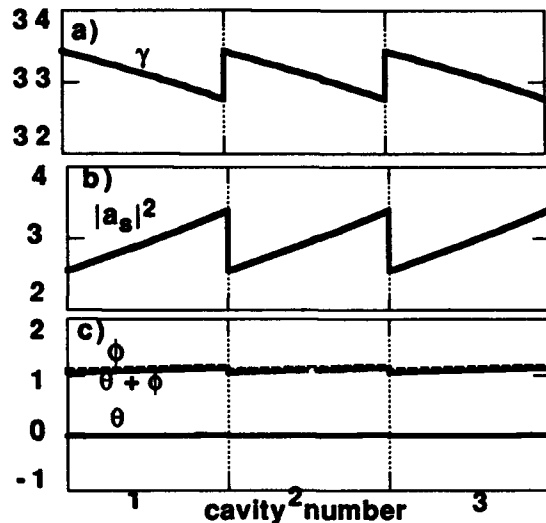


Figure 2. Particle energy (a), field energy (b), particle phase, field phase, and the ponderomotive phase (c) of  $j$ -th particle for the first three cavities. Drift tube regions are not shown, and simply indicated as a vertical dotted line.

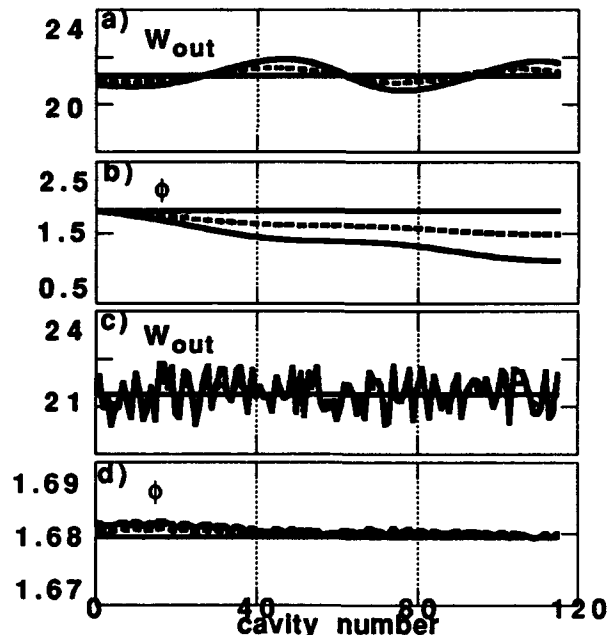


Figure 3. Output energy (a) and field phase (b) versus device length for 0% (straight line), 0.5% (dotted curve), and 1% (solid curve) de-tune in beam energy for the parameters in Table 1. The same quantities are shown in (c) and (d) for 0% (straight line), 2% (dotted curve), and 4% (solid curve) for random cavity errors in  $R/Q$ .

# THE ARGONNE WAKEFIELD ACCELERATOR- OVERVIEW AND STATUS\*

P. Schoessow, E. Chojnacki, W. Gai, C. Ho, R. Konecny,  
J. Power, M. Rosing, J. Simpson  
Argonne National Laboratory, 9700 S. Cass Ave., Argonne IL 60439

## Abstract

The Argonne Wakefield Accelerator (AWA) is a new facility for advanced accelerator research, with a particular emphasis on studies of high gradient ( $\sim 100$  MeV/m) wakefield acceleration. A novel high current short pulse L-Band photocathode gun and preaccelerator will provide 100 nC electron bunches at 20 MeV to be used as a drive beam, while a second high brightness gun will be used to generate a 5 MeV witness beam for wakefield measurements. We will present an overview of the various AWA systems, the status of construction, and initial commissioning results.

## Introduction

The goal of the AWA program is to develop wakefield based high gradient acceleration techniques for future linear colliders. In the process of developing the drive beam previously unexplored regimes of rf photocathode source operation will be investigated.

The AWA project is planned as a series of phases, leading up to a 1 GeV demonstration linac based on wakefield technology. Phase I of the AWA is presently nearing completion, and consists of an L-band 20 MeV drive linac and photocathode source capable of delivering 100 nC, 20 ps (FWHM) pulses, a 5 MeV high brightness photocathode gun to provide a witness beam as a probe of wakefields generated by the drive beam, and associated instrumentation for beam monitoring and wakefield measurements. A plan view of AWA Phase I is shown in figure 1. Additional details of the various AWA subsystems may be found in other papers at this conference ([1-4]).

## High Current Photocathode Source and Drive Linac

At the core of the AWA is a laser photocathode source, capable of delivering 2 MeV, 100 nC electron bunches to the drive linac. The source represents a significant extension of present photocathode gun capabilities, and several novel techniques have been developed to deal with the challenge of generating a beam of this intensity. Details of the gun design and beam dynamics simulations may be found in reference [5].

\*Work supported by U.S. Department of Energy, Division of High Energy Physics, Contract W-31-109-ENG-38

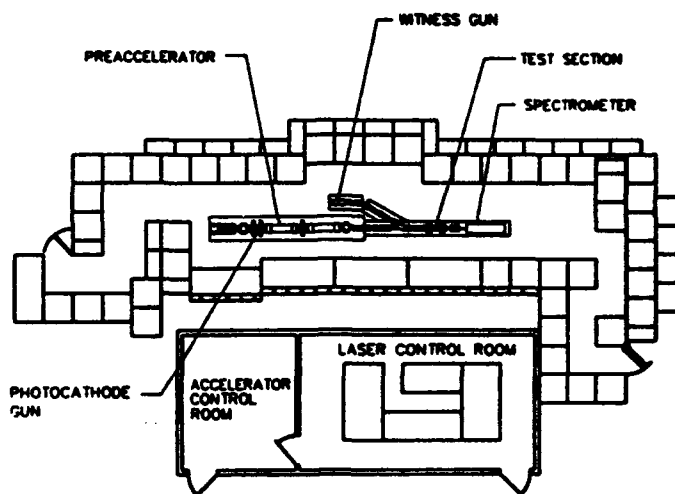


Figure 1. Plan view of AWA Phase I

In order to minimize radial space charge forces during the photoemission process, a large photocathode (2 cm diameter) is used. In addition, a curvature of the laser wavefront is induced using special optics [1]. Simulations indicate an optimal shape for the laser wavefront to be concave (electrons farther out in radius are emitted first), with a sagitta of 17 ps.

There is a strong correlation between the radial position and energy of the electron pulse emitted from the gun. In order to minimize the spot size at the exit of the drive linac, solenoids employing nonlinear focussing (spherical aberration) were designed. The shape of the magnetic field can be modified if necessary by changing the iron pole pieces.

Two standing wave iris-loaded cavities are used to accelerate the drive beam to 20 MeV [3]. In order to minimize wakefield effects in the linac, large diameter (10 cm) irises are used. The drive linac is shown in figure 2.

## Witness gun and wakefield measurement system

The witness gun [4] is used to generate a low current, small emittance pulse which acts as a probe of wakefields generated by the drive bunch. A 6-cell iris-loaded L-band cavity operating in the  $2\pi/3$  mode produces 0.1 nC, 5 MeV bunches with a transverse emittance

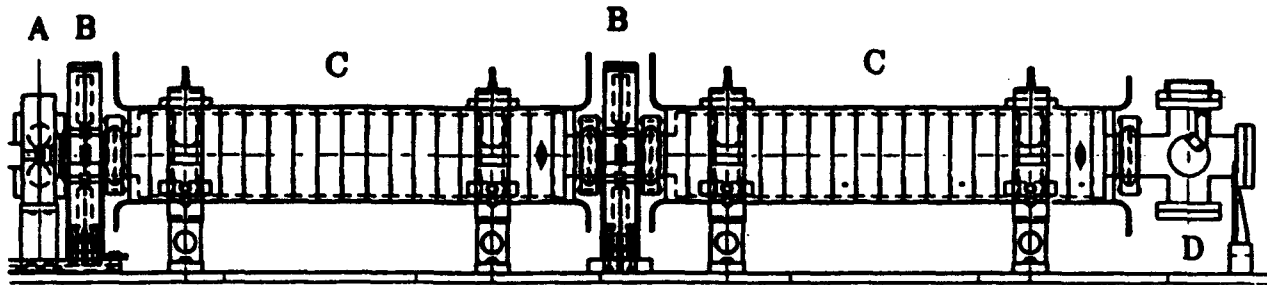


Figure 2. Drive linac. A: Photocathode gun, B: Nonlinear focussing solenoids, C: Linac cavities, D: Laser injection port. The backing solenoid which nulls the magnetic field at the photocathode is not shown.

$\leq 1 \pi$  mm-mrad. The delay between the witness and drive bunches is adjusted by varying the witness gun rf and laser injection phases simultaneously.

A simple chicane is used to transport the drive and witness bunches through the test section containing the wakefield device under measurement. For the initial experiments the drive and witness beams will pass collinearly through the test section. Measurements requiring noncollinear (parallel) drive and witness bunches, such as those involving wakefield transformer structures (see below) are possible with a slight reconfiguration of the beamline.

After passing through the test section, the beams are diagnosed using a magnetic spectrometer. A typical wakefield experiment involves measuring the energy modulation and transverse deflection of the witness bunch as a function of the relative drive-witness delay.

### Laser

The AWA laser system is used for both drive and witness beam generation. The laser can produce 8 mJ, 2 ps pulses at 248 nm. This is sufficient to permit the use of robust but low quantum efficiency photocathode materials such as Yttrium or Copper.

An annular mirror array [1] is used to introduce a curvature of the laser wavefront for drive beam generation. The laser pulse delivered to the witness gun is not shaped.

### Diagnostics

The AWA will make extensive use of luminescent screen beam position monitors viewed by CCTV cameras. The video signal can be digitized for analysis and storage [2]. Button pickups for nondestructive monitoring will be located at various places around the AWA beamlines.

Gas Cherenkov cells are used to diagnose the pulse length of the 20 MeV drive beam. The duration of the Cherenkov light flash can be measured by the streak camera with a 2 ps resolution.

Diagnosing the 2 MeV high current source presents special problems. The transverse bunch shape can be measured using a luminescent screen, but the bunch energy is too low for gas Cherenkov cells to be used as longitudinal diagnostics. Multiple scattering effects in general limit the utility of higher refractive index radiators.

A diagnostic to measure the shape of the leading edge of the drive bunch at the gun exit is under development and is shown schematically in fig 3. A series of quartz beads strung on a thin tungsten wire. Cherenkov light generated by the beam impinging on the bead array is transported to the streak camera. Because of multiple scattering and multiple reflection effects the streak length gives only an upper limit on bunch length at that point. However, the start of each streak gives the time of arrival of the leading edge of the bunch at the corresponding bead.

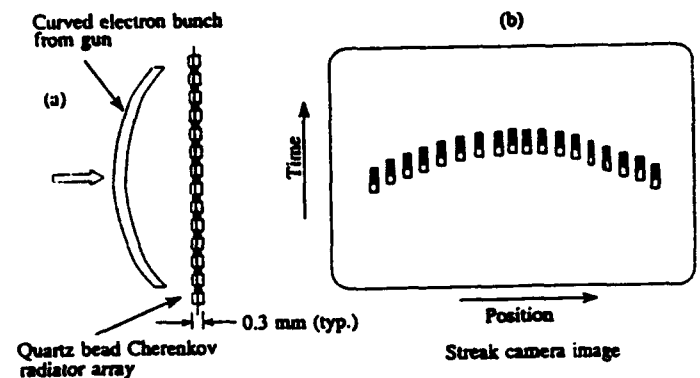


Figure 3. Bead array diagnostic for measuring the shape of the electron pulse emitted from the rf gun.

### Experimental program

The generation of 20 ps, 100 nC electron bunches from the drive linac is in itself an important experiment. Of particular interest is the characterization of the drive gun

and comparison of measured beam parameters with the predictions of the codes used for the design simulations.

The first wakefield experiments will concentrate on the study of breakdown, charging and radiation damage effects in high gradient collinear dielectric structures. These issues will need to be resolved for any practical dielectric-based wakefield accelerator.

The noncollinear drive-witness configuration will be used to investigate wakefield transformer schemes which offer the potential of generating high accelerating gradients without the stringent injection tolerances required by collinear geometries to suppress single bunch beam breakup effects. One particular class of devices being developed by the AWA group are coupled wake tube structures [6]. The wake generated by the drive bunch in a dielectric loaded guide is transferred via quarter wave matching section to a smaller bore accelerating structure. Figure 4 shows a numerical calculation of the gradient step up for a particular geometry as a function of matching section length, demonstrating that the expected transfer efficiency can be attained. Note that the optimum matching section length is, as expected, slightly less than  $\lambda/4$  due to end effects.

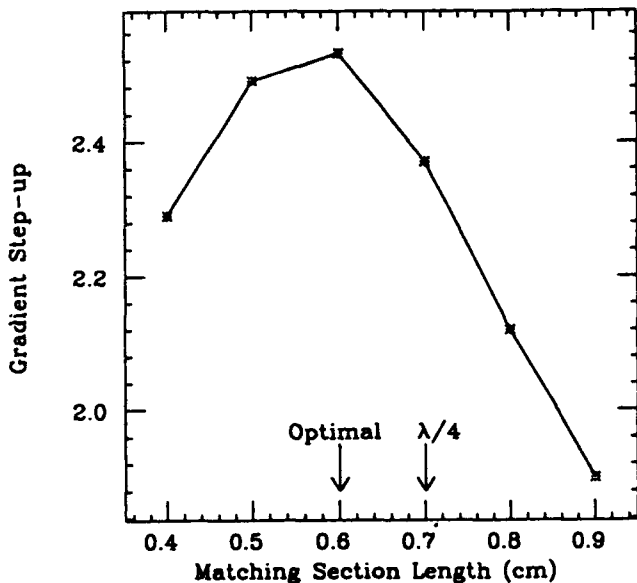


Figure 4. Numerical simulation of gradient step up as a function of matching section length for a 20 GHz coupled wake tube transformer. The expected step up of 2.5 is attained.

The drive bunch generated at the AWA is sufficient to perform the first experimental investigations of the Briezman effect in plasma wakefield acceleration [7]. In this regime all electrons are ejected from the plasma behind the drive bunch, resulting in extraordinary gradients. The plasma wakefield experiment planned at the AWA is predicted to generate gradients of 1 GeV/m.

## Status and Commissioning

The drive linac components have been fabricated and assembled, and witness gun fabrication is underway. After a setback due to the default of the vendor, the rf system is nearing completion, and cavity conditioning is expected to begin this summer. Commissioning of Phase I of the AWA will be completed by the end of CY1993.

## References

- [1] W. Gai, J. Simpson, N. Hill, C. Ho, P. Schoessow, these proceedings
- [2] P.Schoessow, C.Ho, J.Power, E.Chojnacki, these proceedings
- [3] E. Chojnacki, R. Konecny, J. Simpson, M. Rosing, these proceedings
- [4] J. Power and E. Chojnacki, these proceedings
- [5] C.Ho, PhD Thesis, UCLA 1992
- [6] E.Chojnacki et al., Proc. 1991 IEEE Particle Accelerator Conference, pp.2557-2559
- [7] J.Rosenzweig, B.Breizman, T.Katsouleas, J.Su, Phys Rev A 44, R6189 (1991).

# A Self-Consistent Theory of Ferromagnetic Waveguide Accelerators Driven by Electron Beams

Han S. Uhm

Naval Surface Warfare Center  
10901 New Hampshire Ave, White Oak  
Silver Spring, Maryland 20903-5640

## Abstract

A fully self-consistent theory of ferromagnetic waveguide accelerators driven by a relativistic electron beam is developed. The theoretical analysis is based on Faraday's law, which provides a second-order partial-differential equation of the azimuthal magnetic field, under the assumption that  $\mu\epsilon \gg 1$ . Here  $\mu$  and  $\epsilon$  are the permeability and dielectric constant of the waveguide material. The azimuthal magnetic field and axial acceleration field are obtained in forms of integral equations for an arbitrary profile of the drive-beam current  $I(t)$ .

## I. INTRODUCTION

An induced electric field appears whenever the magnetic field changes in time. This induced electric field is an excellent means for charged particle acceleration. One of the most advanced devices for intense electron beam accelerators is the induction linear accelerator (Linac),<sup>1</sup> where each module of many local accelerators applies its electric field to a cluster of traveling electrons. The electric field of each local accelerator in Linac originates from the time varying magnetic field, which is excited by an electrical current carried by a wire. In recent years, there has been a strong progress in the high-current electron-beam technology. Electron beams with an energy of 10 MeV and a current of 10 kA are easily available in the present technology. In addition, a tremendous improvement has been made in the effective control of these electron beams, including the focus, modulation, and a timely termination of the beam current. Thus, the electron beam itself is used as a drive current in the wakefield accelerators, where a short and intense bunch of electrons passes through a plasma<sup>2-4</sup> or dielectric waveguide,<sup>5-7</sup> leaving behind intense electromagnetic field. The axial component of this electromagnetic field accelerates charged particles in the witness beam, which follows the drive electron beam. Based on the transverse magnetic (TM) waveguide modes, a preliminary theory<sup>6,7</sup> has been developed to estimate the acceleration field, which is the fundamental-radial mode in most cases. However, in reality, the acceleration field is a sum of the whole radial modes, which is a complicated function of various physical parameters,

including the geometric configuration, the material properties of the waveguide, and so on. In addition, evolution of the acceleration field in time is again a sum of the every radial-mode evolution. In this regard, we develop a fully self-consistent theory of the wakefield accelerators, which consists of a waveguide with a ferromagnetic material.

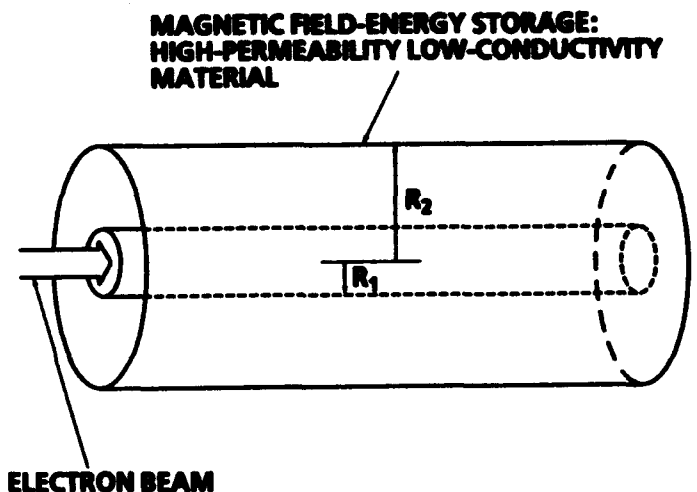


Fig. 1. Ferromagnetic waveguide accelerators.

## II. BASIC ASSUMPTIONS

The theoretical model is based on the induced electric field due to decay of the field energy stored in an energy storage device. As shown in Fig. 1, we assume that an electron beam with current  $I(t)$  propagates through a hole with radius of  $R_1$  in the field-energy storage with radius of  $R_2$ . Note that the electron-beam current  $I(t)$  carries both charge and current, which store the electric- and magnetic-field energies in the energy storage device. The line charge density  $\lambda(t)$  carried by the current  $I(t)$  is given by  $\lambda(t) = I(t)/\beta c$ , where  $\beta c$  is the beam velocity and  $c$  is the speed of light in vacuum. In the subsequent analysis, a polar coordinate system is introduced with the  $z$ -axis along the axis of symmetry,  $r$  represents the radial distance from the axis and  $\theta$  is the polar angle. The system is azimuthally symmetric around the axis. Due to a slowly changing current  $I(t)$ , the azimuthal magnetic field  $B_\theta$  in the energy storage material is given by

$$B_\theta(r,t) = \frac{2\mu I(t)}{cr} \quad (1)$$

This work was supported by the Independent Research Fund at the Naval Surface Warfare Center.

where  $\mu$  is the permeability of the energy storage material. Similarly, the radial electric field  $E_r$  in the range of  $r$  satisfying  $R_1 < r < R_2$  is given by

$$E_r(r,t) = \frac{2I(t)}{\epsilon\beta cr}, \quad (2)$$

where  $\epsilon$  is the dielectric constant of the energy storage material. The field energy associated with the magnetic and electric fields in Eqs. (1) and (2) is stored in the energy storage material.

We note from Eqs. (1) and (2) that the induced electric field due to the radial electric field  $E_r$  is negligible in comparison with that due to the azimuthal magnetic field  $B_\theta$  for the energy storage material with  $\epsilon\mu \gg 1$ , which is common in present applications. In this context, in the subsequent analysis, we use the relation

$$\frac{\partial}{\partial r} E_r(r,t) = \frac{1}{c} \frac{\partial}{\partial t} B_\theta(r,t) \quad (3)$$

in evaluation of the induced electric field resulted from a fast-changing drive current.

### III. ACCELERATING FIELD FOR DRIVE-BEAM $I(t)$

As shown in Eq. (3), the induced electric field increases drastically as the drive current decreases quickly. Remember that a high induced electric field is needed for efficient acceleration of charged particles. When the drive current changes quickly, the induced electric field must be determined in a self-consistent manner. Ampere's law in the Maxwell equation is written as

$$\nabla \times B = \frac{\mu\epsilon}{c} \frac{\partial E}{\partial t} + \frac{4\pi\mu}{c} J_T \quad (4)$$

where  $B$  is the magnetic field,  $E$  is the electric field, and the total current density  $J_T$  represents both the steady-state beam current and the induced current  $J_{in}$ . Assuming that the conductivity of the energy storage material is  $\sigma$ , the induced current density is expressed as  $J_{in} = \sigma E$ . Making use of Faraday's law, the curl of Eq. (4) is expressed as

$$\frac{\partial}{\partial r} \left[ \frac{1}{r} \frac{\partial}{\partial r} (rB_\theta) \right] - \frac{4\pi\sigma\mu}{c^2} \frac{\partial}{\partial t} B_\theta - \frac{\mu\epsilon}{c^2} \frac{\partial^2}{\partial t^2} B_\theta = 0, \quad (5)$$

in the storage device defined by the range of  $r$  satisfying  $R_1 < r < R_2$ . In obtaining Eq. (5), we have neglected the term  $(\partial^2/\partial z^2)B_\theta = (1/\beta^2 c^2)(\partial^2/\partial t^2)B_\theta$ , which is much less than the term proportional to  $\mu\epsilon$  in Eq. (5) provided  $\mu\epsilon \gg 1$ .

The solution of Eq. (8) is expressed as

$$B_\theta(r,t) = \int_0^\infty dk a_k J_1(kr) \exp(-\lambda_k t), \quad (6)$$

where  $J_1(x)$  is the Bessel function of the first kind of order one and  $\lambda_k$  is the generalized frequency. Substituting Eq. (6) into Eq. (5) and defining

$$\gamma_k = \frac{2\pi\sigma}{c}, \quad \alpha_k - i\omega_k = \sqrt{\frac{4\pi^2\sigma^2}{c^2} - \frac{k^2 c^2}{\mu\epsilon}}, \quad (7)$$

we find that the generalized frequency  $\lambda_k$  is expressed as

$$\lambda_k = \gamma_k - i\omega_k \quad (8)$$

Defining the critical wave number  $k_0$  by

$$k_0 = \frac{2\pi\sigma}{c} \sqrt{\frac{\mu}{\epsilon}}, \quad (9)$$

we can express the time profile of the solution in Eq. (6) by

$$q_k(t) = \exp(-\lambda_k t) = \exp(-\gamma_k t) \begin{cases} \exp(\alpha_k t), & 0 < k < k_0 \\ \cos(\omega_k t), & k > k_0 \end{cases} \quad (10)$$

which satisfies the initial and final conditions,  $q_k(t=0) = 1$  and  $q_k(t=\infty) = 0$ . Substituting Eq. (10) into Eq. (6), the desired solution is expressed as

$$B_\theta(r,t) = \int_0^\infty dk a_k J_1(kr) q_k(t). \quad (11)$$

We now calculate the magnetic field  $B_\theta(r,t)$  driven by the current  $I(t) = I(t')U(t-t')$ , where  $U(x)$  is the Heaviside step function defined by  $U(x) = 1$  for  $x > 0$  and 0, otherwise. It is obvious that  $B_\theta = 0$  for  $t < t'$  by the causality. The magnetic field at the time  $t > t'$  is expressed as

$$B_\theta(t) = \frac{2\mu I(t')}{cr} U[(R_2-r)(r-R_1)] + \int_0^\infty dk a_k J_1(kr) q_k(t-t'), \quad (12)$$

where the first term in the right-hand side represents the steady-state solution and the second term represents the time-transient solution. Note that the time-transient solution in Eq. (12) vanishes at the time  $t \rightarrow \infty$ . In obtaining Eq. (12), we have neglected the steady-state solution outside of the energy storage material, assuming that the magnetic permeability of the material is much higher than unity ( $\mu \gg 1$ ).

Making use of the initial condition  $q_k(t-t') = 1$  at  $t = t'$ , we obtain

$$\frac{2\mu I(t')}{cr} U[(R_2-r)(r-R_1)] + \int_0^\infty dk a_k J_1(kr) = 0, \quad (13)$$

from Eq. (12). Multiplying Eq. (13) by  $rJ_1(k'r)$  and making use of the orthogonality of the Bessel function

$$\int_0^\infty x dx J_1(\eta x) J_1(\xi x) = \frac{\delta(\xi-\eta)}{\xi}, \quad (14)$$

we obtain

$$a_k = 2\mu \frac{I(t')}{c} [J_0(kR_2) - J_0(kR_1)], \quad (15)$$

where  $J_0(x)$  is the Bessel function of the first kind of order zero. Substituting Eq. (15) into Eq. (12), the magnetic field at the time  $t > t'$  is therefore expressed as

$$B_\theta(r,t) = \frac{2\mu I(t')}{cr} + \frac{2\mu I(t')}{c} \int_0^\infty dk [J_0(kR_2) - J_0(kR_1)] J_1(kr) q_k(t-t'), \quad (16)$$

for  $R_1 < r < R_2$ .

It is necessary to evaluate the magnetic field due to the drive beam pulse defined by  $I(t) = I(t')U[(t' + \Delta t' - t)(t-t')]$  with the pulse length  $\Delta t'$ . Paralleling the derivation of Eq. (16), the magnetic field at the time  $t > t' + \Delta t'$  is given by

$$\Delta B_\theta(r,t) = -2\mu \frac{I(t')}{c} \int_0^\infty dk [J_0(kR_2) - J_0(kR_1)] J_1(kr) \left( \frac{d}{dt'} q_k \right) \Delta t', \quad (17)$$

which is the magnetic field contributed by a segment  $\Delta t'$  of the drive beam current  $I(t')$ . In obtaining Eq. (17), we have assumed that the pulse length  $\Delta t'$  is very small. Integrating Eq. (17) over the time  $t'$ , we can show that the magnetic field  $B_\theta(r,t)$  due to a continuous drive beam is expressed as

$$B_\theta(r,t) = -\frac{2\mu}{c} \int_0^\infty dk [J_0(kR_2) - J_0(kR_1)] J_1(kr) \int_{-\infty}^t dt' I(t') \frac{\partial}{\partial t'} q_k(t-t'), \quad (18)$$

which determines the magnetic field in the storage material for an arbitrary time profile of the drive beam current  $I(t')$ .

The induced axial-electric field  $E_z$  is proportional to

the time derivative of the azimuthal magnetic field as shown in Eq. (3). Substituting Eq. (18) into Eq. (3) gives

$$\frac{\partial}{\partial r} E_z(r,t) = -\frac{2\mu}{c^2} \int_0^\infty dk [J_0(kR_2) - J_0(kR_1)] J_1(kr) \int_{-\infty}^t dt' \left( \frac{dI}{dt'} \right) \frac{\partial}{\partial t'} q_k(t-t'), \quad (19)$$

where use has been made of the relation  $(\partial/\partial t)q_k = -(\partial/\partial t')q_k$ . Neglecting the azimuthal magnetic field outside the energy storage material ( $r > R_2$ ), we approximate the boundary condition of the axial electric field by  $E_z(r,t) = 0$  at  $r = R_2$ . Integrating Eq. (19) over the radius  $r$ , the axial electric field in the energy storage material ( $R_1 < r < R_2$ ) is given by

$$E_z(r,t) = -\frac{2\mu}{c^2} \int_0^\infty \frac{dk}{k} [J_0(kR_2) - J_0(kR_1)] J_0(kR_2) - J_0(kr) \int_{-\infty}^t dt' \left( \frac{dI}{dt'} \right) \frac{\partial}{\partial t'} q_k(t-t'). \quad (20)$$

Because we neglect the axial electric field due to the azimuthal magnetic field in the hole ( $r < R_1$ ), the axial electric field  $E_z$ , which accelerates the charged particles at the axis, is approximately given by the electric field at  $r = R_1$ . Equation (20), together with Eq. (18), is one of the main results of this article and can be used to determine the acceleration gradient for a broad range of physical parameters, including properties of the energy storage material, geometric configuration of the system, species of the charged particles, and intensity of the drive-beam current. Specific examples of application of Eq. (20) will be presented in the following papers.

#### IV. REFERENCES

- [1] C. A. Kapetanacos and P. Sprangle, *Phys. Today* **38**, 58 (1985).
- [2] P. Chen, J. M. Dawson, R. W. Huff, and T. Katsouleas, *Phys. Rev. Lett.* **54**, 693 (1985).
- [3] J. B. Rosenzweig, *Phys. Rev. A* **40**, 5249 (1989).
- [4] J. B. Rosenzweig and P. Chen, *Phys. Rev. D* **39**, 2039 (1989).
- [5] M. Rosing, E. Chojnaki, W. Gai, C. Ho, R. Konecny, S. Mtingwa, J. Norem, P. Schoessow, J. Simpson, *Proc. of 1991 IEEE Particle Accelerator Conference May 6-9, 1991, San Francisco, Cal. Vol. I*, 555 (1991).
- [6] E. Chojnaki, W. Gai, P. Schoessow, and J. Simpson, *Proc. of 1991 IEEE Particle Accelerator Conference May 6-9, 1991, San Francisco, Cal. Vol. IV*, 2557 (1991).
- [7] S. K. Mtingwa, *Phys. Rev. A* **43**, 5581 (1991).

# Wakefield Accelerator Driven by a Relativistic Electron Beam in a Ferromagnetic Waveguide

Han S. Uhm

Naval Surface Warfare Center  
10901 New Hampshire Ave, White Oak  
Silver Spring, Maryland 20903-5640

## Abstract

A novel high-gradient wakefield accelerator is presented in which the drive-beam current leaves behind a high-gradient wakefield, accelerating the witness beam to very high energy. The theoretical analysis is based on Faraday's law, which provides a second-order partial-differential equation of the azimuthal magnetic field, under the assumption that  $\mu\epsilon \gg 1$ . The accelerating field can be more than one half of one gigavolt/meter in an appropriate choice of system parameters.

## I. INTRODUCTION

In recent years, there has been a strong progress in the high-current electron-beam technology. Electron beams with an energy of 10 MeV and a current of 10 kA are easily available in the present technology. In addition, a tremendous improvement has been made in the effective control of these electron beams, including the focus, modulation, and a timely termination of the beam current. Thus, the electron beam itself is used as a drive current in the wakefield accelerators, where a short and intense bunch of electrons passes through a plasma<sup>1-3</sup> or dielectric waveguide,<sup>4-6</sup> leaving behind intense electromagnetic field. The axial component of this electromagnetic field accelerates charged particles in the witness beam, which follows the drive electron beam. Based on the transverse magnetic (TM) waveguide modes, a preliminary theory<sup>5,6</sup> in a dielectric waveguide accelerator has been developed to estimate the acceleration field, which is the fundamental-radial mode in most cases. However, in reality, the acceleration field is a sum of the whole radial modes, which is a complicated function of various physical parameters, including the geometric configuration, the material properties of the waveguide, and so on. In addition, evolution of the acceleration field in time is again a sum of the every radial-mode evolution. In this regard, I develop a fully self-consistent theory of the wakefield accelerators, which consists of a waveguide with a ferromagnetic material. As will be seen later, the accelerating field is proportional to the square root of the parameter  $\mu/\epsilon$ , where  $\mu$  and  $\epsilon$  are the permeability and dielectric constant of the waveguide material. The higher the permeability, the higher the accelerating field.

This work was supported by the Independent Research Fund at the Naval Surface Warfare Center.

## II. WAKEFIELD FOR THE ACCELERATION

The theoretical model is based on the induced electric field due to decay of the field energy stored in an energy storage device. We assume that an electron beam with current  $I(t)$  propagates through a hole with radius  $R_1$  in the field-energy storage with radius of  $R_2$ . The energy storage device is a waveguide with a ferromagnetic material. Whenever the drive-beam current  $I(t)$  decreases, the induced electric field  $E_z(r,t)$  appears in the system. The induced axial-electric field  $E_z$  is calculated from the Faraday's law and given by

$$E_z(R_1, t) = -\frac{2\mu}{c^2} \int_0^\infty \frac{dk}{k} [J_0(kR_2) - J_0(kR_1)]^2 \int_{-\infty}^t dt' \left( \frac{dI}{dt'} \right) \frac{\partial}{\partial t'} \alpha_k(t-t'), \quad (1)$$

where  $J_0(x)$  is the Bessel function of the first kind of order zero,

$$\alpha_k(t) = \exp\left(-\frac{2\pi\sigma}{\epsilon} t\right) \cos\left(\frac{kc}{\sqrt{\mu\epsilon}} t\right) \quad (2)$$

is the time function and  $\sigma$  is the residual conductivity in the material although it is very small (zero in a practical sense). Substituting Eq. (2) into Eq. (1) and carrying out partial integrations in time and radial coordinate, I obtain the accelerating field

$$E_z(t) = -\frac{2}{c} \sqrt{\frac{\mu}{\epsilon}} \int_{-\infty}^t dt' \left( \frac{dI}{dt'} \right) \int_0^\infty dk [J_0(kR_2) - J_0(kR_1)]^2 \sin\left[\frac{c(t-t')}{\sqrt{\mu\epsilon}} k\right], \quad (3)$$

where the abbreviation  $E_z(t)$  represents  $E_z(0,t)$ . In obtaining Eq. (3), I have neglected the terms proportional to the residual conductivity  $\sigma$ .

For convenience in the subsequent analysis, the normalized times  $\tau_1$  and  $\tau_2$  are defined by

$$\tau_1 = \frac{c(t-t')}{2R_1\sqrt{\mu\epsilon}}, \quad \tau_2 = \frac{c(t-t')}{2R_2\sqrt{\mu\epsilon}}, \quad (4)$$

where we note that  $\tau_1 = R_2 \tau_2 / R_1$ . For  $R_2 \gg R_1$ , the normalized time  $\tau_1$  is much longer than the time  $\tau_2$ . Making use of Eq. (4), we can rewrite Eq. (3) by

$$E_z(t) = -\frac{2}{cR_1} \sqrt{\frac{\mu}{\epsilon}} \int_{-\infty}^t dt' \left( \frac{dI}{dt'} \right) \int_0^{\infty} dx J_0^2(x) \cdot [\sin(2\tau_1 x) + \frac{R_1}{R_2} \sin(2\tau_2 x) - \frac{2R_1}{R_2} \frac{J_0(R_1 x/R_2)}{J_0(x)} \sin(2\tau_2 x)] \quad (9)$$

In the remainder of this article, the analysis is restricted to the case when the inner radius  $R_1$  of the energy storage device is much less than the outer radius  $R_2$ , i.e.,  $R_1 \ll R_2$ . In this limit, we note several points from Eqs. (4) and (5). First, the term proportional to  $\sin(2\tau_1 x)$  in the integrand in Eq. (5) dominates. The corrections associated with other terms are of the order  $(R_1/R_2)^{1/2}$  or less. Second, the peak values of the integration over the variable  $x$  in Eq. (5) occur around the time  $t$  satisfying  $\tau_1 = 1$ ,  $\tau_2 = 1$  and  $\tau_2 = (R_1/R_2)^{1/2}$ , which correspond to the contributions from the terms proportional to  $\sin(2\tau_1 x)$ ,  $(R_1/R_2)\sin(2\tau_2 x)$  and  $J_0(R_1 x/R_2)$ , respectively, in the right-hand side of Eq. (5). In the early stage, the term proportional to  $\sin(2\tau_1 x)$  dominates. In this regard, we keep the term proportional to  $\sin(2\tau_1 x)$  in Eq. (5), neglecting other terms. If needed, the corrections associated with other terms can be calculated in a straightforward manner.

The integration over the variable  $x$  is carried out by making use of the integral<sup>7</sup>

$$\pi \int_0^{\infty} dx J_0^2(x) \sin(2\tau_1 x) = \begin{cases} K(\tau_1), & \tau_1 < 1, \\ \frac{1}{\tau_1} K\left(\frac{1}{\tau_1}\right), & \tau_1 > 1, \end{cases} \quad (6)$$

where  $K(x)$  is the elliptical function of the first kind defined by

$$K(x) = \frac{\pi}{2} \left[ 1 + \left(\frac{1}{2}\right)^2 x^2 + \left(\frac{1 \cdot 3}{2 \cdot 4}\right)^2 x^4 + \dots \right] \quad (7)$$

After carrying out a straightforward calculation, I show that the acceleration field  $E_z$  in Eq. (5) is approximated by

$$E_z(t) = -\frac{2}{\pi c R_1} \sqrt{\frac{\mu}{\epsilon}} \int_{-\infty}^t dt' \left( \frac{dI}{dt'} \right) \cdot [K(\tau_1) U(1-\tau_1) + \frac{1}{\tau_1} K\left(\frac{1}{\tau_1}\right) U(\tau_1-1)], \quad (8)$$

where  $U(x)$  is the Heaviside step function. Equation (8) can be used to calculate the acceleration-gradient field for a broad range of system parameters, where the drive current changes fast. Note that the drive-beam current  $I(t)$  in Eq. (8) is not specified yet.

In order to investigate the long pulse-driven accelerator, we consider the drive current defined by

$$I(t) = \begin{cases} I_m, & t < 0, \\ I_m \left(1 - \frac{t}{\Delta t}\right), & 0 < t < \Delta t, \\ 0, & t > \Delta t, \end{cases} \quad (9)$$

where the parameter  $\Delta t$  is the termination time of the drive beam current. In reality, the drive-beam current  $I(t)$  at  $t < 0$  increases very slowly to  $I_m$  at  $t = 0$ . Thus, Eq. (9) is a good approximation. Substituting Eq. (9) into Eq. (8), and making use of the definitions in Eq. (4) and

$$\tau = \frac{ct}{2R_1 \sqrt{\mu \epsilon}}, \quad \eta = \frac{c \Delta t}{2R_1 \sqrt{\mu \epsilon}}, \quad (10)$$

the acceleration field can be expressed as

$$E_z(t) = -\frac{2I_m}{\pi R_1 c} \sqrt{\frac{\mu}{\epsilon}} q(\tau), \quad (11)$$

where the function  $q(\tau)$  for the drive current in Eq. (9) is defined by

$$q(\tau) = \frac{1}{\eta} \int_0^{\tau} dt' U(\eta - \tau') [K(\tau_1) U(1-\tau_1) + \frac{1}{\tau_1} K\left(\frac{1}{\tau_1}\right) U(\tau_1-1)], \quad (12)$$

and  $\tau' = \tau - \tau_1$ .

Figure 1 presents plots of the function  $q(\tau)$  versus the normalized time  $\tau$  obtained from Eq. (12) for  $\eta = 0.05$  (solid line), 0.1 (broken line), 0.2 (dotted line), and 0.4 (thin broken line). Several points are noteworthy in Fig. 1. First, the shorter the normalized termination time the higher the peak value of the function  $q$ . Second, the peak value of the function  $q(\tau)$  is about 2.5 even for a relatively slow termination time. This peak value occurs at  $\tau = 1$ . Third, the function  $q(\tau)$  is always positive for the choice of the drive current in Eq. (9). Fourth, the value of the function  $q$  in the range of  $\tau$  satisfying  $0 < \tau < \eta$  increases linearly with time  $\tau$ . As we note from Eq. (9), the drive current decreases linearly to zero in this range of  $\tau$ . Because the  $q$  value of this tail portion of the drive beam increases with time, the termination slope stiffens further. This mechanism may decrease the normalized termination time  $\eta$  as time goes by. Finally, we emphasize that the time duration of the high acceleration field is quite broad. This property is important for a long witness beam. In the limit when the normalized termination time  $\eta$  is much less than unity, i.e.,  $\eta \ll 1$ , Eq. (12) is approximated by

$$q(\tau) = \begin{cases} \kappa\left(\frac{\tau}{2}\right) \frac{\tau}{\eta}, & 0 < \tau < \eta, \\ \kappa\left(\tau - \frac{\eta}{2}\right), & \eta < \tau < 1, \\ 1.4 + \frac{1}{2} \ln\left(\frac{2}{\eta}\right), & 1 < \tau < 1 + \eta, \\ \frac{1}{\tau} \ln\left(\frac{1}{\tau}\right), & \tau > 1 + \eta, \end{cases} \quad (13)$$

which agrees reasonably well with the numerical result in Fig. 1 even for  $\eta = 0.4$ .

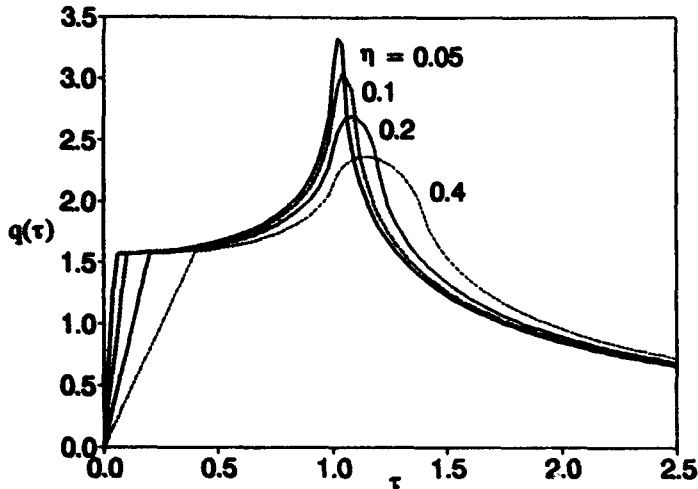


Fig. 1. Plots of the function  $q(\tau)$  versus the normalized time  $\tau$  obtained from Eq. (12) for  $\eta = 0.05$  (solid line), 0.1 (broken line), 0.2 (dotted line), and 0.4 (thin broken line).

As an example, I assume that the current termination parameter is equal to  $\eta = 0.05$ , for which the peak value of the function  $q$  is 3.2 and the accelerating field is given by

$$E_m = \frac{2I_m}{R_1 c} \sqrt{\frac{\mu}{\epsilon}}. \quad (14)$$

Assuming that the drive current  $I_m = 20$  kA, the hole radius  $R_1 = 0.4$  cm and  $\mu/\epsilon = 4$ , we find from Eq. (14) that the accelerating field is given by  $E_m = 0.6$  gigavolt/meter, which is very encouraging number. The current termination parameter  $\eta = 0.05$  corresponds to the real termination time of  $\Delta t = 2.6$  picosecond for  $\mu\epsilon = 4$ . As shown in Eq. (9), the risetime of the drive-beam current must be considerably longer than the termination time. The risetime of 26 picosecond may be enough for present example. The accelerating field in Eq. (14) for a ferromagnetic waveguide is six times of that in a dielectric waveguide<sup>5</sup> for similar system parameters. I remind the reader that the whole pulse length in the example is less than 1 cm, thereby practically indicating that the drive beam is an intense bunch of electrons. The total charge of the drive-beam current in the example is

less than 300 nanocoulomb. Tailoring the beam pulse as mentioned above is very important to achieve a high accelerating gradient. Obviously, the wakefield accelerator in a ferromagnetic waveguide has a great potential for high gradient acceleration of electrons.

In order to achieve the high acceleration field, we must overcome two technical problems. First, the magnetic field in the energy storage material is limited by the saturation field  $B_s$ , which is expressed as

$$B_s = \frac{2\mu I_m}{cR_1}. \quad (15)$$

Once the magnetic field in the storage material is saturated by the drive current  $I_m$ , any additional increase of the current does not help much. Eliminating the current  $I_m$  in favor of the saturation field  $B_s$ , we rewrite Eq. (14) as

$$E_m = \frac{B_s}{\sqrt{\mu\epsilon}}, \quad (16)$$

for the saturation current satisfying Eq. (15). Equation (16) clearly indicates that acceleration field is linearly proportional to the saturation field of the material. The higher the saturation field the higher the acceleration field. Second, reversal time of the magnetization in the storage material must be on the order of nanosecond or less. A sub-nanosecond reversal time has been accomplished several decades ago for a small amount of high-permeability materials with  $\mu$  of 100 or more.<sup>8</sup> However, the wakefield accelerator for a high-current beam requires a bulk storage material. Establishing a short reversal time of the magnetization in a bulk material may require further research on the material science.

### III. REFERENCES

- [1] P. Chen, J. M. Dawson, R. W. Huff, and T. Katsouleas, *Phys. Rev. Lett.* **54**, 693 (1985).
- [2] J. B. Rosenzweig, *Phys. Rev. A* **40**, 5249 (1989).
- [3] J. B. Rosenzweig and P. Chen, *Phys. Rev. D* **39**, 2039 (1989).
- [4] M. Rosing, E. Chojnaki, W. Gai, C. Ho, R. Konecny, S. Mtingwa, J. Norem, P. Schoessow, J. Simpson, *Proc. of 1991 IEEE Particle Accelerator Conference May 6-9, 1991, San Francisco, Cal. Vol. I*, 555 (1991).
- [5] E. Chojnaki, W. Gai, P. Schoessow, and J. Simpson, *Proc. of 1991 IEEE Particle Accelerator Conference May 6-9, 1991, San Francisco, Cal. Vol. IV*, 2557 (1991) and the references therein.
- [6] S. K. Mtingwa, *Phys. Rev. A* **43**, 5581 (1991).
- [7] I. S. Gradshteyn and I. M. Ryzhik, *Table of Integrals, Series, and Products*, (Academic Press, N.Y., New York 1980) Chap. 6.
- [8] M. Prutton, *Thin Ferromagnetic Films*, (Spottiswoode, Ballantyne and Co, London, 1964) Chap. 6.

# Magnetic Field-Decay Accelerator Driven by a Relativistic Electron Beam in a Ferromagnetic Waveguide

Han S. Uhm

Naval Surface Warfare Center  
10901 New Hampshire Ave, White Oak  
Silver Spring, Maryland 20903-5640

## Abstract

A novel high-gradient magnetic field-decay accelerator is presented in which the drive-beam leaves behind a high-gradient accelerating field produced by the magnetic field decay. The electromagnetic fields indicate a decaying function of the time. As an example, we obtain the acceleration field for the case of a short and intense drive bunch, which is represented by a parabolic function of time. With appropriate physical parameters, the acceleration gradient of the magnetic field-decay accelerator can be easily more than 150 megavolt/meter.

## I. INTRODUCTION

In recent years, there has been a strong progress in the high-current electron-beam technology. Electron beams with an energy of 10 MeV and a current of 10 kA are easily available in the present technology. In addition, a tremendous improvement has been made in the effective control of these electron beams, including the focus, modulation, and a timely termination of the beam current. Thus, the electron beam itself is used as a drive current in accelerators. In this presentation, we study the acceleration mechanism based on the magnetic field decay.<sup>1</sup> The magnetic field energy is stored in a high-permeability material by a continuous beam current. If the current drops abruptly, the magnetic field stored in the material decays, thereby generating an acceleration electric field. Physics of the accelerating field arising from the finite conductivity waveguide is very similar to that of the longitudinal resistive wall instability<sup>2,3</sup> which has been investigated for application to circular accelerators. In this presentation, a theory of the magnetic field diffusion is developed, in order to estimate the acceleration gradient whenever the sustaining beam current drops. As an example, we obtain the acceleration field for the case of a short and intense drive bunch, which is represented by a parabolic function of time. The acceleration field is given by  $E_m = 150$  MV/m, for the waveguide hole radius of  $R_1 = 0.5$  cm, the saturation magnetic field  $B_s = 15$  kG, and  $\Delta t = 10^{-10}$  second. Assuming that the parameter  $\mu\sigma = 80$  siemens/m,

the required drive current for the saturation field is given by  $\mu I_m = 660$  kA, which is equivalent to  $I_m = 660$  A for  $\mu = 1000$ . The total charge of this drive beam pulse is  $Q = 85$  nanocoulomb for  $I_m = 660$  A.

## II. EVALUATION OF ACCELERATING FIELD

The theoretical model is based on the induced electric field due to decay of the field energy stored in an energy storage device. We assume that an electron beam with current  $I(t)$  propagates through a hole with radius of  $R_1$  in the field-energy storage with radius of  $R_2$ . If the current drops abruptly, the magnetic field stored in the material decays, thereby generating an acceleration electric field

$$E_z(R_1, t) = -\frac{2\mu}{c^2} \int_0^\infty \frac{dk}{k} [J_0(kR_2) - J_0(kR_1)]^2 \int_{-\infty}^t dt' \left( \frac{dI}{dt'} \right) \frac{\partial}{\partial t'} q_k(t-t'), \quad (1)$$

where the time function  $q_k(\tau)$  is defined by

$$q_k(t-t') = \exp\left[-\frac{c^2 k^2}{4\pi\sigma\mu}(t-t')\right], \quad (2)$$

and  $\sigma$  and  $\mu$  are the conductivity and magnetic permeability of the energy storage material. Substituting Eq. (2) into Eq. (1), we show that the acceleration electric field  $E_z$  is expressed as

$$E_z(t) = -\frac{1}{2\pi\sigma} \int_{-\infty}^t dt' \left( \frac{dI}{dt'} \right) \int_0^\infty dk k [J_0(kR_2) - J_0(kR_1)]^2 \exp\left[-\frac{c^2(t-t')}{4\pi\sigma\mu} k^2\right]. \quad (3)$$

For convenience in the subsequent analysis, we define the normalized times  $\zeta$  and  $\zeta'$  by

$$\zeta = \frac{c^2 t}{2\pi\sigma\mu R_1^2}, \quad \zeta' = \frac{c^2 t'}{2\pi\sigma\mu R_1^2}. \quad (4)$$

This work was supported by the Independent Research Fund at the Naval Surface Warfare Center.

Making use of Eq. (4), Eq. (3) is rewritten as

$$E_z(t) = - \frac{1}{2\pi\sigma R_1^2} \int_{-\infty}^t dt' \left( \frac{dI}{dt'} \right) \int_0^{\infty} dx x [J_0(xR_2/R_1) - J_0(x)]^2 \exp\left[-\frac{(\zeta - \zeta')}{2} x^2\right]. \quad (5)$$

The integration over the variable  $x$  is carried out by making use of the integral<sup>4</sup>

$$\int_0^{\infty} x dx \exp(-\rho^2 x^2) J_p(\alpha x) J_p(\beta x) = \frac{1}{2\rho^2} \exp\left(-\frac{\alpha^2 + \beta^2}{4\rho^2}\right) I_p\left(\frac{\alpha\beta}{2\rho^2}\right) \quad (6)$$

of the Bessel functions. The accelerating field in Eq. (5) is expressed as

$$E_z(t) = - \frac{1}{2\pi\sigma R_1^2} \int_{-\infty}^t dt' \left( \frac{dI}{dt'} \right) \frac{1}{\delta\zeta} \left[ \exp\left(-\frac{1}{\delta\zeta}\right) I_0\left(\frac{1}{\delta\zeta}\right) + \exp\left(-\frac{1}{\delta\zeta} \frac{R_2^2}{R_1^2}\right) I_0\left(\frac{1}{\delta\zeta} \frac{R_2^2}{R_1^2}\right) - 2 \exp\left(-\frac{1 + R_2^2/R_1^2}{2\delta\zeta}\right) I_0\left(\frac{1}{\delta\zeta} \frac{R_2}{R_1}\right) \right]. \quad (7)$$

where  $\delta\zeta = \zeta - \zeta'$ .

The contribution of the second and third terms in the square bracket in the right-hand side of Eq. (7) is less than 20 percent if the parameter  $R_2/R_1$  is larger than five in practical applications. Thus, we neglect these terms and Eq. (7) is simplified to

$$E_z(t) = - \frac{1}{2\pi\sigma R_1^2} \int_{-\infty}^t dt' \left( \frac{dI}{dt'} \right) \frac{1}{\delta\zeta} \left[ \exp\left(-\frac{1}{\delta\zeta}\right) I_0\left(\frac{1}{\delta\zeta}\right) \right]. \quad (8)$$

Recognizing the approximation

$$\frac{1}{x} \exp\left(-\frac{1}{x}\right) I_0\left(\frac{1}{x}\right) = \frac{1}{\sqrt{2\pi x}}, \quad (9)$$

for the variable  $x$  satisfying  $x < 10$ , we can further simplify the acceleration field in Eq. (8) by

$$E_z(t) = - \frac{1}{(2\pi)^{3/2} \sigma R_1^2} \int_{-\infty}^{\zeta} \frac{d\zeta'}{\sqrt{\zeta - \zeta'}} \left( \frac{dI}{d\zeta'} \right), \quad (10)$$

which is one of the main result in this section and can be used to calculate the accelerating field for a broad range of system parameters. Note that the drive current  $I(t)$  in Eq. (10) is not specified yet. I remind the reader that Eq. (10) is valid for  $\zeta - \zeta' < 10$ . This requires that the observation time  $\zeta$  must be close to the time  $\zeta'$ , at which the maximum current-change occurs. As will be seen later, the peak acceleration field occurs right after the maximum current decrease. Therefore, the restriction  $\zeta - \zeta' < 10$  is well justified. Similarly, the azimuthal magnetic field at  $r = R_1$  is obtained from  $B_\theta(R_1, t) = -(\partial/\partial r)A_z(r, t)$  and given by

$$B_\theta(R_1, \zeta) = \frac{\mu}{2\sqrt{2\pi} R_1 c} \int_{-\infty}^{\zeta} \frac{d\zeta'}{\sqrt{\zeta - \zeta'}} K(\zeta'), \quad (11)$$

which will be used to estimate the magnetic field at  $r = R_1$  only for a fast-changing drive current.

As an example, we consider the case when the drive electron beam has a very short pulse with the pulse profile defined by

$$I(t) = I_m \left(1 - \frac{t^2}{\Delta t^2}\right) U(\Delta t^2 - t^2), \quad (12)$$

where  $\Delta t$  is a constant related to the beam pulse and  $U(x)$  is the Heaviside step function. Substituting Eq. (12) into Eq. (11) and carrying out the integration over the time  $t'$ , we obtain the acceleration field

$$E_z(t) = \frac{2I_m}{3\pi c R_1} \sqrt{\frac{\mu}{\sigma \Delta t}} q\left(\frac{t}{\Delta t}\right), \quad (13)$$

where the function  $q(u)$  is defined by

$$q(u) = \begin{cases} \sqrt{u+1}(2u-1), & -1 < u < 1, \\ \sqrt{u+1}(2u-1) - \sqrt{u-1}(2u+1), & u > 1. \end{cases} \quad (14)$$

Shown in Fig. 1 is plot of the function  $q(u)$  versus the normalized time  $u$  obtained from Eq. (14). Value of the function  $q$  at early stage of the drive-beam pulse is negative, indicating that the drive beam transfers its kinetic energy into the field energy in the energy storage device. This large negative value of the function  $q$  inside the drive pulse decelerates the beam itself quickly. In this regard, the pulse profile in Eq. (12) is not appropriate for efficient acceleration of the witness beam. The negative value of  $q(u)$  in the pulse must be minimized by a gradual increase of the drive-beam current. However, this simple profile is good for the feasibility study, which is the purpose of this article. As shown in Fig. 1, the function  $q$  increases from its minimum as the normalized time  $u$  increases from  $u = -0.5$  to 1. By

self-evolution, this portion of the drive pulse will stiffen the termination slope of the current, eventually increasing the peak value of the function  $q$ . The peak value of the function  $q(u)$  occurs at  $u = 1$ , where the drive pulse ends. Electrons trailing the drive beam get their maximum energy gain. In reality, the peak value of the function  $q$  measured at the axis occurs little later than  $u = 1$  because there is a traveling time of the acceleration field from  $r = R_1$  to  $r = 0$ . Eq. (14) (or Fig. 1) exhibits that there is no negative value of  $q(u)$  outside the drive beam pulse ( $u > 1$ ). In this regard, this system is not useful for acceleration of positrons. The positive peak value is about  $q(u=1) = 1.5$ . Therefore, the maximum acceleration field is given by

$$E_m = \frac{I_m}{\pi c R_1} \sqrt{\frac{\mu}{\sigma \Delta t}} \quad (15)$$

from Eq. (13).

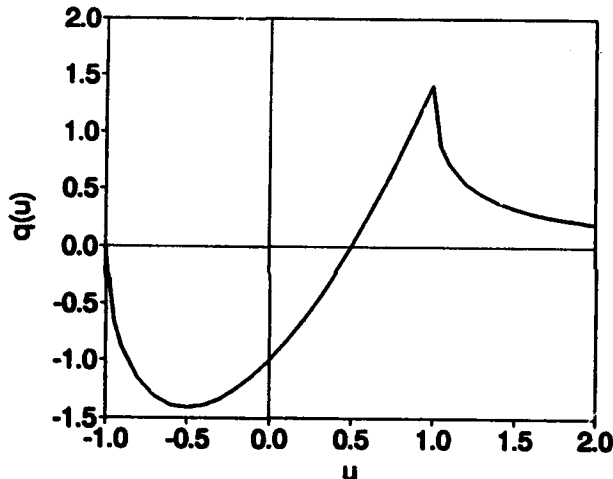


Fig. 1. Plot of the function  $q(u)$  versus the normalized time  $u$  obtained from Eq. (14) for the drive current profile in Eq. (12).

It is important to determine the magnetic field at  $r = R_1$  because the field there must be less than the saturation value  $B_s$ . Substituting Eq. (12) into Eq. (11) and carrying out a straightforward calculation, we obtain

$$B_0(R_1, t) = \frac{2I_m \Delta t}{15\pi R_1^2} \sqrt{\frac{\mu}{\sigma \Delta t}} g\left(\frac{t}{\Delta t}\right), \quad (16)$$

where the function  $g(u)$  is defined by

$$g(u) = \sqrt{u+1}(3+u-2u^2). \quad (17)$$

The magnetic field increases from zero and reaches its peak value of 3.67 at  $u = 0.5$  and decreases as the time progresses from the head of the beam to infinity. Making use of this peak value, we can approximately relate the drive current to the saturation field by

$$B_s = \frac{I_m \Delta t}{2\pi R_1^2} \sqrt{\frac{\mu}{\sigma \Delta t}} \quad (18)$$

Eliminating the beam current in favor of the saturation field  $B_s$ , the maximum acceleration field is expressed as

$$E_m = \frac{2R_1}{c \Delta t} B_s \quad (19)$$

which is remarkably proportional to the hole radius  $R_1$ . For specified saturation field and pulse length, the acceleration field increases linearly as the hole radius increases.

As an example, we consider the case of  $R_1 = 0.5$  cm, the saturation magnetic field  $B_s = 15$  kG, and  $\Delta t = 10^{-10}$  second. The acceleration field for these parameters is given by  $E_m = 150$  MV/m obtained from Eq. (19). Assuming that the parameter  $\mu\sigma = 80$  siemens/m, the required drive current for the saturation field is given by  $\mu I_m = 660$  kA, which is equivalent to  $I_m = 660$  A for  $\mu = 1000$ . The total charge of this drive beam pulse is  $Q = 85$  nanocoulomb for  $I_m = 660$  A. Therefore, the acceleration field per unit charge for these parameters is given by  $E_m/Q = 1.8$  MV/m/nC, which is similar to the result obtained from the wakefield accelerator study for similar physical parameters.

A high-current relativistic electron beam with relatively low energy propagates through a hole bored along the field storage device. Obviously, there should be a physical mechanism to maintain an equilibrium condition of the beam. The axial magnetic field is an excellent means to hold the beam electrons together. However, in this case, the magnetic field may not penetrate well through the high-permeability material. We thus propose to use the ion-focused-regime (IFR) propagation<sup>5</sup> of the electron beam. When a relativistic electron beam propagates through a preionized channel, channel electrons are expelled by the electrostatic force generated by the head of the beam, leaving an ion channel behind. This ion channel partially neutralizes the space charge field of the electron beam, thereby permitting a focused beam. The IFR propagation of a relativistic electron beam has been well demonstrated.

### III. REFERENCES

- [1] H. S. Uhm, Proc. of 1991 IEEE Particle Accelerator Conference May 6-9, 1991, San Francisco, Cal. Vol. IV, 2566 (1991).
- [2] V. K. Neil and A. M. Sessler, Rev. Sci. Instrum. 36, 429 (1965).
- [3] H. S. Uhm, Phys. Fluids 25, 690 (1982).
- [4] I. S. Gradshteyn and I. M. Ryzhik, Table of Integrals, Series, and Products, (Academic Press, New York 1980) Chap. 6.
- [5] R. Smith, R. F. Schneider, M. J. Rhee, H. S. Uhm and W. Namkung, J. Appl. Phys. 60, 4119 (1986).

# Three-Dimensional Simulation Analysis of the First Sections of a Standing-Wave Free-Electron Laser Two-Beam Accelerator\*

Changbiao Wang and Andrew M. Sessler  
Accelerator and Fusion Research Division, Lawrence Berkeley Laboratory  
University of California, Berkeley, California 94720

## Abstract

A 3-D, time-dependent code is used to simulate an array of standing-wave free-electron lasers (SWFELs) in the two-beam accelerator. It is shown that for an array of SWFELs with 9 cavities and a 100.6-nA, 0.5-kA, 7.98-MeV electron beam prebunched at 17.1 GHz, an averaged energy output of 14.7J/m can be obtained with a fluctuation of less than 11%.

## I. INTRODUCTION

In the standing-wave free-electron laser (SWFEL) two-beam accelerator (TBA),<sup>1</sup> a low energy, high current drive beam alternatively loses its energy for generation of microwave power in standing-wave cavities and has its energy replenished in induction cells. The microwave power is coupled into high-gradient rf structures to accelerate an extremely relativistic electron beam of low average current. Hence the drive beam behaves as an energy converter, which converts the energy from the induction cells into rf energy. In the TBA configuration, the extraction of microwave power from each free-electron laser (FEL) cavity is small (usually only a few percent) compared to the electron beam power so that the phase-space distribution of the electrons is not severely distorted by the rf fields. Therefore, if the FEL cavities are periodically set in such a way that the energy-phase phase space of the beam before each cavity has the same distribution, then the fluctuation of the rf output powers from these FEL cavities will be small and the output energy per unit length of the array of SWFELs in the TBA becomes relatively stable.

Many studies have been made on the SWFELs in the TBA using the continuum-cavity model<sup>1-3</sup> and the discrete-cavity model<sup>4,5</sup> and the impedance-based analysis method.<sup>6</sup> These treatments are all based on a one-dimensional assumption. Recently, a three-dimensional, time-dependent code, RKFEL, written based on the code RKTW2D,<sup>7</sup> has been used to investigate a multi-cavity FEL.<sup>8</sup> However, no reacceleration structures were taken into account. In this paper, we use the code RKFEL to study the first sections of a SWFEL/TBA, through which a well-prebunched electron beam is passing. The beam after each cavity is reaccelerated by induction cells so that its average energy remains constant from cavity to cavity. It is shown that for an array of SWFELs with 9 cavities and a 100.6-nA, 0.5-kA, 7.98-MeV electron beam prebunched at 17.1 GHz, an averaged energy output of 14.7J/m can be obtained with a fluctuation of less than 11%.

## II. DESCRIPTION OF THE ARRAY OF SWFELS

So as to be specific, and because of computer cost, for the array of SWFELs we have only used nine identical FEL sections, as shown in figure 1. Each FEL section is 102 cm (6 wiggler periods) long. A beam source provides a 0.5-kA, 7.98-MeV electron beam with a radius of 3.17 mm. The beam is assumed to have passed through a prebuncher and be well bunched at a

\* The work was supported by the Director, Office of Energy Research, Office of High Energy and Nuclear Physics, Division of High Energy Physics, of the U. S. Department of Energy under Contract No. DE-AC03-76SF00098.

frequency of 17.1 GHz and have a peak rf current of 984A. Then the prebunched beam goes into the FEL sections after it passes a 119-cm drift pipe with a 7-period tapered linear wiggler. In each FEL section (figure 2), there is a cavity with a width of 5 cm, a height of 3 cm, and a length of 86.88 cm, a reacceleration cell 6 cm long, and a drift pipe 9.12 cm long. The linear wiggler is uniform and its period is 17 cm. The cavity has a resonance frequency of 17.3 GHz and a wall-dissipation quality factor of 10,000 and an external quality factor of 16, operating at TE<sub>0,1,96</sub> mode. The width and height for all the drift pipes are, respectively, 4 cm and 0.8 cm.

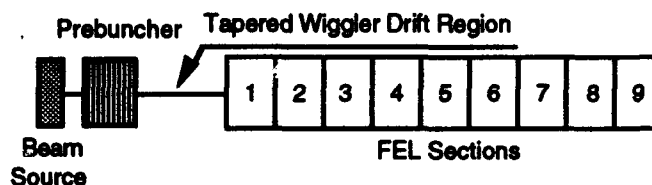


Figure 1. Block diagram of an array of the standing-wave free-electron lasers.

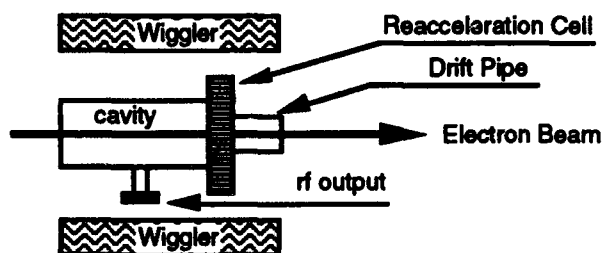


Figure 2. A FEL section.

It should be noted that the length of the FEL section is taken as an integer multiple of the wiggler period to ensure that the beam before each cavity has the same equilibrium distribution in the phase space and thus to reduce variations of output power. In fact, however, the phase-space distributions before the FEL sections can not be made to be exactly the same because of the spread in velocities and the three-dimensional effects of the wiggler magnetic field such as betatron motion.

The vector potential of the linear wiggler magnetic field, provided by parabolically curved magnet pole faces, is given by the following analytic expression<sup>9</sup>

$$A_x = T(z) \frac{B_w}{k_w} \text{ch}(k_x x) \text{ch}(k_y y) \sin(k_w z), \quad (1)$$

$$A_y = -T(z) \frac{B_w}{k_w} \frac{k_x}{k_y} \text{sh}(k_x x) \text{sh}(k_y y) \sin(k_w z), \quad (2)$$

where  $B_w$  is the wiggler magnetic field amplitude on the axis, the wiggler wave number is given by  $k_w = 2\pi/\lambda_w$  with  $\lambda_w$  the wiggler period,  $k_x^2 + k_y^2 = k_w^2$  and the tapering factor is given by  $T(z) = z/7\lambda_w$  when  $z < 7\lambda_w$ , and  $T(z) = 1$  when  $z > 7\lambda_w$ . When  $k_x = 0$ , not only the rf field but also the wiggler field is independent of  $x$ , and the transverse canonical momentum  $P_x$  is a constant, which is used to check the computational precision.

### III. SIMULATION RESULTS

We ran the code RKFEL to simulate the array of the SWFELs with 200 computational particles. The wiggler amplitude  $B_{w0}$  is taken as 0.455 T with  $k_x=k_y$ , corresponding to a detuning frequency of 1.28%. Figure 3 shows the input beam energy and current versus time before the prebuncher. The 100.6-ns pulse has a 4.7-ns rise time, 91.2-ns flat top, and 4.7-ns fall time. We assume that through the prebuncher, a distribution with an initial energy spread  $\Delta\gamma/\gamma=1\%$  and an initial phase spread  $\Delta\omega=0.2\pi$  is loaded, where  $\gamma$  is the electron relativistic factor and  $\omega$  is the drive wave frequency. The 200 particles are randomly distributed within this phase-space rectangle. Figure 4 shows the phase-space distribution for the 50th bucket (about the 60th ns) of the beam right after the prebuncher and before each FEL section. In the tapered wiggler region, the energy spread and the wiggler three-dimensional effect cause increase in the phase spread, and the phase-space rectangle before the tapered wiggler region is changed into a parallelogram before the first FEL section. From the fifth section on, the distributions are quite similar, and the fluctuation of output energy becomes much smaller. The phase spread does not change very much compared with the initial spread. However, simulations indicate that in a state without rf fields, the phase spread can become very large with increase in cavity number because of the spread in longitudinal velocities. So, the FEL interaction has the effect of constraining the phase spread at the expense of increasing the energy spread.

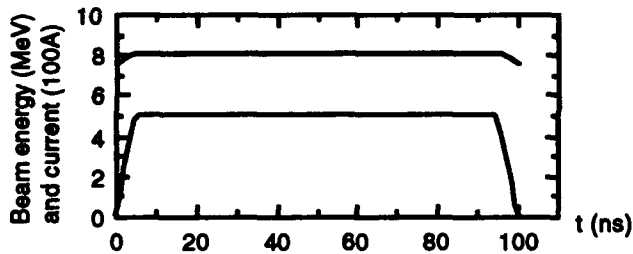


Figure 3. Input beam energy and current versus time.

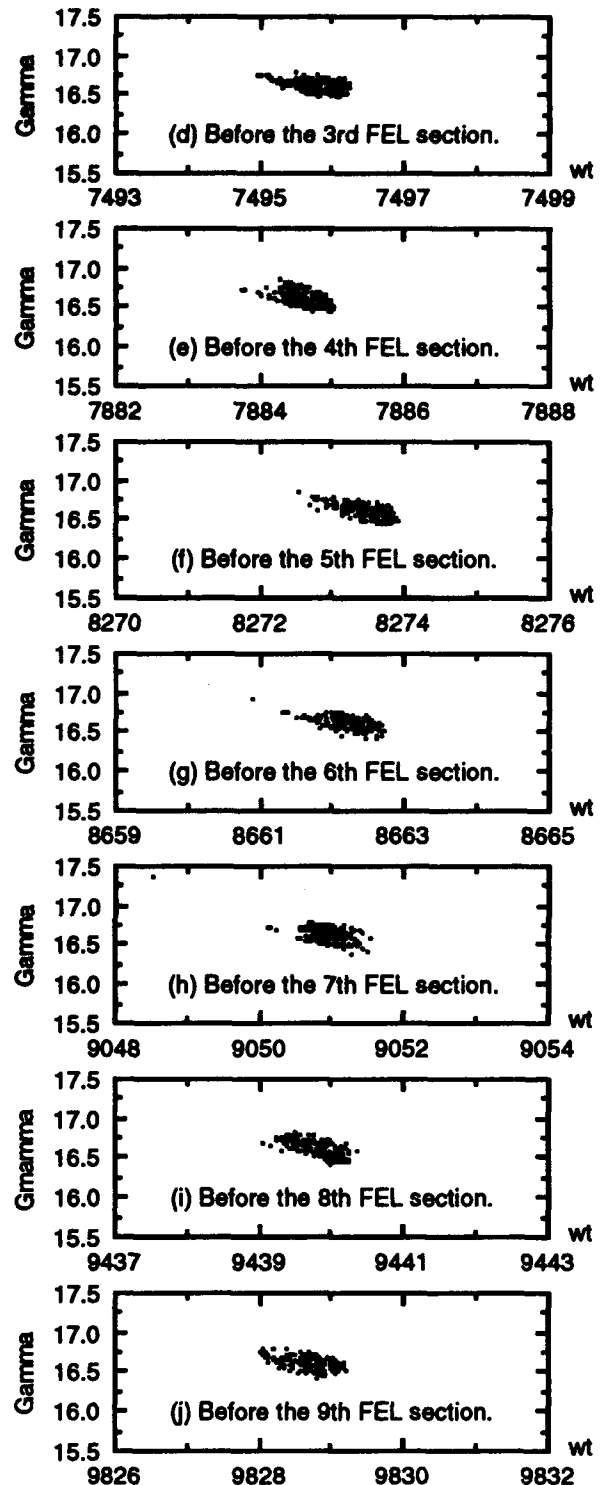
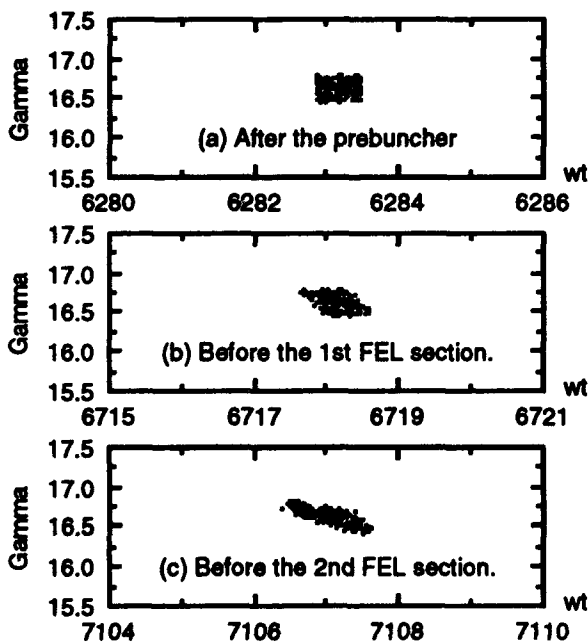


Figure 4. Beam distributions in the  $\omega\gamma$ -space.

Figure 5 shows the dependence of representative cavity output power on time. The output power pulse is a little shortened with increase in the cavity number. However, the power difference between the maximum and minimum is less than 15 MW for the flat part of the pulse. Simulations also indicate that for a too small detuning frequency, the FEL interaction can not lock the phase spread effectively and, further, greatly increase the energy spread so that the output power is rapidly decreased with cavities. For a too large

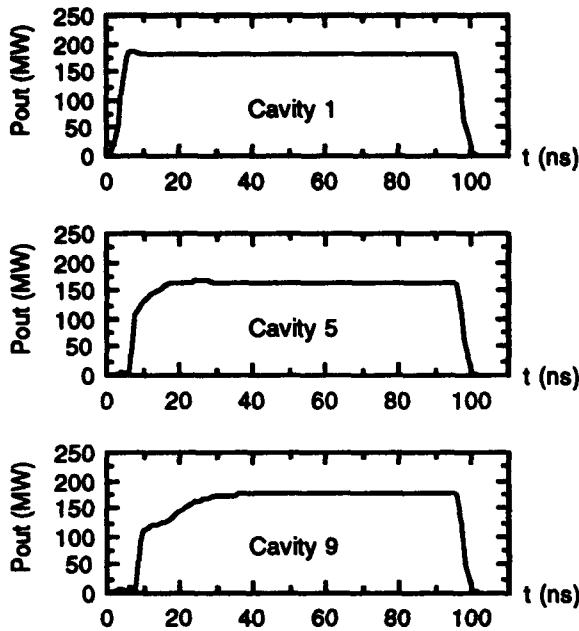


Figure 5. Output power versus time.

detuning frequency, however, the output power for the cavities becomes too small.

Figure 6 shows the electron efficiency and power efficiency versus cavity number for the 50th bucket. The electron efficiency is defined as  $\eta_e = (\langle \gamma_{in} \rangle - \langle \gamma_o \rangle) / \langle \gamma_{in} \rangle$ , where  $\langle \gamma_{in} \rangle$  and  $\langle \gamma_o \rangle$  are the averaged  $\gamma$  before, and after, a cavity. The power efficiency is defined as  $\eta_p = P_{out} / P_b$ , where  $P_{out}$  is the output power of a cavity and  $P_b$  is the input beam power. The electron efficiency is a little greater than the power efficiency because some power is lost on the cavity walls.

Figure 7 shows the output energy and fluctuation versus cavity number (solid circles) during the whole output pulse. The maximum is 16.6 J and the minimum is 14.4 J. The averaged energy output over the array of FEL sections is 14.7 J/m. The fluctuation of the output energy is caused by the non-exact periodicity of the electron beam distribution in the phase space. Many factors may influence the periodicity of a beam distribution. The wiggler three-dimensional effect, energy spread, and action of rf fields can all deteriorate the periodicity. To find out how much different the single-particle model and the multi-particle model<sup>1</sup> are, we ran the code with an initial phase spread of  $0.002\pi$  and a beam radius of 0.0317 mm (1% of the original ones). As shown in figure 7 (hollow circles), they are in reasonable agreement. The averaged output energy is different only by less than 3.5% of the original one. Therefore,

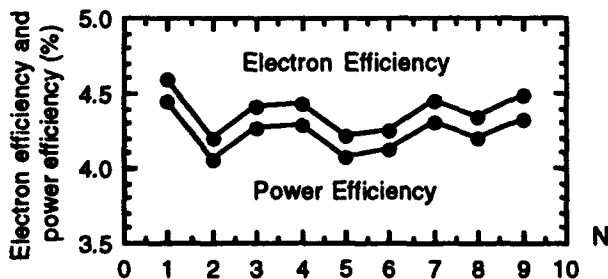


Figure 6. Electron efficiency  $\eta_e$  and power efficiency  $\eta_p$  versus cavity number N.

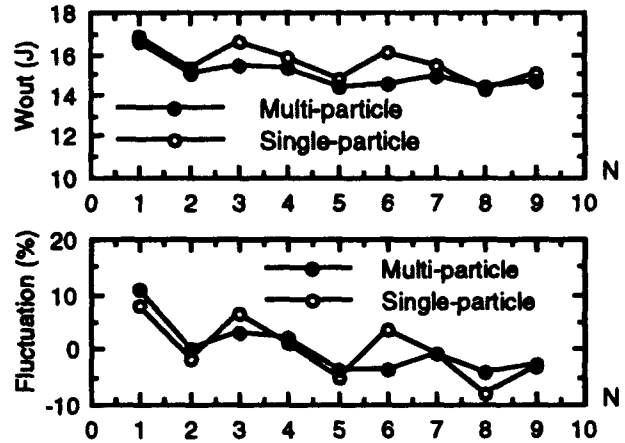


Figure 7. Output energy  $W_{out}$  and fluctuation versus cavity number N.

for a well-bunched beam the single-particle model is a very good approximation.

#### IV. CONCLUSION

In conclusion, for an array of SWFELs with many cavities in the TBA structure, the phase-space distribution before each cavity becomes quite similar after the beam passes through only a few cavities, and a stable energy output can be obtained.

#### V. REFERENCES

- [1] A. M. Sessler, D. H. Whittum, J. S. Wurtele, W. M. Sharp, and M. A. Makowski, "Standing-wave free-electron laser two-beam accelerator," *Nucl. Instr. and Meth.* A306, 592(1991).
- [2] W. M. Sharp, A. M. Sessler, D. H. Whittum, and J. S. Wurtele, "Simulation of a standing-wave free electron laser," *Nucl. Instr. and Meth.* A304, 487(1991).
- [3] W. M. Sharp, G. Rangarajan, A. M. Sessler, and J. S. Wurtele, "Phase stability of a standing-wave free-electron laser," *Proc. SPIE Conference* 1407, 535(1991).
- [4] G. Rangarajan and A. M. Sessler, "Sensitivity studies of a standing-wave free-electron laser," to be published in *Proceedings of the Third Workshop on Advanced Accelerator Concepts*, June, 1992; *Lawrence Berkeley Laboratory Report* LBL-32463, June 1992.
- [5] G. Rangarajan, A. M. Sessler, and W. M. Sharp, "Discrete cavity model of a standing-wave free-electron laser," *Nucl. Instr. and Meth.* A318, 745(1992).
- [6] J. S. Wurtele, D. H. Whittum, and A. M. Sessler, "Impedance-based analysis and study of phase sensitivity in slow-wave two-beam accelerators," to be published in *Proceedings of the Third Workshop on Advanced Accelerator Concepts*, June, 1992; *Lawrence Berkeley Laboratory Report* LBL-31848, June 1992.
- [7] R. D. Ryne and S. Yu, "Relativistic klystron simulations using RKTW2D," *Proceedings of the 15th Int'l LINAC Conference*, 177(1992).
- [8] C. Wang, and A. Sessler, "Three-dimensional simulation analysis of the standing-wave free-electron laser two beam accelerator," to be published in *Proceedings of SPIE on Intense Microwave Pulse*, January, 1993; *Lawrence Berkeley Laboratory Report* LBL-32481, January 1993.
- [9] E. T. Scharlemann, "Wiggler plane focusing in linear wigglers," *J. Appl. Phys.* 58, 2154(1985).

# Reacceleration Experiment to Demonstrate the Concept of Efficiency Enhancement in a Relativistic Klystron Two-Beam Accelerator\*

G.A. Westenskow, and T. L. Houck

Lawrence Livermore National Laboratory  
University of California, Livermore, California 94550

## Abstract

High conversion efficiency of electron beam energy to rf energy can be achieved in two-beam accelerators using reacceleration of the bunched drive beam. To study issues with these designs we are planning a demonstration in which a modulated beam's energy is boosted as it passes through induction accelerator cells. For this experiment we will use the front end of the Choppertron to modulate a 5 MeV electron beam at 11.4 GHz. We have now tested the 5-MeV Choppertron and are reporting on the results. For the reacceleration experiment we plan to use three stages of rf power extraction interspersed with two stages of reacceleration.

## I. INTRODUCTION

We are designing an experiment based on the Choppertron to study the reacceleration of a modulated beam as a verification of the feasibility of building a relativistic klystron two-beam accelerator (RK-TBA). The motivation of our research program at the LLNL Microwave Source Facility is to develop microwave sources which could be suitable drivers for a future TeV linear  $e^+e^-$  collider. The Choppertron<sup>1,2</sup> is a microwave generator which used transverse modulation to generate x-band microwaves. It was originally designed for a 2.5-MV, 1-kA drive beam and configured with two traveling-wave structures (TWS). Although the Choppertron has demonstrated high-power pulses, >150 MW per output at 11.424 GHz with stable phase and amplitude and >400 MW total peak power, the conversion efficiency of beam energy to microwaves was only about 30%. To be a competitive rf source for a collider the conversion efficiency would have to be significantly increased. One means of improving the efficiency is by reaccelerating the beam and extracting additional power. The application of this concept to a linear collider is referred to as the RK-TBA.

\*The work was performed under the auspices of the U.S. Department of Energy by Lawrence Livermore National Laboratory under contract W-7405-ENG-48.

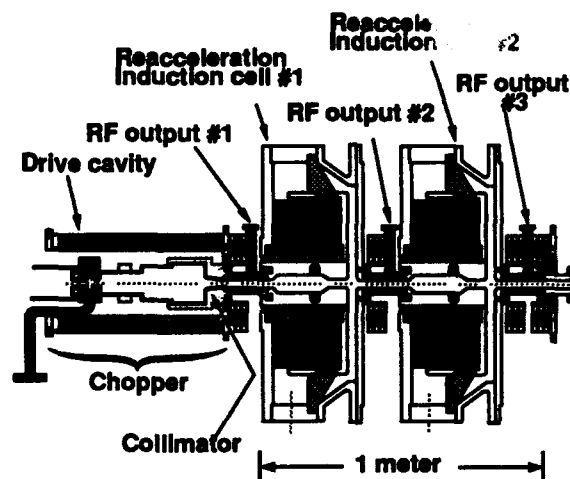


Figure 1. Schematic of the proposed reacceleration experiment.

## II. THE 5-MEV MODULATOR EXPERIMENT

Initial computer simulations<sup>3</sup> for the reacceleration experiment with a 2.5 MeV electron beam showed a significant decrease in the available beam power for extraction due to debunching of the modulated beam by longitudinal space charge effects. Therefore, we added 10 induction cells to our beam line, which increases the beam energy to 5.0 MeV before it enters the Choppertron. We have now tested a modified version of the Choppertron designed for the 5-MeV induction accelerator beam. These modifications included aggressive suppression of higher order modes in the two output structures, and lengthening of the modulation section. Figure 1 shows a layout of the proposed reacceleration experiment. Our simulations indicate relatively consistent power extraction of 100-150 MW from each of the TWS and no beam breakup due to excitation of higher order modes (HOM).

Output rf power in the initial Choppertron was limited by the excitation of HOMs. The HOM damping in the the recent experiments proved effective at reducing this problem. However, operation with the damped structures did not increase

the output power levels to the designed<sup>1</sup> 250 MW. We now believe that beam's emittance is a primary factor in limiting the obtainable output power in the present configuration of the Choppertron. In our experiments, the emittance of the beam determines the beam radius at various positions along the beam line. This is especially important in the modulator section where the betatron resonance and emittance are matched<sup>1</sup> to produce a desired betatron wavelength and beam radius.

A collimator, which consists of a 2-cm diameter 1-m long pipe surrounded by four solenoids, is located after the injector. It serves as an emittance selector allowing only the portion of the incident beam which can maintain a radius equal or smaller than the collimator's pipe radius to pass. By varying the magnetic field of the collimator, the amount of current transported through the pipe is adjusted from the 8 kA emitted from the cathode to the desired beam current. Measurements indicate that at 1 kA the electron beam has a normalized edge emittance of about  $104 \pi\text{-cm-mr}$ , and at 0.5 kA a normalized edge emittance of  $52 \pi\text{-cm-mr}$ .

When the Choppertron was initially being designed, the intention was to operate it on a different accelerator which had a normalized edge emittance of about  $60 \pi\text{-cm-mr}$ . A number of simulations<sup>3</sup> were performed using the relativistic klystron code RKS2<sup>4</sup> to determine the best values of drive power, solenoidal fields, and incident current to maximize output power with no further modifications of the modulator. Figure 2 shows the variation of generated rf current with solenoidal field for about 1.2 MW of deflection cavity drive and at four different values of emittance/current. The emittance values used in these simulations agree with emittance measurements made on the injector at those currents. The rf current produced by the modulator has a broad maximum with magnetic field, drive power and beam current. The 320 amps of rf current shown in Figure 2 is expected to produce about 130 MW of rf power per output structure.

In the recent 5-MeV experiments a combined peak power for the two structures of 260 MW was measured (110 MW in the first TWS and 150 MW in the second TWS). However these high peak power pulses were very narrow, due to electrical breakdown. Wide pulse up to 100 MW could be produced in both output structures (Figure 3). Additional rf conditioning may be required to achieve higher output power. We plan to install other components to the experiment before spending additional conditioning time. We will also

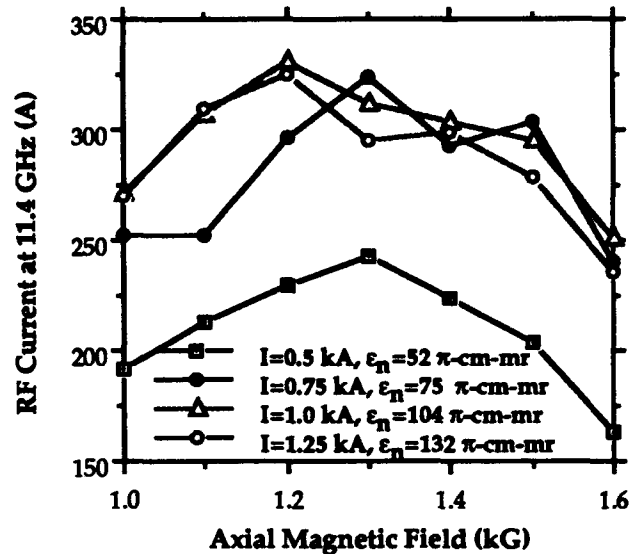


Figure 2. Predicted rf current for different beam emittances and dc currents, drive level = 1.2 MW.

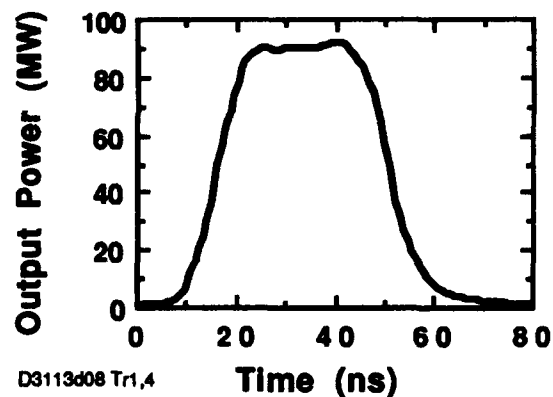


Figure 3. RF power produced in recent experiments.

investigate other possible sources of the electrical breakdown such as the rectangular waveguide flanges and the rf loads used in the experiment.

During the recent experiment we studied the rf power which is reflected off the loads used to absorb the high power rf generated in the output structures. The loads only have a low VSWR close to the 11.424 GHz operating frequency. The leading edge of the rf output pulse has frequency components which are reflected off the loads. This reflected power results in higher electrical fields in the TWS during the leading edge of the pulse and can lead to breakdown. A VSWR of 1.35 for the load experimentally decreased the sustainable output power by ~60%. Similar problems will occur when the output structures are connected to the high energy accelerator structures in a two beam accelerator. A slower ramp in

the front edge of the rf pulse may be desirable to alleviate this problem.

Operation of the Choppertron at low input beam currents (500 amps) has been useful in understanding the operation of the device. At these lower currents the beam has a lower emittance which results in good current transmission through the output structures. Also there are lower electrical field stresses on the surfaces.

### III. MODELING FOR THE REACCELERATION EXPERIMENT

Computer simulations<sup>3</sup> has been performed to study the reacceleration of a modulated beam. Our simulations indicate that approximately 250 MW/m can be achieved (assuming a 1 kA drive beam with normalize emittance of  $104 \pi$ -cm-mr). The two induction cells used for reacceleration should not adversely effect the electron beam dynamics. However, a completely redesigned induction cell which takes advantage of the small bore of the beam line and has significantly reduced impedance characteristics is needed for larger reacceleration experiments. Similarly, the growth of transverse instabilities caused by the traveling-wave structures should not be significant for this experiment, but will require further study<sup>5</sup> as the number of output structures is increased. We intend to use data from a currently operating experiment to improve the modeling for the reacceleration experiment.



Figure 4 . The 12-cell TWS to be tested next.

### IV. NEXT EXPERIMENT

In our next experiment we plan on replacing the two TWSs with one 12-cell TWS designed and constructed by the Haimson Research Corporation (see Figure 4). The structure was designed so that when it is driven with 420 amperes of rf current it will produce 400 MW of rf output in fundamental waveguide. With the 320 amperes of rf current we believe we are now producing with the 5-MeV Choppertron it should produce about 230 MW. This structure has mode suppression similar to the de-Q-ing circuits used in the present Choppertron output structures plus

suppression of higher order modes propagating down stream of the structure. We also hope to test a feed forward phase and amplitude stabilization system with this TWS.

### V. CONCLUSION

Initial experiments using the Choppertron with a 5-MeV drive beam have been completed. Beam breakup due to the excitation of higher order modes in the traveling-wave output structures was successfully suppressed. We have identified the beam's emittance as being a constraint on maximum achievable rf output power. Additional running time will be needed for conditioning the rf surfaces in these output structures to obtain output power greater than 100 MW. We have shown that the front end of the Choppertron can serve as the modulator for the reacceleration experiments which will start later this summer.

### VI. ACKNOWLEDGMENTS

We would like to thank G. Fiorentini for her work on computer simulations of the Choppertron. We would like to thank J. Haimson, B. Mecklenburg, A. Sessler and S. Yu for their continued interest and insights in the Choppertron experiments. For technical assistance, we thank S. Hawkins, A. Myers, S. Petz, and C. Holmes.

### VII. REFERENCES

- [1] J. Haimson, et al., "Design and Construction of a Chopper Driven 11.4 GHz Traveling Wave RF Generator," Conf. Record of the 1989 IEEE Particle Accelerator Conf., pp. 243-245.
- [2] G. Westenskow, et al., "A Chopper Driven 11.4-GHz Traveling Wave RF Generator", Conf. Record of the 1991 IEEE Particle Accelerator Conf., Vol.1, pp. 646-649.
- [3] G. Fiorentini, et al., "Design of a Reacceleration Experiment Using the Choppertron", SPIE Vol. 1872, Intense Microwave Pulses I (1993).
- [4] R.D. Ryne and S.S. Yu, "Relativistic Klystron Simulations Using RKTW2D," Proc. 15<sup>th</sup> Int'l LINAC Conf., Albuquerque, NM, Sep., 1992, pp. 177-179.
- [5] T.L. Houck, "Design Study of a Microwave Driver for a Relativistic Klystron Two-Beam Accelerator," Conf. Record of the 1993 IEEE Particle Accelerator Conf..

# Design Analysis for a 100-MeV Inverse Čerenkov Laser Accelerator\*

J. R. Fontana  
University of California, Santa Barbara  
Santa Barbara, CA 93106

W. D. Kimura and L. C. Steinhauer  
STI Optronics, Inc.  
2755 Northup Way, Bellevue, WA 98004

I. Pogorelsky  
Brookhaven National Laboratory/STI Optronics, Inc.  
ATF/Bldg. 820, Brookhaven National Laboratory, Upton, NY 11973

## Abstract

The analysis of a 100-MeV demonstration experiment based upon inverse Čerenkov acceleration (ICA) is presented. This experiment would use the Accelerator Test Facility (ATF) at Brookhaven National Laboratory. With 50-GW of delivered laser peak power from the ATF CO<sub>2</sub> laser, our analysis indicates the 65-MeV ATF *e*-beam can be accelerated to >165 MeV using three stages of acceleration in ~1 m of total length. The number of electrons accelerated can be raised to ~10<sup>9</sup> by prebunching the *e*-beam using an already available device.

## I. INTRODUCTION

Laser particle acceleration research has been making steady progress. A number of experiments are in progress. The Accelerator Test Facility (ATF) has been constructed at Brookhaven National Laboratory and is available for laser acceleration experiments. This new facility features a 50-MeV linac, which will be upgraded to 65-MeV, and a high peak power (~10 GW) CO<sub>2</sub> laser, which also can be upgraded to generate 100-GW of peak power.

The US Department of Energy (DOE) is interested in a near-term 100-MeV laser acceleration demonstration experiment. The DOE is also interested in the design for a 1-GeV linac based upon laser acceleration.

This paper describes the design of a 100-MeV demonstration experiment that is based

upon inverse Čerenkov acceleration (ICA) and can be performed at the ATF using much of the existing equipment.

## II. EXISTING ICA EXPERIMENT

An inverse Čerenkov laser acceleration experiment is currently being performed at the ATF [1]. Hydrogen gas ( $P = 1.7$  atm) is used in a gas cell to slow the phase velocity of the laser light to match the electron velocity. The beams intersect at a Čerenkov angle of  $\theta_c = 20$  mrad with an interaction length of 20 cm.

The ATF ICA experiments are testing an improved geometry [2] that focuses a radially polarized laser beam onto the *e*-beam. Assuming 5-GW of laser peak power delivered to the interaction region (for a 10-GW input into a 50% efficient optical system), an energy gain of ~12 MeV is predicted. This gain scales as the square root of laser peak power. Thus, a peak power of 50-GW delivered will result in 38-MeV energy gain.

The present gas cell design is already near optimum for the ATF conditions and can be used as the basis for a multistaged 100-MeV ICA demonstration experiment. Since one stage gives 38-MeV energy gain (assuming 50-GW delivered laser peak power), three stages will yield >100 MeV energy gain. The only major changes to the existing ICA experiment needed are upgrading the ATF CO<sub>2</sub> laser to produce 100-GW peak power and modifying the gas cell system to recycle the laser beam. This latter issue is discussed in more detail next.

\* Supported by US DOE Contract Nos. DE-AC06-83ER40128 and DE-FG03-90ER40545.

### III. CONCEPTUAL DESIGN FOR 100-MeV DEMONSTRATION EXPERIMENT

Figure 1 is the simplified conceptual arrangement for the 100-MeV ICA demonstration experiment. A small portion of the drive laser power ( $\sim 120$  MW) is sent to a prebuncher; the rest of the power ( $\sim 100$  GW) is sent to the 3-stage accelerator.

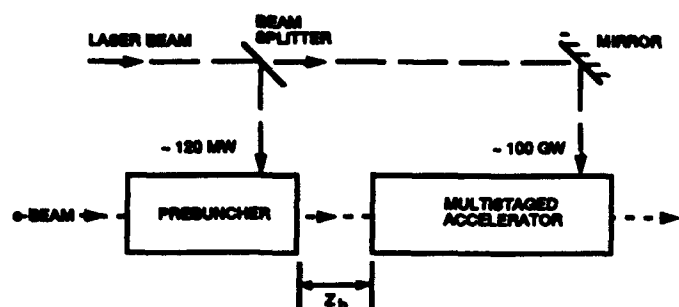


Figure 1. Conceptual arrangement for the 100-MeV demonstration experiment.

Prebunching the  $e$ -beam before it enters the multistaged accelerator will significantly enhance the experiment. Without prebunching the electrons enter the multistaged accelerator at all phases resulting in only a small fraction of electrons being accelerated to the full 100-MeV energy gain. The existing gas cell being used in the current ICA experiments can be used as a prebuncher. Only  $\sim 120$  MW of laser peak power is needed to drive the prebuncher and will give an optimum bunching distance  $z_b \approx 20$  cm. At this point the prebunched  $e$ -beam will enter the multistaged accelerator.

#### A. 3-Stage ICA Accelerator Concepts

Two possible arrangements for the multistaged accelerator are shown in Figures 2 and 3. In the first concept (Figure 2), the incoming radially polarized laser beam reflects off a  $45^\circ$  mirror, which has a small hole in its center for passage of the  $e$ -beam. The laser beam then reflects off a curved axicon and is focused down onto the  $e$ -beam. (The purpose for using a curved axicon will be explained later in Section III.B.) After intersecting the  $e$ -beam in the first stage, the spent laser beam reflects off a slightly conical cylindrical mirror tube. This tube functions the same as the curved axicon and focuses the laser light back onto the  $e$ -beam in the second stage. The process repeats itself for the third stage.

This first concept is very similar in arrangement to the existing ATF ICA experiment [1], which uses a flat axicon rather than a curved one, has only one stage of acceleration, and does not use cylindrical mirror tubes.

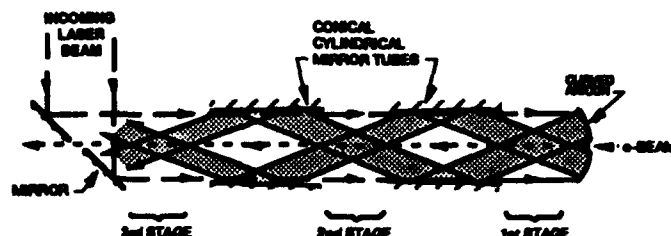


Figure 2. Concept for a 3-stage ICA accelerator.

One disadvantage of the first concept is the length of gas-filled space between the acceleration stages, which leads to additional scattering of the electrons by the gas molecules. Similar to the present ICA experiment, each interaction region is 20-cm long. This means the space between the stages must be  $>20$  cm. Hence, for this first concept the total 3-stage accelerator length is  $\approx 110$  cm.

Figure 3 depicts an alternative concept for the 3-stage accelerator that minimizes the distance between stages. The incoming radially polarized laser beam travels through a  $45^\circ$  mirror with a large hole in its center. The laser beam reflects off a waxicon, which converts the beam

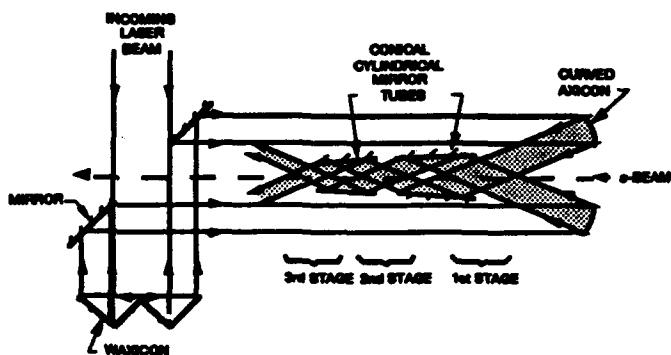


Figure 3. Alternative concept for 3-stage ICA accelerator.

into a hollow one while maintaining its radial polarization characteristics. This hollow beam is directed off the  $45^\circ$  mirror to the curved axicon where it is focused onto the  $e$ -beam. The spent laser beam then immediately reflects off the slightly conical cylindrical mirror tube towards the second stage, and the process repeats itself for the third stage. Since the incoming laser beam

does not need to travel through the mirror tubes as in Figure 2, the diameter of the tubes can be reduced thereby decreasing the space between acceleration stages. The total accelerator length of this second concept is  $\sim 70$  cm.

### B. $\beta$ -Slippage Compensation

In the preceding concepts, the curved axicon helps compensate for phase slippage between the electrons and light wave as the electrons gain energy within each interaction region. The Čerenkov angle  $\theta_c$ , given by  $\cos\theta_c = (1/n\beta)$ , where  $n$  is the index of refraction of the gas and  $\beta$  is the ratio of electron velocity to the velocity of light, changes as the electrons gain energy. By varying the Čerenkov angle within the interaction region it will be possible to maintain near optimum phase matching as the  $\beta$  of the electrons increases. This can be done by using a slightly concave axicon such that the angle of intersection is slightly larger ( $\sim 1$  mrad for the ATF conditions) at the end of the interaction region than at the beginning. The slightly conical shape of the cylindrical mirror tubes also accomplishes this same effect. An alternative method for  $\beta$ -slippage compensation is to use a slightly converging laser beam reflecting off a flat axicon and straight cylindrical mirror tubes.

### C. Recycling Laser Beam

Another issue implied in the preceding concepts is being able to reintersect the laser pulse with the electron bunch in the second and third stages. Due to differences in the electron drift velocity relative to the effective group velocity of the laser pulse, the relative drift distance between the electrons and light pulse over a distance  $L$  is

$$\Delta z_{drift} = \theta_c^2 L. \quad (1)$$

The laser pulse length in space is  $\Delta z_l = c\tau_l$ , where  $\tau_l$  is the laser pulse width in time. Thus, the ratio of these two distances is

$$\frac{\Delta z_{drift}}{\Delta z_l} = \frac{\theta_c^2 L}{c\tau_l}. \quad (2)$$

Hence, if for example,  $\theta_c = 20$  mrad,  $\tau_l = 100$  ps, and  $L = 110$  cm (see Figure 2), then the amount of slippage is 1.5% of the laser pulse length. Therefore, recycling the laser pulse should not be an issue.

## IV. SUMMARY

Table 1 summarizes the estimated performance for the 100-MeV ICA demonstration experiment.

Table 1  
Estimated Performance of 100-MeV ICA  
Demonstration Experiment.

ATF Parameter	Assumed Value
Injector CO <sub>2</sub> Laser Peak Power	65 MeV <i>e</i> -beam 50 GW (delivered)
ICA Parameter	Estimated Performance
Energy Gain # of Accelerated Electrons/Pulse Energy Gradient	95 to 125 MeV (net) >5 × 10 <sup>8</sup> 1st Concept: >92 MeV/m 2nd Concept: >143 MeV/m

The effect on *e*-beam emittance requires additional analysis to extract emittance information from the models. Emittance growth is less of an issue for high- $\gamma$  *e*-beams; however, the ATF *e*-beam energy is relatively low which will impact the emittance growth of the accelerated *e*-beam.

## V. REFERENCES

- [1] W. Kimura, I. Pogorelsky, G. Kim, L. Steinhauer, S. Tidwell, and K. Kusche, "Update on the ATF Inverse Čerenkov Laser Acceleration Experiment," see *Conference Record of the 1992 IEEE Particle Accelerator Conference*.
- [2] J. R. Fontana and R. H. Pantell, *J. Appl. Phys.* 54, No. 8, 4285 (1983).

# An Inverse Free Electron Laser Driven Linear Collider Electron-Positron B-Factory

N. BAROV and C. PELLEGRINI, UCLA, Dept of Physics, Los Angeles, CA 90024

J. SANDWEISS, Yale Univ., New Haven, CT 06511

## Abstract

We discuss an electron-positron linear collider B-Factory using Inverse Free Electron Lasers (IFEL) to accelerate the beams. The requirements on luminosity, larger than  $10^{33} \text{ cm}^{-2} \text{ s}^{-1}$ , and energy spread of a B Factory introduce stringent conditions on the accelerator and the interaction region. We study the longitudinal dynamics through the IFEL, the efficiency of the acceleration process, and the ratio of particles which become accelerated, and fall within the resonance. The device is found to perform well in the presence of large variations in the laser field intensity over the beam. We also discuss the laser system powering the IFEL, and some of the system tolerances.

## Introduction

The set of beam requirements demanded by a linear collider B-Factory, summarized in Table 1 is very difficult to satisfy, and represents a challenge for a novel acceleration technique such as the IFEL. The set of parameters needed at the interaction point (IP) for such a B-Factory were identified in a previous paper [1] on which this work is based. Such an accelerator must meet stringent requirements for the beamstrahlung fractional energy spread, the final energy spread of the accelerator, and the luminosity.

Because the particles are delivered from the injector at a random phase with respect to the optical wave, care must be taken to match these initial particles to the acceleration buckets. This matching is crucial to achieving a final energy spread which has a maximal overlap with the Upsilon(4S) resonance, having a full width of 24 MeV. We examine the efficiency of this matching and present simulation results.

An advantage of the IFEL over conventional accelerators is the efficiency in utilizing the incoming electromagnetic energy. This is the result of having the radiation confined to a region close to the bunch. The efficiency of energy extraction, or beam loading, is influenced by the choice of parameters, such as the beam current. An upper limit on this beam loading must be chosen based on the effect on the acceleration process as a result of modifying the peak electric field. We note that in the IFEL, beam loading does not directly lead to an energy spread, such as in a conventional

linac.

By altering the waveguide dimensions, it is possible to modify the slippage of the bunch relative to the radiation pulse. The zero slip regime offers the possibility of adjusting the tapering to compensate for the loss in power of the radiation. Also, because this approach lends itself more readily to using multiple acceleration sections, the power density required of the drive laser is decreased.

The average power and repetition frequency requirement on the drive laser make a free electron laser the most likely candidate for this task [1]. Driven by a superconducting linac, such as a FEL, assuming 40 percent energy extraction, can insure good wallplug efficiency for the entire system.

Table 1. Beam and Collider Parameters

Beam Energy (GeV)	5
Luminosity ( $\text{cm}^{-2}\text{s}^{-1}$ )	$10^{33}$
Average Beamstrahlung, $\Delta E/E$	$2 \times 10^{-3}$
No. Particles/Bunch	$1.14 \times 10^{10}$
Pulse Repetition Rate ( $\text{sec}^{-1}$ )	$10^4$
$\sigma_t$ ( $\mu\text{m}$ )	0.249
$\beta^*$ at I.P. (mm)	0.31
$\sigma_z$ (mm)	0.31
Disruption Parameter	16
Pinch Enhancement	6
Invariant Emittance (m-rad)	$2 \times 10^{-6}$

## IFEL Designs

We envision an IFEL which begins with an untapered prebunching section, then a set of acceleration modules, and finally a section which reduces the energy spread. We choose a constant period wiggler, which is not the optimum case but the easiest to examine. The resonant phase  $\psi_r$ , describing the particle which does not undergo synchrotron oscillations, is set to  $\pi/4$ , as a compromise between high acceleration rate and sensitivity to parameters. Several studies have been made of the waveguide used to contain the radiation which suggest that low loss propagation is feasible [4,5,6]. With a suitable choice in waveguide parameters, the amount of slippage between the particles and the radiation can be altered. Case A of Table 2 has no slippage control and consists of a single

module, while Case B is an example of zero slip [7] and has 18 modules. The application of the zero slip condition leads to a severely restricted waveguide aperture, (2 mm). While an actual device using these parameters may have problems with beam propagation, this example will demonstrate what is possible using the zero slip approach.

We note that before reaching the IP, it is necessary to wash out the bunching existing on the optical scale with a dispersive section, so as not to exacerbate the beam-beam effects.

**Table 2: IFEL Characteristics**

Parameter	Case A	Case B
Laser Wavelength ( $\mu\text{m}$ )	10	10
Injection Energy (MeV)	500	500
Dimensions of Waveguide (cm)	0.8 x 0.8	0.2 x 0.4
Peak Laser Electric Field (V/m)	$1.04 \times 10^{10}$	$1.84 \times 10^{10}$
Laser Power Density (W/cm <sup>2</sup> )	$1.45 \times 10^{13}$	$4.49 \times 10^{13}$
Laser Pulse Energy (Joules)	104	4.9
Bunch Train Rep. Rate (Hz)	$10^4$	$10^4$
Optical Pulses per Train	1	18
Average Laser Power (Watts)	$1.04 \times 10^6$	$8.8 \times 10^5$
Max. Wiggler B-Field (Gauss)	$5 \times 10^4$	$2.3 \times 10^3$
Wiggler Period (cm)	26.5	160
Total Length of Wiggler (m)	146	282
Acceleration Gradient (MV/m)	31	16

### Initial Matching

In the interest of utilizing the maximum number of 500 MeV initial particles, it is necessary to precondition the beam, increasing the overlap with the acceleration buckets. In addition, the parameters of Table 2 have buckets which are deeper than the allowable energy spread. To avoid problems with this, the beam conditioner can also be used to match the initial distribution to the longitudinal phase space.

The small oscillations near the resonant particle are described by ellipses characterized by,

$$\delta\gamma = \delta\psi \sqrt{\frac{\lambda}{2\pi} \frac{f_b}{2} \frac{\gamma_o^2 a_w a_s}{1 + a_w^2/2} \cos(\psi_r)} \quad (1)$$

where  $\gamma$  is the Lorentz factor,  $f_b$  is the Bessel function factor,  $a_s = eE_0\lambda/2\pi mc^2$  ( $E_0$  is the peak radiation field),  $a_w = eB\lambda_w/2\pi mc^2$  ( $B$  is the peak magnetic field), and  $\psi_r$  is the resonant phase. In order to stay away from the nonlinear parts of the phase space, which may cause filamentation, we wish to match the initial distribution to these ellipses. If an untapered wiggler section is used as a buncher, only a fraction of the particles will be matched, the rest being close to the separatrix or untrapped.

This matching will be undermined by any variation in parameters such as a difference in the

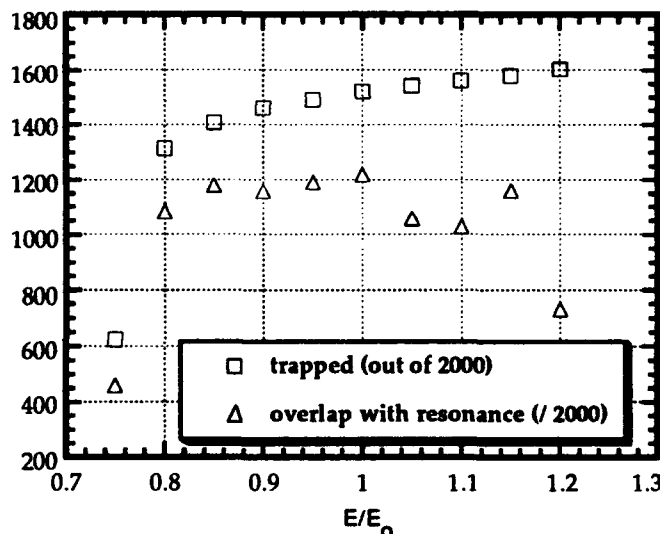
radiation field over the extent of the beam. A slight variation in  $E_0$  will modify  $\psi_r$  and cause synchrotron oscillations for the microbunch. In a more severe case, the nonlinear effects will filament the distribution.

### Numerical Results

We present simulation results motivated by the concerns raised in the last section. To this end, the high radiation intensity and large  $\gamma$  allow us to neglect the optical properties of the beam (guiding, index of refraction, etc.) The system can be modeled through a straightforward application of the wiggler period averaged equations of motion for the particles, found in reference [2]. An extra term containing  $\lambda_c$ , the cutoff frequency of the waveguide, can be added to the usual equation for the phase evolution:

$$\frac{d\psi}{dz} = \frac{2\pi}{\lambda} \left( \frac{\lambda}{\lambda_w} - \frac{1}{2} \left( \frac{\lambda}{\lambda_c} \right)^2 - \frac{1 + a_w^2/2}{2\gamma^2} \right) \quad (2)$$

In this model, we have not considered the effect of betatron motion, and also assume that the particles do not see the variation of the fields off axis.



**Plot 1:** The overlap with the resonance when different sections of the beam see a variation in the laser field  $E$ .

For Case A, the combination of slippage and beam loading assures that the radiation in the vicinity of the beam's leading edge will diminish in intensity. The situation which is simplest to compute is one where each slice of the beam is exposed to a constant intensity throughout the acceleration. For Case B, the interest in keeping the radiation pulse as short as possible again brings unwanted intensity variations. Plot 1 is the result of a series of runs in which the peak electric field was varied. The parameters relevant to Case B were used for this, but the results are also valid for Case A because

here the final energy spread is always slightly smaller. The particles were initially injected in a 1.5 MeV band and with random phases. The prebunching and final energy spread reduction were optimized for the reference electric field, and then kept constant. The final energy spread reduction section consists of a dispersive section and a 9 m untapered section utilizing a  $1.84 \times 10^9$  V/m peak electric field. The effect is to rotate the distribution in the longitudinal phase space so that  $\delta\gamma$  comes to a minimum. The benefit of this energy spread reduction technique is strongly limited by conservation of phase space area and nonlinear dynamics.

These results reveal that the performance degrades gracefully even when the electric field is lowered by as much as 20%. The difference between the number of trapped particles and the number which overlap with the resonance indicates the amount of wasted energy. In summary, effectively 60 per cent of the particles from the injector end up effectively in the resonance. A similar analysis for the trapped particles, which take energy away from the radiation, reveals that 80 per cent of them overlap with the resonance.

The above simulation work did not implicitly treat energy balance. This may seem not to be the correct treatment for Case B, where  $E_0$  is diminished by 5 per cent near the end of each accelerating section. We have carried out additional simulation work to verify that this effect is not very detrimental, but in a more realistic accelerator design the rate of tapering would be adjusted to compensate for this.

## Conclusions

The previous section suggests that the amount of energy extraction from the radiation can safely be made higher - perhaps to the 15 or 20 percent level. Such a change would lead to a favorable impact on the amount of power required of the drive laser. In reference [1], a drive laser design using an FEL is presented, making use of a 23 kA and 9 kA drive beams for Case A and Case B respectively. A twofold increase in efficiency, assuming that any relevant instability issues are studied (such as side bands), would result in lowering these beam requirements to more reasonable levels.

There is ample opportunity to optimize the parameters of this accelerator. For example, the wiggler can have a tapered period, to bring about a reduction in the maximum required magnetic field near the end of the device.

## Acknowledgments

This work was supported by the US Department of Energy under Grant DE-FG03-92ER-40493. We wish to thank J.C. Gallardo for helpful discussions and advice

about the computer code.

## References

- [1] C. Pellegrini, J. Sandweiss and N. Barov, Use of an Inverse Free Electron Laser in a Linear Collider B Factory, Proc. of the Brookhaven Workshop on Advanced Accelerator Methods, 1992.
- [2] E. D. Courand, C. Pellegrini, and W. Zakowicz, Phys. Rev A, 32,2813 (1989).
- [3] U. Amaldi, Pro. US,CERN School on Part. Acc. at So. Padre Island, Texas, October 1986, ed. M. Month (Springer Verlag, 1988).
- [4] R. Palmer, SLAC-PUB-44295, (1987).
- [5] W. Zakowicz, J. Appl. Phys. 55, 9,(1984).
- [6] J. Sandweiss, BNL 35444, August 1984.
- [7] S. K. Ride, Appl. Phys. Lett. 57 1283 (1990)

# 2.5D Numerical Simulation of Relativistic Electron Bunches (REB) Interaction with Underdense and Overdense Plasmas

Oleg V. Batishchev<sup>†</sup>, Vjacheslav I. Karas<sup>‡</sup>, Yurii S. Sigov<sup>†</sup>, Yakov B. Fainberg<sup>†</sup>

<sup>†</sup>M.V.Keldysh Institute of Applied Mathematics  
Russian Academy of Sciences  
125047 Miusskaya Sq., Moscow, Russia

<sup>‡</sup>Kharkov Institute of Physics and Technology  
310108, Kharkov, Ukraine

## Abstract

The results of REB – plasma interaction numerical simulation by means of our relativistic particle EM code are presented. Nonlinear evolution of a single REB injected into underdense and overdense plasmas is studied in detail for cylindrical geometry. It is found that in case of comparable bunch and plasma densities an instantaneous amplitude of excited longitudinal electric field substantially depends on density ratio, relativistic factor and space density distribution of REB. Transversal electric field can considerably exceed the longitudinal one, causing more severe restrictions to initial phase and radial position of particles to be accelerated.

which stops the bunch  $E_{zt}$ . The excitation of nonlinear stationary waves in a plasma by a sequence of periodically spaced electron bunches was studied in ref. [5, 6], where it was shown that the electric field of the wave increases with increasing relativistic factor  $\gamma$ , but only in the case of comparable bunch  $n_b$  and plasma  $n_e$  densities.

The experiments performed in the nonlinear regime of the PWFA displayed interesting three dimensional effects, but only one dimensional treatments of nonlinear plasma wake-fields currently exist (see for example [6] and cited references). In ref. [7] a high-intensity rigid electron beam is used to excite extremely nonlinear, transverse motion dominated plasma oscillations.

## I. INTRODUCTION

The accelerating of charged particles by means of space-charge waves in plasmas and in unneutralized charge-particle beams [1] is a basic direction in collective acceleration methods. One of the main advantages of this method is that it can produce strong electric fields in plasma which are directed along the propagation direction of linear or nonlinear waves with phase velocities  $v_{ph} \leq c$ ,  $c$ -light velocity. This makes possible to keep continuously the wave matched with particles to be accelerated. The possibility of strong accelerating fields achievement simply follows from the circumstance that the field amplitude is proportional to the variable component of the charge density. The last can reach the equilibrium value of the plasma density. Since this density can be made very high, the electric field can reach values up to  $10^7$ – $10^9$  V/cm [1, 2].

Chen et al. [3] suggested a modification of Fainberg proposed acceleration method [1]: switching to acceleration by waves train excited by a finite sequence of periodically spaced REB moving through a dense plasma. The serious difficulty of plasma wake-field acceleration (PWFA) method has been eliminated by Katsouleas [4], who presented a proof that if a bunch with a uniform density distribution is replaced by one asymmetric along it's length, then due plasma wave electric field excited behind a bunch  $E_{ac}$ , accelerating particles injected from the outside of the system, can be many times greater than the electric field

## II. SIMULATION RESULTS

In this work the results of full-scale numerical simulation of a single or a sequence of relativistic electron bunches in plasmas is presented. Excitation of wake fields by them is studied using our 2.5D axial-symmetric electromagnetic code [8]. Recently this code was applied to an induction accelerator [9] and modulated REB simulations [10].

### A. Mathematical model

Dynamics of REB is described by relativistic Vlasov (Beliaev-Budker) equations for distribution functions of plasma species and Maxwell equations for self-consistent  $E$  and  $B$  fields. Two component bulk plasma ( $m_i/m_e = 1840$ ) with density  $n_p$  was initially cold and filled the whole simulation region  $[0, Z] \times [0, R]$ . Usually  $Z$  and  $R$  were taken as 25 and  $3c/\omega_p$  respectively,  $\omega_e$  is Langmuir plasmas frequency. At the plane  $Z = 0$  we organized one or a train of cold relativistic electron bunches injection in accordance with a formula ( $n$  means the injected bunch number)

$$n_b \theta(R_0 - r) \theta(v_b t - z + (n-1)\lambda_p) \theta(z - v_b t + Z_0 + (n-1)\lambda_p)$$

Here beam velocity  $v_b = c(1 - 1/\gamma^2)^{1/2}$ ,  $Z_0$  and  $R_0$  - initial sizes of bunches were equal to  $1/3$  and  $1/6 c/\omega_p$ .  $\lambda_p = 2\pi c/\omega_e$ ,  $n_b = 1/2n_e$  - mean density of REB. Note, that as in experiments [6], initial transversal  $R_0$  and longitudinal  $Z_0$  bunches sizes were less than  $c/\omega_e$ . Bunches could leave the simulation region at it's two corners  $z = 0$

and  $z = Z$  as well as plasma species, which were additionally pumped back into the volume. At the inner surface of cylinder  $r = R$  all particles were reflected. Boundary conditions for fields were the following: metallic at the  $r = R$  and free radiation of  $EM$  waves at corners. In computations we used explicit schemes, time and space steps were constant and equal to  $0.05c/\omega_p$  and  $0.025\omega_p^{-1}$  respectively. So, the mesh size was  $512 \times 64$ , a silent start technique was used. Model particles weight was a function of their radial position, to represent plasma with a less number of particles per cell in less disturbed regions far from axis. The total number of particles was approximately 300000. Note, that all simulations were carried out using *PC/386/20* and we applied the fast modification of particle-in-cell method.

### III. RESULTS AND DISCUSSION

The numerical simulation of one bunch propagation in plasma demonstrates that its transversal size changes in wide range. This leads to essential changes in its density (up to one order) as well as in the wake field excited by them. Longitudinal distributions of transversal  $E_r$  and longitudinal  $E_z$  electric fields corresponding to radius  $r = R_0$  and time  $t = 18\omega_e^{-1}$  are shown at Fig.1 and Fig.2 respectively (in  $m_e c \omega_p / e$  units). You can see that immediately after the REB with  $\gamma = 430$  shapes of radial and longitudinal electric fields differ from sinusoidal, and their amplitudes are not more constant. This is due to transversal oscillations of bunch particles in self-consistent fields connected with an absence of both charge and current compensations. To study a relationship between an excited fields and a number of injected into plasma bunches with initial energy  $mc^2\gamma$  two runs were considered.

#### A. Comparison of two runs

Run 1 is shown at Fig.3 ( $t = 15\omega_e^{-1}$ ) and has the following parameters:  $N = 3$ ,  $\gamma = 430$ . Run 2 (shown at Fig.6 ( $t = 50\omega_e^{-1}$ )) has eight bunches (three ones are shown at a moment) with  $\gamma = 43$ .

At Figs.4,7 longitudinal distributions of radial electric field  $E_r$  and at Figs.5,8 axial electric field  $E_z$  corresponding to Runs 1 and 2 respectively are represented. In addition, the shape of each bunch is shown in magnified scale at top of Figs.3,6. You can see that amplitudes of both longitudinal and transversal fields increase with the bunch injection. This amplitudes nevertheless are not proportional to the number of injected bunches, as it should be for "rigid" bunches. At Fig.9 longitudinal electric field energy time dependence for Run 2 is shown. Each step on the curve corresponds to a moment, when new bunch interacts the simulated system boundary. The non-monotonic character of excited field grow take place after third bunch injection, signifying formation of non-linear regime of train propagation.

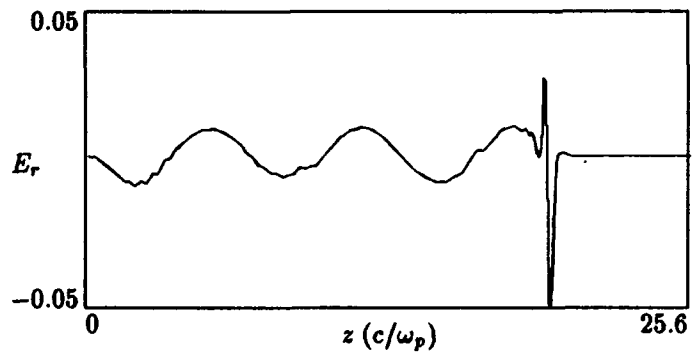


Figure 1: Transversal electric field  $E_r$

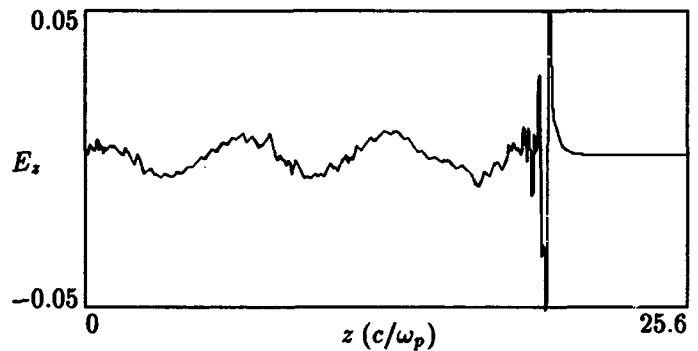


Figure 2: Longitudinal electric field  $E_z$

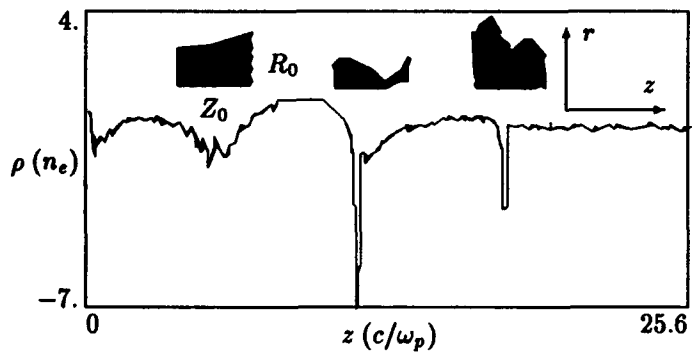


Figure 3: Three bunches, density  $\rho$

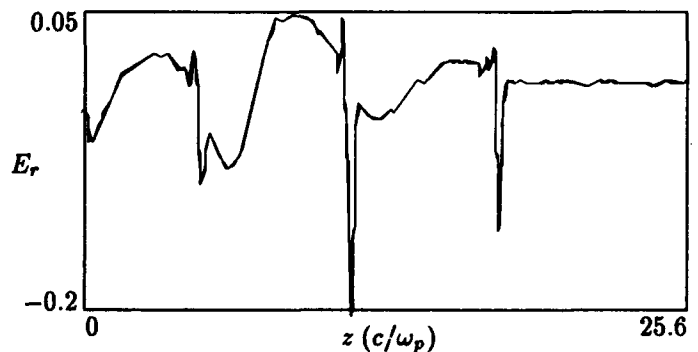


Figure 4: Three bunches, field  $E_r$

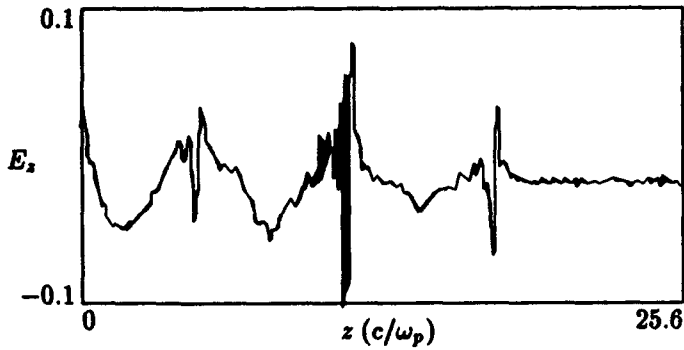


Figure 5: Three bunches, field  $E_z$

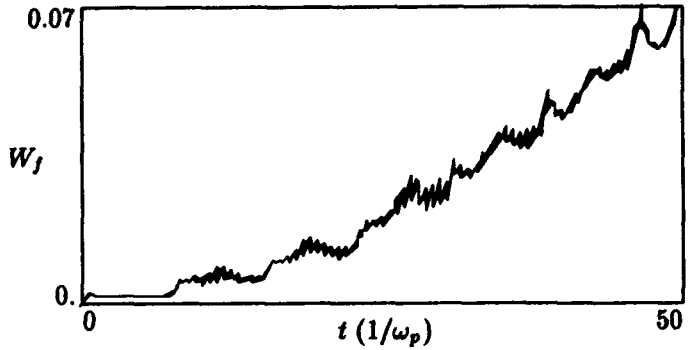


Figure 9:  $E_z$  energy,  $W_f(t)$

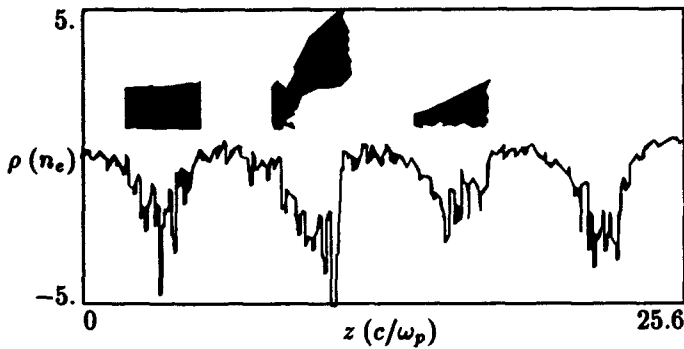


Figure 6: Eight bunches, density  $\rho$

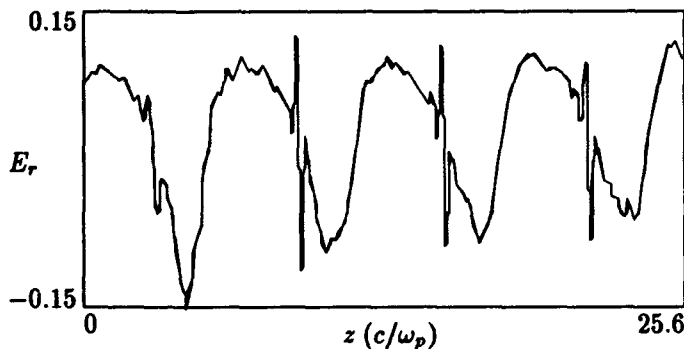


Figure 7: Eight bunches, field  $E_r$

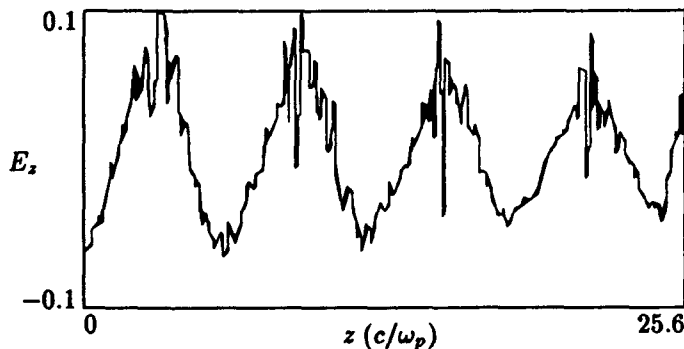


Figure 8: Eight bunches, field  $E_z$

#### IV. REFERENCES

- [1] Ya. B. Fainberg, "The use of plasma waveguides as accelerating structures in linear accelerators", *Proc. Symp. CERN*, Vol. 1, 84 (1956).
- [2] Ya. B. Fainberg, "Acceleration of charged particles by space-charge waves excited on plasmas by laser beams and relativistic electron beams", *Sov. J. Plasma Physics*, 13, No. 5, 350 (1987).
- [3] P. Chen, J. M. Dawson, R. W. Huff, and T. Katsouleas, "Acceleration of electrons by the interaction of a bunched electron beam with a plasma", *Phys. Rev. Lett.*, 54, 693 (1985).
- [4] T. Katsouleas, "Physical mechanisms in the plasma wake-field accelerator", *Phys. Rev. A*, 33, No. 3, pp. 2056-2064 (March 1986).
- [5] A. Ts. Amatuni et al., "Excitation of a high amplitude longitudinal waves in a plasma by electron bunches", *Sov. J. Plasma Physics*, 11, 417 (1985).
- [6] J. B. Rosenzweig, "Nonlinear plasma and beam physics in plasma wake-field", *FERMILAB Conf. 90/40* (February 1990).
- [7] J. B. Rosenzweig et al., "Acceleration and focusing of electrons in two dimensional nonlinear plasma wake fields", *Phys. Rev. A*, 44, No. 10, pp. 6189-6192 (November 1991).
- [8] *Discrete plasma simulation* (ed. Yu. S. Sigov), Keldysh Inst. Appl. Math., Moscow (1990).
- [9] V. I. Karas' et al., "Studies of space-charge neutralized ion beam induction linac for inertial confinement fusion", *Particle Accelerators*, 37-38, pp. 281-288 (1992).
- [10] O. V. Batishchev et al., "Self-focusing of a modulated ribbon REB in a dense plasmas", *Sov. J. Plasma Physics*, 19, No. 6, pp. 738-747 (1993).

# Propagation of Short Electron Pulses in Underdense Plasmas

N. Barov and J. Rosenzweig,  
Department of Physics,  
University of California, Los Angeles, CA 90024

## Abstract

Our program for an experimental plasma wake field accelerator (PWFA) to take place at the Argonne Wakefield Accelerator (AWA) facility, in the recently proposed blow-out regime[1] relies on the propagation of an intense electron beam through an underdense plasma with a minimum of degradation. This paper presents a near-equilibrium model of beam propagation using the Maxwell-Vlasov equations governing the beam's transverse behavior. Numerical results are presented which use this model simultaneously with the plasma electron cold fluid equations. A solenoidal magnetic field, which is necessary for high density plasma containment, also provides an initial beam equilibrium to begin the calculation. We compare the equilibrium model with a discrete beam particle simulation, which verifies the basic conclusions of the equilibrium model, and shows the collisionless damping approach to equilibrium in the beam head. The initial matching requirements for the beam's entry into the plasma are examined. We also discuss the possibility of performing an adiabatic lens experiment.

## Introduction

The recently proposed nonlinear blow-out regime for the PWFA[1], in which all of the plasma electrons become expelled from the region of the beam, has the advantage of linear focusing for the trailing (accelerated) bunch and a very high acceleration gradient. This regime requires a very intense, high quality drive beam. Since the acceleration can be prolonged by using a more energetic drive beam, the long term propagation of this beam through the plasma needs to be addressed.

When an intense electron beam propagates through a plasma in the underdense regime ( $n_0 < n_{\text{beam}}$ ,  $n_0$  is the plasma density), a sufficiently long bunch length will cause complete rarefaction of the plasma electrons, forming an ion channel. This is called the ion focusing regime (IFR) due to the intense magnetic self-focusing forces of the beam as it propagates through the ion channel. For a fully rarefied ion channel, the equilibrium beam radius  $\sigma_r$  is given by,

$$\sigma_r = \left[ \frac{\epsilon_n}{\sqrt{2\pi r_e n_0 \gamma}} \right]^{1/2}$$

where  $\epsilon_n$  is the normalized emittance,  $r_e$  is the classical electron radius, and  $\gamma$  is the Lorentz factor. The beam

can be divided into three qualitatively different regions. The extreme leading edge, or *head* of the beam receives no focusing from the plasma, causing it to expand. The *body* of the beam, which travels in the completely rarefied ion channel, receives the maximum focusing force. In the *transition region* between these two, the beam evolution cannot be described with linear optics, due to the remaining population of plasma electrons. For short pulses ( $\sigma_z \approx k_p^{-1}$ ,  $k_p = \omega_p/c$ ), the evolution of the beam head and the transition region are very important in determining the effective propagation of the beam over long distances.

For the ultra-relativistic case, the beam head expands freely, due to its finite emittance, retarding the response of the plasma electrons at later time steps. This diminishes the focusing force for the next beam slice, leading to what is called emittance driven erosion. A simple 1-d model predicts that after some initial expansion, the erosion happens at a very slow rate. In addition, previous particle-in-cell simulation work by Krall, *et al.* [2] has shown that for emittance-driven erosion, the point on the beam where the plasma becomes completely rarefied, termed the pinch point, moves very slowly, and a near equilibrium develops. Inspired by this result, we develop a model in which beam physics is described by a Maxwell-Vlasov equilibrium and the plasma electrons are described by fully relativistic cold fluid equations. This model also includes the effects of a solenoidal magnetic field. Such a field is required for the containment of the plasma in the PWFA, which can in some cases help to further stabilize this erosion.

## Numerical Treatment of Beam Near Equilibrium

The response of the plasma due to the beam's electromagnetic field is modeled using a technique developed by Breizman [3]. This model relies on a wake field type assumption: any plasma perturbation translates at the beam velocity. Further, the beam velocity is taken to be the speed of light. The plasma electron currents can then be modeled by the cold fluid equation,

$$\frac{\partial \mathbf{p}}{\partial t} + (\mathbf{v} \cdot \nabla) \mathbf{p} = -e \left( \mathbf{E} + \frac{1}{c} (\mathbf{v} \times \mathbf{B}) \right)$$

and the continuity equation. Implicit in using a cold fluid model is the fact that the plasma electron velocity quickly becomes much greater than the initial temperature of the plasma. The plasma can be treated as

a fluid only when the motion is laminar. This is satisfied to a very good approximation in the first half cycle of the plasma motion, making the cold fluid model well suited to studying the effects on the beam. These equations are used along with the Maxwell equations for  $\nabla \times E$  and  $\nabla \times B$ . The speed of light condition,  $\partial/\partial z = -\partial/\partial ct$  is used to eliminate the time variable in these equations, which yield a self consistent instantaneous representation of the plasma disturbance. We use conducting wall boundary conditions in the radial direction and further assume that the plasma is quiescent ahead of the beam.

The body of the beam is assumed to be initially matched to the linear focusing force of the ion channel. For the transition region, the nonlinear focusing brings about a mixing of the transverse phase space in just a few betatron periods. If we assume that the emittance increase, which is very difficult to compute, can be neglected, the phase space can be described by the equilibrium Maxwell-Vlasov equation, setting  $\partial/\partial t = 0$ :

$$\frac{\partial}{\partial t} f(r, p_r) = \frac{p_r}{\gamma m} \frac{\partial f(r, p_r)}{\partial r} + F_r(r) \frac{\partial f(r, p_r)}{\partial p_r} = 0$$

where  $f(r, p_r)$  is the distribution in the transverse phase space,  $p_r$  is the transverse momentum,  $\gamma$  is the Lorentz factor,  $m$  is the electron mass, and  $F_r$  is the radial force arising from the plasma fields. In addition,  $f(0,0)$  must be constant due to conservation of phase space area.

The matching of the beam body implies that the head will undergo betatron oscillations. For the purpose of the model, we assume that the head is itself matched to the solenoid. This is in part justified by the small number of particles which feel no plasma focusing.

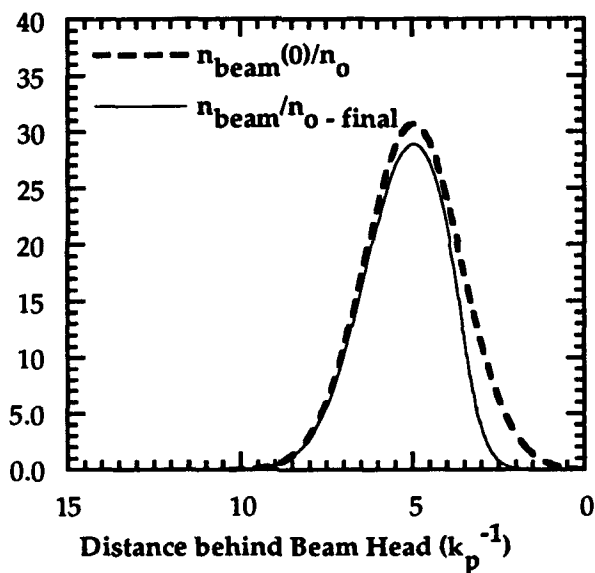


Figure 1. Final (equilibrium) and initial beam density normalized to plasma density using AWA beam parameters,  $n_0 = 10^{14} \text{ cm}^{-3}$ , and a solenoidal field of  $B=2000$  Gauss. The matched equilibrium is achieved very early in the the beam pulse.

In Figure 1, this method is applied to a  $10^{14} \text{ cm}^{-3}$  plasma, using the future AWA beam parameters [4]: 100 nC charge per bunch,  $\sigma_z = .7 \text{ mm}$ ,  $\gamma = 300$ , and  $\epsilon_n = 400 \pi \text{ mm-mrad}$ . The final peak density mimics the initial gaussian density quite well. This run produced a longitudinal wake field capable of sustaining greater than a 1 GeV/m acceleration.

### Initial Matching: Time Dependent Aspects

The equilibrium model of the last section relies on a trumpet shaped beam, an condition which may be difficult to produce from a longitudinally uncorrelated profile. In this section we examine the requirements for initial matching into the focusing channel and present computational results which reveal the efficacy of such matching. In order to minimize the betatron oscillations of the beam head, the largest possible initial beam radius must be used. This is important when the period of these oscillations is longer than the stopping distance of the beam through the plasma. It is therefore advantageous to use the focusing properties of the plasma in such a way as to reduce the radius of the beam body, while leaving the beam head unaffected. The initial ramp in the plasma density at the start of any actual device can be useful for this task. We have studied the effect of a plasma profile which builds up as one side of a gaussian and remains flat afterward. Although this does not represent the ideal focusing scheme, it is a good approximation of the experimental situation.

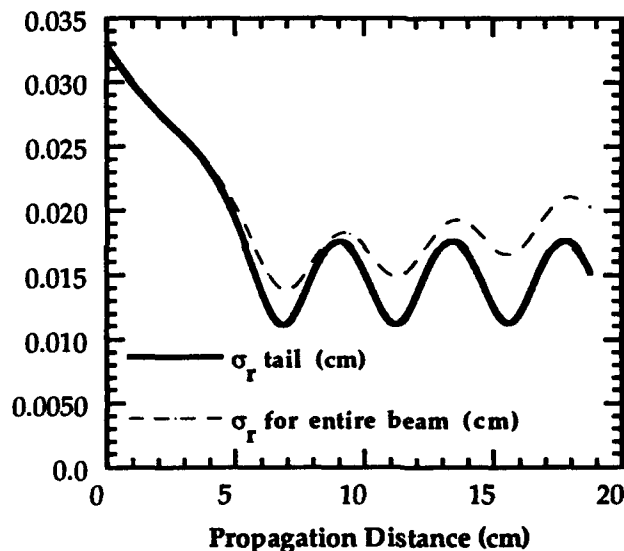


Figure 2. Matching of the beam into plasma with a gaussian ramp,  $\sigma = 2 \text{ cm}$ . For this run, the beam has a virtual waist of 0.026 cm at a position 4 cm into the device. The magnetic field was 2000 Gauss.

To simulate these time dependent effects, we used the same numerical techniques as in the last section to treat the plasma dynamics. The beam in this case was composed of a set of discrete particles, treated self-consistently with the plasma dynamics. It is assumed that the variation in  $n_0$  over the extent of the beam can be neglected. Figure 2 shows results, using the AWA beam parameters, for ramp which builds up as a gaussian from  $n_0 = 10^{12} \text{ cm}^{-3}$  to  $n_0 = 10^{14}$  in 8 cm, and remains flat afterward. A slight mismatch of the beam body is tolerable since it does not diminish the radial force seen by the plasma electrons, which have already left the region of the beam.

Through observing the evolution of the phase space we have witnessed a new mechanism for the suppression of erosion of the beam head. The presence of any erosion diminishes the focusing strength of a given z-slice very slowly. Thus, the slice's  $\sigma_r$  is adiabatically increased until it becomes matched to the solenoid, approximating the equilibrium discussed in the last section. In the case of a weak solenoid, this predicts that a small portion of the beam head will become lost, while the rest of the beam propagates in a near equilibrium.

### Adiabatic Focusing

There has been great interest in using a plasma lens for the final focusing in a linear collider[5]. Chen *et al.* [6] has proposed making such a lens adiabatic, with a smoothly increasing focusing strength. The advantages of adiabaticity are to reduce the effects of synchrotron radiation, lessening impact of the chromatic aberrations, and diminishing the sensitivity to initial optical mismatch. Because the equations governing the plasma motion have a simple scaling with  $n_0$ , the results of a sub-GeV, experiment can yield a good prediction for larger  $\gamma$  and an  $n_0$  of  $10^{18} \text{ cm}^{-3}$ . In addition, as  $n_0$  increases, the condition  $\sigma_z \gg k_p^{-1}$  becomes easier to satisfy. Thus, a proof of principle experiment at low energy would circumvent some of the experimental difficulties of an actual final focus experiment. The AWA beam, with its high peak current, and accompanying access to the underdense regime, can be used to experimentally study such a device. The discrete particle method developed above has been used to numerically study the adiabatic lens. The AWA beam is intense enough to cause blowout at very early times after the arrival of the beam. In addition, the charge and energy can be scaled down to study a large parameter space.

The work by Chen, *et al.*, suggests the use of a lens in which the  $\beta$  function is linearly decreased. This lens has the feature that the plasma density is increasing very rapidly near the end. We have studied a lens whose density increases only exponentially, which we believe

is more realistic experimentally. Figure 3 presents simulation results for such a lens. The body of the beam is focused, in good agreement with the theoretical limit assuming a completely rarefied ion channel. Note that the  $\sigma_r$  averaged over the entire beam never becomes small due to phase differences and the insufficient focusing of the beam head.

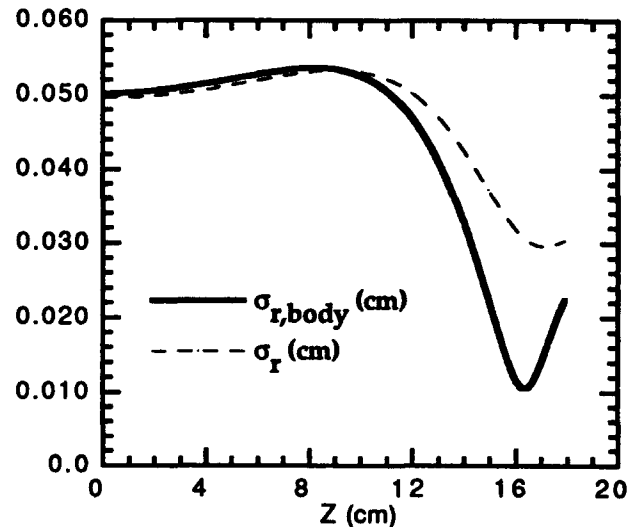


Figure 3: Adiabatic lens for the AWA beam,  $n_0$  starts at  $2.5 \times 10^{11}$  and increases to  $5 \times 10^{13}$  at  $z=15$  cm. The body of the beam (the core population containing half the beam) is focused quite efficiently, down to 100 microns at  $z=16$  cm.

This work was supported by US Department of Energy under Grant DE-FG03-92ER-40493

### References

- [1] J.B. Rosenzweig, B. Breizman, T.Katsouleas and J.J. Su. *Phys. Rev. A - Rapid Comm*, **44**, R6189 (1991).
- [2] J. Krall, K. Nguyen, G. Joyce, *Phys. Rev. A*, **44**, (1991)
- [3] B.N. Breizman, T. Tajima, D.L. Fisher, and P.Z. Chebotaev, University of Texas Fusion Institute Preprint (1991), unpublished
- [4] M. Rosing, *et al.*, An Update on Argonne's AWA, 1991 IEEE Particle Accelerator Conference, P.555
- [5] See B. Barletta, *et al.*, and references therein Plasma Lens Experiment at the Final Focus Test Beam, these proceedings.
- [6] P. Chen, K. Oide, A.M. Sessler, S.S. Yu, *Particle Accelerators*, **31** (1990)

# NUMERICAL SIMULATIONS OF DRIVING BEAM DYNAMICS IN THE PLASMA WAKEFIELD ACCELERATOR\*

Glenn Joyce, Jonathan Krall and Eric Esarey  
 Plasma Physics Division  
 Naval Research Laboratory  
 Washington, DC 20375-5346

## I. INTRODUCTION

Novel plasma based acceleration devices[1,2] have become the subject of active research because of their ability to support acceleration gradients in excess of 10 GeV/m. The plasma wakefield accelerator (PWFA) is one such device which consists of an intense electron beam (the primary beam) whose purpose is to excite a plasma wave which, in turn, accelerates a trailing electron bunch (the secondary beam). Two issues of current interest in the PWFA are 1) the equilibrium and stability of the driving beam and 2) the effect of the wakefield on the quality of the trailing electron bunch. The PWFA is currently the subject of experiments to be performed at the Argonne National Laboratory (ANL)[3] and the University of California, Los Angeles (UCLA)[4].

In the UCLA experiment, a question of particular interest is the equilibrium state of the driving electron beam. Two intriguing suggestions have been made. The first is that in the limit that the beam density greatly exceeds the plasma density, the plasma electrons will be completely expelled from the axis. It was recently pointed out[5] that the resulting ion channel will have a focusing force that varies linearly with radius, preserving the emittance of the trailing electron bunch. The second is that, in parameter regimes of interest, the driving beam will experience a severe radial pinching force. Specifically, Ref. 4 suggested that the electron beam could be pinched via ion focusing in the plasma by as much as a factor of 10 (from  $r_b=300\mu\text{m}$  to  $r_b=30\mu\text{m}$ ). What such extreme pinching does to the beam and whether or not an equilibrium state at  $r_b=30\mu\text{m}$  can be achieved are questions that have yet to be addressed. These ideas suggest that a highly nonlinear wakefield with favorable focusing properties could be produced by a driving electron beam in a tightly focused equilibrium state. Furthermore, this mode of operation may be accessible in new PWFA experiments to be performed at ANL and UCLA. In order to investigate these assertions, we first consider the envelope equation for an electron beam propagating in a plasma with  $n_b \geq n_p$ . We then compare

numerical solutions of this equation to results obtained via two-dimensional axisymmetric (r,z) particle simulation using the FRIEZR particle simulation code.

## II. THE ENVELOPE EQUATION

Consider the envelope equation of Lee and Cooper<sup>6</sup> for an axisymmetric relativistic electron beam:

$$\beta^2 \frac{d^2 R}{dz^2} + \frac{\beta^2}{\gamma} \frac{d\gamma}{dz} \frac{dR}{dz} + \frac{U}{R} - \frac{4\epsilon^2}{R^3} = 0, \quad (1)$$

where  $R$  is the rms radius of the beam,  $\gamma$  is the relativistic factor, and the beam is assumed to be moving in the  $z$ -direction with  $v_z \gg v_\perp$ . We have used as the definition for the rms emittance,  $\epsilon = \epsilon_{rms}/(\beta\gamma)$ .

Each term of Eq. (1) has a physical meaning. The first two terms above account for inertial effects. The third term accounts for self-field effects,

$$U = \frac{1}{c^2} \int_0^\infty r dr \left[ \frac{2\pi r J_b(r)}{I_b} \right] \frac{e}{\gamma m} [E_r - \beta B_\theta], \quad (2)$$

where  $J_b$  is the beam current density,  $I_b$  is the beam current, and  $E_r$  and  $B_\theta$  are electric and magnetic fields. The fourth term represents the expansion of the beam due to emittance. In applying Eq. (1) to this problem, we have assumed that  $r_w > c/\omega_p > R$ , where  $\omega_p = (4\pi n_p e^2/m)^{1/2}$ ,  $n_p$  is the initial plasma density, and  $r_w$  is the radius of the plasma chamber. This condition ensures that return currents do not flow within the electron beam. If we make the additional assumption that  $n_b \geq n_p$ , the plasma electrons will be expelled from the region of the beam.

For a beam with a Gaussian radial profile, we have

$$U = -\frac{W_b [kA]}{17\beta\gamma^3} + \frac{\omega_p^2}{2\gamma c^2} R^2, \quad (3)$$

where our notation is such that  $I_b < 0$  for an electron beam. Assuming  $dy/dz=0$ , Eq. (1) becomes

$$\frac{d^2 R}{dz^2} + \frac{1}{R} \frac{eI_b}{\beta\gamma^3 mc^3} + \frac{\omega_p^2}{2\gamma c^2} R - \frac{4\epsilon^2}{R^3} = 0. \quad (4)$$

With Eq. (4), it is straightforward to solve for the equilibrium radius of a beam with given  $\gamma$ ,  $n_p$  and  $\epsilon$ . For  $\gamma \gg 1$  we have

$$R_{eq} = \left( \frac{8\epsilon^2 \gamma^3 mc^3}{\gamma \omega_p^2} \right)^{1/4} \quad (5)$$

As an example, we consider an electron beam with  $\gamma=40$  (20 MeV), charge  $Q=1nC$ , initial rms radius  $\sigma_r=100 \mu m$ , longitudinal half-width at half maximum  $\sigma_z=600 \mu m$ , and  $\epsilon_n=10mm\text{-mrad}$  propagating through a plasma of density  $n_p=2.0 \times 10^{14} \text{ cm}^{-3}$ . In this case,  $n_{b0}=1.67 \times 10^{14} \text{ cm}^{-3}$  and  $-I_b=0.252 \text{ kA}$ . With these values, Eq. (5) gives  $R_{eq}=41 \mu m$  indicating that the beam is mismatched. Once the beam begins to pinch, we will have  $n_b > n_p$ . Thus, we can integrate Eq. (4) to obtain an estimate of the beam dynamics, shown in Fig. 1. This figure shows severe pinching of the beam, with a minimum radius of  $17 \mu m$ . One might expect significantly strong variations in the wakefield generated by such a beam.

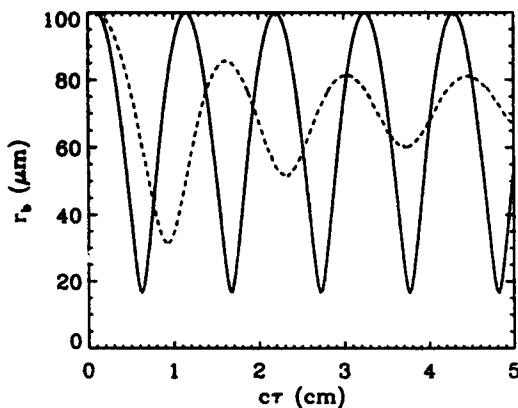


Fig 1. Beam radius  $R$  versus time  $\tau$  from a numerical solution of Eq. (4) (solid line) and from simulation at fixed  $\zeta=0.1 \text{ cm}$  (dashed line).

### III. SIMULATIONS

To address this question in greater detail, we resort to particle simulation. The FRIEZR particle

simulation code is an axisymmetric  $(r,z)$  fully electromagnetic, fully relativistic particle code that makes use of "speed of light" coordinates through a change of variables:  $\zeta=ct-z$ ,  $\tau=t$ . The plasma is represented by particle electrons imbedded in an immobile neutralizing ion background. The relativistic beam, also represented by particles, is injected into the plasma with density

$$n_b(r,\zeta) = n_{b0} \exp\left(-\frac{r^2}{\sigma_r^2}\right) \sin\left(\frac{\pi\zeta}{3\sigma_z}\right). \quad (6)$$

In the  $(\zeta,\tau)$  coordinates, the head of the relativistic beam remains near  $\zeta=0$  with the tail of the beam at  $\zeta=0.18 \text{ cm}$ . The simulation proceeds for  $5 \text{ cm}$ , during which the beam energy remains approximately constant ( $\gamma_{beam}=36$ ). Figure 1 (dashed line) shows the beam radius versus  $\tau$  at  $\zeta=0.1 \text{ cm}$ . It is evident that the beam is being pinched and is undergoing mismatch oscillations. Figure 2 shows the beam density  $n_b$ , the plasma density  $n_p$ , and the axial electric field  $E_z$  on axis at  $ct=5.0 \text{ cm}$ . In this figure,  $\delta n = n_p - n_b$ ,  $E_{z0} = 0.1 E_{wb}$ ,  $E_{wb} = mc\omega_p/c = 1.4 \text{ GV/m}$ . Also, the beam is moving towards the left and  $E_z > 0$  is accelerating. The envelope equation solution and the particle simulation result are in rough qualitative agreement at early times ( $\tau < 1 \text{ cm}$ ). The results then diverge because the plasma electrons are not completely expelled from the axis (see Fig. 2) and because the beam emittance grows as the radial oscillations damp via phase-mixing. This can be seen in Fig. 3, which shows beam emittance at  $\zeta=0.1 \text{ cm}$  plotted versus  $\tau$ . An interesting and somewhat surprising result is contained in this figure, which also shows the peak accelerating electric field  $E_{z,peak}$  versus  $\tau$ . While the beam radius is varying by 50%, the accelerating field is varying by only 20%. We speculate that this occurs for two reasons. Firstly, because the plasma is not entirely expelled from the axis and because the plasma electron density varies over the length of the beam, the simulation shows that the frequency of the radial mismatch oscillations varies as a function of  $\zeta$ . Secondly, in the limit that  $n_b \gg n_p$ , the wake is driven by a large radial electric field that pushes the plasma electrons to  $r \gg R$ . At such large radii,  $E_r$  is function only of the amount of beam charge enclosed within this radius. Additional simulations have confirmed that the wake amplitude is insensitive to the details of the beam profile in this limit.

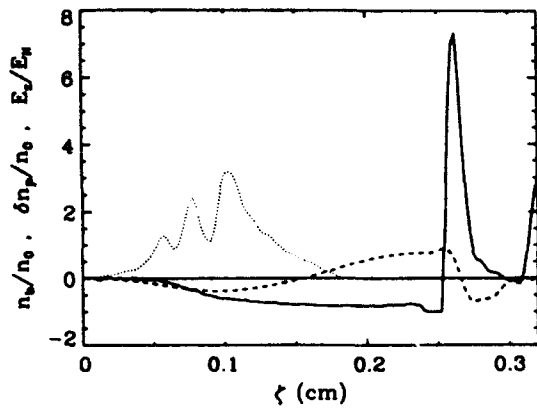


Fig 2. Beam density  $n_b/n_0$  (dotted line), plasma density  $\delta n_p/n_0$  (solid line), and axial electric field  $E_z/E_N$  (dashed line) plotted versus  $\zeta$  on axis at  $c\tau = 5.0$  cm.

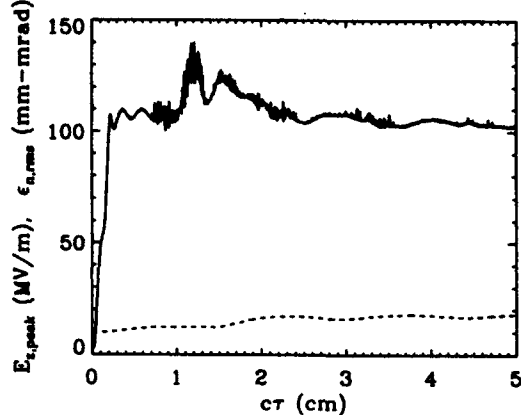


Fig 3. Beam emittance  $\epsilon_n$  (dashed line) at fixed  $\zeta = 0.1$  cm and peak accelerating field  $E_{z,peak}$  (solid line) versus  $\tau$ .

To avoid the oscillations in the wake amplitude that were observed above, we performed a simulation identical to that of Figs. 1-3, but with  $R=R_{eq}=41 \mu\text{m}$  as given by Eq. (5). The results are given in Fig. 4, which shows  $R$  and  $E_{z,peak}$  plotted versus  $\tau$ . This figure shows that, after a transient of 1.5 cm, the beam-plasma system remains in a quasi-equilibrium state, with a slow expansion of the beam radius and a constant peak accelerating field. The radial expansion occurs because a) the beam loses energy ( $\gamma_{final} = 35$ ) and b) the head of the beam, which is not pinched, slowly erodes. Erosion reduces the effectiveness with which the beam expels the plasma electrons such that the plasma electron density inside the beam increases slowly over the length of the simulation. There is no increase in emittance in this case. Note that  $E_{z,peak}$  vs.  $\tau$  in Fig. 4 shows a shorter transient and a significantly higher average value than the corresponding plot in Fig. 3.

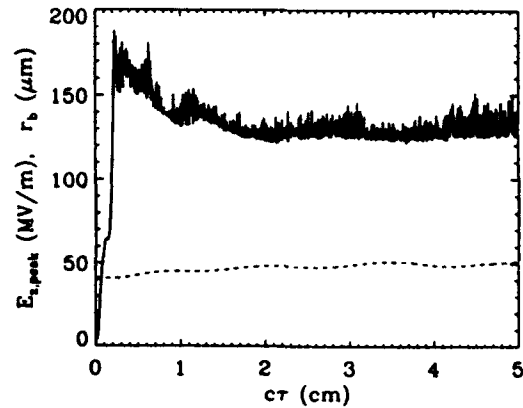


Fig. 4. Beam radius  $R$  (dashed line) at fixed  $\zeta = 0.1$  cm and  $E_{z,peak}$  (solid line) versus  $\tau$  for a simulation with initial  $R=R_{eq} = 41 \mu\text{m}$ .

#### IV. CONCLUSIONS

The radial pinching forces that we have observed in our simulations can be especially severe when  $n_b > n_p$ , where  $n_b$  and  $n_p$  are the beam and plasma densities, respectively. This parameter regime is of interest because of the highly nonlinear wakefields that can be generated. In addition, the filamentation (or Weibel) instability that was observed in the simulations of Keinigs and Jones[7] and Su et al.[8] is avoided in this limit. Our simulations suggest that a highly nonlinear wakefield with favorable focusing properties can be generated by an electron beam in a tightly-focusing equilibrium state.

#### V. REFERENCES

- [1] T. Tajima and J. M. Dawson, Phys. Rev. Lett. **43**, 267 (1979).
- [2] P. Chen, J. M. Dawson, R. W. Huff and T. Katsouleas, Phys. Rev. Lett. **54**, 693 (1985).
- [3] M. Rosing et al., Conf. Record of the 1991 IEEE Particle Accelerator Conference, p. 555.
- [4] J. Smolin, T. Katsouleas, C. Joshi, J. Davis and C. Pellegrini, Bull. Am. Phys. Soc. **35**, 2103 (1990).
- [5] J. B. Rosenzweig, B. Breizman, T. Katsouleas and J. J. Su, Phys. Rev. A **44**, R6189 (1991).
- [6] E. P. Lee and R. K. Cooper, Part. Accel. **7**, 83 (1976).
- [7] R. Keinigs and M. E. Jones, Phys. Fluids **30**, 252 (1987).
- [8] J. J. Su, et al., IEEE Trans. Plasma Sci. **PS-15**, 192 (1987).

\* Supported by ONR/IST/SDIO

# Self-Modulated-Laser Wakefield Acceleration\*

J. Krall, A. Ting, E. Esarey and P. Sprangle

Beam Physics Branch, Plasma Physics Division

Naval Research Laboratory, Washington, DC 20375-5346

**Abstract**—A new configuration of the laser wakefield accelerator is proposed in which enhanced acceleration is achieved via resonant self-modulation of the laser pulse. This requires laser power in excess of the critical power for relativistic guiding and a plasma wavelength short compared to the laser pulse-length. Relativistic and density wake effects strongly modulate the laser pulse at the plasma wavelength, resonantly exciting the plasma wave and leading to enhanced acceleration.

## I. Introduction

Plasma-based accelerators are being widely researched as candidates for the next generation of particle accelerators [1]. One promising concept is the laser wakefield accelerator [2,3] (LWFA), in which a short ( $\tau_L < 1$  ps), high power ( $P > 1$  TW) laser pulse propagates in plasma to generate a large amplitude ( $E > 1$  GV/m) wakefield, which can trap and accelerate a trailing electron bunch. In the standard LWFA, efficient wake generation requires  $L \simeq \lambda_p/2$ , where  $L$  is the full-width-at-half-maximum length of the laser intensity profile on axis,  $\lambda_p = 2\pi c/\omega_p$  is the plasma wavelength,  $\omega_p = (4\pi n_0 e^2/m)^{1/2}$  and  $n_0$  is the ambient plasma density. In this case, the peak axial electric field is given by [2,3]  $E_z \simeq (\pi^2 m c^2/e) a_0^2/(4\lambda_p \gamma_{\perp})$ , where  $\gamma_{\perp} = (1+a_0^2/2)^{1/2}$  and  $a_0 = eA_0/mc^2$  is the normalized amplitude of the laser vector potential field [4] which is assumed to be linearly polarized throughout this paper.

In this paper, we describe a self-modulated-LWFA [5] in which enhanced acceleration is achieved via resonant self-modulation of the laser pulse. This occurs when a) the laser pulse extends axially over several plasma wavelengths,  $L > \lambda_p$ , and b) the peak laser power satisfies  $P \geq P_c \simeq 17(\lambda_p/\lambda_0)^2$  GW, where  $P_c$  is the critical power [6] for relativistic optical guiding and  $\lambda_0$  is the laser wavelength. At fixed laser parameters, both conditions can be met by choosing a sufficiently high plasma density. Operation in the self-modulated regime could have a dramatic impact on LWFA experiments now being planned.

## II. Self-Modulation

In the self-modulated regime, enhanced wakefields are generated, i.e., accelerating fields are more than an order of magnitude greater than those generated by a laser pulse with  $L \simeq \lambda_p/2$ , assuming fixed laser parameters. Acceleration is enhanced for four reasons. Firstly, since a higher

density is required (assuming  $L$  fixed), the wakefield will be increased:  $E_z \sim n_0^{1/2}$ . Secondly, the resonant mechanism excites a very-high-amplitude wakefield in comparison to the standard LWFA. Thirdly, since  $P \geq P_c$ , relativistic focusing further enhances the laser intensity, increasing  $a_0$ . Fourthly, simulations show that a portion of the pulse will remain guided over multiple laser diffraction lengths, extending the acceleration distance.

The mechanism can be understood by considering a long laser pulse,  $L \gg \lambda_p$ , with power  $P \simeq P_c$ , such that the body of the pulse is relativistically guided [3]. The finite rise-time of the pulse will create a low-amplitude wakefield within the laser pulse. In the wakefield, each region of decreased density acts as a local plasma channel to enhance the relativistic focusing effect, while each region of increased density causes defocusing [7]. This results in a low-amplitude modulation of the laser pulse at  $\lambda_p$ . The modulated laser pulse resonantly excites the wakefield and the process continues in an unstable manner. This instability, which is observed to develop on a time-scale associated with laser diffraction, resembles a highly nonlinear 2-D form of the usual forward Raman scattering instability. It is distinguished by its 2-D nature and by its growth rate, which increases dramatically when  $P \geq P_c$ .

In the standard LWFA, the acceleration distance is limited by the diffraction length, or Rayleigh length, of the laser pulse:  $Z_R = (k_0/2)\tau_0^2$ , where  $k_0 = 2\pi/\lambda_0$  and  $\tau_0$  is the radius of the laser waist. At the high plasma densities and extended laser diffraction lengths associated with the self-modulated-LWFA, single-stage acceleration can be limited by detuning due to the reduced group velocity  $v_g$  of the laser pulse, rather than by diffraction. Here,  $v_g \simeq c[1 - (\lambda_0/\lambda_p \gamma_{\perp})^2/2]$ , where  $L \gg \lambda_p$  has been assumed. One-dimensional theory indicates that phase detuning limits the maximum acceleration to  $\Delta\gamma_{max} \simeq \pi\lambda_p^2 a_0^2 \gamma_{\perp}/(2\lambda_0^2)$ , assuming fixed  $a_0$  and  $\lambda_p a_0^2/\lambda_0 \gg 1$ .

We will illustrate the self-modulated LWFA via two numerical simulations. The first is a standard case which is optimized in the usual sense, with  $L = \lambda_p/2$ . The second is a self-modulated case, in which the plasma density is increased such that  $L > \lambda_p$  and  $P > P_c$  are achieved (all other parameters remain unchanged).

## III. Model Equations

These simulations were based on the laser-plasma fluid model described in Ref. 7, which utilizes  $(r, \zeta = z - ct, \tau =$

\*Support by DOE and ONR

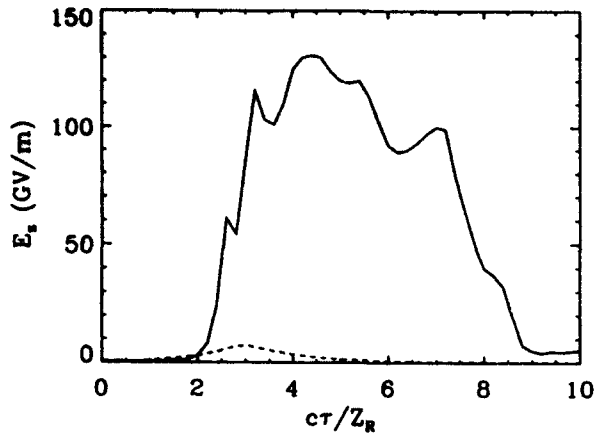


Figure 1: Peak accelerating field versus time for the  $n_0 = 1.4 \times 10^{17} \text{ cm}^{-3}$  case (dashed line) and the  $n_0 = 2.8 \times 10^{18} \text{ cm}^{-3}$  case (solid line).

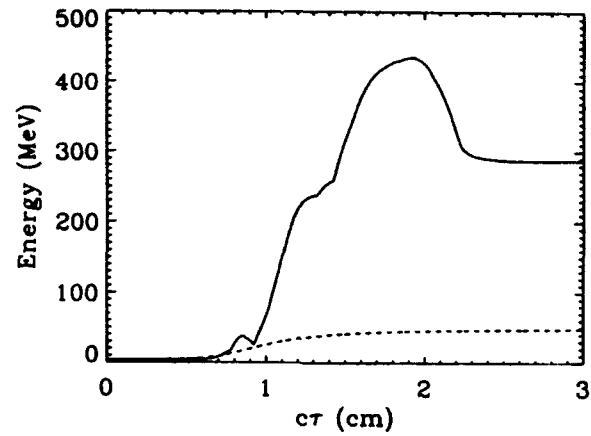


Figure 2: Peak particle energy versus time for the  $n_0 = 1.4 \times 10^{17} \text{ cm}^{-3}$  case (dashed line) and the  $n_0 = 2.8 \times 10^{18} \text{ cm}^{-3}$  case (solid line).

t) coordinates. The laser pulse moves in the positive  $z$  direction such that the front of the laser pulse remains near  $\zeta = 0$ . The physical region of interest extends from  $\zeta = 0$ , where the plasma is unperturbed, to  $\zeta < 0$ . The model is valid when  $Z_R \gg L$ ,  $Z_R \gg \lambda_p$ ,  $\lambda_0 \ll r_0$  and  $\lambda_0 \ll \lambda_p$ . To include phase detuning effects, the  $\partial^2/\partial\zeta\partial\tau$  term is retained in the wave equation, in contrast to Ref. 7. This model neglects certain laser-plasma instabilities. In particular, Raman side-scattering could limit the effective longitudinal extent of a laser pulse with  $P > P_c$  [8].

#### IV. Simulation Results

In these runs, we will consider a Gaussian laser pulse with  $\lambda_0 = 1 \mu\text{m}$ ,  $a_0 = 0.70$ ,  $r_0 = 31 \mu\text{m}$  and  $L = 45 \mu\text{m}$  (150 fs), such that  $Z_R = 0.3 \text{ cm}$ . Here, we define  $a_0$  to be the amplitude of the laser vector potential  $a_f$  at the point of minimum focus in vacuum. In this case, the peak laser power is  $P = 21.5(a_0 r_0/\lambda_0)^2 \text{ GW} = 10 \text{ TW}$  and the energy per pulse is 1.5 J, well within the bounds of present technology [9]. We begin at  $\tau = 0$  with the laser pulse outside the plasma. The plasma density is “ramped up” to reach full density at  $ct = 2Z_R$ . The laser pulse is initially converging such that in vacuum it would focus to a minimum spotsize of  $r_0 = 31 \mu\text{m}$  at  $ct = 3Z_R$ . The simulation continues until  $ct = 10Z_R = 3.0 \text{ cm}$ .

According to standard LWFA theory [2,3], the optimum wakefield will be obtained at a plasma density for which  $\lambda_p \simeq 2L = 90 \mu\text{m}$ , or  $n_0 = 1.4 \times 10^{17} \text{ cm}^{-3}$ . At this density,  $P < P_c \simeq 140 \text{ TW}$ . The presence of the plasma has little effect on the evolution of the laser pulse, which reaches a peak normalized intensity of  $|\hat{a}_f|^2 = 0.56$  at  $ct = 3Z_R$ . This is illustrated in Fig. 1 (dashed line), where the peak accelerating field, plotted versus time, is symmetric about  $ct = 3Z_R$ .

To study the acceleration and trapping of electrons by the wakefield, a particle code is used to accelerate a distribution of 30,000 non-interacting test particles in the

time-resolved electric and magnetic wakefields of the simulation. Here, we consider a continuous electron beam with initial energy of 3.0 MeV and normalized emittance  $\epsilon_n = 130 \text{ mm-mrad}$ . The beam is initially converging such that in vacuum it would focus to a minimum RMS radius  $r_b = 200 \mu\text{m}$  at  $ct = 3Z_R$ . After  $ct = 10Z_R = 3.0 \text{ cm}$ , a small fraction (0.1%) of the original particle distribution has been trapped and accelerated (simulations show that this fraction can be increased by using a lower emittance beam). At  $ct = 3 \text{ cm}$ , the peak particle energy is 48 MeV (see Fig. 2, dashed line).

We now consider a self-modulated-LWFA simulation with parameters nearly identical to those considered above. Here, the plasma density has been increased to  $n_0 = 2.8 \times 10^{18} \text{ cm}^{-3}$  ( $\lambda_p = 20 \mu\text{m}$ ). This reduces the critical power to  $P_c = 6.8 \text{ TW}$ , such that  $P \simeq 1.5P_c$ . As the laser parameters have not been changed, the laser pulse now extends over several  $\lambda_p$ . In this run, one might expect phase detuning to limit the acceleration to  $\Delta\gamma_{\text{max}} \simeq 340$  (170 MeV). However, we will see below that self-focusing enhances the laser intensity by a large factor ( $> 10$ ) such that much higher electron energies can be obtained.

Figure 3 shows the normalized laser intensity at (a)  $ct = 2Z_R$  (just as the laser enters the full-density plasma) and (b)  $ct = 3.2Z_R$  (just beyond the vacuum focal point). The axial electric field at  $ct = 3.2Z_R$  is shown in Fig. 4. The laser pulse has been modulated (three peaks are observable in Fig. 3(b), separated by  $\simeq \lambda_p$ ) and the plasma wave is highly nonlinear. In addition, relativistic and density wake effects have focused the laser to a much higher intensity than was observed in the previous simulation. Figure 1, which shows the peak accelerating field versus time, indicates that the laser pulse is optically guided over  $5.5Z_R$ . Note that the leading portion of the “beamlet” structure, with length  $< \lambda_p/(2\gamma_\perp)$ , diffractively erodes [3,8]. However, the extreme focusing of the laser pulse increases  $\gamma_\perp$  such that the erosion is minimized. In addition, the group velocity within the modulated pulse varies

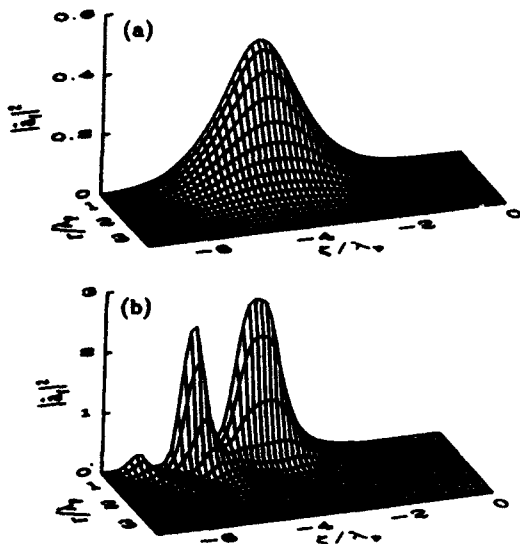


Figure 3: Laser intensity  $|\hat{a}_f|^2$ , sampled over a coarse grid (the numerical grid is much finer), at (a)  $ct = 2Z_R$  and (b)  $ct = 3.2Z_R$ . The laser pulse is moving towards the right.

locally with laser intensity and electron density, further distorting the pulse profile. The laser beamlets continue to distort and erode until  $ct \simeq 7Z_R$ , at which time the laser pulse disintegrates entirely.

Figure 1 (solid line) also shows that as the pulse becomes fully modulated, the amplitude of the peak accelerating field saturates. We have performed further simulations that show that as the wake amplitude increases to the point that the plasma electrons are expelled entirely from the axis of the simulation, the growth of the instability slows. In addition, the 2-D nature of the instability requires that regions of focusing and defocusing occur within the pulse. We find that when defocusing is inhibited, the growth of the instability diminishes.

As before, a beam of noninteracting test particles is injected into the time-resolved wakefield, with approximately 2% of the particles being trapped and accelerated. The peak particle energy of 430 MeV is observed at  $ct = 1.8$  cm =  $6Z_R$ . At  $ct = 3.0$  cm =  $10Z_R$ , however, the peak particle energy has dropped to 290 MeV due to the reduced group velocity of the laser pulse, which causes the electrons to slip out of phase with the wakefield and become decelerated. Figure 2 (solid line) shows acceleration to 430 MeV over 1.8 cm.

## V. Conclusions

We have proposed a new configuration of the LWFA in which enhanced acceleration (by a factor  $> 10$ ) is achieved via resonant self-modulation of the laser pulse (this concept is also discussed in Ref. 10, which was only recently brought to our attention). The self-modulation mechanism requires  $P \geq P_c$  and  $L > \lambda_p$ . We have demonstrated, via simulation, the dramatic advantages of the self-

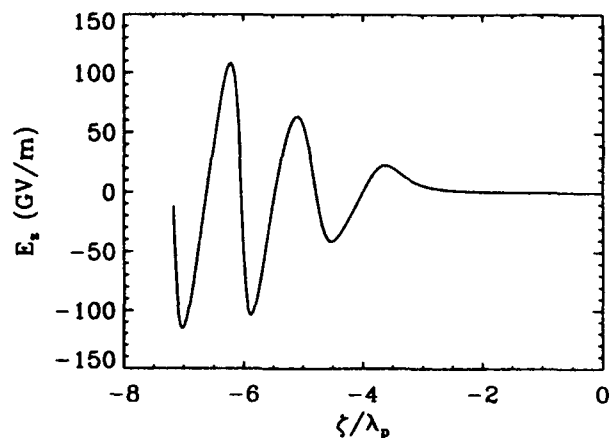


Figure 4: Axial electric field  $E_z$  versus  $\zeta$  plotted at  $ct = 3.2Z_R$ .

modulated-LWFA[5] relative to the standard LWFA [1-3]. We have further demonstrated the feasibility of the self-modulated case by confining our simulations to currently-available laser parameters. It is a notable aspect of these simulations that, by increasing only the plasma density, one can test both the simple linear theory and the highly nonlinear, self-modulation regime described here.

*Acknowledgements*—The authors thank G. Joyce, G. Mourou and D. Umstadter for enlightening discussions.

## VI. References

- [1] See, e.g., Proc. 3rd Intl. Workshop on Advanced Accelerator Concepts, ed. by J. Wurtele, (AIP, NY), to be published.
- [2] T. Tajima and J.M. Dawson, *Phys. Rev. Lett.* **43**, 267 (1979); L.M. Gorbunov and V.I. Kirsanov, *Sov. Phys. JETP* **66**, 290 (1987); P. Sprangle, E. Esarey, A. Ting and G. Joyce, *Appl. Phys. Lett.* **53**, 2146 (1988).
- [3] P. Sprangle, E. Esarey and A. Ting, *Phys. Rev. Lett.* **64**, 2011 (1990); *Phys. Rev. A* **41**, 4463 (1990).
- [4] For a Gaussian laser,  $a_0 \simeq 0.85 \times 10^{-9} \lambda_0 I_0^{1/2}$ , where  $I_0$  is the intensity ( $\text{W}/\text{cm}^2$ ) and  $\lambda_0$  is the wavelength ( $\mu\text{m}$ ).
- [5] J. Krall, A. Ting, E. Esarey and P. Sprangle, submitted to *Phys. Rev. E*.
- [6] C. E. Max, J. Arons and A. B. Langdon, *Phys. Rev. Lett.* **33**, 209 (1974); P. Sprangle, C.M. Tang, and E. Esarey, *IEEE Trans. Plasma Sci.* **PS-15**, 145 (1987).
- [7] P. Sprangle, E. Esarey, J. Krall and G. Joyce, *Phys. Rev. Lett.* **69**, 2200 (1992).
- [8] T. M. Antonsen, Jr., and P. Mora, *Phys. Rev. Lett.* **69**, 2204 (1992).
- [9] G. Mourou and D. Umstadter, *Phys. Fluids B* **4**, 2315 (1992).
- [10] N.E. Andreev, et al., *JETP Lett.* **55**, 571 (1992). The major results of this work are quite similar to our own, but are limited to cases in which  $|\hat{a}_f|^2 \ll 1$ .

# A 100 MeV Proof-of-Principle Laser Wakefield Accelerator Experiment\*

A. Ting, A. Fisher, R. Fischer, J. Grun, J. Krall, E. Esarey and P. Sprangle  
Beam Physics Branch, Plasma Physics Division, Naval Research Laboratory  
Washington, DC 20375-5346

D. Umstadter and G. Mourou  
Center of Ultrafast Optical Science, University of Michigan  
Ann Arbor, MI 48109

**Abstract** We present an initial design of a proof-of-principle experiment on the Laser Wakefield Accelerator (LWFA). The experiment will utilize the NRL Table-Top Terawatt ( $T^3$ ) laser system as the driver for the wakefield in a pulsed-valve gas jet plasma, and a  $\sim 1$  MeV Febetron as the electron beam injector. The LWFA will be operated in the self-modulated regime [1] where enhanced acceleration gradients and extended interaction distances can be achieved. Numerical simulations demonstrate that with the present parameters of the  $T^3$  laser, peak accelerating gradients can reach  $>300$  GeV/m and single stage energy gain of  $>100$  MeV can be attained.

## I. INTRODUCTION

Plasma-based accelerators have recently been the subject of intense research because of their potential for high accelerating gradients, compact size and low cost compared with conventional rf-driven accelerators [2]. While conventional rf-driven accelerators are limited to fields on the order of 100 MeV/m, plasma accelerators have been shown experimentally to support gradients of  $\sim 1$  GeV/m [3] in the Plasma Beat Wave Accelerator (PBWA), and are predicted theoretically and numerically to support gradients exceeding 300 GeV/m [1] in the LWFA.

Two configurations of the LWFA have been proposed, (i) the "standard" LWFA [4] and (ii) the "self-modulated" LWFA.[1] In the recently proposed self-modulated LWFA, enhanced acceleration is achieved via resonant self-modulation of the laser pulse. This occurs when (i) the laser pulse extends axially over several plasma wavelengths,  $L \gg \lambda_p$ , and (ii) the peak laser power satisfies  $P \geq P_c$ , where  $P_c$  is the critical power [5] for relativistic optical guiding,  $P_c[\text{GW}] = 17(\lambda_p/\lambda_0)^2$  and  $\lambda_0$  is the laser wavelength. At fixed laser parameters, both conditions can be met by choosing a sufficiently high plasma density,  $n$ . This is the case since  $P_c \propto 1/n$  and  $\lambda_p \propto 1/\sqrt{n}$ . Operation in the self-modulated regime has very significant advantages over the standard configuration.

The newly developed  $T^3$  laser technology [6] is capable of delivering the short ( $< 1$  ps), ultrahigh power ( $> 1$  TW) laser pulses required by the LWFA. Simulations based on the NRL  $T^3$  laser parameters and the self-modulated LWFA configuration indicate that accelerating fields in excess of 300

GeV/m and electron energies in excess of 100 MeV can be obtained in a single stage.

## II. APPROACH

A schematic of a proof-of-principle LWFA experiment is shown in Fig. 1.

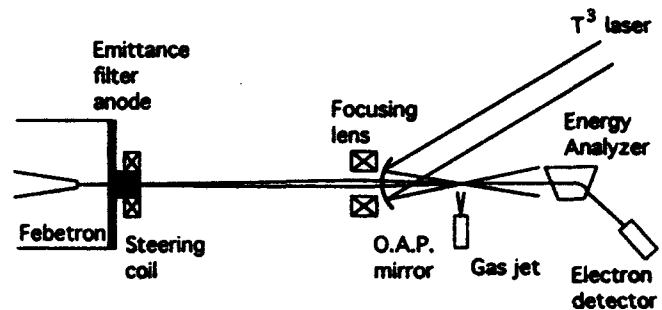


Fig. 1. Schematic of the proof of principle LWFA experiment. An electron beam from a compact injection accelerator is accelerated by the laser plasma wakefield and then energy resolved with an electron spectrometer.

A pulsed-valve is used to deliver a high density gas jet inside an evacuated chamber. The gas jet is ionized through multiphoton ionization to form a plasma column by either a precursor pulse or the prepulse of the driver laser pulse. The driver laser pulse is focused into the plasma column with appropriate optics such as an off-axis paraboloid (O.A.P.) at high intensities to generate the wakefield. The characteristics of the plasma wakefields are measured with the Thomson scattering diagnostics. An electron beam with energy high enough to be trapped by the wakefield is injected into the plasma after being transported and focused. Accelerated electrons are detected and analyzed with a magnetic spectrometer for the energy spectrum. The parameters for the experiment are shown in Table I.

## III. APPARATUS

This experiment consists of five major components: A) the NRL  $T^3$  laser to drive the wakefield, B) the NRL Febetron electron accelerator for electron injection into the wakefield, C) a gas jet plasma source to support the wakefield, D) a Thomson scattering diagnostics for characterizing the

\* Work supported by U.S. DOE and ONR.

wakefield, and E) an electron spectrometer to measure the energy gain of the injected electrons.

#### Laser parameters:

Wavelength	1.054 $\mu\text{m}$
Energy	$\sim 1.5$ J
Pulse length	$\sim 750$ fs
Focal spot radius (F/6 optics)	$\sim 10$ $\mu\text{m}$
Intensity	$\sim 1.3 \times 10^{18}$ W/cm <sup>2</sup>

#### Wakefield parameters:

Plasma density	$\sim 1.25 \times 10^{19}$ cm <sup>-3</sup>
Plasma wavelength	$\sim 10$ $\mu\text{m}$
Acceleration gradient	$> 300$ GeV/m
Interaction length	$\sim 0.2$ cm
Pump depletion length	$\sim 2$ cm
Phase detuning length	$\sim 0.4$ cm
Energy gain	$> 100$ MeV

#### Electron beam parameters:

Energy	$\sim 1$ MeV
Current	$\sim 10$ A
Pulse length	$\sim 50$ ns
Focused beam radius	$\sim 100$ $\mu\text{m}$
Number of electrons trapped	$\sim 10^5$

Table I. Typical laser, wakefield, and electron beam parameters for the proof-of-principle LWFA experiment.

#### A. Laser Diver

The NRL T<sup>3</sup> laser is based on the chirped-pulse amplification (CPA) concept [6] which takes advantage of the fact that laser amplifiers can better amplify a long pulse than a short pulse. By incorporating frequency chirping in a long pulse, the amplified pulse can be compressed by use of gratings into a short pulse with much higher intensity. The NRL T<sup>3</sup> laser system has been operational since Oct. 1992. It has an energy per pulse of  $\sim 1.5$  J and a pulse length of  $\sim 750$  fs, giving a laser power of  $\sim 2$  TW. The high quality laser beam produces a spot size of  $\sim 20$   $\mu\text{m}$  at 1.4 times diffraction limited with an f/6 lens, giving a peak intensity of  $\sim 1.3 \times 10^{18}$  W/cm<sup>2</sup>. It also has a high contrast ratio of  $\sim 10^{-6}$  between the amplitude of the prepulse to the central peak. The repetition rate is one pulse/4 minutes.

#### B. Electron Beam Injector

In a practical LWFA, the electron bunch must be synchronized in both time and space to the wakefield for maximum accelerating gradient and minimum energy spread. However, for a proof-of-principle experiment, the minimum required bunch length is determined by having enough electrons to be accelerated for detection. The NRL Febetron electron beam, which has a pulse length of 50 ns, will behave as if it is CW, and therefore eliminate the problem of

synchronization. The Febetron is capable of producing several kA's of beam current. However, to avoid perturbing the plasma with a high current electron beam, the Febetron beam current will be limited to  $\sim 10$  A by mismatching the diode and collimating the beam with a pinhole aperture (few mm). The collimation also acts as an emittance filter and produces a high quality electron beam which can be focused with a magnetic lens for better matching to the acceptance of the plasma wakefield.

#### C. Plasma Source

By operating the LWFA in the self-modulated regime, substantially higher gradients and longer interaction distances can be achieved. This can be accomplished by using a higher density plasma, while utilizing the same parameters for the laser and the electron beam. By incorporating an ultrasonic nozzle to a pulsed-valve gas jet, neutral gas density of  $> 1 \times 10^{19}$  cm<sup>-3</sup> can be obtained. The corresponding critical power for relativistic focusing for this plasma density is 1.7 TW and the plasma wavelength is only 10  $\mu\text{m}$ . Many periods of plasma wakefields can be excited in the 750 fs laser pulse.

#### D. Wakefield Characterization

Coherent Thomson scattering [7] will be used to detect the plasma wakefields and measure its frequency and amplitude. In this process, a light wave is scattered by a plasma wave. The scattered light wave is frequency shifted by the plasma wave frequency. Thomson scattering from the plasma wave is performed with a synchronized collinear longer laser pulse ( $\sim 20$  mJ,  $\sim 100 - 150$  ps, of either 1  $\mu\text{m}$  ( $\omega$ ) or 0.5  $\mu\text{m}$  ( $2\omega$ ) light) derived from a separate but synchronized transform-limited laser developed at CUOS. The wavelength shift for an electron plasma density of  $10^{16} - 10^{19}$  cm<sup>-3</sup> is found from phase matching conditions to be approximately  $\Delta\lambda = 30 - 950$   $\text{\AA}$  for  $\omega$  and  $8 - 240$   $\text{\AA}$  for  $2\omega$  light, which can be measured with a conventional double grating spectrometer.

The amplitude of the plasma wave,  $\Delta n/n$ , is obtained from the amplitude of the scattered light through the Bragg scattering formula [8]. Assuming a plasma wave amplitude of 10% and probe pulse energy of 20 mJ, as many as  $10^8 - 10^{14}$  photons will be scattered. It is expected that the plasma wave amplitude can be increased to beyond the nonrelativistic cold plasma wavebreaking limit,  $\Delta n/n = 1$ , where nonlinear behavior of the plasma wave is prominent. The nonlinear regimes of wakefield generation can be studied by measuring the harmonics of the plasma wave frequency in the spectrum of the scattered light [9].

#### E. Electron Energy Analyzer

The energy of the accelerated electrons will be measured as a function of laser intensity, plasma density, and acceleration distance. Because the electron bunch is much longer than the plasma wavelength, electrons would interact with the

wakefield at arbitrary points along the wave and thus experience arbitrary gradients. A large energy spread (1 -100 MeV) would be expected regardless of the input electron energy spread. A magnetic electron spectrometer is most suitable for analyzing electron beams with large energy spreads due to its large dynamic range. By allowing a collimated electron beam to enter a narrow gap separating two magnetic poles, the beam velocity can be determined from the resulting radius of curvature. The curved electrons can be detected with solid state detectors, scintillators or Cerenkov detectors. Magnetic monochromators, where the electrons go through fixed radius of curvature, are more suitable for lower energy electrons (1-10 MeV). For higher energy electrons, the energy spectrum can be studied with constant field magnetic spectrometers, attenuation filters, and Cerenkov cells. Direct observation of the electrons in a Wilson cloud chamber is also possible [3].

#### IV. DISCUSSION

The number of electrons that may be trapped by the wakefield can be estimated as follows. Assuming the wakefield has a spatial extent of  $\sim 20 \mu\text{m}$  and an amplitude of a fraction of the nonrelativistic wave breaking field, the acceptance of the wakefield in phase space is typically an elongated vertical ellipse because of the very large radial wakefield that is excited together with the longitudinal accelerating wakefield. On the other hand, the electron beam's phase space area is typically a horizontal elongated ellipse as it comes out of the Febetron accelerator. For a good emittance electron beam ( $\sim 5 \pi \text{ mm mrad}$ ), it can be focused down to  $\sim 200 \mu\text{m}$ . The electron beam's phase space area is thus rotated and squeezed into a vertical ellipse (still wider than the ellipse formed by the wakefield acceptance, and the system is under focused). The overlapping area of the electron beam emittance and the acceptance of the wakefield is approximately given by the square of the ratio of the radial wakefield radius to the focused electron beam radius. The ratio is  $\sim 5 \times 10^{-3}$ . For an electron beam with  $\sim 10 \text{ A}$  of current, a picosecond laser wakefield will overlap with  $\sim 6.2 \times 10^7$  electrons. Taking into account that only one quarter of each wakefield period has both accelerating and focusing wakefields, an interaction length of 2 mm, and the emittance-acceptance overlapping ratio estimated above, the number of electrons that can be trapped and accelerated is  $\sim 2 \times 10^5$ . Such intensities of the accelerated electron may be conveniently detected with solid state detectors or scintillators and photo-multipliers.

Although the minimum injection energy required for trapping of the electrons in the accelerating potential is only  $\sim 200 \text{ keV}$ , higher injection energy is required to overcome scattering of the electrons by the initial radial wakefield in an extended plasma region [10]. A plasma column with sharp boundary will allow a rapid buildup of the wakefield within the scalelength of the plasma boundary when the driver laser arrives. Numerical simulations have demonstrated that with a good quality electron beam and a sharp boundary plasma

column, electrons with  $\sim 1 \text{ MeV}$  will be trapped by the wakefields. The boundary of the gas jet is more well defined at the earlier stages of the gas jet evolution. It is important to synchronize the ionizing laser and the driver laser with respect to the gas jet so as to create a plasma with a sharp boundary. This will facilitate more efficient trapping of the electrons in the injection electron beam.

#### V. CONCLUSIONS

We have presented a preliminary design on a 100 MeV proof-of-principle experiment of the LWFA operating in the self-modulated regime. The experiment is based on the NRL T3 laser driver and the NRL Febetron electron accelerator. We have discussed the various diagnostics for wakefield characterization and electron energy analysis. We have also discussed the importance of using a gas jet as the plasma source, and the propagation and focusing of the electron beam for better trapping of the electrons. A proof-of-principle LWFA experiment that can produce very high accelerating gradients and final energies appears to be feasible.

#### VI. ACKNOWLEDGEMENTS

The authors are grateful to X. Liu, S. Gold, G. Joyce, C. Manka, P. Mora, K. Marsh, C. Clayton and C. Joshi for useful discussions.

#### VII. REFERENCES

- [1] J. Krall, A. Ting, E. Esarey and P. Sprangle, submitted to *Phys. Rev. E*, and these proceedings.
- [2] See, e.g., *Proc. 3rd Intl. Workshop on Advanced Accelerator Concepts, Port Jefferson, NY, 1992*, ed. by J. Wurtele, (AIP, NY), to be published.
- [3] C.E. Clayton, K.A. Marsh, A. Dyson, M. Everett, A. Lal, W.P. Leemans, R. Williams and C. Joshi, *Phys. Rev. Lett.* **70**, 37 (1993).
- [4] T. Tajima and J. Dawson, *Phys. Rev. Lett.* **43**, 267 (1979); L.M. Gorbunov and V.I. Kirsanov, *Sov. Phys. JETP* **66**, 290 (1987); P. Sprangle, E. Esarey, A. Ting and G. Joyce, *Appl. Phys. Lett.* **53**, 2146 (1988).
- [5] C.E. Max, J. Arons and A.B. Langdon, *Phys. Rev. Lett.* **33**, 209 (1974); P. Sprangle, C.M. Tang and E. Esarey, *IEEE Trans. Plasma Sci.* **PS-15**, 145 (1987).
- [6] G. Mourou and D. Umstadter, *Phys. Fluids B* **4**, 2315 (1992).
- [7] C. Clayton, C. Joshi, C. Darrow and D. Umstadter, *Phys. Rev. Lett.* **54**, 2343 (1985).
- [8] R. E. Slusher and C. M. Surko, *Phys. Fluids* **23**, 472 (1980).
- [9] D. Umstadter, R. Williams, C. Clayton and C. Joshi, *Phys. Rev. Lett.* **59**, 292 (1987).
- [10] P. Mora, *Phys. Fluids B* **4**, 1630 (1992).

## Recent Work on Short Pulse Laser-Plasma Accelerators\*

T. Katsouleas<sup>(1)</sup>, W. B. Mori<sup>(2)</sup>, C. Decker<sup>(2)</sup>, T. C. Chiou<sup>(1)</sup>, J. S. Wurtele<sup>(3)</sup>, G. Shvets<sup>(3)</sup>

<sup>(1)</sup>University of Southern California, Los Angeles, CA

<sup>(2)</sup>University of California, Los Angeles, CA

<sup>(3)</sup>Massachusetts Institute of Technology, Cambridge, MA

### Abstract

Theory and simulation of short-pulse laser plasma accelerators is presented. The plasma beat wave and laser wakefield accelerators are examined for the parameters of recently developed high-brightness lasers. For typical parameters, energy gains of .3 to 1 GeV over a few centimeters length appear feasible with a short pulse beat wave design. Issues important for extending these designs to multi-GeV acceleration of beams with high beam quality are examined, including optical guiding of the lasers, non-linear laser and wake velocity shifts, and long-term stability of the laser pulses.

### I. INTRODUCTION

The recent success of the plasma beat wave accelerator at UCLA (see C. Clayton, these proceedings), coupled with the rapid advancement of laser technology point to a promising future for short pulse laser-plasma accelerators. It is natural then to consider what are the key issues for next generation experiments at the 100 MeV to GeV level and beyond. These issues include long-term stability of intense laser pulses, non-linear effects on the laser group velocity and resulting accelerating wake velocity, and techniques for guiding the laser pulses over many diffraction lengths.

First, we illustrate with an example that with present technology it is possible to design a GeV experiment that is a straight forward extension of the UCLA experiment. In the UCLA experiment, it was demonstrated that short pulses could avoid competing instabilities and that the energy gain of approximately 20 MeV was consistent with an acceleration length equal to the laser depth of focus.

Then we take up the long-term stability of laser pulses. The parametric instabilities of radiation in plasmas has been long studied. For pulses shorter than an ion plasma period all of the ion instabilities can be avoided. Thus we consider the coupling to electron plasma noise known as Raman scattering. For pulses shorter than a few times the e-folding time of the Raman backscatter instability ( $\tau_B = 2\sqrt{2} |(V_{os}/c) \sqrt{\omega_0 \omega_p}|^{-1}$ , where  $V_{os}/c = eA_0/mc^2$  is the normalized laser amplitude and  $\omega_0$  is its frequency), this can be avoided. On the other hand, even for pulses shorter than the Raman forward scatter temporal growth time ( $\tau_F \sim 2\sqrt{2} |(V_{os}/c) \omega_p^2/\omega_0|^{-1}$ ) this instability can still be important because the decay waves travel in the direction of the pulse at nearly c. We consider for the first time the *spatial-temporal* growth of the forward Raman instability for arbitrarily intense laser pulses.

Another possible limitation to the energy gain and beam quality in a plasma accelerator is the dephasing between the particle and the wave. Therefore, in laser plasma accelerators it is important to understand the relationship between the laser's parameters (i.e. shape, amplitude, and frequency) and the excited plasma wave phase velocity. In the limit of small laser amplitude, i.e.,  $\frac{V_{os}}{c} \equiv \frac{eA_0}{mc^2} \ll 1$ , the plasma waves phase velocity is equal to the laser pulse's group velocity. However, as the laser amplitude increases these relationships become more complicated because the laser's group velocity ( $v_g$ ) depends on its amplitude and the wake's phase velocity ( $v_w$ ) depends on pump depletion. In Sec. IV we examine the non-linear laser group velocity and wake phase velocity analytically and computationally.

Finally, in Sec. V we examine one technique for guiding laser pulses over many diffraction lengths.

### II. DESIGN EXAMPLE

An illustrative example of a short-pulse beat wave accelerator is given in Table 1 and Figure 1. We call this a hybrid design because it uses very short laser pulses like the laser wakefield scheme but two frequencies as in the beat wave scheme.

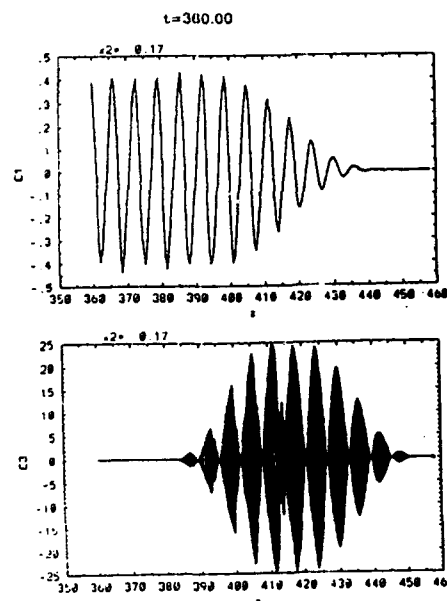


Figure 1. PIC simulation of Plasma wake (above) and laser in hybrid example

\*This work has been supported by the US Dept. of Energy (Grant #DE-FG03-92ER40745)

The parameters are typical of a CPA Nd: Yag laser<sup>1</sup>. As shown in the moving PIC simulation in Fig. 1, the plasma wake grows resonantly, but only over a few plasma cycles. So the homogeneity requirement on plasma density ( $\Delta n_0/n_0 \leq$  one over the number of growth cycles) is greatly relaxed over previous beat wave designs. For this example the energy gain is limited by the laser Rayleigh range to about 300 MeV in 2 cm.

Table 1

Hybrid Wakefield/Beatwave Accelerator	
An Example:	
Laser Wavelengths	1.05, 1.06 $\mu\text{m}$
Laser Pulse Length	1.4 psec
Laser Power	10 TW
Laser Spotsize ( $2\sigma$ )	100 $\mu\text{m}$
Rayleigh Length	0.8 cm
Plasma Density	$10^{17} \text{ cm}^{-3}$
Plasma Homogeneity	+/-20%
Accelerating Field	160 MeV/cm
Acceleration Length*	6.4 cm
Energy	1000 MeV
*Assumes optical guiding. Max energy without guiding is 300 MeV	

### III. FORWARD RAMAN INSTABILITY OF SHORT PULSES

We consider a laser pulse of vector potential  $A \equiv mc^2 a/c$  propagating in a plasma of density  $n_0 \equiv m\omega_p^2/4\pi c^2$ . The coupled equations for the laser potential  $A$  and plasma potential  $\phi \equiv (\chi - 1)mc^2$  are found in the coordinates  $\psi = t - x/c$  and  $\tau = t$ :

$$-2 \partial_\psi \partial_\tau a = \frac{a}{\chi} \quad (1)$$

$$\partial_\psi^2 \chi + \frac{1}{2} \left[ 1 - \frac{1+a^2}{\chi^2} \right] = 0 \quad (2)$$

This is the quasi-static approximation<sup>2</sup>. We expand these for large  $a$  and  $\chi$  about  $\chi = \chi_0 + \delta\chi$  where  $\chi_0^2 = 1 + a_0^2/2$ ,  $a = \frac{a_0}{2}$

$e^{i\theta_0} + \frac{a_+}{2} e^{i\theta_+} + \frac{a_-}{2} e^{i\theta_-} + \text{c.c.}$ ,  $\theta_j = -k_j\psi - (\omega_j - k_j)\tau$ ,  $\delta\chi = \delta\chi_s e^{i\theta}$ , and  $\theta_\pm = \theta \pm \theta_0$ . The details and an exact solution in  $\psi$  and  $\tau$  are given in a longer paper<sup>3</sup>. Here we give the asymptotic growth rate for  $\tau > \psi$  (i.e., distance moved

through the plasma longer than the pulse length) and large  $a_0$ :  $\chi_s$  grows as  $c^\Gamma$  where

$$\Gamma = 2 \gamma_{nl} \sqrt{\psi \tau} \quad (3)$$

$\gamma_{nl} = \gamma_0/\chi_0^2$  and  $\gamma_0$  is the usual small-amplitude temporal growth rate ( $\gamma_0 = a_0\omega_p^2/2\sqrt{2}\omega_0$ )

### IV. NON-LINEAR GROUP AND WAKE VELOCITY

An analytical expression for the nonlinear group velocity is obtained by starting from the conservation of energy equations for a fluid plasma

$$\frac{\partial}{\partial t} \left[ \frac{E^2 + B^2}{8\pi} + n mc^2 \gamma - n_0 mc^2 \right] + \nabla \cdot \left[ \frac{c}{4\pi} E \times B + n mc^2 \gamma v \right] \quad (4)$$

where  $v$  is the electron momentum and  $\gamma \equiv [1 - \frac{v^2}{c^2}]^{-1/2}$ . A group velocity is given by the ratio of the energy flux to the energy density. For long pulses this provides the expression

$$v_g = \frac{c^2/v_\phi}{1 + \frac{\omega_p^2}{2\omega^2} \frac{\gamma_{\perp 0} - 1}{\gamma_{\perp 0}(\gamma_{\perp 0} + 1)}} \quad (5)$$

where  $\gamma_{\perp 0} \equiv (1 + \langle \frac{e A_0}{mc^2} \rangle^2)^{1/2}$ ,  $\langle \rangle$  represents averaging of the laser oscillations and Faraday's law was used to relate  $B$  to  $E$ . An expression for  $v_\phi$  is provided by the well known results of Ahkiczer and Polovin,  $v_\phi^2 = \frac{1}{1 - \frac{\omega_p^2}{\omega^2 \gamma_{\perp 0}}}$ . Therefore,

in the nonlinear limit  $v_\phi v_g$  no longer equals  $c^2$ . Note that expression (4) does reduce to the linear results as  $\gamma_{\perp 0} \rightarrow 1$ . If

we define  $\gamma_g \equiv (1 - \frac{v_g^2}{c^2})^{-1/2}$  then  $\gamma_g = \sqrt{\frac{\gamma_{\perp 0} + 1}{2}} \frac{\omega}{\omega_p}$

while if  $v_g = \frac{1}{v_\phi}$  then  $\gamma_g = \sqrt{\gamma_{\perp 0}} \frac{\omega}{\omega_p}$ . The relationship between  $v_g$  and  $v_w$  was investigated using PIC simulations. Analytical results are difficult because the wake's phase velocity is influenced by  $v_g$ , linear and nonlinear dispersion, photon deceleration (pump depletion), photon acceleration and pulse distortion.

It was found that the group velocity of symmetrically shaped pulsed of length  $\leq 2\pi c/\omega_p$  is always above the linear  $v_g$  but below the nonlinear  $v_g$  of long pulses. However, the wake's phase velocity monotonically decreases from the linear  $v_g$  as the laser's amplitude is increased. We believe this arises from pump depletion which causes the front of the pulse to distort. Furthermore, we have found that pulses with slow

rise times and rapid fall times provide wakes with phase velocities exceeding the *nonlinear* group velocity. We note different conclusions regarding  $v_g$  and  $v_w$  have been reached when the lowest order nonlinearities and times exceeding the pump depletion time were considered. Clearly, further work is needed to fully understand the dependence of  $v_w$  on laser parameters.

### V. HOLLOW CHANNEL LASER WAKEFIELD ACCELERATOR<sup>4</sup>

In order to guide a short pulse over long distances without diffraction we consider a hollow evacuated channel in the plasma. Since the index of refraction in the channel ( $\epsilon = 1$ ) is greater than that in the surrounding plasma ( $\epsilon = 1 - \omega_p^2/\omega_0^2$ ), the channel guides the laser as would an optical fiber. The channel can be formed by a precursor laser (of high frequency, low intensity and long pulse length) or by hydrodynamic means prior to ionization (e.g., a partially blocked gas jet).

The laser excites a wake on the surface of the channel; the fields of the wake extend into the channel where a particle beam can be accelerated. The wake is illustrated in Fig. 2 and the laser pulse, initially and after 13 Rayleigh lengths, is shown in Fig. 3.

The hollow channel scheme presented here has several attractive features: (1) The Rayleigh length limit on acceleration length is overcome. (2) The wake is nearly uniform as a function of radial position in the channel, so beam quality should be good. (3) The laser and wake velocity are higher than in a uniform plasma, so phase slippage is reduced.

Further study of the stability of such pulses is planned.

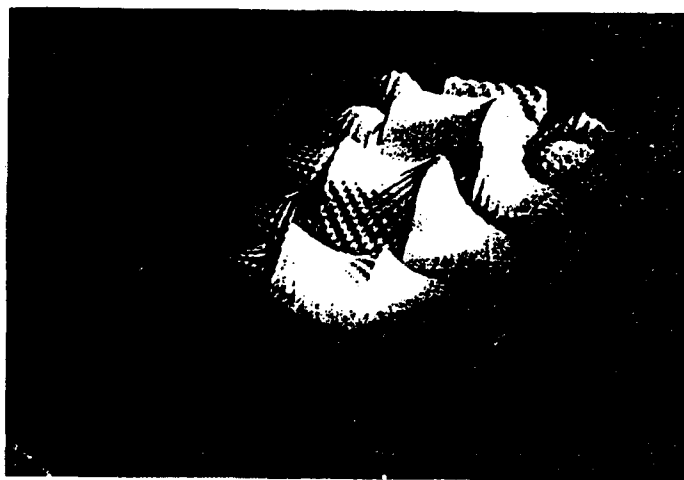
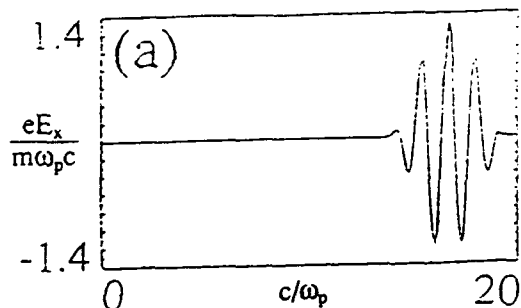
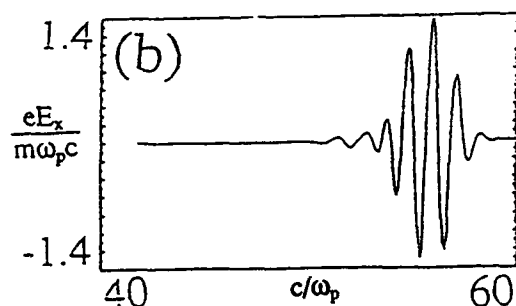


Figure 2. Wake in a hollow plasma channel

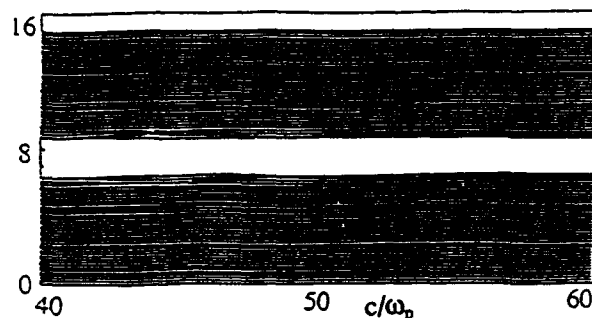
#### Simulations:



(a) Initial laser pulse



(b) Laser pulse after 13 Rayleigh lengths



(c) Plasma channel ( $k_p a = 1$ )

Figure 3.

#### REFERENCES

- [1] G. Morou, in Proc. of Advanced Accelerator Concepts Workshop, J. S. Wurtele, ed., Port Jefferson, June 1992 (AIP, NY 1993).
- [2] See for example P. Sprangle, et al., in Ref. 1.
- [3] W. B. Mori, et al, to be published.
- [4] T. Katsoulcas, et al. in Ref. 1.

# Plasma Lens Experiments at the Final Focus Test Beam\*

B. Barletta<sup>2,4</sup>, S. Chattopadhyay<sup>4</sup>, P. Chen<sup>12</sup>, D. Cline<sup>2</sup>, W. Craddock<sup>12</sup>, W. Gabella<sup>2</sup>, I. Hsu<sup>9</sup>, T. Katsouleas<sup>11</sup>, P. Kwok<sup>2</sup>, P. Lai<sup>11</sup>, W. Leemans<sup>4</sup>, R. Liou<sup>11</sup>, D. D. Meyerhofer<sup>10</sup>, K. Nakajima<sup>8</sup>, H. Nakanishi<sup>8</sup>, C. K. Ng<sup>12</sup>, Y. Nishida<sup>13</sup>, J. Norem<sup>1</sup>, A. Ogata<sup>8</sup>, S. Rajagopalan<sup>2</sup>, J. Rosenzweig<sup>2</sup>, A. Sessler<sup>4</sup>, J. Spencer<sup>12</sup>, J. J. Su<sup>7</sup>, G. Westenskow<sup>5</sup>, D. Whittum<sup>8</sup>, R. Williams<sup>3</sup>, J. Wurtele<sup>6</sup>.

## Abstract

We intend to carry out a series of plasma lens experiments at the Final Focus Test Beam facility at SLAC. These experiments will be the first to study the focusing of particle beams by plasma focusing devices in the parameter regime of interest for high energy colliders, and is expected to lead to plasma lens designs capable of unprecedented spot sizes. Plasma focusing of positron beams will be attempted for the first time. We will study the effects of lens aberrations due to various lens imperfections. Several approaches will be applied to create the plasma required including laser ionization and beam ionization of a working gas. At an increased bunch population of  $2.5 \times 10^{10}$ , tunneling ionization of a gas target by an electron beam - an effect which has never been observed before - should be significant. The compactness of our device should prove to be of interest for applications at the SLC and the next generation linear colliders.

## I. INTRODUCTION

Plasma focusing devices are compact, simple, and very strong focusing elements. The focusing strengths for typical parameters are equivalent to  $\sim 10^9$  Gauss/cm focusing magnets. In principle, such strong fields are capable of focusing beams to very small spot sizes [1-6] and perhaps even capable of avoiding [7] inherent (Oide) limitation [8] in discrete strong focusing. Our goal is to show the effectiveness of plasma lenses in the parameter regime of interest for SLC and the next generation high energy linear colliders. The experience gained is expected to yield new final focus designs capable of producing spot sizes smaller than ever produced before.

There are two low energy, low density beam experimental results which confirm the theory of the beam-plasma interaction performed at ANL [9,10] and Tokyo University [11]. While such experimental results have been useful, however, the beam densities involved in the ANL and Tokyo

experiments were 6 to 7 orders of magnitude lower than the nominal colliding beam density at the SLC and the next generation linear colliders, so that the experience is insufficient to design or evaluate a plasma lens in a high energy collider detector. A beam such as the FFTB offers a unique environment to test all aspects of plasma focusing of high energy, high density, and low emittance beams.

## II. PARAMETER STUDIES

When ignoring the effects due to the return current, the focusing strength for underdense plasma lenses is governed by the plasma density  $n_p$ ,

$$K = \frac{2\pi r_e}{\gamma} n_p \quad (2.1)$$

whereas for the overdense plasma lenses the strength is determined by the beam density  $n_b$ ,

$$K = \frac{2\pi r_e}{\gamma} n_b \quad (2.2)$$

The plasma return current tends to reduce the focusing effect of the lens [12]. The effect is approximately given by

$$K_{rc} = \frac{K}{1 + (k_p \sigma_r)^2} \quad (2.3)$$

where  $\sigma_r$  is the rms size of the beam and  $k_p = \sqrt{4\pi r_e n_p}$  is the plasma wavenumber. The effect is appreciable only when the plasma is considerably denser than the beam.

Beam Parameters	Case 1	Case 2	Case 3
$\mathcal{E}$ [GeV]	50	50	50
$N$ [ $10^{10}$ ]	1.0	1.0	1.0
$\epsilon_n$ [ $10^{-5}$ m-rad]	3.0	3.0	3.0
$\beta_0^*$ [cm]	7.5	7.5	7.5
$\sigma_{r0}^*$ [ $\mu$ m]	4.74	4.74	4.74
$\beta_0$ [cm]	8.03	8.03	8.03
$\sigma_0$ [ $\mu$ m]	4.91	4.91	4.91
$\sigma_z$ [mm]	0.47	0.47	0.47
$n_{b0}$ [ $10^{16}$ cm <sup>-3</sup> ]	5.3	5.3	5.3
Lens Parameters			
$n_p$ [ $10^{17}$ cm <sup>-3</sup> ]	0.2	1.0	10
$k_p \sigma_z$	12.5	28.0	88.5
$s_0$ [cm]	-2.0	-2.0	-2.0
$l$ [cm]	0.3	0.3	0.3
$f$ [cm]	3.80	2.92	3.60
Focused Beam			
$\beta_r^*$ [mm]	3.7	2.1	3.4
$\sigma_r^*$ [ $\mu$ m]	3.35	2.55	3.23
$s^*$ [cm]	1.95	1.07	1.75

Table 1: Round Beam Focusing

\*Work supported by DOE contract DE-AC03-76SF00515.

<sup>1</sup>Argonne National Laboratory, Argonne, Illinois

<sup>2</sup>University of California, Los Angeles, California

<sup>3</sup>Florida A & M University, Tallahassee, Florida

<sup>4</sup>Lawrence Berkeley Laboratory, Berkeley, California

<sup>5</sup>Lawrence Livermore National Laboratory, Livermore, California

<sup>6</sup>Massachusetts Institute of Technology, Cambridge, Massachusetts

<sup>7</sup>National Central University, Taiwan

<sup>8</sup>National Laboratory for High Energy Physics (KEK), Tsukuba, Japan

<sup>9</sup>National Tsing-Hua University, Taiwan

<sup>10</sup>University of Rochester, Rochester, New York

<sup>11</sup>University of Southern California, Los Angeles, California

<sup>12</sup>Stanford Linear Accelerator Center, Stanford, California

<sup>13</sup>Utsunomiya University, Utsunomiya, Japan

### A. Round Beam Focusing

The plasma is created by an intense laser before the arrival of the particle beam bunch. The gas density will be varied to cover all regimes of the plasma lens from underdense to overdense and to the total compensation limit, at which focusing degrades due to return current. Typical parameters corresponding to these lenses are shown in Table 1.

In the table,  $\mathcal{E}$  is the beam energy and  $\epsilon_n$  is the normalized emittance. The initial beta at the vacuum waist is  $\beta_0^*$  and  $s_0$  is the beginning of the lens with respect to this waist. The beta function at the entrance to the lens is  $\beta_0$  and  $l$  is the lens thickness. The focal length of the lens is  $f = s^* - s_0 - l/2$  where  $s^*$  is the distance of the new focal point from the initial one without plasma. The plasma density is  $n_p$  and  $n_{b0}$  is the peak beam density at the entrance to the plasma.

### B. Flat Beam Focusing

With the designed FFTB beam parameters while  $N = 2.5 \times 10^{10}$ , the beam is intense enough to produce a high density plasma by impact ionization and should even reach the tunneling ionization threshold when close enough to the initial focal point. Theory [6] and simulations [13] of such a scheme suggest substantial plasma focusing. Typical parameters for such plasma lenses are shown in Table 2.

In Case 4, the tunneling ionization threshold is reached right from the start of the lens, and the ionization is quickly saturated. With the complimentary impact ionization, we expect that the plasma so produced should be reasonably uniform, and the aberrations should be much mild. In Case 5, the vertical beam size goes down to  $\sim 38$  nm, which is less than 2/3 of the 60 nm designed FFTB minimum vertical beam size.

Beam Parameters	Case 4	Case 5
$\mathcal{E}$ [GeV]	50	50
$N$ [ $10^{10}$ ]	2.5	2.5
$\epsilon_{nx} / \epsilon_{ny}$ [ $10^{-5}$ m-rad]	3.0 / 0.3	3.0 / 0.3
$\beta_{x0}^* / \beta_{y0}^*$ [mm]	3.0 / 3.0	3.0 / 0.12
$\sigma_{x0}^* / \sigma_{y0}^*$ [nm]	1000 / 333	1000 / 60
$\beta_{x0} / \beta_{y0}$ [mm]	4.33 / 4.33	4.33 / 33.5
$\sigma_{x0} / \sigma_{y0}$ [nm]	1200 / 400	1200 / 1000
$\sigma_z$ [mm]	0.47	0.47
$n_{b0}$ [ $10^{18}$ cm $^{-3}$ ]	7.7	2.8
Lens Parameters		
$n_p$ [ $10^{18}$ cm $^{-3}$ ]	2.0	2.5
$k_p \sigma_z$	125.1	139.9
$s_0$ [mm]	-2.0	-2.0
$l$ [mm]	1	1
$f$ [mm]	1.6	1.38 / 0.87
Focused Beam		
$\beta_x^* / \beta_y^*$ [mm]	0.9 / 0.9	0.75 / 0.047
$\sigma_x^* / \sigma_y^*$ [nm]	520 / 165	480 / 38
$s_x^* / s_y^*$ [mm]	0.10 / 0.10	-0.12 / -0.63

Table 2: Flat Beam Focusing

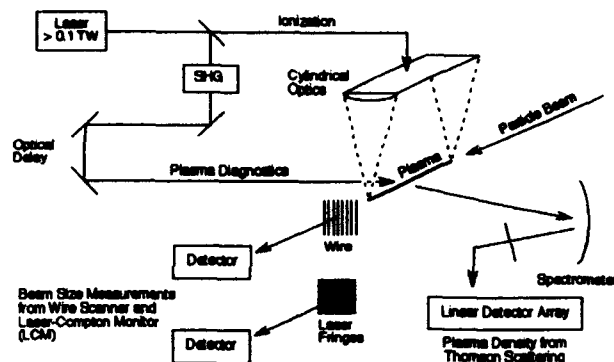


Figure 1: Outline of Plasma Lens Experimental Setup

## III. EXPERIMENTAL DESIGNS

### A. Experimental Setup

The outline of the experiments is shown in Figure 1. The setup mainly consists of a vacuum chamber with a plasma chamber embedded and ports for ionization laser, plasma diagnostics and beam size measuring devices. The setup is to be installed at the FFTB final focus region near Station 1027. An isometric view of the design is shown in Figure 2.

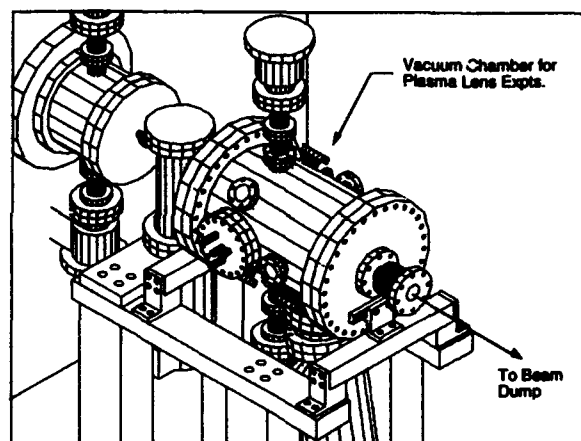


Figure 2: Plasma Lens Experiments at the FFTB.

### B. Plasma Chamber

The plasma chamber is shown in Figure 3. The chamber itself is a small (1 - 3 mm) pipe machined out of a metal block which allows easy variation of lens thickness and good structural integrity. The particle beam enters the gas pipe and exits through 0.01 cm holes at the center of the block. A pressure differential is maintained between the gas connections for a laminar gas flow through the pipe, which should reduce gas loss. Pumping chambers are provided on both sides of the gas pipe to capture most of the leakage before it enters the vacuum chamber. Ionization, diagnostic, and beam size measurement lasers are injected through windows on the chamber. The shield in front of the chamber blocks photons accompanying the particle beam. Hydrogen gas will be used to minimize the background from beam-plasma interaction.

### C. Vacuum System

For the maximum plasma density in Case 5 of  $n_p = 2.5 \times 10^{18}$  cm $^{-3}$ , a H $_2$  pressure of 38.8 torr at room temperature is required. In order to keep pumping requirements

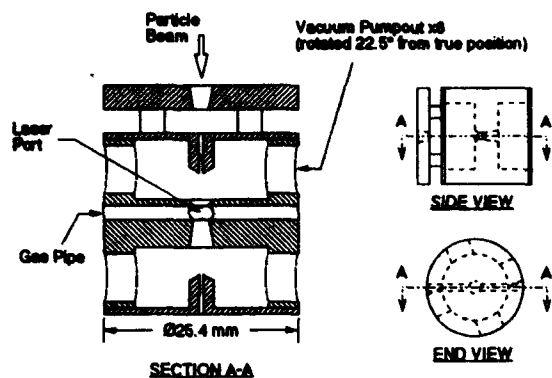


Figure 3: Plasma Chamber

within a practical range, the body of plasma chamber is hollowed out to create two pumping chambers as shown in Figure 3, which enable the majority of the gas to be picked up at a high pressure using a 30 liter/sec mechanical pump. The gas then flows out of the plasma chamber through two narrow, high impedance openings into the vacuum chamber for the experiments. This vacuum chamber is pumped through two 12.7 cm (5") ports by a 1000 liter/sec turbo molecular pump to a pressure of  $1.5 \times 10^{-6}$  torr. The beam line is a very large restriction to the flow of hydrogen out of the vacuum chamber. Approximately  $6 \times 10^{-11}$  gm/sec flows down the beam line where it is captured by two ion pumps. With the small quantities of hydrogen involved, hydrogen safety for the vacuum system should not be a problem.

#### D. Laser Systems

The ionizing laser pulse for the experiments will be generated from the same  $1 \mu\text{m}$  wavelength laser system which is currently being developed for the E-144 [14] experiment at the FFTB. The high-powered Nd:glass laser is based on the concept of chirped pulse amplification and compression (CPA) [15-18], which will produce pulses of 1 ps duration with energies up to  $\sim 2$  J ( $\sim 2$  TW) at 1 Hz. The laser will be synchronized to the electron beam with an accuracy of  $\sim 1$  ps.

For the plasma lens experiments, a small portion of the laser energy will be splitted off and frequency doubled to provide a  $0.5 \mu\text{m}$  wavelength pulse for plasma diagnostics [19]. The bulk of the energy will be focused with a cylindrical lens to form the plasma lens.

#### E. Beam Size Monitors (BSM)

For the round beams of Case 1, 2, and 3, beam sizes of  $\sim 2 - 4 \mu\text{m}$  are involved. The BSM for these cases is a wire scanner using carbon fibers [20]. Fibers of  $\sim 4 \mu\text{m}$  in diameter should allow the measurement of beam sizes to  $\sim 2 \mu\text{m}$  and sustain beam intensity of  $1 \times 10^{10}$ . The bremsstrahlung yields are measured using existing bremsstrahlung detectors installed for the FFTB wire scanners.

For Case 4 and 5, spot sizes with  $\sigma_x$  at  $\sim 0.5 - 1 \mu\text{m}$ , and  $\sigma_y$  of order 40 nm are involved. The BSM for these cases is a version of the Laser-Compton Monitor (LCM) developed by T. Shintake [21]. Since only Mode 1 and 3 of the monitor [22] are sufficient for Case 4 and 5, the implementation will be simpler than the LCM installed for the FFTB. The required

laser is shared with the FFTB version of the monitor by mechanically inserting a beam splitter/mirror into the existing laser transport line.

## IV. CONCLUSIONS

The series of experiments to be performed will serve to characterize plasma focusing devices, and if successful, will lead to practical applications at the SLC and the next generation of linear colliders. The primary goal of our experiments is to study the focusing of high energy and high density particle beams by plasma lenses of various densities and thicknesses. Plasma focusing of positron beams will be demonstrated for the first time. With a bunch population of about  $2.5 \times 10^{10}$  from the FFTB, we will demonstrate the tunneling ionization of a gas target by an electron beam, and establish the plasma lens as a simple, compact and economical add-on device for luminosity enhancement in linear colliders. Furthermore, the total compensation of beam self-fields by the plasma can be of interest for beamstrahlung suppression in future linear colliders.

## V. REFERENCES

- [1] P. Chen, *Part. Accel.* **20**, 171 (1987).
- [2] P. Chen, J. J. Su, T. Katsouleas, S. Wilks, and J. M. Dawson, *IEEE Trans. Plasma Sci.* **15**, 218 (1987).
- [3] J. B. Rosenzweig and P. Chen, *Phys. Rev. D* **39**, 2039 (1989).
- [4] P. Chen, S. Rajagopalan, and J. B. Rosenzweig, *Phys. Rev. D* **40**, 923 (1989).
- [5] J. J. Su, T. Katsouleas, J. M. Dawson, and R. Fedele, *Phys. Rev. A* **41**, 3321 (1990).
- [6] P. Chen, *Phys. Rev. A* **45**, R3398 (1992).
- [7] P. Chen, K. Oide, A. Sessler, and S. Yu, *Phys. Rev. Lett.* **64**, 1231 (1990).
- [8] K. Oide, *Phys. Rev. Lett.* **61**, 1713 (1988).
- [9] J. B. Rosenzweig *et al.*, *Phys. Fluids B* **2**, 1376 (1990).
- [10] J. B. Rosenzweig *et al.*, *Phys. Rev. Lett.* **61**, 98 (1988).
- [11] H. Nakanishi *et al.*, *Phys. Rev. Lett.* **66**, 1870 (1991).
- [12] D. H. Whittum *et al.*, *Part. Accel.* **34**, 89 (1990).
- [13] P. Chen, C. K. Ng, and S. Rajagopalan, SLAC-PUB-5954 (1992); submitted to *Phys. Rev. A*.
- [14] "SLAC Proposal E-144," SLAC (1991).
- [15] S. Augst, D. Strickland, D. D. Meyerhofer, S. L. Chin, and J. H. Eberly, *Phys. Rev. Lett.* **63**, 2212 (1989).
- [16] D. Strickland *et al.*, *Opt. Comm.* **56**, 219 (1985).
- [17] P. Maine, D. Strickland, P. Bado, M. Pessot, and G. Mourou, *IEEE J. Quant. Elec.* **24**, 398 (1988).
- [18] Y. H. Chuang, D. D. Meyerhofer, S. Augst, H. Chen, J. Peatross, and S. Uchida, *J. Opt. Soc. Am B* **8**, 1226 (1991).
- [19] J. Sheffield, "Plasma Scattering of Electromagnetic Radiation," Academic Press, New York (1975).
- [20] C. Field *et al.*, *Nuc. Inst. Meth. A* **295**, 279 (1990).
- [21] T. Shintake, *Nuc. Inst. Meth. A* **311**, 453 (1992).
- [22] T. Shintake *et al.*, KEK Preprint 92-065 (1992).

# A Plasma Lens and Accelerator Based Upon Magnetically Driven Charge Separation

Scott Robertson

Department of Astrophysical, Planetary, and Atmospheric Sciences  
University of Colorado, Boulder, CO 80309-0391 USA

## Abstract

An electrostatic lens is described in which a pulsed magnetic field is used to create a radial charge separation in a cylindrical plasma. The radial field can be made strongly focusing for a positively or negatively charged beam passing along the axis. On a longer time scale, the ions initially in the plasma are accelerated to the axis with energies of up to 0.5 MeV. The device may be useful as a generator of neutrons as well as a lens for charged particle beams. Pulsed radial electric fields exceeding 100 MV/m should be possible from modest magnetic compression fields.

## I. INTRODUCTION

Several collective accelerators have been described and tested in which ions are trapped in the space-charge electric field of a non-neutral rotating electron ring which is subsequently accelerated by a magnetic gradient<sup>1</sup>. The advantage of such schemes is that the space-charge electric field of the electrons can be stronger than accelerating fields created by other means. In this work, we describe a lens based upon a cylinder of charge-neutral plasma in which there is a radial, space-charge electric field due to a pulsed magnetic field acting unequally on the electrons and ions (Fig. 1). We show that potentials of the order of 0.5 MV can be created. The device is similar to a collective lens which has been experimentally demonstrated<sup>2,3,4,5</sup>.

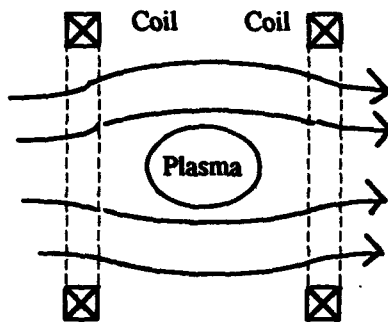


Fig. 1. Schematic diagram of the plasma accelerator. A rapidly rising magnetic field pushes the electrons and ions toward the axis. The difference in masses causes a radial electric field which retards the inward motion of the electrons and which accelerates the ions.

## II. EQUATIONS OF MOTION

We assume a cylindrical plasma having a length much longer than its radius so that axial motion can be neglected. We also assume that the plasma is collisionless and that the canonical angular momenta of the particles are conserved. The angular momentum  $P_\theta$  for the electrons is

$$P_\theta = qrA_\theta + \gamma m_e r^2 \dot{\theta} = -er_0 A_{\theta,0} \quad [1]$$

where  $q = -e$  is the electron charge,  $r$  is the radius,  $A_\theta$  is the time dependent vector potential,  $A_{\theta,0}$  is the initial vector potential which determines the conserved value of  $P_\theta$ ,  $\gamma$  is the relativistic factor,  $m_e$  is the rest mass of the electron, and  $\theta$  is the azimuthal coordinate. The subscript zero denotes the value at the initial time. For a uniform field the vector potential can be written

$$A_\theta = \Phi / 2\pi r = r B_z / 2 \quad [2]$$

where  $\Phi$  is the flux enclosed at radius  $r$  and  $B_z$  is the time dependent axial field. The angular velocity is then determined by the change in the vector potential:

$$\dot{\theta} = \frac{-q}{2\gamma m_e} (B_z - \frac{r_0^2}{r^2} B_{z,0}) = \Omega_{L,e} - \frac{r_0^2}{\gamma r^2} \Omega_{L,e,0} \quad [3]$$

where

$$\Omega_{L,e} = |q| B_z / 2\gamma m_e \quad [4]$$

is the Larmor frequency (half the cyclotron frequency),  $B_{z,0}$  is the initial field which determines the initial canonical angular momentum, and  $\Omega_{L,e,0}$  is the initial Larmor frequency for which  $\gamma = 1$ .

The radial equation of motion is

$$\frac{d}{dt} (\gamma m_e r) - \gamma m_e r \dot{\theta}^2 = -e(E_r + r \dot{\theta} B_z) \quad [5]$$

where  $E_r$  is the space-charge radial electric field. The angular velocity is known from [3] thus [5] becomes

$$\frac{d}{dt}(\gamma m_e \dot{r}) + \gamma m_e r \left[ \Omega_{L,e}^2 - \left( \frac{r_0^2 \Omega_{L,e,0}}{\gamma r^2} \right)^2 \right] = -eE_r. \quad [6]$$

The radial equation of motion for ions is found in the same way with the simplification that the ions can be treated nonrelativistically:

$$m_i \ddot{r} + m_i r \left[ \Omega_{L,i}^2 - \left( \frac{r_0^2 \Omega_{L,i,0}}{r^2} \right)^2 \right] = eE_r. \quad [7]$$

The electric field is found from Poisson's equation. If we assume a sufficiently large plasma density, then a small fractional difference in charge density can provide the electric field. This quasineutrality assumption allows us to set the electron and ion densities equal. The continuity equation then requires that the radial velocities be equal. The equations of motion can then be summed to yield a single equation

$$m_i \ddot{r} = -\gamma m_e r \left( \Omega_{L,e}^2 - \frac{r_0^4 \Omega_{L,e,0}^2}{\gamma r^4} \right), \quad [8]$$

where we have used that  $\gamma m_e \ll m_i$ . This can be further simplified to

$$\ddot{r} = -r \left( \Omega_{L,H}^2 - \frac{r_0^4 \Omega_{L,H,0}^2}{\gamma r^4} \right), \quad [9]$$

where we have defined a hybrid Larmor frequency

$$\Omega_{L,H}^2 = \frac{e^2 B_z^2}{4\gamma m_e m_i} = \Omega_{L,e} \Omega_{L,i} \quad [10]$$

and an initial hybrid frequency  $\Omega_{L,H,0}$ . The electric field is

$$eE_r = -\gamma m_e r \left( \Omega_{L,e}^2 - \frac{r_0^4 \Omega_{L,e,0}^2}{\gamma r^4} \right) - m_e r \dot{\gamma}. \quad [11]$$

The last term in the above equation can be ignored because  $r$  and  $\gamma$  vary on the hybrid time scale. The electric field rises linearly from the center to the edge of the plasma column.

If there is no initial field, [9] is an harmonic oscillator equation at the hybrid frequency. If the magnetic field is instantaneously increased from zero to a value  $B_z$ , both the electrons and ions accelerate to the axis in a time  $\pi/2\Omega_{L,H}$ . The electric field induced by the increasing

magnetic field accelerates the electrons azimuthally and they begin to spiral toward the origin. A radial, space-charge electric field develops which prevents the electrons from moving radially more quickly than the more massive ions. If an initial magnetic field is suddenly decreased, the electrons begin to spiral outward which creates a radial space-charge field of the opposite sign.

### III. OPERATING LIMITS

#### A. Upper bound on charge density

The analysis assumes that the azimuthal current induced in the plasma does not reduce the magnetic field at the axis. This assumption places an upper bound on the plasma density. For relativistic electrons, the current density can be estimated by assuming that the electron tangential velocity is the speed of light. From the current density and Ampere's law we find that

$$\Delta B_z / B_z = \mu_0 n e c r / B_z, \quad [12]$$

where  $\Delta B_z / B_z$  is the fractional change in the field. Requiring this to be small we find

$$r(\omega_{p,e} / c)(\omega_{p,e} / \omega_{c,e}) \ll 1, \quad [13]$$

where  $\omega_{p,e}$  is the nonrelativistic electron plasma frequency and  $\omega_{c,e} = eB_z / m_e$  is the nonrelativistic electron cyclotron frequency.

In the nonrelativistic limit, the electron angular velocity is given by the Larmor frequency and the fractional change in the field is

$$\frac{\Delta B_z}{B_z} = \frac{1}{2} \mu_0 n e \Omega_{L,e} r^2. \quad [14]$$

Requiring this to be small we get

$$(\omega_{p,e}^2 / c^2) \left( \frac{1}{2} r^2 \right) \ll 1 \quad [15]$$

which places an upper bound on the product of the density and the square of the radius. This condition is written to show that it corresponds to having the magnetic skin depth  $c/\omega_{p,e}$  longer than the radius of the plasma. For example, a plasma density of  $10^{12} \text{ cm}^{-3}$  results in  $c/\omega_{p,e} = 3 \text{ cm}$ .

#### B. Lower bound on charge density and upper bound on the magnetic field

The assumption of quasineutrality places a lower bound on the plasma density. If we require that

$$(n_i - n_e) / n_e \ll 1, \quad [16]$$

then Poisson's equation requires

$$\frac{2\gamma\Omega_{L,e}^2}{\omega_{p,e}^2} = \frac{\gamma\omega_{c,e}^2}{2\omega_{p,e}^2} \ll 1. \quad [17]$$

This lower bound on charge density has the effect of being an upper bound on the applied magnetic field.

### C. Combined limits

The greatest electric field is created by operating at the upper bound on density and the upper bound on magnetic field. We estimate the maximum field by setting  $2\omega_{p,e}^2 = \omega_{c,e}^2$  to approximate the upper bound set by [17], by setting  $\omega_{p,e}^2 = 2c^2/r^2$  to approximate the upper bound set by [15], and obtain from [11]

$$eE_r = \frac{1}{4}\gamma m_e r \omega_{c,e}^2 = \frac{1}{2}\gamma m_e r \omega_{p,e}^2 = \gamma m_e c^2 / r. \quad [18]$$

This places an upper bound on the electrostatic potential at the surface of  $e\phi = \gamma m_e c^2$ . Thus the peak potential must be kept below 0.5 MV to avoid violating the assumptions of the derivations.

## IV. APPLICATIONS

In a lens of radius 2 cm, for example, it should be possible to create a potential of 0.2 MV which corresponds to a focusing field of 10 MV/m. The focusing electric field has the same radial force on relativistic particles as a magnetic field of strength  $E/c \cong 0.03$  T. This is less than the field available from magnetic quadrupoles thus there is no advantage in the lens for relativistic particles. For particles below about 0.03 c, the radial force is greater than can be obtained in quadrupoles and there may be an advantage in the electrostatic lens.

A prototype device with a plasma of radius 3 cm and a density of  $10^{11}$  cm<sup>-3</sup> will satisfy the upper bound on

density. The upper bound on magnetic field is satisfied by a field of 500 G. The hybrid Larmor period for a plasma with barium ions is 161 nsec/rad. The magnetic field should rise to a constant value in a time shorter than this period. The period for a hydrogen plasma is much less and a magnetic field with sufficient risetime would be difficult to create. If the plasma radius is increased to 30 cm, the maximum density falls to 10<sup>9</sup> cm<sup>-3</sup>, the maximum field falls to 50 G, and the hybrid period for a deuterium plasma is 139 nsec/rad.

As a radial accelerator, the lens may have promise as a source of fusion neutrons due to the line focus of the accelerated ions. The energy which can be imparted to deuterium or tritium ions is of the order of 0.5 MeV which is well above the threshold for fusion reactions. For this application it may be advantageous to locate a solid cylindrical target on axis. If an initial field is used to confine the plasma, this target should have a radius corresponding to the radius where the ion energy is maximized. The fusion yield without a target depends upon the minimum radius to which the plasma is compressed. In the case of no initial field, the minimum radius is determined by the initial angular momentum from the thermal motion of the ions and electrons.

## V. REFERENCES

- <sup>1</sup>See for example *Collective Methods of Acceleration*, N. Rostoker and M. Reiser, eds., (Harwood Academic Publishers, Chur, Schwiez, 1979).
- <sup>2</sup>S. Robertson, "Collective Focusing of an Intense Ion Beam," *Phys. Rev. Lett.* 48, 149 (1982).
- <sup>3</sup>S. Robertson, "Magnetic guiding, focusing and compression of an intense charge-neutral ion beam," *Phys. Fluids* 26, 1129 (1983).
- <sup>4</sup>G. A. Krafft, C. H. Kim, and L. Smith, "The LBL Neutralized Beam Focusing Experiment," *IEEE Trans. Nucl. Sci.* 32, 2486 (1985).
- <sup>5</sup>S. Robertson, "Collective focusing of a charge-neutral ion beam with warm electrons," *J. Appl. Phys.* 59, 1765 (1986).

# The NRL X-Band Magnicon Amplifier Experiment\*

S.H. Gold, C.A. Sullivan, and W.M. Manheimer  
Beam Physics Branch, Plasma Physics Division, Naval Research Laboratory  
Washington DC 20375-5346

B. Hafizi  
Icarus Research  
7113 Exfair Road  
Bethesda MD 20814

## Abstract

We present a progress report on a program to develop a high-power X-band magnicon amplifier for linear accelerator applications. The goal of the program is to generate 50 MW at 11.4 GHz, using a 200 A, 500 keV electron beam produced by a cold-cathode diode on the NRL Long-Pulse Accelerator Facility. The initial experiment, designed to study the gain from the first (driven) deflection cavity to a second (passive) deflection cavity, has been completed. A gain of  $\sim 15$  dB has been observed in the preferred circular polarization, at a frequency shift of approximately  $-0.18\%$ , in good agreement with theory and simulation. In addition, a design study for a complete magnicon circuit is under way.

## I. INTRODUCTION

The magnicon,<sup>1-3</sup> a "scanning beam" microwave amplifier tube related to the gyrocon,<sup>4</sup> is a potential replacement for the klystron for powering future high-gradient linear accelerators. Scanning beam devices modulate the insertion point of the electron beam into the output cavity in synchronism with the phase of a rotating rf wave. This synchronism creates the potential for an extremely efficient interaction in the output cavity, since every electron will in principle experience identical decelerating rf fields. In the magnicon, the output interaction is gyrotron-like, and requires a beam with substantial transverse momentum about the applied axial magnetic field. The transverse momentum is produced by spinning up the electron beam in a sequence of  $TM_{110}$  deflection cavities, the first of them driven by an external rf source. The output cavity employs an rf mode that rotates at the same frequency as the deflection cavity mode. As a result, the beam entering the output cavity is fully phase modulated with respect to the output cavity mode. The optimum magnetic field in the deflection cavities is approximately twice the cyclotron resonant value at the drive frequency. On the other hand, the output cavity operates as a first harmonic cyclotron device. These two constraints lead naturally to the design of a second-harmonic amplifier, in which the output cavity operates at twice the frequency of the deflection cavities and employs a  $TM_{210}$  mode. The overall design concept is shown in Fig. 1. This circuit will include a drive cavity, two simple half-wavelength deflection cavities, a two-section penultimate cavity, and an output cavity.

\* Work supported by U.S. DOE and ONR.

In this paper, we discuss a preliminary experiment, employing only two 5.7 GHz deflection cavities, the first driven by an external source. We have performed parametric studies of the gain between these two cavities, preparatory to the design of a complete deflection system that will spin up an electron beam to high  $\alpha$  for injection into an 11.4 GHz output cavity. Here,  $\alpha$  is the ratio of perpendicular to parallel velocity.

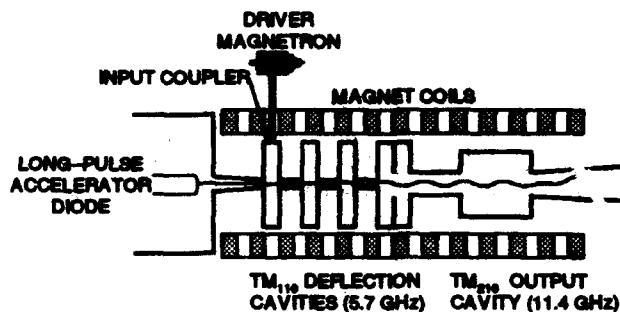


Figure 1. NRL magnicon design concept.

## II. APPARATUS

This experiment was carried out on the NRL Long-Pulse Accelerator Facility.<sup>5</sup> It employed a field-emission diode [see Fig. 2], designed with a flat magnetic field of 1.7 kG in the anode-cathode gap, followed by adiabatic compression to a final magnetic field of 8.1 kG, to generate a 500 keV,  $\sim 200$  A, 5.5 mm diam solid electron beam with low initial transverse momentum. Simulation results using a version of the Stanford Electron Optics Code<sup>6</sup> suggest a mean  $\alpha \sim 0.03$ . This beam was used to power a two-cavity amplifier experiment. The two cavities are of identical pillbox design, with 3.20 cm radius and 2.265 cm length. The length was chosen so that the transit time of a 500 keV electron equals half of an rf period. They are separated by a 1-cm-diam drift space 1.132 cm long. This length is approximately half of an electron gyroperiod. The cavities were fabricated from stainless steel, to permit the penetration of pulsed magnetic fields, with a copper coating on the interior surfaces to decrease the ohmic losses. Each has four coupling pins spaced at  $90^\circ$  intervals in one end-wall. Two adjacent "coupling" pins are "long," for use in driving the two linear polarizations of the cavity, and the remaining two "sampling" pins are "short," in order to measure the cavity fields without significantly loading the cavity. The

first cavity was driven in a circularly-polarized  $TM_{110}$  mode by a C-band magnetron at  $\sim 5.7$  GHz. Circular polarization was generated by driving the two coupling pins with a  $\pi/2$  phase difference using a 3 dB hybrid coupler. In the second (gain) cavity, the two sampling pins led to matched loads, while the two coupling pins were connected through coaxial attenuators to crystal detectors.

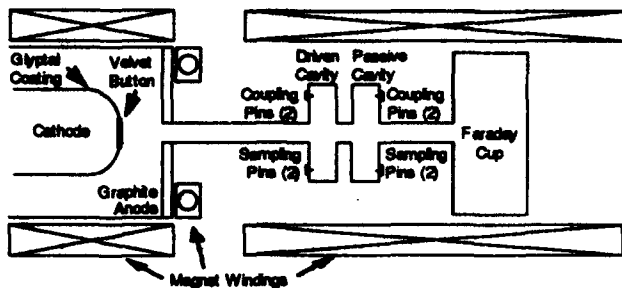


Figure 2. Schematic of the two-cavity experiment.

The cavities, their pickups, and all other microwave components were fully calibrated using a microwave scalar network analyzer. Five microwave signals were monitored on each experimental discharge, including the magnetron signal, signals from each linearly polarized sampling pin of the first cavity, and signals from each coupling pin of the second cavity. In addition, a balanced mixer was used to combine the first cavity signal with the signal from a separate local oscillator tuned as closely as possible to the operating frequency of the magnetron. This "mixed" signal was used to set the exact magnetron frequency (using a mechanical tuner), to adjust the magnetron voltage to avoid excessive frequency chirp, and to guard against frequency drift. In addition, phase or frequency shifts due to the effects of the beam on the drive cavity could be observed.

### III. MAGNICON THEORY AND SIMULATION

The linear theory of the magnetized deflection cavities was first presented by Karliner, *et al.*,<sup>1</sup> and is developed in detail by Hafizi, *et al.*<sup>7</sup> The linear theory has been evaluated for a single on-axis electron, with no initial transverse momentum, and without finite beam radius and finite velocity spreads. Furthermore, it assumes that the electron energy is not changed by transit through the deflection cavities. In order to consider the use of more realistic beam parameters, a numerical simulation code for the deflection cavities was developed.<sup>7</sup> It is a self-consistent steady-state code that propagates particles through the  $TM_{110}$  fields of the first (driven) deflection cavity, through a drift space, and then through successive deflection cavities and drift spaces. The rf field amplitudes are made (by iteration) self-consistent with the finite value of cavity  $Q$  and with the energy lost by the electron beam in transit through each cavity. The rf phase in each of the passive cavities is assumed to be the optimum phase to extract electron beam energy from an initially on-

axis electron, since this should be a good approximation to the phase that is driven by a finite electron beam.

### IV. EXPERIMENTAL RESULTS

The response of the first cavity, and the gain of the second cavity were measured as a function of frequency in each circular polarization of the  $TM_{110}$  mode. The measurements were carried out at 500 keV, with a beam current of  $\sim 170$  A, and a magnetic field of 8.1 kG. This magnetic field corresponds to the theoretical value at which, for the preferred circular polarization (which corresponds to electron gyromotion in the same sense as the rotation of the mode), the beam does not load the cavity  $Q$ .

The predicted and measured response of the first cavity as a function of frequency in the preferred circular polarization are shown in Fig. 3. Simultaneous measurements are made at the cavity sampling pins in each linear polarization of the cavity. The data are normalized to the calculated signal level from the cavity at constant magnetron drive power at the center of the cold cavity resonance in the absence of the electron beam. This normalization is based on cold tests of all components of the system. Theory predicts that the center of the resonance will be shifted by  $-0.18\%$ , and that the beam loading should be very close to zero. This is indicated by a curve whose height is normalized to one, and whose width is consistent with  $Q \sim 1100$ , the value measured in the absence of the beam. The experimental center frequency and resonance width are in good agreement with theory. In addition, while the experimental data for the two linear polarizations consistently differ by  $\sim 3$  dB, perhaps due to cumulative calibration errors, the two data sets bracket the theoretical curve.

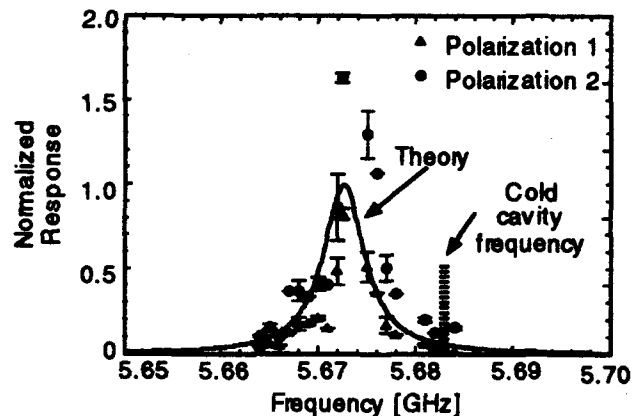


Figure 3. Response of the drive cavity in the preferred circular polarization—theory and experiment.

The predicted and measured gain of the second cavity in the preferred circular polarization are shown in Fig. 4. Theory predicts a gain of  $\sim 15$  dB, with the resonance shifted by  $-0.18\%$  from the cold frequency of the second cavity. The experimental gain measurements are in good agreement with the theoretical curve in amplitude, center frequency, and

bandwidth. However, there is a persistent imbalance in the two linear polarizations, which may be in part calibration error, but also may reflect a true asymmetry in the cavity excitation (elliptical polarization), perhaps due to a small misalignment of the electron beam, or some asymmetry in the mode of the drive cavity.

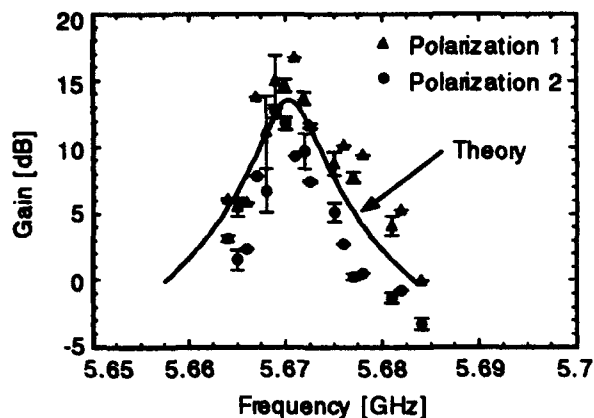


Figure 4. Two-cavity gain in the preferred circular polarization—theory and experiment.

## V. DISCUSSION

The overall purpose of a complete set of magnicon deflection cavities is to coherently spin up an electron beam to high  $\alpha$  for injection into an output cavity. With this goal in mind, the present experiment was designed to measure the gain between a driven and a passive deflection cavity, which could constitute the first section of a complete deflection system. In this two-cavity experiment, high gain ( $\sim 15$  dB) was observed in the preferred circular polarization, in good agreement with the predictions of theory.<sup>8</sup> However, one should note that the present experiment was carried out at very low signal levels, in order to eliminate the possibility of multipactor or breakdown phenomena interfering with the basic gain measurement. Under these conditions, the resulting coherent beam  $\alpha$  should be quite small ( $\leq 0.01$ ). This is less than the initial random  $\alpha$  produced by the diode.

In future experiments, higher drive powers and additional deflection cavities will be employed, in order to achieve a final  $\alpha \geq 1$ . An important requirement in those experiments will be the suppression of multipactor and breakdown effects through a combination of improved cavity design and improved vacuum techniques. The effect of initial

electron radial and velocity spreads on the gain measured in the present experiment is predicted to be quite small. Nevertheless, such spreads may have a large effect on the quality of the final high  $\alpha$  electron beam generated by a full sequence of deflection cavities, resulting in a lowering of the efficiency of the output cavity interaction.<sup>9</sup> In this regard, the real test of the final multicavity deflection system will be to produce a high  $\alpha$  electron beam, while minimizing the spread in energy,  $\alpha$ , and gyrophase. A design study for a complete magnicon circuit is under way.

## VI. ACKNOWLEDGMENTS

The authors are grateful to A. Fisher, A. Fliflet, R. Gilgenbach, O. Nezhevenko, and V. Yakovlev for useful discussions.

## VII. REFERENCES

- [1] M. M. Karliner, *et al.*, "The Magnicon—An advanced version of the gyrocon," *Nucl. Instrum. Methods Phys. Res. A* **269**, 459 (1988).
- [2] O. A. Nezhevenko, "The Magnicon: A New RF Power Source for Accelerators," *Conf. Record—1991 IEEE Particle Accelerator Conf.*, (IEEE, New York, 1991), pp. 2933-2942.
- [3] W. M. Manheimer, "Conceptual design of a high power, highly efficient magnicon at 10 and 20 GHz," *IEEE Trans. Plasma Sci.* **18**, 632 (1990).
- [4] G. I. Budker, *et al.*, "The Gyrocon—An efficient relativistic high-power vhf generator," *Part. Accel.* **10**, 41 (1979).
- [5] N. C. Jaitly, *et al.*, "1 MV Long Pulse Generator with Low Ripple and Low Droop," in *Digest of Technical Papers—Eighth IEEE Int. Pulsed Power Conf.* (IEEE, New York, 1991), pp. 161-165.
- [6] W. B. Herrmannsfeldt, "Electron Trajectory Program," SLAC Report No. 226, 1979 (unpublished).
- [7] B. Hafizi, *et al.*, "Analysis of the Deflection System for a Magnetic-Field-Immersed Magnicon Amplifier," *IEEE Trans. Plasma Sci.* **20**, 232 (1992).
- [8] S.H. Gold, *et al.*, "Study of Gain in C-Band Deflection Cavities for a Frequency-Doubling Magnicon Amplifier," *IEEE Trans. Plasma Sci.*, to be published [August, 1993].
- [9] B. Hafizi, *et al.*, "Nonlinear Analysis of a Magnicon Output Cavity," *Phys. Fluids*, to be published [1993].

# Theoretical Investigation of Magnicon Efficiency<sup>1</sup>

B. Hafizi<sup>†</sup>, S. H. Gold<sup>‡</sup>, W. M. Manheimer<sup>§</sup> and P. Sprangle<sup>‡</sup>

<sup>†</sup>Icarus Research, 7113 Exfair Rd., Bethesda, MD 20814

<sup>‡</sup>Beam Physics Branch, Plasma Physics Division  
Naval Research Laboratory, Washington, DC 20375

<sup>§</sup>Code 6707, Plasma Physics Division  
Naval Research Laboratory, Washington, DC 20375

**Abstract** - In the output cavity of a frequency-doubling magnicon amplifier the electrons interact with a rotating  $TM_{210}$  mode via a gyro-resonant mechanism. The efficiency of a magnicon may be extremely high since the electrons enter the output cavity almost completely phase-bunched and rotate in synchronism with the rf wave. Results from time-dependent simulation of the electron beam-circuit interaction of a magnicon operating at X-band are presented. Efficient ( $> 50\%$ ), accessible and stable operation of an amplifier employing an electron beam with  $\alpha \equiv v_{\perp}/v_{z0} = 1$ , where  $v_{\perp}$  and  $v_{z0}$  are the velocity components transverse to and along the  $z$  axis, is demonstrated.

## I. Introduction

The magnicon<sup>1-5</sup> is an advanced version of the gyrocon<sup>6</sup> and employs a scanning beam that is obtained by the passage of a magnetized pencil beam from the electron gun through a deflection system. The deflection system consists of an input cavity and one or more passive cavities, separated by drift tubes, with the entire system immersed in an axial magnetic field,  $B_0$ . The cavities support a rotating  $TM_{110}$  mode with a frequency that is  $\sim 1/2$  the gyrofrequency,  $\omega_{c0} \equiv |e|B_0/\gamma_0 mc$ . Here,  $e$  is the charge and  $m$  is the mass of an electron,  $\gamma_0$  is the relativistic factor, and  $c$  is the vacuum speed of light. The purpose of the deflection system is to spin the beam to high transverse momentum; i.e.,  $\alpha \equiv v_{\perp}/v_{z0} > 1$ . Here,  $v_{\perp}$  and  $v_{z0}$  are the velocity components transverse to and along the  $z$  axis. After passing through the deflection system, the beam transverse momentum is used to drive a gyrotron-like interaction in the output cavity. The entry point of the electrons in the output cavity rotates in space about the cavity axis at the drive frequency. In the frequency-doubling version, the output cavity supports a rotating  $TM_{210}$  mode

with frequency  $\omega \approx \omega_{c0}$ , which is twice the drive frequency. Since the electrons entering the output cavity are almost completely phase-bunched and rotate in synchronism with the  $TM_{210}$  wave, the transverse efficiency may be extremely high.

## II. Time-Dependent Simulation

The time-dependent simulation results presented here are obtained from the full set of Maxwell-Lorentz equations, following the motion of a single electron through the cavity and studying the build-up of the rf field over a much longer time scale. In Ref. 7 we present a detailed analytical and numerical study of the output cavity. Based on single-electron, steady-state simulation of the reduced and scaled Maxwell-Lorentz system of equations we have identified the regions of parameter space wherein high-efficiency operation may be possible. The time-dependent simulation results herein are intended to demonstrate the accessibility and stability of one such high-efficiency operating mode employing a beam with  $\alpha = 1$ .

Table 1 lists the parameters for the simulation with initial beam  $\alpha = 1$ , the cold cavity frequency being 11.424 GHz. Figures 1(a), (b), and (c) show plots of the electric field amplitude,  $|E_0|$ , the rf phase,  $\beta$ , and the efficiency of energy transfer to the external circuit,  $\eta$ , as functions of time. Observe that the system settles into a steady state after a transient that lasts  $\approx 60$  ns. Figure 1(a) shows that the electric field builds up to about 305 kV/cm, Fig. 1(b) shows that the rf phase settles to an asymptotic value of 1.1 rad, and Fig. 1(c) shows the final efficiency in this field is about 52 %.

Figures 2 (a), (b), and (c) show plots of the axial momentum normalized to its initial value,  $p_z/p_{z0}$ , efficiency, and  $\alpha$  for an electron traversing the output cavity in the final steady-state field. The modulation of the electron momentum is seen to be correlated with the modulation on the efficiency curve. The

<sup>1</sup>Supported by DoE & ONR

scale-length for the modulation is  $\approx 2\pi v_{z0}/\omega$ . The length,  $L$ , of the cavity has been chosen to be 4.75 cm so that, on exiting the cavity, the axial momentum is a minimum, and therefore the efficiency is a maximum. In this sense, the optimal length for the output cavity is  $\approx 2\pi n v_{z0}/\omega$ , where  $n$  is an integer. Figure 2(c) shows that the value of  $\alpha$  declines as the electron spins down on traversing the cavity.

Table 1

Frequency $\omega/2\pi$	11.43	GHz
Voltage	500	kV
Current	180.1	A
Cavity Radius	2.145	cm
Cavity Length $L$	4.75	cm
Cavity Quality Factor	200	
Beam $\alpha$	1	
Magnetic Field $B_0$	6.455	kG
Detuning $(\omega - \omega_{c0})L/v_{z0}$	3.776	
Frequency Shift $\Delta\omega/2\pi$	6	MHz

Table 1: Parameters for time-dependent simulation of an X-band magnicon amplifier output cavity. Initial beam  $\alpha = 1$ .

### III. Conclusions

In conclusion, we may summarize the single-electron simulation results as follows. First, as indicated in Figs. 2, for an ideal beam, it is possible to choose the cavity length so as to convert not only the transverse momentum but also part of the axial momentum into rf field energy. Second, based on the run made with the time-dependent code, we have found a final state that is accessible and stable to an amplifier in which the signal in the output cavity builds up from noise. Third, an efficient ( $> 50\%$ ) final state with  $\alpha = 1$  is achievable.

Multi-electron steady-state simulation using the parameters in Table 1 indicate that the efficiency is sensitive to a spread in the beam parameters, declining by  $\approx 10\%$  as the beam  $\alpha$  spread increases from 0-40%, or the beam radius spread increases from 0-60%, or the energy spread increases from 0-3%.<sup>7</sup>

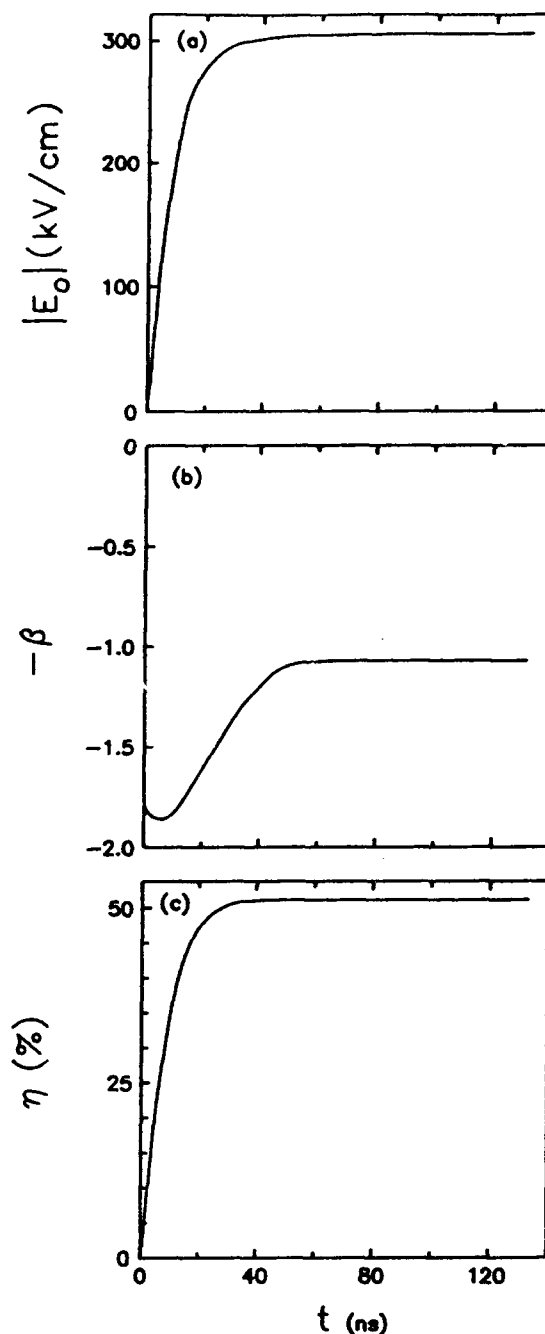


Figure 1: Results from single-electron, time-dependent simulation of X-band magnicon with initial beam  $\alpha = 1$  and detuning  $\Delta = 3.776$ . (a) Electric field amplitude,  $|E_0|$ ; (b) RF phase,  $\beta$ ; (c) Efficiency,  $\eta$ . Abscissa is time.

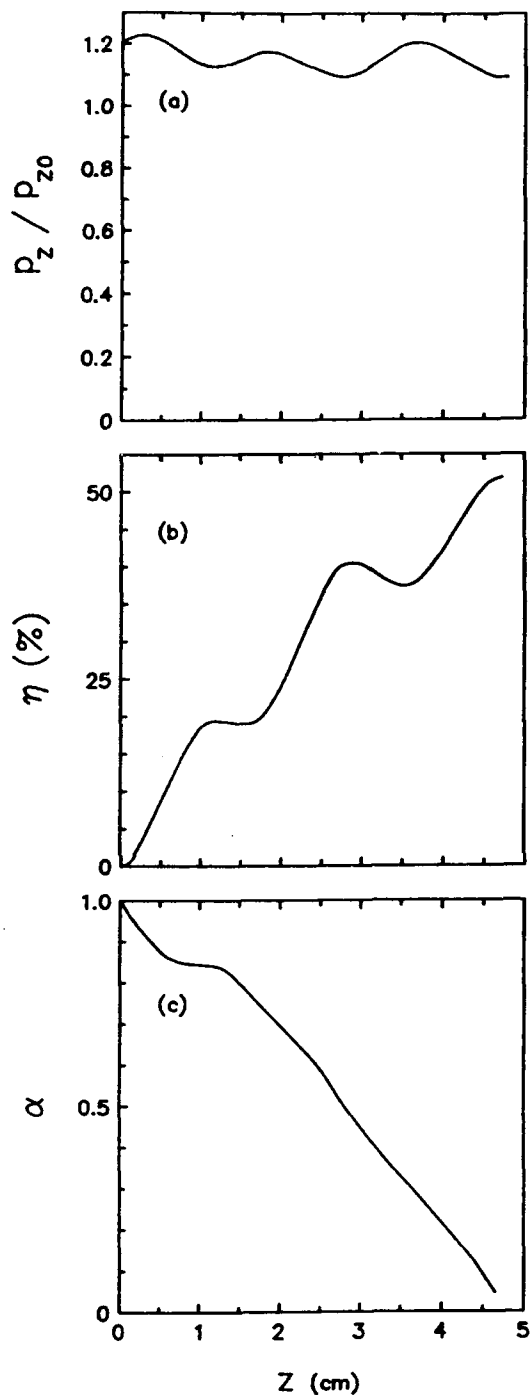


Figure 2: Results from single-electron, time-dependent simulation of X-band magnicon with initial beam  $\alpha = 1$  and detuning  $\Delta = 3.776$ . (a) Axial kinetic momentum normalized to initial value,  $p_z/p_{z0}$ ; (b) Efficiency,  $\eta$ ; (c)  $\alpha$ . Abscissa is distance along cavity. These plots correspond to motion of an electron through cavity in final steady state.

## References

- [1] M. M. Karliner, E. V. Kozyrev, I. G. Makarov, O. A. Nezhevenko, G. N. Ostreiko, B. Z. Persov and G. V. Serdobintsev, Nucl. Instrum. Methods Phys. Res. **A269**, 459 (1988).
- [2] O. Nezhevenko, in Proc. IEEE Particle Accel. Conf., edited by L. Lizama and J. Chen (IEEE, New York, 1991), 2933 (1991).
- [3] W. M. Manheimer, IEEE Trans. Plasma Sci. **PS-18**, 632 (1990).
- [4] B. Hafizi, Y. Seo, S. H. Gold, W. M. Manheimer and P. Sprangle, IEEE Trans. Plasma Sci. **PS-20**, 232 (1992).
- [5] S. H. Gold, C. A. Sullivan, B. Hafizi and W. M. Manheimer, IEEE Trans. Plasma Sci. (1993).
- [6] G. I. Budker, M. M. Karliner, I. G. Makarov, S. N. Morosov, O. A. Nezhevenko, G. N. Ostreiko and I. A. Shekhtman, Part. Accel. **10**, 41 (1979).
- [7] B. Hafizi, S. H. Gold, W. M. Manheimer and P. Sprangle, Phys. Fluids B (1993).

# First Test of the X-Band Pulsed Magnicon.

O.Nezhevenko, I.Kazarezov, E.Kozyrev, G.Kuznetsov, I.Makarov, A.Nikiforov, B.Persov,  
G.Serdobintsev, M.Tiunov, V.Yakovlev, I.Zapryagaev.  
Budker Institute of Nuclear Physics,  
630090, Novosibirsk, Russia.

## I. GENERAL

Magnicon [1,2] belongs to the class of high power RF sources, where a modulation is provided by the beam circular deflection and it is an advanced version of a gyrocon [3].

The first magnicon has been built and tested in Novosibirsk in the middle of 80-ths.

The power of 2.6 MW has been obtained for the frequency 915 MHz and pulse duration 30 msec, the electron efficiency has been 85% [1].

Good results obtained during investigations show that the magnicon can be an adequate RF source for the next generation of accelerators, especially for future linear colliders [4] and accelerators for transmutation of nuclear waste [5].

The magnicon conception described in present paper allows to increase significantly the beam perveance, compared with the first magnicon, and to achieve the pulse power of tens and hundreds megawatts at the beam voltage not greater than 400-600 kV. The device is an amplifier working in frequency doubling mode [2,6] and is a prototype of RF source for linear colliders with high acceleration gradient.

Magnicon is designed for an output power of 50 MW, an operating frequency of 7 GHz and a pulse duration of 2 msec.

## II. MAGNICON DESIGN

The magnicon sketch is shown in Fig 1. The beam source is the diode gun 1 with oxide cathode of 120 mm diameter. The voltage pulse from a step - up transformer is applied to the gun. The main feature of the gun is a high degree of a beam transverse area compression (over 1500). The step - up transformer is placed in the tank with SF<sub>6</sub> under pressure of 4 atmospheres.

The pulse voltage source of the step - up transformer is a modulator based on Blumlein PFN.

The beam from electron gun pass the resonance system, which consists of a beam circular deflecting system and an output cavity. Beam deflecting in the drive cavity 3 and in two passive cavities 4,5 is provided by transverse magnetic field of the TM<sub>110</sub> wave travelling in azimuthal direction (see Fig 1). The cavities are placed into biasing magnetic field that is excited by coils 6.

Drive cavity 3 that is excited by external generator provides a small angle of the beam deflection. Further increase of the

deflection angle up to 50-60 deg is provided in passive cavities exited by a predeflected beam.

A cylindrical output cavity 7 with the TM<sub>210</sub> wave (Fig.1) travelling in azimuthal direction is used to convert the beam energy to RF one. The eigen frequency of the output cavity is twice greater than deflection one [6]. This cavity is placed into biasing magnetic field too, the field value is determined by the conditions which are necessary to achieve an effective long term interaction of the electron beam with RF-field [1,2]. The RF power extraction is provided by two similar slots in side

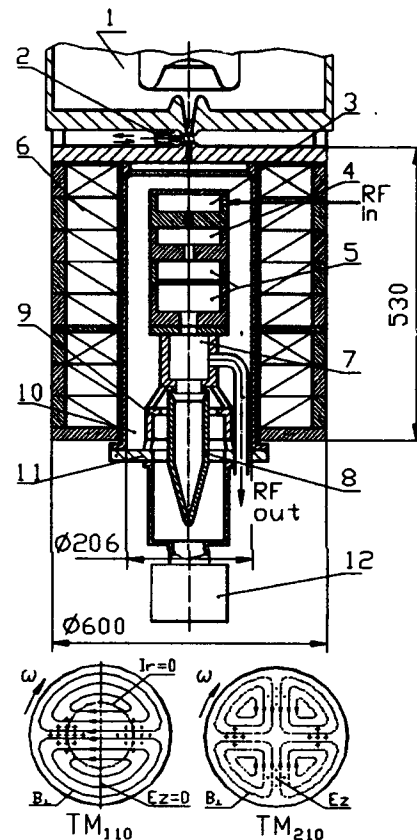


Figure 1. Sketch of the magnicon.

- 1 - electron gun; 2 - gate vacuum valve; 3 - drive cavity;
- 4 - passive deflection cavity; 5 - penultimate cavity;
- 6 - solenoid; 7 output cavity; 8 - collector;
- 9 - pole piece; 10 - vacuum chamber; 11 - flange;
- 12 - vacuum pump.

cavity wall, which are shifted on 135 deg in azimuthal direction to support the wave travelling in azimuthal direction.

The RF system is made of separate cooper parts which are assembled by indium gaskets. A collector is made of cooper, is cooled by water too and is insulated for current measurements.

### III. CHALLENGES

1. Because the electric field in output cavity of magnicon is considerably small [1,2], the main problem with electric breakdown takes place in the last deflecting (penultimate) cavity, where the main beam deflection is produced. In described magnicon design unlike the classic design [1,2] the relevant deflection angle (that is about 50-60 deg) is achieved in the last passive cavity. Here, if a single cavity would be used as a last deflecting one, the surface electric field will exceed reasonable values. To overcome this problem two means are used in present design.

First, because the output frequency is twice higher than the deflecting one, the gaps of deflecting cavities are two times greater than for a magnicon working as an amplifier.

Second, the penultimate cavity 5 (see Fig.1) consists of a pair of coupled cavities, which are excited by a predeflected beam in a counterphase mode. Thus, a "deflection angle addition" mode, or a long term interaction between the beam and deflecting RF field is realized [6].

These means allow to decrease the maximal surface electric field to the value 200 kV/cm (approximately the same as in the output cavity).

2. Some more problems appear because of necessity to have a large deflection angle in the beam deflecting system. In this case it is necessary to have large beam holes in the walls of cavities (the holes diameter must be about four Larmore radii). This holes produce perturbation of RF field distribution, mainly, near the holes there appears the large transverse electric field. In Fig.2 a fringing field distribution near the beam holes for penultimate cavity is shown. (Note

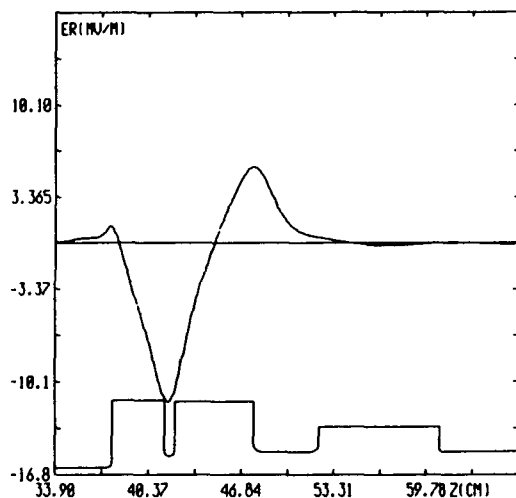


Figure 2. Transverse electric field distribution along the axis of penultimate cavity.

that the surface electric field of the penultimate cavity is determined by these fringing fields.) The action of fringing field on beam dynamics produces two problems.

First, these fields produce beam energy and angle spreads, which lead to the efficiency drop when the beam diameter increases. Simulated picture of behavior of electrons in process of deflecting and deceleration is shown in Fig.3 for initial beam diameter of 2.5 mm. Thus, to obtain high efficiency it is necessary to use the beam with the minimal initial diameter, i.e., with the diameter close to Brillouin one. To overcome this problem a special electron optics system has been developed [7].

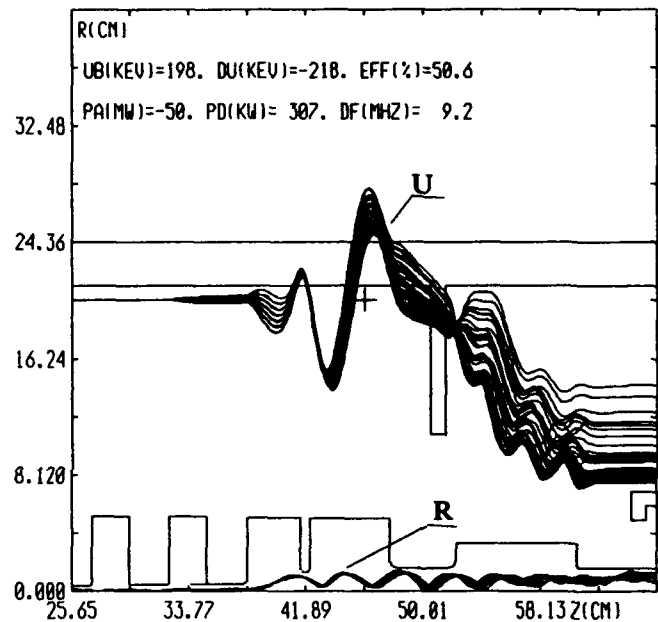


Figure 3. Beam behaviour in process of deflection and deceleration. R - radii, U - energies of the beam particles.

Second, transverse fringing fields decelerate electrons, i.e. near the beam holes electrons of the beam transfer their energy to the RF field. For the beam current of hundreds Amperes, it can lead to an instability, which is specific for magnicon. This instability is realized as self - excitation of a single cavity on the operating RF mode, without any external feedback. For coupled cavities the current threshold is lower than for a single cavity. It is possible to overcome this problem using a special cavity geometry and a biasing field distribution along the tube axis. In particular, decreasing the biasing field near penultimate cavity increases beam loading of this cavity, decreasing its quality factor and so increasing the current threshold of the instability for relevant value. Simultaneously, it allows to reduce a quality factor of other deflecting cavities to obtain compromise between gain and a bandwidth.

3. For coupled cavities there may be a klystron-like instability, i.e. instability with the frequency lower than operating one (on the mode TM<sub>010</sub>). In the first design version of the present magnicon three strongly coupled cavities have been used as the penultimate cavity. The coupling coefficient was about

20% [2,6]. This cavity was selfexcited on the frequency 2.6 GHz when the current reached 50 A. It corresponds to the  $\pi/2$  mode, which has a minimal current threshold because of a large bunching distance. In present design this problem is solved by using two coupled cavities with small coupling (coupling coefficient is 0.5% for TM010). Besides, the relative difference of TM010 mode eigen frequencies for those cavities is greater then coupling value.

#### IV. EXPERIMENT

1. At the first stage of the experiment the electron gun was tested. While testing the following data were obtained: power  $P = 100\text{MW}$  at  $U = 430\text{ kV}$  and microperveance 0.82, pulse width 2 mcsec and the repetition rate up to 5 pps.

The beam diameter, measured with the help of special movable graphite diaphragms [8] is less than 3 mm (i.e. area compression ration exceeds 1500:1 and energy density is  $5\text{ kJ/cm}^2$ ).

The main problem arising in the process of investigation were caused by the last passive cavity. A few different version of this cavity had been examined (with three and two coupled cavities) before succeeded to do away with selfexcitation of both, klystron-like and operating mode TM110.

2. For the time being the very initial test of the magnicon have been carried out. The parameters obtained are listed in Table 1. Figure 4 presents the oscillogram of the output pulse.

Table 1.

Frequency,GHz	7
Power,MW	20
Pulse width,mcsec	1.1
Efficiency,%	25
Repetition rate,pps	2
Drive frequency,GHz	3.5
Gain,dB	47
Beam voltage,kV	400
Beam current,A	200

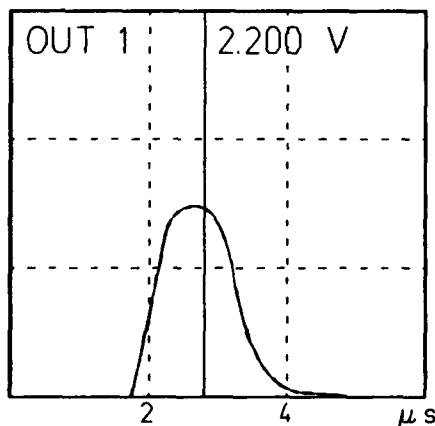


Figure 4. Output pulse oscillogram.

This tests have been started only a month before this conference. The tube is being in the state of conditioning and we expect to get beter parameters in the nearest future.

#### V. REFERENCES

- [1] Karliner M.M. et al. The Magnicon - an Advanced Version of the Gyrocon. *Nuclear Instruments and Method in Physics Reseach*, 1988, v.A269, N3, pp.459-473.
- [2] O.A.Nezhevenko. The magnicon: a new RF power source for accelerators. *IEEE Particle Accelerator Conference, San-Francisco*, pp.2933-2942, 1991.
- [3] G.I.Budker et al. *Particle Accelerators*, v.10,pp.41-59,1979.
- [4] R.Siemann. Overview of Linear Collider Designs. This Conference.
- [5] G.P.Lawrence. High-Power Proton Linac for Transmuting The Long-Lived Fussion Products in Nuclear Waste. *IEEE Particle Accelerator Conference, San Francisco*, pp.2598-2600,1991.
- [6] V.E.Akimov et al.High-Power X-Band Puls Magnicon. *European Particle Accelerator Conference, Nice, Vol.1* pp.1000-1002,1990.
- [7] Y.B.Baryshev et al. Electron Optic System for Forming 100 MW Beam with High Current Density and Microsecond Pulse Duration for X-Band Magnicon. *Proc. of the Eighth International Conference on High-Power Particle Beams, Novosibirsk, Vol.1*,p.598-603, 1990.
- [8] Y.B.Baryshev et al. Electron-Optical System for the Formation of a 100 MW Beam with High Density of Current of a Microsecond Duration for a 7 GHz Magnicon. NIM to be published.

# TM-FEL With a Longitudinal Wiggler and an Annular Beam \*

L. Schächter, T.J. Davis and J. A. Nation  
Laboratory of Plasma Studies and School of Electrical Engineering  
Cornell University, Ithaca, NY 14853 USA

## Abstract

We investigate theoretically the interaction of an electron beam with a *TM* mode in the presence of a longitudinal wiggler. The electron motion is longitudinal and radial therefore adequate for interaction with the electric field components of the mode. There are two facts which make this device unique: firstly, the equations which describe its dynamics are practically identical to the equations of the traveling wave tube (TWT) rather than the free electron laser (FEL) thus its sensitivity to beam quality is significantly lower, and the efficiency in the absence of tapering is higher. Secondly the interaction is possible only with an annular rather than a pencil beam as in a regular FEL - therefore the amount of current it is possible to inject is larger. Optimal operation at 20.56GHz is examined.

## I. INTRODUCTION

From basic electrodynamic arguments it can be shown [1] that the total power of the spontaneous radiation emitted by a charge accelerated parallel to its velocity is larger by  $\gamma^2$  than that obtained if the acceleration perpendicular to the velocity - assuming the same acceleration in both cases. With regard to stimulated (coherent) process the situation is similar. In order to illustrate the problem we shall briefly consider here two devices: first the traveling wave tube (TWT) where the interaction of the electrons is with the *TM* mode - thus the acceleration of the electron is parallel to its main velocity component. The other device is the free electron laser (FEL) - where the acceleration is transverse to its main velocity component.

The equations which describe the dynamics of both TWT and FEL are summarized in Table I - the details can be found in Refs.(2-3) for TWT's and [4] for FEL's. In both cases  $a$  is the normalized amplitude of the electric field,  $\gamma_i$  is the relativistic factor of the  $i^{\text{th}}$  electron,  $\chi_i$  is the phase of the  $i^{\text{th}}$  electron relative to the wave,  $\alpha$  is the coupling coefficient,  $\Omega = \omega d/c$ ,  $K = kd$  is the normalized radiation wavenumber and  $K_w = k_w d$  is the normalized wiggler wavenumber;  $d$  is the total length of the system. The coupling coefficient  $\alpha$  is completely different in the two cases but for the present purpose the explicit expressions are not important. Furthermore, the amplitude  $a$  in the TWT case represents the longitudinal component of the electric field whereas in the FEL it represents the transverse field. In addition we present the spatial growth rate. The major difference between these two sets of equations is the factor  $1/(\gamma\beta)^2$  which appears in both the amplitude and particle equations of the FEL - as a result of the transverse oscillation. In the amplitude equation it introduces a different weighting function

to the phase term which causes a significantly different behavior of the particles relative to the wave.

Although typically an FEL requires a higher quality beam than a TWT, its inherent advantage of a very simple (smooth waveguide) electromagnetic structure has its own appeal - in particular for high power microwave generation where problems of breakdown become significant. It was exactly this issue which triggered the question of whether it is possible to force the electrons to oscillate primarily in the  $z$  direction by means of a magnetic wiggler and to achieve in the upper range of microwave frequencies (10-30GHz) operation similar to a TWT based on a slow wave structure. Our study indicates that this is possible. The wiggler is not the regular wiggler of an FEL but a set of periodic magnetic lens - or practically a longitudinal periodic magnetic field which has zero transverse component on axis and it has an exponentially growing radial component off axis.

The interaction in this kind of device has been investigated in the early eighties by McMullin and Bekefi [5-6] in an attempt to achieve higher frequencies (300-400GHz) than in regular FEL's for the same electrons energy. Some experimental work was done a few years later [7]. The present approach differs from theirs in four aspects: (1) we consider the interaction of the electrons with the *TM* mode rather than the *TEM* mode, (2) our system can operate only with an annular beam rather than a pencil beam. (3) We adopt the single particle equation of motion rather than the fluid approximation to describe the electrons dynamics. (4) The frequency range which has motivated this work is much lower (10-30GHz) than that considered in the past.

## II. SYSTEM DYNAMICS

Let us consider a beam of electrons injected into an uniform pipe of radius  $R$ . The pipe is immersed in a magnetic field which in the interior of the pipe is given by

$$B_r(r, z) = \delta B I_1(k_w r) \sin(k_w z) ,$$

$$B_z(r, z) = B_0 + \delta B I_0(k_w r) \cos(k_w z) ; \quad (1)$$

$B_0$  is the guiding magnetic field,  $\delta B$  is the amplitude of the undulator on axis ( $r=0$ ) and  $k_w = 2\pi/L$  where  $L$  is the spatial periodicity of the wiggler.

Due to the periodicity of the magnetic field it will be natural to expect that the motion of the electrons will follow a similar periodicity. Furthermore, the presence of

	TWT	FEL	TM-FEL
Amplitude Dynamics	$\frac{d}{d\zeta} a = \alpha \langle e^{-jx_i} \rangle$	$\frac{d}{d\zeta} a = \alpha \langle \frac{e^{-jx_i}}{(\gamma_i \beta_i)^2} \rangle$	$\frac{d}{d\zeta} a = \alpha \langle f_i e^{-jx_i} \rangle$
Equation of Motion	$\frac{d}{d\zeta} \gamma_i = -\frac{1}{2} [a e^{jx_i} + c.c.]$	$\frac{d}{d\zeta} \gamma_i = -\frac{1}{2} [a \frac{e^{jx_i}}{(\gamma_i \beta_i)^2} + c.c.]$	$\frac{d}{d\zeta} \gamma_i = -\frac{1}{2} [a f_i e^{jx_i} + c.c.]$
Phase Equation	$\frac{d}{d\zeta} \chi_i = \frac{\Omega}{\beta_i} - K$	$\frac{d}{d\zeta} \chi_i = \frac{\Omega}{\beta_i} - K - K_w$	$\frac{d}{d\zeta} \chi_i = \frac{\Omega}{\beta_i} - K - K_w$
Global Energy Conservation	$\frac{d}{d\zeta} [\langle \gamma \rangle - 1 + \frac{1}{2\alpha}  a ^2] = 0$	$\frac{d}{d\zeta} [\langle \gamma \rangle - 1 + \frac{1}{2\alpha}  a ^2] = 0$	$\frac{d}{d\zeta} [\langle \gamma \rangle - 1 + \frac{1}{2\alpha}  a ^2] = 0$
Spatial Growth Rate	$q = \frac{\sqrt{3}}{2} \left[ \frac{\alpha \Omega}{2} \langle \frac{1}{(\gamma_i \beta_i)^2} \rangle \right]^{\frac{1}{2}}$	$q = \frac{\sqrt{3}}{2} \left[ \frac{\alpha \Omega}{2} \langle \frac{1}{(\gamma_i \beta_i)^2} \rangle \right]^{\frac{1}{2}}$	$q = \frac{\sqrt{3}}{2} \left[ \frac{\alpha \Omega}{2} \langle \frac{f_i^2}{(\gamma_i \beta_i)^2} \rangle \right]^{\frac{1}{2}}$

Table I: The equations which describe a TWT, FEL and TM-FEL.

the magnetic field (and in particular it's modulation) will cause the electrons to gyrate. If we now assume that this gyration is much faster than all other time variations i.e.

$$\frac{eB}{m\gamma\beta} \gg ck_w, ck_{rad} \quad (2)$$

then the effect of this motion on the  $TM_{01}$  mode averages out to zero. Subject to this condition, the trajectory of the electrons can be approximately described by

$$\bar{r} \approx R_0 + R_1 \cos(k_w \bar{z}) \quad (3)$$

in this expression we ignored higher harmonics contributions. The equations which describe the dynamics of such a system (also assuming single mode operation) are presented in the third column of Table I. The filling factor is

$$\bar{f}_i \equiv \frac{1}{2\pi} \int_0^{2\pi} d\theta e^{j p_1 \frac{R_0}{R} \cos\theta} J_1(p_1 \frac{R_1}{R} \cos\theta) \quad (4)$$

If the beam is very thin such that the variations of  $f(R_0)$  are negligible, then the form factor does no longer depend on the index of the particle: at this stage one can redefine:  $a_{new} = a_{old} * f(R_0)$  and  $\alpha_{new} = \alpha_{old} f^2(R_0)$ . With these newly defined quantities the equations of the  $TM-FEL$  are completely identical to those of the TWT.

### III. SYSTEM OPERATION

*Kinematics:* The beam line intersects the electromagnetic mode line in two points. For a given geometry and velocity we conclude from the resonance condition that there could be two resonant frequencies:

$$f_{\pm} = \frac{c}{L} \gamma^2 \beta \left[ 1 \pm \frac{1}{\gamma} \sqrt{(\gamma\beta)^2 - \left(\frac{p_1}{k_w R}\right)^2} \right] \quad (6)$$

subject to the condition  $\gamma\beta k_w R > p_1$ . At the limit  $\gamma\beta k_w R = p_1$  the beam line intersects the EM mode line in a single (tangent) point. In the present study the radius of the pipe is taken to be  $R = 1.6cm$  and the periodicity of the wiggler is  $L = 2.0cm$ . For these parameters the energy of the injected electrons has to be at least  $55keV$  in order to have at least one resonant frequency.

*Magnetic Field:* The ratio between the amplitudes of the wiggler is taken to be  $\delta B = 0.107B_0$ . The trajectory of the electrons was calculated assuming that  $B_0 = 200G$ . The two amplitudes  $R_0$  and  $R_1$  of the electron trajectory are correlated for a given magnetic field. Based on this correlation we have numerically calculated  $\bar{f}(R_0 = 0.57R) = 0.14$ .

*Spatial Growth Rate* We shall now use the analytic expression for the spatial growth rate presented in Table I in order to determine the optimal regime of operation. In Figs.1 and 2 we present the frequency and the growth rate for the low and high resonant frequencies respectively as a function of the normalized velocity  $\beta = V/c$ . The coupling as a function of the initial velocity is calculated assuming a  $200A$  current and a total interaction length of  $d = 30cm$ . In these plots we defined  $q_{\pm}(dB/cm) = q_{\pm} = 20 \log(e^{Im[q(J_{\pm})]})/d$ . The large peak in the gain of the low resonant frequency occurs at the point of zero group velocity. Exactly at cutoff our approximations are no longer valid - however the general trend of operation with low group velocities in order to achieve high gain has been identified also in the beam-wave interaction in metallic corrugated waveguides [8]. The gain per unit length for electrons of energies lower than  $127keV$  is less than  $0.5dB/cm$  therefore it is not attractive. At about the same energies we obtain the maximum gain per unit length for the high resonant frequency waves. The

corresponding frequency is  $f_+ = 20.56\text{GHz}$  and  $q_+ = 1.588\text{dB/cm}$ .

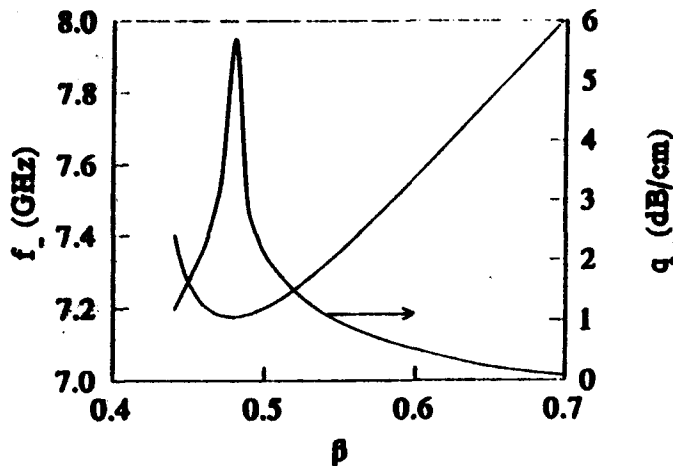


Fig. 1: The lower frequency and the spatial growth rate as a function of the normalized velocity  $\beta$ .

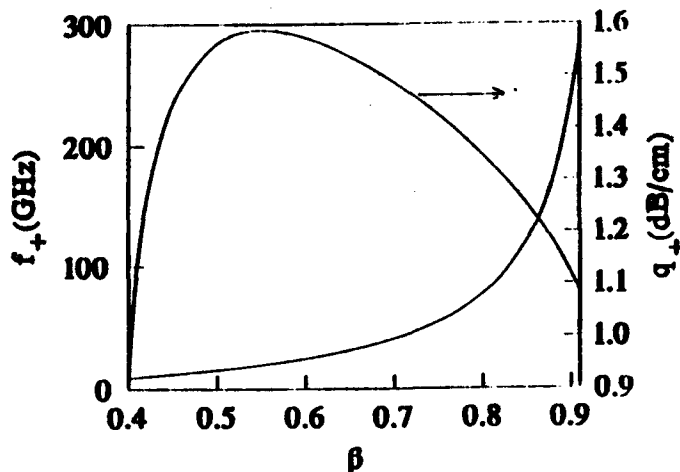


Fig. 2: The higher frequency and the spatial growth rate as a function of the normalized velocity  $\beta$ .

**Quasi-Analytical Approach.** Based on the set of equations presented in Table I, we can simulate the operation of the device as an amplifier. At  $f = 20.56\text{GHz}$ , for  $400\text{A}$  and a  $128\text{kV}$  beam with  $6\text{kW}$  of power at the input the maximum gain is about  $30\text{dB}$  corresponding to more than 11% efficiency. For a prebunched beam the efficiency can be doubled without tapering the magnetic field.

**Particle in Cell Simulations.** The analytical and quasi-analytical results presented above have been tested with the particle in cell code MAGIC -excluding the TE modes. Fig. 3 depicts the trajectories of the electrons. Typically these remain unchanged even when the phase space distribution is significantly altered; the density of particles may vary significantly from one location to another. The system was driven at  $7.2\text{GHz}$  which is, at the input energy, the resonance frequency of the system - close to cutoff ( $7.176\text{GHz}$ ). The spectrum of the radiation generated is

stable and "clean". The Poynting vector integrated over the waveguide cross section indicates about  $2\text{MW}$  (25%).

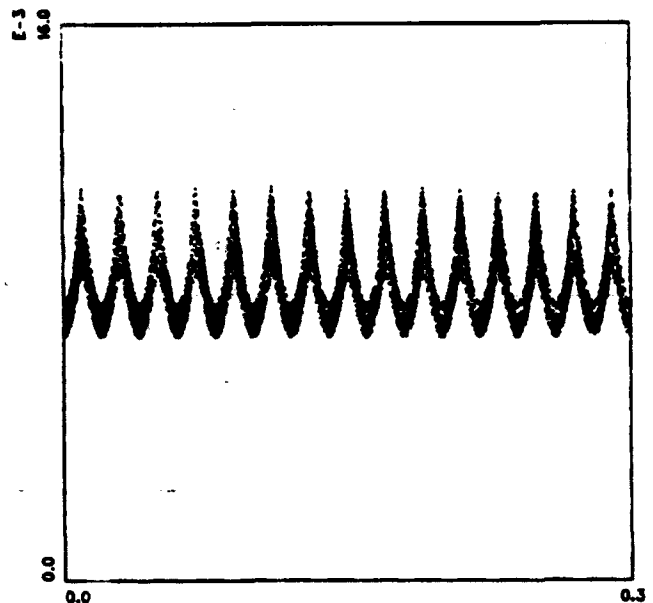


Fig. 3: Electron trajectory as calculated with MAGIC.

#### IV. DISCUSSION AND SUMMARY

We have presented preliminary results from the study of the interaction of a beam with a TM mode in a longitudinal magnetic wiggler. For a thin beam the simplified set of equations which describe the dynamics of such a system are identical to these of a traveling wave tube and differ from the regular transverse wiggler free electron laser. The quasi-analytical model indicates that the TM-FEL has a low sensitivity to initial spread of the kinetic energy - like the TWT and high (11%) "bare" efficiency (no tapering). With a prebunched beam the efficiency can be increased. The trajectories of the electrons are stable even at saturation and are determined by the wiggler. Combining these results with the very simple geometry required for the electromagnetic structure (smooth waveguide), make the device appealing for high power microwave generation in the range of ( $10-30\text{GHz}$ ).

#### V. REFERENCES

- [\*] Work supported by USDOE and AFOSR.
- [1] "Classical Electrodynamics" by J.D. Jackson, John Wiley & Sons, Inc. New York 1962 - p.474-5.
- [2] L. Schächter; Phys. Rev. A 43(7) 3785(1991).
- [3] L. Schächter *et. al.*; Phys. Rev. A. 45 8820(1992).
- [4] C. Roberson and P. Sprangle Phys. Fluids 1,3(1989).
- [5] W.A. McMullin and G. Bekefi; Appl. Phys. Lett. 39(10), 845(1981).
- [6] W.A. McMullin and G. Bekefi; Physical Review A. 25(4), 1826(1982).
- [7] I. Shraga *et. al.* ; Appl. Phys. Lett. 49(21), 1412(1986).
- [8] "Two Stage, High Power X-band Amplifier Experiment", E. Kuang *et. al.*; in this Proceedings.

# CARM and Harmonic Gyro-Amplifier Experiments at 17 GHz\*

W.L. Menninger, B.G. Danly, S. Alberti<sup>†</sup>, C. Chen, E. Giguet<sup>‡</sup>, J.L. Rullier<sup>§</sup>, R.J. Temkin  
Plasma Fusion Center  
Massachusetts Institute of Technology  
Cambridge, Massachusetts 02139

## Abstract

Cyclotron resonance maser amplifiers are possible sources for applications such as electron cyclotron resonance heating of fusion plasmas and driving high-gradient rf linear accelerators. For accelerator drivers, amplifiers or phase locked-oscillators are required. A 17 GHz cyclotron autoresonance maser (CARM) amplifier experiment and a 17 GHz third harmonic gyro-amplifier experiment are presently underway at the MIT Plasma Fusion Center. Using the SRL/MIT SNOMAD II induction accelerator to provide a 380 kV, 180 A, 30 ns flat-top electron beam, the gyro-amplifier experiment has produced 5 MW of rf power with over 50 dB of gain at 17 GHz. The gyro-amplifier operates in the TE<sub>31</sub> mode using a third harmonic interaction. Because of its high power output, the gyro-amplifier will be used as the rf source for a photocathode rf electron gun experiment also taking place at MIT. Preliminary gyro-amplifier results are presented, including measurement of rf power, gain versus interaction length, and the far-field pattern. A CARM experiment designed to operate in the TE<sub>11</sub> mode is also discussed.

## I. INTRODUCTION

### A. Next Generation Collider Requirements

At present, designs for the next generation colliders have settled on 11-30 GHz as a range of reasonable operating frequencies. Some parameterizations put the optimum operating frequency at 17 GHz[1,2]. The typical peak power that will be required per source is in the 500 MW to 1 GW range, with rf pulse lengths in the neighborhood of 25-50 ns[1]. For such a design, accelerating gradients may be on the order of 200 MV/m.

Sources capable of fulfilling the requirements of these accelerators are under development. Promising sources are gyroklystrons[3], free electron lasers[2], CARMs, relativistic klystrons, and gyro-TWT amplifiers.

### B. CRM theory

In cyclotron resonance masers, electrons undergoing cyclotron motion in an axial magnetic field couple to a fast electromagnetic wave. The CRM resonance condition is

$\omega - k_z v_z = s\Omega_e$ , where  $\omega$  is the rf wave frequency,  $k_z$  is the parallel wave number,  $v_z$  is the axial electron velocity,  $s$  is the harmonic number, and  $\Omega_e \equiv q_e B / \gamma m_0 c$  is the relativistic cyclotron frequency. For the gyro-amplifier, the  $k_z v_z$  term in the resonance condition is small, but the CARM makes use of this term to operate at a significantly upshifted frequency with phase velocity close to unity. This operating regime has the unique feature that the electrons maintain resonance with the rf wave even as they lose energy, hence the term, "autoresonance." This autoresonance combined with the upshifted frequency make the CARM an appealing rf source.

A gyro-amplifier using harmonic interactions obtains the same advantage as the CARM—lower magnetic field for a given operating frequency—with the added advantages of being less sensitive to beam quality. For both the CARM and the gyro-amplifier, tapering the magnetic guide field offers the added benefit that the electrons can be kept in resonance as they lose energy, thereby enhancing the efficiency of the amplifier.

## II. DESIGN

Initially, we designed a 17 GHz CARM amplifier utilizing a 500 kV, 500 A, 30 ns flat-top beam pulse generated by the SRL/MIT SNOMAD-II linear induction accelerator[4]. A diagram of the experiment is shown in Fig. 1. A three period bifilar helical wiggler with a wiggler period of 9.21 cm and a field of up to 60 G is used to add pitch to the beam, which is injected by a thermionic Pierce-type gun. The design pitch for the CARM is  $\alpha = 0.4$ . The beam then travels through a region of adiabatic compression where the magnetic field increases to 4 kG for extracting energy via the upshifted CRM resonance. A 17 GHz input signal is injected into the interaction region using a 45° wire-mesh coupler. This signal copropagates with the beam in 1.27 cm radius waveguide, where the signal is resonantly amplified.

Using the experimental setup for the CARM amplifier, we observed a TE<sub>31</sub> gyro-amplifier mode at third harmonic. The beam settings for operation in this mode are 380 kV,  $\alpha = 1.0$ , and a 2.7 kG guide field.

Cold-beam studies predict efficiencies of ~20% for the CARM amplifier [4] in the absence of magnetic field tapering, and ~15% for the third harmonic gyro-amplifier, for this unoptimized design, given our beam parameters. These efficiencies can be improved by magnetic field tapering. Optimized relativistic harmonic gyro-amplifier designs can be expected to yield up to > 40% efficiency at the second harmonic [5]. The gyro-amplifier efficiency drops off much more slowly than that of the CARM as beam quality deteriorates, however. At 10%-15% axial velocity spread, for example, CARM operation is

\*Supported by the Department of Energy, Advanced Energy Projects Office, under contract DE-FG02-89ER14052. Additional support from Science Research Laboratory, DARPA, and LLNL is gratefully acknowledged.

<sup>†</sup>Supported by Swiss National Science Foundation, Fellowship Nr. 8220-30665.

<sup>‡</sup>Also with Thomson Tubes Electroniques, Vélizy, France.

<sup>§</sup>Supported by CEA/CESTA, France.

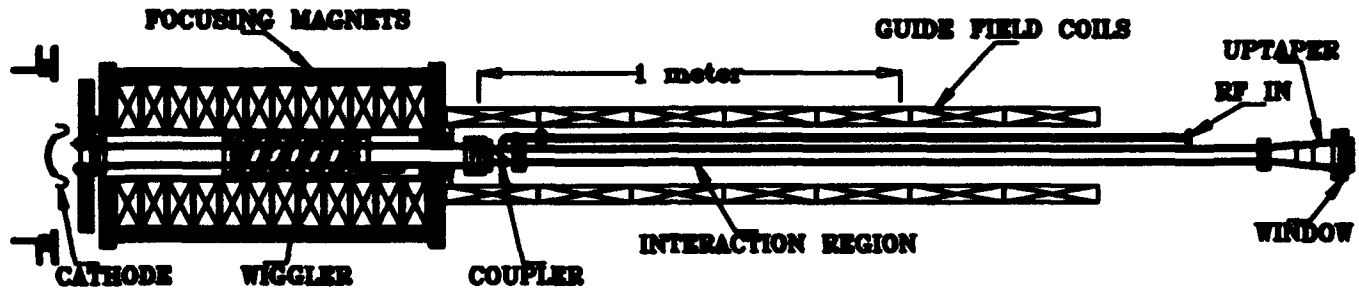


Figure 1: Experimental diagram (to scale).

infeasible, while the gyro-amplifier efficiency still can be as high as 10%.

### III. EXPERIMENTAL RESULTS

#### A. CARM Amplifier

To date, CARM amplifier operation has not been observed. Our beam transport must be improved in order to achieve beam qualities necessary for CARM operation.

#### B. Gyro-amplifier

Operation of the third harmonic gyro-amplifier at high power has been observed, and unprecedented results have been obtained. We measured 5 MW of power in the  $TE_{31}$  mode for a beam voltage of 380 kV and a beam current of 180 A, giving an efficiency of 7%. The current, depending on whether we run the cathode temperature limited or space-charge limited, can be from 150-300 A. Interestingly, increasing the current does not greatly increase the rf power, possibly indicating that at higher current, the space-charge limited electron beam has significantly poorer beam quality than a temperature limited beam. A typical voltage trace and rf pulse for the gyro-amplifier is shown in Fig. 2. Experimental evidence suggests that the rf pulse is narrower than the voltage pulse due to the onset of absolute instability. We observe that as we increase the pitch in the beam, absolute instability occurs at earlier time and has an increasingly detrimental effect on the amplified rf power.

Our output power for the gyro-amplifier was calculated by measuring a 1-D far-field pattern from the output rf window with a calibrated detection horn, attenuator, and diode. We then use the pattern to obtain relative power in the various TE modes. Normally this cannot be uniquely determined from a 1-D pattern, but by ignoring TM modes and the  $TE_{01}$  mode since they have very little coupling to the CRM resonance for an axis encircling beam, we can obtain a unique distribution of power. By integrating the measured pattern, we then obtain absolute power in each of the TE modes. A typical far-field pattern and

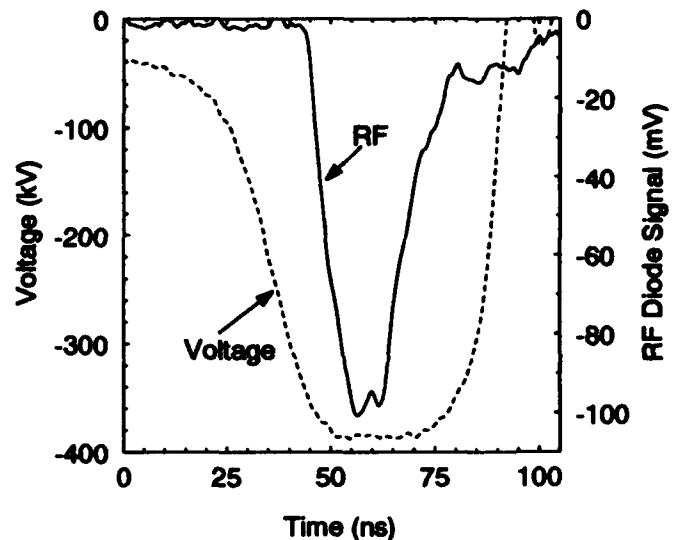


Figure 2: Voltage and rf pulses.

subsequent TE mode content and power calculation is shown in Fig. 3. We estimate the error in this power measurement to be  $\pm 2$  dB. Plans to measure the power using a calibrated directional coupler are in progress.

The injected rf drive power was also measured using a far-field pattern measurement; however, the uncertainty in the measurement is larger since we cannot rule out TM modes from the distribution. The input pattern clearly contains a wide mix of modes, with power in the synchronous  $TE_{31}$  mode estimated at not more than 50 W minimum in order to obtain rf amplification, for a total of over 50 dB of rf gain.

We measured the rf power gain versus interaction distance by sliding a strong "kicker" magnet down our interaction tube to eject the beam at various distances along the interaction. The results of this measurement are shown in Fig. 4. The optimum magnetic field profile is also shown in the figure, verifying that a taper in the field allows increased rf power. The gain history measurement was made by putting the detec-

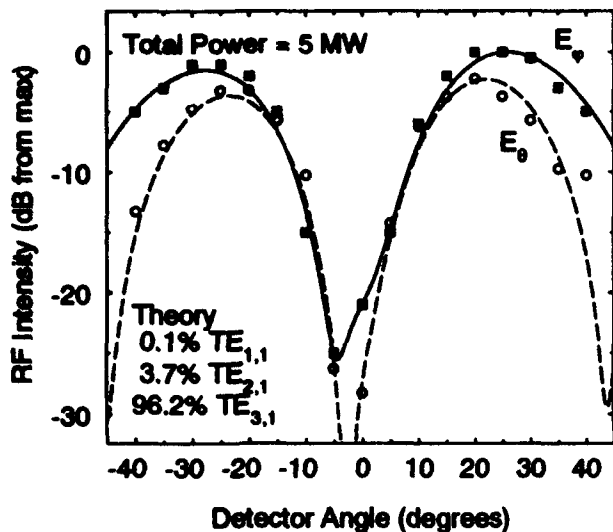


Figure 3: Far-field scan of the amplified rf.

tion diode at the peak angle for  $TE_{31}$  output. Note that at small interaction distances, the signal from the magnetron masks the  $TE_{31}$  signal because the magnetron injects only a fraction of  $TE_{31}$  power. Also, due to limitations in positioning the kicker magnet, the rf drive power is injected into the interaction region 15 cm before the point marked as 0 cm in Fig. 4. Thus the total gain of the system is over 50 dB even though the figure only shows an increase of 48 dB from start to finish.

The theoretical output power of the gyro-amplifier depends strongly on beam pitch. This is a difficult quantity to measure. Simulations predict that our pitch is  $\alpha = 0.75 - 1.0$ . For our beam parameters of 380 kV and 180 A, with  $\alpha$  in this range, predicted output power for a non-tapered magnetic field and a cold beam is 8-12 MW. As we increase our pitch, absolute instabilities occur. For a guide field of 2.7 kG, absolute instability is predicted to occur at  $\alpha \geq 1.1$ , consistent with experimental observation.

#### IV. CONCLUSIONS

Third harmonic gyro-amplifier operation has been observed to produce 5 MW of 17 GHz  $TE_{31}$  rf power at 7% efficiency with a tapered magnetic field. The gyro-amplifier shows a single pass gain of over 50 dB, which allows it to operate with very low power drive sources. This third harmonic gyro-amplifier is presently the planned source for the 17 GHz rf gun experiment at MIT. A second harmonic gyro-amplifier experiment has also been designed and will be tested shortly.

The output power and efficiency of the gyro-amplifier are still much lower than theory predicts, even for very poor quality ( $\sim 15\%$  axial velocity spread) electron beams. Plans for improvement of our beam transport include shortening our bifilar helical wiggler, shortening of the entire system by redesigning the magnetic transport, and minor modifications to the electron gun geometry. Design of a sever to damp absolute instabilities is also in progress.

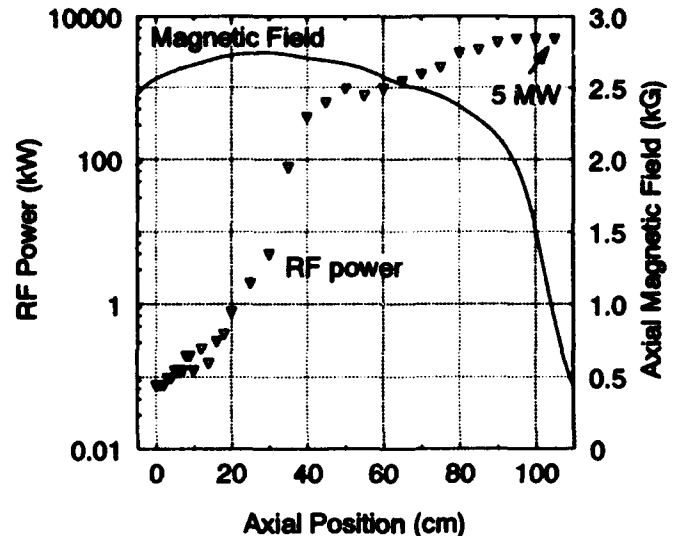


Figure 4: Gain history and magnetic field profile.

Output power of 5 MW at 17 GHz with gain of over 50 dB from a gyro-amplifier operating at third harmonic is unprecedented. Nevertheless, substantial improvement of the operation is expected with optimization of the amplifier for operation on this mode. This power level, combined with the low operating voltage and field, makes the harmonic gyro-amplifier a promising source of rf power.

#### References

- [1] R. Palmer, "The interdependence of parameters for TeV linear colliders," Tech. Rep. SLAC-PUB-4295, Stanford Linear Accelerator Center, 1987.
- [2] R. Jong, R. Ryne, G. Westenskow, S. Yu, D. Hopkins, and A. Sessler, "A 17.1 GHz free-electron laser as a microwave source for TeV colliders," *Nucl. Instr. Methods Phys. Res. A*, vol. 296, pp. 776-783, 1990. Proceedings of the Eleventh International Free-Electron Laser Conference.
- [3] W. Lawson, J. Calame, B. Hogan, P. Latham, M. Read, V. Granatstein, M. Reiser, and C. Striffler, "Efficient operation of a high power x-band gyrokystron," *Phys. Rev. Lett.*, vol. 67, pp. 520-523, July 1991.
- [4] W. Menninger, B. Danly, C. Chen, K. Pendergast, R. Temkin, D. Goodman, and D. L. Sorenson, "Cyclotron autoresonance maser (CARM) amplifiers for RF accelerator drivers," in *Proceedings of the 1991 Particle Accelerator Conference*, pp. 754-756, IEEE, 1991.
- [5] G. Nusinovich and H. Li, "Large-signal theory of gyrotraveling wave tubes at cyclotron harmonics," *IEEE Trans. Plasma Science*, vol. 20, pp. 170-175, 1992.

# Stability of Gyrotwistrons

P.E. Latham, G.S. Nusinovich, and J. Cheng

Laboratory for Plasma Research, University of Maryland, College Park, MD 20742, USA

## Abstract

The stability of gyrotwistrons against the excitation of parasitic modes is studied. A method is described which can be used to compute the nonlinear saturation amplitude of the parasites when the operating mode is present. An example relevant to driving particle accelerators (near 10 GHz and 500 kV) is discussed.

## I. INTRODUCTION

One possible source for driving particle accelerators is the relativistic gyrotwistron,<sup>1</sup> in which the output cavity of a standard gyrokystron amplifier is replaced by a traveling wave section. The primary reason to consider the gyrotwistron over the more conventional gyrokystron amplifier is efficiency: because the interaction region is relatively long, the magnetic field can be tapered to keep the particles in resonance, thereby extracting a large fraction of the available energy. On the other hand, because of the long interaction region gyrotwistrons are highly susceptible to instabilities. In this paper we consider a relativistic gyrotwistron operating in the TE<sub>01</sub> mode and study its stability with respect to the parasitic TE<sub>11</sub> mode. Without the operating mode present the TE<sub>11</sub> mode is unstable when the reflection coefficient at the output cross-section goes above .07%. The question we consider here is: what effect does the operating mode have on the parasite? In the next section, we briefly outline the equations we will use. Section III contains our results for a specific case (425 kV, 160 A, 9.85 GHz, fundamental TE<sub>01</sub>), and Sec. IV contains our summary and conclusions.

## II. EQUATIONS

The equations we use are the Lorentz force equations for the particles and Maxwell's equations for the wave. The electron motion is studied under the following simplifying assumptions:

1. We neglect space charge.
2. We neglect guiding center drift caused by the wave (although we include drift caused by the tapered external magnetic field).
3. We averaged the equations over fast gyrophase.
4. We assume that  $k_{\perp} r_L < 1$  ( $k_{\perp}$  is the perpendicular wave number,  $r_L$  is the Larmor radius).

To simplify Maxwell's equations, we average over a wave period as well as the fast gyrophase, and assume that only two modes are present: the operating mode and one parasite. We consider the case where these two modes are incommensurate; i.e.  $s_1/s_2 \neq \omega_1/\omega_2$  where  $s$  is the harmonic number,  $\omega$  is the frequency, and the subscript "1" and "2" refer to the operating mode and parasite, respectively. And finally, we work in the steady state regime, so the wave amplitudes are fixed in time (but not space).

What we wish to find in this analysis is the amplitude of the parasite as a function of its reflection coefficient at the output cross-section. In fact, there is generally more than one amplitude for each reflection coefficient, and not all of them are stable. The stable solutions are the ones for which the reflection coefficient increases as the amplitude of the parasite increases. Thus, we need to compute the reflection coefficient of the parasite versus amplitude over a range of amplitudes. This computation must be done at frequencies ranging from cutoff to a large enough frequency that the beam and wave lose resonance.

## III. RESULTS

We consider a gyrotwistron relevant to the University of Maryland experiment.<sup>2</sup> This experiment can operate over a range of parameters; for definiteness we consider fundamental operation in the TE<sub>01</sub> mode at a frequency of 9.85 GHz, a voltage of 425 kV, a current of 160 A, a pitch ratio ( $v_{\perp 0}/v_{z0}$ ) of 1.2 and an RMS axial velocity spread of 6%. These are rather easily attainable values. The output waveguide has an initial radius of 1.825 cm and a 0.5 degree taper; the taper helps stabilize the system by ensuring that no mode can remain near cutoff for too long. Instead of an initial cavity, we start the particles uniformly distributed in phase but with a kick in perpendicular momentum, and then let the particle

bunch ballistically in the drift section. As a result of the kick, at the entrance to the output waveguide the distribution in phase  $\psi$  and normalized perpendicular momentum  $u_{\perp}$  are given approximately by

$$\begin{aligned}\psi &= \psi_0 + \frac{q}{K_0}(u_{\perp 0} - 1) + q \cos(\psi_0) \\ u_{\perp} &= u_{\perp 0} - K_0 \cos(\psi_0)\end{aligned}$$

where  $\psi_0$  is uniformly distributed in phase between 0 and  $2\pi$ ,  $u_{\perp 0}$  has a top hat distribution in perpendicular momentum,  $q$  is the standard bunching parameter, and  $K_0$  is proportional to the kick the particles receive in the first cavity.

We first consider the operating mode. Because both the forward and backward waves are excited, there are boundary conditions at both ends of the circuit: the particle phases and momenta are specified at the beginning of the output waveguide according to the above distribution, while the wave amplitudes are specified at both ends (the initial forward wave amplitude and the final backward amplitude are zero). Thus, a hunt and shoot method must be used to find the correct amplitude and phase of the backward wave at the beginning of the circuit. We chose a relatively small bunching parameter,  $q \approx 0.1$ . This made it easy to find an equilibrium satisfying the boundary conditions, although a larger bunching parameter would probably have helped suppress the parasites. In future work we will consider such larger values. The magnetic field had a fairly strong taper; it started at 5.6 kG, and then fell to about half that value in 20 cm. The maximum efficiency was 36%, which occurred at about 18 cm, but the final efficiency was 28%. We integrate past where the efficiency is a maximum because we use the actual experimental coils to specify the magnetic field, so there are constraints on its profile. We should be able to increase the final efficiency by abruptly decreasing the magnetic field at 18 cm, and we are working in this direction.

Analysis of the parasites proceeds as described above. Typically there are a large number of modes that are capable of interacting with the electron beam at the specified magnetic field: 10 to 20 if only the first and second harmonics are considered; more if the third and higher harmonics are also included. To demonstrate our procedure, here we will consider only the parasitic  $TE_{11}$  mode operating at the fundamental cyclotron frequency ( $s_2 = 1$ ). Without the operating mode present, this mode is unstable at 6.4 GHz if the reflectivity at the output cross-section is

above .07%. With the operating mode present the  $TE_{11}$  mode is still linearly unstable; now near 5.2 instead of 6.4 GHz. However, it has a relatively low saturation amplitude: for reflection coefficients up to 50%, the  $TE_{11}$  mode saturates at about 1% of the power of the operating mode. However, even at these low levels it reduces the operating mode efficiency: at 50% reflection, the maximum efficiency falls from 36% to 23%, and the final efficiency falls from 28% to 20%. At lower reflection coefficient, the falloff is similar: at 5% reflection, the maximum efficiency is 26% and the final efficiency is 23%. The parasite was also unstable at other frequencies besides 5.2 GHz, but at those frequencies it had a much lower saturation amplitude.

#### IV. SUMMARY

For the modes we considered ( $TE_{01}$  for the operating mode and  $TE_{11}$  for the parasite), we found that with the operating mode present, the power in the parasite saturated at a level about 100 times lower than that of the operating mode. However, significant degradation in the efficiency of the operating mode was observed; its final efficiency dropped from 28% to about 20% at 50% reflection. We suspect that we can improve this result by using a larger bunching parameter so that the operating mode saturates more rapidly, and by decreasing the magnetic field faster to decrease the operating regime of the parasite. One thing we did not consider was the simultaneous existence of parasites over a range of frequencies. Since the unstable spectrum was fairly narrow, we suspect that it is a good approximation to assume that the parasite is excited at a single frequency; nevertheless, this issue deserves further investigation.

This work was supported by the U.S. Department of Energy.

#### V. REFERENCES

1. G.S. Nusinovich and H. Li, "Theory of the Relativistic Gyrotwistron," *Phys. Fluids B*, **4**, 1058 (1992).
2. W. Lawson, B. Hogan, P.E. Latham, M.E. Read, V.L. Granatstein, M. Reiser, and C.D. Striffler, "Efficient Operation of a High Power X-Band Gyroklystron," *Phys. Rev. Lett.*, **67**, 520 (1991).

# Optimum Operation of Gyrotwistrons

P.E. Latham and G.S. Nusinovich

Laboratory for Plasma Research

University of Maryland, College Park MD 20742, USA

## Abstract

Relativistic gyrotwistrons, which can, in principle, achieve efficiencies in excess of 50%, are promising sources for driving particle accelerators. The optimum operating point for these devices represents a tradeoff between maximizing the available energy and minimizing the deleterious effects of velocity spread. The former increases with Doppler upshift and pitch ratio, while the effects of velocity spread are made worse by both of these quantities. We discuss the issues that go into deciding how to achieve maximum efficiency, with particular attention paid to the role of beam current.

## I. INTRODUCTION

One possible source for driving particle accelerators is the relativistic gyrotwistron,<sup>1</sup> in which the output cavity of a standard gyrokystron amplifier is replaced by a traveling wave section. There are two issues involved in designing a gyrotwistron: stability and efficiency. In another paper ("Stability of Gyrotwistrons," by P.E. Latham, G.S. Nusinovich, and J. Cheng, these proceedings), we consider issues of stability; here we ask the question: what parameters yield the optimum efficiency? In addressing this question, we make the following assumptions:

1. The electron beam voltage and current are fixed.
2. The electron beam has a perpendicular velocity spread,  $\Delta\beta_{\perp 0}/\beta_{\perp 0}$ , that is independent of magnetic field and pitch ratio  $\alpha$  ( $\alpha \equiv \beta_{\perp}/\beta_z$ ).
3. The axial wave number,  $k_z$ , is chosen so that the beam and wave are initially in resonance; i.e. at the beginning of the output waveguide,

$$\omega - s\Omega_c - k_z\bar{v}_z = 0$$

where  $\omega$  is the operating frequency,  $s$  is the harmonic,  $\Omega_c$  is the initial cyclotron frequency and  $\bar{v}_z$  is the initial average velocity.

The first and third assumptions are fairly reasonable; the second needs some explanation. This assumption stems from the observation that the perpendicular velocity spread is an adiabatic invariant. Thus, if a given value of  $\Delta\beta_{\perp 0}/\beta_{\perp 0}$  can be achieved at some value of the pitch ratio, it can be achieved at any other value of  $\alpha$  by adiabatically varying the magnetic field. Since an electron gun can be constructed to produce a beam over an extremely broad range of magnetic fields, it follows that the perpendicular velocity spread is independent of both magnetic field and pitch ratio. Of course, in a particular electron gun this will be true only over a range of magnetic fields.

The task now is, in principle, largely numerical: simply optimize efficiency with respect to initial pitch ratio and magnetic field, with the axial wave number chosen to satisfy the resonance condition given above. This is, however, a big job; especially since the efficiency needs to be optimized with respect to the magnetic field profile. To narrow down the parameter range, in this paper we estimate, using simple physical arguments, the parameters which are likely to yield high efficiency. This will give us a good starting point for a numerical investigation, which will be carried out in future work. In the next section we discuss the issues relevant to high efficiency gyrotwistrons, culminating with a single graph (at each harmonic) which displays our results. Section III contains our summary and conclusions.

## II. DISCUSSION AND RESULTS

As mentioned, the optimum operating point for a gyrotwistron represents a tradeoff between maximizing the available energy and minimizing the effects of velocity spread. The available energy is given by the maximum single particle efficiency,<sup>2</sup>

$$\eta_{sp} = \frac{\gamma_0 + 1}{2\gamma_0} \frac{\alpha^2}{1 + \alpha^2} \frac{\omega}{s\Omega_c}$$

where  $\gamma_0$  is the initial relativistic factor. The single particle efficiency, which is easily derived by noting that the Hamiltonian depends on a single phase

and thus has two conserved quantities, has a simple physical interpretation: the available perpendicular energy increases with pitch ratio, and the available axial energy increases with increasing Doppler upshift (the  $\omega/s\Omega_c$  term).

With no velocity spread, typically one is able to achieve efficiencies on the order of 70% of the single particle efficiency. However, with velocity spread the picture changes dramatically. A good measure of the effect of velocity spread is the spread in phase which it induces. To estimate this, we write down the zeroth order equation<sup>1</sup> for the slow gyrophase  $\psi$ :

$$\frac{d\psi}{d\xi} = \frac{1 - s\Omega_c/\omega - k_z v_z/\omega}{\sqrt{I}\beta_z}$$

where  $I$  is the normalized current and  $\xi = \sqrt{I}(\omega/c)z$  is the normalized length with  $c$  the speed of light. The normalized current for the  $TE_{mn}$  mode is

$$I \equiv \hat{I} [\bar{\beta}_\perp k_\perp c/s\Omega_c]^{2(s-1)} \frac{(k_\perp c/\omega)^2}{k_z c/\omega} \frac{1 - k_z \bar{v}_z/\omega}{\bar{\beta}_z^2}$$

$$\hat{I} \equiv \frac{4eI_b}{m_e \gamma_0 c^3} \left[ \frac{s^{(s-1)}}{(s-1)!2^s} \right]^2 \frac{J_{m\pm s}^2(k_\perp r_g)}{(\nu_{mn}^2 - m^2) J_m^2(\nu_{mn})}$$

where  $I_b$  is the beam current,  $e$  and  $m_e$  are the electron charge and mass, respectively,  $k_\perp$  is the perpendicular wave number,  $r_g$  is the guiding center radius,  $\nu_{mn}$  is the  $n$ th root of the derivative of the Bessel function:  $J'_m(\nu_{mn}) = 0$ . In these units the current appears only in the zeroth order equation of the phase, so we can estimate the effects of the current by looking exclusively at this term. Bars denote an average over the initial velocity distribution.

The phase spread induced by the velocity spread, which we denote  $\Delta_\psi$ , is defined to be

$$\Delta_\psi \equiv \Delta\beta_z \frac{\partial}{\partial\beta_z} \left( \frac{d\psi}{d\xi} \right)_{\beta_z = \bar{\beta}_z}$$

A straightforward calculation yields

$$\Delta_\psi = \left[ \frac{k_z c/\omega}{(1 - k_z \bar{v}_z/\omega)} \right]^{1/2} \frac{(s\Omega_c/\omega)^{s-1} (1 - s\Omega_c/\omega) \bar{\alpha}^2}{\bar{\beta}_\perp^{(s-1)} (k_\perp c/\omega)^s} \frac{\Delta\beta_{10}}{\sqrt{I} \beta_{10}}$$

where we used  $\Delta\beta_z/\bar{\beta}_z = \bar{\alpha}^2 \Delta\beta_{10}/\beta_{10}$  (recall that  $\Delta\beta_{10}/\beta_{10}$  is independent of both pitch ratio and magnetic field).

For large Doppler upshift, i.e.  $k_z$  near one, the most important scaling in this expression is the term  $(k_\perp c/\omega)^{-s}$ , which indicates a rapid increase in  $\Delta_\psi$  as  $k_z$  increases. This is consistent with the

well known fact that large Doppler upshifted devices are sensitive to velocity spread. However, the sensitivity comes not so much from the  $k_z v_z$  term in the resonance condition, but from the weak coupling that occurs when the perpendicular wavenumber becomes small. Note that a slow wave device would have significantly different scaling, as the coupling would not vanish at large  $k_z$ . For small  $k_z$ , the dominant terms are  $\sqrt{k_z c/\omega}$  and  $(1 - s\Omega_c/\omega)$ . The former arises because the normalized current is inversely proportional to  $k_z$ , so the coupling increases as the axial wavenumber decreases. The latter term, which is proportional to  $k_z v_z$  because of the resonance condition, reflects the fact that devices operating near cutoff are insensitive to velocity spread.

The other dependences in this expression are fairly easy to understand:  $\Delta_\psi$  increases as the beam current decreases and velocity spread increases. The dependence on the pitch ratio is slightly more complicated: because of the  $\bar{\beta}_\perp^{(1-s)}$  term,  $\Delta_\psi$  decreases as  $\alpha$  decreases only up to the second harmonic. At the third harmonic  $\Delta_\psi$  depends weakly on the pitch ratio, and at the fourth harmonic and above  $\Delta_\psi$  actually increases as  $\alpha$  decreases. Thus, harmonics above two are not good candidates for operation at small pitch ratio.

In Fig. 1 we plot level curves of both the single particle efficiency and  $\Delta_\psi$  for the first, second and third harmonics (Figs. 1a, 1b and 1c, respectively). The value  $\Delta_\psi = 0.30$  corresponds roughly to the parameters of the University of Maryland experiment<sup>3</sup> (voltage near 425 kV, current near 160 A, pitch ratio near 1, and perpendicular velocity spread near 6%.) At these parameters, numerical simulations indicate that we can achieve gyrotwistron efficiencies on the order of 35%.

The salient feature of these plots is that at a fixed pitch ratio,  $\Delta_\psi$  increases rapidly as we move into the regime of high single particle efficiency; adjacent level curves of  $\Delta_\psi$  increase by a factor of four. For instance, to move from the level curve  $\Delta_\psi = 0.30$  to  $\Delta_\psi = 1.20$  and still extract a large fraction of the available energy, either the velocity spread would have to decrease by a factor of 4 or the current would have to increase by a factor of 16. Both of these are extremely difficult technologically. Thus, since the maximum pitch ratio is generally limited by instabilities and reflected particles, there are severe constraints on the achievable

efficiency in a realistic gyrotwistron.

### III. SUMMARY AND CONCLUSIONS

We have examined, using simple physical arguments, the parameters that lead to optimum operation of a gyrotwistron. The two key concepts in this analysis were the single particle efficiency, which is a measure of the available beam energy, and the phase spread induced on the beam by the velocity spread. We found that large beam current could offset the effects of velocity spread and thus increase efficiency. Thus, high current devices will, in general, yield large efficiencies than those with low current (assuming that the other parameters are fixed).

This work was supported by the U.S. Department of Energy.

### IV. REFERENCES

1. G.S. Nusinovich and H. Li, "Theory of the Relativistic Gyrotwistron," *Phys. Fluids B*, **4**, 1058 (1992).
2. P.E. Latham and G.S. Nusinovich, "Modeling Relativistic Gyroklystron Amplifiers," Proceedings of the Workshop on Advanced Accelerator Concepts, Port Jefferson, NY, June, 1992.
3. W. Lawson, B. Hogan, P.E. Latham, M.E. Read, V.L. Granatstein, M. Reiser, and C.D. Striffler, "Efficient Operation of a High Power X-Band Gyroklystron," *Phys. Rev. Lett.*, **67**, 520 (1991).

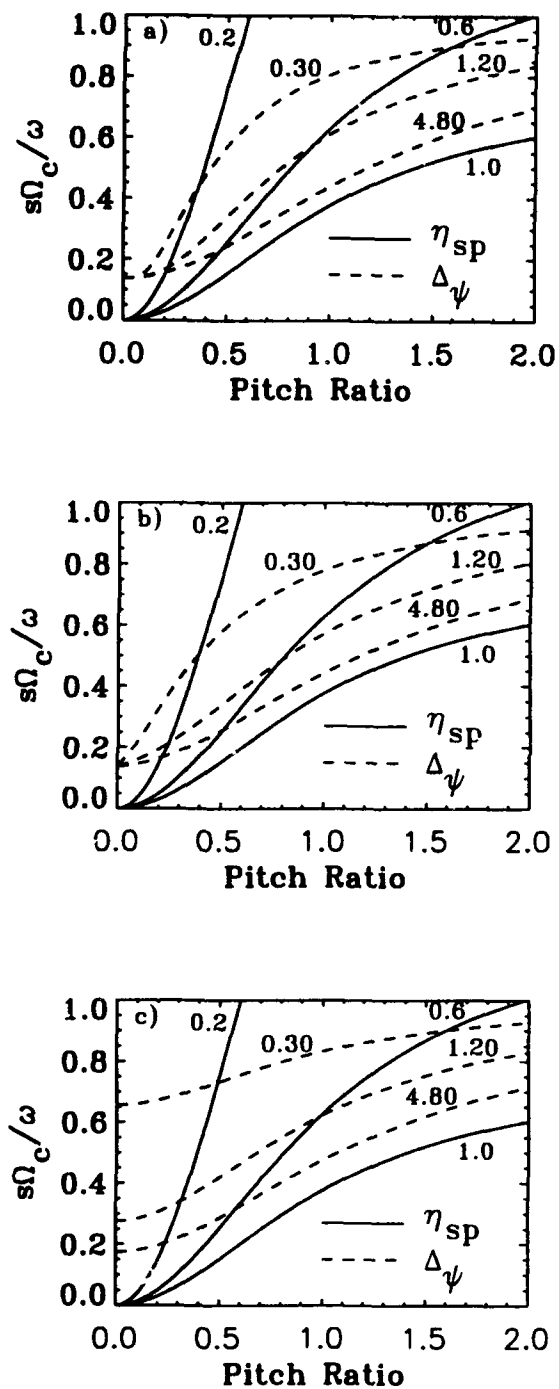


Figure 1: Level curves of single particle efficiency (solid lines) and  $\Delta\psi$  (dashed lines). a)  $TE_{01}$ , fundamental operation; b)  $TE_{11}$ , second harmonic; c)  $TE_{21}$ , third harmonic.

# LARGE ORBIT GYROKLYSTRON DEVELOPMENT AT LOS ALAMOS

R. M. Stringfield, R. M. Wheat, D. J. Brown, M. V. Fazio, J. Kinross-Wright, B. E. Carlsten, G. Rodenz, R. J. Fachl, R. F. Hoerberling

Los Alamos National Laboratory, Los Alamos, New Mexico, 87545

## Abstract

We have designed and are testing a large orbit gyrokylystron amplifier for 1.3 GHz operation in 65 ns pulses. The ultimate power output goal is 500 MW with a gain in excess of 20 dB. This initial investigation is intended to lay the groundwork for operation at 11.4 GHz for particle accelerator applications, and also at frequencies of up to 35 GHz for other uses.

Computational design has been performed with the resonant cavity code MAFIA and the particle in cell codes MERLIN and ISIS. Electron beam optics through a magnetic cusp was also studied with ISIS and MERLIN, and verified experimentally, to develop a suitable electron beam trajectory from the diode into the resonator region. Performance tests of a single stage device have been performed. An unsaturated gain of 43 dB has been observed using 4 kW of input drive, yielding an amplified output of 100 MW.

## Introduction

A large orbit gyrotron (gyroklystron) (LOG) amplifier operating at 1.3 GHz is being developed to operate at powers of up to 500 MW for 65 ns pulses. While this initial investigation is being performed at 1.3 GHz, this device can be scaled to higher frequencies in a straight forward fashion. LOG oscillators have operated at 15 GHz and higher frequencies with comparable performance to that at lower frequencies. Amplifier operation has been examined theoretically and experimentally, but less extensively [1-4].

These devices produce microwaves by the interaction of a helically rotating electron beam with the oscillating fields of a resonant cavity structure. The beam is formed by injecting a hollow, non-rotating beam, born in an axial magnetic field, through a magnetic cusp positioned at the anode plane. An annular slot is cut into the mild steel cusp plate to allow the beam to pass into the downstream resonator. In the cusp, a portion of the axial beam energy is converted to rotational energy. Typical ratios of rotational velocity to axial velocity (defined as alpha) are in the range of 1.5 to 2.5. The electron beam entering the resonator has an energy of 500-700 keV, a current of 1-3 kA, and a radius of 5-8 cm. The device, shown in Figure 1, employs a cylindrical resonator with three vanes in the wall spaced equally in azimuth.

The amplifier is designed as two resonator device, with cylindrical resonators of the type describe above. The vane structure is used to evoke coupling of the rotating electron beam with the TE(0,1,n) resonant cavity mode of the cylindrical structure by modifying the normally circular electric field pattern of the mode into a scalloped pattern, similar to the TE(3,1,n) mode, but near the lower TE(0,1,n) resonant frequency for a non-vaned cylindrical wall with an intermediate radius.

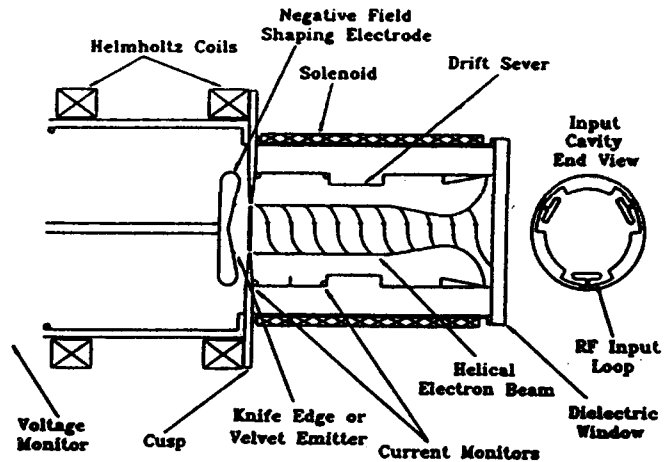


Figure 1. Large orbit gyrotron and gyroklystron geometry. Two resonator stages are shown, although single stage operation also will be investigated.

Rf is fed into the cavity using two loops, one in each of two of the vanes at the axial midplane. The standing wave pattern of the cavity will couple to the rotating beam, provided the beam angular velocity is in synchronism, in such a way that an azimuthal density perturbation will grow on the beam with three density maxima around the azimuth. The magnitude of the density variation will grow as the beam propagates down the length of the resonator, influenced both by the applied oscillating fields, and the space charge self fields of the beam that drive the negative mass instability. The instability will grow as the electron beam propagates through the system. Feedback from the beam instability drives the cavity fields to greater amplitude.

The downstream end of the first cavity has a central opening which forms the entrance to a cylindrical, non-vaned electron beam drift pipe. The pipe is intended to serve the role of an rf isolating sever between the first and second cavities, and also as a region in which the beam bunching can grow by the negative mass instability, independent of applied microwave fields. An optimum drift pipe length will be determined experimentally to maximize azimuthal beam bunching. A second, output resonator designed to be strongly coupled to the beam will be placed downstream of the drift pipe at the point of optimum beam bunching to extract rf energy.

Both 2.5 D particle in cell modeling with the code ISIS was used to design the electron gun, and subsequent experiments were performed that correlated well to the computer design. The electron beam from this design is an annulus 0.5 to 1.0 cm thick, at a radius of 7.1 cm, at an energy of 650 kV, a current of 2 to 3 kA, and an alpha ranging from 1.5 to 2.5, depending upon the magnetic field strength, that ranged

from 300 to 500 G. More detail of the design of the electron beam is contained in a previous paper[5].

### Experimental Studies

The experimental configuration consists of the diode, cusp and magnetic field coils, downstream resonator section, and a dielectric vacuum window for radiating the microwaves into an anechoic volume downstream of the vacuum chamber. A 4 kW 1.3 GHz source provides rf input drive to the resonator in these initial studies. Up to 20 MW is available as input drive but will require device modifications for aperture coupling to accommodate the power. Presently, magnetic loops are situated at the base of two of the vanes for cavity input drive. A loop in the third vane is used to monitor the standing wave field in the cavity. A stub waveguide receiver is positioned in the anechoic volume downstream of the open resonator end to monitor the radiated power in the far field.

We evaluate amplifier performance by comparing the radiated microwave power in three different circumstances. First, the radiated power due to the 4 kW input drive alone is measured. Second, the radiated power with no input drive, but with the electron beam injected, is measured. Finally, the radiated power when both input rf drive and injected electron beam are present in the resonator is measured. Relative power measurements among shots are performed by comparing detected signals received with a waveguide stub placed at a fixed location in the far field downstream of the open ended resonator.

Two significant operating regimes using the single resonator were found. The first regime, operated at a higher ratio of magnetic field to beam voltage (330 gauss/775 kV), appears to be attractive for the two stage gyrokystron (Figure 1) to establish an initiating beam modulation in a first cavity. This ratio is an experimental analog to  $B/\gamma$ , the crucial parameter governing the cyclotron frequency of the rotating beam. The initial bunching in the first cavity would be allowed to grow as the beam drifts to the second cavity. This operating regime showed significant rf production both with and without rf input drive, indicating a tendency for the device to oscillate. However, when rf input drive was present, improvements in the pulse length of the detected rf power signals, pulse energy, frequency purity of the fast Fourier transforms, and the shot to shot statistical consistency were observed. For example, this operating regime yielded rf pulse lengths of only 42 ns when the input drive was off. This effect represents a 55 percent increase in pulse length due to the presence of rf input drive. Table 1 summarizes these results. Figure 2 depicts typical detected power and downconverted mixer signals for the cases of no input drive and 4 kW of input drive.

The second operating regime appears to be most applicable to a single stage amplifier. It uses a slightly lower ratio of magnetic field to voltage (340 gauss/850 kV). In this case we saw a significant increase in output power and energy using input rf drive of 4 kW. Compared with the output when no input rf was used. While final output power determinations have not yet been completed, approximately 100 (+/- 3 dB) MW of additional power is produced from the device when 4 kW of input drive is used. This corresponds to an amplifier gain in

excess of 40 dB. The frequency purity as indicated by the FFT shows the amplified bandwidth to be 25 percent narrower than

RF Input Drive Power (4 kW) ON, Sample Size = 8

	Stub Horn (W)	Duration (ns)	RF Energy (arb)	FFT Freq (MHz)	FFT FWHM (MHz)
Mean	5450	60	3.27	1285	27
Std. Dev.	729	16	0.98	2.5	17

Input Drive Power OFF, Sample Size = 17

	Stub Horn (W)	Duration (ns)	RF Energy (arb)	FFT Freq (MHz)	FFT FWHM (MHz)
Mean	7406	42	3.11	1284	36
Std. Dev.	2089	24	1.98	2.9	25

Table 1. Mean values and standard deviations for several performance characteristics comparing the cases of rf input drive on and off for magnetic field strength and beam voltage of 330 G and 775 kV. Listed are stub horn power amplitude (watts), rf power pulse duration (ns), time integrated rf energy (arbitrary units), and fast Fourier transform (FFT) frequency spectra.

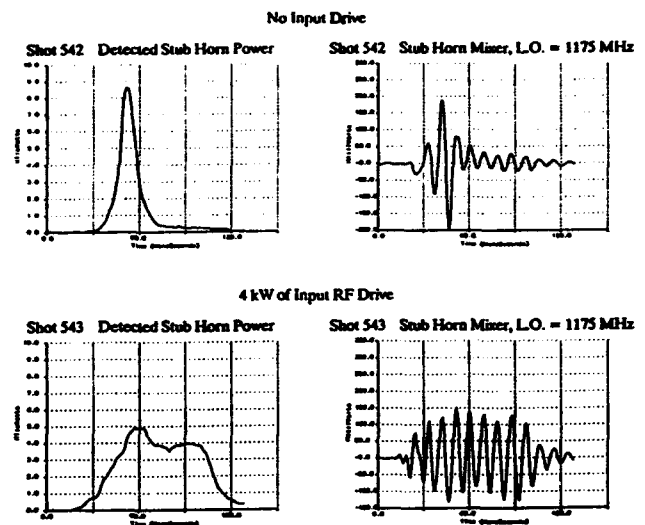


Figure 2. Typical detected diode power and downconverted mixer signals for the cases of Table 1. Stub horn power is 10 kW full scale. The FFT scale is arbitrary, and the same for both cases. The time scale is 20 ns/div.

the bandwidth without input drive (2.0% vs 2.5%), suggesting that the bandwidth is approaching but not quite at the Fourier limit, growing narrower with longer pulse length. Saturated gain has not yet been measured due to temporary difficulty in connecting a more powerful input drive source to the experiment. Hence, device efficiency as a percentage of electron

beam power has not been determined. Table 2 lists the operating conditions which yielded significant power gain in the single resonator amplifier. Figure 3 depicts representative detected power and downconverted mixer signals for the two cases. Using the method described above for estimating amplifier output power from the stub horn power (9807 W) the total power radiated was 157 MW.

### Summary

The study and construction of a large orbit gyrotron and two stage gyrokystron amplifier are underway. Modeling and experiments have been performed to design these devices. Experiments are ongoing to measure and optimize the performance of the single stage device, in preparation for subsequent two stage operation. Improvements in the quality of the rf output pulse produce by the first (rf input) cavity of the device have been found as the result of injecting input rf power into the cavity. This work has been supported by the Los Alamos National Laboratory Independent Research and Development Program, sponsored by the U. S. Department of Energy.

RF Input Drive Power (4 kW) ON, Sample Size = 14

	Stub Horn (W)	Duration (ns)	RF Energy (arb)	FFT Freq (MHz)	FFT FWHM (MHz)
Mean	9807	42.7	2.69	1280	44.1
Std. Dev.	5318	13.3	1.78	14.7	37.9

Input Drive Power OFF, Sample Size = 14

	Stub Horn (W)	Duration (ns)	RF Energy (arb)	FFT Freq (MHz)	FFT FWHM (MHz)
Mean	3060	22.3	0.67	1286	78.8
Std. Dev.	2027	19.1	0.45	17.5	37.9

Table 2. Mean values and standard deviations for several performance characteristics comparing the cases of rf input drive on and off for magnetic field strength and beam voltage of 340 G and 850 kV. This case shows clear amplification from a single stage device.

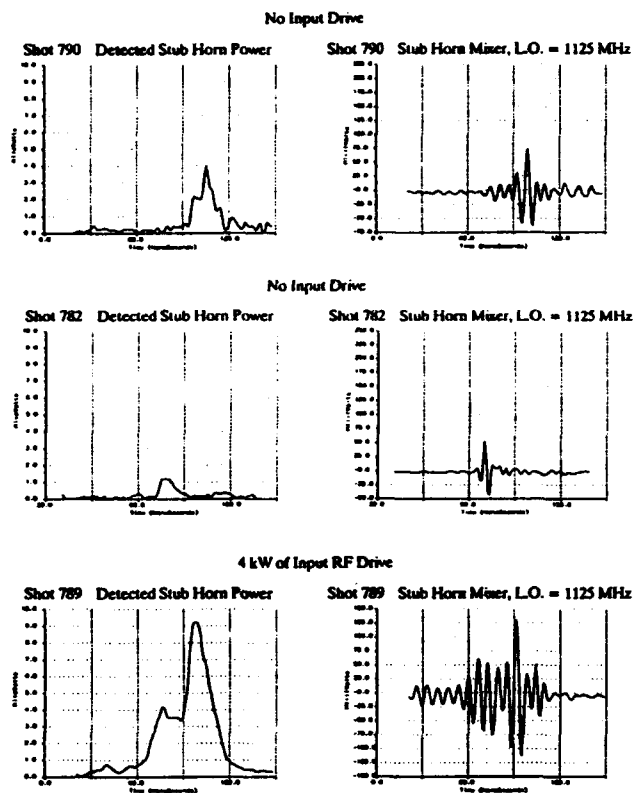


Figure 3. Typical detected power and downconverted mixer signals for the cases of Table 2. Two shots without input drive are shown to indicate the upper and lower limits of self oscillation with no drive power. Stub horn power is 10 kW full scale. The FFT scale is arbitrary, and the same for both cases. The time scale is 20 ns/div.

1. W. W. Destler, et al, "High-power microwave generation from large-orbit devices," *IEEE Trans. on Plasma Science PS-16* (2), April 1988, p71.
2. Y. Y. Lau and L. R. Barnett, "Theory of a low magnetic field gyrotron (gyromagnetron)," *Int. J. of Infrared and Millimeter Waves* 3 (5), 1982, p. 619.
3. J. Y. Choe, K. Boulais, V. Ayres, W. Namkung, and H. Uhm, "Preliminary study of cusptron amplifier," *Microwave and Particle Beam Sources and Directed Energy Concepts*, SPIE 1061 (1989) p. 132.
4. K. R. Chu, et al, "Theory, design, and operation of large-orbit high harmonic gyrokystron amplifiers," *IEEE Trans. on Plasma Science PS-13* (6), December 1985, p 435.
5. R. Stringfield, et al, "Large Orbit Gyrokystron Development at Los Alamos," *Proc. 1992 Linear Accelerator Conf., Ottawa, Ontario, Canada, August 1992, AECL-10728, Vol. p. 190-192*

# Initial Operation of a High Power, K-Band, Harmonic Gyroklystron for Accelerator Applications\*

J.P. Calame, H.W. Matthews, W. Lawson, B. Hogan, M.K.E. Lee, J. Cheng,  
V.L. Granatstein, M. Reiser, and C.D. Striffler  
Laboratory for Plasma Research and Electrical Engineering Department  
University of Maryland  
College Park, MD 20742

## Abstract

Experimental studies of amplification and stability in a series of multi-megawatt, 19.7 GHz, second harmonic gyrokystron amplifier tubes suitable for driving future linear supercolliders are reported.\* Four different two-cavity gyrokystron tubes have been constructed and tested, and each one has exhibited higher power, larger efficiency, and improved stability compared to its predecessor. The latest results include the production of peak output powers in excess of 29 MW, at an efficiency of 27% and a gain of 25 dB.

## I. INTRODUCTION

The economical construction and operation of linear electron-positron colliders with center-of-mass energies in excess of 1 TeV will require the development of a new generation of high-frequency microwave amplifiers. Candidate amplifiers should be capable of producing approximately 100 MW, 1  $\mu$ s pulses with an output frequency in the 10-20 GHz range. Pulse compression techniques would be employed to further increase the output power level to several hundred MW prior to injection into the accelerating structure. One promising candidate source for this application is the gyrokystron amplifier, a device which combines the energy extraction mechanism of the cyclotron resonance maser and the ballistic bunching approach of the klystron. Gyrokystrons can operate with overmoded cavities, which allows the production of high output powers with low current density beams and low cavity electric fields compared to those of klystrons and other conventional sources. Furthermore, the electron source usually employed in gyrokystrons (the magnetron injection gun or MIG) exhibits favorable scaling with frequency compared to linear beam guns. Over the past several years, we have developed a series of two- and three-cavity, 9.85 GHz gyrokystrons which ultimately produced 24-27 MW of output power for 1  $\mu$ s at up to 33% efficiency [1-3]. These devices employed the TE<sub>011</sub> mode in all of the cavities, and produced amplified power via a fundamental cyclotron wave interaction.

In order to increase the output power capability of a gyrokystron at any particular frequency, a larger diameter electron beam, drift tube, and output cavity must be employed. The greater degree of overmoding in these larger structures would almost certainly lead to increased mode competition problems. One way around this problem is to

operate the output cavity at the second harmonic of the drive frequency. In this configuration the input and buncher cavities are designed to resonate at one-half of the desired output frequency. The output cavity extracts energy from the pre-bunched beam via an interaction of the cavity RF fields with the beam's second harmonic cyclotron wave. Further advantages of this device over purely fundamental systems are lower capital costs, simplified cooling, and reduced magnetic field levels. Alternatively, the harmonic gyrokystron can be viewed as a means of doubling the operating frequency with little or no decrease in output power capability compared to a fundamental gyrokystron.

To test the viability of the harmonic concept with our existing beam generation equipment, we have constructed a series of two-cavity, second harmonic gyrokystrons with TE<sub>011</sub>, 9.85 GHz input cavities and TE<sub>021</sub>, 19.7 GHz output cavities. The studies have culminated with peak powers in excess of 29 MW at 19.76 GHz, with 27% efficiency and 25 dB gain. In the following sections we will describe the experimental setup and detail the most recent results.

## II. EXPERIMENT

The modulator, electron gun, magnet system, magnetron input source, and beam dump for the second harmonic experiment are the same as those used in the fundamental experiments. The electron gun produces a rotating, small orbit, annular electron beam which flows into the microwave tube under test. The present group of experiments generally employs beams in the 400-450 kV, 150-250 A range with computed  $\alpha$  ( $v_1/v_2$ ) values near 1.0. The 2nd harmonic gyrokystron tubes are modified versions of our 9.85 GHz two-cavity devices. The old 9.85 GHz, TE<sub>011</sub> output cavities were replaced by TE<sub>021</sub> cavities with resonant frequencies near 19.7 GHz. Cavities with gradual radial transitions were used to avoid mode conversion to the TE<sub>01</sub> waveguide mode and help achieve a high forward-to-reverse power ratio. In addition, the intercavity drift space was modified to improve the attenuation to a 19.7 GHz, TE<sub>01</sub> drift-tube mode while maintaining good attenuations to all other modes in the 6-13 GHz range. This was generally accomplished by modified placements of lossy dielectrics and the addition of resonant traps. A diagram of the third circuit tested is shown in Fig. 1.

The spent electron beam and output radiation pass through a nonlinear uptaper and the beam dump, and the radiation continues through a second non-linear uptaper and

\* Work supported by the U.S. Department of Energy.

a  $\lambda$ -resonant window into either an anechoic chamber or a large directional coupler/liquid calorimeter. New nonlinear tapers which preserve the  $TE_{02}$  output mode were employed in these experiments. In addition, the pickup antenna system in the anechoic chamber and the directional coupler were modified for K-Band operation. Peak power measurements obtained with each of the three measurement systems (anechoic chamber + crystal detector, directional coupler + crystal detector, and liquid calorimetry differential thermal measurements + coupler/crystal detector waveform shape) were found to agree within 7%.

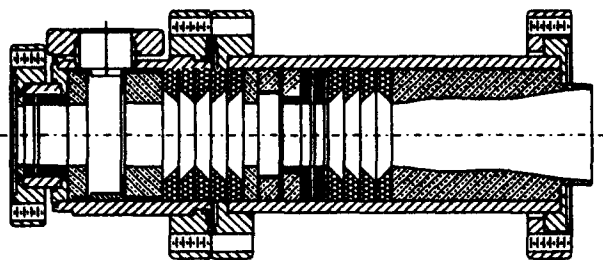


Figure 1. Section view of harmonic gyrokylystron Tube 3.

### III. RESULTS

The first tube employed a long (5 cm) high-Q (650) output cavity and was plagued by severe instabilities that prevented amplification at the second harmonic. The instabilities resulted from fundamental cyclotron interactions in the output cavity region. A second tube was constructed using a shorter (3 cm) output cavity with a somewhat lower Q (500) and a fairly rapid post-cavity radial uptaper. It also employed an improved set of drift tube traps. This circuit produced peak amplified powers near 12 MW at 19.74 GHz with an efficiency of 15%. However, performance continued to be limited by a variety of instabilities. These included a group of 1-4 MW,  $TE_{11}$ -like modes at 6-7 GHz which coexisted with the amplified signal, and a 6.9 GHz oscillation which would "cut" into the amplified signal as the beam  $\alpha$  and/or current were increased.

Based on the assumption that the output cavity region continued to be the source of the instabilities, a third tube with a lower Q (350) and a somewhat steeper post-cavity uptaper was constructed. It produced peak powers in excess of 21.5 MW at 19.76 GHz, with 21% efficiency and 23 dB gain [4]. These results were obtained with a 437 kV, 232 A,  $\alpha \approx 0.9$  electron beam. In addition, at the point of peak power production the amplified signal strongly suppressed the 6-7 GHz background instabilities. Power production and the range of stable beam parameters were still limited by the onset of instabilities at 6.9 and 12.7 GHz. Working on the possibility that the 19.7 GHz resonant trap section of the drift tube was creating reflections at these frequencies, a fourth tube was created by removing the traps from Tube 3 and replacing them with extra lossy dielectric. The change eliminated the instabilities over a broad range of beam parameters. To date we have obtained output powers in excess of 29 MW

at 19.76 GHz, with an efficiency of 27% and a gain of 25 dB. These optimal results were obtained at 455 kV and 238 A, with an  $\alpha$  of about 1.

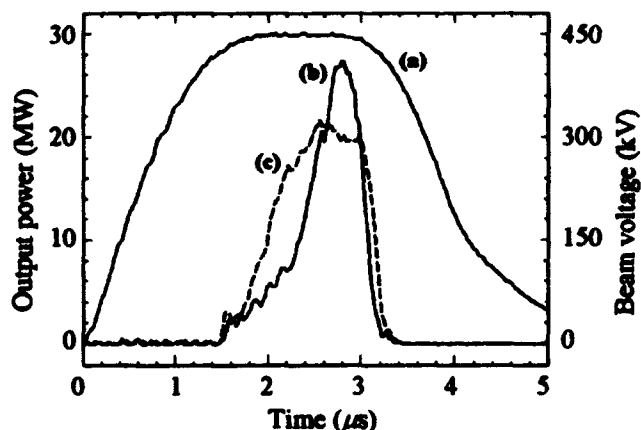


Figure 2. Typical waveforms from Tube 4; (a) voltage, (b) example of a fairly narrow, high power pulse, and (c) a wider, moderate power pulse.

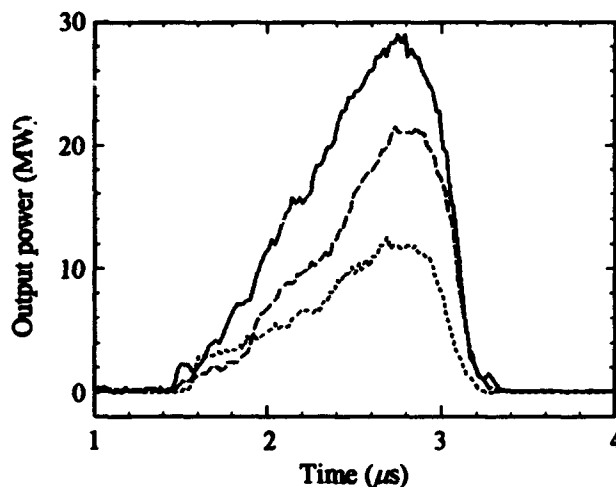


Figure 3. Power vs. time waveforms from Tube 2 (dotted), Tube 3 (dash), and Tube 4 (solid).

Typical output power vs. time waveforms from Tube 4 are shown in Fig. 2. The wider, lower power pulse (c) was obtained by adjusting the magnetic field profile to over-bunch the beam in the input cavity. Fig. 3. shows the highest reproducible peak power waveforms from each tube. In all cases the power builds up slowly over time. This results from a gradual increase in beam  $\alpha$  over the duration of the flattop of the voltage pulse [1]. This effect, due to compensation problems in the resistive divider that drives the modulation anode in the gun, combines with the strong sensitivity of second harmonic gyrokylystrons to changes in  $\alpha$  to produce the triangular pulses observed.

Systematic studies of output power as a function of beam voltage, beam current, and drive frequency in Tube 3 are shown in Figs. 4, 5, and 6, respectively (similar studies at the

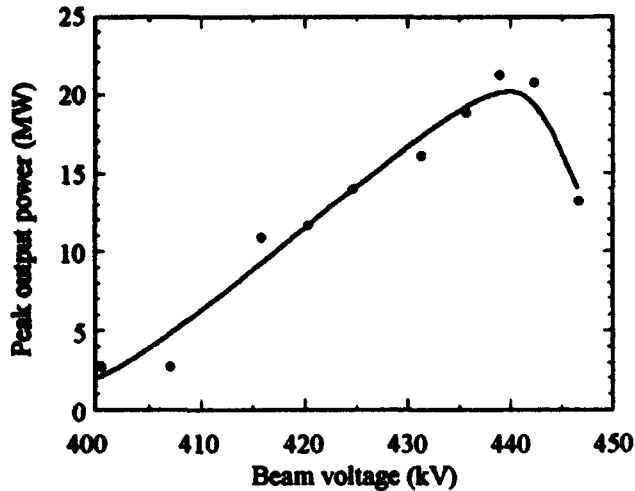


Figure 4. Effect of beam voltage on output power in Tube 3.

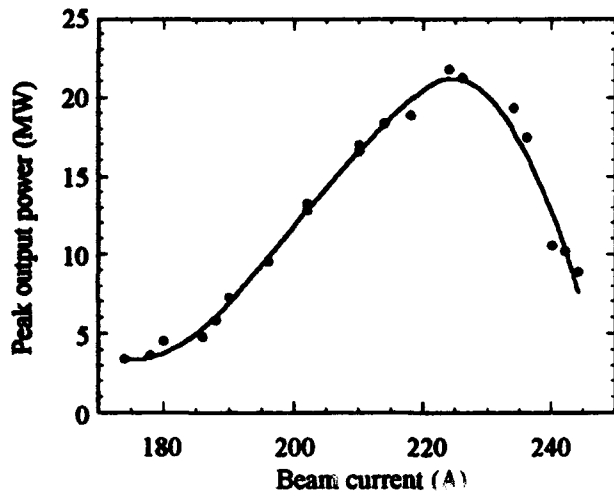


Figure 5. Effect of beam current on output power in Tube 3.

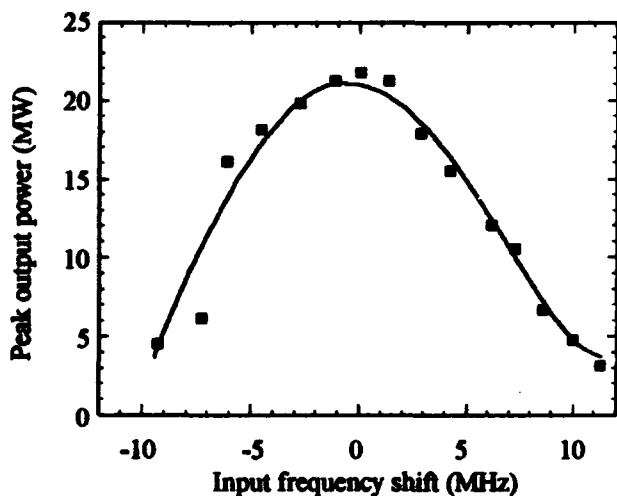


Figure 6. Effect of a shift in drive frequency on output power in Tube 3.

29 MW level in Tube 4 are just getting under way at the time of writing). In each study, only the parameter of interest is allowed to change from the optimal value; the other parameters and the circuit magnetic field profile remain fixed. However, at each point on the graphs the magnetic compression (beam  $\alpha$ ) was adjusted to just maintain stability and therefore maximize power. In the voltage study, the power falls off on either side of the optimal value (440 kV) as the beam-wave interaction slips out of resonance. In the beam current study, the power initially rises as the current increases, due to the existence of additional beam energy. However, at high currents the power falls off for a variety of reasons, including a decrease in beam quality (due to space charge effects), beam-induced detuning of cavity resonances, and the onset of instabilities (which we suppress by reducing  $\alpha$ , and thus the amplified power decreases). In the frequency study, the observed FWHM bandwidth of 14 MHz is only slightly smaller than the value expected on the basis of the cavity  $Q_s$  ( $\approx 17$  MHz).

#### IV. SUMMARY

The results of this proof-of-principle experiment indicate that second harmonic gyrokystrons can produce large amounts of output power with reasonable efficiencies. The powers measured in the latest second harmonic tube are actually higher than those obtained in our earlier two-cavity fundamental experiments (although the efficiency is somewhat lower). These results suggest an advanced capability for driving future linear supercolliders. Future experiments will include studies of harmonic output cavities with discrete radial transitions and experimental measurements of beam  $\alpha$ . A 100 MW output power, 17 GHz, second harmonic experiment with a new electron gun and an upgraded modulator is also under construction [5].

#### V. REFERENCES

- [1] J.P. Calame *et al*, "Experimental studies of stability and amplification in four overmoded, two cavity gyrokystrons operating at 9.87 GHz," *J. Appl. Phys.* 70, 2423 (1991).
- [2] W. Lawson *et al*, "Performance characteristics of a high power X-band two cavity gyrokystron," *IEEE Trans. Plasma Sci.* 20, 216 (1992).
- [3] S. Tantawi *et al*, "High power X-band amplification from an overmoded three cavity gyrokystron with a tunable penultimate cavity," *IEEE Trans. Plasma Sci.* 20, 205 (1992).
- [4] W. Lawson *et al*, "High power operation of a K-band second harmonic gyrokystron," submitted to *Phys. Rev. Lett.* in March 1993.
- [5] W. Lawson *et al*, this conference.

# Design of a 100 MW, 17 GHz Second Harmonic Gyroklystron Experiment

W. Lawson, P.E. Latham, V. Specht, M.K.E. Lee, Q. Qian,  
J.P. Calame, B. Hogan, V.L. Granatstein, M. Reiser, and C.D. Striffler  
Electrical Engineering Department and Laboratory for Plasma Research  
University of Maryland, College Park MD 20742, USA

## Abstract

At the University of Maryland, we are exploring the suitability of gyrokystrons for linear collider applications. In this paper we discuss the design of a two-cavity, coaxial gyrokystron that is designed to produce over 100 MW in 1  $\mu$ s pulses at the second harmonic of the cyclotron frequency. We detail modifications that will be required of our test facility, present the simulated performance of a 400 MW, 500 kV single-anode Magnetron Injection Gun, and describe the design of the coaxial microwave circuit.

## I. INTRODUCTION

In an effort to expand the frontiers of high-energy physics,  $e^-e^+$  colliders with center-of-mass energies approaching 1 TeV are being planned. These machines will require efficient, reliable, pulsed microwave amplifiers with peak power levels that exceed the current state-of-the-art. At the University of Maryland, we have been performing a sequence of experiments based on the cyclotron resonance instability. Initial studies with fundamental mode two-cavity gyrokystrons have produced over 24 MW of power at 9.87 GHz in 1  $\mu$ s pulses with 32% efficiency and 34 dB gain in the TE<sub>01</sub> mode [1]. Recent experiments with two-cavity second harmonic tubes have produced nearly 30 MW of power at 19.76 GHz with 27% efficiency [2]. This performance level represents the maximum we can achieve with our current test facility.

We are currently undertaking a major upgrade of our facility that will enable us to pursue amplifiers in the 100 MW range. Table 1 summarizes the major parameter differences between the current (100 MW) and future (400 MW) test facilities. The facility is shown schematically in Fig. 1. Upgrades to our line-type modulator include doubling the number of PFNs to eight, increasing the

Table 1: System parameters.

Parameter	100 MW System	400 MW System
Beam voltage (kV)	440	500
Beam current (A)	225	800
Velocity ratio	1.0	1.5
Avg. beam radius (cm)	0.78	3.10
Circuit magnetic field (kG)	5.45	5.05
Output frequency (GHz)	19.75	17.14
Drive power (kW)	100	200

current capability of our thyratrons, and reorganizing the HV tank to decrease stray capacitance. The latter modification should yield a 14% increase in our voltage capability, as indicated in Table 1. The eight water-cooled magnetic field coils will remain unchanged but the current capability of the supply which drives the gun coil will be doubled. No modifications are required for the magnetron modulator, but the magnetron itself will be replaced with a lower frequency, more efficient one. Furthermore, the output waveguide (nonlinear tapers, beam dump, and output window) and the microwave diagnostics will have to be replaced. Finally, we will need a new electron gun and microwave circuit. Progress on the designs of these components is described below.

## II. ELECTRON GUN

A single-anode Magnetron Injection Gun (MIG) was selected for the electron gun because of its simpler configuration, wider range [3], and absence of an intermediate voltage requirement. The new beam guiding center (Table 1) was selected to keep the current density in the circuit region equivalent in the two systems. The standard design formalism was followed [4] and EGUN [5] was used to perform the simulations.

Table 2: MIG parameters

A. Specifications	
Cathode radius (cm)	9.58
Emitter strip length (cm)	1.67
Cathode half-angle	40°
Magnetic compression ratio	9.9
Cathode loading (A/cm <sup>2</sup> )	5.95
B. Performance	
Axial velocity spread (%)	6.70
Space-charge limiting current (A)	2,190
Peak electric field (kV/cm)	90.0
Avg. emitter electric field (kV/cm)	51.6
Beam thickness (cm)	1.28

The electrode shapes, together with the beam envelopes, are shown in Fig. 2. The key parameters are listed in Table 2. The magnetic compression is fairly low and the beam voltage and cathode loading have been achieved before [4]. The velocity spread indicated is at the nominal current of 600 A and is due to ballistic considerations only. The emitter strip is curved by  $\pm 4^\circ$  to minimize this spread. The peak cathode field is also comparable to the previous gun. The anode electric field nowhere exceeds 30 kV/cm. The nominal current is less than 28% of the space-charge limit. Beam electrode clearance in the circuit region is approximately 1.1 mm.

The dependence of velocity spread on beam current is shown in Fig. 3. The current affects the velocity ratio due to self-field effects; these are compensated for by adjusting the magnetic field at the cathode. Axial spread approaches 6.4% as the current approaches zero and remains below 9% through the entire current range. This wide current range is directly attributed to laminar flow in the single-anode MIG.

### III. MICROWAVE CIRCUIT

A schematic of the coaxial two-cavity microwave circuit is shown in Fig. 4 and the nominal circuit parameters are given in Table 3. The input cavity is defined by sharp transitions in the radial wall. It is driven in the TE<sub>011</sub> mode at half the output frequency via a slot in the outer

Table 3: Microwave circuit parameters.

Section	Inner radius (cm)	Outer radius (cm)	Length (cm)
A. Input Cavity, Q = 60			
1	2.000	4.205	2.000
B. Drift Tube			
1	2.325	3.825	5.000
C. Output Cavity			
1	2.234	3.920	0.978
2	1.914	4.205	0.922
3	2.358	3.798	0.422
4	2.356	4.415	—

wall. The quality factor is defined in part by two thin carbon-impregnated Aluminum-Silicate rings located against the cavity end walls. The drift tube will be loaded with various lossy ceramics to achieve stable operation. The radii are chosen so that only the TE<sub>11</sub>, TE<sub>21</sub> and TE<sub>31</sub> modes are not cut off at the operating frequency. The output cavity operates predominantly in the TE<sub>021</sub> mode at a point relatively close to cutoff. There is an intermediate step in the radius of the main section to minimize the amount of power in the TE<sub>01</sub> mode which is directed into the drift region.

With an axial velocity spread of 9.5% and a pitch angle of 1.5, this circuit achieved 25% efficiency; with no velocity spread the efficiency was around 35%. The relatively low efficiency is due to interaction with the third harmonic, which accelerates rather than decelerates particles. This places a constraint on the magnetic field and reduces our operating parameter range. We are looking into ways to decrease the effectiveness of the third harmonic interaction and thus increase our efficiency.

We are currently considering two changes in the microwave circuit. The first is to incorporate a TE<sub>031</sub> output cavity. This would increase the separation to neighboring modes and promote stable operation. The second change is to use nonlinear tapers rather than abrupt transitions to define the output cavity. This should help improve mode purity and the left-to-right power ratio.

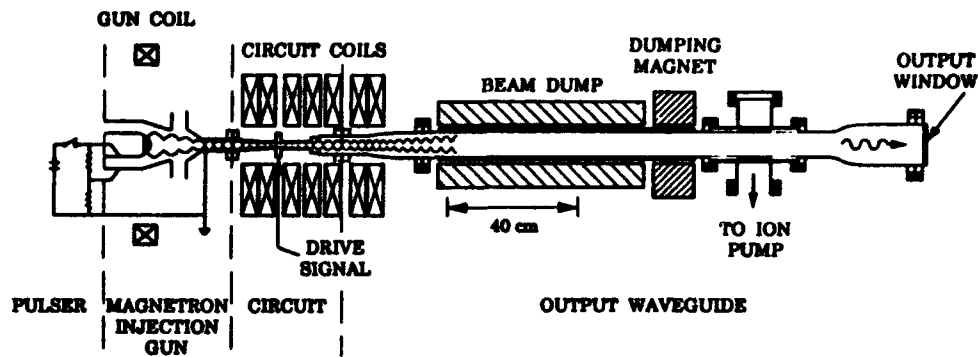


Figure 1: The gyrokystron test facility.

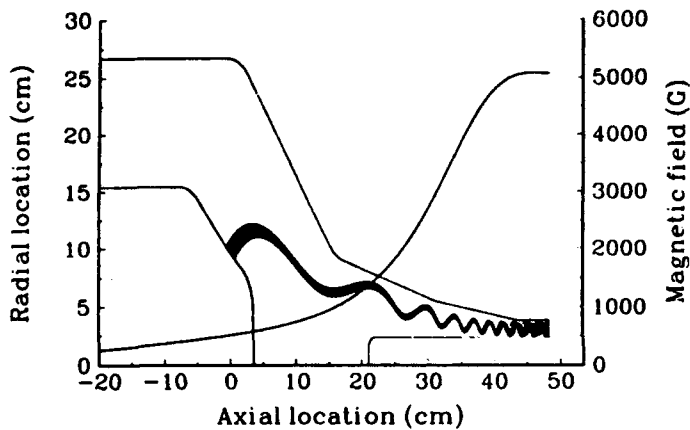


Figure 2: Electrode shapes, axial field profile, and beam envelope of the single-anode MIG.

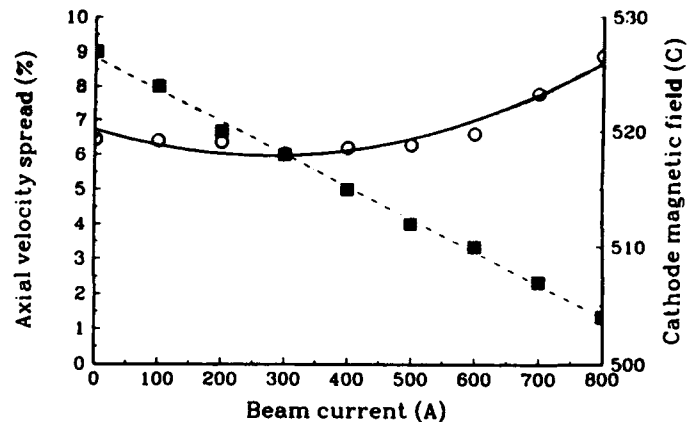


Figure 3: The dependence of velocity spread on current. The circles indicate spread; the squares denote cathode magnetic field.

#### IV. REFERENCES

- [1] W. Lawson et al., "Performance characteristics of a high-power X-band two-cavity gyrokystron," *IEEE Trans. Plasma Sci.*, **20**, 216 (1992).
- [2] J.P. Calame et al., "Initial operation of a high power, K-band, harmonic gyrokystron for accelerator applications," these proceedings.
- [3] W. Lawson and V. Specht, "Design comparison of single-anode and double-anode 300 MW Magnetron Injection Guns," *IEEE Trans. Electron Dev.* (in press).
- [4] J.M. Baird and W. Lawson, "Magnetron Injection Gun (MIG) design for gyrotron applications," *Int. J. Electron.* **61**, 953 (1986).
- [5] W.B. Herrmannsfeldt, "Electron trajectory program," SLAC-Report 226, Nov. 1979.

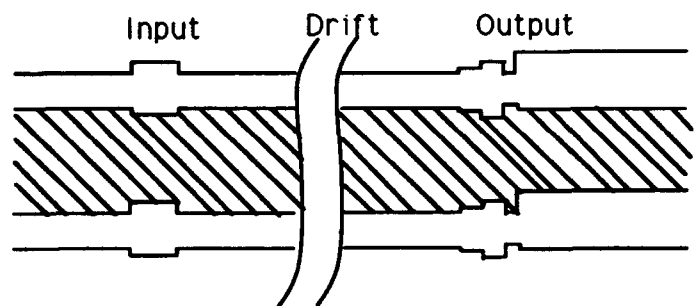


Figure 4: The coaxial microwave circuit.

# Some Concepts of Relativistic Gyroamplifiers for Particle Acceleration

G.S. Nusinovich, P.E. Latham, and V.L. Granatstein

Laboratory for Plasma Research

University of Maryland, College Park, MD 20742

## I. INTRODUCTION

Gyroamplifiers are very promising sources of coherent, phase-controlled, powerful electromagnetic radiation for driving future particle accelerators. At a given wavelength the interaction space in gyroamplifiers is much larger than that for klystrons. Therefore, gyroamplifiers usually operate at short wavelengths ( $\sim 3$  cm) where the problem of miniaturization of the interaction space is, for conventional klystrons, extremely severe.

Two years ago the operation of relativistic gyroamplifiers in a 10 GHz frequency range was successfully demonstrated [1]. The next step in the gyroamplifier development is directed towards improvement of electronic efficiency, enhancement of radiated power and an increase in operating frequency. Some concepts of relativistic gyroamplifiers aimed at improving these output parameters are considered below.

## II. GYROKLYSTRON WITH ZERO TRANSIT ANGLE IN A DRIFT REGION

Electron velocity spread is one of the most important factors reducing the efficiency of gyroamplifiers as well as other microwave tubes. Since in gyroamplifiers the first, modulating cavities are separated from the output cavity with a rather long drift region it is desirable to minimize the effect of electron velocity spread on electron transit through the drift space. We will show that this can be done by minimizing the electron transit angle through the drift space,

$$\Theta_{dr} = \int_0^{L_{dr}} [(\omega - \Omega)/v_z] dz.$$

Here  $\omega$  and  $\Omega$  are the operating frequency and electron cyclotron frequency, respectively,  $v_z$  is electron axial velocity, and  $L_{dr}$  is the length of the drift region.

For a two-cavity gyroamplifier the electron gyrophase relative to the electromagnetic (EM) field phase at the entrance to the output cavity may be written as  $\Theta_{ent} = \theta_0 - q \sin \theta_0 - \Theta_{dr}$ . Here  $\theta_0$  is the initial gyrophase at the entrance to the first cavity and  $q$  is the bunching parameter proportional to the field amplitude in the first cavity and the drift space length,  $L_{dr}$ . Both  $q$  and  $\Theta_{dr}$  depend on electron velocity spread.

We studied the effect of pitch angle spread ( $\alpha = v_{\perp}/v_z$  is the pitch angle, i.e. the ratio of orbital to axial electron velocity components) in a monoenergetic electron beam on the efficiency of relativistic gyroamplifiers. The equations of motion of relativistic electrons averaged over fast electron gyration were used. The axial structure of the output resonator field was described by  $\sin(\pi z/L)$ . The orbital velocity spread was described by a triangular distribution with the width corresponding to a 6% RMS spread. The operating voltage was taken close to 500 kV and both the bunching parameter and the pitch-ratio for the central fraction of the electron beam were equal to one.

First we found the dependence of the electron efficiency, optimized with respect to the phase of the EM field and the cyclotron resonance mismatch in the output cavity, on the field amplitude and the length of this cavity for the ideal electron beam (no velocity spread). Then we considered the effect of

spread for two cases: a) magnetic field constant along the drift region and output cavity, b) magnetic field in the drift region tapered so that the transit angle,  $\Theta_{dr}$ , is close to zero for all electrons. It was found that for parameters predicting 44% efficiency of operation with the ideal beam the velocity spread in the first case reduces the achievable efficiency to 29%. At the same velocity spread the corresponding tapering of magnetic field in a drift region permits one to realize 36% efficiency. So, it becomes possible to mitigate the spoiling effect of velocity spread on the gyrokystron efficiency about 2 times by corresponding tapering of the magnetic field in the drift space.

### III. CONCEPTS OF GYROAMPLIFIERS FOR WAVELENGTH SHORTENING

In general, for gyrodevices operating at the cyclotron resonance condition, to provide the operating frequency increase one has to increase the external magnetic field. That makes the microwave system (including magnets) more expensive. However, there are two possibilities for increasing the operating frequency at a fixed value of the magnetic field. Both of them follow from the cyclotron resonance condition

$$\omega - k_z v_z \simeq s\Omega$$

where  $k_z$  is the axial wavenumber and  $s$  is the resonant cyclotron harmonic number. These are operation at high cyclotron harmonics ( $s > 1$ ) and operation with a large Doppler frequency upshift. The latter gyroamplifiers are known, in the case of moderate frequency upshift, as gyrotwistrons.

Theoretical studies of the cyclotron harmonic and Doppler upshifted operation of gyroamplifiers with the same operating frequency and magnetic field, the same electron beam, the same prebunching cavity and drift space, were started in [2]. It was shown that in the

case of an ideal electron beam the Doppler upshifted operation is more efficient (46% versus 26% for the second harmonic gyroamplifier). Then, electron velocity spread causes the degradation in efficiency which, in principle, for the frequency upshifted operation, is more pronounced than for the harmonic one. The latest studies show that, nevertheless, the optimized efficiency of gyrotwistron operation becomes equal the efficiency of ideal second harmonic operation (26%) only when the RMS value of the pitch-angle spread is about 22% (at this velocity spread the maximum second harmonic efficiency is only 16%). So for a wide range of electron velocity spreads the frequency upshifted operation of the gyrotwistron may be more efficient than that of the second harmonic. This is because in the case of operation with large axial wavenumbers (like in gyrotwistrons) the energy may be extracted from both the rotational and axial electron motion. Note that successful second harmonic operation of the relativistic gyrokystrons has been recently demonstrated [3] and experiments with relativistic gyrotwistrons are planned.

The authors are thankful to O. Dumbrajs for his valuable help in numerical simulations.

This work was supported by the U.S. Department of Energy.

### IV. REFERENCES

1. W. Lawson et al., *Phys. Rev. Lett.* 67, 520 (1991).
2. G.S. Nusinovich, P.E. Latham and H. Li, *Conference Digest of the 17th International Conference on Infrared and Millimeter Waves*, December 1992, p. 136.
3. J. Calame, et al., these proceedings.

# EXPERIMENTAL PROGRESS TOWARD A 1 GW, 1 $\mu$ S PULSE LENGTH, HIGH CURRENT RELATIVISTIC KLYSTRON\*

M. Fazio, B. Carlsten, R. Fachi, W. Haynes, T. Kwan, R. Stringfield  
Los Alamos National Laboratory  
MS H851, Los Alamos, NM 87545

## Abstract

A 1  $\mu$ s pulse-length, high-current relativistic klystron is being developed with a desired peak output power of 1 GW at 1.3 GHz. The tube consists of an input cavity, a single idler cavity, and an output cavity. Power levels as high as 475 MW have been experimentally observed. Current experimental results are presented. Physics and engineering issues affecting klystron performance are discussed.

## I. INTRODUCTION

Los Alamos is developing an L-band high current relativistic klystron amplifier (RKA). Although the present experiments are single pulse, the long term goal is to achieve 1 kJ/pulse with repetitive pulse capability at a PRF of 5 Hz, with a longer term goal of 100 Hz. The RKA has an input cavity, a single idler cavity, and an output cavity. The buncher section, which consists of the input and idler cavities, has been experimentally tested and is performing as designed. The design was done with the help of particle-in-cell (PIC) code calculations using the Los Alamos code ISIS. PIC code modeling has proven to be very important for a successful design because of the highly nonlinear nature of the RKA caused by the intense space charge effects.[1] The most recent efforts involve improving the performance of the output cavity and optimizing the output power and pulse length to reach the design goal of 1 kJ/pulse. A number of expected problems have been encountered with the output cavity that are being systematically addressed. These problems include rf breakdown in the cavity and matching the beam impedance to the cavity gap shunt impedance for the most efficient coupling of modulated beam to microwaves. This paper summarizes the current experimental results. The electron gun and the modulation section consisting of the input and idler cavities have been discussed elsewhere. [2-4]

## II. EXPERIMENTAL WORK

The RKA configuration is shown schematically in Fig. 1. The electron beam is formed from a 6.2 cm-diameter annular field-emission cathode and is slightly compressed by a converging 0.5 T axial magnetic field to a nominal 5.9 cm diameter beam with a 5 mm thickness. The typical beam voltage is 620 kV with the current increasing from 3 to 6 kA during the pulse. This increase is caused by the drop in electron gun impedance due to plasma closure of the anode-cathode gap during the pulse. The input cavity is driven by a 500 kW L-band magnetron. The idler cavity has an annular

tuning ring which gives flexibility in inductively tuning the cavity. The output cavity is a noseless pillbox design with several annular coupling slots near the outer diameter which couples power into a low impedance coaxial transmission line. The coax tapers out into standard 6-inch-diameter, 50  $\Omega$  line where power is measured by a directional coupler with 25 dB directivity and then dissipated in a dummy load.

The complete klystron tube has been assembled and is undergoing testing. The beam modulation section consisting of the input cavity and idler cavity is performing as designed, and is providing a modulated electron beam with a harmonic current  $I_1 = 0.6 I_0$  where  $I_1$  is the fundamental harmonic at 1.3 GHz, and  $I_0$  is the dc beam current. The extracted rf power has been increased from about 10 MW to 475 MW. Currently about 475 MW of peak power is being extracted from the output cavity in a pulse of 1  $\mu$ s duration. The energy residing in the pulse is about 140 J.

A graph showing the output power overlaid with the beam voltage and current is shown in Fig. 2. The rf output power pulse shape approximately follows the beam current shape until the rf output terminates at the peak value of 375 MW. At this time the total rf pulse energy is about 160 J. The rf pulse terminates before the beam voltage and current reach their maximum values. It is not yet certain why the rf pulse is terminating prematurely. The most reasonable explanation is that the output cavity gap field is high enough to reflect electrons back up the beam-line and/or start some oscillation phenomenon such as a virtual cathode. At the time the rf pulse terminates, a highly rf modulated electron beam pulse propagates upstream and is detected by B-dot loops located in the idler cavity and input cavity, and by the directional coupler between the drive magnetron and the input cavity. All of these signals have a spike at the time the rf output power goes away. These signals are bandpass filtered with a bandwidth of several hundred MHz around 1.3 GHz, so the spike appears to be the result of an rf modulation on the beam traveling back up the beam toward the cathode. The interpretation of the observation could be complicated by the fact that the output gap could be breaking down at this time as well. In Fig. 3 is the trace representing the magnetron's reflected power (or power flowing from the input cavity toward the magnetron). The spike at 2.3  $\mu$ s is the result of the electron reflection back upstream. The electron reflection is a manifestation of the intense beam's space charge effects resulting in the severe potential depression of the beam as it is decelerated in the output gap.

\* Work supported and funded jointly by DOE Defense Programs and the Army Research Laboratories.

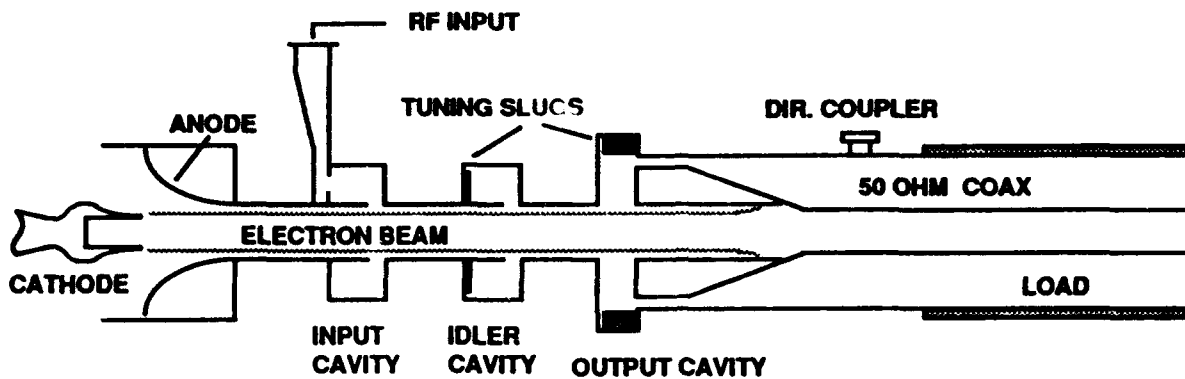


Fig. 1. Schematic diagram of the RKA.

(—) OUTPUT POWER (100 MW/div) : 375 MW peak  
 (—) BEAM VOLTAGE (200 kV/div) : 580 kV peak  
 (- - -) BEAM CURRENT (2 kA/div) : 6.3 kA peak

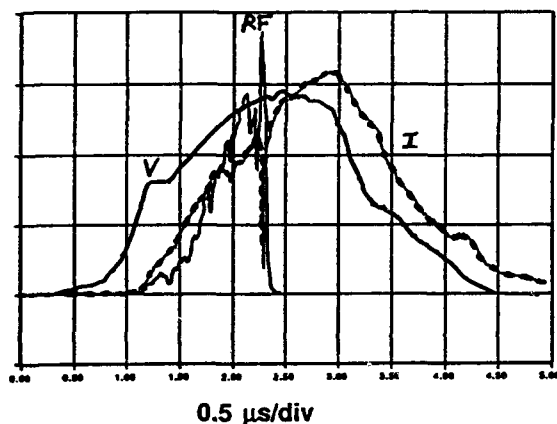


Fig. 2. Rf output power overlaid with the beam voltage and current.

### III. DESIGN MODIFICATIONS

The power extracted can be expressed as

$$P_{ext} = \frac{1}{2} I_1 V_{beam}$$

where  $I_1$  is the beam's average fundamental harmonic current in the output cavity and  $V_{beam}$  is the available voltage that can be extracted from the beam before the space-charge limiting current is reached. To efficiently couple the rf energy from the modulated beam, the output cavity must have a low enough shunt impedance that the gap voltage induced by  $I_1$  does not exceed  $V_{beam}$ . A very low cavity shunt impedance is necessary to efficiently couple to the low impedance beam.

The loaded Q (without beam) of the output cavity in these most recent experiments was about 10. This is obviously not low enough. We have started an overall redesign of the output cavity using a three dimensional rf structures simulator program (HFSS-High Frequency Structures Simulator) to confirm that the new cavity will have the

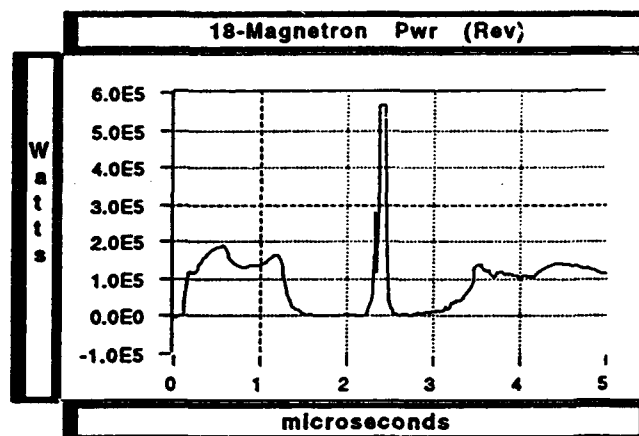


Fig. 3. Magnetron's reflected power signal (power flowing from the input cavity toward the magnetron). The spike at 2.3 μs is the result of the electron reflection in the upstream direction from the output cavity.

desired gap geometry, and a significantly lower shunt impedance and loaded Q. This will lower the output gap voltage, thereby eliminating electron reflection and rf breakdown across the gap. Once the electromagnetic cavity simulations are complete, the new cavity geometry will be compared to the old geometry with the particle-in-cell code ISIS to model the electron beam in the gap to determine if the problems have been sufficiently addressed.

The new pillbox-shaped cavity has a considerably smaller outside diameter which will make the cavity less likely to induce virtual cathode formation caused by the large space-charge bunches passing through the gap. The design Q is about 4. The decreased Q will help prevent the cavity fields from reaching the point where electrons are reflected. The coupling slots have been increased in both height and angular width.

### IV. SUMMARY

A three cavity high-current relativistic klystron is operating at 1.3 GHz with a peak power of 475 MW and an

energy per pulse of about 150 J. The rf pulse length is 1  $\mu$ s. The limit to performance is the output cavity which has a shunt impedance high enough to produce electron reflection, and possibly virtual cathode oscillations, leading to beam disruption and rf termination. An effort is underway to build a new output cavity with a much lower shunt impedance in order to reach the goal of 1 GW peak power and an energy of 1 kJ in a 1  $\mu$ s pulse.

## V. REFERENCES

- [1] B.E. Carlsten, R.J. Faehl, M.V. Fazio, T.J.T. Kwan, D.G. Rickel, R.D. Ryne, R.M. Stringfield, "Effect Of Intense Space Charge In Relativistic Klystron Amplifiers," *Proc. 9th Intl. Conf. on High Power Particle Beams*, Washington, D.C., May 1992, to be published.
- [2] M.V. Fazio, B.E. Carlsten, R.J. Faehl, W.B. Haynes, R.F. Hoerberling, T.J.T. Kwan, D.G. Rickel, R.M. Stringfield, F.W. VanHaften, R.F. Wasierski, A. Erickson, K. Rust, "The Experimental and Theoretical Development of a One Gigawatt, Repetitively Pulsed, One Microsecond Pulse Length, High Current Relativistic Klystron and Modulator," *Proc. 9th Intl. Conf. on High Power Particle Beams*, Washington, D.C., May 1992, to be published.
- [3] D.G. Rickel, , M.V. Fazio, B.E. Carlsten, R.J. Faehl, T.J.T. Kwan, R.M. Stringfield, R.F. Wasierski, "Development of a Long-Pulse 1.3 GHz Relativistic Klystron Amplifier," *IEEE Trans. on Plasma Science Special Issue on High Power Microwave Generation*, 20(3), June 1992, p 373-382.
- [4] M.V. Fazio, B.E. Carlsten, R.J. Faehl, W.B. Haynes, T.J.T. Kwan, R.M. String-field, "Experimental Progress on a Microsecond Pulse-Length Relativistic Klystron Amplifier," *Proc. SPIE 92 Intense Microwave and Particle Beams III*, Los Angeles, Ca., Jan. 1992, 1872, to be published.

# Relativistic Plasma Klystron Amplifier in Connection with Application to High Gradient Accelerators

Han S. Uhm

Naval Surface Warfare Center  
10901 New Hampshire Ave, White Oak  
Silver Spring, Maryland 20903-5640

## Abstract

A novel plasma klystron amplifier is presented in which current modulation of a relativistic electron beam is achieved by the unstable two-stream interaction between the electron beam and a plasma column. A model to describe current modulation is developed. Due to a relatively large growth rate of the instability, required interaction length of the beam and plasma column is short for most applications. A full current modulation can be achieved in the plasma klystron amplifiers.

## I. INTRODUCTION

The generation of intense coherent radiation from the relativistic klystron amplifiers<sup>1-5</sup> (RKA) is one of the renewed interests in the microwave community, because of high-power capability and high efficiency of RKA. High-power relativistic klystron amplifiers have various applications, including the high-gradient RF accelerators and high-power radar. One of the main issues in RKA is enhancement of power and frequency simultaneously. Cavity size and opening should be reduced to increase the excitation frequency. Therefore, a high-power high-frequency klystron amplifier has inherent problems due to reduced size of cavities, including electron emission at the gap opening and shorting, etc. In addition, high-power RF signal is needed in the input cavity for high-power klystrons. In order to eliminate some of these intrinsic problems in the high-power RKA, I present a novel plasma klystron amplifier in which current modulation of the electron beam is accomplished by the two-stream interaction between the beam and plasma column. Because of a large growth rate of the two-stream instability, interaction length of the plasma klystron is short.

As illustrated in Fig. 1, a relativistic annular electron beam with radius of  $R_b$  enters the drift tube with radius of  $R_c$ . In the plasma klystron, there are no intermediate passive cavities, which often present problems associated with self-oscillation and RF breakdown. The electron beam is pre-modulated at the first cavity before it enters a space between the drift tube wall and a plasma column with radius of  $R_p$ .

This work was supported in part by the Independent Research Fund at the Naval Surface Warfare Center and in part by SDIO/IST.

An axial electric field accompanied by the modulated electron beam excites space charge waves in the plasma column, which acts like an inductive medium amplifying the electrostatic waves. The physical mechanism of self-amplification of the electrostatic waves is the longitudinal two-stream instability of the beam-plasma system.

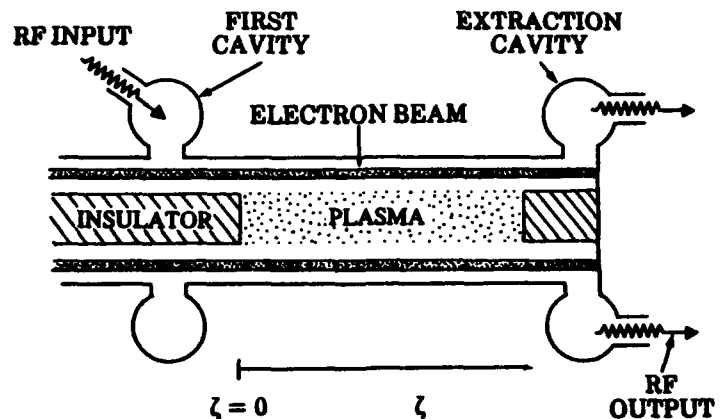


Fig. 1. A Schematic presentation of plasma klystron amplifier.

## II. STABILITY ANALYSIS

Analysis of the two-stream instability of the beam-plasma system is carried out within the framework of the linearized hybrid-Maxwell equations, where beam electrons are described by the Vlasov equation and plasma electrons are described by a cold-fluid model. In the stability analysis, we adopt a normal mode approach in which all perturbations are assumed to vary according to  $\delta\Phi(x,t) = \Phi(r)\exp[i(kz - \omega t)]$ , where  $\omega$  is the eigenfrequency and  $k$  is the axial wavenumber. The eigenfunction of the longitudinal two-stream instability is the axial electric field  $E_z(r)$ .

To solve the eigenvalue equation, we assume that the plasma density is uniform inside and drops abruptly at  $r = R_p$ . For the present purpose, the stability analysis is restricted to the long-wavelength low-frequency perturbations. Under these conditions, the eigenvalue equation is obtained<sup>6,7</sup> and solved, and the dispersion relation of the two-stream instability is expressed as

$$1 - \frac{\epsilon_b(k^2c^2 - \omega^2)}{(\omega - k\beta_b c)^2} + \frac{\epsilon_p(k^2c^2 - \omega^2)}{\omega^2} - \frac{g\epsilon_b\epsilon_p(k^2c^2 - \omega^2)^2}{\omega^2(\omega - k\beta_b c)^2}, \quad (1)$$

where the parameters  $\epsilon_b$  and  $\epsilon_p$  are the beam and plasma dielectric effects, and the geometrical factor  $g$  is defined by  $g = \ln(R_b/R_p)/\ln(R_c/R_p)$ . Equation (1) can be used to investigate properties of the longitudinal two-stream instability in an annular electron beam propagating through a plasma column.

Stability analysis of the dispersion relation in Eq. (1) is carried out in a special case when the beam contacts the plasma, i.e.,  $g = 0$ . Then, the last term in Eq. (5) is neglected and the dispersion relation is significantly simplified. Defining the phase velocity of the unstable wave by  $\omega/k = \beta_p c$ , the instability condition is given by<sup>8</sup>

$$(\epsilon_b^{1/3} + \epsilon_p^{1/3})^3 > \gamma_p^2 \beta_b^2, \quad (2)$$

where  $\gamma_p^2 = (1 - \beta_p^2)^{-1}$ . The electron beam velocity in the plasma klystron amplifier is close to the speed of light ( $\beta_b = 1$ ) for high power. Instability occurs only when the parameter  $\epsilon_p$  is in the order of unity or larger, as we have seen in Eq. (2). In this context, we conclude that the plasma klystron amplifier requires an opaque plasma. The parameter  $\epsilon_b$  is much less than unity for most applications, satisfying  $\epsilon_b \ll \epsilon_p$ . In this case, the phase velocity of the unstable wave is close to the beam velocity and the dispersion relation in Eq. (1) is further simplified.<sup>8</sup> Defining Doppler-shifted frequency  $x = (\omega - k\beta_b c)/kc$ , it is shown that the maximum growth rate occurs at the phase velocity satisfying  $\beta_p/\beta_b = (\epsilon_p/\epsilon_b)^{1/3}/[1 + (\epsilon_p/\epsilon_b)^{1/3}]$  and is given by<sup>8</sup>

$$x_i = \text{Im}(x) = \frac{\sqrt{3}}{2\gamma_b} \left( \frac{\epsilon_b \sqrt{\epsilon_p}}{2} \right)^{1/3}. \quad (3)$$

For the present purpose, we consider an example where an annular electron beam with radius of  $R_b = 2$  cm and energy of  $\gamma_b = 1.67$  enters a drift tube with a radius of  $R_c = 2.5$  cm. The drift tube contains a plasma column whose radius is  $R_p = 2$  cm and density is  $n_p = 6.5 \times 10^{11} \text{ cm}^{-3}$ . For these plasma conditions,  $\epsilon_p$  is calculated to be  $\epsilon_p = 0.7$ . The electron beam current is assumed to be 5.5 kA, which corresponds to  $\epsilon_b = 0.037$  for the beam parameters mentioned above. The normalized electron beam velocity is  $\beta_b = 0.8$ . Note that these beam and plasma parameters satisfy the instability criterion in Eq. (2). Therefore, the normalized growth rate  $x_i$  is estimated to be  $x_i = 0.17$  obtained from Eq. (3). The plasma column needed for the

plasma klystron amplifiers can be produced by thermionic arc discharges<sup>9,10</sup>. These discharge devices are frequently operated at the room-temperature vapor pressure of mercury, which provides plasma densities in the range from  $n_p = 10^9 \text{ cm}^{-3}$  to  $n_p = 10^{13} \text{ cm}^{-3}$  for 10-to-30 cm long discharge tubes.

### III. NONLINEAR MODE EVOLUTION

We now describe the current modulation of an electron beam propagating through the space between the plasma column and drift tube wall. An axial electric field accompanied by the pre-modulated electron beam enters this region and initiates excitation of the space charge waves. Strength of this axial electric field is determined in terms of the system parameters prior to this region.<sup>5</sup> The plasma column responds to the initial perturbations of the axial electric field and amplifies the field strength by acting as an inductive medium. The physical mechanism of the field amplification is the two-stream instability mentioned above. We assume the initial condition that a beam segment labeled by  $t_0$  enters the region at time  $t = t_0$ . Then, the axial electric field  $E_z(z, t_0)$  acting on the beam segment  $t_0$  is expressed as

$$E_z(\zeta, \theta) = -E_0 \exp(x_i \zeta / \beta_b) \sin \theta, \quad (4)$$

where  $E_0$  is the initial axial electric field,  $\zeta = \omega z / \beta_b c$  is the normalized propagation distance,  $\theta = \omega t_0$  is the normalized time and  $x_i$  is the normalized growth rate of the instability obtained in Eq. (3).

Energy modulation of the beam segment labeled by  $\theta$  is obtained from  $d\gamma/dz = -eE_z/mc^2$ . Without loss of generality, we assume that the axial coordinate  $z$  equals zero at the beginning of the plasma column. Integrating along the propagation distance and neglecting the initial modulation, we obtain the relativistic mass ratio

$$\gamma(\zeta, \theta) = \gamma_b + e_0 \exp(x_i \zeta / \beta_b) \sin \theta, \quad (5)$$

of the segment  $\theta$  at the propagation distance  $\zeta$ . In Eq. (5),  $e_0 = \beta_b^2 e E_0 / mc \omega x_i \ll 1$ . The instantaneous velocity  $\beta(\zeta, \theta)c$  of the beam segment  $\theta$  is expressed as

$$\frac{\beta_b}{\beta} = 1 + \frac{\gamma_b - \gamma}{\gamma_b(\gamma_b^2 - 1)}, \quad (6)$$

where  $\beta_b c$  is the beam velocity at the injection point. Making use of the velocity definition  $dz/dt = \beta c$  and the definition  $\varphi = \omega t$ , we obtain

$$\varphi = \theta + \zeta - e \exp\left(\frac{x_i}{\beta_b} \zeta\right) \sin \theta, \quad (7)$$

where use has been made of the fact that the parameters  $\epsilon = \epsilon_0 \beta_b / \gamma_b (\gamma_b^2 - 1) x_i \ll 1$ . Equation (7) relates the present time  $t$  to the initial time  $t_0$ . Differentiating  $\phi$  in Eq. (7) with respect to  $\theta$  gives

$$\frac{d\phi}{d\theta} = 1 - \epsilon \exp\left(\frac{x_i}{\beta_b} \zeta\right) \cos \theta. \quad (8)$$

The beam current at the injection point is a constant value of  $I_b$ . The beam segment  $t_0$  passes the injection point at time  $t = t_0$ . When this segment arrives at  $z$  in time  $t$ , it is stretched by a factor of  $dt/dt_0$ . Thus, the beam current of the segment  $t_0$  at  $z$  is proportional to  $d\theta/d\phi$ . In this regard, the normalized current ratio  $F(\zeta, \theta)$  is expressed as

$$F(\zeta, \theta) = \frac{I(\zeta, \theta)}{I_b} = \frac{N(\zeta)}{|d\phi/d\theta|}, \quad (9)$$

where the normalization constant  $N(\zeta)$  is defined by

$$\frac{2\pi}{N(\zeta)} = \int_0^{2\pi} |d\theta/d\phi| d\theta. \quad (10)$$

The normalization constant  $N(\zeta)$  ensures the charge conservation.

Substituting Eq. (8) into Eqs. (9) and (10) gives the current modulation

$$(11) \quad F(\zeta, \theta) = \begin{cases} \sqrt{1-f^2}/(1-f\cos\theta), & \zeta < \zeta_m \\ N(\zeta)/|1-f\cos\theta|, & \zeta > \zeta_m \end{cases}$$

where the exponential function  $f(\zeta)$  is defined by

$$f(\zeta) = \epsilon \exp(x_i \zeta / \beta_b). \quad (12)$$

the normalization constant  $N(\zeta)$  is calculated from Eq. (10) and the propagation distance  $\zeta_m$  for maximum current modulation is obtained from  $f(\zeta_m) = 1$ . It is obvious from Eq. (11) that the modulated beam current has one peak per period until the beam segment  $\theta$  reaches  $\zeta = \zeta_m$ . If the beam propagates further from  $\zeta = \zeta_m$ , it starts to bunch two peaks per period, thereby providing a possibility of high harmonic modulation.

The propagation distance  $z_m$  of the maximum current modulation is expressed as

$$z_m = \frac{\beta_b c}{\omega} \zeta_m = \frac{\beta_b^2 c}{\omega x_i} \ln\left(\frac{1}{\epsilon}\right), \quad (13)$$

which has a significant meaning because it determines the length of the klystron amplifier. Remember that the parameter  $1/\epsilon$  in Eq. (13) is much larger than unity in general. Several points are noteworthy from Eq. (13). First, the microwave tube length ( $z_m$ ) is inversely proportional to the normalized growth rate ( $x_i$ ) of the two-stream instability. We have observed in the stability analysis that the growth rate  $x_i$  is a slowly changing function of the plasma density, but it is sensitive to the beam current. The growth rate can be significantly increased and the tube length can be considerably shortened, by increasing the beam current  $I_b$  or the ratio of  $R_c/R_b$ . Second, the tube length is proportional to  $\ln(1/\epsilon)$ , indicating that it is a weakly dependent function of the initial energy modulation at the first cavity. In this regard, a relatively low-power microwave input in the first cavity may well excite the two-stream instability in the beam-plasma region and may deliver a highly modulated electron beam to the extraction cavity. Third, the length of the microwave tube is inversely proportional to the frequency. The higher the frequency, the shorter the tube length. Equation (13) also indicates that the tube length can be drastically reduced by decreasing the beam energy. As an example, we consider a system where  $\epsilon = 0.01$ ,  $x_i = 0.13$ ,  $\beta_b = 0.8$ , and the microwave frequency is 3.5 GHz. Substituting these parameters into Eq. (13), we find the tube length  $z_m = 30$  cm. These parameters are easily attainable in the present experimental conditions. There is a broad range of system parameters, which the present technology allows. Obviously, the plasma klystron amplifier has a great potential for high-power high-frequency microwave device. There will be many different plasma configurations, which may be more advantageous for the plasma klystron amplifiers. For example, an electron beam can propagate through a plasma cylinder, providing a large plasma volume.

#### IV. REFERENCES

- [1] M. Friedman, J. Krall, Y. Y. Lau, and V. Serlin, *J. Appl. Phys.* **64**, 3353 (1988).
- [2] Y. Y. Lau, M. Friedman, J. Krall, and V. Serlin, *IEEE Trans. on Plasma Science*, **18**, 553 (1990).
- [3] M. Friedman, V. Serlin, A. Drobot, and A. Mondelli, *IEEE Trans. on Plasma Science*, **14**, 201 (1986).
- [4] M. Friedman, J. Krall, Y. Y. Lau, and V. Serlin, *Rev. Sci. Instrum.*, **61**, 171(1990).
- [5] H. S. Uhm, *Phys. Fluids B* **5**, 190 (1993).
- [6] H. S. Uhm and R. C. Davidson, *Phys. Fluids* **24**, 1541 (1981).
- [7] H. S. Uhm and G. Joyce, *Phys. Fluids B* **3**, 1587 (1991).
- [8] H. S. Uhm, *J. Appl. Phys.* **56**, 2041 (1984).
- [9] N. A. Krall and A. W. Trivelpiece, *Principles of Plasma Physics*, (McGraw-Hill, New York, 1973) Chap. 1.
- [10] H. S. Uhm, J. D. Miller, R. F. Schneider, and D. J. Weidman, *IEEE Trans. on Plasma Science* **19**, 535 (1991).

# Sheet-Beam Klystron RF Cavities\*

David Yu, *DULY Research Inc., Rancho Palos Verdes, CA*  
Perry Wilson, *SLAC, Stanford, CA*

## Abstract

A high-frequency sheet-beam klystron operating at a low perveance per square can produce high peak power at high efficiency<sup>1</sup>. In order to provide beam stability and to maximize power extraction efficiency for a flat beam with a finite width, we have designed rf cavities in which the electric field is nearly constant across the width of the beam (on the order of several wavelengths). However, in such cavities, the electric field in the fundamental mode can couple to the TE propagating mode in the drift section if any cavity or beam asymmetry is present. The dipole field can couple between adjacent cavities even in the absence of these asymmetries as long as the frequency is above cutoff of the drift tube. The effects of coupling between rf cavities are calculated using an equivalent circuit model. Threshold parameters for onset of rf oscillation in the fundamental mode as a result of cavity coupling are obtained. We have designed choke cavities which effectively prevent such possible oscillations.

## Introduction

The sheet-beam klystron (SBK), Fig. 1, can alleviate many limitations on the efficiency of conventional round-beam X-band klystrons. Some of these include space charge effects at high current densities, electrical breakdown across small gaps at high voltages, and potential metal melting due to beam interception at high power densities. By flattening out the beam spatially, the SBK significantly extenuates the space charge effects. It can achieve high power by sustaining a high total current, while keeping a low current density and a moderate voltage. It can also avoid the serious potential problem of metal melting by keeping a low power density. As a function of frequency, the power output of a sheet-beam klystron falls only linearly with wavelength, making it more suitable for high frequency applications.

In an earlier design study<sup>1</sup>, we found that a sheet-beam klystron operating at 11.4 GHz and a low perveance per square (about 0.1 micro-perv.) is capable of producing over 200 MW of power at 65% efficiency. Typical operating parameters of a sheet-beam klystron are: a cross sectional area of 0.4 cm x 16 cm, a moderate voltage of about 400 keV, a strip gun compression ratio of 10:1, a cathode loading of 12 A/cm<sup>2</sup> and a longitudinal focusing field of 3 kG. These results were obtained with CONDOR simulations, in which cavities were treated as ports with proper voltages and phases. The cavity geometry must be established in a detailed design.

We consider in this paper several design issues unique to the sheet-beam klystron cavities. In rectangular cavities, the electric field is not uniform across the transverse direction perpendicular to the sheet beam. Electrons arriving at different points along the gap at the same time would experience different axial forces which could destroy the beam coherence downstream. Another potential problem is rf feedback for the fundamental TM mode between adjacent cavities. If this mode is coupled to an above-cutoff TE mode which is excited in the drift region, power can leak back upstream. This can occur, for instance, if there is asymmetry in the cavity or beam current as a result of manufacturing imperfections. Similar considerations apply to higher order modes, some of which can couple even in the absence of any such asymmetries. Fortunately, this problem can be cured, if necessary, by the use of one or more quarter-wave chokes. The conditions under which the choke joints are necessary will be established.

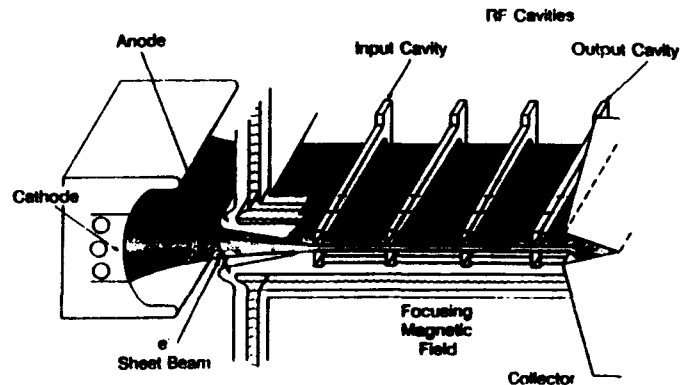


Figure 1 Schematic of Sheet Beam Klystron

## SBK Cavity Design

The electric field of the lowest TM mode of a simple metallic rectangular cavity has a half sine distribution which peaks at the middle and vanishes at the boundaries. In order to accommodate a sheet beam several wavelengths wide, the rectangular cavity must be modified so that the axial electric field, at least in the region where the beam passes through, is approximately constant. One design strategy is to operate the center portion of the cavity near cutoff, with a widened portion about a quarter of a wavelength long at each end<sup>2</sup>. We have used the MAFIA code to design these cavities and found that good field uniformity can be achieved in this way. Fig. 2 shows the axial electric field of the fundamental mode at the midplane (perpendicular to the beam line) of such a "barbell" rectan-

gular cavity, 12.6 cm wide and 6.885 mm high at the mid-section, and 1.3 cm high at the ends. The cavity is connected to a beam pipe 5 mm high. The cavity parameters calculated with MAFIA are  $f=11.42$  GHz,  $Q_0=6438$  and  $R/Q_0=17.3$  ohms. The axial electric field of the fundamental mode as a function of the transverse distance along the centerline of the cavity is shown in Fig. 3.

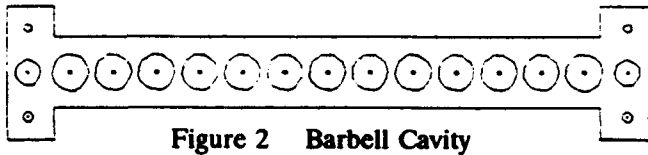


Figure 2 Barbell Cavity

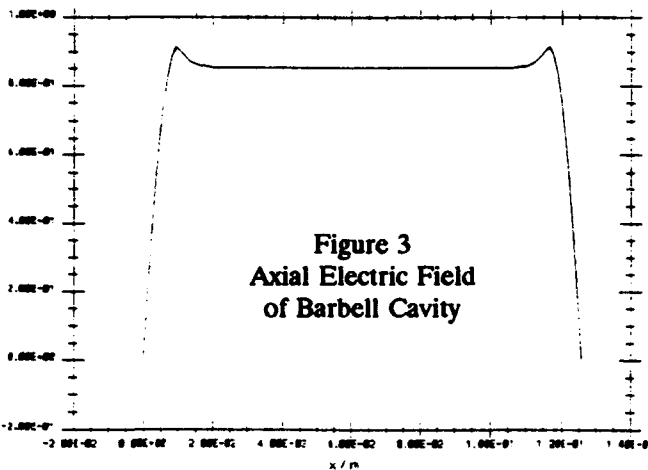


Figure 3  
Axial Electric Field  
of Barbell Cavity

### Coupling between RF Cavities

The electric field of the fundamental mode of two rectangular cavities separated by a distance (2.32 cm) is shown in Figs. 4 and 5. In Fig. 4, each cavity is assumed to be perfectly symmetric about the center plane. The perfect symmetry in this case precludes any coupling between the cavities. In Fig. 5, a large artificial asymmetry is introduced in the cavity geometry: the height of the upper cavity is greater than that of the lower cavity by 14.3%. In this case, the TM cavity mode readily couples to a TE mode in the beam pipe. The coupling of the two cavities via the beam pipe splits the uncoupled frequency into two normal modes: a symmetrical and an antisymmetrical mode. The coupling strength  $k$  between the two asymmetric cavities is directly proportional to the frequency splitting,  $\Delta f$ . For these cavities, we find  $k=\Delta f/f_0=0.0467$ .

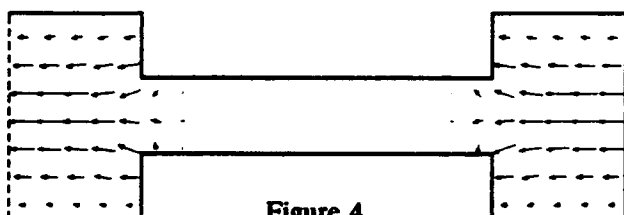


Figure 4  
Fundamental Mode of  
Two Coupled Symmetric Cavities

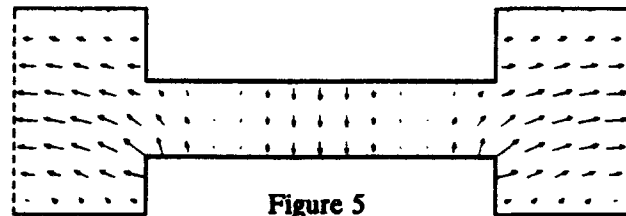


Figure 5  
Fundamental Mode of  
Two Coupled Asymmetric Cavities

Alternately, the external  $Q$  of an asymmetric cavity coupled to the beam pipe can be calculated using the Kroll-Yu (KY) method<sup>3</sup>. Making four URMEL runs with different pipe lengths, we find  $Q_{ext}=246$ .

The electric field of the dipole mode for two coupled symmetrical cavities is shown in Fig. 6. Because the cavity field pattern for this mode reverses directions about the center plane, the asymmetry naturally allows coupling to TE in the beam pipe, resulting in strong coupling between the two cavities. The coupling constant and the external  $Q$  are calculated similarly as above. We find in this case  $k=0.127$  and  $Q_{ext}=11.4$ . Introduction of an artificial cavity asymmetry as in Fig. 5 does not affect these results significantly.

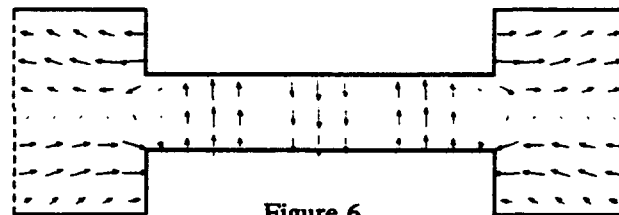


Figure 6  
Dipole Mode of Two Coupled Cavities

The transient and steady-state cavity voltages of two coupled klystron cavities are calculated using an equivalent circuit model shown in Fig. 7. Each cavity is represented by a parallel RCL circuit. The circuit resistance, capacitance and inductance ( $R$ ,  $C$  and  $L$ ) are computed from the shunt impedance, frequency and  $R/Q_0$  of the cavity.

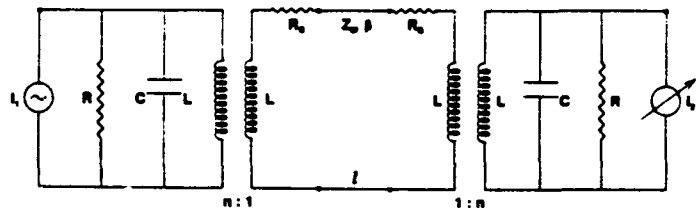


Figure 7 Equivalent Circuit

To simulate the klystron operation, the first cavity is driven by a current source at a frequency,  $\omega$ , at or near the fundamental frequency of the cavity,  $\omega_0=1/\sqrt{LC}$ . The second cavity is driven by a current controlled by the voltage of the first cavity with a gain  $g=I_2/Y_c V_1$ , where  $I$  and  $V$  are the current and voltage of the respective cavity and  $Y_c$  is the cavity admittance,  $Y_c=1/R+1/j\omega L+j\omega C$ . The increased rf current in the second cavity results from

velocity modulation of the beam due to its interaction with the first cavity and with the drift tube. The two cavity circuits are coupled by ideal transformers connected by a transmission line with a characteristic impedance  $Z_0$  and a phase delay,  $\beta l$ , where  $\beta$  and  $l$  are, respectively, the propagation constant and the length of the transmission line. The coupling constant<sup>4</sup>  $\beta_0 (=Q_0/Q_{ext})$  is also equal to the ratio of the transmission line transconductance to the cavity transconductance, divided by the square of the transformer turns ratio, or  $\beta_0 = (1/n^2)(R/Z_0)$ . We use the PSPICE program to simulate the circuit performance. In general feedback in coupled cavities, if unabated, could lead to an exponential rise in voltages. However, with proper choice of parameters, it is possible to essentially uncouple the cavities. Fig. 8 shows a simulation in which the voltages gradually rise and reach steady state in a few rf cycles. The cavity parameters for this case are:  $R=1 \times 10^5$  ohms,  $f=11.424$  GHz,  $R/Q_0=20$ . The transformer is assumed to be perfect, i.e.  $n=1$ . The transmission line is characterized by  $Z_0=1 \times 10^7$  ohms ( $\beta_0=.01$ ) and  $\beta l=\pi/2$ . The second cavity is driven by a current gain of 10 over the first cavity.

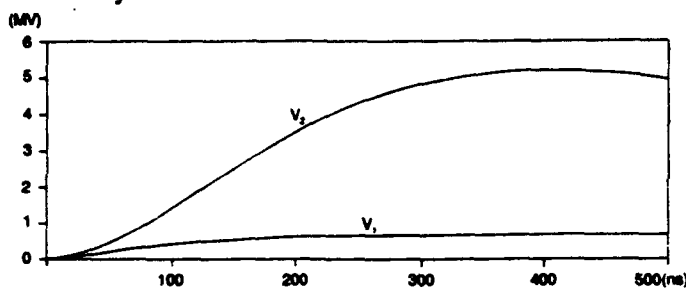


Figure 8 Transient Response from PSPICE Simulation

The allowable gain without onset of oscillation can be derived from the steady-state solution. Thus, we find

$$g = \frac{1}{\sqrt{1+x^2}} \left[ 2 + jx \left( \frac{\beta_0}{y_c} + \frac{y_c}{\beta_0} \right) \right]$$

where  $x = \tan(\beta l)$ , and

$$y_c = Y/G_c = Y_c R^{-1} + j2Q_0 \delta; \quad \delta = (\omega - \omega_0)/\omega_0$$

At critical coupling ( $\beta_0=1$ ) the allowable gain is  $g=2$  for any  $x$ . On the other hand, if  $\beta_0 \ll 1$ , i.e. weak coupling or  $Q_{ext} \gg Q_0$ , then  $|g| \approx 1/\beta_0$  except when  $x$  is close to zero. Thus to facilitate a gain of 10, for instance, the value of  $Q_{ext}$  must be greater than  $6.4 \times 10^4$ .

Parasitic oscillations between cavities can also be prevented using absorptive materials in the drift section, or using choke joints. The latter will be discussed in the next section. To simulate absorption, we add a series resistance,  $R_s$ , on either side of the transmission line in our circuit model. The series resistance has the effect of increasing

the effective value of  $Z_0$  to  $Z_0 + R_s(R_s/Z_0)$ . The cavity voltages can be stabilized in the presence of strong coupling by choosing a suitable value of  $R_s/Z_0$ .

### Choke Joints

A very effective way to decouple adjacent resonating cavities at a given frequency is by placing a choke cavity an odd multiple of quarter wavelengths away from the end of the main cavity. The choke cavity height is about a quarter wavelength. Fig. 9 is an URMEL field plot of the fundamental mode of an asymmetric cavity with a choke joint. Compared with Fig. 5, the TE propagation in the beam pipe has been clearly halted by the choke. Using the KY method, we calculate  $Q_{ext}$  for this waveguide loaded cavity with the choke joint to be  $9.9 \times 10^4$ , sufficient to prevent oscillations up to a gain of 15. A choke joint for the dipole mode can be similarly designed. Fig. 10 shows an URMEL plot for this case. The calculated  $Q_{ext}$  for the dipole mode with choke is  $5.9 \times 10^3$ , compared to 11 with no choke.

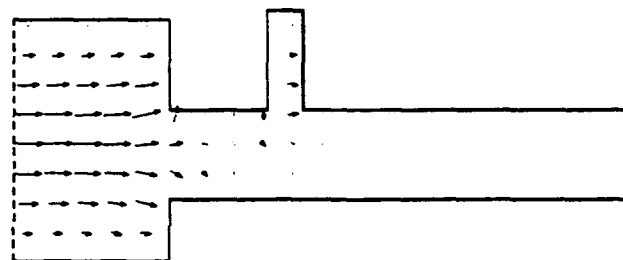


Figure 9 Choke Cavity for Fundamental Mode

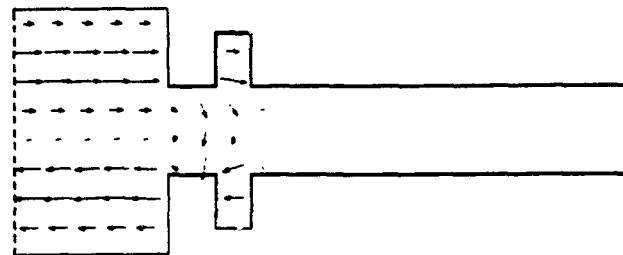


Figure 10 Choke Cavity for Dipole Mode

We thank R. Miller, W. Herrmannsfeldt, K. Eppley and D. Farkas for helpful discussions.

<sup>\*</sup>Work supported by DOE SBIR Grant No. DE-FG03-91ER81116 and DOE Contract No. DE-AC03-76SF00515.

<sup>1</sup>D.U.L. Yu, J.S. Kim and P.B. Wilson, AIP Conf. Proc., Third Advanced Accelerator Concept Workshop, Port Jefferson, Long Island, N.Y., May, 1992.

<sup>2</sup>K.R. Eppley, W.B. Herrmannsfeldt and R.H. Miller, SLAC-PUB-4221, Feb., 1987.

<sup>3</sup>N.M. Kroll and D.U.L. Yu, Part. Accel., **34**, 231 (1990).

<sup>4</sup>P.B. Wilson, SLAC-PUB 2884, Sec. 3.5, Feb., 1982.

# Beam-Wave Interaction in a Quasi-Periodic Structure \*

L. Schächter and J. A. Nation  
 Laboratory of Plasma Studies and School of Electrical Engineering  
 Cornell University, Ithaca, NY 14853 USA

## Abstract

An analytic method to analyze a quasi-periodic disk loaded waveguide is presented. We rely on Cauchy residue theorem to formulate the transmission and reflection from a system composed of radial arms and grooves provided that the inner radius is always the same. The quasi-analytical approach is not limited to slow variations of the geometry.

## I. INTRODUCTION

The constraint imposed by the NLC requirements on the output spectrum of an RF source limits the input section of any system to a very good frequency selective device. From this perspective the klystron cavity or a combination of a cavity with a magnetic field as in the case of the Choppertron<sup>(1)</sup> or an FEL<sup>(2)</sup>, are the natural candidates for the *input section* of any RF system. The *main section* can be a set of isolated cavities as in a klystron, a traveling wave (TW) section or a combination of the two but the breakdown problem will force us to use a TW structure as an *output section* with one or more extraction ports<sup>(3-4)</sup>. A high power traveling wave structure is conceived as a section of a periodic disk loaded structure and its electromagnetic characteristics are determined as if the system was infinitely long. Practically these are a set of cavities which are *coupled* through the disk aperture. At the other extreme, the klystron is a set of a few *isolated* cavities. In the former case the beam interacts with a wave continuously, whereas in the klystron the beam interacts with the field in the close vicinity of the cavity. The interaction in a uniform periodic structure (TWA) or in a few uncoupled cavities (klystron) is relatively well understood. But we lack analytical or even quasi-analytical tools to accurately investigate the interaction in transition region - which is exactly what is required for construction of an adequate output section. For this purpose we have developed an analytical method to investigate the beam-wave interaction in a quasi-periodic structure. The method relies on an arbitrary number of pill-box like cavities of any dimension and an arbitrary number of radial arms. The only constraint is that the radius of the coupling pipe has to be always the same.

## II. BOUNDARY CONDITION PROBLEM

The system described above is illustrated in Fig.1. For the purpose of this presentation we shall describe only the system without the beam and we shall indicate where the differences occur when a beam is present. Unlike in a periodic structure where the field in the inner cylinder ( $0 < r < R_{int}$ ) can be represented by Floquet series

we have to consider the entire spatial spectrum of waves therefore the magnetic vector potential reads

$$A_z(r, z; \omega) = \int_{-\infty}^{\infty} dk A(k) I_0(\Gamma r) e^{-jkz} \quad (1)$$

where  $\Gamma^2 = k^2 - \omega^2/c^2$ ,  $I_0(x)$  is the modified Bessel function of the first kind and the system is assumed to be in steady state ( $e^{j\omega t}$ ). In the arms or grooves the electromagnetic field should be represented by a superposition of modes which satisfy the boundary conditions on the metallic walls. In principle an infinite number of such modes is required. Our experience indicates that as long as the vacuum wavelength is about 5 times larger than the groove/arm width the first mode (TEM) is sufficient for most practical purposes.

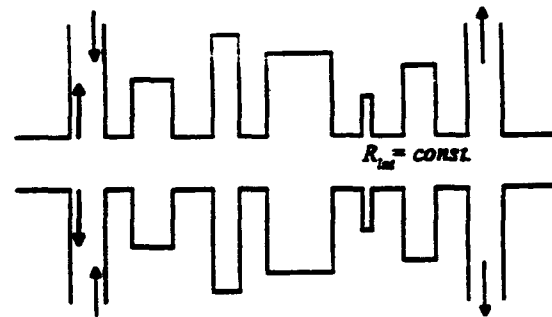


Fig. 1 The schematics of the quasi-periodic system.

This assumption is by no means critical for the present analysis and the arguments are very similar when a larger number of modes is required however we use it since it makes the presentation much simpler. Within the framework of this approximation we can write for the magnetic vector potential in the input arm

$$A_z(r, z; \omega) = A_{in} H_0^{(1)}\left(\frac{\omega}{c} r\right) + D_1 H_0^{(2)}\left(\frac{\omega}{c} r\right) \quad (2)$$

where  $H_0^{(1)}(x)$  and  $H_0^{(2)}(x)$  are the zero order Hankel function of the first and second kind respectively;  $A_{in}$  represents the amplitude of the incoming wave and  $D_1$  is the amplitude of the reflected wave which is yet to be determined. In the  $n^{th}$  ( $1 < n < N$ ) groove we have

$$A_z^n(r, z; \omega) = D_n T_{0,n}\left(\frac{\omega}{c} r\right), \quad (3)$$

$D_n$  is the amplitude of the magnetic vector potential,  $T_{0,n}\left(\frac{\omega}{c} r\right) = J_0\left(\frac{\omega}{c} r\right) Y_0\left(\frac{\omega}{c} R_{ext,n}\right) - Y_0\left(\frac{\omega}{c} r\right) J_0\left(\frac{\omega}{c} R_{ext,n}\right)$  and

$R_{ext,n}$  is the external radius of the  $n^{th}$  groove; later we shall also use the function  $T_{1,n}(\frac{\omega}{c}r) = J_1(\frac{\omega}{c}r)Y_0(\frac{\omega}{c}R_{ext,n}) - Y_1(\frac{\omega}{c}r)J_0(\frac{\omega}{c}R_{ext,n})$ . Finally in the output arm

$$A_s(r, z; \omega) = D_N H_0^{(2)}(\frac{\omega}{c}r). \quad (4)$$

In order to determine the various amplitudes we next impose the boundary conditions in a way which is similar to what is being done in the case of a periodic structure. The main difference is that we no longer can look at what happens in a single cell to characterize the entire system but we have to consider each individual region. The boundary condition problem is formulated next in terms of the amplitudes in the grooves and arms in a matrix form:

$$\sum_{m=1}^N \tau_{n,m} D_m = S_n A_{in} \quad (5)$$

where

$$\begin{aligned} \tau_{n,m} &= \psi_{1,n} \delta_{n,m} - \psi_{0,m} \chi_{n,m}, \\ S_n &= -H_1^{(1)}(\alpha) \delta_{n,1} + H_0^{(1)}(\alpha) \chi_{n,1} \end{aligned} \quad (6)$$

$$L_n(k) = \frac{1}{d_n} \int_{z_n - d_n/2}^{z_n + d_n/2} dz e^{jkz}, \quad (7)$$

$$\psi_{\nu,n} = \begin{cases} H_\nu^{(2)}(\alpha) & n=1 \text{ or } n=N \\ T_{\nu,n}(\alpha) & 1 < n < N \end{cases} \quad (8)$$

and

$$\chi_{n,m} = \frac{d_m \alpha}{2\pi} \int_{-\infty}^{\infty} dk \frac{I_1(\Delta)}{\Delta I_0(\Delta)} L_n^*(k) L_m(k). \quad (9)$$

With  $\nu = 0, 1$ ;  $z_n$  is the location of the center of the  $n^{th}$  groove or arm and  $d_n$  is the corresponding width. Finally  $\alpha = \frac{\omega}{c} R_{int}$  and  $\Delta = \Gamma R_{int}$ .

### III. CAUCHY RESIDUE THEOREM

The next step is to evaluate the integral which defines the matrix  $\chi$  in terms of analytic functions. This is done by using the Cauchy residue theorem. First we substitute the explicit expressions for  $L_n(k)$  from Eq.(7). Second, we examine the integrand we observe that there are an infinite set of poles which correspond to  $I_0(\Delta) = 0$ . Bearing in mind the relation between the modified Bessel function and the regular one ( $J_0(x)$ ) we realize that the condition above is satisfied for  $k^2 = (\frac{\omega}{c})^2 - \frac{p_s^2}{R_{int}^2}$ ; here  $p_s$  are all the zeros of the zero order Bessel function of the first kind i.e.  $J_0(p_s) \equiv 0$ . According to the Cauchy's theorem the contribution to the integral will come from the poles of the integrand hence the integral in Eq.(9) reads

$$\int_{-\infty}^{\infty} dk \frac{I_1(\Delta) e^{jk(x_1-x_2)}}{\Delta I_0(\Delta)} = \frac{2}{R_{int}^2} \sum_{s=1}^{\infty} \int_{-\infty}^{\infty} dk \frac{e^{jk(x_1-x_2)}}{k^2 + \Gamma_s^2} \quad (10)$$

where  $\Gamma_s^2 = (p_s/R_{int})^2 - (\omega/c)^2$ . The last integral is the Green function of a uniform waveguide and is easily evaluated as  $G(x_1|x_2) = \frac{\pi}{\Gamma_s} e^{-\Gamma_s|x_1-x_2|}$ . This result permits us to express the matrix  $\chi$  in terms of analytic functions: for  $n = m$

$$\chi_{n,n} = \frac{\alpha}{R_{int}^2} \sum_{s=1}^{\infty} \frac{2}{\Gamma_s^2} [1 - e^{-\Theta_{s,n}} \text{sinhc}(\Theta_{s,n})] \quad (11)$$

and

$$\chi_{n,m} = \frac{\alpha}{R_{int}^2} \sum_{s=1}^{\infty} \frac{d_m}{\Gamma_s} e^{-\Gamma_s|z_n-z_m|} \text{sinhc}(\Theta_{s,n}) \text{sinhc}(\Theta_{s,m}) \quad (12)$$

otherwise. In this expression  $\text{sinhc}(x) = \sinh(x)/x$  and  $\Theta_{s,n} = \Gamma_s d_n/2$ . The electromagnetic problem has been now simplified to inversion of a matrix whose components are analytic functions. The transmission pattern of the structure fits well the predictions of the dispersion relation of an infinite structure.

In the presence of the beam, using the fluid model, the denominator in Eq.(9) is a more complex function than the  $I_0(\Delta)$ , which in addition to the electromagnetic modes it includes the space charge modes. Once the poles are identified the only aspect which remains to be consider is the fact that the space charge waves, unlike the electromagnetic waves, always propagate along the beam.

### IV. DISCUSSION

Next we shall illustrate the potential of this method. And the first goal is to determine what should be the location of the arms for adequately feed power into a 9 cell narrow band structure ( $R_{ext} = 14.2mm$ ,  $R_{int} = 6.2mm$ ,  $L = 12mm$  and  $d = 6mm$ ). Fig. 2 illustrates the geometry of the narrow band structure with 9 cavities and two arms. In the first case the arms are 6mm from the first cells and we observe that the average transmission coefficient is  $-20dB$ . When the drift region was shortened to 1mm the transmission coefficient increases dramatically to an average value of  $-3dB$  (this result was qualitatively observed in experiment).

Let us now assume for a moment that we have matched the cold system fo a given frequency i.e the gain in dB,  $10 \log(|D_N|^2 d_N / |A_{in}|^2 d_1)$  is zero. We know that in the narrow band structure very high gradients develop in the

interaction process - in particular in the last couple of cells.

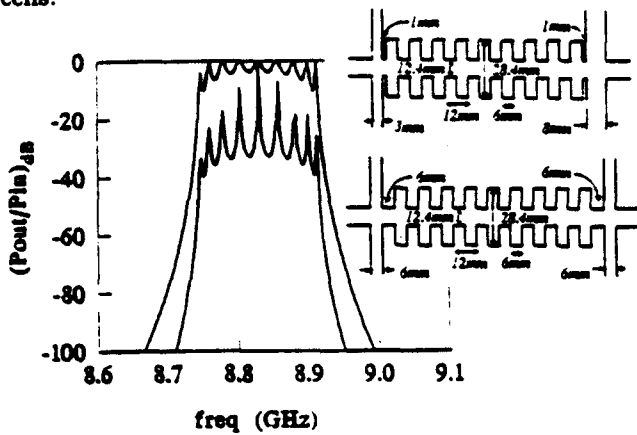


Fig. 2: The transmission coefficient for the two structures shown in the right corner.

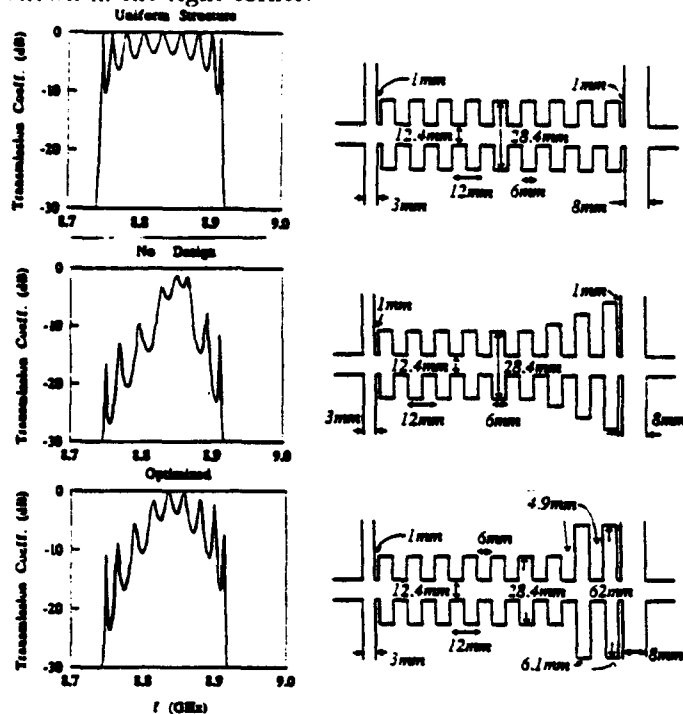


Fig. 3: Transmission coefficient of three structures.

In order to avoid *rf* breakdown we want to increase the volume where the electromagnetic energy is stored and by that we lower the energy density and consequently the field. We started with a "linear" tapering of the external radius (of the last three cells increases linearly). We have varied the width of these cells and their separation in a wide range of parameters to bring the transmission coefficient to 0dB at given frequency and the best we could achieve was -3dB which is not acceptable; see Fig.3. At this stage we returned to the initial geometry only that we have doubled the external radius of the last two cells. These cavities have two (rather than one) resonant frequencies, one of which, is close to that of a cavity in the uniform structure. After some fine tuning we obtained the transmission which is optimized to the required fre-

quency. Fig. 4 illustrates the transmission characteristic of system driven by 1MV, 1kA beam whose radius is 3mm. The two sections are separated by a 3cm long drift region and thus electromagnetically they are completely isolated. In the left we present the geometry and in the right the transmission coefficient. The location of the drift tube is critical as illustrated. The periodic structure was designed with a phase advance of  $2\pi/3$  and we observed that when varying the location of the drift region, each three cells the picture repeats.

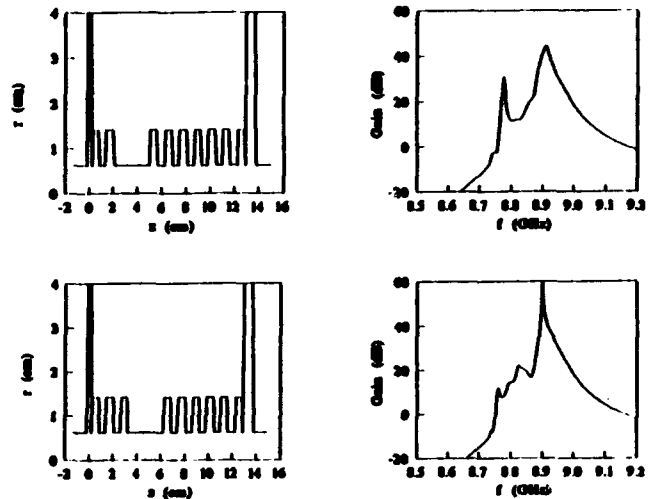


Fig. 4: Transmission coefficient of an active system. The drift region is 3cm long.

In conclusion, we presented a method to calculate the electromagnetic characteristics of a quasi-periodic structure which consists of radial arms and a set of coupled disk loaded cells. The main constraint in this method is that the internal radius has to be kept constant. In the simplified version presented here we used only a single mode to represent the field in the grooves and arms this can be extended to a larger number of modes. However this is necessary only for these grooves or arms whose width is more than  $1/5$  the vacuum wavelength; accordingly the order of the matrix  $\tau$  increases.

## V. REFERENCES

- [\*] Work supported by USDOE and AFOSR.
- [1] "Suppression of beam induced pulse shortening modes in high power RF generator TW output structures"; J. Haimson *et. al.* SPIE Proc. Vol.1629 p.209 (1992).
- [2] "Two-beam linear colliders" by K. Hubner in XV<sup>th</sup> International Conference on High Energy Accelerators, HEACC'92 Hamburg 1992, p. 791.
- [3] "High-gradient electron accelerator powered by a relativistic klystron", M.A. Allen *et. al.* Phys. Rev. Lett. 63 p.2472 (1989). *Rev. Sci. Instrum.*, 57, 855 (1986).
- [4] "Two Stage High Power Traveling Wave Amplifier" D. Shiffler, J. D. Ivers, G. S. Kerslick, J. A. Nation and L. Schächter, *Appl. Phys. Lett.*, 58, 899, (1991).

# Two-Stage, High Power X-Band Amplifier Experiment \*

E. Kuang, T. J. Davis, J. D. Ivers, G. S. Kerslick, J. A. Nation and L. Schächter  
Laboratory of Plasma Studies and School of Electrical Engineering  
Cornell University, Ithaca, NY 14853, USA

## Abstract

At output powers in excess of 100 MW we have noted the development of sidebands in many TWT structures. To address this problem an experiment using a narrow bandwidth, two-stage TWT is in progress. The TWT amplifier consists of a dielectric ( $\epsilon = 5$ ) slow-wave structure, a 30 dB sever section and a 8.8–9.0 GHz passband periodic, metallic structure. The electron beam used in this experiment is a 950 kV, 1 kA, 50 ns pencil beam propagating along an applied axial field of 9 kG. The dielectric first stage has a maximum gain of 30 dB measured at 8.87 GHz, with output powers of up to 50 MW in the  $TM_{01}$  mode. In these experiments the dielectric amplifier output power is about 3–5 MW and the output power of the complete two-stage device is  $\sim 160$  MW at the input frequency. The sidebands detected in earlier experiments have been eliminated. We also report measurements of the energy spread of the electron beam resulting from the amplification process. These experimental results are compared with MAGIC code simulations and analytic work we have carried out on such devices.

## I. INTRODUCTION

Earlier experiments [1] using two-stage ripple wall TWTs with  $\sim 1.8$  GHz bandwidths have achieved output powers in excess of 400 MW at  $\sim 9$  GHz. However at these levels up to 50% of the output power is emitted in asymmetric sidebands. Analytic work [2] has suggested that this process is due to finite length effects and reflections from the transition regions in the slow wave structures. To address this problem we have designed several low group velocity, narrow band structures (NBS) to effectively transit time isolate the input from the output. In addition since the inner diameter of these slow wave structures is beyond cutoff we achieve significant attenuation of any reflected signal from the output. For the forward amplifying wave the attenuation is unimportant because the electron beam couples successive cavities of the amplifier.

The interaction in the narrow band structure has been studied both analytically and with the particle-in-cell code MAGIC. As a result of the interaction process the energy spread of individual electrons can be as high as 60% of the initial beam energy, while the average energy of the beam is reduced by less than 10%. The analytical results indicate that a gain of 5–7 dB/cm can be expected compared to 1–2 dB/cm in the broad passband structure. This results from the high shunt impedance of

the narrow bandwidth structure. In this work the shunt impedance is defined by the relation

$$Z_{sh} = \frac{E_z^2(r = R_b)\pi r_i^2}{2P}$$

where  $E_z(r = R_b)$  is the longitudinal electric field at the beam location,  $r_i$  is the inner radius of the structure, and  $P$  is the total power which flows in the system (both quantities are calculated in the absence of the beam). The high shunt impedance of the narrow bandwidth amplifiers leads to high values of electric field in the structure. Calculations and simulation results show that for output powers of 200 MW the electric field on the wall will be  $\sim 200$  MV/m.

## II. EXPERIMENT

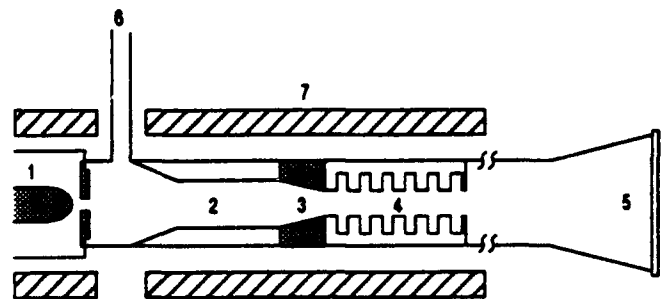


Fig 1. Schematic of the two-stage narrow band amplifier. (1) E-beam diode, (2) dielectric slow wave structure, (3) silicon carbide sever, (4) narrow band structure, (5) output horn, (6) input waveguide, (7) magnetic field coil.

The dielectric first stage of the amplifier (fig. 1) preamplifies the 20–50 kW magnetron input by  $\sim 20$  dB. A silicon carbide sever is used to attenuate by 30 dB the rf wave amplified in the first stage while allowing the space charge wave to propagate into the second stage of the amplifier. In addition, the sever attenuates the reflected wave from the output end of the second stage, and prevents system oscillation due to feedback. The narrow band amplifier serves as the second stage of the system and consists of a ten period iris loaded waveguide. The structure has a 1.2 cm period, and a 1.42 cm external radius. Each iris is 0.6 cm long with an internal radius of 0.62 cm. To couple the power out of the narrow band structure, the width of the last iris is reduced to 0.1 cm. This modification is essential for efficient output coupling. The system is driven by a 950 kV, 1 kA, 50 ns, 0.6 cm diameter electron beam. The output power is determined using far field measurements and has been confirmed calorimetrically.

\* Work supported by USDOE and AFOSR.

As stated earlier substantial electron energy spreads occur during the interaction, with some electrons gaining energy while others lose energy, depending on their phase relative to the wave. The electron energy spread resulting from the amplification process is measured using a small deflection angle magnetic spectrometer. The spectrometer field can be varied to change the energy range of the particles detected by a strip of electron sensitive film. The film is then optically scanned to produce an output electron energy spectrum with the electron deflection calibrated to measure the particle energy.

### III. EXPERIMENTAL RESULTS

The output power of the TWT's is measured using far field measurements of the gain. An independent measurement, up to output levels of 65 MW is obtained from a calorimeter [3].

The output power of the single stage alone is of order 3 MW, and has been increased to 50 MW before rf breakdown occurs on the dielectric. The power from the two stage device is measured as a function of input frequency and is shown in fig. 2. Power levels from the calorimetric measurements are also shown to correlate well with the gain data up to 65 MW. Above this level the pressure transducer in the calorimeter saturated. The maximum output power is ~ 160 MW. At these power levels the rf pulse duration matched that of the driver electron beam.

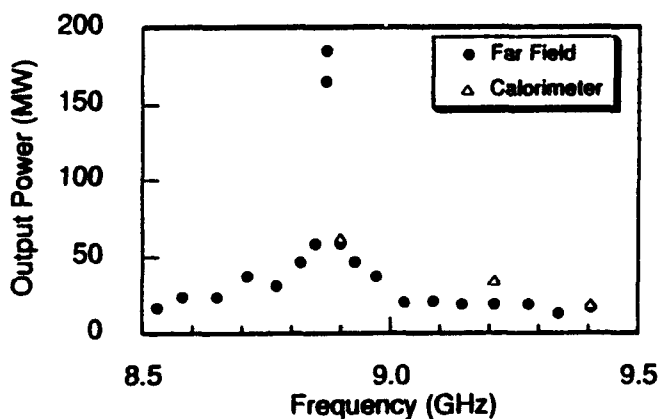


Fig 2. Measured frequency response of the NBS amplifier.

The frequency content of the sampled output signal is measured with a double balanced mixer using heterodyning techniques. A typical fast Fourier transform (FFT) is illustrated in Fig. 3 and is within  $\pm 20$  MHz of the input frequency. Note that the output is single frequency and the sidebands have been eliminated. The electron energy

spectrum is shown in fig. 4 for three sets of conditions.

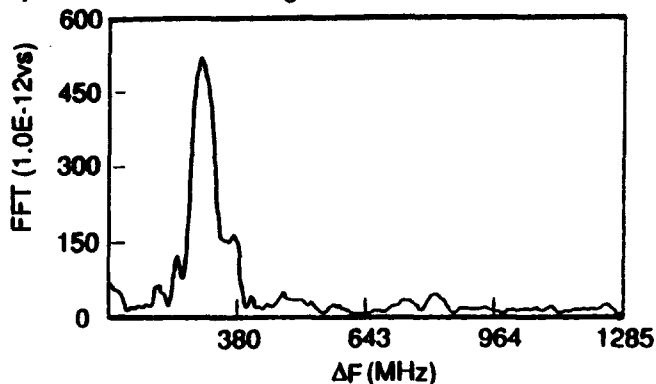


Fig 3. FFT of the measured output signal showing single frequency output.

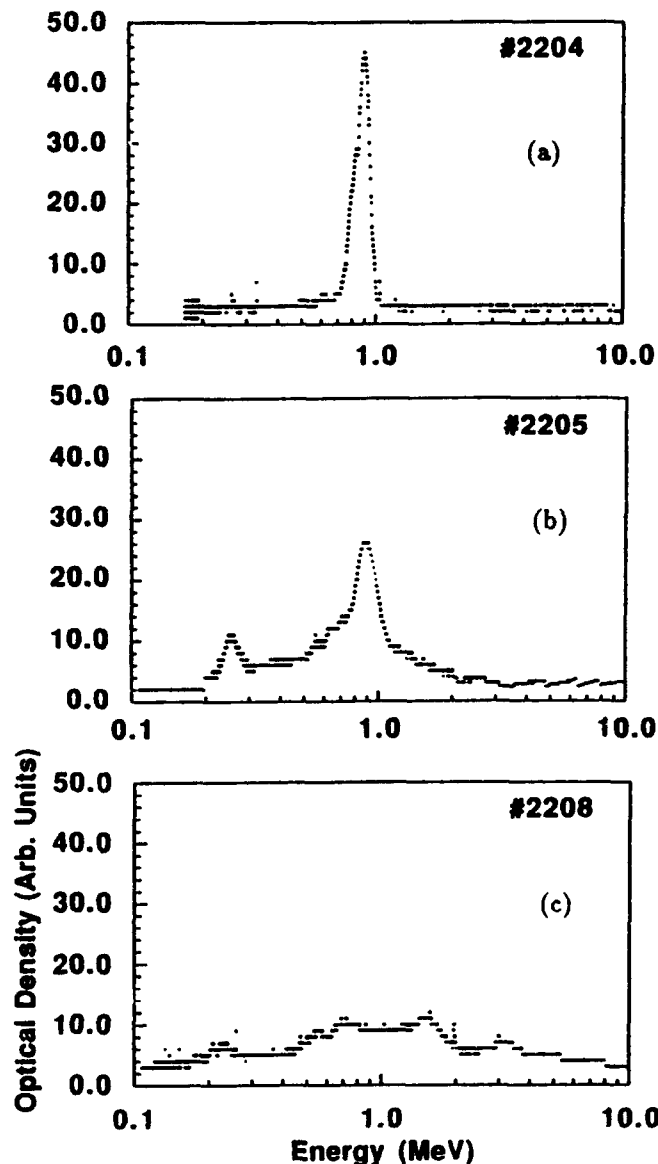


Fig 4. Electron energy spectra at the amplifier output. (a) Injected electron spectrum, (b) output energy spectrum without rf input, (c) output energy spectrum with rf input.

Fig. 4a shows the spectrum of the injected electron beam. In fig. 4b we show the spectrum without any *rf* input. In this case the wave grows in the amplifier structures from noise, causing a substantial change in the electron momentum distribution. The main peak is at the injection energy of 900 *kV*, but there is also a significant component at 250 *kV*. This component is not present in the absence of the amplifier structures and is clear evidence that the wave growing from noise has extracted energy from the electron beam. The spectrum with *rf* input, fig. 4c, shows a larger spread in electron energies extending from 0.25 – 2 *MV* with a clear component at higher energy than that of the injected beam. In addition the lower energy peak has been smeared out, possibly due to the amplifier being too long and some electrons being reaccelerated.

#### IV. DISCUSSION OF RESULTS

The dispersion relation of the narrow band structure compared to our earlier wide bandwidth (1.7 *GHz*) devices is shown in fig. 5. In the wide pass-band structures an electron velocity spread between 0.8 *c* – 1.0 *c* generates noise in a 300 *MHz* frequency range. In the narrow pass-band (200 *MHz*) structure described here the noise generated is restricted to a range of 20–30 *MHz*. This, in effect, overlaps the input signal and eliminates the sidebands. MAGIC simulations of narrow band amplifiers show single frequency output up to high power levels as shown in fig. 6.

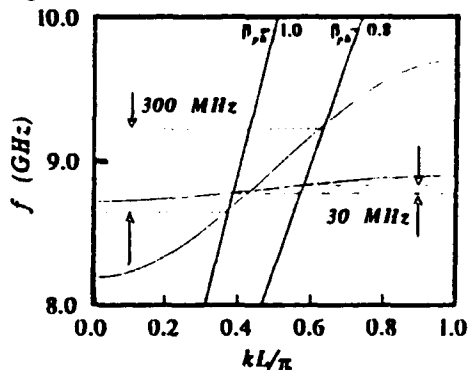


Fig 5. Dispersion relations for a broadband and a narrowband periodic structure.

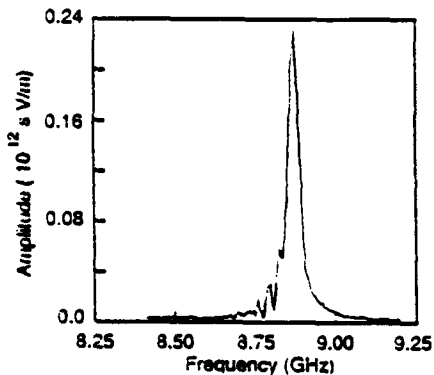


Fig 6. FFT of output signal from narrow band amplifier MAGIC simulation.

The elimination of the sidebands can also be viewed as a transit time isolation. In the 15*cm* long NBS, with a wave energy velocity of  $V_{gr} = 0.007 c$ , it takes about 75 *ns* for a reflected wave to reach the input. This is longer than the electron pulse duration, and consequently the beam is unaffected by the time the reflected wave amplitude becomes significant at the input to the amplifier. At present we are exploring the use of somewhat broader band structures e.g. 400 – 800 *MHz* to identify the limits under which we can operate without sidebands. The shunt impedance of a structure is inversely proportional to the wave group velocity, so the broader band devices will have a lower shunt impedance and hence the electric field of the wave will be lower for a given power flow through the TWT. In addition we are exploring the possibility of interacting with the first space harmonic of a slow wave structure in order to reduce the wave growth rate, and the wave electric field, for a given power flow.

In conclusion, we note that the use of traveling wave tube structures offers an alternate approach for the generation of ultra high power microwave signals. Operation may be in a mode in which a TWT amplifier is used as a stand alone device for microwave generation or as the output structure for a klystron. In the latter scenario the output structure may have additional gain or may be used simply as a device for power extraction. In either case the use of the TWT allows for a reduction in the electric field strength at the output port.

#### V. REFERENCES

- [1] D. Shiffler, J. A. Nation, L. Schächter, J. D. Ivers and G. S. Kerslick, *J. Appl. Phys.*, 70, 106, (1991).
- [2] L. Schächter, J. A. Nation and D. Shiffler, *J. Appl. Phys.*, 70, 114, (1991).
- [3] C. B. Wharton, L. M. Earley, and W. P. Ballard, *Rev. Sci. Instrum.*, 57, 855 (1986).

# Long-Pulse, High-Power, X-Band Relativistic Traveling-Wave Tube Amplifier

T. Kimura, S. Alberti\*, B.G. Danly, and R.J. Temkin

Plasma Fusion Center,  
Massachusetts Institute of Technology,  
Cambridge, MA 02139

## Abstract

A high-power X-band traveling-wave tube (TWT) amplifier has been designed. A disk-loaded circular waveguide is used as the slow wave structure (SWS) for wave interaction with a 450 kV, 80 A solid electron beam. From Pierce theory, the predicted gain at 9.7 GHz is 1.94 dB/cm with an instantaneous bandwidth of 5% and a phase advance of  $\pi/2$  for the  $TM_{01}$  mode. Cold dispersion measurements show good agreement with the simulation.

## Introduction

There has been considerable attention in recent years toward high power microwave devices for applications ranging from heating of fusion plasmas, to drivers for new generation of high energy electron accelerators and radar systems. In the X-band regime, high power TWT experiments have been successful in acquiring large instantaneous bandwidth[1] and producing high power[2]. For our current project, the X-band TWT amplifier is designed for 20 MW peak power, at 9.6 GHz, an instantaneous bandwidth of 5%, and a saturated gain of 30 dB. The electron beam used will have a 2.5  $\mu$ s (1  $\mu$ s flat top) pulse length, 450 kV beam voltage and 80 A beam current. Since the energy per pulse is much greater than in previous experiments, study of interest will include phenomena such as power saturation and sideband effect.

In the following sections we present a description of the experimental design followed by results of simulation and cold-test measurements.

## Experimental Configuration

A high-voltage 2.5  $\mu$ s (1  $\mu$ s flat-top) pulse modulator provides the accelerating potential (450 kV) to the Pierce type thermionic electron gun which has a measured perveance of 0.27  $\mu$ P, resulting in a beam current of 80 A. After being focused by a magnetic field with a maximum intensity of 3 kG, the solid electron beam has a radius of 4 mm with minimal scalloping.

As shown in Fig. 1, the amplifier has three sections: the beam-injection and signal-input section, the slow wave interaction section, and the output section. The input signal comes from a 10 kW magnetron. The input coupler is of the type commonly used for high power TWTs[3]. The coupling from  $TE_{10}$  mode in the feed rectangular guide to  $TM_{01}$  mode in the tube is provided by a sidewall coupler placed in the first cell. A movable stub tuner along the SWS axis serves to match the microwaves into the structure and also allows an optimal coupling over a wide bandwidth.

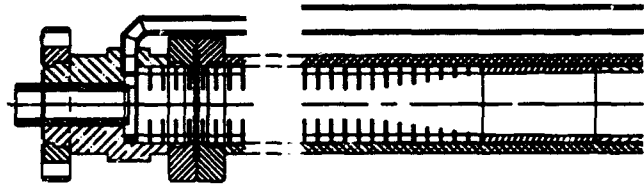


Figure 1: Design of 9.6 GHz Relativistic TWT

Disk-loaded waveguide is used as a slow wave circuit. Two different structures have been designed, one with waveguide radius  $b = 14.5$  mm and disk radius  $a = 8.0$  mm (designated the R8 structure), the other one with  $b = 13.9$  mm and  $a = 7.0$  mm (designated the R7 structure). Both structures have a periodic length of  $L = 6.0$  mm and a disk thickness of  $d = 0.8$  mm. The number of periodic cells can be varied from 32 to 64. In order to minimize reflections from the output sections, a tapered disk-loaded section is placed between the SWS and a smooth cylindrical waveguide. The linear tapering of the disks inner radius occurs over two guide wavelengths. Finally the smooth cylindrical waveguide leads to a conical taper with an output window.

## Simulation Results

The dispersion relation of the slow wave structure is calculated using the URMEL code. The two structures were investigated.

\*Supported by Swiss National Science Foundation, Fellowship No.8220-30665

The  $TM_{01}$  dispersion curves for these two structures are given in Fig. 2. Both curves intersect the 450 kV beam line near  $\pi/2$  point at 9.6 GHz.

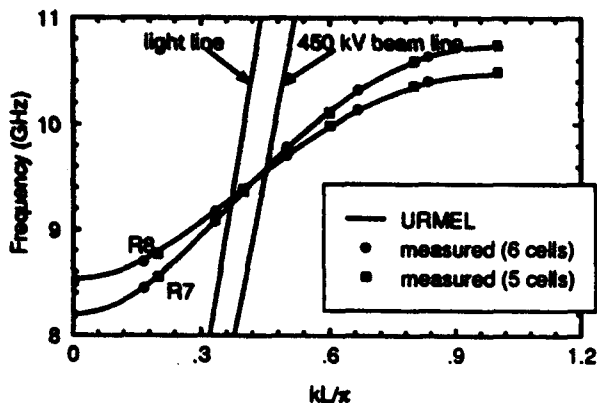


Figure 2: The dispersion curves for the disk-loaded structures.

URMEL is also used to obtain the coupling impedance, which is defined as  $Z_c = E_{z0}^2 / 2k_{\parallel}^2 P$ , where  $E_{z0}$  is the first space harmonic electric field amplitude of the synchronous component of the  $E$  field,  $k_{\parallel}$  is the parallel wave number, and  $P$  is the power flow in the structure. The calculated coupling impedance as a function of frequency for the R8 structure is shown in Fig. 3.

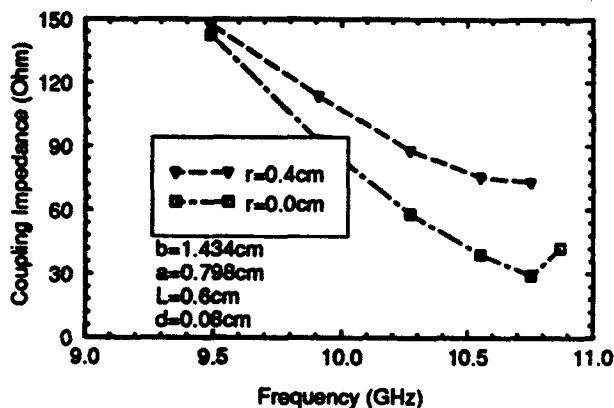


Figure 3: Coupling impedance versus frequency at two different radial positions  $r = 0.0$  mm and  $r = 4.0$  mm obtained from URMEL.

According to Pierce theory[4], when the Pierce space charge parameter  $QC$  is negligible, the TWT maximum gain can be written as,

$$G[dB] = -9.54 + 47.3CN \quad (1)$$

where  $N$  is the amplifier length in number of guide wavelengths and the Pierce gain parameter  $C$  is given by

$$C = \left[ \frac{Z_c}{Z_b} \frac{1}{2(\gamma+1)} \right]^{1/3} \quad (2)$$

where  $Z_b = V_b/I_b$  is the beam impedance, and  $\gamma$  is the relativistic factor of the beam particle. From the values of coupling impedance  $Z_c$  obtained above, the calculated gain at 9.7 GHz for the R7 and R8 structures is 1.94 dB/cm and 1.59 dB/cm, respectively. The total gain for 32 periodic cells of R7 structure is shown as a function of frequency in Fig. 4. It can be seen that the maximum gain is 30 dB with an instantaneous bandwidth of 500 MHz.

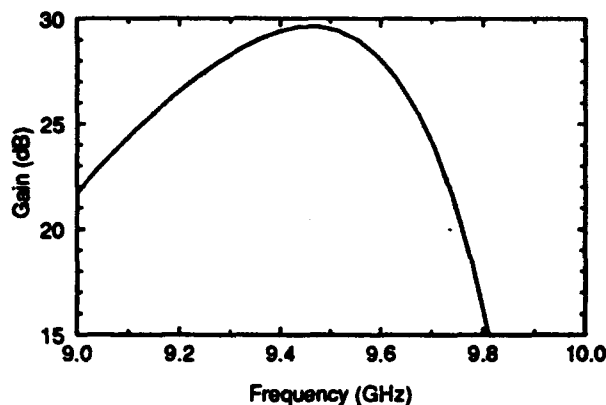


Figure 4: Total gain for 32 cells of the R7 structure as a function of frequency.

## Cold-Test Results

The disk-loaded structures have been cold-tested with an HP8510 network analyzer by measuring the resonant frequencies of the standing waves in a section of the SWS structure composed by five and six cells[5]. The experimental setup for this measurement is shown in Fig. 5. The measured resonant frequencies agree extremely well with the dispersion relation calculated from URMEL, as shown in Fig. 2.

The input coupler has also been cold-tested. The result shows that coupling with less than  $-10$  dB return loss can be achieved with the designed coupler over a frequency range of 9.2 GHz to 9.8 GHz (See Fig. 6). In order to avoid self oscillation of the tube for high gain operation, the implementation of distributed losses and severs is foreseen.

## Conclusion

The design of an X-band traveling-wave tube amplifier has been completed. The structure will be powered by a long-pulsed, high energy electron beam. Simulation indicates a gain of 1.94 dB/cm dB for the structure with an instantaneous bandwidth of 5%. Cold dispersion measurements show good agreement with the simulation. Design of broader instantaneous bandwidth structures as well as theoretical studies of the linear and nonlinear regime using field theory are under way.

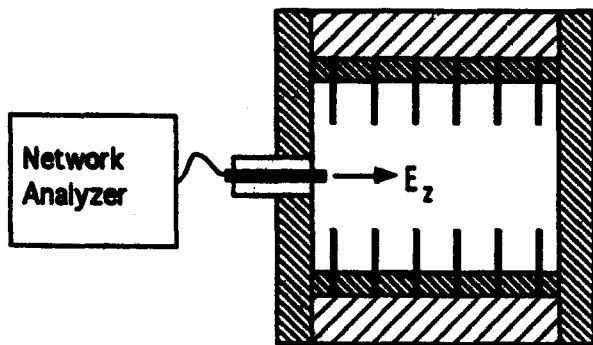


Figure 5: Setup for Cold Test Measurement of the SWS

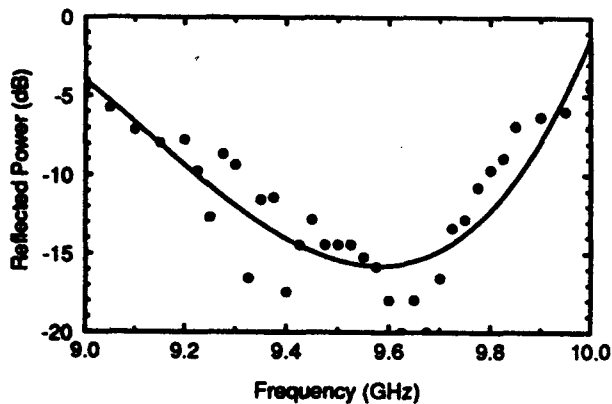


Figure 6: Ratio of reflected power to incident power in dB for TWT input coupler, showing a good match over the frequency range of interest.

## Acknowledgments

W.J. Mulligan and G. Yarworth provided invaluable technical assistance. This work was supported by the U.S. Army Research Laboratory Contract DAAL02-92-K-0054.

## References

- [1] T. Roumbanis, J. Needle, and D.K. Winslow. A megawatt X-band TWT amplifier with 18% bandwidth. In *Proceedings of High-Power Microwave Tube Symposium, The Hexagon, Ft. Monmouth, NJ*, pages 114-129, 1962.
- [2] J.A. Nation, J.D. Ivers, G. Kerslick, D. Shiffler, and L. Schachter. High-gain, high-efficiency TWT amplifiers. In H.E. Brandt, editor, *Intense Microwave and Particle Beams II*, pages 12-22, SPIE, 1990.
- [3] J.F. Gittens. *Power Traveling-Wave Tubes*. American Elsevier Publishing Co., Inc., 1965.
- [4] J.R. Pierce. *Traveling-Wave Tubes*. D. Van Nostrand Co., 1950.
- [5] H.Z. Guo, Y. Carmel, W.R. Lou, L. Chen, J. Rodgers, D.K. Abe, A. Bromborsky, W. Destler, V.L. Granatstein. A novel highly accurate synthetic technique for determination of the dispersive characteristics in periodic slow wave circuits. *IEEE Transactions on Microwave Theory and Techniques*, Vol. 40, No. 11, November 1992.

# Tapered Tube, Microsecond Electron Beam Gyrotron Backward-Wave-Oscillators

R. M. Gilgenbach, M. T. Walter, P. R. Menge, and T. A. Spencer\*  
Intense Energy Beam Interaction Laboratory, Nuclear Engineering Department  
University of Michigan, Ann Arbor, MI 48109-2104

## Abstract

Experiments have been performed to test microwave efficiency enhancement and pulselength extension of the gyrotron-backward-wave-oscillator (gyro-BWO) through the use of a tapered interaction tube. The MELBA accelerator has been utilized to generate electron beams with parameters:  $V = -0.7$  to  $-0.8$  MV,  $I = 1-4$  kA, and pulselengths from  $0.5-1 \mu\text{s}$ . The microwave frequency is magnetically tunable in the range from 4.6-6 GHz. MAGIC code modeling has guided the experimental selection of taper magnitudes to enhance efficiency and pulselength. The optimal taper magnitude found in both the experiment and model has been a 10% downtapered tube, which gave a significant increase in both microwave tube power (factor of  $\sim 2$ , up to about 80 MW) and pulselength ( $\sim 30\%$  average increase up to  $0.38 \mu\text{s}$ ) over uniform tubes. Integrated microwave pulse-energy is also maximized for the 10% downtapered tube. Taper magnitudes larger than 10% gave reduced microwave power and energy.

## I. INTRODUCTION

High power, long-pulse, microwaves have many applications in RF accelerators, defense electronics testing, and plasma heating. One of the major challenges has been to simultaneously generate multimewatt microwaves while maintaining the microwave oscillation mechanism over a fraction of a microsecond. During the past several years, the uniform tube gyrotron-backward-wave-oscillator (gyro-BWO) [1,2] has shown considerable promise for both high

power and long pulse operation [3]. Recently, improvement in gyro-BWO performance has resulted from tapered-interaction tubes [4]. A summary of gyro-BWO experiments on tapered interaction tubes is presented here.

## II. EXPERIMENTAL CONFIGURATION

The experimental configuration is depicted in Figure 1. Electron beams are generated by the Michigan Electron Long Beam Accelerator, MELBA, at diode parameters: voltage =  $-0.7$  to  $-0.8$  MV,  $I_{\text{diode}} = 1-10$  kA, and pulselengths =  $0.5-1 \mu\text{s}$ . A velvet button cathode is utilized, which reduces diode closure, to provide relatively flat current. The diode magnetic field coils are pulsed to generate about 1 kG magnetic field. A graphite anode apertures the e-beam to 5 cm diameter. The beam enters a solenoidal magnetic field coil on the transport tube, which generates 3-8 kG. This range of magnetic field allows the frequency to be magnetically tuned from 4.6-6 GHz. A number of interaction tubes and orientations were run: 1) copper tube with uniform cross section and 1.9 cm radius (20 cm long), 2) tapered tube, average radius of 1.9 cm with 10% decrease in direction of e-beam propagation (defined here as downtaper or -orientation), 3) tapered tube with average radius of 1.9 cm with 23% taper (both + and - orientations tested), 4) tapered tube with average radius of 1.9 cm with 43% taper (both + and - orientations tested). Microwaves were extracted by an S-band waveguide antenna at the diode-end of the machine.

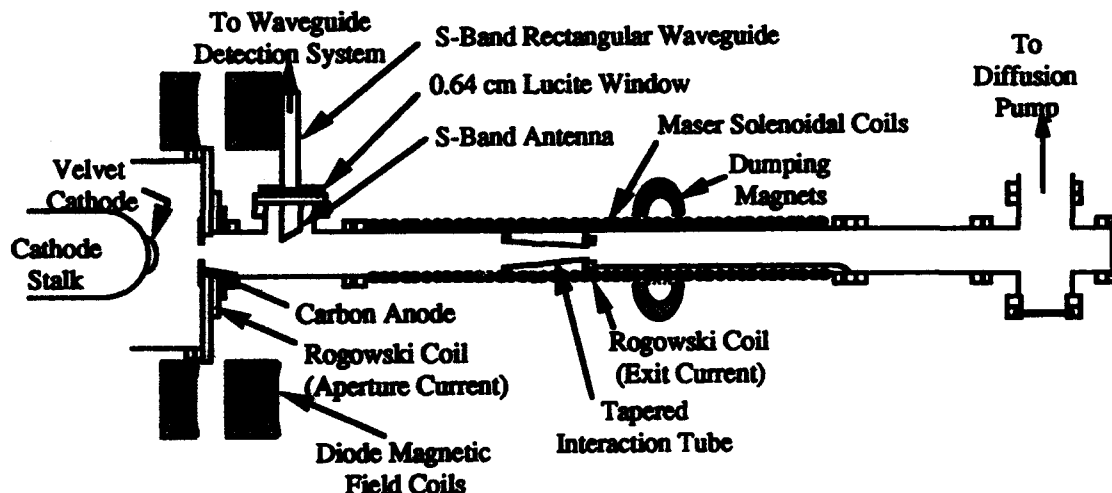


Figure 1. Experimental Configuration for tapered gyro-BWO.

This research was supported by the Air Force Office of Scientific Research, Phillips Lab, and the AFOSR-sponsored MAGIC Code User's Group with Mission Research Corp. P.R. Menge also received a fellowship from the UM Rackham Graduate School.

\* T.A. Spencer's permanent address is the Air Force Phillips Laboratory, Kirtland AFB, NM.

Recent frequency-swept measurements of the microwave coupling have shown a maximum coupling efficiency of -7.5 dB (-18%) between tube microwaves and this antenna. The gyro-BWO microwave output was split by directional couplers and further attenuated for measurement with calibrated diode detectors. Reflected microwaves were typically directed through a lucite window at the far end of the gyro-BWO into a large tank lined with microwave absorber.

### III. EXPERIMENTAL RESULTS

Figures 2 and 3 show examples of gyro-BWO experimental signals detected for the uniform tube and the 10% downtapered tube. Voltage and current signals from MELBA are fairly flat over at least the first microsecond of the e-beam pulse. Generally, the microwave emission was longer and the power was higher for the 10% downtapered tube versus the uniform tube. Assuming the maximum value of coupling (-18%) between the tube and antenna, the peak microwave tube power (up to about 80 MW) for the 10%

downtapered tube is more than a factor of two higher than the peak tube power (~30 MW) found thus far from the uniform tube. The high power microwave emission magnetic tuning band was much larger for the tapered tube, as expected.

MAGIC code simulations predicted that the gyro-BWO power enhancement from tapered tubes was expected to be optimal for the 10% downtapered case, out of all the cases run ( $\pm 10\%$ ,  $\pm 23\%$ ,  $\pm 43\%$ ). This is in qualitative agreement with the experiments, which showed reduced power at tube tapers of  $\pm 23\%$  and  $\pm 43\%$ , relative to the uniform-tube case.

Significant increases in the microwave pulse length were also observed with the 10% downtapered-tube gyro-BWO, as seen in Figure 4. The average pulse length with the tapered tube was 380 ns compared with 300 ns for the uniform tube, about a 30% increase. By integrating digital oscilloscope microwave signals it was found that inferred integrated energy was also greater with the 10% downtapered tube, compared to the uniform case.

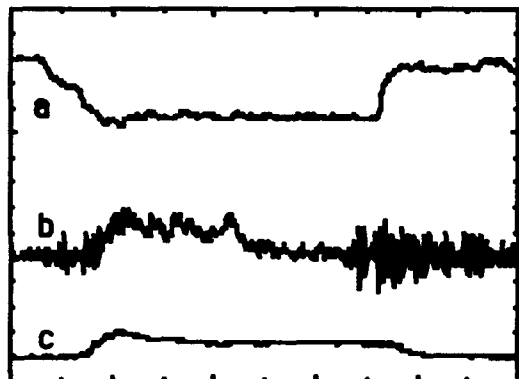


Figure 2. Data for gyro-BWO with uniform tube:  
a) Beam voltage (310 kV/div),  
b) Microwave detector signal (25 mV/div).  
c) Transported beam current (2 kA/div),  
Solenoidal field is 5100 G.  
Time scale is 100 ns/div.

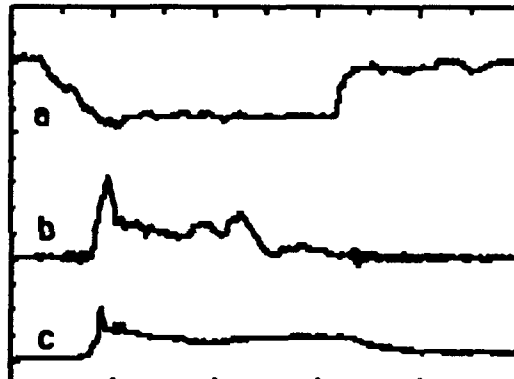


Figure 3. Data for gyro-BWO with 10 % downtapered tube:  
a) Beam voltage (310 kV/div),  
b) Microwave detector signal (100 mV/div).  
c) Transported beam current (2 kA/div),  
Solenoidal field is 5100 G.  
Time scale is 100 ns/div.

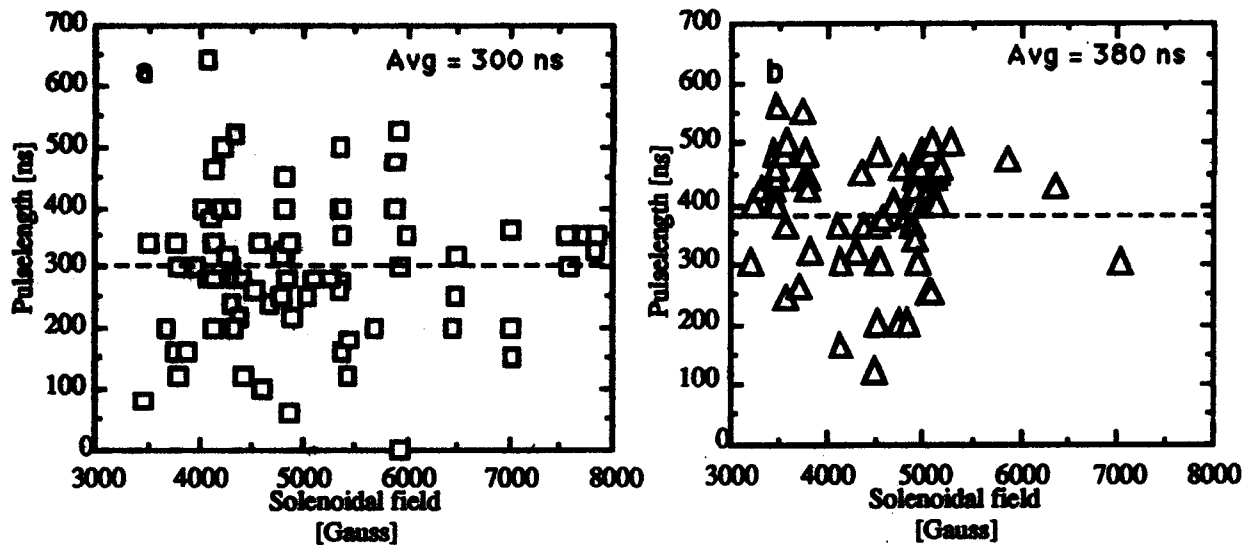


Figure 4. Microwave pulse length for gyro-BWO:  
 a) Uniform tube, and  
 b) Tube with 10% downtaper.

#### IV. ACKNOWLEDGMENTS

We acknowledge valuable discussions with Professor Y. Y. Lau. C. H. Ching and R. A. Lindley are acknowledged for experimental assistance.

#### V. REFERENCES

- [1] S. Y Park, R. H. Kyser, C. M. Armstrong, R. K. Parker, and V. L. Granatstein, *IEEE Trans. Pl. Sc.* Vol. 18, p. 321 (1990)
- [2] A. K. Ganguli and S. Ahn, *Appl. Phys. Lett.* Vol. 54, p. 514 (1989)
- [3] T. A. Spencer, R. M. Gilgenbach, and J. J. Choi, *J. Appl. Phys.* Vol. 72, p. 1221 (1992)
- [4] R. M. Gilgenbach, M. T. Walter, P. R. Menge, and T. A. Spencer, *Proceedings of the 17th International Conference on Infrared and Millimeter Waves*, SPIE Vol. 1929 (1992).

# Quiet Start and Autotasking for PARMELA

J. Gonichon, S. C. Chen, L. C-L. Lin, R. J. Temkin,  
Plasma Fusion Center  
MIT

## Abstract

The simulation code PARMELA has been widely used in the accelerator community for many years. Because of its simplicity, it is still used in many laboratories. When used to simulate the space charge in high current density electron bunches however, the results for the emittance and the other beam parameters can differ considerably from those obtained with PIC codes. This discrepancy comes in part from the noise introduced by the point to point space charge calculation used in PARMELA, when the particle distribution is not uniform. Here we present a new loading scheme which makes the initial distribution in the phase spaces more uniform and reduces greatly the noise introduced by artificial local bunching. At the same time, the code has been slightly modified in order to permit autotasking and vectorization on CRAY computers; the speed up factor obtained for the calculation time is proportional to 4 times the number of CPU available on the computer. Preliminary simulations of a 17 GHz RF Gun with the PIC code MAGIC and PARMELA show relatively good agreement considering that PARMELA does not handle Wakefields and radiations.

## I. INTRODUCTION

In PARMELA, the space charge can be modeled by a point to point calculation: each particle is assigned a super charge and the Coulomb interaction between the particles is evaluated at each time step. When the number of particles in the simulation is large enough, this method gives relatively accurate results; however, because the CPU time scales as the square of the number of particles, it very quickly becomes prohibitive to use more than a few thousand particles. If the initial distribution for the particles is not uniform, artificial local bunching can appear, leading to high charge density areas which are not physical; this phenomenon is enhanced when the charge per macroparticle is increased, or when the number of particles in the simulation, for a constant total charge, is decreased. In Section II of this paper, a new loading scheme,

\*This work is supported by the U.S. Department of Energy, under contracts No. DE-FG02-91-ER40648.

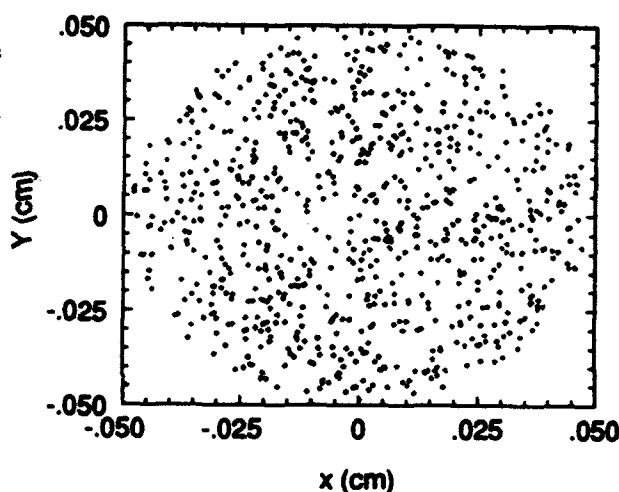


Figure 1: 787 particles sampled randomly in the transverse space.

successfully tested in FEL simulations, which greatly reduces this local bunching is described. Using this scheme, the calculated emittance is far less dependant on the number of particles in the simulation. In Section III, we briefly describe the modification of the source code in order to allow vectorization and autotasking. Finally, Section IV presents a preliminary comparison between the Particle in Cell code MAGIC, and this new version of PARMELA.

## II. QUIET START

Figure 1 shows a typical distribution of the particles on the photocathode area of the 17 GHz Photocathode RF Gun being constructed at MIT [1]. The particles are sampled using the standard Fortran random number generator. It is easy to see "holes" and "bunches" due to the limited number of particles generated. As mentioned earlier this artificial local bunching leads to an increase in emittance which is not real. Figure 2

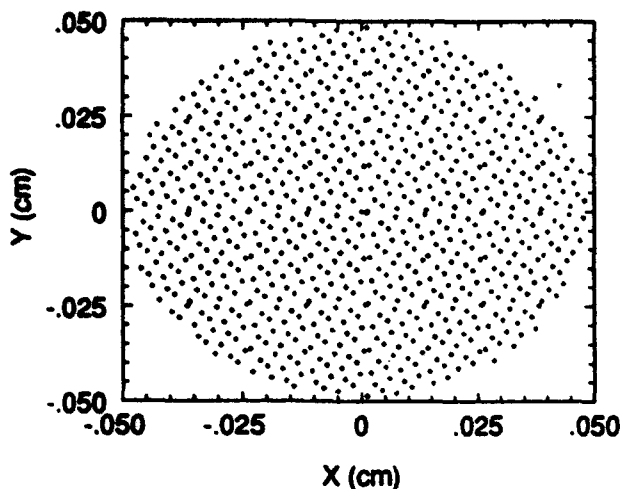


Figure 2: 787 particles sampled in the transverse space using Hammersley's sequence.  $x$  is sampled with  $r=1$  and  $y$  with  $r=2$

shows the same distribution sampled using the Hammersley's sequence [2]. Although there still are a few closely spaced points, the particles are evenly distributed in the transverse space. The Hammersley's sequence is defined as follows:

$$\left\{ \left( j - \frac{1}{2} \right) / N, \Phi_2(j), \Phi_3(j), \Phi_5(j), \dots, \Phi_r(j), \dots \right\}, \quad j = 1, \dots, N$$

where  $\Phi_r(j)$  is the radial inversion function in the base of a prime number  $r$ :

$$\Phi_r(j) = a_0 r^{-1} + a_1 r^{-2} + \dots, \quad j = a_0 + a_1 r^1 + \dots$$

This yields for  $r=2$  and  $r=3$ :  $\Phi_2(j) = 1/2, 1/4, 3/4, 1/8, \dots$ ,  $\Phi_3(j) = 1/3, 2/3, 1/9, 1/3 + 1/9, \dots$

A set of simulations for a 17 GHz photocathode RF Gun cavity was done using the two types of distribution (random and quiet start) and varying the number of particles simulated. Figure 3 shows that the emittance calculated using the Quiet Start (Hammersley's sequence) is lower and much less dependant on the number of particles than the one calculated using the random start.

### III. AUTOTASKING AND VECTORIZATION

When the number of particles in the simulation is more than a few hundred, most of the calculation time is spent in the subroutine used to simulate the space charge effects. This subroutine is composed of two nested loops performing the point to point calculation. By making minor modifications inside the inner loop, and using the Fortran preprocessors available on

Emittance as a function of the number of particles

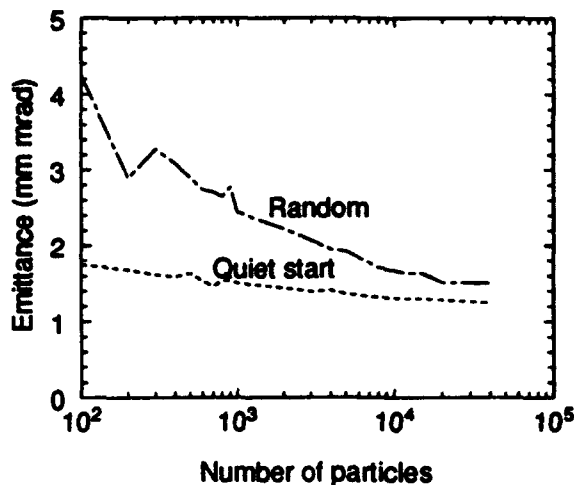


Figure 3: Emittance calculated using random and quiet start.

the CRAY computers [3] [4], the inner loop was vectorized and the outermost loop was parallelized. It should be noted however, that the calculation of the effect of the image charge in the cathode plane had to be eliminated. Work will be done in the future to reimplement this important effect. The speed up factor with only one CPU is 4 due to the vectorization of the inner loop. When using multi-CPU computers, the outermost loop is distributed among the different CPUs and the wall-clock time goes theoretically like the inverse of the number of CPUs. However, because the code is not 100 % parallel and because of the overhead produced by Autotasking, typical speed up factors of up to 10 for the wall-clock time on the 16 Processor CRAY YMP C90 have been observed. The extreme runs shown on Figure 3 correspond to 40000 particles and 113 time steps, corresponding to 12 hours of CPU time with one CPU.

### IV. COMPARISONS WITH MAGIC

The 17 GHz photocathode RF Gun cavity being constructed at MIT has been simulated using the PIC code MAGIC and PARMELA. The fields calculated by MAGIC have been implemented in PARMELA in order to account for non linear RF effects. Figures 4 to 6 show the beam parameters at the exit of the cavity as a function of the charge, calculated by the two programs. The number of particles in the simulation in PARMELA is 500 and the effect of image charge in the cathode plane is included. The cathode radius is 0.5 mm, the laser pulse length 1.4 ps, and the initial phase is 12 degrees. The results for the radius and the divergence agree to within 10 % and those for the emittance and the bunch length agree to within 30 %. The situation is less favorable for the energy spread where the results can differ by a factor of 2 at low

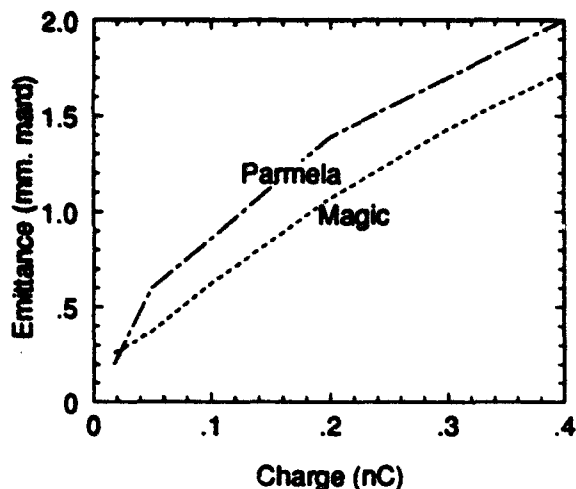


Figure 4: Emittance at exit of RF Gun cavity.

charge. The reason for this discrepancy is still under investigation.

## V. CONCLUSIONS

A new loading scheme (Quiet Start) has been implemented in PARMELA; it makes the distribution of the particles in the transverse space more uniform and consequently reduces the noise level introduced by local bunching. The emittance is then much less dependant on the number of particles in the simulation. The point to point calculation subroutine has been parallelized and vectorized, leading to speed up factors of 4 in CPU time and potentially reducing the wall-clock time by a factor roughly proportional to the number of available CPUs on the computer. Preliminary comparisons with the PIC code MAGIC show an agreement to within 30 % for the emittance. However, it is not yet understood why the energy spread can differ by as much as a factor of 2 between the two codes. The reasons for this discrepancy are still under investigation.

## REFERENCES

- [1] S. C. Chen et al. High gradient acceleration in a 17 GHz photocathode rf gun. *These Proceedings*.
- [2] T. M. Tran and J. S. Wurtele. Free electron laser simulation techniques. *Physics Reports*, 195:1-21, 1990.
- [3] CRAY Research Inc. Vectorization guide (sg-3073 5.0). *CF77 Compiling System*, 3, 1991.
- [4] CRAY Research Inc. Parallel processing guide (sg-3074 5.0). *CF77 Compiling System*, 4, 1991.

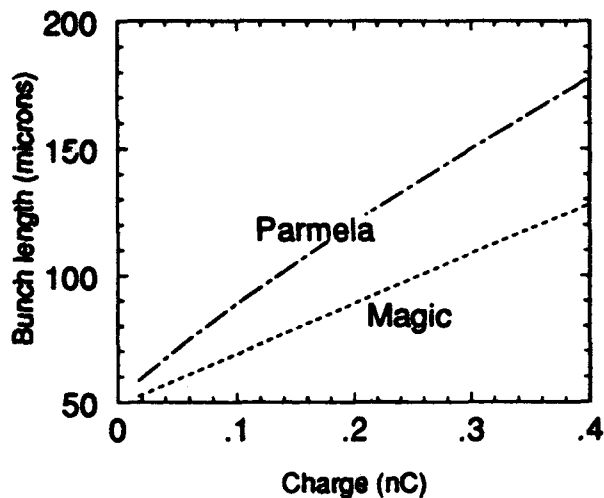


Figure 5: Bunch length at exit of RF Gun cavity.

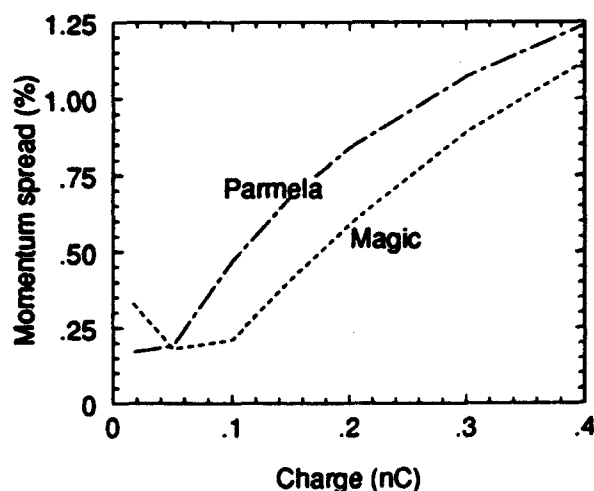


Figure 6: Momentum spread at exit of RF Gun cavity.

# Waveguide Side-Wall Coupling in RF Guns

Leon C.-L. Lin, S. C. Chen, J. Gonichon, S. Trotz, and J. S. Wurtele  
 Plasma Fusion Center  
 Massachusetts Institute of Technology  
 Cambridge, MA02141

## Abstract

Waveguide side-wall coupling for RF guns is investigated both theoretically and experimentally. We model this aperture-coupling problem by an integral equation which is solved by the method of moments. The analysis yields an equivalent circuit representation of the system. Of the two normal modes of cavity resonance, the  $\pi$ -mode and 0-mode, we show that only the  $\pi$ -mode is excited. Experimental results show good agreement with theory.

## I. INTRODUCTION

Photocathode RF guns are promising high brightness electron beam sources for free electron lasers and next generation linear colliders. Among existing systems, the  $1\frac{1}{2}$ -cell RF cavity design with a waveguide-side wall coupling scheme is most widely used[1,2]. This coupling scheme has been shown experimentally to successfully excite the desired  $\pi$ -mode resonance. However, until now there has been no solid theoretical understanding of the coupling. In this paper, we present a theoretical study of the waveguide side-wall coupling. First, we represent this problem by an integral equation based upon the equivalence principle. Next, we solve this integral equation by the method of moments. Then we construct an equivalent circuit representation for this problem: a transmission line shunt with a coupled *GLC* circuit. This circuit can be solved readily. The experimental data[3] are in good agreement with theory.

## II. THEORY AND COLD TEST RESULTS

Consider a  $1\frac{1}{2}$ -cell RF cavity coupled to a waveguide via side-wall apertures, as shown in Fig. 1. The aim is to excite the  $\pi$ -mode resonance for the RF cavity with power

\*This research is supported by DOE under grant DE-FG02-91-ER40048.

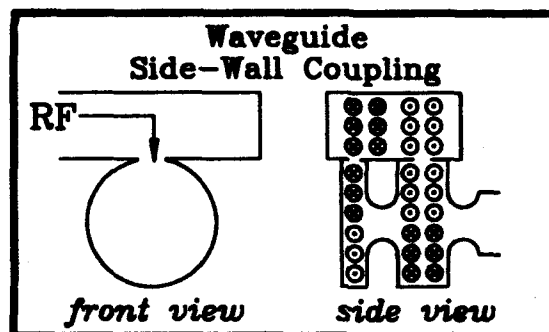


Figure 1: A  $1\frac{1}{2}$ -cell RF cavity coupled to a waveguide via side-wall apertures.

fed through the coupler. It is sufficient, from the equivalence principle, to solve for the unknown tangential electric field on the aperture (denoted as  $E^a$ )[4]. The fields elsewhere can be uniquely determined by  $E^a$ . We introduce an equivalent surface magnetic current  $M_s = E^a \times \hat{n}$ , where  $\hat{n}$  is the unit vector normal to the aperture.  $M_s$  can be expanded by a linear combination of basis functions  $M_j$  ( $j = 1, 2, \dots, N$ ):  $M_s = \sum_j V_j M_j$ . From the continuity of the  $H$  field on the aperture, one obtains

$$[Y^{wg} + Y^{cv}]V = I, \quad (1)$$

with

$$Y_{ij}^{wg} = \iint_S ds M_i \cdot H^{wg}(M_j), \quad (2)$$

$$Y_{ij}^{cv} = \iint_S ds M_i \cdot H^{cv}(M_j), \quad (3)$$

$$I_i = -\iint_S ds M_i \cdot H^{inc}, \quad (4)$$

where  $H^s(M_j)$  denotes the  $H$  field generated by  $M_j$  (for  $x = wg, cv$ ),  $H^{inc}$  denotes the incident  $H$  field, and  $S$  denotes the aperture region. The formulation is greatly simplified if, on either side of the aperture, one has a canonical geometry for which a Green's function in close form exists. In our waveguide side-wall coupling problem, the waveguide is a canonical geometry, but the  $1\frac{1}{2}$ -cell RF cavity is not. However, it is obvious that the two cells are coupled

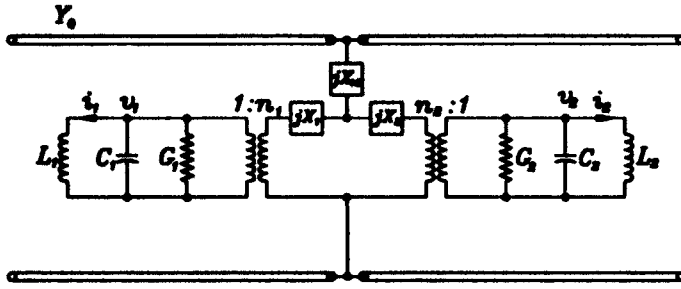


Figure 2: An equivalent circuit for the waveguide side-wall coupling problem.

to each other primarily via the waveguide rather than via the circular iris (note that the circular iris is below cutoff, while the waveguide is not). Therefore, one can adopt the following steps to solve this problem: (1) Simplify by ignoring the iris and by representing each cell as a pillbox cavity — a canonical geometry. (2) Solve the simplified problem by using the moment method and construct an equivalent circuit representation. (3) Include the effects of the iris by introducing a reactive junction in the equivalent circuit.

The details of deriving  $Y_{ij}^{ws}$  and  $Y_{ij}^{cv}$  using Green's functions are given in [5]. Once  $Y^{ws}$  and  $Y^{cv}$  are calculated, the coefficients  $V_j$  can be obtained using Eq. 1. Then one can obtain the reflection and transmission coefficients in the presence of the surface magnetic current  $M_s = \sum_j V_j M_j$  using the Green's function for the waveguide. Then one can construct an equivalent circuit, as shown in Fig. 2, which gives the same reflection and transmission coefficient as those in the original problem. The equivalent circuit elements are

$$X_1 = \left( \frac{\text{Im}\{Y_{11}^{ws}\}}{\text{Re}\{Y_{11}^{ws}\}} - \frac{\text{Im}\{Y_{12}^{ws}\}}{\text{Re}\{Y_{12}^{ws}\}} \right) / 2Y_0, \quad (5)$$

$$X_2 = \left( \frac{\text{Im}\{Y_{22}^{ws}\}}{\text{Re}\{Y_{22}^{ws}\}} - \frac{\text{Im}\{Y_{12}^{ws}\}}{\text{Re}\{Y_{12}^{ws}\}} \right) / 2Y_0, \quad (6)$$

$$X_{12} = \frac{\text{Im}\{Y_{12}^{ws}\}}{2Y_0 \text{Re}\{Y_{12}^{ws}\}}, \quad (7)$$

$$C_i = \frac{\pi \epsilon_0 R_i^2 |J_0'(X_{01})|^2}{d_i}, \quad (8)$$

$$L_i = 1/\omega_i^2 C_i, \quad (9)$$

$$G_i = \omega_i C_i / Q_i, \quad (10)$$

$$n_i^2 = \frac{-2\Delta x_i^2 C_i}{\mu_0 \pi^3 R_i^2 d_i Y_0 \text{Re}\{Y_{ii}^{ws}\}}, \quad (11)$$

where  $R_i$ ,  $d_i$ ,  $\omega_i$ , and  $Q_i$  are the radius, length, resonant frequency, and quality factor of the  $i$ -th pillbox cavity, respectively,  $\Delta x_i$  is the aperture width for the  $i$ -th pillbox cavity, and  $Y_0$  is the characteristic admittance of the waveguide.

From the equivalent circuit, it is obvious that the waveguide must be shorted a quarter wavelength away from the aperture so as to obtain maximum coupling. In that case, by using a  $Y - \Delta$  transformation and transforming the

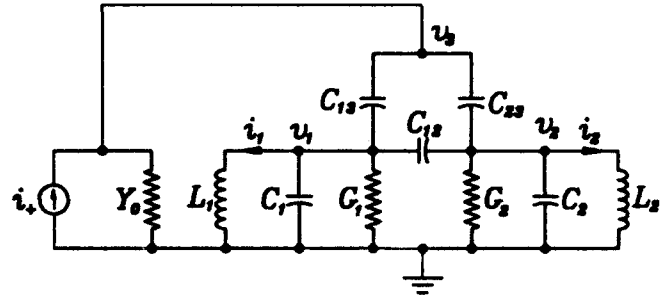


Figure 3: An equivalent circuit for the case when the waveguide is shorted at quarter-wavelength away from the aperture.

GLC circuits to the other side of the transformer, one obtains the circuit shown in Fig. 3.

We define the variables

$$a_i = \sqrt{\frac{C_i}{2}} v_i + j \sqrt{\frac{L_i}{2}} i_i \quad (12)$$

for  $i = 1, 2$  such that  $|a_i|^2 =$  stored energy in the  $i$ -th cell. Because one is interested only in the vicinity of resonant frequencies of both cells, the following approximations can be used: (1)  $1 - (\frac{\omega}{\omega_i})^2 = (1 + \frac{\omega}{\omega_i})(1 - \frac{\omega}{\omega_i}) \cong 2(1 - \frac{\omega}{\omega_i})$ , and (2)  $a_i \cong \sqrt{\frac{C_i}{2}} V_i e^{j\omega t}$ . The circuit is readily solved given the above approximations:

$$\begin{bmatrix} j(\omega - \omega'_1) & -\kappa \\ -\kappa & j(\omega - \omega'_2) \end{bmatrix} \begin{bmatrix} a_1 \\ a_2 \end{bmatrix} = \begin{bmatrix} b_1 \\ b_2 \end{bmatrix}, \quad (13)$$

where

$$\omega'_1 \cong \omega_1 \sqrt{\frac{C_1}{C'_1}} + j \frac{G_1}{2C'_1}, \quad (14)$$

$$\omega'_2 \cong \omega_2 \sqrt{\frac{C_2}{C'_2}} + j \frac{G_2}{2C'_2}, \quad (15)$$

$$\kappa \cong \frac{j\omega C_{12}}{2\sqrt{C'_1 C'_2}}, \quad (16)$$

$$b_1 = \frac{-j\omega C_{13} I_+}{\sqrt{8C'_1(Y_0 + j\omega C'_3)}}, \quad (17)$$

$$b_2 = \frac{-j\omega C_{23} I_+}{\sqrt{8C'_2(Y_0 + j\omega C'_3)}}, \quad (18)$$

$$C'_1 = C_1 + C_{12} + C_{13}, \quad (19)$$

$$C'_2 = C_2 + C_{12} + C_{23}, \quad (20)$$

$$C'_3 = C_{13} + C_{23}. \quad (21)$$

It is convenient to normalize frequencies with respect to the coupling coefficient  $\kappa$ :  $\Omega \equiv \frac{\omega}{j\kappa}$ . Then the eigenvalues and eigenvectors of this system are

$$\Omega_{\pm} = \frac{\Omega'_1 + \Omega'_2}{2} \pm \sqrt{\left(\frac{\Omega'_1 - \Omega'_2}{2}\right)^2 + 1}, \quad (22)$$

$$S = \begin{bmatrix} a_+ & a_- \end{bmatrix} = \begin{bmatrix} \cos \theta & -\sin \theta \\ \sin \theta & \cos \theta \end{bmatrix}, \quad (23)$$

$$\theta = \tan^{-1} \left\{ -\frac{\Omega'_1 - \Omega'_2}{2} + \sqrt{\left(\frac{\Omega'_1 - \Omega'_2}{2}\right)^2 + 1} \right\} \quad (24)$$

The eigenmodes  $a_+$  and  $a_-$  are known as the symmetric ( $\pi$ -) and antisymmetric (0-) mode, respectively. The response  $a$  is a linear combination of  $a_+$  and  $a_-$ :  $a = Sc = c_+a_+ + c_-a_-$  with  $c = S^{-1}A^{-1}b$ . Consider three special cases: (1)  $|\frac{\Omega'_1 - \Omega'_2}{2}| \gg 1$  and  $\Omega'_1 > \Omega'_2$ . Here, the two cells are nondegenerate and the first cell has higher resonant frequency. (2)  $|\frac{\Omega'_1 - \Omega'_2}{2}| \gg 1$  and  $\Omega'_1 < \Omega'_2$ . Here, the two cells are nondegenerate and the second cell has higher resonant frequency. (3)  $|\frac{\Omega'_1 - \Omega'_2}{2}| \ll 1$ . Here, two cells are degenerate. The resonant frequencies  $\Omega_{\pm}$ , normal modes  $a_{\pm}$ , and coefficients  $c_{\pm}$  for these three cases are summarized in Table 1. In general, it is very likely that the cavity will be in either Case (1) or Case (2) before tuning; in either case both the  $\pi$ -mode and 0-mode can be excited. To excite a pure  $\pi$ -mode, one must tune the cavity until Case (3) is reached. Then, if the condition  $c_- \propto (b_2 - b_1) \sim 0$  holds, one can efficiently suppress the 0-mode.

	Case (1)	Case (2)	Case (3)
$\Omega_+$	$\Omega'_1$	$\Omega'_2$	$\frac{\Omega'_1 + \Omega'_2}{2} + 1$
$\Omega_-$	$\Omega'_2$	$\Omega'_1$	$\frac{\Omega'_1 + \Omega'_2}{2} - 1$
$S$	$\begin{bmatrix} 1 & 0 \\ 0 & 1 \end{bmatrix}$	$\begin{bmatrix} 0 & -1 \\ 1 & 0 \end{bmatrix}$	$\frac{1}{\sqrt{2}} \begin{bmatrix} 1 & -1 \\ 1 & 1 \end{bmatrix}$
$c_+$	$\frac{b_1}{\kappa(\Omega - \Omega'_+)}$	$\frac{b_2}{\kappa(\Omega - \Omega'_+)}$	$\frac{b_2 + b_1}{\sqrt{2}\kappa(\Omega - \Omega'_+)}$
$c_-$	$\frac{b_2}{\kappa(\Omega - \Omega'_-)}$	$\frac{-b_1}{\kappa(\Omega - \Omega'_-)}$	$\frac{b_2 - b_1}{\sqrt{2}\kappa(\Omega - \Omega'_-)}$

Table 1: Eigenmodes and their coefficients for three special cases.

We use a network analyzer to measure the reflection coefficient ( $S_{11}$ ) for the 17GHz RF gun cavity. In our experiment, the untuned cavity belongs to Case (2). Also, the two apertures are commensurate in size and, consequently,  $b_1 \sim b_2$ . Therefore, one observes two distinct resonances with comparable magnitude, as shown in Fig. 4. After we tune the first cell to Case (3), only the symmetric ( $\pi$ -) mode is seen, as shown in Fig. 5. Note that the resonance of the symmetric mode is upshifted by an amount  $\kappa$ , which is about 16MHz in our experiment.

### III. CONCLUSION

We have constructed an equivalent circuit representation for side-wall coupling in RF guns. We solved the equivalent circuit and found that, in our coupling scheme, only the  $\pi$ -mode of the  $1\frac{1}{2}$ -cell cavity is excited. Cold tests of our 17GHz gun confirm these predictions.

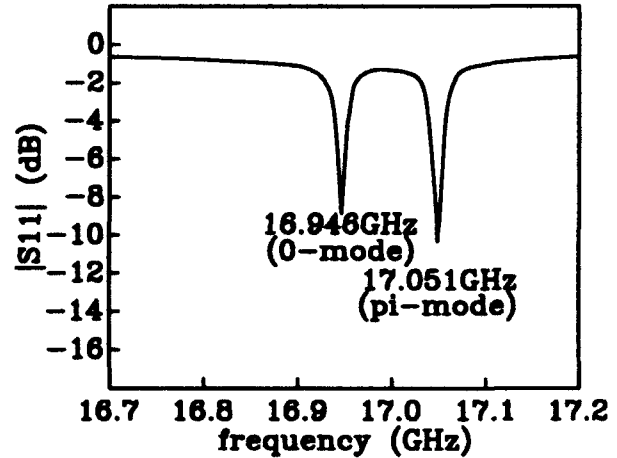


Figure 4: The reflection coefficient for the untuned cavity.

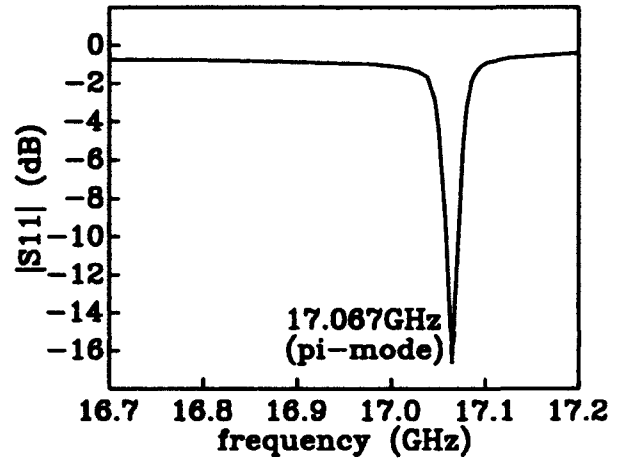


Figure 5: The reflection coefficient for the tuned cavity.

### REFERENCES

- [1] K. Batchlor *et al.*, "Design and Modelling of a 5MeV Radio Frequency Electron Gun," BNL-41766 (1988).
- [2] F. Aghamir *et al.*, "SATURNUS: The UCLA High Gain Infrared FEL project," UCLA-CAA0068-9/90 (1990).
- [3] S. C. Chen *et al.*, "High Gradient Acceleration in a 17 GHz Photocathode RF Gun," These Proceedings (1993).
- [4] R. F. Harrington, *Time-Harmonic Electromagnetic Fields*, New York: McGraw Hill, 1961.
- [5] Leon C.-L. Lin *et al.*, "An Equivalent Circuit Formulation for Waveguide Side-Wall Coupling in RF Guns," to be submitted to *IEEE Trans. Microwave Theory and Technology*.

# A High-Current Micro-Pulse Electron Gun\*

Frederick M. Mako and William Peter

FM Technologies, Inc.

10529-B Braddock Road, Fairfax, VA 22032 USA

## Abstract

A novel concept for a high-current-density micro-pulse electron gun has been studied. The concept employs the resonant amplification of an electron current by secondary electron emission in an rf cavity. We have studied this "multipacting" process in detail, including space charge, and have found the parameters necessary to make use of the phenomenon to produce a micro-pulsed electron beam. One wall of the cavity is made partially transparent to electrons but opaque to the input rf electric field. It is shown from self-consistent analytic theory and two-dimensional, fully relativistic, electromagnetic particle-in-cell (PIC) simulations that the current density scales with frequency cubed. The natural "bunching", or resonant phase selection of the particles gives rise to high current densities (20-5600 A/cm<sup>2</sup>), high charge bunches (up to 100 nC/bunch for a solid beam and up to 1000 nC for a hollow beam), and short pulses (36-3.5 ps) for frequencies from 1.3 to 8 GHz. The beam pulse width is found to be typically 4.6% of the rf period. Beam extraction through the transparent wall was studied using a 2-1/2 dimensional PIC code. Good beam transmission (52-85%) with low normalized emittance (9-18 mm-mrad) could be achieved. The best normalized emittance per charge is 3 mm-mrad/nC. Tuning to the resonant parameters has been shown to be very tolerant. Electrical breakdown is not a problem, and materials are available to satisfy the secondary emission yield requirements for this device. Applications are accelerator injectors and rf generation at a high harmonic of the fundamental frequency.

## I. INTRODUCTION

The development of high-current, short-duration pulses of electrons has been a challenging problem for many years. High-current pulses are widely used in injector systems for electron accelerators, both for industrial linacs as well as high-energy accelerators for linear colliders. Short-duration pulses are also used for microwave generation, in klystrons and related devices, for research on advanced methods of particle acceleration, and for injectors used for free-electron laser (FEL) drivers.

During the last few years considerable effort has been applied to the development of high power linac injectors [1-2] and particularly to laser-initiated photocathode injectors [3-8].

\*Supported by the Small Business Innovation Research Program, US DOE.

The best of these have somewhat higher brightness than the injector in reference [1], but the reliability depends on the choice of photocathode material, with the more reliable materials requiring intense laser illumination.

Summarizing, the methods used to date are rather complex, cumbersome, expensive, and have very definite limits on performance. The method to be described appears to be promising in large part because of a natural bunching process.

## II. CHARACTERISTICS OF THE HIGH CURRENT MICRO-PULSE GUN (MPG)

Micro-pulses or bunches are produced by resonantly amplifying a current of secondary electrons in an rf cavity. Bunching occurs rapidly and is followed by saturation of the current density within ten rf periods. The "bunching" process is not the conventional method of compressing a long beam into a short one, but results by selecting particles that are in phase with the rf electric field, i.e., resonant. One wall of the cavity is highly transparent to electrons but opaque to the input rf field. The transparent wall allows for the transmission of the energetic electron bunches and serves as the cathode of a high-voltage injector. Axial and radial expansion of the pulse is minimized outside the cavity by using rapid acceleration and a combination of electrostatic and magnetic focusing. Inside the cavity, radial expansion is controlled by electric and/or magnetic fields. Both analytic theory and PIC simulation provide verification of this concept. This micro-pulse electron gun should provide a high peak power, multi-kiloampere, picosecond-long electron source which is suitable for many applications.

## III. RESONANCE AND CURRENT DENSITY GAIN

In Fig. 1 is shown an rf cavity operating in a TM<sub>010</sub> mode. Now assume at one of the electrode walls (the screen or grid) of the cavity there is a single electron at rest near the axis. This electron is then accelerated across the cavity and strikes the surface *S*. A number  $\delta$  of secondary electrons are emitted off this electrode. Provided the average transit time of an electron in the cavity is one-half the rf period, and that the secondary electrons are in the proper phase with the rf field, these electrons will be accelerated towards the screen. If  $\delta$  is also the secondary electron yield per primary electron of the screen, then upon reaching the screen,  $\delta T$  electrons will be

transmitted, where  $T$  is the transmission factor. The number of electrons which are not transmitted is then  $\delta(1-T)$ . This is the number of electrons which are stopped by the screen, and can thus produce  $\delta^2(1-T)$  secondary electrons. In order to have a gain of electrons, the number of secondaries produced must be greater than unity, that is,  $\delta^2(1-T) > 1$ . The gain of electrons at time  $t$  after a number of transits is derived to be  $G = [\delta(1-T)^{1/2}]^{(\omega t/\pi)}$ , where  $\pi/\omega$  is the half-period of the radian rf frequency  $\omega$ . If there is a "seed" current density  $J_s$  in the cavity at  $t=0$ , then at time  $t$  the current density will be given by  $J = GJ_s = J_s[\delta(1-T)^{1/2}]^{(\omega t/\pi)}$  until space-charge and saturation limit the current. The current density limit will be shown in later sections. The seed current density can be created by any of several sources including cosmic rays. For a very low seed current density a high current density can be achieved in a very short time. For example, if  $\delta = 8$ ,  $T = 0.75$ , and  $J_s = 14 \times 10^{-10}$  amps/cm<sup>2</sup>, at ten rf periods then  $J = 1500$  amps/cm<sup>2</sup>.

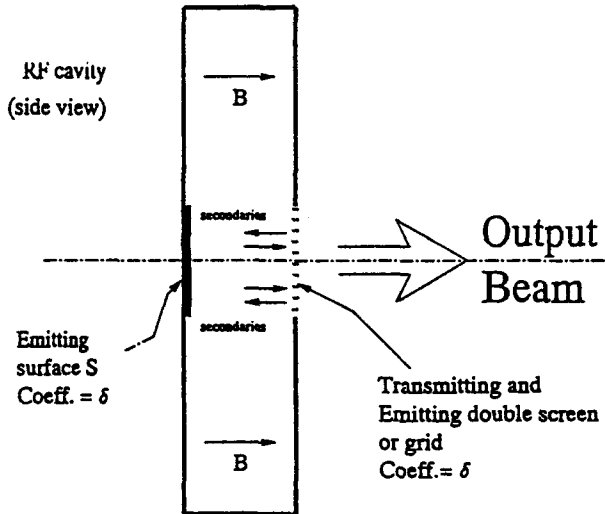


Figure 1: Schematic of micropulse gun for solid beam ( $TM_{010}$ ) mode. A coaxial feed is used for rf input (not shown).

#### IV. STEADY-STATE PARALLEL-PLATE MODEL WITH BEAM (Theory)

In this section we will solve self-consistently for the steady state or saturation current density for a beam (charge slab) that is already "bunched". The axial bunch length or charge slab thickness is  $\Delta$ , the axial gap spacing between the parallel plates or electrodes is  $d$ , and the beam density is  $n$ . We evaluate the equations of motion for electrons "attached" to the front ("f") and back ("b") of the charge slab. The equations of motion are

$$\frac{d^2 x_{f,b}}{dt^2} = (e/m)[E_0 \sin \omega t \pm E_{sc}] \quad (1)$$

with initial conditions  $v_{f,b}(t=t_0) = v_{b0}(t=t_0)$ ,  $x_{f,b}(t=t_0) = 0$ . The subscripts  $f$  and  $b$  refer to the front and back electrons and the top and bottom sign, respectively. The quantities  $E_0$  and  $E_{sc}$  are the magnitudes of the rf and space charge electric fields, respectively.

At resonance when  $\theta = \theta_{f,b} + \pi$ , where  $\theta = \omega t$ ,  $\theta_f = \omega t_{f0}$ , and  $\theta_b = \omega t_{b0}$ , the particles must cross the gap, or  $x_f = d$  and  $x_b = d - x_{f0}$ . Assume that  $v_{f0} = v_{b0} = 0$ . The following expression is obtained from the solution of the equation of motion (1),

$$\theta_{f,b} = \phi - \arccos \left[ \frac{1 \mp \alpha_s (\pi^2/2) - (x_{f0}/d)}{\alpha_0 (\pi^2 + 2^2)^{1/2}} \right] \quad (2)$$

where  $\phi = \arctan(2/\pi)$ ,  $\alpha_0 = \frac{eE_0}{m\omega^2 d}$ ,  $\alpha_s = \frac{eE_{sc}}{m\omega^2 d}$

$E_{sc} = ne\Delta/2\epsilon_0$  and  $\epsilon_0$  is the permittivity of free space.

Consider  $\theta_b$  and therefore the positive quantity in brackets in Eq. (2). If we increase the space charge parameter  $\alpha_s$  with all other parameters fixed, the back electrons will go out of resonance when the quantity in brackets exceeds one. Thus to maintain resonance and the maximum space charge we must satisfy the following equation

$$\alpha_{s,max} = \frac{2}{\pi^2} \left[ \alpha_0 (\pi^2 + 2^2)^{1/2} - 1 + \frac{x_{f0}}{d} \right] \quad (3)$$

The peak steady-state current density can be calculated from the expression  $J = nev$  and the above results,

$$\frac{J}{J_0} = \alpha_s \frac{2\alpha_0 \cos \theta_f + \pi \alpha_s}{(\Delta/d)} \quad (4)$$

where

$$J_0 = \epsilon_0 \frac{m}{e} \omega^3 d \quad (5)$$

From the solution of Eq. (1) we can calculate

$$\left[ \frac{\Delta}{d} \right] = \frac{\alpha_0}{2} \left[ \sin \theta_f - \sin \theta_b + \frac{1}{2} (\theta_b - \theta_f + \pi) \cos \theta_f - \frac{1}{2} (\theta_f - \theta_b + \pi) \cos \theta_b \right] + \frac{\alpha_s}{12} \left[ (\theta_f - \theta_b + \pi)^2 + \frac{\pi^2 + (\theta_f - \theta_b)^2}{\theta_f - \theta_b + \pi} \right] + \frac{x_{f0}}{2d} \quad (6)$$

As will be seen in the section describing the PIC simulations, the  $\omega^3$  scaling of the saturated current derived above is an important scaling law for the micro-pulse gun. This scaling is also derivable from the time-dependent current-voltage relation in a diode first derived by Kadish, Peter, and Jones [9].

## V. CURRENT DENSITY AS A FUNCTION OF TIME (PIC Simulation)

Figure 2 shows a plot of the current density  $J_x$  across the gap ( $d=0.5$  cm) as a function of time for a simulation with an rf frequency of 6.4 GHz and a voltage of 105.2 kV. The current density is measured near the second (right-hand) electrode which, in an actual experiment, would be the exit screen or grid. Hence, this is the current pulse which will exit the device. The top trace, corresponding to a positive current density, is that current which is emitted from the second (right-hand) electrode and propagates back to the first electrode. The bottom trace (negative current density) describes the beam that would leave the cavity. The curves are not symmetric about  $J_x=0$  because the beam pulses have substantially different charge densities and velocities when they cross the position of the probe. In the case for which the current density is positive (i.e., electrons are propagating in the negative  $x$  direction), the electrons have just been emitted from the electrode and form a high-density bunch at a relatively low energy. In the case for which the current density is negative (i.e., electrons are propagating in the positive  $x$  direction), the electrons have already crossed the gap and are at a relatively high energy, and have spread somewhat due to space charge effects. The simulation ran out to a total of 2 ns and reached a peak amplitude of 2.8 kA/cm<sup>2</sup> for  $d=0.5$  cm. At a gap length of 1.0 cm, the resulting current density increased to 7 kA/cm<sup>2</sup>. Both cases use  $\alpha_0=0.453$ .

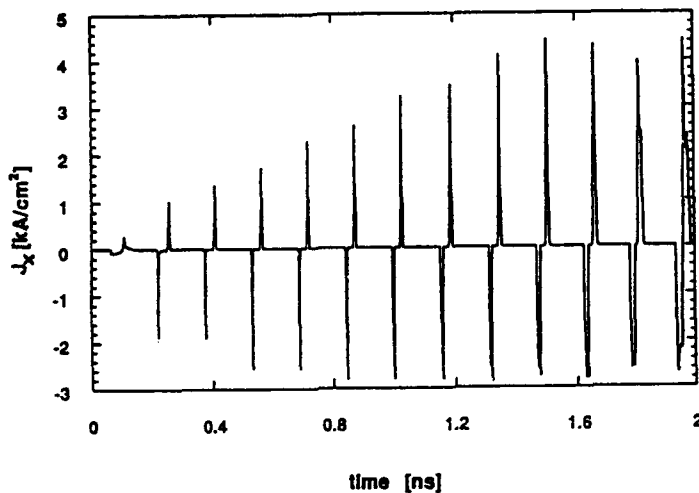


Figure 2: Plot of current density vs. time for simulation with rf frequency 6.4 GHz, voltage amplitude 105 kV,  $d=0.5$  cm, and  $\alpha_0=0.453$ .

## VI. CURRENT DENSITY VS. FREQUENCY

In Fig. 3 we plot simulation results for the peak current density (at saturation)  $J_x$  (kA/cm<sup>2</sup>) vs. frequency for a series

of simulations with gap length 0.5 cm and drive parameter  $\alpha_0=0.453$ . For comparison, we also plot the theoretical curve for  $J_x$  vs. frequency from the theory described in Section IV. Note the excellent agreement between theory and simulation. The  $\omega^3$  scaling for the MPG provides an important characterization of the proposed device. Note that the rf voltage must increase in proportion to  $\omega^2$  to maintain a fixed  $\alpha_0$ .

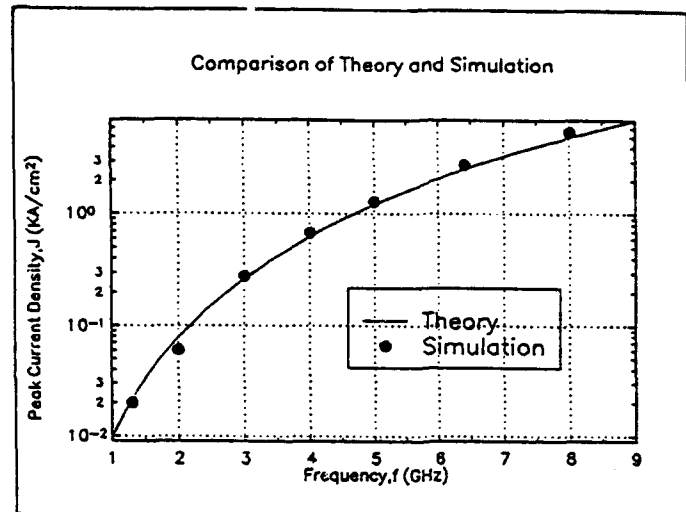


Figure 3: Comparison of peak current density in kA/cm<sup>2</sup> versus frequency for simulation and theory for a gap length of 0.5 cm and drive parameter  $\alpha_0=0.453$ .

We thank Dr.'s L. Len, T. Godlove, and P. Sprangle for useful discussions.

## VII. REFERENCES

- [1] J.L. Adamski et al., IEEE Trans. Nucl. Sci. NS-32, 3397 (1985);
- [2] T.F. Godlove, P. Sprangle, Part. Accel. 34, 169 (1990).
- [3] J.S. Fraser and R.L. Sheffield, IEEE J. Quantum Elec. QE-23, 1489 (1987).
- [4] Proc. 9th Int'l FEL Conf., ed. P. Sprangle, C.M. Tang, and J. Walsh, North Holland Publishing Amsterdam, (1988). R.L. Sheffield, E.R. Gray and J.S. Fraser, p. 222.
- [5] P.J. Tallerico, J.P. Coulon, LA-11189-MS (1988).
- [6] P.J. Tallerico et al, LINAC Proc. 528 (1989).
- [7] M.E. Jones and W. Peter, IEEE Trans. Nucl. Sci. 32 (5), 1794 (1985).
- [8] P. Schoessow, E. Chojnacki, W. Gai, C. Ho, R. Konecny, S. Mtingwa, J. Norem, M. Rosing, and J. Simpson, Proc. of the 2nd Euro. Part. Accel. Conf. (1990), p. 606.
- [9] A. Kadish, W. Peter, and M.E. Jones, Appl. Phys. 25, 2256 (1955)

# Knife-Edge Thin Film Field Emission Cathodes\*

B.Lee, H.P.Demroff, M.M.Drew, T.S.Elliott, T.K.Masumdar,  
P.M.McIntyre, Y.Pang, D.D.Smith, and H.-J.Trost  
Department of Physics, Texas A&M University  
College Station, TX 77843-4242, USA

## Abstract

Cathodes made of thin-film field emission arrays (FEA) have the advantages of high current density, pulsed emission, and low bias voltage operation. We have developed a technology to fabricate knife-edge field emission cathodes on (110) silicon wafers. The emitter geometry is optimized for efficient modulation at high frequency. Cathode fabrication progress and preliminary analysis of their applications in RF power sources are presented.

## I. INTRODUCTION

The RF power sources needed for future  $e^+e^-$  linear colliders and RF-linac-driven FEL's both require an electron source with the capability of emitting electrons in high density pulses. Traditional dispenser cathodes used in klystrons, for example, provide a d.c. current density  $\leq 10$  A/cm<sup>2</sup> and require a buncher to achieve pulsed beams. The bunching process usually increases the beam emittance and introduces instability limits to bunch currents and length. As an alternative, our gigatron project [1] features a gated field emitter array that produces pulsed electron beams in the form of ribbons. The ribbon beams are accelerated in a diode, and then pass through a traveling wave coupler where the RF power is extracted. By eliminating the bunching process and minimizing the transit of bunched beam to the output coupler, extreme beam stability and excellent RF efficiency should be feasible to attain. The first demonstration of emission from FEA's was reported by Spindt *et al.* at SRI [2]. Gray [3] and many others [4] have also actively worked to develop FEA's for vacuum microelectronics. Spindt's FEA's have produced current densities as high as 1000 A/cm<sup>2</sup> from an area of  $\sim 1$  mm<sup>2</sup> [4], but the frequency modulation achieved is below 1 GHz [5]. For the gigatron it is necessary to develop a new type of FEA which can support efficient modulation and high current density at frequencies  $\geq 10$  GHz. The focus of this work is to fabricate knife-edge thin film field emission cathodes on (110) silicon wafers. Preliminary studies show that this cathode can meet the requirements of the gigatron.

## II. FIELD EMISSION ARRAY CATHODES

The Spindt-type FEA is so far the most successful FEA cathode. Its structure is shown in Figure 1(a). The emitter is a metal cone sitting at the center of a cavity formed on a metal-insulator-semiconductor sandwich structure. The top metal layer serves as the modulating gate. When a voltage is applied between the gate and the substrate, a electric field  $E$  concentrates near the tip

of the cone and can support field emission. The emitted current density  $J$  is described by the Fowler-Nordheim equation [6]:

$$J = AE^2 \exp(-B\phi^{3/2}/E)$$

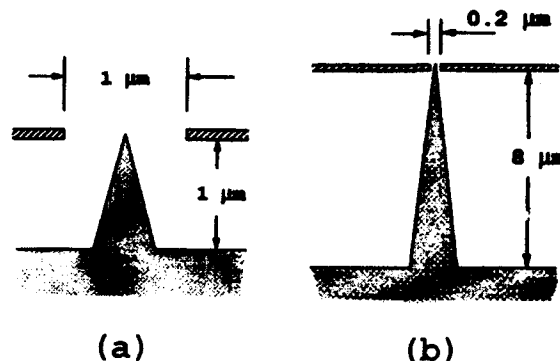


Figure 1. The cross section geometry of Spindt-type FEA (a) and the knife-edge FEA (b).

where  $A$  and  $B$  are two parameters close to constant and  $\phi$  is the work function of the emitter material. For high performance FEA's, it is desired to have large current emission at low bias voltage. This requires that the emitter structure is designed to maximise the field at the emitter apex. This includes a small emitter radius and a small gate opening. The Spindt-type FEA has a tip radius around 500 Å, a gate diameter of about 1 μm, and a gate/base gap of about 1 μm. With these dimensions, the emission starts with  $\sim 100$  V bias. For modulated emissions, however, the Spindt-type FEA's have a drawback: the gap between the gate and the substrate is small and the sandwich structure presents a large parasitic capacitance to the modulation driver. The cutoff frequency is  $f_T = g_m/2\pi C$ , where  $g_m$  is transconductance of the emitter,  $g_m = (\Delta I_c/\Delta V_g)|_{V_c}$ . Spindt has improved the fabrication process to reduce the overlapping area between the gate and the base layers, but this only increases the estimated  $f_T$  to  $\sim 1$  GHz.

The gigatron is designed to operate at 18 GHz or higher frequencies; for this goal, we have proposed a new fabrication approach [7] that makes knife-edge field emission arrays (KEFEA) on (110) silicon wafers. A cross section of the structure is shown in figure 1(b). We have increased the gate/base gap to about 8 μm and reduced the gate opening to  $\sim 0.2$  μm. The capacitance per unit area is reduced thereby by a factor 20 from Spindt-type FEA's. Figure 2 shows a POISSON [8] simulation of the

\* Work supported by U.S. Department of Energy, Office of High Energy Physics, under contract no. DE-FG02-91ER40613

potential distribution in both the Spindt-type FEA and our KEFEA structure. The smaller gate opening in the KEFEA produces higher field for the same voltage bias, with lower parasitic capacitance. Both effects increase the transconductance.

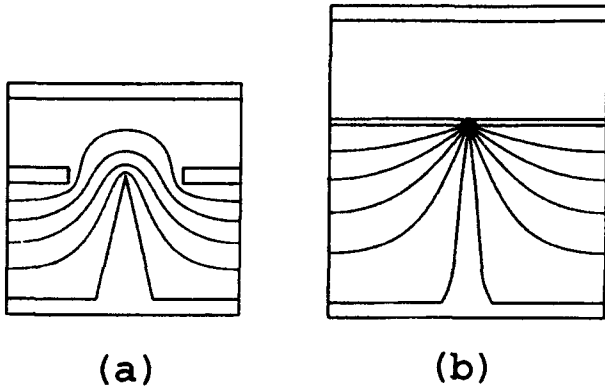


Figure 2. POISSON simulations showing the equipotential lines of Spindt-type FEA (a) and KEFEA (b).

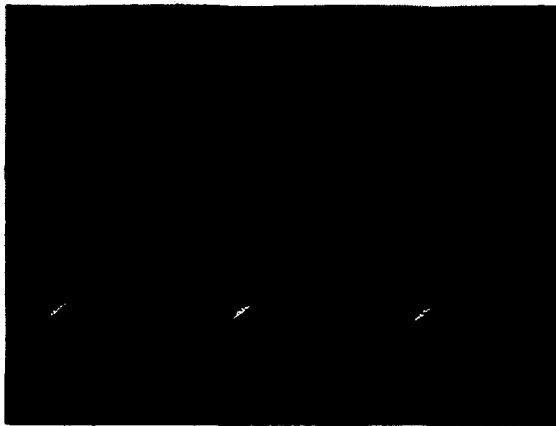


Figure 3. SEM picture showing the wall structure formed by KOH solution etching.

### III. FABRICATED STRUCTURE OF KEFEA

The fabrication starts with a plain (110) silicon wafer. We use photolithography to put down a  $\text{SiO}_2$  pattern of width  $\sim 4 \mu\text{m}$ . Orientation-dependent etching of the wafer in a KOH solution forms a structure as shown in Figure 3. The silicon is etched along crystal planes to produce rectangular prisms  $\sim 10 \mu\text{m}$  high, which serve as the "blanks" from which the knife-edges will be formed. A second etch in a solution made of HF,  $\text{HNO}_3$  and  $\text{CH}_3\text{COOH}$  (Dash etching) sharpens the top portion of the wall-like structure (Figure 4). The cross section of this knife-edge is very similar to that of Figure 1(b), with an edge half angle of about  $5^\circ$ . Our measurement from a scanning electron microscope (SEM) shows that the radii of these etched edges are less than  $500 \text{ \AA}$ . To further reduce the knife-edge radius, we use a thermal oxidation process to grow a surface layer of  $\text{SiO}_2$  into the knife-edge structure. The oxidation

process is carried out at temperatures below  $1000^\circ\text{C}$ , and serves to sharpen the corner at the top of the  $\text{Si}/\text{SiO}_2$  interface. Our measurement shows that the edge radius obtained this way is less than  $200 \text{ \AA}$ . A study by Marcus *et al.* [9] has shown that a radius of  $10 \text{ \AA}$  can be obtained in this way.

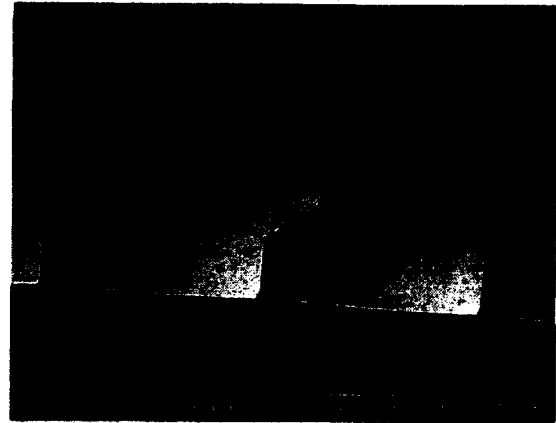


Figure 4. The knife-edge array formed on a (110) silicon wafer.

The insulator material used in the Spindt-type FEA is  $\text{SiO}_2$ , which has a dielectric constant of 3.9. For the KEFEA, we use a layer of polyimide coating (PI). PI has a lower dielectric constant (2.9 to 3.3), giving a further reduction of capacitance. We apply the polyimide as a spin-on liquid with a layer thickness of  $\sim 10 \mu\text{m}$ . This allows us to make the knife-edge structure  $\sim 8 \mu\text{m}$  high. When PI is applied, it planarizes above the knife edges. The PI is then etched in an  $\text{O}_2/\text{CF}_4$  plasma which isotropically removes  $\sim 3 \mu\text{m}$  of the PI material, and exposes the top  $\sim 1 \mu\text{m}$  of the knife edges. The top edges of the native silicon inside the  $\text{SiO}_2$  layer is then located at about the same level as this etched PI surface.

The metal used for the gate layer is applied using RF sputtering, with a thickness of  $\sim 0.5 \mu\text{m}$ . We then apply a layer of photoresist and etch it back to expose the top portion of the metal covered knife-edges. The metal layer is then etched to expose the  $\text{SiO}_2$  layer over the knife edge. Using a HF solution we then strip away the  $\text{SiO}_2$  to expose silicon emitter edge. Since we can precisely control the thickness of the thermally grown  $\text{SiO}_2$  layer, we can produce a gate-emitter spacing  $\sim 0.1 \mu\text{m}$ .

Figure 5 shows the finished structure of our KEFEA. The height of the emitter and the gate/base gap is about  $8 \mu\text{m}$ . The emitter-edge is at the same level as the gate. The metal is etched back and a gap is opened over the knife edge. (This sample was overetched, giving a wider gap than that of our design.)

### IV. DISCUSSION

The challenges for modulating FEA cathodes at microwave frequency are:

- shrinking the control gap to enhance transconductance and reduce transit time;
- isolating the gate from the substrate to reduce parasitic capacitance.

In KEFEA we have devised a means to fabricate knife-edges with extremely small edge radius and gate/edge gap. The thermal oxide process is key to achieving both features. It sharpens the tip radius to  $\sim 100\text{\AA}$ , and provides an accurate means of making a controlled gap of  $\sim 0.1\ \mu\text{m}$  between tip and gate. This process is a new development in vacuum microelectronics and produces the same field enhancement factor at a knife-edge as the best enhancement attained on Spindt-type tips.

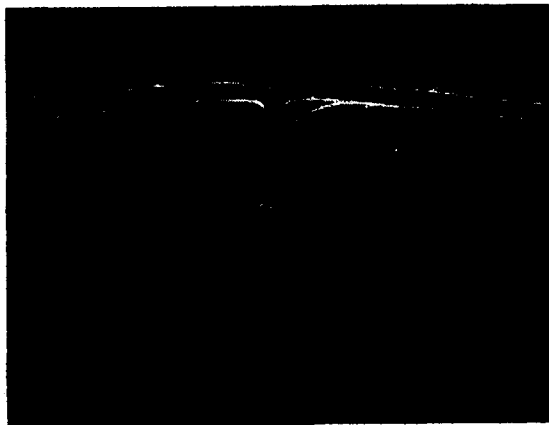


Figure 5. SEM picture of KEFEA structure.

Using orientation-dependent etching to prepare the knife-edge blanks and spin-on polyimide to build the dielectric support for the gate layer, the gate-base separation can be increased and the parasitic capacitance reduced by a factor of 10 compared to Spindt-type tip arrays.

Field emission from any emitter geometry always occurs at a microscopic region (hot spot) where the work function is lowest or the surface features most irregular. Emission from adjacent regions is suppressed by space-charge even as electric field is increased. Studies of field emission from tip arrays have shown that only a single  $\sim\text{nm}$ -sized hot spot emits on each tip. The maximum practical emitter density ( $3\ \mu\text{m}$  tip array) is  $\sim 10^7/\text{cm}^2$ .

By contrast the KEFEA geometry should produce emission from hot spots which are spaced along the edge by a separation comparable to the edge/gate spacing (the spacing at which adjacent regions are isolated from one another's space charge). For a  $10\ \mu\text{m}$  knife-edge spacing and an edge/gate gap of  $0.1\ \mu\text{m}$ , the emitter density should be  $\sim 10^8/\text{cm}^2$ .

The improvements - high field concentration, 10 times less parasitic capacitance, and 10 times more in emitter density - translate directly into improved transconductance and bandwidth. The ultimate high-frequency limit would come from transit time in the edge/gate gap. For a modulation  $\sim 10\text{V}$  and a gap of  $\sim 0.1\ \mu\text{m}$ , the transit time would be  $\sim 10^{-13}$  sec, corresponding to a cut-off frequency  $f_T \sim 400\ \text{GHz}$ .

Present development of the KEFEA technology has achieved all of the process steps. Currently the edge/gate geometry is being fine-tuned in the final etch steps, and initial emission experiments will begin soon. The direction for further development is the possibility of depositing a low-work-function material onto the finished tip surface. Candidate materials include CVD diamond and cermet. The development of modular KEFEA cathodes for the gigatron and other applications is in progress.

## V. REFERENCES

- [1] P.M.McIntyre, H.M.Bizek, S.M.Elliott, A.Nasiri, M.B.Popovic, D.Raparia, C.A.Swenson and H.F.Gray, "Gigatron", *IEEE Trans. Electron Dev.* ED-36, No.11, 2720 (1989).
- [2] C.Spindt, I.Brodie, L.Humphrey and E.Westerberg, "Physical properties of thin-film field emission cathodes with molybdenum cones", *J. Appl. Phys.* 47, No.12, 5248 (1976).
- [3] H.Gray, G.Campisi and R.Greene, "A vacuum field effect transistor using silicon field emitter arrays", *IEDM Tech. Dig.*, 776 (1986).
- [4] Special issue on Vacuum Microelectronics Conference, July 1990, *IEEE Trans. Electron Dev.* ED-38, No.10 (1991); Proceedings of the Fifth International Vacuum Microelectronics Conference, *J. Vac. Sci. & Tech. B* 11, No.2 (1993).
- [5] C.Spindt, C.Holland, A.Rosengreen and I.Brodie, "Field-emitter-array development for high-frequency operation", *J. Vac. Sci. & Tech. B* 11, No.2, 468 (1993).
- [6] R.H. Fowler and L.W. Nordheim, "Electron emission in intense electric fields", *Proc. Roy. Soc. London, ser. A* 119, 173 (1928).
- [7] B.Lee, E.Barasch, T.Mazumdar, P.McIntyre, Y.Pang and H.-J.Trost, "Development of knife-edge field emission cathodes on (110) silicon wafers", *Appl. Surface Sci.* 67, 66, (1993)
- [8] Los Alamos Accelerator Code Group, The POISSON/SUPERFISH Group of Codes, LA-UR-87-115 (January 1987), version 4.12 (17 March 1993).
- [9] R.Marcus *et al.*, "Formation of silicon tips with  $<1\ \text{nm}$  radius", *Appl. Phys. Lett.* 56, No.3, 236 (1990)

# The Oxidized Porous Silicon Field Emission Array\*

D.D.Smith, H.P.Demroff, T.S.Elliott, T.B.Kasprowics, B.Lee, T.K.Masumdar,

P.M.McIntyre, Y.Pang, and H.-J.Trost

Department of Physics, Texas A&M University

College Station, TX 77843-4242, USA

## Abstract

The goal of developing a highly efficient microwave power source has led us to investigate new methods of electron field emission. One method presently under consideration involves the use of oxidized porous silicon thin films. We have used this technology to fabricate the first working field emission arrays from this substance. This approach reduces the diameter of an individual emitter to the nanometer scale. Tests of the first samples are encouraging, with extracted electron currents to nearly 1 mA resulting from less than 20 V of pulsed DC gate voltage. Modulated emission at 5 MHz was also observed. Development of a full-scale emission array capable of delivering an electron beam at 18 GHz of minimum density 100 A/cm<sup>2</sup> is in progress.

## I. INTRODUCTION

### A. Motivation

The gigatron is a project currently under development by the High Energy Accelerator Physics group at Texas A&M University [1]. It is a high-efficiency microwave power source primarily intended for use in the next generation of linear accelerators.

One of the key innovations required for the gigatron design is its cathode, which delivers a directly modulated electron beam. This improvement eliminates the need for beam bunching and greatly improves the system efficiency compared to conventional power systems that rely on d.c. electron sources.

The search for a technology capable of delivering a high-intensity, high-current electron beam at 18 GHz led our group to investigate the use of porous silicon field emission devices.

### B. History of Oxidized Porous Silicon Field Emission Devices

Porous silicon is a remarkable material. By galvanically etching silicon in an HF solution, a dense array of nanoscopic pores are etched in the surface. The pore diameter and spacing are  $\sim 100$  Å; the pores can be etched up to 100  $\mu\text{m}$  deep with remarkably uniform cross-section. A companion paper in this conference [2] describes the morphology of porous silicon.

Dr. W. K. Yue began research on the subject of emissive oxidized porous silicon films while he was a graduate student [3]. He developed a device known as the Oxidized Porous Silicon Field Emission Diode (OPSPED) whose interesting properties led us into this area of study. In a

diode configuration he obtained stable electron field emission from microtips of highly doped silicon left over from the anodisation reaction that creates the porous layer. See Figure 1. Sustained diode currents of  $\sim 20$  A/cm<sup>2</sup> were obtained with a bias voltage of  $\sim 10$  V.

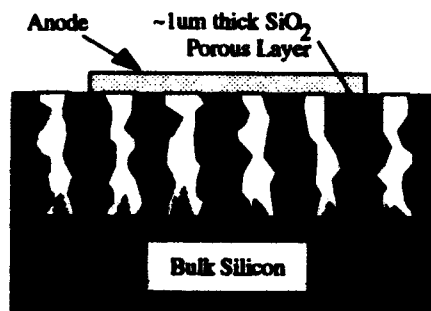


Figure 1. Schematic side view of the OPSFED.

### C. Triode Development

A means of extracting the electron beam from the porous layer needed to be found in order for this approach to be useful for a gigatron cathode. No group had ever succeeded in this endeavor. The key to extraction is to provide a surface metallisation on the (dielectric) porous silicon surface, which would provide a boundary conductor to effectively modulate the field in the pores. The metallisation must however be thin enough to leave the pores open at the vacuum interface.

A metallisation scheme developed at Ford Motor Labs by Dr. R. C. Jaklevic *et al.* was tried [4]. Approximately 40 Å of gold were applied by Dr. Jaklevic's group to the surface of four field-emissive oxidized porous silicon layers we prepared.

After metallization, the samples were diced and tested. All four samples yielded extracted emission current, and a new device was born: the oxidized porous silicon field emission array.

## II. FABRICATION AND TESTING

### D. Fabrication

The proof-of-principle triode prototypes were fabricated in four steps: anodisation, hydrofluoric acid removal, oxidation, and metallization.

Anodisation is the process by which porous silicon is formed. A silicon wafer is immersed in a solution of concentrated hydrofluoric acid and ethanol. A galvanic current is then passed through the wafer. The idea is illustrated in Figure 2.

\* Work supported by U.S. Department of Energy, Office of High Energy Physics, under contract no. DE-FG02-91ER40613

Process parameters include crystal orientation of the wafer, dopant type and concentration, anodisation current density, HF concentration, and time of anodisation. The samples we used for the triodes were  $p<100>$  Si,  $0.001 \Omega \text{ cm}$ . They were anodised for 10 s under 30% wt. [HF], and the current density was varied.

After anodisation the wafers were placed under vacuum for several hours to remove all residual HF from the pores so that no further silicon etching could take place.

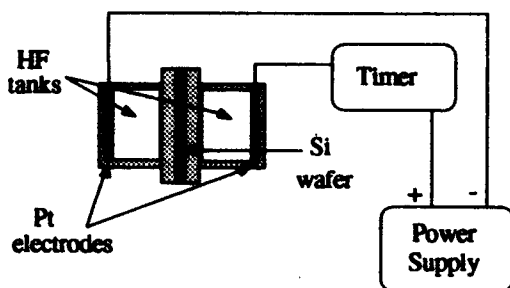


Figure 2. Apparatus to make porous silicon.

Oxidation of the films is carried out in a diffusion furnace. The temperature of the oxidation is kept well below that needed to initiate thermal  $\text{SiO}_2$  growth in the bulk silicon.

The metallisation was an evaporation at ultrahigh vacuum with the substrate held at liquid nitrogen temperature. Forty angstroms of gold were applied. This step was done for us at Ford Motor Research Labs.

The samples were laser-scribed into 2 mm squares and attached to TO-5 transistor headers as shown below. See Figure 3.

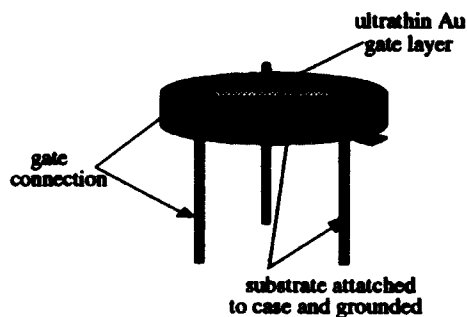


Figure 3. A field emission array ready for testing.

#### E. Experimental Setup

The mounted samples were placed in a vacuum chamber and pumped to a base pressure of  $2 \times 10^{-8}$  Torr. A curved stainless steel tube approximately 2 mm from the gate served as the collector.

A curve tracer and a variable duty cycle pulser provided gate voltage ( $V_g$ ) waveforms to the devices. The collector current ( $I_c$ ) and gate current ( $I_g$ ) were measured as a function of  $V_g$  and collector voltage  $V_c$ .

### III. RESULTS

As mentioned earlier, all four sets of oxidised porous silicon triodes produced extracted emission current. Fowler-Nordheim plots of both  $I_c$  and  $I_g$  as functions of  $V_g$  were made. Peak  $I_c$  for all traces was on the order of several hundred microamperes, and  $V_g$  was below 20 V. The curvature of the  $I_c$ - $V_g$  plots is in qualitative agreement with the model calculations of R. Johnston [4] for emission from extremely sharp silicon tips. See Figure 4.

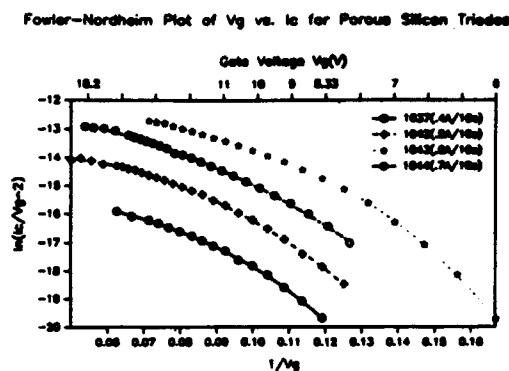


Figure 4. Fowler-Nordheim plot of collector current vs. applied gate voltage for all four samples of oxidized porous silicon field emission arrays.

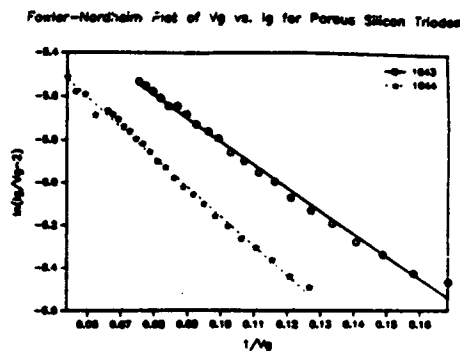


Figure 5. Fowler-Nordheim plot of the gate current vs. the applied gate voltage.

The geometry of the first triodes inevitably led to a large gate current, because many pores were obscured by the connection to the gate layer. We used this data along with the area of the gate connection to determine the emission current density. The gate connection was about 0.5 mm in diameter, and supported currents to above 2 A in pulsed mode, leading to a current density of about  $450 \text{ A/cm}^2$ . Fowler-Nordheim plots of  $I_g$ - $V_g$  show the field-emissive nature of the gate current, as shown in Figure 5. Plate characteristics were measured by holding  $V_g$  fixed and measuring  $I_c$  as  $V_c$  was varied. A typical plate characteristic is shown in Figure 6.

Modulated gate signals were applied to the devices and emission was recorded. Figure 7 shows modulation

of an array at different frequencies. The upper oscilloscope trace is the voltage signal applied to the gate, and the lower trace is the collector current read through a 10 k $\Omega$  resistor. Frequency cutoffs were consistent with the predicted RC cutoffs for the measured resistivities and capacitances of the test devices.

Plate Characteristic for OPS Triode 1042

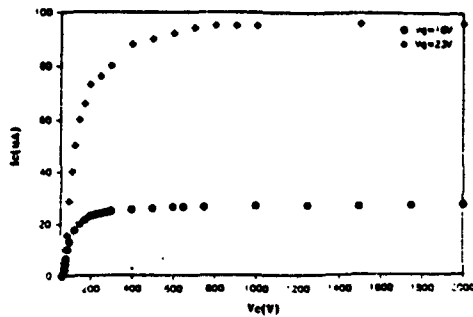


Figure 6. Plate characteristic of the oxidized porous silicon field emission array.

#### IV. SUMMARY

The next generation of field emission arrays will utilize a geometry consisting of alternating emission and bias feed areas. See Figure 8. This geometry radically improves power gain by blocking gate current while increasing the total active emission area. The optimum design parameters are still under consideration. Calculations indicate that a device capacitance of 20 pF/mm<sup>2</sup> is possible

and this results in a 3 dB point above 15 GHz, suitable for gigatron operation.

The use of oxidized porous silicon is a new approach to the fabrication of field emission devices, which holds the possibility of improving both the peak output of large-scale emission arrays and the frequency at which field emission cathodes can operate.

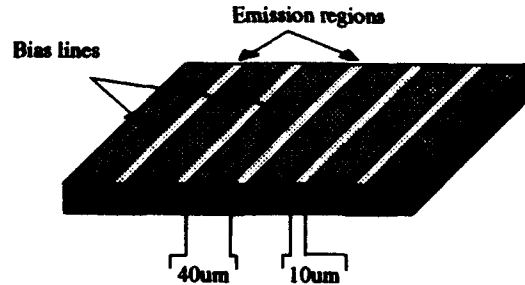


Figure 8. Geometry for the Oxidized Porous Silicon Stripline Field Emission Array.

#### V. REFERENCES

- [1] H.M.Bizek *et al.*, *IEEE Trans. Plasma Sci.* **16**, 258 (1988); P.M.McIntyre *et al.*, *IEEE Trans. Electron Dev.* **36**, 2720 (1989).
- [2] Y.Pang *et al.*, Study of Porous Silicon Morphologies for Electron Transports, these proceedings.
- [3] W.K.Yue, Dissertation, Dept. of Electrical Engineering, Texas A&M University (1991).
- [4] R.C.Jaklevic *et al.*, *Appl. Phys. Lett.* **58**, 1656 (1988).
- [5] R.Johnston, *Surf. Sci.* **246**, 64 (1991).

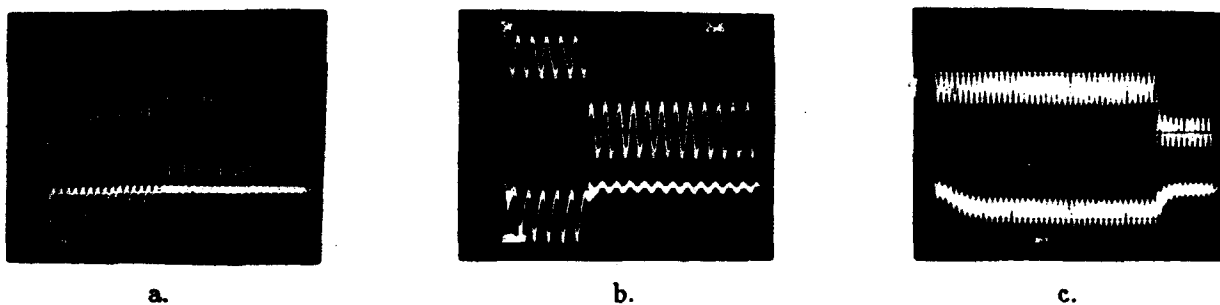


Figure 7. Oscilloscope traces showing modulated emission from an oxidized porous silicon field emission array at (a) 200 kHz, (b) 1 MHz, and (c) 5 MHz.

# Study of Porous Silicon Morphologies For Electron Transport\*

Y.Pang, H.P.Demroff, T.S.Elliott, B.Lee, J.Lu, V.B.Madduri,  
T.K.Masumdar, P.M.McIntyre, D.D.Smith, and H.-J.Trost  
Department of Physics, Texas A&M University  
College Station, TX 77843-4242, USA

## Abstract

Field emitter devices are being developed for the gigatron[1], a high-efficiency, high frequency and high power microwave source. One approach being investigated is porous silicon, where a dense matrix of nanoscopic pores are galvanically etched into a silicon surface. In the present paper pore morphologies were used to characterize these materials. Using of Scanning Electron Microscope (SEM) and Transmission Electron Microscope (TEM) images of both N-type and P-type porous layers, it is found that pores propagate along the  $\langle 100 \rangle$  crystallographic direction, perpendicular to the surface of (100) silicon. Distinct morphologies were observed systematically near the surface, in the main bulk and near the bottom of N-type (100) silicon lift-off samples. It is seen that the pores are not cylindrical but exhibit more or less approximately square cross sections. X-ray diffraction spectra and electron diffraction patterns verified that bulk porous silicon is still a single crystal. In addition, a Scanning Tunneling Microscope (STM) and an Atomic Force Microscope (AFM) were successfully applied to image the 40 Å gold film structure which was coated upon a cooled porous silicon layer. By associating the morphology study with the measured emitting current density of the Oxidized Porous Silicon Field Emission Triode (OPSFET), techniques for the surface treatment of porous silicon will be optimized.

## I. INTRODUCTION

Yue[2] demonstrated that diodes formed using porous silicon films can sustain remarkable transconductance, that the process is field emission, and that the emitted electrons are transported in the vacuum pores of the material. He dubbed this device the Oxidized Porous Silicon Field Emission Diode (OPSFED). Both N- and P-type silicon with different orientations and doping concentrations were used to investigate field emission properties of the OPSFED. Further study [3] showed that the OPSFED field emission current density was higher with P-type than with N-type silicon. With an operation voltage of less than 20 V, the current density reached more than 100 A/cm<sup>2</sup>. Next, an Oxidized Porous Silicon Field Emission Triode (OPSFET) was developed with P-type (100) silicon, anodized with current densities from 40 mA/cm<sup>2</sup> to 70 mA/cm<sup>2</sup>. In order to obtain a smooth gold layer over the porous silicon but keep the fine pores open, a thin gold film was evaporated onto the porous silicon substrate that had been cooled to liquid-nitrogen temperature. The gold

film serves as a gate electrode in the OPSFET to obtain high electronic field strengths for extracting electron emission efficiently. The morphology study presented in this paper is aimed at providing a technological means to distinguish differences in morphologies of the porous silicon samples that were prepared under the same conditions as the porous silicon for OPSFED's and OPSFET's were fabricated.

## II. SAMPLE PREPARATION

The porous silicon samples for morphology study were all anodized in an anodisation cell with a 1:3 mixture of 99% wt. ethanol : 49% wt. HF solution. After baking at 65°C for 10 minutes all the samples were pumped down to 10<sup>-7</sup> Torr vacuum overnight for evacuating the residual HF solution from the pores. Afterwards, samples prepared for SEM, AFM and STM were oxidized in the furnace at 845°C for 45 minutes. STM samples were placed onto a substrate cooled to 77°K and coated with 40 Å gold by thermal evaporation. Both P-type and N-type (100) silicon were investigated.

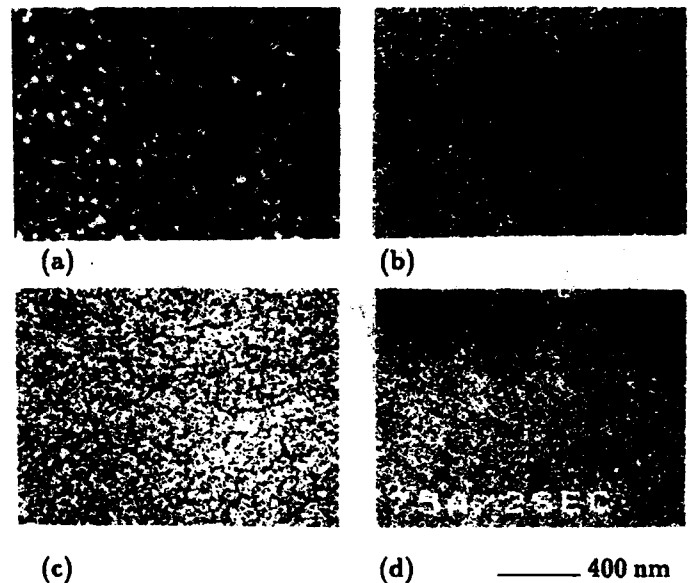


Fig.1 Plan-view SEM images of porous silicon samples before and after RIE. (a) and (b) P-type (100), 0.01 Ω cm, anodisation current density is 40 mA/cm<sup>2</sup>, (a) after 2 min RIE, (b) before RIE. (c) and (d) N<sup>+</sup>-type (100), 0.001 Ω cm, 75 mA/cm<sup>2</sup>, (c) after 1 min RIE, (d) before RIE.

The instruments that we have used in our experiments are: SEM: JEOL 6400; TEM: Zeiss 10C, JEOL

\* Work supported by U.S. Department of Energy, Office of High Energy Physics, under contract no. DE-FG02-91ER40613

### III. EXPERIMENTS AND RESULTS

#### A. Porous silicon in the top layer and main bulk

Fig.1(a) and Fig.1(c) show the plan-view SEM images of the  $N^+$ -type porous silicon surfaces after reactive ion etching (RIE) for 1 minute and 2 minutes respectively by using  $SF_6$  gas at a flow rate of 7 sccm, a power of 200 W and a bias of -550 V. RIE etches the top porous layer about 600 Å /min. The etched thickness was measured using an ALFA stepper. Comparing SEM images before and after RIE etching, it is seen that  $N^+$ -type oxidized porous silicon has different pore densities between the top surface layer and the main bulk.

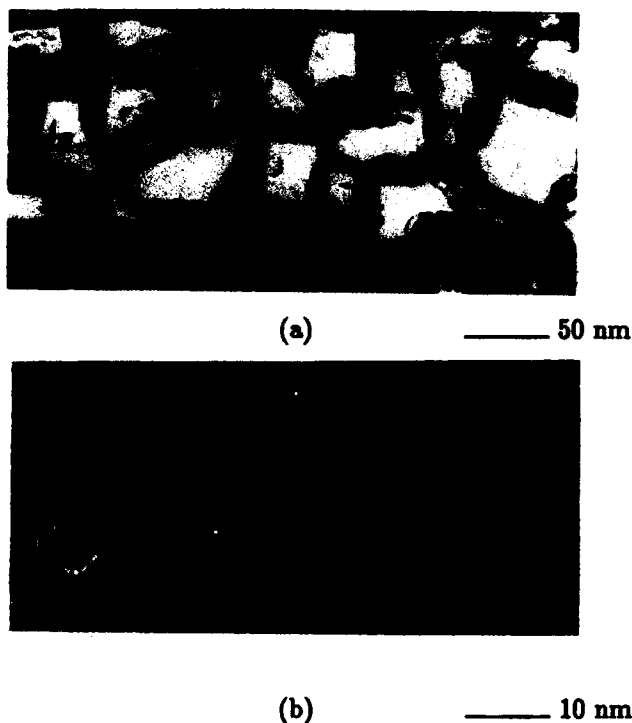


Fig.2 Plan-view TEM images. (a)  $N^+$ -type porous silicon lift-off sample, 0.001  $\Omega$  cm, near lift-off side. (b)  $P^+$ -type porous silicon, 0.001  $\Omega$  cm, anodization current density: 60mA/cm<sup>2</sup>

#### B. Pore shape and propagation

The lift-off technology was used in preparing samples. Anodisation was ended by slowly increasing anodisation current to 350 mA/cm<sup>2</sup> for 1 minute so that the porous silicon membrane was lifted off from the substrate. Fig.2 (a) shows a TEM plan-view image near the lift-off side made from  $N^+$ -type silicon. Pores in this view exhibit mostly square cross-section. Fig.2 (b) shows a TEM plan-view image made from  $P^+$ -type silicon. It is found that pores propagate along the  $\langle 100 \rangle$  crystallographic direction, perpendicular to the surface of (100) silicon wafers.

A similar result was reported by Chuang and Smith [4]. The porous silicon formation mechanisms were discussed by Smith and Collins [5].

#### C. Pore size and density

Samples from  $P^+$ -type, 0.001  $\Omega$  cm, (100) silicon wafers (" $P^+$ ") were anodized at current densities of 20mA/cm<sup>2</sup>, 40mA/cm<sup>2</sup>, 60mA/cm<sup>2</sup>, 80mA/cm<sup>2</sup> and 150mA/cm<sup>2</sup> respectively. These samples were investigated by TEM and AFM. Fig.3 shows pore sizes in cross sectional TEM (XTEM), increasing with the anodisation current density. The pore sizes and densities were measured from both cross sectional and plan-view TEM images, and are listed in Table 1. TEM electron diffraction pattern and X-Ray diffraction spectra indicate that porous silicon is still single crystalline.

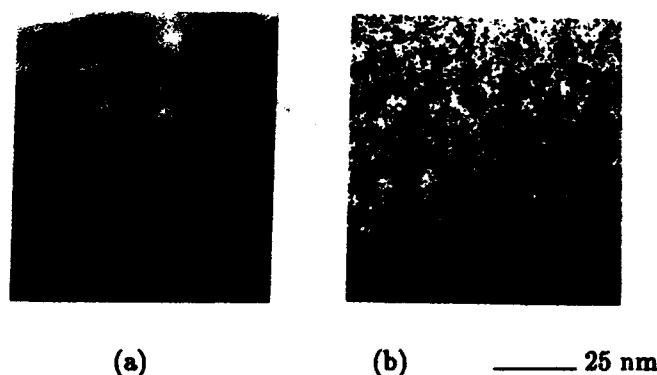


Fig.3 XTEM images of  $P^+$  porous silicon. (a) anodization current density 150mA/cm<sup>2</sup>. (b) anodization current density 80mA/cm<sup>2</sup>.

Table 1 Pores size and density in porous silicon

doping type	anodization current density (mA/cm <sup>2</sup> )	pore size (nm)	pore density (10 <sup>11</sup> /cm <sup>2</sup> )
$P^+$	150	5 - 16	2 - 5.0
	80	4 - 11	2 - 4.5
	60	4 - 9	2 - 4.5
	40	3 - 8	2 - 3.5
	20	3 - 6	
$N^+$	60	4 - 6	6 - 7

#### D. Structure of gold gate electrode layer

A 40 Å gold film was coated onto the surface of porous silicon by thermal evaporation in a 10<sup>-8</sup> Torr oil-free vacuum chamber [6]. The substrates were cooled to liquid-nitrogen temperature during the coating process. The low temperature is expected to limit migration of deposited gold atoms, preventing formation of islands and thereby creating a smooth thin film. This technology has been successfully used with various kinds of dielectric substrates [6]. The coated gold thin film is used as a gate electrode layer, which could be used to extract emitted elec-

tron current from the porous silicon to the anode if those pores remain open after coating. Porous silicon devices which were used in OPSFET's were chosen from those wafers that demonstrated high emission current densities at low operation voltage in OPSFED's.

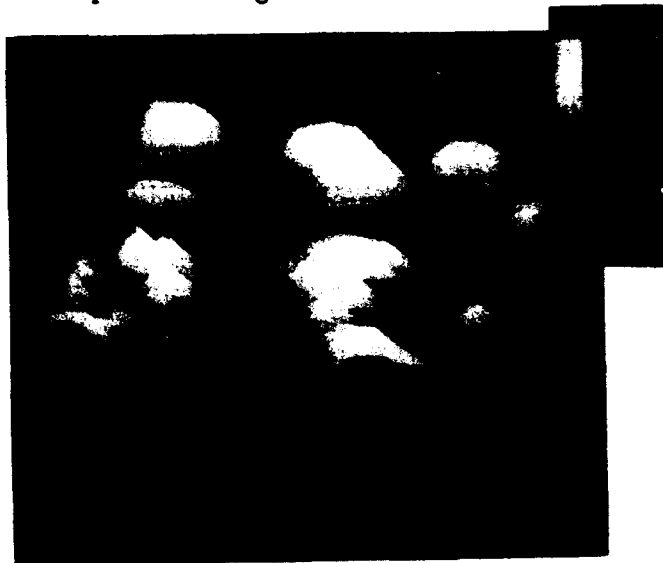


Fig.4 STM image of 40Å Au layer on  $P^+$  porous silicon, 40mA/cm<sup>2</sup>

Fig.4 shows a STM image of the thin gold film coated on the porous silicon which was anodized with a current density of 40 mA/cm<sup>2</sup> in 30% HF solution. Apparently, this coated surface is smoother than the normal coating but still small (~25 nm) gold islands were formed. The TEM plan-view image for the same kind of sample shows that the average size of pores is about 5 nm (Fig.5). By comparing the STM image with the TEM image it can be seen that the gold islands cover some pores and the thin film is not completely continuous. It is speculated that non-uniform deposition may have been caused by an increase in the surface chemical potential during the electrochemical anodization process. Further study is necessary to improve gold deposition on porous silicon and thereby to enhance the efficiency of field emission into vacuum.

#### IV. CONCLUSION

$P^+$  (100) porous silicon shows high field emission properties when produced with an anodization current from 40 mA/cm<sup>2</sup> to 70 mA/cm<sup>2</sup>. The densities of pores are  $2-5 \times 10^{11}$ /cm<sup>2</sup>, pore sizes are 3-10 nm, the pore walls are 5-12 nm in those porous silicon samples. Pore structures exposed with XTEM appear as small channels with numerous "budding" side branches. Those fractal branches form tiny sharp tips with nanometer sizes, which

may be the origin of field emission current. Efforts are being made to deposit a gold gate layer upon the porous silicon without plugging pores. Cold gold evaporation and surface treatment to reduce the surface chemical potential are being studied.

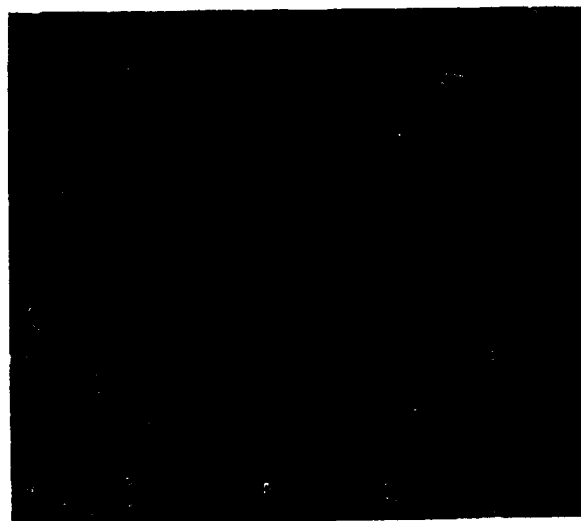


Fig.5 Plan-view TEM image of  $P^+$  porous silicon, 40mA/cm<sup>2</sup>

#### V. ACKNOWLEDGEMENTS

The authors thank the staff in the Electron Microscope Center of Texas A&M University, and V.P.Swenson and Dr. Xueping Xu for the help they have provided.

#### VI. REFERENCES

- [1] P.M.McIntyre *et al.*, "Gigatron", *IEEE Trans. Plasm Sci.* 26, 2581 (1988).
- [2] Y.K.Yue, D.L.Parker, and M.H.Weichold, "Oxidized porous silicon devices", The 3rd Int. Vacuum Microelectronics Conf., Monterey, CA, July 1990.
- [3] D.D.Smith *et al.*, these proceedings.
- [4] S.-F.Chuang and R.L.Smith, "Preferred crystallographic direction in porous silicon layers", The Technical Digest of Solid-State Sensor and Actuator Workshop, Hilton Head Island, SC, p.151, June 6-9, 1988 (IEEE, New York).
- [5] R.L.Smith and S.D.Collins, "Porous silicon formation mechanisms", *J. Appl. Phys.* 71, No.8, 15, R1 (1992).
- [6] R.C.Jaklevic, L.Elle, W.Shen and J.T.Chen, "Ultra-thin Au film studied with the scanning tunneling microscope: Topography of insulating surfaces", *Appl. Phys. Lett.* 52, No.20, 1656 (1988)

# Cold test Measurements of a BWO Slow-Wave Structure

W. Main, Y. Carmel, K. Ogura, J. Weaver and S. Watanabe

Laboratory for Plasma Research  
University of Maryland, College Park, Maryland 20742

## Abstract

Bead-on-string perturbation techniques have been primarily used to study particle accelerator cavities. These techniques are now extended to measure the dispersion relation and axial modes of several transverse magnetic (TM) modes in a slow-wave structure with sinusoidally varying radius. This type of slow-wave structure is commonly used in high power backward wave oscillators (BWO). The dispersion relation is found from the discrete measured resonant frequencies and wave numbers of a cavity containing six periods of the slow-wave structure. The measured axial and radial field profiles are compared with the results of a 2-D code specially developed for calculation of the fields in these generators. For the first three TM modes the frequency error was less than 0.7%.

## I. INTRODUCTION

We present a study of a slow-wave structure which consists of a cylindrical waveguide with sinusoidally varying radius. A similar version of this structure was used in numerous X-band relativistic high-power backward wave oscillator experiments [1,2], however, until now there has not been a systematic analysis of its electromagnetic properties. The purpose of this study is twofold, first to experimentally determine the dispersion relation of the structure and second to test our numerical model of the fields inside the structure.

### Dispersion Relation

A slow wave structure containing N periods will exhibit N+1 resonant frequencies associated with each transverse magnetic mode when shorted at planes of mirror symmetry. Discrete points on each branch of the dispersion relation are found by recording resonant frequencies  $f_r$  and associated axial wave numbers  $\beta_r$  for the set of axial modes associated with each transverse magnetic mode. Figure 1 shows the seven  $TM_{01}$  resonance peaks and derived dispersion relation for a six period slow wave cavity. The

resonant frequencies are easily measured with a microwave network analyzer, but to find  $\beta_r$  we must measure the axial field structure in the cavity. This is done by perturbing the field near the axis of the cavity with a small metal bead. The resulting shift in resonant frequency is related to the E and H fields at the position of the bead. The number of axial variations in the field  $n_r$  can be found by counting number of peaks in a plot of  $\Delta f$  vs. axial bead position. For a structure with N periods of length L this condition for resonance can be stated as

$$NL = (n_r/2) (2\pi/\beta)$$

where  $n_r$  is the number of half wavelengths along the axis of the structure. The axial wave number  $\beta_r$  is then found from  $n_r$  using the above equation. The complete dispersion relation can easily be constructed from these points. For convenience, the dispersion relation was measured on a "cold-test" structure built just for this purpose. This test structure had special end plates with access holes for positioning a bead; and an antenna for launching TM modes. We chose a cold-test structure with six axial periods, giving us seven points on our  $\omega\beta$  diagram.

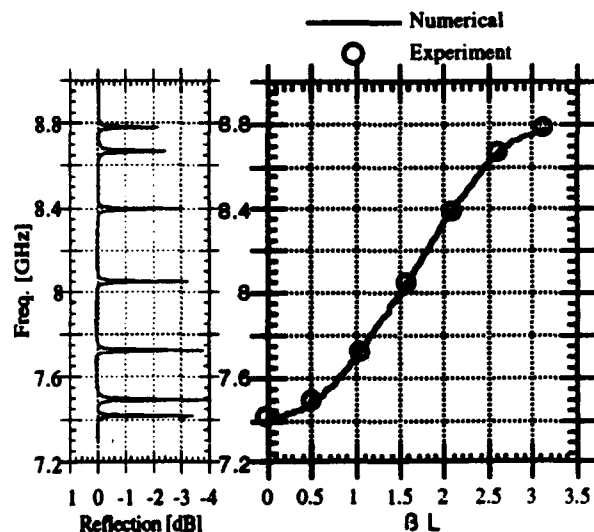


Figure 1. Left graph shows resonances as seen from a one-port measurement on a network analyzer. Right graph shows derived dispersion relation.

### Experimental Verification of Numerical Model

Using the dispersion relation we can find the relation of beam energy and interaction frequency. However, to understand the more complex behavior of an intense beam in a slow wave structure we must use nonlinear particle codes. These codes require an accurate model of the fields in the structure. We use a model developed by Ogura [3] in which the fields are expanded in a spatially harmonic series, according to Floquet's theorem. Solving the dispersion relation for the sinusoidal boundary of the slow wave structure gives us the expansion coefficients. For computational reasons we truncate our expansions at nine terms.

Due to the complexity of this model it is important to experimentally verify the fields at various points in the cavity. Although we cannot directly measure the fields inside the cavity, we can test the numerical model by inserting the same perturbing object in the numerical model and in the experiment. As a perturbing object we introduce a small conducting bead into the cavity. In the experiment, this bead is suspended by a small string, and the resulting frequency shift is measured with a network analyzer. In the numerical model we use perturbation theory to calculate the effect the bead has on the resonant frequency. For a small spherical bead, where the field is almost constant over  $\Delta V$ , integration is unnecessary and the frequency perturbation is given by

$$\frac{\Delta f_r}{f_r} = (2\pi/3) r^3 \left( \frac{1}{2} H_0^2 - E_0^2 \right)$$

where  $E_0$  and  $H_0$  are the field amplitudes normalized to the total field energy in the cavity. By comparing the measured and calculated frequency shift we can judge how well the numerical model agrees with experiment.

Since the only field component on axis is  $E_z$ , the simplest test would be to perturb the field on the cavity axis. But, because of the difficulty in having both the bead and the antenna on axis, the bead was kept 0.543 cm away from the axis. At this radius it was still possible to find  $k_z$  for the  $TM_{01}$  modes by counting peaks in the frequency shift.

### II. EXPERIMENTAL ARRANGEMENT

Three components were required to measure the cavity properties: the mode launcher, the network analyzer and the perturbing object. Figure 2 presents a schematic diagram of the measurement apparatus. The dimensions of the system appear in Table I. The launcher was a simple axial wire which could be moved in and out of the cavity to adjust the coupling. Before making measurements the reflection from the antenna was stored in memory and subtracted from subsequent measurements. This procedure made the resonances easier to identify.

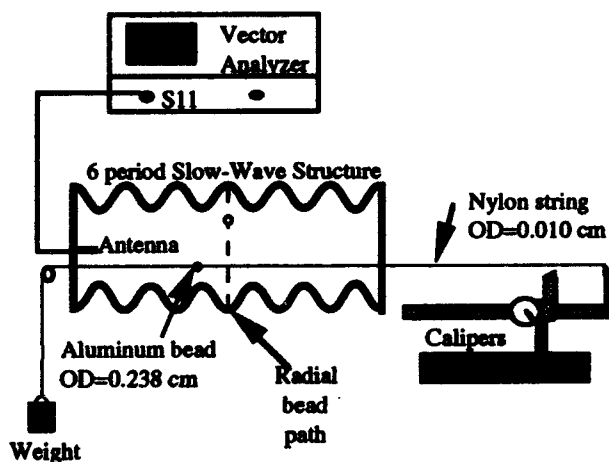


Figure 2. Schematic diagram of measurement apparatus

Table I Dimensions of slow wave structure.

Structure Period	1.667 cm
Total Length	10 cm (6 periods)
Radius[cm]	$1.5 + .41 \sin(3.7z)$
Bead diameter	0.239 cm
string at radius	0.543 cm

The perturbing object used for the majority of this work was an 0.239 cm OD spherical aluminum bead. The bead was suspended by a 0.010 cm OD nylon thread which was connected to the bead through a 0.033 cm ID hole on the bead's axis. Four sets of access holes were drilled in the cavity for the nylon thread. One parallel to the axis of the cavity, at a radius of 0.543 cm and three in the radial direction at axial positions corresponding to the maximum, average and minimum radii. The bead was positioned

in the cavity by connecting one end of the thread to a dial caliper. The other end of the thread was held taught by a small weight. The effect of the nylon string on the resonant frequency was less than 500 KHz in all cases.

### III. RESULTS

#### Dispersion Relation

The dispersion relation results appear both as tables and plots of  $f_r$  and  $\beta_r$ . All measurements are compared with numerical calculation. The dispersion measurements agree very well with the boundary specific calculation of Ogura and the general boundary calculation using the code Superfish [4]. The experimental data for the  $TM_{01}$  mode were on average, 0.17% higher than Ogura's results and 0.03% lower than Superfish, and for the  $TM_{02}$  mode the experimental data were 0.05% lower than Ogura's results. Superfish data was not available for the  $TM_{02}$  modes.

Graphical comparison of the experimental results with Superfish were presented in Figure 1. This figure shows the dispersion curve and reflection data with a common frequency axis. The Superfish results, which were calculated as 7 points are presented as a smooth curve to show the form of the curve and aid in comparing with experiment. In the  $TM_{02}$  case we were not able to experimentally excite the  $\pi$ -mode, although Ogura's code did find this resonance.

#### Field Calculation

Calculations were made for each of seven axial modes on three TM modes. For each of these field structures we calculated the frequency perturbation along the axis and along a radius. We present the results of the cavity field calculation in several forms for the  $TM_{01}$   $2\pi/3$  mode. To help visualize the field structures we present plots of the field lines (Fig. 3a) along with the axial (Fig 3b) and radial (Fig 3c) frequency perturbation plots. The perturbation plots are only used to compare the numerical and experimental results. In these plots the magnitude of the frequency perturbation should not be mistaken to be proportional to the magnitude of the field squared. This is only true when either the E or H field dominates, i.e. on the axis of the structure where  $H = 0$ .

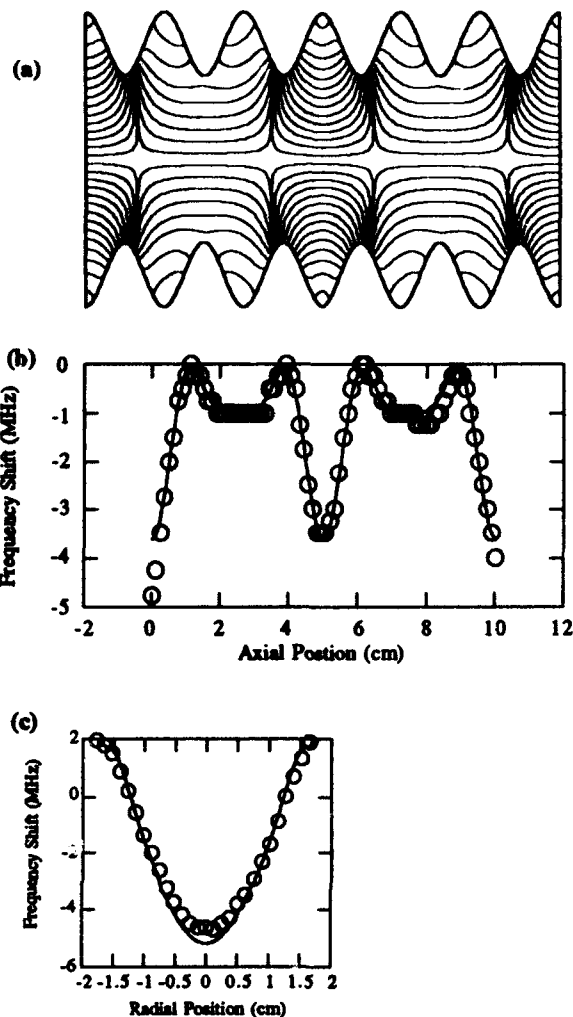


Figure 3. Results for the  $TM_{01}$   $2\pi/3$  mode. (a) Field lines produced by numerical model (Ogura), (b) comparison of measured and calculated field perturbations for axial bead traverse and (c) radial bead traverse.

### IV. REFERENCES

1. N.F. Kovalev et al, JETP Letters, 18, pp138-140, (1973)
2. R.A. Case et al, "High Power BWO driven by a Relativistic Electron Beam", IEEE Trans. Plasma Sci. PS-13 pp. 559-562 (1985)
3. W.Main, Y. Carmel, J. Weaver, K. Ogura, "The Electromagnetic Properties of Finite Length Slow-Wave Structures for Interaction with a Relativistic Electron Beam," IEEE Trans. MTT Submitted.
4. K. Halbach, R. Holsinger, Proceedings, Particle Accelerator Conference pp. 213 (1976)

# COLLECTIVE ACCELERATOR WITH VARIABLE ENERGY AND WIDE SPECTRUM OF ACCELERATED IONS.

R. Meshcherov, B. Batskikh, V. Krasnopolsky,  
V. Rybalko, V. Sazhin, MRTI Russia, 113519.  
A. Vasiliev, MAE Russia.

## ABSTRACT

Experimental results on the slow cyclotron and space charge (plasma) waves excitation in intense relativistic electron beams (IREB) are presented. Large amplitude (10-50 MV/m) and low phase velocity (in order of 0.01 c) waves have been obtained. Collective ion acceleration results, which were received by using microsecond pulse duration electron beams are reported. A concept of a few stage collective accelerator with an energy and particle type control is also considered.

## I. INTRODUCTION

The RF linacs are the most preferable accelerators for producing ions in the energy range of tens and hundreds MeV. However, there are two essential demerits which have to be taken into account when constructing and exploiting linacs, namely, the high cost of the RF supply system and the difficulty to control an energy and type of the accelerated ions in the wide range.

The collective methods of ion acceleration based on the utilization of intense relativistic electron beams may result in development of a new generation of ion linacs (so-called "collective linacs"). It is the most natural way to develop such collective linacs which are similar to the conventional RF linacs, but provide direct transferring a part of the IREB energy to the accelerated ions without using an expensive RF supply system. These linacs may be based on utilization of the slow cyclotron and plasma waves excited in the IREB. As it was shown in the early works [1],[2] the electric fields of the cyclotron and plasma waves are much larger than those in the conventional ion linacs. Moreover, intense ion beams with currents of 1-10 A may be accelerated by the cyclotron and plasma waves. But the most attractive feature of these waves is that their phase velocities may be controlled by a longitudinal magnetic field. The last peculiarity may be used for controlling an energy and a particle type in the wide range.

## II. CYCLOTRON WAVE EXCITATION AND COLLECTIVE ION ACCELERATION

The slow cyclotron waves in the electron beams of a small power [3] or a high power, but a short pulse length [4] had been produced in early experiments by using of the radio-frequency supply from the external powerful generator and the helical guide, as an amplifier structure. In our

experiments the intense relativistic electron beam propagates down a cylindrical copper passive cavity of H-type. The scheme of the experimental set up is shown in Fig.1.

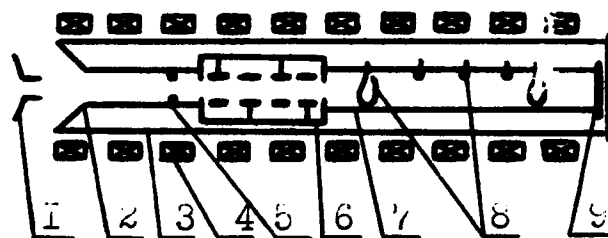


Fig.1. Experimental set up scheme: 1-cathode, 2-anode, 3 - vacuum chamber, 4 - magnetic coils of solenoid, 5 - diaphragm, 6 - cavity, 7 - collective acceleration channel, 8 - magnetic loops, 9 - IREB collector.

The H-cavity length is 0.34 m. The cavity involves 15 drift tubes, which have 4 cm in aperture and are installed with period of 2 cm. The electron beam propagation excites the large amplitude self-sustained RF oscillations in the cavity. The interaction between electrons and cavity fields results in the constrained generation of a slow cyclotron wave. It is found that the beam wave generation is also produced, when an equality between the structure period and the cyclotron wave length is not supported. The generation is occurred in a wide magnetic field range from 0.4 T to 2.0 T. The phase velocity of wave is varied and controlled by value and distribution of magnetic field. When energy of electrons is about 500 keV and beam current equals approximately 1 kA, it is excited a cyclotron wave with amplitude of about 10 MV/m and frequency of 667 MHz. Durations of the wave generation and the cavity oscillation process are about 0.5 - 1.0 nks (beam pulse duration equals 10 nks). A breakdown of the generation process is explained by arising of discharge in the cavity drift tube gap.

To test the effect of the collective ion acceleration by the cyclotron wave field it was proposed to use the collector plasma as ion source and to accelerate the ions opposite to the electron stream (Fig.1) [5]. In carried out experiments the protons were accelerated up to 1.5 MeV. The proton dynamics calculation showed that protons were accelerated up to 0.5 MeV in the acceleration channel and up to 1.5 MeV in the cavity. The current of accelerated protons was about 1 A. It was registered that the ion beam had a RF structure corresponded to the excited wave frequency.

### III. PLASMA WAVE EXCITATION

The problem of plasma wave excitation was solved in early experiments [2],[6]. The experiments of our colleagues [6] were conducted with using the annular IREB of energy 550 keV, current 4.5 kA and pulse duration 100ns. The experimental set up consisted of a disk-loaded waveguide and drift tubes of various diameters. Plasma waves were excited in IREB as a result of the interaction between the IREB and the waveguide. The waveguide had following parameters: relative phase velocity- 0.87, frequency of 3 GHz and shunt impedance of about 20 MOhm/m. The IREB was confined by the longitudinal magnetic field of about 0.7 T. The parameters of plasma waves were measured by magnetic loops mounted inside a drift tube.

The experimental results showed that the slow plasma waves of large amplitudes were excited. The measured values of phase velocities were 0.5 c, 0.27 c and 0.16 c (c - light velocity) when the diameters of drift tubes equaled 4cm, 7cm, and 8cm correspondingly. The estimates made for these cases gave the following values of electric field amplitudes: 4.5 MV/m, 20 MV/m and 50 MV/m. The lowest phase velocity was obtained when  $I_b/I_L = 0.9$ , where  $I_b$  - beam current and  $I_L$  - space charge limiting current. Consequent utilization of plasma waves for ion acceleration is advisable when initial energy of ions is sufficient high (about 20 MeV).

### IV. ION ACCELERATOR CONCEPT WITH AN ENERGY AND PARTICLE TYPE CONTROL

The above experimental research has demonstrated our capabilities of collective ion acceleration by means of the intense electron beams. A rather low value of ion energy experimentally measured can be explained by using collector plasma, as a low energy ion source, and choosing a small value of the synchrotron acceleration phase to demonstrate collective acceleration physical effect. However, acceleration rate about 10 MeV/m can be taken for estimates, if electron beams with parameters described above is used. Energy and current of ions can be increased, if the independent ion injector is applied.

The phase velocity of the cyclotron wave moving together with ions is controlled by the external magnetic field  $B(z)$ :

$$\beta_{ph} = 2\pi\beta\gamma ef/eB(z) \quad (1)$$

$e$ ,  $m$ ,  $\beta$  and  $\gamma$  are charge, mass, relative velocity and energy of electrons respectively,  $f$  - frequency of the propagating wave. The capture of ions with different mass and charge can be produced by varying of  $B_z$  (magnetic field in capture area). The output ion energy can be varied inversely  $B_0$  (output magnetic field). The passive H-cavity has a line spectrum with lower frequency of 230 MHz. Cavity frequency, closely equal to  $f$ , can change according to excited mode and depends on the electron beam parameters. The collective

ion accelerator concept with a velocity and mass control has been developed due to above factors.

The accelerator scheme is the same, as experimental set up scheme. The rather wide spectrum of ions, such as p, d, He<sup>+</sup>, He<sup>2+</sup>, C<sup>+</sup>, C<sup>2+</sup>, N<sup>+</sup>, O<sup>+</sup> can be used for acceleration. Relation of magnetic fields is defined as

$$B_z/B_0 = (1 + 2eEl/W_L)^{1/2}, \quad (2)$$

where  $l$  - relative ion charge,  $E$  - accelerating electric field of wave,  $l$  - acceleration section length,  $W_L$  - injection energy. Maximum value  $B_z$  is limited by the technical capability (2.5 T for that experimental set up). Minimum value  $B_0$  is determined by the electron beam equilibration (about 0.1 T). This magnetic field range is quite enough to capture and accelerate ions of the above spectrum. Using relation (2) one can produce estimates of the accelerator parameters for two boundary cases. The first case is the proton acceleration up to 21 MeV ( $W_L = 1.0$  MeV). It may be obtained, if  $B_z = 1.0$  T,  $B_0 = 0.22$  T and  $f = 667$  MHz. In this case the most "fast" cyclotron wave ( $\beta_{ph} = 0.046-0.21$ ) is creating. In the second case the acceleration of oxygen ions with mass-charge ratio of 16 is produced up to the same output energy and the slowest cyclotron wave ( $\beta_{ph} = 0.008-0.052$ ) is used. It is occurred, when  $B_z = 2.0$  T,  $B_0 = 0.31$  T and  $f = 230$  MHz. In both cases  $\beta\gamma = 2$ ,  $l = 2m$ ,  $E = 10$  MV/m. In order to control the growth rate of wave and the output energy, the respective axial magnetic field distribution must be taken. In our experiments the longitudinal magnetic field gradient was exchanged by means of the solenoid coil commutation and the time displacement of the electron beam pulse relative to the magnetic field pulse. This method of the magnetic field distribution control was used successfully by ourself in the experiments on the collective ion acceleration and the microwave radiation [5],[7].

The output ion energy can be increased by increasing of wave amplitude and acceleration length. The ion energy is risen until 100 MeV, if  $E = 20$  MV/m and  $l = 5$  m.

The acceleration of ions up to hundreds MeV can be realized by using a few stage collective accelerator. For example let us consider a two-stage accelerator which can be based on scheme shown in Fig.2. The first stage consists of an ion injector, a high-intensity electron diode, a passive H-cavity and the first acceleration section. The first stage corresponds to above considered concept and can provide the ion acceleration up to 100 MeV. The second stage consists of an electron diode, a disk-loaded guide and the second acceleration section. The ions accelerated in the first stage are injected into the second stage through the hollow cathode tube of the second diode. The second stage is based on using the plasma waves and can produce a high gradient acceleration because very high fields were obtained in the above described experiments [6]. The phase velocity of plasma waves depends on the relation  $r/R$ , where  $r$  - beam radius and  $R$  - tube radius of acceleration section. In a magnetized electron beam its radius  $r$  is defined by the magnetic field value. Therefore, changing a distribu-

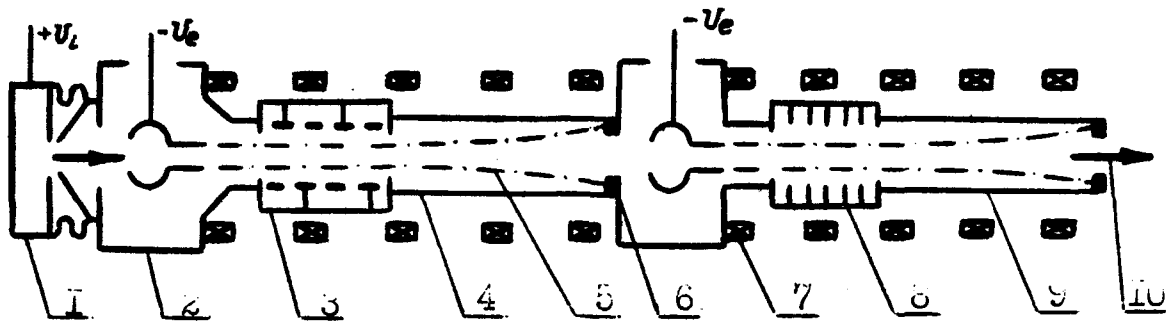


Fig.2. Few stage collective accelerator scheme: 1 - ion injector, 2 - electron diode, 3 - H-cavity, 4 - first acceleration section, 5 - electron beam, 6 - electron beam collector, 7 - magnetic coils, 8 - disk-loaded guide, 9 - second acceleration section, 10 - accelerated ion beam.

tion of the magnetic field one can vary the phase velocity along the acceleration section. This property provides a possibility to accelerate different type ions and to control their energies without overdesigning the accelerating structure. It should be pointed out that the higher is the injection energy of ions the more effective is the acceleration process. Therefore, the injection energy of protons chosen for the above considered example is quite high (1 MeV). In order to produce high energy ions, one can propose to use the resonance accelerating structure driven by an electron beam [8]. Such injector needs no RF

supply system and may provide acceleration of intense ion beams. In this case a single requirement must be fulfilled, namely, the resonance structure frequency must be varied when the mass-charge ion ratio changes. The resonance structure may be driven at different frequencies depending on modulated beam frequency. The electron beam is modulated by means of two gaps coaxial resonator. This method has been described in the papers [8],[9]. According this method the operating frequency may be obtained by means of mechanical tuning the resonator and simultaneously supplying a negative bias to the cavity drift tube.

#### REFERENCES

- [1] M. Sloan, W. Drummond "Autoresonant accelerator concept" *Phys. Rev. Lett.*, v.31, no.20, p.p.1234-1237 (1973).
- [2] A. Anselmo, G. Kerslick, J. Nation, G. Providakes "Space-charge wave propagation in inhomogeneous waveguides", *Phys. Fluids*, v.28, no.4, p.p. 358-365 (1985).
- [3] B. Ivanov, D. Gorozhanin, V. Miroshnichenko, V. Prishchepov "On investigation of the auto-resonant acceleration concept on experimental model devices", in *Proceedings of the 3-rd International Conference on High Power Electron and Ion Beam*, Novosibirsk, USSR, July 1979, v.1, p.p.327-332.
- [4] E. Cornet, H. Davis, T. Starke et al, "Cyclotron wave generation and phase velocity control in intense relativistic electron beam", *Phys. Fluids*, v.24, no.11, p.p. 2039-2048 (1981).
- [5] S. Marichev, A. Markeev, R. Meshchero, P. Mironov, A. Savenko, V. Sazhin "Collective ion acceleration by the space charge waves in intense electron beams", in *Proceedings of the Second European Particle Accelerator Conference Nice, France, June 1990*, v.1, p.p.611-613.
- [6] V. Gapanovich, G. Meskhi, I. Salikhov "The excitation of space charge waves with large amplitude and low phase velocity", in *Sov. Journ.- Problems of Atomic Science and Technique - series: Nuclear and Physical Research*, no.7 (15), p.p.144-148 (1990).
- [7] N. Karbushev, P. Mironov, V. Sazhin, A. Shatkus "Generation of radiation by an intense microsecond electron beam in an axysymmetric wiggler", *Nucl. Instr. and Meth.* A318 p.p.117-119 (1992).
- [8] N. Abramenko, G. Batskikh, N. Gavrilov et al, "Proton acceleration in resonance structures excited by modulated electron beams", in *Proceedings of the Second European Particle Accelerator Conference, Nice, France June 1990*, v.1, p.p. 600-602.
- [9] A. Glazov, V. Krasnopolsky, R. Meshchero, V. Yakushin "Excitation of longitudinal oscillations in intense electron beam for collective ion acceleration", in *Proceedings of USSR Conference on Charge Particle Accelerator*, Dubna, 1989, v.11, p.p.131-133.

# High Gradient Experiments with Nanosecond Pulses

Vincent Baglin, Helmut Haseroth, Jurgen Knott  
CERN, CH-1211 Geneva 23, Switzerland  
Frederic Chautard  
SSCL, Dallas, Texas 75 237, USA

## Abstract

Within the framework of studies related to pulsed accelerating techniques, in particular for the switched power principle, the voltage hold-off for very short pulses has been measured for different materials. Following a presentation of the subject and the requirements, a brief description of the experimental set-up is given. So far gradients of 900 MV/m have been obtained with pulses of two nanoseconds and flat electrodes. The results are compared to measurements based on different experimental techniques.

## I. INTRODUCTION

Future lepton linear colliders, will require much higher accelerating gradients than the ones actually used, in order to obtain a substantial reduction in length as compared to designs based on present technologies. At lower energies, i.e. for high brilliance guns, higher gradients may help to diminish space charge problems.

For conventional r.f. accelerating structures the tendency goes to shorter wavelengths, which are more favourable for voltage hold-off. Different schemes have been proposed to achieve the high gradients. The switched power principle [1] suggests using very short pulses to excite a passive transformer network for producing pulses of 1 MV during 10 ps into 1 mm wide accelerating gaps. The realization presents a series of challenges and we have so far investigated the generation of short pulses and the related voltage hold-off problems.

## II. GENERAL CONSIDERATIONS

### A. Short pulse generation

The idea is to excite a radial transmission line by discharging a photocathode with a fast laser and to amplify the resulting pulse by adiabatic impedance transformation, rather than switching the high voltage directly into the accelerating structure.

According to a study of the transformer effect with a scale model, a gain in voltage by a factor of 20 seems quite feasible [2]. By switching pulses of 50 kV amplitude into the structure one will get 1 MV at the output. We have not yet got the expertise for the very fast laser switching, but in the case of very high current discharges there may be further restrictions for the gain due to saturation effects and the intrinsic impedance of the switch itself.

### B. Voltage hold-off

The highest surface fields will have to be held for only 10 ps in the center of the transformer structure. Another critical place is the input to the structure, where the switch voltage must be held prior to the laser discharge, but possibly only for a few nanoseconds.

Any investigation into the voltage hold-off problems for the very fast pulses in the center requires a transformer network operating with the fast laser switch. We therefore preferred to study first the breakdown problems with more conventional instrumentation in the nanosecond domain. This will correspond to the charge of the laser switch and probably allow for extrapolation to shorter pulse lengths.

### C. Experimental approach

The few experimental results available so far on breakdown limits for nanosecond pulses suggest that gradients of the order of 500 MV/m should be possible [3], depending on the cathode material. Most of the experiments have been done with pointed needle electrodes in order to achieve the required high fields and by measuring the delay to breakdown when submitted to sufficiently long high voltage pulses. The interpretation of these results has to account for changes in the effective cathode radius due to thermal effects during the discharge. Further the small needle points are not really representative for the required large area switching of the switched power principle.

We therefore intended to examine large flat electrodes, at the expense of having to deal with very small gaps to obtain the high gradients. Well defined short pulses are used in order to avoid excessive surface damage.

### III. BREAKDOWN MEASUREMENTS

#### A. Experimental set-up.

We use a coaxial transmission line, about one meter long and 110 mm in diameter, with the outer conductor serving as the vacuum vessel. The line is closed by two impedance-matched glass windows. The operational pumping is done with an ion pump. The experimental spark gap is inserted in the middle of the line and connects via r.f. spring contacts to the inner and outer conductor.

Openings for pumping ports, gauges, broadband voltage probes and observation windows are matched in impedance to give less than 2 % perturbation at 1 GHz. Only the test gap causes 6-7 % reflections because of its relatively high capacitance. We have further tried to keep all possible mismatches sufficiently far away from the test electrodes, in order to avoid perturbations disturbing the breakdown signal.

A coaxial generator of the Blumlein type, loaded by a capacitor bank discharge, delivers 12 kV pulses into the coaxial structure. The rise and fall times are 200 ps and the half-height pulse width is 2.2 ns.

#### B. The spark gap

The test gap forms a compact preassembled block, consisting of the interchangeable flat cathode and the isolated anode.

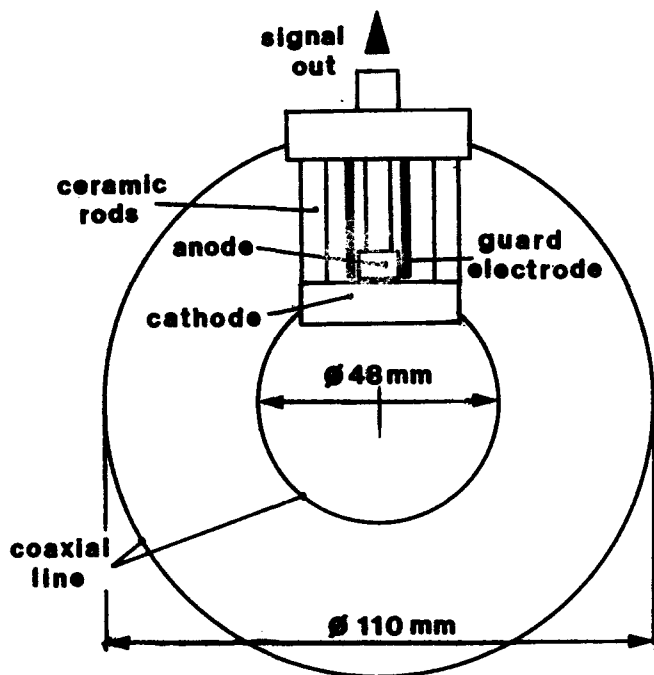


Fig. 1 Schematic cross section of the test gap

The latter is surrounded by a guard electrode to ensure a homogeneous field in the test gap. The surface exposed to the high voltage has an area of  $0.5 \text{ cm}^2$  and the gaps can be adjusted to distances as small as  $10 \text{ }\mu\text{m}$ . The signal from the anode is output via a coaxial UHV feedthrough.

#### C. Signal observation

The detection of breakdowns is done by observing the current collected by the anode with a fast oscilloscope. Due to the large area of the test gap there is unfortunately already a strong capacitive coupling of the high voltage pulse to the anode, even when there is no breakdown.

In the beginning this has raised some problems to distinguish the real breakdowns from the signal pick-up. A differential method using a second probe with a similar time constant as the anode proved to be useful to eliminate the residual signal. In the meantime we have found out how to distinguish the signature of breakdowns from the combined signal.

### IV. EXPERIMENTAL RESULTS

The measurements for a wide range of cathode materials are summarized in Fig.2 and compared to the results from Mesyats and Rohrbach [4] to give a consistent picture for pulses ranging from nanoseconds to microseconds.

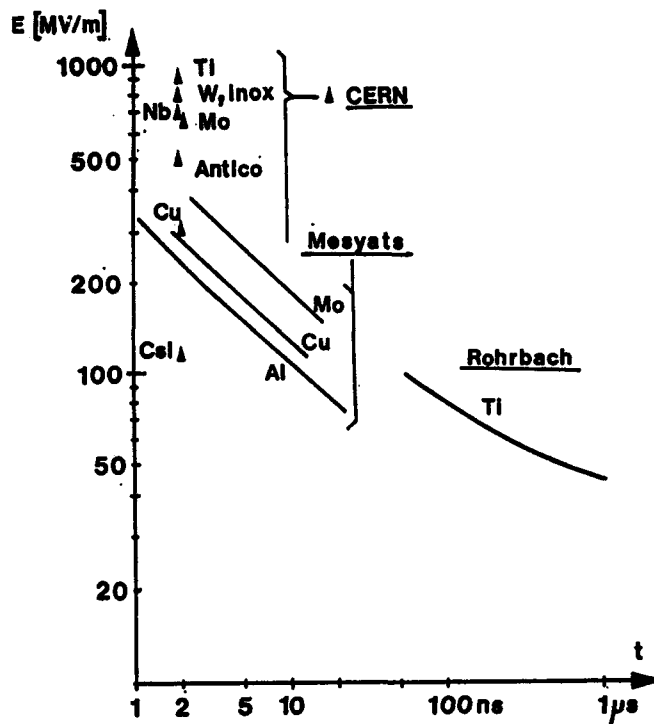


Fig. 2 Results of measurements

The values indicated correspond to the threshold for gradients hold with no breakdown after the initial conditioning of the electrodes.

Most of the measurements have been done with 10  $\mu\text{m}$  gaps, but despite the tricky adjustment the results are well reproducible. For materials with lower breakdown limits we could also prove the surface gradients to be constant for gaps as large as 50  $\mu\text{m}$ .

Our breakdown fields are generally slightly higher than the results obtained by Mesyats, except those for copper cathodes. But both sets of results are in reasonable agreement, if one takes into account the different measurement methods. There may also be a difference in the composition of materials. For example, we used electrodes made from aluminium and titanium alloys instead of pure metals. Probably we also had better vacuum conditions ( $10^{-7}$  mbar). Other explanations for the difference are under consideration, like the influence of surface or thermal treatments of cathodes prior to testing, or the possible impact of the anode material on the cathode initiated breakdown.

An analysis of the electrode surfaces by secondary electron microscopy has shown that the breakdowns during conditioning are equally spread over a large area of the gap, proving the relative flatness of the electrodes. Breakdown currents may amount to several hundred amperes and can produce craters of the order of 5 to 20  $\mu\text{m}$  in diameter and a few  $\mu\text{m}$  deep. Although the surfaces submitted to breakdowns look quite uneven at the microscopic level, there is no obvious reduction in the voltage hold-off.

In addition, we have observed a material transfer between the anode and cathode, which is not yet completely understood. In a few cases local fusion has led to short circuits between the electrodes. This was generally found to be due to accidental discharges of the capacitor bank directly into the test gap, caused by internal sparking in the Blumlein generator.

## V. CONCLUSIONS

The present results confirm that the high gradients required for the switched power principle can be held. But at present the complexity and the low quantum efficiency of the laser switching prevent the application of the switched power principle on a large scale.

We can further conclude that these high fields can for some metals already be achieved with nanosecond pulses. This opens the opportunity for a pulsed device using "slow" switching, possibly without using expensive fast laser technology.

But the longer pulses also have their disadvantages, be-

cause of the increased stored energy in the pulse forming networks and the physical size of the impedance transformer, as the dimension of the latter is proportional to the pulse length.

Therefore, both the fast and the slow version of the switched power concept are for the time being mainly of interest for the design of a single or few stage device, like a high brilliance electron gun. This assumes that the stringent laser requirements or the bigger size of the slow transformer can be outweighed by a significant reduction of space charge effects during extraction.

## VI. REFERENCES

- [1] W. Willis "Laser Acceleration of Particles," *AIP Conf. Proc. No.130, page 421, 1985*
- [2] S. Aronson et al. "Model Measurements for the Switched Power Linac," *Proceedings of the 1987 IEEE Particle Accelerator Conference, Washington, D.C., Vol. 1, page 121-123*
- [3] G.A. Mesyats, "Pulsed Electrical Discharge in Vacuum," *Springer Verlag, Berlin-Heidelberg, 1989*
- [4] F. Rohrbach, "Isolation sous vide," *CERN yellow report 71-5 (TC-L), 1971*

# Development of the Alternate Entry Port for the ATF\*

Zohreh Parsa  
Physics Department  
Brookhaven National Laboratory,  
Upton, NY 11973

## Abstract

We discuss a second entry port for the Accelerator Test Facility (ATF) injection system at Brookhaven National Laboratory, which consists of a photocathode rf gun and a straight-ahead beamline directly into the 50 MeV linac. The proposed second entry port should improve the beam quality and lower the emittance needed for FEL (Free Electron Laser), and laser-acceleration experiments. A discussion on the laser driven high brightness photoelectrons through the primary entry port (a low energy 180 degrees achromatic double bend transport line) now in operation, and a beam analysis for the proposed secondary port is also given.

## I. INTRODUCTION

The high brightness laser driven photoelectron beams (with low emittance and high current) are required for new methods of acceleration such as FEL, IFEL (an inverse free-electron laser) and future development of linear colliders. To achieve high brightness and rapid acceleration, an rf gun operating at 2.856 GHz, with 1-1/2 cells,  $\pi$ -mode resonant, disc-loaded structure (with cathode placed at the start of the first 1/2 cell), has been designed and operating as the injector for the two S-band linac sections at the BNL Accelerator Test Facility (ATF). The cathode is illuminated with a frequency quadrupled Nd:YAG laser with photon energy of 4.65 MeV at the gun exit.

The Accelerator Test Facility at BNL is an experimental Facility for accelerator and beam physics experiments. A major research interest is in the interaction of laser driven photoelectrons with the electromagnetic fields. ATF's present injection system consist of a photoelectron gun and a low energy transport beamline which consists of two sets of quadrupole triplets and a 180° achromatic double bend, (Fig. 1). The photoelectrons are ejected from a photocathode rf gun into the transport beam line and then accelerated through 2 S-band linac sections to 50 MeV [1,2]. The linac consists of two  $\pi/3$ -mode, 3.05 m long, disc loaded, travelling wave SLAC linear accelerator sections that was produced at IHEP, Beijing, China. The gun and the linac are driven by the same XK5 klystron, delivering about 25 MW of peak power with a 3.5 micro-second pulse at 2.856 GHz [2].

With the existing injection system, the beam diverges quickly at the gun exit and gets large in going through the double bend transport line into the linac [3,4]. We have considered and studied various schemes [6] and will present some results for the proposed ATF alternate injection

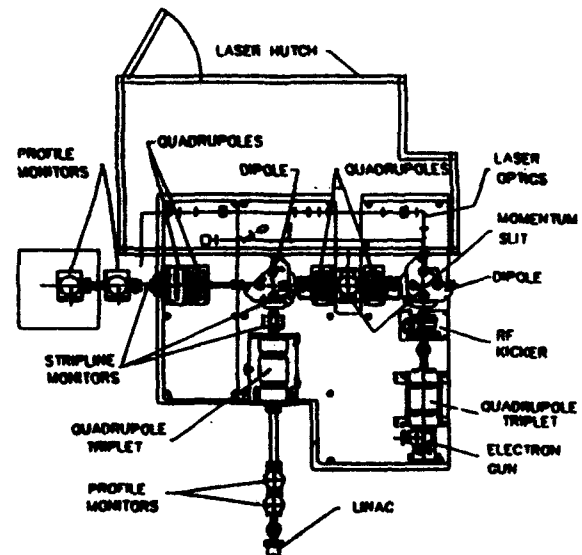


Figure 1: Sketch of the BNL ATF injection system. The transport beamline from the gun to the linac entrance showing the positions of the magnetic elements.

system in section II. A summary and references are given in section III.

## II. ALTERNATE INJECTION SYSTEM

We have considered various schemes to improve the beam quality and preserve the low emittance and high brightness beam needed for experiments at ATF [6]. In this section we present some of our calculations and simulation results obtained for a 2nd entry port for ATF. The alternate (straight-ahead) injection system consists of a solenoid + a gun + solenoid combination that is placed directly into the linac.

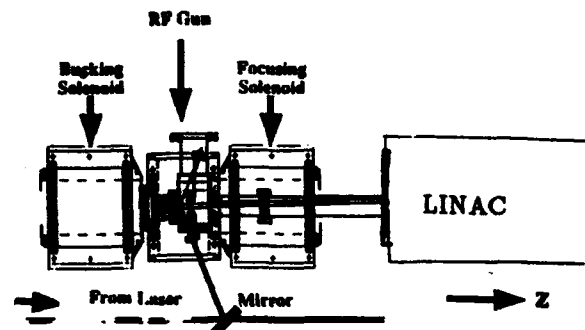


Figure 2: Sketch of the alternate injection system for ATF. A solenoid + gun + solenoid (gun+s) combination is placed in line with the linac. (Not scaled).

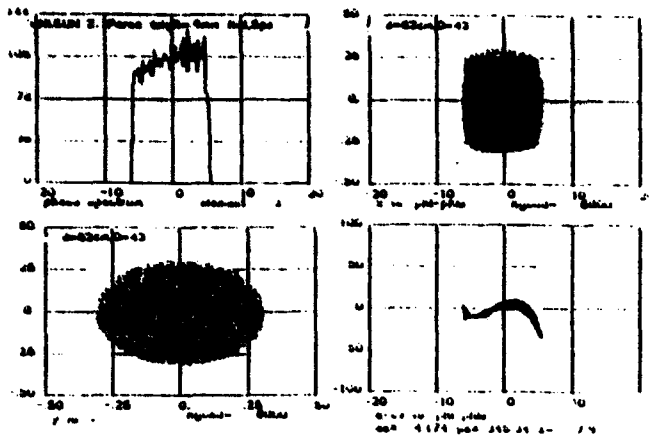


Figure 3a: Shows the beam profile at  $z = 7.9\text{cm}$  (exit of the gun cavity). From the top in c.w.direction: phase spectrum,  $x$  vs change in phase,  $y$  vs  $x$  profile and change in energy vs change in phase with program PARMELA.

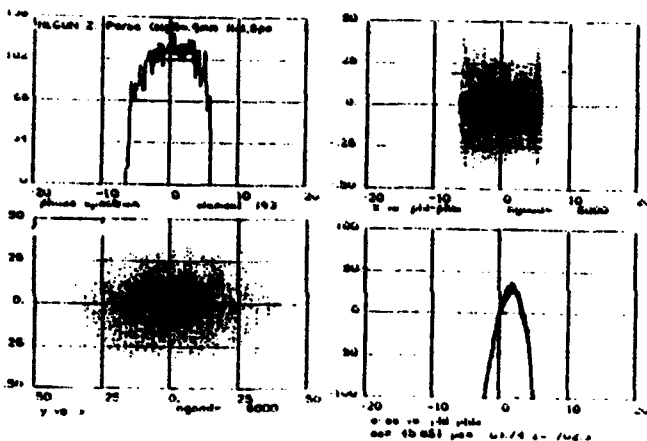


Figure 3b: Shows the beam profile at  $z = 702.3\text{cm}$  (the linac exit). From the top in c.w.direction: phase spectrum,  $x$  vs change in phase,  $y$  vs  $x$  profile and change in energy vs change in phase with program PARMELA.

This scheme would allow the production of the low emittance and high brightness beam needed for the experiments and preserves the present injection system which can be used alternatively for diagnostic measurements etc. Where the beam is injected from a 2nd entry port (using a 2nd gun) directly into the linac without going through the bending magnets.

Selections of  $d$  the distance from the gun (cathode) to the linac entrance and solenoid strength are important and would effect beam quality (see Section III). For other injection schemes and a more detailed analysis see references. In this analysis the fields off axis for solenoids are calculated to sixth order using the expansions:

$$B_z(z, r) = B_z(z, 0) - \frac{r^2}{4} \frac{d^2 B}{dz^2} + \frac{r^2}{4} \left( \frac{d^4 B}{dz^4} \frac{r^2}{16} - \frac{d^6 B}{dz^6} \frac{r^4}{576} \right) \quad (1)$$

$$B_r(z, r) = -\frac{r}{2} \left( \frac{dB}{dz} - \frac{d^3 B}{dz^3} \frac{r^2}{8} + \frac{d^5 B}{dz^5} \frac{r^4}{192} \right)$$

### III. BEAM DYNAMICS AND ANALYSIS

In our analysis of the beam from cathode through the linac exit we have considered various initial charge distributions, laser spot sizes ( $\sigma_r$ ), laser pulse lengths ( $2\sigma_z$ ), field on the cathode  $E$  and accelerating field of the linac, etc.[6]. Table 1 illustrates some of our results obtained with the initial parameters of interest for ATF and the proposed UVFEL project at BNL. For example with initial  $E = 100\text{MV/m}$  on the cathode, laser pulse length ( $2\sigma_z$ ) of 10 ps, and varied spot sizes (e.g. 0.9 mm), various values of  $d$  (e.g. 62 cm, the distance from cathode to linac entrance), solenoid strength of 2.2 KG and initial phase of 43 degrees we can preserve the beam quality and achieve high brightness, low emittance beam at the linac exit, which is needed for the FEL and laser acceleration experiments at ATF. With program PARMELA [5] With  $\sigma_r = 1\text{mm}$  and 0.9 mm (uniform beam distribution) we obtained beam emittance of few tenths of cm-mrad with energies of about 46 MeV and brightness ( $B = I_{\text{peak}}/\pi\epsilon_x^N\epsilon_y^N$ ) of orders of  $10^{13}$  for the beam emerging from the exit of the linac, (Fig.4). We have used 10 ps pulse length in our analysis since  $\sigma_z = 5$  ps is the value noted obtainable at ATF [1].

For  $B_0 = 2.14\text{KG}$ ,  $\sigma_z = 5$  ps,  $\sigma_r = 1$  mm,  $Q = 1\text{nC}$  and an initial uniform distribution, the beam energy and emittance at the linac exit become  $w = 46$  MeV,  $\epsilon_x^{N,rms} = .32$  and  $\epsilon_y^{N,rms} = .276$ . Whereas for the same set of parameters and an initial gaussian distribution the beam emittance grows larger, e.g. at the linac exit. How easy is the production of the uniform distribution (flat beam) depends on the quality and bandwidth of the laser [1]. For detailed beam analysis with Gaussian and Rician distributions see e.g. [1,6].

Fig. 4 shows the change in the beam size along the beamline from cathode through the linac. As can be seen the beam converges to a waist in the linac. Where the change in the solenoid strength or  $d$  would shift the position of the beam waist in the linac and would change the beam parameters. For example a 2% increase in the solenoid strength will increase the emittance from ( $\epsilon_x^{N,rms} = .278$ ,  $\epsilon_y^{N,rms} = .243$ ) to ( $\epsilon_x^{N,rms} = .390$ ,  $\epsilon_y^{N,rms} = .333$ ) at the linac exit. keeping all other parameters fixed [1].

For the proposed alternate injection system for ATF, a pair of solenoids are placed before and after the gun to compensate the beam emittance dilution due to the space charge, such that the coil proceeding the cathode bucks the field due to the second solenoid and produces a zero field on the cathode. To avoid beam loss through the linac a proper matching of the beam into the linac is crucial.

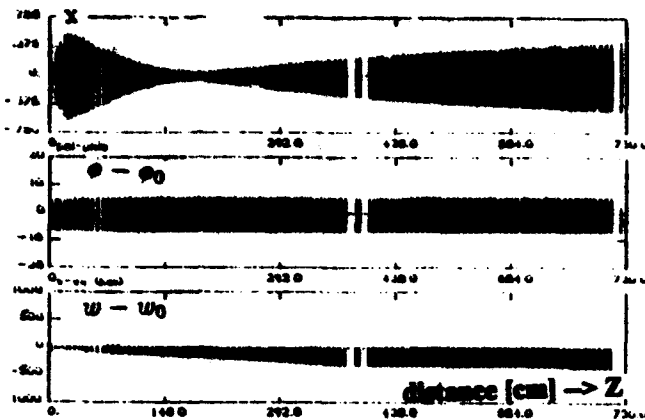


Figure 4: Shows the change in position  $x$  [cm], phase  $\phi - \phi_0$  [degree] and energy  $w - w_0$  [KeV] of particles at each element location, from the cathode through the linac exit. With 2.2 KG solenoid,  $d = 70\text{cm}$ ,  $\sigma_r = .9\text{mm}$  and  $\sigma_z = 5\text{ps}$ .

#### IV. SUMMARY

We presented an alternate injection system for the ATF at Brookhaven National Lab, using a pair of solenoids and an rf gun placed directly into the linac. Earlier results showed that with the present injection system at ATF the beam became too large through the double bend transport line, leading to a large emittance growth and a large beam loss. With solenoid+gun+solenoid straight injection into the linac scheme we can reduce the emittance dilution due to space charge forces, and produce the beam needed for FEL, IFEL and other laser acceleration experiments. We obtained small emittance (few tenths of cm-mrad) and high brightness of orders of  $10^{13}$ . We note that a proper beam matching at the linac entrance is crucial so as to avoid beam loss through the linac. The effects of variations in the solenoid strengths and  $d$  the distance from the cathode to the linac entrance can be detrimental to the beam quality along the transport line and through the linac. The beam converges into a waist after it enters into the linac. The position of this waist changes with the change in initial parameters such as the solenoid strength and the distance between the cathode and the linac entrance. To avoid beam loss or emittance dilution, there must be a careful control of the parameters such as the length and strength of the solenoids, laser spot size and pulse length, distance between the cathode and linac entrance, the accelerator phase and accelerator field. In this analysis the fields off axis for solenoids were calculated to 6th order.

#### VI. REFERENCES

\*Work performed under the auspices of U.S. Dept. of Energy contract DE-AC02-76-CH00016.

1. Z. Parsa, "Preliminary Emittance Measurements and Calculations of the Laser Excited Beam from the BNL Accelerator Test Facility Radio Frequency Electron Gun", Vol. II, Sec. II, p1-54, BNL-52292 (1991) and References therein; K. McDonald et al., Proc.,

Table 1: ATF Solenoid+Gun+Solenoid+Linac system - simulation parameters.

Number of Solenoids	2
Length of Solenoid [cm]	15
Radius of Solenoid [cm]	6
$B_0$ Solenoid [KG]	2.2
Initial phase [degree]	43-45
Laser spot size $\sigma_r$ [mm]	.9, 1 ....
Laser Pulse Length ( $2\sigma_z$ ) [ps]	10
RF Frequency [GHz]	2.856
Radius of Aperture [cm]	1.0
Field on the Cathode [MV/m]	100
Charge [nC]	1
with $d$ [cm]	62 - 70
Linac Accel. Gradient (Ave.) [MV/m]	7.0
At Linac Exit: Energy [MeV]	46 - 47
dp/p [%]	0.18 - 0.2
$\epsilon^N$ [ $\pi$ cm-mrad]	0.2 - 0.4
Brightness ( $B = I^{peak} / \pi \epsilon_x^N \epsilon_y^N$ )	$\times 10^{13}$

- EPAC88, June 1988; A. Fisher, J. Fisher, I. Pogorelsky, private communications on laser performance.; Z. Parsa, "Effects of 3rd Order Maps and Solenoid on a High Brightness Beam", BNL-48397 (1993) and Proc. IEEE PAC May 17-20, Washington D.C. (1993).
2. K. Batchelor, I. Ben-Zvi, I. Bigio, T.S. Chou, R.C. Fernow, J. Fischer, J. Gallardo, H. Kirk, N. Kurnit, K.T. McDonald, R.B. Palmer, Z. Parsa, C. Pellegrini, J. Sheehan, T. Srinivasan-Rao, S. Ulc, A. Van Steenberg, M. Woodle, "Operational Status of Brookhaven Accelerator Test Facility", Proc. March 20-23, 1989 IEEE PAC, Chicago, Ill, #89CH2669-0 (1990).
  3. Z. Parsa, "On Beam Emittance and Invariants - Applications to ATF Beamline", Proc. 2nd EPAC, Nice-France, Nile Ed., Frontiers, (1990); BNL Report BNL-44364 (1990) and Ref. therein.
  4. Z. Parsa, and L. Young, "Modeling of the BNL Photocathode Gun with the Code PARMELA", Nucl. Inst. & Meths. A318 (1992) 254-258.
  5. L. Young, (Private comms.), PARMELA, 1993 version; We thank L. Young for helpful discussions, modifications to the programs and collaborations.
  6. Z. Parsa, "An Alternate Injection System for the BNL Accelerator Test Facility", BNL-48403, APS April 12-15, Washington D.C. (1993); Z. Parsa, "Interactions Between Charged Particles and RF Space Charge and Wake Fields in an Accelerating Structure", Particles and Fields 91, Vol. 2, 1073, Ed. David Axen, Douglas Bayman and Martin Comyn; Z. Parsa, Accelerator Physics and Modeling, BNL- Report BNL-52379, 65-165 (1993).

# Status of Superconducting Magnet Development (SSC, RHIC, LHC)\*

P. Wanderer  
Brookhaven National Laboratory  
Upton, New York 11973

## Abstract

This paper summarizes recent superconducting accelerator magnet construction and test activities at the Superconducting Super Collider Laboratory (SSC), the Large Hadron Collider at CERN (LHC), and the Relativistic Heavy Ion Collider at Brookhaven (RHIC). Future plans are also presented.

## I. INTRODUCTION

This paper reviews the status of the superconducting magnet programs for the RHIC, SSC, and LHC accelerator projects. Most of the focus is on dipole magnets, because of their cost and technical difficulty. Critical technical issues include the quench performance, geometric field quality, and time variation of the fields. Conductor development for these magnets was reviewed last year[1].

The dipoles in these programs embody the same concepts: NbTi superconducting strand in a Rutherford-style partially-keystoned cable,  $\cos \theta$  winding with wedges designed for minimum values of the allowed harmonics, cold iron yoke which helps support the coil against motion, aperture in the range 50 - 80 mm, and length in the range 10 - 15 m. RHIC, with the lowest field requirement, uses only a single layer coil. LHC, with the highest field requirement, will operate at 1.8 K.

## II. SUPERCONDUCTING SUPER COLLIDER

### A. Collider Dipoles

**ASST Dipoles.** Following a difficult but ultimately successful R&D program with 47 mm-aperture, 17 m-long dipoles[2], the aperture was increased to 50 mm. The current lattice has 7964 dipoles of 15 m length and 496 of 13 m length. At 4.35 K, the quench current is typically 7.4 kA (6.7 kA corresponds to 6.7 T central field and 20 TeV).

The task of the R&D program for the 50 mm aperture dipole was to provide magnets built by staff from industry for an Accelerator Systems String Test (ASST) with a half cell of magnets (five dipoles, one quadrupole, one spool piece). At Fermilab, ASST magnets were built by staff from General Dynamics Space Systems (GDSS). At Brookhaven (BNL), ASST magnets were made by Westinghouse Electric Corp. (WEC). A cross section of the Fermilab/GDSS cold mass is shown in Fig. 1; the BNL design is slightly different. The ASST was operated

successfully last summer[3].

The quench performance of both Fermilab/GDSS and BNL/WEC magnets at 4.35 K and 3.85 K was excellent [4]. Measurements of the azimuthal and axial force during cooldown and excitation indicated that the effects of the Lorentz forces were generally as expected[5].

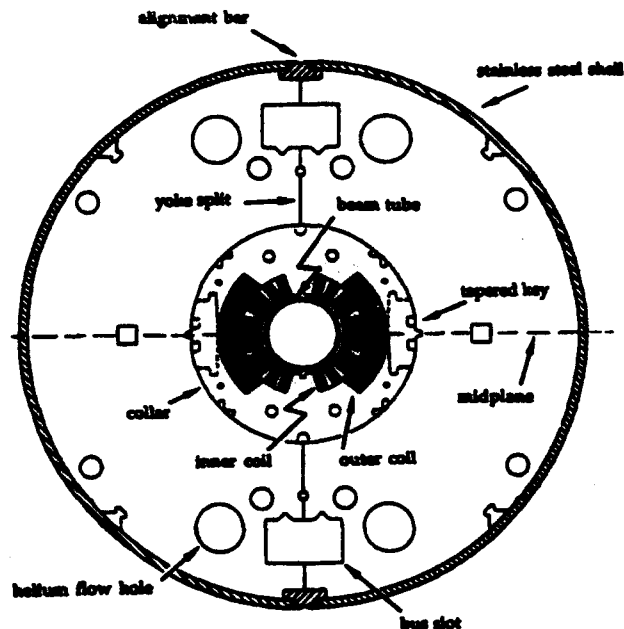


Figure 1. Cross section of SSC Collider dipole cold mass.

The part of the magnetic field that is determined by conductor placement and the saturation properties of iron was well understood in terms of calculations, measurements, and the sizes of the magnet components, within the limitations imposed by low statistics[6,7]. There was good correlation between the "cold" measurements and those at room temperature.

At injection, the expected harmonics due to magnetization were in agreement with calculations for the 6  $\mu\text{m}$ -diameter NbTi filaments[8]. Also at injection, the magnetic field was measured for an hour, the length of time needed for filling both rings of the collider. The drift of the sextupole was within tolerance. The drift of the skew quadrupole needs to be controlled through the basic mechanism underlying this effect, which is not yet

\*Work performed under Contract No. DE-AC02-78CH00016 with the U.S. Department of Energy.

understood.

Magnet quench performance was studied as a function of ramp rate up to 300 A/sec. Harmonics were measured up to 64 A/sec. For the Collider ramp, 4 A/sec, some magnets had acceptable eddy current effects but some did not. All magnets exhibited significant eddy current effects at the High Energy Booster (HEB) ramp rate, 62 A/sec. The effects were strongly correlated with cable vendor. The most obvious source of such effects, for both quench currents and harmonics, is eddy currents, which in turn are a function of the interstrand resistance  $R_i$  of the cable. Studies of the factors which determine  $R_i$  are being carried out as part of the HEB dipole R&D.

**Recent Activity [9]:** At Fermilab, four 15 m R&D dipoles were made by Fermilab staff after the completion of the ASST work. One of these magnets was tested at 1.8 K, where it reached a quench current of 9990A (9.5 T) with little training.

Much of the testing at BNL the past year has focussed on eddy current measurements. Good quench localization information has been provided by a "quench antenna" system, similar to the one first used at the LHC. The ramp rate-induced quenches were found to be located in turns near the midplane, where eddy current effects are largest.

Harmonic measurements were made at the axial location of the eddy current quenches. Current distributions calculated from these harmonics were largest near the midplane. Thus, the recent tests reinforced the conclusion that the ramp rate effects are due to eddy currents in the cable and can be limited by controlling  $R_i$ .

**Future Activity:** As the "leader", GDSS has completed a magnet design taking into account the ASST results and SSC requirements. The first 15 m practice coils magnet have been wound and cured at the GDSS plant. Completion of this magnet is expected in August.

Two 15 m dipoles made at the SSC Magnet Development Lab are scheduled to be tested at BNL this summer. The SSC Magnet Test Facility will be commissioned late in the summer.

### *B. Collider Quadrupole*

Collider quadrupoles will have a central gradient 220 T/m at 6.7 kA, with a 5.2 m magnetic length. Six full-length quadrupoles with 40 mm aperture have been made at Lawrence Berkeley Lab (LBL) by staff from LBL and a Babcock & Wilcox - Siemens collaboration (BW). Initial quenching was in the range 6.6 - 7.2 kA [10]. Typically the magnets trained to about 8 kA and then retrained from 7 kA after thermal cycling. Harmonics were better than the specifications [9]. Correlation between warm and cold harmonics was found at the level of 0.5 units.

The BW quadrupole collared coils are manufactured in Germany and the rest of the magnet in the U.S. Three 1 m models have been quench-tested thus far. The initial quenches in each were at currents near 7.5 kA, with the magnets reaching the conductor limit near 8.4 kA in a few

quenches. Retraining after a thermal cycle began about 8.2 kA. Ramp rates up to 200 A/sec have had negligible effect on the quench currents. Full-length magnets are due this fall.

### *C. High Energy Booster (HEB) Dipoles*

To take advantage of previous R&D, the design requirements are as close as possible to those of the Collider dipoles. The HEB dipoles will have a much larger sagitta than the Collider dipoles. Also, there are two important operational differences: 62 A/sec ramp rate and bipolar operation. Tests at BNL this year confirmed that the magnet quench performance was unaffected by the current polarity, as expected.

The R&D contract for developing the HEB dipole is held by WEC. Based on information from the ASST magnets and other experience, WEC is making magnets with cable of different interstrand resistances (untreated cable, oxide-coated cable, and a third, undesignated, choice that could be alternate untreated and oxide-coated strands). Tests of short models have begun and will run through the end of the year. Production of the first prototype is planned for a year from now.

### *D. Other Superconducting Magnets*

The HEB quadrupoles will operate on the same bus as the HEB dipoles and have design central gradient 190 T/m, length 1.23m, and aperture 50 mm. The industrial design is being developed at Saclay. The first test is expected next year.

Two 1 m models of the insertion quadrupoles have been made and quench tested at the SSC. They trained from an initial quench current of about 7.3 kA to the conductor limit, about 8.4 kA, in a few quenches.

## III. LARGE HADRON COLLIDER

### *A. Dipole Design Parameters*

To make the most effective use of the existing 27 km LEP tunnel at CERN, magnet R&D has been directed toward reaching the highest possible field level. The target range has been 8 T to 10 T. The options include NbTi operated at 1.8 K and Nb<sub>3</sub>Sn at 4.35K. At present, NbTi is foreseen for the magnets, although work continues with Nb<sub>3</sub>Sn high-field models. Space limitations in the tunnel cross section point toward a single cryostat and cold mass, but with two apertures [11] so that the flux passing through one aperture is returned through the other (Fig. 2). With 1300 twin aperture dipoles, each 13.5 m long, a 9.5 T central field yields a beam energy of 7.7 TeV. More detailed information on the lattice and magnets can be found in recent reviews [12,13,14].

Initially, cables for a two-layer magnet capable of 10 T operation were designed. The subsequent R&D program has explored several options for the remainder of the magnet design, as follows: The collars supporting the coils could encompass both coils in a single stamping or just a single

coil. The collars could be aluminum or nonmagnetic stainless steel. The support of the collars by the yokes could be accomplished at room temperature or during cooldown by yokes of several different geometries. For the most part, this work has been carried out by contract with different companies.

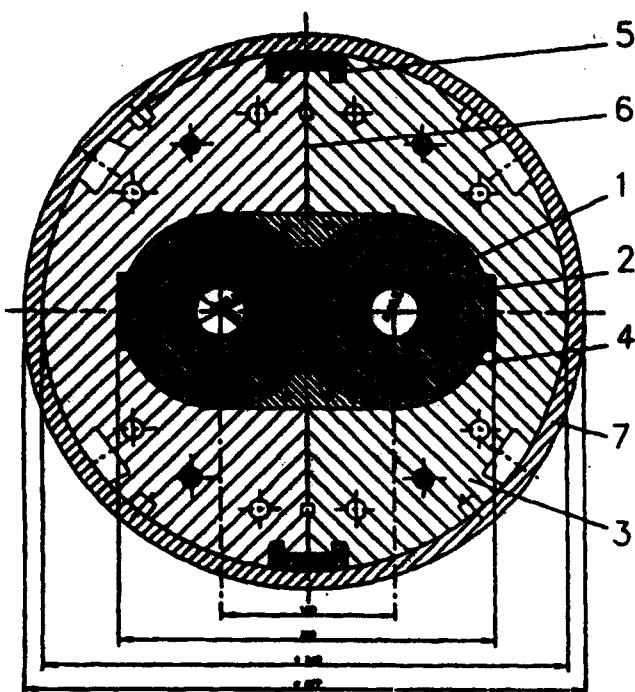


Figure 2. Cross section of LHC twin aperture dipole cold mass, type MTA1. 1. Coils, 2. Collars, 3. Yoke, 4. Iron insert, 5. Clamp, 6. Gap, 7. Outer shrinking cylinder.

### B. Dipole R&D Results

**Short, single aperture models:** Initially, two models with 50 mm aperture were made with HERA-diameter NbTi strand, for speed. At 1.8 K they trained quickly to 9.3 T, the conductor limit. A model with Nb<sub>3</sub>Sn strand was also successfully tested.

A KEK model with fully-keystoned cable and other novel features trained well at 4.35 K but did not reach the conductor limit at 1.8 K.

**Short, twin aperture models:** Using LHC-design cables, four 50 mm aperture models (designated MTA1) have been made by different firms. For each magnet, choices were made among some of the construction features (soldered, partially soldered, and unsoldered cable; common and separate collars; etc.), but all used the same design for the yoke. The quench results of the magnets were quite similar. At 4.35 K they reached 7.9 T within a few quenches. However, at 1.8 K, they trained slowly above 7 T. One reached the conductor limit, 10.02 T, after about 55 quenches [15]. The magnets retrained after a thermal cycle.

It was concluded that the training was due to a common feature of the magnets. To localize the quenches,

the CERN group devised a clever analysis for the field disturbance which occurs during a quench. It was detected by small coils in the bore of the magnet [13]. The analysis was confirmed by voltage tap data from the KEK single aperture magnet [16].

It was found that most of the quenches originated in the ends of the inner layer turns close to the pole, where cable winding is most difficult. Some of the quenches originated in the magnet straight section, also near the pole.

Given the need for rapid turnaround and detailed investigation, a magnet R&D facility was started at CERN about a year and a half ago. Recently, new coils of the MTA1 design were made in industry and assembled at CERN in a three-part yoke. At 4.2 K, this magnet reached the limit of the conductor, 8.1 T, after one quench. At 2 K, the magnet had its first quench above 9 T and subsequently trained to a record central field of 10.5 T. After thermal cycle to room temperature the first quench was at 9.74 T [17].

In twin aperture magnets, the normal quadrupole is an allowed harmonic because left-right symmetry is not preserved in the yoke design. In one magnet, measurements at fixed currents were made to 10 T. The value of the normal quadrupole varied from low to high field in agreement with calculation. The normal sextupole was similarly well behaved. Measurements of the relative dipole angle between the two apertures await completion of the horizontal test facility.

A twin aperture version of the KEK design has been recently tested at 4.35 K [18]. The magnet has separately-collared coils basically similar to the one in the single aperture model. It reached 8.12 T central field after six training quenches. The magnet will be tested in superfluid at CERN.

**10m, twin aperture model:** HERA-type coils were used to construct a twin-aperture prototype (TAP) to gain operational experience with full scale two-aperture magnets. The magnet was tested at CEN, Saclay. At 4.5 K it reached the limit of the conductor, 5.8 T, on the first quench. At 1.8 K, it reached the conductor limit of 8.3 T after five quenches.

### C. Future Dipole Program

**50 mm aperture:** Ten 10 m long twin aperture dipoles have been ordered from four vendors. The magnets will be highly instrumented and four will eventually be assembled into a half cell test. Five of the magnets will have the MTA1 design. One will have the three-part-yoke design recently tested, with additional variants for the other four. The initial magnet is due for delivery soon; the others will follow at two-month intervals.

To explore further the Nb<sub>3</sub>Sn route, a 11.5 T twin aperture model is being built in the Netherlands by a FOM-UT-NIKHEF-CERN collaboration.

**56 mm aperture:** Accelerator studies made following the increase of the design beam intensity indicated the need for a larger physical aperture, so the LHC aperture

has been increased from 50 mm to 56 mm. As a bonus, this also improves field quality. Tooling in the CERN magnet facility is being built for this aperture. A short twin aperture model is being built there by a Finnish-Swedish-CERN collaboration for an operating field of 9.5 T. After a first version with NbTi, this magnet will be equipped with ternary alloy, NbTiTa, coils.

**Reduced field option:** Last fall, a decision was made to design a magnet using cable of the dimensions developed for the SSC. The SSC strands and cables are significantly smaller than those used for the 10 T LHC design (e.g., 0.81 mm vs. 1.29 mm for the inner layer strand). By applying the experience in the construction of the 40 mm and 50 mm SSC magnets to a 56 mm aperture, the effort at CERN could be concentrated on design issues unique to twin aperture magnets. A short twin aperture model built with cable supplied by the SSC is underway. Its operating field is 8.6 T. The high-field version magnet and the SSC-cable magnet will be completed about the end of the year. Details of this program are given by G. Brianti [17].

#### D. Other LHC Magnets

The arc quadrupoles have been designed and built by a CEA, Saclay team in collaboration with CERN. They will be powered in series with the dipoles and have an operating gradient of 250 T/m. Two twin aperture, 3 m prototypes, with 56 mm aperture, are due to be completed in mid-'93. One will be tested at the end of the month.

Prototypes of the correctors have been tested in the UK at Rutherford Lab. Prototypes of tuning magnets are underway in Spain, with testing expected soon.

### IV. RELATIVISTIC HEAVY ION COLLIDER (RHIC)

RHIC magnets stand exactly at the threshold of mass production. Contracts for the 80 mm aperture arc magnets -- about 270 dipoles, quadrupoles, and sextupoles -- have been let, with the first magnets due this year. Production of the arc correctors and the 130 mm aperture insertion quadrupoles at Brookhaven is scheduled to start within the month.

The production cable run of 567 km of 30-strand cable for the arc dipoles and quadrupoles is well underway at Oxford Superconducting Technology (OST) and is due to be completed by the end of the year. The production of 83 km of 36-strand cable for the insertion magnets has begun at OST and Furukawa and will be completed next spring.

A full cell (two dipoles, quadrupoles, sextupoles, correctors) using production designs is scheduled for operation this fall.

#### A. Arc Dipoles

The 9.7 m-long dipoles generate a central field of 3.45 T with a current of 5 kA in the single-layer coil, for 100 GeV/u nuclei (Fig. 3). A total of twelve full-length R&D magnets have been made, with the last two scheduled for test in the next month. These two magnets were used for technology transfer to Grumman Aircraft Corporation (GAC).

None of the 9.7 m magnets has quenched below 3.85 T. Ramp rate effects have been insignificant up to twice the design of 83 A/sec. This insensitivity has been confirmed for the production cable in a short model. With cable production underway, the emphasis is on minimal change.

The time drift of the harmonics is much less of an issue with RHIC than SSC because the filling time is only 1 minute instead of 1 hour. Measurements made on this time scale confirm that drifts are negligible. As a further precaution against magnets with different drift times, the cable will have no cold welds.

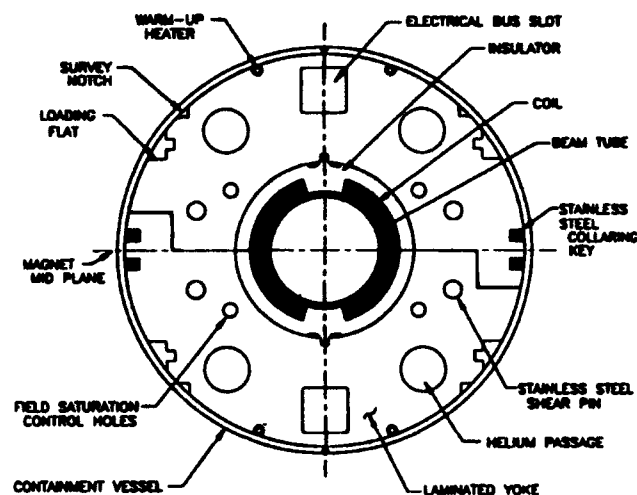


Figure 3. Cross section of RHIC dipole cold mass.

#### B. Arc Quadrupole/Sextupole/Correctors (QSC).

In each half cell, the quadrupole, sextupole, and corrector are assembled into a single cold mass with 80 mm aperture. The arc quadrupoles have a central gradient of 71 T/m at their operating current of 5 kA and a 1.1 m effective length. A series of eight magnets made at BNL is nearly complete. Systematic harmonics have been identified and reduced to acceptable levels. Production will be at GAC.

The arc sextupoles have an integral field of 550 T/m at  $\pm 100$ A, with 0.75 m effective length. Four R&D magnets, built at BNL, have been used to debug the design. Everson Electric Corporation is scheduled to deliver the first of the production models in July.

Four coaxial layers 0.6 m long make up the arc corrector package, providing decapole, octupole, quadrupole, and dipole harmonics. Four R&D models of these have been made using an industrial process for making circuit boards ("Multiwire"). Tooling now set up at BNL will be used for the production run.

### C. Insertion Quadrupoles

The lattice calls for three lengths (1.44, 2.1, 3.4 m) of insertion quadrupoles, but all with the same cross section for economy of tooling. The central gradient is 48 T/m at 5 kA. Two 1.44 models have been successfully tested. The production run of each length is 26 magnets.

## V. GENERAL VIEW OF TRAINING

An interesting parameterization of the quench performance of "well-built" magnets in terms of conductor properties was developed last year [19]. The parameterization quantifies the ability of the copper in the superconducting strands to carry the current during a local heat pulse in terms of an "instability factor",  $\alpha$ , which is proportional to the square of the current density in the copper. Well-built magnets fall on or near a straight line in a log-log plot of  $\alpha$  versus the number of training quenches. For example, the improved quench performance of the most recent MTA1 LHC model at 4.35 K falls on this line.

Thus far, rather few magnets have been tested in superfluid. The 10 T LBL model [15] falls near the line. The LHC TAP dipole and the SSC 50 mm magnet fall directly on the line. The LHC MTA1 magnets lie above the line, possibly indicating that the limitations in 1.8 K quench performance lie in magnet construction rather than in the superfluid helium. It will be interesting to see how well the parameterization stands up when the LHC dipoles made with SSC cable are tested at 1.8 K.

## VI. ACKNOWLEDGEMENTS

I wish to thank these colleagues for helpful discussions: A. Devred, A. Greene, R. Gupta, A. Jain, D. LeRoy, G. Morgan, J. Muratore, T. Ogitsu, R. Palmer, R. Perin, N. Siegel, J. Tompkins, P. Thompson, L. Walckiers, E. Willen

## VII. REFERENCES

- [1] A. Greene, "Recent Status of Superconductors for Accelerator Magnets," *Proc. ICFA Workshop on AC Superconductivity*, KEK Proceedings 92-14, pp. 100-108 (1992).
- [2] A. Devred, "About the Mechanics of SSC Dipole Magnet Prototypes," *AIP Conf. Proc.* 249(2), pp. 1310-1374 (1992) and P. Dahl, "The SSC Dipole: Its Conceptual Origin and Early Design History," report SSCL-320 Rev. 1 (1992).
- [3] W. Robinson, these proceedings.
- [4] W. Nah et al., "Quench Characteristics of 5-cm-Aperture, 15-m-long SSC Dipole Magnet Prototypes," *IEEE Trans. Appl. Supercon.*, Vol. 3, No. 1, pp. 658-661 (1993).
- [5] T. Ogitsu et al., "Mechanical Performance of 5-cm-Aperture, 15-m-Long SSC Dipole Magnet Prototypes," *ibid.*, pp. 686-691.
- [6] P. Wanderer et al., "Magnetic Design and Field Quality Measurements for Full Length 50-mm Aperture SSC Model Dipoles Built at BNL," *Int. J. Mod. Phys. A (Proc. Suppl.)* 2B, pp. 641-643 (1993).
- [7] J. Strait et al., "Magnetic Field Measurements of Full Length 50-mm Aperture SSC Dipole Magnets at Fermilab", *ibid.*, pp. 656-659.
- [8] Y. Zhao et al., "Current Dependence of Harmonic Field Coefficients of 5-cm-Aperture, 15-m-Long SSC Dipole Magnet Prototypes," *IEEE Trans. Appl. Supercon.* Vol. 3, No. 1, pp. 674-677 (1993).
- [9] Many of these results were presented at the Vth International Industrial Symposium on the SSC, San Francisco, CA, May 6-8, 1993.
- [10] A. F. Lietzke et al., "Quadrupole Magnets for the SSC," *IEEE Trans. Appl. Supercon.*, Vol. 3, No. 1, pp. 629-635 (1993).
- [11] Magnets of this type have been successfully tested at BNL: P. Dahl et al., "Performance of Four 4.5 m Two-in-One Superconducting R&D Dipoles for the SSC," *IEEE Trans. Nucl. Sci.*, Vol. NS-32, No. 5, pp. 3675 - 3677 (1985).
- [12] N. Siegel, "Recent Status of LHC Magnets," *Proc. ICFA Workshop on AC Superconductivity*, pp. 6 - 14, KEK Proceedings 92-14 (1992).
- [13] D. Leroy et al., "Test Results on 10 T LHC Superconducting One Metre Long Dipole Models," *IEEE Trans. Appl. Supercon.*, Vol. 3, No. 1, pp. 781-784 (1993).
- [14] R. Perin, "Status Report on the LHC Magnets," *Applied Superconductivity*, Vol. 1, Nos. 10-12, pp. 1487-1502 (1993).
- [15] A 1 m single aperture dipole built at LBL reached essentially the same field, 10.06 T, after 11 quenches at 1.8 K. See D. Dell'Orco et al., "A 50 mm Bore Superconducting Dipole with a Unique Iron Yoke Structure," *IEEE Trans. Appl. Supercon.*, Vol. 3, No. 1, pp. 637-641 (1993).
- [16] A. Yamamoto et al., "Development of 10 T Dipole Magnets for the Large Hadron Collider," *IEEE Trans. Appl. Supercon.*, Vol. 3, No. 1, pp. 769-772 (1993).
- [17] G. Brianti, these proceedings.
- [18] A. Yamamoto, private communication.
- [19] R. Palmer, "Superconducting Accelerator Magnets: A Review of their Design and Training," SLAC-PUB-5899 (1992).

# ELECTRICAL PERFORMANCE CHARACTERISTICS OF THE SSC ACCELERATOR SYSTEM STRING TEST

W. Robinson, W. Burgett, T. Dombeck, J. Gannon, P. Kraushaar, A. McInturff, T. Savord, and G. Tool  
Superconducting Super Collider Laboratory†  
2550 Beckleymeade Avenue, Dallas, Texas 75237

## Abstract

The string test facility was constructed to provide a development test bed for the arc regions of the Superconducting Super Collider (SSC). Significant effort has been devoted to the development and testing of superconducting magnets, spools, and accelerator control systems required for the SSC. The string test facility provides the necessary environment required to evaluate the operational performance of these components as they are configured as an accelerator lens in the collider. This discussion will review the results of high current testing of the string conducted to evaluate magnet element uniformity and compatibility, the splice resistance used to connect the magnets, and system response to various quench conditions. Performance results of the spools, energy bypass systems, energy dump, and the power supply system are also discussed.

## I. INTRODUCTION

The intent of the Accelerator System String Test (ASST) is to obtain data for model verification and information on the magnitudes of pressures and voltages encountered in an accelerator environment. The ASST milestone run was accomplished in August, 1992, and consisted of demonstrating that the accelerator components could be configured together as a system operating at full current.<sup>[1]</sup> Following the milestone run, the string was warmed to correct some design flaws that limited the operational range. The string was again cooled to cryogenic temperatures in October, and a comprehensive power testing program was conducted through the end of January, 1993. This paper describes how the collider arc components operate in an accelerator environment during quenches induced by firing both strip heaters and spot heaters. Evaluation of the data illustrates how variations in the design parameters of magnets used in a string environment can impact system performance.

## II. CONFIGURATION

The ASST is composed of five 50-mm aperture dipole magnets that are 15 meters in length, a five meter long 40-mm aperture quadrupole magnet, and re cooler, feed, and end spools. The dipole magnets used in the string were industrial prototypes constructed by General Dynamics personnel utilizing facilities at Fermi Lab. Those magnets included DCA313, DCA314, DCA319, DCA315, and DCA316. The quadrupole magnet was built at Lawrence Berkeley Lab. The three spool pieces were built to SSCL specification by Meyer Tool (HSPRF), Cryenco (SPR), and Consolidated Vacuum

Industries (HSPRE). A Dynapower Corp. DC current power supply was used to provide a maximum current of 6500 amps. An energy dump was used with the string to evaluate the energy extraction system. A refrigerator with a nominal cooling capacity of 500 watts was used to provide the cryogenics environment. The string cryogenics system is described in another paper presented in this conference.<sup>[2]</sup>

Each dipole magnet consists of four superconducting coils. The differential voltage across each coil is monitored by the quench protection monitor system and a data acquisition system. There are four strip heaters for each magnet that are positioned along the length of the outer coils in a quadrant configuration. The strip heaters in opposing quadrants are electrically connected together in parallel. Each set of strip heaters is independently controlled by a heater firing unit. This configuration protects the magnet by providing a level of redundancy that ensures the outer coils quench despite a failure that may occur in one of the heaters or firing units.

Figure 1 illustrates the electrical configuration of the string. In order to reduce the amount of inductance in the system, each half cell is composed of two independent circuits. Each circuit is powered using one of two power busses that run through the magnets. The first three magnets are powered from the lower bus. The remaining dipoles and the quadrupole are powered through the upper bus. The lower and upper busses are connected together at the HSPRE. Diodes are connected across each set of dipoles to provide the required isolation between circuits during quenching conditions. When a quenching condition is detected in a magnet, the strip heaters contained in the magnets within the quenching circuit are fired, and the power supply is turned off. The large resistive voltage that develops across the magnet circuit from the propagating quench condition places a forward bias voltage across the diodes. Current that is flowing from the non quenching magnets bypasses the quenching magnets through the lower impedance path offered by the diodes. Approximately one second after the quench is detected, the energy dump switch is opened and energy remaining in the string is dissipated through the energy dump. Energy contained in the quenching portion of the string is dissipated into the cryo system through the magnet coils.

## III. ASST TEST SUMMARY

The string was operated at  $T = 4.65$  K partly because of the limitations of the cryogenics plant, but also to keep the amount of operating margin in the magnets small. A total of 66 per tests involving the magnets have been conducted from July 9, 1992, through January 29, 1993. Of those tests, 18 were involved in system commissioning, and 13 were strip heater and spot heater quench tests. One test was the Congressionally mandated milestone demonstration test.<sup>[1]</sup> The remainder of the tests involved energy dump testing or

†Operated by Universities Research Association under contract with the Department of Energy. Manuscript received May, 1993.

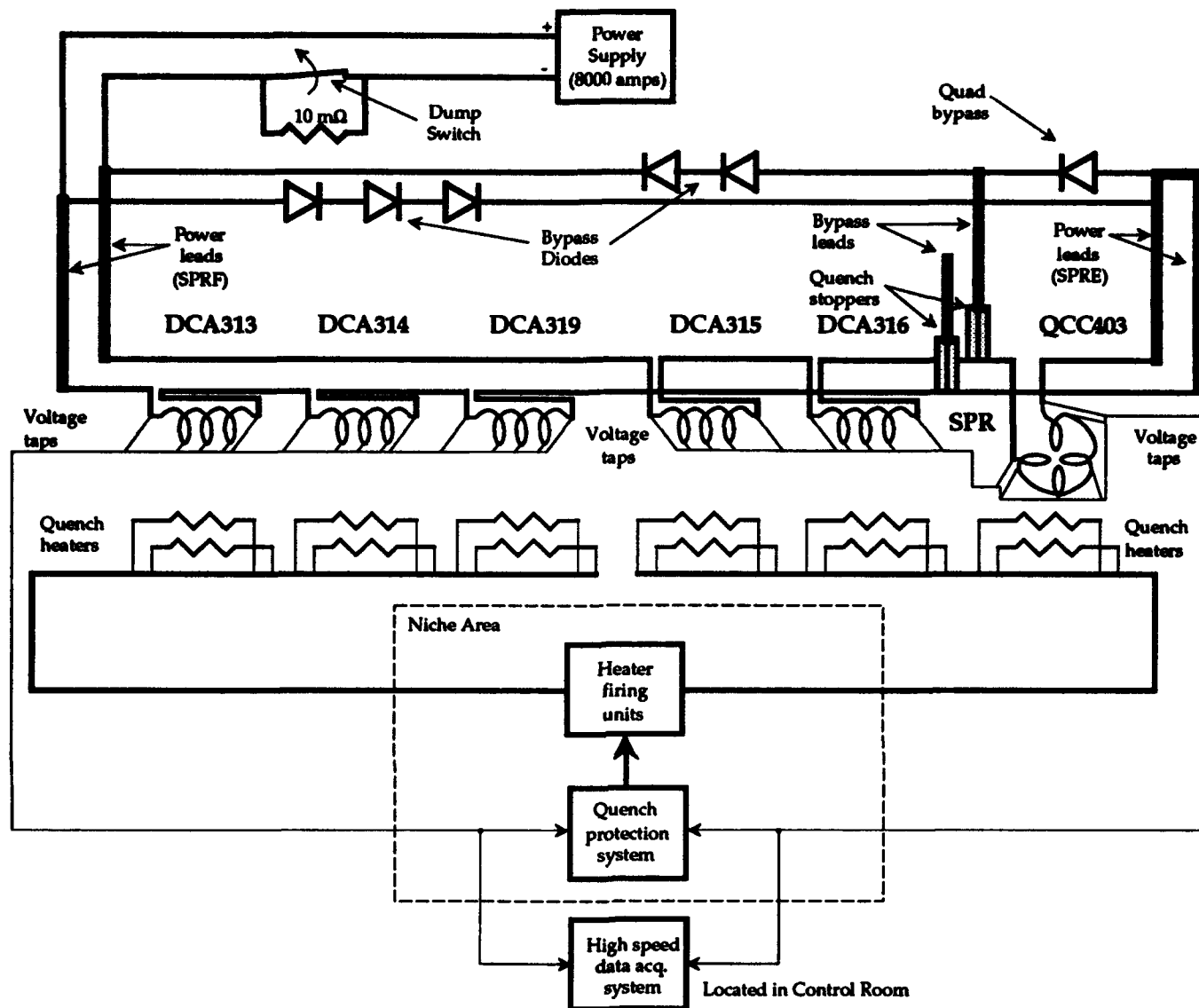


Figure 1. Electrical configuration of the ASST.

bypass lead testing. The opportunities to conduct quench testing were limited because it took the cryogenics system three to four days to recover from a full current quench test. In addition to quench testing, resistance of four splice joints as a function of current were measured.

#### A. Quench Analysis

Peak voltage in the ASST string configuration is of concern because the dielectric strength of the components in the system must be able to withstand this voltage. The peak voltage is influenced by several factors including the method of quench initiation, circuit inductance, string temperature, and differences in the low temperature (non superconducting) resistance between magnets.

Strip heater induced quenches generate higher voltages than spot heater quenches because a larger segment of one

magnet goes resistive in a shorter period of time. The time rate of resistance growth ( $dR/dt$ ) is increased in a strip heater induced quench due to the joule heating of the outer coils, while other magnets in the same circuit remain in a superconducting state. Energy from the other magnets supplies energy to the quenching magnet. By the time the other magnets in the circuit quench, the  $dR/dt$  of those coils is much lower than in the magnet initiating the event.

Operation at lower temperatures increases the operating margin of the magnets. Once a quench is detected by the quench protection system and the heaters are fired in the other non quenching magnets, the time it takes these magnets to reach a normal state is increased due to the additional operating margin. Meanwhile, the quenching magnet that initiated the event continues to build resistance from joule heating.

One of the unexpected results from testing was the effect that differences in the residual resistivity ratio between

magnets had on the system quench response. (The residual resistivity ratio, or RRR, is defined as the 300 K resistance divided by the 10 K resistance.) Problems were encountered during string testing from using magnets with different RRR values in the same circuit. Table 1 outlines the RRR characteristics of the dipole magnets used in the string. From Figure 1, DCA313, DCA314, and DCA319 are grouped together electrically, and DCA315 and DCA316 are wired together. Some magnets in the circuit were dissipating more of the stored energy at a high rate, while other magnets transferred much of their stored energy to the magnets with lower RRR. Figure 2 illustrates the MIITs (millions of amps squared integrated over time) and peak voltage to ground that were attained during strip heater induced quenches on DCA319. The test was terminated at 6000 amps because the voltage was projected to reach 2300 volts at 6500 amps.

RRR VALUES of ASST MAGNETS

Magnet	UI RRR	UO RRR	LO RRR	LI RRR
DCA313	170	174	171	173
DCA314	174	177	174	171
DCA319	105	96	97	108
DCA315	162	173	174	177
DCA316	67	109	109	78

Table 1. UI is the upper inner coil, UO is the upper outer coil, LO is the lower outer coil, and LI is the lower inner coil.

Volts to Ground and MIITs vs Quench Current

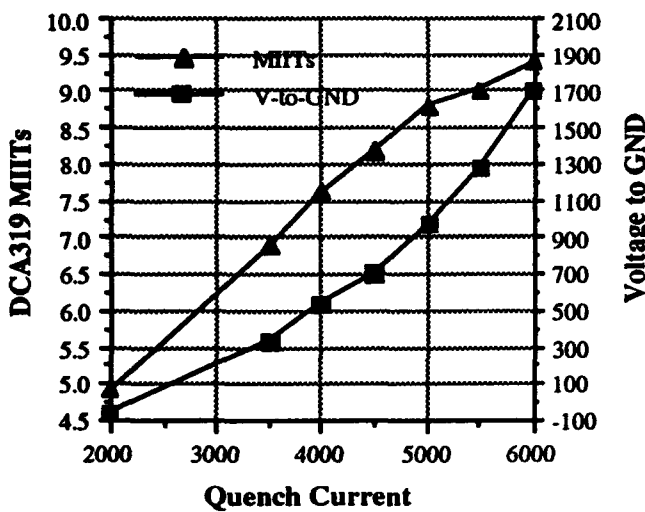


Figure 2. MIITs and voltage to ground as a function current when initiating a string quench by firing the strip heater in DCA319 (T = 4.65 K).

Using the MIITs integral to quantify energy dissipation into heat, it is seen that RRR has an important role in determining the response of the system. The MIITs is determined by

$$\text{MIITs} = 10^{-6} \int_0^{\infty} i^2(t) dt = 10^{-6} A^2 d \int_{T_0}^T \frac{C(T)}{\rho(T, \text{RRR}, B)} dT,$$

where  $i$  is the current,  $A$  is the cross-sectional area,  $d$  is the density,  $C$  is the heat capacity of the conductor,  $B$  is the magnetic field term for the magneto-resistance, and  $\rho$  is the electrical copper resistivity. An approximation for  $\rho$  is

$$\rho(T, \text{RRR}) = \frac{1.545}{\text{RRR}} + \left( \frac{2.32547 \times 10^9}{T} + \frac{9.57137 \times 10^5}{T} + \frac{.62735 \times 10^{-2}}{T} \right)^{-1} \mu\Omega\text{-cm}.$$

The parenthesis on the right is an approximation to the Grüneisen integral formula for the phonon scattering resistivity.<sup>[3]</sup> As the RRR of the material is uniformly reduced, its copper resistivity at low temperatures is increased. The MIITs are reduced because the effective time constant of the system is shorter. Stored energy in the magnets dissipates more rapidly when the cold resistivity of the material is higher. Since the resistivity is increased, the peak voltage attained during quench also increases. In a string environment, quenching magnets with lower RRR experience higher MIITs, voltages, and temperatures than anticipated. These higher values are due to the additional energy dissipated in those magnets that is provided from magnets in the system with higher RRR.

Energy deposition estimates were made using the coil voltage  $V_c(t)$ , which is a combination of the inductive voltage that results from change in current in a coil of inductance  $L_c$  and a resistive voltage resulting from current passing through the copper in the composite superconducting wire. The developed coil resistance  $R_c(t)$  is given by

$$R_c(t) = \frac{(V_c(t) - L_c \frac{di}{dt})}{i(t)},$$

where  $di/dt$  is calculated from the current decay of  $i(t)$ . Given the resistance of each coil, an estimate is made on how the energy is being dissipated in the string. The total energy stored in the string is given by  $W_L = \frac{1}{2} L I_0^2$ , where  $L$  is the string inductance (approximately 75 mH/dipole and 7.5 mH/quadrupole), and  $I_0$  is the string current before a quench occurs. For  $I_0 = 6500$  amps, the energy storage in the string is  $W_L = 8$  MJoules. The energy deposition for each coil is determined by

$$W_{R_c} = \int_{t_0}^{\infty} R_c(t) i^2(t) dt,$$

where  $t_0$  represents when resistance in the coil is detected.

Figure 3 illustrates how the string energy is dissipated in the string during Event #285 when all strip heaters are fired simultaneously. DCA319 dissipated the most energy because it had the lowest RRR of the three dipoles in its circuit (see Figure 1). Although the RRR of DCA316 is similar to DCA319, there was only one other dipole in the DCA316 circuit. The total energy dissipated by Event 285 was 7.79 MJoules. The 3.68% difference from the expected energy of 8.08 MJoules is due to the change in the dipole inductance from the high field iron core saturation.

### Energy Dissipation Profile for Event 285

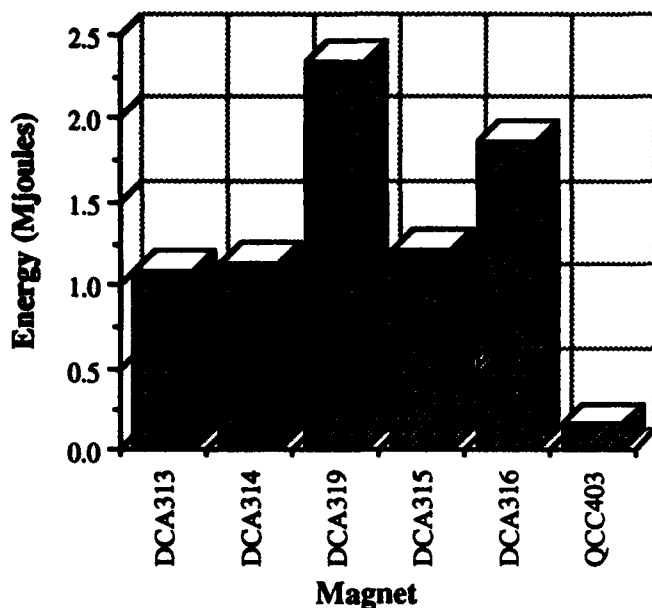


Figure 3. Profile of energy dissipation for Event 285 where all strip heaters were fired simultaneously. Peak current for this event was 6475 amps.

#### C. Ramp Rate Study

Significant effort has been expended on understanding dipole ramp rate sensitivity during single magnet testing. The test facility at used at FNAL did not have an energy dump and was unable to conduct decay ramp sensitivity tests. The baseline dump resistance used in the ASST was increased from 10 mΩ to 16 mΩ in order to reduce the time constant of the system. Table 2 summarizes the result of the test.

Event #	Dump Ω	di/dt [amps/sec]
359	10 mΩ	237.2
375	12 mΩ	276.0
369	16 mΩ	339.3

Table 2. Ramp rate sensitivity tests. DCA313 and DCA315 quenched at 5300 amps during Event 369.

During energy dump using a dump resistance of 16 mΩ, dipole magnets DCA313 and DCA315 quenched due to eddy current heating. Of the magnets used in the string, DCA313 and DCA315 exhibited the highest sensitivity to di/dt during single magnet testing.<sup>[4]</sup> It is possible that if we were operating the string at 4.35 K, we would have been able to successfully dump the system using the 16 mΩ dump impedance without quenching.

Calculations to estimate the resistance change required to obtain a desired ramp rate were performed. The relationship for estimating resistance is

$$R = -\frac{L}{t} \ln \left( 1 - t \left( \frac{di}{dt} \right) / I_0 \right)$$

where  $L$  is the system inductance of 382.5 mH,  $di/dt$  is the desired ramp decay in amps/sec,  $t$  is the time interval, and  $I_0$  is the initial current. Since the initial decay rate at  $I_0 = 6500$  amps for a dump resistance of 10 mΩ was 237.2 amps/sec, the system load including the power bus resistance is calculated to be 14.8 mΩ. Assuming the incremental change in the dump resistance is accurate, the above equation can be used to solve for system inductance. Changing the system load impedance by 2 mΩ, the inductance is 368 mH. Increasing the load resistance by 4 mΩ, the system inductance is approximately 367 mH. The percent change in inductance of 3.79% is consistent with results from the joule deposition calculation presented in the previous section. Using the new inductance in the above equation leads to a system impedance of 14.24 mΩ when using the 10 mΩ dump resistance.

#### D. Spot Heater Testing

The limited operations schedule permitted only two spot heater tests at the full current of 6500 amps. We induced full current spot heater quenches on DCA313 and DCA319. This provided a comparison for voltage to ground and MITTs development between dipole magnets of different RRR values (see Table 1). Table 3 summarizes the comparison between DCA313 and DCA319 as well as lower current spot heater tests conducted on DCA319. As expected, the maximum MITTs developed on DCA319 occurred below 6500 amps.

Magnet	Max current	Volts to GND	MITTs
DCA313	6500	566	11.55
DCA319	6500	1232	10.99
DCA319	6000	923	11.3
DCA319	5000	418	10.95

Table 3. Spot heater test results.

An unexpected event occurred during the spot heater test conducted on DCA313 that was similar to a full current strip heater quench conducted earlier on the same magnet (Event 335). Normally when a quarter cell quenches, the heat from the quench propagates into the magnet in the adjoining quarter cell causing a thermally induced quench. We ordinarily would have expected DCA315 (in the fourth dipole position) to experience a thermal quench. In both cases, when DCA313 was quenched at full current, DCA316 (in the fifth dipole position) experienced a thermal quench. One possible cause could be heating from the recoler in the SPR due to the differential pressure that develops from the induced cryogenic flow impedance. We currently do not have enough data to accurately characterize this process.

#### E. Bypass Lead Testing

The bypass leads located on the SPR are composed of stainless steel that are used to conduct current from the superconducting power bus to the outer cryostat during quenching conditions. The stainless steel is used to provide thermal isolation without excessive heat leak into the cold mass. Since stainless steel is a relatively poor electrical conductor, care must be taken not to overheat the lead during

operation. The lead must be designed to withstand the MIITs developed during an energy dump which is determined by

$$\text{MIITs} = 10^{-6} \int_0^{\infty} i^2(t) dt = 10^{-6} \int_0^{\infty} \left( I_0 e^{-\frac{Rt}{L}} \right)^2 dt = \frac{I_0^2 L}{2R} \times 10^{-6}.$$

For the Collider, the maximum operating current is  $I_0 = 7$  kA, the circuit inductance is 39 H, and the dump resistance is approximately 1  $\Omega$ . The MIITs requirement for the bypass lead is 1000 MIITs. We conducted a series of experiments designed to evaluate bypass lead performance. The lower bypass lead was tested to 1400 MIITs, and the upper bypass lead was tested to 2040 MIITs.

#### F. Splice Joint Resistance

Voltage taps were placed on each side of four splice joints in the string. The voltages across the joints were monitored while ramping the string to full current. Figure 4 illustrates the splice joint resistances from 2000 amps to the full current of 6500 amps. These were also the first joints fabricated in the field so it is expected that the impedance will become lower as our processes continue to improve and experience is gained in joint fabrication. The change in resistance as a function of current is due to the superconducting properties of solder at low currents. The differences between splice impedance at high current is probably due to differences in the solder composition or thickness between joints. The thickness can be thought of as the distance between superconducting composite strands in the opposite sides of the joint with respect to each other.

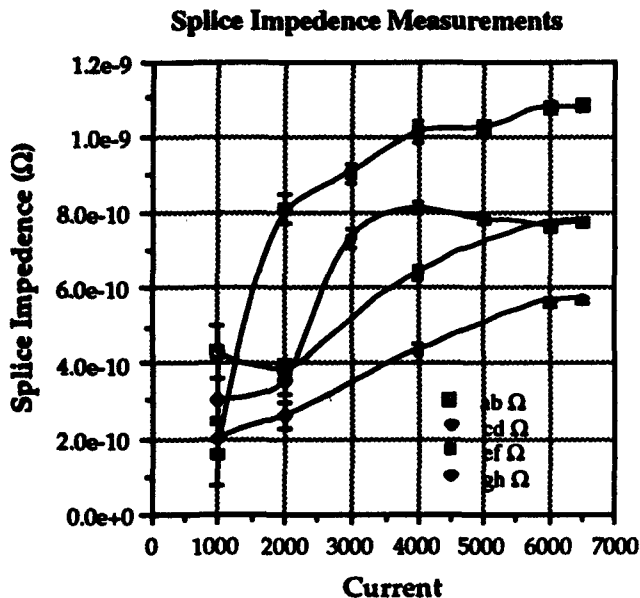


Figure 4. Splice joint resistance as a function of current. The "hump" in the "gh  $\Omega$ " curve is probably due to measurement error.

## IV. FULL CELL RUN

We are currently reconfiguring the string as a full cell that is scheduled for cool down sometime in July. The full cell is composed of 10 dipole magnets and two quadrupole magnets. The dipole magnets are grouped together based on RRR into four families. We expect the energy dissipation of the system to become more balanced as each RRR family is configured together through one bypass circuit. The full cell will be operated utilizing one of the sector refrigerators that has been built for the Collider. The refrigerator will permit operation at lower temperature, and will recover from a full power quench in a much shorter time than the refrigerator used previously. We plan to continue monitoring splice joint resistance and to conduct studies on power bus quenches. A fully instrumented SPR will replace the original SPR. The additional instrumentation allows us to study quench dynamics between half cells. The corrector package in the SPR is operational. The additional instrumentation in the SPR may also allow us to understand how a full current quench in the first dipole induces a thermal quench in the dipole adjoining the SPR.

## V. CONCLUSIONS

Important progress has been made on the Collider design in the past two years. We have identified several problems early enough in the design cycle to have significant impact. With the exception of the problem encountered in matching RRR values between dipoles, we have not encountered any operational problems that would prohibit full current operation of the Collider. The problem encountered with RRR matching is currently being addressed at the design level, and will be solved before magnet production for the Collider has begun.

## VI. ACKNOWLEDGMENTS

The authors wish to recognize the excellent work and significant contribution the many groups and individuals that supported the design, integration, and operations expertise. The string assembly crew led by C. White, the cryogenics crew led by R. Ahlman, and the operations team led by M. Hentges deserve special recognition for their dedicated effort and professional performance.

## VII. REFERENCES

- [1] W. Burgett, et al., "Full-Power Test of a String of Magnets Comprising a Half-Cell of the Superconducting Super Collider," SSCL-Preprint-162, October, 1992. (To be published in the journal *Particle Accelerators*.)
- [2] A. McInturff, et al., "Collider Scenario Implications of ASST Operation," Paper Jc4 of the 1993 *Particle Accelerator Conference*, Washington D. C., May, 1993.
- [3] M. McAshan, "MIITs Integrals for Copper for Nb-46.5 wt% Ti," SSC-N-468, February, 1988.
- [4] J. Kuzminski, et al., "Quench Performance of 50-mm Aperture, 15-m-Long SSCL Dipole Magnets Built at Fermilab," SSCL-Preprint-133, presented at *The XVth International Conference on High Energy Accelerators*, Hamburg, Germany, July, 1992.

# Overview of the Final Focus Test Beam Alignment System\*

V.E.Bressler, R.E.Ruland, D.Plouffe

Stanford Linear Accelerator Center, Stanford University, Stanford, CA 94309 U.S.A.

## Abstract

The Final Focus Test Beam was conceived as a technological stepping stone on the way to the next linear collider. Nowhere is this more evident than with the alignment subsystems. Alignment tolerances for components prior to beam turn are almost an order of magnitude smaller than for previous projects at SLAC. Position monitoring systems which operate independent of the beam are employed to monitor motions of the components locally and globally with unprecedented precision. An overview of the FFTB alignment system is presented herein.

## 1. INTRODUCTION

The primary objective of the Final Focus Test Beam (FFTB) is to consistently and repeatably focus a 50 GeV electron beam onto an area which is 1  $\mu\text{m}$  wide (horizontal) and 80 nm tall (vertical). The FFTB alignment system contributes in three ways.

- (1) Tight initial alignment tolerances reduce the time required to initially focus the beam.
- (2) Sensors which monitor the motions of magnets during a run, independent of the beam, are new tools which improve our ability to focus and control the beam.
- (3) Sensors which monitor motions of the magnets between runs reduce the time required to return to a successful configuration.

## 2. INITIAL ALIGNMENT

### 2.1 Tolerances

The FFTB is composed of four straight sections as shown in figure 1.

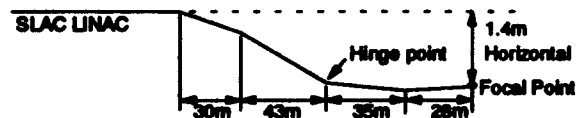


Figure 1. FFTB composed of 4 straight sections.

Initial alignment tolerances for FFTB quadrupoles and sextupoles are quite small: 30 $\mu\text{m}$  horizontally and 100 $\mu\text{m}$  vertically. Additionally, the intersections between adjacent straight sections

must have closest vertical approach of no more than 30 $\mu\text{m}$ .

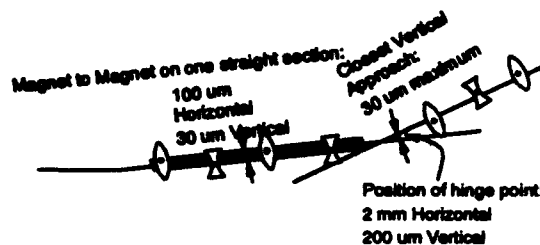


Figure 2. FFTB initial alignment tolerances illustrated.

### 2.2 Tooling plates

The 30 $\mu\text{m}$  vertical alignment tolerance applies to 23 quadrupole magnets and 4 sextupole magnets[1,2]. We have fiducialized these magnets to within 12 $\mu\text{m}$  using a technique developed here at SLAC[3]. The fiducials for these magnets are press fit into invar tooling plates. Two of these tooling plates are kinematically mounted on the horizontal and vertical split planes of each of the 23 quadrupole and 4 sextupole magnets. The mounting scheme of the tooling plates on a quadrupole is illustrated in figure 3. One spherical contact point touches the vertical split plane, two spherical contact points touch the horizontal split plane and 3 spherical contact points press against the magnet in the longitudinal direction. We have found that these tooling

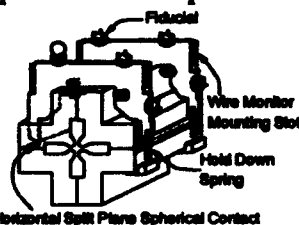


Figure 3. Tooling plates on a quadrupole.

plates may be removed and replaced on the magnet to within 3 $\mu\text{m}$  of their original location.

Mounting slots for 2 wire position monitors (WPMs) are located on each tooling plate. WPMs will be described in section 3.2.

### 2.2 Alignment Instruments

In addition to theodolites, we will use two new alignment instruments for FFTB initial alignment: (1) Laser Tracker (2) Portable Water Hydrostatic Level.

#### 2.2.1 Laser Tracker

The laser tracker[4] is an interferometer whose pointing direction "tracks" a retroreflector mounted

\* Work supported by the U.S. Department of Energy under contract DE-AC03-76SF00515

Contributed to the Particle Accelerator Conference (PAC'93) Washington DC, May 17-20 1993

inside of a 1.5 inch diameter sphere. By moving the sphere between fiducials, one may quickly measure the relative azimuth and elevation between the fiducials, as seen by the tracker, to within a few arcseconds. Relative line of sight distance between fiducials may be measured to within about 10 $\mu$ m.

### 2.2.3 Portable water level

In order to achieve 30 $\mu$ m vertical alignment of the magnets we will use a portable hydrostatic level[5]. The measurement range of this instrument is approximately 25mm, and we typically achieve 10 $\mu$ m repeatability after a series of measurements spanning several meters and taken over the course of an hour. For increased accuracy over large distances, the hydrostatic level, and the laser tracker will use the Fresnel laser system as a global straight line reference.

### 2.3 Fresnel Laser Reference System



Figure 4. A Laser Station.

The SLAC linac Fresnel laser alignment system has been extended to the FFTB[6]. Thirteen new zone plates have been installed and calibrated to within 10 $\mu$ m with respect to fiducials on the outside of their respective laser

stations. By detecting the images produced from these zone plates we may compute to within 5 $\mu$ m[7] the relative offset of each zone plate from a straight line which goes through the center of two zone plates. Thus the relative positions of the laser station fiducials throughout the FFTB may be computed to within about 10 $\mu$ m. These fiducials will serve as a straight line reference extending the length of the FFTB.

## 3. ON LINE MONITORING

### 3.1 Description

On line monitoring is the process by which the stretched wire alignment system monitors the relative motions of the magnets in a straight section while the beam is turned on. Each of the magnets with tooling plates is installed on a mover which can roll the magnet in increments of several  $\mu$ radians and which can move the magnet horizontally and vertically in increments of approximately 1 $\mu$ m. On line monitoring using the stretched wire system will allow us to directly

observe subtle changes in the relative alignment of the magnets in one straight section. Previously such changes were observed indirectly via beam position monitors and other devices which monitor the beam.

### 3.2 Stretched wire alignment system

Our colleagues from DESY have provided a stretched wire alignment system

which will be used for on line (and off line) monitoring of magnet positions. The system consists of a pair of wires for each of the 4 straight sections. Three WPMs are installed on the tooling plates of each of the 23 quadrupoles and 4 sextupoles. Each WPM is similar to a beam position monitor (BPM) in that it contains 4 antenna and the differential signal strength received from opposite pairs of antenna is the quantity of interest. However, unlike a BPM which receives its signal from a packet of charged particles, the WPMs receive their signal from a stretched wire which is excited at the fixed end with a 3 Watt, 140 MHz signal and which is grounded through a 250 $\Omega$  resistor at the pulley end. The wire is centered to within  $\pm$ 150 $\mu$ m inside an 8mm (inner diameter) brass tube. The tube serves as the outer conductor in a coaxial structure which presents a constant impedance to the 3 Watt signal and which shields the signal from the outside world where it would interfere with FM radio broadcasts. A precision made aluminum extrusion provides a straight and rigid support for the brass tube.



Figure 5. The stretched wire

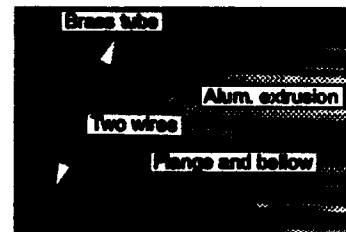


Figure 6. Support structure for the wire system.

The 3 WPMs on each magnet allows us to measure horizontal, vertical, roll, pitch and yaw motions of the magnet. The standard deviation of a set of readings from one WPM is typically less than 1 $\mu$ m. The stretched wire oscillates at approximately 5 Hz with an amplitude of several micro meters. Therefore it is necessary to average readings from each WPM for about a second in order to achieve sub micro meter standard deviation.

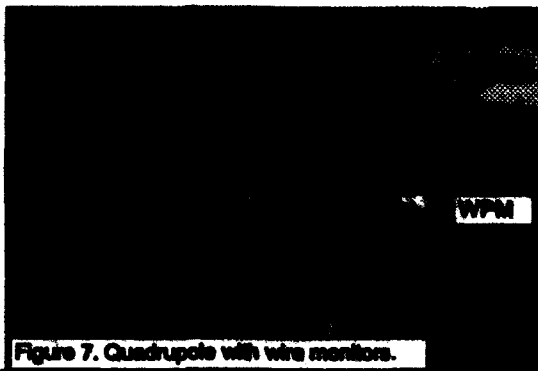


Figure 7. Quadrupole with wire monitors.

## 4. RECONFIGURATION

### 4.1 Description

We anticipate that the FFTB will have runs lasting for one week or less separated by down times of one or more weeks. Therefore, it is important to be able to return the magnets to their previous positions quickly. Our goal is to reconfigure the FFTB to within  $\pm 10\mu\text{m}$  using the alignment system. Reconfiguration applies not only to the alignment of magnets on one straight section but also to the intersection of adjacent straight sections, see figure 2. In order to do this we need a way of monitoring the motions of the ends of the wires.

### 4.2 Bridges

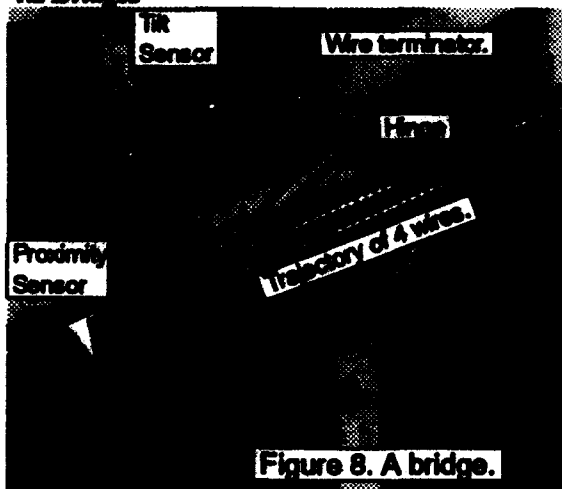


Figure 8. A bridge.

The bridge is a rigid invar structure which transfers the motion of a wire terminator to the top of a laser station whose location may be monitored with respect to other laser stations throughout the FFTB. The bridge rests on a ball which touches the top of the laser station, and the bridge is attached to the wire terminator via a precision hinge. The ends of 4 wires, spanning 2 straight sections, are also mounted on the wire terminator. The roll of the bridge is monitored with sub micro radian precision by a tilt sensor whose temperature is

maintained constant to within 1/1000 degree C. The horizontal displacement of the bridge with respect to the laser station is monitored to within  $2\mu\text{m}$  by a proximity sensor. Using these sensors and a number of temperature sensors located on the wire terminator and the laser station, we will monitor the horizontal and vertical motion of the wire ends with respect to the laser station to within a few micro meters.

### Summary

- Initial alignment of the FFTB will be achieved by supplementing theodolites with two new survey instruments, a laser tracker and a portable hydrostatic leveling system, used in conjunction with the laser reference system.
- On line monitoring of each FFTB straight section will be accomplished using the stretched wire alignment system.
- Reconfiguration of the FFTB after a down time will be accomplished using information from the stretched wire system, the laser reference system and the bridges which connect them.

### References

- [1] These magnets were constructed for the collaboration by the Institute of Physics, Novosibirsk, Russia.
- [2] The FFTB also includes three quadrupoles just upstream of the focal point which are aligned to within  $5\mu\text{m}$  with respect to one another and which are mounted on their own table which may be translated horizontally, vertically, rolled, pitched and yawed with sub-micro meter precision. This entire system provided to the collaboration by KEK laboratory, Japan.
- [3] G.E.Fischer et al., "Precision Fiducialization of Transport Components", Proc. EPAC 1992, p. 138.
- [4] Chesapeake Corp., Lanham, Maryland U.S.A
- [5] Pellissier Instrument Corp., Denver, CO U.S.A
- [6] V.Bressler et al., "High Resolution Fresnel Zone Plate Laser Alignment System", Proc. EPAC 1992, p. 1613.
- [7] V.Bressler et al., "The Final Focus Test Beam Laser Reference System", Proc. PAC 1993

# Long Term Experience with Cryoplant Operation for Superconducting Magnets and RF Cavities at CERN

D. Delikaris, J.-P. Dauvergne, P.K. Frandsen, F. Haug, G. Passardi, J.-M. Rieubland and J. Schmid  
CERN, CH-1211 Geneva 23, Switzerland

## Abstract

Eighteen liquid-helium cryoplants are presently in use at CERN, four of them commissioned in 1992. Unit capacities (entropy equivalent) range from 0.1 to 6 kW/4.5 K. Four even larger cryoplants (12 kW/4.5 K, upgradable to 18 kW/4.5 K) are in the process of installation and commissioning. Apart from feeding laboratories for development and tests of cryogenic equipment, the cryoplants provide cooling for superconducting detector and accelerator magnets and superconducting RF cavities, where their uninterrupted availability is crucial for efficient accelerator operation. Integrated running time in 1992 was of the order of 100 000 hours. This paper summarises experience from all phases of operation, normal running, emergencies, cool-down and warm-up. Some information is given on software controls, data acquisition, and fault analysis, and on conclusions concerning corrective or preventive maintenance and advisability of investments for increased availability of cryogenics.

## I. INTRODUCTION

By the end of 1991, 14 liquid-helium cryoplants were in operation at CERN, totalling a cooling capacity equivalent to 6.6 kW at 4.5 K. Nine of them were used to cool the superconducting magnets of various particle detectors [1] (including low- $\beta$  quadrupoles integrated into the LEP detectors ALEPH, DELPHI, L3 and OPAL [2]), three of them to provide liquid-helium for test facilities, mostly for the development of LEP200 superconducting cavities and superconducting magnets for LHC, and two served for the cooling of superconducting cavities in LEP and SPS [3]. The typical unit capacity of these plants was 500 W.

In the framework of the LEP200 Project [4], two much larger cryoplants of 6 kW equivalent capacity were commissioned in 1992 (and, in addition, two 400 W plants), and another four cryoplants of 12 kW capacity (upgradable to 18 kW by addition of compressors) are presently (in 1993) being installed and commissioned. The cooling capacity installed at CERN has thus nearly tripled in 1992 and will by 1994 have increased by a factor of ten with respect to 1991.

In this paper, experience with operation of the 18 cryoplants in service last year will be reported.

## II. CHARACTERISATION OF THE CRYOGENIC SYSTEM

Table I summarises technical and operational data of the cryoplants. The following points should be noted:

- The cryoplants for experiments are installed close to the detectors in the experimental halls (underground halls for the LEP experiments); compressors are housed in special buildings above ground. Because of the large distances (of the order of 10 km between LEP experiments) centralisation of compressors was possible only for the complex NA35 - NA44 - NA47 - RD5 - LHC magnet test lab and for the complex OMEGA - BOC cryoplant - ex-ISR cryoplant.
- The cryoplants for experiments (with the exception of the OMEGA veteran plant) are usually operated in remote control mode from a central Cryogenic Control Room. Centralisation of cryoplant operation will also be implemented for cavity cryogenics in a later stage (Remote Cryogenics Commissioning Room); in the present LEP200 construction phase involving frequent non-routine operations, local control is often the preferred operational mode. Cryoplants of the test facilities and of the Central Liquefier are controlled locally.
- None of the plants is operated by round-the-clock shifts of operators. At night time and week-ends, operators are, however, on standby duty, and can be called in by an automatic alarm system.
- Table I mentions the year of commissioning of each cryoplant. Note the tremendous increase of plant efficiency (170 kW compressor power for 150 W cooling power, i.e. 1100 W/W, in 1968 versus 2500 kW for 12 kW, i.e. 210 W/W (design value) in 1993. This improvement by a factor of 5 is a very important step forward towards economy in power consumption, which accounts for a substantial part of the operation costs of a superconducting accelerator. The increase in efficiency is probably related to the requirement of utmost compactness for plants to be installed in an accelerator tunnel, where space is at a premium, since compactness requires heat exchangers of highest efficiency, which in turn increase the overall efficiency of the plant.

**Table 1**  
**CERN cryoplants: technical data, operation time and downtime in 1992**

Function	Cryoplant commissioned in	Nominal cooling power at 4.5 K (entropy equivalent) W	Compressor power, kW	Running hours, 1992	Number of accidental full stops		LHe autonomy without cooling hours	Interruption of LHe delivery to users hours
					cryogenic origin	other origin		
<b>Fixed-target experiments</b>								
OMEGA detector	1971	800	850	6200	0	6	0	15
NA35	1976-79	400	450	2200	0	0	0	4
NA44	1979, 1991	400	450	2900	0	0	0	0
NA47	1976-79	400	450	5700	1	1	20	26
RD5	1976-79	400	450	3200	0	0	0	0
<b>LEP collider experiments</b>								
ALEPH (incl. low- $\beta$ quadrupoles)	1988	800	600	6400	3	9	0 (low- $\beta$ : 5)	18 (low- $\beta$ : 10)
DELPHI (incl. low- $\beta$ quadrupoles)	1988	800	600	6800	1	7	0 (low- $\beta$ : 5)	10 (low- $\beta$ : 0)
OPAL low- $\beta$ quadrupoles	1976-79	400	450	6200	1	7	5	10
L3 low- $\beta$ quadrupoles	1976-79	400	450	5950	0	6	5	12
<b>Superconducting RF cavities in the SPS (injection of electrons/positrons into LEP)</b>								
SPS BA4	1989	120	110	5000	0	0	0	0
SPS BA4	1992	400	450	4100	0	1	0	12
<b>Superconducting RF cavities in LEP</b>								
LEP Point 2	1992	6000	1350	6200	1	6	0	Operation according to accelerator requirements
LEP Point 6	(1993)	12000	2500	0				
LEP Point 8	(1993)	12000	2600	0				
<b>Test facilities for superconducting cavities and magnets</b>								
Hall 892: LHC magnet test lab	1976-79	400	450	5550	Intermittent operation according to test requirements			
Hall 180: BOC cryoplant	1977	335	800	4000				
Hall 180: ex-ISR cryoplant	1980, 1990	1200	600	2100				
Hall SM18: LEP200/LHC tests	1992	6000	1800	6000				
<b>Central liquefier and Cryolab</b>								
A.D. Little liquefier	1968	150	170	5370	Intermittent operation according to requirements			
Sulzer liquefier	1992	400	450	7400				

### III. OPERATIONAL EXPERIENCE AND FAULT ANALYSIS

In the last five columns, Table 1 gives the number of running hours of the cryoplants used in regular operation with the accelerator and current experiments, the number of accidental stops of the plant and the duration of interruption of liquid-helium supply to the user. The second last column indicates a certain autonomy for some systems, being cooled from an intermediate dewar and therefore less vulnerable by short-term interruptions of power supply.

Table 1 shows that of a total of 50 interruptions, only 7 were due to malfunctioning of a component of the cryogenic system. That this number is so small is not only due to the quality of the installations, but also to the rapidity and competence of the operators on stand-by duty, who were called in 230 times by an early warning of the automatic alarm system, and who cleared the situation before aggravation led to a breakdown of the system. The total number of lost hours for accelerators and physics experiments was 117 (coincidence of cryogenic downtime with physics data taking), from which only 22 were associated with cryogenic equipment failures. Regarding the 61 000 normal running hours, the fault rate was about  $1.9 \cdot 10^{-3}$  for all stops and only  $3.6 \cdot 10^{-4}$  for the stops caused by cryogenic equipment failures. The high availability of the cryoplants is essentially due to the careful preventive maintenance during shutdowns (Computer Aided Maintenance is being introduced at present), and the competence of the operating team.

Reasons for the interruptions originating in the cryogenic system were the failure of a 24 V power supply (including its backup unit), process software crash, failure of a control valve and impurities in the helium cycle. The remaining 43 interruptions were mostly caused by interruption of water and electric power supplies and by perturbations in the communications network. Looking at these figures, it appears to be good policy to invest, for a reduction of cryogenic downtime, in the reliability of utilities.

It may be worthwhile to comment on this point.

It is a characteristic of cryogenic systems that immediate restart after utility failure is possible only if this failure is of very short duration. (Cryogenic buffering, e.g. by provision of an intermediate liquid-helium dewar for increased tolerance against perturbations, as mentioned, is possible in exceptional cases only, typically when the load is of a nature suitable for cooling in liquefier rather than refrigerator mode). In most cases the time required to restore thermodynamic equilibrium after severe perturbation is a multiple of the utility downtime that provoked this perturbation, in particular if a large and delicate system is concerned, e.g. if the interruption of cooling has led to the quench of a superconducting magnet. Even if interruptions of utilities cannot be excluded, it is of prime importance to keep their duration as short as possible and to make arrangements for their fastest possible reestablishment, with high priority of cryogenics versus other less critical components.

### IV. REFERENCES

- [1] J.P.Dauvergne et al, "Helium Cryogenics at the LEP Experimental Areas", CERN/EF/89-10, 1989 Cryogenic Engineering Conference, UCLA, Los Angeles, USA: Advances in Cryogenics 1990, Vol.35, p.901
- [2] Ph.Lebrun et al, "Operational Experience with the LEP Low-Beta Superconducting Quadrupoles", CERN/AT-MA/92-03, 1992 Third European Particle Accelerator Conference, Berlin, Vol.2, P. 1641
- [3] G.Passardi et al, "Long term Operational Experience and Upgrade of the Cryogenic System for the Superconducting Cavities in the SPS Accelerator", 14th International Cryogenic Engineering Conference (ICEC14), Kiev, Ukraine: Cryogenics 1992, Vol.32, ICEC Suppl. p.146
- [4] M.Barranco-Luque et al, "Status of cryogenics for the LEP200 energy upgrade project at CERN", 14th International Cryogenic Engineering Conference (ICEC14), Kiev, Ukraine: Cryogenics 1992, Vol.32, ICEC Suppl. p.151

# Axial Variations in the Magnetic Field of Superconducting Dipoles and Quadrupoles\*

A.K. Ghosh, K.E. Robins and W.B. Sampson  
Brookhaven National Laboratory  
Upton, New York 11973

## Abstract

A periodic variation in the magnetic field along the axis has been observed in both quadrupole and dipole magnets made from superconducting cable. This oscillation is present in all components of the field and has a wavelength equal to the transposition length of the cable. In general the amplitude of these variations increases with magnet current and is not reversible. The residual field pattern at zero current depends on the energizing cycle and increases with time spent at high field. The decay of the oscillations has a complex time dependence which contains some extremely long time constants. Unbalanced currents in the individual strands of the cable appear to cause these effects and the field variations can only be completely erased by raising the magnet above its critical temperature.

## I. INTRODUCTION

Axial field oscillations were first observed in the sextupole component of HERA dipoles in 1990.<sup>[1]</sup> Similar variations were soon observed at other laboratories and it became apparent that such patterns are present in the field of all magnets made with multistranded conductor.<sup>[2,3]</sup> Since these field variations are small (typically a few gauss) they are most apparent at low fields and can easily be seen when the power supply is turned off after a high field cycle in which the current has been maintained at the peak value for several minutes. The pattern is present at all field levels and in both the normal and skew components of the field.

## II. FIELD DEPENDENCE

The measuring technique used to investigate the axial oscillations has been described elsewhere.<sup>[2]</sup> Most of the measurements reported in this paper concentrate on the first allowed term; sextupole in dipoles and duodecapole in quadrupoles. Figure 1 shows the normal sextupole field for a portion of dipole DCA213, a full length SSC prototype when powered at 7000 amps. The axial variation of approximately 10 gauss peak to peak is much larger than the nominal sextupole field ( $\sim 4$  g) and many times larger than the magnetization sextupole (0.3 g) at this field (7 T). Similar patterns occur in quadrupoles, the variation in the duodecapole component along the axis of RHIC quadrupole QRB003 is shown in Fig. 2.

The amplitude of the oscillations increases with current but generally is not reversible. The magnitude of the axial variation may be smaller on the up-ramp (Fig. 3) or larger (Fig. 4). Similarly when the magnet is maintained at high current the amplitude may increase or decrease with time (Fig. 5). In Fig. 4 the magnet was held at 6000 amps for approximately 1 hour while the amplitude decayed. The cycle depicted in Fig. 3, however, did not have a similar waiting period. A peak to peak amplitude of approximately 2 gauss was present at zero current in both cases due to the previous history of the magnets. For a magnet just cooled into the superconducting state no oscillations would be present and the curves of Figs. 3 and 4 would start at the origin. Once oscillations have been established they can only be completely eliminated by raising the magnet windings above their critical temperature. The difference in behavior exhibited by dipoles 211 and 213 does not seem to be related to any obvious magnet parameter since they were constructed using the same tooling and conductor made to the same specifications.

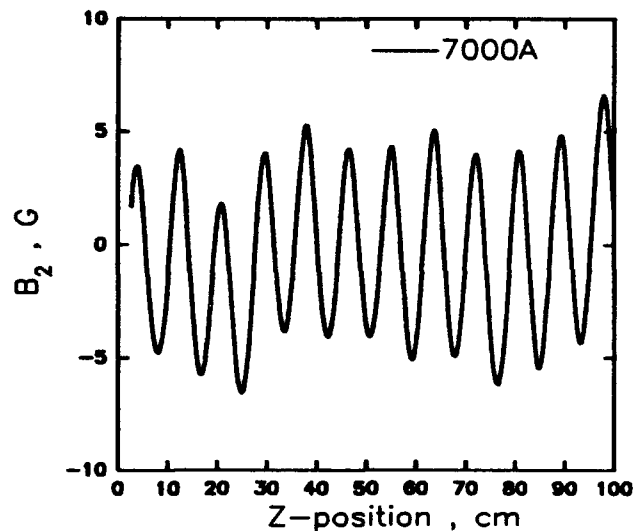


Figure 1. Oscillations in the normal sextupole component of the field of SSC dipole DCA213 near the peak field (7T).

\*Work performed under Contract No. DE-AC02-76CH00016 with the U.S. Department of Energy.

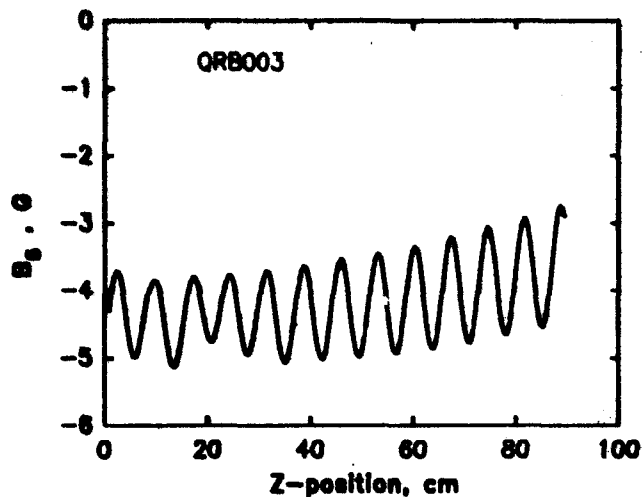


Figure 2. Oscillations in the residual 12-pole component of RHIC quadrupole QRB003.

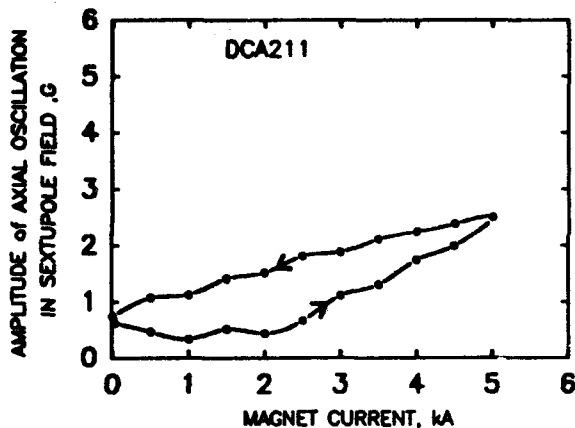


Figure 3. Oscillation amplitude as a function of current for SSC dipole DCA211.

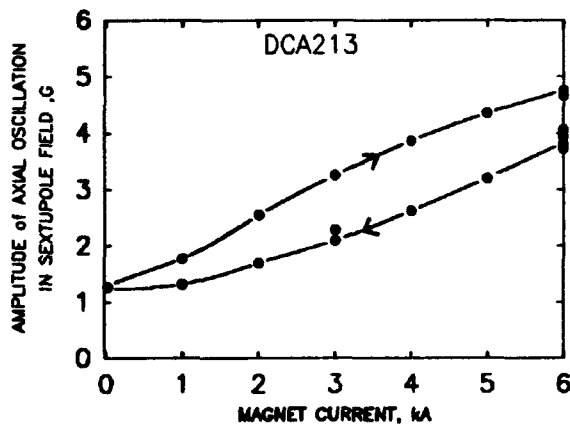


Figure 4. Oscillation amplitude as a function of current for SSC dipole DCA213.

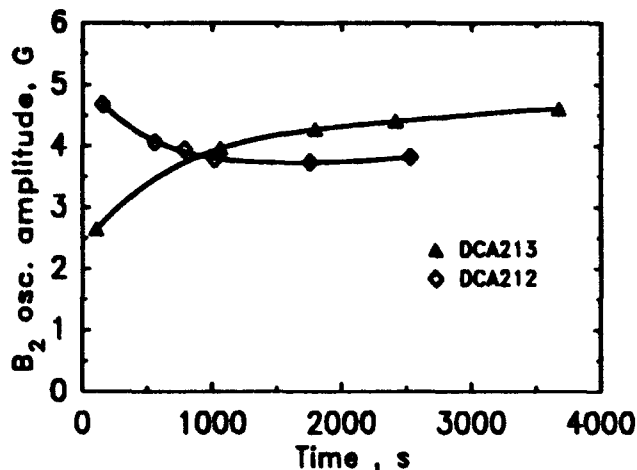


Figure 5. Time evolution of the sextupole oscillation amplitude at 6000 A in the SSC dipoles DCA212 and DCA213.

### III. EFFECT OF LOCAL HEATING

Some of the magnets examined were provided with spot heaters used to initiate normal zones for coil protection studies. One of these heaters was used to see if the axial field pattern could be altered by pulsing the heater without quenching the magnet. Dipole DCA211 was powered to 5000 A and the heater energized to progressively higher values while scanning the region on either side of heater location. No changes in the pattern were observed at any power level below that which provoked a quench. This experiment was repeated with the magnet at 25 A but with a large field oscillation present due to an earlier excursion to high field. Since the pulse power supply was not capable of producing a normal zone at this low field level it was replaced with a dc source. The heater current was increased in one amp increments while scanning the region one half meter on either side of the heater. No change was observed until the heater current reached 10 Amps where the amplitude increased significantly as shown in Fig. 6. This change occurred almost instantly and over the whole region of the scan. No further change was observed with the heater continuously powered on turned off. This increase of almost 50% in the oscillation amplitude decayed back to approximately the original level in about two hours. When the heater current was later increased to 12 Amps another significant jump of 70% occurred in the sextupole oscillation amplitude. Unfortunately higher heater currents were not possible due to limitations in the wiring which was originally only intended for pulsed operation.

One of the 1.8 meter model SSC dipoles DRSK19 was equipped with heaters on its leads at the point where they enter the body of the windings. When these heaters were powered they modified the residual dipole pattern as shown in Fig. 7. In this case the amplitude was dramatically reduced and the average value of the residual field increased.

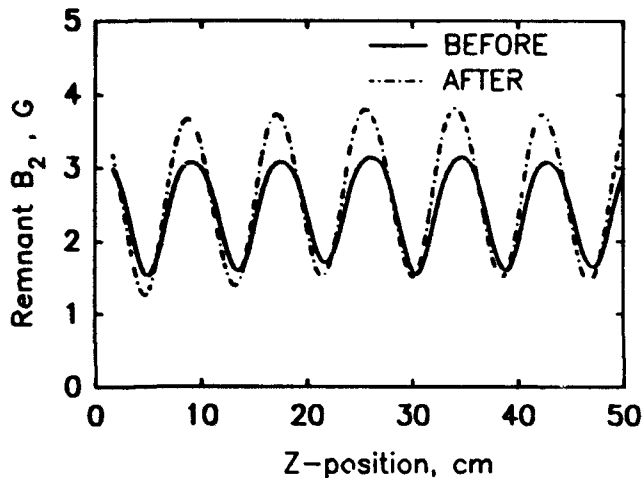


Figure 6. Sextupole oscillations in DCA211 before and after powering the mid-plane spot heater located at 25 cm.

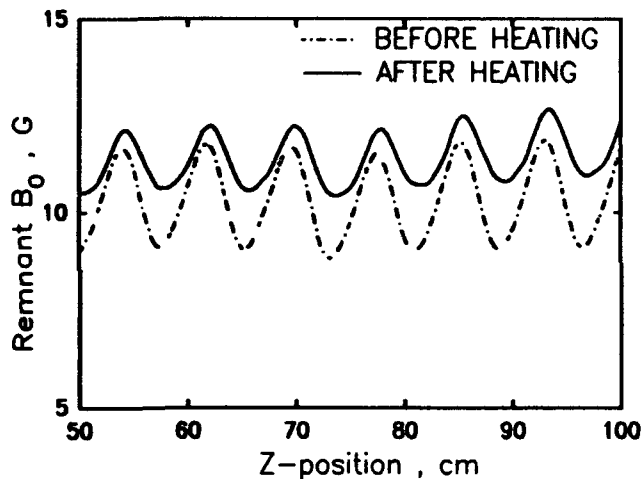


Figure 7. Oscillations in the remnant dipole field of magnet DRSK19 before and after powering the lead heaters.

#### IV. DISCUSSION AND CONCLUSIONS

The fact that field oscillations are present as soon as the magnet is energized and increase with current implies large unbalanced currents in the strands of the cable. A possible mechanism for such periodic currents has been described by A.A. Akhmetov.<sup>[4]</sup> The unusual increase in amplitude observed in the spot heater experiments suggests that the oscillation pattern is the sum of contributions from different portions of the magnet and that the unbalanced currents in a specific length of conductor can be damped out by inducing a small normal zone. Standing waves in each half turn reflecting from the ends of the magnet might explain the experimental observations. When the spot heater raises a small region of the cable above the transition temperature

the current in that half turn dies out leading in this case to an increase in the oscillation amplitude. Higher heater power is required to quench a similar region in the next turn and produce a further change in the amplitude. Presumably spot heaters at other locations in the winding would produce the opposite effect and reduce the oscillation strength. It is not obvious why such standing wave patterns should have the very long time constants observed in these experiments<sup>[3]</sup> which imply an extremely low effective resistance between strands.

The time evolution and the magnitude of the oscillations were also found to be dependent on the ramp rate used to power the magnets. Measurements are underway to try to understand the nature of this ramp rate dependence. The results of this study will be reported in the near future.

The measurements of oscillating fields performed to date are on prototype dipoles developed for various accelerator projects and as such must be done in the time available between quench testing and the more conventional magnetic measurements. Parasitic measurements are always limited by time considerations resulting in a somewhat confusing mixture of data from different magnets. A complete understanding of the exact nature of the current patterns producing these axial variations will probably require the construction of special dipoles equipped with internal heaters and voltage taps and dedicated to resolving the many loose ends in the present understanding of this phenomenon.

#### V. ACKNOWLEDGMENTS

The authors would like to thank the BNL magnet test section for their help in performing these measurements. The Magnet Science group of the Test and Data Management Department of SSCL has supported and encouraged this work.

#### VI. REFERENCES

- [1] H. Brück, et al., DESY HERA, g1-01, 1991
- [2] A.K. Ghosh et al., Supercollider-4, Plenum Press, New York, pp. 765-772, 1992
- [3] A.K. Ghosh, et al., Int. J. Mod. Phys. A (Proc. Suppl.) 2B, pp. 665-667, 1993.
- [4] A.A. Akhmetov and T. Ogitsu, SSCL Report MD-TA-245 (1993).

# Large Aperture Quadrupoles for RHIC Interaction Regions\*

R. Gupta, M. Anerella, G. Ganetis, M. Garber, A. Ghosh, A. Greene, A. Jain, S. Kahn, E. Kelly, E. Killian, G. Morgan, A. Morgillo, J. Muratore, A. Prodell, M. Rehak, W. Sampson, R. Shutt, P. Thompson, P. Wanderer, E. Willen

Brookhaven National Laboratory, Upton, NY 11973, USA

## Abstract

The ultimate luminosity performance of the Relativistic Heavy Ion Collider (RHIC) depends on the field quality in the large aperture (130 mm) superconducting quadrupoles in the interaction regions<sup>1,2</sup>. In this paper we discuss the design features that are incorporated to obtain a good field quality. Coil midplane gap and pole shims may be adjusted to remove certain field harmonics due to systematic errors in construction. Iron tuning shims will be inserted at eight strategic locations in the assembled magnets to correct the measured values of harmonics in each magnet. The performance of two prototype magnets and upgrades under consideration will be discussed.

## I. INTRODUCTION

A total of seventy two 130 mm aperture quadrupoles will be used in 24 focusing triplets in six interaction regions. The parameters of these quadrupoles (Q1, Q2 and Q3) are shown in table 1. The beam will be squeezed to the smallest possible size ( $\beta^* = 1$ ) at the crossing point in the two low-beta interaction regions to obtain the highest possible luminosity. An unavoidable consequence of that squeezing is the increase in the beam size in these quadrupoles. Moreover, a rapid variation in the beam size within the focusing triplet limits the effectiveness of the local and lumped global corrector system<sup>2</sup>. Therefore, good field quality large aperture quadrupoles in the interaction regions are crucial to beam life during the high luminosity operation of RHIC. Since the maximum luminosity is desired at the top energy, the field errors will be minimised at the maximum operating gradient.

In quadrupoles, the skew ( $a'_n$ ) and normal ( $b'_n$ ) field harmonics in prime units are defined as follows :

$$B_y + iB_x = 10^{-4}G \times R \sum_{n=0}^{\infty} [b'_n + ia'_n] \left[ \frac{x + iy}{R} \right]^n$$

where  $B_x$  and  $B_y$  are the field components at  $(x, y)$ ,  $G$  is the gradient at the center of the quadrupole and  $R$  is the reference radius, chosen as 40 mm for these magnets.

## II. BASIC CONSTRUCTION

In the design of these quadrupoles, the yoke also acts as a collar. A 6.35 mm thick stainless steel shell is welded after the collaring keys are inserted in the compressed yoke. The space between the coil and yoke is taken by a thin glass filled phenolic spacer. The magnet contains constant perimeter ends in which the turns are uniformly distributed. The two Q1 quadrupoles of the inner and outer rings will share a common cryostat.

\*Work supported by U.S. Department of Energy.

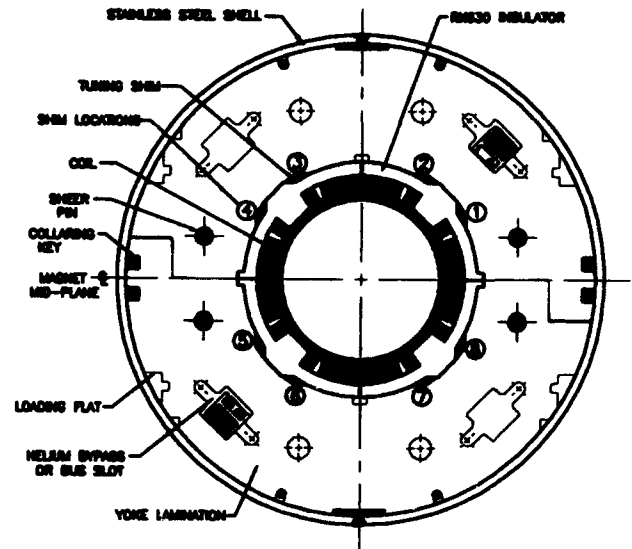


Figure 1: Cross section of the 130 mm quadrupoles for RHIC interaction region.

Table 1: The basic design parameters of the large aperture quadrupoles for RHIC interaction regions.

Parameter	Value
Superconducting wire diameter	0.65 mm
Number of wires per cable .....	36
Copper to superconductor ratio	1.8
Cable mid-thickness/width ....	1.16/11.7 mm
Cable insulation .....	Kapton Ci
Critical current at 5.6T, 4.2°K	≥10100 A
Number of turns per pole .....	27
Coil inner diameter .....	130 mm
Coil outer diameter .....	154 mm
Yoke lamination thickness .....	6.35 mm
Yoke inner radius at midplane .	87 mm
Yoke inner radius at pole .....	92 mm
Yoke outer diameter .....	350.5 mm
Magnetic length, Q1, Q2, Q3 ..	1.44, 3.4, 2.1 m
Min. beam spacing in triplet ..	424 mm
Design current .....	5.0 kA
Design gradient .....	48.1 T/m
Operating temperature .....	4.6° K
Computed quench gradient ....	75.3 T/m
Field margin .....	57%

### III. CROSS SECTION

The quadrupole cross section is shown in Fig 1. The coil has a total of 27 turns per octant in three blocks. The coil midplane gap has been increased from a minimum 0.1 mm to 0.2 mm in the iterated cross section. Any change in coil size in production magnets will be accommodated by changing the midplane gap by about 40% of that amount and the pole shim by about 60%. This would result in the same pre-compression and the same  $b'_5$ . In addition, a variation in midplane gap and a variation in pole shim size provides a simple but powerful tool for tuning the field harmonics in production magnets without changing the basic coil cross section.

In cosine  $\theta$  magnets, the iron aperture is circular. However, in order to reduce  $b'_5$  saturation we have designed a yoke where the aperture is defined by two radii - 87 mm at the midplane and 92 mm at the pole. This has been very effective in reducing the  $b'_5$  saturation from 15 to 1 unit. It forces an early saturation at the yoke midplane and delays/reduces at the pole.

There is a phenolic spacer between the coil outer diameter and yoke inner diameter having a width of 10 mm at the midplane and 15 mm at the pole. However, there are eight places where there is a ~7mm wide space between the spacer and the yoke. These spaces will be used for accommodating the magnetic tuning shims, as shown in Fig. 1. The other holes and cutouts in the yoke have been placed such that the symmetry breaking harmonics are less than 0.1 unit in the design range of operation. The cross talk induced harmonics (by the quadrupole in the other ring) are also less than 0.1 unit.

### IV. SHIMMING

The random errors in harmonics are primarily determined by the limits in the accuracy of the parts and the process used in manufacturing the superconducting magnets. To overcome these limitations, we have developed a method of shimming. The basic principle of this is to insert the iron shims in the eight suitable locations between the phenolic spacer outer radius and the yoke inner radius to reduce the measured harmonics. The approximate angular location of shim No. 1 is 30°, No. 2 is 60°, No. 3 is 120°, etc., as shown in Fig. 1. Since the harmonics will be corrected magnet by magnet, the method will also reduce any systematic value, if present.

Methods based on the same general principle have been used before in conventional magnets. It is more complicated in superconducting magnets because (a) there is usually no access to the iron aperture and (b) when the magnet is opened and assembled again the harmonics are not reproduced at the desired level. However, the design of the RHIC large aperture quadrupoles is such that the eight iron shims can be inserted easily without opening the magnet after the magnetic measurements are performed. The actual shim package will always be molded to the same thickness but a part of it will be made of magnetic steel (laminated and insulated) and the rest will be made of the non-magnetic material brass.

The maximum space available for the magnetic tuning shim is ~6.6 mm. The nominal design has 3.3 mm of magnetic and 3.3 mm of non-magnetic material. All changes in shim size will be made relative to the nominal 3.3 mm of magnetic material. In table 2, we have listed the maximum amount of correction possible in each harmonic with +1 mm and/or -1 mm relative change in shim. The locations which produce a maximum positive value for each harmonic for this relative change is also shown. Some of the harmonics listed in table 2 are coupled to each other, e.g.  $b'_3$  and  $b'_7$  (in general, harmonics  $2n+1$  and  $2n+5$  with  $n=0,1,2,\dots$ ). This means that if  $b'_3$  is changed,  $b'_7$  will also change according to the  $b'_3/b'_7$  ratio given in table 2. Therefore, the eight shims can not be used to make any arbitrary eight harmonics zero. But the correction in the "skew and normal" harmonics and in the "odd and even" harmonics are orthogonal to each other. Therefore, one can still make the desired eight harmonics ( $a'_2, a'_3, a'_4, a'_5$  and  $b'_2, b'_3, b'_4, b'_5$ ) independently zero. Since adequate space for shimming is available, the correction will only be limited by the acceptance in the higher order harmonics generated in the process.

A computer program *SHIMCAL* has been written to compute the values of eight shims to minimize an error function consisting of measured and desired values of field harmonics. The harmonics will be corrected for the top energy operation; at injection there will be about 10% over-correction to account for the loss due to iron saturation. In mass production, the correction will be based on warm measurements. However, a warm to cold (5 kA) correlation will be developed in the beginning.

Table 2: Maximum change possible by +1 mm and/or -1 mm relative change in shim size at the given locations at 5.0 kA. Shim locations 1,2, etc. are shown in Fig 1.

	+1/-1 mm locations	Change (Units)		+1/-1 mm locations	Change (Units)
$a'_0$	1234/5678	18.64	$b'_0$	1278/3456	18.64
$a'_1$	1357/2468	8.37	$b'_1$	All/None	22.50
$a'_2$	5678/1234	9.85	$b'_2$	1278/3456	9.85
$a'_3$	3478/1256	7.37	$b'_3$	1458/2367	6.36
$a'_4$	2358/1467	2.99	$b'_4$	1368/2457	2.99
$a'_5$	2468/1357	2.52	$b'_5$	None/All	1.22
$a'_6$	2358/1467	1.0	$b'_6$	2457/1368	1.0
$a'_7$	1256/3478	0.04	$b'_7$	2367/1458	0.72
$a'_8$	1467/2358	0.25	$b'_8$	2457/1368	0.25
$a'_9$	1357/2468	0.16	$b'_9$	None/All	0.08

### V. MEASUREMENTS, ANALYSIS AND UPGRADES

The quench performance of the two pre-production quadrupoles QRI001 and QRI002 is shown in Fig 2. The first quench occurs at 28% above the maximum operating current. Though not critical to the machine operation, the quench performance is expected to improve significantly

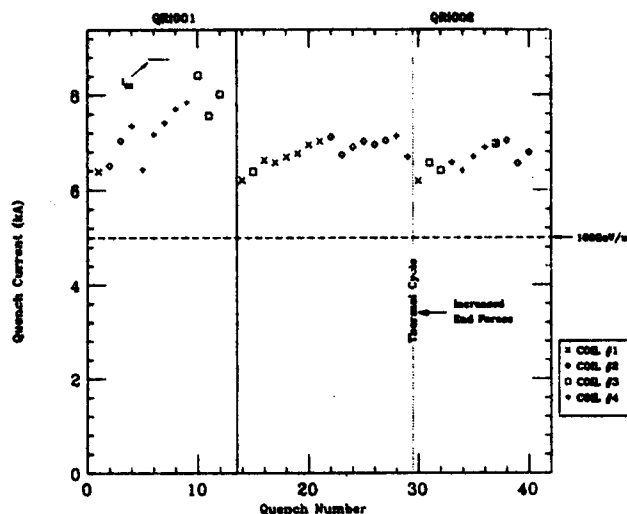


Figure 2: Quench performance of the pre-production quadrupoles QRI001 and QRI002.

in QRI002 rebuild and in production magnets when the pole lead, just coming out of the straight section, is solder filled and thus better supported.

The azimuthal stress on the coil has been measured at all eight pole locations. The average stress was 10.5 kpsi (72.3 MPa) at room temperature. A significantly higher (3 kpsi) stress has been observed in the four strain gauges located nearest to the horizontal plane. After the cool down the average stress was 3.3, 2.1 and 1.5 kpsi at a current of 0, 5 and 6.6 kA; the asymmetry in stress data persisted. The ends were pre-loaded by a varying amount in two magnets and in a rebuild of QRI002; no unusual behavior was noted.

In table 3, we have given the average values of measured harmonics in QRI001 and QRI002. The harmonics in the two magnets were quite close to each other. The body (straight section), lead end and return end harmonics are derived from the measurements at several locations with a 0.229 meter long measuring coil. For computing integral harmonics (in units), the end harmonics must be divided by the magnetic length of Q1, Q2 and Q3 before adding to the body harmonics in table 3. The presence of a large  $b'_3$  in the body will be discussed later. The non-zero  $b'_5$  and  $b'_9$  in the body are due to a change in the insulated cable thickness after the design. The cross section has been iterated to reduce these harmonics for the production magnets. The large  $a'_5$  and  $b'_5$  in the lead end are caused by eight  $\sim 0.2$  meter long leads connecting the four coils. A new lead design is expected to reduce most of these harmonics by a factor of three. A current dependence due to iron saturation has been observed in the allowed quadrupole harmonics. The difference between 2 kA and 5 kA is  $-0.47\%$  in transfer function ( $G/I$ ), 0.3 unit in  $b'_5$  and 0.2 unit in  $b'_9$ . A small value in  $b'_5$  saturation means that the two radii method for reducing iron saturation in quadrupoles has worked well.

Table 3: Average values of the measured field harmonics in the two pre-production magnets QRI001 and QRI002 in the body (see text), lead end and return end.

	Body	Lead end	Return end		Body	Lead end	Return end
	units	units	units		units	units	units
		$\times m$	$\times m$			$\times m$	$\times m$
$a'_2$	0.09	-2.51	1.44	$b'_2$	0.51	-0.10	0.33
$a'_3$	0.28	0.36	0.08	$b'_3$	6.89	-0.29	-0.10
$a'_4$	0.03	0.13	0.23	$b'_4$	0.30	0.13	0.04
$a'_5$	0.39	-4.92	-0.08	$b'_5$	7.02	8.44	1.45
$a'_6$	-0.08	-0.06	0.05	$b'_6$	0.04	0.01	0.05
$a'_7$	-0.02	-0.02	-0.01	$b'_7$	0.03	0.04	0.01
$a'_8$	0.05	-0.01	-0.01	$b'_8$	-0.03	0.04	0.02
$a'_9$	0.02	0.15	0.03	$b'_9$	-1.22	0.26	0.02

The actual position of the wires in the assembled magnet was measured by a coordinate measuring machine from a cross sectional slice cut from the magnet QRI001. The analysis shows that the centers of the upper and lower coil halves were away from the horizontal axis by  $\sim 0.25$  mm. The coils were bent inward by about the same amount in the horizontal plane. Analysis of the yoke inner surface shows a similar behavior. The bending is thought to be the result of applying compression on the coils through the yoke loading flat. The quadrupole symmetry is broken by this deformation, and a positive  $b'_3$  is created. A similar  $b'_3$  has been observed in the 80 mm aperture RHIC arc quadrupoles based on a similar design. This  $b'_3$  was successfully reduced to a small value in those quadrupoles by using an asymmetric midplane gap between the horizontal and vertical plane. However, in these quadrupoles, we can also use the magnetic tuning shims. A final choice, or a combination of the two, would depend on which scheme produces a smaller  $b'_7$ .

## VI. CONCLUSIONS

The field quality in superconducting magnets can be significantly improved by using the techniques described in this paper. The magnetic tuning shims can be used to correct a number of harmonics after the field measurements without opening the magnet. The midplane gap and pole shims can be used to control the field harmonics in addition to accommodating the variations in coil sizes. These techniques are specially suited for the interaction region quadrupoles where a few magnets basically determine the ultimate luminosity performance of the machine.

## VII. REFERENCES

1. R.C. Gupta, et. al., "RHIC Insertion Magnets", Proceedings of the IEEE 1991 Particle Accelerator Conference, San Francisco, May 6-9, 1991 (Page 2239-2241).
2. J. Wei, R. Gupta, S. Peggs, "Magnetic Multipole Compensation for the RHIC Triplets", Paper Ga86, this conference (PAC 1993).

# Design of Superconducting Quadrupole Magnets for CEBAF's Hall A Spectrometer

R. Kreuz, E. Brütch, K. Dreher, H. Grüneberg, H. Lütkehaus,  
W. Nick, H. Peschel, B. Rzezonka, F. Sommer, P. Schäfer  
Siemens AG, KWU, Accelerator and Magnet Technology  
W-51425 Bergisch Gladbach 1 and Mülheim, Germany

by CEBAF [1]. The main parameters are given in Table. 1:

## Abstract

The detailed design for the construction of the Q2/Q3 quadrupole magnets for CEBAF's Hall A High Resolution Spectrometers is presented. The quadrupoles have a warm bore diameter of 600 mm and a cryostat length of 3 m. The quadrupole coil will be wound from a cable conductor carrying a current of 1850 A, the field gradient is 3.5 T/m. A set of eight superconducting multipole coils is positioned in the helium vessel within the bore of the main coil. Each multipole coil is supplied by a separate current lead. The cold mass is suspended by eight support rods of Titanium, sized for a static load of 3 g omnidirectionally, which are fixed at the iron yoke tube surrounding the magnet cryostat. Cold alignment of the quadrupole coil relative to the iron yoke is possible via these supports. The detailed design of the quadrupole coil, the multipole coils, the current leads, the cryostat and of the iron yoke is described.

## 1. Introduction

The Continuous Electron Beam Accelerator Facility (CEBAF) at Newport News, Va. will perform the experiments within three experimental halls. In Hall A two High Resolution Spectrometers are to be installed. Each spectrometer consists of one small quadrupole (Q1) magnet and two bigger quadrupole magnets of identical design, one before (Q2) and one behind (Q3) a 45° dipole magnet.

In November 1991 Siemens got the order from CEBAF for designing, building and testing the four Q2/Q3 quadrupole magnets.

After a period of 10 months for the detailed engineering the design was finished. In chapter 3 and 4 the design of the quadrupole coil and the multipole coils, respectively is described. The current leads are described in chapter 4. In chapter 5 the main features of the iron yoke surrounding the cryostat are given. The design of the cryostat and its components are described in chapter 6.

## 2. Main Parameters and Specifications

The coils and the cryostat of quadrupole magnets were designed according to the specifications given

Table 1: Main Parameters and Characteristics

<b>Magnet:</b>	
• Length of quadrupole coil	232 cm
• Magnetic length	180 cm
• Quadrupole field gradient	3.5 T/m
• Quadrupole gradient uniformity	1 x 10 <sup>-3</sup>
• Operating current	1.85 kA
• Stored energy	592 kJ
• Peak field of main coil	2.5 T
• Superconducting correction (2) and multipole (6) coils max. operating current	100 A
• Weight of cold mass	2.7 t
<b>Cryostat:</b>	
• Diameter of warm bore	60 cm
• Length	295 cm
• Outer diameter	115 cm
• Height	284 cm
<b>Iron Yoke:</b>	
• Outer diameter	150 cm
• Wall thickness	17.5 cm
• Weight approx.	10 t

## 3. Design of the Quadrupole Coil

One eights of the cross section of the quadrupole coil is shown in Figure 1 which is composed of two layers without a splice. Figure 2 shows a top view of the coil ends of a single coil.

The coils are wound from a cable conductor with 30 strands and a cross section of 1.64 mm x 14.7 mm wrapped with Kapton of a total thickness of 0.1 mm and a 0.1 mm thick layer of glass fabric. The conductor is wound around a center post of stainless steel. The three sections of each layer are separated by copper keys in the straight part and 3D shaped copper spacers in the end regions where additional spacer of G10 material will be provided. The head blocks are of copper.

After assembling the four single coils on a mandrel the quadrupole coil will be wrapped with a bandage of epoxy with annular channels left for better helium transparency to the coil. The coil assembly will be surrounded by a tube of aluminium shrunk onto it. It is designed for a 50 MPa prestress in the coil at liquid helium temperature. The thickness of 63 mm of the aluminium tube guarantees an uncircularity resulting from the Lorentz forces of not bigger than  $\pm 0.15$  mm. The circularity for the manufacture and assembly of the quadrupole coil is tolerated with  $\pm 0.25$  mm.

At both ends of the quadrupole coils flanges of Aluminium bound to the Al tube provide for an axial boundary.

#### 4. Correction and Multipole Coils

A set of eight superconducting correction and multipole coils will be installed on the inner tube of the helium vessel. They all are wound on G10 plates with a winding core from a 0.9 mm thick wire capable of carrying a current of 125 A. The inner correction coils (sextupole, octupole) are composed of two layers, the six multipole coils consist only of one layer. In order to save space in radial direction the splices are positioned in the end regions, therefore, the coils are designed for different lengths. The radial thickness of the total set of coils is 25 mm.

#### 5. Current Leads

The current lead for the quadrupole coil are gas cooled and designed for a current of 2 kA. The poles are connected to the leads of the quadrupole coil via flexible copper tapes in order to compensate an axial motion of 4 mm of the coil relative to the current lead which are chosen to be fixed at the head of cryostat tower for reasons of helium tightness at the feedthrough.

The 16 leads of the correction and multipole coils are each coupled to an bundle of insulated brass wires. They are altogether tightly bundled and guided through a tube and cooled by gaseous Helium. At the top of this tube the leads are separated and connected with the feedthroughs.

The arrangement of the current leads can be seen from the cross section of the cryostat tower in Figure 3.

#### 6. Iron Yoke

The iron yoke is made from AISI 1006 steel according to the magnetic material requirement of [1]. It is composed of two half shells and bears the vacuum vessel of the cryostat. It supports the cold mass via eight cold-to-warm supports with titanium rods which are fastened to the iron yoke via a support structure, see Figure 4 and 5. It is the geometrical

reference system for the alignment of the quadrupole coil.

#### 7. Cryostat

A general requirement from [1] for the design of the cryostat was to design for a 3 g omnidirectionally mechanical load.

In order to avoid unacceptable mechanical deformations or high costs for the vacuum vessel the concept of suspending the cold mass at the iron yoke was chosen.

The width of the vacuum vessel tower is nearly of the same size as the diameter of the vacuum vessel in order to have enough space for the current leads, for four cold valves with actuators, a liquid nitrogen vessel for the shield cooling, and the corresponding piping for the cryogenic helium and nitrogen supplies, see Figures 3 through 5.

The cryostat was designed for the required heat load limit [1] of 20 W at 4 K.

The radiation shield is made of copper and cooled by liquid nitrogen. Liquid level sensors for helium and nitrogen are provided.

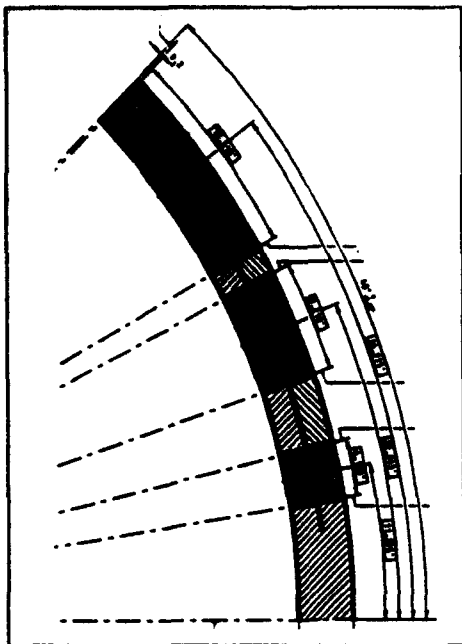
At both ends of the vacuum vessel flanges for the vacuum beam line are integrated.

#### 8. Conclusion

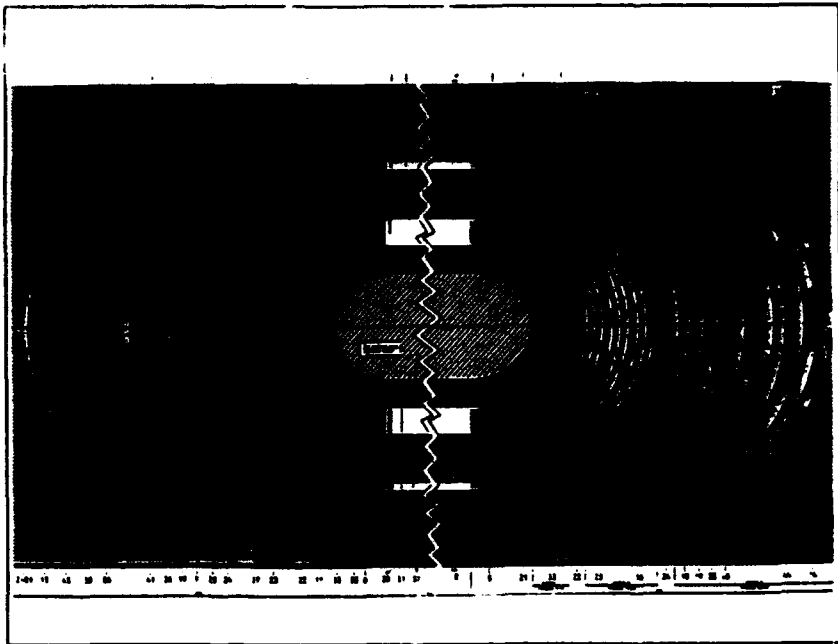
The design of the Q2/Q3 quadrupole magnets was performed according to the global requirements of [1]. These implied a high challenge for the manufacturing design of the quadrupole coils and for the mechanical design of the cryostat under cost saving aspects and with respect to the complexity of the electrical and cryogenic supply, especially under restricted geometrical boundaries in the axial direction.

#### References:

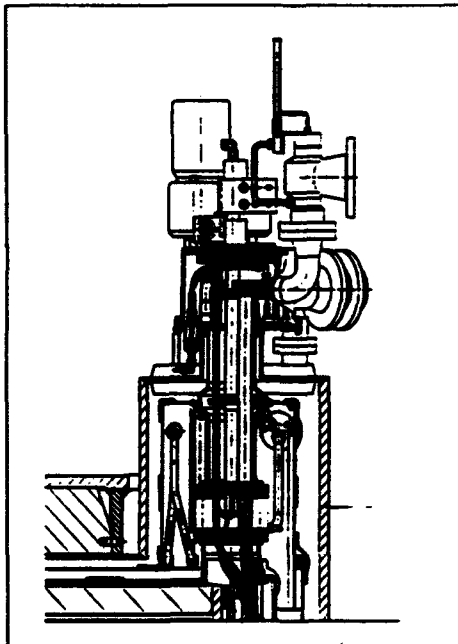
- [1] J. Alcorn et. al.; Technical Specification, TS6521-0001, "Four Superconducting Quadrupoles in the Cosine  $2\theta$  Q2/Q3 Geometry for the 4 GeV/c High Resolution Spectrometers to be Installed within Experimental Hall A at the Continuous Electron Beam Accelerator Facility (1992)



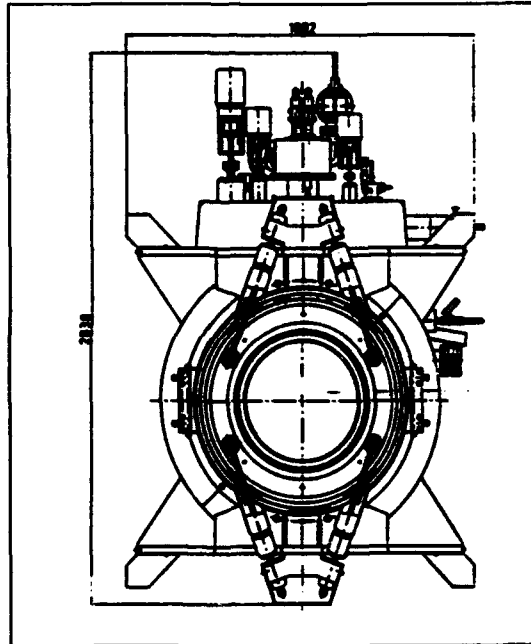
1



2



3



4

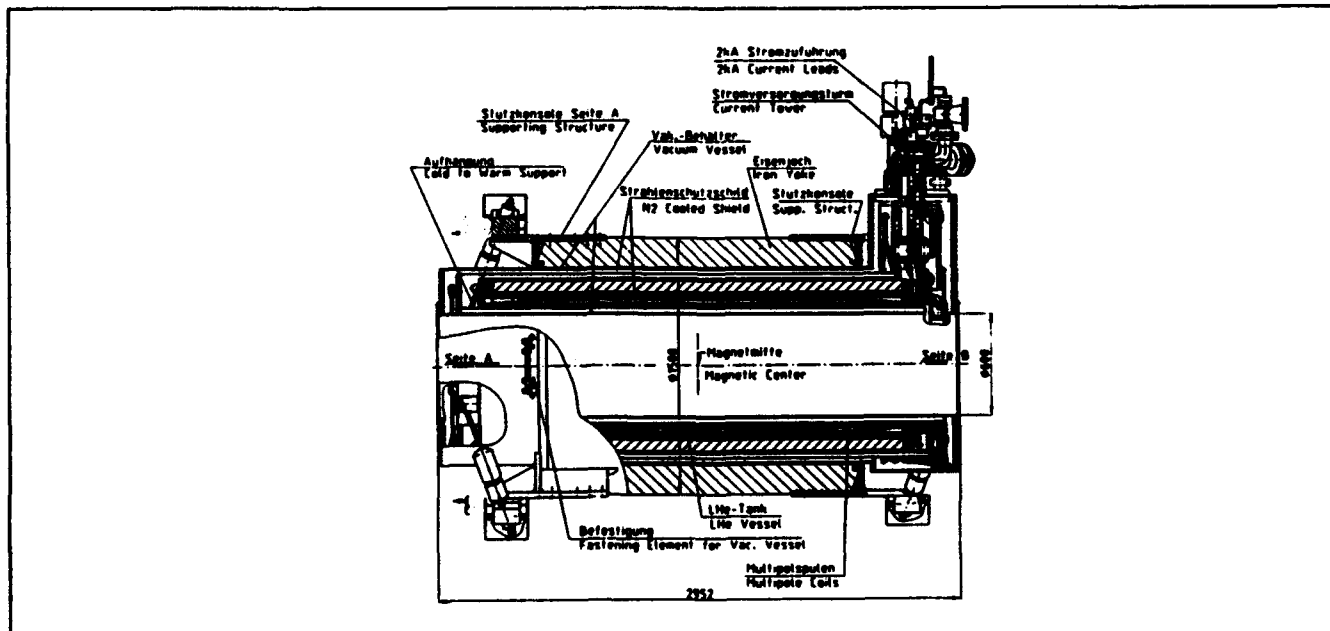
Figure 1:  
Cross section  
of quadrupole coil  
(eights part)

Figure 2:  
Top view of quadrupole  
coil ends

Figure 3:  
Cross section of  
cryostat tower

Figure 4:  
Front view of Q2/Q3  
quadrupole magnet

Figure 5:  
Longitudinal section  
of Q2/Q3 quadrupole  
magnet



5

# Design of a Superconducting Wiggler for the PLS \*

B. K. Kang, Y. M. Koo, D. E. Kim, H. S. Seo, Y. U. Sohn, Y. D. Yun  
Pohang Accelerator Laboratory

Pohang Institute of Science and Technology,  
P. O. Box 125, Pohang, Kyungbuk 790-600, Republic of Korea  
and

P. D. Vobly, N. A. Mezentsev, G. N. Kulipanov  
Budker Institute of Nuclear Physics, Russian Republic

May 14, 1993

## Abstract

The physical engineering design of a 7.5 Tesla superconducting wiggler for the PLS is described. The design is based on three parallel superconducting dipoles. The field is produced by six racetrack NbTi-coils assembled symmetrically above and below the vacuum chamber. The current density for the central pole was chosen to obtain optimal field-current characteristics within the conductor packages. The use of iron poles and return yokes makes it possible to produce higher fields than the corresponding values when no iron is used.

## I Introduction

A strong field wiggler (wavelength shifter) will be installed in a straight section of the Pohang Light source (PLS) storage ring power [1] to enhance the performance of the machine for short wavelength users and to provide new possibilities for SR experiments. The wiggler is not one of the main elements of the lattice and does not reduce the reliability of the machine. However, lattice matching and compensation of wiggler effects on the electron beam dynamics are needed.

A superconducting wiggler is under construction now at the Budker Institute of Nuclear Physics [BINP], Russia and will be delivered to PLS at the end of 1994, which is also the expected completion date for the PLS.

In this article, the design of the Superconducting Wiggler and the radiation properties of the wiggler will be briefly presented.

## II Wiggler Design

A view of the three-pole wiggler is presented in Figure 1. The wiggler design is based on three parallel superconducting dipoles. The magnetic field is produced by six racetrack NbTi-coils assembled symmetrically above and below the vacuum chamber. The conductor is insulated with Kapton film, and the completed coils will be impregnated with epoxy resin. The two central coil packages are split into two

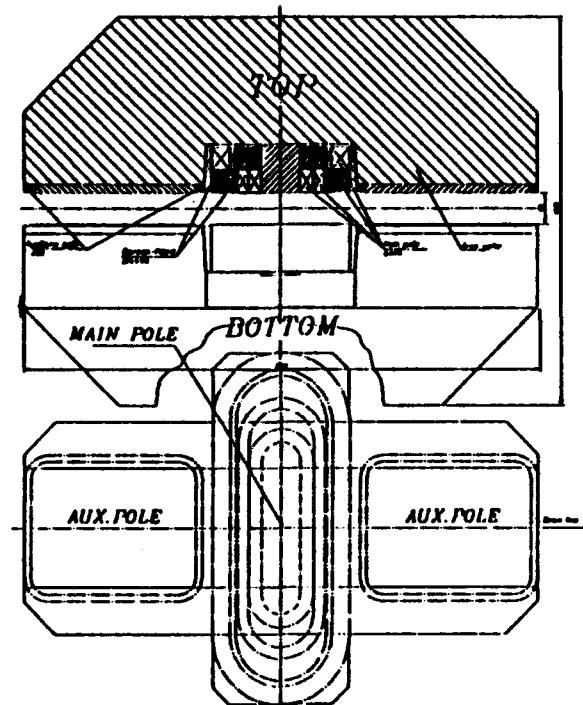


Figure 1: General view of the Superconducting Wiggler

separate coils. The current density in each of the coils was chosen to obtain optimal field-current characteristics.

The iron poles and yoke surround the coils, providing a flux path, and supporting the coils. The use of iron poles and yokes makes it possible to produce a higher field than is possible for similar geometries when no iron is used. In addition, the outer poles act as the mechanical restraint to the very large magnetic forces generated by the main pole coils. The non-magnetic stainless steel slab located between the upper and lower wiggler halves is simultaneously a part of the helium vessel and a support for the halves.

The magnetic field of the wiggler magnet was calculated with the MERMAID code developed at BINP. [2] The flux distribution is shown in Figure 2. The distribution of

\*Work supported by Ministry of Science and Technology, Hyundai Electrical Engineering Co., Ltd. and the Budker Institute of Nuclear Physics

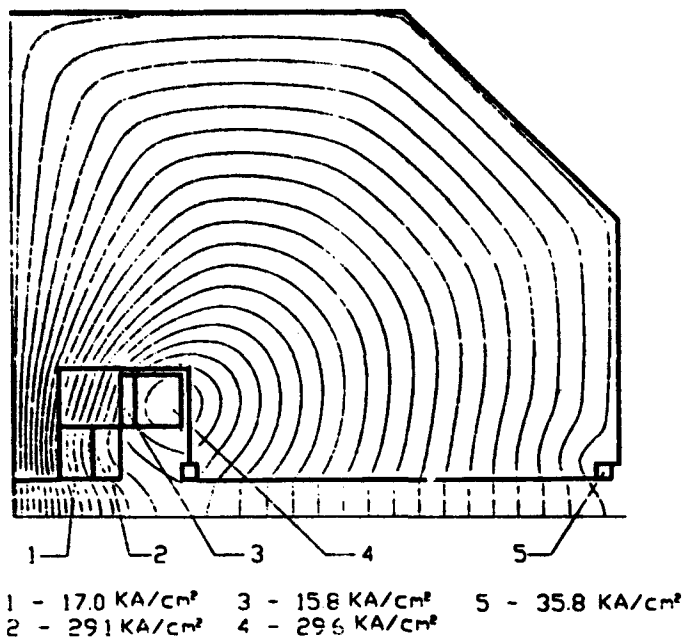


Figure 2: Magnetic flux distribution and overall current densities for each coil region

the magnetic field along the wiggler axis is presented in Figure 3. The maximum central field is 7.5 Tesla and the flux density along the side poles is about -1.7 Tesla. Calculated beam trajectories are also plotted in Figure 3. The maximum deviation from the equilibrium orbit is approximately 15 mm and the maximum slope of the trajectory is 65 mrad, or about 3.8°. The main parameters of the wiggler are summarized in Table 1.

For the central pole coils and the side pole coils, two high stability power supply units are used. Referring to Figure 2, Coil 1 and Coil 3 are connected in series with one supply, and Coils 2, 4, and 5 are excited by the other power supply. Such connection permits us to control the field integral and match it to zero within the required accuracy. We need only one type of superconducting wire which will

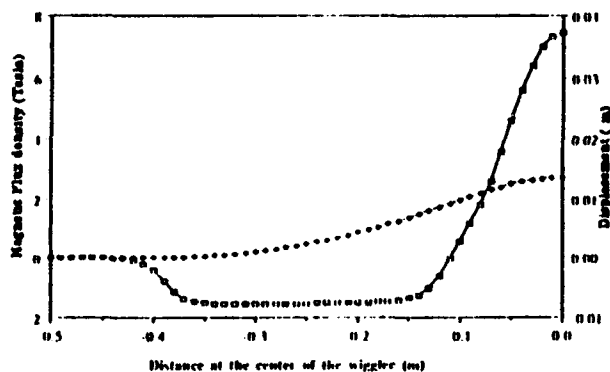


Figure 3: Magnetic field profile and reference orbit

Maximum field on beam axis	
Central pole (T)	7.5
Outer poles (T)	-1.7
Pole gap (mm)	40
Vert. gap of the vacuum chamber (mm)	24
Horiz. gap of the vacuum chamber (mm)	100
Stored energy (kJ)	150
Total weight of cooled parts (Kg)	~ 1000

Table 1: Main parameters of the 7.5 T wiggler

Diameter	0.85 mm (0.95 mm with insul.)
Ratio of Cu:NbTi	0.58:0.42
No. of NbTi filament	8910
Critical Current	360 A (at 7 Tesla)

Table 2: Properties of the superconducting wire

operate with different current density, depending on the coil. We will use the superconducting wire specified in Table 2.

### III Radiation Characteristics

Here and below an electron energy of 2 GeV and an electron beam current of 100 mA are assumed. In Figure 4 the vertically integrated intensity for a 1 mrad horizontal opening angle and 0.1 % bandwidth is shown for a central pole field strength of 7.5 T and side pole field strength of -1.7 T. The spectral photon flux at the critical wavelength  $\lambda_c = 0.62 \text{ \AA}$  (critical energy  $\epsilon = 20 \text{ keV}$ ) is  $I = 3.2 \times 10^{12} \text{ photons/sec/0.1\% BW/mrad}$ .

The total radiation power from the 7.5 T superconducting wiggler is approximately 3.4 kW.

The 7.5 T superconducting wiggler deflects 2.0 GeV electrons in the horizontal plane by a total angle of about  $\pm 3.8^\circ$ . For the case when the wiggler is located in the center of a 6.5 m straight section, the design of the PLS vacuum chamber makes it possible to have a maximum horizontal angular aperture for radiation output approximately equal to  $2\Delta\theta \approx 20 \text{ mrad}$ . This corresponds to an output power of nearly 0.5 kW, with the remainder of the total 3.4 kW emitted power being stopped by several water cooled copper absorbers installed in the vacuum chamber between the wiggler and the beamline port.

Insertion of the special absorber units inside the PLS vacuum chamber will not result in a reduction of the horizontal aperture of the electron beam, which is  $\pm 35 \text{ mm}$ .

The preliminary location of the absorbers has been computed and incorporated into the design of the vacuum chambers.

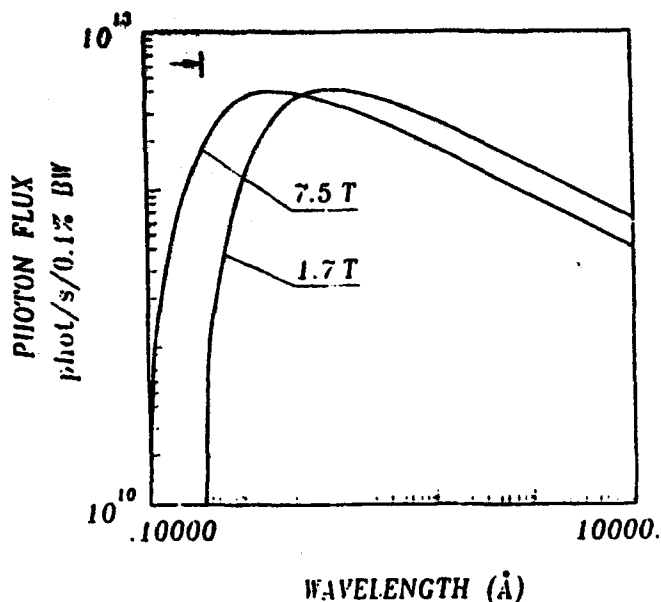


Figure 4: Photon flux integrated over the vertical opening angle.

Maximum output current	2 × 300 A
Maximum output voltage	12 V
RMS Stability	0.01 %
Line voltage	220/380 V-60 Hz
Cooling	water

Table 3: Parameters of wiggler power supply

## IV Miscellaneous

### Cryogenics

The inner helium filled vessel is surrounded by a nitrogen shield to reduce the heat transfer rate between the outside and the helium inner part. The space between the helium vessel and the nitrogen screen, as well as that between the nitrogen screen and the external warm stainless steel vessel, are filled with aluminized mylar insulation to reduce heat transfer rates.

The wiggler coil current inputs are cooled by boiled helium vapors. The vacuum pipe where electrons pass is at room temperature so as not to interfere with the machine. The approximate thermal inflow is 1.4 W, and the expected helium consumption rate is 46 liters/day. Detail design of the cryogenics system is now in progress.

### Power Supply

Two separate power supply units are needed to feed the wiggler coils. Preliminary design parameters of power supply units are listed in Table 3. Each power supply has a three phase thyristor rectifier, a rectifier filter and electronics for the feedback system, as well as current control and monitoring. A zero-flux current transformer is used for high precision output current measurements. The power supplies are computer controlled using 16-bit digital to

analog converters.

## Control System

The wiggler control system has to provide for control and monitoring of the wiggler operation during cooling, ramping on and operation conditions. The main functions of the control system are:

- control and monitoring of the power supply.
- magnetic field ramping.
- control of the quench protection system.
- monitoring of cryogenic equipment.
- wiggler operation statistics.

## V Summary

A superconducting wiggler is being built for the PLS storage ring. The design is based on three parallel superconducting dipoles. The field is produced by six racetrack NbTi-coils assembled symmetrically above and below the vacuum chamber. The current density for the coil about the central pole is optimized to obtain optimal field-current characteristics within the coils. The use of iron poles and yokes makes it possible to produce higher field than the corresponding values when no iron is used. The central field is expected to be about 7.5 T, giving a critical wavelength of  $\lambda_c = 0.62$  Å at an electron energy of  $E=2.0$  GeV. This superconducting wiggler will enhance the performance of the PLS for short wavelength users and provide new possibilities for synchrotron radiation experiments.

## References

- [1] *Conceptual Design Report of Pohang Light Source*, Pohang, POSTECH Press, 1992.
- [2] A. Dubrovina and E. Simonov, *Computer code for magnetic field computation*, preprint from BINP (in printing).

# Calculations of Magnetic Field for the End Design of the RHIC Arc Dipole\*

S.A. Kahn, R.C. Gupta, A.K. Jain, G.H. Morgan, and P.A. Thompson

RHIC Project  
Brookhaven National Laboratory, Upton, NY 11973

## ABSTRACT

This paper describes the results of a 3D calculation of the magnetic field in the end region of the RHIC arc dipole magnet. Multipole harmonics are obtained in the end regions of the magnet. Comparisons of these harmonics are made to the measurements of harmonics on the actual magnets.

## 1. INTRODUCTION

This paper summarizes the 3D calculations performed on the ends of the RHIC dipole magnet. The design of the ends depends both on magnetic and mechanical considerations. The magnetic objectives are to minimise integrated harmonics and to reduce fields at the conductors in the end region. The mechanical consideration is to minimise the strain energy of the cable in the end configuration. The cable can be viewed as a ribbon with an *easy* direction (perpendicular to the ribbon plane) and a *hard* direction (in the plane of the ribbon) of bend. Strain would be minimised if the cable would bend only in the easy direction. In the end, the cable traverses a path where the outer edge is on a cylinder. On the surface which describes the mid-plane of the ribbon the edges of the cable should ideally be geodesic of the surface. The mathematical treatment of the end design is patterned after Bossert et al<sup>1</sup>. The outer and inner edges are assumed to be ellipses when the cylinder on which it lies is unrolled. This procedure of using developed contours for the cable has made the winding of the ends reasonably easy.

The RHIC dipole magnet has a single layer with four blocks in the 2D cross section. Spacers are placed in the ends to spread the positioning of the various turns so as to control the field harmonics. This is performed by a minimisation technique. Fig. 1 shows a projection of the outer edge of the return end of the coil onto a plane. The four blocks merge into seven regions in the end with different spacer sizes.

Calculations of the magnetic fields can be performed based on this model of the ends. Results using the Biot-Savart integration on the conductors are given in section 2. Comparisons are made to measured data for these magnets. Section 3 describes similar calculations that are in progress made with the 3D finite element program TOSCA<sup>2</sup> which takes into account the iron saturation. Also the TOSCA calculations will be used to study the peak field in the vicinity of the conductor.

## 2. CONDUCTOR INTEGRATION

The field at a point in space is obtained by integrating the Biot-Savart relation over the entire conductor path. The coils consist of 32 turns of cable in each half. Each turn is represented by a straight section plus an ellipse in the unrolled cylinder plane for the end region. For field calculations each turn is subdivided by 3 in thickness and by 5 in width with each subdivision being approximated by a filament at its center. The infinite permeability iron is approximated by including the image current to each filament in the iron cylinder. The method of images is not strictly correct since the non-axial components of current do not form images in the cylindrical geometry. However, the non-axial components do not contribute to the field harmonics.

DREK2, Return end outer edges

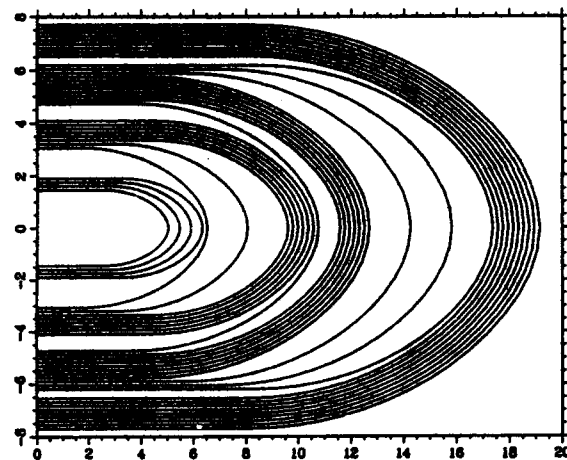


Figure 1: Outer edge of the RHIC dipole return end.

The field is Fourier analysed in terms of harmonics defined as follows:

$$B_y + iB_x = 10^{-4} \times B_0 \sum_{n=0}^{\infty} [b'_n + ia'_n] \left[ \frac{x + iy}{R} \right]^n$$

where  $B_x$  and  $B_y$  are the field components at  $(x, y)$ ,  $R$  is the reference radius chosen to be 25 mm and  $B_0$  is the 2D field at the center of the magnet.  $b'_n$  ( $a'_n$ ) represents the normal (skew) field harmonics. Fig. 2 shows the calculated normal field harmonics as a function of axial position in the end region of the return end (the end without the lead connections) of the magnet. The axial position is somewhat arbitrary with  $x=0$  approximately 3

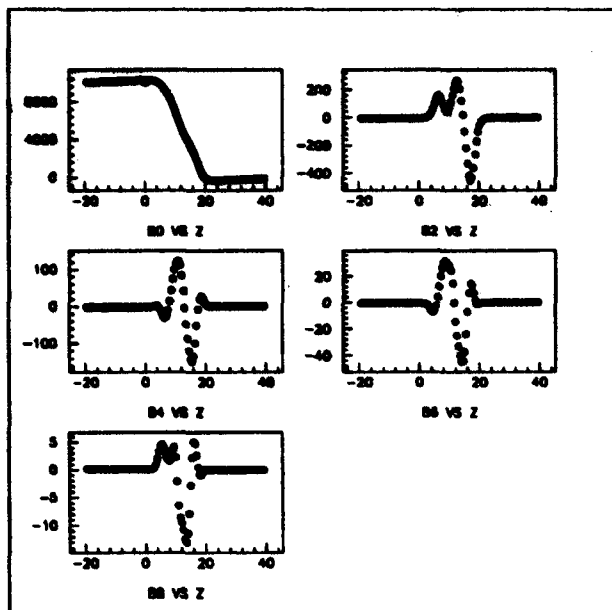


Figure 2: Calculated normal field harmonics for the RHIC dipole return end. Axial position is in cm.

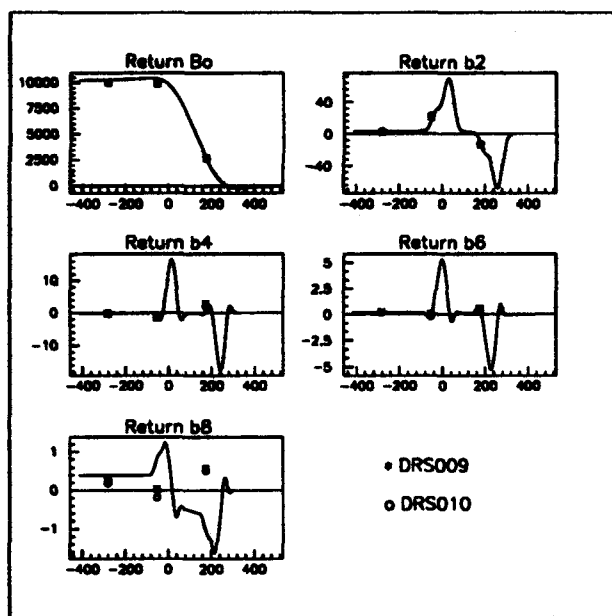


Figure 3: Return end normal harmonics convoluted with 9 inch rectangular function simulate the measurement if it were performed at that  $z$  position. Corresponding harmonics for actual measurements are superimposed. The  $z$  position is quoted in mm in this figure.

cm before the beginning of the curved part of the end. Negative numbers are inside the straight section of the magnet.

Measurements in the end region of a magnet are made with a 9 inch long coil. The measuring coil is stepped in 9 inch increments through length of the

magnet. A sequence of seven steps covers the length of the DRS009 and DRS010 short dipole magnets. To simulate the measurements, a convolution is made of the end calculation at a point  $z$  with a 9 inch band centered around it. Fig. 3 and Fig. 4 show these convoluted calculations for the normal return end and lead end harmonics as the continuous curve. The non-convoluted end effect of the harmonics has an active range of about 15 cm. When this active range is completely within the 9 inch (22.9 cm) band the convoluted harmonics are near zero since the ends were designed to have harmonics that integrate to zero. When upper and lower edges of the 9 inch band pass through the active range a positive and a negative reflection of the profile appear, separated by 9 inches. The measured 9 inch coil data from DRS009 and DRS010 at 2000 amps are also shown in Fig. 3 and Fig. 4. This current is chosen since it is below the turn-on of iron saturation effects and above most of the superconducting magnetization. The arbitrariness of the relative axial position between the measured and calculated harmonics is removed by matching  $B_0$  at the most sensitive 9 inch measurement segment. Furthermore the calculated harmonics are corrected to match the measured harmonics at the position in the middle of the magnet. This is done since the crude representation of the iron in the calculation does not take into account the fine iron details such as notches and other cutouts present in the return yoke. The agreement between the calculation and measurements are remarkably good with the possible exception of  $b_8$ , however higher order harmonics are generally more difficult to calculate.

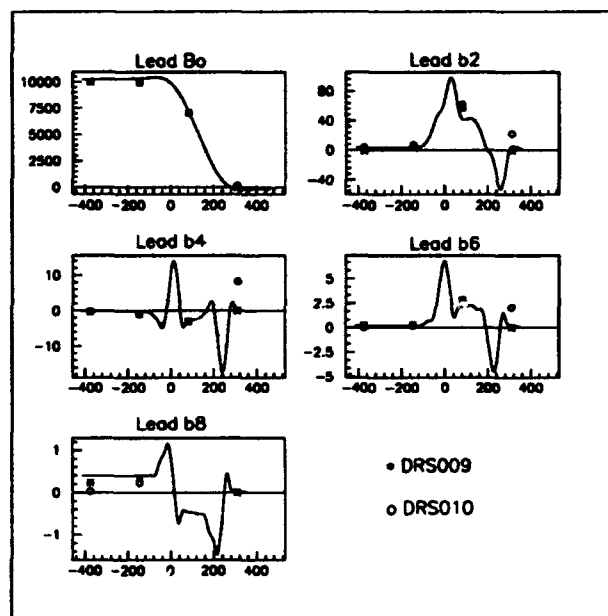


Figure 4: Lead end normal harmonics convoluted with 9 inch rectangular function simulate the measurement if it were performed at that  $z$  position. Corresponding harmonics for actual measurements are superimposed. The  $z$  position is quoted in mm in this figure.

The end harmonics can be defined as

$$b_n^{end} = b_n^{int} - b_n^{body} \times L_{eff}$$

where the effective length,  $L_{eff}$ , is  $10^{-4} \times b_0^{int}$ . This non-standard definition<sup>3</sup> of end harmonics is used to allow the direct comparison of the calculation with the measured data. Using the 9 inch measurements the end harmonics can be separated into contributions from the lead and return ends. The lead and return end harmonics are considered spacially localized contributions to the accelerator lattice in addition to the 2D body harmonics,  $b_n^{body}$ . Table 1 presents the return and lead end harmonics for DRS009 and DRS010 along with the calculated values. The agreement is reasonably good. The skew harmonics,  $a_n^{end}$ , are also given. The calculation of  $a_n^{end}$  are made from the leads alone. The comparison indicates that these skew harmonics are associated largely to these leads. The leads in the measurement test apparatus are unfortunately positioned to give large harmonics. In the accelerator these leads are designed to have minimal effect.

Table 1: Integrated harmonics for return and lead ends. Results are listed as unit-meters.

End	n	DRS9	DRS10	Calc
Return	$b_0$	0.00	2.92	0.00
	$b_2$	0.78	1.43	0.20
	$b_4$	0.39	0.25	-0.01
	$b_6$	0.07	0.06	0.01
	$b_8$	-0.25	-0.22	-0.17
	$a_2$	0.15	0.43	
	$a_4$	0.08	0.22	
	$a_6$	0.00	0.03	
	Lead	$b_0$	0.00	2.79
$b_2$		13.53	14.37	10.12
$b_4$		-0.83	-0.79	-0.55
$b_6$		0.63	0.65	0.51
$b_8$		-0.23	-0.23	-0.15
$a_2$		-7.53	-7.93	-7.41
$a_4$		1.81	1.65	1.26
$a_6$		-0.75	-0.71	-0.28
$a_8$		0.22	0.21	-0.05

### 3. CONCLUSIONS

The good agreement of the low field measured harmonics with the calculations implies that the conductor geometry in the coil ends is as it should be. Currently in progress is an analysis of the RHIC dipole end using the saturable iron computer program TOSCA. This program solves Poisson's equations in 3D using a finite element method. In this program each turn of the coil is

described by a constant perimeter conductor with a developed ellipse in the end region in a similar manner to that which was used in the previous section. The iron is a simple cylinder with the correct inner and outer yoke radii. Other structures in the iron are ignored since the segmentation available on a 3D mesh is not sufficient for such detail. The first part of the study is to understand the behavior of the field harmonics after the onset of iron saturation. The measured harmonics at high field show effects in the  $b_2$  term due to saturation.

The second part of the study is to examine the field in the vicinity of the conductor in the end region. The peak field near a conductor can potentially cause a quench at that location. It is desirable that such high fields not be in the end region where the coil support may be less rigid. Differences of a few percent in field can be important.

### 4. REFERENCES

1. R.C. Bossert et al, *Analytical Solutions to SSC Coil End Design*, Supercollider I, (1990).
2. TOSCA is a computer code marketed by Vector Fields, Ltd.
3. Definition of the end harmonics used for field measurements are described by A.K. Jain and P. Wanderer in an internal note, MDN 482-11 (RHIC-MD-186).

\*Work performed under Contract No. DE-AC02-76CH00016 with the U.S. Department of Energy.

# Collider Scenario Implications of ASST Operation

A. D. McInturff, W. Burgett, M. Christianson, T. Dombeck, J. Gannon, D. Haenni, P. Kraushaar, M. Levin, M. McAshan, G. Mulholland, D. Murray, W. Robinson, T. Savord, R. Smellie, F. Spinos, G. Tool, J. Weisend II, and J. Zatopek  
 Superconducting Super Collider Laboratory<sup>+++</sup>  
 2550 Beckleymeade Avenue, Dallas, TX 75237

## Abstract

After the achievement of the SSCL's Congressionally mandated milestone, the Accelerator System String Test (ASST) half cell under went a series of power tests. These tests involved quenches induced in various configurations and in power levels up to the maximum operation point. These tests have produced data which has defined various parameters and requirements for the individual elements and system.

## I. INTRODUCTION

After careful data analysis of the first operational period of the ASST, and its comparison to previous string data, [1,2] there were a series of unanswered questions and unmeasured or unacceptable parameters that needed to be addressed. [3] There were also a few problems encountered during the preliminary run that experimentally limited the parameter range available. The half end spool's 20K control valve and lines' problem required their rerouting and its replacement. See Fig. 1. These repairs and changes resulted in lower flow rates for the end spool power leads. The required 20K shield flow rate during power cycles decreased by a factor of 5 to 10. The low high voltage breakdown of all the spool's voltage tap connectors required their replacement. See Fig. 2. The ultimate cold hipot limit of the high voltage and current bus plus voltage taps increased from 700 volts to 2.6KV in 4.6K, 4 ATM helium. The ability to reconfigure the half cell for various special tests (i.e., the spool piece containing re cooler "SPR's" safety leads' response) was implemented. There were also a series of special experiments that had been requested and subsequently approved to be done as schedule permitted in addition to the standard verification of the operation range. Induced quenches up to and including the peak operating field were performed. A series of thermal load measurements were taken as well. In addition to the 21 induced quenches that occurred during the initial summer run, the half cell was subjected to 18 more induced quenches including 8 at 6.5KA.

## II. EXPERIMENTAL PROCEDURE

The typical procedure followed first validates the quench protection system. Then the string is powered below the cryostable point and the system's energy is discharged into the dump resistor. Subsequently at a magnet current a few hundred amperes over the cryostable point, at least one heater circuit per magnet is powered to check its ability to drive the coils normal. The third dipole in the string, which is connected to

the lower buss, had in earlier string tests produced the highest quench voltages<sup>[2,3]</sup>. Therefore, it was decided to induce quenches in this dipole at 500 Amps intervals up to 6.5 kilo amps until it was deemed prudent not to, because of high voltage. After completing a series of induced quenches at the maximum operating fields, the energy of the string was dissipated into an external dump in order to bracket the maximum down ramp rate that the half cell could be full field de-energized and stay superconducting. The value of the dump resistor was varied from 12 to 16 mΩ to obtain the various ramp rates. The next experiment was a series of spot heater quenches induced from 5.0KA to 6.5KA in the third dipole to simulate a spontaneous quench. The string was reconfigured such that the current from the power supply (see figure 2) entered the "SPR" safety lead (upper buss) from a group of MCM cables, on the floor parallel to the first 5 dipoles. Once in the cryostat it passed through the quadrupole windings and exited the cryostat through the end spool power lead. After exiting the end spool power lead it returns to the power supply via another set of MCM cables on the floor. The reconfiguration scheme for the lower buss safety lead was for current to enter the lower buss power lead in the end spool and exit the lower buss safety lead in the "SPR." The last experiment was a spot heater induced quench in the first dipole.

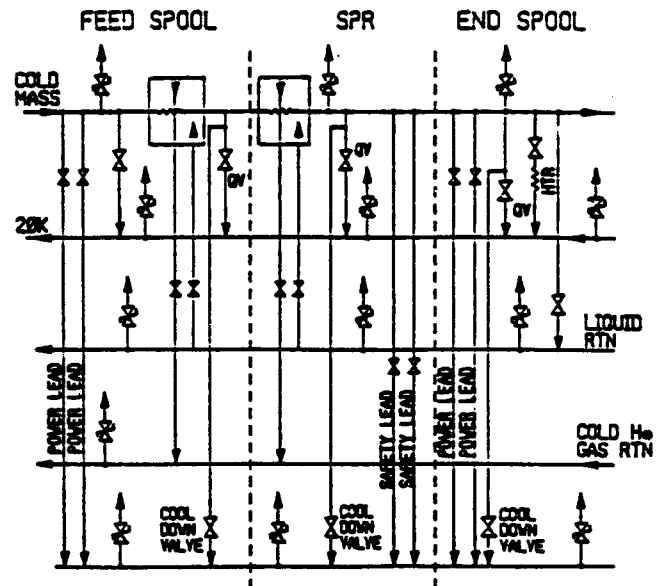


Figure 1. Cryogenic Diagram

The cryogenic loads were measured after the system had been at operational temperature, commissioned, and completed 75% of the experimental program. The system was held at the operating conditions with the notable exceptions of the full

<sup>+++</sup> Operated by Universities Research Association under contract with the Department of Energy. Manuscript received May, 1993.

operational flow and 4.6K instead of 4.25K due to the size of the refrigerator available. There were also a series of load resistors placed in the various cryogenic circuits that loads were to be determined. This allowed an independent heat load measurement calibration and error determination.

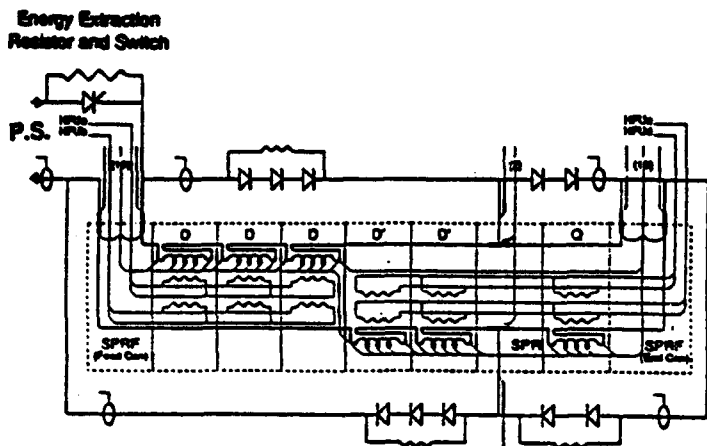


Figure 2. Electrical Diagram

The heat load measurement [4] for the ASST appears to be influenced by end effects originating in the feed spool, re cooler spool piece, and the special end spool. After the end spool repair, the heat load in the return end of the half cell appeared to be significantly reduced.

The sequencing of the quench valve versus position of the initial quenching element evolved during the commissioning. This was done in an attempt to confine the quenched volume to a quarter cell.

### III. RESULTS

The commissioning test and validation checks of the QPS and associated hardware required twelve SCR switched events that resulted in de-energizing the half cell into the "dump resistor." These dumps varied from 500 to 6500 Amps. There were no problems encountered during these dump sequences. There was a mechanical "backup" switch to the SCR's. This being required due to the most common anticipated failure mode being an inability to gate the SCR's off. There were three "mechanically" switched opened events (SCR'S having been not activated for these tests) which were done at 500 Amps, 4000 Amps and 6500 Amps. The mechanical switch performed satisfactorily during these tests. There were also two 6500 Amps dumps made with different values for the dump resistor in order to bracket the maximum down rate that the half cell would operate and not quench in the process. The power lead voltages tripped the "QPS" on two occasions, but did not result in the half cell magnetic elements going normal. The first occurred because of the original 20K valve and lines' problem which required a flow adjustment to correct. This additional flow and shield operation was later reversed on the second run by correction of the end spool problem. The second trip was due to the lead flow being turned up too late before the ramping cycle had started, therefore, leaving the lead cold flag temperature too high.

The additional two higher resistance dumps were performed to determine the maximum rate at which the half cell could be de-energized and stay superconducting. Those values used were 12 and 16 milliohms. These data points indicated that at an operating temperature of 4.6K the half cell would not quench on the down ramp from 6500 amps at a rate of 258 A/sec, however, it would quench on a 328 A/sec one. These results will be repeated and possibly bracketed closer during the next full cell run this summer and at the lower operating temperature of 4.3K. The magnet protection is divided up so that the QPS will quench either the upper or lower buss magnets and bypass them and continue to down ramp the other quarter cell. In the case of the 328 A/sec down rate magnets from both busses went normal. The upper buss (last in the helium coolant path) magnets were slightly ahead of the lower buss magnets, 4.46 and 4.82 seconds into the down ramp, respectively. This resulted in the upper buss magnet (D4) receiving 10.3 Miits and the lower buss magnet (D1) 9.8 Miits. "Miits" is defined as million ampere squared seconds of energy into the original "normal" volume per unit resistance. The quench occurred at a current of 5300 amps and produced only 230 volt to ground. This resulted in a helium pressure wave with a peak of 170 psig which was very typical of 6500 Amp quenches. Therefore, it appears that the planned 200 A/sec down ramp at 4.3K is probably not a constraint, and could be slightly increased.

The commissioning tests comprised a series of twelve protection strip heater induced quenches at 2000 Amps (300 to 500 Amps greater than the cryostable point of the conductor used in the coil windings). These tests were performed to insure that the protection strip heater could indeed drive their associated magnets normal at a low enough current that the magnets were not at risk. The remaining induced quenches were done to study the peak Miits, the maximum voltage to ground and the peak pressure generated in the helium.

There were several interesting aspects to these data; first the voltage to ground which will only be briefly mentioned as it is a subject of another paper this conference [5]. The maximum observed voltage to ground was 1700+ volts during an induced quench at 6000 Amps. This result would have scaled to 2300 volts at 6500 Amps and the system was subsequently hipotted to 2600 volts after this event. This, of course, assumes that the voltage would have continued to rise at its previous rate from earlier quenches at lower currents. The "Miits" appeared to be leveling off in the 9 to 11 region with a solder melt limit being approximately 16+ Miits. The parameter that correlated to this particular magnet producing high voltage was its relatively high low temperature resistance compared to the other elements in the quarter cell that were bussed in series with it. This has lead to an additional requirement that the low temperature resistance of the units in the quarter cells have the same outer coil value within 10%.

The high pressure helium wave front that is generated by the quench was carefully measured to ascertain magnitude and speeds. It appears that there is a large pressure drop across the re cooler when the pressure front passes through it. The peak pressure observed during an induced quench event was 205 psig. This occurred when a quench was strip heater induced in the dipole next to the "SPR" at 6500 amps. The quench valve that had been activated to relieve the pressure was on the opposite side of the re cooler.

The spot heater quench events which simulate some types of spontaneous quenches could be compared to strip heater quenches as follows; a) the Miits at a given current were larger by approximately 10%; b) the peak voltage to ground was about one half plus or minus 10%. These characteristics were valid for both magnets, D1 and D3 for which data existed for comparison.

The "SPR" safety leads' resistance ranged between 0.9 to 1.3 milliohms according to the duration and history of their powering. The thermal time constant for their exit gas temperature appears to be ~20 minutes. The response of the quench stopper located at the base of the safety lead suggests the lead thermal time constant to be on the order of hours. The lead design has a very large safety factor. It was tested to twice the energy input required for a standard ramp down and it did not raise the superconducting cable side of the quench stopper more than a few 100 milliKelvins. Therefore, it would seem possible to reduce its present size and subsequent heat leak. The time to remove the heat from the present safety lead even with the lead gas flow greater than 120 l/sec is on the order of hours. This represents an operational constraint and must be mitigated. The quench stopper in the "SPR" was able to keep the buss stabilized even with  $\Delta T$  of 16K across it.

The thermal measurements on the string are summarized in Table 1 [4].

Table 1. Cryogenic Load for Various Circuits

Circuit /Run #	% Error	Feed Spool **	Watts/(Dipole + Interconnect)						SPR	Bgt
			D1	D2	D3	D4	D5			
Cold Mass/1	± 33	Large Load?	9.5	2.4	0.4	1.7	4.1	(30-40)*	.36	
Cold Mass/2	± 28	Large Load?	9.0	2.4	---	1.5	2.2	(20-6)*	.36	
20K / 2	± 01	---	9.6	4.8	---	5.2	3.8	---	5.1	
80K / 1	± 14	---	27.	29.	26	16	20.	---	37	
80K / 2	± 16	---	23.	25.	23	13	19.	---	37	

\*Very erratic one test to next.

\*\*No Estimate

The minimum total load estimate of the liquid return and cold mass was ~130 watts, therefore, this would indicate the end spools are > 40 w each. As can be seen in the table, there are indications that the high heat leaks present in the end and feed spool pieces corrupt the cold mass thermal load measurement.

#### IV. CONCLUSIONS

These data and those obtained from other experiments not presented have modified our approach to collider operations. Several problems will need to be addressed to limit their impact. The pump out times for the system have been modified. The maximum operating pressure is now determined by the cool down rate not quench pressure. The design of the safety lead will be revised with respect to quench recovery time. The high coldmass heat load will have to be understood.

This is particularly true because of the differences with the earlier lower 40mm string coldmass load measurements. The low temperature <20K resistance of the outer windings of the magnets in a quarter cell will be matched to 10%. There were however no data obtained that would preclude a successful collider operation.

#### V. ACKNOWLEDGMENTS

The authors would like to recognize the contribution of the many individuals and groups to the operation of the half cell during these tests. The cryogenics crew chief, R. Ahlman, the string assembly crew chief, C. White, and operations tech supervisor, M. Hentges, and all the members of their teams deserve a special vote of thanks for the long hours.

#### VI. REFERENCES

- [1] A. McInturff, R. Flora, B. Norris, J. Theilacker, D. Wolff, S. Augustynowicz, C. Dickey, G. Tool, D. Wallis, and J. G. Weisend II. *IEEE Trans. on Mag.* Vol. 28, No. 1, 512 (1992).
- [2] A. McInturff, S. Augustynowicz, W. Burgett, R. Coombes, C. Dickey, T. Dombeck, W. Feitz, R. Flora, J. Gannon, D. Haenni, P. Kraushaar, M. Levin, M. McAshan, G. Mulholland, D. Murray, W. Robinson, T. Savord, F. Spinos, G. Tool, J. Weisend II, D. Wallis, D. Voy, and J. Zbasnik, *IEEE Trans. on Applied Superconductivity*. Vol. 3, No. 1, 622 (1993).
- [3] W. Burgett, M. Christianson, T. Dombeck, J. Gannon, D. Haenni, P. Kraushaar, M. Levin, M. McAshan, A. McInturff, G. Mulholland, D. Murray, W. Robinson, T. Savord, R. Smellie, F. Spinos, G. Tool, J. Weisend II, and J. Zatopek. "Full-Power Test of a String of Magnets Comprising a Half Cell of the Superconducting Super Collider" to be published in *Particle Accelerators*.
- [4] W. Burgett, D. Franks, P. Kraushaar, M. Levin, M. McAshan, A. McInturff, R. Pletzer, D. Revell, W. Robinson, V. Saladin, G. Shuy, R. Smellie and J. Weisend, II. "Cryogenic Characteristics of the SSC Accelerator Systems String Test (ASST)" to be published in *Proceedings of the Fifth IISSC, USA, 1993*.
- [5] W. Robinson, W. Burgett, T. Dombeck, J. Gannon, P. Kraushaar, A. McInturff, T. Savord, and G. Tool, "Electrical Performance Characteristics of the SSC Accelerator System String Test." Paper N3 this conference.

# Preliminary Analysis of Coil Wedge Dimensional Variation In SSC Prototype Dipole Magnets

D. Pollock, G. Brown, S. Dwyer, R. Gattu, D. Warner  
Superconducting Super Collider Laboratory\*  
2550 Beckleymeade Avenue, MS-1004  
Dallas, Texas 75237 USA

## Abstract

The wedges used in SSC Prototype Dipole Magnets determine the relative position of conductor blocks within magnet coils. They serve to compensate partially for the less than full keystoneing of the superconductor cable and to adjust current distribution with azimuth to determine the magnetic field shape. The ability to control the size and uniformity of wedges therefore is an important factor influencing magnet field quality. This paper presents preliminary results of a Statistical Quality Control study of wedge dimensional variation and predicted field quality. Dimensions of samples from outer wedges for magnet DCA102 have been measured using a programmable optical comparator. The data is used to evaluate wedge manufacturing process capability, wedge uniformity, and to predict changes in conductor block position due to wedge deviation. Expected multipole variation attributable to observed wedge variation is discussed. This work focuses on a Prototype Dipole Magnet being built at the SSCL Magnet Development Laboratory (SSCL MDL) in Waxahachie, Texas. The magnet is of the same design as the DCA3xx series magnets built at Fermi National Accelerator Laboratory (FNAL) in 1991-92 and later used in the 1992 Accelerator Systems String Test (ASST).

## I. INTRODUCTION

The SSCL Magnet Systems Division Quality Assurance department (MSD QA) is currently investigating several sources of manufacturing variation in SSC Prototype Dipole Magnets. The work focuses on features of the cold mass production process which are believed to influence magnet field quality including coil azimuthal size and modulus, as well as wedge, collar, and yoke dimensional variation. In this paper we present preliminary results of a study of outer wedge data from wedges made for the DCA3xx and DCA1xx magnets (DSX201B/W6733B cross section) [1, 2]. The method of wedge measurement is described. Measurement error is quantified. A comparison between drawing tolerances and observed results is provided. The relationship between dimensional variation and manufacturing process capability is discussed. Finally, the expected influence of wedge variation on multipoles is described, using the normal sextupole ( $b_2$ ) as an example.

## II. OUTER WEDGE DESCRIPTION

The symmetric outer coil wedge 2D cross section is

\* Operated by the Universities Research Association, Inc., for the U.S. Department of Energy under Contract No. DE-AC35-89ER40486.

described in Figure 1 [3]. The features of the wedge are: (A) Top Width; (B) Delta Width; (C) Large End Height; (D) Bottom Width; (E) Small End Height. The copper wedges are produced using rolling-mill technology in approximately 18 m (60 ft.) lengths. They are cut to intermediate length for shipping and later cut to 1.8 m lengths (6 ft.) for wrapping with kapton insulation. The wedges are installed in the magnet during coil winding.

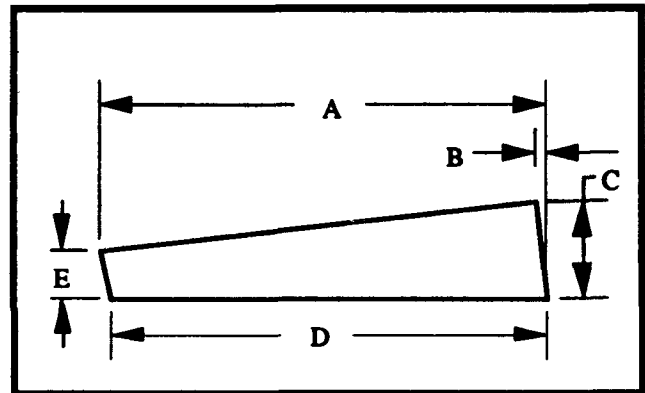


Figure 1. Outer Wedge (2D Cross Section).

## III. WEDGE SAMPLING AND MEASUREMENT

### A. Measurement Method

Several methods are available for verifying wedge dimensions. Two methods have been studied by MSD QA one using a Coordinate Measurement Machine (CMM) and the other using an Optical Comparator (OGP). Due to programming difficulties and schedule limitations only the OGP technique is described at this time.

Sixteen bare outer wedges (each 1.8 m long) were selected at random from SSCL MDL inventory. Small slices were cut from each end of each wedge and mounted on glass microscope slides for measurement. Each feature of the wedge was measured ten times using the automatic mode on the OGP. Details of the measurement method will be distributed in a future MSD QA Note.

### B. Measurement Error

The OGP machine certified accuracy and repeatability are both 0.00254 mm (0.0001"), for individual observations. Calibration accuracy and repeatability have been verified using a NIST traceable certified pin and ten repeat measurements. Measurement capability has been compared to wedge tolerance using the Standard Error of the Mean (SEM)

of the ten repeat measurements on the certified pin. According to this method, the OGP capability is approximately 3.5% of the nominal outer wedge tolerance, as described in Table 1.

Table 1 Optical Comparator Measurement Error

<p><b>Calibration Accuracy and Repeatability</b>          Accuracy (deviation from pin) = 0.00127 mm (0.00005")          1 <math>\sigma</math> Repeatability = 0.00147 mm (0.000058")          SEM = <math>\sigma / \text{sqrt.}(n) = 0.00046 \text{ mm (0.000018")}</math></p>
<p><b>Machine Capability vs. Wedge Tolerance</b>          Nominal Tolerance = +/- 0.013 mm          SEM/Wedge Tolerance = 0.035 (3.5%)</p>

C. Sampling Error

Each feature has been measured 10 times for each of 31 wedge samples (16 from start ends, 15 from finish ends). The average standard error of the slice measurements is typically less than 12 % of the part tolerance, as listed in Table 2.

Table 2 Sample Standard Error (for 10 repeats)

Figure 1 Feature	Average SEM of 31 Samples	SEM / 0.013
A	0.001566 mm	0.1197
B	0.001188 mm	0.0914
C	0.000491 mm	0.0378
D	0.001414 mm	0.1087
E	0.000533 mm	0.0410

Based on One Way Analysis of Variance (ANOVA), "Between" sample (slice-to-slice) variation explains 98.4% of the observed wedge feature variation, on average. "Within" sample variation (sampling error) accounts for only 1.6% of the observed variation. Figure 2 describes the relationship between measurement error and outer wedge variation for the Bottom Width. Each point on Figure 2 shows the wedge slice mean (+ symbol) and standard deviation (error bars) for the start-end of each of the 16 wedges in the study, (tolerance limits are shown as well, 11.66 mm, +/- 0.013 mm).

IV. ESTIMATE OF PROCESS CAPABILITY

A.  $\bar{X}$  Process Limit Calculation

Using the Shewhart  $\bar{X}$  Control Chart for variables [4, 5],  $\pm 3\sigma$  process limits have been calculated for the outer wedge features. The sample size is 16 (wedges in the study) and the subgroup size is 2 (slices measured from the ends of each wedge). The average of 10 repeat observations from each slice is used as the feature value. To demonstrate, Figure 3 shows the Bottom Width for start and finish end of each wedge with the tolerance band, while Figure 4 shows  $\bar{X}$  (the mean of the 2 slices) for each wedge with estimated  $\pm 3\sigma$  process limits.

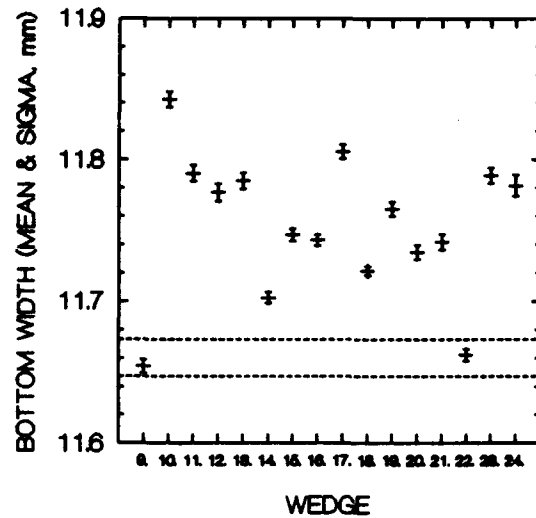


Figure 2. Outer Wedge Bottom Width: Start End Mean and 1  $\sigma$  Error Bars for 10 repeats.

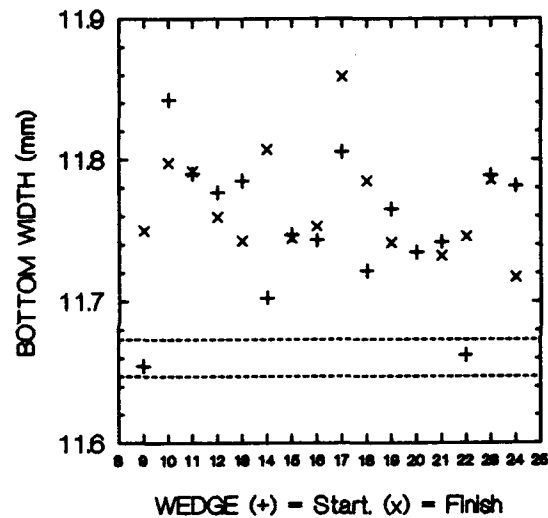


Figure 3. Outer Wedge Bottom Width: Start (+) and Finish End (x) for each Wedge Sample.

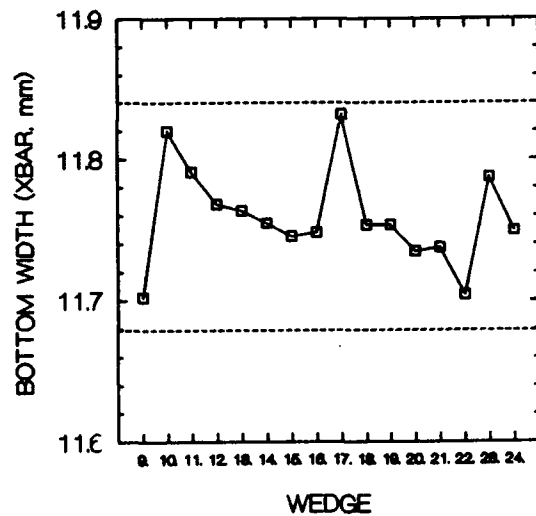


Figure 4. Outer Wedge Bottom Width:  $\bar{X}$  Chart of wedge sample means (subgroup size = 2).

### B. Process Capability Calculation

The Upper and Lower Process Limits calculated for each feature describe the  $3\sigma$  range within which similar samples from the source manufacturing process may be expected to occur 99.73% of the time, if the sample is a fair representative of the process. Typically one would not draw firm conclusions from as small a sample as has been studied so far. But for demonstration purposes and to draw preliminary conclusions we feel the reported results are important. Process Capability ( $C_p$ ) is defined as the ratio of the Tolerance Range (max - min) to the process  $\pm 3\sigma$  range. If this ratio is less than 1, the process is not statistically capable of holding the specification tolerance. Under such conditions, causes for the variation in the process should be investigated and (if possible) eliminated. Table 3 shows the Process Capability estimate for the outer wedge data studied.

Table 3 Outer Wedge Process Capability Estimate

Fig. 1 Feature	$\pm 3\sigma$ Range	Process Capability
A	0.078 mm (0.0031")	0.333
B	0.141 mm (0.0056")	0.184
C	0.054 mm (0.0021")	0.481
D	0.161 mm (0.0063")	0.161
E	0.070 mm (0.0028")	0.371

## V. WEDGE INFLUENCE ON FIELD QUALITY

### A. Estimated Change in $b_2$ Due to Wedge Average Deviation

The wedge angle described by the outer wedge small end height and the outer coil inside radius (to the center of the magnet) is one of the dimensions used to determine normal multipoles ( $b_{even}$ ) for the design cross section [6, 7]. The influence of the average deviation from design nominal for the outer wedge has been estimated for the normal sextupole ( $b_2$ ) multipole harmonic. If the pole angle is fixed (i.e., no pole shims are used, as is the case for the DCA3xx magnets [1]) the change in  $b_2$  has been predicted to be -0.11 units per 0.05 mm change in the outer wedge small end height [2]. For the wedge data in this study, the average deviation of the small end height from the drawing nominal is -0.036 mm. Therefore, the estimated influence of the observed deviation on  $b_2$  is:

$$(-0.036/0.05) \times (-0.11) = 0.079 \times 10^{-4} \text{ units.}$$

### B. Outer Wedge Deviation and Observed Field Quality

Based on the assumption that the wedges studied fairly represent the wedges used in the four outer quadrants of the DCA3xx ASST Prototype Dipole magnets, the fraction of observed  $b_2$  deviation from design nominal attributable to measured outer wedge average deviation has been estimated to be 6.1%, (see Table 4). When results from the three inner wedges are added to the study, the cumulative influence of wedge deviation is expected to be significantly larger.

Table 4. Outer Wedge Deviation vs. Observed  $b_2$ .

Data Source:	DCA311 - DCA319, Z-Scan data
Average $b_2$ (at 2 kA):	1.463 units [8]
Design $b_2$ (at injection):	0.165 units [2]
Average Deviation from Design:	1.298 units
Estimated Outer Wedge influence:	0.079 units
Fraction Attributable to Outer Wedge:	6.1%

### C. Outer Wedge Deviation and Systematic Tolerance

The Systematic tolerance for  $b_2$  at high field is  $\pm 0.8$  units [9]. The influence estimated from outer wedge average deviation (0.079 units) alone represents approximately 10% of the normal sextupole high field systematic tolerance.

## VI. CONCLUSION

Using an approach similar to the one described in this paper, we plan to expand this study to include inner wedges. We plan to estimate the combined influence of variation in all wedges on observed normal multipoles for DCA3xx and DCA1xx Prototype Dipole Magnets. Working with Production Engineering and our wedge suppliers we will also investigate possibilities for improving wedge process capability.

## VII. ACKNOWLEDGMENTS

Ramesh Gupta, Brookhaven National Laboratory, Upton, Long Island, New York.

## VIII. REFERENCES

- [1] SSCL document: MD-MKA-A-93-001, "Requirements and Specifications for SSC 50mm Collider Dipole Magnet (DCA311 - 319, ASST Dipole Magnet Baseline Design)," August 8, 1991.
- [2] R. C. Gupta, S. A. Kahn and G. H. Morgan, "SSC 50 mm Dipole Cross Section," *Supercollider 3*, Plenum Press, New York, 1991.
- [3] FNAL drawing number 0102-MB-292038.
- [4] D. C. Montgomery, "Introduction to Statistical Quality Control, Second Edition," John Wiley & Sons, New York, 1991, pp. 201 ff.
- [5] H. Stenson, "QC STAT: A Supplementary Module for SYSTAT," version 1.1, SYSTAT, Inc., Evanston, IL, 1990.
- [6] R. C. Gupta, "Correcting Field Harmonics After Design In Superconducting Magnets," *Supercollider 4*, Plenum Press, New York, 1992, pp. 773 - 780.
- [7] R. C. Gupta, private conversations, February 1993.
- [8] SSCL document: MD-TA-233, J. DiMarco, "Summary of Axial Multipole Data from 50 mm Dipole Magnet Prototypes DCA311-322," October 7, 1992.
- [9] SSCL document: M80-000001, Revision A, "15 Meter Collider Dipole Magnet, Magnet System Specification," January 10, 1992, p. 14.

# SSC String Test Facility for Superconducting Magnets: Testing Capabilities and Program for Collider Magnets

P. Kraushaar, W. Burgett, T. Dombek, A. McIntarff, W. Robinson and V. Saladin  
Superconducting Super Collider Laboratory\*  
2550 Beckleymeade Avenue, Dallas, TX 75237 USA

## Abstract

The Accelerator Systems String Test (ASST) R&D Testing Facility has been established at the SSC Laboratory to test Collider and High Energy Booster (HEB) superconducting magnet strings. The facility is operational and has had two testing periods utilizing a half cell of collider prototypical magnets with the associated spool pieces and support systems. This paper presents a description of the testing capabilities of the facility with respect to components and supporting subsystems (cryogenic, power, quench protection, controls and instrumentation), the planned testing program for the collider magnets.

## I. INTRODUCTION

The Superconducting Super Collider Laboratory (SSCL) constructed a magnet string testing complex at the laboratory's N15 site in order to fulfill a Congressionally mandated milestone for the project. This milestone was to demonstrate the operation of a half-cell of the Collider lattice under full power conditions. The half-cell tested consisted of five 15 meter, 50 mm aperture dipoles, one 40 mm aperture quadrupole and the necessary spool pieces. This task was successfully completed in August, 1992, when the string was ramped to 6520 amps, six weeks ahead of schedule. The results of this first test run and a discussion of the milestone objectives occurs in reference [1].

The milestone completion marked a transition point in the mission of the ASST facility and the management structure it operated under. The SSCL utilized a task force organization for the milestone effort and once completed, the task force dissolved. Prior to this, a planning effort was started to prepare for the transition of the ASST to testing facility for superconducting accelerator lattice components. The motivation for the organizational structure adopted was simple. The SSC Laboratory required a facility where technical components could be integrated into collider prototypical systems and subsystems for testing and operation. Without this capability, the SSCL could not meet the quality assurance goals stated for the Collider Project. Test verification of the two superconducting accelerator's, (Collider and the High Energy Booster (HEB), level 3B specifications is required[2,3]. Besides providing a facility for system testing and personnel training, the ASST test

program needed to provide for the measurement of critical component parameters that could not be verified in single component testing. Two examples of this would be the heat leak to the 4K cryogenic circuit for collider magnets and the response of spool piece components to magnet quenches.

The Collider Machine Group assumed the responsibility for the program management and the initial operation of the ASST. The ASST Test Group was formed from members of the Collider Machine Group and the Project Management Office (PMO) who participated in the milestone effort, and the support personnel from the ASST Task Force.[4]

## II. THE ASST SYSTEMS CAPABILITIES

The ASST complex consists of the ASST string, the refrigerator, the magnet power supply and the refrigerator compressor buildings. The last three areas are part of the N15 Utility complex that will serve the Collider when in operation. The ASST building consists of a large, 29 m by 9.8 m laydown area for the receiving and checkout of string components, and the magnet string enclosure which is 200 m long and 5.2 m wide. The string enclosure was built with the same curvature as the Collider tunnel. A niche area is provided to contain the quench protection system and other test electronics. Located adjacent to the niche are two trailers, each 5.5 m by 18.3 m. One is configured to provide office space for technical personnel and the other serves as the ASST control room. The remote operation of the string subsystems and the monitoring of the technical components under test is accomplished from this control room. These systems include cryogenics, magnet power, quench protection (QPS), controls (data acquisition and process), and safety.

The initial cryogenics system for the ASST was built around a small 550 watt helium refrigerator (Plan B) which could provide 135 l/hr of liquid helium. This system delivered 50 g/s mass flow of helium to the string.[7] The Plan B refrigerator was adequate to cool and operate a half-cell string and was purchased as a backup to the primary refrigerator, Plan A. Plan B was used in Runs 1 and 2 when the primary system was delayed. The Plan B refrigerator has been removed from the ASST and will be used at the SSCL's Central Facility as part of the spool piece test stand.

The Plan A refrigerator has been commissioned and will support the ASST program from now on. This refrigerator is part of the N15 Arc Sector Refrigerator and will eventually support the operation of the Collider. This system is capable of providing 4000 watts of refrigeration at 0 g/s of liquefaction. During normal operations, the system will

\*Operated by the Universities Research Association, Inc., under contract with the U.S. Department of Energy. Manuscript received May, 1993.

provide 2,200 watts of refrigeration and 22 g/s liquefaction. The maximum liquefaction rate is 40 g/s. The nominal mass flow of helium is 100 g/s with a minimum flow capability expected to be near 20 g/s. The minimum operating temperature is 2.8 K. The operating pressure of the string is 4 bar. This system will be used at the ASST for the first time around June 1993 to cool down and operate the full cell being tested in Run 3.

The magnet power system consists of a high current DC power supply and an energy dump or extraction subsystem. The DC power supply capable of supplying a maximum of 8000 amps of current at up to 40 volts with a total output devaluation of  $\pm 100$  ppm. This supply does not meet Collider requirements but is adequate for the ASST program. A small low conductivity water (LCW) supply system was assembled to provide cooling water for the power supply system. The energy extraction subsystem consisted of a dump resistor which could be placed in series with the magnets. The dump resistor has a maximum resistance of 40 m $\Omega$  with taps at 10, 20, 30, and 40 m $\Omega$ . These taps correspond to the nominal values required for a half-cell, full cell, one and a half cells and two full cells respectively. The resistance values are selectable in 2 m $\Omega$  steps. The dump switch consists of a SCR backed up by a mechanical switch. This switch is rated for currents in excess of 7500 amps.

The magnet power system is controlled by a local processor named the Collider Excitation Controller and Regulator (CECAR), and is monitored from the ASST Control Room. The operators can select the type of ramp, ramp rate and current value. The console display provides a schematic of the string under test and displays key electrical parameters in real time. These observables are stored in data buffers which can be read out and later stored in the ASST database.

The quench protection system (QPS) works in conjunction with the magnet power system. During Runs 1 and 2, the system had one quench protection module (QPM) which monitored quarter coil voltage taps on the string's magnets. This system is being expanded for Run 3 to include a second QPM to allow for tests that require QPM to QPM operations. Like the power system, the QPS is controlled and monitored in the control room. The console displays allow for the monitoring of the voltage taps and other diagnostic information. During a quench event, the voltages and currents which occur in the magnets and the bypass circuits are recorded in data buffers for later display and analysis. The magnet power and quench protection systems used at the ASST are discussed in reference [8].

The ASST has an integrated controls and data acquisition system which records data from the numerous sensors monitoring in the string components and the subsystems supporting the test operations. The Research Instrumentation Data Acquisition System (RIDAS) is the primary data acquisition system for test data. RIDAS is broken down into a VXI based data logging system and a VME based transient data recording system. To support the

tests requested for the full cell configuration, RIDAS will log data from over 420 separate sensor channels. The periodic data logging has been performed at a sample rate of five minutes. The transient data system can accommodate up to 320 channels with its ten A/D modules. This system can accommodate a wide range of sampling rates and collection times. During the half-cell tests, sampling rates and collection times varied from 2000 samples per second for 30 seconds to 10 samples per second for 30 minutes. In addition to RIDAS, the controls system contains the cryogenic process controls system which monitors 80 sensor channels from the string and controls 25 remote devices. There is also a vacuum process controls system which has approximately 40 sensor channels.

### III. COLLIDER MAGNETS TEST PROGRAM

The initial test (Run 1) was the milestone demonstration effort and was successful from that point of view. It was, however, not a test program for determining performance parameters for the half-cell configuration of magnets and spools. During Run 1, some test data was acquired on the thermal behavior of the string and the electrical response during ramping and quench, but only enough to verify that much more was needed to understand the behavior of the components. At the conclusion of Run 1, the string was warmed to room temperature so that equipment modifications and repairs could be made.

The repaired string was cooled down to cryogenic temperatures in October 1992, and the testing program resumed with Run 2. This program ran through January 1993 with a two week break in December when the cryo system was shut down and the string allowed to warm on its own. Over fifteen different test requests received testing time and were able to collect data.

Examples of the type of tests attempted include: measurements of the thermal performance of the magnets and SPR spool; the quench response of the half-cell at various current levels from quenches induced with either spot or quench protection heaters; the evaluation of the SPR bypass lead; the dipole down ramp sensitivity in the string; cold mass vibration monitoring; and superconducting splice joint measurements. Many of these tests and the results are discussed in references [5,6].

The first run of a full cell of ASST magnets will begin in June 1993. Using the results from Run 2, several magnets were changed in the first half-cell and the second half-cell installed. A specially instrumented dipole magnet (DCA323) was added to the first half-cell to measure where heat leaks occur in the dipole cryostat design. The string will include a new re cooler spool (SPR) which is also heavily instrumented to provide data on performance that could not be acquired before. The primary objectives of Run 3 are to acquire data on the thermal performance of the dipole magnets, the electrical response of the string components at 4.25 K, the performance of the SSCL designed SPR spool and finally, to

test two vendor designed and manufactured SPR spools. The first part of this run is expected to last four to five months. At that point, the string will be warmed to room temperature and one of the vendor SPR's installed and tested. This will be repeated two months later for the second vendor spool. This part of the testing program will end in the spring of 1994.

The first three test runs of the ASST magnet string used or will use the ASST style magnets designed by the laboratory and fabricated at either Fermi National Accelerator Laboratory (FNAL) or at Brookhaven National Laboratory (BNL) by industry. The test data will be used by the laboratory's industrial partners (General Dynamics, Westinghouse and Babcock & Wilcox) during the development process of modifying the laboratory design for the dipole and quadrupole into the industrial design that will eventually be manufactured in large quantities and installed in the collider. Planning is in progress for a full cell string test using industry designed and built collider dipole and quadrupole magnets, and spools. This string test has not yet been officially approved by the laboratory management. These magnets will most likely be preproduction units as opposed to prototypes. Assuming that the Collider installation contract is awarded in June 1994, this test could then take place in the first half of FY95. The primary objectives of this string test would be to verify the mechanical design and stability, the thermal and electrical responses under varied ramping and quench conditions and the vacuum performance during cool down for the string. Secondary objectives would be to test the magnet installation techniques and to provide experience to the installation contractor's personnel prior to any installation effort in the actual collider tunnel.

The Early Cryo Loop (ECL) test is another M1 level milestone for the SSCL. The results of M1 milestones are reported back to the DOE and Congress. The ECL test string will be installed in the Collider tunnel. This string will consist of four cells of Collider magnets and spools installed at the N15 Arc Sector Refrigerator feed point and proceeding northward. The four cells will be split between the upper and lower Collider rings. In addition to the dipole and quadrupole magnets, this string will contain two empty cryostats (EC) which provide cold drift space in the lattice. Although the planning for this test is still in the early stages, the basic test objectives are the same as in earlier tests. Those are to verify the operation of the components, subsystems and systems required to operate the Collider accelerator. The ECL test will be the first opportunity to test the ability of the Arc Sector Refrigerator to deliver cryogens to magnets a couple hundred feet underground in a controlled manner to cool down and operate a part of the Collider lattice.

#### IV. SUMMARY

The ASST is an operating test facility for superconducting magnet strings at the SSCL. Two test runs have been completed using prototype magnets in a half-cell

configuration. The test group has a comprehensive and aggressive test program planned for approximately the next three years using a full cell configuration of collider prototype and preproduction magnets. This program is based on the requirements and priorities established by the Collider Machine Group with input from the technical divisions. The results from this program will be fed back into the engineering effort for the superconducting components in the accelerator lattice to improve their operational performance and lifetime. The basic Collider test program will culminate with the Early Cryo Loop Test, which is another M1 milestone for the SSCL. At this point, the HEB Machine Group will be utilizing the ASST surface facility to conduct a HEB magnet string testing program.

#### V. ACKNOWLEDGMENTS

The authors would like to express their appreciation to the many individuals who have contributed to this facility's success. In particular, we would like to recognize the contribution made by J. Grossholz during the construction phase and the continuing contribution by the crews of support personnel working under L. Cromer (CAD and engineering support), H. Carter (cryo operations), C. White (mechanical installation) and M. Hentges (testing and operations).

#### VI. REFERENCES

- [1] W. Burgett et. al., "Full-Power Test of a String of Magnets Comprising a Half-Cell of the Superconducting Super Collider, SSCL-Preprint-162 (1992), to be published in *Particle Accelerators*.
- [2] Project Management Plan for the Superconducting Super Collider, SSCL Document No. P40-000021.
- [3] Element Specification-Collider Accelerator Arc Sections, SSCL Document No. E10-000103.
- [4] P. Kraushaar, "The Accelerator Systems String Test Program", *Proceedings of the Fifth Annual International Industrial Symposium on the Super Collider, 1993*.
- [5] W. Robinson et. al., "Electrical Performance Characteristics of the SSC Accelerator Systems String Test", these proceedings.
- [6] A. McInturff et. al., "Collider Scenario Implications of ASST Operation", these proceedings.
- [7] G. T. Mulholland, "The ASST Cryogenics", *Proceedings of the Fifth Annual International Industrial Symposium on the Super Collider, 1993*.
- [8] G. Tool, "Electrical Systems for the Accelerator Systems String Test", *Proceedings of the Fifth Annual International Industrial Symposium on the Super Collider, 1993*.

# "B" Series RHIC Arc Quadrupoles\*

P. Thompson, M. Anerella, G. Ganetis, M. Garber, A. Ghosh  
A. Greene, R. Gupta, A. Jain, S.A. Kahn, G. Morgan, A. Morgillo  
J. Muratore, A. Prodell, M. Rehak, W. Sampson, P. Wanderer, E. Willen

RHIC Project

Brookhaven National Laboratory, Upton, NY 11973

Table 1: RHIC Arc Quadrupole Parameters

Parameter	Value
Number of Turns/octant	16
Coil ID	80 mm
Design Gradient	71 T/m at 5000 A
Quench Gradient	107 T/m at 7650 A
Magnetic Length	1.11 m
Iron ID	109.2 mm
Iron OD	266.7 mm

## ABSTRACT

A series of pre-production superconducting quadrupoles has been constructed at Brookhaven National Laboratory. These magnets have an operating gradient of 71 Tesla/meter with a coil bore of 80 mm. The eight magnets are exact prototypes of the quadrupoles which will be used in the arcs. These magnets were tested and measured and met the accelerator specifications.

## 1. INTRODUCTION

The Relativistic Heavy Ion Collider (RHIC) will be a colliding beam facility with design energy of 100 X 100 GeV/u for ions as heavy as Au. The necessary focusing will be supplied by 492 superconducting main quadrupoles and 72 superconducting trim quadrupoles. Of these, 420 will have a coil inner bore of 80 mm, and design gradient of 71 Tesla/meter at a design current of 5000 A. The two accelerator/storage rings are divided into "regular arcs" and intersection regions. The arcs contain 276 quadrupoles of bore 80 mm and magnetic length 1.11 meters. In addition the insertion regions contain 144 additional 80 mm quadrupoles with lengths ranging from 0.93 to 1.81 meters. These magnets will use the same superconducting cable and mechanical configuration as the dipoles.

## 2. DESIGN CONSTRAINTS

The basic machine requirement is for quadrupoles with 80 mm bore and design gradient of 71 T/m. Practical considerations force maximum commonality with the dipole magnets. The same 30 wire copper stabilised NbTi superconductor has been used. Thus the quadrupole operating current is nominally equal (5000 A) to that of the dipoles (the quadrupoles are NOT in series with the dipoles). Overall parameters are specified in Table 1.

The overall mechanical structure is very similar to that of the dipoles; the single layer coil is spaced from the cold iron by a 5 mm thick plastic (RX-630) insulator which incorporates the pole spacers. The iron collars are compressed and keyed. Thus the iron serves the purposes of both return yoke and mechanical constraint. Mechanically, the iron has two fold(dipole) symmetry, allowing the use of the same press and techniques for assembly as the dipole. Calculations indicate that the coarser features of this symmetry breaking do not produce significant field perturbations. Detailed study reveals two problems:

**Pole Motion** In the dipole it is possible to key the pole directly to the iron because during assembly, there is no relative motion. This is not possible with a two part quadrupole assembly. The system used in these magnets is to key the insulators at the iron joints; during assembly the insulators and the coils slide within the iron until the tabs on the insulators contact the iron. This is less accurate and more complex than keying directly at the poles.

**Iron Deformation** The necessary prestress is applied with the iron collars. These collars bend under the applied load distorting the inner circumference and the coil. The same distortion occurs during dipole assembly, but produces dipole symmetric terms which are easily compensated by coil design. In the quadrupole this distortion produces  $4\theta, 8\theta, \dots$  terms which can not be easily compensated for in the coil design.

## 3. MAGNETIC FIELD

The magnetic field is computed with a combination of analytic techniques for the coil cross section and finite element codes for the iron yoke. For the central section of the magnet, the allowed harmonics (2,6,10  $\theta$ ) are readily calculated. Fig. 1 shows the calculations and the measurements for the fundamental and the first allowed harmonic (see appendix for definition of units used). The deviations are compatible with the mechanical uncertainties (50  $\mu\text{m}$ ) in the coil at 4 K.

The central harmonics are summarised in Table 2. Aside from the octupole ( $b_3$ ) only the sextupole ( $b_2$ ) is noticeable. The large fluctuation in this term indicates that it is due to some random variation in magnet construction.

**Table 2: Quadrupole Central Harmonics Measured (average for QRB007-012) and Calculated. Values Measured at 3000 A, up ramp**

n	b <sub>n</sub> Calc	b <sub>n</sub> ave	σ b <sub>n</sub>	units
1	1.5107	1.522	0.006	G/A-cm
2	0	-0.822	0.949	b <sub>2</sub> '
3	9.3 <sup>a</sup>	7.443	0.681	b <sub>3</sub> '
4	0	0.040	0.687	b <sub>4</sub> '
5	-9.82	-8.732	0.425	b <sub>5</sub> '
6	0	-0.072	0.096	b <sub>6</sub>
7	0.05	0.095	0.051	b <sub>7</sub> '
8	0	0.005	0.048	b <sub>8</sub> '
9	-1.50	-1.752	0.050	b <sub>9</sub> '
n	a <sub>n</sub> Calc	a <sub>n</sub> ave	σ a <sub>n</sub> n	units
1	0		...	G/A-cm
2	0	0.600	0.537	a <sub>2</sub> '
3	0	-0.535	0.730	a <sub>3</sub> '
4	0	-0.207	0.188	a <sub>4</sub> '
5	0	0.332	0.083	a <sub>5</sub> '
6	0	0.035	0.143	a <sub>6</sub>
7	0	-0.043	0.090	a <sub>7</sub> '
8	0	0.023	0.050	a <sub>8</sub> '
9	0	0.043	0.016	a <sub>9</sub> '

a... see discussion of octupole moment

#### 4. END FIELDS

The ends of these magnets are discussed in more detail by Kahn et al<sup>1</sup>. The fields have been calculated with two different numerical integration programs, with rough agreement. There is significant uncertainty in the shape in the assembled magnet, in addition, one end of the magnet has external leads and cutouts in the iron to accommodate the leads. The fields are varying over distances comparable to the coil radius, which makes measurements difficult. The measurements have been carried out with a rotating coil 229 mm long, which is stepped through the magnet. Fig. 2 compares the calculations with the rotating coil measurements. Even though the calculations have been integrated over 229 mm they show rapid variations. The agreement for b5 is disappointing, but the large contribution from the leads is apparent. The cross section of this series of magnets was adjusted empirically to cancel the b5 contribution of the leads, so that the total would be ~ 0. The calculations can be integrated to produce full length harmonics. The equivalent measurements are done with a 2000 mm long coil. Table 3 presents these data. There are significant random b2/a2 and b4/a4 contributions from the ends. These can arise from differences (~ 2mm) in the coil lengths and twisting of the ends. The difference for b5 is due to the discrepancy for the central section.

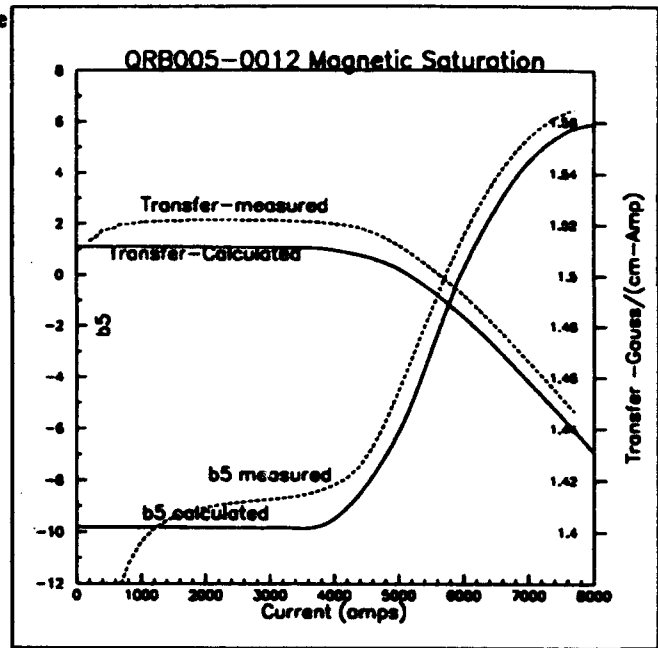


**Figure 1: Central Section Fundamental(B1) and First Harmonic(B5) as a Function of Current, Calculations are Solid Curves.**

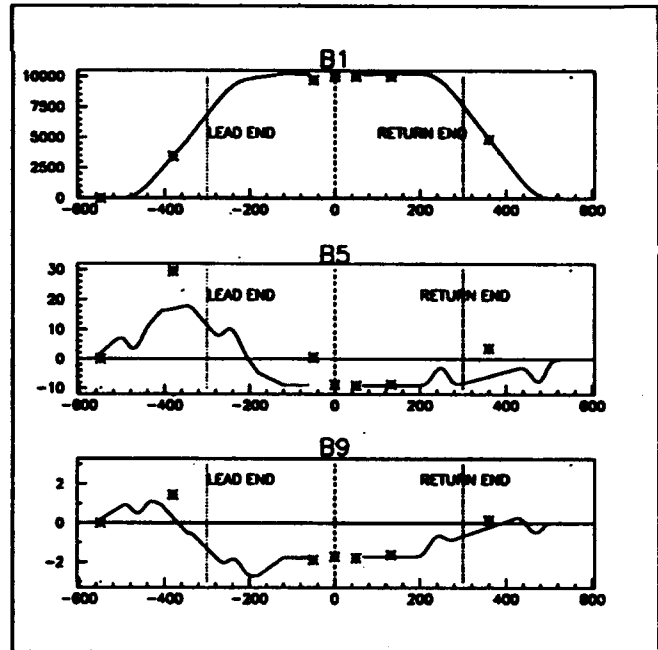


**Figure 2: Comparison of 229 mm Coil Measurement and Calculations for length of magnet. \* are measurements, solid lines END3D calculations. Vertical axis is b<sub>n</sub>', horizontal is mm, the central region has been compressed to 600mm. Dotted lines show the ends of the straight section.**

**Table 3: Quadrupole Integral Harmonics Measured (average for QRB007-012) and Calculated. Values Measured at 3000 A, up ramp**

n	b <sub>n</sub> Calc	b <sub>n</sub> ave	σ b <sub>n</sub>	units
L	1.020	1.097	0.0002 ?	meter
2	0	-1.413	1.398	b <sub>2</sub> '
3	9.3 <sup>a</sup>	7.300	0.592	b <sub>3</sub> '
4	0	0.672	0.613	b <sub>4</sub> '
5	-0.228	2.2582	0.529	b <sub>5</sub> '
6	0	-0.053	0.078	b <sub>6</sub>
7	0.05	0.172	0.049	b <sub>7</sub> '
8	0	-0.133	0.041	b <sub>8</sub> '
9	-1.02	-1.167	0.342	b <sub>9</sub> '
n	a <sub>n</sub> Calc	a <sub>n</sub> ave	σ a <sub>n</sub> n	units
1	39	...	...	a <sub>1</sub> '
2	0	-1.897	1.304	a <sub>2</sub> '
3	0	-0.028	0.731	a <sub>3</sub> '
4	0	2.738	0.522	a <sub>4</sub> '
5	-1.6	-3.708	0.146	a <sub>5</sub> '
6	0	0.172	0.114	a <sub>6</sub>
7	0	-0.027	0.122	a <sub>7</sub> '
8	0	0.048	0.087	a <sub>8</sub> '
9	0.02	0.342	0.023	a <sub>9</sub> '

### 5. OCTUPOLE

Mixing quadrupole(2θ) and dipole(1θ) symmetries produces octupole(4θ) and higher 4n terms. Substantial octupoles have been observed in all RHIC quadrupoles<sup>2</sup>. In the process of clamping the coil with the steel collars the collars are distorted. Detailed measurements of this distortion have been made on a larger aperture quadrupole<sup>3</sup>. These show that the inner radius is reduced, and that the angle (nominally 180°) swept by the half yoke is increased. This appears to account for the observed octupole in the 130 mm quadrupoles. The only mechanical measurements on 80 mm magnets are on dipoles. Since the assembly technique is the same, these are used to calculate the octupole. The measured deformation is 150 μm.

### 6. QUENCH PERFORMANCE

The quench behavior of these magnets is shown in Fig. 3. The design has a large margin, 44%, and the worst case quench is 22% above the design gradient. The I<sub>c</sub> critical current limiting field is calculated in the same way as for dipoles, where it gives a prediction of quench plateau within 2%. Interestingly, these quadrupoles (and others constructed at this laboratory) consistently exceed this limit by ~ 10%. The training may be due to the mechanical constraints on the leads. This will be investigated.

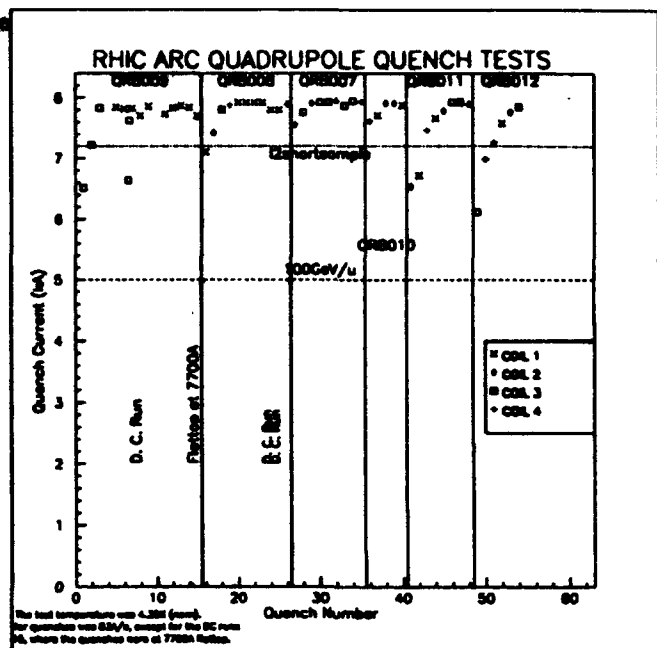


**Figure 3: Quench Currents as a function of event number for these quadrupoles. Design current(5000 A) is indicated with dashed line, predicted critical current limit is shown with dotted line. Legend identifies which of the 4 coils in magnet quenched.**

## APPENDIX

The field on the midplane of a quadrupole can be expressed as:

$$B_y = \text{Grad} \cdot \text{Rref} \cdot b_n' \cdot x \cdot 10^{-4} (z/\text{Rref})^n$$

(the  $\cos(n+1)\theta$  term)

$$B_x = \text{Grad} \cdot \text{Rref} \cdot a_n' \cdot x \cdot 10^{-4} (z/\text{Rref})^n$$

(the  $\sin(n+1)\theta$  term)

Grad = Quadrupole gradient Rref = 25 mm.  
With this definition, the "primed units" represent the field deviation measured at a radius of 25 mm as parts in 10<sup>4</sup> of the Gradient field at 25 mm.

### 7. REFERENCES

1. S.A. Kahn et al, *Calculations of Magnetic Field for the End Design of the RHIC Arc Dipole*, This conference poster Jc3, (1993).
2. P.A. Thompson et al, *Status of the Quadrupoles for RHIC*, IEEE Particle Accelerator Conf., pp. 504-506 (1989).
3. R. Gupta et al, *Large Aperture Quadrupoles for RHIC Interaction Regions*, this conference, paper N8, (1993).

\*Work performed under Contract No. DE-A02-76CH00016 with the U.S. Department of Energy

# FERMILAB-BUILT SSC COLLIDER DIPOLES USING LOW TEMPERATURE CURING INSULATION SYSTEMS WITH AND WITHOUT GLASS TAPE

T. S. Jaffery, R. Coombes, A. Devred, J. DiMarco, T. Ogitsu, R.E. Sims, J.C. Tompkins and M. Wake SSCL, Dallas, Texas USA, R. Bossert, J. Carson, S.W. Delchamps, I. Gonczy, S. Gourlay, R. Hanft, M. J. Lamm, P. Mazur, D. Orris, and J. Strait Fermilab, Batavia, Illinois, U.S.A.

**Abstract--** Polyimide with epoxy impregnated glass tape was used in Fermilab baseline design of several SSC Collider dipole magnets which were used in the SSC Accelerator Systems String Test (ASST). Later in the magnet R&D program several magnets were built using conductor insulation in which adhesive that cures at 140°C was coated directly on the polyimide film. Some alternate materials for coil end parts and coil winding were also tested. The data taken during the tests of these magnets are compared with results from 10-stack studies of the two insulation systems and design expectations and correlated with changes in assembly methods.

## I. INTRODUCTION

Fermilab built and tested several long (15 meter) and model (1.5 meter) collider dipole magnets for the SSC project, based on the baseline design of ASST. The mechanical design of the 2D cross section is discussed in detail in [1,2]. The return yoke of all 50 mm aperture SSC dipoles built at FNAL were vertically split. This gives support to the horizontal mid-plane under all conditions and the collar deflections are minimized under Lorentz ( $I \times B$ ) force [1]. The inner (outer) coils are made of 30(36) strand NbTi cable with six micron filament diameter. Several extensions to the baseline design were incorporated into last 5 short and last 4 prototype SSC dipoles. The primary purpose of these magnets was to study the effect of alternate insulation schemes, various coil end part designs and variation in manufacturing parameter on the performance of magnets under cryogenic conditions. The choice of alternate parts was considered to find ways that are more conducive for mass production of SSC magnets and to demonstrate the alternatives to present manufacturing techniques without altering the existing design. Some important factors in the selection of all polyimide insulation and changes in other magnet parameters,

included their effect on the coil cross-section, magnetic field, quench and mechanical behavior of the magnet. A strong insulation is needed on the coils to avoid turn to turn shorts. Fermilab magnet program for SSC used polyimide, with and without glass tape, in combination with adhesives which cured at low temperatures as compared to the melting polyimide insulation system of CDM baseline design. By using lower curing temperature, for the coils, it is possible to avoid the eddy current heating related to ramp rate sensitivity of these magnets. So, an insulation system with lower curing temperature is desirable. As a backup, some insulation schemes without glass tape were tested in last nine magnets built at Fermilab. Polyimide is more homogeneous so it is easier to handle for mass production of coils. The elimination of glass tape makes the coil smaller. So, another conductor turn, could be added to the coil which could increase the current density and thus the field. Cryorad adhesive has a high resistance to radiation. It was tested in two model magnets. Several materials and techniques were studied for mass production of coil end parts [Table I]. This paper outlines some of the advantages and disadvantages of the above variations. The mechanical behavior of magnets using all polyimide insulation is correlated with changes in the magnet design and assembly methods.

## II. INSULATION SYSTEMS

In Fermilab baseline design the collars are designed to position the conductors as determined by the magnetic field without the use of pole shims [2]. Due to thin polyimide the desired coil size, after curing, carefully calculated pole shims and brass shims on all copper wedges had to be applied. The preload in the coil is created by the oversize pressure of the

**TABLE I. Salient Features of Later Model Collider Dipoles Built by Fermilab**

RTM=molded keys and saddles; 1 = Spaulding part; 2 = Amoco Torlon 5030 with 30% glass fiber part; 3 = Cryorad part:

Magnet	End Parts	Pole Shim (mm) Inner/Outer	Coil Insulation Inner / Outer
DSA 330	G-10CR+RTM-(1)	0 / +0.25	2H+butt LT one side / 2H+2LT one side--scotch 2290 adhesive
DSA 332	G-10CR-as ASST	0 / +0.51	2H+butt LT one side / 2H+2LT one side
DSA 333	G-10CR+RTM-(2)	+0.09 / +0.2	2H+butt LT both side / 2H+2LT both side
DSA 331	G-10CR-as ASST	Lo Inner+0.13 / 0	Apical film with Cryorad adhesive; cured at 140-145°C
DSA 334	G-10CR+RTM-(3)	0 / +0.20	3NP one side / 2NP one side+2NP one side 2NP+butt NP both side / 2NP+2NP both side
DCA 320	G-10CR-as ASST	0 / +0.13	2H+butt LT one side / 2H+2LT one side--scotch 2290 adhesive
DCA 321	G-10CR-as ASST	0 / +0.13	2H+butt LT one side / 2H+2LT one side
DCA 322	G-10CR-as ASST	0 / 0	2NP+butt NP both side / 2NP+2NP both side-2290 adhesive
DCA 323	G-10CR-as ASST	0 / 0	2NP+butt NP both side / 2NP+2NP both side

Work Supported by the U.S. Department of Energy.  
Manuscript received on May 17, 1993.

coil against the collar. Therefore the measured relationship between the coil and shim size with that of prestress was used

to determine the correct molded coil size [6]. The coil size was carefully made to have the same characteristics as Fermilab baseline design magnets.

### Polyimide Insulation System With and Without Glass Tape

The polyimide insulation system with glass tape consists of a layer of 0.025mm x 9.5mm Kapton type H film overlapped by 50% surrounded by one layer of 0.1mm x 9.5mm glass tape impregnated with B-stage epoxy. The coils were cured at 135°C. It was successfully used on Fermilab built ASST magnets which showed very little training [5,8,7].

Low temperature curing insulation system without glass tape was used with different combinations of end parts and shimming on last 9 magnets [Table I,3]. The insulation variations used on these magnets included polyimide only and its equivalent (Apical) cable insulation films of thickness 0.025 mm x 9.525 mm (0.001 in x 0.375 in). The variation in thickness of polyimide films of different kinds is not significant, but presence of glass tape in insulation scheme has a large effect on curing pressure. The thickness of glass tape is 3.5 mil/layer which correspond to 2.6 times of Kapton. In the absence of glass tape as part of the insulation, the coil size becomes smaller for a given pressure. The observed effect of creeping of all polyimide insulation is about twice as normal "Kapton with glass" insulation, and it is comparable to the 10-stack data [5]. Studies show that the thermal contraction and creeping of all polyimide is higher as compared to other insulation systems that were tested [7]. So, there is a large dynamic range for the cured coil size.

The loss in coil pressure after curing (coil creep) can be reduced by using lower number of polyimide insulation layers. Due to thinner insulation, the coils were smaller radially and in azimuth. The poles were shimmed using adhesive backed polyimide, and copper field wedges were shimmed with thick brass to make up the difference in coil size [3]. Despite the use of thinner insulation, the incidents of turn to turn shorts in magnets with all polyimide insulation were not any greater than magnets with polyimide and glass tape insulation.

### III. END PARTS

Several processes and materials were considered for end parts of the magnets for their cost effectiveness, ease in production, uniformity and quality, their strength and radiation resistance. Fermilab baseline design for magnet ends uses a collet clamping system, consisting of a metal can which clamps four azimuthal G-10CR insulating blocks around the coil to provide prestress for the end region [2]. Several materials were molded into end parts except the collets. The details on combination of end parts used on model magnets using all polyimide are given elsewhere [3, Table I].

Resin transfer molding (RTM), compound transfer molding (CTM) and injection molding processes were investigated for use in end parts. The keys and saddles on some magnets [Table I] and test coils [8] were made using RTM. It turns out that end parts made with RTM with fiber glass preform are stronger than CTM parts because in RTM the fibers are aligned in a direction to give maximum strength. Although G-10CR has the highest flexural strength and despite the production complexity of machining G-10CR end parts the tooling is least expensive for this process, molding process is a better way of mass

producing the end parts than machining them [8] particularly when a large number of magnets are to be manufactured.

DSA333 end parts were machined out of Torton injection molded tubes. The quench behavior of this magnet indicates that the bonding between the end parts and the coils might not have been ideal. The epoxy used to bond the end parts with coil seemed to cure very well but its behavior at cryogenic temperatures is not well understood.

Aluminum is a material of choice for the outer end cans. It is cheaper to make and it has a higher coefficient of thermal contraction which allows it to shrink more at cryogenic temperatures.

### IV. COLD TEST DATA

Fermilab-built magnets are instrumented with voltage taps for quench localization. The strain gages located in the collars measure azimuthal stress between the collars and the coils. Four end force gages were used to measure the coil pressure on end plate due to differential thermal contraction during cooldown and the Lorentz force due to magnet excitation.

Tests at liquid helium temperatures were performed on both long and short dipoles. Model magnets were tested in a 3.6 m vertical dewar and long magnets were cryostated. The strain gages on all magnets measured absolute stress at 4K [2,3]. Coil pressures were monitored throughout the cooldown and magnet excitation. The desired prestress was achieved on all magnets. This was possible, by careful handling of the process, even when the glass tape was eliminated from the insulation system. If a layer of thick polyimide was used instead, a large pressure drop could have occurred upon cooldown due to high thermal shrinkage of insulation. The prestress loss due to cooldown is a fraction of a collared coil's initial (295K) pressure [3,7]. The change of pressure due to thermal contraction during cooldown were higher for the inner coils (Fig. 1) than for the outer coils (3,7). There were some unusual behaviors which can be attributed to manufacturing processes.

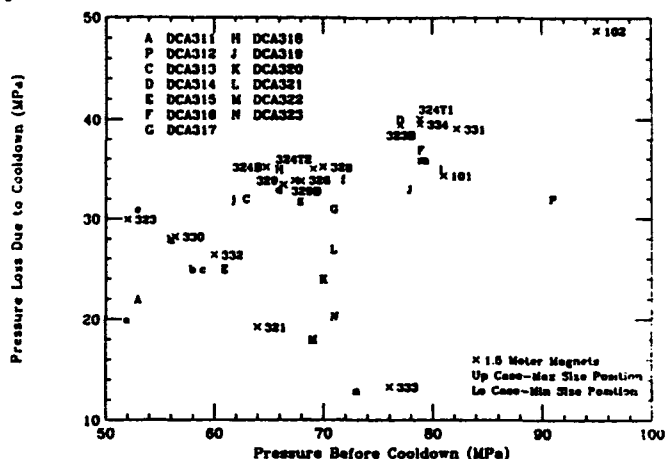


Figure 1: Prestress loss due to cooldown vs coil pressure before cooldown for Fermilab built magnets for the SSC.

### V. EXCITATION BEHAVIOR

The absolute loss in inner coil pressure of Fermilab model and prototype magnets at 7 kA is shown in Fig. 2 The magnets with higher prestress tend to lose more pressure during magnet

excitation. The pressure loss characteristics were maintained in all magnets due to cooldown and excitation [3]. Any unusual excitation behavior, such as DCA311, can be easily observed. DCA311 shows higher than average loss upon excitation, although the prestress is not very high. This unusual change in inner coil pressure, with excitation, is attributed to the diminishing support of the collars from the yoke. This is because the yoke laminations on DCA311 were chevroned due to loose packing.

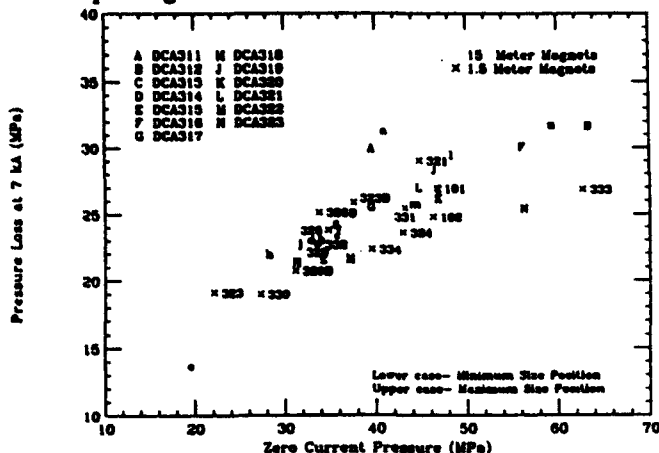


Figure 2: Absolute pressure loss in inner coils as a function of initial coil pressure

The pole stress on all magnets remains positive, during excitation, and there is no sign of unloading [3,5,9] at 7 kA. By maintaining the coil cross-section for all magnets, there does not seem to be any noticeable difference in their excitation behavior due to different types of insulation.

The magnet is partially supported in the axial direction at each end by sets of four bullet load slugs with strain gages. The end force measured, by the bullet gages, increases in proportion to current squared. Fig. 3 shows the total end force experienced by the long and short magnets during excitation. The longitudinal force in the end is expected to increase by approximately 10-15 % of the total electromagnetic force when the magnet is at 6.6T [9]. The total end force is estimated at  $3 \text{ kN} / (\text{kA})^2$ . This is a small fraction of the total electromagnetic force in the coil, as most of the axial force is transferred to the shell through friction between collar and yoke. End force is highly dependent on the collar-yoke

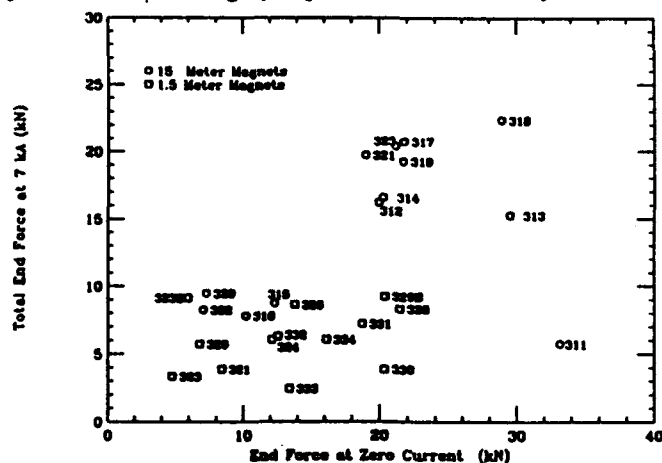


Figure 3: End force at 7kA vs initial end force at zero current.

interaction. Any unusual response is obvious, e.g., DCA311 shows very little end force, at 7 kA, than expected because of smaller collar-yoke interaction as explained earlier. Bullet gage preloads changed over thermal cycle in some magnets, but these changes did not affect the quench performance of Fermilab vertically split yoke magnets, as they have tight collar-yoke interaction.

## VI. CONCLUSION

Quench performance of some of the magnets was not so stable [9]. This could have been due to too many shims, insulation itself or it could also be associated with manufacturing process. A slight modification in manufacturing process can affect the magnet performance, as observed in some magnets with two piece pole end key [3]. Magnets with all polyimide film insulation need to be studied more to fully understand their behavior. We have shown that "thinner insulation without glass tape" with low curing temperature can be used successfully in SSC collider dipoles. One of the magnets of this series DCA322 (all polyimide) was tested at 1.8K at about 9.5 Tesla, showing the Fermilab design to be robust. This gives a confidence in the mechanical design and the choice of insulation for Fermilab built magnets. This is very promising for SSC's future and a success of 2D design. Thermal contraction and coil relaxation is an important design issue for magnets with all polyimide insulation with no glass tape. It is important to use as little insulation as possible without risking turn to turn breakdowns.

We would like to acknowledge the work of many engineers and technicians who made it possible to present these results.

## REFERENCES

- [1] J. Strait et al; "Mechanical Design of 2D Cross-section of the SSC Collider Dipole Magnet", IEEE Particle Accelerator Conference, San Francisco, CA, May 6-9 1991. 4:2176.
- [2] E.G. Pewitt ed. "50 mm Collider Dipole Magnet Requirements and Specifications" Fermilab 16 Aug 1991.
- [3] T. Jaffery et. al. "Test Results of Post-ASST design Fermilab-Built 1.5 meter, SSC Collider Model Dipoles" IEEE Trans. Applied Superconductivity, March 1993, 2:666
- [4] T. Jaffery "Test Results of Post ASST design 50mm SSC Model Dipoles " presented at MSIM, SSCL Internal Tech. Note TS-SSC 92-076.
- [5] R.E. Sims et. al; " A study of variations in dipole cable insulation systems and their effect on creep", submitted to IISSC conference, San Francisco, CA, USA, May 1993,
- [6] M. Wake, et al., "Test of 1.5 meter Model 50 mm SSC Collider Dipoles", submitted to IEEE Particle Accelerator Conference, San Francisco, CA, May 6-9 1991.
- [7] M. Wake, et. al., "Mechanical Behavior of Fermilab/General Dynamics Built 15 m SSC Collider Dipoles" .IISSC Supercollider 4, 1992.
- [8] A.Lipski et. al., "Alternate End Part Materials" Fermilab Internal Tech Note TS-SSC-92-084.
- [9] J. Strait et. al., "Quench Performance of Fermilab/General Dynamics Built Full Length SSC Collider Dipole Magnets" .IISSC Supercollider 4, 1992.

# Design and Tests of UNK Superconducting Correction Magnet Models

E. Rybakov, N. Bogatov, I. Dmitrieva, M. Kosyakin, Yu. Severgin, V. Fedorov, V. Shaan'gin  
D.V. Efremov Scientific Research Institute  
of Electrophysical Apparatus  
189631, St.-Petersburg, Russia

P. Chirkov, S. Kosub, K. Myanikov, V. Sychev  
Institute for High Energy Physics  
Protvino, Moscow Region, Russia

A. Rychagov, V. Sytnikov, A. Taran  
All-Union R & D Institute of the Cable Industry  
Moscow, Russia

## Abstract

At present NIEFA is designing superconducting correction magnets for UNK. UNK magnetic field correction system includes about 1500 various correction windings: dipole, quadrupole, sextupole and octupole. The magnet consisting of 3 concentric saddle type multipole coils with common iron yoke ("spool-piece" type) was selected as basic one. Each of the correction coils has the next optical force: sextupole—600 (T/m<sup>2</sup>)·m, quadrupole—5.5 (T/m)·m, dipole—0.68 T·m. Total length is about 1.6 m, operating current ≤20 A. The 4 full scale models of the basic correction magnet with different types of conductors and various technique of winding have been built. This report describes the main design parameters of models and the particulars of their construction. The results of manufacturing and tests (quench behavior and magnetic field measurements) are discussed.

## I. INTRODUCTION

The basic element of magnetic field correction system of second UNK stage is a superconducting corrector with 70mm diameter aperture. It has 3 correction windings: dipole is to correct the orbit, quadrupole is to correct the betatron frequencies and sextupole is to correct the chromaticity and to compensate the sextupole errors from the main dipoles. These windings has optical forces of 0.68 T·m, 5.5 (T/m)·m and 600 (T/m<sup>2</sup>)·m accordingly. The "spool-piece" conception [1] was chosen as basic. A gabarit size limitations and, particularly, low operating current (≤20A) had led to the necessity of preliminary modelling. Four full-scale models of the correction magnet SCM-1 (2 models), SCM-3 and SCM-4 with different construction of the coils has been designed, built and tested. About 400 correction magnets will be made for the second UNK stage

and therefore the big attention was paid to the fabrication technique in series production conditions.

## II. THE MAIN PARAMETERS AND ASSEMBLY OF MAGNET

Except the difference of coils design, all three models were the same arrangement and similar construction. They consist of 3 concentric saddle shaped windings enclosed in the common cylindrical laminated iron yoke with helium channels on its outer surface. The 4mm stainless steel shell makes outer wall of helium vessel and serves, at the same time, as mechanical bandage. The cross-section of the models is shown in figure 1.

Superconducting wire parameters are given in table 1.

Table 1: Parameters of wire

Diameter of wire (mm)	0.3
Superconductor	NbTi alloy
Matrix	Cu
Cu / NbTi ratio	1.7
Number of filaments	150
Diameter of filament (m)	15
R <sub>300</sub> /R <sub>4.2</sub> ratio	>100
Critical current density at 5 T (A/m <sup>2</sup> )	(2.0-2.2)·10 <sup>9</sup>
Critical current at 5 T (A)	52-57

Chosen wire has a big margin of the critical current (operating current of all models is between 12-20 A in the field, up to 1.3 T). It had been done to avoid the training up to operating current that was one of the main requirements.

The main dimensions of models are given in table 2.

In table 2 the turns density is a number of turns per unit of the coil cross-section. The meanings of the short sample

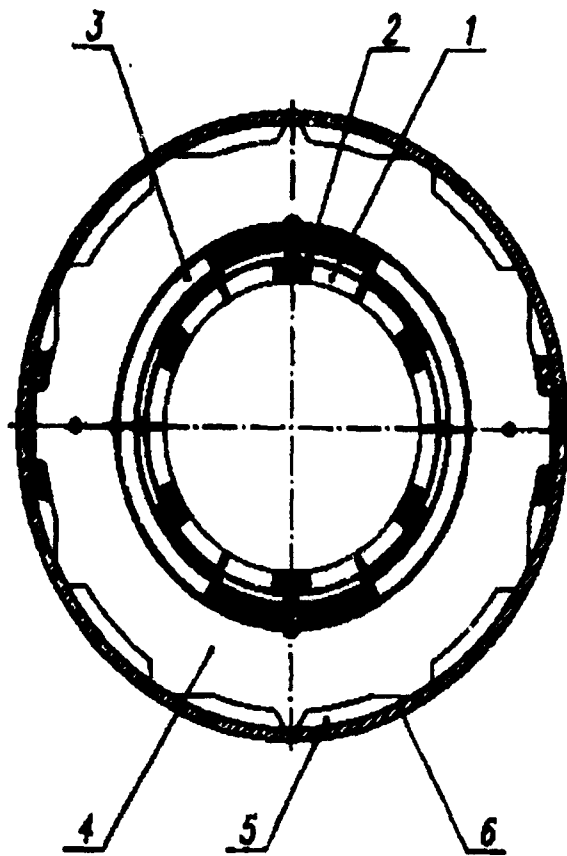


Figure 1: Cross-section of SCM models. 1—sextupole coil, 2—quadrupole coil, 3—dipole coil, 4—laminated iron yoke, 5—helium channels, 6—helium vessel shell

Table 2: Main dimensions of models (mm)

Dimension	Sextu- pole	Quadru- pole	Dipole
<b>COILS:</b>			
Inner radius	40.0	46.5	49.9
Outer radius	46.2	49.6	56.1
Angle dimension (grad)	20.8	27.8	58.9
Total length	1370	1290	1190
Straight length	1320	1220	980
Coils per magnet	6	4	2
Sections per coil (SCM-1 only)	2	4	8
Layers of ribbon per coil (SCM-3 only)	37	58	131
<b>Turns per coil:</b>			
SCM-1	624	408	1760
SCM-3	592	464	1965
SCM-4	384	266	1260
<b>Turns density (1/cm<sup>2</sup>)</b>			
SCM-1		7.3	
SCM-3		6.2	
SCM-4		3.8	
<b>IRON YOKE:</b>			
Inner radius		56.9	
Outer radius		84.0	
Total length		1400	
<b>MAGNET:</b>			
Total diameter		176	
Total length		1440	

limit are given for the joint ramping of all three windings (in more detail see below).

The electrical and magnetic parameters are presented in table 3.

After winding the coils were pressed to the design dimension and were cured at the temperature of 160° C. The fixation of the windings one about another was achieved with the advance assembly of the coils in the semi-blocks consisting of three sextupole, two quadrupole and a dipole coils. Complete coils were assembled in the semi-block on the cylindrical mandrel with epoxy impregnated ground insulation. Then semi-blocks were pressed relatively to the middle plane of the package, were cured again and assembled in the winding package. The top view of the winding package are displayed on figure 2.

Laminated iron yoke was made of the stamped magnetic steel sheets, which in advance were set up in the 100 mm long semi-packages and were welded on outer surface. Semi-packages of the iron yoke were assembled on the complete winding package, pressed along the vertical axis by the pressure of 150 kg/cm<sup>2</sup> and then welded with two seams in the middle plane of the package. Coil connections were made at the top flange of the magnet after

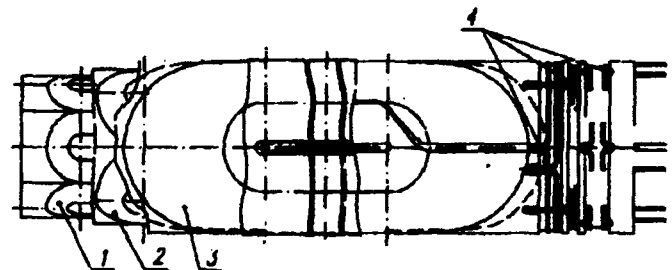


Figure 2: Top view of the winding package. 1—sextupole coil, 2—quadrupole coil, 3—dipole coil, 4—current leads

assembly. Separate wire were twisted together, wrapped with the thin copper wire and then soldered.

The coil resistance measurements and testings of the ground insulation had made after each operation during of the manufacturing and assembly.

Table 3: Electrical and magnetic parameters of models (SCM-1/SCM-3/SCM-4)

Parameter	Units	Sextupole (N=2)	Quadrupole (N=1)	Dipole (N=0)
Optical force	$(T/m^N) \cdot m$	600	5.50	0.68
Centre field (gradient)	$T/m^N$	448	4.37	0.59
Operating current	A	12.2/13.0/20.0	11.7/10.4/18.5	13.1/12.5/20.8
Short sample limit	A		54/56/69	
Constructive current density	$\cdot 10^8$ A/m <sup>2</sup>	0.90/0.80/0.80	0.96/0.66/0.67	0.96/0.73/0.75
Inductance (calculated)	H	3.7/3.2/1.4	1.4/1.9/0.6	15.5/18.8/6.8
Active resistance at 300 K (measured)	k $\Omega$	3.4/3.4/2.4	1.5/0.9/1.1	3.2/3.8/2.5
Stored energy	kJ	0.27	0.10	1.4

### III. PARTICULARITIES OF THE COIL DESIGN

#### A. SCM-1

The coil consists of the several sections with square cross-section. This approach allows to receive the more regular distribution of the turns in the coil. Each section was random wound by the single wire with 25  $\mu$ m polyamidimide enamel insulation in the separate flat mandrel. During the winding the wire was put through the bath with epoxy resin. After the winding the section was pressed to the design dimension, formed on the cylindrical mandrel and cured. After that the complete sections were assembled together around the central G-10 former. Then separate sections were connected serially.

The experience of the two models SCM-1 shown that this technique, on the whole, allows to make the magnets corresponding to presented requirements. However, it is sufficiently complicated and difficult. Besides, it was no possible to avoid completely of the turn shorts, which were observed in approximately 10% of sections.

#### B. SCM-4

In the model SCM-4 for the elimination of the turn shorts was used the wire with combined insulation—15  $\mu$ m polyamidimide enamel and 50  $\mu$ m fiberglass braid. The coil was all random wound in the cylindrical mandrel around G-10 former. In other respects the winding and assembly process was just the same as in the model SCM-1.

Application the add insulation allowed to exclude the turn shorts. Unfortunately, in this case we had to decrease the turn density comparing with the model SCM-1 (see table 2) and to increase the operating current till the limited meaning of 20 A. Besides the random winding brought to the nonuniformity of the turns distribution on the coil cross-section (especially in dipole coil), therefore even after pressing and curing the coil is very friable and needs in vacuum impregnation and special equipment for it.

#### C. SCM-3

One of the ways to reach the regular turns distribution is a winding with the ribbon conductor [2]. Ribbon has the width equal to the radial coil thickness and consists of several parallel secured wires which are connected serially on the coil end. In the model SCM-3 the coils were wound with the ribbon conductor that was made in original method. The ribbon was made with the binding a number of parallel wires by the polyimide thread with following impregnation with the small number of polyamidimide varnish and curing for making ribbon stability during of the winding. The ribbon wires has the increasing diameter from the inner to outer edge of the ribbon to compensate increasing of the coil angle length from the inner radius to outer. The ribbon for the dipole and sextupole coils consisted of 16 wires, and for quadrupole—of 8.

The coils of the model SCM-3 were made like its of model SCM-4. After the curing the separate wires were joined serially. The construction of series connection is similar to the described in above.

The use of the ribbon conductor speeds up the winding process much and allows to increase the turns density in about 1.6 times as compared with the random winding. Polyimide thread securing the separate wire in the ribbon, make the additional insulating distances between its, that allows to exclude the turns shorts. At the same time they make the coils "transparent" for the penetration of epoxy resin. One can suppose that it will make possible to receive the monolithic coils without vacuum impregnation. On the whole, one can say that the winding of the coil with the ribbon conductor is, perhaps, the most preferable of all testing variants.

### IV. THE TESTS

The models were tested in a 3 meter long vertical cryostat at 4.2 K. SCM-1 and SCM-4 models were cooling twice and SCM-3—one time.

Anming He

Superconducting Super Collider Laboratory\*  
2550 Beckleymeade Ave., Dallas, TX 75237 USA

**Abstract**

The quench voltage, especially the turn-to-turn voltage, and the maximal temperature rise due to the quench in 50-mm-aperture Superconducting Super Collider collider correctors are calculated for various currents. The calculation shows a lower copper-to-superconductor ratio gives a lower quench voltage and a lower temperature rise as the result of much higher heat capacity of the superconducting material and lower copper resistivity at lower temperature. It also shows that when the copper to superconductor ratio is 2.2 to 1, each individually powered magnet is self-protected, and for the series of 24 correctors that are powered together in the collider, a parallel 2Ω resistor on each magnet will provide needed protection. The energy loss on these resistors during powering up is less than 5% of the energy stored in the magnet at the operating current.

**I. INTRODUCTION**

When a quench occurs in a superconducting coil, the normal zone starts to grow so that the resistance of the magnet increases until all the stored electro-magnetic energy has dissipated through the ohmic heating[1]. This process causes temperature rise and high voltage in the coil. Can the quenches in the current Superconducting Super Collider (SSC) collider corrector design damage the superconducting windings?

In answering this question, we first study how the normal zone grows in the coil windings under the adiabatic assumption to find the way for calculating the time- and geometry-dependent coil resistance,  $R_{mag}(t)$ . Then we use a computer to simulate the electric circuit that includes the quenching magnet with the resistance,  $R_{mag}(t)$ . Finally, some suggestions on the quench protections will be made for the cases where excessive heat and/or voltage are expected by the simulation results.

**II. NORMAL ZONE GROWTH AND ITS RESISTANCE**

A typical cross section of the SSC collider corrector winding is rectangular, as shown in Figure 1. The area of each unit cell is  $A$ . The longitudinal (along the  $z$ -direction) normal zone growth velocity,  $v_l$ , is determined by the thermal properties of the metal part of the coil; it also depends on the current and conductor packing density [1][2][3]. The transverse velocity,  $v_t$ , is much smaller than the longitudinal one because of the much lower heat conductivity of the insulation. The ratio between the two is [1]

$$\alpha = \frac{v_t}{v_l} = \frac{(\gamma C)_{avm}}{(\gamma C)_w} \left( \frac{k_t}{k_l} \right)^{1/2}$$

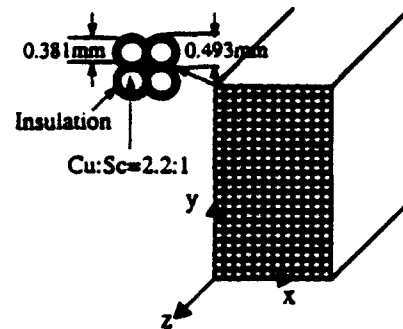


Figure 1. Typical section of coil winding in SSC collider correctors.

where  $(\gamma C)_{av}$  and  $(\gamma C)_{avm}$  are the volumetric heat capacity averaged over the whole coil cross section and the metallic constituents only, respectively;  $k_t$  is the transverse thermal conductivity determined by the insulation; and  $k_l$  is the longitudinal one mainly contributed from the copper and NbTi constituents.  $\alpha$  is around 0.02~0.03 for these corrector coils.

Therefore, at any time  $t$  after a quench starts at time  $t = 0$ , the normal zone is a rotating ellipse centered at the quench starting point. The rotating axis is longitudinal before it hits any coil boundary, or its two ends meet in one of the three directions [4]. The long axis of the elliptic is  $v_l t$  and the two short ones are  $\alpha v_l t$ . When a coil boundary is encountered or two normal zone ends meet, the normal zone stops its growth on that direction, but continues on the other directions until the stored energy is exhausted or the whole coil turns normal, whichever comes first. The resistance  $R(t)$  of this normal zone at any given time  $t > 0$  is evaluated by dividing the whole region into subregions according to their quenching time  $\tau$  and a small time interval  $\Delta t$ . When the coil boundary is not involved, each subregion is a shell in the rotating elliptic, with long axis  $v_l \tau$  and shell thickness  $v_l \Delta t$  on that direction. The MIITS value,

$$MIITS = \frac{1}{A} \int I^2(\tau) d\tau,$$

is computed for each subregion. A comparison of this MIITS value to the temperature-MIITS tables for the copper and NbTi with the given RRR (residual resistivity ratio) value [5] is made to get the temperature rise in this subregion. The semi-empirical expression of the copper resistivity for the temperature range 0~1000K [5],

$$\rho(T, RRR) = \frac{1.545}{RRR} + \left( \frac{2.32547 \times 10^9}{T^3} + \frac{9.57137 \times 10^5}{T^3} + \frac{1.62735 \times 10^2}{T} \right)^{-1}$$

is invoked to find the resistance. A summation of the subregion resistance over the normal zone is carried out to provide the magnet resistance,  $R_{mag}(t)$ .

\*Operated by the Universities Research Association, Inc., for the U.S. Department of Energy under Contract No. DE-AC35-89ER40486.

The submitted manuscript has been authored by a contractor of the U.S. Government under Contract No. DE-AC35-89ER40486. Accordingly, the U.S. Government retains a nonexclusive, royalty-free license to publish or reproduce the published form of this contribution, or allow others to do so, for U.S. Government purposes.

Note that the adiabatic assumption has been used throughout the preceding calculation. There is no heat conducted out of the coil. Inside the coil, heat is also absorbed to produce the normal zone growth, but this latent heat is not deducted when the temperature rise of the conductors is evaluated. So an overestimate of temperature rise and resistance of the normal zone is expected from this procedure.

### III. QUENCH CIRCUIT SIMULATION

The method to calculate the resistance of the corrector magnet coil during a quench was worked out in the previous section. One other important electric parameter is the inductance of the magnet. We use PE2D<sup>1</sup> to do two-dimensional field analysis and stored energy calculation for different currents. The circuit in Figure 2 is for a magnet powered individually. When a quench is detected, the switch is closed and the power supply is shut down. Usually a quench detection has a few millisecond delay to the quench itself, compared to the 100 ms to 200 ms for the whole quench time scale. This delay can be treated as zero without any significant impact on the results. The switch also can be replaced by a diode that introduces  $\sim 0.6$  V voltage across the diode, but that voltage can be ignored compared to the hundreds to thousands of volts inside the magnets across the normal resistance zone.

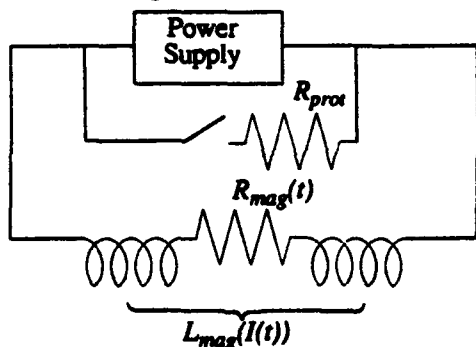


Figure 2. Quench circuit for individually powered corrector.

Assuming the quench starts in a corner of the coil winding at time  $t = 0$  and quench current  $I_0$ , we have the initial conditions,

$$\left\{ \begin{array}{l} \Delta t = 0.001 \text{ sec} \\ z[0] = 0 \\ I[0] = I_0 \\ R_{mag}[0] = 0 \\ \Delta I[0] = -I[0]R_{prot}\Delta t/L_{mag}(I_0) \\ MIITS_i[0] = \frac{1}{A^2} \int_0^0 I^2[t']dt' = 0 \text{ for all integer } i \geq 0, \end{array} \right.$$

where  $z[t]$  is the half-rotating axis of the normal zone ellipse (Figure 1).

At time  $t = n\Delta t$ , the iteration relations become

$$\left\{ \begin{array}{l} z[n\Delta t] = z[(n-1)\Delta t] + \frac{I[(n-1)\Delta t]}{I_0} v_0 \Delta t \\ I[n\Delta t] = I[(n-1)\Delta t] + \Delta I[(n-1)\Delta t] \\ \Delta I[n\Delta t] = I[(n-1)\Delta t] + \Delta I[(n-1)\Delta t] \end{array} \right.$$

and

$$R_{mag}[n\Delta t] = \frac{1}{4} \sum_{i=0}^{n-1} f(i) \frac{\pi \alpha^2 \rho_m (T([i, n\Delta t]), RRR)}{\lambda_m A^2}$$

$\times \{z[(i+1)\Delta t] + z[i\Delta t]\}^2 \{z[(i+1)\Delta t] - z[i\Delta t]\}$  where  $\lambda_m$  is the proportion of the metal constituents in the coil unit cell, and element  $i$  ( $< n$ ) is the subregion of the ellipse mentioned in the previous section, which turns to normal at time  $t' = i\Delta t$ . Its temperature  $T[i, n\Delta t]$  is evaluated via the MIITS iteration formulas.

$$MIITS_i[n\Delta t] = MIITS_i[(n-1)\Delta t] + \frac{I^2[(n-1)\Delta t]}{A^2},$$

and the MIITS tables in Reference [5].

### IV. RESULTS

An SSC collider dipole corrector with the winding configuration shown in Figure 1 has the following additional parameters:

Maximal operating field	2.21 T
Coil width	10.84 mm
Coil height	24.15 mm
Coil length	1.36 m
Number of coils	2
Inductance	2.4 H
Maximal operating current (60% wire short sample)	86 A.

The calculated maximal turn-to-turn voltage, maximal resistive voltage across the normal zone, and temperature rise of the conductor in which the quench starts under various currents are plotted in Figure 3. It shows that the turn-to-turn voltage will not exceed 210 V, the total resistive voltage across the resistance of the normal zone is less than 2000 V, and the temperature rise in the hottest spot is less than 300 K when the magnet is operated below the maximal operating current 86 A. Therefore the magnet is self-protected during the collider operation. Figure 3 also shows that during the magnet quench testing, when the current exceeds 105 A, some protection measure should be taken to prevent any damage in the insulation due to overheating.

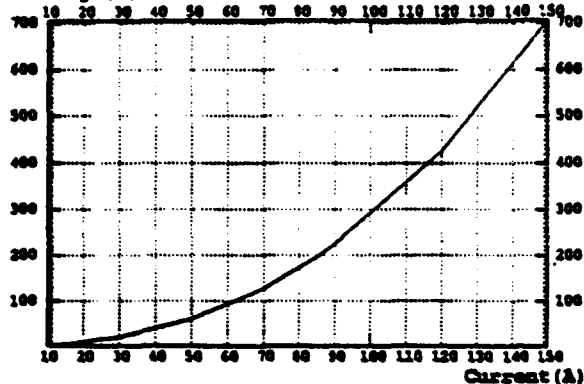
All the other collider arc correction magnets are smaller than the dipole corrector, so they are all self-protected when they are individually powered. But when 24 quadrupole or sextupole correctors are connected in series, the inductance will be higher than 45 H, and the single quenching magnet cannot absorb the tremendous energy stored in all 24 magnets. So a current bypass system is necessary to protect this magnet. A 2- $\Omega$  resistor can be connected parallel to each member in the series for the protection. To minimize the influence of single

<sup>1</sup> PE2D is a trademark of the Vector Field, Inc.

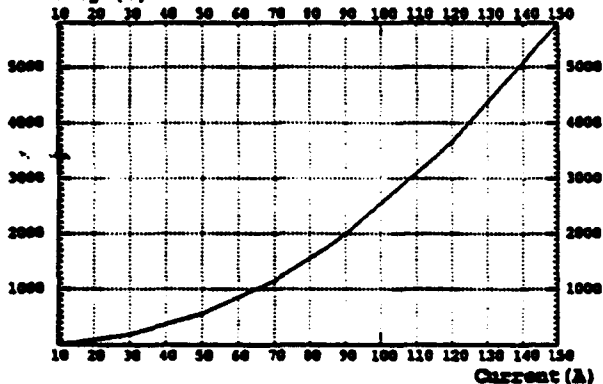
magnet quench on the corrector system operation, two opposite parallel diodes are preferred rather than one resistor for the bipolar current operation.

Quench simulations are also done for different copper-superconductor ratios of the superconducting wire around 2.2:1. It shows that higher superconductor contents lower the quench voltage across the normal resistance zone and the temperature rise caused by the quench. We believe that in our range of study, the much higher heat capacity of the NbTi and lower copper resistivity at a lower temperature are the source of this effect.

a) Maximal Turn to Turn Voltage vs. Quench Current Voltage (V)



b) Maximal Resistive Voltage vs. Quench Current Voltage (V)



c) Maximal Temperature Rise vs. Quench Current Temperature (K)

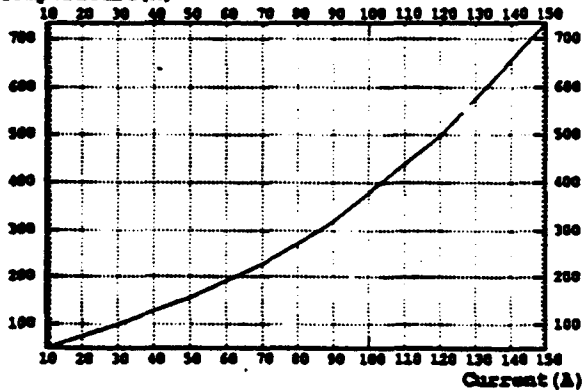


Figure 3. SSC collider dipole corrector quench data.

The simulation code is also checked with the testing data for some prototype correction magnets. A comparison is shown in Figure 4 for the current decay over time. The difference is believed due to ignoring the cooling effect mentioned in Section II.

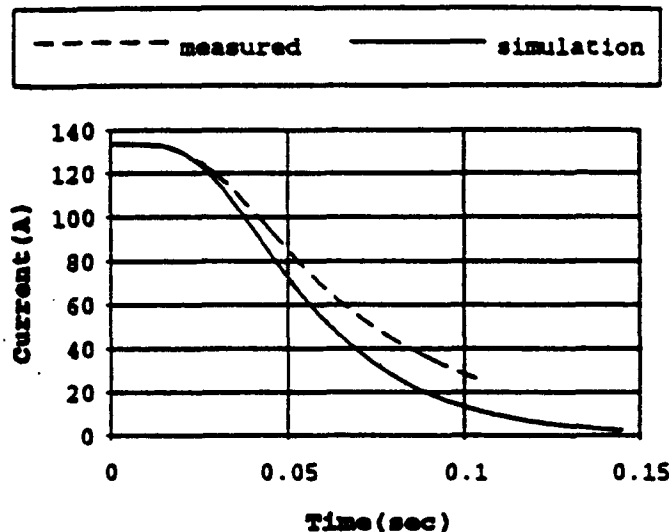


Figure 4. A comparison between the simulation and measured current decay for an SSC corrector dipole prototype.

## V. ACKNOWLEDGEMENT

I would like to thank the staff in the corrector lab of the corrector group in the mechanical engineering department, accelerator division of the SSCL, for the quench testing data. I also want to thank Gustavo López, John Skaritka, and Weijun Shen for their helpful discussions.

## VI. REFERENCES

- [1] M. N. Wilson, "Computing Simulation of the Quenching of a Superconducting Magnet," Rutherford Laboratory Report, RHEL/M151, 1968.
- [2] A. Devred, Waxahachie Lectures on Magnets, Fall 1992.
- [3] A. Devred, "Measurements of Quench Propagation Velocity along a Super-Stabilized Conductor," MT-11.
- [4] M.N. Wilson, *Superconducting Magnets* (Chapter 9), Oxford Science Publications, 1983.
- [5] M. S. McAshan, "MIITS Integrals for Copper and for Nb-46.5wt%Ti," SSC-N-468, February 10, 1988.

# Variation in $a_1$ Saturation in SSC Collider Dipoles\*

Ramesh C. Gupta and Animesh K. Jain

RHIC Project, Brookhaven National Laboratory, Upton, Long Island, NY 11973 USA

## Abstract

Analysis of the variation in the saturation of the skew quadrupole ( $a_1$ ) is presented for the 15m long, 50mm aperture SSC collider dipole magnet prototypes built at BNL. The variations within a magnet are shown to be correlated with local top-bottom asymmetry in the iron yoke weight. On the other hand, magnet to magnet variations in the saturation of integral skew quadrupole are shown to be correlated with the geometric  $a_1$ .

## I. INTRODUCTION

Magnets DCA209-DCA213 are a set of 50mm aperture, 15m long SSC collider dipole models built at BNL[1]. The field quality in these magnets is expressed in terms of the normal and skew harmonic coefficients  $b_n$  and  $a_n$  in dimensionless "units" defined by the multipole expansion

$$B_y + iB_x = 10^4 \cdot B_0 \sum_{n=0}^{\infty} (b_n + ia_n) [(x + iy) / R]^n$$

where  $x$  and  $y$  are the horizontal and vertical coordinates,  $B_0$  is the dipole field strength and  $R$  is a "reference radius", chosen as 1cm for these dipoles. A large amount of variation has been observed in the value of the skew quadrupole field coefficient  $a_1$  as a function of current at different axial positions in a single magnet and also from magnet to magnet. As an example, Fig.1 shows the current dependence of  $a_1$  measured with a one meter long measuring coil in magnets DCA209-DCA213. To facilitate comparison, the curves are offset along the y-axis such that the value of  $a_1$  is zero at 2kA

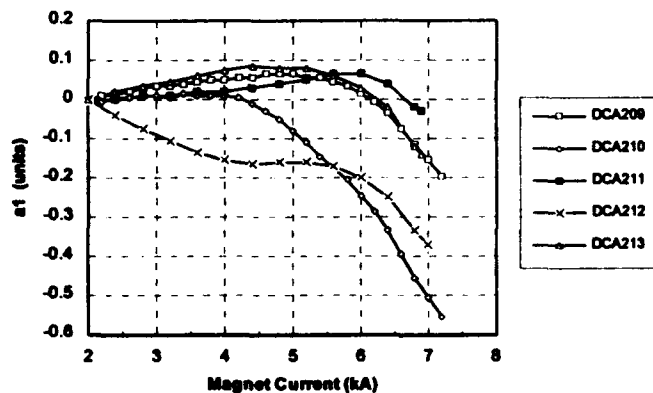


Fig.1 Current dependence of skew quadrupole ( $a_1$ ) in magnets DCA209 to DCA213. The curves are offset such that  $a_1$  at 2kA is zero for all magnets.

for all magnets. The variation with current is commonly referred to as  $a_1$  "saturation" since the major source of this variation is the off-centered placement of the iron yoke in the magnetic cryostat vessel. However, in practice this variation may also include several other sources. In this paper we explain the cause of the measured variations in  $a_1$  saturation and present a simple formula which can be used to predict  $a_1$  saturation in long 50 mm aperture SSC dipole magnets with horizontally split yokes.

## II. SOURCES OF $a_1$ VARIATION

In this section we list some of the sources which may be responsible for the variation in  $a_1$  as a function of current. For each of these sources, we also give estimates of the magnitude of the change,  $\delta a_1$ , between 6600A and 2000A (referred to as "saturation  $a_1$ "). Given below is a brief discussion of some of the sources which may be responsible for the observed  $\delta a_1$ :

### (a) Off-centered yoke in the cryostat :

At high currents the flux lines are not contained in the iron cross section and start leaking outside the yoke. At this stage the magnetic iron in the cryostat vessel provides the additional magnetic path to return the flux lines. However, since the center of cryostat does not coincide with the center of yoke, an up-down asymmetry would be generated in the field at the center of the dipole. The calculations show a noticeable current dependence in  $a_1$  above a primary field of 6.0 Tesla ( $I \sim 6kA$ ) and the computed  $\delta a_1$  is  $\sim -0.2$  unit.

### (b) Difference in the packing factors of the yoke halves :

The packing factor is basically the ratio of the amount of yoke material actually present to the maximum amount of yoke material possible in the design volume. Though the overall difference in the packing factor between the top and bottom yoke halves is well controlled (typically within  $\sim 0.01\%$  in DCA209-213), there may be some local variations along the length of the magnet. The iron weight is measured for each 7.6cm (3") block in the top or bottom yoke. Since the length of the measuring coil is one meter, a top bottom weight difference in the yoke in a one meter region would be seen in the field harmonics. Our 2-d calculations show that a 0.1% higher packing factor in the upper yoke half would give about  $-0.1$  unit of  $\delta a_1$ . This effect is noticeable above 3000A. However, the difference in packing factors is likely to have

\* Work Supported by the U.S. Department of Energy.

opposite sign in neighboring packs to maintain a low overall difference in the packing factor. This implies that 2-d calculations may be over-estimating the effect because in reality the field lines would not only move from bottom to top, but may also move in the axial direction. We will discuss this item in more detail later in Sec.III.

(c) *Off-centered coil in the yoke :*

If the coil center does not match the yoke center, an additional  $\delta a_1$  would be seen. This will also give a geometric  $a_1$ . Our calculations show that for a coil placed 25 $\mu$ m (0.001") above center, there would be an additional  $\delta a_1 \sim +0.1$  unit and the geometric  $a_1$  would be approximately -0.12 unit.

(d) *Difference in the top and the bottom coil sizes :*

A difference between the top and the bottom coil sizes gives a geometric  $a_1$ . The calculations show that if the upper coil half is 25 $\mu$ m larger (which means that the midplane is shifted down by half this amount), the geometric  $a_1$  would be  $\sim +0.7$  unit. It also gives a small additional contribution to the saturation related  $\delta a_1$ , which is about 1% of the geometric  $a_1$ .

There is also a second effect of the coil size difference. It is possible that when there is an initial difference in the size between the top and bottom coil halves, the already displaced coil midplane may shift more as a result of the interaction between the initial mechanical forces and the dynamic ( $J^2$  dependent) Lorentz forces. We have not done the mechanical calculations to compute the amount of this displacement. However, it may be pointed out that merely a 2.5 $\mu$ m additional displacement of the midplane would give a contribution of about 0.14 unit to the observed  $\delta a_1$ .

(e) *Special purpose holes in one yoke pack :*

At about 5m (200 inches) from the lead end, the strain gauges are installed in all the long magnets. In order to bring the wiring out, two 3/8" diameter holes are drilled in one yoke pack from the iron inner radius to the two He bypass holes. This is done only in the bottom half of the magnet. This gives a large local  $a_1$  saturation. Our 2-d estimates suggest that in a 1 meter long measuring coil, an additional  $\delta a_1$  of  $\sim -0.15$  unit should be observed.

(f) *Persistent Currents :*

If an up-down asymmetry is present either in the coil geometry (which also gives geometric  $a_1$ ) or in the coil cables used in the top and bottom coil halves (for example, the cables may have a different  $J_c$ ), an  $a_1$  due to persistent currents would be present. Depending on the amount of asymmetry, the value may be noticeable at 2000A and negligible at 6600A. This would also contribute towards the observed  $\delta a_1$ . We have not done any detailed calculations here, but  $\delta a_1$  due to persistent currents is expected to be within 0.05 unit, based on the measured values of  $a_1$  at 2000A during the up and the down ramps in magnets DCA209-213.

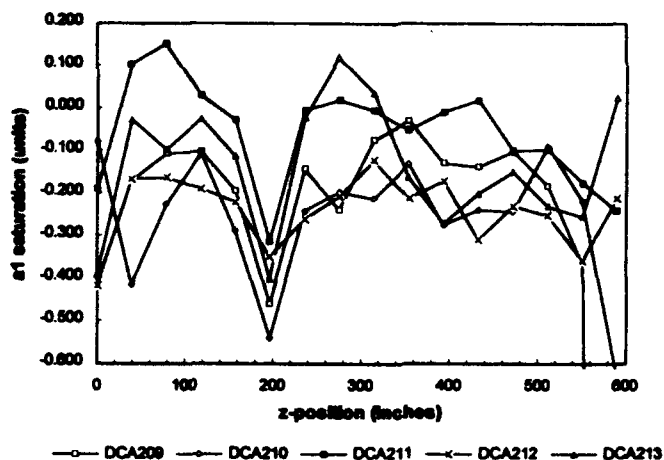


Fig.2  $a_1$  saturation ( $\delta a_1$ ) in DCA209-DCA213 Magnets

### III. $\delta a_1$ VARIATION WITH POSITION

Axial scans have been made in the magnets DCA209 through DCA213 at 2000A and 6600A. It has been found that  $\delta a_1$  varies significantly along the length of a magnet (Fig.2). Amongst the various mechanisms proposed in the previous section, the off-centered yoke in the cryostat and the persistent currents [(a) and (f) in Sec.II] can not account for the variation with position. A difference in the packing factor between the upper and lower yoke halves can be examined most readily from the data on individual yoke block weights. Fig.3 (open boxes) shows the local asymmetry in the top and bottom yoke block weights averaged over the length of the field measuring coil (one meter), as a function of block number (position along the magnet) for the magnet DCA213. The asymmetry is defined as

$$\text{asymmetry} = \frac{\text{wt. of bottom block} - \text{wt. of top block}}{\text{average of top and bottom wts.}} \times 100\%$$

As can be seen from the figure, although the average asymmetry for the entire magnet is nearly zero, there could be a local asymmetry of up to  $\pm 0.1\%$ , when average values over one meter length are considered. The asymmetry is most prominent when the measuring coil center is located around

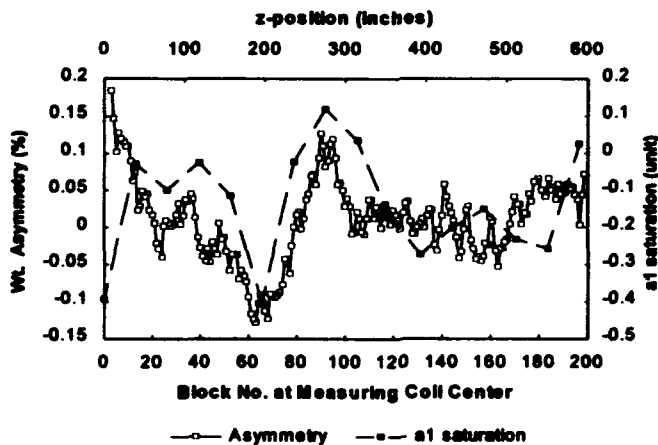


Fig.3 Variation of Top-bottom weight asymmetry and  $\delta a_1$  along the length of the magnet DCA213

block numbers 60 and 90. Fig.3 also shows the variation of  $\delta a_1$  with position (filled boxes, dashed line). A very good correlation between the yoke asymmetry and  $\delta a_1$  is seen. A similar correlation has been obtained for the magnet DCA212 also. This shows that the major cause of  $\delta a_1$  variation along the length of the magnet is a local top-bottom asymmetry in the packing factor. It is interesting to note that a similar axial variation in  $b_1$  saturation is seen in the Fermilab magnets, which may have a left-right asymmetry in the packing factor because of the vertically split yoke design.

An examination of the  $a_1$  saturation profiles for all the magnets (Fig.2) reveals that the maximum  $a_1$  saturation is seen at about 200 inches in all the magnets, which is also the location of special purpose holes [Sec.II(e)]. The location and the magnitude of the dips in  $\delta a_1$  in Fig.2 suggest that the holes are contributing to  $\delta a_1$  at about 200 inches. It should be noted that these holes will not be present in the production magnets.

## V. MAGNET TO MAGNET VARIATIONS OF INTEGRAL $\delta a_1$

Since the total weight in the top and bottom yoke halves is well controlled (within  $\sim 0.01\%$ ) in these magnets, we should not see any appreciable magnet to magnet variations in the integral (or the average)  $\delta a_1$ . Table I lists the average values and RMS variations (along length) in  $a_1(2000A)$ ,  $a_1(6600A)$  and  $\delta a_1$  for the magnets DCA209-213. Only the straight section data are considered for the averaging.

Table I shows that contrary to expectations, the integral  $\delta a_1$  does show some magnet to magnet variation ( $\sigma = 0.085$  units). In fact, there is a strong correlation between the integral values of geometric  $a_1$  and  $\delta a_1$ . We suggest the following mechanism as the possible cause for this correlation. A geometric  $a_1$  implies a mechanical difference between the top and the bottom halves of the coil as seen from the midplane. At high current, the asymmetric Lorentz force due to asymmetric coils could modify this coil asymmetry [Sec.II(d)]. The experimental data are examined in Fig.4 which shows the integral  $\delta a_1$  as a function of integral geometric  $a_1$  in magnets DCA209-213. A linear dependence of  $\delta a_1$  on  $a_1$  is seen, which may be parameterized as

$$\delta a_1 = -0.209 + 0.104 \times a_1(2000A)$$

Table I. Integral  $a_1$  and  $\delta a_1$  in magnets DCA209-DCA213

Magnet	Integral* $a_1(2000A)$	Integral* $a_1(6600A)$	Integral $\delta a_1$
DCA209	$0.26 \pm 0.41$	$0.09 \pm 0.42$	-0.175
DCA210	$-0.23 \pm 0.23$	$-0.47 \pm 0.21$	-0.245
DCA211	$1.76 \pm 0.62$	$1.72 \pm 0.71$	-0.034
DCA212	$-0.19 \pm 0.20$	$-0.42 \pm 0.22$	-0.230
DCA213	$0.61 \pm 0.34$	$0.48 \pm 0.35$	-0.130

\*Error bars refer to RMS variations along the axial position.

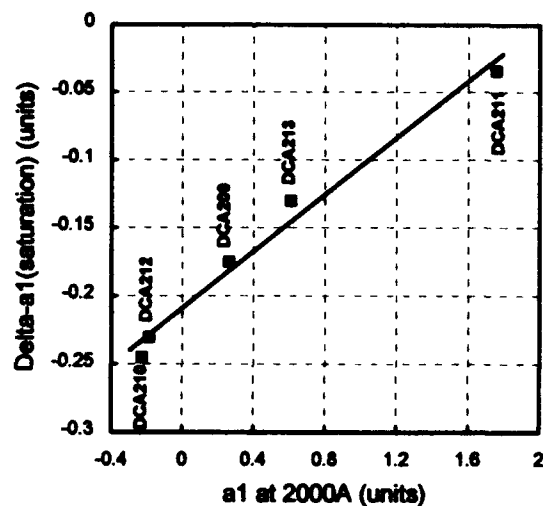


Fig. 4 Correlation between geometric and saturation  $a_1$ .

The constant term in the above equation agrees with the value of -0.2 unit calculated from the effect of off-centered yoke in the cryostat in the absence of any other asymmetry [See Sec.II(a)]. The second term gives the dependence of the integral  $\delta a_1$  on the geometric integral  $a_1$ . A coefficient of 0.104 implies that there is a  $\sim 10\%$  enhancement in coil asymmetry at 6600A due to Lorentz forces. A similar expression, perhaps with a somewhat different coefficient, is expected for magnets built elsewhere.

## V. CONCLUSIONS

We have examined the possible mechanisms for variation of  $\delta a_1$  in different magnets, and at different locations in a given magnet. There are large variations within a magnet which are correlated to the yoke density variations and position of special purpose holes. A good correlation is also found between the integral values of the geometric  $a_1$  and the saturation induced  $\delta a_1$  in the magnets built so far. Since the systematic value of the geometric  $a_1$  is expected to be zero for the production magnets, this variation would only add slightly ( $\sim 10\%$ ) to the random  $a_1$  at high field. The variation of integral  $\delta a_1$  in these magnets has  $\sigma = 0.085$  units, which is small compared to the axial variations and is much smaller than the SSC tolerance of  $\sigma = 1.25$  units for  $a_1$ . This is achieved because the total weights of the upper and the lower yoke halves are very well controlled.

We thank Peter Wanderer for many useful discussions and a critical review of the manuscript.

## VI. REFERENCE

- [1] P. Wanderer et al., "Magnetic design and field quality measurements for full length 50mm aperture SSC model dipoles built at BNL", *Proc. XVth International Conference on High Energy Accelerators*, Hamburg, Germany, July 20-24, 1992 in *Int. J. Mod. Phys. A (Proc. Suppl.)* 2B, pp.641-3 (World Scientific, Singapore, 1993).

# Spool Pieces at the SSCL

T. Clayton, Y. Cai, R. Smellie, S. Stampke  
Superconducting Super Collider Laboratory \*  
2550 Beckleymeade Avenue Dallas, Texas 75237 USA

## ABSTRACT

The basic features of the Superconducting Super Collider lattice are the two beamlines formed by superconducting dipoles (7736) and quadrupoles (1564). The dipoles constrain two 20 TeV proton beams into counterrotating closed orbits of 86.2 Km. The quadrupoles (FODO) require cryogenic cooling to LHE temperatures. This requirement isolates the main magnets from the outside world. The interface required, the Spool, is a crucial component of superconducting lattice design and machine operation. There are over 1588 spools in the Super Collider. We present here SSCL spool designs which consist of 1) housing for superconducting closed orbit and multipole correction magnets, 2) cryogenic function, magnet quench protection, system power, and instrumentation interfaces, and 3) cold to warm transitions for warm magnet and warm instrumentation drift spaces.

## 1. INTRODUCTION

There are two superconducting cryogenic machines in the SSCL complex, The Collider and High Energy Booster (HEB). The Collider is filled with 2 TeV proton beams by The HEB. The HEB is a 10.8 Km superconducting machine. The common task for the Collider and HEB is to design an interface that meets all the requirements of such large machines while maintaining costs and providing reliability in operation. The large quantities of spools and their criticality to machine operation directly effect spool production cost, reliability, and maintainability.

## 2. SPOOL CONCEPTS AND FUNCTIONS

There are three primary types of spools that perform all the functional requirements of the Collider and HEB. These are as follows:

### 1.) Standard Spools

The Standard Spool is found primarily in the arc sections of the Collider and HEB. Its principle functions are cryogenic control, quench (magnet) protection, correction magnet support, and vacuum isolation.

### 2.) Transfer Spools

The Transfer Spools provide most of the functions of the Standard Spool in addition to their principle function of transferring the liquid cryogenics and main power busses to cryogenic bypasses in warm drift regions.

### 3.) Input/Output Spools

The I/O Spools include three types, the Feed, End and Isolation Spools. These three spools have specific functions which are fundamental to the input (Feed), turn-around (End), and separation (Isolation) of cryogenics and main power throughout the Collider and HEB rings.

The top categories of spools (Standard, Transfer, and I/O) do not contain just 5 types of spools as described above. The three primary types multiply into several variations due to limitations in space and the need for special functions in specific locations. One example is the need for a mirror image of all three types of spools. This is not satisfied by just rotating the spool 180 degrees, because the cross-section of any spool and its functions are not symmetrical. An ongoing effort exists to standardize and limit the types of spools. The obvious drivers of such an effort are design costs, spares, and maintenance.

## 2.1 STANDARD SPOOLS AND ARC CELLS

The Standard spools principle location is in the Collider and HEB arc half-cells. A Collider arc half-cell contains a main quadrupole magnet, spool, and five dipole magnets. This spools principle function is cryogenic control, quench protection and housing of correction magnets. This half-cell makes up the fundamental (FODO) cell of the Collider.

A HEB arc half-cell contains a main quadrupole magnet, spool, and two dipole magnets. This spools has the same principle function as the Collider arc spool of cryogenic control, quench protection and housing of correction magnets. This half-cell makes up the fundamental (FODO) cell of the High Energy Booster.

## 3. SPOOL DESIGN

All spools provide an outer cryostat that contains plumbing, temperature shields, an inner cryostat and a beam tube. The Collider ring design has two counter-rotating rings with one above the other. Spool design for the collider must take into account that a second spool will be suspended above a Collider spool.

The HEB ring design is for a bipolar machine. This requirement of being able to accelerate protons in either a clockwise or counter-clockwise direction requires the HEB spool design to consider instrumentation and control differences. The main effect takes place in the location of the Beam Position Monitor (BPM), which is housed in the spool. The requirements for the BPM that directly effect the spool design in the Collider and HEB are that the BPM must be located as close to the main quad of a half-cell as possible. In the case of the HEB a given BPM will be down-stream of a main quad and up-stream of the correction quads while accelerating protons in the clockwise direction. In the next phase of accelera-

\*. Operated by Universities Research Association, Inc., for the U. S. Department of Energy under contract No. DE-AC35-89ER40486.

tion (counter-clockwise) the same BPM will be up-stream of the main quad and down-stream of the spools correction packages. It turns out that operation and control correction schemes are able to handle the differences in clock-wise versus counter-clockwise alleviating the need for special BPM placements in the HEB. This however does not release the requirement of the BPM being positioned close to the main quad. In the Collider and HEB there are locations other than the arc cells that fail to be as straight forward. These locations such as the abort and transfer line straight sections position spools up and down-stream of the main quads. This requires the BPM and other components of the spools to a mirror image.

### 3.1 Spool Design - Standard Spool

#### 3.1.1 General Components, Cryogenic Piping

The Standard spool contains many pipes, valves, power leads, and instrumentation. This is because it is the principle interface into the superconducting rings. The following table lists the basic components of a standard spool:

##### Standard Spool Requirements

Table 1.0

- Beam tube with connections
- Beam tube vacuum port
- Beam tube vacuum valves - warm
- Beam Position Monitor (BPM)
- BPM mounting interface to cryo pipe #1
- Beam Position Monitor lead interface
- Safety lead pair with quench stopper
- Lead port correction element-6 pair, 83 A avg
- Lead port instrumentation function (2)
- Quench vent valve 1-phase to 20K He
- Valve cool-down / warm-up
- Relief valve-cryostat to outside
- Relief valve-liquid helium to outside
- Relief valve-liquid helium return to outside
- Relief valve-gaseous helium return to header
- Relief valve-liquid nitrogen to outside (2)
- Cryostat vacuum pumpout ports w/ valves (2)
- Cryostat vacuum barrier
- Cryo pipe #1-liquid helium cold mass
- Cryo pipe #2-liquid helium return
- Cryo pipe #3-gaseous helium return
- Cryo pipe #4-20K He
- Cryo pipe #5-80K Nitrogen
- Cryo pipe #6-80K Nitrogen
- Shields-20K and 80K
- Multilayer Insulation-20K and 80K
- Insulation vacuum instrumentation
- Correction element supported in cryo pipe #1

The Collider and HEB spool cryogenic piping requirements are the same as the cryogenic piping requirements of their respective main dipole and quadrupole magnets. The HEB pipes are defined in Table 1.0.

The spools as a component of the Collider and HEB are limited to the rate at which heat can be put into the cooling system. These rates are part of a budgeted amount based on cryo plant specifications. The standard spool heat load budgets are as follows:

##### HEB Standard Spool Heat Load Budget

Load Type	Table 2.0			
	Liquif. g/s	4K Watts	20K Watts	80K Watts
Static Heat	0.072	2.73	15.71	57.87
Dynamic Heat		0.29		
<b>Total</b>	<b>0.072</b>	<b>3.01</b>	<b>15.71</b>	<b>57.87</b>

#### 3.1.1 Vacuum Barriers

The standard spool within the HEB has two configurations. The differences are the vacuum barrier and re cooler components. Due to design envelope limits and the complexity and size of both a vacuum barrier and re cooler, only one of these components can be in a single HEB spool. The Collider spool has a longer design envelope than the HEB and is able to contain both a vacuum barrier and re cooler in the same spool. There is a design requirement that a cryogenic machine maintain a vacuum to certain levels within the inner and outer cryostats of all the magnets, spools and drift spaces. By design the vacuum chambers of adjacent magnets and cryogenic components are connected. The vacuum barrier is a component that breaks up the cells of a machine into manageable vacuum chambers. Several design requirements for the vacuum barrier are opposing. The vacuum barrier must be robust enough to withstand fault conditions with atmospheric pressure on one side and evacuated conditions on the other side, and at the same time the heat leak requirements of the barrier want as little mass for heat flow. The vacuum barrier must be able to separate the insulating vacuum between the lead and return end of the spool. This allows for separate vacuum domains in each half-cell of the Collider and each cell of the HEB. All spools have two separate operating vacuum systems. The beam tube vacuum is the principle system and operates at or below  $10^7$  Pa. The other system is the cryostat insulating vacuum which is required to operate at or below  $10^{-4}$  Pa. The systems are independent and maintained by flowing cryogenes around and through the respective evacuated spaces. The vacuum requirements are maintained by cryo-pumping. This is the improvement of a vacuum by means of the adsorption of condensable gases on cold surfaces. Liquid helium at 4.2 K flows around the outer surface of the evacuated beam tube and cryo-pumps. The insulating vacuum is maintained by the 20K helium and 80K nitrogen gas which flow through the cryogenic pipes in thermal contact with the 20K and 80K shields which cryo-pump. At start-up vacuum is achieved by mobile pump carts that pull a vacuum on the beam tube and insulating chambers until cool down with cryogenes enables a cryo-pumping condition.

#### 3.1.2 Recoolers

The re cooler is a component in the spool. It is a heat exchanger that takes 4.25K liquid helium at its inlet and cools it to 4.0K at the outlet. The re cooler is designed to perform at 100 watts @ 4K. The LHe return line supplies the re cooler shell. This liquid helium is sent through the

recooler valve and into the fill port of the re cooler. The GHe that is produced by expansion across the valve is vented to the GHe return line. As a component of the spool the re cooler maintains the cryogenic temperatures required for balance operation throughout the circumference of the Collider and HEB.

### 3.1.3 Quench Stopper / Quench Suppressor

Quenches are the localized increased resistance within a magnet that produces heat and propagates throughout the magnet and ring if left unchecked. Worst case quenching would destroy a magnet. The quench stopper stops the quenches from propagating by directing heat conduction through the bypass lead to the outside of a quenching half-cell. The quench system as a whole includes instrumentation which senses a quench in a local main magnet and initiates a quench stop sequence. The events include the diversion of the propagating quench heat and power on the bus around the quenching half-cell.

### 3.1.4 Correction Magnets and BPM

The Collider and HEB have requirements for correction of closed orbit errors both linear and higher order multipoles. The Spool is required to provide a means of housing and operating these superconducting correction magnets. There is a requirement for Corrector Element Power Leads (CEPL) to power and control the corrector fields. The spool must support the superconducting correctors by means of cooling with liquid helium and alignment and support by rails fiducialized to the spool and BPM. These alignment tolerances require state of the art manufacturing and a fiducialization that will allow alignment to the closed orbit beam when the spool is installed in the tunnel. The Beam Position Monitor (BPM) resides in the interconnect region of the spool. This is outside of the inner cold mass, but as close to the leading end of the corrector package rail support.

## 4.0 SPOOL TYPES

First draft effort at detailing, exceeded 20 types of spools for the Collider and HEB. The Collider counted a quantity of over 1580 spools and the HEB over 340 spools. An ongoing effort to lesson the quantity of types is critical to reliability, design costs, and the quantity of spares that would have to be purchased and stored. The types, quantities, and component functions of the HEB spools are listed in the table that follows:

### 4.1 Transfer Spools

As defined in paragraph 2.0 Spool Concept and functions, the principle purpose of the Transfer Spools is the transportation of liquid cryogens and the main power busses to the cryogenic bypasses. This occurs in areas where warm drift regions are needed. This spool is a T box, where the cryogens and power busses leave the ring to a bypass cryostat. It has the typical interconnect joining

High Energy Transfer Spools

SPOOL	REC	LENGTH	TYPE	LEFT	RIGHT	QUANTITY
				BPM	BPM	
SPRA	YES	3.675m	STANDARD		X	136
SPXA	NO	3.675m	STANDARD		X	135
SPXA <sub>x</sub>	NO	3.675m	STANDARD	X		007
SPRA/SPRA <sub>h</sub>	YES	4.675m	STANDARD	X	X	008
SPRAT/SPRA <sub>t</sub>	YES	4.675m	TRANSITION	X	X	006
SPRST/SPRA <sub>st</sub>	YES	5.000m	TRANSITION	X	X	008
SPRAT/SPRA <sub>t</sub>	YES	3.675m	TRANSITION	X	X	010
SPRE	YES	7.350m	END SPOOL	X		002
SPRF	YES	7.350m	FEED SPOOL	X		002
SPRI	YES	7.350m	ISOLATION	X		002
SPXAR/SPXA <sub>r</sub>	NO	3.675m	RETURN	X	X	002
SPXLR/SPXA <sub>l</sub>	NO	1.000m	RETURN			017
SPXIT/SPXA <sub>i</sub>	NO	1.000m	TRANSITION			007

from the previous cold magnet, and then routes the cryogen plumbing and power busses at a 90 degree angle. There is a cold to warm transitional interconnect that has just the warm beam tube continuing down the rings closed orbit. The straight sections are the locations in the ring that require warm drift sections. These warm sections contain kickers and warm magnets for beam abort, injection, and transfer to Collider. The warm sections also contains Radio Frequency (RF) cavities for acceleration of the proton beams. The table in section 4.0 Spool Types, shows the various configurations and functions of spools that can be of the transfer type.

### 4.2 Feed, End (Return Box), & Isolation Spools

In addition to the same functional requirements as the standard spool, the Feed spool performs the functions as the main connection for power and cryogens to the power control and cryogenic plants. The End spool performs the turn around of power and cryogens for a cryogenic sector. The cryogenic sector is the portion of a ring maintained by a given cryogenic plant. The Collider has 10 cryogenic plants and the HEB two. The Isolation spools are placed periodically around the Collider and HEB rings to allow for isolation of cryogenic sectors in various maintenance, warm-up, and cool-down modes. The Return Box is a variation of the End spool which allows for turn-around of cryogens and power in warm drift areas. The cryogens are only redirected in this case to the cryogenic bypass where they then continue in the nominal flow direction.

## 5.0 ACKNOWLEDGMENTS

The authors would like to thank D. E. Johnson, E. Kindler, J. Austin, D. Strube, E. Cleveland, D. Bryant, G. Shuy, and V. Yarba for their continued support on this design effort.

# Quench Simulation of the 40 mm Aperture SSC-Quadrupole Magnet Connected in Series with 50 mm Aperture SSC-Dipole Magnets

G. López  
 Superconducting Super Collider Laboratory\*  
 2550 Beckleymeade Ave., Suite 125  
 Dallas, TX 75237

## Abstract

The hot-spot temperature is estimated for a Collider Quadrupole Magnet (CQM) connected in series with Collider Dipole Magnets (CDM's) and for a quench appearing in CQM. An active protection system is studied where all magnets except the CQM's have heaters. These heaters cause a spot quench in each of the CDM outer layer conductors. Results indicate that the scheme is safe for a total induced quench time delay of less than 230 ms.

## I. INTRODUCTION

Preliminary simulations of the quench protection system for the SSC [1] considered only the Collider Dipole Magnets (CDM). These simulations were made with the program SSC-RR which calculates the longitudinal quench velocity for each conductor in the coil using the adiabatic quench velocity expression [2]

$$v_q = \frac{J_{co}\sqrt{L_o}}{\gamma(\delta C)_m} \frac{q}{\sqrt{1 - q + \delta\theta/(\theta_c - \theta_o)}} \quad (1)$$

where  $J_{co}$  is the magnetic field dependent critical current density at the bath temperature  $\theta_o$ ,  $L_o = 2.45 \times 10^{-8} \text{ W}\Omega\text{K}^{-2}$  is the Lorentz number,  $\gamma$  is the copper to superconductor (s.c.) ratio,  $\theta_c$  is the critical temperature at zero current,  $q$  is ratio of the operation current density to the critical current density,  $\delta\theta$  is a small shift in the generating temperature,  $\theta_g = \theta_c - (\theta_c - \theta_o)q$ , and  $(\delta C)_m$  is the average of the product of the density  $\delta$  times the specific heat  $C$  of the metal components in the conductor. The temperature  $\theta$  for each conductor is estimated through the solution of the equation

$$(\delta c) \frac{d\theta}{dt} = \rho J^2 \quad (2)$$

where  $\rho$  is the total resistivity of the conductor,  $J$  is the current density flowing in the conductor,  $t$  is the time, and  $(\delta c)$  is the average of the product of the density times the specific heat of all the components of the conductor. The thermal conductivity of the conductor is ignored in equation (2) since the quench velocity is much higher than the thermal diffusion velocity. However, this thermal conductivity effect is considered when calculating the temperature

profile along the conductor [3]. The heat is not transferred to the helium because it has a small effect on the quench characteristics. The transverse quench propagation is estimated using the experimental values (current dependence) from Reference 1. The voltage between the normal zone and the s.c. zone in the magnet is approximated by the following expression

$$V = R_Q I (1 - M/L) + M V_{cs} / L \quad (3)$$

where  $R_Q$  is the total quench resistance in the coil (normal zone),  $I$  is the current,  $V_{cs}$  is the voltage across the magnet,  $L$  is the magnet self inductance, and  $M$  is the mutual inductance between the part of the coil formed by the normal zone and the other part of the coil which is still superconducting (s.c.).

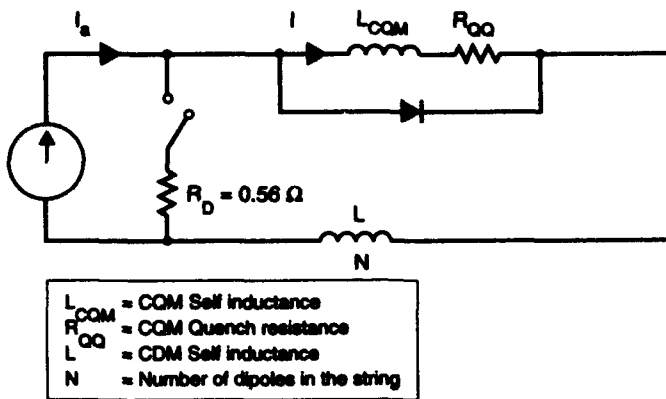
The hot-spot temperature, the highest temperature reached in the coil during a quench (which normally is located where the quench first appears), is the most important parameter affecting magnet safety. The peak voltage between the normal zone and s.c. zone (approximately the peak quench resistive voltage) is the other parameter of importance when internal breakdown voltages are in consideration. The characteristics of the CQM and CDM can be found in Reference [4]. It is clear that the magnetic field in the conductor must be taken into consideration to calculate the quench velocity and resistance developed. In what follows, the analysis of a single CQM passively protected and one CQM with several CDM's connected in series and actively protected will be presented. In the active protection system, CDM's will have heaters but the CQM does not have a heater.

## II. SINGLE CQM (SELF PROTECTED)

The model for the electric circuit can be seen in the Figure 1. The initial current is 6500 A. The inner coil quench appears in the last conductor from the midplane (by symmetry only a quarter of the coil is considered) after the copper wedge in conductor 8. The quench propagates all the way down across the wedge and upward across the insulator layer between the inner and outer coils. The first conductor quenching in the outer coil will be the closest one to inner conductor 8 which is conductor 13. In the outer coil case, the quench starts at conductor number thirteen, and propagates all the way down and into the inner coil, quenching conductor 8 first.

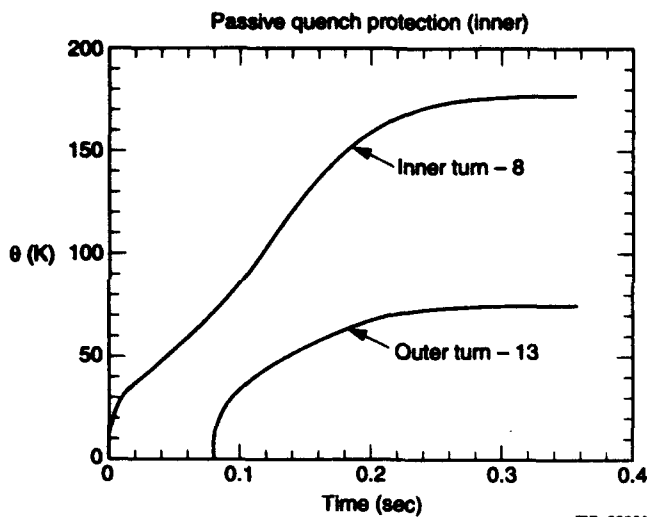
\*Operated by the Universities Research Association, Inc., for the U.S. Department of Energy under Contract No. DE-AC35-89ER40486.

Figures 2 and 3 show the temperature evolution of these conductors for the inner and outer coil quench, indicating the CQM is a self protected magnet (the hot-spot temperature is less than 170 K).



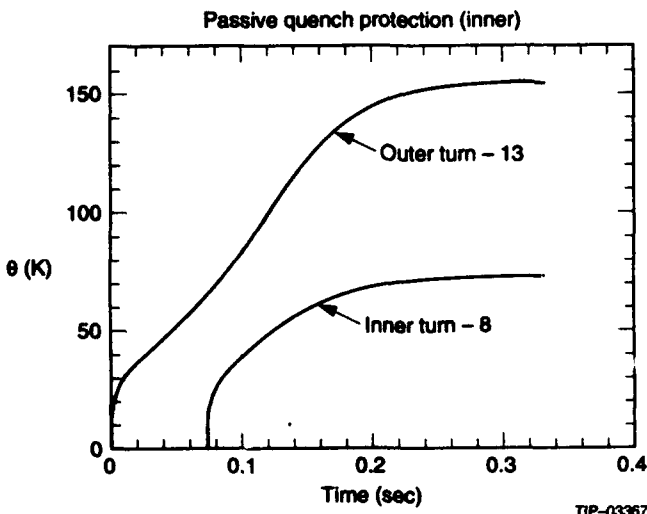
TIP-03365

Figure 1. Passive Protection System Circuit Model.



TIP-03366

Figure 2. Quench Starts in the Inner Coil (turn 8).



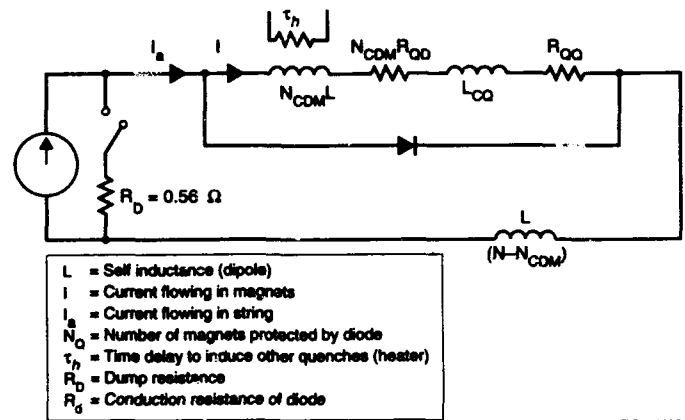
TIP-03367

Figure 3. Quench Starts in the Outer Coil (turn 13).

### III. ACTIVE PROTECTION SYSTEM FOR ONE CQM IN SERIES WITH CDM'S

The model for the electric circuit can be seen in Figure 4. The initial current here is also 6500 A. Since the difference in temperatures for the inner and outer coil quenches is not significant, the inner coil quench case will be the only one presented here. After the CQM quench initiates, the heaters induce a CDM quench at the time "bypass - time +  $\tau_h$ " at a single point (worst case heater performance) on each conductor of the dipole outer coils. The quench velocity on these magnets and all the quench characteristics (temperature, peak voltage, resistance, etc.) are then calculated. Figure 5 summarizes the evolution of the temperature in the CQM for several dipoles connected in series with a quadrupole. Figure 6 shows that when the quadrupole is connected in series with dipoles, the longer current decay time results in a higher and more uniform temperature in the CQM bringing about higher total resistance. This fact is very important for a correct estimation of the quench behavior of the system. An underestimation of this resistance may result in the design of an unnecessarily complicated quench protection system. In the above calculations the heater time delay for the dipole magnets has been set to  $\tau_h = 45$  ms. Figure 7 shows the number of miits developed in the quadrupole magnet for several CDM's connected in series and for three heater delay times. As can be see in this figure, even for a heater delay time of about  $\tau_h = 150$  ms, the hot-spot temperature for the configuration D+D+Q will be about 400 K.

The case for a dipole quench in the system can be seen in the Reference 1. The presence of the quadrupole in this case is irrelevant since its stored energy is one order of magnitude lower, and most of the stored energy is dissipated in the dipoles (mainly in the one where the quench appeared first).



TIP-03372

Figure 4. Circuit Model for the Active Protection System.

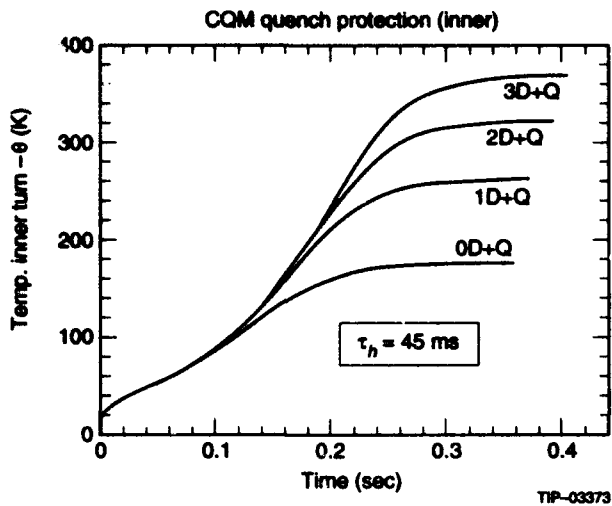


Figure 5. CQM Hot-Spot Temperature Evolution for various CDM's in Series.

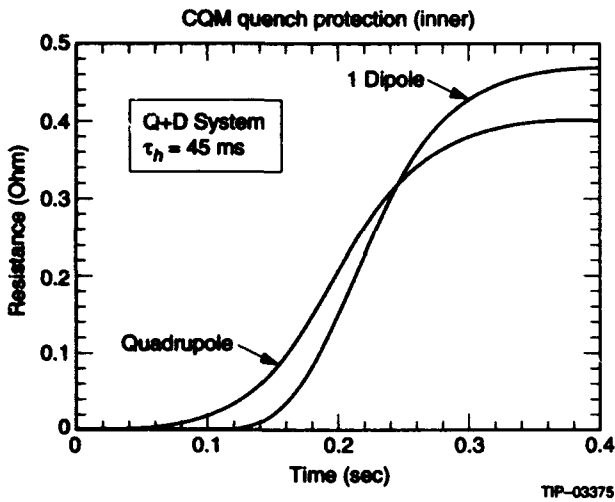


Figure 6. Total CQM Resistance Developed in the System CQM+CDM.

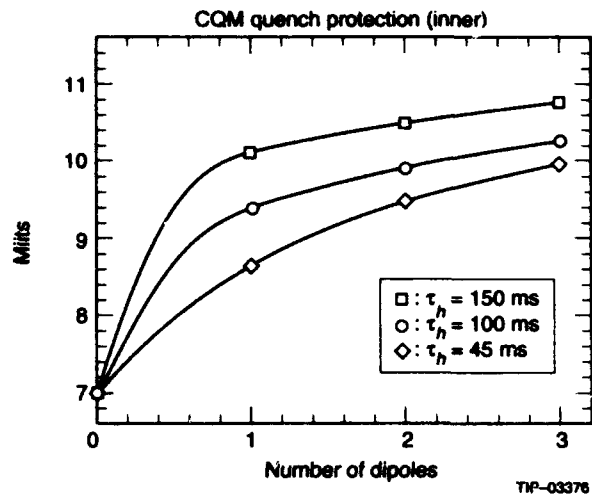


Figure 7. CQM Number of Miits Developed for several CDM's.

#### IV. SUMMARY AND COMMENTS

Passive protection system simulations agree with the experimental fact that the 40 mm aperture quadrupole magnet for the Collider is self protected. Active protection system simulations suggest that the scheme as shown here presented is a safe quench protection scheme. ASST experiments could test this option for the SSC. In the simulations it is assumed that the heaters cause a quench at a single point of each conductor of the outer CDM coil, then the quench propagates according to the longitudinal quench velocity, the time delay for transverse propagation, the magnetic field, *etc.* Actually, the heaters will be capable of quenching a large portion of the outer coil simultaneously. Hence, the assumption taken here should reflect the worst case scenario. Recall that the heater time delay  $\tau_h$  in the simulation is in addition to the approximately 80 ms of delay from the start of the quench in the quadrupole. This is the time required for current in the system (D's+Q) to bypass the magnets and it is assumed in the simulations that at this time the quench is detected. Therefore, the total time delay safe limit, after the start of quench in the quadrupole, is about 80 ms + 150 ms = 230 ms. Finally, it is pointed out that these results will be also valid in case of changing the 40 mm CQM for a 50 mm CQM.

#### V. ACKNOWLEDGEMENTS

I wish to thank Dr. R.Meinke and Dr. R. Schwitters for their support at the SSC.

#### VI. REFERENCES

- [1] G. López and G. Snitchler, SSCL-283, June 1990.
- [2] G. López, SSCL-424, May 1991.
- [3] G. López, SSCL-425, May 1991.
- [4] SCDR, SSCL-SR-1056, July 1990.

# Effective Stress of The SSC 80 K Synchrotron Radiation Liner in a Quenching Dipole Magnet\*

Kent K. Leung, Q. S. Shu, K. Yu, and J. Zbasnik  
Magnet Systems Division  
Superconducting Super Collider Laboratory  
2550 Beckleymeade Ave., Dallas, TX 75237 USA

## Abstract

This paper describes the effective stress on a proposed SSC beam tube. The new issue for the Collider compared to earlier accelerators is the combination of synchrotron radiation with the 4.2-K bore tube of the superconducting magnets [1]. One design option is to use a liner within a bore tube to remove the radiated power and the accompanying photodesorbed gas that impair the beam tube vacuum. Design of the SSC 80-K synchrotron radiation liner requires vacuum luminosity lifetime = 150 hours and liner electrical conductivity,  $\sigma^*t > 2E5 \Omega^{-1}$ . [1]. The bimetallic liner tube is subjected to cool down and eddy current loads [2,3]. The liner tube is a two-shell laminate [4] with Nitronic-40 steel for strength and a copper inner layer for low impedance to the image currents induced by the circulating protons. High electrical conductivity of the copper layer is essential for minimizing the power losses. Perforated holes are used to remove the photodesorbed gases for vacuum maintenance. The tube is cooled by 80-K lines. Structural design of the liner is not covered by the ASME code [5]. The life of the liner involves structural integrity and keeping the copper laminate within yield stress limits to maintain the high surface finish for minimizing the power losses. The copper layer stress governs the structural design of the liner. The liner tube analysis is a three dimensional non-linear stress problem. Thermal transient cool down stress [6] is not considered in this analysis because of the floating support design of the liner. This analysis will address the axial thermal stress, non-axisymmetrical eddy current loads, dynamic and non-linear material effect on the liner that have not been considered in publications on beam tube structural analyses

## I. INTRODUCTION

The proposed SSC liner is a beam tube with two concentric tubes. A perforated liner tube inside a bore tube is designed to remove the photodesorbed gases and synchrotron radiation heat, and to withstand the eddy current and cool down load without stressing the copper beyond yield. The steel bore tube is subjected to external buckling pressure caused by vaporized liquid Helium from the quenching dipole [7]. The liner is designed to have the same reliability level as the ASME code [5]. The liner design can be predicted by nuclear quality code [8] employing adequate finite element modeling [9] to include eddy current load, bimetallic effect, and dynamic amplification.

\*This work was supported by the United States Department of Energy under Contact NO. DE.AC02-89ER40486.

The effective stress analysis employs SSC 50-mm dipole test data to establish the eddy current loadings and response of the liner. By designing the copper stress within the yield strength limit, the liner can be operated over hundreds of quench cycles in 25 years of operation without increasing additional power loss.

## II. LINER TUBE DESIGN

Figure 1 shows the proposed SSC dipole magnet liner system design [4].

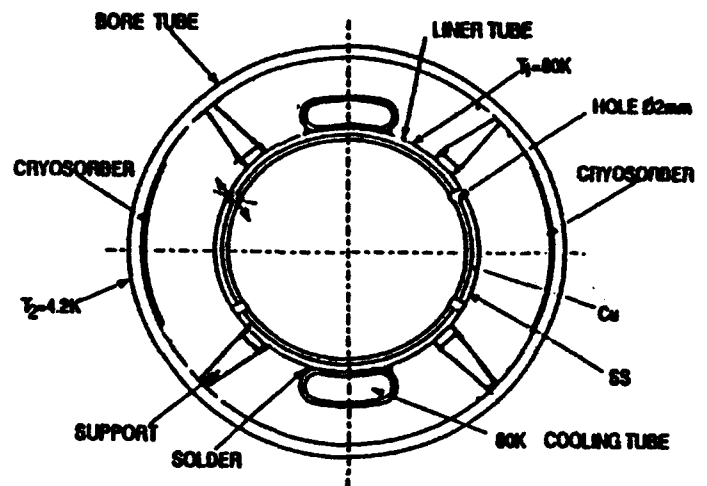


Figure 1. SSC Dipole Liner System.

The liner tube (25.3 mm I.D.) is a bimetallic lamination with a 0.5 mm copper bonded by a steel tube wall of 0.75 mm. Radial standoffs are used to support the liner tube from the bore tube. Torsional restrains are placed in some locations to avoid disturbing the dipole magnetic field. Bellows are used in the liner to reduce the axial load induced by the temperature rise of the tube from the heated coils during quench. Two 80-K cooling tubes are attached to the liner tube for removing synchrotron radiation heat rated as 0.14 watts per meter [4]. The holes are designed to maximize the luminosity lifetime of the liner system. The shape and the pattern of the holes have significant effect on the stress and impedance ( $<170$  mohms/m) of the liner. The present design uses circular holes in a bend pattern with the cut-out area in a ratio of 2/9 along the axial direction. An intensive R and D study is underway to search for the hole shape and pattern.

### III. EDDY CURRENT LOAD

(A) The equation of equatorial eddy current pressure (Maximum Lorentz pressure) [2] is:

$$P_{Lmax} = B * (dB / dT) * b * t * \sigma \dots\dots(a)$$

B (tesla) = dipole field strength.[10]  
 dB/dt (tesla/sec) = rate of change during quench.[10]  
 (also see Figure 2)  
 b (m) = mean radius of the copper layer.  
 t (m) = thickness of the copper layer.  
 $\sigma$  ( $\Omega^{-1} m^{-1}$ ) = copper electrical conductivity at temperature, magnetic flux density and cold-worked condition

SSC 50 mm CDM (DCA320) Experimental Quench Data

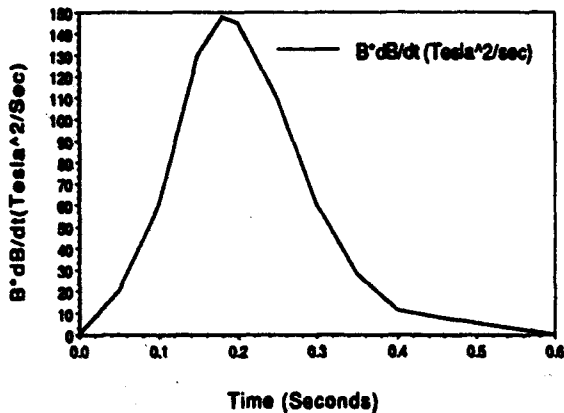


Figure 2. B(t)x[dB(t)/dt] as Function of Time.

From SSC dipole magnet test data and using equation (a) the eddy current pressure is calculated as 0.483 MPa (70 psi) including a dynamic factor of 1.25 as shown in Figure 3:

Load Condition: Quench/Energized

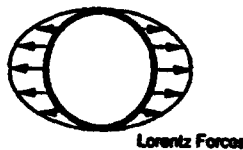


Figure 3. Eddy Current Pressure at Copper Liner.

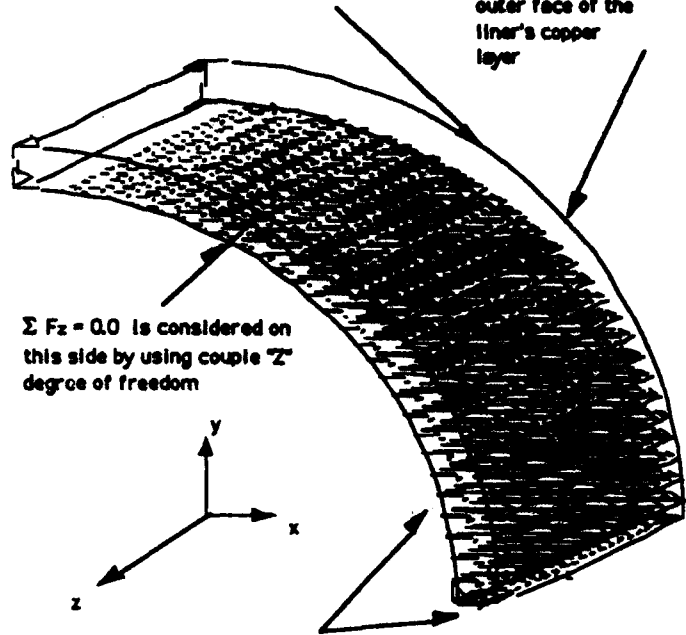
Eddy current torque, or lateral [2, 3,11] force are developed on the liner from geometrical tolerances in the tube forming and copper plating processes. Torque or lateral force induced stresses are used for bellow and torque restraints design to eliminate additional stress to the liner.

### IV. FINITE ELEMENT MODEL

Three-dimensional finite element model (Figure 4) is employed to study the liner because the axial bimetallic effect combined with eddy current load which may collapse the tube, may develop bimetallic bond separation or produce stress beyond the copper yield limit,(Figure 5) that diminishes the thermal and electrical performance of the liner tube and produce unacceptable power loss.

All Z displacement is modeled on this side to represent the thermal centroidal axis in the liner tube

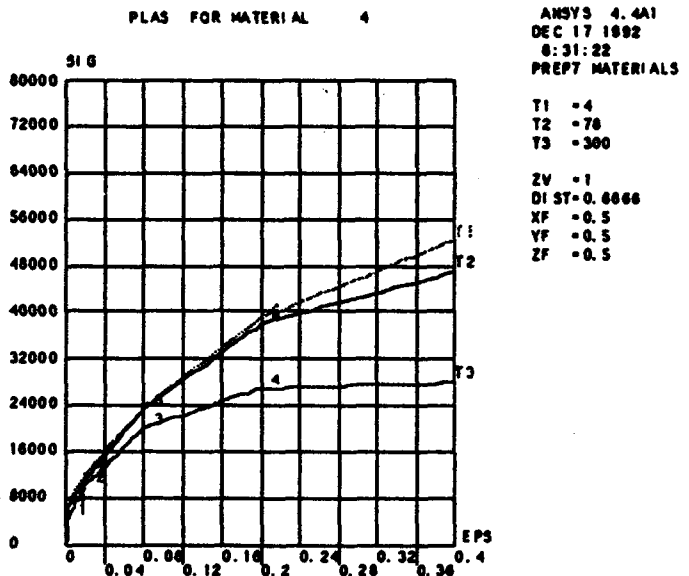
All Lorentz forces are applied at the outer face of the liner's copper layer



$\Sigma F_z = 0.0$  is considered on this side by using couple "Z" degree of freedom

Lorentz Force Edges of the FEM Model is 50% less than the Force at the Center of the FEM Model

Figure 4. SSC Dipole Liner Tube FEM Model.



ASST Perforated Liner(0.75mm SS)0.6t quench, 80K(psi, in)

Figure 6. Non-Linear Copper Stress-Strain.

Effective stress analysis of the liner by the finite element method requires factors obtained from a test. (A) A carry-over factor is used to account for area reduced by the perforated holes. The factor is 1.286. (B) Dynamic factor based on the eddy current pulse shape is 1.25. (C) Stress concentration factor for circular hole is 2.0. The last factor is applied to the result of the finite element analysis is local effect on the overall effective stress.

## V. RESULT OF ANALYSIS

The yield strength of annealed copper depends on grain size and purity. The average yield at 80 K is 44 MPa (6.4 ksi) [7]. The combined stresses for the liner at areas away from the holes are 53.8 MPa (7.8 ksi), see Figure 6, which is over the yield at 80 K [12] but within the ASME specified yield [5]. The stress around the hole will increase to 108 MPa (15.6 ksi) which is within the copper ultimate strength but its affect on the electrical performance of the liner requires additional investigation. The steel tube wall thickness may be increased to keep the copper stress within yield or eliding copper plating around holes. The steel wall stress of the liner is 289 MPa (42 ksi). The stress at the hole area in the steel wall will increase to 578 MPa (83.8 ksi) which is smaller than the 1034 MPa (150 ksi) of the Nitronic-40 steel's yield stress at 80 K.

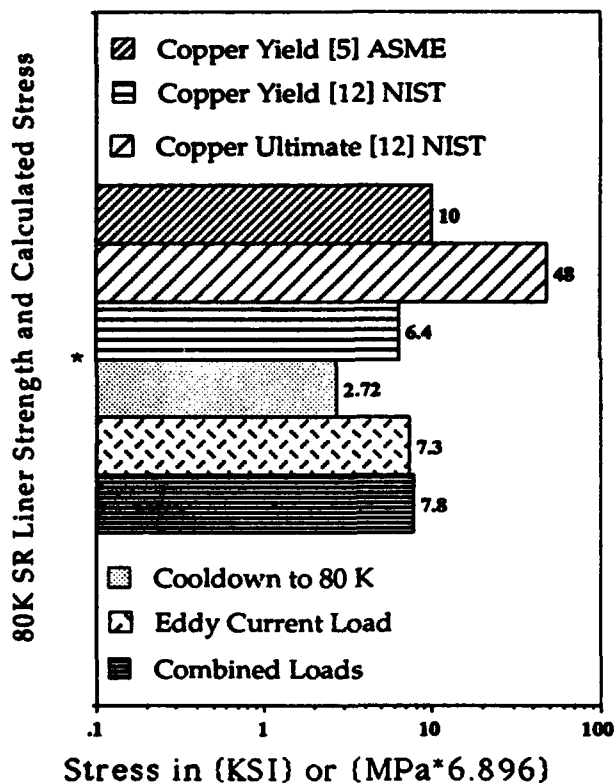


Figure 7. Result of Copper Layer Stress.

## VI. CONCLUSIONS AND DISCUSSIONS

(A) High local stress on the copper layer reduces the level of confidence of the liner for multi-quench because micro-cracks may be developed in the copper surface and increase the power loss from the high frequency image current. Local steel wall may be increased to keep the copper within the yield stress limit.

(B) Analytical result is based on the shape and pattern of the perforated holes in the existing design [4] that induces low stress. Changing the existing circular hole shape to the shape of an ellipse or a square, and rearranging the hole in a random array will increase the copper layer stress. (C) A bellow and torque

stoppers are required to reduce stress on the liner. The high slenderness ratio of the liner tubes ( $l/\gamma > 200$ ) practically deducts the liner to zero axial load capacity. The non-axisymmetrical eddy current Loads [5] will destroy the bellow and liner supports if torque stoppers are not used [3,11]. (D) This analysis is based on annealed copper properties. Cold work or residual stress will rise in post yield. The residual resistivity ratio (RRR) is a measure of the extent of physical defects such as lattice imperfections due to cold-working[12]. Additional analysis shows that stress at hole area is 414 MPa (60 ksi) for hard copper layer which has a yield stress of 207 MPa [30 ksi] and is not recommended to be used. Pure copper wire has an RRR of 50, but very high-purity copper, well annealed, could have an RRR of 2000 [12]. The liner fabrication technique by the electrode-positied method is preferable. It is possible to use high purity copper or gold for the liner using 0.25 mm for the conductive layer, and increasing the steel layer to 1.0 mm from the existing 0.75 mm. If the design guideline [1] for the copper conductivity as  $\sigma = 4E8(\Omega m)^{-1}$  (80K in 6.1T. dipole field) is modified to  $= 8E8(\Omega m)^{-1}$  with identical liner as specified by [4], the liner stress will be reduced to the comfortable level for a indefectible structural designed liner.

## VII. REFERENCES

- [1] W. C. Turner, "Collider Beam Tube Vacuum," Presentation at the Beam Tube Size and Coating Meeting at SSCL, March 31, 1993.
- [2] A. Chao, "More on Copper Coating Considerations," SSCL Report, SSC-N-434, 1988.
- [3] K. K. Leung, "Non-Axisymmetrical Eddy Current Loads on Beam Tube in A Quenching Dipole Magnet," SSCL, Magnet Division Report, MD-TA-243, 1993.
- [4] Q. S. Shu, "Report on the ASST II Liner Status," SSCL Report, SSCL-N-805, Nov. 1992.
- [5] American Society of Mechanical Engineers, "ASME Code Section VIII, Division 1," 1992.
- [6] K. K. Leung, "Transient Cool Down Stress in SSC Dipole Magnet Shell," Supercollider 4, edited by J. Nonte, Plenum Press, N Y and London, 1992.
- [7] K. K. Leung, "Structural Analysis of A 4.2K Beam Tube in A Quenching Collider 50 mm Dipole," Pre-print of 1993 IISCC5, San Francisco, May, 1993.
- [8] J. Swanson, "ANSYS finite Element Code Revision 5.0," Swanson Analysis Systems, Inc. December 23, 1992.
- [9] K. K. Leung, "Seismic Stress of Piping System and Heat Exchanger Structures." *Transaction of The Third International Conference on Structural Mechanics in Reactor Technology*, Section K-7/6, London, 1975.
- [10] Q. S. Shu, "Status of Test on RF Surface & Magneto-Resistance," Presentation at the Beam Tube Size and Coating Meeting at SSCL, March 31, 1993.
- [11] K. Y. Ng, "Allowable Stress in The SSC Beam Tube During A Quench," SSCL, SSC Report, SSC-168, 1988.
- [12] N. J. Simon et al, "Properties of Copper and Copper Alloys at Cryogenic Temperatures," National Institute of Standards and Techn., NIST Monograph 177, February 1992.

# Improved Cable Insulation for Superconducting Magnets\*

M. Anerella, A.K.Ghosh, E. Kelly, J. Schmalzle, E. Willen

Brookhaven National Laboratory

Upton, New York 11973

J. Fraivillig, J. Ochsner, D.J. Parish

E. I. DuPont de Nemours & Co.

Wilmington, Delaware

## I. INTRODUCTION

Several years ago, Brookhaven joined with DuPont in a cooperative effort to develop improved cable insulation for SSC superconducting dipole magnets. The effort was supported by the SSC Central Design Group and later the SSC Laboratory. It was undertaken because turn-to-turn and midplane shorts were routinely being experienced during the assembly of magnets with coils made of the existing Kapton<sup>®</sup>/Fiberglass (K/FG) system of Kapton film overlapped with epoxy-impregnated fiberglass tape. Dissection of failed magnets showed that insulation disruption and punch-through was occurring near the inner edges of turns close to the magnet midplane. Coil pressures of greater than 17 kpsi were sufficient to disrupt the insulation at local high spots where wires in neighboring turns crossed one another and where the cable had been strongly compacted in the keystoning operation during cable manufacture.

In the joint development program, numerous combinations of polyimide films manufactured by DuPont with varying configurations and properties (including thickness) were subjected to tests at Brookhaven. Early tests were bench trials using wrapped cable samples. The most promising candidates were used in coils and many of these assembled and tested as magnets in both the SSC and RHIC magnet programs currently underway. The Kapton CI (CI) system that has been adopted represents a suitable compromise of numerous competing factors. It exhibits improved performance in the critical parameter of compressive punch-through resistance as well as other advantages over the K/FG system:

- Superior manufacturability
  - Relaxation of product storage requirements
  - Reduced coil curing time
  - Improved accommodation of component size variation
  - Reduced mold cleanup after cure
  - Improved coil repair/rework capability
- Increased radiation resistance
- Retention of ductility at cryogenic temperature
- Improved conductor placement uniformity

Figure 1 shows the K/FG system in common use and the new CI system. A technical description of the construction process for SSC magnets is given in Ref. 1.

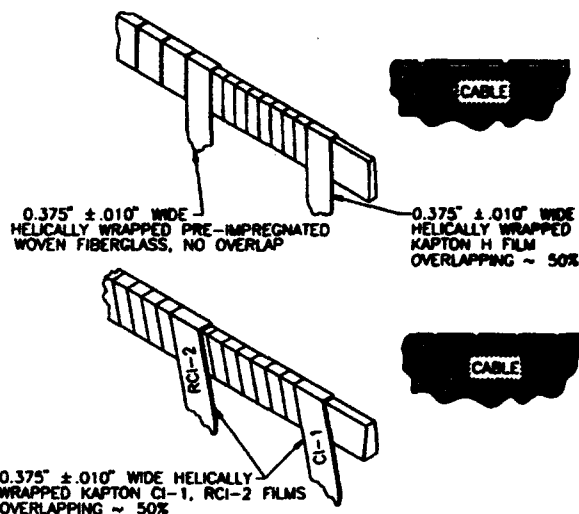


Figure 1. Kapton/Fiberglass insulation (top) and Kapton CI insulation (bottom) as applied to superconducting cable.

## II. DESCRIPTION

Kapton CI is a 100% polyimide cable insulation system. The inner wrap, 120CI-1, is a 0.001" thickness amorphous Kapton film with 0.0002" thickness polyimide adhesive on the outside surface. The outer wrap, 135RCI-2, is a 0.00095" thickness mineral-filled amorphous Kapton film with a total thickness of 0.0004" polyimide adhesive, half on each surface. The adhesive is composed of aromatic diamines plus aromatic and co-aromatic dianhydrides. This all-aromatic product ensures ductility at cryogenic temperature and has superior resistance to ionizing radiation as compared to a system that uses epoxy. Upon reaching a temperature of 217 C, the adhesive bonds in several seconds to form a strong bond (peel strength ~0.2 lb. per inch of width, about half that of K/FG), although some bonding occurs at lower temperatures. It flows out from areas of high compression to fill adjacent voids in the coil structure, thus forming a structure that spreads the compressive coil load over a wider area. It does not, however, lose viscosity nor flow into areas without compressive force. Photomicrographs of coil sections show that the Kapton films and adhesive of this system have, after a coil is molded, merged into a uniform matrix of polyimide material that partially fills the voids and interstitial spaces normally seen in cross sections of coil structure. The adhesive shows no tendency to bond to the wires of the cable, an undesirable

\* Work performed under Contract No. DE-AC02-76CH0016 with the U.S. Department of Energy.

<sup>®</sup> Kapton is a registered trademark of E.I. DuPont de Nemours & Co.

characteristic that could lead to premature magnet quenching if it occurred. Coils made with CI have a per turn thickness  $\sim 0.00075''$  greater than those made with K/FG.

### III. TESTS & CHARACTERISTICS

Compressive punch-through tests were performed with the apparatus shown in Fig. 2. Results of numerous tests can be summarized as follows: CI cables fail in the range of 100 to 150 kpsi, depending on molding history; K/FG cables fail in the range 30 to 40 kpsi. These bench tests are confirmed by the experience with coils and magnets built with CI: no compressive failures have been experienced in over 20 short (1 to 2 m) magnets of various types nor in 4 long (10 m or more) SSC and RHIC dipole magnets. Particularly compelling were the results from coil sections that were compressed with 10 kpsi pressure and that then had turn-to-turn voltage applied to each pair of neighboring turns: CI coils were able to withstand over 5 kV without failure whereas K/FG coils routinely failed by arcing before 2 kV was achieved and before full pressure was applied.

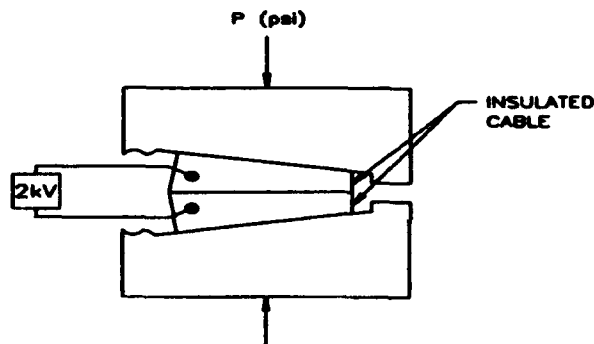


Figure 2. Apparatus for conducting compressive punch-through tests.

A desirable characteristic in the manufacture of coils is the capability to accommodate component (cable, wedge, insulation) thickness variation in such a way that final coil azimuthal size variation is small. This helps to ensure that magnets can be assembled within the required prestress window and that the magnet's field is uniform. Fig. 3 shows the range that was achieved for RHIC arc quadrupole coils (16 turns). Here, it was possible to achieve final coil sizes within an acceptable 0.003" band using a fixed cavity mold despite (intentional) cable thickness variation of 0.00125" by simply varying the coil molding pressure over the range 10.5 to 12.9 kpsi. Alternatively, it was found that for constant cable thickness, the molded coil size could be varied over a range of 0.012" with a molding pressure variation of 6 kpsi (Fig. 4). Coil modulus varied  $\sim 10\%$  for this range of molding pressure. Thus the proper size for CI coils is easily achieved by proportionally adjusting the molding cavity size opposite to the sum of the variations of component sizes, as determined through incoming inspection data. These results cannot be achieved with K/FG coils. For such coils, coil-to-

coil size uniformity can only be achieved for a more limited range of component thickness variation and by using a "double step" process in which molding cavity size is adjusted based on a coil size measurement made during the molding process. A related characteristic is the uniformity of coil azimuthal size along the length of a coil. While strongly tooling dependent, it is found that CI coils are equal to or improved in this important feature with respect to K/FG coils.

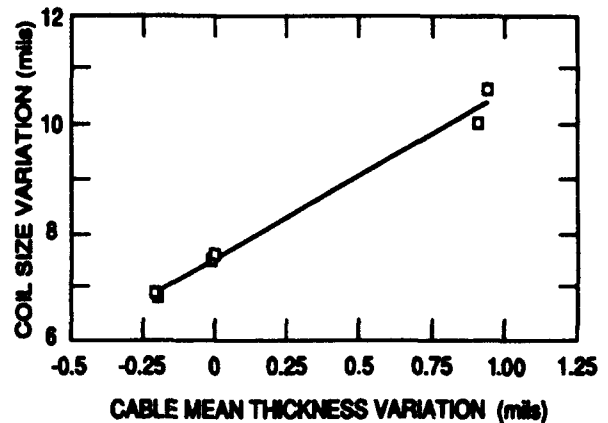


Figure 3. Kapton CI molded coil size variation with variation in cable thickness. The allowable cable thickness variation is  $\pm 0.25$  mils.

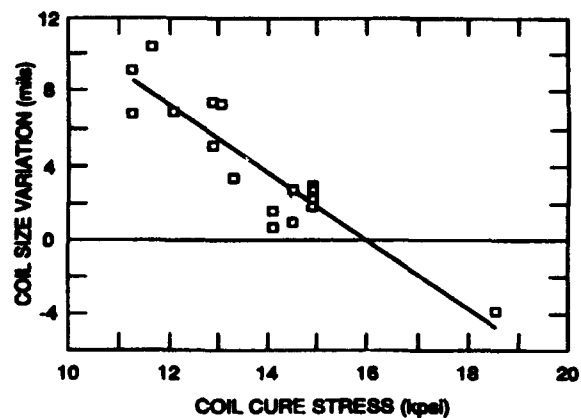


Figure 4. Kapton CI coil azimuthal size variation resulting from variation in the curing stress.

The compressive modulus of CI coils is found to be on the order of 1200 kpsi for 8 cm RHIC dipole coils. This is about the same as that of K/FG coils and it is quite suitable for magnet assembly. Fig. 5 shows the stress vs. strain relation for an SSC 50 mm inner coil. The higher resistance of CI coils to compressive insulation failure gives a safe window for magnet assembly stress of at least 10 kpsi, more than twice that which is safe for K/FG coils. This is highly desirable in a production setting where component size variations within legitimate tolerances must be expected. An

experiment to test coils built with all-polyimide film but using epoxy (3M-2290), which might give improved punch-through resistance without the need for molding at as high a temperature, gave a relatively lower modulus of 750 kpsi and lower punch-through resistance values as compared to CI coils.

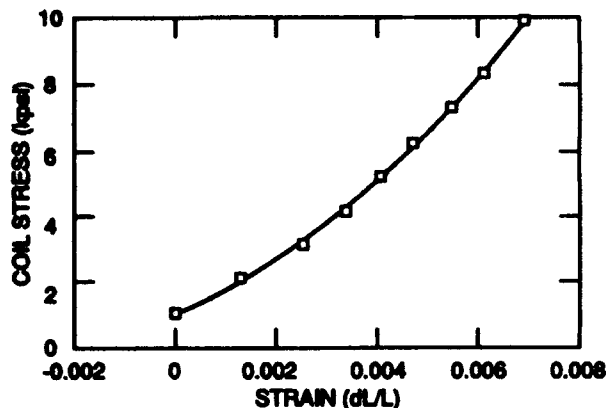


Figure 5. Stress vs. strain for a Kapton CI SSC 50 mm inner coil.

An early concern about coils made with all-polyimide cable insulation was that during a magnet quench, helium might be trapped inside the cable insulation and rupture the insulation as the pressure of the gas increased. Tests were performed on molded coil sections under conditions simulating those in a magnet to measure the impedance to the flow of helium from within the coil. This was done by fitting coil sections with buffer volumes at each end and measuring the flow of helium under various pressures out from the sections while the sections were compressed as they would be in a coil. It was found that the all-polyimide sections leaked helium at approximately 1/7 the rate as the very porous K/FG sections<sup>[2]</sup>, but still sufficient to alleviate concern. In addition, a magnet that had been built with spot heaters to initiate quenching was extensively tested and then dissected to look for insulation damage; none was found. Thus, there is no concern that trapped helium can cause insulation damage during magnet quenching.

Another concern with early all-polyimide coils was that the increased amount of plastic material in these coils would lead to increased loss of coil prestress during cool down to operating temperature. Indeed, it was found that magnets made with early versions of the new insulation system lost 50-60% of their room temperature prestress during cool down as measured with strain gauges monitoring the azimuthal prestress in the magnets. This effect was improved by including a mineral filler in one layer of the cable wrap. Magnets built with the CI system, in which the outer layer of coil insulation is a filled material, lose typically 40-50% of their room temperature prestress, a loss very similar to the loss experienced by K/FG magnets upon cool down and not detrimental to ultimate magnet performance.

Kapton CI coils were initially molded by bringing their temperature up to 225 C, then back to room temperature, while maintaining a pressure on the coils of nominally 10 kpsi in a molding press. It was found that coils made in this way exhibited low interstrand resistance and magnets built with these coils experienced strong and undesirable ramp-rate-dependent effects<sup>[3]</sup>. A modified molding program in which the pressure on the coils was removed during the two temperature ramps between 135 C and 225 C and reduced to a low value at the 225 C temperature plateau was found to ameliorate this effect. In this modified program, coil sizing is accomplished by maintaining high pressure on the coil for 30 min. while at a temperature of 135 C on both the up and down temperature cycles. The interstrand resistance of coils made in this way is similar to that of K/FG coils made with the traditional cycle of 7 kpsi pressure during a temperature cycle to 135 C, and in some cases has been found to result in a higher level of interstrand resistance<sup>[4]</sup>. Extensive investigations into the general question of interstrand resistance have revealed it to be a poorly understood phenomenon dependent on numerous factors including cable manufacturer, manufacturing process, level of oxidation of the wire in the cable, etc., and it has become the subject of extensive investigations in the SSC and RHIC magnet programs. It has been found that the interstrand resistance is quite reproducible if the manufacturing process for the cable is held constant. Thus, magnets that show repeatable and acceptable eddy current effects can be manufactured with either K/FG or CI cable insulation if the cable characteristics are controlled.

#### IV. SUMMARY

The Kapton CI cable insulation system described in this paper has been shown through extensive testing to be robust and reliable. It does require higher molding temperatures but these can readily be accommodated through proper design of the coil tooling. Its characteristics are equal to or superior in all known respects to those of the Kapton/Fiberglass system that has been used to date. In particular, its improved punch-through resistance gives a significant reduction in the probability of electrical faults in the current generation of high field, high prestress accelerator magnets, a characteristic that will be critical for successful operation of large machines built of such magnets.

#### V. REFERENCES

- [1] A. Devred et al, "About the Mechanics of SSC Dipole Magnet Prototypes", AIP Conference Proceedings: The Physics of Particle Accelerators, January 1992 and SSCL-Preprint-6, November, 1991.
- [2] W. Sampson, private communication.
- [3] P. Wanderer, "Test Results from DSA209", presentation at SSC Magnet Systems Integration Meeting, May, 1991 (unpublished).
- [4] M.D. Anerella, A.K. Ghosh, SSC Internal Tech. Note SSC-MD-273, (1991).

# Treatment of the Results of Magnetic Mapping of the SIBERIA-2 Magnets

V.Korchuganov, E.Levichev, and A.Philipchenko  
Budker Institute of Nuclear Physics  
630090 Novosibirsk, Russia

## Abstract

Recently the fabrication and the assembling of all the main magnetic elements for a 2.5 GeV dedicated SR source SIBERIA-2 have been completed. The paper reports a technique for high accurate measuring the field of different types of magnets. The measurement results have been treated statistically and an effective mechanism to correct the magnetic length of the dipoles and quadrupoles has been developed.

## I. INTRODUCTION

The 2.5 GeV SIBERIA-2 storage ring is a dedicated SR source. It has optimized low-emittance lattice with six-fold symmetry [1] which contains 24 zero-gradient dipoles, 72 quadrupoles of three different lengths, 36 sextupoles and 12 octupoles. The design of the magnets was presented in ref. [2]. All the magnets except the quadrupoles were built and installed at the ring. The manufacture of quadrupoles will be completed in the near future. All the magnets were involved in series magnetic measurements. The test procedure and the treatment of the magnetic mapping results are described in this report.

## II. HALL PLATES MEASUREMENT

A familiar Hall probes technique was chosen for magnetic tests. To make point-by-point measurements of the magnetic field the Hall plate bench system for VEPP machines [3] supplied by Karl Zeiss Jena was used. The mechanical positional accuracy along the magnet axis is  $6 \mu\text{m}$ . The single pass scan length available is 0.8 m. To extend the scan length it is possible to shift the initial scanning coordinate without any accuracy reduction. The Hall probes, which have low temperature coefficient ( $5 \times 10^{-5}/^{\circ}\text{C}$ ) do not need special control over the probes temperature. A set of probes was glued on the support, and the distance between adjacent probes was measured at an accuracy better than  $6 \mu\text{m}$ . A sufficiently high output ( $10 \mu\text{V}/\text{Gauss}$ )

makes it possible to read the signal directly with the digital voltmeter. A special constant current source was built for the measurements with the relative current variation  $\leq 10^{-4}$ .

Prior to the measurement Hall probes were calibrated against a high precision NMR probe [4] using a dipole magnet with a high uniform field. The calibration curves were fitted by a spline interpolation technique in the range of  $\pm 2.2 \text{ T}$ .

All the electronics involved was produced in CAMAC standard. The data were read by a microcomputer. The software for analyzing, plotting and storing the measurement results was developed.

The Hall plates array is transversal aligned in the magnet gap with the precision  $\leq 0.2 \text{ mm}$  using the alignment marks.

## III. DIPOLE MAGNETS

The main characteristics of the dipole are given in Table 1. The specific feature of the H-shaped solid Armco-steel magnet is its "soft-end" which is a constant field region with the field equal to one quarter of the main field to produce softer radiation [2]. For symmetry this soft-end pole must be alternatively at the left or at the right end of magnets, thus creating two separate families.

Table 1. Dipole design parameters

	Main pole	Soft-end pole
Bend angle	14.33°	0.67°
Field (2.5 GeV)	1.7 T	0.425 T
Bending radius	4905.4 mm	19622 mm
Magnetic length	1227 mm	230 mm
Gap	42 mm	42 mm
Turns per pole	4	1

Point-by-point measurements have been carried out with an array of 11 Hall probes with 18 mm spacing. Table 2 lists the results of the excitation curve measurements for the central part of the main pole. The optimized yoke geometry has permitted us to reach the nonlinearity of the excitation curve  $\leq 3\%$  at 2.5 GeV.

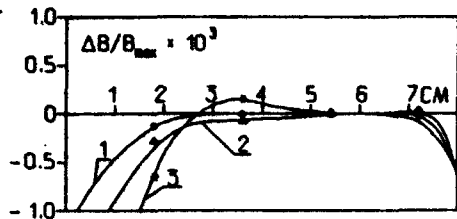


Figure 1: Dipole magnet field uniformity. 1 - 6.5 kA, 2 - 8.5 kA and 3 - 10.5 kA

Table 2. Field versus current for the dipole main pole

I (kA)	1	2	3	4	5
B (T)	.24	.47	.72	.95	1.19
I (kA)	6	7	8	9	10.5
B (T)	1.41	1.64	1.82	1.95	2.17

Fig. 1 shows the field homogeneity at the center of the dipole at several excitation levels. Despite the operation current is 7.3 kA (1.7 and 2.5 GeV), the measurement results demonstrate rather good field quality at 10.5 kA (2.17 T and 3.2 GeV). The field deviation is within the limit  $\pm 5 \times 10^{-4}$  in the region  $\pm 3.1$  cm at the excitation level 7.5 kA and is within the limit  $\pm 5 \times 10^{-4}$  in the region  $\pm 2.8$  cm at the excitation level 10.5 kA. One can see that saturation effects do not seriously degrade the field quality. Due to the large pole width (260 mm) in radial direction the horizontal distribution of the field integral in the working aperture is practically the same as the field profile.

Field mapping was performed directly through the magnet with a 1 cm point spacing. After that, the field profile was calculated using spline interpolation near the electron trajectory which was previously found. The field profile along the electron trajectory is given in Fig. 2. To use

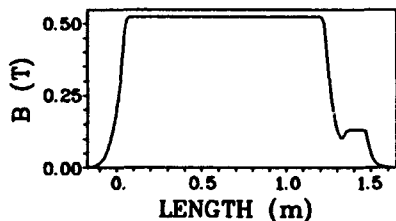


Figure 2: Longitudinal profile of the dipole field.

a hard-edge approximation, the proper ratio between the main and soft-end pole field integrals in the intersection region should be taken into account. Calculations with MERMAID [5] have been done and the integral ratio coefficient was found [6]. The effective length for the appropriate part of the dipole was determined as the ratio of the field integral of this part to the central field amplitude. Unlike the previously used model, a three sectionized magnet (main pole region, zero field region, and soft-end region) has proved to be more convenient. According to the measurement results, the effective lengths variation in the working field interval does not exceed  $\pm 0.05\%$ . The mean effective lengths and their rms deviations over all

the SIBERIA-2 dipoles are presented in Table 3.

Table 3. Dipole effective lengths parameters.

	Main pole section	Zero-field section	Soft-end section
l (m)	1.2422 m	0.052 m	0.175 m
$\sigma_l$	1.196 mm	0.397 mm	0.416 mm
$\sigma_l/l$	$9.6 \times 10^{-4}$	$7.6 \times 10^{-3}$	$2.4 \times 10^{-3}$

Fig. 3 presents the relative deviation of the bend angle of individual dipoles with respect to its average value over all the magnets.

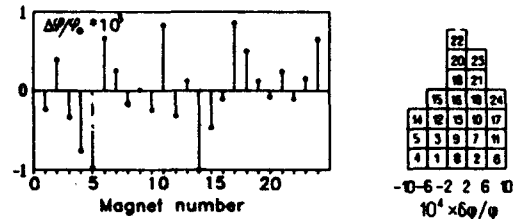


Figure 3: Relative deviation of the bend angle of dipoles with respect to its average value over all the magnets.

## IV. QUADRUPOLE MAGNETS

Three types (A, B and C) of quadrupole magnets differing by their yoke length constitute 6 families [2]. The main parameters of quadrupoles are summarized in Table 4.

Table 4. Main parameters of SIBERIA-2 quadrupoles at 2.5 GeV

Type	A	B	C
Bore radius	28 mm	28 mm	28 mm
Max. gradient	30 T/m	36 T/m	30.5 T/m
Steel length	26.4 cm	36.2 cm	28.8 cm
Turns per pole	15	15	14
Max. current	0.66 kA	0.81 kA	0.67 kA

All the quadrupoles are made of solid Armco-steel. A- and B- types quadrupoles are of the conventional "close-side" design, while the yoke of the C- type quadrupole is split into two symmetric halves - top and bottom - to pass the SR beam lines, without steel connections between them. The halves are joined through strong aluminum spacers. The pole profile is shaped as  $y = 392/x$  hyperbola which is ended by 5-mm-wide strips at  $x = 42.15$  mm. The good gradient region is formed by the pole profile without shimming being inefficient in our case, because the shims iron

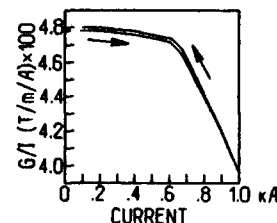


Figure 4: SIBERIA-2 quadrupole excitation curve.

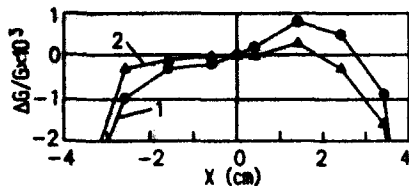


Figure 5: The quadrupole gradient uniformity. 1 - 0.75 kA and 2 - 0.50 kA

is saturated due to the high magnetic field.

The excitation curve measurement results are demonstrated in Fig. 4.

The measurements were performed with a set of 11 Hall probes of 6 mm spacing at several excitation current levels. The set of probes was located horizontally (in the mid plane) and vertically (normal to the mid plane) in the lens aperture, and the field was mapped point-by-point with a 0.5-cm spacing in longitudinal direction.

In Fig. 5 the gradient uniformity for different current levels in the  $A$  - quadrupole center is shown. The quadrupoles edge fields have a considerable effect on the integrated gradient uniformity, and special studies have been carried out to find optimal pole chamfer sizes. Fig. 6 shows the integrated gradient homogeneity for several chamfer sizes. The 6 mm  $\times$  45° chamfer was chosen on the basis of the results

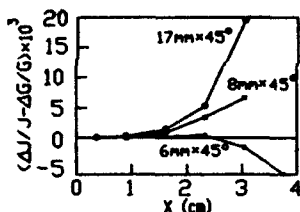


Figure 6: The contribution of the edge field to the integrated gradient homogeneity for several chamfer sizes.

obtained. Fig. 7 demonstrates the integrated gradient homogeneity of the same  $A$  - quadrupole at two excitation levels. The good integrated gradient region (within the specified limits  $\pm 5 \times 10^{-4}$ ) lies within  $\pm 2.2$  cm.

In Table 5 the characteristics which demonstrate the effect of saturation on the quadrupole parameters are listed.  $(\int G(s)ds)/G_0$  determines the dependence of the on-axis effective length on the excitation current, whereas  $(\int G(s)ds)/I$  also incorporates the yoke saturation caused by the transverse magnetic flux. Here  $G_0$  is the gradient

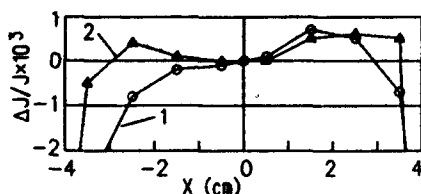


Figure 7: The integrated gradient homogeneity at several excitation levels. 1 - 0.75 kA and 2 - 0.5 kA

in the quadrupole centre and  $I$  is the excitation current.

Table 5. Quadrupole saturation effects characteristics

$I$ (kA)	$\int G(s)ds$ (T)	$G_0$ (T/m)	$\int G(s)ds/I$ (T/kA)	$\int G(s)ds/G_0$ (m)
0.75	9.9010	33.951	13.20	0.291
0.50	6.9697	23.805	13.94	0.293
0.25	3.5046	11.965	14.02	0.293

## V. ACKNOWLEDGEMENT

The contribution of S.Mikhailov to the development of the measurement system and software for treating the results as well as for performing magnets measurements are gratefully acknowledged.

## REFERENCES

- [1] V.Anashin, A.Valentinov et al, "The dedicated SR source SIBERIA-2", The proceedings of the 11-th Russian Particle Conference, Dubna 1989, p.277-280 (in Russian).
- [2] G.I.Erg et al, "Magnetic lattice of SIBERIA-2 - dedicated SR source", Preprint INP 89-174, Novosibirsk 1989.
- [3] P.Vobly et al, "The VEPP magnetic measurements", The Proceedings of the 3-th USSR Particle Conference, Moscow 1973, vol.2, p.87-90 (in Russian).
- [4] N.Zinevitch et al, "NMR field measurement system", The proceedings of the 10-th USSR Particle Conference, Dubna 1986, vol.1, p.342-347 (in Russian).
- [5] A.Dubrovin, "MERMAID Reference Manual, INP Internal Report, Novosibirsk 1992.
- [6] S.Mikhailov, private communication

# Prototype Quadrupole Magnets for the PLS Storage Ring \*

Y. M. Koo, D. E. Kim, Y. G. Nah, H. S. Han, B. K. Kang,  
K. H. Park, J. R. Yoon, H. K. Lee, and J. E. Milburn

Pohang Accelerator Laboratory,  
Pohang Institute of Science and Technology,  
P. O. Box 125, Pohang, KyungBuk 790-600, Republic of Korea

May 13, 1993

## Abstract

Two prototype quadrupole magnets for the 2.0 GeV PLS storage ring have been built and their magnetic properties have been measured. The prototype quadrupoles have a C-shaped core geometry to facilitate installation of the vacuum chambers and photon beam lines. Pole end chamfering experiments to reduce 12-pole and 20-pole errors, and core shimming experiments to compensate the effects of the core asymmetry, have been performed. After compensation, all multipole error levels are less than the tolerances set by the beam dynamics requirements.

## I Introduction

The PLS storage Ring lattice is a Triple Bend Achromat structure with 12 superperiods and a 280.56 m circumference. Each superperiod has mirror symmetry about the central dipole. Each half superperiod contains six quadrupoles; three in the dispersive section and three in the non-dispersive straight section.

There are six different types of quadrupole magnets; Q1 through Q6. All types use same lamination. All SR quadrupole magnets are designed to have a C-shaped core geometry to facilitate installation of the vacuum chambers and photon beam lines. Core lengths are 204 mm for Q1 and Q6, 314 mm for Q3 and Q4, and 494 mm for Q2 and Q5. Magnet types which are the same length differ in their coils. Series powered magnets use a large cross section conductor, and individually powered magnets use a small cross section conductor. Both types of coils have the same exterior dimensions. The major parameters for Q1 and Q2 are shown in Table 1. The end view of the prototype Q2 magnet is shown in Fig. 1 Q1 and Q2 type prototype quadrupole magnets have been built, and the results of the magnetic measurements are summarized. Both prototypes use the smaller cross section conductor.

Type of magnet	Q1	Q2
Max. field gradient [T/m]	18	18
Core length [mm]	204	204
Pole tip radius [mm]	36	36
Good field radius [mm]	30	30
Ampere-turns (efficiency=0.994)	9338	9338
Number of turns/pole	68	16
Current [A]	137.32	583.63
Voltage drop/magnet [V]	35.24	58.86
Current density [A/mm <sup>2</sup> ]	8.39	8.89
Power dissipation/magnet [kW]	4.84	8.08

Table 1. Major parameters of Q1 and Q2 type quadrupole magnets

## II Manufacturing

The poles profile of these quadrupoles is designed by conformally mapping a pole profile from a dipole geometry which satisfies the required field quality.

The steel used is the same low carbon steel material used in our dipole magnet[1]. The bore diameter is 72 mm. Die clearance are kept to within 25 microns along the critical pole profiles. Sorting the laminations within a magnet type will be performed in the production phase. Since the lamination has no symmetry axis for flipping the lamination to remove material thickness variations, the material will be flipped *before* punching.

The core assembly is glued, using a full coverage epoxy film between each lamination. Each core is stacked using a fixture with precision reference surfaces. The epoxy is cured while the core is under compression in the precision fixture. After stacking, the core is compressed by fixture bars which go completely through the core.

The coils are constructed as an inclined pancake. A hollow copper conductor (4.6 mm-square with a 2.5 mm hole) is wound in four layers of 17 turns each. The conductor is insulated with 0.13 mm thick by 20 mm wide Dacron tape, half lapped, and coil pancakes are "ground wrapped" with 0.25 mm thick by 20 mm wide fiberglass tape, half lapped.

After the coil pancakes are installed on each half core, the top and bottom halves are joined with stiff tie bars as shown in Fig. 1. The two halves are aligned by means of steel dowel pins in two V grooves.

\*This work supported by the Ministry of Science and Technology and Pohang Steel Co. Ltd.

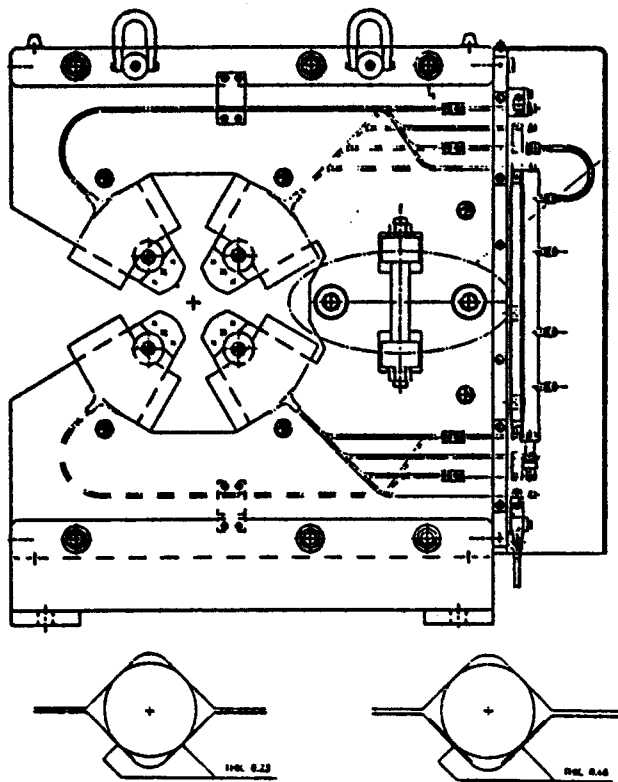


Figure 1: End view of prototype Q2 magnet

### III Magnetic Measurements

#### III-A General

Magnetic measurements are made to investigate magnetic efficiencies at different excitations, to determine an acceptable pole-end profile for the production magnet design, to correct asymmetric core effects on multipole error fields, and to find an appropriate procedure for assembling magnets. A prototype quadrupole rotating coil is used to measure integrated field properties and multipole error levels. The rotating coil has two windings; an inner and an outer winding. The voltage response of each winding is the same for the fundamental field, and is different for multipole error fields. The fundamental field is measured with the outer winding. For the multipole error field measurement, a null measurement is used. The windings are connected in series, with opposing polarities, so that the response of the fundamental field is nulled, resulting in a better signal to noise ratio for the multipole error field measurements.

#### III-B Measurements and Compensations

For the as-assembled (unchamfered) Q2 magnet, the multipole error components are measured. All multipole errors, except  $n=3$  and  $n=6$  are below the tolerance level.

The  $n=3$  multipole error originates from the asymmetric, C-shaped geometry and can be corrected by rotational motions of the poles. The  $n=6$  multipole error is an allowed

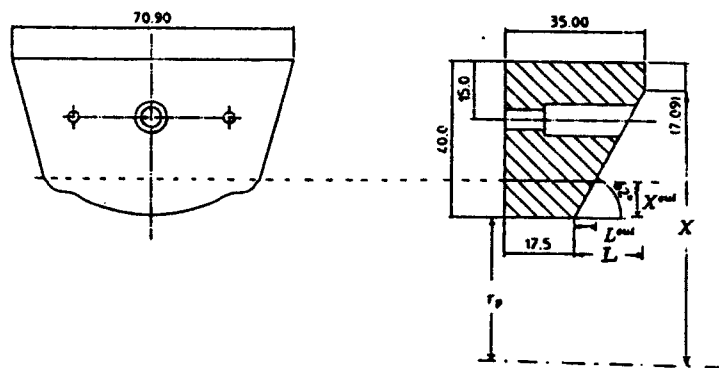


Figure 2: Profiles for pole-end chamfers

harmonic field on quadrupole magnets. Allowed multipole errors ( $n=6,10,14,\dots$ ) are induced either by imperfect pole shaping or by end fields, and can be corrected by choosing a proper profile on the pole-ends.

Pole rotation is achieved by placing shims in the "V"-grooves shown in Fig. 1. The effects of core motions on multipole error fields are given in K. Halbach's [2] perturbation table. For  $r_p = 36$  mm, the optimum required shims for  $90^\circ$  "V"-grooves are calculated to be 0.404 mm for groove 1 and 0.202 mm for groove 2. However, with the intention of slight overcompensation, we chose shims of 0.46 mm for groove 1 and 0.23 mm for groove 2. The expected sextupole error level with these shims is

$$-1.11 \times 10^{-3} + 0.1679 \frac{0.23\sqrt{2} 30}{36} \frac{30}{36} = 1.54 \times 10^{-4}$$

which is well below the specified sextupole random tolerance of  $9.9 \times 10^{-4}$  for the Q2 magnet. The measured sextupole error level after shimming is  $1.1357 \times 10^{-4}$  which is close to the value predicted by the perturbation theory.

Next, the  $n=6$  multipole error is reduced by pole-end chamfering. The measured normal  $n=6$  component at  $I = 100$  [A] and a normalization radius of 30 mm is  $-1.779 \times 10^{-3}$ , and the specified  $n=6$  systematic and random tolerances for the Q2 magnet are  $1.68 \times 10^{-3}$  and  $3.3 \times 10^{-4}$ , respectively. The reason that pole-end chamfers reduce the  $n=6$  multipole error can be understood by an analogy to the correction of  $n=3$  multipole errors in a dipole magnet[3]. In a quadrupole magnet, the length of three dimensional fringe fields will be longest at the center of the pole and shortest at the pole edge where the gap is narrowest. The required cuts can be approximated with a straight chamfer as in Fig. 2. In Fig. 2, the additional iron at each of the pole edges provides a fringe field bump and introduces a  $n=6$  multipole field in opposite polarity to that from the fringe fields of the original unchamfered magnet. The amount of  $n=6$  multipole error compensation with a straight chamfer depends on the depth and the angle cut on the pole. To determine a proper chamfering profile, we test four different chamfer profiles. The optimum cutting depth and cutting angle is found to be  $L = 17.5$  mm and  $62^\circ$ . With this profile, the measured

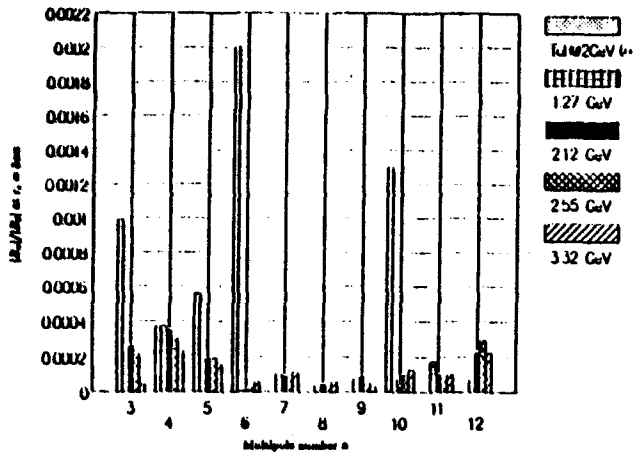


Figure 3: Normalized multipole error vs. multipole number for the shimmed and chamfered Q2 magnet

$n=6$  error is  $-5.25 \times 10^{-5}$ . By designing the pole profile well, so that the contribution of  $n=6$  error in the central region of the magnet is small, the same pole end profile should work on any length quadrupole magnet.

After chamfering the pole-ends and shimming the core, all multipole error levels are measured over the full excitation range, and the results are given in Fig. 3. The results show that the described shims and pole-end profile are good enough to set all multipole error components below the specified criteria.

Quadrupole excitation properties are measured on the unchamfered Q2 magnet and the chamfered Q1 and Q2 magnets. The chamfer angle is  $62^\circ$  with respect to the pole faces, and the depth of cut is 17.5 mm. Before taking data, the magnet current is cycled three times from 0 Amperes to 130 Amperes to condition any hysteresis effects. Then, the magnetic fields are measured at each excitation current. The current normalized quadrupole field  $\int r_o B' dl / I$  is maximum at  $I \approx 82$  [A], and is  $2.277 \times 10^{-3}$  [T-m] for the unchamfered Q2,  $2.062 \times 10^{-3}$  [T-m] for the chamfered Q2, and  $0.885 \times 10^{-3}$  [T-m] for the unchamfered Q1.

A plot of efficiency  $\left( \frac{\int r_o B'(I) dl}{\int r_o B'(I=82.6) dl} - 1 \right)$  versus current is shown in Fig. 4. Assuming that the contributions of fringe fields to the effective length are the same on both the chamfered Q1 and the chamfered Q2 magnets, and using  $(L_{eff} = L_{core} + L_{fringe})$ , and from the field integral measurement  $\frac{L_{eff}^{Q2}}{L_{eff}^{Q1}} = \frac{0.17032}{0.07309} = 2.330$  at  $I=82.6$  [A], we have  $L_{fringe} = 49.0$  mm. Then, the effective length of the Q1 and Q2 magnets are  $L_{eff}^{Q1} = 218$  mm,  $L_{eff}^{Q2} = 508$  mm respectively. The field gradients calculated with these effective lengths compares well with the theoretically ( $\mu = \infty$ ) calculated  $B'$ .

The measured magnet efficiencies are greater than 99.5% for all excitations, indicating that the levels of saturation are acceptable for both magnets.

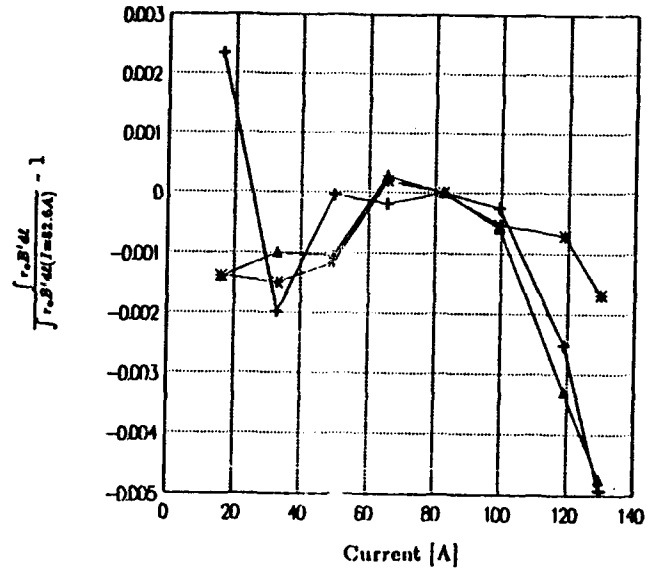


Figure 4: Difference in normalized  $\int r_o B' dl$  versus current: Normalized at  $I=82.6$  A. \*, as assembled,  $\Delta$ ; chamfered and shimmed Q1, and +; chamfered and shimmed Q2.

## IV Conclusion

Prototype quadrupole magnets for the PLS storage ring have been designed and built. They feature asymmetric iron cores to facilitate the installation of the vacuum chambers and photon beam lines. Results of magnetic measurements of the prototype quadrupole magnets are summarized. To meet the specifications set by the beam dynamics requirements, end chamfering and shimming experiments are performed on the Q2 magnet, which has eight removable pole-end pieces. The corrected magnet has an efficiency  $\geq 99.5\%$  for magnetic field gradients  $G \leq 17$  [T/m], and higher order multipole error levels are less than the specified tolerances for all excitations, indicating that the magnet has appropriate properties for the PLS Storage Ring quadrupole magnet.

## References

- [1] *Conceptual Design Report of Pohang Light Source*, Pohang, POSTECH Press, 1990.
- [2] K. Halbach, "Tables and Graphs of First Order Perturbation Effects in Iron Dominated Two Dimensional Symmetrical Multipoles", UCRL-18916
- [3] B. K. Kang et al., PLS-MN067, 1992

# Magnetic Measurement Data of the Injector Synchrotron Dipole Magnets for the 7-GeV Advanced Photon Source\*

K. Kim, S. H. Kim, L. R. Turner, C. L. Doose, R. Hogrefe, and R. Merl  
Argonne National Laboratory  
9700 S. Cass Avenue  
Argonne, Illinois 60439

## Abstract

The magnetic measurement data of the first 34 of the required 68 production magnets for the injector synchrotron are summarized. The magnetic measurement method of the field strength and field shape relative to a reference magnet is described. The standard deviation of the integrated field strength for the 34 magnets is  $3.3 \times 10^{-4}$  and the variation of the integrated field with transverse displacement of  $\pm 25$  mm is less than  $2.5 \times 10^{-4}$ .

## I. INTRODUCTION

The injector synchrotron dipole magnets for the 7-GeV Advanced Photon Source (APS) are to be excited from 0.0447 T to 0.7011 T during a ramp time of 0.25 s. The magnetic length and pole gap are 3.077 m and 40 mm, respectively. The relative tolerance for the integrated field strength is  $2 \times 10^{-3}$  and the tolerances for quadrupole and sextupole coefficients at a radius of 25 mm are  $5 \times 10^{-4}$  and  $1.2 \times 10^{-3}$ , respectively. Detailed descriptions of field shapes of the integrated, 2-D, and end field for the pre-production magnet, including 3-D calculations, are summarized in Ref. [1]. The measured data for the first 34 of the required 68 production magnets are described in this paper.

## II. MEASUREMENT

The integrated field strength, not the local field variation, along the beam orbit is an important parameter to be measured. However, since the 2-D "body" field along the magnet axis for a laminated magnet depends on how smoothly the laminations are stacked, the variation of the vertical field and magnet pole gap are measured. In Figure 1, the field variation, measured every 2.5 cm with a Hall probe, and the inverse of the gap along the beam orbit are plotted. Here, the average measured gap of 39.88 mm and the average measured field of 0.7488 T at 1000 A are used for the plot. It is seen that the field variation closely follows that of the gap. It has been identified that the gap variation is due to displacements of the laminations during welding of the bolting fixtures and support steel plates after the lamination stacking. The local

field variation in Figure 1 is less than  $2 \times 10^{-3}$  and will not be harmful for the positron beam.

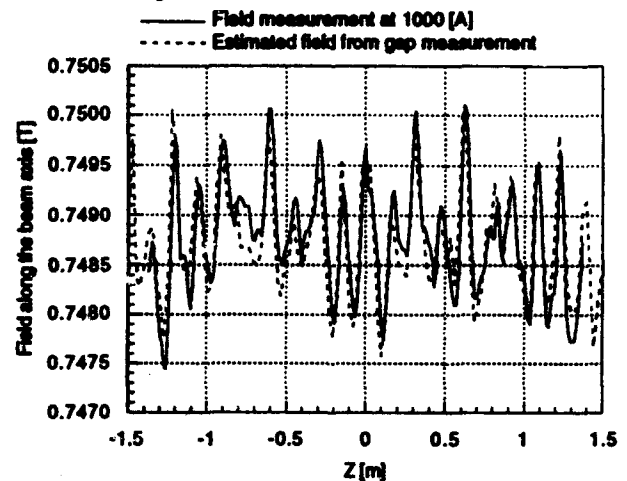


Figure 1. Magnetic field along the beam orbit. The solid line shows the measured field and the dashed line shows the estimated field from the gap measurement.

A general description of the magnetic measurement system is given in Ref. [2]. Two sets of integral coils, one for the reference magnet and one for production magnets, are made by placing two layers of seven printed circuit (PC) coils on an aluminum block along the beam orbit. For measurement of an average magnetic field inside 1.5 m, a short version of the PC coils is placed on top of the full integral coil.

When the magnet current is ramped up and down between 0 A and 1025 A (7.7 GeV) in 120 s, a 0.5-s trigger signal generated by a time-base and gated trigger units is fed into four digital integrators and a digital multimeter. The coil signal from the reference magnet (reference signal) and the bucked signal between the coils for the reference and production magnets are integrated. Then, the integrated data for the reference magnet and the current transducer readings are least-square-fitted to a straight line and the fitting coefficient and the signal form are used to check the measurement condition. The integrated data of the reference and bucked signals are also least-square-fitted to a straight line. The fitting coefficient represents the relative magnetic field strength between the reference and the production magnets. The positioning error of the integrated coil is estimated to be less than  $1 \times 10^{-4}$ , and the repeatability of the fitting coefficient when measured consecutively is better than  $2 \times 10^{-5}$ .

\*Work supported by the U.S. Department of Energy, Office of Basic Energy Sciences, under Contract No. W-31-109-ENG-38.

The integrated field shape is measured by moving the same integral coils in the transverse direction. When the integral coil in the testing magnet is moving in the transverse direction, the trigger signals are generated from a linear encoder and the integral coil signal is measured using the digital integrators.

The measured data for the 34 magnets are listed in Table 1. Magnet BDP003 is used as the reference. The first two columns after the magnet number in the first column are the relative integrated and 1.5-m average 2-D fields, respectively, and are plotted in Figure 2. Except for the magnets BDP006 and BDP007, the relative field strength varies less than  $1 \times 10^{-3}$ .

Table 1.  
Measured data for the 34 production magnets.

Magnet Number	$\frac{\Delta BL}{B_{ref} L_0}$ [ $\times 10^{-4}$ ]	$\frac{\Delta BL_0}{B_{ref} L_0}$ [ $\times 10^{-4}$ ]	Residual Field [Gauss]	Survey Angle [mrad]	$\frac{\Delta BL}{BL}$ in $\pm 25$ mm at 60 A [ $\times 10^{-4}$ ]	$\frac{\Delta BL}{BL}$ in $\pm 25$ mm at 300 A [ $\times 10^{-4}$ ]	$\frac{\Delta BL}{BL}$ in $\pm 25$ mm at 930 A [ $\times 10^{-4}$ ]	$\frac{\Delta BL}{BL}$ in $\pm 25$ mm at 1025 A [ $\times 10^{-4}$ ]
BDP003	0.0	0.0	12.02	0.067	3.0	2.0	1.5	1.5
BDP004	-1.6	0.3	12.24	0.045	1.4	2.0	1.2	1.1
BDP005	0.2	0.1	12.64	-0.171	1.5	1.5	1.0	0.9
BDP006	-13.7	-10.6	12.50	-0.035	1.3	1.8	1.0	1.0
BDP007	-14.8	-11.0	12.90	-0.381	2.2	2.2	1.2	1.0
BDP008	-5.7	-5.3	13.23	-0.027	1.4	1.6	1.0	0.8
BDP009	-5.4	-4.3	12.84	-0.143	1.9	1.6	1.2	1.0
BDP010	-2.3	0.0	12.15	0.156	1.6	1.6	1.1	0.9
BDP011	-3.8	-2.3	12.06	-0.018	1.7	1.5	1.0	0.8
BDP012	-3.6	-2.1	12.21	-0.323	1.8	1.8	1.2	1.0
BDP013	-9.2	-5.7	12.47	-0.065	1.9	2.0	1.3	1.0
BDP014	-3.9	-2.4	12.33	0.046	1.7	1.6	1.1	0.9
BDP015	-1.6	-0.5	12.09	-0.033	1.6	1.5	1.0	0.8
BDP016	-3.6	-3.3	12.65	-0.182	1.3	1.7	1.1	1.0
BDP017	-4.6	-2.8	12.43	0.040	1.3	1.8	1.2	1.0
BDP018	-7.4	-3.0	12.54	-0.139	1.7	1.8	1.2	1.0
BDP019	-1.9	1.8	12.57	0.010	1.9	1.5	1.0	0.8
BDP020	-3.4	-0.7	12.33	-0.095	2.3	2.0	1.4	1.2
BDP021	-7.0	-4.3	12.98	-0.034	2.4	2.1	1.6	1.4
BDP022	-5.1	-1.6	13.35	0.108	2.0	1.9	1.4	1.2
BDP023	-4.9	-1.2	13.15	-0.009	1.9	2.0	1.5	1.3
BDP024	-5.0	-1.7	13.20	0.137	1.5	1.9	1.3	1.2
BDP025	-4.4	-1.4	12.73	-0.059	1.8	1.7	1.3	1.2
BDP026	-3.4	-0.5	12.29	0.104	2.1	1.8	1.2	1.0
BDP027	-3.7	-1.1	12.42	0.032	1.8	1.9	1.5	1.3
BDP028	-1.6	2.7	12.65	-0.042	1.6	2.1	1.4	1.2
BDP029	-4.7	-1.3	12.24	0.458	1.5	1.6	1.0	0.8
BDP030	-1.8	0.2	12.19	0.093	1.9	1.8	1.3	1.1
BDP031	0.4	3.4	13.74	0.091	1.9	1.8	1.2	1.0
BDP032	-4.7	-0.8	11.98	0.090	1.8	2.2	1.5	1.3
BDP033	-2.4	1.6	12.25	0.086	2.0	1.9	1.3	1.1
BDP034	-5.0	-2.1	12.52	0.052	2.5	2.1	1.5	1.3
BDP035	-1.5	0.9	11.91	0.007	2.4	2.2	1.5	1.3
BDP036	-3.7	-0.1	12.42	-0.035	1.6	1.9	1.4	1.2
Average	$-4.3 \pm 3.3$	$-1.7 \pm 3.1$	$12.54 \pm 0.4$		$1.8 \pm 0.4$	$1.8 \pm 0.2$	$1.2 \pm 0.2$	$1.1 \pm 0.2$

( $\Delta BL_0/B_{ref} L_0$  in the third column is the 2-D average field with  $L_0 = 1.5$  m.)

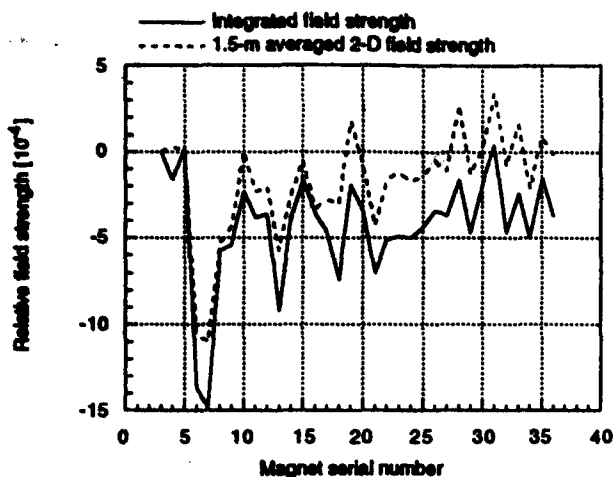


Figure 2. Variation of relative magnetic field strength.

The survey angles in the fourth column in Table 1 are the differences between the angles at the survey reference positions and the average angles for 20 measurements along the magnet length, which are also plotted in Figure 3. The angles vary within  $\pm 0.5$  mrad along the longitudinal positions. There seems to be a systematic tendency in fabrication procedure that at the negative  $z$  end, all but a few of the magnets twist to the same direction.

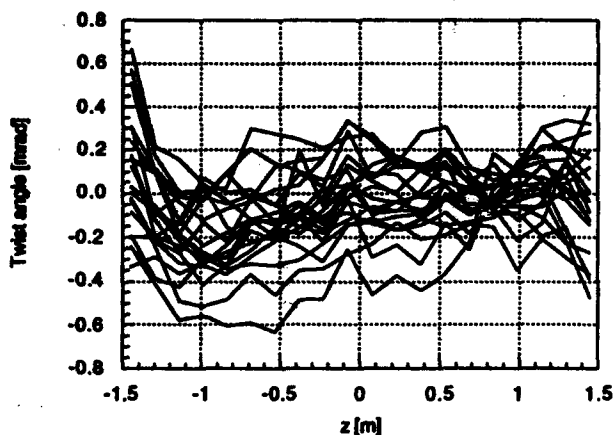


Figure 3. Twist angles along the magnets relative to the survey reference positions for the 20 magnets.

The last four columns in Table 1 are the data for the integrated field variation with the transverse displacement of  $\pm 25$  mm at four excitation currents. The data at the injection and extraction currents are plotted in Figure 4. Slightly less field variation at the extraction energy seems to be due to a slight field saturation at the pole shims. The field variations for the two currents are less than  $2.5 \times 10^{-4}$ .

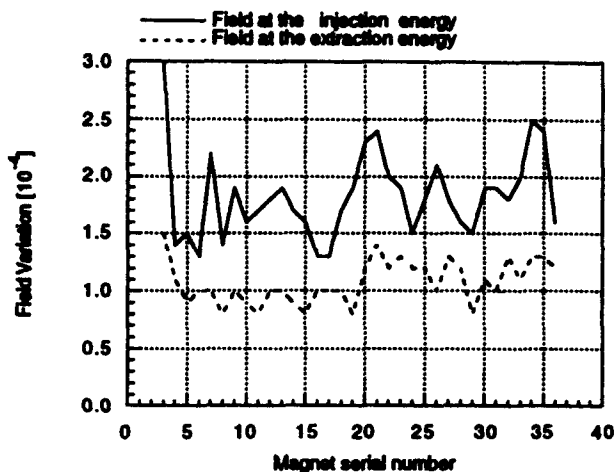


Figure 4. Integrated field variation with the transverse displacement of  $\pm 25$  mm.

### III. CONCLUSION

For the 68 required production magnets for the injector synchrotron of the 7-GeV APS, measured data for 34 magnets show that one standard deviation of the integrated field strength is  $3.3 \times 10^{-4}$  and the integrated field quality with transverse displacement of  $\pm 25$  mm is better than  $2.5 \times 10^{-4}$ . The tendency of the integrated field strength to vary from magnet to magnet seems to be decreasing as magnet production continues.

### IV. REFERENCES

- [1] K. Kim, S. H. Kim, K. Thompson, and L. Turner, "Design and Tests of the Injector Synchrotron Magnets for the 7-GeV Advanced Photon Source," these proceedings.
- [2] S. H. Kim, K. Kim, C. Doose, and R. Hogrefe "Magnet Measurement Facility for the 7-GeV Advanced Photon Source," these proceedings.

# Magnet Measurement Facility for the 7-GeV Advanced Photon Source\*

S. H. Kim, K. Kim, C. Doose, R. Hogrefe and R. Merl  
Argonne National Laboratory  
Argonne, IL 60439 USA

## Abstract

A magnet measurement facility for semi-automatic measurement control and real-time data analysis has been developed to measure more than 1000 magnets for the Advance Photon Source (APS). One dipole and three rotating coil measurement systems and corresponding probe coils are described.

used as the bucking coils for the field-integral and 2-D field measurements. These coils are calibrated against the Hall-cart measurements.

The probe coils are flat printed circuit coils connected in series according to the curvature of the magnet. A printed circuit coil is 0.5 m long with an average width of 6.8 mm, height of 3.3 mm, and 170 turns.

Table 1  
Main Characteristics of the APS Magnets

	Magnetic length(m)	Pole gap, dia.(mm)	Field strength	No. of magnet
SR dipole	3.06	60	0.599T	80
IS dipole	3.10	40	0.696T	68
PAR dipole	0.80	45	1.47T	8
SR quad	.5/.6/.8	80	18.9T/m	400
SR sext	0.24	100	490T/m <sup>2</sup>	280
IS quad	0.60	56.56	9T/m	80
IS sext	0.20	70.01	1.9T/m <sup>2</sup>	68
PAR quad	0.25	120	4T/m	16
PAR sext	0.20	130	10T/m	10

## I. INTRODUCTION

The APS magnet system requires more than 1000 conventional resistive magnets for the storage ring (SR), injector synchrotron (IS), positron accumulator ring (PAR), and beam transports [1]. Main characteristics of the magnets, except those for the beam transport, are listed in Table 1. The magnets are required to measure and evaluate the field strength and field quality to a few parts in  $10^{-4}$  to verify the tolerance requirements. Equally important parameters to be measured for the magnet alignment are the magnetic axis and roll angle with respect to a fiducial within tolerances of  $60 \mu\text{m}$  and  $0.3 \text{ mrad}$ , respectively. The measured data is also being used for the quality control of the magnet fabrication procedures and the correction of some magnets with unacceptable tolerances.

In order to meet the project schedule and technical requirements of the measurements, a magnet measurement facility has been developed. The facility includes a dipole measurement system, three rotating coil systems for quadrupole and sextupole magnets, Hall-probe field mapping, and various types of probe coils. The measurement systems have been extensively tested in parallel with the development of various prototype magnets.

## II. DIPOLE MEASUREMENT SYSTEM

A block diagram of the dipole system is shown in Fig. 1. A 3-D mapping unit with a calibrated Hall probe measures detailed end-field and 2-D field-shape for the prototype and reference magnets. A Hall-cart unit is used to measure the field integral along the designed beam orbit of the reference magnet.

The production dipoles are measured comparatively with respect to a reference dipole. Two sets of curved coils are used, one fixed in the reference magnet and one in the testing production magnet. The two coils in the reference magnet are

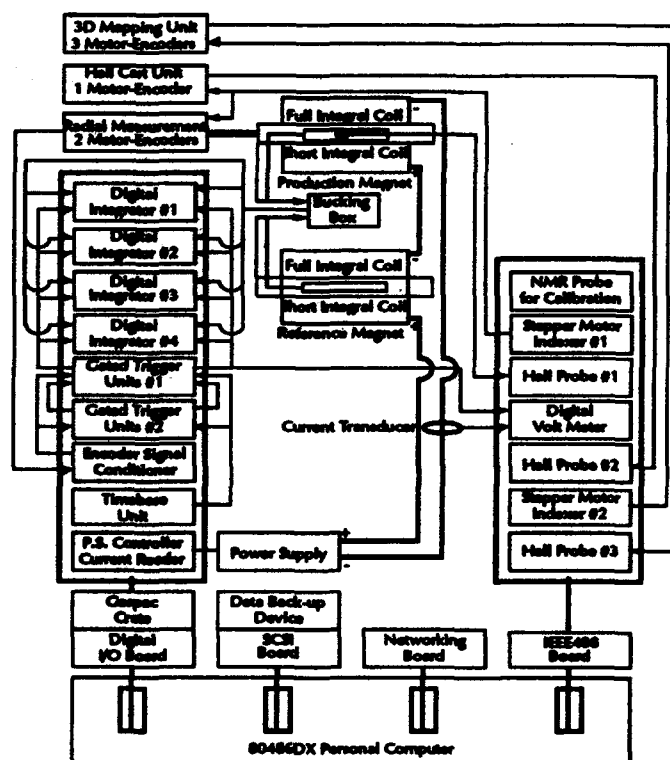


Figure 1. Block diagram of the dipole measurement system.

\*Work supported by the U.S. Department of Energy, Office of Basic Energy Sciences, under Contract No. W-31-109-ENG-38.

The submitted manuscript has been authored by a contractor of the U.S. Government under contract No. W-31-109-ENG-38. Accordingly, the U.S. Government retains a nonexclusive, royalty-free license to publish or reproduce the published form of this contribution, or allow others to do so, for U.S. Government purposes.

Four high-precision digital integrators, which are voltage-to-frequency converters, are used; one each for the field integral and 2-D field of the reference magnet and two for the respective bucking signals between the two magnets. Since the integrator connections conform to G-64 Gespec Crate specifications, IBM digital I/O interfaces and other modules, developed for the measurement control and data acquisition, were modified to configure to Gespec Crate requirements.

An operating system shell on MS-DOS called GPDAS has been developed to provide greater flexibility when taking measurements and performing data analyses [2]. The shell contains the software drivers to interface with GPIB and digital I/O boards, Gespec Crate, and other required PC boards.

The measurement procedures, including control of the magnet current and data analyses in "real-time," are automated. For measurement of IS dipoles, which have an "H-type" cross section, the probe coils are installed and removed manually through one end of the magnet. However, since the pole gap of the "C-type" SR dipole is accessible from one side of the magnet, this measurement procedure is fully automated.

During the prototype and production measurements of IS dipoles, it has been firmly established that relative accuracy and reproducibility of the field strength and field shape measurements are better than  $1 \times 10^{-4}$ .

### III. MULTIPOLE MEASUREMENT SYSTEMS

Two of the three systems are modified versions of the rotating coil measurement bench developed at CERN and fabricated by Danfysik [3]. The third system, developed at Argonne, has additional features for measurement flexibilities

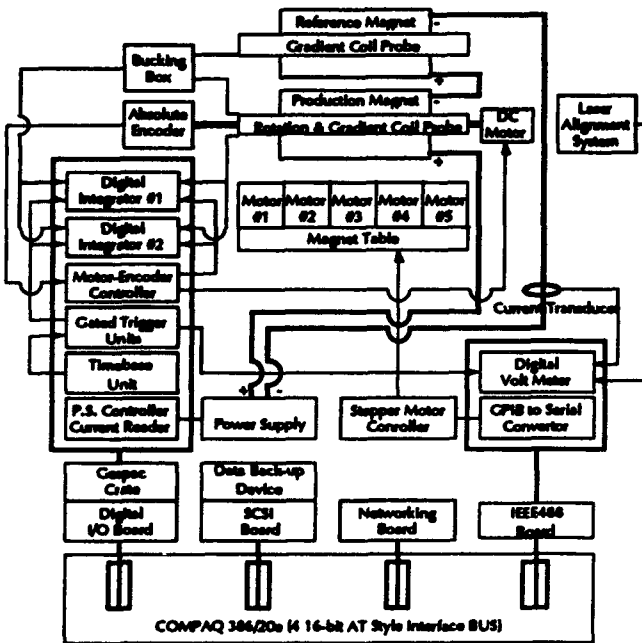


Figure 2. Block diagram of the rotating coil measurement system.

such as different probe lengths. Shown in Fig. 2 is a block diagram of the rotating coil system. A rotating coil cylinder, supported by two air-bearings, is rotated by a DC motor. A 15-bit absolute encoder triggers the integration of the induced voltage in the coil at 256 angular positions per turn.

Since the air-bearing positions are fixed to the base table, the magnet position has to be controlled and pre-aligned to the rotating coil axis using five stepping motors. A precision laser and photo-quadrant detector are used for the alignment. The position of the laser, mounted on one end of the base table, is precisely measured from the axis of the rotating coil cylinder. The detector, mounted in a Taylor-Hopson ball, is placed on top of the testing magnet. From the harmonic analysis of the rotating coil measurements, the magnet is aligned to rotating coil axis. Then, the detector reads the fiducial position with respect to the magnetic center.

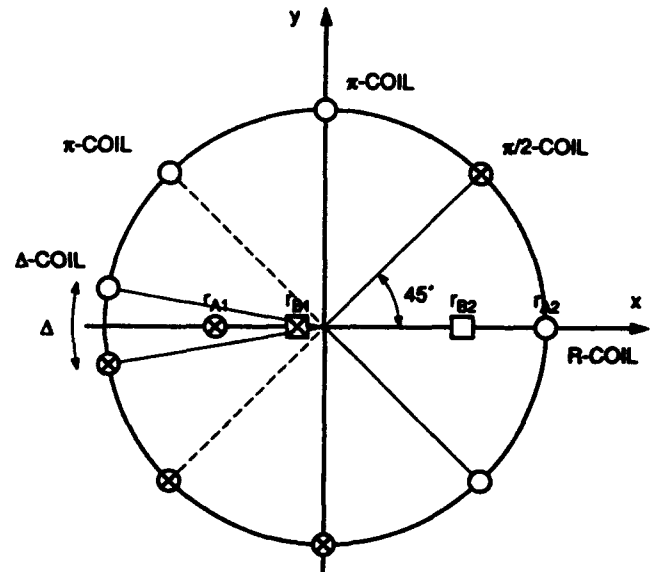


Figure 3. Cross section of the radial and tangential coil geometries.

### IV. ROTATING COIL PROBES

One of the critical components for the multipole measurements is the rotating coil probe. Figure 3 represents the cross section of a rotating coil geometry. The probe in Fig. 3 has two different types of coils: "radial" and "tangential." The radial coil set is located in the plane of the x-axis, while the tangential coil set is installed on the cylinder surface. The radial coil set consists of two separate coils, one for measuring the main field and one for multipole coefficients after bucking the main field.

In Table 2 parameters of the two types of coil sets for quadrupole and sextupole measurements are listed. The ratio of the number of turns and the radii of the coils are denoted as  $N_a/N_b$  and  $r_a/r_b$ , respectively.

The tangential coil set in Fig. 3 consists of a  $\Delta$ -coil,  $\pi$ -coil, and two  $\pi/2$ -coils. The  $\pi$ -coil measures the dipole field component, while the two  $\pi/2$ -coils measure the quadrupole or

Table 2  
Parameters of rotating coils

	quadrupole	sextupole
<b>radial coil</b>		
$N_A/N_B$	1/2	6/21
$r_{A1}/r_{A2}$	0.5	0.5
$r_{B2}/r_{A2}$	0.625	0.6266
$r_{B1}/r_{A2}$	0.125	0.4224
<b>tangential coil</b>		
$N_D/N_A$	1/6	-
$N_Q/N_A$	1/6	1/7
$N_S/N_A$	-	2/7
$\Delta$ -coil	19.471°	15.388°
two $\pi/2$ -coils	measure $B'_z$	measure $B'_z$ , $B''_z$
$\pi$ -coil	measure $B'_z$	measure $B'_z$

sextupole field component, depending on the connection of the two coils. These coils are also used for bucking the main field and measuring lower harmonics.

The advantage of having two types of coil sets on the same cylinder is that the validity of the measurements can be cross-examined at the same condition. For the SR quadrupoles, for example, the measured sextupole coefficients from the two coils agree within  $0.4 \times 10^{-4}$  at a radius of 25 mm.

For the alignment parameters, however, the two coil sets behave somewhat differently. Shown in Fig. 4 is the measured position of the magnetic center for six hours. The laser detector, which is positioned on top of the magnet, monitors the stability of the laser beam. The magnetic center measurements from the two coils agree to within 15  $\mu\text{m}$  and vary less than 10  $\mu\text{m}$  in both the x- and y-axes. The roll angle measurements in Fig. 5 show that the tangential coil measurements are stable to within 0.1 mrad, while those for the radial coil vary  $\pm 0.5$  mrad.

## V. CONCLUSIONS

The magnet measurement facility meets the technical requirements for measurement accuracies. The relative measurement accuracy and reproducibility of the field integrals and field shapes for dipoles are better than  $1 \times 10^{-4}$ . The three rotating coil systems measure the 2-D and 3-D integral values of the main fields and multipole coefficients with relative accuracies of  $\pm 1 \times 10^{-4}$ . The measurement accuracies of the roll angle of the main field and the magnetic center to the fiducial positions are  $\pm 0.3$  mrad and  $\pm 60$   $\mu\text{m}$ , respectively.

## VI. REFERENCES

- [1] "7-GeV Advanced Photon Source Conceptual Design Report," Argonne National Laboratory, ANL-87-15, 1987.
- [2] Y. Chung and K. Kim, "Development and Application of

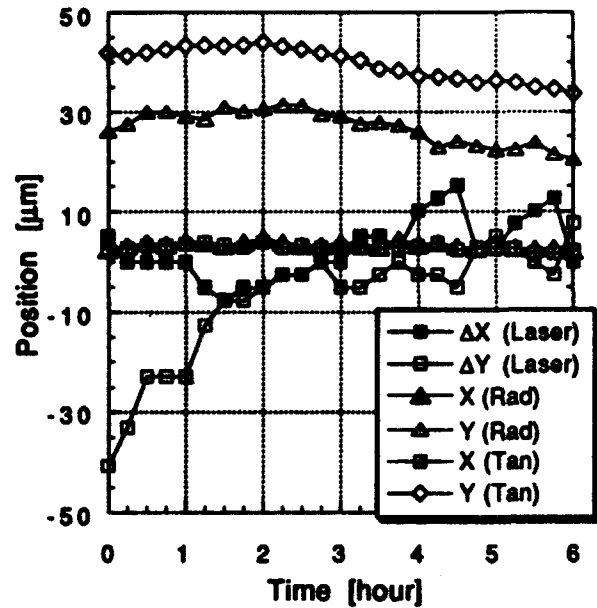


Figure 4. Stability of the laser beam and the magnetic center measurements using radial and tangential coils. The initial data have offsets.

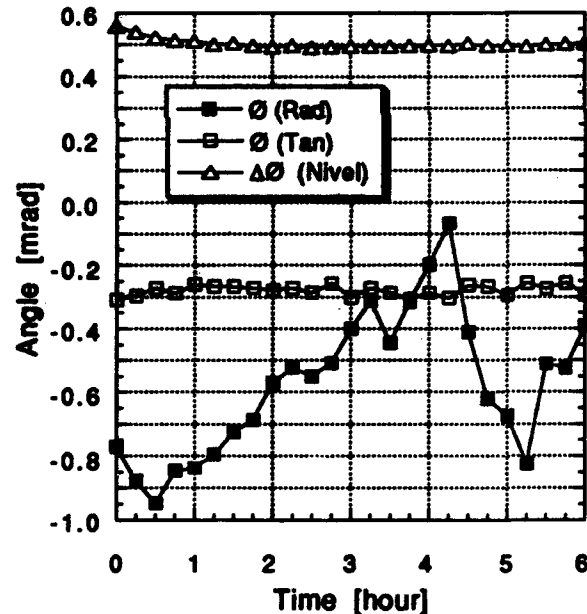


Figure 5. Stability of the magnet roll angle measurements using radial and tangential coils. The electronic tiltometer (Nivel) reading has an initial offset.

General Purpose Data Acquisition Shell (GPDAS) at the Advanced Photon Source," *Conference Record of the 1991 IEEE Particle Accelerator Conference*, Vol. 2, pp. 1299-1301, 1991.

- [3] O. Pagano, P. Rohmig, L. Walkiers and C. Wyss, "A Highly Automated Measuring System for the LEP Magnetic Lenses," 8th Intern'l Conf. on Magnet Technology, *J. de Physique*, Vol. 45, Colloque C1, 949, 1984.

# Magnetic Measurements of the Storage Ring Quadrupole Magnets for the 7-GeV Advanced Photon Source\*

S. H. Kim, K. Kim, C. Doose, R. Hogrefe and R. Merl  
Argonne National Laboratory  
Argonne, IL 60439 USA

## Abstract

The pre-production quadrupole magnet for the Advanced Photon Source (APS) storage ring has been tested. The multipole coefficients meet the tolerance requirements. The field-gradient integrals are measured relative to a reference quadrupole. By using two laser beam units, the magnetic and geometrical axes of the magnet are aligned within 0.2 mrad. The dependencies of the sextupole coefficient and the magnetic center on the excitation current are corrected by shunting the magnetic potentials of the top and bottom yokes.

## I. INTRODUCTION

The APS storage ring (SR) requires 400 normal quadrupole magnets, consisting of five families with three different magnetic lengths [1]. The quadrupoles are conventional resistive magnets; each of them is excited by an independent DC power supply. All the magnets have the same 2-D geometry and bore radius of 40 mm.

In spite of the conventional nature of the quadrupole, the design of the magnet cross section is severely restricted for the accommodation of the vacuum chamber as shown in Fig. 1. The top and bottom halves of the magnet are not connected with flux-return yoke; they are connected mechanically with aluminum spacers between the halves. Each of the top and bottom halves consists of two welded quadrants stacked with 1.5-mm-thick laminations.

In order to maximize the excitation efficiency, the pole bases are asymmetrically widened 22 mm towards the vertical

plane of the magnet as shown in Fig. 1. The magnet has pole-end bevels of 9.6 mm x 17.4 mm and pole chamfers of 16.5 mm [2]. The shims at both edges of the hyperbolic pole face have 6-mm-straight contours perpendicular to each other, and are used as the reference directions for stacking the laminations.

Listed in Table 1 are the design parameters for the five-family quadrupoles, Q1, Q2, Q3, Q4 and Q5, and excitation efficiencies measured for an 0.8-m pre-production magnet at the corresponding operating currents. By asymmetrically widening the poles, the efficiency for the 7-GeV operation is better than 96.5%.

## II. MAGNETIC MEASUREMENTS

### A. Measurement Methods

Field-gradient integrals and multipole coefficients are measured using a rotating coil technique. The probe coil consists of a "radial" integral coil and a 0.4-m-long "tangential" coil on the same cylinder [3]. The latter measures the 2-D "body" multipole coefficients averaged over a 0.4-m axial length of the magnet.

Using a laser beam unit, the rotating coil axis is aligned to the magnetic axis by adjusting the magnet position and minimizing the dipole component of the harmonic analysis. Prior to this procedure, the geometrical axis of the quadrupole is aligned to the axis of two air-bearings as in the following method. A second laser beam unit is installed and aligned with the air-bearing axis. A photo-quadrant detector is placed at the geometrical axis of the magnet aperture. By detecting the beam position along the aperture axis, the magnet is aligned. Since the rotating coil cylinder is supported by the two air-bearings, the coil rotates at the air-bearing axis. This procedure not only ensures parallelism between the geometrical and magnetic axes within  $\pm 0.2$  mrad, but it also enables measurement of the offset of the two axes.

The field-gradient integrals are also measured relative to a reference quadrupole with a measurement reproducibility of  $\pm 1 \times 10^{-4}$ . Figure 2 shows the cross sections of the gradient-coil probes: one on the reference magnet and one on the testing magnet. A probe consists of two flat printed-circuit coils. The probe in the reference magnet is fixed at the geometric or magnetic center supported by a G-10 plate. The probe in the

Table 1  
Parameters for the 400 quadrupole magnets

	Q1	Q2	Q3	Q4	Q5
# mag	80	80	80	80	80
L (m)	0.50	0.80	0.50	0.50	0.60
B' (T/m)	-10.843	15.792	-10.585	-18.902	18.248
B'L (T)	-5.421	12.634	-5.293	-9.451	10.949
I (A)	215	312	210	386	370
e (%)	100	99.5	100	96.5	97.3
I (A) <sup>a</sup>	230	350	225	442	419
e (%) <sup>a</sup>	100	98.3	100	92.5	94.2

<sup>a</sup> for 7.5-GeV Operation

\*Work supported by the U.S. Department of Energy, Office of Basic Energy Sciences, under Contract No. W-31-109-ENG-38.

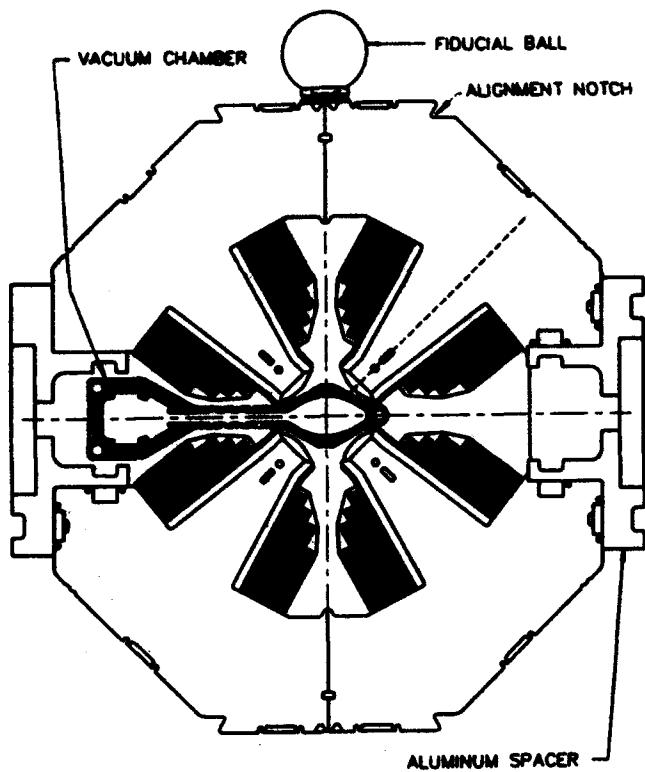


Figure 1. Cross section of the quadrupole and the vacuum chamber. The magnet aperture diameter is 80 mm. A Taylor-Hopson ball and alignment notch for the measurements of magnetic axis and roll angle are shown.

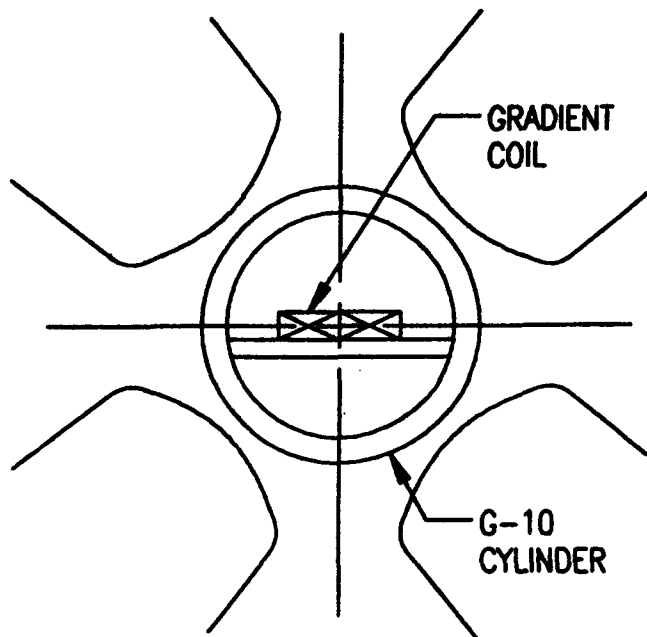


Figure 2. Cross section of the probe for the field-gradient measurements in the testing magnet.

testing magnet is installed in a G-10 cylinder. Since the measurement is conducted after the rotating coil measurements, the probe in the testing magnet is located along the magnetic axis.

### B. Multipole Coefficients

Shown in Fig. 3 are the normal multipole coefficients for the pre-production magnet at four excitation currents. The coefficients, measured at an aperture radius of 35 mm, are calculated at 25 mm. The magnitudes of the coefficients are well within the tolerance of the SR random multipole allowed errors,  $2.5 \times 10^{-4}$ . The measured values of the first two allowable coefficients after the main quadrupole field,  $b_5$  (duodecapole) and  $b_9$ , are  $-0.1 \times 10^{-4}$  and  $-0.45 \times 10^{-4}$ , respectively. The 2-D calculations for the two coefficients agree with the measurements better than  $0.05 \times 10^{-4}$  at a 25-mm radius.

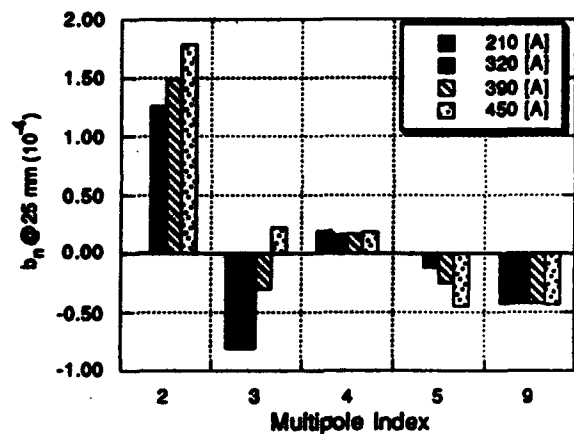


Figure 3. Multipole coefficients at four excitation currents ( $b_2$  = sextupole coefficient).

### C. Ambient Field

Since the top and bottom yokes are not connected magnetically, ambient field (mainly the Earth field) affects the sextupole and dipole coefficients of the magnet. Plotted in Fig. 4 are variations of the sextupole coefficient: with and without shunts of the magnetic scalar potential between the top and bottom yoke, and with three external fields using a Helmholtz coil to compensate for the Earth field. The coefficient  $b_2$  varies  $4 \times 10^{-4}$  between 100 and 450 A without shunts. By shunting with five 1.5-mm-thick and 76-mm-wide straps on both sides of the magnet, the variation of  $b_2$  is corrected to within  $1 \times 10^{-4}$ . Similarly, it was corrected by applying magnetic fields of 0.4 and 0.8 G.

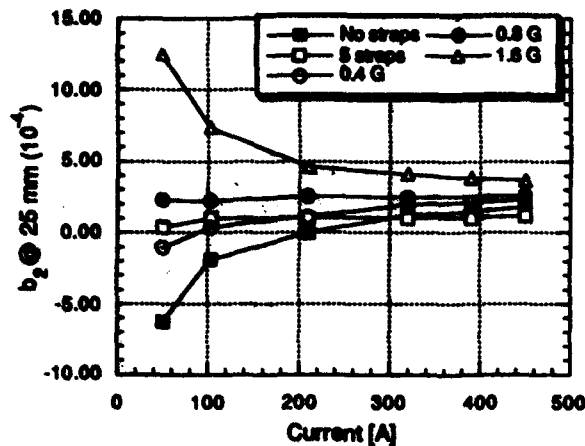


Figure 4. Sextupole coefficients of the quadrupole with no 0.8 and 1.6 G.

Plotted in Fig. 5 are the data for offsets of the magnetic center due to the ambient field. When the yokes are shunted or the ambient field is compensated, the offset in the x-direction does not depend on the magnet excitation currents. As expected, the offset in the y-direction, which is due to a horizontal field, does not depend on the ambient fields.

### III. CONCLUSIONS

The restrictions of the design geometry due to the vacuum chamber have been overcome by widening the pole asymmetrically, and an excitation efficiency better than 96.5% has been achieved. The multipole coefficients are measured at the magnetic axis, which is parallel to the geometrical axis of the magnet within  $\pm 0.2$  mrad. The coefficients are less than  $2.5 \times 10^{-4}$  in magnitude and meet the tolerance requirements. Using two sets of gradient coils, the field-gradient integrals are measured relative to a reference quadrupole to within  $1 \times 10^{-4}$ . The sextupole coefficient and the magnetic axis, which depend on the ambient field, are stabilized by shunting the top and bottom yokes.

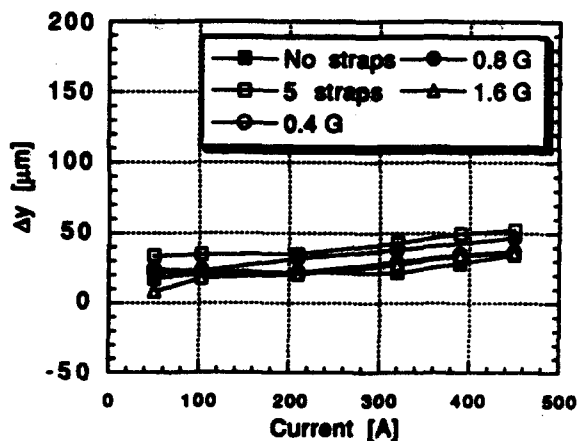
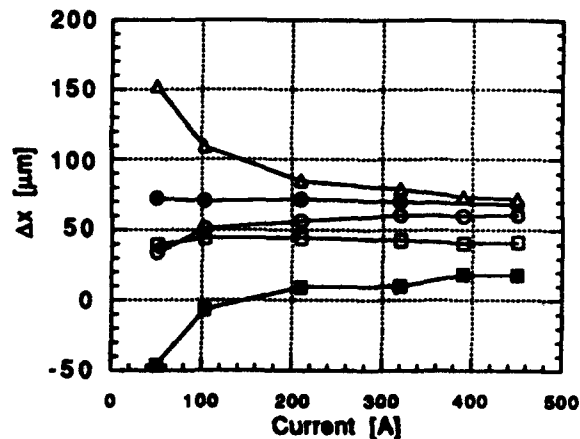


Figure 5. The offsets of the magnetic center in the x- and y-directions due to ambient field.

### IV. REFERENCES

- [1] "7-GeV Advanced Photon Source Conceptual Design Report," Argonne National Laboratory, ANL-87-15, 1987.
- [2] S. H. Kim, K. M. Thompson, E. L. Black and J. M. Jagger, "Fabrication and Tests of Prototype Quadrupole Magnets for the Storage Ring of the Advanced Photon Source," *Conference Record of the 1991 IEEE Particle Accelerator Conference*, Vol. 4, pp. 2375-2377, 1991.
- [3] S. H. Kim, K. Kim, C. Doose, R. Hogrefe and R. Merl, "Magnetic Measurement Facility for the 7-GeV Advance Photon Source," these proceedings.

# Design and Tests of the Injector Synchrotron Magnets for the 7-GeV Advanced Photon Source\*

K. Kim, S. H. Kim, K. M. Thompson, and L. R. Turner  
Argonne National Laboratory  
9700 S. Cass Avenue  
Argonne, Illinois 60439

## Abstract

Design and magnetic measurements of the pre-production dipole, quadrupole and sextupole magnets for the 7-GeV Advanced Photon Source (APS) injector synchrotron (IS) are described.

## I. INTRODUCTION

The APS injector synchrotron requires 68 dipole, 80 quadrupole, and 64 sextupole magnets [1]. The magnets are linearly excited to accommodate the energy of the positron beam between 0.45 GeV and 7 GeV with a ramp time of 0.25 s and an excitation repetition rate of 2 Hz. The main parameters for the three major magnets are listed in Table 1.

Table 1.  
Main parameters for major injector synchrotron magnets.

	Dipole	Quadrupole	Sextupole
No. of magnets	68	80	64
Magnetic length	3.077 m	0.5 m	0.12 m
Pole gap	40 mm	56.56 mm	70 mm
Field strength at Injection	0.045 T (60 A)	0.96 T/m (35 A)	8.8 T/m <sup>2</sup> (4 A)
Extraction	0.701 T (930 A)	16.6 T/m (600 A)	248.0 T/m <sup>2</sup> (116 A)

The 1.5-mm-thick laminations used for the magnets are of low carbon steel with coercive force less than 1.0 Oe. The laminations are coated on both sides with an epoxy.

The magnet cross sections are symmetrical and designed to allow easy installation of the vacuum chamber by lifting the upper half of the magnets. Pre-production magnets have been fabricated and the required magnetic and mechanical tests completed. The pole-end bevels for dipole and quadrupole magnets have been finalized during the pre-production measurements.

\*Work supported by the U.S. Department of Energy, Office of Basic Energy Sciences, under Contract No. W-31-109-ENG-38.

## II. DIPOLE MAGNET

The cross section of the symmetrical dipole is shown in Figure 1. The laminated steel length of the core is 3.0 m. The top and bottom sections of the magnet are clamped together with bolts on both sides. The required tolerances for quadrupole and sextupole coefficients at a radius of 25 mm are  $5 \times 10^{-4}$  and  $1.2 \times 10^{-3}$ , respectively.

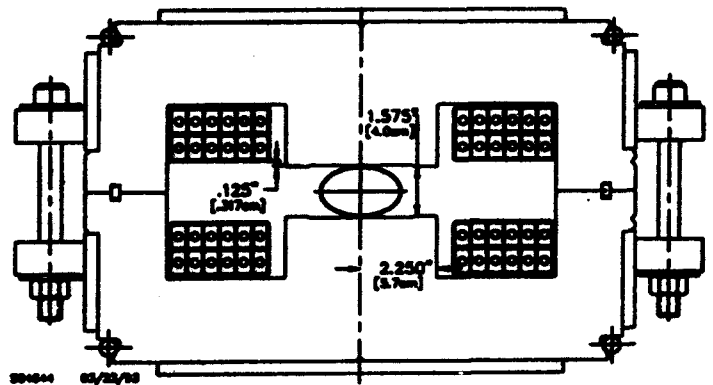


Figure 1. Cross section of the dipole magnet.

The integrated field strength and field variation with transverse displacement are measured using 3.5-m-long curved coils [2]. The integrated and 2-D field shapes at the extraction energy are plotted in Figure 2. The field variations with the transverse displacement of  $\pm 25$  mm at the injection and extraction fields are less than  $2.5 \times 10^{-4}$  and  $1.5 \times 10^{-4}$ , respectively. From the least square fitting of the measured data within  $\pm 30$  mm transverse position, the quadrupole and sextupole coefficients at 25 mm are calculated as  $0.5 \times 10^{-4}$  and  $-0.7 \times 10^{-4}$ , respectively.

The pole-end bevels are designed so that the integrated and 2-D field shapes are not significantly different, as shown in Figure 2. The end field shapes are measured with 0.5-m-long coils extending 0.25 m outside the core end. Figure 3 includes the field shapes for two bevel geometries with the solid line showing the measurement data for the final geometry (bevel #2). The integrated field for the 0.5-m-length found from 3-D computations for bevel #2 is shown in Figure 3 as a dashed line [3]. The calculations agree with the measurements to within 0.1%.

The submitted manuscript has been authored by a contractor of the U. S. Government under contract No. W-31-109-ENG-38. Accordingly, the U. S. Government retains a nonexclusive, royalty-free license to publish or reproduce the published form of this contribution, or allow others to do so, for U. S. Government purposes.

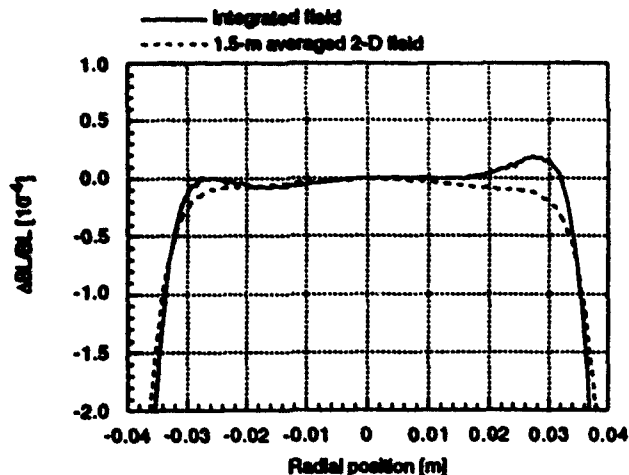


Figure 2. Integrated and 1.5-m averaged 2-D field shape at the extraction energy with respect to the transverse displacement.

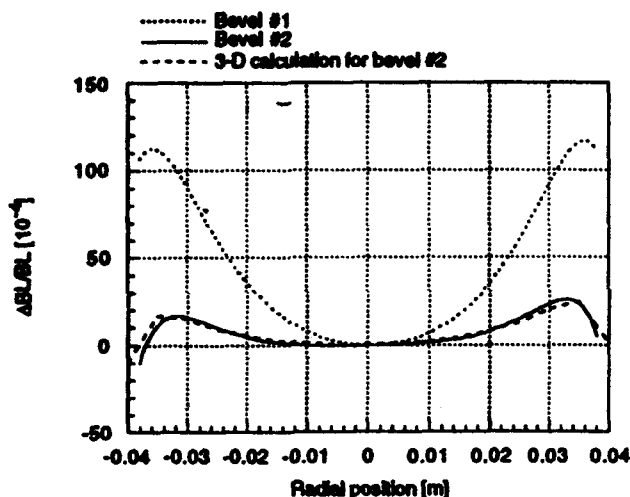


Figure 3. 0.5-m end section field shape at the extraction energy with respect to the transverse displacement.

Table 2.  
Description of the data points in Figure 4.

Measurement Number	Remark	$\frac{\Delta BL}{BL}$
1	initially torqued to 150 ft-lb	$-1.7 \times 10^{-4}$
2	reassembled & torqued to 50 ft-lb	$1.0 \times 10^{-4}$
3	torqued to 100 ft-lb	$0.2 \times 10^{-4}$
4	torqued to 150 ft-lb	$-0.9 \times 10^{-4}$
5	reassembled & torqued to 150 ft-lb	$-0.2 \times 10^{-4}$
6	reassembled & torqued to 150 ft-lb	$0.3 \times 10^{-4}$
7	measurement repeated	$0.3 \times 10^{-4}$
8	reassembled & torqued to 50 ft-lb	$1.7 \times 10^{-4}$
9	torqued to 100 ft-lb	$1.5 \times 10^{-4}$
10	torqued to 150 ft-lb	$0.7 \times 10^{-4}$
11	torqued to 175 ft-lb	$-0.7 \times 10^{-4}$
12	torqued to 200 ft-lb	$-1.7 \times 10^{-4}$

In order to assure the field reproducibility of the dipole before and after installation of the vacuum chamber and associated removal of the upper half of the magnet, the dependence of the field integrals on the clamping force of the bolts in Figure 1 were determined. There are 26 bolts on each side of the magnet. Figure 4 shows the reproducibility of the field integrals for several values of the torques on the bolts. The data indicate that clamping at higher torques distorts the magnet geometry. It was indeed confirmed with gap height measurements that larger torques correspond to increases in gap height and decreases in field integral. Repeatability of the field integral is best achieved within  $0.7 \times 10^{-4}$  at a lower torque of 50 ft-lb.

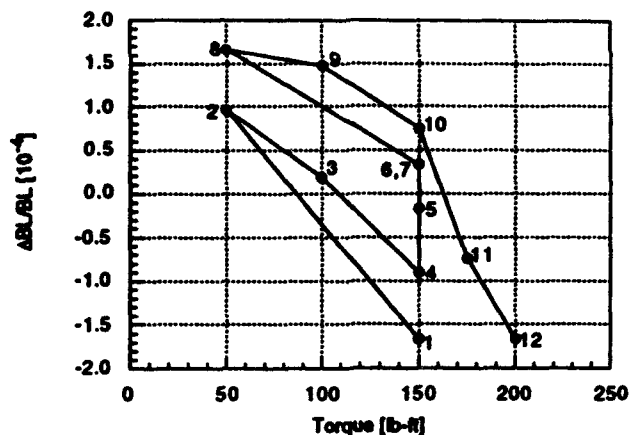


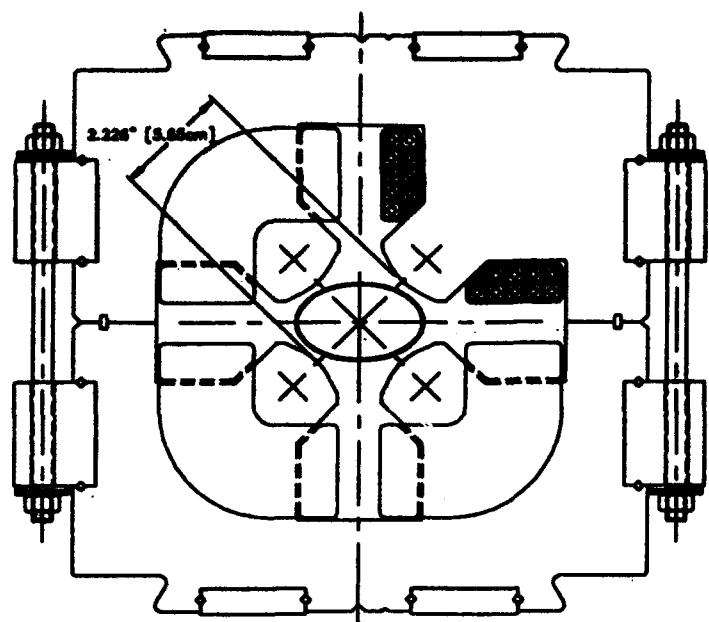
Figure 4. Variation of the dipole field integrals with bolt clamping torques at the extraction energy. (See Table 2 for descriptions of the data points.)

### III. QUADRUPOLE AND SEXTUPOLE MAGNETS

The cross sections of the quadrupole and sextupole magnets are shown in Figure 5 (a) and (b). The quadrupole magnet has pole-end bevels of a 30°-cut on five laminations. The magnetic lengths of the quadrupole and sextupole are 0.5 m and 0.12 m, respectively.

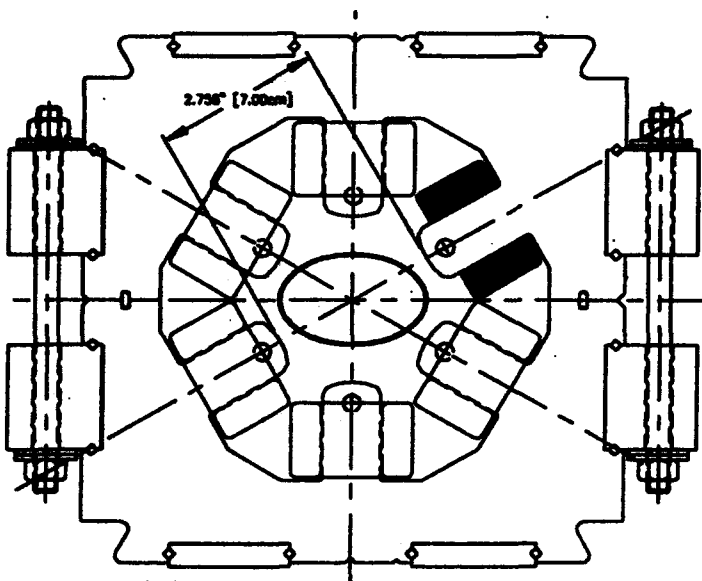
A rotating coil system is used for the magnetic measurements [2]. The measurements are conducted when the rotation coil is aligned to the magnetic axis. The radii of the probe coils for quadrupole and sextupole are both 25 mm.

Relative multipole coefficients of the quadrupole magnet at a radius of 25 mm are shown in Figure 6 at four different excitation currents. The skew and other normal coefficients less than  $1 \times 10^{-4}$  are not included here. There are relatively small variations with current. Since the rotating coil axis is aligned to the magnetic axis, the dipole component, which is not shown in Figure 6, is zero. Since the two poles in each lamination are accurately located, the sextupole component is negligibly small. The bevels increased  $b_5$  (dodecapole) by  $27.0 \times 10^{-4}$  with respect to an unbeveled case, while decreasing  $b_9$  (20-pole) by  $3.1 \times 10^{-4}$ .



304847 03/23/93

(a) quadrupole



304848 03/23/93

(b) sextupole

Figure 5. Cross sections of the magnets

The multipole coefficients of the sextupole are shown in Figure 7. The magnet does not have pole-end bevels, which makes  $b_6$  a relatively large negative value. Since the rotating coil axis is aligned to the magnetic axis, the quadrupole coefficient  $b_1$  vanishes. The measured dipole field of the magnet was less than 0.1 G.

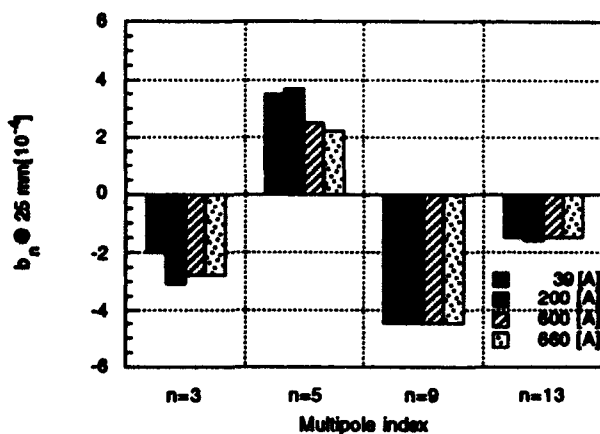


Figure 6. Multipole coefficients of the quadrupole at four different currents. (Index 3 is the octupole coefficient.)

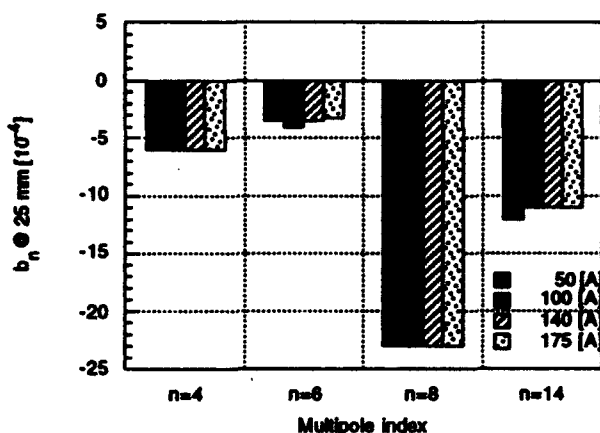


Figure 7. Multipole coefficients of the sextupole at four different currents.

#### IV. CONCLUSION

By choosing correct geometries for the laminations and pole-end bevels, the integrated field shape of the dipole magnet is flat within  $2.5 \times 10^{-4}$  in the required field region. Clamping force between the top and bottom sections of the magnet was optimized to reproduce the field strength to within  $0.7 \times 10^{-4}$ . The geometry of the pole-end bevel for the quadrupole was selected with the multipole measurements. Multipole coefficients of the quadrupole and sextupole magnets satisfy the required field qualities.

#### V. REFERENCES

- [1] "7-GeV Advanced Photon Source Conceptual Design Report," Argonne National Laboratory, ANL-87-15, 1987.
- [2] S. H. Kim, K. Kim, C. Doose, and R. Hogrefe "Magnet Measurement Facility for the 7-GeV Advanced Photon Source," these proceedings.
- [3] L. R. Turner, S. H. Kim, K. Kim, and L. Kettunen, "3-D Field Computations for Accelerator Magnets Using Finite Element and Integral Codes," 1992 *Int. Conf. on Electromagnetic Field Prob. and Appl.*, Oct. 14-16 1992.

# Final Analysis of the ALS Lattice Magnet Data\*

Roderich Keller  
Lawrence Berkeley Laboratory  
University of California, Berkeley, CA 94720

## Abstract

A preliminary analysis of the measured magnet data of the multipole magnets to be installed in the Advanced Light Source (ALS) storage ring had been given in the last conference of this series [1]. That analysis was based on measurements of about one-third of the entire magnet complement, and some of its findings had to be revised after obtaining more data. The present paper gives an account of the integrated fundamental field strengths of all installed storage ring lattice magnets. For the multipole magnets, these values are listed as analytical expressions with four or five parameters, that cover the entire excitation range and include residual strength. Based on this final analysis, all gradient and quadrupole magnets were qualified for installation, whereas the sextupole magnets had to be individually trimmed to bring their effective fundamental strengths into the desired tolerance band.

## I. INTRODUCTION

The measurements of all lattice magnets for the Advanced Light Source (ALS) [2] storage ring have been completed since the last conference of this series [3]. For the production magnets, the main concern lies in the magnet-to-magnet reproducibility of their fundamental excitations, whereas the higher-order multipole errors are largely determined by the given pole shapes, optimized in earlier investigations of engineering models of each basic magnet type [4].

The quadrupole and sextupole magnets were measured using rotating, integrating coils. Their excitation curves are approximated by analytical expressions that include two fitting parameters for the saturation effect and, in the case of quadrupoles, another fitting parameter to compensate for residual excitation. These approximations are more refined than the ones published earlier [1].

All measurements have been taken with rising excitation current, after conditioning every magnet to the maximum power supply current and then reducing the excitation current to zero. For the storage ring gradient magnets elaborate Hall probe scans had to be performed to ascertain sufficient accuracy for the measurements of their quadrupole components. These Hall maps were numerically integrated to derive integrated dipole and quadrupole components, effective lengths, and effective edge angles.

The evaluation procedures and results will be discussed in detail for every magnet type. All nominal magnet parameters given below refer to the standard beam energy of 1.5 GeV.

## II. DEFINITIONS

Integrated strengths of multipole magnets,  $d^{n-1}(BL)/dx^{n-1}$ ,

\*This work was supported by the Director, Office of Energy Research, Office of Basic Energy Sciences, Material Sciences Division, U.S. Department of Energy, under Contract No. DE-AC03-76SF00098.

are listed in the tables below as transfer functions  $T(I)$  of the excitation current  $I$  [A], with  $B$ , local flux density [T];  $L$ , effective length [m];  $x$ , horizontal coordinate [m];  $n=2$  for quadrupoles; and  $n=3$  for sextupoles.

The commonly used  $k$ -values are computed from these values as:

$$k_n = \frac{1}{B_1 \rho L} \frac{d^{n-1}(BL)}{dx^{n-1}} \quad (1)$$

The beam rigidity is always  $B_1 \rho = 5.00536$  [T m].

The tolerance band for the relative errors of integrated magnet strengths was set to  $\pm 1 \times 10^{-3}$  for the  $1\sigma$  width of the actual distribution, with an absolute cut-off limit of  $\pm 2 \times 10^{-3}$  [5].

## III. APPROXIMATION FORMULAE

Magnetic measurements have been carried out on each of the individual lattice magnets after three times cycling the excitation current from zero to the maximum of the power supply and back to zero. Various excitation values were then set by monotonically raising the current from zero to the desired level. This procedure means that in the course of the measurements a transition from the upper to the lower branch of the hysteresis loop has been made, see Figure 1, and this fact is relevant for all quadrupole measurements.

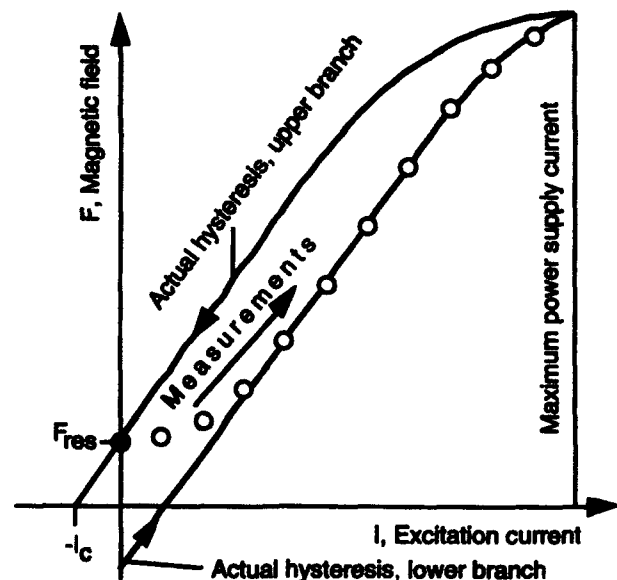


Figure 1. Construction of the lower branch of a hysteresis loop from magnet measurements  $F_{i,meas}$  (open circles) affected by residual fields. Residual field and saturation effects are exaggerated in this illustration.

To reconstruct the lower hysteresis branch for a magnetic quantity  $F$  (e.g. integrated gradient for quadrupoles), the data  $F_{i,meas}$  measured near zero current have to be reduced to ideal data  $F_i$  by subtracting twice the measured residual value  $F_{res}$ . This reduction then must gradually vanish as the measured points approach the actual hysteresis branch. An exponential expression (2) with a fitting parameter  $C$  was developed to provide the reduction, assuming that ten measurements with running number  $i$  have been taken, with beginning saturation effects at the last three values:

$$F_i = F_{i,meas} - 2 F_{res} / \exp \{ I_i / (C I_C) \} \quad [1 \leq i \leq 10] \quad (2)$$

The coercive current  $I_C$  (absolute value) is determined by

$$I_C = F_{res} / T_{raw} \quad (3)$$

with an approximate "raw transfer function" given by:

$$T_{raw} = \langle F_{i,meas} / I_i \rangle \quad [4 \leq i \leq 7] \quad (4)$$

$C$  is recursively optimized such that the reduced value at the first current,  $F_1$ , matches the average reduced transfer function  $T$  of the other values in the linear part of the hysteresis:

$$F_1 / (I_1 - I_C) = T_{lin} \equiv \langle F_i / (I_i - I_C) \rangle \quad [4 \leq i \leq 7] \quad (5)$$

For the three quadrupole families, the individual optimum  $C$  values were separately averaged, and these values were then applied once more to each data set. No residual field measurements had been made with the sextupoles, and therefore the lower excitation values have been given less weight in the evaluation of transfer function coefficients.

To determine a closed expression for the transfer function  $T(I)$  at arbitrary excitation currents  $I$  over the full range of the constructed hysteresis curve, a saturation term is introduced:

$$T(I) = T_{lin} / \{ 1 + ((I - I_C) / I_s)^A \} \quad (6)$$

where  $A$  is a fitting parameter that is kept constant for all magnets of one family ( $A = 3$  for quadrupoles) and the "saturation current"  $I_s$  is individually calculated as:

$$I_s = \langle (I_i - I_C) \times (T_{lin} / T_i - 1)^{-1/A} \rangle \quad [8 \leq i \leq 10] \quad (7)$$

with

$$T_i = F_i / (I_i - I_C) \quad (8)$$

The optimization of  $A$  is performed by minimizing the differences  $R_i$  between all individual  $F_i / (I_i - I_C)$  values and the determined average transfer function  $T(I - I_C)$  from eq. (6):

$$R_i = T(I - I_C) - F_i / (I_i - I_C) \quad [1 \leq i \leq 10] \quad (9)$$

The following expression can then be used to compute actual values of the magnet strength of interest for a given power supply current,  $I$ :

$$F(I) = T_{lin} / \{ 1 + ((I \pm I_C) / I_s)^A \} \times (I \pm I_C) \quad (10)$$

using tabulated values of  $T_{lin}$ ,  $I_C$ ,  $I_s$ , and  $A$ . With Equ. (10) one has to select one of the two branches of the hysteresis curve, depending on operational practice. In the case of ALS,

where magnets are set on the upper hysteresis branch after exciting them with maximum current,  $I + I_C$  is the appropriate choice. For the lower hysteresis branch,  $I - I_C$  is taken.

Figure 2 shows as an example for one quadrupole, the derived fitting curve  $T(I - I_C)$  together with the reduced measured data  $F_i / (I - I_C)$ .

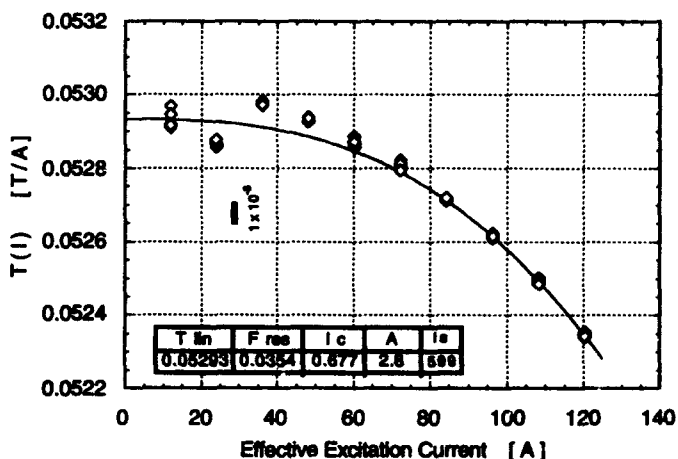


Figure 2. Reduced measured transfer function values and fitting curve for the integrated gradient of quadrupole QF17 as a function of the effective current,  $I - I_C$ .

## IV. RESULTS

### Bend Magnets

The storage ring bend magnet is a straight, parallel-ended combined-function magnet with the following main parameters: bend angle,  $10^\circ$ ; magnetic length, 0.865 m; and effective field edge angles of  $2^\circ$  (wider toward the outer side). From Hall probe scans [1], [3] at 700 A excitation current, the main characteristic data, i.e. integrated dipole field, integrated gradient, core field, and core gradient were evaluated. Core is here defined as the central  $\pm 250$  mm of the magnet. Field integration was performed numerically, with trapezoidal approximation. Statistics for all produced magnets are given in Table 1. One should note that the measured quantities apply to straight paths along the magnet, whereas the beam follows a curved trajectory. Furthermore, after installation on girders the fringe field of the bend magnets is clipped by adjacent magnets, and this effect changes the actual, integrated quantities by a small but significant amount.

Table 1

Storage Ring Bend Magnets Fundamental Parameters

	BL [Tm]	GL [T]	B [T]	G [T/m]
Average	0.9059	-3.420	1.047	-4.039
$\sigma_{rel} [10^{-3}]$	0.58	0.60	0.45	0.57
Max.Rel.Dev. $[10^{-3}]$	1.53	1.91	1.11	1.00

### Quadrupoles

There are three families of quadrupoles with identical cross-sectional shape but different effective lengths: QFA (focus-

ing), 0.445 m; QF (focusing), 0.350 m; and QD (defocusing), 0.200 m. The nominal core gradients,  $G = dB/dx$ , are 15 T/m at 400 A excitation current with 0.621 T pole tip field (QFA) and 13.4 T/m at 89 A with 0.434 T pole tip field (QF, QD). The problems with poor magnet-to-magnet reproducibility, reported earlier [1], were solved by using a better suited rotating integral coil with higher quadrupole sensitivity [3]. Statistics for fundamental strengths and averaged parameters of all produced quadrupoles are given in Tables 2 and 3.

Table 2

Storage Ring Quadrupoles Fundamental Statistics

	Average $T_{lin}$ [T A <sup>-1</sup> ]	$\sigma_{rel}$ [10 <sup>-3</sup> ]	Max. Rel. Deviation [10 <sup>-3</sup> ]
QFA	0.017223	0.49	1.1
QF	0.052922	0.61	1.2
QD	0.028754	0.68	1.3

Table 3

Storage Ring Quadrupoles Average Measured Parameters

	$F_{res}$ [T]	$I_c$ [A]	C	A	$I_s$ [A]
QFA	0.045	2.65	29.51	3.1	2250
QF	0.035	0.661	29.58	2.8	604
QD	0.020	0.711	31.02	4.3	353

### Sextupoles

All sextupoles belonging to the two families, SF (horizontally focusing) and SD (vertically focusing) are built identically. In addition to their main function, they are equipped with trim windings to produce horizontal and vertical steering and a skew quadrupole excitation, but for this report their sextupole functions only are being discussed. The nominal fundamental parameters for 1.5 GeV beam energy are: 0.484 T pole tip field (395 T/m<sup>2</sup>) at 290 A excitation with 0.2 m effective length. After measuring all magnets, the spread of fundamental strengths exceeded the tolerance band by nearly a factor of four. Because the sextupoles are being excited for storage ring operation by two common power supplies it was decided to shunt most of them such as to match the weakest members of each family [6]. Statistics for both cases, without and with shunting, are given in Table 4.

Table 4

Storage Ring Sextupoles Fundamental Statistics

	Average $T_{lin}$ [T m <sup>-1</sup> A <sup>-1</sup> ]	$\sigma_{rel}$ [10 <sup>-3</sup> ]	Max. Rel. Deviation [10 <sup>-3</sup> ]
SF No Shunt	0.5361	3.7	7.1
SF Shunted	0.5323	0.05	0.09
SD No Shunt	0.5362	3.3	5.0
SD Shunted	0.5335	0.18	0.62

Fitting parameters for the transfer functions, separately averaged for the two sextupole families, are given in Table 5. As mentioned above, no actual residual field measurements were made for sextupoles, and the derivation of fitting parameters follows a simpler scheme than outlined in Section III. The effect is insignificant at the operation point of the sextupoles. For the purpose of computing integrated sextupole strengths,  $S = d^2B/dx^2$ , from Tables 4 and 5 for a given current, Equation (11) is to be used:

$$S L = T_{lin} \times I / \{1 + (I / I_s)^A\} + F_{es} \quad (11)$$

Table 5

Storage Ring Sextupoles Average Measured Parameters

	$F_{res}$ [T m <sup>-1</sup> ]	A	$I_s$ [A]
SF	0.221	5	797
SD	0.216	5	796

## V. CONCLUSION

Measured magnetic field data of all ALS storage ring lattice magnets were analysed to judge the variance of their fundamental field strengths. A new algorithm was developed that allows reducing the measured magnet strength values to represent one branch (the lower one) only of the hysteresis curve and further to approximate the saturation part of the hysteresis in one closed expression. All lattice magnets for the ALS storage ring could be qualified for installation without observing a particular placement order; the sextupoles, however, had to be shunted to keep their effective fundamental strengths within the  $\pm 1 \times 10^{-3}$  tolerance band.

## VI. ACKNOWLEDGMENTS

The author would like to thank J. Tanabe for providing the raw data for this analysis work and R. Alvis for her valuable assistance in data processing and preparing graphs of the results. Thanks are also due to A. Jackson and K. Halbach for many discussions and advice in defining the evaluation procedures.

## VII. REFERENCES

- [1] R. Keller, "Magnetic Data Analysis for the ALS Lattice Magnets" Conference Record of the 1991 IEEE Particle Accelerator Conference, Vol. 4, pp. 2113-2115.
- [2] "1-2 GeV Synchrotron Radiation Source, Conceptual Design Report," LBL Pub. 5172 Rev., LBL Berkeley, 1986.
- [3] Measurements performed at LBL Berkeley under the guidance of J. Tanabe, D. Nelson, and M.I. Green.
- [4] J. Tanabe et al., "Fabrication and Test of Prototype Ring Magnets for the ALS," Conf. Record of the 1989 IEEE Particle Accelerator Conference, Vol. 1, pp. 566-568.
- [5] A. Jackson, "Magnetic Field Tolerances in the ALS Storage Ring," ALS LSAP-56, LBL Berkeley, 1989
- [6] J. Tanabe, "Calculation of Shunts," LSME-486A LBL Berkeley (1992).

# Design and Measurement of the Sextupole Magnet for the APS Storage Ring\*

L. R. Turner, K. M. Thompson, S. H. Kim, K. Kim  
Advanced Photon Source, Argonne National Laboratory  
9700 S. Cass Avenue, Argonne, Illinois 60439

## Abstract

A prototype sextupole magnet has been designed, constructed, and measured for the storage ring of the Advanced Photon Source. The design approaches very closely to 120° rotation symmetry, in order to minimize all forbidden multipole components. The core is made of three identical stacks of laminations, each lamination consisting of two poles and the return yoke joining them. The antechamber of the thick aluminum vacuum chamber fits between two neighboring stacks. Computations and measurements of the sextupole strength  $B''$  and multipole field components, both in the central region and integrated in the beam direction, show that the magnet meets the requirements for positron beam dynamics.

## 1. INTRODUCTION

The storage ring of the Advanced Photon Source (APS) produces synchrotron radiation for experiments in material science, biomedical research, and other fields. The ring maintains a 7-GeV positron beam for a lifetime of 10 hours or more. The ring includes 280 sextupole magnets to control the chromaticity of the positron beam. These sextupole magnets operate at a strength of up to 405 T/m<sup>2</sup> and have an effective length of 0.24 m.

The long beam lifetime requires a vacuum of 1 nTorr or better, but synchrotron radiation desorbs gases from the vacuum chamber, leading the vacuum to degrade. For this reason, the vacuum chamber of the APS consists of two chambers; the antechamber entraps the outgassing and high-speed distributed pumping removes it.

This large, two-chambered vacuum chamber makes the design of the magnets for the storage ring more difficult. Earlier designs for the ring sextupole did not exhibit the 1200 symmetry of an ideal sextupole, and both computation and measurement showed the presence of unacceptable dipole and other forbidden multipole components of the field.

## II. DESIGN OF THE SEXTUPOLE

Figure 1 shows a photograph of the ring sextupole magnet, and the cross section is seen in Fig. 2. The design approaches very closely to 1200 rotation symmetry, in order to minimize all forbidden multipole components. Table 1 lists some of the parameters.

\*Work supported by the U.S. Department of Energy, Office of Basic Energy Sciences, under Contract No. W-31-109-ENG-38.

The magnet is excited with six coils made of water-cooled copper conductor insulated with a preapplied polyimide/polyester/glass film and vacuum-impregnated epoxy. The coils extend beyond the ends of the core; no steel need be removed from the core corners under the coils.

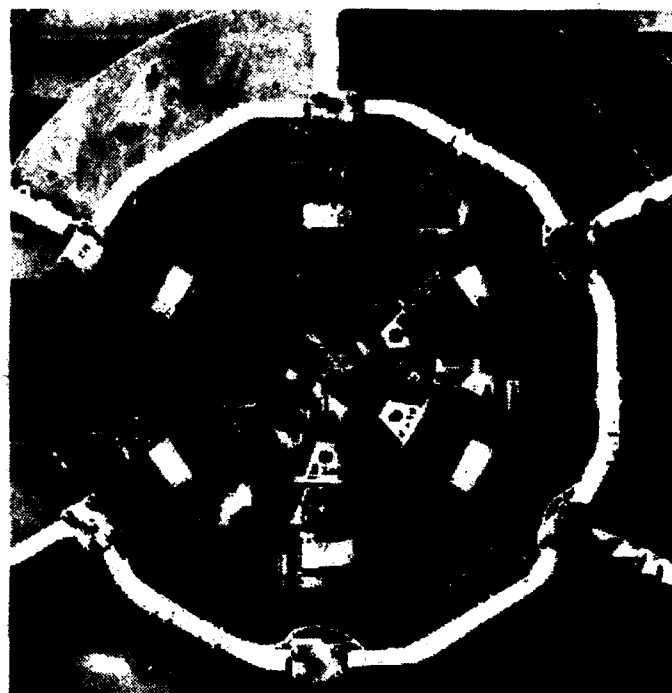


Figure 1. Prototype sextupole magnet for the APS storage ring.

Table 1  
Parameters for the Storage Ring Sextupole  
(7.0 GeV Operation)

Effective Length	0.24 m
Central Field Strength	405 T/m <sup>2</sup>
Bore Diameter	98 mm
Magnetic Core Length	0.21 m
Maximum Current	161 A
Number of Turns per Pole	42
Maximum Power Losses	2.8 kW
Coolant Temperature Rise	8.6 °C

The magnet core is assembled from three identical stacks of laminations, each with two poles and the return path joining them. The antechamber of the thick aluminum vacuum chamber lies in one of the 102-mm air gaps between neighboring stacks. The 1.52-mm-thick laminations are made of low-carbon steel, coated on both sides with a 13- $\mu$ m-thick B-stage epoxy. During curing in a precision fixture, tie bars and tie rods are also epoxy bonded into the core. At each end 12.7-mm-

thick stainless steel plates hold the core sections in position; they are pinned and bolted to the core sections with an assembly fixture.

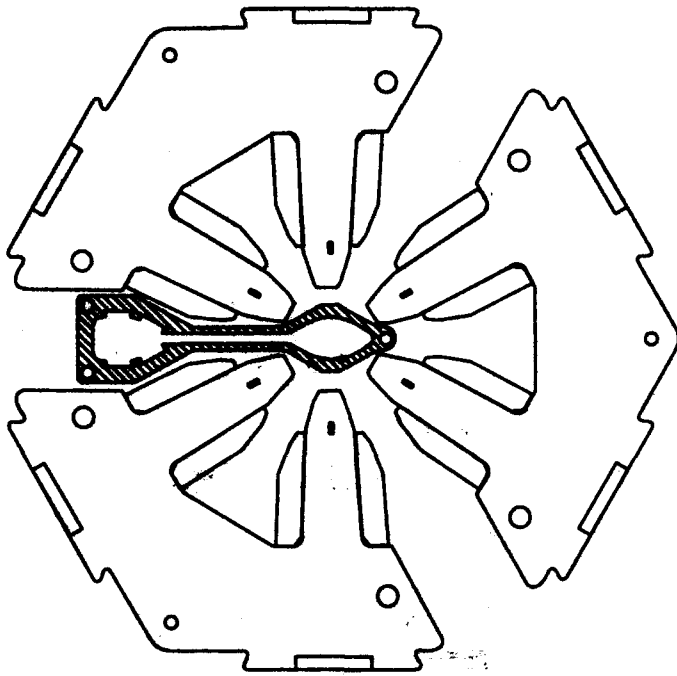


Figure 2. Cross section of the storage ring sextupole magnet with vacuum chamber.

### III. COMPUTATION OF THE SEXTUPOLE

Computations were carried out with the 2-D finite-element code PE2D and the 3-D code TOSCA [1]. As the effective length of the magnet is 0.24 m while the core length is 0.21 m, the flux density is higher in the magnet poles than it would be for a longer magnet with the same ampere-turns. Thus measurement and 3-D computation show the onset of saturation effects where 2-D computation does not.

With this design, in the absence of assembly misalignments there can be no forbidden multipole terms; any that appear in the computation must be artifacts of the mesh and/or of the field evaluation within the mesh. The first allowed multipole beyond the sextupole is the 18-pole. The pole tips were deliberately made narrower than optimum for this magnet to facilitate installing the coils over the poles. A consequence is a negative 18-pole component of about 0.12% at a reference radius of 25 mm. Beam orbit computations show that an 18-pole field of this size has no influence on the dynamic aperture [2]. The multipole field ratios were found by computing the potential over an arc of a circle, and then fitting the potential to a multipole series using the HARM subroutine from the code POISSON [3]. Measured and computed multipoles are compared below in Table 2.

In the bore region, the sextupole field varies quadratically with position. Hence the analysis should be carried out with third-order finite elements, which exhibit quadratic field variation. PE2D, TOSCA, and most other codes support only first- and second-order elements. This limitation can be overcome

in part by using a finer mesh with more elements, but at the cost of more computing time and memory. Even with the finer mesh, computing magnet parameters must be done with care since the computed field varies only linearly within each element.

In the 2-D computations, three kinds of triangular meshes were generated over the bore region and compared: (a) an adaptive mesh automatically generated in the polygonal regions of the bore; (b) a regular annular mesh, defined between radii 5 mm and 42 mm and over 30° of arc, then reflected to fill the 180° or 360° considered; and (c) an equilateral triangular mesh generated over a 60° parallelogram then reflected to form a hexagon. In all three cases, an adaptive mesh was used outside the regions specified. It was predicted [4] that an equilateral mesh gives a potential (at the nodes) correct to sixth order. How the potential varies within a triangular element depends upon the interpolation methods supported by the code. For the 3-D computations, a hexahedral mesh was used, square in the plane perpendicular to the beam direction. This mesh should result in a potential (at the nodes) correct to fourth order [4].

In the bore of a sextupole magnet, the ratio  $B/r^2$  should be constant, where  $B$  is the modulus of flux density and  $r$  is radial distance from the beam centerline. Contour plots of this ratio showed it to vary less for the annular mesh than for the adaptive, and less for the equilateral than for the annular.

### IV. MEASUREMENT OF THE SEXTUPOLES

The sextupole strength and the multipole coefficients (ratio of a specified multipole field to the sextupole field) were measured for the prototype ring sextupole SSS-2. In each case both the integrated (3-D) and body (2-D) fields were measured, using a rotating-coil technique [5]. The probe consisted of an 0.8-m-long radial coil for the 3-D measurements and an 0.08-m-long tangential coil for the 2-D measurements. The radial coil extended well beyond the magnet and the fringe field regions at either end. The tangential coil was located entirely within the magnet, away from the end regions. Measurements were taken at a radius of 35.7 mm, and the multipole coefficients were normalized to a 25-mm radius. Before measurements were made, the magnetic axis of the sextupole was aligned to the axis of the rotating coil.

In Fig. 3, the ratio of integrated sextupole field strength to excitation current is plotted against current. At low currents the ratio is independent of current; the excitation efficiency is said to be 100%. Above 150 A, effects of steel nonlinearity begin to enter, and the excitation efficiency decreases steadily. In Fig. 4 the same ratio is plotted for the body (2-D) sextupole field strength. The 3-D efficiency is seen to be only 0.6% lower than the 2-D efficiency.

Field multipole coefficients were determined from the measurements. Table 2 shows the 18-pole coefficient  $b_8$  is large and negative, it is found to be largely independent of current. The 10-pole component  $b_4$  (both body and integrated) was observed to increase from  $1 \times 10^{-4}$  to  $3 \times 10^{-4}$  as the current increased from 50 to 200 A. All other field multipoles were about  $1 \times 10^{-4}$  or smaller over the total current range.

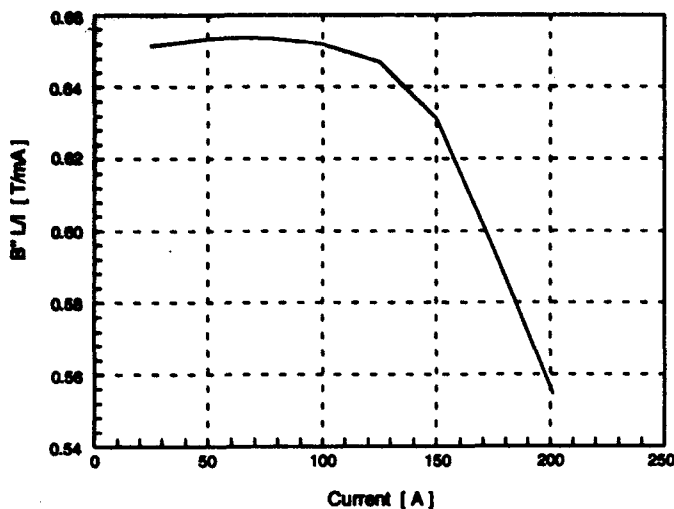


Figure 3. Variation of the ratio of integrated sextupole strength to current ( $B''L/I$ ) with current I.

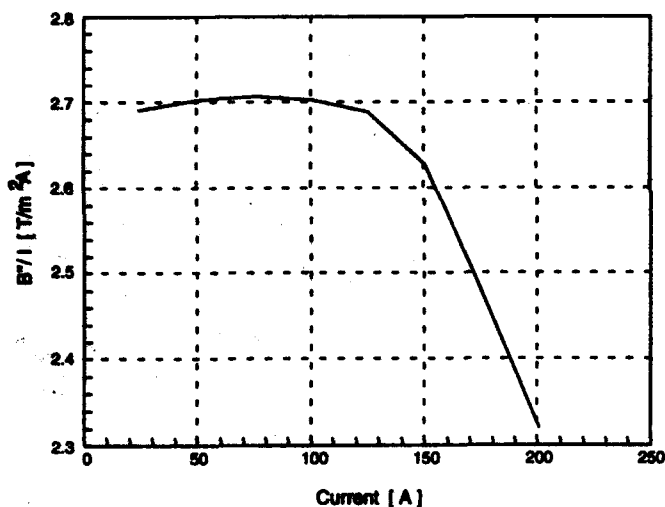


Figure 4. Variation of the ratio of body sextupole strength to current ( $B''/I$ ) with current I.

Table 2  
Ratio of 18-Pole to Sextupole Field at 200 A  
( $\times 10^{-4}$  at the reference radius of 25 mm)

	Computed	Measured
2-D (Body)	-12.2	-11.5
3-D (Integrated)	-13.1	-12.7

## V. CONCLUSIONS

Geometrical and field measurements of the prototype demonstrated that the design and the assembly method will produce magnets that meet the requirements of the positron beam dynamics and production schedule. To reduce the saturation effects demonstrated in the magnetic field measurements, the core length of production magnets will be increased by 6% (12.7 mm). The overall length of the magnets will not be changed.

## VI. REFERENCES

- [1] Codes PE2D (now called OPERA-2D) and TOSCA are available from Vector Fields, Inc., Aurora, IL, USA.
- [2] Eliane Lessner, Argonne National laboratory, personal communication.
- [3] POISSON is available from the Los Alamos Accelerator Code Group, Los Alamos National Laboratory.
- [4] Klaus Halbach, Lawrence Berkeley Laboratory, personal communication.
- [5] S. H. Kim, K. Kim, C. Doose, R. Hogrefe, and R. Merl, "Magnet Measurement Facility for the 7-GeV Advanced Photon Source," these proceedings.

# A Pulsed Septum Magnet for the APS\*

L. R. Turner, D. G. McGhee, F. E. Mills, and S. Reeves  
Advanced Photon Source, Argonne National Laboratory  
9700 South Cass Avenue, Argonne IL 60439, U. S. A.

## Abstract

A pulsed septum magnet has been designed and constructed for beam injection and extraction in the Advanced Photon Source at Argonne National Laboratory. The magnets will be similar for the Positron Accumulator Ring (PAR), the Injector Synchrotron, and the Storage Ring. The septum itself is 2 mm thick and consists of 1-mm-thick copper and S1010 steel explosion-bonded together. The PAR magnet is driven by a 1500-Hz, 12-kA half sine wave current pulse. The core is made of 0.36-mm-thick laminations of silicon steel. The nearly uniform interior field is 0.75 T and the exterior field is 0.0004 T at the undisturbed beam position and 0.0014 T at the bumped beam position. Testing of the magnet awaits the completion of the power supply.

## I. INTRODUCTION

Pulsed septum magnets are used for injection and extraction of the particle beam in circular accelerators. For the Advanced Photon Source (APS), now under construction at Argonne National Laboratory (ANL), these magnets will be used in the 450-MeV Positron Accumulator Ring (PAR), the 450-MeV to 7-GeV Injector Synchrotron, and the 7-GeV Storage Ring. Requirements for the septum magnets include good field homogeneity in the aperture, low stray field, a thin septum, and rapid excitation and discharge. Both transformer-driven and direct driven septum magnets were analyzed. Analysis showed that for a septum consisting of 1-mm-thick copper and S1010 steel strips explosively bonded together, the transformer-driven magnet has lower external fields and more uniform interior fields than the direct driven, if the septum current is constrained to all flow in the gap region.

The design of the septum magnet described here grows out of earlier septum magnets at ANL [1] and Fermilab [2]. Construction of the first magnet is complete, and testing awaits the completion of the power supply. Table 1 shows the parameters of the septum magnet.

## II. COIL AND CORE ASSEMBLY

The core assembly with septum and coil is shown in Figure 1, and the cross section of the septum magnet is shown in Figure 2. The single turn primary coil consists of a continuous length of OFE copper of rectangular cross section, 15.9 mm by 6.35 mm, with a 4.8-mm diameter hole for water cooling. The coil is formed to the final shape in a winding fixture. The lead ends are left long enough to extend beyond the vacuum enclosure, ensuring there are no braze joints within the vacuum system.

\*Work supported by U.S. Department of Energy, Office of Basic Sciences, under Contract No. W-31-109-ENG-38.

Table 1

Septum Magnet Parameters	
Maximum Field	0.75 T
Magnet Length	400 mm
Aperture Width	70 mm
Aperture Height	20 mm
Septum Thickness	
copper	1.0 mm
steel	1.0 mm
Pulsed Current	
drive	5960 A
septum	5954 A
Pulse Shape	half sine wave
Pulse Frequency	1500 Hz



Figure 1. The core assembly with septum and coil, ready for installation in the vacuum enclosure.

Because the coil is inside the vacuum system, polyamide was chosen as insulating material for its good vacuum and dielectric properties. It has good mechanical properties both at operating temperatures and at 260 °C during vacuum bake-out. Insulating sleeve parts are machined from the polyamide and then cleaned by total immersion in an ultrasonic bath. The coil is then enclosed by the sleeve parts, and the laminations are stacked around this assembly in the core stacking fixture to form the core.

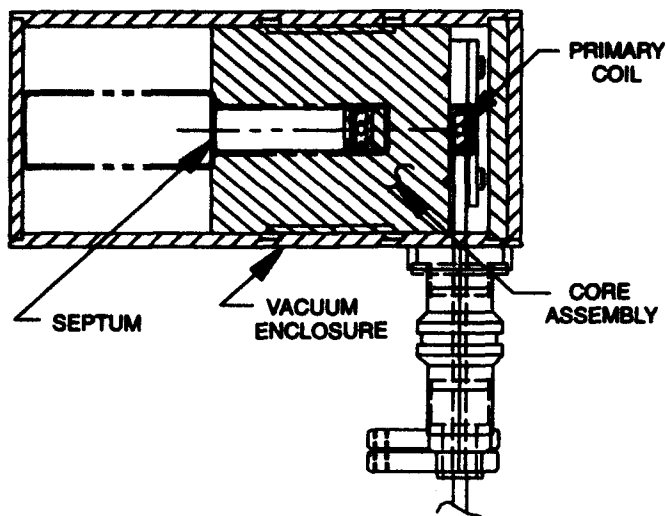


Figure 2. Cross Section of the Septum Magnet.

The core is made of 0.36-mm-thick laminations stamped from AISI type M-22 steel with an AISI C-5 surface insulation coating. The laminations are baked at 750 °C in a vacuum oven at a pressure of  $1 \times 10^{-4}$  Torr, a cleaning process for ultra-high vacuum systems. The laminations are stacked with 13-mm-thick low-carbon-steel end plates in the stacking fixture, which maintains the required surface tolerance. Two 6-mm-thick low-carbon-steel bars are welded to the lamination stack and end plates to constrain the core. The core assembly is structurally robust and can easily withstand the electromagnetic forces it encounters.

### III. SECONDARY TURN AND VACUUM ENCLOSURE

The septum is a crucial part in the design of the magnet. Because it is thin and subject to magnetic, thermal, and machining forces, the proper bonding between copper and steel is essential. Explosion bonding was selected over brazing or roll bonding because it can consistently achieve void-free, very strong mechanical bonds. After 3.2-mm-thick low carbon steel and C102 OFE copper are explosively bonded together, the septum is machined to its final thickness: 1 mm of copper and 1 mm of 1010 steel.

The weld between the septum and the core must carry the combined thermal and magnetic forces. Electron-beam welding was selected for this critical joint because of the dimensional precision that can be attained and because of the depth of penetration of the weld. The resulting welds at the transition between the laminations and the septum steel are very smooth and continuous. Examination of test samples showed that these joints were not contaminated by copper.

The completed core assembly is placed inside the vacuum enclosure, made of plates of the same bonded steel and copper as the septum. The secondary turn is made up of the copper panels that face the inside of the enclosure. The enclosure is welded, then cleaned by total immersion in an ultrasonic bath. The secondary turn is completed by welding the septum to the

copper inner face of the enclosure. After electrical checks are completed, the top of the enclosure is welded in place. Vacuum feedthroughs and flanges complete the assembly.

### IV. ELECTROMAGNETIC DESIGN

The electromagnetic design involved choosing between a directly driven or transformer-driven magnet, choosing the form of the septum, and considering the consequences of current above and below the level of the aperture. The electromagnetic design was carried out with the magnetostatic, steady-state AC, and transient solvers of the 2-D analysis code OPERA-2D (formerly PE2D) [3].

Both directly driven and transformer-driven septum magnets were considered. For the direct drive, the current in the septum of necessity is exactly that which is needed to produce the required field in the gap. For the transformer drive, the driven current determines the field in the gap, and the septum current is somewhat less, just enough to establish a zero current in the exterior region. The transformer-driven case was found to yield an exterior field about a factor of ten lower than the directly driven case, at both the bumped beam position and the undisturbed beam position as seen in Fig. 3.

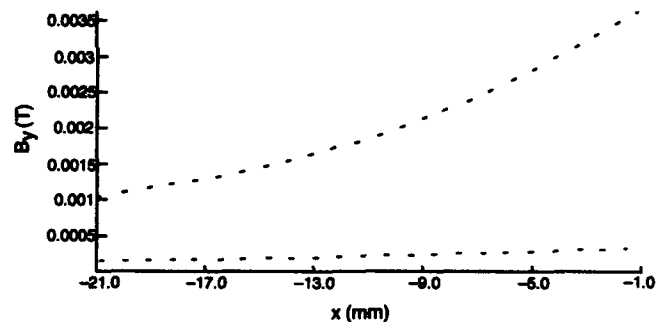


Figure 3. Flux density (T) as function of position (mm) outside the septum. Upper curve: with directly driven septum. Lower curve: with transformer-driven septum.

For the composite septum, the steel part of the septum contains the flux that penetrates the copper part. That effect was found to more than compensate for the fewer skin depths of copper with the composite septum.

It is necessary to locate the septum in slots in the yoke, in order to restrain it against magnetic forces. Consequently, there is some current flow above and below the 20-mm-thick region of the aperture and septum. Some earlier experiences [2] suggested that those currents could lower the homogeneity of the field in the aperture and increase the field leakage outside. But analysis of geometries with and without such currents showed effectively no differences. Uniformity of the field in the aperture is shown in Figure 4.



Figure 4. Flux density within the aperture. Contour spacing: 0.0002 T. Contours above 0.742 T and below 0.7406 T are not shown.

## V. SEPTUM POWER SUPPLY

The four single-turn transformer septum magnets for the PAR, the Injector Synchrotron, and the Storage Ring are powered by capacitor discharge circuits. These are designed to produce half-sine-wave pulses with a base width of 1/3 ms and peak currents repeatable within 0.05% and adjustable from 470 A to 4.7 kA. The capacitor discharge circuits are transformer coupled for impedance matching to the magnet. The peak currents of the transformer secondaries range from 11.4 kA to 16.888 kA. Figure 5 shows a diagram of the power supply. The switch S4 may either be gated or not, depending on the need to reset the magnet steel.

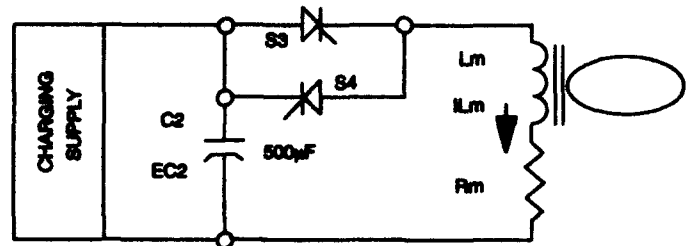


Figure 5. Diagram of the Septum Magnet Power Supply.

## VI. CONCLUSIONS

This design is found to satisfy the conditions required of a septum magnet, both mechanically and electromagnetically. Voltage and inductance testing has begun, and field properties will be measured when the power supply is available.

## VII. REFERENCES

- [1] M. Foss, K. Thompson, and W. Praeg, "A Transformer Septum Magnet," *IEEE Trans. Nucl. Sci.* NS-26, pp. 4024-4026 (1979).
- [2] J. A. Satti and S. D. Holmes, "A Pulsed Septum Magnet for the Fermilab Antiproton Source," *IEEE Trans. Nucl. Sci.* NS-32, pp. 3628-3630 (1985).
- [3] OPERA-2D (PE2D) is available from Vector Fields, Inc. Aurora, IL, USA.

# The ELETTRA Storage Ring Magnets

G. Petrucci, D. Tommasini

Sincrotrone Trieste, Padriciano 99, 34012 Trieste, Italy

## Abstract

24 dipole magnets, 108 quadrupoles, 72 sextupoles and 82 steerers are needed in the storage ring. The very stringent requirements for the magnets field quality were met with the use of a combination of 2D and 3D magnetic design.

The dipoles are combined function elements with a field index  $n=13$  and a maximum magnetic field of 1.5 T at the central orbit. The curved ( $R=5.5$  m) pole profiles were obtained by machining the stacked laminations.

The quadrupoles and sextupoles are made by assembled pole pairs in a C shaped structure with the aperture on the outer side of the ring. To insert the vacuum chamber inside the magnets this structure allows a symmetric opening of the yoke.

The steerer magnets provide both horizontal and vertical magnetic fields; an inverted U shape with a 3D optimization of the vertical field coils sizes and positions was studied to provide space for the connection of vacuum pumps.

## I. INTRODUCTION

### A. General

Elettra has been designed to provide high brightness photon beams over a wide range of energies (10 eV-30 keV) from insertion devices in a low emittance 1.5-2.0 GeV electron storage ring. The machine is now being completed on the Carso plateau near Trieste. The commissioning is foreseen within 1993. The periodicity of the ring is 12, with dispersion free straight sections 6 m long to accommodate insertion devices. The magnets are all room temperature, DC magnets. For the steerer magnets a feedback controlled correction for frequencies up to 50 Hz can be superposed on the DC field controlled by a feedback system. The design of the magnets allows the insertion of the vacuum chamber horizontally from the outside of the ring. The yokes of all the magnets, including the steerers, have been made of low carbon steel laminations, adequately treated in order to keep the coercive force below 0.9 Oe. The dipoles, quadrupoles and sextupoles have been mounted with adjustable feet on a 20 mm thick iron plate, which was fixed to a concrete block well attached to the Carso rock in order to shield the magnets against external vibrations. The steerer magnets have been mounted on aluminum supports on which also the corresponding vacuum pumps are located.

### B. Design method and tests

All the Storage Ring magnets have been designed by using both 2D (POISSON) and 3D (the Cern licensed TOSCA by Vector fields Ltd) packages. The results of the computer

simulations have been compared to experimental measurements which have been made on prototypes [1]. To test the prototypes and to check that the units delivered by the contractors actually complied with the field requirements, two microprocessor controlled measuring systems have been designed and built [2].

## II. DIPOLES

The 24 bending magnets (Figure 1) are C shaped, with a radius of curvature of 5.5 m and parallel end faces. The relevant main parameters are listed in Table 1.

TABLE 1. Dipole magnets main parameters

Number of units	24
Field @ 2.0 GeV	1.212 T
Field index	13
Nominal radius of curvature	5.5 m
Yoke length	1.37 m
Magnetic length	1.44 m
Overall length	1.57 m
Central gap	70 mm
Number of turns	48
Conductor dimensions	23x15- $\phi$ 5.5 mm
Maximum current (@1.49 T)	1950 A
Maximum excitation power	35 kW
Total weight	6 Tons

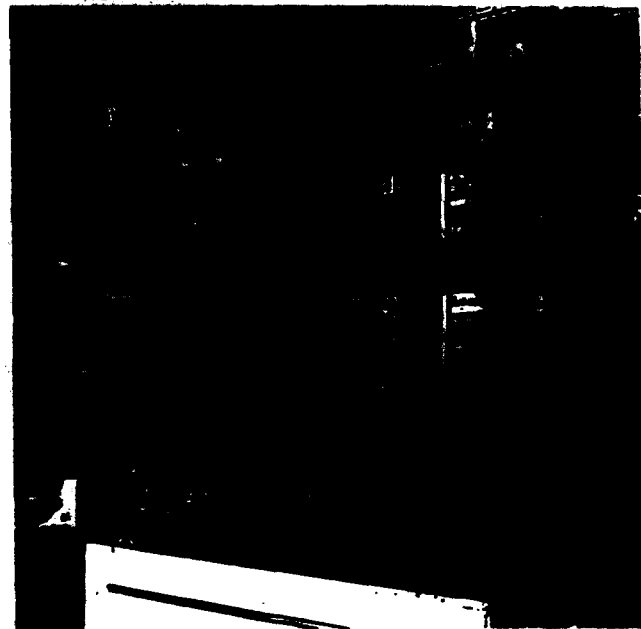


Figure 1. The Storage Ring Dipole on its support.

The yoke is composed of a stack of 1.5 mm thick low carbon steel laminations ending with two 40 mm thick plates. The laminations are kept together by means of 11 longitudinal curved plates welded on its outside surfaces. The insulation between the laminations has been provided by plain blue-steaming.

Being supplied in series, all the dipoles must be as similar as possible to each other. This imposed tight tolerances on the magnetic length ( $\pm 0.2$  mm) and the filling factor (97%). Furthermore, each magnet has been constructed using laminations coming from all the melts, equally mixed. The magnetic properties and the content of impurities of the laminations has been monitored during the manufacture, the melts exceeding a value of coercivity higher than 1.9 Oe for the plates and 0.9 Oe for the sheets have been discarded.

The required tolerance of the pole profile was very high ( $\pm 20$   $\mu$ m). To meet this requirement the manufacturer suggested to machine the profiles of the assembled yokes on a vertical numerically controlled lathe. Unfortunately the result of the machining was not as homogeneous as expected, and two groups of magnets were obtained, ten magnets with a very satisfactory integrated gradient uniformity, and the other magnets with an unacceptable spread (Figure 2). After several attempts the problem was finally solved by adding shims close to the pole ends (gradient and sextupole correction) and by radially displacing the magnets on the ring as needed for field correction [3].

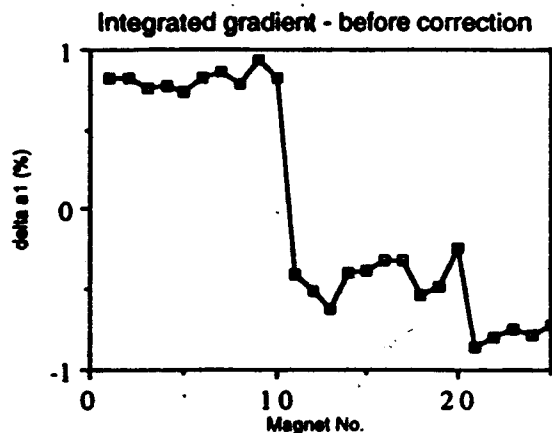


Figure 2. Dipole magnets integrated gradient along the central trajectory before adding the pole-face shims.

Each coil is made by three double pankakes following the curvature of the pole with 24 turns per pole. The coils are insulated with glass tape and radiation resistant epoxy resin. The electrical and hydraulical connections between the pankakes and toward the power leads and the water distribution are made in the center of the coils in order to achieve a good longitudinal symmetry of the magnet.

For alignment two sockets for Taylor Hobson spheres have been fixed on the magnets with a 3D machine with a precision of  $\pm 0.02$  mm with respect to the magnet reference marks which have been used for the magnetic measurements and for the pole profile machining.

All the dipoles are presently installed and aligned in the Storage Ring.

### III. QUADRUPOLES AND SEXTUPOLES

The quadrupoles (Figure 3) and sextupoles (Figure 4) are C shaped magnets with the aperture toward the outer side of the ring, made with the same steel as that of the dipoles. The iron poles are assembled from precision-punched laminations, stacked between two thick end plates and held together by bolts and longitudinal welds on the outside of the stack. The poles are then assembled in independent pairs in order to allow the symmetrical opening of the yoke for the insertion of the vacuum chamber by a horizontal displacement. The opening of the quadrupoles is obtained by a hinge-like rotation, that of the sextupoles by a vertical displacement of the two outer pole pairs. To meet the field quality requirements tight geometrical tolerances have been imposed particularly on the pole surface profile and on the azimuthal position between the pole pairs ( $\pm 70$   $\mu$ m along the whole length).

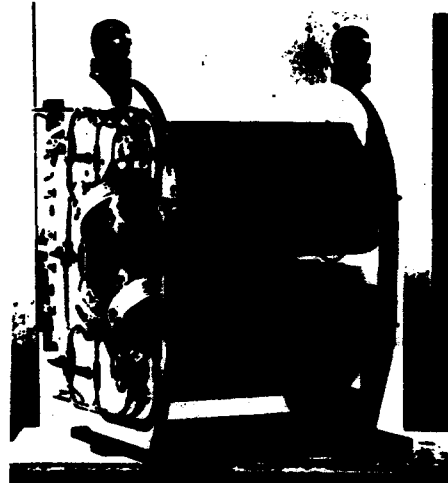


Figure 3. Storage Ring Quadrupole

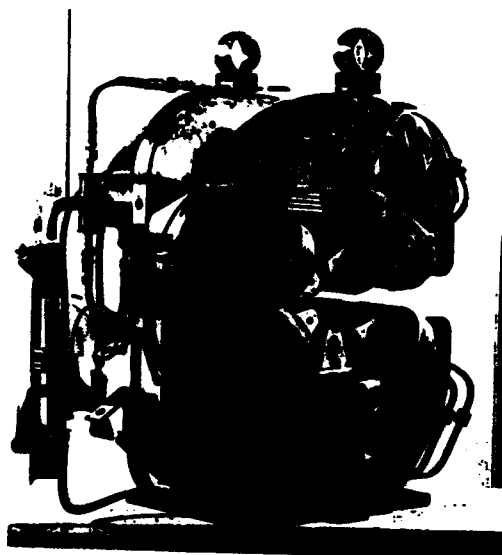


Figure 4. Storage Ring Sextupole

The quadrupoles (Table 2) have been made in three different lengths, the sextupoles (Table 3) in two. The results of the magnetic measurements made on the series production showed acceptable random and systematic harmonic errors (Figure 5 and Figure 6). The dodecapolar field component of the quadrupoles, due to end effects, was reduced by an appropriate chamfer on the end plates.

TABLE 2. Storage Ring Quadrupoles main parameters

	Short	Medium	Long
N. of units	60	24	24
Inscribed diameter	75 mm	75 mm	75 mm
Maximum gradient	19.6 T/m	19.6 T/m	19.6 T/m
Maximum current	300 A	300 A	300 A
Length of iron	230 mm	380 mm	470 mm
Total length	400 m	550 mm	640 mm
Total weight	425 kg	580 kg	700 kg

TABLE 3. Storage Ring Sextupole main parameters

	Short	Long
N. of units	24	48
Inscribed diameter	90 mm	90 mm
Maximum strength	280 T/m <sup>2</sup>	280 T/m <sup>2</sup>
Maximum current	300 A	300 A
Length of iron	125 mm	240 mm
Total length	310 mm	425 mm
Total weight	280 kg	450 kg

118 Quadrupoles, I=200 A, 67% of bore radius

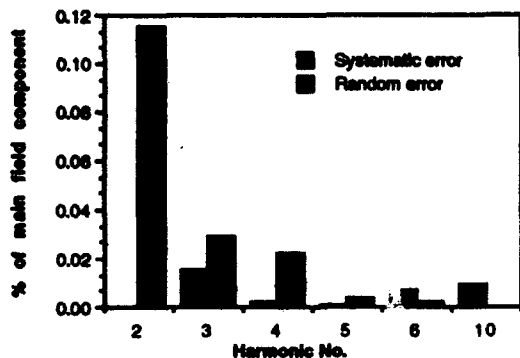


Figure 5. Harmonic measurements on the quadrupoles.  
74 Sextupoles, I=200 A, 50% of bore radius

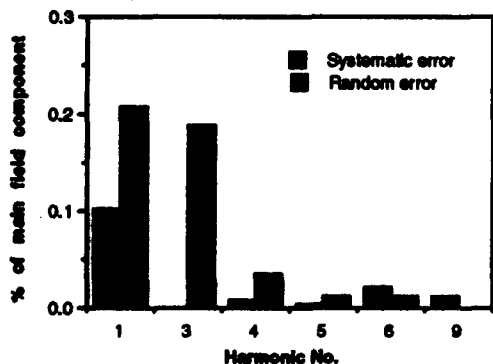


Figure 6. Harmonic measurements on the sextupoles

## IV. STEERERS

The Steerer magnets (Figure 7) provide both horizontal and vertical magnetic fields. The limited longitudinal space available and the need of a complete aperture on the bottom of the magnets in order to allow the connection for the vacuum pump required a detailed 3D design leading to an inverted U shape with an optimisation of the current density distribution in the vertical field coils. An external ferromagnetic screen has been added to shield the lateral fringing field.

TABLE 4. Storage Ring Steerer magnets main parameters.

Number of units	82
Length of iron	150 mm
Total length	220 mm
Horizontal free aperture	110 mm
Maximum magnetic field	500 Gauss (both H and V)
Maximum integrated field	15000 Gauss-cm
Maximum current	16 A
Total weight	60 kg

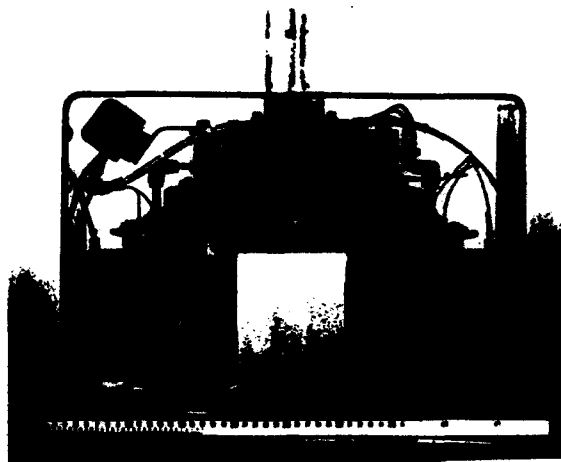


Figure 7. The storage ring steerer magnet.

## V. CONCLUSIONS

All the storage ring magnets have been delivered and have been individually measured [3,4]. The installation and alignment of the magnets are nearly completed, the commissioning of the Storage Ring will start in September 1993.

## VI. REFERENCES

- [1] G.Petrucci et al., "Magnetic measurements of the ELETTRA Storage Ring Prototype Magnets", Proc. of the 3rd EPAC, Berlin, March 24-28, 1992.
- [2] G.Petrucci et al., "The calculation and Measurements of the ELETTRA Magnets", Proc. of the 2nd EPAC, 1990.
- [3] R.P.Walker and D.Zangrando, these Proceedings.
- [4] D.Zangrando and R.P.Walker, these Proceedings.

# Experience with the Source Evaluation Board Method of Procuring Technical Components for the Fermilab Main Injector

D.J. Harding, J.P. Collins, G.R. Kobliska, N.S. Chester, E.G. Pewitt, W.B. Fowler,  
Fermi National Accelerator Laboratory\*,  
P.O. Box 500, Batavia, IL 60510

## Abstract

Fermilab has adopted the Source Evaluation Board (SEB) method for procuring certain major technical components of the Fermilab Main Injector. The SEB procedure is designed to ensure the efficient and effective expenditure of Government funds at the same time that it optimises the opportunity for attainment of project objectives. A qualitative trade-off is allowed between price and technical factors. The process involves a large amount of work and is only justified for a very limited number of procurements. Fermilab has gained experience with the SEB process in awarding subcontracts for major subassemblies of the Fermilab Main Injector dipoles.

## I. INTRODUCTION

Government-funded laboratories have become accustomed to make purchases by the process of awarding subcontracts to the lowest-priced responsive and responsible offeror. Sometimes this involves pre-assigning relative values to various technical elements in order to determine the best price/performance ratio. While this is usually appropriate, in some cases it would be more advantageous to be able to consider the trade-off between price and technical merit. Private industry has this flexibility. In government this can be implemented using a Source Evaluation Board (SEB).

In May 1992 representatives of the Fermilab Main Injector Project (FMI) met with a Department of Energy (DOE) Business Strategy Group (BSG) to discuss the procurement of dipole magnets for the FMI ring. At that time we were advised to consider using the SEB method for selecting the vendors for certain major subassemblies of the dipoles.

\*Operated by Universities Research Association under contract with the United States Department of Energy

## II. PROCEDURE

Since Fermilab had never used an SEB, a procedure had to be developed. The Procurement Department of the Fermilab Business Services Section wrote a procedure which has been reviewed and adopted by the Laboratory. The procedure is based on the DOE SEB Handbook, adapted to Fermilab's requirements. We describe here this procedure, which we have followed over the last year in selecting vendors to be awarded subcontracts for fabrication of major subassemblies of the dipoles. Your organisation's SEB procedure may vary.

### A. Participants

The key participants in the SEB procedure are the Source Selection Official (SSO) and the SEB members. At Fermilab the SSO is usually the Head, Business Services Section (BSS). The SSO appoints the SEB. He reviews the statement of work and qualifications and the evaluation criteria. And, lastly, he makes the final decision (subject to review by DOE) regarding selection of a source.

The SEB at Fermilab consists of three to seven members, preferably an odd number to avoid tie votes. There must be at least one member from the Procurement Department and at least one from the project organisation. Each member is required to sign confidentiality and conflict of interest statements.

### B. Determination

The SEB procedure is only used for "certain major procurements". These procurements are those that have sufficient financial and/or project risk to require the efforts of the SEB. The decision to utilize the SEB depends on the complexity or nature of the procurement, type of subcontract, extent of competition, specialised terms and conditions, and other factors pertinent to the overall risk. The decision is made by the Head, BSS. Most procurements sufficiently major to require an SEB will have required an Advanced Procurement Plan (APP) which discusses, among other things, the decision to use an SEB.

### C. Preparation

The first thing that is required is a full, detailed specification and/or statement of work. The SEB is responsible for reviewing the specification to ensure that it is appropriate. This will become the basis for the Request for Proposal (RFP) that is the vehicle for the solicitation.

The next requirement is a set of qualification criteria. These are minimum requirements for consideration of an offeror's proposal. These qualification criteria must be clearly defined, unambiguous, measurable, and justifiable. All mandatory requirements are listed here. Any proposal which fails to meet any required criterion is not evaluated further. Required criteria are listed as such in the RFP.

The key difference between a usual procurement and the SEB process is that in the latter the award is not necessarily made to the lowest priced responsive and responsible offeror. The SEB process provides for more detailed analysis of evaluation criteria which are used to determine an offeror's understanding of the specification, potential for successful completion of the job, and comparative competitive status. The SEB develops a plan for scoring and ranking the proposals based on the evaluation criteria. The evaluation criteria and their relative importance are included in the RFP. Details of the relative weights are not given.

Evaluation criteria require much thought. To be useful they must be factors that can be objectively evaluated. They must be relevant to the probability of success in performing the subcontract. They must not be absolute requirements; those belong in the qualification criteria. They should provide the SEB members the ability to differentiate the offerors. If all of the acceptable offerors are going to get a high score on a criterion, then it should not be an evaluation criterion but rather a qualification criterion. A typical "good" criterion is the amount of experience the offeror has in doing jobs comparable to the one at hand.

In the SEB evaluation of proposals, cost is not assigned a numerical weight and the technical evaluation is not preassigned a financial value. Whether the cost or the technical factors is more important must be determined initially and stated in the RFP. Neither can be completely ignored, but either one can be more important. The SEB should also state in the RFP how the cost information is to be presented, e.g. on Form SF1411. This is essential to allow comparisons of the proposals on equal footing.

In a procurement that is sufficiently complicated to warrant an SEB, it may be useful to conduct a pre-proposal conference. At that conference there can be a free discussion of the requirements after the potential offerors have had a chance to study the RFP. There certainly can be no private communication with a single potential offeror after the RFP has been distributed.

### D. Evaluation

When the proposals are received, the Procurement representative surveys the proposals to ensure that there

is no cost information in the technical and business/management section. This material is then evaluated independently of the evaluation of the cost material. Any proposal that does not meet the qualification criteria is eliminated from further consideration.

The SEB then ranks the proposals based on the merit of the technical and business/management proposals. Generally this is accomplished by the Board agreeing on a numerical score for the technical evaluation factors. The relative weights of the factors will have been already determined. The cost proposals may then be examined for additional technical information and the scores adjusted, if necessary. The SEB then compares the cost of each proposal to the relative strength of the proposal.

Based on the initial evaluation two courses of action are possible. If there is a clearly superior firm with a low price, then the SEB can recommend that that the proposal be accepted based on the initial offer. This recommendation can be subject to confirmation of the qualifications of the offeror through a visit to the plant to validate the technical proposal. Otherwise, the SEB determines a "competitive range", a list of the initial offerors who have a reasonable chance of improving their proposals to the point of winning the subcontract.

The SEB then enters into "discussions" with the firms in the competitive range. The purposes of the discussions are twofold. First, the Board can elicit additional information from the offerors. It can visit the firms to confirm the information presented and observe the general practices of the firms. A discussion of the proposal can reveal how well the offeror understands the processes proposed and how well they are prepared to deal with them.

Second, the Board must tell each offeror about the deficiencies in its proposal that should be improved. The Board must be very careful in these discussions not to disseminate information from one offeror's proposal to another offeror. The comments must point to the weaknesses but not suggest specific remedies. For example, the Board would say that it believes that a shipping container is not strong enough for the item, not that the offeror should add gussets in the bottom corners. This would be especially critical if another offeror had proposed a shipping container with gussets. Any mandatory submissions or qualifying criteria that the offeror may have missed on the initial submission must be called to their attention during discussions.

Upon completion of discussions, all outstanding questions and concerns about any of the proposals should have been answered. The offerors in the competitive range are then invited to submit Best and Final Offers (BAFO's).

When the BAFO's have been received the SEB evaluates them, following essentially the same procedure as with the original proposals. In some cases there will only be a limited amount of supplementary information. Other offerors will submit new, complete proposals incorporating any changes or additional information.

The SEB must then make a recommendation to the SSO.

This recommendation takes into account their evaluation of the quality of the proposals and the associated costs, considering the agreed upon relative emphasis on the two. The basic criterion is to select the proposal that is in the best interest of the Laboratory, not necessarily the lowest proposed price. The recommendation is written up in a detailed report.

#### *E. Disposition*

The SSO reviews the report from the SEB. He can then take any one of four actions. He may select the recommend source. He may direct the SEB to continue negotiations with all of the firms in the competitive range through BAFO's. He may request further information from the SEB. Or he may make an independent decision to award to an offeror other than the one recommended by the SEB. Whatever the decision, the SSO issues a selection statement. As with any subcontract of this size, DOE approval must be obtained. Finally the Procurement member of the SEB begins the final negotiations with the selected offeror.

### III. EXPERIENCE

After over a year of preparation and work we have awarded six subcontracts for fabrication of three portions of the R&D dipoles for the FMI. We have awarded a subcontract for twelve coils sets for our 12 R&D dipoles, with options for fabrication of bare copper coils for the dipoles. We have awarded subcontracts to three firms for insulating the coils, each firm fabricating three coils sets and Fermilab doing three. We have awarded subcontracts to two firms to stack half-cores from Fermilab supplied laminations.

#### *A. Fermilab Assessment*

Overall we are quite happy with the results of the process. In some cases the firms that were judged most qualified were the lowest price offerors and some cases they were not. In each case the SEB is confident that the best interests of the Laboratory have been served by the selection that was made.

The process has taken much longer than was anticipated. The extra time has come from several sources. In part we were inefficient in executing the process because it was so unfamiliar to us. In part we could not perform as effectively as we might otherwise have because we each had so many other responsibilities at the same time. We suffered from trying to execute three procurements simultaneously. And finally, the process was inherently much more time-consuming than any of us had imagined.

As we gained familiarity with the process the evaluations progressed more smoothly. We have learned about selecting good evaluation criteria. We became comfortable with the level of documentation required to support the recommendations.

Bringing in more people, especially procurement professionals, might seem like the efficient solution to the manpower problem. We do not feel that it would have been advantageous. The issues were technical and required much discussion among the technical staff to reach agreement.

The preparation, the evaluations, the visits to the offerors, the discussions, the documentation, the writing, the editing all took significant amounts of time. A major lesson that we have learned is that one can not undertake an SEB procurement lightly. It requires a major commitment of time from both the procurement staff and from the technical staff.

#### *B. Vendor Reaction*

The reaction to this process from our vendors has generally been favorable. Most of them work with both private industry and with government-funded laboratories. One firm, much more accustomed to dealing with industry, commented that this was the way things were supposed to work. Another firm, seemingly more accustomed to government work, had a difficult time accepting the fact that this was not a straight low bid procurement. The major complaint has been the length of time that our inefficiencies and inexperience introduced into the process.

### IV. CONCLUSIONS

Now that Fermilab is familiar with the SEB process and has an approved SEB procedure, we expect to make additional procurements this way. In some cases the advantages are tremendous. However, the effort involved precludes routine use of SEB's. For most procurements they are not needed.

It is also clear that good communication between the technical and procurement staffs within Fermilab is essential, as is communication between Fermilab and the Department of Energy.

### ACKNOWLEDGMENTS

We would like to thank the members of the DOE Business Strategy Group, who initially guided us in this direction, and particularly the Chairman, Jerry Zimmer. Chicago Headquarters and Batavia Area Office staff have graciously offered valuable guidance. Jim Finks, our Source Selection Official, and Dick Auskalnis, our Procurement Head, have been very supportive of our efforts. Dave Gassman and Greg Wojciechowski have offered pertinent legal advice. Steve Holmes, Fermilab Project Manager for the FMI, has encouraged us throughout the process. We thank Dixon Bogert, Associate Project Manager, for enlightening philosophical discussions.

# Sextupole Magnets for the Fermilab Main Injector

D.J. Harding, N. Chester, and R. Baiod,  
Fermi National Accelerator Laboratory\*,  
P.O. Box 500, Batavia, IL 60510

## Abstract

A sextupole magnet has been designed to satisfy the dynamical, geometrical, and electrical requirements of the Fermilab Main Injector. The steel length is 0.457 m. The top and bottom pole tips are 36.4 mm from the center line; the side pole tips are 48.0 mm from the center line. The design integrated strength is 55 T-m/m<sup>2</sup> at 294 A.

## I. INTRODUCTION

The natural chromaticities of the Fermilab Main Injector [1, 2] (FMI) are -33.65 horizontally and -32.87 vertically. The lattice has been designed to have low  $\beta$  and  $\eta$  (58 m and 1.9 m are the maximum values). Thus, very strong sextupoles are needed to cancel natural chromaticity. The configuration chosen places an F(D) sextupole at each F(D) main quadrupole in the arcs, where  $\eta$  is significant. The sextupoles must also compensate for large sextupole components in the dipole magnets induced by saturation of the steel as the energy approaches 150 GeV and by eddy currents in the beam pipe. These effects produce inherent chromaticities of -77 horizontally (at 150 GeV) and -55 vertically (near 20 GeV).

The chromaticity sextupole magnets for the FMI are a new, nonsymmetrical design, tailored to the geometrical, optical, and electrical requirements of the ring.

## II. REQUIREMENTS

We take as a requirement that the sextupoles be capable of producing a corrected chromaticity of 10 in each plane through the entire ramp, -10 below transition and +10 above transition. The sextupole requirements have been calculated using the natural chromaticity and the measured sextupole contributions from the dipoles[3]. The sextupoles need to have a peak integrated field strength of 55 T-m/m<sup>2</sup>. We were restricted by space to a steel

length of 0.457 m (18 in). This leads to a field strength of 120 T/m<sup>2</sup>. The beam pipe size limits the dimensions of the pole faces.

The cost and complexity of fabrication, installation, and operation of the magnets, the power supplies, and the buses must also be taken into account. The dipole end packs have been designed to provide a sextupole component small enough that the sextupoles may be run on a unipolar power supply. To allow use of 300 MCM cable for the bus work, we want to keep the root mean square current under 200 A during all of the operating modes except the short duration Collider injection cycles. The reduction of the current by the usual technique of increasing the number of turns increases the inductance. The rapid change in the current needed in switching the sign of the chromaticity at transition limits the allowable inductance.

To allow convenient testing of the magnets at peak field, the cooling water circuits must be capable of cooling the coil during DC operation at the peak current.

## III. CONCEPTUAL DESIGN

The conceptual design of the FMI sextupole was done using the spreadsheet program 20/20. A model of the sextupole cross section was built in a worksheet. Input parameters include the required integrated field strength, the magnet length, the number of turns in the coils, and the pole tip radius (distance of closest approach of the pole tip to the central axis). From this we obtain the required current.

Adding the conductor cross section dimensions, including the central hole for cooling water, allows calculation of resistance, power dissipation, water flow, and thus temperature rise. Adding a few additional dimensions and angles allows calculation of corner coordinates of the lamination and conductor. The spreadsheet plots the corners and points along the pole face and presents a fairly good picture of the magnet. It also calculates some critical clearances where the coils will need to slip past the poles during assembly. Material quantities are calculated to provide a cost estimate.

The model was used to try a large number of combinations of magnet parameters. The chosen design satisfies the requirements while striking a balance among the other

\* Operated by Universities Research Association under contract with the United States Department of Energy

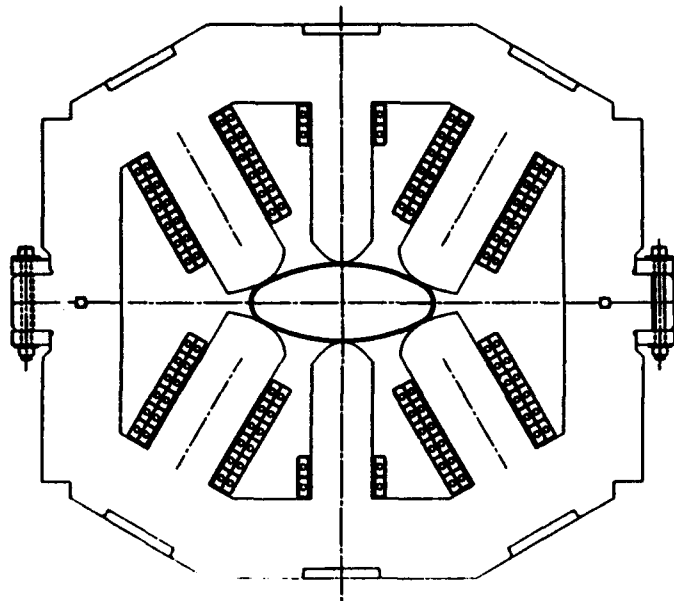


Figure 1: Cross section of the Fermilab Main Injector Sextupole showing the lamination, conductors, and beam pipe

competing design factors. To reduce the resistance and inductance of the magnet the design is not six-fold symmetric, but rather matches the beam pipe with top and bottom poles that are closer to the axis than are the side poles. The number of turns on the top and bottom poles is correspondingly smaller. The cross section of the magnet is shown in Figure 1. The basic magnetic, electrical, and mechanical properties are summarized in Table 1. The six coils are connected in series electrically. In operation the water paths will be connected in series as well. During testing the top and bottom halves will be cooled in parallel to allow running DC at the peak current.

A portion of the worksheet was arranged to generate an input file for the detailed magnetic modeling program PE2D. This allowed maintenance of the full two-dimensional magnetic model in synchrony with the other properties. It allowed testing changes to the magnet model by varying a single worksheet parameter and propagating the changes through to the magnetic model, avoiding typographic errors or inconsistencies.

We have also studied the sensitivity of the field purity to the position of the pole tip. Experience has shown that during production the largest variations in the lamination geometry come in the distance between poles, not in the shape of an individual pole. We moved a single pole tip by varying amounts, ran the model, and analysed the resulting field for its harmonic components. Figure 2 shows the effect on all normal harmonics up to the decapole of moving one pole horizontally by varying amounts. The quantity plotted is the field one inch from the magnet center due to the relevant component normalized to the field due to the sextupole component at one inch. Note the non vanishing decapole field resulting from the asymmetric

cross-section. Figure 3 shows the effect on the skew components of horizontal motion. As expected from the symmetry, all components vanish in the unperturbed case. The effects of vertical motion are comparable.

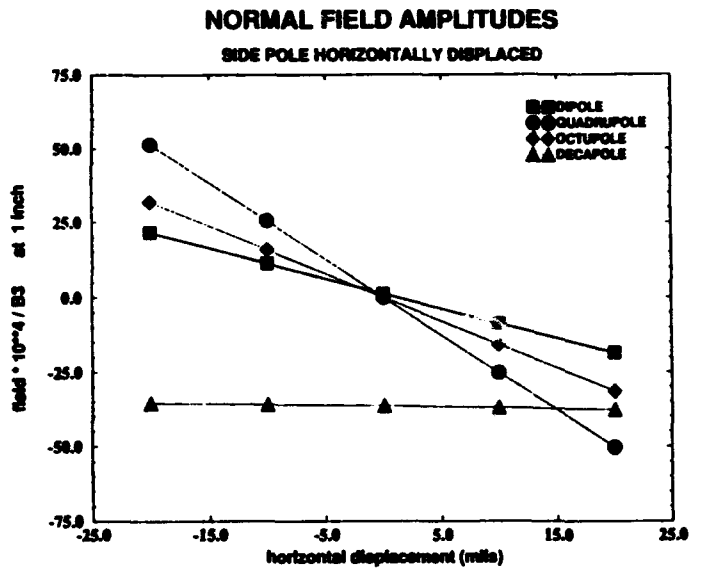


Figure 2: Normal Field Component Amplitudes as a Function of Horizontal Displacement of One Side Pole

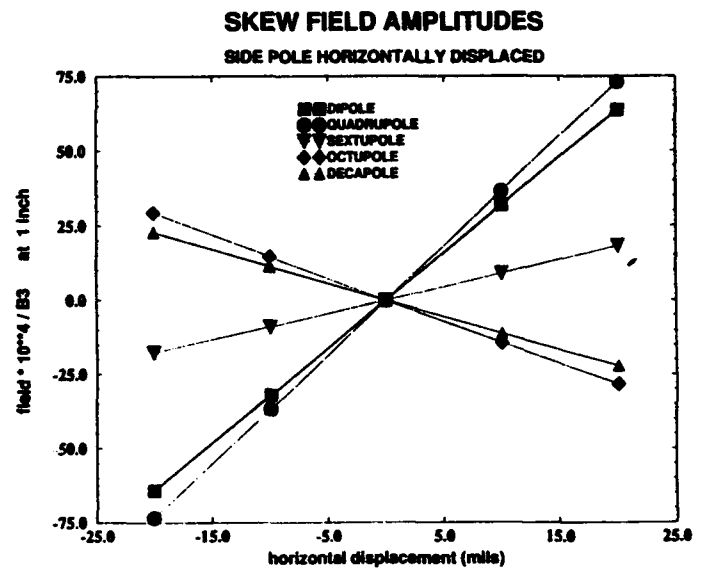


Figure 3: Skew Field Component Amplitudes as a Function of Horizontal Displacement of One Side Pole

#### IV. MECHANICAL DESIGN

The half-cores of the FMI sextupole will be fabricated from stamped steel laminations. The laminations will be

Integrated field (peak)	55 T-m/m <sup>2</sup>
Length	0.457 m (18.0 in)
Field (peak)	120 T/m <sup>2</sup>
Color	Yellow
Pole tip radius top/bottom sides	26.4 mm 48.0 mm
Number of turns top/bottom sides	2 12
Current (peak)	294 A
Conductor	6.35 mm x 12.7 mm (0.250 in x 0.500 in)
Resistance	4.2 mΩ
Inductance	0.7 mH
Water flow	0.019 l/s @ 0.070 kg/mm <sup>2</sup> 0.30 gpm @ 100 psi

Table 1: Main Injector Sextupole Magnet Parameters

stacked on a dedicated fixture and compressed with a screw mechanism. The outside edges will be held together by bars inserted in notches in the laminations and welded down the length of the core. The pole tips will be held in compression by steel rods threaded at one end to accept a nut and washer.

The copper conductor will be insulated as it is wound onto a bobbin. The coil will then be ground wrapped, impregnated with epoxy in a mold, and cured. The coils will be installed into the half cores and brased together in series.

The two half core assemblies will be bolted together to form a complete magnet. After testing, the complete magnet will be stored until it is needed in the tunnel. Installation will require separating the magnet into its halves and reassembling it around the beam pipe in the tunnel.

## ACKNOWLEDGMENTS

We would like to thank Alex Bogacs for his calculations regarding the beam requirements for the sextupoles and Phil Martin for several useful suggestions on the design. Dick Wegforth has done most of the design drawings.

## REFERENCES

- [1] Fermilab Main Injector. Title I Design Report, August 1992.
- [2] V.D. Bogert, W.B. Fowler, S.D. Holmes, P. Martin, and T. Pawlak. Status of the Main Injector Project. In *Proceedings this conference*.
- [3] S.A. Bogacs. Chromaticity Compensation Scheme for the Main Injector. In *Proceedings this conference*.

# Design and Measurements of Prototype Fermilab Main Injector Dipole Endpacks

D.J. Harding, H.D. Glass, J.-F. Ostiguy, B.C. Brown, F.A. Harfoush, C.S. Mishra,  
Fermi National Accelerator Laboratory\*,  
P.O. Box 500, Batavia, IL 60510

## Abstract

The end field regions of the dipole for the Fermilab Main Injector contribute significantly to the overall field quality and magnet performance. The end effects which we must control are the variation in effective length as a function of current and the variation in field shape across the magnet aperture. We employed an iterative process of numerical calculations and prototype testing to refine the design of the endpack steel configuration.

The final design is an approximation to a Rogowski profile, which limits effective length variation to 1.8 mm per end between 0.1 T and 1.7 T, and includes small shims to compensate for the intrinsic negative sextupole of the ends. We discuss details of the design process and present the effective length, field shape, and harmonics measurements for various endpack designs.

## I. INTRODUCTION

The Fermilab Main Injector[1] (FMI) will use dipoles of a new design[2]. There will be 216 6-meter dipoles and 128 4-meter dipoles in the ring. All of the dipoles will be wired in series. In normal operation, beam will be injected at 8.9 GeV/c, accelerated to 120 GeV/c or 150 GeV/c, and extracted. The dipoles must provide a uniform or easily correctable magnetic field over the range of 0.1 T (~ 500 A) to 1.7 T (~ 9400 A).

We have built two prototype dipoles. After testing the bodies, we have built and tested a series of end packs, attempting to optimize the performance. The measurement and analysis techniques are described in Reference [3]. The results are presented in more detail in References [4] and [5].

\*Operated by Universities Research Association under contract with the United States Department of Energy

## II. EFFECTIVE LENGTH OF THE ENDS

### A. Requirements

The parameter of prime interest is the integral through the magnet of the main component of the magnetic field,  $\mathcal{I}(x, y, I)$ . The bend angle of a particle traversing a magnet is proportional to this quantity and inversely proportional to the momentum. The FMI geometry assumes that the 6-m and 4-m dipoles have integrated strengths in the ratio of 3 to 2. To keep the beam on the same path throughout the acceleration cycle, the bend angle must remain the same in each of the magnets. Some variation can be accommodated by the 104 horizontal dipole correctors in the ring. However, it is not prudent to dedicate a large fraction of their range to adjusting for effects that could be avoided with a good magnet design.

Since the momentum of a particle does not vary as it traverses the ring, the relative values of  $\mathcal{I}(I)$  need to remain constant as a function of current. Calling the field at the center of the magnet  $B_0$ , we can characterize the field integral as the product of the central field and an effective length,  $L_{eff}$ . Thus  $\mathcal{I}(I) = L_{eff}(I)B_0(I)$ .

We define the effective length of the ends as the difference between the measured effective length and  $L_c$ , a somewhat arbitrary constant length. For practical purposes we set  $L_0$  to the maximum extent of the magnet steel in the axial direction.

$$L_{end} = (L_{eff} - L_0)/2$$

$$\mathcal{I}(I) = B_0(I)(L_{end}(I) + L_0 + L_{end}(I))$$

$B_0(I)$  and  $L_{end}(I)$  should behave the same way for the 6-m and 4-m dipoles. The steel lengths do not change during the acceleration cycle. Therefore, to maintain the ratio of  $\mathcal{I}(I)$  between the two lengths, we need to keep the effective lengths of the ends constant.

### B. Achievements

If the pole face of a dipole ends (as a function of  $x$ ) with a hard corner, the steel there will saturate at a lower current than will the body. The effective length of the end will fall

as the current increases. To combat this effect, the ends of magnet pole faces are often tapered. The initial design of the FMI dipoles had a single straight cut in the central 50 mm of the pole. The cut angle matched the angle of the sides of the pole. This produced an acceptable variation in the effective length of the end of 2.7 mm per end between 0.1 T and 1.7 T. This variation, along with some other representative endpacks, is shown in Figure 1.

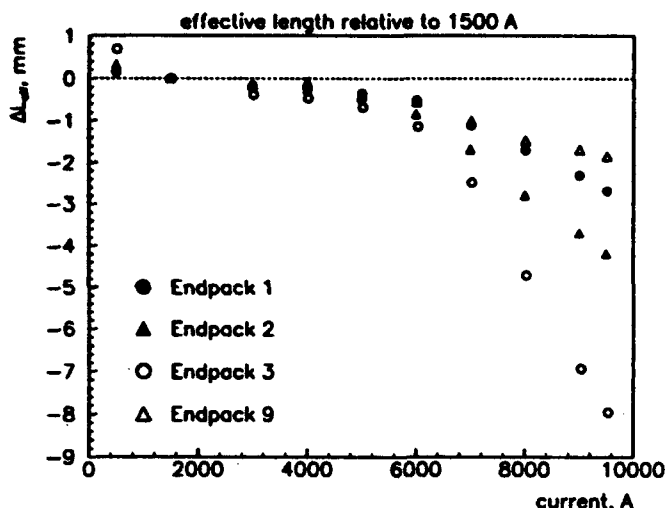


Figure 1: Effective length (relative to 1500 A) vs current for endpacks #1, original straight cut; #2, stepped approximation to straight cut; #3, Borda profile; and #9, Rogowski profile.

The rest of the end pack had a more complicated shape, making machining somewhat expensive. We therefore decided to fabricate the production end packs by building them from laminations trimmed in advance to produce the desired contours. Fermilab has successfully used this technique in the past. We built a set of endpacks that approximated the straight cuts of the initial design with steps three laminations (4.5 mm) deep. This stepped approximation to the straight line produced an unacceptable variation of 4.5 mm per end, as shown in Figure 1.

We then tried an end pack following the Borda profile[6], which we hoped would reduce effective length variations by making the saturation uniform along the pole profile. The stepped approximation to the Borda profile produced an even larger variation of 8.6 mm over the range of interest, as shown in Figure 1. A retrospective analysis showed that we had failed to recognize problems with nonuniform saturation in the bulk of the end pack.

Finally we tried the Rogowski profile[6] and made an end pack which approximated the Rogowski profile (with steps) in the central region. To reduce the iteration time we machined an existing set of end packs, carefully cutting just to lamination boundaries. This shape produces an acceptable variation. After the adjustments described below to the sides of the end pack, the effective length variation is only 2.0 mm, as shown in Figure 1.

Our computer 3-D models have not been able to accurately predict the changes in effective length. We attribute this to difficulty in modeling the anisotropy of the laminations and insufficient computing resources to model a large enough volume with fine resolution.

### III. END FIELD SHAPE

#### A. Requirements

The body field of the FMI dipoles is quite uniform as a function of  $x$ , especially at low current. The goal of the end pack design was to not degrade that uniformity in the total field integral. We expect and ignore a quadrupole component of the end field due to the magnet being constructed with parallel ends rather than as a sector. Any sextupole or higher component is of concern. The end field shape must be studied in concert with the shape of the body field and the shape of the field generated by eddy currents in the beam pipe. We wanted to get the sextupole component of the end field low enough so that the chromaticity correction sextupoles could adjust the chromaticity over the desired range without changing polarity[7].

#### B. Achievements

When it is normalized with respect to its value at  $x = 0$ , the field of a magnet naturally falls off on the sides of the end region. To first order, this effect is purely geometric and introduces an excitation-independent negative sextupole contribution in the integrated field expansion. Since the rate of fall off of the field is larger when the gap to width ratio increases, profiled ends tend to have an even larger sextupole than a plain rectangular end. To compensate for that effect, the original design provided large bumps on each side of the end pack protruding from the flat tapered surface. These provided additional effective length to the sides by keeping the field stronger.

Measurements of the end field shape on the original end pack and the stepped approximation to it agreed quite well with each other[5]. However, the variation with position was unacceptably large, comprising about half of variation in total field integral at the critical injection field ( $I=500$  A). As expected, the shape was not a strong function of current.

The 3-D computer model of the field was able to reproduce the measured field shape qualitatively fairly well. However, the same considerations that limited the effective length calculations affected the shape calculations as well.

We assumed that the shape measurements on the Borda profile endpack, which had no transverse variation in steel profile, would be our best approximation to what the Rogowski profile would produce with no transverse structure. We compared the measured sextupole component of that end field with the sextupole expected (from a 2-D calculation) due to a notch in the pole face. We found that a notch of the depth and length of the first step required

for the Rogowski profile produced approximately the right amount of sextupole to compensate for the corner saturation. While this approach has the advantage of being easier to calculate than a complicated 3-D shape, we expect it to saturate at a lower current. At that point the body sextupole will be dominating the total integral, so a deterioration of the end will be acceptable.

We carefully trimmed off the original bumps, step by step, measuring the end field after each step. We reduced the sextupole component each time, until we were left with only one set of laminations that were not flat. We adjusted the width of the central notch to reduce the sextupole a little more, and declared victory. The final end pack is shown in Figure B.. The resultant field shapes are shown in Figure 1 of [3]. The difference between the final shape and the shape of a tapered endpack with no transverse shaping is in excellent agreement with the integrated field predicted by multiplying the result of a 2-D calculation by the length of the notch.

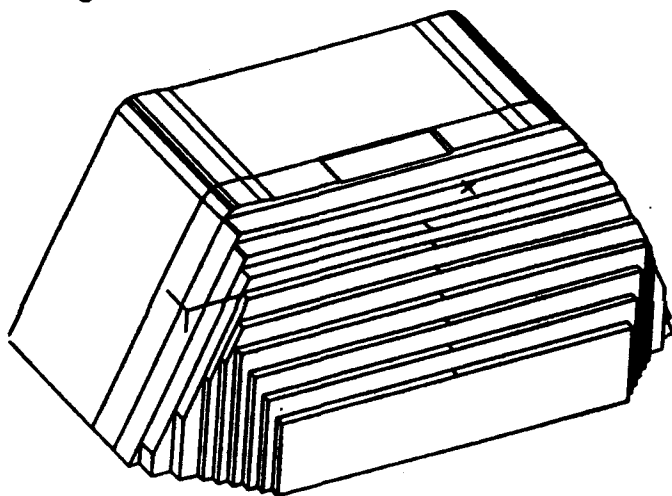


Figure 2: Isometric drawing of the final endpack design.

#### IV. CONCLUSIONS

After a lengthy development program, we have settled on an end pack design for the FMI dipoles and have started production with that design. The design meets all of the magnetic requirements of the accelerator. Figure 3 shows the field at 1500 A of a single end, of the body of the magnet, and of the sum of two ends plus the body. With the simplified method of controlling the sextupole in the end field that we have adopted, machining might have been cost effective compared to building the shape from trimmed laminations. Time constraints prohibited further investigation of that approach.

#### ACKNOWLEDGMENTS

We thank the other participants at the Main Injector Magnet Physics meetings for many stimulating conversations.

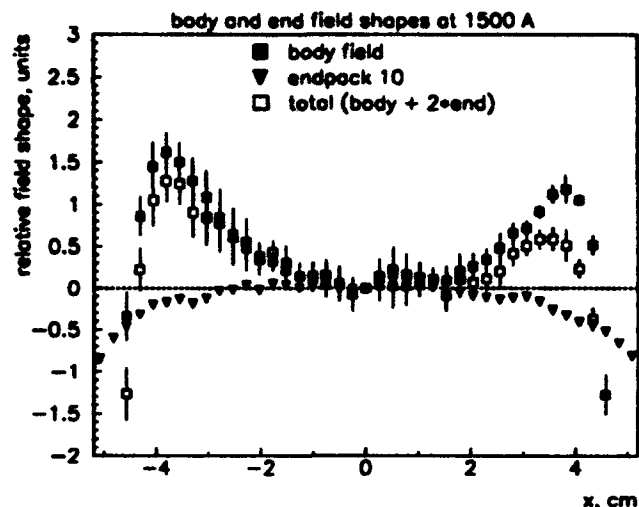


Figure 3: Relative shapes at 1500 A of the body field and integrated field for Endpack 10 (Rogowski profile). The estimated total field shape is superimposed.

We thank Arnie Knauf for his drawings of each end pack in turn and Ron Evans for coordinating the rapid machining of each trial. We thank Dave Hartness, Shree Agrawal, and Mark Thompson for their careful work taking the measurements.

#### REFERENCES

- [1] Fermilab Main Injector. Title I Design Report, August 1992.
- [2] B. C. Brown, N. S. Chester, D. J. Harding, and P. S. Martin. The Design and Manufacture of the Fermilab Main Injector Dipole Magnet. In *Proceedings of the Third European Particle Accelerator Conference, 1992*.
- [3] H.D. Glass. Techniques for Measurement of Dipole Endfields with a Rigid Integrating Coil. In *Proceedings this conference*.
- [4] H.D. Glass, B.C. Brown, and D.J. Harding. Effective Length Measurements of Prototype Main Injector Dipole Endpacks. TM 1815, Fermilab, December 1992.
- [5] H.D. Glass, B.C. Brown, and D.J. Harding. Field Shape Measurements of Prototype Main Injector Dipole Endpacks. TM 1820, Fermilab, December 1992.
- [6] J.-F. Ostiguy. Longitudinal Profile and Effective Length of a Conventional Dipole Magnet. In *Proceedings this conference*.
- [7] S.A. Bogacs. Chromaticity Compensation Scheme for the Main Injector. In *Proceedings this conference*.

# Magnetic Measurement of Quadrupole and Sextupole Magnets for the MIT-Bates South Hall Ring (SHR)\*

D.R. Tieger, J.D. Zumbro\* and W.W. Sapp  
Bates Linear Accelerator Center  
Middleton, MA 01949

## Abstract

Final results of magnetic measurements of 128 quadrupoles and 32 sextupoles are presented. There are many places in the SHR complex where these magnets will be operated from a common power supply. For the quadrupole magnets there are 4 octets, 4 triplets and 18 doublets; these magnets have been matched to  $\pm 0.1\%$  in excitation response for the operating range corresponding to 0.3 - 1.0 GeV. For the sextupoles there are four octets where the (pairwise) matching has generally been made to the  $\pm 0.3\%$  level. Parameterization of the data as well as fits are described and examples of the magnet groupings are shown.

## I. INTRODUCTION

The 190m MIT-Bates South Hall Ring (SHR) will provide both high (85%) duty-factor extracted beams as well as high current (up to 80 mA) circulating beams for internal target physics in the energy range of 300 MeV to 1 GeV. The project has been described elsewhere<sup>[1]</sup>. In order to complete the SHR project, a total of 128 quadrupoles and 32 sextupoles were manufactured. Magnetic measurements have been made on each of these multipole elements in order to determine harmonic content and similarity of response, since many of these magnets will be powered from common power supplies. Previously, we have described these quadrupoles and shown results from the first 24 of them to be measured<sup>[2]</sup>. In that reference we described the magnetic measurement technique and the equipment that was used, thus we shall only summarize this information here. The sextupoles are replicas of LBL Light Source-Booster sextupoles<sup>[3]</sup>, which were fabricated for us by Everson Electric<sup>[4]</sup>.

## II. MEASUREMENTS AND RESULTS

Our multipole magnetic measurement equipment consists of a harmonic analyzer table which was built for us at Chalk River<sup>[5]</sup>. The heart of this system is a ceramic bobbin that contains two tangential coils (one with 90° and one with 45° nominal opening angle) which is rotated on the axis of the multipole. The signal from one of the coils is input to a voltage-to-frequency (V/f) converter with 1MHz per full scale bipolar output. Pulses from the V/f are accumulated in 256 bins per each revolution of the bobbin. Data are accumulated with a PC, which is also used to cycle the power supply controlling the multipole. At each current setting a total of 10 data sets

is obtained, 5 with the bobbin rotating in one direction and 5 with the rotation in the other direction. Prior to a set of measurements, the bobbin is centered on the magnetic axis by minimizing the dipole (quadrupole) term for the quadrupole (sextupole) magnet to be measured, using the 90° (45°) coil.

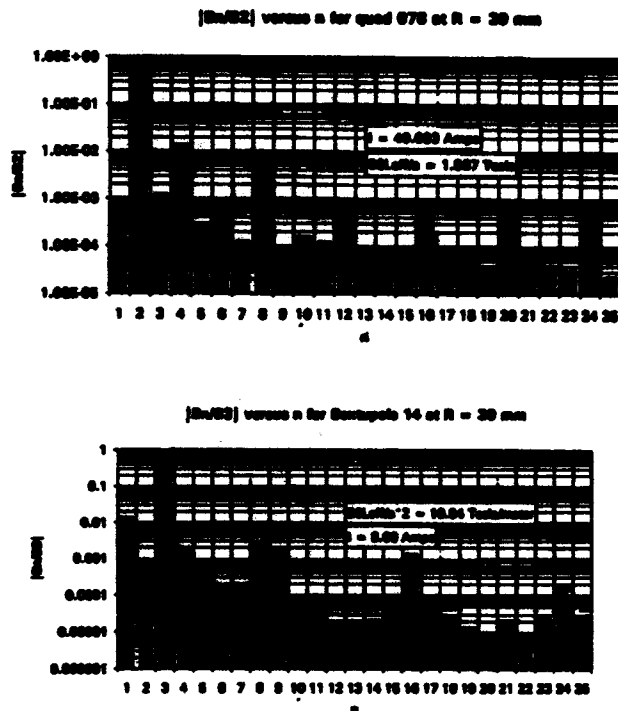


Figure 1. The relative harmonic strengths for a) typical quad at 40 Amps (90° coil not sensitive to  $n=4,8,12,$ etc.) and b) typical sextupole at 8 Amps (45° coil not sensitive to  $n=8,16,24,$ etc.)

The data are then analyzed with a Fast-Fourier Transform (FFT) from which the harmonic strengths are obtained. Figure 1 shows the harmonics relative to the desired one for both a typical quadrupole and sextupole, where in both cases the correct magnet and coil geometry is used. For the quadrupoles the quantity  $B_0 L_{\text{eff}}/a(I)$  is obtained, while for the sextupoles the quantity obtained is  $B_0 L_{\text{eff}}/a^2(I)$ , where in both cases the correct magnet and coil geometry is used. For our quads, the effective length is 300mm and the aperture radius is 32.5 mm, while for the sextupoles, the effective length is 121 mm and

\* This work is supported in part by the U.S. Department of Energy under contract # DE-AC02-76ER03069.

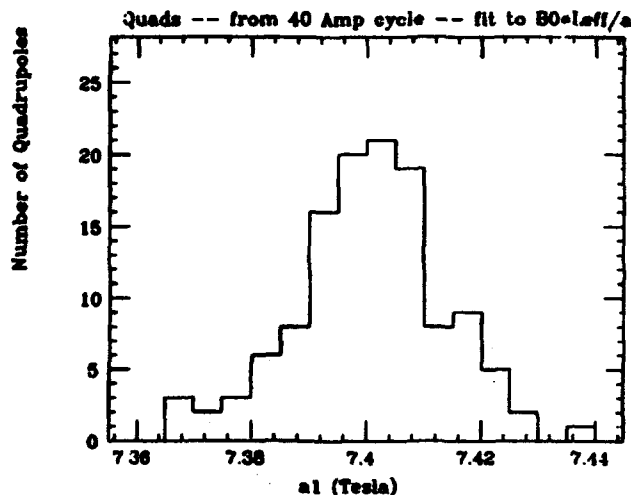
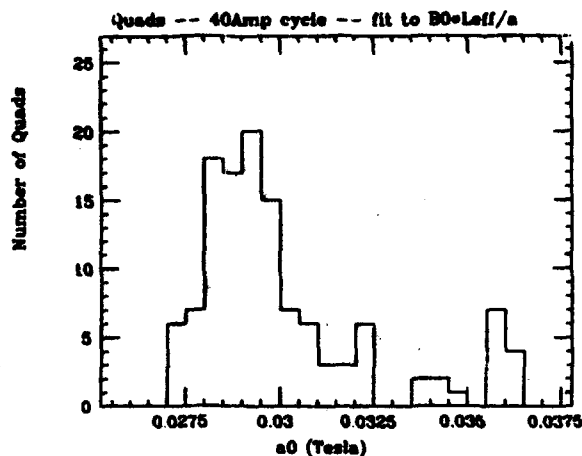
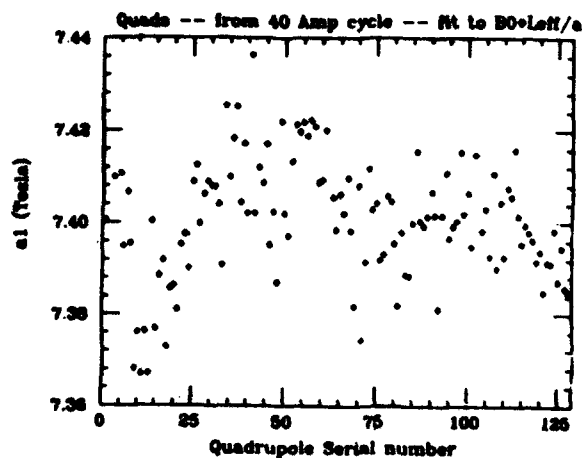
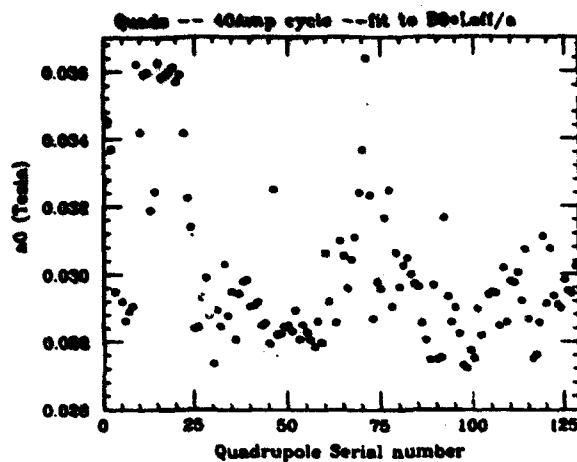


Figure 2. The residual field terms  $a_0$ , obtained from fits to Eq. 1 for the 40 Amp cycle data. a) shows the scatter vs. Serial Number and b) shows the statistics of the distribution.

Figure 3. Similar to Figure 2 for the linear term  $a_1$ , from fits to the data for the 40 Amp cycle data.

aperture radius is 35 mm. We then fit the obtained strengths to the form (e.g. for the quads):

$$B_{\perp} L_{\text{quad}} / a(I) = a_0 + a_1(I/150) + a_2(I/150)^2 + a_3(I/150)^3 + a_4(I/150)^4 + a_5(I/150)^5 \quad (1)$$

from which we can make comparisons and look for matches. Initially, we measured each quad on each of 5 different cycle currents (corresponding to the maximum values of the quad power supplies), which proved to be very time intensive. After approximately two-thirds of them had been measured and we were beginning to make tentative matches, we realized that about one-third of them would require polarity changing. At that point we decided to measure each quad on only one common cycle and make choices based upon that cycle's results. Our SHR lattice, which contains 79 quadrupoles, has four octets—all 32 of these quads are on 40 Amp cycles, which therefore was the cycle of choice. The remaining quadrupoles were all scanned at 40 Amps. Shown in Figure 2 are the residual field terms  $a_0$ , obtained from fits of all our quadrupoles to Eq. 1 for the 40 Amp cycle data. It should be pointed out that with our  $L_{\text{quad}}/a$ , the residual fields are scattered about a value of roughly 30 Gauss. Shown in Figure 3 are the linear terms  $a_1$  in the fit to the data, and one can see that there is a natural

spread of  $\pm 5\%$  in the distribution, which is much narrower than the spread in the residual field term. However, the criterion that the accelerator physicists had given us was to match quads to  $\pm 1\%$ , over the operating range of the SHR. We were able to meet this criterion and two examples are shown in Figure 4. Each arc of the lattice has a triplet (60 Amp positive polarity) in addition to an octet (40 Amp negative polarity). The data in Figure 4 are shown relative to the fit for the reference quad, and one can see that the fit meets the criterion over the range of 8 Amps to 25 Amps, which is the operational range of the octet.

For the sextupoles, all magnets were measured on a single 8 Amp cycle. Half were chosen to be one polarity (deflecting electrons to the right) and half the other. We then pair-wise matched them to approximately  $\pm 3\%$  over the operating range of the sextupoles, which was deemed acceptable to the accelerator physicists. An example of the sextupole matching is shown in Figure 5.

In conclusion, we have met the design criteria of the SHR in the placement of the quadrupole and sextupole multipole elements. From the 128 quadrupoles it was just possible to select the octets, within each of which the

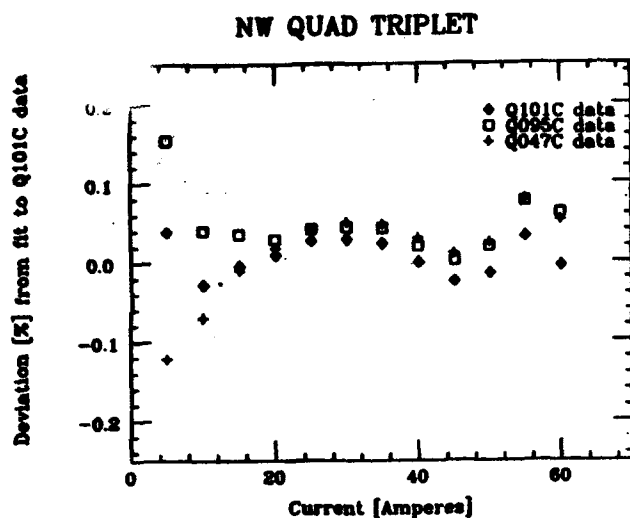
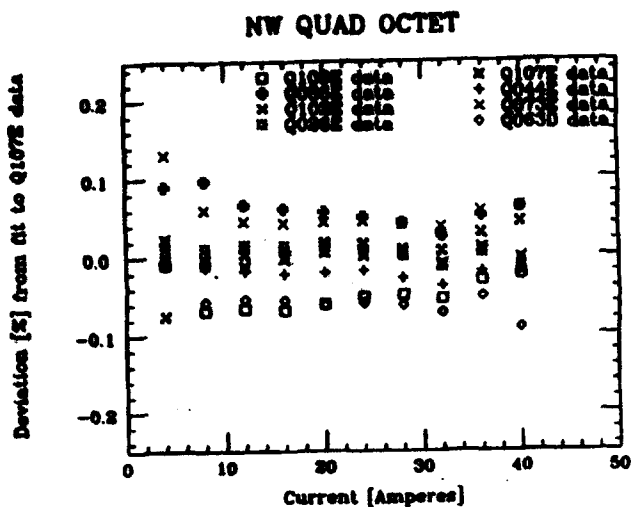


Figure 4. a) Shows the data for the NW Arc octet relative to the fit to the reference quad data. b) shows the data for the triplet in the same arc.

response was matched to  $\pm 0.1\%$ . This was the most stringent requirement. The sextupoles showed a somewhat larger variation in their strengths, but it was still possible to obtain pairs matched to  $\pm 0.3\%$ . The fabrication of both types of multipoles followed standard practices, and there was no post-fabrication machining or selection of materials before final assembly. For applications demanding better matching (than has been demonstrated here), improved fabrication techniques and tighter quality assurance will be necessary.

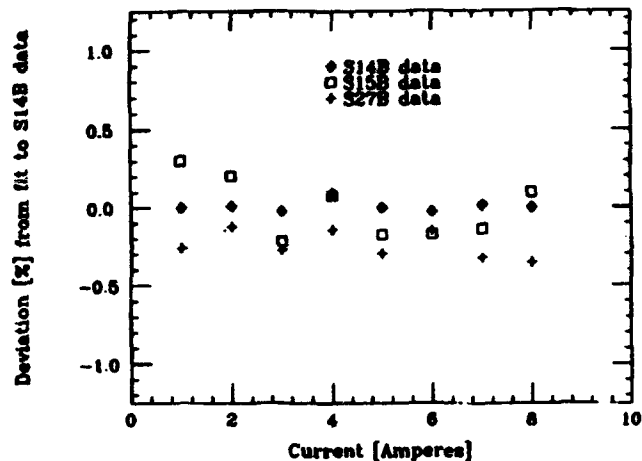


Figure 5. Shows the data from three sextupoles compared to the fit for one of them.

### III. REFERENCES

- [1] J.B. Flanz et al., Proceedings of the 1989 IEEE Particle Accelerator Conf. March 20-23, 1989, p.34.
- [2] J.D. Zumbro et al., Proceedings of the 1991 IEEE Particle Accelerator Conf., May 6-9, 1991.
- [3] J. Tanabe, S. Marks, K. Luchini, Lawrence Berkeley Laboratory, Engineering Note M6816, 1989.
- [4] Everson Electric Company, Lehigh, PA
- [5] W.G. Davies, N. Bray and R. Howard, Chalk River Nuclear Laboratories, Chalk River, Ont., Canada

\* Present Address: LAMPF, Los Alamos National Lab, Los Alamos, NM 87545

# A Permanent Magnet Dipole Correction Element for the Tevatron

J. E. Goodwin, T. Anderson, A. Franck, N. Gelfand, H. Jostlein  
Fermi National Accelerator Laboratory  
P.O. Box 500, Batavia, IL 60510

## Abstract

We have constructed four Halbach-type<sup>1</sup> permanent magnets for use as correction dipoles in the Tevatron. Each magnet consists of 16 trapezoidal prisms of Ferrite, arranged in a cylindrical shell. The magnets may be rotated freely about the beamline by a stepper motor, and are used in pairs to provide any field integral between 0 and 0.6 T-m, in any plane. The correctors buck the dipole component of the static magnetic field caused by the various toroids of the D0 detector, and thus prevent a closed orbit distortion in the Tevatron. The tight space constraints (6" square by 12" long for each pair) and difficulty of getting utilities beyond a dc control cable to the location led us to choose a permanent magnet rather than a Copper-Iron one. We describe briefly the principle of their design and operation. Next the mechanical design, motion control system and field quality are discussed. We conclude with a summary of our operating experience.

## INTRODUCTION

Static magnetic fields capable of perturbing the Tevatron beam at 150 GeV are generated by the EF, CF, and SAMUS toroid components of the D0 detector. At the time the magnets were designed, the integrated field in the D0 detector was anticipated to be as large as 0.4 T-m.<sup>2</sup> This field is expected because the main toroid does not have symmetrically placed excitation coils. Since this is equivalent to a 66  $\mu$ rad bending of the proton beam at 150 GeV (the Tevatron injection energy), or about 15% of the strength of a Tevatron correction dipole, it was decided to correct the field locally with one magnet at each end of the detector. Because of the tight space constraints at the desired location (6" x 6" x 12"), and because an engineering analysis showed that a properly sized electromagnet would be difficult to design, a permanent magnet of the Halbach design was chosen.<sup>1</sup> The magnets were designed and built by Permag Corp., a division of Dexter Magnetics.<sup>3</sup>

A total of four units, dubbed Permanent Dipole Correctors (PDCs) were constructed. See Fig. 1 for an end on view of one magnet. Two PDCs were installed at each end of the D0 detector. A pair of magnets, both having the same strength  $B$ , can create any net field from 0 to  $2B$  by rotating the field direction of each member in a scissors like motion. In addition, the plane of the net field can be chosen by an overall rotation of both members. In practice, one chooses the horizontal and vertical field components desired independently and selects orientations that satisfy both planes simultaneously. Provided  $B_x^2 + B_y^2 < B^2$ , the request can be satisfied.



Fig. 1. The Permanent Magnet Dipole Corrector (PDC) consists of a cylindrical shell filled with ferrite. The magnet is rotated by a stepper motor to any position about the beam axis. The field is normal to the parting plane of the two half shells.

## DESIGN

The design of the PDCs is an approximation to a cylindrical shell of magnetic material with a continuously varying direction of magnetization  $M$ . Such a configuration gives a perfect multipole  $n$  provided that  $\theta$ , the direction of  $M$ , varies as twice the azimuth angle  $\phi$ :  $\theta = 2n\phi$ . For a dipole,  $n = 1$  and so  $\theta = 2\phi$ . In Ref. 1 and references cited therein, Halbach has shown that using piecewise constant approximation to a continuously varying  $M$  gives a reasonably good multipole. We used 16 trapezoidal prisms, each having a constant and properly oriented  $M$  direction, to build up a cylinder.

The geometry of the cylinder is fixed at the inner diameter by the beampipe. The outer diameter is set to achieve the desired field quality and to satisfy geometric constraints. Fortunately, it proved possible to achieve our desired field quality of multipoles not in excess of 1% of the dipole field at 1/2" and to still stay within the 6" square allotted, while using ferrite instead of the more expensive SmCo. The overall parameters of the magnet are given in Table 1.

## MAGNET CONSTRUCTION

The trapezoidal segments were constructed by cutting and grinding triangular prisms having their easy magnetic axis properly orientated. Triangular prisms were then paired to form trapezoidal prisms. The prisms were next epoxied together inside a form consisting of an aluminum half-shell and a thin aluminum coverplate. (The coverplate protects the magnetic surface from ferromagnetic debris that might inhibit free rotation about the beam pipe).

The magnetic field was mapped using a standard rotating coil magnet mapper at the Fermilab Magnet Test Facility. The results are presented in Table 2. The integrated dipole field proved to be consistent to the 1% level. The multipoles were within tolerance for this undemanding application. The most important constraint is how well the dipole fields for each pair can be matched, since this sets the minimum net field in the off (antiparallel) configuration. The mapping results show that by pairing magnets a residual field of 2 Gauss-m is obtainable.

TABLE 1. Parameters of the Permanent Dipole Correctors

Number of units	4
Trapezoidal elements per unit	16
OD of magnetic material	5.600" max.
ID of magnetic material	2.600" min.
PDC unit ID	2.560" min.
Beam pipe OD	2.5" nominal
Magnetic Length	5.875" max.
Min. Integrated Field	12000 Gauss-in

TABLE 2. Field Quality of the PDCs. The PDCs were mapped at the Fermilab Magnet Test Facility using a standard rotating coil magnet mapper. The multipoles higher than dipole are given in Fermilab standard units as a fraction of the dipole field at a 1" radius. 2-pole means quadrupole, 3-pole means sextupole, etc. The magnets are listed in the order installed, proceeding from North to South.

Multipole	UP1	UP2	DN1	DN2
Dipole (T-m)	0.0349	0.0347	0.0353	0.0352
Normal 2-pole	-0.002	-0.012	0.003	-0.003
Skew 2-pole	0.0004	0.002	0.003	-0.001
Normal 3-pole	-0.010	-0.013	-0.007	-0.008
Skew 3-pole	0.005	0.013	-0.0004	0.001
Normal 4-pole	-0.0005	-0.003	-0.0002	-0.001
Skew 4-pole	-0.002	-0.003	-0.0003	0.001
Normal 5-pole	0.001	0.005	-0.008	-0.007
Skew 5-pole	0.008	0.005	0.004	0.003
Normal 6-pole	-0.003	0.001	-0.0005	0.0005
Skew 6-pole	0.003	0.001	0.0002	0.0001
Serial No.	003	001	002	004

## MOTION CONTROL SYSTEM

A stepper motor is used to rotate the PDCs via a pinion and a 7:1 reduction gear cut into the outside surface of the

magnet cylinder. The 3-phase stepper motor makes steps of 360 degrees, but internal gearing includes a 60:1 reduction. Thus, with the external gear, it takes 1260 steps to make one rotation, so the magnets can be positioned to a precision of  $\pm 0.3$  degrees. The magnets' rotation is monitored by a potentiometer that is geared similarly to the stepper motor. In addition, for redundancy there is a microswitch that senses a machined flat on the cylinder surface. There are thus two methods for controlling the angular position—dead reckoning from the microswitch position and reading the potentiometer position. In practice both are used because although the potentiometer gives a more reliable reading than counting steps there is a dead space of a few degrees when the potentiometer "turns over."

The PDCs are controlled by a Fermilab C057 CAMAC card. This card was developed for stepper motors used to control collimators, and thus provides a standard interface to the accelerator control system. Since the present application involves rotary motion, several control signals had to be re-interpreted. In addition, because of size restrictions, a special stepper motor was used. An interface card was designed to translate from the C057 to the commercial stepper motor driver.

When tested at 100 Hz, the motion control system performed satisfactorily but the drive train exhibited excessive vibration. Since the PDCs are designed to be moved infrequently, the step rate was lowered to 10 Hz and no further problems were encountered.



Fig. 2 The PDC with cover removed to show the stepper motor (rear) and potentiometer (front). The stepper motor drives a 7:1 gear cut into the surface of the magnet cylinder via a small pinion. The potentiometer is geared similarly.

## OPERATING EXPERIENCE

The PDCs have been tested, although they are not used operationally, since it has been found that the D0 toroids in fact have a very small effect on the Tevatron beam, about 0.1

mm rms distortion of the beam. The PDC units are capable of producing a 0.7 mm RMS distortion with a cusp at D0 when they are turned to the parallel configuration. The horizontal and vertical planes are sufficiently decoupled that only a 0.1 mm distortion is observed in the orthogonal plane (See Fig. 3). The magnets may find operational use in a planned upgrade of the D0 detector to include a solenoid.

The authors would like to thank R. Stelter of Dexter Magnetics for numerous informative discussions during the design and construction phase; and B. Brown for his assistance in mapping the PDCs. P. Bolan was instrumental in assembling and installing the finished units.

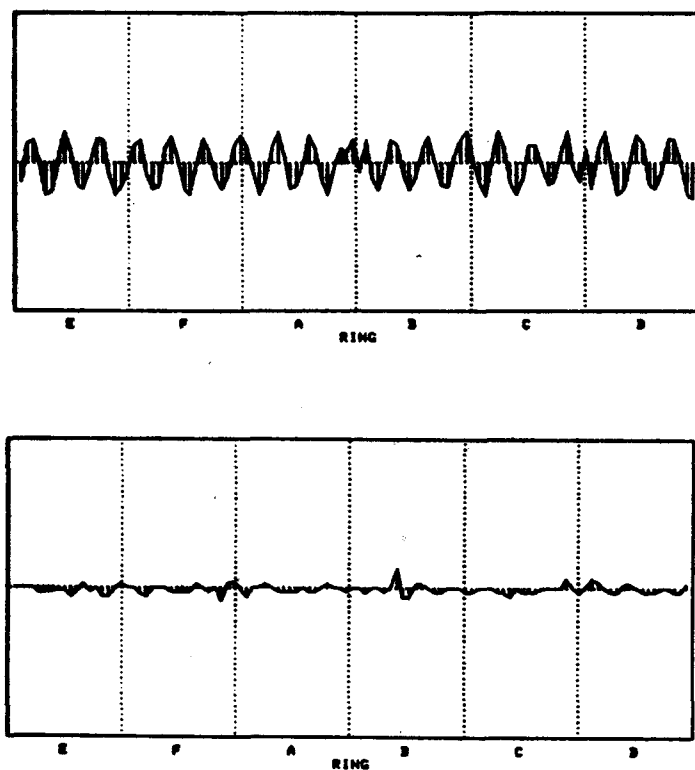


Fig. 3 The upper trace shows horizontal orbit with two PDC magnets parallel, fields vertical. A total orbit distortion of 0.7 mm RMS is observed. In the vertical plane (lower trace) there is hardly any effect. Both orbits are subtracted from the normal closed orbit of the Tevatron. In both cases the scale is  $\pm 5$  mm.

#### REFERENCES

- [1] K. Halbach, Nucl. Instr. and Meth. **169**, 1 (1980).
- [2] H. Jostlein, "Stray Fields from the D0 Muon Toroids: Shielding and Correction Magnets," unpublished memo, April 1989.
- [3] 1050 Morse Ave., Elk Grove Village, IL 60007.

# PRECISION MEASUREMENT OF TRANSPORT COMPONENTS\*

P. Tenenbaum, J.K. Cobb, D.R. Jensen, D. Sawyer, W. Wagner, H.V. Walz, S.H. Williams  
Stanford Linear Accelerator Center, Stanford University, Stanford CA 94309

## Abstract

We report on the methods and results of magnetic measurements of the centers and moments of magnetic focusing elements for the Final Focus Test Beam at SLAC. The magnetic center is located by observing an electromotive force (EMF) generated on a vibrating wire within the magnetic aperture. It is found that the center can be located with a precision of a few microns. The multipole coefficients can also be measured by using a grid of stretched-wire sweeps, and mapping the time-integrated voltage throughout the aperture. By fitting directly to this map, the dipole, quadrupole, and sextupole terms of the magnetic field are extracted. The design fields of quadrupoles and sextupoles can be measured with a precision better than 0.1%, and the resolution of sextupole aberrations of quadrupole magnets is well below design tolerances. This method has been used to process twenty-five quadrupoles and four sextupoles. Results of these measurements are presented.

## I. INTRODUCTION

The Final Focus Test Beam (FFTB) is a transport line designed to test both concepts and advanced technologies for application to future linear colliders. It is currently near completion at SLAC in the straight-ahead tunnel at the end of the linac. The primary optical elements of the FFTB are a family of quadrupole magnets and a family of sextupole magnets used for chromaticity correction. In order to achieve the desired spot sizes at the focal point ( $\sigma_x = 1 \mu\text{m}$ ,  $\sigma_y = 60 \text{ nm}$ ), tolerances on alignment, design field strength, and aberration field strength must be met [1]. We describe below our use of a stretched-wire technique for measuring each magnet's compliance with its tolerances, and discuss our experiences with the apparatus to date.

## II. CONCEPT OF THE METHOD

Figure 1 below depicts a schematic of our apparatus. A computer-controlled Coordinate Measuring Machine (CMM) is used to establish a coordinate system parallel to the mechanical axis of the magnet, with  $x = y = 0$  on the axis and  $z = 0$  at the longitudinal midpoint of the magnet. A thin wire which has been stretched lengthwise down the magnet aperture is then made parallel to the longitudinal axis to within a few tens of microradians.

The technique for measuring the magnetic center of the magnet relative to the mechanical center has been described in detail elsewhere [2]. In brief, the wire is set to vibrate at its resonant frequency  $\omega$ , and the resulting EMF is monitored on a spectrum analyzer. By nulling the EMF at the driving frequency in horizontal and vertical planes, the magnetic center can be located and measured relative to the mechanical coordinate system, via the CMM.

\*Work Supported by the Department of Energy Contract DE-AC03-76SF00515

In order to measure the magnetic moments of the magnet, the wire is swept by a known horizontal or vertical distance ( $\delta_x$  or  $\delta_y$ , respectively) about a point  $(x, y)$ . The expansion to second (sextupole) order of an arbitrary beamline component's magnetic field is:

$$\begin{aligned} B_x &= B_{0x} + G_n y + G_s x + 2S_n xy + S_s(x^2 - y^2), \\ B_y &= B_{0y} + G_n x - G_s y + S_n(x^2 - y^2) - 2S_s xy, \end{aligned} \quad (1)$$

where  $B_{0x}$  and  $B_{0y}$  are the horizontal and vertical field components at the origin, respectively;  $G_n$  is the normal quadrupole (preserving midplane symmetry);  $G_s$  is the skew quadrupole (violating midplane symmetry); and  $S_n$  and  $S_s$  are the normal and skew sextupole components, respectively [3]. When the wire is swept through the magnetic field, the time-integrated EMF across the wire is a function of the center point of the motion and of the total distance traveled in each direction:

$$\int v dt = L \left\{ \delta_x [B_{0y} + G_n x - G_s y + S_n(x^2 - y^2) - 2S_s xy + S_n d_x^2 / 12] - \delta_y [B_{0x} + G_n y + G_s x + 2S_n xy + S_s(x^2 - y^2) - S_s d_y^2 / 12] \right\}, \quad (2)$$

where  $L$  is the effective length of the magnet. The wire is moved to locations throughout the aperture of the magnet, and swept by known amounts, vertically and horizontally. The potential difference across the wire is monitored by an integrating voltmeter, which allows direct measurement of the time-integrated voltage as a function of position and sweep vector. By fitting the mapped measurements directly to the equation above, it is possible to extract the coefficients of the magnetic expansion directly. Note that Eq. (2) is only correct up to an overall sign, which is influenced by the connection between the voltmeter and the wire, among other variables.

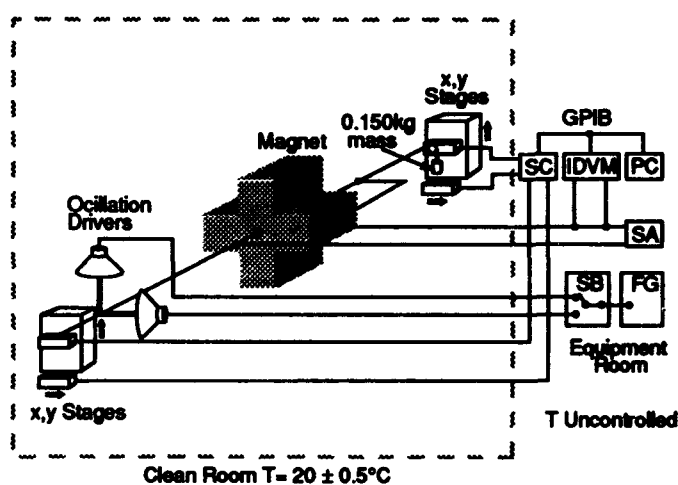


Figure 1. Schematic diagram of apparatus, including Stage Controller (SC), Integrating Digital Voltmeter (IDVM), Spectrum Analyzer (SA), frequency generator (FG) and switch box (SB). Not shown: mounting table and CMM.

### III. DETAILS OF THE APPARATUS

As shown in Figure 1, the principal elements of the measurement apparatus are the wire, the oscillation drivers, the stages which move the wire, the integrating voltmeter, the mounting table upon which the apparatus rests, and the magnets themselves. Many of these components have been described in detail in Reference [2], so for these only supplementary information is given.

#### A. The Wire

The wire employed is a 35  $\mu\text{m}$  gold-plated tungsten wire, of the type often used in drift-chamber applications. Under the conditions of the experiment, the overall sag of the wire is 12  $\mu\text{m}$ . If the height of the wire is measured close to the entrance and exit of a half-meter long magnet, the effective sag correction is about 1  $\mu\text{m}$ . The sag causes no alteration to the fitted field gradients, and an alteration to the sextupole terms that is unmeasurably small.

#### B. The Wire Stages

The wire is moved within the magnet by a set of precision stages made by the Newport Corporation. Four stages were used, one for x-motion and one for y-motion at each end of the wire. The stages were moved independently to align the wire parallel to the magnet, and then in pairs (x or y) to sweep the wire parallel to the magnetic axis for field measurements. The stages are controlled from a PC via a GPIB interface. The stage system has internal monitoring and feedbacks, and in principle each mover is capable of 0.1  $\mu\text{m}$  precision. In practice, this requires that the wires repeatedly iterate their motions, and for our purposes a tolerance of approximately 0.3  $\mu\text{m}$  was chosen. In experimental tests with the wire and CMM, it was found that the x and y motions have a difference in scale of approximately 0.3%, which varies slightly between magnets. This scale factor was determined for each magnet by fitting, and is believed to be due to non-orthogonality between the x-movers and the magnet z-axis. The absolute accuracy of the stages over millimeter-sized motions was highly variable, but always on the order of microns.

#### C. The Integrating Voltmeter

The time-integrated voltage on the wire was measured by a Solartron-Schlumberger Model 7061 Systems Voltmeter. The voltmeter was controlled and read out by a PC via a GPIB interface. The voltmeter has a built-in time-integration function which returns values in volt-seconds. By integrating the voltage in DC mode, the voltmeter rejected high-frequency transients, such as 60 Hz line noise. The integration time was set to 5 seconds, which was found experimentally to be long enough to allow the wire to stop oscillating after being swept.

#### D. The Mounting Table

The magnet, Newport stages, the wire, and the Coordinate Measuring Machine are mounted on a polished flat, 3.2-ton granite block that is seismically isolated from the ground by soft rubber pads in a temperature-controlled clean room. As part of the premeasurement procedure, the magnet is made flat with respect to the table through CMM measurements of the table and the magnet split-planes (see below).

#### E. The Magnets

The outer surfaces of the four quadrupole quadrants were machined with "split-plane" slots to allow access to the mating planes. In all, 30 standard quads were made, of which 28 were destined for installation in the FFTB beamline. After an initial acceptance test using a rotating coil to measure excitation curves [4], each quad was disassembled for installation of a precision Beam Position Monitor (BPM), and reassembled on a remote-controlled mover apparatus for beam-based alignment [5]. At this point, 25 quads were retested using the present technique, both for tolerance-checking and as a final quality control checkout before installation. Two of the quads were not retested because of time constraints, and one was not retested because it had not been split and was downstream of the focal point; therefore, its aberration content was not critical. All measurements were made at a current of 165 amperes on the rising leg of the hysteresis curve.

The standard FFTB sextupoles have a bore diameter of 2.065 cm and an effective length of 25.0 cm. The sextupoles were constructed in a fashion similar to the quadrupoles, and are each capable of producing sextupole coefficients of 7,100 T/m<sup>2</sup>. Each sextupole was subjected to an initial acceptance test similar to that of the quadrupole, and was then mated to a remote-controlled mover. Although the sextupoles were not disassembled after delivery, it was necessary for alignment purposes to mount each sextupole on the apparatus described above, and subsequently each one was measured using a swept wire in the same fashion as the quads. Sextupole measurements were all made at a current of 215 amperes on the rising leg of the hysteresis curve.

### IV. RESULTS

#### A. Vibrating-Wire Measurements

Magnetic center location was accomplished by placing the wire at six different small angles (<1 mr) with respect to the magnet axis, and zeroing the first harmonic EMF signal each time. The resultant six lines were used to find the point at which the average distance from the point to each of the lines was minimized. This fitting would produce a magnetic center point unconstrained by any mechanical reference to the magnet. In all, 28 magnets were measured using this procedure.

Figure 2 shows the distribution of z positions, and the average distance from the fitted center point to the six lines, d. Note that the longitudinal center points are clustered around -2 mm from the mechanical longitudinal centers. The RMS deviation of any line from the point of closest approach was less than 4  $\mu\text{m}$  relative to the external fiducials of the magnet.

#### B. Swept-Wire Measurements

For the swept-wire measurements, the area of the magnet aperture mapped was limited by interference of the apparatus. The total length of each sweep was chosen to be 2 mm, and the centers of each sweep were separated by 2 mm. A square grid was used, containing a total of 25 center points, and each point centered a vertical and a horizontal sweep, for a total of

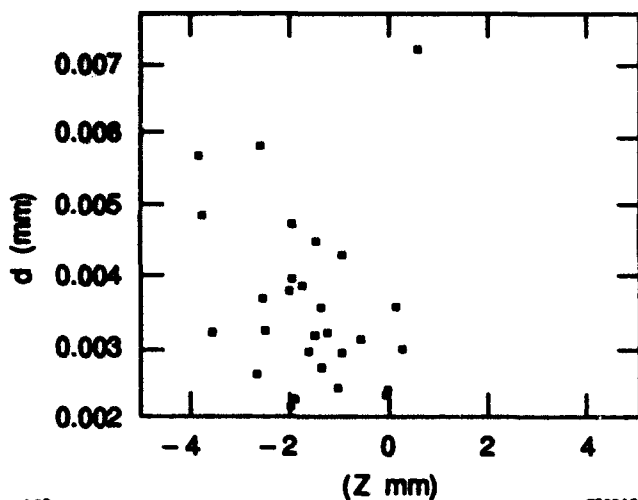


Figure 2. Z and d distributions of magnetic centers relative to mechanical center

50 measurements. This pattern was repeated ten times, and an average and rms deviation was computed for each of the 50 measurements. For most magnetic measurements, the rms was found to be consistent with the measured intrinsic noise of the system, about 80 nV sec, but in some cases it was up to an order of magnitude larger. In the latter cases it was also found that the absolute accuracy suffered, as did the resolution of the measurements. It is believed that high temperatures in the equipment room, which was outside the climate-control area, affected the performance of the Newport stage controller unit. Six out of the 25 quads were so affected; their results are included in the quad strength analysis, but not in the sextupole aberration.

It was also shown that the rms of the measurements did not describe well the deviations of the measurements from fitted values. It was speculated that although the movers have a precision of 0.3  $\mu\text{m}$ , their absolute accuracy might be somewhat lower. We found that an absolute accuracy of approximately 3  $\mu\text{m}$  described the deviations quite well. As the temperature in the equipment room came down, we found that this number also came down, to approximately 1  $\mu\text{m}$ .

Fitting of the magnetic field expansion was done by a special-purpose FORTRAN program utilizing the CERLIB fitting engine MINUIT, which returned fitted values for the parameters, errors on the fitted values, and a final chi-squared for the fit [6]. In fitting the magnetic field expansions, it proved useful to add three parameters,  $x_0$ ,  $y_0$ , and  $\theta$ , corresponding to origin offsets and roll angle, respectively. By introducing these, it was possible to eliminate three magnet parameters from Eq. (1).

The fitted quadrupole coefficients,  $G_n$ , of the normal quads were found to have a resolution of 0.015 T/m at an excitation of approximately 62 T/m, corresponding to a precision of  $2.5 \times 10^{-4}$ . This was dominated by the 3  $\mu\text{m}$  wire mover accuracy. For measurements with better accuracy, the

precision was as good as  $8 \times 10^{-5}$ . With the exception of measurements that were clearly anomalous, there was a systematic deviation of  $0.11 \pm 0.011$  T/m between our results and those obtained with a rotating coil, which has intrinsic resolution similar to our own. This deviation is believed to be due to slightly different absolute calibrations of the two systems.

The construction tolerance on sextupole content of the quadrupole magnets is a sextupole contribution to the magnetic field not to exceed  $1 \times 10^{-3}$  of the quadrupole contribution at 70% of the aperture [7]. This translates to a limit of 7.7 T/m<sup>2</sup> at a quad strength of 62 T/m for our magnets. Out of the 25 magnets tested on our apparatus, we found that 14 met the construction tolerances, five exceeded the tolerances by small amounts, and six gave anomalous readings due to apparatus difficulties. Typical resolutions were 1.0 to 2.0 T/m<sup>2</sup>. Because this was the first sextupole measurement made of these magnets, no comparison figures are available.

The sextupole components of the sextupole magnets were found to have a poorer resolution than those in the quadrupole magnets, typically 4/m<sup>2</sup> at a sextupole strength of 6500 T/m<sup>2</sup>, for a precision of  $6 \times 10^{-4}$ . Because the currents were not recorded during these measurements, no comparison with the rotating coil tests is possible.

## ACKNOWLEDGMENTS

We wish to acknowledge the contributions of many members of the SLAC staff, in particular H. Maxson and O. Dorsey for their help with the apparatus, W. Lockman for his help with MINUIT, and G. E. Fischer for technical and conceptual assistance.

## REFERENCES

- [1] F. Bulos et al., "Review of Tolerances at the Final Focus Test Beam," in the IEEE Trans. of Nuclear Science, Proc. of the Part. Accel. Conf., San Francisco, 1991; SLAC-PUB-5485 (1991).
- [2] G. E. Fischer et al., "Precision Fiducialization of Transport Components," in Proc. 3rd European Part. Accel. Conf., Berlin 1992; SLAC-PUB-5764 (1992).
- [3] We are using so-called "TRANSPORT" units for our expansion. See D. Carey, *Charged Particle Optics*, Harwood, 1987.
- [4] J. K. Cobb and D. Horelick, "A New Precision Measurement System for Beam Transport Type Magnets," Proc. 3rd Int. Conf. on Magnet Technology, Hamburg, 1970; SLAC-PUB-0750
- [5] S. Wagner et al., "Precision Magnet Mover for the Final Focus Test Beam," SLAC-PUB-6132, in preparation.
- [6] F. James and M. Ross, "MINUIT: Function Minimization and Error Analysis," CERN Program Library D506.
- [7] This is the construction tolerance of the standard quads and is significantly tighter than the operational tolerance.

## Measurement and adjustment of CIAE medical cyclotron magnet

M Fan X Zhang T Zhang C Liang Q Tao Z Chao  
C Chu T Li Y Hu Y Chen H Zhang H Jia  
C Jiao J Liu W Zhang C Zhou J Jiao Y Hou  
China Institute of Atomic Energy  
P.O. 275(3), Beijing, 102413, PRC

### Abstract

A 30 Mev compact cyclotron used for medical radioactive isotope production is in construction.

A program controlled mapping instrument with accuracy  $10^{-4}$  was developed. Its probe moves automatically in the 30 mm gap covering a circular area more than 1600 mm in diameter. It makes the mapping efficiency and accuracy.

An iteration method was used for both harmonic and average field shimming. The results were so good that made the first harmonic from more than 10 gauss reduce to about 5 gauss in the most of the radius and 70 gauss to about 10 gauss in the central region. Meanwhile the total phase shift which represents the isochronous from more than  $\pm 90^\circ$  to about  $\pm 20^\circ$ .

### I. INTRODUCTION

In order to keep the most of beam accelerated to the final energy, the magnetic field of a cyclotron should be shimmed to close the isochronous and the imperfect harmonics should be kept as small as possible. There is no trimming or harmonic coils in this cyclotron, the field mapping and shimming become very important.

The field adjustment was implemented by the sector pole edge modified. The aims of the field adjustment are: the first harmonic is limited to 10 gauss or less except central and extracted region where 30 gauss is allowed and the total phase shift is kept in the range less than  $\pm 30^\circ$ .

The full magnetic field survey of the cyclotron at CIAE was carried out based on an automatic mapping system. The sequencing of the probe movement and recording of field value is controlled from a step motor power supply and a PC286. GROUP3 Hall probe was used as the field detector with the accuracy  $10^{-4}$ .

### II. FIELD MEASUREMENT

To make the measurement results more reliable following measures are taken before and during the mapping.

a, To assist in performing the measurement, check list were given for operating the system and preset control switches for each type of measurement planned.

b, Consistency check. The consistent of the rotated center of the instrument and field center is important. But the difference of the two centers exists certainly. To reduce the difference, the probe moved slightly along the radial direction to make sure the probe was located closing to the center that the differences of field value at different azimuthal positions were small enough to be considered as a same point. The limitation in our case is  $\pm 2$  gauss.

c, Radial position check. A azimuthal angle is chosen as  $0^\circ$ . After  $0^\circ$  fixed a serial field data acquired and stored in the different radii from 0 to 84 cm stepped by 2 cm. If the field value in a given field point is not the same as stored before in the mapping process, the warning would be given. Then the radial position will be checked. The data might be given up when the difference is too large.

d, The start point and the final point is a same point for each turn, so is the field. It will be checked if the two value are not the same.

e, The field curve will be displayed on the screen to show whether the shape is reasonable, and whether there is any point is out of the estimation.

### III. HARMONIC ANALYSIS

Harmonic analysis is taken on the range  $[0, 2\pi]$  for each given radius. A code used for Fourier analysis computation is called after mapping. Usually the coefficients up to 40th harmonics are considered.

Fig. 1 shows the imperfect first harmonic distribution along radial direction.

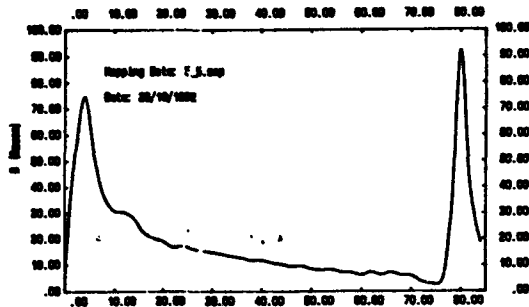


Fig. 1 The amplitude of the first harmonic distribution along radial direction

#### IV. BEAM DYNAMIC ANALYSIS

Fig. 2 shows the Flutter varies with the radius.

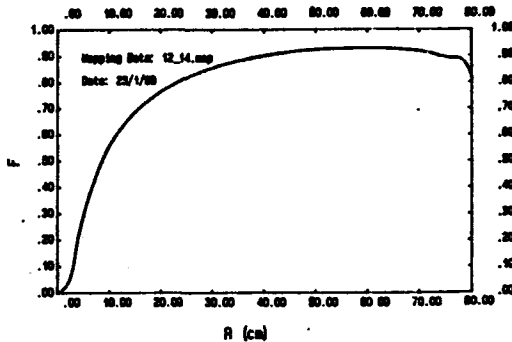


Fig. 2 The Flutter varies with the radius

Based on measured data the phase shift, betatron oscillations in radial and axial direction could be calculated. They are shown in Fig. 3, Fig. 4 and Fig. 5.

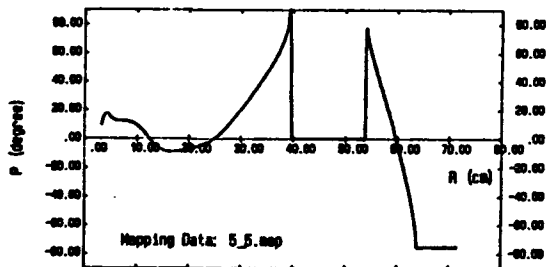


Fig. 3 The total phase shift is calculated at radius

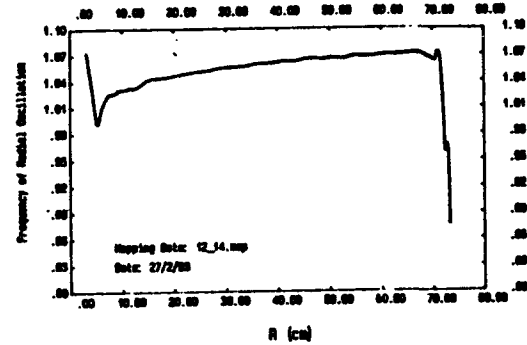


Fig. 4 The radial betatron oscillation

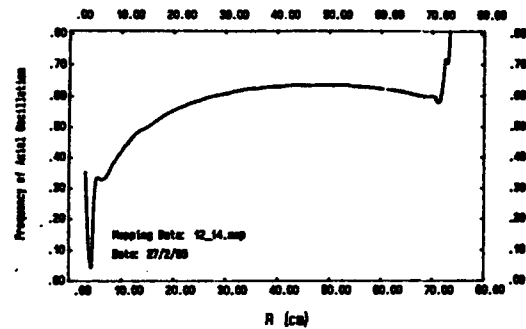


Fig. 5 The axial betatron oscillations

The diagram of data post processor of mapping is shown in Fig. 6

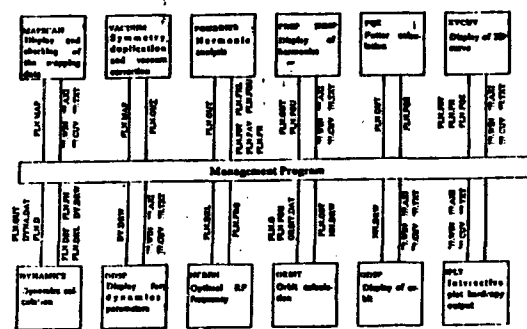


Fig. 6 The diagram of data post processor of mapping

#### V. FIELD ADJUSTMENT AND SHIMMING

The results show that the field is not acceptable

because the imperfect harmonics was too large and the average field drifted out the isochronous much more than the requested. The reason for them was the sectors were not machined on NC machine. The sizes are slightly different each other.

The sectors could not be modified any more. What we were able to do is use the pole edges.

Fig. 7 shows the improving process of the first harmonic after 4 times of the iteration.

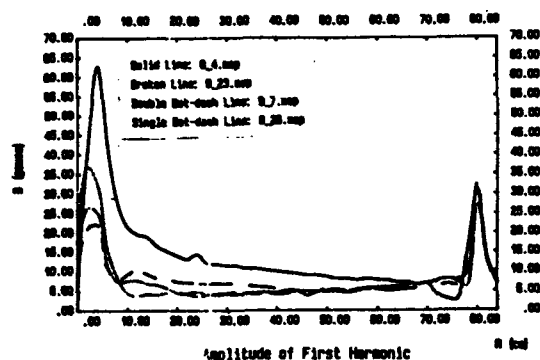


Fig. 7 The improving process of the first harmonic after 4 times of the iteration

After the field succeeded with an acceptable small imperfect harmonics, the average field is ready to be shimmed to meet the requirements from the isochronous. The pole edges are used again for the purpose. But an important matter must be kept in mind is the shimming should not destroy the harmonics which is in the requested amount whenever the pole edges have to be modified to produce the field close to the isochronous. The phase shift would exist if the average field is off the isochronous in a fixed frequency. We can not add some iron to the pole edge but cut in practical modification. In order to make up for such deficiency what we have done is to reduce the frequency a small amount to make the requested isochronous field slightly smaller. Then the modified

amount would become positive using cut only.

Fig. 8 show the process how the total phase shift of the accelerated ion is improving after few times of iteration.

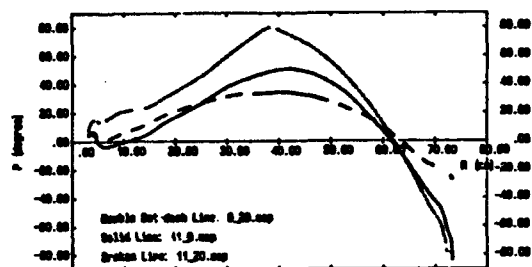


Fig. 8 The process of the total phase shift improving

To make sure the field is acceptable under the possible worst conditions, several assumptions have been added to test whether the field works. No vacuum correction and maximum possible correction have been tested. Also different initial phase angle ( $\pm 30^\circ$ ) for the accelerated particle have been supposed. The results prove that the fields are good enough for a quite large region of the working conditions.

## VI. CONCLUSION

An iteration method was taken for both harmonic and average field adjustment. The results were so good that made the first harmonic from more than 10 gauss reduce to about 5 gauss in the most of the radius and 70 gauss to 20 gauss in the central region. Meanwhile the total phase shift which represents the isochronous from more  $\pm 90^\circ$  to about  $\pm 20^\circ$ .

The quality of the field is acceptable and it would ensure the machine work properly.

# Magnetic Measurement and Alignment of the ELETTRA Storage Ring Quadrupole, Sextupole and Steerer Magnets

D. Zangrando and R.P. Walker

Sincrotrone Trieste, Padriciano 99, 34012 Trieste, Italy

## Abstract

The results of magnetic measurement of the quadrupoles, sextupoles and steerer magnets for the ELETTRA storage ring are presented. The performance of the rotating coil measurement bench and the system used for positioning the reference targets is also described.

## I. INTRODUCTION

The ELETTRA storage ring contains 108 quadrupoles in three families of different lengths, 72 sextupoles of two different lengths and 82 steerers [1,2]. All of the magnets have now been constructed: the quadrupoles and sextupoles by Ansaldo Componenti, Italy, the steerers by Tesla Engineering, England. A previous report dealt with the measurement of the prototype magnets [3]. This report presents the definitive results of the magnetic measurements of all the quadrupole and sextupole series production using the test system developed at CERN [4] and later transferred to Trieste. Also presented are some preliminary results of the steerer magnets.

## II. MEASUREMENT AND ALIGNMENT SYSTEM

### A. General

Magnetic measurements have been carried out with a rotating coil system. The voltage induced in the coil during one constant speed rotation ( $T=25.6$  sec.) is read out by a 3852A HP voltmeter. A FFT analysis is then executed to calculate the harmonic components of the signal. In order to maximize sensitivity different coils have been used for quadrupoles and sextupoles having as large an outer radius as possible - 36.17 mm for the quadrupoles (inscribed radius = 37.5 mm), and 43.69 mm for the sextupoles (radius 45.0 mm). The accuracy of the system is about 0.5  $\mu$ V, which corresponds to between  $2 \cdot 10^{-5}$  and  $10^{-4}$  of the main component at the coil radius at maximum current level, depending on the magnet type. At the reference radius of 25 mm the sensitivity to the higher multipole components is even greater.

Calibrations have been calculated directly from the geometric parameter of the coil. Each coil assembly includes a total of 4 separate coils: divided between left and right, and between outer (radius  $R$ ) and inner (radius  $R/2$ ). Each coil has 8 turns and can be selected separately or together with another coil in order to obtain the sum or the difference of the induced voltage. The alignment of the quadrupole or sextupole magnetic axis to the coil axis is performed using the left and right coils separately, in order to eliminate any compensation

of the alignment errors (i.e. pitch and yaw errors). The inner coils were used to check that the multipole terms scaled correctly with radius, and hence that rotation errors were not introducing false harmonics.

The system also allows a Hall plate to be installed (radius = 29.7 mm) in order to determine the central field strength and hence magnetic length, and also to make a harmonic analysis of the field at any desired longitudinal position.

During routine operation about 4 hours were needed for installation, measurement and alignment of each magnet. Thus, 3 magnets were regularly measured per day, however only 13 magnets per week could be achieved due to need to check the system alignment using a reference magnet (see below). The reproducibility of the system as determined by measurement of the reference magnet, was within 0.01% for both the main and the multipole components.

Since the poles of the magnets have to be opened to install the vacuum chamber, the measurements have been performed after opening of the poles. The reproducibility measured after two successive opening and closing operations was within  $10^{-4}$ .

### B. Alignment System

The location of the magnetic axes of the quadrupole and sextupole magnets must be determined with good accuracy [5] to install and align correctly the magnets in the storage ring. This operation was executed by means of a Micro-Alignment telescope manufactured by Rank Taylor-Hobson. During the magnetic measurements supports for Taylor-Hobson survey targets and an adjustable reference plane were positioned on each magnet. The sensitivity was about 20  $\mu$ m for the targets and 20  $\mu$ rad for the reference plane.

To align the telescope axis to the coil axis so as to define a vertical plane we used the following procedure: align the magnetic axis of a long-quadrupole with the coil axis; centre the Taylor-Hobson spheres with the telescope axis and level the reference plane; rotate the magnet around the vertical axis by  $180^\circ$  and re-align it using the Taylor-Hobson spheres and the reference surface. Then, if the telescope axis is aligned to the coil axis the measured displacement between the magnetic axis and the coil axis is zero. Otherwise a correction is made to the telescope axis and the operation repeated. In practise about 4 magnet rotations were necessary to perform a bench alignment to within 25  $\mu$ m.

Some problems were experienced with maintaining a good alignment of the measurement system even though the measurement area was temperature stabilized within 5  $^\circ$ C. It is presumed that this was caused by ground movements due to either settlement and/or external temperature changes. As a result it was necessary to check the alignment at the beginning and end of each week using a reference quadrupole.

If errors greater than 30  $\mu\text{m}$  were seen a re-alignment of the telescope was carried out. After each re-alignment the magnet was rotated and re-measured to confirm that the survey target positions on the reference magnet had not altered.

The roll angle of each magnet was aligned with respect to the coil within  $0.01^\circ$ . However, the accuracy of setting the coil angle i.e. the effective starting point of the measurement was within  $\pm 0.02^\circ$ , determined by the spirit level that was used.

The maximum alignment error permitted between the quadrupole or sextupole magnetic axis and the coil axis (left and right coil separately) was 10  $\mu\text{m}$ .

### III. QUADRUPOLES

Table 1 presents the main magnetic measurement results for the three types of quadrupole.

Table 1. Main component in the three quadrupole types at maximum current (300 A).

	Short	Medium	Long
Peak gradient (T/m)	19.6	20.4	20.6
Peak integrated gradient (T)	5.07	8.27	10.16
Magnetic length (m)	0.26	0.41	0.49

The specified integrated strengths are obtained with a current of about 295 A, at which level the saturation is 15% for the short quadrupole, 12% for the medium quadrupole and 11% for the long quadrupole.

Tables 2-4 summarize the variations in the main component and the multipole components at 1/3, 2/3 and maximum current level. The numbers of each type of magnet are indicated. Both systematic (average) and random (r.m.s.) parts are given, separately for normal and skew components. The values refer to the percentage field error at a reference radius of 25 mm. Only components with systematic or random components above  $10^{-5}$  are shown.

With respect to the prototype results [3] it can be seen that an improved technique for pole positioning has led to a reduction in components  $n=3,4,5$ , while selection of a suitable end-cut has significantly reduced the dodecapole ( $n=6$ ) component. Some changes in the systematic octupole ( $n=4$ ) and dodecapole with current can be seen; the former due to a small closure of the C-shaped support structure, the latter due to saturation effects.

The performance is within specification [6] apart from the random variation in quadrupole strength and systematic normal octupole component, which are at most two times larger than the specified values. However, calculations have shown that the magnets are acceptable [7].

The magnets were aligned magnetically at 300 A. The centre of the magnetic axis moves slightly with current in both planes, but on average by less than 10  $\mu\text{m}$  between 100 and 300 A, and with a maximum displacement of 50  $\mu\text{m}$ . No appreciable change in angle was seen ( $\leq 0.01^\circ$ ).

### IV. SEXTUPOLES

Table 5 summarizes the main results for the two sextupole types.

Table 2. Multipole content of the short quadrupoles (60)

Normal Components (%)		100 A		200 A		300 A	
n	syst.	rand.	syst.	rand.	syst.	rand.	
2	-	0.125	-	0.134	-	0.174	
3	0.036	0.023	0.027	0.024	0.025	0.026	
4	0.019	0.019	0.024	0.021	0.029	0.023	
5	0.001	0.003	0.001	0.003	0.001	0.003	
6	-0.001	0.002	-0.005	0.002	-0.018	0.003	
10	-0.011	0.0	-0.011	0.0	-0.012	0.0	
Skew Components (%)		100 A		200 A		300 A	
n	syst.	rand.	syst.	rand.	syst.	rand.	
3	0.0	0.027	-0.001	0.026	-0.004	0.029	
4	-0.002	0.003	-0.002	0.004	-0.002	0.004	
5	-0.001	0.003	-0.001	0.003	0.0	0.003	

Table 3. Multipole content of the medium quadrupoles (24)

Normal Components (%)		100 A		200 A		300 A	
n	syst.	rand.	syst.	rand.	syst.	rand.	
2	-	0.065	-	0.064	-	0.083	
3	0.028	0.029	0.019	0.029	0.014	0.034	
4	0.016	0.015	0.025	0.016	0.033	0.017	
5	0.003	0.004	0.003	0.004	0.003	0.004	
6	-0.009	0.002	-0.013	0.002	-0.028	0.002	
10	-0.007	0.0	-0.007	0.0	-0.009	0.0	
Skew Components (%)		100 A		200 A		300 A	
n	syst.	rand.	syst.	rand.	syst.	rand.	
3	-0.009	0.024	-0.010	0.023	-0.015	0.020	
4	-0.001	0.004	-0.001	0.003	-0.001	0.004	
5	0.0	0.002	0.0	0.002	0.001	0.002	

Table 4. Multipole content of the long quadrupoles (24)

Normal Components (%)		100 A		200 A		300 A	
n	syst.	rand.	syst.	rand.	syst.	rand.	
2	-	0.118	-	0.120	-	0.109	
3	-0.012	0.038	-0.019	0.041	-0.020	0.042	
4	0.013	0.027	0.025	0.029	0.038	0.031	
5	-0.003	0.005	-0.003	0.005	-0.003	0.005	
6	-0.004	0.003	-0.008	0.003	-0.022	0.003	
10	-0.006	0.0	-0.006	0.0	-0.008	0.0	
Skew Components (%)		100 A		200 A		300 A	
n	syst.	rand.	syst.	rand.	syst.	rand.	
3	-0.006	0.029	-0.007	0.027	-0.010	0.026	
4	-0.001	0.003	-0.001	0.003	-0.002	0.003	
5	-0.001	0.002	-0.001	0.003	0.0	0.003	

Table 5. Main component ( $B/r^2$ ) in the two sextupole types at maximum current (300 A)

	Short	Long
Peak strength ( $\text{T/m}^2$ )	262	282
Peak integrated strength (T/m)	40	74
Magnetic length (m)	0.152	0.264

The specified strength is reached at 247 A for the short sextupole, and 278 A for the long sextupole, at which level the saturation is 6 % and 4 % respectively.

Tables 6 and 7 summarize the measurement results for the sextupoles, referred to a radius of 25 mm. As for the quadrupoles, an improved technique for pole positioning has led to significant reductions in the  $n=4,5,6$  errors with respect to the prototype [3]. The magnets are within specification apart from the random variation in sextupole strength, and the random normal and skew octupole components, which in both cases are up to two times larger than the originally specified values. Later calculations however showed that the magnets are acceptable.

The sextupoles also contain small systematic and random dipole errors, with maximum values (300 A) of  $1.3 \cdot 10^{-4}$  Tm for the short sextupoles and  $3.2 \cdot 10^{-4}$  Tm for the long sextupoles.

Alignment was carried out in this case at 150 A. The maximum displacement of the magnetic centre in the range 100-300A was 20  $\mu$ m in the horizontal plane and 40  $\mu$ m in the vertical. The maximum angle error was less than  $0.02^\circ$ .

Table 6. Multipole content of the short sextupoles (24)

Normal Components (%)							
n	100 A		200 A		300 A		
	syst.	rand.	syst.	rand.	syst.	rand.	
3	-	0.234	-	0.232	-	0.182	
4	-0.021	0.031	-0.025	0.030	-0.019	0.032	
5	0.001	0.012	-0.001	0.012	0.012	-0.002	
6	0.015	0.013	0.016	0.012	0.018	0.012	
9	-0.023	0.001	-0.023	0.001	-0.024	0.001	
Skew Components (%)							
n	100 A		200 A		300 A		
	syst.	rand.	syst.	rand.	syst.	rand.	
4	0.034	0.046	0.031	0.042	0.022	0.037	
5	-0.014	0.017	-0.015	0.017	-0.014	0.016	
6	0.001	0.003	0.001	0.002	0.001	0.003	

Table 7. Multipole content of the long sextupoles (48)

Normal Components (%)							
n	100 A		200 A		300 A		
	syst.	rand.	syst.	rand.	syst.	rand.	
3	-	0.147	-	0.165	-	0.182	
4	0.001	0.039	0.002	0.038	0.014	0.037	
5	0.008	0.012	0.006	0.012	0.006	0.012	
6	0.018	0.012	0.024	0.012	0.031	0.012	
9	-0.007	0.001	-0.007	0.0	-0.008	0.001	
Skew Components (%)							
n	100 A		200 A		300 A		
	syst.	rand.	syst.	rand.	syst.	rand.	
4	0.020	0.045	0.017	0.046	0.007	0.045	
5	-0.007	0.014	-0.006	0.013	-0.007	0.013	
6	0.0	0.002	0.0	0.002	0.0	0.002	

## V. STEERERS

The steerer storage ring magnets (82 units) [2] have been designed to provide both horizontal and vertical correction. Measurements of the first magnet have been performed with the same rotating coil bench used for the quadrupole and sextupole magnets. The series magnet measurements will be carried out in June. In Table 8 are shown the magnetic measurement results of the prototype.

Table 8. Main field components in the prototype storage ring steerer magnet

	Horizontal Field	Vertical Field
I (A)	12	16
$B_0$ (G)	493.9	450.9
$\int B dl$ (G m)	139.0	126.9
$L_{mag}$ (m)	0.281	0.281

Table 9 shows the integrated field homogeneity of the magnet measured at maximum current, referred to a radius of 25 mm. The harmonic content does not change appreciably with excitation level.

Table 9. Harmonic content of the steerer magnet (%)  
(N) = Normal component, (S) = Skew component

n	Horizontal Field	Vertical Field
2	2.1 (N)	0.1 (S)
3	1.2 (S)	0.8 (N)
4	0.15 (N)	0.02
5	0.02	0.1
6	$\leq 0.01$	0.1
$\geq 7$	$\leq 0.01$	$\leq 0.01$

## VI. ACKNOWLEDGEMENTS

It is a pleasure to acknowledge the contributions of P. del Giusto, R. Ciuch and M. Maselli for the magnetic measurements and for the accuracy in the positioning the fiducial targets.

## VII. REFERENCES

- [1] ELETTRA Conceptual Design Report, April 1989, Sincrotrone Trieste.
- [2] G. Petrucci and D. Tommasini, these proceedings.
- [3] F. Gnidica et al., Proc. 3rd European Particle Accelerator Conference, Berlin, March 1992, p. 1358.
- [4] G. Petrucci et al, Proc. 2nd European Particle Accelerator Conference, Nice, June 1990, p.1139
- [5] A.Wrulich, Sincrotrone Trieste Internal Report, ST/M-TN-90/26, December 1990.
- [6] A.Wrulich, Sincrotrone Trieste Internal Report, ST/M-TN-88/23, October 1988.
- [7] F. Iazzourene, Sincrotrone Trieste Internal Report, ST/M-TN-93/6, May 1988.

# Measurement and Correction of the ELETTRA Storage Ring Dipole Magnets

R. P. Walker and D. Zangrando  
Sincrotrone Trieste, Padriciano 99, 34012 Trieste, Italy

## Abstract

The results of magnetic measurement of the 24 gradient dipole magnets for the ELETTRA storage ring are presented. The method of correcting the variations in dipole, quadrupole and sextupole components using shims is described. Trajectory and path length effects are also considered.

## I. INTRODUCTION

The ELETTRA storage ring [1] contains 24 gradient bending magnets with a nominal field of 1.2 T and field index of 13 at the final operating energy of 2 GeV [2]. A previous report dealt with the measurement of the prototype magnet [3] using the test system developed at CERN for the ELETTRA magnets [4]. The system has since been transferred to Trieste and used to measure the 25 series production magnets, constructed by Ansaldo Componenti, Italy.

## II. FIELD MEASUREMENT AND ANALYSIS

The measurement system consists of an automated three-axis bench with a temperature stabilized probe containing a linear array of 15 SBV-585-S1 Hall plates, with 1 cm spacing. Field maps with a rectangular grid of points were measured in the median ( $x,z$ ) plane of the magnet, with variable density along the longitudinal direction ( $z$ ). A standard measurement (half magnet) contained 38 points in  $z$ , up to  $z=1.06$  m, at which point the field was less than 0.25 % of its central value. The point spacing in  $z$  varied between 5 cm in the magnet centre and 1 cm at the edge. In the  $x$  direction there were 10 points with 1 cm spacing. All 15 plates were read at each point. Subsequent analysis consisted first in averaging the field values at each point. The number of points in  $x$  was such that there were at least 4 measurements of the field at each point in the region of interest.

The trajectory of the electron that starts from the magnet centre and exits with the correct angle ( $7.5^\circ$ ) was determined by iteratively tracking electrons with different energies. Field integrals were then evaluated along a series of curves parallel to the electron trajectory i.e. with constant radial separation,  $r$ . Interpolation between measurement points was carried out using a two dimensional cubic spline. The field integrals were fitted with a third order polynomial in order to determine the multipole field components defined as follows :

$$\int B dl = a_0 + a_1 r + a_2 r^2 + a_3 r^3$$

The rms relative error of the fit over  $\pm 3$  cm was  $10^{-5}$ . Although this method results in a different energy for each magnet, the results are valid also at fixed energy since to a very good approximation small shifts in the  $x$ -direction ( $dx$ ) produce a relative change in field integral, and hence energy, (for fixed bend. angle) given by  $(G_0/B_0)dx$  without significant change in magnetic length or other field components.

Both halves of each magnet were measured at an excitation corresponding to initial operation at 1.5 GeV. A smaller number of magnets were measured at other currents. Linear scans were also carried out in the magnet centre ( $z=0$ ) on each magnet.

## III. MEASUREMENT RESULTS

Table 1 summarizes the average properties of the magnets while figure 1 shows the measured variations in the integrated field components, as well as the field ( $B_0$ ) and gradient ( $G_0$ ) in the centre of the magnets, at 1.5 GeV.

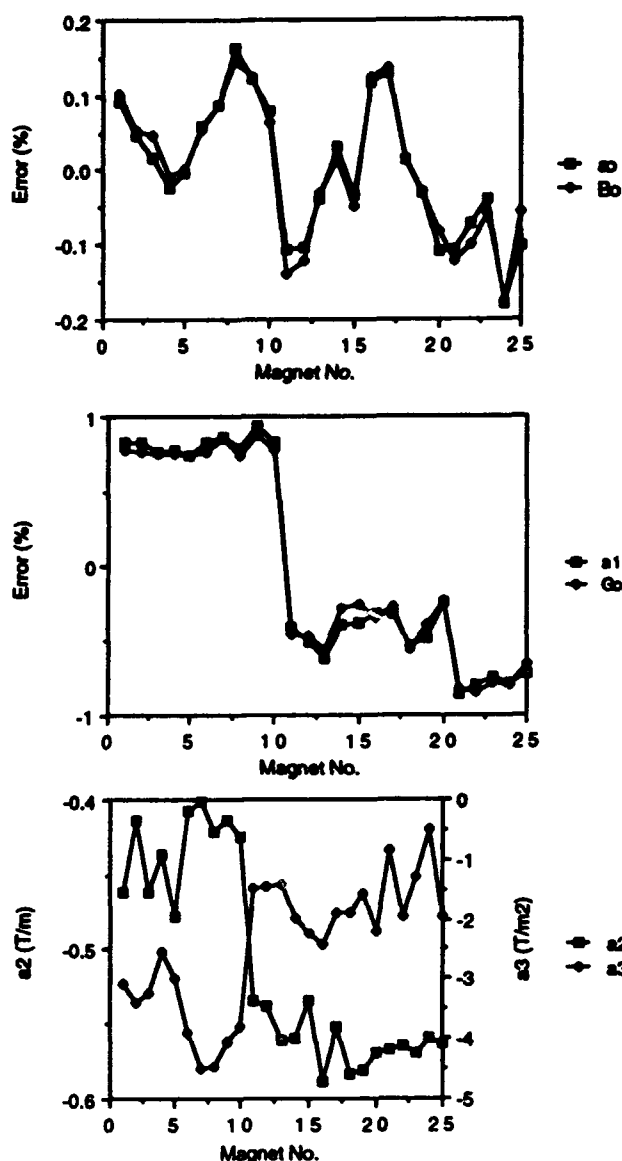


Figure 1. Variation in dipole (upper), quadrupole (middle), sextupole and octupole (lower) field in the dipole magnets.

Table 1. Average magnetic properties of the dipole magnets, before shimming;  $a_1, a_2, a_3$  values refer to 1/2 magnet.

I (A)	E (GeV)	$B_0$ (T)	$G_0$ (T/m)	$L_{mag}$ (m)	$a_1$ (T)	$a_2$ (T/m)	$a_3$ (T/m <sup>2</sup> )
700.0	1.0048	0.6018	1.496	1.4581	1.049	-0.32	-0.5
1050.0	1.5019	0.9008	2.240	1.4560	1.565	-0.51	-2.4
1420.0	2.0021	1.2067	2.993	1.4489	2.059	-1.10	-2.0
1950.0	2.4695	1.5086	3.640	1.4295	2.429	-2.62	-11.3

It is clear from the correlation between  $B_0$  and  $a_0$ , and between  $G_0$  and  $a_1$ , that the variations are caused by differences in the pole profile throughout the whole magnet. The dipole variation of 0.34 % (peak-to-peak) corresponds to a gap variation of 0.24 mm, while the 1.8 % gradient variation is equivalent to a 0.9° change in pole angle. By contrast the magnetic length variation is much smaller, 0.08 %, corresponding to 1.2 mm. It is evident that the errors are due to the final machining operation which was carried out on groups of 5 magnets : numbers 1-5, 6-10 etc. The largest changes occur between the first 10 and the remaining 15 magnets which corresponds to a gap of several months between the machining operations.

The effect of such dipole and quadrupole errors if uncorrected would lead to unacceptable closed orbit and  $\beta$  function errors [5]. The sextupole and octupole components are however small and within specification. The maximum values in fig. 1 correspond to relative field errors at the edge of the good field region ( $\pm 25$  mm) of  $5.8 \cdot 10^{-4}$  and  $1.1 \cdot 10^{-4}$  respectively.

In order to overcome the dipole field variation the magnets will be displaced radially from their nominal positions by up to 0.68 mm. In order to correct the quadrupole (and also sextupole) variation it was decided to adopt the simplest and cheapest solution - a passive correction using shims.

#### IV. SHIMMING TECHNIQUE

Various attempts were made before arriving at a final solution that was sufficiently stable mechanically, and sufficiently independent of magnet current level to be effective over a range of ring energies. Solutions involving additional end plates and washers had to be rejected as being too dependent on magnet excitation, due to saturation in the end-field region. The final solution is illustrated in fig. 2.

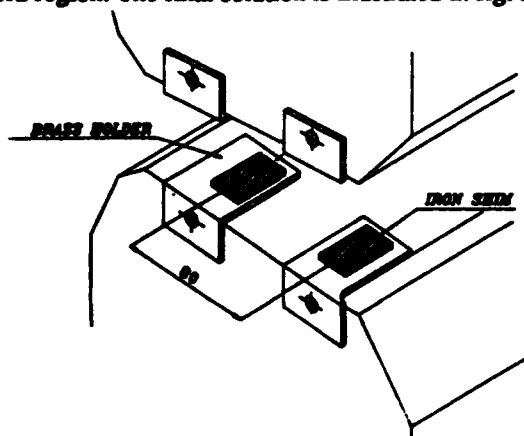


Figure 2. Position of shims for correcting the dipole magnets.

Each shim consists of a piece of magnet lamination, 1.5 mm thick and 20 mm wide, embedded in a brass holder which is bolted onto the magnet end plate so that the lamination lies flat on the pole surface. The centre-to-centre spacing of the shims was a compromise between maximizing the effect on the gradient and minimizing the effect on higher order field components.

Pairs of shims on the open side of the magnet decrease the gradient while those on the closed side increase it; both sets increase the sextupole field. Initial measurements showed that the effect was linear with shim length and that the effects of two pairs of shims added. Shim lengths were then calculated for each magnet to reach a common gradient and sextupole value, chosen in order to minimize the maximum required shim length (61 mm). Shims with similar length were then grouped to obtain an acceptable number of types of shim (7) and magnet groups (5). A prototype was constructed of each pair, and all 5 groups tested on one magnet (no. 16) at excitations corresponding to 1.5, 2.0 and 2.4 GeV. Two shim groups which gave the largest effects of the gradient were also tested on a second magnet (no. 8) with different gradient from the first magnet.

The measured effect of the shims agreed very well with the expected results, with the exception of the shortest shim (10 mm), for which an adjustment of the length was required. The results also demonstrated that the effects were the same for either magnet, and so could be applied to the whole group without the need to test each magnet.

The expected performance of the magnets based on the shim measurement data is shown in fig. 3. It can be seen that the gradient dispersion has been reduced to 0.2 %, within the desired 0.4%. The variation in sextupole value has also decreased significantly. The variation in octupole field has increased, but is considered acceptable.

#### V. PERFORMANCE AT HIGHER ENERGIES

The limited number of measurements that were made at higher energy (7 magnets at 2.4 GeV) are sufficient to show the good correlation between integrated and central field and gradient, as at 1.5 GeV. The *additional* variation at 2 GeV (0.2 %) and 2.4 GeV (0.5 %) with respect to 1.5 GeV is very similar for both field and gradient, and is clearly an effect due to saturation.

Measurements of the shims at different energies show a systematic reduction in the average gradient due to shim saturation, however the maximum variation introduced is only 0.02 % at 2 GeV and 0.08 % at 2.4 GeV, which are therefore small compared to the effects of magnet saturation.

Figure 4 shows the estimated dipole and gradient variations at different energies, taking into account both magnet and shim effects, and assuming a perfect correction of the dipole errors at 1.5 GeV by means of radial positioning.

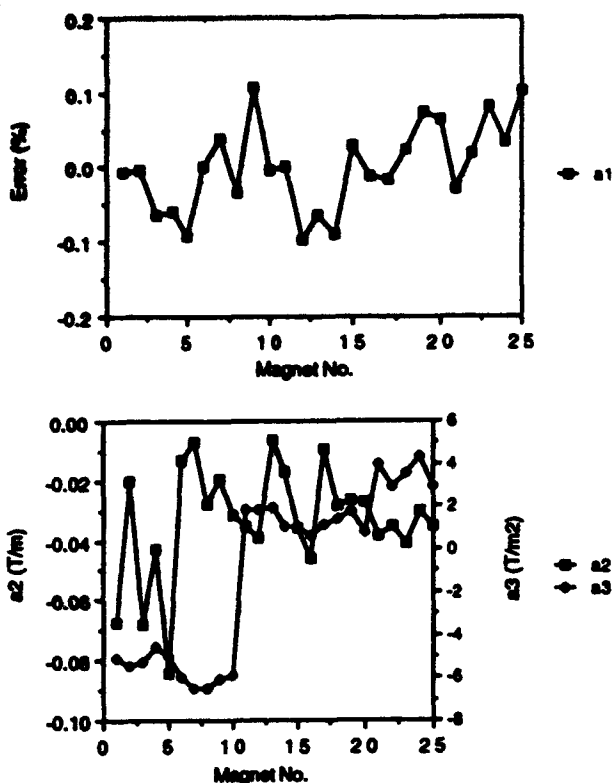


Figure 3. Estimated quadrupole (upper) and sextupole /octupole (lower) field variations at 1.5 GeV after shimming.

At 2 GeV there is little difference to the situation at 1.5 GeV : the dipole variation is 0.14 % and the gradient 0.26 %. At 2.4 GeV however there is a significant increase due to saturation : 0.47 % in field and 0.83 % in gradient. In order to provide for a possible future operation at high energy, it has been decided therefore to distribute the magnets in such a way as to minimize the effects on the optics [6].

## VI. TRAJECTORY EFFECTS

The actual electron trajectory in the magnet deviates significantly from the ideal circular arc with nominal bending radius (5.5 m) due to the fact that the magnetic length and hence the radius of the electron trajectory are slightly greater than the nominal values, and also due to the effect of the fringe field. The result is that the trajectory is displaced in the x-direction ( $\Delta x$ ) and also that the path length is different ( $\Delta L$ ) with respect to the hard-edge case. These quantities have been found to be equal for all magnets and are  $\Delta x = -0.86$  mm,  $\Delta L = -0.089$  mm, at 1.5 GeV. The shims have a negligible effect on both quantities.

The effect of the displacement in x is that due to the gradient, the field and hence current required for a given energy would be different to the measured values. This could be acceptable, however will be corrected along with the path length effect. The total path length error is 4.3 mm, corresponding to a momentum deviation of 1 %, given the ring circumference (259.2 m) and momentum compaction factor ( $1.6 \cdot 10^{-3}$ ). To overcome this effect all ring components

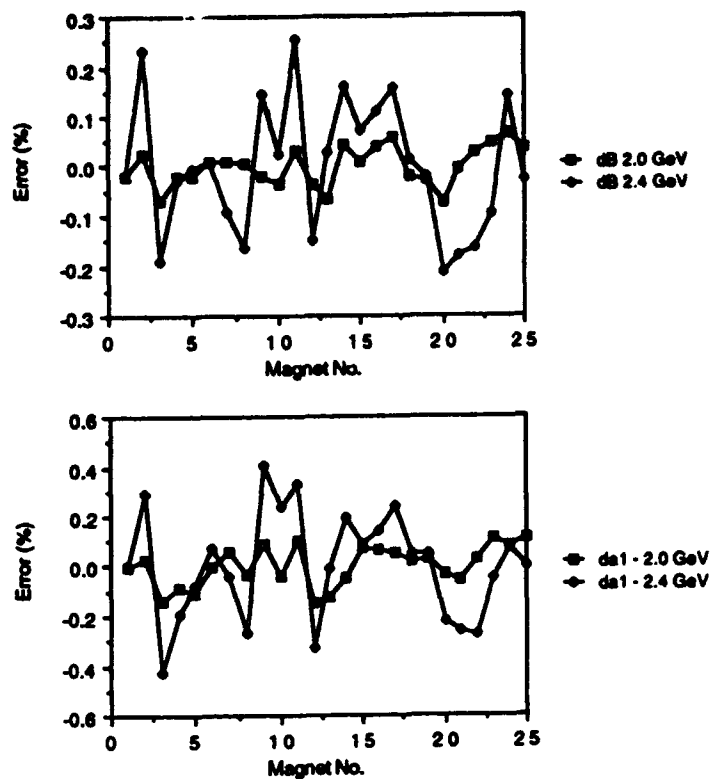


Figure 4. Estimated dipole (upper) and quadrupole (lower) field variations at 2 GeV and 2.4 GeV after shimming.

will be displaced outwards with respect to their nominal positions by  $\Delta L/\sin(\theta) = 0.68$  mm,  $\theta=7.5^\circ$ . To take into account both effects, the dipoles will be displaced inwards by  $0.86-0.68 = 0.18$  mm, in addition to individual displacements to account for the dipole field variations described above.

## VII. ACKNOWLEDGEMENTS

The contributions of G. Petrucci and other CERN staff to the successful transfer of the test system to Trieste is gratefully acknowledged. Magnetic measurements were carried out by A. Gubertini, R. Ciuch and P. del Giusto. D. Tommasini contributed significantly to the mechanical design of the shims and A. Wrulich to discussions on the implications of field errors and trajectory effects.

## VIII. REFERENCES

- [1] ELETTRA Conceptual Design Report, Sincrotrone Trieste, April 1989.
- [2] G. Petrucci and D. Tommasini, these proceedings.
- [3] F. Gnidica et. al., Proc. 3rd European Particle Accelerator Conference, Berlin, March 1992, p. 1358.
- [4] G. Petrucci et. al., Proc. 2nd European Particle Accelerator Conference, Nice, June 1990, p. 1139.
- [5] F. Iazzourene and A. Wrulich, Sincrotrone Trieste Internal Report, ST/M-TN-93/7, May 1993.
- [6] A. Wrulich, private communication.

# Magnet Costs for the Advanced Light Source\*

Jack Tanabe, Jim Krupnick, Egon Hoyer, and Alan Paterson  
Lawrence Berkeley Laboratory, University of California  
1 Cyclotron Road, Berkeley, CA 94720 USA

## Abstract

The Advanced Light Source (ALS) accelerator is now completed. The numerous conventional magnets required for the booster ring, the storage ring and the low and high energy transfer lines were installed during the last two years. This paper summarizes the various costs associated with the quantity fabrication of selected magnet families. These costs include the costs of prototypes, tooling, coil and core fabrication, assembly and magnetic measurements. Brief descriptions of the magnets and specialized requirements for magnetic measurements are included in order to associate the costs with the relative complexities of the various magnet systems.

## I. INTRODUCTION

The ALS is a 1.5 GeV electron storage ring, optimized to take advantage of undulators and wigglers to produce synchrotron light. It is located at Lawrence Berkeley Laboratory (LBL) in the hills above the University of California at Berkeley. Construction began in 1988. All magnets had been installed by the spring of 1992 and commissioning is presently underway. The main components of the accelerator system are a full energy booster ring, with a repetition rate of 1.0 Hertz and a storage ring designed for operation at 1.5 GeV and capable of ramping to 1.9 GeV. The booster magnets were designed for possible operation at 10 Hertz.

## II. MAGNET FABRICATION

All the booster ring magnet cores were assembled using 0.025 inch thick (0.6 mm) M36 silicon steel laminations with C-5 insulation to reduce the effects of eddy currents due to the time varying excitation at a future possible 10 Hertz maximum injection frequency. All storage ring magnet cores were assembled from 0.060 inch thick (1.5 mm) uninsulated low carbon steel laminations to take advantage of the economies of this fabrication technique for large numbers of DC magnets and to distribute systematic variations in steel properties uniformly around the storage ring lattice. With the lone exception of the booster dipole magnet cores, which were welded because of curved geometry, all other cores were fabricated either by gluing, or using mechanical frames combined with a modified gluing technique. It was felt that a higher quality magnet could be achieved by avoiding distortions in the core assemblies due to the thermal effects of welding.

All the ring magnet coils were vacuum potted using rigid reusable molds. The potting compound was an epoxy mixture using Tonox as a flexibilizer in order to avoid the long term development of cracks in the coil insulation. Because of the well known carcinogenic hazards of Tonox, thorough safety

\*This work was supported by the Director, Office of Energy Research, Office of Basic Energy Sciences, Materials Sciences Division, of the U. S. Department of Energy under Contract No. DE-AC03-76SF00098.

precautions including limitation of access to the working areas and the use of protective wear and breathing apparatus were rigidly enforced for the in-house fabrication of the coils. Hazard information and the LBL Operational Safety Procedure (OSP) were also supplied to the industrial coil vendor. These safety precautions added substantially to the cost of coil fabrication. Although the vacuum potting technique was only needed for the booster magnets due to the high voltages generated by pulsed operation, this technique was utilized for the storage ring magnets as well. High quality potting molds were needed for precise coil dimensions required for the storage ring sector chamber cutouts. Also, the economies of fabricating the large coil quantities for the storage ring magnets could easily capitalize the initial high cost of the sophisticated reusable tooling.

In addition to the coil and core fabrication, the magnet effort included the assembly of major parts, busses, interlocks, water fittings and hosing, interlock tests, measurement of electrical parameters, impulse and hipot tests of coils and the magnets. Magnetic measurements and the location of magnet fiducials for survey and alignment are included in the construction costs. Not included in the costs are engineering and design efforts and the detailed design and drafting of magnet components, assemblies and tooling. In addition, the cost of documenting fiducial data and summarizing the results of magnetic measurements and other tests are not included.

## III. BOOSTER MAGNETS

The magnet fabrication for the booster ring peaked during fiscal year 1989. At this time, the average LBL construction fabrication and assembly labor rates were \$36.20/hour.

### A. Booster Dipole

This magnet has a curved core which follows the beam orbit. The curved geometry minimizes the stored energy, to reduce the power supply requirements for the pulsed operation. The coil design includes substantial insulation to ground for the high voltage operation at a future potential 10 Hertz operation.

Prototype Cost	109.6 K\$
Production Cost	567.2 K\$
Tooling Cost	102.5 K\$
Number of production magnets	24+1 spare = 25
Core Weight	3940 lbs
Coil Weight	370 lbs
Magnet Weight	4310 lbs

### B. Booster Quadrupole

Two different lengths of this magnet were required.

Prototype Cost	83.0 K\$
Production Cost	464.5 K\$
Tooling Cost	160.1 K\$
Number of production magnets	2X(16+1 spare)=34
Core Weight	860 and 540 lbs
Coil Weight	65 and 50 lbs
Magnet Weight	925 and 590 lbs

### C. Booster Sextupole

The coils for this magnet were wound from solid conductor.

Prototype Cost	13.5 K\$
Production Cost	137.0 K\$
Tooling Cost	96.3 K\$
Number of production magnets	20 + 1 spare = 21
Core Weight	114 lbs
Coil Weight	18 lbs
Magnet Weight	132 lbs

## IV. STORAGE RING MAGNETS

The magnet fabrication for the storage ring peaked during fiscal year 1990. At this time, the average LBL construction fabrication and assembly labor rates were \$38.55/hour. The unit production cost for the storage ring magnets reflects the increased costs due to inflation and the increased complexity of the magnets fabricated for the storage ring. In general, the field quality and reproducibility requirements for the storage ring magnets were more demanding than the specifications for the booster magnets. In addition, the requirement for providing photon beam clearance and the difficulty in installing magnets along a more congested lattice than the booster ring resulted in substantially more demanding designs. The higher unit costs for the storage ring magnets due to these inflating forces was offset by the experience gained in manufacturing the booster magnets.

### A. Storage Ring Dipole

The storage ring dipole magnet is a gradient magnet. Because of the high precision required for the field quality, it was decided to fabricate the core with a one piece lamination. The field quality requirement forced a wide pole and a narrow throat in the one piece yoke for the gradient geometry. As a result, the coil design required six thin pancakes which could be installed in the core through the narrow throat. Magnet measurements were tedious and costly. Hall probe measurements were made on a finely divided grid for each magnet at an equivalent excitation at 1.5 GeV storage ring operation for 100% of the magnets. In addition, Hall probe maps were required at excitations for storage ring operation at 1.0 and 1.9 GeV storage ring operation for approximately 20% of the magnets.

Prototype Cost	147.5 K\$
Production Cost	1180.6 K\$
Tooling Cost	147.3 K\$
Number of production magnets	36 + 1 spare = 37
Core Weight	6380 lbs
Coil Weight	720 lbs
Magnet Weight	7100 lbs

### B. Storage Ring Quadrupole

The storage ring quadrupole design was a "C" shape variant of the booster quadrupole design. Three different models (lengths) were fabricated, the QFA, the QF and QD families. The QF and QD magnet families used smaller conductor than used for the QFA in order to optimize the design for individual power supplies. The magnet measurement effort required shimming of the two magnet halves in order to reduce the sextupole error introduced by the asymmetric design.

Prototype Cost	134.1 K\$
Production Cost	1054.0 K\$

Tooling Cost	179.8 K\$
Number of production magnets	3X(24 + 1 spare) = 75
Core Weights	2000, 1420 and 750 lbs
Coil Weights	120, 120 and 68 lbs
Magnet Weights	2120, 1540 and 818 lbs

### C. Storage Ring Sextupole

This was perhaps the most complicated magnet design in the entire ALS system. The sextupole had to satisfy four functions. In addition to the sextupole windings, the magnet required coils wound to produce vertical and horizontal steering as well as a skew quadrupole field in the same yoke. As a result, the coil system included twelve separate coils with eighteen separate windings. Electrical bussing needed to be accomplished at both ends of the magnet in order to accommodate the electrical connections for the four separate magnet functions. In addition, the core was divided among three segments. Precision assembly and alignment of the three separate segments was demanding and costly. Magnet measurements included rotating coil measurements to determine the excitation and the error multipole spectrum for each magnet in all its operating modes; sextupole, horizontal steering, vertical steering and skew quadrupole.

Prototype Cost	164.0 K\$
Production Cost	925.1 K\$
Tooling Cost	157.7K\$
Number of production magnets	48 + 1 spare = 49
Core Weight	980 lbs
Coil Weight	120 lbs
Magnet Weight	1100 lbs

## V. DETAILED BREAKDOWNS

Limitations were enforced in the level to which accounting information could be broken down in this extremely large and complex construction project. Thus cost distinctions among the coil fabrication, core fabrication, assembly and magnet testing efforts were not available in the accounting structure. Countless job and purchase orders were issued for the fabrication of each magnet type. It is possible, after very tedious and time consuming effort, to obtain costs for orders in each one of the major effort categories for the fabrication of magnets and add them up in order to get the actual costs of these categories. However, it is felt that a reasonably accurate division of the various effort categories could be obtained by looking at the updated cost estimates which were required periodically throughout the project. In particular, the cost estimate after the evaluation of the prototype and before the expenditure of the production budget would be a fairly accurate projection as to the relative costs among the various effort categories. At the end of the prototype effort, a fairly accurate picture of the fabrication effort as well as the assembly and scope of the required magnet measurement effort is available.

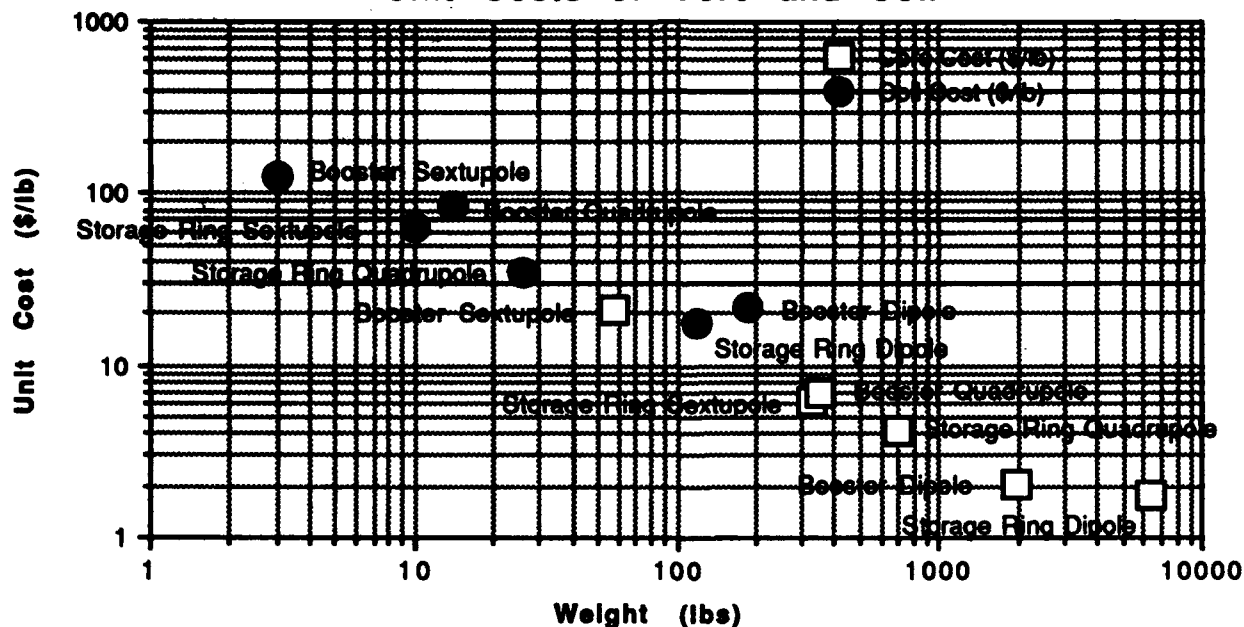
Magnet	Core	Coil	Assy/Test
Storage Ring Dipole	35%	39%	25%
Storage Ring Quadrupole	41%	25%	34%
Storage Ring Sextupole	32%	40%	28%
Average (To be applied to the Booster Magnets)	36%	35%	29%

Applying these numbers to the actual expenditures for all the production magnets, one can develop an approximate unit cost for the coils and cores related to coil and core weights.

Magnet	Number of Magnets	Production Cost	Cost per Magnet	Total Magnet Weight (lbs)	Total Core Weight (lbs)	Total Coil Weight (lbs)
Booster Dipole	25	\$567,165	\$22,687	4310	3940	370
Booster Quadrupole	34	\$464,511	\$13,662	758	700	58
Booster Sextupole	21	\$137,026	\$6,525	132	114	18
Storage Ring Dipole	37	\$1,180,604	\$31,908	7100	6380	720
Storage Ring Quadrupole	75	\$1,054,032	\$14,054	1493	1390	103
Storage Ring Sextupole	49	\$925,096	\$18,880	1100	980	120

Magnet	No. of Core Segments	No. of Coils	Total Core Cost	Total Coil Cost	Core Segment Wt. (lbs)	Individual Coil Wt. (lbs)	Unit Core Cost (\$/lb)	Unit Coil Cost (\$/lb)	Assy & Test (\$/mag)
Booster Dipole	2	2	\$204,179	\$198,508	1970	185	\$2.07	\$21.46	\$6,579
Booster Quad	2	4	\$167,224	\$162,579	350	14	\$7.03	\$83.16	\$3,962
Booster Sex	2	6	\$49,329	\$47,959	57	3	\$20.61	\$126.88	\$1,892
Storage Ring Dipole	1	6	\$413,211	\$460,436	6380	120	\$1.75	\$17.28	\$8,296
Storage Ring Quad	2	4	\$432,153	\$263,508	695	26	\$4.15	\$34.22	\$4,778
Storage Ring Sex	3	12	\$296,031	\$370,038	327	10	\$6.16	\$62.93	\$5,286

Unit Costs of Core and Coil



## VI. SUMMARY

LBL labor rates were quoted for the period of manufacture for each magnet family. The amount of labor should not be implied from these rates. Material and vendor supplied components are included in each of the cost summaries. In addition, LBL employed lower cost contract labor during the various peaks of the fabrication and assembly period. Higher cost professional labor was required during the magnet measurement phase of the effort. Core and magnet assembly efforts were "in house". A vendor, with different labor rates, supplied most of the coil fabrication for the storage ring.

Because of all the special circumstances of manufacture, one must be cautious in the application of these summaries to future estimates. One should only use the numbers herein summarized as general guidelines.

## VII. ACKNOWLEDGEMENTS

The authors wish to acknowledge the help and support of some of the numerous individuals involved in this effort. Alan Jackson and Roderich Keller provided scientific leadership and magnet specifications. Klaus Halbach was always available to lend his special insights on magnet design. John Milburn led much of the engineering effort. Yangmo Koo and Bongkoo Kang were longterm visitors from the Pohang Light Source (PLS) in Korea and contributed significantly to the magnet and magnet measurement system designs. Bob Caylor, Don Yee and Worley Low were lead designers. Kevin Bradley, and Paul Wong were lead technicians. Dick Reimers and John Vertrees provided manufacturing liaison. Michael I. Green, Don Nelson, Steve Marks and Ken Luchini led the magnet measurement effort. We gratefully acknowledge their help and the help of others not herein mentioned.

# Automatic Bench for Precise Magnetic Measurements of Linac Multipole Focusing Elements

V.S.Shachkov, M.A.Kozchekin, R.P.Koujbida, V.I.Lulevich, A.V.Selin, O.S.Sergeeva  
Institute for Theoretical and Experimental Physics  
Moscow, Russia

## Abstract

Automatic Hall-type magnetometer for magnetic measurements of focusing channel elements with arbitrary field configuration is described. Hall probe housing supported around periphery provides 3D precise movement in 75% of aperture space. The measurement technique and mathematical treatment developed to create the spatial model of the field are given. The magnetometer ensures the accuracy 0.3% of maximum field value in a whole magnet working space. Measurement runs for quadrupole lenses of ISTRA linac focusing channel are presented.

## 1 MAGNETOMETER PARAMETERS

The experience of focusing channels development for linear accelerators with given kind of charged particles shows preferable permanent magnet quadrupoles (PMQ) [1,2]. Such magnets require to be careful on a manufacturing stage to ensure tolerances because of wide initial spread ( $\approx 20\%$ ) of its magnetization like both piece-to-piece differ-

Table 1: PMQ main parameters for ISTRA accelerator.

N	Parameter	1 tank		2 tank	
		DT	DT	DT	DT
1.	Aperture, $2r_0$ , mm	$18^{+0.01}$	$18^{+0.01}$	$35^{+0.01}$	$54^{+0.01}$
2.	Lens length, $l_{\text{lens}}$ , mm	50	100	150	
3.	Top field, $B_m$ , T	0.50-0.54	0.29	0.22	
4.	Gradient, $G_0$ , T/m	56-60	32	24	
Tolerances on					
5.	Gradient, %	$\pm 0.5$			
6.	Magnet axis displacement, mm	0.030			
7.	$\frac{\Delta B}{B} _{r^*=0.75r_0}$ , %	0.7			
8.	$\frac{\Delta G}{G} _{r^*=0.75r_0}$ , %	3			
9.	Median displacement	$\pm 30'$			

ences and within volume limits of each magnet element. The main parameters of PMQ for ISTRA proton linac are shown in the Table 1. The tolerances given can be considered typical for such kind of machine.

## 2 MATHEMATICAL APPARATUS

We describe the field  $\vec{B}(r, \varphi, z)$  in a multipole lens working space by a scalar potential function  $U$ :  $\vec{B} = -\text{grad}U$ , which satisfies Laplace's equation in closed volume limited by cylindrical surface. The solution of this equation and hence a field  $\vec{B}$  can be written in terms of Fourier-Bessel series with coefficients depending on boundary conditions.

According to our technique the longitudinal size  $l_m$  of cylinder where the field is measured must be chosen to be long so much that the field value on both sides ( $z = \pm 0.5 \cdot l_m$ ) of cylinder is less than required accuracy (Fig.1). In this case all three spatial components of the field can be calculated in each internal point if we measure only the radial component on cylinder surface. In practice  $l_m$  is greater than geometric lens length  $l_{\text{lens}}$  by approximately  $2a$ . To meet the homogeneous conditions on sides we cut out measured data lower accuracy level (Fig.2) and join a piece of some simple curve (parabola or some other) following down to zero at  $z_0$  (on the left side) and  $z_c$  (on the right side) instead of infinite long actual tail with very small field value. The piece  $l = z_c - z_0$  is the length of a

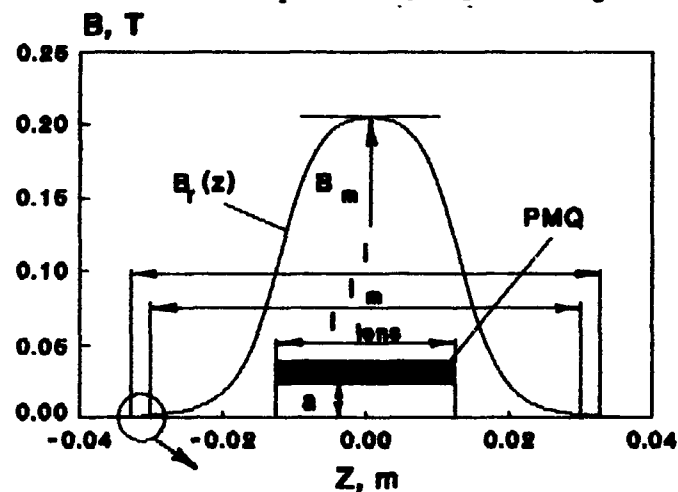


Figure 1: Choice of field expansion length.  $B_r(z)$  - field radial component in a PMQ pole plane at  $r = \text{const}$ .

field expansion into double Fourier-Bessel series.

Representing measured field distribution  $B_r^*(r, \varphi, z)$  on the cylinder surface  $r = r^*$  by corresponding series and on the base of equality

$$B_r^*(r^*, \varphi, z) = \sum_{k=1}^{\infty} \sum_{n=0}^{\infty} R_{k,n}(r^*) \times (\bar{A}_{k,n} \cos n\varphi + \bar{A}_{k,n} \sin n\varphi) \sin \frac{\pi k(z - z_0)}{l}, \quad (1)$$

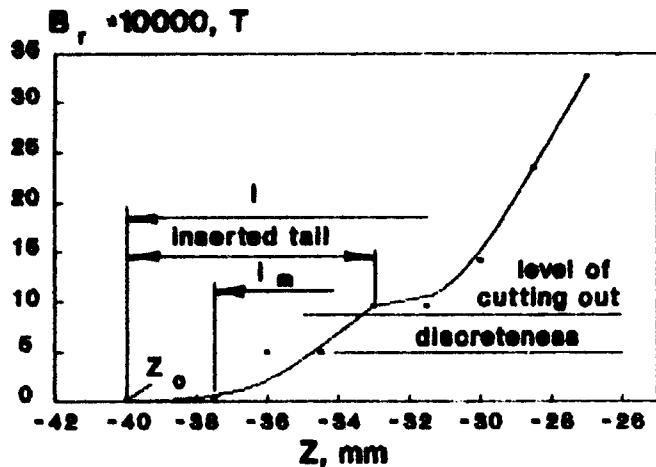


Figure 2: Tail joining. Points - experimental  $B_r$  data, curves - approximating lines.

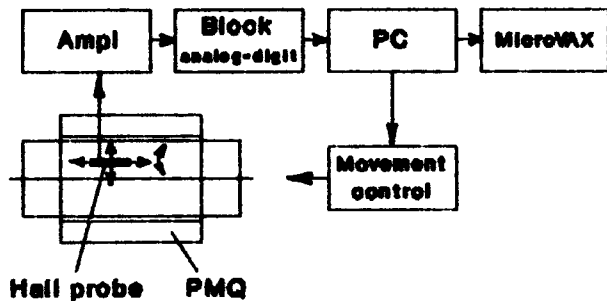


Figure 3: Block diagram of magnetometer.

where

$$R_{k,n}(r) = \frac{d}{dr} \left( \frac{I_n(\frac{rkr}{l})}{I_n(\frac{rkr_a}{l})} \right) = \frac{\frac{n}{l} I_n(\frac{rkr}{l}) + \frac{rk}{l} I_{n+1}(\frac{rkr}{l})}{I_n(\frac{rkr_a}{l})}$$

we determine coefficients  $\bar{A}_{k,n}$ ,  $\bar{A}_{k,n}$  of scalar potential  $U$ .

In our case it is

$$U(r, \varphi, z) = \sum_{k=1}^{\infty} \sum_{n=0}^{\infty} \frac{I_n(\frac{rkr}{l})}{I_n(\frac{rkr_a}{l})} \times (\bar{A}_{k,n} \cos n\varphi + \bar{A}_{k,n} \sin n\varphi) \sin \frac{\pi k(z - z_0)}{l}, \quad (2)$$

and defines the complete distribution of the multipole lens field  $\vec{B}(r, \varphi, z)$  in the whole working space.

### 3 MAGNETOMETER

The 3D movement of Hall probe is carried out by automatic power-driven system which operates in correspondence with control program from computer (Fig.3). Analog signal from Hall probe through amplifier and analog-digit

Table 2: Instrument parameters

N	Parameter	Coordinate		
		R	$\varphi$	Z
1.	Movement range	7 mm	395°	300 mm
2.	Instrument discreteness	10 $\mu$ m	0.08°	15 $\mu$ m
3.	Speed max	5 mm/s	90°/s	10 mm/s
	Speed min	1 mm/s	3°/s	40 $\mu$ m/s
4.	Hall probe housing OD	18 mm		

(1024 bit) block comes to PC hard disk. When measurement cycle is completed all information from PC memory is directed to MicroVAX computer where the mathematical treatment is fulfilled.

The main unit of magnetometer is shown in Fig.4; its main parameters are given in Table 2.

A multipole lens is fixed in the left-side support in such

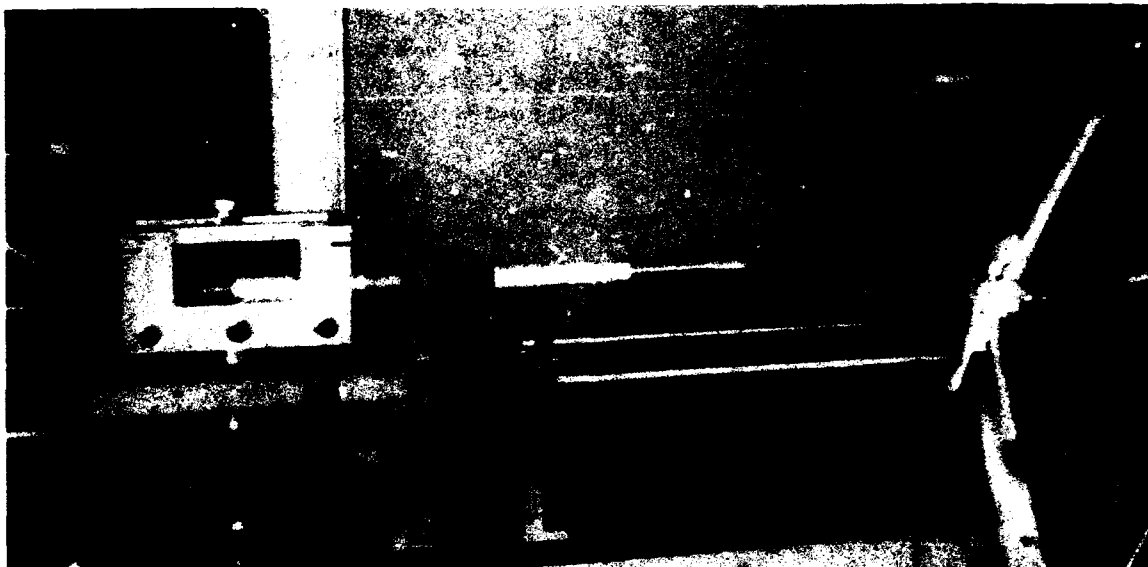


Figure 4: The main unit of automatic bench for multipole lens measurements.

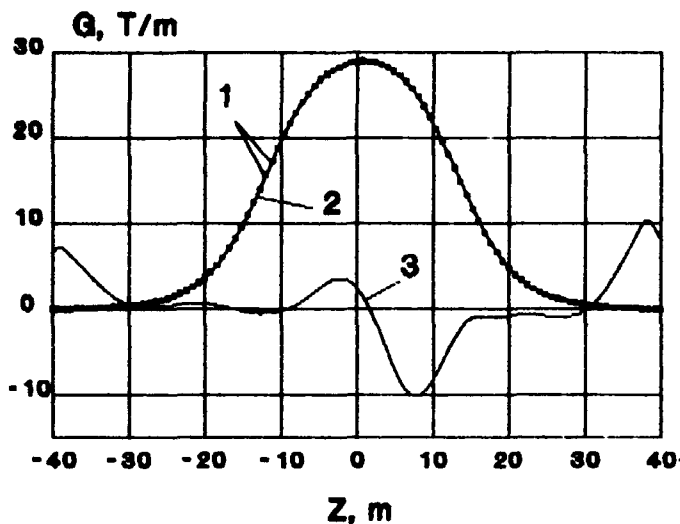


Figure 5: Gradient distribution in 25 mm long rod-type Sm-Co PMQ for ISTRA accelerator. 1 - calculated values (points) from experimental data, 2 - theory dependence, 3 - curve of difference ( $\times 100$ ). r.m.s. deviation =  $6.4 \cdot 10^{-3}$  (0.02%).

a way that its longitudinal axis coincide with axis of two coupling holes by ground finger with accuracy  $10\mu\text{m}$ . The Hall probe is mounted inside the long rod of 18 mm OD 70 mm far from its left end and is oriented with its normal along radial direction. In the right side one can see the movement system with position pickups and the Hall signal preamplifier box.

The measurement procedure runs in following sequence

- Instrument calibration.
- Routine loading into PC memory.
- Field sampling in points of cylindrical surface.
- Data processing and producing of main result.
- Checking the lens measured for quality.

On the instrument calibration stage the special dipole magnet with homogeneous field and NRM device are used. Within 0.3T range of field values it is possible to substitute the real voltage-field Hall probe dependence by linearized one due to small deviation of 0.5 mT (r.m.s.). In the case of wider field range the program simulated regime of voltage-field conversion is provided in accord with real dependence.

Before measurements the necessary sensitivity is chosen by appropriate selection of attenuation factor in amplifier channel to match the maximum loading of analog-digit transformation range at maximum field value in a lens to be measured.

The total running time depends on number of points where the field is measured. It is usually 15 minutes and is provided due to short time response ( $25\mu\text{s}$ ) through Hall probe signal channel. During that period the information in about  $10^5$  points on cylinder surface is accumulated. It gives a possibility to fulfil a statistical treatment of accidental errors on one hand and to provide a detail description

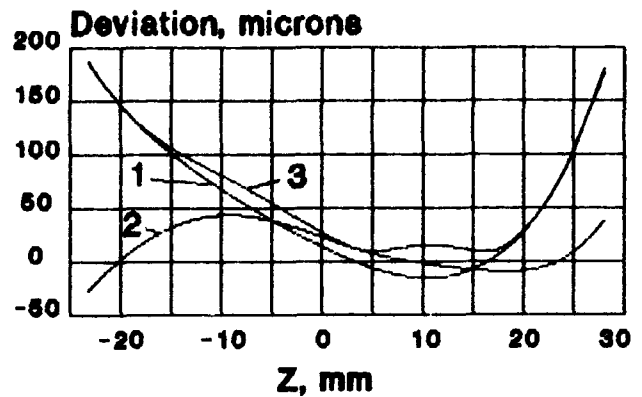


Figure 6: Magnetic axis displacement from geometrical axis. 1 - deviation along x-axis, 2 - deviation along y-axis, 3 - total deviation.

of field distribution on the other.

The total error of absolute measurements does not exceed  $\pm 0.3\%$  of maximum field value. It contains in general digital transformation uncertainty being  $\pm 1$  bit.

#### 4 APPLICATION

The described magnet measurement complex was used as a bench during manufacturing of focusing channel for ISTRA accelerator. It provided both to eliminate errors in magnetization distribution and to carry out computer simulation of beam dynamics. But probable applications of that device are much more wider. It can be used for magnets with arbitrary field configuration as well as for precise field tuning when observation of continuous field changes is desirable. The developed method of spatial modeling gives a possibility to determine all required performance characteristics from spatial harmonics spectral description to integral distributions of a field. On Fig.5 and Fig.6 the longitudinal distribution of gradient and magnetic axis displacement for short PMQ are given respectively. It shows a possibility to detect and localize significant imperfections at low level of values.

#### 5 ACKNOWLEDGMENTS

Authors thank all specialists of division for automatic developments which took part in manufacturing of magnetometer.

#### 6 REFERENCES

- [1] L.M.Kapchinskiy, V.S.Skachkov et al. "Drift Tubes for a Focusing Channel of Ion Linear Accelerator". Proc. of 1998 PAC, IEEE, vol.2, Chicago, USA, p.1073.
- [2] D.J.Liska, and L.B.Dauelsberg. "A Ramped Gradient Drift Tube Linac". Proc. of 1987 PAC.

# Measurements of Loma Linda Proton Therapy Gantry Dipoles

Henry D. Glass, Peter O. Mazur, James W. Sim  
*Fermi National Accelerator Laboratory\**  
*P.O. Box 500, Batavia, IL 60510*

## Abstract

We describe the procedures used by the Fermilab Magnet Test Facility (MTF) to perform tests of dipoles to be installed in the beam lines of the Loma Linda University Medical Center Proton Therapy Facility. The dipoles were manufactured in two styles, one style having a 45° bending angle and the other a 135° bending angle. The tests included magnetic field measurements using a Hall probe and the measurement of coil temperatures, voltages, and water flow rates. The probe was mounted on a movable cart which could be wheeled along the magnet beam pipe; we mounted extensions onto each end of the beam pipe to allow for the probe to measure the magnet end fields. The probe was also mounted at varying transverse positions on the cart to allow for field shape measurements, from which body quadrupole and sextupole coefficients were determined. A longitudinal sampling of the field down the entire length of the magnet allowed us to measure the total integrated field of each magnet. Hall probe measurements were controlled by a C program running on a Unix workstation.

## I. INTRODUCTION

This report describes the procedures used by the Fermilab Magnet Test Facility to perform tests of the Loma Linda gantry dipole magnets, and also to present the measurement results. The dipoles consisted of two classes, a 45° class (of which there are two styles called Type 1 and Type 2), and a 135° class. The tests included magnetic field measurements with a single Hall probe and some auxiliary measurements of coil temperatures, voltages, and water flow rates.

\*Operated by Universities Research Association under contract with the United States Department of Energy

## II. MEASUREMENT APPARATUS

Each magnet was mounted on MTF Test Stand C and powered by two PEI power supplies connected in parallel. Magnet current was measured by a Holec transducer and read out by a digital voltmeter. The Low Conductivity Water (LCW) system provided cooling at a nominal 26.5 liters/minute flow rate. Thermocouples attached to the supply and return monitored coil temperatures. The Hall Probe was read out by a Digital Tealometer (Group-3 Corp. Model DTM-141), which featured a digital display and a GPIB interface for computer readout.

The probe was mounted on a wheeled cart which was positioned longitudinally by rolling inside the magnet's beam tube. Stainless steel extension tubes, having the same cross section as the beam tube (5.08 cm x 2.54 cm), were attached to each end of the magnet to allow the cart-mounted probe to measure the magnet's end fields. The far end of the extension tube on each end extended 54.0 cm beyond the plane of the first lamination.

A cloth tape measure was attached to the cart and ran along the inner radius of the beam tube and out the lead end of the magnet. The longitudinal (*z*) position was measured by reading the tape measure at the end of the extension tube. Transverse (*x*) position was defined to be zero at the center of the beam tube, and to increase toward the convex side of the magnet. Different probe *x*-positions were obtained by using screws to mount the probe at the desired position on the cart. Mounting holes were drilled allowing *x*-positions of 0., ±6.35 mm, and ±12.7 mm.

Figure 1 displays a conceptual topview of a Loma Linda magnet as it was mounted on the test stand. The figure shows the coordinate system used.

## III. MEASUREMENT PROCEDURES

Magnetic field measurements were controlled using the *ptscan* (version 1.22) program, which was developed at MTF for controlling Hall and NMR measurements of Main Injector magnets. This program, which runs on a Unix workstation, operates by reading a set of commands contained in a file called a 'checklist.' The checklist contains all of the commands needed to perform the measurement

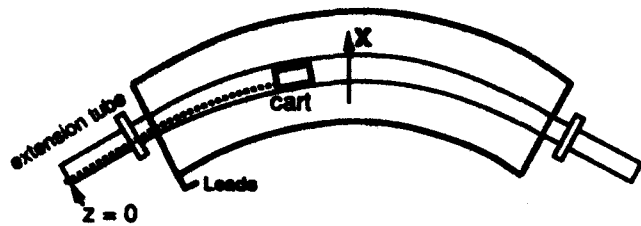


Figure 1: Top view of a typical Loma Linda gantry dipole. The  $z$  origin is at the end of the Lead End extension tube.

sequence. The *ptscan* program, as it executed the checklists, instructed the measurement technician to manually position the probe. Magnet current was set under computer control, and was digitally displayed on the workstation screen. The probe position was entered manually by the measurer, while magnet current and probe reading were obtained by reading GPIB instruments. All data were then recorded to a data file. All current ramps were executed sufficiently slowly (100 A/s typically) to avoid overshoot. In each of the checklists indicated below, we first measured the probe offset by placing the probe inside a mu metal shield. This offset was automatically subtracted from the data by the readout device. Prior to taking field measurements, one or more hysteresis ramps were executed.

#### A. Checklists

1. Central Field Measurement: Position probe in magnet center; loop from  $I=0$  to  $I=3100$  A in 100 A steps; then loop from  $I=3100$  A to 0 in  $-100$  A steps.
2. Body Field Measurement: Loop from  $I=0$  to  $I=2500$  in 500 A steps; then from 2600 to 3100 in 100 A steps. Measure at 3 different longitudinal positions.
3. End Field Measurements: measure longitudinal profile of each end at 12.7 mm intervals. Do at 2000 A and 3100 A.
4. Off-Axis Measurements: At three different longitudinal positions in body, measure field at  $z = \pm 12.7$  mm,  $\pm 6.35$  mm, and 0. Do at 2000 A and 3100 A.
5. Longitudinal Scan: Measure longitudinal variation of field inside body of magnet in 2.54 cm steps (for  $45^\circ$  magnets) or 5.08 cm steps (for  $135^\circ$  magnets). Do at 2000 A and 3100 A.
6. Water Temperature, Coil Voltage, Flow Rate record these quantities as a function of current from 0 to 3000 A in 500 A steps.

## IV. MEASUREMENT RESULTS

The data for each magnet are reported in [1]. The data report includes a tabular listing of the measurements from each checklist, a set of graphs, and a list of calculated results (field integral and harmonics). The tabular listings of magnetic measurements include:  $z$  and  $x$  positions, transducer voltage; magnet current, B field reading from Hall probe, and time from beginning of measurement sequence. Listings of nonmagnetic measurements included the coil voltage, water supply and return temperatures (thermocouple readout), the LCW flow rate, and the water supply and return pressures.

#### A. Field Integral Calculation

The quantity  $\int B dl$  was calculated by combining the data for the end fields and the longitudinal scan. This calculation was performed by the following method:

1. A radius of curvature correction was made to the  $z$ -position measurement. As listed in the data tables,  $s$  is the tape measure reading along the inside radius of the beam tube. To find  $z$  along the center of the beam tube, we calculated

$$z_{\text{center}} = z_{\text{tape}} \cdot \frac{R}{R - w/2}$$

where  $R$  is the beam tube radius of curvature (134.6 cm) and  $w$  is the beam tube width (5.08 cm).

2. We wanted to measure the field at constant current, but the power supply was observed to fluctuate and drift over the course of the measurement, and also the mean measured current was different from the nominal current. For each data point, we calculated the field at the nominal current  $i_0$  from the measured field at current  $i$  by applying the correction

$$B(i_0) = B(i) - (i - i_0) \left( \frac{dB}{di} \right).$$

The field derivative  $dB/di$  was calculated from the Central Field measurements and was assumed to be constant in  $z$ .

3. The corrected  $B$  fields were calculated from two measurement sets: in the 'pass 1' set, the probe sampled the field as it was moved towards increasing  $z$ , and in the 'pass 2' set the probe moves toward decreasing  $z$ . We calculated the average field at each  $z$  and standard deviation from these two sets.
4. We then integrated the field over the  $z$ -range which included the entire magnet and extended 33 cm beyond each end. This was far enough out so the end field had fallen below 1% of the body field. Integration was performed using the trapezoidal rule. The statistical error in the integral was calculated from the

standard deviations in  $B(z)$ . A systematic scale error of 0.2% for the 45° magnets was estimated from the observation that the cloth tape measure reading depended on the tension applied by the measurer. For the 135° magnets, we switched to a fiberglass tape measure, which had an advantage of being much less vulnerable to stretching, and for these magnets we did not list a scale error.

We note that while the Hall probe, whose active area was about 2.5 mm x 2.5 mm, significantly undersampled the  $z$  variation of the field, we believe the error due to undersampling is small.

## B. Harmonics Calculation

We estimated the normal quadrupole and sextupole ( $b_1$  and  $b_2$ ) from the off-axis measurements by fitting the measured field shape to a polynomial. This calculation was performed in the following way:

1. A current correction to the  $B$  fields was made using the Central Field  $dB/ds$  measurement as described in the previous section.
2. At each  $z$  position, the off-axis fields were normalized to the fields at  $x = 0$  by calculating

$$B_n(x) = \frac{B(x) - B(0)}{B(0)}$$

3. The normalized fields  $B_n(x)$  were averaged over all  $z$ 's and standard deviations calculated. This was an attempt to approximate an integrated field shape; since only three  $z$  positions within the body were measured, this approximation is rather coarse, but the field shape did not vary substantially within the body.
4. The harmonic coefficients were estimated by doing a least squares fit to a polynomial

$$B_n(x) = b_1x + b_2x^2.$$

Only the off-axis points ( $x \neq 0$ .) were used in the fit; the  $x = 0$  data point was accounted for by constraining the fit to pass through zero.

The results are reported in *units*, where 1 unit is defined as  $10^4$  times the relative strength of the multipole to that of the dipole at 2.54 cm radius from the center of the beam tube.

## V. OBSERVATIONS

In the 45° magnets, the center of each magnet in  $z$  was characterized by a dip in the field. Figure 2 shows a typical case. This corresponds to the point where the two halves of the magnet lamination packs are joined together. The

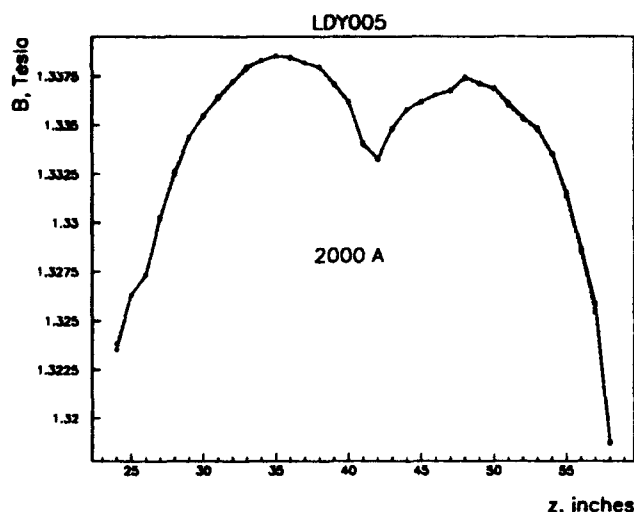


Figure 2: Longitudinal scan of a typical 45° magnet at 2000 A. The two longitudinal segments are joined at  $z = 42$ .

joining is not as tight as would be desired, and a small gap may be observed.

The longitudinal behavior of the 135° magnets is much more complex. The magnets are built from 6 joined sections, plus endpacks, and a 6-fold structure is observable in the body  $z$ -scans. At 2000 A, the amplitude of the modulation in field is about 6 mT out of a 1.332 T mean, or about 0.5% fluctuation. At 3100 A, the magnets are heavily saturated, with a typical sextupole of  $-22$  units.

current, A	$\int Bdl$ , T-m	$b_1$ , units	$b_2$ , units
2000	1.42272	$-3.4 \pm 0.8$	$5.9 \pm 1.7$
3100	1.94910	$-1.7 \pm 1.8$	$-23.9 \pm 3.8$

Table 1: Field integral,  $b_1$ , and  $b_2$  for a typical 45° magnet. The field integral error was  $\sim 5 \times 10^{-4}$  T-m.

## VI. ACKNOWLEDGEMENTS

The authors would like to thank the following individuals at MTF for their contributions to this effort: S. Agrawal, A. Bianchi, J. Garvey, P. Hall, D. Hartness, C. Reid, E. Schmidt, H. Stahl, M. Thompson, and D. Validis. The authors also appreciate useful conversations with G. Coutrakon, J. Johanning and M. Notarus of Loma Linda University Medical Center.

## REFERENCES

- [1] H.D. Glass, P.O. Masur, and J.W. Sim, "Loma Linda Gantry Dipole Measurements," Fermilab Magnet Test Facility Report, MTF-92-014.

# Techniques for Measurement of Dipole Endfields With a Rigid Integrating Coil

Henry D. Glass

Fermi National Accelerator Laboratory\*  
P.O. Box 500, Batavia, IL 60510

## Abstract

The endfield is often one of the most critical regions in conventional accelerator magnets. While the magnetic field structure of dipole ends can be complicated, it can be well described by a few parameters which include the effective magnetic length,  $L_{eff}$ , and the integrated harmonics. Both of these parameters can be measured using a rigid coil which measures  $\int Bdl$  in the endfield region as a function of insertion depth  $z$  and transverse displacement  $x$ . We employ a data analysis technique which uses these measurements to remove body field contributions to the endfield integral, resulting in the effective integrated endfield shape. A least squares polynomial fit is then used to estimate the harmonic coefficients up to decapole. We also present the technique for measuring  $L_{eff}$  as a function of magnet current. These measurement techniques were successfully used in a study to finalize the design of the endpacks for the Fermilab Main Injector Dipole. The techniques are sufficiently general to be useful for other applications, such as the testing of the SSC Medium Energy Booster endpacks.

## I. INTRODUCTION

We describe endfield measurement techniques that were developed for studying various endpack designs for magnet IDM002, the 2nd prototype dipole for the Main Injector[1]. The endpacks were measured using a 2.032 m long rigid probe called a Flatcoil. The probe has 24 turns of 0.254 mm diameter wire wound around an aluminum bar of width 0.635 cm. The turns were spaced in a geometry which minimizes the sextupole contribution of the flux, as expanded about the probe center. The total flux, summed over all turns, is very nearly proportional to the field integral along a path running down the geometrical center of the probe. The probe was mounted on a movable stand which allowed us to insert the probe to various depths inside the magnet. In the *baseline* mode of operation, the

probe records the difference in flux between zero current and current  $i$ .

By aligning the long axis of the probe with the longitudinal ( $z$ ) axis of the magnet, we easily recover the integrated field over the length of the probe:

$$J(z_1, z_2) = \int_{z_1}^{z_2} B(z)dl = \frac{\Delta\Phi}{Nw},$$

where  $N$  is the number of turns and  $w$  is the probe width;  $z_1$  and  $z_2$  are the endpoint coordinates of the probe. We used a coordinate system where  $z$  is zero at the first lamination of the endpack, and is positive going into the magnet. This relation between field integral and flux does not include a correction for the remnant field.

We positioned the probe so that  $z_1$  is far outside the magnet, in a region where the field is negligible. One may therefore approximate  $z_1$  as being equal to  $-\infty$ . The integral then becomes a function solely of the endpoint of the probe that is inside the magnet.

For the endfield shape measurements, data were acquired using Flatcoil probe in the *scan* mode, in which the magnet current is kept constant and the probe scans horizontally across the magnet aperture. By positioning one end of the probe a depth  $z_0$  inside the magnet (the other end being outside the magnet), we measured the field integral as a function of depth and transverse position.

## II. EFFECTIVE LENGTH

### A. Measurement Procedure

We measured the field integral at up to 10 different currents and over a range of probe depths,  $0 < z < 50.8$  cm, stepping every 5.08 cm in  $z$ . At each position the data acquisition program (running on a VAX) recorded the measurements of the current, the  $z$  position, and the flux to a data file. The  $z$  position was the only quantity of the measurement process under manual control, both in terms of positioning (via alignment with a steel ruler mounted on the test stand), and recording.

\*Operated by Universities Research Association under contract with the United States Department of Energy

## B. Effective Length Calculation

The total effective length for a magnet excited to a specified current  $i$  is

$$L_{\text{eff}}(i) = \frac{\int_{-\infty}^{\infty} B(i, z) dz}{B_0(i)} \quad (1)$$

where  $B_0$  is the mean body field. The total integral may be measured using a probe which extends the entire length of the magnet, and  $B_0$  may be measured by a probe which samples only the body field. In a high quality dipole, the body field is very uniform, only falling off as one approaches close to the ends. With this observation in mind, we can re-express Eq. 1 in terms of the steel length,  $L_s$ , and a quantity  $L_{\text{end}}$  which we call the *end effective length*:

$$L_{\text{eff}}(i) = L_s + 2L_{\text{end}}(i) \quad (2)$$

The factor of 2 is present because of our definition that  $L_{\text{end}}$  is the effective length of each end of the magnet.

We used a measurement procedure which measures  $L_{\text{end}}$  using the 2.03 m probe. If the probe is inserted a distance  $z$  into the magnet, then the quantity

$$\ell(z) = \frac{J(z)}{B_0} - z \quad (3)$$

should become constant and approach  $L_{\text{end}}$  as  $z$  becomes larger. The body field,  $B_0$ , is determined by performing a linear fit to  $J(z)$ . The slope is identified as the mean body field in the region  $z_{\text{min}} < z < z_{\text{max}}$  over which the fit is made.

The relative effective length describes the change in  $L_{\text{end}}$  with current and can be determined by choosing a reference current,  $i_0$ , and using Eq. 3 to obtain

$$\Delta\ell(i, z) = \ell(i, z) - \ell(i_0, z) = \frac{J(i, z)}{B_0(i)} - \frac{J(i_0, z)}{B_0(i_0)} \quad (4)$$

The average of  $\Delta\ell(i, z)$  for  $z > z_{\text{min}}$  is used as the value of  $\Delta L_{\text{end}}(i)$ . One may see from Eq. 4 that this quantity is insensitive to positioning errors in  $z$ , a dominant source of systematic errors.

Using the procedure described above we calculated  $L_{\text{end}}(i)$  and  $\Delta L_{\text{end}}(i)$  for each endpack. The results are presented in [2].

## C. Error estimates

A set of measurements was taken in order to understand the contribution of  $z$  positioning errors to the total error in the flux. First, we took four runs at 1500 A with the probe fixed at  $z = 50.8$  cm. These runs produced a standard deviation of the flux equal to  $\sigma_{\Phi}/\Phi = 1.6 \times 10^{-5}$ . This error was identified as being due to a combination of electronic readout noise and accuracy in magnet current readout. Another four runs were then taken, in which the probe was removed and then repositioned at  $z = 50.8$  cm prior to each run. In this case we obtained  $\sigma_{\Phi}/\Phi = 3.6 \times 10^{-4}$ ,

which we attribute to the combined influence of noise plus  $z$  positioning errors. The error due to  $z$  positioning alone is then estimated from these data to be 0.18 mm. Averaging the results of this procedure at selected  $z$  positions gave 0.13mm, which led to a systematic error in  $L_{\text{end}}$  of 0.37 mm.

Some endpacks were measured more than once, usually to determine measurement repeatability or to understand the effect of varying some of the measurement conditions. A test of the long-term repeatability of these measurements was done by comparing measurements of Endpack 1 taken one year apart. During this interval, not only had the endpack been removed and subsequently remounted, but the magnet itself had been removed from the test stand for a period of time. The agreement between the two data sets is very good, being typically 0.2 mm at most currents.

## III. FIELD SHAPE MEASUREMENTS

This section describes how the endfield harmonics were estimated from measurements of  $J(x, z_0)$ . At each selected current we measured  $J(x, z)$  over the longitudinal range  $0 < z < 50.8$  cm in 5.08 cm steps. At each  $z$  position we scanned transversely from  $-6.35$  cm  $< x < +6.35$  cm in 0.254 cm steps. Four scans were made at each  $z$ , and for each  $z$  position we recorded the average of the four scans and the standard deviation in the data file. We inserted the probe at an angle of  $0.6^\circ$  with respect to the lamination face, which coincides with the beam direction.

### A. Body field / End field separation

The first step in the data analysis was to separate the component of the flux that is attributable to the end field from the body field. For probe positions  $z > z_{\text{min}}$ , where  $z_{\text{min}}$  is the location inside the magnet beyond which end effects are unimportant, we can make a linear approximation to the field integral as a function of  $z$ :

$$J(x, z) = \alpha(x) + \beta(x)z \quad (5)$$

The function  $\beta(x)$  can be identified as the body field shape,  $B(x)$ . We can identify  $\alpha(x)$  as the effective end field integral:

$$\alpha(x) = \int_{-\infty}^{\text{end}} B(x, z) dz \quad (6)$$

That is, it is the field integral over some region containing the end of the magnet, with the body contribution subtracted. Note that we do not specify precisely what the upper limit on this integral is, nor do we need to, as long as the probe integrates over a region at least as large as any region in which end effects are important. This is equivalent to choosing  $z_{\text{min}}$  large enough so that  $B(z_{\text{min}})$  contains only body field. For this analysis we chose  $z_{\text{min}} = 25.4$  cm. The error estimated for  $J(x, z)$  was determined from the measured standard deviation in the flux and an estimate of the  $z$  positioning error.

## B. Endfield shapes

Figure 1 shows a superimposed view of all Endpack field shapes at 1500 A. The field shapes are the endfield integrals of Eq. 6 normalised by the quantity  $B_0L$  and multiplied by  $10^4$ . The endfield shapes are observed to be approximately independent of current. The distinct two-hump shape seen in many of the endfields can be parameterised by a large positive sextupole combined with a weaker negative decapole. The magnitude of the sextupole is correlated with the size of the noses on the endpacks. Endpack 10 is seen to have the most desirable shape, in that its deviation from zero is smaller than any of the others.

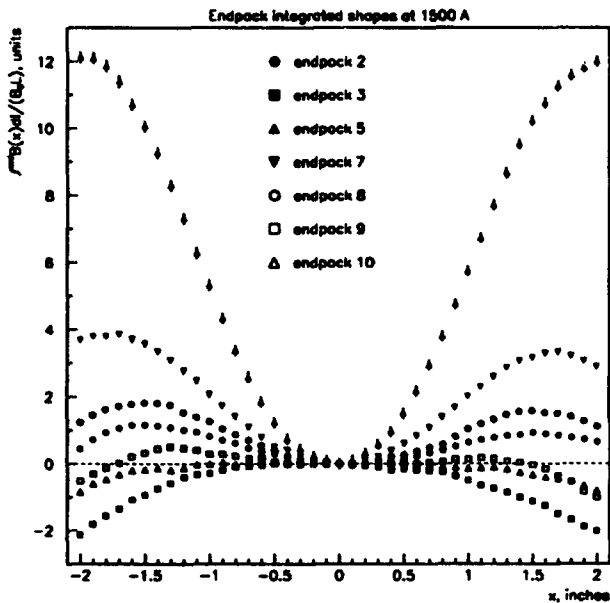


Figure 1: Integrated field shapes for all endpacks.

## C. Estimation of normal harmonics

We obtain the normal harmonics by fitting the function  $\alpha(x)$ , obtained from Eq. 5 to a polynomial:

$$\alpha(x) = \sum_{n=0}^p J_n x^n \quad (7)$$

Prior to performing the fit, the dipole term,  $\alpha(0)$  is subtracted from  $\alpha(x)$ ; this defines an endfield shape function,  $s(x) = \alpha(x) - \alpha(0)$ . In subtracting this constant from  $\alpha(x)$ , we also remove the systematic error due to the probe  $z$  positioning error, since this source of error is the same for all values of  $x$ . We note that there is a simple relation between the effective length due to the endfield and this dipole term[2]:

$$L_{eff} = \frac{\alpha(0)}{\beta(0)} \quad (8)$$

The fit parameters  $J_n$  in Eq. 7 are identified as the integrated normal harmonics over the end region. We chose to report results in terms of normalised harmonics, where the normalisation is relative to the body dipole integrated over the length of the magnet:

$$b_n = \frac{J_n}{B_0L} \quad (9)$$

The value to choose for  $p$  and the region in  $z$  over which to perform the fit were chosen experimentally. Strictly speaking, one may not perform a harmonic fit over a region larger than a circle that just fits within the magnet aperture. Inside the body of the Main Injector magnet, the vertical aperture is 5.08 cm and the horizontal aperture is wide open. Body field shapes are theoretically constrained to be fitted over regions  $x_{min} < x < x_{max}$  such that  $x_{max} - x_{min} < 5.08$  cm. Note that we are only considering regions that are centered vertically ( $y = 0$ ), and therefore skew harmonics can be neglected. At the ends, however, the vertical aperture opens up as a function of  $z$ , and the formal constraints on the fit region become less severe. We chose to fit over the region  $|x| < 5.08$  cm. With regard to the proper choice of  $p$ , we note that for dipoles one may expect important decapole contributions, which suggests choosing  $p$  at least as large as 4; the next "allowed" harmonic after decapole is 14-pole, corresponding to  $p = 6$ . We tried both 4 and 6; the fit to Endpack 10 indicates a need to use  $p = 6$  to achieve a good fit at the higher currents. The results are reported in [3].

## IV. ACKNOWLEDGMENTS

We thank the following individuals for their valuable assistance on this work: S. Agrawal, A. Bianchi, B. Brown, J. Garvey, D. Harding, D. Hartness, S. Helis, P. Masur, J.F. Stiguy, H. Stahl, and M. Thompson.

## REFERENCES

- [1] Fermilab Main Injector, Title I Design Report, August, 1992.
- [2] H. Glass et. al., "Effective Length Measurements of Main Injector Dipole Endpacks," Fermilab TM-1815, Dec. 1992.
- [3] H. Glass et. al., "Field Shape Measurements of Main Injector Dipole Endpacks," Fermilab TM-1820, Dec. 1992.
- [4] D. Harding et. al., "Design and Measurements of Prototype Main Injector Dipole Endpacks," in *Proceedings of the 1993 Particle Accelerator Conference, Washington, DC, May 17-20, 1993*. Institute of Electrical and Electronic Engineers, 1993.

# Lamination and End Plate Design Studies of SSC Low Energy Booster Magnet Prototypes

Nanyang Li

Superconducting Super Collider Laboratory\*  
2550 Beckleymeade Avn. Dallas TX. 75237

## I. INTRODUCTION

The LEB machine includes six kinds of laminated magnets and 4 kinds of laminations. The main quadrupole magnet and low field and high field corrector quadrupoles use the same lamination shape. The chromaticity sextupole, corrector dipole, and main dipole have different lamination designs. To test the physical design and production procedure for the magnets, it is necessary to build 2 or 3 prototypes for each kind of magnet.

The ZVI plant in Moscow, manufactured all 4 kinds of lamination punching dies for the LEB magnets. Each die takes 3 to 5 months to fabricate. SSCL manufactured laser cut laminated magnet prototypes in the SSC shop at the same time.

Since the LEB cycles at 10 Hz, the high frequency current and laminated end plate design causes a delamination problem on the magnet end. This problem is of concern and will be addressed.

## II. LASER CUT LAMINATION

### A. Quality of the laser Cut Lamination

To speed up prototype production and in order to offer some magnetic field information to the Russian collaborators; the SSC shop used laser cut laminations to build the LEB magnet prototypes.

The laser cutting technique is advertised to have a very high machining accuracy of 0.01 mm tolerance over a 200 mm length. But for the 5 kinds of laser cut laminations, only the main quadrupole laminations have reached the  $\pm 0.0125$  mm design tolerance requirements for the critical segments. The corrector quadrupole lamination (the same design as the main quadrupole but made by a different company) pole segment error is around a factor of 10 larger than the requirements. The deviation of the main dipole pole segment on the straight part is around 15 times larger than the design. Even for the very simple shaped trim dipole, one pole on the straight part is still 4 times over the tolerance band. This situation attracted our attention. The laser cutting technique can cut very

complex parts, such as the main quadrupole laminations. But this does not necessarily mean that it will have the necessary accuracy. Industry is familiar with conventional industry standards. It is a rather new thing for them to cut accelerator magnet laminations which are thin and have big transverse dimensions; the shape is rather complicated as well. If we do not carefully choose a good company and do not have a test program for laminations, but just simply believe in the laser cutting technique itself; it is very likely we will have poor quality laminations, even worse than one would expect from conventional tooling methods. When we have poor quality laminations to make the prototype, the physical design problems will be mixed with the mechanical tolerance problems, and it will be hard to separate the physical design errors from the mechanical fabrication errors. The result is that the prototype can only offer a production procedure study but not a physical design study.

From our experience, the conclusion is that using laser cutting techniques to cut laminations may be a good method to build laminated magnet prototypes. It saves time, but it is a very sensitive method as well. Special attention must be paid to the programming and the program running lamination samples.

### B. Different Property between Laser Cut Laminations and Die Punched Laminations

The laser cut laminations have a major difference from the die punched laminations. The laser cut laminations have no burrs, so the stacked core can easily reach almost 100% packing factor. But the die punched lamination core will have a rather lower packing factor. Our laser cut main quadrupole prototype has a 99.8% packing factor and the die punched lamination prototype has a 98.5% packing factor.

The burr characteristic also gives the core stacked from the laser cut laminations a high resistance under high voltage. But the die punched lamination core definitely can not obtain the same value. For the die punched lamination core, the stack resistance is composed of 3 factors: 1. the resistance of lamination coating insulation which is very high; 2. the resistance of steel sheet which is much lower than the coating one, if the stacking

\* Operated by the Universities Research Association, Inc., for the U. S. Department of Energy under contract No. DE-AC 35-89ER40486

compression is reasonable, this resistance can be ignored; 3. the resistance of the lamination edge area which is caused by burrs and can be considered as the steel resistance. When you test the lamination stack insulation, in fact, you can only observe the lamination edge area resistance. Therefore, it is a non-comparable value with the resistance value of laser cut lamination stack. The 10 cm thick stack insulation test shows that the resistance value of the main quadrupole prototype made by the die punched laminations is 2.8 to 4.0 ohm under 5 kg/cm<sup>2</sup> compression at 50 V, the dipole is 0.9 to 1.0 ohm under the same condition. But the 3.0 cm\*3.0 cm\*0.9 cm testing samples obtained  $1.11 \cdot 10^5$  ohm resistance at 1.0 V/mm.

As stated above, the packing factor and the insulation value which were achieved from the prototype made by laser cut laminations can not be used as a criterion to judge the die punched laminations. Otherwise, the two kinds of prototypes made by different laminations should share the same mechanical tolerance and the same magnetic field results.

### III. PUNCHED LAMINATION

#### A. Quality of the Die Punched Lamination

The LEB quadrupole, main dipole, and the chromaticity sextupole lamination punching dies have been developed and several thousands laminations have been punched. Inspections show the laminations have very good quality. All 3 kinds of laminations are qualified for the +/- 0.0125 mm tolerance requirements on the critical segments. It is a real surprise that they are much better than the laser cut laminations. ZVI chose the refined die method for the LEB magnet lamination fabrication. There is no clearance between the guide pins and bushings; pins and bushings are never out of touch with each other; the clearance between the die and the punch is as small as 0.02 mm. ZVI built the main quadrupole lamination die and the punch as one solid piece. ZVI took full advantage of the EDM technique and took the risk as well. If any spot of the die or punch cutting edge is broken, the only way to repair the die is to build a brand new piece. It will cost significant money and time. This adventure obviously supplied a very high quality die and, of course, very high quality laminations. The burrs are as small as 0.02 mm, this means that the deburring procedure can be total eliminated.

#### B. Th Sextupole Lamination

The sextupole laminations show something very interesting. The LEB sextuple design is composed of 2 half cores, i. e. each half has 3 poles, so it is kind of a C shaped lamination.



It is a common knowledge that this kind of lamination tends to open after punching because of the materials inner-stress. In general, it is suggested to use two steps to punch the lamination. First, a rough shape stamp that allows the release of the material's inner-stress and then a punch step to achieve a accurate size pole segments and packing reference segments on the lamination. For the LEB sextupole, its outline dimension is about 479\*220\*0.5 mm; it is rather small and thin. The ZVI plant designed only one die to punch the lamination. They did not adjustments to the die for the opening problem. The inspection results by ZVI in Moscow showed very good quality laminations. Opening did not occur on the laminations at all. The lamination samples were then delivered to the SSC, we re-measured them. The inspection values were different from ZVI report, but in the tolerance band. The interesting thing is that the right and the left poles of the lamination and the right and the left clamping ears of the lamination consistently demonstrated that the lamination did open slightly. I believe there may be ageing. I will continue to study more samples during the sextupole lamination lot production; if the phenomenon indicated above exists in the majority of inspected laminations, it may give us some new information about the opening problem of the C shape lamination. We will get some experimental data between the lamination size and the opening ratio. We may find that we can ignore the opening problem for certain size laminations.

### IV. LAMINATION INSPECTION

#### A. The Principle for Set Up of the Inspection System

There are many ways to set up the lamination inspection system, i.e. the measuring coordinates. But the system that most accurately and directly reflects the possible deviation of the critical part of laminated core after packing should be the favorable one. Such as for the quadrupole magnet, the pole diameter and the gap size between the adjacent poles are the most critical mechanical values to ensure good magnetic field quality. And the datum features of the lamination to reflect these values are the 2 yokes, i. e. the mating surfaces between adjacent quarter cores. So the measuring system should be set on these two features. Then inspection numbers will demonstrate exactly the pole diameter and the gap value. Using the same principle for the dipole

lamination inspection, measurement should use the features which will be chosen for the core packing datum as the X and Y axis. For the sextupole we should choose the bottom most edge and the symmetrical line of the lamination to be the X and Y axis.

To take just the LEB main quadrupole prototype lamination as an example :

The SSC inspection sets up the measuring system as indicated in the left side of figure 2; the ZVI inspection sets up the measuring system as on the right.

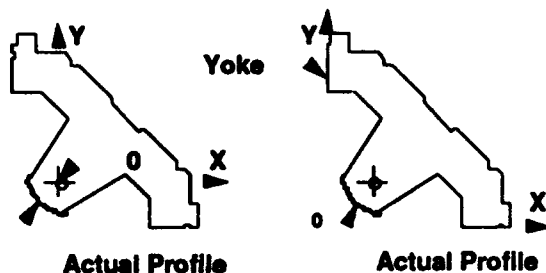


Figure 2. Setup Measurement System

The two inspections show different results. The laminations measured by the SSC system were out of tolerance on the pole tip and the laminations measured by the ZVI system were in tolerance. Of course, the right system is reasonable and reliable. This example shows us that since the magnet laminations have very tight tolerance requirements, an inappropriate measurement system may lead to a wrong conclusion.

The establishment of a lamination inspection system should be thoughtfully considered for each individual magnet .

#### B. The Inspection Programing

Apart from the trim dipole, the LEB magnet lamination poles are a broken line type of design. This kind of design raises a question of lamination inspection: there are two normal lines crossing at the intersecting point of 2 adjacent small straight lines; which one should the inspecting indicator trace? The best way is to write a program which smooths each two intersected broken lines on the pole into an arc and therefore the normal line of the tangent line of this arc will be the trace of the inspecting indicator.

## VI. END PACK DESIGN

To save LEB machine space and avoid eddy currents, the LEB magnets all adopt the glued and laminated end plate type of design. As the LEB is a 10 Hz machine, it is assumed that the high frequency vibration will cause the delamination of the end plates. The glue is not reliable under radiation and for long life times. ZVI made an experiment on a special main dipole model for studying the delamination problem. This model has two different end plates. One is glued and another is not glued. The laminated, unglued end plate was shaking baddly and each lamination was dancing crazily under the 10 Hz power. Just a little tremble could be felt on the glued end plate. But the tear resistance of the glued end plate obviously is a negative factor over the machine life time with such strong split forces.

The INP people proposed a new design to improve the unity property of the LEB dipole magnet end plates. They put a frame of low carbon steel on the top of the laminated end plate and this frame will be welded with the bending plate, which will make it and the core a single element. The frame pushes a solid block of G10 type material toward the laminated end plate and this G10 block is fixed to the pole tip of the end plate by two insulated screws made of non-magnetic stainless steel.

For the main quadrupole end plate, there is a stud through the hole on the pole tip of the core to hold tight the laminated packs and end plate as an entire piece. But since the end plate is chamfered, the end plate will still tend to be split by the 10 Hz vibration. The delamination was observed when we were trimming the end plate chamfer of the main quatrupole prototype even before running AC measurements. The reason is that the glue did not permeate into the gap between laminations thoroughly, and the adhesion was partly destroyed during milling the chamfer. We are going to make some structural change to improve the main quatropole end plate rigidity to ensure it will work as a solid plate. The laminated end plate design was used by Fermi Lab for their DC machine. But there is no experience for use of this design on AC machines. We will continually study problems and find ways to solve them.

# Design and Fabrication of a Multi-Purpose Panofsky Magnet

J. Budnick, T. Hall, D. Li, and S.Y. Lee

Indiana University Cyclotron Facility

Bloomington, IN 47408

## Abstract

A fast, flexible magnet system, consisting of a Panofsky-style ferrite picture-frame magnet and pulsed power supply, has been developed. Magnet specifications are: 8 cm  $\times$  8 cm aperture, 23 cm length, 500 A pulsed/160 A DC, and 1  $\mu$ s risetime. Designed for general accelerator physics studies, the magnet may be quickly converted from dipole to quadrupole or sextupole and higher multipole configurations by easily changing winding end terminations. In the quadrupole configuration a field gradient of 0.5 T/m is achieved at 500 A. This magnet has become an important tool for nonlinear beam dynamics experiments at the IUCF Cooler Ring.

## I. INTRODUCTION

It is well known that beam loss occurs at sum resonances, when the betatron tunes  $\nu_x$ ,  $\nu_z$  satisfy

$$m_x \nu_x + m_z \nu_z = \text{integer},$$

with integer  $m_x$ ,  $m_z$ . Thus, beam dynamics experiments at sum resonances is important in accelerator physics; correction of these sum resonances can improve accelerator performance. A typical beam dynamics experiment is usually performed by measuring the Poincaré map at a resonance condition. However, the beam current within a sum resonance is too small to obtain any useful information; e.g., the stopband width of  $\nu_x + 2\nu_z = 13$  resonance at the IUCF Cooler Ring is typically 0.01. A fast quadrupole capable of producing a tune shift of the order of 0.03 at a rise time of 1  $\mu$ s would serve the purpose for accelerator physics experiments. The method is to jump onto the sum resonance by using the fast quadrupole and observe the beam response as a function of initial betatron amplitudes. Such a process can be achieved by firing a fast quadrupole and then allowing the magnet current (and tune) to die away from the resonance band, back to the original DC tune. One useful operational outcome of such a technique is the ability to jump over intrinsic depolarizing spin resonances and thereby accelerate beam with little polarization loss [1].

To investigate these behaviors and related nonlinear dynamics at the IUCF Cooler Ring we developed a fast ferrite magnet and pulsed power supply. The magnet uses Panofsky-style picture frame construction [2], with solid copper windings embedded along the ferrite inner walls. By designing the windings as separate from the winding end terminations we have achieved a magnet of considerable flexibility. Changing

end terminations allows use as both dipole and quadrupole; modeling also suggests sextupole configurations.

## II. MAGNET DESIGN

We had on hand a large number of 2.54 cm  $\times$  5.02 cm cross-section, 22.9 cm long ferrite slabs. These were cleaned and glued together with a commercial cyanoacrylate ester instant adhesive [3]. The ferrite frame was strengthened by bonding 0.32 cm thick G-10 fiberglass sheets to the ferrite outer walls using silicone RTV. The assembled ferrite frame measured 15.2 cm  $\times$  15.2 cm outside dimensions, 23 cm long, with a 10.2 cm  $\times$  10.2 cm inner aperture (effectively reduced to 8 cm  $\times$  8 cm by the later addition of the copper conductors and fiberglass carrier plates). The top ferrite slabs are free to slide in and out of the lower "U" shaped ferrite frame. This allows insertion around a beampipe by temporarily disconnecting the end termination cables, raising the magnet from below the beampipe, reinstalling the top ferrite/conductor assembly, and reconnecting the end termination cables.

The winding conductors were fabricated from 1.9 cm wide, 0.64 cm thick copper bars. Because the turn-to-turn voltage during the 1  $\mu$ s current ramp-up exceeds several kV, conductor edges were radiused to minimize E-field strength, which otherwise leads to flashover during turn-on. Winding ends were drilled and tapped for #8 screws to form end connections. Carrier plates, constructed of 0.64 cm thick G-10 fiberglass, were milled out to accept the copper bars. These bars were bedded into the G-10 with a thin RTV layer; the G-10 carrier plates similarly attached to the ferrite inner walls (Figure 1).

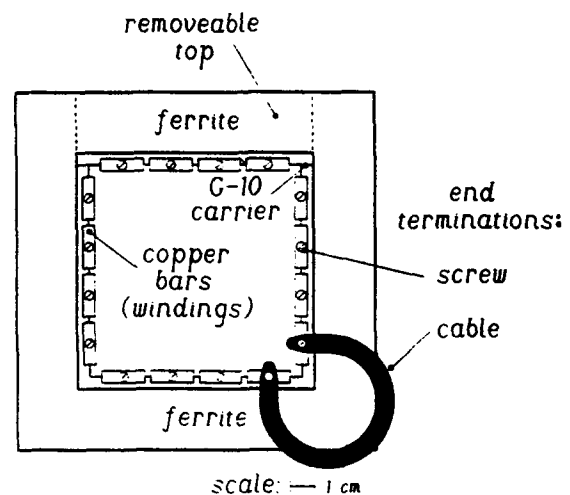


Fig. 1 Magnet construction

Support by U.S. National Science Foundation, NSF PHY 9221402

The completed magnet was mounted on a support base with leveling & centering screws.

For low frequency modulation field monitoring, a demountable, compact field pick-up coil can be attached inside the magnet aperture. This connects to integrator/amplifier electronics mounted on the base plate, providing a high-level field monitor signal over 30 Hz to 300 kHz.

### III. POWER SUPPLIES

For pulsed current work, a supply using capacitor energy storage and ignitron switch tube was designed and built (Fig. 2). Both high- and low-voltage capacitor banks in the supply

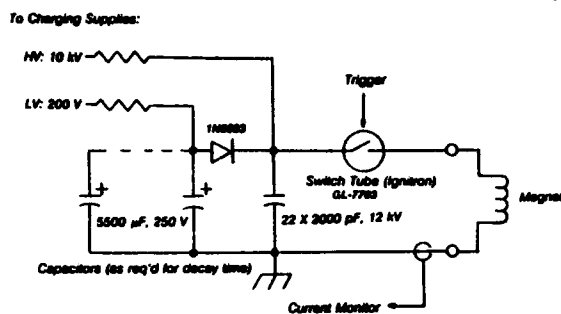


Fig. 2 Pulsed supply topology

are precharged from 10 kV and 200 V charging supplies. A trigger pulse fires the GL-7703 ignitron tube; magnet current resonantly rings up when the charged, 44,000 pF, 12 kV capacitor bank is placed across the magnet. As the magnet approaches peak current at 1/4 cycle (1  $\mu$ s) into the sinusoidal ring, magnet voltage approaches zero crossing. At this point the 1N5603 diode stack forward biases, placing the 22,000  $\mu$ F low-voltage sustaining current capacitors across the magnet. The magnet and capacitors then discharge as a simple RC combination with  $\tau = 3$  ms time constant. Circuit construction utilizes 22 paralleled 2000 pF, 12 kV plastic capacitors for the high-voltage capacitors and four 5500  $\mu$ F, 250 V capacitors for the low voltage bank, allowing considerable flexibility in adjusting rise/decay times for different magnet loads. High- and low-voltage capacitors must be charged in a certain ratio, with a low-voltage offset added for diode forward drop. Tracking is handled by an analog charge programming circuit, adjusted for optimum high-to-low-voltage transition (Fig. 3).

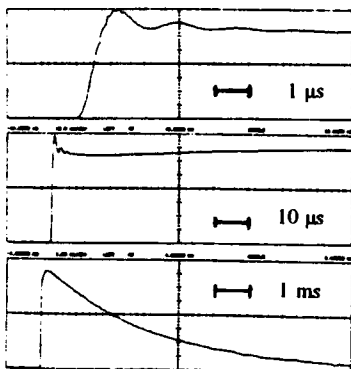


Fig. 3 Pulsed supply current (into quadrupole)

The ignitron approach gives timing jitter of the order of 200 ns over several dozen pulses (and total system delay of about 2  $\mu$ s). Jitter is not as good as with thyratrons but (with Cooler ring single-bunch orbit time of 1  $\mu$ s at 45 MeV) acceptable. Peak ratings for the GL-7703, at 100 kA and 25 kV, far exceed figures for thyratrons of comparable price. Tube robustness and simplicity is another advantage of the ignitron approach, improving reliability by eliminating costly precision filament supplies and reservoir heaters.

Present limitations on higher current performance for the supply/magnet system come from the 1N5603 high-voltage diodes. Extensive testing with  $\tau = 3$  ms has set a peak pulse current rating of 500 A as an upper limit.

For low-current, low-frequency work a bipolar 20 A power supply is used. Measurements on stainless steel beam pipe of 0.23 cm wall thickness gives an upper -3 dB rolloff at 1.2 kHz [4], allowing modulation studies [5] at these low frequencies.

### IV. MAGNET MODELING AND MAPPING

The Panofsky design makes use of conductor images appearing in the ferrite such that, with proper geometry, a symmetrical, infinitely repeating arrangement of current carrying conductors effectively exists. As conductor symmetry is critical in establishing imaging and desired field uniformity,

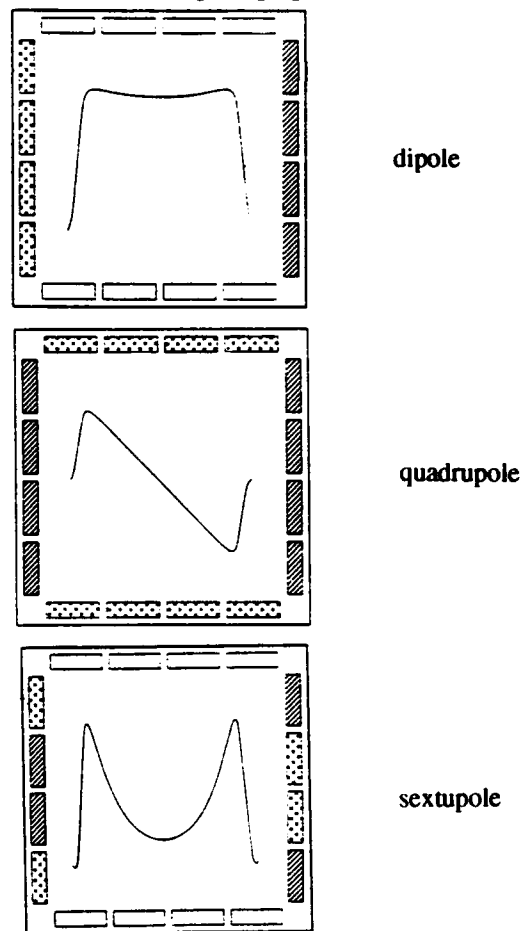


Fig. 4 Magnet multipole configurations ( $B_y(x)$ )

minor misalignments create error multipoles. Although, in principle, single sheet conductors along the ferrite walls could be used to establish field, in practice this has the disadvantages of requiring high currents and causing non-uniform current distribution during short current risetimes. After evaluating supply requirements and mechanical complexity, the compromise of 4 conductors/side was chosen. As seen in Fig. 1, mechanical details prevent the 8 corner conductors from being placed symmetrically with respect to the ferrite (the conductor-ferrite edge gap should be half the conductor-conductor edge gap). This creates, in the dipole example of Fig. 4, about a 6% sextupole component on top of the dipole field. To correct this effect we evaluated the addition of small corrector windings in the corners; optimum results were obtained by making corrector winding current 1/4 of main conductor current, shown in Fig. 5.

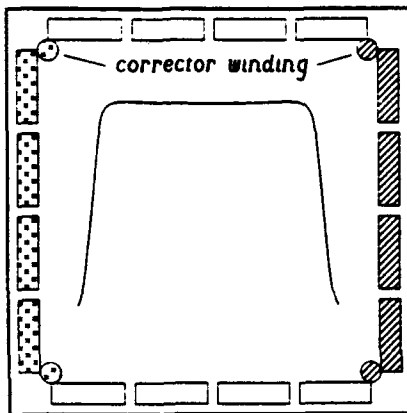


Fig. 5 Dipole with symmetry corrector windings

We used the POISSON modeling code to evaluate DC performance; figure 4 shows dipole, quadrupole, and sextupole results. To establish DC field maps we ran the magnet at its temperature-rise-limited rating of 175 A, with figure 6 showing

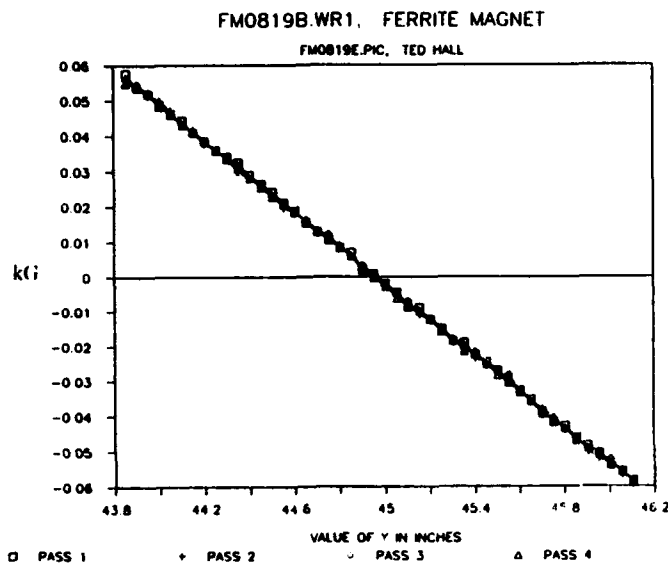


Fig. 6 Quadrupole DC map data (horizontal scan)

good quadrupole field linearity. Four passes smoothed out the mapper data, which is running at about the hardware noise floor here. The 0.19 T/m gradient matched the POISSON result; at a 500 A supply limit this gives 0.5 T/m.

To evaluate pulsed performance, a pickup loop and passive RC integrator was employed to observe the B field pulse leading edge. Figure 7 shows quadrupole results, indicating excellent linearity across the aperture.

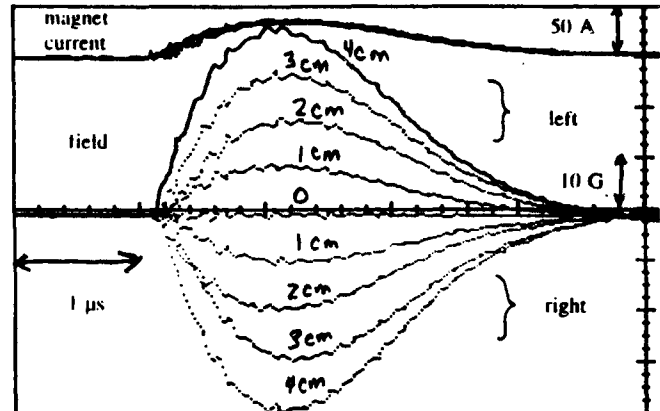


Fig. 7 Quadrupole pulsed field map (horizontal scan)

## V. RESULTS AND FURTHER PLANS

The magnet has been successfully used as both dipole and quadrupole. For low-frequency work the magnet is inserted around normal 0.23 cm wall thickness stainless steel beampipe. High speed pulsed runs require insertion around a 7.6 cm diameter ceramic beampipe. Future work may employ the magnet in quadrupole mode which, in conjunction with a fast kicker, would allow beam echo studies.

## VI. ACKNOWLEDGEMENTS

We thank Dr. Robert Pollock and Terry Sloan of IUCF for use of their ferrite, and Dr. Alan Krisch, Rick Phelps, and the University of Michigan CE-20/40 collaboration for allowing us to use their ceramic beampipe for magnet insertion.

## VII. REFERENCES

- [1] F.Z. Khiari, *et al.*, Phys. Rev. **D39** vol. 1, pp. 45-85 (1989).
- [2] G. H. Morgan, "Shaping of Magnetic Fields in Beam Transport Magnets", in *AIP Conference Proceedings 249: The Physics of Particle Accelerators*, Upton, NY, 1992, pp. 1242-1261.
- [3] Loctite Corporation, Newington CT 06111, Prism Series 410 Black Toughened Instant Adhesive, item no. 41045.
- [4] J. Budnick and G.D. Rondeau, "The IUCF Cooler Ring Betatron Tune Modulation System", in *Conference Record of the 1992 IEEE Nuclear Science Symposium*, Orlando, FL, November, 1992 (in press).
- [5] M. Syphers, *et al.*, "Experimental Simulation of Ground Motion and Power Supply Ripple in IUCF Cooler Ring", this conference.

# Magnetic Septa Design and Performance For Injection And Extraction To And From The MIT-Bates South Hall Ring(SHR)\*

R. Averill, K. Dow, H. Enge, J. Flanz, E. Ihloff, M. Farkhondeh, C. Sibley  
MIT-Bates Linear Accelerator Center  
P.O. Box 846, Middleton, MA 01949

## Abstract

This report discusses the design, construction, testing and installation of 2 magnetic septa in the South Hall Ring Lattice for the injection and extraction of an electron beam of energies from 0.3 to 1.0 GeV. The report covers: magnetic design and performance of the following; steel return frame, electrical coil design, power supply, vacuum vessel, supports, fiducialization, and magnetic measurements.

## I. GENERAL

The magnetic septa specifications are to horizontally bend an electron beam of up to 1.0 GeV energy through 60 mr. The septum width must be less than 8 mm to allow sufficient clearance for the injected and extracted beam and the circulating beam. Multi-turn injection and resonant extraction are planned. The magnet gap, window, and length dimensions were determined to be 1.44 cm, 7.0 cm, and 99 cm respectively. The final configuration for the core was modelled on POISSON<sup>1,2</sup>. The low external side fields outside the septa were reduced further by the addition of a 90% nickel, 0.75 mm thick, cylindrical magnetic shield. The shield tube also acts as a shield for the S-band electron bunches and reduces the beam/tank structure interaction. The watercooled

C-frame septa are mounted on flanges to allow the units to be installed on the vacuum side of the large UHV tanks. Flange mounted support bars support the septum 110 lbs. weight. All connections for electrification and cooling water are external to the vacuum and there are no electrical/water joints inside the vacuum envelope.

## II. STEEL ALLOY RETURN FRAME

The return iron material is 4750 forged alloy obtained from Scientific Alloys Inc. of Westerly, RI. The material was machined to within 1/16" of final dimensions and then annealed at 2150° F for 4 hours and oven cooled to reduce the coercive force of the material. Final dimensions were achieved by Blanchard grinding with water based coolants and then a 0.5 mil thick electroless-nickel plating was applied for corrosion protection and for reduction of surface vacuum outgassing rates. The septum steel consists of 2 plates for top and bottom with dimensions 39.0"x4.53"x1.092" LxWxH. The gap is set by

2 ground bars which allow a space for rear access at the mid point for coil lead passage. The bars dimensions are 19.18"x1.429"x0.567" LxWxH. The frame is bolted together

by 2 parallel rows of bolts to provide clamping of the core assembly. A cross section of the septa is shown in Figure 1. A photograph of the septum assembly mounted on the beam line is shown in Figure 2.

## III. ELECTRICAL COIL DESIGN

Several designs were considered using square OD hollow copper conductor, but the available profiles did not fill the gap with enough copper to maintain the design temperature rise and to help reduce the stray field outside the septum. Consideration was given to rolling a square conductor down to a rectangular profile to obtain more copper in the gap and lower the temperature rise. Our designers, through persistence, located a Finnish supplier, Otukumpu, with the desired profile listed in their catalog. Engineers were able to obtain from the vendor's US offices a small quantity (200 lbs.), which more than supplied our conductor needs. The conductor, an OFHC CDA 102 copper alloy, has dimensions of 6mm x 5mm OD/ 3mm RD-ID. This conductor provides an excellent match to the design gap and septum width specifications.

The conductor has a resistance per foot of 229.1 micro-ohms. The coil length for 2 turns is 20 feet, resulting in a magnet resistance of 4.58 milli-ohms at 20C. To drive the gap to 2000 Gauss requires a current of about 1150 amperes, a voltage of about 6.00 volts and a power consumption of 6.8 kW. Each turn conductor carries 1 GPM of water at 80 psid; such that the temperature rise of the water is less than 13.0C at the maximum current of 1150A for 1.0 GeV operation.

Insulation designs considered for the conductor were: ceramic clips, hard coated aluminum sheets, to flame sprayed alumina. Information from G. Fischer of SLAC<sup>3</sup> on a qualified flame spray vendor, BBC of San Jose, CA. resulted in the selected insulation design of 10 mils ( $\pm 3$ ) mils of AL<sub>2</sub>O<sub>3</sub> being flame sprayed onto the conductor. The coil ends are saddled, turned up/down, to allow the beam to pass through. Early designs called for field clamps/supports for the coil ends, but assembly and

\* This work is supported in part by the Department of Energy under contract #DE-AC02-76ER03069.

testing determined that the coil ends were self-supporting. The coil/frame assembly was high potential tested to 1000 volts DC and no leakage was noted. The four end conductors for the windings come out of the vacuum via a flange with 4 insulating feedthroughs. The conductors slide out through the feedthroughs and are brazed via a matching interface copper disc to the feedthrough after final fit up is achieved. From then on the magnet is tied to the vacuum tank large rectangular flange and is handled as a flanged assembly.

The 2 turns are connected, outside vacuum, in series to produce the required magnetic field and are connected with fittings for parallel turn water cooling supply and return. Temperature sensors are installed on the water outlet conductors and with flow switches are part of the septum interlock protection system. Large tabs are connected to the input terminals so that 6-4/0 AWG flexible cables can be connected to each terminal. The 12 cables for supply and return are interleaved in the path from the power supply to reduce stray fields and couplings to other circuits.

#### IV. VACUUM TANK DESIGN

A rectangular design was chosen based on the availability of a suitable 8"x10"x1/2" wall 304 stainless steel rectangular pipe. Various ports and flangements were provided for; beam entry and exit, vacuum pump port, windows for a beam monitor screen, support and fiducial mounts, and the large side flange for the septum magnet assembly. Articulation of the septum is accomplished over the motion of the entrance and exit bellows and by adjustment of the 6 strut support system, which allows vertical, horizontal and azimuthal motion in an independent way.

The tanks were built by Mill Lane Engineering, Lowell, MA and no problems were noted in fabrication. Cleaning and bakeout processes performed allowed a base pressure  $10 \times \exp(-9)$  Torr to be achieved with an O-ring seal. A Helicoflex Delta Seal is planned to be used for the final assembly sometime in the future.

#### V. POWER SUPPLY

The design of the power supply was specified and an order was placed with Bruker Inc., Billerica, MA. for 2 units rated at 12 Volts and 1300 Amperes DC, with current regulated to 10 ppm/°C long term. The units were delivered, installed, tested and determined to be within specifications without any problems. The power supplies are a distance from the septa due to the radiation associated with the electron beam injection, storage and extraction activities planned.

#### VI. MAGNETIC MEASUREMENTS

The magnetic measurements on the septa were made out of the vacuum tank to allow access to the septum gap and external stray fields using the Bates X-Z table with precision Hall probe. Measurements of the end field, internal gap field, and septum external field were taken versus distance and excitation. The reduction of the stray septum field when the magnetic shield was installed was also measured. Plots of the vertical magnetic fields versus axial distance (z); in the septum for the injected/extracted beam, in the shield for the circulating beam are presented in Figure 3. A photograph of the septum mounted on the main flange is shown in Figure 4.

#### VII. FIDUCIALIZATION

The completed assembly of septum/flange was measured to allow use of external fiducial points on the flange to set the horizontal and vertical position of the septum with respect to the beam position at the septum beam entrance and exit points. The success of this program allowed the beam to be directed through the septum on the first attempt to inject the electron beam.

#### VIII. CONCLUSIONS

The septa were constructed and tested on the injection side of the SHR. Both units performed well with electron injection at about 330 MeV. The first unit was removed to modify some tank dimensions. There are some mechanical improvements in the second unit based on the experience gained with the construction of the first unit.

#### IX. ACKNOWLEDGEMENTS

The authors thank the following: D.McCurley, J.Gostanian, and C.Russo for their efforts in the design phase of the magnetic septa, the Mechanical Group for assembly and test efforts, and the Electrical Group for power supply and cabling efforts.

#### X. REFERENCES

- [1] POISSON/Superfish Group of Codes, Los Alamos National Lab., LA-VR-87-126 (1987).
- [2] J. Bitseveld et al., "DC Septum Magnets for the Damping Ring of the SLC SLAC Linear Collider", IEEE Trans. on Magnetics, Vol. 24, No. 2, March 1988.
- [3] Design Work on Magnetic Septum for the Bates Stretcher Ring, H. Enge, Deuteron, Inc. Sept. 1988.

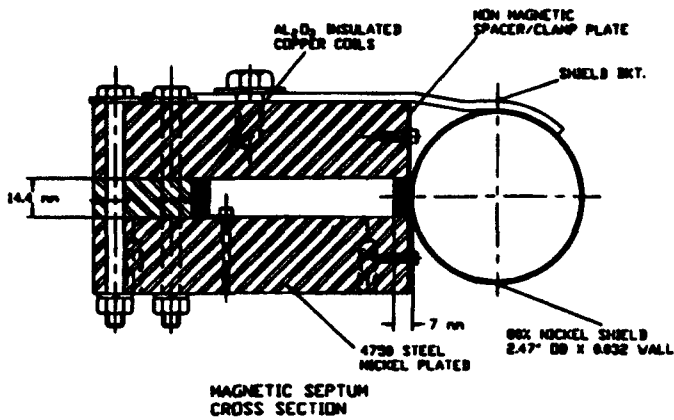


Figure 1. Septum Cross-section.

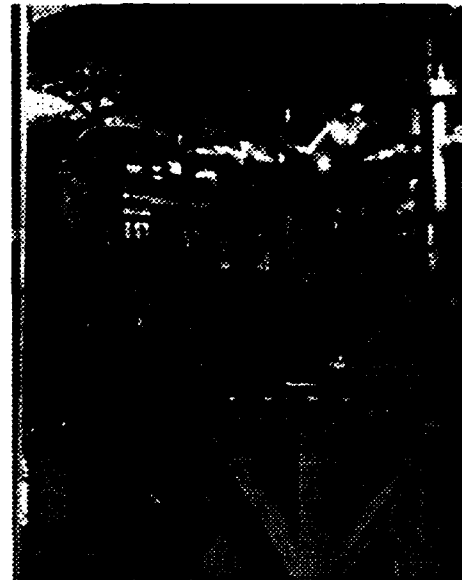


Figure 2. Injection septum installed in Ring.

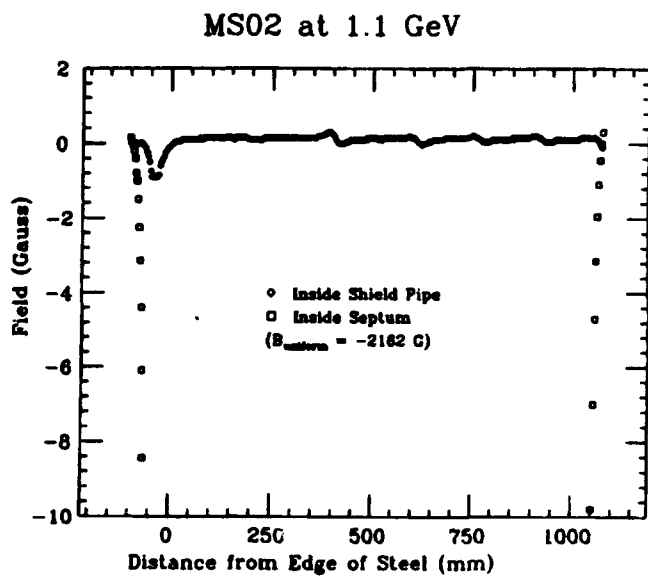


Figure 3.  $B_y(X_2, O, Z)$ ,  $\{+X_1$  inside septum;  $+X_2$  inside shield $\}$  -  $100^{\text{mm}} \leq Z \leq +1050^{\text{mm}}$ . Note: Injected beam along  $(X_1, Z)$ ; circulating beam along  $(X_2, Z)$ .

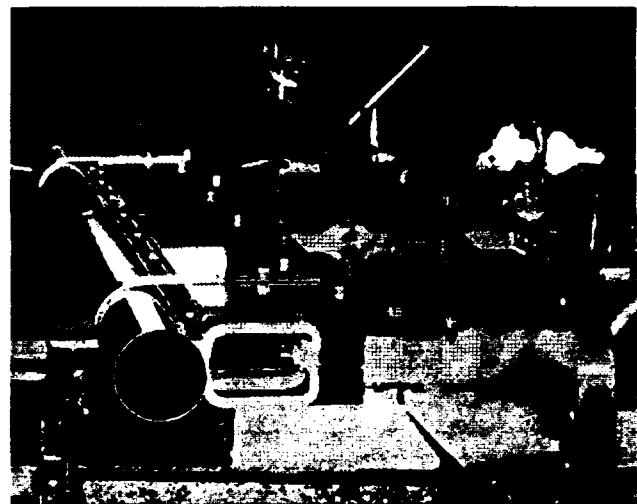


Figure 4. Septum/Shield/Flange Assembly.

# Octupole Magnet Design for the 1/2 Integer Resonant Extraction of Electrons from the South Hall Ring(SHR)\*

R. Averill, J. Flanz, E. Ihloff, D. Tieger  
MIT-Bates Linear Accelerator Center  
P.O. Box 846, Middleton, MA 01949

## Abstract

The MIT-Bates SHR, a 190m long race track shaped electron storage ring with a 9.144m bending radius, is designed for nuclear physics experiments using two modes; the STORAGE mode with internal targets or the PULSE STRETCHER mode, which uses the 1/2 integer resonance and 2 ramped quadrupole magnets and 3 octupole magnets to (smoothly) extract the stored electrons of up to 1.0 GeV energy and 80 mA intensity over a period as short as 1 millisecond into the extraction line.

## I. INTRODUCTION

This report summarizes the design features and results obtained for the octupole magnets, which are characterized by poles of 24.89 cm axial length, located 3.25 cm from the electron beam axis and having variable pole-tip field strengths of up to 6.0 kG, with the pole/coil assemblies mounted in a cylindrical steel return frame.

## II. MAGNETIC DESIGN

The octupole specifications call for a variable octupole field with a minimum of other multi-poles, which is achieved through the appropriate pole tip contour defined by the radius to the pole from the beam axis and by the angle ( $\alpha$ ) from the pole location angle. This radius slowly increases from the minimum  $R_0$  of 3.25 cm according to the following relationship:<sup>(1)</sup>

$$R(\alpha) = R_0 / [\cos 4(\alpha)] \exp(.25)$$

A compromise must be made between the optimum pole angle and the space needed to install the water cooled copper coil and insulation. Iteration of several configurations using the POISSON program<sup>(2)</sup> resulted in the selected design where ( $\alpha$ ) varies from -12 to +12 degrees about each pole tip and which allows a physical space for installation of reasonable coils. Reasonable coil parameters of; turns/pole, current, voltage, power, cooling, and temperature rise were achieved for the selected design.

To determine the required ampere-turns per pole (a-t/p) it is assumed that the field strength varies as the third power of the radius up to the pole-tip where the

design calls for  $B_p = 6000$  Gauss. In the cgs system of units this is also  $H_p = 6000$  Oersted. The assumed variation of  $H(R)$  is cubic and can be expressed as:

$$H(R) = H_p(R/R_0) \exp(3)$$

Integration of this function over  $R$  (0 - 3.25 cm) allows determination of the MMF (gilberts) needed to excite the pole.

$$\text{MMF/p} = H_p(R_0)/4 = 4875 \text{ Gilberts}$$

$$\text{NI/p} = \text{MMF}/0.4(\pi) = 3789.4 \text{ a-t/p}$$

The magnetic efficiency of the magnetic path is assumed to be 0.97, therefore the a-t/p = 3789.4/0.97 or 4000 a-t/p for the coil excitation requirements.

## III. MECHANICAL DESIGN

The return frame is based on a thick wall pipe/tube of 1018 carbon steel with OD/ID of 11.5"/8.5" nominal size, which is "rough machined" to within 1/16" of the final dimensions, annealed at 1500-1800 degrees F for 1-6 hours and oven cooled to relieve internal strains after the auxiliary brackets and support blocks were welded on, then honed to the correct ID. A final electro-less nickel plating of 0.5 mils thickness is added, to provide corrosion protection, completing the frame fabrication.

The poles are made from bar stock of 1003 carbon steel to ensure good permeability at high magnetic field strengths. The poles were rough machined on a CNC Machining Center to within 1/16" of final dimension and then annealed, and finally machined before plating completes the pole(s) fabrication.

The octupole magnet steel parts were preassembled without coils to establish the proper alignment of each pole to the axis and to each other and then bolted up after which the pole/frame interfaces were maked and pinned (Dutchman) to the frame at each end to allow reassembly of the magnet after the coils were mounted on the poles. The magnet final assembly involved the sliding of the coil/pole assemblies non-lead ends into the frame,

\* This work is supported in part by the Department Of Energy under contract #DE-AC02-76ER03069.

locating position by the pins and bolting up tight. Tolerances for the pole locations require the poles to be within  $\pm 0.002''$  to the axis and  $\pm 0.004''$  to each other. Measurements completed indicate that the required tolerances were met in the assembly of the magnetic frame and the poles.

#### IV. COILS

The coil design is based on a copper hollow conductor<sup>[1]</sup> of CDA 102 OFHC alloy with OD/ID dimensions of 0.162 SQ/0.090 RD. The copper is served with a wrap of double dacron/glass fiber to a thickness of 0.006" for turn to turn and layer to layer insulation requirements. Each of the coils have 12 turns per layer for a total of 24 turns per coil. The total magnet resistance is calculated to be 0.202 Ohms at 40 C. The total octupole magnet voltage and power at 167 amperes DC current is calculated to be 33.8 Volts and 5.6 kW respectively. A ground wrap of fiberglass 0.015 thick was placed on the external coil surfaces to provide additional insulation between the coils and the steel frame. The coils were vacuum impregnated with epoxy in a mold. The power supplies chosen to excite the octupole magnets have a rating of 50 Volts and 200 Amperes (10 kW).

#### V. AUXILIARIES

There are attached to the cylindrical steel return frame a number of brackets and blocks to interface the octupoles to the outside world such as; power terminal blocks, interlock box, manifolds for cooling water supply and return, support blocks for support and position adjusters, and fiducial bars for survey and alignment of the octupole magnetic axis on the beam line. The coil ends are arranged to have the cooling water enter and leave the coils in a combined way to reduce the number of hoses to 5 for each manifold.

#### VI. MEASUREMENTS

The octupoles weigh about 200 lbs. The coils resistance has been measured to be 0.024 Ohms and the total resistance measured to be 0.194 Ohms at 24 C. The flow rate at 70 psid was measured at 1.0 GPM total for the first unit delivered. The temperature rise across the manifolds was measured to be 25 C degrees at 179.9 amperes DC with a 1.0 GPM flow rate.

The pole-tip field is linear with current up to 5 kG and then departs from the airgap line by about 10% at 6.0 kG. Measurements of the strength of the octupole and the higher pole content were made on the Magnetic Analyzer at several current excitations including zero. Figure 1 shows the multipole content for the maximum excitation

current and the associated k value  $\frac{B_p L^3}{a^3}$ . Figure 2 shows the k value divided by I vs. I and this curve is fairly constant indicating a linear octupole.

The design effort to produce the three octupole magnets was successful. One unit of 3 delivered has been measured. Figure 3 shows a drawing of the octupole.

#### VIII. ACKNOWLEDGEMENTS

The authors thank H. Enge (MIT) for useful discussions, D. Nicol for the design drafting, and S.Holmburg for the technical support during measurements. Alpha Magnetics, Inc., Hayward, CA fabricated the octupoles in a straight forward manner.

#### IX. REFERENCES

- [1] Parzen, G. Magnetic Fields For Transporting Charged Beams, BNL REPORT BNL 50536 ISA 76-13 January 1976
- [2] POISSON/SUPERFISH Group of codes, Los Alamos Accelerator Code Group, LA-UR-87-115
- [3] Anaconda Hollow Copper Conductor, Technical Publication 56, June 1956

$|B_n/B_4|$  versus  $n$  for Octupole #1 at 179.98 Amps DC  
At  $R = 30$  mm.

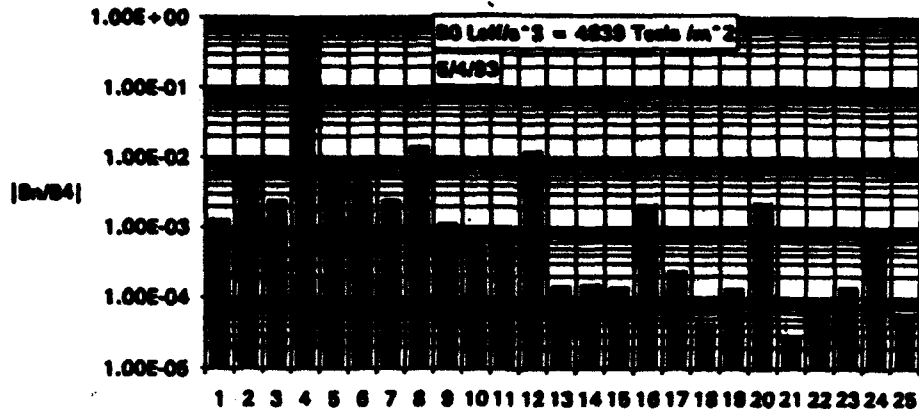


Figure 1. Octupole field harmonic ratios to the octupole field  $n = 4$ .

$B_0 Leff/a^3 = 3(T/m^2) \text{ over } I(\text{Amps})$

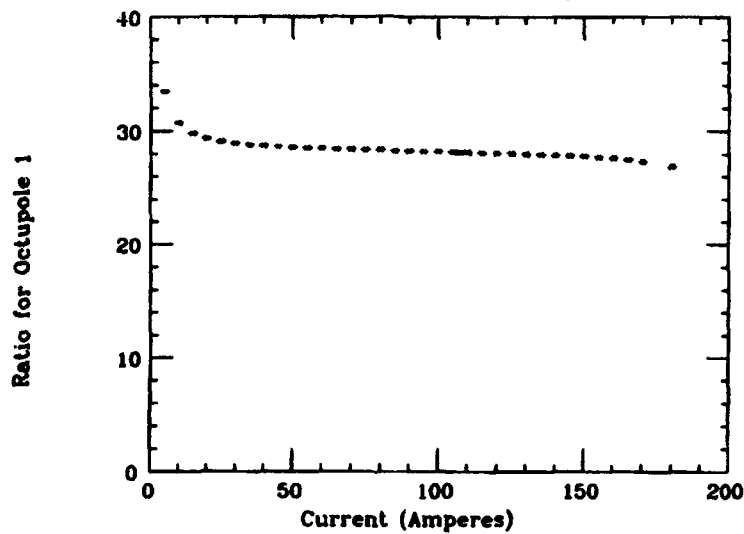


Figure 2.  $k/I$  versus  $I$ .  $k = B_0 Leff/a^3 \exp(3)$ .

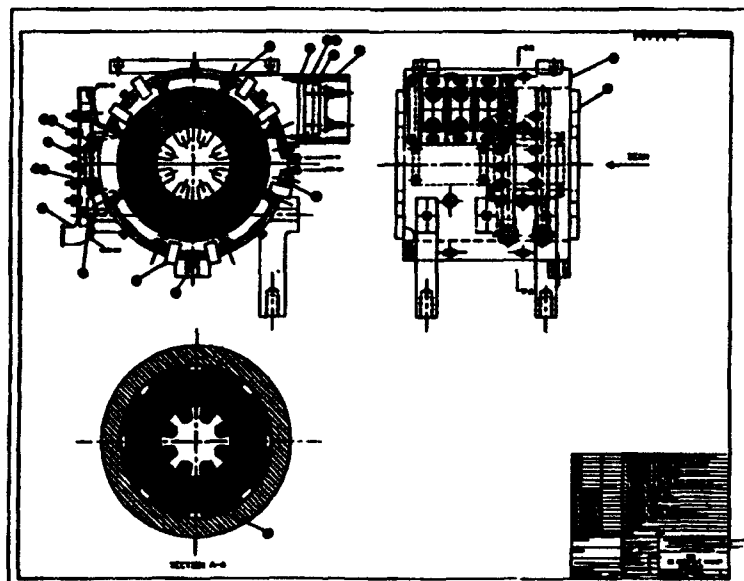


Figure 3. Drawing of the octupole showing 2-views and a section.

# Ramped Quadrupole Design and Performance for the MIT-Bates South Hall Ring(SHR)\*

R.Averill, J.Flaaz, E.Ihloff, D.Tieger,  
MIT-Bates Linear Accelerator Center  
P.O. Box 846, Middleton, MA 01949

## Abstract

This report discusses the design and performance of 2 Ramped Quadrupoles (RQ). They are to be used to rapidly move the horizontal tune close to the half integer (7.5) for extraction of the up to 1.0 GeV electron beam stored in the SHR. The design chosen is an 8 conductor array symmetrically placed about the beam axis at  $\pm 15^\circ$  to the 4 axes and connected to produce a quadrupole field. The conductors are half imbedded in a ferrite shield assembly, outside a ceramic vacuum chamber, and when powered at 250 amperes produce a gradient of about 30 G/cm over the radius of 4.5 cm and along a 30 cm length. The ceramic chamber is internally conductively shielded to present a smooth bore surface for the S-band bunches, but allow the up to 20 kHz quadrupole field components to pass through the shield and influence the electron beam.

## I. GENERAL

The SHR design calls for a half integer beam extraction system to smoothly extract the stored electron beam of up to 80 mA average and up to 1.0 GeV energy during periods as short as 1.0 ms during the interpulse periods of the linac (1000 pps maximum and 1.32 micro-seconds pulse length for 2 turn injection). There are 3 octupoles and 2 ramped quads which make up the resonant extraction beam line components. A review of approaches taken by others in the literature include: current sheets in air<sup>(1)</sup>, current tubes in vacuum, current tubes within flat ferrite plates, and some others with very complex end connections as the number of current elements becomes large. Aircore calculations using MATHCAD determine the resulting field gradients for symmetrically placed current elements about the axis. Calculations were performed for a number of conductors (4,8,12,16,20) at various angles and radii from the beam axis. The selected design was a compromise between a simple configuration and a good field region over a fair fraction of the aperture. By placing the conductors half buried in a ferrite shield, a boost in the internal field strengths by about a factor of 2 and a significant reduction in external stray fields could be expected. This design approach, reduces the required current and power by factors of 2 and 4 respectively, while doubling the inductance.

The horizontal  $\beta$ -function value at the lattice location of the RQs affects the amount of tune shift obtainable.

The planned location has a 20m  $\beta$  value where the expected tune shift per RQ at 250A and 1.0 GeV will be about 0.06, which is conservative given the operating storage nux value of 7.42, which is moved towards the 7.5 half integer value for extraction of the electron beam by the excitation of the RQs.

## II. FERRITE RETURN FRAME

Several manufacturers quoted to the RQ Drawings for the ferrite shield. A contract was placed with NMGI, Bethlehem, PA for a number of ferrite rings (H Material) with 8 half round slots for the conductors to sit into on the ID of the ring. The OD/ID/t of the rings is  $5.40^\circ/3.5^\circ/0.625^\circ$  respectively. The depth of the 8 half round grooves is  $0.125^\circ$  at  $\pm 15^\circ$  to the principle axes to accommodate the OD/ID  $0.250^\circ/0.180^\circ$  hollow hard drawn copper conductors. A prototype assembly of the RQ was constructed to verify  $B_0 \cdot L_{eff}/a$  for the air and shielded design approaches. Because the ferrite shield rings were not available a solid steel pipe was substituted for the shield and proved the expected factor of 2 field enhancement could be approached. The achieved  $B_0 \cdot L_{eff}/a$  at 192.5 Amperes was 0.0852 Tesla. For non-nested conductors a factor of 1.72 was achieved, while placing strips of magnetic material on either side of the conductor to simulate 1/2 buried conductors produced a factor of 1.83 enhancement of the field. The final measurements of the completed final assembly show the field enhancement factor to be about 2. Figure 1 shows a drawing of the unit.

## III. ELECTRICAL DETAILS

The 8 axial conductors are end connected symmetrically as possible to produce the desired quadrupole field and are powered in series. With the ferrite shield outside the conductors the inductance is expected to be about 5.4 micro-Henrys, which is 2 times the inductance without the magnetic shield. The resistance for DC current was measured at 3.4 milli-Ohms and increases with applied frequencies due to eddy currents induced in the water cooled conductors. The maximum current is designed to be about 250 Amperes and the first order current shapes will be trapezoidal or sawtooth. Tune shift control by programming the current to the RQs is required. The period of the excitation will be 1 millisecond or greater depending on the injection-storage repetition rates of the

\* This work is supported in part by the Department of Energy under contract #DE-AC02-ER03069.

injector linac. The final circuit design is not yet finalized, but it is expected that we will drive the current into and out of the ramped quadrupoles by using a linear amplifier to gain experience in the extracted beam behavior at various energies from 0.3 to 1.0 GeV.

#### IV. TESTING

The tests performed on the RQs were done with the ferrite shield and DC current on the Harmonic Analyzer<sup>[2]</sup> to measure the harmonics of the quadrupole fields. Figure 1 shows the relative strengths of the various harmonics as measured at various currents. Measurements of the median plane field and gradient strengths versus radius are shown in Figure 2. Harmonic field ratios for the ramped quadrupole are shown in Figure 3.

#### V. ALIGNMENT

The RQs will be measured to determine their magnetic axes, fiducialized and aligned using MIT-Bates standard methods<sup>[4]</sup>. The RQs can be placed in the SHR lattice to within  $\pm 100$  microns horizontally and vertically using these techniques.

#### VI. CONCLUSIONS

The requirements for a relatively fast quadrupole set to rapidly move the horizontal tune from 7.42 to close to the 7.5 half integer value for smooth resonant extraction from the SHR has resulted in the construction, testing and installation of the above described units. The use of ferrite rings to both boost the internal fields and to provide shielding has proved successful. The array of conductors has provided the required field strengths in a relatively simple arrangement. The excitation circuits while not finalized appear to be feasible and will be constructed in the near future. The system to produce a resonantly extracted electron beam is expected to be tried in the 2nd Quarter of this year.

#### VII. REFERENCES

- [1] H. Ebeling, "Konzeption, Bau und Test eisenloser Quadrupole für die Resonanzextraktion aus ELSA", Bonn Report R-87-35 Sept. 1987.
- [2] J.D. Zumbro et al, PAC91 IEEE Particle Accelerator Conference, Vol. 4, 2125 May 1991.
- [3] S. Sakanaka et al., "Construction of an RF Quadrupole for Suppressing Transverse Coupled-Bunch Instabilities", IEEE Particle Accelerator Conference, Vol. 3, 1836 May 1991.
- [4] M. Farkhondeh et al., "Survey and Alignment of the MIT-Bates South Hall Ring", Proceedings of the 1993 Part. Accel. Conf., May 1993. Poster Session JC71

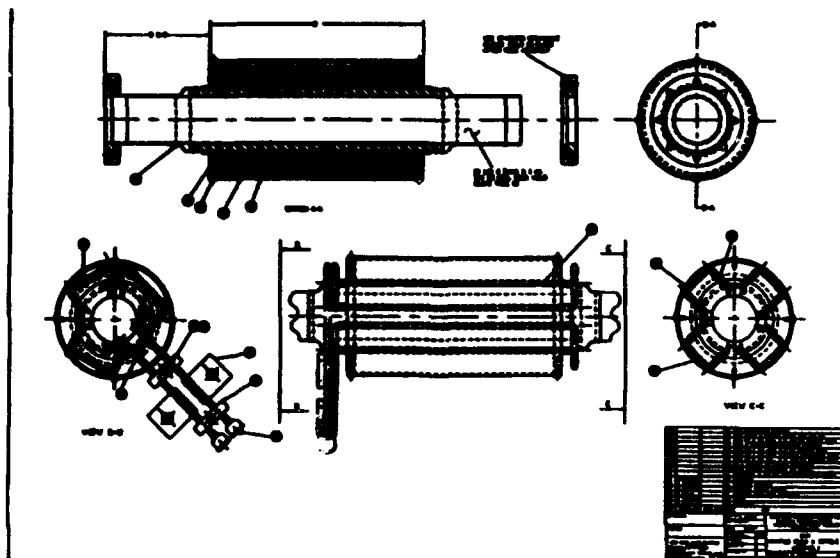


Figure 1.

**$B_y(x)$  and  $dB_y(x)/dx$  versus X for 200 Amps DC for RQ1**

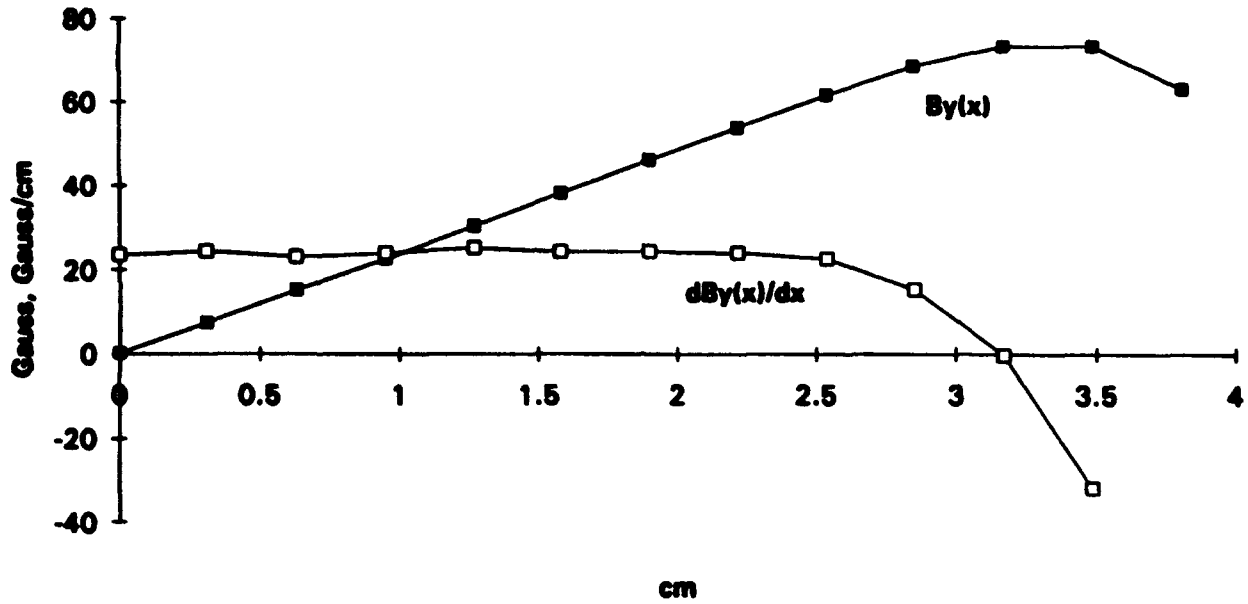


Figure 2.

**$|B_n/B_2|$  versus n for RQ1 at 192.32 Amps at R = 30mm**

$B_{0Left/a} = 0.078324$  Tesla

5/12/93

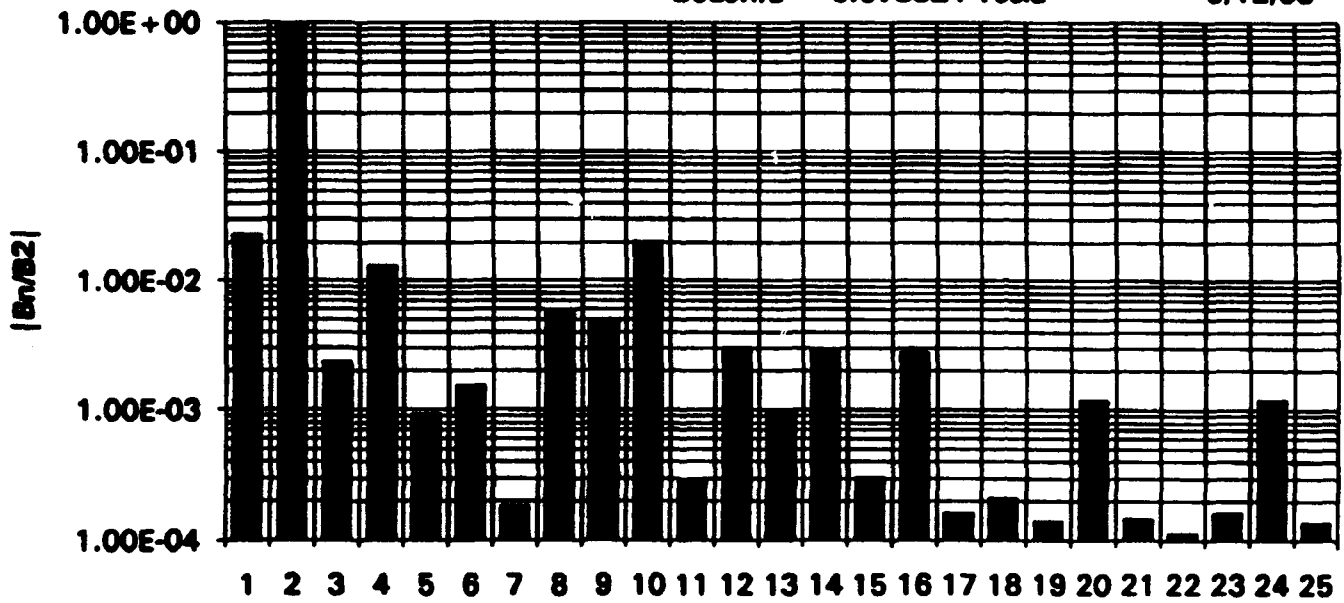


Figure 3.

# LAMBERTSON UPGRADE PROGRAM

Katharine J. Weber

Fermi National Accelerator Laboratory  
P.O. Box 500, Batavia, Ill. 60510 USA

## Abstract

An investigation of a vacuum failure of a Lambertson magnet has resulted in a program to re-evaluate the materials and the method of construction of these magnets. Three additional failures have occurred since the first event. Lambertson magnets are now being built and repaired based on knowledge gained through research aimed at eliminating this type of failure in the future.

## I. INTRODUCTION

A Lambertson consists of an inner core, surrounded by a vacuum skin, an outer core and coils. The inner core, consisting of a stack of laminations, tightly enclosed by a vacuum skin, sits inside an outer core of stacked laminations. There is a cover over the entire top of the magnet.

Over a two year period, four Lambertsons were found to have leaks in the vacuum skin. In addition, three additional Lambertsons are suspected to have leaks. As a result of this, an investigation was conducted and a repair and replacement program was instituted. The conclusion of the investigation was that the stainless steel vacuum skins were failing due to intergranular corrosion.

Intergranular corrosion may occur when the stainless steel undergoes a thermal cycle, called sensitization. When the stainless has been sensitized there is precipitation of a carbide, nitride or other inter metallic phase. This causes the dissolution of the grain boundaries, or closely adjacent regions. If the precipitation is relatively continuous, the depletion renders the stainless steel susceptible to intergranular corrosion.<sup>[2]</sup>

In austenitic stainless steels, such as the type used for vacuum skins, the cause of intergranular attack is the precipitation of chromium rich carbides at grain boundaries. This leaves the stainless steel vulnerable to rapid attack by all forms of corrosion. Certain alloys that are highly resistant to general and localized attack, such as the 300- and 400-series of stainless steels can be affected by intergranular corrosion. Sensitization of austenitic stainless steel can occur when heated in the range of 425 to 870C, with the maximum effect occurring near 675C. Sensitization of stainless often occurs in non-stabilized grades during the welding process.

Stainless steels that have normal carbon content but do not contain any carbide-stabilizing elements are most susceptible to sensitization and intergranular corrosion. Type 304 stainless can be sensitized in about 1 minute at 677C. The most common stabilized grades of stainless are 321, 347, 316Ti, 309Cb and 310Cb. These stabilized grades use titanium, or niobium with tantalum in concentrations of about ten times the carbon content. When these grades are subjected to thermal cycles in the sensitization range, the carbon-stabilizing element forms a precipitate with carbon leaving the chromium in solution. The stabilized grade remains resistant to corrosion.

Stabilized grades of stainless are given a treatment at the mill to ensure that the material is properly stabilized. This treatment consists of heating the material to its solution temperature to dissolve any carbide that may be present. A subsequent heat treatment in the sensitization range precipitates carbides with the stabilizing element, such as titanium, as opposed to chromium.

Although stainless steels are susceptible to several forms of localized corrosive attack, with appropriate grade selection, stainless steel will perform for very long times with minimal corrosion. An inadequate grade of stainless can corrode and perforate more rapidly than plain carbon steel will fail by uniform corrosion. The corrosion performance of stainless steels can be strongly affected by practices of design, fabrication, surface conditioning and maintenance. Corrosion failures in stainless steels can often be prevented by suitable changes in design or process parameters and by use of the proper fabrication technique or treatment.

The vacuum skin on the failed Lambertsons was analyzed and determined to be type 304 stainless steel. This grade could not provide the corrosion resistance required for the application. In addition, the material was sensitized during the fabrication process as well as exposed to corrosives.

The repair and rebuild program effected not only the upgrade of stainless steel used, but re-evaluated all the fabrication processes as well. This program is detailed in the following paragraphs.

## II. MATERIAL SELECTION & PREPARATION

### A. Vacuum Skin Material Selection

Data from log books indicate it was a common occurrence to bake the inner core in the sensitization region. Actual samples removed from the failed skins were examined. They were all found to be sensitized. In addition, samples of the stainless grades used for vacuum jackets were subjected to the conditions outlined in the log book. Under microscopic examination all the samples proved to be sensitized. Type 321 stainless is a grade that has been stabilized with titanium to prevent chromium carbide precipitation. Since this grade is the most commercially available of the stabilized grades, 321 was chosen for the new vacuum skins. Samples of the 321 stainless were subjected to the bake conditions in the log book, and none were sensitized. An additional test was done on the purchased material to verify that the 321 stainless had a sufficient concentration of the stabilizing element, titanium, and that the material had indeed received a stabilizing treatment at the mill.<sup>[2]</sup>

### B. Surface Finish

The optimum surface finish for a satisfactory service life should be one that is smooth and free from surface imperfections, scale and other foreign material. Rough surfaces are more likely to catch dust, salts and moisture,

which can contribute to corrosive attack. An 2BA surface finish is an example of a smooth surface finish.

Type 321 stainless can only be obtained with a 2D finish. In addition, because of the titanium content, this material is difficult to mechanically polish. Electropolishing proved to be the best choice for this application.

Electropolishing can reduce the micro-inch value of a surface by 33% to 66%. Electropolishing removes the "skin" and along with it, all sources of impurities that could become a point for corrosion. This process provides a superior resistance to corrosion as compared to passivation.

In addition, electropolishing is beneficial in vacuum applications by eliminating gases, vapors, and volatiles absorbed on surfaces, which would later be released during pump-down for high vacuum. [2]

#### C. Vacuum Skin Cleaning

Samples taken from the failed vacuum skins revealed significant amounts of chlorine present in the depleted grain boundary areas. Steps were outlined for the new type 321 stainless steel skins to keep them from having contact with any corrosives. [2]

In order to minimize the possibility of corrosion, chemicals should not be used on or near stainless steel whenever possible. Any chemical that does come into contact with the stainless steel should immediately be washed off, followed by a liberal rinsing with alcohol then distilled water. No chemical should be allowed to remain or evaporate on the stainless steel.

The most common corrosive is chlorine, such as in chlorinated solvents, tapping compounds, cutting fluids and fluxes. Chemicals containing chlorine should never be used. Many manufacturers are now distributing these types of products in a non-chlorinated form. [4] Sensitized stainless steel in combination with chlorine is especially likely to exhibit extensive corrosion. Any chlorine residue can initiate corrosion in unsensitized stainless steel, particularly if the steel is subsequently heated. Hydrochloric acid formed from residual amount of a common solvent, trichloroethylene, has caused severe attack in stainless steels.

Oil and grease can be removed by using a detergent and water solution. Weak concentrations of cleaners that contain phosphoric acid have also proved to be successful in removing dirt and grease. [4] All cleaning solutions should be rinsed thoroughly after cleaning. An alcohol rinse will dissolve any cleaner residue left. Follow this with a liberal distilled water rinse, then dry with warm air, dry nitrogen or clean wipes.

#### D. Storage

Parts that will be stored for any period of time should be wrapped in brown Kraft paper and placed in box. The box should be kept in an out of the way area, protected from weather and any accidental spills.

#### E. Lamination Material Selection

Lamination material from the original Lambertsons still remained in stock. Inspection and testing of this material revealed the coating on the material to be protective in nature but not offering any resistive properties. Discussions with physicists and

manufacturers culminated in a specification outlining all required properties for the lamination steel. [12] Criterion was set for acceptance testing of the material. These tests were done by Fermilab or an independent vendor.

It was mandatory that vendors not use any chlorinated solvents on lamination material, since the lamination stack is encased by the 321 stainless skin.

#### F. Lamination Cleaning

Laminations were washed by Fermilab before stacking. They were cleaned in an automated cleaner with a solution of detergent and water. Laminations were rinsed and hot air dried. After washing, laminations were vacuum baked to improve permeability, reduce core loss, reduce absorbed gases and as a final cleaning. [3]

### III. ASSEMBLY MODIFICATIONS

#### A. Stacking

Failed inner core vacuum skins can be replaced by removing the old skin and replacing it with a new skin. Because of the difficulty involved in the reskinning as well as the alarming frequency with the failures were occurring a decision was made to make more spare cores. In the case of a failure the entire inner core could be replaced with a new inner core. The failed inner core could then be allowed to cool to an acceptable radiation level for repair. The reskinning would take place at a more relaxed pace.

Previously built Lambertsons have a press fit between the cores, due to the curvature of the inner stack. Examination of the cores proved this to be true, as indicated by hammer marks as well as laminations out of alignment with the stack.

The failed inner core had relatively deep scratches on the exterior of the vacuum skin, apparently from the process of assembling the inner core into the outer core. Scratches like these can contribute to the failures, by becoming a corrosion site.

Tie bars are welded along the stack of laminations to hold them in alignment. The laminations generally have four tie bar slots, two along the top and two along the bottom. The laminations were previously stacked with two of these slots on top and two on the bottom. This required that the two top tie bars were welded, the stack turned over, and the remaining two tie bars welded. This manipulation of the lamination stack (approx. 20ft long) with little or no support on the three remaining sides caused laminations to move out of alignment. The deformation was permanent and led to the assembly problems, and corrosion sites.

Unfortunately we were not able to change the lamination design. If we had been able to do so, careful reevaluation of the lamination shape could have reduced some stacking problems.

The new replacement inner cores were stacked at 90° from the original stacking position. This left all four tie bar slots exposed. All tie bars are welded before the lamination stack is moved. In addition all welding is alternated to eliminate any heat concentration in one area, which can lead to stack deformation as well. After stacking the core is straight to approximately .002". [5],[6],[9],[10],[11]

After welding, the resulting inner core stack is straight to less than 1/4" from end plate to end plate, approximately 20ft.

In the same manner, the outer core stacking procedure was changed. Outer cores have eight tie bars and three tie plates. The new procedure calls for all tie bars and plates with the exception of the two smallest tie bars to be welded before moving the stack. Welding is done in the same fashion as on the inner core. Outer cores are then surveyed. If the alignment along the inside edge varies by more than .007" over the length of the core, shrink welds are made on the tie plates to bring the core back into alignment.<sup>[5]</sup>

#### B. Skinning

The focus in skinning the inner core was to move the core and handle the materials as infrequently as possible. Every time an inner core is moved during skinning, it is supported on a minimum of two sides. The 'top' skin is placed on a skinning table, then the inner core is placed on this skin. The remaining pieces to form the vacuum jacket are then welded around the inner core. The top skin is tack welded in place before the skinned inner core is turned over and the final welds made.<sup>[5]</sup>

#### C. Baking

After the inner core has been skinned and leak checked, it undergoes a vacuum bake. The core is baked for 14 days. Special controllers on the heat tapes make sure that the temperature never exceeds 400C. After the bake is completed another leak check is done. Ion pumps are then turned on and left to run until the vacuum reaches  $1 \times 10^{-9}$  Torr. The inner core is then ready for assembly or storage.<sup>[5],[8]</sup>

#### D. Assembly

In preparation for assembly, the outer core is placed on the assembly table. The outer core sits on level support bars. The coil is installed in the outer core with spacer insulation in the space between the two cores. The inner core is lifted by four lifting eyes that are welded to the tie bars. The inner core is centered in the beam direction over the outer core and slowly lowered. There is a slight clearance between the two cores if they are both perfectly straight. The inner core is lowered into the outer core as far as it will freely go. If the inner core is not completely seated, bars are then placed across the inner core to help push it into place. There is protective cribbing placed between the bars and the vacuum skin before the bars are bolted to the table. In increments of no more than 1/4" the core is lowered by tightening down the bars, alternating along the length of the core. After the inner core is completely seated, the cover is bolted in place.<sup>[5],[6],[7]</sup>

#### E. Disassembly

In the event a Lambertson needs to be disassembled, such as a vacuum failure or for inspection, a special fixture has been built for this purpose. In the past, the inner core was pulled by the lifting eyes on one end then the other until the inner core was jarred loose. The new fixture pulls on all four lifting eyes with a constant force, eliminating any possibility of plastic deformation from the extraction.<sup>[1]</sup>

#### F. Surveying The Completed Assembly

After assembly there is a final survey of the magnet, to assure the required straightness through the aperture. The magnet is placed on a granite table and a target is pulled through the magnet. Measurements are plotted to determine where the magnet needs straightening. Shrink welds are made on the outer core to pull the magnet into the desired alignment. After each shrink weld has cooled, the aperture is measured again. The data is replotted and shrink welds made as needed. This procedure continues until the entire magnet is within .007" over its entire length.<sup>[5]</sup>

## IV. CONCLUSION

The Lambertson upgrade program has produced magnets which have an increased life expectancy over the previous magnets. After final survey these new magnets are also much straighter through the aperture, since they were much straighter throughout the assembly process. Careful evaluation of every step, from material selection to final assembly procedure is responsible for the success of this program. All steps outlined above are well documented in procedures, sign off sheet and log books. This program is proof that extra time spent in the design and planning phases of a program can produce superior results.

All documents related to this program can be obtained through the author.

## V. ACKNOWLEDGEMENTS

Thanks to M. Kaneshige and R. Kellett for their contributions to the project, and to R. Andrews for his encouragement and support.

## VI. REFERENCES

- [1] R. Kellett, "Lambertson Inner Core Removal Fixture", Fermi Spec. #1323-ES-296052.
- [2] K. Weber, "Corrosion of Stainless Steel Lambertson Skin", Fermi Spec. #1312-ES-296056.
- [3] K. Weber, "Cleaning of Lambertson Laminations", Fermi Spec. #1352-ES-296169.
- [4] R. Kellett, "Mixing & Using Stainless #330 Aluminum & Stainless Steel Cleaner", Fermi Spec. #1301-ES-296069.
- [5] R. Kellett, "A0 D.S.,6" Sym.,F-17,E0 Lambertson Assembly Spec.", Fermi Spec. #1303-ES-296086.
- [6] R. Kellett, "Lambertson Inner Core Lifting Instruction", Fermi Spec. #1303-ES-296092.
- [7] R. Kellett, "Lambertson Outer Stack Lifting Instruction", Fermi Spec. #1303-ES-296093.
- [8] R. Kellett, "Inner Lamination Vacuum Bake", Fermi Spec. #1301-ES-296126.
- [9] M. Kaneshige, "Lambertson Construction Lifting Fixture", Fermi Spec. #1323-ES-296090.
- [10] M. Kaneshige, "Lambertson Inner Core Lifting Apparatus", Fermi Spec. #1323-ES-296097.
- [11] M. Kaneshige, "Lambertson Inner Core Rotating Bars", Fermi Spec. #1323-ES-296098.
- [12] R. Kellett, "Steel Specification for Lambertson Lamination", Fermi Spec. #1351-ES-296025.

# Computer Studies of a Combined-Function Bend Magnet for a Proposed Redesign of the SLAC SLC Damping Rings\*

R. A. Early and T. O. Raubenheimer

Stanford Linear Accelerator Center, Stanford University, Stanford, CA 94309

## Abstract

A proposed redesign of the SLAC SLC Damping Ring requires a combined-function bending magnet. The magnet will operate with a main field of 1.8338 T, and quadrupole and sextupole gradients  $dB_y/dx$ ,  $d^2B_y/dx^2$  of  $-14.1$  T/m and  $-477$  T/m<sup>2</sup>, respectively. Because the orbit sagitta in the magnet is in excess of 2 cm, the pole will be curved with a 2 m radius of curvature. Furthermore, since the current must be variable over a range of  $\pm 2$  percent, we have considered using vanadium permendur poles to avoid adverse saturation effects. Studies were done using POISSON in 2-D and TOSCA for 3-D end effects.

## I. INTRODUCTION

A possible redesign of the Stanford Linear Collider (SLC) damping rings is under consideration [1]. The new ring is designed to have horizontal equilibrium emittances of  $\gamma\epsilon_x = 9 \times 10^{-6}$  m-rad; this is over three times smaller than that in the current SLC damping rings. The reduction in the emittance is achieved by replacing the present bending magnets with combined function magnets. The bends are 68 cm long and operate with a main field of 1.83 T for a beam energy of 1.19 GeV. They have both quadrupole and sextupole gradients of  $dB_y/dx = -14.1$  T/m and  $d^2B_y/dx^2 = -477$  T/m<sup>2</sup>. Each magnet will replace two of the present SLC damping-ring bend magnets which are 30.4 cm long and have peak fields of 2.02 T. Finally, the beam orbit has a 2.2 meter radius of curvature and a sagitta of 2.7 cm in the 68-cm bends. Thus, the pole needs to be curved, following the beam trajectory, to prevent variation of the bending field and gradient through the magnet.

The magnetic gap in the bends was chosen to be equal to the aperture in the quadrupoles, 1.3 cm radius. This allows a constant radius vacuum chamber without the aperture transitions that can increase the impedance of the ring. But, this 2.6-cm gap is 30% larger than the gap in the current damping ring bends, and thus makes it harder to achieve the desired field quality.

We decided to design the pole with vanadium permendur because of its high saturation inductance. This allows us to achieve the desired field quality while reducing the fringe fields. It also prevents differential saturation across the pole so that when the main field is changed by  $\pm 2\%$ , the relative strength of the gradients changes by less than  $10^{-3}$  and higher-order multipoles are not introduced; this would allow the energy of the damping ring to be varied in a straightforward manner.

\* Work supported by Department of Energy, contract DE-AC03-76SF00515.

In the following sections, we describe the design calculations using POISSON [2] and TOSCA [3], then we discuss some of the properties of and experience with vanadium permendur, and finally, we describe the construction tolerance calculations.

## II. DESIGN CALCULATIONS

The bending magnets are 18° sector-bend magnets. The beam enters and exits at right angles to the pole face, although we plan to introduce a rotation to compensate for quadrupole roll-off due to end effects. The first computer studies were done using POISSON, starting from an approximation to the poleface that was obtained with potential theory. The poleface optimization program MIRT [4] was then used to shape the pole such that the required field harmonics were obtained within a 1-cm radius of the beam path. The pole profile is shown in Figure 1. The pole is 11.4-cm wide at the base and has a height of 7.3 cm. It is curved with a 2.2-meter radius of curvature and the beam path is offset 1.6 cm horizontally from the center of the pole where the half gap is 1.3 cm.

A profile of the full magnet is shown in Figure 2. The yoke is only slightly larger than those in the existing SLC damping-ring bend magnets. An extra layer of coil has been used so that the 1.8 Tesla field could be generated with 300 amps; this is well within the capacity of the present power supplies.

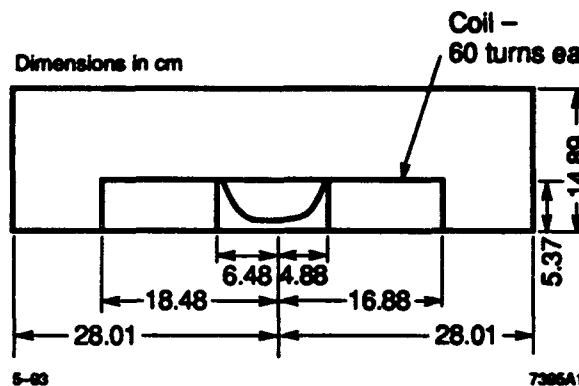


Figure 1 Pole profile of the bending magnet; the main magnetic field is 1.83 T with gradients of  $dB_y/dx = -14.1$  T/m and  $d^2B_y/dx^2 = -477$  T/m<sup>2</sup>.

TOSCA was used to study the effects of the ends on harmonic content. Two views of the mesh are shown in Figures 3 and 4. The coil is a saddle coil because there is very little space between magnets in the damping rings. We used the version of TOSCA that is running on the NERSC CRAY 2 at Lawrence Livermore National Laboratory. The curvature of the magnet was ignored in the

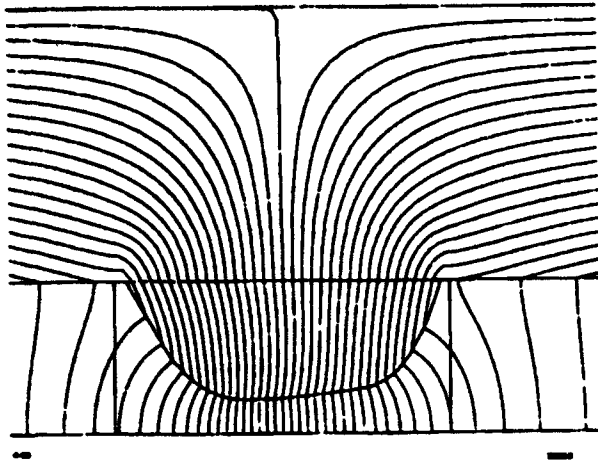


Figure 2 Profile of the bending magnet; the pole is designed with Vanadium Permendur while the yoke is to be constructed of magnet iron; all dimensions are in centimeters.

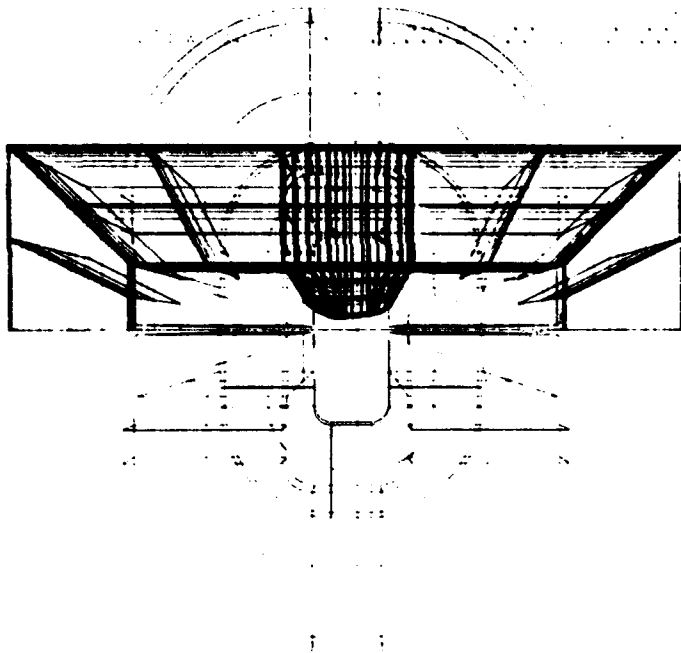


Figure 3 TOSCA finite element mesh for the combined function bending magnet showing the coil position. Only one half of the iron need be modeled, but the full set of coils is required.

3-D modeling. The problem was run with cylindrical symmetry in POISSON with a 2.2-m radius and no significant change was observed in field distribution.

The harmonic content versus longitudinal position in the magnet is shown in Figure 5. Field uniformity within the magnet is good and the fringing fields decay rapidly. Without chamfered nose pieces, the effective length, obtained from TOSCA, is 6% longer than the physical length. The two-dimensional harmonics obtained with TOSCA varied from MIRT results because the number of points on the poleface was smaller. The quadrupole component

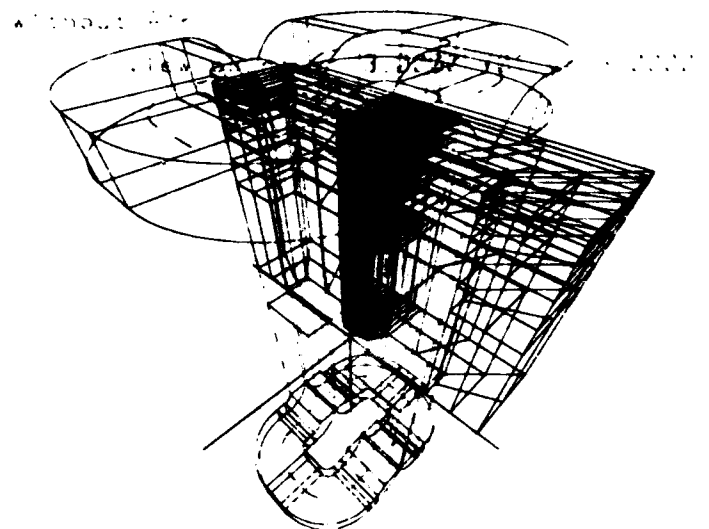


Figure 4 Alternate view of the TOSCA finite element mesh for the bending magnet.

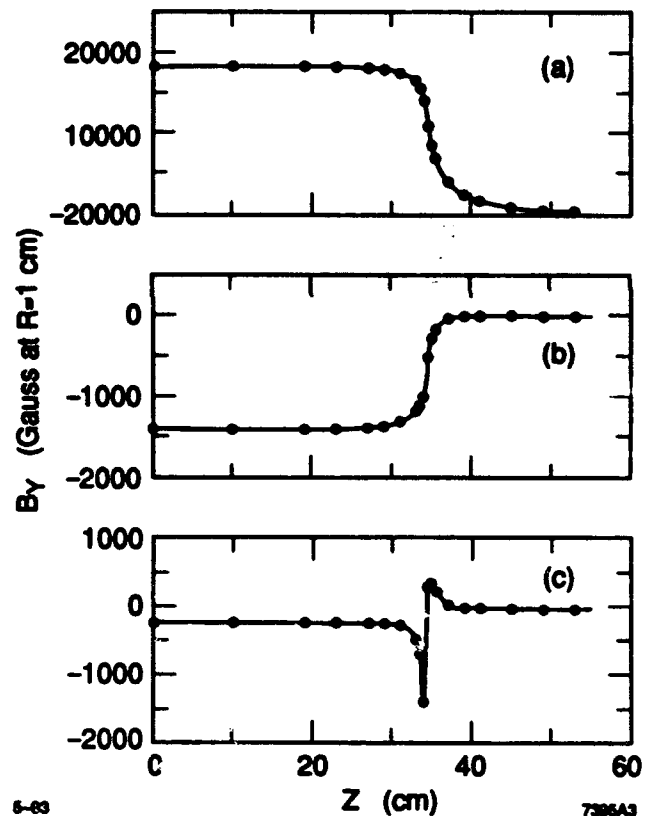


Figure 5 Harmonic content versus longitudinal position in the bend; (a) main field, (b) quadrupole component at  $r=1$  cm, and (c) sextupole component at  $r=1$  cm.

was 0.36 percent higher and the sextupole 5.2 percent lower. When integrated over the length of the magnet, the quadrupole component decreases in absolute value by 6 percent, while the sextupole increases in absolute value by 8 percent. Work is in progress to correct these effects with a combination of pole-end rotation and shaping.

### III. VANADIUM PERMENDUR

Vanadium permendur is an alloy of iron and cobalt in equal proportions with about 2 percent vanadium and has been discussed in previous papers [5,6]. It has a steep  $B-H$  curve and a high saturation induction ( $B-\mu_0 H$ ) near 2.3 T, that makes it useful in the design of magnets in cases where fields are high, but constant magnetic properties are desired.

So far, five magnets using vanadium permendur poles have been built at SLAC. We changed our annealing procedure to a lower temperature than used in Reference 5. Machining can be difficult unless the material is annealed first. At present, our procedure calls for a four-hour anneal at  $750^\circ C$  with a slow cool. A second annealing process is done before the final machining. The procedure leaves roughly 0.5 mm for final machining. One problem which was encountered with our first magnet of this type was that the material had been forged and some distortion was encountered during annealing. This is the reason for doing a second anneal before final machining.

### IV. CONSTRUCTION ERRORS

It was initially thought that the construction tolerances on this combined-function magnet would be very tight. Fortunately, this does not seem to be the case. Dynamic aperture calculations show that random quadrupole and sextupole field tolerances of  $\Delta B_1 \lesssim 0.14$  T/m and  $\Delta B_2 \lesssim 9.5$  T/m<sup>2</sup>, and random and systematic octupole field tolerances of  $\Delta B_3 \lesssim 50$  T/m<sup>3</sup> are acceptable; higher multipoles were not considered. In addition, tuning studies show that recovery is possible from even larger systematic quadrupole and sextupole field errors. Finally, the emittance coupling sets a tolerance of  $\Delta S_1 \lesssim 0.1$  T/m on the skew quadrupole field.

Thus, we have studied five sources of error: accuracy of the alignment fiducials relative to the magnetic center, relative horizontal alignment of the two poles, variation of the magnet gap, flatness of the pole base and the yoke, and the accuracy of the pole contour. The first three sources do not need explanation. The fourth effect, the flatness of the pole base and the yoke, principally changes the quadrupole component and skew quad component because the angle of the pole contour is changed when the pole is bolted to the yoke.

The last effect refers to the accuracy of the pole contour. Assuming a systematic sinusoidal variation of the pole contour:  $f(x) = f_{design}(x) + a \sin(kx + \phi)$ , we can calculate the multipole component using a perturbative expansion:

$$\left| \frac{\Delta B_n}{B_0} \right| = a \frac{k^{n+1}}{\sinh(kh)} \quad (1)$$

where  $h$  is the half gap and  $k$  is  $2\pi/\lambda$  of the error. The tolerance listed in Table 1 corresponds to the sextupole tolerance; the quadrupole tolerance is a factor of three

looser and the octupole tolerance will be tighter. Although this tolerance is tight, it is important to note that it applies only to a systematic error along the entire length of the pole. If the phase of the sinusoidal error varies along the magnet, the effect will average to a smaller contribution. Finally, these results were verified with POISSON calculations.

Table 1. Construction tolerances.

Fiducial: $X$	$\pm 150 \mu\text{m}$
Fiducial: $Y$	$\pm 100 \mu\text{m}$
Pole offset: $x$	$\pm 300 \mu\text{m}$
Full gap: $g$	$\pm 140 \mu\text{m}$
Flatness: $y$	$\pm 50 \mu\text{m}$
Pole contour: $a$ with $\lambda = 2.5$ cm	$5 \mu\text{m}$

### V. DISCUSSION

We described a high-field combined-function bending magnet that uses vanadium permendur for the magnet pole. We conclude that it should be feasible to build the magnet, provided that proper quality control is exercised during construction. Previous experience has shown that vanadium permendur can be used in this application, although it is quite expensive at this time. We plan to measure the field quality by means of a Hall probe mounted on a computer-controlled positioning device. This device has been used to obtain field maps of several magnets at SLAC.

### ACKNOWLEDGEMENTS

The POISSON/MIRT program package was run on both the SLAC IBM 9021 and the NERSC CRAY 1. TOSCA was run on the NERSC CRAY 2 and we are grateful to A. Paul for his support.

- [1] T. O. Raabe, Reimer *et al.*, "A Possible Redesign of the SLAC Damping Rings," presented at this conference.
- [2] K. Halbach, "POISSON Lectures at LBL," unpublished (1972).
- [3] J. Simkin, C. W. Trowbridge, "Three-dimensional Non-linear Electromagnetic Field Calculations, Using Scalar Potentials," *IEEE Proceedings*, vol 27, Pt B, No. 6, Nov, 1980.
- [4] K. Halbach, "A Program for Inversion of Systems Analysis and its Application to the Design of Magnets," UCRL-17436 (1967).
- [5] R. Early, *et al.*, "Design Calculations and Measurements of a Dipole Magnet with Permendur Pole Pieces," SLAC-PUB-4883, *Proc. of 1989 IEEE Part. Acc. Conf.*, Chicago, IL (1989).
- [6] J. Cobb and R. Early, "Some Initial Results from the SLAC Permeameter," SLAC-PUB-5168, *Proc of Acc. Computer Code Mtg.*, Los Alamos, NM (1990).

# COMPARISON OF COMPUTER PREDICTIONS AND MAGNETIC FIELD MEASUREMENTS FOR AN IRON SPECTROMETER MAGNET\*

G.T. Danby, J.W. Jackson, W. Meng, C. Spataro  
AGS Department, Brookhaven National Laboratory  
Associated Universities, Inc.  
Upton, New York 11973

## Abstract

Three dimensional computer calculations using the Program TOSCA have been made for a complex-shaped iron magnet. Precision field measurements were made on this magnet in preparation for its installation in a new Low Energy Separated Beam for the post-Booster high proton intensity AGS at Brookhaven National Laboratory. Point-by-point direct comparisons for field values will be described encompassing the entire useful acceptance. The predictability of higher order multipoles will be described, including the region of the magnet ends. Computer predicted focal properties will be compared with results of experimental data analysis. The method of measurement and analysis, as well as comments on the computer calculations will be described. Conclusions will be drawn on the accuracy of calculations with respect to higher order moments and the impact on future beam optical design and execution of three dimensional computer codes.

## I. DESCRIPTION OF MAGNET

The sector magnet for the LESBIII is shown in Fig. 1. Following the target two quadrupoles form the beam which then enters the sector magnet and is bent through 44.1 degrees. An electrostatic separator follows the sector magnet. The LESBIII, which operates up to 800 MeV/c in momentum, traverses the sector magnet as a parallel beam in the vertical plane and almost parallel in the horizontal plane. Protons which survive the target and two secondary beams are of much higher momentum, so are only deflected slightly by the straight away portion of the sector magnet. Thus the straight away portion has parallel pole edges for the upstream and downstream ends. (See Fig. 1.) The magnet gap is 6 inches and the length of the pole tips in the forward direction is 48 inches.

## II. METHOD OF MAGNETIC MEASUREMENTS.

Point-like search coils were mounted on a moveable trolley. A straight track was used in the forward direction. A curved track which traversed 44.1 degrees with the same radius of curvature as the LESBIII central ray was used for the LESB portion of the field.

Both the straight track and the 44.1 degree track were displaced horizontally to map the entire acceptance of both

beams. For the 44.1 degree beam, data was also taken with the straight track normal to the pole end faces and displaced sideways. With the combination of data the basic and dominant pole edge fringe field can be well described and small discrepancies between mechanical and magnetic lengths can be removed from the ray traces.

Beyond the pole tip ends, both tracks extended outward through the fringe fields in a direction normal to the pole edge face. Hall probe measurements were used to supplement the search coil measurements in the far fringing fields.

NMR was used at the center of the magnet to normalize the search coil signal to absolute Gauss. All data was taken on a down cycle, starting from a few percent above the highest nominal field to minimize magnetization effects.

The field was recorded at a very large number of linearly encoded longitudinal positions. The field was substantially known everywhere relevant in the magnet at a variety of central field values.

## III. COMPUTER PREDICTIONS VERSUS MAGNETIC FIELD MEASUREMENTS.

The requirements for extensive field mapping provided an excellent opportunity to check the precision of computed fields. Calculations were made on TOSCA using mechanical data for the iron and coil geometry and a nominal 1006 permeability table. Figure 2 shows the measured field, passing entirely through the magnet, at the center of the 0 degree forward beam. Superimposed is the TOSCA generated field. At the level of visual inspection, i.e. about 1%, the results including the fringing fields are indistinguishable. Thus the horizontal deflection and vertical edge focusing will be very well predicted by TOSCA. Note that the central field normalization is done based on measurements, since the computations do not include magnetization. However beam optical properties do not depend on absolute magnitudes to high precision in most cases.

Figure 3 shows a point-by-point difference between the measured and computed fields, again for the zero degree central ray.

Figure 4 shows an azimuthal first difference between adjacent measured points. Note the near identity of the first difference on both ends: the peak amplitude and the width at half maximum. Also note the flatness over more than half of the magnetic length. Furthermore, the point-to-point jitter in the data due to either positional error or field measurement error is at the  $1 \times 10^{-4}$  level of field.

\* Work performed under the auspices of the U.S. Department of Energy.

Referring back to Fig. 3, we must conclude that the differences are mainly due to errors in the computed fields. The antisymmetric parts of the peaks at -50 cm and +50 cm could be simply due to a displacement of the  $Z=0$  of the experiment compared to TOSCA. In other words, any  $Z=0$  displacement will qualitatively look like Fig. 4.

Note in Fig. 3 that on either side of  $Z=0$  there is a lack of flatness, at the few parts in  $10^3$  level, which must be in the TOSCA results. Also the peaks which approach greater than 1% difference, do not occur at the regions of the maximum slope of Fig. 2. This indicates slight errors in prediction, not  $Z$  displacement.

Figure 5 shows the experimental field measured along the central ray of the 44.1 degree LESBIII beam. Figure 6 shows the first difference in the direction of the beam of the measured field data. As was seen from Fig. 4, the smoothness of the data shows the measurements are of high accuracy. Note in Fig. 6, the differences are expressed per inch of displacement, whereas in Fig. 4 the differences were per .050 inches. Thus the amplitude of the first difference is 20 times bigger at the peaks in Fig. 6 compared to Fig. 4. The upstream peak is otherwise the same in both cases, since the upstream end is common to both the 0 degree and the 44.1 degree beams. Again, the downstream peak at 44.1 degrees is almost identical to the upstream peak, indicating the magnet has essentially the same fringing field shape entering and leaving both beams. This result strengthens the interpretation that errors in the measured field data are not responsible for the differences seen in Fig. 3.

Table I lists for the 0 degree beam central ray ( $x=0$ ) and at several parallel displaced lines the measured and computed field integral. The calculated field at the magnet center was

normalized to the experimental value, so the differences are due to differences in relative field shape along the length of the magnet, including ends.

The last column indicates TOSCA agrees with experiment to about 1/3 percent discrepancy. The last column is identical to an integration over  $Z$  of the point-by-point differences in Fig. 3. The first column shows the measured field is quite uniform inside the magnet.

#### IV. DISCUSSION

1. Figure 2 shows the agreement of field shape between TOSCA and experiment azimuthally through the magnet is good enough to very well predict horizontal deflection except for the most exacting precision requirements.
2. The vertical or wedge focusing should also be predicted quite well, since the field shape in the rapidly changing end region is quite close to experiment and the vertical focus end impulse is not very sensitive to exact details.
3. Transverse nonlinearities in the horizontal and vertical planes, based on these limited results, may not be adequately known for high precision beams from TOSCA alone.
4. The large body of measurement data that exists on this and other spectrometers will permit further studies of computer predictions of aberrations.
5. It is clear that even at the level demonstrated by these early comparisons, TOSCA does a very good job.

#### Acknowledgement

The magnet was built under the direction of W. Leonhardt of BNL. Members of the first experimental collaboration to use the beam were responsible for the design. (Private communication from A. Otter of TRIUMF.)

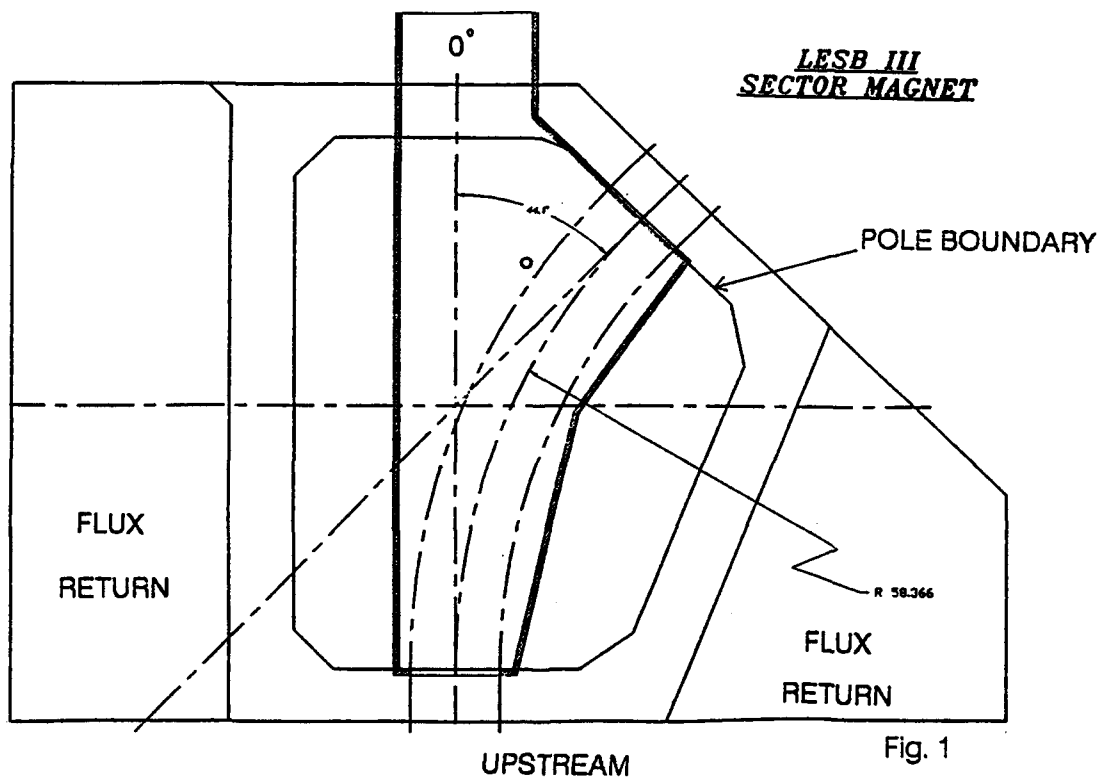


Fig. 1

D1 ZERO DEGREE CENTRAL RAY AZIMUTHAL FIELD  
MEASURED FIELD AND TOSCA PREDICTED FIELD

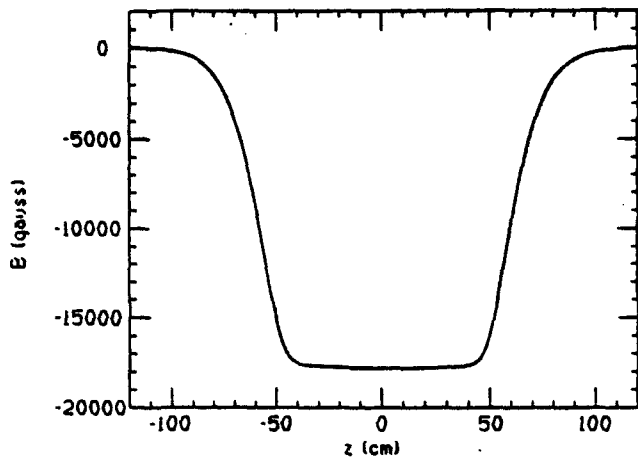


Fig. 2

D1 44.1 DEGREE CENTRAL RAY  
EXPERIMENTAL DATA

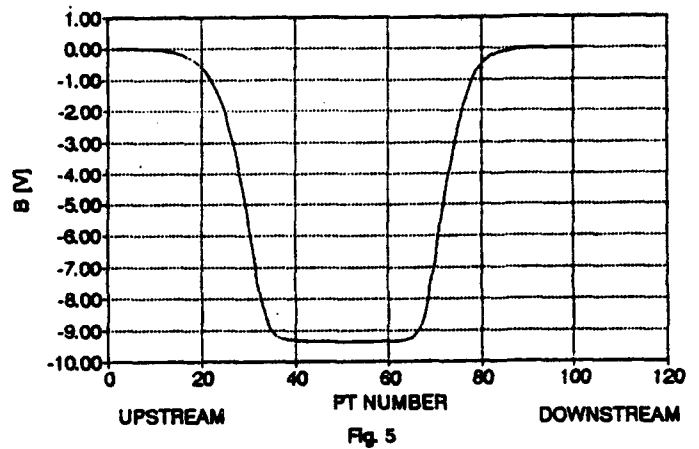


Fig. 5

D1 ZERO DEGREE CENTRAL RAY  
TOSCA - EXPERIMENTAL B AS FUNCTION OF Z

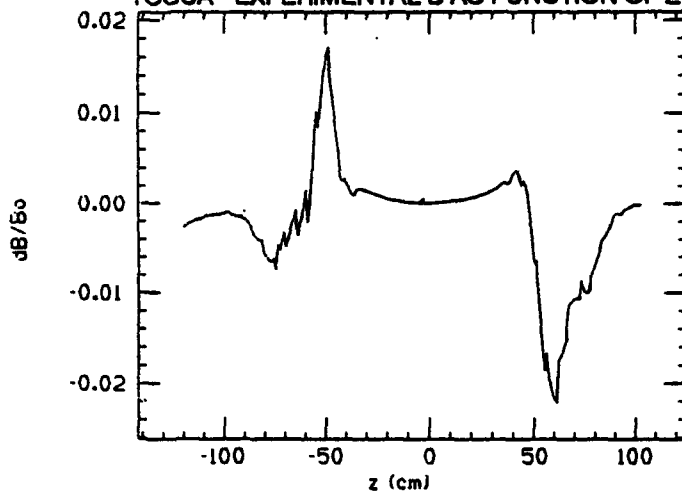


Fig. 3

D1 44.1 DEGREE CENTRAL RAY EXPERIMENTAL DATA  
1ST DIFFERENCE PER Z=1.0°

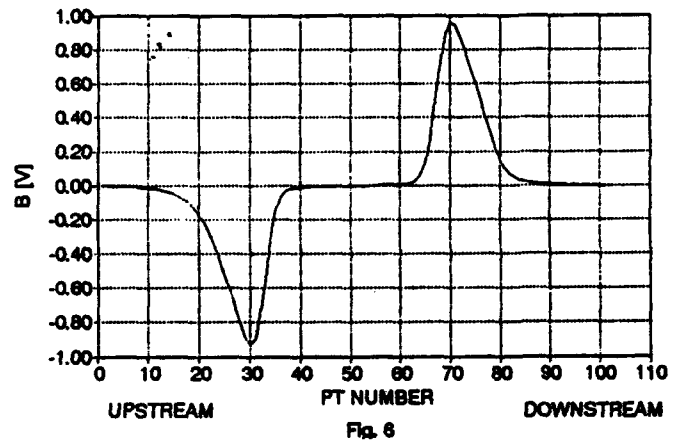


Fig. 6

D1 ZERO DEGREE EXPERIMENTAL DATA  
[1ST DIFFERENCE PER Z=0.050°]

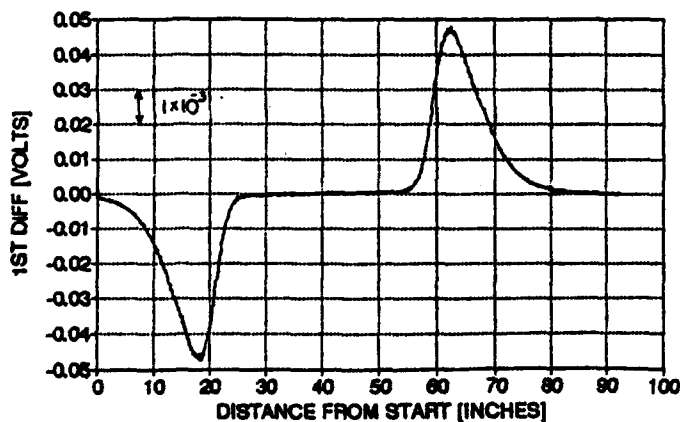


Fig. 4

TABLE I  
TOSCA VS LESBIII EXPERIMENTAL DATA

$Z = +102 \text{ cm}$   
*Normalized*  $\int$  *Comparison*  
 $Z = -120 \text{ cm}$

$B_{\text{point}}$ vs $x$ . [ $z=0$ ]	Integral Path	Tosca Cal. (G-cm)	Measure- ments (G-cm)	Diff. $\Delta/Bdz$ $\int Bdz$
1.0000	$x = 0$	-2227288	-2221776	0.0025
1.0004	$x = -5^\circ$	-2219944	-2211879	0.0036
	$x = -5.5^\circ$	-2216182	-2208336	0.0035
1.0002	$x = -6^\circ$	-2210865	-2204136	0.0030
0.9998	$x = -7^\circ$	-2198551	-2191179	0.0033

# Design and Performance of the Dipole Magnet for the SRRC Storage Ring

C.H. Chang, H.C. Liu, and G.J. Hwang  
Synchrotron Radiation Research Center

No. 1 R&D Road VI, Science-Based Industrial Park, Hsinchu 30077, Taiwan

## Abstract

22 combined function dipole magnets have been fabricated for the SRRC storage ring. The dipole magnet is a curved shaped with rectangular edges which creates a nominal field strength of 1.2407 Tesla and a gradient strength of 1.71 T/m along the magnetic center at 1.3 GeV. The errors of dipole and quadrupole fields in the radial direction is within  $\pm 1 \times 10^{-4}$  and  $\pm 2 \times 10^{-3}$  over the useful aperture. The deviations of the integrated dipole field and the quadrupole field strength for all the 22 magnets are smaller than  $\pm 1 \times 10^{-3}$  and  $\pm 2 \times 10^{-3}$ , respectively. Shims with thickness 3 mm are added on each pole edge for correcting the sextupole component in the end fringe field.

## I. INTRODUCTION

A third generation 1.3 GeV synchrotron radiation accelerator has been constructed in Taiwan by March, 1993. The magnet lattice is designed with a 6-superperiod triple bending achromatic (TBA) structure for a minimum beam emittance machine and easy adjusting optics and tunes. Each superperiod is 20 meter long and contains three combined function bending magnets, eight quadrupoles, four sextupoles and nine correction magnets. The 1.22 m bending magnet is a curved shape with rectangular edges. The radius of curvature of the bending magnet is 3.495 m and it bends the electron beams by 20 degrees. The main nominal characteristics of the dipole magnet are shown in table 1.

Table1 Main characteristics of dipole magnet

Magnetic length	m	1.22
Nominal field	T	1.2407
Field gradient	T / m	1.7102
Magnet gap on center	mm	52
Good field (width x height)	mm	60x24
Number of turns		56
Current	A	939
Current density	A/mm <sup>2</sup>	4.4
Voltage drop	V	14.2

The nineteen dipole magnets are electrically connected in series with a power supply. The dipole magnets must have the same good quality to provide a large dynamic aperture. The typical criteria for the relative integrated field errors are  $\int (\Delta B/B) ds \leq \pm 2 \times 10^{-4}$  and  $\int (\Delta G/G) ds \leq \pm 2 \times 10^{-3}$  in the  $\pm 12$  mm field region.

## II. MAGNET DESIGN

After evaluation of the TBA dipole magnet prototype I with center air gap 50 mm,<sup>[1]</sup> the distribution of the difference between the calculated and measured fields  $\Delta B/B$  and  $\Delta G/G$  in the midplane are quite small. They showed that

the quality of the pole profile is within the tolerance. But the effective dipole length is 9 mm longer the designed value and  $\int G ds / \int B ds$  is found to be 5.3% smaller than the design constant value 1.293 due to edge saturation effects. In order to compensate these deviations. The field gradient is increased from 1.60444 T/m to 1.7102 T/m and the stacking core length is shorten 9 mm. The original 1.8 mm clearance between magnet and vacuum chamber for the prototype I was too tight for the vacuum heater and thermal insulator. The temperature rise of local iron core was over 55<sup>0</sup> C when the vacuum chamber was baked up to 150<sup>0</sup> C. To avoid the core deformation, the nominal magnet gap is modified from 50 mm to 52 mm.

The combined function bending magnet is specified to produce a magnetic field strength of 1.2407 Tesla at the nominal gap of 52 mm and a defocusing field gradient of 1.71T/m for the 1.3 GeV energy. The geometry of pole profile is given by the equivalent magnetic potential line. In the neighborhood of the central orbit, the magnetic potential  $V$  at a point  $P(x,z)$  may be described by  $V(x,z) = -B_0 z (1 \pm kx)$ . The C type magnetic circuit was chosen for easy extraction of the photon beam lines. The configuration of dipole magnet is shown in Fig.1. The two dimensional field distribution was calculated using the "MAGNET" and the "POISSON" computer code. A current density of 4.45 A/mm<sup>2</sup> was chosen for balancing between construction and operation costs.<sup>[2]</sup> The optimal field quality is computed at 1.3 GeV energy to obtain the pole profile in the good field region. The good field region includes the allowance for the required beam stay clear. A good field of width greater than 60 mm for  $\Delta B/B \leq \pm 2 \times 10^{-4}$  and  $\Delta G/G \leq \pm 2 \times 10^{-2}$  is shown in Fig.2 and Fig. 3 respectively.

Several different mesh sizes were calculated for checking the field errors. The field saturation was checked with 1.0 -1.5 GeV energy. The field sensitivity is analyzed with mechanical error of  $\pm 0.025$  mm in the pole profile. The maximum field strength of 1.424 T at orbit center is also calculated for 1.5 GeV operation. The good field width  $\Delta B/B \leq \pm 2 \times 10^{-4}$  was reduced to  $\pm 19$  mm and  $\Delta G/G \leq \pm 2 \times 10^{-2}$  was within  $\pm 18$  mm. The sextupole component due to the field saturation on the pole edge is produced about -0.7 T/m<sup>2</sup>.

## III. MAGNET CONSTRUCTION

### A. Core construction

The magnetic field errors will reduce the performance of the storage ring. The most possible field error in the magnet gap is caused by the accuracy of pole profile. The field variation along the central orbit may be produced by the fluctuation of the permeability and the coercive force of the core materials. In order to produce a uniform and identical magnet, The quality requirement has to be follow strictly in fabrication and assembly of magnets. The magnet cores were

made of 1.5 mm thickness AISI 1006 low carbon steel sheet. The permeability of core material was measured to have a deviation about 5 % at 1.2 Tesla field strength. The laminations have to be shuffled to provide the uniformity of magnetic property.

The laminations were punched to a precision of  $\pm 25 \mu\text{m}$  in the critical profile. To avoid the welding distortion, the laminations were glued with the 3M brand epoxy and kept the epoxy as thin as possible to increase the stacking factor of the core. Before the stacking, half of the laminations were flipped to minimized the top-bottom symmetry error. Blocks of 144 mm thickness were stacked using stacking fixtures. The iron core with a total length of 1152 mm was assembled together with 8 core blocks. The blocks of core were reshuffled for keeping the constant magnet length and weight. 0.5 mm thickness laminations were inserted for compensating the fluctuation of length. The deviation of the length of pole is controlled within  $\pm 0.5 \text{ mm}$ . Detachable end-shims were used for overcoming the sextupole and higher-order field errors at the magnet ends. The non magnetic bolts are used to tightly attach the end-shims on the end blocks for preventing the separation due to magnetic force.

#### B. Coil fabrication

The coil was designed by considering the number of turns, the height of pole gap, the specification of power supply and the water cooling system. The excitation coils are made of 16x16 mm square hollow copper conductor with hollow 7 mm diameter. The coil is insulated by 0.5 mm thickness fiber glass and impregnated with epoxy resin in a vacuum mold. The voltage in an impulse tester up to 5 kV is used to detect the defective coil inter-turn insulation. The waveform patterns were checked and compared to find the defective coil. Each dipole magnet has four pancake-type coils with a total of 56 turns. Auxiliary coils are also provided for trimming 1 % field strength of individual magnets.

#### c. Fiducial work

The beam orbit analysis requires the position deviation of the magnet from the ideal orbit should be within  $\pm 0.1 \text{ mm}$ . In order to ensure the accuracy, the survey and alignment curved fixture has three reference points the entrance, center and exit point of the magnet for fixing the survey pad on the top of magnet. The mechanical fiducial work is measured using a digital 3-D measuring machine. The measuring precision of  $\pm 0.02 \text{ mm}$  allows the magnet geometry transferred from the midplane to the top of fiducial mark. The measurements also check core length and the assembly accuracy of the median plane. The exact magnetic field center is established by the field mapping based on the fiducial mark.

### IV. Field Mapping Results

The magnetic field was measured by Hall probe mapping system. The Hall probe is calibrated using an NMR gauss meter to achieve the accuracy of  $\pm 2 \times 10^{-5}$ . The field distribution mapping was performed in the midplane along the radial direction at the magnet center. The dipole and gradient

field of 2-D measurement results are quite close to the designed value and are shown in Fig. 2 and Fig 3 respectively. That means the precise punching and accurate stacking were done in the pole profile. The mapping trajectory is moved along radial direction. The distribution of integrated dipole and gradient field strength are shown in Fig 4. and Fig 5. The integrated sextupole strength of  $1.075 \text{ T/m}^2$  is close to the tolerance margin at 1.3 GeV and of  $2.492 \text{ T/m}^2$  at 1.5 GeV is out of the tolerance. In order to compensate the strong sextupole field at the end of magnet, different shims at pole edges were added for correcting the sextupole component. According to the measurement results, 3mm thickness (2 by 2 pieces) shims were required on the pole edges of magnet.<sup>[3]</sup> The integrated sextupole strength was then reduced to  $0.262 \text{ T/m}^2$ . The good field region of the integrated dipole and gradient field strength is increased more wider as shown in Fig 4 and Fig 5. This improvement will benefit the quality of beam line and more stable operation at 1.5 GeV. Table 2 lists the summary of dipole magnet at nominal excitation current 939.3 A.

Table 2: Summary of the dipole magnet

Item		Specification	Measurement
B(0,0,0)	(T)	1.24090	1.23999
G(0,0,0)	(T/m)	-1.71084	-1.71609
S(0,0,0)	(T/m <sup>2</sup> )	0	-0.027
O(0,0,0)	(T/m <sup>3</sup> )	0	4.88
D(0,0,0)	(T/m <sup>4</sup> )	0	-105.7
$\int B_{ds}(0,0)$	(T-m)	1.5137	1.5137
$\int G_{ds}(0,0)$	(T)	-1.9574	-1.972
$\int S_{ds}(0,0)$	(T/m)	0	-0.262
$\int O_{ds}(0,0)$	(T/m <sup>2</sup> )	0	14.45
$\int D_{ds}(0,0)$	(T/m <sup>3</sup> )	0	-50.8
Leff dip	(m)	1.22	1.2221

\* The integrated field strength values are rms. value of eighteen dipole magnets

The field errors of all dipole magnet is less than the specified. Although the magnetic effective length is 2.1 mm longer than the designed value. It should not affect the machine performance. The deviation of integrated dipole field strength was measured within  $1 \times 10^{-3}$  and given in Fig. 6 It is found all dipole magnet are uniform and acceptable. The commissioning of the storage ring has been started successfully in April 1993. The first turn beam was run without any exciting the correction magnets. These TBA dipole magnets have been provided a good guiding field in the storage ring.

### V. CONCLUDING REMARKS

The good field region is obtained for all magnet. Because of the construction errors were under control during the fabrication and assembly of magnets. The mechanical tolerance of punching and stacking laminations has been measured within  $\pm 0.025 \text{ mm}$ . The laminations and assembly core blocks were shuffled for averaging the permeability of magnets. The laminations were glued to avoid the welding

distortion. The deviation of core length was measured within  $\pm 0.5$  mm. In order to correct the sextupole field in the end of magnet, 3 mm thickness shims were added on the pole edges. The field quality and the good field region were improved and will benefit the stable operation.

## VI. ACKNOWLEDGMENT

The authors would like to thank our consultant Mr. H.C.H Hsieh for checking the magnet design and valuable discussion during the study and construction of the magnets. Thanks Mr. C.S. Hwang and the field mapping group for their careful magnetic measurements and supplying the measurement data.

## VII. REFERENCES

- [1] C. H. Chang, C.H. Hwang, J.C. Lee, W.C. Chou, J.H. Huang, P.K. Tseng, C.S.Hsue, G.J. Hwang "The TBA Prototype Dipole Magnet of SRRC" 11th International Conference on Magnet Technology, 1989.
- [2] G.E.Fisher, "Iron Dominated Magnets", SLAC-PUB-3726, July 1985.
- [3] P.K. Tseng, C.S. Hwang "The analysis methods of Hall probe mapping system for the combined function dipole magnet", XV th International Conference on High Energy Accelerators, July 20-24, 1992

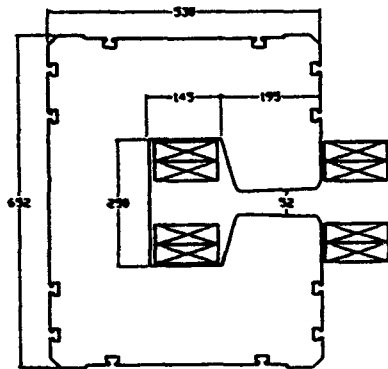


Fig. 1 the configuration of the combined function dipole magnet.

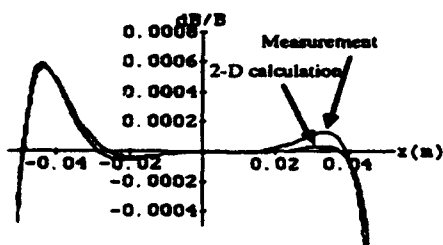


Fig. 2 the dipole field distribution of the calculated and the measured results in the midplane along the radial direction.

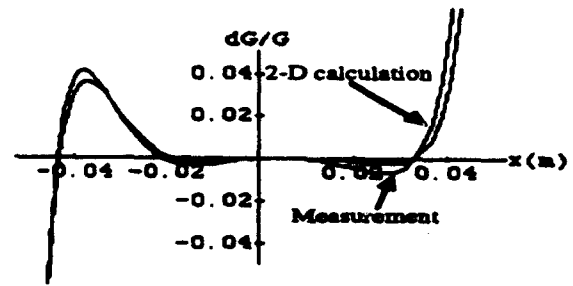


Fig. 3 the quadrupole field distribution of the calculated and measured results in the midplane along the radial direction.

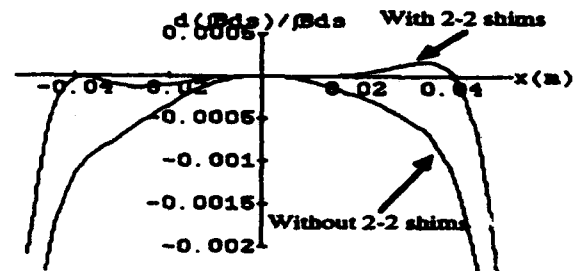


Fig. 4 the integrated dipole field strength distribution in the midplane with and without 3 mm (2-2) shims.

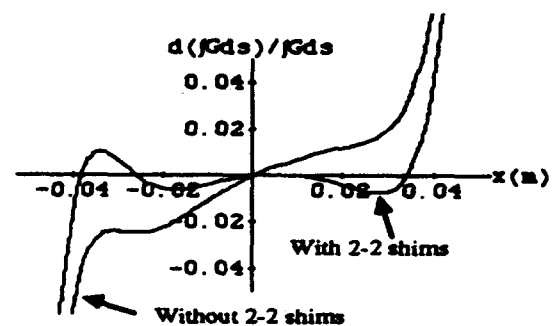


Fig. 5 the integrated quadrupole field strength distribution in the midplane with and without 3 mm (2-2) shims.

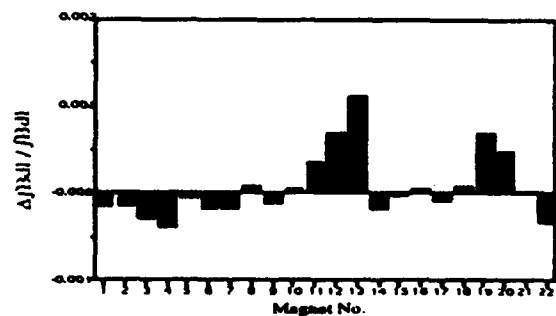


Fig. 6 the deviation of integrated dipole field strength of all the dipole magnets.

# Specific Features of Magnet Design for the Duke FEL Storage Ring\*

B. Burnham, N. Hower, V.N. Litvinenko, J.M.J. Madey, Y. Wu  
Duke University Free Electron Laser Laboratory  
Box 90319 Duke University Durham, NC 27708-0319

## I. INTRODUCTION

The 1 GeV Duke FEL storage ring is dedicated to drive UV and VUV free electron laser devices. The high brightness and low emittance electron beams needed for these devices demand high performance and tight tolerances on the storage ring magnet lattice. Tight tolerances include close spacing of magnetic elements. In this paper we show how combined function magnets are used to eliminate discrete elements and odd shaped end pieces which cause magnetic coupling, saturation and severe undesirable field nonlinearities. Using this scheme we are able to achieve desirable ring dynamic aperture with only minor modification of existing hardware.

Also included is a discussion of a non-standard septum magnet with stray field compensation which will be employed by this storage ring. The design, testing procedures, and preliminary results are outlined for this magnet.

## II. MEASUREMENT PROCEDURES

Magnetic measurements of all magnets were performed prior to installation on the storage ring. In order to facilitate faster data acquisition of large data sets of magnetic fields accurately we make use of a Hall probe array. This array contains eleven individual Hall probes mounted on a non-magnetic plate, each one calibrated using a NMR magnetometer. The elements are separated by approximately 7 mm and the exact distances are measured to within a few microns using a microscope. The voltage signals are sent in parallel to a multiplexer and read by a 20 bit A/D converter in a CAMAC crate to a Macintosh computer running LabView [1]. Magnet power supplies are controlled by 16 and 20 bit DACs and a set of precise shunts and transducers are used for current read back. This particular system was purchased from the Budker Institute of Nuclear Physics in Novosibirsk, Russia, as part of a cooperative effort between Duke University and INP[2].

The high resolution of the array and its electronics yield a magnetic measurement accuracy of better than one part in 10,000 and we can make a two dimensional map with only one pull through each magnet. A set of tracks are used for the precise positioning of the array in each magnet. Since the magnet lattice includes closely spaced elements, it is important that all measurements be taken in a real environment. The magnet test bed at Duke has room to place neighboring magnets around the magnet under test as would be the case when the magnet is eventually placed into the storage ring. In this manner we can better understand the fringe field effects of closely spaced elements.

\*This work supported by APOSR grant #90-0112.

Parameters of the Duke FEL storage ring can be found elsewhere [3-4]. The storage ring arcs and south straight section have bilateral lattice symmetry with respect to dipole, quadrupole, and sextupole fields.

## III. COMBINED FUNCTION QUADRUPOLES

Natural chromaticity should be corrected by a suitable sextupole component of the magnetic field lattice. The most typical method to generate the sextupole component is by discrete sextupole magnets. In the Duke storage ring, with dispersion free straight sections, the sextupole magnets should be placed in the arcs where only 18 cm of space between each dipole-quadrupole pair is available. It was discovered that the initial attempts to use the dipole magnet with "noses and dimples" as main fixed sextupoles coupled with discrete adjustable sextupoles caused major asymmetric saturation of the dipole and a large amount of magnetic flux between the sextupole yoke and the nearby dipole magnet. The stray fields between the magnets also caused severe non-linear components while dipole magnet saturation caused serious orbit distortions. All of these problems taken together would have made it almost impossible to commission a damping storage ring at Stanford.

We decided to use the arc quadrupole magnets as combined function variable strength main quadrupoles and sextupoles. The arc quadrupoles are wired so that the inner pair of poles (toward the inside of the ring) are independent of the outer pair of poles. When the two sets are excited by the same current there is only a quadrupole moment. With more current separation sextupole and dipole moments can be introduced overlapping the quadrupole. The dipole moment in the magnet offsets the magnetic center (2 mm for designed values of sextupole moments). We have therefore designed the ring so that the central orbit will pass through this new magnetic center.

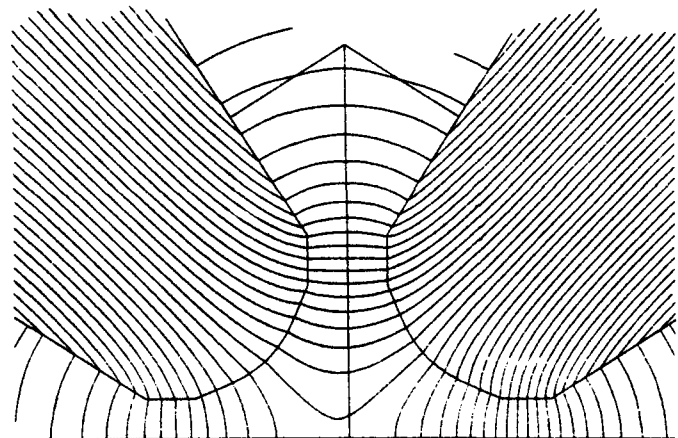


Figure 1. Flux plot from MERMAID.

Using a two dimensional magnetic field computer code called MERMAID [5] we were able to accurately model the effects of asymmetric current excitation of the quadrupole coils. We found we were able to introduce required sextupole moments into the magnets using this method, and from the results of the MERMAID calculations we began testing the magnets in the same configuration. A sample flux plot from MERMAID for asymmetric excitation is shown in Figure 1.

We have taken large data sets of all of the quadrupole magnets in field mappings and current rampings and created a computer routine to fit the multipole moments using spline interpolation in multi-dimensional space. These data will be used in the control system to achieve the desired strengths in the quadrupole. Typical current settings (varying because of the properties of magnet steel) required to maintain quadrupole and sextupole strengths proportional to the electron energy are shown in Figure 2.

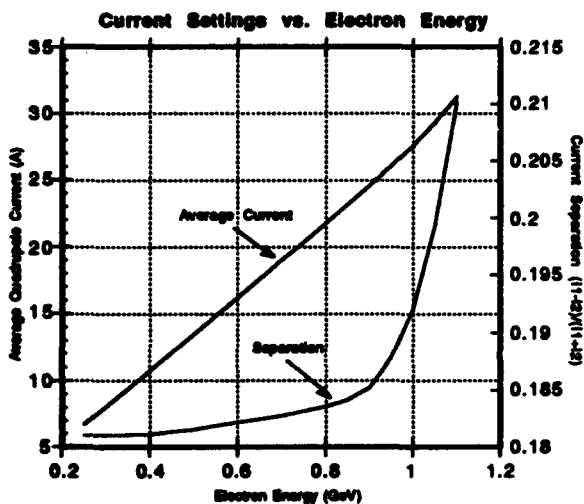


Figure 2. Settings for quadrupole excitation. At 1 GeV gradient is 3.5 kGs/cm, sextupole is 300 Gs/cm<sup>2</sup>.

The typical longitudinal distribution of moments is shown in Figure 3.

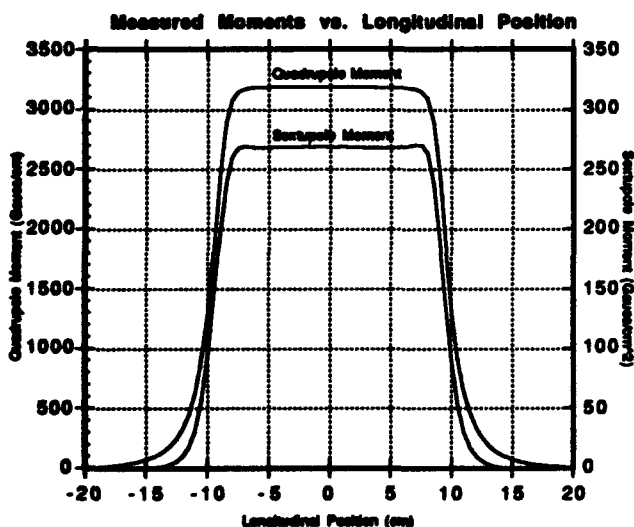


Figure 3. Measured moments in combined function quadrupole.

In order to understand the higher order moments of the quadrupole fields it is necessary to use the measured fields and subtract out the fitted lower order moments. What is left over are the strengths, in this case, for octupole and higher order terms. In the case of the Duke storage ring quadrupoles the lowest moment is dodecapole.

There is a built in correction term for higher orders in these magnets. Figure 4 shows a plot of the integrated moments above sextupole for both the central part of the magnet and the fringe fields. One curve is the integral of the fields inside the magnet steel (without edges), the other for the fringe fields. The two very nearly cancel out overall higher order moments.

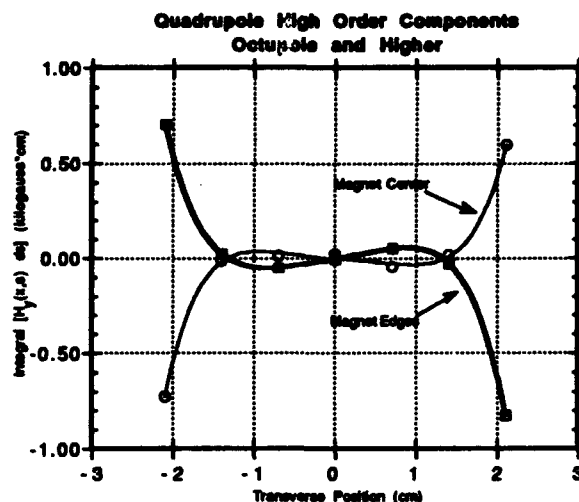


Figure 4. Integrals of higher order moments.

#### IV. COMBINED FUNCTION DIPOLES

We replaced the odd shaped nose and dimple dipole end pieces with new parallel edge smooth symmetric end pieces required to extend dipole magnetic length. This allows us smoothly to reach saturated symmetric magnetic field behavior up to 20.5 kGs (15.9 kGs is required for 1 GeV operation). We have devised a way to make the dipole magnets combined function while maintaining a higher level

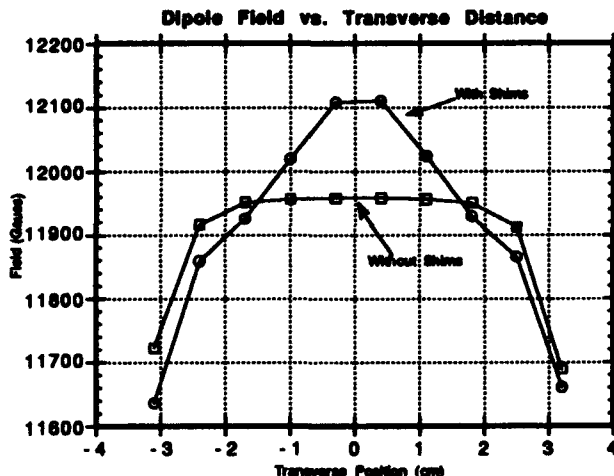


Figure 6. Combined function dipole field.

of symmetry by introducing thin steel shim stock in the center of the magnet. This extra "bump" creates a sextupole field of the desired sign as shown in Figure 5. The steel shims themselves are mounted on aluminum strips, so the whole unit is easily replaced if desired. The steel shim stock measures only 6.4 cm long by 2.5 cm wide in a 33 cm long magnet. The measured sextupole moment as a function of longitudinal distance is shown in Figure 6.

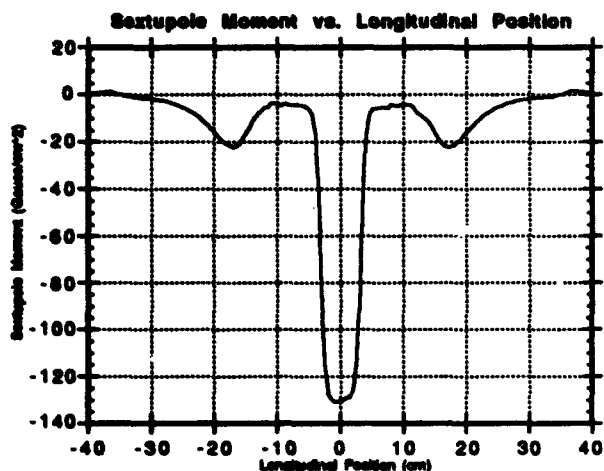


Figure 6. Measured sextupole moment in combined function dipole.

## V. SEPTUM MAGNET

A Lambertson type septum magnet is used for injection into the Duke storage ring. We modified the "V" notch angle to  $45^\circ$  and made the top piece separable for convenience of vacuum chamber installation. The sharp edge measures only 0.5 mm. This magnet employs an 18 turn main coil made from  $2 \times 66 \text{ mm}^2$  copper sheet and cooling plate mounted on the bottom. The coil is fully enclosed by magnet steel. The stray fields from this magnet are very low because of this isolation, no more than 10 gauss in the "V" notch, where the stored beam passes (see Figure 7). It is only 1 mm away from the main gap where the field is 9 kGs. We have found a way to compensate this field both horizontally and vertically down to a level of less than 1 gauss. The horizontal stray field is caused by asymmetrical saturation of the magnet steel and is compensated by using a five turn coil around one half of the magnet to balance saturation effects. This coil has a total of only 10-15 amp-turns.

Using MERMAID we determined that a flat coil laid into the sides of the notch would be sufficient to cancel most of the vertical field component. The single turn coil measures 4 cm wide by 0.05 mm thick by 1.6 m total length and will carry a current of up to 11 amps. An exaggerated view of the septum magnet is shown in Figure 8.

Stray fields are also prevalent in the groove where the walls of the "V" become vertical. Into this notch is placed another one turn compensating coil which carries roughly one half the value of the current in the flat coil. Assuming this ratio to be constant we can make the flat coil and this particular compensating coil from the same piece of copper sheet. In this fashion we can run the compensation from only

one power supply. The magnetic test results confirm the predictions.

The finite permeability of the steel creates a small variation of the magnetic field inside the gap along the pole width which measures 14 cm. This variation was predicted by MERMAID. Even though the field quality satisfies design requirements we suggested one more flat coil ( $2 \times 4 \text{ cm}$  wide) just below the notch above the main pole. Only 15-25 A current is required to make the magnetic field uniform (within 0.5 Gauss) in the area of  $\pm 5 \text{ cm}$ .

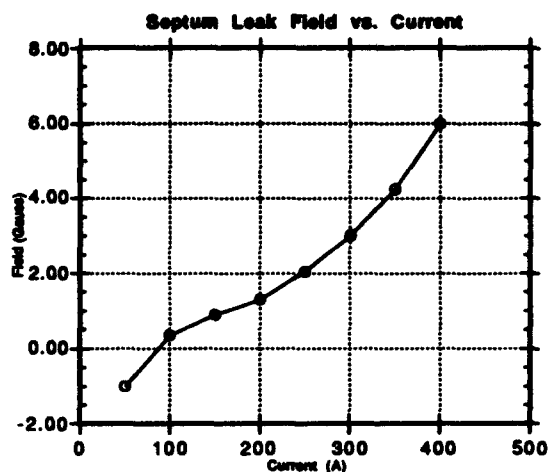


Figure 7. Measured septum leakage field in "V" notch.

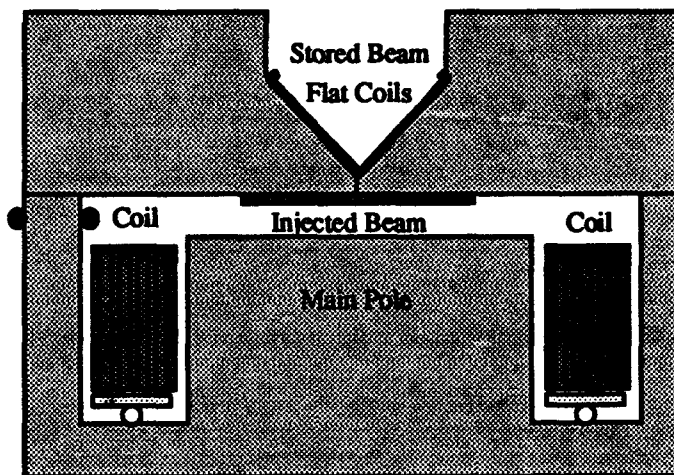


Figure 8. Septum magnet basic design in cross section.

## VI. REFERENCES

- [1] LabView software for Macintosh, National Instruments.
- [2] S.F. Mikhailov, calibration for Duke Hall probe array, private communication.
- [3] V.N. Litvinenko, et al., "UV-VUV FEL Program at Duke Storage Ring With OK-4 Optical Klystron", these proceedings.
- [4] Y. Wu, et al., "Lattice and Dynamic Aperture of the Duke FEL Storage Ring", these proceedings.
- [5] MERMAID software by A.N. Dubrovin for two dimensional magnet design and magnetic field calculations. Budker Institute of Nuclear Physics.

# DIPOLE DESIGN FOR THE EUTERPE STORAGE RING

J.I.M. Botman, C.J. Timmermans, B. Xi, H. Heller,  
H.L. Hagedoorn, P. Brinkgreve, E. Dekkers, J. Moerel,  
Eindhoven University of Technology  
P.O. Box 513, 5600 MB Eindhoven, Netherlands

## Abstract

The magnet system of the Eindhoven synchrotron radiation source EUTERPE (400 MeV) consists of dipoles of unconventional design and construction. Laminated rectangular blocks of transformer steel are fixed together and comprise the dipole magnet (dim. 48x39x35 cm<sup>3</sup>). Apart from a small quadrupole component, a field uniformity  $\Delta B/B$  of  $2 \times 10^{-4}$  over 4 cm at 1 T is obtained in a 2.5 cm gap. The support system is based on static and dynamic analysis. The resultant "six degree of freedom" manipulator (position accuracy = 0.02 mm) can easily adjust 3 positions and 3 angles of rotation of the magnet. Because of the stroke of the adjustable rods being small (= 5 mm), these rods have "elastic hinges" as attachment points. Design and construction have been done at the Central Design and Engineering Facilities of the Eindhoven University. A description of the magnet system, prototype magnetic field measurements and details on the construction, including that of the support system, will be presented.

## I. INTRODUCTION

The Euterpe storage ring is a 400 MeV electron ring under construction at the Accelerator Laboratory of the Eindhoven University (NL). The ring is to be used as an experimental tool for accelerator physics studies as well as for the study of radiation phenomena e.g. in undulators. Limited use of the machine for applications of synchrotron radiation is foreseen. This is a university project with somewhat different objectives as for facility projects. Design, construction and testing is an exercise for the accelerator group of the university and their students, with strong backing from the university workshops. The budget for the machine is small, but there is no time pressure for building it. Many components of the ring, e.g. the complete magnet system, are made in the university itself.

Euterpe has a circumference of 40 m and it has a four-fold symmetric lattice with a triple bend achromatic structure, and 2 m long dispersion free straight sections. Various ion-optical modes for different applications can be set by adjusting the focusing properties [1,2]. The injection takes place from a 75 MeV racetrack microtron [3]. The dipole units are small with a small gap of 2.5 cm. This small value may give rise to limiting effects on the beam lifetime; an account on these effects in Euterpe is given in reference [4]. Alignment requirements for the magnet system, together with the alignment procedure is given separately [5]. Table 1 lists the main Euterpe parameters.

## II. DIPOLE DESIGN

In the philosophy of the Euterpe ring project an attempt was made to be able to store electrons of the highest possible energy using rather small bending magnets. In the present design of the dipoles the maximum magnetic induction is 1.35 T with a bending radius of 1 m, implying a sagitta of 3.4 cm. This leads a rectangular pole area, and also to a rectangular block shaped C-magnet. In this way, making laminated magnets avoids complicated curving procedures.

It is to be mentioned here that the poles are completely flat: no tapering or pole profiling is performed. The width of the pole is sufficient for good homogeneity of the magnetic field. The actual magnet shape has been determined on the basis of POISSON-calculations. According to this, 14 kA-turns is needed for 1.4 T, where saturation plays a role, with a current loss factor of 6.6%.

A technique applied in the transformer industry is the so-called modular core technique to assemble transformers and chokes [6]. Fabrication of the laminated steel core modules is done by collecting equal parts stamped off a flat steel sheet coil, which is available in a range of standard sizes. The sheet coil contains the adhesive for cementing a module.

Circumference	40 m
Max. energy	400 Mev
Inj. energy	75 Mev
Beam current	100 mA
Focusing structure	TBA
Superperiods	4
RF frequency	45 MHz
RF voltage	50 kV
Min. emittance	7.4 nm
Pulse length	3 cm
Crit. wavelength	8.3 nm

Modules to form a transformer or choke are fixed together with rods.

We have bought such modules to compose the C-shaped dipoles. However, the method to fix these together for a complete dipole is different. Because the magnetic forces in the dipoles can be high, clamping the blocks with rods is not possible without unwanted dimensional deformation. Other alternatives were welding the blocks together, or cementing the blocks. Chosen is cementing with epoxy adhesive which is temperature stabilized. Cementing has given very accurate and stress free results. However the film thickness of the epoxy has to be controlled within tight limits.

Since the magnetic properties of the steel sheet depend on the orientation of it (the highest magnetization occurs in the roll direction), the magnetic circuit is optimized by a proper orientation of the laminated modules. In our case 0.35 mm sheet of VM 111-35 iron with a maximum saturation ferric induction of 1.7 T is used. The "pole" blocks with a cross section 12x18.25 cm<sup>2</sup>, two mid blocks of 13.5x9.5 cm<sup>2</sup> and one return yoke block of 13.5x39 cm<sup>2</sup> form the magnet. At the pole ends shimming plates have been attached, whose widths will be adjusted for obtaining equal magnetic lengths of all dipoles.

For the coil construction hollow copper conductor of 6x6 mm<sup>2</sup> and a bore radius of 3.5 mm is used. The coil consists of 7x12 turns with a cross-section of 4.5x8 cm<sup>2</sup>. The coil weight is 20 kg.

Table 2 gives a summary of dipole data.

### III. SUPPORT SYSTEM

The support system is a six degrees of freedom manipulator with the following specifications :- x,y,z stroke  $\pm 5$  mm ; accuracy  $\pm 0.02$  mm-  $\varphi_{xx}, \varphi_{yy}, \varphi_{zz}$  stroke  $\pm 1^\circ$  ; accuracy  $\pm 0.005^\circ$

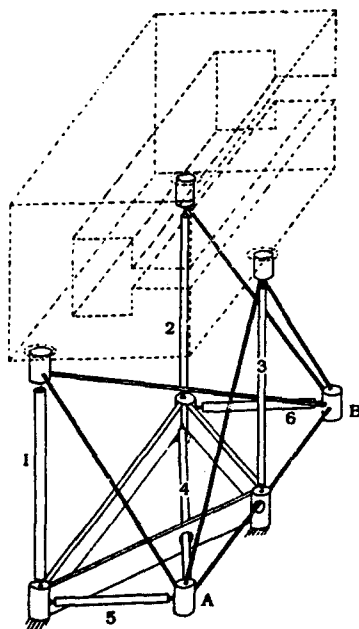


Figure 1 Dipole and support system

Size (lxwxh)	480x350x390 mm <sup>3</sup>
Total Weight	600 kg
Bending radius	1 m
Sagitta	3.4 cm
Effective orbit length	52.4 cm
Pole size	120x480 mm <sup>2</sup>
Gap width	2.5 cm
Coil cross section	4.5x8 cm <sup>2</sup>
Magn. field at 75 MeV	0.25 T
Magn. field at 400 MeV	1.35 T
Power @ 400 MeV	6 kW

In classical mechanical design actual and virtual backlash form the Achilles heel of the behaviour. These have to be avoided or, if not possible, have to be limited to close tolerances. Virtual backlash is the positional inaccuracy as a result of friction combined with limited stiffness. Actual backlash is the positional inaccuracy as a result of clearance.

In this case a solution was aimed for in which :

- All components of the support system are attached to one another by means of welding (clearance free).
- The strokes are realized by means of predetermined elastic deformation (no friction and no clearance) of "elastic hinges".

The basis of this solution for the support system is the "solid mass" of the magnet which is supported by three vertical rods (1,2,3 fig. 1). The movement of the remaining system is transduced to the points A and B. This movement is now limited by rods 4,5 and 6. The six rods mentioned can be varied in length. They actually control the six degrees of freedom the magnet has in relation to the outside world.

The mechanical stiffness of these rods predominantly determines the stiffness of the support system. The rods are dimensioned accordingly. The ends of these rods are attached between the mass of the magnet and the outside world by means of "elastic hinges".

Because of thermal effects (a temperature up to 110° C for the magnet could be allowed) the mechanical elements of the magnet and its support system can change in dimensions up to 0.5 mm. These changes may result in excessive mechanical forces. These forces can cause possible plastic deformation and or creep effects in the mechanical elements of the system. Because of that dimensional changes and inaccuracy will occur. Therefore the magnet is attached to the support system with three leaf springs (A,B,C fig.2). The orientation of these

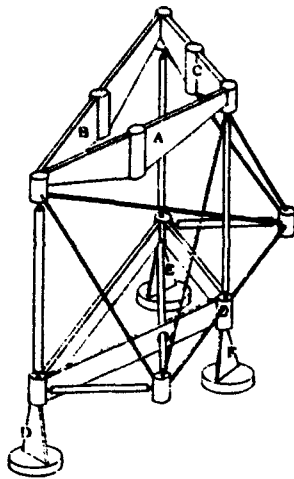


Figure 2 Attachment points support system

springs is such that the relative position of the magnet with respect to the support system remains the same. The same mechanical design concept has been chosen for the attachment of the support system to the ground (D,E,F fig.2).

Mechanical stability is determined with the dimensioning of the stiffness of the support system. A theoretical mechanical resonance frequency of 15 Hz in all directions was chosen (the mass of the magnet is 600 kg). The prototype was measured in three directions and the actual resonance frequency is 14 Hz. Combined with the supposed mechanical noise level of the laboratory these results are adequate for a good dynamical tolerance of place and stability of the dipole mass.

The realized support system has proven to be accurate, cheap to produce and user friendly, even for physicists.

#### IV. PERFORMANCE & FIELD MEASUREMENTS

Measurements have been performed on a completed prototype magnet, consisting however of modules welded together. This procedure leaves about 20% less area for the return flux, compared to the newer cemented types, sooner leading to saturation effects. Figure 3 shows the excitation curve, as calculated by POISSON and also by measurement. The maximum induction is about 1.6 T; the difference in

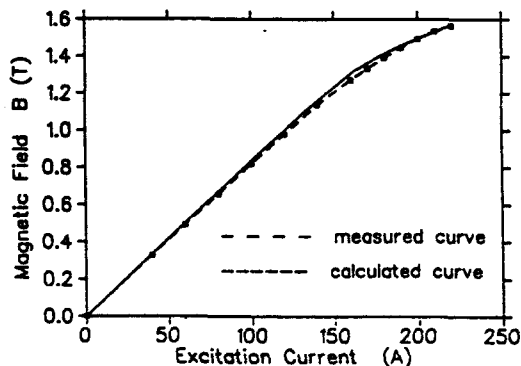


Figure 3 Excitation curve prototype

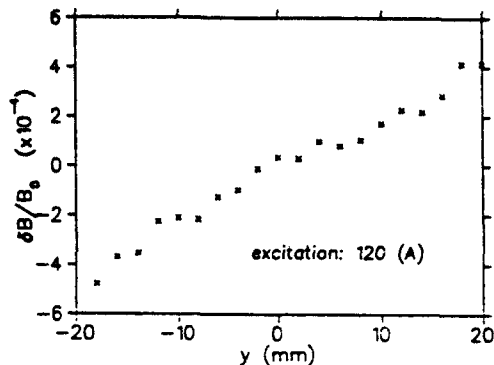


Figure 4 Radial field profile

slope at low excitation for both curves is due to a slightly different gap value. Figure 4 shows the radial field profile at 120 A (1 T). A small quadrupole component is present, which is due to a radially varying gap value. This will be corrected in the cemented versions. Then the expected field uniformity is better than  $10^{-4}$  over 4 cm. The length of the effective field boundary at either side of the magnet is 17 mm. At an excitation of 200 A (1.5 T) a sextupole component of 8 gauss/cm<sup>2</sup> strength is present.

#### V. CONCLUSION

A modular core technique has been applied for the Euterpe dipole magnets. The assembly of modules and of the overall dipole is completely carried out using epoxy adhesive and resin.

A rigid support and manipulating system has been adopted.

Field measurements on a prototype show the expected performance.

#### VI. ACKNOWLEDGEMENT

The authors like to thank the colleagues from the engineering group, in particular J.A.N. Ketelaars, G.J.M. Klitsie and J.M.P. van Laarhoven.

#### VII. REFERENCES

- [1] J.I.M. Botman, et.al., *Rev. Sci. Instr.*, Vol 63 (1) (1992), 1569.
- [2] Boling Xi, et.al., *Nucl. Instr. Meth.*, B68 (1992) 101.
- [3] G. Webers, et.al., these proceedings.
- [4] Boling Xi, et.al., these proceedings.
- [5] S. Wetzels, et.al., these proceedings.
- [6] Magnet modules by Blum GmbH, D-7147 Vaihingen, Germany.

# DESIGN OF A LAMBERTSON INJECTION MAGNET FOR THE RHIC MACHINE\*

E. Rodger, N. Tsoupas, J. Claus, H.W. Foelsche  
Brookhaven National Laboratory  
Associated Universities, Inc.  
Upton, New York 11973

## Abstract

A Lambertson magnet has been designed to serve as an injector into the Relativistic Heavy Ion Collider (RHIC) under construction at Brookhaven National Laboratory. The design is predicted to achieve field uniformity of  $DB/B < 6 \times 10^{-4}$  at  $B_0 = 9.5$  KG transverse to the beam direction over the width of the beam path and stray fields in RHIC's circulating beam pipe of less than 0.2 Gauss. In addition, the magnet is ultra-high vacuum compatible in that only the insides of the beam tubes are exposed to the vacuum and the entire assembly is bakeable in situ to 300°C.

## I. INTRODUCTION

The injection Lambertson magnets described herein will be the last elements in the beam transfer line between the Alternating Gradient Synchrotron (AGS) and the Relativistic Heavy Ion Collider (RHIC) at Brookhaven National Laboratory. They are designed to deflect the injected beam onto a path horizontally parallel to the circulating beam. Two such magnets will be used, each one injecting into one of the counter circulating beams of the RHIC machine. The two magnets will be identical magnetically, but will be physical mirror images of each other.

## II. DESIGN PARAMETERS

Extensive parametric studies arrived at the following design parameters.

1. Bend angle = 38 mrad @  $B\rho = 100$  T·M/rad
2. Length = 4 M ( $B_0 = 9.5$  kG)
3. Field non-uniformity < 6 parts in  $10^4$  over beam path
4. Stray fields < 0.2 Gauss
5. Vacuum level <  $1 \times 10^{-10}$  Torr
6. 26.1 mm vertical aperture
7. 67 mm i.d. circulating beam tube

## III. MECHANICAL DESIGN

### a. Slab Construction

A major consideration from the start was to operate the injection magnet in series (d.c.) with the transfer line dipole

\*Work performed under the auspices of the U.S. Department of Energy.

magnets, thus saving the cost of a separate large power supply. This and the fact, as mentioned in the preceding section, that the geometry changes along the magnet, made laminated construction unnecessary and impractical.

### b. Steel Characteristics

Two and three-dimensional computer modeling showed that the design parameters could be met and exceeded by fabricating the magnet body out of an ultra-low carbon (< 0.005%) steel in the unannealed condition. The material (called "INTRAK" [1]) is available in large slabs and can be machined without significantly altering the magnetic properties.

### c. Beam Tube Materials

The material for the circulating beam is critical as it serves a number of functions. First, it must be ultra-high vacuum compatible, which means pre-firing at a temperature of at least 950°C in a vacuum of at least  $1 \times 10^{-5}$  Torr and should be corrosion-free like stainless steel. In addition, it serves a vital magnetic shielding function. The tube is spaced from the surrounding ultra-low carbon steel by a 1 mm air gap and intercepts leakage fields. For this function, it must have high permeability at low field levels. It must also have sufficient physical strength to resist the vacuum loads with a relatively thin wall. Finally, it helps if the thermal coefficient of expansion is close to that of the magnet body. These conditions are all met by a material called "Permalloy 80" [2]. To reach the required annealed condition, it must be heated to 1150°C after fabrication. This also serves as the vacuum firing.

The injection tube material selected is Inconel 625. It is completely non-magnetic, has good vacuum and thermal expansion properties, and has high stiffness and yield strength to resist vacuum loading. Both the beam tubes can be welded into the common stainless steel downstream chamber (see Figure 1).

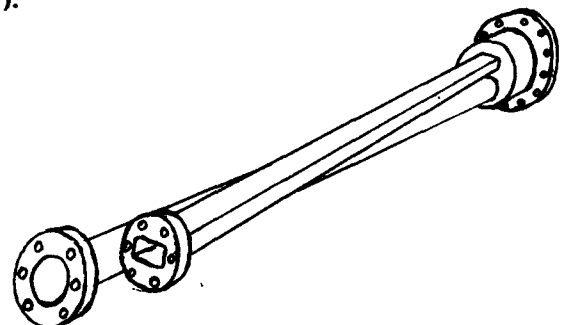


Figure 1.

**d. Bakeout**

Because of the difficulty of trying to heat the injection tube (which is in intimate contact with the poles) independently of the magnet, it was decided to heat the entire magnet. The coil was thermally insulated from the core and is water cooled during bakeout. A covering heater blanket of 20 kW will heat the assembly to 250°C in 12 hours.

**e. Vertical Motion**

During injection, the magnet must be positioned so that the circulating beam almost touches the upper inside surface of the circulating beam tube. This condition represents an aperture restriction for the RHIC machine during the subsequent operating cycle. To solve this problem, provision has been made to raise the entire magnet, after injection, so that the center lines of the circulating beam tube and the circulating beam coincide. This is to be accomplished to an accuracy of ± 0.1 mm by coupling the three support jacks to a common motor with suitable position feedback and limit switches.

### IV. MAGNETIC DESIGN AND PERFORMANCE

The magnetic calculations were separated into two parts. First, the aperture field uniformity and stray fields well within the magnet were modeled in two dimensions using the PE2D code [3]. Next, the field behavior and stray field level within the circulating beam tube near the exit and entrance of the magnet were modeled using the TOSKA [3] three-dimensional code. The two-dimensional study had two purposes. The first was to verify a magnetic field uniformity of  $DB/B < 6 \times 10^{-4}$  transverse to beam direction over the entire beam path, and second, to show that the stray fields inside the circulating beam tube could be held below 2 Gauss. The predicted performance meets or exceeds the goals. This was accomplished by the following means.

1. The ultra-low carbon steel selected for the magnet body saturates at a relatively high field level, thus creating relatively low stray fields in the air. Table I shows the experimental B vs. H curve for this material.

TABLE I	
H(Oe)	B(kG)
1	2.5
2	8.0
4	13.5
10	15.5
100	18.2

2. The magnet length of 4 meters was chosen in part to limit the magnet's gap field to 0.95 Tesla. This choice is compatible with the chosen steel because the steel does not run into saturation in the critical septum region.
3. The pole tip edges were shaped to maximize the good field region. This shaping took into account the aperture geometry, the steel characteristics, and the field levels in the steel.
4. As mentioned in Section III. c., the circulating beam tube material (Permalloy 80") was chosen in part because of its high permeability at relatively low field levels. This enables the circulating beam tube to shield the interior of the tube from the fields leaking from the septum area. These leakage fields are on the order of several Gauss. The 50 mil. thick Permalloy 80 tube is predicted to reduce these down to 0.1 Gauss within the tube.
5. The septum region has been shaped (see Figure 2) to minimize stray fields and make the gap field as uniform as possible. The results of this optimization appear in Figure 3, which shows a cross section of the magnet with zone areas depicting variations of the  $B_y$  gap field. Each zone boundary corresponds to a 5 Gauss field change. The rectangle inside the magnet's aperture represents 2 sigma (standard deviation) of the beam size.

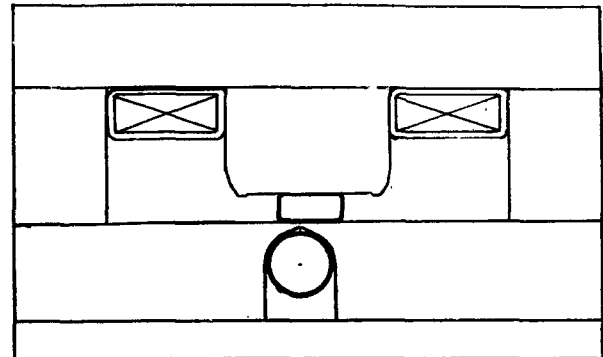


Figure 2.



Figure 3.

A three-dimensional study was undertaken to minimize the stray fields in the circulating beam tube where it enters and exits the magnet. These entrance and exit areas required special attention as they are subject to the stray fields of both the gap and the coil. In addition, the highly permeable (and easily saturated) circulating beam tube must pass through these areas. This study showed that if special protective measures were not taken, the field levels inside the circulating beam tube could reach 1500 Gauss at these areas. Consequently, the following design features were added to the ends of the magnet.

1. The bottom pole piece (septum) was extended 7 cm and 4 cm beyond the top pole piece at the entrance and exit of the magnet, respectively. This shielded the circulating beam tube from the fringe gap field (see Figure 4).
2. "Field clamps" were designed to shield coil end fields (see Figure 4).

The results of the shielding can be seen in Figure 5, which shows the magnitude of the field inside the circulating beam tube on a rectangular surface that is parallel to the top part of the beam starting 30 cm inside the magnet and ending 30 cm outside. The field levels below this rectangular surface, where the beam is, are lower.

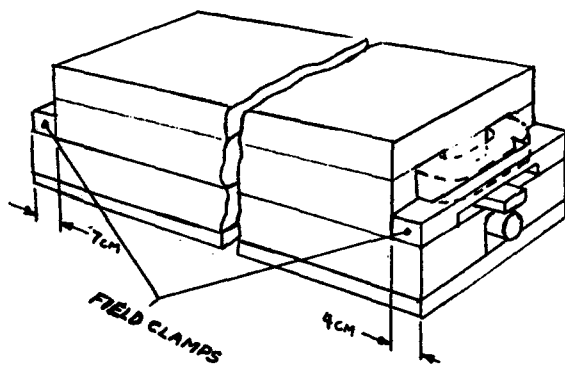


Figure 4.

4.20 Page 7 of 8

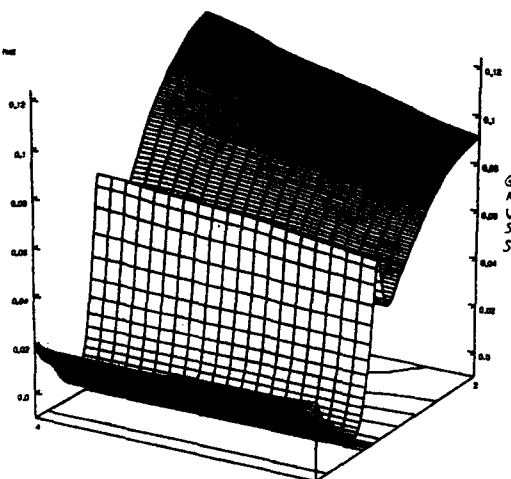


Figure 5.

## V. CONCLUSION

As designed, the RHIC Lambertson magnet has met or exceeded the design goals and represents a state-of-the-art injector in terms of vacuum compatibility, field uniformity, and stray field levels.

## VI. REFERENCES

- [1] Trademark of Inland Steel.
- [2] Trademark of Sprang Specialty Metals.
- [3] Trademark of Vector Fields, Inc.

# Combined ac Corrector Magnets

A.J. Otter, P.A. Reeve<sup>1</sup>,  
 TRIUMF, 4004 Wesbrook Mall, Vancouver, B.C. V6T 2A3  
 N. Marks  
 Daresbury Laboratory, Warrington, England WA4 4AD

## Abstract

Conceptual designs have been made for two types of multipole corrector magnets for use in TRIUMF's proposed KAON Booster ring which operates at 50 Hz. The lack of space in the synchrotron lattice makes it attractive to combine dipole, quadrupole and sextupole correctors in the same yoke structure.

A conventional constant current density winding design is compared with an alternative magnet with twelve poles and windings distributed in slots and at the pole faces. The problem of induced voltages in the windings is discussed.

## I. INTRODUCTION

TRIUMF's Kaon Factory Booster ring design calls for extended families of corrector magnets which operate at 50 Hz. A suggestion to combine dipole and quadrupole correctors was made in 1989 [1] and a preliminary design presented. Further work was carried out in 1992 to add a sextupole field to such a magnet. This paper presents two designs for a combined dipole, quadrupole and sextupole magnet. Each type of field requires independent current control.

The first design presented is for a magnet with a cylindrical yoke and constant current density windings and the second is for a 12 pole magnet with interpole and pole face windings.

## II. REQUIRED FIELD PARAMETERS

It was decided to investigate a magnet with the parameters listed in Table 1 which would cover the magnets in the arcs specified with sextupole fields which would be the most demanding. Production magnets would be made with variations e.g. some magnets would have skew quadrupole windings but not dipole windings.

Table 1 Parameters of Study Magnets

Minimum bore radius	62.0	mm
Good field radius	52.0	mm
Magnetic length	0.3	m
Dipole field	$0.027 \pm 3.1 \%$	T
Quadrupole field	$0.865 \pm 2.3 \%$	T/m
Sextupole field	$17.3 \pm 1.1 \%$	T/m <sup>2</sup>

## III. CYLINDRICAL YOKE MAGNET WITH CONSTANT CURRENT DENSITY WINDINGS

The section shown in Fig. 1a is a conceptual design based on [2] which meets the criteria of Table 1. The winding configuration was chosen to make the most efficient use

<sup>1</sup>also University of Victoria, Victoria, B.C. V8W 3N6

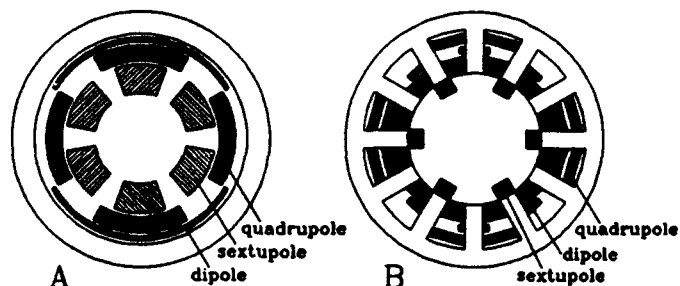


Fig. 1. Magnet Cross Sections: a) Cylindrical Yoke, constant current density windings; b) Multipole with interpole and pole face windings.

of space as the windings requiring the most ampere turns are placed closest to the inner diameter. A radial space of 0.5 cm was maintained between each set of coils and the steel yoke to allow for coil formers which would be nested together in the magnet assembly. The sextupole coil inner radius has a 0.8 cm allowance over the 6.2 cm inner radius specified. Because the steel yoke enhances the fields of the individual coils and its inner radius is not initially known several iterations of the design equations are needed to determine the coil radii. The magnet parameters are given in Table 2.

Table 2 Cylindrical yoke magnet parameters.

Winding	Inner Radius cm	Outer Radius cm	Current Density A/cm <sup>2</sup>	Coil Angle Degrees
Dipole	14.25	14.75	415	60
Quadrupole	11.5	13.75	475	30
Sextupole	7.0	11.0	460	20
Steel Yoke	15.25	18.25	-	-
Magnet Bore	-	6.2	-	-

Calculations from the formulae given in [2] and the POISSON code show that the magnet will produce the specified fields. The field quality requirements are also exceeded although the dipole does have an N=5 component of about 1% and an N=7 component of about 0.2%. It would be possible to reduce these if necessary by modifying the winding configurations [3]. The harmonics are essentially unchanged when the windings are excited individually and simultaneously.

It has been assumed that each component of the magnet would have the same effective length, but in view of the differing coil radii this may not be exactly true. Before a magnet was designed in detail this would be checked using the TOSCA code and if necessary the operating currents would be adjusted. The yoke flux density is low, being about 3.2 kG maximum.

The windings would be made from square hollow copper conductor 0.162 in. square x 0.090 in. ID ( 4.1 mm square x 2.29 mm ID ) each winding would operate at approximately 100 A peak. The coolant temperature rise was limited to 20 C to allow a margin for eddy current losses caused by transverse fields in the conductor material. These losses are estimated at 5.6 Watts/m for this conductor in a transverse field of 3 kG. At this level the losses are similar to the coil resistive losses.

The power supply requirements, Table 3, are estimated from resistive losses and stored energies. Operating margins and any allowance for core losses have not been included. The operating frequency is 50 Hz.

Table 3. Biased power supply requirements.

	A rms	V rms	VA rms
Dipole	60.32	15.7	947
Quadrupole	61.85	101.5	6278
Sextupole	63.2	56.6	3577

Each coil would be cooled with a single cooling circuit except for the quadrupole which might need two circuits per coil because of pressure drop considerations.

#### IV. A 12 POLE MAGNET WITH INTERPOLE AND POLE TIP WINDINGS

An alternative multipole design is shown in Fig. 1b, with parameters listed in Table 4. It is similar in concept to dc magnets used at Daresbury as multipoles in the SRS, but with ac excitation as provided by the programmed quadrupoles in the earlier synchrotron NINA at the same laboratory [4-7].

The sextupole field is superposed on the basic 12 pole geometry with only alternate poles excited. The quadrupole coils each surround two poles with four poles unused. Each dipole coil couples to six poles with a distributed winding that grades the ampere-turns according to the angle of the pole. The magnet bore is larger than specified to obtain adequate field quality for the quadrupole harmonic. The pole face windings on the unused sextupole poles are necessary to offset the field distortion caused by these poles.

Table 4. 12 pole magnet parameters.

Clear bore radius		8.5 cm
Pole tip radius		11.0 cm
Pole width		2.8 cm
Pole height		7.5 cm
Yoke radial thickness		3.5 cm
Outer radius		22.0 cm
Dipole	Number of Turns	30
	Peak Current	81.4 A
	RMS Current	49.8 A
Quadrupole	Number of Turns	38
	Peak Current	109.6 A
	RMS Current	67.1 A
Sextupole	Number of Turns	55
	Peak Current	114.7 A
	RMS Current	70.3 A

The windings use the same conductor at similar current densities as the previous design. Except for the pole tip windings the conductors are in low field regions between the poles so eddy current losses will not be large.

The maximum flux density in the poles and yoke with all coils excited is 1.1 T.

The minimum power supply ratings for each component estimated for the inductive component only, are given in Table 5.

Table 5. 12 pole magnet power supply requirements.

	Dipole	Quadrupole	Sextupole
AC RMS Current (A)	27.78	38.75	40.55
RMS Voltage (V)	14.92	129.0	155.8
kVA Rating (kVA)	0.43	5.0	6.32

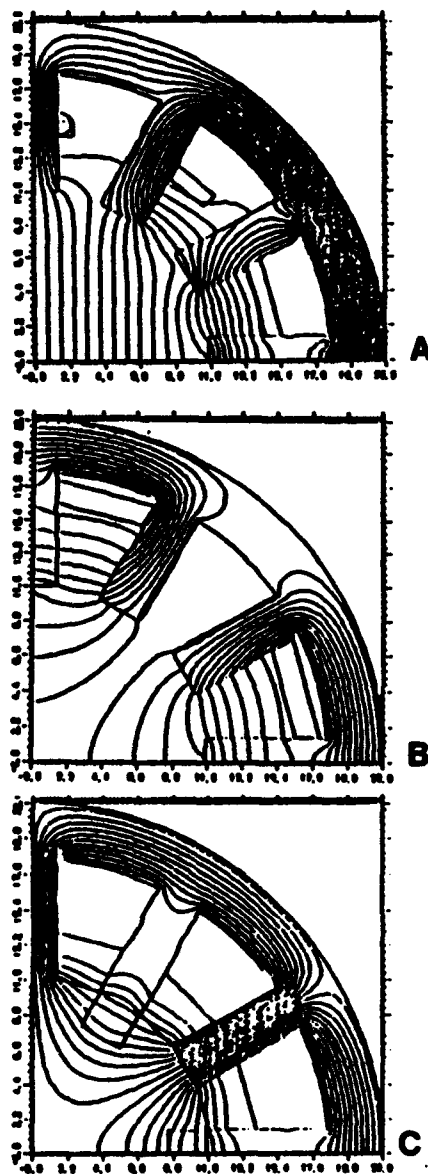


Fig. 2. Multipole Magnet Flux Contours: a) Dipole; b) Quadrupole; c) Sextupole.

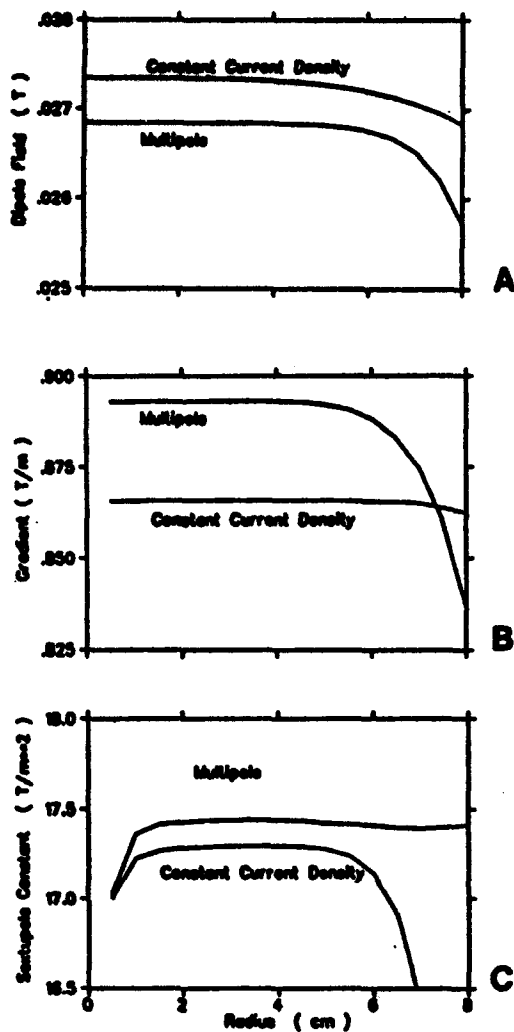


Fig 3. Field Profiles vs Radius: a) Dipole; b) Quadrupole; c) Sextupole.

Figure 2 shows the flux distributions for quarter sections of the magnet with individual coils energised.

The field profiles along the horizontal axis are shown for both magnets in Fig. 3. The apparent drop in value of the sextupole constant at small radii is not real, but is caused by the method of calculation.

#### V. HARMONIC PICKUP BETWEEN COILS

The various coils will act as pickup coils to the driven coils of a different harmonic.

Let the pickup coil have harmonic  $m$  and the driving coil  $n$ , with a phase difference between them of  $\psi$ . Then the pickup coil response is given by

$$S_m = a_m \cos(m\theta + \psi) \quad (1)$$

and for the driving voltage

$$B_n = b_n \cos(n\theta) \quad (2)$$

The voltage output of the pickup coil is the product of eq. (1) and eq. (2). Over  $2\pi$  the integrated output is

$$V = \int_0^{2\pi} a_m b_n \cos(m\theta + \psi) \cos(n\theta) d\theta \quad (3)$$

and if  $m \neq n$   $V = 0$   
but if  $n = m$   $V = \pi a_m b_n \cos \psi$

Therefore in principle each coil will only pickup from its own harmonic. However if the coils are not perfectly made, any imperfection harmonic will be picked up.

This conclusion was confirmed by using the PE2D code and by measurements on a small scale simple models.

#### VI. MANUFACTURING CONSIDERATIONS

Both magnet designs are similar in size and complexity and the choice between them will be made on a cost basis. Detailed engineering designs have not been made. It is anticipated that the coils will be preformed and cast in sub-assemblies that will be assembled together. The length constraint is such that saddle end coils will be specified and it will be necessary to assemble the yokes around them. The laminations for the cylindrical magnet will be made from two overlapping halves and there may have to be six laminations to form the multipole geometry.

#### VII. CONCLUSIONS

We believe that both designs are feasible. They are similar in size and operating current densities and both meet the field criteria specified. The multipole design has a better sextupole and dipole profile but a poorer quadrupole. The power supply kVA rating for the constant current density design is a factor of two lower than for the multipole design mainly due to the smaller radii of the windings.

#### VIII. REFERENCES

- [1] M.R. Harold, "Trim Quadrupoles in the Booster Orbit Correctors", TRI-DN-91-K175, (Jun 1991).
- [2] A. Asner, "Cylindrical Aperture Multipoles with Constant Current Density Sector Windings", CERN, SI/Note MAE/69-15.
- [3] J.H. Coupland, "Dipole, Quadrupole and Higher Order Fields from Simple Coils", Nucl. Instrum. & Methods 78 (1970) 181-184.
- [4] N. Marks, "The SRS Prototype Multipole Magnet", 6<sup>th</sup> Int. Conf. on Magnet Technology, (Bratislava 1977).
- [5] R.P. Walker, "The SRS Multipole Magnets", 7<sup>th</sup> Int. Conf. on Magnet Technology, (1981, Karlsruhe).
- [6] N. Marks, "Nina Programmed Quadrupoles", Proc. Part. Acc. Conf., (1975, Washington, D.C.).
- [7] J.B. Lyall, "Programmed Quadrupole Supplies for Nina", 5<sup>th</sup> Int. Conf. on Magnet Technology, (Rome 1975).

# Longitudinal Profile and Effective Length of a Conventional Dipole Magnet

Jean-François OSTIGUY  
Fermilab\*, P.O. Box 500, Batavia, IL 60510

## Abstract

Magnetic saturation in the vicinity of longitudinal edges results in a small decrease in effective length with increasing excitation current. This phenomenon does not pose any problem in a machine where all dipoles are identical. In the Fermilab Main Injector lattice, dipoles of two different physical lengths are used. The effective length variation is caused by end effects and is essentially independent of the physical length of each type of magnet. However, the relative variation is larger for the short magnets. Since all dipole magnets are on a common bus, the closed orbit is modified in an energy dependent way. Although this effect can be compensated with corrector magnets, a better approach is to design the dipole magnets so as to minimize absolute effective length variations. This can be accomplished with a suitable longitudinal pole profile in the end region. Theoretical considerations and numerical calculations leading to the choice of this profile are presented.

## I. INTRODUCTION

The net (horizontal) angular deflection experienced by a particle of momentum  $p$  going through a dipole magnet is given by

$$\theta = \frac{\Delta p}{p} = \frac{q}{p} \int_{-\infty}^{\infty} \beta_s(s) B_y(x, y, s) ds \quad (1)$$

For highly relativistic particles,  $\beta \simeq 1$ . Accelerator magnets are generally designed in two dimensions. Since by symmetry, the field does not have any axial component in the midplane, a straightforward two-dimensional calculation tends to accurately predict the field in that plane. To separate bulk saturation effects from the small changes in the longitudinal field profile, it is convenient to introduce an "effective" or "magnetic" length  $L_e$ , defined as follows,

with the origin of the coordinate system in the center of the magnet

$$L_e(I) = \frac{1}{B_y(I; 0, 0, 0)} \int_{-\infty}^{\infty} B_y(I; 0, 0, s) ds \quad (2)$$

The deflection can then be written in the form

$$\theta(I) = \frac{q}{p} B_y(I; 0, 0, 0) L_e(I) \quad (3)$$

When the permeability is infinite, the vertical field on axis and the effective length can be estimated by solving in the  $y-s$  plane for the magnetic scalar potential assuming that the poles are equipotential surfaces. Unfortunately, this approach fails when the permeability is finite or when there is saturation; furthermore, it tends to overestimate the field beyond a distance of the order of one gap width away from the physical end of the magnet. A full three-dimensional solution is required to correctly model non-uniform saturation and the faster field decay due to the finite width of the magnet.

It should not be too surprising that a simple rectangular end results in relatively large variations of  $L_e$  with increasing current. The high flux density in the corner region causes non-uniform saturation that tends to make the flux in the end region weaker, resulting in a decreasing  $L_e$ . Clearly, the poles must be profiled longitudinally to control nonuniform saturation effects. As a starting point, it is natural to consider two classical profiles: the Borda and the Rogowski profiles.

## II. BORDA PROFILE

The Borda profile (which has also been attributed to Helmholtz) is well-known in classical hydrodynamics. It corresponds to the curve defined by the streamlines for a fluid issuing from a large vessel by an aperture in a plane wall. In magnetostatics, the streamlines correspond to lines of constant vector potential. When the permeability is infinite, the Borda profile is such that the magnitude of the magnetic flux density along the profile is constant. Since the saturation level depends on the magnitude of the field, it seems reasonable to expect that the Borda profile would help minimizing the variation in  $L_e$  by making the

\*Operated by the Universities Research Association, Inc., under contract with the U.S. Department of Energy.

end region saturate uniformly. We shall see that in practice, this is not really the case. An analytical expression for the Borda profile can be obtained using standard conformal mapping techniques [2]. In parametric form, the result is

$$x = \frac{2g}{\pi} \left\{ \sin \psi - \log \tan \left( \frac{\psi}{2} + \frac{\pi}{4} \right) \right\} \quad (4)$$

$$y = \frac{2g}{\pi} \left\{ \frac{2 + \pi}{2} - (1 - \cos \psi) \right\} \quad (5)$$

where  $0 < \psi < \pi/2$  and  $2g$  is the total gap in the uniform field region. The Borda profile is shown in figure 1. Note that the ratio of the maximum to minimum aperture is  $(\pi + 2)/\pi$ .

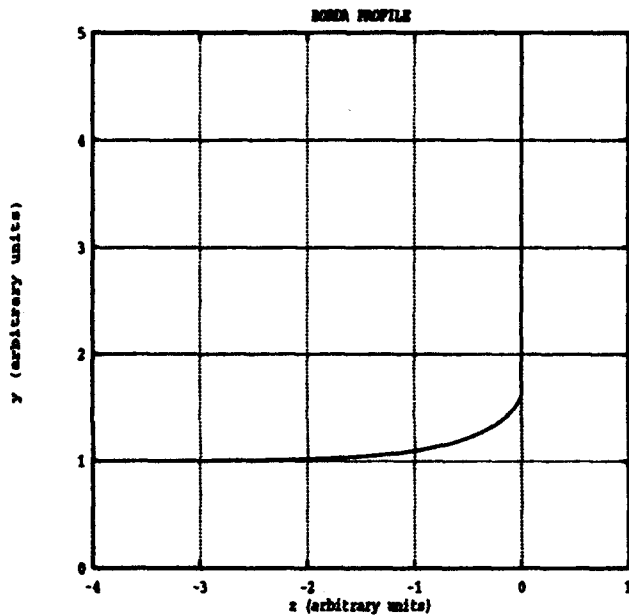


Figure 1: The Borda Profile.

### III. ROGOWSKI PROFILE

This profile was introduced in the context of study of electrical breakdown in gases. Rogowski realized that parallel metal plates of finite dimensions create a problem of electrical stress control at the edges of the plates. Depending upon the material to be tested, the breakdown strength may be very sensitive to local high fields within the whole electrode arrangement. Therefore, the highest stress should only be present in the homogeneous field region, where the plates are parallel. A certain profile of electrodes is necessary outside the plane region but the field strength at the curved edges should never exceed the value  $H_0 = V/2g$  where  $V$  is the applied voltage and  $2g$  the distance between the plates. Rogowski proposed electrodes whose profile follows the analytical function

$$z = \frac{2g}{\pi} (w + 1 + e^w) \quad (6)$$

or, with  $z = x + iy$  and  $w = u + iv$

$$x = \frac{2g}{\pi} (u + 1 + e^u \cos v) \quad (7)$$

$$y = \frac{2g}{\pi} (v + e^u \sin v) \quad (8)$$

where  $-\pi < v < \pi$  and  $-\infty < u < \infty$ . The function 6 was actually first introduced by Maxwell and describes the equipotentials lines of a semi-infinite capacitor. If the field in the uniform region is  $H_0$ , the magnitude of the field is

$$|H| = \frac{H_0}{\sqrt{1 + e^{2u} + 2e^u \cos v}} \quad (9)$$

When  $-\pi/2 < v < \pi/2$ , the field strength has its maximum value in the homogeneous field region and decreases monotonically within the curvature with increasing values  $u$ . Rogowski chose the profile defined by  $v = \pi/2$  and  $-\infty < u < \infty$  because it is the most compact profile that has this property. Since the field in the end region is always weaker than the body field, the end region can be expected not to saturate significantly until the body is well saturated. This should help keeping the effective length constant, at least for excitations below the level required to saturate the end region significantly. This approach turns out to work fairly well in practice. Note in passing that the Rogowski profile can also be defined as the profile which makes the vertical component of the flux density in the pole constant along the pole surface.

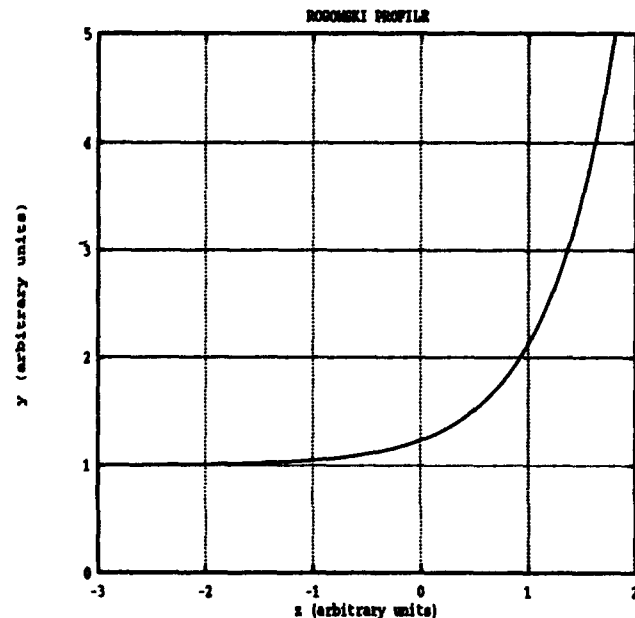


Figure 2: The Rogowski Profile.

The Rogowski profile is shown in figure 2.

## IV. 3D CALCULATIONS

The initial attempts at computing changes in effective length for different profiles were not very successful. As part of the Main Injector magnet R&D program, measurements were therefore performed on endpacks made out of stacked laminations, for both the Borda and Rogowski profiles [2]. The Borda endpack was measured first and the results were not encouraging; however, the Rogowski endpack met the specifications.

Better computer facilities subsequently became available and the calculations were performed again, this time with much improved resolution. The results for one end piece are presented in Table 1. Note that only the changes in length are significant. All calculations were made for one half of a magnet approximately 50 cm long. The agreement with the measurements presented in reference [2] is now relatively good, considering the fact that the computer model is an idealized smooth profile and that no attempt has been made to model the permeability anisotropy introduced by the laminations. For example, at 9500 Amperes, the model predicts a decrease of 6.6 mm per end for the Borda profile. The measured value is 4.5 mm. For the Rogowski profile, the measured decrease is approximately 1 mm and the calculated value is 0.3 mm.

Profile type	$\mu = \infty$	$I = 7000 \text{ A}$	$I = 9500 \text{ A}$
Borda Profile	51.6612 cm	51.6067 cm	51.0017 cm
Rogowski	54.7420 cm	54.7327 cm	54.7116 cm

Table 1. Calculated Effective Lengths (3D Model)

The calculations also demonstrated that the problem with the Borda profile is the presence of rather non-uniform saturation in the bulk of the pole, right above the tapered region. The calculated longitudinal field profiles are illustrated in figure 3. Note the almost linear decrease of the field within the body of the magnet.

## V. ACKNOWLEDGEMENTS

The author would like to thank Dave Harding, Hank Glass and the personnel of the Fermilab Magnet Test Facility for their valuable comments.

## REFERENCES

- [1] J. Simkin and C. W. Trowbridge, "Three-dimensional Nonlinear Electromagnetic Field Computations, using Scalar Potentials", *IEE Proc.*, 127, 6, 368-374 (1980).
- [2] D.J. Harding et al., "Design Considerations and Prototype Performance of the Fermilab Main Injector Dipole", *These Proceedings*.

- [2] Horace Lamb, "Hydrodynamics", Cambridge University Press 1879 (Reprinted by Dover Publications NY 1945).

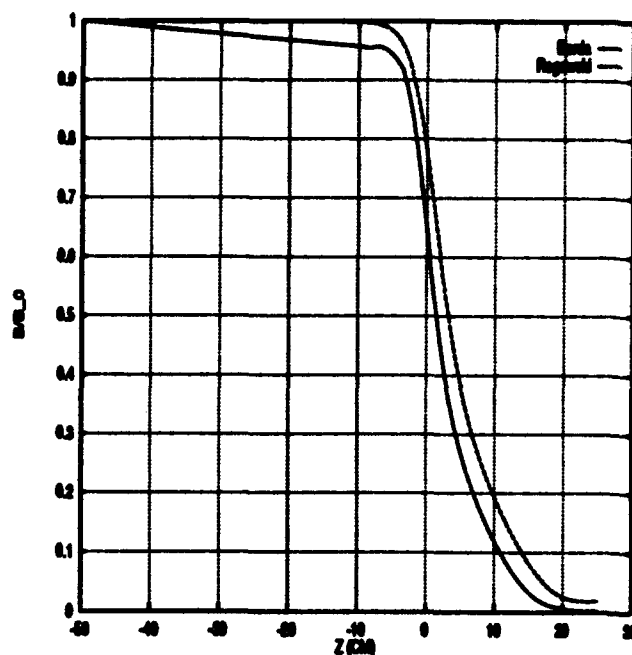


Figure 3: Calculated Longitudinal Field Profiles (3D model).

# Magnetic Flux Shielding for the Precision Muon g-2 Storage Ring Superconducting Inflector<sup>1</sup>

W. Meng, W.B. Sampson, M. Suenaga  
Brookhaven National Laboratory  
Upton, New York 11973

## Abstract

The muon g-2 experiment (E821)<sup>1</sup> at the AGS requires a precision in the magnetic field over muon orbit at the level of 0.1 ppm. Injection is done with a superconducting inflector involving a double cosine theta winding approximately cancels its fringe field. Nevertheless its residual field would effect the homogeneity of the storage ring magnetic field. A method of using a superconducting sheet surrounding the inflector to further reduce the fringe field is being investigated. The experimental program to explore this technique is described and some test results are presented.

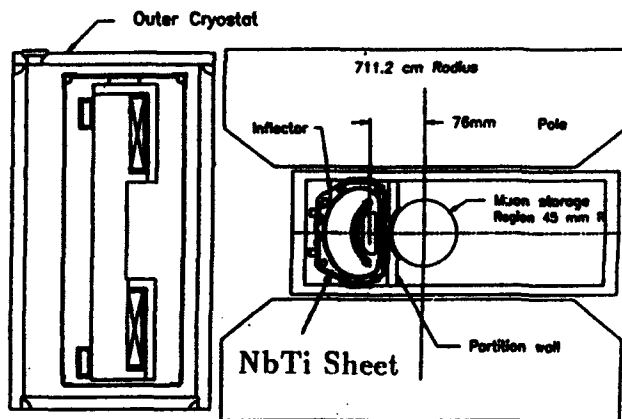


Figure 1: The inflector for the muon storage ring

## I. INTRODUCTION

The goal of BNL AGS E821[1] is a measurement of  $a_\mu$  ( $a_\mu = (g - 2)/2$ ) to 0.35 ppm, a factor of 20 improvement over the CERN experiment which achieved 7.2 ppm in 1977.[2] Improvements include much higher proton beam intensity at the AGS due to the booster, and a superferric storage ring which is to be homogeneous over the storage region to 1 ppm and effective magnetic field average around the ring known to 0.1 ppm. At the ring entrance, differing from the coaxial pulsed device in CERN, a superconducting DC inflector was proposed, which locally cancels the

<sup>1</sup> Work performed under the auspices of the U.S. Dept. of Energy.

field of the main storage ring magnet, so that the beam enters as close as possible and about tangentially to the equilibrium orbit of the ring. The design of the inflector was based on the truncated double cosine principle which minimizes the fringe field by the cancellation of current distributions.[3] In the physical realization, the idea surface current distributions must be replaced by SC windings (Fig.1), hence the cancellation will not be complete due to the discretisation and manufacture tolerance. A fringe field at the order of a few ppm over the storage region is estimated. Since this fringe field is a very rapidly varying function of position, it is quite difficult to correct it by using the conventional iron compensation method. In order to eliminate this residual a superconducting sheet will be used to create a opposite multipole currents.

## II. PRINCIPLE

When a superconducting surface surrounds a magnetic device, currents are induced in the surface which oppose the changes in magnetic field and effectively reduce the field outside the shield to zero. This supercurrent acts very much like the eddy current described by Faraday's Law of induction and Lens's Law, except they do not decay. Such shielding is effective up to the critical current density of the material used and requires that no discontinuities exist in the surface where currents must flow to produce the desired field distribution.

## III. CONCEPTUAL DESIGN

Unlike most applications[4] (in which the aim is to shield relatively large fields), the residual fringe field of the g-2 inflector is fairly low. This suggests the possibility of using a plain NbTi sheet containing no stabilising normal metal as a relatively unsophisticated shield. The ideal location of the SC sheet is on the outer surface of the inflector housing (Fig.1) where the temperature will remain at 4.6 K as long as the inflector is in operation. The magnitude of the field on this surface is estimated at several hundred gauss.

The inflector must stay above the transition temperature when the storage ring magnet is energized, so that the flux of the main magnetic field can penetrate the SC sheet which is in the normal state. After the main field reaches

its stable value (1.45 T), the inflector together with the shield can be cooled to liquid helium temperature. As the current of the inflector increases,  $dB/dt$  induces supercurrents in the sheet, which keep the fringe flux from entering the interior of the sheet.

#### IV. MATERIAL EVALUATION

Magnetisation measurements can be used to determine the critical current density of superconductors in sheet form.

A piece of Nb-46.5w/oTi sheet, 0.5 mm thick, was provided by Teledye Wah Chang. Figure 2 shows the critical current density  $J_c$  as a function of magnetic field at 4.2 K, measured by BNL Materials Science Division. While this current density is very low compared modern multifilamentary composites, it is high enough to provide significant shielding at low field levels.

#### V. SHIELDING TEST

In order to examine the shielding capabilities of this sheet before the completion of the inflector, it was tested in the RHIC Magnet Division, using an existing superconducting SSC sextupole coil to simulate the inflector. Figure 3 shows the experiment arrangement. The NbTi sheet surrounds a superconducting sextupole magnet and is equipped with a heater made from stainless steel ribbon, which controls the temperature of the shield. Two Hall probes  $H_1$  and  $H_2$  were used for monitoring the magnetic flux densities inside and outside of the flux shield. They are situated at position where the flux lines are perpendicular to the shield surface. Figure 4 shows the field seen by the probes, as a function of the sextupole current. The shield was capable of excluding flux from the outer region upto the maximum current of the sextupole coil (256 A) where the field at the sheet surface should be about 1250 gauss. With the sextupole current set at 100 amps, probe  $H_1$  was moved along the total length of the coil with

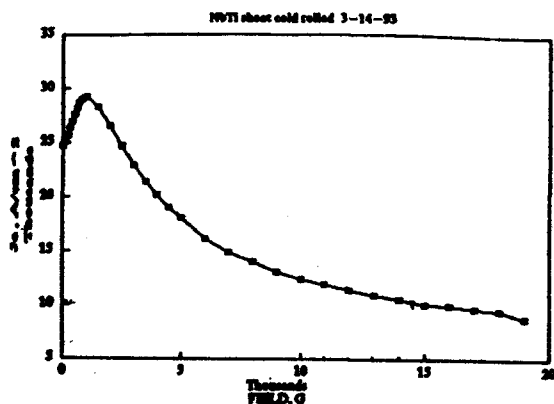


Figure 2: The critical current density of the NbTi sheet deduced from magnetisation measurements

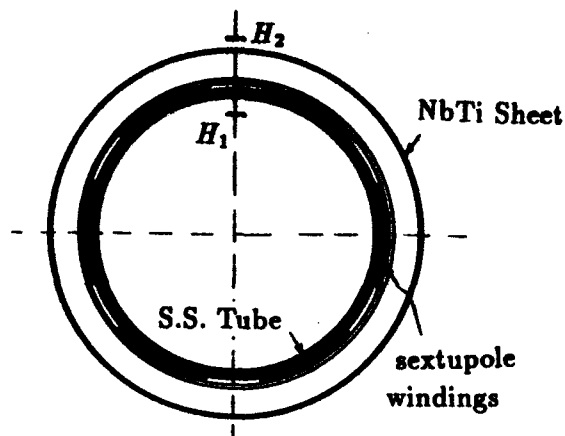


Figure 3: The experiment arrangement used to test the shielding properties of the 0.5mm NbTi sheet.

the shield in both the superconducting and normal states. The results are shown in Fig.5. The sextupole is somewhat longer than the flux shield and is positioned so that one end is not shielded. The transition from the the shielded to the unshielded region occurs smoothly despite the sudden change in the local conditions.

In order to observe some flux penetration, one has to increase the temperature of the sheet by adjusting the power of the heater. This is illustrated in Fig.6 where the maximum current density induced in the NbTi sheet is plotted against temperature. The current density was computed from the flux change inside the sextupole and the temperature estimated from the heater power input. In the temperature range between 4.2 K and 6 K the flux that can be shielded is erratic indicating a lack of stability of the higher current densities in this simple shield.

#### VI. CONCLUSION

The material evaluation and shielding test verified the feasibility of using superconducting material to eliminate the inflector fringe field. Further tests are planned using

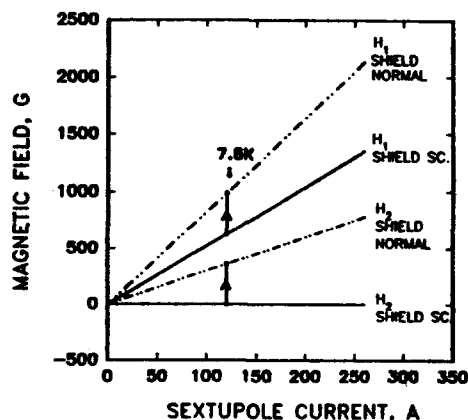


Figure 4: The field at Hall probes 1 and 2 as a function of sextupole current with the flux shield in the superconducting and normal state.

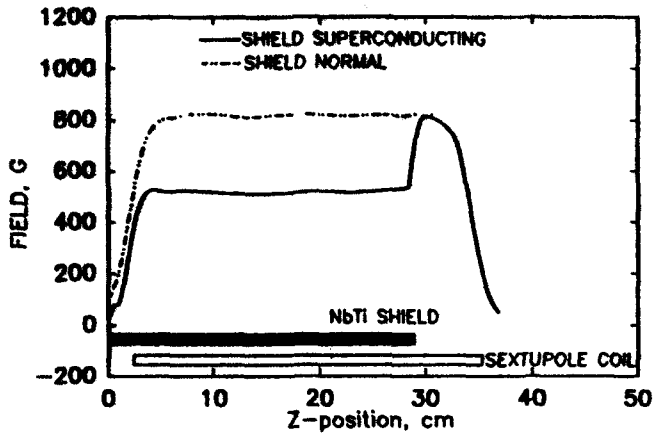


Figure 5: The field distribution along the length of the sextupole at 100 amps with the flux shield in the superconducting and normal state.

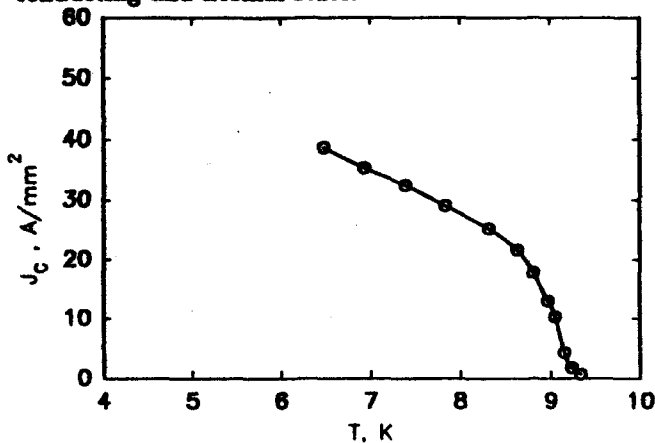


Figure 6: The critical current induced in the superconducting shield as a function of temperature

higher  $J_c$  stabilized NbTi sheet[5] on an inflector prototype made by Japan KEK. These tests will be in a background field of 1.45 T to simulate more accurately the actual conditions the inflector will experience in the storage ring.

## VII. ACKNOWLEDGEMENT

The authors would like to thank G.T. Danby, A.K. Ghosh, M.A. Green, and F. Krienen, for useful discussions and encouragement.

## VIII. REFERENCES

- [1] E821 Design Report, 1992.
- [2] Bailey et al. Nucl. Phys. B150, 1 (1979).
- [3] F. Krienen et al. 1991 IEEE Particle Accelerator Conference.
- [4] F. Martin et al. NIM 103 (1972)503-514.
- [5] I. Itoh and T. Sasaki, Magnetic Shielding Properties of NbTi/Nb/Cu Multilayer Composite Tubes.

# Three Dimensional Field Analysis for the AGS Combined Function Magnets

W. Meng and M. Tanaka  
Brookhaven National Laboratory  
Upton, New York 11973

## Abstract

In order to study the particle trajectories in the fringe field of the AGS ring during the single bunch multiple extraction (or fast extraction) from the the AGS to the muon g-2 experiment and to the RHIC, the magnetic field of the AGS combined function magnets were calculated by using the TOSCA program. The results are compared with the field maps of the previous measurements. The particle tracking is achieved by using the TOSCA program post-processor.

## I. INTRODUCTION

The design of the AGS new fast extraction beam (NewFEB) system for the g-2 experiment and RHIC injection[1] requires detailed magnetic field knowledge about the AGS main magnets, so that one may predict the trajectories of 29 GeV/c protons in the fringe field region during the extraction (Fig.1). 2d and 3d magnetic field computations have been done by using POISSON and TOSCA programs. Partial results are described in this note. The comparisons between calculated field values and measured field maps show that if one properly handles the TOSCA program, high accuracy can be achieved. Further studies will show that particle tracking by using the post process of the TOSCA program is feasible[2].

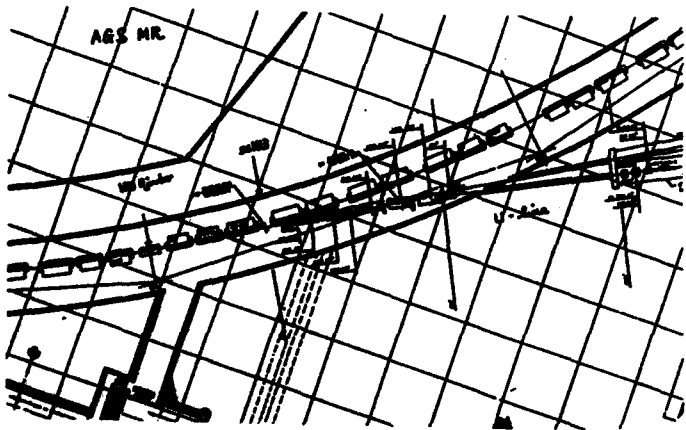


Figure 1: New FEB in AGS

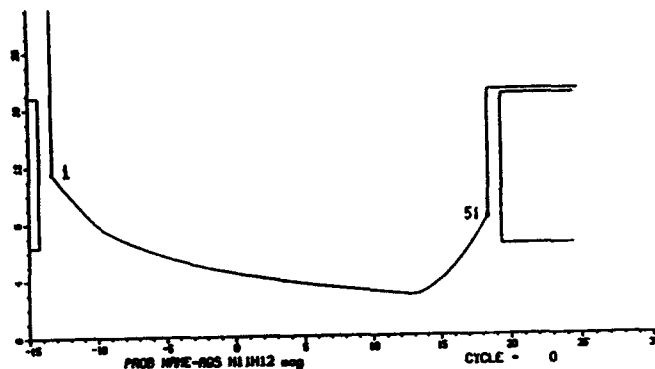


Figure 2: Pole Shape (open type)

## II. AGS MAGNETS

The AGS combined function main magnets perform two functions: a) guiding the proton beam into the circle and b) focusing the beam. Each of the 240 magnets around the AGS ring deflects the protons by 1.5 deg, or 360 deg in all, to complete a nearly circular path. The reference circle is 128.46 meter in diameter. The physical length path of the magnets occupies about two thirds or the circumference, the rest being available as straight sections between magnets for other equipment. According to the principle of alternating gradient strong focus, two types of magnets are utilized - "open" type and "closed" type. Figure 2 shows the pole shape of a "open" type[4]. The pole surface of the AGS magnets was well designed many years ago, based on constant magnetic scalar potential surface. The material of the magnets is the Electrical Grade M-36 Steel Laminations, which contains 1.80% silicon and 0.03% carbon. The laminations are insulated from one another by a coating of varnish to inhibit eddy currents. The stacking factor of the laminations is about 0.98[3]. The B-H data used in calculations was based on a measured magnetization curve. It was interpolated in order to ensure the smoothness of its first derivatives and the continuity of its second derivatives.

## III. TOSCA CALCULATIONS

<sup>1</sup> Work performed under the auspices of the U.S. Dept. of Energy

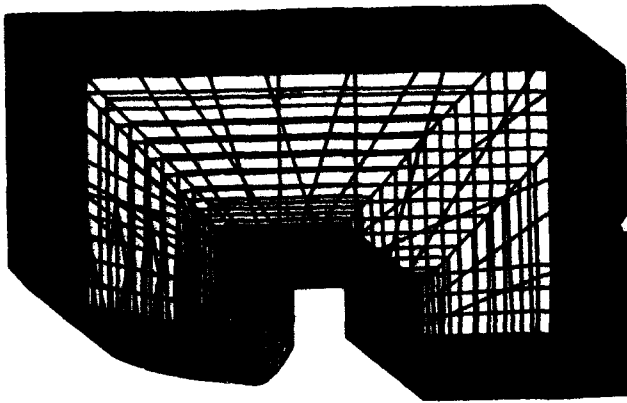


Figure 3: 3d Model

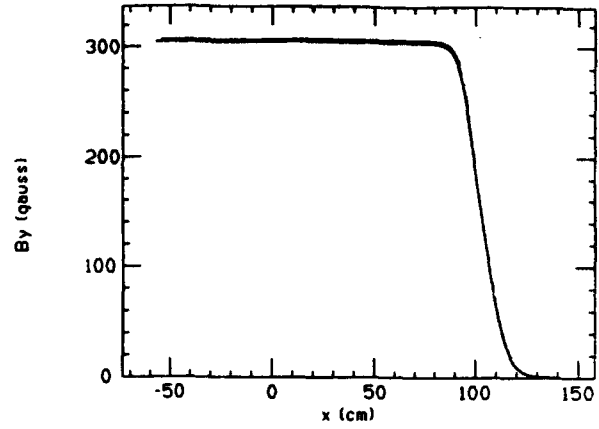


Figure 7: Comparison (fringe field region)

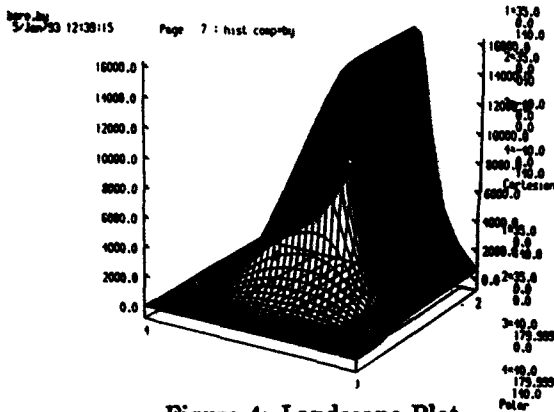


Figure 4: Landscape Plot

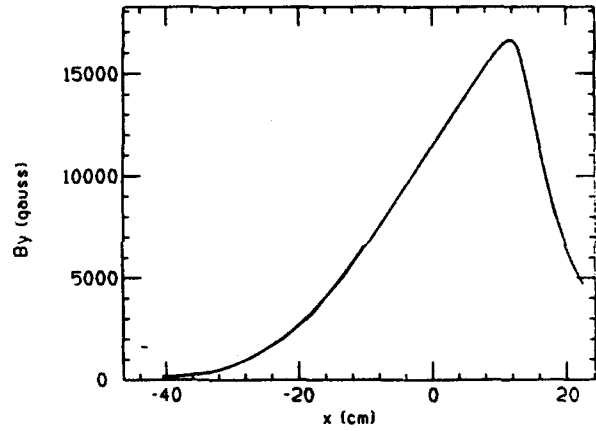


Figure 8: Comparison (high field)

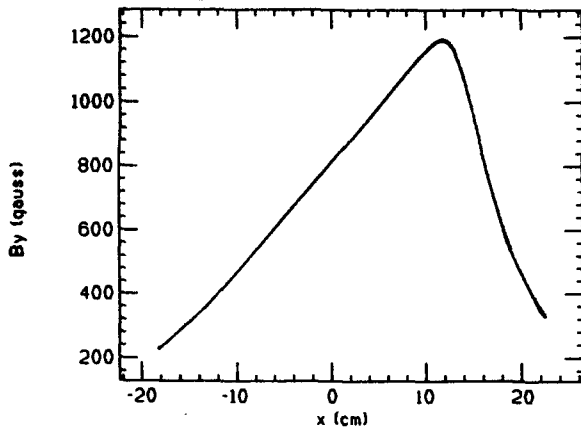


Figure 5: Comparison (median plane)

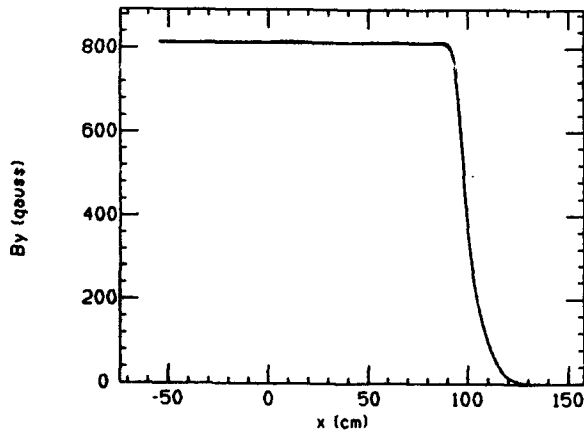


Figure 6: Comparison (beam line)

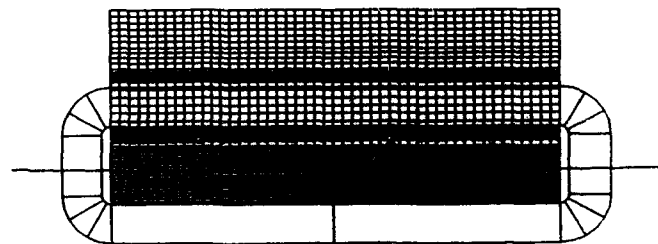


Figure 9: Particle Tracking in Tosca Model

The advent of relatively inexpensive and powerful computers has inspired the development of the large scale three dimensional codes. TOSCA is one of the most well known commercial codes which is widely used in the industry and accelerator field.

Based on the reference [4], a finite element model of one-quarter of the "open" type AGS magnet was constructed. Figure 3 only shows the steel part. The origin of the coordinate system of the TOSCA calculations is in the middle of the magnet and also at the beam center which is 2 inch away from the geometrical center of the pole. The positive  $x$  direction is pointing the ring center.

Figure 4 shows the landscape plot of the vertical components of B-field on the median plane, around the edge of the magnet. The base area 1-2-3-4 stands for the part of the median plane. The cartesian and polar coordinates of these four corners are listed on the right side of the figure. The vertical height of the surface stands for the magnitude of the component  $B_y$  at particular position on the median plane. On the base area, there is a family of curves which represents the equal-height contours (or constant  $B_y$  lines).

Followings are part of the comparisons between the TOSCA results and the measured data.

(a) Compare with the low field measurements:

Measured data file A[5] is the field map with the applied current 2880 ampere per coil. The center field is about 815 gauss, corresponding to 2 GeV/c protons. Figure 5 shows the comparison between the measured data and the calculation, on the median plane, near the center of the magnet. The difference is about 0.6%. Figure 6 shows the comparison along the central beam line; the difference is about 0.7%. Figure 7 shows the comparison in the fringe field region (6 inch away from the center); the difference is about 0.3%.

(b) Compare with the high field measurements:

Measured data file B[5] is the field map of a open type AGS magnet; the applied current is 41000 ampere per coil (5150 ampere per pair), corresponding to 29 GeV/c protons.

Measured data file BF[5] is again the field map of a open type AGS magnet, except it measured only in the fringe field region along the open side of the magnet.

Figure 8 shows the comparison between the above two measured field maps and the TOSCA calculated results. The measured data B covers from  $x = 0$  cm to  $x = 18$  cm. The difference between this measured data and the calculation is about 0.5%.

The measured data BF covers the region  $x$  from -40 cm to 0, along the  $x$  axis. It is noticed that near the point  $x = -9.14$  cm, the second order derivative shows some discontinuity. Accordingly one may estimate that the measurements error could be about 1.1%. These possibly arose from relocating the equipment and remaining magnetization in the steel core during the measurements.

#### IV. DISCUSSIONS

Authors like to comment the TOSCA program and computations on the following points.

(a) Time Consumption. The time cost for constructing the finite element model depends on the problem size, complexity and the experience of the user. The computer CPU time has reduced tremendously since softwares are available on the UNIX machine (IBM RISC System). Generally speaking, to obtain a field map with a reasonable accuracy, it takes less man power by using TOSCA program than by carrying out a measurement. Nevertheless measurements are always indispensable, since it is the most important way to examine the computed results, as long as the magnet is existing and accessible.

(b) The Accuracy of the TOSCA program. The local error at a field point is determined by (1) the size of the elements surrounding the point; (2) the types of these elements (linear or quadratic); (3) the method required to calculate the field value from the potential array (differentiation of shape function, interpolation of nodal averaged values, or integration of magnetization and currents); (4) the far boundary conditions and the potential types. From first glance, one could say that the accuracy is strongly linked to the size of the elements which is limited by the capacity of the program, but this is not the only factor. By making correct choices from factors (2), (3) and (4), reasonably high accuracy is achievable. According to the results presented in this note, the error of the TOSCA computation is within the error of the measurements.

The TOSCA output file contains the complete information of the magnetic field, and its post-processor is capable of performing particle trackings. Figure 9 shows an example of 29 GeV proton trajectory in an AGS open type magnet. Further studies about the beam tracking in the fringe field region will be carried out.

#### V. ACKNOWLEDGMENT

Authors appreciate the AGS initiator G. Danby for his instructive guidance and discussion.

Authors appreciate R. Thern who reserves useful measured data files about the AGS magnets.

#### VI. REFERENCES

- [1] M. Tanaka and Y.Y. Lee, BNL-45344.
- [2] W. Meng and M. Tanaka, to be published.
- [3] Alternating Gradient Synchrotron Project Construction Completion Report, December 1966.
- [4] Engineering Drawing D03-M-666-5, D03-M-667-5.
- [5] R. Thern, private communication.  
File A=AGBU01.MPA; File B=B5150A.MPA; File C=A5150A.MPA.

# Survey and Alignment Data Analysis for the ALS Storage Ring\*

Roderich Keller  
Lawrence Berkeley Laboratory  
University of California, Berkeley, CA 94720

## Abstract

The survey and alignment effort for the Advanced Light Source (ALS) accelerator complex has been described elsewhere [1]. Data analysis for this task comprises the creation of ideal data, comparison of measured coordinates with ideal ones, and computation of alignment values, taking into account the effects caused by finite observation accuracy. A novel approach has been taken, using personal computer spreadsheets rather than more conventional programming methods. This approach was induced by the necessities to create and frequently refine the analysis procedures while measurements were already underway, and further by hardware constraints that limited the use of an available surveying code. A major benefit consists in the ability to identify and deal with discrepancies that occasionally arise when different techniques are used to observe the same object, in a timely and efficient manner. As a result of the performed survey and alignment work, the ALS lattice magnets have been positioned with accuracies well exceeding the original specifications.

The general survey and alignment concept for the ALS [1] is based on a network of fixed monuments installed in the building floor, to which all component positions are referred. Contrary to the original intent, the commercial software package ECDS<sup>®</sup> is being used for data acquisition, bundling, and transformations from observation-station into object coordinate-systems. Theodolites only are used as observation instruments with ECDS, and an absolute scale has to be established by observing some object of precisely known length.

For the tasks of creating ideal data and computing alignment values, spreadsheets were developed by the author using the application EXCEL<sup>®</sup> for Macintosh<sup>®</sup> computers. Choice of a spreadsheet method rather than conventional programming techniques proved very convenient when in the course of this work the sheets had to be progressively modified under severe time pressure to include new effects and help redefine the observation procedures. With spreadsheets, varying input data formats coming from the survey crew could be easily accommodated, and adding numerous consistency checks as well as

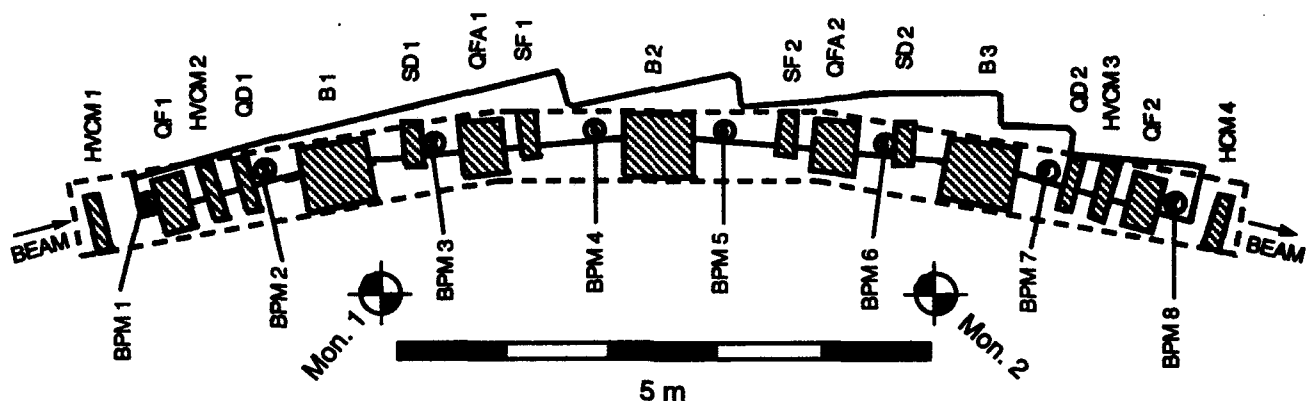


Figure 1. Storage ring magnet lattice in one curved section, with outlines of vacuum chamber (solid line) and girder (broken line). For magnet designations, see Table 1. Four monuments, Mon., are used as survey references; two of them, near the adjacent straight section centers, are not shown in this figure.

## I. INTRODUCTION

The Advanced Light Source (ALS) electron storage ring, now being commissioned at Lawrence Berkeley Laboratory, is the main accelerator of a third-generation synchrotron radiation source designed to produce extremely bright photon beams in the UV and soft X-ray regions [2]. The 1.9-GeV ring consists of 12 superperiods with 196.8 m total circumference and has particularly tight positioning tolerances for lattice magnets and other components to assure the required characteristics.

\* Work supported by the Director, Office of Energy Research, Office of Basic Energy Sciences, Material Sciences Division, U.S. Department of Energy, under Contract No. DE-AC03-76SF00098.

generating additional ideal data for special alignment tasks was possible without much effort. Dedicated spreadsheets were created for each of the 12 curved sectors of the storage ring.

In this paper, the features of these spreadsheets are presented, and the obtained alignment results for lattice and corrector magnets are discussed.

## II. SCOPE AND TOLERANCES

Storage ring objects designated for precision alignment include: a), lattice magnets (36 bend magnets, 72 quadrupoles, and 48 sextupoles); b), 46 corrector magnets; c), special magnets (2 septa and 4 bump magnets); d) 12 storage ring vacuum chambers, represented by 96 beam position monitors

(BPM), 8 per chamber; e), 2 rf cavities; and f), special objects (photon beam-line components and gate valves). A list of required local tolerances for objects discussed in this paper is given in Table 1. These values are understood as 1- $\sigma$  half-widths of every error distribution, with a 2- $\sigma$  cut-off. No strict global tolerance value is established.

Every magnet carries four fiducial posts that are welded to its upper side without attempting to achieve any precise positioning; the positions are determined by a coordinate measurement machine. Different exchangeable targets are used on these posts, either optical targets with engraved circle and center point for surveying or tooling balls, for alignment in combination with dial indicators. The BPMs can be equipped with one target, each.

Table 1  
Local Alignment Tolerances

Object	$\Delta w$ [mm]	$\Delta u$ [mm]	$\Delta v$ [mm]	$\Delta u'$ [mrad]	$\Delta v'$ [mrad]	$\Delta w'$ [mrad]
B	0.15	0.15	0.15	./.	./.	0.25
QD	0.3	0.15	0.15	./.	./.	0.5
QF	0.3	0.15	0.15	./.	./.	0.5
QFA	0.3	0.15	0.15	./.	./.	0.5
SF	0.5	0.15	0.15	./.	./.	./.
SD	0.5	0.15	0.15	./.	./.	./.
HVC	1.0	1.0	1.0	./.	./.	2.0
BPM	0.15	0.15	0.15	./.	./.	./.

B, bend magnet. QD, defocusing quadrupole. QF and QFA, focusing quadrupoles. SF, focusing sextupole. SD, defocusing sextupole. HVC, horizontal and vertical corrector magnet. BPM, beam-position monitor. Tolerances are described in local, beam-following coordinates: w, in beam direction; u, radially away from the ring center; v, vertically up. u', pitch; v', yaw; w', roll. ./ indicates that these values are predetermined by other values in this table.

### III. INSTALLATION AND ALIGNMENT

Magnets and vacuum chambers are mounted on girders spanning one of the twelve curved storage-ring sectors each, see Figure 1. In the first phase of installation, the vacuum chambers are precisely aligned to their girders, represented by 12 girder fiducials. Then the magnets are installed and fine-aligned to the girders as well. As a last step, girders and their objects are aligned to the global 'ALS Coordinate System' represented by the four floor monuments in the immediate neighborhood of every girder. This scheme led to the creation of two families of spreadsheets in which object-alignment data were computed, the so-called 'girder' and 'monument' sheets.

This concept of separation between local alignment of objects (magnets or chambers) to girder fiducials and final global alignment of girders to monuments is well suited in principle to minimize the entire effort, but in reality it failed because the girders bent too much under the weight of the installed magnets, and thus the original girder fiducialization was lost. Therefore, some magnets had to be fine-aligned to girders using survey data related to the global monument

system, and the final alignment of the vacuum chambers was performed using optical tooling methods since most chamber fiducials are hidden by the magnets themselves.

All alignment values are ultimately expressed in local, beam-following coordinates along the main object axes to facilitate the orientation of dial indicators with which the alignment is controlled on every fiducial. Even the alignment to monuments, executed by moving girders only, is monitored on selected magnet fiducials, to achieve final alignment of lattice magnets to the global ALS coordinate system in the most direct manner.

### IV. CREATION OF IDEAL DATA

Ideal data for all objects included in the survey and alignment effort are created in another line of spreadsheets, based on mechanical fiducialization data [3] and magnetic measurements [4]. Special effects are accounted for, such as magnetic-to-mechanical axis offsets for quadrupoles and sextupoles, and roll angles introduced by shimming the two halves of every quadrupole.

These data, together with an accelerator lattice file [5] and the information on the lattice position of any given magnet in the entire ring are being used to convert all fiducial data from local magnet systems into a generic girder system whose origin horizontally coincides with the intersection of the tangents to the ideal beam trajectory on both sides of the central bend magnet. The transformation into the global ALS system is done inside the 'monument sheets,' individually for every storage ring sector.

### V. GIRDER SHEET

The Girder Sheet is the first of the two spreadsheet varieties in which ideal and observed magnet fiducial positions are compared and then adjusted correction values are computed. As a first step, the ideal magnet fiducial data are modified to account for the measured offset of the vacuum chamber center against the ideal girder system. The chambers cannot be moved in this area because they are anchored on a pinned stanchion. After calculating the ideal-to-observed position differences in all three directions of this modified girder system, the longitudinal difference values are compensated for thermal expansion of the girder at the time of surveying. Observed lateral girder deformations, caused by their inner support structures, ultimately made it necessary to maintain the entire storage ring tunnel at the design temperature (23.9  $\pm$  1°C) during surveys, but the longitudinal compensation algorithm is kept in the girder sheets as a safeguard against larger actual temperature excursions.

Two kinds of consistency checks are permanently included in the Girder Sheets, a comparison of the distances between all fiducials of one magnet from both, optical and mechanical measurements, and a comparison of all distances between the four observed monuments with the same values derived from the latest dedicated monument survey. These latter ("ideal") monument distances are included as constants in the ECDS data file to provide absolute scaling.

To facilitate an easy set-up of the dial indicators the derived magnet correction values are transformed from the common girder coordinate system into individual magnet systems. Because of the redundancy of information provided by 12 coordinate values some adjustments are made before the correction values are finalized. The precision of the original installation, compared to magnet dimensions, allows one to compute the adjusted corrections sequentially, rather than as a true rigid-body movement. For every magnet, the average shifts along its own major axes are calculated first, and the remaining correction values are used to evaluate average yaw, pitch, and roll angles which are then translated back into fiducial shifts along the magnet axes, to be superimposed on the average shifts.

## VI. MONUMENT SHEET

The Monument Sheet computes the final alignment values for all magnets, to be executed by moving entire girders only. This implies that all magnet correction values are averaged to yield global girder corrections, i.e. average shifts in three directions and three angular rotations. These global corrections, however, are then expressed as shift values for fiducials on the two focusing quadrupoles at the end of every girder (horizontal directions) and on the central bend magnet in the girder center (vertical direction). Monument Sheets include the same consistency checks as Girder Sheets, but their input and ideal data are expressed in the global ALS coordinate system. One given set of observation data can be easily transformed by ECDS into both, ALS and individual girder systems.

After the initial calculation of ideal-to-observed fiducial position differences in the ALS system, these values are transformed into the corresponding girder system, and the temperature compensation algorithm is applied. At this point there is the option to merge individual magnet corrections, resulting from executing the values obtained from the Girder Sheet, into the Monument Sheet, reducing its remaining corrections accordingly. The average shifts for all magnets are calculated next, and from the remaining correction values the three angular corrections are determined. For pitch and yaw, only magnets at the ends of the girders, including the outer bend magnets, are taken into account, and for roll, only those fiducials are taken that are more than 250 mm away from the girder mid-line. The evaluated angles are then used for a second-order correction, assuring that the average shift for all fiducials resulting from the angular corrections is exactly zero. In addition, the differences between all individual corrections and the effects of the computed global corrections on every magnet fiducial are displayed for visual inspection. All fiducial corrections resulting from the global girder corrections are transformed into local magnet coordinate systems, but the reference fiducial corrections to be used to monitor the girder alignment are together displayed again, for the alignment technicians' use.

## VII. RESULTS

Ideally, 3 surveys and 2 alignments are the minimum number, but due to girder deformation under temperature chan-

ges and mechanical load, changes of the scaling reference, ground motion, and bakeout of two vacuum chambers, it took 7.7 surveys on the average to reach good alignment for all magnets. Two girders actually needed three surveys only, each. The final lattice magnet alignment exceeded the requirements by far. As an illustration, two sets of data are presented in Tables 2 and 3. They represent standard deviations of the remaining position errors for all lattice magnets in absolute, Table 2, and after subtracting a linear fitting line separately for every girder in the transverse coordinates, and the average error in the longitudinal coordinate, Table 3. Roll errors are given as absolute standard deviations, Table 2, and as averages of absolute errors, Table 3.

Table 2  
Final Absolute Alignment Errors

	dw [mm]	du [mm]	dv [mm]	Roll [mrad]
QF	0.17	0.11	0.20	0.07
QD	0.15	0.08	0.20	0.08
QFA	0.14	0.08	0.19	0.08
B	0.14	0.09	0.19	0.07

Table 3  
Final Local Alignment Errors

	dw [mm]	du [mm]	dv [mm]	Roll [mrad]
QF	0.13	0.03	0.04	-0.06
QD	0.10	0.04	0.02	-0.05
QFA	0.05	0.03	0.02	-0.07
B	0.08	0.03	0.02	-0.04

## VIII. ACKNOWLEDGMENTS

T. Lauritzen is the lead engineer for the ALS survey and alignment effort, with responsibilities for all technical and personnel aspects, and it is a pleasure to acknowledge the friendly and efficient collaboration with him in this field over five years. Thanks are also due to the survey crews from LBL, led by W. Baldock and R. De Marco, and from SLAC, led by M. Gaydosh, for their accurate, professional work and many useful suggestions how to improve procedures. Last not least, I want to thank R. Alvis who diligently processed most of the incoming raw data and created several sets of ideal data herself and G. Krebs who took over my responsibilities in this field and contributed some data used in this paper.

## IX. REFERENCES

- [1] R. Keller, T. Lauritzen, and H. Friedsam, 2<sup>nd</sup> Int. Workshop on Accelerator Alignment (DESY Hamburg, 1990).
- [2] 1-2 GeV Synchrotron Radiation Source, Conceptual Design Report, LBL Pub. 5172 Rev. (LBL Berkeley, 1986).
- [3] Magnet fiducialization was performed by members of the ALS Mechanical Engineering group, guided by T. Lauritzen, J. Tanabe, and T. Henderson.
- [4] Magnetic measurements for these purposes were performed at LBL Berkeley, guided by J. Tanabe and D. Nelson.
- [5] H. Nishimura, private comm. (LBL Berkeley 1989).

# A Mechanical System for the Positioning of Accelerator Magnets

Robert Viola and Richard Martin

SSC Laboratory\*

2550 Beckleymeade Ave., Dallas, Texas 75237 U.S.A.

## Abstract

A mechanical support and adjustment system was developed for the precise positioning of the SSC accelerator magnets. This "Ball/Roller" system was designed to be stable, truly kinematic and capable of accommodating a magnet's thermal expansion or contraction. The system's mechanisms are described in detail and its adjustment range, resolution and performance are discussed. Techniques for interfacing the system to magnets of various geometries are presented. A motorized version of the Ball/Roller system was also developed for applications which require magnets to be manipulated remotely. The design and performance of this motorized system are presented.

## I. INTRODUCTION

All particle accelerators require that their lattice elements be located accurately in space. The system which is used to support and position lattice elements is therefore critical to an accelerator's performance. An adjustment system must be capable of micron level movements and yet also be rugged enough to survive the tunnel environment over the life of the machine.

This paper describes a kinematic adjustment system designed to provide stable magnet support while also meeting all key performance requirements associated with alignment. The Ball/Roller design has the flexibility to accommodate either conventional or superconducting magnets with a variety of geometries and weights. Several drive options are available depending on the the particular alignment application.

## II. DESIGN GOALS

The Ball/Roller system was designed with the SSC main ring magnets in mind; it therefore needed to be capable of supporting superconducting dipoles with a mass in excess of 14,000 kg. It was required that the system provide true kinematic support: control of all six of a magnet's degrees of freedom without redundancy<sup>1</sup>. The support also had to allow for thermal expansion of a magnet without buckling or tilting. The range of motion needed to be at least  $\pm 25$  mm with resolution of better than 10 microns. Finally, the geometry of the system had to allow for predictable adjustment of each degree of freedom as well as easy access to its actuator.

## III. BASIC SYSTEM DESCRIPTION

The Ball/Roller is a three-point support and adjustment system patterned after the jack system used to support the LEP dipoles at CERN<sup>2</sup>. A magnet is supported by three identical mechanisms each of which is adjustable in the vertical and one lateral direction but free to move in the other lateral direction. The three mechanisms are arranged to provide a triangular support base with the orientation of one of the mechanism rotated 90 degrees with respect to the other two. By working the mechanisms' actuators in combination, all six degrees of freedom can be controlled.

Details of a single mechanism's design can be seen in Figure 1. A central block slides on a base frame and is threaded to accept a large diameter cup screw. The cup screw

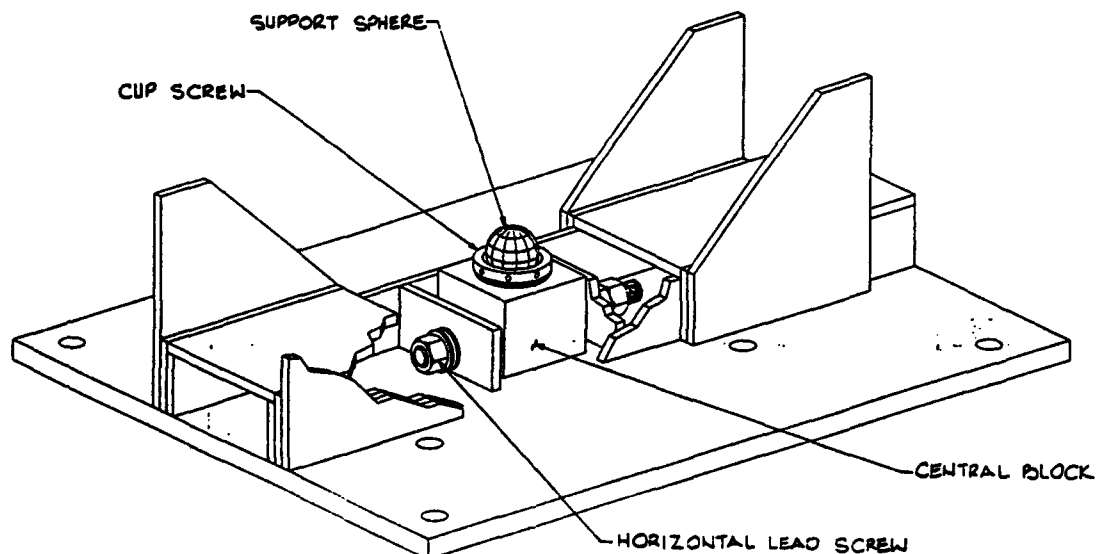


Figure 1. Basic Ball/Roller Mechanism

acts as a jack for adjusting an object's vertical position. The screw's diameter is a function of the load being supported, a full size dipole required a cup screw diameter of 60 mm. The horizontal travel of the block is controlled by lead screw fixed within the mechanism's frame. It should be noted that this horizontal lead screw bears no load; the weight of the object which is being supported is transferred directly from the block to the frame.

A hardened stainless steel sphere acts as the interface between the mechanism and the object being supported. This sphere is captured within the cup screw and fits into a groove in the bottom of the object (Figure 2). This groove is oriented at 90 degrees relative to the direction of the adjacent horizontal lead screw. The steel sphere rolls along this groove and allows an object to translate freely in this direction. The original interface plates developed for SSC magnets used a trapezoidal shaped groove. However, current designs use a semi-circular groove for a more even stress distribution<sup>3</sup>.

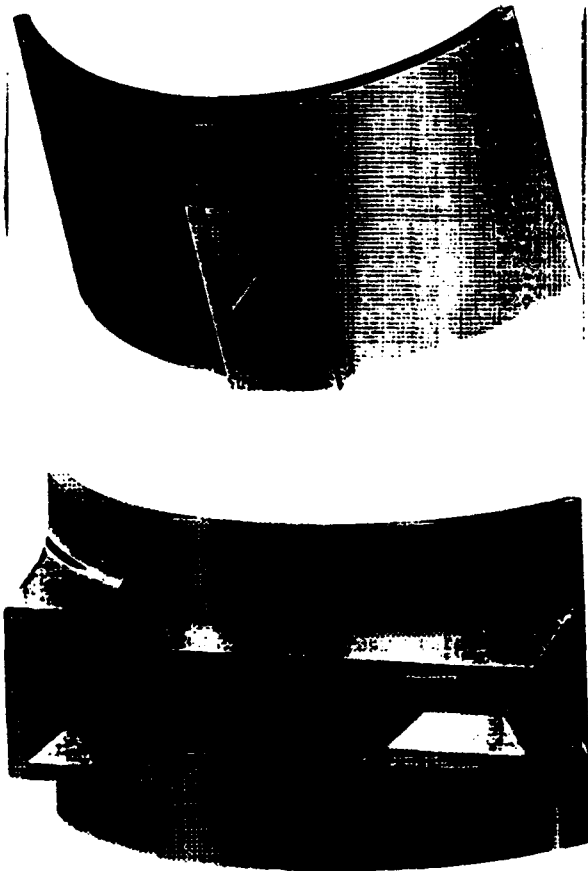


Figure 2. Single and Double Groove Interface Plates

All mechanism components are made of steel and are plated to prevent corrosion and reduce friction. Selected components are hardened as required.

This system is not purely orthogonal, there is cross-coupling between rotations and translations. However, the individual mechanisms are orthogonal thus allowing each degree of freedom to be individually and predictably adjusted.

It should be noted that the preceding discussion assumes that the object which is being supported behaves as a rigid body; in practice, accelerator magnets often have a good deal of flexibility. In the case of long conventional magnets it is sometimes possible to adjust a magnet's roll independently at either end when using a traditional four point support system. While this approach may allow fabrication twist to be adjusted out of the magnet it also leads to a statically indeterminate system and is generally considered undesirable. It is not possible to introduce twist into a magnet using the Ball/Roller system.

#### IV. PERFORMANCE TESTS

Several versions of the basic Ball/Roller adjustment system have been built and tested at the SSC Laboratory. They have been used to support main ring quadrupole magnets as well 40 mm aperture and 50 mm aperture versions of the dipole magnet. Results of these tests indicate that, in general, the Ball/Roller system's performance exceeds design goals.

The geometry of the prototype system was chosen to provide a range of motion of +/- 30 mm in all directions. This value could certainly have been increased but was kept low in order that the individual mechanisms could be made as compact as possible. Motion in all directions was smooth and free of "stiction" over the entire range. The play and run-out of the individual mechanisms was negligible.

The Acme threads used on both the horizontal lead screws and the cup screws had a pitch of six threads per inch. Even with this relatively coarse pitch incremental movements as small as 5 microns were possible after some practice. Since the motion of the magnets was measured directly the Ball/Roller's minimal backlash did not present a problem.

The ball-in-groove interface between the system and the magnet proved to be self centering; magnets could be mounted or removed very quickly with little or no pre-alignment required. The system was stable over time with no locking screws or rings necessary. Lateral and axial "up-set" loads consistent with impact or quench were easily withstood. However, because the Ball/Roll system provides simple support some sort of earthquake restraint would be required in a seismic environment.

Inputs to the system's actuator were made using a standard socket wrench for the horizontal lead screws and with a modified spanner wrench in the case of the cup screws. This technique was satisfactory but not optimal. The torque required to raise and lower the heaviest magnets tested was 450 N-m. This high torque necessitated a rather long "cheater" bar on the spanner which would become awkward in confined spaces. Alternative approaches are currently being explored.

#### V. MOTORIZED ACTUATORS

An automated version of the basic Ball/Roller system has been developed for use in those applications which might require continuous adjustment of an object's position or adjustment of its position in a remote location. An example of this type of application would be the support of the final focus quadrupoles in the SSC interaction regions. The design of this system uses Sumitomo AC Gearmotors to drive the lead and cup screws (Figure 3). The lead screw itself has been

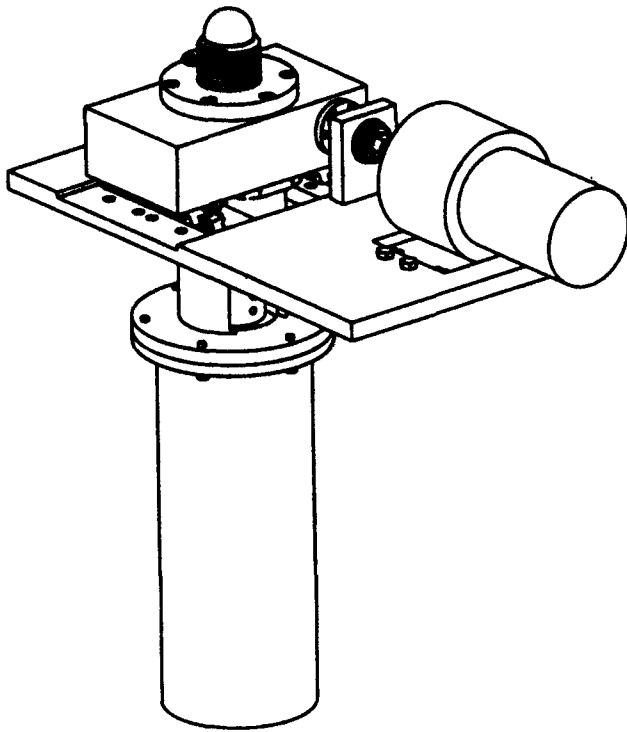


Figure 3. Automated Ball/Roller

off-set in the central block to allow for an in-line connection of the cup screw to its motor via a spline shaft.

Because sliding surfaces were unacceptable in a system subjected to continuous adjustment they have been eliminated from the motorized Ball/Roller. In this version the central block is supported by four THK linear motion guides mounted on a pair of low profile rails. This arrangement not only eliminates sliding friction but also resists the twist which is imparted to the block by the off-set lead screw. The Acme threaded lead and cup screws have been replaced by ball screws of the appropriate sizes which interface to the central block via ball nuts. These ball screw/nut combinations significantly reduce the torque required to move an object, especially in the case of the large diameter cup screw; this in turn reduces the size of the AC motors required.

Results of initial tests on the motorized Ball/Roller system indicate that its range, resolution and load capacity exceed those of the basic system.

## VI. POSITIONING AN OBJECT

For both the basic and the motorized system the general strategy for positioning an object is the same. For any configuration of the support system there exists one and only one corresponding object location in space. In the case of aligning a magnet the magnet's external fiducial targets are

used to define its initial location. The geometry of the magnet and its interface grooves will uniquely determine the coordinates of the three support spheres. For any arbitrary new location in space (as defined by a new set of coordinates for the external fiducials) a corresponding set of new support sphere locations can be computed. The geometry of a Ball/Roller mechanism can then be used to compute the lead screw rotations required to move the magnet to this new location. This procedure is independent of the system's initial configuration.

A variation of this technique allows for the very accurate pre-alignment of magnets. If the ideal coordinates of the magnets external fiducials are known they can be used to compute the ideal coordinates of the support spheres. Prior to the magnet's installation, the support spheres are replaced with target spheres of the same diameter which are equipped with either optical or laser targets. The configuration of the system can then be rapidly adjusted such that these targets are moved to the ideal coordinates. With the support spheres back in place the magnet is set automatically into its proper corresponding location.

Of course, there are other valid strategies for adjusting an object's position; pure translations and rotations could be made in sequence if desired. This approach would be particularly well suited for an automated system using synchronized motors.

## VII. CONCLUSION

It has been shown that the Ball/Roller adjustment system is capable of meeting its performance goals. The design continues to be refined with an eye on improving access to and reducing the torque requirements of the manual actuators. By off-setting the horizontal lead screw in the basic system the cup screw becomes accessible from below. This in turn would allow a standard socket drive to be used rather than the spanner. Incorporating ball screws into the basic system could significantly reduce the torque required to make vertical adjustments. An evaluation of these modifications is currently underway.

The control system of the motorized Ball/Roller will be modified in order to explore "closed-loop" position adjustment.

\* Operated by the Universities Research Association, Inc., for the U.S. Department of Energy under Contract No. DE-AC35-89ER40486.

[1] D. Vukobratovich, "Component Design Choices," *Newport Optics* 1991, pg. B-2 through B-13.

[2] J.P. Quesnel, CERN, Private Correspondence dated March 26, 1992.

[3] E. Kindler, SSCL, "Stress Analysis of Ball Mount Support," 1993

# PRELIMINARY STUDIES ON A MAGNETO-OPTICAL PROCEDURE FOR ALIGNING RHIC MAGNETS\*

M.A. Goldman, R.E. Sikora, T.J. Shea  
AGS Department, Brookhaven National Laboratory  
Upton, NY 11973

## Abstract

Colloid dispersions of magnetite were used at SLAC and KEK to locate multipole magnet centers. We study here possible adaption of this method, to align RHIC magnets. A procedure for locating magnetic centers with respect to external fiducial markers, using electronic coordinate determination and digital TV image processing is described.

## I. INTRODUCTION

Direct measurement of magnetic centers of certain RHIC superconducting quadrupoles and sextupoles is of interest. Mechanical fiducial referencing of coils to external magnet fiducial markers is difficult, and may not be possible after magnet cryostats are sealed. One wishes, for example, to check co-alignment of the low-beta quadrupoles of the insertion region quadrupole triplet, or co-alignment of beam PUE's with sextupole and quadrupole magnets in the arc QSC assemblies, in particular. If one can make such measurements optically, at low magnetic fields and room temperature, installation and alignment of these assemblies is significantly simplified.

Here we examine possibilities for extending magneto-optical alignment methods developed by Cobb and Muray [1], based on work of Johnson [2], and developed by Sugahara, Kubo and Osawa [3], to alignment of RHIC multipole assemblies. These methods use a cylindrical optical cell containing colloidal magnetite between crossed polaroid filters, illuminated by a collimated light beam, to generate a target pattern. The pattern is produced by field-induced optical anisotropy, caused by alignment of magnetite particles along the local magnetic field. An alignment telescope typically views the target pattern, which is symmetric about the magnetic axis of the magnet.

We examine the possibility of using TV digital image processing, together with electronic coordinate measurement, to extend the method to the problems mentioned above.

## II. DESCRIPTION OF THE ALIGNMENT PROCEDURE

Multipole magnet centers are determined as follows. An optical fluid cell is placed in the magnet bore. The cell has accurately flat and parallel windows at each end, and is oriented approximately parallel to the magnet axis. A fiber optic illuminator, with 2 to 5 mm dia. aperture at the end of

\*Work performed under the auspices of the U.S. Dept. of Energy.

the fiber cable is placed at the focal point of a 15 cm focal length,  $f/4$ , achromatic lens to generate the collimated light beam. Polarizing filters are set before and after the cell. Variable iris stops placed along the beam path assist in optical alignment. The cell is observed with a Farrand type 3560 alignment telescope, equipped with horizontal and vertical tilt plate optical micrometers, which displace the image by a calibrated amount, up to  $\pm 0.12''$ , with precision of 0.2 millinch.

The measurement method is shown in Fig. 1. The telescope is mounted to sight the magnet bore. A line of sight is first established on a boresight close to the magnet's geometric axis; precise boresight on axis is not needed. Boresight is established with telescope micrometer tilt plates set for null image displacement reading. This boresight is referenced spatially to external reference fiducials, by setting two Taylor-Hobson balls, each containing a microscopically-centered surveyor's target, along the boresight. The balls sit on kinematic-locating spherical seats, on 2-axis transverse motion translators. The balls can be removed to clear the line of sight and then replaced, or rotated in position, to allow viewing by theodolites, without shift of position of survey target centers.

The cell is mounted on a rail support in the magnet bore, and aligned, by back reflection, with windows normal to the beam. Prior to inserting the cell in the bore, the polarizers are crossed, to give sharp extinction of the light beam. When the magnet is energized, a characteristic cross or spoke shadow pattern is seen, centrally-symmetric about the magnetic axis. Vertical and horizontal components of the axis' displacement from the previously established boresight are measured directly, by displacing the viewed pattern (by tilt of the micrometer plates) until the telescope reticle center (previously set on boresight) coincides with the pattern's center, and reading the micrometers. One can rotate and recross the polarizers to generate a rotated shadow pattern with the same center point, to get an independent remeasurement of the axis. This provides a check, to verify the measurement of transverse displacement of the magnetic axis from boresight.

As an aid to focus the telescope on the cell, we found it helpful to leave an air bubble in the cell. A bright spot is seen in the bubble. One focuses on the spot. Tests involving repeated measurement of location of the shadow pattern center, after defocusing and refocusing the telescope, have demonstrated that parallax is not a problem.

At RHIC we use a LEICA (Heerbrugg, Switz.) ManCAT coordinate measuring system, together with type T-3000 electronic digital-readout theodolites, to acquire, log, and analyze survey data. Typical accuracy of transfer of target position coordinates to external fiducials is 1 to 3 milli-inch. This system can be used to transfer boresight coordinates from Taylor-Hobson ball targets to an external reference coordinate frame. In this system, two or more theodolites equipped with digital angle readout in turn simultaneously view: one another, a calibrated length reference bar, a set of known survey reference fiducial targets and, finally, survey points whose coordinates are to be determined. Theodolite directional data is entered directly into a computer, for coordinate determination in a coordinate frame of choice.

viewing the cell in collimated light, while crossed Ronchi grills were placed in front of the cell window, through the telescope. Refraction gradients appeared as curve distortions of the grill pattern.

Relaxation time for the colloid particles to align to a magnet field was about one second. This was seen by setting the cell onto a V-block, in collimated light, between crossed polarizers. A permanent magnet was held near the cell so that a field of 50 to 100 Oersted passed transversely through the cell, generating a bar shadow pattern. The cell was rotated manually about its axis. The shadow pattern initially co-rotated with the cell, but returned to its initial orientation within two seconds.

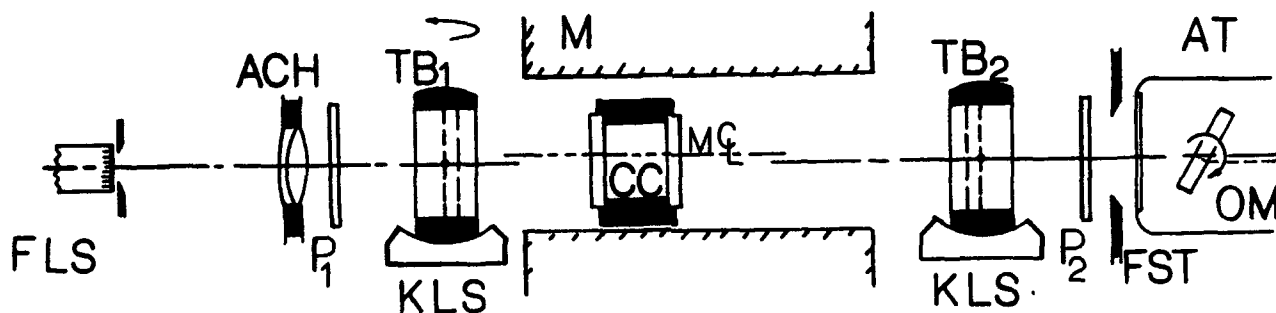


Figure 1. FLS - Fiber Optic Light Source, ACH-Achromatic Collimator Lens; TB - Survey Target Ball, KLS-Kinematic Ball-Locating-Surface; M - Magnet, CC-Colloid Cell, P1 P2 - Polarizer Plates; FST - Field Stops, AT-Alignment Telescope, OM-Optic Micrometer.

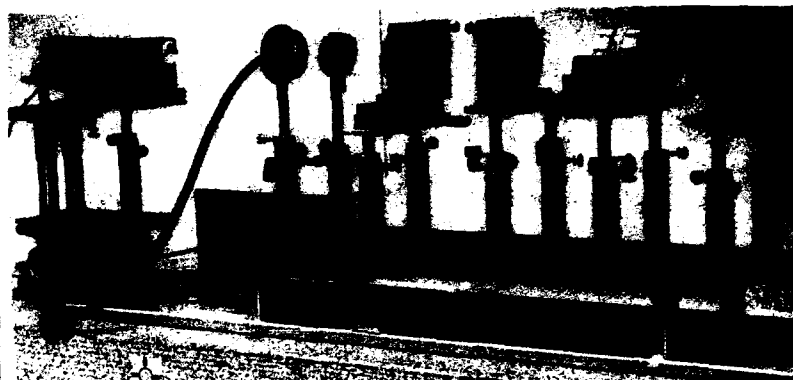


Figure 2. Cell, Magnet, and Optical Setup Used for Colloid Tests.

### III. PREPARATION OF THE COLLOID CELL

The fluid is a suspension in glycerol, of magnetite particles, coated with polydextrose (Pfizer Specialty Chemicals, Clifton, NJ), to prevent aggregation. The suspension was prepared by E. Norton, of the BNL Chemistry Department, using the protocol in [3].

Our fluid differed from that reported in [3] by the fact that the particles could pass through a 0.5 micron Millipore filter; this did not affect optical properties of the fluid adversely, and in fact may have decreased any tendency for particle separation in the strong field gradient of our magnet.

The fluid was checked to eliminate inhomogeneity due to coexisting unmixed aqueous and glycerol phases, so that it was of uniform refractivity, free of striae. This was done by

The cell was tested for separation out of particles in a strong gradient field. The cell sat in a permanent magnet quadrupole's field gradient of 6.6 kOe/cm for 3 hours. No separation to the walls or any change of the optical shadow pattern was seen.

Sensitivity of the cell to low fields was tested by placing a 1.5" long cell inside of a loosely wound solenoid coil, with the cell's axis perpendicular to the solenoid axis. The cell was observed in collimated light, between crossed polaroids. With no solenoid current, the optical field was uniformly dark. At a current sufficient to produce 20 Oersted throughout the cell, the optical field brightened significantly. (Light transmission through a cell depends of course on the particular fluid, and cell length, as well as on magnetic field intensity. Quantitative

studies to optimize cells have not yet been made, but are of future interest.)

#### IV. TEST MEASUREMENTS

Measurements were made first on a permanent magnet quadrupole of type designed by Halbach [4], using a test setup and 1.5" long cell shown in Fig. 2. Development work was done with this simple test set. During development, an opportunity appeared to test the colloid method on a cold SSC 4 cm quadrupole, at BNL. A ¾" long cell using our fluid was built by R. Viola (SSC, Dallas). This cell was built with integrally cemented crossed polaroids, attached collimating lens, and illuminating bulb, and was placed in a warm finger in the bore of a cold SSC 4 cm quadrupole magnet.

The cell was viewed with a jig transit, at 10 meters distance (the alignment telescope was unavailable). The magnetic center was visually located to 0.002" in each coordinate. [We note that the cell, collimation, and telescope had not been optimized for this test; prior observation of the ¾" and 1.5" cells, in the permanent magnet quadrupole showed, in fact, that the shadow pattern for the 1.5" cell was appreciably sharper than for the ¾" cell used in this test.]

A weak trim sextupole magnet was also observed, under conditions of 5 cm pole radius, 72 turns/pole, 24 ampere current. The bore field profile is comparable to that available for warm RHIC sextupoles. A 2.5" long colloid cell was used. A clear shadow pattern was visually observed, but was too wide for direct optical micrometer measurements.

#### V. USE OF PHOTOGRAPHY AND VIDEO DIGITAL IMAGE PROCESSING

The resolution claimed for colloid localization of magnet axes is about 20 micro-meter [1,3]. But published photographs [1,3] show shadow patterns with apparently far worse resolution. Our optical micrometer measurements are consistent with the claimed resolution. To investigate this apparent paradox, we photographed shadow patterns, with a range of exposure times. Photos of a 1.5" long quadrupole cell were taken, both directly behind the polaroid analyzer and at 3m distance, through the alignment telescope. [Figure 3].

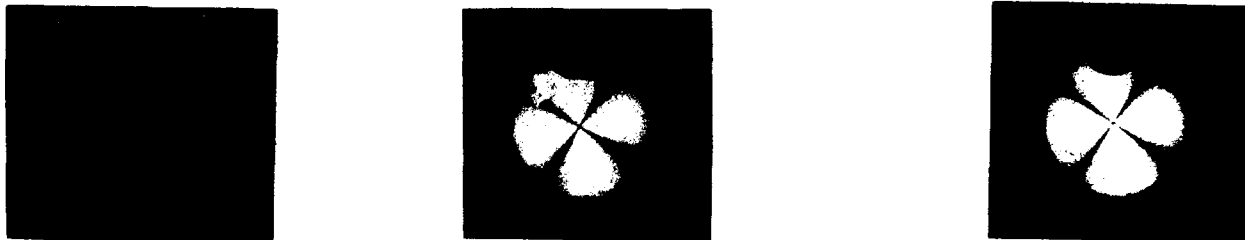


Figure 3. Permanent magnet quadrupole shadow pattern, viewed directly.  
a. Exposure 1/6 sec. b. Exposure 3 sec. c. Exposure 6 sec.

Photographic resolution improves greatly when long exposure is used. This is due to the enormous dynamic range of illumination in the viewed pattern; the crossed polaroids have extinction ratio exceeding 10,000. The brightly illuminated area of the field saturates the film, while the shadow interior remains underexposed unless long exposure is used.

Intrinsic resolution of the measurement is in fact good, when bright illumination is employed. This result encouraged us to examine the possibility of using digital television image processing to extract the axis' location from a digitized TV image of the shadow pattern. This could be of particular value in attempting to perform warm magnet co-alignment of beam pickup electrodes with the RHIC arc sextupoles. Sextupole patterns are wider than quadrupole patterns, because of quadratic dependence of magnetic field intensity with radius; digital image processing then becomes advantageous. Also, when viewing sextupole patterns, the visually dark core of the pattern may exceed the scan range of the optical micrometer. This is not a problem if video digital image processing is used. Preliminary tests with TV imaging are encouraging; work is still in progress. A camera is easily aligned behind the telescope. After the telescope reticle and colloid cell are visually focused on the reticle plane, a real image of cell and cross hair is formed beyond the eyepiece lens of the telescope. The image can be viewed with a target card placed after the telescope eye lens. The camera can be centered on this image. When using video, it is important that no automatic gain control, or other image servo, be employed, so that the fine dark shadow pattern will not be washed out by averaging with adjacent brightly illuminated pixels.

#### VI. DISCUSSION

The fact that our colloid cells switch from light to dark at fields of tens of Oersteds, and that intrinsic resolution is good, as indicated by photographic exposure series, suggests that warm alignment of RHIC insertion quadrupoles, and beam PUE's with arc section QSC assemblies is practical. Studies to optimize optical design are in progress.

#### REFERENCES

- [1] J.K. Cobb and J.J. Muray, Magnetic Center Location in Multipole Fields; Nuclear Instruments and Methods 46 (1967) 99-105.
- [2] R.M. Johnson, Internal Report BeV-687, Lawrence Radiation Laboratory, Berkeley, California (1961)
- [3] R. Sugahara, T. Kubo and Y. Oosawa; A Colloidal

Solution of Fe<sub>3</sub>O<sub>4</sub> Crystallites to Optically Locate the Magnetic Center of Multipole Magnets; KEK Report 89-9, September 1989, National Laboratory for High Energy Physics, Tsukuba, Japan.

- [4] K. Halbach, Strong Rare Earth Cobalt Quadrupoles, IEEE Trans. Nucl. Sci. NS-26. 1979, 3882-3884.

# RHIC SURVEY AND ALIGNMENT\*

F.X. Karl, R.R. Anderson, M.A. Goldman, F.M. Hemmer,  
D. Kazmark, Jr., T.T. Mroczkowski, J.C. Roecklein  
RHIC Project, Brookhaven National Laboratory, Upton, NY 11973

## Abstract

The Relativistic Heavy Ion Collider consists of two interlaced plane rings, a pair of mirror-symmetric beam injection arcs, a spatially curved beam transfer line from the Alternating Gradient Synchrotron, and a collection of precisely positioned and aligned magnets, on appropriately positioned support stands, threaded on those arcs.

RHIC geometry is defined by six beam crossing points exactly in a plane, lying precisely at the vertices of a regular hexagon of specified size position and orientation of this hexagon are defined geodetically.

Survey control and alignment procedures, currently in use to construct RHIC, are described.

## 1. OVERVIEW OF THE RING SURVEY PROCEDURE.

The RHIC survey is performed in local BNL coordinates, directed (for historical reasons) along the BNL road network, at known orientations to the machine lattice and the geodetic (Long Island) NY State Plane Coordinate System [Fig. 1]. The geometry of the RHIC ring and AGS-RHIC transport line are described in [6,7,10].

To generate RHIC geometry, we use a network of control monuments, grout-cemented into the tunnel floor. Each monument is a hollow stainless steel cylinder, of CERN type [Fig. 3], placed into the floor with its axis locally vertical. The monument sockets can receive and precisely locate either a cylindrical bushing holding a centered surveyor's target or a 3.5" diameter steel ball containing a microscopically centered target. The ball connects to a fiber optic jack, to supply bright diffuse target illumination. The ball can be rotated, on the monument bushing, to view its target from either a horizontal or vertical direction, without change of position of its target's cross hair intersection point. The ball target can then be viewed from above, for example, from an exterior survey tower or from the side inside the tunnel.

External control is established by: twelve survey structures spaced around the RHIC ring, with pipe penetrations into the tunnel; towers and penetrations along the injection arcs; and a tall central tower, having clear sight lines to the other towers. Control from the end of the injection bend arcs, into the AGS machine, is established internally, by survey along the beam transport line into AGS.

Survey structures range from simple 4 ft. platforms, to 12 foot wooden double signal platforms, to National Geodetic Survey steel Bilby towers of up to 70 foot height.

The survey structures contain survey instrument support platforms; an aluminum plate bolted onto each platform serves as a support deck of two horizontal motion translation stages. The upper stage holds a tribrach, to locate either a ME-5000 Mekometer EDM, prism retro-reflector, or optical plummet. An opening in each stage allows downward viewing, through the plummet's tribrach support and berm penetration pipe, to the ball target in the tunnel. The aperture

available through the tribrach limits the optical resolution in setting the survey instrument directly above the tunnel survey target at the tunnel primary control monument. Vertical drops to tunnel targets are measured by use of steel tape, with correction for temperature and tape weight. Survey work was done after sundown, when stable atmospheric conditions were available. At each tower station and tunnel monument, temperature was measured to 0.1 deg. C, barometric pressure to 0.1 millibar, and relative humidity to 2% to allow for correction of refractive index.

The external survey was a terrain trilateration of the twelve towers above the tunnel, and the central tower near machine center. The purpose of the survey was to geodetically locate twelve primary control monuments in the tunnel, below the vertical earth berm penetrations, to generate a primary control monument net inside the tunnel. Distances were measured to first and second nearest neighbor towers, and to-and-from the central tower, using the ME-5000 Mekometer. One exception was a line-of-sight blocked by the RHIC office building. Horizontal distances between nearest neighbor towers, and between the ring towers and central tower, were each approximately 610 meter. Adjusted standard error of the distance determinations was one and a half millimeters, with near-circular error ellipses, as expected from the nearly symmetric survey geometry.

A previous survey of seven of the primary monuments and central tower, was performed by the National Geodetic Survey, in 1982, as part of the CBA program at BNL. Adjusted positions of the eight monuments common to the two surveys, separated by ten years in time, were compared by means of a Helmert Transformation, using GEONET survey codes [1,2]. The rms displacement of corresponding stations from one another was one and a half millimeters. This suggests that earth shifts were insignificant, during this time.

## 2. TUNNEL MONUMENTATION AND SURVEY.

To locate position within the tunnel, and to control placement of magnets and support stands, a secondary monument control network has been established in the tunnel, connected to the twelve primary monuments located during the primary external control survey.

The control net configuration is a chain of braced quadrilaterals. Trilateration and triangulation measurements are both used in the control survey. Monuments are installed, typically, opposite centers of ring quadrupole and dipole magnets in the arc sections, and more densely in the insertion sections.

Distances along the tunnel are measured with the Kern (LEICA) Mekometer-5000 [4, 5]. Directions along intermonument lines are measured with the Wild (LEICA) T-3000 theodolite. Each of these instruments is provided with digital electronic readout and an option for either manual or electronic control. The distance mode gap bands, in the Mekometer's, response were calculated in advance,

\*Work performed under the auspices of the U.S. Dept. of Energy

to insure that forbidden distances were not to be measured among the shorter survey distances.

A ZEOS laptop computer, loaded with GEONET [1,2] control and data uplink software, is used for data acquisition, in a format suitable for data basing and reduction by GEONET. Data processing is carried out after data file transfer to a 486 PC or other work station; a local area link allows data transfer to the BNL VAX Cluster mainframe computers, to provide additional data storage and processing capability. When used for control survey, the Mekometer and theodolites are mounted on special tripod stands, bolted to the tunnel floor, at the monuments to be surveyed, on 2-axis horizontal cross feeds. A Kern instrument mount allows each survey instrument to be levelled and force-centered so that the instrument axis coincides with the mount axis. In this way a Mekometer, theodolite or optical plummet can be mounted at the same horizontal position above a monument. The instruments can be located above the target ball at the monument to a horizontal rms radius of two milli-inches.

Magnet stands are installed using the following procedure. A template was fabricated with a circular hole pattern which is the horizontal floor projection of the bolt pattern of the magnet support stand, together with the plan projection of two magnet cryostat fiducial target balls, which will lie adjacent to that stand when the magnet is installed. The template is surveyed into place by surveying the fiducials' floor projection circle centers to their proper horizontal locations. The stand bolt locations are then stencilled onto the tunnel floor from the template. To help in initially locating the magnet on its stand, the centers of the adjacent magnet fiducial ball projections are also located with fine cross marks on the floor. To do the latter operation, one uses an optically-centering transfer punch device (Scribe-Rite, Tool Components, Inc., Gardena CA) to transfer the prism target axis to the punch axis and floor point.

From the magnet-design-specified locations called out for the cryostat fiducial balls on the magnet and the magnet lattice coordinates, a data base set of horizontal survey coordinates for the cryostat fiducials is computed. View directions for theodolite sighting of the floor projections of the cryostat fiducials are computed. Also the slant distances are computed, of a Distomat EDM mounted on the theodolite, to small retro-reflector prisms mounted on the template above the fiducial ball projections. The computed distances and directions are a data base to allow the template to be surveyed into place, from the control monument net.

Survey data acquisition, reduction and adjustment is done using GEONET survey codes [1,2]. After initial data reduction, an independent adjustment is done using STAR\*NET survey codes[3]. The latter codes are convenient for blunder detection and survey graphical presentations, and are a useful complement to GEONET. Model control surveys are simulated using the ERRORP codes of GEONET when control survey procedures are to be examined.

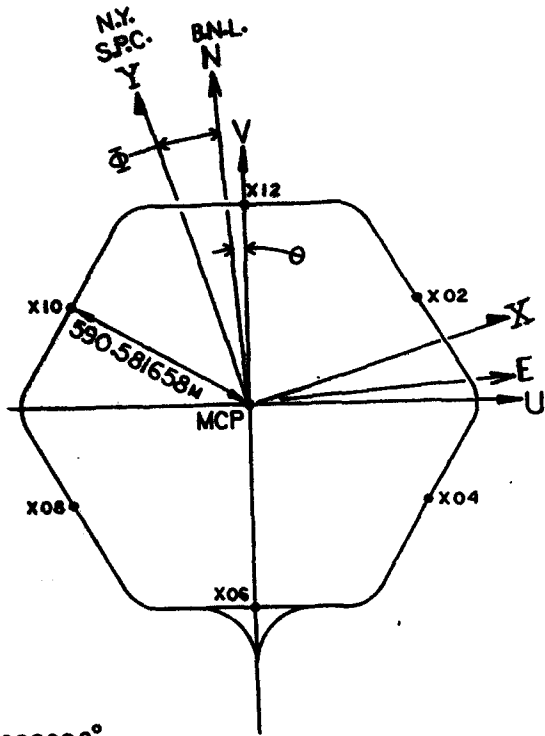
#### References:

1. H. Friedsam, R. Pushor, R. Ruland, A Realization Of An Automated Data Flow For Data Collecting, Processing, Storing And Retrieving - GEONET. Stanford Linear Accelerator Center SLAC-PUB-4142, Nov. 1986.
2. H. Friedsam, Notes (unpublished), Survey And Alignment Workshop On Data Processing Using Geonet For Accelerator Alignment, Stanford Linear Accelerator Center, Stanford, March 1992.
3. STAR\*NET 4.01, Starplus Software, Inc. Oakland CA. 94610.
4. D. Meier and R. Loser, Das Mekometer ME5000 - Ein Neuer Präzisions-distanzmesser. Allgemeine Vermessungs-Nachr. (AIN), Vol. 93, pp 182-190 (1986).

### 3. MAGNET FIDUCIALIZATION AND ALIGNMENT

RHIC dipoles and quadrupoles are provided with two sets of fiducial markers: cold mass fiducials and cryostat fiducials. The cold mass fiducials are balls which seat in fixed position relative to survey notches cut into the magnet cold mass steel plate. These fiducials are well defined relative to the bore circle of the magnet steel. Cryostat fiducials are split balls on shafts which seat onto bushing sleeves on the magnet cryostat body. Cryostat fiducial balls are externally accessible at each end of the magnet. Cold mass fiducials are accessible to survey only before the magnet is fully assembled. Cold mass and cryostat fiducials are surveyed relative to one another before final assembly of the magnet. The ManCAT electronic coordinate measuring system (LEICA GmbH, Heerbrugg, Switz.) will be used to survey cold mass fiducials relative to cryostat fiducials. Magnetic measurements of field center, and field roll orientation relative to cold mass fiducials will be made before magnet assembly. Alignment of magnets in the RHIC tunnel will be made relative to the survey of the cryostat fiducials relative to cold mass fiducials, which in turn relate to the magnetic center and roll of the magnet. The process of aligning magnets in the tunnel consists of setting cryo fiducial marks to lie at their computed locations. Those locations are generated in turn by the lattice, magnet design, measured fiducial point positions relative to the physical structure of the individual magnet, and survey control station absolute positions as determined by tunnel control surveys. This process of setting magnets into position takes no account of relative misalignment of neighboring magnets caused by random error introduced in the installation of individual magnets. Ideally, when ring magnets are installed, the beam closed orbit would be a smooth curve of low degree, within our individual magnet, and would be an arc which joined continuously, to a sufficiently high order of derivative, curve segments through adjacent magnets. But, local relative dislocations and tilts of the axes of successive magnets can cause more serious beam-dynamical problems than global long scale radial or vertical magnet displacements. One then needs a smoothing adjustment of magnet locations to set magnets onto a smooth curve, which lies globally within a tubular envelope of allowable radial and vertical error bounds about the beam trajectory curve specified by the accelerator lattice. The shape of the smoothed curve follows from the particular magnet installation data set to be fitted, rather than from an analytical formalism. Studies of smoothing procedures were carried out at SLAC and CERN [8,9]. SLAC smoothing codes and procedures are being incorporated, into GEONET software; it is expected that they will be available to users in 1993. It is anticipated that a smoothing procedure similar to that used at SLAC will be used at RHIC.

5. T.W Copeland-Davis, The KERN ME5000 Mekometer and Short Distance Measurements, CERN Report LEP/SU 89-2, Feb. 5, 1989.
6. J. Claus and H. Foelsche, Beam Transfer From AGS To RHIC, RHIC Technical Note No. 47, BNL Accelerator Division Report AD/RHIC-47, 1988. See also Jan. 9, 1990 Addendum.
7. R.E. Thorn, Injection Line Geometry, AGS To RHIC Beam Transport Line, BNL Data File ARHIC13, Sept. 12, 1988.
8. T. Hastie, Principal Curves And Surfaces, SLAC Report-276, STAN-LCS-11, UC-32 (M), Stanford Linear Accelerator Center, Nov. 1984.
9. Applied Geodesy For Particle Accelerators, CERN Report 87-01, Geneva, Feb. 9, 1987.



$\theta = 1.999898^\circ$

$\phi = 14^\circ 59' 26.45''$

Fig. 1 The RHIC Ring Geometry

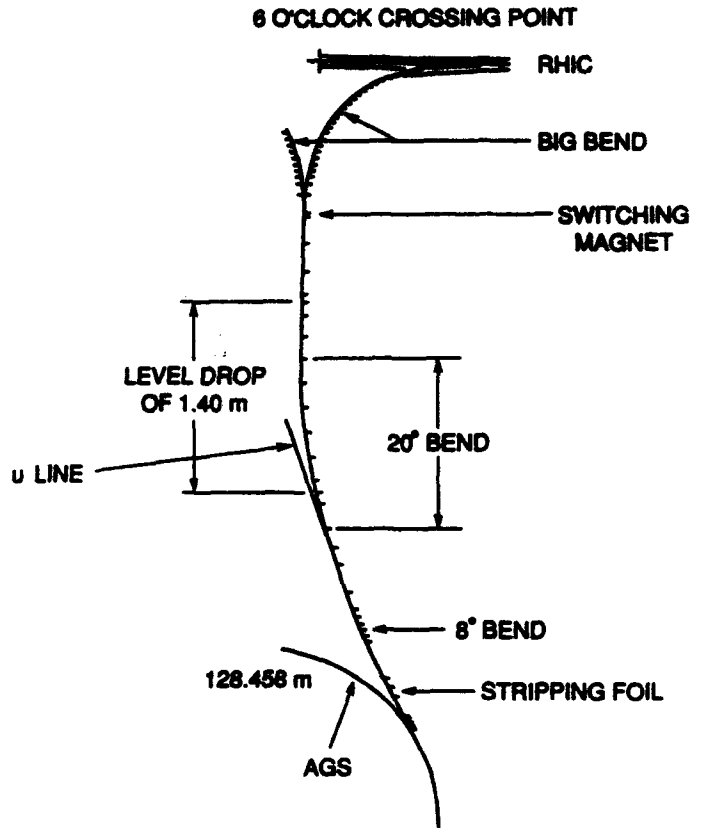


Fig. 2 The AGS to RHIC Transport Line

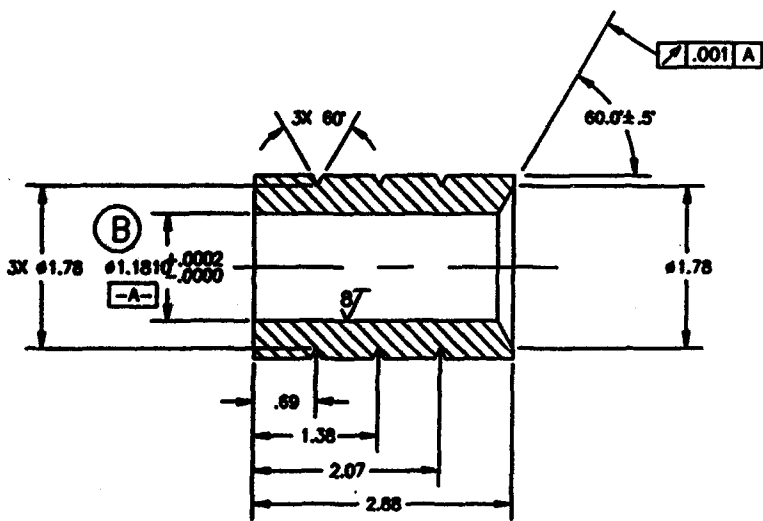


Fig. 3. The Ring Monument and Target Ball



# Effect of Magnet Sorting Using a Simple Resonance Cancellation Method on the RMS Orbit Distortion at the APS Injector Synchrotron\*

F. Lopez, R. Koul, and F. E. Mills  
 Argonne National Laboratory  
 9700 S. Cass Avenue  
 Argonne, Illinois 60439

## Abstract

The Advanced Photon Source injector synchrotron is a 7-GeV positron machine with a standard alternating gradient lattice. The calculated effect of dipole magnet strength errors on the orbit distortion, simulated by Monte Carlo, was reduced by sorting pairs of magnets having the closest simulated measured strengths to reduce the driving term of the integer resonance nearest the operating point. This method resulted in a factor of four average reduction in the rms orbit distortion when all 68 magnets were sorted at once. The simulated effect of magnet measurement experimental resolution was found to limit the actual improvement. The  $\beta$ -beat factors were similarly reduced by sorting the quadrupole magnets according to their gradients.

## I. INTRODUCTION

The method for magnet sorting is based on the Floquet-Fourier decomposition of the orbit in the presence of error fields [1]. The expression for the orbit is:

$$\frac{x}{\sqrt{\beta}} = \sum_{k=-\infty}^{\infty} a_k \frac{v^2}{v^2 - k^2} \exp[i \phi k/v] \quad (1)$$

where  $\phi$  is the betatron phase,  $v$  is the tune, and  $a_k$  is the coefficient given by:

$$a_k = \frac{1}{2 \pi \rho v} \int_0^C ds \sqrt{\beta} \frac{\delta B}{B} \exp[-i \phi k/v] \quad (2)$$

where  $\delta B$  is the measured field error in a dipole magnet,  $B$  is the field, and  $\rho$  is the radius of curvature.

Similar expressions exist for the  $\beta$ -beats where the coefficient is obtained by integrating over the gradient errors at twice integral multiples of the betatron phase. When all  $\beta$  are the same, as in the case for the APS synchrotron, the  $k^{\text{th}}$  coefficient is a vector sum in the complex plane of the field errors multiplied by the exponential factor in (2).

An analytic expression for the rms  $x$  orbit can be derived from the above expressions:

\*Work supported by the U.S. Department of Energy, Office of Basic Energy Sciences, under Contract No. W-31-109-ENG-38.

$$x_{rms}^2 = D \sum_k \frac{1}{(v^2 - k^2)^2} \left[ \sum_i \left( \frac{\delta B}{B} \right)_i^2 + 2 \sum_i \sum_j \left( \frac{\delta B}{B} \right)_i \left( \frac{\delta B}{B} \right)_j \cos \left( \frac{(\phi_i - \phi_j) k}{v} \right) \right] \quad (3)$$

where the  $i, j$  are pairs of magnets and  $D$  is a constant depending on  $\rho, v, \beta$  and the magnet length. The sum on  $i$  and  $j$  is over the  $N$  magnets. The cosine terms of  $N/2$  pairs of sorted magnets can be selected to cancel the first term while uncorrelated pairs of magnets will contribute zero on the average.

## II. SORTING ALGORITHM AND SIMULATION

The lattice functions  $\beta$  and  $\phi$  were generated by the standard transport code COMFORT. Figure 1 displays the horizontal phase as the polar angle, and the radial coordinate is  $\beta$  at the center of each dipole magnet. Dipole magnet sorting is accomplished by minimizing the coefficient of the  $k = 12$  integer resonance for the APS synchrotron since the horizontal tune  $v = 11.76$ .

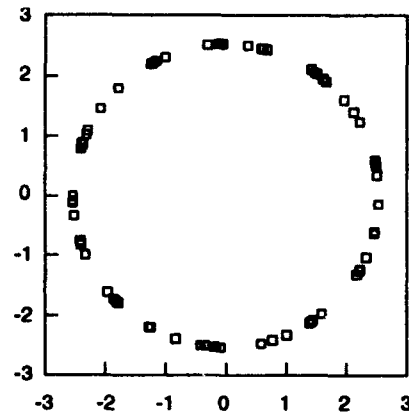


Figure 1. Dipole Phases

The large number of dipole lattice sites approximately 180 degrees apart in phase suggests the simplest algorithm. Magnets with the closest measured errors are assigned to lattice

The submitted manuscript has been authored by a contractor of the U.S. Government under contract No. W-31-109-ENG-38. Accordingly, the U.S. Government retains a nonexclusive, royalty-free license to publish or reproduce the published form of this contribution, or allow others to do so, for U.S. Government purposes.

points with nearly opposite phase on the polar plot. The magnet errors were simulated by a Gaussian distribution as was the magnet measurement resolution.

### III. RESULTS AND DISCUSSION

#### A. Dipoles

The comparison of the random assignment of dipoles with the sorted case of all 68 magnets, assuming zero magnet measurement experimental error, is shown in Figure 2. The mean reduction in rms  $x$  orbit is a factor of approximately four and agrees with (3). The random selection case also exhibits a long tail of upward fluctuations.

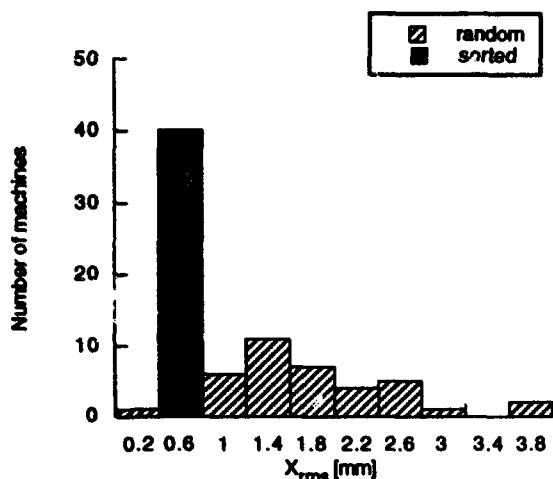


Figure 2. Random vs sorted orbits for 40 machines

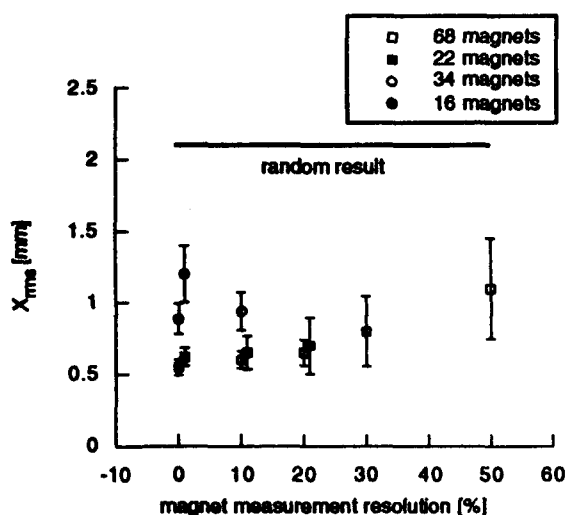


Figure 3. Magnet sorting result for  $\Delta B/B = 10^{-3}$

Identical random field errors were used for both cases. The  $k=1,2,3$  coefficients have the largest contribution to the orbit after sorting. Figure 3 shows the mean rms orbit for different

numbers of dipoles sorted at once. The case of  $N=22$ , one third of the ring, is better than the case of 34 magnets because of reduction of the  $k=2,3$  coefficients due to the periodicity of the lattice. The experimental magnet measurement resolution does not dramatically affect the results for resolution of up to 10% of the rms of  $\delta B/B$ . In comparison, the tolerance specified on the rms  $\delta B/B$  is  $10^{-3}$  and the estimated measurement resolution [2, 3] of the APS synchrotron dipole measurement system is  $10^{-4}$ .

#### B. Quadrupoles

The sorted results for the rms  $\beta$ -beat factors are reduced by a factor of six over the unsorted results. The 40 focusing and 40 defocusing quadrupoles are sorted separately according to their gradients. The difference in sorting improvement compared to the dipoles is primarily due to the properties of the lattice resulting in sites with better cancellation. In the case of the quadrupoles, the best result was obtained by assigning pairs of magnets with opposite gradient errors to the same value of twice the phase on a polar plot. The cancellation using sites with twice the phase approximately 180 degrees apart was not as effective and resulted in a factor of 3.5 average improvement in the beat factor.

### IV. CONCLUSIONS

A simple method for sorting magnets that relies on basic theory yields reduction factors of 4 in orbit for the dipoles and 6 in beat factors for quadrupoles at the APS synchrotron. Similar reductions can be obtained without having the entire sample of magnets to choose from. Analytical estimates and Monte Carlo methods yield the same average results. This procedure can be used to gain an added margin for safety in magnet manufacture. The reductions in  $x_{rms}$  obtained from sorting using a more sophisticated method would be limited by the magnet measurement resolution unless the ratio of rms measurement error to rms field error were smaller than 10%.

### V. REFERENCES

- [1] Courant and Snyder "Theory of the Alternating Gradient Synchrotron," Ann. Phys. 3, 1 (1958).
- [2] K. Kim, S. H. Kim, L. R. Turner, C. Doose, R. Hogrefe, and R. Merl, "Magnetic Measurement Data of the Injector Synchrotron Production Dipole Magnets for the 7-GeV Advanced Photon Source," these proceedings.
- [3] K. Kim, S. H. Kim, K. Thompson, and L. Turner, "Design and Tests of the Injector Synchrotron Magnets for the 7-GeV Advanced Photon Source," these proceedings.

# Optimal Magnet Sorting Procedure and Application to the APS Injector Synchrotron\*

R. K. Koul, Fredrick Lopez and Fredrick E. Mills  
 APS, Argonne National Laboratory  
 Argonne, IL 60439

## Abstract

A magnet sorting procedure for accelerators is developed. It is implemented in two steps. The first step is completely analytical in character while the second step involves the comparison of computed values with the measured error values. The method has been implemented for sorting the Advanced Photon Source (APS) injector synchrotron dipoles and quadrupoles with excellent results.

## I. INTRODUCTION

Suppose we are given a set of magnets whose magnetic field errors have been measured. Then the question arises whether there is some optimal way of placing them around the accelerator ring to minimize the effect of the magnetic field errors.

One of the simplest ways to answer this question is to try all possible permutations of the known errors on the magnet locations and choose the combination which produces the minimum effect. However, the number of combinations grows as  $n!$ , where  $n$  is the number of magnets to be sorted.

In the past, another method has been used for the simulated errors which, for lack of a better name, we will call the "Main Harmonic Cancellation Method" (see Lopez [1]). The idea of this method is as follows. Let us say we want to sort dipole magnets on dipole errors. The magnets of equal strength are selected and placed  $\pi$  radians apart in phase of the particle trajectory so that the equal strength errors make equal but opposite contributions to the particle trajectory.

Sometimes the method of simulated annealing may be used for sorting. This method, also used in simulation for sorting the injector synchrotron dipoles over simulated errors, gave a slight improvement over the Main Harmonic Cancellation Method when used in simulation for the APS injector synchrotron (see Sampson [2]). For details see Kirkpatrick [3] or Flannery[4].

## II. OPTIMAL PROCEDURE

The new sorting procedure is based on solution of the linearized equations of motion. For details see Koul [5] or Courant [6]. The solution characterizing the effect of errors is given by amplitude function  $I$  expressed below.

$$I = C \sum_{i=1}^{i=n} \sum_{j=1}^{j=n} H(\beta_i, L_i) H(\beta_j, L_j) f_i f_j \cos \psi_{ij} \quad (1)$$

$H(\beta_i, L_i)$  is some function of  $\beta_i$  and  $L_i$ , where  $\beta_i$  and  $L_i$  are the beta function of the beam at the  $i$ th element and the length of the  $i$ th element respectively;  $f_i$  is the measured error at the  $i$ th location; and  $\psi_{ij} = (\phi_i - \phi_j)$  is the phase difference of the trajectory between the  $i$ th and the  $j$ th locations phases  $\phi_i$  and  $\phi_j$ .

The optimal procedure has two steps. In the first step a certain linear set of equations has to be solved, and in the second step some matching of the calculated and the measured values has to be performed. The first step can be carried out in either of two ways. Both ways are outlined below under the headings "Procedure 1" and "Alternate Procedure 1."

## III. STEP 1 (PROCEDURE 1)

Suppose we minimize function  $I$  with respect to the phase differences  $\psi_{ij}$ , thereby considering the  $\psi_{ij}$  as variables. Having obtained the equations from variation of  $I$  with respect to  $\psi_{ij}$ , we ask another question: What values should  $f_i$ , (i.e errors) assume, such that the given  $\psi_{ij}$  satisfy the variational equations? If we answer this question, then we have found that for the calculated values of  $f_i$ , given  $\psi_{ij}$  minimize the amplitude function  $I$ . However, it is important to point out the following.

Notice that for  $i \neq j$ ,  $\psi_{ij} = -\psi_{ji}$  and  $\psi_{ii} = 0$ . We are left with only  $n(n-1)/2$  variables, but all of these  $n(n-1)/2$ ,  $\psi_{ij}$  are not linearly independent. Since we are dealing with the phase differences, we can fix a position, say position number '1', and compute  $\psi_{ij}$  for all  $j \neq 1$ , out of the total of  $n(n-1)/2$ ,  $\psi_{ij}$ . Then it is easy to see that for all  $i$  and  $j$ ,  $\psi_{ij} = \phi_{1j} - \phi_{1i}$ . Hence for 'n' positions corresponding to the 'n' magnet, there are only  $(n-1)$  linearly independent  $\psi_{ij}$ . Therefore, to minimize  $I$  with respect to the phase differences we will give variations only with respect to  $\psi_{1j}$ . Carrying out the variation and assuming that at least one of the errors, say  $f_1$ , is known we get,

$$\sum_{i=2}^{i=n} H(\beta_i, L_i) f_i \sin \psi_{ki} = H(\beta_1, L_1) f_1 \sin \psi_{1k} \quad (2)$$

which can be formally written as a matrix equation:

$$\sum_{i=2}^{i=n} M_{ki} f_i = H(\beta_1, L_1) f_1 \sin \psi_{1k} \quad (3)$$

\* Work supported by U.S. Department of Energy, Office of Basic Energy Sciences under Contract No. W-31-109-ENG-38.

The Eq. (2)<sup>1,2</sup> is true for all  $k, k = (2, \dots, n)$ . It is important to remember that the calculated values ( $f_2, \dots, f_n$ ) will be different from the actual measured values in the magnets. However we will delay the discussion of this point.

#### IV. STEP 1 (ALTERNATE PROCEDURE 1)

We assume that at least one of the errors is known and is different from zero. We next consider the rest of the  $f_i$  as variables and take the derivative of the amplitude function  $I$  with respect to these  $f_i$ 's. Let us assume that we know the value of the first error. Then  $\frac{\delta I}{\delta f_k} = 0$  is a set of linear equations whose solution, in terms of the known phases and the known errors, gives the set of unknown errors whose placement at the corresponding phases would minimize  $I$ . Carrying out the above derivative and rearranging the terms, we get for all  $k, k = (2, \dots, n)$ ,

$$\sum_{j=2}^{j=n} H(\beta_j, L_j) f_j \cos \psi_{kj} = -H(\beta_1, L_1) f_1 \cos \psi_{k1}. \quad (4)$$

Comments similar to ones made in "Procedure 1" are valid for this alternate procedure.

#### V. STEP 2

Having solved the set of linear equations obtained from one of the above procedures, we ask how does this information get translated into the placement of the measured error values. It was answered in the following way. We ordered the measured error values and compared the largest measured error value to the calculated values. The measured error was placed in the position of its closest calculated value. Starting from the largest absolute error value we worked our way through towards the smallest error<sup>3</sup>. In this way we associate the measured errors with a position in phase.

#### VI. IMPLEMENTATION OF THE OPTIMAL PROCEDURE

We simulated 45 machines for the dipole errors in dipoles for the APS injector synchrotron. Figure 1 shows the sample random distribution functions used in the simulation. Figures 2 and 3 show the frequency with which the amplification factor  $I$  was improved in each machine, over the randomly placed dipoles and quadrupoles, respectively.

<sup>1</sup> It may be pointed out that it is not necessary to specify only one of the unknowns to start. We can specify more than one measured value at different positions and solve for the remaining ones in terms of the known quantities.

<sup>2</sup> Even though we formally have  $(n-1)$  linearly independent equations in Eq. (2), it may still be that a set of equations is not linearly independent by virtue of the coefficient of the matrix  $M_{kj}$  vanishing for certain values.

<sup>3</sup> Note that as we go from the largest value to the smaller values the number of choices for measured error to be placed keeps decreasing. In particular, the last measured error has only one place to go. Therefore, this may not be an optimal way to relate measured values to the calculated values.

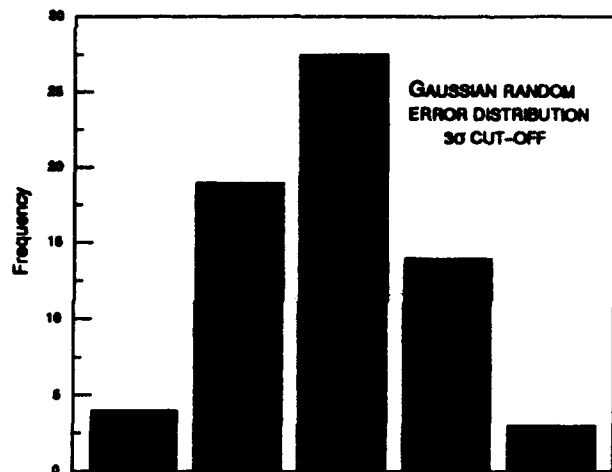


Figure 1

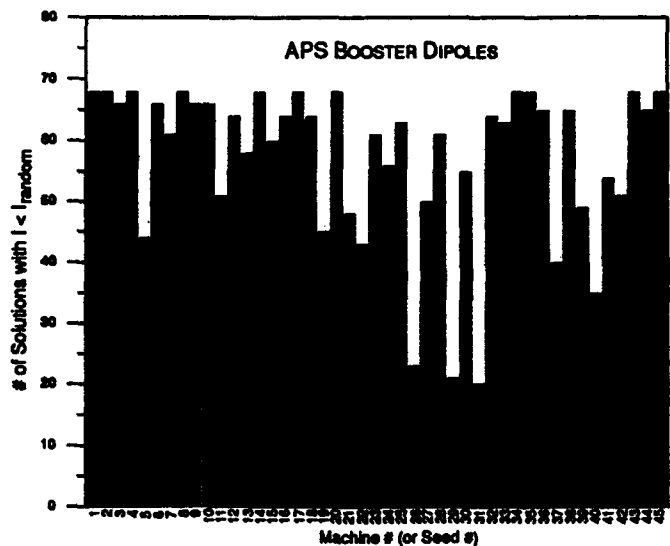


Figure 2

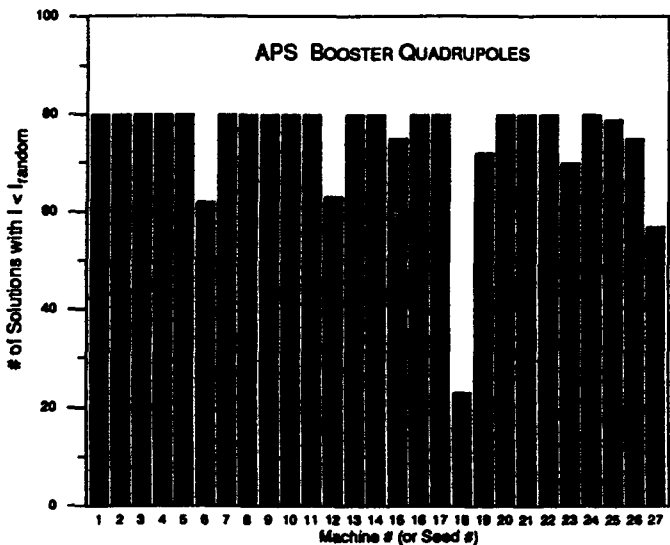


Figure 3

The only comment in favor of this procedure is that it worked extremely well for the simulations run with simulated random errors used for the APS injector synchrotron dipole and quadrupole errors.

The frequency distribution of the amplification factor for sorted and random machines is shown in Figure 4. Figure 5 is a similar plot, but here both sets in the plot refer to the amplification factors obtained after sorting. One corresponds to sorting 68 dipoles at a time and the other corresponds to sorting 34 magnets at a time.

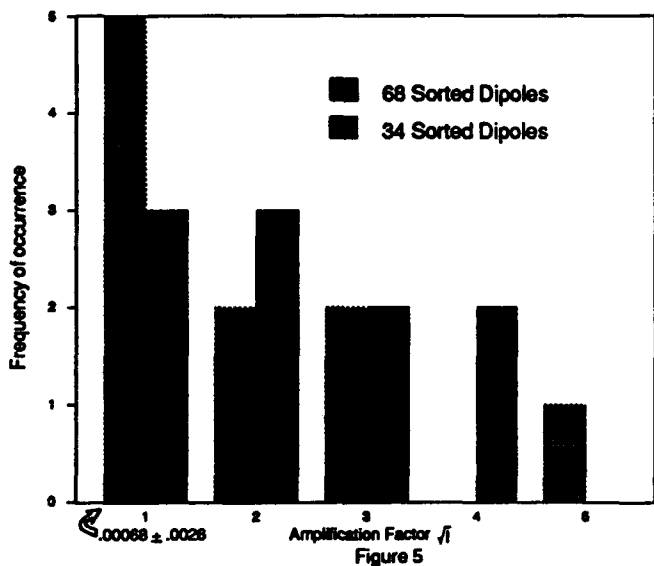
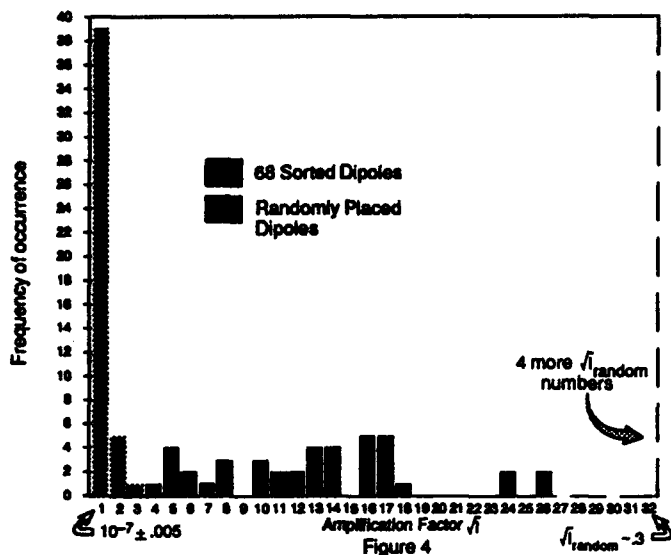
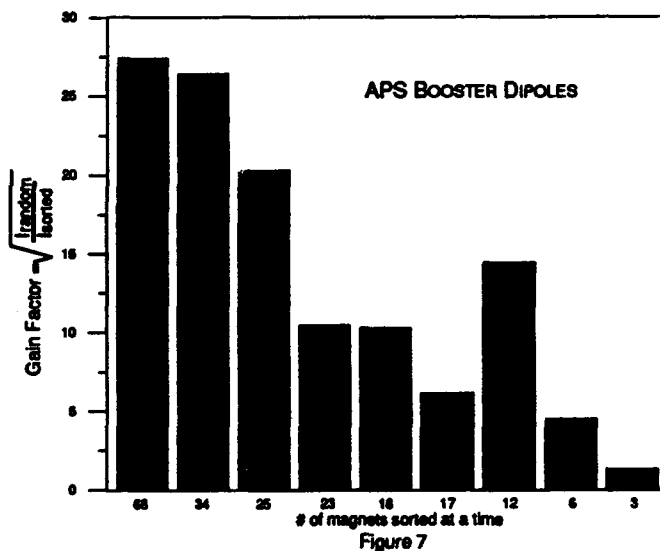
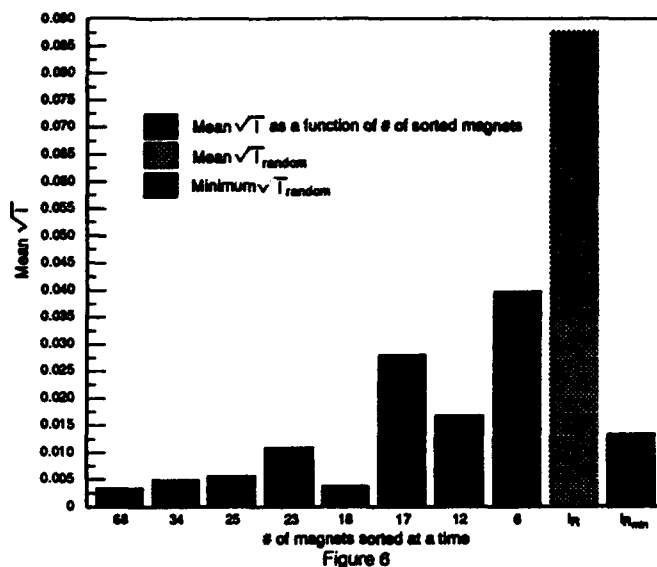


Figure 6 shows the dependence of the result of sorting on the number of magnets sorted at a time. One can easily see that the larger the number of magnets sorted at a time the lower the amplification factor obtained. Figure 6 also shows the mean and the minimum  $\sqrt{I_{\text{random}}}$ . One can easily see that not only is the mean  $\sqrt{I_{\text{random}}}$  much larger than any of the sorted  $\sqrt{I_{\text{mean}}}$ , but the minimum  $\sqrt{I_{\text{random}}}$  out of 45 random machines is much larger than the sorted  $\sqrt{I_{\text{mean}}}$  as long as the number of magnets sorted is at least 18. Figure 7 shows the same result, but here the plot

is for the gain factor, defined as  $\sqrt{I_{\text{random}}/I_{\text{sorted}}}$ , as a function of the number of dipoles sorted.



## REFERENCES

- [1] Frederick Lopez, private communication.
- [2] S. Sampson, "Reduction of Closed Orbit Distortion at the APS Synchrotron by Method of Simulated Annealing," *Internal Summer Student Report*, APS, Argonne, 1992.
- [3] S. Kirkpatrick, "Optimization by Simulated Annealing: Quantitative Studies," *Journal of Statistical Physics*, Vol. 34, p. 975, 1984.
- [4] B. P. Flannery, W. H. Press, S. A. Teukolsky, W. T. Vetterling, *Numerical Recipes in C The Art Of Scientific Computing*, Cambridge University Press, Cambridge, 1989.
- [5] B. K. Koul and Frederick Mills, "Linearized Error Analysis for an Accelerator," (to be published).
- [6] E. D. Courant and H. S. Snyder, "Theory of Alternating Gradient Synchrotron," *Ann. Phys.* 3, 1, 1958.

# Geodetic Concept for the Storage Ring EUTERPE

S.F.C.L. Wetzels\*, C.J. Timmermans\*, G.A. Webers\*, P.H.J. Schellekens\*, J.I.M. Botman\*, H.L. Hagedoorn\*  
\*Cyclotron Laboratory, \*Laboratory of Geometrical Measurement Technology  
Eindhoven University of Technology, P.O. Box 513, 5600 MB Eindhoven, The Netherlands

## Abstract

At present a 400 MeV electron storage ring EUTERPE is being developed at the Eindhoven University of Technology (EUT). It is a University project, set up for studies of beam dynamics, applications of synchrotron radiation and for the education of students in this field. The circumference of the ring is approx. 40 m with 12 dipoles and 32 quadrupoles. The critical wavelength of the emitted photon spectrum is 8.3 nm for the regular dipoles. The major ring components are being constructed at the own University Central Design and Engineering Facilities.

The concept of the geodetical system and the instrumentation are briefly described.

## I. INTRODUCTION

In the Cyclotron Laboratory of the Eindhoven University of Technology (EUT) research is done mainly in two areas, viz. ion beam analysis and its applications, such as proton-induced x-ray emission, and accelerator technology. The Eindhoven University of Technology Ring for Protons and Electrons (EUTERPE), including the injection system consisting of a linear accelerator LINAC 10 MeV and the Race-track Microtron Eindhoven (RTME, up to 75 MeV), is a University project (see Fig. 1) [1,2].

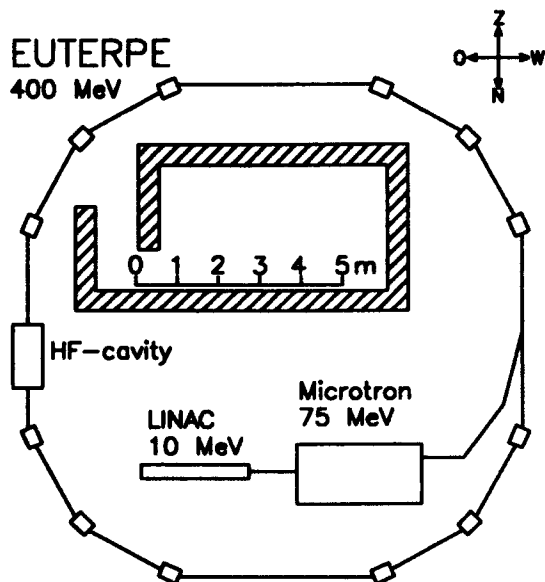


Fig. 1. Lay-out of EUTERPE.

This ring has been designed in the first place as a tool for charged particle beam dynamics studies. In the second place it serves as a facility for studies utilizing the synchrotron radiation and for the education of students who are interested in this field.

The ring will become operational in several phases. In the first phase the synchrotron radiation in the UV and XUV region (the critical wavelength is 8.3 nm) will be provided from the regular dipole magnets. Later on, in the second phase, a 10 T wiggler magnet (corresponding to a critical wavelength of 1.2 nm) and other special insertion devices will be added. In this way other applications and beam dynamic studies will be feasible. Special attention will be devoted to problems relevant to larger facilities, but which cannot be studied there due to a lack of the available beam time.

EUTERPE is a low-energy ring. It is being built by the EUT staff and the Central Design and Engineering Facilities of the EUT within the group budget. In the first phase it will also be supported by EUT stimulation funding. The capital investment, including the UHV system, power supplies, and computer control is estimated at 2.5 million Dfl. Labour costs of the Engineering Facilities are not charged to the group to its full amount.

At present, the LINAC 10 and the RTME are under construction. The dipoles of EUTERPE are in the early test phase. The other components (quadrupoles, sextupoles etc.) are still in development.

## II. TECHNICAL ASPECTS OF THE RING

The magnetic structure of EUTERPE is already known (see Fig. 1) and consists of twelve dipoles (30° bending), 32 quadrupoles for the beam focusing, 8 sextupoles and closed orbit distortion correction magnets. There are four 2 m long dispersion-free straight sections. One of these straight sections will be used for the HF-cavity, necessary to compensate the energy loss due to the synchrotron radiation. Another straight section is allocated for the injection process. The remaining two are useful for insertion devices such as undulators and wigglers, to study fundamental problems.

The bending magnets are of the parallel faced C-configuration which is beneficial for coupling out the synchrotron radiation. The dipole-dimensions are: block length 48 cm, height 39 cm, width 35 cm, pole width 12 cm, gap 2.5 cm and a weight of about 600 kg each. The quadrupoles have an aperture radius of 2.5 cm and a rectangular outer shape of 25 x 21 x 21 cm<sup>3</sup> [3].

The level of the reference beam is about 1.20 m above

the floor. The ring circumference is about 40 m. The EUTERPE project is situated in the hall of the Cyclotron Labs.

### III. THE ALIGNMENT

An overall alignment tolerance for the electron storage ring is specified as  $\pm 0.2$  mm in all directions, a misalignment to neighbouring components of max. 0.1 mm in all directions and a max. twist of 0.2 mrad.

The geodetical basic network will be formed by 8 reference points, the floormarks, fixed just below the surface of the 1½ m thick floor of the hall (see Fig. 2).

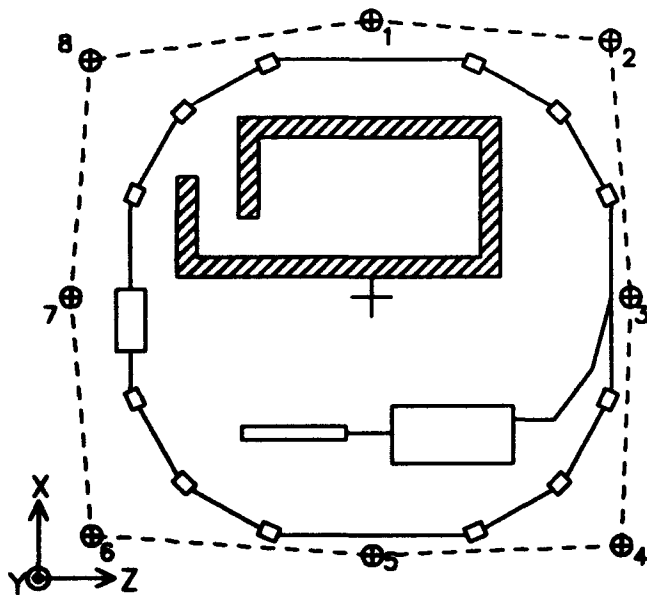


Fig. 2. The geodetical network of EUTERPE.

The position of these floormarks has to be known with at least the same accuracy as is required for the positioning of the components. This is accomplished by measuring the lengths and the angles between points and segments along the complete circumference plus some diagonals of the network. The measurement of the geodetical basic network is only done once, since the floor that contains the floormarks is 30 years old and thus very stable.

The result of the measurement is a rigid network in which the position of the floormarks is indicated by their  $xz$ -coordinates within the main coordinate system. The origin of this coordinate system is chosen in such a way that all relevant points have positive coordinates. Moreover the origin is chosen such that the  $x$ - and  $z$ -coordinates of the centre of the ring are quite different. In this way many simple errors during alignment measurements are prevented. The desired position of the dipoles and quadrupoles, determined by the ion-optical calculations using the program DIMAD, can be converted into  $xz$ -coordinates in the main coordinate system.

By means of an optical plummet, pillars will be centred above the floormarks with an accuracy of 0.02 mm. These pillars (1.60 m high, ensuring a level which is above the level of the components of the ring) will provide a mounting for the theodolite and the optical targets which are used to measure the position of the components (dipoles, quadrupoles etc.) relative to the geodetical network.

One rack with optical targets (Taylor-Hobson spheres), placed reproducibly on each dipole and a similar rack for the quadrupole-assemblies, serves as a reference for the position of these components within the network. The lay-out during the alignment measurement of a dipole is visualized in Fig. 3.

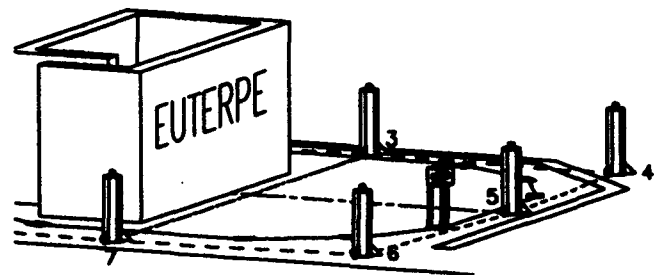


Fig. 3. Overview of lay-out during dipole measurement.

First, the components will be positioned roughly ( $\pm 2$  mm). Then their position will be iteratively measured and adjusted. The measurement is done by spatial intersection. A standard one-second theodolite will be used. Centred over a floormark its position is known. Targets, centred over other floormarks will serve as additional positional references. The angular position of the dipoles and quadrupoles relative to the theodolite can then be determined. By exchanging the theodolite and the targets, the measurement can be done from several points in the network. From all these angular measurements the exact position of the dipoles and quadrupoles within the main coordinate system can be determined.

Finetuning of the six degrees of freedom of the components is provided by the adjustable frames on which they are mounted. This iterative process of measurement and adjustment will finally lead to the desired position of the components.

### IV. REFERENCES

- [1] Boling Xi et al., "Design study of the storage ring EUTERPE," Nucl. Instr. and Methods in Phys. Research, B68 (1992) 101-104.
- [2] J.I.M. Botman et al., "The EUTERPE facility," Review of Scientific Instruments, Vol. 63, No. 1, Jan. 1992.
- [3] J.I.M. Botman, PAC93 contribution.

# ALIGNMENT OF CEBAF CRYOMODULES\*

W. J. Schneider, J. J. Bisognano, J. Fischer, D. R. Douglas, K. Macha, J. Mammosser, W. Oren, J. Preble, J. Robb, M. Wiseman  
Continuous Electron Beam Accelerator Facility  
12000 Jefferson Avenue, Newport News, VA 23606-1909 USA

## Abstract

CEBAF, the Continuous Electron Beam Accelerator Facility, when completed, will house a 4 GeV recirculating accelerator. Each of the accelerator's two linacs contains 160 superconducting radio frequency (SRF) 1497 MHz niobium cavities [1] in 20 cryomodules. Alignment of the cavities within the cryomodule with respect to beam axis is critical to achieving the optimum accelerator performance. This paper discusses the rationale for the current specification on cavity mechanical alignment: 2 mrad (rms) applied to the 0.5 m active length cavities. We describe the tooling that was developed to achieve the tolerance at the time of cavity pair assembly, to preserve and integrate alignment during cryomodule assembly, and to translate the alignment to appropriate installation in the beam line.

## I. INTRODUCTION

The cryomodules for the Continuous Electron Beam Accelerator Facility (CEBAF) located in Newport News, Virginia, will provide a low emittance, 200  $\mu$ A beam with energies up to 4 GeV for fundamental experimental studies in nuclear physics [2]. The acceleration is achieved from a conventional bunched electron source at 500 keV; a superconducting injector, containing 2 1/4 cryomodules, which provide a nominal energy gain of 45 MeV; and two recirculating linacs containing 20 cryomodules, each linac capable of achieving an energy gain of 400 MeV. After five recirculation passes, the two antiparallel linacs produce a beam of 4 GeV to three end stations.

Exercises conducted during the Front End Test in the spring of 1991 indicated significant transverse beam steering by the accelerating cavities. These effects are attributable to cavity cell orientation and cavity pitch and yaw. Measurements taken at that time indicate that cavity misalignment of 1—2 mrad was not uncommon, and one cavity was reportedly at 6 mrad [3].

## II. ALIGNMENT RATIONALE

The original cavity alignment specification was limited to the alignment of the mechanical structure and did not consider the dynamical relevant accelerating field. This specification was in existence at the time of the PCDR [4] and was based on earlier estimates by Leemann and Penner [5]. The model employed for this estimate assumed a uniform accelerating gradient of 5 MV/m over the 0.5 m active length cavity; the transverse beam steering for each cavity was then the cavity

pitch or yaw angle caused by misalignment times the ratio of energy gain to the energy in the cavity. The effect of fringe fields was ignored, which resulted in the original tolerance of  $\pm 1$  mm from the central orbit. This specification was supported by several simulations—York and Tang [6], and Kewisch et al., [7]—which were consistent with the specifications. During a review of the tolerances it became apparent that the models in question [8] were pessimistic in regard to the effect of cavity misalignment since they ignored effects of cavity fringe fields.

A Mafia study was performed to determine the effect of cavity assembly errors. Because of computer mesh limitations, the grid size was constrained to 2.5 to 5.0 mm, minimum size. The cavity manufacturing and assembly tolerances were routinely 10—20 mils (0.2—0.5mm) or an order of magnitude smaller than the mesh size. These studies, concluded that the most critical assembly error is tilts in the cavity equatorial plane. For assembly errors on the 10—20 mil range, one can then expect pitch and yaw errors equivalent to a few mrad.

## III. ALIGNMENT SPECIFICATION

The accelerating field misalignment studies supported the 2 mrad rms tolerance. The simulations were a factor of two too sensitive as they neglected the fringe fields. Similarly the studies were a factor of two too optimistic since they neglected cavity assembly errors. The specification was then set where 2 mrad rms tolerance with a 2  $\sigma$  cutoff was assigned to cavity assembly, measurement, and fiducialization errors. All of these errors, such as cell tilts, electromagnetic axis determination, fiducial transfers to flanges, etc., are to be limited to this level. The factor of two attributable to fringe fields offsets these effects. The remaining 2 mrad rms error with a 2  $\sigma$  cutoff is assigned entirely to mechanical alignment of the cavity. An error budget was then set up consisting of three sources: Individual cavity alignment, cavity pair alignment, and cryomodule alignment. The misalignment was defined in terms of net transverse momentum impulse applied to the beam by a single cavity. Reasonable errors were estimated for the three source terms, which resulted in 0.5 mrad level for cavity alignment, 1.25 mrad for cavity pair and 0.1 mrad level for cryomodule net alignment. When added in quadrature this results in less than 2 mrad, which is in the specified range [9].

## IV. CEBAF CAVITIES

The design, manufacture [10], test and performance [11] of the CEBAF superconducting radio frequency (SRF)

\* supported by U.S. DOE contract DE-AC05-84ER40150

cavities are reported elsewhere. Cavities received from Siemens undergo receipt inspection—which includes tuning, mechanical inspection/measurement and initial chemistry. The cavities then undergo final chemistry, are rinsed, and assembled into pairs on the alignment/installation fixture, Figure 1. Cold ceramic windows, pair parts (elbows, beam pipe), HOM loads and dished head assemblies are attached. One of the larger errors associated with the cavity pair alignment was attributable to the end dish assembly as it mounts to the cavity. A special fixture was manufactured to ensure alignment of the beam pipe to cavity centerline. Errors, for a single cavity, after the inclusion of this additional step, translated into an achievable 0.5 mrad level. The pairs are sealed hermetically while in a class 100 clean room to mitigate cavity contamination that can degrade performance. After this the pair is evacuated, mass spectrometer leak checked, rotated vertically, transferred to a dewar assembly, tested at 2 K in a vertical dewar, where the performance qualification— $Q_0$  versus  $E_{acc}$ —is accomplished. The pair is then warmed up, transferred back to the alignment fixture and turned over for unit assembly. Cavity alignment surveys conducted before and after the vertical tests indicated a repeatability of measurements of better than 1/4 mm total error.

## V. CEBAF CRYOUNITS

Assembly of cryounits [12], each consisting of a cavity pair housed in a helium vessel within an insulated dewar, is accomplished outside of the clean room. Tuners, fundamental power coupler extensions (FPC's) and electrical wiring are installed while the pair is mounted on the fixture. The pair is inserted into the helium vessel, Figure 2, which is supported on a hydraulic adjustable stand. Alignment is maintained by sliding the fixture on bearings riding on Thompson rods through the open vessel. The FPC's are connected to the vessel; wiring is brought out through feed throughs; titanium cavity supports, which match the Niobium thermal expansion, are added, and the alignment and installation fixture is removed. The cavity pair alignment is now preserved by the helium vessel. After leak check of the connections, closure heads are added at both ends, allowing the beam pipe to exit the vessel and thereby providing a fiducial, and the heads are welded up. After leak check of the welded vessel, the magnetic shielding, Multi-Layer Insulation (MLI) thermal shield, and additional MLI are added, and the unit is inserted into the vacuum vessel equipped with additional magnetic shielding. The vacuum vessel is supported on a fixture which allows the beam axis to be preserved through a pair of Thompson rods and bearings, Figure 3. Nitronic rods are installed which support and axially restrain the helium vessel inside the vacuum vessel. Adjustment of the rods aligns the mounted pair inside the cryounit. A top hat assembly, including a pair of waveguides for RF, wiring connections, thermal and magnetic insulation and the top hat cover, completes the installation. Alignment has now been transferred outside of the vessel to the two beam line flanges

and alignment is maintained by the fixturing of the Thompson rails and bearings.

## VI. CEBAF CRYOMODULES

A cryomodule consists of four cryounits, each of which contains a cavity pair, two end cans and five sets of bridging components. In the cryomodule assembly area, a precision assembly bench, consisting of steel "I" beams equipped with Thompson rails, allows the alignment built into the cryounit to be transferred to the module, Figure 4. Initially, a return end can is installed on the rail, then the four cryounits followed by the supply end can. Connections between cryounits are completed under a laminar flow hood, and consist of beam pipes, three helium connections, and thermal and magnetic shielding covered by the bridging cylinder. Access to the beam pipe flange within the vessel is achieved through a port at the midplane on each side of the bridging rings. Special tooling equipped with an optical cross hair is installed on each of the beam pipe flanges which project out to the module midplane. When the assembly bench was installed, four granite blocks were installed at the ends on either side. Scope mounts were set up at one end and targets placed at the other. A rough alignment of the cryounits is performed initially as they are installed. After assembly the bridging rings are welded. Initially we were concerned, as we were for the welding on the helium vessel, that alignment would be compromised. Although we do see movement when welding the helium vessel, the bridging ring welds do not affect alignment. The moment of inertia of the vacuum vessel is large; hence there is little deflection of the cavities. Despite this, final alignment is completed while the welded module is supported at the quarter points, thereby cancelling out this effect. By sighting down both sides simultaneously both the  $x$  and the  $y$  components can be corrected. Typically alignment of the module is better than a 1/4 mm, which when added with the cryounit errors comes in at the 1.25 mrad level.

## VII. CEBAF INSTALLATION

Following the alignment of the cryounits into a cryomodule, a series of external reference points are placed on the outside of the vacuum vessel. These fiducials, which are used to place the cryomodule in its proper position in the tunnel, are surveyed with a theodolite-based industrial measurement system [13]. This procedure, through a rigorous three-dimensional survey and least-squares adjustment, transfers the transverse and angular orientation of the cryomodule centerline as defined by the granite monuments to the reference points. The ideal coordinates in the overall machine coordinate system can then be calculated by knowing the cryomodule's design position on the beam line and the measured target offsets.

Transfer of the cryomodule to the tunnel is accomplished on a specially equipped air ride trailer. Tunnel alignment consists of two steps, both of which utilize a reference control network which defines the machine's position in the tunnel.

This network was measured using standard high-precision surveying techniques developed for particle accelerators [14,15]. The first alignment step, which employs optical tooling techniques, "rough" aligns ( $<1.0$  mm) the cryomodule and its adjacent components for vacuum interconnections. The second step aligns the cryomodule to 0.1 mrad relative to the control network and the design beam line. The beam pipe girders are connected to the module after the second alignment to preclude rotation of the beam line bellows. A third alignment is done to account for tunnel settling.

## VIII. LINAC RESULTS

A limit on the alignment error of the end cavity of the North Linac can be set by the fact that no observable beam spot growth occurs when a 120 MeV beam is energy modulated by a 0.5 MeV using this cavity. The observed down stream steering was  $\leq 1/4$  mm which implied  $\leq 3$  mrad misalignment angle which is consistent with the specification.

## IX. ACKNOWLEDGEMENTS

The authors wish to express their grateful appreciation to D. Machie, B. Carpenter and E. Folts for their extensive help with the design of the alignment tooling, to H. Whitehead for the photography, and to G. Sundeen, who graciously typed the manuscript.

## X. REFERENCES

- [1] P. Kneisel, *et al.*, "Performance of Superconducting Cavities for CEBAF," *Conference Record of the 1991 IEEE Particle Accelerator Conference*, Vol 4 pp. 2384—86.
- [2] H. A. Grunler, *et al.*, "The Continuous Electron Beam Accelerator Facility," *Proceedings of the 1987 IEEE Particle Accelerator Conference*, Vol. 1, pp. 13—18.
- [3] C. Sinclair, private communication.
- [4] CEBAF Pre-Conceptual Design Report, Chap. 4.2, pp. 4—13, December 1985.
- [5] C. Loomann, private communication.
- [6] R. York and J. Tang, unpublished.
- [7] J. Kewisch, *et al.*, "Orbit Correction Techniques for a Multipass Linac," *Proc. 1990 Linear Accelerator Conference*, Sept. 1990.

- [8] D. Douglas, *et al.*, "Transfer Matrix Simulating Motion Through a Linac Cavity," CEBAF-TN-89-0132, 20 June 1989.
- [9] J. Bisognano, *et al.*, "Alignment Tolerances for CEBAF Accelerating Cavities," CEBAF-TN-91-081, 15 Oct. 1991.
- [10] M. Dumas, *et al.*, "Production of Superconducting Niobium Cavities for CEBAF," *Proceedings of the 1991 IEEE Particle Accelerator Conference*, Vol. 4, pp. 2390—92.
- [11] C. Reece, *et al.*, these proceedings.
- [12] J. M. Gaunt, "Bundle Adjustment and Tridimensional Coordinate Determination," SLAC-Pub-4714, 1988.
- [13] R. E. Ruland, "Accelerator and Transport Line Survey and Alignment," Invited Paper at the 5th ICFA Beam Dynamics Workshop, Corpus Christi, TX, Oct. 3—8, 1991.
- [14] S. Turner, editor, CERN Accelerator School Proceedings, "Applied Geodesy for Particle Accelerators," CERN, Geneva, Switzerland, April 1986.

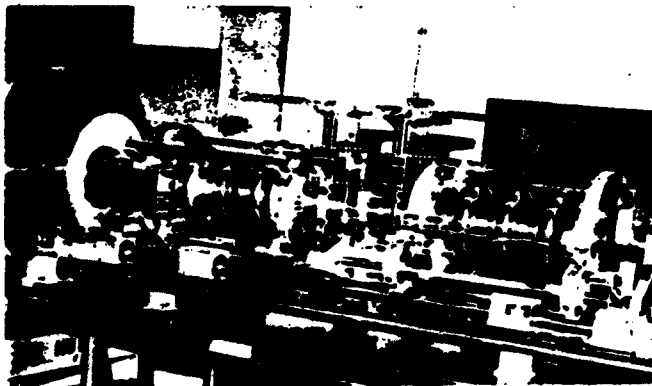


Figure 1. Alignment/installation fixture.

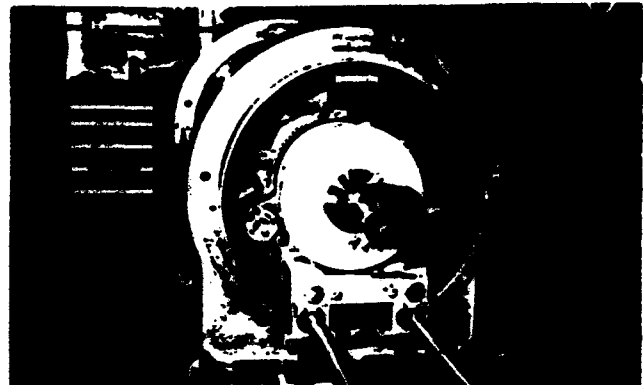


Figure 2. Insertion of cavity pair into helium vessel.

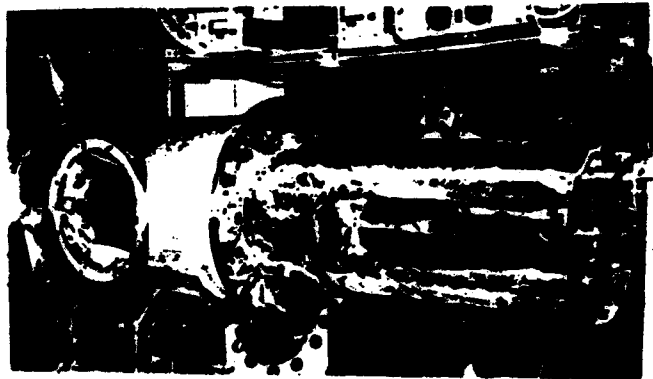


Figure 3. Insertion of helium vessel into vacuum vessel.

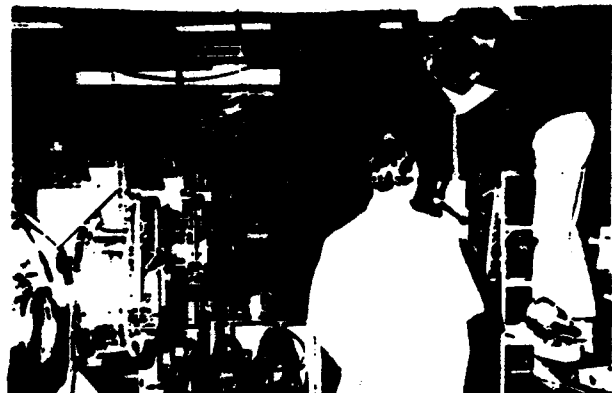


Figure 4. Cryomodule fiducialization.

# The Hydrostatic Levelling System (HLS) / Serve-Controlled Precision Jacks A New Generation Altimetric Alignment and Control System

Daniel ROUX  
European Synchrotron Radiation Facility  
BP220 38043 GRENOBLE FRANCE

## Abstract

In 1987 the ESRF paved the way for a new ambitious accelerator alignment to satisfy demanding and as yet unachieved design specifications. This consists of a permanent realignment of the magnetic elements distributed over the 1km circumference of the storage ring to an absolute horizontal plane with a precision of  $\pm 1\text{mm}$ . Relative alignment precision is specified at  $\pm 0.1\text{mm}$  between two adjacent elements. Realignment operations are performed in less than one day.

In 1989 once laboratory tests confirmed that each of the "Hydrostatic Levelling System" and jack prototypes were capable of achieving the desired results, the series production of the 300 each of HLS and Jacks necessary to align the ESRF storage ring was launched.

From April 1991 thru' January 1992 the installation of girders in local mode was made in record time, to which the HLS made a significant contribution. During the so called storage ring "Commissioning Phase" (running from January 92 thru' June 92) the software was written, installed all equipment connected to the control room.

Today we would like to present the results of the first storage ring alignment which took place on January 10 1993. Results obtained were ten times better than those stipulated in the specifications and duly confirm that in less than one day it is possible to align a 1km circumference storage ring with an absolute precision of  $\pm 0.1\text{mm/km}$  and a relative precision between girders greater than  $10\mu\text{m}$ .



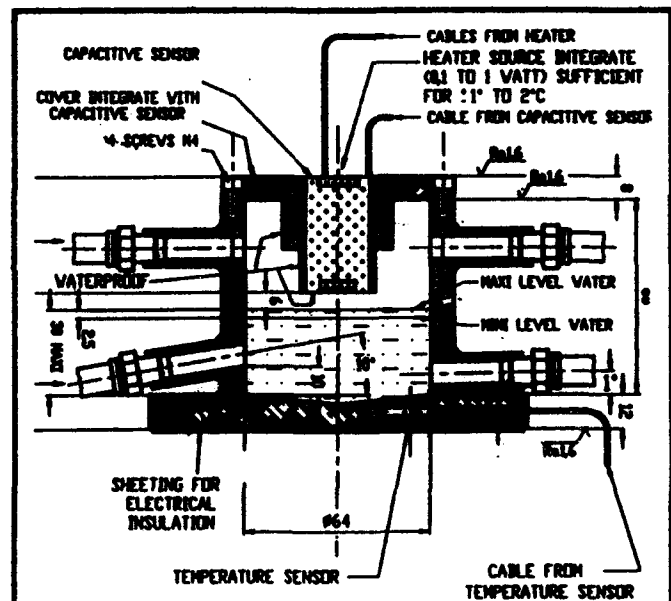
Figure 1 : One of the 96 girder supports for the ESRF storage ring quadrupole and sextupole magnets.

## 1. INTRODUCTION.

We estimated that relative movements over 1km would be of the order of  $1.2\text{mm/year}$  on the geologically homogeneous sub-soil of the Grenoble site. This led us to schedule monthly realignments to satisfy specifications (The estimation was based on information recorded on the scientific polygon over a 15 year period and consolidated by a specific ESRF study made between 1987 and 1988).

From a geometric point of view the ESRF storage ring is composed of 544 sensitive elements distributed on 96 girders of an average weight of 6 tons. Each girder is supported on three jacks and equipped with three HLS located immediately above.

The HLS (Fig. 2) is a measuring instrument based on the principle of communicating vessels. The 288 instruments are interconnected along the circumference of the storage ring by a fluid filled tube which determines the reference plane and an air filled tube which guarantees pressure stability along the network. The design of the capacitive monitoring device was based on high tech satellite developments made by ONERA<sup>1</sup>. This device has a measurement range of  $2500\mu\text{m}$ , analog resolution inferior to  $2\mu\text{m}$  and digital resolution inferior to  $0.1\mu\text{m}$ .



<sup>1</sup> ONERA Office National Etudes et Recherches Spatiales Aéronautiques (Palaiseau, France).

Manufacturer : FOGALE-NANOTECH (Nimes 30000 France)

The pipes which connect the HLS vessels are made of high radiation resistant (20Mrd) transparent material of 8/10mm internal/external diameter.

The servo-controlled jack (Figure 3) is a high precision screw jack, withstanding a nominal load of 3 tons, and with a 40mm displacement capacity (correction estimate over a 20 year period) and resolution under loading of 0.2 $\mu$ m.

The acquisition and control system consists of G64 modules for analog/digital transformation of a 16 byte signal, a VME type transfer bus and an HP type computer operating on UNIX. The acquisition of signals emitted by the 288 HLS on an HP 900/800 work station takes 15 seconds. Transmitting instructions to the 288 jacks takes about two hours, this is due to the procedures and security systems which are operational at present. The intrinsic speed of the system could be 15 minutes.

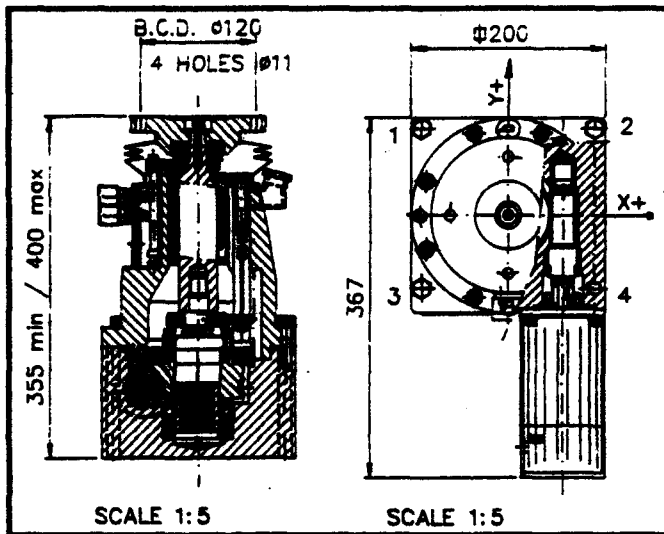


Figure 3 : Cross section of a micrometric screw jack used on the ESRF storage ring.

## II. JANUARY 10 1993 - A WORLD FIRST I.

The first realignment operation required an extremely careful preparation. This was carried out during machine commissioning, we performed a series of monthly filling tests. This test required 60 hours thermal stability in the tunnel. During the first 12 hours we checked the status of the machine prior to testing (<5 $\mu$ m/12h/288 HLS). The following 36 hours were devoted to checking the adjustment of the mean plane before and after filling <10 $\mu$ m/36h/288 HLS. The last 12 hours were spent checking the stability of the machine after testing (Figure 4). We were only able to perform these tests during the long weekends when the machine was shutdown. During the January 10 campaign we performed such tests before and after the realignment operation in order to guarantee optimal safety conditions.

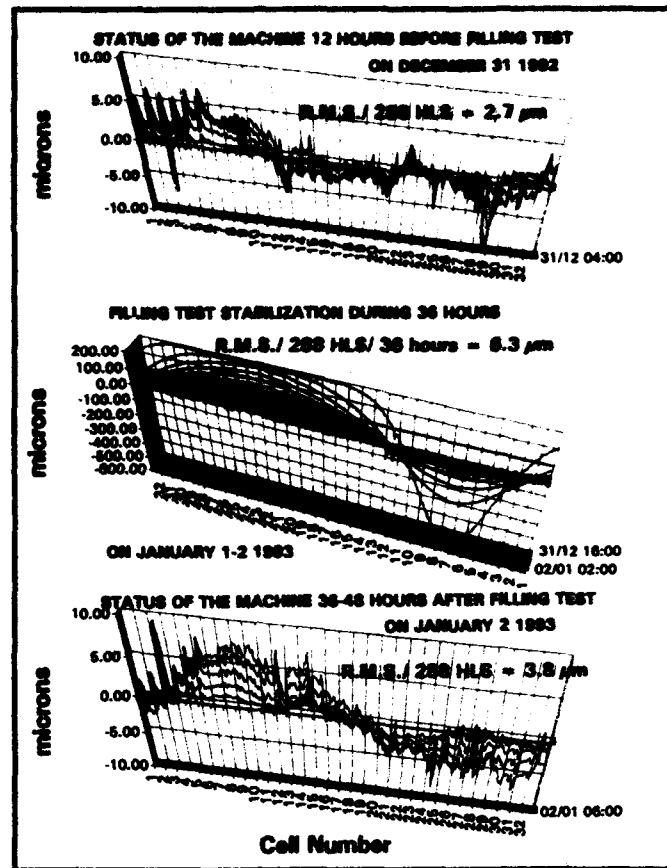


Figure 4 : Precision and stability time of HLS network on ESRF storage ring.

The organization of commissioning of jacks was more complex as confronted with the legitimate reticence of the Operation Team to jeopardize parameters painstakingly achieved over a period of several months. Nevertheless two preliminary tests were performed on July 27 and August 27 1992 during the summer shutdown period. These tests were a uniform displacement of +/- 100mm. They attained a success rate of 92% and 96% respectively and enabled correction of defects, essentially linked to connection problems (absence of cables or motor cards).

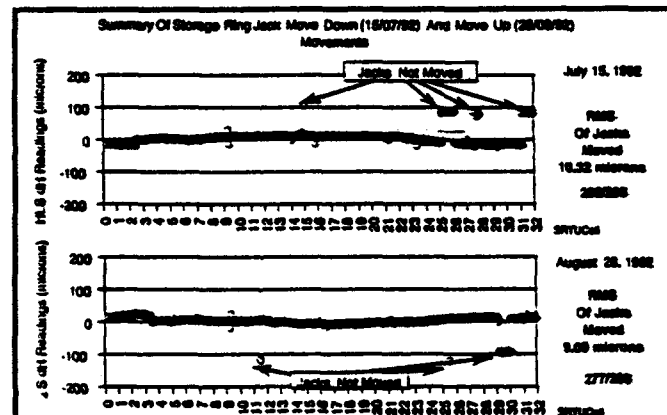


Figure 5 : Curves showing reliability and precision of HLS/jack couples during two commissioning tests.

In view of the large amplitude of displacements to be carried out ( $\pm 1.5\text{mm}$ ) due to numerous earth works we decided to split the hydraulic network into sixteen sectors, composed of two cells each. This was done for two major reasons :

- to prevent loss of signal during adjustments, maximum HLS amplitude being  $2500\mu\text{m}$  ;
- to reduce stabilization time to about two hours instead of thirty six for the whole network

First of all the even then the odd numbered cells of each pair were moved. These operations each took one hour.

The passage of the machine from its position illustrated at the top of figure 6 to that illustrated at the bottom of figure 6 takes two hours. The curve in the middle of figure 6 indicates the differences between orders given to the jacks and the readings recorded by the HLS system.

The RMS value of the jack/HLS pair is  $4.7\mu\text{m}$  and we obtained a 100% success rate on the 288 displacements during this historic alignment operation performed on January 10 1993.

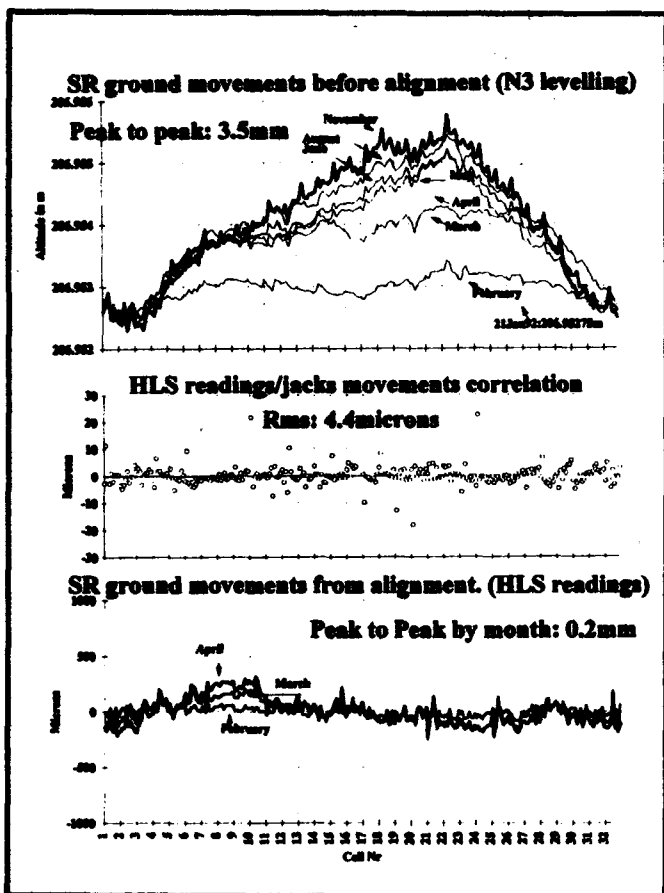


Figure 6 : Status and altimetric evolution of the storage ring before, during and after the January 10 1993 realignment campaign.

### III. CONCLUSION.

Displacements recorded since the January realignment confirm the 1988 estimates concerning differential settlements over one month (Figure 6 bottom).

The success of the HLS/jack pair recorded in January 1993 attests to the feasibility of a monthly realignment enabling the ESRF accelerator to be maintained in an absolute horizontal plane of  $\pm 1\text{mm}$  and adjacent equipment to a value inferior to  $10\mu\text{m}$  during realignment.

When taking account the 1993 - 1994 beamline installation program, it would appear that the optimal realignment schedule will be every four to six months (the next will take place in July 1993). Differential settlement recorded in zones 6 to 13 correspond to beamlines which will be installed this year. In years to come the frequency of realignment campaigns during steady state operation will be monthly. This will guarantee Users on all beamlines with a beam stability of  $\pm 0.1\text{mm}$  around the whole circumference of the ring. Recent HLS connections set up between the machine and recently installed beamlines have given a promising insight to a whole range of new possibilities for control in experimental areas.

### IV. REFERENCES

- [1] Gelman M., Le nivellement hydrostatique, ESGT 1981.
- [2] Roux D., Conception d'un système de contrôle altimétrique automatique et permanent pour le projet ESRF. ALGE-87-03, Octobre 1987.
- [3] Roux D., Alignment and Geodesy for the ESRF project, Proceedings of the first international workshop on accelerator alignment, July 31-August 2, 1989, Stanford Linear Accelerator Center, Stanford University (USA).
- [4] Martin D & Roux D, Real Time Altimetric Control By A Hydrostatic Levelling System, Second International Workshop On Accelerator Alignment, September 10-12, 1990, Deutsches Elektronen Synchrotron (DESY, Germany).
- [5] Martin D, Alignment At The ESRF EPAC (Berlin, Germany, Mars 1992).
- [6] Roux D, Determination Of The Accuracy Of An HLS Network. TS/WR/ALGE/92-22b, Septembre 1992.
- [7] Martin D. & Roux D, Dimensional Control Of The Experimental Hall. June 1992.
- [8] Loffler F, Dobers T, Neubauer G, High Precision Levelling System For The HERA-Detectors And Interactions Quadrupoles. DESY, Hamburg, Germany July 1992.
- [9] Roux D., A New Alignment Design, Application of ESRF Storage Ring. SEE, Paris, France, November 1992.

# Control of Roll in Fiducialization of Quadrupole Magnets for the MIT-Bates South Hall Ring\*

M. Farkhondeh, K. A. Dow and W. W. Sapp

Massachusetts Institute of Technology  
Bates Linear Accelerator Center  
Middleton, MA 01949.

## Abstract

The South Hall Ring (SHR) requires for all 94 quadrupoles in the lattice a roll tolerance of less than 2mr. An important step in achieving this tolerance is the fiducialisation: the relating of the magnetic axes to the position of the survey targets fixed to the magnet. The fiducialisation procedure which we developed involved a harmonic analyser system and the SLAC Industrial Measurement System. After fiducialisation and database generation had been completed for over 1/3 of the elements, and after the precision installation had begun, we noticed a random roll well outside the tolerances. The roll had been overlooked partially because the harmonic analyser system is insensitive to rotations about the coil axis. We were able to overcome the problem through software by developing an extensive algorithm and regenerating the database without a need for refiducialisation. This correction process for both the roll and the pitch will be presented.

## 1 Introduction

The SHR currently under commissioning will be a high intensity pulse stretcher facility providing high quality cw electron beams with energies between 0.3 and 1.0 GeV. It can be operated in storage mode for internal target experiments and in extraction mode for more conventional experiments. A detailed description of the ring is given in ref. [1]

The SHR quadrupoles follow the design of booster ring quadrupoles for the Advanced Light Source at the Lawrence Berkeley Laboratory. The laminated iron yoke consists of two identical cores joined at the horizontal mid-plane. Mechanical imperfections in these cores result not only in non-circular apertures but also in apertures whose profile is a function of position along the magnet axis.

The critical tolerances for the quad positioning are the transverse (XY plane) tolerances of 0.1mm element-to-element and a rotational roll tolerance of 0.1 deg (1.7mr). Rotational misalignment of quads will mix the X and Y components of the field, coupling the phase space in the



Figure 1: A photograph of the Harmonic Analyser table with a quad mounted for magnetic measurement and fiducialisation.

two planes. The specified tolerance should assure that this coupling is less than 10%.

During the initial precision survey and alignment of the quadrupoles [2] in the injection line area, the presence of a random but significant roll and pitch was detected. The problem was soon traced to an oversight in the fiducialisation of the quads and usage of a Harmonic Analyser system which is insensitive to small rotations (a photograph of the table with a quad is shown in Fig. 1). In this report we will describe the issues relevant to the control of the roll and will present solutions to overcome the roll problems as encountered.

## 2 Fiducialization and Rotation

A detailed description of the fiducialisation of these quadrupoles is given in ref. [3] and a schematic of the setup with four Kern theodolite locations is shown in Fig. 2. However, a brief summary of it is given here with an emphasis on the rotation issue. An integral part of this fiducialisation system was a Harmonic Analyser (HA) which was used for magnetically measuring the quadrupoles and is briefly described in ref. [4]. It consists of a rotating

\*Work supported in part by DOE contract DE-AC02-76ER03069.

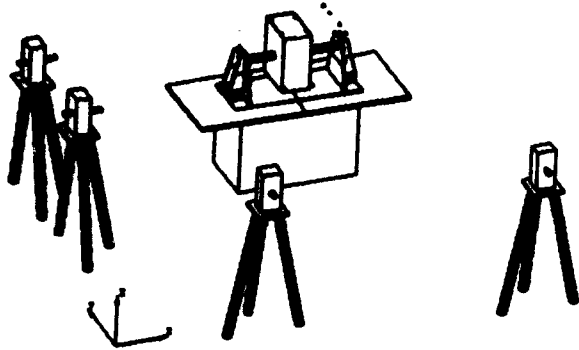


Figure 2: Schematic diagram of quad fiducialisation setup.

cylindrical ceramic bobbin with wire coils wound on it, a moveable support table holding the bobbin and survey targets, and five micrometers for aligning the table supporting the bobbin relative to the quad. The quad is supported by three posts mechanically isolated from the bobbin support.

To position the magnet on the HA for the magnetic measurements and fiducialisation it was first necessary to level the magnet using the three support posts. A precision bubble level was placed on a heavy steel plate (approximately 30 cm square) resting on a thin foam pad which "integrated out" the small surface irregularities of the laminated yoke. It was earlier determined that the top surface was parallel to the mechanical midplane within the needed tolerances. After the magnet had been leveled, the bobbin axis was positioned to coincide roughly with the mechanical axis of the quad. An alignment shaft with custom spacers replaced the bobbin for this operation. The magnet was then energised and the measured dipole component was nulled by fine-tuning the position of the bobbin, being careful to adjust the positioning micrometers such that the axis was only translated and not rotated about any axis.

We also fiducialised the HA table relative to the axis of the bobbin; this one-time survey measured the coordinates of all 11 survey targets affixed to the table relative to the axis of the bobbin as described in ref. [3]. These measured coordinates are fixed relative to the gravity vector as long as the HA micrometers are left alone or changed for only translational movement of the bobbin.

The quad fiducialization was done with the SLAC Industrial Measurement System (SIMS)[5] using a total of four theodolite locations viewing the 11 targets on the HA table, the quad survey targets and the end targets on a precision invar scale bar. A bundle adjustment [6] with the coordinates of the 11 table targets (measured in the table calibration) as input produced a set of coordinates for the quad targets in the bobbin coordinate system. As described above, the bobbin axis is adjusted to coincide

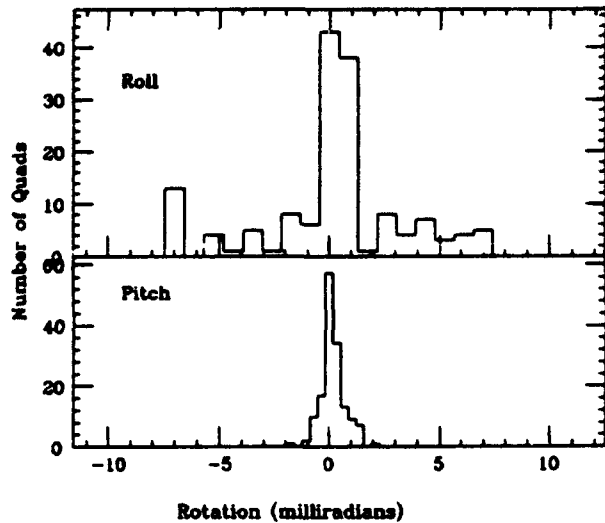


Figure 3: Statistical results of Roll and pitch of the HA table and the quads in the database.

with the magnetic axis of the quad.

An oversight occurred during the rough mechanical alignment of the bobbin in which random table rotations well outside the tolerances were introduced. This occurred in the process of making the custom spacers fit into the quadrupole aperture by randomly changing the micrometers. Since the HA with a long bobbin extending well outside the fringe field regions is insensitive to roll or a small amount of pitch, the subsequent magnetic measurement and dipole minimisation could not detect the rotation of the HA table relative to gravity and the quad.

The oversight was discovered after about 1/3 of the quads were measured and installation began. All quads were installed at the proper survey target heights, but for some, the precision bubble level reported significant amount of pitch and/or roll. These random rotations were as large as 10 mr, well outside the rotational tolerances. Figure 3 presents a statistical analysis of the roll and pitch for nearly all 128 quadrupoles; the roll is typically larger than the pitch. We were able to correct these undesirable rotations by correcting our database without any need for refiducialization. This was possible, primarily because direction of the gravity was implicitly defined by the vertical angles of the theodolites which were recorded in each fiducialization file.

### 3 Control of Roll and Pitch

After the source of the rotation problem was detected we added a procedure for ensuring that during each quad measurement, the HA table orientation relative to the gravity vector was the same as it was during the one-time table fiducialization. We reconstructed this orientation by making the relative differences between the vertical coordinate of the table targets exactly the same as they were in the calibration file. We then installed a ground plate with three point contact on a flat region of the table, leveled

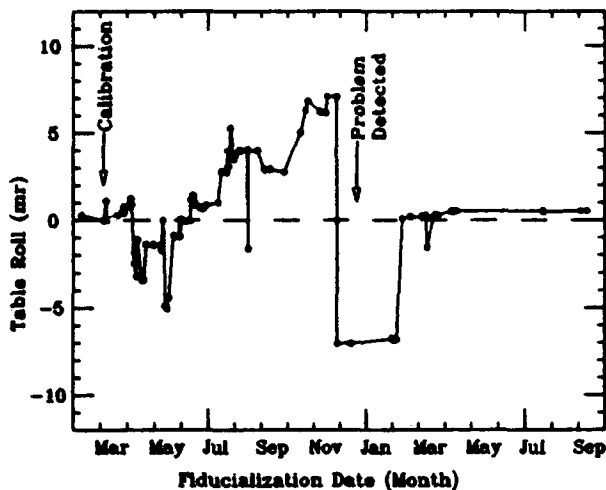


Figure 4: Roll of the HA table as a function of time of quad fiducializations between 1990 and 1992.

the plate with a precision level and permanently attached it to the table. Prior to each quad fiducialisation, the plate was leveled with a precision level, thus ensuring the correct orientation of the table. However, there always were some residual rotations which were corrected in the software.

When the surveying part of the fiducialisation of a quad was completed, the coordinates of the quad survey targets were determined in the table coordinate system by using the survey data and by keeping the calibration coordinates of the 11 table targets (control coordinates) fixed; this step assumes that the table orientation stayed unchanged since the calibration. Since the quads were leveled during the survey, any residual rotation of the table introduced during the mechanical alignment manifested itself as a rotation of the quad in the opposite direction. Denote the coordinates of the  $i^{\text{th}}$  survey target on the quad in the table "object" coordinate system as  $X_o = (x_o^i, y_o^i, z_o^i)$  and the amount of rotation as  $R(\text{oll})$  and  $P(\text{itch})$ . In order to determine the true orientation of the table, we performed a bundle adjustment in the "local" coordinate system of the control theodolite and calculated a set of coordinates for each quad survey target denoted as  $X_l = (x_l^i, y_l^i, z_l^i)$ . Using a 9-parameter coordinate transformation from SLAC between these two sets of coordinate systems we calculated the transformation matrix including  $R$  and  $P$  angles. The rotation angles always were determined with no ambiguity to better than 0.01 degrees. Figure 4. shows a history profile of the the table rotation during the period between 1990 to 1992.

The correct coordinates of the quad targets in the quad system  $X_o^c$  were then calculated by a rotation matrix  $\Gamma = [R][P]$  with  $[R]$  and  $[P]$  the normal  $3 \times 3$  rotation matrices:

$$X_o^c = \Gamma X_o$$

with

$$\Gamma = \begin{pmatrix} \cos P & 0 & \sin P \\ + \sin R \sin P & \cos R & - \sin R \cos P \\ - \cos R \sin P & \sin R & \cos R \cos P \end{pmatrix}$$

The process was automated by a Fortran code which manipulated the coordinate database and performed all the transformations.

## 4 Commissioning Results

The SHR is undergoing its completion and commissioning phase. In March of this year and on the first day of commissioning of the ring lattice, electron beams were stored for as long as 20 ms which corresponds to over 30,000 turns before it was lost due to synchrotron radiation loss with no RF cavity in the ring. With one turn injection, beam currents as high as 40 mA were stored later, meeting the design goal for 1-turn injection.

## 5 Conclusions

We have developed and executed a comprehensive survey and alignment program for controlling the roll and pitch of the SHR quadrupoles. The residual rotations were nulled by correcting the coordinate database, which was based on a fiducialization of individual quads using a harmonic analyser table insensitive to small rotations. The database correction process was automated and the alignment of all 94 SHR quads has been completed to  $\sim \pm 0.25\text{mm}$ . The initial commissioning of the beam verified the success of the handling of the roll.

## References

- [1] J.B. Flanz et al., Proceedings of the 1989 IEEE Particle Accelerator Conference, March 20-23, 1989, p.34.
- [2] M. Farkhondeh et al., Proceedings of the 1993 IEEE Particle Accelerator Conference, May17-21, 1993.
- [3] M. Farkhondeh et al., Proceedings of the 1991 IEEE Particle Accelerator Conference, May17-21, 1991 p.634.
- [4] J.D. Zumbro et al., Proceedings of the 1991 IEEE Particle Accelerator Conference, May17-21, 1991 P.2125.
- [5] A PC-based acquisition and analysis software system for 3-dimensional survey and bundle adjustment, Bernard Bell, Proceedings of the First International Workshop on Accelerator Alignment, July31-August 2, 1989 p. 162, SLAC-PUB-375.
- [6] Bundle Adjustments and Tri-dimensional Coordinate Determination, SLAC-PUB-4717.

# Survey and Alignment of the MIT-Bates South Hall Ring\*

M. Farkhondeh, K. A. Dow, W. W. Sapp and D. R. Tieger

Massachusetts Institute of Technology  
Bates Linear Accelerator Center  
Middleton, MA 01949.

## Abstract

The South Hall Ring (SHR) is a pulse storage/stretcher ring with a circumference of 190m. The complex contains over 200 magnetic elements, most of which must be positioned to tight tolerances to achieve efficient injection and extraction and to obtain storage times of several seconds for internal targets. In particular, the lattice quadrupoles have transverse position tolerances of  $\pm 100$  microns magnet-to-magnet, and the circumference has a tolerance of  $\pm 5$ mm. For the survey and alignment of the ring, we have used automated data capture, data flow and database generation. Alignment of all magnets to approximately  $\pm 1/4$  mm has been completed. The final survey followed by a smoothing of the lattice will begin soon. The present status and issues of the survey and alignment program will be presented, along with the latest alignment aspects of the beam test results.

## 1 Introduction

The SHR, currently under commissioning, will be a high intensity pulse stretcher facility providing high quality cw electron beams with energies between 0.3 and 1.0 GeV. It can be operated in storage mode for internal target experiments and in extraction mode for more conventional experiments. A detailed description of the ring is given in ref. [1]. A plan view of the ring is shown in Fig. 1 and a list of positioning tolerances is given in Table 1.

The design requirements of high quality storage rings demand tight tolerances on the positioning of the adjacent magnets as well as on the overall circumference of the ring. To accomplish this task two options were available: conventional optical tooling and a triangulation system using a database. We adopted triangulation heavily relying on a database, software and automated data capture and data flow with an emphasis on redundancy. Our primary source for software and consulting has been the SLAC alignment group. The survey and alignment of the SHR is based on a network of floor monuments to which all the components are referenced. For data processing, storage and communi-

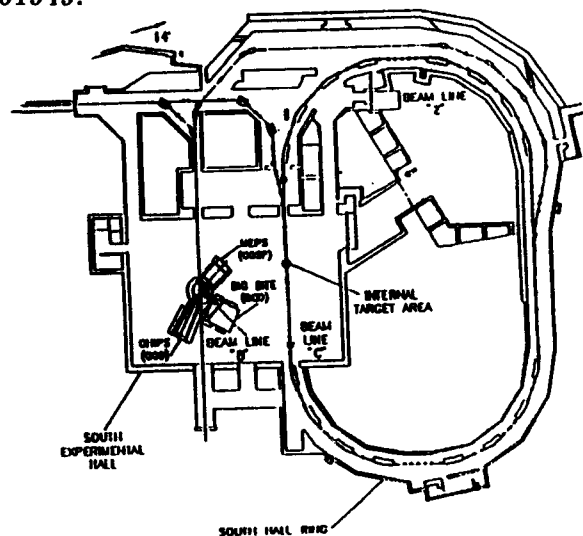


Figure 1: South Hall Ring Complex.

cation we used a customized version of PC-GEONET [2] from SLAC.

The main sources of errors in achieving these design goals are network errors, fiducialization, final survey and smoothing.

Table I  
SHR Alignment Tolerances

Element	Quantity	Tolerance	
		X/Y mm	Roll mr
Quads	128	0.1	2.0
Ring Dipoles	16	0.5	0.7
Dipoles	18	0.5	2.0
Sextupoles	32	0.2	2.0
Octupoles	2	0.2	2.0
Septa	4	0.1	2.0
Kickers	2	0.3	2.0

## 2 Adjustment Systems and Survey Instruments

Whenever possible, three point supports were used for all components and their stands. For adjustment, we adopted the LBL 6-strut system for all but the heavier dipoles,

\*Work supported in part by DOE contract DE-AC02-76ER03069.

which used three struts and three jacks. The 16 main benders have their own built-in adjustment and elevation system. The strut system provided essentially independent adjustments in X, Y and Z except for the short sextupoles, for which some coupling was evident. Motions of more than  $\sim 5$  mm were provided by coarse adjustment systems consisting of machined stainless steel plates and push screws.

Our survey equipment included two Kern electronic theodolites (E2 and E21), a Wild NL optical plummet, a Wild N3 optical level with 10 mm micrometer, a calibrated invar scale kit, a 2m elevation rod, two HP110 laptops, a portable and a stationary 386 PC. For centering systems, we used SLAC type aluminum tripods, three sets of the CERN forced centering system, and SLAC adaptors for merging Kern plates and the CERN system. SLAC-style slanted targets with K&E bullseye targets were used throughout. During the initial survey of the geodetic network, we used an ME5000 distance meter (on loan) from CEBAF.

### 3 SHR Geodetic Network System

For the SHR we have chosen to separate the horizontal coordinates (X,Z) from the vertical (Y) direction. The horizontal locations of all position-sensitive elements were referenced to a global SHR coordinate system. The origin of this geodetic system as shown in Fig. 1 is at the intersection of the west straight and north straight sections. The transverse network consisted of over 80 floor monuments which provided sufficient observation points to overcome sight line obstructions caused by the large benders. The network was surveyed in the Fall of 1990 one year after the completion of the conventional construction and before any floor occupancy. The survey was accomplished with an ME5000 and two theodolites and with help from SLAC and CEBAF. An optimum measurement plan was developed using the GEONET simulation facility. A subsequent measurement of a subset of these floor monuments and some fiducials from the existing beam line was necessary for relating the orientation of the SHR network to the rest of the complex. Fig. 2 shows the monuments and their absolute error ellipses; error propagation caused the enlargement of ellipses further away from the origin. The relative errors are smaller than the absolute errors and have a more uniform size than the absolute ones shown.

A smaller geodetic network of floor monuments was installed for alignment of the Energy Compression System (ECS) dipoles and quads at the end of the linac. This network was surveyed using the SLAC Industrial Measurement System (SIMS) [3], a PC-based bundle adjustment [4] and triangulation system integrated with multiple electronic theodolites.

The SHR and ECS also have a network of elevation monuments for vertical references. This network was periodically resurveyed for seasonal changes in the floor elevation. We have noticed seasonal elevation changes of up to

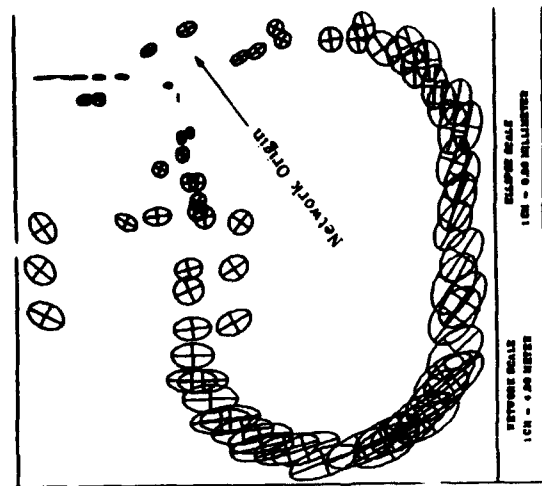


Figure 2: Absolute error ellipses for the SHR geodetic network.

0.8mm over a  $\sim 60$ m long distance in a six month period, well within the tolerances required by relative positioning.

### 4 Fiducialization

The magnetic/mechanical axes of each element were related to several fixed fiducial targets on the element as follows. Survey targets were inserted into drill bushings coarsely positioned on the top surface of the element and their positions were precisely measured using SIMS as described in ref. [5] and [6]. For the dipoles, fixtures were used to precisely position targets in the midplanes and on the design orbit. The coordinates of magnet targets, fixture targets, invar rod targets and some auxiliary targets were measured in the coordinate system of one of the theodolites positioned close to the center of the magnet. A coordinate transformation from the theodolite system to the element system completed the fiducialization. Normally, the transverse positions of survey targets were determined to better than  $50 \mu\text{m}$ .

### 5 Database and "Ideal Coordinates"

The design position of the magnetic axes of each element in the SHR global coordinate system was specified by TRANSPORT optics codes and the output files were transferred to the PC-GEONET. Because the fiducialization files contain the relation between the coordinates of the fixed survey targets and the magnetic axes, combining the two output files with proper rotation of the fiducialization data determined the ideal location of each survey target in the global SHR system. These "ideal coordinates" were actually calculated using customized Fortran codes which also included corrections for dipoles whose measured effective field length was different than the nominal value used

in the TRANSPORT calculations. The ideal coordinates were integrated into the database for use with various survey and alignment software systems.

## 6 Alignment Using Intersection

For alignment of ring elements to an accuracy of  $\sim 1/4$ mm we used triangulation based on intersection of sightlines from two theodolites. This was facilitated by an interactive software package (CLASH) [7] which provided communication between two theodolites and a laptop loaded with the ideal coordinates of the survey targets and the monuments. The accuracy achieved with CLASH is strongly geometry dependent. After a magnet was positioned to within a few centimeters of its ideal location using conventional methods, it was precisely leveled using an optical level and the CLASH database. For horizontal positioning, two theodolites were positioned precisely over two monuments at optimum locations near the element, and CLASH calculated the direction of theodolites pointing at the ideal target. The theodolites were set to those directions and the magnet was moved until the target was at the intersection of the two lines of sight. At the end of this iterative process involving several targets, all survey targets were within  $\pm 1/4$ mm of their ideal positions.

## 7 Final Survey and Smoothing

The remaining tasks are the final survey of every element and the ensuing smoothing of the beam trajectory.

**Final Survey**—Plans are underway for a complete precision survey of the SHR elements with SIMS, simultaneously determining both horizontal and vertical coordinates of all survey targets. The survey includes both the network monuments and the survey targets on the individual components. Overlapping regions will be surveyed in adjacent sections ensuring continuity and redundancy. The bundle adjustment will be done by keeping the nominal coordinates of two endpoint survey targets in a region fixed and letting the monument coordinates vary. If the fixed points are not at their ideal positions, this method can cause a small wrinkle in the beam line, but relative coordinate determinations of adjacent elements will be ensured.

**Smoothing**—The coordinates of each element determined in the bundle adjustment will be used for determining the positional adjustment necessary for creating a "smooth" beam trajectory. We have customized the SLAC smoothing software [8] which is based on a Principle Curves and Surfaces algorithm [9]; this will allow a minimization of the number and the amount of movements while satisfying the  $\pm 100\mu\text{m}$  element-to-element tolerances for the quadrupoles. All necessary software has been written and survey work will begin later this year. The movements will then be made and monitored with three sets of digital dial gages registering three tooling balls on each magnet.

## 8 Commissioning Results

In March of this year on the first day of commissioning of the ring lattice, electron beams were stored for as long as 20 ms corresponding to over 30,000 turns, before they were lost due to synchrotron radiation with no RF cavity in the ring.

## 9 Conclusions

We have developed and executed a comprehensive survey and alignment plan for the SHR by adopting computer based geodetic systems. The quality of our alignment work has been tested in an ongoing commissioning of the ring by successfully storing beams without any need for repositioning a single element or excessive steering. The final survey and smoothing plans have been finalized and will begin soon. Considering all sources of errors in our survey and alignment procedure, we are aiming for overall relative positional uncertainties of  $\pm 0.15$ mm for the quads. The authors would like to thank the SLAC alignment group, particularly Horst Friedsam, now at the Argonne Advanced Photon Source.

## References

- [1] J.B. Flans et al., Proceedings of the 1989 IEEE Particle Accelerator Conference, March 20-23, 1989, p.34.
- [2] H. Friedsam, R. Pushor, and R. Ruland, SLAC-PUB-4142, 1986
- [3] Bernard Bell, Proceedings of the First International Workshop on Accelerator Alignment, July 31-August 2, 1989 p. 162, SLAC-PUB-375.
- [4] Bundle Adjustments and Tri-dimensional Coordinate Determination, SLAC-PUB-4717.
- [5] M. Farkhondeh et al., Proceedings of the 1991 IEEE Particle Accelerator Conference, May 17-21, 1991 p.634
- [6] M. Farkhondeh et al., Proceedings of the 1993 IEEE Particle Accelerator Conference, May 17-21, 1993, Section Jc72.
- [7] A PC based alignment software using intersection with two theodolites, written by Bernard Bell, SLAC Alignment Group.
- [8] Horst Friedsam, Will Oren, Proceedings of the First International Workshop on Accelerator Alignment, July 31-August 2, 1989, p.152, SLAC-PUB-375.
- [9] Principle Curves and Surfaces, SLAC-PUB-276.

# Magnetic Measurement, Fiducialization and Alignment of Large Dipoles for the MIT-Bates SHR\*

M. Farkhondeh, K. A. Dow, W. W. Sapp and J. D. Zumbro †

Massachusetts Institute of Technology  
Bates Linear Accelerator Center  
Middleton, MA 01949

## Abstract

The South Hall Ring (SHR) lattice uses sixteen large dipoles originally designed for the Princeton-Pennsylvania Accelerator. These 3.6m long, 30 ton dipoles have bend radii of over 9 meters and gaps of only 7.6cm. The requirement that the four dipoles be powered in series, as well as other restrictions, resulted in magnetic and mechanical alignment tolerances which are very demanding for magnets of this size and shape. Two independent methods were used for measurement of the field integral along the design orbit. Field integrals were measured on all dipoles using a long coil excited by ramping the field. On four dipoles, the integrals were also measured using Hall probes moving along the design orbit. The techniques and results will be presented. The fiducialization of these dipoles was accomplished using precision-machined fixtures and the SLAC computer-aided Industrial Measurement System. Position corrections due to different measured effective lengths of these magnets will be discussed, and details of fiducialization and alignment will be presented.

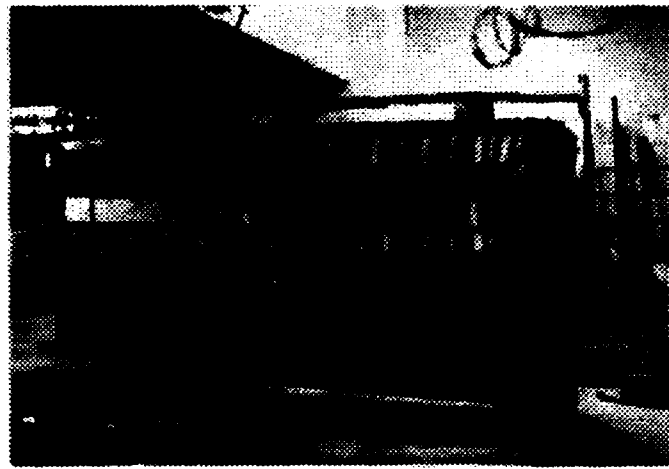


Figure 1: One SHR dipole.

## 1 Introduction

The 190 meter circumference SHR, currently under commissioning, will be a high intensity pulse stretcher facility providing high quality cw electron beams with energies between 0.3 and 1.0 GeV. It can be operated in storage mode for internal target experiments and in extraction mode for more conventional experiments. A detailed description of the ring is given in [1].

The 360 degrees of bend in the ring are provided by 16 C-profile laminated dipole magnets, each 3.6m long with a 7.6cm gap and a nominal  $n$  value of 1/2; one such magnet is shown in figure 1. The yoke of each magnet consists of c-shaped laminates of high  $\mu$  steel with the pole tip field defined by crenelated laminated pole blocks each 2 inches wide. The gap is determined by a vertical spacer plate separating the upper and lower pole pieces; the upper pole pieces are forced onto the spacer plate by pressurized

hoses. A  $\pm 2.2\text{mr}$  relative pole tip inclination produces an  $n = 1/2$  magnet. The pole blocks introduce some small gap variations along the length of the magnet resulting in field variations of  $\pm 0.07\%$  from block to block. The design requirements and magnetic tolerances for these dipoles are summarized in Table I.

Table I  
Magnetic Tolerances

Quantity	Value	Tolerance
Effective length	3.591m	1mm
Gap	7.6cm	0.75mm
Bend angle	22.5deg	0.1mr
Eff. Field Boundary	-	1mm
Field settability	-	$10^{-3}$
Field stability	long term	$10^{-4}$
Field stability	short term	$10^{-5}$

The tolerance on the effective field length is very tight because the beam passes through these dipoles many times and the effective field length enters the overall circumference of the ring which has a tolerance of 5mm. Each of these dipoles has been magnetically measured, fiducialized and aligned.

\*Work supported in part by DOE contract DE-AC02-76ER03069.

†Current Address: Los Alamos National Laboratory, Los Alamos, NM, 87545.

## 2 Magnetic Measurements

After extensive studies two measurement techniques were developed: stepping a Hall probe along the design orbit to produce a field map, and measuring the EMF induced by a ramped field in a coil centered about the design orbit. Two-dimensional field maps with the XZ table provided the  $\int B \cdot dl$  along the beam trajectory,  $n$  value, and an indication of field variations in the uniform region. The long coil measurement determined the effective length along the nominal beam path.

### 2.1 XZ Table Measurement

A two-dimensional mapping table (on loan from NIST) was developed for field measurements using temperature-compensated Hall probes at predetermined points on a plane [8]. Two axes of motion of the table are instrumented and controlled by computer via CAMAC; the vertical axis is controlled manually by a micrometer stage.

The dipoles are so long that the table had to be placed at each end of the magnet. Field maps were made using a long arm holding two Hall probes separated by 54cm, and a complete map of a dipole required joining the four measurements from the two Hall probes from each end of the magnet. This required a good cycling procedure for the magnet, a stable power supply, and an overlap in mapping points of the two probes. The XZ table origin was related to a reference point in the magnet; we chose the intersection of the design orbit with a line parallel to the first lamination in the end pole block. This point was optically referenced using a precision machined fixture holding a survey target. The same fixture was used in the fiducialization of the magnet. The transverse origin was determined using a magnetic blade attached to an aluminum block of precise length with its end registered against the inner land of the upper pole tip. Radial field maps confirmed the design  $n$  value of 1/2; the higher multipoles were consistent with zero in the uniform field region and had high values near the pole faces at each end of the magnet.

### 2.2 Long Coil Measurements

All 16 dipoles were magnetically measured using the long coil. The long coil consists of an arc-shaped aluminum plate with an arc length equal to the physical length of the magnet arc plus 10 gaps, with grooves for the closed loop signal wires. When installed in the magnet for measurement, the long coil form positioned a flat coil of width  $2.055 \pm 0.004$  inches on the midplane, centered about the design orbit. As the current was ramped from 0 to a set point (or from a set point to 0), an EMF was induced in the coil; magnetic flux or the time integral of the induced voltage  $\Phi = \int V dt$  is proportional to the area of the coil and the change in the field,

$$\int V \cdot dt = \int_{B=B_i}^{B=B_f} A \cdot dB = W \cdot L_{eff} \cdot (B_i - B_f)$$

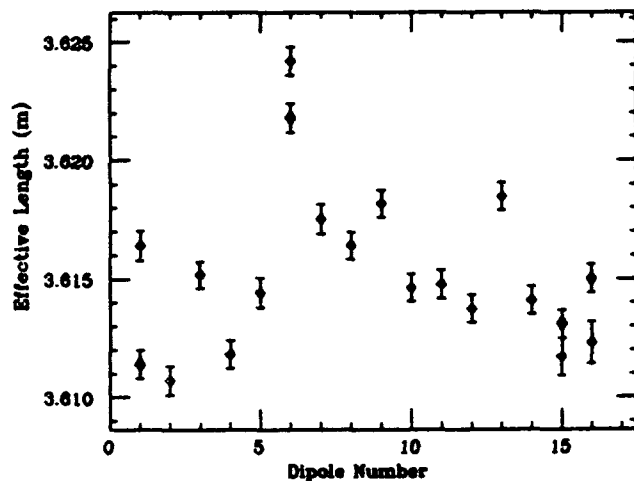


Figure 2: Effective field length for each dipole (solid points are XZ results, open points are Long Coil results).

where  $W$  is the average width of the coil and  $L_{eff}$  is the effective magnetic length of the magnet. The 6 turns of wire in the coil produced a 5 mV signal for a 5 Amp/sec ramp. The field on the design orbit was measured at one location by two NMR probes inserted in a machined slot in the form. Prior to each measurement, the Dymec 2401-A Integrating Digital Voltmeter was calibrated.

The largest uncertainty in determining the effective length was the uncertainty in the average width of the coil, resulting from variations in the placement of the wires in the grooves.

### 2.3 Results and Comparison of the Two Methods

The XZ maps were more time consuming than the long coil measurements and required complicated off-line analysis for deriving the integrated field. The XZ map was used for absolute measurements while the long coil, due to the uncertainty in the absolute value of the coil width, was used for relative measurements of the magnets. Figure 2 shows  $L_{eff}$  for all 16 dipoles for both techniques.

The absolute value of the field integral was measured with the XZ table to  $5 \times 10^{-1}$  to  $1 \times 10^{-3}$  depending primarily on the Hall probe scale used (in other words, depending on the magnet current) and the absolute value of the effective length was measured to  $3 \times 10^{-1}$ . Field integrals were measured at 4 currents corresponding to a range of beam energies between 0.3 and 1.1 GeV. The absolute and relative uncertainties in the long coil measurements of the effective length are  $8 \times 10^{-1}$  and  $3 \times 10^{-1}$ . A polynomial fit to the NMR probe field as a function of magnet current for the long coil data sets produced coefficients which are used by the SHR control system to set the magnets for a given beam energy; the control system also takes into account the varying bend radii  $\rho = L_{eff}/(\pi/8)$  of the magnets.

### 3 Fiducialization

In the fiducialization process, the magnetic and mechanical axes of each magnet were related to five fixed fiducial targets on top of the magnet. Precision fixtures holding survey targets on the midplane were positioned on the pole tip at the edge of last lamination block at either end of the magnet such that one of the targets in each fixture was on the design orbit. We defined the midpoint between these two targets as the magnet origin.

For fiducializing all SHR magnets we used the SLAC Industrial Measurement System (SIMS) [2], with two Kern electronic theodolites. With the help of simulation software, six theodolite locations surrounding a dipole were chosen to achieve maximum sensitivity to both vertical and transverse locations of the survey targets on the magnet and on the design orbit.

The SIMS bundle adjustment software [3] generated the coordinates of magnet targets, fixture targets, targets on either end of a calibrated invar rod [4], and some auxiliary targets with respect to the coordinate system of one of the theodolites positioned close to the center of the magnet. A coordinate transformation from the theodolite system to the origin of the magnet was performed using software from the SLAC Alignment Group. The coordinates of the five fixed targets were stored for the next step, alignment.

The magnet origin found in the fiducialization procedure must be adjusted to account for the different measured effective lengths of the magnets. Each magnet must be positioned such that an electron of the proper energy is bent by  $22.5^\circ$  and its path intercepts the fiducialization targets on the design orbit. Thus, a suitable axis for these dipoles is a line connecting the effective field boundaries of the magnets which are by requirement on an arc of subtended angle  $\frac{\pi}{n}$ . A transverse shift of this axis is necessary because the effective field boundary is further outside the magnet than the design value.

### 4 Alignment

For the SHR survey and alignment [6], we adapted a computer-assisted database survey and alignment system from SLAC [7] which provided sufficient redundancy and error analysis did not require extensive experience with optical tooling techniques. The main steps are:

1. Survey of the network of SIIR floor monuments,
2. Calculation of ideal coordinates of magnet survey targets,
3. Integration of 1) and 2) into a database, and
4. Alignment of magnets using the database and intersecting sight lines of electronic theodolites.

The SHR has a network of over 80 floor monuments whose locations in the ring coordinate system are part of the database. The ideal coordinates of survey targets on

a magnet in the ring coordinate system are achieved by merging the TRANSPORT output of magnet location and the result of the fiducialization. A magnet was positioned to within a few centimeters of its ideal location using conventional methods, then precisely aligned using the monuments and the database. A Wild N3 optical level, 2m survey rod and a network of elevation rivets were used to level and set the magnet at its ideal height. With two theodolites positioned precisely on monuments at optimum locations near a dipole, the CLASH interactive software from SLAC [5] calculated the direction to point the theodolites for each target. In an iterative process, the theodolites were set to the direction for each target, and the magnet moved until that target was at the intersection of the two lines of sight; then the height of the magnet was corrected. In the end, all five targets were within 1/4mm of their ideal positions.

### 5 Conclusions

We have developed and executed procedures for precision magnetic measurements and survey and alignment of 16 very large dipoles for the SHR. The results of the magnetic measurements have been implemented in the ring control system. The success of the measurements and the alignments was confirmed by a successful storage of the beam on the first day of commissioning, for a time limited only by energy losses due to synchrotron radiation, as the cw RF cavity was not installed.

### References

- [1] J.B. Flans et al., Proceedings of the 1989 IEEE Particle Accelerator Conference, March 20-23, 1989, p.34.
- [2] A PC-based acquisition and analysis software system developed at SLAC for tri-dimensional survey and bundle adjustment, SLAC-PUB-375.
- [3] Bundle Adjustments and Tri-dimensional Coordinate Determination, SLAC-PUB-4717.
- [4] Model # 803M, Invar scale kit, Brunson Instrument, Kansas City, Mo.
- [5] PC-based alignment software using intersecting sight lines with two theodolites, developed by Bernard Bell, SLAC Alignment Group.
- [6] M. Farkhondeh et al., Proceedings of the 1993 IEEE Particle Accelerator Conference, May 17-20, 1993.
- [7] H. Friedsam, R. Pushor and R. Ruland, SLAC-PUB-4142, 1986.
- [8] M. Farkhondeh et al., Bates Internal Report B/SHR 90-05.

# Pulsed Taut-Wire Measurement of the Magnetic Alignment of the ITS Induction Cells\*

J.G.Melton, M.J.Burns, D.J.Honabger  
Los Alamos National Laboratory  
Los Alamos, NM 87545

## Abstract

The mechanical and magnetic alignment of the first eight induction-cell, solenoid magnets of the Integrated Test Stand (ITS) for the Dual-Axis Radiographic Hydrodynamic Test (DARHT) facility were measured by observing the deflection of a fine, taut wire carrying a pulsed current. To achieve the required alignment (less than 0.25 mm offset and less than 5 mrad tilt), the magnet design uses quadrifilar windings and iron field-smoothing rings. After detailed measurements of each solenoid magnet, the cells are assembled and then mechanically aligned using a laser and an alignment target moved along the cell centerline. After the cells are in final position, the pulsed wire method is used to verify the magnetic alignment. The measurements show an average offset of the magnetic axes from the mechanical axis of 0.15 mm, with a maximum offset of 0.3 mm. The average tilt of the magnetic axes was 0.7 mrad with a maximum tilt of 1.4 mrad. Tilts are corrected to less than 0.3 mrad, using dipole trim magnets assembled into each cell. Correction is limited by power supply resolution and by background noise.

## I. INTRODUCTION

The Los Alamos ITS electron beam accelerator is a prototype of the DARHT facility and consists of a 4-MV injector and eight 250-kV linear induction cells. Each induction cell contains a solenoidal focusing magnet and x- and y-dipole steering magnets. A cross-sectional view of the induction cell is shown in Fig. 1. Special care was taken in the cell design to control mechanical tolerances so that good mechanical alignment could be achieved. The magnets are referenced with respect to the beam tube, so a good mechanical alignment should result in a good magnetic alignment. The mechanical specification is for the offsets of the individual cells to be 0.25 mm or less and for the tilts to be 5 mrad or less.

The magnet windings are quadrifilar to reduce field errors produced by winding errors and current feeds. Between the magnets and the beam tube are six axially distributed, iron homogenizer rings to further reduce field errors caused by winding errors.<sup>1,2</sup>

The cells are first assembled and mechanically aligned in blocks of four in an alignment fixture. The procedure uses a HeNe laser measurement system and a cart that travels along the bore of the induction cells carrying an alignment target. After the initial alignment and assembly, two blocks of four

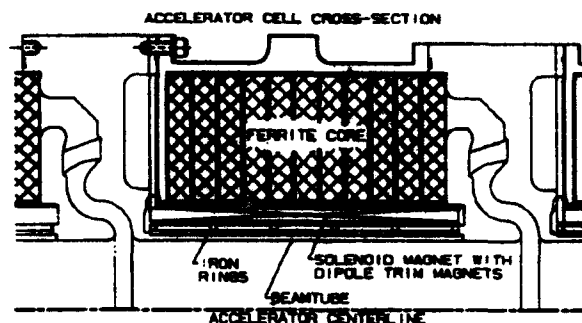


Figure 1. Cross-section of ITS Induction Cell.

cells are moved to their final location and aligned with respect to the injector cathode. The mechanical alignment is measured once again. After final assembly, the pulsed wire method is used to measure and confirm the magnetic alignment.

## II. DESCRIPTION OF THE METHOD

The pulsed taut-wire method of determining magnetic alignment and measuring magnetic field errors has been used by several groups to measure the magnetic fields in accelerator systems.<sup>3,4</sup> Many variations of the basic method have been developed to match the circumstances of the particular experiment. The basic method consists of sending a pulse of current through a taut wire suspended in a steady or quasi-steady magnetic field and observing the motion induced in the wire by the resultant Lorentz force on the wire. If the magnetic field is relatively simple, characteristic patterns of travelling waves are established on the wire that can be easily related to field structure. In particular, the residual magnetic field errors produced by very good solenoidal magnets are typically an offset of the magnetic axis from the mechanical center of the solenoid and a tilt of the magnetic axis from the mechanical axis. The two types of wave patterns produced by these errors are sufficiently different that they can be easily distinguished. Figure 2 shows typical tilt and deflection waveforms before corrections are made. If the fields from several cells are superimposed, however, and if reflections are present due to the ends of the wire, the wave patterns can become too complicated to interpret easily.

Our measurements are done with the induction cells mounted in final position. To accomplish this, we have developed special mounting and positioning fixtures that accurately position the wire with respect to the assembled

\*Work performed under auspices of the U.S. Department of Energy.

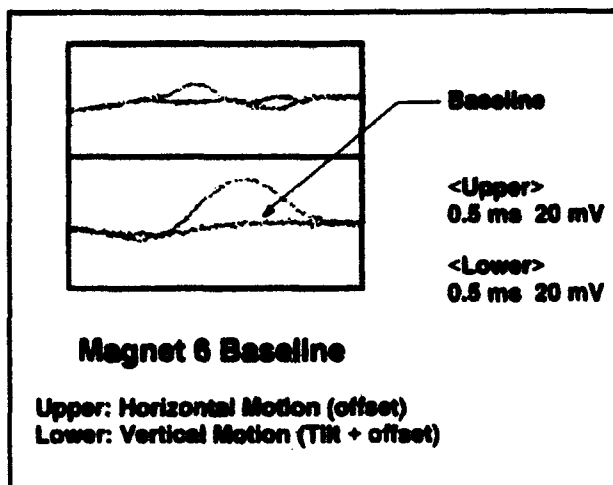


Figure 2. Uncorrected Offset and Tilt Signals

centerline of the cell blocks (to within about 0.05 mm). Also, the measurements must be done with a long wire (over 4 m long) in an acoustically noisy environment, which produces extraneous vibrations in the wire. To subtract these vibrations, we must average over many shots.

Our measurements are made simpler because we only measure the offset of the magnetic axis and correct only for the magnetic tilt. Since we produce a null in the motion detector signal, we do not have to measure the absolute amplitude of the signals. A detailed field map is not produced.

Our procedure consists of the following steps: (1) The wire is carefully tensioned and centered at the centering collars at the two end cells. (2) The optical horizontal and vertical motion detectors and amplifiers are calibrated and set to a region of linear response. (3) Before each cell is examined, a correction is made to the ends of the wire to correct for catenary sag of the wire at the cell of interest. (4) With no power to the magnets of the cell, a zero base line is established for residual room vibrations by applying a pulse of current to the wire and averaging the signal over 20 shots. (5) Current is then applied to the solenoid magnet, the wire is pulsed 20 times, and the averaged waveforms are compared to the reference. (6) The ends of the wire are moved using the x- and y-micrometers until the lack of offset signal indicates the wire is on the magnetic centerline. This measures the solenoid offset. (7) With the wire located on the magnetic centerline, current is applied to the x- and y-dipole steering magnets to null the signals produced by tilt of the solenoid field. (8) The procedure is repeated separately for each cell.

### III. HARDWARE DESCRIPTION

The wire used in these experiments is 0.1-mm-diameter BeCu, 4.2 m long. It is tensioned to about 97% of its breaking strength by a system of low-friction pulleys and suspended fixed weights which hold a constant tension. Elongation of the wire is included in the compensation for catenary sag. Sag is compensated by moving the ends of the wire upward to cause it to pass through the center of the test

cell horizontally and on the mechanical axis.

The ends of the wire are attached to adjustable slides, which can be moved with respect to the fixed mounting fixture by two micrometers on each end controlling horizontal and vertical movement. The mounting fixtures are fixed to the cells at each end by expansion collar arrangements which locate the fixture with respect to the bore of the end cells. Optical detectors to sense vertical and horizontal motion of the wire are mounted on the adjustable slides. Each has independent x- and y-adjustment micrometers. This arrangement allows the detectors to be moved around the centered wire to position the detectors for linear response, and allows the wire to be centered in the beam tube without affecting the detector alignment.

The motion detectors are a pair of orthogonally mounted GaAs LED-phototransistor detector assemblies (Motorola H21A1 9030), amplified by a single operational amplifier. The overall sensitivity of the detector/amplifier circuit is about 50 mV/ $\mu\text{m}$  of deflection. Measured signal levels are 20-50 mV before corrections, corresponding to about 1  $\mu\text{m}$  of deflection at the detector position, and about 5 mV after corrections. Signals produced by room vibrations are typically 20 mV, with a major component at 120 Hz coming mostly from vacuum pumps and ventilation fans.

The current pulse to the wire is supplied by a HP214B Pulse Generator. It produces 0.3 A in the 57- $\Omega$  wire. The current pulse is 1 ms in duration and very square in shape, indicating that the risetime of the current pulse is not limited by the inductance of the wire circuit. The signals are recorded on a LeCroy 9450 oscilloscope that provides real time signal averaging and storage of reference waveforms.

### IV. EXPERIMENTAL PROCEDURE

Before making a series of measurements, the wire is centered in the bore of the two end cells by moving the wire until it makes contact with a straight edge precisely located by locating pins. The straight edge is then rotated 90° to a second set of pins and the wire is moved until contact is made. Contact is detected by electrical continuity. The continuity check has proved to be a very sensitive indicator of contact between the wire and the straight edge positioning tool. It locates the wire to within one wire radius of the line established by the straight edge.

After the wire has been positioned in the center of the beam tube, the detectors are moved with respect to the wire to establish the range of signal and to select an operating point in the center of the linear range. The ends of the wire are then adjusted to compensate for the catenary deflection at the location of the cell under test. Then, with no current applied to the solenoid magnet, an averaged reference base line is recorded. Current is applied to the solenoid magnet of the cell under test, and the averaged signals are compared to the reference waveforms. The ends of the wire are moved to null the deflection signals. Then current is supplied to the x- and y-dipole steering magnets to null the tilt signal. Usually, about

4-12 adjustment steps are required to null all four deflections. A typical set of signals after adjustments have been made to produce a null is shown in Fig. 3.

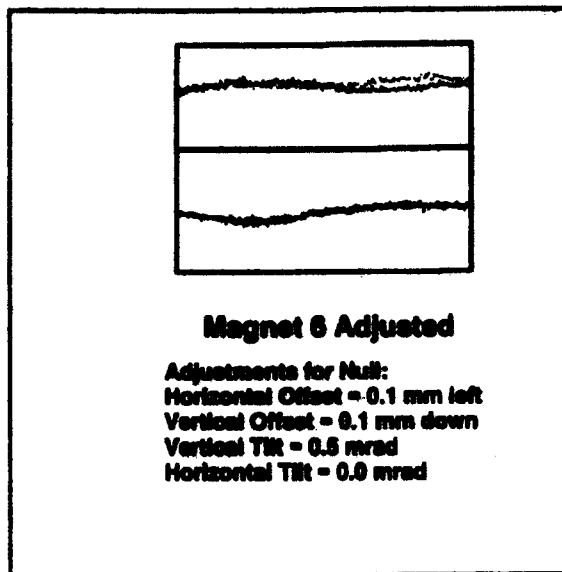


Figure 3. Corrected Deflection Signals

The dipole steering magnet currents needed to correct for tilt are typically very low, about 0.5 A compared to 20 A maximum available from the power supply. Consequently, we are not able to fine tune the steering current better than 0.2 A. However, the full power supply current output could be required if the magnetic tilt were larger. The 20 A current could compensate for 30 mrad tilt.

## V. EXPERIMENTAL RESULTS

The results of the alignment measurements on the eight cells are summarized in Fig. 4. The vectors drawn from each point indicate the tilt of the magnetic axis for that cell. The vectors are scaled to indicate the deflection that occurs over the length of the cell (50 cm). The average value of the radial offset of the eight cells is 0.15 mm, and the maximum offset is 0.3 mm for cell #4. The average tilt of the magnetic axes is 0.7 mrad and the maximum tilt is 1.4 mrad for cell #8.

The accuracy of the method is limited at present by background noise, and by the limit in accuracy to which we can set the steering magnet power supplies. We estimate the accuracy of the method to be about  $\pm 0.1$  mm and  $\pm 0.3$  mrad. Hence, after corrections are made for tilt, there could be a residual tilt of 0.3 mrad. This residual tilt error corresponds to a dipole field of about 0.34 G.

After performing the measurements described here, we tried to improve the signal-to-noise ratio (hence the "accuracy" of the method) by using a larger current pulse through the wire. The 0.3 A pulse was increased to 10 A. While this increased the signal levels and reduced the number of shots over which we had to average, it did not significantly

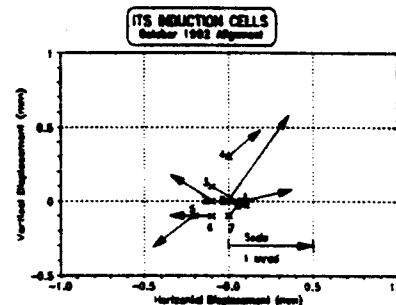


Figure 4. Uncorrected Offsets and Tilts

increase the accuracy with which we could detect the signal null. It introduced the additional complication of frequent wire breakages because of increased mechanical and thermal stress.

## VI. SUMMARY OF RESULTS

The pulsed taut wire method was used to measure the magnetic alignment of the eight induction cells of the ITS facility. The offsets and tilts of the magnetic axes were within the design specification. The design approach taken, to control the magnetic alignment by careful control of mechanical tolerances and assembly, and to reduce the effects of winding errors by using multifilar windings and using field homogenizing iron rings, has produced acceptable field errors. We are developing improved pulsed-wire methods to apply to each of the DARHT accelerators, which will be more than 25 m long.

## VII. REFERENCES

- [1] Michael Burns, et al., "Magnet Design for the DARHT Linear Induction Accelerators," *Conference Record of the 1991 IEEE Particle Accelerator Conference*, 2110.
- [2] M. J. Burns, et al., "Technology Demonstration for the DARHT Linear Induction Accelerators," *9th International Conference on High Power Particle Beams*, Washington, D.C., May, 1992. Also, Los Alamos Report LA-UR-92-1675.
- [3] F. J. Deadrick, L. V. Griffith, "Progress in ETA-II Magnetic Field Alignment Using Stretched Wire and Low Energy Electron Beam Techniques," *1990 LINAC Conference*, Albuquerque, NM, Sept. 1990.
- [4] C. M. Fortgang, et al., "Pulsed Taut-Wire Alignment of Multiple Permanent Magnet Quadrupoles," *1990 LINAC Conference*, Albuquerque, NM, Sept. 1990.

# APPLICATION OF PRECISION MECHANICAL ENGINEERING TECHNIQUES TO THE DESIGN OF A MODERATE ENERGY BEAM TRANSPORT FOR THE FAA EXPLOSIVE DETECTION SYSTEM\*

R. Lujan and K. Christensen  
Los Alamos National Laboratory  
P.O. Box 1663, Los Alamos, NM 87545 USA

## Abstract

This paper discusses the application of precision mounting and alignment techniques to a moderate energy beam transport system (MEBT) used on the exit of a 1.75 MeV RFQ. While frequently found in optical systems, techniques such as kinematic mounting, and degree-of-freedom decoupling, are not as widely used for accelerator components. The MEBT consists of one permanent magnet quadrupole, four electro magnet quadrupoles, and one debuncher cavity. Included in the paper are discussions of design and fabrication considerations as well as, installation, alignment and operations experience during the successful implementation on a working accelerator.

## I. INTRODUCTION

Los Alamos Group N-2 (Advanced Nuclear Technology) has undertaken a project to prototype an accelerator-based system for explosive detection using the nuclear resonance absorption technique. We were asked to provide the mechanical design for a beam transport starting at the end of the 1.75-MeV radio frequency quadrupole (RFQ) to the target location, some 166 cm downstream. The physics design of this moderate energy beam transport (MEBT) called for one rare earth permanent magnet quadrupole (PMQ) at the exit of the RFQ, followed by two electro-magnet quadrupoles (EMQ's), a debuncher cavity, and finally two more EMQ's.

Our goal was to provide a robust mechanical design that would at the same time employ some of the precision alignment techniques found in optical systems for the positioning of the MEBT components in five of the six degrees-of-freedom.

In order to minimize alignment time we attempted wherever possible, to decouple the degrees-of-freedom, thereby eliminating the time consuming "cross talk" between the axes.

## II. DESIGN

The PMQ used for focusing the beam was mounted directly onto the downstream vacuum cover of the RFQ.

\*Work supported by the Federal Aviation Administration under the auspices of the United States Department of Energy.

The four EMQ's and the debuncher cavity were mounted on an adjustable support stand. The support stand consists of a 1.25 inch thick aluminum plate bolted to a structural steel frame adjustable in X, Y, and Z. The MEBT components were aligned to the theoretical beam line within a diametrical tolerance of .002 inch and they were aligned azimuthally to the RFQ within 1.0°. A target assembly, provided by the experimenter, was attached to the downstream end of the accelerator. Figure 1 shows a schematic of the accelerator with the target assembly attached.

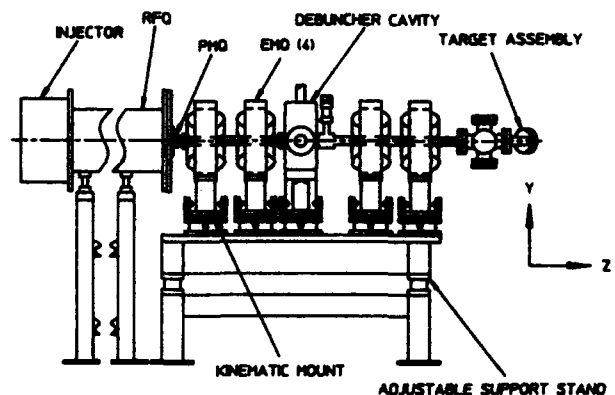


Fig. 1. Schematic of Accelerator.

Several mechanical techniques were used to fulfill the alignment requirements of the accelerator components. The PMQ was held in the center of its holder with a Tolerance Ring.<sup>†</sup> The azimuthal position of the PMQ was fixed by pinning it to the holder using a standard .060 inch diameter dowel pin. Another pair of standard .125 inch diameter dowel pins were used to orient the PMQ and holder assembly to the RFQ end flange.

The EMQ's were attached to kinematic mounts that were designed to allow for adjustment in the Y direction. The kinematic mounts used hardened steel elements for a cone, vee groove, and flat that mated with commercially available hardened steel tooling balls. The relative position in Y of the tooling balls with respect to the magnetic center of the EMQ was adjustable. The tooling balls were each

<sup>†</sup>A product of USA Tolerance Rings, West Trenton, New Jersey.

attached to the end of a 5/8-24 threaded shaft which was preloaded against a base plate. A dial indicator of .001 inch graduations was mounted near each of the threaded shafts. The dial indicators measured the relative vertical displacement of the EMQ. By rotating the three threaded shafts until each dial showed the same amount of movement, true vertical motion was ensured. By using this system, it was possible to resolve the vertical motion of the EMQ to a resolution of less than .001 inch.

To accomplish roll adjustment, each EMQ was mounted in a vee block and the EMQ was rotated with a lever arm attached to the magnet ring. Hardened steel wearing surfaces were attached to both the EMQ and to the vee block to minimize wear and to ensure precise rotation. Rotation was actuated by turning a commercially available threaded ball foot against one side of the lever arm. To eliminate lash, the lever arm was preloaded against the ball with a commercially available spring plunger.

To provide adjustment in the X direction, the assembly was mounted on a commercially available dovetail slide whose axis of travel is perpendicular to the beam direction. Figure 2 shows the EMQ and its mounting system.

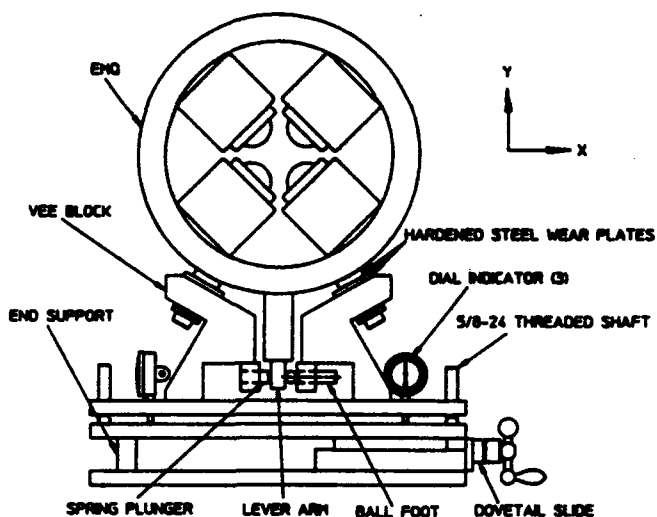


Fig. 2. EMQ and Mounting System.

The debuncher cavity was also mounted on a system similar to that of the EMQ's. Provisions for roll adjustment to the debuncher cavity were not necessary.

### III. FABRICATION

After final magnetic mapping of the permanent magnet quadrupole, a .0643-.0663 groove was machined into its outer aluminum jacket. The groove position was 45° from the north pole of the magnet. Subsequently, the fit and position of the mating dowel pin in the holder were carefully specified, as were the mating conditions of the outer dowel pins for assembly with the end flange of the

RFQ. As a result, fabrication of the PMQ holder was simplified, and the need for active alignment of the PMQ was eliminated. Figure 3 shows the tolerance specifications assigned to the PMQ holder.

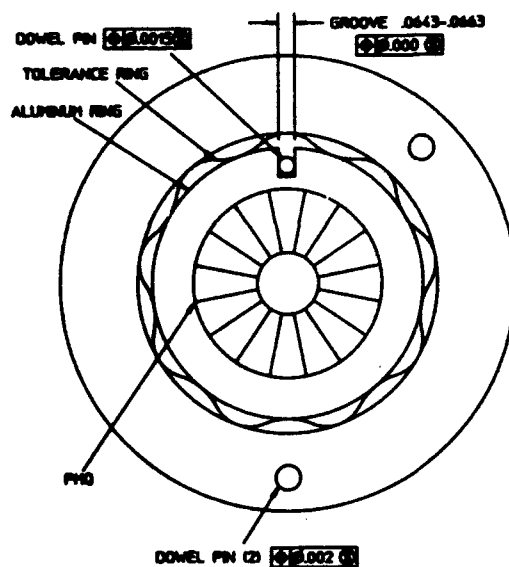


Fig. 3. PMQ and Holder Assembly.

Our previous experience in the design of kinematic systems revealed that cones and vee grooves for kinematic mounting devices having the proper geometry and hardness are not commercially available. Typically, they need to be custom fabricated for each application. However, for the EMQ's and debuncher cavity we determined, that by using other readily available, inexpensive, hardened steel elements, the same kinematic effect could be accomplished for substantially less cost. A cone effect was accomplished by using a steel drill bushing of hardness RC 62-64 and .500 inside diameter mated with a .625 diameter tooling ball. A vee groove effect was accomplished by mounting two standard .500 diameter steel dowel pins of hardness RC 36-42, with their axes parallel to each other and perpendicular to the axis of the 5/8-24 threaded shaft. The flat used in the kinematic mount was a commercially available steel rest button of hardness RC 40-45. Figure 4 shows the three elements of the kinematic mount used for the EMQ's and the debuncher cavity.

The two wear plates on the magnet ring of each EMQ were made from A2 tool steel. They were premachined, hardened, then attached to the EMQ. They were then final ground concentric with a precision alignment pin that was sized to the four inside pole tips of each EMQ. Doing this ensured precise rotation of the EMQ about its magnetic center. ++

++ This mechanical determination of the magnetic axis was used because some of the existing fiducials locating the magnetic axis had been damaged or removed.

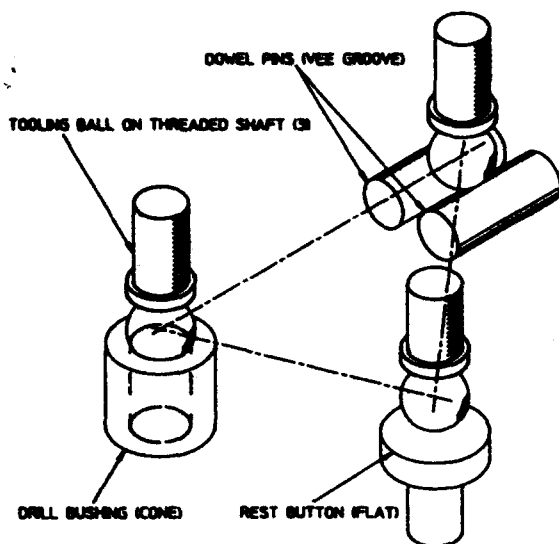


Fig. 4. Elements of Kinematic Mount.

Figure 5 shows the machining technique used for machining the EMQ wear plates.

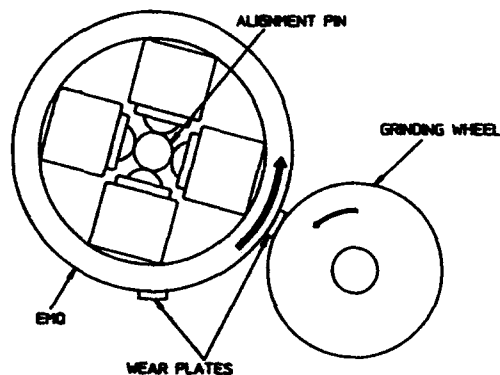


Fig. 5. Grinding EMQ Wear Plates.

#### IV. INSTALLATION, ALIGNMENT AND OPERATION

The next step was to install and align the MEBT components on the beamline. A line of sight through the RFQ was established using a Brunson model 160 line scope sighting through the center of the injector and a backlit pin hole in the exit end of the RFQ. The four EMQ's, the debuncher cavity and their mounts were assembled and pinned to the top plate of the support stand. Initially, EMQ's 1 and 4 were positioned on their mounts so that all adjustments were in mid-range. A precision fit pin having a back-lit pin hole through its axis was inserted into the centers of EMQ's 1 and 4. The line established by the pin

holes at EMQ's 1 and 4 was made colinear with the line scope using the support stand adjustments. The remaining two EMQ's and the debuncher cavity were brought into position by using the X and Y adjustments while sighting on back lit pin holes such as those used on EMQ's 1 and 4. The PMQ and holder assembly was attached to the downstream end flange of the RFQ. A final operation to check the repeatability of the kinematic mounts was then performed by lifting each EMQ and the debuncher cavity completely off their kinematic mounts then replacing them. No measurable X and Y displacement of these elements was observed. The angular alignments of the EMQ's was determined by the experimenters during assembly of the beam tube. A quartz window was installed on the end of selected segments of the beam tube and each EMQ was adjusted until the desired visual beam spot was obtained. The target assembly was installed on the downstream end of the beam tube to complete the assembly. Figure 6 shows the completed accelerator.



Fig. 6. Assembled Beam Transport System.

#### V. CONCLUSION

The accelerator was commissioned and experimental data has been obtained. During initial installation of the beam tube and diagnostics and during routine maintenance it has been necessary to remove and replace the PMQ, EMQ's and debuncher cavity by disassembling them at their kinematic mounts. Each time they have been replaced on the beam line with no measurable shift in their positions. When it is necessary to re-adjust some of the beam elements, each adjustment is made predictably and without concern for coupled motion effects. The application of precision mechanical engineering techniques to the design of this accelerator has proven to be effective.

# The Final Focus Test Beam Laser Reference System\*

V.E.Bressler, R.E.Ruland

Stanford Linear Accelerator Center, Stanford University, Stanford, CA 94309 U.S.A.

## Abstract

The original design for the SLAC linac included an alignment reference system with 270 diffraction gratings situated along the 3000 meter linac. These gratings have provided SLAC with a global reference line repeatable to within 200 micro meters. For the Final Focus Test Beam, this laser system has been extended and 13 new diffraction gratings have been installed. Improvements in the image detection system, in the calibration of the targets and the availability of new instruments allows us to evaluate the performance of the laser reference system at the 5-10 micro meter level. An explanation of the system and the results of our evaluation are presented.

## 1. INTRODUCTION

Components of the FFTB laser alignment system are illustrated in figure 1. A 1 mW HeNe laser provides images with peak intensity of approximately 1 lux at the detector. (Note that all FFTB zone plates are less than 150 m from the laser). The divergent lens is chosen such that the intensity of light at the edges of the zone plate is about 75% of the intensity of light at the center of the zone plate.

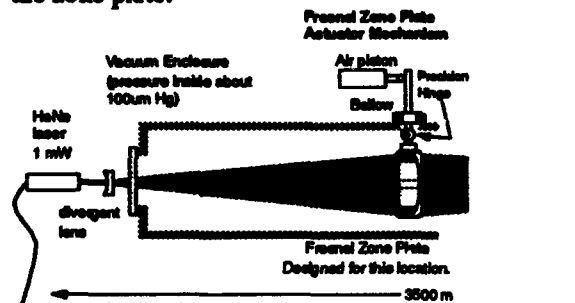


Figure 1a. Components of the FFTB laser alignment system.

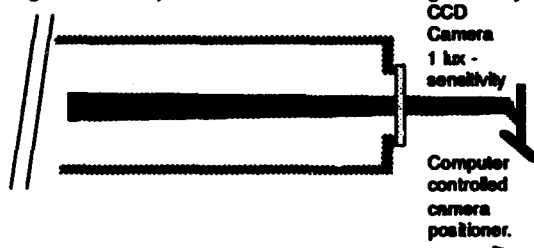


Figure 1b. Components of the FFTB laser alignment system.

A precision hinge which enables the zone plate to return to the same position with each actuation is required; only one zone plate may be lowered into the light at one time.

An inexpensive CCD camera with an array of size 8x6mm is used. FFTB images are much larger than this CCD array. Therefore the camera must be moved many times in order to detect one FFTB image[1]. The accuracy of the camera positioning system is approximately 10 micro meters. However, FFTB images have high sensitivity, figure 2, and need only be detected to within tens or hundreds of micro meters in order to achieve alignment information at the zone plate with precision of a few micro meters.

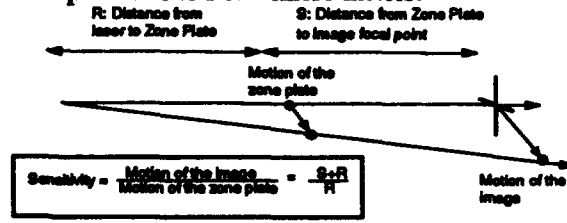


Figure 2. Definition of sensitivity.

## 2. IMAGE MEASUREMENTS

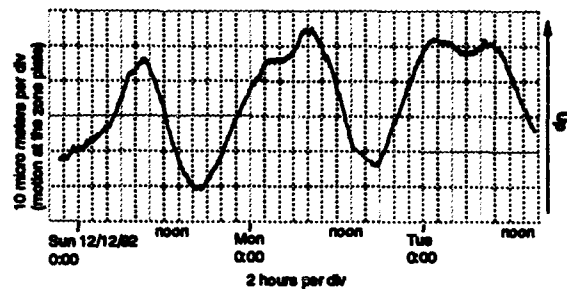


Figure 3a. Measurement of FFTB LSX1 Fresnel zone plate image. VERTICAL LSX1:  $r = 182.8$  m,  $s = 3284.7$  m,  $N = 20$

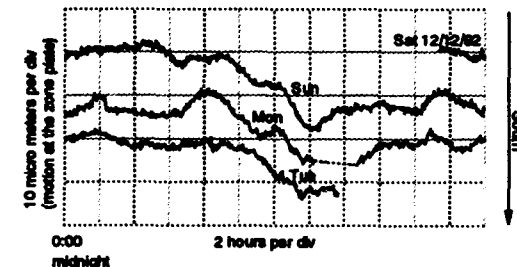


Figure 3b. Measurement of FFTB LSX1 Fresnel zone plate image. (HORIZONTAL)

\* Work supported by the U.S. Department of Energy under contract DE-AC03-76SF00515

Contributed to the Particle Accelerator Conference (PAC'93) Washington DC, May 17-20 1993

Three days of data from the FFTB laser alignment system are shown in figure 3. This data was produced by lowering a *single* zone plate and repeatedly measuring the image from this zone plate. Motions indicated by the data are a combination of motions of the zone plate, the camera and the laser. Motions of the camera and the laser may be eliminated when a set of three or more different images are monitored. However that was not done in this case. The data from figure 3 is useful in order to evaluate the standard deviation or quality of the measurements made by the image detection system. The standard deviation of these measurements, computed in terms of the position of the zone plate, is less than  $5\mu\text{m}$ .

### 3. ACCURACY OF IMAGES

Figure 3 illustrates the *repeatability* of the measurement of zone plate images. However, this data says nothing about the accuracy of these measurements. Notice that the standard deviation of the vertical measurements is less than the standard deviation of the horizontal measurements. The algorithm which is used to detect the center of the image uses (1) the vertical cross section of the image to compute the vertical coordinate of the center of the image and (2) the horizontal cross section of the image to compute the horizontal coordinate of the center of the image.

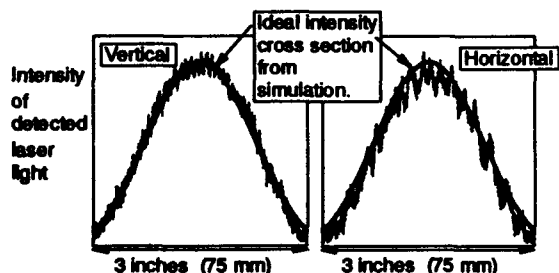


Figure 4. Image intensity cross sections.  
(FTTB Fresnel Target LSX7) 12/08/92

Therefore if the standard deviation of the computed vertical coordinate of the image is less than the standard deviation of the computed horizontal coordinate of the image, we would expect that the vertical cross section of the image would be of better quality than the horizontal cross section of the image. Figure 4 illustrates that this is indeed true.

The imperfection in the images shown in figure 4 are caused primarily by stray light, reflected off the interior of the vacuum enclosure.

These imperfections are stable; cross sections taken on different days contain the same imperfections.

Looking at figure 4, one might wonder if the computed center of such an image is a good measurement of the center of the "ideal" image. Figure 5 illustrates the image detection algorithm.

By varying the Reference Level and remeasuring the center of the image, one may gain a sense of how well we are computing the center of the ideal image.

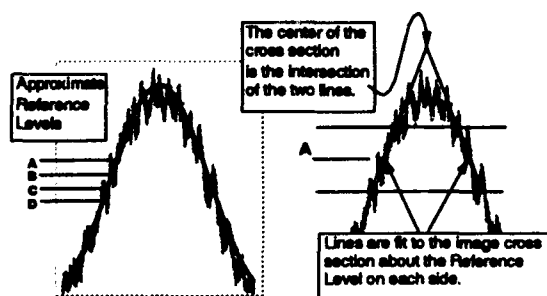


Figure 5. Quick explanation of the image detection algorithm.

The data from figure 6 is taken directly from the database which is attached to the image detection program. This data consists of 12 different measurements of the center of the LSX7 image at 4 different reference levels. X and Y are the horizontal and vertical coordinate of the image in inches as measured in the coordinate system of the image detector. Etime is the time required for the algorithm to converge in seconds. Center Amp determines the effective reference level.

Run	X	Y	Time	MODE	Etime	Center A
32-7	-0.8011	-0.2413	1992 12/09 14:14	TRANS	317	113.0
32-7 B	-0.8174	-0.2428	1992 12/09 14:21	TRANS	139	113.0
32-7 C	-0.8154	-0.2414	1992 12/09 14:24	TRANS	150	113.0
32-7 D	-0.8342	-0.2425	1992 12/09 14:30	TRANS	206	100.0
32-7 E	-0.8368	-0.2432	1992 12/09 14:38	TRANS	273	100.0
32-7 F	-0.8089	-0.2434	1992 12/09 14:43	TRANS	334	100.0
32-7 G	-0.8289	-0.2428	1992 12/09 14:48	TRANS	222	85.00
32-7 H	-0.8239	-0.2435	1992 12/09 14:58	TRANS	268	85.00
32-7 I	-0.8171	-0.2450	1992 12/09 15:00	TRANS	188	85.00
32-7 J	-0.8187	-0.2283	1992 12/09 15:05	TRANS	288	130.0
32-7 K	-0.8238	-0.2305	1992 12/09 15:08	TRANS	148	130.0
32-7 L	-0.8182	-0.2380	1992 12/09 15:12	TRANS	151	130.0

Figure 6. Image measurements at different reference levels.

The total range of all the Y (vertical) measurements is  $440\mu\text{m}$  and  $840\mu\text{m}$  for the X (horizontal) measurements. Translating these measurements into distance at the zone plate we have: *Vertical Range:  $5.6\mu\text{m}$  Horizontal Range:  $2.9\mu\text{m}$* . As far as the image detection algorithm is concerned, these images are quite symmetric. Therefore when we compute the center of the "imperfect" image, we are computing the position

of the center of the zone plate to within about  $5\mu\text{m}$ .

## 6. IMAGE SIMULATIONS

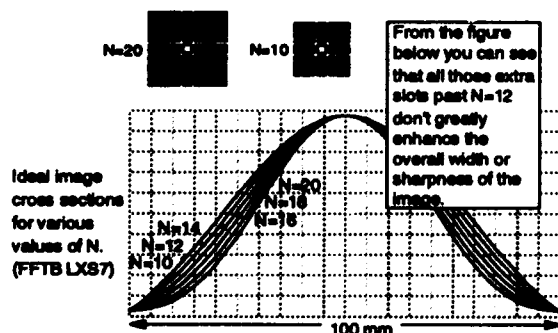
Prior to the construction of the FFTB laser alignment system we investigated the feasibility of a Fresnel zone plate laser alignment system with  $5\mu\text{m}$  accuracy. Several of the questions on our mind were: (Q1) How precisely must the slots of a zone plate be fabricated? (Q2) How large must a zone plate be? (Q3) Does the angle of the zone plate with respect to the incident light wave matter? (Q4) What happens when light from the laser is not symmetrically distributed across the surface of the zone plate?

In order to answer these questions we conducted one and two dimensional simulations which assumed (1) Light incident on the zone plate has a gaussian intensity profile and has spherical phase, originating at the laser. (2) The zone plate is located at distance R from the laser. (3) The zone plate may move horizontally or vertically with respect to the laser line. (4) The zone plate may pitch or yaw with respect to the laser line. (5) The camera is located distance S from the zone plate.

Available space does not permit a description of the simulation algorithm, therefore we will simply present results.

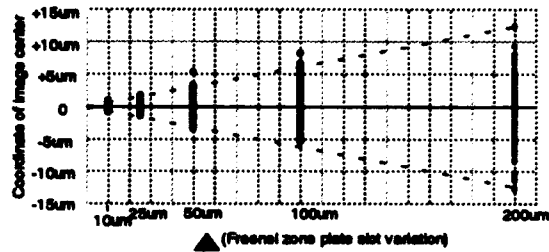
(Q1) How large must a zone plate be.

By "large" I really mean, what is the required number of slots in the zone plate? This is an important issue since as the slots become small, manufacture of the zone plate becomes increasingly difficult and expensive. The number of slots in the zone plate is given by the order of the zone plate, N.

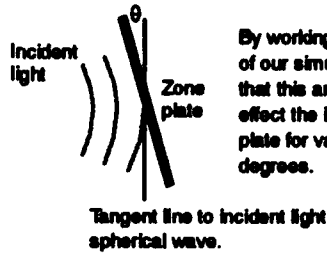


(Q2) How precisely must the slots of a zone plate be fabricated?

Simulations conducted for the FFTB LSX7 ( $r=22.9\text{ m}$ ,  $s=3424.5\text{ m}$ ,  $N=20$ ) Fresnel zone plate. The simulated zone plate has been given random asymmetric imperfections with standard deviation  $\Delta$  and the center of the resultant image has then been computed.

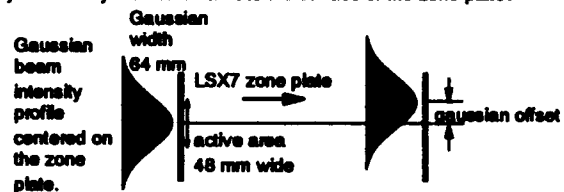


(Q3) Does the angle of the zone plate with respect to the incident light wave matter?



By working through the mathematics of our simulation algorithms we found that this angle  $\theta$  does not significantly effect the image produced by this zone plate for values of  $\theta$  less than several degrees.

(Q4) What happens when light from the laser is not symmetrically distributed across the surface of the zone plate?



Gaussian offset	Image offset
5 mm	3.9 $\mu\text{m}$
10 mm	7.0 $\mu\text{m}$
20 mm	13.5 $\mu\text{m}$

## CONCLUSION:

Fresnel zone plate alignment systems can provide alignment information with relative accuracy from zone plate to zone plate of  $5\mu\text{m}$  without expensive image detection hardware and with zone plates fabricated to  $5\mu\text{m}$  tolerances. FFTB Fresnel zone plate alignment images have been shown to be, (1) Symmetric to within  $5\mu\text{m}$  (2) Re-measurable to within  $5\mu\text{m}$ .

## References

- [1] V.E.Bressler, G.E.Fischer, R.E.Ruland, T.Wang, "High Resolution Fresnel Zone Plate Laser Alignment System", EPAC'92 Conference Proceedings Vol.2 (March 1992), pp. 1613-1615

# Thermal Modeling of Cryogenic Accelerator Structures\*

H. Muller, P. Smith, D. Walend, J. Kirchgessner

Laboratory of Nuclear Studies, Cornell University, Ithaca, NY 14853-5001

## Abstract

A software package has been created for examining the thermal behavior of cryogenic particle accelerator structures. It models the steady state heat flows in waveguides and beampipes while in operation, treating both diffuse and specular infrared reflection. The program runs effectively on small computers, since only a few simple geometries are treated, and the output display options are limited. Overall accuracy for simple test cases is on the order of a few percent, but on short structures with very wide apertures the errors can be up to 10%. An analysis of radiative heat load in the B-factory cavity is presented, and thermal management strategies for the input waveguide are discussed.

## I. INTRODUCTION

Early in the design of the B-factory test cryostat, it was recognized that some features of the cavity would make the design of a low heat leak system a challenge. Specifically, the relatively large beampipe (240 mm diameter) and input waveguide (100mm x 430 mm) could allow a significant amount of infrared radiation into the cavity, and thus introduce a large heat source into the helium coolant bath. Further thermal study was warranted, but no simple analytical technique could treat both specular and diffuse radiative heating, as well as RF heating, wake field heating, and conduction. Sophisticated finite element codes, such as COSMOS/M<sup>1</sup>, were capable of such analysis, but for this task, they would have required too large an investment of time and resources to be cost effective. A software package was developed at Cornell to conduct thermal modeling of accelerator structures. This package, called ASTModeler, provides an inexpensive and useful tool for accelerator design.

## II. PROGRAM DESCRIPTION

To make this software package easy to use, a number of compromises were incorporated into it from the beginning. First, only simple geometries can be accommodated, either cylindrical or rectangular pipes. This avoids the problems of specifying and meshing complex shapes, but still allows the treatment of many structures commonly found in particle accelerators. Because of this restriction on the model geometry, it is also possible to limit the output to simple two dimensional plots without any loss of information. A three

oriented input section prompts the user to describe the modeled section in terms of the following parameters:

- Geometry- rectangular or cylindrical
- Size- length and aperture
- Temperature- endpoint temperatures
- End conditions- open, reflective, or black body
- Material- 304 SS, Cu, Al, or Nb
- Plating- material and thickness
- Surface finish- roughness
- RF environment- frequency and power level

Heat exchangers can also be specified for the section, in terms of tube size, shape, thickness, material, and gas flow rate.

The material data necessary to perform radiative and conductive heat transfer calculations are stored in a library which can be expanded to accommodate any additional materials of interest. Most of these data are available from published literature, but some are not. For example, to accurately treat specular radiation, it is necessary to know both the diffuse reflectivity and specular reflectivity of the material concerned. The data is not available for niobium, the material used in superconducting cavities. This motivated a series of optical measurements on unpolished niobium[1]. The results of this study, which are incorporated in the material properties database contained in ASTModeler, were that niobium has an emissivity of .05, and that it is constant for all wavelengths from 5  $\mu\text{m}$  to 20  $\mu\text{m}$ . In addition, the specular portion of reflected energy varies smoothly from 85% at 5  $\mu\text{m}$  to over 95% at 20  $\mu\text{m}$ .

## III. COMPUTATION TECHNIQUES

The computational package has three main parts; a conduction solver routine, a radiation solver routine, and an additional routine which incorporates RF heating calculations and heat exchanger cooling calculations.

The conduction routine is the starting point of the program. Because of the simple geometry, the conduction problem reduces to one dimensional formalism. This routine segments the model structure and then applies a finite difference form of Fourier's law to these segments. The net heat flow into each segment is calculated by summing the heat flows from the adjacent segments, as well as an external heat flow determined by other routines. In the steady state, all segments but the end ones should see no net heat flow. Each segment temperature is perturbed to see whether this causes an improvement or deterioration in the segment heat balance. This effect is used to estimate the temperature adjustment necessary to balance heat

\* Work supported by the NSF and the US-Japan collaboration

<sup>1</sup> COSMOS/M is a registered trademark of Structural Research

flow through the segment. The iterative adjustment process is stopped when total heat flow for all segments are balanced to some small fraction of the heat flow to an adjacent segment. This convergence criterion is adjustable, and is usually set to a fraction of a percent. With a convergence criterion of 0.1%, this routine agrees with analytical results to within 2%.

The radiation routine uses the segments defined in the conduction routine to define a set of surfaces interacting through radiation and absorption. These surfaces define a greybody enclosure, with temperatures set by the results of the conduction routine. As with the conduction problem, in steady state, the heat flow to and from any surface balance. The problem can be expressed and solved in matrix form through the use of view factors, or geometrical factors quantifying the degree to which radiation from one surface impinges on another. The calculations of these factors is difficult in the general case, especially when specular reflections are considered [2]. These calculations become merely tedious in the simple geometries considered by ASTModeler, and they need only be performed once for each model. The most elaborate of these calculations involves the interaction between the end plates of the model enclosure, and the truncation of this series creates the largest error in the radiation routine. For models in which this end to end interaction is large, as for a short, large aperture beampipe, the disagreement between calculations and analytical results[3] can approach 10%.

The last routine contains the formulas necessary to calculate RF heating in model structures, as well as a heat exchanger modeler. The RF heating formulas[4] incorporate the effects of anomalous skin depth in conductors[5] and of BCS surface impedance in superconductors[6]. The heat exchanger routine determines the heat conducted from each segment to the gas passing through the cooling tube attached to that segment. A boundary layer thermal resistance is calculated from fluid Reynold number, and the series combination of that and wall thermal resistance determines the effective resistance from segment to cooling gas.

The three main routines are executed in series, with the conduction routine determining a trial solution for segment temperatures. Those temperatures are used by the radiation routine to determine radiative heat fluxes for each segment, and by the third routine to calculate any heat flows in, from RF heating, or out, from heat exchanger cooling. The calculated external heat flows are then returned to the conduction routine, and temperatures are altered until the heat flows are again balanced. The process is iterated until adjustments become negligible.

#### IV. DESIGN EXAMPLES

One of the first problems examined with this package was the heat load presented by the B-factory beampipe. Since the cavity connected to that beampipe was not cylindrical, a

cylindrical structure with the same thermal properties as the cavity had to be specified. This was done by using a 2-D Monte Carlo simulation of the behavior of infrared rays propagating in the beampipe and cavity. Each ray was launched from one aperture with a direction determined by a Lambertian weighted random number generator. The ray then experienced either specular reflection or complete absorption at every boundary collision, with absorption probability equal to the boundary emissivity. The simulation indicated that the cavity absorbed more infrared radiation than the beampipe, due to multiple reflections from its concave surface. This absorption pattern could be simulated by a cylinder with a darkened region (lower reflectivity) at the cavity location. The model shape, with an 85% reflectivity in the darkened region and 95% reflectivity elsewhere, was used in ASTModeler to make further thermal calculations. These calculations indicated that the total heat load due to radiation from 300K surfaces was 10.4 W, with another 10.3 W due to conduction along the walls of the beampipe. Since the black body radiation through both beam ports was calculated to be 40 W, it is clear that most radiation simply passed through the cavity without causing heating.

A similar analysis was conducted on the input waveguide bringing RF power into the cavity. In this case, since the rectangular waveguide was terminated by a coupler at the cavity end, much of the IR radiation was absorbed in regions cooled by liquid helium. For mechanical reasons, it was necessary to have two 90 degree E-bends in the waveguide, so it was decided to cool the bend most distant from the cavity to low temperatures with liquid nitrogen. This avoided a line of sight path from room temperature structures to cryogenic ones, but ray tracing simulations indicated that nearly 15 W of radiant energy would be delivered by reflections off the waveguide walls. In fact, the waveguide made an effective light pipe for infrared radiation, due to the high reflectivity of niobium. This effect was controlled by putting small steps inside the waveguide elbow. In both simulations and optical experiments on scale models, nearly 90% of incoming radiation was reflected back to its source, while in ungrooved elbows, less than 3% was returned.

Analysis of this revised waveguide design indicated that 17.2 W would still be conducted into the helium coolant, and that as much as 12 W of this was from RF heating of the waveguide section between the cooled (80K) elbow. This, when added to the heat loads already calculated for the beampipe, was more than allowed by the refrigeration budget. Thus, it was decided to incorporate a helium gas heat exchanger on the waveguide section between the two E-bends. The optimization procedure required a large number of calculations involving various cooling tube geometries, sizes, and flow rates. Semi-circular channels were selected over simple tubes because they exhibited much better heat transfer properties. Rectangular channels were as good as semi-circular ones from a heat transfer standpoint, but they were rejected because of assembly difficulties. Studies of cooling as a function of gas

flow rate indicated that the optimum flow was about 50 mg/s of helium vapor. At this flow rate, total conduction along the waveguide was 3.9 W, an acceptable figure. Additional flow did provide more cooling, but the marginal improvement did not compensate for the reliquification cost of the warmed helium.

## V. REFERENCES

- [1] Measurements performed by Surface Optics Corporation, San Diego, CA
- [2] R. Siegel and J. Howell, *Thermal Radiation Heat Transfer*, New York: McGraw-Hill Book Co., 1981, pg. 220-232
- [3] E. Sparrow and S. Lin, "Radiation Heat Transfer at a Surface Having Both Specular and Diffuse Reflectance Components", *International Journal of Heat and Mass Transfer*, vol. 8, pg. 769-779, 1965
- [4] N. Marcovitz, *Waveguide Handbook*, Lexington, MA: Boston Technical Publishers, 1964, pg. 56-71
- [5] R. Chambers, "The Anomalous Skin Effect", *Proceedings of the Royal Society of London*, A195, pg. 336, 1948
- [6] J. Halbritter, *Externer Bericht 3/70-6*, Kernforschungszentrum Karlsruhe, 1970

# Cryogenics for the LEP200 Superconducting Cavities at CERN

D.Güsewell, M.Barranco-Luque, S.Claudet, W.K.Erdt, P.Frandsen, Ph.Gayet, J.Schmid, N.Solheim, Ch.Titcomb, G.Winkler  
CERN, CH-1211 Geneva 23, Switzerland

## Abstract

The cryogenics for the LEP200 Project cover the cooling requirements of up to 64 modules containing each four superconducting (SC) cavities at 352 MHz RF. This includes bath cooling for the cavities themselves by liquid helium boiling at 4.5 K, and use of cold helium gas for intercepting heat from accessories. Helium refrigeration is provided by separate powerful cryoplants at each of the four interaction points of LEP with 12 kW equivalent refrigeration at 4.5 K and cryogenic distribution lines of up to 810 m length, and by two 6 kW plants for the new test center SM18 where the acceptance tests of both SC cavities and magnets are carried out. Most of the hardware is installed, commissioning of the systems in LEP is progressing and experience in testing the new cavities from industry is accumulating. First conclusions and performance results are reported, and problems listed which require further work.

## I. INTRODUCTION

The LEP200 Project was started at CERN in 1989. By 1995 192 SC cavities should be operational in LEP to boost the  $e^+e^-$  energy above the  $W^\pm$  threshold. The status of the Project is summarized elsewhere at PAC93 [1], and recent results from cavity testing are presented [2]. This paper gives an updated status of the cryogenics for this collider cavity program; a more detailed description was given at ICEC14 [3].

Special solutions had to be adopted to integrate this new large-scale cryogenics into the existing LEP environment without requiring additional underground civil engineering. The LEP200 systems will increase the helium cooling power at CERN almost by an order of magnitude and use about 23% of the 300 MCHF LEP200 Project funds. Compatibility with the operation techniques developed for the numerous smaller refrigerator plants running since years at CERN and contract splitting to avoid dependence on a single vendor were other management targets which determined basic technical choices.

## II. COOLING REQUIREMENTS OF THE LEP200 CAVITIES

For the energy upgrade of LEP to approach 90 GeV, initially forty-eight 4-cavity modules will be installed in the straight sections of LEP, four on each side of points 2 and 6, and eight on each side of points 4 and 8 [1]. At a later stage, points 2 and 6 may also be brought to 8 + 8 modules.

The LEP200 cavities are cooled by a bath of boiling liquid helium (LHe), operated slightly below 1.3 bar or 4.5 K. A few percent (0.2 g/s per cavity) of the evaporated helium is used for intercepting heat conducted along RF couplers, the beam pipe transition to room temperature and the nickel bars used for frequency tuning, before returning at ambient temperature to the refrigerator.

The cryogenic system of the LEP200 cavities was designed to cover the thermal load estimates given in Table 1.

Table 1  
Refrigeration load design figures per 4-cavity module

Static losses	< 90 W
Share of distribution losses	< 60 W
Refrigeration equivalent of gas cooling (Conversion 125 W per 1 g/s)	100 W
RF losses at standard RF conditions (Ref. field of 5 MV/m with $Q=3.10^9$ )	200 W
Spare capacity to cover higher field values or reduced surface quality	>300 W
<b>TOTAL</b>	<b>750 W</b>

## III. BASIC FEATURES OF THE CRYOGENIC SYSTEM

The cryogenic system for the LEP200 Project was mainly designed to cover the LHe bath cooling requirements of up to 4 x 64 RF cavities, made either from niobium (Nb) sheet or Nb sputtered on copper; but it includes already all features to make its main components also suitable for a future proton-proton collider (LHC) in the LEP tunnel.

A major constraint was to avoid new underground civil engineering work in LEP, but to integrate the cavity cryogenics into the existing shaft and tunnel infrastructure of LEP. To allow contract splitting after competitive tendering in CERN member countries and to keep the new systems compatible with the operation practice for the existing refrigerators, CERN ordered control hardware and software separately (ABB, CH/S). An energy saving design was encouraged by a bonus/malus system including electricity cost over 10 years of running. This led to proposals using 6-8 turbines at different temperature levels between 200 and 4.5 K.

Due to the depth (50 - 150 m) of the LEP machine tunnel and the need to operate the cavity bath at constant pressure slightly above atmospheric, LHe production at ground level and the associate static head effects of cold helium had to be excluded.

As a first step, for the prototype cavity string at LEP point 2 and the reception test hall SM18, two very compact 6 kW refrigerators were ordered in May 1990, one each from SULZER (CH, now LINDE) and L'AIR LIQUIDE (F). This was following the concept of an 'horizontal split' with installation of compact cold boxes in both service tunnels close to the cavity strings.

In 1990 the basic concept was changed to better match LHC requirements and to overcome the 2 x limitation given by the space in the service tunnels. A novel concept of a

'vertical split' of the cold boxes near the access shaft was adopted, with a potential of later reaching at least 18 kW of cooling power at 4.5 K.

Four such 12/18 kW cryoplants were ordered in December 1990, two each from SULZER/LINDE and L'AIR LIQUIDE, including screw compressors for all LEP200 cryoplants from the same manufacturer STAL (SE).

The screw compressors and their gas purification system are installed in separate sound-proofed buildings near the LEP access shafts. Each compressor set consists of 2-4 low pressure (LP) and 1-2 high pressure (HP) units, with variable flow in the 30-100% range and a recovery mode using only one unit to limit electric power requirements. All cryogenic components working above about 20 K were grouped into an "Upper Cold Box" (UCB), which could be integrated into the existing surface buildings covering the access shaft (Figure 1).

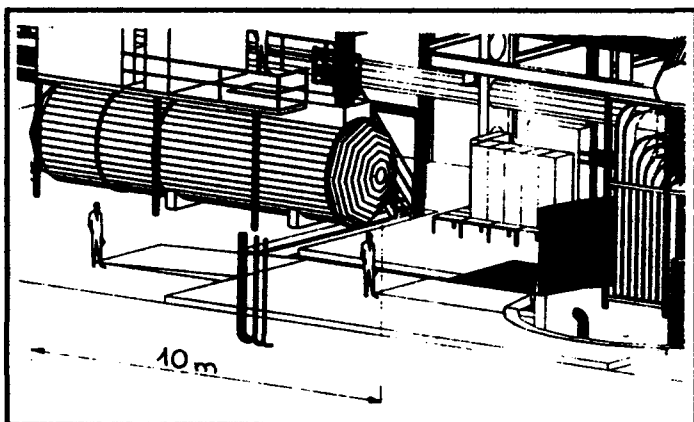


Figure 1  
Integration of Upper Cold Box at top of LEP shaft

Although the space limitations in the surface building were not as stringent as for the compact 6 kW cold box installed in the tunnel, the UCB had to be of horizontal construction too, and use horizontal heat exchangers, but its dimensions were not critical (typical weight 50 t, including 4 turbines).

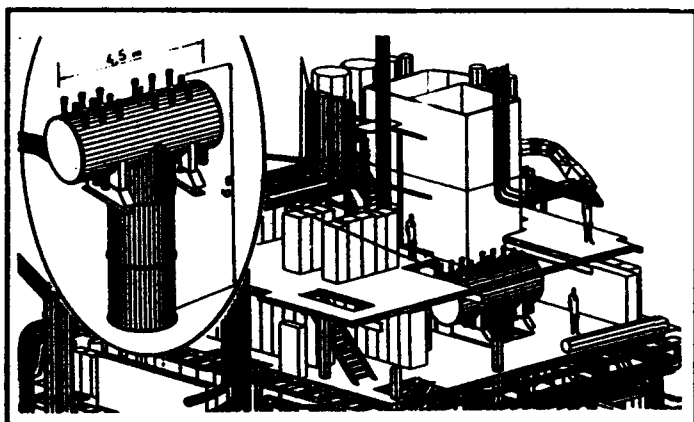


Figure 2  
Integration of Lower Cold Box at bottom of LEP shaft

All components below 20 K were grouped into T-shaped "Lower Cold Boxes" (LCB) for which a position could be found, amidst cable trays and ventilation ducts (Figure 2), in the steel structure at the lower end of the access shaft (typical weight 15 t, including 3 turbines).

The Upper and the Lower cold boxes had to be interconnected by vacuum-insulated transfer lines. The 20 K separation level turned out to be particularly convenient: at this temperature heat insulation is not very critical and gas density is low enough not to give static head problems and not to require big pipe diameters; only four respectively five interconnecting cold pipes were considered necessary: the two main HP and LP pipes, two screen gas pipes, and, in the solution adopted by L'AIR LIQUIDE, one bypass for specific cooldown modes.

Each cavity bath requiring about 200 l of LHe, a total of 16000 l of LHe or 12000 Nm<sup>3</sup> of helium gas must be available at each LEP point with SC cavities. For ease of operation during shutdown periods, it was decided to rely on gas rather than liquid storage. Fifty vertical steel vessels were ordered (75 m<sup>3</sup>, 20 bar), mostly from RUZCHIMMASH (Russia) as a result of agreements between CERN and Russia.

The cold helium distribution is done by a pair of separate transfer lines, one for LHe supply (65 mm inner bore and 25 bar design pressure for LHC service) and a second for the cold gas return (100 mm bore, 16 bar). Both contain also a 22 mm bore screen cooling pipe with helium gas circulating in the 50-75 K range, cooling a 'soft' radiation screen which is made by wrapping of aluminium strips between inner and outer layers of superinsulation and clamping the strips on the screen pipe at regular intervals.

The transfer line pairs for LEP points 2 and 6 with initially 32 cavities each (2 x 275 m length) were ordered from L'AIR LIQUIDE. The lines for LEP point 8 (2 x 405 m length) were ordered from the Russian firm CRYOGENMASH.

#### IV STATUS OF INSTALLATION AND COMMISSIONING

##### A. Cryoplants

Of the two 6 kW plants, only the 7 turbine SULZER/LINDE plant was finally installed underground at LEP point 2, to cool the first cavity modules in LEP before the 12 kW plant will there be available. The 6 kW plant of L'AIR LIQUIDE (3/4 turbines) was installed in the SM18 test hall. Both plants were commissioned in spring 1992 and have since been running most of the time [5]. The SULZER/LINDE plant has a power factor<sup>1</sup> of about 240 W/W, and the L'AIR LIQUIDE plant achieved 290 W/W with only 3 turbines. Reports on both plants will be given at the forthcoming CEC93 [6].

Two of the four 12 kW plants are presently in the process of commissioning, the two others are being installed. The LINDE 12 kW plant at point 6 was first priority for CERN and came already, during tests in April 1993 close to the

<sup>1</sup> expressed as ratio of total electric input to equivalent cooling power at 4.5 K

design performance and a record power factor of 220 W/W, as shown in Table 2.

Table 2 Results of first reception tests of 12 kW cryoplant supplied by LINDE [4]

Suction pressure of compressor set [bar]	1.01
Delivery pressure, compressor set [bar]	19.8
He mass flow [g/s] with suction gas at 295 K	712
Electrical input [kW]	2600
Cooling performance as specified:	
Refrigeration at 4.5 K [kW]	10
Cold gas returned warm ('liquefaction load') [g/s]	13
Screen cooling power at <75 K [kW]	6.7

### B. Cold Distribution Systems

Transfer line systems for 32 cavities at each of the LEP points 2 and 6 have been installed by L'AIR LIQUIDE, partly in the machine and partly in service tunnels, totalling 275 m for LHe and 275 m for cold gas return at each point. Average losses to the 4.5 K pipes were measured, using helium gas circulation at 10-20 K to 0.9-1.0 W/m, including 2 x 8 unshielded flexible connections of 3.5 m length and cryogenic control valves on the manifolds.

At LEP point 8, the 810 m of double transfer lines were built and installed by CRYOGENMASH. Good quality and installation speed were achieved and an identical system is now ordered for LEP point 4. First results with the recently started 12 kW plant from L'AIR LIQUIDE gave about 0.9 W/m, here including losses in 2 x 16 unshielded flexible connections to the cavity modules and their cryogenic valves.

### C. Experience with cavity cooling circuits

During the acceptance tests of cavities and assembled modules, the layout of the cryogenic piping and the cooling passages on accessories inside the cavity modules [3] have been submitted to extensive tests. This design had to take into account severe space constraints due to the planned arrangement of LHC magnets on top of the LEP ring and the slope of the LEP tunnel reaching 1.4%. There was in particular no room for a satisfactory LHe buffer and phase separation volume above the cavity bath.

The module cryogenics worked in general up to expectations. A few corrections had to be made to cope with the presence of helium vapour and partial phase separation in the 10 m long 'liquid' manifold underneath the cavities; this is due to the heat input in the transfer line system and can reach 50% volume fraction. A continuing concern is the limited cooling capacity available for the inner conductor of the Higher Order Mode (HOM) coupler, where RF losses in normal operation are in the mW range but may reach several Watts during conditioning. Active cooling of the cables extracting the HOM power and of the beam pipe transition cones may have to be added to handle the losses expected when LEP will reach total beam current of 8 mA or more.

## V. CONCLUSIONS AND OUTLOOK

The cryogenics for the LEP200 cavities had to be designed, ordered and built on a very short time scale. Competent suppliers could be found, and thanks to their effort and their willingness to accept the particular installation constraints in LEP, almost all required hardware has been installed in time and will be completed in early 1994.

The slower initial pace of cavity module installation in the LEP tunnel is now giving the opportunity of doing a systematic running-in of the new 12 kW cryoplants and of developing fully satisfactory procedures and software for automatic operation from a remote control room. This control room is unattended outside normal working hours, but operators can be called in by an automatic paging system triggered by alarm signals from the plants.

A particular concern is the capability of a fast restart of the cryoplants after accidental stops (in most cases due to a failure of services [5]), to avoid downtime multiplication for LEP by quickly stopping the LHe evaporation to achieve a fast refilling of the cavities baths. A study [7] is under way to find a satisfactory solution for the ' $\Delta T$ ' problem of the biggest heat exchanger in the cryoplants where conservative temperature rules of the manufacturers prevent a quick restart, once cold helium evaporated from the liquid in the cold box and around the cavities has lowered the warm end temperature. An external bypass for the cold gas is installed, and at restart early reliquefaction and a modulated increase of high-pressure flow will be used to save LEP time without reaching dangerous stress levels in the heat exchangers.

Another line of action is the development of systematic preventive maintenance and failure analysis for the new plants to rapidly achieve the low failure rate known from smaller refrigerators [5].

## VI. REFERENCES

- [1] C.Wyss, "Progress of the LEP Energy Upgrade Project", these proceedings
- [2] C.Benvenuti et al., "Superconducting Cavities for the LEP200 Energy Upgrade", these proceedings
- [3] M.Barranco-Luque et al., "Status of Cryogenics for the LEP200 Energy Upgrade Project at CERN", Cryogenics, Vol.32, ICEC Supplement, 151 (1992)
- [4] B.Chromec et al., "A Highly Efficient 12 kW Helium Refrigerator for the LEP200 Project at CERN", Proceedings of IISSC, San Francisco, May 1993
- [5] D.Delikaris et al., "Long-term Experience with Cryoplant Operation for Superconducting Magnets and RF Cavities at CERN", these proceedings
- [6] CEC93 (Cryogenic Engineering Conference and International Cryogenic Materials Conference), Albuquerque, July 12-16, 1993
- [7] G.Owren, "Rapid Temperature Change for Plate-Fin Heat Exchangers", CERN/AT-CR internal report

# Measurements of the Ground Motion Vibrations at the SSC

V. V. Parkhomchuk,\* V. D. Shiltsev, H. J. Weaver  
Superconducting Super Collider Laboratory,†  
2550 Beckleymeade Ave., Dallas, TX 75237-3946

## Abstract

The results of seismic ground measurements at the Superconducting Super Collider (SSC) Accelerator Systems String Test (ASST) site are presented. Spectral analysis of the data obtained in a large frequency band from 0.05 Hz to 2000 Hz was performed.

## I. INTRODUCTION

Vibration effects on collider performance have been theoretically studied in several works [1,2,3,4]. Depending on the frequency of the noise, one can distinguish two mechanisms of beam perturbation. At low frequencies (much less than revolution frequency), the noise produces a distortion of the closed orbit of the beam. The acceptable level of uncorrelated low frequency motion of any single SSC quadrupole is about 0.1–0.3 micrometers [2]. Narrow band high frequency noise centered near a fractional part of the betatron frequency causes direct emittance growth. Depending upon the final value of the fractional part of the tune of the SSC (0.2–0.4) this band center will be located in a frequency range between 700–1200 Hz). For example, high frequency turn-to-turn jitter of every quad with an amplitude about  $10^{-4}$  micrometer will cause emittance doubling after only 20 hours, see Reference [4]. Experimental investigation of underground vibrations at the SSC site at frequencies 1–200 Hz was performed by The Earth Technology Corporation (Long Beach, CA.) in 1989 [5]. At the time of that study the main concern was with the low frequency closed orbit distortion. Since that time, however, there has been a growing interest in the higher frequency emittance growth issue. This paper presents results of recently conducted seismic ground motion measurements at the ASST (located at the N-15 SSC site) in the frequency range from 0.05–2000 Hz.

## II. EXPERIMENTAL

Two types of seismic probes were used in the study. The first was a commercially available model SM-3KV velocity meter which was modified to accommodate a frequency range from 0.05–150 Hz. Two of these probes were used in the study and both have a nominal sensitivity of  $8 \times 10^4$  Volt/m/sec and were calibrated for use in the vertical direction. The second type of probe was a model TA-2 accelerator produced by the Moscow Institute of Earth

Physics. Again, two such probes were used in the study and both had a nominal sensitivity of 0.5 Volt/m/sec<sup>2</sup> in the vertical direction. The dynamic range of these probes (over the frequency band 10–2000 Hz) is 100 dB relative to the acceleration of gravity. Signals from all probes were digitized simultaneously by CAMAC 10-bit ADCs (with a variable sampling frequency up to 32 kHz) and then sent to CAMAC 256 K memory for storing. The maximum memory available for one channel was 64 K 24-bit words. This corresponds to 17.8 hours of permanent measurement time with a sampling rate 1 Hz or about 1 minute with 1 kHz. For long measurements a low pass filter at either 2 Hz or 20 Hz was used; for fast analyses 2000 Hz and 10 000 Hz band filters were applied.

The data was later transferred from the CAMAC memories to an IBM PC/386 for subsequent processing in both the time and frequency domains. The analysis basically consisted of 1) convert the raw data signals from voltage to vibration amplitudes in microns, 2) compute the discrete Fourier transform of the converted signals, 3) calculate the power spectral density (PSD) of the signals, and 4) calculate the spectral correlation between all signal pairs, etc.. In performing the spectral analysis 64 averages were used to reduce the signal noise and statistical errors in the data. The spectral correlation of two signals  $x(t)$  and  $y(t)$  is defined as

$$K(\omega) = \frac{\langle X(\omega) Y^*(\omega) \rangle}{\left( \langle |X(\omega)|^2 \rangle \langle |Y(\omega)|^2 \rangle \right)^{1/2}}$$

where  $X(\omega)$  and  $Y(\omega)$  denote the Fourier transforms of  $x(t)$  and  $y(t)$  respectively. The brackets in the above expression denote the averaging process over the 64 measurements.

## III. RESULTS

The PSD of the ground motion at the SSC site in quiet conditions is shown in Figure 1 (lower curve). This type of data was collected on the slab of the ASST building during the evenings and over weekends when the construction and installation activity were at a minimum. In this figure we see the microseismic peak located at 0.1–0.2 Hz which is the so-called "seven second hum." We note that the actual location of this peak is not necessarily equal to 0.143 Hz (1/7sec) but instead may vary from 0.07 to 0.25 Hz. It may also consist of multiple peaks [6]. The origin of the "seven second hum" is normally associated with ocean waves of the nearest seas (in the case of the SSC – the Gulf of Mexico and the Atlantic Ocean). Consequently, one would expect the amplitude of this peak to change significantly with time and weather conditions. This fact has been verified by filtering all

\* Guest scientist from Budker Institute of Nuclear Physics, 630090, Novosibirsk, Russia.

† Operated by the Universities Research Association, Inc., for the U.S. Department of Energy under Contract No. DE-AC35-89ER40486.

frequency components above 1.0 Hz from the signal and then calculating the rms value of the resulting ground motion signal. This operation was performed on recorded data spanning a three-week observation period from March 2 to March 20, 1993. The result of this analysis is shown in Figure 2. As can be seen, the amplitude of the rms ground motion varies by an order of magnitude from 0.2 to 2.0 microns. The behavior of this value is well correlated with the weather conditions in Florida and over the Atlantic Ocean at the time. Also, sharp peaks on March 5 coincided with small earthquakes. During these earthquakes the amplitude of the seismic motion at a frequency of approximately 0.05 Hz (below the 7 second hum peak) was about 100 microns. The motion from each quake lasted for about an hour.

A second probe was located on the coldmass of a dipole magnet which was resting alone on the support stand at room temperature waiting to be installed in the ASST string. The data taken using this probe was during the day under "noisy" conditions. The resulting PSD function is shown as the upper plot in Figure 1. The dashed line of Figure 1 represents an acceptable level for the 0.1 of beam size beam-beam separation at the interaction point of the SSC due to closed orbit distortions caused by quadrupole motion and emittance growth limitation according to Reference [4]. As can be seen from the figure, the vibrational motion at all frequencies increased. Also, resonant frequencies of the coldmass above 10 Hz become evident. This exercise serves to point out that such resonances must be taken into account when calculating vibrational motion limits for the Collider components. It must be carefully noted that the measurements presented here are for a dipole magnet and the vibrational studies noted in the introduction apply to quadrupole magnets. Preliminary analytical studies indicate that there are no quadrupole coldmass resonant frequencies located within the frequency range of 700–1200 Hz where the emittance growth problem manifests itself. These analytical predictions will soon be examined and evaluated by experimental measurements taken on a quadrupole magnet. Both PSD functions shown in Figure 1 indicate significantly high ground motions below 0.1 Hz. However, the corresponding ground wavelength at these frequencies is on the order of 25 Kilometers which does not present a serious danger to the operation of the machine.

Figure 3 presents real (solid curve) and imaginary (dashed curve) parts of the spectral correlation between two SM-3 KV probes placed a distance of 130 meters apart. As can be seen from this figure there is solid positive correlation in a band around the seven second hum frequency. There is also some correlation (0.5) at frequencies between 1.0–2.0 Hz. However, no other significant correlation was observed over the remaining portion of the spectrum. The decreasing of correlation below 0.1 Hz leads to the need for the underground experiments at the tunnel for careful estimation of the influence of this part of the spectrum on the closed orbit distortion.

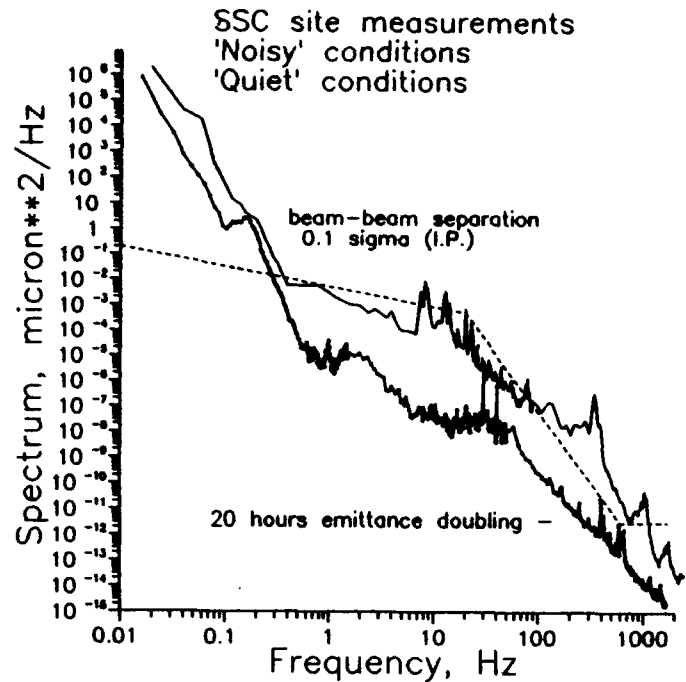


Figure 1. Measured spectra of the ground motion in noisy and quiet conditions.

MDL, ASST, 02–20 of March 1993  
R.M.S. in band 0.1–1 Hz

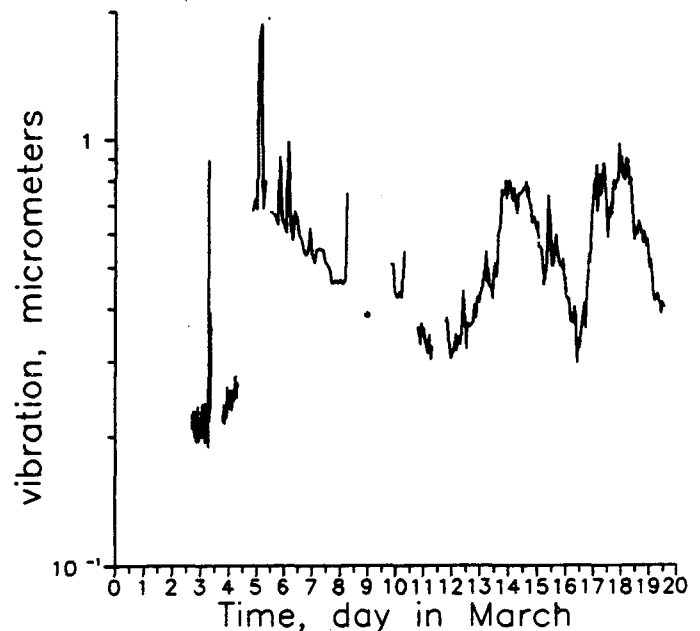


Figure 2. Three week observation of low frequency ground motion.

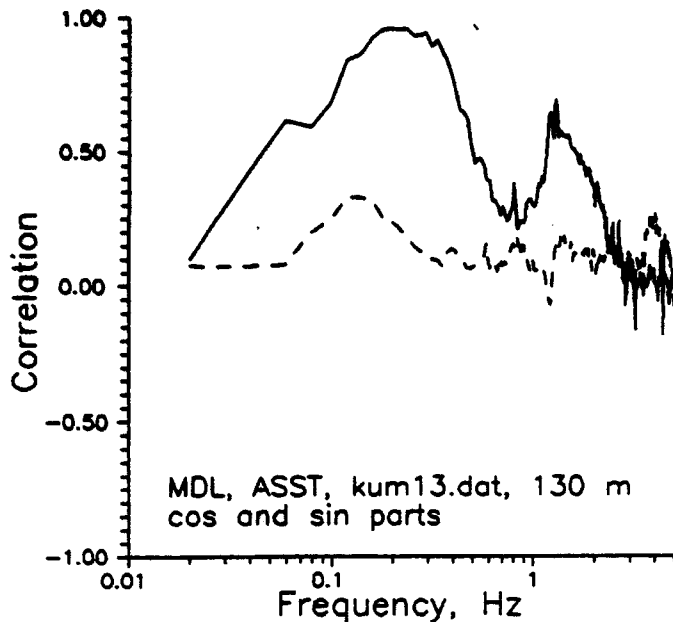


Figure 3. Spectral correlation of ground motion at a distance of 130 meters.

#### IV. SUMMARY AND FURTHER DEVELOPMENT OF EXPERIMENTS

Seismic ground measurements at the SSC site (ASST building) were carried out during March 1993. The equipment used allowed us to obtain data in a very large frequency band from 0.05 Hz to 2000 Hz.

It was found that at high frequencies (above 10 Hz) the main source of vibration is human activity. Analysis shows that under very quiet conditions, ground motion vibrations at high frequency are not dangerous for the SSC transverse emittance growth. Nevertheless, measurements made under noisy conditions show that resonant frequencies of the quadrupole magnet and support stand, if not properly engineered, could lead to fast emittance growth. The measurements in this paper were performed on the surface at the ASST facility and as a result were quite sensitive to various cultural noise. The next set of measurements will be made underground at the bottom of the exploratory shaft and the sensitivity of ground motion to surface activity examined. It is also planned to experimentally measure the resonant frequencies of the quadrupole magnets to verify the analytical predictions that they are outside of the fast emittance growth danger region.

The authors are grateful to Mike Hentges for his assistance with the measurement preparations.

#### V. REFERENCES

- [1] G. E. Fischer and P. Morton "Ground Motion Tolerances for the SSC," SSC-55, 1986.
- [2] K. Y. Ng and J. O. Peterson "Ground Motion Effects on the SSC," SSC-212, 1989.
- [3] V. A. Lebedev, V. V. Parkhomchuk, V. D. Shiltsev and A. N. Skrinsky "Suppression of Emittance Growth Caused by Mechanical Vibrations of Magnetic Elements in Presence of Beam-Beam Effects in the SSC," Preprint-INP 91-120, Novosibirsk, 1991.
- [4] V. A. Lebedev, V. V. Parkhomchuk, V. D. Shiltsev and G. V. Stupakov "Emittance Growth due to Noise and Its Suppression with the Feedback System in Large Hadron Colliders," SSCL-Preprint-188, 1993.
- [5] The Earth Technology Corporation (Long Beach, CA), "Field Measurements and Analyses of Underground Vibrations at the SSC Site," Report No. SSC-SR-1043, Dec. 1989.
- [6] B. A. Baklakov, P.K. Lebedev, V. V. Parkhomchuk, A. A. Sery, V. D. Shiltsev, and A. I. Sleptsov "Investigation of Seismic Vibrations and Relative Displacement of Linear Collider VLEPP Elements," Proc. of 1991 IEEE Part. Accel. Conf., San Francisco, USA, p. 3273, May 1991.

# Performance of Photocathode RF Gun Electron Accelerators\*

I. Ben-Zvi

National Synchrotron Light Source, BNL Upton NY 11973 USA

## Abstract

In Photo-Injectors (PI) electron guns, electrons are emitted from a photocathode by a short laser pulse and then accelerated by intense RF fields in a resonant cavity. The best known advantage of this technique is the high peak current with a good emittance (high brightness). This is important for short wavelength Free-Electron Lasers and linear colliders. PIs are in operation in many electron accelerator facilities and a large number of new guns are under construction. Some specialized applications have emerged, providing, for example, very high pulse charges. PI have been operated over a wide range of frequencies, from 144 to 3000 MHz (a 17 GHz gun is being developed). An exciting new possibility is the development of superconducting PIs. A significant body of experimental and theoretical work exists by now, indicating the criticality of the accelerator elements that follow the gun for the preservation of the PI's performance as well as possible avenues of improvements in brightness. Considerable research is being done on the laser and photocathode material of the PI, and improvement is expected in this area.

## INTRODUCTION

Since the introduction of Photo-Injectors (PIs) [1] about eight years ago, this new field has experienced an exponential growth. It is easy to understand the trend since there is a continuing demand for improved injectors for electron linacs. Free-Electron Lasers (FELs) require high brightness. Linear colliders also require high-charge, low emittance, short pulse bunch trains, either for the accelerated beam or for the generation of rf power. With the rapid growth in the number of projects, the experimental and theoretical results and the diversity of applications, there has been a continued improvement in the performance of these devices. Furthermore, this performance has a considerable influence of the trends in related areas. For example, due to the availability of high-brightness PIs, there is a significant progress in the design of Fourth-Generation Light Sources based on linacs [2]. A number of good recent reviews of microwave guns are available [3,4]

The basic principle of the PI is simple: short bunches of electrons are generated by laser pulses incident on a photocathode located inside an rf accelerating structure. The structure is operated at a high accelerating field to make the electron bunch relativistic in a short distance. Thanks to the combination of the high surface field on the cathode and the

high yield of electrons possible by photo emission, a very large current density,  $J \sim 10^4$  to  $10^5$  A/cm<sup>2</sup>, is possible. This current density is much larger than that possible by thermionic emission (about 10 A/cm<sup>2</sup>). The normalized thermal rms brightness  $B_n$ , (for a cathode effective temperature T) is proportional to the current density:

$$B_n \equiv 2I\pi^{-2}\epsilon_n^{-2} = mc^2 J (2\pi^3 kT)^{-1}.$$

Therefore a PI can deliver a very large brightness. The x-plane normalized rms emittance is defined here as

$$\epsilon_x \equiv \pi \left[ \langle x^2 \rangle \left( \langle (p_x / mc)^2 \rangle - \langle xp_x / mc \rangle^2 \right) \right]^{1/2}.$$

The rapid acceleration also serves to reduce the space-charge induced emittance growth. It also makes the PI a very compact accelerator. For example, the 3 1/2 cell S-band gun designed by a Grumman-BNL collaboration provides 10 MeV electrons in a 20 cm long structure [5].

The mode-locked lasers that drive the PIs provide interesting possibilities. The pulses can be made extremely short (to sub picosecond) and intense (tens of nC at a few ps). The spatial and temporal laser power distributions can be tailored to arbitrary profiles. Particular profiles can lead to the reduction of the emittance of the PI [6]. The pulse format is very flexible and pulse trains of arbitrary length and spacing can be generated.

## THE LASER PHOTOCATHODE RF GUN

A 1 1/2 cell PI is shown in Fig. 1. This 'BNL Gun' design [7,8] and somewhat modified versions are in operation at numerous laboratories around the world. It uses a metal photocathode that forms part of the wall of the 1/2 cell. Cathodes can be changed by using the 'choke joint' access port. The rf gun is a resonant  $\pi$ -mode 1/2 cell cavity operating at 2856 MHz. The 78.75 mm long cavity is 83.08 mm inner diameter and its beam aperture diameter is 20 mm. It has a Q of 11900 and a shunt impedance of 57 M $\Omega$ /m, which corresponds to a beam energy of 4.65 MeV at a structure peak power of 6.1 MW. At this power, the peak surface electric field is 119 MV/m and the cathode field is 100 MV/m. These operating conditions can be achieved after a few days of careful rf conditioning. The rf field contribution to the emittance is minimized in two ways. The first of these uses a choice of an optimal phase of the laser pulses relative to the rf wave for minimum emittance at the gun output. The other involves providing a nearly linear dependence of the transverse fields on beam radius by a suitable cell design. To reduce the non-linear field components, the aperture can be

\* Work supported by the US Department of Energy under contract No. DE-AC02-76CH00016.

shaped to approximate the idealized prescription [8] near the aperture:

$$r = \left[ a^2 - (4d/\pi)^2 \log(\sin \pi z / 2d) \right]^{1/2}$$
 where  $a$  is the aperture radius and  $d$  is the length of the cell. We have verified that this prescription does indeed significantly reduce the non-linear transverse fields [5] but not the (space-charge

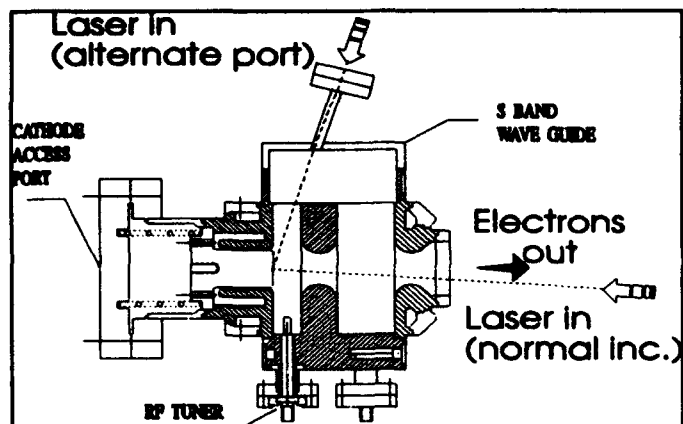


Fig. 1. Cross section of a 2.856 GHz, 1 1/2 cell PI.

dominated) emittance. With the advent of emittance correction schemes this prescription may become more important.

## THE PHOTOCATHODE AND LASER

These subjects are fundamental to the performance of the PI, however they are too vast to be covered here. The ideal photocathode material would have high emission efficiency (for drive laser cost containment) and high ruggedness. A study of various materials [9] for the photocathode has shown that certain metals have a good combination of quantum efficiency, high damage thresholds, and good mechanical and chemical stability. Copper and yttrium metal cathodes proved particularly robust. Yttrium has a work function of about 3.1 eV and a quantum efficiency (QE) of up to  $10^{-3}$  at 266 nm. Copper's work function is 4.3 eV and it has a QE of up to  $10^{-4}$ . Semiconductor cathodes such as Cs<sub>3</sub>Sb or CsK<sub>2</sub>Sb offers a much higher QE, up to several percent at 532 nm [10], but require a much better vacuum and have short lifetimes, a few days at best. Other researchers [11] work on the improvement of the QE of rugged materials such as LaB<sub>6</sub>, achieving QE of up to  $7 \cdot 10^{-4}$  at 355 nm. The laser power required to drive the PI increases as the QE becomes lower, but also as the wavelength used is shorter due to the inefficiency of frequency multiplication ( $\sim 0.5$ ,  $\geq 0.3$  to  $\geq 0.2$  for 2,3 and 4th harmonics of the  $\sim 1\mu\text{m}$  respectively in routine operation). It is reasonable to expect that new materials will emerge with significantly higher quantum efficiencies as well as ruggedness. Furthermore, an increase of the efficiency by a factor of 3 has been observed in a PI using an illumination angle of  $70^\circ$  [12].

The laser plays a significant role in the performance of the PI. High power, short pulse lasers are complicated systems and require considerable attention. Fortunately the state-of-the-art of lasers has been advancing very rapidly. Diode pumped Nd:YLF or Nd:YAG lasers provide short pulses with a considerable power at costs of about \$200k. CW pumped Nd:YLF amplifiers can provide 2 to 4 mJ/pulse in the IR and better than 0.4 mJ/pulse quadrupled ( $\sigma_b$  about 2 ps) at repetition rates of multi kHz. Other laser systems are based on a Ti:sapphire oscillator followed by various amplifiers, such as Ti:sapphire, alexandrite or excimer. While these systems are generally more expensive, they provide several advantages such as higher repetition rates and the possibility of shaping the temporal intensity of the laser.

An important issue is the phase lock stability between the laser and the rf system of the gun (and linac). Sub picosecond phase lock systems are available commercially for Nd:YAG and Nd:YLF lasers. Recently there have been reports of similar or better performance in Ti:sapphire lasers. A technique of direct phase measurement of the rf to laser radiation is being tested [13]. This method may solve the problem of long-term phase drift due to temperature or barometric pressure changes.

## THEORETICAL FRAMEWORK

An analytical model developed by K-J. Kim [14] provides scaling laws that provide insight into the relationship of some of the design parameters of PIs. Using practical units, we have:

$$\epsilon_{sc} \approx 3.8 \cdot 10^3 q (2\sigma_x + \sigma_b)^{-1} (E_0 \sin \phi_0)^{-1}$$

$$\epsilon_{rf} \approx 2.7 \cdot 10^{-5} E_0 f^2 \sigma_x^2 \sigma_b^2$$

where the normalized rms emittance contribution due to rf fields  $\epsilon_{rf}$  and that due to space charge forces  $\epsilon_{sc}$  are expressed in  $\pi$  mm mrad,  $E_0$  is the cathode peak electric field in MV/m,  $f$  is the gun frequency in GHz,  $q$  is the charge in nC, related to the peak current by  $I=q/(2\pi) \cdot 5\sigma_b$ , where  $\sigma_b$  is the rms bunch length in ps and  $\sigma_x$  is the rms transverse size in mm.  $\phi_0$  is the launch phase, typically  $50^\circ$  to  $60^\circ$ .

For a given cathode electric field, charge and beam size, the emittance is optimized by:

$$f_{opt} = 1.2 \times 10^4 (\sigma_b \sigma_x E_0 \sin \phi_0)^{-1} q^{1/2} (\sigma_b + 2\sigma_x)^{-1/2},$$

and then the optimized total emittance (neglecting correlations as well as thermal emittance) is:

$$\epsilon_{min} \approx \left[ \epsilon_{rf}^2 + \epsilon_{sc}^2 \right]^{1/2} \approx 5.4 \times 10^3 q (E_0 \sin \phi_0)^{-1} (\sigma_b + 2\sigma_x)^{-1}$$

Since the minimum emittance is proportional to the charge  $q$  (and thus to the peak current), the highest brightness is not necessarily associated with the highest charge. Since we have left out the thermal emittance in these expressions, one should not conclude that the brightness is maximized for a vanishingly small charge.

The minimum emittance (using the given optimized frequency) is inversely proportional to the electric field. Thus clearly for a given set of beam parameters (charge, bunch size), we would like to apply the highest possible electric field. As we increase the field (*ceteris paribus*) the optimal frequency is lowered. However, for a number of practical reasons the technically achievable field is smaller at lower frequencies. At some field and frequency the PI will operate at the limit of breakdown or available rf power. Once we cross that limit the assumptions of the optimization break down and one can not apply these results.

The beam of a PI has significant correlations of the longitudinal position and transverse phase space. This is the key to 'emittance correction' schemes (discussed later on). When one uses an emittance correction scheme of one sort or another, the space charge emittance is reduced. This will invalidate the conditions of the calculation presented above, pushing the optimum towards lower frequencies, lower electric fields and smaller beam size.

It is instructive to compare the Kim model with beam dynamics modeling. There are a number of codes in use, e.g., PARMELA [15] and MAGIC [16]. The comparison, shown in Fig. 2, has been done with the MAGIC particle-in-cell code [5]. The simulation is for a 3 1/2 cell PI operating at 2856 MHz,  $E_0=100$  MV/m,  $\sigma_x=4$  mm and  $\sigma_b=2$  ps. The output energy is 10 MeV. This code includes the effect of image currents, space charge, and wakefields. The MAGIC simulation was done with truncated Gaussian distributions in  $r$  and  $t$ . This was compared to Kim's model with a full Gaussian distribution. The emittance is sensitive to the distribution details, thus the somewhat better emittance of the simulation is not surprising.

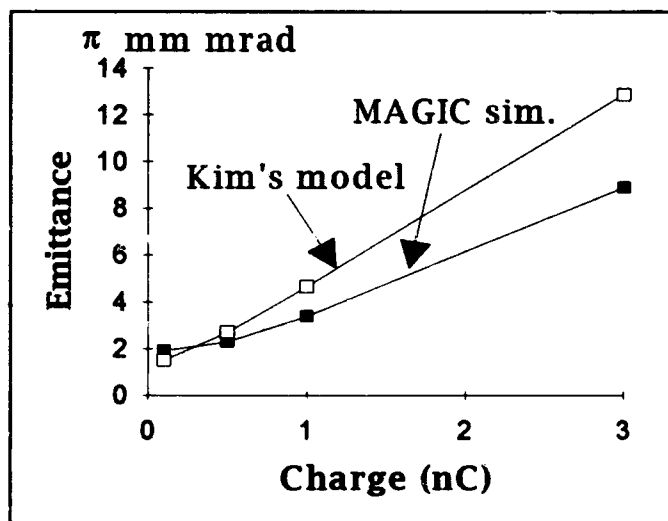


Fig. 2. Normalized rms emittance vs. charge comparing the MAGIC code to Kim's model.

The axisymmetric gun geometry (2-D) was modeled with the exact gun fields. This is accomplished by prescribing the magnetic field for the fundamental  $TM_{01}$

cylindrical cavity mode and allowing the cavity to ring while numerically damping out higher order modes. The fields are then stored and used for later runs with particles. The damping of higher order modes is turned off for the particle runs.

The advantage of using the MAGIC codes is that the field components at the cavity apertures and beam exit are continuous, the method of calculating the space charge forces is inherently more stable and wake fields are included. In the computation the numerical grid for calculating the fields is made very fine near the emission spot and the time steps are small enough to avoid plasma frequency and grid type instabilities, and to properly resolve the temporal behavior of the wakefields. The agreement between simulation and model is quite good for such a closed-form simple model. Thus we may use the model for initial parameter choice. The thermal emittance was left out of the model (but included in the MAGIC calculation). The thermal emittance contribution is difficult to estimate. The effective energy  $E_e$  of the photoemitted electrons is not well determined and may be anywhere between the cathode temperature and the excess energy of the photon relative to the work function modified by the Schottky effect modified. The thermal emittance is given by

$$\epsilon_n = \sigma_r \left[ 2E_e (3mc^2)^{-1} \right]^{1/2}$$

The cathode spot size is set to optimize the total emittance and thus depends on the charge. Experimental results from PIs indicate that the thermal emittance can be neglected at charges larger than 1 nC.

## DESIGN CONSIDERATIONS

In designing a PI one must remember that it is but one component of a larger complex machine including an rf source, laser, diagnostics, beam transport system and an accelerator. In certain designs there is also a cathode preparation system and an UHV system or a cryogenic system. To design a PI one must make use of accelerator physics, laser technology, rf cavity design and more. The objective is not always a high brightness beam, but may be high charge pulses or high duty factor. All of these considerations influence the PI design. The high brightness of the PI will be diluted by any one of a large collection of effects: Wake fields, beam transport aberrations, space charge induced emittance growth (both linear and non-linear), skew quadrupoles and more. For example, ambient magnetic field  $B$  on the cathode (from magnetic lenses or ion pumps), produces an emittance increase given by

$$\epsilon_n \approx \left[ \epsilon_{n0}^2 + e^2 B^2 \sigma_r^4 m^{-2} c^{-2} \right]^{1/2}$$

Thus fields of the order of 10 gauss may be detrimental. The phase space beam parameters of a PI electron bunch are highly correlated, leading to emittance growth on one hand but to emittance correction possibilities on the other. Space-charge forces produce an energy spread in the

bunch. This energy spread may appear in the middle of a magnetic transport system designed to be achromatic and defeat the achromaticity. Good design practices call for a rapid acceleration of the beam to a few tens of MeV before applying dipole fields. Thus, magnetic pulse-compression is better done above, say, 70 MeV. Pulse-compression has always been part of conventional electron gun technology. Although the beam pulses of a PI start out short, the brightness can be further increased by magnetic pulse-compression. A PARMELA simulation of the magnetic pulse-compression at about 80 MeV, the peak current of a 7 ps long, 2.5 nC bunch was increased by a factor of 3 to 800 amp. The emittance, about  $4 \pi$  mm mrad before compression, increased to  $6 \pi$  mm mrad in the bending plane and unchanged off the bending plane [17]. The accepted estimate of the emittance increase due to magnetic compression is

$\Delta \epsilon_n \approx 5I\gamma^{-2}$ . This is much smaller than the simulation result, suggesting that some improvement may be made in the magnetic compressor optics.

An interesting PI subject is emittance correction. We define the 'slice-emittance' as the transverse emittance measured for a short longitudinal slice of the bunch. It has been observed [18,19] that the slice-emittance is considerably smaller than the total emittance (that is integrated over the full length of the bunch). This effect is due to the variation of the space-charge force as a function of longitudinal position in the bunch. Carlsten [18] proposed a simple scheme of reducing the total emittance by using the space-charge force to compensate its own effect. The method employs a lens set to produce a beam size extremum with no cross-over. The electrons 'reflect' relative to the beam axis due to space-charge forces. This condition, that can restore the effects of the linear space-charge force, has been verified in experiments (see next section). It has been assumed that to produce this emittance correction a solenoid lens must be placed in proximity to the cathode and the cathode field must not exceed a certain limit. This assumption has been proven wrong [17,20]. A PARMELA simulation and an analytic-approximate model show that this correction can be applied to a 1 1/2 cell BNL gun operating at 100 MV/m with a solenoid placed at the exit of the gun. A drift space and accelerating structure follow the lens. The acceleration 'freezes' the corrected emittance against further space-charge effects.

The Carlsten technique corrects linear space-charge effects. Other correction schemes have been proposed [6,19,21] to produce the same correction by laser pulse shaping, Radio Frequency Quadrupoles and asymmetric rf cavities, respectively. However the Carlsten scheme is simple and has been tested experimentally. Other correction schemes have been proposed to correct rf time dependent effects [22] and non-linear space-charge effects [21,23]. Finally, a correction scheme for ultra-short, disk-like bunches using an optimized charge distribution has been proposed by Serafini [24].

The emittance correction techniques are expected to exert a significant influence on the design of future PIs. The optimization strategy described above leads a choice of frequency and cathode field. When an emittance correction scheme is in use the optimal frequency will be lower and the usable bunch length longer. Alternately the same gun parameters may be used to produce a higher charge. At the higher charges, more attention will be necessary to non-linear space-charge effects and it is expected that non-linear correction techniques will be necessary.

Another interesting line of R&D is the superconducting PI [25]. This device holds the promise of cw operation at very low rf power. Since the rf power is the largest cost item in a PI, superconducting devices also hold the promise of lower system cost.

### MEASURED PERFORMANCE

By now there have been many experimental results of PI performance. In general, careful experiments are in agreement with the simulation codes, thus it can be concluded that the better computer codes have been benchmarked.

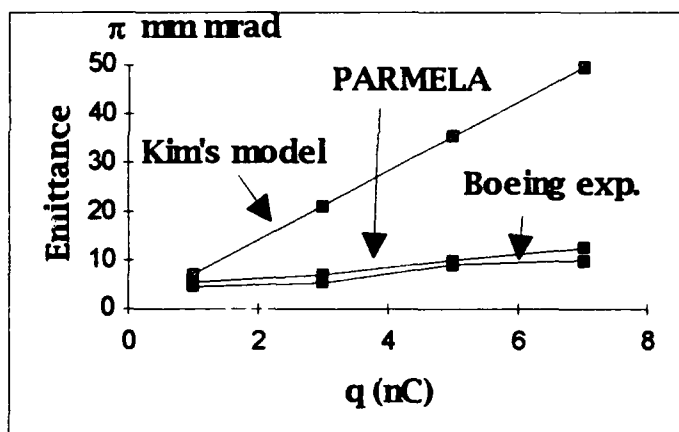


Fig. 3. Normalized rms emittance vs. charge for the Boeing PI compared to Kim's model.

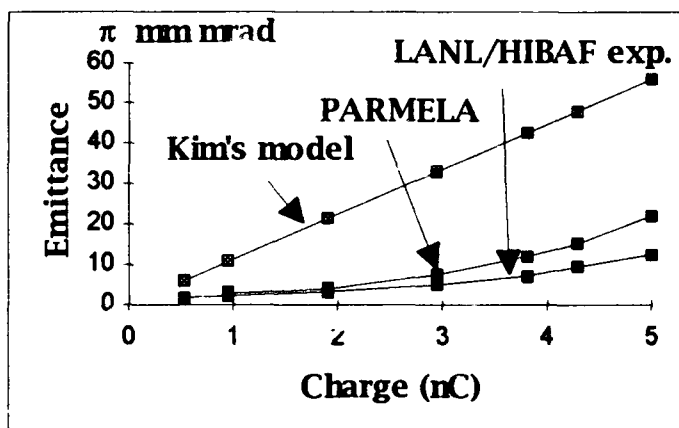


Fig. 4. Normalized rms emittance vs. charge for the LANL/HIBAF PI compared to PARMELA (with wake field) simulation and Kim's model.

Of the most recent results, the Boeing [26] and Los Alamos [27,28] results are noteworthy. The Boeing two cell PI is impressive not only in its emittance results, shown in Fig. 3, but also in its duty factor of 25%. Such a PI would be ideally suitable for very high average power FELs and perhaps linear colliders. It operates at a frequency of 0.433 GHz, a cathode field of 26 MV/m a radial bunch size of  $\sigma_x=2$  mm and longitudinal size of  $\sigma_b=20$  ps. The final energy is 5 MeV. A focussing solenoid is placed between the two cells. From the comparison to Kim's model clearly the emittance correction used in the experiment is very effective. The PARMELA simulation (using the 90% beam emittance) is in good agreement with the experiment.

The Los Alamos gun design has been evolving from the original, single cell design to the six cell HIBAF injector [10] to the 11 cell AFEL integrated gun/linac design [28]. The HIBAF emittance measurements [27] are shown in Fig. 4. This six cell 1.3 GHz PI operated at  $E_0=24.5$  MV/m,  $\sigma_x=3-5$  mm,  $\sigma_b=6.6$  ps. The emittance is measured after acceleration to 36 MeV. This PI has been the first to use the Carlsten emittance correction technique. Fig. 4 shows clearly the correction relative to Kim's model prediction for an uncorrected emittance. The measurement is bracketed by two PARMELA simulations. One, which includes wake-field effects (shown in Fig. 4) predicts a somewhat larger emittance. The other (not shown) predicts a slightly better emittance. Both show clearly the emittance correction at work.

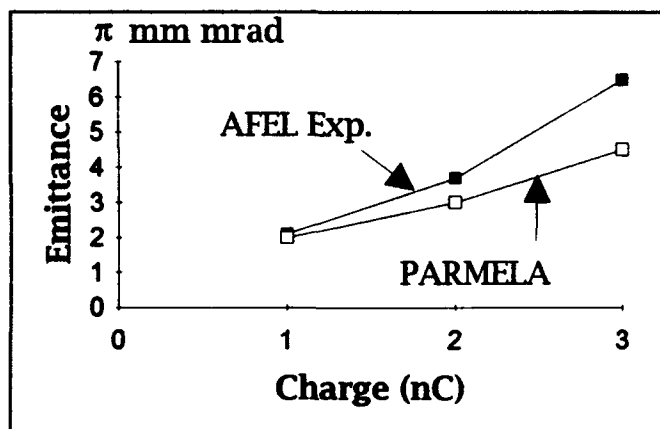


Fig. 5. Normalized rms emittance vs. charge for the LANL/AFEL PI experiment and PARMELA simulation.

The best performance in terms of emittance at a given charge belongs to the LANL AFEL PI [28], shown in Fig. 5. This 11 cell gun operates at  $E_0=20$  MV/m with a  $C_sK_2Sb$  cathode, final energy 12 MeV. The laser FWHM pulse width is 9 ps. The thermal emittance calculated for the 4 mm radius cathode spot-size is  $1.25 \pi$  mm mrad, assuming thermalized photoelectrons. The design final energy is 20 MeV. A better brightness is expected at that energy.

The PARMELA simulation suggests that we may expect even better experimental results from this PI.

## REFERENCES

1. J. Fraser, R. Sheffield, E. Gray and G. Rodenz, *IEEE Trans. Nucl. Sci.* **32** (5), 1791 (1985).
2. I. Ben-Zvi, J. Corbett, E. Johnson, K.J. Kim, R. Sheffield, *Workshop on Fourth Generation Light Sources*, Feb. 24-27, 1992 SSRL 92/02 p. 68, Stanford CA.
3. C. Travier, *Particle Accelerators* **36**, 33 (1991).
4. J. Stovall, 1992 Linac Conf., AECL-10728, 285 (1992).
5. I. Lehrman et. al. *Nucl. Instr. & Meth.* **A318**, 247 (1992).
6. J. C. Gallardo and R.B. palmer, *Proc. Workshop Prospects for a 1Å FEL*, p. 136, BNL 52273 1990, Upton NY 11973.
7. K. Batchelor, J. Sheehan and M. Woodle, BNL-41766 (1988), Upton NY 11973.
8. K. McDonald, *IEEE Trans. Elec. Dev.* **ED-35** 2052, 1988.
9. T. Srinivasan-Rao, J. Fischer and T. Tsang, *Journal Appl. Phys.* **69**, 3291 (1991).
10. P.G. O'Shea et. al. *Nucl. Instr. & Meth.* **A318**, 52 (1992).
11. D.J. Bamford, M.H. Bakshi and D.A.G. Deacon, *Nucl. Instr. & Meth.* **A318**, 377 (1992).
12. P. Davis et. al. 'Quantum efficiency measurements...', *Proc. 1993 Part. Accel. Conf.*, May 17-20, Washington DC.
13. K.P. Leung, L.H. Yu and I. Ben-Zvi, *SPIE Proceedings* Vol. 2013, 1993.
14. K-J. Kim, *Nucl. Instr. & Meth.* **A275**, 201 (1989).
15. K. R. Crandall and L. Young, *Compendium of Computer Codes for Part. Accel. Design and Analysis*, LANL rep. LA-UR-90-1766, May (1990) 137.
16. G. D. Warren et. al. *Proc. Conf. on Computer Codes and the Lin. Accel. Community*, LANL Jan 22-25, 1990, LA-11857-Z (1990) 57.
17. J. Gallardo and X. Zhang, BNL, private communication.
18. B.E. Carlsten, *Nucl. Instr. & Meth.* **A285**, 313 (1989).
19. J.C. Gallardo and R.B. Palmer, *IEEE J. of Quantum Electronics* **26** No.8, 1328 (1990).
20. I. Ben-Zvi and J.C. Gallardo, to be published.
21. L. Serafini, R. Rivolta, L. Terzoli and C. Pagani, *Nucl. Instr. and Meth.* **A318**, 275 (1992).
22. L. Serafini, R. Rivolta and C. Pagani, *Nucl. Instr. and Meth.* **A318**, 301 (1992).
23. J. Gao, *Nucl. Instr. & Meth.* **A304**, 353 (1991)
24. L. Serafini, *AIP Conf. Proc. 3rd Workshop on Advanced Accel. Concepts*, Port Jefferson NY June 14-20 1992.
25. A. Michalke, External Report WUB-DIS 92-5, Wuppertal Univ., FB8 - Physik, 5600 Wuppertal 1, Germany.
26. D. Dowell et.al., 'First operation of...', *Proc. 1993 Part. Accel. Conf.*, May 17-20, Washington DC.
27. P. O'Shea et. al., 'Performance of the APEX FEL at LANL', *Proc. 1992 Int'l FEL Conference*, Kobe, Japan.
28. R. Sheffield et. al., 'Operation of the high brightness ...', *Proc. 1993 Part. Accel. Conf.*, May 17-20, Washington DC.

# First Operation of a High Duty Factor Photoinjector\*

D. Dowell, K. Davis, K. Friddell, E. Tyson, C. Lancaster, L. Milliman, R. Rodenburg, T. Aas, M. Bemes, S. Bethel, P. Johnson, K. Murphy, C. Whelen, J. Adamski, D. Pistoiresi, D. Shoffstall  
Boeing Defense & Space Group, Seattle, WA, and  
G. Busch and D. Remelius - Los Alamos National Laboratory, Los Alamos, NM

## Abstract

Tests of the Boeing Average Power Laser Experiment (APLE) injector have demonstrated first-time operation of a photocathode RF gun electron accelerator at 25% duty factor. The multi-alkali photocathode was illuminated by a frequency-doubled, mode-locked Nd:YLF laser. The cathode was placed in the first cell of four single-cell cavities resonant at 433 MHz. The 4 cavities accelerated the beam to 5 MeV. The pulse duration was 8.3 ns and the repetition rate was 30 Hz. True average beam currents of up to 35 mA have been accelerated to 5 MeV for an average beam power of 170 kilowatts. The 35 mA beam current exceeded previous photocathode performance by a factor of 1000.

## I. INTRODUCTION

In order to increase the output power of free-electron lasers (FELs), it is necessary to increase the electron beam duty factor while maintaining excellent beam quality. In recent years, the photocathode RF gun injector has demonstrated the required beam quality at duty factors in the range of a few hundredths of one percent<sup>1</sup>. However, questions remained concerning photocathode lifetime at high RF duty factor due to vacuum contaminants or damage by the drive laser.

The APLE injector test results presented here demonstrate the successful operation of a photocathode RF gun at duty factors up to 25%. The APLE injector operating parameters are given in Table I.

## II. DESCRIPTION OF THE PHOTOINJECTOR

The APLE RF photocathode gun injector consists of two low beta RF cavities operating at 433 MHz with a K<sub>2</sub>CsSb multi-alkali cathode residing at one end of the first cavity. These two cavities accelerate the electrons to 1.8 MeV and are followed by two additional 433 MHz cavities, which further accelerate the beam to 5 MeV. Solenoids provide an axial magnetic field to contain the electrons during acceleration. The accelerator beamline uses three quadrupole doublets to transport the beam on a path through a three-dipole, doubly-achromatic chicane, or with the chicane dipoles off, straight ahead to a high-power beam dump. The first quadrupole doublet is also used to prepare the beam for the emittance measurements on the view screens SC1 and SC2. Ferrite current monitors and stripline beam position monitors are used to determine the beam charge, current and location without intercepting the beam. The stripline measurements are especially important during high-power operation. A current monitor, CM1, located between the two pairs of RF cavities, and the drive-laser intensity are monitored to determine the photocathode quantum efficiency and lifetime. Figure 1 shows the overall configuration of the APLE injector experiment including both the beamline components and the optical path of the drive laser. The optical path between the laser room and the photocathode in the accelerator pit is approximately 30 meters.

Table I  
Operating Parameters of the APLE Injector

<b>Photocathode Parameters:</b>		<b>Laser Parameters:</b>	
Photosensitive Material	K <sub>2</sub> CsSb Multi-alkali	Micropulse Length	53 ps, FWHM
Quantum Efficiency	5% to 12%	Micropulse Frequency	27 x 10 <sup>6</sup> Hertz
Peak Current	132 amperes	Macropulse Length	10 ms
Cathode Lifetime	1 to 10 hours	Macropulse Frequency	30 Hertz
<b>Gun Parameters:</b>		Wavelength	527 nm
Cathode Gradient	26 MV/meter	Spot Size	3-5 mm FWHM at the cathode
RF Frequency	433 x 10 <sup>6</sup> Hertz	Angle of Incidence	normal
Final Energy	5 MeV	Distribution	gaussian, space and time
Duty Factor	25%	Micropulse Energy	.47 microJoule
Energy Spread	100 to 150 keV	Energy Stability	1% to 5%
Emittance (four x RMS)	20 to 40 pi*mm*mrad		
Charge	1 to 7 nCoulomb		

\*Work supported by USASDC/BMD contract DASG60-90-C-0106.

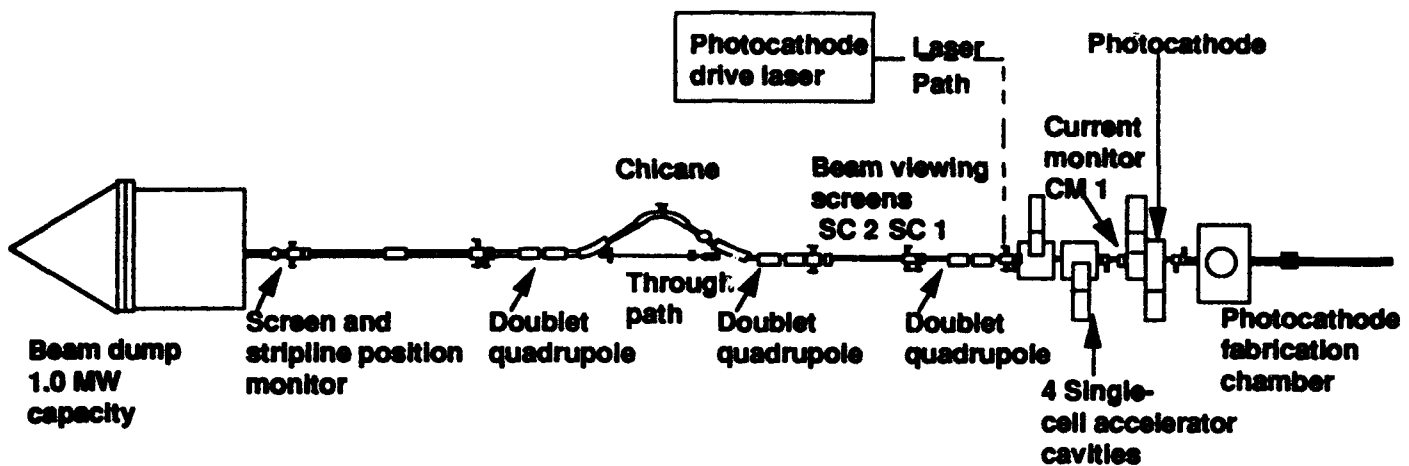


Figure 1. The Average Power Laser Experiment (APLE) RF gun photoinjector. The photocathode resides at one end of the first RF cavity and is illuminated by a 527 nm drive laser. The drive laser is injected using a small off-axis mirror. The emittance growth is controlled by the injector coil and permanent magnet correctors located between the first two cavities.

The photocathode is illuminated by a frequency-doubled, cw mode-locked Nd:YLF drive laser which is injected slightly off axis of the electron beam, striking the cathode at near-normal incidence. The drive laser details have been discussed elsewhere<sup>2</sup>. An optical mask slightly truncates the tails of the gaussian drive laser beam to reduce the beam intensity by only 20 to 30%. Computer simulations<sup>3</sup> indicate the electron beam emittance is sensitive to the drive laser shape and predict that a sharp-edged, top-hat profile leads to the best emittance. Therefore, the emittances presented in this paper are not necessarily the best achievable by this photoinjector.

### III. EMITTANCE MEASUREMENTS

The electron beam emittance was determined using the two-screen method<sup>4</sup>. The beam profiles were verified to be gaussian in shape for 90% to 95% of the beam intensity. This justified quoting the four times rms emittance as the approximate 93% emittance.

Figure 2 shows the emittance measured at charges of 1, 3, 5 and 7 nC per micropulse. For these measurements, the beam pulse format was 1 hertz with 100 microsecond-long macropulses. This format was chosen to limit damage to the view screens. The profiles were obtained by orthogonal projection. The experimental data (shown with error bars) are the best emittances at each micropulse charge. The optimum value was experimentally obtained by tuning the injector coil current. The experimental emittance approximately follows the linear dependence of  $(12.7 \pi + 4\pi Q)$  mm·mR where Q is the micropulse charge in nanocoulombs.

The emittances calculated with a customized version of PARMELA using the experiment conditions are also shown in figure 2.

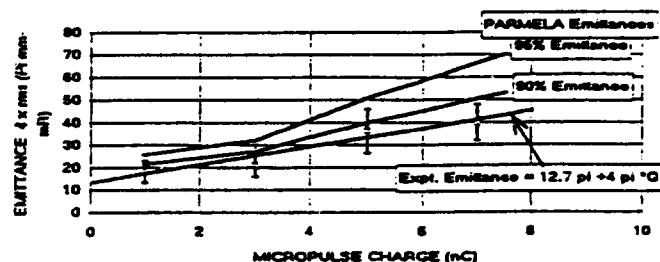


Figure 2. Optimized emittance as a function of micropulse charge. The 90% and 95% PARMELA emittances exceed the measured four times rms emittances.

A customized PARMELA was necessary to properly model misalignments of the injector coil and their correction by permanent magnet dipoles<sup>5</sup>. The emittances are calculated by circumscribing 90% and 95% of the macroparticles (usually numbering 2000) in transverse phase space with ellipses. The ellipse areas are proportional to the emittance.

The calculated emittances are higher than the experimental values at all measured beam charges. A partial explanation involves the five to ten percent of the beam which is outside the assumed gaussian beam shape. Beam halo experiments performed during the high-duty test indicated that the halo emittance at 3 nC per micropulse is approximately  $200 \pi$  mm·mR. Adding this emittance with the four times rms emittance, with each weighted by its respective fraction gives  $38.8 \pi$  mm·mR, only five percent larger than  $37 \pi$  mm·mR, the four times rms value and cannot fully account for the discrepancy with PARMELA.

#### IV. High-Duty Test Results

At average beam powers in the range of 170 kW, it was essential to operate the injector at low emittance and with minimum beam halo. It was equally important to carefully adjust the beam transport to the dump, since only a tenth of the beam power, if focused, would damage the vacuum pipe, or if defocused, would lead to significant vacuum outgassing. Several beam interlocks were used to turn off the drive laser or *crowbar* the RF system in the event of unsafe operating conditions. These interlocks included the RF cavity and beamline vacua, cavity-reflected RF power, beam-loss radiation detectors, and beamline and beam-dump temperature measurements. In addition, the last current monitor in the beamline was used to detect the absence of electron beam when the drive laser was present. This loss-of-beam interlock had a response time of a few microseconds and was especially effective in protecting the beamline during an RF system crowbar. These interlocks allowed safe operation of the injector at the higher beam powers.

Conditioning the APLE injector for high-duty factor operation was quite similar to the seasoning of a high-power klystron. When the duty factor is increased, the accelerator gas load quickly rises and the beam has to be turned off to allow the beamline and beam dump to recover. During repeated high-duty operation, the beamline and beam dump are *scrubbed* by the electron beam, and the improved vacuum allows longer run times. This means that operating time at high beam power depends both upon the beam quality and transport efficiency, and ultimately, on the history of conditioning performed at high power.

Figure 3 shows the electron beam micropulse charge and the average beam power for three successive runs at duty factors between 15% and 25%. The micropulse charge was 5 nC or greater, and the average beam power ranged from 80 to 170 kW. It is significant that these three runs were performed using the same photocathode which survived repeated beam shut down while operating at high beam power. This result demonstrates that high quantum efficiency, multi-alkali photocathodes can be used to generate high current beams for high duty factor free-electron lasers. The cathode 1/e lifetime in this case was 2.7 hours. The second important feature of figure 3 is that the runs lasted one to three minutes, and were not single high-power shots. As discussed before, the length of the runs was limited principally by beamline and beam dump vacuum conditioning and to a lesser extent by RF power system reliability.

The 1/e lifetimes for the photocathodes used during the high-duty test are given as a function of duty factor in figure 4.

The static, or no beam (0% duty factor data), lifetimes range from less than an hour to ten hours, resulting from experiments performed under a wide range of vacuum and cathode conditions. From 1% to 25% duty factor, the average

lifetime is 2.3 hours, which again, demonstrates cathode lifetime is not dependent upon duty factor but depends instead, upon the static or low-power vacuum pressure.

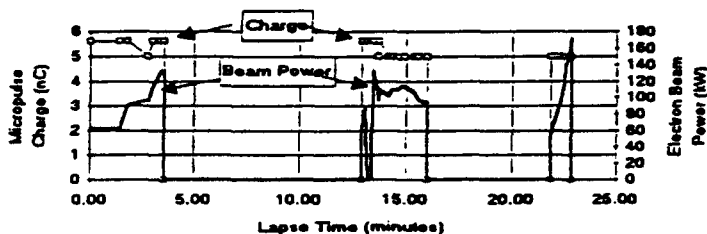


Figure 3. APLE injector accelerated micropulse charge and average beam power for three successive runs on the same cathode. The duty factors ranged between 15% and 25%.

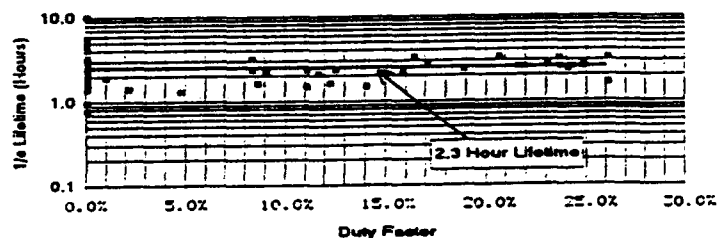


Figure 4. The photocathode 1/e lifetime measured from .1% to 25% duty factor. Above 1%, the average lifetime was 2.3 hours with no significant dependence upon duty factor or beam power.

#### V. SUMMARY AND CONCLUSIONS

This work demonstrates the first-time operation of a photocathode injector at high-average power. The APLE injector has been successfully operated at average beam powers up to 170 kW, with a beam energy of 5 MeV. The average cathode 1/e lifetime was 2.3 hours and was independent of the electron beam duty factor and beam power. Work is currently underway to incorporate this injector into an 18 MeV accelerator as part of an average-power free-electron laser.

#### VI. REFERENCES

1. D.W. Feldman, et al., IEEE J. Quantum Electron. QE-27, 2636 (1991); P.G. O'Shea, et al., Nucl. Instrum. Methods A318, 52 (1992); R. Dei-Cas, et al., Nucl. Instrum. Methods A318, 372 (1992).
2. G.E. Busch, et al., Conf. on Lasers and Electro Optics, 1992, Vol. 12, OSA Technical Digest Series (Optical Society of America, Washington DC), pp 278-279.
3. B.E. Carlsten, et al., IEEE J. Quantum Electronics, Vol. 27, No. 12, December 1991, p. 2580-2597.
4. B. Carlsten, et al., Nucl. Instr. and Meth. A272 (1988) 247 and D.H. Dowell, et al., Nucl. Instr. and Meth. A318 (1992) 447.
5. H. Takeda and B.D. McVey, Nucl. Instr. and Meth. A318 (1992) 644.

# Operation of the High Brightness LINAC for the Advanced Free-Electron Laser Initiative at Los Alamos\*

R. L. Sheffield, R. H. Austin, K. D. C. Chan, S. M. Gierman, J. M. Kinross-Wright, S. H. Kong, D. C. Nguyen, S. J. Russell, and C. A. Timmer  
Los Alamos National Laboratory  
Los Alamos, NM 87545

## Abstract

Free-electron lasers and high-energy physics accelerators have increased the demand for very high-brightness beam sources. This paper describes the design of an accelerator which has produce beams of  $2.1 \pi$  mm-mrad at 1 nC and emittances of 3.7 and  $6.5 \pi$  mm-mrad for 2 and 3 nC, respectively. The accelerator has been operated between 10 and 18 MeV. The beam emittance growth in the accelerator is minimized by using a photoinjector electron source integrated into the design of the linac, a focusing solenoid to correct the emittance growth caused by space charge, and a special design of the coupling slots between accelerator cavities to minimize quadrupole effects.

## Introduction

A new accelerator design that produces a very bright electron beam in a compact form has been constructed through the Advanced Free-Electron Laser Initiative (AFELI) [1] at Los Alamos National Laboratory. State-of-the-art components were incorporated so that the FEL system will be compact, robust, and user friendly.

The design goals for the accelerator were: greater 2 nC charge per micropulse and an effective emittance of less than  $5 \pi$  mm-mrad. Simple design is accomplished by using a single radio-frequency feed to drive the entire accelerator structure. The accelerator (Fig. 1) design has the following features: maximum 20-MeV output energy, maximum average cell gradients of 22 MeV/m, up to 100-Hz repetition rate, up to 30- $\mu$ s long macropulses, 8- to 20-ps long micropulses, and liquid-nitrogen operation capability. The accelerator operates with a 1300-MHz, 17-MW-peak-power klystron.[1]

## Simulations

The following definition is used for the normalized rms emittance in the simulations,

$$\epsilon_n = \beta \gamma \epsilon_x = \pi \beta \gamma [\langle x^2 \rangle \langle x'^2 \rangle - \langle x \cdot x' \rangle^2]^{1/2},$$

where  $\gamma$  is the relativistic factor,  $\beta$  is the particle velocity, divided by the speed of light,  $x$  is the transverse beam size,  $x'$  is the transverse beam divergence, and  $\epsilon_x$  is the unnormalized emittance. The emittance is calculated in two ways. The "full" emittance is calculated in the conventional manner by using the entire micropulse in time and space.

\*Work supported by Los Alamos National Laboratory Institutional Supporting Research, under the auspices of the United States Department of Energy.

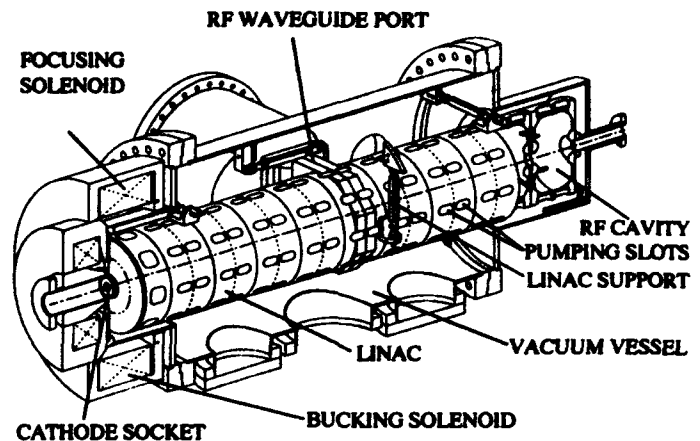


Figure 1. AFEL linac schematic. The focusing solenoid provides compensation of space-charged induced emittance growth. The Bucking Solenoid is adjusted to give zero field at the surface of the cathode. The LINAC is an eleven-cell  $\pi/2$ -mode structure. The LINAC can be operated from 77K to greater than 400K. The support structures allow only rotation of the accelerator on cool-down, not translation.

The "slice" emittance is calculated by dividing a micropulse into slices in time equal to a slippage length (the slippage length is the wavelength of the light times the number of wiggler periods). To ensure enough particles are in a slice to give reasonable statistics, the smallest time slice is limited to 1% of the total pulse length (4000 particles were used in the simulations). We calculate the slice emittance because the electrons are not matched to the wiggler over the entire pulse, but only for the middle portion (in time) of the pulse. Because temporal mixing can occur downstream of the accelerator, the use of slice emittance is only valid at the location of the wiggler.

## Emittance Compensation

Surrounding the first few cells is a large focusing solenoid. The use of a solenoid to correct emittance growth caused by space charge has been discussed in detail in several papers.[2] A brief explanation of emittance compensation follows. As an electron bunch leaves the cathode, the bunch expands radially because of radial space charge forces. Since the space charge force acts continuously on the bunch, no single discrete lens can compensate for the distortion of the distribution in phase space. However, a simple lens can be used to focus the bunch. Then, to the first order, the same forces that acted on the bunch during expansion are present while the bunch is focused. Thus, the emittance growth that has occurred can be significantly reduced by proper lens placement. The position and magnitude of the lens is determined using PARMELA simulations. To accurately render the solenoid

field profiles, we incorporated the POISSON field maps of the solenoid directly into a modified version PARMELA.

### *Coupling Slot Arrangement*

The standing-wave, 1300-MHz,  $\pi/2$ -mode accelerator is designed with on-axis coupling slots [2]. By incorporating MAFIA field maps of the coupling slots into PARMELA, we found that coupling cells with only two coupling-slots produced a quadrupole lens in every accelerator cell. Therefore, it was necessary to change the coupling slot geometries to eliminate asymmetric focusing in the accelerator.

The effect of coupling slots is significant for very high-brightness beams. A single slot produces a dipole lens, two slots produce a quadrupole lens, four slots produces an octupole lens, and so on. Each accelerator cell (except the cells at the accelerator ends) has coupling slots on each half of an accelerator cell. The relative orientation of the slots on either end of the cell will determine the relative angle of the corresponding lens. The two-coupling-slot configuration gives a quadrupole lens at the entrance and exit of the accelerator cell. The orientation of the slots will determine whether the focussing due to the quadrupole lens will add or subtract in each cell. Thus, the coupling cells can be configured such that the fields at each cell end cancel, giving a net effect close to zero for a relativistic beam.

The coupling-slot design for the AFEL accelerator uses a four-coupling-slot arrangement for the first two cells. Because the four-slot arrangement has no quadrupole component, then the first two cells produce no beam asymmetry. The four-coupling-slot arrangement cannot be carried throughout the accelerator. At high currents a dipole mode will build up which is easily coupled through a four-coupling-slot cell and causes beam-breakup for more than two cells. After the beam exits the first two cells, the beam is relativistic, and the remaining cells have a two-coupling-slot arrangement that gives a very small net quadrupole focusing.

### *Other Design Features*

The first cell, a half-cell, is 9 mm longer than one-half of a standard 1300-Mhz cell. A longer injection cell has two advantages. First, the exit phase of the electron bunch depends on the cell length. Since the AFEL linac has a single rf feed, the proper operating phase to minimize energy spread was met by adjusting the first cell length. Second, a longer first cell increases the electron-beam energy at the exit of the first cell. This reduces the space-charge effects and helps improve the final emittance. The exit energy from the first cell is 1.5 MeV instead of 1.0 MeV for a regular half-cell.

Other engineering features of the AFEL accelerator are the capability of operation at 77K; UHV design; and high-Q, high-gradient, long-macropulse accelerator cells.

### *Beam Dependencies*

This type of accelerator is unique in that the electron-beam distribution does not mix longitudinally. With no mixing, the rms emittance calculation for the full pulse overestimates the beam

emittance. Except for statistical noise caused by the limited number of particles in the simulation, the slice emittance is time independent during the micropulse. However, the emittance of the full pulse is significantly larger. The larger full-pulse emittance is caused from the variation in divergence throughout the micropulse.

The AFEL is designed to minimize components and distances and to increase reliability and ease of use. However, the stability of accelerator operation does depend strongly on a few parameters. The parameters that must be tightly controlled are the radius of the cathode; the magnitude of the solenoid field around the cathode region; the accelerator phase; and the magnitude of the accelerator fields.

## **Operation of the Accelerator**

The electron source is a CsK<sub>2</sub>Sb photocathode. The accelerator pressure is maintained at  $8 \times 10^{-10}$  Torr. The beamline directly downstream of the accelerator is at  $2 \times 10^{-8}$  Torr. Because of contaminants produced during operation of the rf, the useful operational lifetime of a single cathode, for a minimum 1 nC, is 2 days. The accelerator has six cathodes available in a cartridge type system. Thus, the cathode cartridge system was refreshed every two weeks. Typical time to replace a cartridge pack was 15 minutes. After replacement, a 4 to 5 hour bake degassed the components exposed to air (typically done during the night).

The drive laser was Nd:YLF. The oscillator produces 50 ps micropulses at 108 MHz. The pulses are then compressed with a grating pair and a fiber-optic line to 8 ps. After compression, two double-pass YLF amplifiers are used to increase the micropulse energy to 25 microjoules. A Pockels Cell is used to obtain macropulses which ranged from a few micropulses to 10 microseconds. A KTP crystal is then used to double the wavelength to 526 nm with a micropulse energy of 8 microjoules. The gaussian spatial profile of the laser beam is sent through an iris that just lets the middle 40% of the light pass. This approximately-uniform spatial profile is then imaged onto photocathode.

The accelerator was initially conditioned for operation from 9 to 16 MeV. Since this initial conditioning, the maximum energy has been extended to 18 MeV through the course of normal operation. However earlier this year, after a year of operation, the accelerator has begun to multipactor. This has limited the minimum beam energy to 14 MeV. Since the FEL requires an electron energy between 15 to 16.5 MeV, cleaning the accelerator to eliminate the multipactoring will be done at later date.

## **Experimental results**

The emittance measurements were taken at an electron beam energy of 13 MeV. A quadrupole is positioned 30 cm upstream from an OTR screen. The FWHM of the electron beam was measured as a function of the quadrupole field strength. The 1 nC data set is shown in Fig. 2. Similar sets were obtained for 2 and 3 nC micropulse charges.

The electron beam produced by this accelerator is characterized by a bright temporal core with high-divergence

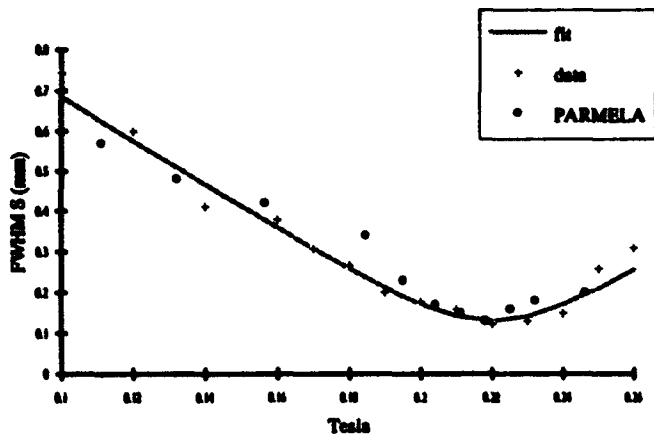


Figure 2. Experimental and simulation data for the 1 nC emittance measurement. The simulation data has statistical uncertainty due to the finite number of particles and the distribution of simulation points into bins. The solid curve is a fit to a quadrupole scan function that gives the beam emittance and other beam characteristics.

wings at the front and back of the pulse. Very little charge is present in these wings, but, due to the large divergence, the wings significantly increase the rms emittance of the beam. Because of the small amount of charge, the wings are too tenuous to be observed in the experimental data.

The only means to characterize the performance of the accelerator is to also simulate the quadrupole scan with PARMELA, and then compare the experimental observable - the beam's FWHM size. Figure 3 compares the full rms emittance with the slice emittance and the emittance as calculated by using the FWHM. The emittance as calculated from the FWHM is very close to the slice emittance (the emittance used by the FEL).

The FWHM simulation results for the 1 nC case is given in Fig. 2. The agreement between the experiment and simulation is good, indicating that the accelerator is performing as designed for 1 nC.

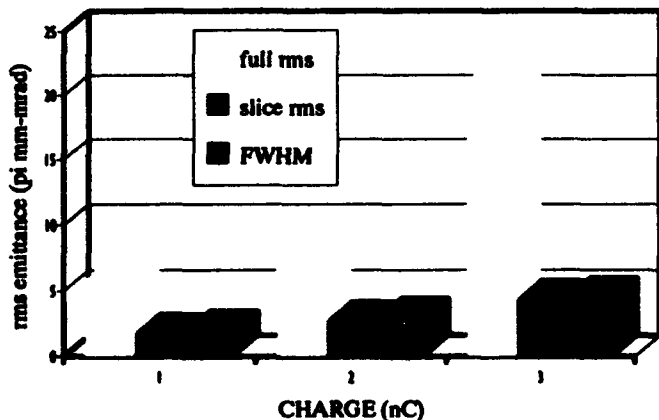


Figure 3. Comparison of PARMELA emittances calculated for the whole beam (full rms), for the rms emittance of a slice (slice rms), and for the FWHM measured from the plot of beam particle number versus transverse dimension (FWHM).

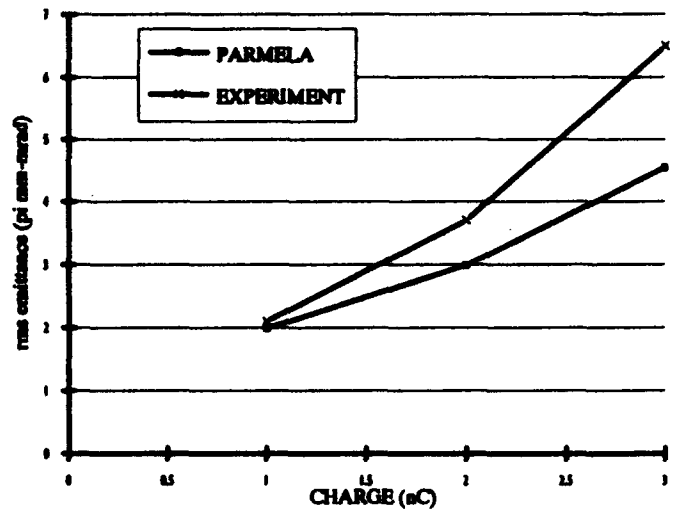


Figure 4. Comparison of experimental and simulation results for several charges.

The emittances for 1, 2, and 3 nC are in Fig. 4. As stated earlier, the agreement is good for 1 nC. However, as the charge is increased the experimental emittance is larger than expected. We have not explored the reason for the increase.

## Summary

At 1 nC, the emittance of  $2.1 \pi$  mm-mrad is in good agreement with PARMELA simulation. The measured emittances for 2 and 3 nC are 3.7 and  $6.5 \pi$  mm-mrad, respectively.

## References

- [1] K. C. D. Chan, R. H. Kraus, J. Ledford, K.L. Meier, R. E. Meyer, D. Nguyen, R. L. Sheffield, F. E. Sigler, L. M. Young, T. S. Wang, W. L. Wilson, and R. L. Wood, Nucl. Inst. Meth. in Phys., A318, 148 (1992). R. L. Sheffield, B. E. Carlsen, and L. M. Young, Proc. Linear Accel. Conf., AECL-10728, 1,46 (1992).
- [2] B. E. Carlsen, Proc. 10th Int. FEL Conf., Jerusalem, Israel, 1988, Nucl. Instr. and Meth., A285 (1989) 313; B. E. Carlsen and R. L. Sheffield, Proc. 1988 Linac Conf., Williamsburg, Va, 1988, CEBAF Report 89-001 (1989) 365; B. E. Carlsen, Proc. 1989 IEEE Part. Accel. Conf., Chicago, IL, IEEE Catalog no. 89CH2669-0 (1989) 313.

# Performance of the SLC Polarized Electron Source with High Polarization\*

J. E. Clendenin, R. K. Alley, H. Aoyagi,<sup>†</sup> J. C. Frisch, C. L. Garden, E. W. Hoyt, R. E. Kirby, L. A. Klaisner, A. V. Kulikov, C. Y. Prescott, P. J. Sáez, D. C. Schultz, H. Tang, J. L. Turner, M. Woods, A. D. Yeremian, and M. S. Zolotarev  
Stanford Linear Accelerator Center, Stanford University, Stanford, CA 94309

## Abstract

For the 1992 operating cycle of the SLAC Linear Collider (SLC), the polarized electron source (PES) during its maiden run successfully met the pulse intensity and overall efficiency requirements of the SLC. However, the polarization of the bulk GaAs cathode was low (~27%) and the pulse-to-pulse stability was marginal. We have shown that adequate charge for the SLC can be extracted from a strained layer cathode having  $P_e \sim 80\%$  even though the quantum efficiency (QE) is  $< 1\%$ . The recent addition of a separate chamber to the PES—which allows cathodes to be loaded into the gun after the vacuum bake and after high voltage (HV) processing without breaking vacuum—increases the reliability for achieving an adequate photoelectron yield. A new SLAC-built pulsed Ti:sapphire laser permits operation of the PES at the required wavelength with sufficient power to fully saturate the yield, and thus improve the  $e^-$  beam stability. The performance of the PES during the 1993 SLC operating cycle with these and other improvements is discussed.

## I. INTRODUCTION

In 1992, during the first SLC run with a polarized beam, the SLC performance was an impressive improvement over previous years. The luminosity of the accelerator and the efficiency of the detector were improved sufficiently for the SLAC Large Detector (SLD) to log over 10,000  $Z^\circ$ s with an average electron polarization at the Interaction Point (IP) of 23% during a run of approximately four months. The average (best) luminosity achieved by the end of the run was 18 (25)  $Z^\circ$ /hour. The goals for 1993 were to achieve at least 50,000  $Z^\circ$ s on tape with an electron polarization  $> 35\%$  at the IP. To meet these goals, it was estimated that the average (peak) luminosity should be about 23 (30)  $Z^\circ$ /hour. As shown in Table 1, the SLC/SLD are well on the way to meeting these goals. As will be discussed in more detail below, the polariza-

tion has been increased to  $> 60\%$  at the IP, and the average (peak) luminosity is now about 35 (45)  $Z^\circ$ /h, or in excess of 500  $Z^\circ$ /day.

For 1993, the SLC peak luminosity has been improved primarily by reducing the betatron coupling in each of the Damping Rings (DR) to produce flat beams. In addition, the average luminosity has been given an added boost by careful attention to reliability details, leading to a significant increase in efficiency. To improve the polarization, the energy of the  $e^-$  DR was increased to produce the correct spin precession to the linac-to-ring (LTR) spin rotator, thus reducing a 5% (relative) depolarization effect to ~2%. However, the primary reason for the increased polarization of the electron beam is the inauguration in the PES of specially designed cathodes that remove the degeneracy at the  $\Gamma$  point between the heavy-hole and light-hole valence bands. Photoexcitation of such cathodes, using circularly polarized light of the proper wavelength, produces highly polarized electrons.

## II. CATHODES FOR HIGH POLARIZATION

The theoretical upper limit for the polarization of photoelectrons from bulk-grown NEA GaAs is 50%. Typically, the actual polarization is much lower unless very thin active layers or cryogenic temperatures are used. For 1992, the SLC PES operated with a bulk GaAs cathode at room temperature, resulting in a polarization at the source of only 27% [1].

Highly polarized electrons from photocathodes have been the focus of efforts at SLAC and other laboratories for many years. The first demonstration of success was at SLAC [2] in 1991, followed soon thereafter by similar results at Nagoya [3]. The technique employed is to introduce a uniaxial tensile strain in the growth direction by growing the active layer on a substrate with an appropriately smaller lattice constant. Above a certain critical thickness, the strain thus induced will decrease, so the active layer must be kept no thicker than a few hundred nanometers.

A crystal cut from an MOCVD-grown [4] 2-inch diameter wafer having a 300-nm active (strained) layer of GaAs(100), Zn-doped to  $5 \times 10^{18} \text{ cm}^{-3}$  and grown on a  $2.5 \mu\text{m}$  p-GaAs<sub>0.76</sub>P<sub>0.24</sub> sublayer, was measured at SLAC to have a peak polarization of ~80% at ~860 nm (room temperature) [5,6]. However, the low intensity QE measured at low voltage was only ~0.1%, which gave rise to concern that it might be difficult to extract the high peak charge needed for the SLC (10 nC per microbunch in the present mode of operation).

A second crystal cut from the same wafer was tested at HV in the SLC gun [7] in a laboratory system having a high power laser tuned to 850 nm, but at present having no polarimeter. The saturated charge (i.e., the maximum charge for high laser power) was found to scale linearly with

Table 1. SLC/SLD Performance/Goals

	Performance		1993	
	1991	1992	Goals	Performance
$Z^\circ$ /h typical		18	23	35
$Z^\circ$ /h peak		25	30	45
$Z^\circ$ /day peak		400	550	600
$Z^\circ$ total	370	1 K	11 K	$> 50$ K
$P_e$ @ IP	0	0	23%	$> 35\%$ ~60%
$P_e$ @ Source	0	0	27%	~80%

<sup>†</sup>Permanent address: Faculty of Science, Nagoya University, Nagoya 464-01, Japan.

\*Work supported by Department of Energy contract DE-AC03-76SF00515.

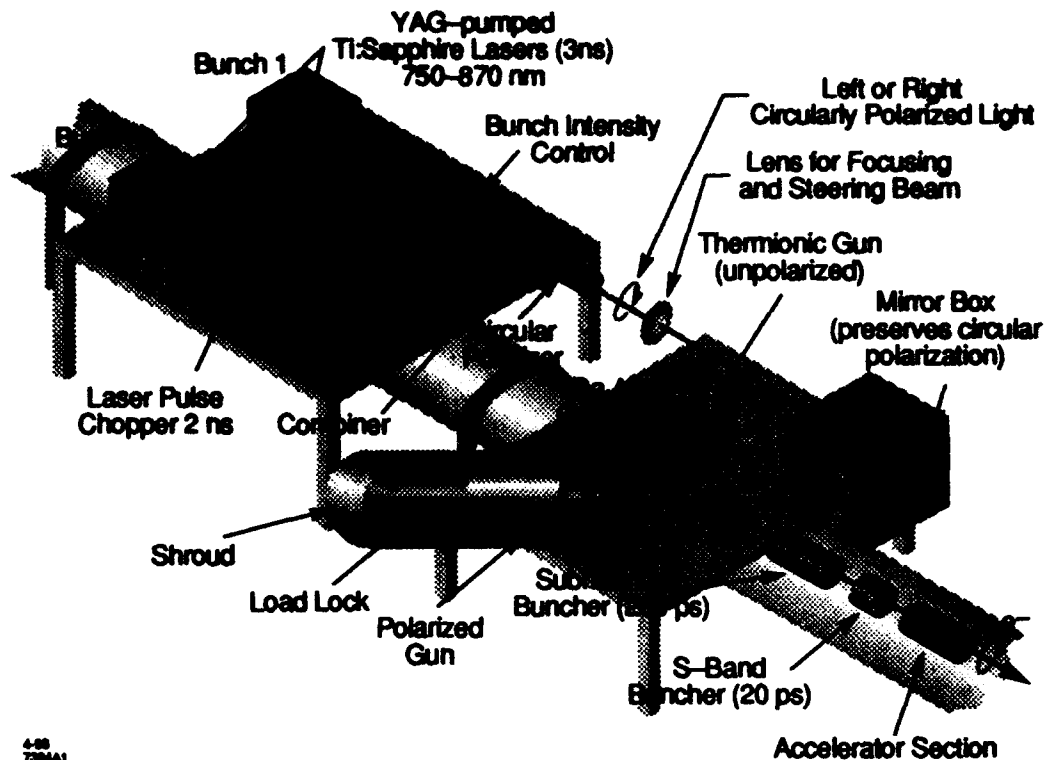


Figure 1. Schematic of the SLC PES for the 1993 SLC/SLD run.

cathode bias, whereas for a low intensity laser, the log of the photocurrent scaled as the square root of the voltage (the expected Schottky effect) [8]. A saturated charge of 19 nC, very close to the space charge limit of ~21 nC, was achieved at 120 kV when the low intensity QE was 1% measured at 830 nm and 120 kV. The improvement in QE was probably due to the use of a load-lock system, as described later. This crystal, together with a third from the same wafer was in the cathode tray of the load lock when the polarized source was installed at the SLC for the 1993 run.

### III. RECENT POLARIZED ELECTRON SOURCE IMPROVEMENTS

The pulsed dye laser used in the 1992 run was limited by power and lifetime requirements to 715 nm, a wavelength too low to permit any polarization gain with the new cathodes. A new Nd:YAG pumped Ti:sapphire laser, Q-switched and cavity-dumped, designed and built at SLAC [9], was installed for this run. This laser, together with associated beam transport optics, provides up to 100  $\mu$ J energy at the cathode in each 2.0 ns FWHM micropulse at wavelengths up to 870 nm.

The addition of a load lock that allows a photocathode to be introduced into the gun chamber after the chamber is baked and HV processed has proven to be a major step in improving the PES performance and reliability [10]. Up to four cathodes can be stored at one time in the load-lock system.

The cathodes are activated in the load-lock system, in part to avoid Cs contamination in the gun itself. Cathode activation

and/or switching of cathodes takes about 8 hours, followed by a period of 10–20 hours in which the gun shroud is purged to remove water vapor before operating at HV. For simple addition of small amounts of Cs to the operating cathode, Cs channels [11] that encircle the  $e^-$  beam are located in the gun chamber just downstream of the anode. The Cs channels are operated remotely through the SLC Control Program (SCP). A schematic of the present PES is shown in Fig. 1. A cross section of the gun is shown in Ref. [12].

### IV. 1993 POLARIZED ELECTRON SOURCE PERFORMANCE

The polarization of the  $e^-$  beam could be measured at 50 GeV by a Møller polarimeter at the end of the linac and by a Compton polarimeter at the IP. The latter was sensitive to the tuning of the Arcs. The wavelength of the PES laser and the Compton polarization were monitored continuously. A sample is shown in Fig. 2. Combined with a Møller measurement made early in the run with the  $e^-$  DR bypassed, the source polarization was found to peak at ~865 nm (cathode at  $-6^\circ\text{C}$ ) with  $P_e \sim 80\%$ .

In its first 10 weeks of operation with a strained layer cathode, the PES was able to provide a highly polarized  $e^-$  beam for the SLC >95% of the time. During the run, the charge limit effect [13] was not a serious limitation [14], although the low-intensity QE following a cesiation touchup was only ~0.5% measured at 830 nm and 120 kV.

The QE was monitored by detecting (using a nanoam-meter attached to the HV electrode) the photocurrent drawn

from the cathode by a modulated 830 nm diode laser (gated off during the beam pulse) attached to a side window of the gun. The nanoammeter was powered and also connected to the SCP through an optical link.

The  $e^-$  intensity was controlled through a feedback system that varied the size of the Ti:sapphire laser spot on the cathode. The laser itself was operated at very high energy so as to keep the cathode always completely saturated. In this manner the  $e^-$  pulse-to-pulse intensity jitter could be kept  $\sim 1\%$ , although the laser energy jitter was often  $>3\%$ . The charge limit did reduce the maximum charge available as a function of cathode surface conditions.

The overall pressure in the gun was  $\sim 10^{-11}$  Torr, dominated by  $H_2$ . As shown in Fig. 3, the rate of decrease of the low intensity QE was not affected the charge extracted from the gun. The QE was found to decrease by  $<0.05\%/day$ . The cathode lifetime was probably extended in this vacuum system by operating the cathode at  $-6^\circ C$  and by the success of the HV processing that reduced the dark current (cathode current at

120 kV with all lasers blocked) to  $<50$  nA [15]. To maintain the required charge, cesium was added in intervals of  $\sim 3$  days.

It was a simple matter to cesiate from the SLC Control Center using the SCP to lower the HV to 1 kV, then to operate the channel cesiator at a fixed 4 A for  $\sim 4$  minutes. To extend the cesiation intervals, the cathode was usually cesiated until the photocurrent dropped  $\sim 20\%$  lower than its peak value. The whole operation took  $\sim 25$  minutes.

## V. NEXT DEVELOPMENTS

Three new developments may improve the source performance even further in the near future. One of the four SLC polarized guns has been modified to double the area of the semiconductor cathode in order to increase the charge limited current. This will be tested soon in the laboratory. Operating the gun at 150 kV instead of 120 kV should also increase the photoelectron emission 25% when charge limited.

Source polarizations  $>90\%$  can be achieved with even thinner strained-layer cathodes [6]. The charge limit for such cathodes is under investigation.

Within the next few months, a Mott polarimeter will be added to the SLC high beam intensity testing system allowing a crystal to be fully qualified for  $P_e$ , QE, charge limit, and lifetime before this same crystal is installed in the operating SLC gun.

## VI. REFERENCES

- [1] D. Schultz *et al.*, "Polarized Source Performance in 1992 for SLC-SLD," presented at the *10th Int. Sym. on H.E. Spin Physics*, Nagoya, Nov. 9-14, 1992.
- [2] T. Maruyama *et al.*, *Phys. Rev. Lett.* **66** (1991) 2376.
- [3] T. Nakanishi *et al.*, *Phys. Lett. A* **158** (1991) 345.
- [4] SPIRE Corp., 1 Patriots Park, Bedford, MA 01730.
- [5] T. Maruyama *et al.*, "Data for Spire 0.3 mm strained GaAs (MO5-1684)," SLAC internal report (1993), unpublished.
- [6] T. Maruyama *et al.*, *Phys. Rev.* **B46** (1992) 4261.
- [7] Active area of SLC cathode has a 14 mm diameter.
- [8] H. Tang *et al.*, "Observation of Non-Linear Photoemission Effects from III-IV Semiconductors," these proceedings.
- [9] J. Frisch *et al.*, "Operation of the New SLC Polarized Electron Source Laser," these proceedings.
- [10] R.E. Kirby *et al.*, "An In-Situ Photocathode Loading System for the SLC Polarized Electron Gun," these proceedings.
- [11] Two SAES Cs channels each with 17 mm active length connected in series.
- [12] D.C. Schultz *et al.*, *Proc. of the Third European Part. Acc. Conf.*, Berlin (1992) 1029.
- [13] M. Woods *et al.*, SLAC-PUB-5894 (1992), to be published in *J. Appl. Phys.*
- [14] The two microbunches required for the SLC were actually produced by separate Ti:sapphire cavities. To minimize charge limiting effects for the second unpolarized microbunch, its laser was tuned to 770 nm.
- [15] P. Sáez *et al.*, "High Voltage Processing of the SLC Polarized Electron Gun," these proceedings.

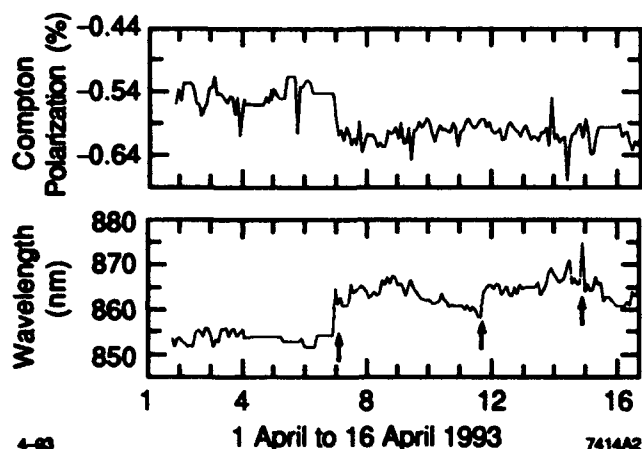


Figure 2. Comparison of PES laser wavelength and Compton polarization over a period of 16 days. The PES wavelength was deliberately changed on April 6, 11, and 14: 853 $\rightarrow$ 865 nm, 859 $\rightarrow$ 864 nm, and 870 $\rightarrow$ 864 nm, respectively.

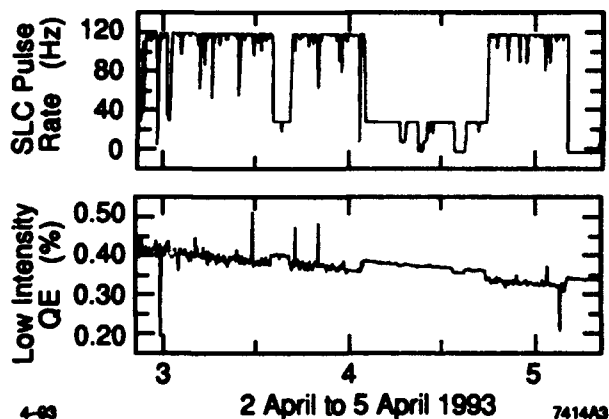


Figure 3. Comparison of the low-intensity QE monitored through a period of  $\sim 15$  hours when the SLC macropulse rate was dropped from the usual 120 Hz to 30 Hz. The offset in the QE is probably an artifact of the instrumentation.

# Quantum Efficiency Measurements of a Copper Photocathode in an RF Electron Gun\*

P. Davis, G. Hairapetian, C. Clayton, C. Joshi  
Electrical Engineering Department, University of California, Los Angeles 90024

S. Hartman, S. Park, C. Pellegrini, J. Rosenzweig  
Department of Physics, University of California, Los Angeles 90024

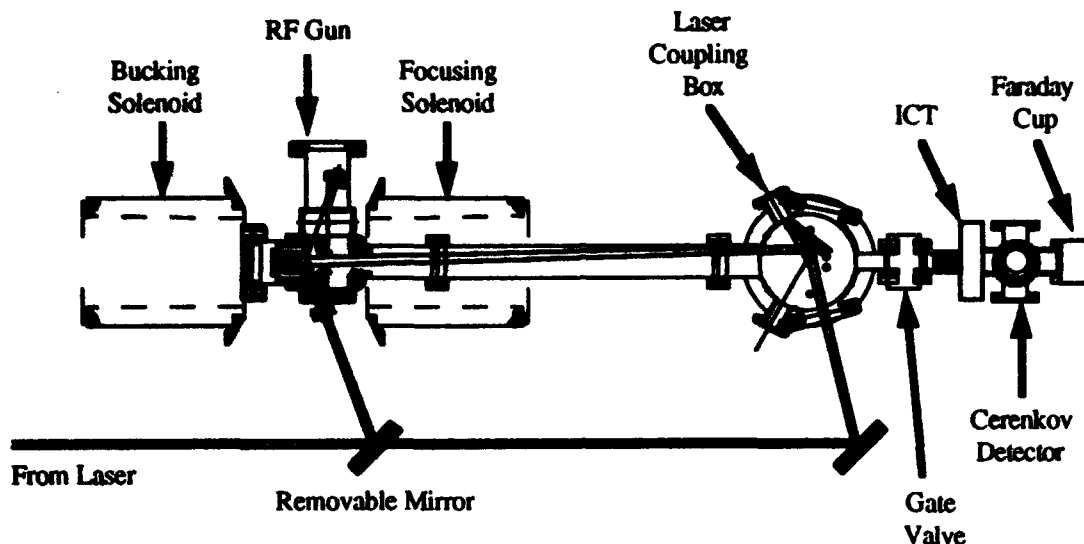


Figure 1: Diagram of the experimental setup

## Abstract

A 4.5 MeV photocathode RF Gun has been commissioned at UCLA. A photo-injector drive laser produces sub 2 ps pulses of UV ( $\lambda=266$  nm) light with up to 200  $\mu\text{J}$ / pulse, and illuminates a copper cathode. The photoelectrons are accelerated to an energy of 3.5 MeV within the gun. The electron beam charge is measured as a function of laser energy using an integrating current transformer (ICT). We present measurements of quantum efficiency as a function of laser polarization for injection angles of  $2^\circ$  and  $70^\circ$  with respect to the cathode normal. At  $70^\circ$  incidence a 50% enhancement in quantum efficiency ( $> 10^{-4}$ ) is observed for p-polarized light over s-polarized light.

## I. INTRODUCTION

The photocathode quantum efficiency is a fundamental parameter in laser driven rf guns. It has been shown that the quantum efficiency depends on the wavelength, injection angle, and polarization of light used in producing electrons[1]. Furthermore, the quantum efficiency is strongly affected by experimental conditions such as the cathode surface, vacuum conditions, and the applied electric field[2].

In most experiments, special consideration is given to the collection of all the charge produced by the injected photons. Since our goal is to create an electron beam, we measure the charge contained in the electron beam at the output of the rf gun and use it in the calculation of quantum efficiency. Therefore, this measurement defines an effective quantum efficiency of the photo-injected rf gun system which incorporates the collection efficiency of the beam.

## II. EXPERIMENTAL SETUP

The photoinjector consists of a Cu photocathode placed at the endwall of the 1/2 cell in a 1 1/2 cell rf gun. After completion of the measurements, the field balance between the 1/2 cell and the full cell was measured to be 1:1.8. This limits the maximum electric field at the cathode to less than 50 MV/m. A solenoid is used to transport the beam to various beam diagnostics. The experimental setup is depicted in Figure 1.

For single photon photoemission, the photon energy must exceed the work function of Cu (4.65 eV)[3]. The photoinjector drive laser was designed to produce  $< 2$  ps laser pulses at 266 nm (4.66 eV) with 200  $\mu\text{J}$ /pulse. This is accomplished using chirped pulse amplification and compression of a mode-locked YAG laser and frequency upconverting using two KD\*P doubling crystals.

\*Work Supported by SDIO/IST through ONR Grant No. N00014-90-J-1952 and US DOE Grant DE-FG03-92ER-40493

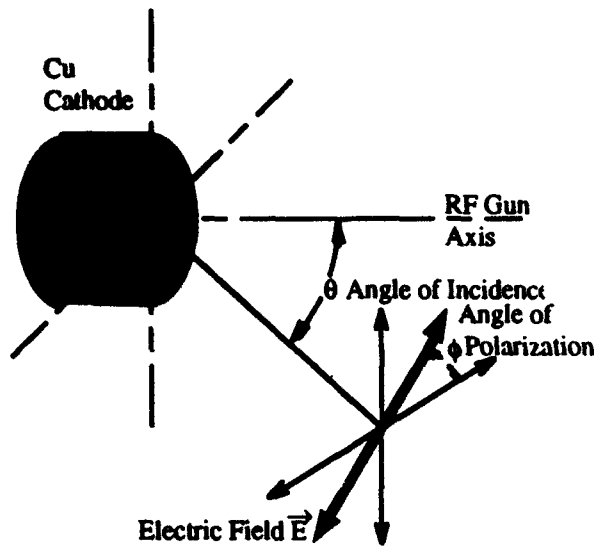


Figure 2: Laser injection geometry

The laser injection geometry is shown in Figure 2. The polarization angle  $\phi$  is the angle the electric field makes with respect to the plane of incidence. Therefore,  $0^\circ$  corresponds to p-polarized light and  $90^\circ$  corresponds to s-polarized light. A  $1/2$  waveplate allows continuous rotation of the laser polarization through a full  $360^\circ$ . The angle  $\theta$  is the angle of incidence of the laser beam with respect to the beam axis of the electron gun. We are limited to only two angles of injection,  $70^\circ$  and  $2^\circ$ .

The electron charge is measured with two independent diagnostics, the Faraday cup and the ICT. Both these diagnostics agree with each other to within 10%. Because the Faraday cup collects significant amounts of dark current, the ICT was used to measure the photo-induced charge per pulse free of the dark current background. A phosphor screen was used to ensure the position of the electron beam was on axis near the center of our diagnostics. The beam energy was

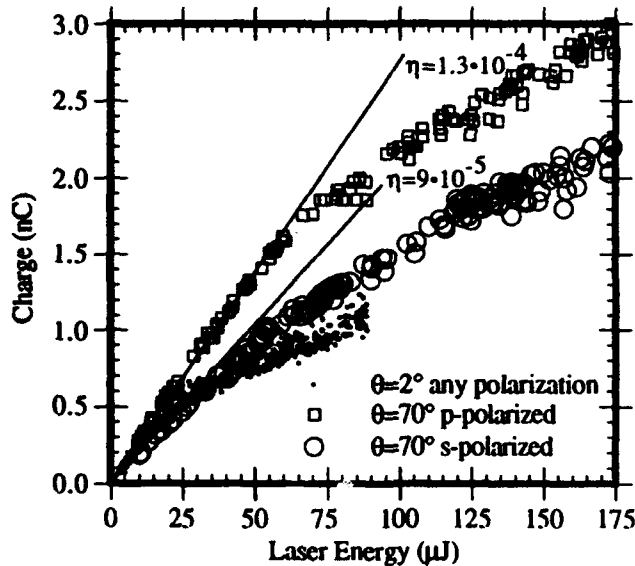


Figure 3: Quantum efficiency measurements

measured to be 3.5 MeV using a dipole spectrometer.

The Cu cathode received no special surface preparation. After machining, the cathode was installed in the rf gun and baked at  $100^\circ\text{C}$  with the gun under vacuum. High power rf conditioning was used to reach a vacuum level of  $10^{-9}$  Torr.

During operation of the gun, the laser spot was focused to sub mm spot sizes on the cathode. The high intensity of the laser pulses damaged the cathode surface further complicating the emission process. The damaged spot is centered on the cathode and therefore all quantum efficiency measurements were made for photoemission from the damaged area.

### III. EXPERIMENTAL RESULTS

Measurements of collected charge vs laser energy for three representative cases are shown in Figure 3. From these measurements it is clear that saturation of the charge occurs at laser energies above  $50 \mu\text{J}$ . Therefore values of quantum efficiency  $\eta$  are taken in the low charge limit. Linear fits for laser energies below  $25 \mu\text{J}$  are presented and labeled with the quantum efficiency ( $\eta$ ) corresponding to the slope of the line. From these fits, an enhancement in quantum efficiency of 50% is observed for  $70^\circ$  p-polarized over  $70^\circ$  s-polarized light.

Measurements of charge vs laser energy were obtained for various polarization angles. For  $2^\circ$  injection, changing the polarization angle did not affect the charge collected. However, for  $70^\circ$  injection, measurements resulted in curves of similar shape to those of Figure 3 but which lie in between the  $70^\circ$  s-polarized and  $70^\circ$  p-polarized curves depending on the angle of polarization. Figure 4 shows the polarization dependence of collected charge for a laser energy of  $100 \mu\text{J}$ . Identical plots are found at different energies. The functional form of this enhancement fits a  $\cos^2 \phi$  dependence which implies that the enhancement is dependent on the energy of p-polarized light rather than its electric field.

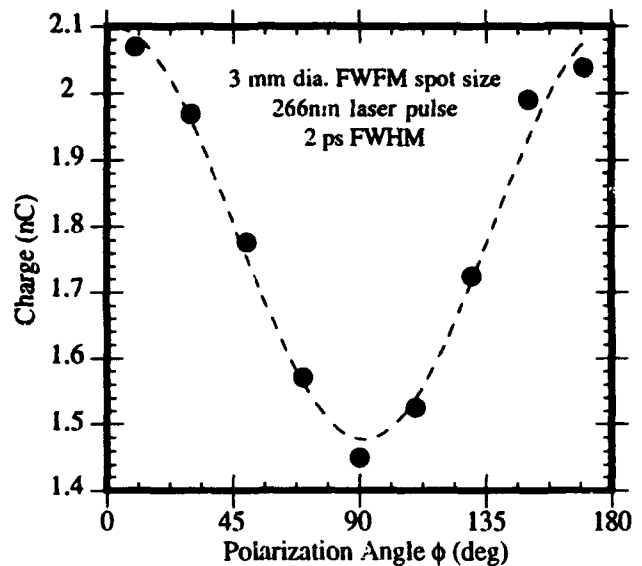


Figure 4: Charge measurements at  $70^\circ$  injection vs polarization angle

For laser spot sizes less than 3 mm in diameter, it was possible to inject the laser pulses at 2° incidence without impinging directly on the damaged area of the cathode. Careful quantum efficiency measurements were not taken under these conditions however a factor of 3 decrease in the quantum efficiency was observed from the undamaged portions of the cathode.

#### IV. DISCUSSION

Quantum efficiencies of  $1 \times 10^{-4}$  are surprisingly high for photoemission from Cu using 266 nm light (4.66 eV) since the photon energy is very close to the work function of Cu (4.65 eV). The quantum efficiency of Cu has been measured to be  $1.5 \times 10^{-5}$  using 248 nm light [4] and  $6 \times 10^{-5}$  using 193 nm light [5]. Typically the quantum efficiency is higher for light of shorter wavelength. Using the Fowler-Dubridge theory for photoemission [6], these previous measurements of quantum efficiency can be scaled for our wavelength of 266 nm predicting  $\eta = 10^{-8}$ . The quantum efficiency can be increased in large electric fields ( $> 10$  MV/m) through the Schottky effect. In order to increase  $\eta$  from  $10^{-8}$  to  $10^{-4}$  electric fields of almost 1 GV/m are necessary at the cathode surface. As was mentioned above, macroscopic fields at the cathode of only 50 MV/m were reached, however, in the damaged area electric field enhancement factors of 20 are possible due to the surface roughness. The enhancement of quantum efficiency from the damaged area over undamaged area could explain the factor of 3 decrease in quantum efficiency observed as the laser spot was directed away from the damaged area.

A more recent measurement of quantum efficiency ( $1.4 \times 10^{-4}$ ) for polished, clean Cu with low applied fields using 266 nm laser pulses was reported by Srinivassan-Rao *et al* [2]. Although this value agrees with our measurement, it implies that field enhanced emission did not occur and does not explain the difference in photoemission between the damaged and undamaged parts of the cathode.

The Fowler-Dubridge theory for one photon photoelectric effect predicts a linear dependence of charge production on incident laser energy. However, the measured charge vs laser energy manifests a saturation of charge output for laser energies above 50  $\mu$ J. The saturation can be explained by space charge effects near the cathode surface. When the electrons are produced by the laser pulse, they are emitted as a thin disk from the cathode: approximately 80  $\mu$ m thick and 1 mm in diameter corresponding to the laser spot size on the cathode. The space charge electric field between the electron bunch and the cathode can be approximated by a surface charge density and its image charge in the cathode. Using this simple model, a space charge field equaling the accelerating field of 50 MV/m results from only .25 nC of charge. This value agrees with the 0° data.

The particle accelerator code, PARMELA[7], has been used to model this space charge effect. This code calculates the space charge forces between a user specified number of test particles as the particles are accelerated from the cathode in an

rf gun. However, experimentally the space charge problem is complicated by the cathode damage. Because of this damage, most of the electrons could be produced from microemitters on the cathode surface. At these emitters the space charge could be worse. Despite these limitations in the computer modeling, the PARMELA simulation showed saturation similar to that of experimental data.

The increase in quantum efficiency for p-polarized vs s-polarized injection is probably due to the difference in the reflectivity of copper at these polarizations. The reflectivity of a copper mirror was measured as a function of incident angle for both s and p polarized 266 nm light. According to the generalized Fowler-Dubridge theory,  $\eta$  is proportional to absorbed laser energy. A 90% increase in absorption was measured for p-polarized light over s-polarized light predicting a 90% improvement of the quantum efficiency for p-polarized injection. The measured enhancement was only 50%. This discrepancy could be due to a difference in the relative reflectivities of the damaged cathode in comparison to those of the copper mirror.

#### V. CONCLUSIONS

The quantum efficiency measurement of Cu in a rf gun resulted in  $\eta = 1 \times 10^{-4}$ . The photoemission from Cu under macroscopic electric fields of 50 MV/m appears to be enhanced by damage on cathode. However, for charge levels greater than .25 nC the quantum efficiency is reduced by space charge near the photocathode. Despite the limitations imposed by space charge, up to 3 nC is produced from the electron gun. For 70° laser injection, p-polarized light results in a 50% increase in quantum efficiency over s-polarized light probably due to their relative reflectivities.

#### VI. REFERENCES

- [1] D.W. Juenker, J.P. Waldron, and R.J. Jaccodine, "Vectorial Photoelectric Effect in Clean Molybdenum," *J. Opt. Soc. Am.* **54**, 216 (1964)
- [2] T. Srinivassan-Rao, J. Ficher, and T. Tsang, "Photoemission studies on metals using picosecond ultraviolet laser pulses," *J. Appl. Phys.* **69**, 3291 (1991).
- [3] Handbook of Chemistry and Physics p. E-78
- [4] Y. Kawamura and K. Toyoda, "Generation of relativistic photoelectrons induced by excimer laser irradiation," *Appl. Phys. Lett.* **45**, 307 (1984).
- [5] S.W. Downey *et al.*, "Simple laser-driven, metal-photocathode electron source," *Appl. Phys. Lett.* **49**, 912 (1986).
- [6] R. Yen, J. Liu, E.P. Ippen, and N. Bloembergen, "Femtosecond Laser Interaction with Metallic Tungsten and Nonequilibrium Electron and Lattice Temperatures," *Phys. Rev. Lett.* **19**, 1837 (1984)
- [7] K.T. McDonald, "Design of the laser-driven rf electron gun for the BNL Accelerator Test Facility," *IEEE Trans. Electron Devices*, ED-35, 2052 (1988)

# High-Efficiency Target-Ion Sources for RIB Generation\*

G. D. Alton  
Oak Ridge National Laboratory  
P. O. Box 2008  
Oak Ridge, Tennessee 37831-6368

## Abstract

A brief review is given of high-efficiency ion sources which have been developed or are under development at ISOL facilities which show particular promise for use at existing, future, or radioactive ion beam (RIB) facilities now under construction. Emphasis will be placed on those sources which have demonstrated high ionization efficiency, species versatility, and operational reliability and which have been carefully designed for safe handling in the high level radioactivity radiation fields incumbent at such facilities. Particular attention will be given to the sources which have been selected for initial or future use at the Holifield Radioactive Ion Beam Facility now under construction at the Oak Ridge National Laboratory.

## 1.0 INTRODUCTION

During the past few years, world-wide interest has developed in the use of radioactive ion beams to address questions concerning the structure of the nucleus and on the nucleosynthesis burn cycles which power stellar processes and which are responsible for heavy element formation. Because many of the nuclear reactions important in nuclear, nuclear structure, and astrophysics are inaccessible to experimental study using stable/stable beam/target combinations, they can only be studied with accelerated radioactive ion beams (RIBs). Such beams, therefore, offer unique opportunities to further our knowledge of the nucleus and the energetics of our solar system. As a consequence, world-wide interest has led to the development and proposed development of RIB facilities in Asia, Europe, and North America [see, e.g., the facilities listed in Ref. 1]. Of the several facilities listed in Ref. 1, only the RIB facility at Louvain-la-Neuve is presently operational [2], while the Holifield Radioactive Ion Beam Facility (HRIBF) at the Oak Ridge National Laboratory has been funded and is now under construction [3].

Our present knowledge of the properties of nuclei far from the region of beta stability can be, in part, attributed to the successful development of reliable, long-lived, and efficient ISOL ion sources with fast release properties. Many ion source developments

have been made over the past few decades for ISOL applications, many of which have been recently included in reviews by Ravn [4] and Van Duppen, et al. [5]. For information on the latest developments in on-line mass separators and target-ion sources associated with their use, readers are encouraged to consult the proceedings of the most recent electromagnetic isotope separator (EMIS) conferences [6,7]. In the present paper, the requirement of brevity places limitations on the number and types of sources which can be included; therefore, the review will be restricted to examples of sources which represent state-of-the-art developments of a particular source type which have demonstrated high ionization efficiencies and reliable performances at ISOL facilities.

## 2.0 CANDIDATE ION SOURCES FOR RIB GENERATION

The ISOL technique is complicated by high-temperature physics, chemistry, metallurgy, diffusion, and surface adsorption processes which take place in the target-ion source; all of these processes add to the delay times which result in losses of the short-lived radioactive species of interest. For RIB generation, the source should ideally exhibit the following properties: high efficiency; high temperature operation in order to minimize the diffusion times from the target and residence times on the surface; low energy spreads; chemical selectivity; flexibility for adaptation to different temperature ranges and modes of operation; target temperature control; long lifetime; and stable electrical and mechanical properties. The source should, as well, be designed for safe and expedient insertion/removal from the ISOL facility to permit changing of the target material and source repairs as required in high radioactivity radiation level fields.

### 2.1 Electron Beam Plasma Ion Sources

*The FEBIAD ion source.* The forced electron beam induced arc discharge (FEBIAD) source, developed at GSI by Kirchner [8-10], differs from conventional plasma discharge sources in that it does not require a minimum pressure for stable operation

\* Managed by Martin Marietta Energy Systems, Inc., under contract No. DE-AC05-84OR21400 with the U.S. Department of Energy.

(commonly referred to as the Langmuir criterion for stable discharge). The source operates at pressures of more than one order of magnitude lower than the Nielsen plasma discharge source [11] as clearly demonstrated by Kirchner and Roeckl [12]. The source is well suited for ISOL applications which involve the use of heavy ions to produce the radioactive species of interest in that it operates stably and efficiently over a pressure range of  $\sim 1 \times 10^{-5}$  to  $\sim 2 \times 10^{-4}$  Torr at elevated temperatures. Several versions of the source have been developed at GSI (see, for example, Refs. 8-10 for specific details on the respective sources); these sources differ in their materials of construction, ionization chamber volumes and achievable target temperatures, depending on the particular source geometry. The efficiency of the FEBIAD ion source is quite high for slow moving heavy ions; for low mass, fast moving atoms with high ionization potentials, the source is not as impressive. For example, the measured ionization efficiencies for the noble gas elements, as reported in Ref. 13, are, respectively, Ne: 1.5%; Ar: 18%; Kr: 36%; and Xe: 54%. The following equation is found to be useful in approximating the ionization efficiencies  $\eta$  for the noble gases:

$$\eta_{\text{calc}} = \frac{4\langle\ell\rangle D_0 N_e}{A_0} \left( \frac{\pi M_i}{8kT_i} \right)^{1/2} \exp \{-I_p / \langle kT_e \rangle\}$$

$$\eta = \frac{4\langle\ell\rangle D_0 N_e}{A_0} \left( \frac{\pi M_i}{8kT_i} \right)^{1/2} \exp \{-I_p / \langle kT_e \rangle\} \quad (1)$$

Where  $\langle\ell\rangle$  = average path length for a particle in the plasma;  $D_0$  = constant ( $\text{cm}^2/\text{s}$ );  $A_0$  = emission area of the source;  $k$  = Boltzmann's constant;  $T_i$  = ion temperature;  $T_e$  = electron temperature;  $I_p$  = ionization potential;  $N_e$  = number of electrons in the valence shell of the atom with a given  $I_p$ ; and  $M_i$  = mass of species. The following values are used for terms in Eq. 1 when estimating ionization efficiencies for the FEBIAD ion source:  $\langle kT_e \rangle = 3$  eV;  $T_i = 2273^\circ\text{K}$ ; and  $4\langle\ell\rangle D_0 / A_0 = 5.39 \times 10^3$   $\text{cm/s}$ .

**The CERN-ISOLDE ion source.** The CERN-ISOLDE on-line source is similar in principle to the FEBIAD source. The design features of several versions of the source have recently been described by Sundell and Ravn [14]. The CERN ISOLDE target/ion source has been utilized extensively for the production of short-lived radioactive species and has been cleverly engineered to enable remote installation and removal from the facility as required for safe handling in high-radiation-level fields. Electron impact ionization sources of the FEBIAD-CERN-ISOLDE type are quite efficient for low-ionization-potential elements and elements which are heavy and,

therefore, move slowly through the ionization volume of the source. The ionization efficiencies for these atoms are close to those measured for the FEBIAD source. For example, the maximum efficiency recorded for Xe is 56% [15]. However, those sources do not appear to ionize low-mass elements or molecular materials efficiently, particularly those with high ionization potentials.

The high-temperature version of the CERN ISOLDE source [16] has been selected as the first source to be used for the generation of radioactive ion beams at the HRIBF because of its low emittance, ( $\sim 2 \pi$  mm.mrad)  $(\text{MeV})^{1/2}$  relatively high ionization efficiency, and capability for producing a broad range of radioactive species. Of equal importance, the source has been cleverly engineered for remote installation, removal and servicing as required in safe handling of highly radioactive contaminated sources, source components, and ancillary equipment. The source design also permits easy modification to lower temperature versions and conversion from electron impact ionization to either thermal or positive and negative surface ionization sources.

The HRIBF version of the CERN-ISOLDE source is described in Ref. 16. The high-temperature target and ionization chamber of the source are shown schematically in Figs. 1 and 2. A collimated ion beam from the ORIC will pass through a thin Re window where it interacts with the refractory target material chosen for the production of the desired radioactive beam. The Ta target material reservoir is lined with Ir or Re metal as is the beam transport tube and internal surfaces of the source.

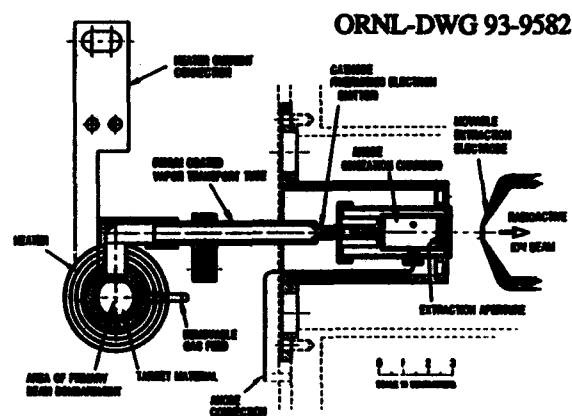


Figure 1. Cross-sectional side view of the HRIBF high-temperature target/ion source showing the target, vapor transport tube, and ionization chamber of the source [16].

The thickness of the target is chosen so that the projectile has an energy spread within the target medium which approximates that required for optimum radioactive species production. The

unreacted beam exits the target through a second Re window, then strikes a cooled C beam stop. This technique reduces the power deposited in the target and thereby simplifies temperature control problems.

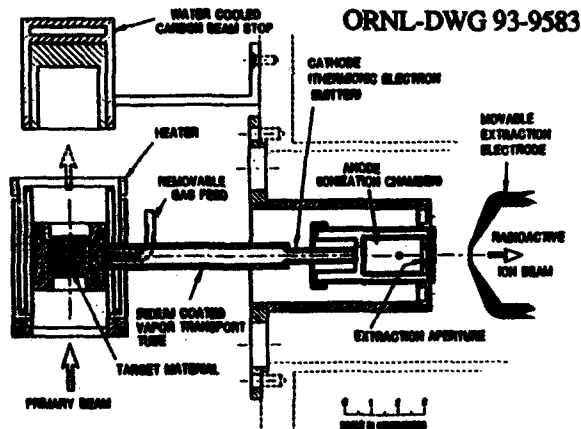


Figure 2. Cross-sectional top view of the HRIBF high-temperature target/ion source showing the target, vapor transport tube, and ionization chamber of the source [16].

The target reservoir is positioned within the inner diameter of a series-connected, resistively heated, three-cylinder, Ta tube. The reservoir can be heated to temperatures exceeding 2100°C by passing a current through the tubular structure. The power required to heat the assembly to 2100°C is estimated to be 5.5 kW (11 V at 500 A). Temperature control will be maintained within  $\pm 2^\circ\text{C}$  by use of feedback circuitry driven by a two-color pyrometer to adjust the current through the heater.

The electron emitter cathode is also made of Ta and is resistively heated to thermionic emission temperatures,  $\sim 2125^\circ\text{C}$ . The electron beam, typically  $\geq 250$  mA, is accelerated through a potential difference of 200-300 V to the perforated anode plate where it passes into the cylindrical cavity of the anode structure and ionizes the gaseous material. Collimation of the electron beam is effected by adjusting the coaxially directed solenoidal magnetic field so as to optimize the ionization efficiency of the species of interest. The cathode power required to achieve thermionic emission temperature will be  $\sim 2$  kW (400 A at 5 V).

The electron beam generated plasma (EBGP) ion source. The electron beam generated plasma (EBGP) ion source, developed for use at the OASIS facility by Nitschke [17] has demonstrated high efficiencies and very high temperature operation ( $\sim 2700^\circ\text{C}$ ). Table 1 compares the efficiencies for a number of elements, as calculated from Eq. 1, with those measured from the EBGP, FEBIAD, and CERN-ISOLDE ion sources.

Table 1. Comparisons of calculated and experimentally measured ionization efficiencies  $\eta$  for electron beam plasma ion sources. Estimated ionization efficiencies were calculated by using Eq. 1.

Z	Element	$I_p(\text{eV})$	$N_0$	$\eta_{\text{calc}}(\%)$	$\eta_{\text{exp}}(\%)$	Ref.
10	$^{20}\text{Ne}$	21.56	8	2.0	1.6	10
18	$^{40}\text{Ar}$	15.78	8	16.6	19	10
24	$^{54}\text{Cr}$	6.77	1	37.0	>20	10
26	$^{57}\text{Fe}$	7.90	2	45.2	30	10
32	$^{76}\text{Ge}$	7.90	4	65.6	41	10
36	$^{84}\text{Kr}$	14.00	8	34.1	35	10
36	$^{84}\text{Kr}$	14.00	8	34.1	36	17
46	$^{100}\text{Pd}$	8.33	18	89.5	>25	10
47	$^{107}\text{Ag}$	7.58	1	36.7	47	10
47	$^{109}\text{Ag}$	7.58	1	36.9	50	10
50	$^{118}\text{Sn}$	7.34	4	74.0	53	10
50	$^{124}\text{Sn}$	7.34	4	74.6	54	10
54	$^{129}\text{Xe}$	12.13	8	54.6	52	10
54	$^{132}\text{Xe}$	12.13	8	54.8	53	10
54	$^{132}\text{Xe}$	12.13	8	54.8	56	15
79	$^{197}\text{Au}$	9.23	1	32.9	50	10
82	$^{208}\text{Pb}$	7.42	4	78.8	52.8	10
83	$^{209}\text{Bi}$	7.29	5	82.9	68.3	10

## 2.2 Thermal Ion Sources

At high temperatures, collisions between gas particles may produce ionization provided that their relative energies exceed the first ionization of the atoms or molecules that make up the gas. For the case of a monoatomic gas, a fraction of the total number of gas particles will be in various stages of ionization at thermal equilibrium. For such reactions, the law of mass action can be used to derive an expression for the ionization efficiency as a function of temperature and pressure [18]. The first reported applications of this technique are described in Refs. [19] and [20]. Such sources are relatively efficient for elements with ionization potentials  $I_p \leq \sim 7$  eV.

Ionization efficiencies for a number of elements, including Ca, Sr, Nb, and La, all of the lanthanides, and U, Pu, and Cm of the actinides have been measured by use of the thermal ionization source described in Ref. 20. The efficiencies for ionizing Ti, Cr, Fe, Ni, Sr, Pb, and U have been measured by Kirchner [21]. The source can be very efficient as indicated. A thermal ion source has also been designed for use at the TRISTAN facility [22]. A thermal source is also now under design at the HRIBF. The vapor transport tube, made of W or Ta, will be resistively heated to  $\sim 2100^\circ\text{C}$ . In addition, the thermal ionization region of the vapor transport tube will be heated to  $\sim 2600^\circ\text{C}$  by electron bombardment.

### 2.3 Surface Ionization Sources

**Positive surface ionization.** For thermodynamic equilibrium processes, the ratio of ions to neutrals that leave an ideal surface can be predicted from Langmuir-Saha surface ionization theory.

**Positive surface ionization sources.** Positive surface ionization sources are quite simple and easy to operate. The principle has been used at CERN-ISOLDE [23] and TSIOL facility [24] to generate ion beams from low-ionization-potential elements. Although they have limited applications in terms of species, the process is highly chemically selective. The CERN-ISOLDE source can be easily retrofitted to accommodate the positive surface ionization source mode of operation, as demonstrated at INS to ionize  $^{38}\text{K}$  [25]. A positive surface ionization source will be used as complementary to the CERN-ISOLDE source at the HRIBF. The ionizer and vapor transport tube will be Ir coated tantalum and heated resistively to  $\sim 1100^\circ\text{C}$ .

**Negative surface ionization.** For thermodynamic equilibrium processes, the ratio of ions to neutrals which leave an ideal surface can be predicted from Langmuir-Saha surface ionization theory appropriate for negative ion formation.

The negative form of surface ionization is also highly chemically selective and, therefore, can be used for the generation of high-electron-affinity elements such as the group VIIA (halogens). Unfortunately, there is limited availability of a wide variety of stable, low work materials.  $\text{LaB}_6$  is the most frequently used low-work-function surface ionizer, having a work function  $\phi = \sim 2.7$  eV for polycrystalline and  $\phi \approx 2.36$  eV for single crystalline material.

**Negative surface ionization sources.** An on-line form of the negative surface ionization source has been developed at CERN-ISOLDE, which is equipped with a  $\text{LaB}_6$  surface ionizer [26]. The CERN-ISOLDE-type source can easily be retrofitted with a  $\text{LaB}_6$  ionizer and used to efficiently ionize high-electron-affinity elements as clearly evidenced by the successful application described in Ref. 26. A spherical-geometry negative-surface source is planned for use at the HRIBF.

### 2.4 ECR Ion Sources

Electrons moving along the field lines of an external magnetic field of flux density  $B$  can be resonantly accelerated by the electric field associated with microwave radiation of the proper frequency which matches the electron-cyclotron resonance condition,  $\omega_{\text{ECR}} = \omega_{\text{rf}} = Be/m$ . The region where the ECR condition is met is referred to as the ECR zone. Several ion sources, based on the ECR

principle, have been developed for ISOL applications including those described in References 27-29.

The ECR ion source is superior in terms of ionization efficiencies for low mass, high ionization potential elements and in terms of their capabilities for producing multiply charged ion beams. Another principal advantage of the ECR ion source is that it does not rely on a negatively biased hot cathode for generating and sustaining the plasma which limits the lifetimes of conventional electron beam plasma sources due to physical sputtering of the cathode material. The principal disadvantage of the source is that, in its present state of development, the discharge chamber can only be operated at modestly high temperatures which severely limits the number of species that the source can be used to process. The ionization efficiencies for condensable materials will be less than those for more volatile elements. However, due to the high probability for ionization during transit through the ionization volume of the source, there is evidence that the efficiencies for condensable materials may be relatively high, as well. The ECR ion source, however, is particularly well suited for the processing of highly volatile or gaseous materials and usually out performs electron beam plasma sources for low atomic number species. The prototype on-line ECR ion source was first developed at Karlsruhe [27] for ISOL applications; the source has demonstrated efficiencies for C of 10%; for N up to 27%; for O up to 55%, for Ne up to 31% and Xe up to 65%. This source was duplicated at TRIUMF [28]. Ionization efficiencies of 18% for N, 37% for C and 14 % for Ne and 35% for Ar have been measured with the on-line ECR ion sources at Louvain-la-Neuve [29-31]. The ionization efficiencies for the ECR ion source are sensitively dependent on the pressure in the discharge chamber as evidenced by the measurements made at Louvain-la-Neuve. These sources are clearly more efficient for low mass, high ionization potential elements than conventional, hot cathode electron beam plasma type sources such as the FEBIAD and CERN-ISOLDE type ion sources. On the other hand, the ionization efficiencies for Xe in this source are close to those recorded at CERN-ISOLDE [15] and GSI [13] for Xe ( $\sim 54\%$ ). These sources are particularly impressive for difficult to ionize elements such as He and Ne. A compact, single stage, permanent magnet ECR ion source is now being developed for on-line use at GANIL for potential RIB applications [32].

### 2.5 Plasma Sputter Negative Ion Sources

The technique of sputtering a surface covered with a fractional layer of a highly electropositive adsorbate material such as cesium has proved to be a universal method for generating atomic and molecular negative ion beams from most chemically active

elements. Positive ion beams, usually formed by either direct surface ionization of a group IA element or in a heavy noble gas (Ar, Kr, or Xe) plasma discharge seeded with alkali metal vapor, are accelerated to energies between a few hundred eV and several keV where they sputter a sample containing the element of interest. A small fraction of the sputter ejected particles leave the adsorbate covered surface as negative ions and are accelerated through an extraction aperture in the source. Several sources predicated on this principle have been developed, some of which are described in Ref. 33. Sources based on this principle are particularly appealing for applications involving the postacceleration of RIBs with tandem accelerators such as at the HRIBF. In particular, sources which use a plasma to sputter the sample [34-37] are especially attractive because this technique assures uniform sputtering and, consequently, good overlap of the bombarding species and the material containing the radioactive ion beam.

Figure 3 displays a schematical representation of a plasma sputter source now under design for use at the HRIBF. The source will be housed in the source vacuum envelope as the CERN-ISOLDE source.

ORNL-DWG 93-9587

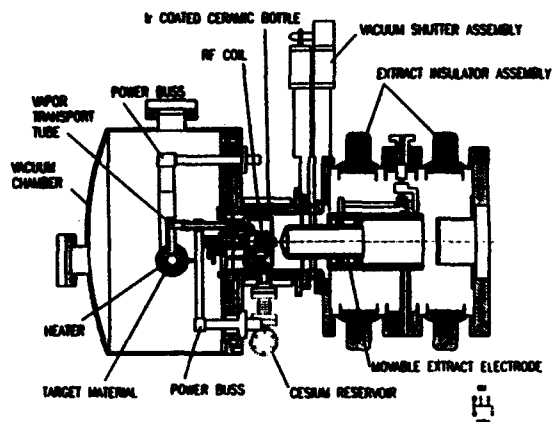


Figure 3. Schematic drawing of a plasma sputter negative ion source now under design for use in the HRIBF. The source will be complementary to the CERN-ISOLDE electron beam plasma source displayed in Figs. 1 and 2.

Radioactive species from the target will be transported at high temperatures through the vapor transport tube into the plasma discharge chamber where the vapor will be condensed on the cold cathode surface. A Xenon plasma, seeded with cesium from an external oven, will be ignited either by a filament or a rf coil. The radioactive ion beam will be formed by sputter ejection of atoms or molecules from the negative biased spherical geometry sputter probe covered with a partial layer of cesium adsorbate material. The

double sheath surrounding the negatively biased sputter probe (spherical radius 30 mm and diameter  $\phi = 12.5$  mm), which is maintained at a variable voltage (0-1000 V) relative to housing, serves as the acceleration gap and lens for focusing the negative-ion beam through the exit aperture (diameter  $\phi = 3$  mm). At this point, the ion beam is further accelerated to energies up to 50 keV prior to mass analysis. The efficiencies of several negative ion species have been estimated by Tsuji and Ishikawa [37]. Their results are shown in Table 2.

Table 2. Estimates of the probability for negative ion formation by xenon sputtering at optimum cesium coverage (Ref. 37)

Negative Ion	C-	Si-	Cu-	Ge-	Mo-	Ta-	W-
Probability (%)	18.3	15.6	12.1	13.6	(0.52)	(1.50)	8.07

The emittance of the source is quite good ( $\sim 8\pi$  mm.mrad  $[\text{MeV}]^{1/2}$ ) as measured by Mori for the compact plasma sputter described in Ref. 36 when operated with mA beams of  $\text{Cu}^-$ . The emittance is much lower than the acceptance of the 25-MV tandem accelerator [38] and, therefore, should be easily transported to the terminal stripper in the machine.

## 2.6 Multi-photon Resonance Ionization Sources

Multi-photon resonance ionization spectroscopy (RIS) has been utilized for a number of years to selectively ionize atoms [39]. The scheme is, in principle, very simple; the difficult challenge is to find the most efficient scheme for ionizing a particular atom. Two or more lasers are used to selectively ionize the species of interest. Because the ionization process requires the precise matching of the photon energies to each of the energy levels of the particular atom, the process is resonant and uniquely species selective; the RIS scheme is, therefore, highly discriminatory against potential contaminants. Thus, RIS offers a means of generating fully ionized, isotopically and isobarically pure RIBs. Approximately 80% of the elements in the periodic chart can be resonantly ionized with the RIS technique with existing lasers.

Several groups are actively developing RIS laser ion sources for future ISOL applications. The RIS scheme has been applied to resonantly ionize atoms released from an ISOL target and effused through tubular or insulated cavities which are operated at high temperatures to prevent condensation. Two or three tunable dye laser beams are collinearly focused through the cavity with their wave lengths chosen to resonantly ionize the species of interest. This source is handicapped by the fact that some of the atoms are in excited states or may be thermally or surface

ionized due to the high temperatures required to prevent condensation on the walls of the cavity. The otherwise chemical selectivity character of the RIS process is, therefore, compromised. Nevertheless, the hot cavity-RIS technique has been used off-line by Andreev, et al. to selectively ionize Sr to efficiencies of 17% [40] and by Ames, et al to ionize Tc to efficiencies of 13% [41]. These groups both employed Cu vapor lasers which operate at high repetition rates to pump tunable dye lasers. This RIS scheme has been duplicated by Alkhazov, et al. to study the ionization of the rare earth elements Yb, Ho, Tl, and Sm [42]. Mishin, et al. used the RIS technique to determine the ionization efficiencies for Sn, Tm, Yb, and Li [43]. Efficiencies up to 15% were recorded for Yb. In these studies, it was found that the initial chemical selectivity factor for Tm, compromised by surface and thermal excitation/ionization processes, could be increased from 10 to 10000 by the proper choice of cavity material and by reducing the cavity temperature; the gain in selectivity was made by suppressing thermal and surface ionization processes. Furthermore, it was found that another factor of 10 could be gained by using gated detection techniques on the bunched beam. The laser desorption technique has been used to desorb Pt and Au which were ion implanted into samples and to study the Pt-Au isobar contamination problem by using the RIS technique. Ionization efficiencies for this study only reached  $5 \times 10^{-3}$  [44]. However, the desorption efficiencies for the process reached 60%.

### 3.0 Conclusions

ISOL ion source development continues to be driven by needs for sources with improved chemical selectivity, high duty factors, and more universal species capabilities. Despite the fact that electron beam plasma ion sources have poor chemical selectivity characteristics, they have a decided advantage in that they are closer to being universal than other ISOL sources that have been developed to date. Of the electron beam sources, the CERN-ISOLDE source is very appealing for RIB generation applications.

Although ECR ion source development has made considerable progress, this source type still suffers from the fact that no really satisfactory solution to the low wall temperature/condensation problem has been found; as a consequence, the source, in its present state of development, has very limited species capabilities for ISOL applications. However, there is ample incentive to solve this problem because of the obvious advantage of the ECR source over conventional source types in terms of ionization efficiency.

The results from the testing of RIS laser sources has been rather encouraging and it is expected that

this technology will rapidly advance in the future. The RIS technique offers the idealistic prospect of eliminating the need for expensive isotope and isobar electromagnetic separation devices.

Plasma or cesium sputter ion sources offer another possibility for the efficient formation of negative ion beams from high electron affinity elements. Sources, based on this well developed technology, do not suffer from poisoning effects as do direct negative surface ionization sources and are very appealing for use at tandem accelerator based RIB facilities such as the HRIBF.

Thermal and surface ionization sources have reached a certain degree of maturity in their development but still play important roles for the efficient generation of ion beams from specific elements. Surface ionization sources, in particular, offer a high degree of chemical selectivity and are simple and easy to operate.

### Acknowledgments

Specials thanks are extended to J. Dellwo, D. L. Haynes and G. D. Mills for supplying several graphic illustrations included in the manuscript. The author, as usual, is indebted to Ms. Jeanette McBride for typing and assembling the manuscript.

### References

- [1] D. K. Olsen, Nucl. Instr. and Meth. **A328**, 303 (1993).
- [2] P. Van Duppen, P. Decrock, M. Huyse, Th. Delbar, W. Galster, P. Leleux, I. Licot, E. Lienard, P. Lipnik, M. Loiselet, C. Michotte, G. Ryckewaert, J. Vervier, P. Duhamel, and J. Vanhorenbeeck, Nucl. Instr. and Meth. **B70**, 393 (1992).
- [3] A Proposal for Physics with Exotic Beams at the Holifield Heavy Ion Research Facility, eds. J. D. Garrett and D. K. Olsen, Physics Division, ORNL, March 1991, unpublished.
- [4] H. L. Ravn, Nucl. Instr. and Meth., **B70**, 107 (1992).
- [5] P. Van Duppen, P. Decrock, M. Huyse, and R. Kirchner, Rev. Sci. Instr. **63**, 2381 (1992).
- [6] Proceedings of the Eleventh Int. Conf. on Electromagnetic Isotope Separators and Techniques Related to Their Applications, Ed. W. L. Talbert, Jr., Nucl. Instr. and Meth. **B26** (1987).
- [7] Proc. of the Twelfth Int. Conf. on Electromagnetic Isotope Separators and Techniques Related to Their Applications, Eds. M. Fujioka, T. Shinozuka, and Y. Kawase, Nucl. Instr. and Meth. **B70** (1992).

- [8] R. Kirchner, D. Marx, O. Klepper, V. T. Koslowsky, T. Kühli, P. O. Larsson, E. Roeckl, K. Rykaczewski, D. Schandt, J. Eberz, G. Huber, H. Lochmann, R. Menges, and G. Ulm, *Nucl. Instr. and Meth.* **A234**, 224 (1985).
- [9] R. Kirchner, K. Burkhard, W. Hüller, and O. Klepper, *Nucl. Instr. and Meth.* **186**, 295 (1981).
- [10] R. Kirchner, K. Burkhard, and O. Klepper, *Nucl. Instr. and Meth.* **B70**, 56 (1992).
- [11] O. Almen and K. O. Nielsen, *Nucl. Instr. and Meth.* **1**, 302 (1957).
- [12] R. Kirchner and E. Roeckl, *Nucl. Instr. and Meth.* **133**, 187 (1976).
- [13] R. Kirchner, *Nucl. Instr. and Meth.* **B70**, 186 (1992).
- [14] S. Sundell and H. L. Ravn, *Nucl. Instr. and Meth.* **B70**, 160 (1992).
- [15] G. D. Alton and S. Sundell, unpublished.
- [16] G. D. Alton, D. L. Haynes, G. D. Mills, and D. K. Olsen, *Nucl. Instr. and Meth.* **A328**, 325 (1993).
- [17] J. M. Nitschke, *Nucl. Instr. and Meth.* **A236**, 1 (1985).
- [18] M. N. Saha, *Philos. Mag.* **40**, 472 (1920).
- [19] G. J. Beyer, E. Herrmann, A. Piotrowski, V. I. Raiko, and H. Tyroff, *Nucl. Instr. and Meth.* **96**, 347 (1971).
- [20] P. G. Johnson, A. Bolson, and C. M. Henderson, *Nucl. Instr. and Meth.* **106**, 83 (1973).
- [21] R. Kirchner, *Nucl. Instr. and Meth.* **A292**, 203 (1990).
- [22] A. Piotrowski, R. L. Gill, and D. McDonald, *Nucl. Instr. and Meth.* **224**, 1 (1984).
- [23] T. Bjørnstad, E. Hagebø, P. Hoff, O. C. Jonsson, E. Kugler, H. L. Ravn, S. Sundell, and B. Vosicki, *Phys. Scripta* **34**, 578 (1986).
- [24] M. Dombaky, L. Buchmann, J. M. D'Auria, P. McNeely, G. Roy, H. Sprenger, and J. Vincent, *Nucl. Instr. and Meth.* **B70**, 125 (1992).
- [25] N. Ikeda, Y. Shirakabe, J. Tanaka, T. Nomura, S. Ohkawa, S. Takaku, M. Oyaizu, H. Kawakami, I. Katayama, and T. Shinozuka, *Nucl. Instr. and Meth.* **B70**, 150 (1992).
- [26] B. Vosicki, T. Bjørnstad, L. C. Carraz, J. Heinemeier, and H. L. Ravn, *Nucl. Instr. and Meth.* **186**, 307 (1981).
- [27] V. Bechtold, H. Dohrmann, and S. A. Sheikh, *Proc. of the 7th Workshop on ECR Ion Sources*, Jülich, 1986, p. 248.
- [28] M. Dombaky, J. M. D'Auria, L. Buchmann, H. Sprenger, J. Vincent, P. McNeely, and G. Roy, *Nucl. Instr. and Meth.* **A295**, 291 (1990).
- [29] P. Decrock, M. Huyse, P. Van Duppen, F. Baeten, C. Dom, and Y. Jongen, *Nucl. Instr. and Meth.* **B58**, 252 (1991).
- [30] M. Huyse, P. Decrock, P. Dendooven, J. Gentens, G. Vancraeynes, P. Vandenberghe, and P. Van Duppen, *Nucl. Instr. and Meth.* **B70**, 50 (1992).
- [31] M. Gaelens, et al., to be published.
- [32] A. Chabert, P. Bricault, A. Joubert, and P. Sortais, *Proc. of the 2nd Int. Conf. on Radioactive Nuclear Beams*, Louvain-la-Neuve, Belgium (1991).
- [33] G. D. Alton, *Nucl. Instr. and Meth.* **B73**, 221 (1993).
- [34] G. D. Alton, Y. Mori, A. Takagi, A. Ueno, and S. Fukumoto, *Nucl. Instr. and Meth.* **A270**, 194 (1988).
- [35] G. D. Alton, *Rev. Sci. Instr.* **63**, 2455 (1992).
- [36] Y. Mori, *Nucl. Instr. and Meth.* **A328**, 146 (1993).
- [37] H. Tsuji and J. Ishikawa, *Rev. Sci. Instr.* **63**, 2488 (1992).
- [38] J. D. Larson and C. M. Jones, *Nucl. Instr. and Meth.* **140**, 489 (1977).
- [39] G. S. Hurst and M. G. Payne, *Principles and Applications of Resonance Ionization Spectroscopy* (I.O.P., London, 1988).
- [40] S. V. Andreev, V. I. Mishin, and V. S. Letokhov, *Opt. Commun.* **57**, 317 (1986).
- [41] F. Ames, T. Brumm, K. Jäger, J.-H. Kluge, B. M. Suri, H. Rimke, N. Trautmann, and R. Kirchner, *Appl. Phys.* **B51**, 200 (1990).
- [42] G. D. Alkhazov, L. Kh. Batist, A. A. Bykov, V. D. Vitman, V. S. Letokhov, V. I. Mishin, V. N. Panteleyev, S. K. Sekatsky, and V. N. Fedoseyev, *Nucl. Instr. and Meth.* **A306**, 400 (1991).
- [43] V. I. Mishin, V. N. Fedoseyev, J.-H. Kluge, V. S. Letokhov, H. L. Ravn, F. Scheerer, Y. Shirakabe, S. Sundell, and O. Tengblad, *Nucl. Instr. and Meth.*, to be published.
- [44] U. Krönert, St. Becker, G. Bollen, M. Gerber, Th. Hilberath, H.-J. Kluge, and G. Passler, *Nucl. Instr. and Meth.* **A300**, 522 (1991).

# Performance of SSC LINAC Injector\*

K. Saadatmand, G. M. Arbique, F. Guy, M. Haworth, J. Hebert, J. Hurd, J. Lenz, N. Okay, D. Raparia

Superconducting Super Collider Laboratory  
2550 Beckleymeade Avenue, Suite 260, MS1043  
Dallas, Tx 75237-3946

## Abstract

The Superconducting Super Collider (SSC) LINAC Injector consists of an Ion Source, Low Energy Beam Transport (LEBT) and Radio Frequency Quadrupole accelerator (RFQ). The LINAC Injector is required to provide 25 mA of  $H^-$  beam (pulse width of 9.6- 48  $\mu$ s at 10 Hz repetition rate) at 2.5 MeV with transverse normalized rms emittance ( $\epsilon_{t-n-rms}$ ) of less than  $0.2 \pi$  mm-mrad and longitudinal normalized rms emittance ( $\epsilon_l$ ) of less than  $0.82 \cdot 10^{-6}$  eV-s. An RF-driven volume source was chosen for the initial commissioning of the SSC LINAC Injector. The RF volume source generates beams with  $\epsilon_{t-n-rms}$  as low as  $0.06 \pi$  mm-mrad while meeting all other SSC ion source operating requirements (30 mA at 35 keV). The highly converging input beam required by the SSC RFQ is provided by a dual einzel lens. The initial experimental results from commissioning of the SSC LINAC Injector and experimental results pertinent to the performance of the SSC ion source and LEBT will be discussed.

## I. INTRODUCTION

Figure 1 is a functional diagram of the SSC LINAC Injector (Injector) showing the  $H^-$  Ion Source, LEBT, and RFQ. Figure 2 shows the Injector at its temporary location at our R&D laboratory in Waxahachie, Texas. The Injector is scheduled to be moved to its permanent tunnel location later this year. First beam was successfully accelerated through the Injector on April 8th, 1993. With 30 mA from the 35 keV ion source, the Injector output current was 18 mA. After a brief description of the Injector subsystems, details of experimental results from the Injector output beam characterization will be presented.

## II. INJECTOR SUBSYSTEMS

### A. SSC $H^-$ RF Volume Source

Multicusp plasma sources provide volume production of low energy ( $<2$  eV)  $H^-$  ions leading to low emittance, high brightness beams. An RF driven volume  $H^-$  source, based on RF induction discharge, was developed for SSC by LBL [1]. A schematic of the SSC RF volume ion source is shown in Figure 3. The plasma is confined by the longitudinal line-cusp field produced by samarium-cobalt magnets that surround the source chamber and back flange. A pair of water-cooled permanent magnet filter rods placed near the plasma electrode creates a narrow region of transverse magnetic field which

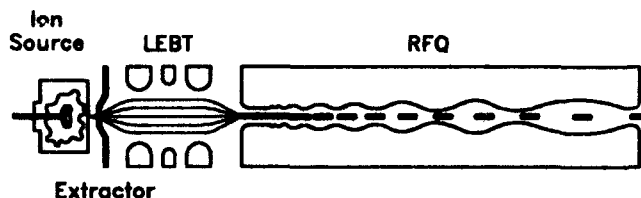


Figure 1. Functional diagram of SSC LINAC Injector

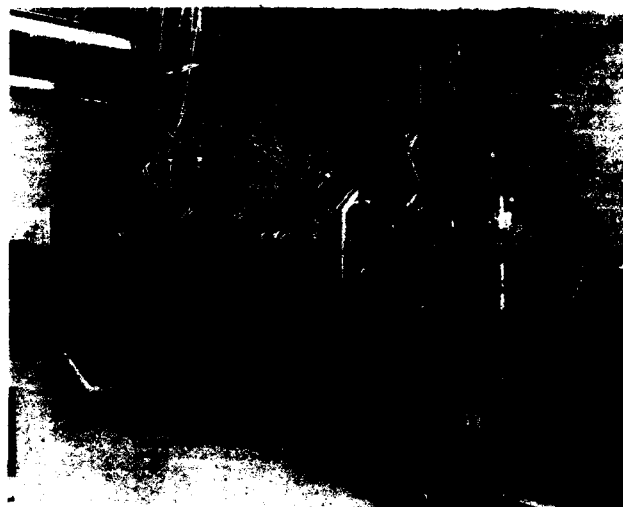


Figure 2. SSC LINAC Injector

divides the source chamber into discharge and extraction regions. The 2 MHz RF power, with electrons supplied by a hairpin tungsten filament plasma starter, excites and ionizes the hydrogen gas molecules in the discharge region. The RF power is inductively coupled to the mixture via a two turn ceramic coated copper antenna. The magnetic field of the filter rods prevent the energetic plasma electrons from entering the extraction region. Cold electrons, the positive and negative ions, and the vibrationally excited hydrogen molecules can drift across this magnetic field forming a plasma in the extraction region with a low electron temperature. The cold plasma enhances the formation of  $H^-$  ions by dissociative attachment [2].

We have extracted  $H^-$  beam currents as high as 40 mA at 35 kV. The volume source has a high extracted electron to  $H^-$  ratio (30:1). These unwanted electrons are separated from the  $H^-$  beam by a 4 cm long magnetic spectrometer at the extractor electrode exit (Figure 3). The spectrometer's magnets are

\*Operated by the University Research Association, Inc. for the U.S. Department of Energy, under contract No. DE-AC35-89ER40486.

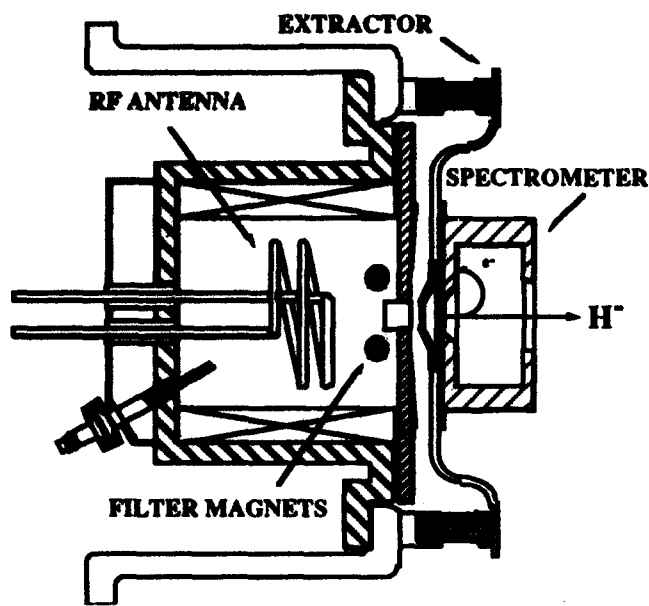


Figure 3. SSC H<sup>-</sup> RF Volume Source

housed inside a soft iron envelope to prevent fringe field from penetrating the extraction gap and the volume source. Figure 4 is a close up of the RF volume source as part of the Injector assembly (the LEBT vacuum shell and portions of the RFQ are also shown).



Figure 4. RF volume source as part of the Injector assembly.

Emittance measurements, at an axial position corresponding to the LEBT entrance ( $\sim 5$  cm downstream of extractor electrode), yield  $\epsilon_{t-n-rms}$  (rms normalized emittance extrapolated to 100% of the assumed Gaussian beam [3]) of  $0.10 - 0.15 \pi$  mm-mrad. Smaller emittance [4],  $\epsilon_{t-n-rms} = 0.06 \pi$  mm-mrad, has been measured in the presence of Xe neutralizing gas which minimizes space charge effects. The actual H<sup>-</sup> beam emittance out of the ion source is believed to

be closer to  $0.06 \pi$  mm-mrad. Figure 5 shows a typical horizontal phase-space emittance contour plot of beam out of the volume source. The beam is highly diverging and is about 0.8 cm in radius.

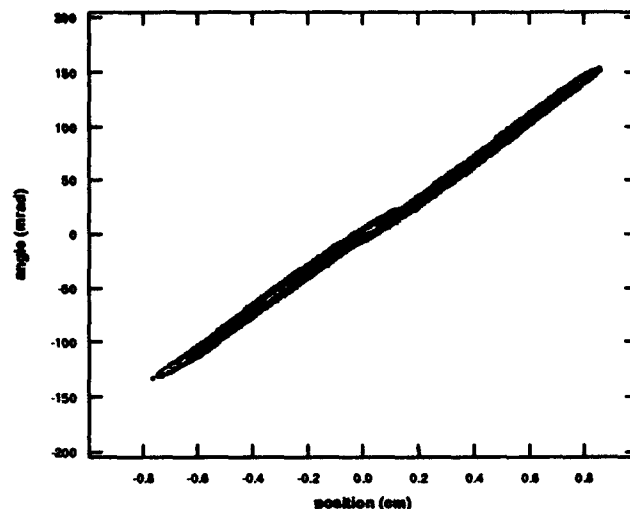


Figure 5. A typical ion source horizontal phase-space emittance contour plot

#### B. LEBTs

The divergent ion source beam is matched into the RFQ by the LEBT. The LEBT housing also contains source diagnostics and provides the differential pumping between the source and the RFQ. The SSC RFQ requires a highly convergent input beam. The Twiss parameters for the design input beam are  $\alpha_{x,y} = 1.26$  and  $\beta_{x,y} = 0.018$  mm/mrad (140 mrad convergence and  $\sim 4$  mm in diameter).

A gas neutralized LEBT is not an option for SSC since the neutralization time ( $\sim 50 \mu\text{s}$ ) is longer than the SSC pulse length. Thus, electrostatic LEBTs were the only viable option. The 30 mA operating current is low enough that several electrostatic focusing concepts can be considered. The einzel lens and helical electrostatic quadrupole (HESQ) lens are the leading candidates for the SSC LINAC and their characteristics are being evaluated at the SSCL. The University of Maryland is investigating a straight electrostatic quadrupole (ESQ) LEBT concept [5] on our behalf and LBL is investigating a very compact single ring lens concept [6].

The einzel lens is probably the most mature technology for this application. Unfortunately this LEBT requires voltages similar to the source voltage which results in nonlinear aberrations. For the initial commissioning of the Injector, we are using an existing dual einzel lens LEBT optimized to meet the SSC magnetron ion source requirements. This choice was not the most desirable one but, in the interest of meeting our schedule, it was the logical choice.

The 30 mA output beam of the volume source and einzel LEBT configuration was characterized at 35 keV. Figure 6 shows a typical horizontal beam phase-space emittance contour plot out of the einzel lens at an axial location corresponding to the RFQ entrance. Nonlinear aberrations are quite pronounced. However, the shape of the vertical and horizontal phase-space

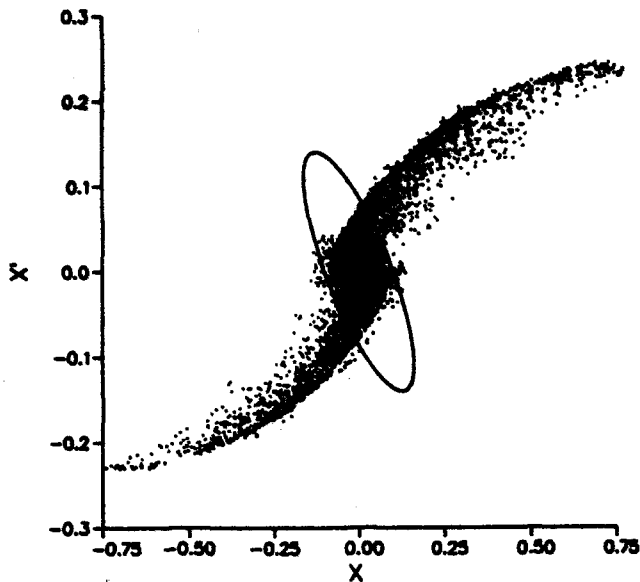


Figure 6. LEBT Phase-space horizontal emittance contour plot

emittance contour plots are similar. The measured  $\epsilon_{t-n-rms}$  ranges between  $0.38 \pi$  mm-mrad in the vertical plane to  $0.79 \pi$  mm-mrad in the horizontal plane. This is 3-5 times the ion source emittance. However, most of this LEBT induced effective emittance growth is due to the large, low particle-density, phase-space wings. As shown in Figure 6, the converging core of this beam, which contains the majority of particles, fits within the nominal acceptance space of the RFQ. Computer simulations [7] have indicated a 40-65% transmission of this beam through the RFQ. A 50% transmission, will provide a more than adequate Injector beam (15 mA) to commission the following stages of the SSC LINAC. Figure 7 is a close up of the einzel lens housing assembly as installed in the Injector. The ion source extractor and magnetic spectrometer are also shown in this figure.



Figure 7. Einzel lens housing assembly

### C. RFQ

The SSC RFQ is a four vane structure designed and built for SSC by LANL [8]. The design parameters of the SSC RFQ are given in Table I. The SSC RFQ has two unique features. First, the design included the effects of higher multipoles by using an 8-term electric field potential to optimize transmission. Second, the intervane voltage is ramped along the length of the RFQ to minimize the beam losses and structure length.

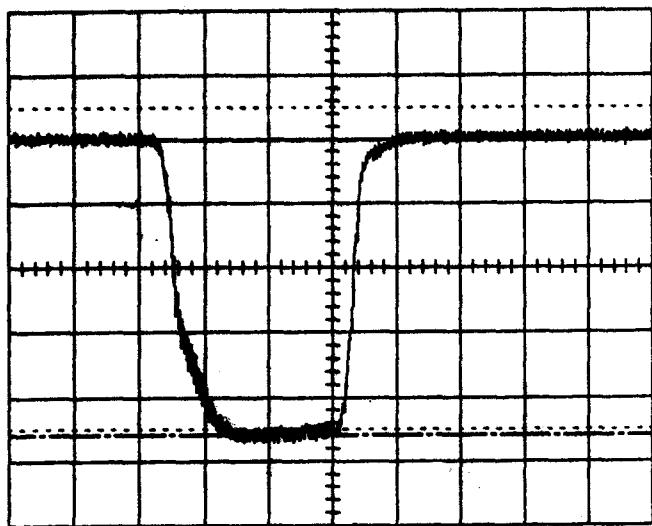
Table I  
RFQ Design Parameters

Frequency	428 MHz
Injection Energy	35 keV
Output Energy	2.5 MeV
Injection current	30 mA
Output current	28 mA
RFQ length	218 cm
Input aperture radius	0.198 cm
Final aperture radius	0.240 cm
Final modulation factor	1.93
Intervane voltage	54.82 to 88.5 kV
Peak surface field	36 MV/m (1.8 K)
Cavity peak rf power	<300 kW
Input $\epsilon_{t-n-rms}$	< $0.2 \pi$ mm-mrad
Output $\epsilon_{t-n-rms}$	< $0.2 \pi$ mm-mrad
Output $\epsilon_j$	< $0.82 \cdot 10^{-6}$ eV-s.
Output beam radius (rms)	0.75 mm

### III. INJECTOR OUTPUT BEAM CHARACTERIZATION

A set of toroids and Faraday cups (FC) placed in various axial locations along the Injector are used to measure the output beam current and beam transmission through the RFQ. A Faraday cup can be inserted between the ion source and the LEBT to measure the ion source beam current and to block the beam from the rest of the Injector. A non-intercepting toroid in the LEBT measures the RFQ input beam current. At the RFQ output, the Injector current is measured by a toroid and a downstream FC. The Injector output beam current, as measured by the RFQ output FC is shown in Figure 8. The measured output beam shape is an exact duplicate of the measured ion source output beam current (Figure 9). The highest Injector output beam current achieved to date is 20 mA (for 30 mA input), this translates to a 66% transmission through the SSC RFQ.

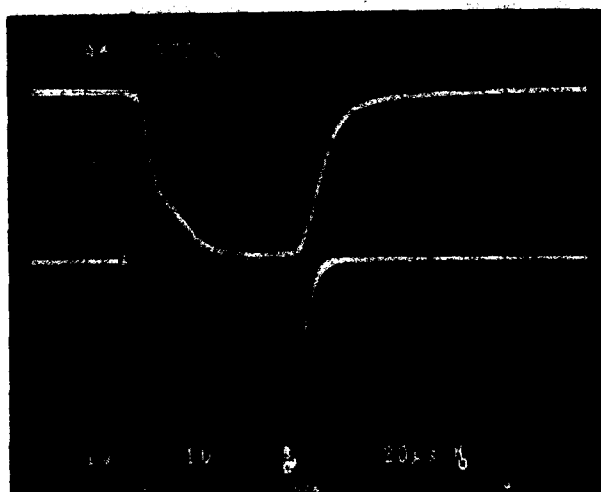
An absorber-collector experiment has bracketed the output beam energy to a value between 2.1 MeV and 3.3 MeV. In this experiment a 2.1 MeV range-thick foil, placed upstream of the output F.C., allowed the whole Injector output beam to be collected while a 3.3 MeV range-thick foil stopped the entire beam. This experiment also indicated a 100% accelerated beam at the nominal RFQ design field.



Vertical Axis : 4 mA/div  
Horizontal axis : 20  $\mu$ s/div

Figure 8. Injector output current time profile

A slit & collector diagnostic [9] system has been used to measure the Injector beam emittance 21.6 cm downstream of the RFQ. Typical horizontal and vertical phase-space emittance contour plots of the Injector output beam are shown in figures 10 and 11, respectively. The elliptical contours are well defined and the measured emittance in the transverse planes are  $\epsilon_{x-n-rms} = \epsilon_{y-n-rms} = 0.25 \pi$  mm-mrad. These values are



Top trace :  $H^-$  current 10 mA/div  
Bottom trace : electron current 500 mA/div  
Horizontal axis: 20  $\mu$ s/div

Figure 9. Ion source output current time profile

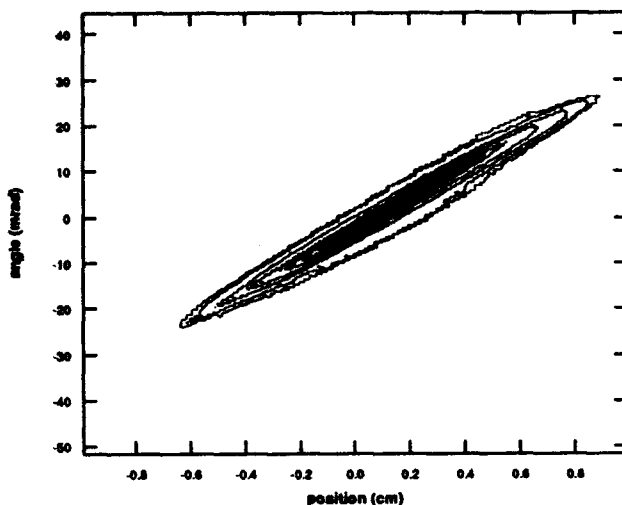


Figure 10. An Injector output beam horizontal phase-space emittance contour plot

25% larger than the SSC LINAC Injector goal. However, the large emittance is believed to be due to the use of the non-optimized LEBT. We expect to improve the Injector output beam current and transverse emittance once the Injector is fully optimized and tuned.

A bunch shape monitor diagnostic built by INR [10] was used to determine the micro-bunch longitudinal phase profile. The beam hits a thin wire at a 10 kV potential and secondary electrons are emitted proportional to the beam intensity. The electron beam is collimated and "time stamped" with an rf deflector. The deflector phase (w.r.t. the output beam phase) is scanned, measuring the intensity of the electron beam at different times during the micro-pulse to produce an intensity versus phase profile. The first measurements of the SSCL bunch shape monitor are in good agreement with theory. Figure 12 shows a comparison of measured results with the theoretical model at nominal RF power, 15 cm downstream of

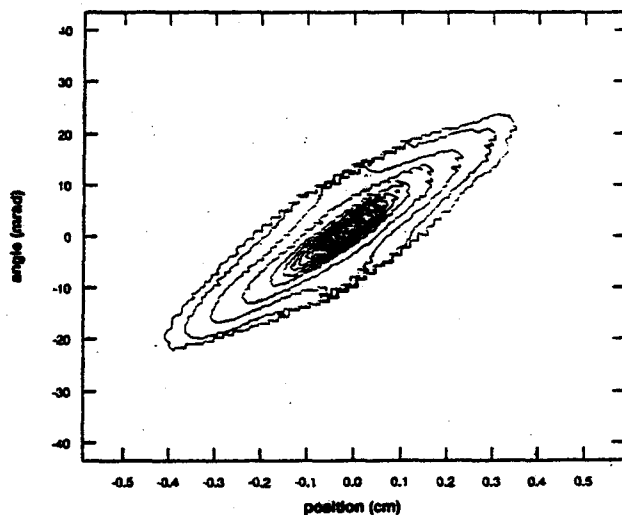


Figure 11. An Injector output beam vertical phase-space emittance contour plot

### Theoretical and Experimental Bunch Shape at 100% RF Amplitude

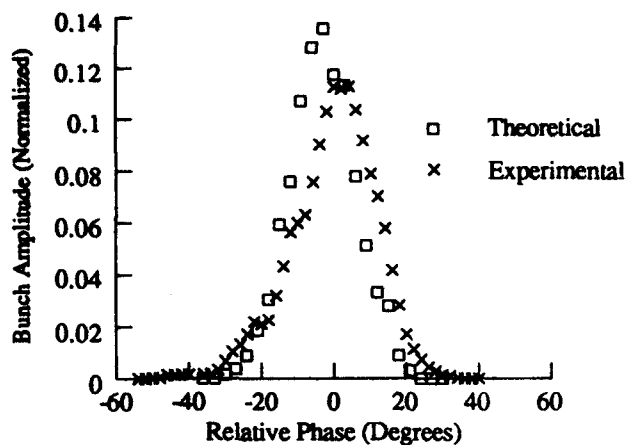


Figure 12. Theoretical bunch shape predicted by PARMTEQ simulation and experimental data as measured by the bunch shape monitor for nominal vane voltage. The intensity is normalized for a unit area.

the RFQ. The measurements indicate a well bunched beam with an rms micro-bunch length of 10 degrees.

## IV. FUTURE WORK

In the near future, we are planning to measure the output beam energy more precisely using a magnetic spectrometer and Rutherford scattering diagnostics. We will continue the injector output beam studies in an attempt to optimize the output beam characteristics in the next few months.

## V. ACKNOWLEDGEMENTS

The authors thank W. Funk, G. Leifeste, K.N. Leung, and D. Swenson for many instructive and constructive discussions. We also thank R. Brown, C. R. Chang, C. Cuevas, C. Crist, P. Datte, A. Feschenko, P. Ferrel, G. Jamieson, J. Sage, S. Volz, and W. Whittenberg for their assistance in running the injector experiments.

## VI. REFERENCES

- [1] K.N. Leung, et al., Rev.Sci.Instrum., 62, 100(1991).
- [2] A. T. Forrester, "Large Ion Beams Fundamentals of Generation and Propagation", p276, John Wiley & Sons, Inc., 1988.
- [3] P. A. Allison, AIP Conference Proceeding NO. 158, P465 (1987).

- [4] K. Saadatmand, et al., AIP conference Proceedings of Sixth International Symposium of Production and Neutralization of Negative Ions and Beams (1992), to be published.
- [5] S. Guharay, et al., this Conference
- [6] C.-F. Chan, et al., this Conference
- [7] F. Guy, et al., this Conference
- [8] T.S. Bhatia, et al., Conference Record of the 1991 IEEE PAC, Vol. 3, P1884.
- [9] Stanley Humphries Jr. "Charged Particle Beams" published by John Wiley & Sons, Inc., 1986, p 79-159.
- [10] J. W. Hurd, et al, this conference

# Proposal for a Pulsed Optically Pumped Polarized $H^-$ Ion Source For High Energy Accelerators

A.N. Zelenski

Institute for Nuclear Research, Russian Academy of Sciences, 117312 Moscow, Russia

C.D.P. Levy, P.W. Schmor W.T.H. van Oers, and G. Dutto  
TRIUMF, 4004 Wesbrook Mall, Vancouver, B.C., Canada V6T 2A3

Y. Mori

KEK, Oho 1-1, Tsukuba-shi, Ibaraki-ken 305, Japan

## Abstract

The acceleration of polarized protons in multi-GeV machines is a great challenge for accelerator physicists. An essential part of such development is the primary source of polarized  $H^-$  ions. Recent studies at TRIUMF and INR, Moscow, showed that pulsed Optically Pumped Polarized Ion Source (OPPIS) could produce up to 1.2 mA  $H^-$  ion beam with polarization in excess of 80% within 1.5  $\pi$  mm-mrad normalized emittance. This current is ten times higher than the best currently available from atomic beam sources. The pulsed OPPIS is quite inexpensive in comparison with atomic beam source, and is ideally suited for high energy accelerator applications.

## I. INTRODUCTION

The importance of spin effects in the multi-GeV range of energies has been realized in recent years and as a result a number of experiments employing accelerated polarized proton beams have been proposed for KAON [1], FNAL [2], BNL [3], and SSC [4]. Accelerator physicists have met this challenge by implementation of the "Siberian snake" technique of preserving the polarization during acceleration [5]. Another important part of such facilities is the primary source of polarized  $H^-$ . Conventional atomic beam sources are gradually being improved, and recent progress on a D- plasma ionizer will probably lead to increased polarized  $H^-$  currents of up to 100  $\mu$ A in 1.5  $\pi$  mm-mrad emittance, even though  $H^-$  is not a favored ion for atomic beam sources [6]. Typical currents of unpolarized  $H^-$  ion injectors are about 50 mA [7]. A big difference in the polarized and unpolarized current will substantially restrict the possibilities of studying polarization phenomena at the low duty-factor high energy accelerators.

## II. PROPOSAL FOR A PULSED HIGH CURRENT OPPIS

An alternative to the atomic beam source is the comparatively new technique of optically pumped polarized ion sources, which is particularly suitable for  $H^-$  production. In the last few years optically pumped polarized  $H^-$  sources have been put into routine operation at KEK [8], LAMPF [9] and TRIUMF [10]. This has improved substantially the facilities for polarization studies at these laboratories.

Two basic OPPIS configurations are in use. At KEK, LAMPF and TRIUMF, ECR sources are used for producing the primary proton beam. Very similar results have

been obtained with this arrangement for both pulsed and cw modes of operation, and presently the  $H^-$  current is limited to less than 200  $\mu$ A in a 1.0  $\pi$  mm-mrad normalized emittance. This limitation is to occur as a result of the ECR plasma temperature (higher than 2 eV). The KEK pulsed OPPIS, for example, nearly achieved this current limit [8]. The influence of rubidium ion space charge on emittance degradation is also very important and is not yet well understood. Another approach, implemented at INR, Moscow overcomes these problems [11] (see Fig. 1.). In this technique a high intensity neutral atomic hydrogen beam is injected into a strong longitudinal magnetic field, where it is ionized in a pulsed gas helium (or neon) cell. The resulting proton beam is then injected into an optically pumped Na (or Rb) cell, which is situated in the same solenoidal field as the ionizer. In effect, the ionizer cell acts as a proton source in a high magnetic field. The proton yield from He at hydrogen beam energies of 5-8 keV is about 70% and about 40% for neon. The He cell is isolated and biased at -1 kV, allowing energy separation of the protons from the primary neutral hydrogen beam. A conventional electromagnetic pulsed gas valve cannot be used in a high magnetic field and a piezoceramic or pneumatic valve must be used. A very bright neutral injector (the prototype was developed at the Budker INP, Novosibirsk) produces up to 30 mA equivalent transmitted atomic beam current through the ionizer cell and the optically pumped cell. It is based on production of a low divergence proton beam, which is extracted by a four-electrode multiwire system from an expanded plasma [12]. The proton beam is focused by a solenoidal magnetic lens and neutralized in a pulsed hydrogen or alkali vapour cell. The geometry of the source extraction system and focusing lens has to be chosen carefully to provide the conditions for space-charge compensation during beam formation, in order to avoid increasing the beam divergence.

The resulting polarized current is very close to estimates obtained from the measured initial beam and the efficiency of ionization and charge-exchange processes in helium and sodium. The polarized current doesn't depend on the magnitude of the magnetic field in the optically pumped cell, but there is a loss of about 30%, because some additional divergency is introduced during deceleration of the proton beam at the exit of the He ionizer. The polarized  $H^-$  current obtained at INR for a maximum polarization of 65% is 400  $\mu$ A in an emittance of 1  $\pi$  mm-mrad. At higher Na thicknesses in the optically pumped cell, the current

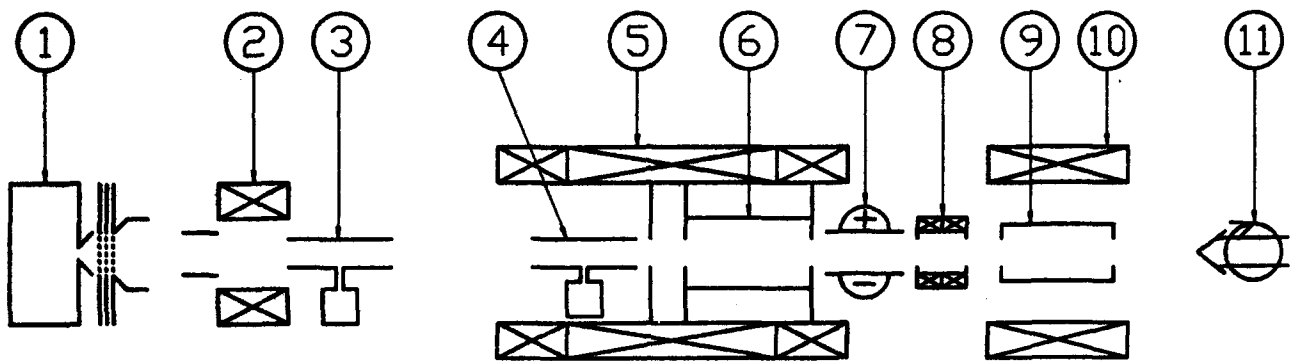


Fig. 1. Schematic layout of the pulsed optically pumped polarized  $H^-$  ion source: 1-source of primary protons; 2-focusing lens; 3-neutralizer cell; 4-pulsed helium ionizer cell; 5-superconducting solenoid 25-30 kG; 6-optically pumped Rb cell; 7-deflecting plates; 8-Sona transition magnetic shield and trim coil; 9-sodium ionizer cell; 10-ionizer solenoid 1.5 kG; 11-pulsed Ti:Sapphire laser.

increases to  $600 \mu A$  but the polarization drops to 45%, because of radiation trapping within the sodium vapour.

Recent progress in OPPIS development has been the result of switching from dye lasers and optical pumping of sodium to solid state Ti:sapphire lasers and optical pumping of rubidium [13] and potassium [9]. The advantages of Rb as a medium for optical pumping and the high power of Ti:sapphire lasers have greatly improved the OPPIS parameters. At TRIUMF even in a cw mode of operation, up to  $8 \times 10^{13}$  Rb atoms/cm<sup>2</sup> with an electronic polarization of over 95% was produced. An efficiency of 50% for capture of polarized electrons by the incident proton beam was obtained. A high power pulsed Ti:sapphire laser was tested in the INR source, where a 90% neutralization efficiency at the highest polarization was achieved, nearly doubling the polarized  $H^-$  current compared with using sodium. In such a way, it should be possible to produce at least  $800 \mu A$  polarized  $H^-$  beam in a  $1.0 \pi$  mm-mrad emittance. This current is expected to scale with emittance and, if  $1.5 \pi$  mm-mrad emittance is acceptable - such emittance is specified in the FNAL proposal on acceleration of polarized protons [2] -  $1200 \mu A$  could be available from a pulsed OPPIS. As for possible improvements, the current scales with the neutral beam intensity and development in that area is definitely not exhausted. For example, the above current of  $400 \mu A$  was measured at only half the neutral hydrogen beam intensity, which has been obtained from the Budker Institute prototype source.

This technique is particularly suitable for high energy accelerators having low repetition rates of 10-15 Hz (FNAL, SSC). At such low rates, the ionizer helium consumption is only  $3 \times 10^{17}$  atoms/sec and vacuum pumping of the He ionizer cell is accomplished easily by one 1000 l/sec turbomolecular pump. A very simple, inexpensive laser system

based on a pulsed Ti:sapphire laser could be used to produce high polarization of the Rb vapor. The INR pulsed Ti:sapphire laser produces up to 1 kW power in a pulse duration of 200  $\mu sec$ , with a linewidth of 10-12 GHz and a repetition rate up to 25 Hz. A longer pulse duration could be realized by using two such lasers, or an alexandrite laser.

Very important results have been obtained recently at TRIUMF [14]. Proton polarization of over 80% was obtained in a cw mode of operation, at a high magnetic field of 25 kG in the optically pumped cell. In the INR-type source, energy separation of the protons produced by ionization of the primary neutrals provides better background conditions and the polarization should be even higher.

Combining the INR results of highest current production and the experience with pulsed Ti:sapphire lasers and the TRIUMF results of highest polarization, we propose the development of a pulsed polarized ion source which will produce high current polarized  $H^-$  beam having the specifications shown in Table 1.

Table 1. Pulsed OPPIS parameters.

Repetition rate	10-15 Hz
Pulse duration	100 $\mu sec$
Pulsed polarized $H^-$ current	> 1.0 mA
Pulsed polarized $H^+$ current	10 mA
Polarization	80-85%
Normalized emittance	$1.5 \pi$ mm-mrad

Such a pulsed OPPIS will produce at least a factor of ten times higher polarized  $H^-$  current than the best atomic beam source currently available. It's construction is less expensive than that of an atomic beam source and we believe it is ideally suited to be used at high energy ac-

celerators. An important feature of the proposed OPPIS is the capability of further development by using a spin-exchange technique of polarization [15]. In that technique there is no space-charge current limitation, since polarization takes place in collisions between neutral hydrogen and alkali-metal atoms. Future spin-exchange optically-pumped sources will likely produce polarized  $H^-$  ion currents in excess of 10 mA, and may finally solve the problem of a polarized injector for high energy accelerators.

### III. CONCLUSION

There is a great deal of interest in high energy spin physics experiments at fixed target, collider and storage ring setups. The development of a high performance pulsed optically pumped polarized  $H^-$  ion source should be considered for the most efficient use of these facilities with polarized beams.

Anderson (Univ. of Wisconsin USA) and Mori (KEK National laboratory, Japan) were awarded the 1993 IEEE Particle Conference Technology Award for their invention and development of the optically pumped polarized negative ion source and in recognition of successes of the first generation OPPIS. We believe the optically pumped polarized  $H^-$  ion sources of the next generation, which have been discussed in this paper, will produce polarized  $H^-$  ion currents of 1-10 mA, i.e. close to the currents of unpolarized ion sources.

### IV. REFERENCES

- [1] W.T.H. vanOers, "Spin-physics at KAON", in *Proc. 9<sup>th</sup> Intern. Symp. on High Energy Spin Physics* edited by K.H. Althoff (Springer Verlag, 1991) p. 335.
- [2] *Report on Acceleration of Polarized Protons to 120 and 150 GeV in the Fermilab Main Injector*, SPIN collaboration, Michigan, Indiana, Fermilab, N. Carolina/TUNL, Protvino, Moscow, KEK, March 1992.
- [3] S.Y. Lee, *Particle and Field Series 42*, AIP Conf. Proc. No. 223, 30, (1990).
- [4] *Proc. 1985 Ann Arbor Workshop on Polarized Beam at the SSC*, AIP Conf. Proc. 145 (AIP New York 1986).
- [5] Ya.S. Derbenev, A.M. Kondratenko, *Proc. 10<sup>th</sup> Intern. Conf. on High Energy Accelerators*, IHEA, Serpukhov (Protvino, USSR 1977), Vol. 2, 70.
- [6] A. Belov *et al.*, "A source of polarized  $H^-$  ions with deuterium plasma ionizer" (to be published in *Proc. 10<sup>th</sup> Intern. Symp. on High Energy Spin Physics*, (Nagoya, Japan 1992).
- [7] J.G. Alessi *et al.*, *Rev. Sci. Instr.*, **61**, 625, (1990).
- [8] Y. Mori, *Proc. 8<sup>th</sup> Intern. Symp. on High Energy Spin Physics*, (Minneapolis 1988), AIP Conf. Proc. 187, 1200, (1989).
- [9] R.L. York *et al.*, *Operation of the OPPIS at LAMPF*, Proc. 1991 IEEE PAC, p. 1928.
- [10] C.D.P. Levy *et al.*, "Status of the TRIUMF OP-PIS", in *Proc. 13<sup>th</sup> Intern. Conf. on Cyclotrons and Their Applications*, (World Scientific, Singapore, 1992) p. 322.
- [11] A. Zelenski *et al.*, *Nucl. Instrum. and Methods A245*, 223, (1986).
- [12] V.I. Davydenko *et al.*, *Dokl. Akad. Nauk, USSR*, **271**, 1380, (1983).
- [13] C.D.P. Levy *et al.*, "A dc OPPIS based on optically pumped rubidium", in *Proc. 4<sup>th</sup> Intern. Conf. on Ion Sources*, ed. B.H. Wolf (Bensheim 1991) *Rev. Sci. Instr.* **63**, 2625, (1992).
- [14] A. Zelenski *et al.*, "Optimization studies of proton polarization in the TRIUMF OPPIS", (to be published in *Nucl. Instrum. and Methods*).
- [15] A. Zelenski *et al.*, *Proc. Intern. Workshop on Polarized Ion Sources and Jets KEK Report*, No. 90-15, 310, (1989).

# Design and Performance of the Inter-RFQ Beam Transport and Matching Section for the SAIC PET Isotope Production Accelerator\*

W. D. Cornelius, Science Applications International Corp.  
4161 Campus Point Court, San Diego CA 92121

## Abstract

The SAIC PET isotope production accelerator is comprised of a 1 MeV  $^3\text{He}^+$  radio-frequency quadrupole (RFQ) accelerator followed by a charge-doubler and pair of RFQ accelerators to produce 8 MeV  $^3\text{He}^{++}$  ions. The inter-RFQ section consists of a stripper and a transport system in order to match the beam into the following RFQ. This inter-RFQ section is functionally equivalent to a single-sided beam funnel where the bend magnet has been replaced with a stripper cell. The operating frequency is doubled from 212.5 MHz to 425 MHz and the beam must be matched transversely and longitudinally to the 425 MHz RFQ acceptance. The transverse matching is accomplished using permanent magnet quadrupoles and the longitudinal matching is accomplished using a buncher cavity. Our particular design is unique in that the transverse x:y diameter ratio can be as high as 4:1. Initially this asymmetry was thought to complicate the transport, however the system can be designed to exploit the unique features of a large aspect ratio and has important implications at other facilities.

## I. INTRODUCTION

The SAIC PET isotope production accelerator is illustrated in figure 1. The  $^3\text{He}^+$  ions produced in an ion source are accelerated to 1 MeV by a 1 meter "PreStripper" RFQ operating at 212.5 MHz.[1] The 1 MeV ions are stripped of the second electron in the "charge-doubler" section and further accelerated by a 425 MHz "PostStripper" RFQ (2.8 meters) to a final energy of 8 MeV. The 8 MeV beam is focused into the isotope production target by a combination of quadrupole and multipole electromagnets to produce the four common PET isotopes.

The matching of the ion beam between the two RFQs is accomplished in the charge-doubler section using a combination of permanent magnet quadrupoles (PMQs)[2] and a buncher cavity. In order to simplify the transport and matching of the beam through this region, the final few cells in the PreStripper RFQ were modified.[1]

\*Work sponsored by Strategic Defense Initiative Organization Contract Number SDIO 84-89-C-0046.

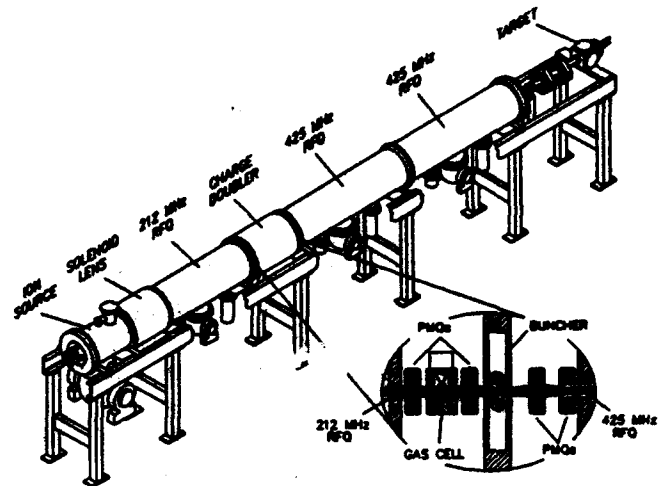


Figure 1. Line drawing of the PET accelerator. The  $^3\text{He}^+$  ion beam is produced in a duoplasmatron ion source and accelerated to 1 MeV in the PreStripper RFQ operating at 212.5 MHz. The ions are stripped of the second electron in the charge-doubler and matched into the PostStripper RFQ. The PostStripper RFQ is divided into two segments by an aperture plate. The first segment accelerates the beam to 5 MeV and the second to 8 MeV. Upon exiting the PostStripper RFQ, the beam is directed into the isotope production target.

## II. TRANSPORT DESIGN

In the charge-doubler region, the 1 MeV  $^3\text{He}^+$  ion beam exiting the PreStripper RFQ, passes through the first PMQ and enters the gas cell where the second electron is stripped to make  $^3\text{He}^{++}$  ions. These ions are focused through the buncher cavity and matched to the PostStripper RFQ acceptance using three additional PMQs.

A conventional pillbox cavity operating at 212.5 MHz would be very large and bulky. Also the small longitudinal distance available would result in a very inefficient cavity. Hence the PET buncher cavity was designed as a quarterwave stripline resonator. This design minimizes the longitudinal distance required and the drift-tube geometry provides two rf gaps, effectively halving the rf voltage required. The resonant frequency is controlled by moving a sliding short along the "stem" of the drift tube.

### III. EXPERIMENTAL RESULTS

The original transport solution performed poorly. Although the emittance orientation of the 1 MeV beam exiting the PreStripper RFQ agreed with the theory,[1] the transmission of the beam through the PostStripper RFQ was less than 20%. The reason for this poor performance was inadequate performance of the buncher cavity.

The difficulty with the original transport solution is that the rf defocusing produced by the buncher cavity must be within 3.4% of the theoretical value to maintain a transverse match. This means that insufficient bunching leads to not only a longitudinal mismatch, but a transverse mismatch as well.

Fortunately the features of the beam transport solution provide a simple means of measuring the degree of rf defocusing produced by the buncher cavity. Because the effective focal distance of the second PMQ is substantially altered by rf defocusing, the degree of defocusing can be derived from the change in quadrupole field required to refocus the beam ions on a viewer downstream of the buncher cavity. In addition it is not necessary to strip the beam ions to the  $2^+$  state to observe this effect. Therefore a relatively simple experiment can be performed to measure the degree of rf defocusing produced by the buncher and also calibrate the effective on-axis voltage as a function of rf power without requiring measurement of the longitudinal emittance, phase, or energy spread.

To measure rf defocusing, the PostStripper RFQ was replaced with a drift space and a beam viewer with an electromagnetic quadrupole between the buncher and the viewer. The  $^3\text{He}^+$  beam was accelerated in the PreStripper RFQ and focused onto the viewer using the electromagnetic quadrupole. As the phase of the buncher was varied, the quadrupole magnet was adjusted to refocus the beam onto the viewer and the current required was recorded for a variety of rf power levels.

Figure 2 shows a typical result of quadrupole focusing current as a function of buncher phase at a fixed rf power level. The amplitude of the refocusing current was derived by fitting the data with a sine wave shown as the solid line in the figure. The effective rf defocusing produced by the buncher cavity was derived from the refocusing current and compared with results from TRACE3D.[3]

### IV. THEORY

The theoretical rf fields were derived using electrostatic field codes to compute the electric field amplitude and fitting that amplitude with a time-varying Gaussian function. Although the electric fields are not precisely Gaussian, this difference does not lead to significant errors and the Gaussian expression can be integrated analytically to yield the effective rf gap voltage ( $E_0\text{TL}$ ) used by TRACE3D. This effective gap voltage was used to generate rf defocusing according to the defocusing model internal to TRACE3D. The quadrupole

gradients required to refocus the beam could then be derived from TRACE3D.

The original buncher drift tube had a 5 cm bore to reduce geometric aberrations. However analysis of this geometry indicated that a drift-tube voltage of 1.5 MV would be required to achieve proper performance. Reduction of the drift-tube bore diameter did not appreciably improve on this performance.

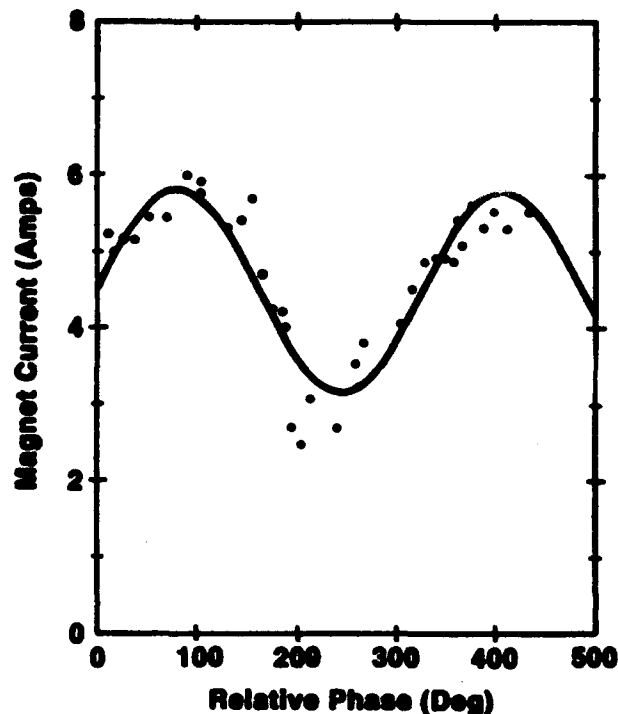


Figure 2. Typical data plot of quadrupole refocusing current as a function of buncher rf phase. The data were fit with a sine function. The resulting amplitude is the change in quadrupole magnet current required to refocus the beam onto the viewer and is proportional to the degree of rf defocusing induced by the buncher.

The solution to this problem is based on abandoning the circular-aperture geometry. Although this approach runs contrary to common practice, the key factor to consider is the necessity of increasing the effective on-axis rf voltage without sacrificing additional rf power. The on-axis voltage is very sensitive to the relationship between the rf gap and the inner diameter of the drift-tube. The narrow rf gap necessitated by the low-energy ion beam places severe restrictions on the inner diameter of the drift tube if high efficiency is to be maintained.

This situation is improved considerably by substituting a "slit" for the circular drift-tube aperture. In this situation, the effective on-axis voltage is determined by the geometry of the smallest dimension of the slit and can easily attain more than 90% of the drift-tube voltage. A significant additional benefit of this approach is that rf defocusing can be neglected in the direction parallel to the long axis of the slit.

Substituting a 0.9 cm by 3.5 cm vertical slit for the circular drift-tube aperture increased the effective on-axis voltage to 93% of the drift-tube voltage and reduced the required rf power to less than 20 kW.

This situation represents a considerable improvement in the stability of the beam transport solution because it virtually eliminates the sensitivity of the transverse beam matching to buncher operation. The horizontal beam transport was already insensitive to rf defocusing and, with the slit geometry, the vertical focusing is insensitive as well. Hence the new beam transport solution does not depend on achieving a precise rf-defocusing effect from the buncher cavity and the beam is always well-matched in the transverse planes regardless of the status of the buncher cavity.

## V. EXPERIENCE

The theoretical transmission of the original transport solution was 6% without an operating buncher cavity. The measured value was about 20%. The discrepancy is probably due to modelling the performance with TRACE3D rather than a more precise code like PARMILA.[4] Without an operating buncher, the debunching of the beam exiting the PreStripper RFQ is nearly complete by the time the ions arrive at the entrance to the PostStripper RFQ. Hence the tail and head of the leading and following bunches overlap the bunch in the middle. This overlap adds additional current to the central bunch that can be captured and accelerated but is not accounted for by the theory. Adding one-third of the ions captured from the overlap of the leading and following bunches to the beam captured from the central beam bunch boosts the theoretical transmission from 6% to 18% and is in much better agreement with the measured value.

The performance of the new transport design has not yet been quantified. Simulations indicate substantially improved performance, but these predictions have not yet been verified.

## VI. IMPLICATIONS

The potential implications of the slit drift-tube apertures are very interesting. Abandoning a circular geometry could have a significant impact on design of accelerators. For example using a slit geometry in a conventional drift-tube linac (DTL) could significantly improve the performance at the low-energy end where the drift-tubes and rf gaps are "short" relative to the required apertures. The inlet end of DTLs has always been a design problem because the drift-tubes in this region can be too short to include quadrupole magnets. The invention of the RFQ accelerator partially solved this problem by boosting the injection velocity, but this solution is difficult to implement for heavy ions because the RFQs producing the required injection velocities get very long at the low frequencies required for heavy ion acceleration. Additionally it is desirable to increase the rf frequency to improve the effective acceleration gradient and to support beam funneling. Doubling the frequency halves the distance

between drift tubes and halves the length of the drift tubes, effectively reintroducing the low-energy end problem.

Designing these DTLs could be simplified with slit-apertures because the rf defocusing can be neglected along the long axis of the slit. In this case one needs only relatively weak focusing to keep the edges of the "ribbon beam" confined. The strong focusing required in the other direction might be achievable by shaping the edges of the drift tube around the slit to produce the desired focusing components in the rf electric fields. The efficiency of "short" drift-tubes is also improved by the slit geometry because the effective gap voltage is a greater percentage of the rf voltage on the drift-tube. Transitioning from a ribbon beam to a circular beam could be accomplished at higher energies where the drift-tubes have sufficient volume to include magnetic focusing elements.

## VII. CONCLUSIONS

The poor performance of the original charge-doubler section was traced to inadequate buncher operation. Transverse and longitudinal matching of the beam into the PostStripper RFQ required a precise degree of rf defocusing from the buncher. When this effect was not produced, the quality of the match was poor. Redesigning the buncher drift-tube with a slit aperture resulted in substantially improved theoretical performance and the rf power required by the buncher decreased by a factor of 13. In addition, the new transport solution always matches the transverse emittances regardless of the condition of the buncher. This solution decouples longitudinal matching from transverse matching and provides a much better solution to the inter-RFQ beam transport.

### *Acknowledgements*

Successful operation of this accelerator facility is a result of the combined efforts of many people. In particular I want to acknowledge the efforts and contributions of Steve Schmidt, Mike Donovan, Russ Parker, Phil Young, Steve Ringler, John Klaus, and Don Young.

### *References*

- [1]W. D. Cornelius and P. E. Young, Nucl. Instr & Meth. **B72**(1993)933
- [2]Field Effects Inc. Acton Massachusetts
- [3]K. R. Crandall, TRACE3D Documentation, revised by D. P. Rusthoi, LAUR-90-4146. Code available from the Los Alamos Accelerator Code Group, Los Alamos National Laboratory, Los Alamos NM 87545
- [4]PARMILA (Phase And Radial Motion in Ion Linear Accelerators), Code available from the Los Alamos Accelerator Code Group, Los Alamos National Laboratory, Los Alamos NM 87545

# Electron Cyclotron Resonance Sources of Multiply Charged Ions Last Developments at Grenoble

G.Melin, F.Bourg, P.Briand, M.Delaunay, A.Girard, D.Hitz,  
P.Ludwig, T.K.Nguyen, M.Pontonnier  
CEA/Département de Recherche Fondamentale sur la Matière condensée/PSI  
85X, 38041 Grenoble Cédex, France

## Abstract

The behavior of compact electron cyclotron resonance ion sources (ECRIS) is emphasized in this article, and more specifically the Caprice ECRIS concept: a high B field ( $\geq 1$  T) source offering good performances both in extracted ion charge states and intensities, in a rather small volume, a source easy to handle and to operate. This concept like the ECRIS concept itself originated from the Grenoble group; it is quite attractive to continuous regime cyclotrons requiring high stability ion beams, but it is also well suited to delivering very high intensity particle pulses (today a few  $\mu\text{A}$  of  $\text{Pb}^{28+}$  or  $\text{Au}^{27+}$  ion beams, a few ms long) of interest for synchrotron bunching. Finally the developments and activities in the field of ECRIS at Grenoble, are shortly surveyed while giving some trends and prospects.

## I. INTRODUCTION

The ECRIS are now widely used by the accelerators. The Grenoble group which developed the first high charge state ECR source [1], although not directly associated with an accelerator facility, keeps on strongly working on ECRIS development for improving their performances, and on other plasma applications where radiofrequency waves-plasmas interactions are very important.

The ECR ion sources, an outgrowth of the fusion plasma studies in the so called open-ended mirror machines [2] can be shortly described as follows. It is made of a magnetic configuration able to trap hot electrons heated by a resonant rf wave-electron interaction; as a consequence, in order to satisfy the charge neutrality condition, the ions get electrostatically trapped and undergo successive ionizations; the extracted ion beams out of an ECRIS are actually the losses of this magnetic configuration. This is why tuning an ECR ion source in order to obtain high charge state and high intensity ion beams, results in a difficult compromise owing to opposite requirements: (i) confining a high density plasma for ionizing high charge states, but consequently having low losses and offering low intensity ion beams, (ii) having high plasma losses and possibly high intensity ion beams, which evidently does not allow the plasma density to build up, and may seriously jeopardize the ionization efficiency for high charge states!

Various concepts of ECR ion sources have been constructed, while trying to overcome this contradiction as well as other difficulties both from the technology and from the plasma physics. The Grenoble group built Minimafios,

one of the most performant sources as to the 16-18 GHz prototypes [3] for delivering special ion beams; Neomafios [4], a source using only permanent magnets for its magnetic configuration; and Caprice, a compact source which got gradually improving [5].

## II. THE CAPRICE CONCEPT

Although the Caprice source is not the best today source as to the performances of the multiply charged ion beams it can deliver, nevertheless it offers an outstanding compromise between the so many desirable characteristics of a multiply charged ion source that physicists of modern accelerators may wish to work with: high charge states, high intensities, high stability, wide range of ion species, reliability and longevity (no cathode, no filament), simplicity and modularity in the design (easy change of parts), a source easy to handle and to operate.

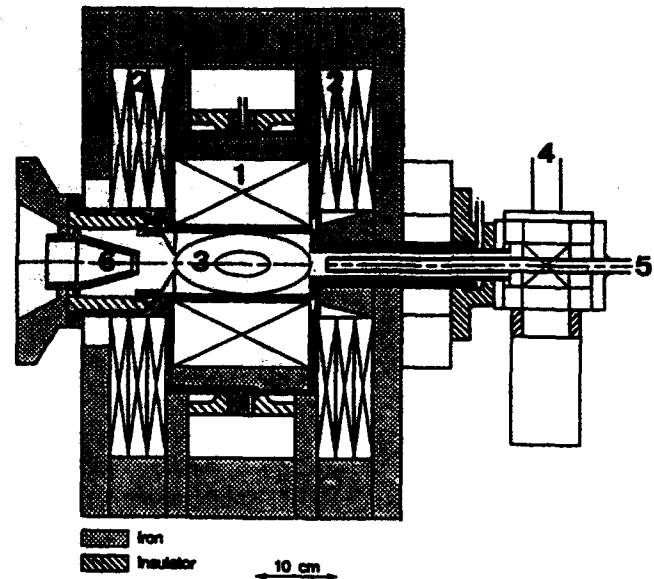


Figure 1: Caprice source, 1-permanent magnet hexapole, 2-solenoid coils, 3-closed mod-B surfaces, 4-rf power input, 5-gas inlet, electric oven feedthroughs, 6-ion extraction.

### A. Description and main features

A sketch of the source is given in figure 1. The source is characterized by a small plasma chamber (16 cm long, 6.6 cm diameter) highly magnetized (i) by using electrical coils for the axial field,  $\sim 1.2$  T at the mirror throat owing to a strong and thick iron yoke and to other iron parts such as the puller electrode, (ii) by a high remanent induction

permanent magnet hexapole for the radial field,  $\sim 0.9T$  at the plasma chamber radius.

The rf power is launched by a coaxial feeder, and the source equally works at 10 GHz and 14 GHz (at a higher axial field) with quite similar performances.

The measured emittances at a constant extraction voltage vary in between 80 to 150 mm.mrad (for 80% of the beam intensity) for charge states below 10; at higher charge states the emittance gets better not only because of the increased ion beam velocity, but also because the high charge state ions are actually originating from the plasma center along the main axis (electrostatic confinement).

### B. Results in continuous regime

This is one of the main advantages of the Caprice concept: it behaves exceptionally stable for long runs, i.e. tens of hours of continuous operation, with usually no more than 1 kW of rf power. The data set shown in figure 2 gives the optimized results with a few gases obtained with a Caprice source at 10 GHz.

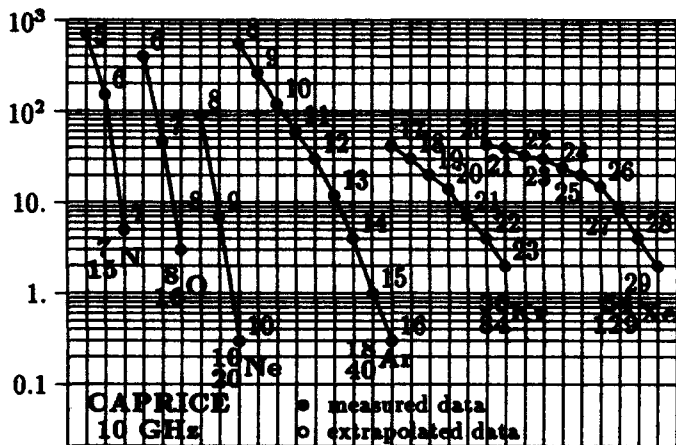


Figure 2: Optimized ion currents ( $e\mu A$ ) for some gases.

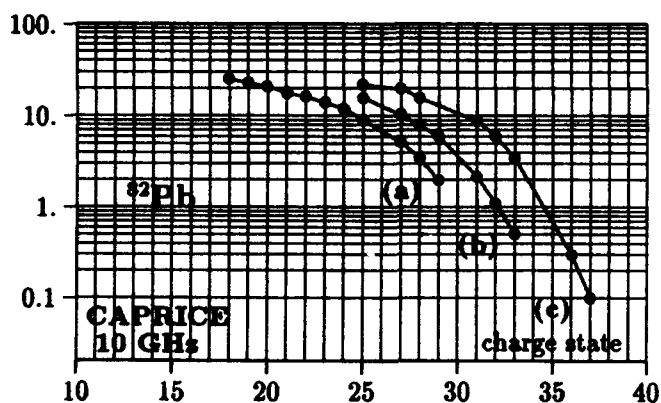


Figure 3: Optimized lead ion currents ( $e\mu A$ ) from Caprice (a)4kG hexapole, Pb plasma-vaporized, (b)8kG hexapole, Pb plasma-vaporized, (c)9.3kG hexapole, Pb oven-vaporized

Recently for atomic physics studies, the Caprice source proves its capability of delivering  $Ar^{17+}$  ions in the 1 nA range, and  $Ar^{18+}$  ions in the 20 epA range, which ranks it well above other sources.

The figure 3 illustrates how much progress has been

made with optimized lead ion beams, as an example, when increasing the hexapole magnetic field and varying the technique of production of the metal vapor. The technique of independently heated micro-oven considerably improved the capability of the source for delivering high charge state high intensity ion beams, as compared to the former technique of metal/oxide samples directly heated by the hot electron plasma; the main drawback of this former technique was to kill some hot electrons, and then to reduce the ionization efficiency of the source, as well as not to separate the functions of (i) vaporizing the metal and controlling its pressure, from (ii) the ionization and plasma formation. A few instantaneous charge state distributions are shown for lead and gold in figure 4, both obtained by this specific high temperature oven technique.

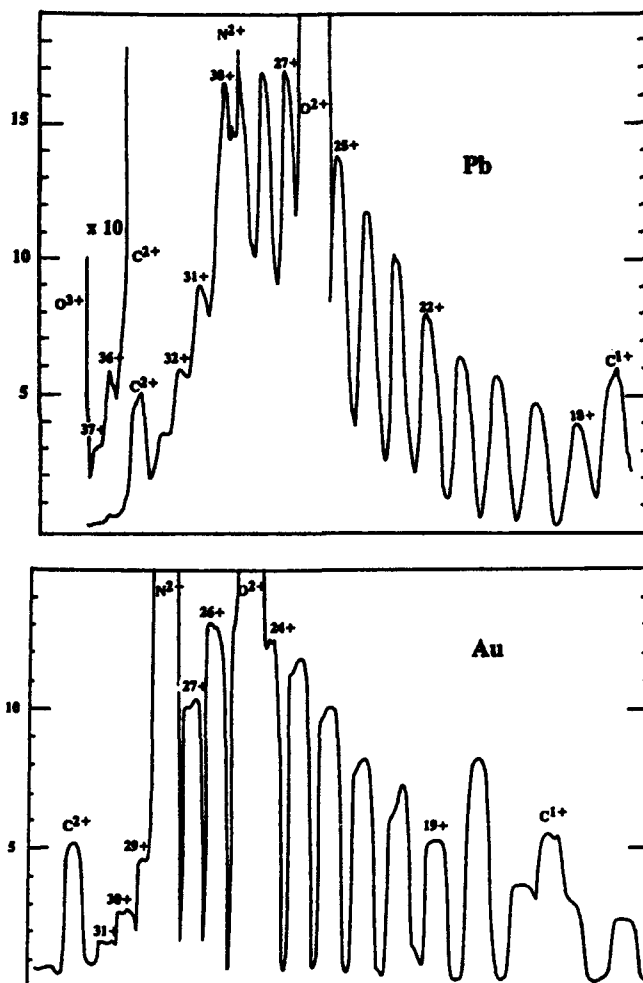


Figure 4: Charge state distributions from a 10 GHz Caprice source for lead (optimized on  $Pb^{31+}$ ) and gold (optimized on  $Au^{26+}$ ), vertical scale in  $e\mu A$ .

### C. Results in pulsed mode: the afterglow effect

The pulsed mode of operation of the Caprice source is even more impressive than the cw mode; this specific afterglow mode, which the Grenoble group was first to investigate [3], is a consequence of the electrostatic confinement of the ions in the space charge well of the magnetically con-

finned hot electrons within the source, that makes it similar to the EBIS. Once the ECR discharge has reached a steady state regime, turning the rf power off causes the electron population to collapse: the cold electrons leave the trap faster than the hot ones, and as the discharge is no longer sustained by the rf field, i.e. not refuelled by new cold electrons, the confined ions are compelled to leave the trap because of the charge neutrality condition. This effect occurring in the afterglow plasma is quite impressive; it may be optimized so as to obtain a few particle  $\mu\text{A}$  pulses of charge state  $\sim 30$ , a few ms long, at a frequency  $\sim$  a few tens of Hz: so far 2  $\mu\text{A}$  pulses of  $\text{Pb}^{28+}$  ions, 1  $\mu\text{A}$  pulses of  $\text{Au}^{27+}$  ions (see figure 5); the pulse intensity is essentially limited by the metal vaporization process (here the oven technique), it should be possible to reach  $\sim 3 \mu\text{A}$  for these ions.

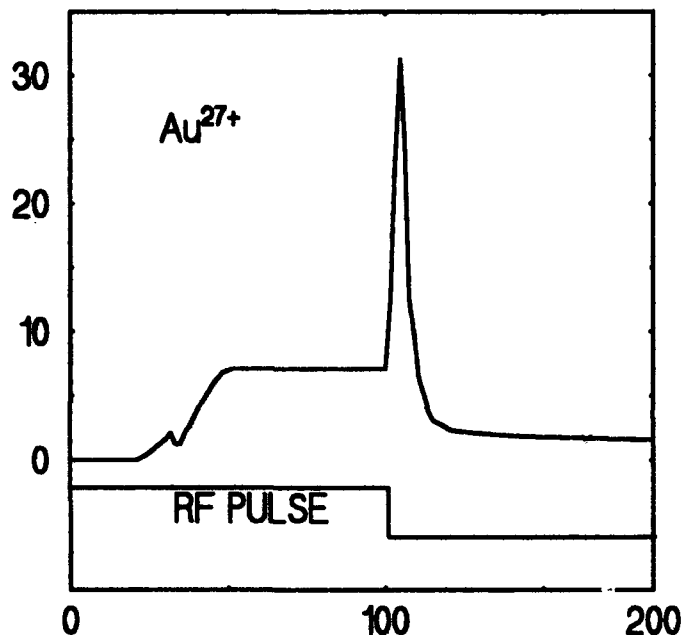


Figure 5: Afterglow pulse of  $\text{Au}^{27+}$  ion current ( $e\mu\text{A}$ ), horizontal scale in ms.

### III. ECRIS R&D AND PROSPECTS

As already mentioned above the Grenoble group has developed other sources, among which the only permanent magnet built ECRIS Neomafios 8 & 10 GHz [4] and soon 2.45 GHz are quite interesting because of their reduced power consumption, however offering lower performances than the Caprice source.

Today the main activity in Grenoble concentrates on the following efforts, which will hopefully give new orientations to the ECRIS.

#### A. The Quadrumafios facility

This facility specially designed for plasma measurements, and evidently not a compact one, aims at featuring and understanding the multiply charged ion production. Plasma and atomic physics diagnostics are developed in order to measure and control the most important plasma parameters: microwave interferometry for the electron den-

sity, bremsstrahlung and line X-ray spectrometry for the electron energy and the ion characterisation, diamagnetic loops for the plasma energy content, electron cyclotron emission for the electron energy, electron and ion losses electrostatic analyzer, visible light and VUV light spectrometry, etc. . . The first data obtained at the frequency of 10 GHz are currently being processed.

#### B. Superconducting ECRIS

In a joint venture INFN-LNS-Catania/CEA-DRFMC-Grenoble, the building of a superconducting source for the K-800 cyclotron has just started. The source is designed so as to reach the highest magnetic fields so far used in an ECRIS: 1.4 T radially at the chamber wall and 2.2 T axially at the mirror throat. This facility is expected to deliver at high charge states the highest extracted ion currents,

(i) because of its capability of trapping a higher electron density, and thus of delivering larger intensity ion beams, than the today ECRIS;

(ii) because of its large plasma volume, that should enhance the plasma losses and the extracted ion currents (assuming a constant rf power per unit volume).

#### C. Prospects for Caprice

When considering the question how to get enhanced performances with Caprice, it seems like, partly from observations and partly from speculations, that turning the knob up for the rf power is not the solution. Thus the only serious possibility would be to increase the plasma volume, while keeping constant the other parameters. Nevertheless this leads to increase the input rf power, so as to maintain the same rf power per unit volume. But may Caprice be upgraded in size without ruining the concept itself and its compromise? This is actually another challenge the Grenoble group is facing with.

### IV. REFERENCES

- [1] R. Geller, "ECR Multiply Charged Ion Sources", IEEE Trans. Nucl. Sci., vol. NS-23, pp. 904-912 (1976); *ibid.*, vol. NS-26, pp. 2120-2127 (1979).
- [2] T.C. Simonen, "Experimental Progress...", Proceedings of the IEEE, vol. 69, pp. 935-957 (1981).
- [3] G. Melin, F. Bourg, P. Briand et al., "Some particular aspects...", Rev. Sci. Instrum., vol. 61, pp. 236-238 (1990); C. Barué, P. Briand, A. Girard et al., "Hot electron studies...", *ibid.*, vol. 63, pp. 2844-2846 (1992).
- [4] P. Ludwig, R. Geller, G. Melin, "The 10-GHz Neomafios upgraded ECR ion source", Rev. Sci. Instrum., vol. 63, pp. 2892-2893 (1992).
- [5] B. Jacquot, F. Bourg, R. Geller, "Source d'ions lourds...", N.I.M., vol. A254, pp. 13-21 (1987); *ibid.*, vol. A269, pp. 1-6 (1988); *ibid.*, vol. A287, pp. 341-347 (1990); *ibid.* vol. A295, pp. 5-11 (1990); in 10th Int. Workshop ECRIS Proceedings, Report ORNL CONF-9011136, pp. 133-155 (1990); *ibid.*, pp. 173-175 (1990).

# Design and Construction a Full Copper Photocathode RF Gun\*

X.J. Wang, K. Batchelor I. Ben-Zvi D. Lynch, J. Sheehan and M. Woodle  
Brookhaven National Laboratory  
Upton, New York 11973

## Abstract

The design and construction of an all copper S-band one-and-half cell photocathode electron gun without a choke joint is described. The methods utilized to determine the field balance at the operational frequency without usage of the bead pulling perturbation measurement is given together with the computational data.

## I. THE ATF INJECTION SYSTEM

One of the major development in accelerator technology in the last decade is the development of photocathode RF electron gun for Free Electron laser and other applications. At the Brookhaven National Laboratory Accelerator Test Facility(ATF), an S-band, one and half cell, photocathode RF gun is now in operation.<sup>1</sup>

As part of ATF R&D program, extensive study has been performed to investigated the various options of improving the ATF injection system.<sup>2</sup> It was found that the large divergence of the electron beam from the RF gun and the mismatch caused by the space charge are major sources of the emittance growth. Two simple techniques<sup>3</sup> were studied to reduce the beam divergence. Making the half cell field 80% of the full cell's, the beam divergence can be reduced by half. It is also possible to reduce the emittance growth due to the beam divergence in the injection line using an elliptical laser spot, it matches better to the strong focusing injection line. Recent study<sup>4</sup> suggested by using two solenoid magnets and place the RF gun directly at the entrance of the linac, significant emittance reduction can be achieved.

The distance between the cathode and linac is about 75 cm for the new injection system, the arrangement was made in such way, that the old injection system will be left untouched for RF gun studies, second gun was built for the new injection system.

## II. THE FULL COPPER RF GUN

Comparing the BNL one-and-half cell gun<sup>5</sup> and Grumman-BNL multi-cell gun,<sup>6</sup> a modified BNL gun was chosen for its proved performance. The BNL one-and-half cell RF gun had achieved its designed parameters at both ATF<sup>1</sup> and other labs.<sup>7</sup> The BNL RF gun is operated routinely at lower field than designed value, because of the break down near the choke joint and the beam loading caused by the field emission current. The experimental results showed<sup>1</sup> that copper cathode can satisfy the demands of the the ATF experiments, modify the BNL one-and-half cell gun to a full copper RF gun will make it much more reliable. The full copper RF gun may also reduced beam loading effect. It was demonstrated that

S-band linac structure can operate at field much higher than 100 MV/m,<sup>8</sup> the dark current beam loading could be reduced if the RF gun can be conditioning at higher field.

## III. THE RF GUN CAVITY CONSTRUCTION AND TUNING

The calculated frequency using SUPERFISH is about 15 MHz higher than 2856 MHz before any tuning work. Based on the experience of building the first BNL RF gun, following steps were taken for the construction of the full copper RF gun:

**Target frequency.** We first determined the target resonant frequency of the cavity in the air at room temperature(24°C) is 2856.3 MHz. From both calculation and measurement, the temperature coefficient of the resonant frequency is 50 KHz/deg., and the frequency change from air to vacuum is about 800 KHz. In order to operate the gun near 45°C of the SLAC-type linac operating temperature, the target frequency should be near 2856.3 MHz.

**Tuning range.** There is a loop type tuner at each cell, the tuning range of the half cell is about 1 MHz, and the full cell's range is about the half of the half cell's.

**Size of the coupling hole.** We estimated that to lower the resonant frequency from 2871 MHz near the target frequency and realize reasonable coupling between the waveguide and the cavity, a coupling hole size 1 cm by 2 cm is adequate for each cell(see Fig. 1).

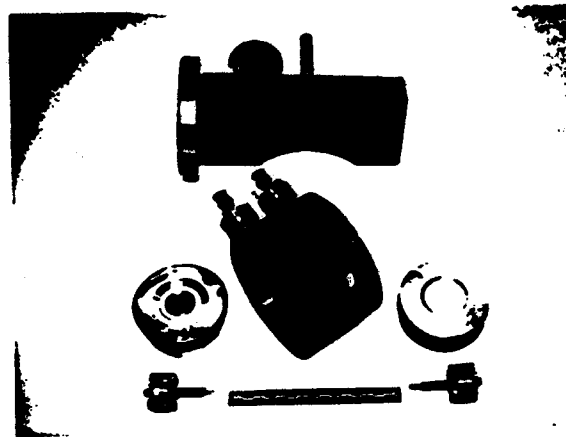


Figure 1: Parts for the RF gun.

**Frequency tuning.** After the coupling holes were machined, the resonant frequency was about 8 MHz lower than the target frequency. We can either machine the cylinder of the cavity or the end wall of the each cell. We decided work on the end wall because its flexibility. Near

\* Work supported by U.S. DOE.

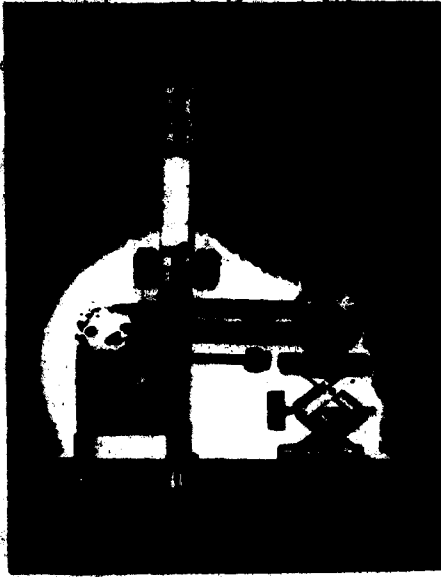


Figure 3: The ATF full copper RF gun.

the cavity resonant frequency, the cavity can be described by an equivalent LC circuit whose resonant frequency is,

$$\omega = \frac{1}{\sqrt{LC}} \quad (1)$$

Changing the depth of the cathode (or anode) penetration into the cavity is equivalent to adjusting the capacitance, since the cathode is located in the strong electric field region. The resonant frequency can be reduced by increasing the capacitance through increasing the penetration of the cathode. Similarly, an increase of the resonant frequency can be achieved by decreasing the cathode penetration. The radius of the areas were machined off is about 2.3 cm(Fig. 1).

**Critical coupling.** After the gun cavity was tuned near the target frequency, the gun was under coupled. We can open the coupling to increase the coupling, which also affects the resonant frequency. The method we used to achieve the critical coupling is equivalent to add another reactive load to the waveguide, so the total load for the wave guide is resistive. We placed a cooper block across the broad side of the wave guide across from the coupling holes. By adjusting the thickness of the block and it's position, the critical coupling was obtained (Fig. 2).

S:1  
REF 1.0 Units  
2 200.0 mUnits.  
49.414  $\Omega$  0.084  $\Omega$   
AP

MARKER 2  
2.86015 GHz

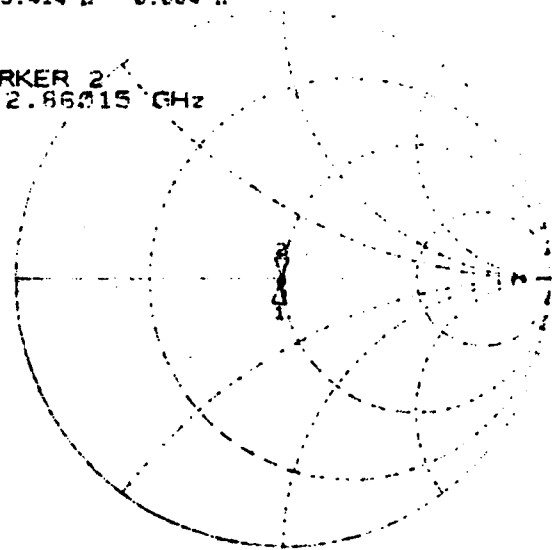


Figure 2: The Smith chart of the waveguide.

**Final assembly.** The full copper RF gun was brazed together at SLAC(Fig. 3).

**The Field balancing.** The performance of the RF gun will be affected by the accuracy of balancing the fields between the two cells. The perturbation method is usually used to balance the field, it is reliable but inconvenient. We have been used following two techniques to balance the gun.

- **Q-measurement.** We studied how the difference of the peak fields in the two cells affects the properties of the cavity.

$$Q = \frac{\mu}{\mu_0} \left( \frac{V}{\delta S} \right) \times (\text{Geometrical Factor}) \quad (2)$$

where  $\mu$  and  $\mu_0$  are permeabilities,  $\delta$  is the skin depth,  $V$  is the cavity volume, and  $S$  is the surface area enclosing the volume. Eq. (2) shows that, since the ratio of surface area to the volume in the half cell is larger than that of the full cell, the higher field in the half cell will lower the Q of the whole cavity. Table 1 is the calculated results using SUPERFISH, where  $E_c$  is the field at cathode surface and  $E_2$  is the peak field on axis of the full cell. It shows that field balancing can be measured by measuring the loaded Q (assuming the gun is at critical coupling).

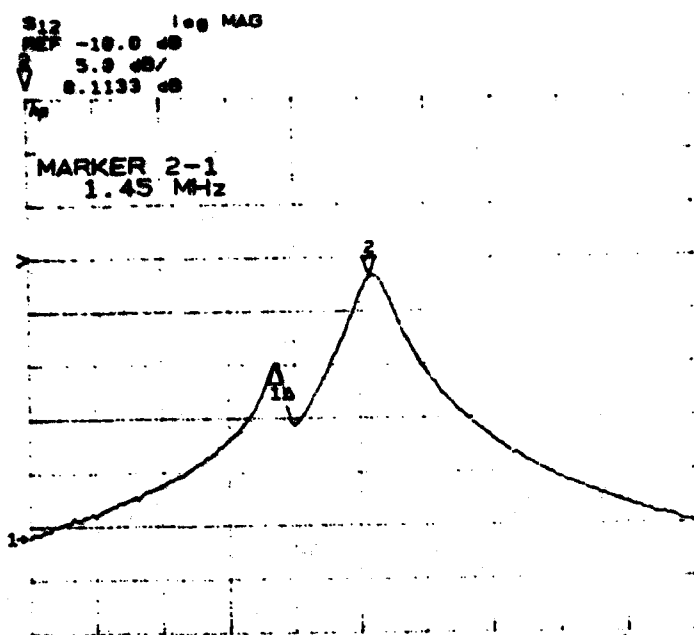


Figure 5: The mode separation for balanced fields.

Table 1: RF Cavity properties and Field relation

Q <sub>0</sub>	R	E <sub>c</sub> /E <sub>2</sub>
11113	52.57	1.25
11887	56.76	1.02
11915	56.89	0.99
12387	58.83	0.86

• Modes separation The frequency difference of the  $\pi$ -mode and zero-modes can be expressed as,<sup>7</sup>

$$f_{\pi} - f_0 = kf \quad (3)$$

where  $k$  is the coupling factor of the gun, and  $f$  is single cell resonant frequency.  $k$  is determined by the coupling factor of each cell, and hence determined by the field strength. Eq. (3) is usually used to calculate the coupling factor  $k$ , we can use perturbation method to calibrate the coupling factor, and use the mode separation to determine the field balance. Fig. 4 is the field distribution of the RF gun on axis obtained using the perturbation method. Fig. 5 is the corresponding mode separation for the balanced field.

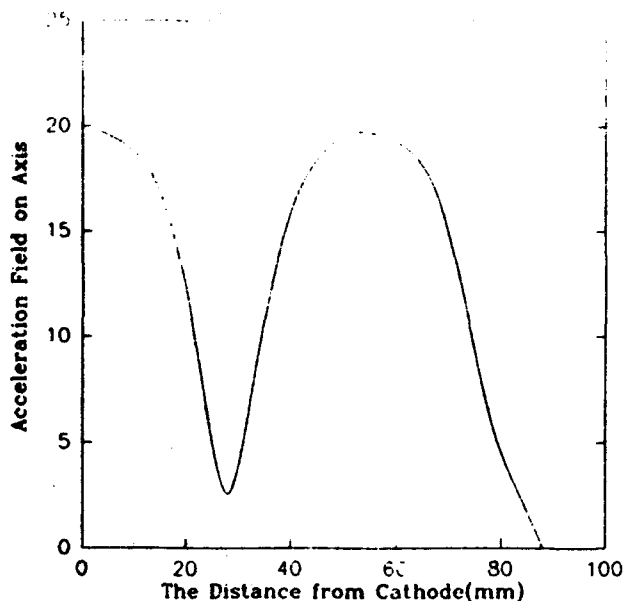


Figure 4: On-axis field distribution of the gun.

We wish to thank C. Biscardi and R. Harrington on the construction of the gun. We are very grateful to the help provided by Dale Sartan and Carl Rago of SLAC in brazing the gun in short notice.

#### IV. REFERENCES

1. H.G. Kirk *et al.*, Experimental results from the BNL ATF photocathode gun, Proceeding of 13th Int. FEL Conf.(1991).
2. X.J. Wang *et al.*, The Brookhaven Accelerator Test Facility Injection System, p.307, Proc. of Part. Acc. Conf.(1989).
3. X.J. Wang and K. Batchelor, RF Gun Studies, CAP-ATF-Tech. Note # 11, April 1991.
4. J.C. Gallardo and H.G. Kirk, The ATF straight-ahead injection system, this proceeding.
5. K. Batchelor *et al.*, Design and Modelling of a 5MeV Radio Frequency Electron Gun, BNL-41766(1988).
6. I.S. Lehrman *et al.*, Design of a High-brightness, high-duty factor photocathode electron gun, Nucl. Inst. and Meth. A318(1992) 247.
7. R. Bossart *et al.*, RF-Gun Construction, Tuning and High Power Tests, CERN PS 92-19(LP).
8. J.W. Wang, RF Properties of Periodic Accelerating Structures for Linear Collider, SLAC-Report-339(1989).

# Streak Camera Measurements of Electron Bunch Length from a Copper Photocathode in an RF Gun\*

G. Hairapetian, P. Davis, M. Everett C. Clayton, C. Joshi  
Electrical Engineering Department, University of California, Los Angeles 90024

S. Hartman, S. Park, C. Pellegrini  
Department of Physics, University of California, Los Angeles 90024

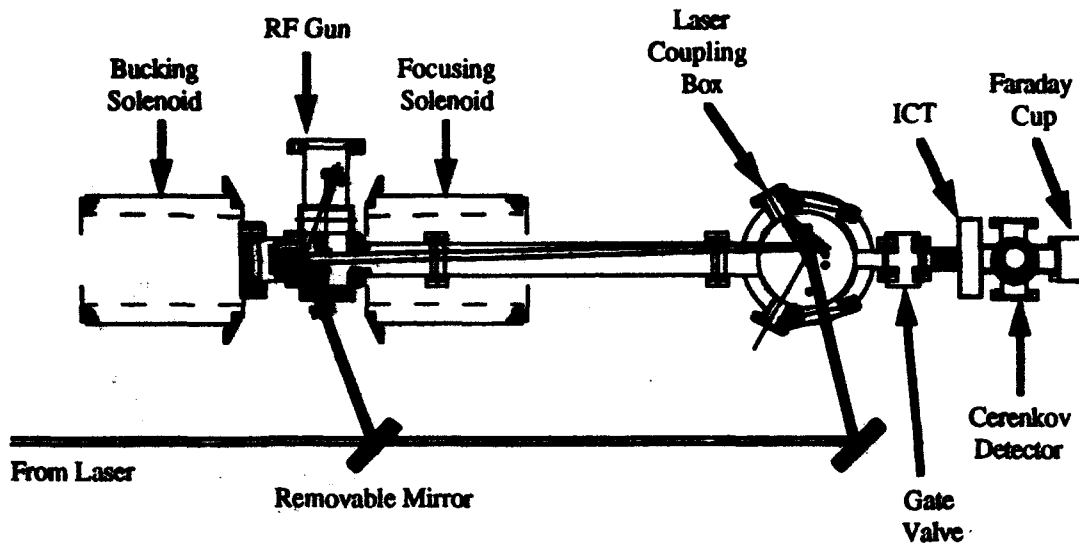


Figure 1: Diagram of the experimental setup

## Abstract

Short laser pulses (sub 2 ps) of UV ( $\lambda=266$  nm) light with 200  $\mu\text{J}/\text{pulse}$  are used to produce electrons from a copper cathode in a rf gun. The electron bunch length is measured by streaking the Cerenkov radiation ( $\lambda=530$  nm) from a thin (250  $\mu\text{m}$ ) fused silica etalon. Streaks for both  $0^\circ$  and  $70^\circ$  laser incidence angles with respect to the cathode normal are presented with a temporal resolution of 3.6 ps. The shortest electron bunch length measured was 9 ps.

## I. INTRODUCTION

Although photoemission is a prompt process down to sub picosecond time scales, the production of very short ( $< 2$  ps) electron beams from a photocathode rf gun cannot be taken for granted. Photocathode rf guns are constructed to minimize bunch length growth by allowing the creation of the electron bunch in high electric fields (up to 100 MV/m). Under these fields the electrons are accelerated to relativistic velocities in less than one centimeter. Most of the bunch length growth occurs before the beam becomes relativistic and before the beam exits the rf gun.

The electron bunch length is measured using a Cerenkov radiator viewed by a streak camera. The radiator is placed as close to the exit of the rf gun as possible given physical

constraints. Only a solenoid is used to transport the beam to the radiator. The streak measurements presented indicate typical electron bunch lengths of about 15 ps.

## II. EXPERIMENTAL SETUP

The photoinjector consists of a Cu photocathode placed at the endwall of the 1/2 cell in a 1 1/2 cell rf gun. After completion of the measurements the electric field ratio between the 1/2 cell and the full cell was measured to be 1:1.8. This limits the maximum electric field at the cathode to less than 50 MV/m and the electron energy to 3.5 MeV. Electrons are created by a laser pulse incident on the photocathode at either  $2^\circ$  or  $70^\circ$ . The experimental setup is shown in Figure 1.

For single photon photoemission, the photon energy must exceed the work function of Cu (4.65 eV)[1]. The photoinjector drive laser was designed to produce  $< 2$  ps laser pulses at 266 nm (4.66 eV) with up to 200  $\mu\text{J}/\text{pulse}$ . This is accomplished using chirped pulse amplification and compression of a mode-locked YAG laser ( $\lambda=1.064$   $\mu\text{m}$ ) and frequency upconverting using two KD\*P doubling crystals.

A 250  $\mu\text{m}$  thick fused silica etalon served as the Cerenkov radiator. The etalon side where the electron beam entered was sanded forming a diffuse surface to prevent bunch lengthening due to multiple reflections. Furthermore, the beam entrance side of the etalon was covered with a 0.005" thick aluminum foil which provides grounding of the Cerenkov radiator and

\*Work Supported by SDIO/IST through ONR Grant No. N00014-90-J-1952 and US DOE Grant DE-FG03-92ER-40493

prevents any scattered laser light from entering the field of view of the Cerenkov light. The etalon was attached on a mount which was externally rotatable about an axis perpendicular to the beam. For a relativistic electron beam, the angle of Cerenkov radiation with respect to the beam axis is

$$\theta_c = \cos^{-1}\left(\frac{1}{n}\right),$$

where  $n$  is the index of refraction of the medium. For fused silica  $n = 1.46$  and therefore  $\theta_c = 47^\circ$ . The Cerenkov radiator setup is depicted in Figure 2.

This Cerenkov radiator allows 1 ps time resolution. The limiting factor in the bunch length measurements is the streak camera. We used a Hadland Imacon 500 streak camera. At the fastest sweep speed of 20 ps/mm, the time resolution is no better than 3.5 ps.

The streak camera cannot be installed directly viewing the Cerenkov detector because of the high levels of radiation inside the lead shielding. Therefore the Cerenkov light is transported through a maze in the lead shielding. Because the light intensity levels are near the detection limits of the streak camera, the Cerenkov image is reduced by a factor of 4 when focused on the streak camera slit. To achieve 3.5 ps resolution, a 25  $\mu\text{m}$  slit is used at the entrance to the streak camera. Accounting for the 400% reduction in image size, the 25  $\mu\text{m}$  slit infers a 100  $\mu\text{m}$  acceptance at the Cerenkov radiator. The maximum time delay possible between any two Cerenkov photons created by an infinitely small thin electron beam is 1 ps. When combined with the resolution of the streak camera, the overall resolution of the Cerenkov streak system is 3.6 ps.

The streak camera resolution was verified by streaking the laser pulses. This streak camera cathode is sensitive to green 532 nm light but not to UV 266 nm light. Therefore, the

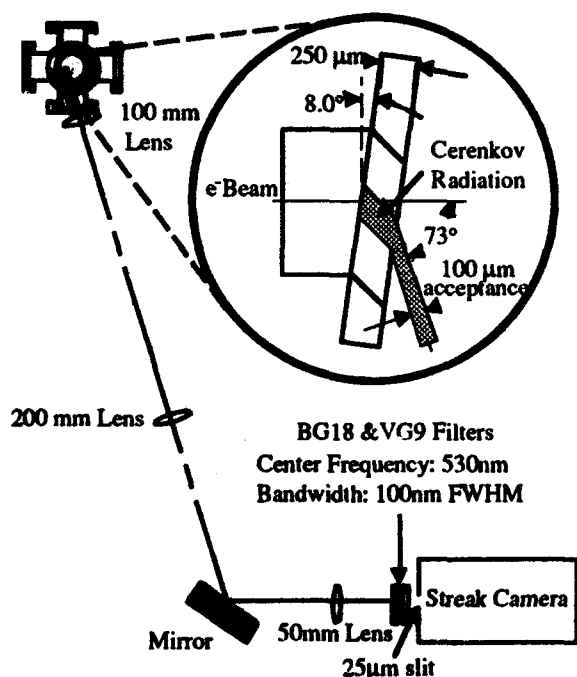


Figure 2: Cerenkov detector setup

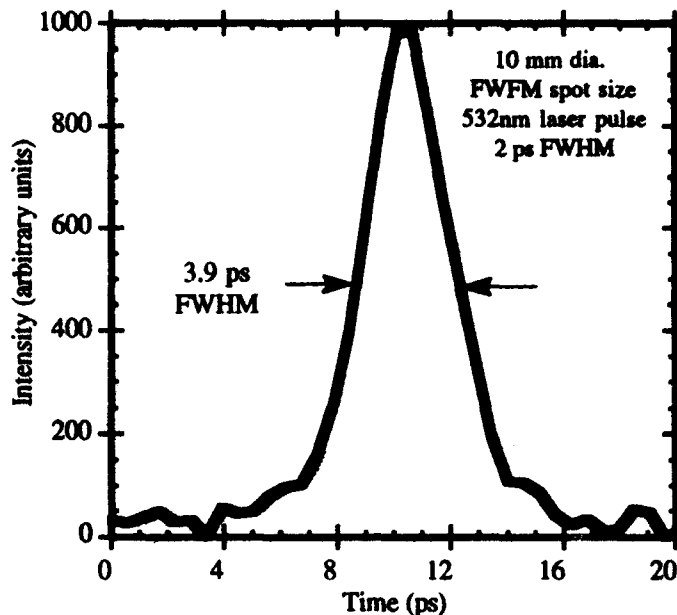


Figure 3: Laser streak indicating streak camera resolution

laser pulses were streaked after the first doubling crystal. A  $\sqrt{2}$  reduction in pulse width should occur when the green light is doubled to UV. In streaking short pulses, care is taken to avoid space charge saturation within the streak camera which can result in erroneous measurements. Figure 3 depicts a typical laser streak and its corresponding integrated intensity plot.

The laser pulse streak resulted in a pulse width of 3.9 ps FWHM. Since the resolution of the streak camera is 3.5 ps, the actual laser pulse width is 1.7 ps. Autocorrelation measurements of the CW mode-locked YAG laser beam result in pulse widths of 2 ps FWHM. After doubling to green light, the pulse width is expected to decrease by  $\sqrt{2}$ , producing 1.4 ps pulses in reasonable agreement with the streak camera measurements.

### III. EXPERIMENTAL RESULTS

The streak images appear spotted due to the low light levels incident on the streak camera. Low light levels are required to avoid space charge lengthening in the streak camera and to achieve 3.5 ps resolution. In analyzing Cerenkov streaks, the images are integrated along the space axis to provide better statistics. Each array element corresponds to .56 ps. Since the Cerenkov streak system resolution is 3.6 ps, a smoothing algorithm is used to average over the 6 nearest neighbors in the integrated array.

The first streak measurements were taken with 70° laser injection. Laser injection at 70° produces bunch lengthening from a time delay across the cathode as the laser wavefront strikes it. This produces an electron beam with a linear space time correlation. This correlation is present in the Cerenkov streak shown in Figure 4. A laser spot size of 2 mm produces a time delay of

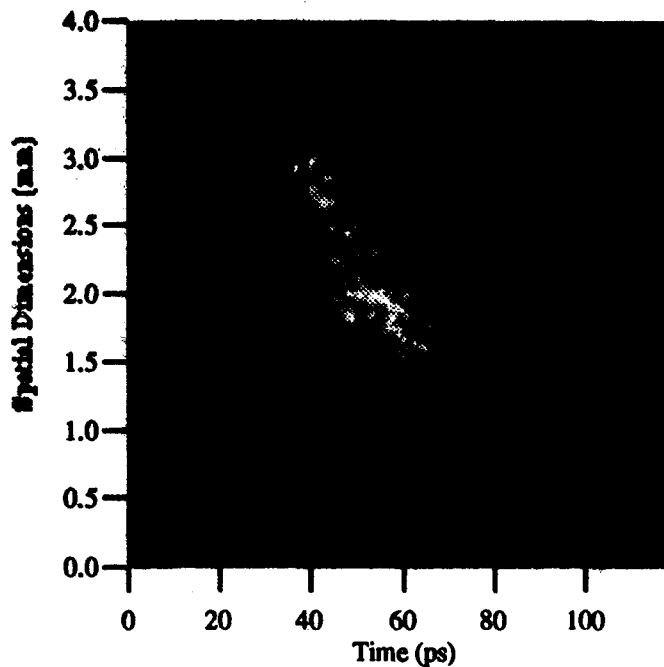


Figure 4: Electron beam streak with 70° laser injection

$$\tau \approx \frac{2\text{mm}}{c \cos(70^\circ)} \approx 20\text{ps}$$

The measured delay from the streak in Figure 4 was 25 ps. When the streak is corrected for the delay across the wavefront, the measured pulse width becomes 13 ps.

At 2° injection, the time delay across the cathode is insignificant and the Cerenkov streaks indicate the electron bunch length directly. By focusing the laser spot to 2 mm, we were able to move the laser spot to an undamaged portion of the cathode. A streak from the undamaged cathode is depicted in Figure 5. Streaks from the damaged portion of the cathode resulted in slightly longer bunches due to an elongated tail.

Bunch length measurements with the Cerenkov radiator and streak camera resulted in 9 ps to 15 ps FWHM for various charge levels from .2 nC to 2.6 nC, however, no correlation was found between the bunch length and the charge output from the rf gun.

#### IV. DISCUSSION

All the streak camera measurements indicate electron bunch lengths longer than 8 ps. Measurements for 2° incidence on the undamaged portion of the cathode provide the shortest bunch length measurements averaging 12 ps. However, the 2° measurements from damaged parts of the cathode clearly characterize longer bunches with more time structure and long tails. These measurements contradict the assumption that electron bunches will mimic the laser pulses in time.

One source for bunch lengthening is space charge. The quantum efficiency data indicated significant reductions in charge production due to space charge[2]. Microemitters can further aggravate this problem possibly accounting for pulse

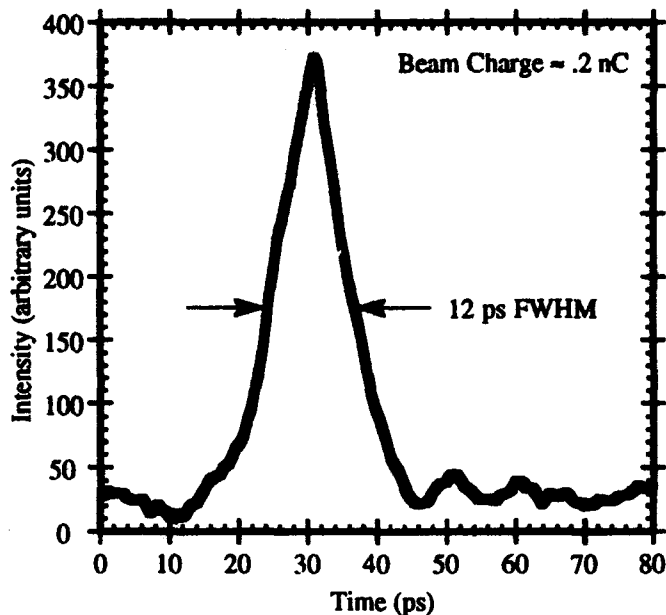


Figure 5: Electron beam streak for 2° laser injection on the undamaged part of the cathode

lengthening and time structure of the streaks from damaged portions of the cathode. PARMELA[3] simulations were performed for various output bunch charge levels from 100 pC to 1.3 nC. These simulations show a bunch lengthening as output charge is increased. For typical charge levels between .4 nC and 1.0 nC PARMELA predicts bunch lengths from 9 ps to 15 ps. These bunch lengths predictions are within the scatter of the measured bunch lengths, however, the measurements did not indicate a correlation with charge level.

#### V. CONCLUSION

In the present experiments, the electron bunch length does not mimic the laser pulse length. The shortest Cerenkov streak measurements indicate 9 ps bunch lengths. The physical mechanism for this bunch lengthening is under investigation. PARMELA simulations showed that bunch lengthening on the order of 10 ps can occur due to space charge, although, the bunch length measurements did not show a correlation between bunch length and charge output from the gun. However, even with the bunch lengthening, beam currents of 100 A are produced.

#### VI. REFERENCES

- [1] Handbook of Chemistry and Physics p. E-78
- [2] P. Davis *et al*, these proceedings
- [3] K.T. McDonald, "Design of the laser-driven rf electron gun for the BNL Accelerator Test Facility," *IEEE Trans. Electron Devices*, ED-35, 2052(1988)

# Possible Efficiency-Enhancement of Metal Photocathode for DISKTRON Electrostatic Accelerator

T. Tanabe, Y. Kawamura, D. Li† and K. Toyoda

The Institute of Physical and Chemical Research (RIKEN)

2-1 Hiroseawa, Wako, Saitama 351-01, Japan

## Abstract

Possibility of increasing quantum efficiency of metal photocathodes by geometric alteration is being investigated. The fourth harmonic light of Nd:YAG is used to produce photoelectrons on a metal surface. The pulse length is about 50 ps (FWHM) and the peak current is greater than 2 A at 0.7 MeV. This scheme employs grooved surface with adjusted polarization and other pertinent parameters such as extraction voltage. The measurements are done after acceleration by

DISKTRON<sup>®</sup> electrostatic accelerator which, with a combination of a laser-induced photocathode, gives fairly controllable bright short-pulse-electron-beam up to the energy of over 1 MeV. This configuration permits us to find the overall improvement of e-beam characteristics for the future laser-undulator-experiment.

## I. INTRODUCTION

In the last few years laser-induced photocathodes have become one of the most preferred methods to generate a bright short-pulsed electron beam. However no material that possesses both a high quantum efficiency and high ruggedness so far has been found. Therefore one could either improve the properties of the efficient but weaker materials or employ other means to enhance the efficiency of rugged ones. We have chosen to use the latter method for the improvement due to a rather moderate vacuum level in our experimental facility and our operational requirements such as high stability of operation and low maintenance.

## II. PRINCIPLES

There are several ways to improve photoelectron-emission-efficiency of a metal. One is to use surface plasma waves (SPW) excitation that can also be explained by Brewster angle reflection by modulated surfaces of complex refractive index [1-3]. This method appears to be very promising as long as the wavelength, incident angle of the laser light, and the pitch of the surface modulation are properly tuned. The second one is to employ multiphoton process that requires a laser with high power and short pulse [4].

The easiest and most general way to enhance the emission efficiency is to change the geometric shape of the target to fully utilize the surface emission, namely to choose the direction of the light polarization and the shape of the target to maximize the probability that electrons can escape the surface of the metal.

It has been known that the quantum efficiency of photoelectric effect depends on the relative relation between electric field and the plane of incidence [5]. In this experiment we have shown a simple but effective way to increase the emission efficiency of a photocathode, especially at low power level of the input laser. In order not to degrade the beam emittance, a finely grooved target is used. The dimension of the grooves is much larger than the wavelength of the input laser to avoid unexpected interference. Fig. 1 shows the microscopical picture of the edge and surface of the target. The angle of the slope with respect to horizontal direction is 55 degree and the area with grooves is 50% of the illuminated surface. This method can be used in many of existing FEL photo injector just by replacing the target and adjusting the polarization of the laser.

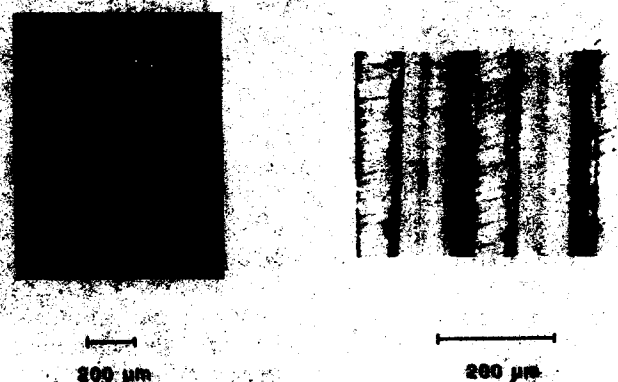


Fig. 1 Microscopical pictures of Al photocathode.

†Permanent address: Changchun Institute of Optics and Fine Mechanics, Chinese Academy of Sciences, P.O. Box 1024, Changchun, PRC

### III. EXPERIMENT

A series of experiments was conducted in the configuration of relativistic electron beam source (DISKTRON<sup>®</sup> electrostatic accelerator and a laser-induced photocathode) for the future laser undulator experiment at the Institute of Physical and Chemical Research (RIKEN) [6]. Fig. 2 shows a schematic of the experimental configuration. The fourth harmonics light of a mode-locked Nd-YAG laser illuminates the target to produce an electron beam which is subsequently accelerated by static electric field to the energy of 0.7 MeV. The e-beam is wholly collected by a piece of graphite and the current is fed to 50Ω input. The laser power is initially measured by a power meter for calibration and is monitored by a PIN diode during the measurements. A half-wave plate is placed in front of the entrance-beam-port to alter the direction of the polarization of the laser light. The degree of polarization of the fourth harmonic of the Nd-YAG has been measured to be more than 90% and the use of the half-wave plate does not cause any difference in terms of transmitted laser power on the target in two cases of which the direction of the light polarization is perpendicular each other. The grooves are lined vertically to the experimental plane so that the horizontally polarized light is regarded as P-polarization.

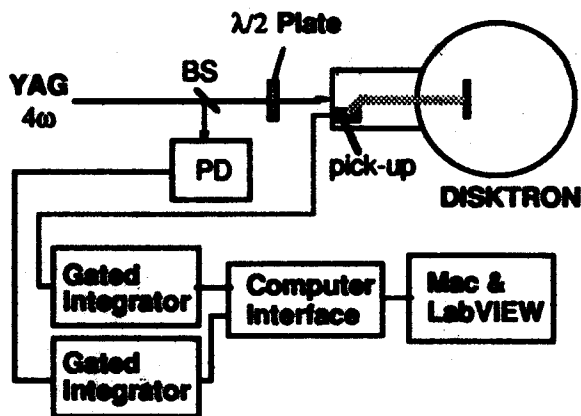


Figure 2. Schematic of the experimental configuration.

Fig. 3a and 3b show the relations between laser power density and produced e-beam current density for an aluminum target which has a flat surface. There is no clear difference between two cases with perpendicular polarization as is expected. Fig. 4a and 4b are the results of the same kind of measurement after replacing the target with the one having a grooved surface. It is distinctly shown that the case of P-polarized light yields higher than that of S-polarized light. Compared to the flat target the former case gives slightly more than three times higher quantum efficiency. Even though the available surface area is increased for the grooved target, after taking into it into the account that only 50% of the surface has slopes, the real yield increase appears to be more than three times. No noticeable degradation of emittance was observed after comparing the sizes of e-beam spots at the focus in two cases.

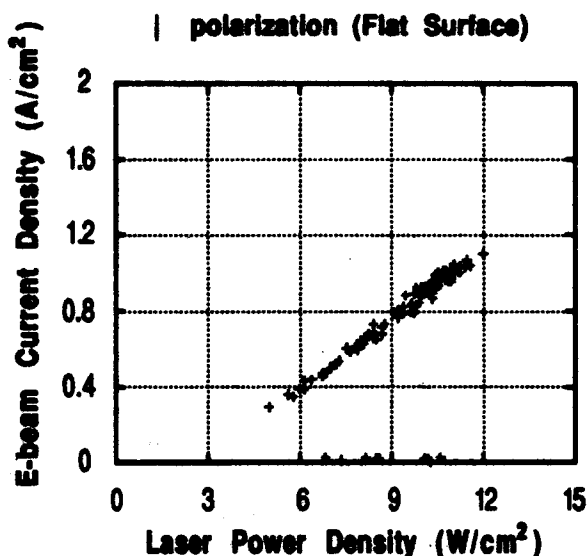


Fig. 3 (a) Laser power density v.s. e-beam current for the light of vertical polarization using the flat target.

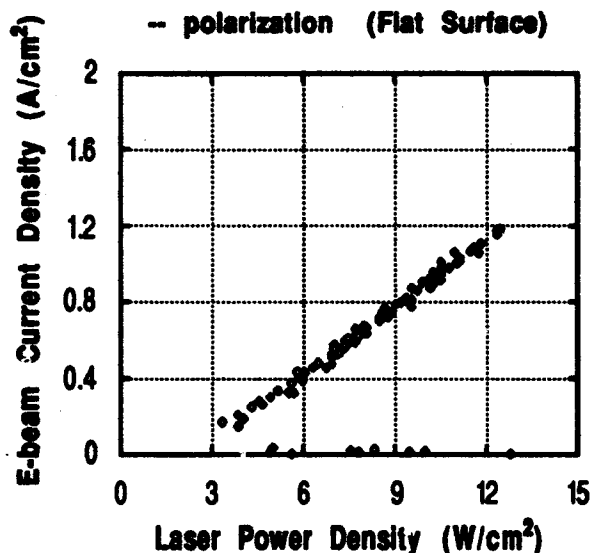


Fig. 3 (b) Laser power density v.s. e-beam current for the light of horizontal polarization using the flat target.

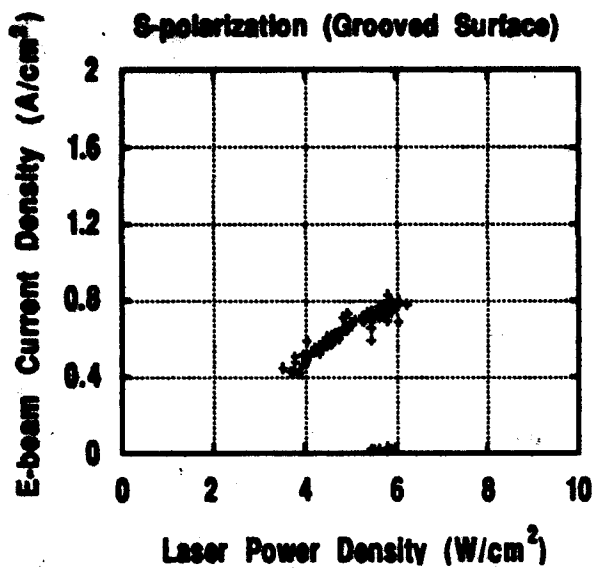


Fig. 4 (a) Laser power density v.s. e-beam current for the light of S-polarization using the *grooved* target.

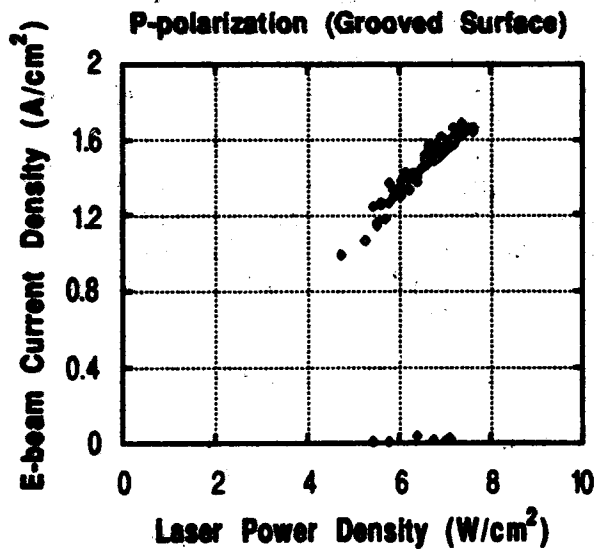


Fig. 4 (b) Laser power density v.s. e-beam current for the light of P-polarization using the *grooved* target.

#### IV. CONCLUSION

It has been shown that the quantum efficiency of a metal photocathode can be easily enhanced up to a factor of three simply by replacing a flat target with a grooved one. Unlike other enhance methods such as surface-plasma-wave method this method requires no resonance condition so that it can be adapted in the most of existing photo-injectors without many modifications.

#### V. REFERENCES

- [1] J.G.Endriz and W.E.Spicer, Phys. Rev. B4, 4144 (1971)
- [2] G.Hincelin, Phys. Rev. B24,787 (1981)
- [3] M.C.Hutley and D.Maystre, Opt. Comm. 19, 431 (1976)
- [4] Gy. Farkas, Z.Gy.Horvath and I.Kertesz, Phys. Lett. 39A, 231 (1972)
- [5] R.Rohí, Verh. d.D. Phys. Ges., 11, 339 (1909)
- [6] Y.Kawamura, T.Tanabe, D.Li and K. Toyada, 14th Int. FEL Conf. Proc., to be published in Nucl. Instr. and Meth.

## Cold Test of Rocketdyne RF Gun

Michael Lampel  
Rocketdyne Division  
Rockwell International Corporation  
6633 Canoga Av., Canoga Park, CA 91303

Ranshan Zhang  
Physics Department  
UCLA  
405 Hilgard Av., Los Angeles, CA 90024

### Abstract

The RF gun to be used in the Rocketdyne 1 kW FEL was cold tested at UCLA. This gun follows the two cavity BNL design. Data was taken, using a HP8510B network analyzer, on frequency tuning with a rotating paddle in the first (half) cavity and on frequency shift due to axial movement of the LaB<sub>6</sub> photocathode. Results and analysis will be presented.

"Design of the Laser-Driven RF Electron Gun for the BNL Accelerator Test Facility", K. T. MCDONALD, IEEE TRANS. ELECT. DEV., VOL. 35, NO. 11, NOV 1988

### I. INTRODUCTION

Rocketdyne has been developing components for a kW class FEL [1], [2]. The recent delivery of the radio-frequency power assembly (RFA), which consists primarily of a SLAC 5045 klystron and a command charge, feed forward modulator [3] allows testing of the RF gun at high power. Preliminary to this the gun was checked out at the UCLA High Frequency Laboratory to verify its operating characteristics. This paper will present the data obtained and analyses which verifies that nominal operating specifications had been met and calibration data for diagnostics.

### II. THE GUN

The RF gun consists of two resonant cavities, highly coupled both through side slots which allow

RF power input from the RFA and an axial hole through which the accelerated electron beam also passes.

The electron beam is generated in a quarter wavelength cavity, off of a 3 mm dia. LaB<sub>6</sub> cathode. The cathode is mounted on a linear feedthrough so that its position can be changed axially to allow fine tuning of electron beam parameters. To compensate for the frequency shifts cathode motion induces the cavity is also equipped with a small tuning paddle on the side wall which tunes the cavity inductively. The gun is coupled to the RFA by a waveguide which ends with a half wavelength stub past the coupling slots to set boundary conditions correctly for the cavities. The stub also has a pumpout port in it to allow approximately 100 1/s conductance from the cavities. Finally both cavities have RF pickup loop diagnostics.

### III. THE MEASUREMENTS

A Hewlett Packard model 8510B Network Analyzer was used for the measurements. The maximum power output of +20 dBm allowed pickup of the signals through the high attenuation RF pickup loops installed into the two cavities of the gun. The RF probe was inserted into the waveguide through the pumpout port, so that coupling into the cavities would be the same as high power operation, while minimizing the path the low signal RF had to travel.

All measurements were performed at atmospheric pressure and

approximately 75° F.

The measurements were made with the Network Analyzer were: Frequency as a function of axial cathode placement for both 0-mode and  $\pi$ -mode (tuning paddle fixed); frequency as a function of tuning paddle position (cathode position fixed); VSWR with the cathode in position and removed; and pickup loop attenuation.

VSWR measurements were 2.16 with the cathode removed and the tuning paddle at 172°, and 1.93 with the cathode in place and the tuning paddle at 208°, a position for which the  $\pi$ -mode and 0-mode are degenerate.

Table I gives data for frequency vs. cathode position.

TABLE I

Dial (in)	$\pi$ -mode (GHz)	0-mode (GHz)
.223	2.8551875	2.8525750
.222	2.8551875	2.8525750
.220	2.8551875	2.8525750
.215	2.8552125	2.8527375
.210	2.8552250	2.8528250
.205	2.8552500	2.8529250
.200	2.8552625	2.8529875
.199	2.8552625	2.8529875

with the tuning paddle position 172°

Cathode position as measured on indicator from linear feedthrough, with .205" corresponding to the cathode flush with the wall of the cavity, so that travel corresponds to .018" into the cavity to .006" recessed back into the wall.

Table II gives data for frequency vs. tuning paddle position.

TABLE II.

Paddle Pos. (°)	$\pi$ -mode (GHz)
75	2.8565000
170	2.8552000
208 (degen)	2.8557250
245	2.8565525
245 (1 rot.)	2.8564875
248	2.8565000
250	2.8565125
252	2.8565125
252 (1 rot.)	2.8565125
258	2.8565125
340	2.8551875
348	2.8551875

with the cathode fixed at .200" (slightly retracted)

These data show the doubly periodic frequency tune shift of the paddle with respect to rotation, with the nominal midpoint (where the paddle has no net effect on cavity frequency) near 208° an odd multiple of 90°.

#### IV. DATA ANALYSIS

The RF gun was specified to operate at 2.8560 GHz  $\pm$  100 kHz at 35° C in vacuum. In order to compare the raw data presented it is necessary to correct for differences in temperature and pressure. The dielectric effect of dry air in changing the frequency is about 800 kHz, and the gun was originally tuned at the manufacturer (Schonberg Radiation Corp.) for a central frequency of 2.8552 GHz. This was done at the nominal operating temperature of 35° C. From the formula:

$$f = 2.405 / (n \cdot R)$$

with  $f$ =freq.,  $n$ =index of refraction, and  $R$ =radius of cavity. The change in frequency w.r.t. temp,  $T$ , is:

$$\delta f / \delta T = -(f/R) \cdot dR/dT$$

With  $R \cdot dR/dT = 5 \cdot E-6$  cm/°C for Copper and taking  $f=2.856$  GHz then the calculated change of frequency with temperature is:

$$\delta f / \delta T = 14.3 \text{ kHz}/^\circ\text{C}$$

This leads to a downshift of 0.514 MHz in going from 24° C (75° F) to 35° C (95° F.) The central frequency, corrected for temperature is then:

$$2.85534 \text{ GHz}$$

The manufacturer's measured central frequency is:

$$2.85520 \text{ GHz}$$

The difference of 0.14 MHz is within

tolerances for agreement.

#### V. CONCLUSION

The Rocketdyne RF gun was measured first at the manufacturer's and then at the High Frequency Lab. at UCLA with good agreement after appropriate corrections. Additional information needed for calibration of rf pickups and the tuning loop were also performed. This work has prepared the rf gun for installation onto the power distribution system from the radio frequency power assembly, RFA, allowing the Rocketdyne FEL program to proceed to high power test and evaluation of the RF gun.

#### VI. REFERENCES

- [1] R.A. Cover, G.T. Bennett, R.J. Burke, M.S. Curtin, M.C. Lampel, G. Rakowsky, "Simulations of the Rocketdyne free-electron laser with a 4 m wiggler," Nuc. Inst.&Meth. in Phys. Res. A318 (1992) 623-627.
- [2] R.A. Cover, G.T. Bennett, R.J. Burke, M.S. Curtin, M.C. Lampel, G. Rakowsky, J.P. Stone, "Rocketdyne FEL For Power Beaming Using a Regenerative Amplifier," OE LASE '93 SPIE Proceedings Vol.1868, Jan. 18, 1993.
- [3] M.C. Curtin, these proceedings

# Design and Construction of a High-Duty Factor Photocathode Electron Gun\*

LS. Lehrman, I.A. Birubanna, M. Cole, R.L. Hoyer, E. Sheedy  
Grumman Aerospace Corporation, 4 Independence Way, Princeton, NJ 08540 USA

I. Ben-Zvi, K. Batchelor, J.C. Gallardo, H.G. Kirk, T. Srinivasan-Rao  
Brookhaven National Laboratory, Upton, NY 11973 USA

## Abstract

Under a joint collaboration between Grumman and BNL, a high-duty factor ( $> 1\%$ ) photocathode electron gun is being constructed for use at the ATF facility at BNL. This gun was designed as the electron source for the proposed UV FEL Users' Facility at BNL. The thermally induced stresses exceed the yield strength of OFHC copper. For this reason, the gun is fabricated from GlidCop, an aluminum oxide dispersion strengthened copper alloy.

## I. INTRODUCTION

The proposed UV FEL User's Facility at BNL[1] will require a photocathode electron gun capable of producing short ( $< 6$  psec) bunches of electrons at high repetition rates (5 kHz), low energy spread ( $< 1.0\%$ ), peak currents in excess of  $> 300$  A (after compression) and a total bunch charge in excess of 3 nC. The emittance of the electron bunches is required to be below  $7 \pi$  mm-mrad (normalized RMS).

The construction of such a gun (Gun II) is nearing completion under a joint Grumman-Brookhaven National Laboratory research collaboration [2]. The starting point for our design is the present 1-1/2 cell BNL photocathode RF gun (Gun I) shown in Fig. 1. Figure 2 shows the layout of Gun II. Gun II consists of 3-1/2 cells which allows beam energies in excess of 9 MeV to be achieved. The beam dynamics of the gun were modeled with the MAGIC[3] particle-in-cell code. This code is used to study the emittance growth of the electron bunches as they are accelerated through the gun, as well as to determine how the operational parameters effect its characteristics (i.e. divergence, momentum spread, energy, current).

The thermal and mechanical properties of the gun were modeled with the ANSYS[4] finite element code. Power deposition profiles were calculated with SUPERFISH[5]. A thermal/structural analysis was performed to determine the temperature profiles and the pressure and thermally induced stresses.

## II. BEAM DYNAMICS MODELING

The MAGIC code includes the effects of image currents, space charge and wakefields. The axisymmetric gun geometry (2-D) was modeled with exact gun fields. This is

\*This work supported by the Grumman Corporation and the Brookhaven National Laboratory under US DOE contract.

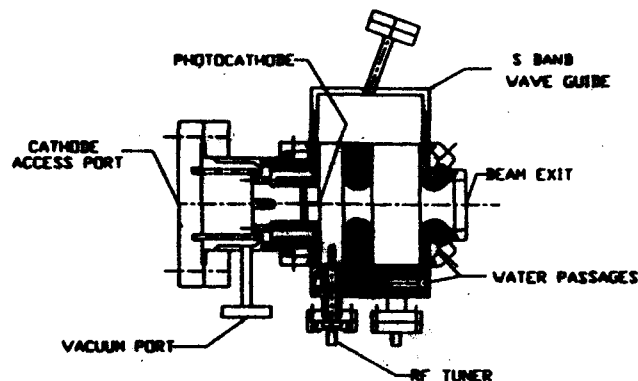


Figure 1. Present BNL 1-1/2 cell gun (Gun I).

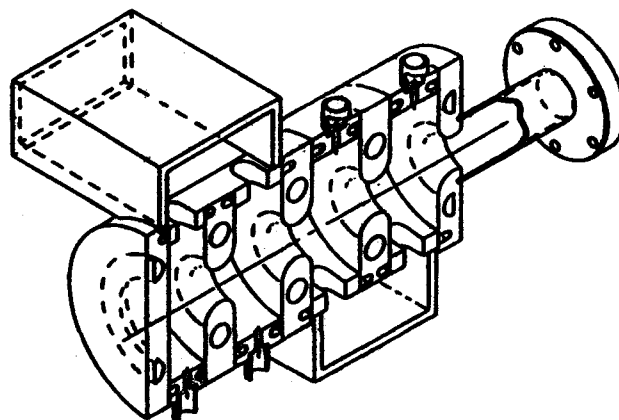


Figure 2. Cutaway view of Gun II showing the locations of the water cooling channels.

accomplished by prescribing the magnetic field for the fundamental  $TM_{01}$  cylindrical cavity mode and allowing the cavity to ring while numerically damping out higher order modes. The fields are then stored and used for later runs with particles. Figure 3 shows a vector plot of the electric fields for Gun II.

The advantage of using the MAGIC code is that the field components at the cavity apertures and beam exit are continuous and the method of calculating the space charge forces is inherently more stable. Typical simulations for a 3-1/2 cell gun consisted of a grid  $2000 \times 90$  (Z x R) with 1500

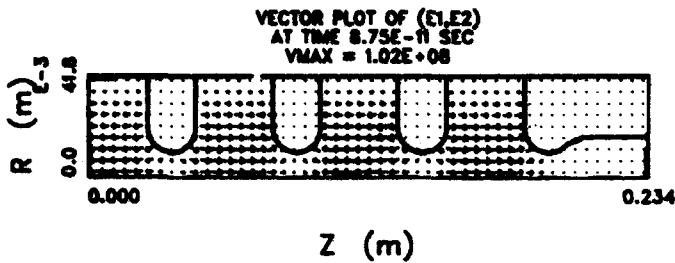


Figure 3. Vector plot from MAGIC of the electric field in the 3-1/2 cell gun (Gun II)

particles. Particles are emitted in nearly any functional form in radius and time to model the laser illumination of the cathode. Table 1 lists the operational parameters for Gun II.

Table 1. Operational parameters of Gun II

Number of cells	1
Laser radius ( $1\sigma_r$ )	4 mm
Pulse length ( $\pm 2\sigma_t$ )	8 psec
Cathode electric field (nominal)	100 MV/m
Beam momentum	10 MeV/c
Peak power	12.5 MW
Duty factor	1%
RF frequency	2.856 GHz

Most of our simulations were done for a 1-1/2 cell gun since they require 1/4 of the computer time and uncover most of the underlying physics. The brightness,  $B$ , was used as one figure of merit for our gun design. We use the definition:

$$B = \frac{I}{e_n^2} \cdot I = \frac{Q}{\sqrt{2\pi} \sigma_b}$$

where  $I$  is the peak current,  $e_n$  is the RMS invariant emittance,  $Q$  is the total charge, and  $\sigma_b$  is the bunch length (divided by the speed of light). After the beam exits the gun, it enters a transport line whose function is to match the beam to the linac. In addition, the transport line may serve to magnetically compress the bunch length, resulting in peak currents >1000 amps. The compressibility was determined analytically and used to determine the ideally compressed current.

The divergence of the beam is inversely proportional to  $\gamma$ , the relativistic factor, and the space charge forces are inversely proportional to  $\gamma^2$ . Simulations of the full 3-1/2 cell gun show that the addition of 2 full cells for the gun (Gun II) will double the momentum of electrons to 10 MeV/c which should result in a bunch that is more easily transported and compressed.

A study was made to determine the effect of varying the length of the half cell on the emittance, divergence and compressibility. It was found that by increasing the length of the half cell from 2.625 cm ( $\lambda/4$ ) to 3.5 cm, the divergence was reduced by 20%, the compressibility increased by a factor of 2, and the effect on the emittance was negligible. The 3.5 cm first cell offers a number of other advantages. The peak

electric field is on the cathode rather than on the aperture as in the previous case. This should allow the cathode field to reach 110 MV/m with the same conditioning that it takes to reach 100 MV/m in the present BNL gun. Table 2 summarizes the beam dynamics modeling for Gun II.

Table 2. Modeling results for Gun II

Charge (nC)	0.5	1.0	3.0
Emittance ( $\pi$ mm-mrad)	2.3	3.4	8.9
Divergence ( $x'$ mrad)	7.9	8.3	9.5
Momentum spread	~ 0.2% - 2.0% (selectable)		
Launch phase	55°	59°	63°
Peak current			
Uncompressed (A)	118	220	571
Compressed (A)	2705	4224	7429

### III. THERMAL AND MECHANICAL DESIGN

Operation at duty factors of 1% present significant challenges in the heat removal aspects of the gun as well as the pressure and thermally induced stresses and deformations. The half cell of the gun will be 3.5 cm long followed by 3 full cells each 5.25 cm ( $\lambda/2$ ) in length. The longer cell simplifies the construction of the gun by reduced the space constraints. The peak power in the gun is 12.5 MW, thus an average power of 125 kW must be removed from the structure. Since Gun II will utilize a copper cathode, the cathode wall will be constructed of a solid GlidCop plate without penetrations. The cathode plate, four cylindrical spool pieces and four aperture pieces will be brazed together. The cathode plate is a 0.75 cm long cylinder 12.25 cm in diameter, with coolant channels milled in a circular pattern. A second 0.75 cm long cylinder is brazed on the back to enclose the channels. A 2.5 cm long cylindrical spool piece is used to connect the photocathode to the aperture. The spool pieces for the full cells are 3.25 cm long. All of the spool piece are cooled by circular channel machined into each end. Each aperture is designed as two cylindrical pieces, 1.0 cm long with two coolant channels milled in a circular pattern, which are brazed together. The aperture opening is a separate machining operation.

We have chosen to use GlidCop-25, an aluminum oxide dispersion strengthened copper alloy, which combines good thermal, electrical, and structural properties. The GlidCop will be electroplated with OFHC copper to provide the good electrical conductivity for the cavity and a barrier for the silver based braze alloys.

The thermal management of the gun requires heat removal from a cavity only 8.31 cm in diameter with peak power densities of 22 kW/cm<sup>2</sup>. The mode of heat transfer chosen is turbulent forced convection, the Dittus-Boelter heat transfer correlation was used. The heat removal is provided by pumping pressurized water through strategically placed coolant channels.

The power density was supplied by the SUPERFISH code for the cavity configurations evaluated. The power density in the longer half cell is decreased by nearly 15%. The operating

pressure and temperature distributions are input to the structural model and the pressure and thermally induced deformations and stresses are calculated. The resulting displacements are evaluated to determine the variation in cavity deformations impacting the frequency and tuning of the cavity. The stresses are evaluated and compared to the various stress categories in the ASME Boiler and Pressure Vessel Code.

The temperature distribution (3-D) shows that the peak temperature of the gun should reach about 144 °C which corresponds to a frequency shift of 4.4 MHz. The maximum Von Mises stress is less than 21 ksi (145 MPa) with an allowable of 31 ksi (214 MPa). 3-D modeling indicates no significant increases in either the temperatures or stresses occur near the coupling slots. Though these stress levels are well within the allowable levels for GlidCop, they exceed the allowable levels for OFHC copper (Yield Stress = 11 ksi).

#### IV. RF DYNAMICS

The design of Gun II requires that  $\pi$ -mode phasing be maintained between cells 1 and 2 and between cells 3 and 4. In addition, we would like to vary the phase smoothly between cells 2 and 3. The arrangement of the coupling slots and the distance of the waveguide short from the coupling slots ( $\lambda/4$ ) preferentially couples to the  $\pi$ -mode. Figure 4 shows the mode separation and relative amplitudes for the 0 and  $\pi$ -modes when two adjacent cells are driven with a single loop coupler or with the waveguide. Notice that the single loop excites the 0-mode most strongly by aperture coupling to the second cavity. By comparison, the waveguide most strongly excites the  $\pi$ -mode. The coupling constant is approximately  $5 \times 10^{-4}$ .

In order to match the waveguide to the gun, the coupling slots must be sized for critical coupling. The coupling is dependent on the Q of the cavity, therefore, the coupling slots will be slightly undersized and the gun will be brazed together. The final matching of the waveguide to the gun will then be achieved by shimming the height of the waveguide above the coupling slots. This method is preferred over cutting the coupling slots since the resonant frequency of the cavity is significantly influenced by the size of the coupling slots.

#### V. GUN STATUS

The GlidCop aperture sections and cathode plates have been brazed into assemblies and have been leak checked. A 1 cm thick disk was brazed between the aperture halves of the aperture which separates cells 2 and 3. This additional thickness was found to sufficiently reduce the coupling between cells 2 and 3. The apertures were then machined to achieve the final dimensions. The apertures and cathode were polished with diamond paper to achieve better than a 4 micro-inch finish. The ring sections have been completed as well. The apertures and rings have been clamped together and final tuning is nearly complete. We have been able to achieve better than 20% field tilt between adjacent cells.

After the rings have been polished, all of the GlidCop pieces will be copper plated with 0.0015" of copper. The

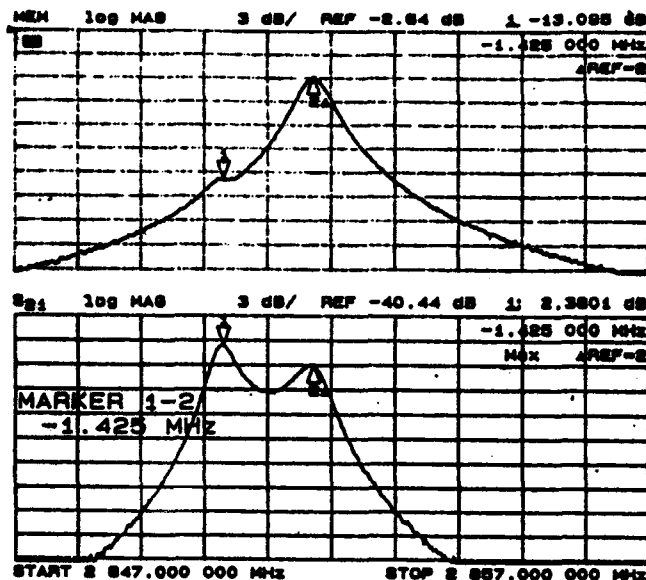


Figure 4. Network analyzer plots of the mode structure in Gun II. Points 1 and 2 indicate the locations of the 0-mode and  $\pi$ -modes, respectively. Waveguide driven (top) and loop driven (bottom).

assemblies will then be remeasured and tuned by polishing with copper wool in order to achieve 5% field tilt between adjacent cells.

Once the rings and apertures are in final form, the stainless cooling tubes (~60 pieces) and exit tube will be brazed to the GlidCop sections. The aperture and ring sections will then be brazed together and final frequency measurements will be made on the gun. If it is necessary to correct for the frequency of the cells at this point, material can be removed from the coupling slots to lower the frequency of the cells. A shim will be fitted and sized in the waveguide to increase the coupling to slightly beyond critical coupling. The final step will be to braze the waveguides to the gun.

#### VI. REFERENCES

- [1]I. Ben-Zvi, L.F. Di Mauro, S. Krinsky, M.G. White and L.H. Yu, Nucl. Instr. and Meth. A304 (1991) 181.
- [2]I. S. Lehrman, I. A. Birnbaum, M. Cole, *et al*, Proceedings of the 1992 Linear Accelerator Conference, Ottawa, CA, August 24-28, 1992 (1992)280.
- [3]G.D. Warren, L. Ludeking, J. McDonald, K. Nguyen and B. Goplen, Proc. Conf. on Computer Codes and the Linear Accelerator Community, Los Alamos National Laboratory, Jan 22-25, 1990, ed. R. Cooper, LA-11857-Z (1990) 57.
- [4] ANSYS engineering analysis system, Rev 4.3A, Swanson Analysis Systems Inc. Houston, Pa. (1987).
- [5] M.T. Menzel and H.K. Stokes, Users guide for the POISSON/SUPERFISH group of codes, Los Alamos Natl. Lab. Rep. LA-UR-87-15 (Jan. 1987).

### Abstract

The positron/electron linac for the Advanced Photon Source (APS) at Argonne National Laboratory can be used to accelerate electrons to 650 MeV. As part of a project to use this linac to test the quality of insertion devices, work has been done to develop a higher-brightness thermionic microwave gun of the SSRL [1] type. The new gun design has smaller emittance by a factor of 3 to 4. The ratio of cathode field to maximum surface field is more than doubled. The new alpha-magnet-based transport line design produces negligible emittance degradation due to chromatic aberrations, in spite of the  $\pm 5\%$  momentum spread.

## I. INTRODUCTION AND MOTIVATION

The advantages of using RF fields to accelerate electrons off of a gun cathode are increasingly well-known. At S-band, surface electric fields in excess of 300 MV/m are feasible [2], more than an order of magnitude greater than possible with DC fields. The resultant rapid acceleration of electrons leads to reduced space-charge effects in the gun. RF guns produce beams with energies of several MeV, giving reduced space-charge effects during beam transport.

Most RF gun work involves the use of laser-pulsed photocathodes to produce relatively short beam pulses directly at the cathode. While this has a number of advantages, cost, simplicity, and reliability are not currently among them. In contrast, the thermionic gun built at the Stanford Synchrotron Radiation Laboratory (SSRL) and its associated systems are based on simpler technology, yielding reliable performance that exceeds that of simple DC-gun-based injectors in beam brightness [3].

The primary mission of the APS is to provide X-ray beams from the 7-GeV positron storage ring. Many of the beamlines will use undulators, which must be carefully constructed in order to produce the desired X-ray beam properties for the user without negatively impacting the positron beam dynamics. The primary purpose of the APS RF gun is to provide a high-brightness electron beam to test insertion devices prior to installation. It will also allow characterization of novel insertion devices prior to installation. The gun will be coupled with the 650-MeV APS linac [4], now under construction.

A number of testing techniques are under consideration. One can determine the transport properties of a device by measuring the coordinates of a beam exiting the device as a function of the input coordinates. The beam emittance can be measured before and after the device, to ascertain whether there has been degradation. The spectral properties and angular distribution of the radiation can be used as sensitive measures of the quality

of the device. The last two techniques require a low-emittance electron beam, but not necessarily a high-current one.

The normalized RMS emittance of the electron beam in the horizontal plane is defined as  $\epsilon_{n,x} = \pi \sqrt{\langle x^2 \rangle \langle p_x^2 \rangle - \langle p_x x \rangle^2}$  where  $p_x = \beta_x \gamma$  is the normalized transverse momentum in the horizontal plane. For a sufficiently mono-energetic beam, the geometric RMS emittance is  $\epsilon_x \approx \epsilon_{n,x}/\gamma$ . It is well known that a necessary condition for coherent undulator radiation is  $\epsilon_{n,x}/\lambda \leq \lambda/4$ , and similarly in the y plane, where  $\lambda$  is the wavelength of the radiation. At the boundary of this regime, the angular and spatial distributions of the radiation are roughly equally determined by the properties of the electron beam and of the undulator.

Using the usual expression for the wavelength of undulator radiation, one sees that coherent radiation is obtained only when  $\gamma \leq \lambda_u (1 + K^2/2) / (8\epsilon_n)$ , where  $\lambda_u$  is the undulator period and  $K = x'_{max} \gamma$ . Hence, for a given normalized emittance, one can obtain coherent radiation by reducing the beam energy. However, this is at odds with the desire to produce short wavelength radiation.

Various undulators will be used at APS, with periods from 23 mm to 200 mm and K values between 0.3 and 2.7 [5]. With beam energies between 50 and 650 MeV, a normalized emittance of  $10\pi \cdot m_e c \cdot \mu\text{m}$  gives coherent radiation in the UV to IR for these undulator parameters. This emittance was chosen as the goal for the new gun and transport line design.

## II. GUN DESIGN CRITERIA

As with the SSRL gun, the APS gun is a side-coupled,  $\pi/2$ -mode, standing-wave structure, resonant at 2856 MHz, with a normalized load impedance of about 4. In order to reduce the beam emittance, a number of aspects of the SSRL design needed to be improved. In considering what follows, the reader may wish to refer to Figures 1 and 2, which show the new cavity phase and field profiles, respectively.

1. *Nonlinear radial dependence of fields.* The SSRL gun cavity was based on a design optimized for high shunt impedance, so that the gun has rather long, sharp cavity noses. These have been altered in the new design to produce a smoother variation in the on-axis longitudinal field. This is directly related to the magnitude of the non-linear transverse dependence of the fields [3], which has a strong effect on the emittance.

As in the SSRL design, the APS design incorporates a modification of the cathode end-wall to produce radially-focusing electric fields. In the present design, the structure producing these fields is further from the beam and less abrupt, giving a more linear dependence of  $E_r$  on  $r$ . Evaluated at the cathode radius of 3 mm, the peak nonlinear content of the radial and longitudinal fields have been reduced by a factor of three to four.

\* Work supported by U.S. Department of Energy, Office of Basic Energy Sciences under Contract No. W-31-109-ENG-38.

The submitted manuscript has been authored by a contractor of the U. S. Government under contract No. W-31-109-ENG-38. Accordingly, the U. S. Government retains a nonexclusive, royalty-free license to publish or reproduce the published form of this contribution, or allow others to do so, for U. S. Government purposes.

2. *Magnitude of  $E_z$  at the cathode.* Since both the SSRL and APS guns are designed for use with a magnetic compression system, the output longitudinal phase-space must exhibit a monotonic dependence of momentum on exit time. This requires that particles arrive in the second cell of the gun behind the RF crest, which in turn requires either lowering the first-cell fields relative to the second [1, 3], or else moving the cathode end-wall back. In the SSRL gun, the peak on-axis fields in the two cells were in the ratio  $\alpha = E_{p2}/E_{p1} \approx 3$ . In the APS gun, the cathode end-wall was moved back 6 mm, and the first-cell fields were increased to give  $\alpha = 1.63$ . The ratio on the peak surface field to the cathode field has been increased from 0.13 to 0.28. For the same peak surface field, the maximum beam momentum is about 75% higher. However, for the same maximum momentum, the cavity wall power is approximately the same.

### III. GUN SIMULATIONS

In this section, I report on the results of simulations of the gun using the fully electromagnetic PIC code `spiff` [6]. The simulations were of the entire gun with a single bunch emitted from the cathode. Resistive effects in the cavity walls were not included, so the fields were created by ringing the individual cells, not by driving them to steady state.

Because the fields are time-varying, particles exiting the gun have a momenta from some maximum down to essentially zero; 45% to 55% of the charge is in the top 10% of the energy range. The transport line will incorporate a momentum filter to select just this "useful" portion of the beam.

Figure 3 shows the normalized RMS emittance of the useful beam versus the useful-beam charge, for a range of excitation levels and beam currents. The maximum current for each level corresponds to a current density of  $J = 30 \text{ A/cm}^2$ , which gives an approximate matched condition for the  $\beta \approx 4$  cavity. As in the SSRL gun, the cathode has a 3 mm radius.

The emittances predicted are well below the desired level, particularly at low current. Note that the emittance of the useful beam *decreases* with current for  $E_{p2} = 80 \text{ MV/m}$ . This is a result of the selection of a fixed fractional momentum interval, which does not correspond to a fixed emission phase interval.

Additional simulations were done to assess the space-charge-induced emittance growth for the gun beam in a drift following the gun. These indicate that significant emittance growth can occur, particularly at the higher current levels. For  $E_{p2} = 60 \text{ MV/m}$  and  $J = 20 \text{ A/cm}^2$ , the emittance increases 60% in a 50-cm drift. This effect motivates a short gun-to-linac transport system, which is in conflict with the needs of magnetic compression.

### IV. TRANSPORT LINE

As at SSRL, APS will employ an alpha-magnet-based magnetic bunching system [7, 3]. The optimal system for low space-charge consists of an alpha-magnet and a total of 2 FA of longitudinal drift space. A significantly shorter drift length would require a much stronger alpha-magnet, since the optimal gradient is inversely proportional to  $L^2$ . Because of the magni-

tude of space-charge effects on the drifting beam, however, a shortening of the transport line is under consideration, probably at the expense of increasing the bunch lengths from 1 to 2 ps to about 5 ps.

One significant problem at SSRL was emittance degradation due to quadrupole chromatic aberrations, particularly because a large momentum spread ( $\pm 10\%$ ) was utilized. Simulations predicted emittance increases by factors of 5 to 10, and these were born out by experiment. As implied above, the present project will use a smaller momentum spread ( $\pm 5\%$ ). In addition, a strategy for correcting the chromatic aberrations was developed.

The common approach to correcting aberrations is to make a first-order design with the desired optical properties, usually building in symmetry to give cancellation of certain aberrations [8]. One then adds nonlinear elements to compensate as many of the remaining aberrations as possible. It was found that such a procedure was very difficult for the present case. In particular, a system with first-order optical symmetry tends to be longer, have greater phase advance, and have more elements than the solution used.

The solution adopted was to optimize the first- and higher-order properties of the transport line simultaneously. More precisely, the tracking program `legant` [6] was used to optimize the beam transport by tracking the initial phase-space calculated with `spiff`.

To understand this further, consider that the initial phase-space of the gun beam is roughly described by  $x' = \alpha x$ , with  $\langle x\delta \rangle = \langle x'\delta \rangle = 0$ , where  $\delta = \Delta p/p_0$ . For simplicity, I assume that  $\alpha$  is constant, giving an initially zero emittance beam.

If such a beam is sent through a thin-lens quadrupole of focal length  $f_0$ , then the slopes become  $x'_1 = x' - \frac{1-\delta}{f_0}$ , and the geometric RMS emittance becomes  $\epsilon_1 = \pi x_{rms}^2 \delta_{rms} / f_0$ . The immediate conclusion from this result is that one should avoid strong focusing and large beam sizes in designing the beamline. This is one reason that optically symmetric systems are more difficult, since obtaining a  $-I$  matrix from the start to midpoint requires strong quadrupoles or a relatively long system. One ends up seriously degrading the emittance simply by attempting to obtain the first-order optics solution.

Another lesson that can be drawn from this example is that the emittance degradation can be restored by another quadrupole. For example, if the initial beam has  $\alpha = 0$ , then following the first quadrupole by another of equal but opposite strength at a distance of  $2f_0$  will result in an emittance proportional to  $\delta_{rms}^2$ —i.e., the degradation is essentially cancelled.

Unfortunately, this quadrupole pair does not form a useful optical element. The point of the example is to convince the reader that it is possible to recover the emittance even after degradation, and therefore that a beamline can be designed without separate chromatic correction elements. Figure 4 shows the RMS beam sizes and normalized emittances in the transport line designed for APS, using the optimization method just discussed. The initial phase space is from a `spiff` simulation with  $J = 5 \text{ A/cm}^2$  and  $E_{p2} = 60 \text{ MV/m}$ . This gives just over 50 pC

of useful beam per pulse, which is adequate for our primary application. Future work will attempt to extend these results to transport with space charge.

## V. ACKNOWLEDGEMENTS

The author wishes to acknowledge valuable consultations with Eiji Tanabe of AET, who built the gun, and with Jim Weaver of SSRL.

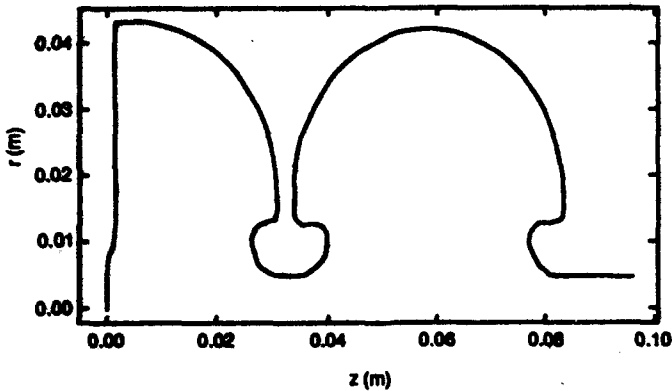


Figure 1  
Cavity shape for the RF gun

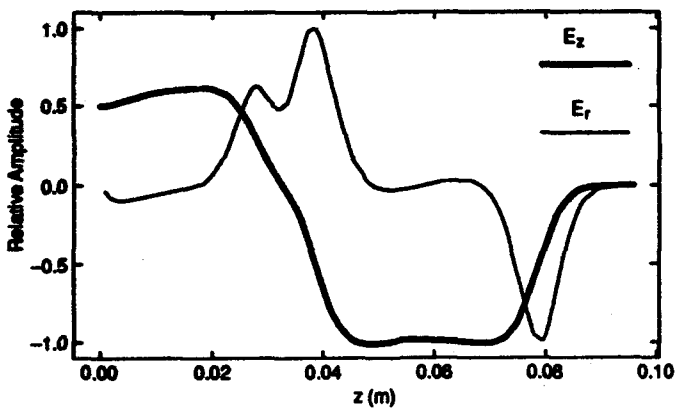


Figure 2  
Electric field profiles for the gun cavity

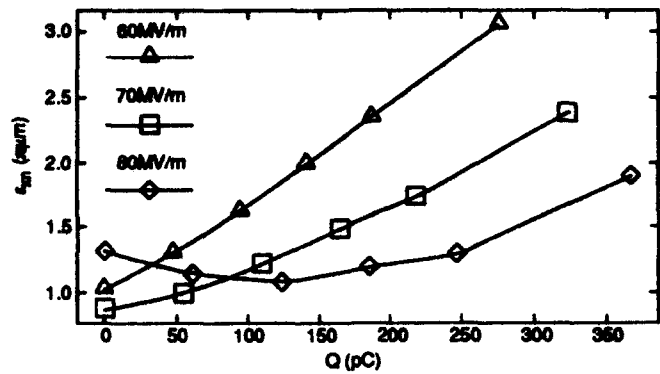


Figure 3  
Normalized RMS emittance at the gun exit vs. useful charge per bunch

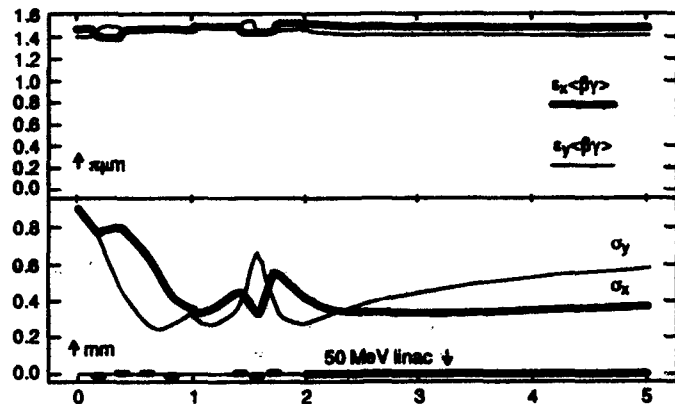


Figure 4  
Geometric emittance along the transport line

## VI. REFERENCES

- [1] M. Borland, *et al.*, "Performance of the 2 MeV Microwave Gun for the SSRL 150 MeV Linac," in *Proceedings of the Linear Accelerator Conference*, September 1990.
- [2] J. W. Wang, *et al.*, "RF Breakdown Studies in Copper Electron Linac Structures," in *Proceedings of the Particle Accelerator Conference*, March 1989.
- [3] M. Borland, "A High-Brightness Thermionic Microwave Electron Gun," SLAC-Report-402, 1991. Stanford University Ph.D. Thesis.
- [4] A. Nassiri, *et al.*, "The Linac Injector for the ANL 7 GeV Advanced Photon Source," in *Proceedings of the Linear Accelerator Conference*, September 1990.
- [5] "Advanced Photon Source Conceptual Design Report," ANL-87-15, 1987.
- [6] M. Borland. Unpublished program.
- [7] H. A. Enge, "Achromatic Magnetic Mirror for Ion Beams," *Review of Scientific Instruments*, Vol. 34, No. 4, 1963.
- [8] K. L. Brown, "A First- and Second-Order Matrix Theory for the Design of Beam Transport Systems and Charged Particle Spectrometers," SLAC-Report-75, 1982.

# EXPERIENCE WITH A RADIO FREQUENCY GUN ON THE SSRL INJECTOR LINAC\*

J. N. Weaver, R. D. Genin, P. Golceff, H. Morales and J. Sebek

Stanford Synchrotron Radiation Laboratory at

Stanford Linear Accelerator Center, Stanford University, Stanford, CA 94309 USA

## Abstract

A-SSRL/Varian-Associates-built, one-and-a-half cavity, microwave, thermionic-cathode gun has operated on the SSRL Injector Linac reliably without changing the cathode for over 10,000 hours, with no significant decrease in emission. Thus, for a pulsed electron beam, with a maximum of 0.5 A peak at 2 to 3 MeV from a 3.5 MW peak rf pulse of 2  $\mu$ s pulse width at 10 pps, the apparent but small amount of back bombardment of the cathode has been tolerable. Use of a bunch-compression alpha magnet and a stripline chopper after the gun produces the required S-band 3 to 5 microbunches of electrons for injection into a standard 10-m-long linac and on into a booster synchrotron, which in turn is used to fill SPEAR. Component limitations and operating characteristics of the gun and the linac's rf system are discussed.

## I. INTRODUCTION

There are four thermionic-cathode, microwave guns of the SSRL/VA/AET type [1,2,3] in existence, designated by the following model numbers: SSRL 1, SSRL 2, MG-200, and MG-300, and listed here in the order in which they were built. SSRL 1 is being used as the source for SSRL's injector for SPEAR, and has logged over 10,000 hours of operation on the linac. SSRL 2 has been operating for over 1000 hours as the source for a couple of experiments at HEPL on the Stanford campus [4]. Both MG-200 and MG-300 were built for ANL's new APS facility that is still under construction, and have not been tested yet. After testing, one is expected to serve as a secondary source [5]. Some discussion of the operating characteristics of SSRL 1 follows. The complete layout of the SSRL linac's rf system has been described elsewhere [6,7]. This system has behaved reasonable well, with the exception of some modulator reliability problems, and some outgassing and arcing problems. The arcing problems, described below, seem mainly to have been associated with one particular accelerator section and load.

## II. THE LINAC'S RADIO FREQUENCY GUN PERFORMANCE

The linac receives nominally three 120 MeV bunches of  $4 \times 10^8$  electrons each, with a bunch spacing of 350 ps, at a repetition rate of 10 Hz from a chopper, alpha magnet and rf gun source. Thus, the gun only has to produce a steady beam for a relatively short time during its

\*Work supported by Department of Energy contract DE-AC03-76SF00515 and the Office of Basic Energy Sciences, Division of Material Sciences.

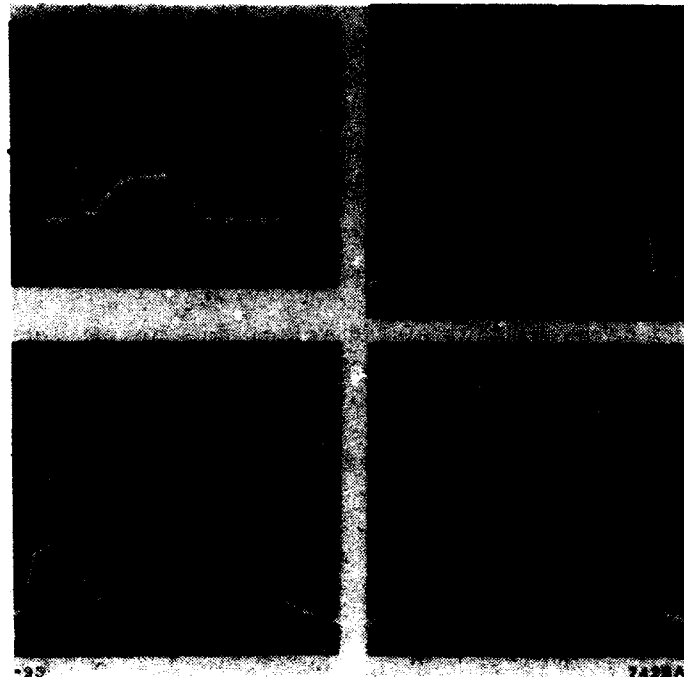


Figure 1. Incident (full pulse) and reflected (with a porch) rf power pulses from the rf gun, 0.5  $\mu$ s/div, (a) [upper left] with the heater off and a 10 mW peak pulse from a signal generator (the incident pulse is not shown in the oscilloscope), (b) [upper right] with the heater off and a 3.5 MW peak incident pulse, (c) [lower left] with the heater on at its normal, 9.0 W, operating level and a 3.5 MW peak incident pulse and (d) [lower right] with the heater at 10 W and a 3.5 MW incident pulse.

pulsed time on. The rf gun and accelerator section fill times are factors that have to be coordinated, since the same klystrons and modulators supply the whole rf network. Five time constants for the rf gun standing-wave cavities are about 1.5  $\mu$ s, and the linear fill time of the travelling-wave accelerator sections is about 0.8  $\mu$ s, so a 2- $\mu$ s-long rf pulse with a nominal 1.5  $\mu$ s flat top is sufficient for operation. The gun cavity  $Q_0 = 14,000$ , as calculated from a slotted line measurement of  $\beta = 4.4$  and from determining the pulse decay time from Fig. 1(a), which shows the reflected signal from the rf gun with the heater off and a square, signal-generator-level, incident pulse. Within measurement accuracy, the values of  $Q_0$  and  $\beta$  are the same after 10,000 hours of operation as when built. Figure 1(b) shows the incident and the reflected signals from the gun, also with the heater off, but with a high-power incident pulse. The reflected signal is much less

ideal with the much-less-than-square incident pulse from a modulator pulse forming network. Figure 1(c) shows the same signals with the heater set at its normal operating point, which result in a beam-loaded reflected signal. It should be noted here that the cathode is run temperature-limited in order to obtain the desired current from rf accelerating fields that allow the alpha magnet-to-bunch length compress a few microbunches most effectively for injection into the linac [2],[3]. If the heater power is increased by 10%, the same signals are as shown in Fig. 1(d).

It seems that the heavier the beam-loading, the earlier the beginning of the rise in the reflected signal (from a steady, beam-loaded state to the cavity discharging state that accompanies turn off of the incident pulse). This phenomenon, together with the continually rising shape of the gun output current pulse, as seen in Fig. 2(a), may be an indication of the effects of back bombardment [8], and/or off-resonance-rf driving, or something else. The SSRL 1 gun has never had to use a bias or deflecting magnet to divert the back-bombarding beam away from the cathode to prevent overheating. The SSRL 2 gun, which is being run at higher power and is being studied extensively for such effects, is operated with a deflecting magnet [8], as was one of the earliest rf guns [9].

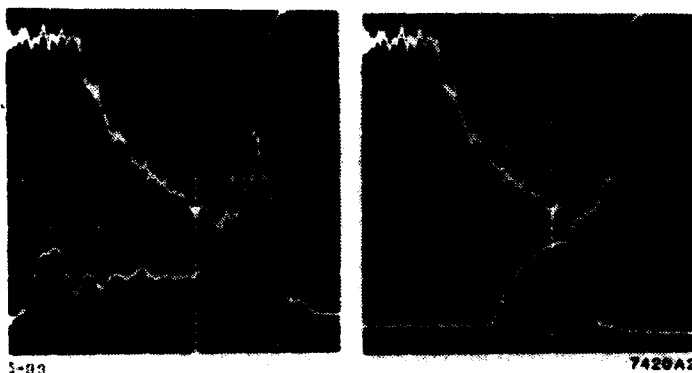


Figure 2. Current pulse (upper and inverted) directly out of the rf gun as compared in time,  $0.5 \mu\text{s}/\text{div}$ , to (a) [left] the gun reflected rf power pulse (lower), and (b) [right] the current pulse (lower) after being scraped and compressed by the alpha magnet.

Another complication occurs with the timing of the compressed current pulse out of the alpha magnet, in comparison with current directly out of the gun, as seen in Fig. 2(b). The amplitude of the former is reduced from that of the latter by a low-energy tail scraper. Computer calculations undoubtedly predict that the maximum in the high energy portion of the current pulse occurs before full beam loading. However, since measurements of the rf field levels in the two cells of the gun during operation is only possible with MG-200 and MG-300 (which have coupling loops built into them), this will have to wait for computer model verification. It turns out that, for 3.75 MW of incident power some component (a faulty vacuum window?)

in the gun's drive, rectangular waveguide network arcs occasionally, abruptly dropping the incident signal's amplitude. As a result, the reflected signal (actually only an emitted signal from the cavity remains) rises sharply, then decays with the cavity's time constant, as the theory says. Thus, there is reason to believe that the unexplained pulse shapes of some of the previous figures are real.

The gun's first cathode died at an early age while undergoing initial beam tests in one of Varian Associates' Clinac test cells under high rf fields and a long pulse length (close to 6 MW for  $6 \mu\text{s}$ ). The initial test setup was not fully instrumented with vacuum interlocks, so the apparent cause of failure was from poor vacuum during excessive processing discharges and excessive heating of the cathode due to back bombardment. The gun's rectangular-waveguide ceramic window cracked and the poisoned cathode was found to be severely crevassed in some areas. Before the failure, the heater power supply could be completely turned off once emission was established, which is a good indication of self-heating from back bombardment. With a long pulse and high fields, the current out of the gun was found to increase exponentially after about 3 or  $4 \mu\text{s}$  into the pulse. Thus the initial plateau value that was reached some 2 to  $3 \mu\text{s}$  into the pulse would rise to triple or quadruple the current before pulse breakup occurred at about 4 to  $5 \mu\text{s}$ , from yet some other undiagnosed instability. Subsequent tests of the gun on the linac have resulted in relatively stable operation with less than 4 MW of peak rf drive power to the gun at 10 pps and a  $2 \mu\text{s}$  pulse width. The more than 10,000 hours now logged on the second cathode have been under these less strenuous running conditions. It seems that rf guns with thermionic-cathodes do have some interesting quirks that could bear further study.

### III. ACCELERATOR SECTION AND RADIO FREQUENCY LOAD PERFORMANCE

The linac's three, 3-m-long, accelerator sections and rf loads were purchased from IHEP in Beijing, PRC. They have performed very well, with the exception of a not-very-well understood arcing and outgassing problem that occurred almost exclusively with one load. This problem manifested itself in terms of high reflected power signals from either within the guide or from the kanthal-coated, vacuum, rectangular-waveguide load of the SLAC-type. Most kanthal loads of this type are notorious sources of prolonged outgassing and multipactoring. Thus, to be safe after exposure to air and before rf processing, all the loads are treated with a  $160^\circ\text{C}$  dry nitrogen bake for 24 hours and then with a  $160^\circ\text{C}$  vacuum bake for several days. The duration of the vacuum bake depends upon the pump down rate.

Some tests of a load on a SLAC klystron test stand indicated a VSWR that increased from 1.05:1 at signal generator power levels to 1.26:1 at 0.1 MW peak, and to over 4:1 at 8 MW peak. A permanent magnet passed along the length of the load could change the VSWR and the outgassing rate considerably, suggesting some sort of discharge

phenomenon. The high reflected power signals could be processed away, but they have also occasionally returned, so the problem load has been replaced by a water load with double ceramic windows with a "guard vacuum" in between. The guard vacuum is instrumented to hopefully give an early warning of any impending water-to-vacuum leaks. An improved, high peak power, high vacuum load with external water cooling is being sought. Some ideas and designs are on the horizon [10]; currently, they are in the process of being incorporated into a readily available proven product [11].

### ACKNOWLEDGEMENTS

The dogged and intuitive efforts of the SSRL operators to get and to keep the rf gun going in the face of only a little enlightened instruction is to be praised, especially since the gun is still running!

### REFERENCES

- [1] E. Tanabe et al., SLAC-PUB-5054 (1989).
- [2] M. Borland et al., "Performance of the 2 MeV Microwave Gun for the SSRL 150 MeV Linac," *Proc. 1990 Linac Conf., 761-3, Albuquerque, NM or SLAC-PUB-5333* (1990).
- [3] M. Borland, Ph.D. thesis, Stanford University, 1991.
- [4] Private communication with R. H. Pantell and H. Wiedemann, Stanford University, Stanford, CA 94305.
- [5] M. Borland, "An Improved Thermionic Microwave Gun and Emittance-Preserving Transporting Line," *Proceedings of the 1993 Particle Accelerator Conference, Washington, D.C.*
- [6] M. Borland et al., "Design and Performance of the Travelling-Wave Beam Chopper for the SSRL Injector," *Conference Record of the 1991 IEEE Particle Accelerator Conference, Vol. 2, pp. 976-8.*
- [7] J. N. Weaver et al., "The Linac and Booster rf Systems for a Dedicated Injector for SPEAR," *ibid.*, pp. 969-71.
- [8] J. F. Schmergie et al., "An Eight Centimeter Long Accelerator for a Far Infrared FEL," to be published in *Nuclear Instruments and Methods in Physics Research, A320* (1994).
- [9] G.A. Westenskow et al., "Owner's Manual for the Microwave Electron Gun," HEPL TN-86-1, Stanford University, Feb 1986, unpublished.
- [10] *Proceedings of the Workshop on Microwave-Absorbing Materials for Accelerators, at CEBAF, Newport News, VA, Feb. 22-24, 1993.*
- [11] Private communication with A. A. Zante of Titan Beta, Dublin, CA 94568, and with L. J. Nielsen of Premier Microwave of California, Santa Clara, CA 95054.

# Design of a High Duty Cycle, Asymmetric Emittance RF Photocathode Injector for Linear Collider Applications

J. B. Rosenzweig, Eric Colby  
UCLA Department of Physics  
405 Hilgard Ave, Los Angeles, CA 90024  
G. Jackson and T. Nicol  
Fermi National Accelerator Laboratory  
P.O. Box 500, Batavia, IL 60510

## Abstract

One of the attractive features of the superconducting approach to linear collider design is that the transverse emittances demanded are much larger than in normal conducting schemes. For TESLA design parameters, the damping rings appear to be relatively large and expensive, and it is therefore of some interest to look into alternative sources. For electrons, a promising source candidate is an rf photocathode. In this paper, we present conceptual design work towards development of an asymmetric emittance rf photocathode source which can operate at the TESLA repetition rates and duty cycle, and is capable of emitting beams with the required emittances and charge per pulse.

## 1. INTRODUCTION

In linear colliders, the transverse emittances are generally asymmetric, for a variety of reasons. The most compelling have to do with ameliorating the effects of the beam-beam interaction by colliding "flat" beams ( $\sigma_x \gg \sigma_y$ ). This allows the beamstrahlung energy loss and spurious pair creation to be minimized, while at the same time loosening the constraints on the final focus system and allowing the beams to collide at a small angle, easing the task of disposing the beam exhaust. In addition, the standard way of obtaining low emittance  $e^+$  beams is through the use of damping rings, which naturally give horizontal emittances which are much larger than vertical ( $\epsilon_x \gg \epsilon_y$ ).

For the TESLA design parameters, however, the higher average current allows for relaxation of the beam sizes at the final focus. This in turn implies that the emittances can be substantial larger in an SRF linear collider. In fact the TESLA parameter sets usually specify horizontal and vertical normalized emittances of 25-50 and 1 mmrad, respectively. These numbers are nearly two orders of magnitude larger than the corresponding normal conducting linear collider designs specify. These numbers are, in fact, near the present state of

the art in rf photo-cathode technology. This state of affairs naturally has prompted the suggestion that the electron beam in an SRF collider might be created by an rf photocathode source, doing away with the electron damping ring.

## II. ASYMMETRIC EMITTANCE RF PHOTOCATHODE GUNS

There is considerable experience in producing symmetric high brightness photocathode sources, whose charge per bunch and product of transverse emittances  $\epsilon_x \epsilon_y$  are near that demanded by TESLA designs. Unfortunately, it is not possible to produce an asymmetric emittance beam from a symmetric beam which has a smaller emittance in one plane than the original symmetric emittance (see discussion in the Appendix). Thus one must start with an asymmetric beam,  $\sigma_x \gg \sigma_y$ .

The scaling of the emittances with beam and rf parameters of photocathode sources has been examined in previous work.[1] The emittances arise from three sources: the effective temperature of the photoelectrons (which is usually ignorable), the time-dependence of the transverse rf fields, and space charge.

The rf contribution to the rms emittances is, following Kim[2]

$$\epsilon_{x,y}^r = \frac{1}{\sqrt{2}} W k_{rf}^2 \sigma_z^2 \sigma_{x,y}^2$$

where  $W = eE_{rf} / m_e c^2$ , and  $E_{rf}$  and  $k_{rf}$  are the rf electric field amplitude and wave-number, respectively. This scaling pushes one to longer rf wavelength and impacts the large dimension (x in our case) emittance much more severely than the small dimension.

The space charge contribution has been estimated from simulations and model calculations to be, with laser injection phase  $\phi_0$ ,

$$\epsilon_{n(x,y)}^{sc} = \frac{2N_b r_e}{7\sigma_{x,y} W \sin(\phi_0)} \exp(-3\sqrt{W\sigma_y}) \sqrt{\frac{\sigma_y}{\sigma_x}}$$

It is also interesting to note that the product of the emittances takes the form

$$\varepsilon_x^x \varepsilon_y^x \equiv \left[ \frac{2N_b r_e}{7W} \right]^2 \frac{\exp(-3\sqrt{W\sigma_y})}{\sigma_x \sigma_z}$$

The exponential term is on the order of unity, and so, at first glance, it would seem that one can make the emittances arbitrarily small by raising  $\sigma_x \sigma_y$ , but this option is suppressed by the scaling of the rf component to the emittance. In addition, the minimizing of  $\varepsilon_y$  is ultimately constrained by the longitudinal space charge limit on minimum beam spot size[1], which is

$$\sigma_x \sigma_y \geq \frac{2N_b r_e}{W \sin(\phi_0)}$$

This limit has been verified experimentally[3]. Use of a beam at this limit allows us to rewrite the emittance product as

$$\varepsilon_x^x \varepsilon_y^x \equiv 0.04 \left[ \frac{N_b r_e}{W} \right] \frac{\sigma_y}{\sigma_z}$$

This points out the need to maximize the beam length, which can be exploited if one can circumvent the scaling of  $\varepsilon_{n(x,y)}^f$ . This point will be returned to below.

### III. DESIGN: BEAM DYNAMICS

It is clear that we would like to design a source at as low a frequency as possible since we are pushed towards large  $\sigma_z$ . We also need, however, large accelerating gradients (large  $W$ ), which implies higher frequencies. A good optimum appears to be at 1300 MHz, which is conveniently the TESLA rf frequency. We have examined the behavior of an asymmetric beam in a 1.5 cell 1300 MHz standing wave  $\pi$ -mode gun, with parameters as listed in Table 1, by inputting an asymmetric beam profile into a form of PARMELA which uses a point-by-point space charge calculation algorithm.

Beam sizes ( $\sigma_x, \sigma_y, \sigma_z$ )	8, 0.25, 2 mm
Beam population $N_b$	$5 \times 10^{10}$
Accelerating field $E_f$	90 MV/m
Final energy $E_b$	8 MeV
Final emittances $\varepsilon_{nx}, \varepsilon_{ny}$	95, 4.5 mm-mrad

Table 1. parameters for PARMELA design calculation of asymmetric emittance rf photocathode source.

For the input beam charge and dimensions given, our final scaling law gives  $\varepsilon_x^x \varepsilon_y^x \equiv 400$  (mm-mrad)<sup>2</sup> which is in fact very close to what is obtained by the simulation. We have fallen short of

the TESLA design goals ( $\varepsilon_x \varepsilon_y \leq 50$  (mm-mrad)<sup>2</sup>) by a factor of 2 to 4 in both transverse dimensions. This is not as discouraging as it may seem, since both the rf and space charge contributions to the emittance can be mitigated. Dynamical correction of the space-charge derived emittance is practiced at LANL and preliminary calculations[4] indicate that it may allow TESLA design emittances to be obtained in a 1300 MHz photoinjector. In addition, we are presently examining the effects of using an asymmetric cavity, using the 3-D electromagnetic code ARGUS, to minimize  $\varepsilon_x^f$ .

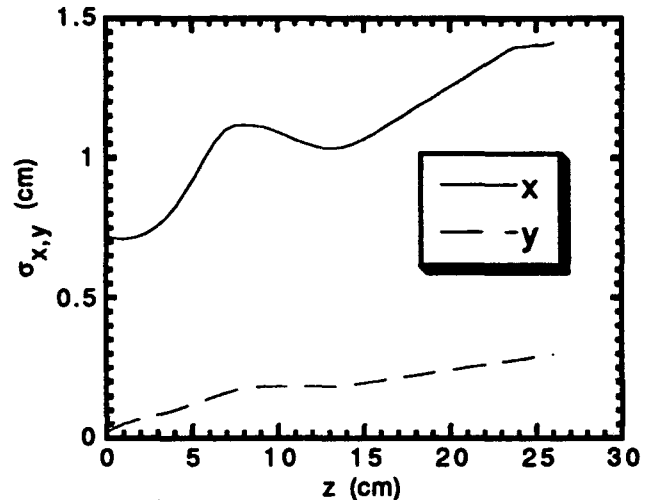


Figure 1: Evolution of the rms beam envelopes in 1.5 cell gun.

The beam dynamics in the gun are dominated by the alternating gradient rf focusing<sup>5</sup>, as is shown in Figure 2. Beam transport after the gun must also be optimized to produce no emittance degradation. One common focusing element which is not allowed is the solenoid. Even if one achieves a linear  $n\pi$  rotation to uncouple the beam, chromatic focusing (and rotation) effects, as well as space-charge effects (even at 8 MeV, the transverse electric field will produce an  $\vec{E} \times \vec{B}$  rotation dependent on position in the beam), will destroy the smaller emittance  $\varepsilon_y$ .

### IV. DESIGN: DUTY CYCLE EFFECTS

The TESLA duty cycle presents some difficult challenges to rf photocathode source design. The most obvious is in rf power, both average and peak. The shunt impedance of our gun design is  $ZT^2 = 27 \text{ M}\Omega / \text{m}$ , and thus the peak power is 15 MW. This peak power must be applied for about 1 msec, with a one percent duty cycle. During each pulse 800 bunches are extracted at a one MHz rate.

This is problematic in terms of both obtaining and dissipating the rf power. A thermal and structural analysis was performed, in which the average power (150 kW) was not found to be difficult to handle. This is not surprising, as the Grumman/BNL gun[6] has a similar average power, with a smaller mass. The peak power and the long rf pulse, may be more serious an issue. Fig. 2 shows the maximum temperature in the structure for the transient case, and we see that the peak temperature rise per pulse is only 15 degrees. The structural analysis is not complete, however, and so the issue of the effect of the heating on rf performance is not resolved. Also of impact on this design is the lack of a commercial klystron with the required specifications; the closest models in performance are presently the Thomson TH 2115 and TD2104U.

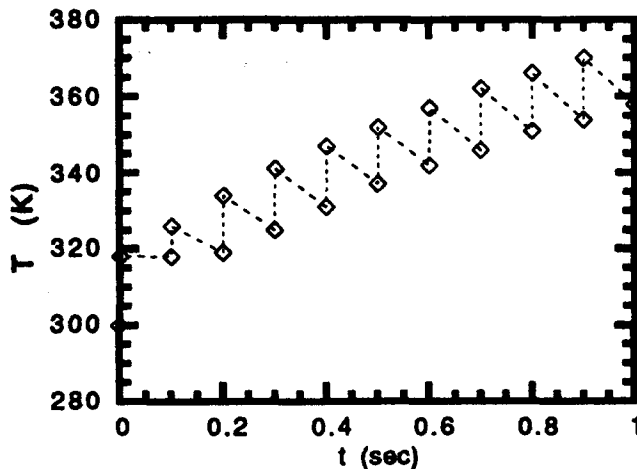


Figure 2. Transient profile of maximum temperature in rf photocathode gun structure.

The other major problem associated the TESLA time structure is that of obtaining a uniform (in laser energy) 800 pulse train at a 1 MHz rate during the rf pulse. This subject is still under study.

*Appendix: Impossibility of reducing the minimum emittance in a transverse phase plane*

The normalized rms emittances are constrained to evolve in certain ways. In particular the invariance of the determinant of the beam  $\sigma$  matrix under linear transport gives the condition

$$\epsilon_x \epsilon_y = \text{constant} \equiv \epsilon_0^2.$$

where the rms emittances are defined by

$$\epsilon_x^2 = \langle x^2 \rangle \langle x'^2 \rangle - \langle x x' \rangle^2$$

$$\epsilon_y^2 = \langle y^2 \rangle \langle y'^2 \rangle - \langle y y' \rangle^2.$$

There are also many invariants associated with higher moments of the Vlasov equation, as discussed by Rangajaran, et al.[7] Of particular

interest is a second order moment, which considering only transverse phase space is

$$\epsilon_2^2 = \epsilon_x^2 + \epsilon_y^2 + 2\langle xy \rangle \langle x' y' \rangle - 2\langle xy' \rangle \langle x' y \rangle.$$

This invariant moment is a constant of the motion even if the  $x$  and  $y$  phase space planes become coupled. Note that if one introduces an infinitesimal coupling to a previously uncoupled system, it must be by applying a skew quadrupole kick, which only changes the last term in the above equation. In that case, it is easy to show that a kick of this form causes this additional term to be positive,  $\langle xy' \rangle \langle x' y \rangle > 0$ . Thus the rms emittances must grow if one couples the phase space planes, in order to preserve the invariance of  $\epsilon_2$ .

Because of this, if one begins with uncoupled phase space planes, one must always completely uncouple the phase space planes in order to obtain a minimum sum of squares of the emittances. Now we have a second constraint on the emittances, derived from the second order invariant,

$$\epsilon_2^2 = \text{constant} = \epsilon_x^2 + \epsilon_y^2.$$

If we now apply both constraints on the emittances, we can derive a condition for the final state emittances in terms of the initial emittances  $\epsilon_x$  and  $\epsilon_y$ , as follows. We have

$$\epsilon_2^2 = \epsilon_{x0}^2 + \epsilon_{y0}^2 \quad \text{and} \quad \epsilon_0^2 = \epsilon_{x0} \epsilon_{y0}.$$

Solving this system for the final emittances, we have

$$\epsilon_{x,y}^2 = \frac{\epsilon_2^2 \pm \sqrt{\epsilon_2^4 - 4\epsilon_0^4}}{2} = \epsilon_{x0}^2 \quad \text{or} \quad \epsilon_{y0}^2.$$

The final emittances, under this uncoupled condition, can take on only the value of either of the initial emittances. Leaving the emittances unchanged is obtained by any total transformation which contains a rotation of  $n\pi$ , and exchange of the two emittances by any transformation containing a rotation of  $(n + \frac{1}{2})\pi$  ( $n$  integer).

**REFERENCES**

1. J. Rosenzweig and S. Smolin, to be published in *Proceedings of the Port Jefferson Advanced Accelerator Concepts Workshop* (AIP, 1993).
2. K.J. Kim, *Nucl. Instr. Meth. A* 275, 201 (1989).
3. P. Davis, et al., these proceedings.
4. R. Sheffield, private communication.
5. S. Hartman and J. Rosenzweig, *Phys. Rev. E* 47, 2031 (1993).
6. I. Lehrman, et al., *1992 Linear Accel. Conf., Proc.*, 280 (AECL-10728, Chalk River 1992).
7. G. Rangajaran, et al., *Proc. of 1989 IEEE Part. Accel. Conf.*, 1280 (IEEE, 1989).

# Design of a High Brightness RF Photoinjector for the SLAC Linac Coherent Light Source

J. Rosenzweig

UCLA Department of Physics, 405 Hilgard Ave, Los Angeles, CA 90024

L. Serafini

INFN-Milano, Milan, Italy

## Abstract

The electron injector for the SLAC Linear Coherent Light Source[1] (LCLS) must produce a low jitter, high brightness beam. This beam must be accelerated and longitudinally compressed to yield a sub-picosecond beam which radiates a burst of self-amplified spontaneous emission x-rays upon passing through a long undulator. As the gain of this amplifier is very sensitive to the emittance, energy spread and peak current the electron source and subsequent transport, acceleration, and compression systems must reproducibly give a very high quality beam. The conceptual design of an rf photocathode gun which satisfies the requirements of the LCLS is presented here.

While the design peak current emitted by this gun is above 200 A, the requirements of gain length in the undulator are such that the beam must undergo longitudinal compression to raise the peak current by an order of magnitude. This compression is very much dependent on both the phase of the accelerating rf wave and the longitudinal wake-fields in the linac, and so the final bunch length will not be reproducible if the time of beam emission (laser beam injection) and/or the charge per bunch have large variations. Because of concerns on reliability and feasibility of the photoinjector, a design which takes maximum advantage of proven technology, and recent experience in photoinjector development has been explored, and is outlined below.

## I. INTRODUCTION

The proposed SLAC LCLS is designed to be an R&D facility based on the FEL principle which provides sub-picosecond pulses of x-rays in the 2-4 nm spectral region. The LCLS injector, which must produce the electron beam which is then accelerated in the SLAC linac to an energy of  $\leq 7$  GeV, must satisfy fairly stringent requirements on beam quality. The beam emittance must be very small, while producing a nanocoulomb of charge in a picosecond bunch length. The parameters of the injector we have studied are listed in Table 1.

## II. RF DESIGN

The rf gun structure chosen is of a type evolved from the high gradient guns in use at BNL and UCLA. It is a three-and-one half cell standing wave  $\pi$ -mode cavity, which is nominally operated with a peak accelerating gradient of  $E_{rf} = 100$  MV/m. The frequency was chosen to coincide with the that of the SLAC linac structure, mainly because of ready availability of the power source, but also because of the proven ability to reach high fields in other S-band structures. The large accelerating field is chosen to minimize the contribution of space charge to the emittance growth the beam undergoes during acceleration. Both a replica of the BNL structure and a modified structure with larger iris openings were examined for use in this gun; the modified structure, with its higher intercell coupling, allowed superior mode separation, more linear transverse rf fields, and greater flexibility in regard to coupling of the cavity to the wave-guide.

The high field levels in the gun imply that a peak power of 13.6 MW must be supplied to the structure, well within the reach of a SLAC XK5 klystron. Assuming a maximum repetition rate of 120 Hz, and a minimum pulse length of 2.25 microseconds (three rf fill times), the average rf power in the structure is 50 kW, which is

Final energy $E$	10 MeV
Norm. emittance $\epsilon_n$	3 mm-mrad
Number of electrons $N$	$6 \times 10^9$
Bunch length $\sigma_t$	2 psec
Rf structure	$3 + \frac{1}{2}$ cell, $\pi$ -mode
Shunt impedance $ZT^2$	40 M $\Omega$ / m
Rf frequency	2856 MHz
Laser wavelength $\lambda$	248 nm
Cathode material	LaB <sub>6</sub>

Table 1: Parameters of SLAC LCLS photoinjector.

approximately one-half that dissipated in a similar, optimally cooled gun designed by Grumman and BNL[2].

The use of a high gradient standing wave accelerating field also mitigates the need for external focusing, due to the strong ponderomotive (alternating gradient, AG) rf focusing provided by the backward wave[3]. A design with a lower field in the initial half-cell was also studied, to enhance the rf focusing effect, and yield a smaller beam, with a smaller divergence at the exit of the gun.

### III. BEAM DYNAMICS

The beam dynamics in the gun were analyzed using the simulation codes PARMELA, which calculates the particle trajectories using an approximate (radiation free) treatment of the beam self-fields, and ITACA[4], an axisymmetric particle-in-cell (PIC) code which calculates the fully self-consistent electromagnetic cavity, space-charge and (radiation) wake-fields.

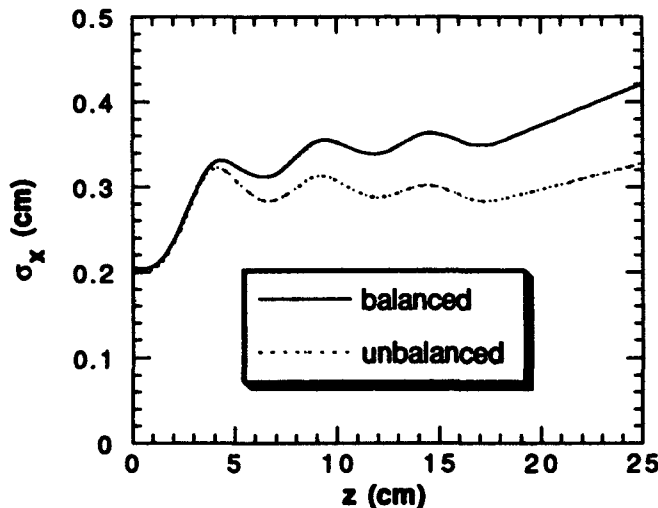


Figure 1: The rms transverse beam envelope, calculated by PARMELA, for the cases of equal (solid) and unequal (dots) field in half and full cells.

The behavior of the beam envelope, obtained from 1000 particle PARMELA simulations, is shown in Fig. 1. The dotted line corresponds to a uniform 100 MV/m field, and the AG rf focusing provided (which is equivalent to a solenoidal magnetic field of  $B_z = E_{rf} / \sqrt{2} = 2.3$  kG) controls the beam expansion inside of the gun. The exit of the gun is effectively a powerful unmatched defocusing lens of focal length  $f = 2E_b / E_{rf} = 20$  cm[5]. It is thus desirable to keep the beam even smaller at this point, which can be accomplished by using a smaller field at

half-cell, so that the kicks are unmatched at the first iris, and the focusing there is made stronger than the balanced AG focusing. This case is shown by the solid line, where the half-cell field amplitude is 82 MV/m, and the full cells are run at 108 MV/m. The beam size and divergence at exit of the gun are reduced by a factor of two over the balanced field case. These reductions are quite important, as too strong of focusing employed after the gun tends to give significant transverse emittance growth from chromatic effects.

These effects can also be minimized by controlling the energy spread at the gun exit. The longitudinal phase space at the gun exit, as calculated by PARMELA for an optimum initial launch phase of 62 degrees, is shown in Fig. 2. The energy spread in this case is  $\delta p / p = 0.18\%$ . This phase space distribution was used as input for the transport and longitudinal compression simulations performed by Seeman, *et al.*[6]

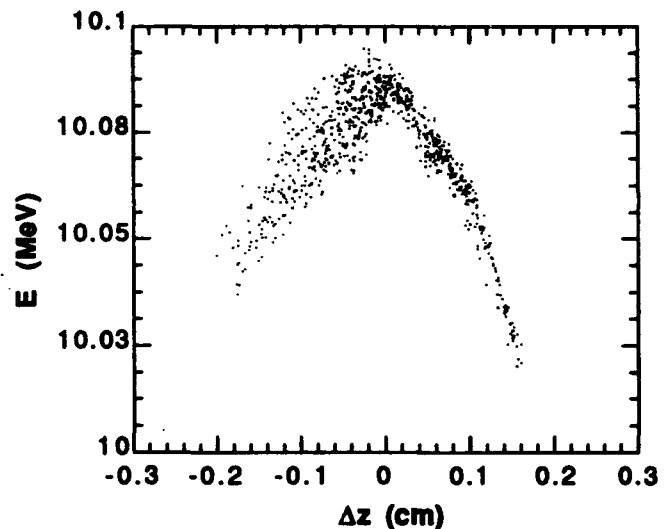


Figure 2: Longitudinal phase space at gun exit, from PARMELA simulation.

For the accurate calculation of the expected emittance the PIC code ITACA, with its lower inherent numerical noise level, was used. Several methods of tailoring the beam distribution were used to minimize the final emittance, including use of a longitudinally uniform beam pulse, and a cutoff transverse gaussian distribution. The latter can be trivially achieved by collimation; the former is perhaps more problematic, but might be achieved by use of a saturable optical element.

The normalized rms emittance calculated by ITACA using a nonoptimized beam distribution was 3 mm-mrad. If an optimized distribution[7], which employs a beam with a transverse gaussian cut-off at  $1.5\sigma$ , is used, then the transverse emittance is below 1.5 mm-mrad,

which is near the thermal limit. This is shown in Fig. 3. Only the dynamics in the first half of the gun, where nearly all of the emittance growth occurs, is shown. due to the excessive computing time demanded for analyzing the full structure.

The beam transverse dynamics after the gun are still investigation. The preservation of the emittance during subsequent transport and acceleration must be examined in detail. This region of the beamline does not just present a challenge in preserving emittance, however. There are schemes which have been studied and implemented[8] in which the space-charge derived emittance has been removed by appropriate beam transport.

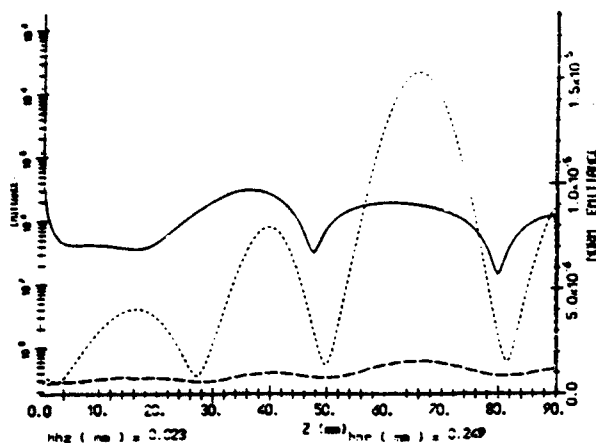


Figure 3: ITACA simulation of the evolution of the transverse rms emittance for the optimized beam distribution, in the first half of the gun. Shown: rms normalized (whole beam, solid; beam core, large dash) and unnormalized (small dash).

#### IV. LASER AND PHOTOCATHODE

The reproducibility of the x-ray pulse derived from the LCLS is critically dependent on the beam peak current. In order for the pulse compression to work properly, the beam's bunch-to-bunch charge fluctuations must be below one percent, and the timing jitter of initial injection (which is dependent on the laser) must be somewhat less than one picosecond (a degree of rf phase).

These requirements have not been met by photoinjectors in the past mainly because of difficulties associated with the laser. With the advances made recently in the technology of diode pumped solid-state, short pulse lasers, this may no longer be the case.

As an example of a system developed recently in industry, Lightwave Electronics has tested a diode pumped Nd:YLF regenerative amplifier which amplifies 1047 nm, 8 psec FWHM (3

psec rms) pulses derived from a mode-locked diode pumped Nd:YLF oscillator[9]. The oscillator produces a 500 kHz pulse train which has very small energy fluctuations, and which are, by a phase feed-back system, timing stabilized with respect to the rf phase to within 0.7 picoseconds. The energy output per pulse of the amplifier is 92  $\mu$ J, which after two stages of frequency doubling through nonlinear crystals, yields 10  $\mu$ J at 262 nm. The fluctuations in output energy, even with the nonlinear elements in the system, are at the 0.5% level.

In order for this laser to be useful for exciting a photocathode, the cathode material must have a relatively high quantum efficiency. Recent work by Bamford, *et al.*, [10] has shown that a quantum efficiency of 0.1% with 266 nm light at 45 degree incidence on a properly prepared  $LaB_6$  cathode is possible. This choice of cathode is well suited to our application, since it is rugged (like a relatively low quantum efficiency metal) but has no lifetime problems or stringent vacuum requirements (like a multi-alkali cathode). Using this cathode material and the Lightwave laser system, one can expect about 2.1 nC of charge, which is well above our design criterion.

Using these emerging technologies, this photoinjector design should be able to produce a high brightness electron beam which meets the stringent beam quality and jitter requirements of the LCLS project.

#### REFERENCES

1. H. Winick, *et al.*, these proceedings (abstract F7).
2. I. Lehrman, *et al.*, 1992 *Linear Accel. Conf., Proc.*, 280 (AECL-10728, Chalk River 1992).
3. S. Hartman and J. Rosenzweig, *Phys. Rev. E* 47, 2031 (1993).
4. L. Serafini, *et al.*, 1992 *Linear Accel. Conf., Proc.*, 796 (AECL-10728, Chalk River 1992).
5. R. Miller and R. Helm, in *Linear Accelerators*, ed. P.M. Lapostolle and A.L. Septier, 115 (North-Holland, Amsterdam, 1970).
6. J. Seeman, K. Bane, and T. Raubenheimer, these proceedings (abstract Jb19).
7. L. Serafini, *et al.*, 1992 *Linear Accel. Conf., Proc.*, 796 (AECL-10728, Chalk River 1992).
8. J. Gallardo and H. Kirk, these proceedings (abstract Pa150).
9. M. Gifford, *et al.*, *Optics Lett.* 17, 1788 (1992).
10. D. Bamford, *et al.*, *Nucl. Instr. Meth. A* 318, 377 (1992).

# Performance of the SLC Polarized Electron Source and Injector with the SLAC 3 km Linac Configured for Fixed Target Experiments\*

A. D. YEREMIAN, R. K. ALLEY, J. E. CLENDENIN, J. C. FRISCH, C. L. GARDEN, L. A. KLAISNER, A. V. KULIKOV, R. H. MILLER, C. Y. PRESCOTT, P. J. SAEZ, D. C. SCHULTZ, H. TANG, J. L. TURNER, M. B. WOODS  
M. ZOLOTOREV

Stanford Linear Accelerator Center  
Stanford, CA 94309

## Abstract

The SLC polarized electron source (PES) can be modified to produce  $\mu\text{sec}$ -long pulses for injection into the unSLEDded SLAC 3 km linac, with a duty factor considerably higher than for SLC. Such beams are desirable for fixed target experiments at SLAC requiring polarized electron beams of up to 50 mA within an energy spread of 0.5%, at energies of up to 26 GeV. During the fall of 1992, the SLAC linac was operated continuously for two months unSLEDded with the PES dye laser (715 nm) modified to produce a 1  $\mu\text{sec}$  pulse at 120 Hz. An AlGaAs photocathode was installed in the electron gun to achieve 40% polarization, and a prebuncher was added to the SLC injector to improve capture for long pulse beams. We discuss the performance of the polarized electron beam for long pulse operation.

## I. INTRODUCTION

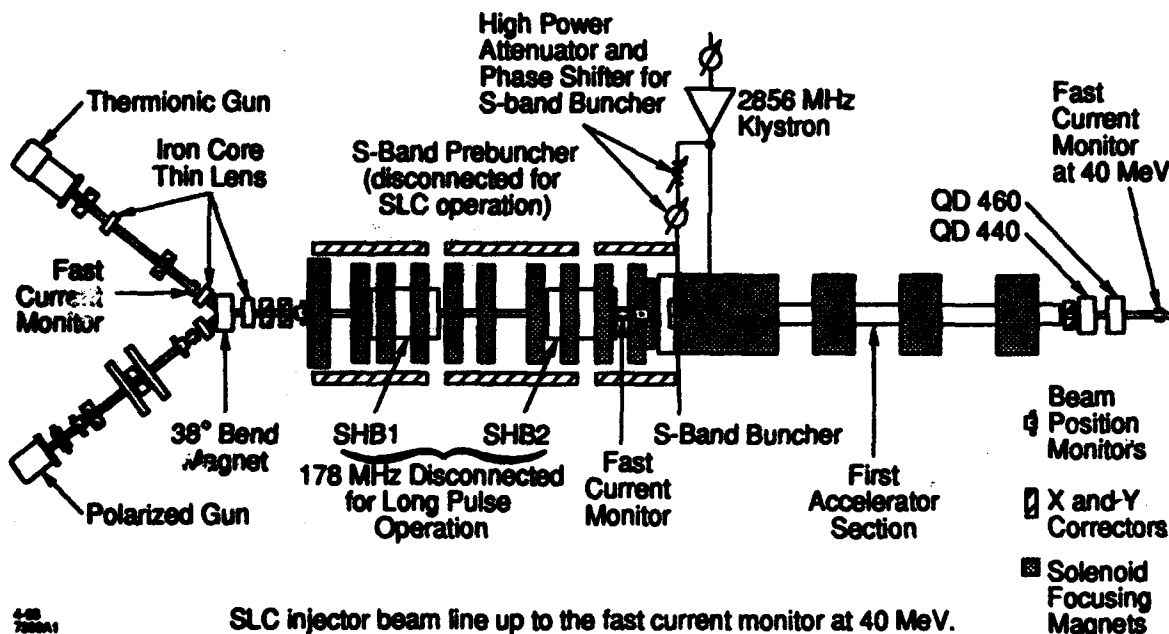
A fixed target experiment (E-142) was conducted at SLAC for which a 1–2  $\mu\text{sec}$  electron pulse of 10–20 mA at

the target at a repetition rate of 120 Hz and with at least 40% polarization was required. To accommodate these requirements, the Candela dye laser at the SLC Polarized Electron Source (PES) was modified to produce a low intensity laser pulse  $>1 \mu\text{sec}$ . To improve the electron capture by the injector, an S-band pre-buncher was installed upstream of the S-band buncher and capture section. The layout of the polarized gun and the first few meters of the beam line are shown in Fig. 1.

The PES was operated at 60 kV to produce a 1  $\mu\text{sec}$ , 30 mA electron pulse at 120 Hz from the source.

## II. LASER

The Candela flash lamp-pumped dye laser used for the SLC 1992 run was modified to produce a pulse width  $>1 \mu\text{sec}$  (Ref. 1). This was accomplished by decreasing the laser cavity losses by making two changes: 1) the dye concentration was reduced from 3 to  $2 \times 10^{-4}$  mol/l; and 2) the reflectivity of the output coupler was increased from 55% to 80%. The laser output



SLC injector beam line up to the fast current monitor at 40 MeV.  
Figure 1. SLC injector beam line up to the fast current monitor at 40 MeV.

\*Supported by Department of Energy contract DE-AC03-76SF00515.

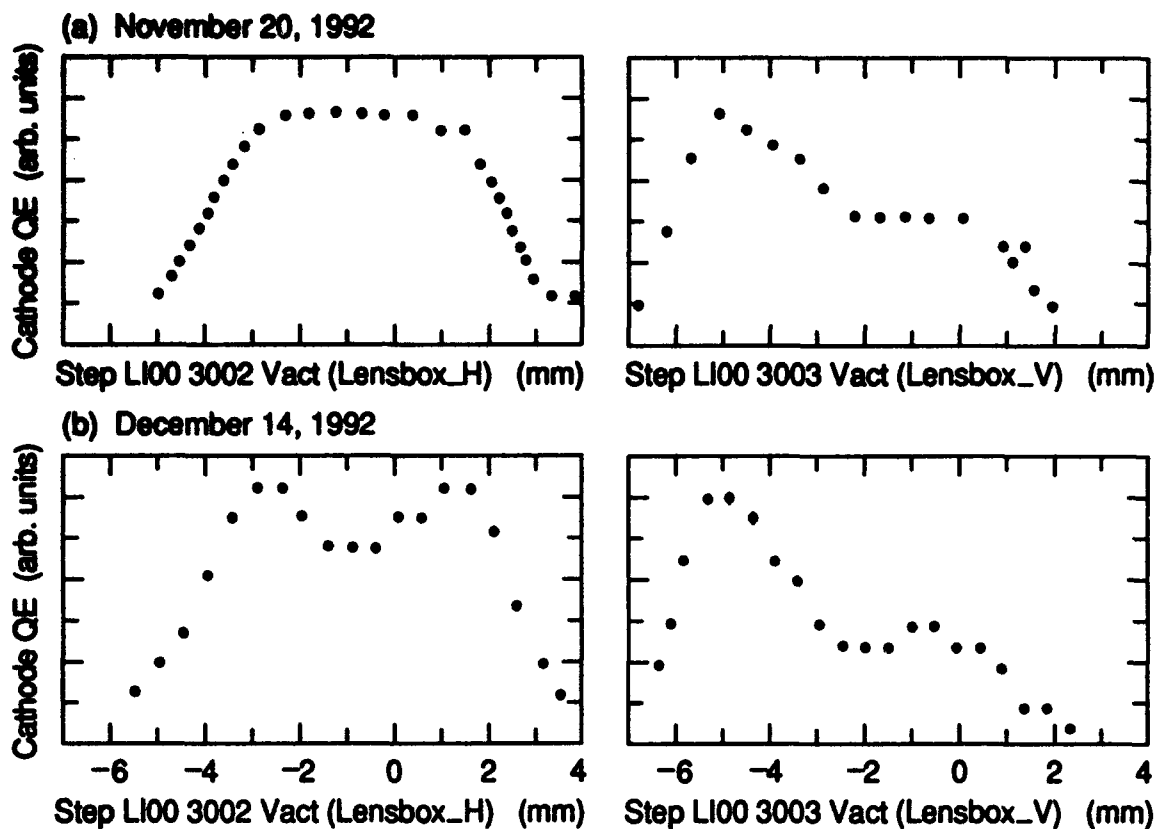


Figure 2. Horizontal (LENSBOX H) and Vertical (LENSBOX V) QE scans of the cathode.

pulse was chopped and flat-topped with a pulsed-Pockels cell and crossed-polarizer system, TOPS (Top Hat Pulse Shaper), to produce the desired light pulse. Although the system was capable of producing a 2  $\mu\text{sec}$  long pulse under optimum conditions, during the E-142 run, the laser was operated in the 1.0–1.3  $\mu\text{sec}$  range. A fast pulser, LPC (Laser Pulse Chopper), upstream of TOPS, could produce a narrow SLC-type pulse that was detectable by the SLC linac beam position monitors. Normally the short pulse was run at 1 Hz with the production pulse operating at 119 Hz. To optimize laser power and dye lifetime, the Candela was operated at 715 nm with Oxazine 720.

### III. CATHODE

The active layer of the photocathode was 0.3 mm of  $\text{Al}_{0.12}\text{Ga}_{0.88}\text{As}$ , Be doped to  $6 \times 10^{18} \text{ cm}^{-3}$ . At final activation of the cathode by heat cleaning and cesiation the initial quantum efficiency (QE) was 1.5% at 750 nm (at low V), rapidly dropping to 0.8% (at 60 kV). The cathode temperature throughout the run was maintained at 0°C, which in the SLC gun is thought to increase the lifetime of the cathode. The gun for this run was Diode Gun 1.

For the SLC 1992 run, a thick GaAs cathode was used, for which the bandgap at 0°C is about 1.44 eV (860 nm) (Ref. 2). At 715 nm, the polarization at the source was ~27%. For E-142 the expected polarization at the source was increased by using a cathode with a larger bandgap.

Adding 12% Al to the active layer increases the bandgap at 0°C to about 1.63 eV (760 nm). By using a 0.3 mm thick  $\text{Al}_{0.12}\text{Ga}_{0.88}\text{As}$  cathode operated at 0°C, the source polarization at 715 nm was expected to be ~40% (Ref. 3). The typical electron polarization measured by Møller in End Station A (ESA) was 41%.

During the entire run the QE did not change significantly. The QE profile across the cathode surface started with a large peak on the "+" vertical side. Near the end of the run, a dip in the middle of the horizontal scan was observed (see Fig. 2). The horizontal (LENSBOX\_H) and vertical (LENSBOX\_V) scans of the cathode were made with a HeNe laser (spot diameter ~2 mm) on November 20th and December 14th. The abscissa indicates motion of the lens box in mm.

The average QE as measured at 60 kV with a modulated diode laser operating at 750 nm varied over a period of many days between 0.7% and 0.9%. These variations may have been entirely instrumental.

It is not known why the QE held constant. Certainly the lower voltage helped. The dark current at HV (laser blocked) was typically about 10 nA, a factor of 5 to 10 lower than during SLC 1992 run (for which the voltage was 120 kV with a different gun). The gun vacuum was also extremely low: the mass 4 (28) peak was about  $6(1) \times 10^{-12}$  Torr, unchanged with HV on or off. The low peak currents (compared to SLC 1992) may have helped reduce electron stimulated molecular desorption from the

vacuum components near the source cathode. All the vacuum components except the cathode were at about 35°C, the temperature of the accelerator housing.

## V. ELECTRON BEAM INTENSITY

The laser beam intensity at the cathode was kept constant by a hardware feedback system integral to TOPS. To compensate for changes in the QE, provision was made for a software feedback system which monitored the electron beam intensity at the first BPM (Beam Position Monitor) and could adjust the attenuation of the laser beam using the BIC (Bunch Intensity Control) located just downstream of TOPS. Since the QE was essentially constant, the software feedback was not activated, the BIC being adjusted only occasionally and in manual mode in response to changed beam requirements or sometimes, near the end of a lamp/dye cycle, when TOPS could no longer provide the desired laser intensity.

Since E-142 was the first fixed target experiment with the full SLC linac, it is perhaps not surprising that although the instrumentation for tuning the beam was adequate, it was not optimal. Midway into the run, the transmission of the beam from the polarized gun cathode to the beam switchyard through the 0.7% energy defining slits was increased from 25% to 55%. This was accomplished by adjusting the injector bunching and steering using the entire linac as a monitor.

For most of the experiment, the Candela beam diameter on the cathode was maintained at about 6 mm. (The active area of the cathode has a diameter of 14 mm.) Thus the maximum current density drawn from the cathode was about  $0.2 \text{ A cm}^{-2}$ .

The Candela is a multimode laser with an intensity jitter of 3 to 4%. TOPS reduced this jitter by about a factor of  $\sim 2$ . The electron beam intensity jitter as measured on the linac toroids at 40 and 200 MeV was typically the same as the laser jitter at the TOPS output.

## V. SUMMARY

There were about 1062 total hours in the E142 run. The PES was available to provide full intensity beams to the linac for 96% of that time. The downtime attributed to the PES totaled only 41 h, of which 32 h were associated with scheduled lamp and dye changes followed by restoration of the injector beams.

The timing of the lamp and dye changes was driven by downtimes scheduled as part of the turn on for the SLC 1993 run, and thus was not optimum for PES efficiency. Nonetheless, the average interval between these changes was about 200 h (8.4 days).

Other than for maintenance tasks such as lamp and dye changes, the PES was operated entirely from the SLC Main Control Center by the SLC operators.

## REFERENCES

1. "Polarized Light Sources for Photocathode Electron Guns at SLAC," M. Woods, J. Frisch, K. Witte, M. Zolotarev, Dec. 1992, SLAC PUB 5965, submitted to the 10-th Int. Symp. on H.E. Spin Physics, Nagoya, Japan (1992).
2. "Polarized Source Performance in 1992 for SLC-SLD," D. Schultz, R. Alley, J. Clendenin, J. Frisch, C. Garden, E. Hoyt, L. Klaisner, A. Kulikov, C. Prescott, P. Saez, H. Tang, J. Turner, M. Wicks, M. Woods, D. Yeremian, M. Zolotarev, February 1993, SLAC-PUB-6060, submitted to the 10-th Int. Symp. on H.E. Spin Physics, Nagoya, Japan (1992).
3. "Electron Spin Polarization in Photoemission From the Thin  $\text{Al}_x\text{Ga}_{1-x}\text{As}$ ," T. Maruyama, E. L. Garwin, R. A. Main, R. Prepost, J. S. Smith, J. D. Walker, SLAC-PUB-5367, 1992, to be published in Journal of Applied Physics.

# An In-situ Photocathode Loading System for the SLC Polarized Electron Gun

R. E. Kirby, G. J. Collet, K. Skarpaas  
Stanford Linear Accelerator Center  
Stanford, CA 94309 USA

## Abstract

An ultra-high vacuum loadlock system capable of operating at high voltage has been added to the SLC Polarized Electron Gun. The unit incorporates facilities for heat cleaning, activating and measuring the quantum efficiency of photocathodes. A tray of up to four photocathodes can be exchanged without bringing the activation unit or gun up to atmosphere. Low voltage quantum efficiencies of 20% have been obtained for bulk GaAs at 633 nm and 6% for a 0.3 micron GaAs layer at 755 nm. Results for other cathodes as well as operational characteristics are discussed.

## I. INTRODUCTION

Polarized laser photoemission from GaAs, or related III-V compound, photocathodes form the basis for most polarized electron sources currently in use. Extremely clean vacuum conditions are required to extend the usable lifetime of these cathodes between re-activations. In addition, sources such as the SLC Polarized Electron Gun (PEG) [1] must function under high voltage conditions (peak fields of  $\sim 10\text{kV/mm}$ ). A high voltage discharge occurring in the gun is capable of irreversibly damaging the cathode, an event which is enhanced by the presence of Cs used to activate the photocathode to negative-electron affinity. In the past, the PEG has been baked and high voltage-processed to eliminate breakdown sites on the gun electrodes. The cathode was then installed and the gun re-baked. It has been shown [2] that baking reactivates some breakdown sites, requiring re-processing with potential for cathode damage. Also, we have observed that quantum efficiencies (QE) tend to be higher for cathodes that have not been baked in large systems for long time periods. Cathode replacement requires a lengthy and expensive reprocessing of the gun itself.

A cathode-loading system ("LoadLock") has been added to the PEG to address the concerns detailed above, but its use also adds a valuable capability to the polarized source program: As new, higher polarization cathodes become available, they may be easily introduced into the PEG operating on the accelerator. This approach has proven immediately successful with a thin GaAs strained-layer cathode structure [3].

## II. OPERATIONAL REQUIREMENTS

Two identical LoadLock units were constructed: one for use at the SLC injector and the second at the Gun Test Facility which consists of a PEG, laser and duplicate electron beam line

\*Supported by Department of Energy contract DE-AC03-76SF00515.

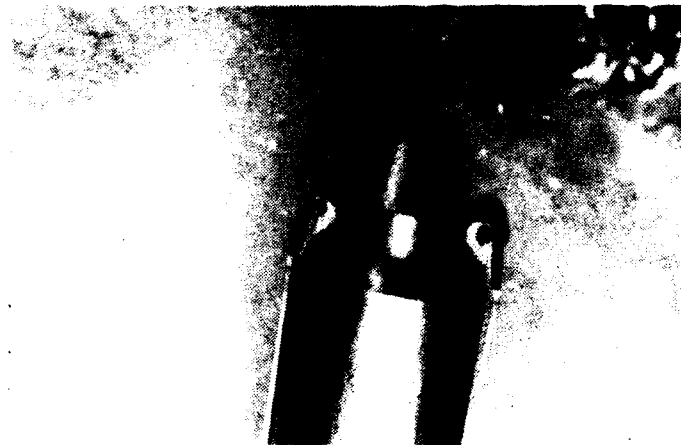


Figure 1. Cathode emitter tube. Mo leaf springs with sapphire roller bearings engage carrier tightly onto the plug end.

up to the first bend magnet. Each LoadLock and PEG incorporates an isolation valve, allowing each to remain independently under vacuum. Connection is via a low-volume short spool piece which can be evacuated and baked-out in a few hours. The functional requirements defined for LoadLock were:

- Heat clean and activate cathodes to negative-electron-affinity using Cs and  $\text{NF}_3$ .
- Measure quantum efficiency.
- Preserve ability to cool the cathode to  $0^\circ\text{C}$  while in the PEG.
- Vacuum environment consistent with that of the PEG.
- Require no changes to PEG electron optics.
- Be able to introduce cathodes into LoadLock for use in PEG, preferably without bringing LoadLock itself up to atmospheric pressure.

The cathode cooling requirement has been satisfied by preserving the PEG cathode emitter tube design without modifying the gun structure. The photocathode is mounted on the vacuum side of the tube, and cooling gas is injected from the atmosphere side [4]. Cooling has been useful for extending the period between re-cesiation of cathodes. This requirement, however, means that the LoadLock unit itself is at cathode high voltage during electron beam injection.

## III. LOADLOCK DESIGN

The structure of LoadLock consists of three sub units: mechanical drive, cathode activation chamber, and cathode tray. Cathode wafers are mounted onto individual Mo carriers using a Ta ring clamp. The carriers can be shuttled between the emitter tube (Fig. 1) and the cathode tray (Fig. 2) using a system of bellows-sealed linear motions.



Figure 2. Photocathode carrier tray shows both a position occupied by a Mo wafer carrier (1) and an empty position (2).

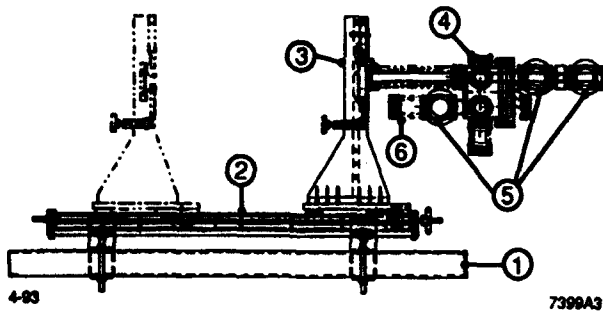


Figure 3. Mechanical drive. 1-Support beam, 2-Rail, 3-Emitter tube transfer assembly, 4-Activation chamber (services not shown), 5-Isolation valves, 6-Carrier tray, Item 3 also shown in emitter tube-retracted position for cathode activation/exchange (dashed).

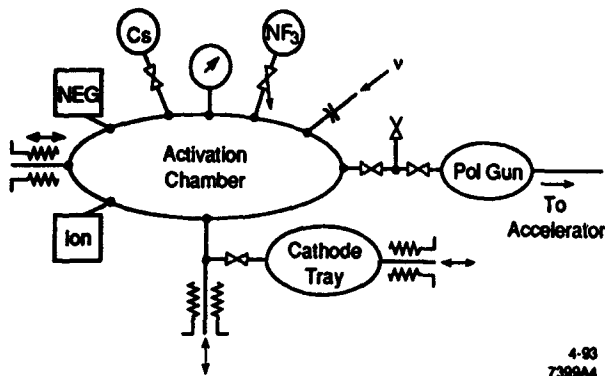


Figure 4. Schematic structure of LoadLock.

The main mechanical drive (Fig. 3) moves the emitter tube through the activation chamber and into the PEG. After insertion, the drive unit is removed and the remaining LoadLock components are enclosed by a corona shield and a high voltage insulating gas containment vessel. After several hours of dry air flow-through, the unit continually stands off a 120kV potential.

Figure 4 is a schematic of the services available in the cathode activation chamber. The activation chamber is pumped

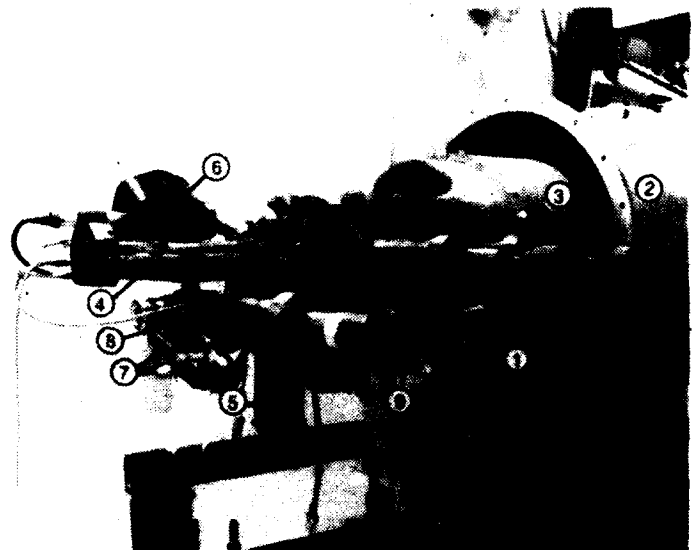


Figure 5. LoadLock attached to the PEG. 1-Isolation valves, 2-Part of HV gas container, 3-G10 support cylinder, 4-Emitter tube and bellows, 5-Cathode exchange linear motion, 6-Ion pump, 7-NEG pump, 8-Cathode tray, corona shield and high voltage container not shown.

by a combination of an 8 l/s diode ion pump (powered by a fiber-optic-isolated supply) and by a room temperature ST707 non-evaporable-getter pump [5]. The residual gas composition is >99.9% H<sub>2</sub> at a pressure of <1x10<sup>-10</sup> torr. A gas heater unit inserted into the emitter tube allows heating of SLC 15 mm diameter cathodes to ~600°C. During heating, the evolved gas (>99%) is H<sub>2</sub>, which has been shown [6] to be beneficial for removing oxides and hydrocarbons from GaAs surfaces. A completed LoadLock unit connected to a PEG at the Gun Test Facility is shown in Fig. 5.

The cathode tray is separated from the activation chamber by an isolation valve so that a total of four carriers may be used in LoadLock. A laser alignment screen in a carrier is occasionally used for system alignment and then removed from PEG for cathode replacement. The tray stays connected to, and is pumped by, LoadLock during operation.

#### IV. PERFORMANCE

LoadLock units were tested in two stages: initially by connection to a simple vacuum chamber containing a cathode-anode electrode structure, photo-electron current collector and light window, and finally, by connection to a PEG at the Gun Test Facility. Bulk GaAs(100) was used in the first system. QE's and life times were measured down to 0°C. QE's as high as 20% at 633 nm and 9% at 755 nm were achieved with life times at 0°C, identical to previous PEG performance [4].

Measurements at the Gun Test Facility concentrated on thin GaAs (300 nm) and 300 nm GaAs strained-layers. The latter were used on the accelerator when the first LoadLock/PEG combination was moved into operation. The thin GaAs QE at 120kV was 6% at 755 nm, measured at the Gun Test Facility. Full details of SLC cathode performance are reported elsewhere [3], but the current LoadLocked SLC strained-layer

cathode on the linear accelerator produces 80% polarization and ~1% QE at 830 nm, 120kV.

## V. CONCLUSION

The addition of LoadLock to the SLC electron source has resulted in a marked improvement in source capability and reliability. Large amounts of Cs, associated with high voltage breakdown, have been excluded from the gun. A small channel cesiator has replaced the effusion cell on the gun proper. This allows remote additions of Cs to the cathode during the running cycle when a full re-activation is not required. LoadLock has also allowed a rapid upgrade of source polarization from the 28% of the 1992 SLC/SLD experimental program toward 80% in 1993.

## VI. REFERENCES

- [1] D.C. Schultz, J. Clendenin, J. Frisch, E. Hoyt, L. Klaisner, M. Woods, D. Wright and M. Zolotarev, "The Polarized Electron Gun for the SLC," 3rd European Particle Accelerator Conference, Berlin, 1992.
- [2] S. Bajic and R.V. Latham, "A New Perspective on the Gas Conditioning of High-Voltage Vacuum-Insulated Electrodes," *Journal of Physics D* 21, 943 (1988).
- [3] J. E. Clendenin, R.K. Alley, H. Aoyagi, J.C. Frisch, C.L. Garden, E.W. Hoyt, R.E. Kirby, L.A. Klaisner, A.V. Kulikov, C.Y. Prescott, P.J. Sáez, D.C. Schultz, H. Tang, J.L. Turner, M. Woods, A.D. Yeremian and M.S. Zolotarev, "Performance of the SLC Polarized Electron Source with High Polarization," these proceedings.
- [4] D. Schultz, R. Alley, J. Clendenin, J. Frisch, C. Garden, E. Hoyt, L. Klaisner, A. Kulikov, C. Prescott, P. Sáez, H. Tang, J. Turner, M. Wicks, M. Woods, D. Yeremian, and M. Zolotarev, "Polarized Source Performance in 1992 for SLC-SLD," 10th Int. Symp. on High Energy Spin Physics, Nagoya, 1992.
- [5] SAES Getters U.S.A., Inc., Colorado Springs, CO 80906.
- [6] R.W. Bernstein and J.K. Grepstad, "Removal of the Surface Contamination Layer From CF<sub>4</sub> Plasma Etched GaAs(100) Substrate by Thermal Annealing in Hydrogen," *J. Appl. Phys.* 98, 4811 (1990).

# HIGH VOLTAGE PROCESSING OF THE SLC POLARIZED ELECTRON GUN\*

P. SÁEZ, J. CLENDENIN, C. GARDEN, E. HOYT, L. KLAISNER,  
C. PRESCOTT, D. SCHULTZ, AND H. TANG  
Stanford Linear Accelerator Center  
Stanford, CA 94309 USA

## Abstract

The SLC polarized electron gun operates at 120 kV with very low dark current to maintain the ultra high vacuum (UHV). This strict requirement protects the extremely sensitive photocathode from contaminants caused by high voltage (HV) activity. Thorough HV processing is thus required. X-ray sensitive photographic film, a nanoammeter in series with the gun power supply, a radiation meter, a sensitive residual gas analyzer and surface x-ray spectrometry were used to study areas in the gun where HV activity occurred. By reducing the electric field gradients, carefully preparing the HV surfaces and adhering to very strict clean assembly procedures, we found it possible to process the gun so as to reduce both the dark current at operating voltage and the probability of HV discharge. These HV preparation and processing techniques are described.

## I. INTRODUCTION

The polarized electron gun is essential for a new series of experiments at SLAC [1]. It uses a cesium activated GaAs photocathode to produce a longitudinally polarized electron beam which is injected into the accelerator. The activated photocathode is extremely sensitive to contamination and so must reside in an UHV environment (total pressure  $\sim 2 \times 10^{-11}$  Torr). HV of 120 kV is required to produce a sufficiently high intensity electron beam and to properly inject the electrons into the accelerator. These conditions must coexist in a gun that will operate continuously for several months with minimal intervention.

The early SLC polarized guns (prior to 1992) had unacceptable HV problems. A single HV breakdown can reduce the QE [2] in the photocathode. Reactivation, as opposed to mere cesiation, is often required to restore the QE and is not always successful in doing so. High pressure levels associated with high dark current accelerate the drop in QE with time. We will first discuss how we diagnosed some of the HV problems and then describe the material preparation and HV processing techniques that have given us stable and reliable guns.

## II. DIAGNOSTICS

One of the major sources of high voltage breakdown is field emission from metal surfaces. At very high electric fields ( $E \sim 3 \times 10^9$  V/m) the surface potential barrier for metals is small and thin enough for electrons to tunnel out, producing field emission [3]. Figure 1 shows the inside structure of the gun. EGUN [4]

\* Work supported by Department of Energy contract DE-AC03-76SF00515.

simulation of the gun electrodes gave a maximum electric field of  $7 \times 10^9$  V/m on the cathode electrode [5] at 120 kV. Microscopic surface irregularities and/or contaminants can enhance this electric field in such a way to produce field emission [3].

A nanoammeter in series with the gun HV power supply was used to study the behavior of the gun dark current at high voltage. Figure 2 shows that these data are well represented by a Fowler-Nordheim form, where the slope of the curve indicates an electric field enhancement of  $\beta \sim 500$  at the field emitting point.

The field emitted electrons are accelerated to the anode surfaces where they desorb gases and generate x-rays. Figure 3 shows the spectrum of x-rays emitted from the electrode region at 110 kV. The data approximate a Bremsstrahlung energy loss distribution. X-ray sensitive photographic film [6] was used to map the x-ray emitting sites inside the gun. X-rays going through a small aperture on a lead plate fiducial, external to the gun, would cast an image on film arranged around the electrode area. Multiple small spots on the film indicated that the field emitting sources were discrete point sources. Ray tracing analysis showed that most field emitting points came from the cathode electrode and the cathode electrode support tube.

Surface samples taken from a gun after HV processing were viewed under a microscope and analyzed using an energy dispersive x-ray spectrometer (EDAX). Figure 4 shows the copper surface of the cathode electrode support tube in Gun #1. The highly polished copper surface has been disturbed, probably by ion bombardment during HV nitrogen processing (see below). Figure 5 shows a fragment of stainless steel on the polished cathode electrode, presumably the

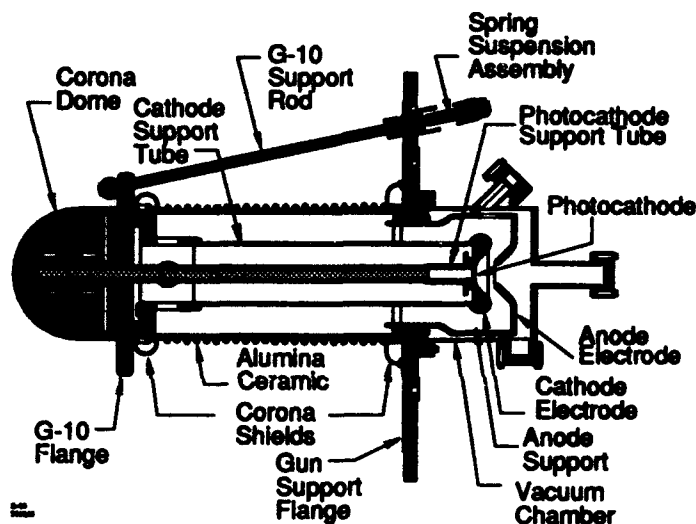


Figure 1. Schematic of the polarized electron gun.

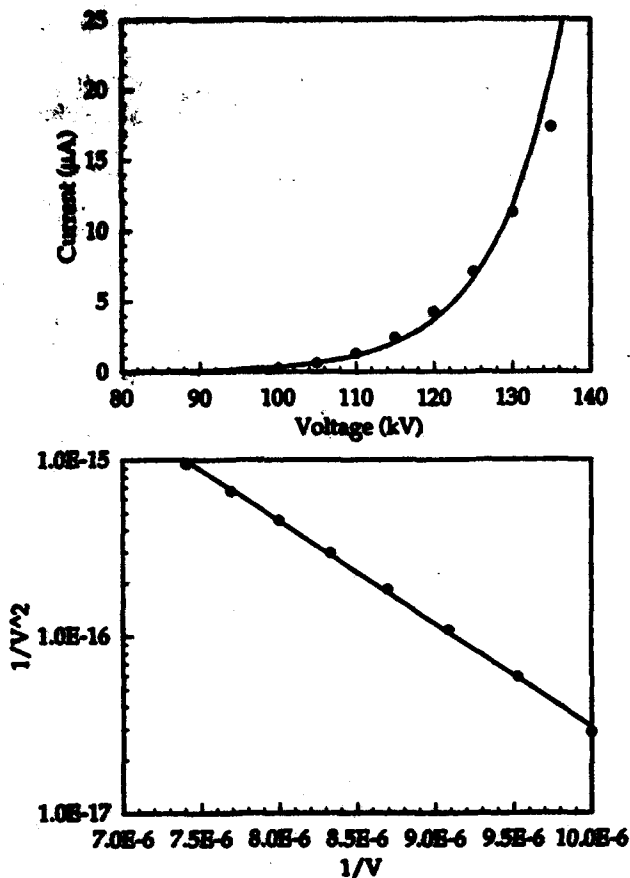


Figure 2. (a) Current versus voltage plot for Gun #3 (b) Fowler-Nordheim plot for Gun #3 with electric-field enhancement of  $\beta \sim 500$ .

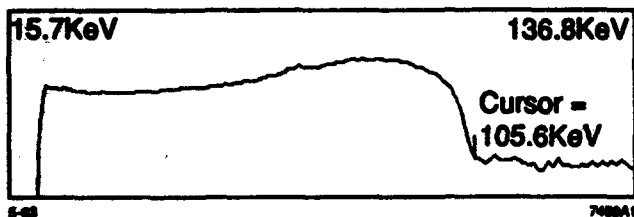


Figure 3. Energy distribution of emitted x-rays for 110 kV.

fragment is a remnant from HV arcing. Figure 6 shows evidence of HV arcing activity on a polished electrode surface contaminated with potassium chloride. The potassium chloride contamination must have been introduced during the gun assembly.

Fowler-Nordheim plots and spectra of emitted x-rays indicate that the HV activity comes from electron field emission. The EGUN simulation and xray film analysis point to the electrode area as the source of these electrons. The EDAX study shows that contamination during assembly can harm the HV performance.



Figure 4. Copper surface of cathode support tube.

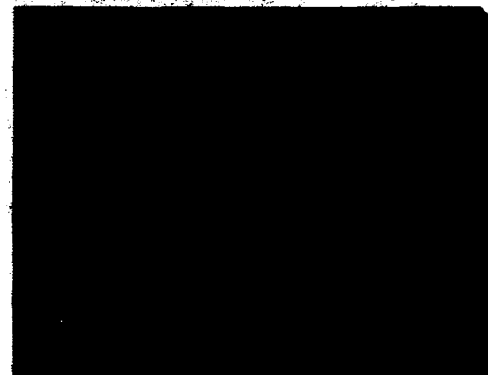
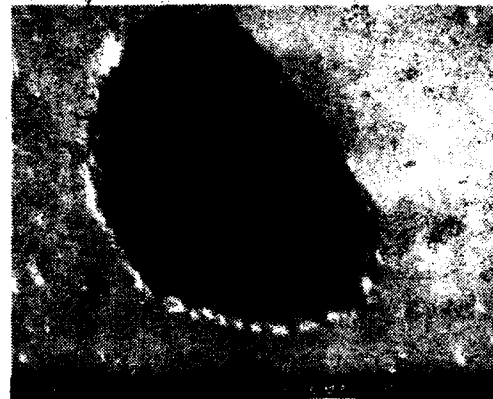


Figure 5. (a) Stainless steel fragment on polished cathode electrode and (b) EDAX plot of fragment contents.

### III. MATERIAL PREPARATION

Selection and preparation of materials to be used for high field areas is critical. The material used in these areas is certified low carbon vacuum arc remelted stainless steel 304, 316, and on the electrodes 317. All tubing was seamless stainless steel 304L or 316L. Samples of these materials were metallographically evaluated for inclusion content and grain size. After the electrodes are machined using UHV procedures, they are chemically cleaned and hydrogen fired to 1050°C for 10 minutes. Then they are polished to a one micron finish. The material is cleaned again, inspected and

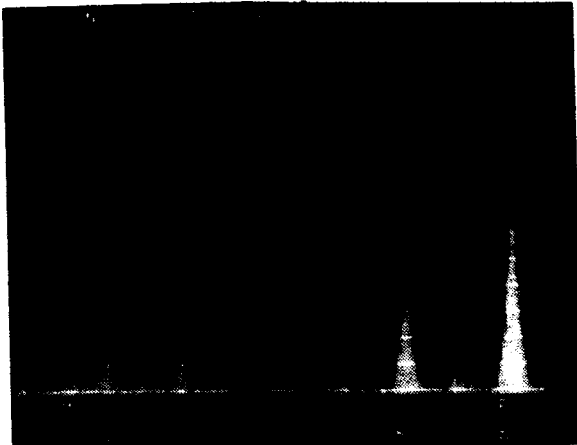
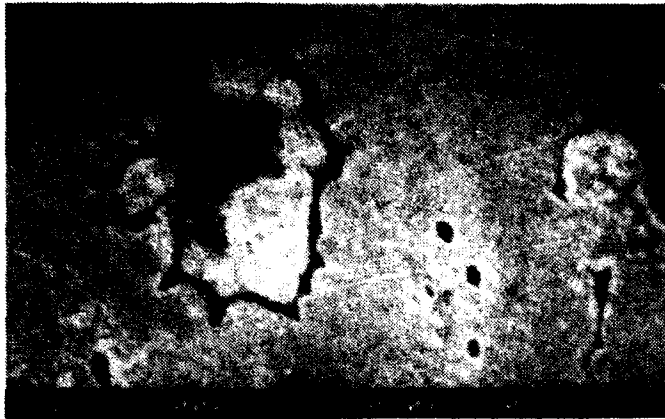


Figure 6. (a) High voltage arcing activity on polished electrode surface and (b) EDAX plot showing contamination with potassium chloride.

vacuum fired at 450°C until outgased. Finally we inspect the surfaces, and assemble all the components in a class 1000 clean room. Extreme cleanliness is emphasized throughout the process. Fixtures made of teflon are used for holding components during transport and extreme care is taken to prevent any contact with polished surfaces. The gun assembly is baked at 250°C for a minimum of 100 hours until outgased. The gun is then ready for high voltage processing.

#### IV. HIGH VOLTAGE PROCESSING

The gun HV processing is intentionally conservative; we minimize the amount of dark current ( $< 20 \mu\text{A}$ ) to prevent permanent damage to the electrode structure. The main diagnostics used during processing are the nanoammeter in series with the HV power supply, a xray detector, and a Residual Gas Analyzer (RGA) which measures the partial pressures of gas species in the gun vacuum.

Our experience with HV processing of the guns has been as follows. The voltage is slowly raised to 60 kV with only minor discharge (spikes in the current together with small, short bursts of CO, H, and other gases). Above  $\sim 60$  kV the guns start drawing 1-20  $\mu\text{A}$  of current. Constant voltage is maintained until the current

decreases, which may occur gradually or may occur suddenly after a HV discharge. To attain a dark current of less than 50 nA at the operating voltage of 120 kV, the guns are processed to 180 kV. The rate of raising the voltage varies, taking from a few hours to a few days. One technique that speeds the processing is to introduce dry nitrogen from liquid nitrogen boil-off into the gun to  $10^{-6}$  Torr. When processing with nitrogen, 180 kV can be reached in a few hours [7].

Gun #3 showed unusually good behavior. It had very few arcs during the initial processing. After introducing and then pumping out some nitrogen without HV, the gun achieved 180 kV in just one hour with much less than 1  $\mu\text{A}$  of dark current [8]. The other guns were more problematic and needed a few days of HV processing.

#### V. CONCLUSION

Good HV performance of the SLC guns begins with a design of low electric field gradients, continues with the choice of the cleanest materials and their proper outgasing at high temperature bakes, and ends with careful monitoring of dark current, xrays and gas pressures. The assembly process requires extreme cleanliness to optimize HV performance as well as UHV performance. The chief diagnostics, the nanoammeter and the RGA, are used on the accelerator during beam operations to keep track of the dark current, the ultra high vacuum and any high voltage problem that might occur. At present there are three guns which can operate at 120 kV, with a total pressure of  $\sim 2 \times 10^{-11}$  Torr and a dark current of 10-50 nA.

#### REFERENCES

- [1] Moffeit, K. C., "Polarized Electron Beams at SLAC", SLAC-PUB-6005 (1992).
- [2] Quantum efficiency or photoelectron yield is the number of emitted electrons per incident photon.
- [3] Latham, R. V., "High Voltage Vacuum Insulation: The Physical Basis", Academic Press, London (1981).
- [4] Herrmannsfeldt, W. B., "EGUN- An electron optics and gun design program", SLAC-REPORT-331 (1988).
- [5] Schultz, D., et al., "The Polarized Electron Gun for the SLC," SLAC-PUB-5768 (1992), Proceedings of the Third European Particle Accelerator Conference, Berlin, (1992).
- [6] Polaroid TPX System, Polaroid Corporation.
- [7] Pure xenon was also used in HV processing.
- [8] Following processing, gun #3 was used for the 1992 SLC-SLD run. See Schultz, D., et al., "Polarized Source Performance in 1992 for SLC-SLD", SLAC-PUB-6060 (1993).

# Study of Non-Linear Photoemission Effects in III-V Semiconductors\*

H. Tang, R.K. Alley, H. Aoyagi<sup>†</sup>, J.E. Clendenin, J.C. Frisch, C.L. Garden, E.W. Hoyt, R.E. Kirby, L.A. Klaisner, A.V. Kulikov, C.Y. Prescott, P.J. Saz, D.C. Schultz, J.L. Turner, M. Woods, and M.S. Zolotarev  
Stanford Linear Accelerator Center, Stanford University, Stanford, CA 94309, USA

## Abstract

Our experience at SLAC with photoemission-based polarized electron sources has shown that charge limit is an important phenomenon that may significantly limit the performance of a photocathode for applications requiring high intensity electron beams. In the process of developing high performance photocathodes for the ongoing and future SLC high energy physics programs, we have studied the various aspects of the charge limit phenomenon. We find that the charge limit effect arises as a result of non-linear response of a photocathode to high intensity light illumination. The size of the charge limit not only depends on the quantum efficiency of the cathode but also depends critically on the extraction electric field. In addition, we report the observation of charge oversaturation when the intensity of the incident light becomes too large.

## I. INTRODUCTION

Polarized electron beams have been in continuous use for the SLC high energy physics program at SLAC since the spring of 1992 [1,2]. The polarized electrons are generated by the Polarized Electron Source (PES) consisting of an electron gun with a GaAs-based photocathode and a laser operated near the cathode band gap. In addition to the requirement of high polarization, the SLC program also demands high beam intensities, i.e., two 2 ns electron bunches separated by 60 ns with up to  $10^{11}$  electrons in each. The gun is operated at 120 kV so that the amount of charge extractable in the space charge limit is about  $1.2 \times 10^{11}$  electrons per bunch for a fully illuminated photocathode (14 mm diameter), which is well above the desired intensity. If a photocathode responds linearly to the excitation light intensity, then, the amount of photoemitted charge will increase proportionally with the light intensity until the space charge limit is reached. In contrast to this expectation, earlier studies [3] indicated that, when the quantum efficiency (QE, defined as the ratio of the number of emitted electrons over the number of incident photons) of the cathode drops below a certain level, the total amount of charge extractable within 2 ns from a fully illuminated cathode saturates to a value that is smaller than the space-charge limited value, a phenomenon becoming known as charge limit (CL). We report in this paper a more detailed study of this nonlinear effect and other important properties in a variety of III-V semiconductor photocathodes.

## II. EXPERIMENTAL

All of the experiments were performed by using the Gun Test Facility at SLAC which is essentially a duplicate of the first few meters of the SLC injector. The facility consists of a polarized electron gun with a loadlock system for easy cathode change [4], a YAG-pumped pulsed Ti:Sapphire laser tunable between 750 nm and 870 nm [5], and an electron

beam line with a beam position monitor, a fast gap monitor and a Faraday cup. Very high vacuum is maintained in the gun by means of nonevaporative getter pumping as well as ion pumping. A residual gas analyzer (RGA) is used to monitor the gun vacuum. During normal operation, the total pressure in the gun is about  $1 \times 10^{-11}$  Torr and the CO level is about  $1 \times 10^{-12}$  Torr. A large number of III-V semiconductor photocathodes were studied, including 0.3  $\mu$  strained lattice (high polarization) GaAs/GaAs<sub>0.76</sub>P<sub>0.24</sub>, 0.3  $\mu$ , 1  $\mu$ , and bulk GaAs, and 0.3  $\mu$  Al<sub>0.12</sub>Ga<sub>0.88</sub>As, where the thickness refers to the active layer, all doped with either Be or Zn to a concentration of  $5 \times 10^{18}$  to  $2 \times 10^{19}$  /cm<sup>3</sup>. The cathodes are activated by first heating to 610 °C for one hour, then applying Cs until the photocurrent peaks, and followed by codeposition of Cs and NF<sub>3</sub>. Two continuous wave diode lasers of wavelengths 750 nm and 833 nm operated at low power (< 1 mJ) were used for QE measurements. Unless otherwise stated, the cathode temperature was always kept at 0 °C. All of the data presented below are obtained from the 0.3  $\mu$  strained GaAs cathode, whose results are qualitatively representative of those of the other cathodes.

## III. RESULTS AND DISCUSSION

Figure 1 shows the charge versus laser pulse energy data, or saturation curve, for the 0.3  $\mu$  strained GaAs cathode. The Ti:Sapphire laser is tuned to a wavelength of 850 nm for the measurement. The QE is 1.51% and .57% at 750 nm and 833 nm, respectively, measured with the laser spot fully illuminating the cathode area. The difference in the QE

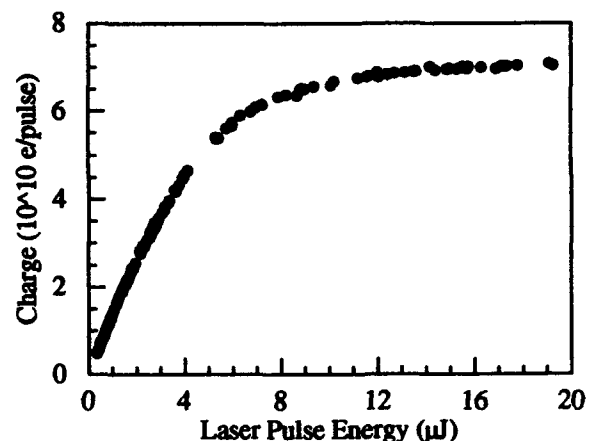


Fig. 1. Photoemitted charge as a function of laser pulse energy at a wavelength of 850 nm.

measured at the two wavelengths can primarily be attributed to the different number of photons actually absorbed by the 0.3  $\mu$  thick cathode for an equal number of incident photons at the two wavelengths. From the figure it is seen clearly that for low laser intensities the amount of emitted charge per pulse is

linearly proportional to the laser pulse energy. However, the dependence quickly becomes nonlinear for higher energies and the amount of emitted charge eventually saturates to a limit of  $7 \times 10^{10}$  electrons/pulse. This behavior is consistent with the results reported in Reference [3]. As the QE drops with time, the charge limit decreases almost proportionally.

The nature of the charge limit is more clearly elucidated in the time resolved electron intensity measurement with the gap monitor. Two temporal profiles of the electron bunch with low and high intensity laser illumination, corresponding to non-charge-limited and charge-limited cases, respectively, are shown in Figure 2. At low laser energy, the electron pulse shape is symmetric and closely resembles that of the laser pulse, indicating that the cathode response to the laser illumination is approximately linear. At the high laser energy when the charge limit is reached, the electron pulse shape becomes asymmetric and peaks at a significantly earlier time than the light pulse. This behavior is very different from the space charge limit manifested by a flat-topped symmetric pulse with the flat top amplitude determined by the space charge limit effect. For our gun operated at 120 kV, the space charge limit is about 10% higher than the peak in the charge limit pulse shown in Figure 2.

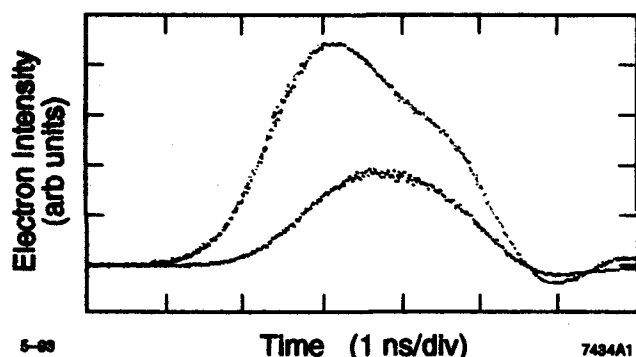


Fig. 2. Charge pulse shapes for incident laser pulse energies at  $30 \mu\text{J}$  (top trace) and  $3 \mu\text{J}$  (lower trace), showing charge limit and linear response behaviors, respectively. The laser wavelength is at  $850 \text{ nm}$ .

The decreased photoemission in the later part of the pulse as revealed by the time profile in Figure 2 is characteristic of the charge limit effect. In the deep charge limit regime, the suppression of photoemission after the electron pulse peaks may be so strong that the electron pulse becomes significantly shorter than the light pulse. These results suggest that as a large number of electrons are excited from the valence band into the conduction band in the cathode, the work function at the cathode surface increases and reduces the escape probability of the excited electrons. Several models have been proposed to account for the induced work function increase [6-8]. Although at present it is unclear which model is correct — and it is possible that more than one mechanism may be responsible — the photovoltaic effect [9] does appear to be the primary cause for the charge limit effect.

To further explore the properties of the charge limit, we studied its dependence on the gun high voltage. The data shown in Figure 3 demonstrate that the charge limit is strongly dependent on the high voltage, although less so than the  $V^{3/2}$  dependence for space charge limit. The almost linear relation between the charge limit and the high voltage may be

coincidental. However, it is clear that the strong dependence cannot be explained by the Schottky barrier lowering effect [10], which, as shown below, models very well the voltage dependence of QE measured at low laser power (i.e., in the linear response regime).

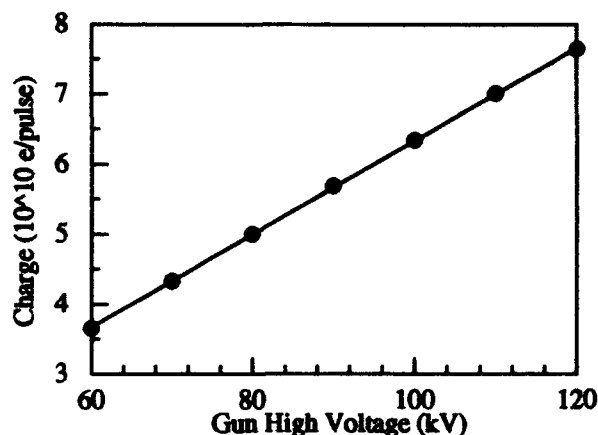


Fig. 3. Charge limit as a function of gun high voltage measured with a  $30 \mu\text{J}$  laser pulse at  $850 \text{ nm}$ .

Figure 4 shows two sets of data in the form of  $\ln(\text{QE})$  versus  $E^{1/2}$  (the square root of the extraction electric field at the cathode surface) for two excitation wavelengths [10]. Both can be satisfactorily fit to a linear relation, establishing the validity of the following expression:

$$\text{QE} = (\text{QE})_0 \times \exp(BE^{1/2}), \quad (1)$$

where  $B$  is the slope of the linear fit. The reduction in the work function due to Schottky effect is proportional to  $E^{1/2}$  [11].

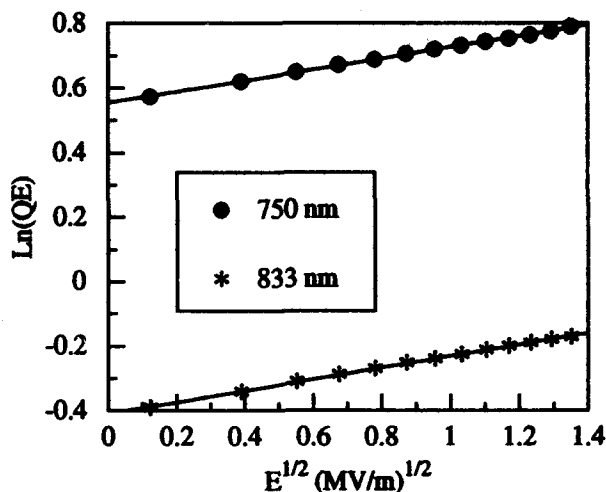


Fig. 4. Quantum efficiencies measured at  $750 \text{ nm}$  and  $833 \text{ nm}$ , respectively, versus the extraction electric field. The lines are the best fits to the data.

Therefore, equation (1) demonstrates that the excited electrons can be characterized by an effective temperature when reaching the cathode surface [12]. For the  $750 \text{ nm}$  and  $833 \text{ nm}$  excitation photons, we find the effective temperatures to be  $201 \text{ meV}$  and  $193 \text{ meV}$ , respectively. The fact that the effective temperatures for electrons excited by the  $750 \text{ nm}$  and

833 nm photons are almost the same shows that the excited electrons undergo rapid thermalization to the conduction band minimum, i.e., the  $\Gamma$  point, via phonon exchanges with the lattice, whose temperature is about 23 meV at 0 °C. The thermalized electrons are then accelerated in the band-bending region and become hotter when reaching the surface. The weak dependence of the effective temperature on the wavelength of the excitation photons may be attributed to the incompletely thermalized electrons.

The rather different voltage dependencies exhibited by the charge limit and QE indicate that QE is not the only important parameter that determines the charge limit, as suggested in reference [3]. In addition to the surface barrier lowering due to Schottky effect, the external field appears to affect the electron extraction efficiency critically.

We now discuss the effect of the laser wavelength on the charge limit. When the excitation wavelength is changed from 760 nm to 865 nm, the charge limit for the 0.3  $\mu$  strained GaAs cathode (at -8 °C) is found to decrease by only about 20% while the QE as evaluated from the linear response region in the saturation data decreases by more than an order of magnitude. Meanwhile, the laser pulse energy required for achieving the charge limit increases by more than an order of magnitude. These observations again show that the excited electrons are rapidly thermalized with the lattice and therefore become largely indistinguishable although at the beginning they may have very different kinetic energies depending on the excitation wavelength. Thus, the charge limit is only weakly dependent on the excitation wavelength mainly due to the incompletely thermalized electrons which are expected to be more energetic for higher photon energies. On the other hand, the number of incident photons required to achieve the charge limit strongly depends, as does the QE, on the wavelength because of the strong wavelength dependence of the optical absorption coefficient near the band gap.

Finally, we show in Figure 5 a saturation plot with the laser pulse energy extending well over the level required for achieving the charge limit. It is striking to see that, after reaching a maximum, the photoemitted charge decreases substantially as the laser energy further increases. Temporal

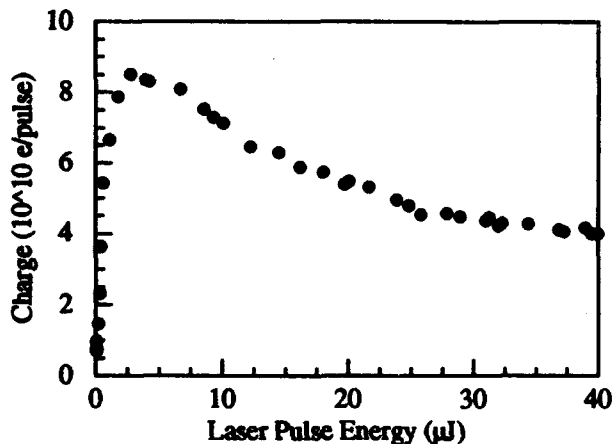


Fig. 5. Photoemitted charge as a function of laser pulse energy (at 760 nm) over an extended energy range.

profiles of the charge pulses measured with the gap monitor at various laser energies show that in the oversaturated regime, i.e., for laser energy greater than 4  $\mu$ J, the width of the charge

pulse decreases dramatically with increasing laser energy. Although there is also a small, but observable, decrease in the pulse height, it is the decreased pulsewidth that is primarily responsible for the decrease in the emitted charge. The oversaturation phenomenon further illustrates the complicated nature of the non-linear photoemission effect.

#### IV. CONCLUSIONS

In conclusion, we have studied the various aspects of the charge limit phenomenon. The non-linearity in the photocathode response at high laser intensities arises from the induced increase in the work function. The strong voltage dependence of the charge limit points to the advantage of operating the gun at the highest possible voltage, for high intensity and high polarization electron beams are produced only in very thin cathodes which are almost always operated in the charge limit.

\* Work supported by DOE contract DE-AC03-76SF00515.

† Permanent address: Faculty of Science, Nagoya University, Nagoya 464-01, Japan.

#### V. REFERENCES

- [1] D.C. Schultz, *et al.*, "Polarized source performance in 1992 for SLC-SLD", presented at the 10th Int. Sym. on H.E. Spin Physics, Nagoya, Nov. 9-14, 1992.
- [2] J.E. Clendenin, *et al.*, "Performance of the SLC polarized electron source with high polarization", these proceedings.
- [3] M. Woods, *et al.*, "Observation of a charge limit for semiconductor photocathodes", SLAC-PUB-5894, J. Appl. Physics, in press.
- [4] R.E. Kirby, *et al.*, "An in-situ photocathode loading system for the SLC polarized electron gun", these proceedings.
- [5] J. Frisch, *et al.*, "Operation of the new SLC polarized electron source laser", these proceedings.
- [6] M. Zolotarev, "Nonlinear effects in photocathodes", SLAC-PUB-5896 (1992).
- [7] A. Herrera, *et al.*, Stanford University, private communication.
- [8] H. Tang, *et al.*, "Modeling of the charge limit effect based on the photovoltaic effect", unpublished.
- [9] Photovoltaic effect refers to the reduction in the band bending due to the photoexcitation-induced accumulation of charges at the surface of opposite sign (electrons in our case) to that of the original surface charges (positively charged ions in our case) which leads to a reduction in the net amount of surface charges.
- [10] The extraction electric field at the cathode is proportional to the gun high voltage. At 120 kV, the extraction field is 1.827 MV/m.
- [11] See, for example, S.M. Sze, *Physics of Semiconductor Devices*, p. 250 - 254, John Wiley & Sons, 1981.
- [12] The effective temperature  $T_e$  is related to  $\beta$  through the following expression:

$$T_e = (e^3/4\pi\epsilon_0)^{1/2}/k_B\beta,$$

where  $e$  is the electron charge,  $\epsilon_0$  the electric permittivity in vacuum, and  $k_B$  the Boltzmann constant.

# Photocathode Performance Measurements for the SLC Polarized Electron Gun\*

C. L. Garden, E. W. Hoyt, D. C. Schultz, H. Tang  
Stanford Linear Accelerator Center  
Stanford, CA 94309, USA

## Abstract

A low-voltage test system is used to qualify various III-V semiconductor materials as photocathodes for the SLC. The system features a load lock to introduce samples, high pumping speed, a sensitive residual gas analyzer, and an infrared temperature detector. Heat cleaning, cesiation, and oxidation procedures have been studied to optimize cathode activation for achieving an optimum NEA surface. VGF GaAs, MBE-grown AlGaAs, MBE GaAs layered on AlGaAs, and MOCVD GaAsP cathodes with different active layer thicknesses and doping concentrations have been tested for quantum efficiency and lifetime. New higher-polarization strained-layer GaAs on GaAsP photocathodes have also been tested. Results and operational experience are discussed.

## I. INTRODUCTION

The cathode test system (CTS) was established in August 1990, for materials qualification of different III-V semiconductor photocathodes with a quick turn-around time, and to test different activation procedures in an environment that closely simulates the Polarized Electron Source (PES) Gun [1]. Experience gained here is

used to maximize quantum efficiency (QE) and QE lifetime, and aid in photocathode choice in the PES Gun. Materials come from different suppliers [8], and vary in structure, doping level, and dopant. This system is intended to compare the QE of different materials, but is not equipped to measure polarization. A new system that will also measure polarization is under development. See Figure 1 for an overview of the CTS.

## II. SYSTEM COMPONENTS

The chamber vacuum level is monitored with a residual gas analyzer (RGA) that has mass range of 0-200 AMU and is sensitive to partial pressures of  $10^{-13}$  Torr[2]. Cathode temperature (above 450 °C) is measured with an infrared temperature detector specially designed for work with GaAs [3]. An emissivity value of 0.7 for GaAs is used, which was calibrated by observing the congruent evaporation of GaAs at 663 °C [4]. The temperature measurements are accurate to  $\pm 5$  °C.

There are two different cesium sources on the CTS: a set of channel cesiators [5] and a SLAC-built effusion cell cesiator. No difference between the performance (peak QEs achievable) of the two was observed, but the

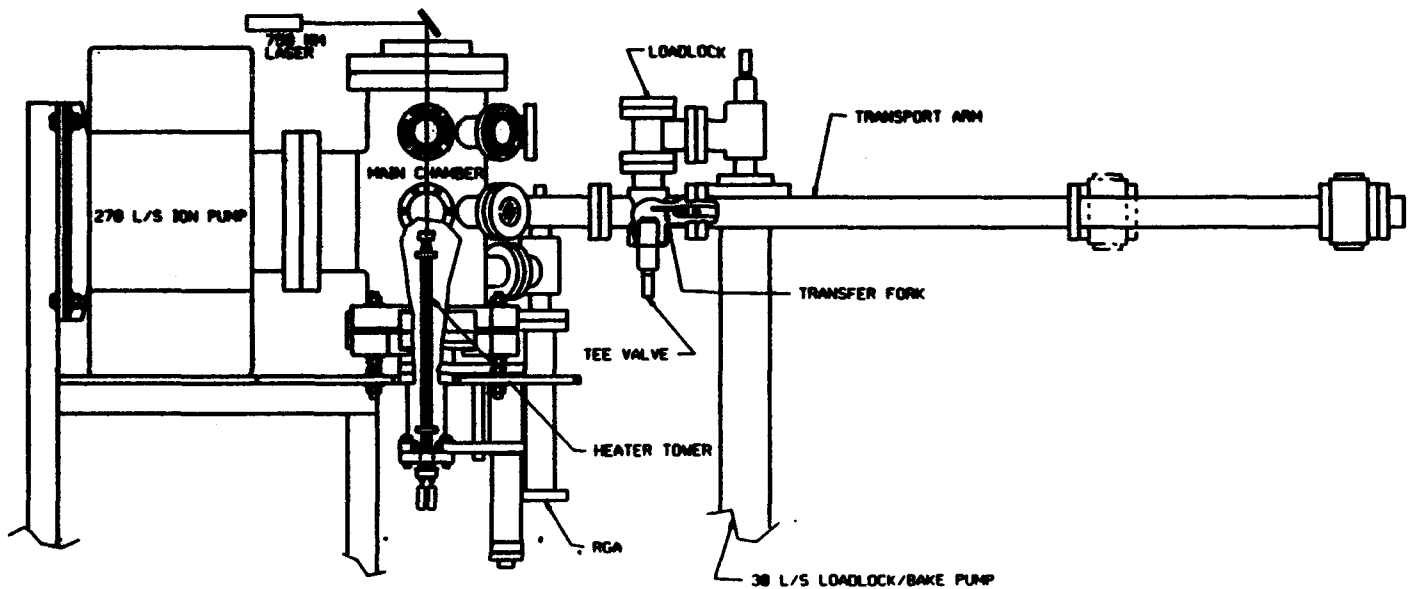


Figure 1. Cathode Test System.

\* Work supported by Department of Energy contract DE-AC03-76SF00515.

channels are much simpler to use. The channels heat up and cool down rapidly, giving much greater control of the amount of cesium deposited.

The load-lock (and bake) pump is a thirty-l/s ion pump. There is also a twenty-l/s ion pump used to pump out the NF<sub>3</sub> lines.

QE is monitored using a 750-nm diode laser, and occasionally a 633-nm helium-neon laser. QE versus wavelength data is taken using a white light and a series of 10-nm bandwidth interference filters. The extraction voltage on the cathode is -132 V, supplied by a battery box. The electrons are collected by a wire loop anode one in ch above the cathode.

Individual components were pre-baked to 450 °C. The entire system has been baked several times, initially to 160 °C and later to 250 °C. Following bake the total pressure is typically  $5 \times 10^{-11}$  Torr. The spectrum is dominated by hydrogen, with a partial pressure of 2 to  $3 \times 10^{-12}$  of CO. Figure 2 shows a typical RGA spectrum after a bake.

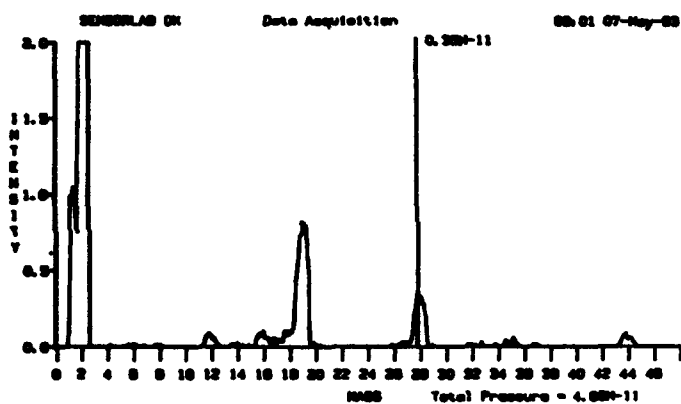


Figure 2. RGA spectrum after bake.

### III. SAMPLE PREPARATION

Cathode materials are shipped overnight in a N<sub>2</sub> atmosphere and are waxed to a glass cover immediately upon receipt. The glass cover facilitates cutting the wafers with a diamond wire saw (into 18–22-mm diameter discs), and protects the surface from contamination until use. The wax and glass cover are removed in four Pyrex beakers of boiling semiconductor-grade trichloroethane, then the wafer is rinsed with semiconductor-grade methanol and blown dry with nitrogen.

VGF GaAs cathodes are then etched for ten seconds in a 4:1:1 solution of semiconductor-grade sulfuric acid, hydrogen peroxide, and de-ionized water. They are rinsed with de-ionized water and semiconductor-grade methanol and blown dry with nitrogen. All beakers and tools used to prepare cathode materials are Teflon to reduce the possibility of contamination.

Manufacturers add a 50–100 Å arsenic cap to the thin active-layer MBE grown structures, as these can not be etched before they are used. The arsenic cap layer is removed by heat cleaning in the system. The same procedure is used in preparing cathodes for the SLC injector.

### IV. LOAD-LOCK OPERATION

Cathodes are installed through a small volume (1/2 liter) load-lock (see Figure 1). The view port on the top of the load-lock volume is removed and a photocathode on a molybdenum tray is lowered onto the seat of the closed tee valve. During this operation the load-lock is purged with 2–3 psi positive pressure of dry N<sub>2</sub>. The top view port is then replaced, and the load lock is roughed down using a turbo pump.

Pressure is low enough to switch to the thirty-l/s ion pump in about thirty minutes. To transfer the cathode into the main chamber, the tee valve on the load-lock area is opened, lowering the cathode to where it can be picked up by a transfer fork and brought into the main chamber. The transfer fork is on a long magnetically coupled arm [6]. When the fork is moved, a pressure rise due to gas desorption along the bearing of the arm is seen, and pumps out almost immediately. There is no rise in the main chamber pressure after a cathode transfer is completed. It takes thirty minutes to install the cathode onto the heater tower, after which the tee valve to the load lock is closed.

The cathode rests on a molybdenum tray during transport and when installed, this molybdenum tray rests on the heater tower. Figure 3 shows a close-up view of the cathode on the heater tower, and the positions of the anode ring and cesiators.

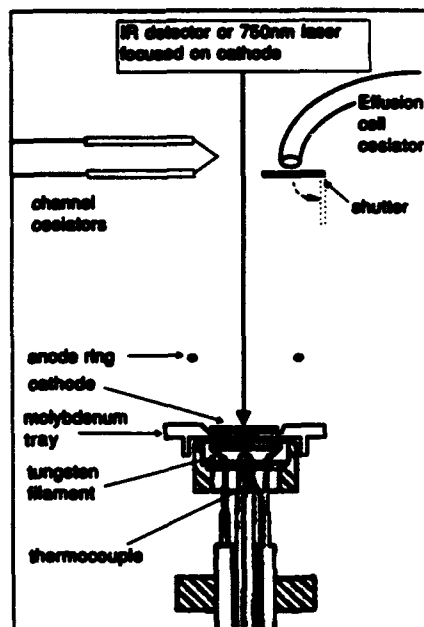


Figure 3. Close-up of cathode on heater tower, showing cesiators and anode ring.

## V. TYPICAL ACTIVATION

The typical activation cycle is as follows. The cathode is heated to 600 °C for one hour. Cesium is added (three minutes at five amps on two 17-mm channel cesiators). The temperature is ramped up to 640 °C in thirty seconds, and the power is cut as soon as 640 °C is reached. The cathode is allowed to cool one hour, until the cathode temperature is 30 °C or cooler. Using a 750-nm diode laser to monitor the photocurrent, cesium is added ( between four and five amps on the channel cesiators, depending on their age) until the photocurrent peaks, then NF<sub>3</sub> co-deposition is begun. The level of NF<sub>3</sub> is adjusted to maintain a positive slope. For optimal NF<sub>3</sub> deposition a  $1 \times 10^{10}$  Torr partial pressure (sum of mass 33, 52, and 71 peak heights) is used, with cesium channels at four to five amps. The NEA layer deposition takes about one hour.

## VI. ACTIVATION EXPERIMENTS

The photocathode is heat cleaned at high temperature for 60 minutes. Heat cleaning to very high temperature is essential for attaining high QE's. Heat cleaning to 600° C is much (300 percent better than 500 °C, and 620 °C is somewhat (10–30 percent) better than 600° C. Better QE (by about 10 percent) was obtained by adding some cesium near the end of the heat cleaning when the heat cleaning temperature is 600 °C.

## VII. SUMMARY OF RESULTS

Peak QE results for various cathode materials are

summarized in Table 1. QEs as high as 14 percent at 750 nm(20 percent at 633 nm) have been obtained for GaAs and GaAsP. The results depend somewhat on chamber history, the laser power used (influencing electron desorption rate), and the number of previous activations of that cathode. Results using different cathodes cut from the same wafer can vary 2 percent in QE.

Electron polarization of these photocathode materials is measured as  $\geq 40$  percent, except for the strained GaAs material, which gives electron polarization  $\geq 80$  percent [7].

## REFERENCES

- [1] "The Polarized Electron Gun for the SLC," D. C. Schultz et al., *Proc. of the Third European Part. Acc. Conf.*, Berlin(1992) 1029.
- [2] V. G. Quadrupoles, model MSL200D5NUT, through Fisons, Danvers MA.
- [3] MODLINE V Series, operates at 950 nm, IRCON Inc., Niles, IL
- [4] B. Goldstein et al., *Surface Science* 57 (1976) 733.
- [5] SAES Getters, Colorado Springs, CO.
- [6] MDC Vacuum Components, Hayward, CA.
- [7] T. Marayuma et al., *Phys. Rev. B* 46 (1992) 4261; and H. Aoyagi et al., *Phys. Lett. A* 167 (1992) 415.
- [8] Photocathode Vendors:  
 AXT, American Crystals Technology, Dublin, CA.  
 SPIRE, Spire Corporation, Bedford, MA.  
 EPI, Epitaxial Products International, Ltd., Cardiff, UK.  
 NSI, Northeast Semiconductor, Inc., Ithaca, NY.  
 UCB, University of California at Berkeley, Berkeley, CA.  
 QED, Quantum Epitaxial Designs, Bethlehem, PA.

Material	QE	Vendor	Active Layer		
			Composition	Thickness	Doping
VGF GaAs	13.90%	AXT	GaAs	635.0 $\mu$ m	2 E+19 Zn
Strained GaAs	0.85%	SPIRE	GaAs on GaAsP	0.2 $\mu$ m	5 E+18 Zn
GaAsP	14.40%	EPI	GaAs <sub>.87</sub> P <sub>.13</sub>	2.0 $\mu$ m	6 E+18 Zn
GaAsP	13.00%	EPI	GaAs <sub>.87</sub> P <sub>.13</sub>	4.0 $\mu$ m	2 E+19 Zn
AlGaAs	7.10%	NES	GaAs <sub>.88</sub> Al <sub>.12</sub>	1.5 $\mu$ m	6 E+18 Be
AlGaAs	6.00%	UCB	GaAs <sub>.88</sub> Al <sub>.12</sub>	0.3 $\mu$ m	5 E+18 Be
AlGaAs	6.10%	QED	GaAs <sub>.88</sub> Al <sub>.12</sub>	0.3 $\mu$ m	1 E+19 Be
AlGaAs	5.10%	NES	GaAs <sub>.88</sub> Al <sub>.12</sub>	0.3 $\mu$ m	1 E+19 Be

Table 1: Summary table of results for various materials.

# Electron Quantum Yields from a Barium Photocathode Illuminated with Polarized Light\*

M. E. Conde, S. Chattopadhyay, K.-J. Kim,  
S.-I. Kwon<sup>†</sup>, K.-N. Leung, and A. T. Young  
Lawrence Berkeley Laboratory  
University of California, Berkeley, CA 94720 USA

## Abstract

Photoemission measurements with a barium photocathode and a nitrogen laser are reported. The cathode is prepared by evaporating barium onto a copper disc. Radiation from a nitrogen laser (337 nm, 10 ns) is polarized and strikes the cathode surface at variable angles. An electron quantum yield as high as  $1 \times 10^{-3}$  is observed. The dependence of the quantum yield on the beam polarization and angle of incidence is investigated. The results indicate that higher quantum yields are achieved when the laser beam is incident at an angle of  $\sim 55^\circ$  and is polarized perpendicular to the plane of incidence.

## I. INTRODUCTION

The laser driven RF photocathode [1] holds great promise as a source of tightly bunched high-brightness electron beams. This is important for many accelerator applications, as well as for the generation of shortwave electromagnetic radiation. It is therefore important to improve and optimize the photocathode efficiency.

It has been shown [2] that barium is an attractive candidate for use as a photocathode material. It has a low work function ( $\sim 2.5$  eV) and provides relatively high electron quantum yields. This paper reports work on the optimization of the performance of barium photocathodes. Studies are conducted on the dependence of the quantum yield on laser beam incident angle and polarization. The results shown here may be relevant to other photocathode materials as well.

## II. EXPERIMENTAL SETUP

A 22 cm diameter stainless-steel vacuum chamber pumped by a cryosorption pump houses the photocathode. The typical base pressure in the chamber is  $2 \times 10^{-7}$  Torr. The cathode consists of a solid copper disc (20 mm in diameter) onto which a thin layer of barium is vapor deposited. The anode, a graphite disc (15 mm in diameter), is located directly in front of the cathode. They are mounted on a stainless-steel shaft by means of small ceramic rods and separated by a distance of 40 mm (Fig. 1). The rotation of the shaft allows for the variation of the laser incident angle on the cathode surface, while keeping the cathode-anode distance fixed.

The photocathode is prepared by evaporating barium from commercially available getter wires (SAES). A moveable support, holding twenty 1.6 cm-long segments of barium

getter wire, is placed directly in front of the cathode surface. The passage of electric current through the wires (approximately 5 Amperes per segment) raises their temperature and causes the barium to evaporate. Some of the barium vapor adheres to the cathode surface, forming a barium layer that is a few microns thick. The getter assembly is then moved away from the cathode. The whole process of barium deposition is performed in vacuum, and the pressure is kept in the  $10^{-7}$  Torr range.

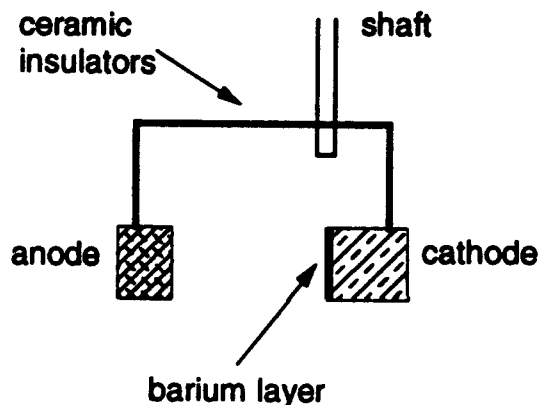


Figure 1. Schematic of the cathode and anode.

A schematic of the experimental setup is shown in Fig. 2. Nitrogen laser radiation at 337 nm with a pulse width of approximately 10 ns and a repetition rate of 22 Hz is used to excite the photocathode. An iris limits the diameter of the beam to approximately 4 mm. The laser beam is directed through a spatial filter to improve the beam quality and polarized by a calcite Glan prism. The beam power is then attenuated to  $0.05 - 1 \mu\text{J}/\text{pulse}$  and enters the vacuum chamber through a quartz window. The photoelectrons are collected by the anode, which can be biased to a maximum potential of 6 kV.

A photodiode monitors the laser power by using the small fraction of the beam that is reflected at the quartz window. It is important to note that this reflection occurs at near-normal incidence, making the reflection coefficient insensitive to the polarization state of the beam. This reflected beam is subsequently deflected to the photodiode by a prism. (This process is also insensitive to the beam polarization.)

## III. MEASUREMENTS

The time-averaged photocurrent is measured by a picoammeter connected to the cathode. The quantum yield is then calculated as the ratio between the number of emitted electrons and the number of incident photons. A calibrated thermopile detector (Scientech, model S-3610) is used to mea-

\* This work was supported by the Director, Office of Energy Research, Office of Fusion Energy, Development and Technology Division, of the U.S. Department of Energy under Contract No. DE-AC03-76SF00098.

<sup>†</sup> Permanent address: Department of Physics, Kyonggi University, Suwon, Korea.

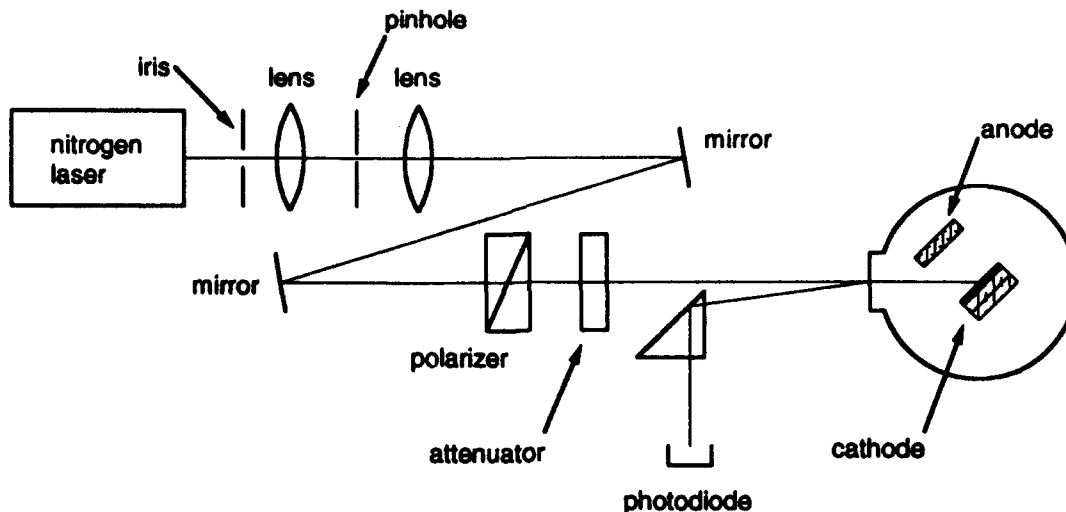


Figure 2. Schematic of the experimental setup.

sure the time-averaged laser power, thereby determining the number of photons.

Figure 3 presents the measured quantum yield as a function of anode bias voltage and barium layer age. The graph shows that the voltage applied to the collecting anode has to be sufficiently high to overcome the space-charge limit at the cathode. For high enough voltages the measured quantum yield is independent of the anode voltage, indicating that all the emitted electrons are collected. The figure also illustrates the decrease of the quantum yield as a function of the cathode age, which is presumably a consequence of the contamination of the barium surface.

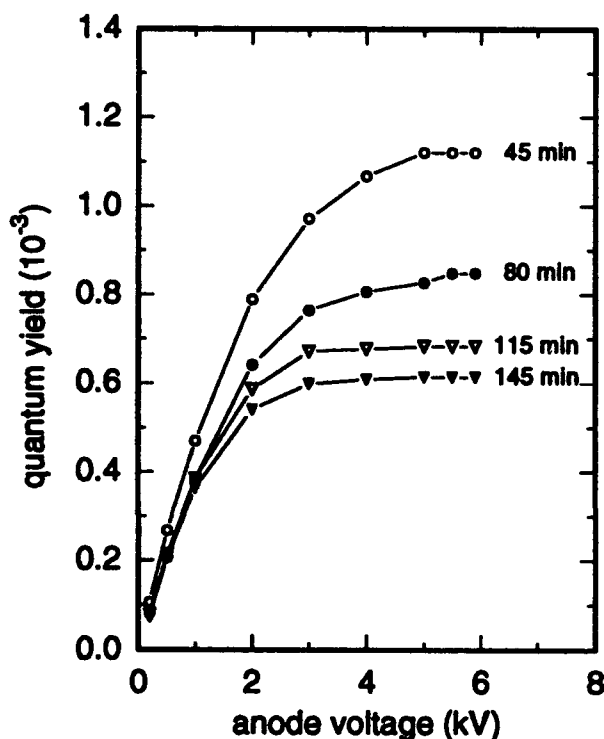


Figure 3. Electron quantum yield as a function of anode voltage and barium layer age.

Absolute values of the laser beam energy are measured with the above mentioned thermopile detector. The precision of these power measurements is  $\sim 20\%$  at these low average power levels ( $< 0.5$  mW). More precise (although only relative) power measurements are obtained with a photodiode (see Fig. 2). In the next paragraphs we present the quantum yield dependence on the polarization and angle of incidence of the laser beam. In both cases the laser power is measured with the photodiode, therefore the quantum yield values are just relative measurements.

Figure 4a shows the relative quantum yield as a function of laser beam polarization (for a fixed angle of incidence). The quantum yield reaches a maximum value when the polarization state is such that the component of the electric field normal to the cathode surface is maximized (cf. Fig. 4b). Conversely, the quantum yield has a minimum value when the electric field in the laser beam is parallel to the cathode surface.

Figure 5 illustrates the dependence of the quantum yield on the laser beam incident angle. Two curves are shown, corresponding to two polarization angles of the beam (perpendicular to each other). The difference between the quantum yield of each polarization becomes larger as the incident angle is increased. The maximum quantum yield is reached at an incident angle of  $\sim 55^\circ$ , with the beam polarized perpendicular to the plane of incidence. Small angles of incidence cannot be explored because the anode would block the laser beam. Measurements with very large angles are also difficult; a fraction of the beam can easily "miss" the cathode surface.

#### IV. DISCUSSION

In these experiments electron quantum yields of  $10^{-3}$  have been measured with a barium photocathode at a wavelength of 337 nm. These values are comparable to results in similar experiments employing barium cathodes and at a number of excimer laser wavelengths [2]. Thus, it has been demonstrated that barium is a very attractive candidate for use as a photocathode material. Barium presents quantum yields much higher than the values obtained with bare copper, with vacuum requirements that are only slightly more stringent

( $\sim 10^{-7}$  Torr). Cesium semiconductors [3] can achieve higher quantum yields, but ultra-high vacuum is required for their operation ( $< 10^{-9}$  Torr).

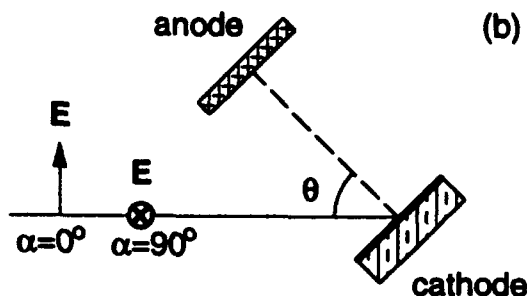
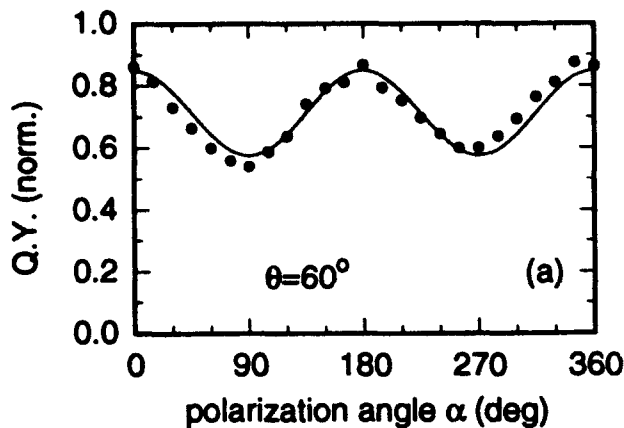


Figure 4. Effect of the laser polarization on the quantum yield: (a) normalized quantum yield as a function of polarization angle; (b) diagram indicating the angles of polarization ( $\alpha$ ) and incidence ( $\theta$ ).

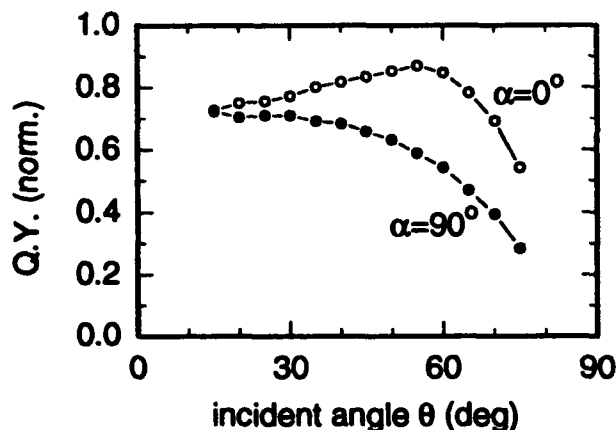


Figure 5. Normalized quantum yield as a function of angle of incidence.

An enhancement of the photoemission has been observed when the laser light is polarized such that the electric field of the laser beam has a component normal to the cathode surface. This effect is small at near-normal laser incidence, and is more pronounced for larger incident angles.

The effect of the beam polarization on the quantum yield must be, in part, due to changes of the reflection coefficient of the barium as a function of the angle of incidence and the polarization of the light. Thus, a smaller reflection coefficient allows a larger fraction of the incident photons to interact with the barium layer, yielding a larger number of photoelectrons. We are presently investigating this topic. Preliminary calculations of the reflection coefficient are consistent with the measured curves. These estimates are limited by the uncertainty in the values of the optical constants of barium, and also by the unknown effect of the roughness of the actual cathode surface.

We have also observed these polarization effects with laser power levels that differ by an order of magnitude. This suggests that the effect cannot be attributed to field-assisted photoemission in an obvious way.

## V. ACKNOWLEDGEMENTS

We thank Wim Leemans for advice on the optics and for lending us the photodiode. We are also grateful to John Edighoffer for helpful discussions.

## VI. REFERENCES

- [1] R. L. Sheffield, "Photocathode RF Guns," AIP Conference Proceedings #184, Physics of Particle Accelerators, edited by M. Month and M. Dienes, AIP 1989, p. 1500.
- [2] M. D. Vanloy, A. T. Young, and K.-N. Leung, "Measurements of Barium Photocathode Quantum Yields at Four Excimer Laser Wavelengths," (submitted to Appl. Phys. Lett.).
- [3] P. E. Oettinger, R. E. Shefer, D. L. Birx, and M. C. Green, "Photoelectron Sources: Selection and Analysis," *Nucl. Instrum. Methods A272*, 264 (1988).

# The 1992 Polarized Light Source

R. Alley, M. Woods, M. Browne, J. Frisch, M. Zolotorev

Stanford Linear Accelerator Center, Stanford University, Stanford, CA 94309 USA

## Abstract

We describe the Polarized Light Sources used at SLAC during the 1992 runs of the experiments SLD and E142.

## I. Introduction

Polarized electron sources utilizing photocathodes are currently in use at many accelerators around the world. Two experiments utilizing polarized beams at SLAC are SLD, run with the SLAC Linear Collider (SLC) at the  $Z^0$  resonance, and E142 which is a fixed target experiment running in End Station A. The Polarized Light Source (PLS) performance for these experiments is summarized in Table I.

## II. The PLS for the 1992 SLD Experiment

In 1992, there were a five month SLD run and a two month E142 run at SLAC. The Polarized Electron Source used for the SLD run is shown in Fig. 1. The laser used was a flashlamp-pumped dye laser operating at 120 Hz and 715 nm. A current pulse, 15 J in 1.5  $\mu$ s, is sent to each of two flashlamps and produces (typically) a 5 mJ laser pulse with a pulse width of 750 ns.

A Laser Pulse Chopper (LPC) system consisting of a Pockels Cell between crossed polarizers is used to produce two 2 ns pulses separated by 60 ns from the initial 750 ns pulse. The first of these pulses produces an electron bunch for  $e^+e^-$  collisions, while the second laser pulse produces an electron bunch for positron production. Following the Laser Pulse Chopper, a Bunch Intensity Control (BIC) system consisting of a Pockels Cell between aligned polarizers is used to regulate the intensity of laser light on the photocathode.

The laser beam is linearly polarized through the BIC system. A linear polarizer followed by a Pockels Cell oper-

ating at its quarter-wave voltage compose the Circular Polarizer System (CPS) to produce circularly polarized light. A positive HV pulse on the CPS Pockels Cell produces positive helicity light, while a negative HV pulse produces negative helicity light. The sign of the HV pulse is set by a random number pattern generator, which updates at 120 Hz. This effectively eliminates any false asymmetries due to time-dependent behaviour of the accelerator. The absolute helicity of the laser light was determined using total internal reflection in a prism to generate a known helicity laser beam.

After the CPS system, the laser beam enters a 20-meter-long vacuum transport line to the photocathode. This transport line contains a 6 m focal length imaging lens approximately midway between the CPS Pockels Cell and the photocathode. It also contains four mirrors to redirect the laser beam to the photocathode while preserving circular polarization.

Table I. PLS Performance

	SLD	E142
Repetition Rate	120 Hz	120 Hz
Pulse Energy	5 $\mu$ J	20 $\mu$ J
Pulse Length	2 ns	1.2 $\mu$ s
Circular Polarization	99%	99%
Intensity Jitter	5% rms	2% rms
Helicity Dependent Intensity Asymmetry	$< 10^{-3}$	$< 10^{-4}$

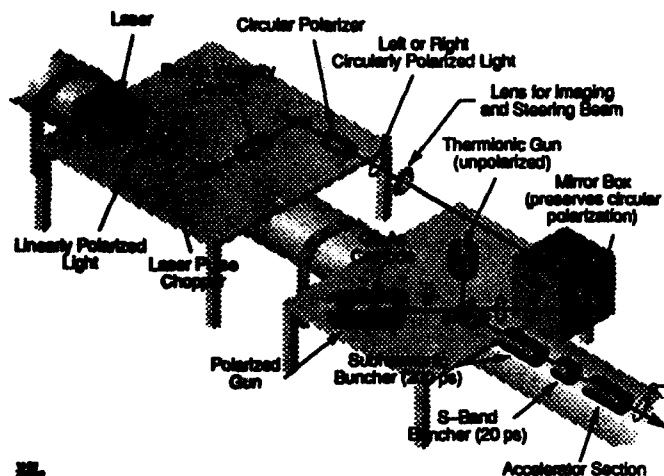


Figure 1. The Polarized Electron Source at SLAC.

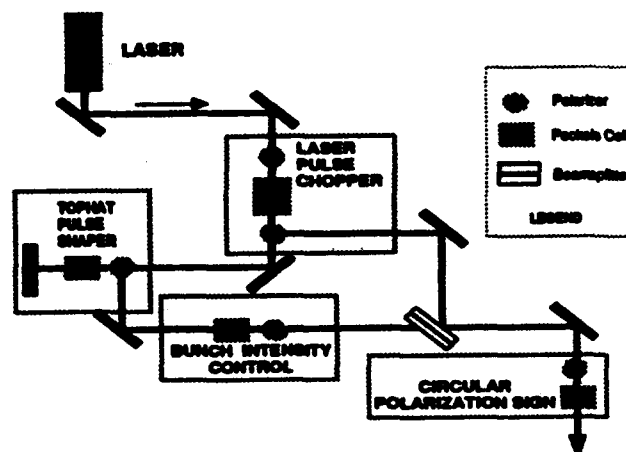


Figure 2. The Polarized Light Source for E142.

The PLS ran continuously at 120 Hz for the five month SLD run in 1992, with only a four hour scheduled downtime every ten days for dye and flashlamp changes. The PLS delivered usable beams for SLD running with about 95% efficiency for the run, including the scheduled downtime. Typically, 5  $\mu\text{J}$  in a 2 ns bunch was delivered to the photocathode with 99% circular polarization. The helicity-dependent intensity asymmetry was determined to be less than  $5 \cdot 10^{-4}$  from monitoring of the electron beam. The GaAs photocathode used had a typical quantum efficiency of 5% and produced  $6 \cdot 10^{10}$  electrons per 2 ns bunch (5 A peak current). The electron beam polarization was 28%.

### III. The PLS for the 1992 E142 Experiment

Following the SLD run, the PLS was reconfigured for E142 as shown in Fig. 2. For long pulse operation, the dye laser was modified to produce longer output pulses at lower peak power. Two beams from the pulsed dye laser are produced — a 1.2- $\mu\text{s}$ -long pulse for the experiment, and a 2 ns short pulse for accelerator diagnostics and tuning. Normal operating conditions during E142 were concurrent running of the long pulse at 119 Hz and the short pulse at 1 Hz.

The Laser Pulse Chopper Pockels Cell system is similar to the one described above for the SLD experiment, except that now the Pockels Cell is between aligned polarizers, and only one pulse is produced. The Tophat Pulse Shaper (TOPS) system shapes the dye laser pulse into a 1.2  $\mu\text{s}$  long flattop pulse. A fast feedback system determines a correction voltage to the TOPS Pockels Cell such that a photodiode signal following the TOPS system matches a reference waveform.

After TOPS is the BIC system which serves the same purpose as for the SLD experiment, which is to regulate the laser light on the photocathode and hence the intensity of the long pulse electron beam. After the BIC system, the short and long laser pulses are combined and sent to the CPS system, which is identical to that used for SLD. From the CPS on, the PLSs for E142 and SLD are identical.

The PLS efficiency for E142 is similar to its efficiency for SLD, with typically four hours of scheduled maintenance every 10 days for dye and lamp changes. The PLS delivers about 20  $\mu\text{J}$  in a 1.2  $\mu\text{s}$  pulse to the photocathode with 99% circular polarization. Helicity-dependent intensity asymmetries as large as  $1.5 \cdot 10^{-4}$  have been measured during E142 running. This helicity asymmetry is believed to arise from two effects—residual linear polarization in the laser beam coupled with a small transmission asymmetry in the laser transport optics from the CPS to the photocathode, and steering of the laser beam by the CPS Pockels Cell due to misalignment of the laser beam with respect to the Pockels Cell.<sup>1</sup> For E142, an AlGaAs photocathode was used. It had a typical quantum efficiency of 0.8% and produced  $3.5 \cdot 10^{11}$  electrons in a 1.2  $\mu\text{s}$  pulse. The electron beam polarization was 40%.

### VI. Conclusions

We have described the Polarized Light Source used to produce a polarized electron beam at SLAC. PLS operation for the 1992 SLD and E142 experiments was very successful, having an uptime efficiency of 95% averaged over seven months of running.

### References

1. These effects are described in detail in G. Cates et. al., *Nucl. Inst. Meth. in Phys. Res.* A278, 293 (1989). This article points out that the transmission asymmetry in the optics transport line can be minimized by using pairs of phase compensating mirrors, such as is done in the SLAC PLS Mirror Box. The article also points out that steering effects from the helicity Pockels Cell can be minimized by 1:1 imaging of the laser beam from the helicity Pockels Cell to the cathode. This is approximately accomplished in our setup with the 6 m imaging lens between the CPS and photocathode.

# Operation of a Ti:Sapphire Laser for the SLAC Polarized Electron Source\*

Josef Frisch, Ray Alley, Mike Browne, Mike Woods  
SLAC Stanford CA 94309

## Abstract

A new laser system has been developed as the light source for the SLAC polarized electron source for the 1993 SLD physics run. A Q-switched and cavity-dumped Ti:Sapphire laser, pumped by a doubled YAG laser is used. This laser delivers typically 50μJ to the photocathode with the required 2 nanosecond, double pulse, 120Hz time structure. The laser operates at wavelengths between 760nm and 870nm. The laser was installed on the SLAC linac in January 1993, and is currently in use.

## I. INTRODUCTION

The polarized electron source for the SLAC linac uses a semiconductor photocathode driven by a laser. For the 1992 physics run, a flashlamp pumped dye laser was used[1]. The new high polarization strained-lattice cathodes[2] intended for the 1993 run required higher optical pulse energies and longer wavelengths than the dye laser could deliver. The requirements for the new laser were:

Table 1. Laser Operating Parameters

Operating wavelength	760nm - 870nm
Pulse energy to cathode	>50μJ
Pulse length	2.0ns
Timing jitter	<50ps RMS
Pulse structure	2 pulses, 62ns apart
Repetition rate	120Hz
Energy stability	<3% RMS
Pointing stability	<5μR RMS
Reliability	>95% uptime
System Lifetime	>10,000 Hours

No commercial lasers were available which could meet these parameters, so a system was developed at SLAC.

## II. LASER SYSTEM DESIGN

### A. Optical layout

Titanium doped sapphire ( $Ti^{3+}:Al_2O_3$ )[3] is the only commercially available solid state laser material which can operate over the required wavelength range at the required powers and repetition rates. Frequency doubled YAG was chosen as the most practical pump source for Ti:Sapphire.

We decided to use 2 Ti:Sapphire cavities to produce the first and second pulses. This allowed

independent control of pulse timing and intensity. Commercial YAG lasers with the required output energy (5mJ at 532nm) were not available with repetition rates greater than 60Hz. This necessitated the use of 2 YAG lasers operating interleaved to pump each of the Ti:Sapphire cavities. Figure 1 shows the overall system layout.

SLAC Ti:Sapphire Polarized Source Laser System Layout

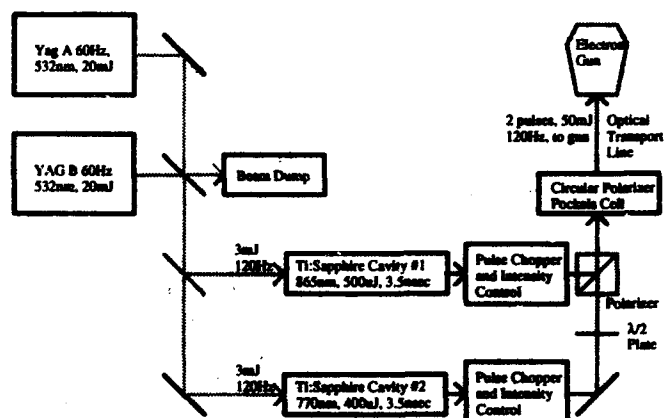


Figure 1. Laser System Layout

### B. Optical Cavity Design

The Ti:Sapphire cavities are Q-switched[4] and cavity dumped[5] with an intra-cavity Pockels Cell and polarizer (Figure 2). When high voltage is applied to the Pockels cell, the polarization of the light in the cavity is rotated and lasing is inhibited. Removing the high voltage allows build-up of light in the cavity to begin. When the intra-cavity optical power reaches maximum, a fast high voltage edge is applied to the Pockels cell. This causes the circulating light to be extracted through one of the cavity polarizers. This produces a pulse whose length is the round trip length of the optical cavity.

SLAC Polarized Source Ti:Sapphire Cavity

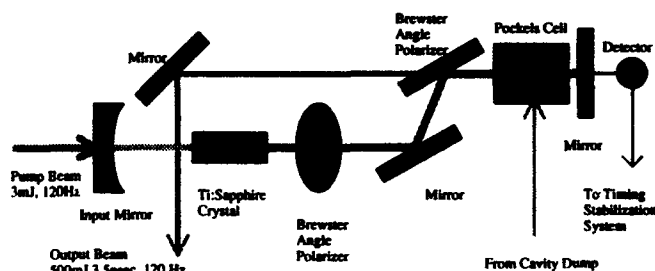


Figure 2. Laser Cavity Layout.

\* Work Supported by U.S. Department of Energy Contract DE-AC03-76SF00515

A Pockels cell with a fast (150psec rise and fall time) avalanche transistor driver chops the output pulse to the required 2ns width. An additional Pockels cell after each cavity is used to control the output intensity.

### B. Feedbacks

The Polarized source laser is required to run for long periods of time (weeks) without adjustment. A number of feedbacks have been incorporated into its design to allow long term stable operation (Figure 3.)

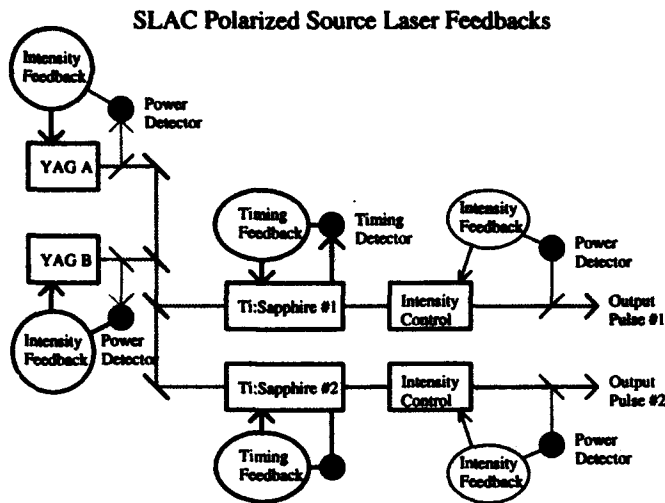


Figure 3. Laser feedbacks

A pair of feedback loops stabilize the output energy from each of the YAG lasers. A photodetector monitors the output energy and adjusts the flashlamp high voltage. Drifts in the YAG output beam steering are removed by optics which image the YAG rods onto the Ti:Sapphire crystals.

The primary source of intensity jitter in the Ti:Sapphire cavities is variations in the optical gain causing the timing of the Q-switched pulse to change. As the cavity dump time is fixed by the accelerator timing, these variations in build-up time cause variations in output intensity. Feedback loops which measure the build-up time of the light, and control the stop time of the Q-switch pulse are used to maintain the cavity-dump time at the peak of the optical pulse. The gain variations due to changes in each of the YAG lasers on each of the Ti:Sapphire cavities are independent so 4 separate timing feedback loops are used. Without the timing stabilization, the output intensity jitter from the Ti:Sapphire lasers is approximately 12% RMS. The feedbacks reduce this to approximately 5% RMS.

The output power from the Ti:Sapphire cavities is stabilized by intensity feedbacks which read the optical energy and control the high voltage to a

Pockels cell. Separate feedbacks are used for pulses generated by each of the pump lasers.

### C. Fast Feedforward

After the slow timing feedbacks have removed drifts in the build-up time of the optical power, the major remaining source of jitter is pulse to pulse fluctuations in gain due to intensity jitter in the pump YAG lasers. A "Fast Feedforward" system is used to eliminate this effect to first order. The fast feedforward measures the YAG output energy, and on the same pulse, adjusts the stop time for the Ti:Sapphire Q-switch to reduce the build-up time jitter. The fast feedforward reduces the output jitter from the Ti:Sapphire cavities to <3% RMS.

## III. SYSTEM PERFORMANCE

### A. Electron Beam Current

The laser system is currently installed on the SLAC polarized source driving a strained lattice GaAs photocathode. The maximum charge which can be extracted in nanosecond pulses from semiconductor photocathodes saturates as a function of incident laser energy[6]. A charge saturation curve for the source cathode at a wavelength of 863nm is given in figure 4.

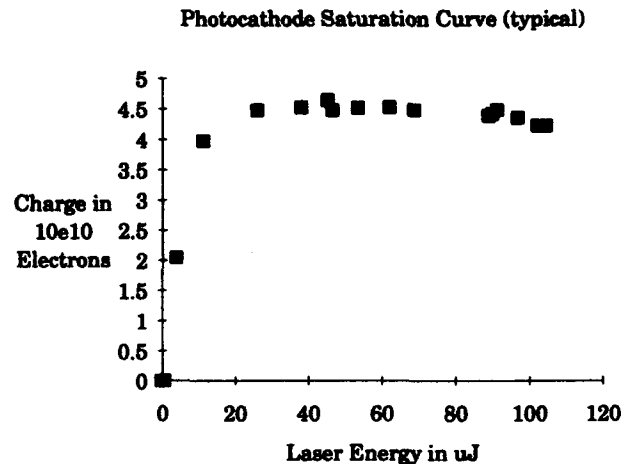


Figure 4. Photocathode charge saturation

This saturation in the charge extracted from the photocathode reduces the sensitivity of the electron beam current to fluctuations in the laser intensity. The laser is typically operated at the maximum of the saturation curve (approximately 50uJ) with a resulting output current stability of <1.6% RMS. The total current from the gun is adjusted by changing the spot size of the laser on the photocathode.

The charge limit for the first bunch reduces the available total charge for the second bunch. The charge limit is larger for shorter laser wavelengths. As the polarization of the second electron bunch is not important ( it is used to generate positrons), we are able to operate the Ti:Sapphire cavity #2 at

shorter wavelengths (770nm). This increases the charge limit for the second bunch to allow production of equal intensity bunches.

### B. Position Stability

Position instabilities of the laser spot on the photocathode are the result of two primary sources. Motion of the YAG pump beams, and drift and vibration of the optical transport system. The Ti:Sapphire cavities themselves do not introduce significant beam motion.

Motion of the pump beams causes the position of maximum gain in the Ti:Sapphire cavity to move and the mode position to shift. This is particularly troublesome because the drifts of the two YAG lasers are independent, and the result is an output beam position which alternates at 60Hz. This motion is typically 40 $\mu$ m RMS (for a 8mm FWHM spot) at the photocathode. Vibration of the laser transport system produces similar amplitude motions. Under normal operating conditions, these motions do not significantly effect electron beam operation.

### C. Wavelength and Polarization

At the present time there is no polarimeter to measure the electron beam polarization directly from the photocathode gun. A combination of measurements on the 50GeV beam and laboratory measurements on similar cathodes can be used to estimate the source polarization as a function of laser wavelength. Note: the laser polarization is >99%. For wavelengths longer than 860nm, the electron polarization at the gun is believed to be 80 $\pm$ 5%[7]. For shorter wavelengths, the polarization decreases at about 1% per nanometer.

The only wavelength tuning in the laser system is due to the limited bandwidth of the polarizers. The combination of polarizers in transmission and reflection produces a bandwidth of about 4nm FWHM. The center wavelength drifts (dependent on humidity) by  $\pm$ 3nm on a timescale of days.

The charge limit decreases and the optical energy required to saturate the cathode increases when the wavelength is increased. We operate the laser at wavelengths between 862nm and 868nm to maintain good polarization and charge limit.

### D. System Reliability

The laser system was commissioned on the SLAC linac at the end of January 199. Table 2 lists system downtime since that time. 19% run uptime with the flashlamp pumped dye laser source are listed for comparison.

Table 2. Laser System Uptime

System Performance	1992	1993
Total hours	3980	2230
Uptime	97.0%	97.4%
Downtime - scheduled	2.0%	1.6%
Downtime - unscheduled	1.0%	1.0%

Scheduled maintenance of the laser has been dominated by wavelength and transport system changes to optimize polarization. In the future, scheduled downtime will probably be dominated by YAG laser flashlamp changes: 4 hours every 45 days or 0.4%. The laser system uses 4 planar triode tube pulsers. Maintenance on these units will probably increase scheduled down time to approximately 0.5%.

The largest unscheduled maintenance item has been avalanche transistor Pockels cell driver failures. These units produce the 150psec rise time, 2ns wide, 3KV pulses to chop the optical beam. The electrical performance of these units is excellent, and we are working to improve their reliability. Other unscheduled failures totaled 0.4%.

### D. Overall Performance

This laser system has been used as the source for the SLAC linac for the production of >15,000  $Z_0$  bosons (as of 5/1/93) with approximately 60% electron polarization at the SLD detector.

## IV. REFERENCES

- [1] M. Woods et. al. "Polarized Light Sources for Photocathode electron guns at SLAC" *SLAC PUB 5965*. Submitted 10th intl. Symp. on H.E. Spin Physics - Nagoya 1992
- [2] T. Maruyama et. al. "Electron-spin polarization in photoemission from strained GaAs grown on GaAs<sub>1-x</sub>P<sub>x</sub>" *Physical Review B*, Vol. 24, No. 7, 15 Aug. 1992
- [3] A. Sanchez et. al. "Crystal Growth, Spectroscopy, and Laser characteristics of Ti:Al<sub>2</sub>O<sub>3</sub>", *IEEE J. of Quantum Electron.*, Vol. 24, No. 6, (995-1002) 1998
- [4] W. Koechner "Solid State Laser Engineering" *Springer-Verlag* 1976 (411-421)
- [5] W. Koechner "Solid State Laser Engineering" *Springer-Verlag* 1976 (441-445)
- [6] M. Woods et. al., "Observation of a Charge Limit for Semiconductor Photocathodes" *SLAC PUB 5894* (Submitted to *J. Applied Physics*)
- [7] J. Clendenin et al. "SLC Source Polarization" *SLAC SLCPOLSOURCE-TN-93-11* April 23, 1993 (unpublished)

# The Argonne Wakefield Accelerator (AWA) Laser System and Its Laser Pulse Shaper

W. Gai, N. Hill, C. Ho, P. Schoessow and J. Simpson  
Argonne National Laboratory, Argonne, IL 60439

## Abstract

Generating a 100 nC, 20 ps (FWHM) pulse length electron beam at the AWA requires a stable laser system capable of producing 1 - 3 ps, 1 mJ pulses at 248 nm and the capability of shaping the wave front. A wave front shaping device has been designed and built. It consists of nine concentric cylindrical mirrors. Each cylinder's position can be adjusted relative to the others by a system of computer controlled stepping motors. The reflecting surfaces were optically polished and dielectric coated. Detailed characterizations of the laser pulse shaper's performance using a streak camera and its associated optics are presented.

## 1. Introduction

The Argonne Wake-field Accelerator (AWA) is under construction. Phase I of the AWA includes a linac which can produce 100 nC, 20 ps (FWHM) electron bunches at 20 MeV. An L-band photocathode gun and standing wave preaccelerator are used to generate such high electron beam currents. One of the key components of the gun is a pulsed laser system which produces 2 ps, 1 mJ pulses at 248 nm and operates at a maximum repetition rate of 30 Hz. A laser system constructed jointly by Coherent-Lambda Physik has been purchased to fulfill these requirements. Details of AWA design and construction status are discussed in reference [1]. The design requires that the electron beam have a roughly spherically concave shape as it is emitted from the cathode, with the first electrons emitted from the outer diameter of the cathode. A sagitta of about 17 ps has been identified as a reasonable starting point. This curvature has two important benefits. First, it reduces significantly the radial space charge forces as the electrons are accelerated because of relativistic effects. Second, it produces an energy and radial spatial correlation which permits a smaller beam spot at the end when combined with nonlinear focussing.

In this paper, we discuss the laser set up and the laser pulse shaping device. The pulse shaper consists by nine concentric cylinders. The axial position of each cylinder can be adjusted relative to its neighbor by a

stepping motor. The front surface of each cylinder is optically polished and coated with dielectric to increase UV reflectivity. Laser pulses are incident normally on these surfaces. By adjusting each cylinder's axial position, the reflected wave front is shaped accordingly. This scheme is flexible in its configuration and permits the production of nearly arbitrary wavefront shapes.

## 2. Laser system configuration

The schematic diagram of the laser system is shown in the Figure 1. The system uses well known technologies<sup>2</sup>. The central component of the "front end" is a synchronously pumped mode locked dye oscillator (Coherent 702). The dye laser is tuned to the desired wavelength of 497 nm by a single-plate birefringence filter. Coumarin 102 dissolved in benzyl alcohol and ethylene glycol is the lasing medium, and DOCI dissolved in benzyl alcohol and ethylene glycol is the saturable absorber. A harmonic tripled mode locked Nd:YAG laser is used to pump the dye laser. The frequency of the mode locker is 40.625 MHz which is the 32nd harmonic of 1.3 GHz rf frequency exactly.

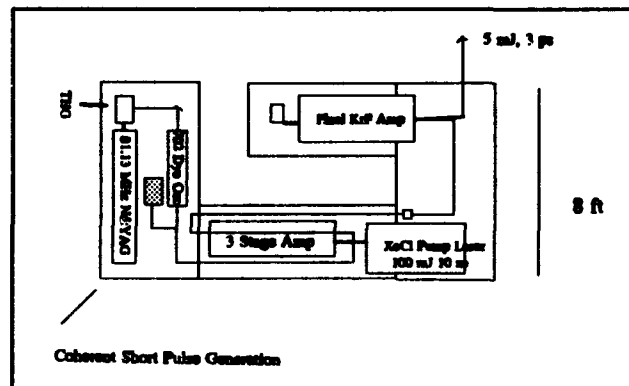


Figure 1 Schematic Diagram of the AWA laser system

A single pulse from the dye laser output train is amplified to 300  $\mu$ J through a three-stage dye amplifier. The dye amplifier is Lambda-Physik FL2003 pumped by 100 mJ, 308 nm pulses from a Lambda-Physik LPX105i

excimer laser. The duration of the pump pulse is shortened to 10 ns so only one pulse from the dye oscillator is selected and amplified. The output from the dye amplifier is frequency doubled in a 3x3x7mm angle matched BBO crystal. Output at 248 nm is typically 25 - 30  $\mu$ J.

Amplification of the ultra-short UV pulses is done in a single stage KrF excimer laser (Lambda-Physik LPX105i). The input pulses pass through the amplifier twice in order to utilize its fully stored energy. The output energy from final amplifier is measured by using Moletron J25 joule meter. An output energy of 8 - 10 mJ is obtained routinely. Depending on the discharge HV, the ASE is ~ 5 - 10% measured at 20 cm from the output window. The length of the final pulse is measured by Hamamatsu streak camera (model C1587) which has resolution of 2 ps. The typical measured pulse length (FWHM) is 3 - 4 ps. No satellite pulses are observed. The repetition rate of the laser can be as high as 35 Hz.

### 3 Laser Pulse Shaper and Its Characterizations

Figure 2 shows the mechanical drawing of the laser pulse shaper. All the cylinders have a wall thickness of 1 mm except the 4 mm diameter center rod. The diameter of the outer most cylinder is 2 cm. The cylinders are made of carbon steel and machined for a lapped fit inside each other. Each cylinder is controlled by a stepping motor with 1/2 inch of motion with increments of 0.001 inch. The front surfaces of the cylinders were optically polished at Argonne's machine shop, and subsequently a high reflection coating was applied at CVI lab. The measured reflection at 248 nm is about 65 % for normal incidence.

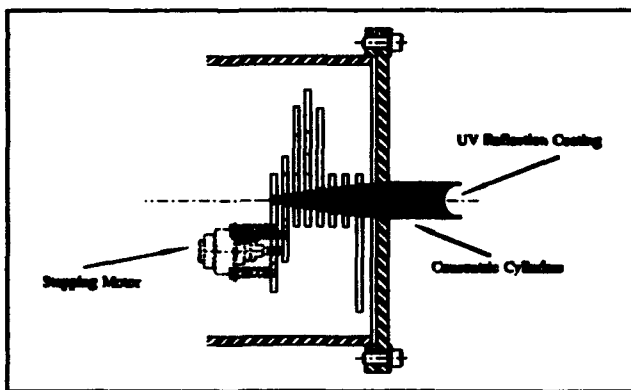


Figure 2 Mechanical drawing of the pulse shaper

The configuration for the initial tests of the

shaper is shown in Figure 3. A small amount of the laser beam were split off from output of the final amplifier for the test because of full intensity laser beam would damage the streak camera. The laser beam passed through a diffuser, and illuminated the pulse shaper. In order to preserve the timing and spatial distribution of the reflected laser beam, a focusing lens was used to image the pulse shaper at the target. For these tests, the target was the input window of the streak camera. The lens was made of CaF<sub>2</sub> and had a focal length of 15 cm, and the arrangement produced a spatial magnification of 1/7. The data acquired by the streak camera were sent to the data acquisition system and stored in a computer for further analysis<sup>2</sup>.

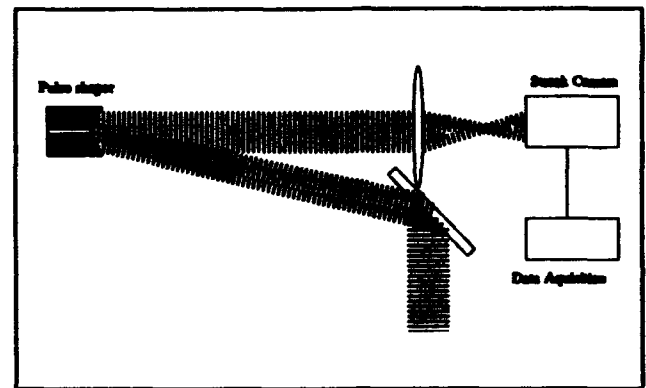


Figure 3 Experimental setup for pulse shaper measurement

As discussed in the introduction, the near optimal design parameters for short electron beam generation requires a circularly shaped laser pulse with sagitta of about 17 ps. Figure 4 shows the reflected image on the streak camera monitor for this case. The laser pulse width is about 3 ps. The apparently longer pulse is a result of the slit of the streak camera being opened wider than normal in order to capture all the image (the slit width is not exactly uniform across its width and streak tube sensitivity also varies due to the years of abuse. This explains why intensity of the data is not uniform). The full scale from top to bottom is 170 ps, and detailed data analysis show the pulse does indeed have a 17 ps sagitta.

We also have taken the data for a circular shaped laser pulse front with a 30 ps sagitta. The streak camera image for this case is shown in Figure 5.

A mountain range plot of the data in figure 6 was done to show the detailed reflected laser pulse shape.

Some other forms of laser wave front were also

tested, for example, parabolic and linear etc. All the data show good agreements with experimental set up.

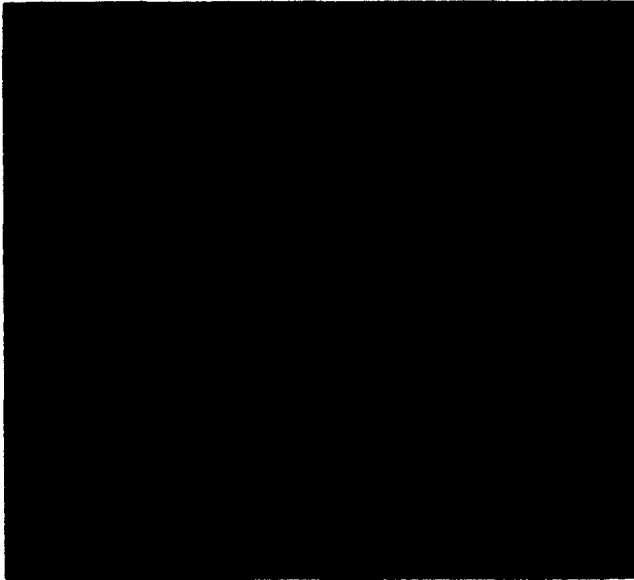


Figure 4 The streak camera image of 17 ps sagitta setting.



Figure 5 Streak image of circular shaped 30 ps sagitta setting

#### 4. Summary

The AWA laser system has been installed and tested. The results show that the system is ready for

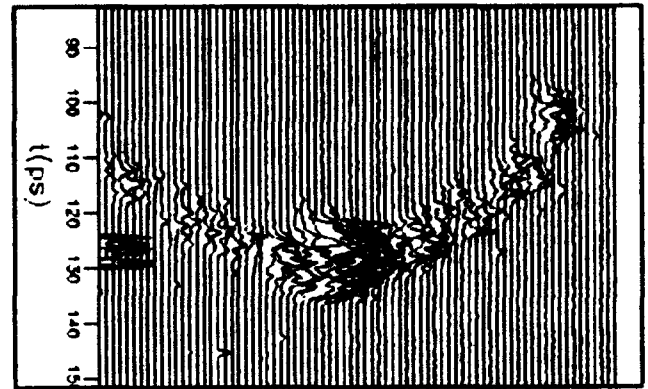


Figure 6 Mountain range plot of data in Figure 5.

initial AWA operation. The laser pulse shaper was designed and fabricated. Laboratory testing shows that this laser pulse shaping method will satisfy our present demands. A higher reflection coating is planned to further enhance the system's performance.

This work is supported by US Department of Energy, High Energy Physics Division under contract No. W-31-109-ENG-38.

#### References:

1. P. Schoessow et al, "The Argonne Wakefield Accelerator: Overview and Status", these proceedings.
2. J. P. Roberts, A. J. Taylor, P. H. Lee, "High-irradiance 248-nm laser system", Optics Letter, Vol 13, p734 (1988)
3. P. Schoessow, C. Ho, J. Power, E. Chojnacki, "Control, Timing, and Data Acquisition for the Argonne Wakefield Accelerator", these proceedings.

# CANDELA Photo-injector: the Drive Laser\*

P. Georges, P. Thomas

IOTA, Institut d'Optique Théorique et Appliquée, Bât. 501,

B. Leblond, C. Travier

LAL, Laboratoire de l'Accélérateur Linéaire, Bât. 200,

UPS, Centre d'Orsay

F-91405 Orsay CEDEX

## Abstract

In view of the future linear colliders, a bright photo-injector named CANDELA is being constructed at LAL Orsay. To illuminate the photo-cathode, a femtosecond Ti:sapphire laser has been developed. It consists of an oscillator that delivers a continuous train of femtosecond pulses at a repetition rate of 100 MHz. This train is then amplified in a regenerative amplifier pumped by a second harmonic Q-switched Nd:YAG laser. The status of the overall RF gun experiment is also mentioned.

## I. INTRODUCTION

Since the beginning of 1990, the "Laboratoire de l'Accélérateur Linéaire" (LAL) at Orsay, has started to develop a high-brightness photo-injector [1,2]. The project, named CANDELA ("CANon Déclenché par LAser"), consists of a two cavity 3 GHz microwave electron gun. These cavities are independently powered: the first one is designed to minimize the linear emittance growth and the second one is used to reduce the energy spread. The details of the calculations that led to this design are given in reference [3].

The photocathode is illuminated by a Ti:Sapphire picosecond laser designed by the "Institut d'Optique Théorique et Appliquée" (IOTA) and presented in this paper.

## II. LASER DESCRIPTION

The laser system, we have developed is based on the Titanium Sapphire crystal which has been proved to be the best material to produce very short and high energy pulses in the near infrared [4-6]. This crystal combines the advantages of the dyes with a large fluorescence bandwidth (700-1000 nm) and those of the solid state medium with a saturation fluence of  $1 \text{ J/cm}^2$ .

The laser consists of an oscillator followed by an amplifier as shown in the Figure 1.

The femtosecond oscillator is a self mode locked Ti:Sapphire laser based on that originally produced by Spence et al. [4] and producing 100 fs at 780 nm. In the linear cavity the two curvature mirrors are used off axis in order to compensate the astigmatism introduced by the Brewster angle

cut crystal. The pump beam is focused on the crystal with a curvature mirror through a dichroic mirror.

The two prisms arrangement is used to compensate the positive Group Velocity Dispersion (GVD) in the rod and to obtain very short pulses. The mode locking is produced by non linear effect (Kerr effect) in the crystal itself. This effect introduces a positive lens in the cavity that changes the cavity beam waist in the mode locked regime compared with the cw regime. By properly aligning the laser, we are able to have a large beam in cw regime that decreases in size when the laser operates in femtosecond regime. By using an aperture (slit) in the cavity, we introduce losses that are more important in the cw regime. To start the laser in pulsed regime, we mount the high reflective plane mirror on a piezoelectric transducer to create a modulation in the laser signal that initiates the non linear regime and so the mode locking.

The transducer is also used to synchronize the optical pulses with the RF wave in the cavity. The phase locking of the laser is achieved by mixing the output of a monitor photodiode with a reference signal to derive a phase-error signal. Amplification, integration, and level comparison of this signal allow a suitable error signal to be supplied to the piezoelectric transducer controlled cavity mirror. The output of the laser is so maintained in phase with the reference signal that also drives the RF cavities. We have experimentally recorded an rms jitter of 2 ps between the optical pulses and the reference signal.

The oscillator produces pulses in the range of 100 fs to 1 ps at a 100 MHz repetition rate but with an energy of a few nanojoules. In order to increase the pulse energy, we have to amplify the pulses to the millijoules level. This amplification is obtained in a regenerative amplifier pumped by the second harmonic of a Q-switched Nd-Yag laser working at 10 Hz repetition rate.

The amplifier consists of two high reflective mirrors, a Ti:Sapphire crystal, a broadband polarizer and a Pockels cell. A Faraday isolator is used to discriminate the input and the output of the amplifier. The pulse trapping and dumping is accomplished as follows : initially the pockels cell is oriented to give a quarter wave of static birefringence in order to prevent any lasing effect in the cavity. One pulse of the oscillator is then trapped in the amplifier by applying a quarter wave voltage step on the Pockels cell. The pulse then travels into the amplifier, its energy increases until it reaches the saturation. At this level, the pulse is ejected from the cavity by applying a second quarter wave voltage step on the

\* Work supported by IN<sub>2</sub>P<sub>3</sub> and ULTIMATECH under the contract number 90N89/0018

Pockels cell. The energy of the output pulse is typically 6 mJ. However, in order to avoid non linear effects in the components of the amplifier (such as self focusing) we have to decrease the peak power of the amplifier pulses by using the well-known Chirped Pulse Amplification (CPA) technique.

This technique consists of a stretcher that temporally broadens the pulse before the amplifier and a compressor after the amplification in order to return to the initial pulse duration. The stretcher consists of a single grating (2000 grooves/mm used at Littrow angle) and a lens that introduces a positive GVD. The stretching factor is of the order of 1000 to 5000. At a few hundred of ps, the peak power is decreased by the same amount and the pulses can be amplified safely. The compressor is based on a two parallel gratings arrangement (same as in the stretcher also at Littrow angle) giving the opposite (negative) GVD. The overall transmission of the compressor is more than 50 % and so the compressed pulse energy is typically 3 mJ. Furthermore by slightly disaligning the compressor we are able to vary the pulse duration of the amplified pulses and so it will be possible to study the performance of the photo-injector as a function of the temporal characteristics of the light pulses.

By using non linear effect (second and third order harmonic generation) in BBO crystals, we will produce ultrashort pulses in the UV and so take advantage of the better quantum efficiency of the photocathode at this wavelength. With 3 mJ in the near infrared (780 nm) we expect to obtain 0.3 mJ at 260 nm.

The laser was assembled in August 1992, and has been working since then.

### III. CANDELA STATUS REPORT

Some problems with the RF power source (modulator, klystron, RF network components) did not allow to start the gun conditioning in the fall of 1992 as scheduled. These problems are now solved and the gun will be conditioned starting in May 1993 with the first photo-electrons scheduled for the summer 1993.

The gun was baked for 20 days at 150°C. After that the vacuum measured just at the gun exit in the beam pipe was  $3 \cdot 10^{-10}$  Torr. This indicates that the vacuum inside the cavities is probably very near  $10^{-10}$  Torr.

A U-shape beam transport line is being assembled. It will support several diagnostics used to characterize the beam properties. These diagnostics will include Wall Current Monitors for charge and position measurements, slit and Faraday cup for energy, and OTR monitors for transverse profile measurements. For these last measurements, we are also trying to develop a gaz ionization monitor which has the advantage to be non-destructive for the beam and the laser.

### IV. ACKNOWLEDGEMENTS

All the people that participated in the construction of CANDELA RF gun are acknowledged.

### V. REFERENCES

- [1] C. Travier, J. Gao, Proc. of the 1990 European Particle Accelerator Conf., Nice, June 12-16, 1990, Ed. Frontières, pp. 706-708.
- [2] J. Gao et al., Proc. of the 1992 European Particle Accelerator Conf., Berlin, March 24-28, 1992, Ed. Frontières, pp. 1020-1022.
- [3] J. Gao, Nucl. Instr. & Meth. A297 (1990), pp. 335-342.
- [4] D. Spence, P. Kean, and W. Sibbett, Opt. Lett. 16, 42 (1991)
- [5] J. Squier, F. Salin, G. Mourou, and D. Harter, Opt. Lett. 16, 324 (1991)
- [6] J. Kmetec, J. Macklin, and J. Young, Opt. Lett. 16, 1001 (1991)

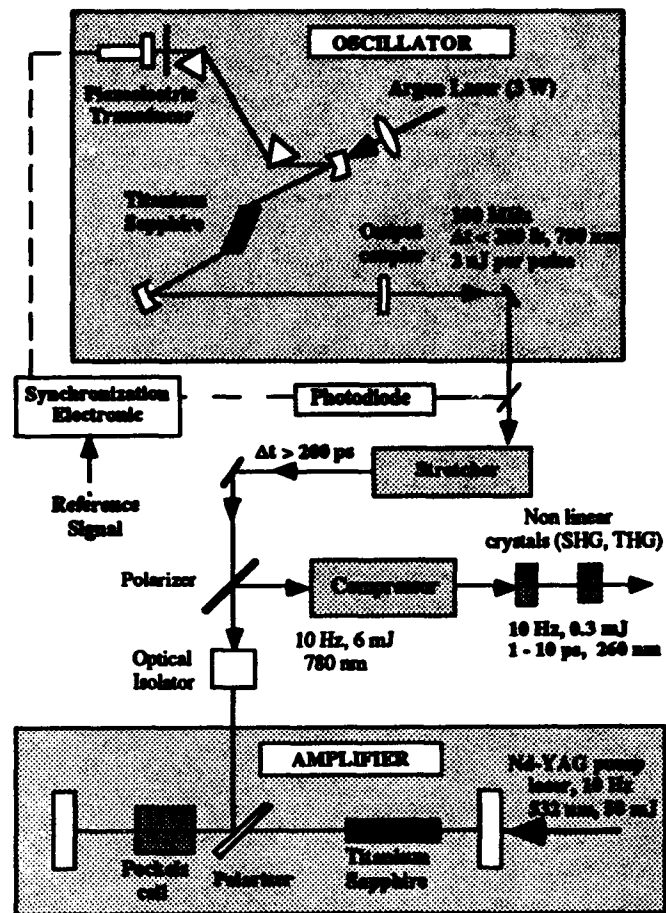


Figure 1: Schematic of the Ti:Sapphire laser system

# A Flat-Cathode Thermionic Injector for the PHERMEX Radiographic Facility

T. Kauppila, L. Buita, M. Burns, W. Gregory, D. Honabeger, and S. Watson  
Los Alamos National Laboratory  
P.O. Box 1663  
Los Alamos, New Mexico 87545  
and  
T. Hughes  
Mission Research Corp.  
1720 Randolph Road SE  
Albuquerque, NM 87108

## Abstract.

The PHERMEX (Pulsed High-Energy Radiographic Machine Emitting X-rays) standing-wave linear accelerator is a high-current electron beam generator used for flash-radiography. An improved electron gun has been designed employing a flat-thermionic cathode to replace the existing Pierce-geometry gun. The flat cathode yields increased current with the same applied voltage and cathode area as the Pierce gun. The ISIS code simulations indicate a beam current of 1.5 kA at 600 kV<sup>1</sup> vs. 500 A for the old gun. The new geometry also reduces the probability for high voltage breakdown in the A-K gap. A re-entrant magnet captures the expanding electron beam and a bucking coil nulls cathode-fringe field. A third coil is used to optimize the extraction field profile and reduce the effect of nonlinear space charge on the beam emittance. Time-resolved measurements of beam current and voltage have been made. In addition, a streak camera was used to measure beam emittance and spatial profile. Comparisons of measurements with simulations are presented.

## I. INTRODUCTION.

The PHERMEX accelerator at Los Alamos National Laboratory is used for a variety of flash radiographic experiments. The electron injector used a Pierce geometry gun employing a b-type thermionic cathode. This injector has remained relatively unchanged, and has performed reliably for over 25 years. To increase the injected current without increasing the probability of high-voltage breakdown, a new gun has been designed with a planar A-K gap. This type of geometry has been used successfully on the REX<sup>2</sup> injector at LANL. The beam is generated on a field-free thermionic cathode, extracted with a system of three solenoidal magnets and transported with an additional three solenoids to the entrance of the accelerator. We report experiments measuring current, voltage and emittance. The experimental data is also modeled with SPEED<sup>3</sup>, a 2D static beam-trajectory code.

Work performed under the auspices of the U.S. Department of Energy.

## II. EXPERIMENT.

The electron gun consists of a 5.08-cm-diam thermionic cathode with a 7.5-cm A-K gap spacing. The anode hole diam is 16 cm. High voltage isolation is provided by 2 convoluted Al<sub>2</sub>O<sub>3</sub> ceramic insulators. A schematic of the gun A-K gap and solenoidal extraction magnets is shown in Fig. 1.

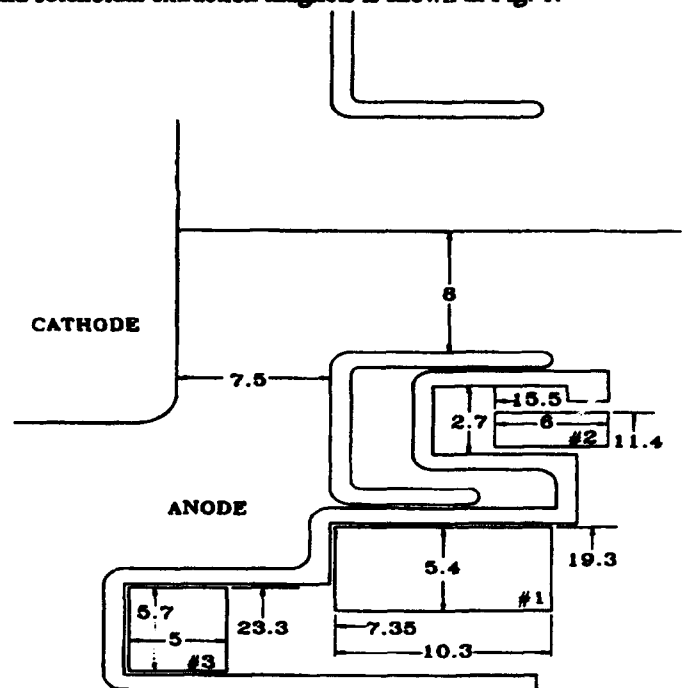


Figure 1. Schematic of gun A-K gap

The gun mechanical structure and ion plus-cryogenic vacuum pumping system are the same for the existing Pierce gun<sup>4</sup>. Vacuum pressure during operation is approximately  $5 \times 10^{-7}$  torr and cathode temperature is 1300 C. Both cathode field-forming structure and anode structure are molybdenum while the vacuum vessel is water-cooled stainless steel. The pulse power drive for the gun is a 275  $\Omega$ , 11-stage open-air cable Marx bank, which is capable of producing a 500-kV, 200-ns pulse into a matched load. Multiple-stage Marx banks of this type are inherently high impedance and inductance

pulsers, and therefore with the capacitance of the A-K gap, form an LRC circuit that exhibits damped ringing.

Voltage was measured with a 945-Ω resistor with an 0.1 Ω divider in parallel with the gun. Extracted current was measured with four-way summed and integrated b-dot sensor-loops. A Tektronix RTD-720 digitizer with a 2-ns sample rate was used to record the data. Typical voltage and current waveforms are shown in Fig. 2.

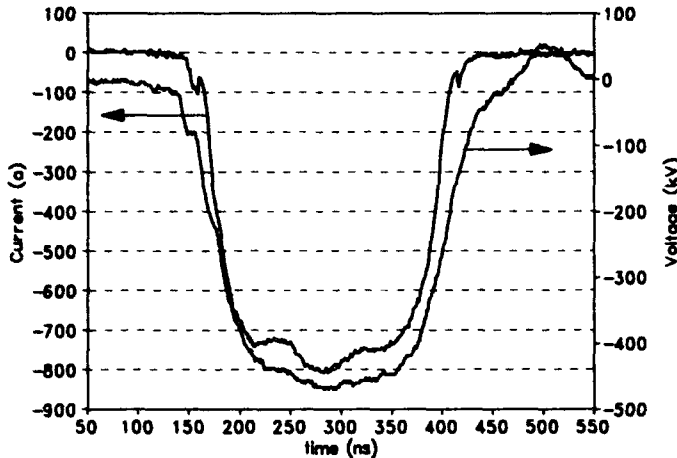


Figure 2. Plot of current and voltage waveforms

The beam was extracted with a system of three air core solenoidal magnets. The first solenoid is a 19.3-cm-diam coil with 116 turns. The second is 11.4-cm diam. with 26 turns. The third coil is 22.3-cm-diam. with 52 turns. All coils are quadrupole wound using 0.65-cm square copper wire with water cooling jackets. The third coil was placed with the magnetic pole at the cathode-surface plane, bucking the first extraction magnet. Current on the bucking coil was adjusted to produce a field null on the cathode. The extraction magnet was placed in a re-entrant anode to capture the expanding electron beam as close to the cathode as mechanically possible. The second coil was also bucking the extraction magnet. It tailors the radial field-profile by flattening  $B_z(r)$  which reduces spherical aberration. The beam was then transported with three solenoidal magnets and matched to the entrance of the accelerator. The transport magnets contain six iron homogenizing rings to reduce magnetic field tilt due to random winding errors.

Emittance was measured by intercepting the electron beam with a stainless-steel mask containing 0.4-mm-diam holes spaced 8.0 mm apart. The transmitted beamlets drift 203 mm to a Bicon-422 scintillator and produce light proportional to electron intensity. The light is relayed through a turning mirror and telescope to the streak camera photo-cathode with a Thompson-CSF large format streak camera with a velocity of 4 ns / mm. To measure radial current distribution the emittance mask was replaced by a mask containing a 0.75-mm slit. The streaked images were then captured by an optically coupled, cooled, 1024x1024 pixel back-thinned, 16 bit CCD camera and stored on a 486 PC. Analysis was

performed using an IDL computer code<sup>5</sup>. The code displays the streak image and provides rapid analysis for shot-to-shot comparison.

### III. RESULTS

A plot of extracted current vs voltage is shown in Fig.3. Initial calculation of gun perveance overestimated the extracted current (20 %). Measurement of the A-K geometry

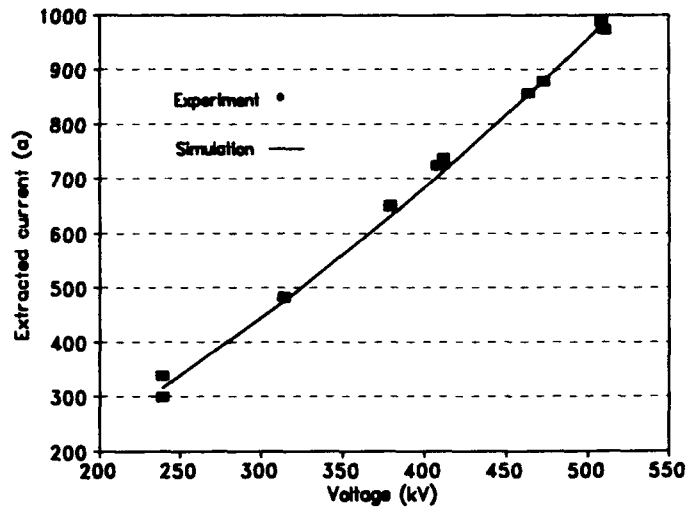


Figure 3. Extracted current vs. voltage

determined that the cathode was inset 1.5-mm from the field-forming electrode. This reduced the electric field on the outer annulus of the cathode where a substantial fraction of the beam current was generated. Subsequent recalculation with the correct geometry matches the experimental results. A plot of the calculated radial current distribution from the cathode with flush and inset cathodes is shown in Fig. 4. At 400 kV the flush cathode produces 790 A while the recessed was 690 A.

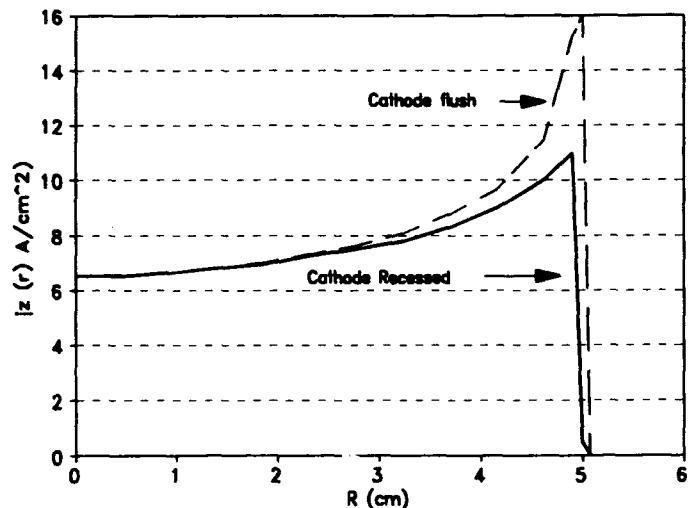


Figure 4 Current density with flush and inset cathodes

A significant contribution of the electron beam emittance is caused by curvature or "twist" in phase-space. This twist is produced by both nonlinear space-charge and solenoidal over focusing, and is compensated by the introduction of the second solenoid. An emittance plot showing the twist reduction by the second coil is shown in Fig. 5.

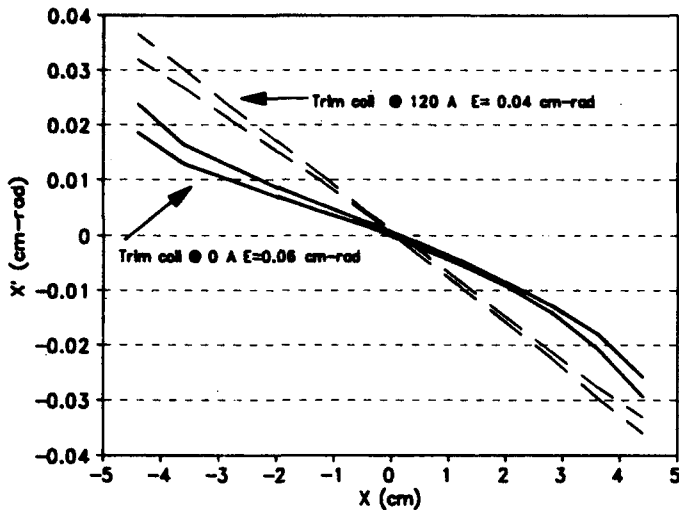


Figure 5. Phase space plots showing improvement in phase-space curvature

The emittance was determined by measuring the parametrically-fit Gaussian distributions of the streaked beamlet widths. From the average positions, the radial velocity of the beamlets can be calculated, while the line widths are related to the transverse beam temperature. The emittance is calculated according to the relation<sup>6</sup>

$$E = 4 \beta \gamma x_{rms} x'_{rms}. \quad (1)$$

The center beamlet is used to determine the effective cathode temperature by fitting it to a Gaussian function and correcting (deconvolving) the data for the finite hole size in the mask to yield the angular spread. The spread is then corrected for beam compression by the ratio of cathode to beam diam. at the mask. This angle when normalized to the beam voltage is the angular spread at the cathode surface. The effective cathode temperature is given by

$$T_{eff} = .511 \times 10^6 (\beta \gamma \theta_{rms})^2 = 6.0 \text{ eV}. \quad (2)$$

The corresponding Lapostolle emittance at the cathode is

$$E_L = 2 \times R_{cathode} * \beta \gamma \theta_{rms} = 0.03 \text{ cm-rad}. \quad (3)$$

The radial current distribution is peaked at the outer radius where space-charge depression on the cathode is smallest. As the beam is transported through the remaining three solenoids the beam undergoes charge redistribution and flattens considerably. A plot of the radial current distribution at 225 cm is shown in Fig. 6.

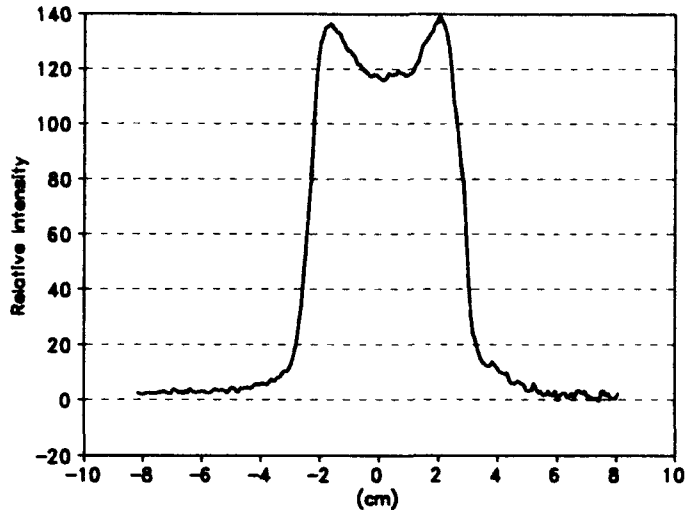


Figure 6. Beam distribution after transport  
V= 475 kV, I=860 A

#### IV. CONCLUSIONS.

The total current the injector produces is slightly lower than predicted. This difference is attributed to the inset of the cathode from the cathode field forming electrode and predicted by SPEED calculation. A new mechanical design will bring the cathode forward and flush. The normalized rms emittance measured with the streak camera was 0.04 cm-rad, which compares favorably with the SPEED calculation of 0.05 cm-rad. The effective cathode temperature is 6.0 eV. The injector voltage of 500 kV nominal produces 950 A. This corresponds to a perveance of 2.7  $\mu\text{P}$ . To produce the necessary current density the cathode must be run at higher than desired temperature, which reduces cathode lifetime and requires the heater filament to be run at correspondingly large input power. A new Spectra-Mat 311 barium ratio cathode with a scandate-dopant will lower cathode operating temperature. Based on the experimental results we expect this new gun may double the output X-ray dose of the PHERMEX accelerator.

#### V. REFERENCES.

- [1] T. Hughes, D. Moir, R. Carlson, "Upgrade of the PHERMEX Accelerator," Proc. 1991 IEEE Part. Accel. Conf. p. 245
- [2] T.P Hughes, R.L Carlson, and D.C Moir, "High-Brightness Electron-Beam Generation and Transport," J. Appl. Phys. 68 (6) pp. 2662-2571, September 1990.
- [3] SPEED was written by J. Boers, Thunderbird Simulation, Inc.
- [4] L.A. Buita "PHERMEX electron gun development" Proc. 1983 Part. Accel. Conf.
- [5] EMIT was written by S. Watson, Los Alamos National Laboratory.
- [6] S. Humphries, Charged Particle Beams (Wiley-Interscience, 1990), pp 93-101.



The edge synchronized start and stop pulses are used to generate a gate whose width is determined by the time between the leading edges of the start and stop pulses from the ALS Timing System. A coincident circuit which follows generates a burst of 125 MHz RF signal with this gate. In the mean time the trailing edge of the 300 ns start pulse starts a 950 ms time out gate which is used to disable the RF gate generator for that duration of time. When this gate is activated via a jumper on the circuit board, there is a 950 ms dead time after one burst of gun pulses. This is used to safeguard the gun from being accidentally pulsed more than once per second from external sources.

The output from the RF gate is amplified and used to drive an optical transmitter which operates at the wavelength of 820nm. A fiber optic cable transmits the optical signal to a RF optical receiver on the high voltage deck. The output from the optical receiver is amplified and filtered before it is used to drive a 25 watts wide band RF amplifier whose output in turn drives the gun cathode. The grid bias control for the gun is also optically coupled to the high voltage deck and the bias level can be set and read back via fiber optical cable.

An external RF shut down control has been implemented to accommodate various operating requirements. The system will accept an external differential TTL logic level signal and shut down the RF gate generator. No signal will be generated to drive the cathode under this condition.

### III. CURRENT PULSE WIDTH

An Eimac tube, 8847A[4], was used to simulate an electron gun for the current pulse width measurement. A toroidal transformer was used to monitor the current pulse width and amplitude when various bias levels were applied to the grid under certain drive conditions. Using a 50V peak, 125 MHz sinusoidal drive signal, the measured transfer functions of the current pulse width and amplitude versus the grid bias is given in fig. 2. The anode voltage was set at +400V for this measurement, at which point  $V_g$  (see below) was -5V. Although this measurement cannot represent the actual ALS gun performance, it does show the bias can be used to lower the current pulse width with a reduction in pulse current amplitude. The deviation of the measured pulse widths at high bias voltages could be partly due to measurement instrumentation bandwidth limitation.

The current pulse width generated by a sinusoidal drive signal with a triode whose grid is biased beyond cutoff can be represented by the following expression:

$$T_w = \frac{90 - \sin^{-1} \left( \frac{(V_b - V_g + V_p)}{2V_p} \right)}{180 f}$$

- where
- $T_w$  = Output current pulse width at FWHM
  - $-V_b$  = Grid bias
  - $-V_g$  = Bias voltage at which the triode starts to conduct at the operating electric field gradient
  - $-V_p$  = Drive signal peak voltage
  - $f$  = Frequency of drive signal in Hertz

Figure 2 also shows the limitation of this mode of operation. Other limiting parameters in the supporting system

also enter the picture when higher current pulse amplitude and narrower current pulse width are required. Different schemes of generating a higher amplitude and narrower current pulse width may be necessary if such requirement should exceed the capability of the present system. Figure 3 shows a typical pulse train produced by the ALS electron gun as monitored by a Wall Current Monitor[3].

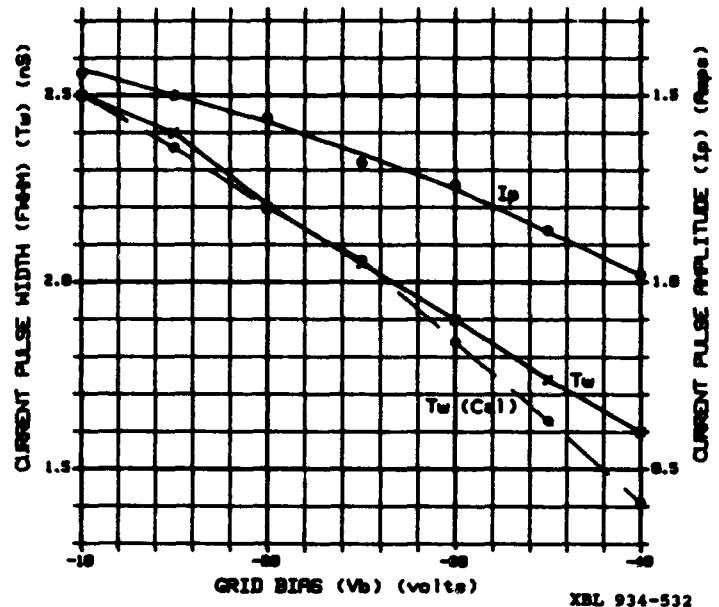


Figure 2. Current pulse width and amplitude vs grid bias.

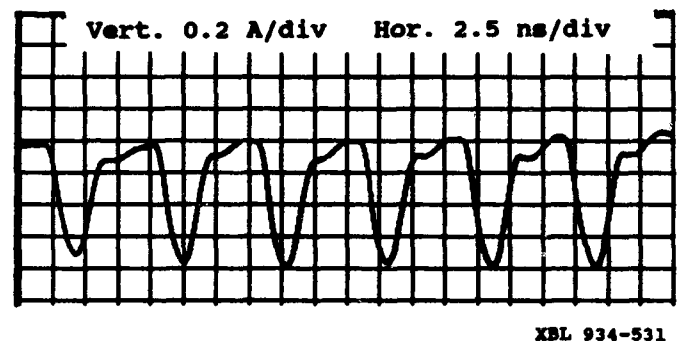


Figure 3. ALS gun pulses as monitored by the Wall Current Monitor

### IV. CONCLUSION

The Gun Electronics System was developed to provide the ALS with single or multiple electron bunches with low time jitter performance. ECL devices are used in all timing and logic circuits to ensure low time jitter for the electron bunches. The time jitter has been measured at better than 50 ps FWHM with available instruments on hand. The processing of most signals on the ground end helps reduce the power requirement at the high voltage deck, and also reduces the optical component count of the system. The system has been operating for many months without any problem. Further work on producing a narrower current pulse width and a higher current pulse amplitude may be needed if such parameters are desired in future operations.

## V. ACKNOWLEDGMENT

This work was funded by the director, Office of Energy Research, Office of Basic Energy Sciences, Material Science Division of the U.S. Department of Energy under Contract No. DE-AC03-76SF00098 with Lawrence Berkeley Laboratory. Reference to a company or a product name does not imply approval or recommendation of the product by the University of California or the U.S. Department of Energy to the exclusion of others that may be suitable.

## VI. REFERENCES

- [1] Hermosa Electronics, Instruction Book For LBL Electron Gun.
- [2] M. Fahmie, Design of the Advanced Light Source Timing System. To be presented in this Conference.
- [3] J. Hinkson, Performance of Advanced Light Source Particle Beam Diagnostics. To be presented in this Conference.
- [4] Brian Taylor, Private communication.

# Witness Gun for the Argonne Wakefield Accelerator

J. POWER, J. SIMPSON and E. CHOJNACKI

Argonne National Laboratory, Argonne, IL, 60439, USA

## Abstract

In order to probe the wakefields of the Argonne Wakefield Accelerator (AWA) a beam of medium energy (4 - 6 MeV) and relatively low charge (100 pC - 1 nC) is needed. Two options for a witness gun meeting these specifications are currently under study. The first is a conventional iris loaded multicell gun. The second is a dielectric-lined cylindrical cavity operating in a pure  $TM_{01n}$  mode. Since a more accurate probing of the wakefields can be obtained by improving the witness beam quality, this factor of merit will determine which gun is better suited for the experiment. It is thought that a brighter beam may be obtained using the dielectric gun. Since the dielectric gun will operate in a single accelerating mode, higher order modes will not be present. This in turn may lead to a slower emittance growth. This potential benefit comes at the cost of a lower cavity Q and dielectric charging considerations. Details of design, bench test and simulation results will be presented.

## I. INTRODUCTION

The AWA group is considering two options for an electron gun for generation of a witness beam for use in the AWA project. After briefly describing why we are considering both options, the physical layout of each accelerating structure will be presented. Simulation results done with PARMELA will then be presented here for both options in an attempt to compare the guns. Bench test have already been done on the dielectric-lined gun using a network analyzer and a relatively high cavity Q was found. The paper will end with some concluding comments about the future course for the AWA witness gun.

## II. MOTIVATION

It is shown<sup>(1)</sup> that two major causes of emittance growth are due to space charge and the nonlinearities present in the fields of an accelerating structure. For this reason, we feel there may be some benefit in using a structure operating in a pure  $TM_{01n}$  mode. The fields in the dielectric-lined cavity have been calculated<sup>(2)</sup> and are very nearly linear in the region of acceleration. Whereas conventional slow wave structures using irises create large nonlinearities in the region of the irises. However, since the AWA project MUST have a functioning witness gun for its experiments, we have decided to also design a conventional copper cavity, for insurance purposes. The design being studied is a scaled up version of the MARK IV accelerator.

## III. GUN CONSTRUCTION

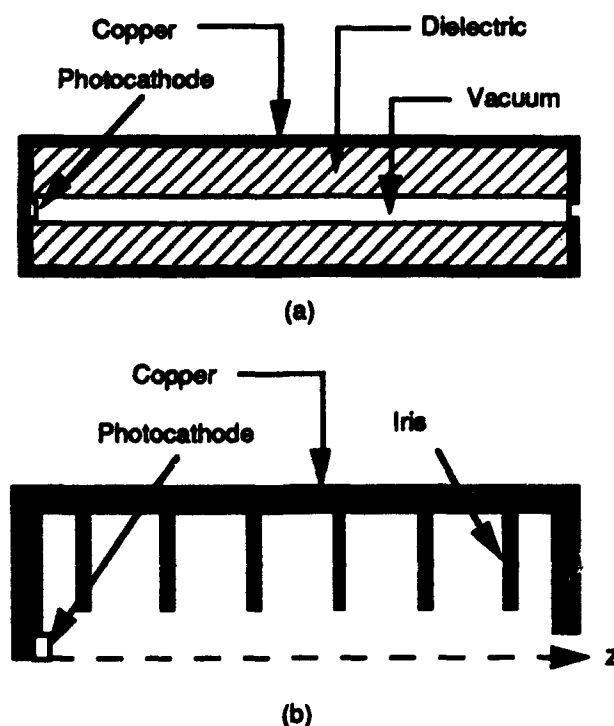


Fig. 1) Schematic views of both guns. a) Dielectric-lined gun b) 6 cell, Mark IV gun

### A. Dielectric Gun

For our initial test cases we designed the dielectric gun to run in a  $TM_{013}$  mode and we chose the dielectric to be quartz. Since the rf power available has a frequency of 1.3 GHz and we will operate at a phase velocity of 98% the speed of light, all dimensions of the cavity are fixed. The inner radius of this gun is 1 cm. The inner radius is the radius of the region labeled vacuum in Fig 1a. Solving for the outer radius by requiring the particular phase velocity we obtain a radius of 5.44 cm. The outer radius is from the center of the vacuum section to the copper/dielectric boundary. Lastly, the length of the cavity is determined to be 32.57 cm.

### B. Mark IV Gun

The Mark IV accelerator (an s-band structure) was the predecessor to the two mile accelerator at SLAC. We chose this design for several reasons. Since we will be running off

the same modulator used to drive the preaccelerator<sup>(3)</sup>, we will have limited power available to operate the witness gun, about 4-6 MW. Due to both power and spatial limitations (not much room for the gun, about 1 m) the gun will be operated in a standing wave mode. We also wanted an iris loaded cavity optimized for low bunch charge that would provide a 4-6 MeV beam. With only minor modifications the Mark IV gun proved to be an excellent choice. Since the modulator will operate at 1.3 GHz we needed to scale the dimensions of the original Mark IV gun up from s-band to l-band. The dimensions are as follows, the length is 46 cm, the radius to the irises is 2.48 cm, the radius to the outer walls is 9.05 cm, the gap between irises is 7.68 cm and the thicknesses of the irises is 1.28 cm.

### III. COMPARISON OF GUNS

In 1992 we performed a bench test to measure the cavity Q of the dielectric lined gun. Using alumina as the dielectric we made the measurements at room temperature with a network analyzer. The alumina tube was purchased from Coors and was quoted to have a loss tangent of  $10^{-4}$ . Given this value and the dimensions of the cavity, we expected a Q of about 7000. The result of the bench test however was a Q of 12,500. We felt that this was due to the particular sample we received from Coors having a loss tangent of  $0.5 * 10^{-4}$ . In any case, we now feel reasonably confident about being able to find high Q dielectrics for our gun. For simulation purposes, however, we used a very conservative (low) value of Q.

Simulations are being carried out with a modified version of PARMELA<sup>(4)</sup> for both guns. For our initial studies we have chosen quartz as our dielectric and to run in a TM<sub>013</sub> mode ( $\epsilon = 3.87$  &  $Q = 6880$ ). With this low value of Q the dielectric gun is power consumptive, needing about 15 MW to produce a 5.2 MeV bunch energy. However, the other figures of merit, emittance, energy spread and bunch length show the beam to be of high quality (see table 1).

For the Mark IV gun we have chosen to use a 6 cell, standing wave gun operating in a  $2\pi/3$  mode (see fig 1b). This gun gives acceptable beam quality at low power. For 4 MW of power the emerging beam has an energy of 5.4 MeV and sufficient beam quality (see table 1).

For comparison purposes a list of output parameters is given in table 1. A bunch charge of 100 pC is being run through each gun. Both beams have an initial phase launch angle of 70° and the size of the laser pulse on the photocathode is 2 mm in the dielectric gun and 1 mm in the Mark IV gun.

	Dielectric	Mark IV
Energy	5.20 MeV	5.42 MeV
Emittance	1.01 mm*mrad	1.86 mm*mrad
Energy spread	0.69%	3.28%
Bunch length	1.8 ps	3.57 ps

Table 1) Comparison of the dielectric and Mark IV guns done with PARMELA.

Although the modified PARMELA code fully calculates space charge effects, it does not take wakefields into account. The primary effect of the wakefields are to increase the energy spread of the bunch. We have estimated the energy spread due to wakefields in both guns analytically. The energy spread calculated by PARMELA and due to the wakefields are given in table 2.

	Dielectric	Mark IV
Wakefields	1.1%	0.2%
PARMELA	0.69%	3.28%
Total	1.79%	3.48%

Table 2) Energy spread due to wakefields and PARMELA.

### IV. THE FUTURE

For the purposes of the AWA experiment we will probably have to use the Mark IV gun since the dielectric gun is too power consumptive. This does not rule it out altogether though. It still may be useful to someone looking at generation of a high quality beam of medium energy in a small space. As long as power is not your main limitation, the dielectric gun may prove to be a viable option. Since there are so many parameters that can be adjusted for the dielectric gun, We fully expect the beam parameters to improve further. Simulations on the dielectric gun will continue. The immediate plan is to first build the Mark IV gun so we have a working witness gun for the AWA project. We will then build and run the dielectric gun both at low power (4-6 MW) and at high power (15 MW) for further investigation into the feasibility of a dielectric lined electron gun.

### IV. REFERENCES

1. Kwang-Je Kim, Nuc. Inst. and Meth. in Phys. Research (1989) pg. 201-218, 'rf and space charge effects in laser-driven rf electron guns'
2. J. Power, Argonne HEP Division, Wakefield Note (1993)
3. M. Rosing *et. al.*, Argonne Wakefield Accelerator Update '92, Proc. 1992 Linear Accelerator Conf. (Ottawa, Ontario, Canada) Vol. 1, pg. 79
4. C. H. Ho, Ph.d. Thesis, UCLA (1992)

# PARAMETRIC STUDIES WITH PARMELA TO IMPROVE SLC PERFORMANCE\*

T.A. Jones, A.D. Yermian, R.H. Miller  
Stanford Linear Accelerator Center  
Stanford University  
Stanford, CA 94309

## Abstract

The PARMELA particle dynamics code has been used at SLAC to simulate the SLC injector from the electron gun through the first accelerator section. The strength of injector components was set and tuned based on the simulation results. Parametric studies with PARMELA were conducted in which injector components were varied in an incremental fashion to study their effects on beam parameters such as transmission of current, capture of the charge in 20° of S-Band, required for satisfactory spectrum, and emittance. We discuss the results of our simulation and its application to optimizing the performance of the injector.

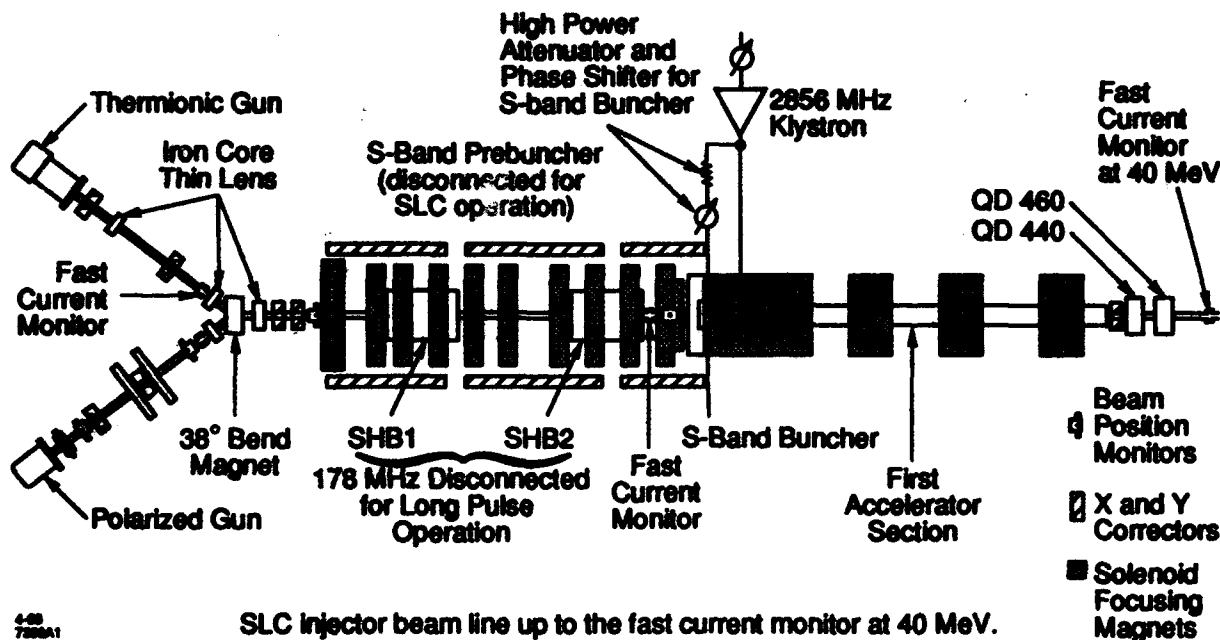
## I. Introduction

The SLC Injector is designed to deliver two bunches of electrons to a damping ring whose energy is nominally 1.2 GeV. These bunches must be 61 ns apart, with greater than  $6 \times 10^{10}$  electrons in 20 ps per bunch, at a repetition rate of up to 120 Hz, with less than 2% intensity jitter [1]. We try to reduce the intensity jitter due to individual components to less than 0.2%. In an effort to fulfill these conditions, the

PARMELA simulation has been used to study the stability and optimization of various parameters in the injector, most recently the amplitude of the S-Band (2856 MHz) buncher.

## II. The Injector

The Injector, Fig. 1, consists of two electron guns, each at a 38 degree angle from the accelerator centerline, a switching magnet to allow operation of either gun, a bunching section consisting of two subharmonic bunchers at 178.5 MHz, a 4 cell S-band (2856 MHz) buncher, and a 3 m traveling wave S-band accelerating section which contributes to bunching as well as accelerating the beam to 40 MeV. The power into the S-Band buncher is obtained from the Klystron to the first accelerator section through a 7 dB coupler. There are a high power attenuator and a phase shifter to adjust the amplitude and phase of the S-Band buncher RF independently of the accelerator section. The injector compresses the beam from 2.5 ns at the gun to less than 20 ps at 40 MeV. Beyond the gap intensity monitor at 40 MeV, there is a series of accelerating sections which further accelerate the beam to 1.2 GeV [2]



SLC injector beam line up to the fast current monitor at 40 MeV.

Figure 1. SLC injector beamline up to the current monitor at 40 MeV.

\*Supported by Department of Energy contract DE-AC03-76SF00515.

### III. The Simulations

#### A. Simulation Procedure

PARMELA, a 3D ray trace code with a 2D space charge model, was used to simulate the beamline [3] and the beam parameters at the gun were calculated with EGun [4]. The magnetic field profile due to magnet optics was calculated using POISSON [5]. Results of these codes show good correspondence to past experiments [6].

Using our simulation tools we optimized the bunching and the magnet optics to maximize electron capture into 20° of S-Band starting with a gun pulse of  $12.4 \times 10^{10}$  e- in a 3.2 ns FW, 2.5 ns FWHM truncated Gaussian distribution.

Using PARMELA, the S-Band buncher amplitude was varied in an incremental fashion, with all other electric field parameters optimized and held constant. The corresponding effects on capture, transmission of total current, and emittance were noted at the location corresponding to the intensity monitor at 40 MeV, where the beam is well bunched and relativistic.

#### B. Simulation Results

The damping ring acceptance is  $\leq \pm 1\%$  energy spread. For this study, we define capture to include only those particles falling within a final bunch length of 20° of S-Band, resulting in an energy spread of about  $\pm 0.75\%$ .

We plotted the fraction of electrons captured in 20° S-Band as a function of S-Band buncher amplitude. As shown in Fig. 2, the resulting graph has an almost parabolic dependence, although a fourth order equation was used in order to closely fit the points around the peak. The peak lies at an amplitude of 6 MV/m.

Figure 3 shows the percent intensity change per percent amplitude change as a function of amplitude for charge captured within 20° of S-Band, and shows the sharp rise in jitter that occurs as we move away from the optimum amplitude.

The amplitude jitter of the S-Band buncher is 0.4%, mostly due to multipactor in the high power phase shifter. We are particularly concerned with how this amplitude jitter affects the intensity jitter as a function of S-Band buncher amplitude. That is, if the S-Band buncher is set at some nominal amplitude around which it is allowed to vary by 0.4%, by how much does the intensity vary?

Using Taylor series expansion and the fourth order polynomial fitted to the capture vs. S-Band buncher amplitude curve, we calculate that for 0.4% amplitude jitter, the captured electron intensity jitter is essentially zero at the optimum amplitude setting of 6 MV/m. At 3.5 MV/m, where the amplitude was set, before the PARMELA simulations of the injector were conducted, the calculated captured electron intensity jitter is 0.3%.

We also plotted total charge as a function of S-band buncher amplitude (Fig. 4). Total charge is of interest since it is easily observed on the toroids, and is often used as a diagnostic in actual machine tuning. Total charge has a parabolic dependence on amplitude and peaks somewhere around an amplitude

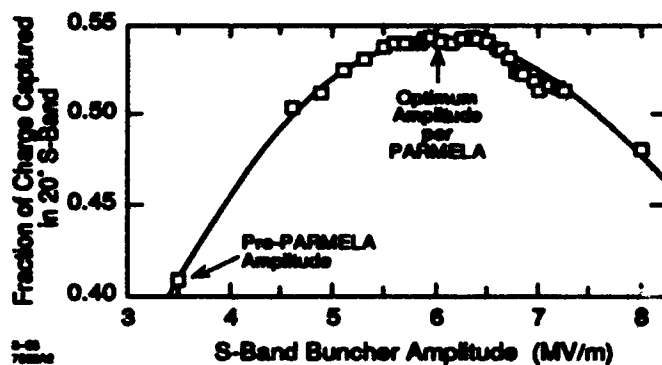


Figure 2. Capture vs. S-Band buncher amplitude.

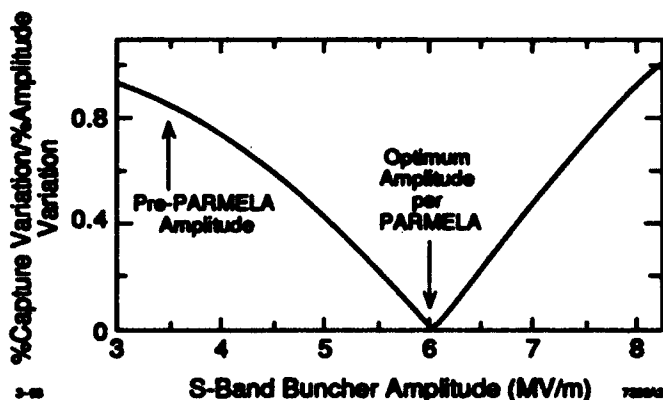


Figure 3. Percent intensity change per percent amplitude change vs. S-Band buncher.

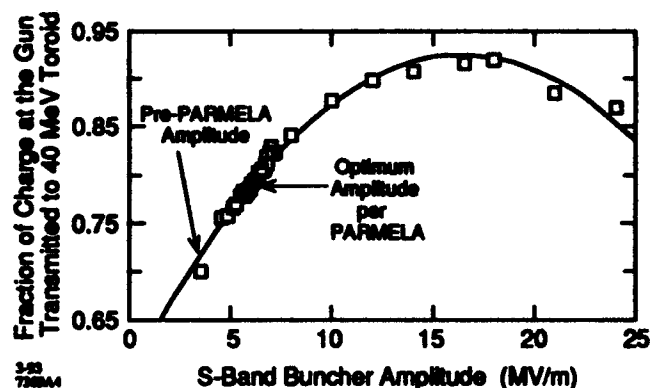


Figure 4. Total charge vs. S-Band buncher amplitude.

of 15 MV/m, which is much higher than the amplitude for optimum bunching. This graph, together with the capture vs. amplitude graph, demonstrates that tuning for optimum bunching will actually mean less total transmission from the gun to the 40 MeV point. This is because the gun pulse width at 3.2 ns FW is too long for 100% capture by the 178.5 MHz subharmonic buncher system.

X and Y normalized emittances for RMS and for 90% of transmitted particles were plotted (Figs. 5, 6, 7, and 8). These graphs show that the emittance rises as the S-Band buncher amplitude is increased, leveling off somewhere around 15 MV/m.

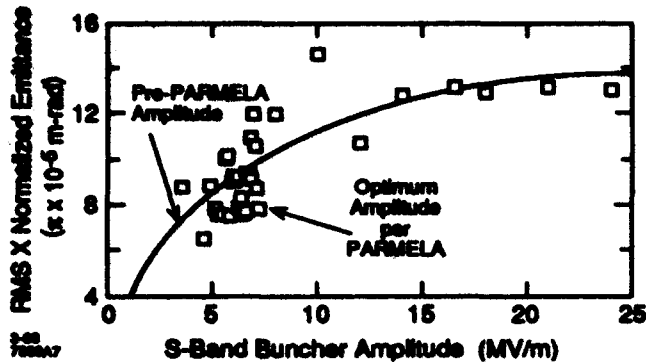


Figure 5. RMS X normalized emittance vs. S-Band buncher amplitude.

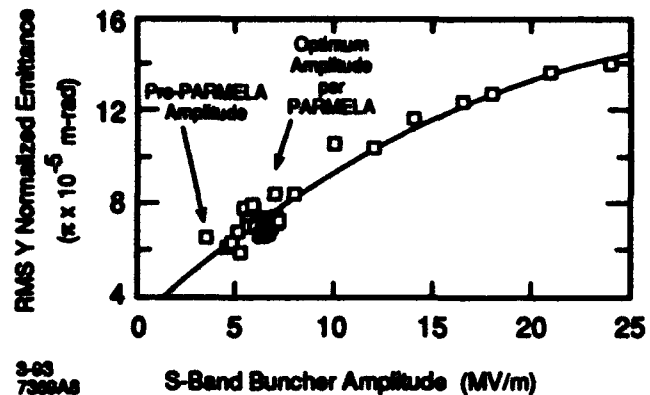


Figure 6. RMS Y normalized emittance vs. S-Band buncher amplitude.

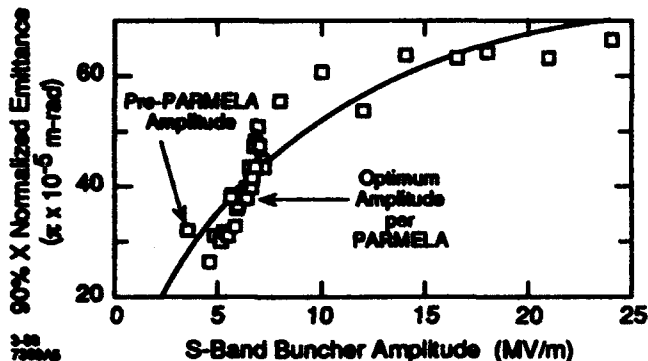


Figure 7. 90% X normalized emittance vs. S-Band buncher amplitude.

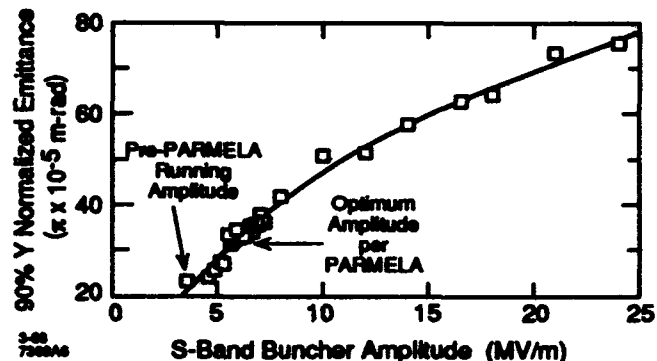


Figure 8. 90% Y normalized emittance vs. S-Band buncher amplitude.

#### IV. Summary of Results

The nominal gradient in the S-Band buncher for the SLC injector before modeling with PARMELA was 3.5 MV/m. On the basis of PARMELA-derived results, we have been running with a gradient of about 6 MV/m. This has improved bunching and allowed for larger S-Band buncher RF amplitude jitter tolerances.

Machine studies designed specifically to support or refute these results have not been performed. However, we do have history plots of the S-Band buncher RF amplitude which show that during the period in which the S-Band buncher was set to 3.5 MV/m, it was necessary to have amplitude jitter tolerances of 0.03% to minimize intensity jitter in the captured charge. Recently, with the buncher set to 6 MV/m, S-Band amplitude jitter reached as high as 0.6% with no noticeable ill effect on the intensity jitter. This difference of greater than an order of magnitude seems to support the model results.

#### V. References

- [1] M.B. James and R.H. Miller, "A High Current Injector for the Proposed SLAC Linear Collider," *IEEE Trans. Nucl. Sci.*, NS-28, (3), 3461 (1981).
- [2] A.D. Yeremian et. al., "SLC Injector Simulation and Tuning for High Charge Transport," *Linac '92 Conference*.
- [3] K. Crandall and L. Young, "PARMELA: Phase and Radial Motion in Electron Linear Accelerators," Private communication.
- [4] W.B. Herrmannsfeldt et.al., "EGUN, Electron Trajectory Program," SLAC-PUB-331 (1988).
- [5] K. Halback, "POISSON Lectures at LBL", 1972 (unpublished).
- [6] A.D. Yeremian et. al, "Boeing 120 MeV RF Linac Injector Design and Accelerator Performance Comparison with PARMELA," *Proceedings of the 1989 IEEE Particle Accelerator Conference*, Vol. 1, p. 657, 1989.

# High Current, Low Energy Electron Beams Produced During the High Current Phase of a Pseudospark\*

T-Y Hsu, R. Liou, G. Kirkman\*\*, and M. A. Gundersen  
Department of Electrical Engineering-Electricphysics  
University of Southern California  
Los Angeles, CA 90089-0484 USA

## Abstract

Electron beams produced by the superemissive cathode of a back-lighted thyratron (BLT) or pseudospark are reported. The cathode is highly emissive, or superemissive during conduction, producing a current density of  $>10^4$  A/cm<sup>2</sup> over an area of  $\sim 1$  cm<sup>2</sup>. During conduction, electrons produced by the cathode are accelerated through the anode central hole, forming a beam that can be extracted. An electron beam of 120 A has been observed with an efficiency of 10%. The beam current increase with increasing applied voltages and decreasing gas pressure. A pulse forming network can transfer energy to an electron beam with a duration of the discharge pulse. The superemissive beam has energy of  $\sim 400$  eV corresponding to the cathode sheath voltage. Beam extraction into a low pressure area ( $<7$  mTorr) was achieved by a differential pumping scheme with a guiding magnetic field. A flat-top spatial profile of the beam current distribution is obtained after the beam propagation through a narrow dielectric tube.

## I. INTRODUCTION

The back-lighted thyratron (BLT) or pseudospark structure have been studied for producing pulsed electron beams and proposed as a potentially high-quality beam source for high power applications. Pseudospark-produced electron beams during and briefly before voltage breakdown have been reported, and is related to the hollow cathode (HC) discharge.[1-4] Electron beams generated by the back-lighted thyratron (BLT) during the conduction phase, which is related to the superemissive cathode (SEC) discharge, also have been reported.[5-7] The SEC in the BLT is self-heated, very robust, and produces extremely high, uniform current.[8-10] In the low pressure glow discharge mode, typical of the BLT and the pseudospark, high current density on the order of 10 kA/cm<sup>2</sup> over an area of 1 cm<sup>2</sup> have been observed. New evidence and theory show that vacuum arc type discharges also present on the cathode surface near the center hole during the SEC conduction phase.[11] During the conduction of the BLT, the voltage across the gap is dropping down to the order of a hundred volts. Most of the voltage drop is across the cathode fall region which forms a thin layer of few micron on the cathode surface. The electrons generated by the superemissive cathode are accelerated across the cathode fall region and inject into the bulk plasma. The formation and extraction of the SEC electron beam was simulated and predicted by Bauer and Gundersen.[12,13] In this report, we present further data

related to characteristics of the SEC beam, the influence of operation parameters, extraction of the SEC beam into low pressure area, and the effect of dielectric tube.

## II. EXPERIMENTS AND RESULTS

The experimental setup for the SEC beam diagnostic is the same as in reference.[5] Figure 1 shows typical discharge currents and beam currents produced by the BLT with an external capacitor for energy transfer. The beam current extended well into the falling portion of the discharge current indicating a SEC beam, as distinct from a HC beam. These electrons are injected from the cathode fall region of the BLT during the high-current conduction phase. The beam current terminates shortly after the maximum of the discharge current, which is a result of fast voltage decay across the BLT during conduction. Experiments also show that the beam current increases with applied voltage (Figure 1) and with decreasing gas pressure within the operation range of 60 to 20 mTorr argon gas. This suggests that the voltage holdoff capability of the BLT, thus the SEC-produced beam current, can be scaled by a multiple-gap structure.[14]

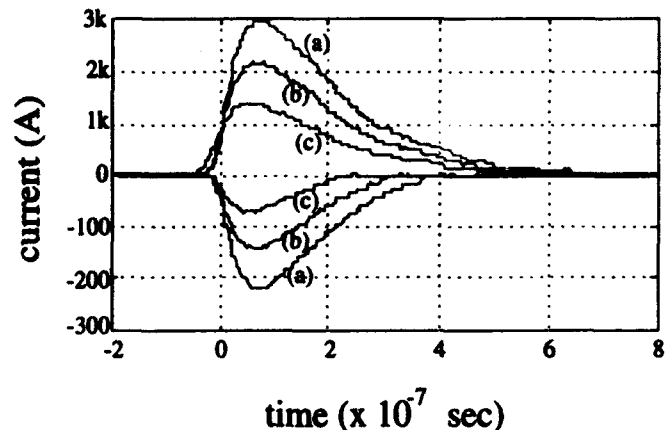


FIG. 1 The discharge currents (positive) and the beam currents (negative) at 50 mTorr argon, applied voltages of (a) 10 kV, (b) 15 kV, and (c) 20 kV, using a 40 nF charging capacitor and a 5 ohm load resistor.

The beam characteristics has been studied with several different pulse forming network (PFN) as energy transfer unit. Figure 2 shows typical beam pulses and the discharge current at different gas pressures. The beam has about the same duration as the discharge current. The magnitude of beam pulse also increases with increasing applied voltage and with decreasing gas pressure as shown in Figure 2. A voltage measurement shows a significant amount of voltage ( $\sim$  few hundred volts) is maintained and not decaying across the BLT

\* This work was supported in part by the U.S. Army Research Office, SDIO through the U.S. Office of Naval Research, and the Lawrence Livermore National Laboratory.

\*\* G. Kirkman is with Integrated Applied Physics, Inc., Waltham, MA.

during current discharge. Measurements indicate that the voltage across BLT increases with increasing applied voltage.

Another setup with crossed glass drift tube, which provide a portion of drift region with wider cross section, is constructed to look at the Larmor radii of beam electrons at different applied voltage. The magnet is placed right below the crossed region of the glass drift tube. Results show that the Larmor radius of the SEC beam increases with increasing applied voltage, indicating the energy of the SEC beam, just like the energy of the HC beam, increases with applied voltage. The data shows the Larmor radius of the SEC electrons is 0.85 cm at applied voltage of 20 kV. Knowing the magnetic field at tube center ( $\sim 80$  Gauss), the estimated energy of the SEC beam is 420 eV. At applied voltage of 13 kV the SEC beam energy is 170 eV.

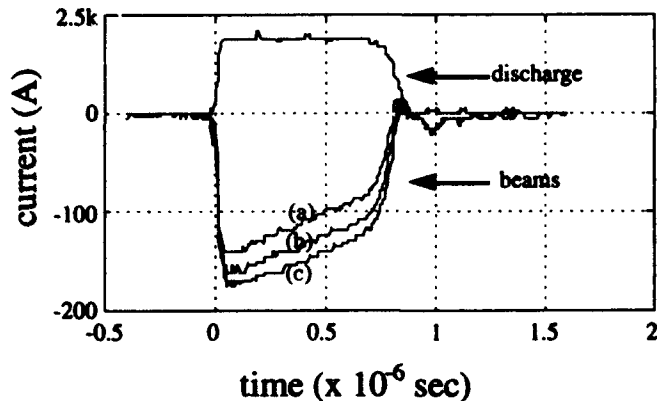


FIG. 2 The discharge and the beam currents at 15 kV applied voltage and argon pressures of (a) 50, (b) 40, and (c) 30 mTorr, using a PFN of 750 ns pulse for energy transfer.

The behavior of the SEC electron beam in the low pressure ( $< 10$  mTorr) area is studied by a differential pumping scheme. The gas is fed in from the BLT cathode side and pumped out from the diagnostic region. The differential pumping effect results from the central holes of electrodes and anode back wall. A longitudinal magnetic field is generated for focusing the electron beam. Figure 3 shows the increase of

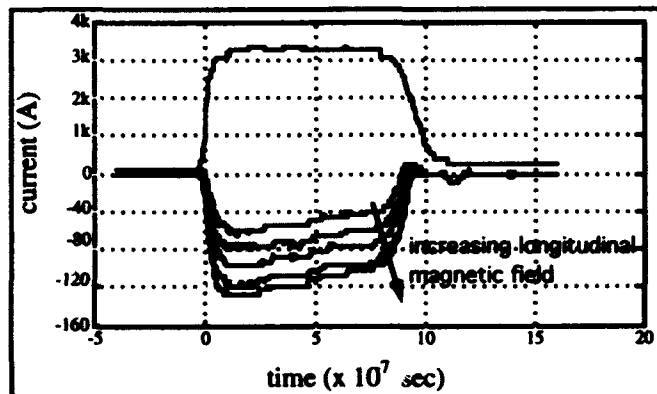


FIG. 3 The discharge current (positive) and beam currents (negative) at 15 kV applied voltage and 6 mTorr argon pressure in the diagnostic region when the magnetic field increases from 0 to 400 Gauss.

beam current with increase of magnetic field at argon pressure of 7 mTorr in the diagnostic region. An electron beam of

$>120$  A is extracted into low pressure area by this simple setup. An electron beam transporting through a dielectric tube results in beam collimation and focusing. This is mainly due to the impinging of the electron beam front on the tube walls, resulting in surface breakdown and positive ion ejection, compensating the space charge of beam electrons.[15-17] In this case, the tube diameter should not significantly exceed that of the beam exiting the anode, since the charge compensation effect is drastically reduced. The SEC beam has been guided through a glass tube of 12 cm in length and 1 cm in diameter right behind the anode back wall. The spatial profile of the BLT electron beam was measured 18 cm away from the anode back wall with and without the glass tube (Figure 4). Based on the data, it is evident that the beam is effectively collimated when using the small diameter dielectric tube. At 18 cm downstream, the central area of  $\sim 1$  cm<sup>2</sup> of the collimated electron beam is very uniform, with a current density exceeding 60 A/cm<sup>2</sup>.

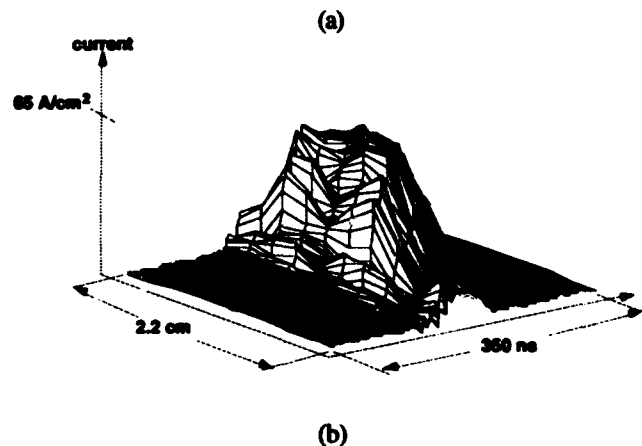
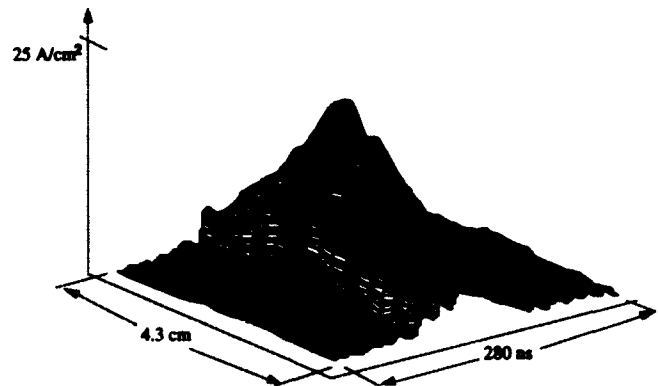


FIG. 4 The spatial and temporal profile of the BLT produced electron beam (a) without and (b) with the glass tube.

### III. CONCLUSION

An SEC electron beam produced by the BLT with a capacitive energy storage is terminated shortly after the maximum of discharge current and is a result of fast decay of voltage across the BLT. With a PFN as the energy storage, the BLT maintains a significant amount of voltage during the whole discharge pulse and generates a beam pulse of equal duration. The energy, current, and duration of the SEC

electron beam can be modified through the control of external circuit elements and operation parameters. The spatial uniformity of the SEC beam is improved by the guiding of a dielectric tube. The fact that the SEC electron beam has extremely high current density and can be modified by adjusting several different operation parameters makes the BLT an attractive candidate as a high power electron beam source for many applications, including accelerators and laser ionization.

#### IV. REFERENCES

- [1] W. Benker, J. Christiansen, K. Frank, H. Gundel, W. Hartmann, T. Redel, and M. Stetter, "Generation of intense pulsed electron beams by the pseudospark discharge," *IEEE Tran. Plasma Sci.*, **17** (5), 754 (1989).
- [2] E. Boggasch, T. A. Fine and M. J. Rhee, "Measurement of Pseudospark Produced Electron Beam," *Bull. Amer. Phys. Soc.*, **33**, 1951 (1988).
- [3] P. Choi, H. H. Chuaqui, M. Favre, E. S. Wyndham, "An Observation of Energetic Electron Beams in Low Pressure Linear Discharges," *IEEE Trans. Plas. Sci. PS-15*, 428 (1987).
- [4] H. Pak and M. Kushner, "Multi-beam-bulk model for electron transport during communication in an optically triggered pseudospark thyatron," *Appl. Phys. Lett.*, **57**, 1619 (1990).
- [5] T-Y Hsu, R-L Liou, G. Kirkman-Amemiya, and M. A. Gundersen, "Electron beam generation from a superemissive cathode," *Proceedings of the 1991 Particle Accelerator Conference*, 1990 (1991).
- [6] T-Y Hsu, R-L Liou, G. Kirkman-Amemiya, and M. A. Gundersen, "Electron beams produced by the superemissive cathode," *Proceedings of the Eighth IEEE International Pulsed Power Conference*, 567 (1991).
- [7] T-Y Hsu, and M. A. Gundersen, "A high-power electron beam source based on the superemissive cathode," *Appl. Phys. Lett.*, **61** (21), 2515 (1992).
- [8] W. Hartmann and M. Gundersen, "Origin of anomalous emission in superdense glow discharge," *Phys. Rev. Lett.*, **60**, 2371 (1988).
- [9] W. Hartmann, V. Dominic, G.F. Kirkman, and M.A. Gundersen, "Evidence for large area super-emission into a high current glow discharge," *App. Phys. Lett.* **53** (18), 1699 (1988).
- [10] W. Hartmann, V. Dominic, G. Kirkman, and M.A. Gundersen, "An analysis of the anomalous high current cathode emission in pseudo-spark and BLT switches," *J. Appl. Phys.*, **65** (11), 4388 (1989).
- [11] A. Anders, S. Anders, and M. A. Gundersen, "Model for explosive electron emission in a pseudospark superdense glow," submitted to *Phys. Rev. Lett.*
- [12] H. Bauer and M. A. Gundersen, "Penetration and equilibration of injected electrons into a high-current hydrogen pseudospark-type plasma," *J. Appl. Phys.*, **68** (2), 512 (1990).
- [13] H. Bauer and M. A. Gundersen, "High current plasma based electron source," *Appl. Phys. Lett.*, **57** (5), 434 (1990).
- [14] T-Y Hsu, G. Kirkman-Amemiya, and M. A. Gundersen, "Multiple-gap back-lighted thyatrons for high power applications," *IEEE Trans. Elec. Devices*, **38** (4), 717 (1991).
- [15] R. G. Little, R. Lowell, and J. R. Uglum, "Cavity current enhancement by dielectrics", *IEEE Trans. Nuc. Sci. NS-21*, 249 (1974).
- [16] R. G. Little, J. R. Uglum, and R. A. Lowell, "Cavity IEMP enhancement by dielectric walls", *IEEE Trans. Nuc. Sci. NS-22*, 2351 (1975).
- [17] B. A. Koval, and G. E. Ozur, "Transport of a nonrelativistic high-current electron beam in a vacuum dielectric channel in a external magnetic field", *Sov. Phys. Tech. Phys.* **31**, 726 (1986).

# Theoretical and Experimental Study of Pseudospark Electron Beam Generation\*

L. Pitchford and J. P. Boeuf  
University Paul Sabatier, France

V. Puech  
University De Paris-Sud, France

R. Liou and M. Gundersen  
University of Southern California, USA

## Abstract

Pseudospark hollow cathode discharges (HCD) are sources of intense electron beams. Reported in this paper are theoretical and experimental studies of the HCD processes and the related electron beam production. The purpose of the work is to develop a predictive model to guide the development of this high brightness electron beam. According to the model, the initial, rapid current rise is associated with the formation of a plasma and its expansion in the hollow cathode region (HCR). The space charge distortion of the applied field just as the plasma begins to fill the HCR is such that electron multiplication is maximum at this point in time, and there is a consequent rapid increase in the charged particle densities. The electron beam observed experimentally during the current rise is predicted by the model. Electrons created in the HCR are largely confined by the high field sheaths until they lose most of their total energy in collisions. These low energy electrons are trapped in the low field region on axis behind the cathode hole through which they diffuse into the cathode-anode gap, and then are accelerated in the remaining potential within the gap. These electrons comprise the observed electron beam. The model indicates that the beam is a direct consequence of HCD and is therefore produced by a plasma cathode. The difficulty in modeling an actual electron emitting metal surface can therefore be overcome. Experimental results of a hydrogen HCD electron beam are also presented. The pulse-length is usually 10's of nsecs, peak beam current of 170 A, efficiency of 21% was measured at -20 kV applied voltage. The experimental results and model predictions are in good qualitative agreement, and demonstrate the potential for developing a first principles predictive model for electron beam current, emittance and brightness.

## I. INTRODUCTION

Pseudosparks are transient gas discharges which occur in a special hollow cathode geometry and can produce electron beams of very high brightness ( $>10^{10}$  A/m<sup>2</sup>rad<sup>2</sup>). [1-3] Two electron beam components can be observed in a pseudospark discharge. The first one is produced immediately following the breakdown event (which is usually triggered), and is typically a beam with energy comparable to the voltage switched, and peak current of ~ 10-1000 A. The width of this component in time and its spread in energy depend on the evolution of the plasma produced in the discharge, or more

precisely, the evolution of the potential distribution in the gap. Measurements of the properties of this component of the electron beam provide not only data needed for its eventual optimization in terms of current and brightness, but also provide a stringent test of the prediction of numerical model of pseudospark discharges.

A second component of the pseudospark electron beam is related to the operation of super-emissive cathode mode. [4,5] An electron beam with current  $\approx$  200 A, duration on the order of  $\mu$ secs, energy of several hundred eV has been experimentally observed. [6]

Our focus to date is to develop a predictive model to guide the development of high energy, high brightness electron beams generated in the initiation phase of the pseudospark discharge. In this paper we present a semi-qualitative description of this component of the electron beam and show comparison between model prediction and measurements.

## II. THEORETICAL MODEL

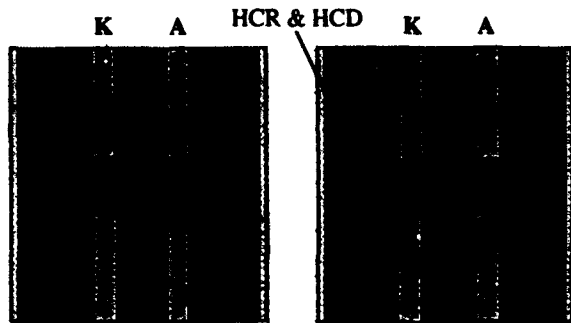
An essential phenomena during the initiation phase of pseudospark discharge is the development of space charge. At this moment the plasma is collisional even though the electron mean free path can be on the order of the discharge dimension. The collisions between electrons and neutrals will dominate and the coulomb collisions between charged particles can be neglected. The energy distribution of electrons is therefore more energetic than that of ions. The result is a non-Maxwellian electron energy distribution. For this reason the model must be able to take into account the non-equilibrium charged particle transport and electric field distribution in a self-consistent manner.

A two dimensional, self-consistent model of the electrical properties of transient HCD which is used to describe the initial phases of a pseudospark discharge has been developed. The model consists of Poisson equation for the electrical field coupled to a fluid description of the electron and ion transport, with the important feature that the ionization source term in the electron and ion fluid equations is determined through a Monte Carlo simulation. The fluid equations determine the time and space dependence of the charged-particle densities. The space charge and self-consistent field from Poisson equation yield the particle currents. With the knowledge of electron current density distribution leaving the cathode and the electrical field distribution within the cathode-anode gap, the Monte Carlo simulation determines the ionization source term which, in turn, is input to the fluid equations. This model is referred as a hybrid fluid-particle model. [7]

Figure 1 shows a snap shot of both the equipotential contours and the electron density contours for a 0.6 Torr helium at a constant applied voltage of 2 kV. The contours

\* The work supported in part by the U.S. Army Research Office, SDIO through the U.S. Office of Naval Research, the Joint Services Electronics Program through the Air Force Office of Scientific Research, NATO and DRET.

were taken at 50.4 nsec after the application of voltage. In this particular calculation, the geometry is symmetrical (with a hollow cathode and a hollow anode). The electrode thickness and cathode-anode separation is 2.5 mm and 4.5 mm. Both electrode central holes are 5 mm in diameter. The HCR has a dimension of 3 cm in diameter and 0.7 cm in length. A trigger pulse is assumed to produce a uniform initial charged particle density in the HCR at the time when the voltage is applied ( $t=0$ ). The electrical field at  $t=0$  is almost uniform in the gap, with a small distortion in the region of the holes. As the initial electrons are pulled out of the cathode and towards the anode, they produce ionization in the gas. The secondary electrons are accelerated towards the anode, leaving behind a growing ion space charge field. If the trigger pulse is of sufficient amplitude, a plasma will form in the gap and distort the geometrical field. This will in turn increase the potential in the HCR as shown in Figure 1-a. The space charge distortion of the applied field just as the plasma begins to fill the HCR is such that the electron multiplication is a maximum at this point in time, and there is a rapid increase in the charged particle densities. The result is shown in Figure 1-b where a high electron density core (on the order of  $10^{13} \text{ cm}^{-3}$ ) can be observed. During this time a large displacement current spike has also been observed due to the increase in the field corresponding to this space charge.



(a) Equipotential contours (b) Electron density contours  
 FIG. 1 Snap shot of equipotential contours and the electron density contours in a 0.6 Torr helium gas with 2 kV applied voltage. The pictures were taken at 50.4 nsec after the application of voltage.

In general, with the application of a high enough voltage the plasma will begin to form first in between the cathode-anode gap or close to the cathode hole. The plasma expands from this point of formation towards the cathode. The potential which existed at the position where the plasma is first formed is pushed into the HCR as the plasma expands. Electrons created in the HCR are largely confined to oscillate between the high field sheaths until they lose most of their total energy in collisions. These low energy electrons are trapped in the low field region on axis behind the cathode hole through which they diffuse into the gap and then are accelerated in the remaining potential within the gap. These electrons comprise the observed electron beam. From simulation an electron beam with current density  $\approx 20 \text{ A/cm}^2$  and peak energy of 700 eV was observed at 30.8 nsec after the trigger with an applied voltage of 2 kV.

### III. EXPERIMENTAL RESULTS

Figure 2 shows the experimental setup. The HCR was made of copper with a cylindrical structure, a cathode on one end and a quartz window on the other. The HCR has a dimension of 3.5 cm in diameter and 2.5 cm in length. The electrode central hole size and the thickness of insulators were both 3 mm. The discharge was initiated with a UV flash lamp at the back of cathode near the central hole through a quartz window. Cathode current was monitored through a  $5 \text{ m}\Omega$  current viewing resistor (CVR) and the cathode voltage through a Tektronix P 6015 high voltage probe. The electron beam was generated with an RC discharge circuit ( $22 \Omega$ ,  $16 \text{ nF}$ ). The electron beam current was measured with a fast Rogowski coil ( $\leq 1 \text{ nsec}$ ) at  $\approx 1 \text{ cm}$  behind the anode hole. A fast Faraday cup ( $\leq 2 \text{ nsec}$ ) is also available. Permanent magnets were used only for beam energy measurements.

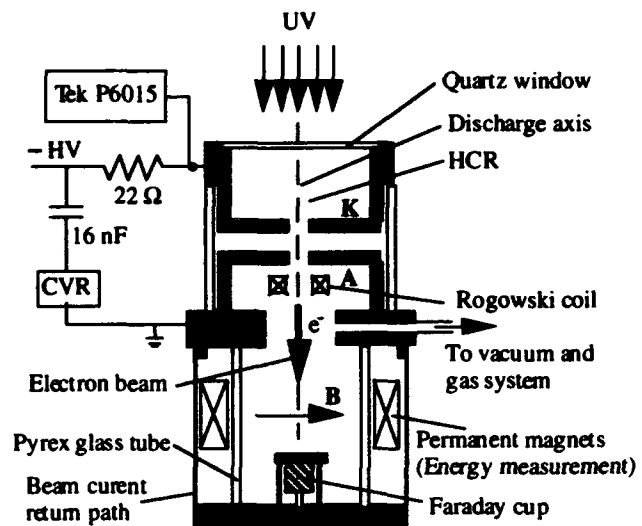


FIG. 2 The experimental setup for electron beam measurement.

The drift tube is a 41 mm Pyrex glass tube. Two copper screen cylinders were used to cover both sides of the glass tube. The inner copper screen was to provide the plasma electrons return path and was directly connected to the grounded anode. The outer screen provides the beam current return path to the anode and can be detached from the anode when necessary.

Figure 3 shows the typical discharge current and the electron beam current with -20 kV applied voltage with 80 mTorr  $\text{H}_2$ . The peak of the discharge current is  $\approx 800 \text{ A}$  and the electron beam  $\approx 170 \text{ A}$  which gives a beam current to discharge current ratio of 21%. The pulse length is  $\approx 50 \text{ nsec}$ . The pulse length is associated with the plasma formation processes within the cathode-anode gap and not readily controllable with external circuitry. The discharge current has a slower rise at the beginning of the pulse which corresponds to the build-up phase of the transient HCD. After this moment the discharge current increases over-exponentially as a result of fast increase of charge multiplication inside the HCR. The electron beam current has a similar behavior and the peak is coincided with the peak of discharge current.

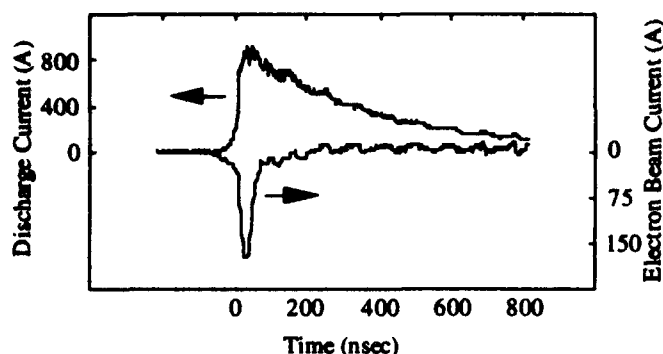


FIG. 3 The discharge current and the beam current at 1 cm behind anode. The turn-off of beam current is associated with the decrease of cathode voltage.

Beam current dependence on gas pressure was also studied. A dramatic increase was observed when operated at lower gas pressure. The beam current increases by a factor of 4 with a pressure reduction of only  $\approx 40\%$  (from 140 mTorr to 80 mTorr). The beam current was also found to increase with increasing applied voltages. The beam current increases from 10 A to 45 A when the voltage is varied from -14 kV to -20 kV in a 135 mTorr  $H_2$ . These results suggest that when operated at a -40 kV voltage and 50 mTorr hydrogen, an electron beam with current of kA is feasible.

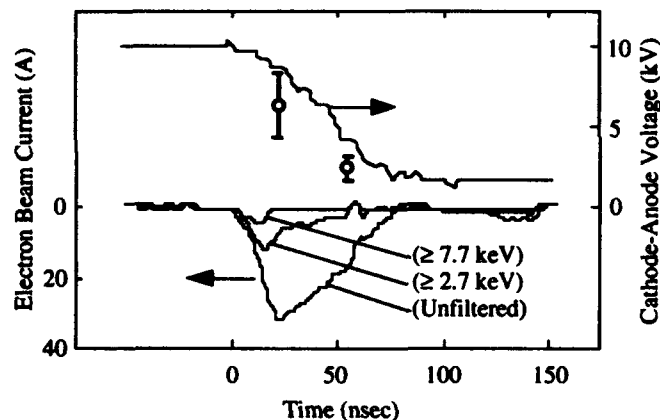


FIG. 4 Electron beam energy measurement with high-pass filtering method.

The electron beam energy was estimated with a high-pass filtering technique. The technique utilizes the  $V \times B$  deflection that beam electrons experience when traversing a transverse magnetic field. Only those electrons with high enough energies can survive the deflection and still be collected by the Faraday cup. With different strength of the magnetic field different electron energy can be estimated. The spatial distribution of the magnetic field was measured and used as the prescribed field for a single electron trajectory computer simulation with electron energy as input parameter. With a 16 nF and 500  $\Omega$  capacitor discharge at -10 kV in 400 mTorr He gas the peak beam current is  $\approx 32$  A at 2 cm behind anode. With increasing transverse magnetic the beam current is observed to decrease accordingly. The electron beam decreases both in beam current and pulse length. The latter portion of the beam current is observed to diminish first and the vanishing point represent electron beam with minimum energy set by the magnetic field. Figure 4 shows the

experimental results. The minimum beam energy is found to be  $1.2 \text{ keV} \leq E_1 \leq 2.7 \text{ keV}$  for one pair of the permanent magnets and  $4.2 \text{ keV} \leq E_2 \leq 7.7 \text{ keV}$  for two pairs of magnets. The source of error comes from the possible uncertainty of the precise position of Faraday cup in the transverse direction ( $\approx \pm 1 \text{ mm}$ ). The upper curve of Figure 4 is the cathode voltage. On the same curve the minimum energy from trajectory simulation was plotted at the time where electron beam corresponding to different magnetic field vanished. The results indicate that the electron beam has energy close to and below the cathode voltage as predicted from the theoretic model.

The propagation of this electron beam in an 80 mTorr  $H_2$  was studied with radiachromic films at various locations behind anode. The method is time-integrated in nature and a beam divergence half angle  $\approx 5.0^\circ$  is measured. Emittance can also be estimated with the assumption that the beam waist is at the anode position.[8] At 170 A and instantaneous energy of 10 keV a normalized emittance of 25 mm-mrad is found and a normalized brightness of  $2.7 \times 10^{10} \text{ A/m}^2 \text{ rad}^2$  is calculated.

#### IV. CONCLUSION

In conclusion a theoretical model for the initiation phase of the pseudospark discharge has been developed. The results of the simulation correlate with the experimental observations. The evolution of the discharge and the observed electron beam are found to be in good qualitative agreement. The model is important because the electron beam generated from HCD is basically from a plasma cathode. The emission can therefore be modeled with microscopic details which are usually difficult to obtain when associated with a metal cathode. In principle the model can be developed to predict beam parameters including emittance and brightness based on a microscopic description of collisional, dissociative and ionizational processes. The future work will include the theoretical study of beam emittance, dependence on circuits, applied voltage, gas pressure, and gas species.

#### V. REFERENCES

- [1] D. Bloess, I. Kamber, H. Riege, G. Bittner, V. Bruckner, J. Christiansen, K. Frank, W. Hartmann, N. Lieser, C. Schultheiss, R. Seebock, and W. Steudtner, *Nucl. Instru. Methods* **205**, 173 (1983).
- [2] K. Jain, E. Boggasch, M. Reiser, and M. Rhee, *Phys. Fluids B* **2**, 2487 (1990).
- [3] M. Favre, H. Chuaqui, E. Wyndham, and P. Choi, *IEEE Trans. Plasma Sci.* **PS-20**, 53 (1992).
- [4] H. Bauer and M. A. Gundersen, *J. Appl. Phys.* **68**, 512 (1990).
- [5] H. Bauer and M. A. Gundersen, *Appl. Phys. Lett.* **57**, 434 (1990).
- [6] T.-Y. Hsu and M. A. Gundersen, *Appl. Phys. Lett.* **61**, 2515 (1992).
- [7] J. Boeuf and L. Pitchford, *IEEE Trans. Plasma Sci.* **PS-19**, 286 (1991).
- [8] C. Lejeune and J. Aubert, *Advances in Electronics and Electron Physics*, **13A**, edited by A. Septier, Academic Press, New York, 159 (1980).

# A Variable Pulse-Length Electron Beam from the Back-Lighted Thyatron\*

R. Liou, T. Hsu, G. Roth, M. Gundersen and G. Kirkman\*\*  
University of Southern California  
Los Angeles, CA 90089-0484

## Abstract

A variable pulse-length electron beam source capable of 100's  $\mu\text{sec}$  pulse to DC operation is reported. Long-pulse electron beam generation was based on the steady-state hollow cathode discharge mode of operation of the back-lighted thyatron and achieved by modification of circuit parameters that control the discharge. Three different discharge circuits were used in the experiment. An RC circuit (16 nF, 1 k $\Omega$  at -20 kV) was used to generate an electron beam with duration  $\approx 100 \mu\text{sec}$ . The energy of the beam is associated with the cathode voltage and a current density  $\approx 10 \text{ A/cm}^2$  was measured. To further increase the pulse-length a discharge circuit with 100  $\mu\text{F}$  and 500  $\Omega$  was used. The pulse-length was extended to 50 msec FWHM. The third circuit was a pulse forming network which generated a non-decaying amplitude electron beam with a duration of 200 msec FWHM. DC operation has also been achieved. The results demonstrate the feasibility of controlling the electron beam pulse-length with modifications of external circuitry. The device is simple, robust, and compatible with a plasma environment. Applications include electron beam ionized lasers, electron beam ion trap, electron beam assisted atomic layer epitaxy and plasma-filled microwave generators.

## INTRODUCTION

Plasma compatible electron beam sources are of interest in current research areas that include plasma-filled microwave generation, electron beam ionized lasers and a long duration electron beam is also essential for electron beam ion trap (EBIT) experiments.[1-6] Electron beam generation is usually achieved through using thermionic cathodes, field emitters or photocathodes. The plasma cathodes are of particular interest in the generation of long pulse electron beam. In a glow discharge, electrons can be generated by ion bombardment and then accelerated through the cathode fall.[7,8] This feature makes glow discharge a promising candidate for applications mentioned above.

Recently the back-lighted thyatron (BLT) and pseudospark have been developed for high current pulsed power switching applications.[9] The BLT and pseudospark have several modes of operation, including a mode that is essentially a hollow cathode discharge (HCD).[10] This is achieved with electrodes that are parallel discs, each with a circular central hole and separated by insulators. With the application of sufficiently high voltage, a very low current (typically  $< 10^{-6} \text{ A}$ ) Townsend discharge develops on axis due to the focusing effect of the electric field. A positive space

charge builds up inside the hollow cathode region (HCR) as a result of low mobility of the ions produced by electron-neutral collisions. The release of a sufficient number of starting electrons inside the hollow cathode initiates a *transient* HCD. The short-pulse ( $\sim 10\text{-}100 \text{ nsec}$ ) electron beam generation during this transient HCD has also been subjected to some extensive studies.[11-14] In the process towards a high discharge current operation, the increasing plasma density eventually shields the electric field from the HCR. The discharge current will then be taken over by the cathode surface at the aperture, the HCD ceases and the super-emissive process becomes dominant.[15-17] In this work the BLT was running under a HCD condition (low current) and not the super-emissive condition. The low current condition prevents the BLT from entering into the super-emissive mode of operation and a *steady-state* HCD is achieved.

## II. RESULTS AND DISCUSSION

### A. Experimental Setup

Figure 1 shows the experimental setup. A single-gap BLT was directly built on a standard 2-3/4" conflate flange and mounted on a 15 cm diameter vacuum chamber. The HCR is a copper cylinder, with a cathode on one end and a quartz window on the other. The HCR is 3 cm in both the diameter and length. The cathode central hole size and cathode-anode gap are 3 mm and 5 mm. The cathode-anode gap spacing is maintained with a 44-mm glass insulator.

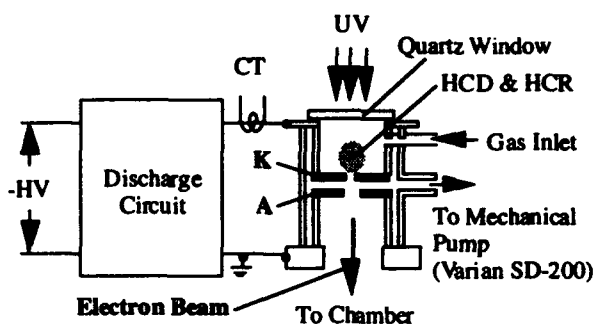


FIG. 1 Experimental setup. The chamber is evacuated with a Varian 80 liters/sec turbo pump. Beam current was measured with a Faraday cup.

The discharge (and therefore the electron beam emission) is initiated with UV light illuminated on the cathode back surface through the quartz window. During the experiment a working gas will flow into the cathode back space and be evacuated through the cathode hole. The cathode-anode gap is evacuated with a Varian SD-200 mechanical pump and the chamber a V-80 Turbo pump. Pressure in the chamber was monitored with a cold cathode gauge. Time-resolved beam current was measured with a Faraday cup which could be moved along the discharge axis. The Faraday cup has a resistance of 0.25  $\Omega$  and a rise time  $\leq 2 \text{ nsec}$ . The area of

\* This work was supported in part by the U.S. Army Research Office, SDIO through the U.S. Office of Naval Research, and the Lawrence Livermore National Laboratory.

\*\* G. Kirkman is with Integrated Applied Physics, Inc., Waltham, MA.

Faraday cup is  $\approx 1.25 \text{ cm}^2$ . The electron beam is self-extracted with no extraction voltage nor axial guiding magnetic field (except for the DC operation). Cathode voltage is monitored with Tektronix P 6015 high voltage probe. Various discharge circuits have been used to generate electron beam with different pulse-length.

### B. 100 $\mu\text{sec}$ pulse-length Electron Beam Generation

An RC circuit (16 nF, 1 k $\Omega$ ) operated at -20 kV was used to generate the electron beam with pulse-length of 100  $\mu\text{sec}$ . The 1 k $\Omega$  resistor was chosen as a ballast resistor to limit the discharge current so that a prolonged HCD can be sustained.

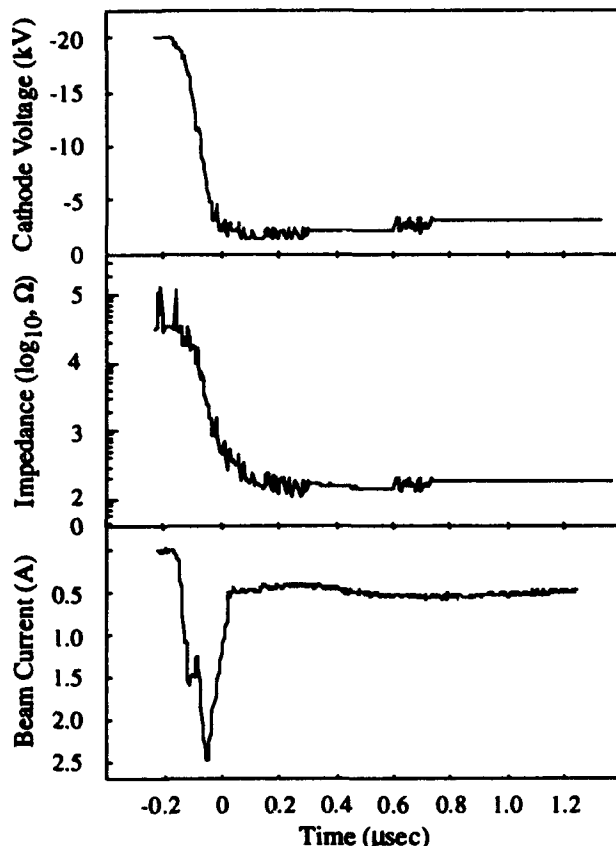


FIG. 2 The cathode voltage, BLT cathode-anode impedance, and the beam current at 2 cm behind anode for a 100  $\mu\text{sec}$  pulse electron beam generation with both the transient and steady-state phases shown.

The top trace of Figure 2 shows the BLT cathode voltage. The discharge voltage drops from the initial -20 kV in about 170 nsec; roughly equals to the duration of the transient electron beam. The discharge voltage then decays with a time constant of  $\approx 12 \mu\text{sec}$ . The BLT impedance was determined from the ratio of discharge voltage to discharge current. This varies from a blocking state (order of M $\Omega$ ) to about 200  $\Omega$  during the voltage transient. Since the BLT is maintained in a low discharge current operation the impedance is much higher than what was usually found in a typical high current operation (order of 10 m $\Omega$ ). On the same time axis also shown is the electron beam current measured at 2 cm behind anode. A correlation between the discharge voltage and the electron beam currents is clearly seen. The transient electron beam had a wide energy variation, from an

initial 20 keV down to 2 keV. The long-pulse electron beam on the other hand had a much slower energy variation in time. The measurements indicate a two-phase operation. The transient phase of electron beam has a peak current  $\approx 2.5 \text{ A}$  and duration  $\approx 130 \text{ nsec}$  FWHM. The steady state phase of the electron beam has shape and duration follow the discharge current. The discharge current is highly overdamped with peak current  $\approx 16 \text{ A}$  and duration  $\approx 100 \mu\text{sec}$ . The long-pulse electron beam has a duration of  $\approx 100 \mu\text{sec}$  and current of several hundred mA. The minimum current density is estimated to be  $\approx 10 \text{ A/cm}^2$  with the beam area assumed to be anode aperture. The ratio of electron beam to discharge current is  $\approx 4\%$  at the peak of discharge current.

### C. 100 msec Electron Beam Generation with RC Discharge

An RC circuit with 100  $\mu\text{F}$  capacitor and 500  $\Omega$  resistor was chosen to extend the pulse-length. Figure 3 shows the electron beam current, discharge current and the cathode voltage when operated at -2 kV (capacitor rating : 2.5 kV).

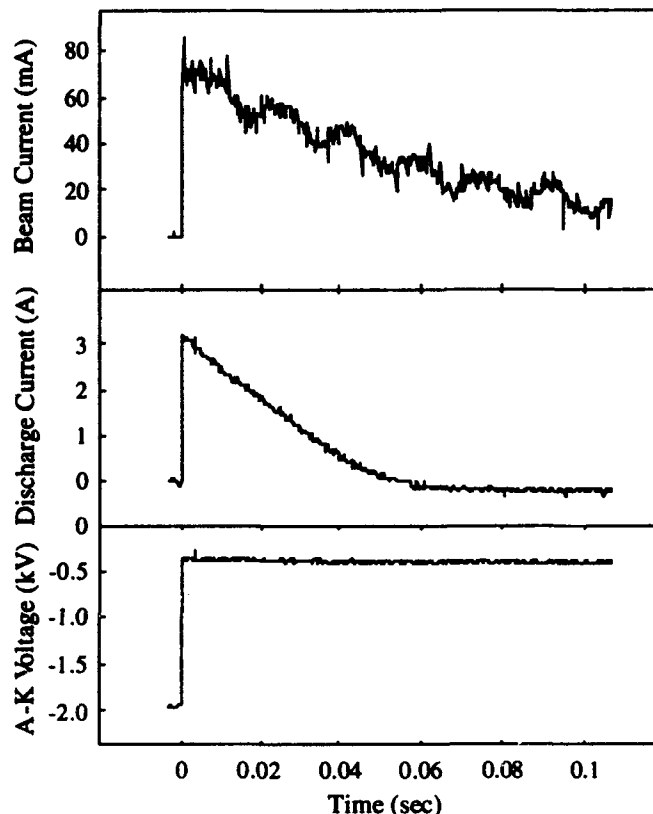


FIG. 3 Electron beam generated with a low-voltage RC discharge circuit (100  $\mu\text{F}$ , 500  $\Omega$ ). Beam current was measured at 5 cm behind anode.

The discharge current is overdamped with a peak current of  $\approx 3 \text{ A}$ . With  $\approx 800 \text{ mTorr}$   $\text{H}_2$  in HCR and  $\approx 8 \text{ mTorr}$  inside the chamber the self-extracted electron beam has peak current of 75 mA and FWHM pulse-length of 50 msec. The beam current to discharge current ratio is  $\approx 2.5\%$ . The cathode voltage drops from an initial applied voltage of -2 kV to  $\approx -400 \text{ V}$  and remains at that value for the rest of the discharge. This behavior is similar to the familiar "normal glow discharge" between two planar electrodes where the discharge

voltage is found to be constant with a wide range of discharge current.[18]

Visual observation of cathode-anode gap through the glass insulator indicates that discharge near the cathode side is confined within a radius about the size of the cathode hole. This fact confirms that electron emission comes solely from the HCR as expected. In this case the cathode hole acts like an electron beam focusing lens which brings the broad-area electron beam from HCR to a much smaller dimension with a compression ratio more than 400. The present geometry presents a simple device which, together with a proper magnetic guiding field, can produce electron beam density on the order of  $100 \text{ A/cm}^2$ .

#### D. 100 msec Electron Beam Generation with PFN Discharge

A pulse forming network consisted of four  $100\text{-}\mu\text{F}$  capacitors and two 5-H inductors was used to generate electron beam with FWHM  $\geq 200$  msec with an applied voltage of  $-2.5 \text{ kV}$ . A beam current of  $70 \text{ mA}$  was measured at  $2 \text{ cm}$  behind anode with a  $2\text{-A}$  discharge current. The self-extraction efficiency was  $\approx 3.5\%$ . The beam energy is confirmed with a retarding field measurement to be  $\geq 400 \text{ eV}$  as indicated from the cathode voltage measurement. Beam currents measured with Faraday cup at various positions indicate a beam divergence half-angle of  $\approx 13^\circ$ .

A DC operation has also been achieved. An axial magnetic field of  $\approx 200$  Gauss was used to guide the low-energy electron beam. At  $2 \text{ cm}$  behind anode the efficiency is  $\geq 90\%$ . The beam energy spectrum was measured at  $18 \text{ cm}$  behind anode. The majority of the electrons have energy  $\leq 40 \text{ eV}$ . Since electrons with energies more than a few eV play an important role in electron-enhanced chemical reactions on surfaces, it is of interest to apply this BLT DC electron beam in an electron beam assisted atomic layer epitaxy experiment (EBALE) to locally assist the growing processes.[19]

### CONCLUSION

In conclusion, we have demonstrated the generation of a long pulse electron beam (from  $100 \mu\text{sec}$  to DC) from a simple device. The self-extracted beam current density is on the order of  $10 \text{ A/cm}^2$ . The results indicate that the electron beam pulse-length can be controlled through the modification of the external circuit, i.e. the discharge current pulse. Future work will seek to increase the beam current through proper differential pumping, magnetic guiding, and extraction structure. The device is simple, robust and compatible with a plasma environment. Possible applications include electron beam ionized lasers, plasma-based microwave generation where a plasma compatible electron beam source may be preferred, EBIT and EBALE.

### REFERENCES

- [1] Y. Carmel, K. Minami, R. A. Kehs, W. W. Destler, V. L. Granatstein, D. Abe, and W. L. Lou, *Phys. Rev. Lett.*, **62**, 2389 (1989).
- [2] J. Daugherty, *Principles of Laser Plasma*, edited by G. Bekefi, John Wiley and Sons, New York, 369, (1976).
- [3] J. J. Rocca, J. D. Meyer, and G. J. Collins, *Phys. Lett. A*, **90**, 358 (1982).
- [4] T. Sara, Y. Sadamoto, M. Hamagaki, T. Ohgo, and T. Dote, *Jpn. J. Appl. Phys.* **22**, L379 (1983).
- [5] M. A. Levine, R. E. Marrs, J. R. Henderson, D. A. Knapp, and M. B. Schneider, *Phys. Scr.* **T22**, 157 (1988).
- [6] B. M. Penetrante, J. N. Bardsley, M. A. Levine, D. A. Knapp, and R. E. Marrs, *Phys. Rev. A*, **43**, 4873 (1991).
- [7] B. B. O'Brien, Jr., *Appl. Phys. Lett.* **22**, 503 (1973).
- [8] J. J. Rocca, J. D. Meyer, M. R. Farrell, and G. J. Collins, *J. Appl. Phys.* **56**, 790 (1984).
- [9] K. Frank, E. Boggash, J. Christiansen, A. Goertler, W. Hartmann, C. Kozlik, G. Kirkman, C. Braun, V. Dominic, M. A. Gundersen H. Riege and G. Mechttersheimer, *IEEE Trans. Plasma. Sci.* **PS-16**, 317 (1988).
- [10] J. Delcroix and A. Trindade, *Advances in Electronics and Electron Physics*, edited by L. Marton, Academic Press, New York, **35**, 87.(1974).
- [11] D. Bloess, I. Kamber, H. Riege, G. Bittner, V. Bruckner, J. Christiansen, K. Frank, W. Hartmann, N. Lieser, C. Schultheiss, R. Seebock, and W. Steudtner, *Nucl. Instrum. Methods* **205**, 173 (1983).
- [12] W. Benker, J. Christiansen, K. Frank, H. Gundel, W. Hartmann, T. Redel, and M. Stetter, *Proc. SPIE* **873**, 249 (1988).
- [13] K. Jain, E. Boggasch, M. Reiser, and M. Rhee, *Phys. Fluids B* **2**, 2487 (1990).
- [14] M. Favre, H. Chuaqui, E. Wyndham, and P. Choi, *IEEE Trans. Plasma Sci.*, **PS-20**, 53 (1992).
- [15] W. Hartmann and M. A. Gundersen, *Physics and Applications of Pseudospark*, Edited by M. A. Gundersen and G. Schaefer, Plenum Press, New York, 77 (1990).
- [16] J. Boeuf and L. Pitchford, *IEEE Trans. Plasma Sci.* **PS-19**, 286 (1991).
- [17] B. M. Penetrante and J. N. Bardsley, *Proc., XXth International conference on Phenomena in Ionized Gases*, edited by V. Pallechi and M. Maselli (Istituto di Fisica Atomica e Molecolare, Pisa), 1027 (1991).
- [18] G. Francis, *Encyclopedia of Physics*, Vol. XXII, Gas Discharge II, edited by S. Flugge, Springer-Verlag, Berlin, 53 (1956).
- [19] Q. Chen and P. D. Dapkus, *J. Electrochem. Soc.*, **138**, 2821 (1991) and the references within.

# One-Dimensional Simulation Studies of Breakdown and Electron Beam Generation Processes for a Hollow Cathode Pseudospark Discharge\*

S. Y. Cai and C.D. Striffler

Laboratory for Plasma Research

University of Maryland, College Park MD 20742, USA

## Abstract

We have developed a 1-D model to study the importance of some of the basic physical processes involved in a low pressure discharge. Our results show that during the early stage of the discharge, the emitted electron current comes mainly from the secondary emission off the cathode. Meanwhile, a quasi-neutral plasma column is being formed in the gap via ionization. The growing plasma oscillations are excited by the fast electrons from the cathode as they pass through the plasma due to the two-stream instability. The oscillation heats the background electrons to energies above the ionization threshold and ultimately leads to a rapid increase in both the plasma density and electron current at the anode. To our knowledge previous pseudospark models have not included ionization of the ambient gas due to the heated background charged particles within the dense quasi-neutral plasma region. Under this 1-D model, the discharge approximately satisfies a Paschen's Law in the low pressure regime.

## I. INTRODUCTION

There has been an increasing interest in pseudospark devices [1-5]. One of the potential applications of this kind of a device is as a high current, high brightness electron beam source. At the University of Maryland a series of experiments were performed to determine some of the properties of such a pseudospark discharge. It was found that electron beams of current on the order of 1 kA/cm<sup>2</sup> and brightness as high as 10<sup>10</sup> A/m<sup>2</sup>rad<sup>2</sup> can be produced from a low pressure discharge in a hollow cathode geometry [4,5].

Besides experiments, progress has also been made in theoretical studies of pseudospark discharges [6-8], although no existing theory is comprehensive. A recent model, based on the experimental observation that a melted area was found on the cathode surface, proposed that the high current originates from electric-field-enhanced thermionic emission from the cathode [9]. However, in order to melt the cathode surface, an ion flux of the order of 10<sup>9</sup> W/cm<sup>2</sup> is required over a

10 nsec period [10]. Such a flux is equivalent to 100 A/cm<sup>2</sup> if the applied voltage is 10 kV. Also, in order for the electric-field-enhanced thermionic emission to emit the measured current, the electric field at the cathode surface has to be above 10<sup>6</sup> V/cm. The mechanism which brings the discharge to reach the required high current flux and electric field is still unclear.

The present study is aimed at determining the most important basic physical processes involved in the pseudospark discharge. While the hollow cathode has a 2-D structure, we believe that the basic physics involved should not be sensitive to the actual geometry. Thus a rather simple 1-D model is used. The description and the results of the study are given in the following two sections.

## II. NUMERICAL MODEL

The numerical model is a 1-D particle-in-cell (PIC) model, which simulates an infinite parallel plate system with a background helium gas maintained at pressure  $p$ . A constant negative voltage  $-V_0$  is applied on the cathode which is located at  $z = 0$ , and the anode located at  $z = d$  is grounded. An initial uniform plasma of 10<sup>8</sup>/cm<sup>3</sup> is present between the plates. The motion of the charged particles is non-relativistic and is governed by the equation of motion

$$\frac{d^2z}{dt^2} = \frac{q}{m}E(z), \quad (1)$$

where  $z$  is the location of the particle,  $q$  and  $m$  are the charge and mass of the particle, respectively,  $E(z)$  is the electric field at  $z$ . The electric field  $E(z) = -dV/dz$  is obtained by solving the Poisson equation

$$\frac{d^2V(z)}{dz^2} = -\rho(z)/\epsilon_0 \quad (2)$$

with boundary conditions  $V(z = 0) = -V_0$ ,  $V(z = d) = 0$ , and where  $\rho$  is the net charge density.

Because pseudosparks usually operate at low gas pressure and high voltage, we only take into account ionizing collisions. The ionization cross-sections for electrons and ions in He are obtained from Ref. [11].

When an ionization occurs, the incident particle's energy is reduced. In addition, when ions hit the cathode, secondary electrons are emitted. The secondary emission coefficient is dependent on the ion energy and is obtained from Ref. [12], assuming that the cathode is made of Mo. When a new particle is created, we assume that it has no initial kinetic energy.

### III. SIMULATION RESULTS

The 1-D PIC code is used in a series of simulations of high voltage, low pressure discharges. Figure 1 shows a typical plot of electron current collected at the anode versus time. The total current is composed of contributions resulting from ion-neutral ionizations, electron-neutral ionizations, and secondary emissions. In Fig. 1, a rapid increase in the total current occurs at about 108 nsec after the onset of the  $-20$  kV voltage. The simulation was stopped when the current reached  $\sim 1$  kA/cm<sup>2</sup> where the number of particles in the system becomes computationally prohibitively large. It is also observed that during the early stage of the discharge, the current mainly is a result of the secondary emission. But just before the sudden increase in the total current, the contribution from the electron-neutral ionizations becomes dominant. This new observation can be explained as follows.

Figures 2(a) and 2(b) show the potential and the charged particle densities in the gap at  $t = 105.8$  nsec. By this time, a quasi-neutral plasma column has formed in the gap. The plasma density in this case is of the order of  $2 \times 10^{13}$ /cm<sup>3</sup>. When the high energy electrons emitted from the cathode pass through this plasma, it can excite a plasma oscillation due to the two-stream instability. The growing plasma oscillation is clearly shown in Fig. 3, where the electric field at  $z = 0.85$  cm from the cathode is plotted as a function of time. Note that the oscillation frequency  $f \sim 3.3 \times 10^{10}$  Hz matches well with the electron plasma frequency, taking  $n_e = 2 \times 10^{13}$ /cm<sup>3</sup>. The plasma oscillation heats the background electrons. Figure 4 is a plot of the electron energy distribution at  $t = 105.8$  nsec. It shows that at this time, a large portion of the plasma electrons have been heated to above the threshold energy of 24.6 eV. The electron ionization cross-section increases rapidly when the electron energy is above the ionization threshold and reaches a maximum at about 100 eV. When a significant amount of electrons are heated to above the threshold, ionizations due to these hot electrons will also rapidly increase and further increase the electric field associated with the plasma os-

cillation. This in turn leads to a rapid increase in the electron current.

In addition to the above typical case where "breakdown" occurs, we have also performed parametric studies of the pseudospark discharge with this 1-D model. We looked for a critical voltage where the typical breakdown behavior is observed for a given gap length  $d$  and gas pressure  $p$  and plotted the results in Fig. 5. We see that our simple 1-D model obeys Paschen's Law fairly well, namely that the critical voltage for breakdown is a function of the product of the gap length  $d$  and gas pressure  $p$ . More studies need to be done on this subject to quantify the dependence on  $d$  and  $p$ .

\* This work is supported by U.S.D.O.E.

### IV. REFERENCES

1. *Physics and Applications of Pseudosparks*, edited by M.A. Gundersen and G. Schaefer (Plenum Press, New York and London, 1990).
2. W. Hartmann and M.A. Gundersen, *Phys. Rev. Lett.*, **60**, 2371 (1988).
3. M.J. Rhee and B.N. Dong, *Phys. Fluids B4*, 764 (1992).
4. K.K. Jain, E. Boggasch, M. Reiser, and M.J. Rhee, *Phys. Fluids B2*, 2487 (1990).
5. W.W. Destler, Z. Segalov, J. Rodgers, K. Ramaswamy, and M. Reiser, *Appl. Phys. Lett.* **62**, 1739 (1993).
6. H.R. Bauer, G. Kirkman, M.A. Gundersen, *IEEE Trans. Plasma Sci.* PS-18, 237 (1990).
7. H. Pak and M.J. Kushner, *J. Appl. Phys.* **71**, 94 (1992).
8. J-P Boeuf and L.C. Pitchford, *IEEE Trans. Plasma Sci.* PS-19, 286 (1991).
9. W. Hartmann, V. Dominic, G.F. Kirkman, and M.A. Gundersen, *J. Appl. Phys.* **65**, 4388 (1989).
10. T.J. Sommerer, H. Pak, and M.J. Kushner, *J. Appl. Phys.* **72**, 3374 (1992).
11. R.K. Janev, W.D. Langer, K. Evans, Jr., D.E. Post, Jr., *Elementary Processes in Hydrogen-Helium Plasmas* (Springer-Verlag, 1987).
12. B. Chapman, *Glow Discharge Processes* (Wiley & Sons, 1980) p. 87.

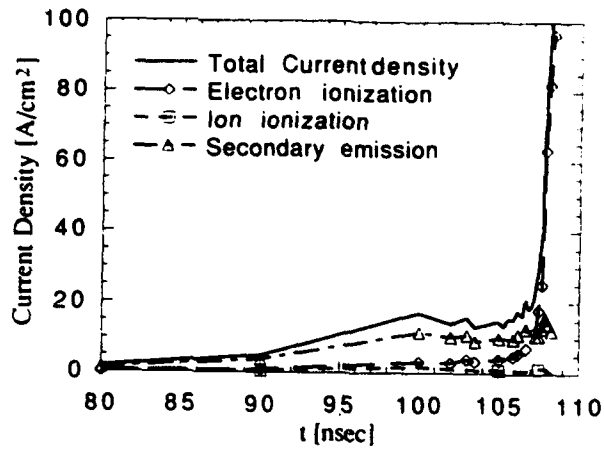


Figure 1: Total electron current density at the anode and its components versus time. The system parameters are  $p = 2$  torr,  $V_0 = 20$  kV,  $d = 1$  cm and an initial plasma density of  $5 \times 10^7 / \text{cm}^3$ .

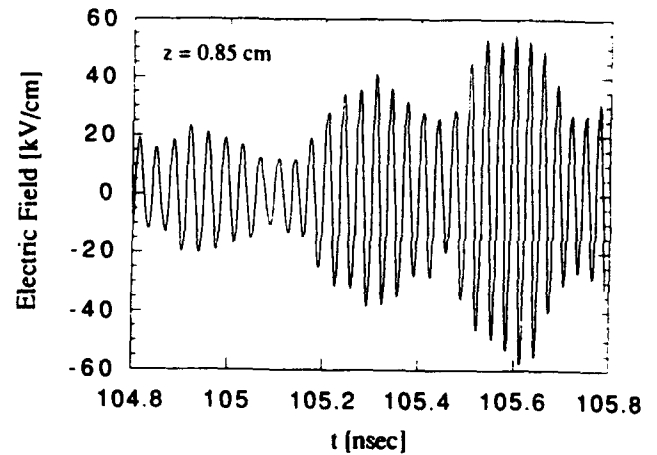


Figure 3: The electric field at  $z = 0.85$  cm versus time. Note the growing plasma oscillation. Same system parameters as in Fig. 1.

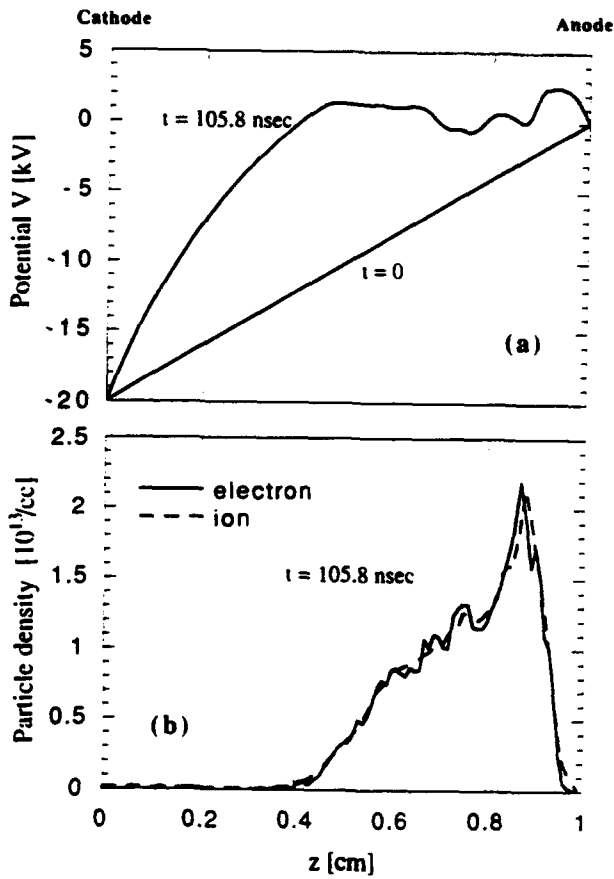


Figure 2: Electric potential (a), and charged particle densities (b) versus position at  $t = 105.8$  nsec. The  $t = 0$  potential profile is shown for reference. Same system parameters as in Fig. 1.

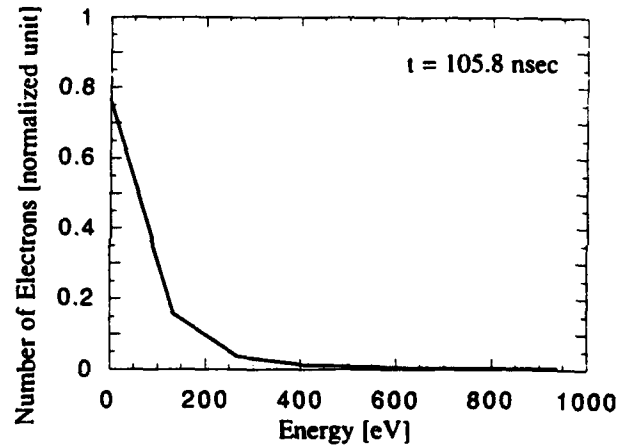


Figure 4: The electron energy distribution at  $t = 105.8$  nsec. Same system parameters as in Fig. 1.

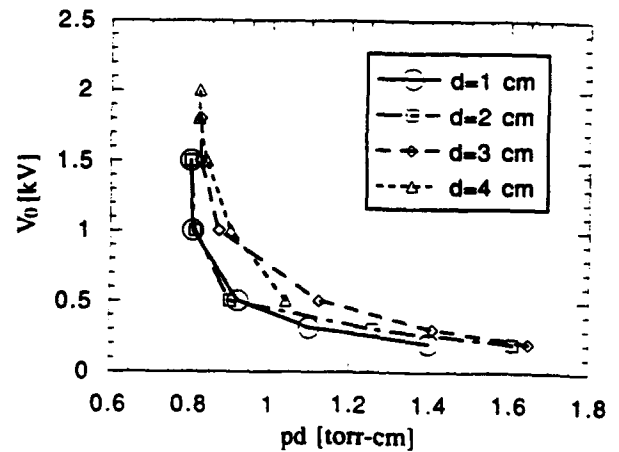


Figure 5: Breakdown Voltage as a function of gas pressure times gap length for gap lengths from 1 to 4 cm.

# A High Brightness Electron Beam Produced by a Ferroelectric Cathode\*

B. Jiang, G. Kirkman and N. Reinhardt  
Integrated Applied Physics, Inc.  
50 Thayer Road, Waltham, MA 02154 USA  
Tel. (617) 489-1818

## Abstract

We report experimental measurements of a high brightness electron beam produced by a ferroelectric cathode. The experiments were carried out with a cathode of area  $3.7 \text{ cm}^2$ ; up to  $36 \text{ A}$  of current ( $10 \text{ A/cm}^2$ ) were obtained at a voltage of  $22.5 \text{ kV}$ . The emission of the electron current was carried out with a DC voltage held between the cathode and ground anode. Emission was gated by a  $1\text{-}2 \text{ kV}$ , pulse applied across the sample by a solid state or krytron switch. The beam emittance was measured with a mask, phosphor screen and CCD camera; it was found to be  $5\pi \text{ mm mrad}$  yielding a normalized rms beam brightness of  $1.2 \times 10^{11} \text{ A/m}^2 \text{ rad}^2$ . This is the first reported measurement of the brightness of a ferroelectric cathode beam; it exceeds that of a thermionic cathode and is close to that of a photocathode. The results for the ferroelectric cathode may be directly compared with a preliminary experiment carried out in the same geometry with a thermionic cathode. The ferroelectric cathode yielded higher current density.

## I. Introduction

Ferroelectric materials such as lead lanthanum zirconium titanate (PLZT) and lead titanate-zirconate (LTZ or PZT) become spontaneously polarized when cooled below their Curie temperature resulting in a high charge density at their surface which is normally screened by a layer of surface charge. The spontaneous polarization can be as high as  $20 \mu\text{C/cm}^2$  resulting in the accumulation of a screening charge density of  $10^{14}$  elementary charges/ $\text{cm}^2$ . Altering the spontaneous polarization rapidly results in emission of the surface charge layer. This emission mechanism is unique and has potential advantages over emission mechanisms presently considered for high brightness sources. Fast polarization change and electron emission are accomplished by applying a fast high voltage pulse to the ferroelectric disk. In our experiment, the electrodes are deposited silver coatings; one side is solid while the other is in a grid pattern leaving areas of the ferroelectric surface exposed. A  $1\text{-}2 \text{ kV}$  fast pulse is applied to the ferroelectric disk by a solid state or krytron switched pulse generator to change the polarization in the ferroelectric disk.

Electron emission from PLZT and PZT has been previously observed. Gundel and Riege [1], [2] of CERN

\* This work was supported by National Science Foundation Grant No. ISI-9160797 through the SBIR Program.

obtained electron densities of  $10 \text{ A/cm}^2$  and Ivers et al. [3] of Cornell obtained  $70 \text{ A/cm}^2$ . Both groups have measured electron beam current, current density, repetition rate capability and temporal evolution of the emission. In our work we have for the first time measured the quality of the beam produced by a ferroelectric cathode --- emittance and brightness. We have obtained a beam current density similar to that of CERN and have shown that the beam is produced with low emittance.

## II. Experimental Design

Electron emission is produced from LTZ ferroelectrics by rapidly changing the polarization of the ferroelectric with a fast rising high voltage pulse. The emitted electrons are then accelerated by an electron gun held at a DC potential by an external circuit. The ferroelectric electron gun consists of a ferroelectric disk with specially prepared contacts, an electron gun and two driving circuits --- one to provide the fast high voltage pulse to induce the electron emission and the second to accelerate the beam in the electron gun. The electron gun and driving circuits are shown schematically in Figure 1.

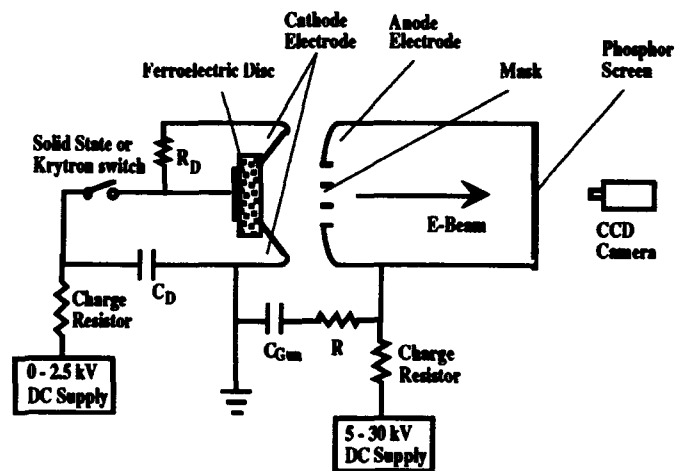


Figure 1. Electron gun and driving circuit for the ferroelectric experiment.

The driving circuit for inducing electron emission from the ferroelectric must produce a fast rising voltage pulse of  $1\text{-}2 \text{ kV}$  across the ferroelectric disc. The ferroelectric disc has a capacitance of about  $6 \text{ nF}$ ; therefore a high current pulser is required. Two tested pulsers are a commercial solid

state switched pulser capable of producing 20A at 2kV and a simple krytron switched pulser switching the charge stored in a 10 nF capacitor to the ferroelectric.

The electron source is a disc of LTZ-2 obtained from Transducer Products, Inc. The discs are 2.5 cm in diameter and 1 mm thick, with about 10 to 20  $\mu\text{m}$  thick silver contacts on both sides. The samples are pre-polarized in an electric field of 4 kV/cm. To be used as an electron source the discs must have one contact in a grid pattern exposing the surface of the ferroelectric. At Integrated Applied Physics (IAP), we prepared this grid pattern by a photochemical etching process to give a pattern of 200  $\mu\text{m}$  wide silver strips separated by 200  $\mu\text{m}$  wide spaces of bare surface. A ring of solid silver material was left at the edge of the sample for electrical contact to the grid.

### III. Preliminary Experiments with a Thermionic Cathode

The electron gun was designed to operate as a thermionic cathode at 5 - 50 kV with space charge limited current for a flat thermionic cathode of a few  $\text{A}/\text{cm}^2$ . The space charge limited current of this gun was measured using the thermionic cathode to allow a direct comparison with the performance of the ferroelectric source. Results for the thermionic cathode are shown in Fig. 2. The gun has obtained its design perveance up to the limits of this measurement which are 40 kV and  $\sim 3\text{A}/\text{cm}^2$  for a total current of 10A and a perveance of  $1.2 \mu\text{Perv}$ .

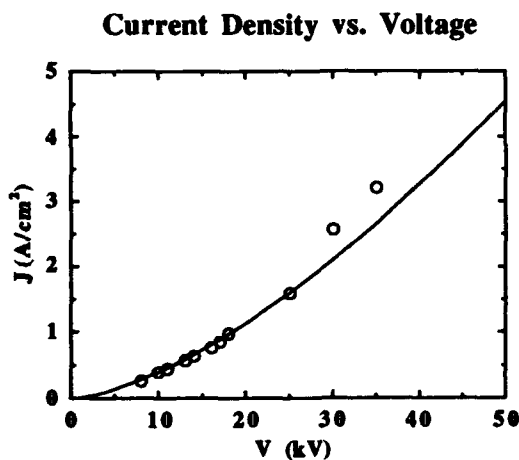


Figure 2. Electron gun results for the thermionic cathode. The curve is the theory for a  $1.2 \mu\text{Perv}$  gun; the open circles are the experimental results. To obtain the electron beam current, multiply  $J$  by the cathode area,  $3.7 \text{cm}^2$ .

The ferroelectric electron gun was fabricated using high vacuum ceramic-metal techniques which we have developed for the fabrication of high power switches. All electrodes are stainless steel, the insulator is  $\text{Al}_2\text{O}_3$  ceramic

which is brazed to a Kovar ring, the entire assembly is welded together using TIG welding techniques developed at IAP. The final assembly is made using high vacuum flanges and the entire system is pumped on a diffusion pump to a base pressure of  $10^{-7}$  Torr. For this work, we kept the electrode geometry of the thermionic electron gun, but replaced the thermionic cathode with the ferroelectric disk.

### IV. Experimental Results for a Ferroelectric Cathode

The measurements of the electron beam current versus applied gun voltage for the ferroelectric cathode are shown in Figure 3. The current increases linearly with the applied gun voltage and is higher than the result for a space charge limited thermionic cathode electron gun in the same geometry. The highest peak current observed was 36A at a 22.5 kV gun voltage, which is a current density of about  $10 \text{A}/\text{cm}^2$ . The current observed is about 10 times larger than the expected space charge limited current for a thermionic cathode gun. At 15 kV the ferroelectric source gives 24A compared with the previously measured space charge limited current of 2.2A at 15 kV using a thermionic cathode. The results shown in Figure 3 qualitatively agree with the observations of the Cornell group (Ref. 3). However, our peak beam current is lower than the expected circuit limit indicating that the electron gun or the ferroelectric source may be limiting the current.

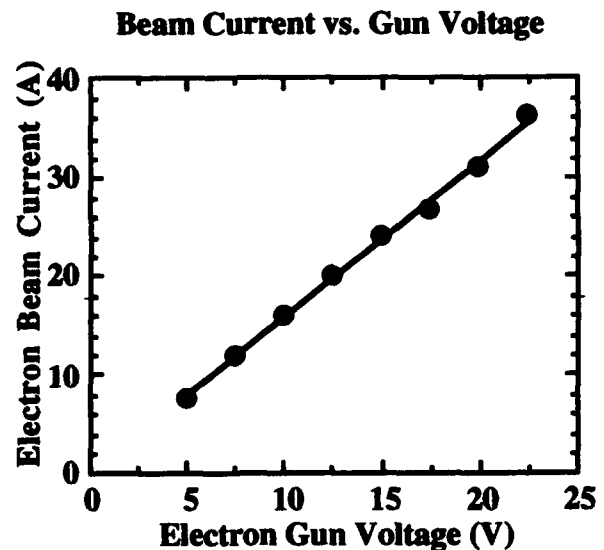


Fig. 3. Electron beam current produced versus applied gun voltage. In all cases the ferroelectric was pulsed at 2kV.

Beam emittance has been measured by using the pepperpot emittance meter. In our implementation of this measurement, the pepperpot mask is a thin copper disk with an array of diameter  $d=200\mu\text{m}$  holes separated by 1 mm. It is placed at the center of the anode electrode of the electron gun. A portion of the electron beam passes through the holes on the

mask and drifts freely to a phosphor screen a distance  $D=214$  mm away. The beam image on the phosphor screen is then recorded for analysis of the beam emittance. The beam is observed on the phosphor screen by using a CCD camera interfaced to a Macintosh computer. The image is captured and analyzed by using the program NIH Image 1.41. The combined resolution of the camera and the phosphor screen is better than 0.2 mm which allows us to measure beam emittance to about  $\pm 10\%$ . The raw data of a density profile obtained by analyzing the beam image captured by the CCD camera are shown in Fig. 4.

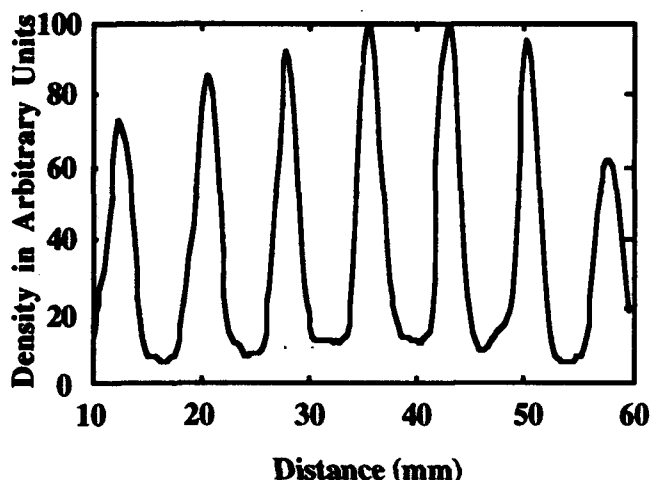


Fig. 4. Raw data of density profile.

Under the assumption that the electron beam produced by the ferroelectric cathode is axisymmetric, not rotational and with a Maxwellian transverse velocity distribution, the data analysis approach of Rhee [4] is used to obtain the rms emittance of the beam. The normalized emittance at 10 kV is  $5\pi$  mm·mrad. Emittance measurements were taken at several values of beam current between 3 and 15A. In this range, the emittance was observed to be constant. The normalized brightness at 10 kV, 15A is  $1.2 \times 10^{11}$  A/m<sup>2</sup>·rad<sup>2</sup>.

## V. Discussion and Conclusions

The present experiments have produced pulsed electron beams of very high quality from a novel, ferroelectric cathode. Operation was demonstrated at beam voltages of 5 to 22.5 kV and currents up to 36A. At 10 kV and 15A, the normalized emittance was measured to be  $5\pi$  mm mrad yielding a normalized beam brightness of  $1.2 \times 10^{11}$  A/m<sup>2</sup>·rad<sup>2</sup>. These are, to our knowledge, the first reported measurements of the beam emittance and brightness of the electron beam produced by a ferroelectric cathode. A number of important applications appear promising for the ferroelectric cathode because of the demonstrated high beam quality.

The cathode was successfully prepared from a commercial specimen of LTZ-2 by etching a grid pattern. The ferroelectric disk was mounted in an electron gun geometry and sealed using high vacuum, ceramic-metal techniques. The final package is rugged and stable and should be capable of long life operation. The ability to demonstrate a rugged package for the novel ferroelectric cathode is another important factor in applying the cathode in research and commercial applications.

The ferroelectric cathode has many advantages over the conventional thermionic cathode which is widely used in microwave tubes, x-ray tubes, switches, etc. The present research gives direct experience in comparing the ferroelectric and thermionic cathodes in the same configuration. A thermionic cathode was able to produce about 3A of current at 20 kV; in the same package, a ferroelectric cathode produced up to 30A at 20 kV, an order of magnitude improvement. Furthermore, the quality of the ferroelectric beam was higher than that of the thermionic beam. The ferroelectric beam quality corresponded to an effective cathode temperature near room temperature; the effective temperature of the beam from a thermionic cathode is generally above 1000C.

## VI. References

- [1] H. Gundel, H. Riege, E. Wilson, J. Handerek and K. Ziotus, *Ferroelectrics* 94, 337 (1989).
- [2] H. Riege "New Ways of Electron Emission for Power Switching and Electron Beam Generation," in "Physics and Applications of Pseudosparks," NATO ASI Series B, Vol. 219, Edited by M. A. Gunderson and G. Schaefer, Plenum, New York, 1990.
- [3] J. D. Ivers, R. Advani, J. A. Nation and L. Schachter, "Electron Emission from Ferroelectric Ceramics, 1991 Particle Accelerator Conference, San Francisco, CA, May, 1991.
- [4] M. J. Rhee and R. F. Schneider, "The Root-mean-square Emittance of an Axisymmetric beam with a Maxwellian Velocity Distribution", *Particle Accelerators*, 1986, Vol. 20 pp. 133 - 141.

## Acknowledgment

The authors would like to thank Dr. R. J. Temkin for helpful suggestions during the course of this work.

# THE UV-FEL AT THE NSLS: STRAIGHT INJECTION CONFIGURATION

Xiaohao Zhang and Juan C. Gallardo  
National Synchrotron Light Source and Physics Department  
Brookhaven National Laboratory, Upton, New York 11973

We present a design of a colinear RF-photocathode gun and linac sections for the ultraviolet free-electron laser under study at the National Synchrotron Light Source. Inverse Helmholtz solenoid pair is used to control the divergence of the electron beam and present a slightly convergent and small beam into a conventional SLAC linac. The relative distance of the gun to the linac and the strength of the solenoidal field are chosen to minimise the emittance growth of the beam due to space charge. The simulation codes PARMELA and TRACE-3D are used to model the beam from the cathode to the entrance to the wiggler.

## I. INTRODUCTION

The National Synchrotron Light Source (NSLS) is studying the design and construction of an ultraviolet free-electron laser (UV-FEL) capable of providing tunable coherent radiation from 3000 to 750 nm. [1,2]

In this design study we use the by now well known BNL RF-photocathode gun [3] supplemented with an inverse Helmholtz solenoid pair [4] to control the divergence of a few picosecond and highly correlated electron pulse. The coils are located symmetrically with respect to the cathode to insure  $B_x = 0$  at the plane where the electrons are emitted. In the low energy section, the main cause of emittance dilution is the space charge. [5] We will show in the next section that an interplay between (linear) solenoidal focusing forces and de-focusing space charge fields lead to a minimum of the transverse emittance inside of the linac. [6]

The well known simulation codes PARMELA [7] and TRACE-3D [8] have been used as design tools.

## II. LONGITUDINAL BEAM SLICES AND EMITTANCE CORRECTION

To study the causes of emittance dilution in the transport and acceleration of a high brightness electron beam, it is desirable to divide the few picosecond bunch in longitudinal slices ( $\leq 10$ ) of equal length. We follow each slice through the transport system and observe that the intrinsic emittance is small ( $\approx 4 - 5\pi$  mm - mrad) but the projection in 2-D phase space of all slices gives rise to the typical fan plots. Although the area swept by each

slice is relatively small, the area covering all slices is significantly larger as is, consequently, the total emittance. It is easily seen that the space charge is greater in the core of the beam than at the ends and as a result, the core tends to have larger radius and  $x'$  than the ends which leads to ellipses in phase space of different orientation or slope with the larger slope corresponding to the core of the beam.

In Ref. [5], it was proposed ways to force the fan to close and effectively correct the emittance. Here we follow the suggestion in Ref. [6]; we use a solenoid to compensate the de-focusing forces of space charge. As discussed in Ref. [9], the optimal situation leading to a minimum of emittance corresponds to an ellipse in phase space that rotates from the first to the fourth and back again to the first quadrant with the particles in the tail with larger  $x$  and  $x'$  than the corresponding coordinates of the particles in the core of the pulse. In this condition space charge alone tends to close the fan and consequently to decrease the total emittance of the bunch. At this point, if the beam is left to drift, space charge will eventually spread the fan again and restore the emittance to its previous higher value. However, in our design the waist occurs inside of the linac. As the beam is accelerated, the slice ellipses are frozen with respect to each other due to a decrease of space charge  $O(\frac{1}{\gamma^2})$ . The final result after appropriate tuning is an emittance for the entire beam which is essentially the slice emittance. The initial parameters of the electron beam are shown in table I.

TABLE I. Parameters used in the PARMELA simulations for an axially symmetric  $1\frac{1}{2}$ -cell gun in a  $\pi$ -mode configuration with a solenoid pair.

RF frequency [MHz]	2856
Radius of aperture [cm]	1.0
Radius of nose [cm]	1.0
First cell length [cm]	2.625
Second cell length [cm]	5.23
Field on cathode [MV/m]	100.0
Initial phase [degree]	45.0
Laser spot size (Uniform top-hat profile) [cm]	0.1
Laser pulse width (Uniform top-hat profile) [ps]	7.0
Charge (2.4 nC with a chicane) [nC]	2.5
Solenoidal field $B_0$ [kG]	2.2
Solenoid length [cm]	15.0

The emittance correction scheme just described only corrects linear forces. Therefore, a uniform laser illumination of the cathode with sharp edges is required, as only this type of distribution leads to linear space charge forces. [10,11] An emittance (rms - normalise) plot as a function of the longitudinal coordinate  $z$  is shown in Fig. 1. In that figure we observe a fast increase of the emittance  $\epsilon^{norm}$  occurring immediately after the gun and a subsequent reduction to a rather broad minimum (in some cases there is a gentle asymptotic decrease) located inside the first linac section. This behavior of  $\epsilon^{norm}$  reflects the interplay of (linear) solenoid focusing and de-focusing space charge fields and illustrates the mechanism discussed above.

### III. ELECTRON BEAM LINE DESCRIPTION

The beam line consists of a high brightness electron source, an accelerating and a transport section. The total length of the beam line is about 25 meters. The 2.4 nC electrons are produced by an RF-photocathode gun with a pair of symmetric solenoids. A length adjustable drift ( $\approx 75$  cm) after the gun is followed by the first linac section which increase the beam energy from 4.0 MeV to 70 MeV. The strength of the solenoids and the drift length between the gun and the first linac section are adjusted to have a convergence beam going into the linac and a double waist at the end of it. The initial phase of the cavity is tuned for the beam to have the correct longitudinal phase space for magnetic compression. The compression is achieved by a chicane designed to reduce the length of the electron pulse by a factor of 2 and to increase the current of the front of the pulse by a factor of 3. After compression the electron are accelerated to 360 MeV by four additional linac sections. The beam is accelerated a slightly off the peak of the RF wave to reduce the energy spread of beam. At the entrance of each linac section, a quadrupole triplets is located to provide necessary focussing to keep the beam size small. It also provide a flexibility for later improvement and modifications.

### IV. PARMELA RESULTS

We present results with and without magnetic compression.

*With magnetic compression:* Fig. 2 depicts the pulse length in picosecond and rms (global) energy spread of the pulse. Fig. 3 illustrates the current of individual slices as the beam progresses through the transport line. We notice that the tail of the beam carries less than 25 % of the total charge.

The characteristics of the electron beam presented to the wigglers is summarise in table II.

TABLE II. Electron beam parameters at the end of the transport line (case with a chicane) SLICES 1 AND 2

Average energy [MeV]	362
$\gamma$	710
Q first two slices (80% of 2.4 nC) [nC]	1.88
Energy spread [%]	0.14
Length of the pulse [ps]	2.75
Current ( $820 \times 0.75 + 276 \times 0.25$ ) [A]	684.0
rms $\epsilon^{norm}$ [ $\pi$ mm-mrad]	6.0
rms radius [mm] (x,y)	0.8 , 0.4
rms divergence (x,y)	-0.04 , -0.025

*Without magnetic compression:* The electron beam parameters at the end of the transport line are in table III, notice we are retaining only 90 % of the 2.5 nC.

In a work under preparation, we will include errors, such as solenoids misalignment, stability of the coil power supply and wake fields in the linac.

TABLE III. Electron beam parameters at the end of the transport line

Average energy [MeV]	326
$\gamma$	640
rms Global energy spread [%]	0.3
rms Local energy spread [%]	0.06
rms length of the pulse [ps]	3.1
Current ( $I = \frac{Q}{\sqrt{2\pi\sigma_z^{rms}}}$ ) [A]	290
rms $\epsilon^{norm}$ [ $\pi$ mm-mrad]	5.7
$\alpha$ (x,y)	4.7 , 4.2
$\beta$ [cm] (x,y)	6.4 , 6.4
rms radius [mm] (x,y)	0.85 , 0.8
rms divergence (x,y)	0.06 , 0.05

### V. SUMMARY

We have presented the design of a high-brightness injection line for the proposed UV-FEL at the NSLS, Brookhaven National Laboratory. The study of slices of the electron pulse is essential to tune the compensating effects of the solenoid (focusing) and space-charge forces (de-focusing) as emittance correction scheme. Furthermore, magnetic compression leads to a pulse with  $\approx 685$  A, global energy spread of 0.14 and normalised emittance of  $\approx 6.0 \pi$  mm - mrad.

### ACKNOWLEDGEMENTS

The authors wish to thanks B. Palmer and H. Kirk for illuminating discussions. We also acknowledge the active support and encouragement of I. Ben-Zvi. This research was supported by the U.S. Department of Energy under Contract No. DE-ACO2-76-CH00016.

## VI. REFERENCES

- [1] *UV Free-Electron Laser. Conceptual Design Report*, BNL Report No. 48565, February (1993).
- [2] X. Zhang, Juan C. Gallardo, *Low energy beam transport in the NSLS UV-FEL*, BNL report, unpublished.
- [3] K. Batchelor et al., *Nucl. Instr. and Meth.*, **A318**, 372 (1992)
- [4] R. L. Sheffield, *AIP Conference Proceedings*, **184**, 1502 (1990) and reference there in; K. McDonald, unpublished; Zhi-Yu Jiang and C. Pellegrini, private communication.
- [5] Juan C. Gallardo and Robert B. Palmer, *Nucl. Instr. and Meth.*, **A304**, 345 (1991)
- [6] R. L. Sheffield et al., *Nucl. Instr. and Meth.*, **A318**, 282 (1992) and references there in.
- [7] L. Young, private communication.
- [8] K. R. Crandall, TRACE-3D, LA-UR-90-4146 Los Alamos Accelerator Code Group, December (1990).
- [9] Juan C. Gallardo and H. Kirk, *An injection scheme for the Brookhaven ATF utilizing space-charge emittance growth compensation*, this Proceedings.
- [10] S. Humphries, Jr., *Nucl. Instr. and Meth.*, **A258**, 548 (1987)
- [11] Juan C. Gallardo, *Control of non-linear space-charge emittance growth*, BNL-43862 (1990)

FIG. 1. History of the rms normalized transverse emittance  $\epsilon^{norm}(x,y)$  vs. distance  $z$  without compression.

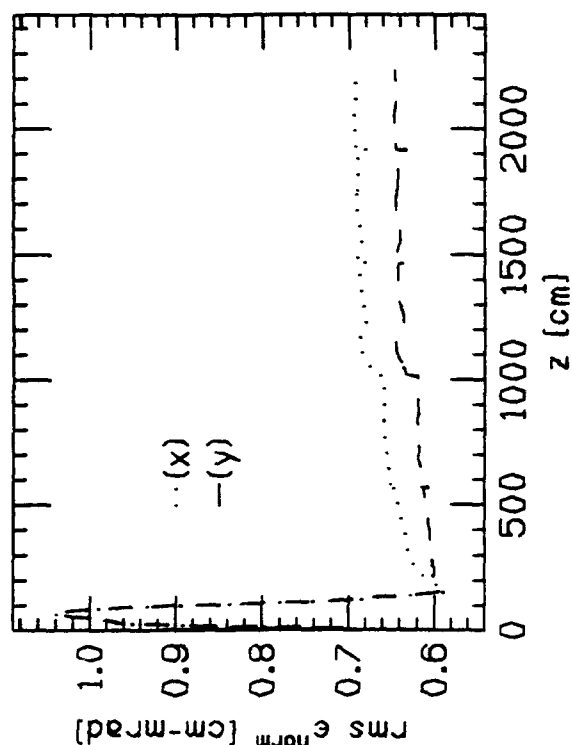


FIG. 2. a) History of the rms pulse length in picosecond without compression.

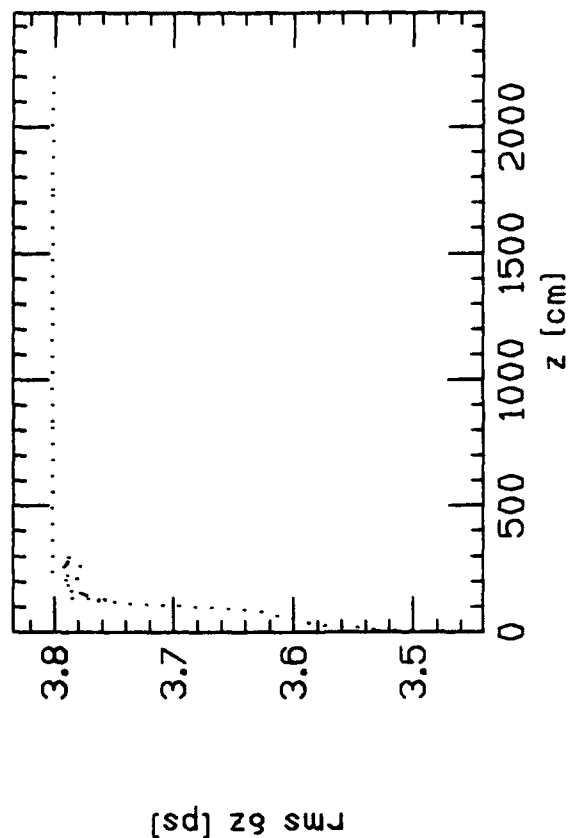
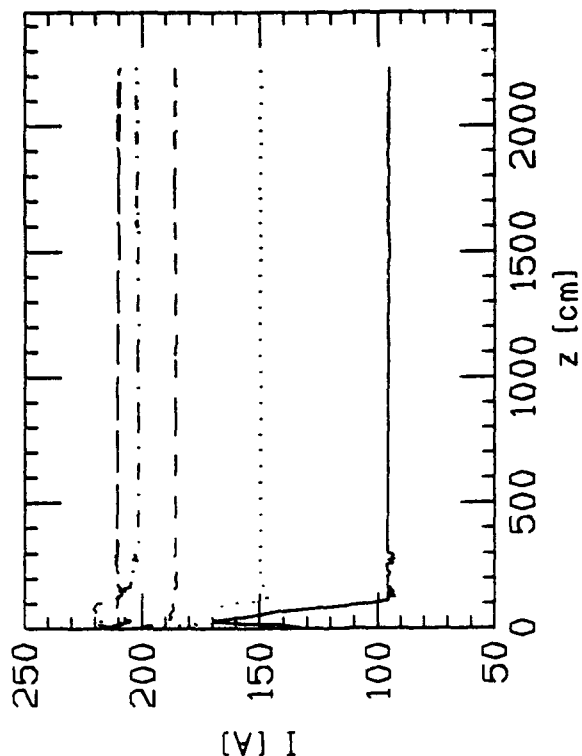


FIG. 3. History of the current of 5 slices along the-transport line without compression.



# Progress on PEP-II Injection R&D\*

E. Bloom, F. Bulos, T. Fieguth, G. Godfrey, G. Loew, R. Miller  
Stanford Linear Accelerator Center  
Stanford, CA 94309 USA

## I. ABSTRACT AND INTRODUCTION

The R&D program described in this paper focuses on an improvement of the SLAC linac designed to extract and study a 9 GeV electron beam under stringent control of energy, energy spread, emittance, optical parameters, and timing.

The extraction system begins with an on-axis pulsed magnet, followed by a magnetic lattice and diagnostic equipment required for the measurement and optimization of the above beam qualities. Design, construction, and installation of this system is the first step in the development of the overall PEP-II  $e^\pm$  injection system.

This system is required to fill 1658 bunches of 9 GeV electrons (0.99A stored) and 3.1 GeV positrons (2.14A stored) in two separate rings in a total of about 6 minutes from zero ring current (i.e., full-fill mode, 0 to 100%) or in about 3 minutes from 80% ring current (i.e., topping-off mode, 80 to 100%).

This unprecedented rate of filling can be met<sup>1</sup> by a judicious use of the SLC linac, damping rings, and positron source.

## II. ROLE OF R&D PROGRAM IN OVERALL PEP-II INJECTION

The overall goals of the PEP-II Injection System are summarized in Table 1. These differ from those given in earlier papers<sup>2,3</sup> in that the current of the electron ring (HER) was recently lowered from 1.48 to 0.99A, and that SLC operation showed that the transverse beam emittance can be decreased by going to flat beams ( $\epsilon_y \sim \epsilon_x/8$ ). These two factors both ease the injection process.

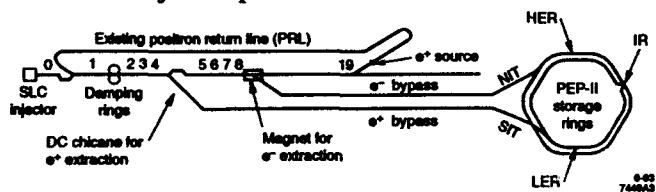


Fig. 1. Schematic of the B Factory  $e^\pm$  injection system, based on use of the SLC linac with bypass lines.

Figure 1 shows a diagram of the entire injection system using the SLC. Alternate linac pulses accelerate the electrons for HER on one 60 Hz time slot, and the positrons for LER together with the electrons which make the positrons on the next 60 Hz time slot. The electrons are stored in the North Damping Ring (NDR) for 1/120th of a second, the positrons are stored in the South Damping Ring (SDR) for 1/60th of a second. The first eight sectors of the linac are pulsed at 120 Hz, the remaining sectors up to the  $e^\pm$  source are pulsed at

60 Hz. The extraction of the positrons takes place by means of the DC chicane in Sector 4. The extraction of the electrons takes place in Sector 8 by means of the slow pulsed bending magnet and lattice described in this paper.

The correct injection timing of the bunches, which in PEP-II are spaced 4.2 ns apart, is obtained by adjusting the timing of the damping-ring extraction kickers and the phase of the DR rf (714 MHz) during the damping interval. The linac rf frequency (2856 MHz) and the PEP-II rf frequency (476 MHz) are harmonically related and locked together.

TABLE 1: Selected PEP-II Injection Parameters.

Beam energy	
High-energy ring (HER)	9 [range:8-10] [GeV]
Low-energy ring (LER)	3.1 [range: 2.8-4] [GeV]
Beam Current	
High-energy ring (HER)	0.99/4518 [A/10 <sup>10</sup> e <sup>-</sup> ]
Low-energy ring (LER)	2.14/9799 [A/10 <sup>10</sup> e <sup>+</sup> ]
Particles per bunch	
High-energy ring (HER)	2.7 [10 <sup>10</sup> e <sup>-</sup> ]
Low-energy ring (LER)	5.9 [10 <sup>10</sup> e <sup>+</sup> ]
Linac repetition rate	
Linac current range during filling	60/120 [Hz]
Invariant linac emittance	0.1-3 [10 <sup>10</sup> e <sup>±</sup> /pulse] <sup>a</sup>
$\epsilon_x$	4x10 <sup>-5</sup> [m · rad]
$\epsilon_y$	0.5x10 <sup>-5</sup> [m · rad]
Normal filling time	
Topping-off (80-100%)	3 [min.]
Full fill (0-100%)	6 [min.]
Revolution period	
Harmonic number	7.336 [μs]
Number of bunches <sup>b</sup>	3492
Vertical damping time	1746-5%=1658
HER	38 [ms]
LER, with wigglers	40 [ms]
LER, without wigglers	68 [ms]
Nominal beam emittance	
HER, horizontal/vertical	48/1.9 [nm · rad] <sup>c</sup>
LER, horizontal/vertical	64/2.5 [nm · rad] <sup>c</sup>

<sup>a</sup> Assuming 75% filling efficiency. The SLC routinely delivers  $2.8 \times 10^{10}$   $e^\pm$  per linac pulse at the detector.

<sup>b</sup> For filling, the rings are divided into nine equal zones. A 5% gap leaves one zone partially unfilled.

<sup>c</sup> Unnormalized, or geometrical, values.

## III. EXTRACTION SYSTEM AND LATTICE

The geometry and optical lattice of the extraction system design<sup>4</sup> are influenced by the desire to accomplish extraction without significantly perturbing the optics of the linac. This

\* Work supported by Department of Energy contract DE-AC03-76SF00515.

will be conducive to the operation of interlaced beams and to switching operating modes between SLC, beams for fixed target experiments, and the PEP-II studies.

The extraction lattice has a phase advance of  $90^\circ$  per cell. Extraction dipoles are placed in pairs having equal but opposing bends, and are separated by four cells or  $360^\circ$  in phase advance. The extracted beam is thus made to be parallel to, but offset from, the linac beam, and the induced dispersion is suppressed overall.

Figure 2 shows the optical functions of the beam line and Fig. 3 is a schematic of its components. Four regions are indicated. The first, Region I, where the beam is dispersed, will be used for measurements pertaining to the beam energy. Also in this region, capability is provided to correct errors in the dispersion without modifying the overall monoenergetic parameters (i. e., beta and alpha functions).

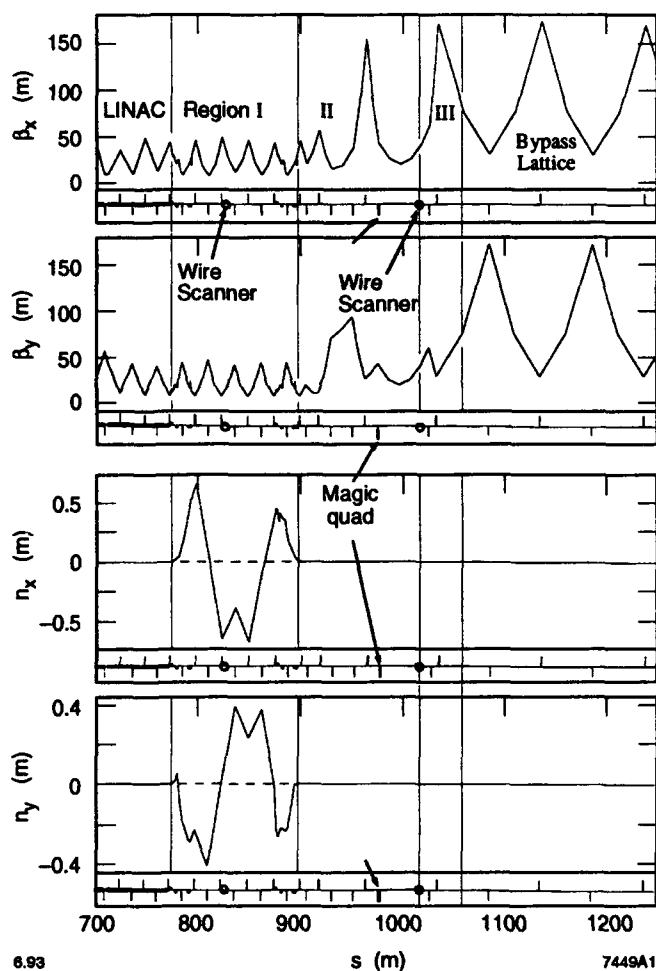


Fig. 2. Machine function for the PEP-II, 9 GeV electron beam extraction system.

Region II provides the facility to correct the errors in these latter parameters, but again in an orthogonal manner, that is, without changing the dispersion. This region is equipped with a wire scanner and a single "magic" quadrupole<sup>5</sup> (see below) for the purpose of measuring beta, alpha and the emittance of the beam in each plane. Region III

is a matching section which matches the linac lattice to the Bypass lattice.

Finally, the first two cells of the Bypass lattice are represented in the last region, which can be continued by repeating this lattice until the end of the linac housing is reached, and the beam line is connected to the existing north PEP transport line going to the ring housing. The Bypass lattice also has a phase advance of  $90^\circ$  per cell with the cell length designed so that there is one cell per linac sector. This short section of Bypass line is terminated by a beam dump and can be extended at a later time.

#### IV. EXTRACTION LINE BEAM-POSITION MONITORS

Every quadrupole in the extraction system, and in the subsequent transport lines, will be equipped with a beam-position monitor (BPM) capable of measuring beam position in the x- and y-plane, but only one coordinate will be measured from each instrument. A measurement of the orbit—at  $90^\circ$  intervals in phase advance—throughout the dispersive and non-dispersive regions will allow separation of betatron oscillations from energy dependent effects. These latter changes in position due to energy will be monitored by a feedback system to hold the energy constant.

Because of their importance to the beam parameter measurements and their relatively large number and cost, the BPMs must be engineered very carefully. In the linac housing, wherever possible, two cables (for x or y) will be run from each new BPM to a nearby existing linac BPM to which they will be coupled with  $\sim 10$  dB loss couplers. This multiplexing, which is already being used for the existing Positron Return Line in the linac housing, will save greatly on the cost.

The position resolution of the extraction and transport line BPMs is determined by the need to steer the beam through apertures and to match it to the acceptance<sup>6</sup> in position, angle and energy of PEP-II. If the BPM resolution is better than the beam  $\sigma_x$  and  $\sigma_y$  everywhere in the extraction and transport line, then the beam position will be known well enough with respect to their apertures. The minimum  $\beta_x$  or  $\beta_y$  of the  $\beta$ -function maxima (where the BPMs will be used) is  $\sim 40$  meters. For a beam emittance of  $2.5 \times 10^{-9}$  m · rad, this minimum size corresponds to a  $\sigma$  of 0.3 mm. The closest (in mm) object to the injected beam is a PEP-II septum at 3.5 mm ( $\sim 10 \sigma_y$ ). The PEP-II energy acceptance is  $\pm 5\%$ . This corresponds to  $\pm 2$  mm position resolution in x in the dispersive region ( $\eta_x \sim 0.4$  meters) at the beginning of the extraction line where the beam energy will be stabilized by the feedback loop. An easily attainable resolution of  $100 \mu\text{m}$  for all BPM position measurements will be comfortably less than these minimum  $\sigma$ s. This specification of a  $100 \mu\text{m}$  resolution will apply for a pulse of  $1 \times 10^9$  electrons, a value representing the smallest quantum of charge that is planned to be injected.

#### V. MEASUREMENT AND ADJUSTMENT OF BEAM PARAMETERS

As mentioned above, the parameters of the extracted electron beam will be measured and adjusted in the first two regions shown in Figs. 2 and 3.

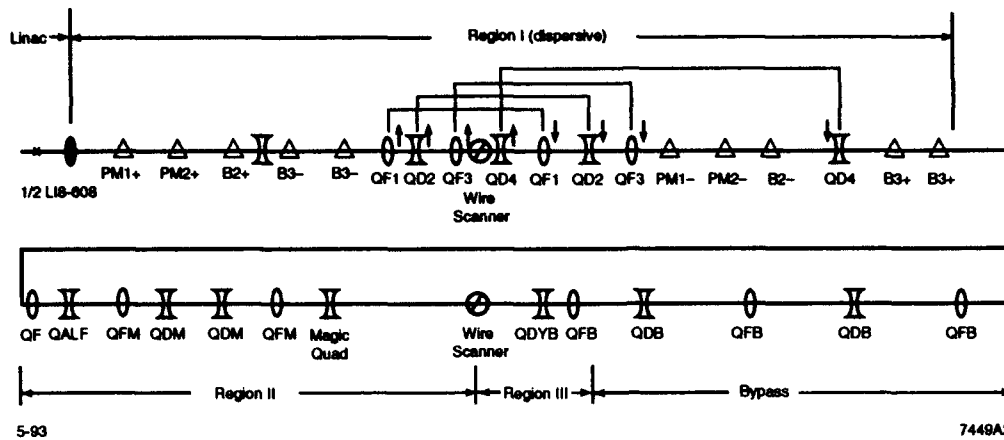


Fig. 3. Schematic of optical components for electron extractor system.

In Region I, where the dispersion is maximum, it contributes as much as 15 times the monochromatic beam size ( $\sqrt{\beta E}$ ). A wire scanner, located at a point of almost maximum and equal dispersion in both x and y, will be used to measure the energy distribution. The expected scanner accuracy is  $\sim 50 \mu\text{m}$  and the beam size from dispersion is  $\sim 2500 \mu\text{m}$ . Thus  $\Delta E$  will be measured to  $\pm 2\%$ , and  $\Delta E/E$  to about  $\pm 0.01\%$ , assuming an incoming beam spectrum of  $\pm 5\%$ .

As shown in Fig. 3, in Region I there are four pairs of quadrupoles ( $180^\circ$  per cell apart in each pair) which are used to correct for errors in the dispersion. By changing the strength of these quadrupoles in each pair equally but in opposite direction, it is possible to eliminate the anomalous residual dispersion at all points in the dispersion-free Region II downstream. This scheme has the virtue of leaving  $\beta$ -functions unchanged in the downstream region, eliminating the need for retuning.

In Region II a second wire scanner and a single quadrupole are used to measure the emittance and Twiss parameters of the beam. This quadrupole is called magic because, unlike the behavior normally associated with quadrupoles, it does not change the shape of the beam which for equal (unequal) emittance in both planes will always be round (flat). Thus, at its nominal setting the beam is round (flat) and a minimum in size; it will stay round (flat) but become larger for any change of the quadrupole strength in either direction. This allows measurement of the size of the beam about its minimum in both planes simultaneously with reasonable changes in quadrupole strength.

The quadrupoles in the dispersion-free Region II will be independently controlled to provide the capability of correcting the Twiss parameters, and matching the proper conditions for launch into the Bypass lattice.

The addition of instrumentation for measurement of beam charge and timing will complete the instrumentation. The controls will be provided by utilizing the existing SLC control system and its application programs.

## VI. CONCLUSION

The proposed electron extraction system will be capable of measuring all beam parameters important to the development of an injection system for the PEP-II asymmetric collider. Modifications to the linac and its operations will be quite modest.

## REFERENCES

- [1] E. Bloom et al., "A Critical Examination of the PEP-II Injection System and Alternative Proposals." SLAC-PEP-II-AP-NOTE-1-92, Sept. 1992.
- [2] LBL-PUB-5303, SLAC-372, CALT-68-1715, UCRL-ID-106426, UC-IIRPA-91-01 (1991).
- [3] E. Bloom et al., "The Proposed Injection System for an Asymmetric B Factory in the PEP Tunnel." *Proc. of IEEE Particle Accelerator Conference*, San Francisco, CA, Vol. 2, p. 982, (1991), SLAC-PUB-5771 (1991).
- [4] T. Fieguth et al., "Injection System for the PEP-II Asymmetric B Factory at SLAC," *Proc. of Third European Particle Accelerator Conference*, Berlin, Germany, Vol. 2, p.1443 (1992), SLAC-PUB-5771 (1992).
- [5] T. Fieguth, "Comments on Optics for Electron Extraction," PEP-II Technical Note No.12, May 1993.
- [6] F. Bulos et al., "Optimizing the Injection Straight of PEP-II Asymmetric B Factory at SLAC," contributed to the *International Conference on B Factories*, Stanford, CA, April 1992, SLAC-PUB-5800 (1992).

# New Pre-injector of the KEK 2.5-GeV Linac and its Performance

S. Ohsawa, I. Abe, S. Anami, J.-Y. Choi, A. Enomoto, K. Furukawa, H. Hanaki, K. Kakihara, N. Kamikubota, T. Kamitani, H. Kobayashi, Y. Ogawa, T. Oogoe, I. Sato, T. Suwada, Y. Yamazaki, M. Yokota, KEK, National Laboratory for High Energy Physics  
Oho, 1-1 Tsukuba-shi, Ibaraki-ken, 305 Japan  
and A. Asami

Naruto University of Education  
Takashima, Naruto-cho, Naruto-shi, Tokushima-ken, 722 Japan

## Abstract

The injection system (pre-injector) of the KEK 2.5-GeV linac has been upgraded so that we can investigate intense beam acceleration for the KEK B-factory project. It requires intense beams to achieve a short injection time in practice. An outline of the new pre-injector and its performance is given.

## I. INTRODUCTION

The pre-injector of the 2.5-GeV linac was extensively upgraded during the summer of 1992 [1]. We installed the new pre-injector during the summer maintenance period from July 11 to September 27, 1992. At first we completely removed almost all of the previous system in the tunnel. Entire devices, including a supporting girder, were replaced with new ones, except for 2 quadrupole magnets and 2 accelerating guides. The first test operation with beams was performed on September 24 to 25, as scheduled. Everything was completed within the period, except for some small items. Normal operation started well on September 28, as prearranged.

This is the first step toward upgrading the linac to meet the requirements of the KEK B-factory [2], which is presently under consideration as a future project. It requires intense beams, especially an intense  $e^-$  beam for producing positrons. It is, therefore, important to understand how high-intensity  $e^-$  beams can be accelerated in the linac, as well as any instabilities of the beams.

## II. NEW SYSTEM CONFIGURATION

The layout of the new pre-injector is shown in Fig. 1. Improved items extended over a wide area [3]. The main items are described in the following.

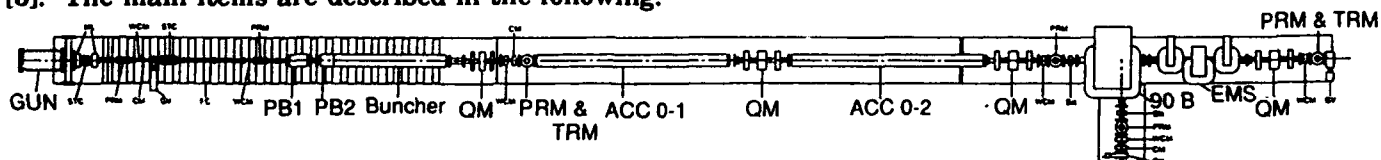


Fig. 1 Layout of the new pre-injector of the 2.5-GeV linac

## A. Electron Gun

We changed the electron gun to a newly designed one, which is under operation at 190 kV. A ceramic insulator was changed from one 130 mm long with ICF-203 flanges to at one of 300 mm long with ICF-253 flanges. The cathode is a commercially available one (EIMAC Y-796).

## B. Bunching System

We adopted a multiple bunching system that comprises double prebunchers and a high field buncher [1]. Our new system has several features: (1) The distance between the 2nd prebuncher and the buncher was made as short as possible in order to obtain short bunches. This is also important to minimize any effect resulting from beam loading in the gun. If the beam energy is gradually reduced at the gun, multiple bunches are made at different phases. The shorter distance requires a stronger modulating field, which makes the loading effect relatively small. (2) The prebunchers were designed to have very low shunt impedances and large group velocities. The aim is to reduce any wake-field effects caused by an intense beam. (3) The buncher comprises two sections, each of which has a high field (15 MV/m). The beginning part is the bunching section, which has 6 cavities, including an input coupler. Each cavity has a different phase velocity, varying gradually from  $0.77c$  to  $0.99c$ . A normal section with a phase velocity of  $c$  directly follows the bunching section. (4) All of the prebunchers and buncher are of the traveling-wave type. (5) The field asymmetry in the coupler cavities was compensated for by offsetting the coupler cylinders instead of making a counter slot on the cylinder wall [4].

The field strengths and phase velocities of the bunching system were determined by simulations

with PARMELA. An example is shown in Figs. 2a and 2b. The simulation predicts a bunch length of  $5^\circ$  (FWHM) at the buncher exit for a 200 keV/ 8A beam from the gun [5]. The particles plotted in these figures reach just 90% of the initial particles, which indicates a high bunching efficiency.

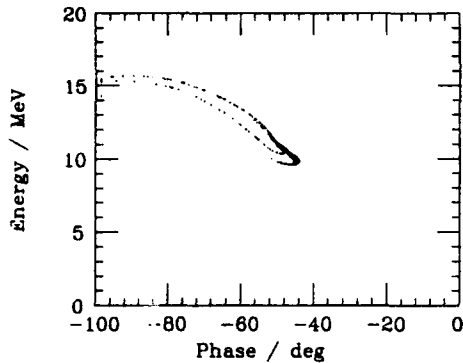


Fig. 2a Simulation example of energy distribution versus the buncher rf phase.

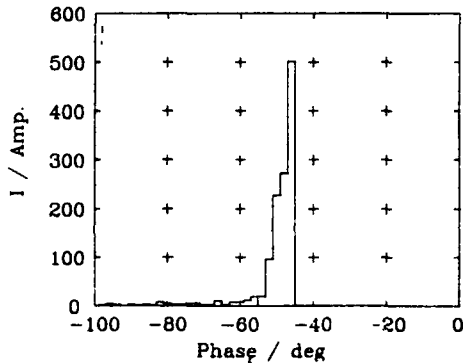


Fig. 2b Current density versus the rf phase in the same case. Each bin has a width of  $2^\circ$ .

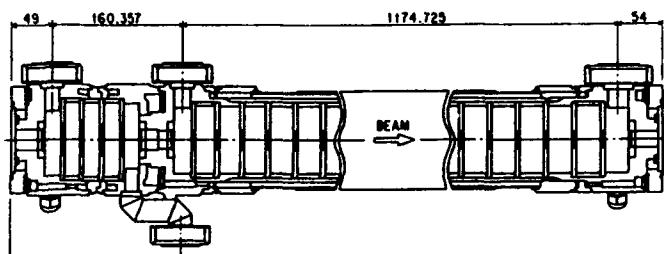


Fig. 3 Structure of the 2nd prebuncher and buncher, which are connected mechanically, but separated electrically.

### C. RF Adjusting System

It is necessary to optimize the power levels and phases of microwaves fed into the prebunchers and the buncher. We employed equipment that is capable of changing the power level and the phase independently [3],[6]. This is useful for simplifying the rf optimization in the bunching section. Since a

double prebuncher system was adopted, one more unit became additionally necessary for the rf adjusting system. This time we did not just add one unit for the system, but also rearranged the entire system.

The new rf adjusting system is shown schematically in Fig. 4. It has the following additional features: (1) The power dividing ratio for the 2nd prebuncher and buncher, which is controlled by the first unit, can be changed continuously without any phase shift. (2) When the same unit is driven as a phase shifter, all of the rf phases in the bunching system are shifted simultaneously by the same amount. This property is very useful for phasing the beam with respect to the fixed rf phases in the following accelerating guides, since it does not affect the beam bunches.

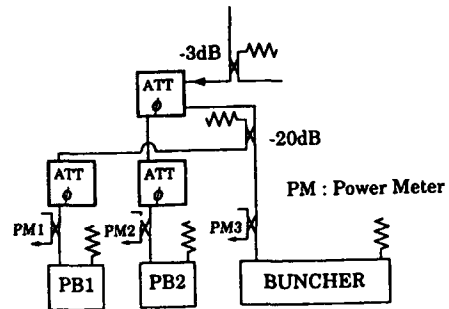


Fig. 4 Schematic diagram of the new rf adjusting system

### D. Beam Monitors

As the beam intensity increases, it becomes more important to transport beams at the centers of the accelerating cavities in order to reduce some of the transverse wake-field effects. We added some fluorescent screen monitors, two of which have additionally polished stainless steel as the transition light emitter. A streak camera is used to analyze the transition light for measuring the bunch lengths [7].

## III. PERFORMANCE TEST

### A. High-Current Acceleration

After the pre-injector upgrade, high-current beam acceleration was performed with an 8-A/ 4-ns beam, which contained  $9.3 \times 10^{10}$  electrons. The transport system was carefully adjusted only to the center of the 2nd sector, since the positron-production target had been assumed to be installed somewhere up to that point. Electrons of 83% were accelerated to the 1st sector entrance and 73% to the 2nd sector entrance. The results are given in Fig. 5. Monitor No. 11 is located at the 2nd sector center. After the upgrade, the beam currents increased as well as the transmission rate, as was expected.

Up to the center of the 2nd sector, beam profile deformation was not obvious on the screen monitors. In the following sectors, however, deformed profiles were observed, and the beam charge was decreased to 5.0 nC at the center of the 4th sector. The deformation that depended on the beam positions indicates that it was caused by wake fields.

Beams that contained much more charge were accelerated as a trial. They were longer beams with lower densities. As can be seen in Fig. 5, electrons of high rate (83 to 89%) were accelerated to the pre-injector exit. The beams were, however, considerably lost in the following sectors, especially in the first unit of the 1st sector. We are planing to install a quadrupole magnet there in order to improve the transmission rate. Beam loss is caused by a heavy beam-loading effect as well as transverse wake fields.

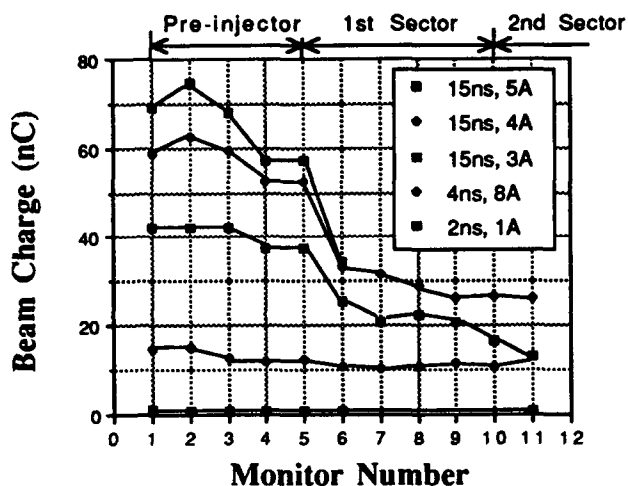


Fig. 5 High-charge beam acceleration after the pre-injector upgrade.



Fig. 6 One of the bunches of the 8-A/ 4-ns beam measured with a streak camera. It is a single-shot measurement.

### B. Bunch Length

Beam bunch lengths were measured at the end of the pre-injector using the streak camera. Figure 6 shows one of the bunches in the 8-A/4-ns beam, which

was taken, while analyzing the transition light. The measured bunch length (FWHM) is 9.8 ps, which is about twice as large as a prediction by a PARMELA simulation. The reason for the discrepancy is under investigation. Some reasons can be suggested: (1) incorrect bunching parameters, (2) wake-field effects, and (3) bunch-monitor performance.

### C. Emittance

The beam emittance was measured just downstream from the buncher by the usual method with a screen monitor and a quadrupole magnet. The beam sizes were measured on the screen varying a focusing strength of the quadrupole magnet. Beam sizes were defined by the full width at half maximum in the beam-density distribution. For a 4-A/15-ns beam, the obtained emittances were  $\epsilon_x = 45$  (mm mr) and  $\epsilon_y = 52$  (mm mr).

## V. FUTURE

The KEK B-factory requires for injection an s-band single-bunched  $e^-$  beam and an  $e^+$  beam of two or three bunches that are about 100 ns apart. Toward obtaining a single-bunched beam, we are presently preparing a 476-MHz SHB and its driver, which will be installed this summer. We will investigate soon what will occur in high-density single-bunched  $e^-$  beam acceleration at the present state of the 2.5-GeV linac. The purpose is, of cause, to determine what should be improved so that our linac will meet its requirements.

## VI. REFERENCES

- [1] S. Ohsawa et al., "Improvements to the Injection system of the KEK 2.5-GeV Linac," *Conference Record of the 16th International Linac Conference*, 1992, pp. 91-93.
- [2] A. Enomoto et al., "Linac Upgrade Plan for the KEK B-Factory," these proceedings.
- [3] Photon Factory Activity Report 1992, KEK, to be published.
- [4] H. Hanaki et al., "Computer Design of Coupler Cavities for a Traveling-Wave-Type Buncher," *Conference Record of the 3rd European Particle Accelerator Conference*, Vol. 2, pp. 910-912.
- [5] T. Kamitani et al., "A Simulation Study on Beam Bunching in the KEK 2.5-GeV Linac New Pre-injector," these proceedings.
- [6] S. Ohsawa et al., "High-Power Hybrid Attenuator & Phase-Shifter Systems," *Conference Record of the 15th International Linac Conference*, 1990, pp. 159-161.
- [7] Y. Ogawa et al., "Beam Monitor Utilizing Transition Radiation," these proceedings.

# Hydrodynamic Calculations of 20-TeV Beam Interactions with the SSC Beam Dump

D. C. Wilson, C. A. Wingate, J.C. Goldstein, and R.P. Godwin  
Los Alamos National Laboratory, Los Alamos, New Mexico, 87545  
and N.V. Mokhov

Superconducting Super Collider Laboratory, 2550 Beckleymead Ave., Suite 125, Dallas, Texas, 75237-3946

## Abstract

The 300 $\mu$ s, 400 MJ SSC proton beam must be contained when extracted to the external beam dump. The current design for the SSC beam dump can tolerate the heat load produced if the beam is deflected into a raster scan over the face of the dump. If the high frequency deflecting magnet were to fail, the beam would scan a single strip across the dump face resulting in higher local energy deposition. This could vaporize some material and lead to high pressures.

Since the beam duration is comparable to the characteristic time of expected hydrodynamic motions, we have combined the static energy deposition capability of the MARS computer code with the two- and three-dimensional hydrodynamics of the MESA and SPHINX codes. EOS data suggest an energy deposition threshold of 15 kJ/g, below which hydrodynamic effects are minimal. Above this our 2D calculations show a hole boring rate of 7 cm/ $\mu$ s for the nominal beam, and pressures of a few kbar. Scanning the nominal beam faster than 0.08 cm/ $\mu$ s should minimize hydrodynamic effects. 3D calculations support this.

## I. INTRODUCTION

Two- and three-dimensional hydrodynamic calculations using very high energy (TeV) particle deposition are required to understand the behavior of the SSC beam dump under abnormal beam aborts. The dump is currently designed as an 800 cm long, 160 cm square rectangular block of pressed graphite. The 20 TeV beam enters the dump about once a day through a 0.2cm thick titanium window. The other faces are contained by an aluminum cooling vessel. For simplicity, our modeling approximated this structure as a graphite block. Normally the beam spot will be raster scanned across the beam dump face, keeping the temperature of the dump below 1300K. If the scanning magnets fail, a worst case scenario allows the beam spot to remain at a single location. A more realistic case has some linear spot motion across the face, due to the droop of the kicker magnet field.

We consider a limited set of beam characteristics: 20 TeV protons delivered in 290 microseconds at two fluences,  $4.5 \times 10^{17}$  and  $1.0 \times 10^{19}$  protons/s. The first is the nominal SSC design, the second, a higher value we used to explore scaling effects. The SSC upgrade design has an intermediate fluence 3 times the nominal. Because of the long distance from the kicker magnet to the dump, the standard deviation of the beam's transverse Gaussian profile has expanded to 0.2 cm.

Preliminary 2-D hydrodynamic calculations with mocked energy depositions led us to expect that the 400 MJ (energy equivalent to 100 kg of TNT), could have explosive consequences. The small spot size could also lead to boring a hole through solid material in the beam path. To study these phenomena and to guide mechanical designs for controlling these effects, we sought to create a 3D hydrodynamic code which

correctly modeled energy deposition. We chose the MARS<sup>1</sup> energy deposition code and both the Eulerian MESA<sup>2</sup> and Lagrangian SPHINX<sup>3</sup> hydrodynamics codes.

## II. COMPUTER CODES

### A. MESA

MESA is a two- and three-dimensional Eulerian hydrodynamics code<sup>2</sup>. While originally developed for simulating the interactions of military projectiles with armor, it is easily adapted to other hydrodynamic applications. A variety of analytical and tabular equation-of-state, material strength, and fracture models is available to complement the hydrodynamics. The numerical hydrodynamics is divided into two phases. The first phase is Lagrangian; the second is an Eulerian advection. The Lagrangian phase is subcycled for increased computational efficiency. The Youngs interface reconstruction<sup>4</sup>, which assures that materials are advected in the correct order, is a powerful feature of MESA. It minimizes the numerical diffusion characteristic of Eulerian codes. This interface treatment allows fewer computational cells to be used for the same numerical accuracy than earlier codes because it handles the mixed material cells at material interfaces so effectively. This feature is particularly important in 3-D simulations with relatively coarse meshes.

### B. SPHINX

Smooth Particle Hydrodynamics (SPH) is a gridless Lagrangian computational technique in which "particles" represent mathematical points at which the fluid properties are known. SPH was first derived by Lucy<sup>5</sup> as a Monte-Carlo approach to solving the hydrodynamic time evolution equations. Later it was reformulated in terms of interpolation theory, which was shown to better estimate the error scaling of the technique. Gradients that appear in the fluid equations are obtained via analytic differentiation of smooth interpolated functions, or kernels. Each kernel is a spherically symmetric function centered at the particle location and generally resembling a Gaussian in shape. The interpolation is accomplished by summing each equation or variable at any location over nearby known values at particle locations, each weighted by its own kernel weighting function. By appropriately modifying the normalization condition, the same code can easily switch between 1D, 2D, and 3D, spherical or cylindrical configurations. The computer code SPHINX is our implementation of SPH.

### C. MARS

MARS<sup>1</sup> is a Monte Carlo program for inclusive simulation of three-dimensional hadronic and electromagnetic cascades in matter and of muon transport in radiation shielding, accelerator and detector components at energies up to 30 TeV

It allows fast cascade simulation with modest memory requirements, providing the availability of complex geometries with composite materials, presence of magnetic fields, and a variety of scoring possibilities. To construct a cascade tree only a fixed number of particles from each vertex is chosen (four in MARS12), and in the simplest case each carries a statistical weight which is equal to the partial mean multiplicity of the particular event. Energy and momentum are conserved on the average over a number of collisions.

MARS is well suited for use with a 3-D hydrodynamics code. It was easily modified to allow arbitrary material densities, and runs quickly (five minutes of one CRAY YMP processor can give a meaningful calculation). Since MARS may be called hundreds of times in a calculation, speed was crucial. However MARS only needs be called by the hydrodynamic code when the distribution of mass has changed enough to change the energy deposition calculation. This time between MARS calculations we estimated as 0.2 times the beam spot radius ( $1 \sigma$ ) divided by the maximum radial velocity in the deposition region. This time step control allowed us to reduce by factors of 2 to 10 the time spent in MARS calculations. Nevertheless an unoptimized 2D MESA/MARS calculation at nominal fluence required 12 CRAY YMP cpu hours to reach a time of 150  $\mu$ s.

#### D. Equation of State

In order to perform hydrodynamic calculations we require the dependence of pressure and specific internal energy on a material's temperature and density. The Sesame Equation-of-State (EOS) Library is a standardized, computer-based library which contains tables of thermodynamic properties for a wide range of materials over a wide range of physical regions (from ambient to astrophysical conditions). The library currently contains data for about 150 materials, including simple elements, compounds, metals, minerals, polymers, mixtures, etc. However for the beam dump application a new equation of state had to be created for compressed, porous, powdered graphite. An EOS for full density graphite was created using data from shock measurements at 1.948 g/cm<sup>3</sup>, a melt temperature of 4530K, and a vapor pressure of 0.01GPa at 4500K. These gave a critical temperature of 8204K, critical pressure of 2.04 GPa, and a critical density of 1.00 g/cm<sup>3</sup>. A threshold crush pressure of 0.1 GPa is assumed with a linear ramp in pressure as the porous graphite of density 1.71 g/cm<sup>3</sup> is crushed up to the 2.25 g/cm<sup>3</sup> full density of graphite.

The resulting EOS displayed an important characteristic. Below a specific energy of 10 to 15 kJ/g, the pressure remained very low. Above this threshold the pressure rapidly increased to values above 1 GPa (10 kbar). This specific internal energy corresponds roughly to that needed for melt and evaporation. Above this energy deposition threshold substantial hydrodynamic effects will occur.

### III. 2-D CALCULATIONS

Although we ultimately desire a 3-D calculational ability, we performed 2-D calculations to test the codes and study the consequences of the beam remaining stationary on the dump face. With the MESA/MARS code we modeled the beam dump

as a 800 cm long, 4 cm radius graphite cylinder. We studied two beam fluences,  $4.5 \times 10^{17}$  (Figs. 1,2,3) and  $1.0 \times 10^{19}$  protons/s with  $\sigma_x = \sigma_y = 0.2$  cm. Figure 1 shows the temperature along the beam axis at 20, 60, and 150  $\mu$ s. The curve at 20  $\mu$ s shows the temperature rise from energy deposition in static, homogeneous material. Material at the peak energy deposition, 210 cm, has just vaporized. By 60  $\mu$ s vaporization extends from 90 to 500 cm; by 150  $\mu$ s to the end of the dump. Figure 2 at 60  $\mu$ s shows why. Density on axis has been reduced allowing the beam to propagate farther into the dump. Figure 3 shows the pressure causing this expansion away from the beam axis. Peak pressures of 1 to 2 kbar are present not only at this time, but throughout the problem. Figure 4 shows the density variation with radius and length at 20  $\mu$ s in a SPHINX/MARS calculation of a 2 cm radius cylinder at high fluence. The teardrop shape to the low density hole is qualitatively similar to the MESA/MARS calculation. Because SPHINX had not incorporated the Sesame EOS, results differ quantitatively. Temperature is approximately uniform within the low density region, the pressure somewhat less so. The MESA/MARS calculation at the nominal intensity gives temperatures of about 4500 K and pressures of 1-2 kbar. Although some of the graphite has been vaporized, the dump might be designed to contain these pressures. At the high fluence the temperatures are about 11000 K and peak pressures, 30-35 kbar. The existence of an EOS threshold suggested we should get little motion before 15  $\mu$ s in the nominal case and 0.7  $\mu$ s for the high fluence. This was observed in the calculations.

These calculations show the SSC beam first depositing its energy into cold material, which as it evaporates creates pressures opening an axial density hole which expands outward. Because the density is low on axis, the beam penetrates farther into the dump, heating new material, and boring a hole through the dump. At the nominal fluence the penetration rate is about 7 cm/ $\mu$ s; at high fluence, 70 cm/ $\mu$ s. Since the beam strikes the dump for 290 microseconds, these rates are unacceptable.

### IV. 3-D CALCULATIONS

The beam is not planned to dwell in one spot, but rather to perform a raster scan across the dump face. By moving the beam deposition into fresh, cold material, the deposition in any one location should be below the threshold for hydrodynamic effects. By integrating the lateral distribution of beam energy deposition over radius at the position of peak deposition and applying the hydrodynamic threshold, we obtain a minimum scanning speed. Below this speed hydrodynamic effects occur. For our nominal SSC beam on graphite this speed is 0.08 cm/ $\mu$ s; for high fluence, 1.7 cm/ $\mu$ s.

So far we have performed only one calculation, with SPHINX, to test three dimensional effects. Figure 5 shows density after 20  $\mu$ s with the beam ( $\sigma_x = \sigma_y = 0.2$  cm) sweeping in the z direction at 0.1 cm/ $\mu$ s from 0 to 2 cm at high fluence (well below the minimum scanning speed). The dump is simulated by a graphite cylinder 2.0 cm in radius and 400 cm long. As expected the beam creates a hole between 120 and 400 cm and an asymmetrical expansion. Temperatures are reduced by a factor of 0.75 compared to the non-moving beam calculation.

V. REFERENCES

- [1] N.V. Mokhov, "The MARS12 Code System. Proc. of SARE Workshop, Santa Fe, 1993. N.V. Mokhov, "The MARS10 Code System", Fermilab FN-509, 1989.
- [2] D. J. Cagliostro, D. A. Mandell, L. A. Schwalbe, T. F. Adams, and E. J. Chapyak, "MESA 3-D Calculations of Armor Penetration by Projectiles with combined Obliquity and Yaw," *Int. J. Impact Engng.*, 10, pp. 81-92, 1990.
- [3] R. F. Stellingwerf and C.A. Wingate, "Impact Modeling with Smooth Particle Hydrodynamics," Los Alamos Rpt. LA-UR-92-1981. To be published in 1992 Hypervelocity Impact Symposium.
- [4] D. L. Youngs, "Time dependent multi-material flow with large fluid distortion", in *Numerical Methods of Fluid Dynamics*, K. W. Morton and J. H. Banes, eds. (Academic Press, 1982).
- [5] L. Lucy, "A Numerical Approach to Testing the Fission Hypothesis", *Astron. J.*, 48, pp. 1013-1024, 1977.

VI. ACKNOWLEDGEMENTS

We thank Sean Clancy, Bill Harvey, and Bob Stellingwerf for their assistance with the hydrodynamic codes and Stan Lyon and J.D. Johnson for the SESAME EOS work. The MESA code was developed at Los Alamos National Laboratory with DARPA./Army/Marine Corps support. This work was supported by the DOE through the Superconducting Super Collider Laboratory.

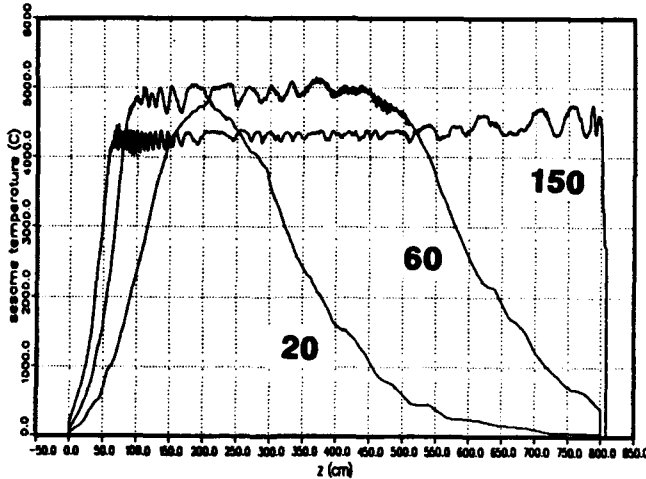


Figure 1 Axial Temperature, 2D MESA at nominal fluence

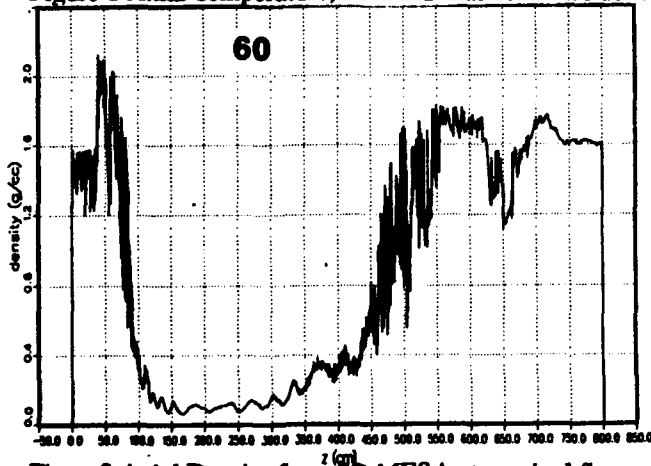


Figure 2 Axial Density from 2D MESA at nominal fluence

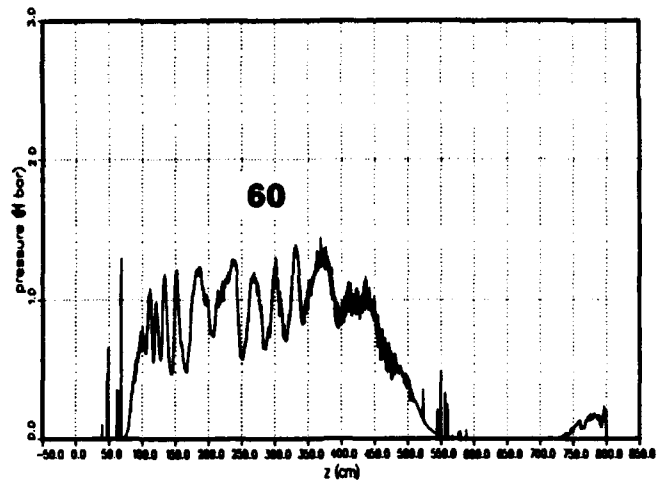


Figure 3 Axial Pressure from 2D MESA at nominal fluence

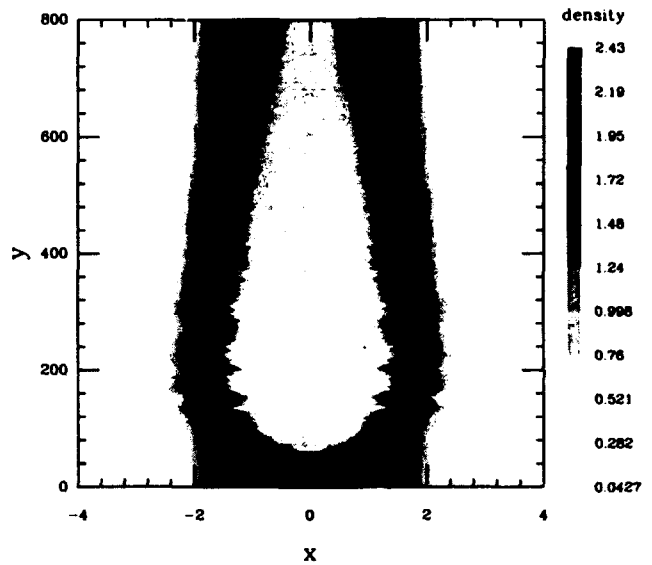


Figure 4 Density from 2D SPHINX at high fluence

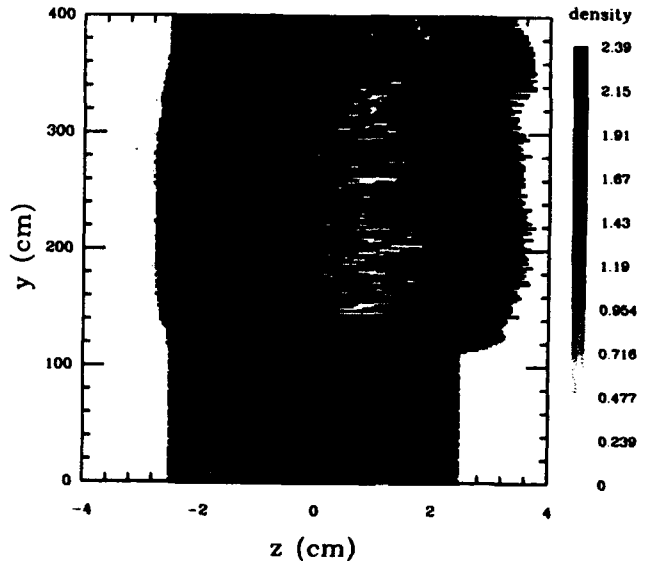


Figure 5 Density from 3D SPHINX at high fluence

# First Results concerning a Crystal Radiator dedicated to Positron Production by Photons from Channeled Multi-GeV Electrons

R.Chehab, T.Baier\*, P.Jean  
LAL - IN2P3 - CNRS - Univ. Paris-Sud - 91405 Orsay, France  
X.Artru, M.Chevallier, R.Kirsch, J.C.Poizat, J.Remillieux  
IPNL - IN2P3 - CNRS - Univ. Lyon-1 - 69622 Villeurbanne, France  
A.Jejcic, J.Maillard, J.Silva  
LPC, Collège de France - IN2P3 - CNRS - Place M.Berthelot, 75005 Paris, France  
E.Hourany, G.Renou, J.P.Didelez, A.Elayi, L.Rosier  
IPN - IN2P3 - CNRS - Univ.Paris-Sud - 91405 Orsay, France  
V.N.Baier, V.M.Katkov, V.M.Strakhovenko  
BINP - 630090 Novosibirsk, Russia  
K.Maier  
Max Planck Institute, Stuttgart, Germany

## Abstract

Starting from extensive simulations of photon emission by channeled electrons in tungsten crystals, a test experiment has been proposed. It concerns a 2 GeV electron beam impinging on a 1 mm tungsten crystal oriented along its  $\langle 111 \rangle$  axis. Radiation measurements are ensured by a preshower detector followed by a lead-plexiglas calorimeter. Channeling data are compared to those obtained for random incidence. They can be associated with simulations using shower codes (GEANT) for estimating performances of positron sources based on this principle.

## I INTRODUCTION

Extrapolation of conventional positron sources to the parameters required for linear colliders led to the utilization of high energy electron beams impinging on thick targets. Adequate set-up (high gradient RF sections, damping rings) is necessary to minimize longitudinal and transverse phase space extensions. Moreover thermic effects are important and represent serious limitations[1, 2]. A different way to generate positrons has been initiated for VLEPP colliders and adopted in the DESY-THD linear collider project: they use intense photon beams created in helical wigglers by very energetic electron beams, to produce electron-positron pairs in thin targets[3, 4]. Such a method, though bringing lower emittance and weaker power deposition in the target, requires a very high energy beam (100-250 GeV) and a very long wiggler (50-150 m). Instead of using a magnetic wiggler we may use an atomic wiggler of millimeter scale to generate the powerful photon beam to be sent onto the pair generation target. Channeling of multi-GeV electrons in oriented crystals could produce enough photons to reach the expected

value of more than one accepted positron per incident electron which represents the current design value for linear colliders[5, 6].

Channeling radiation may be more intense than classical Bremsstrahlung in a given crystal thickness for specific incident energies. For a tungsten crystal oriented along the  $\langle 111 \rangle$  axis, the ratio between the intensities due to channeling and bremsstrahlung reaches unity for an energy of 0.7 GeV and a value of 2 at 2 GeV.

A test experiment using the 2 GeV Orsay linac with a 1 mm thick tungsten crystal, oriented on its  $\langle 111 \rangle$  axis has been proposed; the first results are presented hereafter.

## II PRELIMINARY SIMULATIONS

The fundamental physical process on which the proposed set-up is grounded, i.e. photon generation produced by channeled electron in a crystal, has been simulated by a Monte-Carlo code[7]. From calculated electron trajectories in a given crystal lattice the photon emission probabilities and their complete kinematics are computed according to the quasi-classical Baier-Katkov formula for radiation in a non uniform field[8]. The multiple scattering is taken into account.

Simulation was done in the software environment usual in High Energy Physics. The detector simulation code GEANT[9] was adopted as the basis for working out the needed calculations. In this framework the code simulating channeling was introduced as event generator. The main physical processes involving electrons, positrons and photons were taken into account.

Considering an electron beam having normal distribution with rms value of 1 mm (radial) and 0.5 mrad (angular) simulations on photon production have been worked out. Photon yield as well as radiated intensities were evaluated in the energy domain 2 - 20 GeV and systematically

\*on leave of absence from BINP - Novosibirsk

compared for a crystal and an amorphous target of the same thickness[6]. Enhancement above 3 for the photon yield and 2 for the radiated intensity were reported simulating the experimental conditions. Equivalent positron yield increase was evaluated when putting an amorphous tungsten (1 mm thick) located after the crystal [6].

### III EXPERIMENTAL SET-UP

The lay-out, represented on figure 1, comprises the following elements:

- The tungsten crystal was grown at the Stuttgart Max-Planck Institute für Metallforschung. Mosaic spread controlled by  $\gamma$  - diffractometry is no more than 0.5 mrad; this value is lower than the Lindhard critical angle, 1 mrad for 2 GeV beam on  $\langle 111 \rangle$  axis.
- The goniometer from Microcontrole, has an angular resolution of  $10^{-3}$  degree. Rotation around two perpendicular axes and translation are controlled by a microcomputer.
- The detection of photons transmitted through a 2 cm diameter collimator is provided by a scintillator - for photon counting - and a lead-plexiglas calorimeter.
- Electron beam diagnostics for intensity and transverse profile are provided
- Bending magnet is used for electron beam sweeping before the detector.

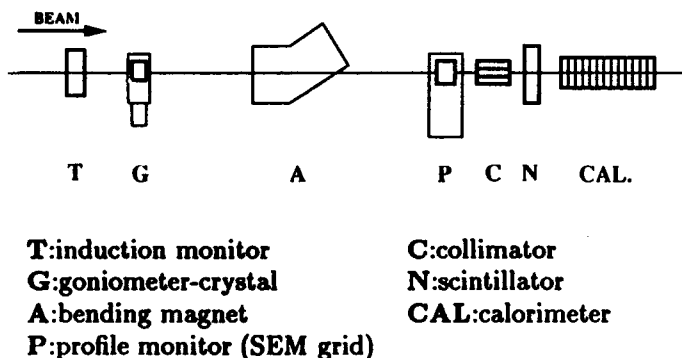


Figure 1: Lay-out of the experiment

Step by step goniometer motion as measurement data gathered on the scintillator (number of photons) and the calorimeter (radiated energy) are processed by two microcomputers. Beam pulse number and integrals of elementary goniometer steps could be chosen; angular limits of motions are also usually fixed before starting an angular scan. Multiscale spectra for photon number, radiated energy and incident electron beam intensity allow full observation of these parameters during the angular scans. Moreover, photon data normalization by incident electron beam intensity will ensure efficient monitoring.

## IV EXPERIMENTAL RESULTS

### A Experimental conditions

Recalling that efficient channeling needs an angular divergence for the electron beam smaller than 1 mrad, particular attention was given to this problem. Two collimators with  $4 \times 4 \text{ mm}^2$  aperture and distant 60 meters apart allowed maximum divergence better than 0.1 mrad. Electron beam dimensions were controlled through a multiwire secondary emission profile monitor[10]. Typical FWHM values were about 1.5 mm; crystal lateral dimensions being 6 mm. Additional emittance monitoring using Optical Transition Radiation at the crystal location is installed.

### B Results

Angular scans for both rotation axes (vertical Z and horizontal Y) are registered. Crossing of the electron beam along the chosen  $\langle 111 \rangle$  axis in the crystal requires that the beam direction be perpendicular to the entrance face (111). This condition is met for particular values of the rotation angles around the axes. At rather large angular distance ( $\sim 1$  degree) from these values, the crystal is seen as a disordered structure (amorphous) by the beam.

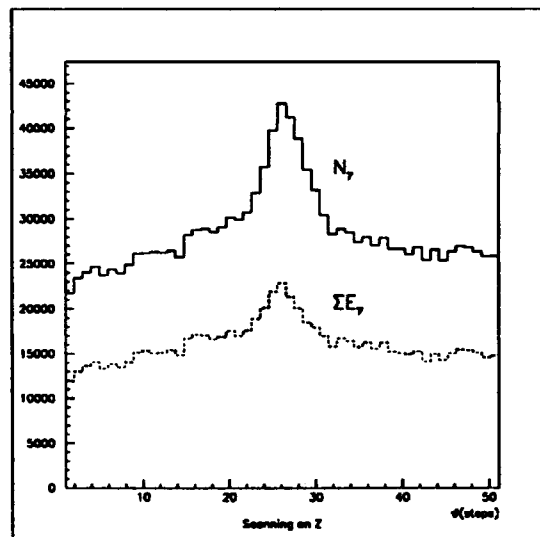


Figure 2: Angular scan around Z axis for scintillator ( $N_\gamma$ ) and calorimeter ( $\Sigma E_\gamma$ )

Scanning around the vertical axis, for this particular value of the rotation angle around the horizontal axis, is shown on figure 2 which gives the relative number  $N_\gamma$  of photons detected by the scintillator. On this figure, angular steps represent 0.05 degree. Enhancement by a factor  $2 \div 2.5$  may be observed when comparing the peak value (channeling conditions) and the quasi constant value (amorphous). Corresponding enhancement ( $\sim 1.8$ ) for radiated energy  $\Sigma E_\gamma$  is also observed for the same angular parameters (figure 2). From these results, we can obtain

the average photon energy,

$$\langle E_\gamma \rangle = \frac{\sum E_\gamma}{N_\gamma},$$

the orientation dependence of which is presented on figure 3. One observes that this average energy exhibits a minimum in alignment conditions.

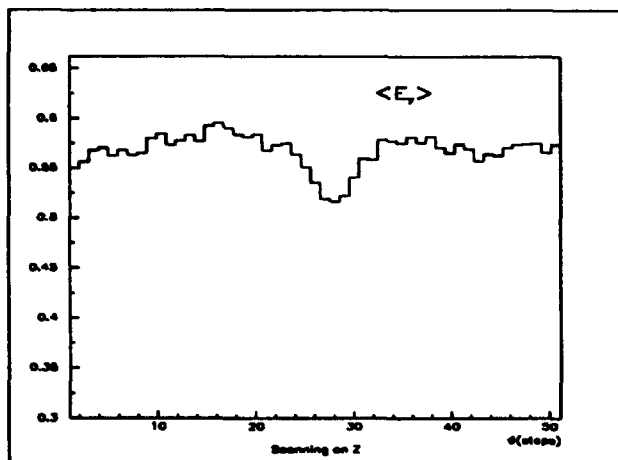


Figure 3: Angular scan of the average energy of photons

A convenient representation may also be observed on figure 4. Scanning on both vertical and horizontal axis shows the maximum for the relative number of photons.

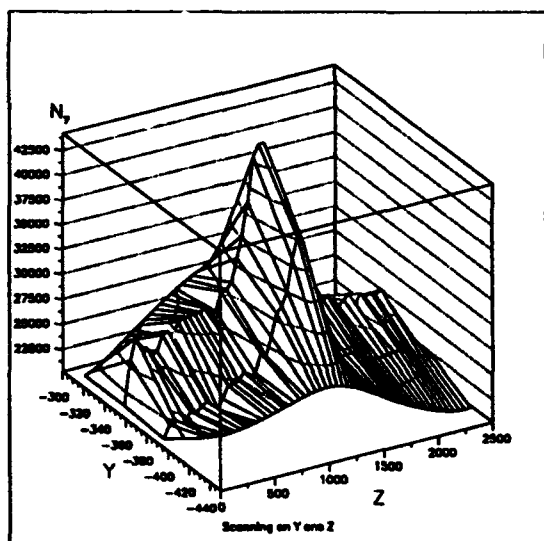


Figure 4: Angular scans around axes Z and Y of the photon yield

## V COMMENTS ON THE RESULTS

Maxima in relative photon number and radiated energy as well as minimum of average photon energy occur for the same crystal orientation corresponding to channeling.

FWHM value of the angular scans corresponds to 6 mrad when collimating the photon beam before the detector with  $\pm 1$  mrad. Photon enhancement persists beyond

the nominal Lindhard angle for 2 GeV (1 mrad). This is connected mainly with the contribution to the radiation process of above-barrier particles, i.e. slightly beyond channeling conditions. This has been previously observed in other experiments [11].

Enhancement in photon production is slightly below computed estimates.

These first results constitute quite encouraging observations concerning the photon radiation. They could be improved in the future particularly by background subtraction.

Nevertheless, the enhancement of the photon yield allows equivalent improvement in positron production if one refers to shower simulations.

A rough estimate of the cumulated number of incident particles on the crystal shows a total fluence of  $\sim 10^{15}$  electrons/mm<sup>2</sup>. No radiation damage is observed.

Further measurements are foreseen.

## VI ACKNOWLEDGMENTS

We are indebted to Profs. M.Davier, J.Haissinski, M.Froissart and Dr. F.Richard for constant support and interest. We acknowledge constant technical assistance from J.Barth, G.Reinmuth, R.Lacroix and from the technical staff of the LURE linac.

## VII REFERENCES

- [1] S.Ecklund, SLAC PUB 4427 (October 1987) Stanford, USA
- [2] J.L.Cledenin, "High-Yield Positron Systems for Linear Colliders", Proceedings of IEEE PAC, Chicago, IL, March 1989.
- [3] T.A. Vsevolozhskaya et al., "Helical Undulator for Conversion system of the VLEPP Project". Preprint 86-129 INP Novosibirsk, Russia.
- [4] K.Flötman and J.Rossbach, Proceedings of LC91 Workshop on Linear Colliders, Protvino, Sept 1991, Russia.
- [5] R.Chehab et al., "Study of a Positron Source Generated by Photons from Ultrarelativistic Channeled Particles". Proceedings of IEEE PAC, Chicago, IL, March 1989 and LAL-RT 89-01.
- [6] X.Artru et al. "Overall simulation of a positron beam generated by photons from channeled multigeV electrons". Proceedings of IEEE PAC, San Francisco, March 1991 and LPC 91-12, LAL-RT 91-07.
- [7] X.Artru NIM B48(1990) 276
- [8] V.N.Baier and V.M.Katkov, Soviet Physics JETP 26(1968)854 and 28(1969)207.
- [9] L.Dufflot et al., "Operating HEP simulation codes on the T.Node Paraliel computer", Conference on Computing in HEP, March 1991, Tsukuba, Japan.
- [10] R.Chehab et al., "A multiwire secondary emission Profile Monitor for small emittance beams", LAL-RT 85-05, May 1985, Orsay (France).
- [11] A.Belkacem et al., Phys. Lett B177(1986)211.

# New Target Results from the FNAL Antiproton Source\*

S. O'Day, F. Bieniossek, K. Anderson  
Fermilab, P.O. Box 500, Batavia, IL 60510

## Abstract

Nickel and compressed rhenium powder targets have been installed in the FNAL antiproton source target station. Ni was chosen for its high melting point energy and resistance to stress wave fractures. As well, compressed powdered rhenium segments were constrained by a thin-wall Ti jacket to insure resistance to stress fractures. The  $\bar{p}$  yield of these new targets is compared with that of copper—the previous standard production target. The target depletion characteristics of nickel and rhenium for a beam intensity of  $1.6 \times 10^{12}$  protons per pulse are also presented.

## I. Introduction

The requirements placed on the antiproton production target at Fermilab become more stringent as the linac upgrade and Main Injector projects come to fruition. To understand how to meet the yield and durability requirements that these projects will impose, a variety of targets have been considered. The targets which were installed for production and study in February of 1992 were selected carefully based on their material properties.

The properties which are the most interesting are yield strength, melting point and shock wave limit energies and the Gruneisen parameter (which relates the differential pressure to energy changes). Ideally, one would like to have a target material with a high yield strength and shock wave limit energy, but a small Gruneisen parameter to minimize local pressure gradients. The melting point energy should be as high as is necessary to eliminate or at least minimize localized melting at the beam spot for a single beam pulse. Melting will reduce the density thus diminishing the yield. Data for various target materials are given in Table 1.

Calculating the expected yields for various targets is difficult. Efforts in the past have produced results which are only within a factor of 2 of measured yields<sup>1</sup>. The antiproton yield is only weakly dependent on the absorption length (table 1) complicating even relative yield estimates. As more data is collected, modeling efforts will show improved results. Qualitative statements can however be made regarding the material dependence of  $\bar{p}$  production. While targets with shorter absorption lengths experience a greater number of interactions with 120 GeV protons, the yield gain is tempered by the greater fraction of produced  $\bar{p}$ s which are re-absorbed in the target. Also, primaries from proton-nucleon inelastic scattering and secondaries

\* Operated by the Universities Research Association under contract with the U.S. Department of Energy

Table 1  
Target Material Properties

Tgt	Iridium	Rhenium	Tungsten	Nickel	Copper	Iron
$A^2/\rho$	.255	.271	.295	.437	.446	.486
Melting Pt. E(J/gm)	458	614	634	1044	613	1036
Yield Strength(Pa)	160000	270000	500000	230000	72000	134000
$\rho\Gamma$ (Pa Kg/J)	80600	66000	31000	15800	17200	15900
Shock Wave Limit(J/gm)			200		600	

from primary hadron-nucleon interactions both contribute to the  $\bar{p}$  yield. The admixture of these processes is both geometry and material dependent. Figure 1 shows the target stack geometry which was used for this experiment.

In  $\bar{p}$  production running, a 120 GeV beam of  $1.6 \times 10^{12}$  protons per pulse (80 full bunches per pulse) impinges on a selected target. A lithium lens approximately 20 cm downstream collects and focuses the 8 GeV secondaries. These secondaries are then kicked horizontally 3 degrees by a pulsed dipole into the aperture of the AP2 beamline and transported to the Debuncher storage ring.

During optimum running conditions, there may be as many as  $2.1 \times 10^{12}$  protons per pulse on target and the operating gradient of the lithium collection lens may be as high as 890 T/m. Under such conditions, the measured absolute yield into the Debuncher was measured to be  $1.9 \times 10^{-8}$   $\bar{p}/p$  or  $4.0 \mu\text{A}$  of current per pulse.

## II. Measurements

### A. Yield Measurements

The yield measurements were made in the Debuncher using both a dynamic signal analyser(dsa) and a d.c. beam current transformer(dcct). The signal analyser does an FFT of the longitudinal Schottky power spectrum and integrates it over a specified bandwidth. The signal analyser is calibrated to the dcct and is accurate to a few percent. A summary of the results may be found in Table 2. The yield is normalized to the proton intensity on target as given by the toroid in the 120 GeV beamline(AP1) closest

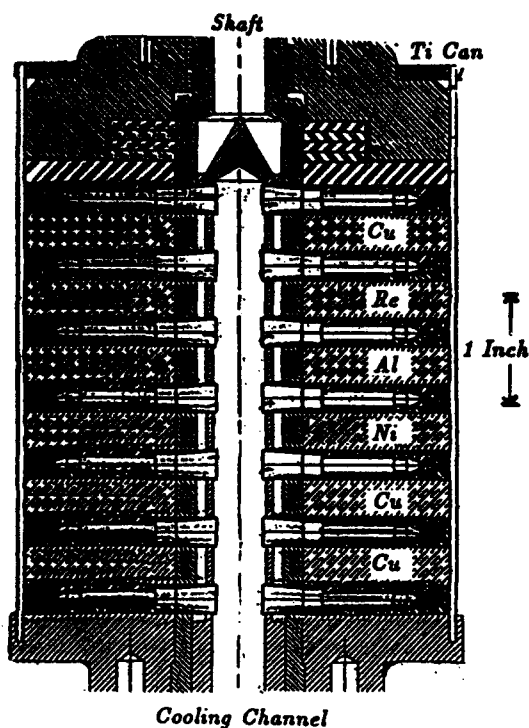


Figure 1. Target Stack. Note that the target stack has vertical motion for changing targets, horizontal motion perpendicular to the beam for changing the length of target which the beam intersects and motion along the beam so that the lens focal point may be varied. The beam direction is into the page.

Table 2  
Yield Data Normalized to Ni

Material	DSA/AP1 Toroid	DCCT/AP1 Toroid
Nickel	1.000	1.000
Copper	0.979	0.997
Rhenium	0.994	0.998

to the target. These data show no statistically significant differences between the  $\bar{p}$  yields of the three targets.

### B. Target Edge Yield Study

The  $\bar{p}$  yield was measured when the beam hit near the interface between copper and aluminum. Copper is much denser than aluminum. The study attempted to find out whether or not the yield was enhanced by allowing roughly a third of the solid angle of primarily produced  $\bar{p}$ s to escape through a lighter material thus lowering the probability of

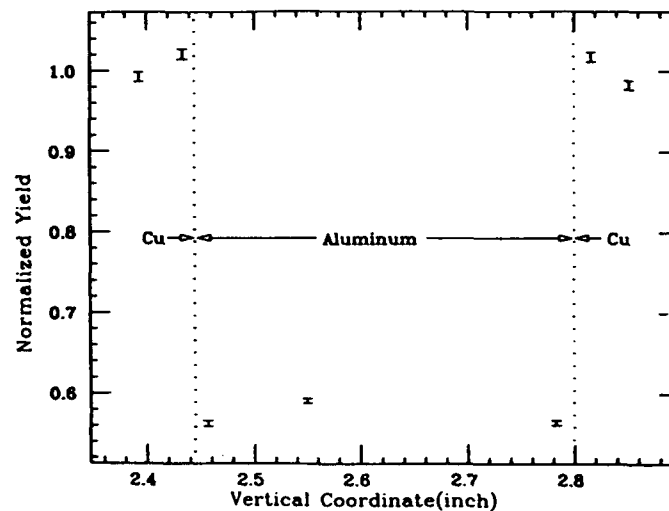


Figure 2. Yield enhancement at the target vertical edge.

$\bar{p}$  absorption. At the same time however, the probability of producing  $\bar{p}$ s from energetic pions is reduced because these will also escape through the aluminum with a much lower probability of inelastic interaction.

To compare with theoretical predictions which ignore secondary  $\bar{p}$  production, the collection lens was focused on the upstream end of the target. Here, a larger fraction of the  $\bar{p}$ s produced would be primary hadrons. Figure 2 shows that edge enhancement on the order of 4-5 % is observed. The overall yield is however reduced by 30 %. Future studies will include a 1 mm diameter wire target which should further enhance this effect and possibly increase the overall  $\bar{p}$  yield.

### C. Target Density Depletion Study

A large energy deposition on target is expected to locally melt target materials. This will result in a diminished hadron yield from those bunches of protons which arrive after this melting has occurred. Since rhenium has a calculated melting point energy below our energy deposition level, we performed a study to demonstrate density depletion using this target.

The FNAL Main Ring provided a beam with an intensity of  $1.6 \times 10^{12}$  protons per pulse and a transverse width ( $\sigma$ ) of .14 mm on target. Using a resistive wall monitor in the Debuncher, the bunch structure of the beam during the first turn was measured. As well, a similar wall monitor was used to measure the incoming proton bunch structure. By integrating the individual bunches, the charge associated with each bunch was determined. Comparing the production bunch charge with the corresponding proton bunch charge provides a measure of the

pressed-powder target material and the seams of the titanium can. Radioactive xenon nuclei would then have decayed to the daughter products observed (iodine and tellurium). A similar, although much smaller, release occurred with an intensity of  $1.2 \times 10^{12}$  protons per pulse.

It should be noted that no target depletion effects were observed for Ni (the standard production target at this time). This is what one would expect since the energy deposition in Ni for an intensity of  $1.6 \times 10^{12}$  protons per pulse is  $615 J/gm$  while the melting point energy is  $1100 J/gm$ .

#### IV. Conclusions

From the measurements made, one can conclude that the yields from quite different materials- Ni and Cu as compared with Re, are similar. Also, the calculations and measurements made were in agreement on the issue of target density depletion. The yield enhancement measurement leads naturally to a more sophisticated target geometry experiment. Specifically, a wire target surrounded by a low  $z$  material will be constructed sometime in the future to get more data on the admixture of primary and secondary yield contributions. Further work, both theoretical (Monte Carlo) and experimental is planned to improve the understanding of  $\bar{p}$  production. This work will lead to the optimization of future target and collection lens designs.

#### V. References

1. C. Hojvat, A. Van Ginneken, "Calculation of Antiproton Yields for the Fermilab Antiproton Source", Nucl. Instrum. Meth. 206:67, 1983.
2. A. Leveling, AD Radiation Safety, FNAL. Private Communication. (January 1993.)
3. T.W. Eaton, C.D. Johnson, E. Jones, CERN/PS/868-15, 1986.

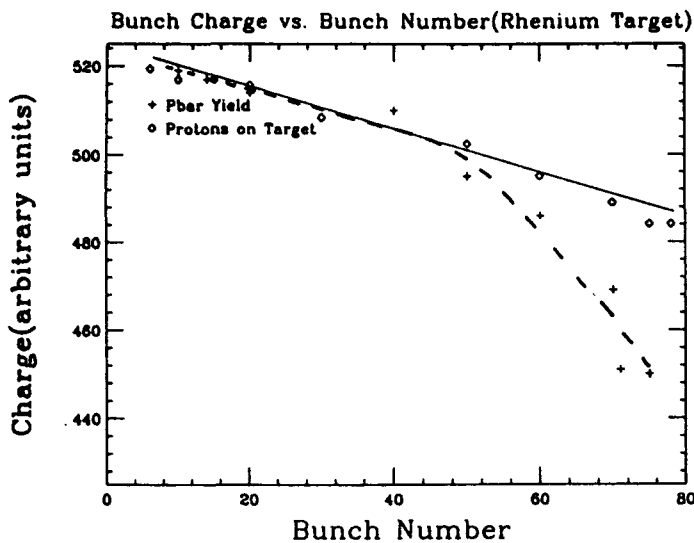


Figure 3. Yield vs. Bunch Length

yield. The charge in arbitrary units for protons on target and  $\beta = 1$  particles in the Debuncher as a function of bunch number is given in figure 3. The yield from the last 25 % of the bunches shows an obvious deficit which increases with bunch number. By the eightieth bunch, the yield is down  $8\% \pm 4\%$  as compared with the first.

Also interesting is the number of bunches which hit the target before the yield began to drop. The yield began to drop after  $45 \pm 5$  bunches or after a Casim calculated energy deposition of  $600 \pm 65 J/gm$ . This is consistent with the melting point energy for rhenium from table 1 of  $614 J/gm$ . A more sophisticated model assuming the relationship  $d\rho/dT = -.0001\rho$  for liquid rhenium and a 25% beam absorption rate in the central beam region predicts that  $\Delta\rho/\rho = -21\%$ . Since the melting point of rhenium is  $3180^\circ C$  and a density drop of this magnitude corresponds to a temperature of  $5280^\circ C$ , this implies that the melting began after 60% of the pulse hit the target. This is once again consistent with the data.

Analysis of the target station airborne radiation monitor filter revealed the presence of radionuclides (largely iodine, with smaller amounts of tellurium, sodium and potassium) in the airborne radiation monitor<sup>2</sup>. The total release was quite small (about 5 mCi). This release is a by-product of the spallation reactions between the 120 GeV protons and the target nuclei<sup>3</sup> and the subsequent nuclear fission. These reactions produce noble gases (xenon in this case) and result in void formation, swelling and embrittlement of solid target materials. We hypothesize that the xenon, normally trapped in the solid metal target, was released as the target melted and escaped through the voids in the

# High Current Radioisotope Production with Solid Target System

W.Z. Gelbart, N.R. Stevenson, R.R. Johnson, F. M. Nortier\*, J. Orzechowski and F. Cifarelli  
TRIUMF, 4004 Wesbrook Mall, Vancouver,  
B.C., V6T 2A3, Canada

## 1. Introduction

Remotely manipulated solid target systems have been developed at TRIUMF for the production of  $^{201}\text{Tl}$ ,  $^{67}\text{Ga}$ ,  $^{111}\text{In}$  and  $^{57}\text{Co}$  radioisotopes. An extension of these systems to accept a  $400\ \mu\text{A}$  30 MeV proton beam has been designed. The design criteria included keeping the temperature of the water-cooled silver face of the target below  $140^\circ$  during irradiation. A combination of computer modeling and actual measurements employing thermocouples indicate the temperature to be significantly lower thereby permitting even higher beam currents. This paper will present these results and conclusions and also summarise the refinements and changes made to the hardware of the target stations and transfer system which feature high radiation hardness components to minimize maintenance and improve reliability.

## 2. Isotope Production at TRIUMF

Two isotope production cyclotrons (42 and 30 MeV) are operated at TRIUMF for Nordion Int. Inc. A total of four external beam solid target stations are in use (in addition to gas and PET targets). The solid target irradiation and transfer system was designed and built at TRIUMF a decade ago and a few minor improvements have been made over the years of operating these systems although the basic concept has remained the same [1,2].

A new target system [3] is being designed which, while still being based on the existing setup, incorporates several significant changes and improvements following past experience and the demand arising from the increase in beam capacity available (up from 6 to 12 kW per beamline). Construction of a prototype station was started last year with completion and installation scheduled for later this year.

## 3. Target

Figure 1 shows an unassembled 12 kW solid target with its shuttle in the background:

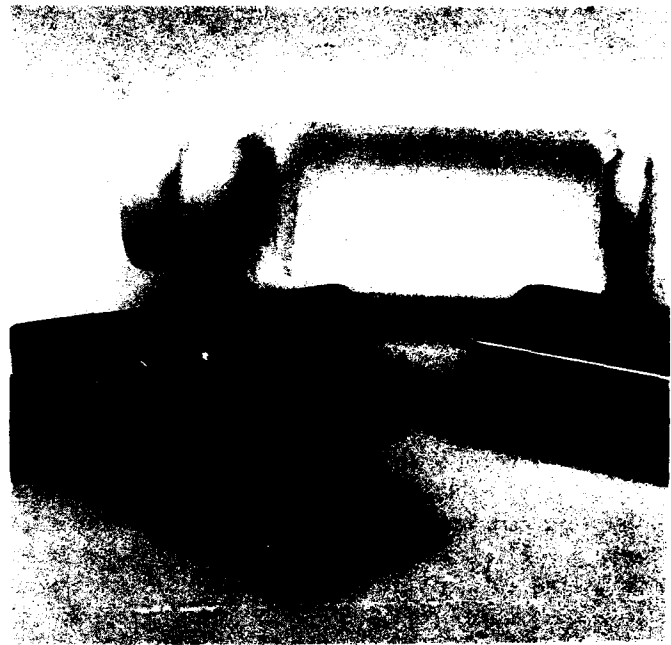


Fig. 1. The new  $400\ \mu\text{A}/30\ \text{MeV}$  (12kW) target.

The target is assembled from two major components: a pure silver substrate incorporating integral water cooling channels, and a copper plated aluminum body. These two parts are soldered together to form one assembly. The target material is electroplated onto the silver face and exposed to the particle beam at a  $7^\circ$  angle to spread the beam out over the  $43 \times 100\ \text{mm}^2$  active area. The cooling water flow patterns were optimized

\*On leave from the National Accelerator Center, Faure, S. Africa.

by the shape of the cooling channels in the silver to keep the surface temperature below  $140^{\circ}$  at the center for a 12 kW beam. This criterion is essential where low melting point target materials are used. In practice,  $400\mu\text{A}$  represents about 90% of the beam at the target station since about 10% of the beam is trimmed off on four collimators which form a rectangle shadowing the edges of the target face. After the removal of the electroplated target material these targets can be reused (about 10 times) after a short cooldown period.

#### 4. Target Station

The station is shown in Figs. 2 and 3. Three modular subassemblies are mounted on an aluminum stand:



Fig. 2. The higher power (12kW) solid target station.

landing terminal, vacuum/irradiation chamber and manipulator. By designing the target in such a way as to take maximum advantage of the geometrical limitations imposed by the existing hot cell receive terminals and the transfer lines to the irradiation areas it was possible to leave these components of the solid target system

unchanged.

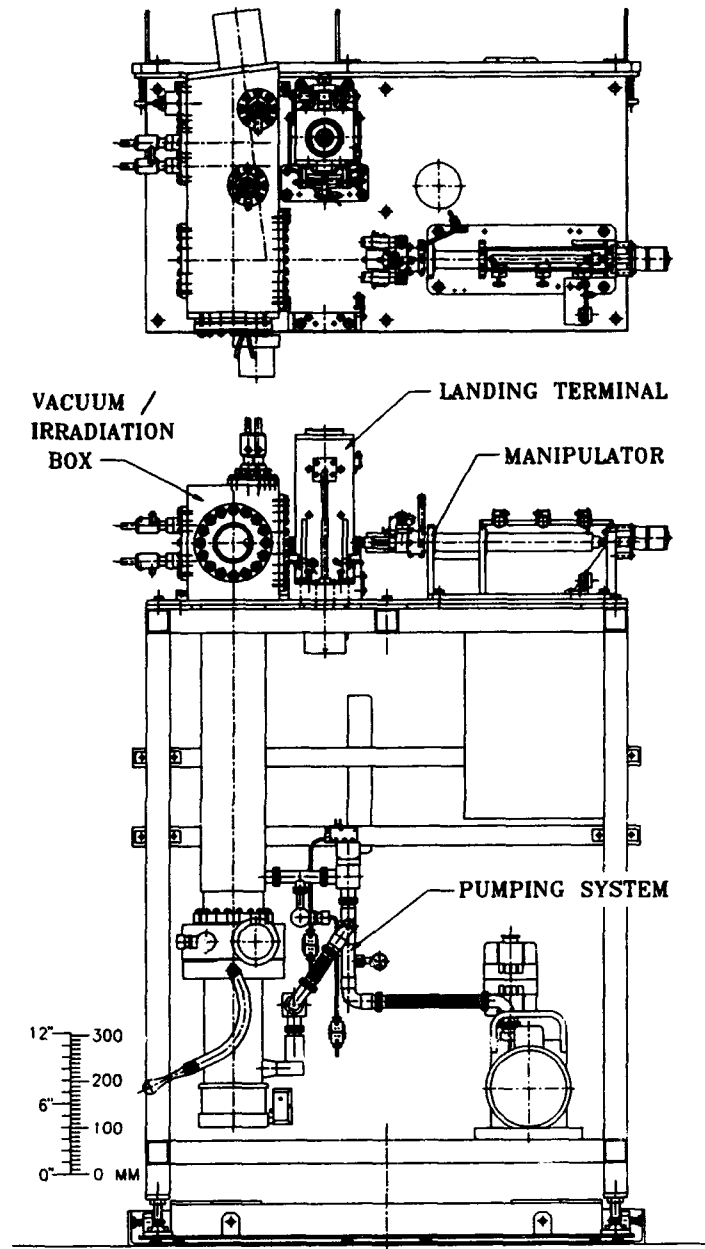


Fig. 3. Front elevation and top view of the 12 kW target station.

During operation the target (in its shuttle or "rabbit") is transferred via an air chute between the hot cell terminal and the target station. Its progress along the transfer line is monitored by a series of detectors actuated by a permanent magnet attached to the rabbit. The final detector, located close to the station, actuates a reverse air flow inside the landing terminal which acts to slow the rabbit to a "soft landing". During its descent the rabbit is oriented the required way (i.e. to face the extraction manipulator) by permanent magnets placed

inside the terminal walls.

As the target is removed from the rabbit by the manipulator grabber cooling water connections are engaged. After the empty rabbit is returned to the receive terminal in the hot cell the target is moved into the irradiation position in the vacuum chamber and the chamber is then pumped down before beam is put on the target.

The complete operational cycle, as well as all interlocks, are controlled by an industrial programmable logic controller. Typically, complete target changes from the end of an irradiation on a target to the start of beam on the subsequent target take about 20 mins.

### 5. Radiation Hardness

Past experience with the existing 6kW target system has shown some downtime caused by radiation damage to certain components. Bearing this in mind the present high current design had the aim of minimizing this damage by prudent choice of materials and locations of components with respect to the beam and target. Pneumatic cylinders, for example, are fitted with graphite pistons and rod seals. The vacuum chamber employs metal seals in specially designed seats (Helicoflex) on all ports except the target flange. The elastomer O-ring on the target is used only for one irradiation. Electrical isolation is achieved by hard anodizing on aluminum or polyimide plastic ("Vespel" from Dupont) components.

Long-term testing under actual operating conditions for these materials (as well as others chosen for electrical wiring, water connections, etc.) proved their radiation hardness and suitability for this application.

### 6. Target surface temperature

An essential parameter in the target design was the surface temperature which should be kept below 140° [1]. Finite element analyses were made [4] of the heat flux and temperature distributions in the solid targets under different operational conditions. The existing target configuration and operational parameters were taken as a departure point and the various parameters were varied in order to establish limitations and ways of improving the thermal performance of the design.

To actually measure the temperature a special target was constructed. The silver face was coated with kapton except for certain spots which were masked off. The kapton was then cured and a thin layer of nickel was plated on top to produce a series of Ni/Ag thermal junctions with which the actual surface temperature (at the various locations) could be directly measured. The concept was tested on a running production target up to 7.5 kW and will be repeated up to 12 kW or more when the high current target system is in place. Extrapolation of the results (see Fig. 4) indicate a surface temperature

actually lower than that expected by calculation. We anticipate a temperature rise of 70° above that of the inlet cooling water (~ 20°).

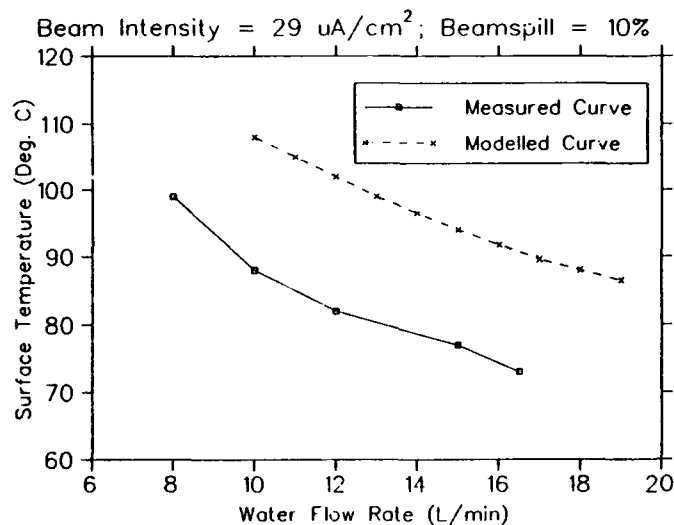


Fig. 4. Surface temperature predictions and measurements.

### 7. Conclusion

The existing solid target system at TRIUMF will be replaced with a high power system in the near future. This will permit full usage of the beam available from high current cyclotrons such as the EBCO TR30, installed at TRIUMF two years ago.

### 8. REFERENCES

- 1) Pinto, G., *et al.*, "Target Systems for Radioisotope Production," in **Proceedings of the 7th Conf. on the Applications of Accelerators in Research and Industry**, Denton, Texas, 1982.
- 2) Burgerjon, J.J., *et al.*, "A High Power Target System for Radioisotope Production," in **Proceedings of the 11th Conference on Cyclotrons and their Applications**, Tokyo, 1986.
- 3) Stevenson, N.R. and Gelbart, W.Z., "External High Current Targetry for Radioisotope Production," in **Proceedings of the 13th Int. Conf. on Cyclotrons and their Applications**, Vancouver, Canada, 1992, p 196, Ed. G. Dutto and M.K. Craddock, World Scientific Press.
- 4) Nortier F.M. and Stevenson N.R., "Thermal Analysis of the TRIUMF Solid Target", Symposium on Isotope Production and Applications in Medicine, Science and the Environment, Vancouver, Canada, 1993.

## ISOSPIN TARGET-ION SOURCE SHIELDING

Marcel M. Barbier

Marcel M. Barbier, Inc., 3003 Rayjohn Lane, Herndon, VA 22071

We will study a shielding casemate built closely around an isospin target for a radiation level of 1 mrem/h ( $2.778 \text{ n/sec.cm}^2$ ), i.e. one where people can work 8 hours a day. We assume a proton beam of  $6.25 \cdot 10^{14}$  p/sec., and an energy of 600 MeV, i.e. a beam power of 60 KW. Taking the values measured at CERN for a beam of this energy, we find a secondary high energy neutron production of .6 per steradian and proton at  $0^\circ$ , .1 at  $60^\circ$  and .04 at  $90^\circ$  from the forward direction. One calculates the following numbers of mean free paths to attenuate the resulting neutron fluxes to the value mentioned above: 20.6 at  $0^\circ$  and 18.76 at  $60^\circ$  for a distance of 4 meters and 18.42 at  $90^\circ$  for a distance of 3 m. To keep dimensions small, we will take steel, and surround it with 3 ft. of ordinary concrete (2 mean free paths) to absorb the iron window neutrons. Then we find the thicknesses of steel needed: 3.23 at  $0^\circ$ , 2.91 m at  $60^\circ$  and 2.84 m at  $90^\circ$ . The bunker would have the shape shown in figs. 1 (plan), 2 (transverse section), 3 (longitudinal section). The shielding needed on top can be calculated to be 14.4 mfp for skyshine to have 25 mrem/yr at a site boundary 50 meters away, which can be divided in 2.15 m of steel and 0.9 m of concrete. The philosophy of placing the whole shielding at the target gives the minimum shielding volume and dimensions. When this is achieved, one has more freedom in the placement of several target stations to be served by the same accelerator, and to engineer the front end in order to distribute the radioactive beams from the different ion-sources to all the analyzing systems.

Fig. 1. Plan

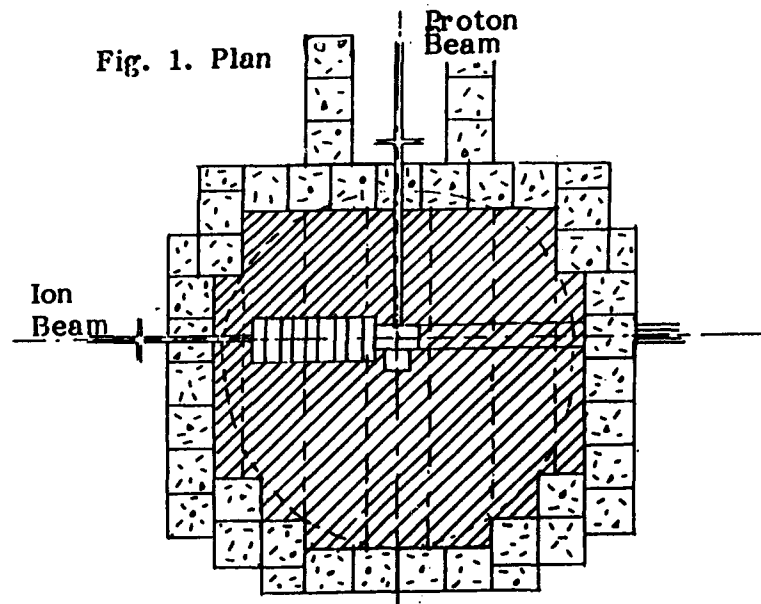


Fig. 2. Transverse Section

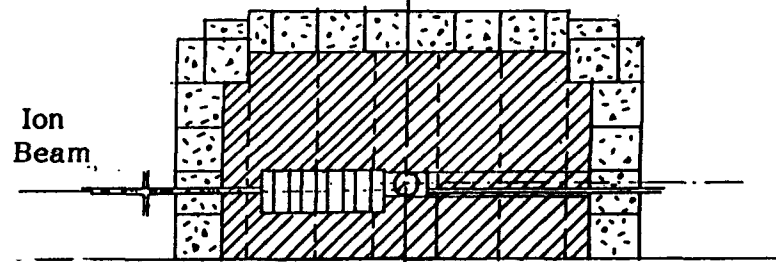
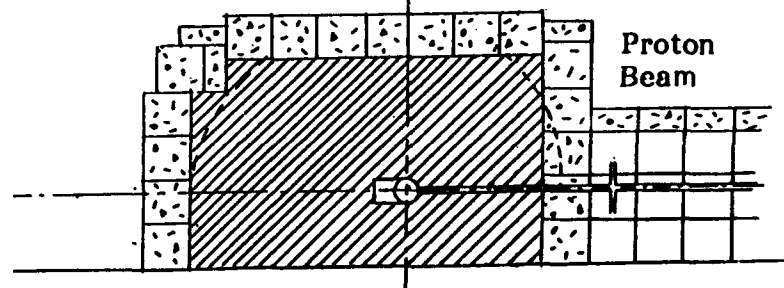


Fig. 3: Longitudinal Section



# Beam Raster System at CEBAF

C. Yan, J. Beaufait, P. Brindza, R. Carlini, W. Vulcan, and R. Wines  
CEBAF, 12000 Jefferson Avenue, Newport News, VA 23606

## Abstract

A cascade raster system will be used in Hall C at CEBAF to generate a variable rastering pattern on the polarized target, the cryogenic hydrogen target, and the beam dump with adjustable frequency up to 10 kHz and variable deflection angle from 0.05 mr to 1 mr. Each raster consists of two air-core bedstead coils providing transverse and vertical scans. The magnets are energized by individual MOS power amplifiers controlled by a scan generator which determines frequency, amplitude, and phase shift between the cascade rasters.

## I. INTRODUCTION

### A. Heating effect in the solid target

Assume that a beam current is 200  $\mu\text{A}$  and the target periphery is kept fixed at the initial target temperature 20 K. The beam spot size is about 0.2 mm diameter. A thin molybdenum target of  $2 \times 2 \text{ cm}^2$  is considered. The target thickness is 0.2 mm, which corresponds to about 0.15% radiation length ( $0.204 \text{ g/cm}^2$ ) for molybdenum. In this case thermal conduction through the metal target material and the metal frame is considered as the major means of releasing the heat deposited by the beam. With eliminating the blackbody thermal radiation the steady state beam spot temperature reaches 2500 K when the beam spot is fixed at the center of the target. If the beam scans the target with a sinusoidal motion having frequency 100 Hz and amplitude 9.6 mm in one direction, the steady temperature is about 300 K over the target area except the four vertex points of the motion [1]. A further simulation by [2] shows that if a fast two dimensional rastering ( $f_1 = 2 \text{ kHz}$  and  $f_2 = 0.1176 \text{ kHz}$ ) is applied to an aluminium target (20 mm  $\times$  20 mm), the temperature distribution on the target will be quickly saturated after 1 second exposure to 200  $\mu\text{A}$  electron beam. The temperature rise  $\Delta t$  is below 70 K at an initial temperature 300 K. For the iron target a

temperature rise of 500 K occurs due to the worse thermal conductivity and the smaller specific heat.

### B. Heating effect in the cryogenic target

In the case of a 10 cm liquid hydrogen target operating at 20 K the power dissipation due to the energy loss in the target cell by 200  $\mu\text{A}$  beam is about 1 kW. The liquid hydrogen is overheated by the deposited beam energy and bubbles are formed, therefore, a density variation is eventually generated. In order to minimize this bubble formation effect and reduce forced flow velocity to a reasonable level (1 to 10 m/s), the best solution is beam rastering. The global and local beam heating analysis by [3] shows a 18 kHz rastering with 2 mm amplitude is preferable.

### C. Heating effect in the beam dump

As discussed by [4], for an instantaneous spot size of 100  $\mu\text{m}$ , the critical time constant for drilling a hole into the window is 100  $\mu\text{s}$ . Also, any window material loses its strength after an energy deposition of  $10^{18} \text{ ergs/gram}$  by the beam. Therefore, the rastering speed and pattern have to be selected carefully to avoid long dwell times. Tentatively, a spot size of  $4 \times 4 \text{ cm}^2$  at the dump was adopted. The spot size at the beam dump entrance can be increased nearly arbitrarily by using high speed magnetic rastering.

### D. Rastering on the polarized target

The polarized target will have a useful width and height of 2.5 cm. To make full use of it, the rastering of the beam on the target should cover at least  $2.5 \times 2.5 \text{ cm}^2$  [5]. An adjustable offset of rastering current is desirable for the beam alignment. In the polarized target experiment the current density is only 100 nA; it is reasonable to require 1 kHz rastering. The Moller polarimeter requires a linear rastering pattern on the iron target with amplitude of 2 mm instead of moving the target [6]. The linear scan of the beam will effectively reduce the temperature rise of the target and keep the polarisation at a higher level in the beam current range from 10 to 100  $\mu\text{A}$ .

Table 1 gives rastering parameters required by different target materials.

\*This work was supported by the U.S. Department of Energy, under contract No. DE-AC05-84ER40150.

Table 1: Raster frequency and amplitude, FR: fast raster, SR: slow raster

Parameter	Cryogenic Target	Polarised Target	Beam Dump materials
Position(m)	146.25	146.25	200.65
Current( $\mu$ A)	200	0.1	200
Area (cm <sup>2</sup> )	0.2x0.2	2.5x2.5	4x4
Frequency(kHz)	10-18	0.1-1	0.1
Operation	FR	FR+SR	SR

Table 2: Specification of SR and FR magnets

Design Parameter	SR	FR
Central field (Gauss)	438.8	80.1
Bending angle at 6 GeV	0.84 mr	0.0588
$\int Bdl$ (kG cm)	16.8	1.2
Field uniformity	$10^{-2}$	$10^{-2}$
Effective length (cm)	38.34	15
Physical dimension (cm)	48	25
Inner radius (cm)	1.905	1.27
Number of turns	200	20
Ampere-turns (A-T)	4000	240
Current density (A/cm <sup>2</sup> )	148	100
Stored energy (Joules)	6.944	0.0167
Inductance (H)	$34.7 \times 10^{-8}$	$84 \times 10^{-6}$
DC resistance ( $\Omega$ )	0.916	$3.02 \times 10^{-3}$
RMS power (kW)	2.18	0.528
Type of conductors	Awg 8	Litz
Rastering frequency (Hz)	60	10,000

## II. RASTER MAGNET DESIGN BY TOSCA

Two bedstead air core coils are used as the raster magnets. Based on TOSCA calculation, the specifications of these coils are listed in Table 2.

The geometry of the raster magnet is shown in Figure 1. The bedstead shape of the raster coil will generate a larger uniform field region and keep the high order field components, mainly the sextupole component, as small as possible. In order to reach a higher rastering frequency up to 10 kHz, neither iron nor laminate iron material can be used as the raster magnet. A ferrite magnet is also not preferable because its small hysteresis makes it difficult for phase control.

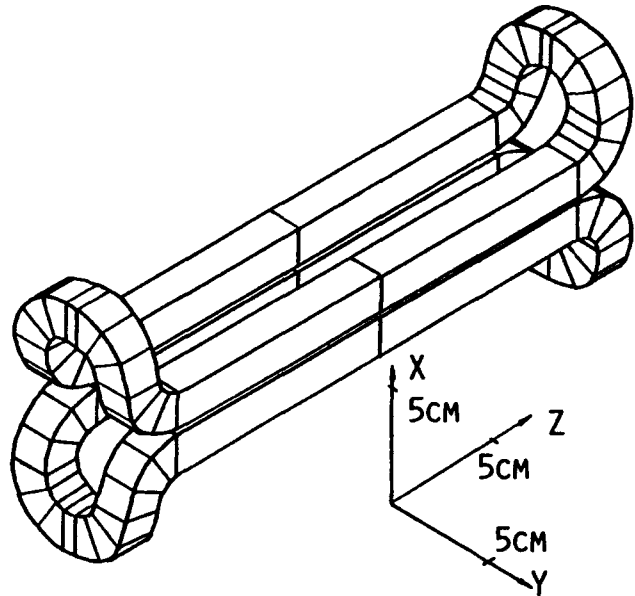


Figure 1: TOSCA layout of the fast raster magnet (FR).

## III. FREQUENCY CHARACTERISTICS OF RASTER COIL

A triangle waveform is selected to drive the raster coil. Based on the Fourier theorem, an arbitrary function  $F(x)$  can be expressed

$$F(x) = \sum_{n=1}^{\infty} [A_n \sin n\omega_n x + B_n \cos n\omega_n x] \quad (1)$$

where  $\omega_n = 2\pi f_n$ , the amplitude of the n-harmonic is  $\sqrt{A_n^2 + B_n^2}$  and the intensity of the n-harmonic is  $A_n^2 + B_n^2$ . In the case of an identical triangle waveform

$$y = \begin{cases} -T-x & -T \leq x \leq -T/2 \\ x & -T/2 \leq x \leq T/2 \\ T-x & T-x \leq x \leq T \end{cases} \quad (2)$$

the Fourier expansion of the triangle waveform is

$$y = \frac{4T}{\pi^2} \sum_{n=1}^{\infty} \frac{(-1)^{n-1}}{(2n-1)^2} \sin \frac{(2n-1)\pi x}{T} \quad (3)$$

$$y = \frac{4T}{\pi^2} \left[ \sin\left(\frac{\pi x}{T}\right) - \frac{1}{9} \sin\left(\frac{3\pi x}{T}\right) + \frac{1}{25} \sin\left(\frac{5\pi x}{T}\right) - \dots \right] \quad (4)$$

therefore, the ratios of the amplitudes and the intensities of the first, the third, and the fifth harmonic components are  $1 : \frac{1}{9} : \frac{1}{25}$  and  $1 : \frac{1}{81} : \frac{1}{125}$  respectively.

The 20 kHz triangle waveform generated from the Tektronix FG 501A 2 MHz function generator was experimentally analyzed by an HP network analyser. The frequency spectrum is displayed in Figure 2. The ratio of relative amplitudes of the fundamental frequency and the third and

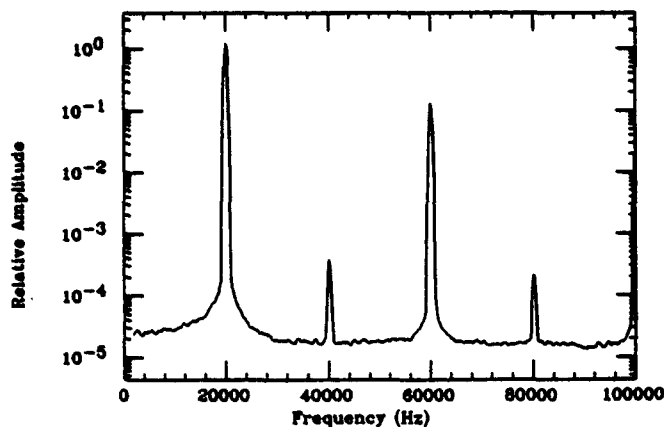


Figure 2: Frequency spectrum of the triangle waveform

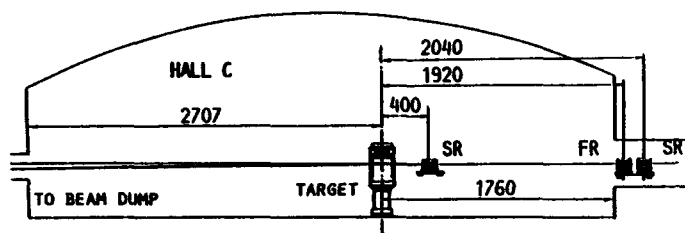


Figure 3: The raster system in Hall C beam line

the fifth harmonics is as the same as the computation from Fourier analysis mentioned above. The frequency range of a triangle waveform should cover 3-order harmonic.

Losses in a conductor due to the skin effect and proximity effect should be considered. For the FR magnet, a round Litz cable 660/36 is used for the winding. For the SR magnet, Litz cable is replaced by awg 6 solid cable because the skin depth in copper conductors is 8.5 mm at lower frequency (60 Hz).

#### IV. OPERATIONAL PERFORMANCE

The Hall C raster system is arranged as shown in Figure 3.

A fast raster (FR) system is placed at the entrance of Hall C, just in front of the first chicane magnet (BE). With a bending power 0.0588 mr at 6 GeV it is able to provide  $2 \times 2 \text{ mm}^2$  rastering area on the cryogenic target. A combined SR system which is located in front of the FR scans the beam on the polarised target with rastering area  $2.5 \times 2.5 \text{ cm}^2$ . The second SR near the target chamber, executes two functions: in the absence of the polarised target it scans the beam to a safety size ( $4 \times 4 \text{ cm}^2$ ) on the beam dump, and in the operation of the polarised target, it de-rasters the beam with opposite phase in order to reduce the large amount background generated from scattered

beam at the beam pipe walls.

Each raster system consists of two pairs of bedstead coils, one for horizontal scan, another for vertical scan. Different rastering patterns have been simulated and compared by two dimensional oscilloscopic Lissajous figures. The best ratio (1.721) of the two rastering frequencies was found, which gives the longest trajectory traversal and fast uniform distribution.

The FR magnet is driven by PA03 MOS power amplifier (APEX MICROT TECHNOLOGY CORPORATION), which has excellent features of high supply voltage (150 V), high output current (30 A), and high internal dissipation (500 W). The SR magnet is driven by a resonance circuit, which consists of a  $\pi$ -type LC resonance circuits, impedance match network, and low frequency power amplifier. Both of those drivers are under development.

A ceramic duct should be used as the vacuum pipe of FR magnet. The ceramic vacuum duct avoids the heating-up effect and the field attenuation due to eddy currents induced by alternating magnetic field. A very thin metal coating layer should be applied in the inner wall of the duct conducting the image current produced by the beam.

#### REFERENCES

- [1] Conceptual Design Report on Basic Experimental Equipment (revised), CEBAF, April 13, 1990.
- [2] Javer Gomes, Private communication, December 1992.
- [3] J. Mitchell, "Global and Local Beam Heating in the Hall C Cryo Target", CEBAF, March 2, 1993.
- [4] B. Mecking and C. Sinclair, Memorandum, Meeting on Beam Lines to Experimental Area, 28 November, 1992
- [5] D. Day and I. Sick, Memorandum, "Considerations Concerning Chicane for  $G_{en}$ ", July 23, 1992.
- [6] Matthias Loppacher, Progress Report of the CEBAF Hall C Moller Polarimeter, November 1992.

# Monitoring Production Target Thickness\*

Michael A. Othoudt  
Clinton P. Anderson Meson Physics Facility  
Los Alamos National Laboratory  
Los Alamos, NM 87545 USA

## Abstract

Pion and muon production targets at the Clinton P. Anderson Meson Physics Facility consist of rotating graphite wheels. The previous target thickness monitoring procedure scanned the target across a reduced intensity beam to determine beam center. The fractional loss in current across the centered target gave a measure of target thickness. This procedure, however, required interruption of beam delivery to experiments and frequently indicated a different fractional loss than at normal beam currents. The new monitoring procedure compares integrated upstream and downstream toroid current-monitor readings. The current monitors are read once per minute and the integral of readings are logged once per eight-hour shift. Changes in the upstream to downstream fractional difference provide a nonintrusive continuous measurement of target thickness under normal operational conditions. Target scans are now done only when new targets are installed or when unexplained changes in the current monitor data are observed.

## I. INTRODUCTION

The Clinton P. Anderson Meson Physics Facility (LAMPF) provides a high power beam of up to 1 mA of 800 MeV protons to Experimental Area A production targets. Pions, muons, and neutrinos are provided to secondary channels for six or more concurrent experiments. The pion and muon production targets consist of rotating ATJ graphite wheels 3- to 4-cm thick. Figure 1 shows a sketch of the production target at the A2 location.

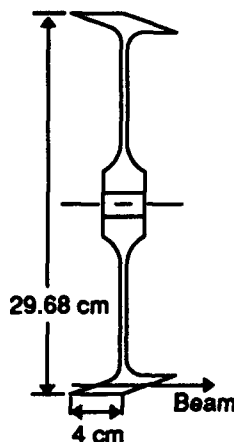


Figure 1. A cross section of the A2 production target. The beam passes through the 4-cm-thick rim. The nonrectangular shape of the rim optimizes production of muons and pions relative to the secondary channel acceptance.

During recent operating periods at LAMPF, a vacuum leak in the A2 target box has caused abnormally rapid erosion in the thickness of the A2 target. The erosion produces pits going completely through the thin edges of the target, which in one case reduced the effective target thickness by 50%. Large segments have broken off when the erosion was allowed to continue too long. Target replacement makes beam unavailable to experiments for up to three days to allow short-lived activation to die down, removal of the old target, installation of a new target, vacuum pump down and retuning the beam.

Attempts to fix the vacuum leak have been unsuccessful and a complete replacement of the target box is planned. Until this replacement is performed, however, it is necessary to optimize running conditions for experiments. Erosion of the A2 target reduces pion and muon fluxes to the two experiments running off the A2 target. Raising beam current to compensate for reduced target thickness increases the rate of erosion and forces a three-day beam off period for six or more experiments while the target is replaced. Thermal fluctuations in the A2 target box change the vacuum leak and therefore erosion rates, making it difficult to pick a single optimal operating current. The optimal strategy would be to continuously monitor the target, adjusting beam current for maximal secondary particle production for experiments while delaying the need for target replacement until scheduled maintenance periods when the beam would be off for other reasons.

## II. Original Monitoring Procedure

The original procedure for monitoring target thickness made use of a Hardware Transmission Monitor [1] (HWTM), which compared the outputs of toroidal current monitors upstream and downstream of the target. The HWTM compares the difference between the current monitors to an Expected Loss set with a potentiometer on the module; the difference between the measured and expected losses is the Loss Deviation. For the A2 target, the full 4-cm thickness corresponds to an Expected Loss of approximately 12%. Variation in the Loss Deviation could indicate

- missteering of the beam, causing part of it to miss the rim of the target;
- change in beam spot size also causing part of it to miss the rim of the target;
- shift in target position with respect to the beam; or
- change in target thickness.

\* Work supported by U. S. Department of Energy Contract W-7405-ENG-36.

The first two possibilities could be checked by observing the beam with wire scanners and harps without making beam unavailable to experiments. Target position shifts have been observed, due either to malfunction of the target positioning mechanism or thermal expansion of the 24-foot-long steel arm that supports the target. The original procedure checked all four possibilities:

1) Using wire scanners and harps, steer beam upstream and downstream of the target to within 0.1 mm of centerline. Also check spot sizes.

2) Reduce beam current to 70  $\mu\text{A}$  to reduce thermal stresses on the target in the next step. This makes the beam unsuitable for most experiments.  
 3) Scan the target by driving it across the beam, recording the change in beam loss as a function of target position. Figure 2 is a plot of such a scan.  
 4) Center the target on the beam.  
 5) Reset HWTM Expected Loss potentiometer to give zero Loss Deviation.  
 6) Raise beam current back to normal levels (200-800  $\mu\text{A}$  for 1992 running).

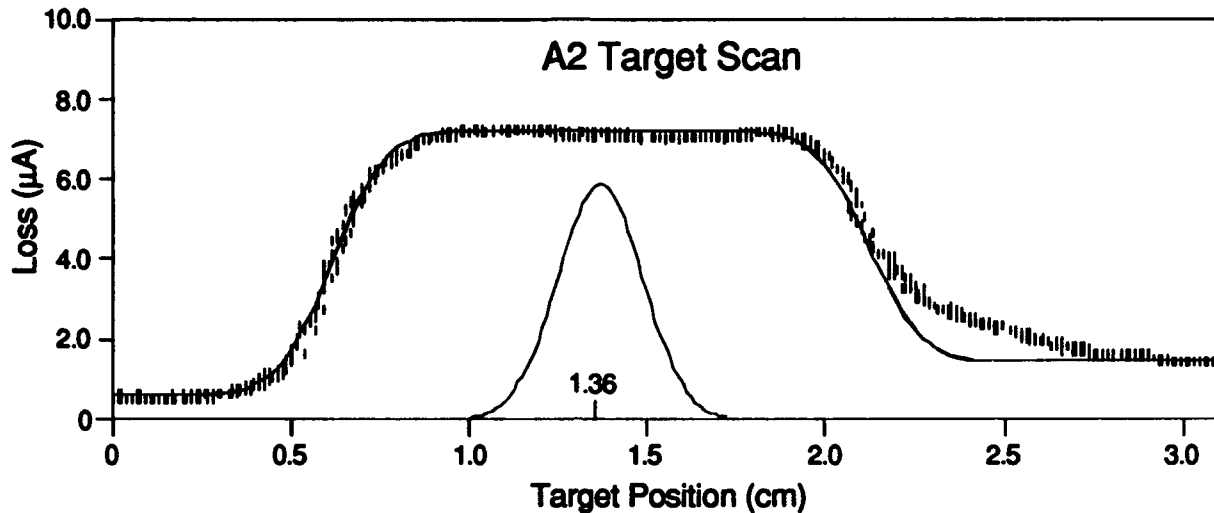


Figure 2. Result of an A2 target scan. Short vertical lines indicate the reproducibility of the data. The solid line is a fit to the data based on a Gaussian beam profile convoluted with the shape of the target. The Gaussian resulting from the fit is shown at the position which centers the target on beam. The centering position (1.36 cm) is used in step 4 of the scanning procedure. The target-shape model does not include the material in the radius between the rim and central web of the target; this causes the large deviation of the fit from the data near 2.4 cm.

The HWTM Expected Loss setting is the measure of target thickness from this procedure. The procedure has several undesirable features:

- Beam is unavailable to experiments for up to half an hour.
- Scanning the target causes stresses in the target drive and rotation mechanisms. Failure of these mechanisms could require up to three days of beam downtime to repair.
- Scanning the target even at low currents exposes the target to thermal stresses as the beam crosses the inner and outer edges of the rim. Such stresses could prematurely fracture an eroded target.
- The HWTM Loss Deviation changes significantly when the beam current is raised to normal levels. (This may be due to a change in the ratio of electrons to protons passing through the current monitors. Electrons are produced by beam halos intercepting nearby beam collimators.) This change makes it difficult to interpret the meaning of later changes in the Loss Deviation.
- To minimize loss of beam time for experiments, this procedure was done no more often than weekly. The infrequent measurements made accurate extrapolation of target lifetime difficult.

### III. New Procedure

The new procedure also makes use of the upstream and downstream toroidal current monitors, but samples the data continuously and does not make beam unsuitable for experiments. The current monitors are sampled by computer once per minute, summed and recorded periodically. Plotting the fractional difference in upstream and downstream currents versus integrated current delivered to the target then gives an indication of target thickness. During 1992, the fractional loss was calculated daily. Figure 3 shows a plot of data for the A2 target taken with this procedure for the LAMPF 1992 operating period. Data were also taken for the 3-cm target at the A1 location; better vacuum at A1 resulted in no detectable erosion of the A1 target.

The new procedure was implemented near the end of the lifetime of the first A2 target used during 1992. Earlier data for the first target were extracted from archival records. Because of the continuous nature of this procedure, confidence in the state of the target was much higher and extrapolations of thickness were considered more trustworthy. Thus the second target was allowed to erode much further than the first before replacement. Target scans were done

## A2 Target Erosion in 1992

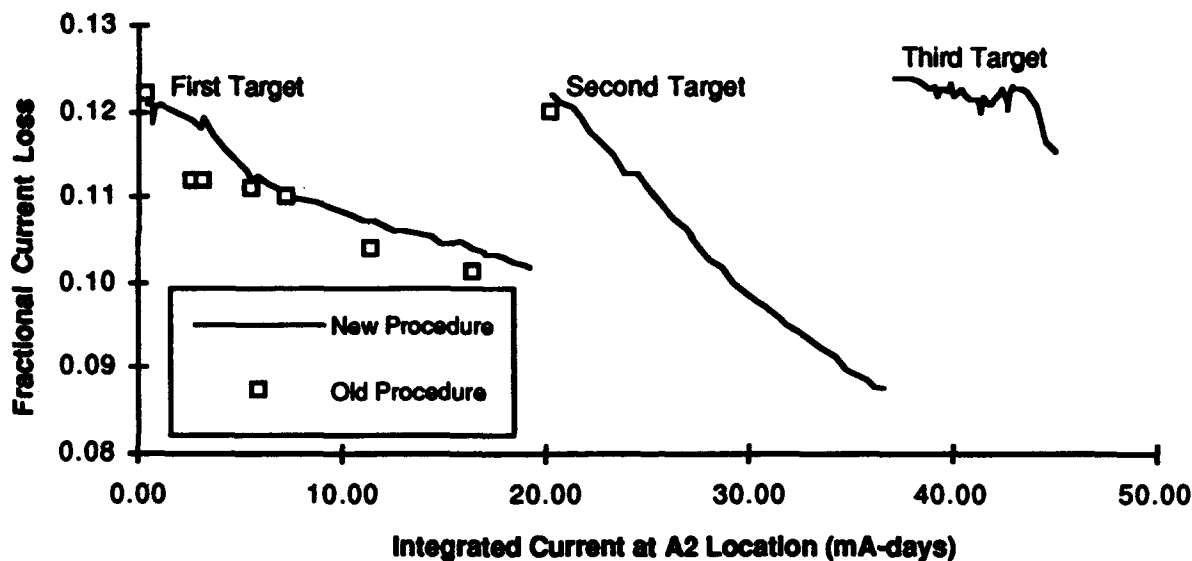


Figure 3. The fractional current loss across the A2 target as measured by the new procedure plotted against integrated current on target. The fractional loss is a measure of target thickness. Also shown is the fractional loss measured by the old procedure. Three different targets were used during 1992 running. The low rate of erosion of the third target was due to low beam currents ( $200 \mu\text{A}$ ) run during this time period.

only when new targets were installed. Plans were to perform scans if unexplained changes in the losses were observed to check for lurches in target position; however, no significant deviations from gradual erosion were observed and no intermediate scans were done.

Based on these data it was possible to correlate target erosion with beam current and A2 vacuum pressure. It was found that at currents below  $500 \mu\text{A}$ , target erosion was small at all pressures observed. Below pressures of 0.2 microns, target erosion was also very slow for currents up to  $700 \mu\text{A}$ . However, for pressures above 0.2 microns, the erosion rate increased rapidly for beam currents above  $500 \mu\text{A}$ .

### IV. Conclusions

Use of the new procedure provided greater confidence on the status of the A2 target and permitted better scheduling of beam currents. Significant amounts of beam time were saved

by avoiding the lengthy target scan procedure. Continuous monitoring of erosion also allowed correlation of with beam current and vacuum pressure.

Future uses of this technique may include recording current-monitor data as often as minute-by-minute to better understand short term fluctuations in the losses. Use of ion chambers located near the production targets will be investigated to see if data from them can be used as a cross check on the current monitor data. In addition it may be possible to use pairs of current monitors upstream and downstream of beamline collimators to better monitor beam losses during beamline tuning.

### V. REFERENCES

- [1] A. Browman, "LAMPF Hardware Beam Transmission Monitor Systems," *IEEE Trans. Nucl. Sci.* NS-28, NO. 3, 2237 (1981).

# Beam Loss Handling at the SSC

I.S. Baishev, A.I. Drozhdin, and N.V. Mokhov  
 Superconducting Super Collider Laboratory\*  
 2550 Beckleymeade Ave., Dallas, TX 75237 USA

## Abstract

A scraper/collimation system is required to localize the beam loss in the Collider of the Superconducting Super Collider to a few predefined locations and by doing so to minimize the irradiation of superconducting magnets, to sustain favorable background conditions in the Interaction Regions (IR), and to reduce the impact of radiation on other equipment, personnel, and the environment. Results of full-scale simulation are presented for various systematic and accidental beam loss.

## I. INTRODUCTION

A fraction of the beam lost in the Collider due to pp-collisions at interaction points, beam-gas scattering, beam halo scraping, various instabilities and errors will result in the irradiation of conventional and superconducting components of the machine [1]. Catastrophic effects of the accidental beam loss should be minimized with some special measures. A very reliable beam collimation system is required to protect accelerator equipment against irradiation, to sustain favorable background conditions in the IRs, and to reduce the impact of radiation on personnel and the environment.

Calculated beam loss rate due to beam-gas interaction is about  $3 \times 10^3$  p/m/s at the baseline parameters. It is distributed almost uniformly along the Collider. Local sources such as pp-collisions and scrapers add some peaks to the above "pedestal". Results on beam loss distribution in this paper are presented for those peaks only.

## II. SCRAPER SYSTEM

The first approach to the Collider beam scraper system is described in [2]. Primary features follow Tevatron [3], UNK [4] and LHC [5] schemes. A current betatron collimation system [6] is situated in the Collider west utility straight section and consists of horizontal and vertical scrapers and a set of collimators (Figure 1). Scrapers and collimators have movable jaws controlled by high-precision motors. The jaws are surrounded with radiation shielding. Tungsten targets, 1-mm thick, are used to deflect halo particles deeper into the scraper front face. The target-scraper offset is approximately 0.05 mm. The essential part of the

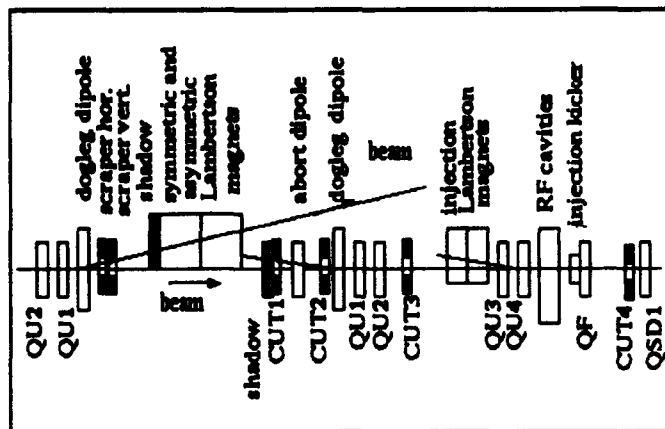


Figure 1. Scraper System in the West Utility.

beam collimation system is a horizontal dogleg structure, which provides a complete interception of neutral and low-energy charged particles out of the scrapers. The horizontal dogleg is created by two superconducting dipoles and a set of warm magnets including symmetric, asymmetric Lambertson, and resistive magnets. To provide a fine tuning of the beam on the scrapers existing in the utility straight, eight spool pieces are used. A high-precision feedback system will be used to control a scraping intensity.

The expected scraping rate is rather high [6]: about 1% of intensity at the very beginning of acceleration and then at flat-top  $3 \times 10^9$  p/s over the first 15 minutes and  $4 \times 10^8$  p/s during the collisions (24 hours). The overall design of the jaws, cooling system and radiation shielding is not a trivial engineering problem. The west utility straight has near zero dispersion, so modifications to the east utility for off-momentum scraping are under consideration.

## III. IR COLLIMATORS

A set of collimators is required in the Interaction Regions to protect the final focus triplet and vertical bending magnets. The current set for the East IRs consists of 14 collimators with movable jaws and 4 collimators of the fixed aperture. Optimal jaw position for the first group is  $20 \sigma$  from the circulating beam axis. Each collimator includes a steel jaw 3 m long surrounded with radiation shielding.

The fixed aperture collimators (CIR01-04) are placed in the experimental halls just upstream from the low- $\beta$  quadrupoles. They deal with relatively low energy sec-

\*Operated by the Universities Research Association, Inc., for the U.S. Department of Energy under Contract No. DE-AC35-89ER40486.

ondaries produced at the interaction points (IP). Other collimators intercept high energy protons (mainly diffractive) produced in beam interactions all around the machine. Collimators CIR1 and CIR5 are used to intercept secondaries produced by beam-gas interactions. For each ring, one collimator (CIR1) is situated upstream IP and two more (CIR2, CIR3) – downstream IP, just down the common vertical bending magnets. Collimator CIR4 is placed in the middle of the hinge region at a nonzero dispersion point. Collimator jaw positions at injection and top energies are shown in the Table 1 and 2, respectively.

Table 1  
Scraper and Collimator Jaw Positions at Injection.

	Beta hor.(m)	Beta ver.(m)	Position hor.(mm)	Position ver.(mm)
Scraper	611	430	-5.4	-4.5
CUT1	422	584	+7.1	+8.4
CUT2	423	621	-7.1	-8.7
CUT3	480	287	+7.5	
CIR1	316	142	-6.2	-4.1
CIR01	64	63	12.5	12.5
CIR02	64	65	12.5	12.5
CIR2	178	462	-4.6	-7.5
CIR3	140	222		-5.2
CIR4	103	185	-3.5	
CIR5	318	141	-6.2	-4.1
CIR03	63	65	12.5	12.5
CIR04	65	65	12.5	12.5
CIR6	177	476	+4.6	+7.5
CIR7	138	230		+5.2

Table 2  
Scraper and Collimator Jaw Positions at Top Energy.

	Beta hor.(m)	Beta ver.(m)	Position hor.(mm)	Position ver.(mm)
Scraper	611	430	-1.7	-1.4
CUT1	422	584	+2.8	+3.3
CUT2	423	621	-2.8	-3.4
CUT3	480	287	+3.0	
CIR1	4108	1554	-8.9	-5.5
CIR01	799	791	12.5	12.5
CIR02	791	799	12.5	12.5
CIR2	2457	6389	-6.7	-11.0
CIR3	1007	2605		-7.0
CIR4	103	174	-1.4	
CIR5	4097	1591	-8.9	-5.5
CIR03	796	812	12.5	12.5
CIR04	812	796	12.5	12.5
CIR6	2448	6554	+6.7	+11.0
CIR7	1001	2675		+7.0

#### IV. BEAM LOSS DISTRIBUTION

With no movable collimators in the IRs a maximum beam loss rate in superconducting magnets due to only

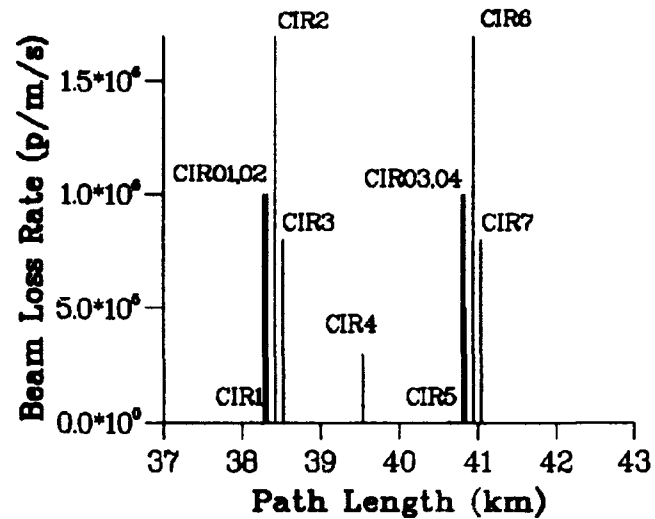


Figure 2. Beam Loss in IRs at Collisions (Collimators are ON).

pp-collisions is a few times  $10^5$  p/m/s. Being added to other sources this exceeds any possible limits [1, 6]. With the collimators at  $20\sigma$  calculated beam loss distribution in the IRs is shown in Figure 2. Beam loss rate is decreased down to  $(4-8) \times 10^3$  p/m/s at all the IR superconducting magnets. Most of loss is intercepted by CIR2 and CIR6 collimators.

It turns out that the IR collimators can't protect completely the beta-peak region against protons outscattered of the scrapers. Beam loss distributions due to that component calculated with and without collimators are shown in Figure 3 and 4, respectively. Even with the collimators on, beam loss rate in QL3 quads is unacceptably high. The solution is three additional collimators in the West Utility downstream of the abort Lambertson's magnets. They provide good interception of most of the scraper protons.

#### V. ACCIDENTAL BEAM LOSS

The unsynchronized injection and abort system kicker misfire/prefire result in the additional beam loss in the Collider components. The above collimation system is intended to protect superconducting magnets in those cases also, if the injection timing error is shorter than  $0.7 \mu\text{s}$ . For the larger errors, the injected beam is lost in a few superconducting magnets causing the catastrophic consequences.

In case of injection kicker misfire, the beam must be aborted from the Collider within one or two turns, because the transverse damping system is not designed to damp injection beam displacement in this case to an acceptable level. The IR collimators are used to protect superconducting magnets in this case.

The abort kicker prefire results in coherent betatron oscillation of the beam with rather high amplitude. Collimator CIR5 is used to protect the low- $\beta$  quads against ir-

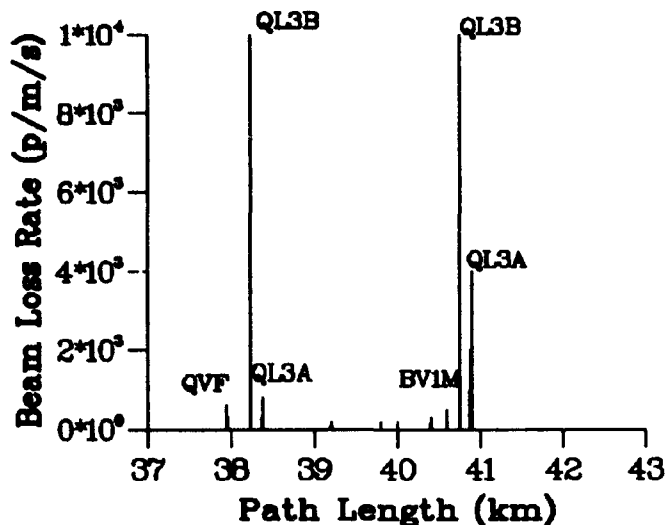


Figure 3. Beam loss in IRs at Scraping (Collimators are OFF.)

radiation in this event. Without that collimator the beam loss rate in the final focus triplet is 50 to 100 times higher of the quench level.

## VI. CONCLUSIONS

The designed measures should provide the reliable protection of superconducting components against excessive irradiation.

## VII. REFERENCES

- [1] I.S. Baishev, A.I. Drozhdin, and N.V. Mokhov, SSCL-306 (1990).
- [2] M. Maslov, N. Mokhov, and I. Yazynin, SSCL-484 (1991).
- [3] A.I. Drozhdin, M. Harrison, and N.V. Mokhov, Fermilab FN-418 (1985).
- [4] I.S. Baishev, V.N. Chepegin, A.I. Drozhdin et al., *Proc. of the 14th Int. Conference on High Energy Accel.*, Japan (1989), part III, p.667.
- [5] L. Burnod, J.B. Jeanneret, CERN SL/91-39 (EA), Geneva (1991).
- [6] N.V. Mokhov, Collider Utility Sections PDRR, SSCL, January 1993.

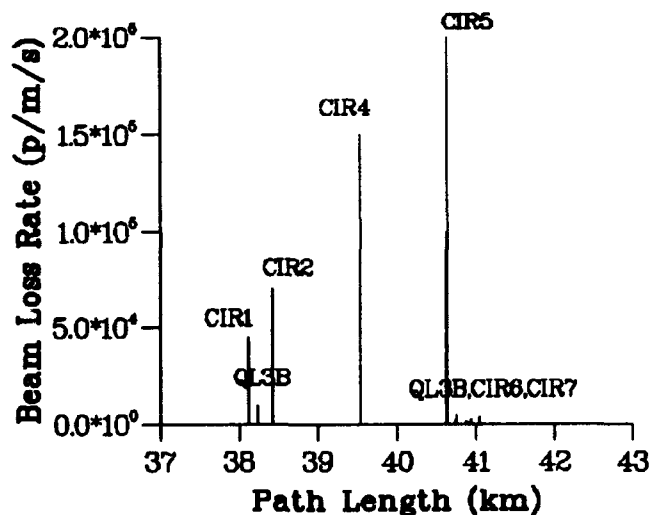


Figure 4. Beam loss in IRs at Scraping (Collimators are ON).

ANALYTICAL STUDY OF RFQ CHANNEL  
BY MEANS OF THE EQUIVALENT CHARGES MODEL

Vitaly M. Pirozhenko and Oleg V. Plink

Moscow Radiotechnical Institute  
113519 Moscow, Russia

Abstract

A simple model of RFQ channel is proposed. The model represents the periodic chain of twin point charges with a screw symmetry axis and alternating sign of the charges. For this approach the expressions both for longitudinal and azimuthal potential harmonics are determined in closed forms. The relationship of model parameters with RFQ geometry is defined. The results of calculations for different vane shapes are given including idealized electrodes and electrodes with extremely large modulation.

1. INTRODUCTION

In most cases the well-known concept of idealized electrodes or two terms potential is used when calculating the main parameters of RFQ accelerator [1]. Further more accurate definition is accomplished by means of computer simulations [2]. The use of electrodes with large modulation was supposed to increase both acceleration rate and output energy of RFQ accelerators [3,4]. However the difficulties of analytical and numerical studies of the RFQ with large modulation restrict the application of this system.

In this paper the equivalent charges model is proposed to calculate the RFQ parameters. The method of the equivalent charges was earlier used to study axisymmetric channel with alternating sign accelerating field [5]. It allowed to define harmonic contents of the field in explicit form, the channel capacitance per unit length, the transit time factor and the field enhancement factor. Optimization of the axisymmetric channel was also carried out by means of the equivalent charges description of the channel [5].

The equivalent charges model of the RFQ channel is described and studied below. On base of this, RFQ geometry is defined for the various vane shapes. A number of expressions was earlier obtained in the paper [6].

2. MODEL DESCRIPTION

To model the RFQ channel an endless periodic chain of twin point charges is used (fig.1). The system has a screw symmetry axis. The sign of charges alternates along the channel axis. The charges of similar polarity are located periodically in pairs. The period of the system is  $2h = \beta\lambda$ . The distance from the charges to the channel axis  $b$  and the value of the point charge  $Q$  are the fitting model parameters. For this approach various vane configurations can be generated by means of metalizing different isopotential surfaces for different values of  $b$ . The value of  $Q$  is arbitrary as a matter of fact.

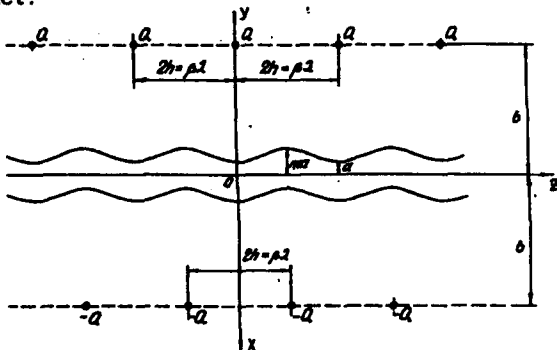


Figure 1. RFQ equivalent charges model

The minimal distance from the longitudinal profile of a chosen equipotential to the channel axis gives the channel bore radius  $a$ . The maximum distance defines the modulation factor  $m$ .

3. LONGITUDINAL HARMONICS OF POTENTIAL

The potential for the system in cylindrical coordinates can be expressed in the following form:

$$\varphi(r, \theta, z) = \frac{Q}{4\pi\epsilon_0} \sum_{n=-\infty}^{\infty} \sum_{l=0}^3 (-1)^l ((\nu_{ln} h - z)^2 + R_l^2)^{-1/2}$$

where  $\epsilon_0 = 8.85 \text{ pF/m}$ .

$$R_l^2 = r^2 + b^2 - 2rb \sin(\theta + i\pi/2).$$

$$\nu_{ln} = \begin{cases} 2n & \text{for } l = 0, 2 \\ 2n+1 & \text{for } l = 1, 3 \end{cases}$$

The longitudinal Fourier series expansion of the potential is

$$\varphi(r, \theta, z) = \tau \sum_{l=0}^{\infty} A_l(r, \theta) \cos l k z.$$

where  $\tau = Q/(2\pi\epsilon_0 h)$ ,  $k = \pi/h$ .

Taking into account the relations

$$\int_0^{\infty} ((c_1^2 + x^2)^{-1/2} - (c_2^2 + x^2)^{-1/2}) dx = \ln c_2/c_1,$$

$$\int_0^{\infty} (c^2 + x^2)^{-1/2} \cos \lambda x dx = K_0(\lambda c).$$

where  $K_0(x)$  is the modified Bessel function, we have the expressions for longitudinal harmonics of the potential:

$$A_0(r, \theta) = h^{-1} \int_0^h \varphi(r, \theta, z) dz = 0.5 \sum_{l=0}^3 (-1)^{l+1} \ln R_l.$$

$$A_1(r, \theta) = 2h^{-1} \int_0^h \varphi(r, \theta, z) \cos l k z dz = \sum_{l=0}^3 (-1)^{l+1} K_0(l k R_l).$$

The axis potential distribution coincides with the axisymmetric case [5]:

$$\varphi(z) = 4\tau \sum_{l=0}^{\infty} A_{2l+1}(0) \cos((2l+1)kz).$$

with  $A_{2l+1}(0) = K_0((2l+1)kb)$ .

4. AZIMUTHAL HARMONICS OF POTENTIAL

For further transformations the following addition theorems are used:

$$\ln R/b = - \sum_{s=1}^{\infty} (r/b)^s s^{-1} \cos s\theta$$

$$K_0(\lambda R) = K_0(\lambda b) I_0(\lambda r) + 2 \sum_{s=1}^{\infty} K_s(\lambda b) I_s(\lambda r) \cos s\theta.$$

where  $R^2 = r^2 + b^2 - 2rb \cos\theta$ ,  $r < b$ .

$I_s(x)$ ,  $K_s(x)$  are modified Bessel functions.

Then the longitudinal Fourier coefficients are connected with azimuthal ones

$$A_0 = - \sum_0^{\infty} A_{0,2s+1}(\alpha) \cos 2(2s+1)\theta.$$

$$A_{21} = -\beta \sum_0^{\infty} A_{21,2(2s+1)}(\beta, \gamma) \cos 2(2s+1)\theta.$$

$$A_{21+1} = 4A_{21+1,0}(\beta, \gamma) + 2 \sum_1^{\infty} A_{21+1,4s}(\beta, \gamma) \cos 4s\theta.$$

where  $A_{0,s}(\alpha) = \alpha^{2s}/s$ .  $A_{1,s} = K_0(1\beta)I_0(1\gamma)$ .

$$\alpha = r/b. \quad \beta = kb. \quad \gamma = kr \quad \text{for } r < b.$$

$$\alpha = b/r. \quad \beta = kr. \quad \gamma = kb \quad \text{for } r > b.$$

### 5. RFQ EQUIVALENT PARAMETERS

For proper choice RFQ geometry it is desirable to define the following characteristics of the channel.

The effectiveness of acceleration in RFQ is characterized by

$$\xi = 2 \cdot \phi(0)T/V.$$

where  $V$  is the intervane voltage.

$$T = \pi \cdot A_1(0) / (4 \sum_{l=0}^{\infty} A_{2l+1}(0))$$
 is the transit time factor.

The effectiveness of focusing in RFQ is characterized by

$$\chi = 2 \cdot \tau A_{0,1}(a/b)/V$$

where  $a$  is the bore radius of the channel.

When choosing RFQ geometry, it is necessary to know the coefficients of nonlinearity and asymmetry of focusing field:

$$\delta = |1 + E_r(a, \pi/2, 0)a/(xV)|.$$

$$\eta = |1 + E_r(a, \pi/2, 0)/E_r(a, 0, 0)|.$$

The above obtained results leads to

$$\xi = 2 \cdot \pi \tau K_0(kb)/V. \quad \chi = 2 \cdot \tau (a/b)^2/V.$$

$$T = \pi \cdot K_0(kb) / (4 \sum_0^{\infty} K_0((2l+1)kb)).$$

One can consider  $T = \pi/4$  for  $kb \geq 2$ . This result corresponds to the one term potential distribution along the channel axis.

### 6. ANALYSIS AND RESULTS

The different electrodes shapes can be synthesized by means of changing of the generating parameter  $kb$ . As examples the results of calculations of isopotential surfaces (electrodes shapes) are given at Fig.2 - 5 for  $kb = 5$ ,  $kb = \pi$  and  $kb = \pi/2$ .

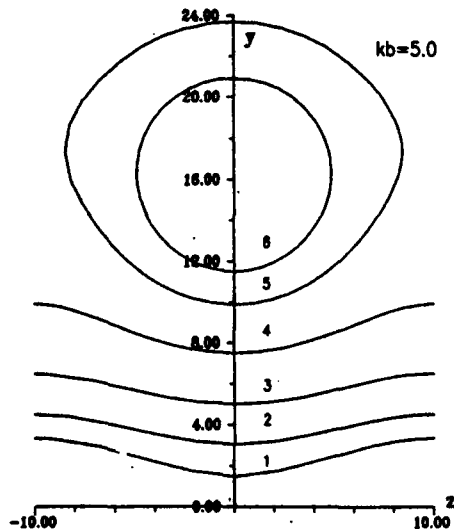


Figure 2. Equipotentials for  $kb = 5$

The equipotentials of the system can be either enclosed configurations or surfaces which are continuous along the channel axis. For the systems with large value of  $kb$  the part of equipotentials is enclosed. The others are the unenclosed surfaces modulated periodically in the longitudinal direction. These types of equipotentials are separated from each other by the boundary surface - the space separatrix (the curve number 3 at Fig.3). The cross sections of the electrodes in  $X - Z$  plane are shown at Fig.4. For  $y < ma$  the  $X - Z$  equipotentials are closed, for  $y > ma$  they are unenclosed.

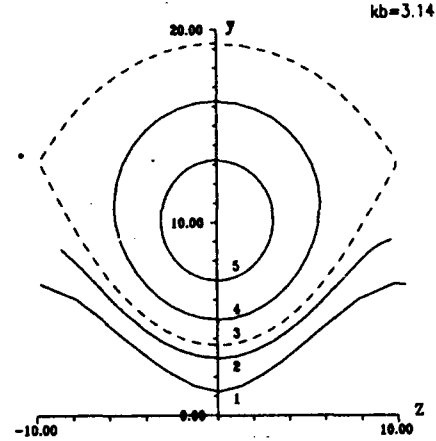


Figure 3. Equipotentials for  $kb = \pi$

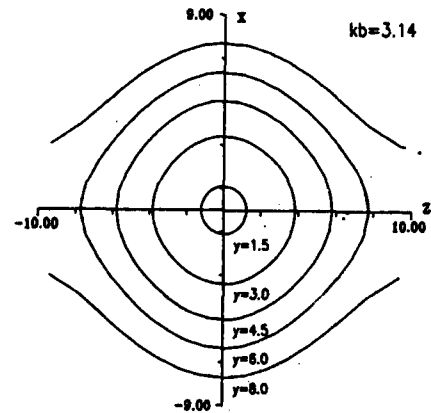


Figure 4. Equipotentials for  $kb = \pi$

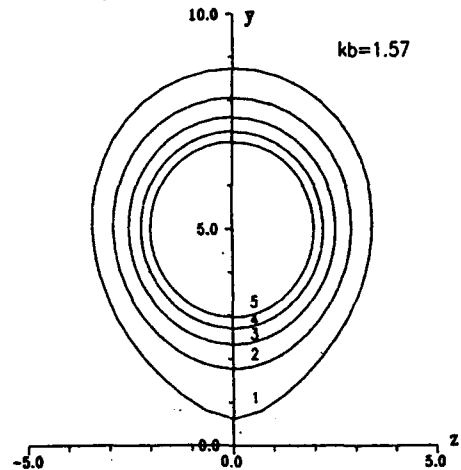


Figure 5. Equipotentials for  $kb = \pi/2$

For small values of generating parameters  $kb$  (Fig.5) equipotentials have the closed configuration. This case corresponds so called stem electrodes or the electrodes with extremely large modulation.

The results of calculations are summarized in Tables 1 - 3.

Table 1  
Results of calculations for  $kb = 5$

Curve number	1	2	3	4	5	6
$ka$	0.468	0.958	1.57	2.36	3.10	3.61
$m$	2.23	1.47	1.30	1.32		
$x_1$	0.360	0.661	0.773	0.794		
$4E_1/\pi$	0.606	0.272	0.132	0.070		
$x$	0.359	0.661	0.772	0.776	0.692	0.587
$4E/\pi$	0.603	0.266	0.116	0.051	0.027	0.017

Table 2  
Results of calculations for  $kb = \pi$

Curve number	1	2	3	4	5
$ka$	0.390	0.933	1.15	1.57	2.20
$m$	5.50	3.07	3.62		
$x_1$	0.105	0.350	0.466		
$4E_1/\pi$	0.862	0.528	0.393		
$x$	0.111	0.361	0.425	0.474	0.403
$4E/\pi$	0.860	0.488	0.379	0.225	0.098

Table 3  
Results of calculations for  $kb = \pi/2$

Curve number	1	2	3	4	5
$ka$	0.193	0.560	0.732	0.848	0.930
$x$	0.018	0.114	0.156	0.174	0.182
$4E/\pi$	0.912	0.685	0.548	0.457	0.395

In Tables 1 - 2 the effectivenesses of acceleration and focusing for the idealized electrodes are also given. They were calculated in accordance with [1]:

$$x_1 = (I_0(ka) + I_0(mka)) / (m^2 I_0(ka) + I_0(mka)).$$

$$4E_1/\pi = (1 - x_1) / I_0(ka).$$

These relations can be used for the unenclosed configurations with  $ma < b$ . For such systems the relationship of the effectiveness of focusing with the model parameters has the simple form:

$$x = (1 + 4(b/a)^2 K_0(kb) I_0(ka))^{-1}.$$

$$\delta = \eta/2 = (kb)^2 \cdot K_0(kb).$$

## 7. CONCLUSION

The equivalent charges model allows to describe various RFQ electrodes configurations beginning with the idealized electrodes up to the electrodes with extremely large modulation - the stem electrodes. The use of electrodes with large modulation may allow to increase an acceleration rate in RFQ. The additional advantage of such a system is small value of capacitance per unit length. But the increase of the modulation leads to rise of nonlinearity of focusing field. A final choice of the RFQ channel parameters requires analysis of influence of this effect on beam dynamics.

## 8. ACKNOWLEDGMENTS

The authors wish to thank A.A.Krasnoborodko and T.S.Berkovich for their help and assistance in conducting the computer simulations.

## 9. REFERENCES

- 1.I.M.Kapchinskiy. "The theory of linear resonance accelerators". Moscow. 1982 (in Russian).
- 2.K.R.Crandall. R.S.Mills and T.P.Wangler. "Radio - frequency quadrupole vane-tip geometries". IEEE Trans. on Nucl. Sci. NS-30. No.4, p.3554-3556 (1983).
- 3.Donald A. Swenson. "Superconducting RFQ's in the 100 MeV range", IEEE Trans. on Nucl. Sci. NS-32. No.5. pp.3240-3242 (1985).
- 4.I.Ben-Zvi. A.Jain. H.Wang and A.Lombardi. "Electrical characteristics of a short RFQ resonator". Proceedings of the 1990 Linear Accelerator Conference. pp. 73 - 75.
- 5.O.Plink. "Electric field in the channel with alternating sign accelerating field". Journal of Technical Physics. vol.59. pp.196-198 (1989).
- 6.B.Bondarev. A.Durkin. V.Pirozhenko and O.Plink. "Development and study of the opposed vibrator resonator for RFQ compact ion linacs". Proceedings of the Third European Particle Accelerator Conference. pp. 1337 - 1339 (1992).

# Design of an 80-MHz RFQ Linac for Heavy Ions

O. Takeda, Y. Tanabe, K. Satoh and S. Kawazu  
Toshiba Corporation

2-4, Suehiro-cho, Tsurumi-ku, Yokohama, 230 Japan

Y. Oguri, M. Okamura and T. Hattori

Tokyo Institute of Technology

2-12-1, Ohokayama, Meguro-ku, Tokyo, 152 Japan

## Abstract

At the Tokyo Institute of Technology (TIT) a four-vane RFQ is to be applied for inertial confinement fusion research[1]. The RFQ (TIT RFQ) is designed for acceleration of particles with charge to mass ratio ( $q/A$ ) of 1/16 from 5keV/amu to 213keV/amu. The planned maximum injection beam current is 10mA for  $^{16}\text{O}^+$ . Beam dynamics was calculated using a PIC (Particle-In-Cell) code which can take influence of the multipole components in the intervane potential into account. For input beam current of 10mA transmission of 60% was obtained.

A half-scaled cold model was fabricated to investigate fundamental rf characteristics. In the cold model experiment, the difference in electric field strength between each quadrant was minimized to  $\pm 3\%$  by using side tuners and flat field distribution along the beam axis was achieved by adjusting end tuners.

## I. INTRODUCTION

In a previous paper[1] a design of the TIT RFQ with the vane-tip curvature radius of  $0.75r_0$  was presented. The computer code PARMTEQ was used to simulate the beam dynamics in the RFQ and the computer code GENRFQ was used to generate the vane parameters for PARMTEQ calculation. For this old design the beam transmission was expected to be 72% for the injection current of 10mA.

In the meantime, one of the authors of this paper developed a new simulation code "QLASSI (Quadrupole Linear Acceleration Simulator with Space and Image charge effect)"[2] which can simulate the beam dynamics including influence of the multipole components in the intervane potential. This code was applied to calculation of the beam dynamics for the old design. Since the result of this calculation showed very poor transmission efficiency of 34%, the TIT RFQ had to be redesigned.

In this paper we describe the modifications of vane-tip design as well as the cavity geometry, which are necessary to improve the beam dynamical performance. The beam transmission performance for the new design is presented. Recent results on a half-scaled model including development of tuning device are also reported.

## II. NEW SIMULATION CODE QLASSI

In computer code QLASSI, the equation of motion in the RFQ is expressed as

$$\frac{d^2 \mathbf{r}}{dt^2} = q \mathbf{E} / m = - (q/m) \nabla (U_{rfq} + U_{sc} + U_{ic}), \dots (1)$$

where  $U_{rfq}$ ,  $U_{sc}$  and  $U_{ic}$  are the external RFQ potential, the space charge potential and the image charge potential, respectively. In the calculation, eq.(1) is numerically integrated for each particle using fourth-order Runge-Kutta method. Harmonics up to the dodecapole moment are taken into account in  $U_{rfq}$ .  $U_{sc}$  is given by the sum of monopole Coulomb potential from all other particles.  $U_{ic}$  is determined by solving a 3D Dirichlet's boundary problem defined by the beam space charge and the metallic electrode surface.

Figure 1 shows axial transmission profile calculated using QLASSI for the old design. For the injection beam current of 10mA the transmission is only 34%, which is less than half of the one calculated using PARMTEQ.

## III. NEW DESIGN OF THE TIT RFQ

The TIT RFQ was redesigned since the predicted transmission was limited to 34%. In the new design the curvature radius of vane-tip was increased from  $0.75r_0$  to  $r_0$  in order to suppress the multipole components. Parameters of the new design are summarized in Table 1. In order to increase rf focusing effect  $r_0$  was decreased from 0.495cm to 0.466cm. The vane length becomes 20cm longer than that of the old design owing to the reduction of  $r_0$ . The total vane length is 422cm which corresponds to 273 cells including a radial matching section with 20 cells. Figure 2 shows axial transmission profile calculated using QLASSI for injection current of 10mA. The transmission is improved up to 60%.

The cavity geometry was determined using computer code SUPERFISH. Main rf parameters are summarized in Table 2. The operating frequency is 80MHz which is same as that of the old design. The cavity diameter was decreased from 76.6cm to 72.5cm in order to keep a resonant frequency to be 80MHz. The wall loss increased

Table 1  
Design Parameters of TIT RFQ

Charge-to-mass ratio	≥1/16
Operating frequency (MHz)	80
Input energy (keV/amu)	5
Output energy (keV/amu)	213
Normalized acceptance (cm·mrad)	0.05π
Vane length (cm)	422
Total number of cells	273
Characteristic bore radius, $r_0$ (cm)	0.466
Minimum bore radius (cm)	0.294
Margin of bore radius, $a_{min}/a_{beam}$	1.1
Maximum modulation, $m_{max}$	2.05
Focusing strength, $b$	3.4
Maximum defocusing strength, $\Delta_b$	-0.051
Synchronous phase, $\phi_s$ (deg.)	-90 → -20
Intervane voltage (kV)	79
Maximum field (Kilpat.)	2.2
Transmission (%)	(0mA input) 87 (10mA input) 60

Table 2  
Main rf parameters of TIT RFQ

Resonant frequency (MHz)	80
Calculated Q value	20000
Wall loss (at nominal intervane voltage, kW)	89
Shunt impedance (MΩ/m)	29.5
Calculated maximum field (Kilpat.)	2.2
Vane-tip radius (cm)	0.466
Cavity diameter (cm)	72.5
Cavity length (cm)	440

from 81kW to 89kW.

The structure of the TIT RFQ is illustrated in Figure 3. Each quadrant of the cavity has six plunger-type tuners, only one of which is movable because other five plungers are fixed after adjustment. End regions consist of inductive end cuts and a capacitive tuner like a pan (called an end cap hereafter). Since it is impossible to machine the 4m long vane with sufficient accuracy, three tanks with 1.4m long vanes are connected in series.

#### IV. COLD MODEL TEST

A cold model without vane modulation and a radial matching section was fabricated. The tank length and the tank diameter are 1.7m and 32cm respectively. Each quadrant has six plunger-type side tuners to obtain the quadrupole mode. Two kinds of capacitive tuners, plunger-

type end tuners and an end cap, were equipped on each end plate and dimensions of these tuners were tested.

Although alignment of four vanes was carried out using two end jigs and reamer pins, setting accuracy was too poor to observe the quadrupole mode. Re-alignment using a pin-gauge achieved the gap difference between vanes within 30μm along the whole vane length. The quadrupole mode could be excited after this re-alignment but the measured electric field strength of this mode was quite different in each quadrant.

The side tuners were adjusted in order to make the electric field strength equal in each quadrant. The electric field near the beam axis was measured with the bead-perturbation method. The resonant frequency of quadrupole mode is 192.0MHz and the frequency shift due to the bead-perturbation is shown in Figure 4. This result shows that the difference in electric field strength between each quadrant is within ±3%. It is possible to make the difference smaller by repeating the fine side tuner adjustment.

Flat electric field distribution along the beam axis is achieved by using the end caps illustrated in Figure 5. One end cap faces the side of four vanes and the capacity of end region becomes much higher than that of the plunger-type tuner, because the facing area is much larger.

The flatness  $F$  is defined as

$$F = \frac{\hat{E}_{end}}{E_{cent}}, \quad \dots(2)$$

where  $E_{cent}$  is the electric field strength at center and  $\hat{E}_{end}$  is the mean electric field strength of both ends, respectively. In Figure 4, the distance between end cap and vanes is 5.4mm and the flatness  $F$  is 0.97. If the end tuners were adopted, the gap between end tuner and vane would be only 1.5mm in order to obtain the same  $F$ . It is clear from this result that the end cap is preferable to avoid an electric discharge and concentration of wall loss in the end region.

#### V. SUMMARY

Since the transmission performance calculated using QCLASSI was very small, the TIT RFQ was redesigned. In the new design the curvature radius of vane-tip was determined to be  $r_0$  in order to suppress the multipole components. The characteristic bore radius  $r_0$  was decreased to 0.466cm in order to increase rf focusing effect. Due to these modifications, the beam transmission recovered to 60%.

The cavity dimensions were also redesigned to maintain the resonant frequency to be 80MHz. Owing to this change, the power dissipation increased by a factor of 10%.

A half-scaled cold model was fabricated without vane modulation and a radial matching section. In the cold

model experiments, the difference in electric field strength between each quadrant was minimized to  $\pm 3\%$  and the flatness of the field distribution along the beam axis was 0.97. In addition, useful results on the vane cutting method were acquired and applied to the design work of the actual cavity.

## VI. REFERENCE

- [1] O. Takeda et.al., "Design Study on an 80MHz RFQ Linac for Heavy Ion", Proc. European Particle Accelerator Conf., Berlin, March 1992, 1334-1336
- [2] Y. Oguri et.al., "Beam Tracking in an RFQ Linac with Small Vane-Tip Curvature", J. Nucl. Sci. And Tech., to be published

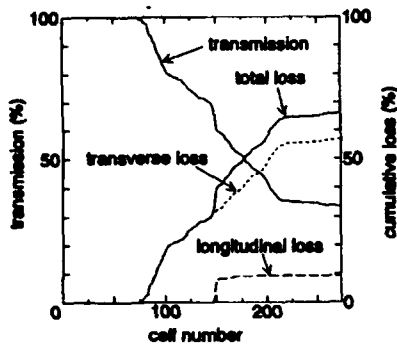


Figure 1 Axial beam transmission profile calculated using QLASSI for the old design (Injection current is 10mA)

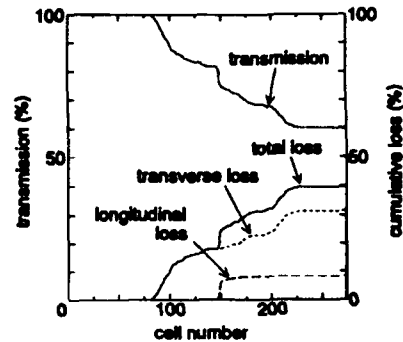


Figure 2 Axial beam transmission profile calculated using QLASSI for the new design (Injection current is 10mA)

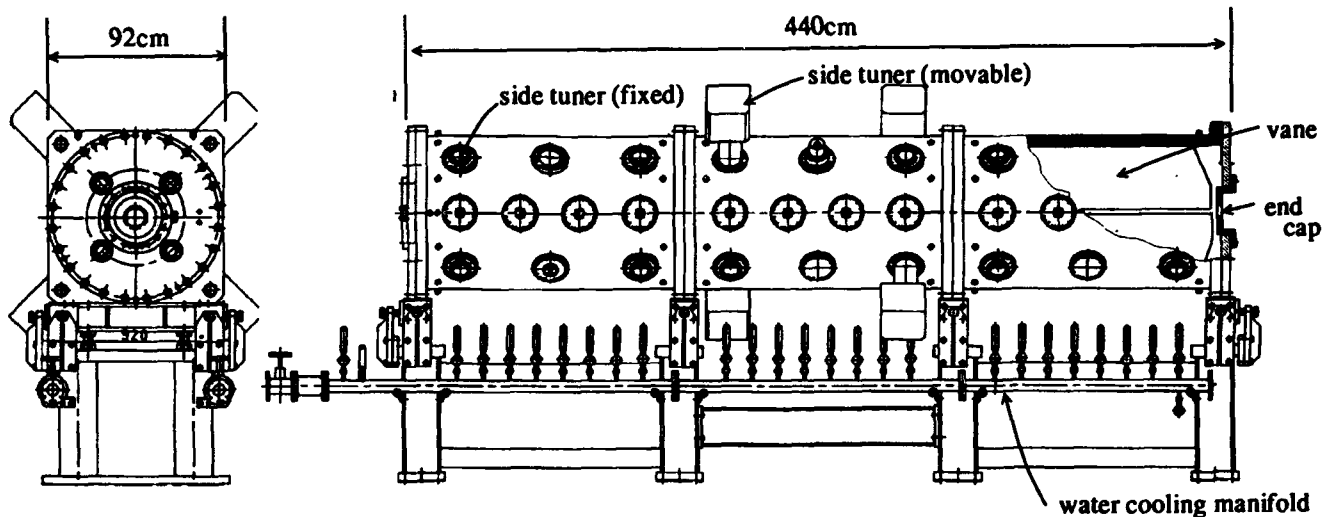


Figure 3 The TIT RFQ

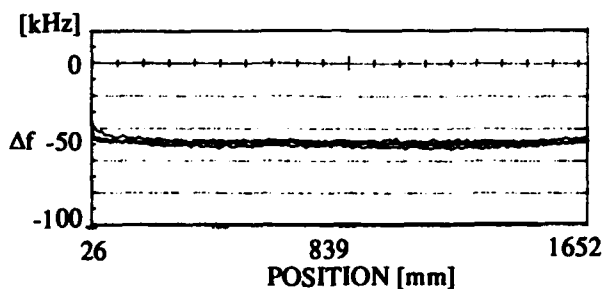


Figure 4 Frequency shift due to bead-perturbation

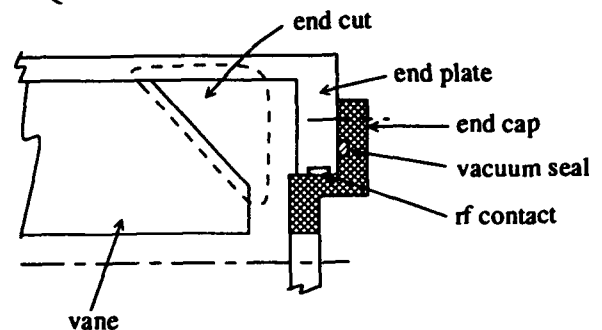


Figure 5 Schematic drawing of the end cap

# Operational Characteristics of a 100-mA, 2-MeV Radio-Frequency Quadrupole\*

K. F. Johnson, W. B. Cottingham, G. O. Bolme, C. M. Fortgang, W. Ingalls, J. Marquardt, D. P. Rusthoy, O. R. Sander, M. Smith, and G. T. Worth  
Los Alamos National Laboratory, MS H818  
Los Alamos, NM 87545 USA

## Abstract

A 100-mA, 2.07-MeV Radio-Frequency Quadrupole (RFQ III) has been commissioned and operated routinely on the Accelerator Test Stand (ATS) [1] at Los Alamos National Laboratory. To characterize the RFQ output beam dynamics, measurements were made of the beam transmission and of the transverse and longitudinal phase-space distributions. Data were taken for different RFQ III operating conditions and compared to simulations.

## I. INTRODUCTION

The ATS experimental program had the objective of comparing measured performance of an accelerating structure to predicted performance. The evaluation was made by comparing measured and predicted beam transmission, position and angle centroids, energy and phase centroids, and transverse and longitudinal phase-space distributions. RFQ III was the third RFQ in a series of RFQs [2,3] to be tested on the ATS. Pertinent RFQ III design parameters: frequency is 425 MHz, number of cells is 358, length is 289.23 cm, design vane potential is 111 kV, average radius is 0.4047 cm, final radius is 0.278 cm, final modulation is 1.83, initial synchronous phase is  $-90^\circ$ , final synchronous phase is  $-30^\circ$ , peak surface field is 32.7 MV/m, nominal current limit is 167 mA, and design acceptance at 100 mA is  $0.232 \pi$  cm-mradian. This paper presents the RFQ III commissioning results.

## II. EXPERIMENTAL TECHNIQUE

The  $H^-$  input beam to the RFQ was obtained from the ATS, 100-keV source and accelerating column [4]. A low-energy, beam-transport section (LEBT) followed the column. The LEBT consisted of four permanent magnet quadrupoles (PMQs) and two electromagnet horizontal and vertical steerers. The PMQs could be moved along the beam axis. Moving the PMQs varied the input match to the RFQ. The RFQ was operated at a low duty factor (0.025%).

The experimental objective was to fully characterize the output beam of the RFQ to allow for a detailed comparison to the simulation codes. To achieve this end, the output-beam current, beam transmission, and transverse and longitudinal phase-space distributions were measured for a variety of RFQ operating conditions.

Diagnostics for these measurements included broad-band toroids (current and transmission), a LEBT Faraday cup (current), an electric-sweep emittance scanner in the LEBT [5], two pairs of slit-collectors (transverse emittance), Laser

\*Work supported and funded by the US Department of Defense, Army Strategic Defense Command, under the auspices of the US Department of Energy.

Induced Neutralization Diagnostic Approach (LINDA) [6] (longitudinal emittance), a momentum spectrometer (momentum centroid and spread), and an x-ray detector [7] (RFQ rf field).

## III. EXPERIMENTAL RESULTS

The RFQ vane potential is the only adjustable variable of the RFQ. It affects the transverse and longitudinal focusing of the beam. The RFQ vane potential was determined from end point measurements of the x-ray energy spectrum generated by electrons accelerated across the vane gap [7]. The x-ray energy spectra were measured versus cavity rf power and used to calibrate rf pickup loops in the RFQ. The pickup loops were used to set the RFQ vane potential. The RFQ operating voltage range was 95 to 138 kV.

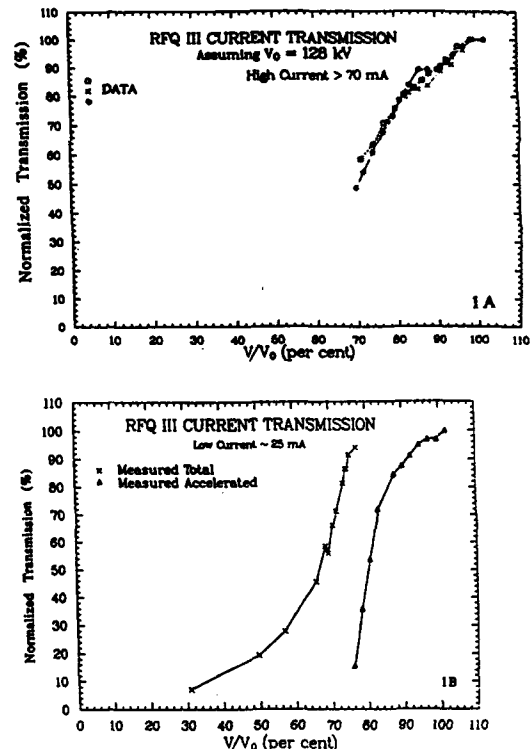


Figure 1. Normalized beam transmission versus normalized vane potential  $V$  for high- and low-beam currents.

The RFQ III beam transmission was measured versus the vane potential for various input beam currents. Figure 1A shows the total beam transmission for beam currents  $>70$  mA. Figure 1B shows the total and accelerated beam transmissions for currents  $\sim 25$  mA. At high currents, the plots have the same shape, regardless of input beam conditions. Although not shown, simulations show the same vane potential

dependence as the data. The magnitude of the measured high current transmission never exceeded ~85%, whereas simulations predict ~90% transmission. Typically the measured transmission was 65% to 70% due to a beam mismatch at the RFQ entrance. The transmission knee occurs at a vane potential of 128 kV rather than the design value of 111 kV.

The beam momentum was measured with a focusing spectrometer that consisted of two quadrupoles, primarily for vertical containment, and a horizontal 60° bending magnet with circular pole tips [3]. At the design vane potential the beam had the predicted energy of 2.07 MeV.

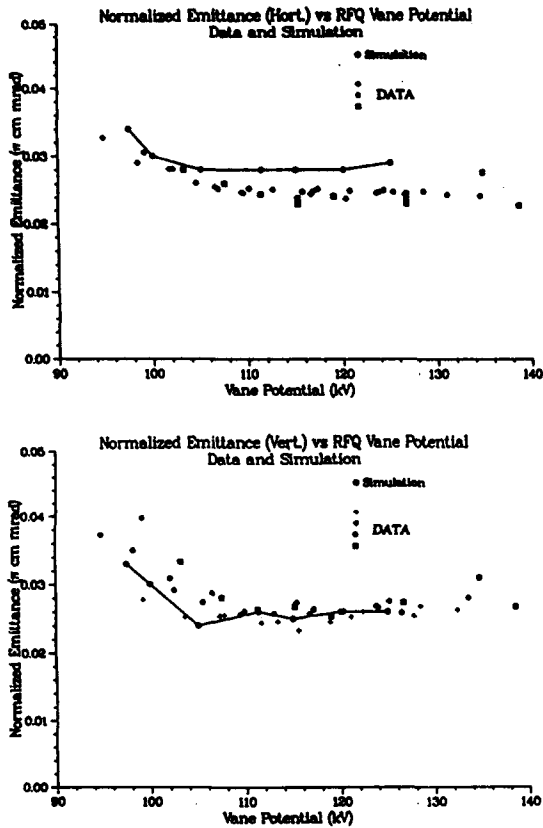


Figure 2. Measured and simulated transverse emittances versus normalized vane potential  $V$  for 78% of the beam.  $V_0$  equals 128 kV. Horizontal and vertical data are shown.

The output RFQ transverse phase-space distribution was measured versus vane potential. The phase-space distributions (horizontal and vertical) were measured with a standard slit and collector technique [8]. The rms normalized emittances were measured for the vertical and horizontal planes. The RFQ input beam was matched in all cases. Figure 2 shows data and simulations. The data sets correspond to measurements made on different days. The scatter in the data gives the typical day-to-day reproducibility of the beam. The measurement error was 5 to 8% with background subtraction being the dominant component. The agreement between data and simulations was better in the vertical plane than in the horizontal. In both planes, the emittance flattens off at ~110 kV which is consistent with the design value of 111 kV but inconsistent with beam transmission results.

The measured Courant-Snyder (CS) parameters were compared to simulations. The data are shown in Fig. 3. The

data sets correspond to measurements from different days. There was qualitative agreement between data and simulations as the vane potential was varied. For RFQ II the agreement was good [1]. The discrepancy for RFQ III probably is due to differences between the as-built and as-designed RFQ, which have not been incorporated into the simulations. A determination of these discrepancies will require off-line checks of RFQ III at a future date.

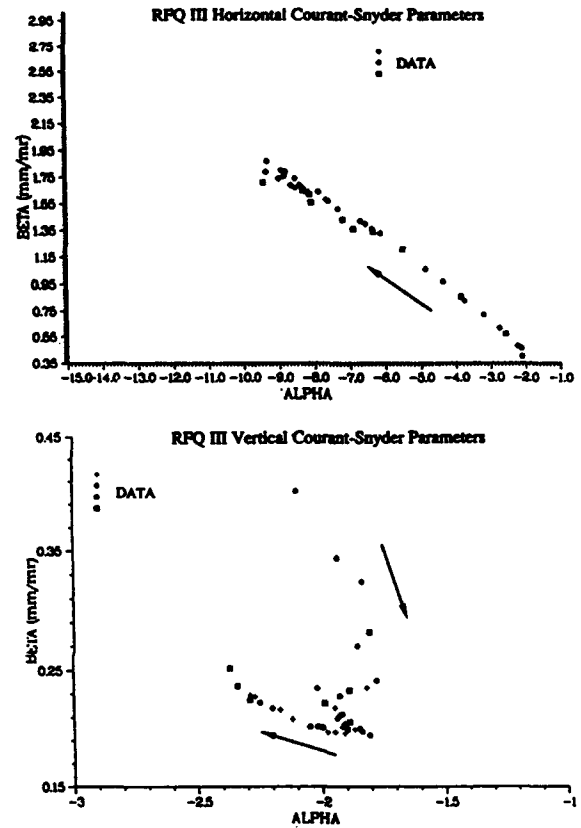


Figure 3. Horizontal and vertical CS parameters versus RFQ III vane potential for 78% of the beam. The arrows indicate the direction of increasing vane potential.

Figure 4 shows the vertical phase-space distributions for data and simulations. The parallelogram shapes at lower vane potentials are due to off-energy particles.

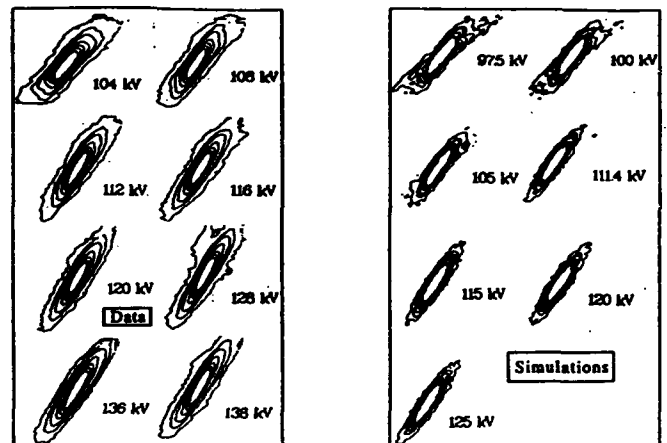


Figure 4. The vertical phase-space distributions for data and simulations for different vane potentials.

The RFQ output transverse phase-space distribution was measured versus the match of the input beam. For large variations in the input mismatch factor [9] (i.e., in the shape of the input beam), the output CS parameters and emittance remained nearly constant; agreeing with simulations. The beam transmission varied with the input match resulting in decreased beam brightness for large mismatches.

Longitudinal phase-space distributions were measured using the LINDA technique [6]. The measured and simulated distributions appear similar (Fig. 5), but the measured emittance is ~60% of the simulated emittance (Fig. 6). The difference is many times the uncertainty in the data which is estimated to be ~5%. This difference between the data and simulations is not understood, but a likely explanation is the difference between the as-built and as-designed RFQ. For the GTA RFQ, there was good agreement with data and simulations [10] giving confidence in the measurement technique and simulations codes. For power levels  $\leq 120$  kV the longitudinal phase-space distributions begin to change from elliptical to crescent-shaped (Fig. 5). The change is caused by off-energy particles. These data indicate that RFQ III should be operated at 128 kV rather than the design value of 111 kV.

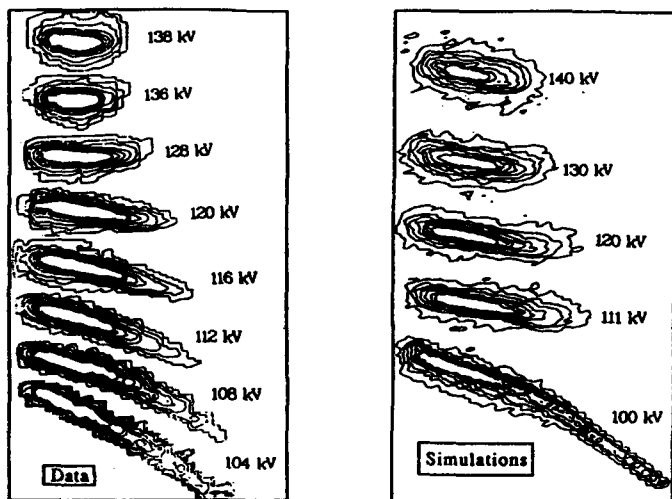


Figure 5. Measured and simulated longitudinal phase-space distributions versus vane potential.

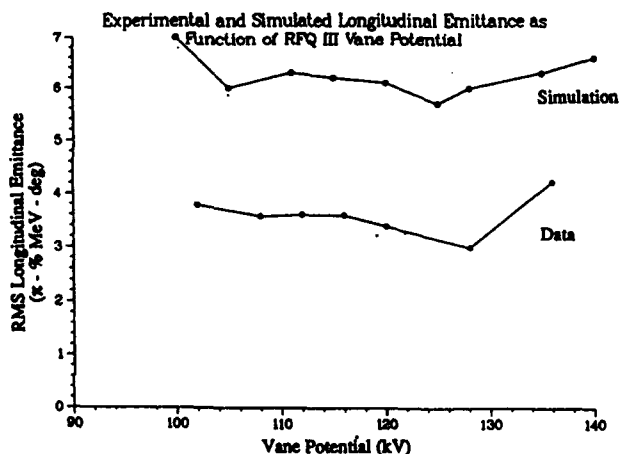


Figure 6. The rms longitudinal emittance for data and simulation versus vane potential.

## IV. SUMMARY AND CONCLUSIONS

RFQ III was successfully commissioned and operated routinely and reliably. The RFQ performance was largely as expected. The longitudinal-emittance discrepancy between data and simulations is not understood but appears to be real.

## IV. ACKNOWLEDGMENTS

The commissioning of the ATS RFQ would not have been possible without R. D. Patton and the ATS rf team; S. D. Orbesen and the ATS injector personnel; M. L. Milder and the ATS facility support team; and the LINDA personnel.

## VI. REFERENCES

- [1] O. R. Sander, et al., "Review of the Accelerator Test Stand Performance and Expectations," Los Alamos National Laboratory report LA-CP-89-489 (July 1989).
- [2] F. O. Purser, et al., "Operating Characteristics of a 2.0-MeV RFQ," Proc. 1983 Particle Accel. Conf., IEEE Trans. Nucl. Sci. 30, No. 4, (1983), p. 3582.
- [3] O. R. Sander, et al., "Operational Parameters of a 2.0-MeV RFQ LINAC," Proc. 1984 Linear Accelerator Conf., Gesellschaft für Schwerionenforschung report GSI-84-11, May 1984, p. 54.
- [4] P. W. Allison and J. D. Sherman, "Operation Experience with a 100-keV, 100 mA H<sup>-</sup> Injector," Proc. Production and Neutralization of Negative Ions and Beams, edited by Krsto Prelec, (AIP Conf. Proc. No. 111, 1984), p. 511.
- [5] P. W. Allison, et al., "An Emittance Scanner for Intense Low Energy Ion Beams," Proc. 1983 Particle Accel. Conf., IEEE Trans. Nucl. Sci. 30, No. 4, (1983), p. 2204.
- [6] V. W. Yuan et al., "Measurement of Longitudinal Phase Space in an Accelerated H<sup>-</sup> Beam Using a Laser-Induced Neutralization Method," Nucl. Instr. and Meth., A329 (1993) 381.
- [7] G. O. Bolme et al., "Measurement of RF Accelerator Cavity Field Levels at High Power from the Characteristic X-ray Emissions," Proc. 1990 Linear Accelerator Conf., Los Alamos National Laboratory report LA-12004-C, March 1991, p. 219.
- [8] O. R. Sander, "Transverse Emittance: Its Definition, Applications, and Measurement," Proc. Accelerator Instrumentation, edited by E. R. Beadle and V. J. Castillo, (AIP Conf. Proc. No. 212, 1989), p. 127.
- [9] J. Guyard and M. Weiss, "Use of Beam Emittance Measurements in Matching Problems," Proc. 1976 Linear Accel. Conf., Atomic Energy of Canada, AECL-5677 (1976), p. 254.
- [10] K. F. Johnson et al., "Commissioning of the Ground Test Accelerator RFQ," 1992 Linear Accel. Conf. Proc., AECL Research, Chalk River Laboratories Report, AECL-10728 (1992), p. 64.

# Analysis of the End Regions of the CERN Lead-Ion 4-rod RFQ

V.A. Andreev

ITEP, Bolshaja Chermomushkinskaja 25, 117259 Moscow, Russia

A. Lombardi, G. Parisi

INFN, Laboratori Nazionali di Legnaro, via Romea 4, I-35020 Legnaro (PD), Italy

M. Vretenar

CERN, PS Division, CH-1211 Geneva 23, Switzerland

## Abstract

A 4-rod-like Radio Frequency Quadrupole for the new CERN lead-ion injector will be built at the Laboratori Nazionali di Legnaro, Italy [1].

By means of 3D simulations with MAFIA codes [2] and measurements on a cold model, an asymmetry was found in the gap between the end plate and electrodes, yielding a non-zero longitudinal component  $E_z$  on the axis of the RFQ and therefore a potential barrier in the gap.

In this paper an explanation is given for this fact and possible solutions are proposed for end cell tuning, which allow to eliminate the undesirable  $E_z$  component and also to obtain good inter-electrode voltage distribution along the structure. Results of MAFIA calculations and cold model measurements are shown.

## 1 INTRODUCTION

We considered the structure shown in Fig. 1, representing a part (4 supports instead of 14) of the Lead-Ion RFQ as modelled by MAFIA codes; the end plates are not shown for the sake of clearness. It is a 4-rod structure, similar to the ones developed in Frankfurt [3] but having double symmetric supports and "vane-like" shaped rods.

By means of the MAFIA codes, it was found that the voltages at the end of the electrodes are not balanced with respect to the external tank; actually, at their end, one pair is near the full potential  $V_e$ , oscillating at RF, while the other pair remains near the ground potential.

This doesn't affect the quadrupolar symmetry inside the accelerating channel, but determines on the axis a potential difference  $V_e/2$  between the end of the electrodes and the end plates. As a consequence, a longitudinal component  $E_z$  of the electric field arises, and such region behaves like a RF gap that may accelerate the particles passing through it.

## 2 ANALYSIS OF THE PHENOMENON

We evaluated the  $\vec{B}$  field distribution for the above structure. In Fig. 2 the longitudinal section at the vertical symmetry plane is shown; Fig. 3 displays two transverse sections: through a support and in the center of a cell.

We can see that middle cells are filled with magnetic field, whose lines are closing around the supports and the electrodes, while there is almost no field in the end cells. This absence, confirmed by measurements on cold models, is not peculiar of our "double support" structure, although

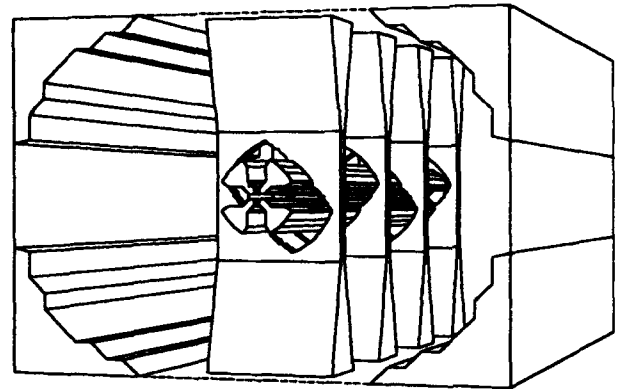


Fig. 1: MAFIA plot of the CERN Lead-Ion 4-rod RFQ

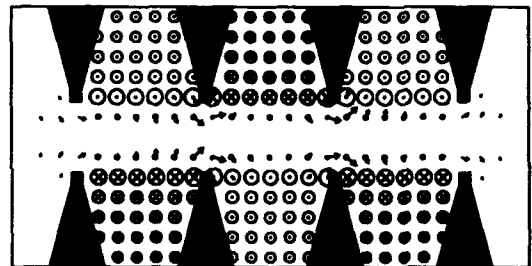


Fig. 2: MAFIA plot of  $\vec{B}$  field (longitudinal section)

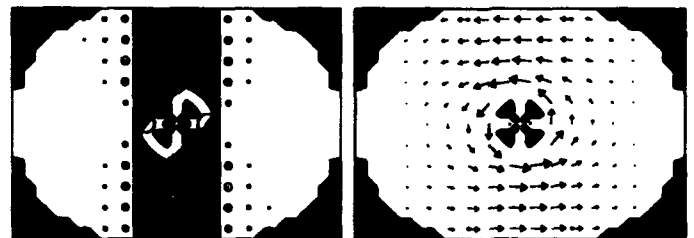


Fig. 3: MAFIA plots of  $\vec{B}$  field (transverse sections)

it depends on the geometry used and in our case happens to be more evident than in other RFQ's.

In order to understand this phenomenon, we investigate the behaviour of our RFQ by considering the electrical properties of a chain of five coupled oscillators: from the RF point of view, it consists of coupled resonant cells, all equal to each other except the ending ones, that have half length and are terminated with a metallic plate, separated by a gap from the end of the electrodes.

When the middle cell is excited (by a feeder loop) it resonates at a certain  $\omega_0 = 1/\sqrt{L_0 C_0}$ , where  $L_0$  and  $C_0$  are its equivalent inductance and capacitance. The adjacent cells have the same  $L_0$  and  $C_0$  and are strongly coupled, while

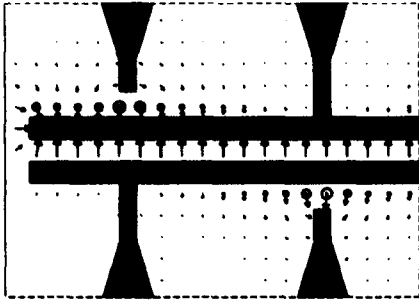


Fig. 4: MAFIA plot of  $\vec{E}$  field (detail)

the end cells have half the inductance ( $L_{end}$ ) and a lower capacitance ( $C_{end}$  is half of  $C_0$  plus the small capacitance between the end plate and electrodes). Their resonant frequency is therefore much higher and the consequence is that there is no  $\vec{B}$  field (or just a small one) and no induced currents (or small ones) in the ending regions, due to the absence of a time-varying magnetic flux.

Another complementary effect is that the inter-electrode voltage  $V_e$  drops in the middle of the structure (see Fig. 9-left), also due to the difference in the end cells behaviour.

In Fig. 4 it is shown a detail of  $\vec{E}$  field in a longitudinal section through a pair of electrodes; we can see that the potential symmetry condition ( $+V_e/2$  on one pair of electrodes and  $-V_e/2$  on the other one, relatively to the end plate) is not fulfilled at the end of the electrodes.

This is also illustrated by Fig. 7-left, where a detail of  $\vec{E}$  field in the gap is shown (in a transverse section near end plate): on the axis, MAFIA codes evaluated a longitudinal component  $E_x$  which integrated along the gap leads to a voltage  $V_e/2$ .

To explain this phenomenon, let us consider the simplified equivalent lumped circuit of an end cell shown in Fig. 5-left, where four rods are presented, for simplicity, as a two-wire line. As seen before, there are almost no  $\vec{B}$  field nor currents in the ending regions, so that we can evaluate potentials  $V_{A0}$  and  $V_{B0}$  of the points A and B with respect to point 0 (ground) as:

$$V_{A0} \approx V_{AC'} + V_{C'C} + V_{C0} \approx 0 \quad (1)$$

$$V_{B0} \approx V_{BC''} + V_e + V_{C''C} + V_{C0} \approx V_e \quad (2)$$

While beam dynamics calculations were carried on in order to analyse the effect of this asymmetry on the heavy ion beam [4], we concentrated on finding an end cell configuration achieving the condition:

$$V_{A0} = -\frac{1}{2}V_e \quad V_{B0} = +\frac{1}{2}V_e \quad (3)$$

To reach such goal on our RFQ, different versions of end cell tuning were simulated using MAFIA codes and the best one was then tested on a cold model.

### 3 POSSIBLE SOLUTIONS

In order to cope with the above effects, which are due to the difference between middle and end cells, we need to

tune the latter, so to have there a proper electromagnetic field. Thus, the  $E_x$  component arising in the gap between end plate and electrodes disappears.

Our approach follows from the one proposed by Pirkel [5], attempting to include the equivalent terminating reactance elements at the end of the electrodes relatively to end plate. We analyse his proposal from the point of view of end cells tuning, i.e. of electromagnetic fields in the end cells.

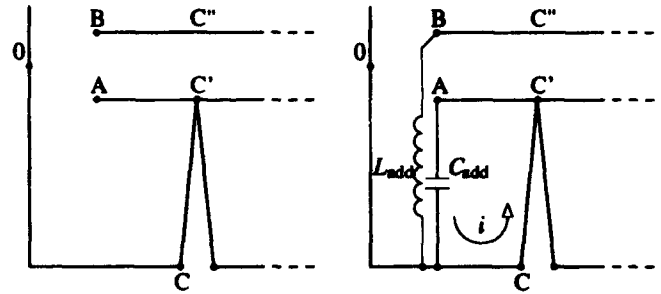


Fig. 5: Equivalent lumped circuits

As a first attempt, we can try to connect "hot" ends of electrodes (B) to the external tank by means of conductive strips, i.e. we add an inductance  $L_{add}$  (Fig. 5-right). The choice of  $L_{add}$  is limited by two conditions:

- To reach a balance between the cells, the resonant frequency of the end cell should be equal to the middle cell one:

$$(L_{end} + L_{add})C_{end} = \omega_0^{-2} \quad (4)$$

As in our case the end cell length is half of the middle one, for symmetry reasons we have  $L_{end} = \frac{1}{2}L_0$  and  $C_{end} = \frac{1}{2}C_0$ ; thus, to fulfill (4), it must be:

$$L_{add} = \frac{3}{2}L_0 \quad (5)$$

- In order to fulfill (3), the voltage drop on  $L_{add}$  should be equal (in module) to the one on  $L_{end}$ . As the same current passes through both inductances, it means:

$$L_{add} = L_{end} = \frac{1}{2}L_0 \quad (6)$$

It is not possible to satisfy both conditions (3) and (4) changing only the inductance of the last cell, in fact we obtained (5) and (6) which are incompatible. Therefore one has to act simultaneously on both inductance and capacitance, adding  $L_{add}$  at the "hot" electrodes and  $C_{add}$  at the "cold" ones. Inductance can be further increased by changing the shape of the last support; capacitance by a vane-connecting ring or adding some plates between the end of the "cold" electrodes (A) and the end plate, i.e. a capacitance  $C_{add}$ .

By MAFIA simulations, many different combinations of strips, plates and rings were tested on the cold model geometry. Modifying their dimension and position, each version allowed to obtain a good longitudinal  $V_e$  distribution (flatness within  $\pm 1\%$ ) and to reduce 4 ÷ 15 times the

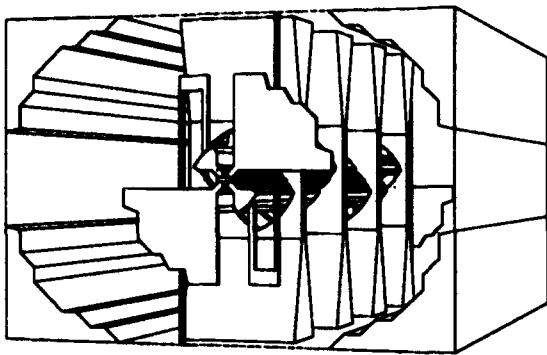


Fig. 6: MAFIA plot of a possible solution

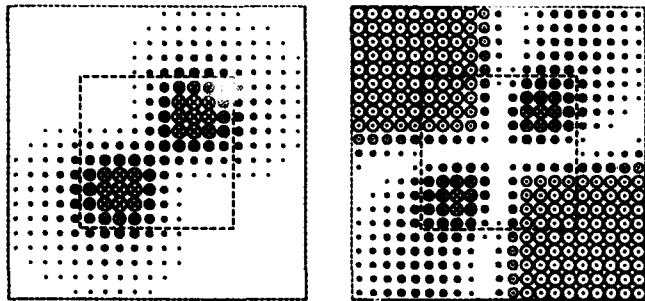


Fig. 7: MAFIA plot of  $\vec{E}$  field in the gap (detail)

$E_z$  component in the gap. In principle, there are no limitations to reach an ideal tuning.

The solution shown in Fig. 6 (two strips and two plates) gave quite good results: Fig. 7 shows  $\vec{E}$  field in a transverse section near end plate for the initial configuration (left) and for the modified geometry (right); notice  $E_x = 0$  on the axis. The smaller squares define the "interesting" region for beam dynamics.

#### 4 MEASUREMENTS

To check proof of principle we used the geometry of Fig. 6, but it should be noted that in practice it is necessary to change the shape of the last stems, in order to increase  $L_{add}$ ; in fact, as the end plate is very close to the electrodes, it is not easy to reach a high value of  $L_{add}$  with a reasonable shape. Besides, large plates should be avoided.

The electric field between end plate and each electrode was measured on a cold model, using a perturbing bead; Fig. 8 shows normalised  $|E_x|$  field measured on the model in its initial configuration (left) and after the tuning (right); here #1 and #3 are the "hot" electrodes. These results confirm the situation described by MAFIA.

Bead-pull measurements of the inter-electrode voltage all along the structure were performed on the cold model, using an automatic computer-controlled system [6]. The results before and after tuning are shown in Fig. 9; a comparison with MAFIA simulations (continuous lines) emphasizes a quite good agreement, the small discrepancy being due to the slightly different position of the bead during measurements with respect to the path used in simulation, and to mechanical misalignments of the electrodes.

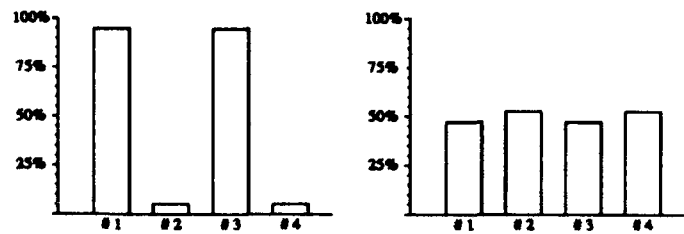


Fig. 8: Normalised  $|\vec{E}|$  field in the gap

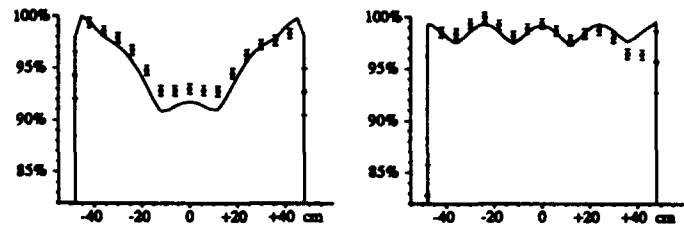


Fig. 9: Inter-electrode voltage distribution  $V(z)/V_e$

#### 5 CONCLUSIONS

The main result of this study is that both a good voltage symmetry in the region between end plate and electrodes and a good longitudinal inter-electrode voltage distribution can be reached by proper tuning of the end cells.

A more detailed analysis of the phenomenon is still needed to find a shape that could be used in practice, under working conditions (high power and vacuum problems): the aim of this paper is just to give hints of possible solutions and proof of principle of the adopted methodology.

#### 6 ACKNOWLEDGMENTS

The authors are very grateful to W. Pirkl and M. Weiss for their essential help in understanding the phenomenon, and to A.M. Porcellato for her assistance.

#### 7 REFERENCES

- [1] A. Lombardi, G. Parisi, M. Vretenar, "Comparison Study of RFQ Structures for the Lead-Ion Linac at CERN", Proc. 1992 European Particle Acc. Conf., Berlin, Germany, March 1992, pp. 557-59.
- [2] R. Klatt et al., "MAFIA - A Three-dimensional Electromagnetic CAD System for Magnets, RF Structures and Transient Wake-field Calculations", Proc. 1986 Linear Acc. Conf., Stanford, California, June 1986, pp. 276-78.
- [3] A. Schempp, H. Deitinghoff, M. Ferch, P. Junior, H. Klein, "Four-Rod- $\lambda/2$ -RFQ for Light Ion Acceleration", Nucl. Instr. and Meth. in Phys. Res., B10/11, 1985, pp. 831-34.
- [4] M. Comunian, A. Pisent, "Longitudinal Dynamics at the Input of a Four-Rods RFQ", LNL-INFN Internal Note (REP) 61/92, April 1992.
- [5] W. Pirkl, "Balancing the End Cell of a 4-Rod RFQ", CERN-PS Informal Note, March 1992.
- [6] A. Porcellato, A. Battistella, S. Marigo, "Automation of the Cavity Parameter Measurements", Proc. 1990 European Particle Acc. Conf., Nice, France, June 1990, pp. 1109-11.

# 90°-apart-stem RFQ Structure for Wide Range of Frequencies

V.A. Andreev

ITEP, Bolshaja Chermomushkinskaja 25, 117259 Moscow, Russia

G. Parisi

INFN, Laboratori Nazionali di Legnaro, via Romea 4, I-35020 Legnaro (PD), Italy

## Abstract

At present, many different resonant RFQ structures for accelerating both light and heavy ions are successfully used. Usually they are divided into two well known groups: 4-vane and 4-rod structures, each of them having its merits and drawbacks. In this paper a new resonant structure is considered, which combines the advantages of both. It may be seen as a 4-vane structure with holes ("windows") in the vanes, or as a 4-rod one having stems located 90° apart from each other and from the beam direction. Thus, changing the window size, such a structure can be modified from a typical 4-rod resonator, working at 50 MHz or less, to a typical 4-vane one, working at higher frequencies (up to 500 MHz) and having a better frequency distinction between operating and unwanted dipole modes, due to the magnetic coupling between neighbouring quadrants through the holes. It also should be noted that no voltage arises on the beam axis in the gap between end plate and electrodes, provided that horizontal and vertical windows have the same longitudinal position. Computer simulations with MAFIA codes are presented and compared with cold model measurements.

## 1 INTRODUCTION

The well known idea of "spatially uniform strong focusing", proposed by Kapchinsky and Teplyakov [1], is very widely used for accelerating both light and heavy ions.

A suitable arrangement of accelerating and focusing fields can be provided by different RFQ resonant structures, usually distinguished between resonant cavities (as 4-vane, Double-H and Split-Coaxial) and resonant LC-structures (as 4-rod, Spiral and Split-Ring) [2].

A new version of 90°-apart-stem RFQ structure, henceforth called "4-ladder", which combines the merits of 4-vane and 4-rod RFQ's, has been developed in the framework of a collaboration between ITEP and INFN-LNL in contact with the CERN design group of the "Lead Ion Linac Facility".

During 1992, a full scale cold model of a 100 MHz structure was built in ITEP (Fig. 1) and MAFIA simulations were carried out at LNL. Both simulations and measurements showed a reliable mode separation without any Vane Coupling Rings (VCR) and with a good RF efficiency.

## 2 4-VANE, 4-ROD AND 4-LADDER RFQ

The main parameters taken into account, for a proper design of an RFQ structure and its outer resonator, are:



Fig. 1: Full scale 100 MHz cold model built at ITEP

- RF power losses (to be minimized);
- mode separation (to be maximized);
- end region effects (properly controlled);
- dimensions (feasibility);
- mechanical features (feasibility).

To reduce RF power losses, it is necessary to choose structures with a high shunt-impedance  $Z_{sh}$ , defined as  $V_e^2/P$  where  $V_e$  is the inter-electrode voltage and  $P$  is the dissipated power. In general, the 4-vane RFQ has an higher  $Z_{sh}$  with respect to the 4-rod one: in fact the whole inner tank surface is a part of the resonant system and this allows to decrease the current density and hence to reduce power losses. The same happens for our 4-ladder structure: from the point of view of RF efficiency, it should be just a little worse than a 4-vane.

The need for a negligible emittance growth requires a very stable RF field distribution inside the structure; it means first of all a good separation of the operating quadrupole mode from the dipole ones. It's known that a 4-rod RFQ (particularly a "double support" one) has absolute freedom from undesired dipole components, due to the coupling effect of the frames, so  $f_{dip}$  is quite higher than  $f_{quad}$  (even double). On the contrary, in a 4-vane RFQ the difference is only of a few percent (with  $f_{dip} < f_{quad}$ ) and VCR or other coupling mechanism have often to be used to reject undesired dipole modes; furthermore, there are some problems with mode separation in long resonators ( $L > 2\lambda$ ). In the 4-ladder structure this separation is expected to be rather larger than in the 4-vane resonator, due to the strong magnetic coupling between neighbouring quadrants through the windows.

A correct end regions tuning is needed in order to guarantee a flat inter-electrode voltage distribution along the structure. Moreover, a recent investigation [3] showed that some types of 4-rod RFQ's have a longitudinal  $E_z$  component of the electric field on the axis in the region between end plate and electrodes; this effect is in principle negative as it perturbs the matching of the beam, nevertheless it can be controlled and even used to provide a velocity modulation of the particle beam in order to reduce the emittance growth in the accelerating channel [4]. From the point of view of end region effects, our 4-ladder structure is close to the 4-vane one, because the tuning may be obtained by changing the size of the last window; nevertheless we expect to have an  $E_z$  component, because of the shift between vertical and horizontal windows (i.e. of the shift of the points exciting the accelerating channel). This effect depends on the ratio between the distance of these points and the wavelength  $\lambda$  and we found that it is easily eliminated if we install the windows in the same longitudinal position.

The dimension of a 4-vane structure is larger in comparison with a 4-rod resonator, and it becomes impractically large at frequencies lower than 100 MHz. The 4-ladder structure is smaller in comparison with the 4-vane one and a little larger than the 4-rod one.

From the point of view of mechanical stability, rigidity and simplicity, the 4-vane resonator is more attractive, combining a very high accuracy in manufacture and alignment. The 4-rod structure, though being quite simple in manufacture, has many joints (by means of welding, brazing or bolt connections) between supports and electrodes. From this point of view, the 4-ladder structure is similar to a 4-vane, because it has no joints between electrodes and stems, thus keeping the same rigidity and accuracy of manufacture.

It should be noticed that a  $90^\circ$  arrangement had been used earlier in the low energy  $\beta\lambda/2$  RFQ at Frankfurt, where two orthogonally placed stems with a connecting strip are a typical inductance (having in contrast to the "90°-apart-stem" structure practically no coupling with the tank) and in the Split-Coaxial Resonator, where stems are elements of joint that connect separated fingers to suitable RF potential points of the resonator [5]. Besides, during the comparison study of RFQ structures for the Lead-Ion Linac at CERN [6], a version of "90°-apart-stem" structure had been considered, having cylindrical stems located  $90^\circ$  apart from each other and from the axis, which connect opposite electrodes by means of frames.

### 3 NUMERICAL SIMULATIONS

Using the MAFIA codes [7], the structure shown in Fig. 2 has been studied with respect to all the previous features.

First of all it was optimized from the point of view of RF efficiency: the tank diameter was not changed, but both the size of the windows and their position were adjusted (keeping the same distance between their centers);

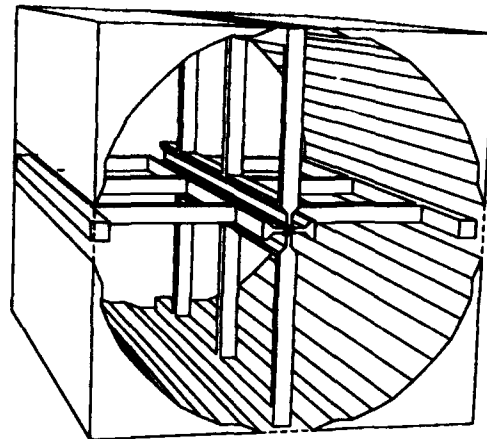


Fig. 2: MAFIA plot of the 100 MHz 4-ladder RFQ

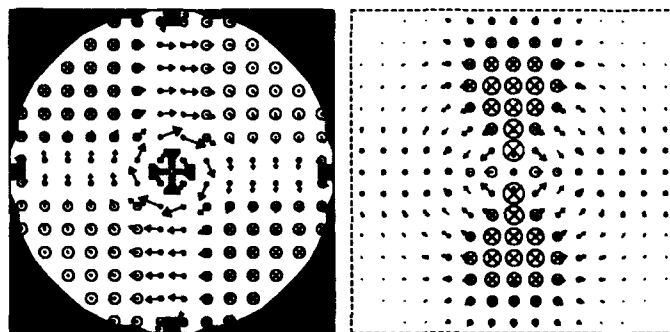


Fig. 3: MAFIA plot of  $\vec{B}$  field through the windows (left) and detail of  $\vec{E}$  field in the end region (right)

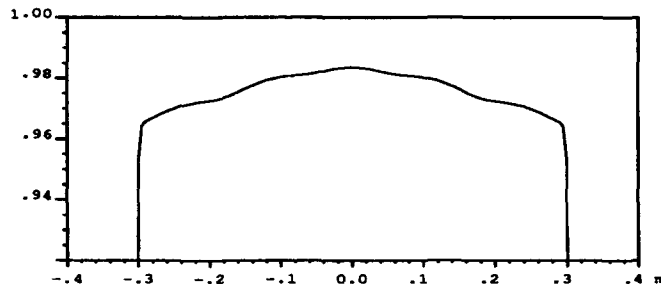


Fig. 4: MAFIA plot of normalized  $V_e(z)$

actually three versions of the structure were tested. In the best case, the specific shunt-impedance  $R_{sh} = 340 \text{ k}\Omega\cdot\text{m}$  was achieved, with  $Q = 1.5 \times 10^4$  (full copper structure).

As foreseen, the dipole modes were found more than 20 MHz higher than the quadrupole one; this separation is enough to guarantee their suppression. A plot of the harmonic magnetic flux density is presented in Fig. 3-left; notice the  $\vec{B}$  lines coupling a quadrant to another.

An electric field  $E_z$  was found on the axis, in the gap between end plate and electrodes, as shown in Fig. 3-right; on the other hand, simulations confirmed that it can be eliminated by moving the horizontal and vertical windows to the same longitudinal position. The inter-electrode voltage distribution  $V_e(z)$  is shown in Fig. 4; the small drop on the ends ( $\sim 2\%$ ) disappears with a proper tuning of the end regions.

In Tab. 1 the results from simulations are presented (copper tank and aluminium electrodes).

width×height (m)	$f_{\text{quad}}$ (MHz)	$f_{\text{dip}}$ (MHz)	Q-value ( $10^3$ )	$R_{\text{sh}}$ ( $k\Omega \cdot m$ )
0.17×0.13	119.91	139.79	10.9	202
0.20×0.135	110.21	132.74	11.6	235
0.22×0.17	99.93	124.90	12.7	291

Tab. 1: Computed parameters in function of window size

This work is presently continuing for another structure, working around 400 MHz; first results show the possibility to tune end regions.

#### 4 MEASUREMENTS ON COLD MODELS

In order to determine the accuracy of calculations, measurements were performed on the cold model shown in Fig. 1, (without modulation of the electrodes) using all the three simulated versions. The dimensions of that structure are:

- Inner tank diameter - 0.44 m
- Length of the structure - 0.64 m
- Length of the electrodes - 0.60 m
- Aperture radius - 0.003 m
- Curvature radius of electrode tip - 0.003 m
- Gap between end plates and electrodes - 0.02 m
- Distance between the centers of the windows - 0.24 m
- Material of the electrodes - aluminium
- Material of the tank (and end plates) - copper

Copper strips were used to connect the vanes to the tank by means of screws.

The electric field distribution between each pair of electrodes has been measured with the "bead-pull" technique. The measurement results are just coinciding with the simulation ones.

A small discrepancy ( $\sim 3\%$ ) was observed concerning the calculation of frequencies: the measured ones are a little bit lower than the computed ones, mainly because the MAFIA approximation of the electrode tip was rather rough. Notice the split of the dipole mode into two distinct modes, due to mechanical asymmetries.

The measured Q-values are within  $2.7 \div 3.9 \times 10^3$ ; this poor result is due to bad contacts. The same applies for specific shunt impedance.

In Tab. 2 the measurements results are presented.

#### 5 CONCLUSIONS

The investigation of the 4-ladder structure, as one of the possible versions of the  $90^\circ$ -apart-stem RFQ, showed that it can be used in accelerator technique: it has good RF efficiency (quite reliable mode separation and field distribution) and maintains such merits of a 4-vane structure as simplicity of manufacture and mechanical stability.

width×height (m)	$f_{\text{quad}}$ (MHz)	$f_{\text{dip}}$ (MHz)	Q-value ( $10^3$ )	$R_{\text{sh}}$ ( $k\Omega \cdot m$ )
0.17×0.13	116.03	135.0 135.8	3.9	76
0.20×0.135	106.60	128.5 128.9	3.3	70
0.22×0.17	97.06	124.0 124.3	2.7	63

Tab. 2: Measured parameters in function of window size

The idea of an orthogonal arrangement allows to design structures for wide range of frequencies; indeed, for low frequency RFQ, one can use spirals instead of stems. The stems can be connected directly to the electrodes without any frames, or by means of frames. In the first case, there is no limitation to install neighbouring orthogonal stems (in our case windows) at the same longitudinal position and hence to eliminate completely the  $E_z$  component on the axis in the end regions.

It should also be noted that MAFIA codes are a very good instrument of investigation for resonant structures, allowing to get reliable information about all the parameters of interest.

#### 6 ACKNOWLEDGEMENTS

The authors are grateful to A. Lombardi for very useful discussions, and to V.N. Sidorenko and K.V. Vosnecensky for their help in cold model design and measurements.

#### 7 REFERENCES

- [1] I.M. Kapchinsky, V.A. Tepliakov, "Linear Ion Accelerator with Spatially Homogeneous Strong Focusing", translated from *Pribory i Tekhnika Eksperimenta* N. 2, pp. 19-22, March-April 1970.
- [2] H. Klein, "Development of the Different RFQ Accelerating Structures and Operation Experience", Proc. 1983 Particle Acc. Conf., Santa Fe, NM, March 1983, IEEE Trans. Nucl. Sci., vol. ns-30, no.4, pt.2, pp. 3313-22 (August 1983).
- [3] V.A. Andreev, A. Lombardi, G. Parisi, M. Vretenar, "Analysis of the End Regions of the CERN Lead-Ion 4-rod RFQ", these proceedings.
- [4] A.I. Balabin, V.S. Kabanov, G.N. Kropachev, D.G. Skachkov, "On the Possibility of Reduction of Beam Emittance Growth in RFQ Linac", Preprint ITEP 57-91, Moscow, Russia, 1991.
- [5] R.W. Muller, "MAXILAC - A High-current Linear Accelerator for Heavy Ions at Low Charge States", GSI-90-25 Report, October 1990, ISSN 0171-4546.
- [6] A. Lombardi, G. Parisi, M. Vretenar, "Comparison Study of RFQ Structures for the Lead-Ion Linac at CERN", Proc. 1992 European Particle Acc. Conf., Berlin, Germany, March 1992, pp. 557-559.
- [7] R. Klatt et al., "MAFIA - A Three-dimensional Electromagnetic CAD System for Magnets, RF Structures and Transient Wake-field Calculations", Proc. 1986 Linear Acc. Conf., Stanford, California, June 1986, pp. 276-278.

# The SSCL RFQ System Integration<sup>1</sup>

G. Arbique, A. Calo, C. Cuevas, P. Datte, D. Evans, J. Hurd, E. Marsden, K. Saadatmand and J. Sage  
Superconducting Super Collider Laboratory  
2250 Beckleymeade Avenue, Dallas, TX 75237-3997 USA

## Abstract

The integration and performance of subsystems on the Superconducting Super Collider Laboratory (SSCL) 428 MHz, 0.1% duty factor radiofrequency quadrupole accelerator is reported. Results of low- and high-power rf measurements on the RFQ cavity are compared to design specifications. Operation of the integrated RFQ vacuum, temperature and supervisory control systems are described.

## I. INTRODUCTION

The radiofrequency quadrupole (RFQ) accelerator for the SSCL Linac is designed to accelerate up to 50 mA of H<sup>+</sup> ions from 35 keV to 2.5 MeV. The SSCL RFQ is the first to use a ramped inter-vane voltage to maintain high transverse (focussing) field strength through the accelerating sections [1]. The vane profile was designed using an eight-term potential and the maximum peak surface fields were limited to a conservative 36 MV/m (1.8 Kilpatrick).

The SSCL requirement for a high-reliability, low-risk and low-cost RFQ design was satisfied by the choice of demonstrated technology and fabrication techniques from the Los Alamos National Laboratory (LANL) [2]. The RFQ cavity is a 2.2 m ( $\approx$  three wavelengths) structure fabricated from tellurium-copper. The structure comprises two axial segments bolted together to form the resonant cavity. Each segment is a near copy of an existing LANL cavity design, fabricated by electro-forming, at room temperature, four identical vane/cavity quadrant sections together. The resulting monolithic assembly features a stress-free integral vacuum vessel with no cross-sectional rf joints.

Following shipment from LANL in August 1992, the RFQ was assembled at the SSCL Central Facility (CF), in Waxahachie, for final acceptance low level rf tests. The structure was then integrated with the vacuum and temperature control [3], 600 kW rf amplifier [4] and computer control subsystems. After passing an integrated operational safety review in early December 1992, DOE approval was granted to start high-power rf conditioning. By the end of 1992, the cavity was rf conditioned to fields up to 115% of design (i.e., 2.1 K<sub>p</sub>). Details of the cavity conditioning and acceptance tests on the rf amplifier are presented in a companion paper [5].

The RFQ accelerated first beam in early April of this year. Presently, the RFQ is undergoing beam acceptance testing to verify the design energy, transmission and emittance. A companion paper [6] discusses the preliminary acceptance test results and describes the ion source/LEBT arrangement.

Figure 1 is a photograph of the RFQ as installed at CF, showing vacuum, temperature control and rf connections.

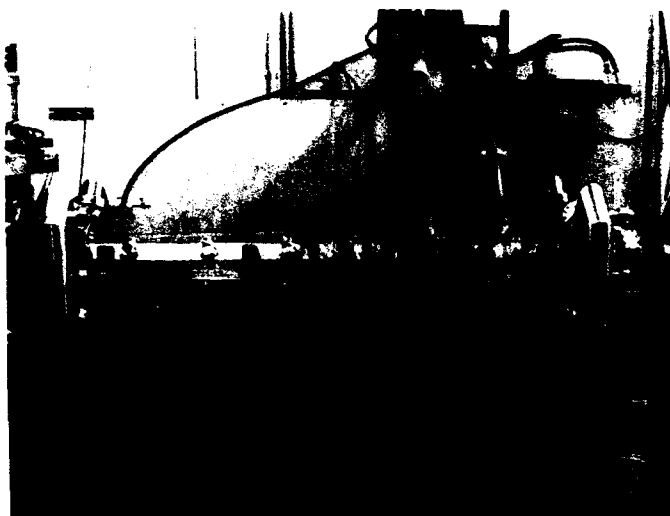


Figure 1. Photograph showing the RFQ as installed at the SSCL Central Facility.

## II. RF TUNING AND SUBSYSTEM INTEGRATION

### A. RF Tuning

The RFQ was first assembled at LANL for low level rf tuning of the cavity [2]. LANL personnel reverified cavity tuning after the RFQ was assembled on the support stand at SSCL. No significant post-delivery tuning deviations were measured, and the RFQ met the field balance and voltage ramp design requirements.

The design requirement for the unloaded cavity Q for the SSCL RFQ was 7500. At LANL, the unloaded cavity Q of  $\approx$  7150 was measured. By installing aluminum and copper substitutes, it was determined that the low Q was due to the SSCL endwall assemblies. At SSCL, the highest Q value measured was  $\approx$  6850. The assemblies are stainless steel with electro-deposited Cu rf surfaces; the quality/uniformity of the plating is suspect (the design requirement was a minimum thickness 15  $\mu$ m, or three skin depths). The lower-than-design Q values were considered acceptable as they represent, at most, a 10% increase in the rf power requirement.

The RFQ cavity is required to operate at a resonant frequency of 427.617 MHz. The cavity was tuned to resonate at this frequency at 40.5°C. Figure 2 shows a plot of the resonant frequency versus cavity temperature for the completed cavity assembly. At 40.5°C, the resonant frequency

<sup>1</sup>Operated by the University Research Association, Inc. for the U.S. DOE, under contract No. DE-AC35-89ER40486.

is  $\approx 50$  kHz higher than the design value. The difference is attributed to vacuum isolation plugs, in the endwall bead-pull holes, which were not installed when the cavity was tuned. Unless the cavity is retuned, an operating temperature of  $\approx 46.5^\circ\text{C}$  is required to operate at the required frequency.

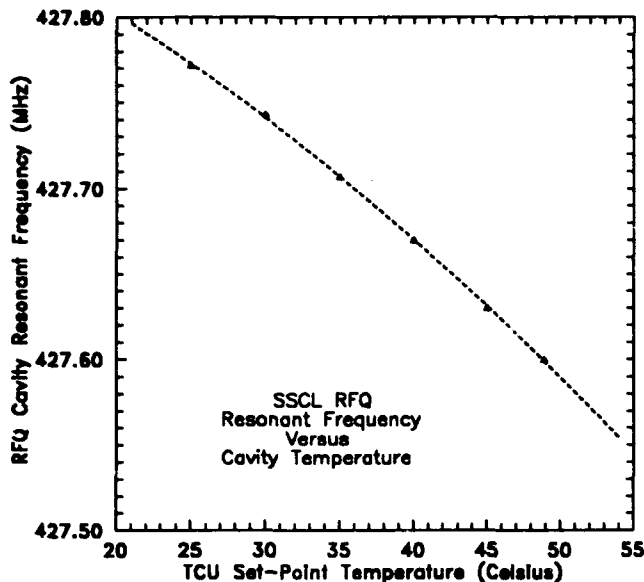


Figure 2. SSCL RFQ resonant frequency versus cavity temperature.

### B. Vacuum and Temperature Control

Two parallel 450 l/s turbopump systems provide vacuum pumping on the RFQ [3] through vacuum manifolds at the high- and low-energy ends. The manifolds connect through bellows to 143 l/s conductance vacuum pumping ports on each of the four cavity quadrants. Gate valves provide vacuum isolation between the pump systems and the manifolds. Sentry valves and molecular sieves prevent migration of oil from the backing pumps to the RFQ cavity. Beam-line isolation valves were custom-designed to fit in to the tightly-confined endwall spaces at the entrance and exit of the RFQ.

At the operating temperature, the base vacuum pressure (measured in the manifolds) is typically  $\approx 5 \times 10^{-6}$  Pa, well within the  $1.3 \times 10^{-5}$  Pa base pressure design requirement (at room temperature, the pressure falls by a factor of five). The pressure is also within the  $6.5 \times 10^{-5}$  Pa operating pressure design requirement when the isolation valve to the source is open. The system has operated now for over 3000 hr, and base pressures are routinely achieved within 15 minutes of starting a pump down from atmosphere (the RFQ is only back-filled with dry  $\text{N}_2$ ). The endwall isolation valves provide an adequate vacuum seal, and total cavity leak rates are less than the  $2 \times 10^{-10}$  Pa  $\text{m}^3/\text{s}$  design requirement.

A temperature control unit (TCU) [3] supplies temperature-controlled, low-conductivity water (LCW) to the RFQ to frequency-stabilize the resonant cavity. The TCU system comprises a pump and heater to recirculate heated

LCW through a network of channels in the RFQ vanes. An elevated LCW temperature,  $40.5^\circ\text{C}$  design, was chosen to simplify the system by eliminating the need for a chiller. A temperature controller regulates the LCW temperature by operating a heater or by bleeding in cooler water ( $30^\circ\text{C} - 35^\circ\text{C}$ ) from the primary LCW supply. Resistive temperature devices (RTD's) in the cavity walls monitor the temperature of the RFQ structure.

The TCU was designed for a  $35^\circ\text{C} - 45^\circ\text{C}$  operating range. However, satisfactory operation has been demonstrated at operating temperatures up to  $50^\circ\text{C}$ . To avoid retuning the cavity, a  $46.5^\circ\text{C}$  operating temperature was established as the nominal operating temperature (see Section II A). Temperature stability is well within the  $\pm 0.5^\circ\text{C}$  design requirement and the cavity temperature can be raised from ambient to the operating setpoint within one-half hour (better than the one hour design requirement).

### C. Computer Control

The vacuum system and TCU are computer controlled through a UNIX/CAMAC based, distributed control system. The system is based on TACL (Thaumaturgic Automatic Control Logic) software, developed at the Continuous Electron Beam Accelerator Facility [7]. The system provides the operator with control/monitoring functions including: display screens, hardware access routines and datalogging.

To simplify operation, the vacuum system is fully automated. TACL provides a set of start-up, shutdown and valve control sequences through "point-and-click" buttons on a display screen. System pressures, valve positions and vacuum pump conditions are also displayed. The TCU recirculating pump and temperature set-point are computer controlled, and LCW flows and temperatures are monitored. Note: All safety interlock functions are hardwired.

To date, TACL has provided satisfactory control and monitoring functions for the RFQ vacuum and TCU subsystems. However, TACL will be replaced by an VME based EPICS<sup>2</sup> global control system which will be the SSCL standard. EPICS is currently used to control the rf amplifier.

### D. RFQ Beam Diagnostics

Diagnostic instrumentation consisting of segmented apertures, Faraday cups and wire scanners are installed in the RFQ endwalls. A companion paper describes these devices and outlines the current commissioning status [8].

## III. RFQ CAVITY HIGH POWER OPERATION

The RFQ cavity was successfully conditioned to cavity fields up to  $\approx 115\%$  of the 1.8 Kilpatrick design after only 10 hr [5]. Once conditioned, cavity power can be raised to design

<sup>2</sup>Software produced under US Government Contracts: W-7405-ENG-36 at LANL and W-31-109-ENG-38 at Argonne National Laboratory.

levels almost immediately. Presently operation is virtually spark free, and spark-rates are unaffected by the source gas load. A reflected power trip on the rf amplifier (active after the cavity fill time) has proven critical to maintain cavity conditioning; the trip level is typically set at 10%.

Figure 3 shows a plot of the RFQ peak inter-vane voltage at the high-energy end versus peak cavity power (the dashed curve is a fitted square root function). The peak voltage was determined from measurements of the vane-tip, x-ray bremsstrahlung endpoint energy (viewed through an exit end vacuum port) using a collimated, Ge spectrometer system. Cavity power was determined from the rf amplifier forward and reverse power, and is in agreement with measurements using the calibrated rf cavity probes [2]. Absolute errors on the plotted values are estimated to be  $\pm 5\%$  on power and a few percent uncertainty in voltage.

At the 1.8 Kilpatrick design field, the inter-vane voltage at the high-energy end is 89 keV. Figure 3 shows that 330 kW of cavity power is required to establish design field levels. Considering measurement errors, and the lower than design Q (Section II A), the required power of 330 kW is within acceptable limits of the  $< 300$  kW design power requirement. Low- to high-energy end ratios of the x-ray endpoint energies are in good agreement with the 0.62 value calculated from the design voltage ramp.

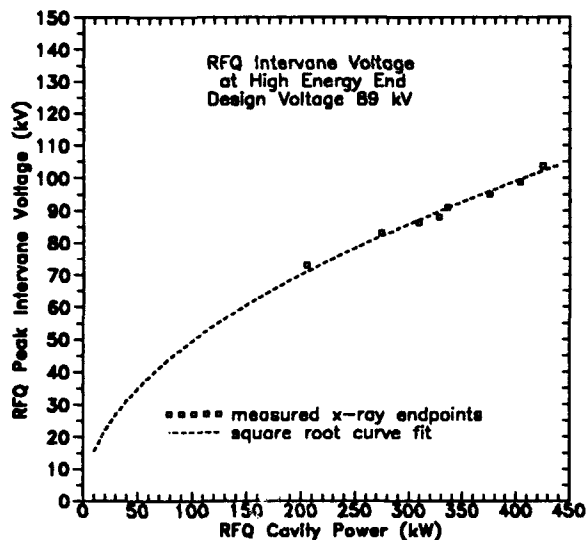


Figure 3. SSCL RFQ peak inter-vane voltage, at the high-energy end, versus peak cavity power.

The low ( $< 0.1\%$ ) duty-factor of the RFQ results in low average x-ray field emissions from the structure. In general, contact dose-rates are  $< 0.5 \mu\text{Sv/hr}$ . Higher dose-rates are measured at the vacuum port manifolds where the cavity shielding is minimal. At the high-energy end manifold, where inter-vane voltages are the largest, dose-rates are  $< 10 \mu\text{Sv/hr}$ .

Due to the low duty-factor, there is little effect on the cavity temperature from rf power. At design power levels, only a slight ( $\approx 0.3^\circ\text{C}$ ) temperature increase in the cavity wall is measured, due to differential heating. This temperature

increase is well within the  $\pm 0.5^\circ\text{C}$  design stability requirement. At design power, the increased cavity pressure is within a factor of three of the  $5 \times 10^{-6}$  Pa base pressure (well within the  $6.5 \times 10^{-5}$  Pa operating pressure design requirement).

#### IV. CONCLUDING REMARKS

The SSCL RFQ has been successfully assembled and integrated with its ancillary supports, rf amplifier and computer control systems. High-power operation of the RFQ has been demonstrated to 130% of the design power and beam operation has commenced. Operations at the SSCL Central Facility will continue until the RFQ injector is moved to the permanent tunnel location later this year.

#### V. ACKNOWLEDGEMENTS

The authors thank the many individuals involved in the integration of the RFQ. A few bear particular mention: J. Langstrand for assembly and assistance in low level rf measurements; J. Butteris, Q. Lui and L. Plesea for TACL displays and programming; J. Katchinska for controls wiring; F. Ross for assistance in x-ray endpoint measurements; S. Revell for radiation monitoring; and T. Benke for system integration documentation.

#### VI. REFERENCES

- [1] T.S. Bahtia, et al., "Beam Dynamics Design of an RFQ for the SSC Laboratory", *Conference Record of the 1991 IEEE Particle Accelerator Conference*, 91CH3038-7, Vol. 3, pp. 1884-1886.
- [2] D.L. Schrage, et al., "Radiofrequency Quadrupole Accelerator for the Superconducting Super Collider", *Paper presented at the 12th International Conference on the Applications of Accelerators in Research and Industry*, November 2-5 1992, Denton, TX.
- [3] D. Evans, R. Valicenti and F. Wood, "Integrated Design of the SSC Linac Injector", *Conference Record of the 1992 Linear Accelerator Conference*, May 5-12, Ottawa, Ontario, Canada, AECL Research Report AECL-10728, pp 238-240.
- [4] R.I. Cutler, et al., "SSC Linac RFQ RF System", *Conference Record of the 1992 Linear Accelerator Conference*, May 5-12, Ottawa, Ontario, Canada, AECL Research Report AECL-10728, pp 380-382.
- [5] R. Cutler, et al., "Rf Commissioning of the Superconducting Super Collider Radio Frequency Quadrupole Accelerator", *these conference proceedings*.
- [6] K. Saadatmand, et al., "Operation of the SSCL Injector", *these conference proceedings*.
- [7] R. Bork, et al., "CEBAF Control System", *Conference Record of the 1988 Linear Accelerator Conference*, October 3-7, Newport News, VA, CEBAF-Report-99-001, June 1989, pp 415-417.
- [8] P. Datte, et al., "Beam Instrumentation for the SSC RFQ", *these conference proceedings*.

# SSC Radio-Frequency-Quadrupole Beam: Comparison of Experimental and Simulated Results\*

F.W. Guy, J.W. Hurd, D. Raparia, K. Saadatmand, W.A. Whittenberg  
Superconducting Super Collider Laboratory  
2550 Beckleymeade Avenue, Dallas, Texas 75237

## Abstract

Simulations of the SSC RFQ output beam, run on the RFQ multiparticle code PARMTEQ, are compared with measurements from the SSC linac injector system. Some simulated RFQ input beams are generated from experimental observations of the output beams of the SSC einzel-lens Low Energy Beam Transport (LEBT) that focuses the beam from the ion source into the RFQ; this is the first LEBT to be tested with the RFQ.

## I. INTRODUCTION

Now that operation of the SSC RFQ has begun [1], experimental beam output data from this machine can be compared to beam-dynamics simulation results from the PARMTEQ multiparticle code. These comparisons are important in the preliminary setup of the RFQ and its diagnostics and are used extensively to establish whether the RFQ is operating as expected. They can establish credibility for simulations of current RFQ operating conditions, and by extension, to simulations of other operating conditions or input beams; for instance in error studies [2]. Finally, they can be used to verify, and if necessary to adjust, simulated RFQ beam outputs to accurately represent the RFQ output beam for simulations of downstream components of the SSC Linac.

## II. CALCULATIONS

The RFQ simulation code used in these calculations is derived from the Los Alamos National Laboratory VAX version of the PARMTEQ particle-following code [3]. The LANL code was modified at the SSC to allow input from a file of particle coordinates, to use an eight-term expansion of vane field potential [4] rather than the original two-term potential, to produce specialized outputs and to run on UNIX. A special version of the resulting SSCL code was further modified to investigate the effect of 3-D space-charge and image-charge effects, because these have been shown to result in decreased simulated beam transmission in some RFQs [5]. This version of the code was adapted to the SSCL Hypercube multi-processor computer because of its long running time.

The nominal input beam used in the RFQ design [4] was a matched 4-D waterbag of 30 mA with  $\epsilon_{rms,n} = 0.2 \pi$  mm-mrad. Test runs with the SSCL version of PARMTEQ gave virtually the same results with this beam as were obtained at LANL, 95% transmission and unchanged normalized emittance. The 3-D space-charge, image-charge version produced slightly higher transmission but within statistical error and we consider the results to be essentially identical.

\* Operated by the University Research Association, Inc. for the U.S. Department of Energy, under contract No. DE-AC35-89ER40486.

Many parameter study simulations (such as error studies) have been run at LANL and SSC with the nominal design beam in the course of design and analysis. We now have recent experimental LEBT output beam data that can be used in simulations [6]. Files of particle coordinates are generated by random sampling from experimental slit-and-collector data files. These coordinate files are used for input to simulation codes and for plotting in the same format as simulation code output for easier comparison.

Simulated RFQ output particles were transported through the RFQ fringe field and drifted to the slit position of the slit-and-collector (22 cm) or the wire position of the bunch shape monitor (15 cm) by the particle-following code PARMILA [7]. There is a vertical (y) waist in the beam about 8 cm from the RFQ output with an x-y aspect ratio of more than 3 to 1, therefore a 3-D space-charge subroutine was used.

## III. RESULTS

### A. Input Beam

An einzel-lens LEBT is presently being used to focus and steer the volume ion source output beam into the RFQ. Slit-and-collector emittance data was taken at the output of the LEBT with the einzel lens focusing and steering voltages adjusted to give the best apparent match of the central beam Twiss parameters to the RFQ input acceptance. This is the input beam that was used in the simulations reported in this paper. The resulting experimental distributions are shown in Fig. 1 with the nominal input beam ellipse.

After the LEBT was mated to the RFQ and the RFQ was turned on, LEBT focusing and steering voltages were adjusted by hand to the settings that gave the highest beam transmission through the RFQ. Beam transmission was found to be quite sensitive to LEBT voltages (set using analog meters), therefore the RFQ input distribution used for the calculations in this paper may be somewhat different from that measured at the LEBT output. Input current for the simulations was 30 mA; measurements were made at approximately the same or perhaps slightly higher current.

Simulations were also done with an input beam derived from earlier measurements on a previous, slightly different, version of the source-LEBT combination. Simulated RFQ transmission of that beam was significantly better, up to 65%. We believe the difference in the input beams is due primarily to dissimilar settings of the focusing and steering electrodes rather than to the mechanical differences of the devices. As time permits, we intend to remove the present source-LEBT from the RFQ and more completely characterize the LEBT output beam with variations in focusing and steering. These measurements will provide data for further simulations.

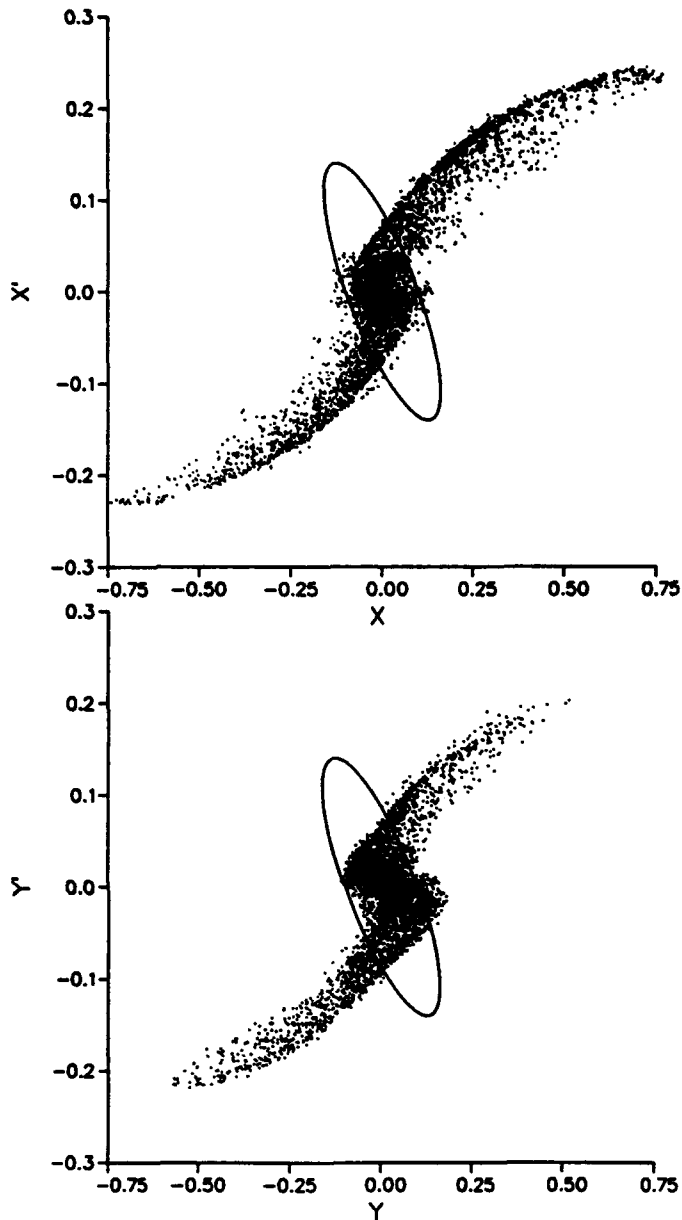


Figure 1. Experimental particle distributions (in cm and mrad) from the einzel lens LEBT. The design specification beam emittance ellipse is shown.

*b. Output Beam: Transverse*

In Figs. 2 and 3,  $y-y'$  particle plots of simulated and measured output beams at the slit position are shown. The  $y$ -projection was chosen because it is more compact than the  $x$ -projection. Emittance ellipses of equivalent uniform beams ( $5 \cdot \epsilon_{rms}$ ) are shown for measured and simulated beams. Table I gives beam parameters. As can be seen, Twiss parameters are similar but transmitted current and emittances are larger for the measured beam. This may be a result of differences in the RFQ input beam between the LEBT measurements at the LEBT output and that used for the RFQ measurements.

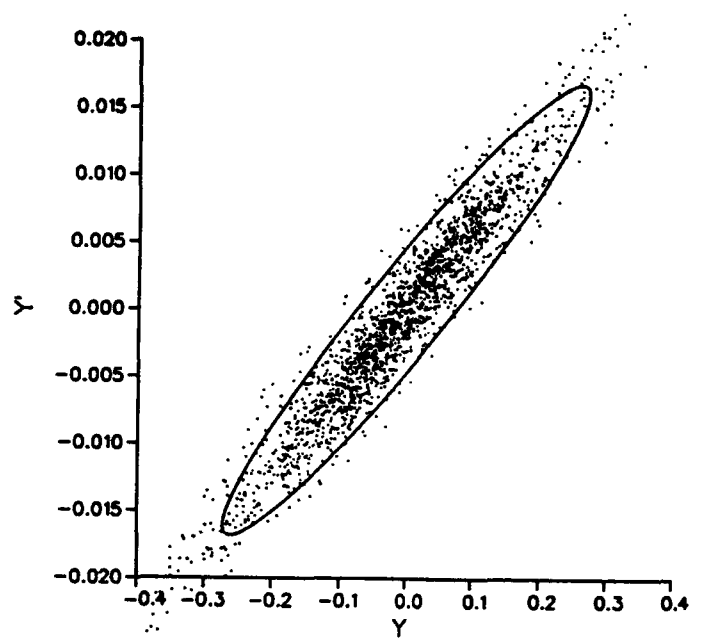


Figure 2. Transverse ( $y-y'$ ) particle plot in cm and mrad of simulated output beams at the slit position.

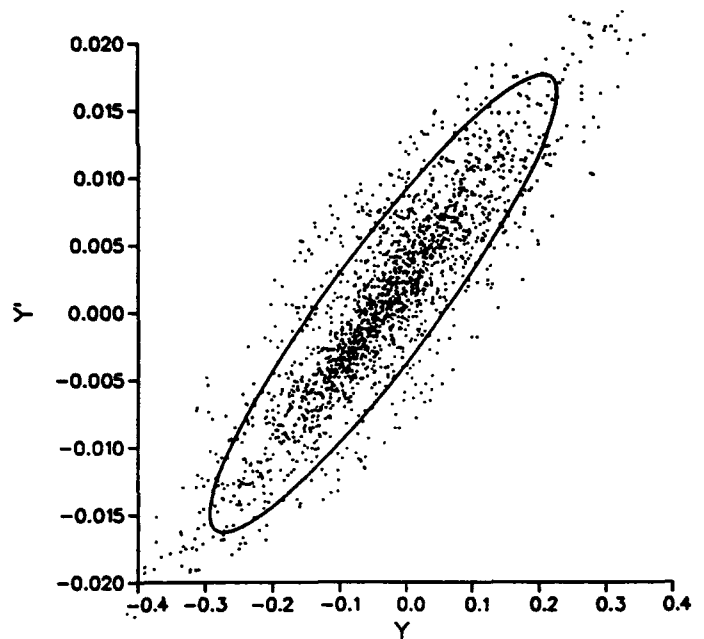


Figure 3. Transverse ( $y-y'$ ) particle plot (in cm and mrad) of measured output beam at the slit position.

TABLE I.

SIMULATED AND MEASURED BEAM PARAMETERS

	Alpha	Beta,	Emittance,	Current,
		mm/ $\pi$ -mrad	$\pi$ -mm-mrad	mA
			(rms-norm.)	
Simulated x	-8.65	2.53	0.172	11.7
y	-3.43	0.58	0.187	
Measured x	-10.5	3.00	0.247	16
y	-2.39	0.40	0.249	16

## B. Output Beam: Longitudinal

The longitudinal profile of the simulated beam bunch for a full-current beam is compared with data from the bunch shape monitor in Ref. [8] and shows qualitatively good agreement, with a smooth shape. Bunch shape monitor measurements were also taken with the LEBT defocused to reduce beam current to a small value below the range of the RFQ output toroid. At this low current, the bunch length monitor was easily able to resolve a good signal, as shown in Fig. 4. It contained much more structure than the high-current beam signal.

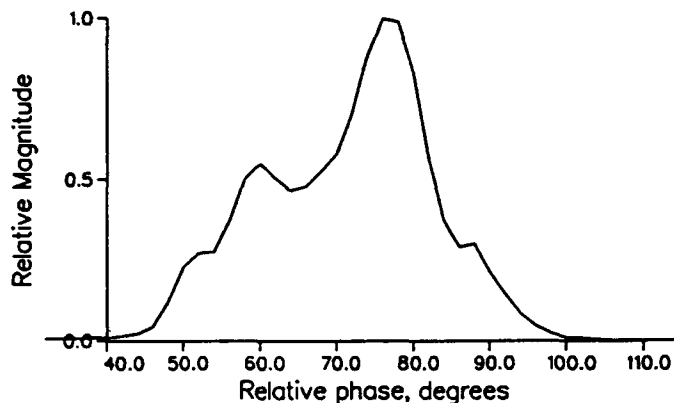


Figure 4. Measured longitudinal phase signal from the bunch shape monitor.

A simulation was done with the experimental RFQ input particle distribution with input current reduced to 1 mA. About half of this current was transmitted through the RFQ. After the drift the longitudinal distribution is shown in Fig. 5.

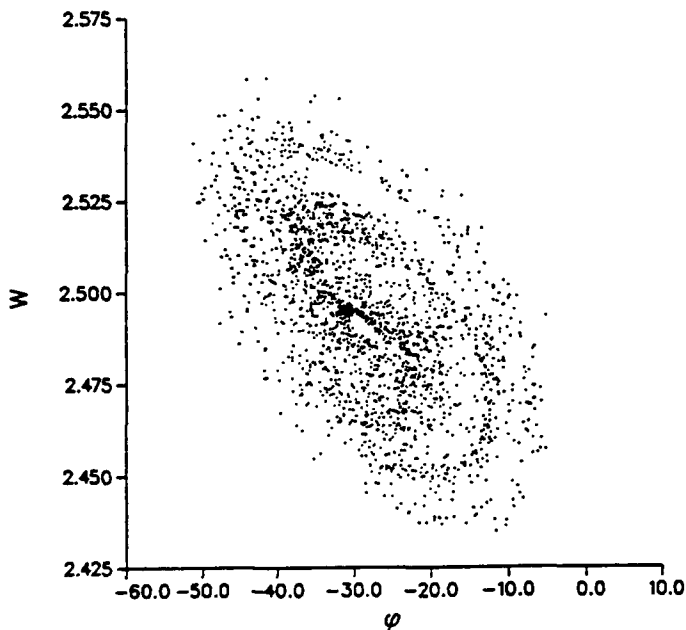


Figure 5. Longitudinal particle plot in phase and energy of simulated RFQ output beam at bunch shape monitor.

It is clearly evident that for the very-low-current case, structure is produced in the RFQ output longitudinal phase distribution by "wrap-around" of the initial monoenergetic beam in the RFQ bucket. This structure is destroyed by space-charge effects if beam current is more than a few milliamperes. The details of the phase distribution of the RFQ output beam are influenced by the input beam distribution and current, and by the RFQ vane voltage, of which only the vane voltage was known with any certainty. A comparison of the detailed structure of the measured vs. simulated low-current beams is likely to be unproductive until actual conditions can be better determined. Nevertheless it is interesting that the bunch shape monitor can be used for such a comparison.

## IV. CONCLUSIONS

These preliminary comparisons between measured and simulated output data for the SSC RFQ show remarkably good agreement for an accelerator in the early stages of commissioning. However, much work needs to be done with detailed measurements and corresponding computer runs to investigate the parameter range of this source-LEBT-RFQ combination and to prepare for commissioning of downstream linac components.

The SSC plans to test the Helical ElectroStatic Quadrupole (HESQ) [9] in the near future, and this will provide an opportunity to use measured HESQ LEBT outputs in RFQ simulations.

## V. ACKNOWLEDGEMENT

The authors thank K. Crandall of AccSys Corporation for his guidance and advice, and J. Hebert and J. Lenz of the SSCL Linac Group for their help and cooperation.

## VI. REFERENCES

- [1] K. Saadatmand et. al., "Performance of the SSC LINAC Injector," these Proceedings.
- [2] D. Raparia et. al., "Error and Tolerance Studies for the SSC Linac," these proceedings.
- [3] K.R. Crandall, "PARMTEQ—A Beam-Dynamics Code for the RFQ Linear Accelerator," *AIP Conference Proceedings 177, Linear Accelerator and Beam Optics Codes*, La Jolla Institute, pp. 22-28 (1988).
- [4] T.S. Bhatia et.al., "Beam Dynamics Design of an RFQ for the SSC Laboratory," *Proc. 1991 IEEE Particle Accelerator Conference*, Vol. 3, pp. 1884-1886.
- [5] F.W. Guy, "Three-Dimensional Space Charge and Image Charge Effects in Radio-Frequency-Quadrupole Accelerators," *Proc. 1991 IEEE Particle Accelerator Conference*, Vol. 5, pp. 3032-3034.
- [6] J. Lenz et. al., "Comparison of Experimental and Simulated Results for the SSC LEBT," these proceedings.
- [7] G.P. Boicourt, "PARMILA — An Overview," *AIP Conference Proceedings 177, Linear Accelerator and Beam Optics Codes*, La Jolla Institute, pp1-21 (1988); Los Alamos National Laboratory Report LA-UR-88-1544.
- [8] J.W. Hurd et.al., "Bunch Shape Monitor for SSCL Linac," these Proceedings.
- [9] D. Raparia, "Beam Dynamics of the Low Energy Beam Transport and Radio Frequency Quadrupole," Ph.D. Thesis, University of Houston, Houston, TX (1990).

# Mechanical Integration of an RF Volume Source and Einzel Lens LEBT to the SSC RFQ\*

R.A. Valicenti, J. Lenz, N.C. Okay, L. Plesea, and K. Saadatmand  
Superconducting Super Collider Laboratory  
2550 Beckleymeade Avenue, MS 4008  
Dallas, Tx 75237-3946 USA

## Abstract

The Superconducting Super Collider (SSC) LINAC Injector is currently operating with an RF-driven volume ion source coupled with an einzel lens Low Energy Beam Transport (LEBT). The ion source, LEBT and beam diagnostics are integrated into a compact vacuum enclosure which is mounted to the upstream endwall of the Radio Frequency Quadrupole (RFQ). Beam dynamic requirements imposed a minimum longitudinal space of only 23.5 cm, thus creating a very challenging packaging problem. In addition, optimum beam matching to the RFQ specified a maximum gap of 1 cm between the LEBT and the entrance endwall face, thereby excluding the use of a bellows between the LEBT chamber and the RFQ. Vacuum system induced loads and vibrations are isolated from the beamline components by the use of a straddling support frame which is an integral component of the vacuum system/support cart. This paper will describe some of the unique aspects of the mechanical design resulting from beam requirements, high gas load, availability of the vacuum system and the need for unconstrained attachment to the RFQ. In addition, the mobile installation cart and the fully automated vacuum control system will be discussed.

## I. INTRODUCTION

Figure 1 shows the SSC LINAC Injector set up for commissioning at its temporary location at the SSC Central Facility. The first 2.5 MeV output beam was successfully produced on April 8, 1993. With 30 mA at 35 keV out of the source, the Injector output current was 18 mA, 60% of specified transmission. An extensive experimental schedule is planned to fully characterize all injector subsystem components in order to maximize their performance and reliability, thereby insuring the long term availability of the LINAC.

The ion source and LEBT subsystems of the Injector are not configured as fixed, floor mounted devices, but instead are integrated into a mobile vacuum system/support cart which is designed for rapid installation and removal to the RFQ as a unit. This feature permits off-line operation for fine tuning of the ion source and LEBT when necessary, while the RFQ remains under vacuum and RF conditioned. Mobility of the ion source/LEBT installation also allows for improved access to the RFQ downstream endwall when servicing beam instrumentation modules and endwall isolation valves.

\*Operated by the University Research Association, Inc. for the U.S. Department of Energy, under contract No. DE-AC35-89ER40486.

## II. ION SOURCE & LEBT SUBSYSTEMS

Parallel R&D programs were used to evaluate the performance and reliability of both a Magnetron and RF Volume H<sup>-</sup> sources for near term LINAC Injector commissioning. An RF Volume H<sup>-</sup> ion source, based on RF induction discharge, developed for the SSC by LBL[1] was the best performing near term candidate. Beam is extracted at 35 keV and at a current as high as 40 mA of H<sup>-</sup>. High electron current which is an inherent characteristic of this type of ion source is deflected out of the beam by a spectrometer assembly. This ion source was chosen not only because of its favorable beam performance[2], but also due to its high reliability, simplicity of its controls and extremely short start up time.

Since the SSC LINAC requires short pulses, electrostatic LEBT candidates were suitable options. The 30 mA operating current is small enough that several LEBTs using electric field focusing can be used. An einzel lens, HESQ and ESQ have been fabricated and tested, and are currently undergoing further R&D. The einzel lens was the best characterized LEBT[3] of the three at the present time and offered the simplest integration for near term Injector commissioning.

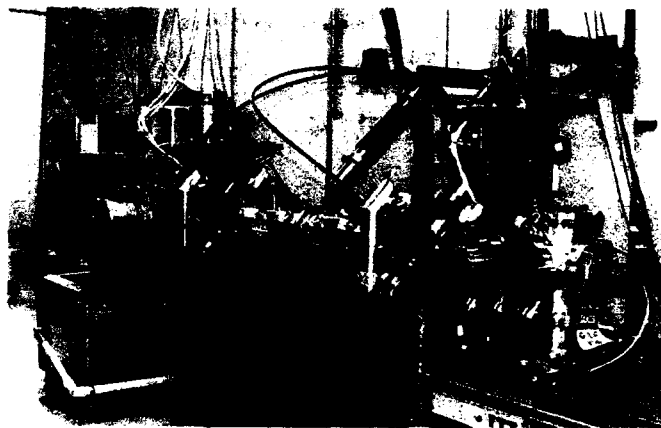


Figure 1. SSC LINAC Injector.

## III. MECHANICAL INTEGRATION

### A. Design Requirements & Features

The design requirements evolved early on as a combination set of worst case requirements for the two ion source and the three LEBT candidate integration schemes. A universal and upgradable approach was utilized for the final support frame and vacuum system installation concept. Many of the solutions applied to the RF Volume source installation were developed originally for the Magnetron/einzel lens combination.

Three primary requirements drove the design and overall

configuration of the system. 1) The vacuum capacity (pumping speed) at the chamber of 2000 l/s was a function of the ion source's gas load and the maximum allowable operating pressure of  $7.0 \times 10^{-4}$  Pa in the LEBT. 2) Beam divergence and matching as a function of LEBT type, and the spacial relationship of components - this dictated the minimum length of the vacuum chamber. 3) Existing mounting features on the endwall and minimum induced loads at the RFQ. A cross section of the packaging scheme that is used is shown in figure 2. All other features unique to the integration scheme were determined from beam diagnostics, availability and serviceability of the subsystems, and general LINAC commissioning requirements. Table 1 summarizes the main features incorporated into the design.

Table 1  
**MECHANICAL INTEGRATION FEATURES**

- \* Compact vacuum enclosure (23.5 cm Lg)
- \* Vacuum enclosure cantilever mounted to the RFQ
- \* Vacuum system supported independent from chamber
- \* (2) Pairs of opposing bellows (no induced vacuum loads)
- \* (4) 900 l/s ( $H_2$ ) Turbopumps with ceramic bearings
- \* (4) Automatic Vacuum Gate Valves with Iso 160 Flanges
- \* Fully automatic vacuum control system
- \* (1) Current Toroid & (1) Deployable Faraday Cup
- \* (8) LEBT externally accessible alignment adjusters
- \* Cart supports vacuum enclosure for off-line use
- \* Source alignment adjustment in X, Y & Z axis

#### B. Vacuum Enclosure

The vacuum enclosure is designed as a minimum envelope, just large enough (35 cm ID) to prevent arcing from the 35 keV reentrant flange of the ion source and to provide sufficient vacuum conductance for differential pumping of the LEBT. The front flange provides a 12 bolt hole pattern and o-ring groove for hard mounting to the RFQ endwall. The rear flange is designed to interface with the ion source assembly. Enclosure length is a function of optimized beam matching requirements - an 8 mm gap between the electron separator and LEBT is available for locating a Faraday cup. Figure 2 depicts the chamber and the internal relationship of all the components.

For ease of fabrication, and to make maximum use of commercially available flanges, the chamber was made from 304 & 316 stainless steel. Four Iso 160 flanges, spaced  $90^\circ$  apart allowed for compact installation of the vacuum pumps, in addition to providing 3000 l/s of conductance at the chamber. The requirement of minimizing distortions of the RFQ specified a 82 kg and 26 kg-m limit for the total cantilevered mounted assembly. Figure 3 shows the integrated chamber installed to the RFQ endwall.

#### C. Component Alignment & LEBT Support Scheme

The LEBT can be aligned externally to a precision of  $\pm 0.1$  mm with the use of long piloted set screws acting inboard on the LEBT's casing. These adjusting screw are located con-

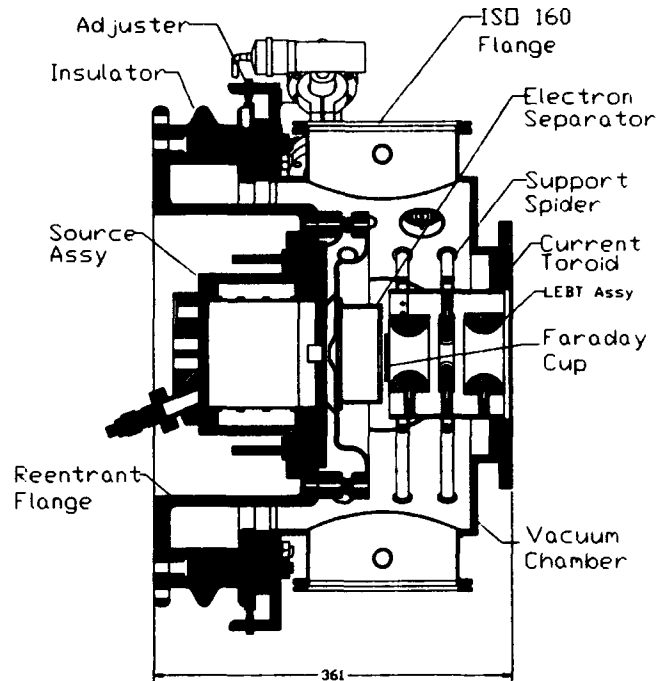


Figure 2. General Arrangement of RF Volume Source & einzel lens LEBT Integration scheme.

centrically within the support tubes spanning from the LEBT's support ring to mini conflat flanges welded to the chamber. Four support tubes are bolted radially to each ring and after their mounting bolts are fully tensioned, the assembly forms a rigid support spider. Since the spiders consist of a mechanical assembly only, they can be replaced to accommodate different size LEBT lens.

The ion source is aligned to the LEBT in the transverse plane within  $\pm 0.1$  mm with the aid of four bucking screws acting on the source's rear flange. Axial position of the ion source assembly can be adjusted with a machined spacer. Component alignment can be referenced to either a datum on the chamber or directly to an RFQ reference. Prealigned installation to the RFQ is maintained and provided by two brass bushing/inserts.

#### D. Beam Instrumentation

A single current toroid is located at the exit end of the LEBT to monitor current transmission thru the LEBT. The toroid was sized so it would mount directly on the LEBT casing, allowing it to move with the LEBT during alignment. A graphite Faraday cup was located in the 8 mm gap between the electron separator and LEBT's first element. The cup is mounted on the end of a pivoting arm and is deployed by a 1" travel linear actuator. A rotational deployment scheme created a more compact mechanism, along with limiting the external dimension of the actuator.

#### E. Support Frame and Vacuum System Cart

An existing general purpose diagnostic cart was utilized for integrating design specific structural elements and all vacuum components. The bare cart is a heavy duty welded aluminum structure that offered many mounting options. The

packaging scheme adopted allows the ion source/LEBT subsystem to be fully mobile and functional in both Injector, and off-line modes. Design specific structure consists of aluminum adapting plates and mounting shelves. A welded aluminum frame straddles the vacuum enclosure and carries all vacuum induced loads and the weight of the pumps and gate valves. The gate valves and bellows are mounted on plates with adjustable mounting locations. Provision for aligning the cart and frame are incorporated into the design. The cart is designed for multi mode use - it has provisions for supporting the vacuum chamber while being installed and removed from the RFQ, as well as for off-line testing (operating while removed from the RFQ). Figure 4 represents the as-built hardware.

#### F. Vacuum System

The vacuum system utilizes four 900 l/s ( $H_2$ ) ceramic bearing turbopumps. Space limitations required pumps which could be mounted in any orientation. Since the pumps are mounted to the support frame which are connected to the chamber via bellows, frequent separation of the bellows from the chamber, necessitated the use of Iso flanges due to their quick disconnect feature. Automatic gate valves are used at each location to allow removal of a failed pump without bringing the entire system up to air. The use of four pumps provides an additional 1000 l/s of redundancy, allowing the ion source/LEBT to continue operating with one failed pump. Two identical roughing pump strings service each pair of turbopumps. Sentry valves, electro-pneumatic in-line valves, automatic vent valves, seven convectron gauges and a single ion gauge are incorporated into the system, and are hardwired and interlock to a fully automated control system. Figure 4 shows the arrangement of the vacuum system components.



Figure 3. Volume Source/LEBT installed to RFQ.

#### IV. VACUUM CONTROL SYSTEM

The Ion Source vacuum control system is fully interlocked and automated. A hardwired interlocking scheme was implemented for machine safety. The control system software is TACL (Thaumaturgic Automatic Control Logic, developed at CEBAF). The control system includes one supervisor/database computer and one slave, which in turn controls a CAMAC

crate. All the signals required for operation are generated by general purpose CAMAC boards. This control system also controls the RFQ vacuum system. The pumpdown sequence, failure detection, recovery and stop sequence are completely automated. The Controls Group has selected EPICS (developed at LANL) as the control software which will be used at the SSC, and VME as the bus technology. EPICS is ideally suited for controlling large systems and VME will allow increased density, as well as a large base of available products. The ion source vacuum control system will be ported to VME and EPICS in the near future.

#### V. CONCLUSIONS

The successful mechanical integration of the RF volume ion source and einzel lens LEBT to the RFQ, along with the extensive development of all other subsystems has created a world class Injector at the SSCL. Improved LEBTs are in development which will be installed and operated to increase the beam current transmission of the RFQ.

#### VI. ACKNOWLEDGMENTS

The authors wish to acknowledge the technical assistance of A. Hessong and K. Johnson in the design, modeling and drafting of the ion source/LEBT integration hardware, and K. Jones for the Finite Element Analysis of the support structure and vacuum chamber.

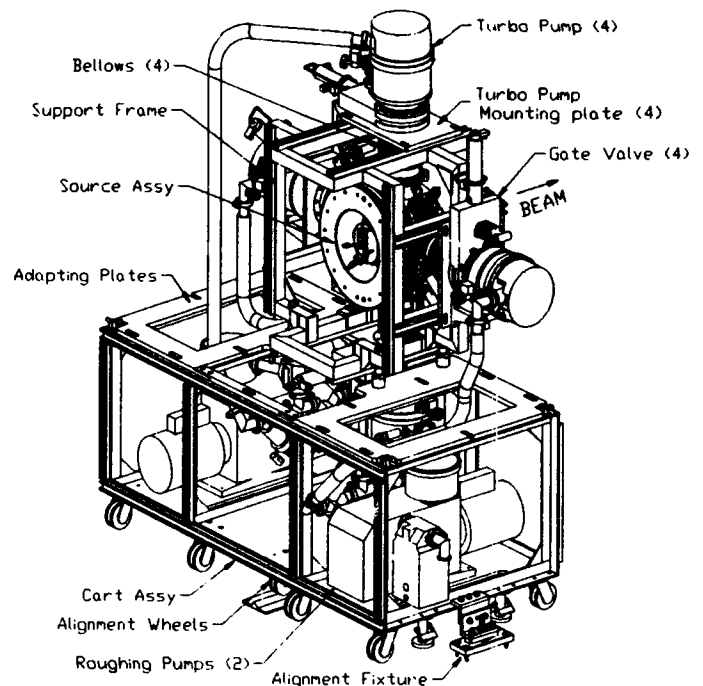


Figure 4. Vacuum cart assembly.

#### VII. REFERENCES

- [1] K.N. Leung, et al., Rev.Sci.Instrum.,62, 100(1991).
- [2] K. Saadatmand, et al., these Proceedings.
- [3] J. Lenz, et al., "Comparison of Experimental and Simulated Results for the SSC LEBT," these Proceedings.

# Segmented Resonantly Coupled Radio-Frequency Quadrupole (RFQ)\*

L. M. Young  
Los Alamos National Laboratory  
Los Alamos, NM 87545

## Abstract

In this experiment a 4-m-long radio-frequency quadrupole (RFQ) resonating at 348 MHz was split into two 2-m-long RFQs. The two RFQs were then rejoined with resonant coupling<sup>1</sup> to form a segmented 4-m-long RFQ. This coupling improved both the longitudinal and transverse stability of the 4-m-long RFQ. The frequencies of all the modes near the RFQ mode and the sensitivity of the RFQ mode to perturbations were measured. This paper presents the results of these measurements and compares them with measurements of the original 4-m-long RFQ. Both the original RFQ and the resonant-coupled RFQ use four rods (dipole stabilizers) on the end plates to adjust the frequencies of the dipole modes. Slug tuners distributed along its outer walls tune the RFQ. Modifications to the program RFQTUNE<sup>2</sup> allow its use for tuning the segmented RFQs. This paper also describes the tuning procedure.

## INTRODUCTION

The Continuous Wave Deuteron Demonstrator (CWDD) RFQ cold model was originally built to determine the feasibility of building the 4-m-long CWDD RFQ.<sup>3</sup> The model has four 1-m-long sections that are bolted together to form one continuous structure. The modifications for resonant coupling consisted of (1) machining undercuts on the end of the vanes at the center joint and (2) joining the resulting two 2-m-long segments with a coupling plate (see Figure 1) that separates the two segments. Each segment is a complete RFQ with vane undercuts and dipole stabilizers on each end.

Although each segment can be tuned to the correct frequency and field distribution before they are joined, in this experiment the two segments were joined before tuning. The coupling plate has a large center hole through which the vane ends, above the undercut, partially extend. When the two segments are joined, the vane tips almost touch. The distance between the vane tips is adjusted to provide the correct amount of capacitance between the two segments. The coupling plate has dipole stabilizers on both sides.

Figure 1 shows the details of the resonant-coupling joint in the 8-m-long RFQ designed for the Accelerator for the Production of Tritium (APT) project. The coupling plate has stabilizer rods mounted on both sides of it that are identical to the stabilizer rods at the ends of the RFQ. These rods

adjust the frequency of the dipole modes to minimize the mixing of dipole modes with the operating frequency. The APT RFQ requires cooling channels for cw operation. Some of the cooling channels are shown in Figure 1.

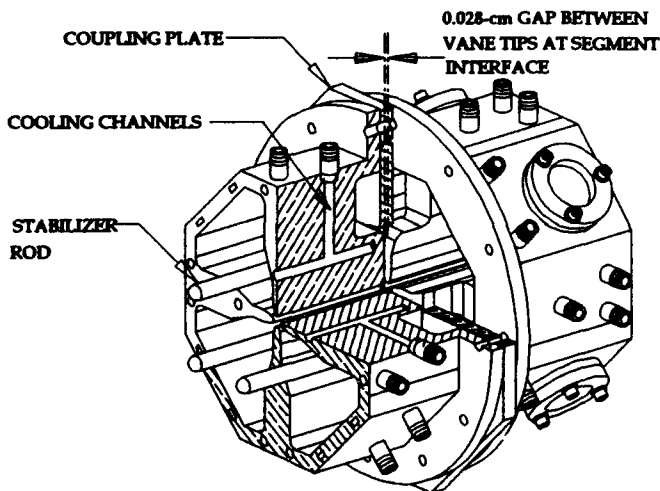


Figure 1 Details of the joint between segments

## RESONANT COUPLING

Resonant coupling in a segmented RFQ provides longitudinal field stabilization. In this RFQ design resonant coupling also provides a stop band in the dipole mode dispersion curve around the operating frequency of the RFQ. This stop band improves the transverse stability of the RFQ by eliminating the dipole modes close to the frequency of the operating mode.

Figure 2 shows the modes in the 4-m-long CWDD RFQ cold model without segments. The modes labeled "1-3 dipole" are dipole modes with fields that are predominantly in the quadrants labeled 1 and 3; the modes labeled "2-4 dipole" have fields in the quadrants labeled 2 and 4. The quadrants are labeled clockwise from 1 to 4 with the lower left quadrant labeled 1, when viewed from the low energy end of the RFQ. Figure 2 also shows where the estimated frequencies of the additional modes that are found in an 8-m-long RFQ would lie if its dispersion curves were superimposed on those of the 4-m-long CWDD RFQ cold model. Figure 3 shows the dispersion curves of this same RFQ after it was modified with resonant coupling. This Figure also shows the estimated frequencies of additional modes labeled "8-m RFQ," that occur in the 8-m-long RFQ with resonant coupling. There are twice as many modes in a given frequency range in the 8-m-long RFQ as in the 4-m-

\*Work supported by the U. S. Department of Energy, Office of Defense.

long RFQ. The mode numbers shown at the bottom of Figure 2 are for the 4-m-long RFQ. The two orientations of the dipole modes are degenerate in a perfectly symmetric RFQ and the dipole dispersion curves lie on top of each other in both figures.

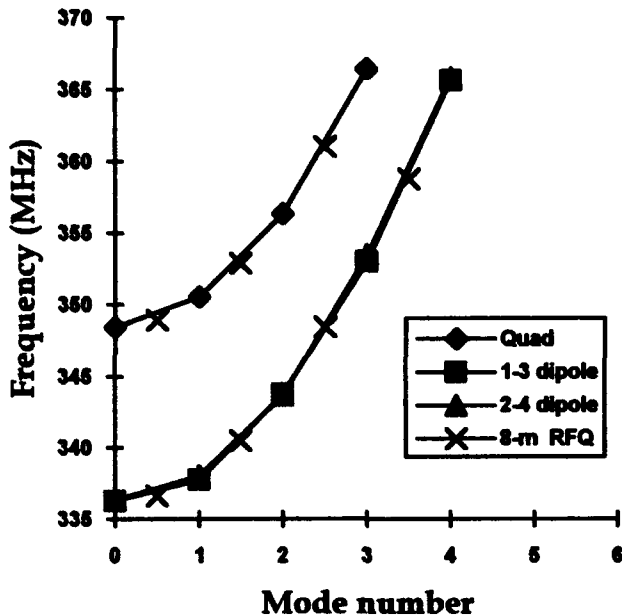


Figure 2 Modes found in CWDD RFQ cold model.

The operating mode is the quadrupole mode near 348 MHz in these figures. In Figure 2 the operating mode is the quadrupole mode number 0. In Figure 3 the operating mode is the quadrupole mode with 0 phase shift per segment. Note that the mode nearest the operating mode in both cases is a quadrupole mode. In the CWDD cold model the nearest mode is the quadrupole mode number 1 which is 2.1 MHz higher than the operating mode. Doubling this RFQ in length would make the nearest quadrupole mode only 0.5 MHz higher than the operating mode. This slight difference would probably make the 8-m-long RFQ difficult if not impossible to tune. The dipole mode could be moved away from the quadrupole mode in an 8-m-long RFQ but not by more than 2 MHz.

In the resonantly coupled CWDD RFQ cold model the modes nearest the operating mode are at  $\pm 4.45$  MHz. In the APT RFQ the nearest modes are at  $\pm 2.2$  MHz. Therefore, perturbations will tend to mix these modes equally but with opposite sign with the operating mode. These modes will have similar characteristics. Thus, the effect of mixing one of these modes with the operating mode is canceled by the other mode. This cancellation is one way of describing the stabilization of the fields in a compensated resonantly coupled system. However, in a RFQ with 2-m-long segments, the modes are different enough that there is only partial cancellation. In places where the modes actually add, the amplitude of the modes is small.

In a resonantly coupled RFQ of this type the nearest dipole is about 8 MHz from the operating mode. This separation of the dipole modes from the operating mode is a factor-of-two improvement over the CWDD RFQ. This separation of modes is also better than the mode separation in the 2.2 m long Superconducting Super Collider (SSC) RFQ<sup>4</sup> which has dipole modes at  $\pm 6.4$  MHz from the operating mode.

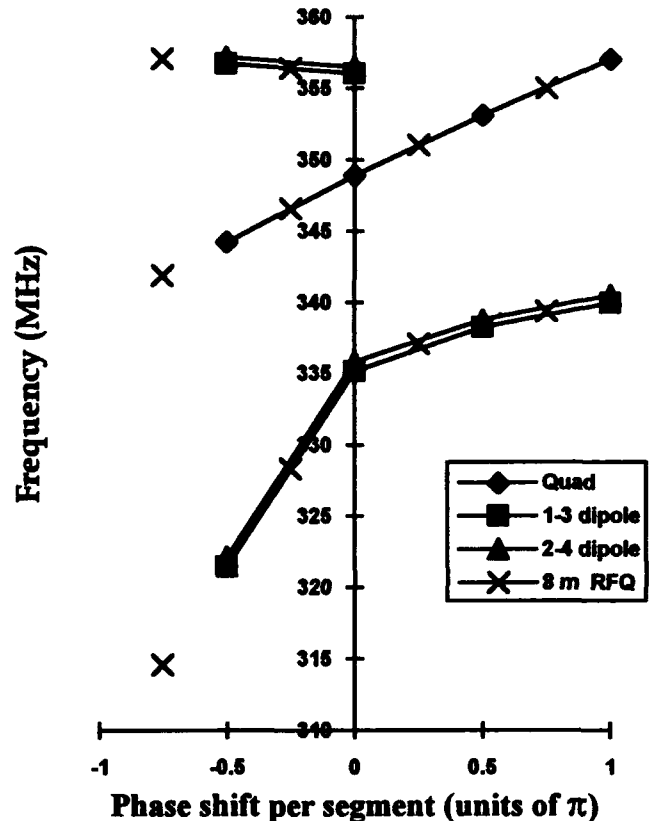


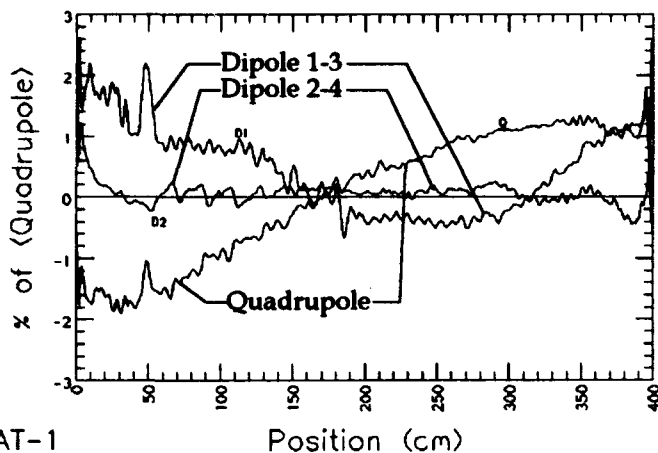
Figure 3 Dispersion curves of the modes found in the resonantly coupled CWDD RFQ cold model.

### SENSITIVITY TO PERTURBATIONS

The effect of perturbations was measured in the CWDD RFQ cold model before (Figure 4) and after the RFQ was modified with resonant coupling (Figure 5). Figure 4 shows the percentage change in the fields from a 25-kHz perturbation. Figure 5 shows the percentage change in the fields from a 100-kHz perturbation that consisted of two 50-kHz perturbations.

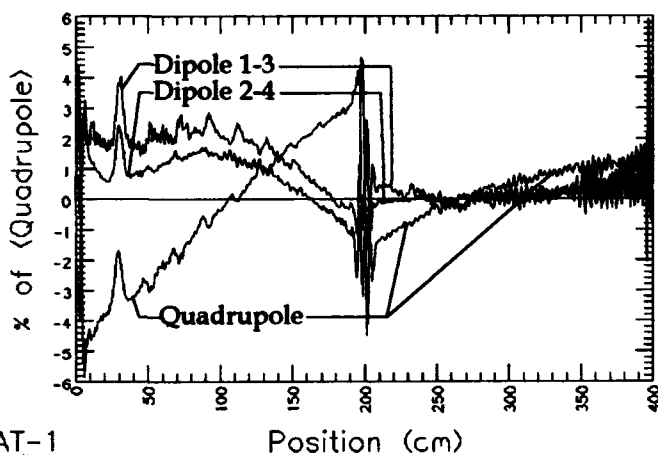
Note that the vertical scale in Figure 4 is  $\pm 3\%$ , while in Figure 5 it is  $\pm 6\%$ . The perturbation in the resonantly coupled RFQ cavity is four times greater than that in the continuous RFQ's cavity. These perturbations distort the quadrupole fields differently. However, the maximum change in the coupled RFQ cavity is only twice as great for a four times greater perturbation. In addition, this comparison also shows that the average field in the two halves of the

resonantly coupled RFQ is almost unchanged, whereas the average field in the first two meters in the CWDD RFQ is about 2% less than in the second two meters.



AT-1  
Los Alamos

**Figure 4** Percent change in fields in CWDD RFQ (25-kHz perturbation).



AT-1  
Los Alamos

**Figure 5** Percent change in fields in resonant coupled RFQ (100 kHz perturbation).

In the resonantly coupled CWDD RFQ, the effect of the perturbations on the dipole fields appears to be localized to the segment containing the perturbation. As shown by the perturbation measurements, which were performed about every 50 cm throughout the first segment, this localization of the perturbation effects held true for all measured locations.

## TUNING

The field strength in an RFQ is measured with the bead-perturbation technique.<sup>5</sup> In this technique a metal bead is suspended on a nylon line and is drawn through the four quadrants near the RFQ's outer wall. The bead perturbs the structure and changes the resonant frequency, depending on the electric and magnetic field strength. In RFQs with constant capacitance between the vane tips and constant cross section the electric field strength, in the bore of the

RFQ, is directly proportional to the magnetic field strength. The technique actually measures the magnetic field strength because the magnetic field dominates the perturbation near the outer wall.

The desired magnetic field profile as well as the bead-perturbation data is input to the program RFQTUNE. The measured frequency of all the nearby modes must also be input to RFQTUNE so that it can calculate the shape of each mode and the effect of a perturbation at each slug tuner. Then, RFQTUNE calculates the position of each tuner to adjust the fields in the RFQ to the desired profile. The program has tuned the following RFQs: CWDD, the Ground Test Accelerator,<sup>6</sup> SSC, and the 4-m-long resonantly coupled CWDD cold model. The CWDD RFQ and the 4-m-long CWDD cold model each have 80 tuners.

Final rf tuning includes the following:

1. Machine the undercuts on the vane ends to achieve the desired shape of the fields at the end of the vanes.
2. Machine the end of the vanes at the segment joints to adjust the resonant coupling. This process adjusts the frequency of the nearby dipole modes to equalize the spacing of the dipole modes.
3. Machine the dipole stabilizers to the proper lengths to establish the optimum frequencies of the dipole modes.
4. Machine the slug tuner lengths to achieve the required frequency, the required quadrupole field profile, and the minimum dipole field.

## REFERENCES

1. M. Jean Browman and Lloyd M. Young, "coupled Radio-frequency Quadrupoles as Compensated Structures," in *Proceedings of the 1990 Linear Accelerator Conference*, (Albuquerque, NM, September 10-14, 1990), pp. 70-72.
2. L. Young, "Tuning and Stabilization of RFQ's," in *Proceedings of the 1990 Linear Accelerator Conference*, (Albuquerque, NM, September 10-14, 1990), pp. 530-534.
3. G. E. McMichael, "High-Current CW RFQ's," in *Conference Record of the 1991 IEEE Particle Accelerator Conference*, (San Francisco, CA, May 6-9, 1991), pp. 2093-2097.
4. T. S. Bhatia, J. H. Billen, A. Cucchetti, F. W. Guy, G. Neuschaefer, L. M. Young "Beam Dynamics Design of an RFQ for the SSC Laboratory" in *Conference Record of the 1991 IEEE Particle Accelerator Conference* (San Francisco, CA., May 6-9, 1991), pp. 1884-1886
5. E. L. Ginzton, "Resonant-cavity Characteristics: Measurement of  $R_0/Q_0$ ," in *Microwave Measurements*, (McGraw Hill, 1957), Chapter 10, pp. 435-461.
6. K. F. Johnson, et al., "Commissioning of the Ground Test Accelerator RFQ," in *1992 Linear Accelerator Conference Proceedings*, (Ottawa, Ontario, Canada, August 24-28, 1992), pp. 64-66.

# Experiments with the High Current RFQ Prototype for GSI\*

A. Kipper, A. Schempp, H. Deitinghoff, J. Madlung, T. Ludwig, K. Volk, O. Engels, A. Firjahn-Andersch, H. Vormann  
Institut für Angewandte Physik  
Johann Wolfgang Goethe-Universität  
D-60054 Frankfurt, FRG

## Abstract

A new high current injector (HSI) for the UNILAC and the SIS synchrotron for all ions up to Uranium is planned at GSI [1],[2]. The Spiral-RFQ accelerator accepts low energy (2.2 keV/u), high current (25 mA) beams with low charge states ( $U^{2+}$ ) at an operating frequency of 27 MHz. Results of particle dynamics calculations and structure development for the first crucial part of the HSI-RFQ, where all bunch forming is done, are presented together with results of rf measurements and first beam tests.

## I. Introduction

The GSI upgrading program [3],[4] consists of the new 18 Tm heavy ion synchrotron SIS, the experimental storage ring ESR and the two new injectors HLI (Hochladungsinjektor) and HSI (Hochstrominjektor). With these new components and the UNILAC it is possible to accelerate all elements up to Uranium to energies above 1 GeV/u. The SIS and the ESR are now working for more than 2 years. The HLI for the nuclear physics research program at the UNILAC is also successfully working since June 92. Figure 1 shows the plan view of the extended GSI accelerator facility.

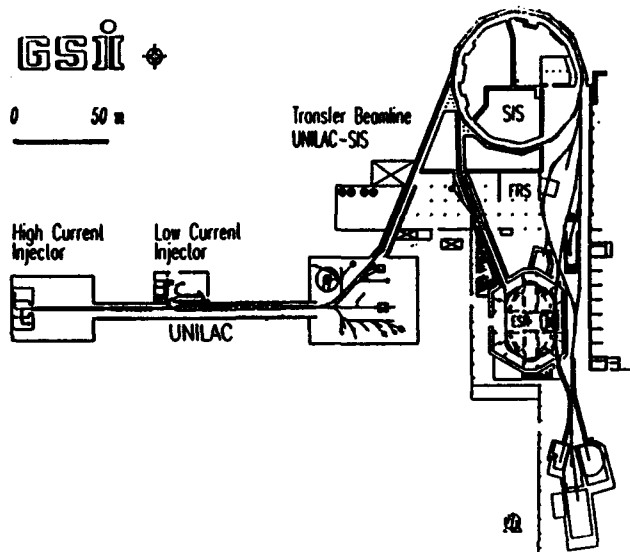


Figure 1 Plan view of the extended GSI accelerator facilities

The high charge injector HLI [5] consists of a combination of an ECR ion source, a 4 Rod-RFQ [6] and an IH-structure [7], both operating at a frequency of 108.5 MHz. The HLI enables direct injection of  $U^{28+}$  into the Alvarez part

of the UNILAC at an energy of 1.4 MeV/u without stripping. This injector is designed for a beam current of 5  $\mu$ A at a duty cycle up to 50 %.

The high current injector HSI is designed to fill the SIS up to the space charge limit and will accept e.g.  $U^{2+}$  beams with currents as high as 25 mA at low initial particle energies of 2.2 keV/u. The accelerator structure works at the Wideroe frequency of 27 MHz, which allows a beam transfer without frequency jump. A gas stripper at 216 keV/u produces a reasonable fraction of the necessary charge state of  $U^{10+}$  for acceleration in the second Wideroe part of the UNILAC. The second gas stripper at 1.4 MeV/u between the Wideroe and the Alvarez part provides the  $U^{28+}$  beam for postacceleration and injection into the SIS.

## II. The Spiral-RFQ-Structure

A 4 Rod-RFQ with spiral shaped supports [8] is suitable for operation at the Wideroe frequency (27 MHz). The length of a spiral arm is 1180 mm, the height is 450 mm. Using the spiral stems for the RFQ-accelerator allows the application of a very compact vacuum chamber (e.g. with a diameter of only 600 mm). Figure 2 shows a scheme of the spiral structure.

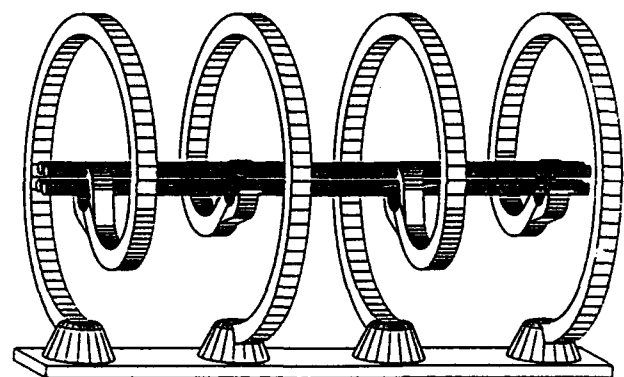


Figure 2 Scheme of the spiral structure

The whole HSI-RFQ will have an overall length of about 35 m to reach an ion velocity corresponding to an accelerator voltage of 26 MV. To achieve the space charge limit of 0.2 mA times the ratio mass over charge state the electrode voltage has to be 180 kV for  $U^{2+}$ . A short test resonator of 1 m length had been operated with even higher voltages [9].

\* supported by the BMFT and the GSI

### III. The Spiral-RFQ-Prototype

#### A. Layout

A 4 m prototype of the 4 Rod-Spiral-RFQ with 20 spiral supports has been built for both, rf and beam test purposes [10],[11]. The electrodes consist of the first 231 cells, one third of the HSI's total cell number. These 231 cells cover the crucial low-energy part of the HSI-RFQ, where the dc-beam is converted into a bunched beam. Therefore the 4 m prototype can give relevant information on beam properties e.g. emittance growth. Figure 3 shows the beam dynamics layout of the 4 m RFQ-Prototype. A survey over the main parameters of the RFQ-Prototype is given in table 1.

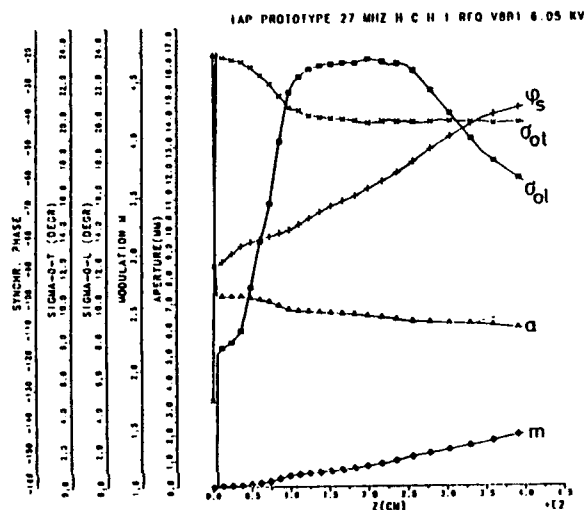


Figure 3 Beam dynamics layout

Table 1  
Main Parameters of the RFQ

f	27.1 [MHz]	Q <sub>0</sub>	5400
cells	231	R <sub>p</sub>	520 [kΩm]
T <sub>in</sub>	2.2 [keV/u]	T <sub>out</sub>	17.6 [keV/u]
φ <sub>s</sub>	-90 to -39 [°]	a	7.0 - 6.02 [mm]
m	1 - 1.458	α <sub>synchr</sub> (norm)	0.9 π [mm mrad]
ε <sub>in</sub>	0.3 π [mm mrad]	length	3950 [mm]
U <sub>el</sub>	1.51 A/ξ [kV]	spirals	20
I <sub>max</sub>	0.23 A/ξ [mA]	A/ξ <sub>max</sub>	130

#### B. Alignment of the RFQ

For the RFQ-Prototype a rectangular vacuum chamber made of aluminium has been chosen. Ten large lids simplify the mounting and adjustment of the RFQ structure. The structure has been aligned with an opto-mechanical system. For reasons of manufacturing each 4 m-electrode consists of 21 pieces. To achieve a high stability the electrodes are fixed and brazed on ten electrode carriers, each about 100 mm long. The electrodes are adjusted by washers with a precisely milled thickness. The precision of the electrode alignment is better than 0.12 mm, less than 3 % of the aperture radius.

#### C. Rf-Measurements

From low level measurements the quality factor of Q<sub>0</sub>=5400 could be observed. The field distribution along the beam axis has a maximum deviation of less than 2 %. Rf-tests have been performed upto 35 kW pulsed input power (67 kV) and 7.2 kW in cw operation, no mechanical and cooling problems could be observed. From beam- and rf-measurements an R<sub>p</sub>-value of 520 kΩm could be determined which has been checked with x-ray spectroscopy.

### IV. Beam experiments with He<sup>+</sup>

First beam experiments have been done at the Institut für Angewandte Physik. Due to the limited rf-power and extraction voltage light ions (He<sup>+</sup>) have been used for the experiments. The corresponding electrode voltage and beam current are 6 kV and 0.8 mA, respectively. Figure 4 gives a view of the experimental setup.

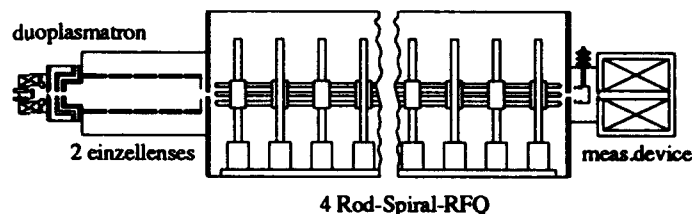


Figure 4 Scheme of the experimental setup

The beam was extracted from a duoplasmatron source and injected into the RFQ by two electrostatic einzel lenses. For beam analysis an emittance-measurement-device, a fast Faraday-cup and an analyzing magnet had been installed.

Figure 5 shows the rf-signal of a pickup loop and beam bunches behind the RFQ recorded with a fast Faraday cup.

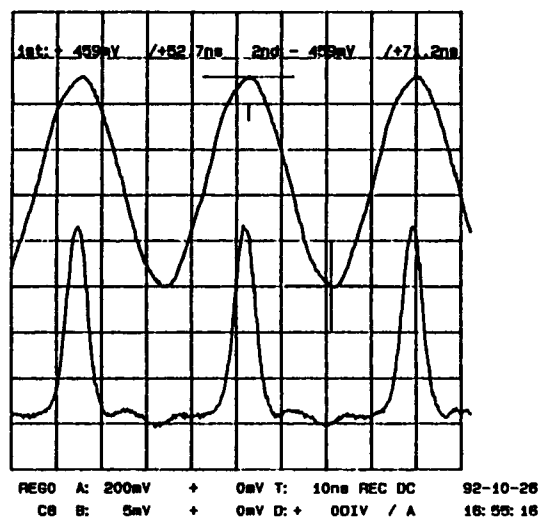


Figure 5 Measured rf-signal and beam bunch behind the RFQ.

Corresponding to the synchronous phase of 42° - 38° in the final part of the prototype, the proper output energy is reached at about 70 % of the design electrode voltage, as can

be seen in Figure 6. Measurements and calculations are in good agreement.

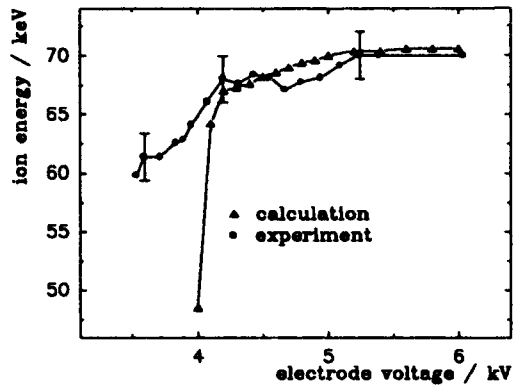


Figure 6 Ion energy vs. electrode voltage.

The maximum transmitted beam current was 980  $\mu\text{A}$ , but due to the input emittance with the typical aberrations of einzellenses as shown in Figure 7 the transmission at design voltage has been less than 40 %. PARMTEQ calculations with this input emittance delivered transmission curves which are in good agreement with the measurements [12]. Figure 8 shows the calculated transmission curves vs. electrode voltage for the design input emittance ( $\epsilon_{\text{norm}}=0.3 \pi \text{ mm mrad}$ ,  $\alpha_x=0.8$ ,  $\beta_x=0.1 \text{ mm/mrad}$ ), the emittance with the aberrations of the einzellenses ( $\epsilon=0.5 \pi \text{ mm mrad}$ ,  $\alpha_x=-0.8$ ,  $\beta_x=0.04 \text{ mm/mrad}$ ) and the measured transmission.  $\text{N}^+$  in the beam, caused by a leaky valve in front of the ion source, is responsible for the tail of the measured transmission curve. The calculated transport of  $\text{N}^+$  is also shown in Figure 8.

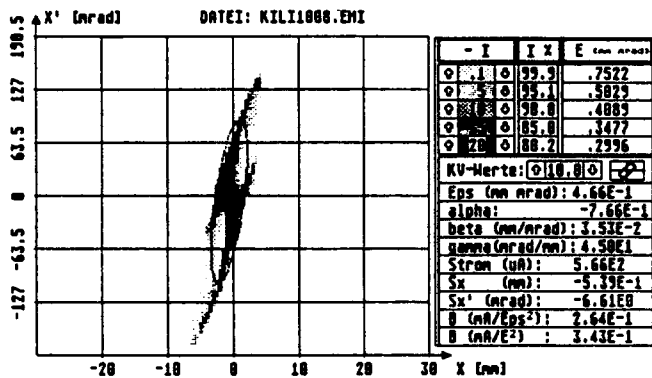


Figure 7 Measured Emittance at RFQ input.

## V. Status and Schedule

The  $\text{He}^+$  experiments in the institute have been successfully finished. Next plans are to operate the prototype at the high current injector test stand at GSI with heavy ions to check the full specifications.

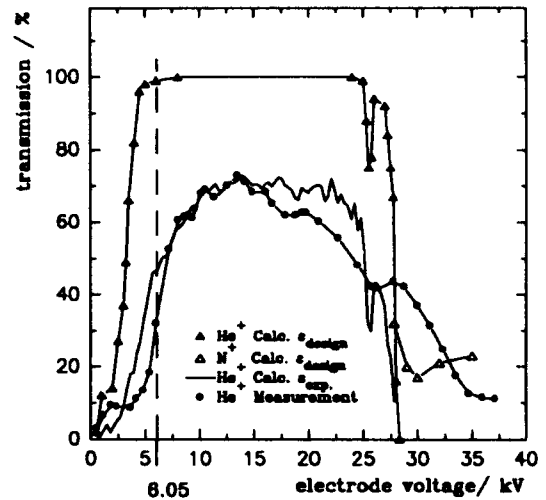


Figure 8 Calculated and measured transmission curves.

## VI. References

- [1] R. Bock, Gesellschaft für Schwerionenforschung, Scientific Report, GSI-89-41, 1989
- [2] D. Böhne et al., "The Performance of the SIS and Developments at GSI", Proc. 2nd EPAC, Nice, p. 18, 1990
- [3] J. Klabunde, "The UNILAC Upgrade Project", Proc. LINAC, CEBAF-Rep. 89-001, p. 242, 1989
- [4] N. Angert et al., "The UNILAC Modifications for an Improved Synchrotron Performance", Proc. 2nd EPAC, Nice, p. 503, 1990
- [5] J. Klabunde, "The High Charge State Injector for GSI", Proc. LINAC, Ottawa, p. 570, 1992
- [6] J. Friedrich et al., "Performance of the GSI HLI-RFQ" Proc. LINAC, Ottawa, p. 609, 1992
- [7] U. Ratzinger, "A Low Beta RF Linac-Structure of the IH-Type with Improved Radial Acceptance", Proc. LINAC, CEBAF-Rep. 89-001, p. 185, 1989
- [8] A. Schempp et al., "Development of a 27 MHz Heavy-Ion-Spiral RFQ", NIM A278, p. 169, 1989
- [9] A. Kipper et al., Gesellschaft für Schwerionenforschung, Scientific Report, GSI-90-1, p. 339, 1989
- [10] A. Schempp et al., "The GSI High Current RFQ Prototype", Proc. of the 12th Int. Conf. on the Application of Accelerators in Research and Industry, Denton, 1992
- [11] A. Kipper et al., "The High Current Spiral-RFQ Prototype", Proc. LINAC, Ottawa, p. 416, 1992
- [12] H. Deitinghoff, this Conference

# Transport of Ions in RFQ - Accelerators\*

J. Dehen, W. Barth<sup>1</sup>, A. Schempp and H. Deitinghoff  
Institut für Angewandte Physik der J. W. Goethe - Universität, Robert-Mayer-Str. 2-4  
D 6000 Frankfurt am Main, BRD  
<sup>1</sup>now at Institut für Biophysik der J. W. Goethe-Universität

## Abstract

Radio Frequency Quadrupole (RFQ) structures [1,2] are well suited to accelerate all kinds of ions at low particle energies with high transmission efficiency even at high beam currents. Like other rf-accelerators they normally have a fixed velocity profile and corresponding fixed input and output energies per nucleon of the accelerated ions. But - due to the strong transverse focusing - the RFQ-accelerators can also capture and transport very efficiently ions with energies and specific charge states even far away from the design values [3]. Results of calculations will be presented and compared to measurements.

## I. INTRODUCTION

RFQs serve today in manifold functions as pre- and postaccelerators, injectors, implanters for light and heavy ions, for low and high currents with small duty cycles up to dc operation [4]. Also RFQs with unmodulated electrodes have been built for beam transport experiments [5] to investigate current limits and instabilities. Here the beam behaviour of transported beams will be described in RFQs, which were designed and built for the acceleration of ions. The RFQ design has to be made for the lowest charge to mass ratio of the ions to be accelerated, input and output specific energy or velocity resp. are fixed and the cell length of the RFQ must fulfill the Wideroe resonance condition  $l = v_p/2f = \beta_p \lambda_v/2$ . Energy variable RFQs [6] can be built, when the frequency varies with the particle velocity  $v_p \sim f$ . The electrode modulation will be adjusted for simultaneous transverse focusing and longitudinal bunching and acceleration along the RFQ. The applied electrode voltage depends on the specific charge and is chosen in such way, that  $\zeta/AU\cos\phi_s$  is matched to the designed  $v_p$  of the RFQ cell considered. Small deviations  $U$  will be automatically corrected by the ions slipping to another rf phase  $\phi_s$ . Ions with input energies much higher or smaller than the design value cannot fulfill the Wideroe condition and get out of the acceleration process, the same happens for too small electrode voltages. The beam behavior for these cases has been studied and some possible applications are discussed.

## II. TRANSPORT EXPERIMENTS

Transport experiments have been carried out with a small proton RFQ [7]. The experimental setup is shown schematically in fig. 1. The proton beam is extracted by an accel-decel-system from a plasma beam ion source, which delivers a high fraction (80%) of protons. The focusing of the beam into the RFQ is done by a solenoid. The RFQ which is of the split coaxial type [8] consists of 32 cells only and bunches and accelerates protons from 6.5 to 50 keV at an design electrode voltage  $U_{des} = 9$  kV. The shaper is omitted for a shorter length, which causes longitudinal losses. The RFQ operates at 50 MHz, the total length is 58 cm.

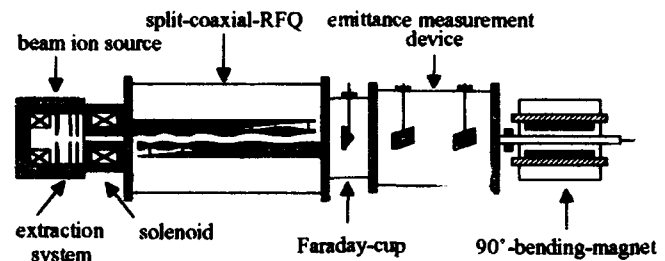


Fig. 1. Schematic drawing of the experimental setup

For the beam diagnosis behind the RFQ a Faraday cup, a bending magnet and an emittance measurement device could be used. First the operation at design values has been checked. Fig. 2 shows the measured transmission curve as function of electrode voltage for the design input energy of 6.5 keV.

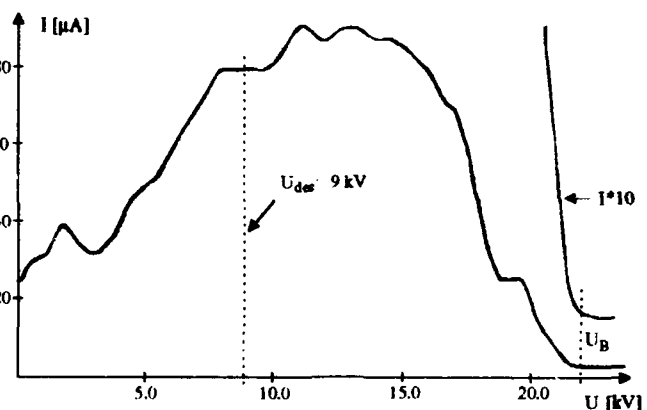


Fig. 2. Measured transmission vs. electrode voltage for design input energy,  $T_{in} = 6.5$  keV

\* Work supported by the BMFT under contract nr. 06OF3511

As can be seen from the plot some fraction of the beam is transmitted already, when no electrode voltage is applied, due to the short total length. With increasing voltage the transmitted beam rises already before acceleration starts ( $U_{\text{acc}}=9$  kV), the protons being transported through the RFQ. At high voltages the beam motion gets transversally unstable and the transmission is breaking down at  $U_B$ . The same behaviour can be observed in fig. 3, where the measured transmission is plotted as function of the electrode voltage for proton beams with input energies far lower than the design value of 6.5 keV.

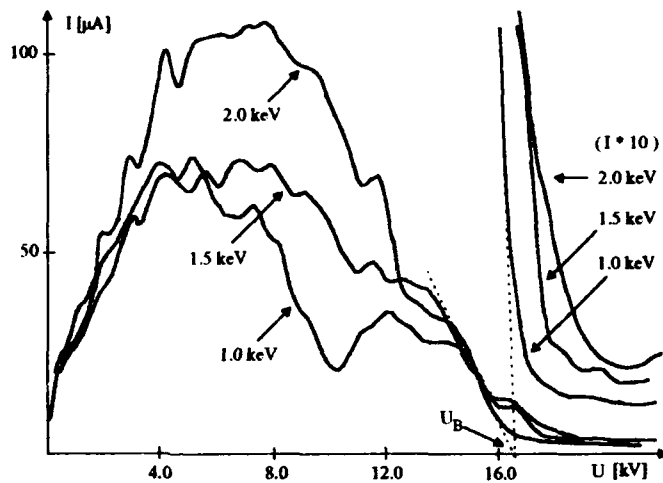


Fig. 3 Transmission vs. electrode voltage for three beam input energies: 1.0, 1.5 and 2.0 keV

Again the transmission first rises and drops at high voltages, but now the break-down voltage  $U_B$  is only 16.4 kV instead of 21.7 kV as before. This lower voltage can be explained by the change in the transverse rf defocusing, when the beam is transported instead of being accelerated. Fig. 4 gives a plot of the measured energy spectra for three different electrode voltages and  $T_{\text{in}} = 1.5$  keV. At the low voltage of 5.4 kV only some energy spread had been introduced into the beam, at the high voltage a partial acceleration to 10 keV ( $T_{\text{acc}}=50$  keV) took place.

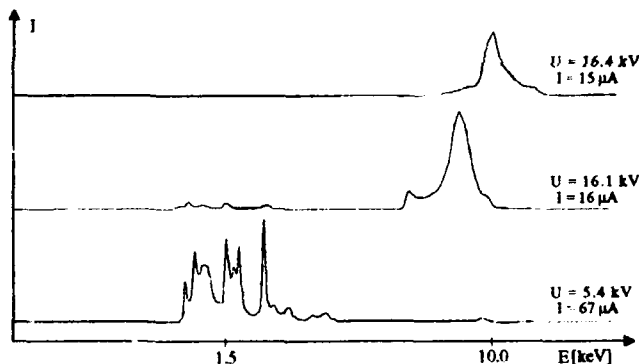


Fig. 4 Energy spectra for different electrode voltages and  $T_{\text{in}} = 1.5$  keV

At the point of breakdown of the transmission the transverse phase advance is  $180^\circ$ , to which a certain focusing gradient belongs. If the radius is known precisely, from this value the electrode voltage can be determined. This could be an additional method for checking the shunt impedance and efficiency of a RFQ [9]. As a final example the measured energy spectra for the transport of protons as function of the electrode voltage are presented in fig. 5 for constant input energy.

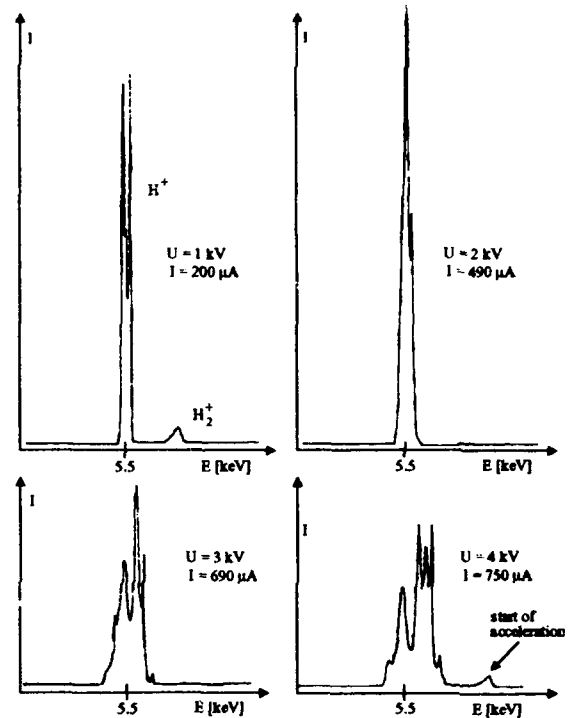


Fig. 5 Measured energy spectra for the transport of a proton beam with  $T_{\text{in}} = 5.5$  keV for different electrode voltages below the design voltage.

As can be seen from this curves the output energy is constant, which means that transport takes place. The width of the curve, i.e. the energy spread, is directly proportional to the applied electrode voltage.

### III. RFQ WITH DIFFERENT OUTPUT ENERGIES

In the measurements steps in the output energy of the beam could be observed, when the electrode voltage was varied from low values to the design value for a beam with design input energy. These steps could be reproduced for certain constant voltages and were better marked at voltages closer to the design voltage. This effect can be explained as follows: for voltages below the design voltage the ions must change to a lower synchronous phase to be stable accelerated. If the voltage is such low, that no stable phase could be found, particles can no longer reach the design energy. For a bunched beam with a small bunch width the whole bunch will be decelerated and can loose once, twice or even more

often the electrode voltage times charge state times acceleration factor in energy. PARMTEQ calculations came out with the same results. This effect could be used for the design of a RFQ with different output energies. Fig. 6 shows as an example the longitudinal and transverse beam behaviour along a RFQ. In the first part the beam is mainly captured and bunched before acceleration can start.

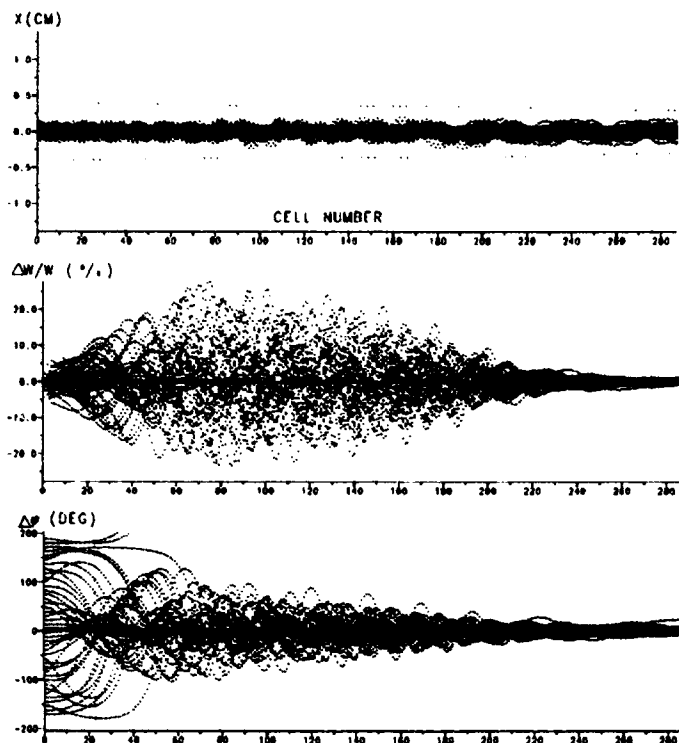


Fig. 6. Transverse and longitudinal beam behaviour along a RFQ

If the RFQ at the end of the bunching process is cut into two pieces, already two final energies are available: The bunched beam can be transported with the output energy of part 1 through part 2 at low electrode voltages to maintain transverse focusing, or can be accelerated in part 2 to the original final energy at design voltage. Two more intermediate energies can be adjusted, when the voltage in part 2 is varied. Fig. 7 a shows the result of PARMTEQ calculations for  $U_{el} = 0.8U_{des}$ , fig. 7 b for  $U_{el} = 0.62U_{des}$ . The final energies in these examples are 30 and 40% lower than the energy with acceleration. Together with the transport energy of 50% beyond, four different output energies are available with high transmission and good beam quality.

#### IV. CONCLUSION

Measurements and calculations show, that transport of ions with good beam quality in RFQ accelerators is possible. One possible application is the design of RFQs with different end energies without frequency variation e.g. for ion implantation.

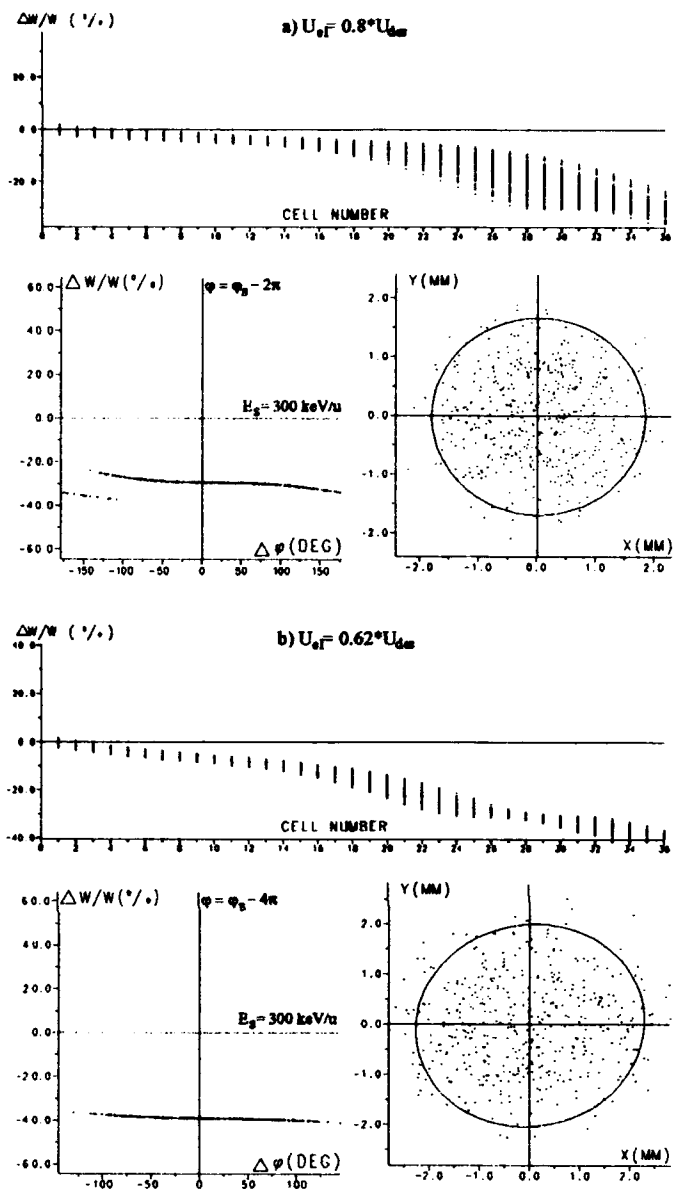


Fig. 7. Example of longitudinal motion and output emittances for lowered electrode voltage

#### V. REFERENCES

- [ 1 ] I. M. Kapchinskij, V. Teplyakov, Pribori Tekh. Eksp. 119,2 (1970) 17
- [ 2 ] K. R. Crandall, R. H. Stokes, T. P. Wangler, BNL-51143 (1980) 205
- [ 3 ] J. Dehen et al., Ed. Frontiers, Vol. 2 (1992) 967
- [ 4 ] e.g. A. Schempp, Habilitationsschrift (1991)
- [ 5 ] N. Zoubek, Thesis, Frankfurt university (1987)
- [ 6 ] A. Schempp, LA-12004-C (1991) 535
- [ 7 ] P. Leipe et al., NIM A278 (1989) 213
- [ 8 ] R. W. Müller, BNL-51143 (1980) 148
- [ 9 ] J. Dehen, Thesis, Frankfurt university (1993)

# An ESQ Lens System for Low Energy Beam Transport Experiments on the SSC Test Stand

S. K. Guharay, C. K. Allen, M. Reiser

Laboratory for Plasma Research, University of Maryland, College Park, MD 20742, USA  
and K. Saadatmand

SSC Laboratory, Dallas, TX 75712, USA

## Abstract

A low-energy beam transport system is designed with the aim of transporting a 30 mA, 35 kV  $H^-$  beam from a volume source and focusing it into an RFQ. The characteristics of the beam from the source are determined analyzing the emittance data. The behavior of the beam through the LEBT is studied using simulation codes. The system parameters are optimized so that the LEBT has a very modest contribution to the emittance growth (here a factor of about 1.5) and the emittance budget of the linac section is maintained.

## I. INTRODUCTION

One of the vital considerations in modern high-energy accelerators is related to the design of an efficient low-energy beam transport (LEBT) section so that an intense, high-brightness beam (here we consider an  $H^-$  beam) can be transported over certain distance and finally focused into the commonly used RFQ accelerator in the linac section. The emittance growth in the LEBT is the key issue in developing a good scheme at the low-energy end of the accelerator chain. Thus, in order to achieve a good beam quality and match it to the acceptance of an RFQ a systematic study of beam dynamics in the preceding sections including the extraction optics of the ion source is warranted. We have experienced that emittance measurements of the beam from an ion source and an analysis of the data to characterize the beam at the extraction electrode are two important problems in the context of designing an efficient LEBT. Earlier we reported [1,2] on the beam characterization and beam dynamics through a LEBT for  $H^-$  beams from a Penning-Dudnikov type [3] and magnetron type sources. In recent years significant progress has been made in the performance of volume sources [4,5]; normalized beam brightness approaches about  $10^{11}$  A/(m-rad)<sup>2</sup> for  $H^-$  beams. This article highlights on the study of  $H^-$  beams

0-7803-1203-1/93\$03.00 © 1993 IEEE

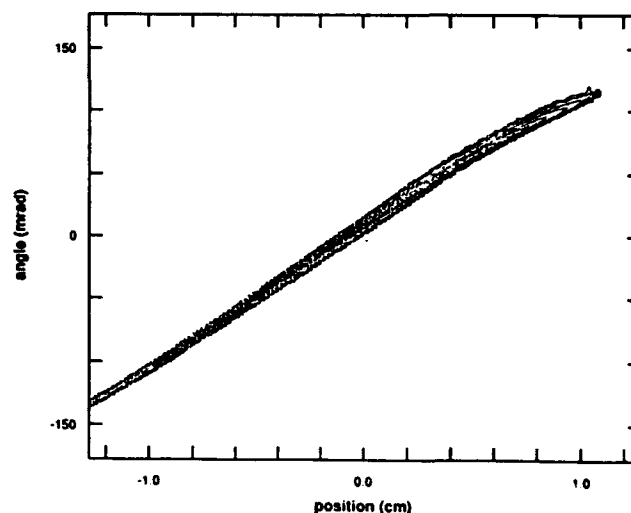


Figure 1: Contour emittance plot.

from the SSC volume source with the aim of designing a LEBT system to deliver a 30 mA, 35 kV beam matched with the RFQ input.

## II. BEAM CHARACTERISTICS

### A. $H^-$ Beam from the Ion Source

The  $H^-$  beam from the SSCL volume source is measured at 10.13 cm downstream after the electrons (ratio of initial electron to ion current  $\sim 40$ ) are deflected away from the extracted beam current by a 10 cm long magnetic trap. Figure 1 shows the contour plots in the  $x - x'$  space from emittance diagnostics; the flattening of the distribution in the upper half is possibly caused by the space-charge force due to the electrons deflected upward. The beam parameters at  $z = 10.13$  cm are: beam size  $D = 2.38$  cm, full divergence  $\Delta\theta = 260$  mrad,  $\pi\epsilon_n = 0.1537\pi$  mm-mrad. These data are used in an envelope simulation code to estimate the beam characteristics at the extraction electrode; space-charge effects due to the electrons in the extraction region are included. Figure 2(a) shows the assumed space-charge correction factor,  $f$ , due to the electrons. Note that  $f$  is

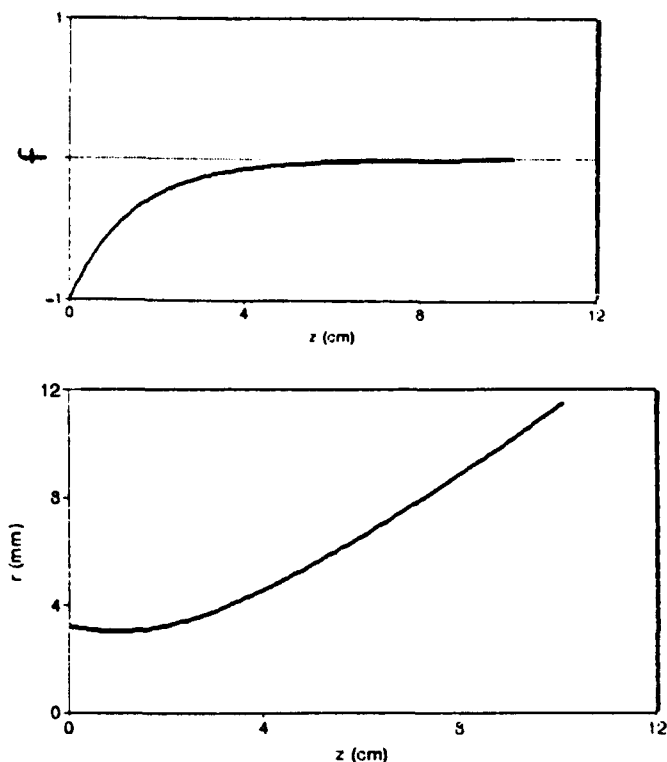


Figure 2: (a) Space-charge correction factor  $f$ ; (b) beam envelope.  $z = 10.13$  cm corresponds to the location of emittance measurements.

negative here and the beam perveance is to be multiplied by the factor  $(1 - f)$ . The beam envelope in Fig. 2(b) is evaluated by integrating the K-V envelope equations using a fourth-order Runge-Kutta method. This analysis suggests that the beam at the extraction electrode emerges nearly parallel, and the beam size is close to the aperture radius ( $= 4$  mm).

### B. Desired Output Beam Parameters from the ESQ LEBT

The purpose of the LEBT section is to isolate the RFQ from the ion source for a clean operation and also to deliver a matched beam to the RFQ. The SSC RFQ acceptance for a 30 mA, 35 kV  $H^-$  beam is given by the Twiss parameters:  $\alpha = 1.26$ ,  $\beta = 1.86$  cm/rad,  $\pi\epsilon_n = 0.2\pi$  mm-mrad. As the normalized rms emittance of the  $H^-$  beam from the source is about  $0.1537\pi$  mm-mrad (Fig. 1), the LEBT is to be designed under a very tight emittance budget. The matching condition dictates that the beam parameters at the tip of the RFQ vane should be: beam radius = 1.3 mm and the corresponding slope of the beam envelope =  $-89$  mrad; this is located at about 3 cm downstream from the front wall of the

RFQ. It has been shown earlier that a short (about 5 cm long) single einzel lens module between an ESQ LEBT and the RFQ will be a good choice in satisfying the aforementioned stringent conditions of the RFQ [2]. The ESQ LEBT transforms the highly diverging beam from the ion source into a moderately converging one without any significant emittance dilution, and the einzel lens provides the final strong focusing. This analysis showed that the parameters of the output beam from the ESQ LEBT should follow: beam radius  $\sim 3$  to 5 mm, the corresponding slope of the beam envelope  $\sim -30$  to  $-50$  mrad.

### III. BEAM TRANSPORT THROUGH THE ESQ LEBT

The design principles of the ESQ LEBT follow the scheme as discussed earlier [1,2]. The present configuration of the magnetic trap in the extraction region of the SSCL volume source restricts the ESQ LEBT's distance to the extraction aperture to about 10 cm. This causes the beam to blow up significantly (Fig.1). After a detailed analysis with such a beam it is recognized that the goal to deliver a matched beam to the RFQ for the full beam current (30 mA) is a very difficult task. Our analysis suggests that a shorter magnetic trap (about 5 cm long) will be a better choice. Figure 3 shows the beam envelope through the ESQ LEBT when a hard-edge focusing function for the external field is assumed. An initial drift space of 5 cm long is considered, and a profile of the space-charge correction factor due to the electrons (Fig. 3, bottom) is assumed. The beam parameters at the extraction aperture are taken from the analysis of Fig. 2. The maximum aperture radius of the quadrupoles is 22 mm; it was taken as 12 mm when the LEBT was closer (1.5 cm) to the extractor [1].

The distribution of the beam particles through the ESQ LEBT is estimated using a modified PARMILA code [6]. Figure 4 shows the particle distribution in phase space for  $I = 30$  mA. The estimated output beam parameters are:  $X = 3.5$  mm,  $Y = 3.5$  mm,  $X' = -51.7$  mrad,  $Y' = -50.8$  mrad,  $\epsilon_n^f/\epsilon_n^i = 1.5$ . The emittance growth is primarily due to chromatic aberrations.

### IV. CONCLUSIONS

Emittance measurements of a 30 mA, 35 kV  $H^-$  beam from the SSCL volume source have been studied. The simulation results suggest that the  $H^-$

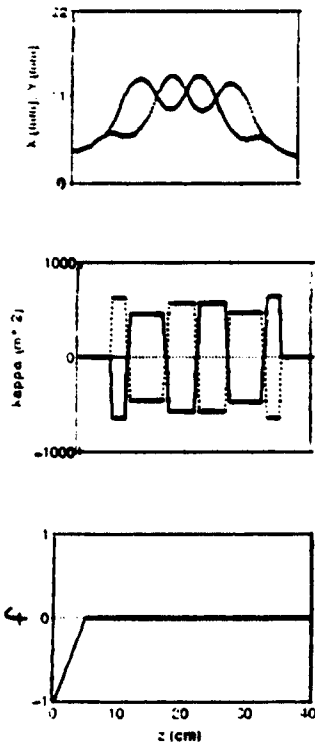


Figure 3: K-V envelope solution.

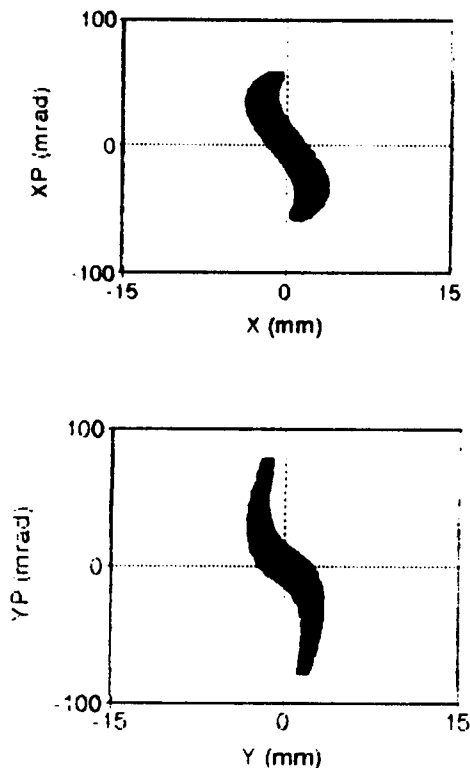


Figure 4: Particle distribution at the output of the ESQ LEBT.

beam envelope has a waist at the extraction aperture. With this definition of the input beam and a given set of characteristic parameters of the RFQ acceptance, we have designed a LEBT system. The particular design of the LEBT consisting of six ESQ lenses and a short einzel lens can transport the full beam current and match it to the RFQ.

Beam transport experiments with a prototype ESQ LEBT will be conducted to validate the simulation predictions. Further, the 3-D LAPLACE simulation scheme is being improved using a method of moments where any arbitrary boundary can be represented numerically and the practical problems will be simulated more realistically [7].

This work was supported by ONR/SDIO and DOE.

#### IV. REFERENCES

- [1] S. K. Guharay, et. al., *Proc.1991 Particle Accelerator Conf.*, p. 1961.
- [2] S. K. Guharay, et al., *BNL Conf. on Production and Neutralization of Negative Ions and Beams*, Nov. 1992 (to be published in AIP Proc.).
- [3] P. G. O'Shea, et al., *Nucl. Instrum. & Meth. in Phys. Res. B40/41*, 946 (1989).
- [4] K. N. Leung, *BNL Conf. on Production and Neutralization of Negative Ions and Beams*, Nov. 1992 (to be published in AIP Proc.).
- [5] K. Saadatmand, these proceedings.
- [6] C. R. Chang, Ph. D. Thesis, Univ. Maryland, 1989.
- [7] C. K. Allen, et al., these proceedings.

# Test of the Transport Properties of a Helical Electrostatic Quadrupole and Quasi-Octupole\*

L. Xiu, S. Ohnuma, K. Wang  
Physics Dept., University of Houston  
Houston, TX 77204-5504 USA

and

C.R. Meitzler, Y. Xu  
Physics Dept., Sam Houston State University  
Huntsville, TX 77341 USA

## Abstract

A third-generation continuous helical electrostatic quadrupole (HESQ) lens has been built and tested. The new HESQ is 21.5 cm long and has a 3.6 cm diameter aperture. The HESQ has been tested under two separate conditions: with a pulsed 25 keV, 0.5 mA proton beam; and a 25 keV, 10 mA proton beam. The input emittance was fixed using a multi-aperture collimator. A comparison is made between experiment and numerical simulations for a wide variety of operating conditions. A second possible operating mode is the quasi-octupole mode[1] which offers significantly reduced aberration when compared to the quadrupole mode. The results of preliminary tests in this operating mode will be presented.

## I. Introduction

The helical electrostatic quadrupole lens was originally proposed by Raparia[2] in 1990 as a way to transport a low-energy  $H^-$  beam from an ion source to a radio-frequency quadrupole accelerator. Several "proof-of-principle" tests[3] had been performed using a discrete helical structure which showed that the basic principles of Raparia's design were valid. These tests had shown that the lens would provide relatively strong focusing. Numerical tracking studies of this early HESQ have shown that various types of beam shape deformations in phase space are observed, with chromatic aberration being the dominant cause of distortion.

A continuous-type HESQ was used by Mori et al.[4] in 1991 to focus a 1 mA beam of  $Cu^-$  ions with much less emittance growth than was observed when an einzel lens was used in a similar test. Mori's test with copper ions was significant in demonstrating the potential of the HESQ to

transport intense negative ion beams. Encouraged by KEK's success, we had designed a new continuous-type HESQ in January 1992. A summary of the design was presented in Reference 1. The present paper presents a summary of a series of in-beam tests during the fall and winter of 1992/93.

## II. Quadrupole Operating Mode

A continuous HESQ was designed using both the experience gained from both experimental studies of the discrete HESQ, and from numerical simulations of it. Table 1 presents a summary of the basic design parameters.

For the testing program, a duoplasmatron proton source[5] was used to produce the ion beam. The duoplasmatron source had a single gap extraction system capable of being biased up to 25 kV. The extractro was followed immediately by an einzel lens operated in decel mode. A 2.5 cm diameter collimator mounting flange was located 20 cm from the einzel lens. Inside the collimator mounting flange, we were capable of installing a multi-aperture set of slits to generate a controlled emittance which was somewhat independent of the source's operating condition. For large diameter beams, this set of slits was removed from the mounting flange. Immediately after the collimator was a zero-length faraday cup[6] constructed on a PC-board. The HESQ was mounted with the alignment of each of the four segments being independent.

Table 1. Parameters for third generation HESQ.

Number of segments	4
Length of segment	5 cm
Helical pitch	1.5 cm
Gap between segments	0.5 cm
Rod radius	1.5 cm
Aperture	36 mm
Total length	21.5 cm

\* This work supported by the Texas National Research Laboratory Commission under grant RFGY9203.

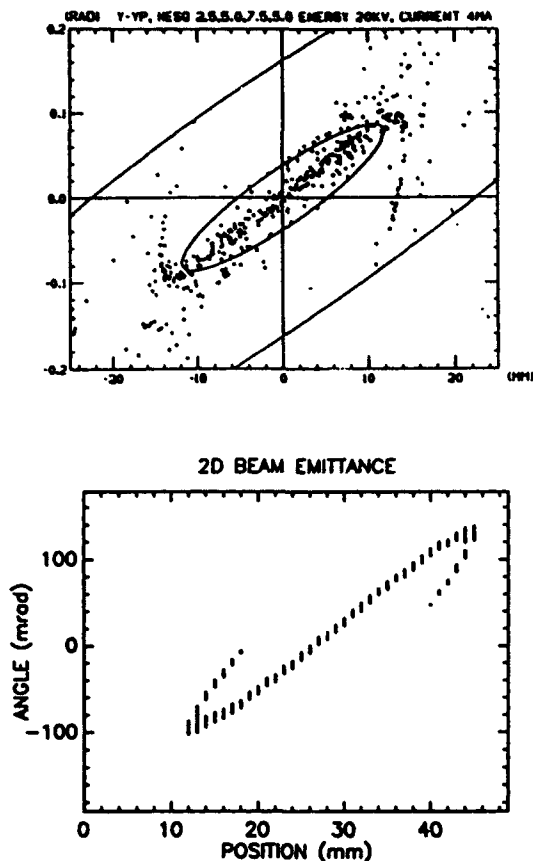


Figure 1 Comparison of numerical simulation (top) and experimental data (bottom) for a large diameter beam incident on the HESQ.

### A. Large Diameter Beams

A large diameter beam of protons was injected into the HESQ. The emittance of the beam was measured without any voltage being applied to the HESQ. The electrode voltages were then set to 2.5, 5.0, 7.5, and 5.0 kV on first through fourth segments, respectively. The beam emittance was then measured one more time. (The other plane was not measured at this time due to a problem with the current pick-up in the emittance scanner: this measurement will be performed in the future.)

The results of an emittance measurement in one plane for a 30 mm diameter, 10 mA proton beam is shown in Figure 1a. A numerical simulation, which includes space charge, of the beam transport through the HESQ using the known initial source emittance is shown in Figure 1b. The qualitative agreement between the experiment and simulation show that we are properly including space charge in our calculation.

### B. Low-Current Tests

A four-aperture collimator was constructed to simulate the emittance of the beam extracted from a magnetron ion source. The beam from the duoplasmatron was focussed onto the collimator. Due to the low acceptance of the aperture system, the beam was reduced from approximately 10 mA to 0.5 mA. This reduction in the intensity permitted us to examine the HESQ's transport properties when space charge was not a dominating factor.

A set of over 1000 low-current measurements were undertaken to map as much of the operating space as possible. The procedure followed in these measurements was similar to that used in Section A: the beam emittance was determined; voltage was applied to the HESQ electrodes; the final beam emittance was measured again. The results of a typical emittance measurement for both the X- and Y-planes are shown in Figure 2. The measured and calculated unnormalized beam emittances for this case are summarized in Table 2.

During the course of our measurements, we had noted that there was considerable steering as voltage was applied to the electrodes. After the measurements, we dis-assembled the HESQ and checked the alignment of the electrodes. We discovered that some of the electrodes were severely misaligned. This problem has been corrected, and a new set of measurements are underway.

Table 2. Measured unnormalized emittances in units of  $\pi$  mm-mrad.

	X	Y
Source	13.6	17.8
After HESQ	16.1	20.0
calculated	24.7	40.3

### III. Quasi-Octupole Operating Mode

The quasi-octupole operating mode for the helical electrostatic quadrupole structure was proposed in 1992 by Xiu et al.[1] The advantage of the quasi-octupole mode was that the lens would be able to transport higher currents with low electrode voltages. The HESQ was operated in quasi-octupole mode by connecting the four electrodes to a single power supply. The polarities of the power supplies for each segment were positive, and the potentials on the four segments were 4.0 kV, 10.0 kV, 7.5 kV, and 20.0 kV, respectively. A 25 kV proton beam was injected into the lens, and the output emittance was measured with the Allison-type electrostatic emittance scanner. We observed that we needed to apply 20 kV to the final electrode in order for the lens to focus the beam. This seems to imply the quasi-octupole mode for the operated as a thick einzel lens.

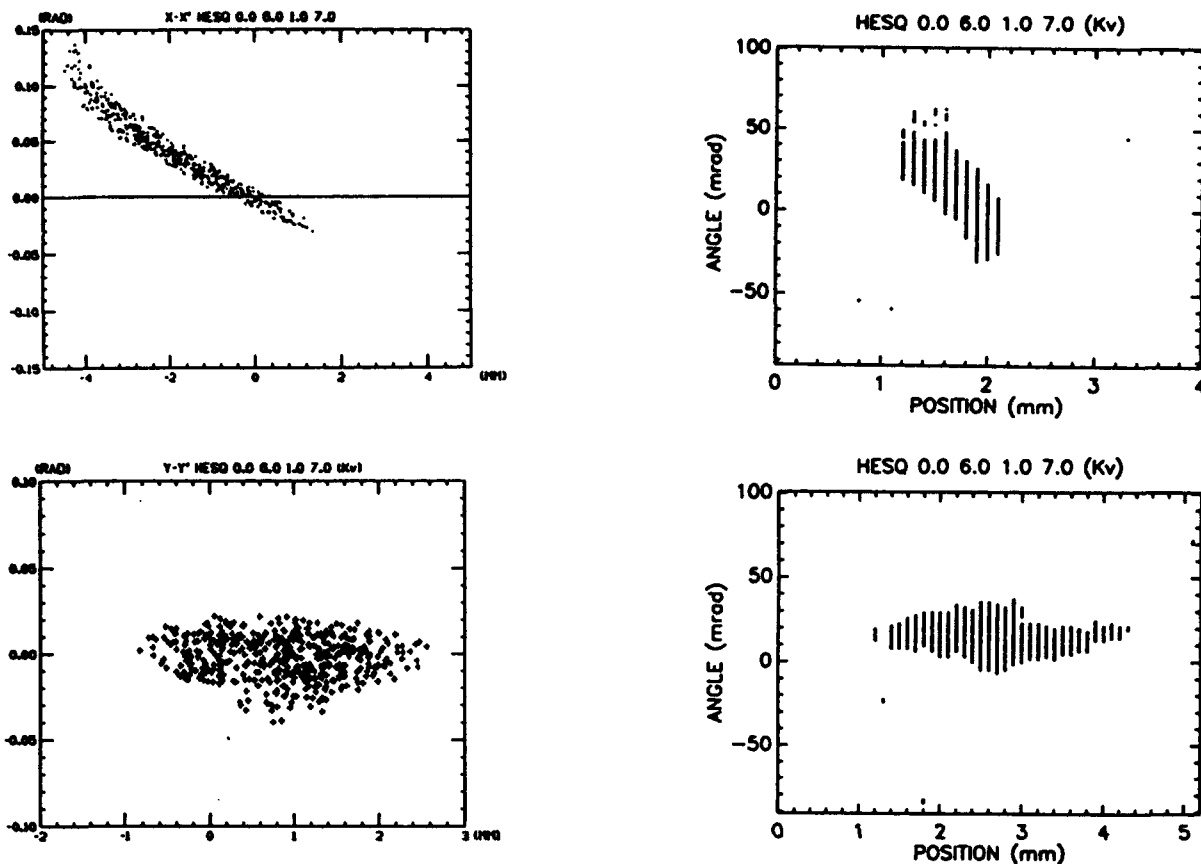


Figure 2 Measured and calculated emittances of a low-current proton beam transported through the HESQ. RIGHT: measured, LEFT: calculated

#### IV. Summary

Based on our experience with the first HESQ, we designed a new, continuous HESQ. The operating parameter space of the HESQ has been explored. There was some emittance growth of the beam as it passed through the lens; however, due to misalignments of the electrodes it is not clear how much the misalignments contributed to this growth. The quasi-octupole mode of operation did not provide the improved performance anticipated from numerical simulations.

#### V. Acknowledgements

The authors wish to thank the Dr. Peter McIntyre and the staff of the Texas Accelerator Center at the Houston Advanced Research Center for enabling us to perform these measurements at their facility. We would also like to thank Larry Crowe for his help with maintaining the equipment for this experiment. We would also like to thank Chuck Carlson of Brookhaven National Laboratory for lending a duoplasmatron to us.

#### VI. References

- [1] L. Xiu, L. Dong, S. Ohnuma, and C.R. Meitzler, *Proceedings of the Third European Particle Accelerator Conference*, Berlin, 24-28 March 1992, p. 1533.
- [2] D. Raparia, Ph.D. Dissertation, University of Houston, Houston, Texas, USA (1990).
- [3] C.R. Meitzler, K. Antes, P. Datte, F.R. Huson, and L. Xiu, *Conference Record of the 1991 IEEE Particle Accelerator Conference*, May 1991, San Francisco, p. 1958.
- [4] Y. Mori, A. Takagi, T. Okuyama, M. Kinsho, H. Yamamoto, T. Ishida, and Y. Sato, *Proceedings of the 8th Symposium on Accelerator Science and Technology*, Saimata, Japan (1991), p. 182.
- [5] General Ionex Corporation, 19 Graf Road, Newburyport, Massachusetts, USA.
- [6] J.M. Bogaty, R.C. Pardo, and B.E. Clift, *Proceedings of the 1990 Linear Accelerator Conference*, Los Alamos Report LA-12004-C (1991) p. 465.

# Comparison of Experimental and Simulated Results for the SSC LEBT

J.W. Lenz, J. Hebert, N. Okay, D. Raparia, K. Saadatmand  
Superconducting Super Collider Laboratory\*  
2550 Beckleymeade Avenue, Dallas, Texas 75237

## Abstract

The SSC LEBT (Low Energy Beam Transport) device focuses and steers a divergent 30 mA  $H^-$  beam extracted at 35 KV from the volume ion source into a strongly converging beam to match the acceptance of the 2.5 MeV RFQ. Of the LEBT candidates, an einzel lens and HESQ (Helical Electro-Static Quadrupole) are presently under study at the SSC. The experimental emittance results for the einzel lens at the RFQ acceptance plane are compared to AXCEL simulations. A comparison is made between the PARTEQ simulated percent of beam transmitted through the RFQ with the experimentally measured beam and with the simulated AXCEL beam.

## I. INTRODUCTION

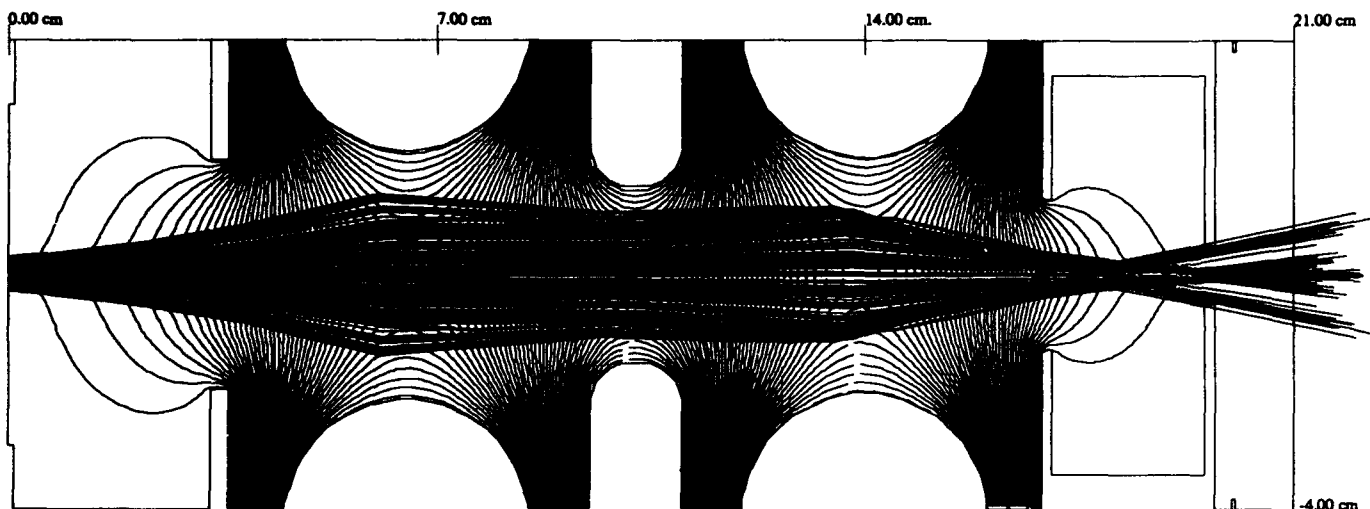
The SSC LEBT focuses the divergent 30 mA  $H^-$  beam from the volume  $H^-$  ion source[1] into the 2.5 MeV RFQ as part of the SSC Injector for the Linac. Electrostatic focusing LEBTs were chosen because of the SSC requirement of a short pulse length (9.6-48  $\mu$  sec) beam. For such a short pulse length it was decided to avoid a LEBT using magnetic solenoids and neutralization gas focusing. The electrostatic lenses were well understood and were suitable for arbitrarily short pulses. A photograph of the ion source-einzel lens-RFQ entrance assembly is shown in Fig. 1. The RFQ acceptance requirements are quite demanding, requiring a strongly



Fig.1 Ion Source-LEBT-RFQ entrance Assembly.

converging (140 mrad)-4 mm diameter beam. The acceptance Twiss parameters are:  $\alpha_{x,y} = 1.26$ ,  $\beta_{x,y} = 0.0186$  mm/mrad, and  $\epsilon_{rms,nor} < 0.20 \pi$  mm-mrad. See Fig. 5.

The beam optics geometry, potential lines, and beam ray traces are shown in Fig. 2. Reference Fig. 2 for the following dimensional location descriptions. A magnetic dipole electron separator occupies the axial space 0.0 to 3.2 cm. The axial space between 3.2 and 16.9 cm is expandable and depicts the



COMMENT: LENS#1=30,948V LENS#2=33,016V

CYCLE: 10. PLOT: 3. DATE: 3-MAR-93

Fig. 2 Einzel lens geometry, potential lines, beam trajectory.

\* Operated by the University Research Association, Inc. for the U.S. Department of Energy, under contract No. DE-AC35-89ER40486.

LEBT. The center electrode of the einzel lens is a split quadrant used both as a quasi ground plane for the lenses and to steer the beam vertically and horizontally. The acceptance plane for the RFQ is at 20 cm (as shown by the indentation in Fig. 2). The axial space between 17 and 20 cm is reserved for diagnostic insertion. This drift space does limit the beam convergence of this LEBT design.

## II. CALCULATIONAL METHOD

An experimental phase-space plot of the extracted beam is shown in Fig. 3. The  $H^0$  beam has been subtracted. The Twiss parameters are:  $\alpha_x = -21.38$ ,  $\beta_x = 0.1217$  cm/mrad, and  $\epsilon_{rms,unmor} = 1.59$  cm-mrad at the 91.8% contour line, assuming a gaussian beam. The Y-plane phase-space plot is very similar except angled upward at 22 mrad because of the electron separator magnet. Because AXCEL[2] assumes cylindrical symmetry, the X-plane plot was used for this simulation input. The experimental ion source phase-space plot was generated within AXCEL. With the experimental voltages applied to the lenses (nominally 31KV upstream and 33KV downstream), the phase-space plot of Fig. 4 was simulated at the RFQ acceptance plane. Ten iterations with 1,000 rays was used. The experimental phase-space plot from a slit and collector is shown in Fig. 5. In both Figs. 4 and 5 the nominal RFQ acceptance ellipse is shown. The particles within the described RFQ acceptance ellipse are transmitted through the RFQ. The other particles are not transmitted, due mainly to transverse mismatching [3].

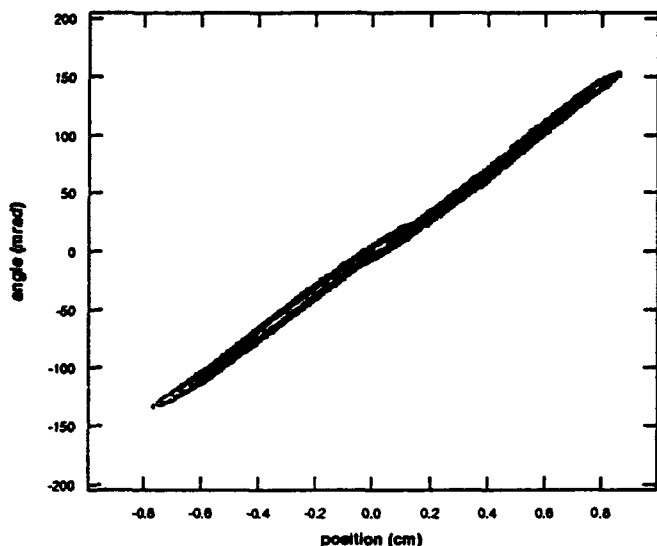


Fig. 3 Experimental beam extracted from the ion source

## III. CONCLUSIONS

For comparison, the resultant Twiss parameters for all the particles are shown in Table 1. Included is the important comparison of the sub-set of particles transmitted through the RFQ, simulated by the multiparticle code PARTEQ [4].

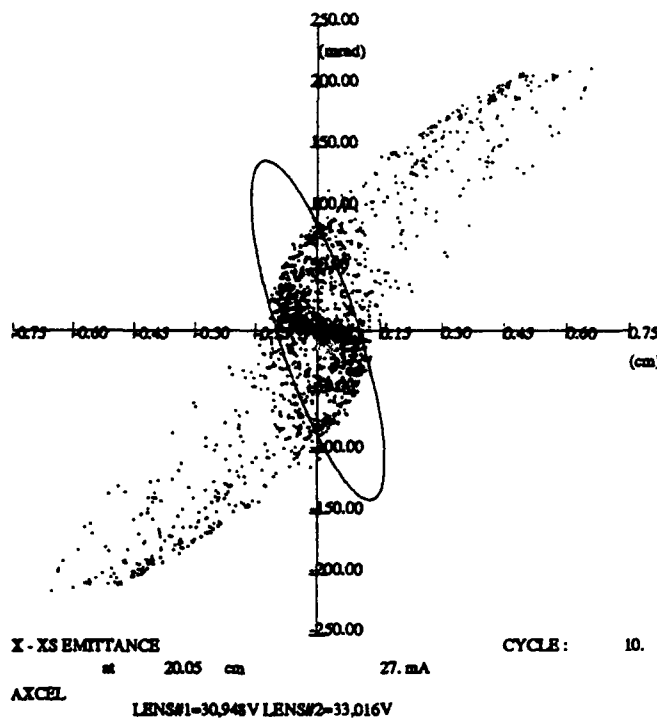


Fig. 4 AXCEL phase-space plot

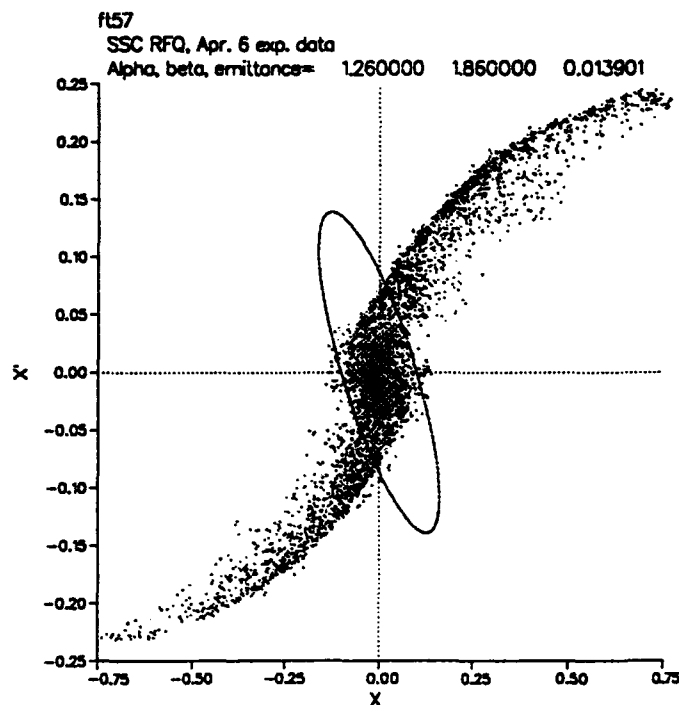


Fig. 5 Experimental phase-space plot

Table 1.

	$\alpha$	$\beta$ cm/mrad	$\epsilon_{rms,unmor}$ cm-mrad	RFQ % trans. simul
Exper. 91.8%cont	-2.018	0.0040	9.240	38.8
AXCEL 90%cont	-2.029	0.0054	10.722	62.

#### IV. ACKNOWLEDGEMENTS

We wish to acknowledge the efforts of Jun Wu in revising the AXCEL SSC code from a VAX to a UNIX operatable code.

Considering that neither the spacial and angular translations of the experimental beam nor the steering voltages were included in the AXCEL simulation, the comparison in Table 1 indicates reasonable agreement of the Twiss parameters for all the particles (a macro comparison). However in the region of special interest, that portion of the emittance plot whithin the RFQ acceptance ellipse, the PARMTEQ simulated percent transmission through the RFQ using AXCEL simulated and experimental beam as input is only whithin ~60% agreement.

The AXCEL input file asks for the Twiss parameters ( $\alpha$ ,  $\beta$  and  $\epsilon$ ) of an input beam then a particle-by-particle input file is created from these parameters. When one knows the particle-by-particle parameters, such as in our slit-collector emittance data, one might enter these data directly into the input file. This method may improve the accuracy of AXCEL when a particle-by-particle emittance is known, incorporating spacial and angular translation.

#### V. REFERENCES

- [1] K. Saadatmand, et al, AIP conference Proceedings of the Sixth International Symposium of Production and Neutralization of Negative Ions and Beams (1992), to be published.
- [2] P. Spadte, GSI-Report 9, GSI, West Germany, 1983 (Version 85/2 used). Revised by Deepak Raparia and Jun Wu for the Unix system
- [3] F.W. Guy, J.W. Hurd, D. Raparia, K. Saadatmand, W..A. Whittenberg, "SSC Radio-Frequency Quadrupole Beam: Comparison of Experimental and Simulated Results", these Proceedings.
- [4] K.R. Crandall, "PARMTEQ A Beam Dynamics Code for the RFQ Linear Accelerator, AIP Conference Proceedings 177, Linear Accelerator and Beam Optics Codes, La Jolla Institute, pp. 22-28 (1988). Modified to include multipoles by Frank Guy, SSC

# Axial Magnetic Field Lens with Permanent Magnet

Yoshihisa Iwashita  
 Accelerator Laboratory  
 Nuclear Science Research Facility  
 Institute for Chemical Research, Kyoto University  
 Gokanosho Uji, Kyoto 611, JAPAN

## Abstract

A compact Permanent Magnet Symmetric (PMS) lens which produces the axial magnetic field is studied. The proposed lens has no iron pole piece except for the return poles on both ends. It can produce the magnetic field on the axis more than the remanent field of the magnet material by the perpendicular field superimposition.

## I. INTRODUCTION

A 7-MeV proton linac was constructed at Institute for Chemical Research, Kyoto University.[1,2] The linac is consisting of a 2-MeV RFQ linac and a 7-MeV Alvarez (DTL). The operating frequency is 433.3 MHz and the structure dimension is compact. Because of the poor vacuum property of the RFQ cavity, two evacuation ports are located at both the entrance and exit side of the cavity.

In order to match the RFQ acceptance, the input beam has to be focused strongly to the RFQ. Unfortunately, the entrance side of the RFQ is occupied by the vacuum port and the final focus element has to be installed into the hole in the end plate of the RFQ. The hole has diameter of 40 mm and the depth of 60 mm. A compact focusing device which can fit in this size had to be devised.

For future study of the simultaneous acceleration of both positive and negative ions, einzel lenses are not preferable. The RFQ requires the round beam in X-Y plane at the entrance, and the quadrupole lenses are not adequate in this respect. A magnetic lens which produces the magnetic field of axial symmetry was picked up as a candidate for the purpose. The field can be produced by a "solenoid". Applications of anisotropic magnet have been studied for charged particle beam manipulations [3,4,5]. With a careful study of the radially oriented anisotropic magnets, it was found that a compact strong Permanent Magnet Symmetric (PMS) lens can be fabricated in the limited size by application of the perpendicular field superimposition.

## II. PERPENDICULAR FIELD SUPERIMPOSITION

Let us consider the anisotropic magnet configuration in the two dimensional space as shown in Figure 1. The magnetic field has the direction of Z, and the maximum at the center. The analytical expression for the maximum field is calculated as follows;

$$B_{\max} = \frac{Br}{\pi} \left\{ \log \left( 1 + \frac{l^2}{b^2} \right) - \log \left( 1 + \frac{l^2}{r^2} \right) \right\}. \quad (1)$$

0-7803-1203-1/93\$03.00 © 1993 IEEE

It can be shown that the value is not finite when  $l/b \rightarrow \infty$  keeping  $l/r$  finite. Because the produced field is perpendicular to the easy axis of the magnet, the operating point in the B-H curve will stay in the upper half. If the magnet material has no knee in the second quadrant of the B-H curve, which is easy requirement for almost rare earth magnet materials, no demagnetization is expected. Although it is only a logarithmic increase, it seems to have no limitation.

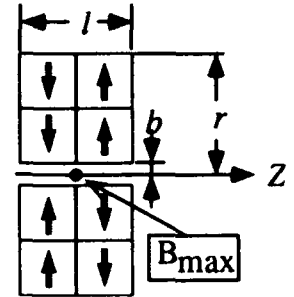


Figure 1. Geometry for field concentration test.

The field concentration by perpendicular filed superimposition is verified by a rough experiment. Eight pieces of 10 mm x 10 mm x 30 mm magnets made of NEOMAX 35H, which has  $B_r$  of 1.1 [T], are placed as shown in Figure 1. One block is consisted of four pieces which attract each other. Two of the blocks are fixed on jaws of a vice which is made of iron, and put close by pressing with the vice to the gap of 2 mm. The maximum field is measured by an axial Hall probe as 1.6 [T] which is more than  $B_r$ .

Neglecting the second term of the equation (1) and substituting the values for  $l$  and  $b$ , we get  $B_{\max}=1.6$  [T]. Because the jaws of vice is made of iron, it acts like return yoke. The magnetic field produced by the magnets with the iron return yoke is also calculated by PANDIRA [6]. It also shows the value 1.6[T] as a maximum.

## III. PROPERTY OF MAGNETIC FIELD LENS

The focal strength  $1/f$  for charged particles with the energy of  $eV$  in a magnetic field lens of axial symmetry is given by

$$\frac{1}{f} = \frac{e}{8m_0V^*} \int_{-\infty}^{\infty} B^2 dz \quad [m], \quad V^* = V \left( 1 + \frac{|eV|}{2m_0c^2} \right), \quad (2)$$

where  $e$  and  $m_0$  are the charge and the mass of the particles at rest respectively.[7] It should be noted that the focal strength is proportional to  $B^2$  and 20% increase in the focal strength will be obtained by 10% increase of the remanent field which will be achieved by material developments. The drawback is that the temperature coefficient of the focal strength is twice as large as that of the remanent field. On the other hand, this property can also be used as a focal strength adjustment by means of the temperature control. The typical temperature coefficient of the Nd-B-Fe magnet is 0.1% / °C.

#### IV. MAGNETIC FIELD PRODUCED BY A RADIALLY MAGNETIZED MAGNET

Let us consider a radially oriented permanent magnet ring as shown in Figure 2.

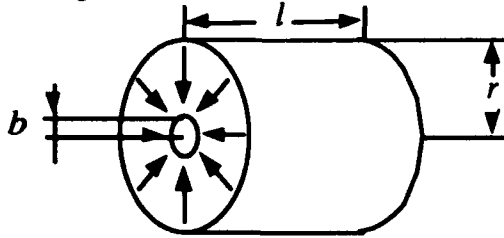


Figure 2. Radially oriented permanent magnet ring

Integrating over the magnetic dipole, the magnetic field on the axis of the magnet is given as

$$B(z) = \frac{Br}{2} \left\{ \frac{1}{r_1} - \frac{1}{b_1} - \frac{1}{r_0} + \frac{1}{b_0} + \log \frac{(1+r_0)(1+b_1)}{(1+b_0)(1+r_1)} \right\},$$

$$r_0 = \sqrt{1 + \left(\frac{z}{r}\right)^2}, \quad b_0 = \sqrt{1 + \left(\frac{z}{b}\right)^2},$$

$$r_1 = \sqrt{1 + \left(\frac{z+l}{r}\right)^2}, \quad b_1 = \sqrt{1 + \left(\frac{z+l}{b}\right)^2} \quad (3)$$

The magnetic field has a maximum at  $z=0$ , where the end of the magnet is located. The value is

$$B(0) = \frac{Br}{2} \left\{ \frac{r}{\sqrt{r^2+l^2}} - \frac{b}{\sqrt{b^2+l^2}} + \log \frac{1+\sqrt{1+l^2/b^2}}{1+\sqrt{1+l^2/r^2}} \right\}. \quad (4)$$

Again, it can be shown that the logarithm term is not finite if keeping  $l/r$  finite, and  $l/b \rightarrow \infty$ . In the real applications, two kinds of rings with different magnetization will be placed alternatively. In the case, the magnetic field should be superimposed and the maximum field is doubled. The principle of the perpendicular field superimposition should work here again. For example, a lens of two rings ( $b=5$  mm,  $r=2$  cm, and  $l=2 \times 2$  cm) has the maximum field of  $1.22 Br$ .

#### V. PMS LENS

To fabricate the real magnet, one has to consider several constraints. The ring should be segmented to realize the radially oriented anisotropic property. The return iron yoke has to be located around the magnet to reduce the leakage field on the axis particularly to the RFQ side. The case of the magnet can be made of iron, and acts as the return yoke. The corners of the magnets are rounded so that the lens has less aberration. The bore hole of the iron case at entrance side is made large to accept a beam with large diameter. The magnet material is NEOMAX 40 which has the remanent field  $Br$  of 1.29 T nominal. The final dimensions are shown in Table 1. Photo 1 shows the assembled PMS lens.

The field calculated by PANDIRA is shown in Figure 3. Figure 4 show the magnetic field distribution plots on the axis

both the calculated value by PANDIRA and the measured value. The measured peak value is about 10 % smaller than the calculated one. There are three reasons that can decrease the field. 1) The azimuthal segmentation reduces the field. 2) Because of the repulsive force and the tolerances, the bore radius is larger than the designed value. 3) Because of the surface finish for Ni plating on the magnet, the corners of the magnet are rounded. It makes the effective bore radius larger. According to the PANDIRA calculation, 2 % increase of the bore radius will result the 1 % magnetic field decrease. The first one is thought to be the main factor in our model magnet case.

number of ring	2
outer radius of a ring magnet	17 mm
length of a ring magnet	25 mm
number of segments in a ring	16
bore radius	5 mm
corner radius of a segment	8 mm
outer radius of iron case	20 mm
length of iron case	60 mm
corner radius and thickness of lids	3 mm
bore radius of entrance lid	7.5 mm
remanent field	1.29 T

Table 1. Model PMS dimensions

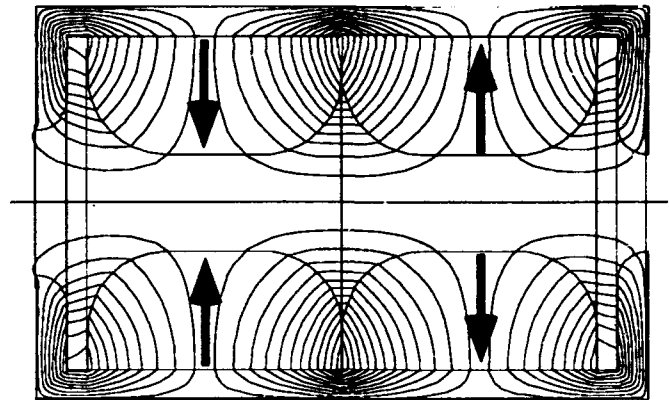


Figure 3. PANDIRA result

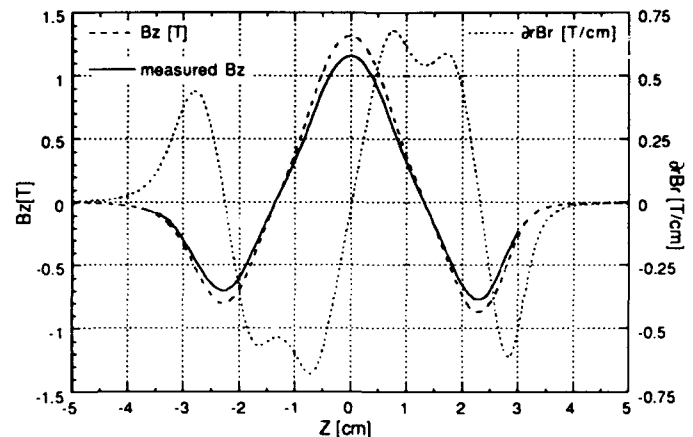


Figure 4. Magnetic field distribution

## VI. BEAM OPTICS

The beam dynamics simulations based on the calculated magnetic field distribution by PANDIRA are performed. The equations of motion in the cylindrical coordinate are

$$\begin{cases} m_0 \dot{v}_r = -q v_\theta B_z + m_0 v_\theta^2 / r, \\ m_0 \dot{v}_\theta = -q (v_z B_r - v_r B_z) - m_0 v_r v_\theta / r. \end{cases} \quad (5)$$

The equations are integrated numerically. For less aberration, the  $r$  dependence of  $B_z$  and  $\partial B_r$  should be small. One typical result is shown in Figure 5.  $B_z$  and  $\partial B_r$  at 10 different radii are shown on the Z axis. The parallel beams on the x axis with 0.4 mm equally spaced radii start at  $z=-6$  cm ( left edge ), and go through the PMS whose center is located at  $z=0$ . The  $x-x'$  phase space plots are also shown at the initial point and the



Photo. The assembled PMS lens

focal point calculated by equation (2). Because the integral over  $B_z$  on axis of PMS lens is zero, the image does not rotate. In this calculation, the space charge is not included yet. Further study will include the space charge effect.

## VII. ACKNOWLEDGMENT

The author would like to thank R. A. Jameson for the useful information. The model magnet was fabricated by Sumitomo Special Metal Co. LTD.

## VIII. REFERENCES

- [1] Y. Iwashita, et. al. "7MeV PROTON LINAC", Proc. 1990 Linear Accel. Conf., Albuquerque, p.74
- [2] A. Noda, et. al. "Improvement of the Proton Accelerator System", Bull. Inst. Chem. Res. Kyoto Univ. Vol.70, No.1 (1992)
- [3] O. C. Dermois, "The external injection system for the Groningen cyclotron", Proc. Fifth Int. Cyclotron Conf. Oxford, 620 (1969)
- [4] K. Halbach, "Physical and Optical Properties of Rare Earth Cobalt Magnets", Nucl. Instr. and Meth., 109 (1981)
- [5] K. Halbach, "Magnet Innovations for Linacs", Proc. 1986 Linac Conf., Stanford, SLAC-Report-303, 407 (1986)
- [6] User's Guide for the POISSON/SUPERFISH group of codes., LA-UR-87-115, LANL (1987)
- [7] C. Fert and P. Durandeu, "Magnetic Electron Lenses" in "Focusing of Charged Particles", Edited by A. Septier; Academic Press, 309 (1967)

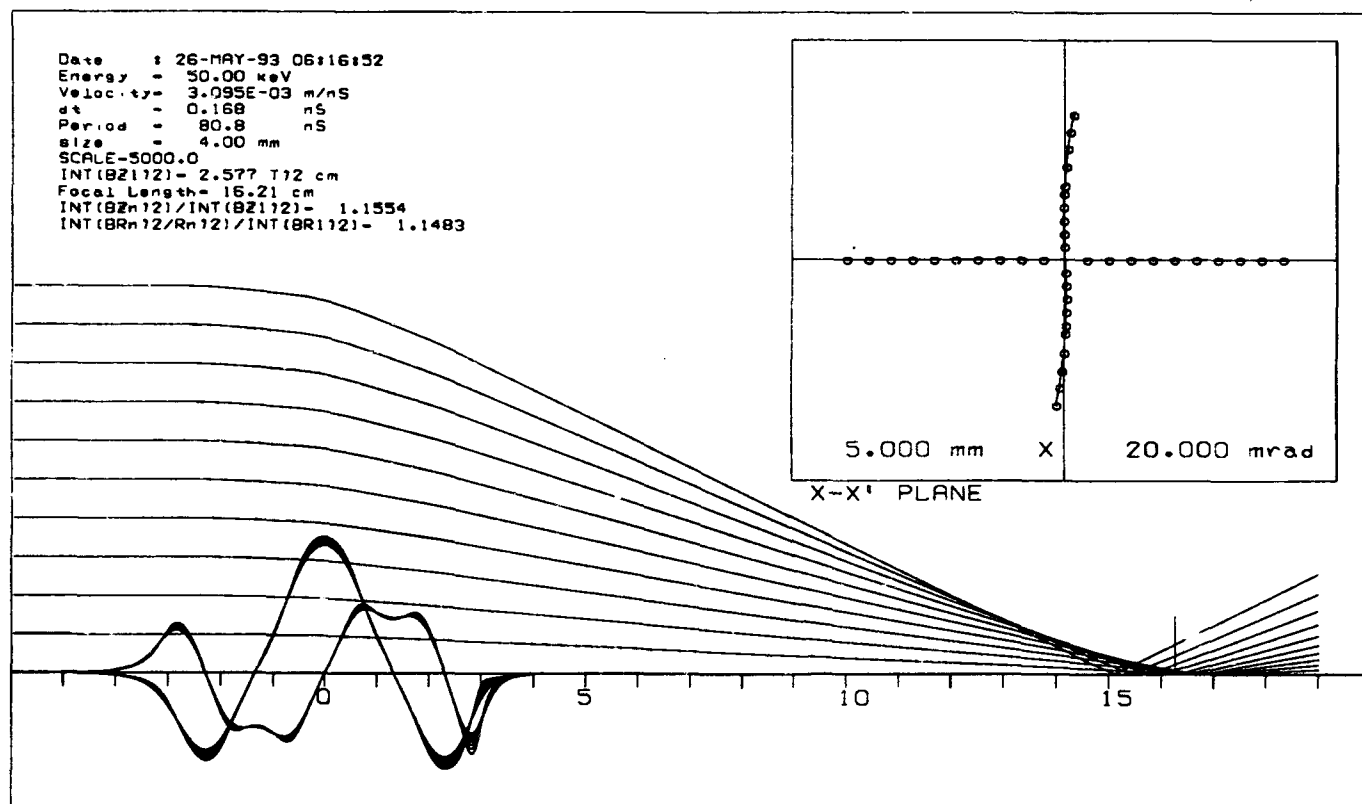


Fig 5. Beam dynamics simulation based on PANDIRA result.

# DESIGN OF A MERGING BEAMLET PRE-ACCELERATOR FOR AN ELECTROSTATIC QUADRUPOLE ACCELERATOR (ESQ)

C. F. Chan and M. C. Vella  
Lawrence Berkeley Laboratory, Berkeley CA 94720

## Abstract

An experiment is planned to merge 200 mA of multi-beamlet  $H^-$  at 100 keV into a single channel electrostatic quadrupole accelerator (ESQ), which will boost the beam to 200 kV. The experiment is a collaboration based on a Japan Atomic Energy Research Institute (JAERI) volume  $H^-$  plasma source and focused multi-aperture extractor, mated to the LBL 200 kV prototype ESQ. A 2D particle code (WOLF) has been used to design a merging beamlet pre-accelerator. The key merging elements are a focus ring to enhance the focusing of the extractor and a gradient grid to produce a merged beam profile which matches ESQ acceptance and minimizes emittance growth.

## I. INTRODUCTION

This paper presents a design for an experiment to demonstrate merging of the beamlets from a multi-aperture extractor into a prototype ESQ. The experiment will use a JAERI volume generation  $H^-$  plasma source and focused extractor [1], mated to the LBL 200 kV, 200 mA ESQ prototype [2]. If successful, this combination can be scaled to amperes of megavolt negative ion based neutral beams, for heating and current drive in future tokamak such as the International Thermonuclear Experimental Reactor (ITER).

Two types of negative ion accelerators are under development. Conventional electrostatic (ES) Pierce type dc accelerators have the advantage of being proven with low currents up to several megavolts. Also, they directly match the capabilities of available  $H^-/D^-$  cesiated volume plasma sources. The reactor relevant challenges for ES accelerators are voltage holding and insulator lifetime. Electrons stripped from the negative ion beam by gas, plus secondaries, can generate a high x-ray flux. The LBL group is developing the ESQ accelerator because it is mechanically compatible with long, low (electrical) stress high voltage insulators ( $\leq 4$  kV/cm). Also, the quadrupole fields are expected to filter out energy mismatched particles, reducing x-ray loads.

The practical challenges for a multi-beamlet merging experiment are: (1) Match the ESQ acceptance requirements; (2) Demonstrate  $H^-$  current density that scales to ITER requirements; (3) Achieve acceptable emittance growth within the ESQ.

## II. LBL 200 KV ESQ

Matching requirements for the LBL 200 kV, 200 mA (proton equivalent) ESQ are: 100 keV input energy; Input radius  $\leq 1$  cm; and Convergence -10 mrad to -30 mrad for a circular beam. Previous experiments used single channel positive and negative ion beams. The nominal 200 mA current was demonstrated with a space charge equivalent 100 mA  $He^+$  beam [2].

This ESQ has three quadrupoles in the matching section, and two quadrupoles forming a 100 kV acceleration section, as illustrated in Fig.1. The design is modular, and could be expanded in 100 kV sections to over 1 MV. The ESQ has a 3.5 cm diameter aperture. If the input conditions are met, the beam envelope can be kept within 80% of the aperture diameter, and emittance growth due ESQ electric field non-linearities should be minimal [3]. The short length of the 200 kV configuration makes it very tolerant of input emittance.

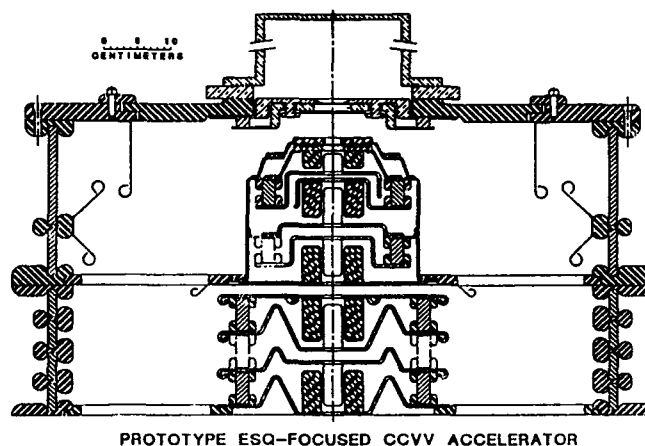


Figure 1. Drawing of the LBL 200 kV, 200 mA ESQ. The first three modules are used for matching, and the second two modules for acceleration from 100 keV to 20 keV.

## III. JAERI FOCUSED EXTRACTOR

The JAERI plasma source will be similar to the type tested at JAERI and Cadarache, and planned for JT-60U [3]. The usual cesium seeding is planned to increase output and reduce gas pressure. The JAERI focused extractor [1] uses curved plasma and extraction grids, with nineteen apertures and embedded magnets for electron suppression. Three sets of grids were built with nominal geometric focal lengths of 10 cm, 15 cm and 20 cm (i.e., plasma grid radius of curvature).

The 15 cm and 10 cm grids were tested at JAERI in 1992 [1]. Except for curvature, these are similar to the flat grids used in the large JAERI injectors [4], including embedded magnets to bury electrons in the extraction grid. The beamlets are defined by 0.45 cm radius holes in the plasma and extraction grids. A side view of the nominal 15cm grid set is shown in Fig.2a, and a flat projection is shown in Fig.2b.

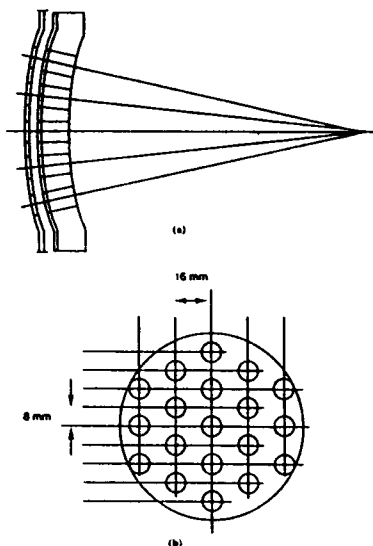


Figure 2. The layout of the JAERI focused plasma and extraction grid design is illustrated: (a) Side view, 15 cm focal length; and (b) Projection of the beamlet layout, with one, six, and twelve beamlets rings.

#### IV. 2D SIMULATION OF BEAM MERGING

The goal of these studies is to provide a conceptual design for a beamlet merger which would match the JAERI extractor and the LBL ESQ. The merged beam should satisfy the acceptance requirements of the latter as mentioned in Sec. II above. To accomplish this we propose two additional optics elements: (1) focus ring; and (2) gradient grid. A focus ring on the exit side of the extraction grid, just outside the last ring of beamlets, increases the curvature of the potential contours for the outer beamlets. The gradient grid is used to tune the envelope convergence. A relatively long gap to the ESQ is required to get a good input match, which should experience low emittance growth, even in a long acceleration channel.

As mentioned previously, limiting emittance growth due to ESQ non-linearities requires that the envelope radius remain within  $\leq 80\%$  of the nominal aperture. This will be possible if the ESQ acceptance requirements are met, but also requires that the merging be accomplished in a way which minimizes the electrostatic energy of the merged beam. This means we should stack the beamlets against each other with minimal overlap. In the planned experiment, given the 0.45 cm beamlet radius and the  $\leq 1$  cm ESQ acceptance radius, beamlet overlap after merging is unavoidable.

To adapt to the 2D symmetry of WOLF[5,6], the simulated beam geometry was a set of concentric, focused cylindrical ringlets, which were set at radii equivalent to the beamlets from the JAERI extraction grid. The ringlets were

launched with the energy expected for the beam at the extraction grid during the LBL experiment, 6.5 keV. They were given a Maxwellian distribution equivalent to a temperature of 1 eV.

Results for two geometries are presented: (1) Two ringlets, which corresponds to seven apertures with total current  $\leq 100$  mA; and (2) Three ringlets, which corresponds to using the nineteen available apertures with total current  $\leq 200$  mA. Current in the ringlets was distributed in the same ratio as the number of apertures of the JAERI layout, i.e., 1:6, for two ringlets (seven holes), or, 1:6:12, for three ringlets (nineteen holes). This distribution most closely resembles the current distribution of the beamlet layout, but perhaps introduces some extraneous effects on emittance. For comparison with the experiment, it is convenient to refer to these configurations as "seven holes" and "nineteen holes".

The effect of a gradient grid on convergence of the seven hole trajectories is illustrated in Fig.3a, where a large aperture, 60 kV gradient grid with a thickness of 1 cm is added 6.0 cm from the center of the extraction grid and 12.0 cm from the ESQ entrance. The corresponding phase space is illustrated in Fig.3b. Envelope convergence is greatly reduced after the beam pass through the second gap. The 0.9 cm radius is a good match to the ESQ. A quantitative measure of the collective beam envelope was obtained from WOLF by calculating the rms parameters of the projectional phase space ellipse. These rms parameters were used to calculate the convergence angle of a K-V beam with equivalent projectional emittance. Based on this procedure, the beam in Fig.3a has a K-V equivalent envelope convergence of  $-24$  mrad, which matches the acceptance of the 200 mA ESQ. In general, increasing the gradient grid voltage (with respect to the extractor) increases the beam envelope convergence, with a small change in the envelope radius.

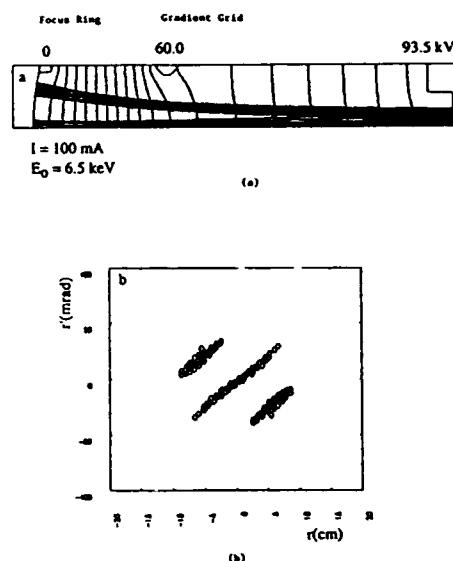


Figure 3. WOLF simulations for a 100 mA  $H^+$  beam with a center beam and one ringlet, accelerated from 6.5 keV to 100 keV. Beam trajectories are plotted in (a) and the  $r$ - $r'$  phase space is shown in (b).

Trajectories and phase space diagrams for a nineteen hole (i.e., three ringlet) design are illustrated in Fig.4a and b. Changes from the previous design are an increased gap between the extraction grid and gradient grid (to 10 cm). Beam radius at the ESQ entrance is about 1 cm and convergence is acceptable, -30 mrad.

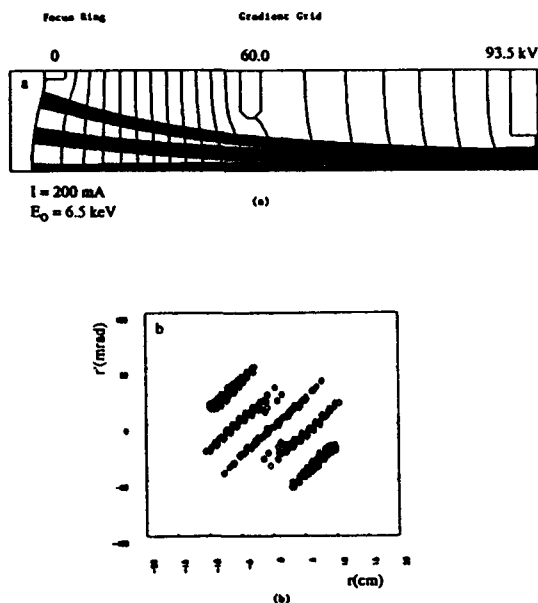


Figure 4. WOLF simulations for a 200 mA  $H^-$  beam with a center beam and two ringlets, accelerated from 6.5 keV to 100 keV. Beam trajectories are plotted in (a), and the  $r$ - $r'$  phase space is shown in (b).

The large gap layout illustrated in Fig.4a, with focus ring and gradient grid, has been chosen for the joint experiment between JAERI and LBL. Assuming the plasma grid is masked and the appropriate focus ring installed, this design has been shown computationally to also work well with seven beamlets. WOLF simulations indicate that for seven beamlets, the gradient grid should be at 90 kV. With 100 mA  $H^-$  the envelope was 0.65 cm in radius, with a -12 mrad convergence. This is an easy match to the 200 kV ESQ.

The long path from the extraction grid to the ESQ in the experimental layout raises concerns about stripping losses. However, progress in volume source technology has significantly reduced operating pressure in recent years. Also, this ESQ was designed with a high conductance to handle gas from older sources, with higher pressure than now expected. Estimates are that stripping losses associated with the longer path length will be a small fraction of the losses within the extractor.

The conceptual design for the nineteen hole merger shown in Fig.4a offers a good match to the acceptance of the 200 kV ESQ, and the expected current should scale to an ITER proof of principal demonstration. The key optics elements are a focus ring at the perimeter of the extraction grid and a large aperture gradient grid. The focus ring effectively increases the curvature of the extraction grid, and the gradient grid insures

the flexibility to match the ESQ acceptance. This design is adaptable to also testing seven beamlets. Self-consistent 3D simulations are planned in the future to refine the design and to study emittance growth.

## ACKNOWLEDGMENT

The authors are pleased to acknowledge constructive technical suggestions from W. S. Cooper at LBL, and Y. Okumura and T. Inoue at JAERI. This work was supported by the Director, Office of Energy Research, Office of Fusion Energy, Development and Technology Division, of the U.S. Department of Energy under Contract No. DE-AC03-76SF00098.

## REFERENCES

- [1] T. Inoue, M. Hanada, M. Mizuno, Y. Okumura, Y. Ohara, M. Tanaka, Y. Suzuki, and K. Watanabe, "Development of a Multi-Ampere  $H^-$  Ion Source at JAERI," Proc. Sixth Intl. Symp. on Production and Neutralization of Negative Ions and Beams, Upton, New York, USA, November 9-13, 1992. (to be published)
- [2] J.W. Kwan, G.D. Ackerman, O.A. Anderson, C.F. Chan, W.S. Cooper, G.J. deVries, W. B. Kunkel, K.N. Leung, P. Purgalis, W.F. Steele, and R.P. Wells, Rev. Sci. Instrum. 62 (6), p. 1521 (1991).
- [3] I. Haber, "Simulation of Low Emittance Transport", Proc. INS Intl. Symp. on Heavy Ion Accelerator and Their Application to Inertial Fusion, Tokyo, p.451 (1984).
- [4] Y. Okumura, "Negative Ion Based Neutral Beam Injector for JY-60U," Proc. Sixth Intl. Symp. on Production and Neutralization of Negative Ions and Beams, Upton, New York, USA, November 9-13, 1992. (to be published)
- [5] W. S. Cooper, K. Halback and S. B. Magyaryi, Proc. 2nd Symp. on Ion Sources and Formation of Ion Beams, Berkeley, LBL-3399 (1974).
- [6] C.F. Chan, W.S. Cooper, J.W. Kwan, and W.F. Steele, Nucl. Inst. and Meth. in Phys. Res. A306, p. 112 (1991).

# Low-Energy H<sup>-</sup> Injector Design for SSC RFQ\*

Chun Fai Chan and Ka-Ngo Leung

Lawrence Berkeley Laboratory  
University of California  
Berkeley, CA 94720

## Abstract

We present a design for the low-energy H<sup>-</sup> injector. It is used in conjunction with a rf-driven multicusp source and will deliver 30 mA of H<sup>-</sup> at 35 kV, at a pulse length of less than 1 msec to a RFQ downstream (used in the LINAC booster of the SSC, for example). It has several distinguishing features and meets the goal of having an outgoing beam free of electron contamination, with small radius, large convergent angle and small projectional emittance.

The specific example presented meets all the requirements of the injector for SSC RFQ. However, the principle and method used should easily be adapted for the designs of injectors with similar requirements for other purposes.

## I. INTRODUCTION

Advances [1] have been made with the recent works on the rf-driven, cesium free volume production multicusp H<sup>-</sup> source which operates at relatively low gas pressure ( $p \sim 10$  mT), and yields high ion current density ( $j_i \sim 100$  mA/cm<sup>2</sup>) with low extracted electron to ion ratio ( $j_e/j_i \sim 10$ ) and low ion temperature ( $kT_i \sim 1.5$  eV). In this paper we describe a design of an injector that would couple with such a source and would deliver a useful H<sup>-</sup> beam to a RFQ, for example, with desirable matching parameters. In the specific example provided, the exiting H<sup>-</sup> beam of 30 mA at 35 kV has to meet the following requirements in order to match the Twiss parameters for the RFQ: beam radius = 0.2 cm, convergent angle = 139 mrad, and  $\epsilon = 0.018 \pi$ -cm-mrad. The injector consists of four electrodes and is operated in an accel-decel-accel scheme similar to the other injector design [2]. The first two electrodes employ an acceleration voltage of 50 kV to extract the negative ions and the unwanted electrons. The latter are swept away by a pair of permanent magnets embedded in the first electrode. (The reason to choose the 50 kV value is to provide enough gap spacing for those deflected electrons to reach the second electrode.) The H<sup>-</sup> beam is then decelerated by the third electrode (normally biased at the same voltage as the first one). The beam expands as it slows down. It is then reaccelerated and

compressed by the fourth electrode, which is also the entrance to the RFQ. Several technical improvements have been made over the preliminary version reported earlier [3]. They are described in Sec. II-IV below. Further improvements and extensions of the design are discussed in Sec.V.

## II. SPECIAL TECHNIQUES USED IN THE DESIGN COMPUTATION

We use an axisymmetric 2-D ion beam optics code to compute the charged particle trajectories. In order to be precise, we include the effect of the attenuation of the H<sup>-</sup> beam due to gas stripping by modifying the current density along the z axis with the function  $f_i$  shown in Fig.1. This survival function of  $j_i$  is a fit to the numerical result based on the stripping cross-section of H<sup>-</sup> by neutral molecules, the pressure profile of which comes from a molecular flow calculation performed previously[3]. For the extracted electrons, a method has to be devised to simulate their space charge effect, at least in the direction of the symmetry axis. We use the function  $f_e$  shown in Fig.1. It accounts for the full effect near the source aperture and is gradually turned-off about 1 cm away.

In order to compute the rms projectional emittance, it is necessary to use the "skew beam dynamics" described in Ref.[4]. It also gives more accurate numerically convergent results.

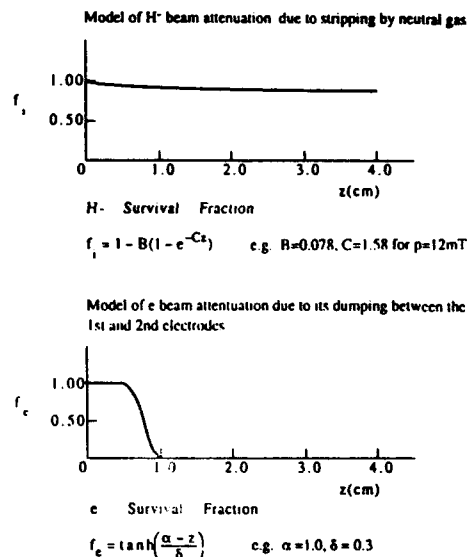
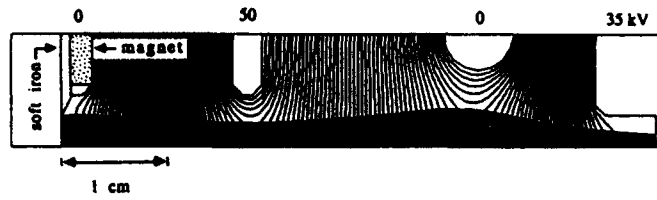


Fig. 1 Models of Beam Attenuations

\* Supported by SSCL and by U.S. DOE contract DE-AC03-76SF00098.

### III. DESIGN GOALS AND THE RESULTS

The specific goal mentioned in Sec.I is fulfilled with the design shown in Fig.2.



Extraction aperture radius = 0.3 cm

$I_{H^-} = 30$  mA at exit  
 $\epsilon_{1rms} = 0.009 \pi$ -cm-mrad at exit  
 $j_e/j_{H^-} = 11/1$  at the source aperture

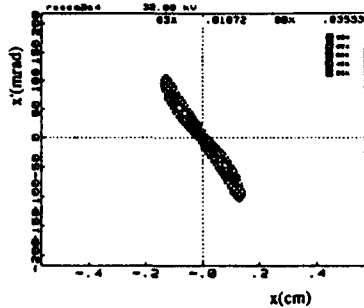


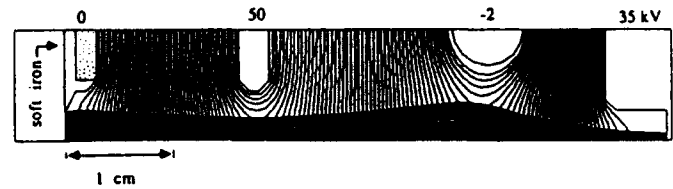
Fig. 2 Axisymmetric Beam Trajectory Plot and Exit Phase

An  $H^-$  current density  $j_j = 115$  mA/cm<sup>2</sup> is assumed at the source aperture which has a radius  $r = 0.3$  cm. As the beam travels about 6 cm to the exit, it retains about 92% of its current according to the function  $f_j$  shown in Fig.1. We also assume a uniform current density distribution at the aperture and an ion temperature of 1.5 eV. Thus the initial rms emittance is 0.006  $\pi$ -cm-mrad at that location. The  $x-x'$  phase plot in Fig.2 shows 90% of the emittance as the beam enters the last electrode. The length of the first gap is chosen in such a way that it nearly saturates the Child-Langmuir limit, once the acceleration voltage of 50 kV is chosen. The shape of the first electrode is optimized to ensure a flat plasma emitter, which is defined by the once-integrated Poisson equation, and there is a relatively low electric field ( $E \sim 1000$  kV/cm) across this emitter. (The voltages of the four electrodes are 0, 50, 0, and 35 kV. Alternatively, they can be labelled as -35, 15, -35 and 0 kV).

The potential of the third electrode is normally equal to that of the first one. However, if a larger convergent angle of the beam into the RFQ is desired, it should be biased at a few kV negative. Thus one can adjust the beam angle continuously to provide the proper entrance angle for a particular RFQ requirement. An example is shown in Fig.3.

### IV. DUMPING OF THE ELECTRONS

One of the problems of extracting negative ions from a volume source is that the beam contains a large amount of unwanted electrons. Putting a pair of permanent magnets (e.g. SmCo) inside the first electrode can sweep those electrons out of the beam at the early stage of acceleration. However, a closer examination of this solution[3] reveals



Extraction aperture radius = 0.3 cm

$I_{H^-} = 30$  mA at exit  
 $\epsilon_{1rms} = 0.010 \pi$ -cm-mrad at exit  
 $j_e/j_{H^-} = 11/1$  at the source aperture

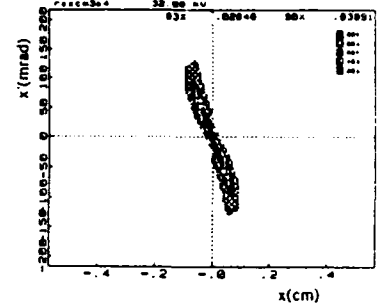


Fig. 3 Axisymmetric Beam Trajectory Plot and Exit Phase with a Larger Convergent Angle

that the magnets of proper size and strength to achieve this result would also produce a B field of about 500 gauss at the source aperture, extending and gradually diminishing into the source chamber. Fig.4 shows the calculated and measured B field as a function of axial position. This penetration would have a destructive effect on the  $H^-$  production there.

A method is found to solve this problem. We replace the usual material copper for making the first electrode with soft iron, with the location of the magnets shown in Fig.2 and 3. This soft iron housing has the effect of shifting the peak of the B field away from the source and greatly reduces the penetration, as shown in Fig.5.

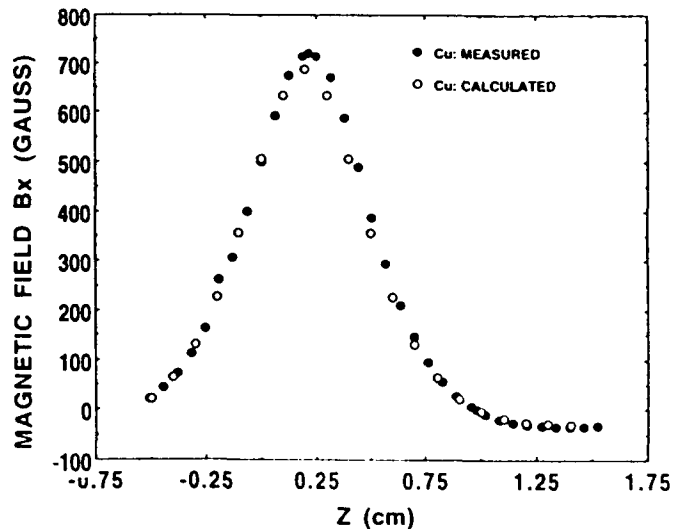


Fig. 4 Comparison of the Axial B Fields: Calculated and Measured, both with Copper Housing

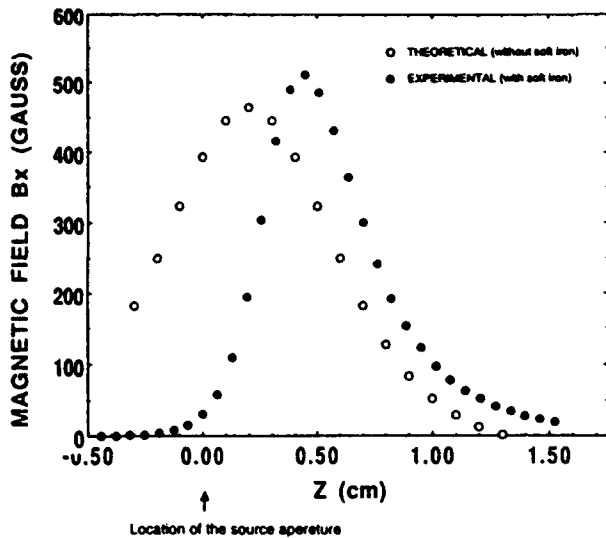


Fig. 5 Comparison of the Axial B Fields: Calculated (with Copper Housing) and Measured (with Soft Iron Housing)

In Fig. 6 we simulate this shifted B field in a planar calculation to study the trajectories of the electrons. The exact landing location of the electrons on the second electrode is not critical as long as they are stopped from going further downstream. Since the present design is for short pulse operation (less than 1 msec.) and low duty factor, the heat loading should not pose a problem, especially if active cooling is employed.

There is one further advantage of the accel-decel design. There exists an electric field reversal before and after the second electrode. Any secondary emission of electrons produced by the impact of the extracted source electrons on the upstream face of the second electrode would be confined to the first gap and would not migrate downstream to cause head-loading damage or to produce x-rays.

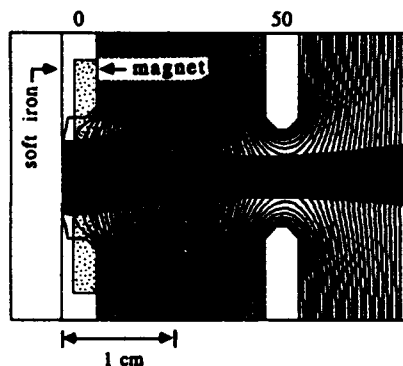


Fig. 6 Planar Calculation Showing the Effect on the Extracted Electrons due to a Pair of Magnets Located Inside the 1st Electrodes

## V. DISCUSSIONS AND CONCLUSIONS

We have shown in Sec. III and IV a design of a compact injector to produce an  $H^-$  beam with large convergent angle and low emittance. The overall arrangement, including the source, is shown in Fig. 7. The exit emittance is about a factor of two smaller than the SSC RFQ injector requirement. This is achieved by good ion beam optics and the low  $H^-$  ion temperature. In this study we have ignored the contribution of the emittance growth due to the perturbation of the ion trajectories by the magnetic field, as well as its steering effect on the beam as a whole. However, we don't expect these effects to be dominant factors. We intend to investigate them in 3-D calculations in the future.

The question of how to dump the electrons without interference with the source performance and ion beam optics is a long standing problem for  $H^-$  extraction. We believe we have found a simple method, described in Sec. IV, to decouple those issues. The modification of the present design to accommodate dc operation is under study and shall be reported elsewhere.

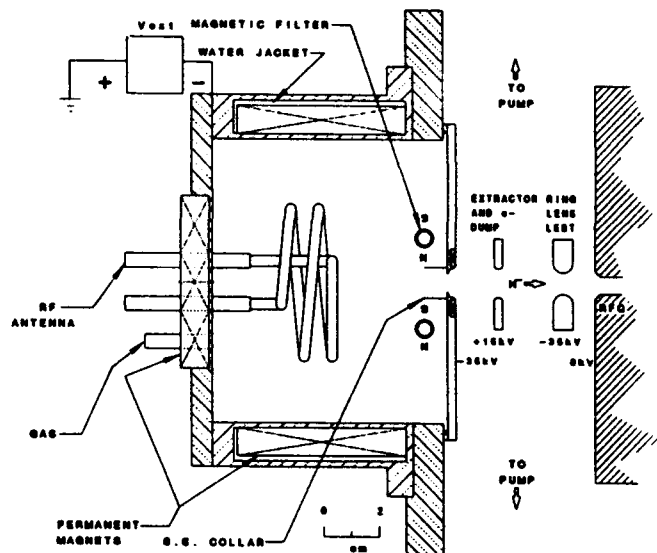


Fig. 7 Schematic Diagram of the RF Multicusp Ion Source

## REFERENCES

- [1]. K. N. Leung, G. J. DeVries, W. F. Divergilio, R. W. Hamm, C. A. Hauck, W. B. Kunkel, D. S. McDonald, and M. D. Williams, *Rev. Sci. Instrum.* **62**, 100 (1991). D. S. McDonald, D. A. Bachman, W. F. Divergilio, W. B. Kunkel, K. N. Leung, and M. D. Williams, *Rev. Sci. Instrum.* **63** (4), 2741 (1992).
- [2]. C. F. Chan and A. F. Lietzke, *Bull. Am. Phys. Soc.* **34**, 9, 2116 (1989).
- [3]. O. A. Anderson, C. F. Chan, K. N. Leung, L. Soroka, and R. P. Wells, *Rev. Sci. Instrum.* **63** (4), 2738 (1992).
- [4]. C. F. Chan, W. S. Cooper, J. W. Kwan and W. F. Steele, *Nucl. Instr. Met. Phys. Res.* **A306**, 112 (1991).

# Lithium Lens for Focusing Protons on Target in the Fermilab Antiproton Source

F.M. Bieniosek and K. Anderson  
Fermi National Accelerator Laboratory \*  
P.O. Box 500  
Batavia, Illinois 60510

## Abstract

A lithium lens will be used to focus the 120 GeV proton beam on the antiproton production target to a spot size of about 0.1 mm, as part of the planned upgrade to the FNAL antiproton source target station. Improved focusing increases antiproton yield and corrects for possible future emittance dilution of the incident proton beam. The lens, with a radius of 3 mm and length of 8 cm, is expected to operate at a gradient of 2667 T/m and a current of 120 kA. The lens is similar in design to the antiproton collection lens.

## I. INTRODUCTION

A lithium lens is a cylindrical current-carrying conductor. If the current density in the lithium is uniform, the strength of the focusing magnetic field is linear with radius, and the device acts as a simple lens on high energy particle beams. Such lenses have been used routinely at FNAL for antiproton collection downstream of the antiproton production target. This paper describes the design and operational parameters of a lithium lens to be installed upstream of the antiproton production target. The upstream (proton) lens design is based on the design of the downstream (collection) lens. In addition, the proton lens design incorporates improvements which may be used in future versions of the collection lens such as improved optical quality and enhanced mechanical design of the beryllium window and titanium cooling jacket.

## II. DESIGN CONSIDERATIONS

### A. Lens Optics

A short focal length final focus lens minimizes the spot size on target for an incident proton beam. In addition, a short focal length reduces local heating of the beryllium entrance window of the downstream collection lens by the proton beam. The lithium lens was chosen over alternate focusing technologies (e.g., plasma lens, pulsed quadrupoles) because the design of the lens can borrow extensively from experience at FNAL gained in fabricating and operating the antiproton collection lens. For a given magnetic field gradient, the radius

of the lens should be as small as possible to minimize stresses encountered in the cooling jacket which surrounds the lithium core. Experience at FNAL [Ref. 1] and elsewhere [Refs. 2,3] indicates that lithium lenses can be made to operate reliably if the magnetic field at the outer radius of the lens ( $r_0$ ) is maintained below 10 T. The minimum radius is dictated by the properties of the 120 GeV proton beam and transport line. TRANSPORT [Ref. 4] calculations for a  $0.2\pi$  mm-mrad emittance beam with  $\Delta p/p = 0.2\%$  (95% limits) in the transport line retuned for the proton lens yield a half-beam size of 1.7 mm at the upstream entrance of the lens. Allowing for beam sweep on target, variations in emittance, and drift in beam position, a 3 mm lens radius should be adequate for efficient beam transport. A lens of 8 cm length located at the first collimator module of the target station (approximately 168 cm upstream of the target) and operated at a gradient of 2667 T/m would focus the beam to an RMS spot size on target of  $\sigma_x = \sigma_y = 0.1$  mm. At the design radius, the edge field will be 8 T. To provide flexibility in placement of the lens, the design is based on a maximum operating field of 10 T. If the emittance of the proton beam should be larger than expected, it will be possible to maintain the desired spot size by placing the lens closer to the target and operating at a field higher than 8 T.

A pulsed power supply delivers a half-sine wave current to the lens described by  $I(t) = I_0 \cdot \exp(-\alpha t) \cdot \sin(\omega t)$  ( $0 < \omega t < \pi$ ), where  $I_0$  is the peak current without damping,  $\alpha$  is the damping constant, and  $\omega$  is the angular frequency determined by the capacitance and inductance of the pulser circuit. The current and magnetic field diffuse into the lithium core on a time scale that depends on the ratio of the skin depth to the lens radius  $\delta/r_0$  [Ref. 5]. Aberrations in the lens are minimized when the magnetic field approaches a linear radial dependence. Aberrations  $\Delta r$  at the focal point may be written as a function of radial position at the lens  $r$  as:

$$\Delta r(r) = \left( \frac{H(r)}{rG} - 1 \right) \cdot r \quad (1)$$

where  $H(r)$  and  $G$ , the magnetic field at a given lens radius and the gradient of the linear component of the field, respectively, may be calculated from the analytic solution of Reference 5. We calculate the RMS value of the aberration  $\langle \Delta r^2 \rangle^{1/2}$  as:

\*Operated by the Universities Research Association Under Contract with the U.S. Department of Energy

$$\langle \Delta r^2 \rangle^{1/2} = \frac{1}{G} \langle (H - rG)^2 \rangle^{1/2} \quad (2)$$

where

$$\langle (H - rG)^2 \rangle^{1/2} = \frac{2}{r_0^2} \int_0^{r_0} (H - rG)^2 r \cdot dr \quad (3)$$

which is solved in Fig. 1 for  $\delta/r_0 = 0.6, 0.65, 0.7,$  and  $0.75$  ( $\alpha = 6760 \text{ sec}^{-1}, \omega = 41\,000 \text{ sec}^{-1}$ ).

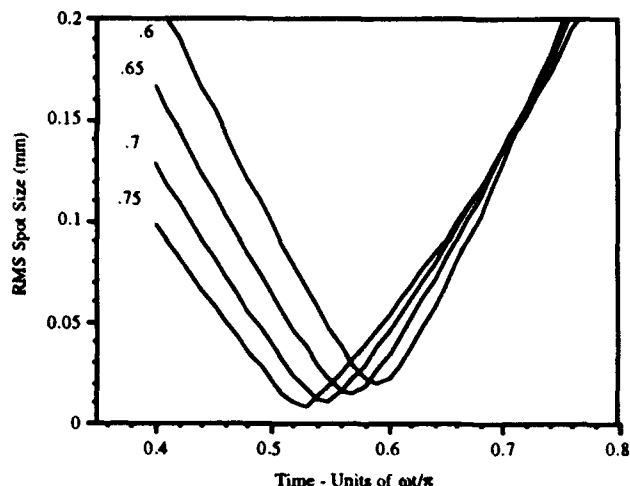


Figure 1. Proton lens field linearity.

This calculation assumes that the incident proton beam is free to wander across the aperture of the lens. The ratio  $\delta/r_0$  is set at 0.7 to allow for jitter in the trigger circuit of the lens pulser;  $\langle \Delta r^2 \rangle^{1/2}$  remains less than 0.02 mm in radius over a  $5 \mu\text{s}$  time window.

The ratio  $\delta/r_0$  changes as the lithium is heated during the pulse. Temperature and conductivity both vary significantly as a function of radius during the pulse; typical curves for the temperature distribution are shown in Fig. 2.

The solution of Ref. 5 neglects the conductivity profile in the lithium; solving the complete coupled equations requires a numerical solution [Ref. 6]. The full solution has not yet been completed in this case; however, if the conductivity profile is parabolic, one can show that the spot size is not significantly degraded, although the timing of minimum spot size may change slightly.

Multiple scattering, which amounts to about  $27.5 \mu\text{rad}$ , is the dominant contributor to spot size growth from beam interaction with the proton lens. The quadrature sum of all lens contributions, including multiple scattering, finite depth of focus, and optical aberrations, to spot size is about 0.05 mm. This value is smaller than the limiting spot size for the expected emittance of the proton beam delivered to the lens (0.1 mm). As a result, lens imperfections are not expected to

be a significant factor in determining the attainable spot size. The total beam absorption loss is 7.5% (i.e., 5.8% in the lithium and 1.7% in the beryllium windows).

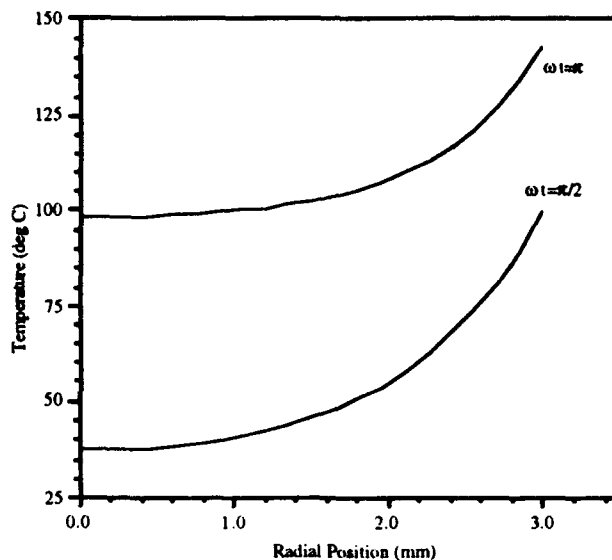


Figure 2. Temperature profile in lithium core at peak current and after pulse during cyclic operation.

### B. Mechanical Design

A cross-section of the proton lens is shown in Fig. 3. The current is introduced to the lithium through 1018 steel, which has relatively low resistivity, adequate strength, and is compatible with liquid lithium.

The cooling jacket is machined from Ti 6Al-4V ELI billet bar stock. The various pieces of the water circuit septum are joined by electron beam welding. Great care is exercised in preparing and joining the septum components to minimize weld embrittlement and avoid formation of deleterious microstructures. The central core of lithium is constrained by a 1 mm thick Ti 6Al-4V conductor tube which provides the path for heat exchange between the lithium core and the cooling water. The thickness of the conductor tube was selected such that it carries only a small fraction (i.e.,  $<5\%$ ) of the total current, minimizes the combined stresses in the tube during operation, and minimizes the temperature gradient across the tube wall. Calculations indicate that the largest stress in the cooling jacket occurs just after the pulse and is due primarily to the thermal expansion of the lithium core. The largest radial stress occurs at the inner wall of the conductor tube and is estimated to be 14.7 ksi. The highest tangential stress (i.e., maximum principal tensile stress) also occurs at the inner wall of the conductor tube and is calculated to be 52 ksi, which is well below the endurance limit of the material for  $10^7$  cycles. As delineated in Fig. 2, the temperature of the lithium core remains well below the melting point of  $186^\circ \text{C}$  during cyclic operation.

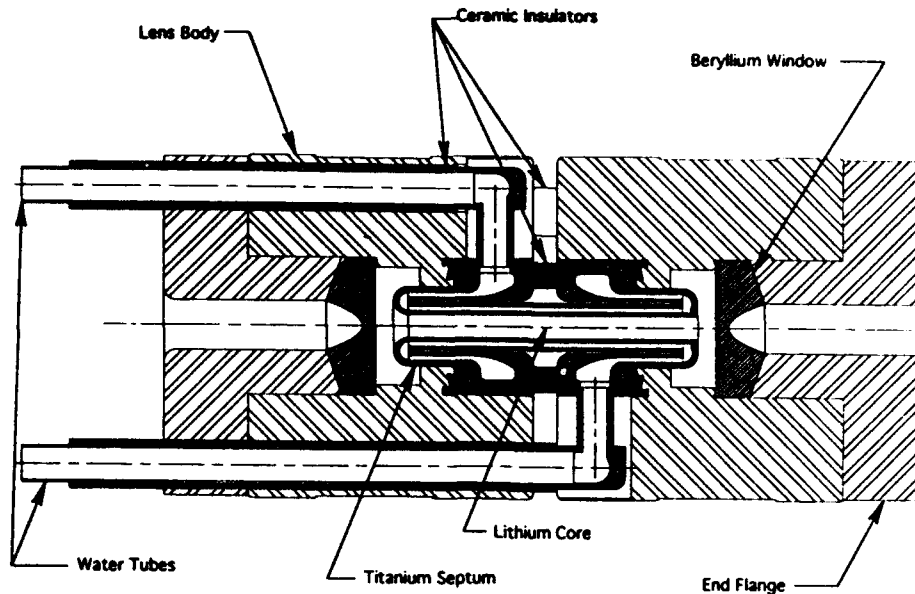


Figure 3. Cross-Sectional View of Proton Lens Assembly

The septum endcaps feature a uniform gradation in cross-section to provide the transition in wall thickness of 1 mm in the conductor tube to 1.5 mm thickness in the outer current director base. Such design minimizes stress concentrations due to changing wall thickness and provides adequate strength in the critical endcap region.

As delineated in Fig. 3, the beryllium window features a parabolic profile which minimizes the window thickness and consequently beam absorption while maintaining adequate strength to prevent fracture. Beryllium was selected to minimize beam absorption and multiple scattering which could dilute the effective spot size on target. The minimum window thickness is 3 mm. The peak axial pressure exerted on the window (about 30 ksi) is primarily due to the sum of axial pressures generated by radially flowing currents in the end region and by Poisson effect loads associated with radial compression of the central lithium core. The inclined boundary of the window serves to minimize the maximum principal tensile stress at the center of the window and results in a more homogeneous state of stress in the window. The window was modeled using the finite element program ANSYS® [Ref. 7]. The resulting equivalent stress in the window is estimated to be below the  $10^7$  cycle endurance limit for notched specimens of S65 beryllium of 24 ksi.

The steel lens bodies are separated by 95% alumina ceramic standoffs. The lens current will be monitored by a Rogowski coil placed around the center of the lens body in the transformer package. The entire assembly is constrained against axial loading by 8 Ti 6Al-4V preloaded fatigue studs.

Lithium will be introduced into the lens in a procedure similar to that used for the collection lens [Ref. 5]. The lithium will be extruded such that a compressive preload of

210 atm will be maintained at ambient conditions to counteract the maximum z-pinch at  $\omega t = \pi/2$ .

The proton lens body current contact area was designed to accommodate the same transformer package as that used in the 2 cm diameter collection lens. The total inductance of the secondary pulser circuit is expected to be 30 nH; the secondary circuit resistance is 490  $\mu\Omega$ , of which the lithium central conductor contributes 330  $\mu\Omega$ . The primary circuit consists of a power supply capacitance of 260  $\mu\text{F}$ , an equivalent circuit inductance of 2.5  $\mu\text{H}$ , and an equivalent circuit resistance of 35 m $\Omega$ . For a nominal operating field of 8 T, the charge voltage on the capacitor bank is  $V = 2.0$  kV, the peak primary circuit current is 15 kA, and the current pulse is 80  $\mu\text{s}$  long. The corresponding lens current is 120 kA.

### III. REFERENCES

- (1) G. Biallas, et al., "Power Tests of the Fermilab Lithium Lens for Antiproton Collection", Proceedings of the 12th International Conference on High Energy Accelerators, Batavia, IL, 1983, pp. 591-593.
- (2) D.C. Fiander, "Beam Tests of a 2 cm Diameter Lithium Lens", IEEE Transactions on Nuclear Science, Vol. NS-32, 1985, pp. 3063-3065.
- (3) B.F. Bayanov, et al., "A Lithium Lens for Axially Symmetric Focusing of High Energy Particle Beams", Nuclear Instruments and Methods, Vol. 190, p.9, 1981.
- (4) D.C. Carey, "High Energy Charged Particle Optics Computer Programs", Nuclear Instruments and Methods, Vol. 187, pp. 97-102, 1981.
- (5) A.J. Lennox, "The Design Parameters for a Lithium Lens as Antiproton Collector", IEEE Transactions on Nuclear Science, Vol. NS-30, 1983, pp. 3663-3665.
- (6) H. Knoepfel, Pulsed High Magnetic Fields, North-Holland Publishing Company, 1970, p. 88.
- (7) ANSYS Engineering Analysis System, Swanson Analysis Systems, Inc., Houston, PA, 1990.

# Injector Design for High-Current CW Proton Linacs\*

Ralph R. Stevens, Jr., Joseph D. Sherman, and J. David Schneider  
Los Alamos National Laboratory, Los Alamos, NM 87545

## Abstract

We present an injector design for high-power cw proton linacs with particular emphasis on intense neutron-spallation sources. Long-term operational reliability and availability dominate over specific beam parameters for these accelerators. We discuss technical requirements for the ion source and low-energy beam transport line and compare different options. A prototype design for a 75-kV, 110-mA cw proton injector is presented.

## I. INTRODUCTION

The development of radio-frequency quadrupole (RFQ) accelerators has provided an effective match between dc ion source injectors and radio-frequency, drift-tube accelerators which greatly enhances the practicality of building high-current cw proton linacs for intense neutron spallation sources [1]. These RFQ accelerators reduce the required injection energy to a limit set by beam perveance rather than by linac beam dynamics and can support long-term, cw operation. Accelerator-based conversion (ABC) of weapons-grade fissile materials, accelerator transmutation of nuclear waste (ATW), and accelerator production of tritium (APT) are possible applications of this technology. After discussing the design considerations for these injectors, we present a preliminary design for these applications.

## II. INJECTOR SPECIFICATIONS

The cw injectors for neutron-spallation sources must provide stable proton beams with high availability. The total number of protons on target will be an important measure of operation. These injectors will have to provide >100-mA cw proton beams at energies up to 100 keV with a 95% beam fraction normalized emittance of 1.2  $\pi$ mm-mrad at the RFQ match point.

A design for an accelerator to produce tritium is being developed at the Los Alamos National Laboratory (LANL). This accelerator is expected to be on line for 7800 hours/year with an overall availability of 85%. Injector availability must exceed 98% during the scheduled on-time. Periodic ion-source maintenance may be done no more often than once a week during a single scheduled 8-hour maintenance period. The injector fault rate (primarily high-voltage faults) must be limited to less than one per hour. Means must be provided in the injector to reestablish the beam in the linac quickly with minimal perturbation and beam spill. The low-energy beam transport (LEBT) line must provide proper matching and centroid control at the RFQ entrance. Non-interceptive beam diagnostics are needed to ensure proper tuning and on-line monitoring of the injector beams.

## III. ION SOURCE

The choice of ion source for these cw applications will be made on the basis of proven performance for long-term availability and operational stability as well as current and emittance requirements. Ion source gas and power

efficiencies are useful criteria for cw source selection. We define the ion-source gas efficiency,  $\eta$ , as

$$\eta = 6.95 i_{H^+} (A) / Q_{H_2} (\text{sccm}) \quad (1)$$

where the proton current is expressed in Amperes (A) and the hydrogen flow is given in standard cubic centimeters per minute (sccm). The power efficiency,  $\zeta$  is given by

$$\zeta = j_{H^+} (\text{mA/cm}^2) / P_d (\text{kW}) \quad (2)$$

where  $j_{H^+}$  is the proton current density at extraction and  $P_d$  is the discharge power. Other important operating parameters of interest for a cw ion source are the proton current, proton fraction, beam emittance, and source lifetime.

Table I summarizes the demonstrated characteristics of a few candidate sources. These are the multicusp source with filament drive [2], the multicusp source with 2.0 MHz rf drive [3], the monocusp ion source [4], and the 2.45 GHz electron-cyclotron resonance (ECR) ion source [5]. Emitter radii are given immediately below the source description in the first column, and the extraction voltage is given in the second column. The total beam current (proton current in parentheses) is given in the third column. A high proton fraction (the ratio of the proton current to the total current) is desirable to limit beam perveance and to eliminate mass analysis prior to RFQ injection. Note that the monocusp source results are for deuterium. The discharge power is presented in the fourth column, while the power efficiency,  $\zeta$ , is shown in the fifth column. The duty factor (df) employed for the data is shown in the sixth column while the gas efficiency,  $\eta$ , is in the seventh column. Finally, the measured normalized emittance at the 95% beam-fraction level is shown in the last column. A Gaussian beam-emittance model has been used to obtain the 95% beam-fraction emittance values.

Table I  
Comparison of Candidate Ion Sources for CW Linacs

	$V_{\text{ext}}$ (kV)	$i$ (mA)	$P_d$ (kW)	$\zeta$ (mA/cm <sup>2</sup> /kW)	df (%)	$\eta$	$\epsilon$ (95%) ( $\pi$ mm-mrad)
Multi-cusp [2] (filament) $r_e = 0.4$ cm	60	56 (45)	7.1	13	100	0.07	0.59
Multi-cusp [3] (2.0 MHz rf) $r_e = 0.32$ cm	35	82 (70)	18	12	.3	0.02	0.60
Monocusp [4] (filament) $r_e = 0.65$ cm	200	200 (120) D+	1.5	60	100	0.14	-
ECR proton [5] (2.45 GHz) $r_e = 0.35$ cm	42	96 (67)	0.6	290	100	0.31	0.60

The ECR ion source developed at the Chalk River Laboratory is a promising candidate for this application based on proven cw performance and high gas and power efficiencies [6]. A schematic diagram of this ECR source is shown in Fig. 1. The basic ECR geometry has been modified to optimize the production of protons by eliminating the axial confinement geometry. The 2.45-GHz microwave frequency is sufficiently low that the required axial magnetic field of 875

\*Work supported by an Exploratory Research & Development Initiative under the auspices of the US Dept. of Energy.

Gauss does not dominate the beam emittance after extraction. Current densities up to 500 mA/cm<sup>2</sup> at 90% proton fraction have been obtained. This source has been used for several years with the RFQ1 project at Chalk River and has demonstrated sufficient lifetime and stability at a 90 mA total current level to support extended operation of their cw RFQ [7].

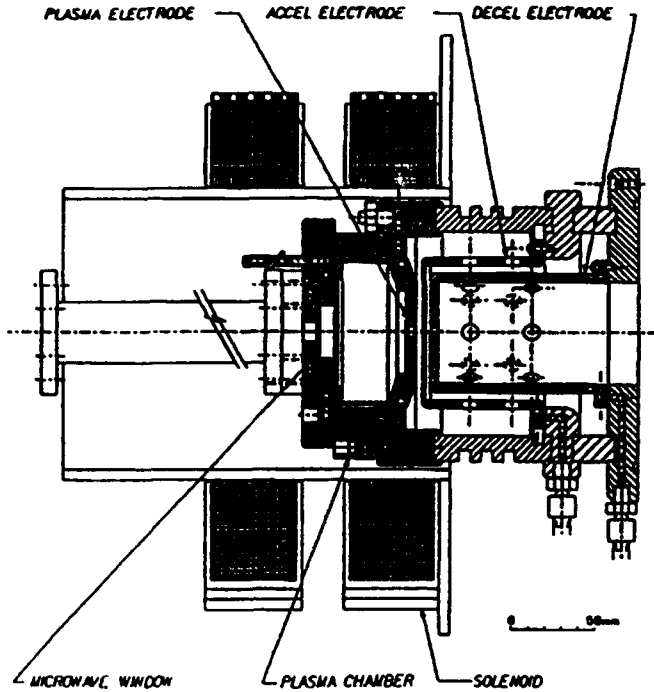


Fig. 1. Schematic Diagram of the Chalk River ECR Ion Source.

Another promising ion source for this application is the rf-driven, multicusp, volume source [3,8]. A 2.0-MHz version of this source has been tested and has demonstrated 85% proton fraction for low-duty-factor beams [3]. The gas efficiency of this source is expected to increase for cw (100% d) operation. Tests are needed to extend the operation of this source to full cw operation.

Our initial preference for the ECR ion source over the rf-driven volume source is based largely on the improved power efficiency. The ECR source operates with <1 kW of 2.45 GHz microwave power, while the volume source may require >20 kW of 2 MHz rf power to produce similar beam current densities. Additional testing of several candidate ion sources under expected cw operating conditions is required before a final choice can be made.

An injection energy of 75 keV has been selected based on previous experience with the Fusion Materials Irradiation Test (FMIT) injector [9]. We have designed an ion-extractor system to produce the required 110 mA of protons assuming a proton fraction of 85% and H<sub>2</sub><sup>+</sup> and H<sub>3</sub><sup>+</sup> fractions of 7.5% each. This design entails a total extracted current of 130 mA. The extracted current density is chosen to be 235 mA/cm<sup>2</sup>, so the emitter radius, r<sub>e</sub>, is 0.42 cm. The equivalent electron pervance of this beam is 0.29 μP. The extractor design was done using the SNOW code [10]. The electron trap is a proven design used in the FMIT injector. Calculations have been made varying the injected current from the ion source; this geometry has a minimum emittance at the design current of 130 mA. Additional designs for lower proton fractions have also been developed.

## LOW-ENERGY BEAM TRANSPORT SYSTEM

The LEBT system transports and matches the beams extracted from the ion source to the RFQ accelerator. The design beam predicted by the SNOW simulation has an envelope radius of 0.43 cm and an envelope divergence of 46 mrad, while the input beam required by the RFQ has an envelope radius of 0.21 cm and an envelope convergence of 41 mrad.

There are two basic approaches that can be used for the beam-transport system depending on whether electric or magnetic optics are employed. Electrostatic-transport systems have been used to transport 100-mA, 100-keV H<sup>+</sup> beams and could be used in this application for proton beams [11]. This option is less sensitive to beam noise and beam instabilities but is limited by space-charge effects for high-pervance beams.

Magnetic-transport lines, on the other hand, generally entail space-charge neutralized beams. A two-solenoid, magnetic-lens system [12] preserves the cylindrical beam symmetry and is extremely versatile in beam matching to the RFQ. This transport system requires that the beam be space-charge neutralized to ≥95%. Figure 2 shows a layout of the preferred two-solenoid lens, direct-injection LEBT. Beam dynamics simulations with 85% proton fraction show that <0.5 mA of H<sub>2</sub><sup>+</sup> and H<sub>3</sub><sup>+</sup> contaminant ions enter the RFQ for this design. These currents are much less than the expected proton losses in the RFQ and should not pose an operating problem.

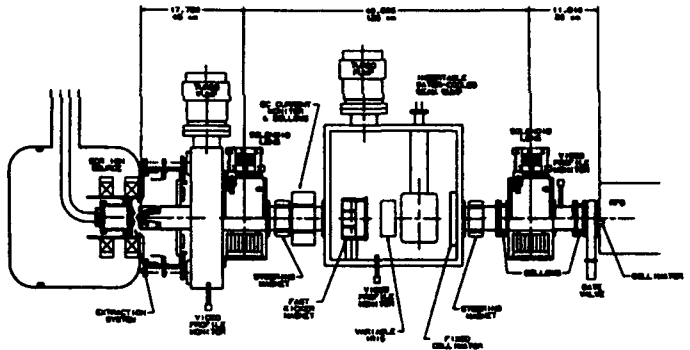


Fig. 2. Layout of the High-Current Proton Injector.

In addition to the focusing lenses, steering elements are needed to correct for minor alignment errors. Steering algorithms have been developed to provide independent control of both centroid position and angle in both transverse planes using two steering pairs. This control is needed to provide optimum tune into the RFQ [13].

A fast kicker magnet provides a means to turn off the proton beam within several microseconds if a fault should occur anywhere in the accelerator or target systems. There is provision to insert a variable iris at the midpoint of the LEBT to limit the beam current to the accelerator and to facilitate beam turn-on. We plan to employ an accelerator design in which the tune is relatively insensitive to beam current so that the accelerator will be brought up to full power by ramping up a low-current, cw beam. This mode of turn-on entails less transient loading of RF systems and permits continuous adjustment of beam tune during ramp-up.

Non-interceptive, beam-diagnostic elements are included in the injector to facilitate beam tuning and to diagnose operating problems. Optical profile monitors provide continuous, on-line beam profile monitoring. Tomographic techniques can be used to deduce the beam emittance [14].

Proper setting of the ion-source parameters can be achieved by tuning for optimum beam profiles. The tune of the focusing and steering elements can also be monitored on line by these profile monitors with a positional accuracy of  $\pm 0.2$  mm. Optimal monitoring locations are at the LEBT midpoint and at the RFQ entrance. A dc transducer will provide continuous monitoring of the LEBT beam current. An insertable beam dump is provided for limited off-periods when it is undesirable to turn off the ion source. Water-cooled collimators and apertures will be used throughout the transport line to intercept any errant beam. The  $H_2^+$  and  $H_3^+$  molecular ion beams in large part will be intercepted on the collimators at the entrance of the RFQ and on the fixed collimator at the LEBT midpoint.

This design was done for a nominal current density of 235 mA/cm<sup>2</sup>. Designs have also been carried out for other current densities ranging from 200 mA/cm<sup>2</sup> to 500 mA/cm<sup>2</sup>. The two-solenoid-lens LEBT has sufficient flexibility to match any of these beams to the RFQ. Figure 3 shows the  $\alpha$ - $\beta$  tuning diagram for the 235-mA/cm<sup>2</sup> design. This diagram shows loci of match-point parameters at the RFQ entrance that can be obtained for a given excitation of the first solenoid as the strength of the second solenoid is varied. The use of two solenoids provides an adequate tuning range in  $\alpha$ - $\beta$  space to accommodate tuning variations in the proton beams. In these simulations, the input beam is assumed to be fully neutralized. The emittance parameters were obtained by scaling the 235-mA/cm<sup>2</sup> results from SNOW to the maximum emittance allowed by the RFQ and then requiring the beam envelope size and divergence to be unchanged. These calculations were done for a total emittance of  $6\epsilon_{rms}$  which corresponds to 95% beam fraction for a Gaussian beam. Similar tuning diagrams were found for beams with 95% neutralization (7 mA effective current) and for  $\pm 15\%$  current variations from the nominal 130 mA extracted beam.

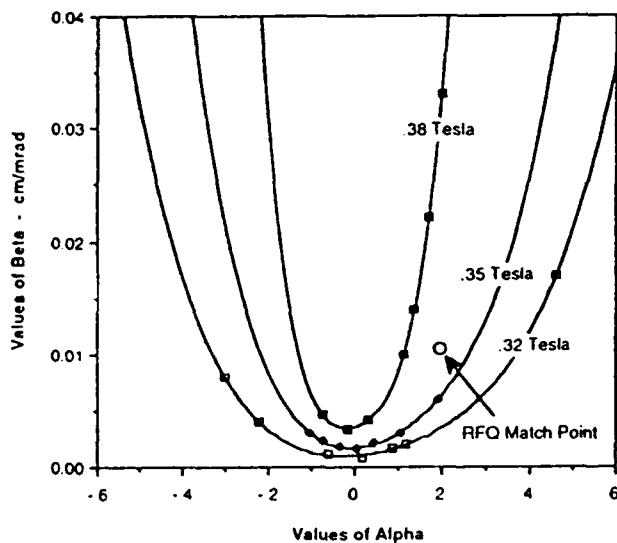


Fig. 3.  $\alpha$ - $\beta$  Tuning Diagram at RFQ Entrance for the High-Current Proton Injector.

Error studies indicate that beam centroid positioning errors should be less than  $\pm 0.50$  mm and  $\pm 10$  mrad at the RFQ match point. Optical aberrations are limited by conservative solenoid-lens designs with the beam filling less than half the magnet bore. The use of adequate pressure in the transport line ( $1 \times 10^{-5}$  torr of a suitable background gas) ensures that beam neutralization limits non-linear, space-charge-induced emittance growth in the LEBT.

#### IV. SUMMARY

A basic injector design for high-current, cw, proton linacs is presented. With the advent of RFQ accelerators, the required injectors can be designed for much lower injection energies with most of the ion-source, ancillary systems at ground potential. An ECR ion source operating with a standard high-voltage column feeding a magnetic-transport line using solenoid lenses appears to be a suitable design. Particular attention must be paid to long-term, operational stability and reliability. Further testing of this injector system is needed to prove that the required long-term operation can be achieved.

#### V. REFERENCES

- [1] G. P. Lawrence, 1991 Particle Accelerator Conference, Vol. 4, p 2598, San Francisco, California (1991).
- [2] Y. Okumura, T. Inoue, H. Oguri, and H. Tanaka, 1992 Linear Accelerator Conf. Proceedings (Ottawa, Canada) AECL-10728, 645 (1992), and Y. Okumura and K. Watanabe, JAERI-M, 92-104 (March, 1992)..
- [3] J. Sredniawski and T. Debiak, Grumman Corporation, Internal Report 92-10 (Dec., 1992) and private communication (1993).
- [4] J. P. Brainard and J. B. Hagen, Rev. Sci. Instrum. **54** (11), 1497 (1983) and private communication.
- [5] T. Taylor and J. S. C. Wills, 1992 Linear Accelerator Conf. Proceedings (Ottawa, Canada) AECL-10782, 347 (1992) and AECL-10782, 350 (1992).
- [6] T. Taylor and J. S. C. Wills, Nuclear Instruments and Methods in Physics Research **A309**, 37 (1991).
- [7] G. M. Arbique, B. G. Chidley, G. E. McMichael, and J. Y. Sheikh, 1992 Linear Accelerator Conf. Proceedings (Ottawa, Canada) AECL-10728, 55 (1992).
- [8] K. N. Leung, D. A. Bachman, and D. S. McDonald, Third European Particle Accelerator Conference (Berlin, Germany), 1038 (1992).
- [9] J. D. Schneider and D. D. Armstrong, IEEE Trans. on Nuclear Science, **NS-30**, no. 4, 2844 (1983).
- [10] J. E. Boers, "SNOW - A Digital Computer Program for the Simulation of Ion Beam Devices," Sandia National Laboratory report SAND79-1027 (1980).
- [11] O. A. Anderson, L. Soroka, J. W. Kwan, and R. P. Wells, Second European Particle Accelerator Conference (Nice, France), 1288 (1990).
- [12] R. R. Stevens, Jr., "High-Current Negative-Ion Beam Transport," submitted to Sixth International Symposium on the Production and Neutralization of Negative Ions and Beams, Brookhaven National Laboratory (1992).
- [13] S. K. Brown and W. H. Atkins, "Beam Steering in the Ground Test Accelerator Low Energy Beam Transport," LANL report, LA-UR-93-358 (1993).
- [14] D. P. Chamberlin, G. N. Minerbo, L.E. Teel, and J. D. Gilpatrick, IEEE Trans. on Nuclear Science, **NS-28**, no.3, 2347 (1981).

# A High Power Long Pulse RF-driven H<sup>-</sup> Source

J. W. Kwan, G. D. Ackerman, W.S. Cooper, G. J. deVries, K.N. Leung, R. P. Wells  
Lawrence Berkeley Laboratory, University of California,  
Berkeley, CA 94720

## Abstract

We have tested the radio-frequency driven H<sup>-</sup> source and have shown that the H<sup>-</sup> production efficiency and the beam emittance are similar to those obtained from the filament discharge. Typically the numbers are 2.8 mA/cm<sup>2</sup>/kW and 0.017  $\pi$ -mrad-cm (which corresponds to 1.9 eV) respectively. So far we have operated RF pulses of  $\approx 10$  kW for  $\approx 50$  ms with a porcelain-coated antenna and  $\approx 15$  kW for  $\approx 1$  s with additional layers of quartz sleeving. It is necessary to develop better antenna coating material that can withstand the intense plasma heating and sputtering in order to operate at higher power with longer pulse length.

## I. INTRODUCTION

In the last Particle Accelerator Conference, Leung et al<sup>1</sup> reported some encouraging results using a radio-frequency driven multicusp source to produce H<sup>-</sup> ions. More than 30 mA of H<sup>-</sup> current was obtained with a 5.4-mm-diam extraction aperture and with an RF input power of 50 kW. As explained by the authors, the RF discharge has many advantages over the filament discharge; these include longer lifetime, ease of operation at high power, fast start-up etc. Similar to filament discharges, the H<sup>-</sup> yield can be enhanced by introducing cesium vapor into the RF-driven discharge. Using the same RF power, Leung et al<sup>2</sup> obtained more than 90 mA of H<sup>-</sup> current in a later experiment which confirms a factor of 3 enhancement by the cesium injection. The above experiments were done with discharge pulses typically less than a couple of ms long. The purpose of our experiment is to test the ion source for a longer pulse length extending up to many seconds

at a practical cw power level (e.g. at  $\approx 20$  kW).

## II. APPARATUS

A schematic diagram of the ion source is shown in Fig. 1. The source dimension is similar to the one described in reference 1. It has a multicusp chamber 10-cm-diam by 10-cm-deep surrounded by 20 columns of samarium-cobalt magnets. The central field-free region is approximately 6 cm in diameter. Two pairs of filter rods (which have permanent magnets embedded inside) are used to generate the magnetic field in front of the extraction aperture. When needed, cesium can be released into the ion source by SAES dispensers<sup>3</sup> mounted inside the source. The inner surface of the source is covered with molybdenum liners in order to minimize cesium condensation on the cold copper surfaces. Since we are operating at  $\approx 20$  kW instead of 50 kW, the H<sup>-</sup> current density is much lower than that obtained in reference 1 and 2. For this reason, a larger aperture (15 mm in diameter) was selected in order to produce sufficient H<sup>-</sup> beam current. Description of the 100 keV preaccelerator with the electron trap can be found in reference 4.

In the past, the same ion source was driven by two tungsten filaments. In this study, the filament unit has been replaced by an RF antenna. It has the shape of a two-turn induction coil (6 cm in diameter) and is made of 4.7-mm-diam copper tubing coated with a thin layer of hard porcelain material. A small tungsten filament is used as a starter to pre-ionize the hydrogen gas before the RF discharge occurs and it can be turned off after the RF discharge has started.

Apart from the antenna, the ion source itself is designed to

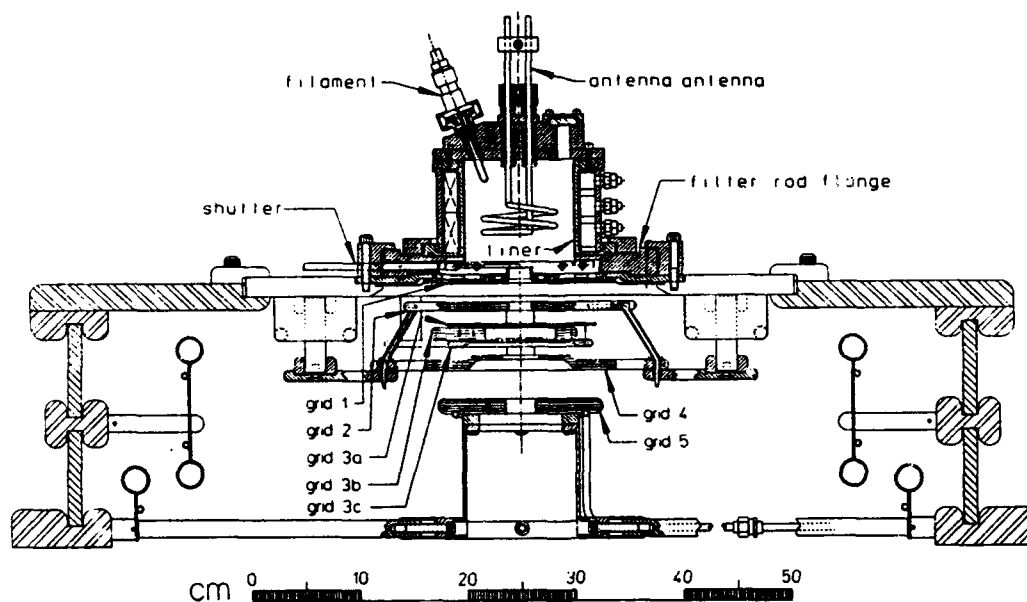


Fig. 1. Schematic diagram of the ion source with an RF antenna.

handle 36 kW of steady-state input power. During the initial testing, we found that the original RF antenna used in Leung's experiments began to fail (at the porcelain coating) when the power exceeded 7 kW for pulses over a second long or for 10 kW pulses over a few hundred ms. In our experiment, we found that adding one or two layers of quartz sleeving over the porcelain-coated antenna can improve the antenna's operating range. However the quartz sleeving introduces another adverse effect to the production of  $H^-$  ions. We will discuss this in more detail in the next section.

The RF circuit diagram is shown in Fig. 2. The RF power supply is capable of delivering 100 kW of cw RF power at  $\approx 2$  MHz. The RF power is transmitted from the power supply via a 50 ohm co-axial cable to a 5-stage 100 kV isolation transformer. The final stage of the transformer is coupled to a LC matching network. As usual, the antenna itself can be represented by a transformer with a single turn secondary while the plasma acts as a resistor in series with an inductor. During operation, the RF frequency is tuned (in the neighborhood of 2 MHz) to obtain resonance in the matching network such that the voltage and the current at the input of the isolation transformer are in phase. The turns ratio of the isolation transformer is adjusted to bring the transformer input impedance (with the plasma load) close to 50 ohms. According to a power balance calibration, the isolation transformer only has a power transmission efficiency of  $\approx 70\%$  (probably due to the lossy core material).

$H^-$  beam current is measured by a current transformer downstream of a dipole magnet which eliminates all remaining electrons in the beam. The average current density reported here is defined as the beam current measured by the current transformer divided by the area of the source aperture. At a typical source operating gas pressure of 10 mT, our Monte Carlo gas flow computation predicted a 45% stripping loss of  $H^-$  ions in the preaccelerator.

### III. EXPERIMENTAL RESULTS

Our first interest was to compare the  $H^-$  yield between filament driven and RF driven discharges. Previously, the ion source had been operated to obtain 75 mA of  $H^-$  beam current from a 14-mm-diam aperture using 17 kW of dc filament

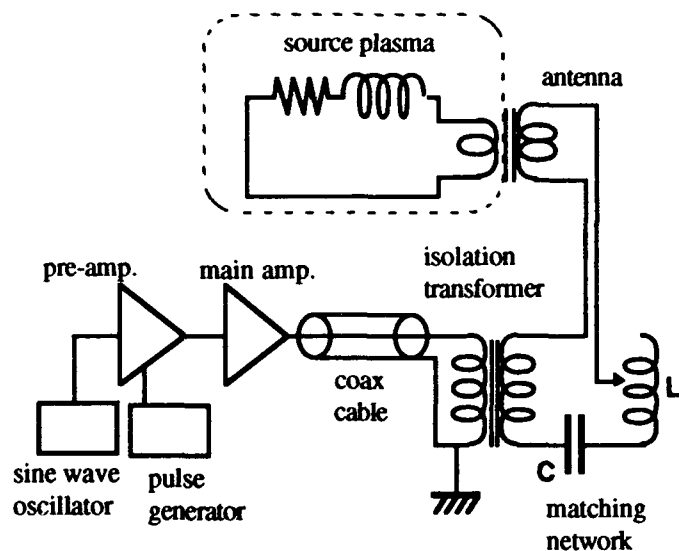


Fig. 2. A circuit diagram of the RF system.

discharge<sup>4</sup>. The  $H^-$  production efficiency in that case was equal to  $2.81 \text{ mA/cm}^2/\text{kW}$ . The pulse length was 270 ms. With a slightly reduced power of 14 kW and a smaller aperture (10 mm diameter), we have obtained up to 2.5 s of  $H^-$  beam; the beam current started at 32 mA, stayed constant for about 1 s and then drooped down to 29 mA at the end of the 2.5 s pulse. We believe that this reduction of  $H^-$  yield is due to the accumulation of tungsten vapor on the cesiated surfaces during the very long pulse.

We typically accelerate the  $H^-$  beams to more than 70 keV energy, thus it is necessary to minimize the electrons extracted from the ion source. In order to do this, the plasma electrode must be biased positively with respect to the source anode. Unfortunately, a positive bias has the adverse effect of reducing the  $H^-$  yield. The electron problem is more severe in the case of RF discharge than the filament discharge and therefore a high positive bias is required which further reduces the  $H^-$  yield. This situation is different from that in Leung's experiments<sup>1,2</sup> in which a negative bias was applied to the plasma electrode.

Fig. 3 shows the  $H^-$  yield as a function of RF power with and without cesium injection. The three series of data are labeled as "no cesium", "some cesium" and "more cesium" because we had no means of quantitatively measuring the amount of cesium vapor in the discharge. Interestingly, the  $H^-$  output current was proportional to the RF power without showing any sign of saturation at high power. Comparing the performance between "no cesium" and "more cesium", the  $H^-$  yield was enhanced by more than a factor of 3. Given that the aperture has an area of  $1.77 \text{ cm}^2$ , the  $H^-$  production efficiency for RF is  $2.76 \text{ mA/cm}^2/\text{kW}$  (when there is plenty of cesium vapor in the discharge). This number is very close to the one found for filament discharge mentioned earlier. These beam data were obtained with discharge pulses that were  $\geq 50$  ms long.

The pressure in the source was reduced from 15 mT in the case of "no cesium" to  $< 10$  mT in the case of "more cesium". The plasma electrode was typically biased at +10 V for all

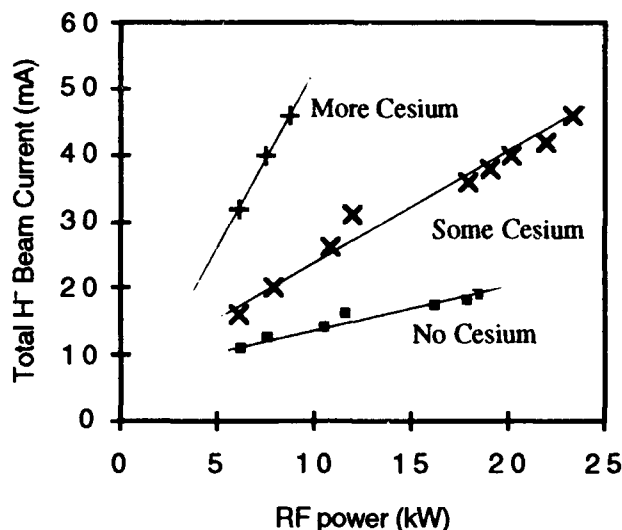


Fig. 3.  $H^-$  yield as a function of RF power into antenna.

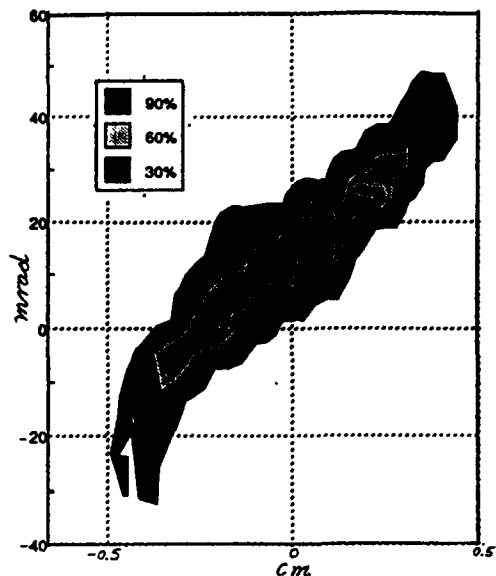


Fig. 4. An emittance diagram of a 70 keV, 41 mA  $H^-$  beam.

cases. The ratio of leakage electron to  $H^-$  current varied with discharge power and cesium concentration. For example at 8.5 kW, the ratio was 4:1 in the case of "more cesium" and 8:1 in the case of "no cesium".

Fig. 4 shows an emittance diagram of a 41 mA  $H^-$  beam obtained with 8.4 kW of RF input power. The pulse length was equal to 50 ms. The normalized rms emittance was  $0.017 \pi$ -mrad-cm which corresponds to an equivalent ion temperature of 1.92 eV at the 15-mm-diam aperture. This ion temperature is certainly within the same range as the ones obtained in our previous experiment using filament dc discharges<sup>4</sup>.

As mentioned earlier, the original antenna design was unable to withstand cw operation exceeding 7 kW of RF power. The first place to show damage was the porcelain coating at the center of the induction coil where the plasma density was expected to be at its maximum. By moving the antenna "return leg" to the outside of the loop, the situation was improved but we are still unable to operate at  $> 10$  kW cw. Another approach that we have tried was to add quartz sleeving over the porcelain-coated antenna. Apparently, the quartz sleeving provided enough thermal shielding to the antenna that it could operate at up to  $\approx 15$  kW cw without incurring damage. Unfortunately we found that the quartz sleeving was responsible for depositing a thin layer of insulating material (most likely quartz) all over the inside of the source. For this reason, the cesium enhancement effect was suppressed and subsequently the  $H^-$  yield was very low.

#### IV. DISCUSSION

So far the result in testing the RF-driven multicusp  $H^-$  source showed that the  $H^-$  production efficiency and the beam emittance are similar to those obtained from the filament discharge; they are typically at  $2.8 \text{ mA/cm}^2/\text{kW}$  and  $0.017 \pi$ -mrad-cm (which corresponds to 1.9 eV) respectively.

The present porcelain coating on the antenna surface works well only for short pulses or for cw low power applications. In order to operate at high power (e.g.  $\geq 15$  kW) with long

pulses (e.g.  $\geq 500$  ms), it will be necessary to develop better antenna coating material to withstand the intense plasma heating and sputtering.

#### V. ACKNOWLEDGEMENT

We would like to thank D. Moussa, S. Wilde, B. Leonard and W. Steele for technical assistance. This work is supported by USASDC under contract No. W31RPD-9D4039 and by U.S. DOE Office of Fusion Energy under contract No. DE-AC03-76SF00098.

#### VI. REFERENCES

- [1] K.N. Leung, W.F. DiVergilio, C.A. Hauck, W.B. Kunkel and D.S. McDonald, Proc. of 1991 IEEE Particle Accelerator Conference, (May 1991, San Francisco, CA) p.1919.
- [2] K.N. Leung, D.A. Bachman and D.S. McDonald, to be published in Rev. Sci. Instrum., April 1993
- [3] Dispensers were manufactured by SAES GETTERS U.S.A. Inc., Colorado Springs, CO.
- [4] J.W. Kwan, G.D. Ackerman, O.A. Anderson, C.F. Chan, W.S. Cooper, G.J. deVries, W.B. Kunkel, K.N. Leung, P. Purgalis, W.F. Steele, and R.P. Wells, Rev. Sci., Instrum., 62, 1521, (1991).

# Initial Operation of the CW 8X H<sup>-</sup> Ion Source Discharge\*

H. Vernon Smith, Jr., Paul Allison, Carl Geisik, David R. Schmitt,  
J. David Schneider, and James E. Stelzer  
Los Alamos National Laboratory  
Los Alamos, NM 87545

## Abstract

A pulsed 8X source was built and the H<sup>-</sup> beam current, emittance, and power efficiency were measured. These results were promising, so a cooled, dc version designed for operation at arc power levels up to 30 kW was built. Testing of the CW 8X source discharge is underway. The design dc power loading on the cathode surface is 900 W/cm<sup>2</sup>, considerably higher than achieved in any previous Penning surface-plasma source (SPS). Thus, the electrode surfaces are cooled with pressurized, hot water. We describe the source and present the initial operating experience and arc test results.

## I. INTRODUCTION

The 8X source is under development for possible use in the neutral-particle beam program. It may also be of interest to other projects that require either dc or high-duty-factor, high-quality H<sup>-</sup> beams. The pulsed-8X source design and measured performance are described in Ref. [1]. Grumman Space Systems built [2] a cooled version of the 8X source, the CW 8X source [3], that is designed to operate with dc arc. The source is now installed on the high-current test stand (HCTS) at Los Alamos for dc arc tests. The HCTS was modified to accommodate the additional equipment necessary for these tests, including installation of a water-cooling system and a Macintosh IIfx-LabView™-based set-point, data-archiving computer system [4]. Previous work on cooled or long-arc-pulse Penning sources is described in [5], [6], and [7].

## II. SOURCE DESIGN

We observed a cathode power efficiency  $\zeta = 640$  mA/kW in our pulsed 8X source measurements [1] ( $\zeta = j_{H^-}/F_C$ , where  $j_{H^-}$  is the emission current density and  $F_C$  is the cathode power loading). Researchers at Novosibirsk claim [8] dc operation of an H<sup>-</sup> planotron SPS at cathode power loads  $F_C = 1$  kW/cm<sup>2</sup>. Thus, we speculate that  $j_{H^-} \geq 640$  mA/cm<sup>2</sup> would be possible for dc operation of the 8X source (a Penning SPS).

The CW 8X source predicted performance, based on the measured pulsed-8X-source performance [1], is shown in Table I of Ref. [3]. We assume that for the dc source the effective H<sup>-</sup> transverse temperature is 6.7 eV, the value found in the pulsed-8X-source emittance measurements [1]. For a 0.40-cm-diam emitter, 60-mA dc H<sup>-</sup> beams with rms normalized emittances  $\epsilon \approx 0.01 \pi$  cm mrad are anticipated. We estimate a cathode power density of 900 W/cm<sup>2</sup>, low enough to permit dc operation. However, the discharge power is 88 V  $\times$  340 A = 30 kW, with 20 kW estimated to go to the cathode and 10 kW to the anode. Vigorous cooling of all surfaces contacting the source plasma is provided.

The approach taken to cool the cathode and anode [2,3] operating at power loads as high as 1.4 and 0.26 kW/cm<sup>2</sup>, respectively, is illustrated in Fig. 1. To cool the cathode, water

is transported up seven squirt tubes (0.22 cm o.d.  $\times$  0.013 cm walls) to the end of each cathode tip. The water then reverses direction (180° bend) and is transported down the annulus between the squirt tube and the 0.30-cm-i.d. cavity machined into the cathode. The power deposited on the cathode is transported through a 0.17-cm-thick layer of molybdenum to the coolant passages. Good heat transfer is achieved by using the fluid velocity to suppress local burnout. The heated water from the annuli surrounding the 14 squirt tubes (7 in each tip) is returned to a common plenum. The water is then transported to a specially built unit capable of removing up to 46 kW. Because the anode power loading is four times lower than the cathode loading, and because the emission-aperture-cap power loading is assumed to be the same as for the anode, both are cooled using conventional coolant passages [3]. A conical collar in the drift region (Fig. 2) provides maximum e<sup>-</sup> suppression with no degradation of the H<sup>-</sup> beam output [9]. The anode, cathode, and emission-aperture cap are molybdenum, which has good thermal and structural properties in addition to excellent H<sup>-</sup> production. More design details, and the results of the design calculations, are given in [2] and [3].

Figure 2 shows a CW 8X source assembly drawing. The variable magnetic field is provided with an electromagnet coil. Cesium vapor is provided by heating a mixture of titanium and cesium-chloride powders contained in a separate oven (not shown). The source is heated initially to 185°C by the water system. Once the arc is struck, the water temperature is kept  $\geq 150^\circ\text{C}$  to maintain the proper cesium coverage on the electrode surfaces.

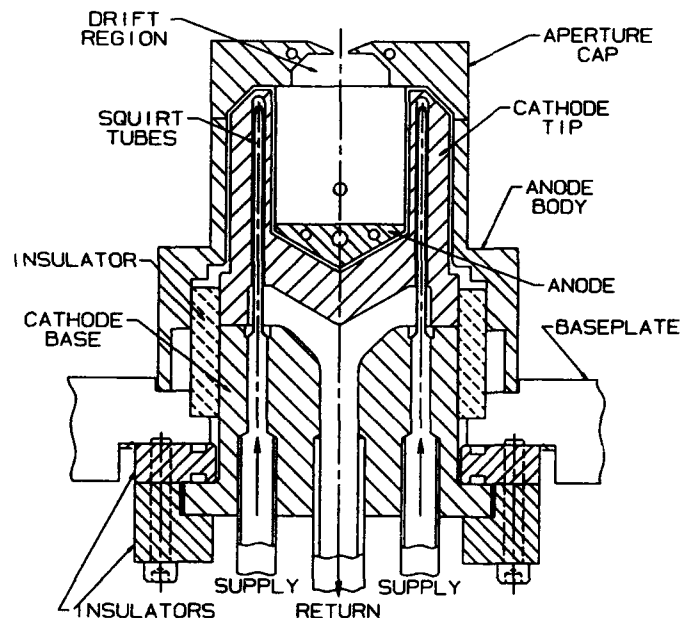


Figure 1. A cross-sectional view of the CW 8X source cathode, anode, and emission-aperture cap [2,3].

\* Work supported by the Dept. of Defense, US Army Strategic Defense Command under auspices of the US Dept. of Energy.

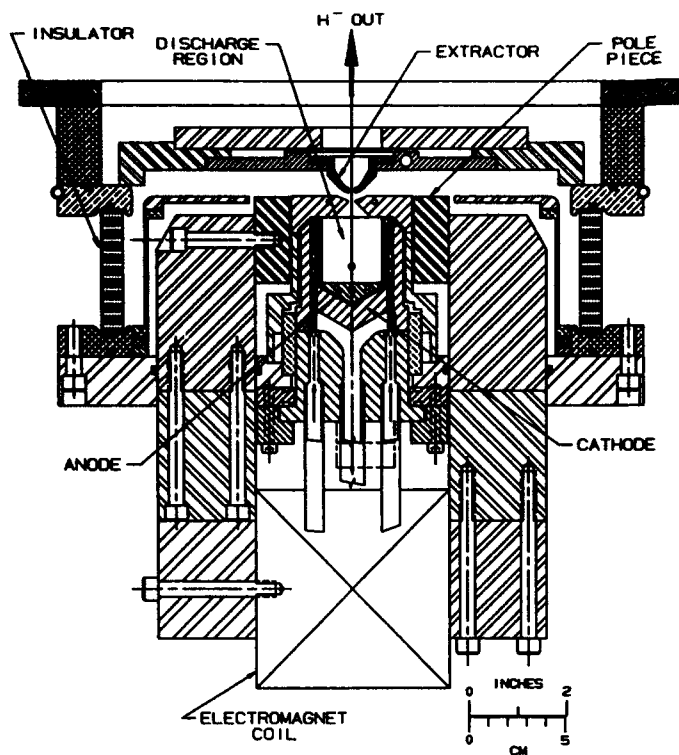


Figure 2. An assembly drawing of the CW 8X source [3].

### III. WATER SYSTEM

Figure 3 shows the layout of the HCTS. The 500 psi (3.4 MPa), 200°C water system, purchased from Wellman Thermal Systems in Shelbyville, IN, provides the deionized, high-temperature water. During start up, the water is heated by a 12-kW electrical heater coil. A 22-gpm (83-lpm) pump circulates the water to the source through the manifolding. Once the operating temperature is reached, a Honeywell UDC 5000 controller maintains the water temperature at the preset

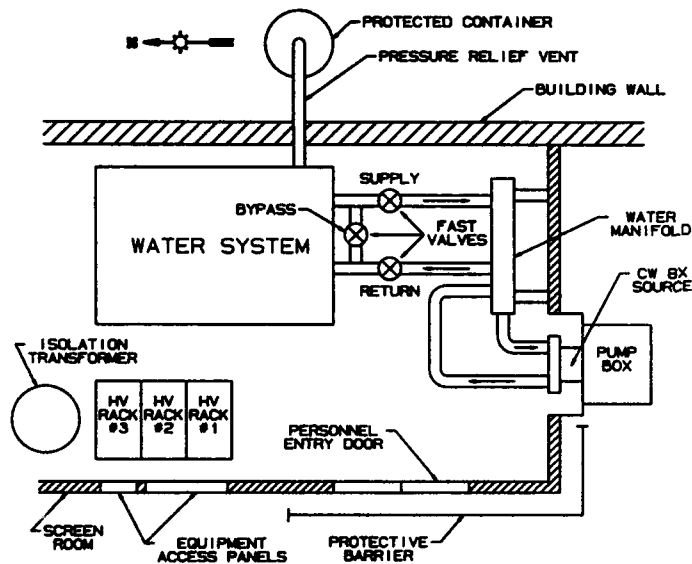


Figure 3. Schematic of the test-stand layout, including the water system.

value by sending a portion of the water through a heat exchanger that has 46-kW cooling capacity. If a water leak is sensed, air-actuated fast valves isolate the water system from the manifolding and the source. Pressure-relief valves automatically protect against over-pressure conditions.

### IV. SOURCE ELECTRONICS

In addition to the requirements imposed by having to cool a 30-kW dc discharge, an additional complication is introduced by the arc requirements. Approximately 400 V is needed to initiate the Penning SPS discharge. We estimate that 350 A of arc current is needed to produce the desired H<sup>-</sup> current. One option is to use a 400-V, 350-A dc power supply to start and to sustain the discharge. Instead, we use a 600-V arc pulser to strike the discharge and two 30-kW dc power supplies (one rated at 150 V, 200 A and the other at 200 V, 150 A, arranged in parallel) to sustain it (Fig. 4). Schematics of the expected CW 8X source discharge voltage ( $V_d$ ) and discharge current ( $I_d$ ) waveforms are shown in Fig. 5.

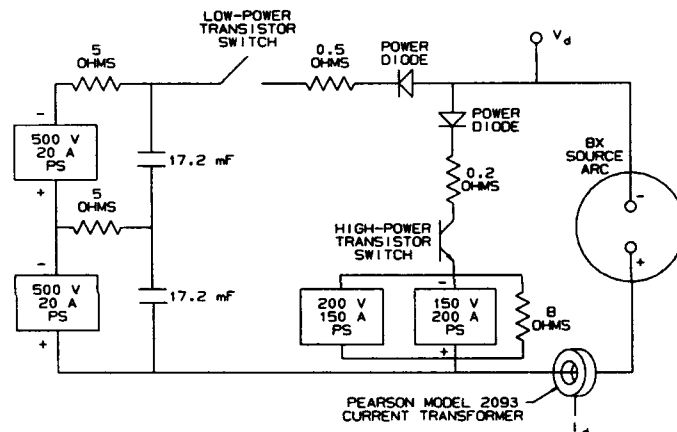


Figure 4. CW 8X source electronic circuit schematic.

Two power supplies charge the 17.2-mF arc-pulser capacitors. Zener diodes placed in the control circuits of the 500-V power supplies limit their outputs to 300 V. At time  $t = 0$ , the low-power transistor switch closes initiating the source discharge. The 150-V, 350-A power supply continually draws current through the 8-Ω resistor to improve its response to the pulsed current demand. That demand comes at  $t = 1.0$  ms, when the high-power transistor switch closes and the low-power switch opens. Large power diodes prevent crosstalk between the 150-V, 350-A power supply and the arc pulser. The 150-V, 350-A power supply keeps the discharge running until the high-power transistor switch is opened.

### V. INITIAL OPERATING EXPERIENCE

NiOro brazing compound (82% Au, 18% Ni) was used to join the molybdenum components together. A silver-copper over-braze was used to provide a vacuum seal for the cathode and anode assemblies (the emission-aperture cap did not need the over-braze). Before the source was assembled, pressure tests at 750 psi (5.2 MPa) revealed no leaks in the cathode, anode, and aperture cap assemblies. After 70 hours of pulsed operation, the braze joints are still intact. The cathode assembly must be electrically isolated from source ground (the anode, emission-aperture cap, and water system) in the high-

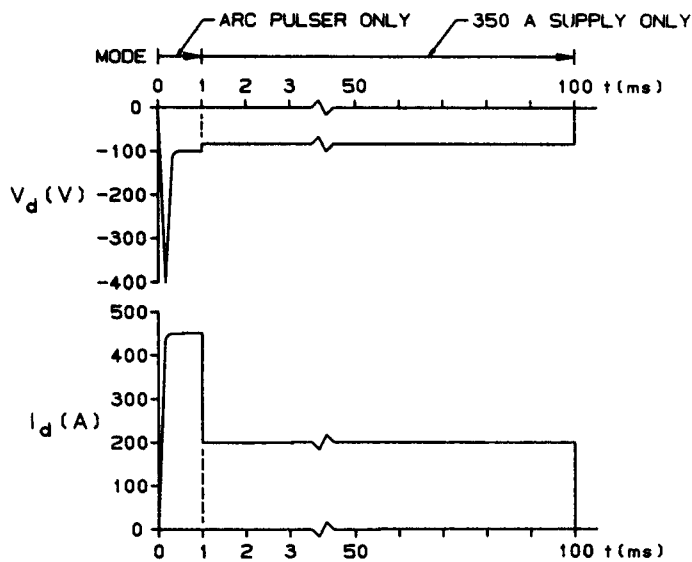


Figure 5. Expected  $V_d$  and  $I_d$  waveforms.

temperature water loop. This is done with KEVLAR™-reinforced, silicone-rubber hose assemblies that were specially made for this application by Preece, Inc. of Irvine, CA. We have not had any hose failures at temperature. The hose crimp joints developed leaks after several thermal cycles. Recrimping the hose connectors sealed these leaks—no failures have occurred in the recrimped assemblies.

A heater power of 9 kW maintains the water unit, the manifolding, and the source at 184°C, leaving 3 kW to raise the temperature further if necessary (200°C is the design maximum). We add 5 ppm each of  $\text{NaNO}_2$  and  $\text{Na}_2\text{MoO}_4 \cdot 2\text{H}_2\text{O}$  to the deionized water to suppress corrosion of the molybdenum components. We also add 30 ppm of  $\text{NaOH}$  to the deionized water to elevate the pH of the water from  $\approx 6$  to  $\geq 9$  to prevent corrosion of all the materials that contact the water: 316L, 304L, and 316 stainless steels; molybdenum; copper; silicone; teflon; KALREZ™ and Parker compound E962 O-rings; PEEK™ seals in the ball shut-off valves; and NiOro and silver-copper brazing compound.

Cathode material is worn away by sputtering. In our pulsed 8X source tests, the sputtered molybdenum occasionally bonded poorly to the anode and aperture cap, causing flakes to form which degraded source performance. Thus, erosion of the cathode can present a problem for long-term, dc operation. Based on the 4X source pulsed operation data [10], we project that the erosion of the CW 8X source cathode due to sputtering will be  $\approx 0.02$  mm/h. Experience does not necessarily indicate a problem with this level of sputtering, but long-term effects are unknown. The dc erosion rate may be much less than the pulsed rate because the dc discharge voltage is normally lower than the pulsed voltage. So far in our tests, we have immeasurably small erosion of the CW 8X source cathode, and the very-thin layers of sputtered molybdenum that deposited on the anode bonded securely (no flaking has been noted).

## VI. INITIAL RESULTS

Figure 6 shows the measured discharge voltage and current waveforms for 1-ms-long arc-pulser and 4-ms-long dc-power-supply pulses. The source parameters for the waveforms shown in Fig. 6 are arc magnetic field = 420 G,

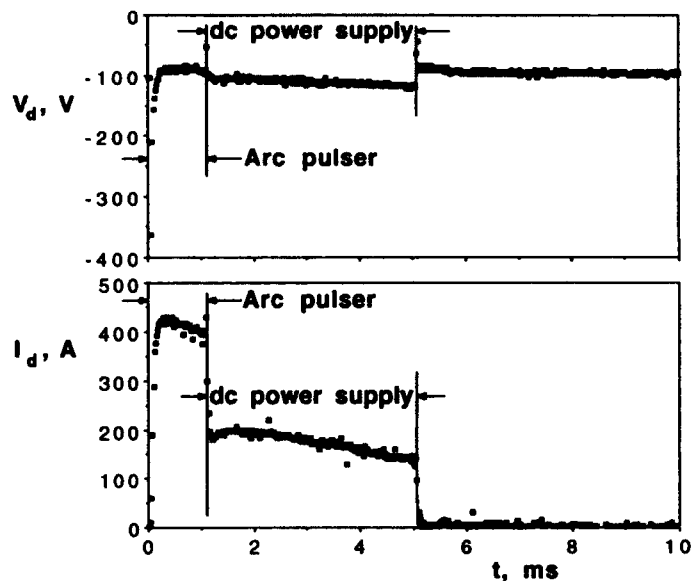


Figure 6. Measured  $V_d$  and  $I_d$  waveforms for a 1-ms-long arc-pulser pulse and a 4-ms-long dc-power-supply pulse.

pulse repetition rate = 1 Hz, and  $\text{H}_2$  and  $\text{N}_2$  gas flow = 100 and 1 sccm, respectively. The droop in the arc-pulser-driven discharge current is due to the RC drain of the pulser capacitor bank. The droop in the dc power-supply-driven current pulse is the turn-on response of the power supplies; the same shape is measured when the source arc is replaced with a short.

## VII SUMMARY

The dc version of the 8X source is installed on the HCTS at Los Alamos and the arc tests have begun. The arc pulse length will be extended from 6 ms to  $>1$  s before we prepare to extract dc  $\text{H}^-$  beam from this source.

## REFERENCES

- [1] H. V. Smith, Jr., P. Allison, and J. D. Sherman, "Penning Surface-Plasma Source Scaling Laws - Theory and Practice," Proc. 6th Intl. Symposium on the Production and Neutralization of Negative Ion and Beams, Brookhaven National Laboratory, November 9-13, 1992 [to be published in the AIP Conf. Proc. series, 1993]. Also LA-UR-92-3664.
- [2] R. Heuer, J. Porter, I. Birnbaum, T. Schulties, and J. Sredniawski, "Final Design of the 8X CW Negative Ion Source," Grumman Aerospace Corporation, Bethpage, NY, Report, 1991.
- [3] H. V. Smith, Jr., et al., "CW 8X Ion Source Development," in Ref. 1. Also LA-UR-92-4075.
- [4] C. Geisik, D. R. Schmitt, J. D. Schneider, and J. E. Stelzer, "Computer System for the High-Current Test Stand," Los Alamos National Laboratory report LA-CP-92-232.
- [5] R. B. McKenzie-Wilson, K. Prelec, and R. Hrudá, IEEE Pub. No. 79CH1441-5 NPS, 225 (1979).
- [6] W. K. Dagenhart, C. C. Tsai, W. L. Stirling, P. M. Ryan, D. E. Schechter, J. H. Whealton, and J. J. Donaghy, AIP Conf. Proc. No. 158, 366 (1987).
- [7] H. V. Smith, Jr., N. M. Schnurr, D. H. Whitaker, and K. E. Kalash, IEEE Catalog No. 87CH2387-9, 301 [1987].
- [8] Yu. I. Bel'chenko, G. I. Dimov, V. G. Dudnikov, and A. S. Kupriyanov, Revue Phys. Appl. 23, 1847 (1988).
- [9] H. V. Smith, Jr. and P. Allison, "Electron Suppression in the  $\text{H}^-$  Beam from a Penning Surface-Plasma Source," Rev. Sci. Instrum. 64, (June, 1993). Also LA-UR-92-3337.
- [10] W. B. Ingalls, Los Alamos National Laboratory, private communication.

# Volume H<sup>-</sup> Ion Source Development at LAMPF

R. L. York, D. Tupa, D. R. Swenson, and R. Damjanovich  
Los Alamos National Laboratory, Mail Stop H838, Los Alamos, NM 87545

## Abstract

One method of increasing the intensity of the LAMPF Proton Storage Ring is to use a brighter H<sup>-</sup> ion source. To develop such a source, the performance of the small LBL dipole filter and the BNL toroidal filter volume H<sup>-</sup> sources are being investigated. Results of testing a new high-duty-factor design of the BNL toroidal filter volume source are discussed. Results of experiments to reduce the electron to H<sup>-</sup> ratio and modulate the beam intensity in the small LBL source are presented.

## I. INTRODUCTION

The LAMPF Proton Storage Ring, PSR, and proposed new projects, such as the National Center for Neutron Research, NCNR, require a high-duty-factor H<sup>-</sup> ion source capable of producing a 35 mA beam with an emittance of 0.04 cm-mrad at 95% beam fraction. The LBL dipole-filter [1] and the BNL toroidal-filter [2] volume H<sup>-</sup> sources have both demonstrated, at low duty factors (<1%), the beam intensity and quality necessary for these facilities. A development program to determine the high-duty-factor capabilities of these sources has been in progress for one year. LAMPF has operational experience and facilities to evaluate high-duty factor H<sup>-</sup> ion sources.

Reducing the ratio of electrons to H<sup>-</sup> ions is essential to minimize operational problems and maximize the quality of the H<sup>-</sup> ion beam. Operational experience at LAMPF has shown that, at duty factors greater than 5%, impinging even a small amount of electron beam on the accelerating lenses can produce an arc down rate that can devastate the operational reliability of the source. Reducing the electron ratio at the source is especially important at high duty factors.

## II. BNL TOROIDAL FILTER SOURCE

The BNL toroidal volume H<sup>-</sup> source, with its unique conical shape magnetic filter, has been under study at BNL since 1988 and its performance is well documented [2]. This source is very attractive for high-duty-factor applications because it produces H<sup>-</sup> beam in excess of 30 mA with an electron ratio of less than 5:1. With the assistance of Jim Alessi at BNL, a high-duty-factor version of this source has been designed and constructed. A drawing of this source is shown in Figure 1. Extensive magnetic field calculations were performed using PE-2D [3] to preserve the magnetic-cusp and filter-field geometry while incorporating the necessary changes to obtain reliable high-duty-factor

performance. The interior of the source housing is stainless steel with individual recesses for each magnet arranged in circular patterns. The outer housing is aluminum rather than iron for maintenance and construction considerations; the PE-2D calculations indicated that the major features of the magnetic confinement and filter fields could be maintained without an iron return. The filament feedthroughs are of a concentrically cooled design that has been used reliably in the production operation of our surface source for 10 years. The cylindrical cavity at the back of the source makes it possible to optimize the filter strength by changing filter magnets without breaking vacuum. The unique clamshell design of the vacuum housing makes maintenance of the inside of the source possible without opening water passages. This design also permits the plasma electrode position to be optimized.

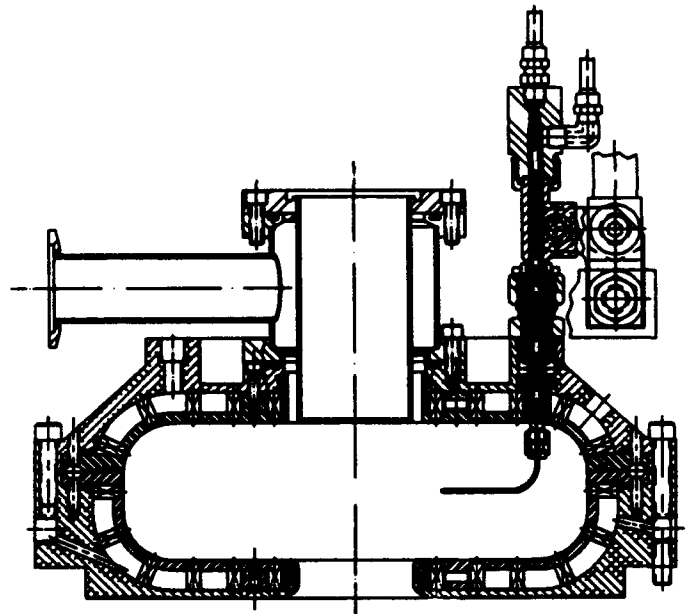


Figure 1. The LAMPF high-duty factor version of the BNL toroidal filter source.

For evaluation, the new source was installed in the H<sup>-</sup> Cockroft-Walton dome[4]. To optimize the magnetic filter, different sizes and strengths of filter magnets were tested. The polarity of the magnets was changed from attracting (the filter magnets are opposite in polarity to the innermost ring of cusp magnets on the source front plate, as in the BNL design) to repelling (the filter magnets are the same polarity as the cusp magnets). A representative sample of these data is shown in Figure 2. Unlike BNL, for our source design, the performance of the repelling magnetic configuration is superior to the attracting one. In this configuration, the extracted H<sup>-</sup> current and electron ratio are

\*Work performed under the auspices of the U.S. D.O.E.

comparable to the BNL results. An iron plate was added to the front of the source and the plasma electrode was moved to the inside front edge of the source to better simulate the BNL design, but this was detrimental to the source performance for both filter polarities.

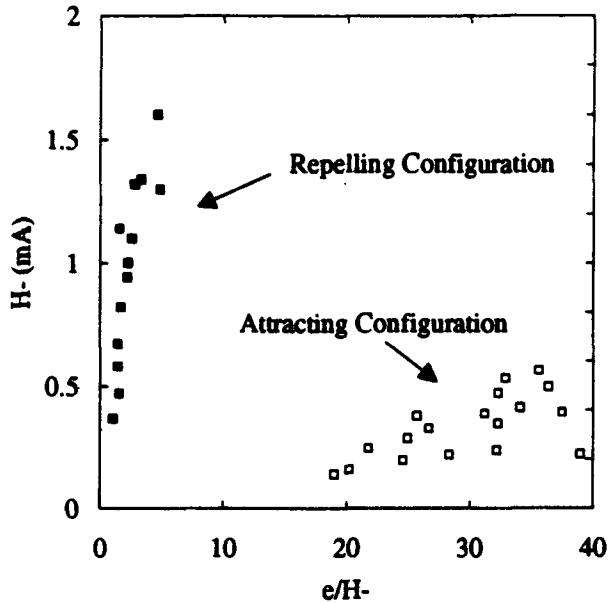


Figure 2. H<sup>-</sup> current vs. electron ratio for attracting and repelling filter magnet configurations and filter strengths.

For these studies, two 1.5 mm diameter tungsten filaments shaped in semicircle loops with a radius of 6.5 cm were used. The performance of the source depended on the filament's heater current directions. The optimum heater current pattern was different for two filter polarities. This supports the BNL observation that there is an interaction between the filter magnetic field and the local magnetic fields produced by the filaments.

Plasma electrode positions beginning at the inner front face of the source and spacing outward 1.0, 1.5, and 2.0 cm were studied. Over this range, the H<sup>-</sup> current only varied 10%, but electron ratio increased a factor of 5 as the plasma electrode was moved away from the source. However, the extraction optics are more difficult when the plasma electrode is more reentrant.

The plasma aperture was opened to 0.4 cm<sup>2</sup>. The H<sup>-</sup> current and electron ratio as a function of arc current are plotted in Figure 3. The pulse length was 800 μsec. Data taken at 4, 60, and 120 Hz showed no dependence on duty factor. The H<sup>-</sup> current and electron ratio produced after cesium is added to the source are also plotted in this figure. Without cesium, the source produces an 8 mA beam, which corresponds to 20 mA/cm<sup>2</sup> with an electron ratio of 5:1. When cesium was added to the discharge, the H<sup>-</sup> current increased to 40 mA/cm<sup>2</sup> with an electron ratio of 2:1.

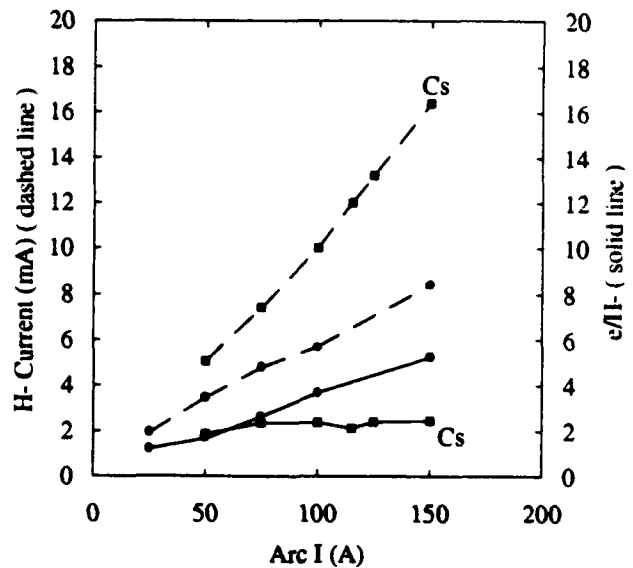


Figure 3. H<sup>-</sup> current and electron ratio vs. arc current with and without cesium.

The emittance was measured using a slit and collector emittance station 1.5 meters from the source. For arc currents of 50 to 150 A, the 95% values of the emittance are plotted in Figure 4. This shows that the emittance increases almost linearly with arc current. The reason for this increase is not understood, but the beam emittance did not appear to be increased by aberrations. The emittance of an 8 mA beam with cesium at 100 A of arc current is also plotted. We were unable to measure the emittance of the 40 mA/cm<sup>2</sup> beam because the high-voltage electrode spacing was inadequate to transport a beam of this density.

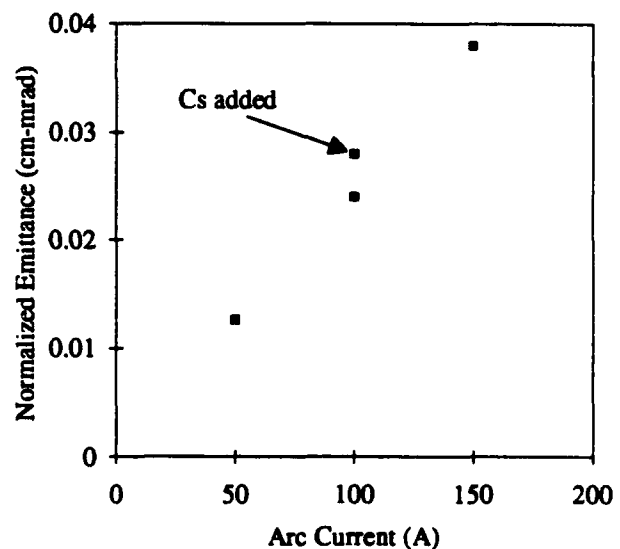


Figure 4. Normalized emittance vs. arc current.

### III. SMALL LBL VOLUME SOURCE

The small LBL volume  $H^-$  source also has very impressive performance at low-duty factor. The 2 MHz rf driven version of this source has produced currents greater than 40 mA without cesium at a 1% duty factor[1]. However, reducing the electron ratio of this source would enhance its reliability for high-duty operation. Studies have shown that using a plasma electrode aperture with an aspect ratio (aperture diameter/thickness) of one greatly increases the ability to reduce the electron ratio by biasing the plasma electrode. This technique reduces the electron current by a factor of 10 while reducing the  $H^-$  current by only a factor of 2. The effects of magnetic filter strength, plasma electrode spacing from the filter, and the use of a collar have also been studied. These studies have revealed the effect of electron ratio on the beam emittance. Figure 5 shows how the beam brightness increases as the electron ratio is reduced. For the 240 A case, when the electron ratio was reduced by a factor of 7, the beam brightness increased by a factor of 5 while the  $H^-$  current only decreased 25%. Using a combination of these techniques, we have measured current densities in excess of 35 mA/cm<sup>2</sup> with a normalized emittance of 0.03 cm-mrad at 95% beam fraction and an electron ratio of less than 5:1 without cesium. To study the high-duty-factor performance of this source, a 2 MHz, 100 kW rf drive capable of 10% duty operation has been ordered.

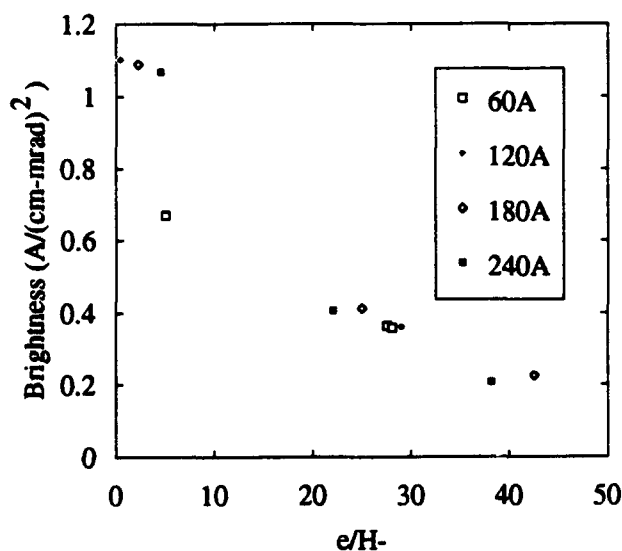


Figure 5. Beam brightness vs. electron ratio at different arc currents.

### IV. BEAM MODULATION

Neutron spallation sources such as PSR require 100 to 200 ns gaps in the beam for extraction purposes. Designs of the NCNR accelerator propose this chopping at energies of approximately 100 keV. Calculations indicate that space-charge effects will make this process very difficult.

Modulating the beam intensity at the source with rise and fall times of 100 ns or less would make final beam chopping easier by reducing the space-charge effects. This capability would also be useful at accelerators such as SSC where beam pulses with sharp rise and fall times are desired.

Our studies show that the beam intensity of the small LBL Volume  $H^-$  source can be modulated by biasing the plasma electrode. The geometry of the plasma electrode is very important to this process. For these tests, a collar[1] and plasma electrode aperture that is 3 mm in diameter and 3 mm thick were biased at the same potential with respect to the source housing. The tests showed that, with an arc current of 150 A, 90% of the extracted beam current could be suppressed if the plasma electrode was biased at -150 or +40 volts. Using a simple Hexfet modulator circuit, the plasma electrode can be pulsed to -150 volts in approximately 100 ns. The time response of the beam intensity was measured to exactly correspond to the applied voltage. This result proves that the plasma response is adequate to modulate the beam intensity at the source with a beam turn-off time of 100 ns. The plasma electrode discharge time and beam turn-on time of 100 ns were also been measured. Developing a voltage modulator with faster response that operates reliably floating at 80 kV has proven to be quite challenging. We hope to determine the time response limit of the beam-intensity modulation. We are also studying the geometry dependence of the beam modulation.

### V. CONCLUSION

Both types of volume  $H^-$  sources show the potential of providing the brighter beams required for PSR and NCNR. If the toroidal filter source beam intensity continues to scale with plasma aperture, it will provide adequate beam current with small electron ratio. If the techniques to reduce electron ratio work as well for the rf driven source as for the filament source, it will also produce adequate beams. Modulating the beam intensity at the source on a time scale of less than 100 ns has numerous applications.

### VI. ACKNOWLEDGEMENTS

We would like to acknowledge the contributions of J. Wieting, H. Williams, W. Potter, and J. D. Paul to this work.

### VII. REFERENCES

- [1] K. N. Leung et al., *Rev. Sci. Instrum.* **64**, 970,(1993).
- [2] J. G. Alessi and K. Prelec, "The BNL Toroidal Volume  $H^-$  Source," *Conference Record of the 1991 Particle Accelerator Conference*, Vol. 3, pp. 1913-1915.
- [3] Vector Fields Limited, 24 Bankside, Oxford OX5-1JE, England.
- [4] Ralph R. Stevens Jr. et al, *Proceedings of the 1984 Linear Accelerator Conference*, pp. 226-228.

# Further Development with Heavy Ion Sources at Brookhaven National Laboratory's Tandem Van de Graaff Facility

M. J. Zarcone, D. B. Steski, K. S. Smith, and P. Thieberger  
Brookhaven National Laboratory  
Upton NY, 11973 USA

## Abstract

The Ion Source Test and Development Group at Brookhaven National Laboratory's Tandem Van de Graaff Facility has been evaluating the Peabody Scientific [1] PSX-120 negative ion cesium sputter source for use as the source of pulsed negative ion beams for injection of the Brookhaven synchrotrons. The decrease in emittance due to the use of a spherical ionizer, as recently reported [2], may lead to improved brightness of the beam injected into the MP Tandem resulting in improved beam output. Emittance measurements with the PSX-120 are presented for dc beams and some of the first pulsed beam results are also discussed.

## I. INTRODUCTION

The two MP Tandem Accelerators at Brookhaven National Laboratory are, at present, the only devices [3-5] that can satisfy the requirements for injection of heavy ions into the AGS and will be used when the Relativistic Heavy Ion Collider, RHIC, now under construction comes on line. With the commissioning of the BOOSTER in 1992, the mode of operation of the Tandems has permanently changed from a three stage mode of operation [6] using both MP Tandem Accelerators to a two stage mode that uses only one of the MPs. This changes the conditions under which the ion sources can be run. In addition, although the current ion sources provide adequate intensities of negative ions for the Heavy Ion Physics Program, increased intensity and lower emittance from the ion source will enhance the program, providing a wider range of operating conditions and a greater margin for less than optimum performance.

## II. MULTIWIRE BEAM PROFILE MONITORS

The emittance measurements taken on the test bench were a first approximation but nonetheless a valid and reasonable representation based on the profiles of the beams. Two multiwire beam profile monitors or harps were constructed using 14 - 0.040" stainless steel rods set on 0.200" centers, in both the vertical and horizontal planes contained in a 3.5" square frame of Macor®. The two harps are located at distances of 1.21m and 2.78m from the center of an Einzel lens (Ortec Model 345 Gridded Einzel Lens [7]) which is approximately 0.6m from the extraction electrode of the source. Current measurements were made in the 'source' cup located 0.3m from the extraction electrode of the source and in the 'object' cup located 0.2m before the downstream harp.

The signals from the wires are fed into a standard HITL/AGS instrumentation package [8] for processing and display on an oscilloscope. These electronics are capable of reading all four sets of fourteen wires but sampling was usually done in the horizontal plane on one harp at a time.

The observed profile of positive currents for the negative ion beam is due to the secondary electron emission from those wires that intercept the ion beam superimposed onto the profile of the electrons picked up as 'cross-talk' from one wire to the adjacent ones.

The cross-talk of emitted electrons tends to skew the relative currents from one wire to the next and needs to be eliminated or at least greatly reduced. Studies [9] show that the majority of these secondary electrons have kinetic energies of less than 50 eV. The most prominent peak in the energy spectrum of the secondary electrons being the 'slow' peak, which occurs at very low energies, less than 6 eV.

The method of reducing the cross-talk uses both planes of wires on the harp, one to measure the current and one to apply a bias voltage. The upstream plane of wires was positively biased and the current measured on the downstream plane of wires. The electron cross-talk is not altogether eliminated but is greatly reduced with a positive bias of 20 Volts. Modeling the harps with SIMION [10], an electrostatic lens analysis code, shows that the small number of electrons still being picked up are those that are emitted from the outermost edges of the wires.

## IV. EMITTANCE MEASUREMENTS

Emittance as used in this paper is defined as  $\pi\epsilon$  which is the area of the phase ellipse. Values quoted are for the normalized emittance given by  $\pi\epsilon E^{1/2}$  with units of mm mrad MeV<sup>1/2</sup> where E is the energy of the ion beam in MeV.

The formula used to obtain a value for the emittance can be derived from the transport matrices using a lens followed by a drift region [11]. The one used for these emittance calculations is given by:

$$\epsilon = (W_2^2 / (L_2 - L_1)) \sqrt{(W_1^2 / W_2^2 - L_1^2 / L_2^2)}$$

This formula computes the emittance using the half widths of the beam profiles on the two harps,  $W_1$  (upstream harp) and  $W_2$  (downstream harp) and the distances of the harps from the center of the Einzel lens,  $L_1$  and  $L_2$ . This formula is derived for a configuration where there is a minimum spot size (not a waist) on the second harp.

The procedure was to minimize the beam on the down-

stream harp, record the profile, read the current on the object cup, put in the upstream harp without any adjustments of parameters and record its profile, then read the current on the source cup. The data was then fit to a Gaussian distribution where the standard deviation was determined. The half width used in the formula is obtained from 80% of the beam profile.

Several sets of data were taken on the test bench using the PSX-120 with the helical and spherical ionizers for gold and a few for silicon.

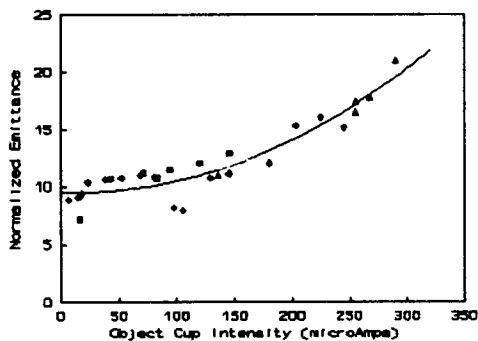


Figure 1. Emittance Measurements for the Helical Ionizer.

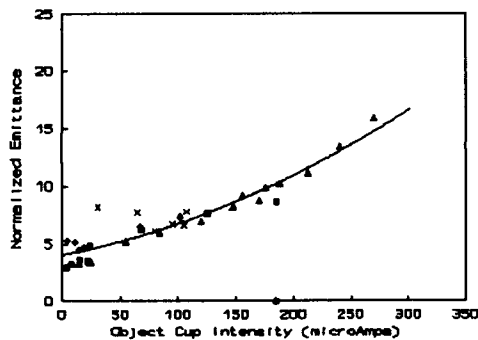


Figure 2. Emittance Measurements for the Spherical Ionizer.

In Figures 1. and 2. above, the data for the normalized emittance of the gold beams using the helical and spherical ionizers is shown. The energy of the extracted ions was 30 kV with cesium accelerating voltages of 3.8 - 10 kV. The spread in the data is representative of the difficulty in determining the emittance by this method. These difficulties are due to 1) moderate resolution on the harps from the diameter and spacings of the wires, 2) the deviation of the beam from a purely gaussian shape, and 3) measuring emittance of a beam before mass analyzing (only trace amounts of elements other than gold but  $Au_2^-$  and  $Au_3^-$  each have an intensity of up to 10% of that of the  $Au^-$  beam). In addition, the secondary electron emission coefficient of each wire can change as the wires are coated by the ion beam.

The normalized emittance as measured with both ionizers can be seen to increase with intensity. A quadratic line was fit to the data points using a least squares program. The emittance growth is a result of the increase in space charge forces but the form of this dependence is not straight forward [12] and will be addressed in a later paper.

If we compare the two graphs we can conclude that the emittance of the gold beams with the spherical ionizer is 45% of that with the helical ionizer at lower intensities, but gradually increases to 75% over the range of intensity shown. A few measurements of 30 kV  $Si^-$  beams with both ionizers have also been made over the same range. These data average, for 80% of the beam, to about  $3.5\pi$  mm mrad  $MeV^{1/2}$  for the spherical ionizer and  $8.2\pi$  mm mrad  $MeV^{1/2}$  for the helical ionizer. The number of measurements are too few to determine how the emittance grows but is definitely less than that for gold. This is consistent with space charge arguments for lower vs. higher mass ion beams.

### III. PULSED BEAMS

Most of the data taken on the test bench and at the Negative Ion Injector of the Tandem has been for the dc mode. A 15 kV, 500  $\mu$ sec pulser was built, tested and added to the test bench in November 1992.

The PSX-120 with the spherical ionizer was run in the pulsed mode with a gold target. Although in-depth studies have not yet been done, some initial results and observations deserve mention. The procedure was to characterize the pulses in the source and object cups while working toward improved transmission to the object cup.

The input to the pulser is usually a 500  $\mu$ sec square pulse at a repetition rate of 2 Hz. This high voltage pulser is capable of producing up to a 15 kV, 500  $\mu$ sec pulse or an equivalent voltage-time combination. The output voltage from the pulser has a 30  $\mu$ sec rise time and a 60  $\mu$ sec fall time. In addition, there is an initial 6% overshoot with a settling time of 110  $\mu$ sec.

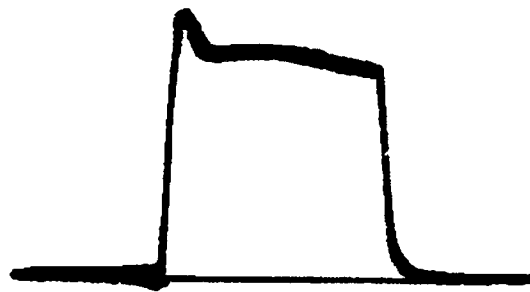


Photo 1. 920  $\mu$ A Pulse as seen in the Source Cup.

Photo 1. above, taken from the oscilloscope display shows a 920  $\mu$ A, 500  $\mu$ sec negative gold beam pulse observed at the source cup close to the source. The extraction voltage was 35 kV and the cesium acceleration voltage was pulsed to 10 kV from a base of 600 VDC. Part of the apparent beam pulse overshoot is due to electrical cross-talk but otherwise the rise and fall times are similar to the ones of the high voltage cesium acceleration pulse. The other feature that distinguishes the source cup pulse from the HV source pulse is that the intensity falls off from the max of 920  $\mu$ A to about 840  $\mu$ A. This, it is believed, is due to the change in cesium and/or

target conditions during the pulse. It remains to be studied if this can be compensated for by adjusting the trace voltage, heating the cesium boiler or some combination of both.

The 920  $\mu\text{A}$  pulse was sent down the line through the

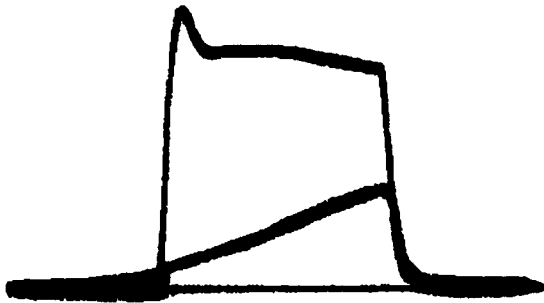


Photo 2. Object Cup Pulse showing Time-Dependent Space Charge Effects.

Einzel lens to the object cup. Photo 2., above, shows what was seen at the object cup overlaid on the pulse from the source cup. This pulse rises from 100  $\mu\text{A}$  up to about 375  $\mu\text{A}$  and would probably continue to rise if the pulse width was longer. The slow increase in the intensity suggested a process that was occurring during the pulse. Space charge neutralization was the suspected process. Since vacuums are usually in the  $10^{-7}$  through the  $10^{-6}$  Torr range space charge neutralization might be enhanced if one or more of the cryopumps on the beam line was closed off. After trying a few combinations, the best results were produced when the cryopump 0.2m downstream of the source (at the source cup) was closed off. The difference in vacuum at the source cup went from  $3 \times 10^{-6}$  Torr with the cryopump opened to  $3 \times 10^{-5}$  Torr with it

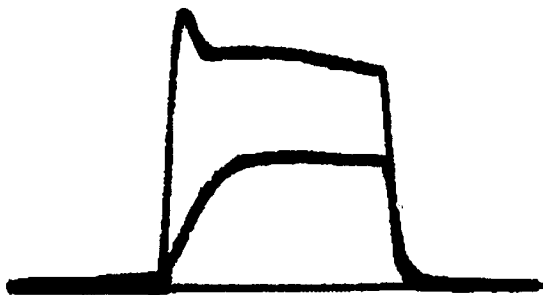


Photo 3. Object Cup Pulse with Enhanced Space Charge Neutralization.

closed. This translated to the object cup where the vacuum went from  $5 \times 10^{-6}$  Torr (opened) to  $9 \times 10^{-6}$  Torr (closed). The results are shown in Photo 3. where the object cup pulse is overlaid on the 920  $\mu\text{A}$  source cup pulse. As can be seen in this photo the intensity rises to 500  $\mu\text{A}$ , where it is sustained for 300  $\mu\text{sec}$ . The rise time is roughly 120  $\mu\text{sec}$  which is comparable to that seen on the low energy faraday cup at the entrance to the MP-7 Tandem accelerator.

## V. FUTURE PLANS

Clearly there is a need for further in-depth studies of the source with pulsed beams. More time needs to be devoted to learning about space charge neutralization and improving transmission. There should be a complete study of emittance measurements for gold at various extraction energies and pulser voltages. These should be made with both the spherical and helical ionizers using harps with greater resolution and some computer assistance.

## VI. ACKNOWLEDGEMENT

A special thanks to John Benjamin for the many useful discussions and help with the research and this paper.

## VII. REFERENCES

- [1] Peabody Scientific, Peabody, MA, USA.
- [2] K. S. Smith, D. B. Steski, M. J. Zarcone, and P. Thieberger, "Heavy Ion Source Development at Brookhaven National Laboratory's Tandem Van de Graaff Facility," *Sixth Int. Symp. on the Prod. and Neut. of Neg. Ions and Beams*, Nov. 1992, in press.
- [3] K. Prelec, M. J. Rhoades-Brown, P. Thieberger, and H. E. Wegner, "Comparative performance study of heavy-ion injector systems for high-energy synchrotrons," *Nucl. Inst. and Meth.*, A295, pp. 21-33, (1990).
- [4] P. Thieberger, "The Brookhaven Double MP Facility: Recent developments and plans for the future," *Nucl. Inst. and Meth.*, 220, pp. 45-53, (1984)
- [5] P. Thieberger, "Possible use of synchrotrons as post-acceleration boosters for Tandems," *Nucl. Inst. and Meth.*, 220, pp. 209-210, (1984)
- [6] P. Thieberger and H. E. Wegner, "The Brookhaven National Laboratory Three-Stage MP Tandem Facility", *Nucl. Inst. and Meth.*, 122, pp. 205-212, (1974).
- [7] EG&G ORTEC, Oak Ridge, TN, USA.
- [8] R. L. Witkover, W. Buxton, V. Castillo, I. Feigenbaum, A. Lazos, Z-G Li, G. Smith, and R. Stoehr, "Beam Instrumentation for the BNL Heavy Ion Transfer Line", *Proc. of the 1987 IEEE Part. Acc. Conf.*, pp. 567-569, (1987).
- [9] J. Schäfer, R. Schoppe, J. Hölzl, and R. Feder, "Experimental and Theoretical Study of the Angular Resolved Secondary Electron Spectroscopy (ARSSES) for W(100) in the Energy Range  $0 < E < 20$  eV", *Surf. Sci.* 107, pp. 290-304, (1981).
- [10] D. A. Dahl and J. E. Delmore, SIMION Version 4.02, Idaho National Engineering Laboratory, EG&G Idaho Inc., Idaho Falls ID, USA.
- [11] H. Ploss and L. N. Blumberg, "Methods of Emittance Measurement in External Beams Using Ellipse Approximations", AGS Internal Report, BNL, (1968).
- [12] R. G. Wilson and G. R. Brewer, "Ion Beams with Applications to Ion Implantation," Wiley and Sons, NY, USA.

# A Dual-Optically-Pumped Polarized Negative Deuterium Ion Source

Y. Mori, M. Kinsho\*

National Laboratory for High Energy Physics (KEK)

Oho 1-1, Tsukuba-shi, Ibaraki-ken 305, JAPAN

\*Graduate University for Advanced Studies

Oho 1-1, Tsukuba-shi, Ibaraki-ken 305, JAPAN

(abstract)

Acceleration of polarized deuterons in the KEK 12-GeV proton synchrotron is under discussion. To get a highly vector polarized deuteron beam, a new type of optically pumped polarized ion source (OPPIS) with dual optical pumping has been developed. In the preliminary experiment, we found that the dual-pumped polarized scheme had a large potential to generate highly nuclear-spin polarized negative deuterium ions.

## I. INTRODUCTION

Polarized protons have been successfully accelerated in the KEK 12-GeV proton synchrotron (KEK-PS) since 1985. Many experiments have been carried out with polarized proton beams so far. Recently, several proposals for the physics experiments with polarized deuteron beams in the KEK-PS are under discussion.

An ordinary deuteron beam was successfully accelerated to an energy of 11.2 GeV (5.6 GeV/u) in the KEK-PS, the limiting energy of the ring, in 1992. [1] The beam intensity of the accelerated deuterons reached more than  $2 \times 10^{12}$  ppp which was almost the same as that for protons. Acceleration of polarized deuterons in the synchrotron is rather easier than that of polarized protons. Since the anomalous magnetic moment (G) of the deuteron is -0.1426, which is 10 times less than that of the proton, the number of depolarization resonances that are caused by the betatron motions of the beam and imperfection of the ring are quite few during the acceleration of polarized deuterons in the synchrotron compared with polarized protons.

As for polarized ion source, an optically pumped polarized ion source (OPPIS) has been used for generating nuclear-spin polarized negative hydrogen ions so far. It has been believed that this type of polarized ion source is not useful to produce a highly nuclear-spin polarized (vector and tensor) deuterium ions. In this paper, we report the preliminary experimental results which showed that the highly vector polarized negative deuterium ions could be produced by OPPIS with dual-optimally-pumped technique.

## II. OPPIS FOR DEUTERONS

An OPPIS has been used for acceleration of polarized proton beams in the KEK-PS until now. The idea of this type of polarized ion source was proposed by Anderson[2] and the first operational ion source has been successfully developed at KEK. [3] Afterwards, various institutes have developed the OPPIS for their accelerators. [4][5][6]

In Fig.1, a block diagram of the dual-optimally-pumped polarized ion source is shown schematically. An energetic electron-spin polarized hydrogen beam is generated via pickup of a polarized electron by a proton beam of a few keV in an optically pumped alkali vapor. Then the atomic polarization of the hydrogen beam is transformed into nuclear polarization by a diabatic transition between hyperfine sub-levels (Sona transition). Finally, the nuclear-spin polarized hydrogen beam is ionized.

Although OPPIS is very useful to generate polarized protons, it has been thought that OPPIS is inadequate for making highly polarized deuterons. In deuterium atoms, because the nuclear spin,  $I=1$ , three hyperfine sub-levels ( $I_z=+1,0,-1$ ) exist. High polarization can not be expected if only a Sona transition is used because of the  $I_z=0$  state. The theoretical maximum polarizations, in this case, are  $+2/3$  for vector polarization ( $P_v$ ) and  $-1/3$  for tensor polarization ( $P_{zz}$ ).

To achieve a high polarization, a new scheme which selects a pure nuclear-spin state is necessary. In 1988, Schneider and Clegg[7] proposed a new nuclear-spin state selection scheme. Their idea is as follows: After picking up the polarized electrons from optically pumped alkali atoms, deuterium atoms are electron-spin polarized, for example, in the state of  $m_j=+1/2$  as shown in Fig.2. These electron-spin polarized deuterium atoms equally populate three hyperfine sub-levels  $I_z=+1, 0$ , and  $-1$  in a high magnetic field, which are labeled the states 1, 2, and 3, respectively in Fig.2. Using the Sona transition, the state 1 ( $m_j=+1/2, I_z=+1$ ) goes to the state 1' ( $m_j=-1/2, I_z=-1$ ), the state 2 ( $m_j=+1/2, I_z=0$ ) goes to the state 2' ( $m_j=+1/2, I_z=-1$ ), and the state 3 goes to the state 3' ( $m_j=+1/2, I_z=0$ ), respectively as shown in Fig.2. Therefore, the deuterium atoms with only the hyperfine level of  $I_z=-1$  (state 1' in Fig. 2) has an opposite electron-spin state,  $m_j=-1/2$ , of the other two sub-levels (2' and 3') after Sona transition. When the alkali atoms in the ionizer are also optically pumped and their electrons are to be spin polarized in the  $m_j=+1/2$  state, only deuterium atoms with the electron-spin state of  $m_j=-1/2$  (state 1') can form negative ions because of the Pauli exclusion principle. This process is shown in Fig.3 schematically. The nuclear-spin state of the negative deuterium ions in this case is  $I_z=-1$ , the nuclear vector polarization becomes  $-1$ . The nuclear tensor polarization is, in this case,  $-1$ . Using a proper rf transition simultaneously, a pure nuclear tensor polarization of  $-2$  may become possible.

In spite of this possibility of making a highly polarized deuteron beam by optical pumping, they concluded eventually in their paper that this dual optical pumping scheme might be

serious problem and highly polarized deuterons could be obtained with the dual-pumped scheme.[8]

Recently, a preliminary experiment for proving the principle of the dual-pumped scheme has been carried out at KEK. The result of the experiment is shown in Fig. 4. The vertical axis in the figure presents the nuclear vector polarization of negative deuterium ions. The horizontal axis shows the relative change of the beam intensity of the negative deuterium ions by switching the optical pumping of the alkali atoms in the ionizer on and off. Deuterium atoms in only one hyperfine sub-level can become negative deuterium ions by picking up polarized electrons from the optically pumped alkali atoms in the ionizer. Thus, the beam intensity of negative deuterium ions depends upon the population of deuterium atoms in each hyperfine sub-level after the Sona transition. This means that the deuteron vector polarization ( $P_D$ ) and the electron-spin polarization of optically pumped alkali atoms in the ionizer ( $P_{IONZ}$ ) affect the beam intensity of negative deuterium ions. These values are related each other as expressed in the following equation.

$$P_D = -2\varepsilon/P_{IONZ}(1-\varepsilon). \quad (2)$$

Here,  $\varepsilon = (I_{off} - I_{on})/I_{off}$ , where  $I_{off}$  and  $I_{on}$  are the beam intensities of negative deuterium ions when the optical pumping of the alkali atoms in the ionizer is turned off and on, respectively. The solid line in Fig.4 presents the relation between  $P_D$  and  $\varepsilon$  when  $P_{IONZ} = 1$ . The closed circle in the figure shows the experimental result. The electron-spin polarization of alkali atoms

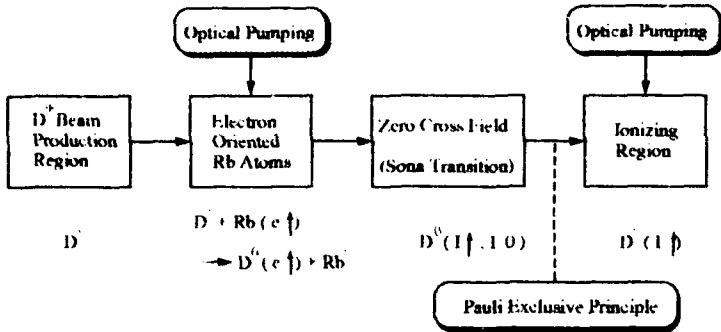


Fig.1 Block diagram of the dual-optically-pumped polarized ion source.

not practical because efficient optical pumping of the thick target in the ionizer is difficult due to radiation trapping. Radiation trapping is a re-absorption process of fluorescence photons in optical pumping and it limits the maximum polarization of the pumped atoms. However, their conclusion was qualitative and they did not estimate quantitatively the effect of radiation trapping. Recently, we have re-examined the dual-pumped scheme in detail and found that radiation trapping was not a

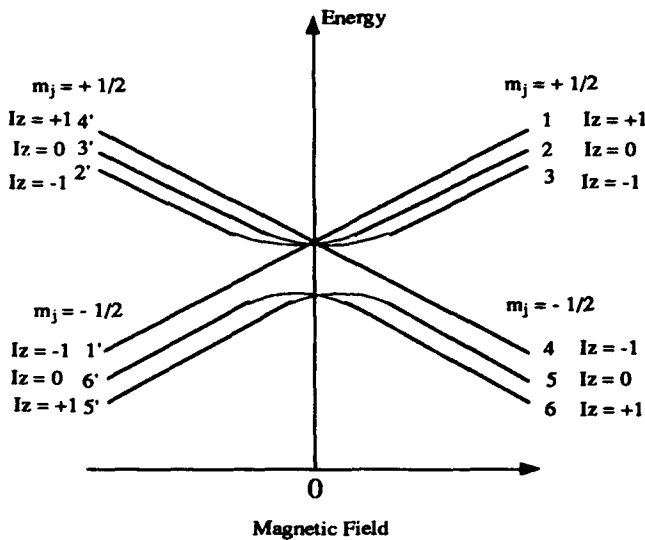


Fig.2 Hyperfine sublevels of deuterium atom in Sona transition.

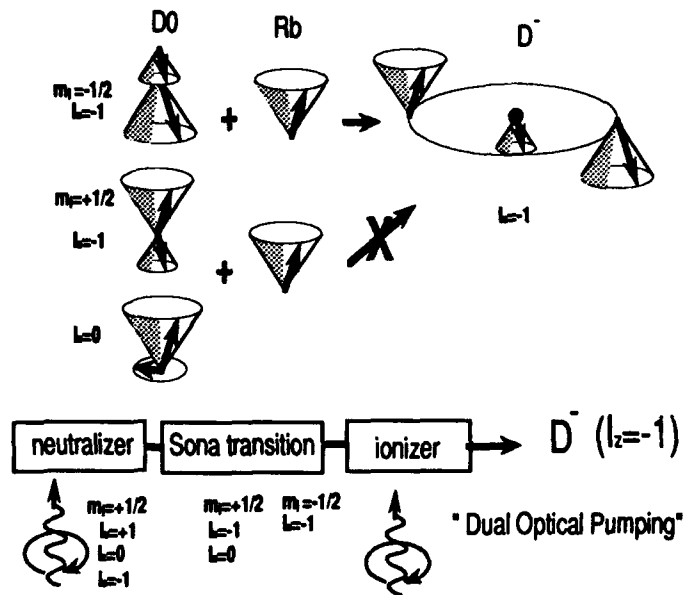


Fig. 3 Principle of dual-pumped polarized negative deuterium ion source.

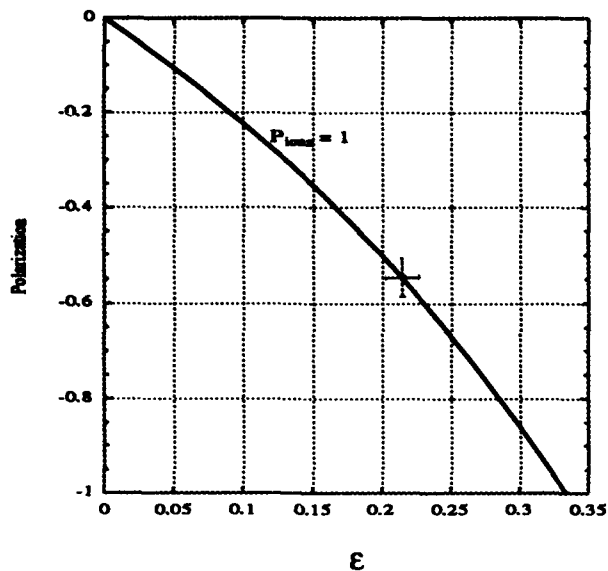


Fig.4 Relation between  $P_D$  and  $\epsilon$  when  $P_{\text{IONZ}} = 1$ . The closed circle in the figure shows the experimental result.

in the ionizer ( $P_{\text{IONZ}}$ ) was measured using a Faraday rotation method. The errors shown in the figure present the fluctuations of the data taken at different times.

In the preliminary experiment, we obtained  $P_D = -0.55 \pm 0.04$ . In the present apparatus where the magnetic field strength at the neutralizer is 1.1T, the theoretical maximum polarization is limited to less than 80%. This is because the spin-orbit coupling in neutral deuterium atoms, created by picking up polarized electrons from the optically pumped alkali atoms in the neutralizer, reduces the electron-spin polarization at this magnetic field strength. Thus, the obtained deuteron-spin polarization was almost 70 % of the maximum limiting value. This is very encouraging and it may be said that the dual-optically pumped scheme for producing highly polarized negative deuterium ions has worked in principle.

### III. CONCLUSION

A new dual-optically-pumped scheme to obtain a high deuteron-spin polarization in an optically pumped polarized ion source has been examined in detail. The results of the preliminary experiment are very encouraging and it is shown that the new scheme, in principle, has worked. It was previously thought that the optically pumped polarized ion source was not useful for producing highly polarized deuterons. Our results may open up a new possibilities for the optically pumped polarized ion sources.

There seems to be no fundamental problem for polarized deuteron acceleration in the KEK-PS.

The authors would like to appreciate Profs. M.Kihara,

Y.Kimura, and H. Sugawara for their continuous encouragement. They are indebted to Mrs. K.Ikegami, and A. Takagi for their helps in the experiments. They are also grateful to Drs. A. Zelenskii and C.D.P.Levy for their valuable suggestions.

- [1] Y.Mori et al ; contributions for this conference.
- [2] W.L.Anderson: Nucl. Instr. and Meth. 167,363(1979).
- [3] Y.Mori, K.Ikegami, Z.Igarashi, A.Takagi, and S.Fukumoto: AIP Proc. 117, New York(1983)123.
- [4] R.L.York, O.B. Van Dyck, D.R.Swenson and D.Tupa: Proc. of the Int. Workshop on Polarized Ion Sources and Polarized Gas Jets, KEK Report 90-15(1990),page 142.
- [5] L.Buchmann,C.D.P.Levy, M.McDonald, R.Ruegg, and P.W.Schmor: ibid page 161.
- [6] A. Zelenskii, S.A.Kokhanovskii, V.G.Polushkin and K.N. Vishnevskii:ibid page 154.
- [7] M.B.Schneider and T.B.Clegg: Nucl. Instr. and Meth.,A254,630(1987).
- [8] Y.Mori ; submitted to Nucl. Instr. Meth.

# THE IUCF HIGH INTENSITY POLARIZED ION SOURCE PROJECT

M. Wedekind, R. Brown, V. Derenchuk, D. Friesel, J. Hicks, P. Schwandt

## Abstract

The IUCF high intensity polarized ion source has been completed and installed in the 600 kV terminal. The design is based on the source in operation at TUNL, which employs cold ( $\sim 30$  K) atomic beam technology and an electron cyclotron resonance ionizer. It is expected to produce 100  $\mu$ A DC  $\text{H}^+$  and  $\text{D}^+$  ion beams with a polarization of 75% or greater. Coupled with a wideband and resonant bunching system and a high transmission beam line into the injector cyclotron, the source should allow  $10^{10}$  protons to be stored in the Electron Cooled Storage Ring in a few seconds. Results from source development and project status will be described.

## I. INTRODUCTION

To further enhance the unique opportunities in spin physics research using the Cooler ring, circulating beam intensities of  $10^{16}$  particles/sec are required because internal polarized target densities and/or reaction cross sections are very low.

In order to meet these experimental requirements, a high intensity source of polarized ions, coupled with a high efficiency bunching system and high transmission beam line<sup>1</sup> to the injector cyclotron, should allow  $10^{10}$  protons to be stored in the Cooler ring in a few seconds.

The design for the high intensity polarized ion source (HIPIOS) was based on the source at TUNL<sup>2</sup>, developed by Tom Clegg and associates, which utilizes cold (30 K) atomic beam technology and an electron cyclotron ionizer (ECR).

HIPIOS deviates from the TUNL configuration in three significant ways: the first sextupole is 50% longer to provide stronger focussing, the cesium charge exchange canal is replaced by a gridded, single-gap RF buncher with a ramp waveform, and ion beam extraction from the source is achieved by raising the internal structure of the ECR ionizer to 20 kV potential. The latter was dictated by the necessity of operating the source assembly at local ground potential in the 600 kV terminal and has significantly complicated the design.

HIPIOS was initially built and tested off-line, the results of which are described in the 1992 Cyclotron Conference Proceedings<sup>3</sup>. The source has since been installed in the high voltage terminal with modifications based on the knowledge gained from initial testing. The improvements achieved with those modifications, and the current status of the entire project are described here.

## II. HIPIOS OPERATION

### A. Atomic Beam Development

During initial testing of the ECR it was noticed that the beam intensity from the dissociator drops by a factor of two during the first few hours of operation. The drop in atomic beam intensity with time is due to the coating of the cold nozzle with a white powdery substance analyzed to be  $\text{SiO}_2$ . Discussions with other groups that have had long-term operating experience with RF dissociators led us to conclude that the powder accumulation was directly correlated with the time integral of the RF discharge power, and therefore the temperature of the dissociator tube during dissociation.

Several design modifications were made to the dissociator in order to address this problem: a  $-20^\circ\text{C}$  closed loop alcohol cooling system was installed in place of the water cooling system, the dissociator tube was modified to provide cooling within 1 cm of the accommodator, and the  $\text{N}_2$  buffer gas which prevents recombination in the cold nozzle is mixed with the  $\text{H}_2$  upstream of the dissociator, rather than being introduced directly into the accommodator. The dissociator now runs stably without any powder formation with the following operating conditions: 25 SCCM  $\text{H}_2$ , .030 SCCM  $\text{N}_2$ , 33.5 K nozzle temperature,  $-10^\circ\text{C}$  alcohol return temperature and 100 W RF power (with 23 W reflected). We have consistently measured an atomic beam intensity of  $2.0 \times 10^{16}$  atoms/sec with a density of  $3.3 \times 10^{11}$  atoms/cm<sup>3</sup>. New development projects include mixing  $\text{O}_2$  with the hydrogen to further increase the beam intensity, and a modification to cool the downstream end of the dissociator tube to 100 K since the rate of recombination reaches a minimum at that temperature.

A collaboration between IUCF and Dr. Alexander Belov from the INR, Moscow has resulted in the construction of a time-of-flight mass spectrometer which will be installed immediately upstream of the ECR to measure the dissociated fraction of the beam. Dr. Belov also participated in the modifications to the ECR extraction system design.

### B. ECR Ionizer Development

Operation of the ECR at ground potential while the permanent magnet sextupole was biased at 20 kV presented several problems - primarily one of radial and downstream ion extraction resulting in excessive current draw on the high voltage power supplies. Attempts to solve this problem by

reverse biasing an entrance cone and screen around the permanent magnets was not entirely successful. Inspired by the ECR ionizer design at PSI, a quartz tube was installed as a liner for the permanent magnet sextupole to further reduce the radial extraction of beam from the ECR plasma.

Since the quartz tube restricts radial pumping of the plasma region, the extraction system has been redesigned to allow for improved axial pumping (Fig. 1). The first design, with an emittance limiting aperture of 1 cm, has been replaced by three molybdenum grids with 95% transmission in a diameter of 4.45 cm. The three grids are electrically isolated and attached to independent high voltage supplies to allow for testing of accel-accel and accel-decel extraction from the ECR.

Testing of the modifications has just begun, with encouraging results. With an atomic beam intensity of  $2.0 \times 10^{16}$  atoms/sec as measured in a compression tube 10 cm upstream of the ECR, a total beam current of 1.2 mA was extracted at 10 kV as measured on a beam stop 10 cm downstream of the ECR. With the atomic beam valve closed, the total beam current was measured to be 0.6 mA.

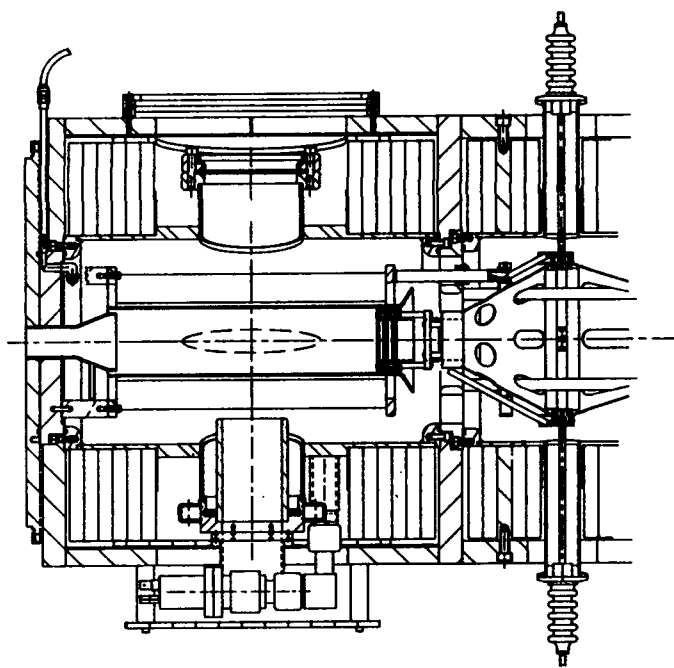


**Figure 1.** ECR and Buncher assembly with quartz tube and gridded extraction system.

#### C. RF Transition Units

Since we do not yet have a way to measure beam polarization, the strong and weak field RF transition units for hydrogen were tested on the atomic beam source in Madison, WI. The cavities performed as expected, but a polarimeter will be essential for maximizing proton polarization out of the source. A design for a 5-10 keV metastable atom polarimeter was passed on to us by Anatoli Zelenski from the INR. We are anxious to build this polarimeter and install it in the

HIPIOS diagnostics line as soon as funding and our work load allows.

#### D. Buncher

Tests of the gridded single-gap buncher with the 600 W wideband RF power amplifier were very promising. Although the load is very reactive, a suitable coupling method was found which yielded the required waveform linearity at voltages even higher than anticipated. This higher voltage leads to a greater range of allowed beam energies in the bunching region. Further testing with beam will determine the optimal beam energy.

Initial bunching factor measurements were taken before the source was moved into the terminal using a gridded pickup. The minimum phase width observed was  $100^\circ$  and with the addition of a second molybdenum photo-etched grid we expect the system to operate as designed. We hope to compress all the beam into a  $30^\circ$  phase width, which would consequently lead to linear bunching in the following resonant (sinusoidal waveform) buncher.

#### E. Control System

The Vista control system<sup>4</sup> has been almost completely implemented for HIPIOS and is working very reliably. We are now controlling the source elements with DACs and are developing a "combo" to run all of the extraction element high voltage supplies with one DAC.

### III. 20 keV BEAM TRANSPORT

The 20 keV ion beam emerging from the source is electrostatically focussed and magnetically steered through the 4 m long beam transfer line to the entrance of the acceleration column. This beam line incorporates three principal systems of note. A combination of a  $90^\circ$  bend, spherical electrostatic channel and a pair of spin rotation solenoids, placed at beam waists, is used to change the spin alignment axis of the polarized beam from the axial orientation at the source exit to vertical at the end of the transfer line. A doubly focussing, doubly achromatic magnetic beam translation system produces a 0.5 m vertical parallel drop of the ion beam in the terminal to match source beam height to the acceleration column. A unit magnification electrostatic zoom lens system matches the fixed transfer line optics to the variable acceleration column optics to provide controlled ground potential beam line injection over a wide range of terminal voltages. Assembly of the beam line is proceeding as manpower is available and is scheduled to be completed by the middle of August.

### IV. HIGH VOLTAGE TERMINAL

The 14' x 30' x 12' high stainless steel high voltage terminal (significantly larger than our existing terminals, but

getting smaller every day) houses HIPIOS and the 20 keV beam transport line with room for an additional ECR source. The space will initially be used for the polarimeter so that polarization studies can be done without having to accelerate beam from the terminal. The terminal operates at 600 kV and is supported on eleven insulating legs, each consisting of three ceramic insulators separated by two spun aluminum corona rings. Two of the legs have a conductive surface glaze to provide 900 Megohms voltage grading to ground, and the corona rings are cross-connected so that all surfaces at the same elevation have the same voltage. This design should require very little maintenance, unlike the water path grading system used on our existing terminals. AC power is delivered to the terminal by a 125 kVA alternator driven by a 200 hp motor connected to a G-10 filament-wound drive shaft - a design which we hope will require much less maintenance than the hydraulic system used to power the other terminals.

The terminal has been successfully tested at 600 kV without sparking or excessive leakage current. Fabrication of the AC drive system is now underway with installation scheduled for July. First beam extraction from the terminal is scheduled for mid-September.

## V. 600 kV BEAM LINE

The 30 m beam line (BL1C) will transport beam from Terminal C to the injector cyclotron. BL1C was designed with the goal of increasing the beam transmission efficiency from the source through the main stage cyclotron from the present 10% to over 30%. The beam line is composed of four 180° betatron phase advance sections between each 45° dipole which leads to alternating sections of high and vanishing dispersion, followed by a section to match beam phase space to the injector cyclotron acceptance. This symmetry also suggests a natural ordering for steering dipole and beam position monitor pairs (i.e. modula 90° in betatron phase advance).

Beam manipulation and diagnostic systems integrated into the beam line design will measure the beam transverse distribution at the beginning of the line, the beam envelope and dispersion throughout the line, and the cyclotron transverse acceptance. The diagnostic systems will also provide the operator with easy to use tools to match the beam properties to the measured acceptances. These tools will operate in an auto-tuning mode during routine operation after being tested in a "manual" mode. Longitudinal diagnostic systems will measure and provide hardware control of both the first and second moments of the beam longitudinal distribution.

The new diagnostics hardware required from Terminal C to the injector consists of 30 beam position monitors, two wire scanners, four beam stops, four slit systems, two phase pickups, four longitudinal profilometers and a 600 keV <sup>6</sup>Li (p,x) polarimeter.

The double-gap resonant waveform BL1C buncher, in conjunction with the terminal buncher, will reduce the energy spread caused by the bunching process by a factor of 4 from

the present system, while providing a sharper phase focus ( $\pm 3^\circ$ ). This should enhance transmission through the injector cyclotron inflector system and actually eliminate the need for precise dispersion matching. The existing buncher will also be used to provide three stage bunching, allowing adjustment of the beam phase width at the longitudinal focus to optimize matching to the injector. A prototype buncher element has been fully tested, and the mechanical design for the tuneable elements is underway.

All the beam bunching systems will be phase-locked to the beam using hardware phase feedback loops, thus eliminating the otherwise-required precise regulation of power supplies and beam properties. The phase feedback loops will have bandwidths of 10 kHz or higher. The beam phase detectors require a dynamic range of over 40 dB for operation with beam currents in the range 1 - 100  $\mu$ A. An additional hardware feedback loop will modulate the buncher voltage in proportion to the square root of the beam current to compensate for space charge effects.

All of the elements for BL1C have been fabricated with the exception of the buncher and the slit assemblies. Installation of the beam line is underway, and the required modifications to the existing beam line upstream of the injector cyclotron will take place during the upcoming shutdown (May 24 - July 14). First beam into the injector from BL1C is scheduled for the end of September.

## VI. ACKNOWLEDGEMENTS

The authors express their appreciation to Alexander Belov, Tom Clegg, Anatoli Zelenski and the entire technical staff at IUCF. The HIPIOS project is supported by NSF Grant PHY-891440.

## VII. REFERENCES

- [1] W.P Jones et al., "Beam Transport System for the IUCF High Intensity Polarized Ion Source," Proceedings from the 13th International Conference on Cyclotrons and Their Applications, Vancouver, 1992, pp. 609-611.
- [2] T.B. Clegg et al., "A New Atomic Beam Polarized Source for the Triangle Universities National Laboratory: Overview Operating Experience and Performance," submitted to NIM.
- [3] V. Derenchuk et al, "Performance and Status of the IUCF High Intensity Polarized Ion Source," Proceedings from the 13th International Conference on Cyclotrons and Their Applications, Vancouver, 1992, pp. 330-333.
- [4] T. Capshaw et al, "The IUCF High Intensity Polarized Ion Source Control System," Proceedings from the 13th International Conference on Cyclotrons and Their Applications, Vancouver, 1992, pp. 641-643.

# The High Current Ion Source System HOLCROSS

Nikolai R. Lobanov<sup>†</sup>  
Moscow Engineering Physics Institute  
Kashirskoye Chausse 31, Moscow 115409, Russian Federation

## Abstract

The model HOLCROSS ion source is designed for the production of high current and brightness ion beams for application in particle accelerator injection and ion implantation. The cross type hollow cathode device in which the cross size of the cathode is greater than a longitudinal size is described. This system allows the creation of a quiet, cold and stable plasma of all cross sections. Compared with traditional hollow cathode systems this one is characterised by improved technical and operational performance. In the case of a duoplasmatron ion source the cross hollow cathode is optimised for gaseous charges such as noble gases, nitrogen, oxygen etc. A description of the source is given, together with some recent results. With a one aperture extraction system in which the square of the anode hole equals  $0,25 \text{ mm}^2$  this source will produce more than  $15 \text{ mA H}_1^+$  at  $8 \text{ keV}$  and  $200 \text{ mA}$  discharge current.

## I. INTRODUCTION

In the field of ion implantation and particle accelerator's injection, there is a growing interest in ion beams of different mass with high brightness and high current. The project using an original hollow cathode ion source for a MeV- RF implanter has been developed at the Moscow Engineering Physics Institute [1]. Preliminary studies have been performed using only a cross-type hollow cathode device. This article summarises the investigations on a duoplasmatron ion source with cross-type hollow cathode (150-mm diam) performed in MEFPI.

## II. THE CROSS TYPE HOLLOW CATHODE ION SOURCE

The experimental setup has already been described in a previous article [2], (see Figure 1). In brief, the hollow cathode is fabricated from a air-cooled cylindrical stainless steel chamber (150 mm diam, 0-30 mm depth). The cross size of the hollow cathode is greater than the longitudinal size. At the back of the cathode chamber, the operational gas is let in through a tube 4 mm in diameter and is pumped away through the anode aperture by a diffusion 1500 l/s oil pump. The square of the anode hole equals  $0,25 \text{ mm}^2$ . Technical hydrogen was used.

<sup>†</sup>Correspondence should be send: Australian Institute of Physics, 1/21 Vale Street, North Melbourne VIC 3052

The duoplasmatron ion source consists of few discharge chambers, followed by an small expansion cup. The expander (7 mm diam and 5 mm depth) with the extraction electrode form the modified Pierce's system [2]. In the region between intermediate electrode and anode, an axial magnetic field, obtained by a permanent magnet, is applied. The magnetic flux lines are guided by ferromagnetic material. The influence of the magnetic field on the cathode region is negligible.

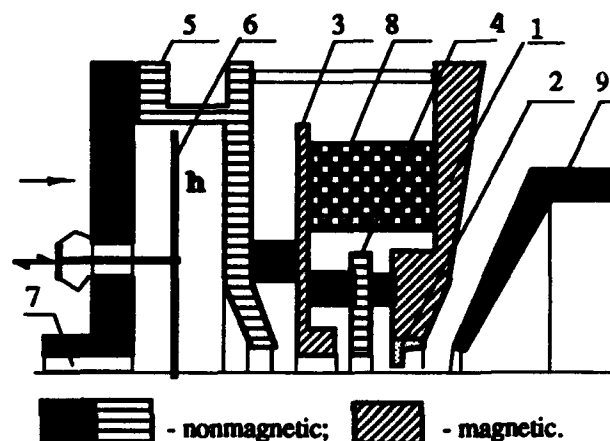


Figure 1. The experimental setup: 1- anode; 2- expander; 3- intermediate electrode; 4- additional electrode; 5- cathode chamber; 6- circle plate; 7- gas inlet; 8- magnets; 9- extractor.

An electronic system has been developed and built to run a hollow cathode and duoplasmatron ion source in dc mode. Cathode and anode are connected to the power supply. The cathode chamber is negatively biased with respect to the anode. The potentials of the intermediate and additional electrodes are floating.

All the measurements were performed with the source and extraction operated in dc mode. The ion optic system consists of an Einzel lens. The beam current was measured by a Faraday cup at a distance of 120 cm from the lens. The beam energy was varied between 5 and 15 keV.

## III. EXPERIMENTAL RESULTS

In order to determine the optimal conditions for generating a plasma the effect of the discharge current ( $I_d$ ), discharge voltage ( $U_d$ ) and the source pressure ( $P_a$ ) on the distribution of the charged particles were investigated. In this experiment the intermediate and additional electrodes

were pulled out. A cross hollow cathode discharge is easily established when the operating pressure is of the order of 10 Pa. It is very stable discharge and transition into an *arc* discharge is not observed for the discharge current up to hundreds mA in dc mode.

Figure 2 shows the anode (discharge) voltage as function of the source pressure for a constant discharge current and a

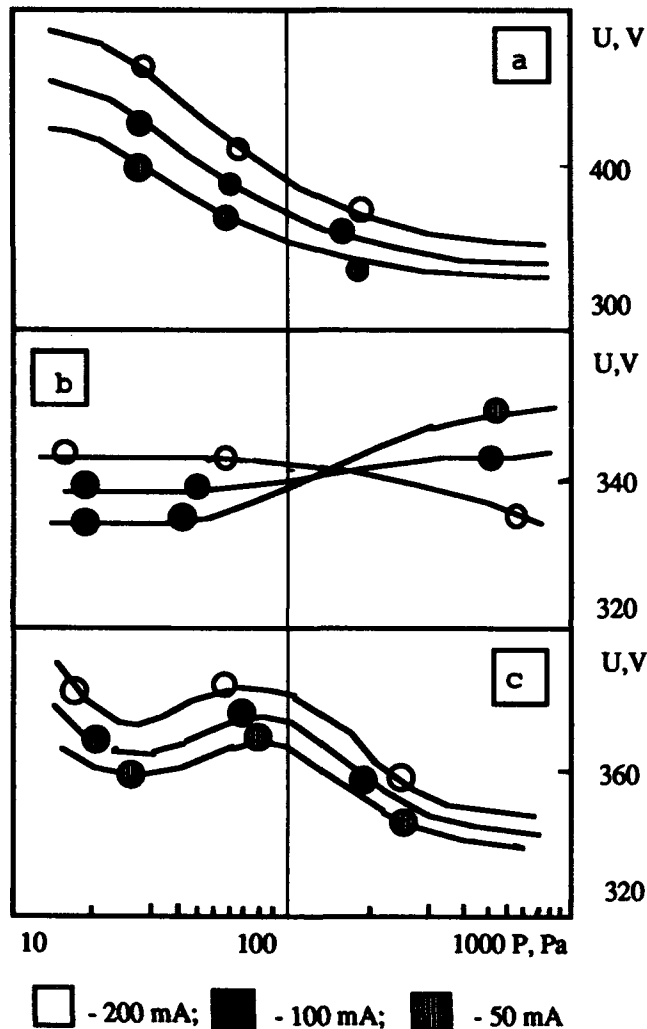


Figure 2. Dependence of the discharge voltage  $U_d$  on the source pressure  $P_a$  for a constant discharge current  $I_d$ : a)-  $h = 0$  mm; b)-  $h = 6$  mm; c)-  $h = 16$  mm.

cathode chamber depth  $h$ . It can be seen that for  $h = 0$  mm (fig. 2a) and for  $h = 16$  mm;  $P_a > 50$  Pa (fig. 2c) the curves repeat the same dependence for a glow discharge. The voltage dependency of the pressure on Figure 2c is divided into two parts. For a pressure below 50 Pa and larger than 30 Pa the voltage is decreasing with the pressure decreasing. But for pressures below 30 Pa the situation is reversed. Now the voltage is rising and a glow

discharge is transmitted into the high voltage (electron beam) mode.

Figure 2b illustrates the relationship of the discharge voltage to the discharge current for another hollow cathode configuration. In this case, the hollow cathode's depth is 6 mm. For a wide ranges of pressure and discharge current, the discharge voltage remains approximately constant.

The average discharge voltage  $\langle U \rangle$  on hollow cathode depth  $h$  is plotted in Figure 3 for a constant source pressure. The results show that there is an optimal value of  $h$  corresponding to the minimal discharge voltage. Voltage of 340 V can be obtained for a hollow cathode depth of about 6 mm.

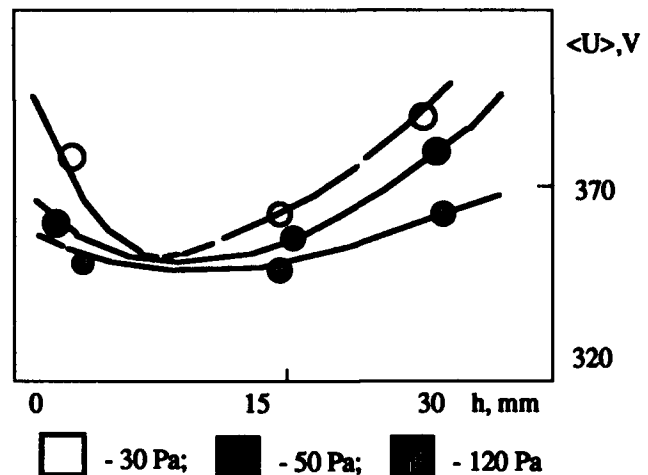


Figure 3. Dependence of the average discharge voltage  $\langle U \rangle$  on the hollow cathode depth  $h$  for a constant source pressure.

In the second part of the experiment, the visual observation of the discharge through the transparent cathode flange was conducted. A metal screen was installed instead of the circle plate. The results are shown in Figure 4a-f. One can see that the plasma occupation of the cathode chamber can be efficiently achieved due to the choice of combination of  $I_d$ ,  $P_a$  and  $h$  values corresponding to the electron oscillation mode of the discharge.

The duoplasmatron type plasma generator is an example of use of the cross hollow cathode with the duoplasmatron ion source [2]. This system allows the creation of a quiet, cold and stable plasma of all cross sections. Compared with traditional hollow cathode systems this one is characterised by improved technical and operational performance. In the case of a duoplasmatron ion source the cross hollow cathode is optimised for gaseous charges such as noble gases, nitrogen, oxygen etc. With a one aperture extraction system this source will produce more than 15 mA  $H_1^+$  at 8 keV and 200 mA discharge current. For other monatomic

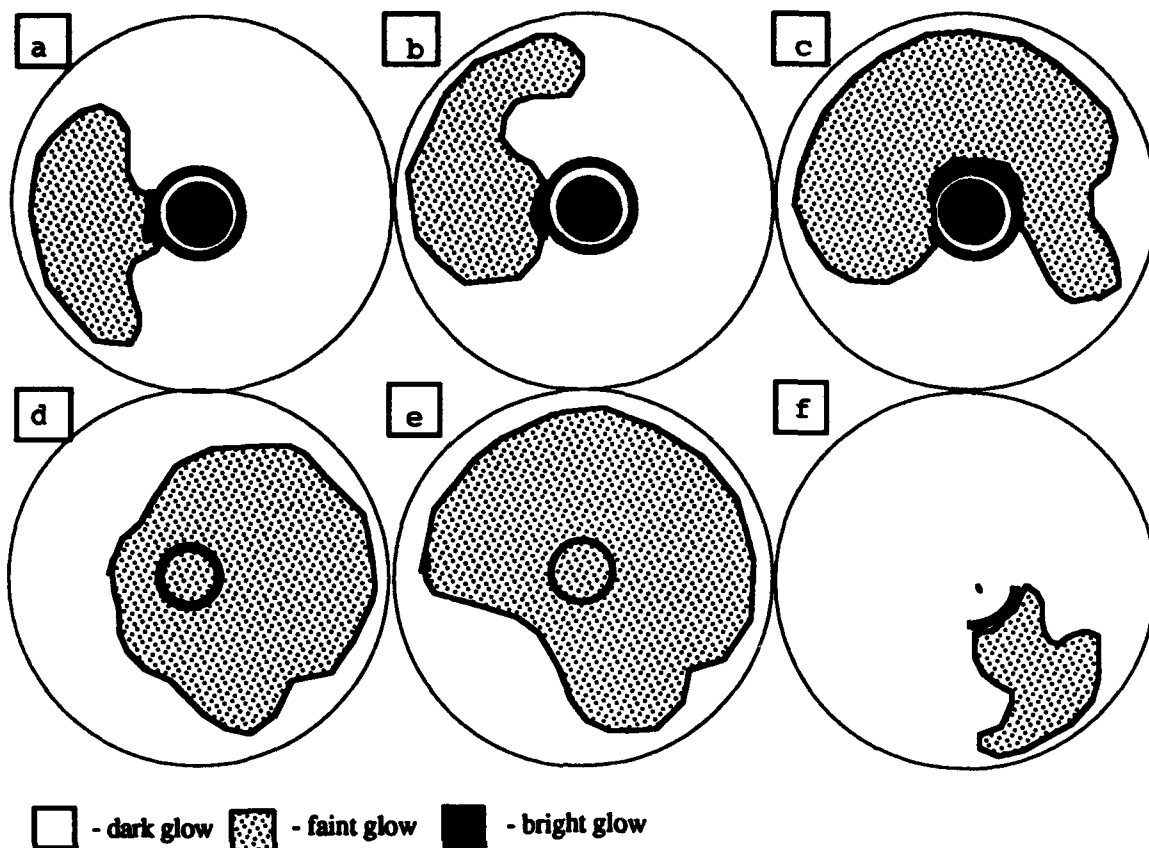


Figure 4. Depiction of the plasma occupation of the cross hollow cathode's cavity for  $h = 6$  mm;  $I_d = 100$  mA ( for direction of vision see the arrow on fig. 1 ) : a-  $P_a = 10$  Pa,  $U_d = 360$  V; b- 30, 340; c- 50, 330; d- 60, 335; e- 100, 350; f- 400, 370

gases the beam currents scale as the inverse square root of the mass number  $A$ .

#### IV. CONCLUSION

The cross hollow cathode system has certain advantages over the source of the previous article [2] of the same power dissipation, such as: high ionisation efficiency with low gas flow rates and good power efficiency. Due to the modular construction of the HOLCROSS system, it is fairly easy to introduce modifications. One special version uses an internal negatively biased sputtering target to produce ions from elemental metal samples. Another alternation is equipped with an additional cross type hollow cathode system placed between the auxiliary plasma generator and the extractor. A negative voltage is applied to the cathode so

that dependent low pressure gas discharge is observed. All these advantages secure the application of the cross hollow cathode as an effective long-lived plasma generator. Further investigations of the cross hollow cathode system will be published.

#### V. REFERENCES

- [1] N.R. Lobanov, "Plasma source of charge particles," Inventor's certificate N163467, *Byull. Izobret.* N9, (1991).
- [2] A.A. Glazkov, N.R. Lobanov, V.T. Barchenko et.al., "Duoplasmatron-type ion source with improved technical and operational performance for linear accelerator," *Conference Record of the 1992 Third European Particle Accelerator Conference*, Vol.2, pp.993-995.

# Positive Hydrogen Ion Beam Production by an RF-driven Multicusp Source\*

K. N. Leung, D. A. Bachman, P. R. Herz, D. S. McDonald, M. Olivo†, and L. T. Perkins

Lawrence Berkeley Laboratory  
University of California  
Berkeley, CA 94720

## Abstract

A 10-cm-diam rf-driven multicusp ion source has been tested for positive ( $H^+$ ) ion production in cw mode for future use in the 870 keV Cockcroft-Walton preinjector at Paul Scherrer Institute. The source is optimized for the best atomic hydrogen ion species and extractable current. It is found that the porcelain coating on the antenna is very durable and stays intact after days of continuous operation. It is expected that the antenna will have a very long lifetime for an rf input power of  $\sim 6$  kW.

## I. INTRODUCTION

An rf-driven source has recently been developed at Lawrence Berkeley Laboratory to efficiently produce  $H^-$  ion beams for use in the injector unit of the Superconducting Super Collider. Under optimum conditions, an  $H^-$  beam current as high as 40 mA has been obtained from a 5.6 mm diameter aperture [1]. The same source has also been tested for other ion beam production and the results are reported in Ref. [2].

The cyclotron at Paul Scherrer Institute (PSI) requires a long lifetime positive hydrogen ion source that can generate high current and high proton percentage. The present PSI source utilizes tungsten filaments for the plasma discharge. The lifetime of the cathode is limited to about one month of low arc power and about ten days of higher arc power source operation. Results of the rf-driven source testing in pulsed mode indicate that it can satisfy both the current and ion species requirement for the PSI Cockcroft-Walton injector [2]. The objective of this experiment is to investigate the extractable current, hydrogen ion species distribution and the durability of the antenna when the rf-driven source is operating in cw mode.

The durability of the antenna is an important factor when considering the long-term performance of ion sources. Antenna lifetime has been demonstrated for high power ( $>50$  kW) pulsed operation at LBL, Grumman Corporation, and SSCL, but has not been tested for cw operation in a plasma environment until now. The results are encouraging. The porcelain-coated copper antenna has been observed to have a high durability after continuous plasma exposure. It is expected that the antenna will have a very long lifetime when the source is operated with an rf input power of  $\sim 6$  kW.

† Paul Scherrer Institute (PSI), CH-5232 Villigen PSI, Switzerland

\* Supported by Paul Scherrer Institute and by U.S. DOE contract DE-AC03-76SF00098.

## II. EXPERIMENTAL SETUP

A schematic diagram of the rf ion source is shown in Fig. 1. The source chamber was a copper cylinder (10 cm diameter by 10 cm long) surrounded by 20 columns of samarium-cobalt magnets that formed a longitudinal line-cusp configuration. The magnets were enclosed by an anodized aluminum cylinder with cooling water circulating between the magnets and the inner housing. The back flange had four rows of magnets cooled by water passages drilled in the copper.

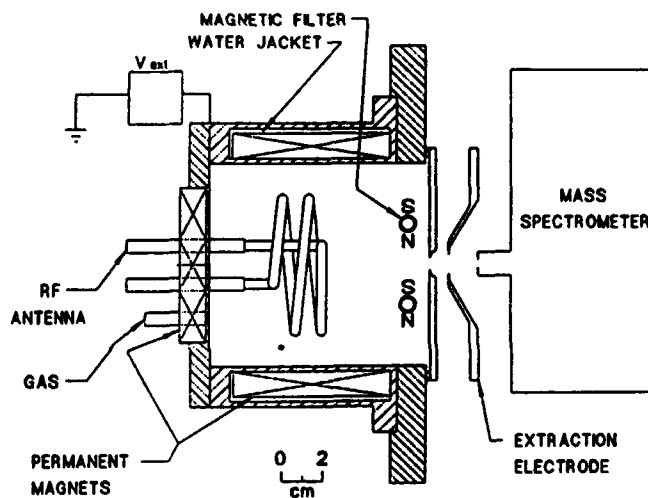


Fig. 1 Schematic diagram of the rf-driven multicusp source.

The open end of the source chamber was closed by a two-electrode extraction system. Positive or negative ion beams were normally extracted from the source through a 2 mm diameter aperture. A permanent magnet mass analyzer was used with a Faraday cup to measure the electron, positive or negative ion currents in the accelerated beam. When multiple ion species were present, an electromagnetic mass analyzer was used to determine the species distribution.

The rf antenna was fabricated from 4.7 mm diameter copper tubing and was coated with a thin layer of hard porcelain material. The thin coating was slightly flexible and resistant to cracking. The rf system consisted of a series circuit of capacitive and inductive components with a plasma acting as the resistive load (Fig. 2). Rf power was delivered to the system by means of an isolation transformer with a step-down ratio of 10:1. To assure maximum power dissipation in the plasma and minimal power reflection, the matching circuit's impedance was adjusted to minimize the phase difference between the current and voltage. This

tuning was done at an rf operation frequency of approximately 1.8 MHz.

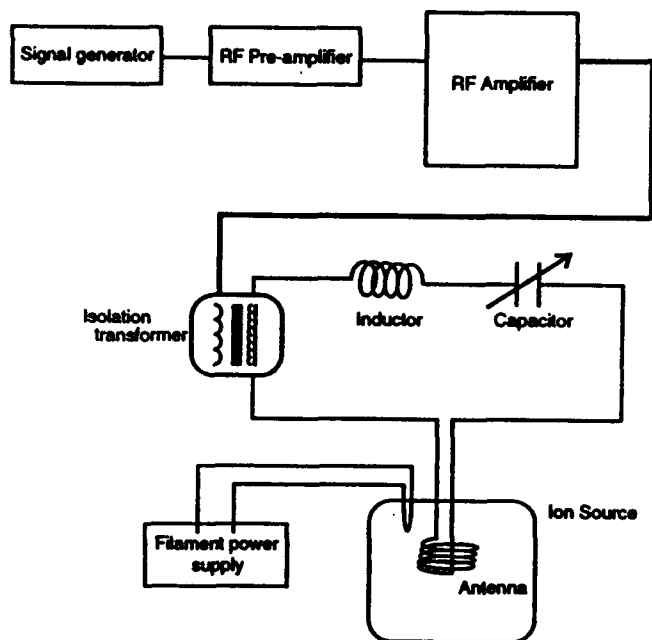


Fig. 2 Schematic diagram of the complete rf power system.

In the initial operation of the system, a moderate rf power of 4.8 kW could be coupled to the plasma in cw mode with only a small amount of power being reflected from the matching circuit. However, as the source operation continued, a shift in the rf coupling gradually developed. The current and voltage phase difference began to increase, thereby delivering less power to the plasma. The remainder of the power was then dissipated as heat in the matching circuit's components. The phase difference eventually became so pronounced that the system's circuit breakers tripped due to excessive reflected power.

When the impedance of the matching circuit was remeasured, a significant change in phase had occurred. In addition, the isolation transformer had become exceedingly hot. To try remedy the situation, the circuit was retuned while hot and a plasma reignited. It soon became apparent though, that the hot circuit was less efficient and that the circuit components could be damaged. A cw rf discharge became difficult to maintain for any duration of over twenty minutes.

The majority of heat dissipation occurred within the isolation transformer. Approximately 70 watts of the input power was being dissipated in the primary and secondary windings of the transformer. This heat may appear small in comparison with a 5 kW input power but the cumulative effect on the electrical components becomes significant when there is no cooling to carry this heat away. The increasing temperature changed the transformer's ferrite core permeability and accordingly the system became unstable.

As a solution to this problem, an external blower was installed to cool the isolation transformer by forced air convection. The system performance improved markedly. Since then, the ion source had been operated in cw mode at ~ 6 kW of rf power for over two weeks. Daily operation was maintained at two hours or longer (total integrated time for source operation > 24 hours). After running for this duration, the source chamber was opened. The antenna showed no signs of deterioration with the only visible effect being a grayish coating caused by vaporization of the starter tungsten filament. There was no measurable change in the thickness of the porcelain coating. It appeared that continued operation with the same antenna was still possible for an extended period of time.

### III. EXPERIMENTAL RESULTS

Multicusp generators are capable of producing large volumes of uniform and quiescent plasmas with densities exceeding  $10^{12}$  ions/cm<sup>3</sup>. For this reason, there was a great interest in the early 1980s in applying such devices as ion sources for neutral beam injection systems and for particle accelerators. To increase plasma penetration by a neutral beam, a high percentage of H<sup>+</sup> or D<sup>+</sup> ions is required. It has been demonstrated that atomic species as high as 85% can be obtained routinely if a multicusp source is operated with a magnetic filter [3]. The magnetic field generated by the filter magnet is strong enough to prevent the primary electrons from reaching the extraction region. The absence of energetic electrons will prevent the formation of H<sub>2</sub><sup>+</sup> in

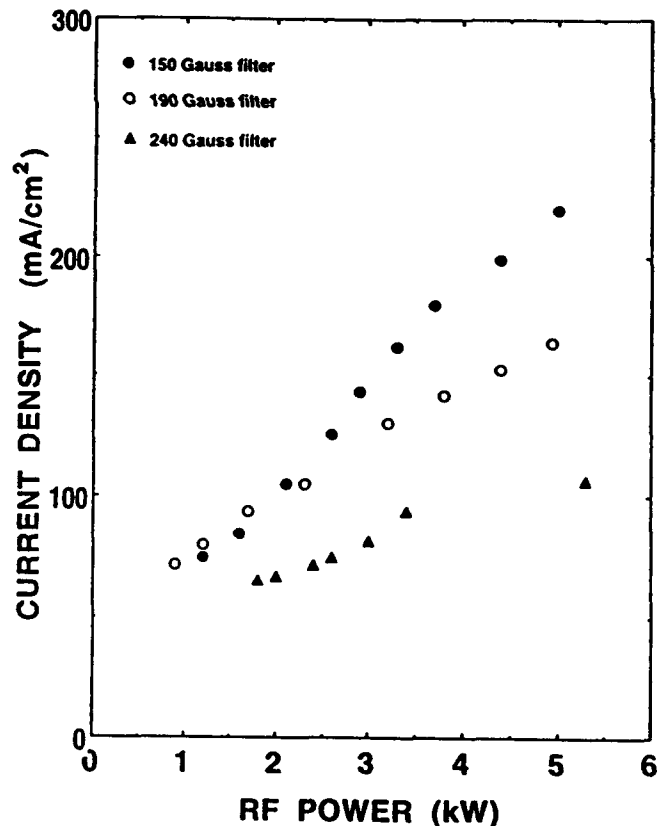


Fig. 3 Hydrogen ion current density as a function of rf power.

the extraction region, but dissociation of the molecular hydrogen ions ( $H_2^+$ ,  $H_3^+$ ) can still occur. As a result, the atomic ion species ( $H^+$ ) percentage in the extracted beam is enhanced.

We have investigated the extractable current density and the hydrogen ion species composition in the rf-driven source with different source parameters. Source operating pressure was maintained between 4 to 6 mTorr. Figure 3 shows the hydrogen ion species as a function of rf power for three different filter field strengths (The B-field is measured at the mid-plane of the filter). As expected, the weaker the filter field, the higher the extracted positive hydrogen ion current density. The data indicates that a nominal current density of  $150 \text{ mA/cm}^2$  can be achieved by both the 150 G and 190 G filters at about 4 kW of rf power. Source operation with the 240 G filter can produce a current density of only  $100 \text{ mA/cm}^2$ .

Figure 4 shows a plot of  $H^+$  ion percentage versus rf power for the three different filter fields. The  $H^+$  ion concentration increases as the rf power is varied from 1 to 5 kW. In the range of rf power considered, the 190 G filter provides higher proton percentage than the other two filters. According to the results shown in Figs. 3 and 4, one can conclude that by using the 190 G filter, an  $H^+$  current density of  $\sim 100 \text{ mA/cm}^2$  can be obtained by operating the rf source at  $\sim 4 \text{ kW}$  of power. The  $H^+$  output current should exceed the present PSI source performance and should have

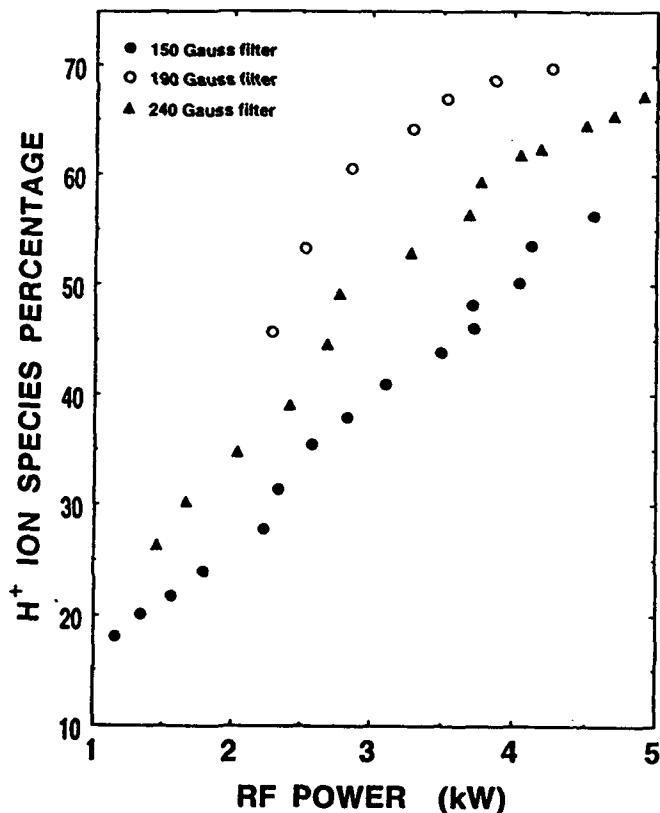


Fig. 4  $H^+$  ion species percentage as a function of rf power.

a much longer source lifetime. As a result, routine source maintenance will be much reduced.

Based on the results of this source testing, we are now designing and fabricating a new rf-driven multicusp source for positive ( $H^+$ ) ion production in cw mode for future use in the 870 keV Cockcroft-Walton preinjector at PSI. Operational characteristics of this new ion source will be reported in the near future.

## ACKNOWLEDGMENTS

We would like to thank S. Wilde, G. DeVries, R. Wells and members of their group for technical assistance and B. Thibadeau and W. Scharff for preparing this manuscript. This work is supported by the Paul Scherrer Institute and the Director, Office of Energy, Office of Fusion Energy, Development and Technology Division, of the U.S. Department of Energy under Contract No. DE-AC03-76SF00098.

## REFERENCES

- [1]. K. N. Leung, D. A. Bachman, C. F. Chan, and D. S. McDonald, Proc. XVth Int. Conf. on High Energy Accelerators, Hamburg, Germany (July, 1992) p.200.
- [2]. K. N. Leung, D. A. Bachman and D. S. McDonald, Proc. 3rd European Particle Accelerator Conf. Berlin, Germany (March, 1992) p.1038.
- [3]. K. N. Leung and K. W. Ehlers, Rev. Sci. Instrum., 52, 1452 (1981).

# Measurements of Emittance and Species Fractions of a Positive Hydrogen Ion Beam Extracted from an RF-Driven Multicusp Source\*

G. Gammel, T.W. Debiak, S. Melnychuk, and J. Sredniawski  
Grumman Aerospace Corporation  
1111 Stewart Ave., Bethpage, NY 11714 USA

## Abstract

Measurements of the  $H^+$ ,  $H_2^+$ , and  $H_3^+$  fractions and emittances of a hydrogen beam extracted from an RF-driven multi-cusp source were made using a bending magnet and an electrostatic emittance scanner. The  $H^+$  fraction increased with RF power. Fractions in excess of 90% were obtained. At a given RF power, the  $H^+$  fraction increased with decreasing source pressure and increasing filter rod separation. When the "collar" surrounding the extraction aperture (used for  $H^-$  operation) was removed, the  $H^+$  current increased by a factor of  $\sim 4$ , without changing the  $H^+$  fraction at a given RF power. With a large filter rod separation,  $H^+$  currents on the order of 100mA were achieved at  $\sim 20$  kW of RF power. Using a modified extractor [1] operating at 35kV,  $H^+$  currents on the order of 60mA were obtained with a 90% normalized rms emittance of  $0.012\pi$  cm-mrad.

## I. INTRODUCTION

CW  $H^+$  accelerators are receiving increased attention recently due to increased interest in projects such as accelerator transmutation of waste (ATW), accelerator production of tritium (APT), and accelerator-based conversion of nuclear weapons (ABC). The accelerators envisioned for these projects require a reasonable emittance and an ion source with a high  $H^+$  fraction. This paper describes a technique used for measurements of the  $H^+$ ,  $H_2^+$ , and  $H_3^+$  fractions in a positive hydrogen ion beam, and presents some emittance, current, and  $H^+$  fraction measurements. For all data, the beam was pulsed for 1 ms at 0.3% duty factor.

The emittance scanner on the Grumman Test Stand [2] was used with a dipole bending magnet after the extractor to measure emittance and hydrogen species fractions as shown in Fig. 1. The scanner entrance slit was 17 cm from the extractor. Current was measured using a 2-7/8" ID x 9" long cup. The ion source for most of the measurements was a 10 cm ID RF-driven multi-cusp source with a variable strength magnetic dipole filter field [3]. The strength\*\* was changed by varying the spacing between the filter rods. The ID of the RF coil was 5.8 cm, and the aperture diameter was 6.4 mm.

\*Work supported under Grumman IR&D project #7256-2709.

\*\* All references to filter field strength refer to the strength on axis in the midplane of the filter rods, which contain the magnets.

$\int B dl$  for the bending magnet was 4070 G-cm, which nicely resolved all three species. For some measurements, a 7.5 cm ID source was used with a 4.3 cm ID RF coil (reduced by the same ratio as the chamber ID's). The filter field strength was fixed at 120 G, the aperture diameter was 5.6 mm, and  $\int B dl$  for the bending magnet was 3325 G-cm, which resolved the  $H^+$  peak, but the  $H_2^+$  and  $H_3^+$  peaks were still overlapping.

Typical raw data for a scanner sweep at one position, using the large source, is shown in Fig. 2. The horizontal axis is proportional to time and deflection angle - i.e. the peaks are separated in angle rather than in spatial position. The three species are resolved, and a small impurity of mass 17 or 18 ( $OH^+$  or  $H_2O^+$ ) is usually observed. With a well baked out and pumped out gas line, the impurity is  $< 1\%$  of the total current. The current in each species is proportional to the area under each peak summed over all sweeps as the scanner moves through the beam. The fractions are obtained from the ratios of the summed areas, and the current in each species is the fraction for that species times the Faraday cup current. The analysis program also calculates the emittance of each species separately.

For small source operation, the most deflected particles entered the scanner at angles greater than the angular acceptance. Therefore, emittances are not quoted for this source. Also, the actual  $H^+$  fractions are slightly higher than shown because relatively more  $H^+$  was missed than the other species since  $H^+$  is the most deflected. For large source operation, the problem was corrected by tilting the scanner 75 mrad, as shown in Fig. 1.

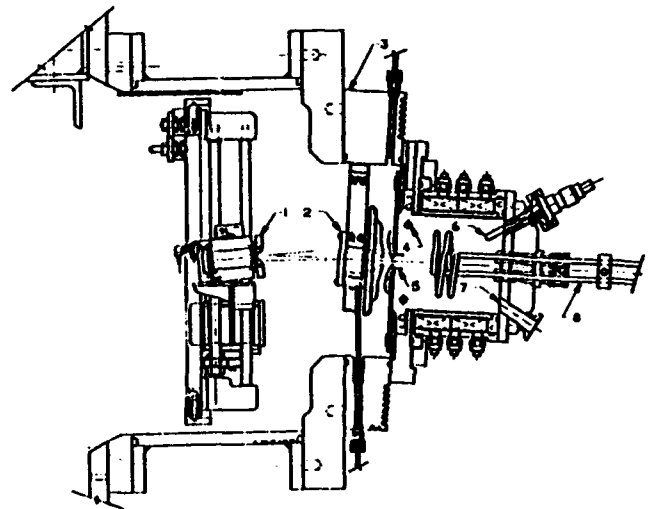


Fig. 1 Scale drawing of experimental apparatus. 1 = emittance scanner (tilted 75 mrad); 2 = bending magnet; 3 = 60° wedge plate; 4 = filter rod; 5 = collar; 6 = starter filament; 7 = gas inlet; 8 = RF antenna.

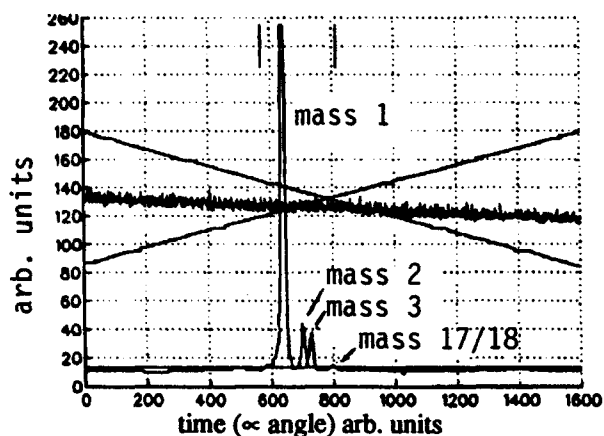


Fig. 2 Raw data from emittance scanner, showing the three species and a small impurity. The crossing lines are the voltages on the two deflection plates ( $\Delta V = \theta = 0$  at the crossover point), and the hashy line in the middle is the current hitting the front face of the scanner.

## II. RESULTS

### A. Current and $H^+$ Fractions

Fig.'s 3 - 5 show total current density and  $H^+$  fraction vs RF power for different filter field strengths. For the large source, at a given RF power, both the total current and the  $H^+$  fraction increased as the filter field was decreased by pulling the filter rods apart. In future studies, we will increase the separation even further. We will also vary the filter field by changing magnets at a fixed spacing. Fig.'s 3 and 5 show that adding the collar (see Fig. 1) reduced the current by a factor of four without affecting the  $H^+$  fraction. The current densities in Fig. 4 should therefore increase by a factor of four at a given RF power by removing the collar.

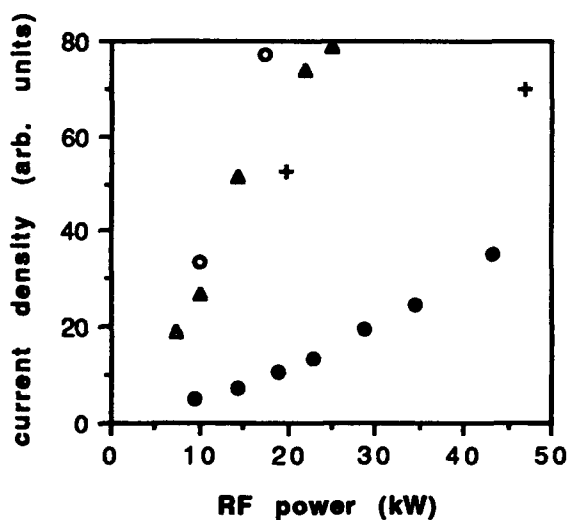


Fig. 3 Relative current density vs RF power for the large source. + = 400 G, no collar;  $\Delta$  = 280 G, no collar; o = 190 G, no collar; • = 300 G, with collar.

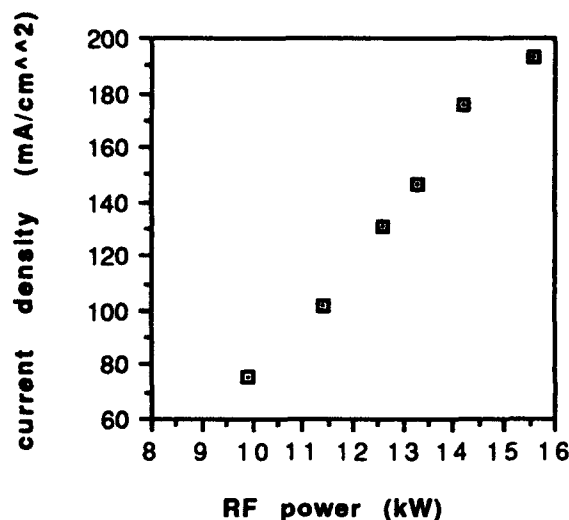


Fig. 4 Current density vs RF power for the small source with a collar. Aperture radius = 2.8 mm.

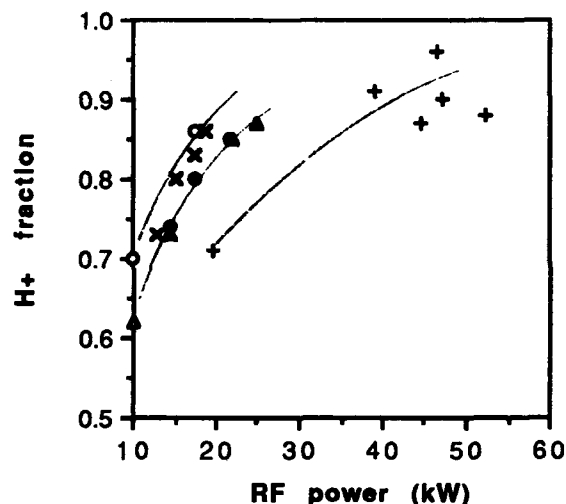


Fig. 5  $H^+$  fraction vs RF power for some of the data from Fig. 3 plus additional small source data (x) with collar.

As the  $H^+$  fraction rose with power, we found that the  $H_2^+$  fraction remained roughly constant, while the  $H_3^+$  fraction decreased. Fig. 6 shows that the  $H^+$  fraction starts decreasing if the source pressure is too high.

### B. Emittance

Fig. 7 shows results of a typical emittance scan for the large source at 35 kV. The results for  $H_2^+$  and  $H_3^+$  are similar, except the centroids shift due to the mass differences. The measured angular centroids scaled approximately as  $1/\sqrt{\text{mass}}$  as expected, and were close to the predicted values based on the measured  $|\partial B|$  of the bending magnet:

$$\Delta\theta = (\sqrt{e/2m_p})|\partial B|/\sqrt{AV_{\text{ext}}}$$

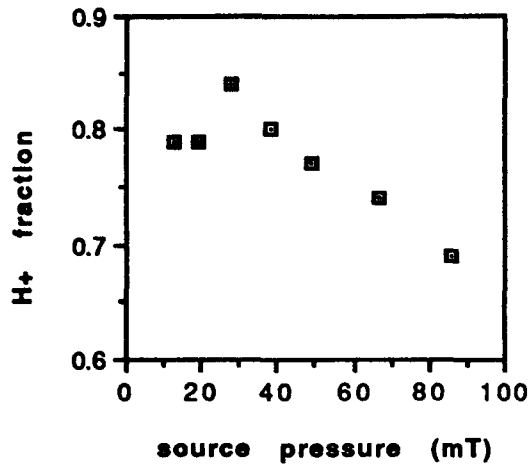


Fig. 6 Pressure scan using the small source.

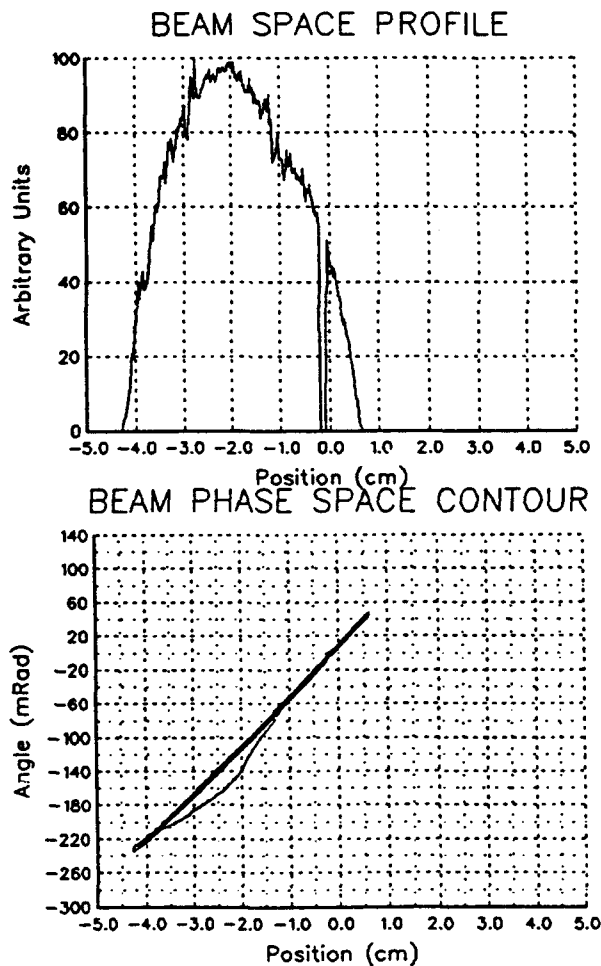


Fig. 7 Typical emittance scan data for the H<sup>+</sup> peak only. The plots for the other species show the centroid shifts, but are otherwise similar. The wedge plate angle (60°) must be added to obtain the net deflection.

We observed that the H<sup>+</sup> phase space is bowed (see Fig. 7). At least part of the reason for this is that the scanner moves vertically through the beam, which is not transverse to the H<sup>+</sup> beam since H<sup>+</sup> emerges from the dump at a downward slant. Since the heavier species are not deflected as much, they come out more on axis, so the bow should be less obvious in their phase space plots. We do, in fact, observe this. The bow makes the rms emittance artificially high.

Fig. 8 shows the normalized 90% H<sup>+</sup> rms emittance after straightening out the bow in the analysis program, vs RF power at 30 kV and 35 kV. The extractor was running overdense at 30 kV, and on perveance to overdense at 35 kV. The highest power corresponds to an H<sup>+</sup> current on the order of 60 mA.

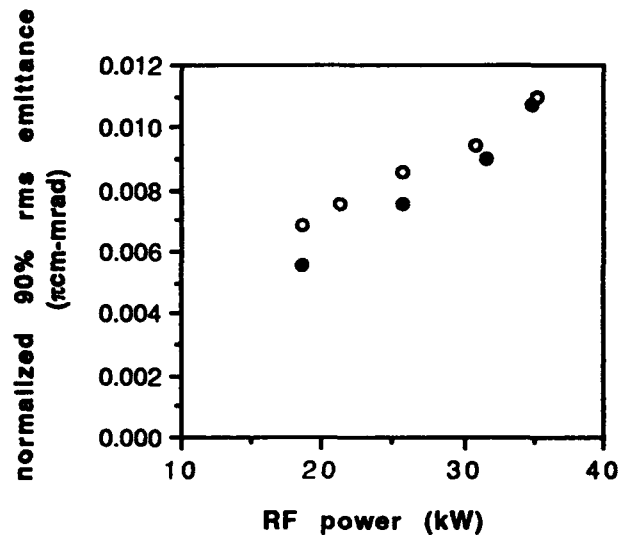


Fig. 8 Large source; ○ = 30 kV, ● = 35 kV.

### III. SUMMARY

Based on the large source species measurements, it is clear that increasing the filter separation is desirable for obtaining a high H<sup>+</sup> fraction at low power, but the effect on emittance must still be determined. It is also clear that the H<sup>+</sup> fraction increases with power, and that a collar around the emission aperture cuts down the current by a factor of four without affecting the H<sup>+</sup> fraction.

Further work is planned to optimize the geometry and operating parameters of the RF-driven source for high H<sup>+</sup> fraction and high current at low power for ATW/APT applications, including full CW testing by late '93.

### IV. REFERENCES

- [1] design provided by C. Geisik (LANL)
- [2] R. Heuer et al., "A New Stand-Alone Beam Emittance Measurement System", *Nucl. Instrum. and Meth. in Phys. Research*, B42 (1989), p. 135.
- [3] K. Leung et al., "RF-Driven Multicusp H<sup>-</sup> Ion Source", *Rev. Sci. Instrum.* 62(1), Jan. 91, p. 100.

# A New Design of the Sputter type Metal Ion Source and its Characteristics of Ion Beam Extraction

W. Kim, B.H. Choi, J.T. Jin, K.-S. Jung  
Korea Atomic Energy Research Institute, Taejon, 305-606, Korea  
S.H. Do  
Pusan National Fishers University, Pusan, 608-737, Korea  
and  
K.H. Chung  
Seoul National University, Seoul, 151-742, Korea

## Abstract

In an attempt to get a high current metal ion beam of various solid elements including refractory metals, a gaseous duoPIGatron ion source was modified by placing a grid type cathode and a sputter target in the PIG chamber. Tungsten mesh was adopted as the cathode grid, and Ar gas was used for a support gas for sputter induction. For Cu, Fe, and Al, ion current and ratio of the metal ion were obtained at various conditions of sputtering voltage, support gas pressure, arc current, magnet current, and beam extraction voltage. Results showed that the metal current density is linearly changed with the sputtering voltage and magnet current. Ratio of the metal ion in the total current is larger at lower support gas pressure. Current densities for Al, Cu, and Fe were  $4 \text{ mA/cm}^2$ ,  $5.5 \text{ mA/cm}^2$ , and  $2 \text{ mA/cm}^2$ , respectively, at an arc current of 3 A, extraction voltage of 20 kV, and a sputtering voltage of 1 kV. Ratios of the metals in the extracted ion currents were 9%, 8%, and 5% for Al, Cu, and Fe, respectively.

## I. INTRODUCTION

Metal ion source technology has been developed for the separation of isotopes, preparation of isotope targets for nuclear physics, doping of semiconductor materials, and the injector section for the heavy ion accelerators. Studies on the modification of surfaces as metals, ceramics, or polymers were started more than twenty years ago and parts of the results are applied to the industry[1]. For example, ions of Cr, Mo, and Ti are used to strengthen the corrosion resistances and wear properties of engineering materials like steels[2].

Ion sources capable of producing currents of tens of mA or current densities of a few  $\text{mA/cm}^2$  are required for the wider utilization of the technology in industries. However, those ion sources as Freemann type or CHORDIS type[3,4] thus far developed until now have extraction current capabilities for the metal ions of only a few milliamperes. The conventional heating-evaporation type ion sources have the problem of metal condensation. The trend of the development of ion sources are thus centered on those producing large currents like MEVVA type ones[5].

## II. PRINCIPLES OF PLASMA GENERATION BY THE ION INDUCED SPUTTERING

The concept and principle of the sputter type plasma generator with a single discharge chamber are shown in Fig.1. Arc discharge is maintained in the chamber filled with an inert gas by applied voltage between the filament and the mesh-type grid. Application of a few kV between grid and the target induces ion acceration from plasma to the target. Sputter-generated electrons and neutral particles enter the chamber through the grid spacings. The neutral particles further ionizes in the chamber, thus being extracted as ion beams or induces next sputtering. For a cylindrical target, average sputtering angle of the secondary neutral particles is normal to the target surface and particle density is expected to be maximum at the centre of axis.

## III. SPUTTER TYPE ION SOURCE

A variance of the dual discharge chamber DuoPIGatron ion source is made for the implementation of the ion induced sputtering[Fig.2]. This modification composed of the intermediate electrode with a filament inside, the main Penning discharge chamber for the plasma generation, and the ion beam extraction system.

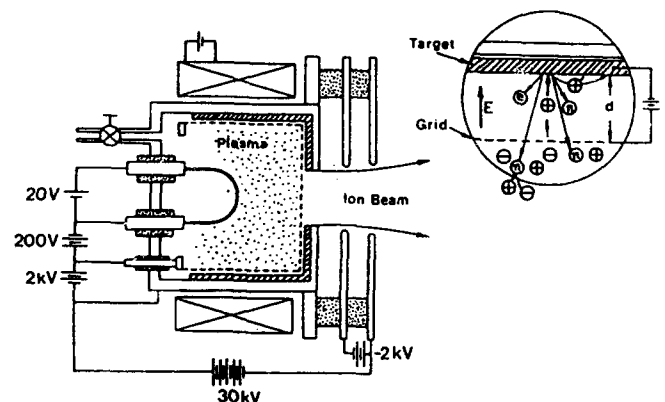


Fig.1 Principle of a Sputter Metal Ion Source

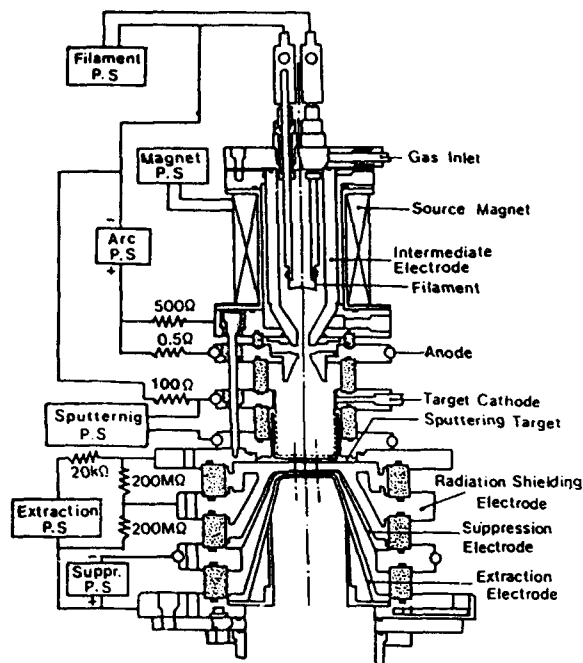


Fig. 2 Schematic Diagram of a Sputter-Type DuoPIGatron Metal Ion Source

#### A. Plasma Generation

The PIG discharge chamber consists of one anode and a grid-type cathode. Electrons entering through the hole of the intermediate electrode to the PIG chamber are accelerated and produce ions through collision with neutral particles. Others reach the cathode and re-accelerated to the anode, making another collisions with neutral particles. This multiple ionization process is enhanced by the axial magnetic field formed by the source magnet. The target section to produce the metal ions consists of a grid and a target. Wall side and bottom side of the grid cathode are meshes of nickel and tungsten, respectively. Target is bucket-shape holding the grid inside and has a hole at the bottom. Application of 1-2 kV between grid and target induces acceleration of ions from the plasma to the target. Secondary electrons, ions, and neutral particles are ejected from the bombarded target and the ejected electrons and neutral particles pass through the grid to enter the PIG chamber, thus making added ionizations. Within the experimental conditions that the yield of the ejected neutral particles is larger than 1, self-sustained discharges with only sputtered particles become possible.

#### B. Ion Beam Extraction System

Ion beam extraction is made possible by the proper attachment of an accelerating electrode and a decelerating electrode to the rear of the target. The target has a hole of 5.5 cm in diameter and an accelerating electrode is distanced 6 mm from the target. Behind the accelerating electrode, the decelerating electrode is located at 2 mm apart.

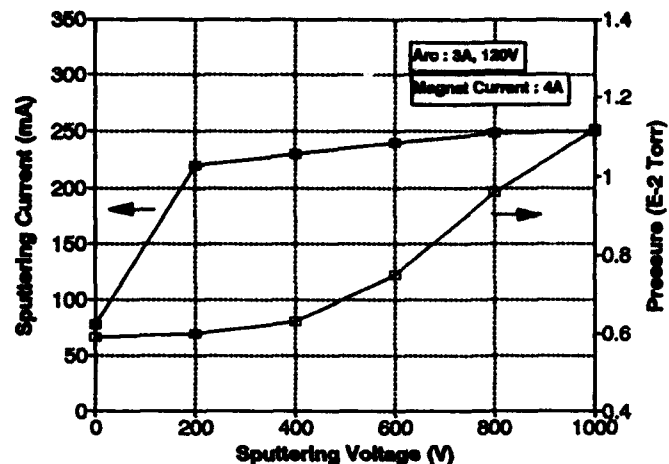


Fig. 3 Pressure in PIG Chamber and the Sputtering Current depending on the Sputtering Voltage

Collisional losses of ions with the electrode walls are minimized by the proper ion-optical designing of the electrodes dimensions. Neutral particles through the system were rapidly removed through vacuum slots.

### IV. CHARACTERIZATION EXPERIMENTS

The 100 kV gas ion implanter in operation at KAERI was replaced of its ion source by the metal ion source.

A power supply(5kV, 1A) was added to the system for the sputtering. Discharge pressure, extraction current, and the ion masses were measured for targets of Al, Cu, Fe, and C. Ion mass separation was performed by a magnetic dipole composed of a permanent magnet. Extraction currents were measured with the scanning Faraday cup.

#### A. Characteristics of the plasma formation

Each of the targets was tested for the plasma characteristics using Ar as the support gas. Sputtering current and pressure were measured for voltage variations using Al as the target at an Ar pressure maintained at  $7.5 \times 10^{-3}$  torr(Fig.3). Increase of the neutral particles with the sputtering energy would be the cause of the increased pressure at high voltages. Saturation of the sputtering current at larger than 200 V is thought to be from the space charge limit effect.

#### B. Beam Extraction Characteristics

Extraction currents for each kind of ions with the Al target at a constant discharge condition are shown in Fig.4. Total ion current is constant for the sputtering voltage variations, but Al ion current increases with sputtering voltages. The increase can be ascribed by the increase of sputtering yield. In comparison with the Al ion current and the sputtering yield at various voltages, the increase of the current with sputtering voltage is thought to be resulted from the increased sputtering yield with voltage. Efficient confinement of ions and electrons by the strengthened magnetic field can increase the resultant current densities(Fig.5).

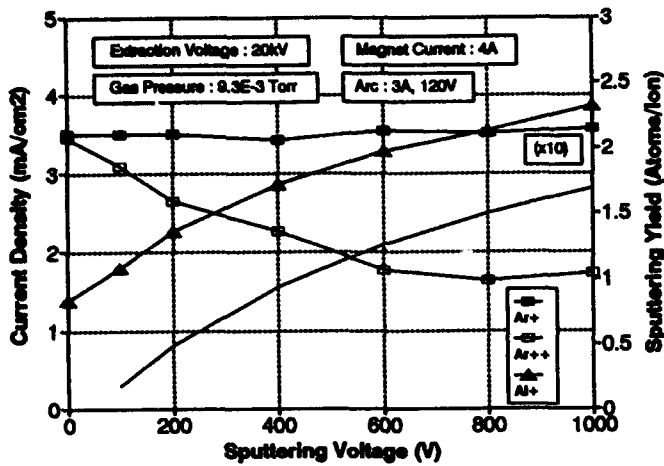


Fig. 4 Ion Current Densities and Sputtering Yield as a function of Sputtering Voltage

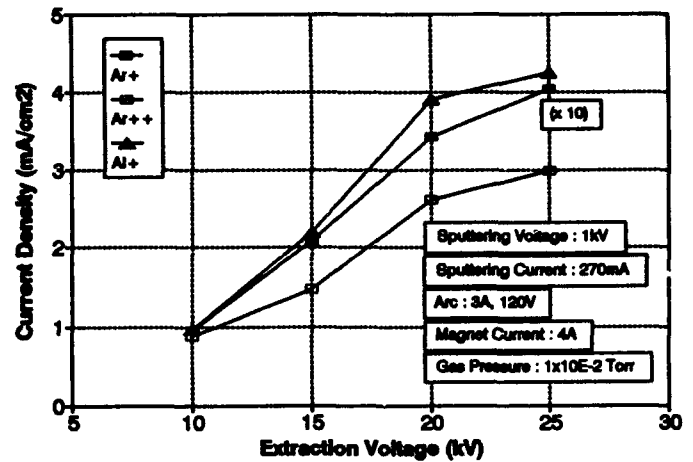


Fig. 7 Ion Current Density with Aluminum Target System depending on Extraction Voltage

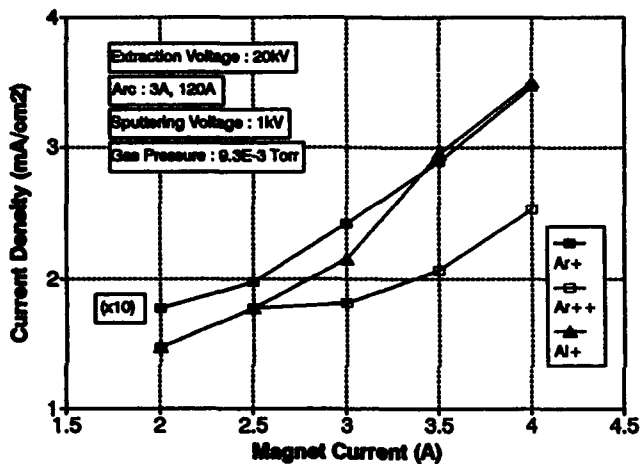


Fig. 5 Ion Currents with Al Target System depending on Magnet Current

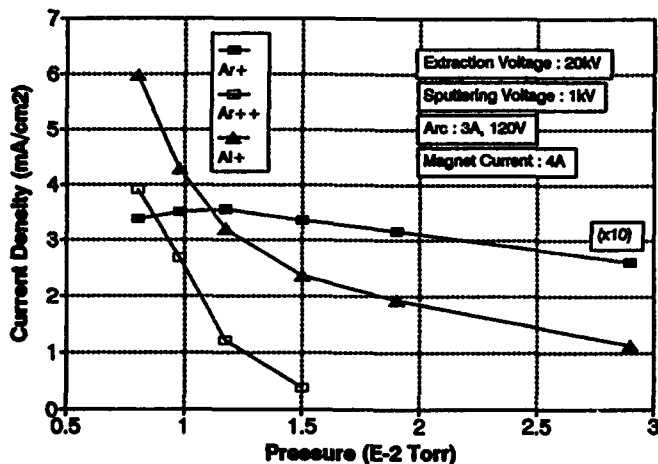


Fig. 6 Ion Current Density in Aluminum Target System as a function of Feed Gas Pressure

Each component of the ion current depending on the feed gas pressure is shown Fig.6. The total Ar ion current shown as Ar<sup>+</sup> is constant for the pressure range. The figure shows the self-sustained discharge as the major mechanism for the generation of the neutral particles. Fig.7 shows the ion current densities depending on the extraction voltage. For Al, Cu and Fe, the current densities were 4 mA/cm<sup>2</sup>, 5.5 mA/cm<sup>2</sup>, and 2 mA/cm<sup>2</sup>, respectively, at similar operational conditions.

## V. CONCLUSION

A sputter-type ion source which can produce ion beams of the most metallic elements including refractory ones has been developed by applying the principles of ion induced sputtering and reflex arc discharge. Results of the performance test showed that the pressure of the discharge chamber and the extracted current density of the metal ion components were increased linearly with the sputtering voltage. Extraction current density of the metal ions were a few mA/cm<sup>2</sup> and the ratio of the metal ions and total ions was about 10 %. Continuous metal ion beams with current of a few mA were obtained.

## VI. REFERENCES

- [1] P. Siosansi, Mat. Sci. & Eng., 90, 373 (1987)
- [2] M.I. Guseva, M.V. Atamanov, Private Communications (1992)
- [3] D.J. Chivers, Rev. Sci. Instrum., 63(4), 2501 (1992)
- [4] R. Keller, P. Spadtke and H.Emig, Vacuum 36, 833 (1986)
- [5] I.G. Brown, Rev. Sci. Instrum., 63(4), 2531 (1991)

# K<sup>+</sup> Ion Source For The Heavy Ion Induction Linac System Experiment ILSE\*

S. Eylon, E. Henestroza, W. W. Chupp, and S. Yu

Lawrence Berkeley Laboratory  
1 Cyclotron Road  
Berkeley, California 94720

## Abstract

Low emittance singly charged potassium thermionic ion sources are being developed for the ILSE injector. The ILSE, now under study at LBL, will address the physics issues of particle beams in a heavy ion fusion driver scenario. The K<sup>+</sup> ion beam is emitted thermionically into a diode gap from alumino-silicate layers (zeolite) coated uniformly on a porous tungsten cup. The Injector diode design requires a large diameter (4" to 7") source able to deliver high current (~ 800 mA) low emittance ( $E_n < .5 \pi$  mm-mr) beam. The SBTE (Single Beam Test Experiment) 120 keV gun was redesigned and modified with the aid of diode optics calculations using the EGUN code to enable the extraction of high currents of about 90 mA out of a one-inch diameter source. We report on the 1" source fabrication technique and performance, including total current and current density profile measurements using Faraday cups, emittance and phase space profile measurements using the double slit scanning technique, and life time measurements. Furthermore, we shall report on the extension of the fabricating technique to large diameter sources (up to 7"), measured ion emission performance, measured surface temperature uniformity and heating power considerations for large sources.

## I. INTRODUCTION

The potassium thermal Ion Source is being developed at LBL for the HIFAR (Heavy Ion Fusion Accelerator Research) 2 MV Injector Program and the ILSE (Induction Linac System Experiments) experiment. The Injector [1] consists of a diode of up to 1 MV followed by electrostatic quadrupoles (ESQ) to simultaneously focus and accelerate the ion beam to 2 MV. A 2 MV Marx pulse generator is used to drive the injector ESQ-diode system. The Injector diode design requires a large diameter (4" to 7") curved source capable of delivering a high current (~ 0.8 A) low emittance ( $E_n < .5 \pi$  mm-mr) singly charged potassium K<sup>+</sup> beam. The size of the source together with the tight injector emittance budget imply that the source emittance must be nearly temperature-limited. Furthermore, as a critical component of the ILSE and driver injector, the source must have sufficient reliability, life time and reproducibility.

Two types of sources have been studied [2], namely plasma sources and a thermal surface sources. The alumino silicate surface thermal source was found to meet the above

requirements. The K<sup>+</sup> ion beam is emitted thermionically into a diode gap from alumino-silicate layers (zeolite) coated on a porous tungsten cup. An improved potassium alumino-silicate (Spodumene analog) uniform coating technique was developed leading to a source with a uniform high emission current density and a high depletion charge density. A 1" diameter K source was fabricated and tested in the SBTE injector setup. Initial measurements showed a maximum space charge limited extracted ion beam current of 95 mA, corresponding to a density of 19.5 mA/cm<sup>2</sup>. The maximum density achieved thus far is limited by the source diode optics, and not by source emission. The normalized emittance measured was 0.059 $\pi$  mm-mrad, corresponding to a transverse temperature of 0.2 eV. Nondestructive life tests showed that the source can be operated under ILSE continuous operating conditions for more than a month (twenty, eight-hours days with 1  $\mu$ s long pulses at 1 second repetition rate). D. C. destructive life tests showed that ~ 30% of the total stored K can be ionized and extracted, allowing for years of ILSE operation. Following these encouraging results, larger sources with diameters of 4" and above have been fabricated and tested.

## II. SOURCE FABRICATION

The source uses a porous (80%) tungsten cup with a high heating efficiency. The potassium alumino silicate (zeolite) is spread on the porous tungsten cup surface and fired in a vacuum oven to a temperature of 150° C allowing it to melt and soak into the curved surface pores. The source is cooled slowly at a rate of 150° C/hr allowing the crystallization of the alumino-silicate into a uniform thin cristobolite phase layer. The coating is mechanically bonded to the cup surface allowing high current density and charge depletion out of the source. This technique is used to coat the 1" source as well as the large diameter curved surface sources.

## III. SOURCE CURRENT MEASUREMENTS

The total ion current was measured using a Faraday cup collector. The current waveform is monitored across a 50 ohm resistor using the Tektronix 2440 oscilloscope. Looking for the source emission and space charge limits the current was measured at various source diode voltages and heating powers. The SBTE injector consists of the source emitter and a series of accelerating planar electrodes. The extracted current depends mostly on the first electrode voltage and distance, to which we shall refer to as U<sub>gap</sub> and D<sub>gap</sub>. The other electrodes are used mostly for controlling the beam optics.

\* Work supported by the Director, Office of Energy Research, Office of Fusion Energy, U.S. Department of Energy under Contract No. DE-AC03-76SF00098.

EGUN calculations were used to design the source configuration including gap voltages, gap distances and different Pierce electrode geometries to maximize current extraction from the source and transport through the series of electrodes into the Faraday cup.

The results presented in Figure 1 represent a set of current measurements taken using a Dgap of 2.05 - 2.25 cm Pierce electrode with focusing angle of 55° - 67.5°. Ugap is set to .3 - .4 of the full MARX voltage. The heater power varied from 50 - 150 W (980°). There is a grid in the exit ground electrode. A total current of 95 mA was measured leading to a current density of 19.5 mA/cm<sup>2</sup>. The source emission limit was not reached. A further increase in the source current may be possible with additional modifications to optimize the beam optics. A source perveance k of 5.48 nPerves was obtained from the measurements which obeyed the Child-Langmuir Law. The EGUN calculated k was 5.72 nPerves.

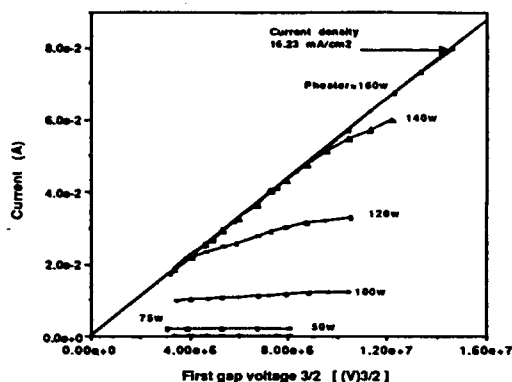


Figure 1. SBTE source current vs. diode voltage to the 3/2 showing the source emission limit for given heater powers (surface temperature)

The beam transverse current density profile was measured using a varying diameter aperture across the beam (Figure 2). The measurement was taken at a MARX voltage of 120 kV gap voltage of 31 kV, total current of 20 mA, Dgap = 3 cm, and a Pierce electrode angle of 67.5°. One can see that the beam has a uniform current density profile in agreement with EGUN simulations.

Recently we ran emission tests on a newly fabricated four inch diameter source. A curved graphite extraction electrode was designed and placed to obtain a planar diode configuration with a 6 mm gap. Ten parallel 20x2 mm slits were cut in the extraction electrode to allow current density measurements using a Faraday cup and temperature measurements using a hot wire pyrometer. The extraction voltage pulse up to about +15 kV is supplied to the source, allowing the extraction electrode to be at ground potential. Figure 3 shows the source surface temperature and current density profiles found to be uniform. The measured source perveance was found to be 24.7 nPerves; the calculated source perveance for a 6 mm gap planar diode is 22.5 nPerves. The

difference of 6% between the measured and calculated perveance could be because of uncertainty in the diode gap distance.

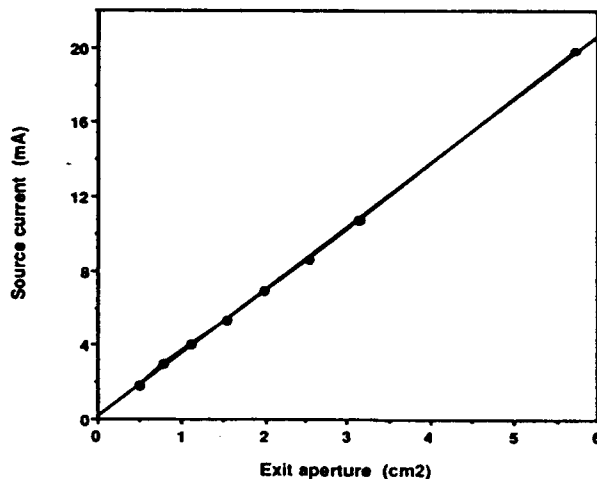


Figure 2. SBTE diode current vs. beam aperture area, showing a uniform current density profile.

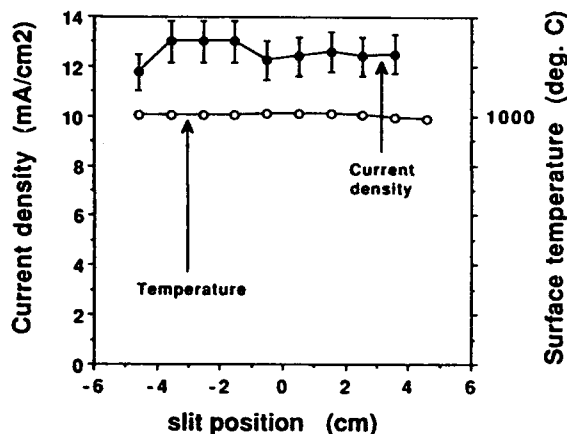


Figure 3. Four inch source current density and surface temperature profiles.

#### IV. TRANSVERSE EMITTANCE AND TEMPERATURE

The beam transverse rms unnormalized emittance was measured using the double slit scanner. We have used the usual SBTE setup, as in the current density measurements. The measured unnormalized emittance is 6π mm-mrad, leading to a normalized emittance E<sub>n</sub> of 0.059π mm-mrad.

The source intrinsic temperature kT in eV can be calculated [3] knowing the measured normalized emittance (Figure 4):

$$kT = E_n^2 (C/2R)^2 mi/q = 0.2 \text{ eV}$$

where  $C$  is the light velocity ( $3e+8$  m/sec),  $R$  is the beam radius ( $1.25e-2$  m), and  $mi/q$  for the potassium ion is  $4.08e-7$ . The measured source surface temperature is about  $980^\circ\text{C}$ , i.e.,  $0.13$  eV within 60% of the evaluated  $0.2$  eV.

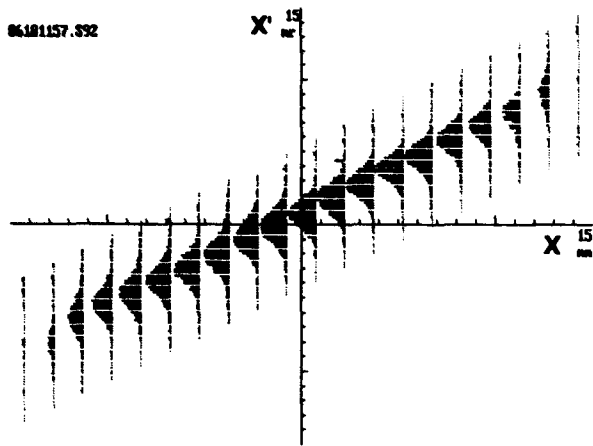


Figure 4. Beam phase space profile in  $x$  (radius) and  $x'$  (angle).

## V. LIFE TESTS

The objective of the test was to show the source performance during experiments that are the equivalent of a one-month of continuous ILSE operation, i.e., twenty eight-hour days with  $1 \mu\text{s}$  long pulses at a one second repetition rate. The source was fired about 50,000 times with extended pulse duration of 7 to 40 microseconds with repetition rates from one in 12 seconds to one per second, extracting a total charge of over  $3.7 \text{ mCb/cm}^2$  above the required  $2.4 \text{ mCb/cm}^2$ . The source was kept at a temperature  $980^\circ\text{C}$  for over 160 hours. We have not observed any depletion or evaporating effects during and after the test.

A D. C. depletion destructive life experiment was performed on small  $1/4$ " sources. A total depleted charge (25 micro Amp. 12 hour) of  $1.6 \text{ Cb/cm}^2$  was extracted, more than is needed by ILSE over years of operation.

## VI. CONCLUSIONS

Alumino silicate  $\text{K}^+$  sources were evaluated for applications in the ILSE injector and in a possible driver in an Heavy Ion Fusion (HIF) scenario. The measured source transverse emittance and current density were found to meet ILSE requirements. Beam transverse emittance and temperature were found to be consistent with the source intrinsic temperature and emittance within a factor of two. Our new Zeolite coating technology was successfully extended to the coating of large diameter, up to 17 cm, curved surface sources. This technique allows a uniform coating with lasting mechanical bond to the source surface. Life test showed that the source can be operated under ILSE conditions for more than one year and for about one month in a fusion scenario driver. Destructive deletion tests showed that more than 30% of the K atoms estimated to be stored in the alumino silicate coating can be extracted as K ions. One can see that the alumino silicate K zeolite sources can meet the special requirements given by the ILSE experiments. The fabrication of a new ILSE source, the design of which is presented above, is to be tested soon in a diode configuration.

## VII. REFERENCES

- [1] S. Yu et al., Intl. Symp. Heavy Ion Inertial Fusion, Frascati, Italy, May 1993.
- [2] H.L. Rutkowski et al., *The Berkeley Injector*, Particle Accelerators 37, 61 (1992)
- [3] J.D. Lawson, *The Physics of Charged Particle Beams*, p. 201 (Clarendon Press, Oxford), 1978.

# On the Magnetic Compression of Electron Beams in E.B.I.S. or E.B.I.T.

J.L. Bobin, G. Giardino\*, E. Mercier,  
 Université Pierre et Marie Curie, T. 12, E. 5, 4, place Jussieu, 75252, Paris, FRANCE.  
 \* L.P.A.N. associé au C.N.R.S.

## Abstract

Conditions for compression of a laminar non-relativistic dense beam by an inhomogeneous magnetic field  $B$  are investigated theoretically and numerically. A generalized Brillouin regime is defined in which an efficient beam compression may proceed according to the scaling  $Br = \text{const}$ , provided the field undergoes slow variations: adiabaticity condition. The initial density profile and radial velocity are found critical for subsequent laminarity.

## I. INTRODUCTION.

A large electron density in the beam of an E.B.I.S. or E.B.I.T. is of paramount importance to obtain a large number of multiply charged ions. Adiabatic magnetic compression starting for example at the gun exit or further downstream in a Brillouinlike beam is a way to reach this goal. It will be shown in section II that numerical simulations referring to actual devices indicate an unfavorable  $Br^2 = \text{const}$  scaling law. Furthermore "beam scalloping" easily occurs depending on initial conditions and beam geometry. It appears then worthwhile to investigate magnetic compression both theoretically and numerically. An important requirement is the laminarity of the electron flow. Since the whole analysis deals with electron trajectories, laminarity is defined by nonintersecting trajectories.

## II. IDEAL BRILLOUIN BEAM AND MAGNETIC BEAM COMPRESSION

We need to use an electron beam in Brillouinlike conditions ( $\approx 0.5$  mm envelope beam radius, constant beam profile all along the beam section, 3000 Gauss axial magnetic field) and to increase

by 100 the current density, using magnetic compression in Brillouin mode ( $Br = \text{const}$  in a rigid rotator beam) up to 3 Tesla axial magnetic field (Fig.1).

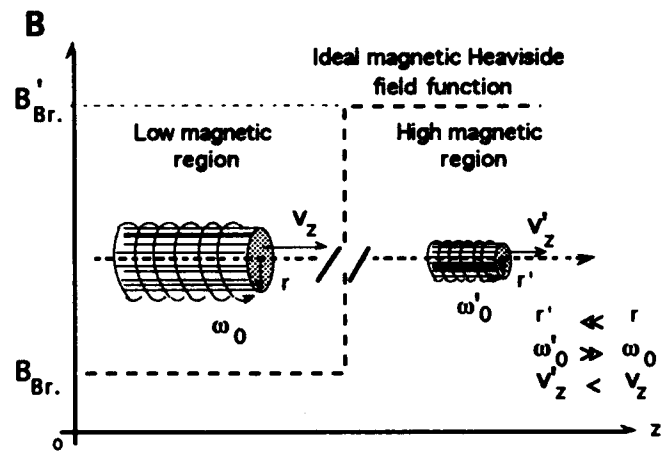


Fig 1

In our E.B.I.S. design and with the beam conditions at 3000 Gauss, the computed trajectories (2D-axisymmetric Thomson-CSF-TTE code with space charge) lead to a  $Br^2 = \text{const}$  (Fig. 2) beam compression scaling (constant flux) instead of the expected  $Br = \text{const}$  law (Brillouin mode).

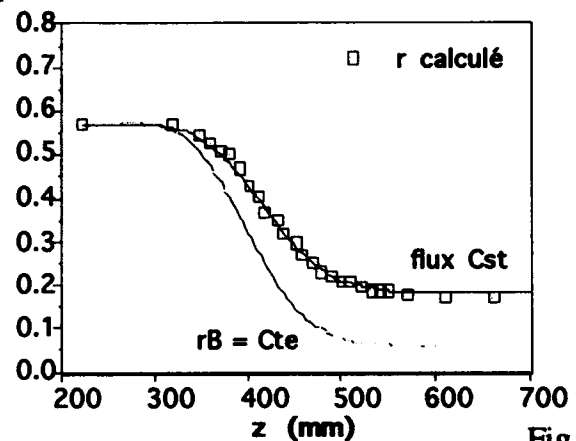


Fig. 2

Beam envelope when the magnetic field increases from 3000 Gauss to 3 Teslas. Squares are computed values. Vertical scale in millimeters.

We then investigate the better way to reach high current density beam, with a special emphasis on initial beam conditions. Two simulations were performed starting with a perfect Brillouin beam (0.5 mm, 10 kV, 0.054 A, 386 Gauss, constant current density). We used a 2D-Thomson code and alternatively a Runge-Kutta procedure integrating the equations of motion. It appears immediately a beam envelope scalloping (Fig. 3) corresponding to the inhomogeneous magnetic field structure (a gradient of the radial magnetic component is associated with any axial magnetic field component rise).

Two computed radius envelope electron beam in inhomogeneous magnetic field with space charge with Brillouin injection conditions:

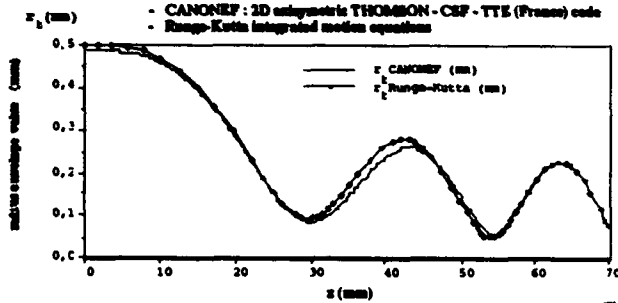


Fig. 3

When analysing accurately the motion of an electron in an axisymmetric magnetic structure with space charge (beam charge density), trochoidal trajectories are found with conspicuous beam translaminarities (Fig. 4).

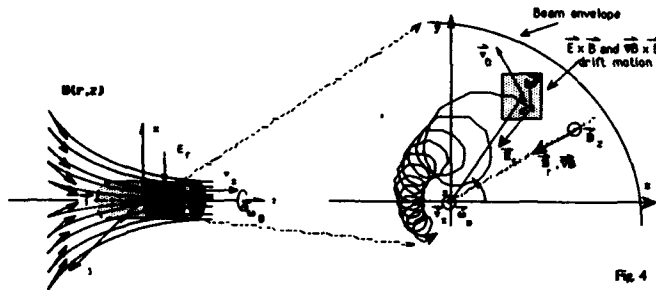


Fig. 4

We can explain these results using the transverse reduced effective potential energy leading to extended laminar flow expressions (low magnetic fields up to high magnetic fields).

### III. A GENERALIZED BRILLOUIN REGIME

In a uniform magnetic field parallel to the beam, the so-called Brillouin flow corresponds to the limit:

$$\omega_p^2 = \frac{\Omega^2}{2}, \quad \omega = \omega_B = \frac{\Omega}{2} \text{ (Larmor frequency)},$$

where  $\omega$  is the angular velocity around the beam axis,  $\omega_p$  is the plasma frequency and  $\Omega$  is the gyro frequency of the electrons. The beam then behaves like a rigid rotor: perfectly laminar flow. Now, Busch's theorem holds, i.e., for every electron trajectory

$$\omega = \frac{d\varphi}{dt} = \frac{e}{2\pi m r^2} (\Phi - \Phi_0).$$

$\Phi$  is the magnetic flux through a disk centered on the beam axis with radius is  $r$ , the distance of the electron to the axis.  $\Phi_0$  is a constant of the motion which vanishes in the Brillouin regime. Now in a non uniform field with azimuthal vector potential  $A_\varphi$ , assuming an homogeneous compression and an almost constant longitudinal velocity  $v_z$  (this is close to reality), a radial electric field is

$$E_r = -\frac{m}{e} \frac{W_0}{r}, \quad \text{where } W_0 = \int_0^r \omega_p^2(r') r' dr'.$$

In the case  $\Phi_0 = 0$ , a transverse reduced effective potential energy is

$$E_{\text{eff}} = \left( \frac{eA_\varphi}{m} \right)^2 - 2W_0 \ln\left(\frac{r}{r_0}\right).$$

This potential has a minimum at  $r_{\text{min}}$  such that

$$r_{\text{min}}^2 = \frac{\Omega(0,z)}{d^2 \Omega(0,z)} \left( 1 - \sqrt{1 - \frac{8 W_0}{\Omega^3(0,z)} \frac{d^2 \Omega(0,z)}{dz^2}} \right),$$

which in the "superadiabatic" limit

$$\frac{8 W_0}{\Omega^3(0,z)} \frac{d^2 \Omega(0,z)}{dz^2} \ll 1,$$

reduces to

$$r_{\text{min}} = \frac{2 \sqrt{W_0}}{\Omega(0,z)}, \quad \text{i.e. } B(0,z) r_{\text{min}} = \text{const.}$$

A laminar flow (generalized Brillouin regime) is obtained when every electron trajectory follows the bottom of such a potential valley (line C Fig. 5).

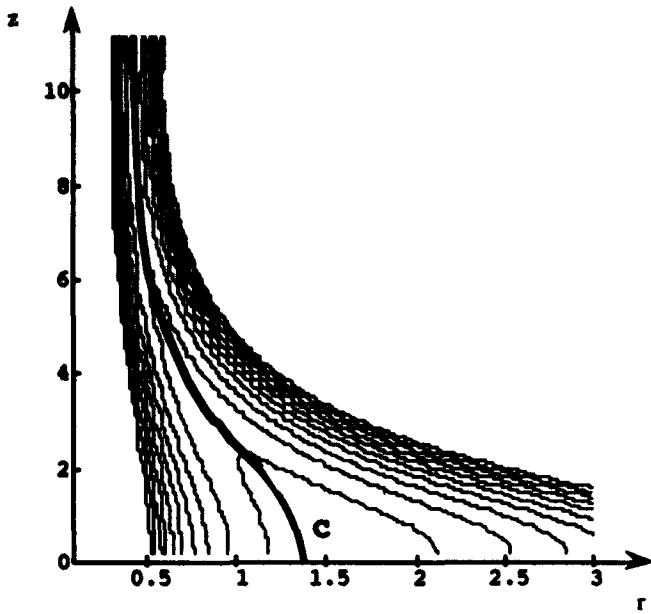


Fig. 5

The corresponding requirements are:

i) 
$$r_0 = r_{\min}(z=0),$$

$$\omega_0(r_0) = \frac{e}{2m} B_z \left( \frac{r_0}{\sqrt{2}} \right),$$

$$n(r_0) = \frac{\epsilon_0 m}{e^2} \frac{\Omega^2(0,0)}{2} \left( 1 - \frac{r_0^2}{\Omega(0,0)} \frac{d^2 \Omega(0,0)}{dz^2} \right)$$

and since

$$\Omega^2(r_0,0) = \Omega^2(0,0) \left( 1 - \frac{r_0^2}{2\Omega(0,0)} \frac{d^2 \Omega(0,0)}{dz^2} + \dots \right).$$

The Brillouin matching  $\omega_p^2 = \frac{\Omega^2}{2}$  holds only on the beam axis.

ii) the ratio of initial radial vs longitudinal velocities has to be carefully optimized.

These initial beam conditions (longitudinal and angular beam velocity for each beam radius) added to the  $\Phi_0 = 0$  Busch condition allow a favourable compression mode of electron beams in inhomogeneous axisymmetric magnetic fields (Fig. 6).

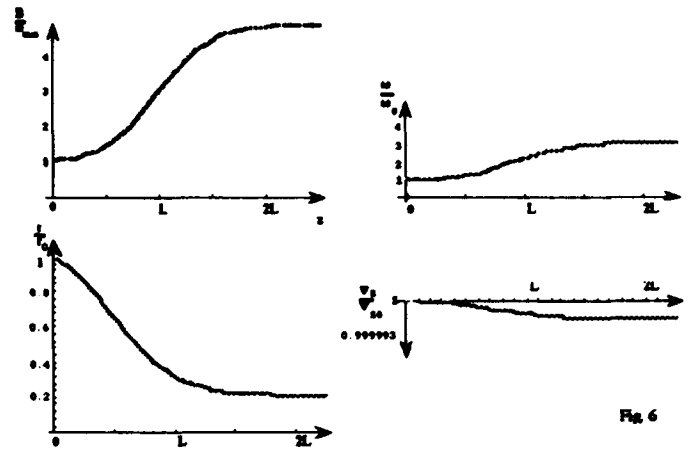


Fig. 6

### III. CONCLUSION

Although the better way to transport electron beams with space charge in a constant magnetic field is to use a constant profile density beam in the Brillouin regime (rigid rotator conditions), the laminarity of such a beam is not conserved along an increasing field. Looking then for laminarity conservation, we have shown that suitable conditions are  $\Phi_0 = 0$  for every electron trajectory at the initial field increase, a parabolic density beam profile, an inhomogeneous rotating beam and an adiabatic magnetic field increase.

#### References:

R.C. Davidson, in: *The Physics of Nonneutral Plasmas*, Addison Wesley (New-York, 1990)

J.D. Lawson, in: *The Physics of Charged-particle Beams*, Oxford (England, Oxford, 1977) § 2

L. Brillouin, *Phys. Rev.* 67 (1945) 260

E.D. Donets, *IEEE Trans. Nucl. Science* 23 (1976) 897

R.E. Marrs, M.A. Levine, D.A. Knapp and J.R. Henderson, *Phys. Rev. Lett.* 60 (1988) 1715

H. Busch, *Annalen der Physik* 81 (1926) 974

E. Durand, *Electrostatique et Magnétostatique*, Masson (France, Paris, 1953)

G. Giardino, *Etude de réalisation d'une sources d'ions du type super EBIT*, Doctorate thesis Université Paris 7 (France, Paris, 1992)

# Choice of Hexapole Parameters for ECR Ion Source

V. P. Kukhtin, E. A. Lamsin, Yu. P. Severgin, S. E. Sytchevsky  
D. V. Efremov Scientific Research Institute of Electrophysical Apparatus  
189631, St.-Petersburg, Russia

## Abstract

Some results of optimization of NdFeB hexapole parameters, carried out on the base of analytical and numerical calculations for a 14 GHz compact ECR ion source are presented. On providing the required value and distribution of magnetic field it has been enabled to minimize the magnetized volume of the hexapole. The number of bars and outer radii of Halbach hexapole magnetic rings at fixed inner radius, defined by outer radius of the plasma chamber, have been varied.

## I. INTRODUCTION

At present, in ion beam physics a considerable progress is seen. It is directly attributed to the development and construction of ECR ion sources with the operational principle based on ions extraction from hot electron plasma heated by electron-cyclotron resonance to the temperature necessary for the generation of multicharged ions of the working substance.

For stable plasma confinement a magnetic field of "minimum  $B$ " configuration, increasing to all sides from the region occupied by the plasma, is used. Such field configuration in the ion source results from the superposition of the fields produced by coaxial coils and a multipole structure. Usually, a hexapole, made of permanent SmCo or NdFeB magnets, is employed as a multipole structure. The hexapole produces magnetic field increasing in radial direction. A coil system is a simple mirror trap with the mirror ratio of 1.5-2 and provides field increase in the axial direction.

Lack of the axial symmetry in the magnet system necessitates the 3-dimensional calculations of the hexapole field, in particular, the identification of the character of edge fields distribution because of probable appearance of the spurious resonances in the area of the ion beam extraction and RF power input.

This paper presents the investigation and optimization results for the permanent magnet hexapole for the ECR source of multicharged ions at 14 GHz microwave frequency, corresponding to the 0.5 T resonance magnetic field.

## II. OPTIMIZATION OF HEXAPOLE PARAMETERS

The hexapole represents a set of segmented magnet rings, whose magnetization vector  $M$  lies in the plane perpendicular to the longitudinal axis. Continuous law of the magnetization distribution over the ring in the azimuthal direction, corresponding to the ideal hexapole case, is defined as

$$M = M_0 (e_\phi \cos 3\phi - e_r \sin 3\phi) ,$$

where  $e_\phi$ ,  $e_r$  are the orthonormal basis of the polar system of coordinates. In an actual construction it is approximated with a polyline in accordance with the number of segments assembled of a homogeneously textured material.

For the case of an ideal hexapole with a given inner radius  $R_1$  and outer radius  $R_2$ , magnetic induction dependency upon the coordinates in presentation  $B = H + 4\pi M$ , where  $H$  is the magnetic field strength, is the following:

$$B = \begin{cases} \frac{6\pi M_0 (R_1^2 - R_2^2) r^2}{R_1^2 R_2^2} (e_r \sin 3\phi + e_\phi \cos 3\phi) , & 0 \leq r < R_1 \\ 2\pi M_0 \left[ 3 \left( \frac{r^2}{R_1^2} - 1 \right) e_r \sin 3\phi + \left( \frac{3r^2}{R_1^2} - 1 \right) e_\phi \cos 3\phi \right] , & R_1 \leq r \leq R_2 \\ 0 , & R_2 < r \end{cases}$$

Simple analysis of these expressions permits to make the following conclusions:

- Magnetic induction in the hexapole aperture ( $r < R_1$ ) is  $B \sim r^2$ ;
- In the case of  $R_2 > \sqrt{3}R_1$ , near to the points  $r = R_1$ ,  $\phi = \frac{\pi k}{3}$ ,  $k = 0, 1, \dots, 5$ , a working point on the magnetization curve  $B = B(H)$  lies in the 3-rd quadrant. For the contemporary magnet materials it can produce the unwanted effects of the hexapole inner layers demagnetization by outer layers.
- Neglecting the demagnetization effects, maximum probable induction in the hexapole aperture on its inner surface is  $B_S = B_{\max} = 1.5 B_0$ , where  $B_0 = 4\pi M_0$  is the residual induction. In a particular case at  $R_2 = \sqrt{3}R_1$ ,  $B_S = B_0$ .

For the analysis of the hexapole edge fields, the 3-dimensional calculations have been done. The program complex DIAMOND has been developed for the calculation of permanent magnet systems.

Table 1: Dependency of the magnetic field on the number of segments

Number of sectors, $N$	12	18	24	2400
$B_S/B_0$	0.8696	0.9404	0.9662	1.0000

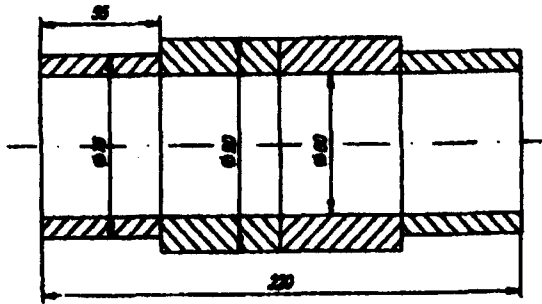


Figure 1: The longitudinal cross-section of the hexapole for the ECR ion source

Design optimisation of the hexapole with the specified length and radius  $R_1$ , determined by the ionisation chamber outer radius and length, consists in the variation of  $R_2$ -radii and the number of magnet rings segments. As a criterion, the efficiency of the permanent magnet material use was considered on condition that the requirements for the magnetic field magnitude and profile distribution were kept. The table 1 gives the dependency on the number of segments of the magnetic field value, reduced to the surface value  $B_S = \left(\frac{R_1}{r_s}\right)^2 B_0$ , for the ratio  $R_2 = \sqrt{3}R_1$  and  $r_s = 0.75 R_1$ .

The number of segments  $N = 18$  seems to be optimal in technological aspect. Fig.1 shows schematically the longitudinal cross-section of the accepted hexapole construction for the ECR source of multicharged ions. The hexapole is composed of 4 rings of equal length with the  $N = 18$  segments made of  $NdFeB$  magnets with the residual induction of  $B_0 = 10.5$  kGs. The outer diameter of the extreme rings can be reduced proceeding from the plasma stability conditions. The magnetic field distribution for the hexapole aperture in the longitudinal direction is shown in Fig.2 as a function of radius.

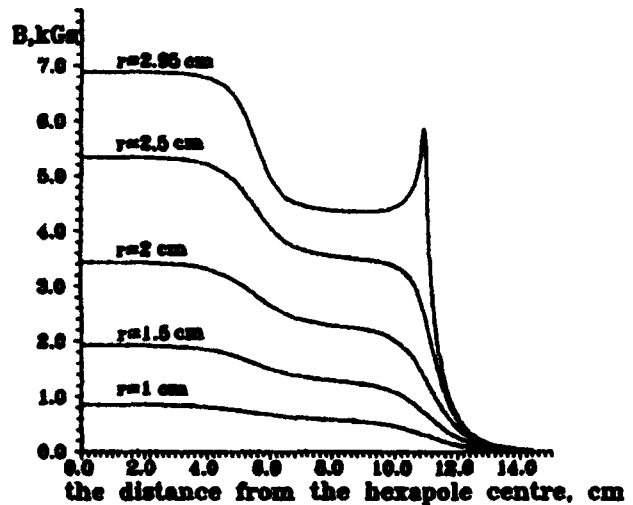


Figure 2: The magnetic field distribution in the longitudinal direction

# Stripping Efficiencies for 277 MeV/amu Gold Beam on Copper Foils\*

Thomas Roser

AGS Department, Bldg. 911B, Brookhaven National Laboratory  
Upton, NY 11973 USA

## Abstract

Stripping efficiencies were measured for 277 MeV/amu Au<sup>33+</sup> ions with Copper foils ranging in thickness from 25 μm to 100 μm. The charge state distribution was analyzed using the beam line magnets of the transfer line between the AGS Booster and the AGS at Brookhaven. The relative charge state abundances were analyzed to find the optimum foil thicknesses for fully stripped Au<sup>79+</sup> and Helium-like Au<sup>77+</sup>. It was also possible to extract electron stripping and pick-up cross sections.

## 1 Introduction

For the first acceleration of Gold ions in the AGS complex to 11 GeV/amu Au<sup>33+</sup> was accelerated in the AGS Booster to 277 MeV/amu and then transferred to the AGS where the final acceleration to the top energy took place[1]. Typically a 50 μm thick Copper foil was used in the transfer line between the Booster and the AGS to strip Au<sup>33+</sup> to Au<sup>78+</sup>. The higher charge state allows acceleration to much higher energy in the AGS but is also required because the relatively bad vacuum in the AGS would lead to excessive beam loss due to stripping by the residual gas. However, it is expected that Helium-like Au<sup>77+</sup> can be accelerated in the AGS without significant losses and, as shown below, can be produced with higher efficiency than fully stripped Au<sup>79+</sup>.

## 2 Measurement of Stripping Efficiencies

By varying two dipole magnets following the stripping foil in transfer line between the Booster and the AGS the relative abundance of the charge states Au<sup>77+</sup>, Au<sup>78+</sup> and Au<sup>79+</sup> could be studied with a multi-wire profile monitor. Measurements were made for 25, 37.5, 50, and 100 μm thick foils. One profile alone did not cover the full charge state distribution. Therefore, several profiles had to be taken with different settings for the analyzing magnet. The profiles for different magnet settings were then combined by fitting all profiles with a single distribution made up from three gaussians corresponding to the three charge

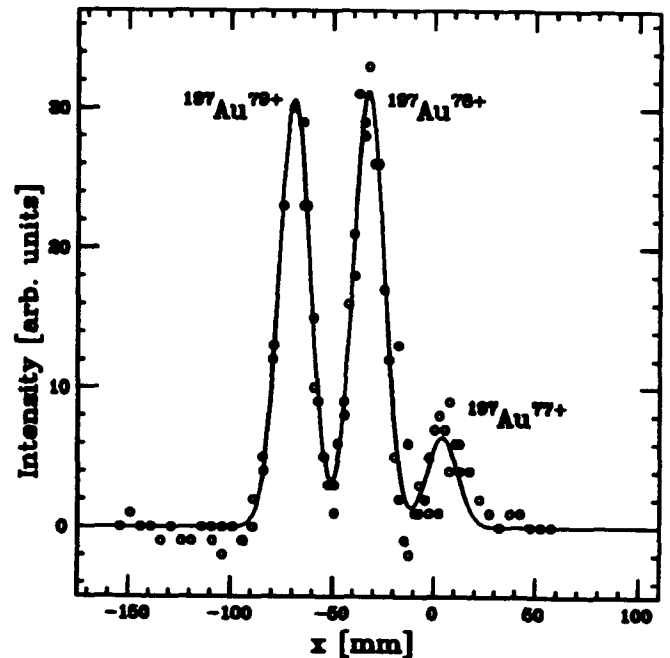


Figure 1: Fit to the charge state distribution of the measurements with the 50 μm thick Copper foil.

states 77+, 78+, and 79+. The gaussian distributions all had the same width and were separated by equal distances. A typical result is shown in Figure 1 and Table 1 gives the fitting parameters for the four foil measurements.

From the variation of the peak position of charge state 77+ with the foil thickness one can extract the energy loss in the Copper foil of  $99 \frac{\text{MeV/amu}}{\text{g/cm}^2}$ . The expected value obtained from the Bethe-Bloch equation[2], which leads to the scaling law

$$\left. \frac{dE}{dx} \right|_{Axz} = \frac{Z^2}{A} \times \left. \frac{dE}{dx} \right|_{proton} \left( p = \frac{pX}{A} \right), \quad (1)$$

is  $80 \frac{\text{MeV/amu}}{\text{g/cm}^2}$ , in good agreement with the measured value. The total energy loss for the 100 μm foil was therefore about 9 MeV/amu.

The increase of the width of individual charge state peaks is due to multiple scattering in the foil which leads to an increase of the divergence and of the energy spread

\*Work performed under the auspices of the U.S. Department of Energy

Foil Thickness [ $\mu\text{m}$ ]	25	37.5	50	100
Center of 77+ Peak [mm]	$22.6 \pm 0.2$	$7.2 \pm 0.2$	$3.9 \pm 0.2$	$-18.7 \pm 0.3$
Width of Peaks [mm]	$8.2 \pm 0.3$	$9.1 \pm 0.2$	$10.7 \pm 0.3$	$13.6 \pm 0.4$
Abundance of 77+ [%]	$51 \pm 5$	$13 \pm 1$	$9 \pm 1$	$4 \pm 9$
Abundance of 78+ [%]	$40 \pm 5$	$44 \pm 1$	$46 \pm 1$	$42 \pm 4$
Abundance of 79+ [%]	$10 \pm 1$	$44 \pm 1$	$45 \pm 1$	$54 \pm 5$

Table 1: Fitting parameters for the four foil measurements

of the beam. In gaussian approximation the multiple scattering adds in quadrature to the initial beam width which results in the following dependency of the beam width  $\sigma$  on the foil thickness  $d$ :

$$\sigma = \sqrt{\sigma_0^2 + \alpha d} \quad (2)$$

The result of a fit is  $\sigma_0 = 4.8 \text{ mm}$  and  $\alpha = 1.7 \frac{\text{mm}^2}{\mu\text{m}}$ . The contribution to  $\alpha$  from increased divergence based on the gaussian approximation to Moliere's theory[3] is only  $0.92 \frac{\text{mm}^2}{\mu\text{m}}$ , where we used the calculated projection factor of  $9.8 \frac{\text{mm}}{\text{mrad}}$  for the beam transport between foil and monitor. This suggests that half of the increase in the beam width is due to increased energy spread.

Clearly the foil leads to a significant beam emittance blow-up of up to a factor of 8. A more optimized situation should include a thinner foil, as discussed below, and a smaller beam spot at the foil.

### 3 A Simple Model

The relative abundance of the three charge states can be understood within the framework of a simple model if we assume that after a short distance  $d_0$  all electrons except the K shell electrons are stripped off. Beyond this initial stripping foil thickness the relative abundances of the three charge states are then determined solely by single electron pick-up and stripping between the three charge states 77+, 78+, and 79+[4]. This can be described by a set of coupled differential equations:

$$\frac{d}{dx} \begin{pmatrix} r_{79} \\ r_{78} \\ r_{77} \end{pmatrix} = \begin{pmatrix} -p_1 & s_1 & 0 \\ p_1 & -(s_1 + p_1) & s_2 \\ 0 & p_2 & -s_2 \end{pmatrix} \begin{pmatrix} r_{79} \\ r_{78} \\ r_{77} \end{pmatrix} \quad (3)$$

where  $r_{79}$ ,  $r_{78}$ , and  $r_{77}$  are the relative abundances as listed in Table 1.  $s_1$  and  $s_2$  are stripping probabilities for  $78 \rightarrow 79$  and  $77 \rightarrow 78$ , respectively, whereas  $p_1$  and  $p_2$  are the pick-up probabilities for  $79 \rightarrow 78$  and  $78 \rightarrow 77$ , respectively. The system of linear differential equations can easily be solved. The eigenvalues are:

$$\begin{aligned} \lambda_1 &= 0 \\ \lambda_2 &= \frac{a - (p_1 + p_2 + s_1 + s_2)}{2} \\ \lambda_3 &= \frac{-a - (p_1 + p_2 + s_1 + s_2)}{2} \end{aligned} \quad (4)$$

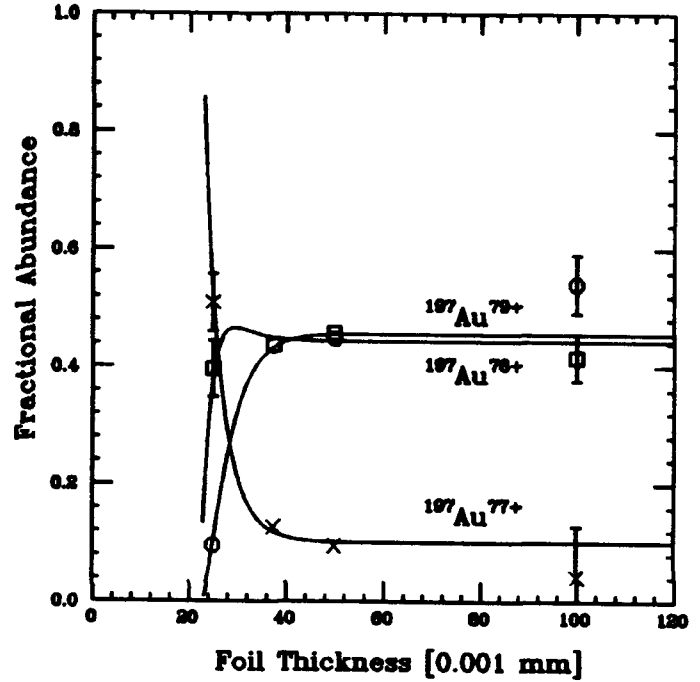


Figure 2: Relative charge state abundance vs. foil thickness. The  $\text{Au}^{79+}$ ,  $\text{Au}^{78+}$ , and  $\text{Au}^{77+}$  abundances are shown as circles, squares and crosses, respectively, together with the model calculations. The model is based on rate equations between these three charge states only.

with

$$a^2 = p_1^2 + p_2^2 + s_1^2 + s_2^2 - 2p_1p_2 + 2p_1s_1 + 2p_2s_1 - 2p_1s_2 + 2p_2s_2 - 2s_1s_2$$

A fit to the data is shown in Fig. 2 and gives the following results:

$$\begin{aligned} d_0 &= 22.4 \pm 0.5 \mu\text{m} \\ s_1 &= 0.20 \pm 0.04 \mu\text{m}^{-1} \\ s_2 &= 0.27 \pm 0.07 \mu\text{m}^{-1} \\ p_1 &= 0.19 \pm 0.04 \mu\text{m}^{-1} \\ p_2 &= 0.06 \pm 0.02 \mu\text{m}^{-1} \end{aligned} \quad (5)$$

This simple model describes the dependency of the abundances on foil thickness very well, which is reflected in a confidence level of 40% of the  $\chi^2$  distribution. For a very

thick foil these probabilities result in asymptotic abundances of

$$\begin{aligned} r_{77} &= 10\% \\ r_{78} &= 44\% \\ r_{79} &= 46\% \end{aligned} \quad (6)$$

The probabilities calculated above can be used to determine absolute cross sections:

	This experiment	Predicted
$\sigma(78 \rightarrow 79)$	$(24 \pm 5) \times 10^{-21} \text{cm}^2$	$9 \times 10^{-21} \text{cm}^2$
$\sigma(77 \rightarrow 78)$	$(32 \pm 8) \times 10^{-21} \text{cm}^2$	$22 \times 10^{-21} \text{cm}^2$
$\sigma(79 \rightarrow 78)$	$(22 \pm 5) \times 10^{-21} \text{cm}^2$	$12 \times 10^{-21} \text{cm}^2$
$\sigma(78 \rightarrow 77)$	$(7 \pm 2) \times 10^{-21} \text{cm}^2$	$6 \times 10^{-21} \text{cm}^2$

The predicted cross sections are based on the relativistic Bethe-Bloch theory[2] for the stripping cross sections and on an extrapolation of eikonal calculations of non-radiative-capture for a Xe projectile on a Cu target[5]. Note that the prediction for the contribution of radiative capture is a factor of 10 smaller for a heavy target such as Cu.

## 4 Conclusion

This analysis shows that, even with this relative high energy beam, it is possible to produce Helium-like  $\text{Au}^{77+}$  ions with high efficiency. This can be achieved with a thin  $22 \mu\text{m}$  thick foil which also introduces only minimal emittance growth.

## References

- [1] L. Ahrens et al., Proc. of the XV<sup>th</sup> Int. Conf. on High Energy Accelerators, Int. J. Mod. Phys. A (Proc.Suppl.) 2A, 109 (1993)
- [2] H.A.Bethe, Ann.Phys. (Leipzig) 5, 325 (1930); C.Moller, Ann.Phys. (Leipzig) 14, 531 (1932)
- [3] W.T.Scott, Rev.Mod.Phys. 35, 231 (1963)
- [4] H.Gould et al., Phys.Rev.Lett. 52, 180 (1984)
- [5] W.E.Meyerhof et al., Phys.Rev. A 32, 3291 (1985)

# Management of High Current Transients in the CWDD Injector 200 kV Power System\*

John A. Carwardine, Geoff Pile, AEA Technology, Culham Laboratory, Abingdon, England  
Thomas E. Zinneman, Argonne National Laboratory, Argonne, IL

## Abstract

The injector for the Continuous Wave Deuterium Demonstrator is designed to deliver a high current CW negative deuterium ion beam at an energy of 200 keV to a Radio Frequency Quadrupole [1]. The injector comprises a volume ion source, triode accelerator, high-power electron traps and low-energy beam transport with a single focusing solenoid. Some 75 Joules of energy are stored in stray capacitance around the high voltage system and discharged in a few microseconds following an injector breakdown. In order to limit damage to the accelerator grids, a magnetic snubber is incorporated to absorb most of the energy. Nevertheless, large current transients flow around the system as a result of an injector breakdown; these have frequently damaged power components and caused spurious behavior in many of the supporting systems. The analytical and practical approaches taken to minimize the effects of these transients are described. Injector breakdowns were simulated using an air spark gap and measurements made using standard EMC test techniques. The power circuit was modeled using an electrical simulation code; good agreement was reached between the model and measured results.

## I. INTRODUCTION

High current ion injector systems have frequently suffered from reliability problems associated with grid conditioning of the dc accelerator. As requirements head towards higher ion currents, higher duty factors, and increased energies, the reliability problems have become more evident and seemingly more difficult to overcome.

During initial testing of the injector system at Culham Laboratory, reliability problems occurred when operating above 150 kV, with both power and control circuits being frequently damaged. A program was initiated to solve these problems after the system was installed at Argonne National Laboratory. The nature of these problems are now better understood, and hardware modifications have been implemented to improve reliability. The system is now operating routinely at and above the design energy of 200 keV. In this paper, the High Voltage Power Supply (HVPS) is used to illustrate techniques and solutions that were implemented. These same techniques and solutions were also used on other subsystems of the injector.

## II. TEST METHODOLOGY

When a breakdown occurs, energy stored in stray capacitance of the high voltage circuit is discharged, exciting resonances in the low megahertz range. The result is a radio frequency transient of several hundreds of amperes flowing around the power circuit, generating huge RF voltages across stray inductances and coupling into all parts of the system. The currents are so large that even very weakly coupled circuits can be catastrophically affected.

*Bulk-Current Measurement* and *Bulk-Current Injection* are used in Electromagnetic Compatibility (EMC) testing to measure conducted emissions and conducted susceptibility of equipment [2]. It has been established in previous tests at Culham and in similar tests at JET [3] that conducted interference was by far the most significant problem on this equipment, even though radiated levels in excess of 140 dB $\mu$ V have been measured. *Bulk-Current* techniques were used to measure RF currents flowing in power and control circuits during actual breakdowns and simulated breakdowns at low voltage to allow measurements within the high voltage equipment, and quantify the level of susceptibility of various equipment. In order to provide a consistent test scenario, an air sparkgap was used to simulate injector breakdowns.

Figure 1 shows the main components of the injector high voltage power circuit. Transient currents are shown for a sparkgap setting of 56 kV; peak breakdown currents are in amperes. The current transient is principally a damped sinusoid at 1 MHz lasting approximately 6  $\mu$ s, produced as stray capacitance in the high voltage isolation transformer and the high voltage feedthrough are discharged through the busbar system.

Surprisingly large currents were measured in the high voltage power supply switched-mode electronics (HV Controller). These can be explained when it is realized that considerable voltages are generated along the machine *ground* busbar. The busbar between the machine *star-point* and the HVPS 0v connection had an inductance of 15  $\mu$ H. At 1 MHz, the impedance of this connection was 94  $\Omega$  and could, therefore, be expected to develop approximately 20 kV across it. This voltage then appeared as a differential across the HVPS isolation transformer, which coupled the transient by way of stray capacitance and an imperfect primary screen.

\*Supported Under U.S. Government Contract No. W31 RPD-2-D4072.

Significant transients (up to one ampere) were measured on control cables between the injector and the control room, even though they are DC isolated. However, for RF, these cables are in parallel with the busbar connecting the machine star-point to building ground and, therefore, carry a portion of the feedthrough discharge currents.

### III. CIRCUIT ANALYSIS

A simplified equivalent circuit of the injector high voltage power system is shown in Figure 2. Most of the capacitance values were obtained by measurement, whereas the inductance values were calculated.

An analog circuit analysis program for personal computers, Micro-Cap IV [4], was used to generate current and voltage waveforms for various nodes of the circuit. For comparison, generated waveforms are shown in Figure 2 at the same locations as the measured waveforms in Figure 1. Both the measured and calculated waveforms decayed exponentially, reaching equilibrium in 6-10  $\mu$ s. Overall, the analysis agreed well with reality, although peak values of the calculated waveforms were generally higher than those of the measured waveform. One possible reason is that small resistive components were not included in the model except around the HV controller.

A major component of the HV circuit is the magnetic snubber. This device is designed to absorb much of the available energy generated during an arc discharge. The energy is dissipated by means of eddy current losses in a transformer core. The CWDD snubber is similar to the snubber developed by Lawrence Berkeley Laboratory [5]. In the analysis, the snubber has been represented by a resistor in parallel with an inductance.

The Berkeley paper assumes a nonoscillatory current suggesting that the value of inductance,  $L$ , is so large that it can be neglected, and that the resistance is a function of time. For large values of  $L$ , breakdown transients should decay exponentially, similar to overdamped or critically damped circuits. However, observed transients on the CWDD injector are oscillatory, similar to that of an underdamped circuit. Attempts to measure the snubber inductance produced values in the 10 to 40  $\mu$ H range. Using the lower value of  $L$  in the circuit analysis resulted in calculated waveforms more closely resembling measured waveforms than when using higher values.

### IV. SOLUTIONS

It became clear that the grounding system must be modified to minimize impedances and, hence, voltage drops. To reduce currents in the HV controller, the HVPS elements must all be connected to the same ground point. Breakdown current paths must be localized as much as possible, to reduce coupling to other circuits.

An existing aluminum skin covering the walls and floor of the high voltage areas offered a low impedance ground system and was close to an ideal *coaxial* arrangement. Power system ground connections were removed from the bus bar and connected to this skin. Since this skin is so wide, the limiting factor in minimizing ground impedance became the connections from the equipment to the skin. In addition to ground system modifications, each subsystem was modified to improve internal grounding for radio frequencies, and filtering was installed to shunt transient currents to ground.

Sparkgap testing was repeated at 56 kV and then at 200 kV. Unwanted currents had been reduced by at least a factor of four, and in the case of the busbar currents to ground, a factor fifty improvement had been made. Indeed, at 200 kV, the HVPS currents are now lower than previously measured at 56 kV.

Modeling of the new arrangement was made in order to predict improvements in unwanted currents. Accurate modeling was found to be more difficult since the new ground system impedance was difficult to calculate. However, the model did predict improvements comparable to those seen when sparkgap tests were performed.

### V. SUMMARY

Conventional power system approaches are clearly inadequate when designing high voltage systems for today's injectors. Further considerations are necessary to successfully manage the transients resulting from dc accelerator breakdowns.

Breakdown transients have been measured on the CWDD injector and their effects are now understood. Dramatic improvements have been made in the reliability as a result of modifications, such that the high voltage systems now operate more reliably at 200 kV than previously at any voltage.

The system's behavior has been modeled to first order using relatively simple circuits. These proved helpful in understanding failures caused by breakdowns. Proposed modifications were tested on the model before implementation on the real system. Overall improvements predicted by the model compared favorably with those obtained in practice.

The effect of the magnetic snubber on a *resonant* circuit needs further work. At 1 MHz, the CWDD snubber is clearly less effective than expected—far less energy is dissipated, and peak currents appear to be limited as much by stray inductance as by the snubber itself.

Experience on CWDD has shown that with proper management of transients, a high level of reliability can be achieved on high voltage, high power injector systems.

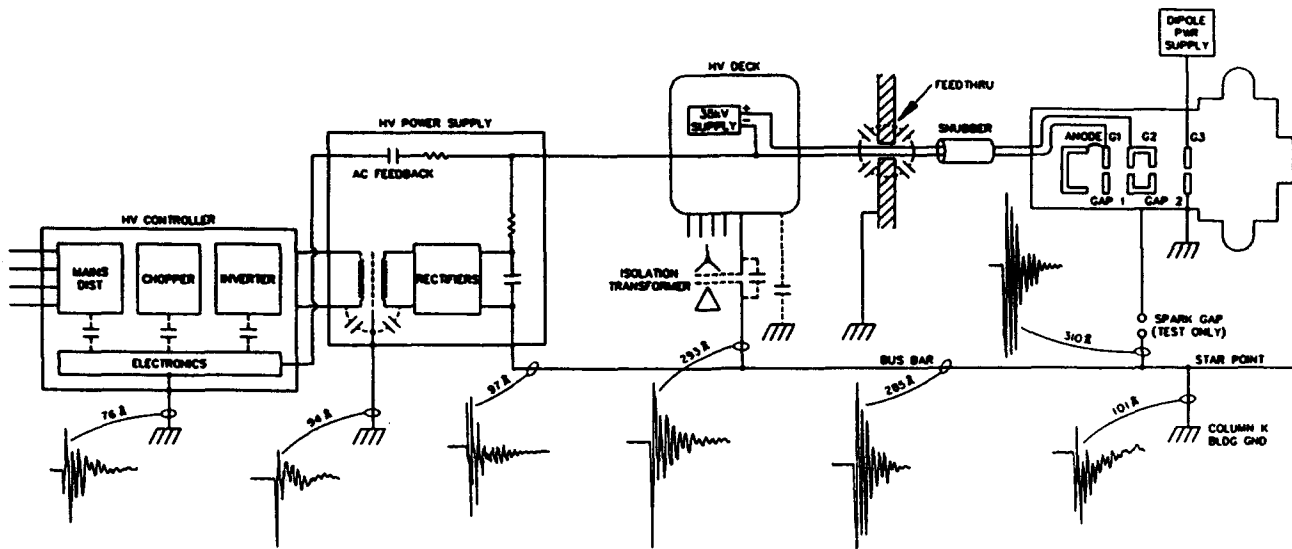


Figure 1. Injector High Voltage Power Circuit

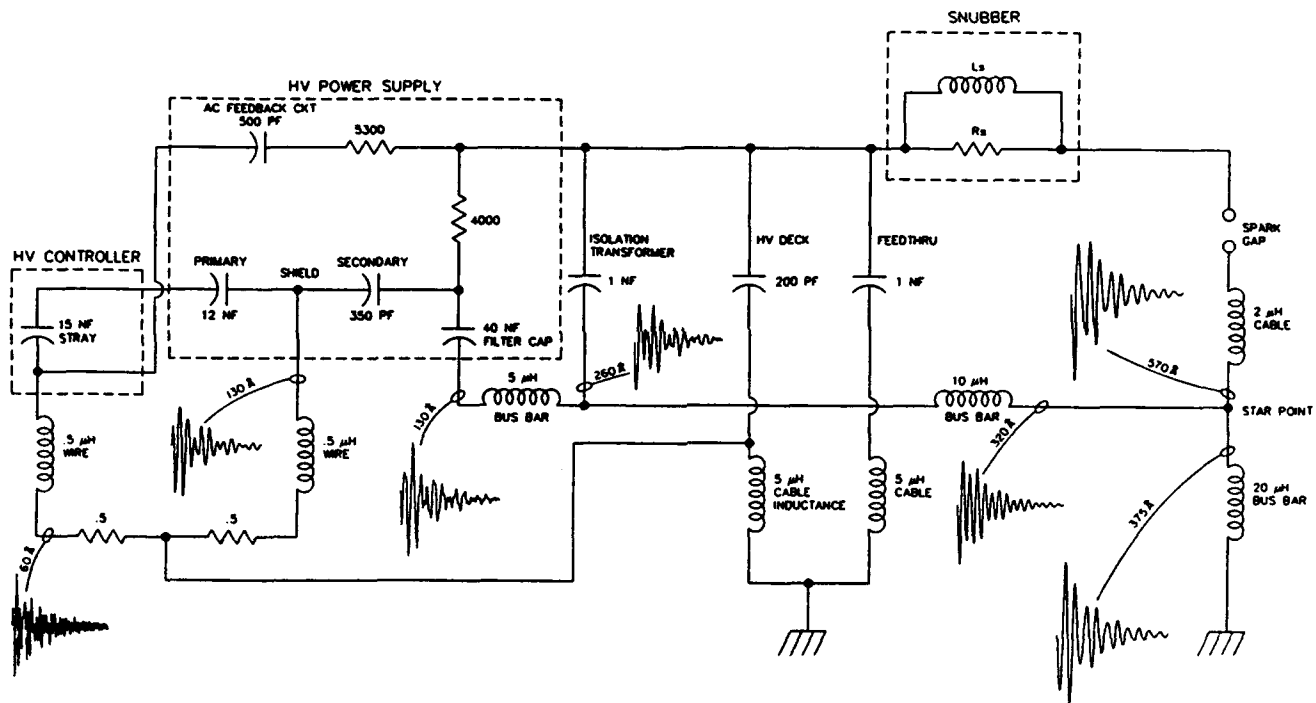


Figure 2. Equivalent Circuit of Injector High Voltage Power Circuit

## VI. ACKNOWLEDGMENTS

The authors recognize and appreciate contributions made by other members of the Argonne, Culham, and Grumman CWDD team to this effort.

## VI. REFERENCES

- [1] P. Den Hartog et al., "Commissioning Status of the Continuous Wave Deuterium Demonstrator," Proceedings of the 1993 IEEE Particle Accelerator Conference, Washington, D.C. (May 1993).
- [2] MIL-STD-462D, "Electromagnetic Interference Characteristics, Measurement of" (U. S. Dept. of Defense, Jan. 1993).
- [3] J. A. Carwardine, "Upgrade of the Neutral Injection Test Bed Power Supplies for Electromagnetic Compatibility at 160 kV," JET Report No. JET-1R(89)04.
- [4] Micro-Cap IV, Electronic Circuit Analysis Program, Spectrum Software.
- [5] J. H. Fink et al., "Analysis and Application of a Transformer Core that Acts as an Arc Snubber," IEEE Transactions on Plasma Science, Vol. PS-8, No. 1, March 1980.

# Design and Results of the Radio Frequency Quadrupole RF System at the Superconducting Super Collider Laboratory

J. Grippe, E. Marsden, and O. Marrufo  
Superconducting Super Collider Laboratory\*  
2550 Beckleymeade Ave., Dallas, TX 75237 USA

A. Regan, D. Rees, and C. Ziomek  
Los Alamos National Laboratory

## Abstract

The Superconducting Super Collider Laboratory (SSCL) and the Los Alamos National Laboratory (LANL) entered into a joint venture to design and develop a 600 kW amplifier and its low-level controls for use in the Radio-Frequency Quadrupole (RFQ) accelerating cavity of the SSC. The design and development work has been completed. After being tested separately, the high power amplifier and low level RF control system were integrated and tested on a test cavity. Results of that tests are given. Tests were then carried out on the actual RFQ with and without the presence of the accelerated beam. Results of these tests are also given, along with the phase and amplitude information.

## I. INTRODUCTION

The RFQ cavity requires 225 kW of power at each of two RF input ports at a frequency of 427.617 MHz. To provide this power with an adequate amount of safety margin and enough drive to ensure a fast cavity fill time, a 600-kW amplifier was designed and built. The requirements [1] placed upon the amplifier are as shown in Table 1.

Table 1  
RFQ Amplifier Requirements

Operating Frequency	427.617 MHz
Bandwidth	300 KHz Minimum
Power Output	600 kW peak
Gain	77 dB nominal
Pulse Length	100 microseconds
Pulse Repetition Rate	0-10 Hz
Pulse Droop	1% maximum
Linear Range	<0.5 db within any one hour period
Phase Stability	<10 deg. within any one hour period

The purpose of the low level RF, along with providing the drive power to the amplifier, is controlling the phase and amplitude of the cavity RF. The RF field in the RFQ cavity is to be maintained within 0.5 degrees of the desired phase and 0.5% of the desired amplitude.

A block diagram of the RFQ RF System [2-4] is shown in Figure 1.

\*Operated by the Universities Research Association, Inc., for the U.S. Department of Energy under Contract No. DE-AC35-89ER40486.

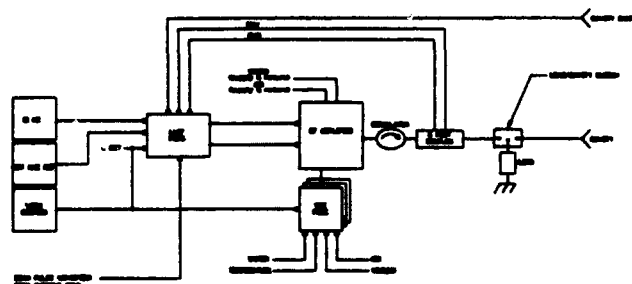


Figure 1. RFQ RF System.

## II. TOPOLOGY

The amplifier consists of three stages of RF amplification. The first stage is a solid-state amplifier which takes the input RF and amplifies it by approximately 48 dB. The intermediate amplifier consists of a cathode-modulated Eimac 8938 Triode, cavity, and a high voltage power supply. The tube is air cooled and has a gain of approximately 15 dB. The final power stage consists of a Burler 4616 tetrode and its associated cavity, a 25 kV anode power supply rated at 2 kW average power output, and the necessary grid supplies. The tetrode operates in Class AB with approximately 5 mA of bias current from the high voltage power supply. At the 600 kW output level the efficiency is approximately 60%.

The low level RF circuitry is VXI based and uses the in-phase (I) and quadrature signal components (Q) or more commonly called an I&Q detection system. The cavity field sample is downconverted to 20 MHz, where a vector detector performs I&Q detection. The resulting I&Q baseband signals are fed to a pair of Proportional Integral Differential (PID) controllers, one for the I signal and another for the Q signal. The setpoints for the I&Q channels are also fed to the PID controllers where the cavity field error signals are generated and processed. The outputs of the I&Q PID controllers are fed to a 20 MHz vector modulator, the output of which is upconverted to the 427.617 MHz operating frequency. The output of the upconverter passes through a fast RF switch and additional amplification before driving the high power amplifier.

Many signals in the low level RF crate are available as analog signals on the module front panels and, once per beam pulse, are monitored through sample and hold circuits which are then sent to slow speed, on board A/D's. Additionally, certain critical analog signals can be remotely selected and fed across the VXI backplane to a twisted pair line driver for remote viewing or fast digitizing. All timing pulses for low level RF

circuitry and the high power amplifier gate are derived on board each VXI module through the use of a programmable timing generator triggered by a single 10 Hz pulse from the Linac timing system.

RF transmission components at the output of the power amplifier consist of a high power circulator to isolate the amplifier from the high reflected power during the cavity fill time, a six-port coupler to provide amplifier reverse and forward power to the low level RF, and a manual high power waveguide switch that can be used to direct the RF energy to a dummy load for test purposes.

### III. TEST RESULTS

Table 2 lists the results obtained when testing the amplifier into a high power water load.

Table 2  
Amplifier Test Results

Gain	77.4 dB
Linear Range	200 to 500 kW
3 dB Bandwidth	900 kHz
1 dB Bandwidth	550 kHz
Maximum Power Output	625 kW
Efficiency	63%

The frequency response data for the amplifier is listed in Table 3. The data is plotted in Figure 2.

Table 3  
Frequency Response

FREQ (MHz)	Po (kW)	Pin (kW)	GAIN (dB)
427.1	228	12.5	71.1
427.2	323	12.5	72.6
427.3	443.2	12.5	74
427.4	546	12.5	74.9
427.5	611.8	12.5	75.4
427.6	620	12.5	75.4
427.7	615	12.5	75.4
427.8	566.5	12.5	75
427.9	498.6	12.5	74.5
428.0	432.2	12.5	73.8
428.1	343.6	12.5	72.9
428.2	261.4	12.5	71.7

Tests of the RF system, LLRF and amplifier are shown in the following figures. Figure 3 illustrates the field in a test cavity without a simulated beam. After initial cavity filling and settling time the phase is controlled to within 0.1 degree and the

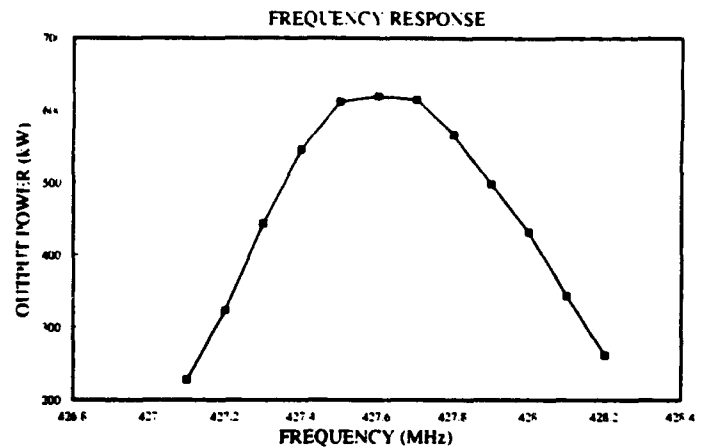


Figure 2. RFQ amplifier.

amplitude is controlled within 0.1%. Figure 4 illustrates the field in the test cavity with simulated beam loading, with both LLRF feedback control and feedforward consisting of a square input pulse to the PID controllers 0.2 microseconds before the beam pulse. The maximum phase variation in this case is 0.2 degrees and the maximum amplitude variation is 0.4%. These tests prove that the SSC RFQ RF system can meet its phase and amplitude performance requirements with a combination of feedback and feedforward in the control system.

The photograph of Figure 5 was taken, open loop, with the RF amplifier delivering 365 kW of power at 427.617 MHz into the RFQ cavity. A 20-milliampere, 2.5-MeV beam was present. The lower trace of the photo shows the high VSWR during the cavity fill time. Immediately after the fill and before the beam arrives, the mismatch of the cavity to the amplifier can be seen. During the beam the improved match is apparent followed by the high reflection at the end of the pulse. The upper trace shows the effect of beam loading on the cavity RF.

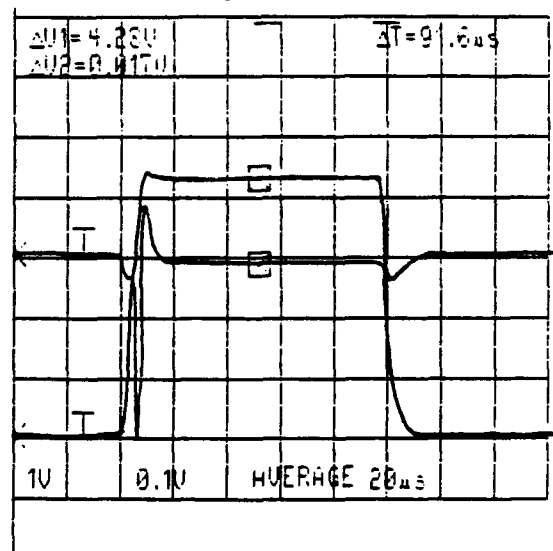


Figure 3. Amplitude (Upper Trace) and Phase (lower trace) of a test cavity without beam loading simulation. Phase 1 degree per division.

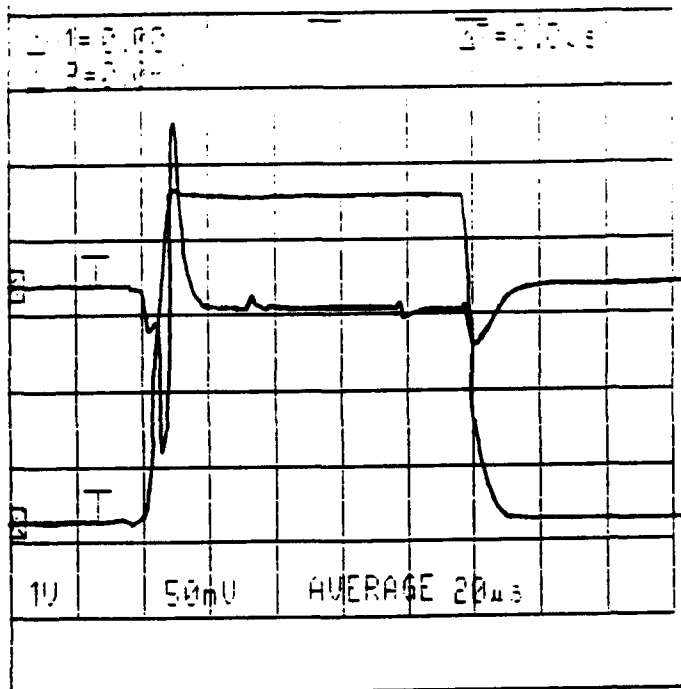


Figure 4. Cavity amplitude (upper trace) and phase (lower trace) of test cavity with beam loading simulation. Feed forward and feedback present. Phase 1 degree per division.

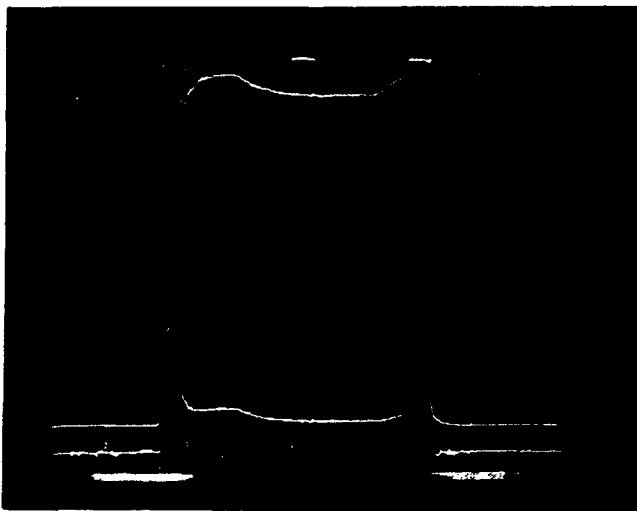


Figure 5. Photograph of amplitude (upper trace) and reflected power (lower trace) taken during 20 milliamperes beam in RFQ cavity. System is running open loop.

#### IV. SUMMARY

From the data taken during the testing of the RFQ RF subsystem it has been shown that the system meets all the design requirements placed upon it. Testing into a test cavity was done by using a 60-dB coupler from the main RF power line since the test cavity was only capable of accepting 2 watts. Testing into the RFQ cavity is ongoing at the SSC central facility. As of this writing the 2.5 Mev, 20 milliampere design goal has been achieved.

#### V. REFERENCES

- [1] Element Specification (Level 3B) For the Linear Accelerator of the Superconducting Super Collider Laboratory, No. E10-000025, July 22, 1991, W.B.S. 1.1.2.1 p. 45.
- [2] R.I. Cutler, et al., "SSC Linac RFQ RF System." Conference proceedings of the 1992 Linear Accelerator Conference, Vol 1, pp. 130-132.
- [3] J.M. Grippe, et al., "The Superconducting Super Collider Linac RF System," Conference Record of the 1992 Twentieth Power Modulator Symposium, pp. 53-56.
- [4] A. H. Regan, et al., "RF System Description for the Ground Test Accelerator Radio-Frequency Quadrupole," 1992 Linear Accelerator Conference Proceedings, pp. 680-682.

# Initial Operation and Beam Characteristics of the UCLA S-band RF Photo-Injector\*

C. Pellegrini, N. Barov, S. C. Hartman, S. Park,  
J. Rosenzweig, G. Travish, R. Zhang

Department of Physics, University of California, Los Angeles 90024

P. Davis, C. Joshi, G. Hairapetian

Electrical Engineering Department, University of California, Los Angeles 90024

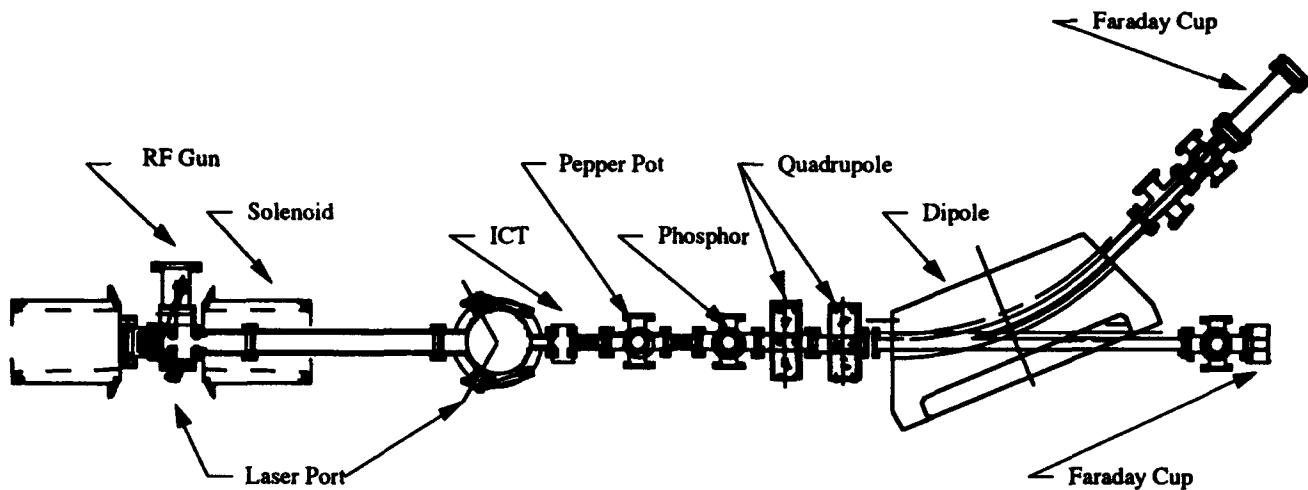


Figure 1.

## Abstract

The UCLA rf photo-injector system has been commissioned(1). All of the sub-components such as the high power rf, pico-second laser, rf photo-injector cavity, diagnostics, and supporting hardware have been tested and are operational. We briefly discuss the performance of the various components since the details of each subsystem are very lengthy. The laser delivers a sub 4 ps pulse containing 0-300 $\mu$ J of energy per pulse. The photo-injector produces 0-3 nC per bunch with an rf induced emittance of 1.5  $\pi$ (mm-mrad).

## I. INTRODUCTION

We report the initial results of the operation of the UCLA 4.5 MeV Photocathode RF gun. This electron source is part of a 20 MeV compact electron linac described before(1). It will be used for studies of the interaction of relativistic beams, plasmas and the generation of coherent radiation. All the components of this system have been built and tested. Full assembly will be completed during the fall of 1993. Our initial work has been dedicated to a characterization of the photocathode rf gun, which is the electron source for the system. As part of this work we have measured the electron beam emittance and the quantum efficiency of a copper cathode under different conditions. Detailed descriptions of the results of these measurements and the techniques used are reported in other papers presented at this conference. We will limit this

paper to a summarization of the overall performance of the gun and our plans for its' future development. The photocathode rf gun has also been used to study a thin plasma lens(2). This experiment demonstrated electron beam focusing and confirmed theoretical expectations.

## II. ACCELERATOR SYSTEM DESCRIPTION

### A. RF System

The gun is powered by a SLAC XK5 type klystron producing 24 MWatts of rf power with a pulse duration of 4  $\mu$ s. The rf system is driven by a signal produced by a master oscillator clock at a frequency of 38.08 MHz. This signal is multiplied 75 times to produce the klystron operating frequency of 2.856 GHz and is then sent to a 1 kwatt solid state amplifier. The amplifier signal in turn feeds the klystron. This ensures the timing and a feed back loop stabilizes the laser pulse to rf jitter to less than 4 ps.

### B. RF Photo-Injector

The photocathode rf gun is based on the Brookhaven design(3). It consists of a one and a half cell standing wave accelerator producing a beam with an energy up to 4.5 MeV. Producing accelerating gradients of up to 100 MV/m are achieved.

### C. Laser System

The drive laser is a mode locked Nd-YAG oscillator cavity. To compress the pulse the laser is matched into a 500m fiber to produce a frequency chirp. The chirped pulse is then amplified a million times by a regenerative amplifier and

\*Work Supported by SDIO/IST through ONR Grant No. N00014-90-J-1952 and US DOE Grant DE-FG03-92ER-40493

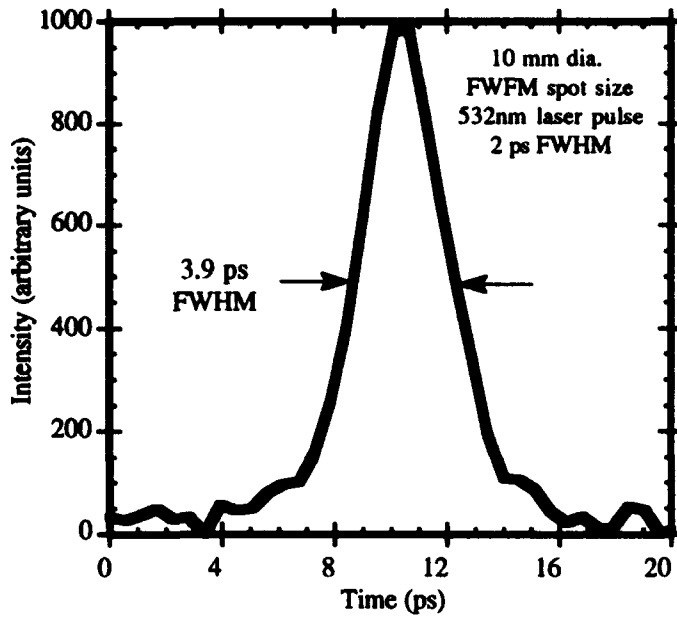


Figure 2.

sent to a grating pair where it is compressed. Once it leaves the compression stage the laser beam is frequency upconverted to green by a KD\*P crystal. Then it is doubled again to UV, 266 nm, by a second frequency doubling crystal. The up conversion efficiency is typically 10%. The laser was measured with a streak camera and is shown in figure 1.

#### D. Diagnostics

The electron beam diagnostics are as follows. The main diagnostics are the phosphor screens which monitor the spot size. An Integrating Current Transformer, ICT, is used to measure the electron beam charge along with faraday cups at various locations. Some of the phosphor screens are floated so that they can double as faraday cups. A dipole is used to

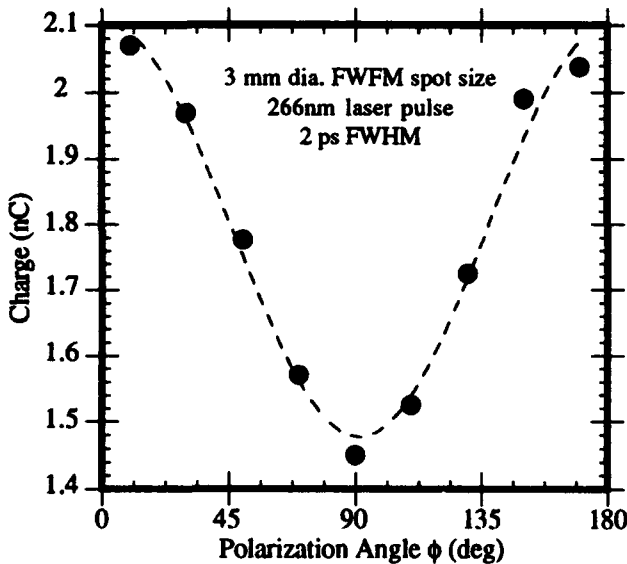


Figure 3.

measure the energy and energy spread of the beam.

## II. QUANTUM EFFICIENCY

### A. Quantum Efficiency Results

The quantum efficiency measurements are described in detail in (4). The quantum efficiency has been measured as a function of input laser energy, illumination angle, and polarization. In the first series of measurements the cathode was initially damaged by over focusing the laser to a small spot size. This produced local melting and damaged the copper cathode surface. The damage limited the possibility of producing a beam with the design spot size of about 3 mm, since most electrons were produced by the damaged area. The resulting effective spot size was about 0.3 mm. This small spot size led to large space charge effects at small charge, so in this series of measurements space charge was always a dominant effect.

Angle of Incidence, Degrees	Polarization	Quantum Efficiency
2	S	$9 \times 10^{-5}$
2	P	$9 \times 10^{-5}$
70	S	$9 \times 10^{-5}$
70	P	$1.3 \times 10^{-4}$

Table 1.

The main results for the damaged cathode quantum efficiency are given in Table 1. One can see that the quantum efficiency depends on the incidence angle and the light polarization. The largest quantum efficiency,  $10^{-4}$ , is obtained for 70 degrees incident angle and P polarized light. The dependence of the quantum efficiency on the polarization angle  $\phi$  is shown in Fig. 3 and can be fitted with a  $\cos^2\phi$  dependence which implies single photon emission.

## III. ENERGY and ENERGY SPREAD

### Dark Current Peak Momentum Fluctuations

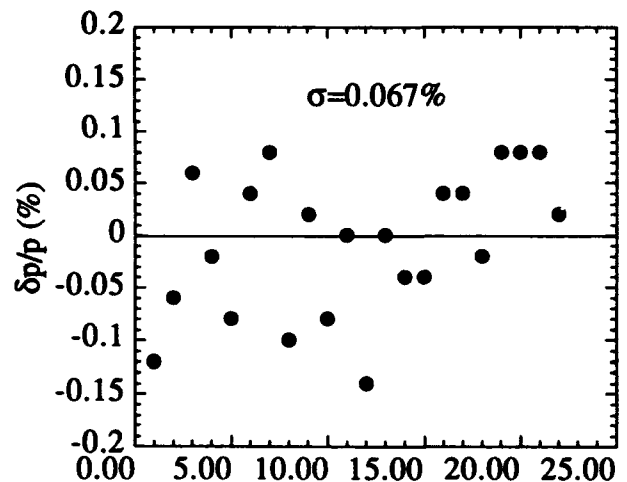


Figure 4.

The time jitter of the laser pulse and the fluctuations in the rf voltage are of deep concern for future FEL experiments. In Fig. 4 we show the fluctuations in the dark current energy end point, showing the level of the rf system fluctuations. In Fig. 5 we show the jitter in peak momentum of the photoelectrons, which includes also the laser pulse jitter. One can see that the resulting rms momentum fluctuation is 0.25% and is due mainly to the residual laser pulse jitter. The dependence of the bunch energy on the initial rf phase is shown elsewhere(5). This dependence shows that the accelerating field in the two cells is unbalanced with a larger field in the full cell. Introducing this unbalance the data can be fitted using the analytical theory of Kim. From the beam energy measurements we can also determine the gun shunt impedance which is evaluated to be 36 M $\Omega$ /m, smaller than the value expected from the Superfish calculations. The beam energy spread measured at low current, 50 pC, is less than 0.2%. However, due to the large space charge effects it increases rapidly with charge, when using the damaged cathode.

#### IV. EMITTANCE

The emittance has been measured(5) using a pepper pot. Measurements at a charge smaller than 50 pC, show an emittance dominated by rf effects with a minimum of 1.5  $\pi$ mm-mrad rms. At larger charge the emittance is dominated by space charge effects, in the case of the damaged cathode and unbalanced gun. These results as well as the results for the energy spread are compatible with the assumption of an initial spot size of 0.3mm radius, rms. The rf photoinjector is clearly a very brilliant electron source, capable of producing beams with time structures determined by the incident laser pulse. Metal cathodes are very robust but put strong requirements on the laser fourth harmonic generation efficiency. Importance of reducing amplitude fluctuations and time jitter is also noted. The photoinjector produces a beam of superior quality as exemplified by the successful plasma lens

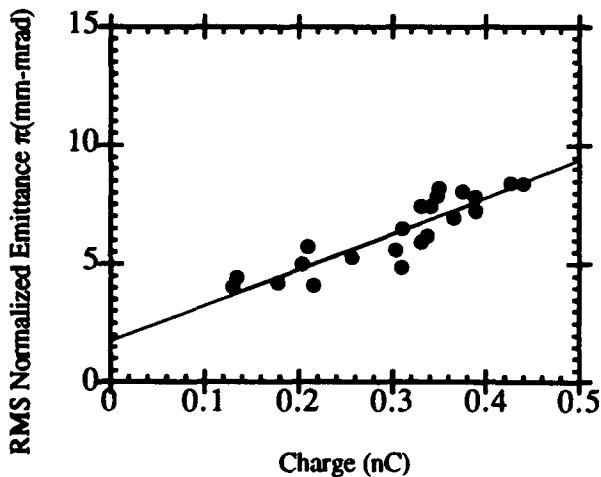


Figure 6.

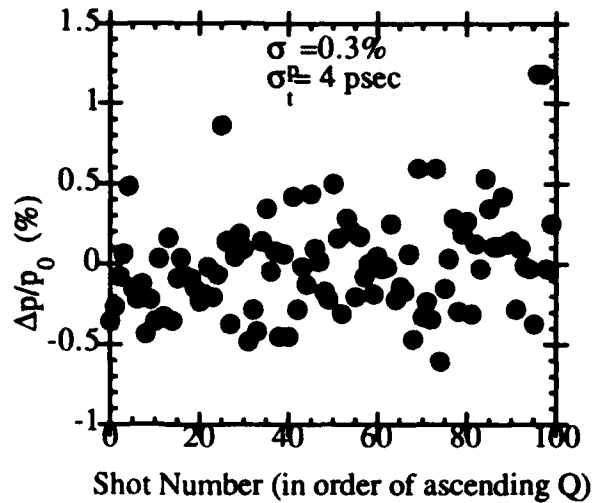


Figure 5.

experiments completed at UCLA.

#### V CONCLUSION

The UCLA photo-injector has been operated successfully. The measurements show that the emittance scales as expected. The important thing to note is that for these set of emittance runs the rf photo-injector had a field imbalance. The filled in the full cell was 1.8 times that in the half cell. This contributed to emittance blowup as did the phosphor screens used to measure the emittance. The phosphor screens were placed onto the beamline at a 45° angle. This created broadening of the line widths

#### References

1. S. C. Hartman et al., Photocathode Driven Linac at UCLA for FEL and Plasma Wakefield Acceleration Experiments, Particle Accelerator Conference Sanfransisco, CA., 1991), pp. 2967.
2. G. Hairapetian et al, Experimental Demonstration of Plasma Lens Focusing, Particle Accelerator Conference Washington, DC., 1993),
3. K. Batchelor et al, European Particle Conference Accelerator Conference Rome, Italy, June 7-12, 1988),
4. P. Davis et al, Quantum Efficiency Measurements of a Copper Photocathode in an rf Electron Gun, Particle Accelerator Conference Washington, DC., 1993),
5. S. C. Hartman et al., Emittance Measurements of the 4.5 MeV UCLA rf Photoinjector, Particle Accelerator Conference Washinton, DC., 1993),

# Conference Author Index

## A

Aas, T. 2967  
 Abbott, S. 3748  
 Abe, I. 3087  
 Abrahamsson, K. 1735  
 Acerbi, E. 1524  
 Ackerman, G. D. 3169  
 Adam, S. R. 3639  
 Adams, F. P. 829, 832, 835, 1039  
 Adamski, J. 2967  
 Adler, R. J. 1306  
 Adney, J. 3745  
 Adolphsen, C. 414, 417, 543, 2019, 3342  
 af Ugglas, 1735  
 Ahrens, L. 3633  
 Ahrens, L. A. 3763  
 Aiello, G. R. 2322, 2367  
 Aiello, R. 2118  
 Aizawa, K. 1468  
 Akai, K. 769, 992, 3450  
 Akbari, H. 2492  
 Akchurin, N. 32  
 Akemoto, M. 1309  
 Akre, J. 1572  
 Alberti, S. 2656, 2690  
 Aleksandrov, A. 3243  
 Alessandria, F. 1524  
 Alexandrov, V. 2042  
 Alimov, A. S. 2059  
 Allen, C. K. 3145, 3648  
 Allen, L. J. 1689, 1691  
 Allen, S. L. 1551, 1554  
 Alley, R. 3045, 3047  
 Alley, R. K. 2978, 3027, 3036  
 Allison, P. 3172  
 Allison, S. 1884, 2106  
 Alton, G. D. 2979  
 Amidei, D. 2199  
 Amiranoff, F. 2450  
 Amiry, A. 173  
 Anami, S. 590, 1163, 1193, 1416, 3087  
 Anamkath, H. 608, 611  
 Anashin, V. 3876  
 Anashin, V. V. 2022  
 Anders, A. 1390  
 Anders, S. 1390  
 Anderson, D. 3745  
 Anderson, D. E. 1354  
 Anderson, K. 3096, 3163  
 Anderson, R. R. 2919  
 Anderson, S. 1421  
 Anderson, T. 2835  
 Andler, G. 1735  
 Ando, M. 1468  
 Andreev, V. A. 3121, 3124  
 Andreev, V. G. 980  
 Andreev, V. V. 297  
 Anerella, M. 2744, 2766, 2790  
 Annala, G. 3808  
 Annala, J. 354  
 Anne, R. 1789, 1792

Anthouard, P. 670, 697  
 Antoine, C. 798  
 Antropov, V. 2042  
 Aoki, T. 2039  
 Aoyagi, H. 2978, 3036  
 Arai, S. 1780, 1783, 1786  
 Arakaki, Y. 41  
 Araki, M. 1518  
 Arbique, G. 827, 3127  
 Arbique, G. M. 2124, 2426, 2986  
 Arbuzov, V. 1226  
 Archie, C. N. 480  
 Arcioni, P. 772, 1524, 1569  
 Arinaga, M. 2292, 3552  
 Arkhipov, O. 2042  
 Arnaudon, L. 44  
 Arnold, D. E. 989  
 Arnold, N. D. 1957, 1960  
 Artiomov, A. S. 2166, 2169  
 Artru, X. 3093  
 Asami, A. 3087  
 Askew, D. R. 1336  
 Assang, A. 2187  
 Asseev, A. A. 315, 318, 320, 322, 324  
 Assmann, R. 44  
 Åström, J. 2068  
 Atkins, W. H. 1669  
 Aurerbach, E. H. 1872  
 Ausset, P. 858  
 Austin, R. H. 2970  
 Averbukh, J. 824  
 Averill, R. 1372, 2054, 2331, 2868, 2871, 2874, 3851  
 Awaji, N. 1515, 1518  
 Ayvazian, H. 1750  
 Azuma, O. 1202

## B

Baartman, R. 3330  
 Baba, H. 959  
 Babenko, E. 2423  
 Baccaglioni, G. 1524  
 Bachman, D. A. 3190  
 Bachmor, R. 1178  
 Badano, L. 32  
 Bagge, L. 1735  
 Baglin, V. 2720  
 Bai, X. 3237  
 Baier, T. 3093  
 Baier, V. N. 3093  
 Baik, K. H. 679  
 Bailey, J. 3757  
 Bailey, R. 1937, 2001, 2013  
 Baiod, R. 2826  
 Baishev, I. S. 3109, 3772  
 Bak, J. 581  
 Bak, J. S. 593  
 Balabin, A. I. 3675  
 Balandin, V. 441, 444, 477  
 Ball, M. 29, 224, 227, 420, 2289, 3745  
 Ball, M. S. 2243, 3536  
 Balleyguier, P. 1136  
 Baltrusaitis, R. M. 2400  
 Band, A. 2240  
 Bane, K. 543, 1445, 3240, 3375  
 Bane, K. L. 596  
 Bane, K. L. F. 3339, 3342, 3432  
 Baptiste, K. 1238  
 Baranovsky, A. E. 682  
 Barbier, M. M. 3102  
 Bardy, J. 670, 697  
 Barklow, T. 2019  
 Barletta, B. 2638  
 Barletta, W. 2010, 3836  
 Barletta, W. A. 775, 1524, 1988, 3817  
 Barlow, D. 1703  
 Barlow, D. B. 2480  
 Barnard, J. 703, 706  
 Barnard, J. J. 712, 715, 733, 3612  
 Barnes, M. J. 1148, 1181, 1330, 3402  
 Barnes, P. 763, 886, 889, 892, 918, 921, 977, 995, 1399  
 Barov, N. 561, 2617, 2623, 3216  
 Barr, D. S. 2163  
 Barranco-Luque, M. 2956  
 Barry, W. 2109  
 Barsotti, E., Jr. 3294  
 Barsotti, E. L. 2531  
 Bartalucci, S. 778  
 Bartelson, L. 918, 1342  
 Barth, W. 3142  
 Barts, T. 3444  
 Bar'yakhtar, V. 1480  
 Basseti, M. 2048  
 Batchelor, K. 2486, 3000, 3012  
 Batishchev, O. V. 2620  
 Batskikh, G. 2717  
 Batskikh, G. I. 980  
 Batygin, Y. K. 50  
 Bazzani, A. 273  
 Be, S. H. 3845  
 Bearzatto, C. 1184  
 Beaufait, J. 3103  
 Beckert, K. 1645, 1738  
 Beebe, E. 1735  
 Beechy, D. 2118  
 Behrsing, G. 83  
 Belk, A. 1937  
 Belkacem, A. 3751  
 Bell, R. A. 1039, 2010  
 Bellomo, G. 775, 1001, 1524  
 Belloni, F. 3839  
 Belomestnykh, S. 1226  
 Belomestnykh, S. A. 3669  
 Belomestnykh, S. E. 2022  
 Beloshitsky, P. 2042  
 Belov, V. 2042  
 Belov, V. P. 3820, 3822  
 Belova, N. G. 664, 3546  
 Bemes, M. 2967  
 Benaroya, R. 3857  
 Benes, S. J. 1957  
 Benesch, J. 1016

Benesch, J. F. 748, 781, 947  
 Bengtsson, J. 567, 1488, 2272, 3312  
 Benke, T. 1706  
 Bennett, G. 2070  
 Bennett, L. F. 667  
 Bennett, M. 3748  
 Bennett, P. 1916  
 Benson, S. 3663  
 Benvenuti, C. 806  
 Ben-Zvi, I. 849, 1439, 1602, 2486, 2962, 3000, 3012  
 Berg, J. S. 291  
 Berg, W. 605  
 Bergher, M. 3708  
 Bergmann, U. 2145  
 Bernard, D. 2450  
 Bernard, M. 694  
 Bernard, P. 806  
 Bernardini, M. 3842  
 Beroud, Y. 784  
 Bertrand, P. 1789  
 Bertsche, K. J. 1727  
 Berz, M. 155, 164  
 Bethel, S. 2967  
 Bethke, S. 2172  
 Betto, A. 1220  
 Bhandari, R. 381  
 Bharadwaj, V. 2228, 3806  
 Bhat, C. M. 405, 787, 1223  
 Biagini, M. E. 2048  
 Bickley, M. 1835, 1895  
 Bieniosek, F. 3096  
 Bieniosek, F. M. 3163  
 Bieri, R. L. 742  
 Bieth, C. 1789  
 Bijleveld, J. 2343  
 Billan, J. 68  
 Billen, J. 1712  
 Billen, J. H. 790, 793  
 Billquist, P. 1694  
 Birattari, C. 1524  
 Birnbaum, I. 2420  
 Birnbaum, I. A. 3012  
 Biscardi, R. 1419  
 Biscari, C. 2048  
 Bishop, D. 1148, 1181  
 Bisoffi, G. 1747  
 Bisognano, J. 512, 3663  
 Bisognano, J. J. 179, 2364, 2929, 3246, 3473, 3515  
 Bixio, A. 1063  
 Bizek, H. 1485  
 Blaker, G. 1300  
 Blasche, K. 357, 3736  
 Blaskiewicz, M. 3321, 3324  
 Blell, U. 357  
 Bleser, E. 3766  
 Bleser, E. J. 3763  
 Blewett, J. P. 2546  
 Blind, B. 56  
 Blockus, D. 2172  
 Bloess, D. 806  
 Blokland, W. 2528  
 Blondel, A. 44  
 Bloom, E. 3084  
 Bluem, H. 1451  
 Blum, E. 3579  
 Blum, E. B. 1599, 2246, 2307  
 Blumberg, L. N. 3579  
 Bobin, J. L. 3202  
 Bobyleva, L. 2042  
 Boden, A. 2051  
 Boers, J. E. 327  
 Boeuf, J. P. 3039  
 Bogacz, S. A. 74, 77, 2587  
 Bogatov, N. 2769  
 Bogaty, J. M. 1694  
 Böge, M. 460  
 Bogert, D. 3793  
 Bohl, T. 2001  
 Bohn, C. L. 838, 1715, 3666  
 Boiteux, J. P. 2358  
 Bollinger, L. M. 1694  
 Bolme, G. O. 1669, 3118  
 Bondarev, B. I. 980  
 Boni, R. 611, 778  
 Bonifacio, R. 1524  
 Bonin, B. 798  
 Bonnafond, C. 670, 697, 2115  
 Bordoley, M. 1867, 2313  
 Bordry, F. 44, 2001  
 Bordua, M. 3748  
 Borer, J. 2103, 2492  
 Borisov, O. N. 518  
 Borland, M. 285, 2028, 3015  
 Bosch, F. 1645  
 Bosch, R. A. 3369  
 Boscolo, I. 1524  
 Bosotti, A. 1524  
 Bossert, R. 2769  
 Bossingham, R. 3751  
 Botlo, M. 128  
 Botman, J. I. M. 1072, 1820, 2062, 2065, 2892, 2927, 3423, 3645  
 Bourg, F. 2997  
 Bourgarel, M. P. 1789  
 Bourianoff, G. 128, 203, 515  
 Boussard, D. 2376, 2379  
 Bovet, C. 2492  
 Bowling, B. A. 1895, 2298, 2477  
 Bowling, S. 1669  
 Boyce, R. 1445, 1608  
 Boyce, R. F. 543  
 Boyd, J. K. 463  
 Boyes, J. 667  
 Bozoki, E. 105, 2284, 3636  
 Brabson, B. 29, 224, 227, 420  
 Bracco, R. 1587  
 Bradley, S. 2054  
 Brandeberry, F. 824, 880  
 Brandt, D. 3429  
 Branson, B. H. 1220  
 Brau, C. A. 1448  
 Brauer, S. O. 1217  
 Braun, A. 354  
 Bravar, A. 32  
 Brennan, J. M. 1241, 3763  
 Brennan, M. 2286  
 Bres, M. 1184  
 Bressan, M. 772, 1524, 1569  
 Bressler, V. E. 2736, 2950  
 Briand, P. 2997  
 Brianti, G. 3917  
 Bridges, J. 285, 1013  
 Bridges, J. F. 766, 910, 913, 1157, 1408, 1906  
 Briegel, C. 1914  
 Briggs, R. J. 3922  
 Brindza, P. 3103  
 Brinkgreve, P. 2892  
 Brinkmann, R. 3742  
 Brittain, D. L. 1169  
 Broggi, F. 1524, 1569  
 Brooks, T. 1154  
 Broome, W. 1419  
 Brouk, V. 2382  
 Browman, A. 1683  
 Browman, M. J. 3267  
 Brown, B. 3757  
 Brown, B. C. 351, 2829  
 Brown, D. 2181  
 Brown, D. J. 2664  
 Brown, G. 2760  
 Brown, I. 1390  
 Brown, K. 384  
 Brown, K. L. 333, 378  
 Brown, N. 62  
 Brown, P. 2358  
 Brown, R. 2507, 3184  
 Browne, M. 3045, 3047  
 Brownman, M. J. 800  
 Bru, B. 1789, 1792  
 Brüttsch, E. 2748  
 Bruhwiler, D. L. 59, 3624  
 Brumwell, F. 3757  
 Brunelle, P. 1465  
 Bruns, W. 904, 1133, 3714  
 Bryant, H. 369  
 Bu, S. 1411  
 Buchanan, E. 3533  
 Buda, S. 1419  
 Budlong, J. 3533  
 Budnick, J. 29, 224, 227, 420, 2865  
 Budzko, A. 3642  
 Budzko, A. V. 3784  
 Builta, L. 3055  
 Bull, J. 1369  
 Buller, T. L. 1075  
 Bulos, F. 3084  
 Bultman, N. 1712  
 Bulyak, E. 300, 1480  
 Bulyak, E. V. 3512  
 Buon, J. 469, 2513  
 Burgett, W. 2731, 2757, 2763  
 Burke, D. 2019  
 Burke, D. L. 543  
 Burkhardt, H. 2001  
 Burnham, B. 2889  
 Burns, A. 2103, 2301  
 Burns, M. 3055  
 Burns, M. J. 2944  
 Burtin, G. 2495  
 Burton, R. J. 829, 832  
 Busch, G. 2967  
 Bushuyev, A. 1226  
 Butterworth, A. 1903  
 Büttig, H. 1477  
 Byrd, J. 2349, 3315  
 Byrd, J. M. 2109, 3318, 3408  
 Byrne, T. 567

## C

- Cai, S. Y. 3075  
 Cai, Y. 203, 2781  
 Calabrese, R. 3243  
 Calame, J. P. 2667, 2670  
 Calderon, M. 3836  
 Callahan, D. A. 730, 733, 3660  
 Callin, R. 543, 620, 1106  
 Calloway, D. 2172  
 Calo, A. 3127  
 Calvert, J. 1160, 3748  
 Camas, J. 2498  
 Cameron, P. 1166  
 Cameron, P. R. 2328  
 Campbell, B. 1402  
 Campisi, I. E. 1115, 1220  
 Capista, D. 2252  
 Caporaso, G. 703  
 Caporaso, G. J. 712, 715  
 Cappi, R. 3570  
 Cardito, M. 2154  
 Cardman, L. S. 3246  
 Carey, D. C. 47  
 Carlé, P. 1735  
 Carlini, R. 2136, 3103  
 Carlisle, L. 1718  
 Carlson, R. L. 661  
 Carlsten, B. 2675  
 Carlsten, B. E. 2537, 2664  
 Carmel, Y. 2714  
 Carpenter, J. 3757  
 Carr, R. 1596  
 Carroll, F. E. 1448  
 Carron, G. 1066, 3426  
 Carson, J. 2769  
 Carter, A. 2054  
 Carwardine, J. 1709  
 Carwardine, J. A. 3210  
 Caryotakis, G. 543, 1106, 1259  
 Casella, R. 1277  
 Caspers, F. 2157, 3381  
 Cassel, R. 543, 1318  
 Castellano, M. 573  
 Castro, P. 2103  
 Catani, L. 573  
 Caussyn, D. 3745  
 Caussyn, D. D. 29, 224, 227, 420, 3536  
 Cavallari, G. 806  
 Celata, C. M. 724, 3748  
 Cerniglia, P. 2310  
 Chabert, A. 1789  
 Chae, Y. 282  
 Chae, Y. C. 182  
 Chamberlain, O. 2172  
 Champion, M. 809, 918, 1127  
 Champion, M. S. 989  
 Chan, C. F. 3157, 3160  
 Chan, K. D. C. 2970  
 Chanel, M. 2157  
 Chang, C. H. 1943, 2886  
 Chang, C. R. 122, 812, 3585  
 Chang, H. P. 1943  
 Chang, J. S. 1345  
 Channell, P. J. 38  
 Chao, A. 3781  
 Chao, A. W. 29, 224, 227, 420, 3345, 3348  
 Chao, Y. 587  
 Chapman, L. 1914, 2249  
 Chappelier, J. 158, 161  
 Charruau, G. 858  
 Chase, B. E. 2355  
 Chattopadhyay, S. 83, 2638, 3042  
 Chautard, F. 267, 2720  
 Chechetenko, V. 1480  
 Chehab, R. 3093  
 Chel, S. 855  
 Chen, B. 3345, 3348  
 Chen, C. 2656  
 Chen, H. 2151  
 Chen, J. 1095  
 Chen, J. R. 1635  
 Chen, J. S. 1878  
 Chen, P. 617, 2638  
 Chen, S. 200, 3255  
 Chen, S. C. 2575, 2696, 2699  
 Chen, S. J. 1878  
 Chen, T. 3479  
 Chen, Y. 303, 718, 2841  
 Chen, Y. J. 703, 706  
 Cheng, J. 2659, 2667  
 Cheng, W. 221  
 Cheng, Y. 1262, 1393, 2269  
 Chepurinov, A. S. 2059  
 Chesnokov, Y. A. 454  
 Chester, N. 2826  
 Chester, N. S. 2823  
 Chevallier, M. 3093  
 Chiaveri, E. 806, 849  
 Chida, K. 41  
 Chimenti, V. 3906  
 Chin, J. 1572, 1584  
 Chin, Y. H. 3347, 3414  
 Ching, C. H. 3351  
 Chiou, T. C. 2635  
 Chirkov, P. 2769  
 Chmielewski, A. G. 1890  
 Cho, C. 2151  
 Cho, M. 581, 1521  
 Cho, M. H. 593, 1315  
 Cho, Y. 399, 3757  
 Cho, Y. S. 679  
 Choi, B. H. 679, 3196  
 Choi, J. 2516, 3273  
 Choi, J.-Y. 3087, 3705  
 Chojnacki, E. 815, 1844, 2596, 3061  
 Chou, P. J. 3363  
 Chou, W. 818, 2281, 3444, 3609, 3781, 3888  
 Christensen, K. 1712, 2947  
 Christiansen, C. F. 1098, 2139  
 Christianson, M. 2757  
 Chu, C. 306, 2841  
 Chubar, O. V. 1626, 2474, 2510  
 Chubarov, O. V. 2059  
 Chugun, T. 2205  
 Chung, K. H. 679, 3196  
 Chung, Y. 188, 1814, 2112, 2263, 2266, 2275, 2304  
 Chupp, W. W. 703, 3199  
 Church, M. 330  
 Chuvilo, I. V. 1675  
 Ciapala, E. 1903, 2358  
 Ciardullo, D. J. 1241  
 Ciarlette, D. 285  
 Ciarlette, D. J. 1814  
 Cifarelli, F. 3099  
 Ciullo, G. 3243  
 Claborn, G. 2222  
 Clark, D. 369, 3888  
 Clark, D. J. 1724, 1727  
 Clark, S. L. 543  
 Clarke, J. A. 1494, 1638, 3594, 3672  
 Claudet, S. 2956  
 Claus, J. 2895  
 Clay, W. 3888, 3891  
 Clayton, C. 2976, 3003  
 Clayton, C. E. 558, 2551, 3543  
 Clayton, T. 1369, 2781  
 Clément, M. 1363  
 Clendenin, J. 3033  
 Clendenin, J. E. 2978, 3027, 3036  
 Clerc, G. 1184  
 CLIC Study Group 540  
 Clift, B. E. 1694  
 Cline, D. 2051, 2638  
 Clout, P. 1801  
 Clozza, A. 3906  
 Coacolo, J. C. 3567  
 Coadou, B. 798  
 Cobb, J. K. 2838  
 Codutti, A. 1587  
 Cohen, S. 369  
 Colby, E. 3021  
 Colchester, R. J. 2495  
 Cole, B. 128, 203  
 Cole, M. 821, 3012  
 Cole, R. 1669  
 Coleman, P. 824  
 Coleman, P. D. 1033, 1256, 3252  
 Colestock, P. 3294  
 Colestock, P. L. 3303, 3306, 3384, 3540  
 Collet, G. J. 3030  
 Collet, P. 1187  
 Collier, P. 1937, 2001  
 Collins, J. 29, 224, 227, 420  
 Collins, J. P. 2823  
 Colton, E. 3297  
 Combs, C. 1703  
 Combs, C. M. 846  
 Conciauro, G. 1524, 1569  
 Conde, M. E. 3042  
 Condé, H. 1771  
 Connolly, R. 1669  
 Conte, M. 32, 438  
 Conway, P. 2388  
 Coombes, R. 2769  
 Cooper, R. 3297  
 Cooper, R. G. 2400  
 Cooper, R. K. 3267  
 Cooper, W. S. 3169  
 Coosemans, W. 44  
 Corbett, J. 173  
 Corbett, W. J. 108, 114, 1483, 2275  
 Cork, C. 1575  
 Corlett, J. N. 2109, 3318, 3408, 3411  
 Cornacchia, M. 173  
 Cornelis, K. 2001, 3429

Cornelius, W. D. 2994  
Corredoura, P. 2370, 3240  
Corsini, R. 626, 1524  
Cottingame, W. B. 3118  
Courant, E. 3778  
Courant, E. D. 137  
Cover, R. 1605  
Craddock, W. 2638  
Crandall, K. R. 1042, 3585, 3657  
Crane, M. 1922, 1966  
Cravey, W. R. 739  
Crawford, A. 1223  
Crawford, C. 886, 918  
Crawford, C. A. 3540  
Crawford, J. F. 1771  
Crawford, K. 1925, 3757  
Crist, C. 2121  
Crist, C. E. 2124, 2130, 2426,  
2456, 2501  
Crockford, G. 2504  
Crofford, M. 587  
Crofford, M. T. 2364  
Crosbie, E. 285, 1485  
Crosbie, E. A. 282, 506  
Crouch, R. 2199  
Cuevas, C. 1838, 3127  
Culwick, B. 1277  
Cuneo, M. E. 694  
Curbow, J. 941  
Curry, B. P. 375  
Curtin, M. 1154, 1244  
Cutler, R. 3509  
Cutler, R. I. 827, 1250

## D

Dabrowski, J. 1274, 1855, 1858,  
1861  
Daclon, F. 1378, 3842, 3873  
Dalesio, L. R. 1806  
D'Alsace, R. 1419  
Daly, R. 1960, 2142  
Damjanovich, R. 3175  
Damm, R. 1166  
Danared, H. 1735  
Danby, G. T. 2883  
Danilov, V. 3429, 3711  
Danly, B. G. 2575, 2656, 2690  
Dasbach, D. 1080  
Datte, P. 1703, 2118, 2483, 3127  
D'Auria, G. 953, 956, 1145  
D'Auria, J. M. 1641  
Dauvergne, J.-P. 2739  
Davidson, A. D. 1175  
Davis, K. 2967  
Davis, P. 561, 2976, 3003, 3216,  
3543  
Davis, T. J. 2653, 2687  
Dawson, J. 2462  
Dawson, R. 1733  
Deadrick, F. 703  
Debiak, T. 821  
Debiak, T. W. 2420, 3193  
Decker, C. 2635  
Decker, F. 3582  
Decker, F.-J. 414, 2019, 2278,  
2435, 2507, 3234, 3240, 3576

Decker, G. 188, 2196, 2263,  
2275, 2304  
Decker, G. A. 1814  
Deckers, R. 1820  
DeFord, J. 3450  
Degen, C. M. 2310  
DeHaven, R. 1021, 1683  
Dehen, J. 3142  
Dehning, B. 44  
Deitinghoff, H. 3139, 3142  
de Jong, M. S. 829, 832, 835,  
1039  
Dekkers, E. 2892  
de Lamare, J. 1318  
Delaunay, M. 2997  
Delayen, J. R. 288, 838, 1715,  
3666  
Delchamps, S. W. 2769  
Delcourt, B. 2513  
Delhez, J. L. 1820, 2062, 2065,  
3423  
Delikaris, D. 2739  
Dell, G. F. 171  
Delmere, C. 2492  
Delsart, P. 670, 697  
de Mascureau, J. 670, 697, 2115  
de Menezes, D. 858  
Demmel, E. 1178  
Demos, P. T. 829, 832  
Demroff, H. 2711  
Demroff, H. P. 2705, 2708  
Demsky, M. I. 682  
Deng, D. P. 1172  
Denney, P. 1154, 1669  
Denney, P. M. 1232, 2391  
Depaola, F. 1013  
Derenchuk, V. 29, 224, 227, 420,  
3184  
de Rijk, G. 1937, 2001  
Deruyter, H. 543, 620, 907, 986,  
1121  
Derwent, P. F. 2199  
De Salvo, L. 1524  
Desforges, B. 2001  
Despe, O. D. 1864  
Destler, W. W. 685  
Devin, A. 670, 697, 2115  
Devred, A. 2769  
deVries, G. J. 3169  
Dewa, H. 1697  
Dey, J. 405, 1223  
Diamond, W. T. 1381  
Dickey, C. 1339  
Didelez, J. P. 3093  
Didenko, A. A. 2022  
Dienel, S. 1477  
Dikansky, N. 3243  
Dikansky, N. S. 2022, 3684  
DiMarco, J. 2769  
DiMarco, J. N. 1021  
Di Massa, G. 2154  
Dinkel, J. 1357  
Dinova, K. 1620  
Diviaco, B. 1587, 1590, 1593  
Dmitrieva, I. 2769  
Do, S. H. 3196  
Dobeck, N. 587  
Doble, N. 1363  
Doi, M. 1783, 1786

Dolinsky, A. V. 3822  
Dolique, J.-M. 3567  
Dombeck, T. 2731, 2757, 2763  
Dombrowski, R. 2459  
Donahue, J. 369  
Donald, M. 131  
Dong, W. W. 1448  
Dooling, J. 1709  
Doolittle, L. R. 748  
Doose, C. 2802, 2805  
Doose, C. L. 2799  
Dorfan, J. M. 2010  
Dortwegt, R. 3857  
Douglas, D. 587, 1895  
Douglas, D. R. 584, 2929  
Dovbnaya, A. 1480  
Dow, K. 2054, 2868  
Dow, K. A. 2935, 2938, 2941  
Dowell, D. 2967  
Dreher, K. 2748  
Drew, M. M. 2705  
Drobot, A. 3267  
Drozhdin, A. I. 1360, 3109, 3772  
Drury, M. 841  
Ducar, R. 2199  
Dugan, G. F. 3717  
Dunbar, A. 1166  
Dunn, A. 2199  
Dunnam, C. R. 578, 2394  
Dutt, S. 29, 224, 227, 267, 420,  
3609  
Dutto, G. 2991  
Duval, M. 1789  
Dvornikov, V. A. 844  
Dwinell, R. 3748  
Dwyer, S. 2760  
D'Yachkov, M. 3330  
Dykes, D. M. 3594, 3672  
Dylla, H. F. 748, 3867  
Dymnikov, A. 206, 3618  
Dyshkant, A. 454

## E

Early, R. 620, 2025  
Early, R. A. 2880  
East, G. 29, 224, 227, 420  
Eaton, L. 1154  
Eaton, L. E. 2391  
Ebihara, K. 673  
Eden, J. R. 3485  
Edwards, D. A. 134  
Edwards, H. 918  
Edwards, H. T. 537  
Efimov, S. 300, 1480, 2057  
Egan-Krieger, G. V. 1887  
Ehrlich, R. 995  
Ehrnstén, K. 1735  
Eickhoff, H. 357, 1645, 1738  
Eidelman, Y. 450  
Einfeld, D. 149, 152, 1477  
Eisen, N. 2076, 2352  
Ekdahl, C. A. 2400  
Elayi, A. 3093  
Elia, R. 2172  
Elkins, J. 1160  
Elkonin, B. V. 849

Elliot, T. S. 2705  
Elliott, T. S. 2708, 2711  
Ellis, S. 1718  
Ellison, J. 423  
Ellison, J. A. 387, 3588  
Ellison, M. 29, 224, 227, 420  
Ellison, M. J. 3536  
Ellison, T. 29, 224, 420, 3745  
Ellison, T. J. P. 2243, 2289, 3536  
Elmgren, K. 1771  
Elsener, K. 1363  
Emery, L. 2266, 3360  
Emma, P. 116, 429, 635, 2019, 2160  
Emma, P. J. 98, 100  
Emoto, T. 546  
Endo, K. 1291  
Enegren, T. 846, 877, 941, 1703  
Enge, H. 2868  
Engels, O. 3139  
Engström, A. 1735  
Enomoto, A. 546, 590, 2516, 3087, 3705  
Eppley, K. 1106  
Eppley, K. R. 1190  
Erdman, K. 1733  
Erdt, W. K. 2956  
Erg, G. 1384  
Erickson, J. 1669  
Esarey, E. 2626, 2629, 2632  
Esin, S. 2426  
ESRF Project Team 1427  
Evans, D. 3127  
Evans, K., Jr. 188, 2263, 2275  
Evans, L. R. 1983  
Everett, M. 2551, 3003  
Evsstigneev, A. 1384  
Eyhart, P. 670, 697  
Eyl, P. 670, 697  
Eylon, S. 703, 706, 709, 712, 3199

## F

Fabbricatore, P. 1001  
Fabris, A. 953, 956, 1145  
Fabris, R. 1333, 1378  
Facco, A. 849  
Faehl, R. 2675  
Faehl, R. J. 2664  
Fahmie, M. 1869  
Faillon, G. 1184  
Fainberg, Y. B. 2620  
Faltens, A. 703, 721, 724  
Fan, J. Y. 1943  
Fan, M. 306, 1721, 2841  
Fang, J. 2578  
Fant, K. 543, 1106  
Fant, K. S. 620  
Farias, R. H. A. 1089  
Farkas, Z. D. 620, 1121, 1196, 1208  
Farkhondeh, M. 1372, 2054, 2868, 2935, 2938, 2941  
Fasanello, T. 2397  
Fathizadeh, M. 1288  
Faugier, A. 2001

Faure, J. 1465  
Faus-Golfe, A. 2045  
Fawley, W. M. 724, 1530  
Fazio, M. 2675  
Fazio, M. V. 2664  
Fedele, R. 209, 212  
Fedorov, V. 2769  
Fedotov, Y. S. 315, 318  
Feinberg, B. 2187, 3748, 3751  
Felker, B. 1551, 1554  
Fenstermacher, M. 1551  
Fenstermacher, M. E. 1554  
Ferguson, M. 1294  
Ferguson, S. W. 1551, 1554  
Feroli, G. 2498, 2504  
Fero, M. 2172  
Ferrario, M. 573, 968, 3279  
Ferry, J. 3745  
Feschenko, A. 2426  
Fessenden, T. 703  
Ficklin, D. 1318  
Fieguth, T. 3084  
Fields, S. 1551  
Fields, W. F. 1554  
Filimonov, M. Z. 2208  
Filtz, M. 901, 1036  
Fink, C. L. 375  
Finley, D. A. 3721, 3806  
Fiorito, R. B. 1620, 2397, 2453  
Firebaugh, J. 1817, 1912  
Firjahn-Andersch, A. 3139  
Fischer, C. 2504, 3597  
Fischer, G. E. 44  
Fischer, J. 2929  
Fischer, R. 2632  
Fischer, W. 246, 2301  
Fisher, A. 2632  
Fisher, A. S. 2578  
Fishler, Y. 1297  
Fitzgerald, D. 366, 369, 2216, 2219, 3297  
Fitzgerald, D. H. 3739  
Flannigan, J. 1852  
Flanz, J. 2868, 2871, 2874, 3851  
Flanz, J. B. 1875, 2054, 2331  
Fleck, R. 1080  
Flora, R. 1914  
Flynn, T. 889  
Foelsche, H. W. 2895  
Foerster, C. 3836, 3876  
Foley, M. 852, 3294  
Fomin, M. 1226  
Fong, B. 1483  
Fong, K. 1139  
Fontana, J. R. 2614  
Force, R. 3748  
Forest, E. 131, 291  
Fortgang, C. M. 2480, 3118  
Fouaidy, M. 855  
Fougeron, C. 858  
Fowkes, R. 1106  
Fowke, W. R. 620, 1259  
Fowler, W. 3793, 3796  
Fowler, W. B. 2823  
Fox, J. 2352  
Fox, J. D. 2076, 2109  
Fox, W. 995, 1712  
Fraivillig, J. 2790  
Franck, A. 2249, 2835

Franczak, B. 1645, 3736  
Frandsen, P. 2956  
Frandsen, P. K. 2739  
Frankle, S. 366, 369, 2216, 2219, 3297  
Franzke, B. 357, 1645, 1738  
Frias, R. 3748  
Friddell, K. 2967  
Friedman, A. 105, 703, 727, 730, 1599, 2284  
Friedrichs, C. 803, 824  
Friesel, D. 29, 224, 227, 420, 3184  
Frisch, J. 3045, 3047  
Frisch, J. C. 2978, 3027, 3036  
Frischholz, H. 1247, 2358  
Fritsche, C. T. 2501  
Fu, S. 1686  
Fugitt, J. 939, 1109  
Fuja, R. 605  
Fujita, H. 1697  
Fujita, Y. 2260  
Fukuda, S. 1193  
Fuller, R. 543  
Fullett, K. D. 3309  
Funakoshi, Y. 3497  
Funk, L. W. 812, 1700, 1706, 2130  
Funk, W. 1703, 1765, 3585  
Furman, M. A. 3485  
Furukawa, K. 2516, 3087, 3705  
Fuzesy, R. 2172

## G

Gabella, W. 420, 2051, 2638  
Gabella, W. E. 233  
Gagliardi, P. 1063  
Gai, W. 2596, 3050  
Gallardo, J. C. 2578, 3012, 3081, 3615  
Gallo, A. 778  
Galloway, C. 620  
Galluccio, F. 209, 2154  
Galyaev, N. A. 454  
Gammel, G. 3193  
Ganetis, G. 2744, 2766  
Gannon, J. 1898, 2731, 2757, 3870  
Gao, J. 862, 865, 868  
Gao, S. 745, 3521, 3696  
Garavaglia, T. 3591, 3609, 3769  
Garber, M. 2744, 2766  
Gardelle, J. 626  
Garden, C. 3033  
Garden, C. L. 2978, 3027, 3036, 3039  
Gardner, C. 3633, 3763  
Gardner, M. 1439  
Gareyte, J. 246  
Garnett, R. 1712  
Garoby, R. 3570  
Garren, A. 2051, 3778  
Garren, A. A. 137  
Gath, B. 1572  
Gatignon, L. 1363  
Gattu, R. 2760

- Gavrilov, N. 1226  
Gayet, P. 2956  
Geisik, C. 3172  
Gelbart, W. Z. 3099  
Gelfand, N. 2835  
Gelfand, N. M. 3790  
Geller, J. 1277  
Gemme, G. 775, 1001, 1524  
Genesio, F. 806  
Genin, R. D. 3018  
George, M. J. 661  
Georges, P. 3053  
Gerasimov, A. 3276, 3291  
Gerig, R. 267, 3558  
Gerig, R. E. 333  
Geschonke, G. 2358  
Gevchuk, A. 1480  
Ghosh, A. 2744, 2766  
Ghosh, A. K. 2742, 2790  
Giacuzzo, F. 3842  
Giannini, M. 1378  
Giardino, G. 3202  
Gierman, S. M. 2970  
Giguët, E. 2656  
Gilgenbach, R. M. 2693, 3351, 3354  
Gillespie, G. H. 86  
Gillier, R. 3900  
Gilpatrick, J. D. 1669, 2163, 2316, 2334, 2480  
Giovannozzi, M. 246, 273, 500  
Giove, D. 1524  
Girard, M. 2997  
Gjaja, I. 3387  
Gladkikh, P. 1480, 2057  
Gladkikh, P. I. 194  
Gläser, W. 1477  
Glass, H. D. 351, 2829, 2856, 2859  
Glenn, J. W. 3633, 3763  
Glock, H.-W. 614, 623  
Gluckstern, R. L. 221, 1545, 3219, 3387, 3390  
Godden, D. 1709  
Goderre, G. 354, 3482  
Godfrey, G. 3084  
Godwin, R. P. 3090  
Goetz, T. 1477, 2534  
Golceff, P. 3018  
Gold, S. 1318  
Gold, S. H. 2644, 2647  
Goldberg, D. A. 871, 874  
Goldin, L. 1771  
Goldman, M. 1166  
Goldman, M. A. 2916, 2919  
Goldstein, J. C. 3090  
Golubeva, N. 441, 444  
Gonçalves da Silva, C. E. T. 252, 390, 1454  
Gonczy, I. 2769  
Gonichon, J. 2575, 2696, 2699  
Gonzalez, R. E. 2322  
Goodwin, J. E. 2835  
Goren, Y. 824, 846, 877, 880, 883, 1703, 3405, 3888  
Gormley, M. 1127  
Gorniker, E. 1226  
Gould, H. 3751  
Gourber, J.-P. 68  
Gourlay, S. 2769  
Govil, I. M. 1753  
Gower, E. 1244  
Grabner, J. 886, 889, 892, 918  
Grafström, P. 1363  
Granatstein, V. I. 2572  
Granatstein, V. L. 2667, 2670, 2673  
Gras, J. J. 2495, 2504  
Grau, M. C. 2328  
Gray, E. 1021  
Green, K. 998  
Greene, A. 2744, 2766  
Greenwald, Z. 3690  
Gregory, W. 3055  
Greiner, P. 798  
Greiser, M. 1747  
Grelick, A. 605, 2412  
Grenier, J. 626  
Gribov, I. V. 2059  
Griffin, J. 405  
Griffin, J. E. 408  
Grigor'ev, Y. 2057  
Grimm, T. 824, 1083  
Grimm, T. L. 3252  
Grippe, J. 827, 1250, 3213  
Grippe, J. M. 1169  
Grishanov, B. I. 2022  
Grossberg, P. 2106  
Grote, D. 703, 709  
Grote, D. P. 727  
Groupe d'Etudes des Cavités Supraconductrices 796  
Groves, T. 2249  
Grüneberg, H. 2748  
Grua, P. 670, 697  
Gruber, A. 1645  
Grudzien, D. M. 2213  
Grun, J. 2632  
Grusell, E. 1771  
Guharay, S. K. 3145, 3648  
Guidee, P. 1184, 1187  
Guidi, V. 3243  
Guigli, J. 1238  
Guignard, G. 3336, 3426, 3600  
Guirlet, R. 2450  
Guk, I. 2057  
Gulley, M. 369  
Gundersen, M. 3039, 3072, 3537  
Gundersen, M. A. 3066  
Günther, C. 3381  
Guo, Z. Y. 3237  
Gupta, R. 258, 2744, 2766  
Gupta, R. C. 2754, 2778  
Guratzsch, H. 1477  
Gurd, D. P. 1916  
Güsewell, D. 2956  
Gutscher, W. D. 1154  
Guy, F. 1703, 2986, 3585  
Guy, F. W. 122, 2124, 2127, 2426, 2483, 3130
- H
- Haas, A. 2222  
Haber, C. 2199  
Haber, I. 724, 727, 730, 3612, 3627, 3660  
Haberichter, W. 2462  
Habs, D. 1747  
Haebel, E. 806, 898  
Haenni, D. 2757  
Hafizi, B. 1560, 1623, 2584, 2644, 2647  
Hage-Ali, M. 1363  
Hagedoorn, H. L. 1072, 2062, 2065, 2892, 2927, 3423, 3645  
Hahn, A. 2193  
Hahn, K. 3285  
Hahn, R. v. 1747  
Hairapetian, G. 561, 2976, 3003, 3216, 3543  
Halbach, K. 1445, 1581, 1599, 1608, 1727  
Halbleib, J. A. 691  
Halka, M. 369  
Hall, J. 32, 1244  
Hall, T. 2865  
Halling, A. M. 472, 474, 2193  
Halling, H. 1253  
Halling, M. 3814  
Halliwell, J. 3748  
Hamilton, B. 29, 224, 227, 420, 3745  
Hamilton, B. J. 2243, 2289, 3536  
Hamm, C. 962  
Han, H. S. 2796  
Hanaki, H. 590, 1163, 3087  
Hancock, S. 3570  
Hanft, R. 2769  
Hanna, B. 354, 1357  
Hanna, S. 1419  
Hanna, S. M. 895, 1118  
Hansberry, E. 1154  
Hansen, S. 1229  
Hanson, D. L. 694  
Haraguchi, M. 1518  
Hardek, T. 2319, 3297  
Hardek, T. W. 2240  
Hardekopf, R. A. 3760  
Harding, D. J. 2823, 2826, 2829  
Harfoush, F. A. 342, 345, 348, 351, 2829  
Harkay, K. 3258  
Harkay, K. C. 3306  
Harkewicz, R. 1694  
Harmer, P. 1916  
Harms, E. 3533  
Harms, E., Jr. 3803  
Harris, K. 1318  
Hart, R. 1901  
Hartley, R. 1527  
Hartman, S. 575, 2976, 3003, 3357, 3543  
Hartman, S. C. 561, 3216  
Hartmann, B. 1477  
Hartog, P. D. 1709  
Hartung, W. 898, 921, 3450  
Haseroth, H. 2720  
Hashimoto, Y. 1780, 1783  
Hassenzahl, W. 1572  
Hassenzahl, W. V. 1575, 1584  
Hatton, V. 2001  
Hattori, T. 1783, 1786, 3115  
Haug, F. 2739

Hauviller, C. 3854  
Hawkins, S. A. 739  
Haworth, M. 1703, 2124, 2986  
Hayashi, S. 2039  
Hayes, T. 1241  
Haynes, W. 2675  
Hays, T. 3450  
Hayward, T. D. 1075  
Hayworth, M. D. 846  
He, A. 2775  
Hebert, J. 2986, 3151  
Hébert, J. E. 2483  
Heefner, J. 1838  
Heese, R. 608  
Heifets, S. 543, 3456, 3459  
Heifets, S. A. 3462  
Heinrichs, H. 995  
Hellborg, R. 206, 3618  
Heller, H. 2892  
Helm, R. 92, 131, 185  
Helser, A. 1399  
Hemmer, F. M. 2919  
Hendrickson, L. 1972, 2106  
Hendry, G. O. 1730  
Henestroza, E. 703, 709, 3199  
Henke, H. 549, 901, 904, 1133,  
2593, 3288  
Henrichsen, K. 44  
Henriot, C. 798  
Herr, S. 2187  
Herrlander, C. J. 1735  
Herrup, D. 2199  
Herrup, D. A. 2249  
Herz, P. R. 3190  
Hettel, R. 2275  
Heuer, R. 1439, 2420  
Heuer, R. L. 1527, 3012  
Hewett, D. 703  
Hewett, D. W. 706, 718  
Heydari, H. 411  
Hicks, J. 3184  
Higgins, C. S. 2298  
Higo, T. 1027, 3503  
Hildreth, M. 2019  
Hilke, J. 1735  
Hill, B. W. 86, 1762  
Hill, J. 1154  
Hill, N. 3050  
Hill, S. F. 3594, 3672  
Hiller, M. 921  
Hilleret, N. 806  
Himel, T. 1972, 1975, 2019,  
2106, 2373  
Himeno, Y. 546  
Hindi, H. 2076, 2352  
Hinkson, J. 2097, 2109  
Hipple, R. 703  
Hiramatsu, S. 673  
Hiramoto, K. 309  
Hirano, K. 546  
Hirao, Y. 1291, 1686  
Hirata, K. 466, 3491  
Hirota, J. 309  
Hirshfield, J. L. 2584  
Hitz, D. 2997  
Ho, C. 1844, 2596, 3050  
Hoag, H. 543, 1106  
Hoag, H. A. 620, 907, 1121  
Hochadel, B. 1747

Hodgson, J. A. 1039  
Hoerberling, R. F. 2664  
Hoehn, M. 3739  
Hoffberg, M. G. 1957  
Hoffstaxter, G. H. 164  
Hofler, A. 587, 1895  
Hofler, A. S. 2298  
Hofman, J. M. A. 3423  
Hofmann, A. 44, 173, 3429  
Hogan, B. 2667, 2670  
Hogan, M. 3494  
Hogrefe, R. 2799, 2802, 2805  
Holdener, F. 3836  
Holmes, S. 3793  
Holt, J. A. 80, 3806  
Holtzapfle, R. 638  
Holtzapfle, R. L. 3234, 3564  
Honaberger, D. 3055  
Honaberger, D. J. 2944  
Honma, H. 1416  
Hooper, E. B. 1551, 1554  
Horan, D. 1294, 3757  
Hori, T. 602  
Hori, Y. 3903  
Horton, T. E. 1413  
Hou, Y. 2841  
Houck, T. L. 2590, 2611  
Hourany, E. 3093  
Hovater, C. 587, 3515  
Hovater, J. C. 2364  
Howard, D. 1160, 3748  
Howell, J. 1497, 1500  
Hower, N. 2889  
Hoyer, E. 1572, 1575, 1581,  
1584, 2850  
Hoyt, E. 3033  
Hoyt, E. W. 2978, 3036, 3039  
Hs, I. C. 2465  
Hseuh, H. C. 3897  
Hsieh, H. 611, 3906  
Hsu, I. 2151, 2638  
Hsu, K. T. 2031, 2091  
Hsu, T. 3066, 3072  
Hsue, C. S. 1943, 3369  
Hu, K. H. 2091  
Hu, Y. 2841  
Huang, H. 29, 224, 227, 420, 432  
Huang, T. H. 2465  
Huang, Y. 3558  
Hughes, E. 2172  
Hughes, E. A. 3594, 3672  
Hughes, T. 3055  
Hughes, T. P. 661  
Hui, M. 1160  
Hui, Z. 1557  
Hulsey, G. 803, 824, 877, 1083  
Hulsey, S. 1551  
Hulsey, S. D. 1554  
Hülsmann, P. 614, 623  
Humphrey, R. 543  
Humphries, D. 1572, 1575, 1581  
Humphries, S. J., Jr. 1199  
Hunt, D. 3748  
Hunt, S. 128, 1823, 1826, 1829,  
1838  
Hunter, T. 393  
Hur, J. 1327  
Hurd, J. 1703, 2986, 3127, 3509

Hurd, J. W. 122, 2124, 2127,  
2130, 2426, 2444, 3130, 3585  
Hurh, P. 2148, 2459, 3533  
Husmann, D. 152  
Hutcheon, R. M. 829, 832  
Hutson, R. 363, 366, 369, 2216,  
2219, 3297  
Hutton, A. 527  
Hwang, C. 1393  
Hwang, G. J. 2886  
Hyodo, K. 1468

## I

Ieiri, T. 2292, 2295, 3333  
Igarashi, Z. 1163  
Ihloff, E. 2054, 2331, 2868,  
2871, 2874, 3851  
Iida, T. 1515  
Ikegami, M. 1697  
Ikezawa, M. 1614, 1617  
Iliev, A. 3784  
Imanishi, A. 1783  
Ingalls, W. 3118  
Ingalls, W. B. 1669  
Ingold, G. 1439, 1602  
Inoue, M. 1697  
Irwin, J. 92, 95, 116, 119, 131,  
185  
Ishi, K. 1614, 1617  
Ishida, T. 2540  
Ishimaru, H. 3885  
Ishizuka, H. 676, 1566  
Ishkhanov, B. S. 2059  
Itano, A. 1291, 1686  
Ivanov, A. S. 555  
Ivanov, P. M. 2022  
Ivanov, S. 3561  
Ivers, J. D. 1312, 2687  
Iwashita, Y. 1697, 3154  
Izawa, M. 930

## J

Jach, C. 1297  
Jachim, S. P. 1154, 1232, 2391  
Jackson, A. 1432  
Jackson, G. 402, 1366, 2148,  
2418, 2525, 3021, 3363, 3366,  
3533  
Jackson, G. P. 3799  
Jackson, J. W. 2883  
Jackson, L. T. 1265  
Jackson, M. C. 1554  
Jacobs, K. 3851  
Jacobs, K. D. 1875, 2054, 2331  
Jacobsen, R. 44  
Jaquet, F. 2450  
Jaenker, P. 1019  
Jaeschke, E. 1474, 1747  
Jaffery, T. S. 2769  
Jahnel, L. 390  
Jain, A. 2744, 2766  
Jain, A. K. 2754, 2778  
Jakob, H. 2301

Jameson, R. 1683  
 Jameson, R. A. 3926  
 Jamieson, G. 1703, 2118, 2127  
 Jan, G. J. 1878, 2091  
 Janssen, D. 1477  
 Jason, A. 1683  
 Jason, A. J. 56, 3760  
 Jean, P. 3093  
 Jeanjean, J. 2513  
 Jeansson, J. 1735  
 Jecic, A. 3093  
 Jenner, D. 1421  
 Jensen, C. 1357  
 Jensen, D. R. 2838  
 Jensen, K. 1300  
 Jerng, D. 3757  
 Jia, H. 2841  
 Jiang, B. 1327, 3078  
 Jiang, S. 3390  
 Jiao, C. 2841  
 Jiao, J. 2841  
 Jin, J. T. 3196  
 Jobe, R. K. 2234, 2423  
 Joh, K. 71, 89  
 Johnson, A. 939  
 Johnson, A. M. 1220  
 Johnson, C. D. 626  
 Johnson, D. 236, 378  
 Johnson, J. 2109  
 Johnson, K. F. 1669, 3118  
 Johnson, P. 2967  
 Johnson, R. P. 1451, 1949  
 Johnson, R. R. 3099  
 Johnstone, C. 1912  
 Johnstone, J. 342  
 Jones, A. 2118  
 Jones, C. M. 1660  
 Jones, R. M. 936  
 Jones, T. A. 3063  
 Jones, W. P. 29, 224, 227, 420  
 Jonker, M. 2001  
 Joshi, C. 561, 2551, 2976, 3003,  
 3216, 3543  
 Jost, W. 998  
 Jostlein, H. 2835  
 Joubert, A. 1789, 1792  
 Jowett, J. M. 2013  
 Joyce, G. 1560, 2626  
 Judd, D. 703  
 Judkins, J. 3240  
 Judkins, J. G. 1039  
 Juillard, C. 3429  
 Juillard, J. C. 2358  
 Julian, J. 1238  
 Junck, K. 3540  
 Jung, J. 3654  
 Jung, K.-S. 3196  
 Jung, R. 2202, 2495, 2498, 2504  
 Junk, T. 2172  
 Junquera, T. 855  
 Juras, R. C. 1660  
 Jurgens, T. 852

## K

Kadnikov, A. 564, 1348  
 Kadokura, E. 2540

Kahana, E. 1814, 2112, 2237,  
 2304  
 Kahn, S. 2744  
 Kahn, S. A. 2754, 2766  
 Kaiser, H. 944  
 Kakigi, S. 1697  
 Kakihara, K. 3087  
 Kako, E. 992, 1024  
 Kalbfleisch, C. 1823, 1826, 1829  
 Kalbreier, W. 2013  
 Källberg, A. 1735  
 Kalnins, J. 3748  
 Kaltchev, D. 2042  
 Kamada, S. 1468  
 Kamikubota, N. 3087  
 Kamitani, T. 590, 2516, 3087,  
 3705  
 Kamiya, Y. 930, 1509, 2260,  
 2295, 2337  
 Kanai, T. 1614, 1617  
 Kanazawa, K. 3860  
 Kanazawa, M. 1291, 1686  
 Kang, B. K. 2751, 2796  
 Kang, H. 1521  
 Kang, Y. G. 1268  
 Kang, Y. W. 549, 766, 910, 913,  
 1057  
 Kapchinskiy, I. M. 1675  
 Kapustin, A. A. 3822  
 Karabekov, I. P. 457  
 Karas', V. I. 664, 2620, 3546  
 Karl, F. X. 2919  
 Karlner, M. 824  
 Karnaukhov, I. 1480, 2057  
 Kasha, D. 1166  
 Kashihin, V. S. 3822  
 Kasproicz, T. B. 2708  
 Kasuga, T. 2409  
 Katalev, V. 916  
 Katayama, T. 41, 1783, 1786  
 Katkov, V. M. 3093  
 Kato, R. 1614, 1617  
 Kato, S. 3518  
 Kato, T. 1291  
 Kato, Y. 2556  
 Katsouleas, T. 2635, 2638, 3543  
 Katsura, T. 2257, 2260, 2295,  
 2337, 2409  
 Kauffman, S. 267  
 Kauffmann, K. 3609  
 Kauffmann, S. 2489  
 Kauffmann, S. K. 137, 197  
 Kauppila, T. 3055  
 Kawakubo, T. 2540, 2556, 3552  
 Kawamura, M. 1163  
 Kawamura, Y. 3006  
 Kawasaki, S. 676, 1566  
 Kawazu, S. 3115  
 Kazacha, V. 2042  
 Kazarezov, I. 2650  
 Kazarinov, N. 2042  
 Kazimi, R. 599, 939, 1109  
 Kazmark, D., Jr. 2919  
 Keane, J. 608, 1118, 1419, 1852  
 Keating, P. 369  
 Keeney, D. S. 706  
 Kehne, D. 62, 65, 3282, 3627  
 Keller, F. 2811  
 Keller, R. 2910

Kelley, E. 2790  
 Kellogg, N. 1160  
 Kelly, E. 2744  
 Kennedy, W. L. 838, 1042  
 Kerns, C. 1214  
 Kerns, Q. 1127, 1214  
 Kersevan, R. 3842, 3848, 3888  
 Kerslick, G. S. 1312, 2687  
 Kersteins, D. 1669  
 Kewisch, J. 1835, 1895  
 Kheifets, S. 543, 635  
 Kheifets, S. A. 3462  
 Kick, R. 233  
 Kiehlmann, D. 1080  
 Kijima, Y. 1518  
 Killian, E. 2744  
 Kim, C. H. 2036  
 Kim, D. E. 2751, 2796  
 Kim, G. H. 2564  
 Kim, J. 2593  
 Kim, J. M. S. 1112  
 Kim, J. S. 3288  
 Kim, K. 2799, 2802, 2805, 2808,  
 2814  
 Kim, K.-J. 83, 1445, 1533, 3042  
 Kim, S. H. 2799, 2802, 2805,  
 2808, 2814  
 Kim, W. 3196  
 Kimura, T. 2690  
 Kimura, W. D. 2564, 2581, 2614  
 Kimura, Y. 673  
 Kincaid, B. 1572, 1575, 1578,  
 1581  
 King, R. 2172  
 Kinross-Wright, J. 2664  
 Kinross-Wright, J. M. 2970  
 Kinsho, M. 3181  
 Kipper, A. 3139  
 Kirbie, H. C. 739  
 Kirby, R. E. 2978, 3030, 3036  
 Kirchgessner, J. 763, 769, 886,  
 889, 892, 918, 921, 977, 995,  
 1399, 2953, 3450  
 Kirchman, J. 2266  
 Kirk, H. G. 3012, 3615  
 Kirkman, G. 1327, 3066, 3072,  
 3078  
 Kirsch, R. 3093  
 Kiselev, V. A. 2022  
 Kishimoto, T. 1515, 1518  
 Kishihiro, J. 673  
 Kitagawa, A. 1291  
 Kitagawa, S. 1686  
 Kitagawa, Y. 2556  
 Klaisner, L. 3033  
 Klaisner, L. A. 2978, 3027, 3036  
 Klamp, L. 3384  
 Kleb, R. 3757  
 Kleeven, W. J. G. M. 1072, 2065,  
 3423  
 Kleffner, C. M. 1747  
 Klein, H. 614, 623  
 Kleman, K. J. 924, 1235  
 Klepper, O. 1645  
 Kloeppel, P. K. 2298  
 Kneisel, P. 927, 947, 1010, 1016,  
 1060, 3867  
 Knobloch, J. 889  
 Knott, J. 2720

Knott, M. 1960  
Knowles, H. B. 1762  
Knox, A. 3757  
Knox-Seith, J. F. 255  
Ko, I. 581, 1521, 3654  
Ko, I. S. 593  
Ko, K. 936, 986, 1039, 1121  
Kobari, T. 3903  
Kobayashi, H. 3087  
Kobayashi, M. 3903  
Kobayashi, T. 3552  
Kobayashi, Y. 215, 1321  
Kobliska, G. R. 2823  
Kocur, P. 236, 1369  
Kodaira, M. 1515, 1518  
Kodama, R. 2556  
Koechlin, F. 798  
Koepke, K. 918, 1127  
Kohno, T. 1291, 1686  
Koiso, H. 3497  
Kokorin, A. M. 3822  
Kolomiets, A. A. 1675  
Kondakov, A. 1226  
Konecny, R. 815, 2596  
Kong, S. H. 2970  
Kononenko, S. 1480, 2057  
Koo, Y. M. 2751, 2796  
Koontz, R. 543, 620  
Koontz, R. F. 1318  
Koop, I. 3711  
Koopman, J. 2504  
Korchuganov, V. 230, 564, 1384,  
2793  
Korenev, I. L. 2543  
Koscielniak, S. R. 3506, 3639  
Koseki, S. 1291  
Koseki, T. 930, 1509, 2295  
Koshelkin, A. V. 1629, 1632  
Kostas, C. 3267, 3270  
Kosyakin, M. 2769  
Kot, N. C. 3243  
Kotov, V. I. 454  
Koujbida, R. P. 2853  
Koul, R. 2922  
Koul, R. K. 2924  
Kourbanis, I. 35, 405, 3630, 3799  
Koutchouk, J. P. 44, 68  
Kovachev, V. 3888  
Kowalski, S. 2054  
Kowitt, M. 2172  
Kozchekin, M. A. 2853  
Kozin, V. 1480, 2057  
Kozub, S. 2769  
Kozyrev, E. 2650  
Krafft, G. A. 426, 587, 599,  
1895, 2298, 2364, 3246, 3515  
Kraimer, M. 1960  
Krall, J. 2626, 2629, 2632  
Krämer, D. 1436, 1474  
Krasnopolsky, V. 2717  
Krasnopolsky, V. A. 933  
Krasnykh, A. 552, 2042  
Kraus, R. 1669, 1703  
Kraushaar, P. 2731, 2757, 2763,  
3888  
Krauter, K. 1922  
Krawczyk, F. 1712  
Krebs, G. 2187  
Kreiser, H. 32

Krejcik, P. 2019, 2370, 2373,  
3240  
Kreutz, R. 2748  
Krinsky, S. 492, 1439, 1491,  
1545, 1599, 1602, 1852, 3375  
Krishnaswamy, J. 1527  
Kroc, T. K. 1689  
Kroes, F. 1998, 2343  
Krogh, M. 2124, 2130  
Krogh, M. L. 2501  
Kroll, N. 620, 936, 1039, 1121,  
2559  
Kroll, N. M. 543, 983, 1196, 3453  
Kropachev, G. N. 3675  
Krueger, W. 1004, 3267  
Krug, H. 1477  
Krupnick, J. 83, 2850  
Krycuk, A. 939, 1109  
Krylov, Y. 564  
Kryshkin, V. I. 454  
Kuang, E. 2687  
Kubo, H. 1291  
Kubo, K. 992, 1027, 2364, 3503,  
3515  
Kubo, T. 1163  
Kubota, C. 1163  
Kuchnir, M. 918  
Kudelainen, V. 3243  
Kudelainen, V. I. 2022  
Kudo, H. 1509  
Kudo, K. 1163  
Kudryavtsev, V. 916  
Kukhtin, V. P. 3205  
Kulikov, A. V. 2978, 3027, 3036  
Kulinski, S. 336, 573, 611, 968  
Kulipanov, G. 564, 1384  
Kulipanov, G. N. 2751  
Kumada, M. 1291, 1686  
Kumazawa, R. 2205  
Kunkel, W. B. 1727  
Kuo, C. C. 1635, 1943  
Kuo, C. H. 2091  
Kuo, T. 372  
Kuo, T. T. Y. 1730  
Kuprianov, A. P. 682  
Kuptsov, I. 1226  
Kuramoto, R. 1300  
Kurennoy, S. S. 3417, 3420  
Kurkin, G. 1226  
Kurochkin, I. A. 2190  
Kuroda, S. 2340  
Kurokawa, S. 294, 2004, 2073  
Kurz, M. 614, 623  
Kusche, K. P. 2564  
Kushin, V. V. 1798  
Kushnick, P. 1016  
Kuske, B. 1474  
Kuske, P. 1474  
Kustom, R. 285, 549, 1013, 1057,  
1294, 3757  
Kustom, R. L. 766, 910, 913,  
1217, 2213, 3393, 3396  
Kuzmin, I. A. 844  
Kuznetsov, G. 2650  
Kuznetsov, N. A. 2022  
Kuznetsov, S. 564, 1506, 1955  
Kvashonkin, I. 2042  
Kwan, C. M. 2385  
Kwan, J. W. 3169

Kwan, T. 2675  
Kwiatkowski, S. 824, 941  
Kwok, P. 2638  
Kwon, S. 1832  
Kwon, S.-I. 3042

## L

Labrousche, J. 670, 697  
Lackey, J. 2228  
Lackey, S. 1912, 1914  
Laclare, J. L. 1427  
Lahey, T. 1969  
Lai, P. 2638  
Laird, R. J. 1814  
Lal, A. 2551  
Lamanna, G. 3243  
Lambert, G. 2376  
Lambertson, G. 1039  
Lambertson, G. R. 2109  
Lamm, M. J. 2769  
Lamont, M. 1937, 2001  
Lampel, M. 3009  
Lamzin, E. A. 3205  
Lancaster, C. 2967  
Landis, R. 2222  
Langdon, A. B. 730, 733, 3660  
Lange, F. 3864  
Langenbeck, B. 3736  
Langenbrunner, J. 1021  
Lanni, C. 3876  
Lanz, P. 1151  
Lapitsky, S. N. 2190  
Lapostolle, P. 3606  
Larsen, R. 2070  
Larsson, B. 1771  
Laslett, L. J. 724  
Lasnier, C. J. 1551, 1554  
Lath, A. 2172  
Latham, P. E. 2659, 2661, 2670,  
2673  
Latushkin, S. T. 1795  
Lau, Y. Y. 3351, 3354  
Launspach, J. 670  
Launspach, J. 697  
Laverly, M. 1139  
Lavine, T. 543  
Lavine, T. L. 620, 1121, 1196,  
1208  
Lawson, W. 2667, 2670  
Lawson-Chroco, L. 44  
Laxdal, R. E. 372  
Lazarev, N. V. 1675  
Lebedev, V. A. 2022, 3243  
Leblond, B. 3053  
Le Diberder, F. 2513  
Le Duff, J. 2045  
Lee, B. 2705, 2708, 2711  
Lee, E. P. 3678  
Lee, H. 581  
Lee, H. K. 2796  
Lee, H. S. 593  
Lee, J. C. 1943  
Lee, M. 173, 1483  
Lee, M. J. 108  
Lee, M. K. E. 2667, 2670

- Lee, S. Y. 6, 29, 102, 224, 227, 420, 432, 435, 2865, 3291  
 Lee, T. 841, 1106, 1457, 3273  
 Lee, T. G. 1259  
 Lee, Y. Y. 360, 3633  
 Leemans, W. 83, 567, 2638  
 Lefrancois, M. 3900  
 Legg, R. 587  
 Lehrman, I. 1439  
 Lehrman, I. S. 1527, 3012  
 Leibfritz, J. 3864  
 Leifeste, G. T. 2124, 2130, 2426  
 Lemaitre, E. 798  
 Lenisa, P. 3243  
 Lenkszus, F. 1960, 2304  
 Lenkszus, F. R. 1814  
 Lennox, A. J. 1666, 1756  
 Lenz, J. 2986, 3133  
 Lenz, J. W. 3151  
 Leonhardt, W. J. 3882  
 Leonov, V. V. 1795  
 Leontein, S. 1735  
 Lepeltier, V. 2513  
 Leroy, R. 1789, 1792  
 Lessner, E. 1485, 3757  
 Lessner, E. S. 399  
 Le Taillandier, P. 670, 697  
 Leung, K. 3888  
 Leung, K. K. 1503, 2787  
 Leung, K. N. 1727, 3169, 3190  
 Leung, K.-N. 3042, 3160  
 Level, M. P. 1465  
 Levichev, E. 230, 564, 1384, 1506, 2793  
 Levin, M. 2757  
 Levitt, S. 1969  
 Levy, C. D. P. 2991  
 Lewis, S. 3748  
 Lewitowicz, M. 1792  
 LHC Machine Group 3917  
 Li, C. Y. 1727  
 Li, D. 29, 224, 227, 420, 1439, 2865, 3006  
 Li, G. X. 3237  
 Li, M. 38, 236  
 Li, N. 2862  
 Li, Q. 1620  
 Li, R. 1909, 3473  
 Li, T. 2841  
 Li, X. 3527  
 Li, Z. 179, 1721  
 Liang, C. 2841  
 Liang, C. F. 1792  
 Liang, D. 3696  
 Lidbjörk, P. 2068  
 Liebmann, J. 1747  
 Lien, E. 1106  
 Liger, P. 3663  
 Likhachev, V. 1480, 2057  
 Liljeby, L. 1735  
 Lima, S. 1892  
 Limberg, T. 429, 2019, 2025, 2435, 3240  
 Lin, K. K. 2031  
 Lin, L. 252  
 Lin, L. C.-L. 2575, 2696, 2699  
 Lin, X. 3453  
 Lindner, A. 1160  
 Lindner, A. F. 2210
- Linnecar, T. P. R. 2376  
 Linnemann, J. 1477  
 Linscott, I. 2076, 2352  
 Liou, R. 2638, 3039, 3066, 3072, 3537  
 Lipkin, I. M. 1675  
 Lipnicky, M. 1151  
 Lippmann, G. 944  
 Lipsett, M. G. 1039  
 Liska, D. 1718  
 Littmann, B. 1133  
 Litvinenko, V. N. 218, 1442, 2889  
 Liu, B. 1611  
 Liu, C. J. 688  
 Liu, H. 279, 512, 1563, 3663  
 Liu, H. C. 2886  
 Liu, J. 182, 285, 2841  
 Liu, K. 1262  
 Liu, Y. 2151  
 Liu, Y. C. 1635  
 Liu, Z. 2070  
 Lo, C. C. 1142, 1238, 3058  
 Lobanov, N. R. 3187  
 Lockner, T. R. 667  
 Loew, G. 1445, 3084  
 Loew, G. A. 543, 620, 644  
 Logachov, P. 3243  
 Loiselet, M. 1672  
 Lom, C. 821, 2133  
 Lombardi, A. 3121, 3606  
 Lopez, F. 2922, 2924  
 López, G. 200, 2784, 3255, 3467  
 Lorello, M. 1709  
 Lorenz, R. 1133, 2325  
 Losito, R. 2154  
 Low, K. 1823, 1826, 1829  
 Lu, J. 2711  
 Lu, J. J. 1303  
 Lu, X. 3366, 3799  
 Lu, X. P. 472  
 Lublinsky, B. 1817, 2249  
 Luccio, A. 438, 1872, 2175  
 Luchini, K. 1265  
 Ludewigt, B. A. 1759  
 Ludmirsky, E. A. 315  
 Ludwig, P. 2997  
 Ludwig, T. 3139  
 Luginsland, J. W. 3354  
 Luijckx, G. 1998  
 Lujan, R. 2947  
 Lukasiewicz, J. 1890  
 Lulevich, V. I. 2853  
 Lumpkin, A. 2304  
 Lumpkin, A. H. 2086, 2112  
 Luo, G. 1211  
 Lütkehaus, H. 2748  
 Lutz, I. 1265  
 Lyashchenko, V. 1480  
 Lynch, D. 1439, 3000  
 Lynch, M. T. 1683, 2391  
 Lyons, S. 608, 611  
 Lysenko, A. 3711  
 Lysenko, W. P. 1669
- Ma, Y. 1611
- Maas, R. 1901, 1998  
 Macek, R. 363, 366, 369, 2216, 2219, 2319, 3297  
 Macek, R. J. 3739  
 Macek, R. W. 3760  
 Macha, K. 2929  
 Machida, S. 176, 255, 3724, 3558  
 Maciga, B. 3243  
 Maciszewski, W. 1890  
 Mackenzie, G. H. 372  
 Mackenzie, R. 1966  
 MacKenzie, R. 1969  
 Mackerrow, E. 369  
 MacLachlan, J. 405  
 Maddocks, J. 3879, 3888, 3891  
 Madduri, V. B. 2711  
 Madey, J. M. J. 218, 1442, 2889  
 Madlung, J. 3139  
 Maeda, H. 676  
 Magyaray, S. 1811  
 Mahale, N. 423, 3769  
 Mahale, N. K. 877  
 Mahoney, K. L. 2298  
 Maier, K. 3093  
 Maillard, J. 3093  
 Main, W. 2714  
 Maisheev, V. A. 315, 322  
 Majima, T. 1321  
 Makarov, A. A. 3822  
 Makarov, I. 2650  
 Mako, F. M. 2702  
 Makowski, M. 1551  
 Makowski, M. A. 1554  
 Makulkin, A. V. 3702  
 Malitsky, N. 128  
 Malone, R. 2486  
 Malyshev, O. 3876  
 Mammosser, J. 781, 947, 1016, 2929  
 Manarin, A. 2492  
 Manca, J. 608, 611, 1244  
 Mane, V. 3435, 3438  
 Mangino, J. 2382  
 Manheimer, W. M. 2644, 2647  
 Manini, P. 3839  
 Mankofsky, A. 3267  
 Mann, J. 2498, 2504  
 Mao, N. 333  
 Mapes, M. 3882, 3897  
 Mariam, F. G. 384  
 Marin, M. 1063  
 Marin, P. 1465  
 Marino, M. 3839  
 Markov, V. 1480, 2057  
 Marks, N. 2898  
 Marks, S. 1572, 1575, 1578, 1581  
 Marneris, I. 1277  
 Maroli, C. 1524  
 Marquardt, J. 3118  
 Marquardt, N. 1471  
 Marrufo, O. 827, 1169, 3213  
 Marsden, E. 3127, 3213  
 Marsden, S. 827  
 Marsh, K. A. 558, 2551  
 Marsh, W. 1912  
 Marshall, J. 841, 1396  
 Martens, M. 405  
 Martens, M. A. 1963, 3300  
 Martin, D. 1703, 2118, 3888
- M

Martin, K. 1914  
 Martin, P. 3793  
 Martin, R. 2913  
 Martini, M. 3570, 3699  
 Maruyama, T. 2172  
 Maruyama, X. K. 1620, 2397  
 Marziali, A. 950  
 Mashiko, K. 602  
 Maslennikov, I. 3876  
 Massarotti, A. 953, 956, 1145  
 Masuda, H. 1780, 1783  
 Masullo, M. R. 2154  
 Masunov, E. S. 1681, 2474  
 Mathae, J. C. 2432  
 Matheisen, A. 918  
 Mathewson, A. G. 3828  
 Mathieson, D. 1823, 1826, 1829  
 Matsumoto, H. 959, 1124  
 Matsumoto, S. 1291, 3491  
 Matsuoka, M. 1024  
 Matthews, H. W. 2667  
 Matuk, C. 83  
 Matumoto, M. 3903  
 Matveev, Y. 1348, 1384  
 Matz, W. 1477  
 Mavrogenes, G. 549, 605  
 May, R. 2184  
 Mayoud, M. 44  
 Mazarakis, M. G. 667  
 Mazumdar, T. K. 2705, 2708, 2711  
 Mazur, P. 2769  
 Mazur, P. O. 2856  
 McAllister, B. 2054  
 McAllister, B. G. 1875  
 McAshan, M. 2757  
 McCammon, D. 1421  
 McCauley, G. 1718  
 McCormack, F. 2187  
 McCormick, D. 1975, 2160, 2423  
 McCrory, E. S. 1691, 1952  
 McDonald, D. S. 3190  
 McDowell, C. 2477  
 McDowell, W. 1960  
 McGhee, D. 1864, 3757  
 McGhee, D. G. 1271, 2817  
 McGill, J. 378, 381, 384  
 McGill, J. A. 333  
 McGinnis, D. 35, 2100, 2228, 2231, 2361, 3533, 3787  
 McGinnis, K. 2124, 2130  
 McInturff, A. 2731, 2763  
 McInturff, A. D. 2757  
 McIntyre, P. M. 2705, 2708, 2711  
 McKenzie-Wilson, R. 1172  
 McMahan, M. A. 2187  
 McMichael, G. E. 1175  
 McMurry, D. 1669  
 McNerney, A. 1166  
 McNerney, A. J. 1241  
 McPherson, J. 32  
 Meads, P. F., Jr. 3825  
 Meddahi, M. 1488, 3312  
 Medvedko, A. 1297  
 Meigs, M. J. 1660  
 Meinke, R. 203, 2468, 2489  
 Meisner, K. 405, 2519, 2522, 2525  
 Meitzler, C. R. 3148  
 Melin, G. 2997  
 Meller, R. E. 578  
 Mellors, W. 1039  
 Melnychuk, S. 3193  
 Melton, J. G. 2944  
 Mendelsohn, S. L. 1774  
 Menegat, A. 543, 620, 1121, 1196, 1208  
 Meng, W. 2883, 2904, 2907  
 Menge, P. R. 2693, 3351  
 Menninger, W. L. 2656  
 Men'schikov, L. 552  
 Mercier, E. 3202  
 Merl, R. 2799, 2802, 2805  
 Merle, E. 670, 697, 2115  
 Merminga, L. 599, 2184, 2364, 3515  
 Merz, W. 1841, 1898  
 Meshchero, R. 2717  
 Mestha, L. K. 2382, 2385  
 Meth, M. 1166, 1241, 2286  
 Metty, P. 1244  
 Metzger, D. 918, 995, 1399, 3450  
 Meuth, H. 962, 1253, 3381  
 Meyer, D. 3888  
 Meyer, F. 1841, 1898  
 Meyer, R. 1703  
 Meyer, R. E. 2334, 2480  
 Meyer, W. 1551  
 Meyer, W. H. 1554  
 Meyerhof, W. E. 3751  
 Meyerhofer, D. D. 2638  
 Mezentssev, N. A. 1494, 2751  
 Michelotti, L. 80, 495  
 Michizono, S. 1193  
 Micklich, B. J. 1715  
 Miele, G. 209, 212  
 Miertusova, J. 3842, 3873  
 Migdal, W. 1890  
 Mihelic, R. 3888  
 Milburn, J. E. 2796  
 Miles, J. 44, 2001  
 Militin, B. L. 2022  
 Militsyn, B. 3711  
 Miller, E. 1972  
 Miller, J. 3612  
 Miller, R. 608, 608, 611, 611, 3084  
 Miller, R. H. 543, 620, 3027, 3063  
 Miller, W. 369  
 Millich, A. 965, 3426  
 Milliman, L. 2967  
 Millo, D. 1587  
 Mills, F. 285, 549, 3757  
 Mills, F. E. 2817, 2922, 2924  
 Mills, M. R. 2322  
 Mills, R. S. 3657  
 Millsom, D. 1966  
 Milstead, I. 2301  
 Milton, B. 1733  
 Mimashi, T. 2340  
 Miné, P. 2450  
 Ministrini, M. 573, 968  
 Minty, M. 224, 227, 447, 2019, 2370, 2373, 2435, 3240  
 Minty, M. G. 29, 420  
 Miram, G. 1106  
 Mironov, V. 2042  
 Mirzozan, A. 2426  
 Mishin, A. V. 971  
 Mishnev, S. I. 2022  
 Mishra, C. S. 342, 345, 348, 351, 2829  
 Mitchel, G. R. 2415  
 Mitra, A. K. 974, 1303  
 Mitsuhashi, T. 215  
 Mitsui, H. 2205  
 Miura, A. 959, 1124  
 Miura, I. 1650  
 Miwa, H. 1024  
 Miyahara, Y. 653  
 Mizuno, A. 602  
 Mizuno, H. 1202, 1321  
 Mocheshnikov, N. 1480, 2057  
 Mock, R. C. 691  
 Modéer, J. 2034  
 Moe, H. 3757  
 Moe, H. J. 2213  
 Moerel, J. 2892  
 Moffat, D. 763, 769, 886, 889, 892, 918, 921, 977, 995, 3450  
 Moffeit, K. 2172  
 Moiseev, V. A. 3249  
 Mokhov, N. V. 1360, 1369, 3090, 3109, 3772  
 Moller, J. 1551  
 Moller, J. M. 1554  
 Møller, S. P. 1363, 1741  
 Molodkin, V. 1480  
 Momose, T. 3885  
 Mondelli, A. 1004, 3267, 3270  
 Montès, B. 2450  
 Montuclard, J. 3900  
 Morales, G. 3888, 3891  
 Morales, H. 3018  
 Morano, R. 2450  
 Moravec, K. 3864  
 Morcombe, P. 1339  
 Morduev, A. 1672  
 Moretti, A. 1127, 1214  
 Morgan, G. 2744, 2766  
 Morgan, G. H. 2754  
 Morgillo, A. 2744, 2766  
 Mori, W. B. 2635  
 Mori, Y. 2991, 3181, 3754  
 Morillo, J. 2450  
 Morishita, O. 1686  
 Moritz, G. 3736  
 Morpurgo, G. 2103  
 Morse, W. 2070  
 Mortazavi, P. 1419  
 Morton, P. 1445  
 Moshhammer, H. 131, 2025  
 Moskalenko, V. 1480, 2057  
 Mosnier, A. 629, 855  
 Mottershead, C. T. 1669  
 Mourou, G. 2632  
 Moz, S. 1063  
 Mroczkowski, T. T. 2919  
 Mudiugin, B. 2042  
 Mud'jugin, B. G. 3822  
 Mukugi, K. 1515, 1518  
 Mulholland, G. 2757  
 Muller, H. 889, 918, 995, 2953  
 Müller, R. 1887  
 Munson, F. H. 1694  
 Murakami, T. 1291, 1686

Muratore, J. 2744, 2766  
Murin, B. P. 980  
Murphy, J. B. 1477  
Murphy, K. 2967  
Murray, D. 1838, 2757  
Murray, J. 1274, 1855, 1858, 1861  
Musenich, R. 1001  
Mustaine, R. E. 1033  
Myae, E. A. 318, 322  
Mynk, J. 1250  
Mytsykov, A. 1480, 2057  
Myznikov, K. 2769

## N

Nadji, A. 1465  
Nagaenko, M. 2057  
Nagafuchi, T. 2039  
Nagaitsev, S. 29, 224, 227, 420,  
3524, 3745  
Nagaitsev, S. S. 3536  
Nah, Y. G. 2796  
Nakagawa, S. 1468  
Nakahara, Y. 1566  
Nakajima, K. 2556, 2638, 3552  
Nakajima, S. 676  
Nakamura, H. 2260  
Nakamura, K. 3537  
Nakamura, N. 2257, 2295, 2337  
Nakamura, T. 3464  
Nakanishi, H. 2556, 2638, 3552  
Nakao, K. 1193  
Nakayama, H. 2340  
Nakazato, T. 1614, 1617  
Nam, S. 581  
Nam, S. H. 593, 1315  
Namkung, W. 581, 593, 1315,  
1521  
Nantista, C. 543, 620, 983, 1196  
Napoly, O. 632, 3347  
Nassiri, A. 605, 2142, 2412  
Nation, J. A. 1312, 2653, 2684,  
2687  
Natter, E. F. 1154, 2391  
Nawrocki, G. J. 1957  
Nawrocky, R. 2246  
Nawrocky, R. J. 2145  
Nazmov, V. 3876  
Neil, G. 279, 3663  
Neil, G. R. 1563  
Nelson, E. M. 983, 1086  
Nelson, J. 1916  
Nelson, W. R. 185  
Nemoshkalenko, V. 1480  
Neri, F. 56  
Nesterenko, I. 3711  
Nesterov, N. A. 1798  
Nett, D. 611  
Neuffer, D. 2136, 3297, 3663  
Neumann, W. 1477  
Neuschaefer, G. 1683  
Newberger, B. S. 387, 3588  
Newman, W. 2133  
Newton, M. A. 739  
Nexsen, W. 2468, 2489  
Nezhevenko, O. 564, 2650  
Ng, C. K. 986, 1039, 2638, 3432

Ng, K. Y. 29, 35, 102, 224, 227,  
405, 420, 3300, 3630  
Ng, L. S. B. 1949  
Ng, Y. 2133  
Nguyen, D. C. 2970  
Nguyen, T. K. 2997  
Nguyen-Tuong, V. 1007  
Nick, W. 2748  
Nicol, T. 3021  
Nicol, T. H. 989  
Nielsen, R. 3757  
Nightingale, M. P. S. 1777  
Niki, K. 1780, 1783, 1786  
Nikiforov, A. 2650  
Nilsson, A. 1735  
Nilsson, B. 1771  
Ninan, L. 599  
Nishi, M. 309  
Nishida, Y. 2556, 2638, 3552  
Nishimura, H. 111  
Noda, A. 41, 1291, 1697  
Noda, K. 1291, 1686  
Nodarse, F. F. 1892  
Noguchi, S. 992, 1024  
Nolden, F. 1645, 1738  
Nolen, J. A. 71, 89, 1694  
Nomura, M. 546  
Noomen, J. 1998  
Noomen, J. G. 2343  
Nordberg, E. 995  
Norem, J. 2462, 2638  
Nortier, F. 3099  
Nosochkov, Y. 125, 143, 239,  
3778  
Novak, J. 1021  
Novak, W. 2462  
Nuhn, H.-D. 173, 1445, 1608  
Nurushev, S. B. 315  
Nusinovich, G. S. 2572, 2659,  
2661, 2673  
Nyman, M. 3748

## O

Oasa, K. 1554  
Obert, J. 1792  
Obina, T. 2409  
Ochsner, J. 2790  
O'Connell, J. S. 3657  
O'Day, S. 330, 2459, 3096  
Oeftiger, U. 2157  
Oehme, W. 1477  
Oganessian, R. 1672  
Ogata, A. 2556, 2638, 3552  
Ogawa, H. 1291, 1686  
Ogawa, Y. 2516, 3087, 3705  
Ogitsu, T. 2769  
Ogiwaru, N. 1566  
Ogloblin, A. A. 1795  
Ogren, H. 2172  
Ogura, K. 2714  
Oguri, Y. 3115  
Oh, J. S. 593, 1315  
Ohkuma, H. 1509  
Ohmori, C. 3297  
Ohnuma, S. 3148, 3603  
Ohsawa, S. 2516, 3087, 3705

Ohsawa, Y. 2205  
Oide, K. 466, 2340, 3339  
Oikawa, Y. 3845  
Okamoto, H. 221, 1545, 1697,  
3390  
Okamura, M. 3115  
Okay, N. 2986, 3151  
Okay, N. C. 2483, 3133  
Oku, Y. 1468  
Okuda, S. 650  
Olchowski, F. 32  
Oldfather, D. E. 2210  
Oliphant, V. 1706  
Olivier, R. 44  
Olivo, M. 3190  
Ollis, C. W. 739  
Olsen, D. K. 1660  
Olsen, R. 44, 1274, 1855, 1858,  
1861  
Olson, R. E. 667  
Onel, Y. 32  
Onillon, E. 2379  
Onischenko, L. 2042  
Onischenko, L. M. 518  
Ono, M. 546, 1024, 1163  
Oogoe, T. 3087  
Oothoudt, M. A. 3106  
Oren, W. 2929  
Orlov, Y. 3488  
Orr, N. 1792  
Orris, D. 2769  
Orthel, J. L. 1762  
Orzechowski, J. 3099  
Oshita, H. 546  
Osipov, V. 3876  
Ostiguy, J. 2901  
Ostiguy, J.-F. 2829  
Ostreiko, G. 564  
O'Sullivan, M. 1925  
Otis, A. 1241  
Otter, A. J. 2898  
Ovchinnikov, V. P. 555  
Owens, T. L. 1689, 1691  
Oxoby, G. 2076, 2352  
Oyamada, M. 1614, 1617  
Ozaki, T. 673, 2205

## P

Paál, A. 1735  
Padamsee, H. 763, 769, 886, 889,  
892, 918, 921, 977, 995, 998,  
1399, 3450  
Page, T. 2459  
Page, W. 2222  
Palkovic, J. A. 21, 3261  
Palmer, D. 620  
Palumbo, L. 212, 778  
Pan, C. 44  
Pang, Y. 2705, 2708, 2711  
Papash, A. 372  
Papash, A. I. 3822  
Pappas, G. C. 1336  
Papureanu, S. 962, 1747  
Pardo, R. C. 1694  
Paris, P. 1792  
Parish, D. J. 2790

Parisi, G. 3121, 3124  
Park, K. H. 2796  
Park, S. 561, 570, 2976, 3003, 3216  
Park, S. S. 593, 1315  
Parker, B. 1360, 3772, 3775  
Parkhomchuk, V. V. 2022, 2959  
Parodi, R. 775, 778, 1001, 1524  
Parry, R. 2222  
Parry, R. R. 2225  
Parsa, Z. 509, 2723  
Parshin, I. O. 1798, 3675  
Parzen, G. 483, 486, 489  
Pasotti, C. 953, 956, 1145  
Pasquinelli, R. 3533  
Pasquinelli, R. J. 2081, 2355, 2361  
Passardi, G. 2739  
Paterson, A. 2850  
Paterson, J. 1445  
Paterson, J. M. 543  
Patteri, P. 573  
Patterson, D. 2112  
Paulson, C. C. 1774  
Pauluhn, A. 270  
Pavlov, S. N. 3822  
Pawlak, T. 3793  
Paxson, V. 1940  
Payet, J. 1465  
Payne, A. N. 736  
Payne, J. 3870  
Pearce, W. J. 1949  
Pearson, C. 543, 907, 1106, 1259  
Pearson, C. C. 620  
Pedersen, F. 2370, 3240  
Peggs, S. 35, 168, 233, 258, 261, 351  
Peggs, S. G. 74  
Pei, X. 29, 224, 227, 420, 1421, 1424  
Peiniger, M. 1080  
Pekeler, M. 918  
Pellegrini, C. 173, 561, 570, 575, 1445, 1533, 1608, 2617, 2976, 3003, 3216  
Pelligrini, C. 3543  
Pendleton, R. P. 1039  
Penner, S. 381  
Penzo, A. 32  
Perelstein, E. 2042  
Perevedentsev, E. 3429, 3711  
Perkins, L. T. 3190  
Perregrini, L. 772  
Perret, R. 2202  
Perry, J. 587, 1925, 2184  
Persov, B. 2650  
Pescharadt, E. 1903, 2358, 3429  
Peschel, H. 2748  
Pestrikov, D. 294  
Pestrikov, D. V. 3681, 3684, 3687  
Peter, W. 2702  
Peters, C. 703  
Petersen, D. 1551, 3836  
Petersen, D. E. 1554  
Peterson, D. 809, 3533  
Peterson, D. W. 3573  
Peterson, E. 2400  
Peterson, J. 203, 2281, 3769, 3781  
Peterson, T. 809

Petillo, J. 1004, 3267  
Petradza, M. 2172  
Petrov, E. 2042  
Petrov, S. 1297  
Petrov, V. 824, 1226  
Petrov, V. M. 877, 941  
Petrucci, G. 2820  
Pettersson, O. 1771  
Pewitt, E. G. 2823  
Peyromaure, J. 858  
Pfeffer, H. 918  
Philipchenko, A. 564, 1384, 2793  
Phillips, H. L. 1007  
Phillips, R. 543, 1106  
Phinney, N. 116, 2019  
Pianetta, P. 1445, 1536  
Picard, M. 1477, 2534  
Pickens, D. R. 1448  
Pierini, P. 1524, 1569  
Piestrup, M. A. 1620, 2397  
Pikin, A. 1735  
Pilat, F. 143, 203, 239, 515  
Pile, G. 1709, 3210  
Pimiskern, K. 944  
Pindyurin, V. 3876  
Pinkow, J. 357  
Piovella, N. 1524  
Pipersky, P. 1572  
Pirkl, W. 1172, 1241  
Pirozhenko, V. M. 3112  
Pisent, A. 32  
Pistoresi, D. 2967  
Pitchford, L. 3039  
Pivarc, J. 3894  
Placidi, M. 44  
Plate, D. 1572, 1575  
Platt, R. C. 2456  
Plesea, L. 3133  
Plesko, M. 149, 152, 1477, 2534  
Plink, O. V. 3112  
Plotnikov, S. V. 1798  
Plotnikov, V. K. 1675  
Plouffe, D. 2736  
Ployard, G. 2115  
Plum, M. 366, 2181, 2319, 3297  
Pogorelsky, I. 2564, 2614  
Poilleux, P. 2450  
Poirier, R. L. 753  
Poizat, J. C. 3093  
Poliakova, R. V. 1892  
Poll, D. 3533  
Pollock, D. 2760  
Poloni, C. 1587  
Pontonnier, M. 2997  
Poole, M. W. 1494, 1638, 3594, 3672  
Popkov, Y. 1480, 2057  
Popov, A. 2042  
Popov, Y. 552  
Popovic, M. B. 1214, 1689, 1691  
Porro, M. 3839  
Porter, J. 2133, 2420  
Portmann, G. 1572, 2272  
Postiau, N. 1672  
Potter, J. 1004  
Potts, C. 3757  
Potukuchi, P. N. 1045  
Poukey, J. W. 667, 691, 694  
Power, J. 1669, 1844, 2596, 3061

Power, J. F. 2334  
Powers, T. 1007, 1010, 1016  
Pozdeev, E. 3711  
Pradal, F. 3842  
Preble, J. 841, 1396, 2929  
Preger, M. A. 2048  
Preist, D. H. 1103  
Prescott, C. 3033  
Prescott, C. Y. 2978, 3027, 3036  
Price, E. 587  
Price, R. R. 1448  
Primdahl, K. 766, 1013, 1294  
Pripstein, D. 2172  
Proch, D. 758  
Prodell, A. 2744, 2766  
Pröhl, D. 1477  
Propp, A. 824, 941  
Prosnitz, D. 1445  
Prusakov, V. 552  
Pruss, S. 2252  
Pruss, S. M. 3802  
Ptitsin, V. 3711  
Puech, V. 3039  
Pullia, M. 1524  
Pusterla, M. 32  
Putaux, J. C. 1792  
Puzo, P. 2513

## Q

Qian, G. 745, 3521, 3696  
Qian, Q. 2670  
Qin, J. 3237  
Qin, Q. 3237  
Qiu, X. Z. 1439  
Quinn, P. D. 1638, 3594, 3672  
Qunell, D. 1357

## R

Raabe, P. 1645  
Raffone, G. 2048, 3906  
Rahn, J. 1887  
Raimondi, P. 98, 100, 116, 2019  
Rajagopalan, S. 2638, 3555  
Rakowsky, G. 1605  
Ramamoorthy, S. 1849, 1852  
Ramaswamy, K. 685  
Rambaldi, S. 273  
Ramirez, G. 1419  
Ramseier, G. 44  
Ranganathan, R. 1402  
Rao, M. G. 927, 3867  
Raparia, D. 122, 1765, 2127, 2426, 2986, 3130, 3151, 3509, 3585  
Rathke, J. 1709  
Ratner, L. 432  
Ratti, A. 1166, 1172  
Raubenheimer, T. 417, 1445, 2019  
Raubenheimer, T. O. 11, 596, 635, 2025, 2880  
Rauchas, A. 3757  
Rawlins, A. 1727  
RD22 Collaboration 26

Reece, C. 1007, 1016  
Reece, R. K. 1277, 3763  
Reed, L. 2462  
Rees, D. 3213  
Rees, D. E. 1169, 1199, 1205  
Rees, G. 3297  
Rees, G. H. 3731  
Reeve, P. A. 2898  
Reeves, S. 2817  
Regan, A. 1683, 3213  
Regan, A. H. 1154, 2391  
Reginato, L. 703, 1351  
Reginato, L. L. 656  
Rehak, M. 2744, 2766  
Reich, H. 1645  
Reid, C. 809  
Reilly, R. 1357  
Reimund, J. A. 1280  
Reinhardt, N. 1327, 3078  
Reiniger, K. W. 1112, 1283  
Reiser, M. 62, 65, 685, 2667,  
2670, 3145, 3282, 3627, 3648,  
3660  
Reist, H. 1771  
Reistad, D. 1744, 3745  
Remelius, D. 2967  
Remillieux, J. 3093  
Remondino, V. 68  
Remy, M. A. 1089  
Rendon, A. M. 2480  
Renou, G. 3093  
Rensfelt, K.-G. 1735  
Repnov, R. 1747  
Reusch, M. F. 59, 1527, 3624  
Rhee, M. J. 688  
Ricaud, C. 1789  
Rice, D. 1978, 3479  
Rice, D. H. 2007  
Richardson, R. D. 2456, 3772  
Richter, R. 1160  
Richter-Sand, R. J. 1306  
Ride, S. K. 1623  
Riedel, C. 3736  
Rietdyk, H. 2397  
Rieubland, J.-M. 2739  
Rifkin, J. 543  
Rimmer, R. 1039  
Rimmer, R. A. 871, 874, 3411  
Rinckel, T. 32  
Ringwall, A. 1703  
Ringwall, A. D. 846  
Riordon, J. 2118  
Risselada, T. 246  
Ritchie, A. L. 2210  
Ritson, D. M. 125, 143, 3778  
Riunaud, J. P. 3570  
Rivkin, L. 3429  
Rivoltella, G. 1524  
Rizzi, V. 1145  
Robb, A. 1575  
Robb, J. 2929  
Robertson, S. 2641  
Robin, D. 131, 173  
Robins, K. 1439, 1602  
Robins, K. E. 2742  
Robinson, W. 2731, 2757, 2763  
Roche, C. T. 1715  
Ródenas, J. 647  
Rodenburg, R. 2967

Rodenz, G. 2664, 3267  
Rodger, E. 2895  
Rodgers, J. 685  
Rodrigues, A. R. D. 1454  
Rodriguez, J. P. 798  
Rodriguez, R. 827, 1250  
Roecklein, J. C. 2919  
Rogdestvinsky, B. V. 3822  
Rogers, J. D. 1033, 1256  
Romero, A. 128  
Rondeau, G. 420  
Rönnqvist, T. 1771  
Root, L. 372  
Ropert, A. 1512  
Roques, A. 670, 697  
Rose, C. 1669  
Rose, C. R. 2334  
Rose, J. 1172  
Rosengård, U. 1735  
Rosenthal, S. E. 694  
Rosenzweig, J. 233, 561, 1445,  
1548, 2623, 2638, 2976, 3024,  
3216, 3357, 3494  
Rosenzweig, J. B. 3021  
Roser, T. 2286, 3207, 3633, 3763  
Rosier, L. 3093  
Rosing, M. 815, 2596  
Ross, M. 522, 1975, 2019, 2234,  
2435  
Ross, M. C. 1972, 2160, 3564  
Rossa, E. 2432, 2492, 3429  
Rossi, C. 953, 956, 1145  
Rossi, L. 1524  
Rossmannith, R. 32, 429, 457, 1477  
Rostamzadeh, C. 1405  
Rotela, E. 1497  
Roth, G. 3072  
Rothman, J. L. 2307  
Rouaud, C. 3900  
Roux, D. 2932  
Rowson, P. 2172  
Roy, A. 1045  
Rubin, D. 921, 3450, 3479  
Rubingh, M. J. A. 1072  
Rudchik, A. T. 3822  
Rudd, H. 65  
Rudenko, V. 552  
Rudolph, K. 1019  
Ruggiero, A. G. 700, 3530  
Ruggiero, F. 503  
Ruiz, E. 3405  
Ruland, R. E. 2736, 2950  
Rule, D. W. 1620, 2397, 2453  
Rullier, J. L. 2656  
Ruschman, M. 809  
Rusnak, B. 1021  
Russell, S. J. 2537, 2970  
Russell, T. 605  
Russell, T. J. 1324  
Russo, D. 2286  
Rusthoi, D. P. 1669, 3118  
Ruth, R. D. 291, 543, 620, 907,  
1196, 3693  
Rutkowski, H. 703  
Rutkowski, H. L. 706  
Ryan, W. A. 2310, 2328  
Rybakov, E. 2769  
Rybalok, V. 2717  
Rychagov, A. 2769

Ryckewaert, G. 1672  
Ryder, R. 3739  
Ryne, R. 3267  
Ryne, R. D. 3229  
Ryu, C. 581  
Rzaev, R. A. 454  
Rzezonka, B. 2748

## S

Saadatmand, K. 2124, 2127,  
2426, 2483, 2986, 3127, 3130,  
3133, 3145, 3151  
Sacepe, B. 697  
Sachtschale, R. J. 1339  
Saeki, H. 3885  
Sáez, P. 3033  
Sáez, P. J. 2978, 3027, 3036  
Safranek, J. 1491, 2275  
Sagalovsky, L. 288, 838, 1715  
Sagan, D. 53, 3470, 3479  
Sage, J. 1838, 2444, 2483, 3127  
Saint Laurent, M. G. 1792  
Saito, K. 673, 1024  
Saito, Y. 1193  
Sajaev, V. 230  
Sakamoto, K. 1566  
Sakamoto, S. 676, 1321  
Sakanaka, S. 1027, 3503  
Sakaue, H. A. 3845  
Sakawa, Y. 2556  
Saladin, V. 2763  
Sale, K. E. 1663  
Salimov, A. 3876  
Sampayan, S. E. 1554  
Sampson, W. 1439, 1602, 2744,  
2766  
Sampson, W. B. 2742, 2904  
Sandberg, J. 1277  
Sander, O. R. 1669, 3118  
Sanders, R. 1241  
Sanders, R. T. 1166  
Sandoval, D. P. 1669  
Sandweiss, J. 2578, 2617  
Sanford, T. W. L. 691  
Sannibale, F. 611  
Sapozhnikov, L. 2076, 2352  
Sapp, W. 1372, 2054  
Sapp, W. W. 2832, 2935, 2938,  
2941  
Saraniti, D. 921  
Saritepe, S. 354  
Sarkar, S. 1841, 1898, 1916, 1919  
Sasaki, Y. 2039  
Sass, R. 2106  
Sass, R. C. 1946  
Sathe, S. 1846, 1852  
Sato, H. 1291  
Sato, I. 546, 590, 1193, 1416,  
2516, 3087, 3705  
Sato, K. 1291, 1686  
Sato, Y. 1291, 1686  
Satogata, T. 261  
Satoh, K. 3115  
Sauer, L. 3863, 3864  
Saulter, Q. 841  
Saunders, C. 1864

Saversky, A. J. 1030  
 Savord, T. 1914, 2731, 2757  
 Sawada, K. 1686  
 Sawyer, D. 2838  
 Sazhin, V. 2717  
 Scala, R. G. 2519  
 Scandale, W. 16, 246  
 Schachinger, L. 1940  
 Schachter, L. 1312  
 Schächter, L. 2567, 2653, 2684,  
 2687  
 Schaefer, J. 907  
 Schäfer, P. 2748  
 Schaffer, G. 1033, 1256  
 Schaille, R. 236, 378, 1360, 1369  
 Scharlemann, E. T. 1530, 1533,  
 1551  
 Scharlemann, T. 1445  
 Scheer, M. 1474  
 Schegolev, L. 1384  
 Schellekens, P. H. J. 2927  
 Schempp, A. 3139, 3142  
 Schimmel, F. 1901  
 Schlenk, R. 1477  
 Schlueter, R. 1572, 1575, 1581  
 Schlueter, R. D. 1727  
 Schmalzle, J. 2790  
 Schmickler, H. 2001  
 Schmid, J. 2739, 2956  
 Schmidt, C. W. 1655, 1689, 1691  
 Schmidt, F. 246, 500, 2301  
 Schmidt, R. 44, 2103, 2133  
 Schmitt, D. R. 3172  
 Schmor, P. W. 2991  
 Schmöser, P. 886, 918  
 Schnase, A. 962, 1253, 3381  
 Schneider, J. D. 1669, 3166, 3172  
 Schneider, L. X. 1354  
 Schneider, W. 841, 1396  
 Schneider, W. J. 2929  
 Schoessow, P. 1844, 2596, 3050  
 Scholz, T. 1036  
 Schriber, S. O. 3760  
 Schukeilo, L. A. 3822  
 Schultz, D. 3033  
 Schultz, D. C. 2978, 3027, 3036,  
 3039  
 Schultz, S. 2559  
 Schumm, B. 2172  
 Schürmann, M. 264  
 Schwalm, D. 1747  
 Schwandt, P. 3184, 3745  
 Schwarz, H. D. 1039  
 Schweppe, E.-G. 1178  
 Schwettman, H. A. 950  
 Schwitters, R. 3781  
 Sciuotto, W. 1063  
 Sears, J. 763, 769, 886, 889, 892,  
 918, 921, 977, 995  
 Sebek, J. 3018  
 Sedlacek, M. 3745  
 Sedlyarov, I. 1226  
 Seeman, J. 1445, 1608, 2019  
 Seeman, J. T. 414, 596, 638,  
 2423, 2507, 3234, 3564  
 Segalov, Z. 685  
 Seidl, P. 721  
 Seifrid, P. 3533  
 Seleznev, V. S. 2190  
 Selin, A. V. 2853  
 Sellyey, W. 2112, 2237, 2304  
 Selph, F. 83  
 Semertzidis, Y. 2070  
 Sen, T. 134, 137, 140, 143, 146,  
 239, 3778  
 Senichev, Y. 3509, 3642  
 Seo, H. S. 2751  
 Serafim, P. 1560  
 Serafini, L. 3024, 3279  
 Serdobintsev, G. 564, 2650  
 Serebrennikov, D. 2042  
 Sereno, N. S. 3246  
 Sergeeva, O. S. 2853  
 Serio, M. 778, 2076, 2352  
 Servranckx, R. 236, 255  
 Servranckx, R. V. 167, 3784  
 Sessler, A. 2638  
 Sessler, A. M. 1530, 2593, 2608,  
 3288, 3527  
 Sethi, R. 1703  
 Settles, M. 2172  
 Severgin, Y. 2057, 2769  
 Severgin, Y. P. 2208, 3205, 3820,  
 3822  
 Shafer, B. E. 1285  
 Shafer, R. E. 2316  
 Shaimerdenov, E. 564  
 Shako, V. V. 2406  
 Shalz, L. 3748  
 Shan, J. 405  
 Shan, J. P. 35, 74, 3787  
 Shan'gin, V. 2769  
 Shankland, L. W. 1175  
 Shapiro, G. 2172  
 Sharma, S. 1497, 1500  
 Sharp, W. M. 733, 2593  
 Shatunov, Y. 3711  
 Shchedrin, I. S. 1030  
 Shcherbakov, A. 1480, 2057  
 She, K. 995  
 Shea, T. 3438  
 Shea, T. J. 2310, 2328, 2916  
 Sheedy, E. 3012  
 Sheehan, J. 1439, 1439, 1527,  
 3000  
 Sheffield, R. L. 2970  
 Sheikh, J. Y. 1175  
 Shen, J. 2178, 2438  
 Sheng, I. C. 1497, 1500  
 Shepard, K. W. 1042, 1045, 1694  
 Shephard, W. 821  
 Sherman, J. D. 3166  
 Sherwin, G. 1881  
 Sheynin, S. 393  
 Shi, J. 242, 243, 3603  
 Shibata, H. 3552  
 Shibata, Y. 1614, 1617  
 Shidara, T. 590, 1416  
 Shih, H.-J. 387, 3588  
 Shiho, M. 676, 1566  
 Shiltsev, V. D. 2959  
 Shinoe, K. 1509, 2295, 2337  
 Shintake, T. 1048, 1051  
 Shiraga, H. 2556  
 Shirai, T. 1697  
 Shishido, T. 992, 1024  
 Shiwaku, H. 1468  
 Shoae, H. 1946, 2106  
 Shofstall, D. 2967  
 Shoji, T. 2556  
 Shoji, Y. 3633, 3763  
 Shpak, A. 1480  
 Shrader, M. B. 1103  
 Shtirbu, S. 1934  
 Shu, Q. S. 921, 2787  
 Shu, Q.-S. 3888, 3891  
 Shutt, R. 2744  
 Shvedunov, V. I. 1069, 2059  
 Shvets, G. 2635  
 Sibley, C. 1372, 2054, 2868  
 Siddons, D. P. 2145  
 Siemann, R. 2019, 2370  
 Siemann, R. H. 532, 2373, 3240  
 Siergiej, D. 3482  
 Sievers, W. 1916  
 Siffert, P. 1363  
 Sigov, Y. S. 2620  
 Sikora, R. E. 2328, 2916  
 Sillanoli, M. 2492  
 Silva, J. 3093  
 Sim, J. W. 2856  
 Simmons, J. 3888  
 Simpson, J. 815, 2596, 3050,  
 3061  
 Simrock, S. 1925, 2184  
 Simrock, S. N. 599, 1909, 2364,  
 3515  
 Sims, R. E. 2769  
 Sinclair, C. 3663  
 Sinclair, C. K. 1109, 3246  
 Singh, O. 2254, 2284  
 Sissakian, A. 2042  
 Skachkov, D. G. 3675  
 Skachkov, V. S. 2853  
 Skarpaas, K. 1039, 3030  
 Sladen, J. P. H. 2346  
 Sloan, T. 29, 224, 227, 420, 1421  
 Sluijk, T. 2343  
 Smellie, R. 2757, 2781  
 Smirnov, Y. 2042  
 Smith, B. H. 1175  
 Smith, D. D. 2705, 2708, 2711  
 Smith, D. L. 667  
 Smith, D. R. 1075, 2559  
 Smith, H. V., Jr. 3172  
 Smith, J. 1852, 2222, 2284  
 Smith, J. D. 1846, 1849  
 Smith, J. R. 694  
 Smith, K. S. 3178  
 Smith, L. 3678  
 Smith, M. 1669, 3118  
 Smith, P. 1718, 2953  
 Smith, S. L. 1494, 1638, 3594,  
 3672  
 Smolucha, J. 1817, 1912  
 Smolyakov, N. V. 1626  
 Smythe, W. R. 1054  
 Snee, D. 1013  
 Snitchler, G. 3888  
 Snyder, D. 1620  
 Snyderstrup, L. 3897  
 So, I. 2275  
 Sobczynski, S. 1372, 3851  
 Sohn, Y. U. 2751  
 Sokolov, S. V. 318, 320  
 Sokolowski, J. S. 849  
 Solensten, L. 2133

- Solheim, N. 2956  
 Solomon, L. 1439, 1602, 1605  
 Solomons, R. 3748  
 Sommer, F. 2748  
 Sommer, M. 1465  
 Somov, L. 552  
 Song, J. 1057, 2142  
 Song, J. J. 2213, 3393, 3396  
 Song, T. 2199  
 Sortais, P. 1789, 1792  
 Soukas, A. 1277, 3633  
 Soukas, A. V. 1345  
 Soundranayagam, R. 1360  
 Spädtko, P. 1645, 1738  
 Spalek, G. 1021  
 Spanggaard, J. 2492  
 Spata, M. 841  
 Spataro, B. 611, 778  
 Spataro, C. 2883  
 Spayd, N. 880, 3405  
 Specht, J. E. 1694  
 Specht, V. 2670  
 Specka, A. 2450  
 Spence, W. 2019  
 Spence, W. L. 3234, 3576  
 Spencer, J. 543, 2025, 2638  
 Spencer, J. E. 396  
 Spencer, N. 1884, 1969, 1975  
 Spencer, T. A. 2693  
 Spinos, F. 2757  
 Spitz, R. 1166, 1241  
 Sprangle, P. 1560, 2584, 2629, 2632, 2647  
 Sredniawski, J. 821, 2133, 3193  
 Srinivasan-Rao, T. 3012  
 Stagno, V. 775, 1524  
 Stallard, B. 1551  
 Stallard, B. W. 1554  
 Stampke, S. 203, 2781  
 Staples, J. W. 1759  
 Stapleton, G. 2184  
 Starker, J. 1735  
 Starkovich, V. S. 1075  
 Steck, M. 1645, 1738  
 Steckmeyer, J. C. 1792  
 Stefan, P. M. 895  
 Stege, R. E., Jr. 2234  
 Steimel, J. M., Jr. 2100, 2231  
 Steinbach, C. 339  
 Steiner, H. 2172  
 Steinhauer, L. C. 2564, 2581, 2614  
 Stelzer, J. E. 3172  
 Stepanov, A. 2426  
 Stepp, J. D. 1157, 1408, 1906  
 Teski, D. B. 3178  
 Stevens, J. 3357  
 Stevens, R. R., Jr. 3166  
 Stevenson, N. 1733  
 Stevenson, N. R. 3099  
 Stiening, R. 143, 239, 3778  
 Stillman, A. 2471  
 Stittsworth, D. 2124, 2130  
 Stoker, J. 703  
 Stover, G. 1351  
 Strait, J. 2769  
 Strakhovenko, V. M. 3093  
 Strelkov, M. 1480, 2057  
 Strelkov, M. A. 194  
 Striffler, C. D. 2667, 2670, 3075  
 Stringfield, R. 2675  
 Stringfield, R. M. 2664  
 Struckmeier, J. 1645  
 Stuart, M. E. 1727  
 Stucki, H. 339  
 Stupakov, G. V. 197  
 Su, G. 1411  
 Su, J. J. 2638  
 Subbotin, S. 552  
 Sudou, M. 1291, 1686  
 Suemine, S. 650  
 Suenaga, M. 2904  
 Sueno, T. 1291  
 Suetsugu, Y. 3860  
 Sugahara, R. 2340  
 Suhring, S. 587  
 Sulgin, I. 916  
 Suller, V. P. 1494, 1638, 3594, 3672  
 Sullivan, C. A. 2644  
 Sullivan, M. 131  
 Sulyaev, R. M. 454  
 Summers, L. K. 1220  
 Sun, D. 1127  
 Sun, H. 3696  
 Sun, N. 515  
 Sun, T. 1411  
 Sundelin, R. M. 1092  
 Sundquist, M. 3745  
 Surma, I. V. 2059  
 Susta, J. 1060  
 Suwada, T. 2516, 3087, 3705  
 Suzuki, H. 2039  
 Suzuki, K. 2556  
 Suzuki, S. 602  
 Suzuki, T. 1024  
 Svandrlík, M. 953, 956, 1145  
 Svinin, M. P. 555  
 Swartz, M. 2172  
 Swenson, D. 1703  
 Swenson, D. A. 812, 846, 2426  
 Swenson, D. R. 3175  
 Sychev, V. 2769  
 Symon, K. 285  
 Syphers, M. 29, 203, 224, 227  
 Syphers, M. J. 38, 134, 137, 140, 146, 420, 3588  
 Sytchevsky, S. E. 3205  
 Sytnikov, V. 2769
- T
- Tacconi, E. J. 1098, 2139  
 Tadokoro, M. 309  
 Tagawa, S. 3552  
 Tajima, T. 1024, 2556  
 Takada, E. 1291, 1686  
 Takada, Y. 1291  
 Takahashi, N. 546  
 Takahashi, S. 3845  
 Takahashi, T. 1614, 1617  
 Takaki, H. 1509  
 Takamuku, S. 650  
 Takasaki, E. 1163  
 Takayama, K. 673, 2205  
 Takeda, O. 3115  
 Takeda, S. 1309  
 Takeda, Y. 1783  
 Takenaka, T. 1163  
 Takeo, T. 2409  
 Tallerico, P. 1683  
 Tallerico, P. J. 1199  
 Talman, R. 203, 236  
 Tamezane, K. 602  
 Tamura, K. 2409  
 Tanabe, J. 2850  
 Tanabe, T. 1291, 3006  
 Tanabe, Y. 3115  
 Tanaka, M. 360, 2907  
 Tang, C. 1623  
 Tang, H. 2978, 3027, 3033, 3036, 3039  
 Tang, Y. 1852, 2275  
 Tang, Y. N. 492, 1846  
 Tanii, T. 2205  
 Tantawi, S. 543, 936, 1106  
 Tantawi, S. G. 620, 1121, 1130, 1196  
 Tao, Q. 2841  
 Taran, A. 2769  
 Tarasenko, A. 1480, 2057  
 Taratin, A. 2489  
 Tarovik, M. N. 3822  
 Tarrant, M. 1937  
 Tatchyn, R. 1445, 1536, 1539, 1542, 1608, 2429  
 Taylor, B. 1142, 1238  
 Taylor, L. 824  
 Tazzari, S. 573, 968  
 Tazzioli, F. 573, 3279  
 Tecchio, L. 3243  
 Tecker, F. 2432, 3429  
 Tekawa, M. 3748  
 Telegin, Y. 1480, 2057  
 Temkin, R. J. 2575, 2656, 2690, 2696  
 Temnykh, A. B. 2007, 3476  
 Tenenbaum, P. 2838  
 Teng, L. 224, 285, 420, 1485  
 Teng, L. C. 182  
 Tepikian, S. 168, 420  
 Terrien, J. C. 1187  
 Terzi, F. 1063  
 TESLA Collaboration 537  
 Thern, R. E. 2471  
 Thevenot, M. 670, 697  
 Thiagarajan, V. 3372  
 Thieberger, P. 3178  
 Thielheim, K. O. 276  
 Thiessen, H. 3297  
 Thiessen, H. A. 1021, 3760  
 Thivent, M. 339  
 Thomas, M. G. 1419  
 Thomas, P. 3053  
 Thompson, K. 3757  
 Thompson, K. A. 543, 3342, 3693  
 Thompson, K. M. 2808, 2814  
 Thompson, P. 2744, 2766  
 Thompson, P. A. 2754  
 Thorndahl, L. 1066, 3426  
 Thuot, M. E. 1806  
 Tidwell, S. C. 2564  
 Tiefenback, M. 587  
 Tiefenback, M. G. 426  
 Tieger, D. 2054, 2871, 2874

Tieger, D. R. 2832, 2938  
Tighe, R. 2370, 2373  
Tigner, M. 769, 918, 921, 977,  
995, 3450, 3479, 3690, 3931  
Timmer, C. A. 2970  
Timmermans, C. J. 1072, 1820,  
2892, 2927, 3645  
Ting, A. 2629, 2632  
Titcomb, C. 2956  
Tiunov, A. V. 1069, 2059  
Tiunov, M. 2650  
Tkatchenko, A. 1465  
Tobiyama, M. 2409  
Todd, A. M. M. 1774, 1777  
Toge, N. 98, 100, 116, 3912  
Tojyo, E. 1783  
Tokuchi, A. 676  
Tokuda, N. 1783  
Tokumoto, S. 1202  
Toldo, F. 1241  
Tolstun, N. G. 555  
Tomassini, D. 1477  
Tomizawa, M. 41, 1780, 1783,  
1786  
Tomkins, J. C. 2769  
Tomlin, R. 2228, 3787  
Tommasini, D. 1375, 1378, 2820  
Tompkins, P. A. 1448  
Tooker, T. F. 1706  
Tool, G. 1405, 2731, 2757  
Tornoe, R. N. 1103  
Tosolini, P. 1333, 1378  
Towne, N. A. 2415  
Toyama, S. 546  
Toyoda, K. 3006  
Tran, H. J. 3402  
Tran, P. 173  
Tran-Ngoc, T. 829, 832, 1039  
Travier, S. 3053  
Travish, G. 561, 1445, 1533,  
1548, 3216  
Trbojevic, D. 102, 168  
Treas, P. 608, 611  
Tribendis, A. 977, 3450  
Tribouillard, C. 1792  
Trifonov, D. E. 682  
Tron, A. M. 2403, 2406  
Tronc, D. 1768  
Trost, H.-J. 2705, 2708, 2711  
Trotsenko, V. 1480  
Trotz, S. 2575, 2699  
Trzeciak, W. 285  
Tsai, H. J. 1943  
Tsang, K. T. 3270  
Tsarik, S. V. 454  
Tschalaer, C. 2054  
Tsiang, E. Y. 3621  
Tsoupas, N. 2895  
Tsuchidate, H. 1515  
Tsuchiya, M. 3845  
Tsumori, K. 650  
Tsyganov, E. 2468, 2489  
Tuckmantel, J. 806  
Tuli, M. 3888  
Tupa, D. 3175  
Turchetti, G. 273  
Turlington, L. 939, 1109  
Turner, J. L. 2978, 3027, 3036

Turner, L. R. 2799, 2808, 2814,  
2817  
Turner, W. 3876, 3888  
Turner, W. C. 3833  
Tyrroff, H. 1477  
Tyson, E. 2967

## U

Ueda, A. 215  
Ueda, S. 3903  
Ueda, T. 3552  
Ueng, T. S. 2031  
Ueyama, Y. 2039  
Uggerhøj, E. 1363  
Uher, T. 2382  
Uhm, H. S. 2599, 2602, 2605,  
2678  
Ulc, S. 2578  
Umezawa, H. 1024  
Umstadter, D. 2632  
Underwood, K. 1884, 1969  
Unser, K. B. 2394  
Urano, T. 2516, 3705  
Urasawa, S. 1614, 1617  
Ushakov, V. 564, 1384  
Ushkov, V. 564  
Utino, K. 1291  
Utterback, J. 1928, 1931

## V

Vaccarezza, C. 3906  
Vaccaro, V. 2154  
Vaidya, M. 1010  
Vakhrushin, Y. P. 682  
Valbuena, R. 2202  
Valicenti, R. A. 3133  
Val'kov, A. E. 3822  
van Asselt, W. 3633, 3763  
van den Berk, F. 1820  
van der Heide, J. A. 1072  
van der Laan, J. 1901, 1998  
van der Stok, P. D. V. 1820  
Vandeusen, A. 2124, 2130  
Van Deusen, A. L. 2121  
van de Vijver, Y. 1820  
van Dyck, O. 369  
Vanecek, D. 703  
van Garderen, G. 1901  
van Laar, J. 3645  
van Oers, W. T. H. 2991  
VanOlst, D. 1884  
van Steenberg, A. 2578  
Van Straagen, P. K. 86  
Van Westrum, D. C. 1054  
van Zeijts, J. 587  
Variante, V. 775, 1524  
Varisco, G. 1524  
Vasil'ev, A. N. 315  
Vasiliev, A. 2717  
Vasserman, I. 3711  
Vaughn, G. 1669  
Vejcik, S. 2199  
Vella, M. C. 3157

Verdier, A. 158, 161, 249  
Verdú, G. 647  
Vergamini, A. 1205  
Vescovi, M. 611  
Veshcherevich, V. 977, 1226,  
3450  
Vetter, A. M. 1075  
Vignola, G. 611, 1993, 2048  
Villate, D. 670, 697, 2115  
Vinnik, V. 1297  
Vinokurov, N. A. 1442  
Viola, R. 2913  
Vishnevsky, I. N. 3822  
Visnjic, V. 3811, 3814  
Vlieks, A. 543, 1106  
Vlieks, A. E. 620, 1121, 1196,  
1208  
Vobly, P. D. 2751  
Vodopianov, F. A. 1078  
Vogel, H. 1080  
Volk, K. 3139  
Volzhev, A. A. 682  
Vong, F. C. 1906  
Vormann, H. 3139  
Vorobjov, I. A. 1675  
Voroshilov, A. N. 2022, 3669  
Vos, L. 2301  
Voss, D. 285  
Votaw, A. 2112  
Votaw, A. J. 1814  
Vouillot, J. M. 2495  
Vretenar, M. 3121  
Vulcan, W. 3103  
Vylet, V. 543, 1445

## W

Wadlinger, E. A. 1669  
Wagner, W. 2838  
Wait, G. D. 1148, 1181, 1330,  
3402  
Wake, M. 2769  
Walend, D. 2953  
Walker, N. 2019  
Walker, N. J. 92, 95, 98, 100,  
116, 119  
Walker, R. P. 1587, 1593, 2844,  
2847  
Wallace, J. D. 1033, 1256  
Walling, L. 824, 877, 880, 1083,  
3405, 3888  
Walstrom, P. 1021  
Walter, M. 3351  
Walter, M. T. 2693  
Walz, D. 185  
Walz, H. V. 2838  
Wan, W. 155  
Wanderer, P. 2726, 2744, 2766  
Wang, C. 1575, 1578, 2608  
Wang, C. J. 1878  
Wang, D. 2013, 2331, 3429, 3851  
Wang, D. X. 62, 3282, 3627, 3660  
Wang, D. Y. 1451, 1949  
Wang, F. 378, 381, 1360  
Wang, J. G. 62, 3282, 3627, 3660  
Wang, J. M. 1419

- Wang, J. W. 543, 620, 907, 1086, 1208  
 Wang, K. 3148  
 Wang, M. H. 1943  
 Wang, S. 1411  
 Wang, T. 3297  
 Wang, T. F. 883, 3500  
 Wang, T.-S. 2319  
 Wang, X. 2051, 2112, 2237  
 Wang, X. J. 2486, 3000  
 Wang, X. Q. 1033, 1256  
 Wang, Y. 29, 224, 227, 420, 3845  
 Wang, Y. L. 546  
 Wangler, T. P. 1712, 3606, 3657  
 Warn, C. E. 2400  
 Warner, D. 2760  
 Warnock, R. L. 291, 3378  
 Warren, D. S. 2480  
 Watanabe, A. 1566  
 Watanabe, K. 3845  
 Watanabe, M. 1515  
 Watanabe, S. 41, 1291, 2714  
 Watanabe, T. 41  
 Waters, G. 1148, 1181  
 Waters, J. W. 1448  
 Watson, S. 3055  
 Watson, S. A. 2447  
 Weaver, H. J. 2959  
 Weaver, J. 2714  
 Weaver, J. N. 3018  
 Webber, R. 2118  
 Webber, R. C. 2094, 2382  
 Weber, K. J. 1387, 2877  
 Webers, G. A. 2062, 2065, 2927, 3423  
 Wedekind, M. 3184  
 Wei, J. 258, 3527, 3651  
 Wei, K. 312  
 Weihreter, E. 1474  
 Weingarten, W. 806  
 Weisend, J., II 2757  
 Weiss, R. 1669  
 Weissenburger, D. 1439  
 Weisz, S. 26  
 Welbourne, L. A. 1494, 1638, 3594, 3672  
 Welch, D. R. 661, 3549  
 Welch, J. J. 2007, 3476  
 Wells, F. D. 2316  
 Wells, R. P. 1727, 3169  
 Weng, W. T. 3264, 3633, 3726, 3763  
 Wenninger, J. 44  
 Werkema, S. J. 3303, 3309, 3573  
 Wesolowski, W. 605  
 Westenskow, G. 2638  
 Westenskow, G. A. 2611  
 Wetherholt, D. M. 2483  
 Wetzels, S. F. C. L. 2927  
 Wheat, R. M. 2664  
 Whelen, C. 2967  
 White, G. R. 1881  
 White, M. 605  
 Whitham, K. 608, 611, 1244  
 Whittenberg, W. A. 2483, 3130  
 Whittum, D. 2638, 3552  
 Whittum, D. H. 673, 3288, 3399  
 Wienands, U. 255, 393  
 Wiik, B. H. 1
- Wildman, D. 405, 1223, 3258  
 Wilke, M. D. 2480  
 Wilkinson, C. 366, 369, 2216, 2219, 3297  
 Willeke, F. 3742  
 Willen, E. 2744, 2766, 2790  
 Williams, R. 2638  
 Williams, S. H. 2838  
 Wilson, D. C. 3090  
 Wilson, I. 641  
 Wilson, P. 2681  
 Wilson, P. B. 543, 620, 1208  
 Winans, J. R. 1957  
 Wines, R. 3103  
 Wingate, C. A. 3090  
 Winick, H. 173, 1445, 1608  
 Winkler, G. 2956  
 Wiseman, M. 841, 1060, 2929  
 Wisnivesky, D. 1089, 1454  
 Witherspoon, S. 599  
 Witherspoon, S. D. 2364  
 Won, S. C. 1832  
 Wood, F. 2118  
 Wood, R. 1551, 1712  
 Woodbury, K. 1912  
 Woodle, M. 1439, 2578, 3000  
 Woodley, M. 92, 95, 119, 2019  
 Woodley, M. D. 3576  
 Woods, M. 2172, 2978, 3036, 3045, 3047  
 Woods, M. B. 3027  
 Woods, R. 3760  
 Woodworth, E. 2184  
 Worm, T. 1363  
 Worth, G. T. 3118  
 Wright, B. 998  
 Wright, E. 1106  
 Wright, E. L. 1259  
 Wright, S. 2124, 2130  
 Wu, B. 1611  
 Wu, D. 173  
 Wu, G. 2228, 2252  
 Wu, X. 255, 393  
 Wu, Y. 218, 1901, 1998, 2889  
 Wuensch, W. 641, 2346  
 Wuppertal, U. 995  
 Wurtele, J. 2638  
 Wurtele, J. S. 2575, 2635, 2699, 3327, 3399  
 Wüstefeld, G. 1474  
 Wyss, C. 2016
- X
- Xi, B. 2892, 3645  
 Xie, M. 1445, 1533  
 Xiu, L. 3148  
 Xu, C. Y. 3845  
 Xu, G. 3237  
 Xu, Y. 3148
- Y
- Yakimenko, V. 450  
 Yakovlev, S. 824  
 Yakovlev, V. 2650  
 Yakovlev, V. P. 877, 941  
 Yamada, S. 1291, 1686  
 Yamada, T. 1291, 1686  
 Yamaguchi, S. 959  
 Yamakawa, T. 215, 1614, 1617  
 Yamamoto, N. 466, 2340  
 Yamamoto, T. 650  
 Yamashita, Y. 676  
 Yamazaki, Y. 3087  
 Yampolsky, I. 1327  
 Yan, C. 2136, 3103  
 Yan, Y. 236, 3402  
 Yan, Y. T. 29, 38, 224, 227, 242, 243, 420, 423, 515  
 Yanagi, Y. 3845  
 Yanagida, K. 602  
 Yandon, J. C. 1916  
 Yang, B. 3243  
 Yang, X.-F. 2462  
 Yao, C. G. 812  
 Yao, C. Y. 122, 2444  
 Yarba, V. 236  
 Yarosh, V. E. 1795  
 Yartsev, D. I. 1795  
 Yelk, J. 2070  
 Yen, E. 1460  
 Yeremian, A. 543  
 Yeremian, A. D. 2978, 3027, 3063  
 Yeung, K. S. 2385  
 Yin, Y. 2441  
 Yokomizo, H. 602, 2039  
 Yokota, M. 3087  
 Yokouchi, S. 3845  
 Yokoya, K. 3441  
 Yoneda, C. 620  
 Yonehara, H. 2039  
 Yoneyama, S. 2039  
 Yoon, J. R. 2796  
 Yoon, M. 3273  
 York, R. 236, 255, 393, 3739  
 York, R. L. 3175  
 Yoshida, K. 1780, 1783  
 Yoshida, Y. 3552  
 Yoshikawa, H. 602  
 Yoshioka, M. 1614, 1617  
 Yoshizawa, J. 1291, 1686  
 Yoshizawa, M. 41, 1783, 1786  
 Young, A. 1205, 1285  
 Young, A. T. 1727, 3042  
 Young, L. M. 790, 3136  
 Youngman, B. 543  
 Yu, D. 2388, 2681  
 Yu, D. U. L. 936  
 Yu, J. X. 1727  
 Yu, K. 2787, 3888, 3891  
 Yu, L. H. 1439, 1602  
 Yu, S. 703, 709, 3199  
 Yu, S. S. 712  
 Yu, X. T. 3327, 3399  
 Yuan, V. 1669  
 Yücel, A. 3879  
 Yudin, I. P. 191, 297, 1892  
 Yudin, L. A. 2543  
 Yudin, L. I. 1795  
 Yugami, N. 2556, 3552  
 Yule, T. 1709  
 Yule, T. J. 1777  
 Yunn, B. 3663

Yunn, B. C. 179, 1092, 1909  
Yupinov, Y. 564  
Yvlov, T. 2042

## Z

Zach, M. 1151  
Zagel, J. R. 2193  
Zakhvatkin, M. N. 2022  
Zaltsman, A. 1241  
Zangrando, D. 1587, 2844, 2847  
Zante, T. 608, 611  
Zapalac, G. 2172  
Zapolsky, V. N. 454  
Zapryagaev, I. 2650  
Zarcone, M. J. 3178  
Zarucheisky, V. G. 454  
Zatopek, J. 2757  
Zbasnik, J. 2787, 3888, 3891  
Zelanzny, M. 1884  
Zelazny, M. 1966  
Zelenski, A. N. 2991

Zelinsky, A. Y. 194, 1480  
Zelynsky, A. 2057  
Zenkevich, P. 2073  
Zhabitsky, V. M. 2543  
Zhang, B. 1001  
Zhang, C. 312, 3237  
Zhang, H. 2841  
Zhang, M. 1411  
Zhang, P. 176  
Zhang, P. L. 29, 224, 227, 420  
Zhang, Q. 1411  
Zhang, R. 561, 575, 3009, 3216  
Zhang, S. Y. 1277, 3264  
Zhang, T. 306, 2556, 2841  
Zhang, W. 2841  
Zhang, X. 312, 1439, 1599, 1721,  
2841, 3081  
Zhang, X. L. 3237  
Zhang, Z. 303, 1611  
Zhao, Y. 1033, 1256  
Zhao, Z. 2841  
Zhao, Z. T. 3237  
Zhmendak, A. V. 3822  
Zholents, A. 131

Zhou, C. 2841  
Zhou, J. 3396, 3772  
Zhou, P. 3303, 3309, 3540, 3573  
Ziemann, V. 98, 100, 108, 114,  
116, 498, 1483, 3909  
Zinchenko, A. 2468, 2489  
Zinkann, G. P. 1694  
Zinneman, T. 1709  
Zinneman, T. E. 3210  
Ziomek, C. 1154, 3213  
Ziomek, C. D. 2391  
Zisman, M. S. 2010  
Zolfaghari, A. 829, 832, 2331,  
3851  
Zolfaghari, Z. 2054  
Zolotorev, M. 2172, 3027, 3045  
Zolotorev, M. S. 2978, 3036  
Zoni, G. 1063  
Zotter, B. 3347, 3429  
Zu, D. 1095  
Zumbro, J. 1021  
Zumbro, J. D. 2832, 2941  
Zyngier, H. 1465



